SLAC NATIONAL ACCELERATOR LABORATORY

U.S. DEPARTMENT OF ENERGY | Office of Science

Stanford University

International BEAM INSTRUMENTATION Conference

Monterey, California, USA
September 14-18, 2014













The 3rd International Beam Instrumentation Conference, IBIC 2014, was held in Monterey, California, USA on September 14-18, 2014.

Like its predecessors, BIW and DIPAC, this conference was dedicated to exploring the physics and engineering challenges of beam diagnostics and measurement techniques for charged particle beams.

IBIC 2014 was hosted by SLAC National Accelerator Laboratory. The four day scientific program included tutorials, invited and contributed talks, three poster sessions, a vendor exhibition, and an opportunity to tour SLAC National Accelerator Laboratory.

IBIC 2014 Program Committee

Steve Smith (SLAC, Chair)
Wim Blokland (SNS)
Mark Boland (SLSA)
Mairo Ferianis (Sinc. Trieste)
Doug Gilpatrick (LANL)
Hitoshi Hayano (KEK)
Andreas Jansson (ESS)
Rohdri Jones (CERN)
Kevin Jordan (TJNAF)
Patrick Krejcik (SLAC)
Bob Lill (APS)
Sergio Marques (LNLS)
Guenther Rehm (DLS)
Tom Russo (FRIB)
Jim Sebek (SLAC)
James Sedillo (LANL)
Om Singh (BNL)
Victor Verzilov (TRIUMF)
Jonah Weber (LBNL)
Kay Wittenburg (DESY)
Jim Zagel (FNAL)

IBIC 2014 JACoW Editorial Team

David Button (ANSTO)
Isidre Costa (CELLS)
Magdalena Montes-Loera (SLAC)
Ian Martin (DLS)
Volker RW Schaa (GSI)



International Beam Instrumentation Conference (IBIC '14)
September 14-18, 2014
Monterey, California, USA

The International Beam Instrumentation Conferences are dedicated to exploring the physics and engineering challenges of beam diagnostics and measurement techniques for charged particle beams. Like that of its predecessors, the Beam Instrumentation Workshops (BIW), held 1989 through 2012, and the Diagnostics and Instrumentation for Particle Accelerators Conferences (DIPAC), held 1993 through 2011, the goal of this conference is to share and spread knowledge and to help develop the next generation of experts in the field.

IBIC '14, was hosted by the SLAC National Accelerator Laboratory at the Portola Hotel in Monterey, California. The four day scientific program consisted of two tutorials, 11 invited talks, 19 contributed talks, and 127 posters in three poster sessions. Twenty-one industrial sponsors exhibited at the conference. All sessions were in plenary format to enable participants to attend all sessions. The two tutorials, given by Mike Gruchalla of Los Alamos National Labs presenting "Managing Electromagnetic Interference in Large Instrumentation Environments" and Thomas H. Lee of Stanford University presenting "Dark (and Bright) Secrets of RF Design" were very well received. Kent Irwin (SLAC and Stanford University) presented an exciting talk on superconducting detectors spanning their applications from X-ray beamlines to the recent announcement of detection of evidence for gravitational waves in the early universe.

Each evening a reception, made possible by the generous sponsorship of our industrial exhibitors, concluded the day's program. These receptions enabled the workshop participants to continue the discussions generated during the day by the conference talks and posters. On Tuesday a reception honoring "The Faraday Cup Award and its Transition into the Care of the IBIC Organizing Committee" was sponsored by Bergoz Instrumentation and GMW Associates. The conference banquet was held on a beautiful evening outdoors in the Memory Garden of the Monterey State Historic Park. After the official closing of the conference, most of the participants boarded busses for the long drive to SLAC and took advantage of the organized tour to visit many of the SLAC accelerator facilities.

Conference attendance included 175 participants. Notably, fewer than one third of the participants were from the host continent. Two-thirds of the participants travelled from Asia, South America, and especially Europe which alone was responsible for one half of the attendees, likely reflecting the vibrancy of the European accelerator scene with projects such as the European XFEL, the European Spallation Source, FAIR, and LHC underway.

IBIC '14 continued the tradition of the Beam Instrumentation Conferences in soliciting nominations for the Faraday Cup Award. This prize, sponsored by Bergoz Instrumentation, is given for a novel beam instrument of proven (published) performance for charged-particle beams with preference given to candidates early in their career. The Program Committee heatedly debated the merits of the nine nominations submitted. All submissions were excellent in many of the criteria established for the

Faraday Cup, but as we did not find any one nomination that met all of the award's exacting criteria we chose not to award the Faraday Cup this year.

The success of a conference such as IBIC '14 depends on the hard work of many people. We thank the JACoW collaboration and the editors: David Button (Australian Light Source), Isidre Costa (CELLS-ALBA Synchrotron), Ian Martin (Diamond Light Source), Maggie Loera (SLAC), and Volker RW Schaa (GSI Helmholtz Center for Heavy Ion Research) for their excellent work assembling and polishing these proceedings on a very tight schedule. We also thank their home institutions and funding agencies for supporting their participation here.

Many thanks to the Program Committee for guiding the development of an excellent agenda of tutorials, invited and contributed talks. (The only complaint I heard about the agenda was that the talks were so interesting that participants could not find any time to enjoy a walk along the Monterey beachfront.) The committee consisted of Wim Blokland (Spallation Neutron Source), Mark Boland (Australian Light Source), Mario Ferianis (Sincrotrone Trieste), Doug Gilpatrick (Los Alamos National Lab), Hitoshi Hayano (KEK), Andreas Jansson (ESS), Rhodri Jones (CERN), Kevin Jordan (TJNAF), Patrick Krejcik, (SLAC), Bob Lill (ANL), Sergio Marques (LNLS), Guenther Rehm (Diamond Light Source), Tom Russo (FRIB), Jim Sebek (SLAC), James Sedillo (Los Alamos National Lab), Om Singh (BNL), Steve Smith (SLAC), Victor Verzilov (TRIUMF), Jonah Weber (LBNL), Kay Wittenburg (DESY), Jim Zagel (FNAL). Thanks also to the Local Organizing Committee: Suzette Escobar, Patrick Krejcik, Jim Sebek, and Steve Smith, and to Stanford University, especially Stanford Conference Services, SLAC National Accelerator Laboratory, the Portola Hotel & Spa (especially Eddie Guice and Phil Pennington), the City of Monterey, and the SLAC tour guides and organizers.

Also many thanks to Keshia Abeyta, Terry Anderson, Nick Arias, Ryan Auer, Lauren Barbieri, Collette Barss, Suzanne Bennett, Angelica Buridos, Charlotte Chang, Ambrose Chu, Teri Church, Lorna Cisneros, Sarah Cobbett, Stephanie Corsino, Chet DeRouin, Jerry Diaz, Mike Early, Laurissa Ellis, John Escudero, Laurie Escudero, Steven Erickson, Cynthia Faulkner, Alan Fry, Danna Gianforte, Phillip Gin, Eddie Guice, Kristi Hollman, Norbert Holtkamp, Kari Horwath, Ellin Kohler, Terri Lahey, Megan Laughton, Atilla Lazar, Raymond Lo, Cindy Lowe, Jennifer Luu, Thomas Mathis, Joline McQuillan, Diana Merino-Tillman, Robyn Mosset, Brigid Neff, Jeanne Nicholas, Simon Ovrahim, Phillip Pennington, Hector Prado, Laura Ramirez, Anthony Renteria, Jennifer Sarbahi, Jo Anne Thorne, Kelvin Tom, Vena Tse, Cecilio (Chico) Vazquez, Tanya Walker, Jennifer Wilhelmsen, Stephanie Weitzenkamp, Sharon West, and especially Suzette Escobar, who brought it all together. We also, once again, thank our industrial exhibitors/sponsors.

The next three instances of the International Beam instrumentation Conference will be the IBIC '15 September 13-17, 2015 in Melbourne, Australia, the IBIC '16 September 11-15, 2016 in Barcelona, Spain, and the IBIC '17 in East Lansing, Michigan, USA. We look forward to your participation in these conferences!

Steve Smith,
IBIC '14 Chair

Contents

Preface i
Foreword iii
Contents v
Committees ix
Group Photo x

Papers 1
MOIXB1 – Welcome to the 2014 International Beam Instrumentation Conference 1
MOCYB1 – Non-Destructive Vertical Halo Monitor on the ESRF's 6GeV Electron Beam 2
MOCYB2 – Design and Initial Commissioning of Beam Diagnostics for the KEK Compact ERL 7
MOCYB3 – Longitudinal Laser Wire at SNS 12
MOIZB1 – NSLS2 Diagnostic Systems Commissioning and Measurements 16
MOCZB1 – A Picosecond Sampling Electronic "KAPTURE" for Terahertz Synchrotron Radiation 24
MOCZB2 – Reference Distribution and Synchronization System for SwissFEL: Concept and First Results 29
MOCZB3 – Comparison of Feedback Controller for Link Stabilizing Units of the Laser Based Synchronisation System used at the European XFEL 34
MOPF02 – RHIC-Style IPMs in the Brookhaven AGS 39
MOPF03 – NSLSII Photon Beam Position Monitor ElectronicsTesting and Results 42
MOPF04 – RHIC Injection Transport Beam Emittance Measurements 45
MOPF05 – Instrumentation for the Proposed Low Energy RHIC Electron Cooling Project with Energy Recovery 49
MOPF07 – Construction and Operational Performance of a Horizontally Adjustable Beam Profile Monitor at NSLS-II 55
MOPF08 – Beam Profile Measurements in the RHIC Electron Lens using a Pinhole Detector and YAG Screen 59
MOPF09 – Absolute Beam Emittance Measurements at RHIC Using Ionization Profile Monitors 64
MOPF10 – A Compact In-Air X-Ray Detector for Vertical Beam Size Measurement at ALBA 69
MOPF13 – Wire Scanner Installation into the MicroTCA Environment for the European XFEL 73
MOPF14 – Vertical Beam Size Measurement at CesrTA Using Diffraction Radiation 77
MOPF15 – Status of and Future Plans for the CERN LINAC4 Emittance Meter based on Laser Electron-Detachment and a Diamond Strip-Detector 83
MOPF16 – CERN-SPS Wire Scanner Impedence and Wire Heating Studies 88
MOPF17 – Methods for Measuring the Transverse Beam Profile in the ESS High Intensity Beam 93
MOPF19 – Design of a Profile Monitor with 12 Inches of Actuation for FRIB 97
MOPF20 – Diagnosing NSLS-II: A New Advanced Synchrotron Light Source 100
MOPF22 – Simultaneous Operation of Two FEL Undulator Beamlines at FLASH 103
MOPF27 – Simulation and First Results of the ELBE SRF Gun II 106
MOPF28 – Beam Diagnostics and Timing Monitoring for SuperKEKB Injector Linac 110
MOPF30 – Diagnostics of the TPS Booster Synchrotron for Beam Commissioning 114
MOPF31 – Overview of Beam Instrumentation Activities for SwissFEL 119
MOPD01 – RHIC p-Carbon Polarimeter Target Lifetime Issue 124
MOPD02 – The Electron Backscattering Detector (eBSD), a New Tool for the Precise Mutual Alignment of the Electron and Ion Beams in Electron Lenses 129
MOPD03 – Performance and Upgrade of the Fast Beam Condition Monitor at CMS 134
MOPD04 – Synchronisation of the LHC Betatron Coupling and Phase Advance Measurement System 139
MOPD05 – Dual Transverse and Longitudinal Streak Camera Imaging at ELSA 144
MOPD06 – Electron Beam Diagnostics for Short Pulse FEL Schemes at CLARA 147
MOPD07 – New MTCA.4-based Hardware Developments for the Control of the Optical Synchronization Systems at DESY 152
MOPD08 – A Double-Prism Spectrometer for the Longitudinal Diagnosis of Femtosecond Electron Bunches with Mid-Infrared Transition Radiation 157
MOPD09 – Longitudinal Phase Space Tomography Using a Booster Cavity at the Photo Injector Test Facility at DESY, Zeuthen Site (PITZ) 161
MOPD10 – New Results Of FERMI FEL1 EOS Diagnostics With Full Optical Synchronization 165
MOPD11 – Near-Saturation Single-Photon Avalanche Diode Afterpulse and Sensitivity Correction Scheme for the LHC Longitudinal Density Monitor 169
MOPD12 – Novel Femtosecond Level Synchronization of Titanium Sapphire Laser and Relativistic Electron Beams 174
MOPD15 – CW Beam Stability Analysis in Time and Frequency Domain 179

MOPD17 – Single-Shot Electro-Optical Diagnostics at the ANKA Storage Ring . . . 182
MOPD18 – ALS Timing System Upgrade . . . 187
MOPD19 – Bunch Arrival Time Monitor for PAL-XFEL . . . 191
MOPD21 – Bunch Pattern Measurement via Single Photon Counting at SPEAR3 . . . 195
MOPD23 – Development Status of SINAP Timing System . . . 199
MOPD24 – Diagnostics of and with Laser-Induced Energy Modulation at the DELTA Storage Ring . . . 202
MOPD25 – Time Domain Pickup Signal characterization for Low Charge Arrival-Time Measurements at FLASH 209
MOPD26 – A Bunch Extension Monitor for the Spiral2 LINAC . . . 212
TUIXB1 – The Beam Instrumentation and Diagnostic Challenges for LHC Operation at High Energy . . . 216
TUTUB1 – Managing Electromagnetic Interference in Large Instrumentation Environments . . . 224
TUIYB1 – Diagnostics for High Power Accelerator Machine Protection Systems . . . 239
TUCYB1 – Study of scintillation stability in KBr, YAG:Ce, CaF2:Eu and CsI:Tl Irradiated by Various-Energy Protons 250
TUCYB2 – Pulsed Green Laser Wire System for Effective Inverse Compton Scattering . . . 254
TUCYB3 – SwissFEL Beam Profile Monitor . . . 259
TUIZB1 – Radiation Sources and Their Application for Beam Profile Diagnostics . . . 263
TUCZB1 – Novel Emittance Diagnostics for Diffraction Limited Light Sources Based on X-ray Fresnel Diffractometry 274
TUCZB2 – Measurements of Small Vertical Beamsize using a Coded Aperture at Diamond Light Source . . . 279
TUCZB3 – A Quantum Gas Jet for Non-Invasive Beam Profile Measurement . . . 284
TUPF01 – NSLS-II RF Beam Position Monitor- System Test and Integration . . . 289
TUPF02 – Proposed Pulse Stretching of BPM Signals for the Position Determination of Very Short and Closely Spaced Bunches . . . 294
TUPF03 – Overview of the Geometrical Non-Linear Effects of Button BPMs and Methodology for Their Efficient Suppression . . . 298
TUPF04 – Numerical Calculations for the FAIR Proton Linac BPMs . . . 303
TUPF05 – Production Process for the European XFEL Re-Entrant Cavity BPM . . . 307
TUPF06 – Commissioning of the Electronics for HOM-based Beam Diagnostics at the 3.9 GHz Accelerating Module at FLASH . . . 311
TUPF07 – FLASH Undulator BPM Commissioning and Beam Characterization Results . . . 315
TUPF08 – Design, Development and Commissioning of a MTCA-Based Button and Strip-Line BPM System for FLASH2 . . . 320
TUPF09 – Calibration of OLYMPUS/DORIS Beam Position Monitors . . . 324
TUPF10 – Stability Study of the Higher Order Mode Beam Position Monitors at the Accelerating Cavities at FLASH 327
TUPF11 – Mechanical Design of Cryogenic Vacuum Feedthroughs for X-FEL Button BPMs . . . 332
TUPF12 – First Tests of a Micro-TCA-Based Downconverter Electronic for 5GHz Higher Order Modes in Third Harmonic Accelerating Cavities at the XFEL . . . 337
TUPF13 – Diamond-Based Photon BPMs for Fast Electron-Beam Diagnostics in Synchrotron Radiation Sources 342
TUPF14 – Newly Developed 6mm Buttons for the BPMs in the ESRF Low-Emittance-Ring . . . 346
TUPF15 – First Results with the Prototypes of New BPM Electronics for the Booster of the ESRF . . . 351
TUPF16 – FRIB Beam Position Monitor Pick-Up Design . . . 355
TUPF18 – Development of a Button BPM for the LCLS-II project . . . 361
TUPF19 – Beam Position Monitor Electronics Upgrade for Fermilab Switchyard . . . 365
TUPF21 – NSLS2 Visible Synchrotron Light Monitor Diagnostic Beamline Commissioning . . . 369
TUPF23 – Beam Size Measurements using Synchrotron Radiation Interferometry at ALBA . . . 374
TUPF25 – Characterization of the Laser Beam for HHG Seeding . . . 380
TUPF26 – Linear Focal Cherenkov-Ring Camera for Single Shot Observation of Longitudinal Phase Space Distribution for Non-Relativistic Electron Beam . . . 385
TUPF27 – Optical System for ESS Target Protection . . . 389
TUPD01 – Distinct Transverse Emittance Measurements of the PXIE LEBT . . . 393
TUPD02 – Electron Beam Profiler for the Fermilab Main Injector . . . 398
TUPD03 – Terahertz and Optical Measurement Apparatus for the Fermilab ASTA Injector . . . 403
TUPD04 – Third Generation Residual Gas Ionization Profile Monitors at Fermilab. . . . 408
TUPD05 – Optimization of Beam Induced Fluorescence Monitors for Profile Measurements of High Current Heavy Ion Beams at GSI . . . 412
TUPD06 – CUPID: New System for Scintillating Screen Based Diagnostics . . . 417
TUPD07 – Performance Demonstration of the Non-Invasive Bunch Shape Monitor at GSI High Current LINAC . 421
TUPD08 – YAG:Ce Screen Monitor Using a Gated CCD Camera . . . 426

TUPD09 – Vacuum Improvement of Bunch Shape Monitor for J-PARC Linac . . . 430
TUPD10 – An Ultrafast Linear Array Detector for Single-Shot Electro-Optical Bunch Profile Measurements . . . 435
TUPD11 – LANSCE 1L Harp Data Acquisition System Upgrade . . . 438
TUPD12 – Development of Non-Invasive Electron Beam Position Monitor Based on Coherent Diffraction Radiation from a Slit . . . 442
TUPD13 – Experience with and Studies of the SNS Target Imaging System . . . 447
TUPD16 – Development of the Transverse Beam Profile Monitors for the PAL-XFEL . . . 452
TUPD21 – AC Coupling Studies and Circuit Model for Loss Monitor Ring . . . 455
TUPD22 – Beam Loss Monitor at SuperKEKB . . . 459
TUPD23 – Real-Time Display System for the Optical Fiber Beam Loss Monitor for the PHIL and ThomX Facilities 463
TUPD24 – Installation of a Beam Loss Monitoring System at the S-DALINAC* . . . 468
TUPD25 – Cryogenic Beam Loss Monitors for the Superconducting Magnets of the LHC . . . 471
WEIXB1 – LCLS Beam Diagnostics . . . 475
WEIYB1 – Direct (Under)Sampling vs Analog Downconversion for BPM Electronics . . . 486
WECYB1 – Development of a Modified Six-Port Discriminator for Precise Beam Position Measurements . . . 495
WECYB2 – NSLS-II RF Beam Position Monitor Comissioning Update . . . 500
WECYB3 – Status of the Sirius RF BPM Electronics . . . 505
WECZB1 – A SQUID-Based Beam Current Monitor for FAIR/CRYRING . . . 510
WECZB3 – Measurement of Beam Losses Using Optical Fibers at the Australian Synchrotron . . . 515
WEPF02 – A Toroid Based Bunch Charge Monitor System with Machine Protection Features for FLASH and XFEL 521
WEPF03 – Upgrade of the Fast Beam Intensity Measurement System for the CERN PS Complex . . . 525
WEPF04 – A Cryogenic Current Comparator for the Low Energy Antiproton Facitities at CERN . . . 530
WEPF05 – Simulation of the Beam Dump for a High Intensity Electron Gun . . . 536
WEPF06 – A New Integrating Current Transformer for the LHC . . . 540
WEPF07 – Optimization of a Short Faraday Cup for Low-Energy Ions Using Numerical Simulations . . . 544
WEPF08 – Dosimetry of Pulsed Beams in Proton Therapy . . . 548
WEPF09 – Introduction to the Test Result of Turbo-ICT in PAL-ITF . . . 553
WEPF10 – Range Verification System Using Scintillator and CCD Camera System . . . 558
WEPF12 – A Diagnostics of Ion Beam from 28 GHz Electron Cyclotron Resonance Ion Source . . . 561
WEPF13 – The Status of Beam Diagnostics for the Hie-Isolde Linac at Cern . . . 565
WEPF15 – Status of the Standard Diagnostic Systems of the European XFEL . . . 569
WEPF16 – Algorithm to Improve the Beta-Function Measurement and its Evaluation in Storage Rings Lattices . 574
WEPF17 – Error Analysis for Pepperpot Emittance Measurements Redux: Correlated Phase Spaces . . . 579
WEPF18 – Precise Digital Integration of Fast Analogue Signals Using a 12-Bit Oscilloscope . . . 584
WEPF19 – Fast Transverse Phase Space Measurement System for GunLab - A Compact Test Beamline for SRF Photoinjectors . . . 588
WEPF21 – Electron Cloud Density Measurements Using Resonant Microwaves at CesrTA . . . 592
WEPF23 – Dosimetric Verification of Lateral Profile with a Unique Ionization Chamber in Therapeutic Ion Beams 597
WEPF24 – Development of Three-Dimensional Dose Verification System using a Fluorescent Screen in Ion Beam Therapy . . . 601
WEPF25 – A Fast Quadrupole Magnet for Machine Studies at Diamond . . . 605
WEPF26 – The Brookhaven LINAC Isotope Production Facility (BLIP) Raster Scanning Upgrade . . . 608
WEPF28 – Failure Mode and Effects Analysis of the Beam Intensity Control for the SPIRAL2 Accelerator . . . 613
WEPF29 – Progress on the Beam Energy Monitor for the SPIRAL2 Accelerator. . . . 617
WEPF30 – Study of General Ion Recombination for Beam Monitor used in Particle Radiotherapy . . . 620
WEPF31 – Sensor Studies for DC Current Transformer Application . . . 624
WEPD01 – Observations of the Quadrupolar Oscillations at GSI SIS-18 . . . 629
WEPD03 – Conceptual Design of Elliptical Cavity Beam Position Monitors for Heavy Ion Storage Rings . . . 634
WEPD04 – High Position Resolution and High Dynamic Range Stripline Beam Position Monitor (BPM) Readout System for the KEKB Injector Linac Towards the SuperKEKB . . . 637
WEPD05 – Improvement of Data Transfer Speed of Large Memory Monitors . . . 642
WEPD07 – Evaluation of Libera Single Pass H for ESS LINAC . . . 647
WEPD08 – Beam Jitter Spectra Measurements of the APEX Photoinjector . . . 652
WEPD09 – Development of a High Speed Beam Position and Phase Monitoring System for the LANSCE Linac 655
WEPD10 – Front End Concept for a Wake Field Monitor . . . 660

WEPD11 – Beam-Based Calibration and Performance Optimization of Cavity BPMs for SwissFEL, E-XFEL and FLASH2 . . . 665
WEPD12 – Low-Q Cavity BPM Electronics for E-XFEL, FLASH-II and SwissFEL . . . 670
WEPD13 – Development of the SwissFEL Undulator BPM System . . . 675
WEPD17 – Commissioning Results of MicroTCA.4 Stripline BPM System . . . 680
WEPD21 – BPM Data Correction at SOLEIL . . . 684
WEPD22 – Design of a New Blade-Type XBPM . . . 687
WEPD23 – Commissioning of the ALBA Fast Orbit Feedback System . . . 691
WEPD24 – New Features and Measurements using the Upgraded Transverse Multibunch Feedback at Diamond 696
WEPD25 – Upgrade Development Progress for the CERN SPS High Bandwidth Transverse Feedback Demonstrator System . . . 700
WEPD26 – Bunch-by-Bunch Feedback Systems at the DELTA Storage Ring used for Beam Diagnostics . . . 703
WEPD27 – Commissioning of Bunch-by-Bunch Feedback System for NSLS2 Storage Ring . . . 707
THIXB1 – Commissioning of the FLASH2 Electron Beam Diagnostics in Respect to its use at the European XFEL 712
THCXB1 – Cross-Calibration of Three Electron Cloud Density Detectors at CesrTA . . . 722
THCXB2 – Performance Evaluation of the Intra-Bunch Feedback System at J-PARC Main Ring . . . 727

Appendices **731**
List of Authors . . . 731
Institutes List . . . 739

IBIC 2014 CONFERENCE COMMITTEES

Program Committee:

Steve Smith (SLAC, Chairperson)
Wim Blokland (Spallation Neutron Source)
Mark Boland (Australian Light Source)
Mario Ferianis (Sincrotrone Trieste)
Doug Gilpatrick (LANL)
Hitoshi Hayano (KEK)
Andreas Jansson (ESS)
Rhodri Jones (CERN)
Kevin Jordan (TJNAF)
Patrick Krejcik (SLAC)
Bob Lill (ANL)
Sergio Marques (LNLS)
Guenther Rehm (Diamond Light Source)
Tom Russo (FRIB)
Jim Sebek (SLAC)
James Sedillo (Los Alamos National Lab)
Om Singh (BNL)
Victor Verzilov (TRIUMF)
Jonah Weber (LBNL)
Kay Wittenburg (DESY)
Jim Zagel (FNAL)

Local Organizing Committee –
SLAC National Accelerator Laboratory:

Steve Smith (SLAC)
Jim Sebek (SLAC)
Patrick Krejcik (SLAC)
Suzette Escobar (SLAC)

JACoW Editorial Team

David Button (ANSTO)
Isidre Costa (CELLS)
Maggie Loera (SLAC)
Ian Martin (DLS)
Volker RW Schaa (GSI)

JACoW External Help

Todd Satogata (TJNAF)
Christine Petit-Jean-Genaz (CERN)
Jan Chrin (PSI)
Matt Arena (FNAL)
Joe Chew (LBNL)



WELCOME TO IBIC14

Stephen Smith, SLAC National Accelerator Lab, Menlo Park, CA, USA

The 3rd International Beam Instrumentation Conference (IBIC 2014) in Monterey's Portola Hotel is dedicated to exploring the physics and engineering challenges of beam diagnostics and measurement techniques for charged particle beams. The International Beam Instrumentation Conferences, first held in Tsukuba (2012) and Oxford (2013) are the successors of the former Beam Instrumentation Workshops (BIW) held from 1989 through 2012 and the Diagnostics and Instrumentation for Particle Accelerators Conference series (DIPAC) held from 1993 through 2011.

We have scheduled two tutorial sessions, 12 invited talks, 20 contributed oral talks, 180 posters, and a tour of SLAC facilities that will be presented during the 4 day scientific program. Twenty-one exhibitors are ready to connect with you to share information on their latest products and services.

On behalf of SLAC, the program committee, the local organizing committee, Stanford Conference Services and the Portola Hotel, it is my pleasure to welcome you to IBIC14!

Copyright © 2014 CC-BY-3.0 and by the respective authors

ISBN 978-3-95450-141-0

NON-DESTRUCTIVE VERTICAL HALO MONITOR ON THE ESRF'S 6GeV ELECTRON BEAM

B.K. Scheidt, ESRF, Grenoble, France

Abstract

The population density along the electron's beam vertical profile at far distance from the central core (i.e. the far-away tails or "Halo") is now quantitatively measurable by the use of bending magnet X-rays. An available beam-port is equipped with two specific adapted absorbers, an Aluminium UHV window, an X-ray light blocker, an X-ray imager, and a few motorizations. The simple and inexpensive set-up (resembling much that of an X-ray pinhole camera system for emittance measurements in Light Sources, but much shorter in length) allows to record images of the electron density profile over the 0.5 to 6mm distance range from the core. Results, obtained under various manipulations on the electron beam to vary either Touchek or residual Gas scattering and thereby the Halo levels, will be presented, to fully demonstrate that this Halo monitor is exploring those realms of the beam where other diagnostics can not reach ...

NON-DESTRUCTIVE MEASUREMENTS OF VERTICAL BEAM HALO

The European Synchrotron Radiation Facility runs a 6GeV electron beam at nominally 200mA and with a vertical emittance typically below 10pm.rad. The typical (natural) lifetime of the beam is above 50hrs, and the ESRF presently only uses 'slow' top-ups at intervals up to 12hrs. The small vertical emittance implies that the vertical size of the electron beam is in a range of roughly 13 to 50um [fwhm] depending on the local vertical Beta value which varies from >45m in some dipole sections to <3m in the straight sections reserved for Insertion Devices. [1]

However, it is known that a non-negligible beam population exists at many millimetres vertical distance from the beam-centre. [2, 3]

This is easily verified by using a vertical scraper and measuring the signal from a down-stream Beam Loss Detector (BLD). The progressive insertion of such a scraper jaw at 10mm above the beam-centre shows the so induced electron beam-losses thanks to the high sensitivity of such BLD. But this method is destructive to the beam and not useable for assessing the Halo population while serving normal users operation.

A prototype of a non-destructive Halo monitor based on imaging the X-rays from an available bending magnet beam-port was successfully operated to demonstrate the principle and the strait forwardness of a practical implementation. [4]

Since the above mentioned prototype device shared this beam-port with other (incompatible) usages we decided to build a dedicated Halo monitor on one of the still un-occupied bending magnet beam-ports, and to optimize both the associated X-ray absorbers and the distances between the main components in this new set-up that are illustrated in Fig.1 and Fig.2.

Long-distance X-rays Projection with Specific Central Absorbers to Attenuate Those Coming from the Intense Beam Core

The ESRF dipoles (0.86T, Ec=20KeV) provide an angular X-ray fan of 6.25degrees that is absorbed mainly in the crotch-absorber indicated at point 1 in Fig.1. Such crotch-absorber lets through about 15mrad of horizontal beam fan from its bending magnet, and normally this beam goes through a Front-End first and then further down-stream to a User's beam-line.

But in our case for this Halo beam-port there is neither Front-End nor beam-line, instead a second horizontal absorber (2) limits the horizontal fan of the X-rays to about 1.6mrad. About 10cm further down-stream is the third absorber (3), positioned vertically such that it takes fully the X-rays beam. However, its upper edge is only 0.7mm above the vertical heart of the beam.

The X-rays that are emitted from electrons that are >0.7mm above the centre of the electron beam will pass over this vertical absorber, and their first (and only) obstacle is a 2mm thick Aluminium window (5cm behind the vertical absorber) before hitting a scintillator screen. This scintillator screen is part of a sensitive X-ray imager that includes focussing optics and CMOS camera and covers a field of view 6.9x5.2mm (hor. x vert.).[5]

The total path length of X-rays is about 4.2m from their source-point in the dipole to the screen.

The X-rays emitted from the centre of the electron beam will hit that 28mm thick Copper vertical absorber. This small absorber is water cooled and evacuates about 240W of heat-load coming from the 1.6mrad wide X-ray beam fan. It protects the Aluminium window behind it that is not cooled.

The 28mm thickness of the Copper absorber is enough to fully take the heat-load but totally insufficient to stop all the X-rays. Therefore a 7mm thick Tungsten blade is positioned behind the window to further attenuate these X-rays coming from the core of the electron beam. This 7mm thickness was chosen so that the intensity of the traversing X-rays (28mm Cu, 2mm Al and 7mm W), coming from the central beam-core, will produce a light signal on the imager system of roughly comparable intensity to that of the Halo signal (created by X-Rays traversing only 2mm Al).

Copyright © 2014 CC-BY-3.0 and by the respective authors

ISBN 978-3-95450-141-0

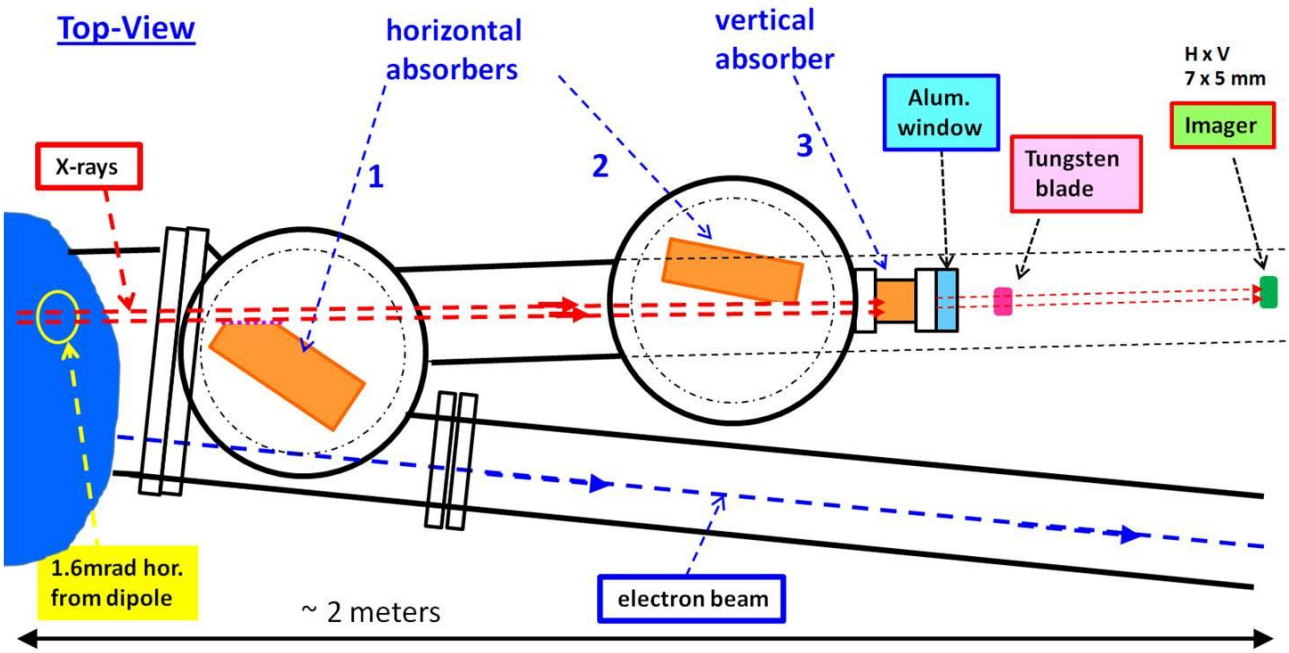


Figure 1: Top-view of the set-up with the dipole at far left and the (red) X-rays going to the right towards detector.

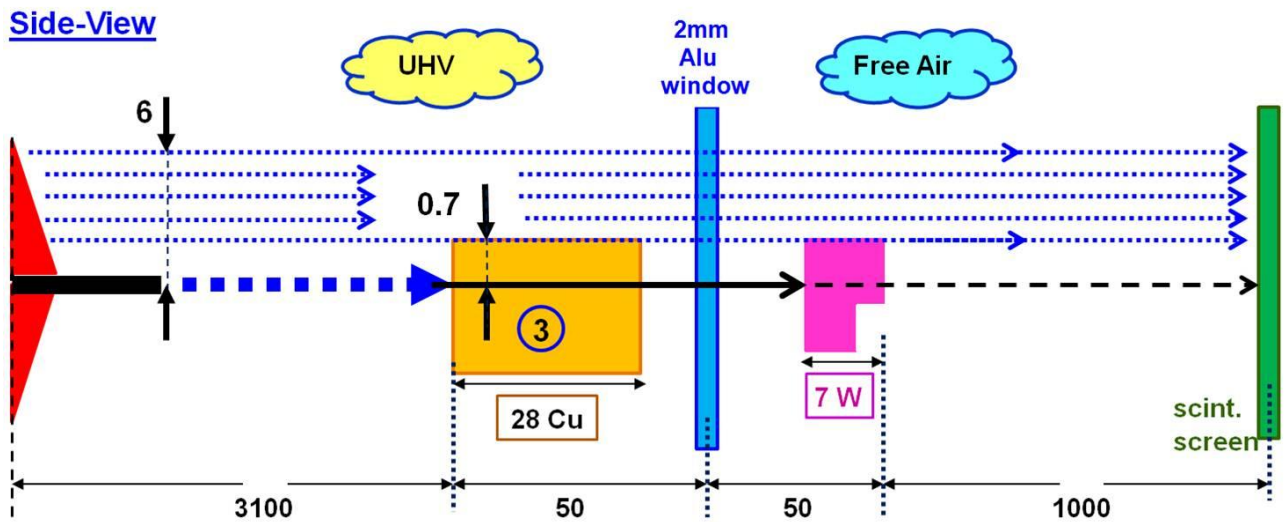


Figure 2: Side-view with emphasis on the down-stream parts with the 28mm Copper vertical absorber, the aluminium UHV window, the 7mm Tungsten light-blocker, and the detector. The latter 2 devices are equipped with hor. and vert. remote control translation stages.

The Fig.3a shows a typical image obtained under normal operation conditions of our electron beam. Horizontally the image provides no information on the electron beam, it simply represents the (1.6mrad) width of the fan of the dipole radiation. Nevertheless, the width of this fan is proportional to the signal strength and thus to sensitivity and overall resolution of the system.

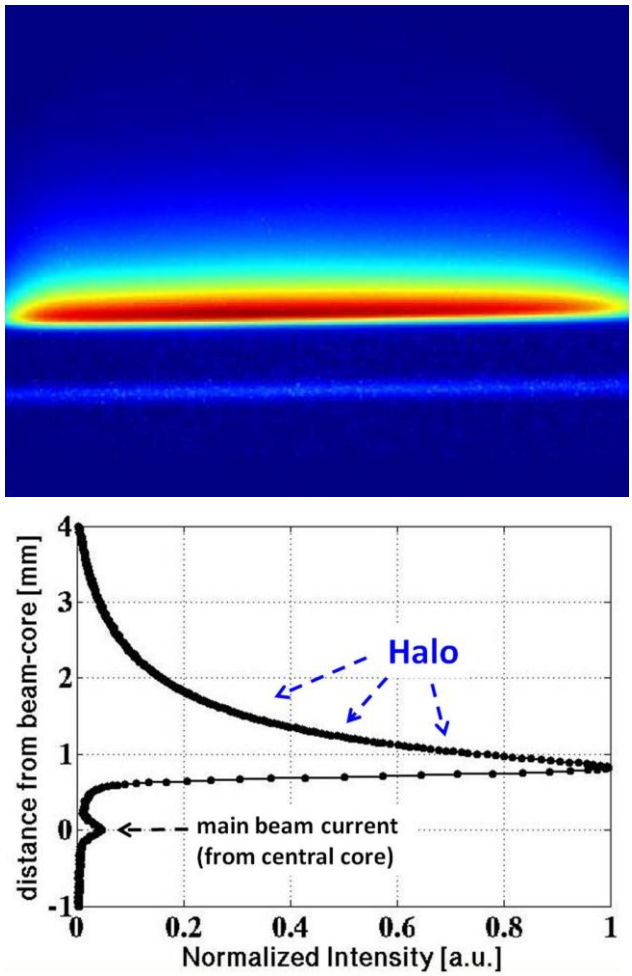
Vertically the narrow stripe in the lower part represents the intensity of the beam-core, it is relatively weak since taken with 75mA beam current (16 bunch mode) in the Ring.

The bright zone in the middle is the contribution of the Halo. This image was taken with that 7mm thick Tungsten light blocker positioned exactly as indicated in the side-view here above in Fig.2 : its top-edge vertically at the same level as the top-edge of the Copper absorber i.e. 0.7mm above the beam-centre. It should be noted that the vertical position of the Tungsten light blocker can be remotely adjusted.

The Fig.3b shows the profile of that image along the vertical axis in which both the (strong) Halo contribution and the (small) contribution coming from the central main beam are easily resolved.

ISBN 978-3-95450-141-0

Copyright © 2014 CC-BY-3.0 and by the respective authors

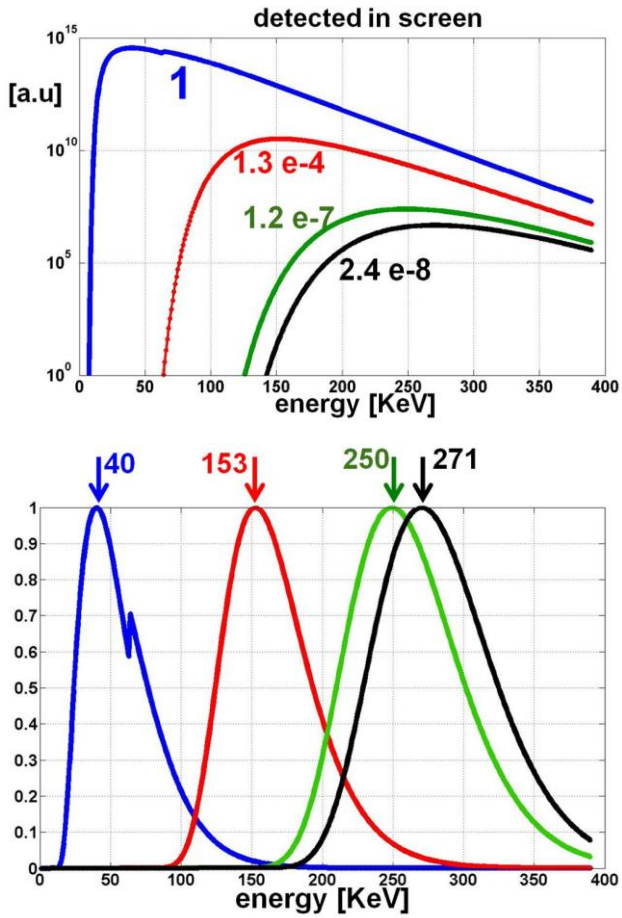


Figures 3a & 3b: Halo-monitor image covering a 6.9x5.2mm field of view (top), and the profile (bottom) along the vertical axis showing the Halo level (big peak) and the main beam current (small peak).

The Characteristics of the X-rays Traversing Four Different Paths of Material Attenuation

As said before, the X-rays emitted from the Halo part of the electron beam (i.e. between 0.7 and 5mm above beam-core) will traverse much less material then those from the central beam-core. Knowing precisely the spectral characteristics of synchrotron light from the 0.86T bending magnet and the absorption characteristics of the used scintillator (1mm thick Prelude) we can calculate the detected signal. The Fig.4a and 4b show the energy spectra of 4 distinct cases and the relative numbers of detected signal. These 4 cases correspond to :

- 2mm Al (blue curve) only,
  peak-energy=40KeV, relative intensity=1
- 28mm Cu plus 2mm Al, (red curve)
  peak-energy=153KeV, relative intensity=1.3E-4
- 28mm Cu plus 2mm Al plus 5mm W (green curve)
  peak-energy=250KeV, relative intensity=1.2E-7
- 28mm Cu plus 2mm Al plus 7mm W (black curve)
  peak-energy=271KeV, relative intensity=2.4E-8



Figures 4a & 4b: Energy spectra of the X-rays (detected by 1mm of Prelude scintillator) for the 4 different cases of beam paths and absorption in the system.

Since the Tungsten blade is on a remote control vertical translation stage it can be positioned as shown in Fig.2 (at level with the Copper absorber) but it can also be completed lowered (corresponding to the red curve case) or be put so that the X-rays from the central beam-core go through 5mm of Tungsten (instead of 7mm). This arrangement allows us to verify (in different steps) the theoretical values of detected signal with the reality of the measured values. It also allows to cross-check the linearity of the X-ray imager system that now uses a CMOS camera. In these sensitivity calibrations & verifications we make use of the camera offering an effective exposure time range of about 4 decades (600mS to 0.06mS) and a gain range of 10 (20dB).

Such verifications have allowed assessing the errors of the above reported detection sensitivity values to be within 30%.

In the explanation of the concept and with the illustration of Fig.2 it was so far simplistically presented that the X-rays do not diverge (at all). However, while the vertical divergence of the X-ray beam at energies shown in Fig.4b is small, their real values do impose some limitations on the system :

The spatial resolution at the X-ray imager (at 4.2m) is approx. 300um (fwhm) for the divergence of about

Copyright © 2014 CC-BY-3.0 and by the respective authors

ISBN 978-3-95450-141-0

75urad (fwhm) of the "soft" spectra shown by the blue curve (peaking at 40KeV).

The second limitation is on how close to the beam-core this system is able to operate. The height offset of 0.7mm of the vertical absorber is determined also by this vertical divergence of the X-rays : Those coming from the intense beam-core will at 225urad angle still have a relative intensity of 1E-9. In order to enable the system to detect real Halo levels down to below 1E-8 with respect to the central beam-core intensity, and limiting false contributions to <10% we have decided to put this value at 0.7mm which represents roughly 225urad at 3.1m.

The real Halo levels during Users' mode are in the range of 1E-6 (113nA / 75mA) as is shown in Fig.5 which is a measurement at 75mA in 16 bunch mode. Using the above reported sensitivity factors for the different energies of the X-rays we can indeed express the Halo level directly in current (e.g. nA). With Halo level is meant here the integrated value in the distance range of 0.7 to 4mm (from centre).

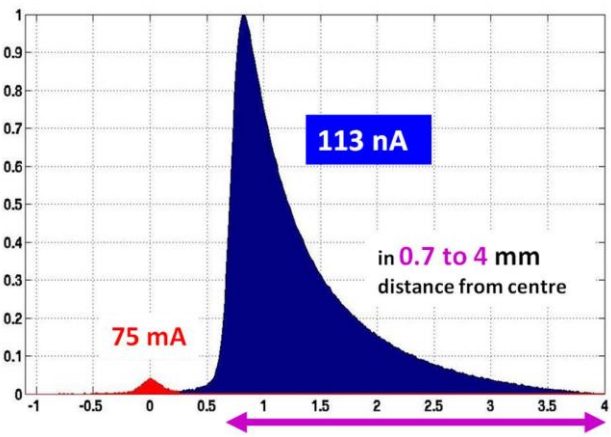


Figure 5: Profile with the main current contribution in red and the (integrated) Halo level expressed in nano-amps.

VERIFICATIONS BY SCRAPING THE ELECTRON BEAM

Since the difference in Halo level and that of the beam-core is of many magnitudes (~1E6) it could be suspected that the signal obtained on the X-ray imager is not really constituted by X-rays emitted from the electrons in these far away tails of the electron beam but instead due to some combined artefacts like scattering, reflection, leakage etc.

In fact in the earlier moments of commissioning and aligning the system some phantom signals were observed in the image that clearly seemed to come from the surface of one of the up-stream horizontal absorbers. Some of the surfaces here are unavoidably at grazing incidence angles and therefore prone to scattered propagation. We have managed to locate the origin points of these and be able to re-align the system (horizontally) thereby avoiding such scattered X-rays reaching the scintillator screen.

An efficient way of verifying that the observed signal in the image is indeed entirely coming from the electron's beam and without any phantom contributions is to remove the electron's beam tails by a scraper. One of the available scraper jaws in our Ring was used during some time dedicated to drive it in a sequence of steps close to the beam-centre and to record the Halo-monitors' images at the same time. A typical sequence is driving the scraper from 10mm to 1mm and then back out to 10mm with 0.5mm steps and staying at each step only a few seconds. The loss of the total beam current is only fractional (i.e. <0.1%) by such measurement sequence.

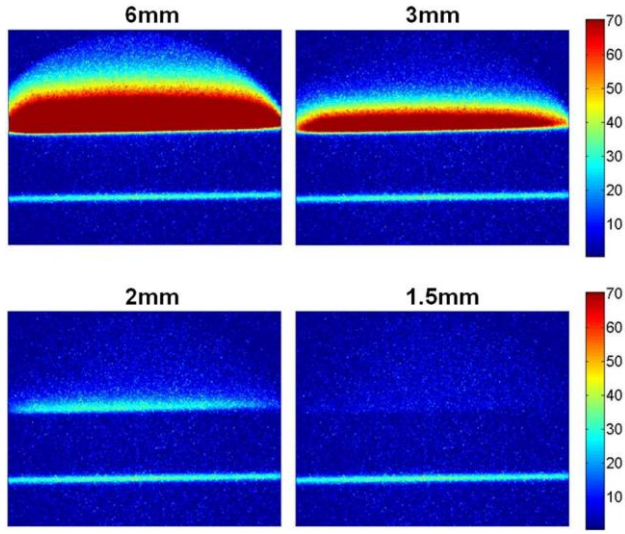


Figure 6: Images for 4 vertical scraper positions.

The 4 images in Fig.6 show only a part of such sequence i.e. the Halo images with the scraper at 6, 3, 2 and 1.5mm. In the lower part of each image one can observe that the main current (central beam-core) is not affected while the Halo signal disappears. This measurement was done with the Tungsten blade raised to 1.5mm height (instead of 0.7mm), this allowed reducing the amplitude of the Halo signal and thus increasing the camera's gain and so to get more signal of that main current. The Fig.7 shows the profile plots of such measurement.

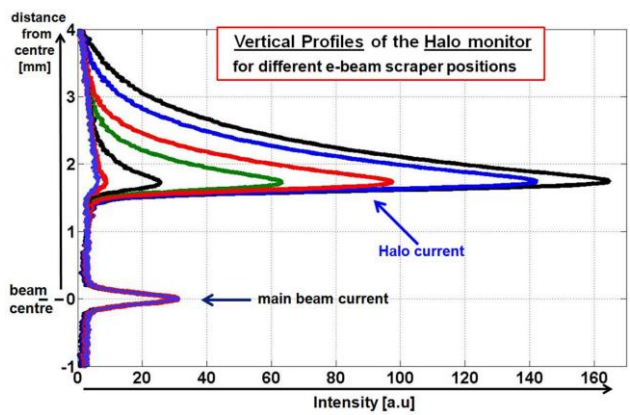


Figure 7: Profiles of the Halo for different positions of the vertical beam scraper (in Cell 5).

ISBN 978-3-95450-141-0

Copyright © 2014 CC-BY-3.0 and by the respective authors

MANIPULATIONS WITH THE BEAM AND THE INSERTION DEVICES

The Halo monitor essentially measures the rate of electrons suddenly leaving the central dense beam-core and subsequently describing oscillations at large distances from that centre before then damping down and re-integrating this beam-core again. During this damping time (~7ms for our lattice) they occupy this Halo zone and thus contribute (via X-ray synchrotron radiation) to the signal of the here described device.

The two main reasons of this scattering is by energy exchange between 2 electrons (known as Touchek scattering) and by the deflection of the electron by a residual gas molecule of a non-perfect vacuum in the chamber. The Touchek scattering is very much favoured by the density of the electron bunches, while scattering due to gas is proportional to the vacuum pressure.

During normal User's operation we observe that the Halo monitor is extremely sensitive to the slightest increase of the vacuum pressure. When comparing these recordings with that of our set of local Beam Loss Monitors at the occurrence of such tiny gas outburst we see in addition to the good correlation that the signal-to-noise ratio of the Halo monitor is superior to that of the BLDs.

The Touchek scattering varies with beam charge per bunch and with the beam-size. The latter can be easily manipulated (blown-up) by adding some white-noise oscillation to the beam in the vertical plane by the use of a so-called shaker.

In addition to these manipulations on the electron beam we have also investigated how the Halo level varies under different scraper (both horizontal and vertical) settings and this again for different beam conditions (intensity, vertical emittance). An example is shown in Fig.8.

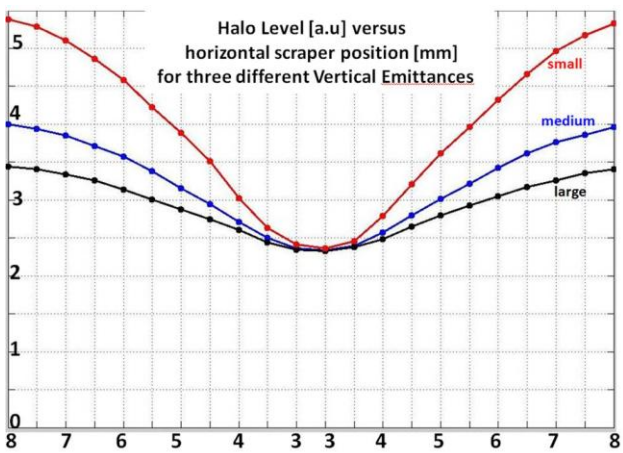


Figure 8: scraping the beam with a horizontal scraper.

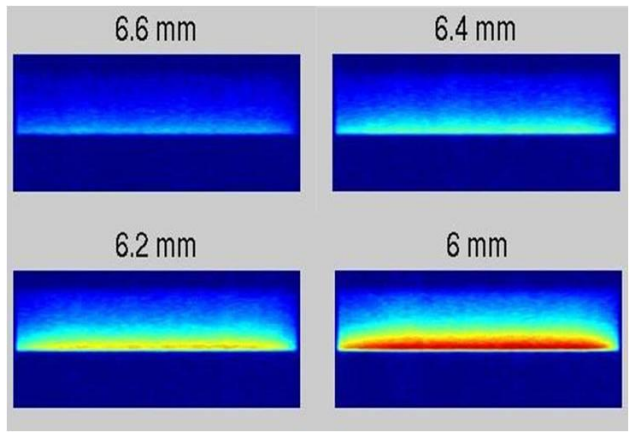


Figure 9: four differential Halo images when closing the ID15 In-Vac undulator down to its minimum of 6mm.

Finally, an interesting application is to see how the In-Vacuum undulators (12 installed in the Ring) can affect the Halo levels when their gaps are set to small values (i.e. 6mm). An illustration is shown in Fig.9 with differential images at 4 different gap settings. A differential image is obtained when subtracting the image when gap_fully_open from the image with a small gap setting.

ACKNOWLEDGMENT

The author wishes to thank N.Benoist for taking care of the mechanical designs, the installation work and for the realisation of the adequate protection and housing of the image/detector system. The help and support in the initial design concept received from B.Ogier and J-C.Biasci is also acknowledged. Thanks are also expressed to F.Ewald and J-M.Chaize for support given to the device-server aspects of various new cameras that have been used and tested.

REFERENCES

[1] F.Ewald et al., "Vertical Emittance Measurement at the ESRF", MOPD61, DIPAC'11, Hamburg, May 2011. http://accelconf.web.cern.ch/AccelConf/DIPAC2011/papers/mopd61.pdf

[2] A.Zholents, W.Decking, "Non-gaussian beam tails at the Advanced Light Source", 04-01-2000. http://escholarship.org/uc/item/54z1j750

[3] T.Mitshuhashi, "Beam Halo Observation by Coronograph", ITMM03, DIPAC'05, Lyon, May 2003. http://accelconf.web.cern.ch/AccelConf/d05/PAPERS/ITMM03.PDF

[4] B.K.Scheidt, "Recent Development of Novel Beam Diagnostics at the ESRF", TUOCB201, IPAC'13, Shanghai, May 2013. http://accelconf.web.cern.ch/AccelConf/IPAC2013/papers/tuocb201.pdf

[5] Saint-Gobain, Cerium doped Lutetium based scintillation crystal, http://www.crystals.saint-gobain.com

Copyright © 2014 CC-BY-3.0 and by the respective authors

ISBN 978-3-95450-141-0

DESIGN AND INITIAL COMMISSIONING OF BEAM DIAGNOSTICS FOR THE KEK COMPACT ERL

R. Takai#, T. Obina, H. Sagehashi, Y. Tanimoto, T. Honda, T. Nogami, M. Tobiyama,
KEK, 1-1 Oho, Tsukuba, Ibaraki 305-0801, Japan

Abstract

A compact energy-recovery linac (cERL) was constructed at KEK as a test accelerator for the ERL-based light source. Standard beam monitors such as beam position monitors (BPMs), screen monitors (SCMs), and beam loss monitors (BLMs) have been developed for the cERL and used in its commissioning. For the main BPMs, we adopted the stripline type, the time response of which is improved by using a glass-sealed feedthrough. The SCMs are equipped with two types of screens and an RF shield for wake-field suppression. Optical fibers with photomultiplier tubes (PMTs), covering the entire cERL circumference, are used as the BLM. CsI scintillators with large-cathode PMTs are also prepared for detecting local beam loss. The design and some initial commissioning results of these standard monitors are described in this paper.

INTRODUCTION

The energy-recovery linac (ERL) has recently received significant attention as one of the promising candidates for next-generation light sources [1]. The Compact ERL (cERL), which is a test accelerator aimed at demonstrating the key technologies for the ERL-based light source, was constructed at KEK, and the complete system was commissioned in December 2013. The commissioning proceeded without troubles, and we successfully accelerated 6.5-μA CW beams to energies reaching 20 MeV; the beams recirculated without major loss, and they were guided to the beam dump after energy recovery in only two months [2]. In such an early phase of commissioning, standard beam diagnostics such as the monitoring of beam position, beam profile, and beam loss plays a central role. In this paper, we describe the design of our standard beam monitors that have contributed to the efficient cERL commissioning, and we report the initial commissioning results.

The beam monitors used for the cERL are listed in Table 1, and Fig. 1 shows their schematic layout. Four sets of fiber loss monitors cover the entire cERL circumference. Because the CsI-scintillator-based beam loss monitors described later are still under development, they are not listed in Table 1. Four current transformers (CTs) and a DCCT are currently not used, because of the low beam current. The beam current is measured by using not only the three movable Faraday cups (FCs) listed in Table 1 but also two beam dumps: injector and main dumps. In addition to these monitors, a slit scanner and a deflecting cavity are installed along the diagnostic line following the injector for the emittance and bunch-length measurements, respectively [3].

Table 1: List of cERL Beam Monitors

Monitor Type	Objective	#
BPM (Stripline/Button)	Position, Charge	45
SCM (Ce:YAG/OTR)	Position, Profile	30
BLM (Fiber&PMT)	Loss	4
CT	Charge	4
DCCT	Current	1
Movable FC	Charge	3

BEAM POSITION MONITOR

A beam position monitor (BPM) is a very useful tool especially for monitoring high-intensity ERL beams because it can non-destructively measure the beam centroid displacement in the transverse plane. The cERL has 45 BPMs, which are roughly classified into five types according to the duct structure and electrode type. This section describes the design of the BPM duct in the straight section, which contains the largest number of

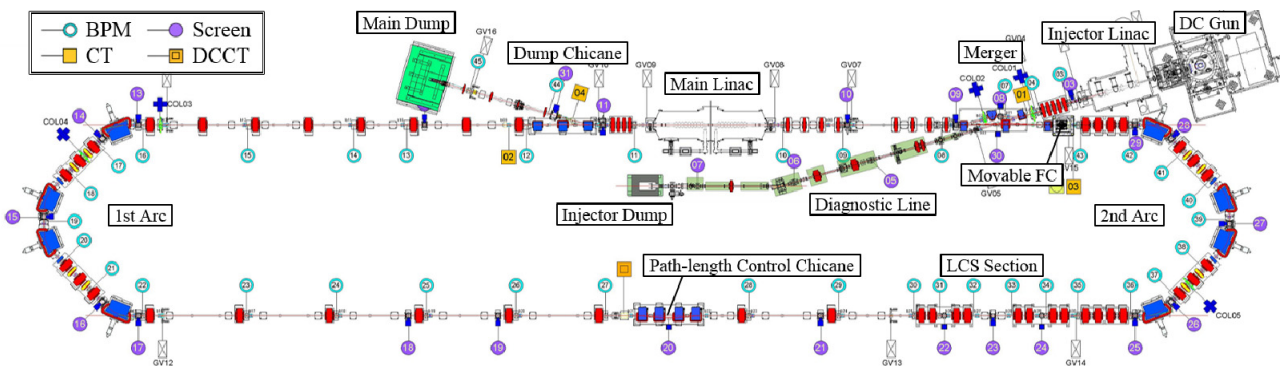


Figure 1: Layout of cERL beam monitors.

#ryota.takai@kek.jp

ISBN 978-3-95450-141-0

Copyright © 2014 CC-BY-3.0 and by the respective authors

BPMs, and its electronics used for detecting the beam signals. To demonstrate the use of BPMs in the commissioning, we also report the result of measuring two-color beams before and after the circulation for energy recovery.

Design of the BPM Duct

Figure 2(a) shows a schematic of the BPM duct in the straight section. Stripline electrodes are disposed on the top and bottom as well as right and left inner walls of the duct, which has an inner diameter of 50 mm. The length of each electrode was fixed as 28.8 mm to maximize sensitivity to the frequency component of 2.6 GHz, which is the beam's maximal repetition frequency. As for BPMs installed along the injector line and the dump line where the repetition frequency is only 1.3 GHz even when future upgrades are considered, the electrode length was set to 57.6 mm, which is twice the length of the above electrodes. The electrode width was selected such that the opening angle relative to the beam axis is 20° for all BPMs. The characteristic impedance of each electrode was designed to be 50 Ω, and it was confirmed using time domain reflectometry (TDR). The electrode end at the downstream side was directly welded to the duct wall and grounded. Beam signals induced on the electrode are extracted to the outside through a feedthrough welded at the upstream side end of the electrode. In this feedthrough, low-permittivity glass (BHA, ε_r = 5.0) is used for insulation and sealing to improve the time response [4]. The wake fields excited by the beam and the beam coupling impedance were evaluated in advance by using GdfidL [5]. In the simulations of an electron beam with a bunch length of 1 mm (3.3 ps), the longitudinal loss factor was calculated to be 59.1 mV/pC. After conversion into the power loss for the beam average current of 10 mA, the loss factor becomes 4.6 mW. For vacuum flanges at both ends of the BPM duct, we used special gapless and stepless flanges developed to reduce the wake fields [6]. A cylindrical boss on the top surface is useful for precise alignment because it can be used to mount a level and a reflection target of the laser tracker on the duct. Figure 2(b) shows a photograph of the stripline electrodes inside the BPM duct.

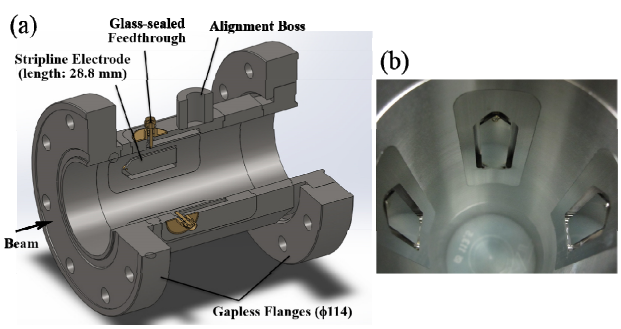


Figure 2: (a) Schematic drawing of the BPM duct in the straight section. (b) Photograph of the stripline electrodes taken from the upstream side.

Detection Circuit & Digitizer

BPMs for the ERL require a broad dynamic range rather than high measurement accuracy. Therefore, we adopted a log detection circuit with a bandwidth of 10 MHz to detect the beam signals. Although the preferable center frequency for wave detection with noise reduction is 2.6 GHz, it was taken to be 1.3 GHz because the cut-off frequency of the octagonal duct in the arc section is approximately 2.6 GHz. The block diagram of the detection circuit is shown in Fig. 3. Output signals from one BPM are processed in one NIM module including four detection circuits. When a variable attenuator following an input port is set to 0 dB, the detection circuit log-linearly responds to the input voltage in the range of -90 to -30 dBm. The rise time of the output signals for a pulse input of width 1 μs is about 200 ns. A commercial high-speed data acquisition unit and insulating input modules were employed as a digitizer (Yokogawa, SL1000). This digitizer has a sufficiently wide analog bandwidth and a resolution of 12 bit. It can be utilized for beam current monitoring by inputting the output signal of a Faraday cup, in addition to other waveform analyses.

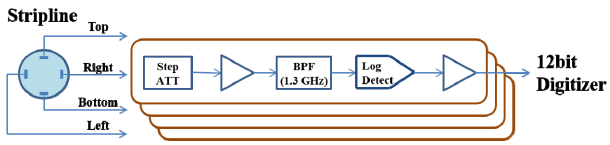


Figure 3: Block diagram of the detection circuit.

Examples of BPM Usage

Beam positions measured by the BPM are shown in Fig. 4(a) in red as a function of time. In this experiment, we changed the beam position stepwise by using a steering magnet located upstream from the BPM. The blue line indicates the nominal beam positions calculated on the basis of the measurement obtained using a screen monitor. The two measurements are in a good agreement. If the BPM resolution, including the beam position jitter, is evaluated from the variation of the measurement data, the obtained value is about 150 μm. Figure 4(b) shows the mapping results calculated using CST PARTICLE STUDIO [7]. The sensitivity curve obtained by fitting the fifth degree polynomial to this map was used for converting the detected signal into the beam position.

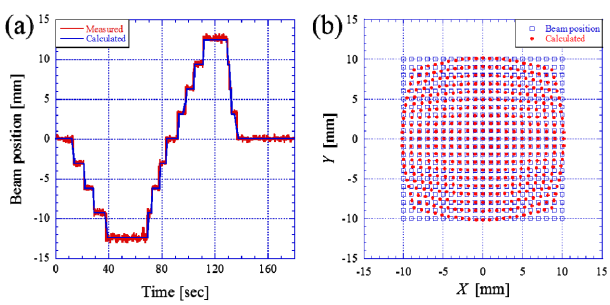


Figure 4: (a) Comparison of beam positions measured by the BPM with those obtained using a screen monitor. (b) BPM mapping results.

Copyright © 2014 CC-BY-3.0 and by the respective authors

ISBN 978-3-95450-141-0

In the section between the merger and the dump chicane, destructive monitors such as screen monitors cannot be used to observe the post-circulation high-energy beam, because the pre-circulation low-energy beam is simultaneously propagating in the same section. Therefore, we focused on the fact that the post-circulation beam signals superimpose on the pre-circulation signals with a constant delay corresponding to the circulation time, and we devised a simple method to detect the positions of these beams individually by using a BPM. This method is schematically illustrated in Fig. 5(a). In the case of burst mode with macro-pulse beams that is commonly used in the commissioning, the head and tail parts of the detected signal contain only pre- and post-circulation beam signals, respectively, because of the above delay. Ideally, there are no signals between these parts because the 2.6-GHz component produced by the superimposition of the beam signals dephased by 180° relative to each other for the energy recovery is removed by the bandpass filter in the detection circuit. Figure 5(b) shows the measurement results of the two-color beams obtained upstream and downstream of the main linac. Each detected signal from four circuits has a step-like profile, and we can clearly distinguish the two different energy beams. The width of each part depends on the beam's circulation time, which for the cERL is about 300 ns. The difference between the rise times of detected signals is caused by the characteristic difference between the detection circuits used in this measurement. The reason for the appearance of finite signals between these parts is that the phase difference of 180° shifts in proportion to the distance from the main linac because of the beam energy difference. In other words, the signals in this part can be used as a beam phase monitor. This simple and reliable method worked very well in adjusting the beam orbit after the circulation. If a negligible blank area with no beam is added periodically, this method can be applied to the CW beams.

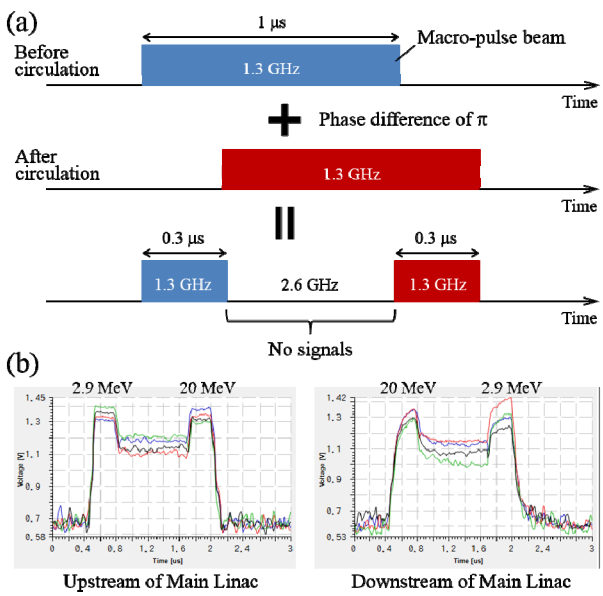


Figure 5: (a) Schematic of the measurement of two-color beams by using a BPM. (b) Measurement results obtained upstream and downstream of the main linac.

SCREEN MONITOR

While a screen monitor (SCM) is a typical destructive monitor, it is one of the essential instruments, especially for the linac commissioning, because it enables the precise measurement of the beam position and profile even for low-intensity beams. The SCM is also useful for estimating the beam quality by combining it with a magnet or a deflecting cavity located upstream of it. As shown in Fig. 1, 30 SCMs are present in the cERL. The internal structure of the SCM differs depending on the installation section and can be classified into six types. In this section, we describe the details of the SCM installed in the straight section and report the emittance measurement results obtained by using it.

Design of the SCM Duct

A schematic of the SCM duct in the straight section and a photograph of the screen holder are shown in Fig. 6. The duct's internal structure was designed on the basis of that employed at JLab and BNL [8, 9]. The two-stage screen holder allows us to use two different screens according to the beam energy and intensity. The first screen is a 100-μm-thick Ce:YAG scintillator. The beam is normally incident on the scintillator's surface. Fluorescent light emitted from the scintillator is guided to a side viewport through a thin SUS mirror arranged at 45° relative to the beam axis. The beam incidence surface is coated with a 3-nm-thick aluminum layer to avoid damage due to charge-up. The second screen is a metal foil used for generating an optical transition radiation (OTR). We adopted an aluminum-coated silicon wafer as the OTR radiator so that the radiation surface is flat. The thickness of the wafer and coating are 70 μm and 40 nm, respectively. To prevent overlapping of the forward OTR emitted from the wafer's rear surface and the backward OTR emitted from the mirror's front surface, this screen was arranged at 45° relative to the beam axis. Both apertures of these screens are 28 mm in diameter. Four

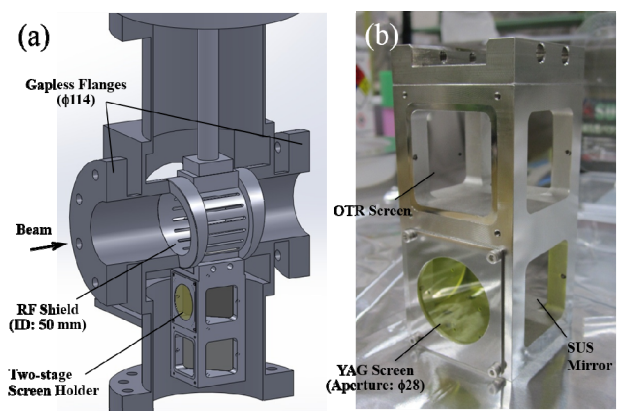


Figure 6: (a) Schematic of the SCM duct in the straight section. (b) Photograph of the two-stage screen holder.

Copyright © 2014 CC-BY-3.0 and by the respective authors

ISBN 978-3-95450-141-0

holes of diameter 1 mm each are located at peripheral parts of the screens and used for the focus adjustment and the magnification calibration for the imaging optics. These screens are concealed behind a cylindrical RF shield when not in use. The RF shield is smoothly connected with the adjacent beam ducts only with physical contact through high-precision fitting. According to the GdfidL estimation, this RF shield reduces the longitudinal loss factor to 1/100 (10 mV/pC) or below for an electron beam with 1-mm bunch length. These components are driven by a pneumatic actuator with a positioning precision of 0.1 mm or less. As in the BPM duct, gapless flanges are also used for the SCM duct.

Imaging Optics & CCD Camera

As mentioned above, the light emitted from the screen is extracted in the direction perpendicular to the beam axis and then relayed via an optical window and a flat mirror to a CCD camera (Allied Vision Technologies, Prosilica GC650). The flat mirror in the middle of the optical path is useful for adjusting the optical axis and protecting the camera from radiation-induced damage. A low-distortion CCTV lens with a diaphragm is mounted on the camera's front (Myutron, HS5028J3). Figure 7 shows a focused image of a calibration pattern obtained using the imaging optics with a magnification that is actually used in the commissioning. The spatial resolution of the YAG screen was estimated by accounting for the depth of field and multiple scattering of electrons in the Ce:YAG crystal in addition to the edge width of this image. Assuming the image bleeding to be on the order of the crystal's thickness, the spatial resolution was estimated to be 62 μm. Because the OTR screen is not affected by the multiple scattering of electrons, it is expected that the resolution is improved up to about 40 μm.

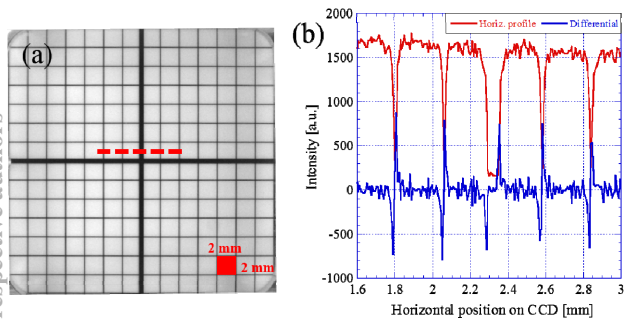


Figure 7: (a) Focused image of the calibration pattern. (b) Horizontal profile on the dashed line and its position differential.

Examples of SCM Usage

Thus far, we primarily used the YAG screen in the commissioning with low-energy and low-intensity beams. The linearity of the fluorescence intensity in the range of beam densities achieved in the commissioning was confirmed experimentally in advance. The exposure time of the camera was typically set to 100 μs. In this setup, noise signals caused by a dark current emitted from the superconducting cavities tuned for the acceleration up to 20 MeV were negligibly small.

The beam tuning effect clearly appears in the beam's normalized emittance. It was measured by employing the quadrupole-scan (Q-scan) method using the SCM. An example of the Q-scan result acquired at the downstream section of the first arc is shown in Fig. 8. The bunch charge was approximately 20 fC/bunch. The space charge effect in the bunch can be negligible. The quadrupole magnet used for the measurement, in other words the length of the drift space between the quadrupole magnet and the SCM, was selected such that the beam size at the waist position of the graph was not lower than the spatial resolution of the YAG screen. The camera's gain and the density of ND filters were adjusted carefully to prevent the saturation of CCD pixels even at the waist position. The normalized emittance can be calculated from some coefficients obtained by fitting the theoretical function to these measurement data by using the weighted least squares method. Although the initial emittance was over 0.4 mm·mrad in both horizontal and vertical directions, it gradually reduced as the beam tuning proceeded and reached the value of 0.14 mm·mrad. This was almost the same as the design value for low-bunch-charge beams. In the latter part of the commissioning, the normalized emittance for high bunch charge (7.7 pC/bunch) was also measured by employing the same method. While the measured value is still larger than the target value at present, it is decreasing steadily because of elaborate optics matching using the SCM.

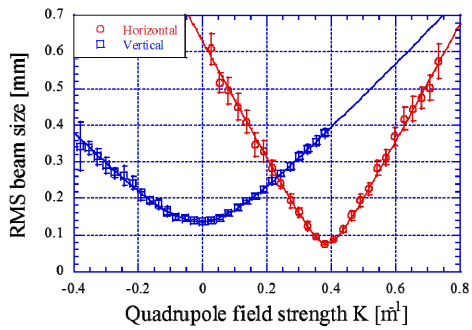


Figure 8: Example of the emittance measurement using the Q-scan method (for a low bunch charge of ~20 fC/bunch).

BEAM LOSS MONITOR

Fast Beam Loss Monitors

Throughout the commissioning, typical beam tuning was performed with a 1-μs macro-pulse beam with 20 fC/bunch and 770-ps (1.3 GHz) bunch spacing. Because the electron source of the cERL is a 500-kV DC photocathode gun, high-charge beams with pulse length greater than expected may be produced in the case of a trouble of the laser. To avoid serious damage to screen monitors or other accelerator components, it is essential to

Copyright © 2014 CC-BY-3.0 and by the respective authors

ISBN 978-3-95450-141-0

have a fast interlock system for stopping the gun laser by using beam loss monitors (BLMs). The first goal of our fast BLM is to attain time response on the order of 1 μs.

Four 30-m long optical fibers were installed along the vacuum chamber as one of the fast BLMs, covering the entire cERL circumference [10]. Photomultiplier tubes (PMTs, Hamamatsu, H10721-110) were attached at both ends of the fiber, and two oscilloscopes were used to analyze the time structure of the output signal. This monitor is primarily used to estimate the beam-loss point along the circumference.

We have also developed a fast BLM by using a pure CsI crystal for local beam loss detection [11]. The dimensions of the CsI crystal are 10 mm×10 mm×25 mm, and it is attached to a large-size PMT cathode (Hamamatsu, R11558). Figure 9(a) shows an example of beam loss detection at the first arc section. The green and blue lines indicate output signals of the PMT with a CsI scintillator and of a post-stage integration circuit for the interlock system, respectively. A time response sufficiently fast for detecting 1-μs-wide macro pulses is clearly obtained. Note that this measurement was performed before the precise optics matching, and the signal was caused by a loss of the beam's tail. When the beam's core is lost (e.g., when the screen is inserted), the output signal voltage is much higher than that shown in Fig. 9(a). After matching the arc section optics, the beam loss drastically decreased, as shown in Fig. 9(b). Since a thallium-doped CsI crystal has longer time response but higher sensitivity, it will also be utilized for small beam loss detection.

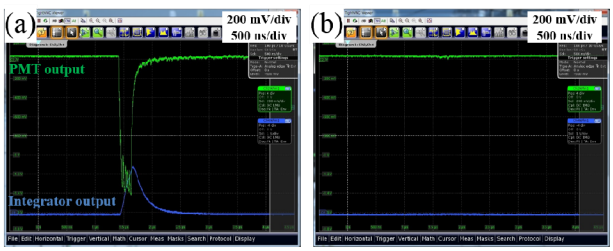


Figure 9: Example of beam loss detection at the first arc section. Before (a) and after (b) the optics matching.

Slow Radiation Monitors

Twelve area monitors were used to measure the gamma dose rate inside the accelerator shield. As a second-order time response is sufficient for this purpose, we adopted ALOKA MAR-782, which utilizes a silicon semiconductor detector to measure gamma rays with energies ranging from 50 keV to 6 MeV. Each area monitor can be arbitrarily set at a threshold level of interlock for stopping the gun laser. A 4-port RS232 device server embedded with EPICS was developed to remotely observe the radiation levels measured by each area monitor [12], and it worked without troubles for over half a year.

Low-energy gamma rays with energies above 7 keV were primarily detected using an ion chamber survey meter, Fluke 451B, which was also used to cut off the gun's high voltage when the radiation dose exceeded a threshold level.

SUMMARY AND FUTURE PLAN

The details of BPMs, SCMs, and BLMs for the cERL, which are the most standard and the most important beam monitors, were described. Commissioning toward the experimental utilization of pulsed X-rays generated by laser Compton scattering (LCS) will start in January 2015. By that time, we plan to add two button-type BPMs at both sides of the LCS collision point and a large-aperture SCM at the dump line. In addition, we are also preparing for bunch-length measurement using coherent transition radiation and a Michelson interferometer to confirm the effect of bunch compression with the first arc [13].

ACKNOWLEDGMENT

The authors would like to thank all members of the cERL commissioning team for their collaborative efforts during this work. We would also like to thank T. Michikawa and H. Kameta for their continuing support in the construction of the control system for beam monitors and other components.

REFERENCES

[1] N. Nakamura, "Review of ERL Projects at KEK and around the World," IPAC'12, New Orleans, p. 1040 (2012).
[2] S. Sakanaka et al., "The First Beam Recirculation and Beam Tuning in the Compact ERL at KEK," LINAC'14, Geneva, TUPP075 (2014).
[3] S. Sakanaka et al., "Construction and Commissioning of the Compact-ERL Injector at KEK," ERL'13, Novosibirsk, p. 16 (2013).
[4] M. Tobiyama et al., "Development of Button Electrode with Improved Time Response," BIW'08, Tahoe City, p. 205 (2008).
[5] http://www.gdfidl.de
[6] Y. Tanimoto et al., "Design of the cERL Vacuum System," IPAC'13, Shanghai, p. 3315 (2013).
[7] https://www.cst.com/Products/CSTPS
[8] P. Evtushenko et al., "Electron Beam Diagnostics of the JLab UV FEL," PAC'11, New York, p. 1446 (2011).
[9] D. M. Gassner et al., "BNL Energy Recovery Linac Instrumentation," ERL'11, Tsukuba, WG4003 (2011).
[10] T. Obina et al., "Optical Fiber Based Loss Monitor for Electron Storage Ring," IBIC'13, Oxford, p. 638 (2013).
[11] H. Sagehashi et al., "Test of Detection Unit for the cERL High-speed Loss Monitor," the 11th Annual Meeting of PASJ, Aomori, SUP083 (2014) [in Japanese].
[12] T. Obina et al., "Development of Compact Device Server with EPICS," the 11th Annual Meeting of PASJ, Aomori, MOOL08 (2014) [in Japanese].
[13] Y. Honda et al., "Development of Bunch Length Monitor System at the Return Loop of KEK ERL Test Accelerator," the 11th Annual Meeting of PASJ, Aomori, SAP089 (2014) [in Japanese].

ISBN 978-3-95450-141-0

Copyright © 2014 CC-BY-3.0 and by the respective authors

LONGITUDINAL LASER WIRE AT SNS

A. Zhukov, A. Aleksandrov, Y. Liu
Oak Ridge National Laboratory, Oak Ridge, TN 37830, USA

Abstract

This paper describes a longitudinal H- beam profile scanner that utilizes laser light to detach convoy electrons and an MCP to collect and measure these electrons. The scanner is located in MEBT with H- energy of 2.5MeV and an RF frequency 402.5MHz. The picosecond pulsed laser runs at 80.5MHz in sync with the accelerator RF. The laser beam is delivered to the beam line through a 30m optical fiber. The pulse width after the fiber transmission measures about 10ps. Scanning the laser phase effectively allows measurements to move along ion bunch longitudinal position. We are able to reliably measure production beam bunch length with this method. The biggest problem we have encountered is background signal from electrons being stripped by vacuum. Several techniques of signal detection are discussed.

INTRODUCTION

The Spallation Neutron Source accelerator complex consists of an H- linac where a one mS long train of ~1us mini-pulses is accelerated to 1GeV to be injected into a storage ring. The mini-pulses are accumulated in the ring and extracted to hit a mercury target as an intense ~700nS long pulse. Every mini-pulse is bunched at a 402.5MHz frequency. The SNS accelerator runs at 60Hz with average current of ~1.6mA resulting in over 1MW of beam power on target. Such a machine requires low loss operation, thus careful matching of longitudinal and transverse planes becomes important. The SNS uses several diagnostics devices and techniques for longitudinal profile measurements [1] including classical wire based Bunch Shape Monitor [2] and Laser Bunch Shape Monitor (LBSM) installed in MEBT. Also a method for measuring longitudinal Twiss parameters with Beam Position Monitors (BPM) was recently developed [3]. The LBSM is the only beam dynamics model independent device that allows non-invasive measurements while the accelerator is running at full power in neutron production mode.

THEORY OF OPERATION

A mode-locked laser running at 80.5MHz – in sync with the 5th sub-harmonic of 402.5MHz – detaches the electrons from the 2.5MeV negative hydrogen ions in the MEBT. The detached electrons are deflected by a magnet to be collected by an MCP as shown in Fig.1. While changing the laser phase we effectively move longitudinally along the ion beam and strip the ions that have a corresponding beam phase only. Using the 5th sub-harmonic results in 72° of scanned laser phase for a full sweep of 360° of ion beam phase.

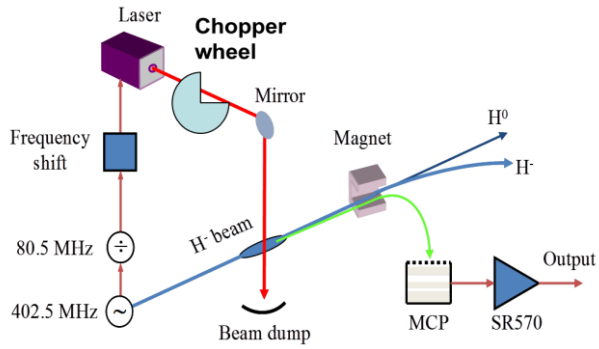


Figure 1: A layout of the Laser Bunch Shape Monitor.

In order to use this technique we need to precisely measure the laser phase vs. the base 402.5MHz carrier. We developed two approaches: frequency offset and phase shift.

Frequency Offset

If we change laser pulse repetition frequency by a tiny Δf on the order of 1kHz it will result in a phase drift with the period of ~1ms. Since the ion pulse length is 1ms it will experience all possible values of laser phase along its length. This will effectively plot longitudinal bunch distribution against time along the macro-pulse where 200us (1ms/5) corresponds to 360° of ion beam phase. Figure 2 shows the bunch profiles for different Δf.

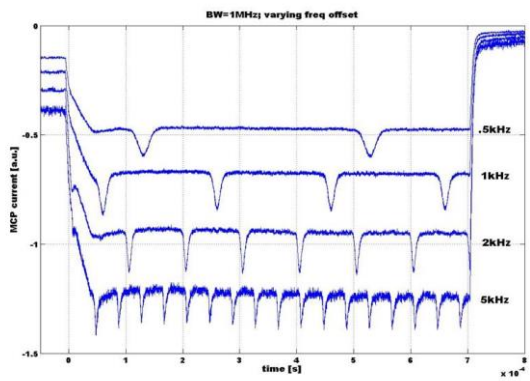


Figure 2: Bunch profile measurements with different frequency offsets in the frequency offset mode.

This method allows measuring bunch profile instantly by capturing one ion beam macro-pulse. It is very convenient because no additional equipment is needed and a scope waveform shows the bunch profile. It also doesn't require any precise measurement of Δf and actually even locking to 402.5MHz is not necessary.

Unfortunately this approach only works for long ion beam pulses. It is impossible to run full-length pulses

Copyright © 2014 CC-BY-3.0 and by the respective authors

ISBN 978-3-95450-141-0

during experimental setups where high loss is expected. Thus this method is applicable for production optics only.

Phase Shift

An alternative way to scan laser phase relative to beam phase is to insert a controllable phase shifter between the base 80.5 MHz clock and the laser. This way one sets the phase and records MCP signal for every phase value. So to obtain a profile consisting of N points it requires N macro-pulses to be measured.

While this method works with any macro-pulse length, implementing it requires a much more sophisticated setup including automated phase shifting and measuring its actual value. Figure 3 shows a typical bunch length measurement with a phase shifter.

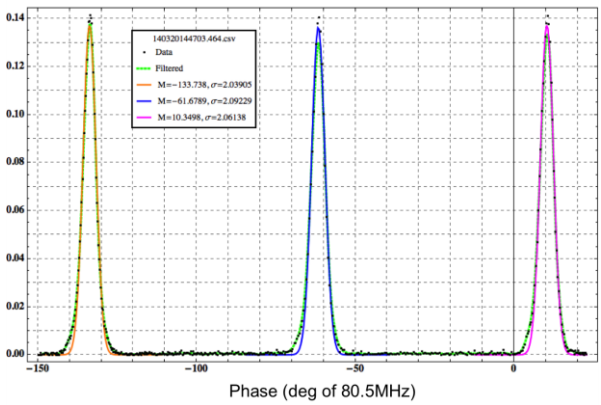


Figure 3: Typical bunch profile taken with phase shift technique. Peaks are distributed 72° apart.

LASER AND TRANSMISSION LINE [4]

SNS uses a Mira 900 Ti:sapphire mode-locked laser (pumped by a 10W Verdi-V10 solid-state laser) as the light source. The laser is synchronized to a stable external radio frequency (RF) source at 80.5MHz with a Coherent Synchro-Lock controller. The laser has pulse width (FWHM) of 2.5pS. The laser's peak power is variable up to 5kW.

The laser itself is located on the third floor of SNS front end building, so the light has to be transported to the beam line from there. Initially a free propagation transport line was used, but it was adding significant vibration and temperature effects. So it was replaced with a 30 m long polarization-maintaining LMA fiber (PM-LMA) from Nufern. The fiber significantly increases laser beam stability in the interaction point but broadens the laser pulse to ~10 ps. With the current laser spec (800nm wavelength/0.6W average power/80.5MHz rep. rate) and ion beam spec (2mm transverse and 80ps longitudinal, all of sigma size), the photoionization efficiency was estimated to be about $3x10^{-6}$ at the MEBT. For a typical SNS ion beam macro-pulse, the photo-ionized electron charge over one macro-pulse was estimated to be about 10pC.

A chopper wheel is used to intercept the laser beam and collect the background signal of the MCP with no laser present. We also experimented with a shutter instead of the chopper in order to have full control of the number of background measurements.

A motorized stage allows transverse scans in the horizontal plane, so it's possible to build 2D distribution in the X-Z plane.

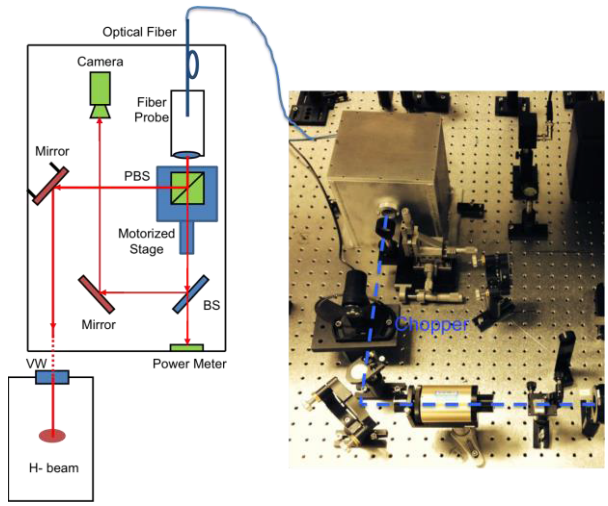


Figure 4: Laser transport line layout.

EXPERIMENT SETUP

In order to implement the phase shifting scheme we used a custom built analog chassis that relies on two RVPT0003MAC phase shifters. The shifters are connected in series to provides more than 400° at 80.5MHz. The base 402.5MHz is down converted to 80.5MHz and connected to the phase shifting chassis. The output of the chassis is sent into the laser synchronization module.

The phase shifter's dependence on bias isn't linear (Fig. 5). Chaining two phase shifters also adds non-linearity due to amplitude variations for differing bias, so phase readback is necessary.

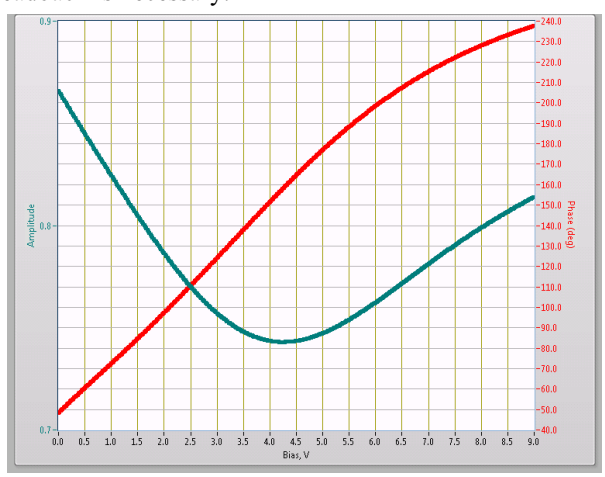


Figure 5: Phase shifter output vs. controlled bias.

The actual laser phase is monitored from an internal photodiode by an SR844 lock-in amplifier that is locked

ISBN 978-3-95450-141-0

Copyright © 2014 CC-BY-3.0 and by the respective authors

to the same 80.5MHz. We found out that we needed to buffer the shifter's inputs with ZFL-500LN amplifiers to avoid reflections that contaminated the base frequency of the lock-in amplifier – Fig. 6.

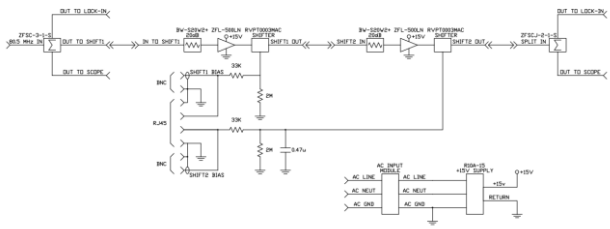


Figure 6: Schematics of phase shifter chassis.

Collected electrons are amplified by an MCP (Photonis APD 1 MA 40/12/10/8 D 60:1) and further amplified with an SR 570 current amplifier. The signal bandwidth is ~ 1MHz. The amplified signal is digitized with an NI 5105 card. The MCP's high voltage is controlled by a custom made HV power supplied that is controlled by an NI 6229 card and typically runs at negative 2.3kV.

The chopper wheel is synchronized to the ion beam trigger, so every even pulses have laser-induced signal and odd ones are used for background (that is subtracted in software). This effectively halves the ion beam repetition rate, as two ion pulses are required for each data point taken.

Everything is controlled form LabVIEW based software that manages data acquisition, background subtraction, phase scanning, and phase read back measurements. It also provides control over the MCP HV and magnet current.

Background Considerations

The laser signal is ~20% of the background in the maximum of bunch profile. The main source of background signal is from H- stripping on residual gas. It makes measurements extremely sensitive to background pulse to pulse deviations. Fig. 7 shows the typical signal in phase shifting measurement in the middle of the bunch.

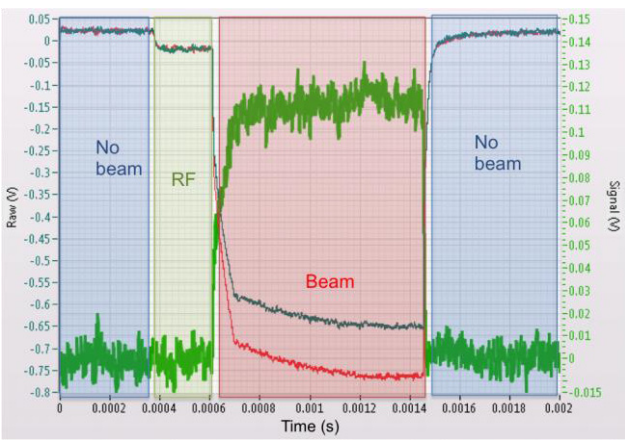


Figure 7: Macro-pulse structure during production. Red trace shows the MCP signal with laser hitting the ions and the grey-blue trace represents signal with laser being blocked by chopper. Green trace is the difference.

The first "step" of the waveform corresponds to cavities switching on and generating x-rays. The second step is actual ion-beam induced signal.

For a better understanding of the noise structure we collected 10 minutes of waveform data at 60Hz during beam production. The data was partitioned into batches of 1000 subsequent pulses and waveforms were averaged over every batch – Fig. 8. From this we obtained a slow evolution of the background waveform over time and concluded that it makes sense to average over several macro-pulses as it decreases signal deviation according to $1/\sqrt{N}$.

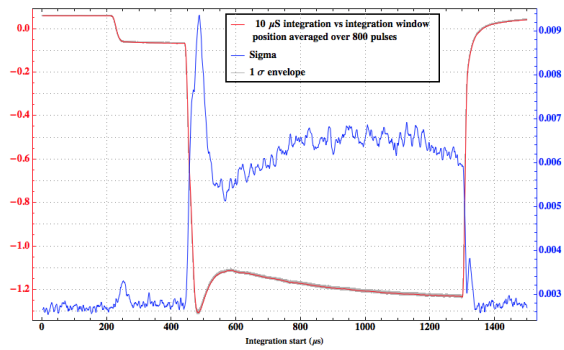


Figure 8: Background waveform averaged over 1000 macro-pulses. Sigma refers to standard deviation of every waveform point for one batch statistics.

The Fig. 9 demonstrates how 10 pulse averaging works for production beam.

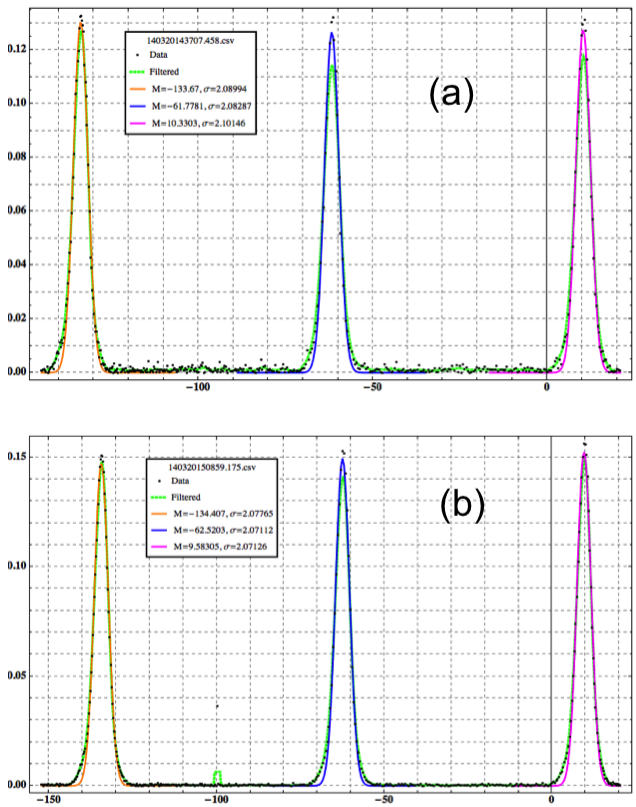


Figure 9: (a) no averaging, (b) averaged over 10 macro-pulses.

Copyright © 2014 CC-BY-3.0 and by the respective authors

ISBN 978-3-95450-141-0

We experienced significant problems with the short ion beam pulses that are used for accelerator studies – 50 uS length. We considered several ways of statistically improving the profiles. One can either increase the ion beam length up to 50 us and run scans at 1 Hz repetition rate or alternatively we can run 10 us beam at 5 Hz rate to stay below dangerous beam power levels. In the first scenario we can average along macro pulse (in the beam window) and in the second scenario we can average over several macro-pulses. Unfortunately we weren't able to obtain conclusive results of which technique is better. We observed that the pulse-to-pulse background deviation is significantly higher than during production. Figure 10 demonstrates an example noise pattern during a 50 us scan.

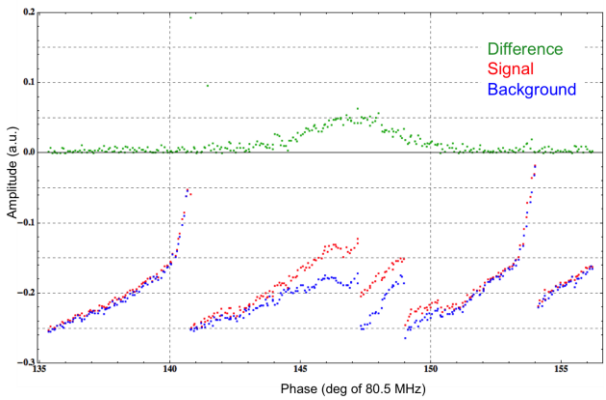


Figure 10: Short pulse scan.

Currently there is no understanding what mechanism can cause such background behavior.

We also tried to detect the 80.5 MHz component in MCP signal hoping that this component won't be prone to noise issues, but we failed since the bandwidth of our existing MCP appeared to be significantly lower.

REBUNCHER SCAN

In order to see if we can achieve meaningful results that can be predicted by beam dynamics models, we successfully applied the well known quadrupole scan technique [5]. Normally it is used to measure transverse emittance by plotting transverse size vs. quadrupole field strength and fitting it with a parabola.

The same technique can be used for plotting the longitudinal size vs. RF amplitude. The results of scanning upstream rebuncher amplitudes are shown on Fig. 11. They provide a good sanity check that the device produces physical results, but couldn't be used for emittance calculation because of space charge. Attempt to perform similar scan with lower beam current (no space charge effects) was unsuccessful due to background issues mentioned above.

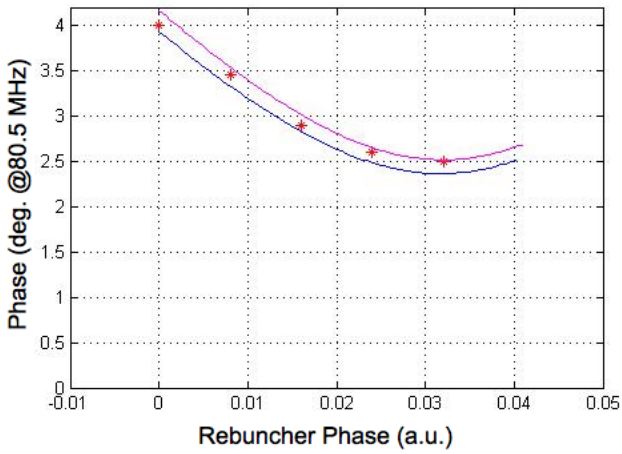


Figure 11: Experimental results compared to model generated for two different input Twiss parameters.

CONCLUSIONS

The SNS LBSM scanner is operational and can be used for reliable measurement of production beam longitudinal size. The measured beam size is around 10°, but the reference design size is ~15°. Currently there is no explanation for this discrepancy, although it's hard to imagine a flaw in the measurements that could lead to smaller beam size.

Significant background signal and its time deviation currently limit the use of this device for short pulses and low current setups. We plan to consider replacing the MCP with a high bandwidth detector and also investigate the bending magnet's ability to reject background electrons.

ACKNOWLEDGEMENT

ORNL/SNS is managed by UT-Battelle, LLC, for the U.S. Department of Energy under contract DE-AC05-00OR22725.

REFERENCES

[1] A. Aleksandrov, *et al.* Proc of IBIC2013, p. 163.
[2] A. Feschenko, *et al.*, Proc. PAC2001, p. 517.
[3] A. Shishlo *et al.*, Phy. Rev. Lett. 108, 114801, (2012).
[4] C. Huang, *et al.*, Applied Optics / Vol. 52, No. 19, p.4462-4467, (2013).
[5] M.G. Minty, F. Zimmermann, "Measurement and Control of Charged Particle Beams", Springer, (2003).

Copyright © 2014 CC-BY-3.0 and by the respective authors

ISBN 978-3-95450-141-0

NSLS2 DIAGNOSTIC SYSTEMS COMMISSIONING AND MEASUREMENTS*

W. Cheng#, Bel Bacha, Danny Padrazo, Joe Mead, Marshall Maggipinto, Kiman Ha, Yong Hu, Huijuan Xu, Om Singh, NSLS-II, Brookhaven National Laboratory, Upton, NY 11973

Abstract

As the newest and most advanced third generation light source, NSLS2 commissioning has started recently. A total of 50mA stored beam was achieved in the storage ring. Most of the diagnostic systems have been commissioned with beam and proved to be critical to the success of machine commissioning. This paper will present beam commissioning results of various diagnostic systems in the NSLS2 injector and storage ring, including profile monitors, current monitors and position monitors. We will discuss some preliminary machine measurements as well, like beam current and lifetime, tune, beam stability, filling pattern etc.

INTRODUCTION

NSLS2 is an advanced third generation light source recent constructed at Brookhaven National Laboratory. It includes a 200MeV S-band LINAC, 200MeV to 3GeV Booster, LINAC to Booster (LtB) transfer line, Booster to storage ring (BtS) transfer line and 3GeV storage ring.

Injector commissioning was carried out from Nov 2013 to Feb 2014. 3GeV ramped beam was established in the Booster on last day of 2013. The injector is capable to deliver high charge in multi-bunch mode, as well single bunch beam to the storage ring. So far the storage ring had finished two phases of commissioning. The phase 1 beam commissioning, from Mar 26 to May 12, was using PETRA 7-cell normal conducting cavity. Small gap damping wiggler chambers were installed in three long straight sections. For the phase 1 commissioning, 25mA stored beam was achieved after fixing issues like hanging springs in the vacuum chamber. Many of the storage ring diagnostic systems had seen beam and commissioning during this period. Super-conducting RF cavity was installed during the shutdown together with several other in-vacuum undulators and beamline front end, and beam commissioning was resumed from Jun 30 to Jul 14, 50mA stored beam was achieved with super-conducting RF cavity. To eliminate the effect of insertion devices, all damping wigglers and IVUs were fully open. Beam commissioning will be continued in coming months to close the insertion devices and send X-rays down to beamlines.

Figure 1 shows the storage current and lifetime when 50mA beam was achieved. The stored average current was measured by in-flange type DCCT which is commercially available [1]. Filling pattern monitor system was used to measure the bunch to bunch current, BPM buttons SUM signal was send to high speed digitizer or oscilloscope. Figure 1 bottom snapshot gives the oscilloscope filling pattern at around 50mA, when one long bunch train was filled. Green trace (Ch2) is storage ring revolution clock while yellow trace (Ch1) is four button SUM signal from dedicated BPM.

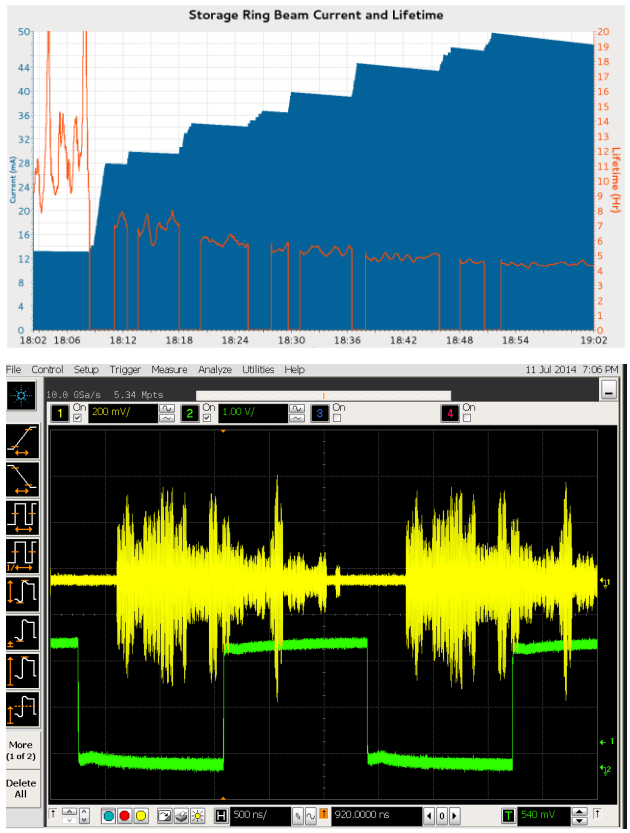


Figure 1: (top) storage ring DCCT measured current and lifetime history plot when fill up to 50mA; (bottom) filling pattern at around 50mA.

Table 1 lists major parameters of NSLS2 storage ring. There are 30 double bend achromatic (DBA) cells in the ring with bare emittance of 2 nm.rad. Horizontal emittance decreases to < 1 nm.rad with three damping wigglers.

* This material is based upon work supported by the U.S. Department of Energy, Office of Science, Brookhaven National Laboratory under Contract No. DE-AC02-98CH10886.

#chengwx@bnl.gov

Copyright © 2014 CC-BY-3.0 and by the respective authors

ISBN 978-3-95450-141-0

Table 1: NSLS2 Storage Ring Parameters

Energy	3.0 GeV
Circumference	792 m
Number of Periods	30 DBA
Length of Straights	6.6 & 9.3 m
Emittance (h,v)	< 1nm, 0.008 nm
Momentum Compaction	0.00037
Dipole Bend Radius	25 m
Energy Loss per Turn	< 2 MeV
Energy Spread	0.094 %
RF Frequency	499.68 MHz
Harmonic Number	1320
RF Bucket Height	> 2.5 %
RMS Bunch Length	15ps – 30ps
Average Current	500 mA
Current per Bunch	0.5 mA
Charge per Bunch	1.3 nC
Touschek Lifetime	> 3 hrs
Top-Off Injection	1/min

NSLS2 DIAGNOSTICS

Various diagnostic systems have been built and installed in the NSLS2 machine complex to measure electron beam position, current, profile and other parameters. Table 2 is a summary of diagnostics in NSLS2 machines.

Table 2: NSLS2 Diagnostics Systems

	LN	BR	LtB	BtS	S.R.
Button BPM	5	37	6	8	180
ID BPM					2 or 3 per ID
Photon BPM					1 or 2 per BL
Faraday cup	1		2	1	
WCM	5				
FCT/FPM		1	2	2	1
ICT			2	2	
DCCT		1			1
Screen	6	6	9	9	1
X-ray diag. BL					1
Visible diag. BL		2			1
Energy slit			1	1	
Tune monitor		1			1
BxB feedback					1H, 1V
Scraper					3H + 2V
BLM					5 CBLM 2 NBLM

Button type beam position monitors (BPM) are widely used to measure beam centroid along the injector and in the storage ring. Different button sizes and chamber profiles are available, details of the button BPM design and performance can be found in earlier papers [2, 3]. There is 1 or 2 photon BPM planned for each user's beamline, only one photon BPM is installed at this time and it will be commissioned together with the beamline commissioning. In-house developed BPM electronics [4-6] report raw ADC data, turn-by-turn data, 10kHz fast acquisition data as well as 10Hz slow acquisition data. Same hardware platform works for single-shot beam and circulating beam.

Faraday cup in LINAC front end, wall current monitors (WCM), fast current transformers (FCT) are used to measure bunch to bunch currents in LINAC, Booster and transfer lines. Broadband pickup signals (> 1GHz) were feed to high speed digitizers with sampling rate up to 8GHz. Processed filling patterns are updated on control's operational panel at 1Hz injector ramping rate. Faraday cups and integrated charge transforms (ICT) in the LtB/BtS transfer lines are used to measure beam charge per shot at selected locations. ICTs were calibrated before the commissioning started. There is one DCCT in Booster and storage ring, to measure the average current of circulating beam. DCCTs are well calibrated like ICT. In-situ calibration is possible with standard DC calibrator current source and related control software. DCCTs and ICTs are considered to be reliable tools to measure beam current/charge. Beam transfer efficiency and injection efficiency can be calculated based on the measured data on the same injection cycle.

Different types of screen monitors are used to measure the beam profile. LINAC and Booster screen monitors use YAG:Ce material, plenty of photons are generated even at very low charge. However the YAG screen resolution is not as good and saturation had been observed at high charge. LtB/BtS profile monitors have two selectable screens – YAG and OTR. OTR screen has less photon but improved resolution. Screens are moved by pneumatic actuators. There is a multi-position screen monitor in the storage ring injection straight, located right after the pulsed septum [7]. The screen is controlled through a linear stage and motor to see injecting beam, one turn beam or bumped stored beam. To measure stored beam size and emittance, one X-ray diagnostic beamline was constructed with source point at non-dispersion location. A second planned X-ray diagnostic beamline at dispersion was not fully built due to budget constraints. Energy spread measurement will be possible utilize the visible synchrotron light monitor (SLM), where the source point locates at the beginning of second bend in DBA cell. SLM beamline is equipped with streak camera to measure bunch length as well as other setups [8, 9]. Two synchrotron light monitor ports are available in the Booster ring to measure beam profiles during ramp.

Besides three major types of diagnostics to measure beam position, current and profile. There are other diagnostics to measure the betatron tune, beam losses, transverse bunch-by-bunch feedback etc. In the following sections, beam commissioning results and some physics measurements using these diagnostics will be discussed.

Copyright © 2014 CC-BY-3.0 and by the respective authors

ISBN 978-3-95450-141-0

BPM COMMISSIONING RESULTS

Incorporating the newest digital technologies, BPMs in NSLS2 are capable to measure 117MHz ADC raw data, turn-by-turn (TbT) data, 10kHz fast acquisition (FA) and 10Hz slow acquisition (SA) data. LINAC and transfer line BPMs measure the beam position in single shot mode, hence the raw ADC data and first turn of turn-by-turn data are particular interesting for these BPMs. 10kHz data was used to measure the beam orbit during booster energy ramping. There are six BPMs in the each storage ring cell, with total of 180 BPM mounted in multipole chambers. ID straight sections and injection straight have BPMs installed and see the beam. Storage ring BPMs' FA data is streaming out the fiber port to cell controller and used for fast orbit feedback. SA data is always available for orbit monitor and correction. ADC, TbT and FA waveform data are available from BPM IOCs. The waveform data can be retrieved on Internal/External triggers. External trigger to all BPMs around the ring guarantee sampling beam position/trajectory synchronized.

BPM Synchronization

Due to BPM pickup physical location and cable length difference, BPM electronics need to be timed well to get real turn-by-turn data. At the early stage of commissioning, before BPMs timed well, raw ADC waveform supplied powerful diagnostic information. Fig. 2 shows an example of storage ring BPMs ADC waveform data. The data was acquired when beam survived for 5-6 turns. One can see 180 storage ring BPMs were roughly timed but not perfect aligned.

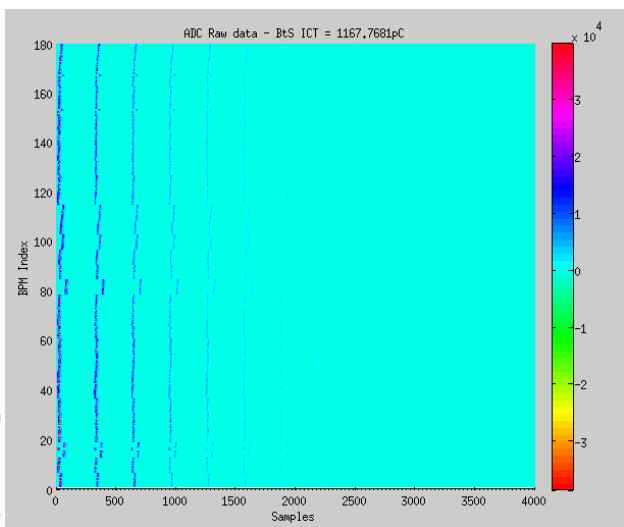


Figure 2: ADC waveform data from 180 SR BPMs, beam survived for about 5 turns. There are 310 ADC samples per turn.

Once BPMs timed well, all BPMs in the ring will see exactly same turn data. Fig. 3 shows all Booster BPMs 4-button SUM signal when timed right. Upon injection, all Booster BPMs saw the first turn beam on TbT sample #4. Beam was ramped for about 382ms in the Booster, BPMs have sufficient memory to capture turn-by-turn data during the whole ramp. Near extraction, only half of the ring sees beam on the extraction turn. Note that to read the extracted position data, BPM DDR memory had offset of 719236 turns. Beam was extracted on turn #3966 where only half of the Booster ring BPMs saw beam on that turn. Beam was circulating in the Booster for 723199 turns.

SUM Signal Diagnostics

From previous section, one might see 4-button SUM signal can be very useful to diagnose not only the time, but also the beam loss between BPMs. Even with same charge passing through the pickups, SUM signal varies due to BPM button size and chamber geometry difference, cable length and attenuation difference, SUM signal position dependency, attenuator settings etc. All these effects can be corrected to have meaningful comparison of beam charges from BPM to BPM.

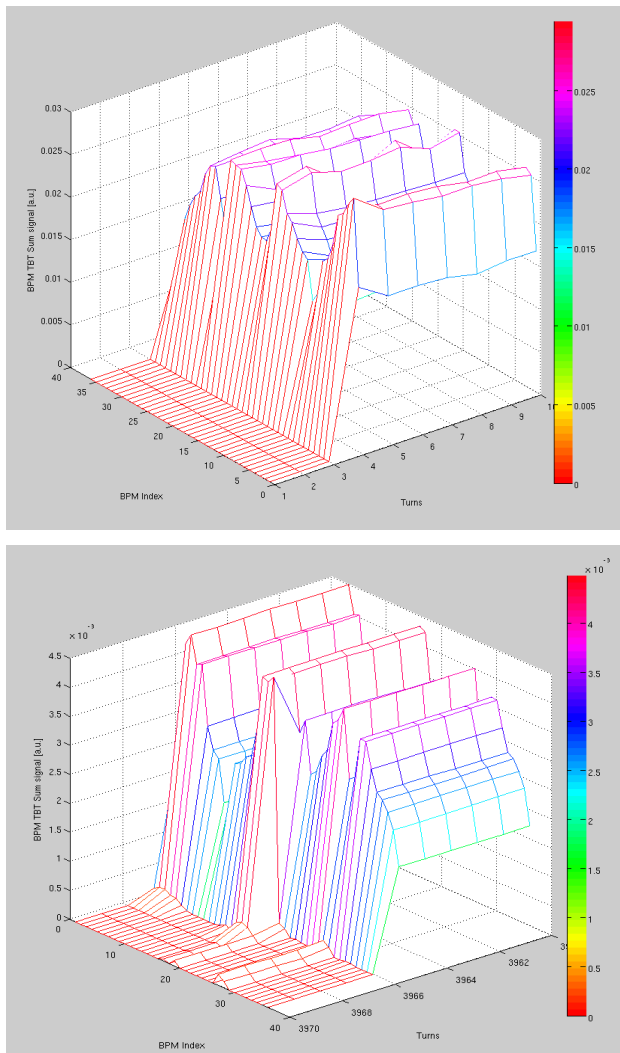


Figure 3: Booster BPM 4-button SUM signal in TbT mode. (top) Beam was injected on TbT sample #4, which is the first turn in Booster. All Booster BPMs saw the beam at same turn. (bottom) Beam was extracted on turn sample #3966 (Offseted by 719236 turns), only the first 18 BPMs saw beam on that turn.

Copyright © 2014 CC-BY-3.0 and by the respective authors

ISBN 978-3-95450-141-0

At early stage of storage ring commissioning, before the beam circulating the ring, BPM timing was roughly adjusted to capture the beam signal. First turns beam position and SUM signal was retrieved from ADC data. Shown in Fig. 4, are button A,B,C,D signals, x/y position and SUM signal processed from ADC waveform data. The SUM signal was corrected for button geometry, cable losses, attenuators and beam positions. The data was recorded when beam was circulating for less than 10 turns. Beam trajectory had large horizontal offset, likely came from mis-matched injection kickers. From all BPMs 4-button SUM signal, one can see there was partial beam lost at BPM #90 (C10 BPM4), this is the location where later an RF spring obstacle was found. With this BPM SUM signal beam loss tool, together with other evidence like limited local aperture, elevated radiation level in area when beam dumped, it was convinced there was obstacle in vacuum chamber. A hanging RF spring was found after break the vacuum in C10, at upstream of BPM 4.

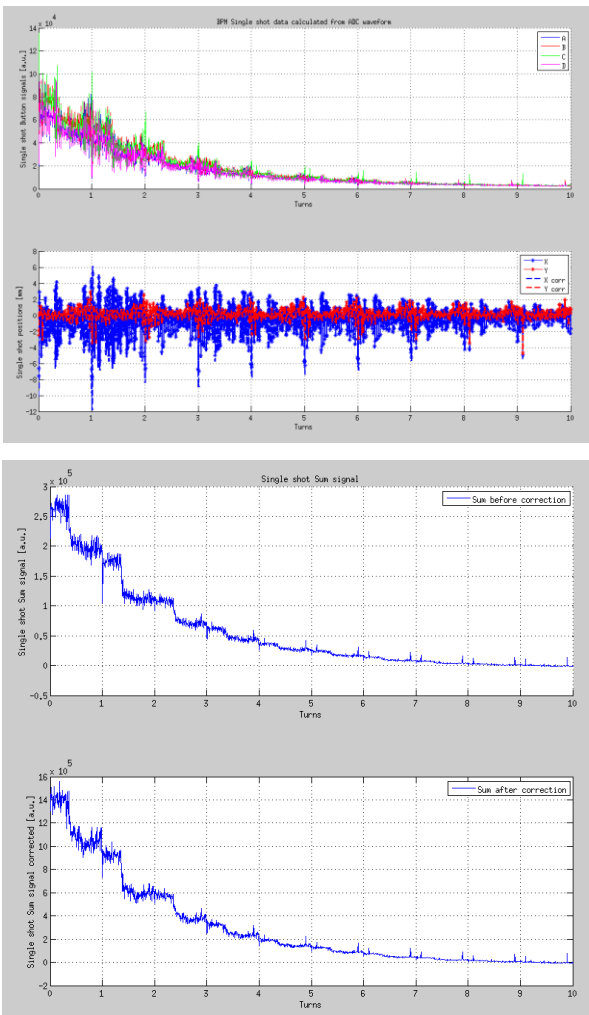


Figure 4: Beam circulating the storage ring for several turns, first turn trajectories and SUM signal from ADC data. There are 180 BPM data points in one turn. (top) four button signals and calculated x/y positions; (bottom) BPM SUM signal before and after corrections.

Electronics Resolution Measurements

BPM resolution measurements were performed using an extra BPM button assembly and electronics module installed in Cell 28 [10]. The electronics module was connected to the 4 BPM buttons using a combiner/splitter assembly to make the measurements independent of transverse beam motion. With this connection scheme each of the 4 channels of the electronics will see the same signal and electronics performance can be measured independent of beam motion.

The resolution measurements were performed for different fill patterns. A typical measured FA resolution at different single bunch current can be seen in Fig. 5, where single bunch was stored to and decayed while taking the data for analysis. At around 0.9mA, electronics resolution was measured to be ~2 μm.

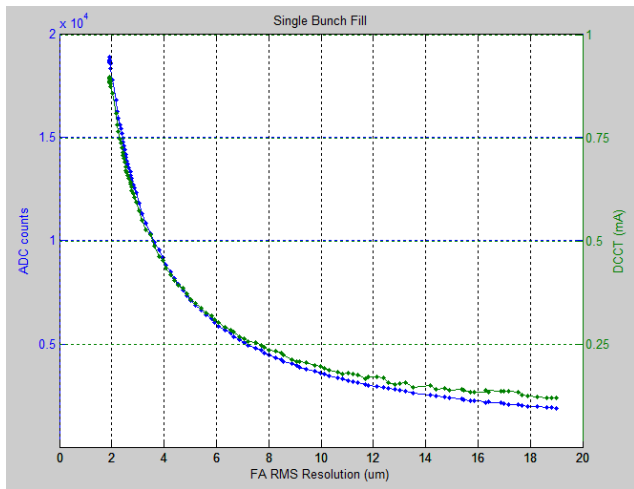


Figure 5: BPM FA data resolution with single bunch stored.

Beam Motion Spectrum

Using BPMs data, many physics measurements/ applications have been realized. BPMs are critical diagnostics for lattice measurement and correction; injection optimization; BPM TbT spectrum and tune measurement; beam based alignment; beam dynamics studies; beam instabilities studies etc. In this paper, we are not going to discuss details of these measurements. Only beam motion spectrum analyzed from BPM TbT/FA data is being presented.

Figure 6 gives a typical spectrum from storage ring BPMs TbT data. The spectrum was averaged for 180 storage ring BPMs. Beam was stored at 23mA in multi-bunches. Beam was unstable so that betatron sidebands were clearly visible. On horizontal spectrum, synchrotron sideband appeared at dispersive BPMs. From the integrated power spectrum density, there was about 3.6um w/o betatron motion in horizontal plan. The RMS motion

ISBN 978-3-95450-141-0

Copyright © 2014 CC-BY-3.0 and by the respective authors

will be ~26 um include betatron motion. In vertical plane, the RMS motion was 2.1um w/o betatron motion and 9.8um include betatron motion. To characterize the lower frequency beam motion spectrum, 10kHz FA data is more suitable.

Similarly to TbT spectrum, BPM FA data spectrum was analyzed with better precision. Beam motion was about 2 um for x/y spectrum, not including the synchrotron motion contributions. Extra 3-4 um was added to dispersive BPMs. Assume dispersion at BPMs was around 0.4m, energy jitter was ~ 0.001%. Hopefully this can be improved by optimize the low level RF controller. RMS beam motion up to 1kHz was measured to be ~ 1% of beam size horizontally and ~20% of beam size vertically. Fast orbit feedback, once commissioned, will keep the motion within 10% vertical beam sizes.

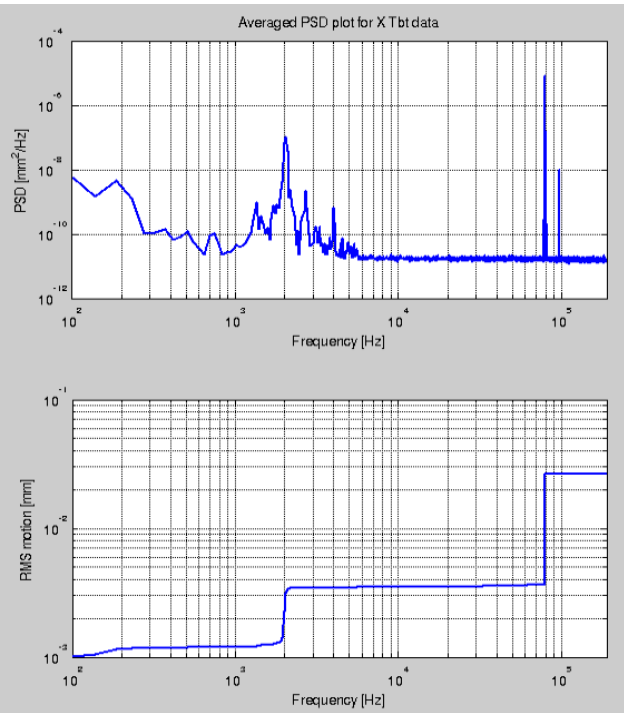


Figure 6: Averaged power spectrum density spectrum and integrated RMS motion plot from storage ring X TbT data. Beam was stored at 23mA.

CURRENT MONITORS

As shown in Table 2, there are different types of current monitor sensors to measure the AC/DC beam current. Many of these sensitive current monitors saw noises from pulse magnets and ground loops. Adding ferrite beads helped to kill common mode noises. Figure 7 gives Booster FCT signals measured when beam was circulating for multi-turns. FCT beam signal appeared each turn on top of the noises caused by Booster injection kickers. Zoom in gives the typical 20 bunches pattern in the train. Digitizer was configured at 8GHz sampling rate, there was about 16 samples per 2ns RF bucket period.

Storage ring filling pattern was measured from a dedicated 4-button BPM SUM signal. Broadband hybrid SUM signal was send to high speed digitizer or 20GHz oscilloscope. Bunch filling pattern was calculated from pulse area or peak amplitude. Meanwhile bunch centroid can be used to measure beam synchronous phase. This could be useful tool to detect the transient beam loading effect with long bunch train and ion gap fill. Shown in Fig. 8 is a typical bunch pulse observed on storage erring filling pattern monitor, using 20GHz oscilloscope. Red diamonds are the raw sampled data with 50ps separation. To retrieve the peak amplitude and location with better resolution, 10 times interpolation was applied to the raw data. Interpolated data points are plotted as blue circles. Searched peak of interpolated point gives the green square in the figure, its amplitude was considered to be bunch current and its position was measured synchronous phase. Interpolated points have 5ps separation, the measured synchronous phase shall have accuracy better than 5ps, not including the trigger jittering.

To validate the synchronous phase measurement method, preliminary study was done by varying RF cavity voltage and recording the synchronous phase. From the synchronous phase vs. cavity voltage curve, energy loss per turn was estimated to be ~ 275 keV, this is close to theoretical value of 287 keV.

Copyright © 2014 CC-BY-3.0 and by the respective authors

ISBN 978-3-95450-141-0

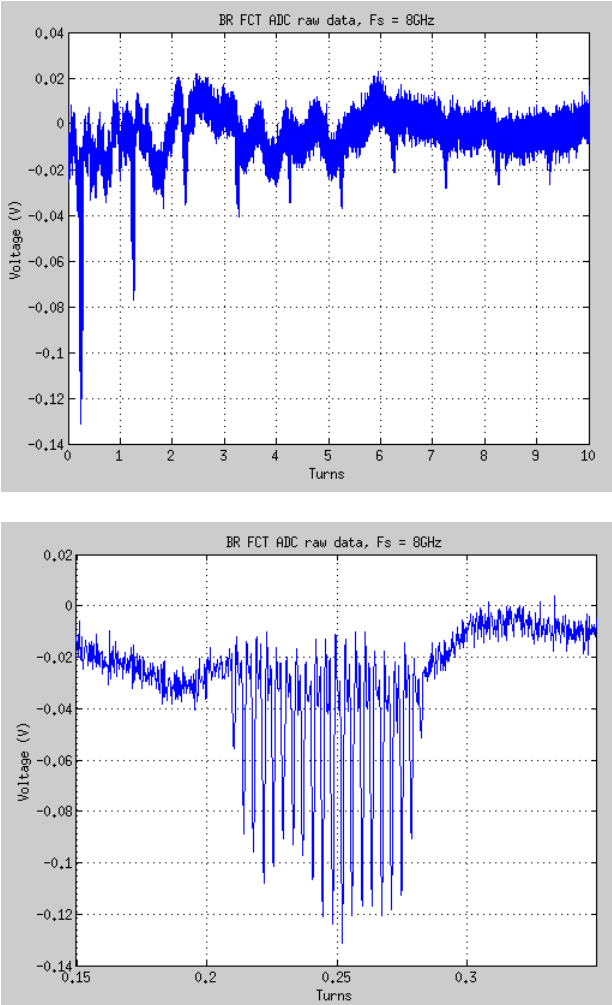


Figure 7: Booster FCT measurements shown beam was circulating for multi-turns (top). 20 bunches were detectable from 8GHz sample rate data (bottom).

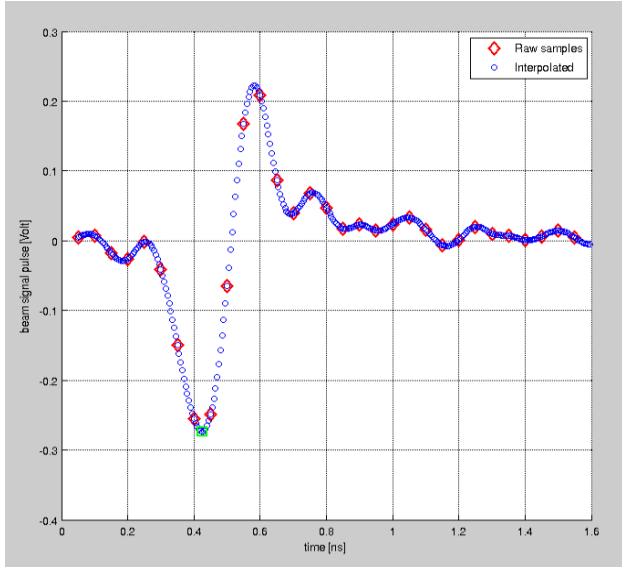


Figure 8: Storage ring filling pattern monitor signal from 20GHz real time sampling scope. Red diamonds were raw sample data points while blue circles were interpolated points by a factor of 10. Green Square is the searched peak of interpolated point, its amplitude was considered to be bunch current and its position was measured synchronous phase.

There is one in-flange type DCCT installed in Booster and storage ring. The DCCT sensor has same chamber profile to nearby sections to minimize the beam impedances. CompactPCI digitizer ICS 710A is used to sample the DCCT output signal. The digitizer can be programmed to have different anti-alias low pass filter. Maximum sampling rate of the digitizer is 216 kHz. Storage ring beam current decays due to: 1) Elastic scattering (Columb scattering) or inelastic scattering (Bremsstrahlung) with residual gas; 2) Collisions between electrons (Touschek scattering); 3) Photon emission (Quantum lifetime) or 4) Trapped ion or macro dust in beam potential. High brightness synchrotron light sources operating at low emittances and large beam current are usually lifetime limited from Touschek scattering. For a short period of time much less than beam lifetime, one can linear fit the measure bunch current data point, linear fit slope will be $-1/\tau$. During SR phase-1 commissioning, large noise signals were picked up by DCCT electronics. A programmable low pass filter was added before the digitizer to eliminate the noises. DCCT noise was able to decrease from 40uA to 3uA.

PROFILE MONITORS

As described there are many screen (flag) monitors in the injector to measure transverse beam profile. Transfer line profile monitors have selectable YAG or OTR screens. Beam emittance and energy spread can be measured. Figure 9 is an example of LtB second flag monitor which is located with dispersion. Assume dispersion is known, beam energy spread can be measured from the profile distribution. Absolute beam energy was measured based on the upstream dipole current settings.

Copyright © 2014 CC-BY-3.0 and by the respective authors

ISBN 978-3-95450-141-0

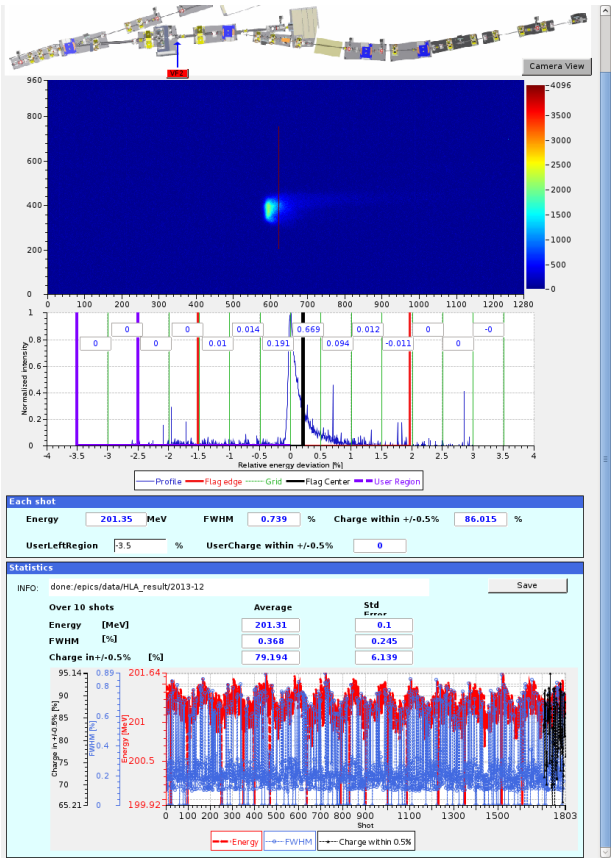


Figure 9: LINAC beam energy jitter and energy spread measurement using LtB VF2.

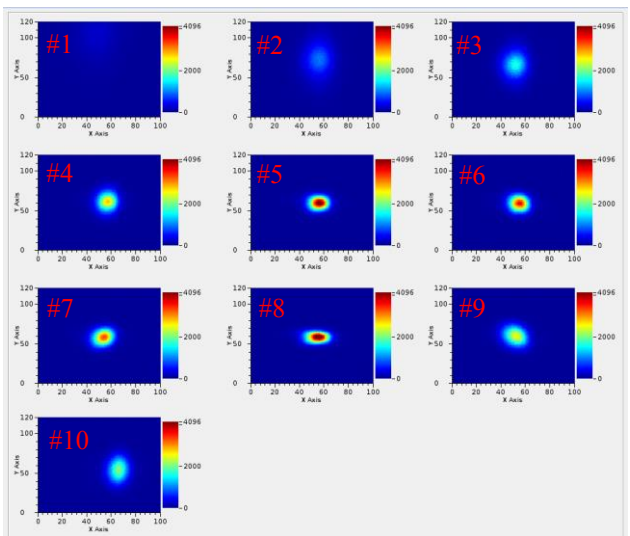


Figure 10: Booster A1 SLM ten burst images during energy ramp. The images were acquired with separation of 40ms.

Two synchrotron light monitors in the Booster tunnel were able to capture beam profiles during energy ramp. CCD camera can be triggered with a burst of pulses so that same ramp profiles at different energy ramp time can be captured. As seem in Fig. 10, ten burst images were captured from the same ramp, the burst images were separated by 40ms.

Storage ring visible synchrotron light monitor (SLM) diagnostic beamline utilizes the radiation from C30 BM-B, which is the second dipole after injection. Nominal source point is ~2.75mrad into the dipole. The beamline has acceptance of +/-1.5mrad horizontal and +/-3.5mrad vertical. Visible light from the dipole synchrotron radiation is reflected by in-vacuum mirror. The visible light is then relayed into SLM hutch locates on the C30 experimental floor. There are various optics setups on the 4'x10' optical table, currently there are three branches setup: CCD camera branch; fast gated camera branch and streak camera branch. Visible light can be guided to different cameras. Due to excellent alignment work, SLM beamline was able to see the first synchrotron light even for first turn beam. More information for the SLM commissioning is available at [9].

OTHER DIAGNOSTICS

Different methods have been used to measure the betatron tune. It can be measured by BPM turn-by-turn data Fourier spectrum of kicked beam doing betatron oscillation. Tune can be measured from Bunch-by-bunch feedback system by watching the notch on the spectrum. NSLS2 storage ring has dedicated sweeping tune measurement system (TMS). The system uses button BPM delta signal from Hybrid to detect the horizontal and vertical betatron motion. Mixer IF output baseband signal is sent to a network analyzer to measure the transfer function. Beam is excited by 15cm stripline with diagonal kicks. Two 75W broadband amplifiers are used to feed the stripline. Network analyzer can be controlled through EPICS CSS panel, sweeping time of the NA is programmable and it's typically takes seconds. TMS operation panel with measured tune spectrum is given in Fig. 11. RTD sensors are installed to monitor the stripline feedthrough and chamber temperatures.

Scraper blades are controlled with linear motors with 1um resolution and 3um repeatability. When electron particle hits the scraper, it losses energy hence will be bend inward towards the chamber wall. Glass rods are installed at selected locations to detect the lost electrons outside the vacuum. When electron passes through the Glass rod, it generates Cherenkov light which will be reflected towards the end of glass rod. Optics setups in the end boxes include photo diode and PMT and related signal condition electronics. Cherenkov light converted in to electrical pulse signal to be detectable with digitizers. There are 2 neutron detectors as part of the beam loss monitoring system installed on top of the injection septum. During the beam commissioning, scrapers had been used for fault studies as well as limit the beam lifetime for some shifts. Cherenkov and neutron beam loss monitors had been calibrated with injecting beam.

Copyright © 2014 CC-BY-3.0 and by the respective authors

ISBN 978-3-95450-141-0

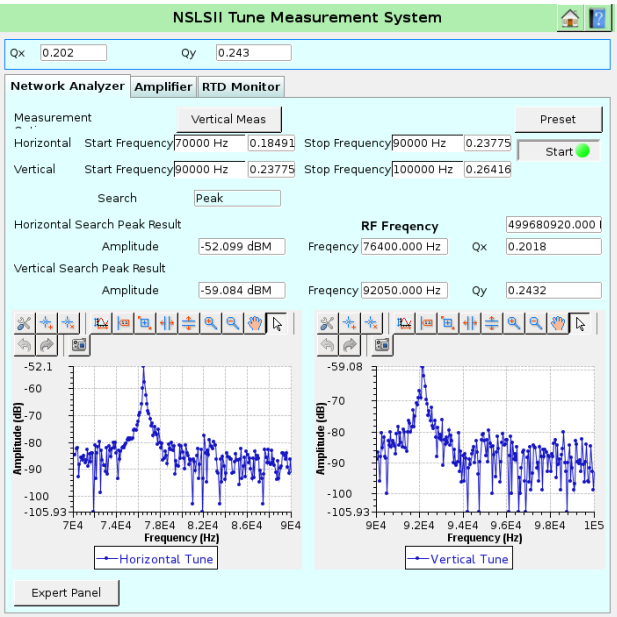


Figure 11: Storage ring sweep tune measurement system operational panel showing the x/y tune spectrums.

There are fiver scrapers and five Cherenkov beam loss monitors (CBLM) installed in C30 and C01, where high density concrete is used for better shielding. The purpose of this configuration is to have beam losses in a controllable manner near injection area so that beam loss at other part of the ring is minimized. [11]

Transverse bunch by bunch feedback system installed at C16 has been commissioned. The system helped to suppress multi-bunch instabilities which are likely ion induced. Single bunch instability was suppressed by the feedback system and threshold bunch current can be increase from 1mA to more than 6mA. [12]

SUMMARY

During past months of NSLS2 injector and storage ring commissioning, Most of the diagnostic systems have seen beam and commissioned. 50mA stored beam were achieved in the storage ring. Varity of diagnostic tools has proved to be critical for the success of beam commissioning. We expect these tools to continue play important roles for the future high intensity, high stability commissioning and operation of NSLS2.

We thank the diagnostic group for enormous construction, installation and testing work and operation team for commissioning the machine.

REFERENCES

[1] http://www.bergoz.com
[2] W. Cheng, et. al., “NSLS2 Beam Position Calibration”, BIW’2012.
[3] W. Cheng, et. al., “Performance of NSLS2 Button BPMs”, IBIC’2013.
[4] K. Vetter, et. al., “NSLS-II RF Beam Position Monitor”, PAC’2011.
[5] K. Vetter, et. al., “NSLS-II RF Beam Position Monitor Update”, BIW’2012.
[6] O. Singh, et. al., “NSLS-II BPM and Fast Orbit Feedback System”, IBIC’2013.
[7] B. Kosciuk, et. al., “Construction and Operational Performance of a Horizontally Adjustable Beam Profile Monitor at NSLS-II”, IBIC’2014.
[8] W. Cheng, et. al., “Design of Visible Diagnostic Beamline for NSLS2 Storage Ring”, PAC’2011.
[9] W. Cheng, et. al., “NSLS2 Visible Synchrotron Light Monitor Diagnostic Beamline Commissioning”, IBIC’2014.
[10] J. Mead, “NSLS-II RF Beam Position Monitor Commissioning Update”, IBIC’2014.
[11] S. Kramer, “Beam Loss Monitors for NSLS-II Storage Ring”, PAC’2011.
[12] W. Cheng, et. al., “Commissioning of Bunch-by-bunch Feedback System for NSLS2 Storage Ring”, IBIC’2014.

Copyright © 2014 CC-BY-3.0 and by the respective authors

ISBN 978-3-95450-141-0

A PICOSECOND SAMPLING ELECTRONIC "KAPTURE" FOR TERAHERTZ SYNCHROTRON RADIATION

M. Caselle, M. Brosi, S. Chilingaryan, T. Dritschler, N. Hiller, V. Judin, A. Kopmann, A.-S. Müller, J. Raasch, L. Rota, L. Petzold, N. J. Smale, J., L. Steinmann, M. Vogelgesang, S. Wuensch, M. Siegel, M. Weber, KIT, Karlsruhe, Germany

Abstract

The ANKA storage ring generates brilliant coherent synchrotron radiation (CSR) in the THz range due to a dedicated low-a_c-optics with reduced bunch length. At higher electron currents the radiation is not stable but is emitted in powerful bursts caused by micro-bunching instabilities. This intense THz radiation is very attractive for users. However, the experimental conditions cannot be easily reproduced due to those power fluctuations. To study the bursting CSR in multi-bunch operation an ultra-fast and high-accuracy data acquisition system for recording of individual ultra-short coherent pulses has been developed. The Karlsruhe Pulse Taking Ultra-fast Readout Electronics (KAPTURE) is able to monitor all buckets turn-by-turn in streaming mode.

KAPTURE provides real-time sampling of the pulse with a minimum sampling time of 3 ps and a total time jitter of less than 1.7 ps. The KAPTURE system, the synchrotron operation modes and beam test results are presented in this paper.

INTRODUCTION

At the synchrotron light source ANKA, up to 184 electron bunches can be filled with a distance between two adjacent bunches of 2 ns corresponding to the 500 MHz frequency of the accelerating RF system.

Since a few years, special user operation with reduced bunch length in the order of a few picoseconds has been available to research communities. In this mode, coherent synchrotron radiation is generated for electro-magnetic waves with a wavelength in the order of or longer than the electron bunch length. Due to this, one usually observes a strong amplification of the radiation spectrum in the THz band. Moreover, above a certain current threshold, a coherent modulation of the longitudinal particle distribution (microbunching) occurs due to CSR impedance [1]. This particle dynamic effect changes the characteristics of the CSR tremendously. The microbunching structures fulfil a coherence condition for shorter wavelengths. This leads to an instantaneous increase of the radiated THz power. Observation in the time domain shows bursts of radiations which occur with different periodicities depending on the bunch current. The characteristics of the bursting patterns are unique for different sets of accelerator parameters [2].

The KAPTURE (KArlsruhe Pulse Taking and Ultrafast Readout Electronics) system opens up a possibility to monitor the THz radiation of all bunches in the ring over a principally unlimited number of turns, realising a new type of measurement at ANKA. In this paper we present the KAPTURE system, the synchrotron applications and the measurements of CSR at the ANKA synchrotron light source.

KAPTURE SYSTEM

The KAPTURE system records individual pulses continuously with a sub-millivolt resolution and a relative timing resolution between two consecutive pulses in the order of picoseconds. KAPTURE is a flexible system and can be easily configured for the requirements of others synchrotron facilities.

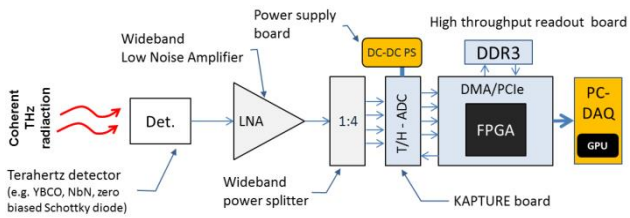


Figure 1: KAPTURE system for the detection of coherent THz radiation generated at ANKA.

The KAPTURE system is shown in Fig. 1. It consists of a Low Noise Amplifier (LNA), a power splitter, a picosecond pulse sampling stage called "KAPTURE board", a high throughput readout board and a high-end Graphics Processing Unit (GPU). The signal from the detector is fed into a LNA and then divided in four identical pulses by a wideband power splitter. The KAPTURE board acquires each pulse with 4 sample points at a programmable sampling time between 3 and 100 ps. The basic concept of the picosecond KAPTURE board and the architecture have been reported previously [3,4]. The high throughput readout board uses a new bus master DMA architecture connected to PCI Express logic [5] to transfer the digital samples from the KAPTURE board to a high-end GPU server. For continuous data acquisition a bandwidth of 24 Gb/s (12 bits @ 2 ns * 4 digital samples) is necessary. The DMA architecture has been developed to meet this requirement with a high data throughput of up to 32 Gb/s. The GPU computing node is used for real-time reconstruction of the pulse from the 4 digital samples. Afterwards, the peak amplitude of each pulse and the time between two consecutive pulses/buckets with a picosecond time resolution are calculated. The GPU node performs also an on-line Fast Fourier Transform (FFT) for the frequency analysis of the CSR fluctuations.

Copyright © 2014 CC-BY-3.0 and by the respective authors

ISBN 978-3-95450-141-0

The internal organization of the KAPTURE system and its components is shown in Fig. 2. The detector signal is connected to the LNA by a wideband V-connector and then propagated to the power divider by a tee-bias device.

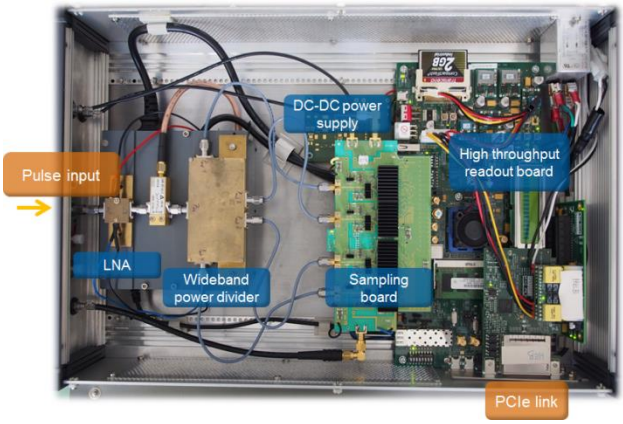


Figure 2: View inside the KAPTURE system.

Matching of the high bandwidth required to design a novel wideband power divider architecture [6]. The LNA gain has been developed in order to compensate the power divider insertion loss with minimum additional noise contribution. The readout board is equipped with a Virtex 6 FPGA that receives the digitalized samples, tags them with the current bunch number, and sends the data to the GPU server via the PCIe data uplink.

KAPTURE PERFORMANCE

The KAPTURE system is designed for continuous sampling of very short pulses (minimum FWHM of few tens of picosecond) with a trigger frequency synchronous with the RF-system of synchrotron machines (500 MHz for ANKA). Moreover, the amplitude of the pulses are typically in the order of some tens of millivolts. Due to ultra-fast and low amplitude pulses, KAPTURE has been designed with special precautions regarding component selection and layout technologies. The RF/ microwave analog front-end is operating at an analog input frequency range of DC - 50 GHz. The RF technologies used are described in previous work [6]. For a better control of the characteristic impedance of the line, especially at high frequency, special wideband coplanar waveguide transmission lines have been designed using a via fence technique. To achieve this performance special substrates have been used, respectively Duroid 5880 for the analog front-end and Roger 4003 for digitalization circuits [3,6].

The digitizer circuits use a picosecond time chip to control the timing between two adjacent samples. In this way, the picosecond sampling time can be programmed by FPGA. Low skew sampling time and clock distributions have been optimized with a total skew that does not exceed 6 ps.

KAPTURE is very flexible and can operate in both real time and equivalent sampling modes. In the real time mode each pulse is acquired by four sample points with a flexible sampling time between 3 and 100 ps. In the equivalent sampling method the KAPTURE is able to acquire a periodical waveform with a sampling rate that exceeds 300 GS/s with a total observation time up to 2.2 ns. A very low noise layout design guarantees a Gaussian shape of the total time jitter with a standard deviation (Std-Dev) measured to be less than 1.7 ps [4]. The picosecond time characterization is fundamental for understanding the performance of the KAPTURE system. For this purpose, very short pulses with a FWHM of few tens of picosecond and a time jitter of few picoseconds are required. Due to limitations of commercial pulse generators, we have performed the characterization using short pulses generated by an YBCO detector [7] illuminated with coherent synchrotron radiation. The input pulse with a FWHM of 42 ps and an amplitude of 45 mV was previously measured with a real-time oscilloscope. For the time characterization we configured the KAPTURE system to operate in an equivalent sampling mode with a sampling time of 3 ps. In this way, we have acquired the input pulse with an equivalent sampling rate of more than 300 GS/s. The acquired pulse shape is in agreement with the previous measurement by a real-time oscilloscope; all results are reported in the previous work [6].

The analog channel and the ADC circuits exhibit a wide dynamical range of ± 2.5 V with a noise below 2 mV (RMS) [4].

To sustain a continuous data acquisition a bandwidth of 32 Gb/s is necessary. A high-throughput readout system is used to transfer the sampled data from the digitizer stage to the high-end GPU-DAQ system. The readout architecture and the FPGA firmware are presented [6].

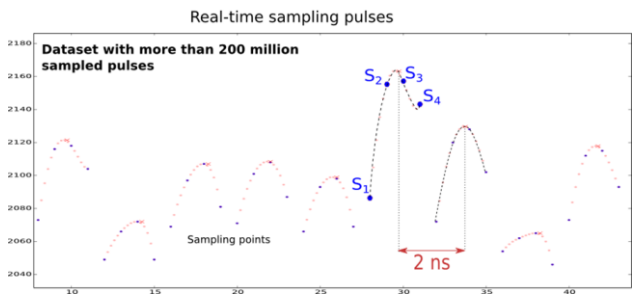


Figure 3: Details of reconstructed pulses, the x-axis shows the sampling points and the y-axis the ADC counts.

The real time data analysis is based on GPU node. The GPU is used for the pulse reconstruction; the measurements of the pulse amplitude and the time of arrival of each pulse, and also performs an on-line fast Fourier Transform (FFT) for the frequency analysis of the coherent synchrotron radiation fluctuations. Fig. 3 shows a dataset acquired in real time acquisition mode by a fast cryogenic YBCO detector. For each pulse the four sampling points S1, S2, S3 and S4 are acquired with a time distance of 15 ps respectively between the first sample S1 and the second S2, 9 ps between S2 and S3 and 15 ps between S3 and S4, while the time distance between two consecutive pulses is 2 ns.

ISBN 978-3-95450-141-0

Copyright © 2014 CC-BY-3.0 and by the respective authors

KAPTURE – OPERATION MODES

The KAPTURE system has been designed with four individual wideband analog inputs. In this way, the system is flexible and can be used to acquire the fast detector signal from one or up to four detectors in parallel. Additional data flow logic can be instantiated in the FPGA for an additional real-time data processing on the detectors pulses. Fig. 4 shows the possible configurations and the number of sampling points per individual pulse.

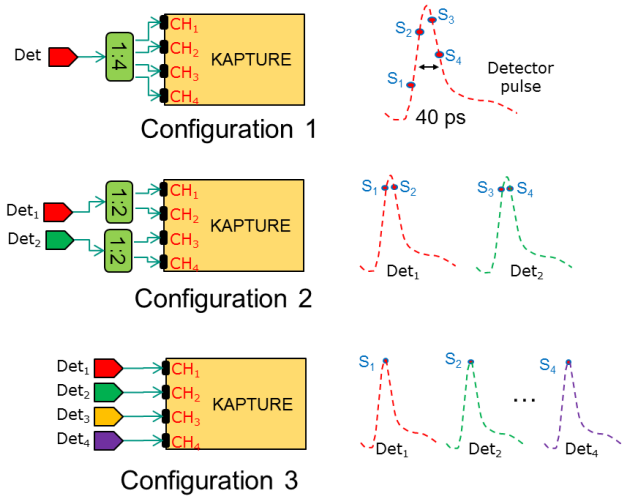


Figure 4: KAPTURE configuration modes, the connection between the detectors, power splitter and KAPTURE are made by wideband cables.

With configuration 1 the power splitter can be mounted internally within the system as shown in Fig. 2. This configuration allows for the acquisition of a very short pulse coming from a detector with a very high temporal resolution (e.g. YBCO). In configuration 2 and 3, KAPTURE uses a wideband power splitter with two outputs which have been developed for these measurements. These configurations are suitable for the acquisition with two or more detectors in parallel. Configuration 2 has been used for the measurements of the CSR with two zero-biased Schottky diodes. For the correct measurements of the detector pulse the sample points must be located in the peaking time region. The system assists the user to select the correct timing for the best position of the sample points for each analog input. Moreover, this configuration allows for additional real-time data processing between signals if necessary.

MEASUREMENTS AT ANKA

All measurements were performed at ANKA's infrared beamlines IR1 and IR2, which have an acceptable transmission grade for THz radiation. Fig. 5 shows a typical data set taken by KAPTURE. It shows the bursting regime in multi-bunch mode with four trains consisting of 33-35 bunches. The colour density plot shows the evolution of the intensity of all 184 buckets in the time domain. Only around 120 thousands turns are displayed here for the better visualisation of the bursting behaviour. The whole data set contains about 1 second of data, corresponding to 2.7 million turns. On the left side the calculated mean of the THz intensity and the measured bunch currents are shown. For the determination of bunch current a single photon counting method is implemented at ANKA [8].

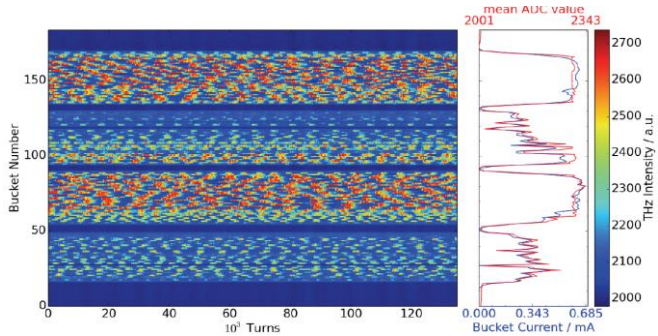


Figure 5: The THz signal measured with a fast Schottky Diode detector by the KAPTURE system with four trains consisting of approx. 33 bunches are shown on the left side for around 140 thousands consecutive turns. The intensity is colour coded. At the right side the corresponding bucket current is shown in blue and the mean THz signal in red by KAPTURE.

The filling pattern was tailored using the recently installed Bunch-by-Bunch Feedback system [9]. The measurement shows different bursting behaviours (Fig. 5, left) at different bunch currents (Fig. 5, right). For the investigation of bursting effects a frequency analysis using an FFT of the time domain data can be performed. These frequency domain data sets displayed for long-term decaying bunch currents in 2D gives a spectrogram. In Fig. 6, spectrograms of three arbitrarily chosen buckets within the similar properties. For the same time range are shown with the dashed line marking the same bunch current in every picture. Only marginal differences can be observed. It seems that the bunches show similar bursting behaviour for similar bunch currents. The investigation of similarities and differences of bursting spectrograms will provide a useful tool for the study of bunch-bunch interactions.

Copyright © 2014 CC-BY-3.0 and by the respective authors

ISBN 978-3-95450-141-0

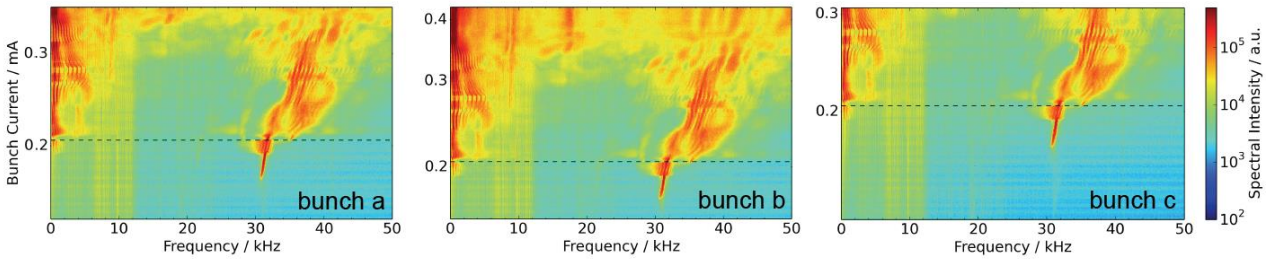


Figure 6: A frequency analysis of the time domain signal taken simultaneously for different bunches in the same fill gives insight into the bursting behaviour of each bunch in a multi-bunch environment. Here three bunches with different initial currents were taken. The horizontal dashed lines mark the different points in time where the bunches have the same current. The differences in the spectrograms are not obvious and have to be investigated thoroughly. The studies of bunch-bunch interactions are in progress.

Dependency of Bursting Threshold and Momentum Compaction Factor

Another measurement studies is the bursting threshold at different momentum compaction factor (a_c) and at constant RF settings based on KAPTURE. The bursting threshold is defined by the current at which the emitted CSR intensity starts to fluctuate. If the single-bunch mode is used, the complete bunch current range needs to be observed. Instead of waiting for a single bunch to pass through the whole current range, it is also possible to use multiple bunches with different bunch currents to save time. This kind of instant bursting threshold measurement method using the mean of the THz signal for all 184 buckets and corresponding single bunch currents has been used in the past with KAPTURE [10]. However another method using the standard deviation of the THz signal has shown higher reliability. Above the threshold, the standard deviation is increasing significant due to the initiated fluctuations. This allows to scan the machine parameters and to observe almost in real-time the change of the bursting threshold.

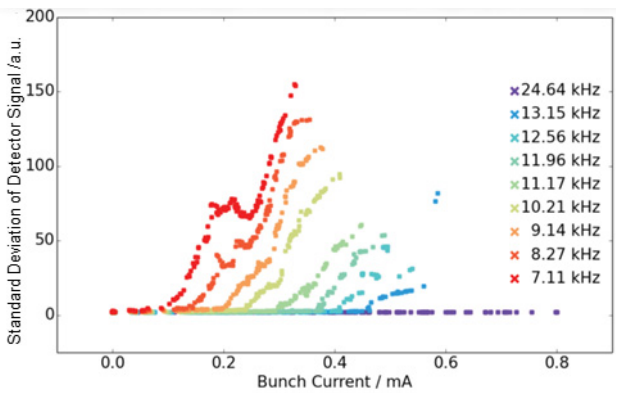


Figure 7: The bursting threshold study for different momentum compaction factors at constant RF-conditions is shown. The KAPTURE system allows monitoring of the bursting threshold during changes of the beam optics.

The standard deviation of the signal in dependence of the single bunch current is displayed in Fig. 7 during a reduction procedure of α_c at ANKA, where the strengths of focusing magnets are changed in steps while keeping the RF-voltage constant. Each colour indicates a data set, which corresponds to beam optics with the given synchrotron frequency f_s. For beam optics with lower a_c (corresponds to a lower f_s) the instability threshold is significantly reduced. Due to different bursting regimes the standard deviation does not increase constantly. Especially for f_s = 7.11 kHz, a change of bursting regime is visible at 0.2 mA.

Simultaneous Measurement with two Detectors

Operating KAPTURE in configuration 2 (see Fig. 4) we are able to measure simultaneously with two detectors. Bursts of radiation emitted due to micro-bunching instabilities in the ANKA storage ring have been observed continuously with both detectors for every bunch and every turn. Radiation split by a wire grid and detected with two Schottky diodes is shown in Fig. 8.

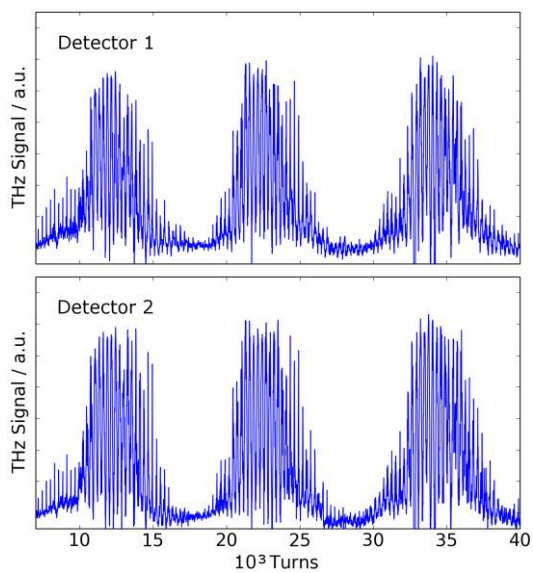


Figure 8: Simultaneous measurement of bursting instabilities with Schottky detectors.

For long-term observations over several hours we implemented a data reduction method in KAPTURE's. Only every 10th turn is saved, which limits the instability dynamics frequency to 270 kHz. Also only one second

ISBN 978-3-95450-141-0

Copyright © 2014 CC-BY-3.0 and by the respective authors

out of 10 seconds is stored, resulting in 1 Hz frequency resolution. With these settings, we are able to observe both, the dynamics of the high frequency changes in the kHz-range due to electron bunch phase space rotations as well as the slowly changing beam-current depending on the bursting behaviour. The resulting data rate is kept below 100 MB/s and can easily be stored on standard hard disks.

ACKNOWLEDGMENT

The authors would like to acknowledge the infrared group at ANKA for their support during the beam times at the infrared beamlines IR1 and IR2. This work is supported by the German Federal Ministry of Education and Research (Grant No. 05K13VKA) and the Helmholtz Association (Contract No. VH-NG-320).

REFERENCES

[1] G. Stupakov and S. Heifets, “Beam instability and microbunching due to coherent synchrotron radiation”, Phys. Rev. STAB, 2002, Vol. 5, Nr. 5, DOI:10.1103/PhysRevSTAB.5.054402.

[2] M. Schwarz et al., “Bursting Patterns of Coherent Synchrotron Radiation in the ANKA Storage Ring”, WEPEA011, IPAC’13, Shanghai.

[3] M. Caselle et al., “Ultra-fast data acquisition system for coherent synchrotron radiation based on superconducting terahertz detectors”, WEOBB202, IPAC 2013, Shanghai.

[4] M. Caselle et al. “An ultra-fast data acquisition system for Coherent Synchrotron Radiation with terahertz detectors “, TWEPP 2013, Perugia, *JINST* **9** C01024 doi:10.1088/1748-0221/9/01/C01024.

[5] L. Rota, M. Caselle et al. “A New DMA PCIe Architecture for Gigabyte Data Transmission", 19th Real-Time conference IEEE-RT, Nara, Japan.

[6] M. Caselle et al. “An Ultra-fast Digitizer with Picosecond Sampling Time for Coherent Synchrotron Radiation”, 19th Real-Time conference IEEE-RT, Nara-Japan.

[7] P. Thoma et al., “High-speed Y-Ba-Cu-O Direct Detection System for Monitoring Picosecond THz Pulses”. IEEE Transactions on terahertz science and technology, vol. 3, NO.1, January 2013.

[8] B. Kehrer et al., "Filling Pattern measurements at the ANKA storage ring", TUPC087, IPAC’11, San Sebastián.

[9] E. Hertle et al., "First Results of the New Bunch-by-bunch Feedback System at ANKA", TUPC087, IPAC’14, Dresden.

[10] A.-S. Müller et al., "Studies of Bunch-bunch Interactions in the ANKA Storage Ring with Coherent Synchrotron Radiation using an Ultra-fast Terahertz Detection System", MOPEA019, IPAC’13, Shanghai.

Copyright © 2014 CC-BY-3.0 and by the respective authors

ISBN 978-3-95450-141-0

REFERENCE DISTRIBUTION AND SYNCHRONIZATION SYSTEM FOR SwissFEL: CONCEPT AND FIRST RESULTS

S. Hunziker#, V. Arsov, F. Buechi, M. Kaiser, A. Romann, V. Schlott,
Paul Scherrer Institut, CH-5232 Villigen PSI, Switzerland
P. Orel, S. Zorzut, Instrumentation Technologies d.d., SI-5250 Solkan, Slovenia

Abstract

The development of the SwissFEL [1] reference distribution and synchronization system is driven by demanding stability specs of LLRF-, beam arrival time monitors (BAM) and laser systems on one and cost issues, high reliability/availability and flexibility on the other hand. Key requirements for the reference signals are <10fs$_{rms}$ jitter well as down to 10fs$_{pp}$ temporal drift stability (goal) for the most critical clients (BAM, pulsed lasers). The system essentially consists of a phase locked optical master oscillator (OMO) with an optical power amplifier/splitter, from which mutually phase locked optical reference pulses as well as RF reference signals are derived. Optical pulses will be transmitted to pulsed laser and BAM clients over stabilized fiber-optic links whereas the RF signals are transmitted over newly developed stabilized cw fiber-optic links. Both s- and c-band reference signals use s-band links, whereupon the C band receiver incorporates an additional ultra-low jitter/drift frequency doubler. Furthermore, ultra-low noise analog laser PLLs have been built. We are presenting concepts and first results of sub-10fs$_{rms}$ jitter and 20fs$_{pp}$ long term drift cw links, tested in the SwissFEL Injector Test Facility (SITF).

REFERENCE DISTRIBUTION CONCEPT

Generation of Mutually Stable Reference Signals

High mutual short as well as long-term stability is required between all clients of the reference distribution system. On the other hand the SwissFEL RF system uses three different RF frequencies ($f_{s\ band}$ = 2998.800MHz, $f_{C\ band}$ = 5712.000MHz and $f_{X\ band}$ = 11'995.200MHz = 4x2998.800MHz). The S and X band frequencies are very close to the European standards, whereas 5712.000MHz is a US C band frequency. $f_{C\ band} \neq 2xf_{S\ band}$, which complicates fs-stable electrical reference generation, i.e. mutual stability between C band, S band, X band and various pulsed lasers and BAMs. The European standard S band frequency has been slightly detuned to the above mentioned value in order to find an as high as possible common subharmonic base frequency (f_b = 142.800MHz).

The idea of the SwissFEL reference system is to start with this base frequency and derive laser reference pulses as well as RF reference frequencies from it. It has been shown that a mode locked laser OMO ($f_{rep} = f_b$ = 142.800MHz), synchronized to a stable microwave source, can provide reference signals with extremely high temporal stability, pulses as well as RF harmonics, where the latter can be extracted from the OMO's pulse train (Fig. 2) or are delivered by a microwave oscillator synchronized to the latter [2]. Carefully deriving all reference signals from the OMO laser pulses yields high mutual stability.

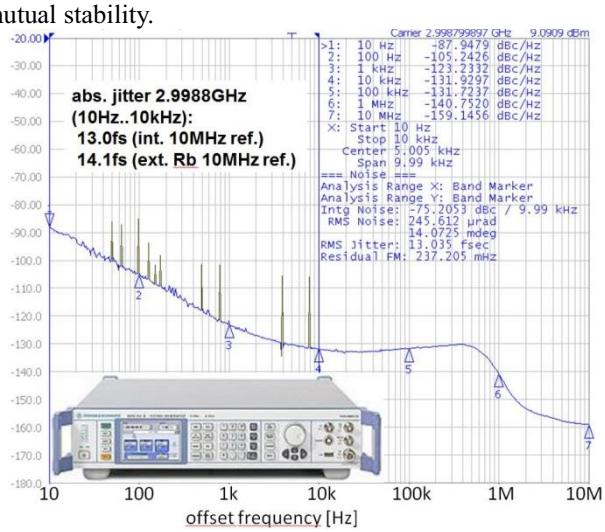


Figure 1: Measured phase noise spectrum timing jitter of the SwissFEL RF MO (Rohde + Schwarz SMA 100A.) Locking with a 10MHz Rb frequency standard (SRS FS725) slightly increases jitter from 13.0 fs to 14.1fs.

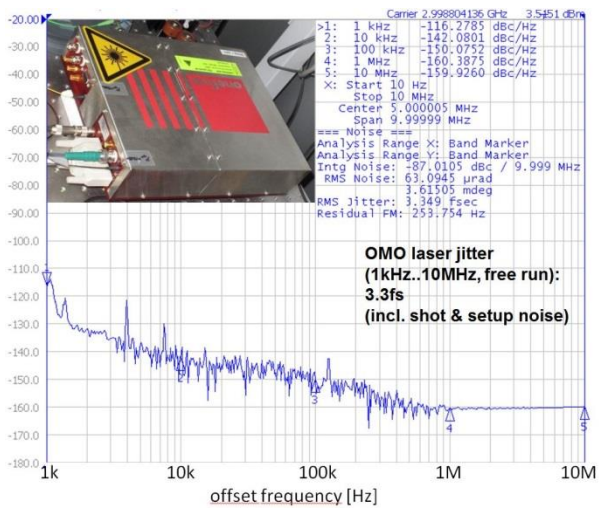


Figure 2: Measured phase noise spectrum and timing jitter of the free running SwissFEL OMO laser (Onefive Origami 15, 1560nm, 142.8MHz repetition rate; Discovery DSC50 photodiode).

Figure 3 shows a schematic overview of the system. The OMO laser is locked on the 10th harmonic to the RF master oscillator (RF MO, Fig. 1), which is itself locked

ISBN 978-3-95450-141-0

Copyright © 2014 CC-BY-3.0 and by the respective authors

to a 10MHz Rb standard to achieve high long-term frequency stability. Phase noise spectrum and jitter of the 21st harmonic of the free running OMO (1kHz … 10MHz) are given in Fig. 2. It confirms that extremely clean RF signals can be derived by extracting harmonics using direct photodetection from the laser pulse train. Potential phase drifts due to amplitude variations can be supressed using a voltage variable optical attenuator with constant optical path length and a control loop keeping the photocurrent constant.

For the RF reference distribution 4 RF frequencies are required: $f_{S\ band}$ = 2998.800MHz, $f_{C\ band}$ = 5712.000MHz, $f_{X\ band}$ - $f_{S\ band}$ = 8996.400MHz (for LLRF X band downconverter LO), $f_{X\ band}$ = 11'995.200MHz. $f_{S\ band}$ and $½f_{C\ band}$ = are extracted and transmitted via group delay stabilized radio-over-fiber links described below. C band signals require subsequent frequency doubling. SwissFEL requires 6 S band and 27 C band links. X band reference, X band downconverter LO and an S band reference signal, all required by the X band LLRF system are extracted from the photodetected pulse train of a stabilized pulsed link in the X band LLRF station. Alternatively the extracted harmonics could be used to lock low noise floor VCOs or a balanced optical to microwave phase detector based PLLs, fed directly with the optical pulses as reference, could lock VCOs [2].

A 142.8MHz reference signal is also extracted for the BPM reference distribution. The latter is based on a non-phase-stabilized low cost fiber-optic links with coaxial sub-distribution inside the accelerator tunnel.

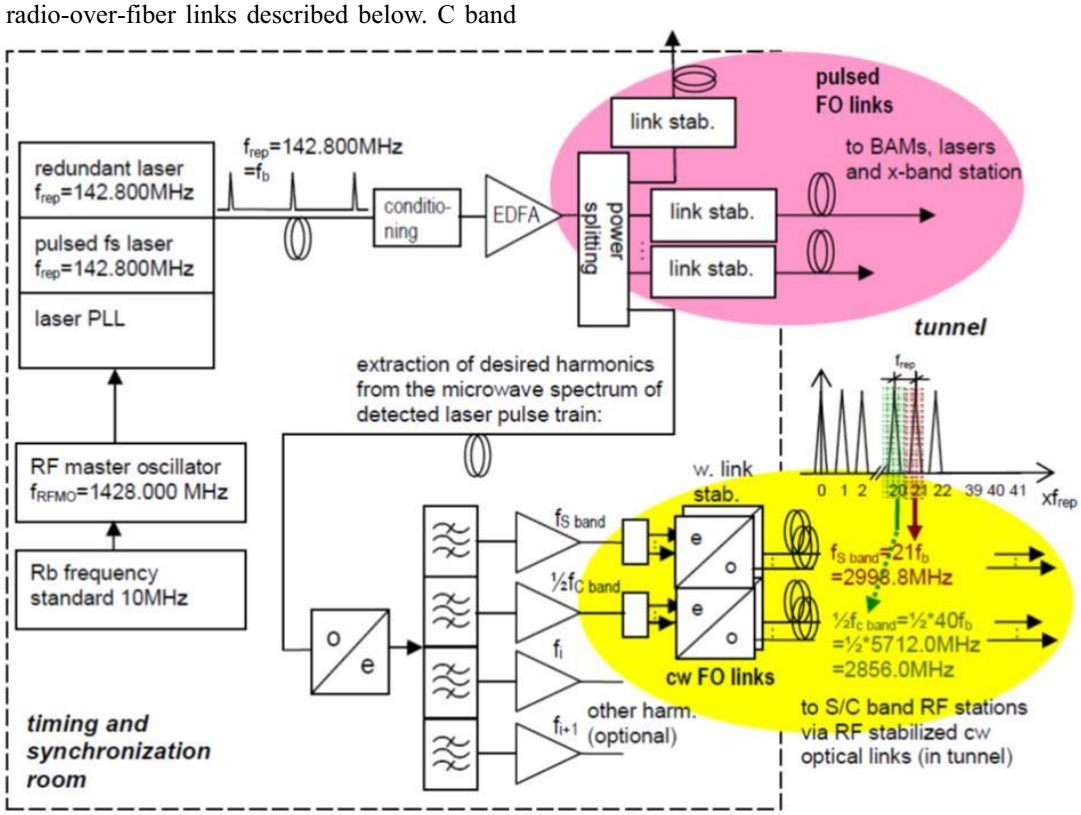


Figure 3: Concept of the SwissFEL reference generation, distribution and synchronization system.

CW FIBER-OPTIC LINKS FOR RF REFERENCE DISTRIBUTION

In the past, basically two approaches have been presented to achieve fs-stability in the distribution of reference signals: 1) Transmission of mode-locked fs-laser pulses and group delay stabilization by means of a balanced optical cross-correlator (BOC) [3]. 2) Intensity modulation and optical phase stabilization [4]. Both technologies potentially yield extremely high long-term timing stability (<10fs_{pp}/d) for link length up to 1km or even more. Particularly 1) has been optimized, ruggedized and even commercialized [5] over the last years. This type of link transmits laser pulses, but not RF signals, which makes it - together with its exceptional short and long term stability - the first choice for direct optical synchronization of stability-critical pulsed lasers, to derive stable RF signals from the pulses, requires additional effort. Drawbacks of this link type are that it requires relatively complicated optics, components that are expensive and operated in modes for which they were not manufactured and qualified and for many critical components no second source exists. Running the system reliably requires qualified personnel. Moreover the fibers need careful dispersion compensation and the system is rather sensitive. Using group delay stabilized radio-over-fiber links (RF input, RF output) was considered to be a straight forward and promising approach to distribute RF

#stephan.hunziker@psi.ch

Copyright © 2014 CC-BY-3.0 and by the respective authors

ISBN 978-3-95450-141-0

reference signals. The basic technology has already been established for decades [6] and high quality reliable cots components designed for telecom and sensing applications are available from various suppliers at reasonable cost.

Group Delay Stabilized Radio-Over-Fiber Links

A radio-over-fiber type fiber-optic link, named "Libera Sync 3" has been developed in collaboration between PSI and Instrumentation Technologies d.d. The idea was to develop a fiber-optic link, based on classical intensity modulation of (cw) telecom laser diode light ("cw link") but with additional group delay stabilization. It is conceptually based on the detection of the RF phase between the transmitter input signal and the photo-detected light reflected at the link end. . The operating frequency for the first prototype is 2998.8MHz (SwissFEL S band frequency).

Even in a carefully designed bi-directional fiber-optic link Rayleigh scattering [7] causes a weak noise floor (uncritical in telecom applications), significantly increasing the jitter in the received signal, still at 1550nm wavelength. Therefore the system incorporates two distinct fibers. One fiber is operated in a bi-directional mode providing a stable medium … long term (>seconds) phase, whereas the other is uni-directional. RF phase detectors are also key components, the performance of which has been optimized by taking care of high symmetry and temperature stabilization. As opposed to pulsed optical links phase noise and drift due to AM-PM conversion in the photodetector can be eliminated in RF intensity modulated cw light by operating it at an optimum photocurrent, as many photodiodes exhibit sweet spots in the phase-vs.-photocurrent characteristic for this type of modulation. An optimized prototype of the Libera Sync 3 has been tested recently at PSI and results are presented here. Details on the system architecture can be found in [8,9,10]. Transmitter (TX) and receiver (RX) units are in compact 19"/2HU housings and can be remote controlled and monitored via Ethernet (Fig. 1). After installation, the units can be tuned-on and the link automatically phase-locks after a warm-up phase of <2h.



Figure 4: Libera Sync 3 cw fiber-optic link receiver (top) and transmitter (bottom).

The TX Input power level is +15dBm. The RX has two outputs with +15dBm each and a tapped output for testing.

Libera Sync 3 Prototype Measurement Results

Measurements of phase noise, timing jitter, long term timing drift and link gain drift have been made. Two 453m (max. SwissFEL RF reference link span is ≈500m) long meandering fiber loops installed on a cable tray have been spliced in the 65m long SITF tunnel to establish a realistic environment for the tests. TX and RX units were located in the SITF gun laser hutch, which is temperature and relative humidity controlled (typ. ±<0.25°C, ±<1%RH) and was usually rather crowded during all tests. The tunnel temperature is stabilized during operation but not its relative humidity.

The phase noise/jitter contribution of the link was measured by tapping part of the reference signal that feeds the TX input and mixing it in quadrature with the RX output. This relative phase noise measurement carries the risk of adding phase noise from the reference source at offset frequencies >10kHz, as the output noise higher spectral components' correlation decreases after transmission over a certain distance. Therefore a Poseidon/Raytheon DRO with a low noise floor of -170dBc/Hz has been chosen as reference source to reduce this overestimation of phase noise.

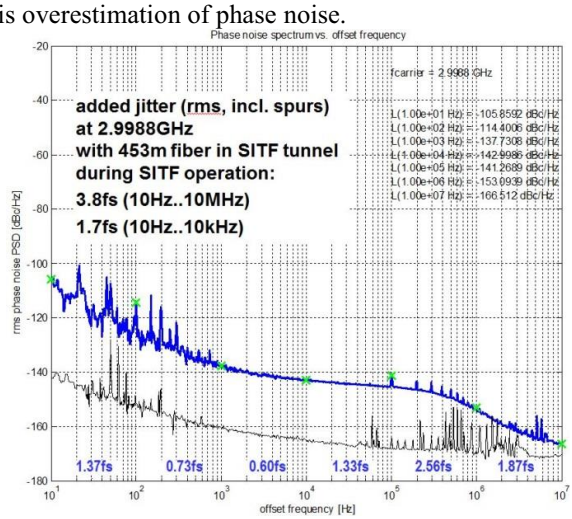


Figure 5: Libera Sync 3 measured phase noise and jitter at 2998.8MHz. Thin black curve: setup noise limit (mixer Pulsar ML-04-LC, SSA Agilent E5052B baseband).

Fig. 5 shows the measured phase noise and jitter as well as the jitter values for each decade between 10Hz and 10MHz. The added jitter of $3.8fs_{rms}$ (10Hz … 10MHz) or $1.7fs_{rms}$ in a smaller range relevant for many reference signals (10Hz … 10kHz) for this S band fiber-optic link in a realistic accelerator environment is below the envisaged $\approx 7fs_{rms}$.

The link phase and gain drift measurement setup is shown in Fig. 6. The phase/gain detector is based on the well-known Analog Devices AD8302, which incorporates a Gilbert cell mixer and input log amps. With additional temperature stabilization this integrated detector is

ISBN 978-3-95450-141-0

Copyright © 2014 CC-BY-3.0 and by the respective authors

extremely stable (given there are no significant differential input signal variations) as shown in Fig. 7. The cabling for this measurement has been laid out as symmetric as possible using low temperature drift RF cables (Micro Coax UT-85C-FORM). Two dummy couplers have been added to optimize cabling symmetry.

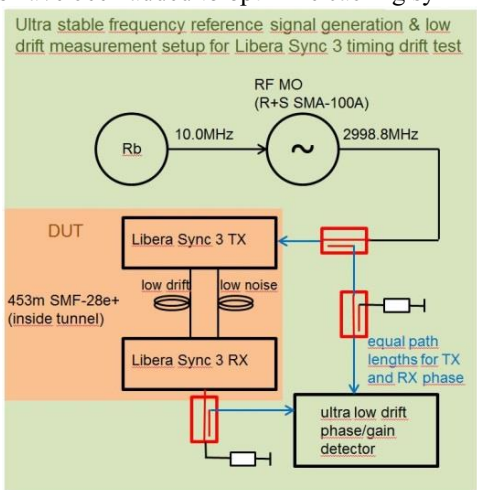


Figure 6: Setup for the link phase and gain drift measurements.

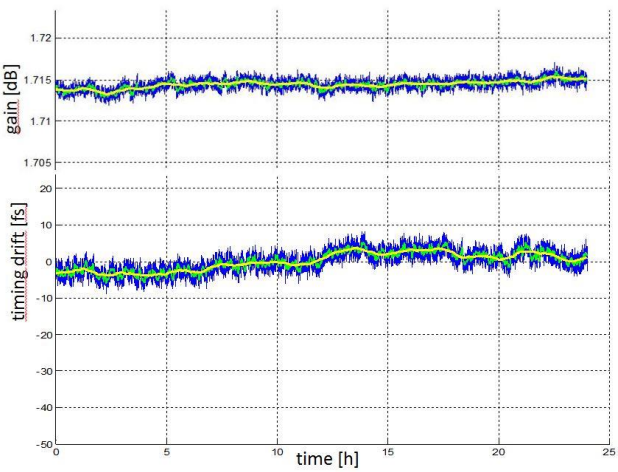


Figure 7: Phase/gain det. drift over 24h (f=2998.8MHz): Gain det. (top), phase det. (bottom). Blue: raw (2.2s sampling period); grn.: 2.2min avg.; yellow: 1h avg. Timing/gain drift:11.4fs_{pp}/0.003dB_{pp} (2.2min avg.), 7.6fs_{pp}/0.002dB_{pp} (1h avg.).

The reference source is the SwissFEL RF MO SMA 100A (Fig. 2), locked to a Rb standard. TX and RX units, reference source and phase detector were installed in a vibration damped rack, the front of which was partly covered to shield it from direct air flow and exposure to lamps that are frequently turned on and off.

Two typical link phase and gain drift measurements for relatively stable environmental conditions and crowded hutch during the measurement periods are shown in Figs. 8 and 9. RH in the tunnel is varying by 11.5% (Fig. 8)/9% (Fig. 9) and the temperature by about 0.4°C (Figs. 8 and 9). The measured drifts are well within the spec (<a few tens of fs_{pp}/d and <0.05dB_{pp}/d).

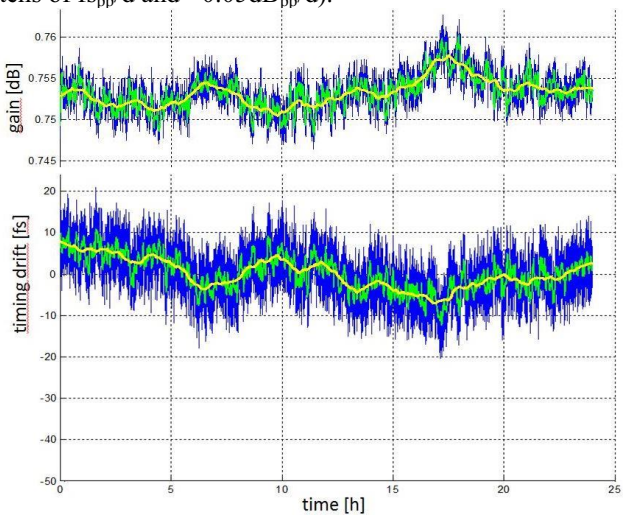


Figure 8: Libera Sync 3 phase/gain drift over 24h (453m link in SITF tunnel, f=2998.8MHz): Gain det. (top), phase det. (bottom). Blue: raw (2.2s s.p.); grn.: 2.2min avg.; yellow: 1h avg. Timing/gain drift: 23.7fs_{pp}/0.012dB_{pp} (2.2min avg.), 15.0fs_{pp}/0.007dB_{pp} (1h avg.).

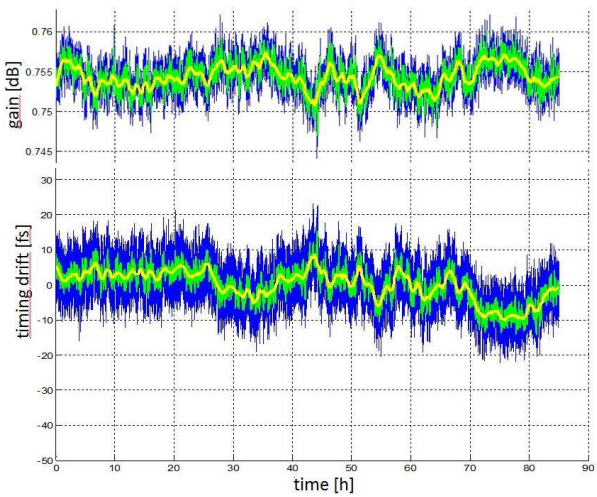


Figure 9: Libera Sync 3 phase/gain drift over 85h (453m link in SITF tunnel, f=2998.8MHz): Gain det. (top), phase det. (bottom). Blue: raw (2.2s s.p.); grn.: 2.2min avg.; yellow: 1h avg. Timing/gain drift: 29.5fs_{pp}/0.013dB_{pp} (2.2min avg.), 18.6fs_{pp}/0.007dB_{pp} (1h avg.).

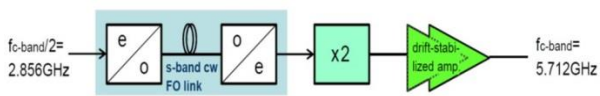


Figure 10: C band reference distribution using S band cw radio-over-fiber link Libera Sync 3.

Using Libera Sync 3 for C Band Reference Signal Distribution

Apart from S band also C band reference signals have to be distributed (SwissFEL LINAC). The optics of the Libera Sync 3 system is designed for S and C band

Copyright © 2014 CC-BY-3.0 and by the respective authors

ISBN 978-3-95450-141-0

frequencies f>6GHz but the RF part would require a new design for direct C band transmission. As the long term stability requirements for the C band reference signals are somewhat relaxed in case of SwissFEL, we decided to use the S band link also for the C band reference signals but to transmit $f_{C\ band}/2$ = 2856.000MHz and use a stable RF frequency doubler and a drift stabilized amplifier at the end of the link (Fig. 7). Measurements have shown that low noise Schottky diode 3GHz→6GHz frequency doublers do not add measurable jitter to an ultra-low noise 3GHz signal as provided at the Libera Sync 3 RX output. Furthermore this type of switched frequency doubler is potentially relatively immune to AM-PM conversion (timing drift due to input amplitude variations, which are very low anyway with stabilized links) [11]. A frequency doubler/amplifier is currently under development at PSI.

PULSED OPTICAL LINKS

Some clients that require ultimate long term stability (<10fs_{pp}) will finally be fed with pulsed optical reference signals (SwissFEL phase 1: 4 BAMs, experiment and gun lasers, X band RF). Therefore 7 stabilized pulsed optical links will be installed as well. As this technology is commercially available today, the pulsed optical links including the optical pulse power amplifier/splitter system will be purchased from a commercial vendor.

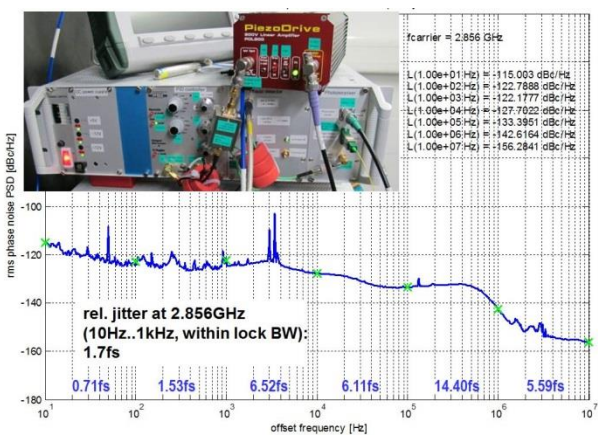


Figure 11: Relative phase noise/jitter of Onefive Origami 15 OMO, locked to a R+S SMA 100A with the analog PSI laser PLL vs. frequency doubled RF MO reference signal ($2xf_{ref\ RF,MO}$=1428MHz).

PULSED LASER SYNCHRONIZATION

The relative phase noise of the locked Origami 15 OMO (142.8MHz rep rate) is shown in Fig. 11. The reference signal is at 1428MHz (10x rep rate) from an SMA 100A and the relative phase noise is measured at the 20th harmonic vs. the frequency doubled reference signal. The analog ultra-low noise PLL locks a laser harmonic to an RF reference. The measurement shows that very tight lock is possible up to a few kHz. Above the loop bandwidth of few kHz the phase noise of the SMA 100A reference source dominates in this relative measurement. Vector modulator based superperiod lock and coarse frequency tuning are controlled via the EPICS control system. A versatile digital PLL incorporating these functionalities and sequentially locking the laser to superperiod, RF and optical pulses (BOC) is currently under development.

CONCLUSION

We have presented the core of the planned SwissFEL reference generation, distribution and synchronization system which provides high mutual phase and amplitude stability for all RF and optical reference signals. Test results for a radio-over-fiber link prototype (<4fs_{rms} jitter, <20fs_{pp} w. 1h avg. phase drift over 85h) as well as for RF MO (14fs_{rms} abs. jitter) and OMO harmonic (3.3fs_{rms} free run abs. jitter 1kHz..10MHz) have been reported.

ACKNOWLEDGMENT

Support by the SwissFEL project and discussions with colleagues from PSI, Elettra, Desy, PAL-FEL and SLAC (diagnostics, T&S, LLRF) are gratefully acknowledged.

REFERENCES

[1] http://www.psi.ch/swissfel/
[2] J. Kim, F. X. Kaertner, and F. Ludwig, “Balanced optical–microwave phase detectors for optoelectronic phase-locked loops,” *Opt. Lett.*, 31, no. 24, pp. 3659-3661, 2006.
[3] F. Loehl, J. Chen, F. X. Kaertner, J. Kim, F. Wong, J. M. Mueller, and H. Schlarb, “Sub-10 Femtosecond Stabilization of a Fiber Link Using a Balanced Optical Cross Correlator,” *PAC*, FROAC04, 2007.
[4] R. Wilcox, J. M. Byrd, L. Doolittle, G. Huang, and J. W. Staples, “Stable transmission of radio frequency signals on fiber links using interferometric delay sensing,” *Opt. Lett.*, 34, no. 20, 3050-3052, 2009.
[5] http://www.menlosystems.com/products/timing-distribution-solutions/tds/
[6] C.H. Cox, “Analog optical links: theory and practice,” Cambridge Univ. Press, Cambridge, 2004.
[7] T.H. Wood, R.A. Linke, B.L. Kasper, and E.C. Carr, “Observation of coherent Rayleigh noise in single-source bidirectional optical fiber systems,” *J. Lightwave Technol.*, 6, no. 2, 1988.
[8] P. Lemut, R. Hrovatin, P. Orel, S. Zorzut, S. Hunziker, and V. Schlott “Next generation cw reference clock transfer system with femtosecond stability,” *NA-PAC*, THPMA04, Pasadena, CA (USA), 2013.
[9] S. Zorzut, P. Orel, P. Lemut, E. Janezic, S.G. Hunziker, and V. Schlott, “Test results of the Libera Sync 3 cw reference clock transfer system,” *IPAC*, TUPRI079, Dresden (Germany), 2014.
[10] http://www.i-tech.si/
[11] R.A. Baugh, “Low noise frequency multiplication,” *Proc. 26th Ann. Frequency Control Symp.*, Atlantic City (USA), pp. 50-54, 1972.

ISBN 978-3-95450-141-0

Copyright © 2014 CC-BY-3.0 and by the respective authors

COMPARISON OF FEEDBACK CONTROLLER FOR LINK STABILIZING UNITS OF THE LASER BASED SYNCHRONIZATION SYSTEM USED AT THE EUROPEAN XFEL

M. Heuer, S. Pfeiffer, H. Schlarb, DESY, Hamburg, Germany
G. Lichtenberg, HAW, Hamburg, Germany

Abstract

The European X-ray Free Electron Laser will allow scientists to perform experiments with an atomic scale resolution. To perform time resolved experiments at the end of the facility it is essential to provide a highly stable clock signal to all subsystems. The accuracy of this signal is extremely important since it defines limitations of precise measurement devices. A laser based synchronization system is used for the synchronization with an error in a sub-femtosecond range. These light pulses are carried by an optical fiber and exposed to external disturbances which changes the optical length of the fiber. For that reason the fiber is actively stabilized using a controller implemented on the new MicroTCA Platform. Due to the high computation resources of this platform it is possible to attack the time delay behavior of the link system with well known model based control approaches. This contribution shows how to design a model based controller for such a system and compares the control performance of the previously used PID controller with advanced control algorithms at the currently installed laboratory setup.

INTRODUCTION

The European X-ray Free-Electron Laser (XFEL), is currently under construction at the Deutsches Elektronen Synchrotron (DESY) in Hamburg, Germany. This device with a length of 3.5 km will generate extremely intense and short X-ray laser light pulses with a duration of a few femtoseconds. Technical specifications of the facility can be found in [1]. The intense and ultra-short X-ray laser pulses are generated by an electron bunch which is feed through an undulator. They will provide scientists from all over the world the possibility to take a closer look into tiny structures on an atomic scale with a repetition rate of up to 4.5 MHz. This provides the ability to e.g. film the folding and formation of complex biomolecules [2]. One of the main challenges is to distribute a timing signal with a frequency error of less than 10 fs for all devices within the free-electron laser to achieve the required precision. In [3] a laser based synchronization system was proposed for that purpose, it is used for FLASH, and will be implemented for XFEL [4].

This paper is organized as follows: The first section gives an overview of the Laser based Synchronization system (LbSynch) and explains the Links Stabilization Unit (LSU). The second chapter introduces at set of possible control strategies and the dead time compensation. The experimental results and a comparison between the controller is given in section three. The paper closes with a short outlook how to improve the performance further.

Laser Based Synchronization System

Figure 1 shows a simplified version of the laser based synchronization system with the beamline.The injector laser triggers a detachment of electrons at the cathode of the gun, which generates an electron bunch. This bunch is than accelerated by 101 superconducting modules (I0 and I39H, A1.M1-4, ..., A25.M1-4). At the end of the beamline the bunch is lead through the undulator, which forces the electron bunches on a sinusoidal trajectory. This causes the so-called Self-Amplified Spontaneous Emission (SASE) process, which generates the high energy X-ray pulse. Other important devices within the beamline are e.g. the Bunch Arrival time Monitors (BAM) [5], which are used to measure the relative time of the electron bunch crossing a certain position w.r.t. the timing pulse of synchronization system.

To provide a clock signal to these devices the laser based synchronization system is used. It consists of two parts, the Master Laser Oscillator (MLO) generates the laser pulse train at a frequency of 216.66 MHz. This is the timing signal of the system, which is distributed through fibers to the different end station in the facility. This fiber is exposed to temperature and humidity changes as well as vibrations, which results in small changes of its optical length. To stabilize this length, the second part of this system, the so-called Link Stabilizing Unit (LSU) is used.

The lower right part of Fig. 1 shows the control scheme of a LSU. If a pulse enters the LSU, one small fraction of the laser pulse is branched off and the main part goes through a piezo stretcher into the fiber and further to the device in the accelerator. A piezo stretcher allows to slightly change the length of the fiber, hence it is used as an actuator in this scheme. At the device the pulse is partly reflected by an Faraday Rotating Mirror (FRM) and travels back the way to the LSU. This returning pulse and the fraction of the subsequent pulse pass an Optical Cross Correlator (OXC) two times. Each time a new pulse of the shape of the correlation of both incoming pulses is generated. Inside the OXC both polarizations have a different velocity and therefore both new correlation pulses are different. A balanced detector can measure the timing difference between both incoming pulses by measuring the intensity difference of the correlation pulses. If the pulses within the pulse train are equidistant and the signal of the balanced detector is zero, the length of the attached fiber is a multiple of the MLO repetition rate. With this scheme it is possible to suppress the error of the timing signal induced by length changes of the fiber caused by stress, temperature and/or humidity changes acting on the fiber.

Copyright © 2014 CC-BY-3.0 and by the respective authors

ISBN 978-3-95450-141-0

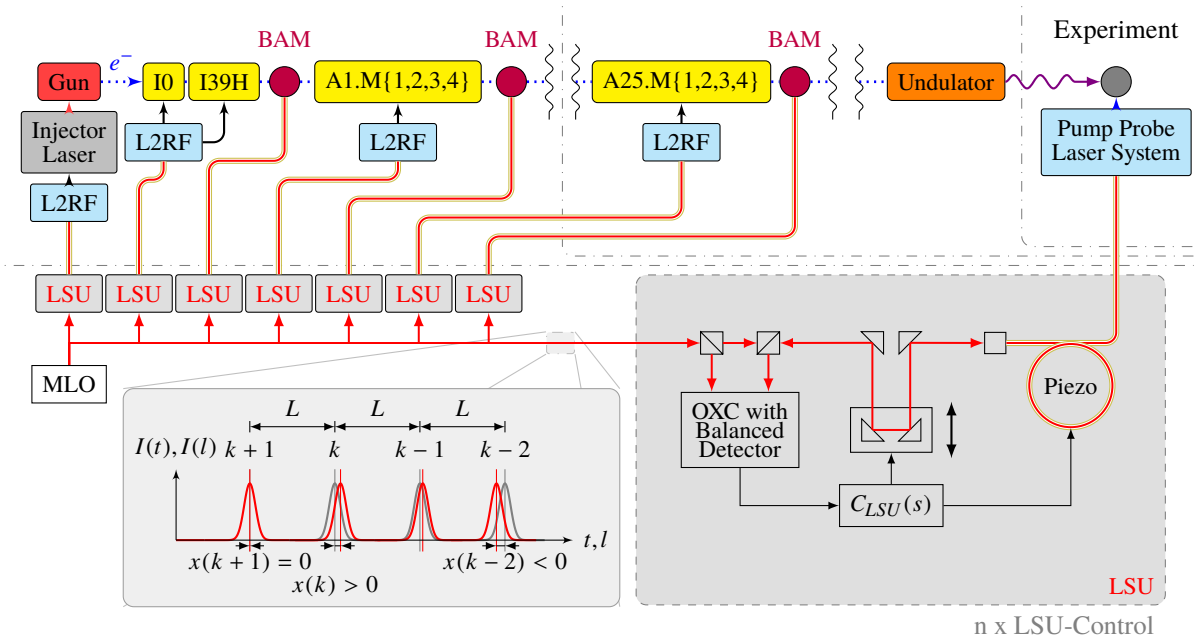


Figure 1: Block Diagram of the Laser based Synchronization System.

Link Stabilizing Unit

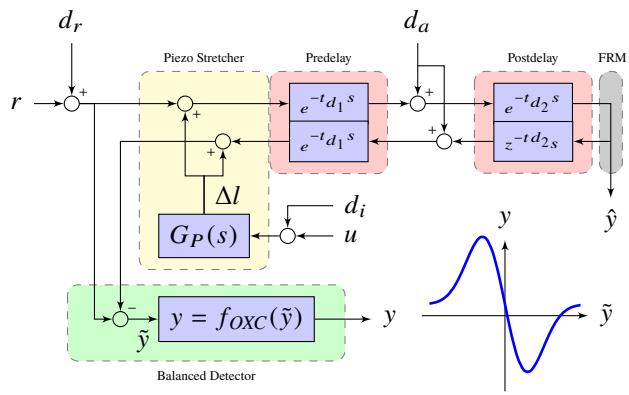


Figure 2: Block Diagram of the LSU.

The block diagram of the Link Stabilizing Unit is given in Fig. 2. All signals in this diagram are relative timing changes of the current laser pulse with respect to perfect pulse at the same time instance. A model of the piezo actuator is given by the transfer function G_p, the time delay effect of the fiber link by the delay blocks and the combination of optical cross correlator and balanced detector is given by the nonlinear function f_{OXC}. In this paper we assume, that we are in the linear range of this function. The plant $P(s)$, where s denotes the Laplacian operator, has the input u and the output $\hat{y}$. For a very short link length the the transfer function of $P(s)$ is given by $2 \cdot G_p(s)$, whereas if the link length increases the second response is delayed and changes the dynamic behavior.

General Control Loop

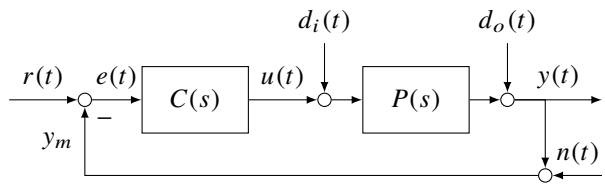


Figure 3: General setup of a control loop [6].

The general control loop is shown in Fig. 3. The two main elements are the plant $P(s)$ with the output $y(t)$ and the controller $C(s)$. The controller should generates a signal to the input of the plant $u(t)$ in such a way, that the difference between the plant output and a given reference $r(t)$, called the control error $e(t)$, goes to zero. Moreover unwanted disturbance and noise effects which influences $y(t)$ should be suppressed. Those effects are:

1. The input disturbance $d_i(t)$ effects the value $u(t)$, e.g.
   - Ripple and other effects on the supply voltage
2. The output disturbance $d_o(t)$ directly effects the controlled value $y(t)$, e.g.
   - Movement of the coarse tuning motor
   - Vibrations and temperature changes of the optical table on which the optical setup is mounted
   - Vibrations of the fiber inside the accelerator
3. The noise $n(t)$ effects the measurement but not the controlled value $y(t)$, e.g.
   - Thermal noise of the photo diode
   - Noise and quantization errors of the ADC

ISBN 978-3-95450-141-0

Copyright © 2014 CC-BY-3.0 and by the respective authors

PID Controller

In the current setup a proportional integral derivative (PID) controller is used to stabilize the timing error of the link. This well known controller type uses the amplified control error as well as the integration and derivation of the control error to generate the required plant input. It is easy to obtain a sufficient performance for a wide class of plants via heuristic tuning or with tuning rules from [7] even without the knowledge of the plant. For that reason this controller type is most commonly used in the industry, like shown in [8].

In this paper a PID controller will be used as a reference for the model based LQG controller.

LQG Controller

The linear quadratic gaussian (LQG) controller is well known in control theory and combines an optimal state observer with an optimal state feedback gain.

In the following, all systems $P(s), C(s), \ldots$ are represented in the state space form,

$$\dot{x}(t) = Ax(t) + Bu(t), \tag{1}$$

$$y(t) = Cx(t) + Du(t), \tag{2}$$

and abbreviated with

$$P(s) = \left[\begin{array}{c|c} A & B \\ \hline C & D \end{array}\right], \tag{3}$$

where $x(t) \in \mathbb{R}^n$ are the states (internal energy storage's), $u(t) \in \mathbb{R}^m$ the inputs and $y(t) \in \mathbb{R}^l$ the outputs of a system. The matrices $A \in \mathbb{R}^{n\times n}$, $B \in \mathbb{R}^{n\times m}$, $C \in \mathbb{R}^{l\times n}$, $D \in \mathbb{R}^{l\times m}$ representing the dynamic behavior of the system. The linear quadratic regulator (LQR) is an optimal controller of the form $u(t) = -Fx(t)$ which minimizes the cost function

$$V = \int_0^\infty x(t)^T Q x(t) + u(t)^T R u(t)\, dt\,, \tag{4}$$

$$Q \in \mathbb{R}^{m\times m} \geq 0\,, \quad R \in \mathbb{R}^{n\times n} > 0, \tag{5}$$

where $x(t)$ are the states and $u(t)$ are the inputs of the closed loop system. The matrices Q and R are tuning parameter and can be freely choose if they satisfy (5).

The optimal feedback gain F is computed with Matlab by

```
F = lqr(A,B,Q,R);
```

With this controller it is possible to change the eigenvalues of the closed loop system, i.e. the dynamic behavior of the system. [6]

In most cases not all states $x(t)$ are measurable. Therefor one has to estimate them using an observer

$$O(s) = \left[\begin{array}{c|cc} A - LC & B & L \\ \hline I & 0 & 0 \end{array}\right], \quad u_o(t) = \begin{bmatrix} u(t) \\ y(t) \end{bmatrix}, \tag{6}$$

which computes the states from the known input $u(t)$, the measurement $y(t)$ and the known system defined by the matrices A, B, C, D. The feedback gain L for the observer can be calculated by

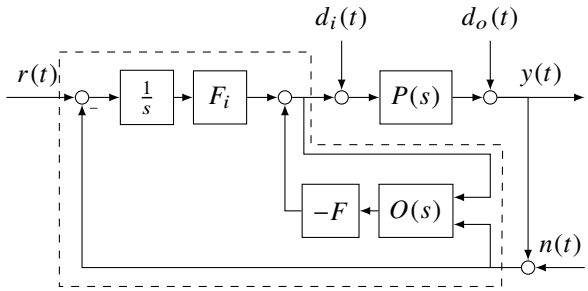


Figure 4: Block Diagram of the LSU in the current experimental setup.

```
L = lqr(A',C',Q_o,R_o)';
```

It is important to choose the observer tuning parameter Q_o and R_o in such a way, that the dynamics of the observer are faster than those of the closed loop state feedback system.

In order to reach a steady state control error of zero ($\lim_{t\to\infty} e(t) \to 0$) it is necessary to include integral action to the controller if the plant itself is without integral behavior. Figure 4 shows the block-diagram for such a controller with the integrator $\left({}^1/_s\right)$ and the additional feedback gain F_i. To design such a controller the augmented system

$$P_a(s) = \left[\begin{array}{c} \dot{x} \\ \dot{x}_i \\ \hline y \\ x_i \end{array}\right] = \left[\begin{array}{ccc|c} A & 0 & B & \\ C & 0 & 0 & \\ \hline C & 0 & D & \\ 0 & I & 0 & \end{array}\right] \left[\begin{array}{c} x \\ x_i \\ \hline u \end{array}\right] \tag{7}$$

can be used to design the gains F and F_i in the same synthesis step.

Smith Predictor

The presence of a time delay inside the plant $P(s)$ reduces the performance of the closed loop, it is even possible that the closed loop is unstable. To compensate this delay, the well known structure in Fig. 5 is used. If the plant model $\hat{P}$ and the time delay $e^{-\hat{t}_d s}$ model are perfect, the time delayed system is compensated and the controller reacts on the perfectly matched plant model. Further effects, if plant and the model are not equal are analyzed in [9]. In the case of long fiber links, a smith predictor can be added if the length of the link reaches a length where the time delay of the returning pulse influences the dynamic behavior of the plant.

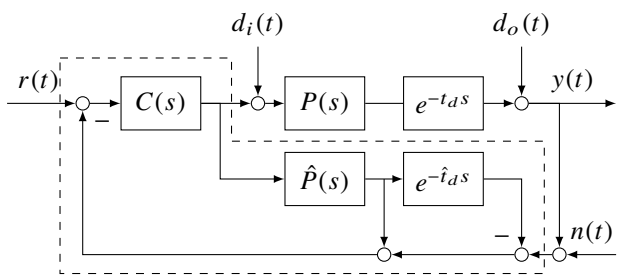


Figure 5: Control loop with a smith predictor [10].

Copyright © 2014 CC-BY-3.0 and by the respective authors

ISBN 978-3-95450-141-0

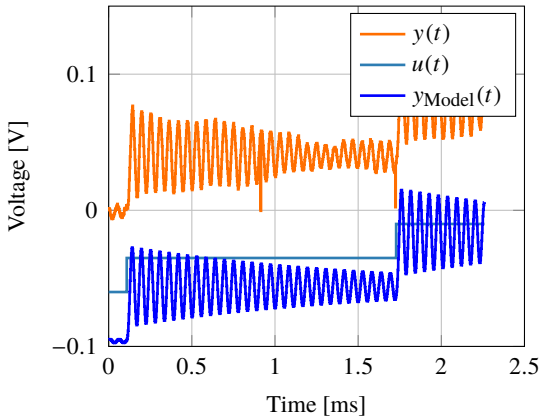


Figure 6: Validation of the identified model.

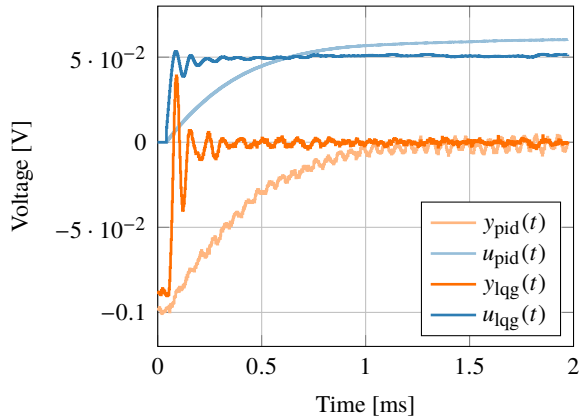


Figure 7: Dynamic behavior of the controller start.

EXPERIMENTAL RESULTS

In the following section the experimental results are presented. The control system is based on the new MicroTCA standard used for XFEL. A SIS8300L board at 81 MHz is used to compute the control algorithm and to feed the control value $u(t)$ to the piezo amplifier. A SIS9000 connects the the balanced detector to the SIS8300L. The control algorithm itself is designed in Matlab/Simulink and is implemented on an FPGA using the Simulink to VHDL Toolchain developed in [11]. This tool is based on the SysGen Toolbox by Xilinx which is extended to a fully automated code generation and deployment environment for FPGA based MicroTCA board.

The first step of a model based controller design is to identify and verify a suitable model for the plant. In this case a black box identification is performed. An excitation signal is applied to the plant input $u(t)$ and the response of the plant $y(t)$ is measured. With those measurement it is possible to derive the continuous time state space model

$$A = \begin{bmatrix} -253.8 & 1.133 \cdot 10^5 & 935.9 \\ -1.133 \cdot 10^5 & -1138 & -2017 \\ 935.9 & -4035 & -1.346 \cdot 10^5 \end{bmatrix},$$

$$B = \begin{bmatrix} 112.9 & 237.9 & -209.5 \end{bmatrix},$$

$$C = \begin{bmatrix} 225.8 & -475.9 & -418.9 \end{bmatrix}$$

with A as the system matrix, B as input matrix and C as output matrix, for the 300 m link currently setup in the laboratory. The direct feedthrough matrix D is set to zero, the usual case for physically realizable plants. Figure 6 shows the validation of this model. The dynamic behavior as well as the decay of the model matches well with the measurement $y(t)$. The remaining offset is caused by a very slow drift behavior of the link and will be treated with an integral behavior of the controller.

In the next step we compare the dynamic behavior of both controllers.

For a minimum rms value at the output $y(t)$ just the integrator of the PID controller is used. This value is increased as long as no oscillation occur, like it is done in the past.

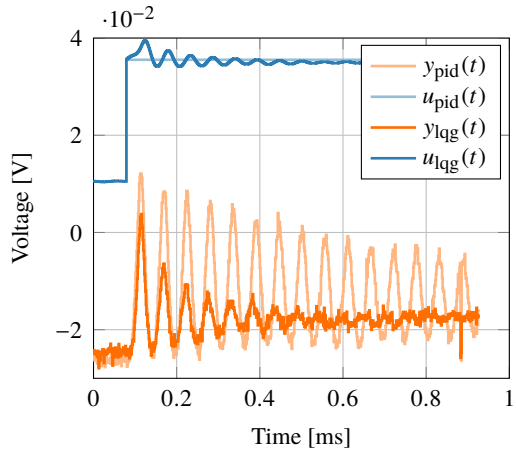


Figure 8: Response to an input disturbance $d_i(t)$ step of the state feedback controller without integrator.

The model based LQG controller designed with the methods shown in the previous section and implemented in the FPGA.

Figure 7 shows the dynamic behavior of both controllers in the moment of the start. One can see that the LQG controller acts faster and reaches the steady state much earlier than the PID controller. In this measurement the LQG controller starts much closer to the final value. Nevertheless, the PID controller also requires more time to reach the final value if different initial values are considered. The reason for that is, that the LQG controller provides a component which directly acts on the change of the value and doesn't need time to act like an integrator would do.

The effect of the state feedback is shown in Fig. 8. Due to the knowledge of the plant, it is possible to change the eigenvalues of the closed loop system in such a way, that the dynamics have the required properties. In the case of the fiber links we would like to suppress the oscillation of the piezo crystal. Figure 8 shows exactly this behavior. With the activated controller the damping of the system is much faster.

The dynamic behavior of the LQG controller with an integrator is shown in Fig. 9. The state feedback part of the

ISBN 978-3-95450-141-0

Copyright © 2014 CC-BY-3.0 and by the respective authors

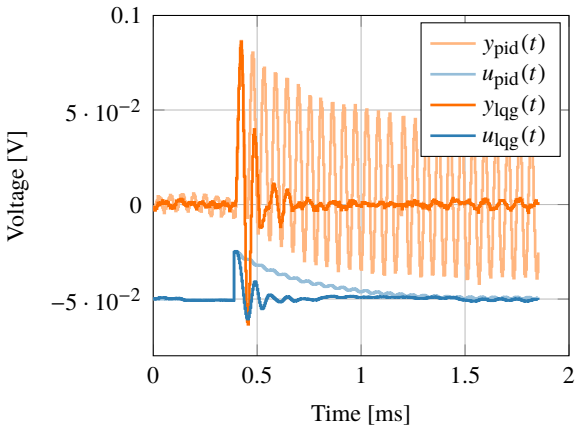


Figure 9: Response to an input disturbance $d_i(t)$ step of the augmented state feedback controller with integrator.

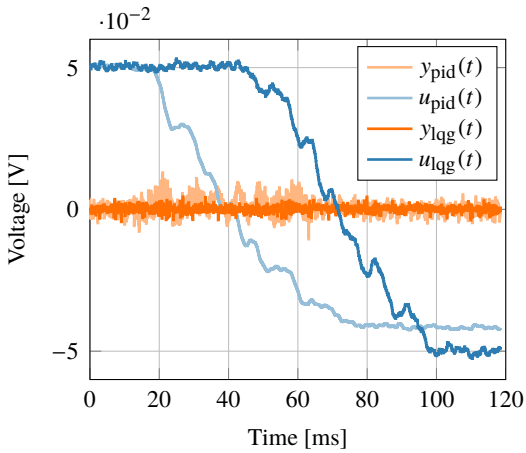


Figure 10: Response to a step of the coarse tuning motor, down-sampled by 42, $u_{lqg}(t)$ and $u_{pid}(t)$ are shifted to keep the graphs within the figure.

controller suppress the oscillation whereby the integration part pushes the output value $y(t)$ back to the reference value $r(t) = 0$. The PID controller also reaches a non offset steady state but oscillations of the piezo crystal are not attacked in an appropriate way.

The piezo crystal, used in the LSU control scheme, adjusts the length of the fiber. This helps to cope with the disturbances mentioned earlier. The range of this actuator is limited and a motorized delay stage is used to adjust larger timing variations by a stepper motor. This behavior is shown in Fig. 10. The PID controller is to slow to suppress the influences due to the motor, whereas the fast response of the LQG controller is suitable to cope with this influences and no changes on the output $y(t)$ are visible.

CONCLUSION

In this paper a model based LQG controller design with integral action is shown. Furhermore, a smith predictor is included to cope with time delayed signals. The controller is tested at the Stabilizing Fiber Links in the experimental laboratory setup. The time domain responses to disturbances shows that such a model based LQG controller is well suitable for such a system and has an superior performance with respect to a heuristically tuned PID controller.

REFERENCES

[1] M. Altarelli et al., XFEL, The European X-Ray Free-Electron Laser, Technical design report, DESY, Hamburg, Germany, 2007.

[2] C. M. Günther et al., Sequential femtosecond X-ray imaging, Nature Photonics 5, 2011, pp. 99-102.

[3] J. W. Kim et al., Large scale timing distribution and RF-synchronization for FEL facilities, FEL Conference 2004, Trieste, Italy, 2004.

[4] Sebastian Schulz et al., Past, Present and Future aspects of Laser-Based Synchronization at FLASH, Proceedings of the International Beam Instrumentation Conference 2013, Oxford, U.K., 2013.

[5] M. K. Bock, Measuring the Electron Bunch Timing with Femtosecond Resolution at FLASH, University of Hamburg, Hamburg, Germany, 2012.

[6] S. Skogestad, I. Postlethwaite, Multivariable Feedback Control: Analysis and Design, Wiley, Chichester, U.K., 2001.

[7] J. B. Ziegler, N. B. Nichols, Optimum settings for automatic controllers, ASME Transactions, v64 (1942), pp. 759-768.

[8] H. Takatsu, T. Itoh, M. Araki , Future needs for the control theory in industries — report and topics of the control technology survey in Japanese industry.

[9] J. E. Normey-Rico, E. F. Camacho, Control of Dead-time Processes, Springer, London U.K., 2007.

[10] O. Smith, Closer control of loops with dead time, Chem. Eng. Progress, vol. 53, no. 5, 1957, pp. 217–219.

[11] P. Predki, M. Heuer, L. Butkowski, A. Napieralski, Rapid FPGA development framework using a custom Simulink library for MTCA.4 modules, 19th IEEE Real Time Conference, Nara, Japan, 2014.

Copyright © 2014 CC-BY-3.0 and by the respective authors

ISBN 978-3-95450-141-0

RHIC-STYLE IPMs IN THE BROOKHAVEN AGS*

R. Connolly, C. Dawson, J. Fite, H. Huang, S. Jao, W. Meng,
R. Michnoff, P. Sampson, S. Tepikian, Brookhaven National Lab, Upton, NY, USA

Abstract

Beam profiles in the two storage rings of the Relativistic Heavy-Ion Collider (RHIC) at Brookhaven National Lab (BNL) are measured with ionization profile monitors (IPMs). An IPM measures the spacial distribution of electrons produced in the beam line by beam ionization of background gas. During the 2012 shutdown we installed a RHIC IPM in the Alternating-Gradient Synchrotron (AGS) to measure horizontal profiles and tested it during the 2013 run. This test was successful and during the 2013 shutdown a vertical IPM was built. This paper describes the new AGS IPMs and shows detector data.

INTRODUCTION

The Relativistic Heavy-Ion Collider (RHIC) at Brookhaven National Lab is a pair of concentric synchrotrons in which counter-rotating beams intersect at six points [1]. Beams of ions from protons (E_{max}=250 GeV) to fully-stripped uranium (E_{max}=100 GeV/nucleon) are accelerated and stored for several hours. There are detectors at two of the six intersection points for physics experiments with colliding beams.

Beam is injected into RHIC from a network of five accelerators. There are three primary accelerators: a tandem Van de Graaff, a 200-MeV H^- linac, and the new Electron-beam Ionization Source (EBIS). One of these three accelerators injects beam into the booster synchrotron, which injects into the AGS which injects RHIC.

Ionization profile monitors (IPMs) have been developed at BNL to measure transverse beam profiles in RHIC [2]. An IPM measures the distribution of electrons in the beam line resulting from residual gas ionization during a bunch passage. The electrons are swept transversely from the beam line and collected on 64 strip anodes oriented parallel to the beam axis.

In 2012 we installed a RHIC IPM into the AGS for horizontal profile measurements. The commissioning tests in the 2013 run were successful so for the 2014 run we built and installed a vertical IPM. The vertical AGS IPM is different from the horizontal to accommodate the required large horizontal aperture of the AGS. Also we added electrical coils on the permanent-magnet dipole detector magnets for beta-function measurements.

*Work performed by employees of Brookhaven Science Associates, LLC under Contract No. DE-AC02-98CH10886 with the U.S. Department of Energy

DETECTOR

Figure 1 is a schematic of the detector and electronics in the accelerator tunnel, fig. 2 is a photo of the detector, and fig. 3 shows the beam installation. An electric field to accelerate the signal electrons toward the collector is generated in the 100mmx150mm rectangular beam pipe by biasing the top electrode at -6kV. The electrons are forced to travel perpendicularly to the measurement plane by a permanent dipole magnetic with field of 1.4kG. A second, reversed, magnet corrects the AGS beam trajectory.

A signal-gating grid is located between the beam and the collector. This is normally biased at the sweep voltage of -6kV to prevent the signal electrons from passing. To make measurements the grid is pulled to ground by a Behlke transistor switch to allow the signal electrons to pass through to the input of a microchannel plate (MCP) which amplifies the electron flux by 10^4 to 10^7. Because each channel of an MCP has a dead time of 1ms after firing, the MCP can become dynamically depleted if the input electron flux is left on continuusly. Periodically the signal electrons are gated off, with the MCP bias on, so the plate can recharge.

The amplified electron flux falls on an anode circuit board with 64 channels spaced 0.53mm apart. Each channel is connected via vacuum feedthrough to an amplifier mounted on the beam pipe, fig 3. Each amplifier output drives a shielded twisted-pair transmission line to a 50MSPS VME digitizer channel.

A screen-covered rectangular opening in the grounded half of the beam pipe decouples the electron gate from the beam. The collector board with attached MCP is located in a Faraday enclosure with an opening for the electrons covered by a grounded stainless steel honeycomb grid which attenuates rf by 80dB.

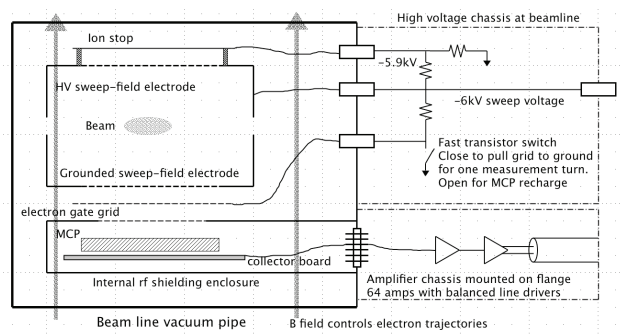


Figure 1: Schematic of detector and electronics located at the beam line.

Copyright © 2014 CC-BY-3.0 and by the respective authors

ISBN 978-3-95450-141-0

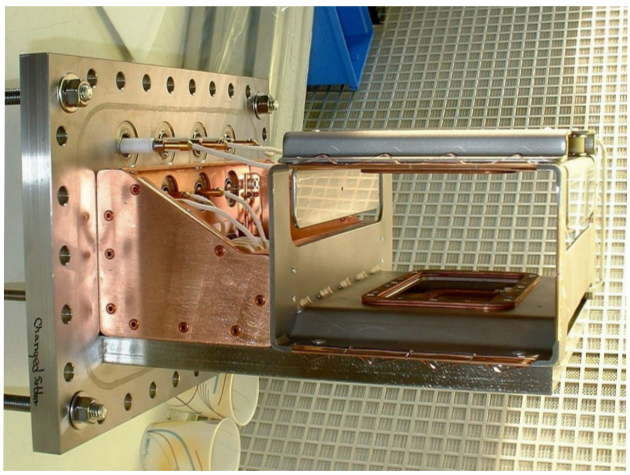


Figure 2: Assembled IPM transducer.

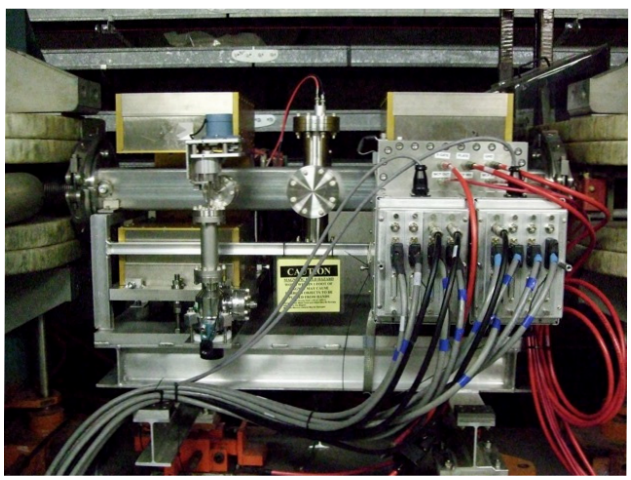


Figure 3: The horizontal detector in the beam line.

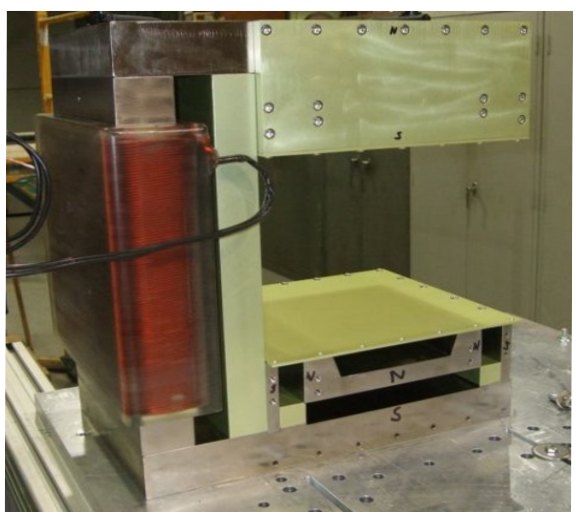


Figure 4: The horizontal detector magnet with the backleg winding.

In 2014 we added electrical coils to the backleg of the dipole magnet, fig 4. These will be used to measure the beam beta function at each IPM. If a steering angle of $\Delta\theta$ is placed at the detector and the beam moves by Δx then the beta function is,

$$\beta = 2 \tan(\pi Q) (\Delta x/\Delta\theta) \quad (1)$$

where Q is the tune. To measure the beta function through the acceleration cycle the coil current follows the same program as the main dipoles so the deflection angle, $\Delta\theta$, remains constant and the beam center is measured through the ramp. This capability is still under development.

DETECTOR COMMISSIONING

One known challenge is the horizontal orbit stability in the AGS. All events in the AGS cycle are timed from the t_0 event. Beam injection is at 143ms, the energy ramp ends at 580ms, and extraction is at 1.4s after t_0. During the cycle the beam moves around horizontally over a range up to 6cm. Since the IPM measurement aperture is 3.4cm, the beam is out of this aperture much of the time.

The profile in fig. 5 was taken at t_0+425ms. The beam was outside of the measurement aperture from injection until halfway up the acceleration ramp. The measurement sequence in fig. 6 shows the beam centers and widths from 375ms, when the beam moved into the aperture, until 1.2s. The red crosses show the beam sigmas and the blue circles show the beam centers.

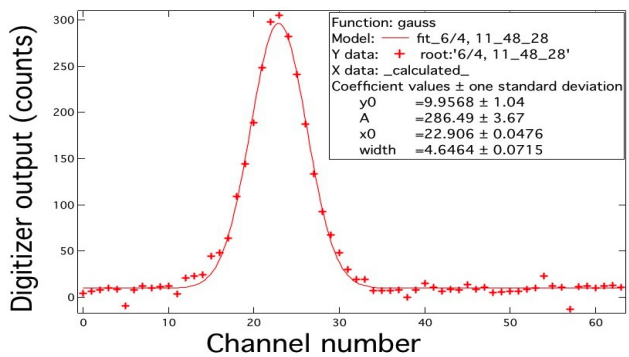


Figure 5: Beam profile during the acceleration ramp.

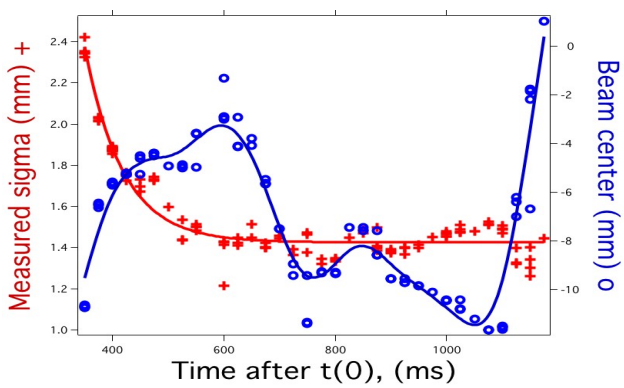


Figure 6: Beam widths (red +) and beam center (blue o) from second half of acceleration ramp to extraction.

Copyright © 2014 CC-BY-3.0 and by the respective authors

A vertical IPM was installed in 2014. This detector is identical to the horizontal except the aperture spacing between the sweep electrode and collector electronics is increased by 5cm to accommodate the need for a larger horizontal aperture. Figure 7 shows horizontal and vertical profile mountain-range plots from one AGS cycle. The horizontal orbit is moving while the vertical orbit is stable.

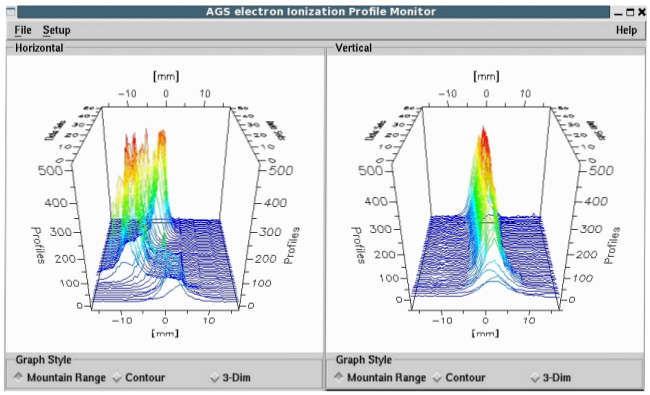


Figure 7: Horizontal and vertical profiles during a single AGS cycle.

The IPM digitizers are triggered at the peak of the beam-bunch signal on each turn. The profiles in fig. 7 are averages over 200 turns. To study injection matching we take several hundred single-turn profiles and fit Gaussians to each turn. With proton beams we need to create a pressure bump to get a statistically adequate number of signal electrons.

Each IPM has a controlled leak that stabilizes the chamber pressure at the desired level. Figure 8 shows data taken during tests. The chamber pressure is raised in steps from $2x10^{-8}$ to $8x10^{-7}$ torr. During actual machine operation the chamber base pressure was $5x10^{-10}$ torr and was raised to 10^{-8} torr for measurements.

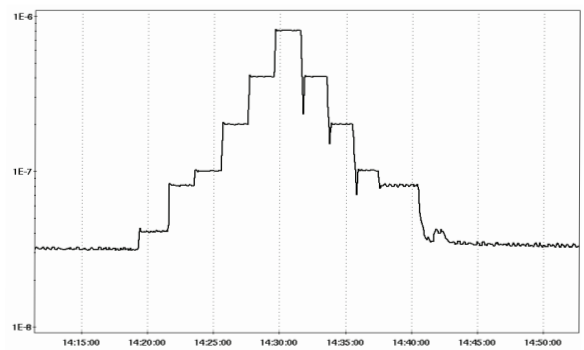


Figure 8: Chamber pressure vs. time for testing of the controlled leak.

Figure 9 is a typical data set showing results of 210 turn-by-turn profile measurements at injection taken with the vertical IPM. The beam was within the aperture of the vertical IPM during the entire cycle, fig. 7. The top plot shows the beam centers vs. turn and the second plot is the FFT of these data. The vertical tune peak is at 0.11. The third plot shows the beam widths vs. turn and the fourth plot is the FFT of these data. There is a weak quadrupole peak at twice the tune frequency and a strong peak at the tune frequency. This pattern is typical of all the measurements taken.

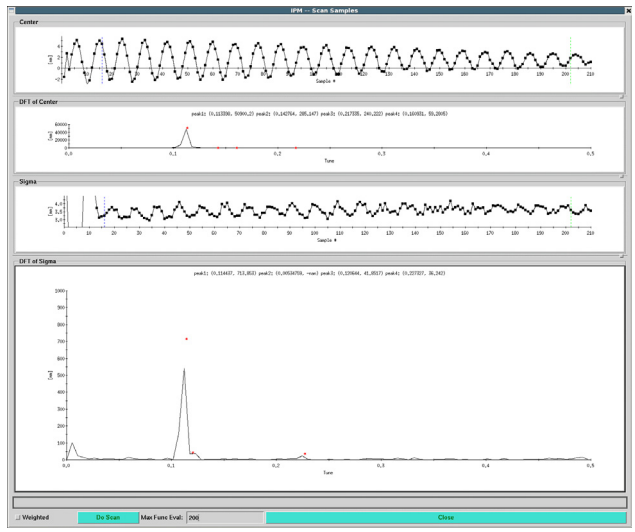


Figure 9: Turn-by-turn of centers (top) and widths (third plot) with FFTs of these data.

SUMMARY

We have installed two RHIC-style IPMs into the AGS. These are operated in turn-by-turn mode for injection studies and multiple averaged profiles measurements for profile evolution up the ramp. The RHIC signal amplifiers are not optimum for AGS operation so we are designing charge-sensitive amplifiers which will integrate over the long AGS bunches. Coils placed on the flux return backleg of the permanent-magnet dipoles will allow measurement of the beta functions.

REFERENCES

[1] http://www.rhic.bnl.gov/

[2] http://accelconf.web.cern.ch/AccelConf/BIW2010/PAPERS/TUPSM010.PDF

Copyright © 2014 CC-BY-3.0 and by the respective authors

ISBN 978-3-95450-141-0

NSLSII PHOTON BEAM POSITION MONITOR ELECTRONICS TESTING AND RESULTS

A. DellaPenna, Om Singh, Kurt Vetter, Joseph Mead, Marshall Maggipinto

Brookhaven National Laboratory, Upton, NY 11973, USA

Abstract

Simulated and real beam data has been taken using the new NSLSII Photon BPM electronics. The electrometer design can measure currents as low as 10's of nanoamps and has an ability to measure a current as high as 300mA. The 4 channel design allows for internal calibration and has both a Negative and Positive bias ability. Preliminary bench testing results has shown excellent resolution.

INTRODUCTION

At NSLSII we have installed a 4 blade design X-ray beam position chamber. The focus of this paper will be on the electronics and tests performed in the lab and with beam using diamond detectors installed @ NSLS beamlines. The design requirements of the electronics were to measure beam currents from 500nA to 1mA. With the Blade Chamber design, signals levels we could expect, were to be in this range. The electronics also required both a positive and negative Bias. The blade current transfer function reveals that without bias we would see ~ 0.5ua for every 1ma of stored beam. This number would double with a bias present. A block diagram is shown in Fig 1. The electronics were designed with the same idea of a AFE (Analog Front End) and a DFE(Digital Front End). As shown in - Fig. 2. This allowed the design to move forward quicker, utilizing what was done with the NSLSII RF BPM. The initial testing used the exact same DFE as the RF BPM electronics, but have since evolved and a new DFE was designed using the ZYNQ FPGA. The electronics PC boards also used the same chassis as the RF BPM.

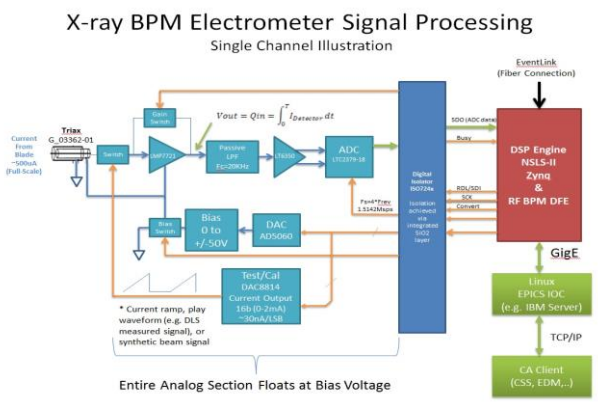


Figure 1: Block diagram of AFE/DFE.

ANALOG ELECTRONICS

The Analog Front End (AFE) was designed as a 4 channel electrometer. The first stage of the design required converting the current into a voltage. The lowest bias current amplifier in the industry was selected as the transimpedance front end. Because of the wide dynamic range mentioned previously 5 gain stages were developed. For the most sensitive gain stage, a range of 10's of nanoamps to 1uA was developed. The other gain stages are 1uA – 10uA, 10uA – 100uA, 100uA -1.2mA and a high gain stage 1mA – 250mA. The switching of the gain stage is done with a very low resistive CMOS switch. A reset switch was also included to discharge the signal before taking a fresh measurement. A simple two pole anti aliasing filter was also included before the digitizer. The digitizer chosen, was a 18bit 1.6Mhz serial device however, a new 20bit version has come out, which has the same footprint and would only require a small software change. Because a Bias was also required we decided to float our entire receiver section. This involved isolators for all signals coming in and out of the receiver. The bias was limited to less than 50V for safety reasons. We ensure that the voltage cannot exceed this by two means. One, our Bias supply control signal is set by a DAC. The reference for this DAC was limited to limit the output to 43V. A 43V Zener diode was also added to provide additional protection. The Xbpm chamber also has a provision for an additional "Electrode". Because of this, the design was modified to allow a bias to also be present on that plate as well. The board also has a provision for on board calibration using a 4 channel 14bit current DAC which allows for testing currents from 100nA to 1.5mA.



Figure 2: AFE and DFE connected together.

To determine what our signal might look like from the blades, a trip to the Diamond Light Source (DLS) was

Copyright © 2014 CC-BY-3.0 and by the respective authors

done. Beam current was very similar to what we would see here at NSLSII (250-300mA). With that current we measured a blade current of 60uA. DLS runs without bias on XBPM blades, causes factor of 2 decrease in signal level from ~ 500ua to 250uA. This is still plenty of signal to obtain a few 10's nanometer resolution at 100- 200Hz processing bandwidth. Looking at a single blade signal directly into a 40Gsps scope terminated into 50ohms, the scope was also band-limited to 1Ghz. We observed that most of the blade signal was "DC" (Fig. 3). Because of these results, most of the testing was done with DC current or pulses. However, Sine and Square wave measurements were also performed.

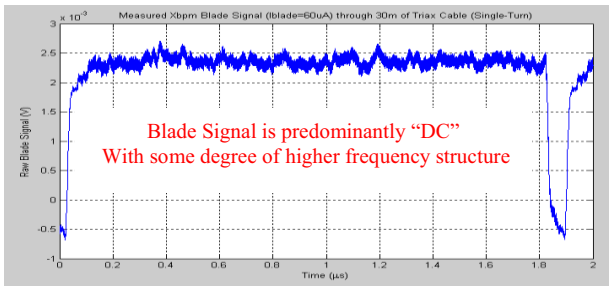


Figure 3: Temporal Blade Signal over 1-turn from Diamond Light source.

LAB TESTING

To prepare for our lab testing a Keithley current source was purchased (model 6621). This model had enough dynamic range to test the full range of our electronics. Also this model would allow both pulse and sweep measurements. These tests would be repeated using the on board current DAC as well. With the 18bit digitizer we had a full scale of ~260k counts. Next step was converting the counts to current for calibration. Our gain stages typically were set up for 0-2.5V out, this equated to 25,000 counts per nanoamp. Starting with the most sensitive gain stage (500nA)We quickly found that our electronics greatly outperformed our design requirements. Our noise floor was -120 dB which allowed us to resolve 10's of nanoamps. Of course at those low currents the resolution would be degraded. Because of the extreme sensitivity we were also able to measure the noise floor of our current DAC. Even with the DAC set to "zero" we would still record 50-60nA. The accuracy and linearity at each gain stage was measured as well as channel to channel coupling. We could not detect any coupling channel to channel with DC and pulse measurements. The error in the measured current compared to actual was less than 1% (Fig. 4) for each gain stage except at the upper and lower limits. Various DC levels were examined along the full range of the electronics. Test data confirmed that data was linear along the data range unless it was taken at the highest or lowest gain stage. To ensure that one would never be in a non-linear range a gain switch would be required.

1 Ua Gain stage		counts /.1uA	ave error
DC current in	digitizer counts		
20nA	-122460	2260	10%
100nA	-103600	25000	0.01%
200nA	-78540	25000	0.01%
400nA	-28440	25000	0.01%
500nA	3460	25000	0.01%
1uA	129300	24000	4%
10uA Gain stage			
1uA	-100900	25000	0.01%
2uA	-75800	25000	0.01%
3uA	-50850	25000	0.01%
10uA	129200	24000	4%
1mA Gain Stage			
.1mA	-103650	22000	0.01%
.2mA	-81650	22000	0.01%
.3mA	-59650	22000	0.01%
.4mA	-37670	22000	0.01%
.6mA	6325	21980	0.01%
1mA	94250	21990	0.01%

Figure 4: Data taken during lab measurements.

BEAM TESTING X28 (NSLS)

Because we don't have our Xray beam lines ready for beam, an alternate beam line for testing was necessary. Fortunately for us here at BNL we still have an active light source at NSLSI. We were given the opportunity to test our electronics on one of the Xray beam lines (X28). The only concern was that detector that we were going to use to get our signal was a Diamond Detector rather than a Blade design. Signal levels were expected to be much larger than we would like. Using filters to bring the signal into our range was done and currents in the 100's of nanoamps were measured. Using the most sensitive gain setting, the results looked very promising however, results showed 3khz component. A possible explanation is the pinhole aperture and the diamond detector were not mounted together, so this component was likely due to relative movement between them. (Fig.5) The Diamond detector was moved relative to the beam in 100um steps from -300um to +300um. First in vertical, then in horizontal. ADC data for the 4 channels was recorded. The sampling rate was 378khz and record length was 32k samples. Sensitivity plots were done to find Kx, Ky. Position plots showed very good correlation compared to motor movements.(Fig. 6)

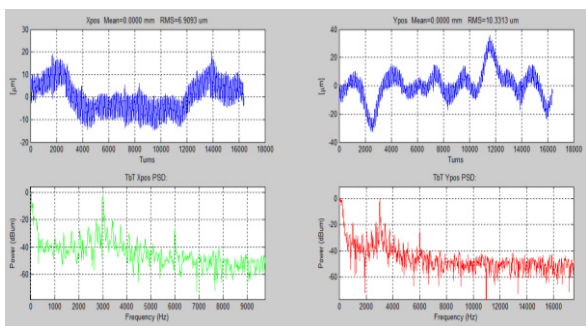


Figure 5: Time domain plot and corresponding PSD sampled at 378khz.

Copyright © 2014 CC-BY-3.0 and by the respective authors

ISBN 978-3-95450-141-0

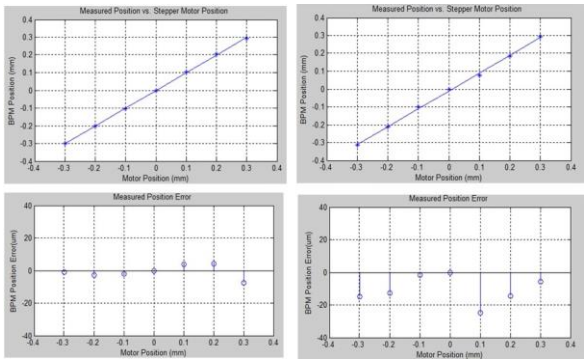


Figure 6: Using the Kx and Ky values computed, the difference over sum position calculation was scaled to mm and plotted.

BEAM TESTING X15 (NSLS)

Within less than one month after testing at X28 another beam line became available X15. This beam line was available for us to test our electronics as well as test other diamond detectors. Two types of diamond detectors were available (Fig. 7). We also knew that the mounting of those detectors was critical for us to take precise measurements. The mounting bracket was adjusted however, it did still create a concern with stability. The white beam tests taken at X15 also allowed us to test a "hotter" beam. Removing all the filters to try to measure the largest beam signal was done. Even with all filters removed the total beam current was still limited by the pin hole aperture which acted like a collimator. Still, we did measure currents in the 100's of micoamps. Numerous scans were done with both detectors to evaluate sensitivity of the detectors. As shown in - Fig. 8. The scans showed that with such a large beam (~350uA , 300um beam) only a small number of steps were achievable due to the aperture.

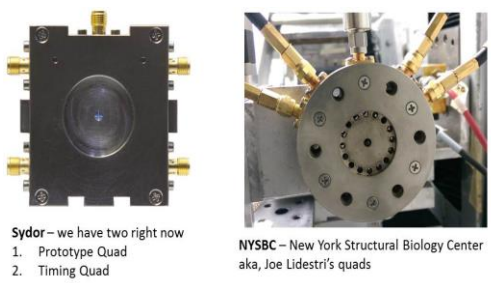


Figure 7: two types of diamond detectors used to test electronics.

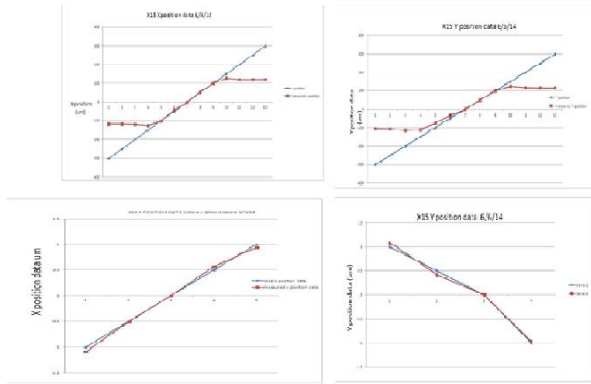


Figure 8: X and Y measurements done with both detectors.

CONCLUSION

The Photon Beam Position Monitor electronics have shown to perform very well in different beam conditions however, our beam results were done with a diamond detector not a blade emission design at NSLS. We expect confident that based on the results from beam testing and the lab results the electronics will perform as expected with the actual Xray chamber. The second revision of the design has just been completed and is undergoing testing now. The changes were very minor and based on bench tests I don't see any degradation in performance. The next step is to work on interfacing the electronics into the control network. Currently I am working on CSS pages as well as an IOC for the control. I look forward to testing on NSLSII.

ACKNOWLEDGEMENTS

Joseph Mead, who has been the backbone of the digital end as well as most of the software used for testing. Kurt Vetter, for his extensive expertise and help in so many aspects. Marshall Maggipinto for his technical help. Erik Muller, John Smedley and Jennifer Bohon for allowing me to test my electronics using their beam lines.

Copyright © 2014 CC-BY-3.0 and by the respective authors

RHIC INJECTION TRANSPORT BEAM EMITTANCE MEASUREMENTS*

J. Huang#, Duke University, Durham, North Carolina 27708, USA
D.M. Gassner, M. Minty, S. Tepikian, P. Thieberger, N. Tsoupas, C. Zimmer
Brookhaven National Laboratory, Upton, New York 11973, USA

Abstract

The Alternating Gradient Synchrotron (AGS)-to-Relativistic Heavy Ion Collider (RHIC) transfer line, abbreviated AtR, is an integral component for the transfer of proton and heavy ion bunches from the AGS to RHIC. In this study, using 23.8 GeV proton beams, we focused on factors that may affect the accuracy of emittance measurements that provide information on the quality of the beam injected into RHIC. The method of emittance measurement uses fluorescent screens in the AtR. The factors that may affect the measurement are: background noise, calibration, resolution, and dispersive corrections. Ideal video Offset (black level, brightness) and Gain (contrast) settings were determined for consistent initial conditions in the Flag Profile Monitor (FPM) application. Using this information, we also updated spatial calibrations for the FPM using corresponding fiducial markings and sketches. Resolution error was determined using the Modulation Transfer Function amplitude. To measure the contribution of the beam's dispersion, we conducted a scan of beam position and size at relevant Beam Position Monitors (BPMs) and Video Profile Monitors (VPMs, or "flags") by varying the extraction energy with a scan of the RF frequency in the AGS. The combined effects of these factors resulted in slight variations in emittance values, with further analysis suggesting potential discrepancies in the current model of the beam line's focusing properties. In the process of testing various contributing factors, a system of checks has been established for future studies, providing an efficient, standardized, and reproducible procedure that might encourage greater reliance on the transfer line's emittance and beam parameter measurements.

INTRODUCTION

The beam emittance measurements that were performed in various sections along the 580 m long AtR transfer line rely on a series of profile monitors equipped with mostly CCD cameras [1] to help determine the values of the beam parameters prior to injection into RHIC. Two sections of the AtR transfer line are being used to make beam emittance and beam parameter measurements between the machines that are of particular importance given that lower emittance allows for more frequent collisions, in turn producing a desirably higher luminosity.

The beam emittance and beam parameters' measurements are derived from measurements of the horizontal and vertical beam sizes at three separate locations together with the known strengths of the magnets in the AtR [2, 3].

*Work supported by the auspices of the US Department of Energy
julia.y.huang@duke.edu

By testing the sensitivity of emittance on factors such as calibrations, resolution, dispersion, and noise under uniform conditions, a straightforward method of measurement that can be applied to future studies was established.

OFFLINE EMITTANCE ANALYSIS

During the RHIC run we collected beam profile data from a variety of flags in the AtR line that were measured under different conditions. This beam profile information was logged for later use because a majority of our analysis was performed offline after the run cycle ended. In order to calculate and test the dependence of emittance to different parameters, we used the logged data and a script file that reads the saved input files and outputs the measurements in the form of the standard deviation (sigma) of the beam profiles. Given that emittance has a dependency on horizontal and vertical sigma values, we tested each potential factor by applying its impact, measured as a ratio or multiplier, to sigma. After editing a file of sigma's to adjust for the factor of interest, we ran the emittance script to determine the corrected measurements and re-evaluate the emittance.

INITIAL CONDITIONS

The beam emittance and beam parameter measurements in the AtR transfer line rely on VPMs which are plunged in and removed from the beam pipe through the FPM controls application which is an interface that allows users to alter configuration settings while viewing immediate results in one of four equally capable frame grabbers, or viewing windows. While inserted, the beam hits and illuminates the phosphor (Gd_2O_2S:Tb) screen; the image data is displayed and automatically logged. The 12 flags are distributed along the transfer line and separated into four sections named the U, W, X, and Y lines. Based on location, flags of interest for this study are UF3, UF4, UF5, WF1, WF2, and WF3 of the U and W-lines, corresponding to the transfer line between the AGS up to the switching magnet that deflects beams into either of the two RHIC accelerators.

The goal of our work was to test factors that affect emittance measurements as a means to produce an efficient method of acquiring accurate data during future run cycles. Before delving into these properties, however, ideal and uniform initial conditions were necessary. The FPM application offers a user-controlled environment for optimizing measurement conditions by way of optional background subtraction, intensity adjustment, and Range of Interest (ROI) selection. Previous research has elaborated on the potentially harmful effects of imperfect background subtraction and on the advantages of the ROI

Copyright © 2014 CC-BY-3.0 and by the respective authors

ISBN 978-3-95450-141-0

function [4]. Background subtraction was therefore switched off for all scans.

Image intensity settings relate to gain and offset, or contrast and brightness, respectively. Using a python tape sequence, we acquired and plotted data sets to determine the effects of varying offset and gain settings on vertical and horizontal sigma and center of the beam profile. As an example, Fig. 1 illustrates the ideal offset range of 242-252 for which sigma remains constant. To avoid saturation, values on the lower end of this range were considered ideal. In the second scan, the gain was confirmed as having little effect on sigma while remaining in the viable range of 80-160. To confirm that accurate beam parameters were independent of beam intensity variations, we performed a scan of beam intensity and employed neutral density filters to conclude that there was no dependence of the beam profile for very low intensities and a maximum charge of 2 e11 protons per bunch.

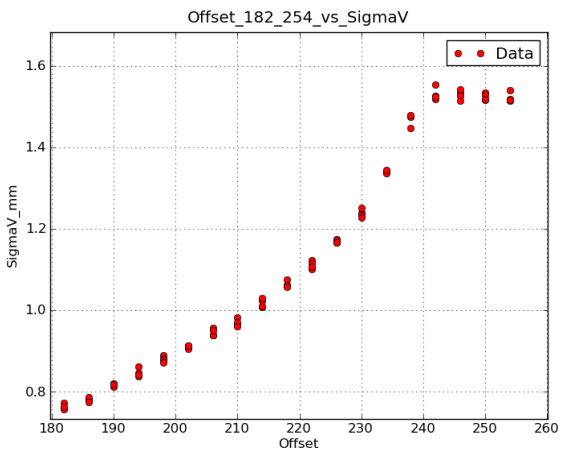


Figure 1: UF4 Flag with 1E11 protons per pulse, offset vs. vertical sigma intensity plot.

CALIBRATION

When discussing highly precise machinery and technology, it is reasonable to expect natural changes in positioning or accuracy of individual monitors and camera lenses. To counter this inevitable adjustment, we conducted a recalibration of flags in the U and W-lines using screen fiducial drawings from the commissioning of the transfer line. Marks on each drawing correspond to those on the phosphor screen of each flag and the comparison of theoretical and measured distances on these screens produced a corrective ratio.

Precise measurements of distance on flag screen images required a saved "bitmap" image from FPM. Since these images were Unix executable files, using an additional image processing software tool was necessary. ImageJ [5], a freeware available online, recognizes this file type, and offers the capability of viewing coordinate pixels on any imported image. Using the line tool and pixel display in ImageJ, we calculated the mm/pixel relationship to match existing calibrations using appropriate conversion factors.

By taking a ratio of the updated calibration over the existing value for each flag, we obtained corrective ratios. Since the measurement of interest in this study was emittance, we multiplied these ratios by measured sigma's from the initial scan to derive input data that demonstrated calibration effects on emittance measurements. These new values are shown in Fig 5.

PROFILE MONITOR RESOLUTION

The resolution of the AtR video profile monitor system is measured using a translation of the Modulation Transfer Function (MTF) for a bitmap under ideal intensity conditions with no suppression of the baseline. MTF is defined in equation 1.

$$MTF = \frac{(Peak - Valley)}{(Peak + Valley)} \tag{1}$$

Plot profiles of ruler sections on bitmaps in ImageJ provided average peak and valley values for each flag of interest. Resulting MTF amplitudes (contrast) ranged from 0.214 to 0.445, with four flags falling short of the ideal ratio 0.33, which corresponds to 200 micron resolution. As a result, we used a "PatternCalc" Excel program to generate a resolution coefficient, or Line Spread Function, from the contrast percentage. Using the adjusted input files, we corrected the emittance measurements based on the resolution of each flag.

DISPERSION

In the fall 1995 commissioning of the AtR transfer line, an early attempt to measure dispersion was made by adjusting magnet strengths to different extraction energies [6]. Unfortunately, too many influential variables were involved, thereby compromising the validity of results.

During the 2013 run cycle, we performed a dispersion scan at BPMs and flags by changing the AGS extraction frequency by 1 Hz steps for a range of -5 Hz to +5 Hz (Fig. 2). A correlation plot of this energy change ($G\gamma$) and BPM position (Fig. 3) provides a slope equal to the dispersive contribution [eq. 2a-2d]

$$x = a \cdot G\gamma + b \tag{2a}$$

$$a = \frac{\partial x}{\partial G\gamma} \tag{2b}$$

$$Dx = \frac{\frac{\partial x}{\partial G\gamma}}{G\gamma} \tag{2c}$$

$$Dx = a \cdot G\gamma \cdot 10^{-6} \tag{2d}$$

where $G\gamma$ is a convenient energy scale, G is the anomalous part of the proton magnetic moment (1.7928), γ=E/m with E as beam energy and m as proton mass. Equation 2d represents horizontal dispersion in meters.

Similarly, the dispersion at each flag was calculated with a correlation of $G\gamma$ at each flag plotted against

Copyright © 2014 CC-BY-3.0 and by the respective authors

position (horizontal center in pixels). This method required additional conversion factors to apply previously determined calibrations and convert units from pixels to meters. Dispersive contribution was measured using two methods at two locations for assurance, but this preferred method was applied to each flag location for additional corrective values.

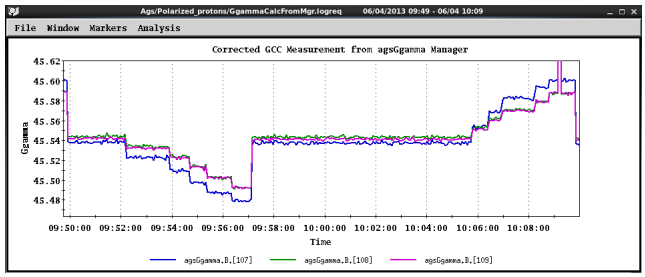


Figure 2: $G\gamma$ values for each time/frequency step.

Interestingly, the introduction of dispersive corrections had negligible effects on emittance, suggesting future studies can plausibly ignore this correction as shown in Fig 5.

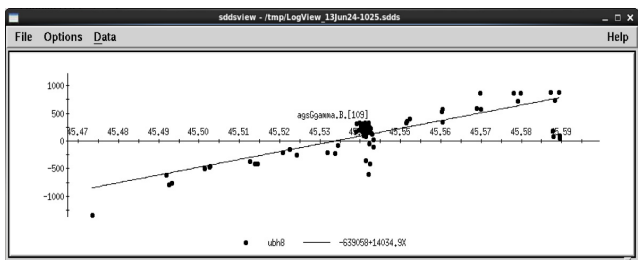


Figure 3: $G\gamma$ vs. BPM position fitted correlation plot.

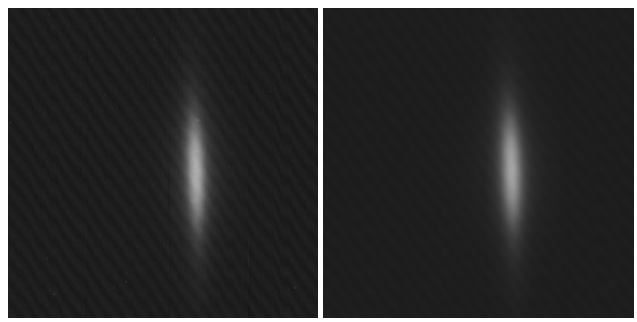
BACKGROUND NOISE

Figure 4a shows a high frequency noise pattern, or electromagnetic interference (EMI) drifting diagonally through the digitized image. This pattern is likely the result of upper harmonics in the switching power supply coupling to our analog video signal, but time has not yet been allocated to study this for confirmation. Background subtraction as a function in FPM was deemed overpowering in the 2011 study [4], but an alternative could be use of software filters like the Gaussian blur. This low pass filter blurs the EMI noise while maintaining integrity of the beam spot, in effect removing disruptive frequencies from raw data as shown in Fig 4b.

In this study, EMI noise suppression is performed on the bitmap of each flag with the most noticeable noise for optimal corrections in emittance. We use ImageJ to obtain initial standard deviations as well as new values after applying a Gaussian blur with a tested sigma (radius) of 3.0. A ratio of initial to final standard deviation produces the corrective ratio, which is then multiplied by sigma values already corrected for the previous three factors. Refer to Figure 5 for noise-corrected emittance results.

RESULTS/CONCLUSIONS

Beam emittances and beam parameters were measured at two different intensities along both horizontal and vertical planes to test the effects of calibration, resolution, dispersion, and EMI noise corrections. Both lower intensity and noise suppressed beams generally produced lower emittance measurements, whereas calibration and resolution corrections adjusted emittance on a case-by-case basis. Since our data collection method demonstrates no immediate problems, it is possible that the existing model of the magnetic optics of the transport line holds some inaccuracies. Future studies might then benefit from closer examination of actual magnet performance between the flags, together with the code used to evaluate emittance and the beam parameters.



Figures 4a-4b: WF2 bitmap with and without Gaussian blur of radius 3.0. Image at right is after the filter is applied.

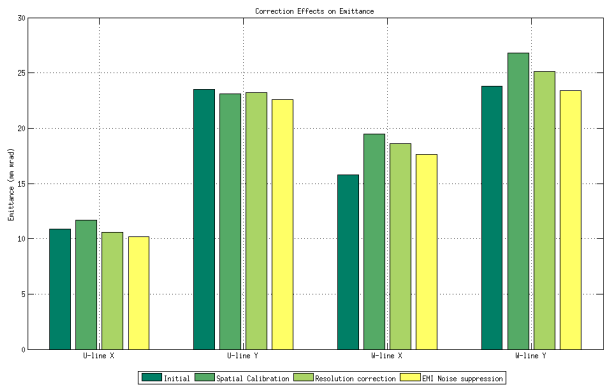


Figure 5: Average horizontal and vertical emittance measurements (in mm-mrad) for varying factors at U and W-lines. Dispersive corrections are not shown because they are negligible.

ACKNOWLEDGMENTS

Thanks to the operations staff in the Main Control Room for their cooperation and help with data acquisition during the 2013 run cycle.

Copyright © 2014 CC-BY-3.0 and by the respective authors

ISBN 978-3-95450-141-0

REFERENCES

[1] R. L. Witkover, "Design of the Beam Profile Monitor System for the RHIC Injection Line", TPB26, PAC'95, Dallas, Texas, USA, (1995).

[2] N. Tsoupas et al., "A Computer Code to Measure the Beam Emittance and Beam Parameters of the ATR Line", BNL C-A/Accelerator Physics note 42, March 2001.

[3] M.C. Ross et al., "Automated Emittance Measurements in the SLC", p. 725, PAC'87, Washington DC, USA, (1987).

[4] P. Thieberger et al., "Baseline Suppression Problems for High Precision Measurements Using Optical Beam Profile Monitors", MOP208, PAC'11, New York, USA, (2011).

[5] http://imagej.nih.gov/ij/

[6] T. Satogata et al., "Physics of the AGS-to-RHIC Transfer Line Commissioning", MOP006G, EPAC'96, Sitges, Spain, (1996).

Copyright © 2014 CC-BY-3.0 and by the respective authors

INSTRUMENTATION FOR THE PROPOSED LOW ENERGY RHIC ELECTRON COOLING PROJECT WITH ENERGY RECOVERY*

D. M. Gassner #, A. Fedotov, R. Hulsart, D. Kayran, V. Litvinenko, R. Michnoff, T. Miller, M. Minty, I. Pinayev, M. Wilinski, BNL, Upton, NY 11973, USA

Abstract

There is a strong interest in running RHIC at low ion beam energies of 7.7-20 GeV/nucleon [1]; this is much lower than the typical operations with 100 GeV/nucleon. The primary motivation for this effort is to explore the existence and location of the critical point on the QCD phase diagram. Electron cooling can increase the average integrated luminosity and increase the length of the stored lifetime. A cooling system is being designed that will provide a 30 – 50 mA electron beam with adequate quality and an energy range of 1.6 – 5 MeV. The cooling facility is planned to be inside the RHIC tunnel. The injector will include a 704 MHz SRF gun, a 704 MHz 5-cell SRF cavity followed by a normal conducting 2.1 GHz cavity. Electrons from the injector will be transported to the Yellow RHIC ring to allow electron-ion co-propagation for ~20 m, then a 180 degree U-turn electron transport so the same electron beam can similarly cool the Blue ion beam. After the cooling process with electron beam energies of 1.6 to 2 MeV, the electrons will be transported directly to a dump. When cooling with higher energy electrons between 2 and 5 MeV, after the cooling process, they will be routed through the acceleration cavity again to allow energy recovery and less power deposited in the dump. Special consideration is given to ensure overlap of electron and ion beams in the cooling section and achieving the requirements needed for cooling. The instrumentation systems described will include current transformers, beam position monitors, profile monitors, an emittance slit station, recombination and beam loss monitors.

INTRODUCTION

The Low Energy RHIC electron Cooling (LEReC) project is presently in its design stage and scheduled to begin commissioning components in 2017, with operations planned for 2018-19. The electron and ion parameters are shown in Table 1 and 2. This will be the first bunched beam electron cooler and the first electron cooler in a collider. The goal is to achieve an efficient cooling system for Au+Au collision beams at 7.7, 11.5 and 20 GeV/u in the center of mass corresponding to electron energies of 1.6, 2.7 and 5.0 MeV. An effective cooling process would allow us to cool the beams beyond their natural emittances and also to either overcome or to significantly mitigate limitations caused by intrabeam scattering and other effects. It also would provide for longer and more efficient stores, which would result in significantly higher integrated luminosity.

Cooling of ion and hadron beams at low energy is also of critical importance for the productivity of present and future Nuclear Physics Colliders, such as RHIC, eRHIC and ELIC.

Table 1: Electron Beam Parameters

Electron Parameters	
Electron Beam Energy	1.6-5 MeV
Electron Bunch Charge	100-300 pC
Electron Average Current	30-50 mA
RMS Norm Emittance	≤ 2.5 mm mrad
Bunch Rep Rate	704 MHz
Bunch Train Rate	9.1 MHz
RMS Energy Spread	$\leq 5 \times 10^{-4}$
RMS Bunch Length	100 ps
RMS Trans beam size	2-4 mm
Max power with ER	100 kW

Table 2: RHIC Ion Beam Parameters

Ions with gamma = 4.1	
Particles per Bunch	0.75×10^{9}
Peak Current	240mA
RMS Norm Emittance	2.5 mm mrad
Rep Rate	75.9 kHz
RMS Energy Spread	$\leq 5 \times 10^{-4}$
RMS Bunch Length	3.2m
RMS Trans beam size	4.3 mm
Space charge tune shift	0.02

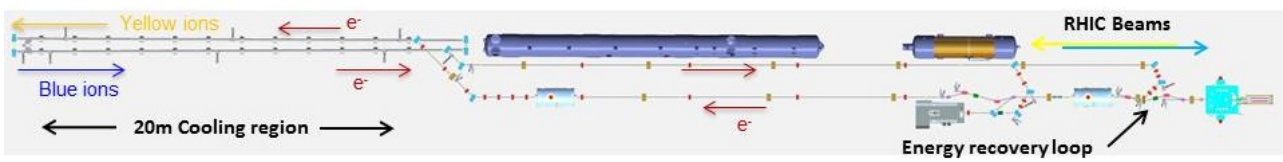


Figure 1: LEReC beam line layout for electron cooling with energy recovery. The Blue and Yellow adjacent 20 m ion cooling beam lines shown at left are located in a RHIC region without superconducting magnets.

* This material is based upon work supported by the U.S. Department of Energy, Office of Science, Brookhaven National Laboratory under Contract No. DE-AC02-98CH10886.

gassner@bnl.gov

ISBN 978-3-95450-141-0

Copyright © 2014 CC-BY-3.0 and by the respective authors

Electron Guns and Bunch Patterns

We are moving forward with two electron gun alternatives to ensure a reliable source is available for the LEReC project. We are planning to purchase a copy of the latest design 500 kV DC electron gun [2] from Cornell as a backup plan if the BNL ERL 704 MHz SCRF gun [3] does not meet the LEReC schedule or beam requirements. If the DC gun is chosen as the electron source, one option is to use the cavity of the SCRF gun as a booster.

An example of co-propagating electron-ion bunch patterns during the cooling process with 4.1 gamma ions are shown in Figs. 2 and 3. For the highest ion energy of 10.7 gamma we can place 18 electron bunches on a single ion bunch.

Electron Beam Path for Cooling

The LEReC project is planned to be carried out in two phases. The first phase will use 1.6-2MeV electrons to cool 7.7-9.1 GeV gold ions. The electron beam path for this phase will be from the gun through a 5-cell SCRF Linac and 2.1 GHz cavity, and then ~20 m of beam transport to the RHIC beam line, cool both RHIC beams, and then back to a dump.

The instrumentation proposed for the original LEReC design without energy recovery can be found in this reference [4]. It has recently been decided to use many of the BNL R&D Energy Recovery Linac (ERL) [5] components in the LEReC project for a variety of reasons primarily driven by equipment cost savings.

During phase 2 scheduled for the following year, the plan is to modify the upstream beam lines to include two zig-zag emittance compensation regions, and install an additional beam transport to allow energy recovery and therefore reduced power deposited in the dump. This configuration is shown in Figs. 1 and 4.

Electron Beam Merging and Splitting

There will be two zig-zag emittance compensation beam transports in injection portion of the LEReC facility when the energy recovery upgrade is installed. They are located upstream and downstream of the SCRF 5-cell 704 MHz cavity as shown in Fig. 4. Both zig-zags are similar, they each utilize four dipoles.

The main function of the merger upstream of the Linac is to combine two beams with different energies to allow

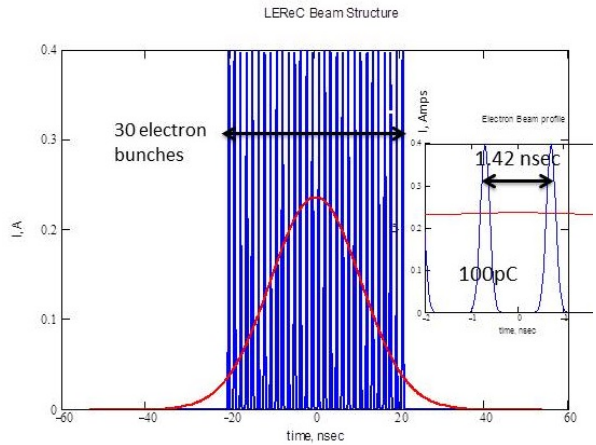


Figure 2: Thirty electrons bunches (blue, 1.42 ns apart) overlap a single ion bunch (red). Example for ion long bunches with 9 MHz RHIC RF at gamma = 4.1.

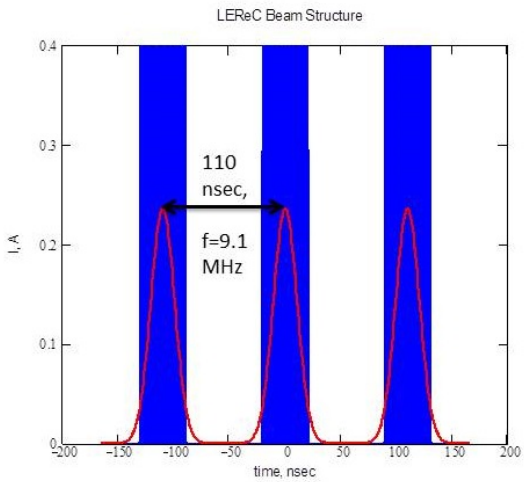


Figure 3: Electron bunches (blue) overlap ion bunches (red) spaced 110ns apart utilizing the 9 MHz RHIC RF.

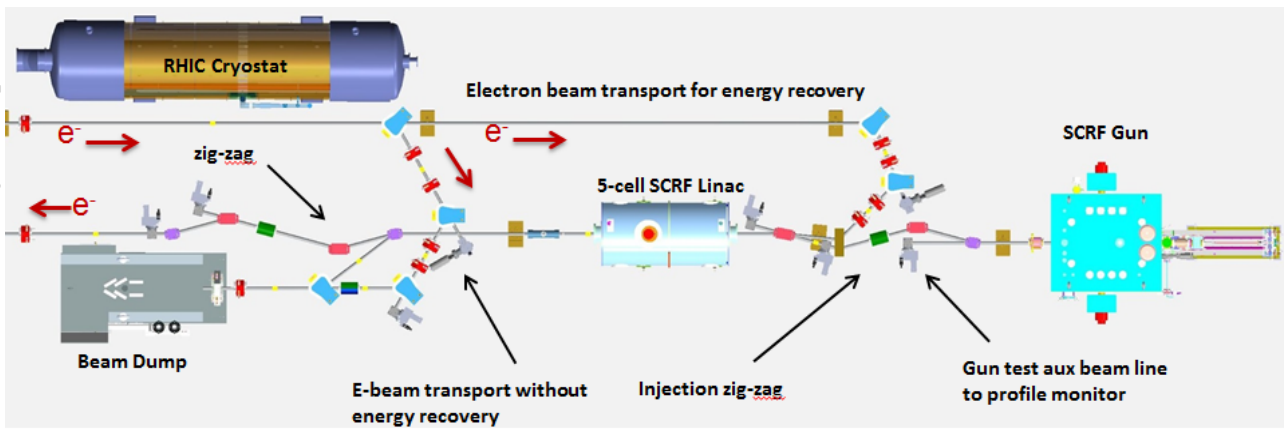


Figure 4: LEReC beam line detailed layout showing additional beam transport and two zig-zag matching sections that allow recirculation through the Linac for energy recovery when cooling with 2 to 5 MeV electrons.

Copyright © 2014 CC-BY-3.0 and by the respective authors

ISBN 978-3-95450-141-0

energy recovery, and conversely the main function of the separator downstream of the Linac is to extract the low energy beam and steer it towards the dump and allow the higher energy beam to continue while maintaining its emittance. The zig-zag for existing ERL configuration was proposed to preserve the emittance of the low-energy high-charge electron beam [6].

Since each beam has an energy spread a single dipole would not only separate the high and low energy beam but also introduce a transverse growth of emittance, proportional to the initial energy spread. By matching the "dispersion function" to be zero after the merge this is avoided.

The combination of low energies (less than 10 MeV) and high bunch charge is another effect that blows up the emittance. The space charge forces repel particles from each other. Hence, the particles in the head of the bunch gain energy, while the particles at the tail of the bunch lose energy. If an electron changes energy inside the bump then the dispersion matching is disrupted. However, by adding a second bump in the opposite direction the disruption in the first bump is cancelled in the second bump. A zig-zag is the compact form of two bumps.

ELECTRON BEAM DIAGNOSTICS

The electron beam diagnostics systems will provide measurements to:

- Commission the 704 MHz SCRF gun with a maximum energy of 2 MeV beam and commission the SCRF Linac.
- Ensure the beam transport of electron bunches without significant degradation of beam emittance and energy spread throughout the 1.6 to 5 MeV energy range.
- Ensure low transverse angular spread for the electron beam in the cooling section.
- Ensure that the quality of the beam is preserved through the entire beam transport and both cooling sections.

The preliminary distribution of the beam diagnostics is shown in Figs. 7 and 8.

Electron Beam Position Monitors

As we are still in the early stages of the system design, the development of a detailed commissioning plan is still underway. There are 24 dual plane position monitor pick-up stations planned. We plan to reuse the 9 mm buttons from ERL and purchase additional 15 mm buttons from MPF Inc. These will be installed at key locations along the ~70 meter beam line. The proposed BPM locations and quantity may vary as the simulations and specifications evolve. We plan to use Libera Brilliance Single Pass [7] electronics from Instrumentation Technologies; these will also be repurposed from the ERL project. The allowable transverse error for a single pass of 100 pC bunch is 10 microns (angular resolution of one microradian with a cooling section length of 20 meters). The angle between the electron and ion beam should not be more than 50 microradians, this specification comes from the limitation of 50 microradian difference over the 2 m distance between cooling section solenoids, and it allows 100 microns transverse deflection. Averaging position data over multiple passes and increasing number of bunches will increase the measurement accuracy.

To measure the short electron bunch train position while it co-propagates with the long ion bunches, electronics with an input band-pass filter frequency of 500 MHz can be used so the signal from the ion bunches (3 m rms bunch length, 7.5 e8 ions) that have lower frequency components will be suppressed. These units will require lower band-pass filter frequency (10-100 MHz). The effect of the electron beam can be subtracted from the data from ion BPM receivers. Calibration can be done by running each beam independently. The electron-ion beam transverse alignment in the cooling section needs to be ~2% of the 5 mm electron beam sigma, or ~100 microns.

We plan to utilize new in-house designed VME based BPM electronics modules in the cooling region, these are presently under development. These modules are based on a Xilinx Zynq processor programmable logic array combination which allows for greater flexibility in designing custom processing algorithms for a variety of bunch frequencies and types. The present design incorporates 500 MHz and 707 MHz band pass RF filters in the analog input section which are suited for electron beam measurements. A different configuration also allows the use of a 39 MHz low pass filter instead for hadron beam measurements. A set of four A/D converters can be clocked at rates up to 400 MHz and provide four channels of measurement on each VME board which will correspond to each dual-plane BPM module. Each VME module has its own Ethernet connection to the network which allows direct access to data from standard Controls software tools. The first series of hardware boards have been received at BNL and are currently under testing and evaluation.

Electron Beam Transverse Profile Monitors

Transverse beam profiles will be measured at a variety of pneumatically plunging stations using 0.1 X 30 mm YAG:Ce screens. Images from the YAG screens are transported through a mirror labyrinth to a GigE CCD camera in a local enclosed optics box.

A pair of specially designed YAG dipole profile monitors [8] will be provided in the zig-zag transport sections. This design is necessary due to tight space constraints. They will plunge into the beam path inside of the two 30º y-shaped dipole vacuum chambers as shown in Figs. 5 and 6. These instruments are presently being designed and fabricated by Radiabeam Technologies. Precise YAG screen positioning will be provided by a stepper motor actuated plunging mechanism, with a 4-inch stroke, that has a long YAG screen holder that extends into the dipole magnet chamber through an auxiliary port to intercept the electron beam. The beam can be imaged at different places on the crystal including the edge depending on the plunge depth. This can be useful for semi-destructive beam halo monitoring.

ISBN 978-3-95450-141-0

Copyright © 2014 CC-BY-3.0 and by the respective authors

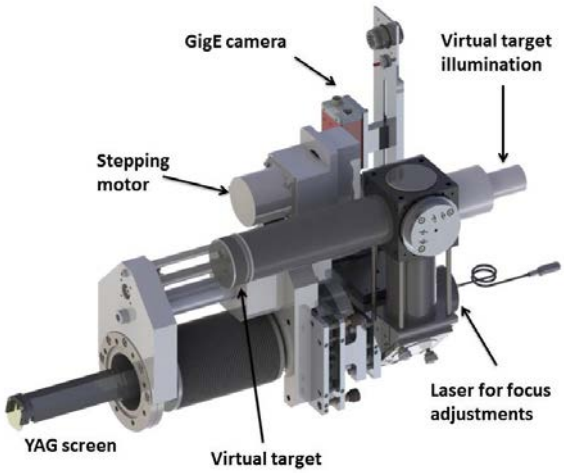


Figure 5: Dipole Profile Monitor assembly, drawing courtesy of Radiabeam Technologies.

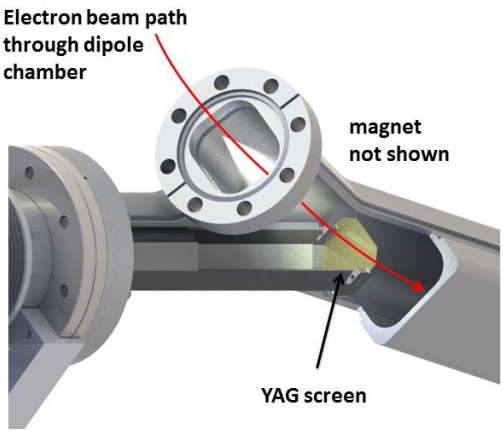


Figure 6: Dipole Profile Monitor shown with YAG screen inserted into the beam path, drawing courtesy of Radiabeam Technologies.

Electron Beam Emittance

There are several techniques planned to measure beam emittance. The expected rms normalized emittance is 2.5 mm-mrad. Several emittance slit stations will be used to measure the electron beam emittance. The first station with be located just downstream of the gun to ensure the gun performance meets the requirements. The second station will be located just before the electron beam merges with the ion beam to ensure the emittance is adequate for cooling. These stations will be comprised a multi-position plunging tungsten mask with a slit pattern upstream of a YAG profile monitor. A calibration laser will be installed upstream of each slit mask to ensure the slits are properly aligned with the electron beam.

Electron Bunch Charge and Current

Bunch-by-bunch and bunch train charge will be measured by a Bergoz [9] in-flange Integrating Current Transformer (ICT). Beam charge signals will be processed by standard BCM-IHR Integrate-Hold-Reset electronics feeding a beam-synch triggered digitizer. In order to increase the range of commissioning modes that this system will be compatible with, the 10 kHz measurement rate option was included. The ICT will be installed in the upstream portion of the electron transport near the gun.

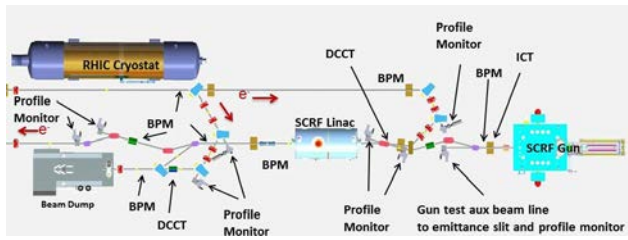


Figure 7: Electron beam diagnostics in the injection transport from the SCRF Gun to the 5-cell SRF Linac, and the transport to the beam dump after energy recovery.

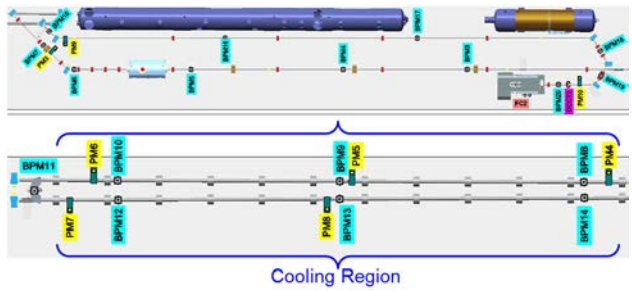


Figure 8: Top, BPMs (blue) and profile monitors (yellow) in the transport to and from the cooling region. Bottom, diagnostics are shown in the cooling and U-turn region.

There will be a pair of Bergoz NPCT DCCTs configured in differential mode, installed to measure the absolute beam current and transport efficiency, one near the injector and one near the dump. We plan to employ a similar system that is presently being designed for use at the BNL ERL [10].

The low and high power dumps will be electrically isolated to allow direct current measurements of the collected beam using current meters or gated integrators.

Electron Beam Loss Monitors

Efficient beam transport needs to be maintained and protection against possible damage to the equipment needs to be provided in the electron beam transport and in the common sections. Photomultiplier tube (PMT) based loss monitors are a candidate to be the primary loss detector and will be installed at a variety of locations. The design of the detector and signal processing electronics [11] are based on ones developed at Jefferson Lab and used at CEBAF. At the LEReC facility we plan to use the Hamamatsu R11558 PMT in these loss detectors. Based on experience we will obtain at the ERL, we also plan use some long heliax cable detectors and RHIC style ion chambers.

Electron Beam Stability

The stability requirement for bunch intensity variations is better than 7%. Shot-to-shot charge variations at this level can be monitored with an ICT and beam charge monitor electronics by Bergoz which has a dynamic range

Copyright © 2014 CC-BY-3.0 and by the respective authors

ISBN 978-3-95450-141-0

over 800. The bunch phase jitter requirement can tolerate 100 ps which is comparable the 100 ps rms electron bunch length we are planning. We have measured the RHIC ion beam jitter to be less than 25 ps.

Ion Clearing

The preliminary design included plans for ion clearing electrodes in the beam transport line every 5m. An alternative clearing method could be produced by simply making few microsecond clearing gap in electron bunch current. We will have a 100 ns gap between electron bunch trains, which may be enough to clear away unwanted ions. Future simulations will confirm the best strategy to use with the LEReC beam parameters to avoid the impact of ionized residual gas that is considered a source for instabilities in accelerators.

Energy Spread, Halo, and Bunch Length

Simulations and tracking will be done to determine the best method and location to measure and collimate the beam halo. Early determinations show a preference to locating halo related instruments after the first bend.

By accelerating off-crest in the accelerating cavity and viewing the transverse beam profile images on a downstream YAG screen we will get information about the bunch length from the measured growth of the beam energy spread.

Electron-Ion Energy Match

The diagnostics and method to match the electron energy to the ion energy has to be detailed. The strategy for synchronization between the bunches needs to be determined, an early estimate of accuracy/resolution of ~10 ps. We will need a transducer that can provide this level of accuracy, a BPM pick-up may be useful depending on the type chosen.

Beam Dump Diagnostics

The 1 MW water cooled dump [12] constructed for the BNL Energy Recovery Linac project will be repurposed to absorb the 100 kW LEReC electron beam power. Typically a set of distributed dump vessel temperature sensors would be used to monitor and help avoid any concentrations of dumped beam power and damage. This dump is designed with a dual layered water cooling jacket to provide a forward and return cooling path making distributed spatial temperature monitoring impractical.

A variety of diagnostics will be provided upstream of the dump to monitor the incoming beam in addition to loss monitors around the dump vessel to measure the radiation distribution pattern from the dumped beam [13]. During dump commissioning and while operating at low power, x-rays will be detected by set of 7/8" heliax ion chambers that encage the dump both in circular and axial directions as shown in Fig. 9. When running higher power levels RHIC style ion chambers installed outside of the dump shielding layer will be used because the internal heliax ion chambers will likely saturate.

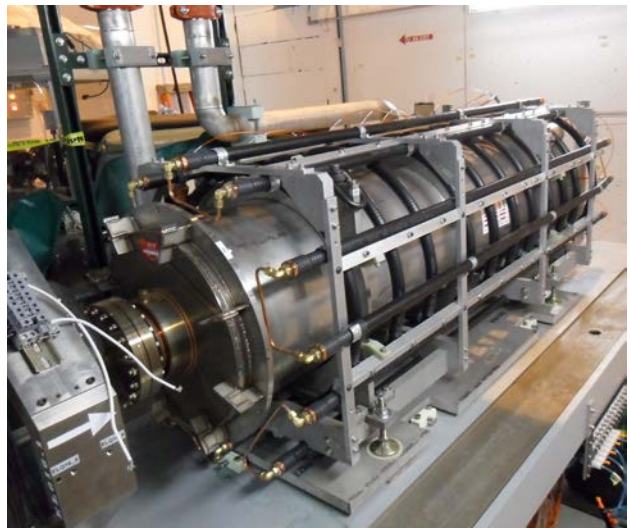


Figure 9: Electron beam dump shown with heliax cable ion chambers installed to monitor x-ray levels and ensure uniform distribution of the collected beam.

RHIC ION BEAM DIAGNOSTICS

The primary diagnostics for monitoring of the cooling process will be the RHIC Wall Current Monitor [14] and Schottky monitors. A new wideband Schottky pick-up is being designed for improved monitoring of the longitudinal stochastic cooling characteristics that may also be useful for LEReC. The valuable experience gained using these instruments during the successful stochastic cooling commissioning and Coherent electron Cooling Proof of Principle [15] will be applied to the LEReC effort.

The existing RHIC DX BPMs will be used to center the 10^9 ions per bunch, 2.5 mm-mrad rms norm emittance ion beam in the cooling regions. The RHIC closed loop orbit system will ensure ion beam position stability.

Recombination Measurement

In order to measure the number of ions that have accumulated electrons while co-propagating with the electron bunches during the cooling process, a detector will be located near the place where simulations determine these ions with non-ideal charge state will be lost. This is most likely to be near the RHIC collimators. The detector planned is a scintillator coupled to a photomultiplier tube and signal processing electronics (counting) and/or pin diode loss monitors, both types can provide scalar data that can be logged versus time. A calculated estimate of the recombination rate is about 5 e6 ions/sec.

ACKNOWLEDGMENTS

The authors would like to thank LEReC team for the concept development, simulations and support, J. Fite for engineering support, J. Kewisch for helpful discussions, Marcos Ruelas from Radiabeam, and S. Picataggio for the beam line drawings.

ISBN 978-3-95450-141-0

Copyright © 2014 CC-BY-3.0 and by the respective authors

REFERENCES

[1] A. Fedotov et al., “Bunched Beam Electron Cooler for Low-Energy RHIC Operation”, PAC2013, TUOAA1, http://jacow.org

[2] B. Dunham et al., “Performance of the Cornell High-Brightness, High-Power Electron Injector” IPAC2012, MOOAA01.

[3] D. Kayran et al., “First Test Results from SRF Photoinjector for the R&D ERL at BNL” IPAC2014, MOPRI064.

[4] D. Gassner et al., “Instrumentation for the Proposed Low Energy RHIC Electron Cooling Project”, IBIC 2013, TUPF24.

[5] D. Kayran et al., “Status of High Current R&D Energy Recovery Linac at BNL”, PAC2011, THP006.

[6] D. Kayran et al., “Merger System Optimization in BNL’s High Current R&D ERL” Proceeding of PAC 2007, THPAS097.

[7] http://www.i-tech.si/

[8] D. Gassner et al., “Status of the BNL ERL Instrumentation”, ERL2013, PS11

[9] http://www.bergoz.com/

[10] P. Cameron et al., “Differential Current Measurement in the BNL Energy Recovery Linac Test Facility”, Newport News, Virginia ERL2005.

[11] T. Allison et al., "New Beam Loss Monitor For 12GeV Upgrade”, ICALEPCS2009, WEP092.

[12] A. Hershcovitch “R&D ERL: Beam Dump”, PAC99, C-A/AP/#378 January 2010.

[13] T. Miller et al., “Instrumentation Designs for Beam Distribution Measurements in the ERL Beam Dump at BNL”, ERL2013, PS14, Sept 2013.

[14] P. Cameron et al., “The RHIC Wall Current Monitor System”, PAC1999, WEA116.

[15] D. Gassner et al., "Coherent Electron Cooling Proof of Principle Instrumentation Design”, BIW2012, WEAP01.

Copyright © 2014 CC-BY-3.0 and by the respective authors

ISBN 978-3-95450-141-0

CONSTRUCTION AND OPERATIONAL PERFORMANCE OF A HORIZONTALLY ADJUSTABLE BEAM PROFILE MONITOR AT NSLS-II*

B. Kosciuk#, A. Blednykh, S. Seletskiy, Brookhaven National Laboratory, Upton, NY 11973, USA

Abstract

The NSLS-II Synchrotron Light Source is a 3 GeV electron storage ring currently in the early stages of commissioning at Brookhaven National Laboratory. In order to observe the electron beam cross section in the injection region of the storage ring, a specially designed, horizontally adjustable beam profile monitor was installed at the downstream end of the injection septum. It allows the profile of the injected, bumped or single turn beam to be viewed and measured. In this presentation, we discuss the final design, construction challenges, and operational performance of this novel device.

DESIGN REQUIREMENTS

The primary design requirements for the NSLS-II beam profile monitor [1] or "flag" are as follows. Insert a scintillator screen into the beam path at three different horizontal positions within the vacuum chamber, allowing the beam cross section and rough position to be captured. The chamber length and internal aperture are defined by the space between the upstream septum chamber and downstream kicker chamber. In this case the overall chamber length is 357mm with 150mm CF (Conflat) flanges. The upstream and downstream internal apertures are different and require a tapered transition over the chamber length.

In order to capture the beam at three different locations, the horizontal screen position needs to be precisely controlled to a resolution of 250µm. It is also desirable to have the screen position infinitely adjustable as opposed to just three discreet positions. A position read back device is also required to verify horizontal position.

Due to space constraints in the injection region, the choice was made to incorporate two sets of RF BPM (radio frequency beam position monitor) button assemblies into the flag chamber. One set of BPMs located 24.25mm from chamber center is intended to measure position of the injected beam while the other set located 15mm from chamber center is intended to measure bumped beam position.

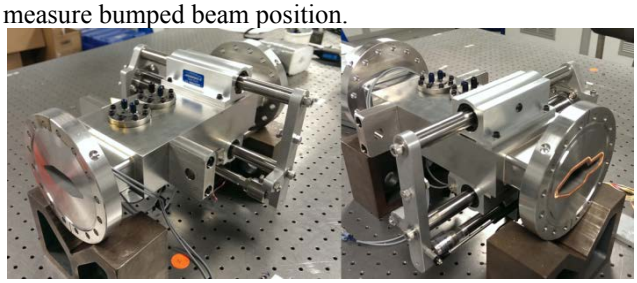


Figure 1: NSLS-II SR Flag in final assembly configuration.

*Work supported by … DOE Contract No: DE-AC02-98CH10886
#bkosciuk@bnl.gov

CHAMBER CONSTRUCTION

The construction of the flag chamber was by far the most challenging aspect of this design. The final design consists of a three piece stainless steel assembly with two brazed joints. The body of the chamber is a rectangular stainless steel "slab" 57mm x 120mm in cross section. The internal aperture is rectangular and is 25mm x 80mm on the upstream side and tapers to 25mm x 76mm over the 230mm length. The internal aperture was precisely cut via a wire EDM (electro discharge machining) process. Ports were machined into the top, bottom and side of the slab to accept the BPMs and bellows assembly. These ports are designed to be used with HelicoFlex® Delta-type UHV (ultra high vacuum) seals and require a specially prepared surface to mate with. The surface finish requirement for these seals is 16 micro inch with a circular lay. Delta-type seals are used extensively in the NSLS-II storage ring with great success.

To simplify the chamber assembly, both the upstream and downstream flanges are a one piece fabrication, each is machined from a slug of 304 stainless steel. This eliminated the need for welding Conflat flanges after the brazing was complete. The upstream aperture has a complex internal geometry, tapering from an asymmetric shape corresponding that of the downstream aperture of the septum chamber to a rectangular aperture that matches the central chamber. Machined into the face of the upstream flange is a dovetailed groove designed to accept a slant coil RF spring, the purpose of which is to shorten any cavities where high order modes can exist. The downstream flange tapers from a rectangular shape to the standard NSLS-II 25mm x 76mm hexagonal aperture. The apertures of both flanges were also cut using EDM. Fiducial targets were machined into the circumference of both flanges for in-situ survey and alignment after installation in the storage ring.

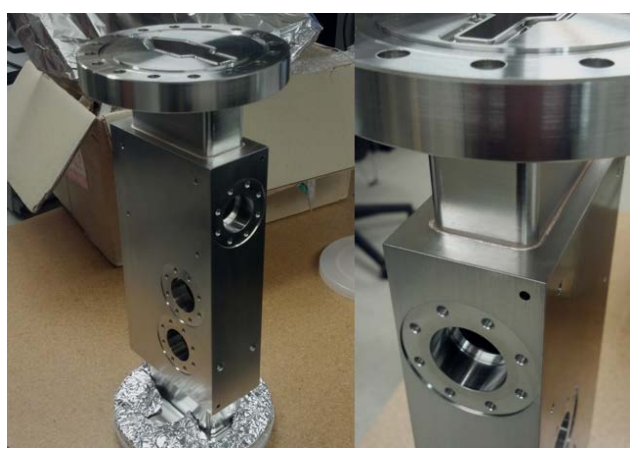


Figure 2: Successfully brazed flag chamber.

Copyright © 2014 CC-BY-3.0 and by the respective authors

ISBN 978-3-95450-141-0

The chamber assembly and brazing (Fig 2) were performed in-house and took place in two stages, a high temperature braze for the upstream flange using an 82%Au-18%Ag braze alloy (Premabraze 131) followed by a low temperature braze for the downstream flange using a 56%Ag-42%Cu-2%Ni (Braze 559). Both braze joints were successful after the first attempt as the subsequent leak check revealed.

SCREEN CARRIER ASSEMBLY

The primary component of the flag is a Cerium doped YAG (Yttrium-Aluminum-Garnet) scintillator screen with a 20mm calibration pattern and is produced by Crytur [2]. The elliptically shaped, 200µm thick screen is mounted into a custom machined aluminium screen carrier such that the angle of the screen with respect to the incident electron beam is 45°. The screen carrier assembly consists of the screen carrier optical tube, the YAG screen and the screen retainer. An aperture is cut into the screen carrier tube to allow the injected beam to pass through when viewing the bumped or single turn beams (Fig 3).



Figure 3: Screen carrier assembly and a beam's eye view of the YAG screen in the first turn position.

The screen carrier assembly is installed in a custom bellows which is mated to the side of the flag chamber via a custom flange and HelicoFlex seal. The free end of the bellows is capped with a fused silica viewport to allow the beam image to be observed by the optical system.

A special provision was designed into the screen retainer. A rim which when the flag is in the parked or home position bears up against a slant coil spring installed in the chamber (Fig 4). This feature serves to shield the cavity inside the bellows and suppress high order modes.

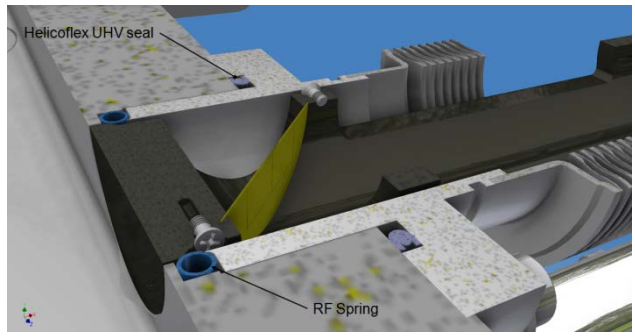


Figure 4: Screen in the parked position showing the RF spring. The HelicoFlex seal is also shown.

MOTION CONTROL

A set of linear bearings secured to the top and bottom of the flag chamber constrain the bellows and screen carrier to purely horizontal motion. These bearings were assembled with a special radiation resistant grease to avoid the problems commonly experienced with organic grease in high radiation environments.

In order to accurately position the screen, a radiation hardened, stepper driven linear actuator with a 100mm stroke was chosen. This type of actuator was employed in other NSLS-II systems and provides resolution of 10µm or better and high repeatability. Precision limit switches are installed at the travel limits, one of which is used for homing. These switches have a repeatability of 2 µm. Finally, a position read back device was installed to report the horizontal screen position. A linear potentiometer was chosen for this purpose since it is resistant to radiation damage and influence from stray magnetic fields and has adequate resolution and repeatability.

FINAL ASSEMBLY OF THE FLAG

Final assembly of the flag took place inside a portable clean hood following standard UHV vacuum practices (Fig 5). A critical aspect of the final assembly was to insure the screen carrier was centered within the bellows and side port of the chamber and that it could traverse the entire 75mm horizontal aperture of the chamber without impediment.



Figure 5: Final assembly of the NSLS-II SR Flag inside a portable clean hood.

Copyright © 2014 CC-BY-3.0 and by the respective authors

ISBN 978-3-95450-141-0

OPTICAL TRANSPORT ASSEMBLY

The optical transport for the flag is constructed primarily of commercial off-the-shelf components and has an optical path length of 900mm (Fig 6). It consists of an LED illuminator coupled directly to a kinematic right angle mirror. A remotely controlled filter wheel is mounted to an extruded aluminium rail along with a CCD and lens mounted atop a 100mm focusing stage. The focusing stage is a critical element in the optical assembly due to the fact that the YAG screen is dynamic and can be positioned anywhere within the 75mm range of the chamber aperture. The control system is programmed so the focusing stage follows the linear actuator that controls the screen position. The entire optical transport was pre-assembled remotely and then installed, aligned and tested in-situ.

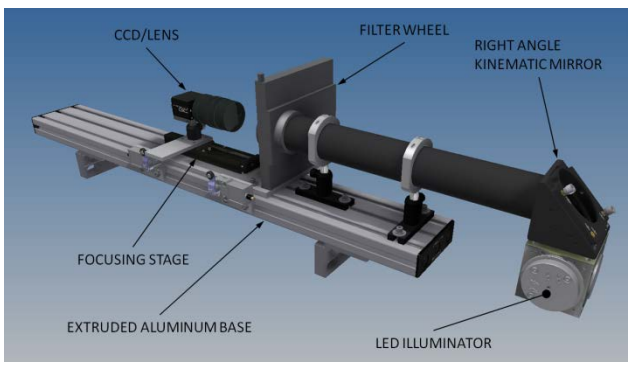


Figure 6: Details of the NSLS-II SR Flag optical transport.

INSTALLATION

Installation within the injection straight took place in stages. The flag itself was installed and vacuum connections made between the upstream septum chamber and the downstream bellows (Fig 7). The system was then leak checked and a bake-out was performed to insure the vacuum satisfied NSLS-II specifications. The optical transport was then installed, aligned and tested followed by the installation of semi-rigid SiO_2 coaxial BPM cables (Fig.8).

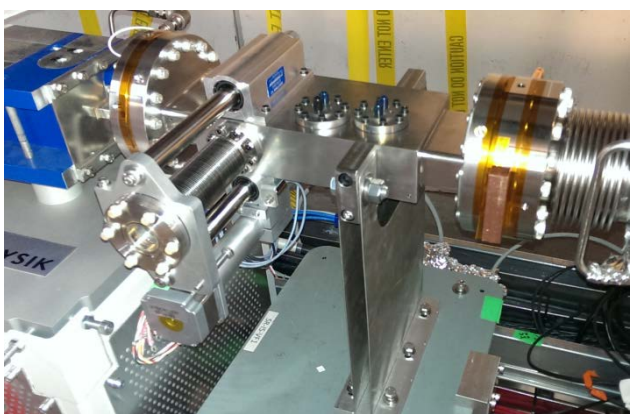


Figure 7: Installation of NSLS-II flag in the injection straight.



Figure 8: Final configuration of NSLS-II SR flag.

COMMISSIONING

The horizontally adjustable flag proved very useful during the commissioning phase of injection. The position and beam cross section were easily obtained using this device. Fig. 9 shows the CSS (Control Systems Studio) screen used to interface with the flag. The Flag Controls toolbar allow the user to move the screen to one of three pre-programmed positions corresponding to the injected, bumped or single turn beam or an arbitrary position can be entered within the physical limits of the chamber. The Camera toolbar shows the image capture with X and Y calibration in terms of μm per pixel as well as filter wheel information.

The pulsed septum injection channel is 1.3 m long and has 20 mm x 10 mm horizontal x vertical inner transverse size. The nominal horizontal size of the beam at the exit of the septum is about 6 mm (6σ) and the design trajectory of the beam is such that at septum exit the beam almost touches the septum wall.

Copyright © 2014 CC-BY-3.0 and by the respective authors

ISBN 978-3-95450-141-0

From the above, it is easy to see that even small errors can cause partial loss of the beam. Indeed, on many occasions we observed a clipped beam image on the flag, and in a few extreme cases, the complete loss of the beam. By monitoring the beam image on the flag and tuning the two injection septa and the beam correctors we were able to correct the trajectory of injected beam and to improve the injection rate.

The injection straight flag was also used together with flags in the Booster to Storage Ring transfer line for proper matching of the injected beam envelope.

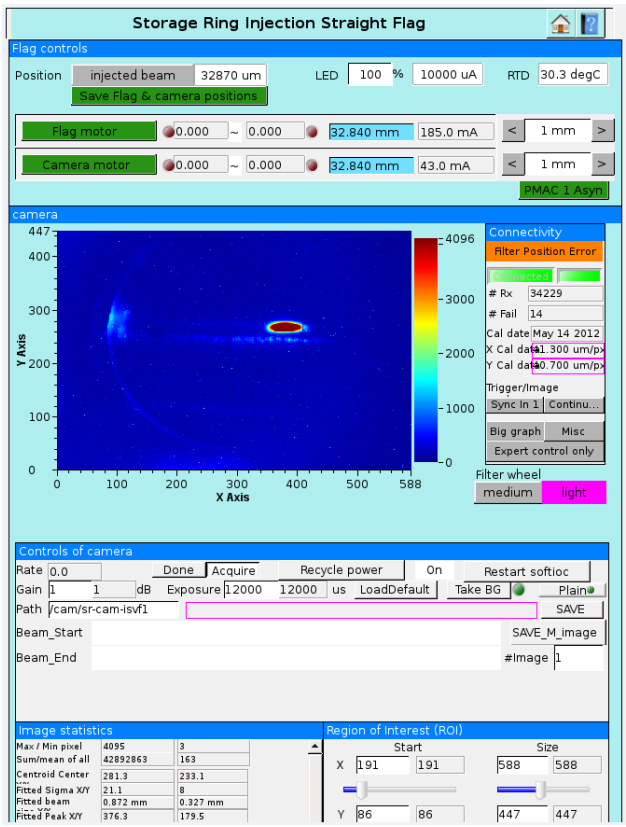


Figure 9: The interface control screen for the NSLS-II SR flag showing an image of the injected beam.

CONCLUSIONS

The overall design of the NSLS-II storage ring flag was adequate to satisfy the performance requirements specified by accelerator physicists. The fabrication and assembly took place with few if any problems. The brazed stainless chamber proved to be a solid design given the complexity of the internal and external features and should be considered for similar applications in the future. The novel aspect of the NSLS-II storage ring flag, the ability to position the screen anywhere within the chamber aperture is shown to be both feasible and useful during commissioning and will be potentially useful during beam studies.

REFERENCES

[1] B. Kosciuk, "Development of a Horizontally Adjustable Beam Profile Monitor for the NSLS-II Storage Ring", MEDSI-2012, Shanghai, May 2010

[2] Crytur, www.crytur.cz

Copyright © 2014 CC-BY-3.0 and by the respective authors

BEAM PROFILE MEASUREMENTS IN THE RHIC ELECTRON LENS USING A PINHOLE DETECTOR AND YAG SCREEN*

T. Miller†, M. Costanzo, W. Fischer, B. Frak, D. M. Gassner, X. Gu, A. Pikin,
C-AD, BNL, Upton, NY, 11973, U.S.A.

Abstract

The electron lenses installed in RHIC are equipped with two independent transverse beam-profiling systems, namely the Pinhole Detector and YAG screen. A small Faraday cup, with a 0.2mm pinhole mask, intercepts the electron beam while a pre-programmed routine automatically raster scans the beam across the detector face. The collected charge is integrated, digitized and stored in an image type data file that represents the electron beam density. This plungeable detector shares space in the vacuum chamber with a plunging YAG:Ce crystal coated with aluminium. A view port at the downstream extremity of the collector allows a GigE camera, fitted with a zoom lens, to image the crystal and digitize the profile of a beam pulse. Custom beam profiling software has been written to import both beam image files (pinhole and YAG) and fully characterize the transverse beam profile. The results of these profile measurements are presented here along with a description of the system and operational features.

INTRODUCTION

In order monitor the quality of the electron beam in the electron lens used to compensate for the effects of head-on Beam-Beam interactions in the collider [1], two parallel methods of beam profile measurement were developed and tested on a test bench [2] toward the end of 2011. Final designs were made and these systems were installed during the shutdown beginning in the summer of 2012 on the electron lens prepared for the RHIC blue beam [3]. Installation of both the electron lenses, one for blue and one for yellow RHIC beams, continued throughout the rest of 2012. The two beam profile measurement instrumentation systems were tested, along with applications for single-bunch beam-beam compensation, during the 2013 polarized-proton run in RHIC [4].

Table 1: Beam Parameters During Measurement

Parameter	YAG	PinHole
Beam Energy	6 keV	6 keV
Beam Current	70 mA	210 mA
Pulse Width	1 μs	12.5 μs
Rep Rate	1 Hz	10 Hz
Resolution	~40 pixels/mm	~8.5pts/mm

In this paper we present the final design and function of the YAG and pinhole scan system and the results of the profiles measured using the two methods. Table 1 summarizes the electron beam parameters, reduced from normal operation during the two profile measurements.

YAG SCREEN IMAGING

A mono-crystalline Cerium doped YAG crystal is used as the scintillating screen. Measuring 30mm diameter and 0.1mm thick, it is coated with a 100μm layer of evaporated aluminium to drain accumulated charge. The mechanical arrangement used on the test bench, presented earlier [5], was repeated in the installation in RHIC. The Gigabit Ethernet camera was upgraded from a Manta G201B to a G145B. The 21% larger sensor has 1.4 megapixels (MP) instead of 2 MP and thus provides increased sensitivity due to the larger pixel size on its SonyICX285 2/3 image sensor. The camera is used in its external trigger mode and is synchronized to the pulsed electron beam by the timing system.

Although two lenses were compared during tests on the test bench [5], the Sigma 70-200mm f/4-5.6 APO DG Macro lens with C-mount adapter was chosen. Its large aperture mates well with the high sensitivity of the camera. The drawback of this commercially available low cost lens is its fragile plastic body and lack of locking mechanism. The focus adjustment was very sensitive as the depth of field was very shallow with the aperture wide open. Sitting 86cm downstream of the YAG crystal, the zoom lens was adjusted to fill the camera's view with the 20mm useable area of the YAG screen. At this zoom, the focus adjustment was at its limit, suggesting an imperfect but sufficient setup of the optical system. The resulting resolution of the 20mm screen projected onto the camera's sensor was measured to be 39.4 pixels/mm. Fig. 1 shows the result of the high-resolution image of the

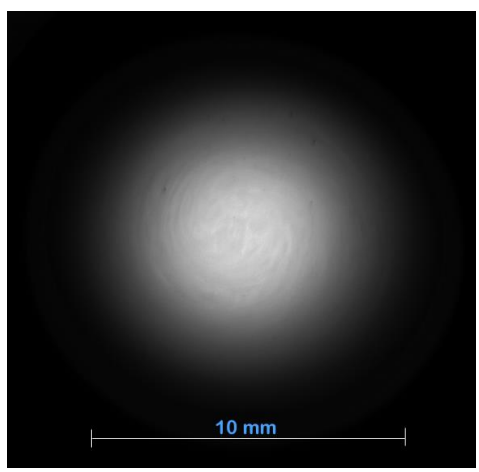


Figure 1: YAG screen profile of the electron beam.

*Work supported by Brookhaven Science Associates, LLC under Contract No. DE-AC02-98CH10886 with the U.S. DOE
†tmiller@bnl.gov

Copyright © 2014 CC-BY-3.0 and by the respective authors

ISBN 978-3-95450-141-0

electron beam. Notice the structure seen in the image that is likely indicative of variations in quantum efficiency of the thermionic cathode's surface coating.

Some diagnostics were included to check the health of the YAG crystal since damages from over-exposure to beam occurred several times in the past. A 450nm high-brightness, focused LED was used to flood the YAG crystal with a wavelength of light at which it fluoresces most efficiently. Figure 2a shows a uniform fluorescence of the YAG crystal during a 500ms exposure with a camera gain of 20dB, under 80mA of LED current. The motive is to look for cracks or reduced fluorescence due to over heating, as was found during the YAG crystal damage discussed previously [5]. The bright spot in the image is believed to be an unwanted reflection that appeared with a long exposure time.

A 405nm, 4mW laser was also injected through the lens onto the crystal. Figure 2b shows the structure in the inexpensive laser beam as it appears on the YAG crystal. This structure was used as a focusing aid during set up.

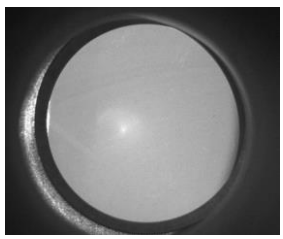
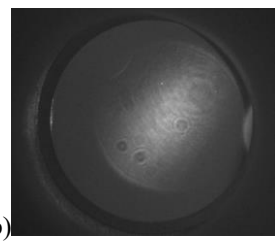
a)  b) 

Figure 2: YAG crystal illuminated with a) uniform 450nm LED light and b) 405nm expanded laser beam.

PINHOLE SCAN IMAGING

An image of the electron beam is created by taking current measurements throughout a matrix of positions over the cross-section of the electron beam. The pinhole scanning system is comprised of a faraday cup plunged into the beam via a pneumatic actuator and with a 0.2mm diameter pinhole mask. As this electrode sits at a fixed position at the center of the beam pipe, the electron beam is raster scanned over it and the beam current is recorded at each position in the matrix.

The pinhole faraday cup electrode sits in an instrument cluster mounted to the opening of the beam dump. Thus, the instrument cluster is biased at the potential of the beam dump (up to +/-10kV). Consequently, the pinhole motion control and signal integrating electronics must also sit in a chassis biased above ground potential. The current signal from the masked faraday cup is carried to the integrator electronics through nearly 80m of Belden 9311 coaxial cable, in a high voltage sleeve inside steel conduit.

Control System

An array of positions is created from parameters defining the minimum & maximum steering currents for the horizontal and vertical coils and the number of points along each axis. The timing system coordinates power supply settings and data acquisition hardware. There are four major BNL standard custom hardware components as described below and shown in the block diagram of Fig. 3.

- Waveform Generators – pair of modules comprised of a controller with waveform table, coupled via fiber to a remote power supply controller module having an analog output as well as 4 analog input channels for power supply readbacks. The generator pair generates the scanning waveforms and supports external timing signals to synchronize stepping through the waveform table.
- Data Acquisition Module – Module having 4 Analog input channels and is isolated from its controller by a bidirectional fiber optic link. The controller contains a readback buffer for the data as well as external timing inputs to synchronize data acquisition times.
- Trigger Generator – Multi-channel module that utilizes a widely-distributed master clock and event link to generate output pulses with programmable delays and widths that have deterministic timing.
- Front End Computer – VME-based controller running the VxWorks Operating system, used to control the other three components above and to bridge their parameters and data with the rest of the controls system infrastructure over an Ethernet network.

Scan parameters are entered into the application GUI, including (but not limited to) the number of points to be scanned, the horizontal and vertical current limits of the scan, and the frequency at which the system advances through measurement points. The application software begins executing steps to execute the scan. Waveform tables are generated with the appropriate steering magnet currents in sequence to generate a raster-scan pattern. These tables are loaded into the horizontal and vertical waveform generator internal memories. The trigger generator channels are configured to generate a trigger sequence to advance the waveform generator points, allow the steering coil currents to settle, generate an electron beam pulse, initiate one or more data acquisition pulses including control of the integrator (reset and gate), and finally transfer data back to the application software to be buffered. The pinhole scan is then initiated by enabling an appropriate event on the trigger generator event link. At this point events begin occurring at the predetermined rate on the link and the trigger generator channels respond to each event in turn advancing the steering magnets, firing the electron beam, gating the integrator equivalently to the length of the beam pulse and triggering the data acquisition. When the appropriate number of points has been scanned through, the events cease and the data is stored in a linear array.

The speed of the scan is limited by the settling time of the current in the steering coils after each step change. The settling time is directly affected by the step size. In

Copyright © 2014 CC-BY-3.0 and by the respective authors

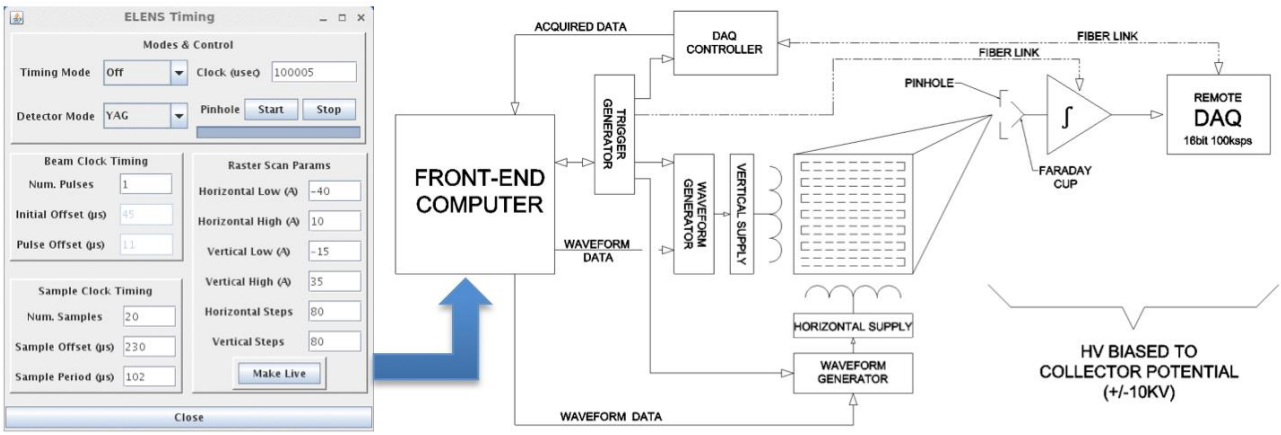


Figure 3: Block diagram of Pinhole scan hardware and software control GUI.

order to minimize the step size in the horizontal scan sequence, the horizontal scan lines alternate in direction. Note the serpentine dashed lines depicting this in Fig.3. The steering coils, embedded in water-cooled solenoid magnets, have power supplies capable of up to 400A. The steering coils have a steering effect of ~0.2mm/A. Thus, beam can be scanned over more than the full aperture of the beam pipe. A 100x100 scan running at 10Hz requires just under 17 minutes to complete; however, tests have shown that scan rates of up to 100Hz with steps under 13A are possible.

As each scan line alternates in direction, the linear array is picked apart and reassembled into an 2D-array with the original number of horizontal and vertical points. Although this tightly packed array of intensity data point does represent an image of the beam, it must be scaled in each direction as a function of the strength of the steering coils in order to represent the actual beam size. To accomplish this, a calibration procedure using the YAG crystal and camera is used to define deflection coefficients for each axis (in A/pixel) and then to measure the number of pixels per mm in order to calculate A/mm.

Calibration Using YAG Imaging

The size calibration of pixels/mm is found by drawing a reference circle on an image of the YAG crystal, illuminated to see the crystal support frame, as shown in Fig. 4. Controls are provided to position the circle and adjust its radius to match the known 20mm diameter of the frame's bezel. Once defined within the image, the scaling coefficient can be calculated. It is shown in Fig. 6 in the calibration interface as 39.4 pixels/mm.

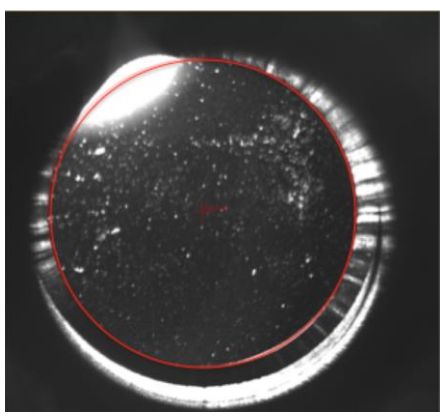
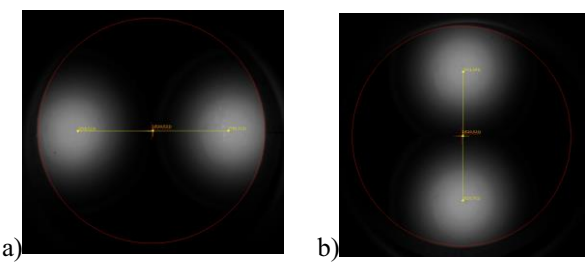


Fig. 4: Calibration circle defined along the 20mm inside diameter of the mounting fixture bezel.

Deflection coefficients for both the horizontal and vertical axes are found by a procedure of steering the beam to the maximum and minimum scan limits for the pinhole scan and taking the four corresponding images of the beam with the YAG profiling system. Software developed to control all parameters of the pinhole scan first finds the center of gravity of the beam profiles. It then overlays the two images taken for each of the two horizontal and vertical axes, generating two new images. A line is drawn between the centers of gravity of the two deflected beam spots. The distance is measured in pixels and then translated to millimetres from the pixels/mm factor found using the reference circle. Figure 5 shows the resulting two images. Offset coefficients are also generated for the horizontal and vertical axes.



a) b)

Figure 5: Composite images for calculation of deflection coefficients, skew angles, and offsets for the a) horizontal and b) vertical axes.

Moreover, a skew angle is measured from the horizontal or vertical for each image. These skew angles are used to correct the image data for coupling between the horizontal and vertical steering coils. These calibration coefficients are shown in the screen shot of the calibration interface in Fig. 6.

Copyright © 2014 CC-BY-3.0 and by the respective authors

ISBN 978-3-95450-141-0

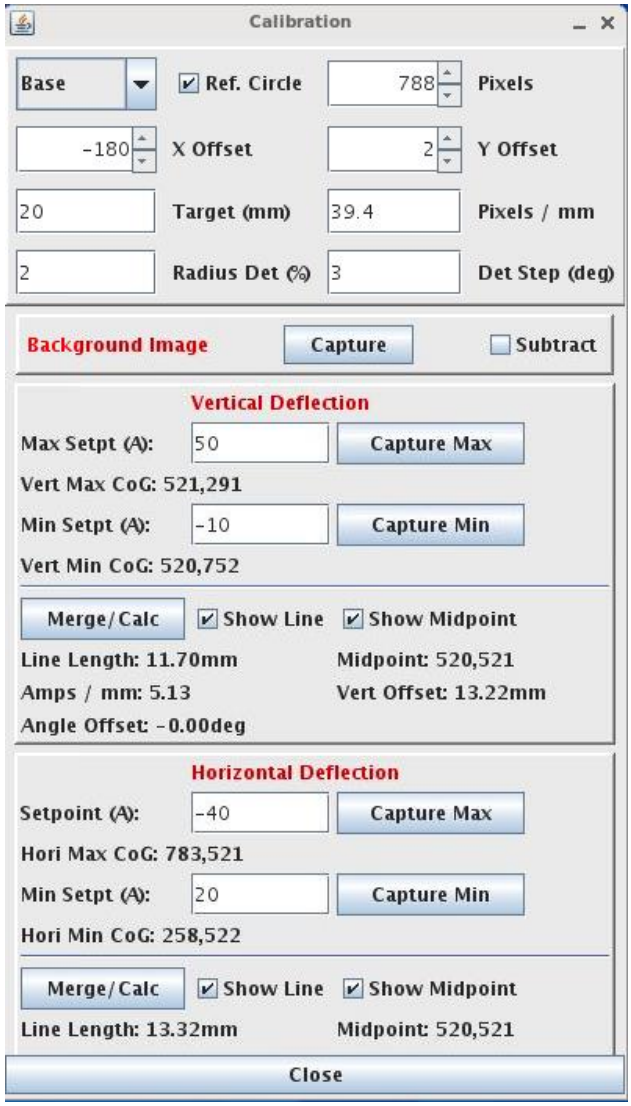


Figure 6: Calibration procedure software interface screen.

Example Scan

With the parameters shown in the GUI in Fig.3, the span of the steering magnets in the horizontal and vertical directions was 60A while the array size was 100 x 100.

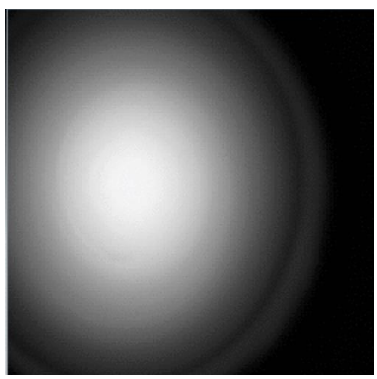


Figure 7: 100x100 point pinhole scan rendered to an image.

Thus an array of 10,000 points with a step size of 600mA was created. Once the image is generated from the data array, it is scaled by the deflection coefficient constants using standard java image library functions. This accounts for in-equivalent gains of the two steering coils. Also, the horizontal and vertical axes of the image are skewed by the negative of the skew angles to compensate for coupling between axes. Finally, a smoothing algorithm is applied and the final image is rendered in the same format as the image taken from the YAG screen camera so that the profiles of the two images can be measured using the same set of tools. Figure 7 shows the rendered image resulting from the scan.

IMAGE ANALYSIS

The images of the beam profile, whether taken by the YAG screen camera or rendered from a pinhole scan, can be sliced along the X, Y or user defined arbitrary axes. The software developed for this application determines the center of gravity of the locus of points and then allows the user to define an arbitrary axis about that center. The axes are then divided into segments over which the intensity is averaged.

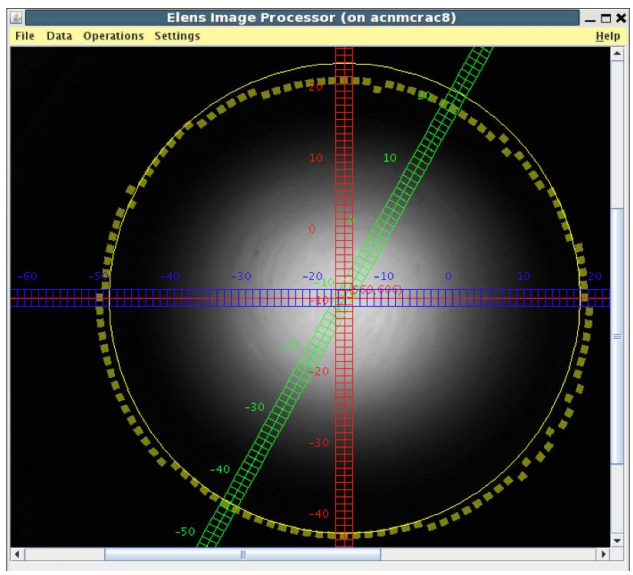


Figure 8: YAG beam profile, magnified, with analysis axes and beam radius boundary shown.

Figure 8 shows the beam profile taken from the YAG screen camera with the axes added and the averaging segments shown as blocks along the axes. Also, the beam radius boundary is automatically defined by a fitted circle through points that lie at 2.5% of the intensity.

A 2D plot is then made of the average intensity versus distance. The distance calibration came from the reference circle definition and the image scale factors from the deflection coefficients. Figure 9 shows the profile along the arbitrary axis of the rendered pinhole scan. The program overlays a fitted Gaussian curve and displays

Copyright © 2014 CC-BY-3.0 and by the respective authors

statistical data about the curve, such as its formula, radius, sima, and X^2 parameters.

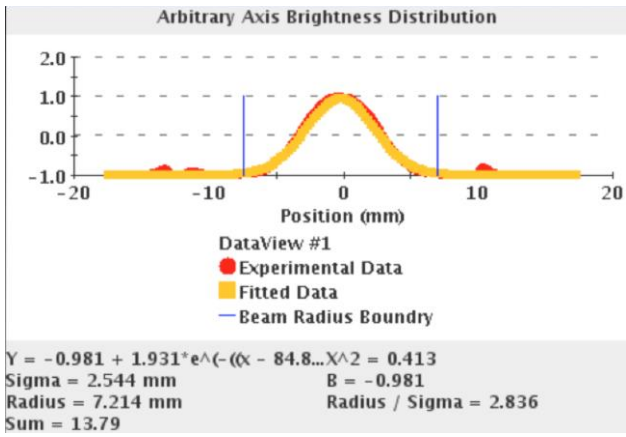


Figure 9: Profile of the electron beam taken through the arbitrary axis, here defined at 60° from Fig 8.

Comparison of Methods

Two profiles were measured and compared, one taken with the YAG screen camera and the other rendered from a pinhole scan, each with the parameters shown in Table 1. Excellent agreement can be seen in the comparison of the profiles from the two methods. Although the two measurements were taken at different beam currents, previous tests on the eLens test bench showed the YAG screen profile to scale linearly with beam current, thus retaining its Gaussian shape. A comparison of the two is shown in Fig. 10.

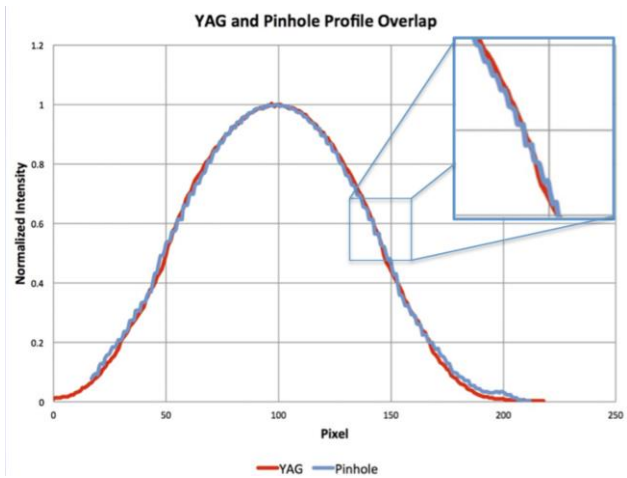


Figure 10: Comparison of the YAG vs PinHole generated profiles.

Note the coarser resolution of the pinhole data (~8.5 pts/mm) compared to that of the YAG screen data (~40 pixels/mm) as shown in the magnified window in Fig. 10.

CONCLUSION

Two successful methods of measuring the electron beam profile are now operational on two electron lenses installed in RHIC. Since results from the two methods concur, the YAG screen method will be the instrument of choice as provides is a faster measurement. However, due to the fragile nature of the YAG crystals, the pinhole scan system will remain as a back-up system of measurement. Plans are underway to upgrade the YAG crystal holder to a multi-crystal system that will allow a choice of several redundant crystals to be selected and provide for testing of alternate scintillating media.

ACKNOWLEDGEMENTS

The authors would like to thank J. Hock, K. Hamdi, C. Liu, B. Lambiase, and members of the controls group, especially Z. Altinbas, A. Fernando, J. Jamilkowski,, P. Kankiya, R. Olsen, & C. Theisen, and recognize the support of the Accelerator Components & Instrumentation Group, especially N. Baer, J. Carlson, J. Citro, T. Curcio, S. Jao, B. Johnson, J. Kelly, D. Lehn, J. Siano, D. Von Lintig, & A. Weston.

REFERENCES

[1] W. Fischer, *et al.*, “Status of head-on beam-beam compensation in RHIC”, RHOBBC, proceedings of BB3013: The ICFA Mini-Workshop on Beam-Beam Effects in Hadron Colliders, March 2013, CERN, CERN-2014-004, pp. 109-120, 17 July 2014, ISBN 978-92-9083-404-5

[2] T. Miller, *et al.*, “Instrumenting the e-Lens Test Bench with a scanning pin-hole detector and YAG imaging for comparing beam profiling methods ”,TUPG039, proceedings of BIW2012, Newport News, VA, USA, (2012).

[3] W. Fscher, *et al.*, “Commissioning Progress of the RHIC Electron Lenses”, TUPFI077, proceedings of IPAC2013, Shanghai, China, (2013).

[4] X. Gu, *et al.*, “Commissioning RHIC’s Electron Lens”, TUOCA2, proceedings of PAC2013, Pasadena, CA, (2013).

[5] T. Miller, *et al.*, “Electron’Lens Test Stand Instrumentation Progress”, THCB01, proceedings of IBIC2012, Tsukuba, Japan, (2012).

Copyright © 2014 CC-BY-3.0 and by the respective authors

ISBN 978-3-95450-141-0

ABSOLUTE BEAM EMITTANCE MEASUREMENTS AT RHIC USING IONIZATION PROFILE MONITORS*

M. Minty#, R. Connolly, C. Liu, T. Summers, S. Tepikian, BNL, Upton, NY, USA

Abstract

In this report we present studies of and measurements from the RHIC ionization profile monitors (IPMs). Improved accuracy in the emittance measurements has been achieved by (1) continual design enhancements over the years, (2) application of channel-by-channel offset corrections and gain calibrations in the beam profile measurements and (3) use of measured beta functions at the locations of the IPMs. The removal of systematic errors in the emittance measurements was confirmed by the convergence of all four planes of measurement (horizontal and vertical planes of both the Blue and Yellow beams) to a common value during beam operation with stochastic cooling. Consistency with independent measurements (luminosity-based using zero degree counters) at the colliding beam experiments STAR and PHENIX was demonstrated.

INTRODUCTION

In the past, comparisons between emittance measurements from ionization profile monitors, Vernier scans (using as input measured rates from zero degree counters, ZDCs), the polarimeters and the Schottky detectors evidenced significant variations of up to 100%. In this report we present studies of the RHIC ionization profile monitors (IPMs). After identifying and correcting for systematic instrumental errors in the beam size measurements, we present experimental results showing that the remaining dominant error in beam emittance measurements was imprecise knowledge of the local beta functions. After application of measured beta functions, thanks to full 3-D stochastic cooling we demonstrate that precise measurements of the absolute emittances result. Also, consistency between the emittances measured by the IPMs and the ZDCs was demonstrated.

BRIEF HISTORY OF THE RHIC IPMS

The design of the RHIC IPMs has evolved over time with continuous improvements. The first prototype was built and tested in 1996 [1] with first measurements in RHIC in 1999 [2, 3]. In 2002 two changes were made motivated by experiences with beam: shielding was added upstream of the detectors to prevent signal contributions from upstream beam losses and the electrodes were made longer to avoid electron clouds from migrating into the region of the detector [4]. In 2005 fast signal gating was added to avoid depletion of the multichannel plate (MCP) detector and better isolation of the detector from the electromagnetic fields of the beam was implemented [4]. As the beam intensities increased, this latter effect was further suppressed with a new design in 2007 which placed all electronics inside a Faraday cage outside of the path of the beam's image current [5]. The prototype for this new design [5] was implemented for the Yellow Ring vertical plane (YV) in 2008. In 2010 the new design [5] was implemented for both the Blue and Yellow Ring horizontal planes (BH, YH) and these IPMs were moved to locations where the beam sizes were larger. The new IPM design [5] was implemented in the last remaining plane, Blue Ring vertical (BV), in 2013.

* Work supported by Brookhaven Science Associates, LLC under Contract No. DE-AC02-98CH10886 with the U.S. Department of Energy

minty@bnl.gov

INSTRUMENTAL SYSTEMATIC ERRORS

During the FY11 RHIC run [6], it was found that when the beams were brought into collision at a new third experiment (AnDY), the vertical beam size measurements from the IPMs changed considerably. To investigate further, measurements were taken while scanning the beam across the area of the detector. The measurements revealed significant damage to the multi-channel plate detectors (MCP) due to depletion [7] however with corrections applied, the position sensitivity still remained (since the beam sizes at full energy were small compared to the region of the MCP depletion). Other issues concerned variations between measurements, which were not small compared to expectation based on the statistical properties (i.e. ionization cross sections) of the measurements, and channel-to-channel variations within a single measurement.

CHANNEL-BY-CHANNEL OFFSET CORRECTION AND GAIN CALIBRATIONS

A conceptual view of the IPM and photographs are shown in Fig. 1. The signals from the MCP (bottom left) are processed through 64 channels as seen on the anode board (bottom right) and transferred to amplifiers through 64 ceramic-beaded wires (bottom left). Using the previously acquired data (beam size measurements as a function of beam centroid position), the channel offsets were determined by measurements with beam passing across the MCPs but not above the specific channels of interest. After applying the offset corrections to all the measured profiles and removing bad channels, the gain calibrations were obtained using the following automated procedure. For each IPM:

(1) Fit each of the (20 to 30 or so) profiles in the calibration scan with a Gaussian and compute the chi-squared, χ^2.

Copyright © 2014 CC-BY-3.0 and by the respective authors

(2) Calculate a figure of merit equal to the mean chi-squared $< \chi^2 >$.
(3) For a given channel (the RHIC IPMs have 64 readout channels), scale the channel gain and repeat steps 1-2.
(4) Iterate steps 1-3 over a range of channel gain scale factors.
(5) Perform a polynomial fit to the resultant $< \chi^2 >$ versus scaled channel gain. Examples are shown in Fig. 2.
(6) Implement the channel gain so found (with minimum $< \chi^2 >$).
(7) Repeat steps 1-6 for all 64 channels.

Figure 3 shows IPM profile measurements from the FY11 RHIC run [5] without channel-by-channel corrections (top) and from the FY12 RHIC run with corrections (bottom). The new and simplified header display now includes a fit error which until these corrections were applied was not useful in evaluation of the quality of the profile measurements. As can be seen, the Gaussian fit algorithm was considerably better constrained after implementing the channel-by-channel offset corrections and gain calibrations.

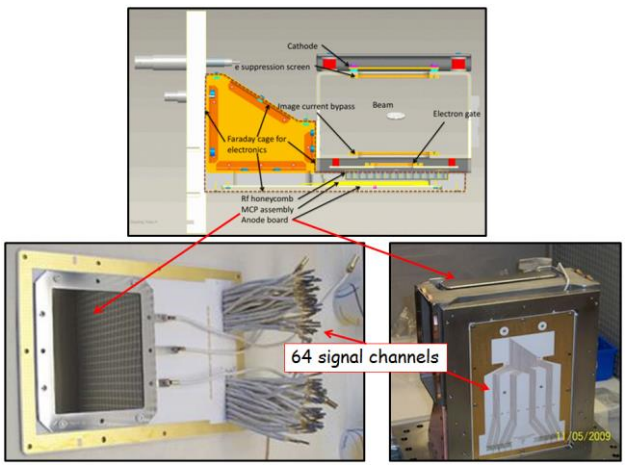


Figure 1: Conceptual view (top) and photographs (bottom) of new RHIC IPM [5]. The MCP (left) dimensions are 8 cm by 10 cm. The signals from the MCP are collected by the 64-channel anode board (right) and read out through the ceramic-beaded wires (left).

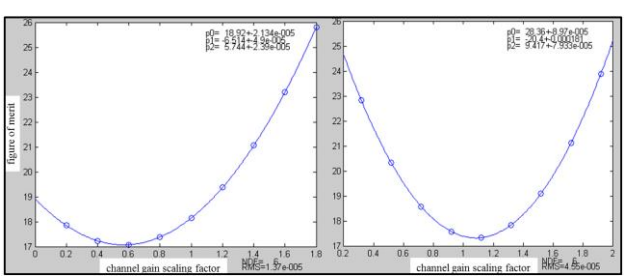


Figure 2: Examples of polynomial fit to figure of merit, $< \chi^2 >$, versus channel gain scaling factor for two different IPM channels.

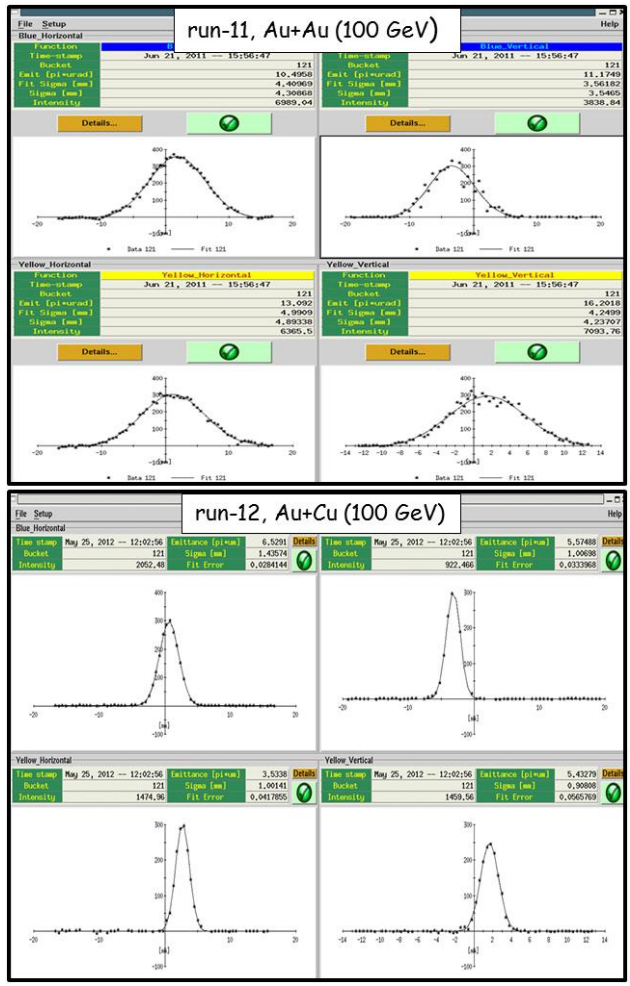


Figure 3: Example beam profile measurements before (top) and after (bottom) implementation of IPM offset and gain corrections. In each subplot, shown in the top row are the Blue ring horizontal (left) and vertical (right) profiles and in the bottom row the Yellow ring horizontal (left) and vertical (right) profiles.

EMITTANCE MEASUREMENTS USING MEASURED BETA FUNCTIONS

After removal of the systematic measurement errors in the measured beam sizes, the presence of another significant systematic error became apparent (e.g. unphysical shrinking emittances without accompanying beam loss during acceleration in FY12 and FY13 and during the "rotator ramp" with a special E-Lens optic in FY13). Since the emittance ε is given by the ratio of the square of the rms beam size σ_β to the beta function β at the location of the IPM, the value assumed for the beta function was suspect. As an illustration, the reported horizontal and vertical emittances of both the Blue and Yellow beams did not converge to equal values which with stochastic cooling [8] is expected to result [8, 9]. This was the case in the FY11 RHIC Run when stochastic cooling was applied in the vertical planes with damping of both transverse planes achieved through betatron

Copyright © 2014 CC-BY-3.0 and by the respective authors

ISBN 978-3-95450-141-0

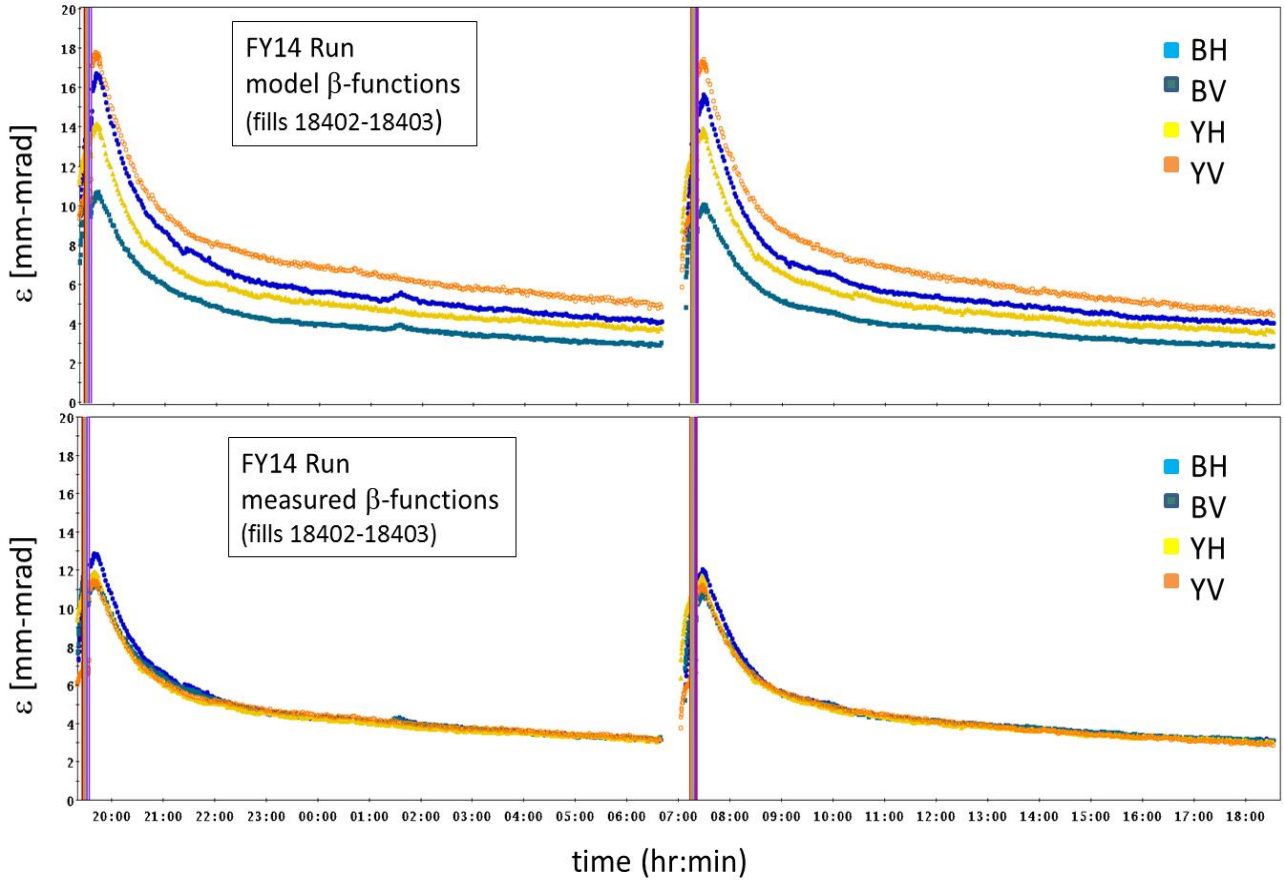


Figure 4: Evolution of the transverse beam emittances with 3D stochastic cooling [9] during the FY14 RHIC Run derived from the IPM profile measurements in all 4 planes (horizontal and vertical in the Blue and Yellow Rings) during two physics stores derived using model beta functions (top) and, for the same two stores, using beta functions interpolated from measurements from nearby beam position monitors (bottom).

coupling [8]. Similarly, in FY14 with full 3-D stochastic cooling [9], the emittances did not converge to identical values as shown in Fig. 5 (upper plot).

During the FY13 and FY14 RHIC Runs, the beta functions measured at the beam position monitors bracketing the IPMs were used to interpolate to the positions of the IPMs [10]. A comparison between the model beta functions (used to date for derivation of the emittances from the beam profile measurements) and the measured beta functions obtained early in the FY14 Run is given in Table 1. The measured beta functions were used to correct the measurements (by scaling by the ratio $\beta_{model}/\beta_{meas}$). Shown in Fig. 4 (bottom) are the emittances obtained using the measured beta functions rather than the model beta functions (which were used in Fig. 4 (top)). The two physics stores shown here correspond to a time late in the FY14 Run at which time RHIC operations was fully optimized with only occasional adjustments over the course of a physics store to stochastic cooling. The adjustments were made by Operations based on observed relative increased emittances, which was indicative of over-cooling of one beam relative to the other (examples of this are visible in Fig. 4 at ~01:30 and ~10:00). The convergence of the measurements in all 4 planes to a common value gives good confidence that the emittances are now accurately determined.

Table 1: Model and Measured Beta Functions at Store Energy During the FY14 Au+Au RHIC Run

	Blue Horizontal	Blue Vertical	Yellow Horizontal	Yellow Vertical
β_{model} (m)	202	118	206	112
β_{meas} (m)	262	109	245	174
$\beta_{model}/\beta_{meas}$	0.77	1.08	0.84	0.64

COMPARISON OF EMITTANCE MEASUREMENTS FROM THE RHIC IPMS AND FROM THE RHIC ZDCS

As mentioned in the introduction, emittance comparisons using different methods have in the past shown disparities. Here we compare the emittance measurements from the IPMs to those inferred using the experiment's ZDC counters [11] as input and analyzed in the application StoreAnalysis [12], which among other things computes the effective beam emittance taking into account the measured ZDC rates, the model beta

Copyright © 2014 CC-BY-3.0 and by the respective authors

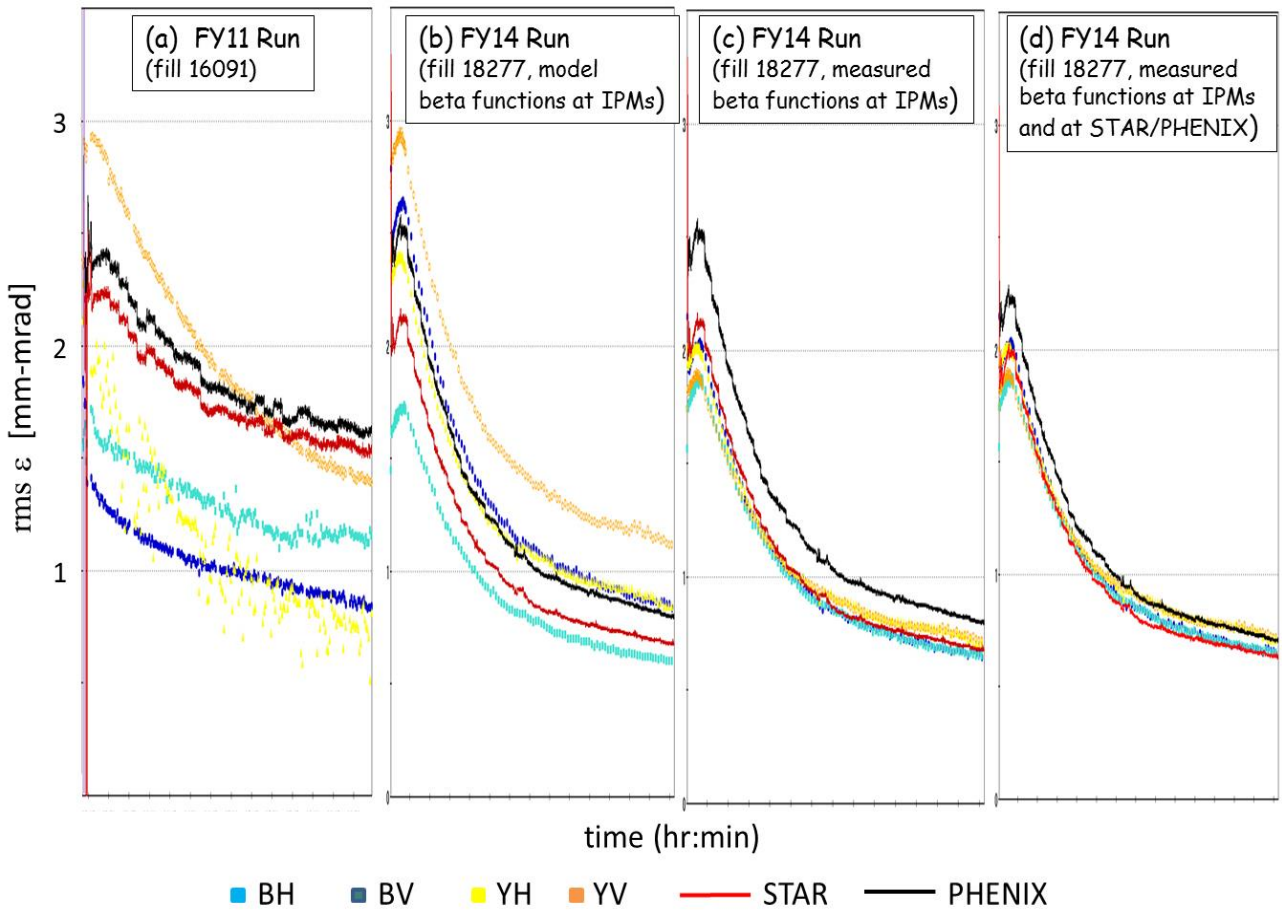


Figure 5: Comparison of rms emittance measurements during Au+Au, 100 GeV operations from the RHIC IPMs and from the experimental ZDCs (red and black lines) from the FY11 Run (Fig. 5a, no channel-by-channel offset corrections and gain calibrations), from the FY14 Run (Fig. 5b, with channel-by-channel corrections and model beta functions at the IPMs), the same data from the FY14 Run (Fig. 5c, with measured beta functions at the IPMs only) and the same data from the FY14 Run (Fig. 5d, with measured beta functions at the IPMs and at STAR and PHENIX). The horizontal time scale is 3.5 hours in all cases.

functions (assumed equal in all 4 planes), and the bunch length (for evaluation of the hourglass effect). Shown in Fig. 5 are the rms emittance measurements from the RHIC IPMs and from the ZDCs. In Fig. 5a (FY11 Run - Au+Au, 100 GeV), the IPM measurements did not at that time have channel-by-channel offset corrections or gain calibrations. In Fig. 5b (FY14 Run – Au+Au, 100 GeV) the channel-by-channel offset corrections were applied (with unity gain corrections as these were found not to be necessary since removal of certain unused electronics during the preceding shutdown [13]). Figure 5c shows the same data as Fig. 5b now with the measured beta functions applied at the IPMs. Figure 5d shows the same data as Fig. 5b using measured beta functions at the IPMs and at the ZDCs. For the latter, the measured beta functions were used (1) to determine the beam sizes at the interaction points and (2) for a small (<2%) correction to the geometric luminosity reduction due to finite bunch length (hour glass effect) [14]. From these results we observe that with all corrections applied the agreement between emittance measurements from the RHIC IPMs and the ZDC counters is considerably improved

SUMMARY

The accuracy of emittance measurements using the RHIC IPMs has been greatly improved by the following: (1) continual design enhancements over the years [1-5], (2) application of channel-by-channel offset corrections and gain calibrations in the beam profile measurements and (3) use of measured beta functions at the locations of the IPMs. The removal of systematic errors in the emittance measurements was confirmed by the convergence of all four planes of measurement (horizontal and vertical planes of both the Blue and Yellow beams) to a common value during beam operations with stochastic cooling (Fig. 4). Consistency with independent measurements (based on the ZDCs) at STAR and PHENIX was shown to be within ~ 15% (Fig. 5).

Copyright © 2014 CC-BY-3.0 and by the respective authors

ISBN 978-3-95450-141-0

Future studies will involve continued efforts towards more precise measurements of the beta function during acceleration and optics correction during acceleration [15-17] so that, together with measurements from the injectors, a better understanding of sources of emittance dilution between the injector synchrotron, the AGS, and RHIC and during acceleration in RHIC can be better characterized and localized and, eventually, corrected.

ACKNOWLEDGEMENTS

The RHIC IPM design and evolution thereof has been led by R. Connolly. The beautiful 2008 design had fabrication support by J. Fite, S. Jao, D. Kipp, T. Russo and C. Trabocchi and support from Vacuum, Controls and Instrumentation for installation and integration. S. Tepikian, author of the fitting algorithm, provided continuous enhancements to the online data processing application. T. Summers championed implementation of the online calibration measurements. C. Liu's development and automation of the beta function interpolation routine has been invaluable.

REFERENCES

[1] R. Connolly et al, "A Prototype Ionization Profile Monitor for RHIC", PAC97, Vancouver, B.C., Canada, May 1997, p. 2152 (1997).
[2] R. Connolly et al, "The RHIC Ionization Profile Monitor", PAC99, New York, NY, Mar 1999, p. 2144 (1999).
[3] R. Connolly et al, "Beam Profile Measurements and Transverse Phase-Space Reconstruction on the Relativistic Heavy-Ion Collider", Nucl. Instr. and Meth. in Phys. Res. A443, pp. 215-222 (2000).
[4] R. Connolly et al, "Residual-Gas Ionization Profile Monitors in RHIC", PAC05, Knoxville, TN, May 2005, p. 230 (2005).
[5] R. Connolly et al, "Residual-Gas Ionization Beam Profile Monitors in RHIC", BIW10, Santa Fe, NM, May 2010, TUPSM010, p. 116 (2010).
[6] G. Marr et al, "RHIC Performance for FY2011 Au+Au Heavy Ion Run", Proc. of IPAC2011, San Sebastian, Spain, Sept 2011, TUPZ038, p. 1894 (2011).
[7] R. Connolly, M. Minty and S. Tepikian, "Calibration Scans on IPMs", APEX Weekly Meeting, http://www.cadops.bnl.gov/Instrumentation/InstWiki/index.php/File:APEX_IPM_presentation.pdf (2011).
[8] M. Blaskiewicz, J.M. Brennan and F. Severino, "Operational Stochastic Cooling in the Relativistic Heavy-Ion Collider", Phys. Rev. Lett. 100, 174802 (2008).
[9] M. Blaskiewicz, J.M. Brennan and K. Mernick, "Three-Dimensional Stochastic Cooling in the Relativistic Heavy Ion Collider", Phys. Rev. Lett. 105, 094801 (2010).
[10] C. Liu et al, "Global Optics Correction in RHIC Based on Turn-by-Turn Data from ARTUS Tune Meter", NA-PAC13, Pasadena, CA, Sept 2013, TUPBA06, p.532 (2013).
[11] C. Adler et al, "The RHIC Zero Degree Calorimeters", Nucl. Instr. and Meth. in Phys. Res. A 470, pp. 488-499 (2001).
[12] W. Fischer, private communication.
[13] C. Dawson, private communication.
[14] M. Minty et al, "Absolute beam emittance measurements at RHIC using ionization profile monitors", BNL-105970-2014-IR, C-A/AP/522 (2014).
[15] M. Minty et al, "Measurement of Beam Optics During Acceleration in the Relativistic Heavy Ion Collider", NA-PAC13, Pasadena, CA, TUPBA08, p. 538 (2013).
[16] C. Liu, A. Marusic, M. Minty, "Implementation of Optics Correction on the Ramp in RHIC", NA-PAC13, Pasadena, CA, TUPBA05, p. 529 (2013).
[17] C. Liu, A. Marusic, M. Minty, "Optics Measurement and Correction during Beam Acceleration in the Relativistic Heavy Ion Collider", BNL-106065-2014-IR, C-A/AP/528 (2014).

Copyright © 2014 CC-BY-3.0 and by the respective authors

A COMPACT IN-AIR X-RAY DETECTOR FOR VERTICAL BEAM SIZE MEASUREMENT AT ALBA

A. A. Nosych, U. Iriso, ALBA CELLS, Barcelona, Spain

Abstract

An in-air x-ray detector (IXD) was developed for ALBA to study the residual x-rays after traversing copper crotch absorbers. The device prototype is placed in-air after such an absorber, mounted flush with the vacuum pipe. The remaining x-rays (above 120 keV) generate a visible footprint if they impinge upon a sensitive enough scintillator. After unsuccessful testing different screens, we are using a Cerium doped PreLude420 (LuYSiO:Ce) screen, whose the image is observed with a simple optics system mounted on a commercial CCD camera. This measurement allows evaluating the vertical electron beam size with exposure times in the order of 1 second. Similar instruments are used at ESRF and ANKA storage rings. This paper presents the results of the first measurements with IXD (March-July 2014), and describes its potential to be used as a full diagnostics tool for the 3 GeV storage ring of ALBA.

INTRODUCTION

At ALBA, as it is widely used in most 3rd generation synchrotron light sources, the emittance in both planes is measured with the usual pinhole method [1]. However, this only provides a local measurement of the vertical emittance, thus a local measurement of the ver/hor coupling. In order to infer the global coupling, readily available measurements of the vertical beam size are desirable.

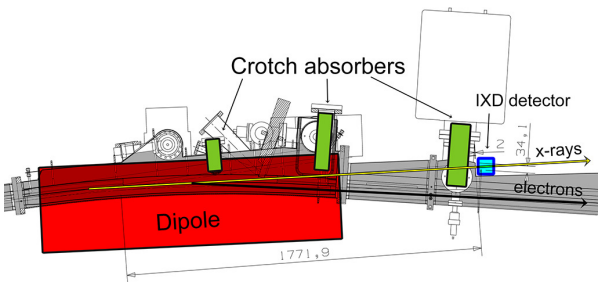


Figure 1: Tunnel section layout, showing a bending magnet with water cooled absorbers and paths of the electron and photon beams.

In-air X-ray Detectors (IXD), developed first at ESRF [2] and ANKA [3], are cheap and simple devices that can provide such measurements. They use the "left-over" hard x-rays produced by the dipoles and going through the absorbers to obtain an image of the synchrotron radiation fan, from where the vertical beam size can be inferred.

At ALBA, the unused excess of x-rays generated by 32 1.4 Tesla dipoles are damped by water cooled absorbers, which are mounted by sets of three into each dipole (Fig. 1). The absorbers are thick large-toothed copper jaws, half-open to form a crotch geometry (Fig. 2), with a minimum thickness of 35 mm and are aimed at complicating the path of x-rays traversing through. Only a fraction of low intensity higher-energy flux can penetrate the absorbers; however, if detected, it can serve as an alternative diagnostics tool for real-time monitoring of vertical beam size and emittance.

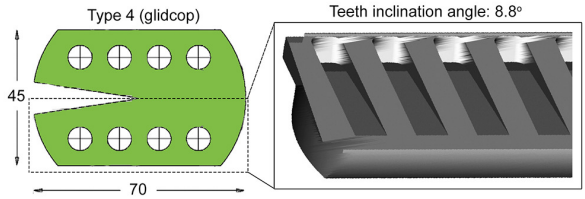


Figure 2: Transverse cross-section of the crotch absorber and a model of its lower jaw.

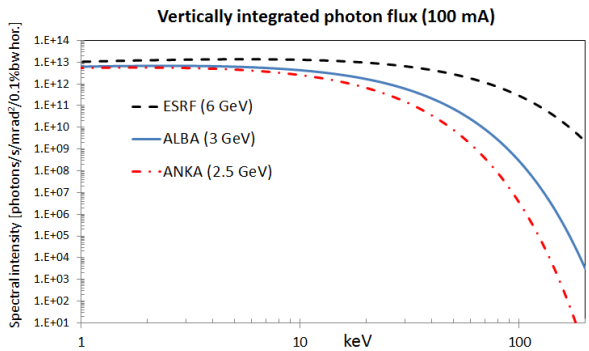


Figure 3: Vertically integrated x-ray spectrum emitted by bending magnets for machines using iXD detectors.

At ESRF and ANKA the combination of beam energy and absorber thickness offer favorable conditions for these detectors: the 6 GeV ESRF has 40 mm absorbers, and 2.5 GeV ANKA has 8 mm absorbers. ALBA is the first 3 GeV 3rd generation synchrotron light source where this technology is applied, which has become possible after choosing the appropriate scintillating material.

The total photon emission, summed over all vertical angles, emitted when an electron beam of energy E crosses a dipole is:

$$N = 2.46 \times 10^{13} E I_b \int_{\frac{\epsilon}{\epsilon_c}}^{\infty} K_{5/3}(u)\, du \qquad (1)$$

in units of photons/second/h-mrad/0.1%BW, where I_b is the electron beam current and $u = \epsilon/\epsilon_C$ is the ratio between the photon energy ϵ and the machine critical energy ϵ_C. For reference, Figure 3 compares this flux to other synchrotron light machines for fixed intensity $I_b = 100$ mA, while Fig. 4

Copyright © 2014 CC-BY-3.0 and by the respective authors

ISBN 978-3-95450-141-0

compares the flux remained after traversing an absorber corresponding to each machine.

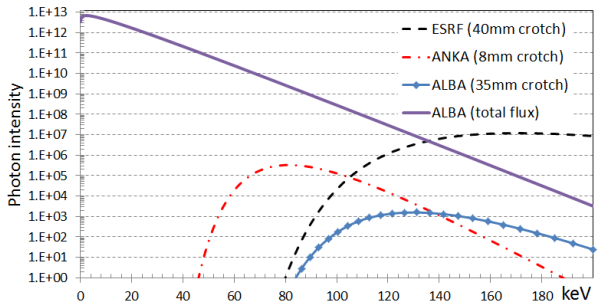


Figure 4: Photon flux before and after traversing crotch absorbers at ALBA (solid lines), compared with the flux after traversing corresponding absorbers at ESRF and ANKA (dashed lines). Note that ALBA flux after the crotch absorber is between 2 and 4 orders of magnitude lower.

DETECTING X-RAYS IN THE AIR

The prototype in-air x-ray detector (IXD) is placed downstream of a 3rd absorber of one of the storage ring dipoles (absorber Type 4 in Dipole 02 of Sector 01), and intercepts the remaining photons after they pass through a minimum of 35 mm of copper and 2 mm of steel anti-chamber wall (Fig. 2).

The IXD consists of a short optics line which provides a 18×14 mm field of view over a 1034×779 px sensor of a commercial Basler Scout CCD camera, and a 0.8 mm thick PreLude420 scintillating screen, which converts the detected x-rays to visible light. We have selected the PreLude material (Cerium doped LuYSiO5) for its sensitivity to higher energy photons compared to other common scintillators like e.g. CdWO4 used at ANKA and ESRF (Fig. 5). We also tested the available YAG screens, with unsuccessfuls results.

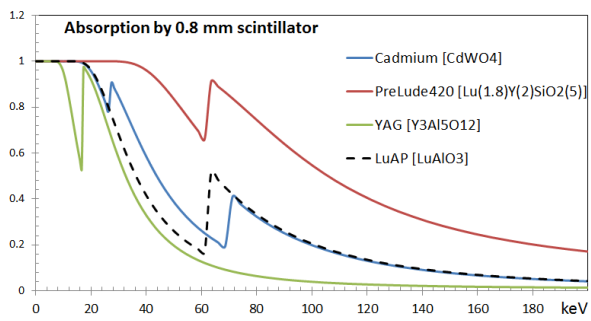


Figure 5: Photons absorption in various 0.8 mm scintillators.

Ray tracing study indicates that IXD observes a part of the x-ray fan corresponding to 4.35^o of bending curvature, which is equivalent to a 150 mm arc inside a 1370 mm bending magnet. LOCO simulation ("Linear Optics from Closed Orbit" software) of the electron beam size variation along the magnet (Fig. 6) is fully compatible with the electron beam size measurement done by the pinhole monitor [1]: $\sigma_{y,e}^{loco} = \sigma_{y,e}^{pinhole} = 24\mu$m.

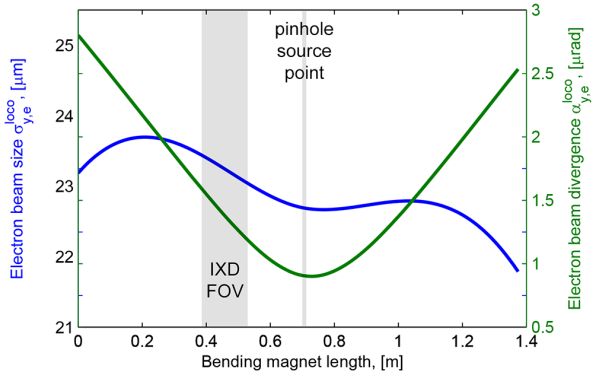


Figure 6: Vertical beam size (mean) and divergence in the considered bending magnet. The gray-highlighted section is the field of view of the IXD (15 out of 140 cm)

The photon source point for the pinhole monitor is located in another sector of the ALBA storage ring, in particular, in the central part of a dipole with identical characteristics to the one used for IXD.

The dipole spectral characteristics before ($\epsilon_{crit} = 8.5$ keV) and after absorption ($\epsilon_{max} = 130$ keV) indicate the reduction in total flux of the remaining x-rays by a factor of 10^9 with respect to the initial intensity, see Fig. 4 calculated with XOP [4]. In particular, ALBA's absorbers reduce the 130 keV flux by a factor of 5×10^5, luckily, enough to leave a footprint on the PreLude screen.

Under the assumption of a Gaussian symmetric distribution of electrons in the bunch we calculate the vertical angular distribution of the photon radiation as a function of photon energy [5], Fig. 7:

$$\sigma_r = \sqrt{\frac{2\pi}{3}} \frac{1}{\gamma} \frac{\int_{\frac{\epsilon}{\epsilon_c}}^{\infty} K_{5/3}(u)\, du}{K_{2/3}^2(\epsilon/_{2\epsilon_c})} \qquad (2)$$

and make a first estimation of the photon beam divergence at 130 keV (for $\psi = 0$): $\alpha_{ph} = 30$ μrad, which corresponds to the remaining x-rays after passing through center of the absorber (exactly 35 mm of copper and 2 mm of steel). A more precise value of photon divergence can be derived by integrating the total remaining flux over all energies: $\alpha_{ph} = 25.2$ μrad. An analysis of photon divergence and total transmitted flux as functions of Cu thickness is shown in Fig. 8.

FIRST IXD MEASUREMENTS

Due to low flux and thin PreLude screen, it is difficult to reach sub-second response of the IXD with quantitative results. A typical acquired image with a 10 second exposure time is shown in Fig. 9. The background noise can be removed by subtracting the image acquired at 10 seconds without beam (darkness).

Several unexpected observations were carried out from the first experiments. Firstly, a noticeable tilt (around 1^o)

Copyright © 2014 CC-BY-3.0 and by the respective authors

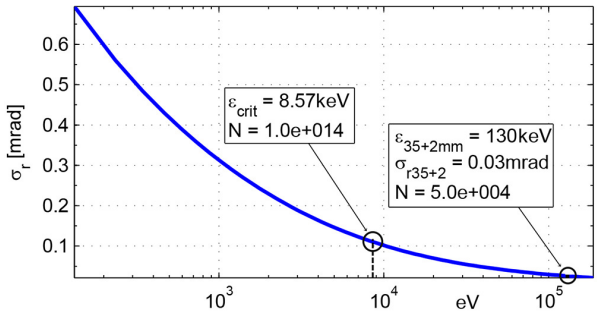


Figure 7: A plot of σ_r versus $\frac{\epsilon}{\epsilon_c}$ for ALBA beam.

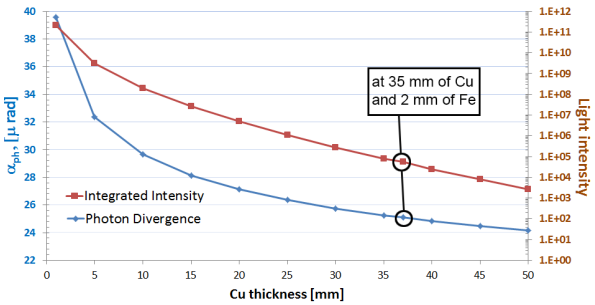


Figure 8: Relation between integrated flux transmission and photon divergence as functions of Cu thickness.

of the photon imprint can be explained by inaccuracy of camera alignment done by hand, or the vertical beam orbit variation within the 150 mm length of the observed dipole arc.

Secondly, the photon beam is observed with spots of different intensities. These can not be related neither to cooling tubes inside the absorbers (they are located below and above the photon beam), nor by the fan from upstream bending. However, they can be explained by the design of the absorber and its "teeth", in particular in the path of the x-rays: the more intense part of the beam traverses less copper. An indication of this can be the fact that the gap of 6 mm of least light intensity in the central part of the IXD image corresponds to the 6 mm width of a "tooth" (Fig. 2).

Lastly, by measuring the vertical photon beam size in Fig. 9 in three different regions of the fan we obtain a value of around $\sigma^{\mathrm{ixd}}_{\mathrm{y,ph}} = 70\mu$m. By deconvoluting it down to vertical electron beam size we obtain a value of

$$\sigma^{\mathrm{ixd}}_{\mathrm{y,e}} = \sqrt{(\sigma^{\mathrm{ixd}}_{\mathrm{y,ph}})^2 - R^2(\alpha^2_{ph} + \alpha^2_e)} = 56\ \mu\mathrm{m}, \qquad (3)$$

where $\alpha_e = 1.6\ \mu$rad is the theoretical electron beam divergence in the considered dipole. The explanation to the factor of 2.3 difference between $\sigma^{\mathrm{ixd}}_{\mathrm{y,e}}$ and both $\sigma^{\mathrm{pinhole}}_{\mathrm{y,e}}$ and $\sigma^{\mathrm{loco}}_{\mathrm{y,e}}$ is yet to be found. The focus of the study is on a possible optical effect, created by elements in the x-ray path, i.e. an underestimation of copper thickness and photon scattering inside copper itself.

The IXD images obtained within 10 to 1 second exposure times measure identical photon beam size. At sub-second shutter speeds the central part of the beam imprint (with least intensity) saturates in the background noise.

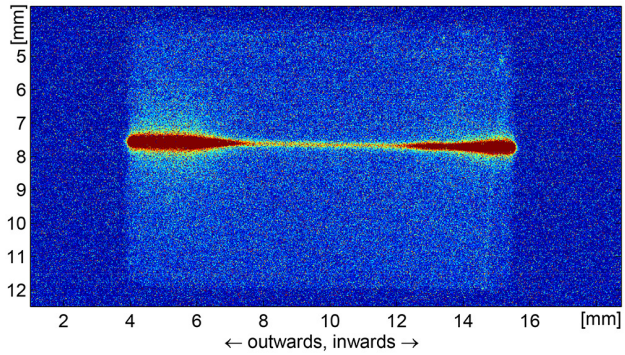


Figure 9: IXD images with and without background, for 10 and 1 sec exposure.

BEAM SIZE TESTS

As part of a beam test, the IXD vertical photon beam size $\sigma^{\mathrm{ixd}}_{\mathrm{y,ph}}$ was calibrated against the vertical electron beam size by the pinhole $\sigma^{\mathrm{pinhole}}_{\mathrm{y,e}}$ while changing the beam coupling. The coupling factor κ (vertical to horizontal emittance ratio) was increased to 1.28% and decreased to 0.3% from the nominal value of 0.5%. It can be seen that at low coupling the photon beam size (red curve) measurement saturates, while the pinhole (blue curve) remains highly sensitive to small beam size changes. This measurement makes it possible to evaluate experimentally the α_{ph} to better understand the uneven photon imprint on the IXD screen.

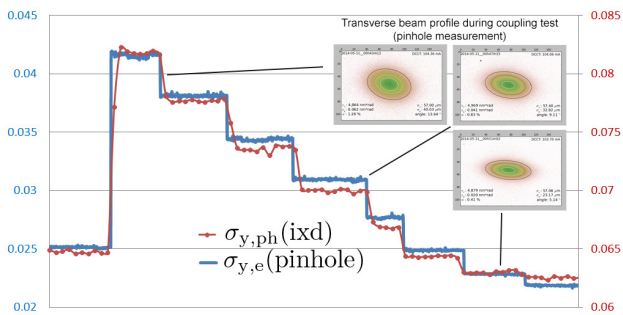


Figure 10: Calibrating vertical photon beam size against the electron beam size.

CONCLUSIONS

We have successfully developed and tested an in-air x-ray detector which measures the vertical photon beam size from the flux remaining after traversing the copper absorbers. The measurement results reveal the full potential of IXD to become a promising powerful diagnostics tool for the ALBA storage ring.

The limits of its application and several uncertainties were identified, e.g. a "tooth-shaped" fan profile and the electron beam size discrepancy with theoretical value, which will

Copyright © 2014 CC-BY-3.0 and by the respective authors

ISBN 978-3-95450-141-0

be investigated and improved. Currently the tests are ongoing with scintillating screens of different materials (e.g. CRY19) and thicknesses to reach sub-second response time and higher output light intensity.

We are also looking into Fluka/Penelope simulations of photon scattering in copper to verify its role in changing photon divergence, which could explain the photon fan profile.

ACKNOWLEDGMENTS

We would like to thank the ALBA Computing, Engineering and Experiments divisions, in particular S. Blanch, J. Montero and I. Sics for all invaluable assistance, Z. Marti and M. Quispe for LOCO calculations and ray tracing, and K.B. Scheidt of ESRF for important discussions and advise.

REFERENCES

[1] Beam size and emittance measurements using the ALBA Pinhole, U. Iriso, ALBA Project Document No. AAD-SR-DI-PINH-01, 2011.

[2] Detection of hard x-rays in air for precise monitoring of vertical position and emittance in the ESRF dipoles, B. K. Scheidt, Proc. DIPAC-2005, pp. 238-240, 2005.

[3] Precise measurements of the vertical beam size in the ANKA storage ring with an in-air x-ray detector, A.-S. Mueller, I. Birkel, E. Huttel, P. Wesolowski, Proc. EPAC-2006, pp. 1073-1075, 2006.

[4] X-ray Oriented Programs (XOP 2.3), www.esrf.eu, 2014.

[5] The science and technology of undulators and wigglers, James A. Clarke, Oxford Publications, 2004.

Copyright © 2014 CC-BY-3.0 and by the respective authors

WIRE SCANNER INSTALLATION INTO THE MICROTCA ENVIRONMENT FOR THE EUROPEAN XFEL

T. Lensch*, A. Delfs, V. Gharibyan, I. Krouptchenkov, D. Nölle, M. Pelzer,
H. Tiessen, M. Werner, K. Wittenburg, DESY†, Hamburg, Germany

Abstract

The European XFEL (E-XFEL) is a 4th generation synchrotron radiation source currently under construction in Hamburg. The 17.5 GeV superconducting accelerator will provide photons simultaneously to several user stations [1]. For the transverse beam profile measurement in the high energy sections Wire Scanners are used as an essential part of the accelerator diagnostic system, providing the tool to measure small beam size in an almost nondestructive manner. The scanners will be operated in a fast mode, starting from a trigger the wire will be accelerated to 1 m/s and hitting about 100 bunches out of the long bunch train of E-XFEL within a single macropulse. Slow scans with single bunches are also possible. In the first stage 12 stations are planned to be equipped with Wire Scanners where each station consists of two motion units (horizontal and vertical plane). The new concept uses linear servo motors for the motion of the wires and a new mechanical design has been developed at DESY [2].

This paper describes the electronics developments for the motion part of these Wire Scanners and the integration into the MicroTCA environment.

MOTIVATION

At DESY wire scanners have been used for diagnostic purposes for many years in HERA or Flash, operated with the control systems TINE and DOOCS. Rotating motors or pneumatic cylinders had been used as drive units [3]. The goal was to build the E-XFEL wire scanner as an improved system based on these experience. The new system has to be based on MicroTCA (MTCA.4) in order to be well integrated into the controls hard- and software as well as the timing infrastructure.

OVERVIEW

It is planned to start the commissioning of the E-XFEL with 12 wire scanner stations and about 60 screen monitors. Each station consists of a set of two motion units (horizontal and vertical plane). These wire scanner stations are placed in groups of three stations with well designed phase advance before the collimation system and before each of the 3 SASE undulators, allowing to measure emittance and twiss parameters without changing the magent settings. Additional 15 positions can easily be equipped later with wire scanners if this turns out to be useful.

* timmy.lensch@desy.de
† Deutsches Elektronen Synchrotron

Mechanics and Motor

For the E-XFEL wire scanners the mechanics of the motion unit was developed from scratch. A lot of experience from FLASH and HERA wire scanners went into the design to ease service and thus improve the availability. As a driver for the wire scanner forks linear motors from LinMot [4] were chosen. A catch unit had been added into the design to keep the fork mechanically out of the beam area during times of no scans. The catch unit has to be opened electrically to be able to move the fork into the beam. An end switch inside indicates, when the fork is in parking position and locked. Furthermore magnetic springs guarantee moving the fork back to this out-position in case of failure. Figure 1 shows the mechanical setup of the wire scanner prototype with almost complete cabling and safety housing. Table 1 gives some basic specifications of the device [5].

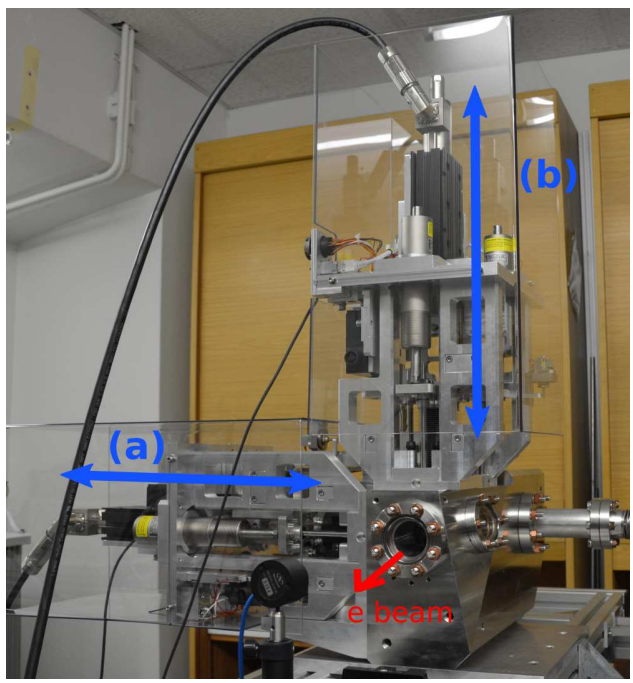


Figure 1: Mechanical Prototype station with horizontal (a) and vertical (b) motion unit.

Wire Scanner Forks

The wire scanner forks are made of titanium to improve the weight im comparison to steel by an comparable rigidity. From experience with former fork designs a lot of detailed improvements were made to ease wire assembly and adjustment. Five wires are installed in total to be able to use different wire thicknesses and to have spare wires. Three

Copyright © 2014 CC-BY-3.0 and by the respective authors

ISBN 978-3-95450-141-0

Table 1: E-XFEL Wire Scanner Specifications

Parameter	Value
Stroke	53 mm
Scanning Modes	Fast (1 m/s), Slow
Number of wires per fork	5 (see Fig. 2)
Motor to beam sync	$< 10\ \mu s_{rms}$
Wire material	Tungsten
Fork gap	15 mm
Wire - wire distances	5 mm (90°)

of these wires are mounted in 90° and one pair in ±60° in relation to the fork gap. It is planned to use Tungsten wires with thicknesses between $10 - 30\,\mu s$.

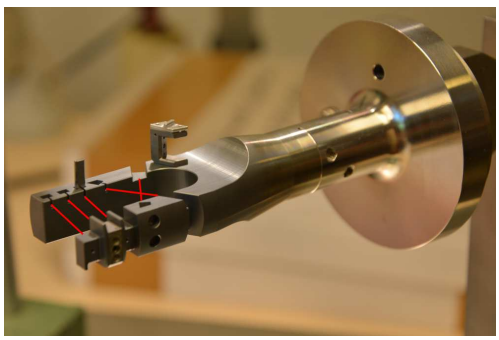


Figure 2: Titanium fork at assembly workstation. Wires are indicated by red lines.

Planned Detector Layout

In the current lattice of the machine there are four reasonable positions for detectors, one for each of the wire scanner groups. Each position will be equipped with two detectors to measure the particles scattered by the wire. The readout will be realized using MTCA.4 standard components, in this case four STRUCK SIS8300 ADC [6] with a custom made Rear Transition Module (RTM) which holds the analog signal conditioning and additional interfaces for controlling the High Voltage Power Supplies of the detectors. Since the detectors might be distributed along the accelarator, each SIS8300 ADC with RTM will control two detectors and a high voltage supply only to prevent long cable distances.

MicroTCA for the E-XFEL

The MTCA.4 standard will be used as a base of the electronics hardware of the E-XFEL and thus will also be used for the E-XFEL Wire Scanners [7]. The MTCA.4 standard defines modules, power supplies, cooling, racks, etc. Advanced Mezzanine Boards (AMC) are connected typically by PCIe to the control system. Multi LVDS connections over the backplane are used for connection to the timing system or between dedicated AMCs. Rear Transition Modules (RTM) connect to an AMC from the rear side. Many commercial products are available. More information can be found at [8] and [9].

WIRE SCANNER ELECTRONICS HARDWARE

For the implementation of the wire scanner motion control electronics the DAMC2 digital AMC FPGA board was chosen. This board is a non commercial DESY development [10]. Its FPGA firmware framework [11] implements the control system interface via PCIe, backplane interfaces to the timing system and connections to the RTM. Figure 3 shows a block diagramm of AMC and RTM for the wire scanner motion unit. Figure 4 shows a pre-series RTM.

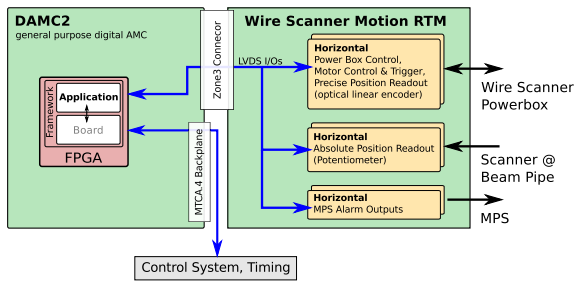


Figure 3: Couple of DAMC2 digital board and wire scanner motion RTM.

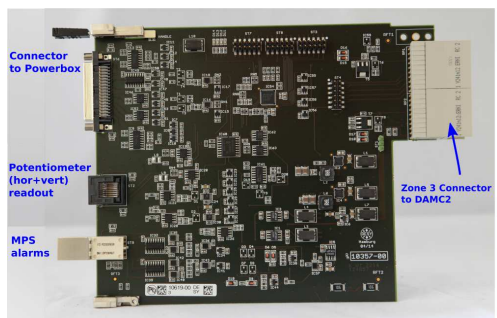


Figure 4: Pre-Series Wire Scanner motion RTM.

Wire Scanner Motion RTM

The interfaces to the scanner hardware (position readouts, motors, end switches, etc.) are implemented on a RTM which is under development at DESY. For high precision position read out a Heidenhain optical linear encoder [12] is used. This device achieves an accuracy of 0.5 µs. Hence this encoder gives a relative position value without initialization a linear potentiometer [13] with a resolution of 50 µs is used for safety purposes. The potentiometer value is captured by an ADC on the RTM. Furthermore the RTM implements motor control and trigger interfaces as well as Machine Protection System (MPS) outputs. One RTM implements the interfaces for two channels of one station with horizontal and vertical motion unit.

Wire Scanner Power Box

The RTM is connected to a 19" 5HU so called power box, which houses motor controllers and power supplies (which

Copyright © 2014 CC-BY-3.0 and by the respective authors

are volumious and have weights about 12 kg) for a set of horizontal and vertical motion unit. Additionally the power box implements some electronics for galvanic isolation of signals. A microcontroller is used to reduce the number of cables between RTM and power box by transmitting slower and uncritically signals over a serial data link. Figure 5 shows an overview of a complete wire scanner station. Figure 6 shows the prototype power box during assembly.

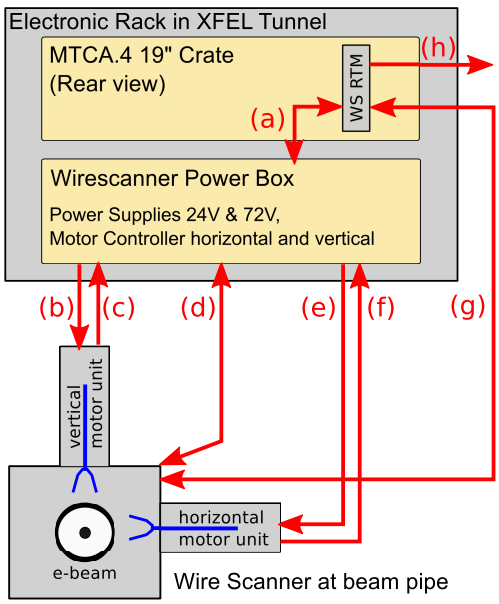


Figure 5: Overview of a complete wire scanner motion unit with RTM to Powerbox cable (a), motor cables (b, e), Heidenhain linear encoder readout cables (c, f), end switches and catch units cable (d), potentiometer readout cable (g) and cable with alarms to MPS (h).

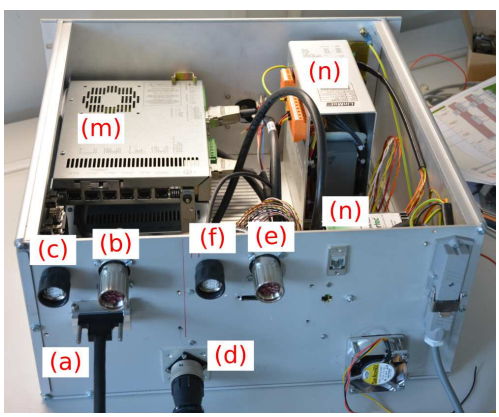


Figure 6: Prototype of Wire Scanner Powerbox (rear view) with LinMot Motor Controllers (m), Power Supplies (n), horizontal and vertical Heidenhain linear encoder readout cables (c, f) and motor cables (b, e), RTM to powerbox cable (a) and cable for end switches and catch units at the scanner (d).

MOTION APPLICATION FIRMWARE

Wire scanner related functionalities for motion units are implemented in the application part of the VHDL framework mentioned above.

Scan Modes

A fast scan is performed by receiving a pre-trigger (from timing system) 60 ms before arrival of the first bunch. Derived from the pre-trigger a configurable delayed trigger in dependency of the beam position and the desired wire to be hit is generated. This trigger is transmitted from the FPGA, through RTM to the corresponding motor controller into the wire scanner power box. Upon reception of a trigger the motor controller starts the motor with a jitter of $< 1\,\mu s$. To achieve a repetitive high accuracy of the motion (motor to beam sync) a special trigger input had been implemented into the motor controller firmware by LinMot company on request by DESY. For slow scans the motor is moved to certain positions or by incremental steps. This mode can also be used for calibrating the Beam Loss System.

Data Readout

If a fast scan is performed the encoder position is sampled and stored into an FPGA internal buffer with the bunch frequency (4.5 MHz). Figure 7 provides a sketch of a wire scanner station with a corresponding detector readout system. Both installations can be seen as two independent systems where the synchronisation of position and detector data on a bunch by bunch basis is done with the help of makro pulse numbers provided by the timing system.

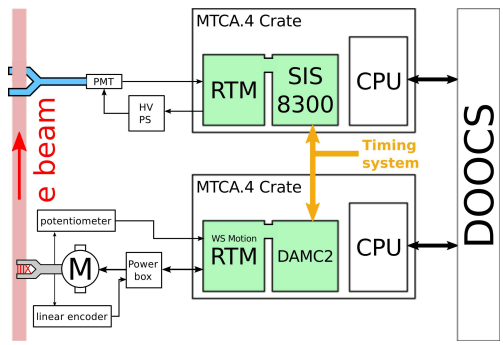


Figure 7: Overview of wire scanner station with corresponding detector readout. Only one motion plane is displayed. The detector can be meters apart from the motion unit.

Safety Aspects

Protecting the wires is an essential part of the system. To prevent the wire from melting the firmware has to make sure that number, frequency and charge of the bunches (bunch pattern received from timing system inside FPGA firmware) are limited and the fork achieves the design speed of 1 m/s in a certain position range (where the wire could hit the beam) in fast scan mode. For slow scans only single bunch is allowed. In case of incompatible bunch pattern the scan

Copyright © 2014 CC-BY-3.0 and by the respective authors

ISBN 978-3-95450-141-0

will not start. In case the speed is too slow due to motor failure during fast scan the beam will be stopped within the makropulse by an alarm given to the MPS. As the precision incremental linear encoder needs an initialisation the position and speed for the safety functionalities is measured with the linear potentionmeter as this is the only device in the system which gives an absolute value. Furthermore the potentiometer is radiation resistant. The end switch inside the catch unit masks the MPS alarm outputs electrically independend of the status of the wire scanner electronics so that system failures have no impact on the machine operation if the fork is out of the beam inside the parking position. To start a fast or slow scan the catch unit has to be opened electrically to allow the motor moving the fork out of the parking position.

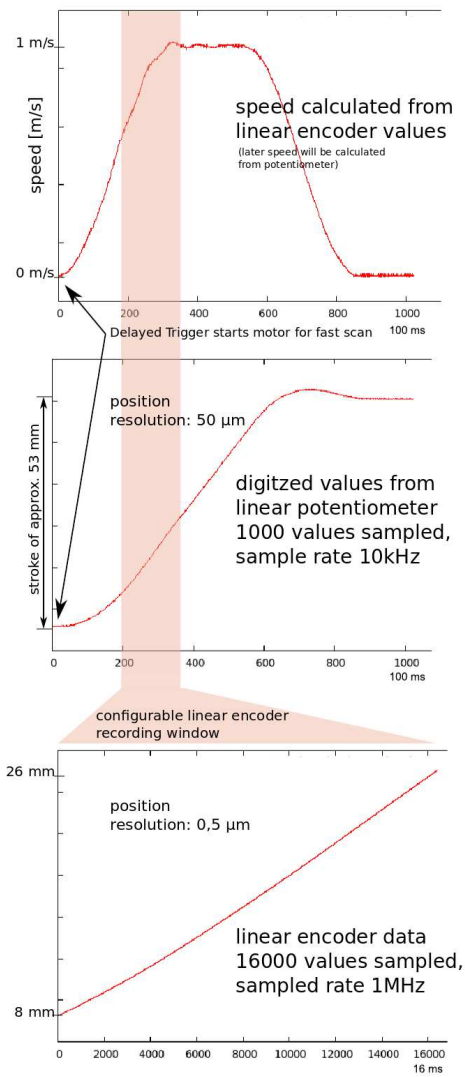


Figure 8: Complete triggered stroke showing speed, linear potentiometer data and high precision linear encoder data.

STATUS AND FIRST TESTS

Tests with mechanical design including the motor controller and motor itself has been evaluated and discussed in [5]. Based on this, first tests had been done with a prototype RTM and a first application firmware on a DAMC2 board. Figure 8 shows position readout of the linear potentionmeter, the more precise readout of the linear encoder and the calculated speed. By configuring thresholds for speed and position range an MPS alarm could be demonstrated.

OUTLOOK

After the first tests a two channel (horizontal and vertical) RTM has been designed and a pre-series has been built. Lose wired components like power supplies and LinMot motor controllers are currently installed into a prototype power box so that an initial test of the almost complete system of MTCA.4 crate, power box and mechanics will follow by the end of 2014 in the lab without beam.

REFERENCES

[1] "XFEL Technical Design Report", DESY 2006-097, http://xfel.desy.de/technical_information/tdr/tdr

[2] D. Nölle, "Overview on E-XFEL Standard Electron Beam Diagnostics", BIW 2010, Santa Fe/NM, USA

[3] M. Werner, "A New Wirescanner Control Unit", DIPAC 2001, Grenoble, France

[4] http://www.linmot.com

[5] V. Gharibyan, "Twisting Wire Scanner", IBIC2012, Tsukuba, Japan

[6] http://www.struck.de/sis8300.html

[7] http://tesla.desy.de/doocs/doocs.html

[8] http://www.picmg.org/openstandards/microtca

[9] http://mtca.desy.de

[10] http://fe.desy.de/fea/projects/tca_developments/damc2

[11] http://fe.desy.de/fea/projects/tca_developments/fpga_framework

[12] http://www.heidenhain.com

[13] http://www.gengethoma.ch

Copyright © 2014 CC-BY-3.0 and by the respective authors

VERTICAL BEAM SIZE MEASUREMENT AT CESRTA USING DIFFRACTION RADIATION

L. Bobb, JAI, Egham, Surrey, UK; DLS, Oxfordshire, UK
T. Aumeyr, P. Karataev, JAI, Egham, Surrey; Royal Holloway, University of London, Surrey, UK
E. Bravin, T. Lefevre, S. Mazzoni, H. Schmickler, CERN, Geneva, Switzerland
M. Billing, J. Conway, Cornell University, CLASSE, Ithaca, NY, USA

Abstract

Over recent years the first Diffraction Radiation (DR) beam size monitor has been tested on a circular machine. At CesrTA, Cornell University, USA, the sensitivity and limitations of the DR monitor for vertical beam size measurement has been investigated. DR emitted from 1 and 0.5 mm target apertures was observed at 400 and 600 nm wavelengths. In addition, interference between the DR signals emitted by the target and mask has been observed. In this report, we present the recent observations and discuss areas for improvement.

INTRODUCTION

Diffraction Radiation (DR) describes photons which are emitted when a charged particle passes through a target aperture. In this case the charged particle does not intersect the boundary of the medium but interacts with the medium via its electric field. The field of the charged particle excites atomic electrons of the medium. Polarisation currents are produced which are accompanied by the emission of electromagnetic waves called diffraction radiation [1].

The DR spectral angular distribution can be calculated using Eq. 1 where the wave number is defined as $k = 2\pi/\lambda$ and $E_{x,y}$ are the polarisation components of the radiation integrated over the target surface. The total field of the radiation is dependent on the incident charged particle field [1, 2].

$$\frac{d^2W}{d\omega d\Omega} = 4\pi^2 k^2 \left(|E_x|^2 + \left|E_y\right|^2\right) \tag{1}$$

The far-field zone defined by the far-field condition in Eq. 2 where L is the distance from the target to detector, γ is the Lorentz factor and λ is the DR wavelength [3] is the region at which the angular distribution of DR is observed. The prewave zone is the region near the target where the far-field condition is not satisfied.

$$L \gg \frac{\gamma^2 \lambda}{2\pi} \tag{2}$$

As shown in Fig. 1, DR is emitted in two directions. Forward Diffraction Radiation (FDR) is emitted in the direction of the charged particle trajectory. Backward Diffraction Radiation (BDR) is emitted in the direction of specular reflection relative to the incident charged particle trajectory and the target tilt angle θ_0. For high energy beams the emission of DR is considered to be non-invasive. The energy loss of the charged particles to DR is much less than the energy of the fast moving charged particle. For this reason the particle velocity can be treated as constant to a good accuracy [1] and DR, particularly BDR, can be used for non-invasive beam diagnostics.

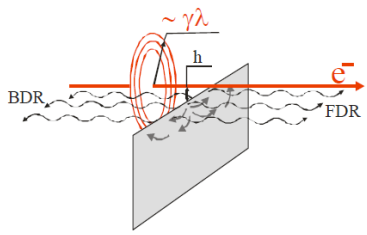


Figure 1: Schematic of DR emission from a particle moving in the vicinity of a medium where $\gamma\lambda$ is the effective electric field radius and h is the impact parameter [2].

EXPERIMENT SET-UP

The DR monitor is located in the L3 straight section of CesrTA (see Fig. 2). The X-ray beam size monitor (xBSM) [5] located at the CHESS synchrotron radiation (SR) station is used to measure the vertical beam size σ_y. The visible beam size monitor (vBSM) [6] located in L3 approximately 10 m upstream of the DR target is used to measure the horizontal beam size σ_x [7, 8].

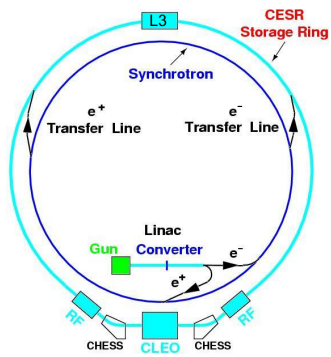


Figure 2: Layout of CesrTA [4].

An overview of the DR tank is shown in Fig. 3. Inside the tank the target is attached to a mechanism with two degrees of freedom: translation IN/OUT and rotation about this axis. DR escapes from the DR tank via a viewport at the top which is connected to the optical system.

In Fig. 4 a schematic and photograph of the optical system are shown. The optical system is a dual purpose system providing direct imaging of the target surface using the achromat

Copyright © 2014 CC-BY-3.0 and by the respective authors

ISBN 978-3-95450-141-0

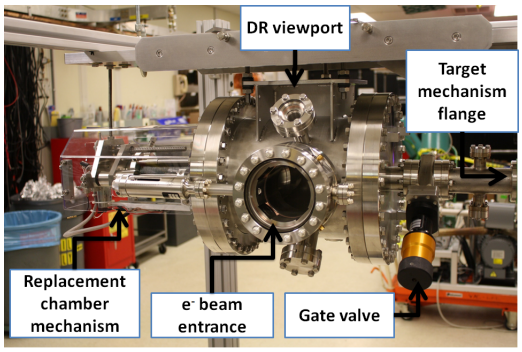


Figure 3: View of the DR target vacuum chamber from the upstream direction. The target is inserted from right to left.

and far-field imaging such that the angular distribution of DR can be observed using the planar convex (or biconvex) lens. In the latter case, since the compact optical system is within the prewave zone [3], the camera must be positioned at the back focal plane of the planar convex lens.

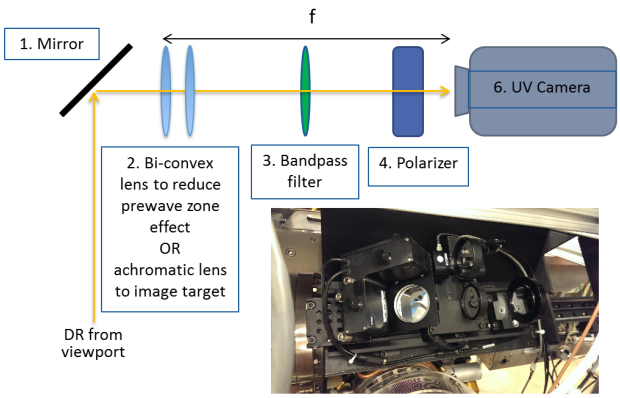


Figure 4: Schematic and image of the optical system.

Targets used on circular machines must be modified to have a fork-like shape since they must be retracted from the storage ring during injection and then inserted to the stored beam. The roughness, aperture size and coplanarity of the target must be controlled during fabrication to avoid distortions in the DR angular distribution.

Bonding by molecular adhesion is a technique that enables two substrates having polished surfaces to adhere to one another, without the application of adhesive [9]. The upper and lower tines of the target are machined separately in sets. The tines are then paired together in all variations to identify which upper/lower pairs result in the best coplanarity and attached to a flat mounting block. In effect, the molecular adhesion target consists of three individually machined pieces: two tines and the mounting block.

In this experiment a 0.5 mm molecular adhesion target made of Suprasil fused Silica (SiO_2) glass with an Aluminium (Al) and Chromium (Cr) coating was used. This target was paired with a Silicon Carbide mask with 1 and 2 mm apertures. The mask was positioned 15.5 mm upstream of the target to reduce the synchrotron radiation (SR) background (see Fig. 5).

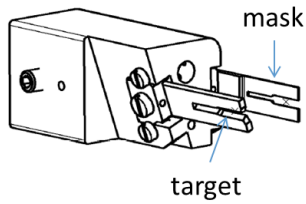


Figure 5: Schematic of the mask and target assembly.

OPTICAL DIFFRACTION RADIATION (ODR) MODEL WITH PROJECTED VERTICAL POLARISATION COMPONENT (PVPC)

The author of [10] has shown that the vertical polarisation component is sensitive to beam size. It is assumed that electron beam has a Gaussian distribution [2].

In [11], the expression for the ODR vertical polarisation component convoluted with a Gaussian distribution is given and shown here in Eq. 3 where α is the fine structure constant, γ is the Lorentz factor, θ_0 is the target tilt angle, $t_{x,y} = \gamma\theta_{x,y}$ where $\theta_{x,y}$ are the radiation angles measured from the mirror reflection direction, λ is the observation wavelength, σ_y is the rms vertical beam size, a is the target aperture size, $\overline{a_x}$ is the offset of the beam centre with respect to the slit centre and $\psi = \arctan\left[\frac{t_y}{\sqrt{1+t_x^2}}\right]$. This model is applicable when the TR contribution from the tails of the Gaussian distribution scraping the target is negligible i.e. approximately $a \geq 4\sigma_y$.

The projected vertical polarisation component (PVPC) takes the vertical (y) projection of the 3-dimensional (θ_x, θ_y, intensity) DR angular distribution. The y-projection is obtained by integrating over the horizontal angle θ_x. The visibility (I_{min}/I_{max}) of the y-projection is sensitive to the beam size of the electron beam. The reader should refer to [11] for detailed steps to obtain the vertical beam size measurement.

OPTICAL DIFFRACTION RADIATION INTERFERENCE (ODRI)

FDR produced by the mask interferes with BDR emitted by the target. Both of these DR sources will also interfere with background SR. The ODRI model uses Eq. 4 with parameters:

$$k = \frac{2\pi}{\lambda} \qquad f = \sqrt{k_x^2 + \eta^2}$$
$$k_x = k\sin\theta\cos\phi \qquad \beta = \sqrt{1 - 1/\gamma^2}$$
$$k_y = k\sin\theta\sin\phi \qquad \Phi_0 = \frac{2\pi d}{\beta\lambda}(1 - \beta\cos\theta)$$
$$\eta = \frac{k}{\beta\gamma} \qquad \Phi_1 = \frac{2\pi\Delta}{\lambda}$$

Copyright © 2014 CC-BY-3.0 and by the respective authors

$$\frac{d^2W_y^{slit}}{d\omega d\Omega} = \frac{\alpha\gamma^2}{2\pi^2}\frac{\exp\left(-\frac{2\pi a\sin\theta_0}{\gamma\lambda}\sqrt{1+t_x^2}\right)}{1+t_x^2+t_y^2}\times\left\{\exp\left[\frac{8\pi^2\sigma_y^2}{\lambda^2\gamma^2}(1+t_x^2)\right]\cosh\left[\frac{4\pi\overline{a_x}}{\gamma\lambda}\sqrt{1+t_x^2}\right]-\cos\left[\frac{2\pi a\sin\theta_0}{\gamma\lambda}t_y+2\psi\right]\right\} \quad (3)$$

$$E_y = \frac{ie}{4\pi^2 c}\left\{\left[\frac{\exp[-(\frac{a_1}{2}+y-\delta)(f-ik_y)]}{f-ik_y}-\exp(i\Phi_1)\frac{\exp[-(\frac{a_1}{2}-y+\delta)(f+ik_y)]}{f+ik_y}\right]\right.$$
$$\left.-\exp(i\Phi_0)\left[\frac{\exp[-(\frac{a_2}{2}+y)(f-ik_y)]}{f-ik_y}-\exp(i\Phi_1)\frac{\exp[-(\frac{a_2}{2}-y)(f+ik_y)]}{f+ik_y}\right]\right\} \quad (4)$$

where Δ is the coplanarity of the target tines in the longitudinal direction (i.e. along the trajectory of the electron), a_1 is the mask aperture size, a_2 is the target aperture size and d is the distance between the mask and target [12]. To observe the vertical angular distribution $\phi = \pi/2$ and a suitable range of θ is chosen. This model should be used when $a_1 < 4a_2$.

BEAM SIZE SENSITIVITY

The xBSM was used as the reference beam size monitor from which we could compare the DR monitor measurements. A variety of beam sizes were measured at 600 nm wavelengths. From DR theory it is known that the sensitivity to beam size scales inversely with wavelength. However as aforementioned, at $\lambda = 400$ nm the SR background was too high causing distortions to the DR angular distribution and inhibiting further analysis.

ODR with PVPC Technique

In Fig. 6 the DR angular distribution in the case of negligible interference is shown. As expected, the central lobes have a greater intensity compared to the side fringes. In Fig. 7 the beam size sensitivity is demonstrated. The visibility of the vertical projections at 45 μm beam size were larger than that at 17 μm as expected. The 45 μm line profile with a known beam offset relative to the target centre also had a greater visibility than that of the centred beam. Thus in Fig. 7 the ambiguity and contribution due to beam offset in the target aperture to the beam size measurement can be observed. The beam offset was observed from direct imaging of the target surface.

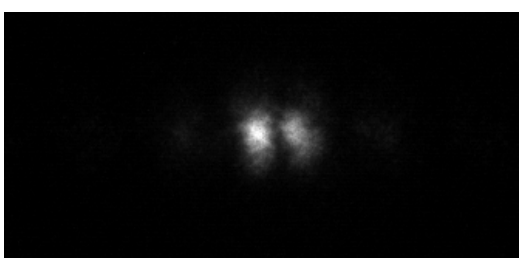


Figure 6: An example of the DR angular distribution: λ = 600 nm, 0.5 mm target and 2 mm mask.

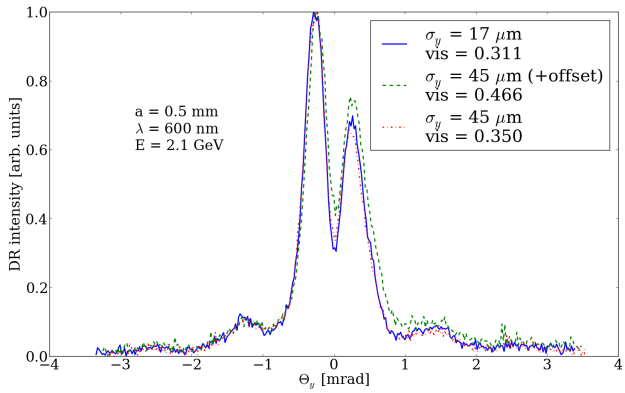


Figure 7: A comparison of projected vertical polarisation components (PVPCs) for different beam sizes.

Using the ODR model and PVPC technique, the expected visibility curves were simulated by obtaining the visibilities from simulated angular distributions using Eq. 3 for different beam sizes at 600 nm wavelength and 0.5 mm target. The simulated visibility curve assumes zero background thus the curve passes through the origin. The expected theoretical visibility curve was fitted to Eq. 5 [2] to obtain the coefficients $A_{0,1,2}$. The coefficient A_0 defines the crossing point on the visibility axis. For real data measurements there will be some background contribution to the DR signal. Thus A_0 will be larger than zero and this baseline represents the background contribution to beam size measurement.

$$R = A_0 + A_1\sigma_y + A_2\sigma_y^2 \quad (5)$$

Images at 17 and 45 μm beam size and 600 nm wavelength were analysed. In Fig. 8 the measured visibility from each image was plotted (red crosses). The average visibility at each beam size was also plotted (green circles). From the simulated visibility curve the coefficients obtained were $A_1 = -15.49$ and $A_2 = 2.130\times10^7$. Using the data and performing a least squares fit given A_1 and A_2, the background offset for the real data was found to be $A_0 = 0.292$. This background offset was predominantly due to the SR.

As discussed, a significant SR contribution to the beam size measurement was observed at 600 nm wavelength. In

Copyright © 2014 CC-BY-3.0 and by the respective authors

ISBN 978-3-95450-141-0

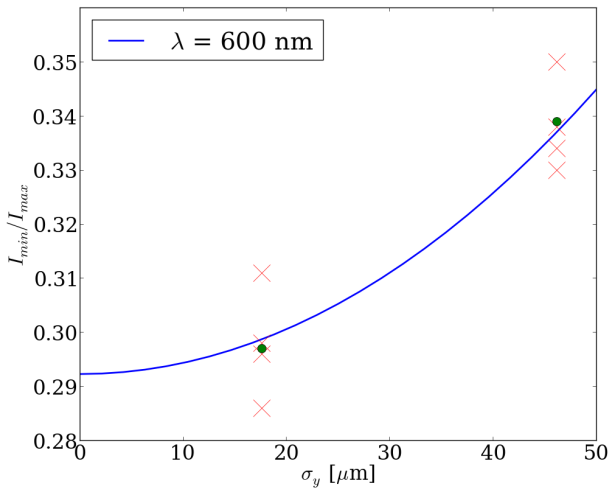


Figure 8: Resultant visibility curve at 600 nm wavelength and 0.5 mm target aperture from a least squares fit of the average visibility (green circles) at different beam sizes from individually measured visibilities (red crosses) corresponding to separate images.

this regime, it was found that SR contributed primarily as a background offset and did not modify the DR interference fringes noticeably. The beam size sensitivity improves with decreasing wavelength. However, in this experiment the SR contribution increased with decreasing wavelength. At 400 nm it was not possible to accurately measure the visibility due to the modification of the DR angular distribution due to SR. In Fig. 9 the distortion to the angular distribution at 400 nm in the 0.5 and 2.0 mm target and mask apertures respectively is shown.

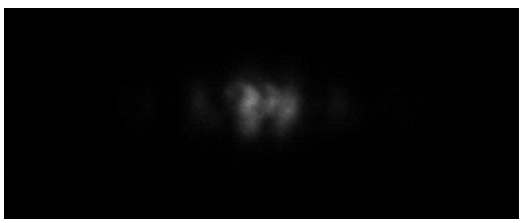


Figure 9: DR angular distribution at 400 nm wavelength and 0.5 mm target aperture.

ODRI

In addition to beam size sensitivity, the ODRI model is also sensitive to the beam divergence. In the Monte Carlo application of the ODRI model, the summation of the DR intensity distribution for each electron of the beam is simulated. Therefore each electron is assigned a transverse position and divergence in the beam satisfying the user-defined beam profile. The beam profile and beam divergence are assumed to be Gaussian. To fit the beam size only, a reasonable estimate of the beam divergence was calculated. This was done by calculating the vertical beam emittance using the beam size measurement from the xBSM and the machine optics.

Table 1: Table of Beam Size and Divergence at the ODR Monitor

$\sigma_y(xBSM)$ [μ m]	ε_y [m]	$\sigma_y(ODR)$ [μ m]	$\sigma'_y(ODR)$ [μrad]
22.2	3.06E-11	17.6	4.08
46.1	1.70E-10	36.6	8.46
58.2	2.71E-10	46.2	10.7

The natural vertical emittance ε_y was calculated to be $\sigma_y^2(xBSM)/\beta_y(xBSM) = 3.96 \times 10^{-11}$ m. From the vertical emittance the beam size and beam divergence were calculated as 17.6 μm and 4.08 μrad respectively. These results are summarised in Table 1.

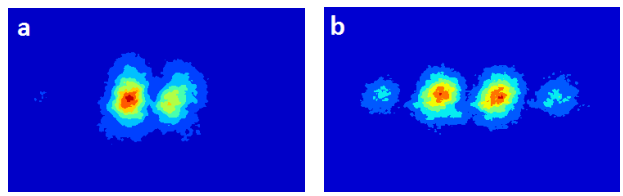


Figure 10: Contour plots of the angular distributions for a) ODR and b) ODRI.

In Fig. 10 the ODR and ODRI angular distributions may be compared. Fig. 10(a) shows the non-interference case (ODR) using a 0.5 mm target and 2.0 mm mask. Fig. 10(b) shows the interference case (ODRI) using a a 0.5 mm target and 1.0 mm mask. As expected, an enhancement of the side fringes was observed due to the interference between FDR and BDR from the mask and target respectively.

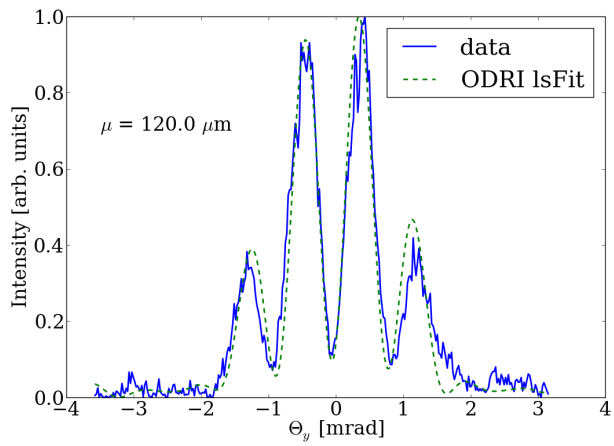


Figure 11: A beam offset of 120 μm obtained using a least squares fit for ODRI data given parameters: σ_y = 17.6 μm, σ'_y = 4.08 μrad and coplanarity offset 40 nm.

As aforementioned in addition to beam size, a beam offset relative to the centre of the target aperture also contributes to the visibility measurement. To quantify this beam position offset the line profile was fitted using the method of least squares. The result of the least squares fit is shown in Fig. 11.

Copyright © 2014 CC-BY-3.0 and by the respective authors

The beam offset relative to the target aperture centre was found to be 120 μm.

SHADOWING OF THE ELECTROMAGNETIC FIELD

In the formation zone ($L_f \approx \gamma^2\lambda/2\pi$) the Coulomb field of the ultra-relativistic ($\gamma >> 1$) electron and FDR from the aperture cannot be measured separately [13].

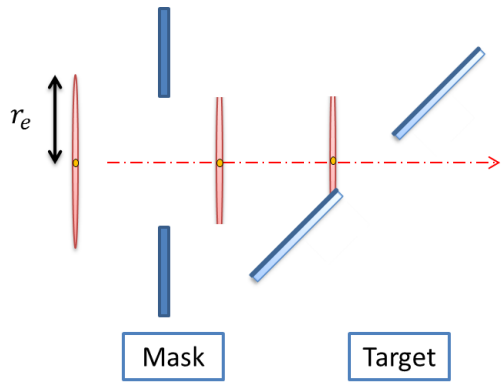


Figure 12: Shadowing of the Coulomb field of an electron passing through the mask and target.

In the Coulomb field point of view, the electric field associated with the electron beam is considered to consist of quasi-real photons. Scattering of the Coulomb field by the mask gives rise to FDR. Positioned downstream, the target is in the shadow of the mask (see Fig. 12). Thus it emits almost no radiation. The Coulomb field is gradually "repaired" during the formation zone [13].

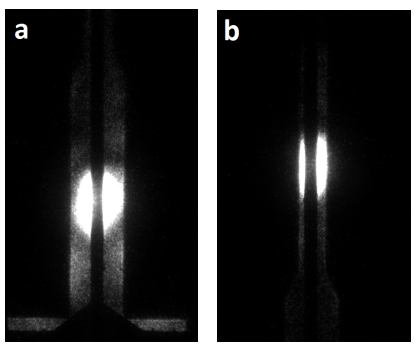


Figure 13: Images of the 0.5 mm target surface: (a) with negligible shadowing from a 2 mm mask and (b) with significant shadowing from a 1 mm mask where λ = 600 nm.

In Fig. 13(a) negligible shadowing was observed and the measured radius of the illuminated DR disc in the vertical direction (perpendicular to the target edge) was 0.96 mm. The effective field radius for an electron $r_e \approx \gamma\lambda/2\pi$ given γ = 4110 and λ = 600 nm was 0.4 mm. A factor of two difference was obtained between the calculated and measured radii of illumination of the DR disc in the vertical direction.

Fig. 13(b) shows significant shadowing. The vertical width of the illuminated region has reduced from 2×0.96 = 1.92 mm to 1 mm defined by the mask aperture. Here the reader should note the significance in this observation of clear evidence of the shadowing effect on the target surface. The mask is separated from the target and the optical system only images the target surface. Therefore although it is expected that SR cannot extend into the shaded regions of the target due to being blocked by the mask positioned upstream, DR emitted by the target should not have this boundary unless as a result of shadowing.

CONCLUSION

In this paper vertical beam size measurements from the Diffraction Radiation monitor installed at CesrTA are presented. Using a 0.5 mm target and 600 nm wavelength, interference effects in the angular distribution between the mask and target have been investigated. Further study of these interference effects have been explored via direct imaging of the target surface. These observations show evidence for the presence of shadowing.

ACKNOWLEDGMENT

The author would like to thank the numerous colleagues who have participated in the project from CERN, Cornell University and Royal Holloway, University of London and the support of Diamond Light Source in presenting this research to the accelerator community.

Copyright © 2014 CC-BY-3.0 and by the respective authors

ISBN 978-3-95450-141-0

REFERENCES

[1] A. P. Potylitsyn et al., *Diffraction Radiation from Relativistic Particles*, (Springer, Berlin Heidelberg, 2010)

[2] P. Karataev, "Investigation of Optical Diffraction Radiation for Non-Invasive Low-Emittance Beam Size Diagnostics", Thesis, 2004.

[3] P. V. Karataev, "Pre-wave zone effect in transition and diffraction radiation: Problems and solutions", Physics Letters A, 345 (2005) p. 428-438.

[4] Cornell Electron Storage Ring, LEPP, Cornell University, http://www.lepp.cornell.edu/Research/AP/CESR/

[5] N.T. Rider, et al., "Operation of a Single Pass, Bunch-by-Bunch X-ray Beam Size Monitor for the CESR Test Accelerator Research Program", IBIC'12, Tsukuba, Japan, WECD01, p. 585.

[6] S. Wang, et al., "A Turn-by-turn Beam Profile Monitor using Visible Synchrotron Radiation at CESR-TA", IPAC'13, Shanghai, China, MOPWA073, p. 849.

[7] L. Bobb et al., "UV/X-ray Diffraction Radiation for Non-intercepting Micron-scale Beam Size Measurement", IBIC'12, Tsukuba, Japan, MOCC01, p. 24.

[8] L. Bobb et al., "Diffraction Radiation Test at CesrTA for Non-Intercepting Micron-Scale Beam Size Measurement", IBIC'13, Oxford, UK, WEAL3, p. 619.

[9] S. Kerdiles, C. Duret, A. Vaufredaz and F. Metral, "Process for bonding by molecular adhesion", Patent (2012), http://www.google.com/patents/US8158013

[10] M. Castellano, "A new non-intercepting beam size diagnostics using diffraction radiation from a slit", Nucl. Instr. and Methods in Phys. Res. Sec. A: Accelerators, Spectrometers, Detectors and Associated Equipment, 394, 3, (1997), p. 275-280.

[11] P. Karataev, R. Hamatsu, T. Muto, S. Araki, H. Hayano, J. Urakawa, G. Naumenko, A. Potylitsyn and T. Hirose, "Application of optical diffraction radiation to a non-invasive low-emittance high-brightness beam diagnostics", QUANTUM ASPECTS OF BEAM PHYSICS. SINGAPORE : WORLD SCIENTIFIC PUBL CO PTE LTD, (2004) p. 111-118

[12] A. Cianchi, M. Castellano, L. Catani, E. Chiadroni, K. Honkavaara and G. Kube, "Nonintercepting electron beam size monitor using optical diffraction radiation interference", Phys. Rev. ST Accel. Beams, 14, (2011), 10, p. 102803-102812.

[13] G. Naumenko, X. Artru, A. Potylitsyn, Y. Popov, L. Sukhikh and M.Shevelev, "Shadowing of the electromagnetic field of relativistic charged particles", Journal of Physics: Conference Series, 236, (2010), 1, p. 012004.

Copyright © 2014 CC-BY-3.0 and by the respective authors

STATUS OF AND FUTURE PLANS FOR THE CERN LINAC4 EMITTANCE METER BASED ON LASER ELECTRON-DETACHMENT AND A DIAMOND STRIP-DETECTOR

T. Hofmann*, E. Bravin, U. Raich, F. Roncarolo, F. Zocca, CERN, Geneva, Switzerland
S. Gibson, K.O. Kruchinin, A. Bosco, G. Boorman
John Adams Institute at Royal Holloway, University of London, Egham, United Kingdom
E. Griesmayer, CIVIDEC Instrumentation, Vienna, Austria

Abstract

LINAC4 has started its staged commissioning at CERN. After completion it will accelerate high brightness H^- beams to 160 MeV. To measure the transverse profile and emittance of the beam, a non-destructive method based on electron photo-detachment is proposed, using a pulsed, fibre-coupled laser to strip electrons from the H^- ions. The laser can be focused and scanned through the H^- beam, acting like a conventional slit. A downstream dipole separates the neutral H^0 beamlet, created by the laser interaction, from the main H^- beam, so that it can be measured by a diamond strip-detector. Combining the H^0 beamlet profiles with the laser position allows the transverse emittance to be reconstructed. A prototype of this instrument was tested while commissioning the LINAC4 at 3 and 12 MeV. In this paper we shall describe the experimental setup, challenges and results of the measurements, and also address the characteristics and performance of the diamond strip-detector subsystem. In addition, the proposal for a permanent system at 160 MeV, including an electron detector for a direct profile measurement, will be presented.

INTRODUCTION

In the context of the High-Luminosity upgrade of the LHC (HL-LHC), CERN needs to upgrade its LHC injector chain, to deliver higher brightness beams. LINAC4 will replace the ageing LINAC2, the first injector in the chain, aiming to accelerate H^- ions from 45 keV at the source front-end to 160 MeV at the injection into the PS-Booster (PSB). Using a H^- beam makes injection via the charge-exchange scheme into the PSB possible [1]. With the brightness of the PSB proton beam is expected to double with respect to the present configuration based on protons injected at 50 MeV from LINAC2.

The transverse emittance has to be measured precisely at the machine's top-energy of 160 MeV. It is not possible to do so with a conventional slit & grid method as at this energy the H^- ions will travel through any possible slit material. Other methods, such as three-profile measurement, can be heavily influenced by space-charge effects while the secondary emission monitors typically used for this cannot handle the nominal LINAC4 pulse length of 400 µs.

To overcome these problems, a non-destructive method based on laserwire technology was proposed [2]. A pulsed laser with a peak power of about 1 kW can be focused to a diameter of less than 200 µm in the interaction region with the H^- beam. Since the outer electron of the H^- is very weakly boundeded to the atom, it can easily be stripped by a low energy photon [3]. Having neutralized a slice of the H^- beam, the H^0 move straight forward to a detector while the H^- are deflected by a bending magnet between the laser and the H^0 detector. By scanning the laser beam across the H^- beam, the H^0 profiles measured can be used to reconstruct the transverse emittance. Figure 1 shows the prototype setup that has been developed for tests during the LINAC4 commissioning at 3 and 12 MeV.

EXPECTED SIGNAL AND BACKGROUND

The H^0 background is expected to be dominated by H^- stripping upstream due to collisions with residual gas atoms particularly where the laser H^- interaction region is not preceded by a dipole magnet. This has been simulated in order to estimate the signal to background ratio at the H^0 detector. The simulation results are shown in Table 1 for different beam energies (3 and 12 MeV during commissioning and 160 MeV for the final system). The signal values are calculated assuming a laser pulse with an energy of 67 µJ when crossing the center of the H^- beam and a diamond strip detector with an area of 18 mm x 3.5 mm, used to integrate the arriving H^0 . The signal variation for different energies comes from the different time of flight of the H^- in the laser light (the slower the H^- the larger the stripping for similar stripping cross-sections) and the varying H^- beam sizes at different energies. The reduction of the background for increasing energy follows from the lower expected rest gas concentration. More details can be found in [2].

Table 1: Comparison of Simulation Results for Signal and Background in Different Commissioning Stages

H^- Beam Energy [MeV]	3	12	160
Laser Stripped [H^0 / ns]	1549	408	2400
Background [H^0 / ns]	105	69	67
SNR	**14.7**	**5.9**	**35.8**

* thomas.hofmann@cern.ch

ISBN 978-3-95450-141-0

Copyright © 2014 CC-BY-3.0 and by the respective authors

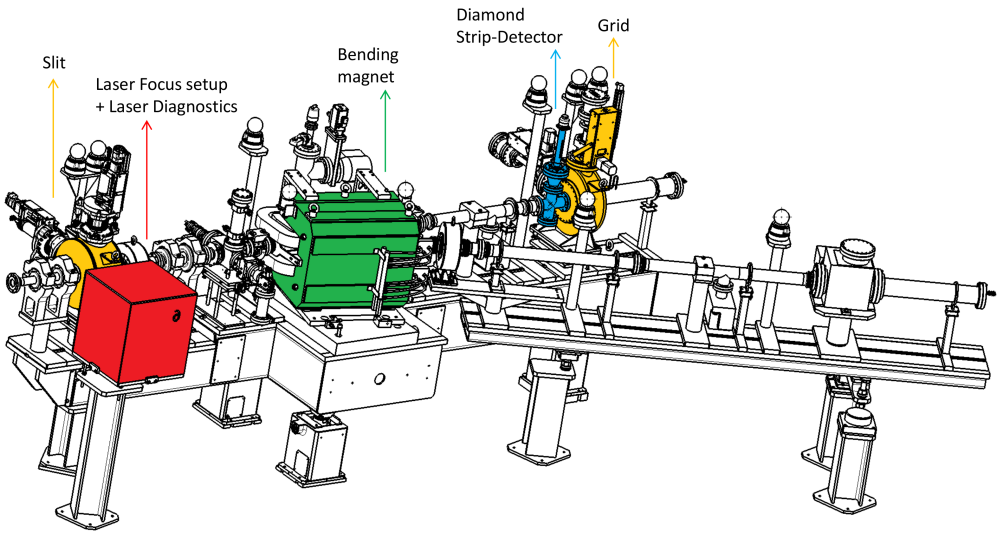


Figure 1: LINAC4 test bench. The laser is transported by an optical fiber to the red box and then focused into the beampipe. The bending magnet separates the H^0 from the H^- . The H^0 profiles are measured by a diamond strip detector. The laser-diamond measurements can be directly compared to the operational slit-grid system scans.

PROTOTYPE TEST AT THE LINAC4 3 MeV AND 12 MeV BEAM

A prototype system was developed for tests during the LINAC4 3 MeV and 12 MeV commissioning. The nominal beam parameters are summarized in Table 2. However, during the 3 and 12 MeV tests the H^- source managed to deliver only up to 8.5 mA.

Table 2: LINAC4 Beam Parameters

Parameter	Value
Particle type	H^-
Top Energy	160 MeV
Pulse Frequency	0.83 Hz
Pulse Length	400 µs
Nominal current	40 mA
RF-frequency	352 MHz

In the measurement setup shown in Fig. 1, the laser source, a diode pumped Master Oscillator Power Amplifier (MOPA) fiber-laser generates 80 ns FWHM pulses [4]. It was operated with a repetition frequency of 30/60 kHz and a pulse energy between 75 and 150 µJ. The transport of the laser beam to the LINAC4 beam pipe was accomplished by using a Large Mode Area (LMA) optical fiber [5]. This method is on one hand limiting the maximum laser-pulse power but on the other hand a very effective and simple method, when compared to high power, open air lasers. Finally the laser is collimated after the fiber and focused into the beam pipe so that the H^- beam sees it as a laser wire with an almost constant 150 µm diameter. After the interaction of the H^- ions with the laser, the H^0 atoms created drift for 3.35 m towards the diamond strip-detector shown in Fig. 2. The detector is a 20 x 20 mm, 500 µm thick disc of polycrystalline diamond. The front side is covered by 5 strip-shaped aluminium electrodes while on the back side a 500 V bias is applied to the whole surface. When a H^0 particle hits the detector, the remaining electron is stripped in the first few nanometers with the resulting proton traversing the diamond material, creating carrier and whole pairs. At 3 MeV the proton is absorbed in the diamond after about 50 µm, while at 12 MeV it can cross the complete 500 µm and exit the detector. The signal produced is proportional to the energy deposited inside the diamond. The detector read out, shown at the bottom of Fig. 2, includes a 1 µF capacitor used to rapidly recharge the diamond when electrons are read out. The signal from the diamond is digitized with a 1 GS/s oscilloscope.

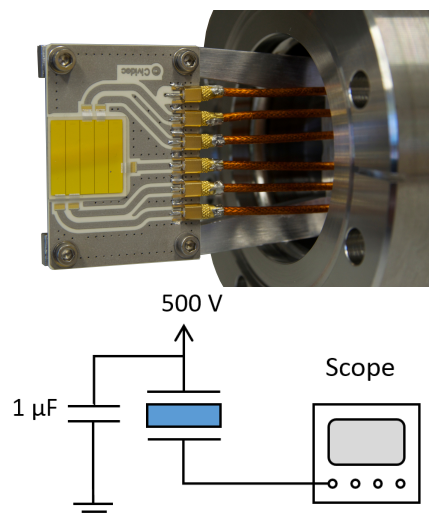


Figure 2: Top: Polycrystalline diamond detector with 5 aluminium electrodes. Bottom: Readout schematic for one diamond channel [6].

Copyright © 2014 CC-BY-3.0 and by the respective authors

ISBN 978-3-95450-141-0

3 MeV Results

The comparison between the diamond signal and the beam current during a beam pulse is shown in Fig. 3. The signal peaks correspond to the 30 kHz laser pulses. The slight increase of the signal floor can be explained by the H^0 atoms created by residual gas collisions. The ratio between the peak signal and baseline value is fairly constant (between 10 and 11). Given the uncertainties of the simulation input (e.g. gas pressure, detector time response etc...), this value compares well to the simulated value of 14.7 (see Table 1).

Even though in some cases the signal from the diamond detector reproduced well the beam current evolution [7], in most cases, as presented here, the agreement was poor in the second part of the beam pulse. The reason for this is not yet fully understood, but proton implantation in the diamond is likely to play a key role. From simulations, the predicted number of protons implanted by the background for one LINAC-pulse is 3.7×10^7. The variation of the electrostatic field inside the diamond could thus lead to a decreased Charge Collection Efficiency (CCE) during the LINAC pulse. This might also explain the signal amplitude of just a few mV, which is significantly lower than expected by calculations not considering implantation. All measurements at 3 MeV were therefore performed with a 46 dB preamplifier to achieve an acceptable signal level.

Despite the non-optimized diamond detector, it was still possible to complete some emittance scans. Due to the inhomogeneous response of the different diamond channels the reconstruction of beam profile and emittance was performed with the data of just one channel. Details on the analysis of the acquired data can be found in [8]. An example of the measured phase space distribution is shown in Fig. 4. This result was compared to the operational slit-grid system and the agreement in terms of normalized emittance was found to be within 2 % [7].

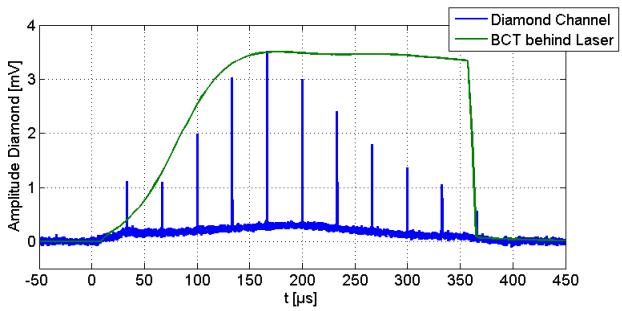


Figure 3: Signal of one diamond detector channel at the 3 MeV test compared to Beam Current Transformer (BCT) signal (normalized to the diamond channel signal).

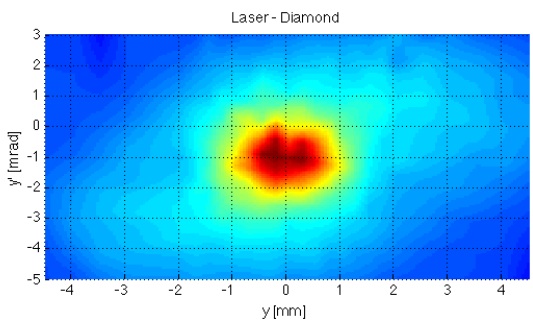


Figure 4: Transverse emittance of the LINAC4 beam at 3 MeV measured with laserwire & diamond detector.

12 MeV Results

At the time of writing just the very first tests at 12 MeV were accomplished. Figure 5 shows the signal from one channel of the diamond detector, compared to a beam current transformer signal, recorded with a similar setup as used for the measurements at 3 MeV. The signal amplitude of the diamond detector is now much higher than at 3 MeV and the shape now follows the beam current measured with the BCT. Since at 12 MeV proton implantation into the diamond is expected to be negligible, this preliminary results would confirm the hypotheses discussed above for the 3 MeV case. The signal to background ratio is also decreased as predicted in Table 1. More measurements at 12 MeV are foreseen in the next few months and will be used for performing emittance scans and to check the homogeneity of the different diamond detector channels.

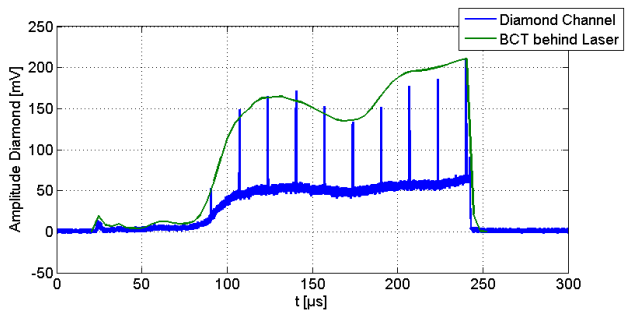


Figure 5: Preliminary result from a 12 MeV beam test. Comparison of one diamond detector channel with a BCT signal (normalized to the diamond channel signal).

DESIGN OF THE 160 MeV SYSTEM

The final emittance meter will be installed in the 160 MeV section of LINAC4 as shown in Fig. 6. It is foreseen to install two independent systems. Both shall be able to measure the beam emittance in the x and y plane. Due to the high beam energy and proximity to the main dump the radiation level has to be considered when planning the installation, and therefore the laser source will be situated in a cabinet on the surface, about 10 m above the tunnel. The laser beam will again be delivered to the H^- beam line through a LMA fiber, of about 20 m in length. The design of laser optics and diagnostics can be reused with only minor changes from the 3/12 MeV prototype [4].

H^0 Detector

The first candidate for H^0 monitoring in the final system at 160 MeV is the diamond strip detector tested at 3 and 12 MeV.

Copyright © 2014 CC-BY-3.0 and by the respective authors

ISBN 978-3-95450-141-0

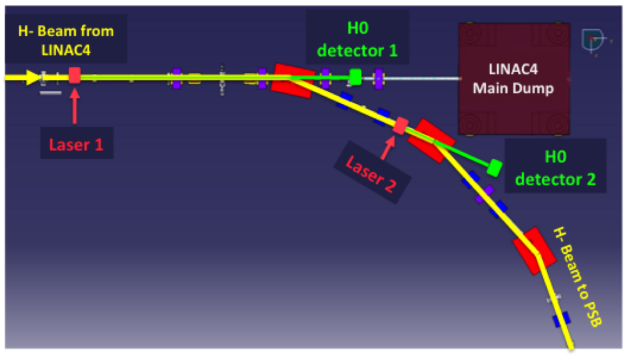


Figure 6: Layout of the 160 MeV section of LINAC4 showing the transfer line towards the PS-Booster and the locations reserved for two laser profile and emittance meter systems.

The number of channels can be increased by changing the design of the front electrodes. Instead of the five existing electrodes with a width of 3.5 mm, it is possible to use a metallisation pattern with up to 35 stripes and a width of 500 µm per channel. Due to the H^0 bombardment and the radiation from the dump, the radiation hardness of the detector has to be carefully examined. When considering 160 MeV protons, diamond detectors are rated about 10 times more radiation hard than silicon detectors [9]. But even this seems to be on the borderline for the LINAC4 requirements. A test carried out with an alpha source in the laboratory after the measurement campaign at the 3 MeV H^- beam, already showed a degradation of the detector. In order to measure a correct profile despite this ageing due to radiation, a calibration procedure would need to be performed periodically and possibly automatically. Tests to find the most reliable calibration procedure are ongoing.

Alternative H^0 detection concepts such as the use of Gas Electron Multiplier (GEM) [10] are also under investigation.

Profile Measurement by Electron Collection

Measuring the number of stripped electrons during a laser scan allows the transverse beam profile to be reconstructed. This can be achieved by installing a weak bending magnet just after the laser-beam interaction point, so that the electrons are steered to a Faraday cup detector. A system including stripped electron counting has already been implemented at the Oak Ridge Spallation Neutron Source (SNS) [11].

At 160 MeV the stripped electrons have a kinetic energy of just 87 keV. A magnetic field of less than 0.02 T along a 8 cm long gap is therefore sufficient to deflect them by 90^o. The unstripped H^- ions travelling through the same magnet will be deflected by less than 1 mrad, for which an identical corrector magnet with opposite polarity placed just after the electron extraction point will transparently re-steer the main beam to the original orbit.

The challenge for the Faraday cup will be to achieve sufficient time resolution. The Faraday cup as well as its read out electronics will have to be designed to resolve the 80 ns laser-pulses to distinguish it from the background. The design of the Fadaday cup and the magnets is currently ongoing.

CONCLUSIONS AND OVERVIEW

A laser-based emittance meter prototype was successfully developed and tested in LINAC4 at both 3 and 12 MeV. At 3 MeV the H^- stripping was found to agree well with prior simulations but the implantation of protons into the detector caused a very weak response of the detector. Nevertheless, a comparison of emittance measurements with the slit and grid system showed very good agreement.

The first tests at 12 MeV, where proton implantation is negligible, show that H^0 detection with a diamond detector can work with high sensitivity. If confirmed by further measurement campaigns at 12 MeV, this would also apply to the final system at 160 MeV.

The next year will be dedicated finalizing this development and producing the final system to measure beam profiles and emittances at the top energy of LINAC4.

ACKNOWLEDGMENTS

We acknowledge the support of the Marie Curie Network LA^{3}NET which is funded by the European Commission under Grant Agreement Number GA-ITN-2011-289191.

In addition, we would like to acknowledge the contribution to this work and to the general development of laser-stripping technologies by Christoph Gabor, who sadly passed away before these results could be published.

REFERENCES

[1] W. Weterings et al., "Status of the 160 MeV H^- injection into the CERN PSB", TUPPR091, Proceedings of IPAC2012, New Orleans, Louisiana, USA

[2] T. Hofmann et al., “Laser based stripping system for measurements of the transverse emittance of H^- beam at the CERN LINAC4” MOPME075, Proceedings of IPAC2013, Shanghai, China

[3] J.T. Broad and W.P. Reinhardt, "One- and two-electron photoejection from H^- : A multichannel J-matrix calculation", Physics Review A 14, 2159 (1976)

[4] S. Gibson et al., "Overview of laserwire beam profile and emittance measurements for high power proton accelerators", TUPF15, Proceedings of IBIC2013, Oxford, UK

[5] Datasheet, "20/130 Passive LMA Double Clad Fiber", www.nufern.com

[6] CIVIDEC Instrumentation GmbH, www.cividec.at

[7] F. Roncarolo et al., "Transverse profile and emittance measurements with a laser stripping system during the CERN LINAC4 commissioning at 3 and 12 MeV", Proceedings of LINAC2014, Geneva, Switzerland

[8] S. Gibson et al., "A fibre coupled, lowpower laserwire emittance scanner at CERN LINAC4", Proceedings of IPAC2014, Dresden, Germany

[9] Wim de Boer et al., "Radiation hardness of diamond and silicon sensors compared", Phys. Stat. Sol. A 204, No. 9, 3004–3010 (2007)

Copyright © 2014 CC-BY-3.0 and by the respective authors

[10] S. Duarte Pinto et al., "GEM-based beam profile monitors for the antiproton decelerator", J. Instrum., Volume 7, March 2012

[11] Y. Liu et al., "Laser wire beam profile monitor in the spallation neutron source (SNS) superconducting linac", Nucl. Instr. and Meth. in Phys. Res. section A 612, 241, (2010).

Copyright © 2014 CC-BY-3.0 and by the respective authors

ISBN 978-3-95450-141-0

CERN-SPS WIRE SCANNER IMPEDANCE AND WIRE HEATING STUDIES

E. Piselli, O. E. Berrig, F. Caspers, B. Dehning, J. Emery, M. Hamani, J. Kuczerowski, B. Salvant, R. Sautier, R. Veness, C. Vuitton, C. Zannini,
CERN, Geneva, Switzerland

Abstract

This article describes a study performed on one of the CERN-SPS vertical rotational wire scanners in order to investigate the breakage of the wire, which occurred on several occasions during operation in 2012. The thermionic emission current of the wire was measured to evaluate temperature changes, and was observed to rise significantly as the wire approached the ultimate LHC beam in the SPS, indicating the possibility of strong coupling between the beam's electromagnetic field and the wire. Different laboratory measurements, complemented by CST Microwave Studio simulations, have therefore been performed to try and understand the RF modes responsible for this heating. These results are presented here, along with the subsequent modifications adopted on all of the operational SPS wire scanners.

INTRODUCTION

Beam Wire Scanners (BWS) are instruments used for precise transvere profile measurements in the LHC and its injector chain.

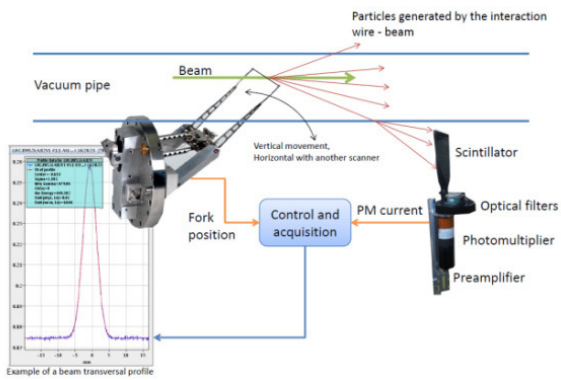


Figure 1: BWS working principle.

During the scan, a thin carbon wire is moved through the beam, with the interaction of beam and wire generating a cascade of secondary particles. For a high energy primary beam these secondary particles are energetic enough to exit the vacuum chamber and can be detected by a scintillator/photomultiplier assembly. With appropriate settings the amplitude of the light produced by the scintillator is proportional to the intercepted beam intensity (Fig. 1).

As the scitillator/photomultiplier signal is fast compared to the revolution frequency, synchronising the acquisition of the wire position and the measured light intensity allows the transverse beam profile to be reconstructed as the wire moves across the beam over multiple turns.

The CERN-SPS is equipped with 6 rotating BWS fitted with a carbon wire of 30µm diameter and which can scan at a maximum speed of 6 ms^{-1}.

SPS WIRE BREAKAGE MECHANISMS

The CERN-SPS rotational wire-scanners are used on a regular basis by machine operators to perform beam size measurements to verify and optimise the beam emittance.

During the run in 2012, there were many more abnormal wire breakages during the use of these scanners compared to previous years. Table 1 summarize these failures. Since the SPS machine was being pushed to provide high intensity beams for LHC, the first suspected cause of these events was due to these higher intensites, as had previously been observed in the high intensity run of 2002 [1]. During this 2002 run, there were observations of a large current induced in the wire, leading to wire breakage, when the scanning fork was in its parking position. This was finally explained by radio-frequency (RF) modes developing in the scanner tanks with the wire acting as an antenna. This was though to be solved by the addition of ferrites to the scanner tanks to damp these modes.

Table 1: BWS SPS Wire Failures During in 2012

Scanner	Beam induced failures	Mechanical failures
416.H	0	0
416.V	2	0
519.H	1	2
519.V	1	0

To try and understand the failures of 2012, the evolution of the wire current of one of the first breakage event observed was plotted as function of the time. Fig. 2 shows four consecutive wire-scans for vertical scanner 416, one before, one during and 2 after wire failure. The first two clearly indicate a current increase in the wire as the wire approaches and then crosses the beam (at 0.008 s as can be seen on the corresponding profile measurements). A current as high as 12 mA is observed when the wire has passed the beam and is close to its IN position. The wire breakage occurs during the second wire-scan (shown in blue). It can be seen that the

Copyright © 2014 CC-BY-3.0 and by the respective authors

evolution is similar to the previous wire-scan (in red), until 14 ms where the wire breaks.

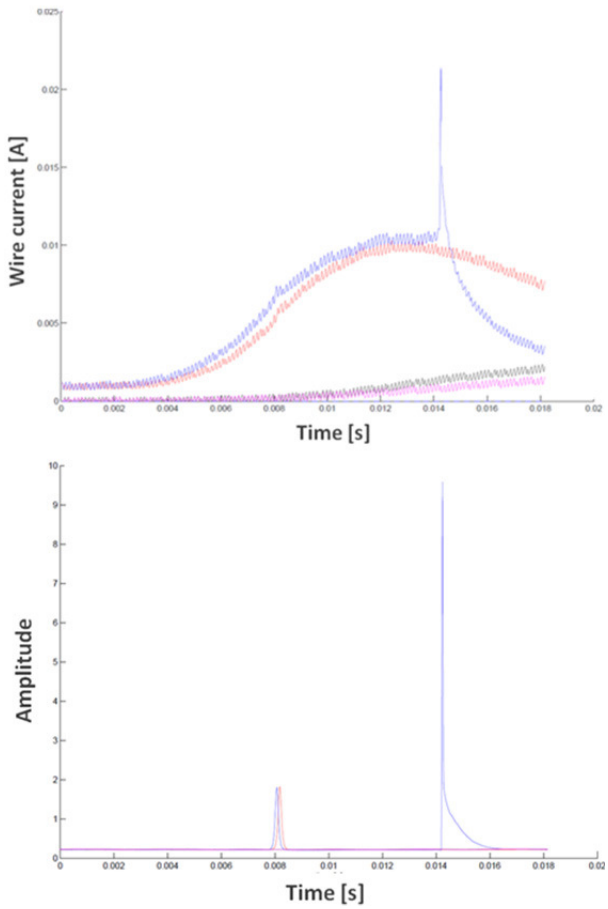


Figure 2: Scanner 416 vertical wire current versus time during four movements around the time of wire breakage (top) and corresponding profile measurement (bottom).

After these first observations, an off-line analysis based on the logged wire-scanner data and beam current transformer (BCT) data was performed for almost all the 2012 run. The goal was to determine the severity of this induced current for the four different scanners (two vertical and two horizontal) in use in the machine.

Fig. 3 shows the results for one of the scanners for all scans performed during the year. The beam intensity during the scan is plotted against the average wire current measured during the 18ms of the scan. The plot shows a correlation between the beam intensity and the induced wire current, with a threshold for the onset at around 2×10^{13} protons.

Table 2 summaries the analysis results for the four operational scanners. The scanner which did not have any wire breakage during the run (416H) is confirmed to not show signs of any beam induced current. All other scanners show induced currents higher than the injected current of 2 mA used for checking the wire integrity.

Observing the mechanical implementation of this scanner (416H), it is found that the main difference is an aperture limit due to inserted field plates. The scanner 416V is the only scanner which shows a clear correlation of the wire current with the beam current and experienced two wire breakages during the run. The other scanners also show a wire current increase without a clear beam intensity dependence. It is suspected that the different behaviour depends on the tank geometry, the subsequent RF modes this can generate and how the wire then samples these modes during a scan.

Table 2: Results of the Off-line Analysis of the Wire Current Versus Beam Current for the Four Scanners

Scanner	Beam aperture [mm]	Current increase	Correlation to Intensity	Peak current [mA]
416.H	461x220x340 plates 100	NO	NO	2
416.V	220x461x318	YES	YES	16
519.H	461x220x455	YES	PARTIAL	16
519.V	220x461x433	YES	PARTIAL	5

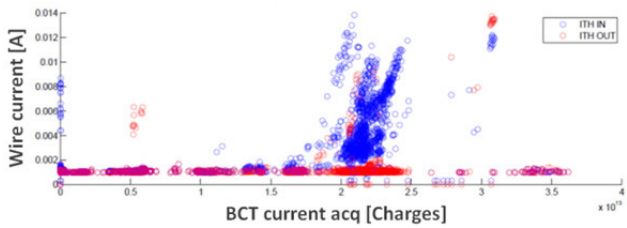


Figure 3: Scanner 416 vertical averaged wire current versus beam current for the whole of the 2012 SPS run.

SOLUTION PROPOSED

Following the results of the studies on 2012 data it is again believed that these wire breakages are related to RF coupling between the beam and the wirescanner, but this time due to RF modes sampled during the actual wire scans as opposed to those sampled in the wire parking position. Solutions to the problem have therefore concentrated on this phenomenon.

A charged particle beam circulating in the accelerator generates an electromagnetic field with a frequency spectrum which, in the case fo the SPS may extend up to several GHz. If the resonating modes of the wirescanner tank are within this beam spectrum, RF power can be transmitted from the beam to the wire.

The first modification adopted to try and reduce the power coupled to the wire was the installation of a tungsten wire of 0.5mm diameter placed across the fork at a distance of 40mm from the shaft (Fig. 4).

The idea behind this thicker, more robust tungsten wire was to try use this as an additional coupling antenna to “deviate and absorb” some of the higher RF modes generated in the tank cavity and dissipate the energy in

Copyright © 2014 CC-BY-3.0 and by the respective authors

ISBN 978-3-95450-141-0

the body of the fork/shaft structure. This would then reduce the RF coupling to the carbon measurement wire, leading to a lower induced current.

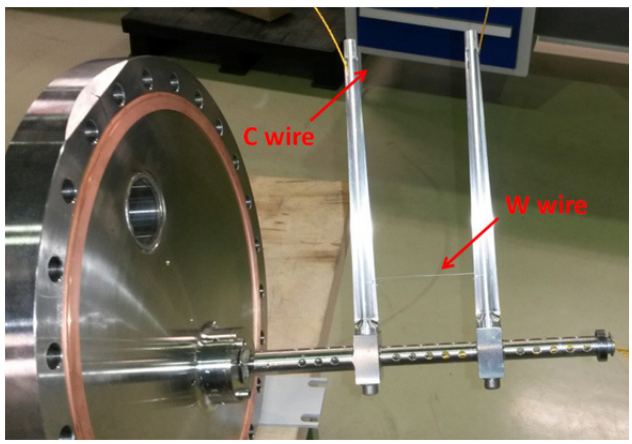


Figure 4: SPS BWS with additional tungsten wire.

The second modification adopted was intended to decrease the overall RF power building up in the vacuum tank. Two vertical, aluminium plates were installed to avoid discontinuities and reduce the volume of the tank seen by the beam. (Figs. 5,6).

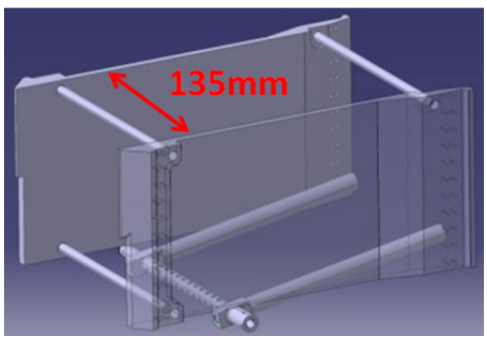


Figure 5: New vertical insertion plate drawing.

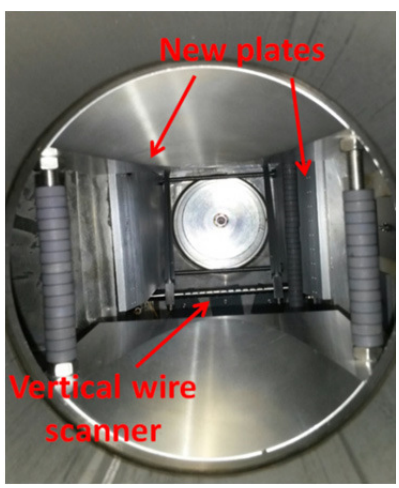


Figure 6: New vertical insertion plate.

LABORATORY MEASUREMENTS

Both the above modifications were applied to the SPS 416V scanner for tests in the laboratory. The scanner was also equipped with a probe antenna powered by a Vector Network Analyzer (VNA) in order to excite the high frequency modes in the beam spectrum (Fig. 7). The two ends of the carbon wire were connected to a Δ-Σ RF hybrid coupler [2], with the resulting sum (Σ) and difference (Δ) signals measured by the VNA. The difference signal being the eventual signal that would generate a current in the carbon measurement wire.

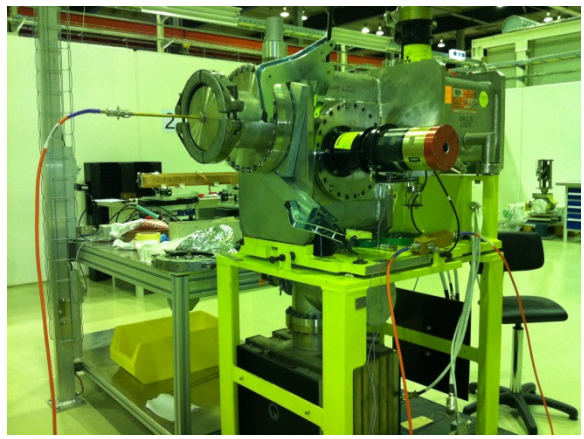


Figure 7: SPS BWS tank with the probe and the hybrid system.

Measurements were performed for three different configurations:

1) the original unmodified wirescanner
2) with a tungsten wire added to the fork
3) with a tungsten wire added and vertical plates incorporated

Measurements were taken in all configurations with the fork in both the IN and the OUT (parking) positions.

We assume that the delta signal gives a signal proportional to the induced current on the carbon wire. Figs. 8 and 9 show the measured delta signals in the IN and OUT position respectively, for the frequency range from 300 kHz to 2 GHz. Two regions of high coupling can be identified, one between 200 MHz and 400 MHz and the other between 600 MHz and 800 MHz.

Figs. 10 and 11 show the difference in the measured Δ signal between the original configuration, that with only the additional tungsten wire and the configuration with both tungsten wire and side plates, for the two different frequency ranges of interest.

This is plotted at various wire positions for two different probe positions, one with the 40 cm long probe inserted by 15 cm in the tank and the other with the probe inserted by 25 cm (confl and conf 2 respectively in Figs.10 and 11).

Copyright © 2014 CC-BY-3.0 and by the respective authors

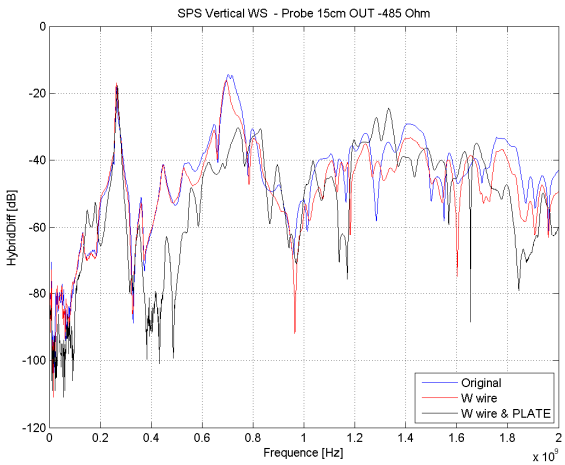


Figure 8: Δ signal on the fork for the IN position.

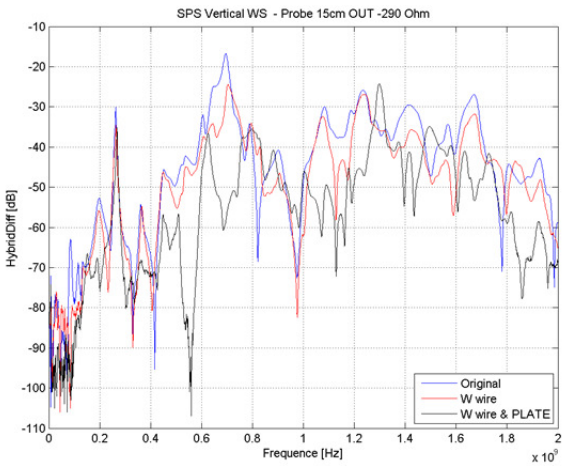


Figure 9: Δ signal on the fork for the OUT position.

The angular position of the fork where it would normally meet the beam is marked with a red line.

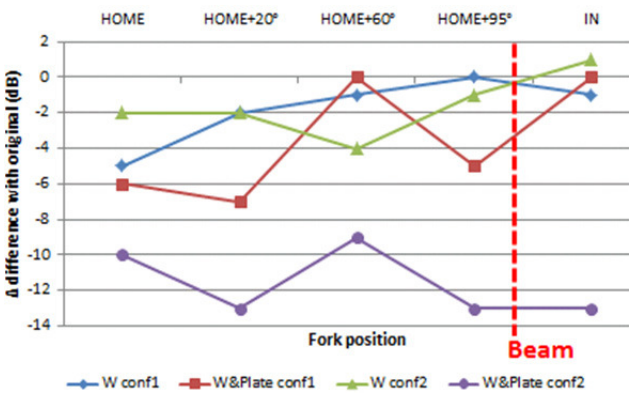


Figure 10: Δ signal difference in the range 200-400MHz.

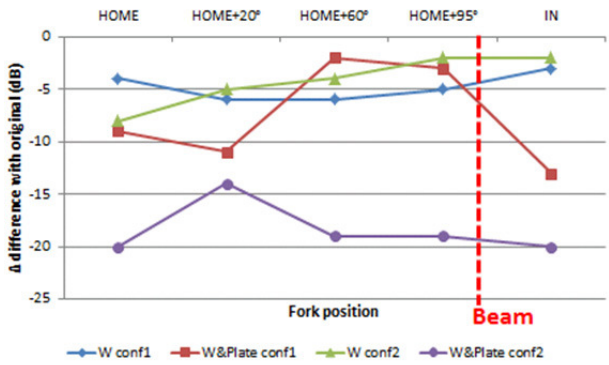


Figure 11: Δ signal difference in the range 600-800MHz.

It is clear that with both modifications in place there is a reduction in the coupling in both frequency ranges of interest over the whole fork range. However the degree of reduction achieved depends heavily on the probe position with respect to the tank.

CST SIMULATION

The measurement set-up was also simulated using the CST STUDIO SUITE [3], with the 3D model used for the simulation shown in Fig. 12.

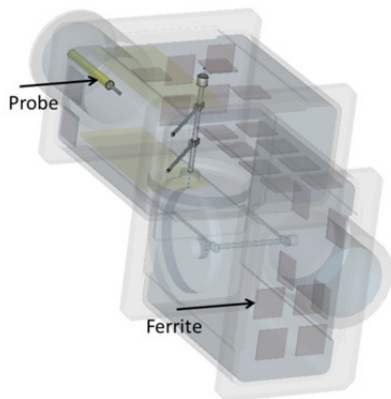


Figure 12: CST 3D model of the SPS BWS.

The model contains all the main features of the device, including the measurement probe and the carbon wire with its connecting wires with the fork. The sum and difference signals were simulated using the frequency domain solver of CST Microwave STUDIO with tetrahedral mesh cells. The results show two resonant peaks in the 200-400MHz range and a broader resonance in the 600-800MHz range in good agreement with the measurements (Figs. 13,14,15,16).

The solution "wire and plates" and "plates" both show significant improvement over the original design.

Copyright © 2014 CC-BY-3.0 and by the respective authors

ISBN 978-3-95450-141-0

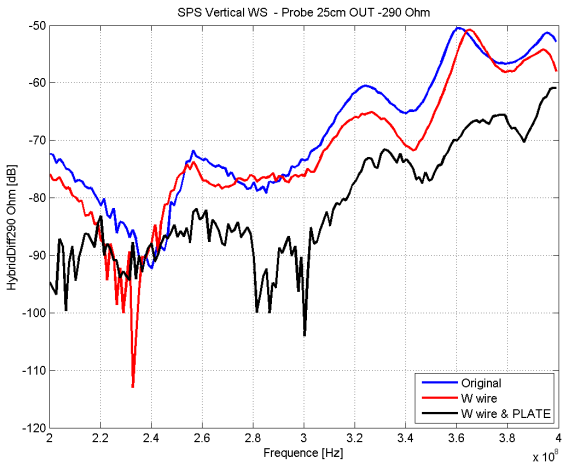


Figure 13: Measured Δ signal on the fork for the OUT position in the range 200-400MHz.

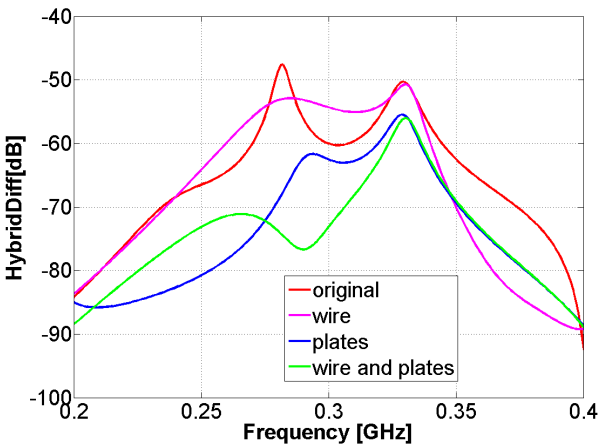


Figure 14: Simulated Δ signal on the fork for the OUT position in the range 200-400MHz.

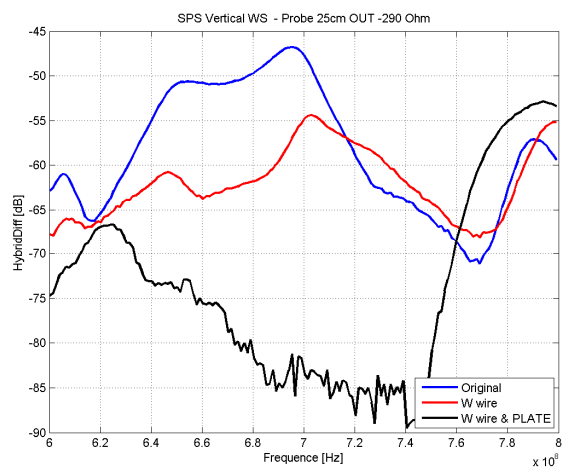


Figure 15: Measured Δ signal on the fork for the OUT position in the range 600-800MHz.

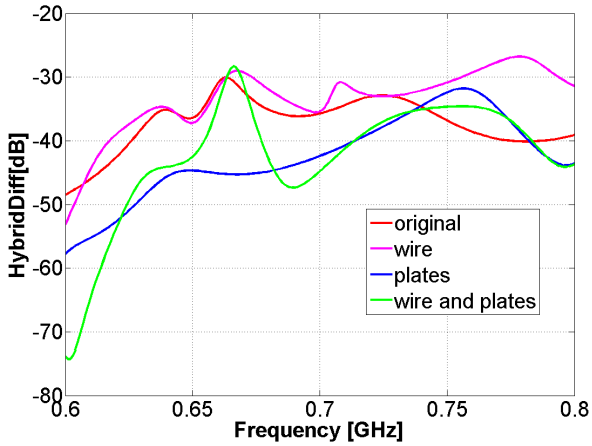


Figure 16: Simulated Δ signal on the fork for the OUT position in the range 600-800MHz.

CONCLUSIONS AND PERSPECTIVES

Laboratory measurements and simulations have been performed to try and understand the wire breakage of the SPS wirescanners during high intensity operation, thought to be linked to beam induced currents in the measurement wire. A good agreement is observed, with significant RF coupling expected in the case of the original tank set-up. A marked reduction in the RF power absorbed by the structure is also seen by both measurement and simulation when adding a tungsten wire to the fork and vertical shields to the tank. Both modifications have now been carried out on the installed SPS scanner 416 vertical and the tungsten wire on all the wire scanners. The effect on wire lifetime will be investigated during the 2014 and 2015 SPS runs.

REFERENCES

[1] F. Caspers, B. Dehning, E. Jensen, J. Koopman, J.F. Malo, Roncarolo F., "Cavity mode related wire breaking of the SPS Wire Scanners and loss measurements of wire materials", Proc. DIPAC 2003, Mainz, Germany.

[2] F. Roncarolo, "Accuracy of the Transverse Emittance Measurements of the CERN Large Hadron Collider", PhD Thesis (2005), http://lphe.epfl.ch/publications/theses/these.fr.pdf

[3] CST Microwave Studio, http://www.cst.com

Copyright © 2014 CC-BY-3.0 and by the respective authors

METHODS FOR MEASURING THE TRANSVERSE BEAM PROFILE IN THE ESS HIGH INTENSITY BEAM

C. Roose*†, I. Dolenc Kittelmann, A. Jansson
European Spallation Source AB (ESS), Lund, Sweden

Abstract

The European Spallation Source (ESS), currently under construction, consists of a partly superconducting linac which will deliver a 2 GeV, 5 MW proton beam to a rotating tungsten target. Beam transverse profile monitors are required in order to insure that the lattice parameters are set and the beam emittance is matched. Due to the high intensity of the beam and the constraint to perform non-disturbing measurements, non-invasive techniques have to be developed. The non-invasive profile monitors chosen for the ESS are based on the interaction of the beam with the residual gas. Two different devices are developed, one utilises the fluorescence process, the other one the ionisation process. The paper presents their latest preliminary developments.

INTRODUCTION

The ESS [1] is a multi-disciplinary research centre based on the world's most powerful neutron source. With an average flux of 1.6×10^{15} neutron cm^{-2} s^{-1} and a peak flux of 40×10^{15} neutron cm^{-2} s^{-1}, ESS will be around 30 times brighter than today's leading facilities. The spallation will occur by bombarding a tungsten target with protons accelerated by a linac up to 2 GeV with an average power of 5 MW. The ESS accelerator, illustrated in Fig. 1, consists of:

- an ECR source which will produce 75 keV protons,
- a warm linac part consisting of a Low Energy Beam Transport line (LEBT), a Radio Frequency Quadrupole (RFQ), a Medium Energy Beam Transport line (MEBT) and a Drift Tube Linac section (DTL), which will accelerate the protons up to 90 MeV,
- a cold linac part, made of a spokes section and elliptical cavities (called Medium β and High β) which will accelerate the protons up to 2 GeV,
- a High Energy Beam Transport line (HEBT) and an upgrade part which transports the beam to the target.

The linac will create a pulsed beam with an average pulse current of 62.5 mA, pulse duration of 2.82 ms and repetition rate of 14 Hz.

In beam diagnostics, it is important to measure the beam transverse profile in order to insure that the lattice parameters are set properly and the beam emittance is matched. Two different kinds of devices are currently been designed [2, 3] for the ESS linac, an invasive and a non-invasive one, which will both be located in the same module. The invasive device will be a wire scanner [4] and will be used during the commissioning at low beam current and short pulse. However the invasive system would get damaged by the beam at its full power, therefore the non-invasive profile monitors are being developed as well in order to provide the profile information without disturbing the beam during normal operation.

NON-INVASIVE TRANSVERSE PROFILE MONITORS

The ESS Non-invasive transverse Profile Monitors (NPMs) [5] are based on the interaction processes between the proton beam and the vacuum chamber residual gas, primarily composed of H_2 (65-80%) and the rest being a mixture of CO, CO_2, CH_4, Ar and H_2O. They exploit the secondary excited/ionised particles produced by these interactions to reproduce the transverse profile. For the ESS linac, two designs are being developed. The main parameters influencing the design are the residual gas pressure in the vacuum chamber, the excitation/ionisation cross sections between the primary proton beam and the hydrogen molecules and the space allocated for the devices.

In the warm linac and HEBT, Beam Induced Fluorescence monitors (BIFs) will be used. While the cold linac will host Ionization Profile Monitors (IPMs). The position and the number of the NPMs along the whole linac are showed in Fig. 1. Both technologies are already well developed by others facilities [6–9] however they have to be adapted to the ESS main constraints i.e. the beam intensity, the H_2 residual gas and the radiation level.

BEAM INDUCED FLUORESCENCE PROFILE MONITOR

In the warm linac, the main constraint is the 10 cm available space for the NPM. The BIF monitor [10], based on the fluorescence emission of the excited residual gas, is a good choice to that issue as both horizontal and vertical profile measurements can be performed at the same place. Furthermore, its optical design is quite simple and can be easily changed, since all the device components, except for the beam pipe viewport, are outside the beam pipe.

For this monitor, the major worries are the light yield level and the optical design. If the first question will be partially answered below, the second has still to be addressed as it is strongly depended on the ambient radiation levels which still have to be studied.

Fluorescence Light Yield

As previously said, the residual gas present in the beam pipe is expected to be composed of 65-80 % of H_2. In the warm linac and the upgrade part, the pressure is expected

* charlotte.roose@esss.se
† Marie Curie Fellow oPAC Project

Copyright © 2014 CC-BY-3.0 and by the respective authors

ISBN 978-3-95450-141-0

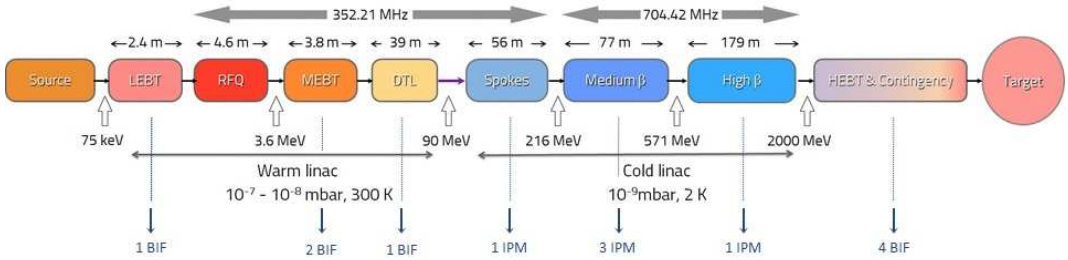


Figure 1: Schematic of the ESS linac and layout of the NPMs.

to be 10^{-7}–10^{-8} mbar and the temperature 300 K. One issue currently studied for the development of the BIF is the fluorescence yield and the H_2 wavelength spectrum. From the work of B. Pottin [11], the more intense spectral lines of the H_2 residual gas are expected to be the Balmer lines from the atomic hydrogen, see Fig. 2. His experiments were performed with 95 keV protons. For such energy, the dissociation cross section is much higher than the excitation one. Therefore the fluorescence process coming from the secondary hydrogen atom, produced by the dissociation of the hydrogen molecule, is much more probable than the one coming from the H_2. The cross section at 95 keV for the production of the H_α Balmer line (wavelength = 656.2 nm) is $\sigma = 3.4\,10^{-18}$ cm^2.

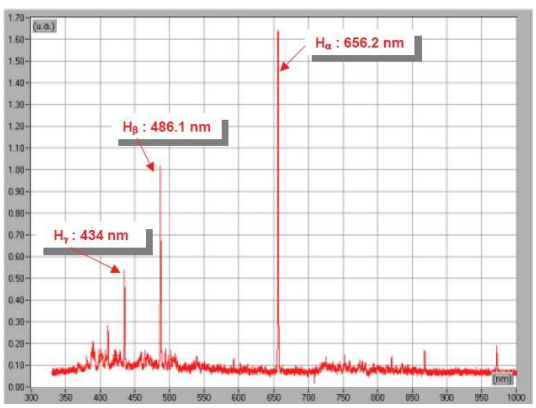


Figure 2: Spectrum analysis of a residual gas composed of 98 % of H_2 [11].

The number n of H_α photons produced per N_{inc} incident particles is given by $\sigma \cdot \rho \cdot N_{inc} \cdot L$, where ρ is the H_2 residual gas density and L the gas length through which the beam is passing.

With the result of B. Pottin, a first estimation of the H_α light yield can be performed at 95 keV. The gas density ρ is calculated from the ESS linac parameters by transforming the well-know ideal gas law

$$\rho = \frac{p}{\mathrm{R} \cdot T} \cdot \mathrm{N_A}$$

where p and T are respectively the pressure (10^{-7}–10^{-8} mbar) and the temperature (300 K) in the beam pipe, R is the ideal gas constant and N_A the Avogadro number. Table 1 presents the photon flux produced by a 95 keV beam pulse (1.1×10^{15} protons) passing through a gas of 1 cm length. In the worst case, (10^{-8} mbar and 65% of H_2), $6{\times}10^5$ photons would be produced with a wavelength of 656 nm.

Table 1: Estimation of H_α Photons Flux Produced by a Pulse of 95 keV Protons Passing Through the H_2 Gas

p [mbar]	ρ_{H_2} [cm^{-3}]	n [photons/s]
10^{-8}	$1.57\,10^8$	$5.87\,10^5$
10^{-7}	$1.57\,10^8$	$5.87\,10^6$
10^{-8}	$1.93\,10^8$	$7.22\,10^5$
10^{-7}	$1.93\,10^8$	$7.22\,10^6$

This calculation gives a first approximation of fluorescence yield for the low energies. As the warm linac accelerates protons from 75 keV to 90 MeV, further investigations have to be done to approximate and measure the fluorescence yield at higher energies.

IONIZATION PROFILE MONITOR

In the cold linac, the pressure is expected to be 10^{-9} mbar and the temperature 3 K. For this part of the accelerator, another type of NPM has to be used since the gas density is lower than in the warm part and so less secondary particles will be produced. Therefore, more space is allocated for the devices between the cryogenic modules than in the warm linac.

The IPM monitor is based on the secondary charged particles production during the interaction of the beam with the residual gas in order to obtain the profile of the beam. In the current model [5], shown on Fig. 3, these secondary ions are accelerated by an electric field from the centre of the device to a scintillator screen. Outside the beam pipe, an optical system collects the photons produced by the screen. Currently the electric field is produced via 2 symmetric plane electrodes on which a voltage of ± 30 kV is applied and lateral electrodes keep the electric field straight. The dimensions of the electric cage (10 cm × 10 cm × 10 cm) are restricted by the size of the tank hosting the transverse profile monitors and the space taken by the wire scanner. 327 mm in the spoke section and 359 mm in the Medium β and High β are allocated for the two IPM devices. In both cases the diameter of the tank is 246 mm.

Due to the expected energy deposition on the collecting plate which could easily damage electronic components,

Copyright © 2014 CC-BY-3.0 and by the respective authors

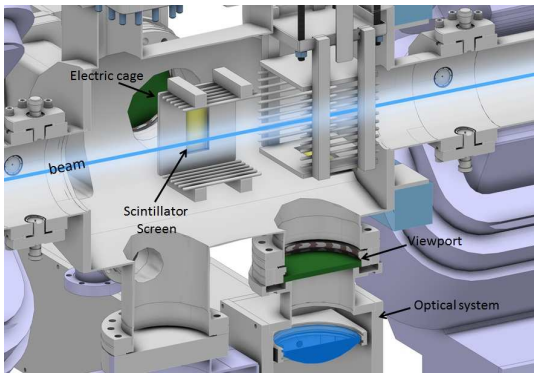


Figure 3: Longitudinal cutting plane of the current IPM monitor design.

scintillator screens [5] are preferred to collect the secondary ions. Like in the case of the BIF, the radiation background will influence the choice of the screen and the optical system design.

Space Charge Influence on the IPM Design

The electric field created by the IPM cage has two purposes. The first one is, as said before, to accelerate the secondary ions to the scintillator screen. The second one is to decrease the bunch space charge effect which disturbs the ion trajectory and distorts the profile. In order to determine the electric field required to compensate the space charge effect, rough approximations were previously made [3] and came to the conclusion that the electric strength should be around 600 kV/m.

To support that result, more detail calculations were performed. First, the dynamic electric field strength produced by a moving bunch in the IPM was simulated with the use of the Particle-in-Cell (PIC) solver of the CST STUDIO SUITE software [12]. After extraction of the electric field components calculated by CST, a custom made MATLAB routine was used in order to track H^+ secondary ions until they reach the screen in the total electric field, composed of the beam dynamic electric field and the static electric field of the IPM cage. The tracking was finished when the ions reached the screen. The static electric field of the IPM cage was chosen to be perfectly straight in these simulations[1].

The CST simulations were performed with the following parameters:

- 500 MeV, 1 GeV and 2 GeV bunches were simulated where one-side RMS bunch lengths of 6, 4.5 and 3 ps are respectively expected,
- the proton bunch was assumed to have a 3D gaussian distribution of charge with an RMS size equal in both vertical and horizontal planes to 2.2 mm,
- the total bunch length (distance between two bunch) is 2860 ps.

[1] When the best suitable field will be selected, simulation with the Electrostatic solver of CST will be performed in order to take in account the imperfections of the static field in the tracking of the secondary particles.

An example of the calculated electric field is shown on Fig.4 and the maximum electric field strength at the longitudinal centre of the bunch produced by a bunch for the three considered energies is shown on Fig. 5.

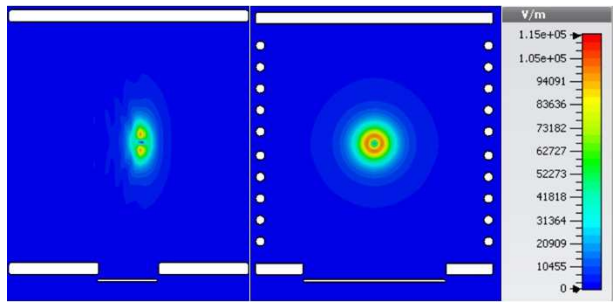


Figure 4: Calculated bunch dynamic electric field strength in the IPM cage for the 500 MeV proton beam. From the left to the right: longitudinal and transverse cutting plane.

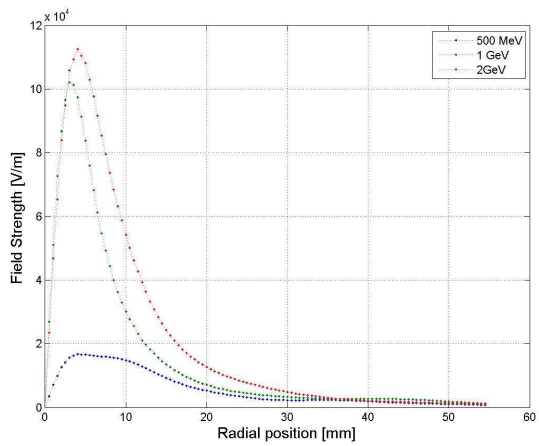


Figure 5: Maximum electric field strength at the longitudinal centre of the bunch produced by a bunch for three different energies.

For the MATLAB tracking, the parameters were:

- the secondary particles were created on a 2D plan, transverse to the beam trajectory, with a 2D Gaussian distribution of 5 RMS radius. This 2D tracking is a first approximation and a fully 3D tracking is planned in the future.
- the H^+ ions were tracked in 4 different static electric fields: -600, -300, -150 and -50 kV/m.
- the tracking finished when the particles arrive at the screen, i.e. at 57 mm of the centre of the beam.

Table 2 presents the maximum transverse deviation with respect to the expected position without space charge effect of the secondary particle. Even for -50 kV/m the deviation is not significant. Therefore it is planned to perform simulations where the field is gradually decreased to te point where the static electric field stops to compensate the space charge effect.

Copyright © 2014 CC-BY-3.0 and by the respective authors

ISBN 978-3-95450-141-0

Table 2: Maximum Deviation of an H^+ Ion Present in the Beam Pipe at 57 mm of the Centre of the Beam

Beam Energy [GeV]	Cage electric field strength [kV/m]	Deviation [%]
0.5	-600	0.09
0.5	-300	0.13
0.5	-150	0.18
0.5	-50	0.31
1	-600	0.02
1	-300	0.03
1	-150	0.05
1	-50	0.08
2	-600	0.08
2	-300	0.08
2	-150	0.17
2	-50	0.20

These results show that the electric field which has to be applied on the IPM electrodes could be significantly reduced. However the results are preliminary and are planned to be rechecked. But the result may be explained with the fact that ions are affected by the bunch space charge only in a small fraction of the drift length(approximately 5 RMS). The fact that the expected ESS bunches are short additionally supports these results since short bunches lead to short time for ions to be influenced by the space charge compared to the whole drift time.

CONCLUSION AND FUTURE WORK

Two designs are currently under development for the ESS NPMs. The first one is a BIF monitor which will be used in the warm linac and the HEBT section. The fluorescence yield at 95 keV for the Balmer line is expected to be at around 6×10^5 photons/(s cm). Additional investigations have to be performed in order to estimate the fluorescence yield at higher energies. The optical design, which depends mainly on the ambient radiation level, will be studied in the following months as well. The second NPM type is an IPM monitor which will be used in the cold part of the linac. The preliminary study of the space charge effect shows that the perturbation of the transverse profile by the dynamic electric field of the beam is not an issue for an cage electric field strength higher than -50 keV/m. In-depth studies have to be performed to confirm these results. In parallel, scintillator screen hardness is planned to be tested and the optical device will be developed.

ACKNOWLEDGEMENT

This project has received funding from the European Union's Seventh Framework Programme for research, technological development and demonstration under grant agreement no 289485.

REFERENCES

[1] S. Peggs et al., "ESS Technical Design Report", Lund, Sweden,2013

[2] B. Cheymol et al., 'Overview of the European Spallation Source Warm Linac Beam Instrumentation.', IBIC'13, Oxford, United Kingdom, September 2013, TUPC01, p 346, http://jacow.org/IBIC2013/papers/tupc01.pdf

[3] C. Böhme et al., "Beam Instrumentation in the ESS Cold Linac", IBIC'13, Oxford, United Kingdom, September 2013, WEPC06, p 667, http://jacow.org/IBIC2013/papers/wepc06.pdf

[4] B. Cheymol et al., "Wire Scanner Design for the European Spallation Source", IBIC'13, Oxford, United Kingdom, September 2013, WEPF10, p 830, http://jacow.org/papers/wepf10.pdf

[5] C. Roose et al., "Development of Non-Invasive Transverse Profile Monitors for the ESS Linac", IPAC2014, Dresden, Germany, June 2014, THPME167, p 3656, http://jacow.org/IPAC2014/papers/thpme167.pdf

[6] P. Forck et al., "Beam induced fluorescence profile monitor developments", HB2010, Morschach, Switzerland, 2010, WEO1C03, p 497

[7] G. Burtin et al., "The luminescence profile monitor of CERN SPS", EPAC2000, Vienna, Austria, 2000, p 256

[8] D. Bartkoski, "Analysis, Prototyping, and Design of an Ionization Profile Monitor for the Spallation Neutron Source Accumulator Ring", PhD diss., University of Tennesse, USA, 2013

[9] T. Giacomini et al., "Ionization Profile Monitor - IPM @ GSI", DIPAC2011, Hamburg, Germany, 2011, TUPD51, p 419

[10] F. Becker, "Non-destructive Profile Measurement of Intensive Heavy Ion Beams", PhD diss, Darmstadt, Germany, 2010

[11] B. Pottin, "Etude d'un Profileur Optique de Faisceaux Intenses de Protons par Absorption Laser", PhD diss, Université de Paris XI - Orsay, France, 2002

[12] www.cst.com

Copyright © 2014 CC-BY-3.0 and by the respective authors

DESIGN OF A PROFILE MONITOR WITH 12 INCHES OF ACTUATION FOR FRIB*

S. Rodriguez#, G. Kiupel, I. Nesterenko, D. Sattler FRIB, Michigan, USA

Abstract

Actuated diagnostics present additional challenges that static diagnostics devices do not such as alignment, stability, and incorporating an appropriate drive mechanism. These challenges become even more apparent as the actuaded length increases. At the Facility for Rare Isotope Beams (FRIB) we plan on using a number of actuated diagnostics devices including a Profile Monitor (AKA: Wire Scanner) with 12 inches of actuation. The Profile Monitor uses tungsten wires to traverse the beam pipe aperture to measure the beam intensity with respect to it's location in the X-Y plane. This paper will detail the design of the 12 inch Profile Monitor and how it is able to overcome the stability, alignment, and drive issues that come with the 12 inches of actuation.

INTRODUCTION

The FRIB beam line has three folding segments where the beam pipe increases to up to 6 inches in diameter. This profile monitor design scans the whole aperture while maintaining the fork outside the aperture at all times. Due to cross-talk between sense wires, these wires are typically separated such that only one wire is inside the beam pipe aperture at a time. Having a fork in this configuration scanning a 6 inch aperture would result in over 16 inches of stroke which is why the task has been separated into two separate profile monitors; one would scan the horizontal "X-axis" and the other would scan the vertical "Y-axis" as well as an additional axis 45° from the vertical axis. This paper focuses on the latter which results in a minimum stroke requirement of 11.39 inches.

*This material is based upon work supported by the U.S. Department of Energy Office of Science under Cooperative Agreement DE-SC0000661, the State of Michigan and Michigan State University. Michigan State University designs and establishes FRIB as a DOE Office of Science National User Facility in support of the mission of the Office of Nuclear Physics.

#rodrigus@frib.msu.edu

†Presently at Facility for Rare Isotope Beams, Michigan State University.

‡Presently at Department of Physics, University of Chicago.

DESIGN

FRIB first explored the idea of using an off-the-shelf mechanical feedthrough and it was low in cost. Upon testing a purchased unit, it was apparent that the actuator would wobble during its motion. This wobble is unacceptable to FRIB which is why a custom design was pursued.

Overall Design

The design of the Profile Monitor attempts to maintain all key components axially aligned so that the motion of actuation is as linear as possible. *Figure 1* shows the overall design of the profile monitor. Although shown in a horizontal position, this device gets mounted in a vertical orientation onto a 10-inch port of a vacuum vessel.

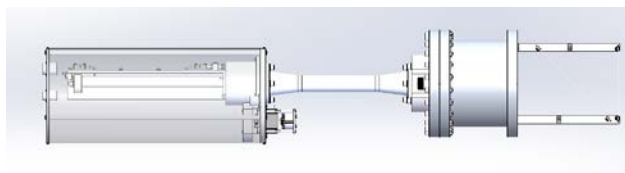


Figure 1: Overall Design.

The nipple in the front serves as a housing for the fork to retract into. This keeps the size of the vacuum vessel smaller as the flange to center distance is reduced. As it can be seen on *Figure 2*, many of the components have a piloting feature to maintain alignment.

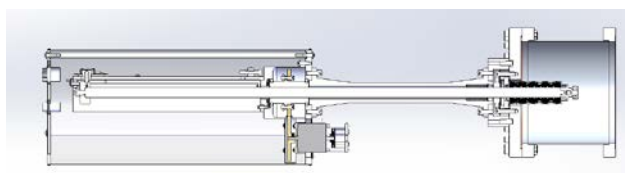


Figure 2: Section view of the profile monitor.

Fork

As previously mentioned, this fork utilizes two wires to scan the vertical axis and an axis at a 45° angle from the vertical axis. *Figure 3* shows the design of the fork.

Assuming that the first wire is tangent to the aperture of the beam pipe, and the second wire must fully traverse this 6-inch aperture, the total minimum stroke results in 11.39-inches.

Copyright © 2014 CC-BY-3.0 and by the respective authors

ISBN 978-3-95450-141-0

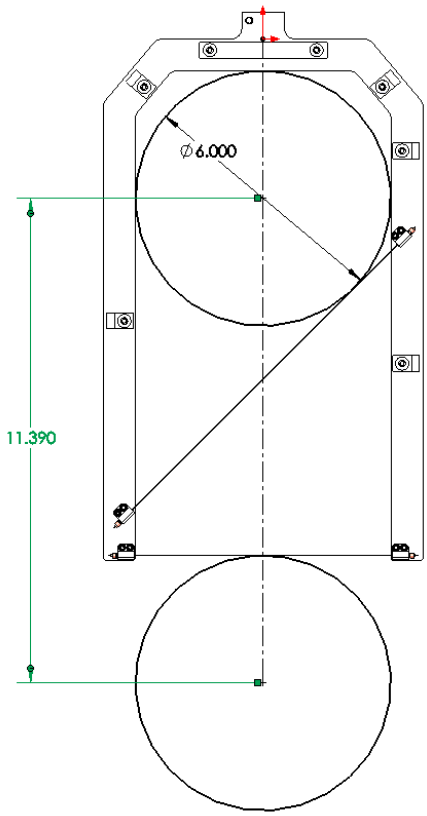


Figure 3: Fork design.

Drive System

The drive system consists of a ball-screw/ball-nut set up where the nut is driven by a motor-gear system while the screw actuates linearly. *Figure 4* shows the detailed drive system. In order to maintain stability and concentricity, the ball-nut is held in place by two radial bearings resting on features precisely machined for this purpose.

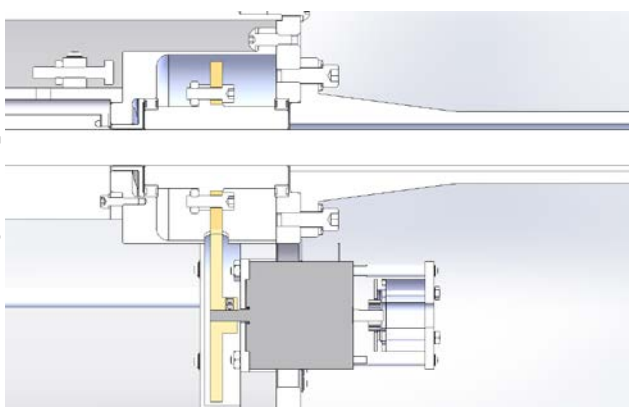


Figure 4: Drive system.

As mentioned above, this design implements a ball-screw which has very high efficiency and back-drives easily. For this reason, a brake is implemented in this design mounting directly on the rear shaft of the motor. This is a power-off brake that engages when power is cut off. This works both as a safety feature when the actuator is at rest and in the case of a power outage.

Typical actuators will have the nut driven by a rotating screw. This allows for a higher load to be actuated but also has its setbacks. Because of its length, rotating the screw would require much more torque to achieve the required speed than if it is driven by rotating the nut.

Concentricity

In order to maintain concentricity, many components are piloted into their mating counterparts. This method can be seen in the frame-to-flange interface shown in *Figure 5*. Here, the part mating to the 10-inch flange is located using two round pins (shown in green).

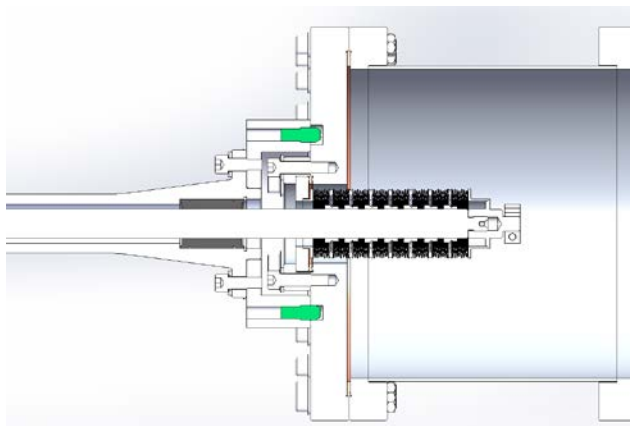


Figure 5: Frame piloting interface.

Additionally, the main frame piece (shown in the far left) pilots into the intermediate piece maintaining concentricity. Lastly, the actuated shaft is supported and guided by the linear bearing shown in grey.

Limit Switches

Part of the limit-switch bracket can be seen on the left side of *Figure 4* where the ball nut housing pilots into the bracket to maintain alignment. *Figure 6* shows a picture of the mentioned bracket. This design, includes two limit switches in the “OUT” position and one in the “IN” position. Additionally there is a guide that travels through the slot in the center of the bracket. The clearance between these two features is such that it keeps the screw from rotating while allowing it to actuate.

Copyright © 2014 CC-BY-3.0 and by the respective authors

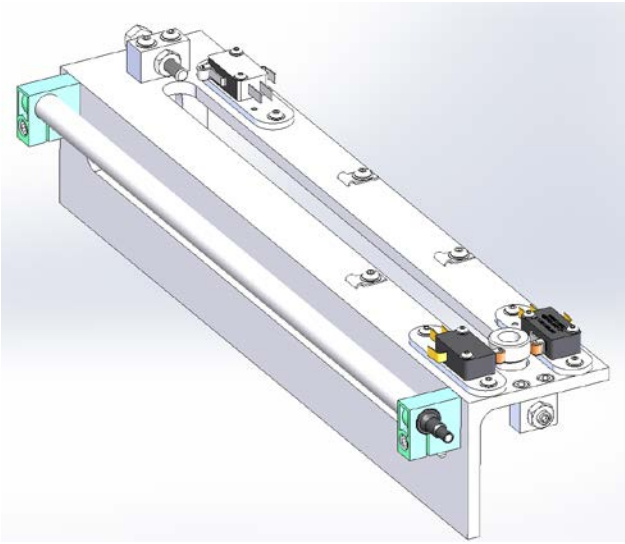


Figure 6: Limit Switch Bracket.

On the side of this bracket there is a linear potentiometer. This Potentiometer serves as position feedback to plot the beam intensity against wire position. This is also actuated by the movement of the ball-screw.

CONCLUSION

While designing an actuator for a stroke this long, under the environmental conditions of FRIB, many drive systems and components were considered. This design was based off of a design that Los Alamos National Laboratories developed, has successfully tested and is currently procuring for their LANSCE accelerator.

What makes this design work is how each component aligns with the next one to keep a concentric path for the ball screw. Additionally, the extra support from the linear bearing near the bellows allows a straight motion rather than a wobbly one seen in other designs and even off-the-shelf actuators.

FRIB plans on building at least two other variations of this profile monitor. Because of how this was designed, many parts can be interchanged between designs. This allows easier maintainability and less volume of spare parts needed in stock.

Copyright © 2014 CC-BY-3.0 and by the respective authors

ISBN 978-3-95450-141-0

DIAGNOSING NSLS-II: A NEW ADVANCED SYNCHROTRON LIGHT SOURCE*

Yong Hu#, Huijuan Xu, Om Singh, Leo Bob Dalesio, BNL, NSLS-II, NY 11973, U.S.A.

Abstract

NSLS-II, the successor to NSLS (National Synchrotron Light Source) at Brookhaven National Lab, is scheduled to be open to users worldwide by 2015 as a world-class advanced synchrotron light source because of its unique features: its half-mile-circumference (792 m) Storage Ring provides the highest beam intensity (500 mA) at medium-energy (3 GeV) with sub-nm-rad horizontal emittance (down to 0.5 nm-rad) and diffraction-limited vertical emittance at a wavelength of 1 Å (<8 pm-rad). As the eyes of NSLS-II accelerators to observe fascinating particle beams, beam diagnostics and controls systems are designed to monitor and diagnose the electron beam quality so that NSLS-II could be tuned up to reach its highest performance. The design and implementation of NSLS-II diagnostics and controls are described. Preliminary commissioning results of NSLS-II accelerators, including Linac, Booster, and Storage Ring, are presented.

INTRODUCTION

The construction of NSLS-II (NSLS-2) began in Mar. 2009. Three years later, preliminary Linac commissioning started in Mar. 2012. The Injector, which includes Linac, Booster and transfer-lines in between, has been successfully commissioned by Feb. 2014. The Storage Ring commissioning is on going and in good progress -- 50 mA stored beam was achieved in July 2014. When the whole machine is fully commissioned and tuned up, NSLS-II will be the most advanced third-generation light source in terms of the following parameters:

1) The lowest horizontal emittance at 0.5nm-rad;
2) The smallest beam size at ~3um;
3) The highest beam current (intensity) at 500mA;
4) The highest photon spectral brightness due to the lowest emittance, the smallest beam size, and the highest beam current as stated above.

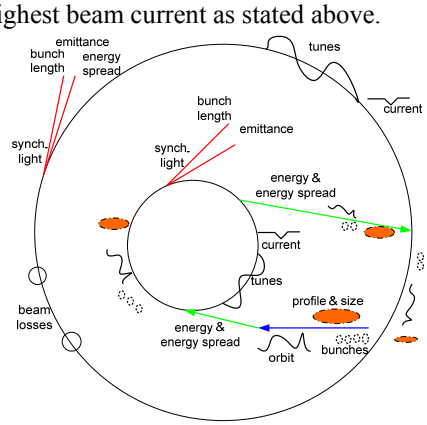


Figure 1: Beam Parameters Measured at NSLS-II.

Machine commissioning and tuning up is all about diagnosing. To achieve the exceptional performance of NSLS-II, beam diagnostics and control systems are designed to monitor and diagnose the electron beam of NSLS-II accelerator complex. Diagnosing NSLS-II means measuring a variety of beam parameters (~10 types), including beam charge/current, filling pattern, beam position/orbit, beam size/profile, energy spread, tunes, emittance, bunch length, beam losses, etc., via a variety of beam monitors (~16 types, ~370 total device counts as shown in Table 1 below) distributed around the whole machine. Figure 1 briefly shows how the NSLS-II accelerators are diagnosed, i.e. what kind of beam parameters is measured from Linac to Storage Ring.

Effective diagnosing of NSLS-II accelerator depends on the effective combinations of a variety of beam monitors, control and data acquisitions (DAQ), and high level physics applications. Figure 2 shows how beam instrumentation, controls, and physics work together to diagnose the NSLS-II machine.

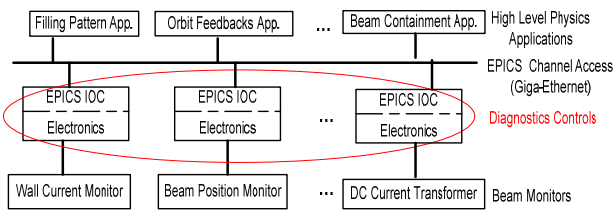


Figure 2: NSLS-II diagnostics and control architecture.

BEAM MONITORS AND SUBSYSTEMS

NSLS-II accelerators consist of one Injector and one Storage Ring (SR). According to the functionality as well as geographical distribution, the Injector is divided into 4 sub-accelerators: Linac, Linac to Booster (LtB) transfer line (including 2 beam dumps), Booster, Booster to Storage ring (BtS) transfer line (including 1 beam dump). Table 1 gives a summary of the beam monitors distributed over the whole machine.

From system functionality and application point of view, the variety of beam monitors as shown in Table 1 could be classified into a few subsystems such as beam position monitor (BPM), filling pattern (Wall Current Monitor, Fast Current Transformer), beam intensity (Integrating Current Transformer, DC Current Transformer), loss control and monitoring (Beam Loss Monitor, Scraper), beam profile (Screen, Visible Light Monitor, Streak camera), tunes, etc., as shown in Figure3.

*Work supported by DOE contract No: DE-AC02-98CH10886
#yhu@bnl.gov

Copyright © 2014 CC-BY-3.0 and by the respective authors

ISBN 978-3-95450-141-0

Table 1: Beam Monitors at NSLS-II

	Linac	Ltb	Booster	BtS	SR
WCM	5				
Screen/Flag	6	9	6	8	1
BPM	5	6	37	8	180
FCT / FPM		2	1	2	1
Bergoz ICT		2		2	
Energy Slit		1		1	
Faraday Cup	1	2		1	
Bergoz DCCT			1		1
Streak Camera					1
Visible Light Monitor			1		1
X-ray diag. beam-line					1
Tune Monitor			1		1
Transverse Feedback					1
Beam Loss Monitor					5
Beam Scrapers					5
Photon/x-ray BPM					1 or 2 per BL

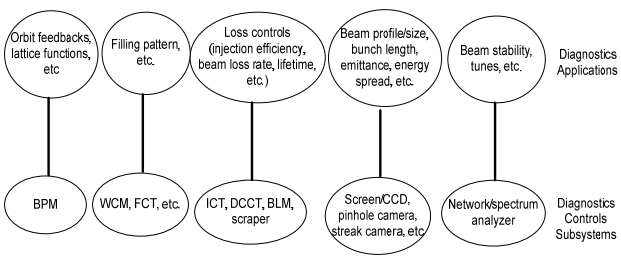


Figure 3: Diagnostics subsystems and applications.

CONTROLS AND DATA ACQUISITIONS

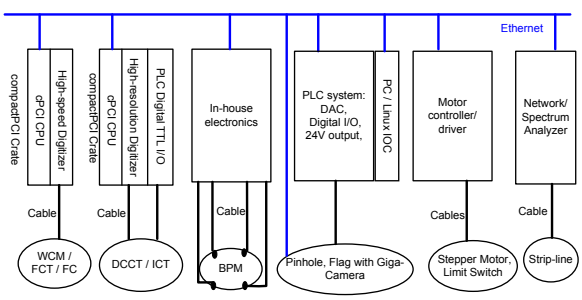


Figure 4: Diagnostics control interfaces.

NSLS-II beam diagnostics control system is completely EPICS-based [1]. Each type of beam monitor requires electronics to process its output signal. The electronics for beam monitors and associated EPICS IOC platform are listed in Table 2. Figure 4 shows the control interfaces for various beam monitors at NSLS-II.

Table 2: Diagnostics Electronics and IOC Platform

Beam Monitor	Diagnostics Electronics	IOC platform
WCM & FCT	Acqiris DC252 (2GHz bw, 10-bit, 4~8GS/s)	cPCI/Linux
DCCT & ICT	1)GE ICS-710-A (24-bit, 200KS/s, 8-ch) 2)Allen-Bradley PLC (DAC, Digital I/O)	cPCI/Linux
BPM	In-house BPM receiver [3]	PC/Linux
Profile / camera	PC/Linux	PC/Linux
Slit & scraper	Delta Tau GeoBrick LV	PC/Linux
Tune	Network analyzer	PC/Linux

PRELIMINARY DIAGNOSING NSLS-II

NSLS-II Storage Ring commissioning started in March 2014. A total of 50-mA stored beam in the Storage Ring was achieved with super-conducting RF recently (see Fig. 5). Although this is still far away from the designed value at 500 mA, it is a major milestone for the NSLS-II Project because the accelerators, including Linac, Booster, and Storage Ring, have been proven working in principle.

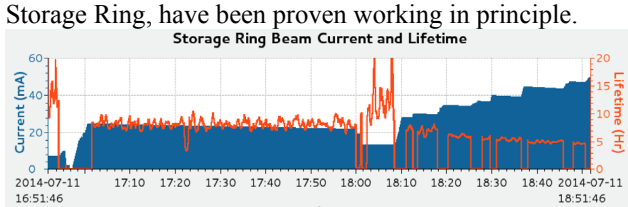


Figure 5: NSLS-II milestone -- 50-mA stored beam.

Beam Intensity Measurement

Beam intensity, also named beam charge (Q) or beam current (I_b), is one of the most important beam parameters for synchrotron light sources. 500-mA stored beam circulating in the Storage Ring is the ultimate goal, which is one of the factors making NSLS-II a world-class light source.

For single-pass accelerators including Linac and transfer-lines (LtB, BtS), the beam intensity is measured as beam charge (Q, nC) via the beam monitor Bergoz ICT. For ring-based circular accelerators including Booster and Storage Ring, the beam intensity is measured as beam current (I_b, mA) via the beam monitor Bergoz DCCT. The charge of circulating beam is actually the beam current multiplying the ring revolution period: $Q = I_b * T_{rev}$. In a sense, beam current and beam charge is interchangeable. Various injection efficiencies, such as

ISBN 978-3-95450-141-0

Copyright © 2014 CC-BY-3.0 and by the respective authors

Booster injection, Booster ramping, Booster extraction, and Storage Ring injection, are calculated by the synchronized shot-by-shot charge ratio between two adjacent ICTs or DCCTs along the beam path.

During NSLS-II accelerator commissioning, the beam current monitors, i.e. Bergoz ICT and DCCT, have been proven very useful and reliable instruments for measuring absolute beam charge with accuracy ~1%. We had noise issues on the ICT & DCCT systems. But we managed to reduce the noise as low as possible by various methods such as adding ferrite beads around the cable, adding low-pass filter (50 Hz) for the Storage Ring NPCT / DCCT, adjusting trigger delay for the BCM / ICT, etc.

Filling Pattern

To achieve ultra-high stored beam current, i.e. 500 mA and meet various beam-line users' requirements, NSLS-II Injector is capable of delivering flexible filling patterns (also named bunch pattern or bunch structure): multi-bunch (80~150 bunches) beam with total charge up to 15 nC or single-bunch with beam charge up to 1 nC per shot. High-bandwidth beam monitors, such as Wall Current Monitors, Fast Current Transformers, together with high-speed digitizers (max. 8GS/s) are used for filling pattern measurement, which provides data of number of bunches, bunch-to-bunch variation, turn-by-turn bunch charge, etc.

During NSLS-II Storage Ring commissioning, we successfully filled any RF bucket using different patterns as shown in Fig. 6.

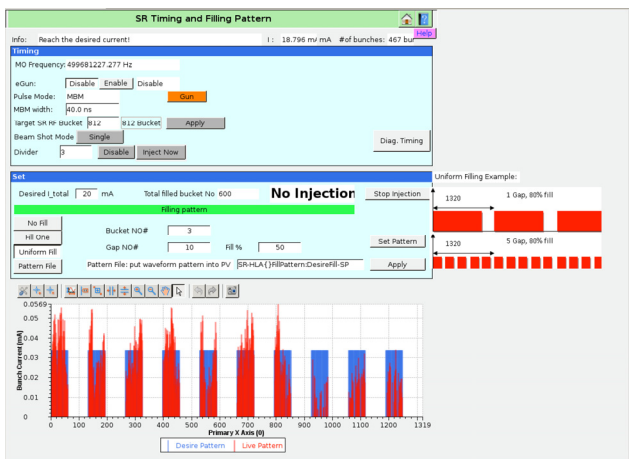


Figure 6: Storage ring filing pattern.

Beam Position Monitor

BPM is the largest as well as the key sub-system for NSLS-II beam diagnostics and controls. Eventually, NSLS-II Storage Ring will reach the lowest emmittance and the smallest beam size at ~3 um, which requires BPM resolution at 0.3 um (10% of beam size) to monitor beam position stability. This requirement for the BPM system is quite challenging. Huge efforts have been put in the development of in-house BPM electronics [2], which has demonstrated excellent long-term resolution performance and provided flexible data flows (see Table 2) for various physics applications during machine commissioning.

The BPM has played a vital role during NSLS-II machine commissioning: by using all BPMs' ADC raw data and turn-by-turn data, we made the first-turn beam in the Booster and Storage Ring quickly; by analysing BPMs' turn-by-turn sum signal drop, we found a hanging RF spring in the vacuum chamber, which resulted in the sudden beam loss [3]; The slow orbit feedback was tested and proved to be working as shown in Fig 7.

Table 2: BPM Data & Physics Applications

Data Flow	Data Rate	Applications	Requirements
ADC	117 MHz	diagnostics, debugging	on demand; ~ 3.8K samples
TBT	378 kHz	tunes, phase advance, injection damping, etc.	on demand; 1 um resolution; ~ 380K samples;
FA	10 KHz	fast orbit feedback, machine protection	continuous; 0.4um resolution;
SA	10 Hz	beam-based alignment, response matrix, closed orbit, life-time	continuous; 0.3um resolution;

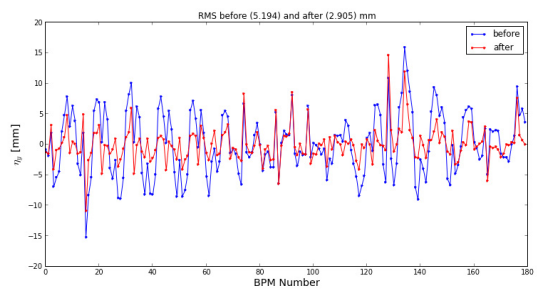


Figure 7: Preliminary test of slow orbit feedback.

CONCLUSIONS

Although we have made a very good start of commissioning NSLS-II accelerators, there are still lots of improvement opportunities for us to make the machine reach its highest performance and make it a world-class light source in the near future. Beam diagnostics and control systems have been tested with beam, proven to be functional, have played and will continue to play important roles for diagnosing NSLS-II.

REFERENCES

[1] http://www.aps.anl.gov/epics/
[2] Joe Mead, et al., "NSLS-II RF Beam Position Monitor Commissioning Update", Proceedings of IBIC14, Monterey, CA, USA.
[3] Weixing Cheng, et al., "NSLS2 Diagnostic Systems Commissioning and Measurements", Proceedings of IBIC14, Monterey, CA, USA.

Copyright © 2014 CC-BY-3.0 and by the respective authors

ISBN 978-3-95450-141-0

SIMULTANEOUS OPERATION OF TWO UNDULATOR BEAMLINES AT FLASH

S. Ackermann*, V. Ayvazyan, B. Faatz, E. Hass, K. Klose, S. Pfeiffer, M. Scholz, S. Schreiber
Deutsches Elektronen-Synchrotron (DESY), Hamburg, Germany

Abstract

In the last few years, first tests have been performed to show that two FLASH undulator lines can deliver FEL radiation simultaneously to users with a large variety of parameters, such as radiation wavelength, pulse duration, intra-bunch spacing etc. In order to achieve this, FLASH has the possibility to have two injector lasers on the cathode of the gun with different parameters, and the accelerator can vary gradient and phase within one RF-pulse to guarantee optimal performance for both beamlines. In this contribution, we show the flexibility which can be achieved with this system.

INTRODUCTION

FLASH, the free-electron laser at DESY in Germany has been in operation as a user facility since summer 2005 [1]. Since then, the request for beamtime has been growing steadily over the years, with a factor of 4 overbooking in the recent user periods. A description of the FLASH facility can be found in Ref. [2].

In order to meet the increased demand, a study started in 2006 to look at the feasibility to add an undulator line to the existing accelerator. In order to double the beamtime, both users would need the 10 Hz repetition rate. A fast kicker in combination with a DC septum is used to deflect the beam into the second undulator line. In addition, the large variety in beam parameters should be possible at both beamlines independently in order to ensure a maximum flexibility in planning of the beamtime. For this reason, it was decided to use two cathode lasers, each with its own bunch train. A variable delay between the two lasers within the RF pulse of gun and modules ensures that the two users get their own set of parameters. In addition, the start time of kicker pulse is shifted with the start time of the laser pulse and the RF-phase and amplitude of gun and each of the modules can be tuned for optimal conditions for both users.

The layout of the facility including the new beamline is described in Ref. [2] and shown in Fig. 1. In addition to a new undulator line with variable gap undulators, a new experimental hall has been built which has space for an additional 5 to 7 experimental stations. In Table 1, the parameters expected for FLASH2 are shown. They are similar to those for FLASH with the exception of the energy spread, which is increased due to coherent synchrotron radiation and the large separation angle of 12° [3, 4].

That the RF-system is able to handle the flexibility needed to compress the beam independently for FLASH1 and FLASH2 has already been presented earlier [5]. Also the fast kicker system has been tested and is behaving according to specifications. What we want to present in this paper is that we are able to get two independent bunch trains to radiate with different charges and a variable delay in time.

Table 1: Expected Parameters for FLASH2

Electron Beam	**Value**
Energy Range	0.5 – 1.25 GeV
Peak Current	2.5 kA
Bunch Charge	0.02 - 1 nC
Normalized Emittance	1.4 mm mrad
Energy Spread	0.5 MeV
Average β-function	6 m
Rep. rate	10 Hz
Bunch separation	1-25 µs
Undulator	**Value**
Period	31.4 mm
K	0.5 - 2
Segment length	2.5 m
Number of segments	12
Photon Beam SASE	**Value**
Wavelength range (fundamental)	4 - 60 nm
Average single pulse energy	1 - 500 µJ
Pulse duration (FWHM)	10 - 200 fs
Peak power (from av.)	1 - 5 GW
Spectral width (FWHM)	≈ 0.5 - 2 %
Peak Brilliance	10^{28} - 10^{31} B

SIMULTANEOUS OPERATION OF FLASH1 AND FLASH2.

User demands vary in almost all respects. A significant increase in beam time can only be achieved, if the parameters between the two undulator lines can be varied independently. For the wavelength, this is clear and straightforward. For other parameters, such as the bunch length, this is not so trivial. Figure 2 shows, how the bunch length was varied by varying the charge. The measurements were performed with a standard diagnostics implemented in FLASH1 and foreseen for FLASH2 [6, 7].

The next tests show the possibility to produce SASE for different parameters. For these tests, only RF parameters were changed within the RF-pulse and orbit was adjusted behind the FLASH2 extraction point. Because the FLASH2 beam line was under construction, the tests presented in this section were all performed at FLASH1. This means, that a certain freedom, which one normally has for lasing with two pulse trains, such as adjustment of orbit and optics in the part of the machine which the beamlines do not have in common, is not available for these tests.

* sven.ackermann@desy.de

ISBN 978-3-95450-141-0

Copyright © 2014 CC-BY-3.0 and by the respective authors

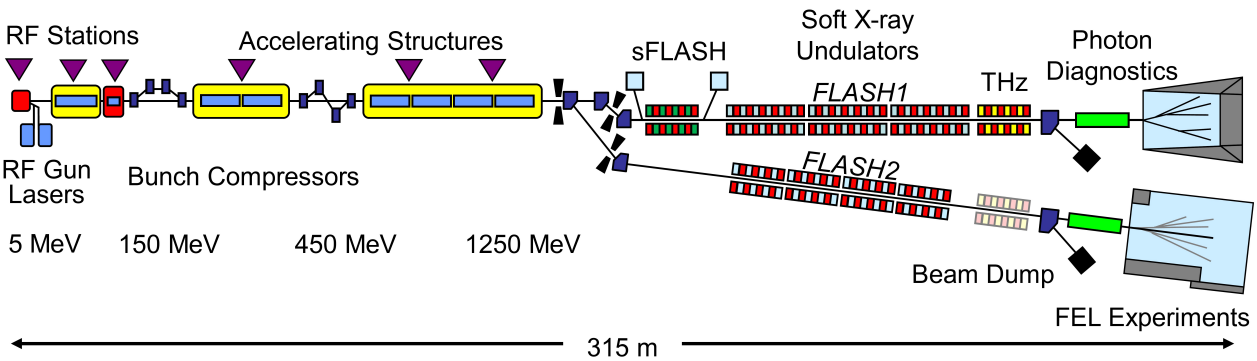


Figure 1: Schematic layout of the FLASH facility. The electron gun is on the left, the experimental hall on the right. Behind the last accelerating module, the beam is switched between FLASH1, which is the present undulator line, and FLASH2, which is the upgrade.

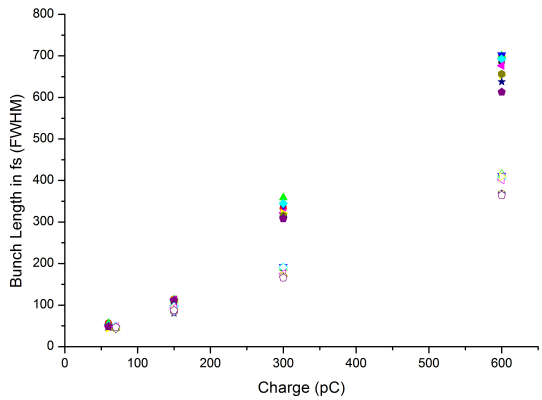


Figure 2: Bunch length for different charges. Measurements have been performed for a beam energy of 0.7 (top) and 1.1 GeV (bottom)

Table 2 shows the SASE level, which was achieved at these different bunch lengths. For the same compression, one would assume that the SASE level is proportional to the charge. As can be seen, towards higher charge, the pulse energy does not increase anymore linearly. A reason could be that space charge reduces the peak current and therefore the pulse energy. For the high energy of 1.1 GeV, corresponding to around 5 nm in FLASH1, optimization of the orbit in the undulator is needed, which may not be equally good for each charge. Details can be found in Ref. [8].

Table 2: SASE Level for Different Charges and Bunch Lengths

Charge in nC	SASE 0.7 GeV in µJ	SASE at 1.1 GeV in µJ
0.6	200	165
0.3	170	90
0.15	110	75
0.07	40	35

So far, all tests were performed with a single injector laser. The next tests show lasing with two injector lasers, separated in time by 80 μs.

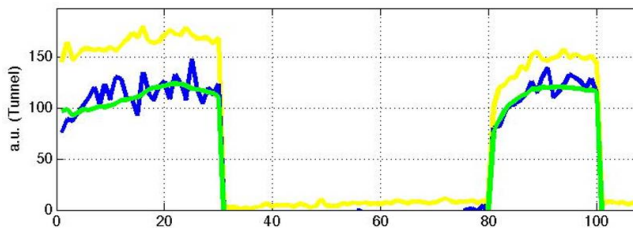


Figure 3: Lasing of two bunch trains with the same charge of about 0.5 nC. The horizontal scale is µs. The blue line indicates the actual SASE pulse energy produced by each individual electron bunch in the macro pulse. The green line is the time average of this signal. The yellow line indicated the maximum SASE level which occured since the measurement was started.

Figure 3 shows lasing of the two bunch trains in the SASE undulators in FLASH1 with the same charge of around 0.5 nC. In the example shown here, both bunch trains have a repetition rate of 1 MHz. The number of bunches in this case was 30 and 20 respectively. As can be seen, the SASE level is more or less equal. Great care was taken to make sure that both injector lasers hit the cathode on the same spot and under the same angle to make sure that the electron beams have the same trajectory. This condition will be relaxed in the later situation, since the orbit in the FLASH1 and FLASH2 undulators can be adjusted independently to optimize lasing.

In Fig. 4, the charge of the second bunch train was reduced by a factor of 2. In order get SASE at the level shown in Fig. 5, mainly compression phases had to be adjusted in the second part of the RF-pulse. The entire change was done in a matter of minutes, mainly given by finding the new optimum in compression settings. As can be seen, the first pulse train was not changed.

A more accurate characterization of both bunch trains has not been done. Of special interest is, what the difference

Copyright © 2014 CC-BY-3.0 and by the respective authors

ISBN 978-3-95450-141-0

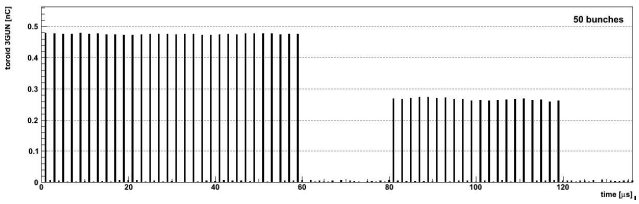


Figure 4: Two trains of bunches, generated by two injector lasers shifted in time.

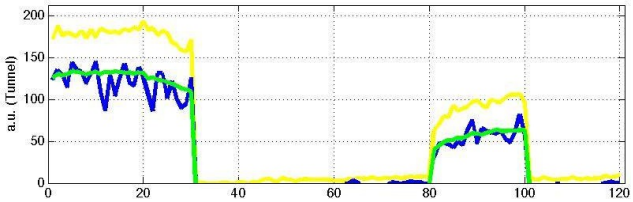


Figure 5: Lasing of two bunch trains with a factor of 2 difference in charge, e.g. of 0.5 nC for the first and 0.25 nC for the second bunch train. The horizontal scale is µs. The blue line indicates the actual SASE pulse energy produced by each individual electron bunch in the macro pulse. The green line is the time average of this signal. The yellow line indicated the maximum SASE level which occured since the measurement was started.

in bunch length was between first and second bunch train. However, the spectral measurements showed, that the wavelength of both bunch trains were the same within each others bandwidth.

Recently, first tests have been performed with FLASH1 and FLASH2 in operation. In Fig. 6, the spot of the FEL radiation produced in FLASH2 is shown [9]. While these tests were done, SASE was delivered in FLASH1 at the same time. This shows, that the fast kicker is working in combination with the DC-septum, the two injector lasers produce FEL radiation simultaneously in FLASH1 and FLASH2.

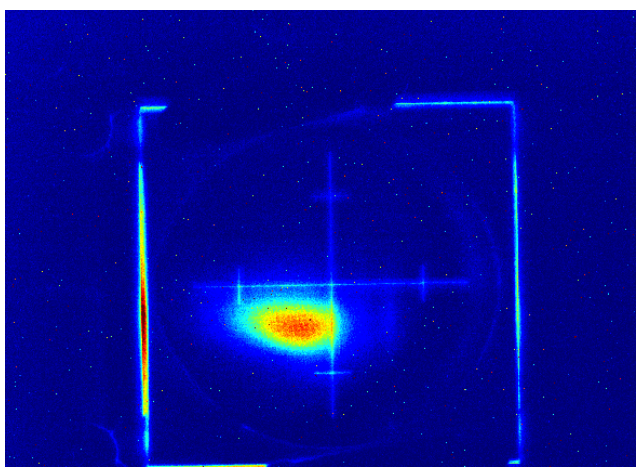


Figure 6: First Lasing at FLASH2. Shown is the spot on the YAG-screen.

SUMMARY AND OUTLOOK

Several tests have been performed to show that simultaneous operation of two beamlines is possible. After having shown that the fast kicker system can deliver bunch trains with a flattness and stability that does not influence the overall stability of FLASH and that also changes in RF-settings within an RF-pulse can be achieved that allow for different compression settings for different charges (and therefore different bunch lengths), it has now also been shown that we can get both bunches to radiate at the same wavelength.

The FLASH2 commissioning in 2014 has resulted in first lasing during the summer. The remainder of the year is dedicated to beam time showing that we can actually deliver this in two different beamlines.

REFERENCES

[1] W. Ackermann et al., Nature Photonics 1, 336 - 342 (2007)

[2] K. Honkavaara et al., "FLASH: First Soft X-ray FEL Operating Two Undulator Beamlines Simultaneously", in Proc. 36th Int. Free-Electron Laser Conf., Basel, 2014, WEB05.

[3] M. Scholz et.al., "Extraction Arc for FLASH II", Proceedings of the FEL 2012 Conference, Nara, Japan.

[4] M. Scholz et.al., "OPTICS MEASUREMENTS AT FLASH2", Proceedings of the FEL 2014 Conference, Basel, Switserland.

[5] B. Faatz et.al., "Simultaneous Operation of a Multi Beamline FEL Facility", Proceedings of the FEL 2011 Conference, Shanghai, China.

[6] E. Hass et al., "Longitudinal Bunch Profile Reconstruction Using Broadband Coherent Radiation at FLASH", Proceedings of IBIC2013, Oxford, UK.

[7] H. Delsim-Hashemi et al., "Single-Shot Longitudinal Diagnostics with THz Radiation at the Free-Electron Laser FLASH", Proceedings of the FEL 2006 Conference, Berlin, Germany.

[8] S. Ackermann et. al., "Simultaneous Operation of a multi beamline FEL facility", Proceedings of the FEL 2012 Conference, Nara, Japan.

[9] S. Schreiber, B. Faatz, "First Lasing at FLASH2", presented at 36th Int. Free-Electron Laser Conf., Basel, 2014.

Copyright © 2014 CC-BY-3.0 and by the respective authors

ISBN 978-3-95450-141-0

SIMULATION AND FIRST RESULTS OF THE ELBE SRF GUN II

P. Lu, H. Vennekate, HZDR & TU Dresden, Germany
A. Arnold, U. Lehnert, P. Murcek, J. Teichert, R. Xiang, HZDR, Germany

Abstract

Recently a new SRF gun has been installed at HZDR, which is named of ELBE SRF Gun II. Stable operation at 8 MV/m RF Gradient has been achieved. The energy and energy spread have been measured for different laser phases. And the results are compared with the beam simulations in this publication. The minimum energy spread is 10 keV at a laser phase of 50°, this is true for both simulation and measurement. In addition, the phase space has been measured and compared to simulation. The determined transverse emittance is in the order of 0.4 µm.

At present the bunch charge is less than 1 pC generated by a bare cooper cathode, which has been installed for first tests of the SRF cavity. In future, the installed UV laser is planned to be operated in either the 13 MHz mode or the 500 kHz mode. The bunch charge will be respectively 77 pC or 1 nC. A simulation based study is in progress, aiming to look for the according "high bunch charge" parameters of the gun and an optimization of the beam transport to the ELBE accelerator.

The code packages ASTRA and elegant are combined in a Labview interface to perform the simulation studies. A 1D model, including space charge effect, is applied to the electron emission and the low energy beam transport in ASTRA. From the exit of the gun cavity, elegant takes charge of the beam transport simulation in the ELBE accelerator. The requirement for the SRF gun to realize 1 nC operation mode is discussed.

INTRODUCTION

ELBE SRF Gun II

The ELBE (Electron Linac with high Brilliance and low Emittance) SRF Gun II [1]has been set up at Helmholtz-Zentrum Dresden-Rossendorf (HZDR) in May 2014. This SRF Gun is an improved version of the ELBE SRF Gun I [2] with a fine grain 3½-cell Nb cavity for realizing higher beam energy up to 9 MeV , and a superconducting solenoid for an improvement in emittance compensation [3]. Figure 1 shows the section view of the gun cryostat.

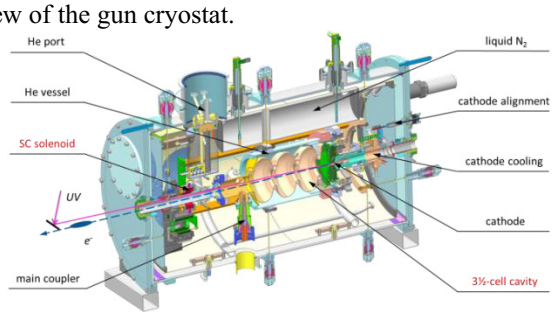


Figure 1: construction of the ELBE SRF Gun II.

The standard material for the gun cathodes is Cs_2Te[4], which has been used in the ELBE SRF Gun I. In this paper all measurement results are from a copper cathode, which has been installed for the current commissioning phase. New Cs_2Te cathodes are under preparation and will replace the copper cathode in the near future.

Compared to the old cavity, the new Niobium SRF cavity generates higher fields at the cathode position in the half-cell. This feature reduces the range of the space charge effect dominated region for low energy bunches near the cathode. Furthermore, the reduced power dissipation on the cavity wall is another improvement, which allows higher gradients in the superconducting cavity at similar helium consumption.

A 258 nm UV laser is used to excite electrons from the cathode cooled by liquid Nitrogen. The laser parameters have serious impacts on the gun's behavior. The synchronization between the laser and the RF generation, characterized by the laser phase, influences both the energy gain of the beam and the emittance. The initial structure of the extracted bunch is directly determined by the laser pulse shape itself. A uniformly distributed, large laser spot is expected to exploit the quantum efficiency of the cathode. Meanwhile for a certain bunch charge, a larger laser spot results in a reduced space charge effect. This direct dependency of the beam quality on the laser spot size could be reproduced by the simulations.

Beam Transport

Electron bunches from the ELBE SRF Gun II are supposed to be transported through a dogleg beam line and into the linac beam line of the ELBE, which is primarily designed for a thermionic gun. Therefore, it is necessary to simulate the entire beam transport to get the optimized parameters for this particular setup.

The longitudinal phase space can be manipulated by two accelerator modules and two chicanes. The beam should be focused longitudinally at the final target position and kept defocused in transport to reduce the space charge effect. Since the longitudinal elements also have a significant influence on the transverse beam parameters, they have to be optimized first. Proceeding on the basis of fixed cavity phases and chicane bending angles, transverse elements like a super conducting solenoid and in total 35 quadrupoles can be used to achieve the desired transverse phase space.

The bunch emission from the cathode and the acceleration in the gun are simulated with ASTRA, and further beam transport is computed using elegant[5]. The Coherent Synchrotron Radiation (CSR) effect[6] in the bending magnets, as well as the following short drifts, and the Longitudinal Space Charge (LSC) effect[7] in other

Copyright © 2014 CC-BY-3.0 and by the respective authors

ISBN 978-3-95450-141-0

drifts are considered. Besides, a simplex optimization procedure is applied for the transverse elements.

MEASUREMENTS FOR LOW BUNCH CHARGES

Although at the moment only a bare copper cathode is applied with low bunch charge of < 1 pC, it is still sufficient to perform the beam based alignment and the energy measurements.

The laser position on the cathode is scanned to determine the center of the electric field of the cavity. When the beam position on the downstream YAG screen does not change with the laser phase, the laser spot is considered to be centered. After that, the position of the superconducting solenoid is adjusted by two perpendicular steppers with the goal, that the beam position remains stable for different solenoid currents. Alignments of further elements still need to be done. As Figure 2 shows, the energy and energy spread are measured in the diagnostics beamline by using the 180° dipole.

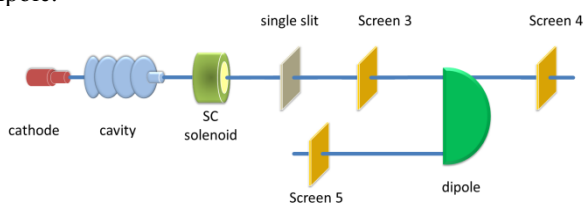


Figure 2: Diagnostics beamline for ELBE SRF gun II.

After the beam has been centered on screen 4 using the solenoid, the bending dipole is used to focus it on screen 5. The current of the dipole corresponds to the beam's kinetic energy while the beam spot size on screen 5 is related to the energy spread. The transverse size and divergence of the beam also contributes to the beam spot size on screen 5. However, to estimate this error requires the detailed phase space analysis at the entrance of the dipole, which is not measurable with the present beam line. Instead, the beam spot size on screen 5 has been determined by simulation and was compared with the measurement results.

As shown in Figure 3, the measured and simulated curves of the energy versus laser phase have the same trend, but a systematic error exists. The calibration of the dipole current to the energy might be the reason.

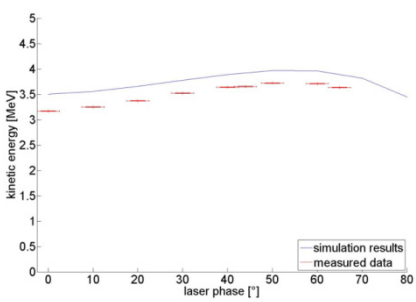


Figure 3: Measured and simulated kinetic energy of the beam versus laser phase.

Figure 4 plots the simulated standard deviation of the electron energy statistics, as well as both measured and simulated energy spread calculated from the beam spread on Screen 5, which includes the influence from beam divergence. According to the simulation, the contribution of the beam divergence will enlarge the beam size spread on Screen 5 by about 35%.

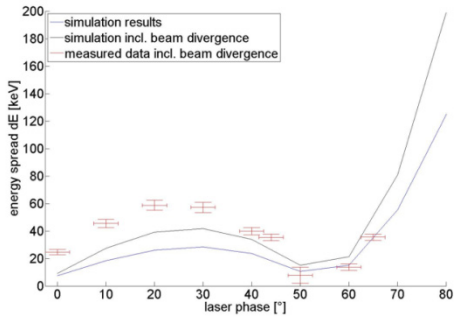


Figure 4: Measured and simulated energy spread with different laser phase.

As shown in Figure 2, a single slit is used to sample the beam while the beam lets are recorded on Screen 3 in order to calculate the transverse emittance. Figure 5 gives the emittance versus laser phase at a gradient of 6 MV/m. The simulation here has been performed with an estimated value for the initial laser spot size of 0.3 mm.

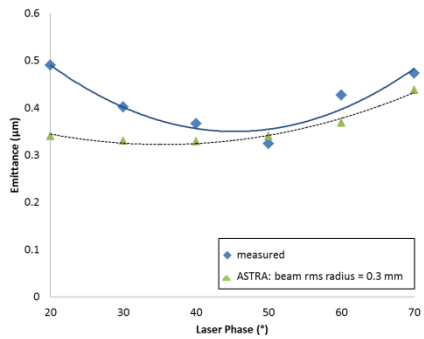


Figure 5: Transverse emittance versus laser phase.

SIMULATION FOR HIGH BUNCH CHARGES

As mentioned above, new Cs_2Te cathodes will be installed to achieve an increased bunch charge of 77 pC in 13 MHz mode and 1 nC in 500 kHz mode. The 77 pC beam optimization of the gun and the beam transport system has already been discussed in reference [8]. In this contribution the focus is on the task of the 1 nC operation mode.

It is of great importance to determine the minimal cavity energy/gradient to realize the desired bunch charge, since the field emission from the cavity wall increases exponentially with the field; and the dissipated RF power on cavity requires more helium cryogenic power. Also, when operating at high gradient, to compensate the strong Lorenz force detuning is a big challenge for the tuning system.

ISBN 978-3-95450-141-0

Copyright © 2014 CC-BY-3.0 and by the respective authors

Sufficient quantum efficiency of the cathode and laser power is assumed for the 1 nC task. A large initial bunch size with a uniform distribution is recommended in order to minimize the space charge effect, which will strongly expand the 3D bunch size, as shown in Figure 6. What is also shown is that higher laser phase corresponds to smaller beam size after the cavity, but enlarges the bunch's longitudinal expansion.

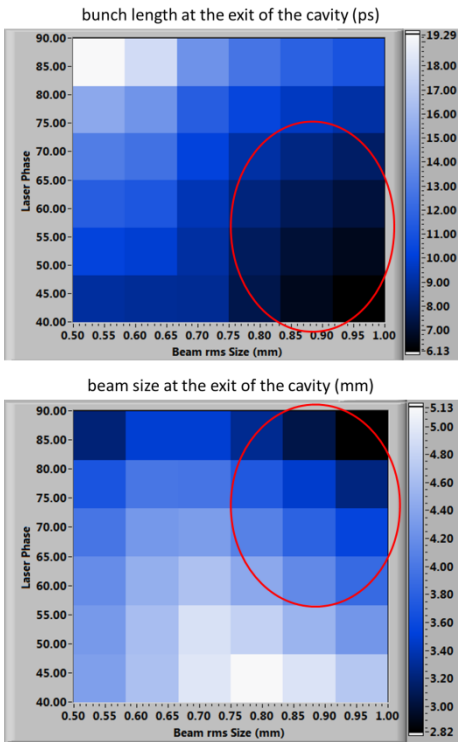


Figure 6: Simulation results: Expansion of the 3D bunch size at the exit of the SRF gun versus initial beam size. Different laser phases are scanned. Red areas are proper parameters.

For the reason mentioned above, a uniform laser spot is applied with the radius of 2.0 mm (in ASTRA, σ_x/σ_y=1.0 mm). A 2D scan of the RF gradient and the laser phase has been performed, and some results at the gun exit are plotted in Figure 7.

As of experience of the further beam transport in the dogleg from simulation, a bunch exiting the SRF cavity should be less than 5 mm of rms radius to be able to pass though the dogleg. Otherwise, the large beam halo in the dipoles and quadrupoles will result in a significant emittance increase. In Figure 7, from the beam size distribution at the exit of the gun, a triangular shaped area of the parameter space of cavity gradient and laser phase is selected. However, the energy spread distribution shows a valley-like area that has a comparable small energy spread. The overlap of these two areas has a minimum gradient of roughly 10 MV/m, while the emittance in this area is over 5 µm.

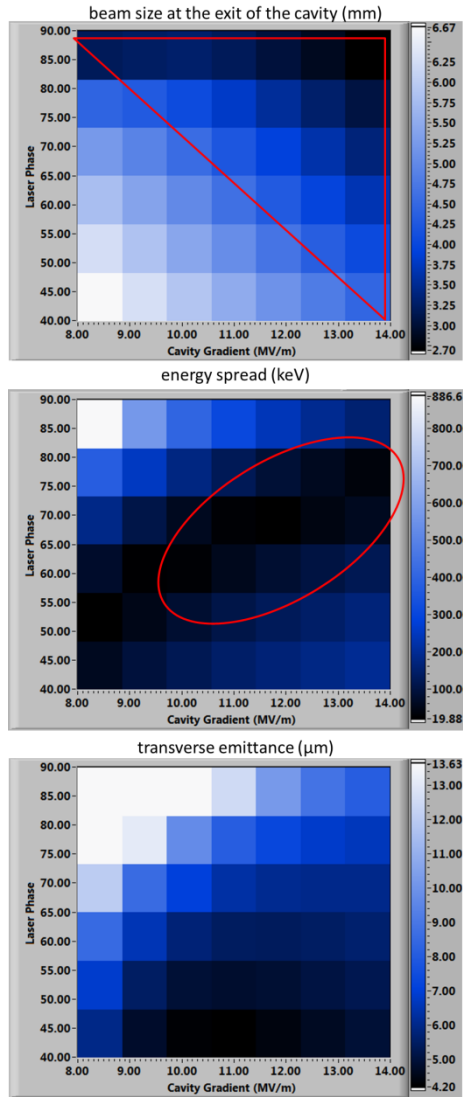


Figure 7: Simulation results: RF gradient and laser phase scanning for the beam with bunch charge of 1 nC. Results are given for the exit of the SRF cavity.

According to this simulation, it is assumed that higher than 10 MV/m is the limit for the gradient, Therefore, we made a simulation of the beam transport in this case. The kinetic energy of the beam after the ELBE SRF Gun II is 4.9 MeV, the transverse emittance has a value of 5.6 µm, the bunch length is 11.2 ps (5 ps from cathode) and the energy spread is 46 keV.

The maximum of the beam size is located in the first solenoid of the dogleg, where the dimension halo almost equals the beam pipe's inner diameter and the nonlinear effect of the quadrupole increases the horizontal emittance by 6 µm. The chicanes also increase the transverse emittance, if the CSR effect is considered for their dipoles. The dispersion out of the bending beam line is minimized to be zero. At the end of the simulation, after the second chicane, the beam energy is at 29 MeV, the transverse emittance is 30 µm in the horizontal plane and 13 µm vertical, the bunch length is compressed to 2.8 ps and the energy spread is 317 keV.

Copyright © 2014 CC-BY-3.0 and by the respective authors

ISBN 978-3-95450-141-0

Figure 8 illustrates the beam size profile and the different phase spaces. Results show, that at this gradient a 1 nC bunch is possible to be generated by the SRF Gun II and can transported through the ELBE beam line. However, the transverse emittance needs to be optimized and the maximum beam size might cause beam loss and serious radiation in reality.

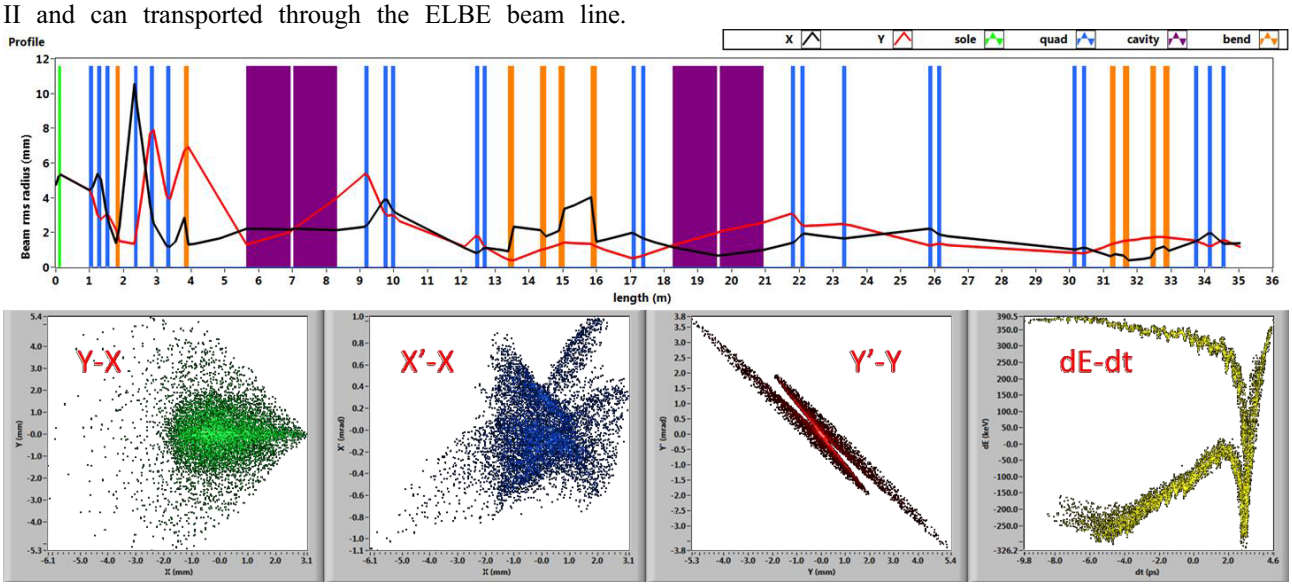


Figure 8: Beam transport and phase spaces of 1 nC, 10 MV/m. The massive X phase space is due to the CSR effect and the nonlinear longitudinal phase space is the result of LSC effect and the bunching of the chicanes.

CONCLUSION

The ELBE SRF Gun II has been installed at HZDR and its commissioning is in progress. The work of pushing the cavity's gradient is continued. Up to now, low bunch charge measurements have been performed and compared with beam dynamics simulations. The simulation work is focused on the 1 nC bunch charge operation. As a first result of these studies, with the present beam line arrangement, 10 MV/m turns out to define the minimum gun gradient for this high bunch charge mode for the ELBE accelerator facility.

ACKNOWLEDGEMENT

We would like to thank the whole ELBE team for their help and assistance with this project. The work is supported by the European Community under the FP7 programme (EuCARD-2, contract number 312453, and LA3NET, contract number 289191), and by the German Federal Ministry of Education and Research grant 05K12CR1.

REFERENCES

[1] P. Murcek, *et al.*, *The SRF Photoinjector at ELBE – Design and Status 2013*, SRF 2013 – 16th Int. Conf. on RF Superconductivity, September 23-27, 2013, Paris, France.
[2] A. Arnold, *et al.*, Nucl. Instr.and Meth. A 577 (2007) 440-454.
[3] H. Vennekate, *et al.*, Transverse Emittance Compensation for the Rossendorf SRF Gun II, IPAC 2014 proceedings, TUPRI015.
[4] R. Xiang, *et al.*, Phys. Rev. ST Accel. Beams 13, 043501, (2010).
[5] M. Borland, Advanced Photon Source LS-287, September 2000.
[6] M. Borland, Physical Review Special Topics - Accelerators and Beams, Volume 4, 070701, (2001).
[7] Ahmed M. Al-khateeb, *et al.*, Phys. Rev. E 63, 026503.
[8] P. Lu, Simulation of the ELBE SRF Gun II, IPAC 2014 proceedings, MOPRI024.

Copyright © 2014 CC-BY-3.0 and by the respective authors

ISBN 978-3-95450-141-0

BEAM DIAGNOSTICS AND TIMING MONITORING FOR SUPERKEKB INJECTOR LINAC

F. Miyahara#, K. Furukawa, R. Ichimiya, N. Iida, M. Ikeno, H. Kaji, M. Satoh, M. Shoji, T. Suwada, M. Tanaka, Y. Yano, KEK, Tsukuba, Ibaraki, Japan
T. Okazaki, EJIT, Tsuchiura, Ibaraki, Japan

Abstract

The KEK e^+/e^- linac has multiple operation modes for the electron beam injection into three rings, the SuperKEKB HER (High Energy Ring), PF (Photon Factory) Ring and PF-AR, and the positron beam injection into the damping ring (DR) and the SuperKEKB LER (Low Energy Ring). The operation modes can be switched every 20 millisecond, repetition rate of 50 Hz, with arbitrary order. The beam parameters such as charges, energies are different for each of the rings. Moreover, the bunch charges of the electron beam for HER, 5nC, is 5 times higher and the transverse emittance of ~10 mm mrad is 30 times lower than those of the KEKB injector.

Thus, the development for the BPM readout system with a wide dynamic range, the installation of optical fiber detectors with a good S/N ratio for the wire scanners and bunch-length monitor have been performed. For stable operation of the linac, many timing signals have to be monitored as well. To that end we have developed 32-bit multi-hit time-to-digital converters (TDCs) with 1-ns resolution. The first beam tests of those systems are reported.

COMPONENTS OF THE LINAC

The SuperKEKB injector linac is under development to achieve the required performance [1]. The layout of the linac with energy evolution from downstream of the 180-degree arc for each operation modes is shown in Fig. 1. The linac consists of eight sectors (A – C, 1 – 5). Each sector has eight accelerating units except for sector A, 1, and 4. The black square represents an accelerating unit which provides an average energy gain of 160 MeV. In sector A, a new photocathode RF gun designed to obtain high charge (5 nC) and low emittance (10 mm mrad) electron beam [2-3] is set on beginning of the sector. The linac also has a conventional thermionic gun which is dedicated to PF/AR in sector 3. Thus, electron source for PR/AR rings can be exchange. A magnetic chicane to give an energy chirp for bunch compression in the arc section and a diagnostic beamline are located on downstream of the RF gun.

A new positron source which consists of a tungsten target with a 2-mm diameter beamline-centered hole for electron, a beam spoiler, a flux-concentrator and six large-aperture S-band (LAS) accelerating structures inside DC solenoids have been installed in sector 1 [4,5]. In case of beam injection to PF or HER, the electron beam goes through the hole of the target. To obtain positron beam, an electron/positron separator chicane has been installed at downstream of the last LAS accelerating structure. To reduce the geometric emittance down to 41(horizontal)/2(vertical) nm, the positron beam injected to the damping [6] is stored 40 ms, the store time depends on the injection rate, then return to the linac. Thus, trigger timing of upstream (sector A – 2) and downstream (sector 3 - 5) for the RF system and the BPMs will be controlled independently [7].

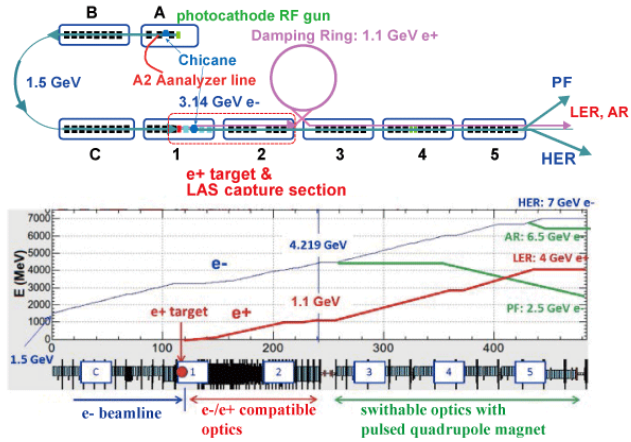


Figure 1: Schematic layout of the linac and energy-evolution patterns for each operation mode.

MONITORING SYSTEM

The beam positions and charges are monitored by stripline BPM. There are more than 90 BPMs and 23 oscilloscopes for fast BPM data acquisition (DAQ) system [8]. The position resolution of the BPM system is about 50 μm. To achieve emittance preservation of high bunch charges of 5 nC electron beam, the alignment error of 0.1 mm for each section and a dedicated orbit correction are required. These specifications require less than 10 μm position resolution for the BPM, but current DAQ system does not satisfy it. Then, we have been developed a VME-based readout system. The position resolution of 3 μm was achieved that was measured on the basis of 3-BPM method in the linac [9]. To measure the beam size and emittance, Al_2O_3 ceramic screen (30 μm thick) is set in the vacuum chamber at the chicane downstream of the gun, 4 sets of four successive wire

#fusashi.miyahara@kek.jp

Copyright © 2014 CC-BY-3.0 and by the respective authors

ISBN 978-3-95450-141-0

scanners are installed in sector B, C, 2, 5 [10]. The temporal laser profiles for the RF gun and electron bunch length are monitored by using streak camera. In order to confirm bunch compression at the arc section and orbit correction, an X-band RF deflector will be set at the end of the linac.

OPTICAL FIBER LOSS MONITOR

The optical fiber is already used as a beamloss or/and a profile monitor in TTF1 [11], FLASH [12] and many facilities. In the KEK linac, the fiber loss monitors have been installed around a pulsed bending magnet for PF ring and the end of sector 5. So far, photomultiplier tube without any scintillator, the glass in front of the photocathode works as dielectric medium for Cherenkov radiation, has been used as the detector for the wire scanner. But, the way is not suited to the measurement at the location with heavy beamloss.

Beam Loss Monitor at the End of the Linac

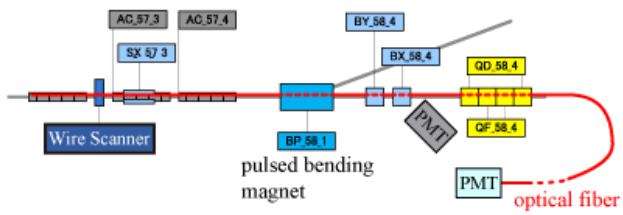


Figure 2: Schematic Layout of the linac end (sector 5).

The schematic layout of the linac end is shown in Fig. 2. The optical fiber is set along the beamline. The fiber passes through the pulsed bending magnet, steering magnets (BX, BY) and quadrupoles (QF, QD). It was revealed that the electron beam tail hits the vacuum chamber installed in the pulsed bending magnet from analysis of the signal of the fiber. The beam sizes measured by a wire scanner are shown in Fig. 3. The signals measured by the PMT without fiber is deteriorated due to the background of heavy beamloss. On the other hand, the data measured by the fiber shows clear beam profile. That good S/N ratio has been achieved by to set appropriate ADC gate timing that corresponds to quadrupoles. It appears that the fiber passed through in

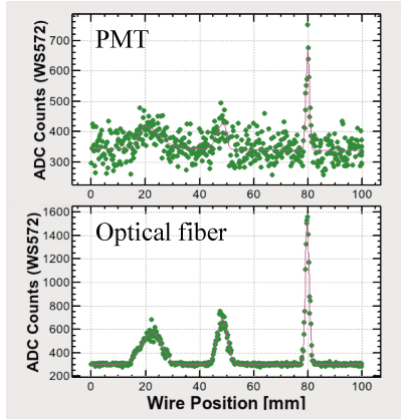


Figure 3: Signals from a PMT without any scintillator (top) and a PMT coupled to the optical fiber (bottom) vs wire position. The left, center and right peaks correspond to vertical, oblique and horizontal beam profiles. These scales of the vertical and horizontal should be divided by $\sqrt{2}$.

quadrupoles is much closer to beam axis and recoil electrons which lose energies are over focus or defocus in the quadrupole.

Loss Monitor in Downstream of the Positron Source

The target system for positron production was changed that electron beams go through a small hole with 2.0 mm diameter on axis, while the beam had been bypassed the target in the KEKB injector. Although the radius of the hole is designed so that the electron beam passes through without any beamloss, the target could cause beamloss due to any position jitter, beam halo or other reasons.

The construction of positron source was started in 2013 and wire scanner system in sector 2 had been installed. Then, initial positron beam commissioning has started. To find the good S/N position for wire scanner, the optical wire was set along the beamline (Fig. 4). The background signal originating from beamloss at the target is shown in Fig. 5. Although, the primary electron beam passed through the target hole without any clear charge losses monitored by BPMs, six strong signals that corresponds quadrupoles were observed. The bottom in Fig. 5 presents signals with insertion of the wire scanner. The growth of 5th and 6th signal indicates electron beam

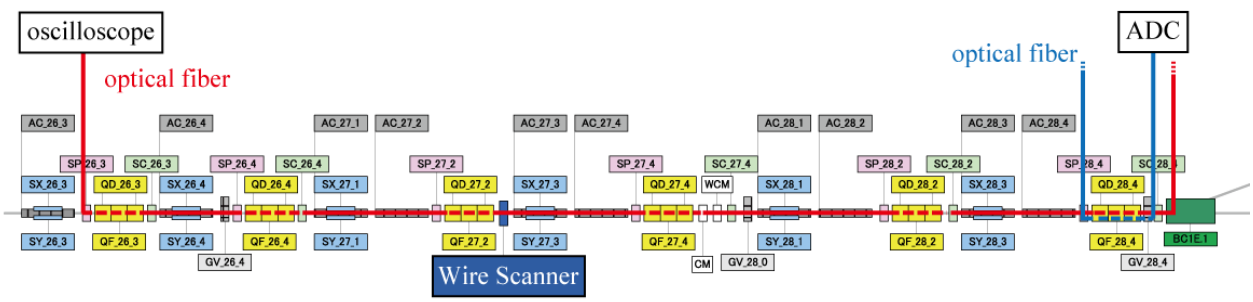


Figure 4: Layout of the beamloss monitor at sector-2 end which located ~100 m-downstream of the positron source.

ISBN 978-3-95450-141-0

Copyright © 2014 CC-BY-3.0 and by the respective authors

scattering in the wire. In case of two-bunch operation, those peaks are overlap other. Thus, the optical fiber dedicated to beamsize measurement using wire scanner has been set in last quadrupoles (QF_28_4, QD_28_4 in Fig. 4). The beam profile was measured, nevertheless high background as shown in Fig. 6.

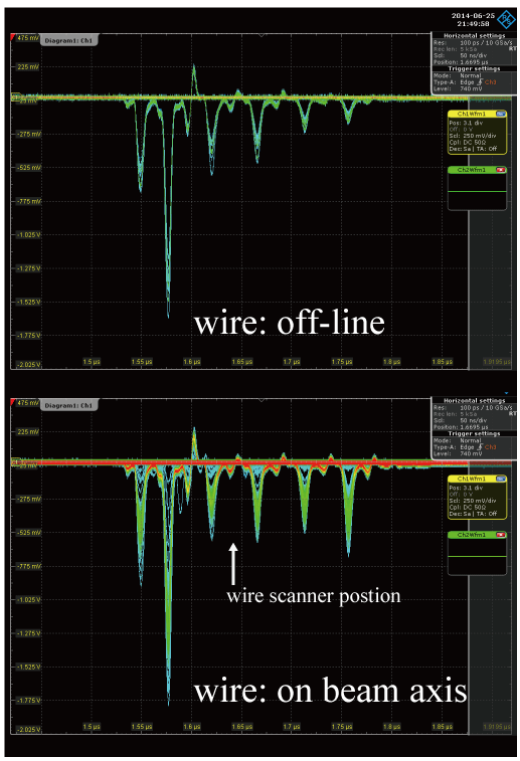


Figure 5: Background signals due to a beamloss at the positron source, in case of the primary electron beam passes through the target hole. The top/bottom corresponds to without/with insertion of the wire scanner.

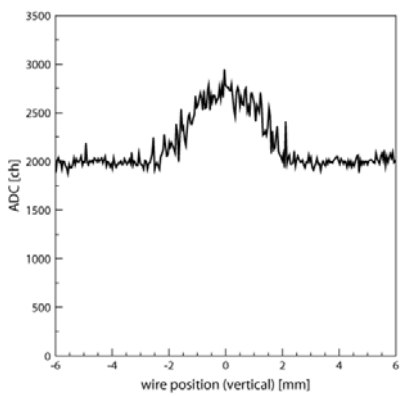


Figure 6: Vertical beam size at the wire scanner.

TIMING MONITORING SYSTEM

The trigger timing system of the linac is based on Event Timing System on VME [13]. The timing system distributes trigger timings and parameters for the linac components, such as RF phases, currents of magnets, etc., through event code and data buffer. The injection beam for the HER and LER requires timing jitter of less than 30 ps. It is confirmed that the system satisfies that the requirement under a variation of temperature in the linac [14]. To accomplish multiple injections to HER, DR, LER, PF ring and PF-AR, sequence of injection will be put every ~2 s. The trigger timings and parameters are decided by each beam mode. Those trigger timings range from ns to several hundred μs and the interval between the beam pulses is 20±1 ms and should be scheduled precisely. Thus, timing monitoring system with a wide dynamic range of more than 20 ms and a resolution of 1 ns is required. Then, a FPGA-based TDC has been developed [15].

FPGA-BASED TDC

The basic specification of the FPGA-based TDC listed in Table 1. The TDC has a common strat input and 16 multi-stop input channels. The inputs to the modules are standard NIM logic levels. Since handling FPGA with 1 GHz is not easy, the 4X oversampling technique is employed to the TDC with a 250MHz clock. The timing charts are shown in Fig. 7. Four clocks which have π/2 relative phase reference, then the time duration T is given by $T=NT_{clk}+\Delta T_1+\Delta T_2$ and a resolution of $T_{clk}/4$ is obtained.

Table 1: Margin Specifications

Parameters	Value
Number of common start	1
Number of stop channels	16
Number of multi-stops	4
Dynamic range	4.3 s
Resolution	1 ns
Clock	250 MHz

The performance test has been performed by using the TDC and the Digital Delay generator (SRS, Model DG645, rubidium time base) from the delay time of 1 ns to 800 ms. The accuracy which is given by the absolute time difference divided by the setting delay time and variations in the time difference of the measured to the setting delay time are shown in Fig. 8. The accuracy is 0.13 ppm up to ~3 ms which corresponds to the roll-off point. Those results are acceptable in our trigger timing monitoring system.

Copyright © 2014 CC-BY-3.0 and by the respective authors

ISBN 978-3-95450-141-0

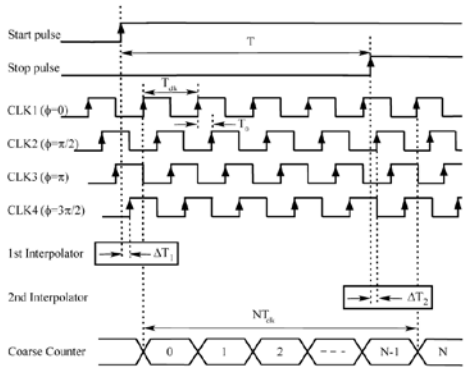


Figure 7: Schematic timing diagram for the FPGA-based TDC.

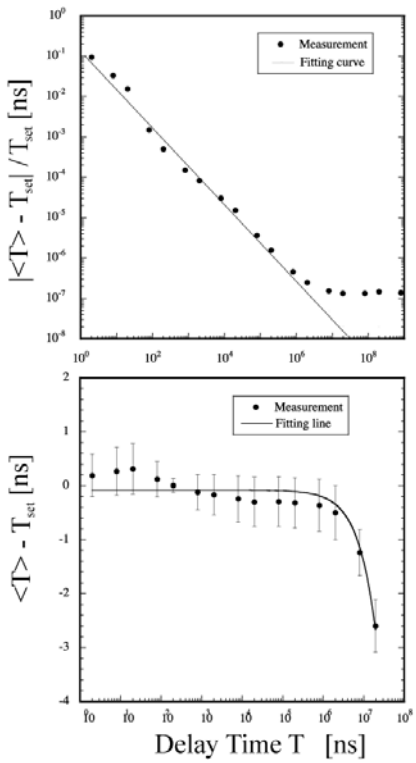


Figure 8: Accuracy and timing jitter. The bar shows standard deviation.

CONCLUSION

In the SuperKEKB injector linac, a new RF gun for low emittance, high bunch charge electron beam and a new positron source had been installed. Although the beam commissioning was just started, in case of the electron beam passes through the hole on the positron target, a beamloss was found by using the optical fiber set along the beamline. The optical fiber dedicated to beamsize measurement by using wire scanner has been also installed. A clear beam profile was obtained by using the system under the background which stems from the target. Trigger timings for the linac components ranges from ns to several hundred μs and the modulators of high power klystron should be triggered by 20±1 ms. Thus, wide dynamic range TDC with 1 ns resolution has been developed. The TDC shows good performance enough to monitor the linac timing system.

REFERENCES

[1] T. Miura et al., "Upgrade Status of Injector Linac for SuperKEKB", MOPRO001, IPAC'14, Dresden, Germany (2014).
[2] T. Natsui et al, "Quasi Traveling Wave Side Couple RF Gun for SuperKEKB", TUOCB103, IPAC'13, Shanghai, China (2013).
[3] M. Yoshida et al., "Generation and acceleration of low-emittance, high-current beams for SuperKEKB", MOIOB03, LINAC14, Geneva, Switzerland (2014).
[4] L. Zang et al., "Positron Yield Optimisation by Adjusting the Components Offset and Orientation", MOPRI003, IPAC'14, Dresden, Germany (2014).
[5] T. Kamitani et al., "SuperKEKB Positron Source Construction Status", MOPRI004, IPAC'14, Dresden, Germany (2014).
[6] M. Kikuchi et al., "Design of Positron Damping Ring for SuperKEKB", TUPEB054, IPAC'10, Kyoto, Japan (2010).
[7] H. Kaji et al., "Construction and Commissioning of Event Timing System at SuperKEKB", TUPRI109, IPAC'14, Dresden, Germany (2014).
[8] M. Satoh et al., "EPICS IOC of WindowsXP-based Oscilloscope for Fast BPM Data Acquisition System", WEP086, ICALEPCS2009, Kyoto, Japan (2010).
[9] R. Ichimiya et al., "High Position Resolution and High Dynamic Range Stripline Beam Position Monitor (BPM) Readout System for the KEKB Injector Linac Towards the SuperKEKB", WEPD04, these proceedings, IBIC2014, Monterey, California, USA (2010).
[10] N. Iida et al., "Recent Progress of Wire Scanner System for the KEKB Injector Linac and Beam Transport Lines", WEP5A15, EPAC2000, Vienna, Austria (2000).
[11] E. Janata, "Determination of location and intensity of radiation through detection of Cherenkov emission in optical fibers", Nucl. Instr. and Meth. A 493, 1 (2002).
[12] M. Korfer et al., "Fiber optic radiation sensor systems for particle accelerators", Nucl. Instr. and Meth. A 523, 256 (2004).
[13] Micro-Research Finland Oy website: http://www.mrf.fi/index.php/vme-products
[14] H. Kaji et al., "Upgrade of Event Timing System at SuperKEKB", THCOCA04, ICALEPCS2013, San Francisco, USA (2013).
[15] T. Suwada et al., KEK-Preprint 2014, in press.

Copyright © 2014 CC-BY-3.0 and by the respective authors

ISBN 978-3-95450-141-0

DIAGNOSTICS OF THE TPS BOOSTER SYNCHROTRON FOR BEAM COMMISSIONING

C. H. Huang, C. Y. Liao, Y.S. Cheng, Demi Lee, P. C. Chiu, C. Y. Wu, S. Y. Hsu, K. H. Hu, Jenny Chen, C. H. Kuo, K. T. Hsu
NSRRC, Hsinchu 30076, Taiwan

Abstract

Booster synchrotron for the Taiwan photon source project is in commissioning. Diagnostics which consist of screen monitors, intensity monitors, beam position monitors, tune monitors, visible light synchrotron radiation monitors and radiation-sensing field-effect transistors are integrated with accelerator control system. Integration and functionality check were done recently. Details of these diagnostics and preliminary test results will be summarized in this report.

INTRODUTION

Taiwan Photon Source (TPS) is a low emittance, third-generation light source in NSRRC [1]. It consists of a 150 MeV S-band linac, linac to booster transfer line, 0.15 to 3 GeV booster ring, booster to storage ring transfer line, and 3 GeV storage ring. The booster has 6 FODO cells which include 7 BD dipoles with 1.6 m long and 2 BH dipoles with 0.8 m long in each cell. Its circumference is 496.8 meters and it is concentric with the storage ring in the same tunnel. The radio frequency is 500 MHz with 828 harmonic numbers. The ramping repetition rate is 3 Hz which is locked with the frequency of the power system. Preliminary commissioning of the booster synchrotron is being proceeded and it shares some windows for installation and system-integrated test from mid-August 2014. Diagnostics which equips in booster to help the beam commission will be described in the report, and preliminary results will be summarized as well.

DIAGNOSTIC DEVICES IN THE BOOSTER

There are seven screen monitors in the booster ring to monitor the beam profile and beam position, shown in Fig. 1. The average beam current is measured with a Bergoz's new parametric current transformer (NPCT) and the pulse current is observed by a fast current transformer (FCT). Sixty beam position monitors (BPMs) can be used to measure beam position and rough beam intensity along the longitudinal position. For the tune monitor, the beam is shaken by stripline electrodes or a magnetic shaker using narrow band white noise; the beam motion signal is picked up by BPMs. Two visible light synchrotron radiation monitors (SRMs) are used to measure the synchrotron radiation profile. They are set up in the opposite side of the booster with a camera inside the tunnel and one outside the tunnel. In order to investigate applicable of radiation-sensing field-effect transistors (RadFETs) for measuring the local beam loss, several RadFETs are installed at the injection area of the booster ring.

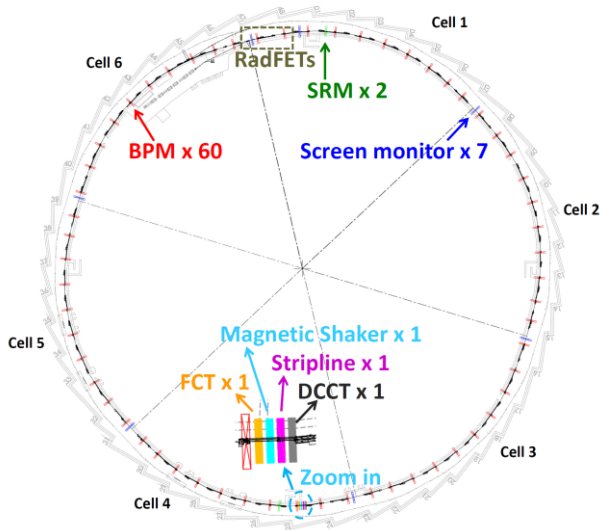


Figure 1: The layout of the diagnostic devices in the booster ring.

SCREEN MONITOR

Seven screen monitors are designed in the beginning of six cells of the booster and behind the 1st DB dipole of the 1st cell for booster commissioning. The screen monitor assembly consists of a hollow tube, a Yag:Ce screen with 25 mm in diameter and 0.5 mm in thickness. The YAG:Ce screen is mounted at 45° angle in one side to intercept the beam. A vacuum-sealed window is in the other end of the tube to extract the light. A CCD camera is mounted at a supporting tube with LEDs installed beside the CCD camera for illumination. A pneumatic device is used to move the whole assembly in or out. All of these devices are controlled remotely including the on/off of the LED. The structure of the screen monitor assembly is shown in Fig. 2. The power over Ethernet (PoE) switches are used to connect the cameras and uplink to the vision system in the input / output controller (IOC) of the experimental physics and industrial control system (EPICS) [2]. The IOC is constructed based on Linux operating system with areaDetector EPICS module and a compiled Matlab analysis program is used as a graphical user interface, shown in Fig. 3. The camera trigger comes from TPS timing system. Exposure time and camera gain are adjustable to meet various beam conditions. This scheme is simpler than the complicated attenuator design.

Copyright © 2014 CC-BY-3.0 and by the respective authors

ISBN 978-3-95450-141-0

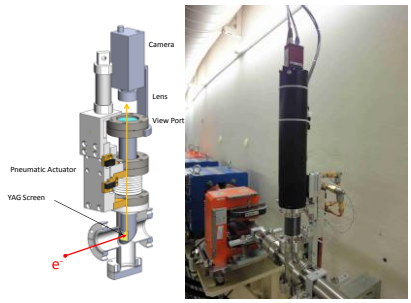


Figure 2: Screen monitor assembly.

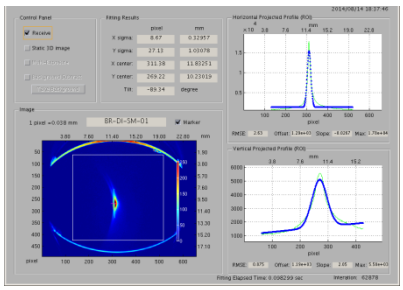
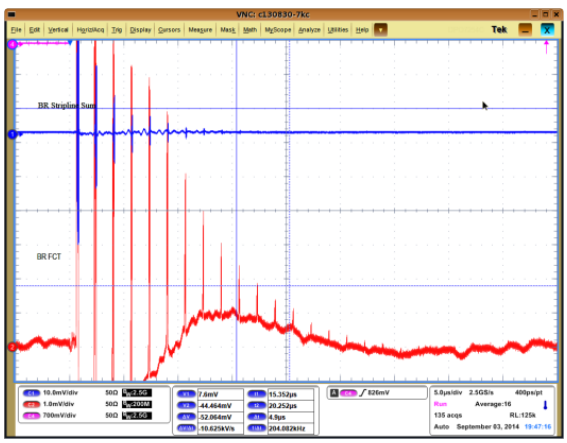


Figure 3: The image profile as the beam passes through the 1st screen of the booster ring.

CURRENT INTENSITY MONITOR

A FCT is used to observe filling pattern via an oscilloscope. Trigger of the oscilloscope is controlled by the timing system which can shift to the timing of any ramping energy. The singles of the FCT and stripline sum are shown in Fig 4. From this figure, it is clear that the electron beam circulates more the ten turns. Average beam current is measured by a NPCT in which current waveform can be obtained using analog-to-digital converters (ADCs) and the averaged beam current can be obtained using digital voltmeters. Beam current data is acquired from an EPICS IOC.



Fiugre 4: Beam singles observed by a fast current transformer (FCT) and stripline .

BEAM POSITION MONITOR

The booster synchrotron equips with 60 button-type BPMs. All BPMs accompany with Libera Brilliance+ electronics [3-4]. There are 60 sets of phase-trimmed 0.240" form polyethylene coaxial cables which connect the button to BPM electronics. The gain variation of BPM electronics is less than 5%. The same attenuation for all BPMs benefits from the equal length of all cable sets. It also makes possible to use the sum signal of a BPM as an intensity indicator. The error would only come from position dependence of the beam. All parameters of BPM electronics are accessible from the EPICS control system.

BPM electronics supports beam position and intensity data for commissioning and routine operation. The raw data of an ADC is useful for checking the timing of the beam and beam property especially in the first turn. The single pass, turn-by-turn, 10 kHz and 10 Hz beam position data will also be deployed and accessed by EPICS process variables (PVs). 10 Hz rate data is only useful for the injection energy at the direct current (DC) operating mode in the booster synchrotron. The BPM data is useful for beam commissioning. To demonstrate usage of the BPM during commissioning, several examples are presented here.

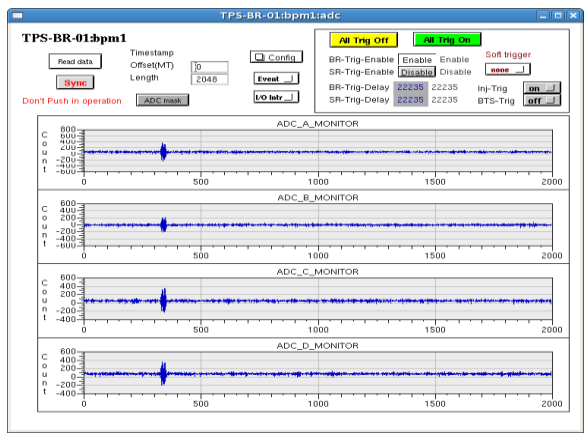


Figure 5: The ADC data when beam passes through the 1st BPM of the booster synchrotron.

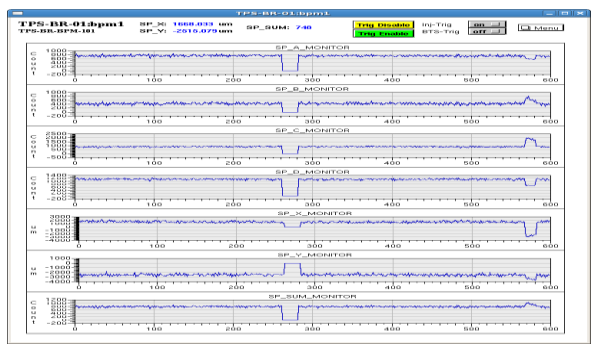


Figure 6: Beam position and intensity trend observed by the 1st BPM of the booster synchrotron. The change of the data is caused by the injection condition.

The first beam which passed through the injection septum and kicker and then arrived the 1st BPM of the booster ring is shown in Fig. 5 and Fig. 6. Beam losses along the longitudinal position can be easy extracted from the ADC data. Figure 7 shows the sums of the ADC count

ISBN 978-3-95450-141-0

Copyright © 2014 CC-BY-3.0 and by the respective authors

of various BPMs as the beam attempts to circulate the first turn.

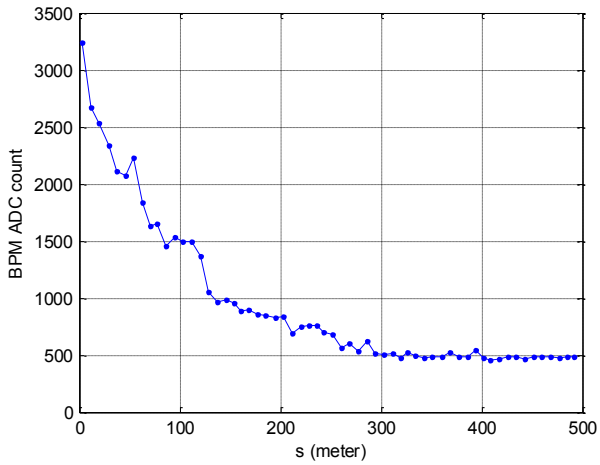


Figure 7: Beam intensity along the booster synchrotron when attempting to circulate the first turn.

After correcting the orbit, the beam, which has completely circulated more than 5 turns, can be clearly observed from the button signals of the BPM ADC raw data in the 1st cell as show in the Fig. 8. The trajectory of the first 3 turns is shown in Fig. 9. It can be identified clearly that particular beam loss happens as the beam passes through the first 3 BPMs of the first turn. A great deal of beam loss at the first cell can be identified by a step change of beam intensity in Fig. 9(c). Large horizontal oscillation is clearly observed at the second turn because the beam sees the injection kicker post-pulse ripple. Horizontal trajectory is large than 5 mm. Vertical oscillation can keep within +/- 2 mm.

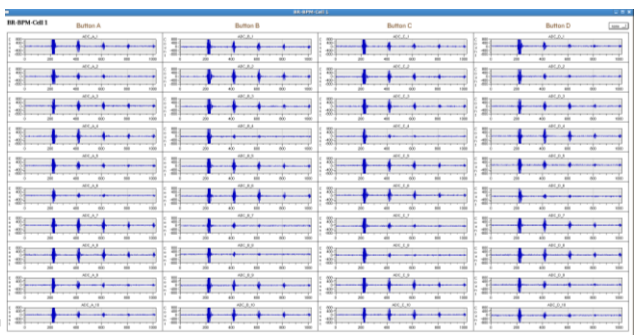


Figure 8: The ADC data as the beam circulates complete 5 turns in the booster.

In order to reduce the beam loss at the first 3 BPM, the chamber is realigned and some further orbit correction has been done. The trajectory variation in the horizontal and vertical plane, shown in Fig. 10, becomes fewer and the beam loss at first turn is around 20%, which is significant improve comparing to previous results. However, the horizontal trajectory in the second turn still remains around +/- 5 mm and the loss between the adjacent turn is still large. To store beam and ramp the energy into 3 GeV are our short-term goals.

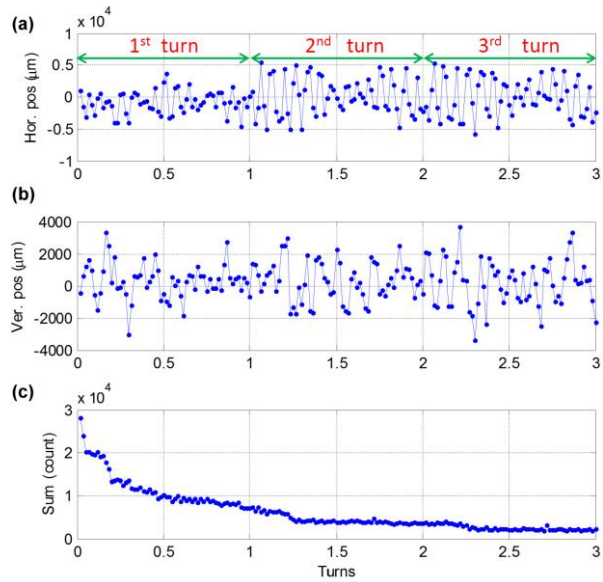


Figure 9: The trajectory in the (a) horizontal plane and (b) vertical plane. (c) Sum of the first three turns.

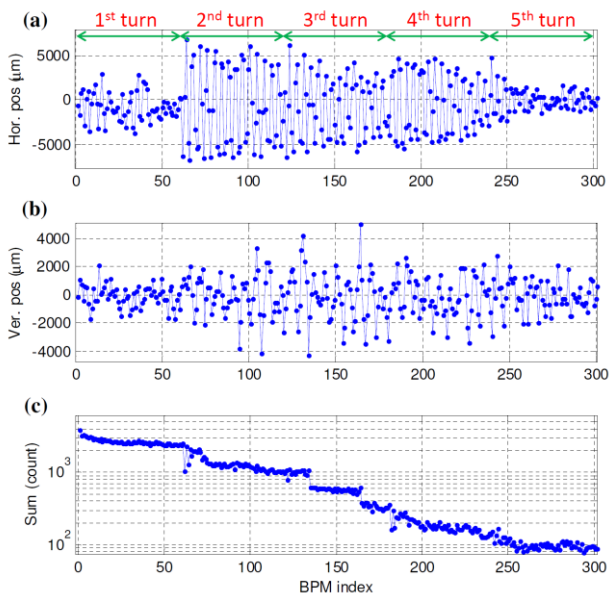


Figure 10: The trajectory in the (a) horizontal plane and (b) vertical plane. (c) Sum signal of the BPMs after aligning the booster chamber and doing the orbit correction.

TUNE MONITOR

Damped oscillation caused by the injection kicker can be used to extract tune information at the injection energy or commission for the DC mode. The injection tune can be extracted from the Fourier analysis of the turn-by-turn data of the selected BPM.

Tune variation during ramping can be measured by a continuing beam excitation and doing spectra analysis of the turn-by-turn data as the energy is ramped up and beam survives. Therefore, when the extraction of booster is not actived, tune measurement during the ramping down

Copyright © 2014 CC-BY-3.0 and by the respective authors

ISBN 978-3-95450-141-0

energy is also available before beam loss. To excite stored beam for tune measurement, a stripline kicker was original proposed to install. However, because it cannot meet commissioning schedule, a magnetic shaker using handy spare parts is installed as Fig. 11 as the current solution. The stripline will be installed later. The magnetic shaker is without bunch-by-bunch capability. It is used to continuously exciting the beam now and is acceptable for tune measurement. The shaker consists of two multi-turn coils mounted on the ceramic chamber in the horizontal and vertical planes of the shaker, which is enclosed by a ferrite box. The kickers with 50 Ω terminated loads have a calibration factor of 3 mG/A. An arbitrary signal, which is provided by a band-limited, amplitude-adjustable signal generator, is amplified by a power amplifier to drive the shaker in each plane. Turn-by-turn beam oscillation data is acquired by the BPM electronics. The functional block diagram of this tune monitor system is shown in Fig. 12.

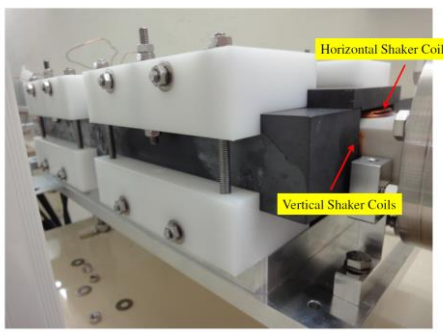


Figure 11: Magnetic shaker.

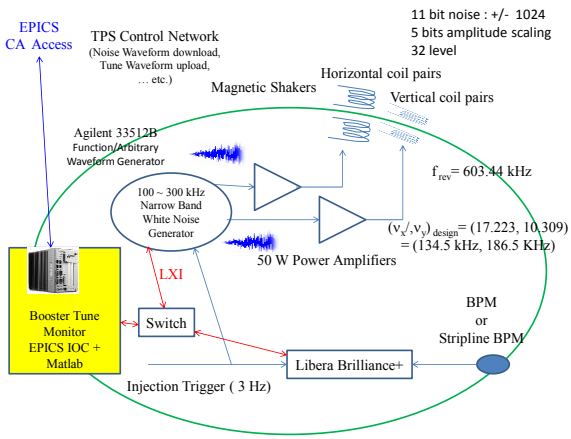


Figure 12: Functional block diagram of the tune monitor.

Preliminary tests in Taiwan Light Source show that the beam can be excited effectively during the whole ramping cycle [5]. The betatron sideband is observed by a BPM with acceptable signal to noise ratio as in Fig. 13. The spectrogram of the horizontal and vertical BPM turn-by-turn data could identify the tune variation clearly. Peak identification from the spectrogram could extract the varying tunes during one ramping cycle.

Tracking of the dipole filed and strength of quadruple families to keep the tune value within the tolerance is important. A large tune shift will degrade the operating performance of the booster synchrotron and even lead to the beam loss. Minimize tune variation can be realized by observing tune variation during energy ramping and be used to correct quadruple settings. The beam currents of the magnets for the TPS booster synchrotron are excited by a 3 Hz sine-like waveform which is in corporation with the radio frequency (RF) system. Tune monitor can provide tune variation during the ramping for tracking compensation.

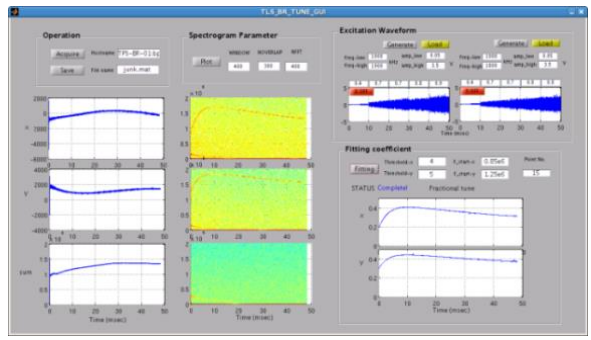


Figure 13: Graphical user interface of the tune monitor.

SYNCHROTRON RADIATION MONITOR

There are two SRMs in the booster synchrotron and their extract ports were installed at the 2nd BD dipole magnet of 1st cell and 4th cell. One port can extract light to the shielding wall for the measurement of a streak camera as shown in Fig. 14. The designed beam emittance at 150 MeV is 0.167 mm-mrad and 0.01 mm-mrad when ramping to 3 GeV. Beam size (σ_x, σ_y) will shrink ten times from (0.7 mm, 1.5 mm) to (0.15 mm, 0.1 mm). To ensure better resolution at small beam size part in 3 GeV, unit conjugate optics for both monitors is adopted. This optic design will ensure that the diffraction is not deleterious to beam size measurement at 100 μm level. The beam size of the booster synchrotron radiation is captured a GigE Vision CCD camera using external trigger which is synchronized with the machine cycle. The PoE switches are also used to connect the cameras and uplink to the vision system EPICS IOC.



Figure 14: The setup of a synchrotron radiation monitor (SRM) after the 2nd BD dipole in the 1st cell.

ISBN 978-3-95450-141-0

Copyright © 2014 CC-BY-3.0 and by the respective authors

REAL-TIME DOSE MONITORING USING RADFETS

A RadFET is a p-channel metal-oxide-semiconductor field-effect transistor with an aluminium gate and thick layer of silicon dioxide as a dosimeter [6-7]. A RadFET changes its electrical characteristics under the influence of ionizing, i.e., removal of electrons and leaving a stationary positive charge in the silicon dioxide layer. The relaxation of the positive charge would be several months, which makes it measure the total dose, not dose rate. The trap charges shift the gate threshold voltage as the reader uses a constant current through the transistor.

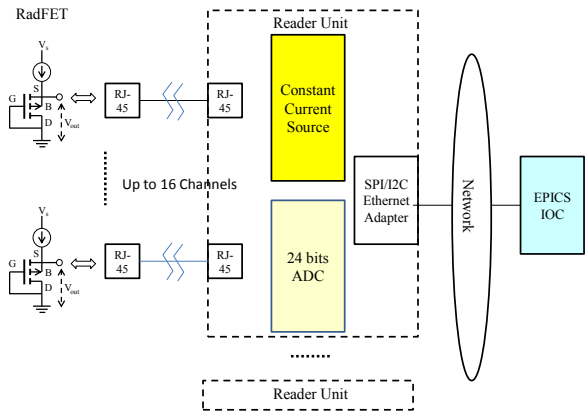


Figure 15: Block diagram of RadFET reader.

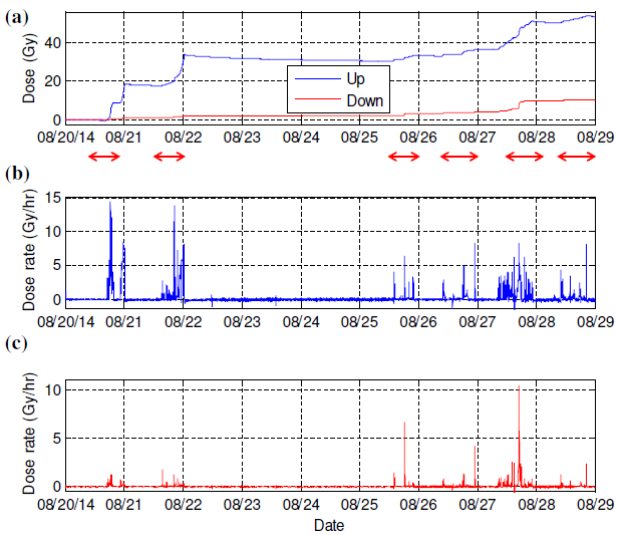


Figure 16: Loss pattern during beam commissioning window from August 20th to 28th, 2014. The RadFETs are installed at the up side and down side of the vacuum chamber after the injection kicker of the booster synchrotron. The red arrow in (a) is the beam commissioning windows.

A prototype RadFET reader which accommodates up to 16 RadFETs has been implemented, shown in Fig. 15. The connection between a RadFET and reader unit is an unshielded-twisted-pair network cable with RJ-45 connectors due to its popularity and easy to handle. Currently reading rate is 60 seconds. The measured doses are published in EPICS PVs format and saved in the archiver for further usage. The dose rate can be easily obtained by taking time derivative of the recoded dose data.

From the radiation dose or dose rate measured by the RadFET installed in the upside and down side of chamber after injection kicker of the booster in Fig. 16, the dose increases at the commissioning windows due to the beam loss during beam test. The dose in the other windows, which is available for continue installation works, is slightly decay due to the annealing effects. The decay rate is around 4% for 24 hours without exposing to the radiation. The position and period of high dose rate which indicates the beam loss may provide some information to the operator to adjust the beam.

CURRENT STATUS

Final system integration test of booster with the installation of the storage ring and preliminary beam commissioning of the booster synchrotron is in progress now. Beam was circulated one turn soon after commissioning work started. To store beam and ramp the energy into 3 GeV are the recent efforts. Diagnostics for the booster synchrotron has been exercised with beam during last several weeks. Functionality and supporting tools of software have been revised. Preliminary results show the diagnostic support fulfills its role.

REFERENCE

[1] TPS Design Handbook, version 16, June 2009.
[2] C. Y. Liao, et. al., "Image profile diagnostics solution for the Taiwan photon source", IBIC 2012, Tsukuba, Japan.
[3] www.i-tech.si
[4] P. C. Chiu, et. al., "TPS BPM electronics Performance measurement and statistics", IBIC 2012, Tsukuba, Japan.
[5] P. C. Chiu, et. al., "New booster tune measurement system for TLS and TPS prototype", IBIC 2013, Oxford, UK.
[6] L. Frohich, et. al., "DOSFET-L02: An advanced online dosimetry system for RadFET sensors", IBIC 2013, Oxford, UK.
[7] L. Frohich, et. al., Nucl. Instr. And Meth. A 703 (2013) 77-79.

Copyright © 2014 CC-BY-3.0 and by the respective authors

ISBN 978-3-95450-141-0

OVERVIEW OF BEAM INSTRUMENTATION ACTIVITIES FOR SwissFEL

R. Ischebeck, R. Abela, V. Arsov, R. Baldinger, H. Braun, M. Calvi, R. Ditter, C. Erny, F. Frei, R. Ganter, S. Hunziker, Y. Ivanisaenko, P. Juranić, B. Keil, W. Koprek, R. Kramert, D. Llorente Sancho, F. Löhl, F. Marcellini, G. Marinkovic, B. Monoszlai, G.L. Orlandi, C. Ozkan, L. Patthey, M. Pedrozzi, P. Pollet, M. Radovic, M. Roggli, M. Rohrer, V. Schlott, A. Stepanov, J. Stettler, PSI, Villigen, Switzerland
P. Peier, DESY, Hamburg, Germany
F. Ardana-Lamas, I. Gorgisyan, C.P. Hauri, L. Rivkin, EPFL, Lausanne & PSI, Villigen, Switzerland

Abstract

SwissFEL will provide users with brilliant X-ray pulses in 2017. A comprehensive suite of diagnostics is needed for the initial commissioning, for changes to the operating point, and for feedbacks. The development of instrumentation for SwissFEL is well underway, and solutions have been identified for most diagnostics systems. I will present here an overview of the instrumentation for SwissFEL, and give details on some recent developments.

INTRODUCTION

A comprehensive diagnostics suite has been designed to assist in the commissioning and operation of SwissFEL [1]. The normal-conducting accelerator will run at a repetition rate of 100 Hz, generating two electron bunches separated by 28 ns in each RF pulse. The bunch charge can be adjusted between 10 and 200 pC, depending on the operation mode. A significant effort has been put into designing instrumentation suitable for the low-charge mode, which generates the smallest signals in the pick-ups, but has the tightest tolerance goals.

Instrumentation for SwissFEL has been tested at the SwissFEL Injector Test Facility [2]. Detailed measurements demonstrate the suitability for the SwissFEL design parameters [3].

CHARGE MONITORS

For calibration of the FEL photon pulses, an absolute charge measurement accuracy of 1% is desired. We currently have two possibilities: 1) in-house developed BPMs; 2) Bergoz Turbo-ICT-2 with BCM-RF-2 readout electronics. The BPM is a highly sensitive but not a calibrated device. The charge related signals of the BPM still need to be calibrated. The Turbo-ICT-2 is a calibrated device. It is an upgrade of the Bergoz Turbo-ICT with 2-bunch resolving capability and can accomplish these requirements with negligible beam position and bunch length dependence. It is insensitive to dark current due to its fast readout of the beam induced current (3 ns) at higher bandwidth. The resolution of the Turbo-ICT-2 is comparable to that of the BPM at charges > 10 pC (Fig. 1). Hence, the ICTs can still be mounted with the BPMs in every dispersive section of the machine and used to calibrate the BPMs.

The second option for calibrating the BPMs is the Bergoz ICT with BCM-IHR readout electronics. This is a calibrated device that gives the total charge in an integration window of 5 µs and cannot resolve the two bunches at SwissFEL. It measures the total charge, including the dark current. The single-shot resolution of this device is 20 pC; however, it can be used to calibrate the BPMs by first measuring the dark current and subtracting this value from the total integrated charge, one bunch at a time, to ascertain the charge of a single bunch.

BEAM POSITION MONITORS

SwissFEL will use cavity beam position monitors (BPMs) to align the beam along the linac, and to measure the electron energy in dispersive sections [4]. The proper alignment of the beam is important to reduce emittance growth due to wake fields, and to ensure overlap of the electron bunch with the radiation in the undulators. The BPMs consist of dual-resonator cavities. The dipole cavity determines the position, while the monopole cavity is used as a charge reference measurement. This measured charge value is also used for other monitors that exhibit a strong bunch charge dependence, such as bunch compression monitors.

There will be three types of cavity BPMs in SwissFEL, taking into account vacuum chamber diameters of 38, 16, and 8 mm in the gun, the linac and the undulator lines, respectively. For the cavities designed for a vacuum chamber diameter of 38 and 16 mm, a frequency of 3.3 GHz and a low quality factor of about 40 was chosen to minimize the crosstalk between the two bunches separated by 28 ns. The BPMs with 8 mm diameter will be deployed in the undulator lines, where only single bunches will be present in each RF pulse. For this reason, a higher quality factor will be chosen.

The resolution of the BPMs has been determined by comparing the measurements of several monitors installed in series. The residual of the SwissFEL cavity BPM (BPM16) is 0.8 µm rms for a 0.35 mm beam offset (Fig. 2).

BUNCH ARRIVAL MONITORS

Two bunch arrival monitors (BAMs) have been commissioned in the SwissFEL Injector Test Facility [5]. The first BAM upstream of the bunch compressor (FINXB-DBAM10) was commissioned in 2012. Two pick-ups were used there

ISBN 978-3-95450-141-0

Copyright © 2014 CC-BY-3.0 and by the respective authors

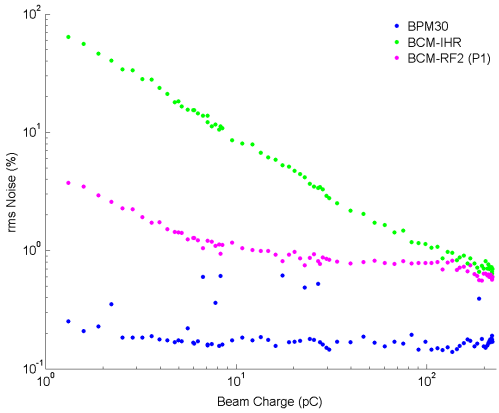


Figure 1: Signal-to-noise ratio measurement as a function of bunch charge, comparing resonant strip line sum signals (BPM30) with charge monitors BCM-IHR and BCM-RF2.

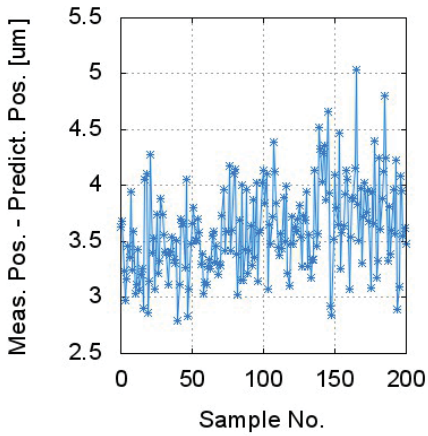


Figure 2: Beam position monitor resolution, measured by comparing several BPMs installed in series.

– a button with 80 GHz intrinsic bandwidth (vacuum side) and a Ridge Waveguide (RWG) with 16 GHz bandwidth and potentially stronger response at low charge. The bandwidth of both pick-up types was limited to 20 GHz by the vacuum feedthroughs, the highest bandwidth feedthroughs available on the market. In addition, the EOMs in the tunnel front-end had a bandwidth of 10 GHz and the acquisition ADC card was 12 bit, AC coupled. With this BAM, the best resolution achieved with the button pick-up was 18 fs in the range 60 to 200 pC and 30 to 170 fs in the range 10 to 60 pC. Several improvements were made in the second BAM commissioned in 2014 downstream the bunch compressor. Installed were button pick-ups equipped with 40 GHz vacuum feedthroughs. Used were EOMs with 33 GHz bandwidth (40 Gs/s) and small half-wave voltage (4.6 V). A DC-offset DAC allowed utilization of the full ADC dynamic range. The improved photoreceiver design allowed higher input optical powers and adjustable RF-amplification. Thus even with a 12 bit ADC a resolution of 10 fs to 13 fs was demonstrated in the range of 90 to 200 pC and 13 to 40 fs in the range of 20 to 90 pC. This measurement satisfies the specification for SwissFEL at high charge (Fig. 3). Two further improvements are due to be

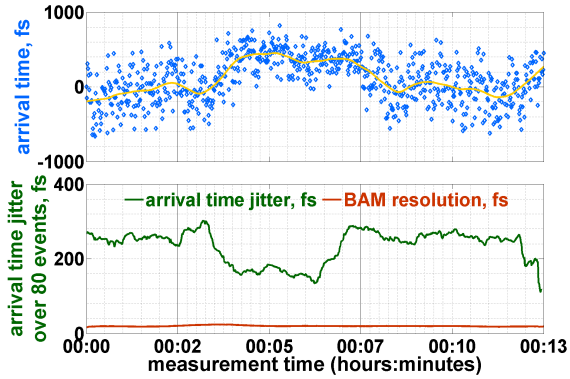


Figure 3: The bunch arrival time monitor has been used to measure arrival time jitter and drift in the SwissFEL Injector Test Facility.

tested in September 2014 before decommissionig of SITF: use of a 16 bit ADC card and a button pick-up mounted on a vacuum chamber with 16 mm inner diameter. With the utilization of the full dynamic range of the 16 bit ADC and the stronger signals of the 16 mm beampipe pick-up, at least factor 4 improvement in the resolution is expected, thus meeting the requirements for SwissFEL also for small charge.

BUNCH COMPRESSION MONITORS

Bunch Compression Monitor BC1

At the first bunch compressor of SwissFEL, the electron bunches will be compressed to a bunch duration of 250 to 500 fs. Dependent on the bunch shape and length, this implies coherent edge as well as coherent diffraction radiation up to the few THz spectral range. A bunch compression monitor (BCM) detecting relative bunch length changes is based on measuring two different spectral bands (0.26 to 2 THz and 0.6 to 2 THz) by using “thick grid” high pass THz filters and fast Schottky diodes.

The response of these detectors on accelerator parameters has been measured, applying small variations around the operating point [6]. The radiation detected behind the two filters shows a slightly different dependency on S-band and X-band phase (Fig. 4). Further investigations will aim at increasing the ratio between the two detectors, in order to achieve a linearly independent measurement of the relevant parameters.

Bunch Compression Monitor BC2

In a second magnetic chicane, the electron bunches will be further compressed to 3…75 fs. Therewith, the coherent radiation emitted by the electron bunch is extending up to the infrared spectral region. To cover the wide spectral range required, the design of a prism based spectrometer, using a mercury cadmium telluride (MCT) array as detector, is currently under investigation.

Copyright © 2014 CC-BY-3.0 and by the respective authors

ISBN 978-3-95450-141-0

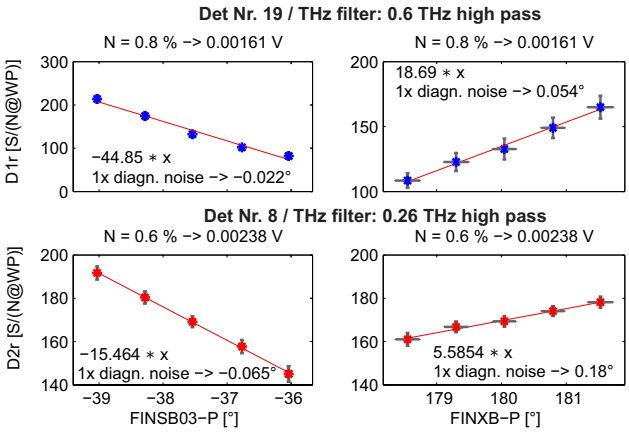


Figure 4: Measurement of the dependency of terahertz radiation in two spectral bands, as a function of S-band and X-band phases.

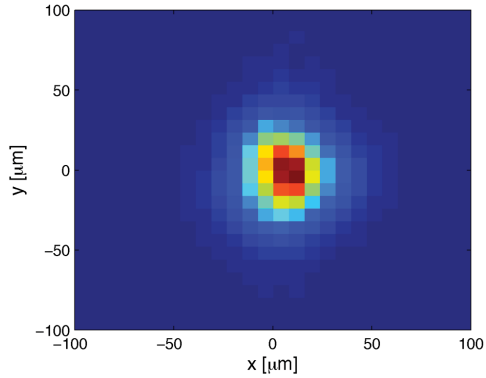


Figure 5: Measurement of a beam with 15 µm rms size.

ELECTRO-OPTICAL MONITORS

We have developed a non-invasive, compact and cost effective longitudinal profile monitor based upon the electro-optic effect. A chirped laser pulse propagates through a GaP crystal parallel to the electron beam in the beam pipe. Electric field of the electron bunch induces birefringence in the crystal. The laser light polarization is rotated proportionally to the electric field in the part of the laser pulse that temporally overlaps with the electron bunch. Polarizers convert the polarization angle into an intensity modulation, measured with a spectrometer. This modulation can be mapped into time by measuring the laser pulse chirp. Electron bunch longitudinal profiles as short as 300 fs were measured at SITF using this technique.

TRANSVERSE PROFILE IMAGERS

The transverse profile is measured by three diagnostics: screen monitors using a fluorescent crystal, synchrotron radiation monitors, and wire scanners.

The screen monitors consist of a cerium doped yttrium aluminum garnet (Ce:YAG) crystal that can be inserted into the vacuum chamber. It is imaged through an in-vacuum mirror onto a CCD or CMOS detector. The imaging is be set up with different magnifications, accounting for the change in beam size along the accelerator. In each case, the imaging is set up according to Snell's law of refraction to achieve a resolution that is not affected by the thickness of the crystal (Fig. 5), and observing the Scheimpflug imaging condition, such that a large field of view can be obtained [7].

A system to read out the cameras at the beam rate of 100 Hz has been set up [8]. It allows for a bunch-synchronous data acquisition and processing.

SYNCHROTRON RADIATION IMAGERS

In SwissFEL four synchrotron radiation monitors will be used to measure the transverse profile of the electron beam in the charge range 10…200 pC. Two of them – installed in BC1 and BC2 – will monitor at 100 Hz the beam energy at 350 MeV and 2.1 GeV, respectively, and the related energy spread. The SR monitors installed in BC1 and BC2 will image in the visible the SR light emitted by the 3rd dipole of the magnetic chicane by means of CMOS cameras equipped with an f = 300 mm lens. The projected pixel size corresponds to a relative energy spread resolution of $1.13 \cdot 10^{-4}$ for BC1 and $1.54 \cdot 10^{-4}$ for BC2. In a second phase, the two SR-monitors of BC1 and BC2 will be equipped with a two-bunches camera system, to resolve the 28ns time structure of the 100Hz two-bunches train of SwissFEL. This will be accomplished with a beam splitter, internal optics and two fast switchable micro channel plate image intensifiers.

Two SR monitors will be also installed in the Aramis High-Energy Collimator and in the ATHOS switchyard to monitor the beam transverse size in the UV radiation or X-ray. The conceptual design of the SR monitors in the Aramis High-Energy Collimator and the ATHOS switchyard is under development.

WIRE SCANNERS AND LOSS MONITORS

In SwissFEL, YAG screens and wire scanners will be used to monitor the electron beam in the charge range 10…200 pC and in the energy range 0.340…5.8 GeV. In particular, wire-scanner will be used to resolve the 28 ns time structure of a 100 Hz two-bunches train. Design criteria of the SwissFEL wire-scanner are: use a single UHV linear stage to scan beam profile in the X,Y and X-Y directions; use Tungsten wire with different diameters 5-13 µm to ensure a resolution in the range 1.5-3.5 µm; equip each wire-scanner with spare/different-resolution wires; detect the wire-losses with scintillator fiber downstream the wire; Beam-Synchronized-Acquisition (BS-ACQ) of the read-out of both the encoder wire position and the loss-monitor; wire-fork designed for routine beam scanning during FEL operations (no beam interception with the wire-fork); wire-fork equipped with different pin-slots (distance of wire-vertex from vacuum-chamber axis: 8, 5.5, 3 mm) in order to reduce the scanning time as a function of the position of the wire-scanner along the machine. Bench and beam tests of prototypes of wire-scanner have been carried out. The results of the

ISBN 978-3-95450-141-0

Copyright © 2014 CC-BY-3.0 and by the respective authors

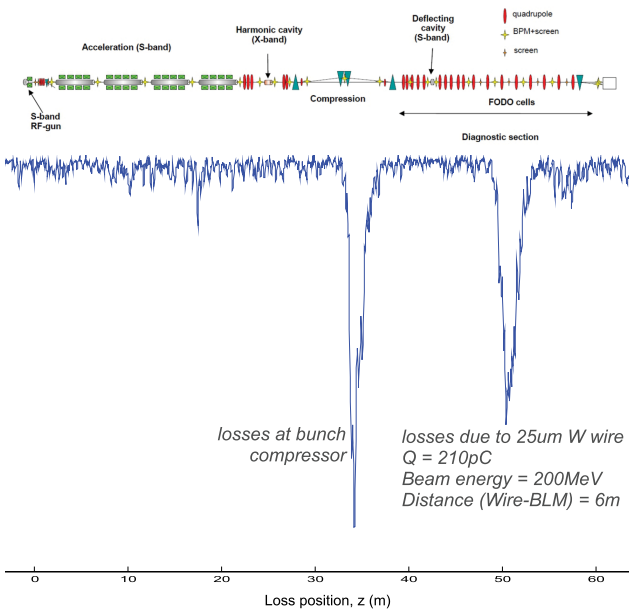


Figure 6: The longitudinal loss monitor uses the arrival time of the Cherenkov photons at the detector to infer the location of the losses.

wire vibration tests indicate that, in the wire velocity range 0.2…2 mm/s, the measured vibration of the wire is below the intrinsic resolution limit which is expected for a wire scanning the transverse profile of a beam [9]. Beam tests of wire-scanners confirmed the reliability of the wire-scanning technique in comparison with OTR screen measurements.

The interaction of the electron beam with the wire causes a scattering of the initial beam - scattered primary electrons and secondary particles which is proportional to the number of the electrons sampled by the wire. The scattered secondary particles and photons reach the Beam loss monitor mounted at a certain distance to the wire-scanner. A Beam Loss Monitor (BLM) is composed of 1mm diameter polystyrene scintillator fibers. The scintillation light is carried away from the tunnel to be detected by photomultiplier tubes (PMTs), located in the electronics racks outside, via plastic waveguide fibers. Due to the fast decay time (2 ns) of the scintillators and the fast PMTs (Hamamatsu H10720), the BLMs are able to discriminate the 28 ns time structure of the two bunches.Tests carried out at SITF show that the BLMs can detect the wire losses down to an input bunch charge of 1 pC and resolve the 28 ns time structure of the electron beam. A second system is composed of a fiber installed along the accelerator. Lost particles generate Cherenkov radiation, which is detected by a PMT at the upstream end of the fiber (Fig. 6). Measurements have also shown that beam size measured with OTR screens versus WSC scans show an excellent linearity (less than 2% deviation) and the comparison of the WSC-BLM and OTR measurements show an agreement within 8% (Fig. 7) [10].

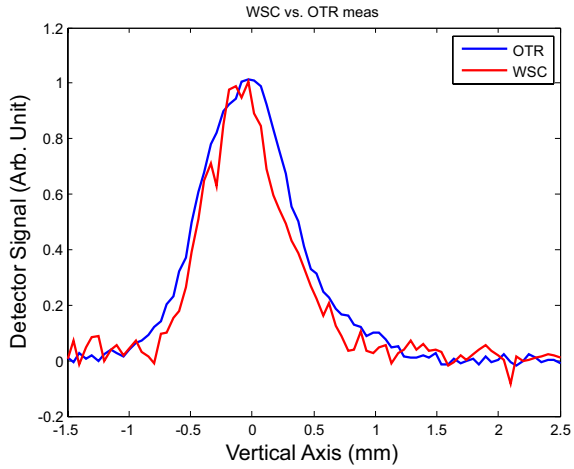


Figure 7: A measurement of beam size with a wire scanner. For comparison, the beam size measured by optical transition radiation is shown.

DOSE RATE MONITORS

The SwissFEL requires monitoring of radiation doses to prevent radiation-induced demagnetization of its in-vacuum Undulators. To this purpose, integrating dosimeters called the Radiation-sensing field-effect transistors (RADFET, RFT-300-CC10 RADFET, REM Oxford Ltd) will be placed on each Undulator flange, close to the beam pipe. Regular readings from 30 RADFETs over the years of operation of the accelerator will track and locate periods of high and low dose. A dosimetry system DOSFET-L02, developed at Elettra, allows reading out 4 RADFETs at a time [11]. The system has performed well at the SITF during the U15 test measurements, acquiring one dose reading per 20 seconds. The REM RFT-300 sensors were set in 25V bias mode, as the application of a positive bias to the sensors vastly increases their response at the expense of limiting the measurable dose range [12]. This choice of mode allows the measurement of integrated doses up to 110 Gy. The readings from the RADFET system were found to be in good agreement with Gafchromic XR-RV3 film dosimeters which were also mounted on the undulator flanges, behind the RADFETs. A measurement performed during the undulator experiment is shown in Figure 8.

X-RAY PULSE ARRIVAL TIME AND LENGTH MONITORS

The X-ray pulse arrival time and length will be measured by terahertz streak cameras in the SwissFEL end stations [13]. This device has only a small absorption, and can be placed in front of the user experiments.

The terahertz streak camera is based on the ionization of Xenon clusters that are injected into the beamline through a pulsed piezo valve. The energy of the photoelectrons is modulated by a terahertz potential generated by the experimental laser, and measured by two time of flight spectrometers, oriented at opposite sides of the chamber. Due to the time-

Copyright © 2014 CC-BY-3.0 and by the respective authors

ISBN 978-3-95450-141-0

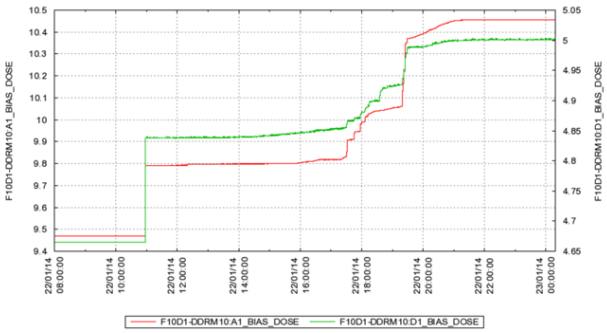


Figure 8: Measurement of dose rate at the undulator installed in Summer 2014. About half of the dose accumulated in this particular day has been deposited during two short time periods, demonstrating the need for a fast interlock system.

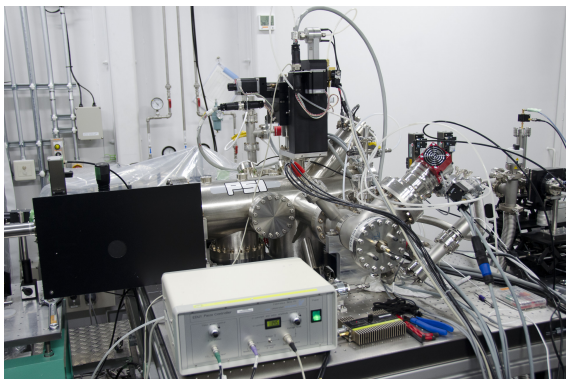


Figure 9: Installation of the terahertz streak camera at SACLA.

dependent nature of the terahertz field, an arrival time shift then manifests itself as a relative change of the electron energy in the two spectrometers. The X-ray pulse length can be measured by the width of the spectra. We have tested the prototype of the terahertz streak camera at SACLA (Fig. 9), and measured arrival time and pulse length at photon energies up to 10 keV.

REFERENCES

[1] SwissFELConceptual Design Report. Technical report, Paul Scherrer Institut, April 2012.

[2] M Pedrozzi. SwissFEL Injector Conceptual Design Report. *PSI Bericht*, 10(05), 2010.

[3] R Ischebeck et al. Instrumentation Activities at the SwissFEL Injector Test Facility. In *Proceedings of IBIC2013, Oxford, UK*, 2013.

[4] B Keil et al. Design of the SwissFEL BPM System. In *Proceedings of IBIC2013, Oxford, England*, 2013.

[5] V Arsov et al. Commissioning and results from the bunch arrival-time monitor downstream the bunch compressor at the SwissFEL Injector Test Facility. In *Proceedings of FEL2014, Basel, Switzerland*, 2014.

[6] F Frei et al. Experimental results of diagnostics response for longitudinal phase space. In *Proceedings of FEL2014, Basel, Switzerland*, 2014.

[7] R Ischebeck and V. Thominet. Transverse Profile Imager for Ionizing Radiation. EP 2 700 979 A1, February 2014.

[8] D Llorente Sancho. CameraLink High-Speed Camera for Bunch Profiling. In *Proceedings of FEL2014, Basel, Switzerland*, 2013.

[9] P Mohanmurthy, GL Orlandi, and R Ischebeck. Vibration Measurements of the Wire Scanner for the SwissFEL. *APS Division of Nuclear Physics Meeting Abstracts*, -1, October 2012.

[10] GL Orlandi et al. Design and Test of Wire-Scanners for SwissFEL. In *Proceedings of FEL2014, Basel, Switzerland*, 2014.

[11] L Fröhlich, K Casarin, E Quai, A Holmes-Siedle, M Severgnini, and R Vidimari. Online monitoring of absorbed dose in undulator magnets with RADFET dosimeters at FERMI@Elettra. *Nuclear Instruments and Methods in Physics Research Section A: Accelerators, Spectrometers, Detectors and Associated Equipment*, 703:70–79, March 2013.

[12] L Fröhlich, S Grulja, and F Löhl. DOSFET-L02: an advanced online dosimetry system for RADFET sensors. In *Proceedings of IBIC2013, Oxford, England*, 2013.

[13] P N Juranić et al. A scheme for a shot-to-shot, femtosecond-resolved pulse length and arrival time measurement of free electron laser x-ray pulses that overcomes the time jitter problem between the FEL and the laser. *Journal of Instrumentation*, 9(03):P03006–P03006, March 2014.

Copyright © 2014 CC-BY-3.0 and by the respective authors

ISBN 978-3-95450-141-0

RHIC p-CARBON POLARIMETER TARGET LIFETIME ISSUE*

H. Huang, I.G. Alekseev, E. Aschenauer, G. Atoian, A. Basilevsky, K.O. Eyser, A. Fernando, D. Gassner, D. Kalinkin, J. Kewisch, G. Mahler, Y. Makdisi, S. Nemesure, A. Poblaguev, W. Schmidke, D. Steski, D. Svirida, T. Tsang, K. Yip, A. Zelenski
Brookhaven National Laboratory, Upton, NY 11973, USA

Abstract

RHIC polarized proton operation requires fast and reliable proton polarimeter for polarization monitoring during stores. Polarimeters based on p-Carbon elastic scattering in the Coulomb Nuclear Interference(CNI) region has been used. Two polarimeters are installed in each of the two collider rings and they are capable to provide important polarization profile information. The polarimeter also provides valuable information for polarization loss on the energy ramp. As the intensity increases over years, the carbon target lifetime is getting shorter and target replacement during operation is necessary. Simulations and experiment tests have been done to address the target lifetime issue. This paper summarizes the recent operation and the target test results.

INTRODUCTION

The collision of polarized proton beams at RHIC (at up to $\sqrt{S}$ = 510 GeV energy) provides a unique physics opportunity for studying spin effects in hard processes at high luminosities, including the measurement of the gluon polarization and the quark and anti-quark spin flavor composition.

RHIC is the first polarized proton collider where the Siberian snakes were successfully implemented to maintain polarization during beam acceleration [1]. The fast polarization measurements are critical for the accelerator setup and physics programs during the physics stores. The pC CNI polarimeters in RHIC are based on elastic proton scattering with low momentum transfer in the CNI region and measurement of asymmetry in recoil carbon nuclei production [2]. This process has a large cross-section and sizable analyzing power of a few percents which has weak energy dependence in the 24-255 GeV energy range. A very thin (5-10 µg/cm^2, 5-10 µm wide) carbon ribbon target in the high intensity circulating beam produces high collision rate and a highly efficient DAQ system acquires up to 5×10^6 carbon events /sec. The absolute beam polarization was measured with a polarized H-jet polarimeter which is also based on elastic proton-proton scattering in the CNI region [3]. These calibration measurements have been done at various energies, such as 24 GeV, 31 GeV, 100 GeV, 250 GeV and 255 GeV. The results showed weak energy dependence, especially above 100 GeV. The simultaneous measurements in pC and H-jet polarimeters provide the calibration for pC polarimeter analyzing power. A typical store would result a ±3% statistical error in the polarized jet measurement. The fast pC polarimeter measures polarization profiles in both transverse planes, which are used to derive the polarization at collision points for experiments. The pC polarimeter also measures possible polarization losses during the energy ramp and possible polarization decay during the RHIC store.

POLARIMETER ASSEMBLY

RHIC polarimeters have evolved in past ten years [4]. Two identical polarimeter vacuum chambers are located in the warm RHIC sections which are separated for the two rings and have the separate vacuum systems. Due to the complexity of the chamber and the electronics, it is not practical to bake the chamber. A non-evaporable getter cartridge pump is added to each chamber to provide additional continuous pumping. As a result, the pump down speed is greatly improved, which allows the target replacement during maintenance day. A full intensity physics store can be resumed within 24 hours (vacuum down to 10^{-9} Torr).

It is desirable for the polarimeter to measure both horizontal and vertical beam polarization profiles, which requires separate targets scanning both vertically and horizontally. Since the thin carbon target has a relative short lifetime at the full RHIC beam luminosity, it would be advantageous to mount multiple targets on the driving mechanism (spaced so that the beam sees one ribbon at a time) to extend the time between maintenance periods. Each polarimeter consists of six horizontal targets and six vertical targets. Simulation shows that the expected equilibrium temperature at 255 GeV with full loaded intensity (2.4×10^{13}) for a typical carbon ribbon target would be around 1800°K. It is generally inadvisable to run the fiber at temperatures exceeding 2000°K, which is the onset of thermionic emission, since this would shorten the lifetime of the fiber.

The large aspect ratio of the thin carbon target (2.5 cm long, 10 µm wide and 25-50 nm thick) is essential for polarization measurement. First, it increases heat dissipation rate so that the target can survive the high intensity beam. Second, it reduces multiple scattering for recoil carbon ions and also keep the event rate within the detectors and DAQ capabilities. However, the ultra thin target is very fragile and has limited lifetime. Good targets survive in the RHIC beam for 50-100 measurements at the full beam intensity and 255 GeV. The ultra-thin carbon target production procedure was developed at Indiana University [5] and it is a routine now at BNL [6]. The target positioning accuracy is about ±0.5 mm and limited by the target straightness. The accuracy is required due to limited detector acceptance.

The time-of-flight and recoil carbon energy measurements are required for elastic scattering identification. The silicon-

* Work performed under contract No. DE-AC02-98CH1-886 with the auspices of the DOE of United States

Copyright © 2014 CC-BY-3.0 and by the respective authors

ISBN 978-3-95450-141-0

strip detectors are used in the polarimeters since they allow measurements of energy and arrival time of Carbons in the RHIC ring vacuum environment. The late arrival time of the recoiled carbons is advantageous since the detection can be done with much less noise after all beam-induced disturbances are gone. In addition to one pair of detector sitting in the horizontal plane, two pairs of detectors sitting at 45° are added, which allow measurement of both vertical and radial polarization components. At full RHIC designed intensity, the rms bunch length is about 2 ns and bunch spacing is 106 ns. To avoid the prompt background, the carbon nuclei should arrive the detectors between two bunches. The Si detector can detect carbons with kinetic energy as low as 200 keV, which can travel about 20 cm in 100 ns. The distance between detectors and interaction point is set as 18 cm. There are RF shields at the surface of the chamber to cover the detector ports to reduce the impedance impact [7].

The preamplifier boards are mounted on the polarimeter vacuum chamber and directly connected to the vacuum feedthroughs to minimize the distance to the signal source. The amplified analogue signals are transferred through the RHIC tunnel on coaxial cables for about 90 m to a counting room located next to the tunnel. A wave form digitizer is utilized in the DAQ to handle the high-rate and minimize dead-time.

TARGET LIFETIME ISSUES

Usually, a good carbon target breaks after usage of 50 to 100 times. But the variation of target lifetime is relative large: many targets have been lost before seeing beam, or just broke after a few uses. This is especially the case when a target was lost at store, and a new target has to be used right away. Polarimeter chamber has to be opened to replace targets during maintenance day twice in past two polarized proton operations. The broken targets were checked under microscope. About 2/3 of the broken targets were broken near the ends. The rest 1/3 were broken near the center. A lot efforts were put in to understand the mechanism for the target breakage. It was found that the targets survived beam operation are graphitized and have smaller resistances, about a few MΩ while the resistance of unexposed targets is a few hundreds MΩ. It was also found that the exposure to flash light can greatly reduce the target resistance. About 1/3 targets used in run13 were exposed to high power flash light to reduce the resistance. Since some new targets lost at store in first a few uses, one hypothesis is that the targets need to be "conditioned" with modest beam intensity before using at store energy. This is the similar effect as the high power flash, but probably more powerful. In run13, all targets have been used first at injection with gradually increased total intensities: 0.5, 1 and 2×10^{13}. Then they were put into use at store. However, this effort did not yield significant improvement in the target lifetime. The target temperature is expected to be around 1500-2000°K, visible light emission is expected at these temperatures. The polarimeter target chamber has several viewports to check targets during maintenance day.



Figure 1: A glowing target when crossing beam. The central bright spot is due to beam.



Figure 2: A target with glowing ends when it is off beam. Note that the nearby target end (on the right side) is also glowing in the dark. Due to the limited aperture, the camera can not cover more targets.

A few cameras were installed to take video when targets crossing beam. The observation surprised all of us. The glowing light was brightest when the target crossed the beam center. This is understandable, as beam heating generates high temperature and black body radiation could be the main source of the glowing light from target portion hit by beam. In addition, the ends glow when the beam is far away (a few cm) from the target. Figure 1 showed the captured picture of a glowing target when it crossed the beam center. Figure 2 is when target was far away from beam and at park position, where the target sat for hours between polarization measurements. The persistent glowing over a store (8-10 hours) could be a source of relative short target lifetime for these targets.

Light filters with different spectrum ranges were put into one camera. The idea was to get the relative strength of the light emission at different wave length ranges. Comparing with black body radiation power distribution, one can get

ISBN 978-3-95450-141-0

Copyright © 2014 CC-BY-3.0 and by the respective authors

the nature of the light (black body radiation or not) and the temperature. The glowing light spectrum at the target tails when crossing the beam or at park position does not consistent with black body radiation. But to make detail spectral analysis, a spectrometer is needed.

One possible mechanism to explain the glowing target tails is the induced electric-magnetic fields due to the beam passing by. The target chamber is like a RF cavity and the target frame is like an antenna. The induced high frequency electrical fields move electrons back and forth along the target frame as weel as targets. Heat is generated due to the resistance of the targets, which in turn causes black body radiation and emit lights.

At store energy(250 or 255 GeV), the high frequency RF cavities (200 MHz) were turned on to generate shorter bunches for luminosity gain. The high peak current associated with the short bunches should make the glowing worse. Indeed, the 200 MHz cavity was ramped to lower value and the glowing light disappeared. This observation is consistent with the induced field hypothesis, as higher peak current with higher 200 MHz cavity voltage is expected to induce stronger electric fields. In run13, the 200 MHz cavity voltage was ramped down during the polarization measurements. This procedure not only reduced the glowing light, but also reduced the electronic noises in the preamp circuitry. The ramping down 200 MHz cavity voltage only reduces the light during measurements when the effect is strongest. The target glowing at park position is still a problem. Due to the space constraint, only half of the targets can be parked far enough from the beam. The other half targets have to endure the chronic effect of the induced electric-magnetic fields throughout the stores. These targets indeed have shorter lifetime compared to the other half which could be parked further away. To prolong the target lifetime for these half and probably to all targets, something needs to be done.

SIMULATION OF TARGET HEATING

If the problem is due to the induced electric-magnetic fields, the effect should be proportional to the electric fields along the target wire. One possible solution is to provide surface for the field lines to "spread out". These surface should have smooth curvature to avoid sharp edges. One design is to add fins to both ends of the target frame. In general, the larger the surface, the larger the reduction, but the fins must fit into the limited space in the tank and the clearance from the target-beam interaction region to the Si detectors have to be maintained, too.

The simulations were done with CST-studio [8]. The real mechanical drawing of the polarimeter chamber (as shown in Fig. 3) was used in the simulation. The peak current of beam is used in the simulation. Three cases of target relative to beam positions were simulated: the first one was when a target crossing the beam center; the second and third ones were when all targets were away from the beam by 2.5 cm transversely at either inner or outer positions. There was not much difference in the last two cases.

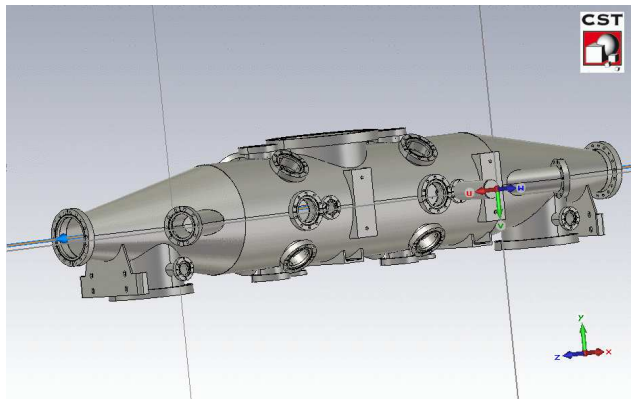


Figure 3: The 3D drawing of the polarimeter chamber. The tape structure (5:1) is to reduce the impedance impact on the overall RHIC ring impedance budget. The two view ports on both tape structure are used to monitor the target operation. The big view port on the top is for target installation. Three cameras are mounted on these view ports to monitor the polarimeter target operation. There are two sets of six Si detectors ports surrounding the chamber on both sides of the big view port. There are vertical and horizontal targets for each set.

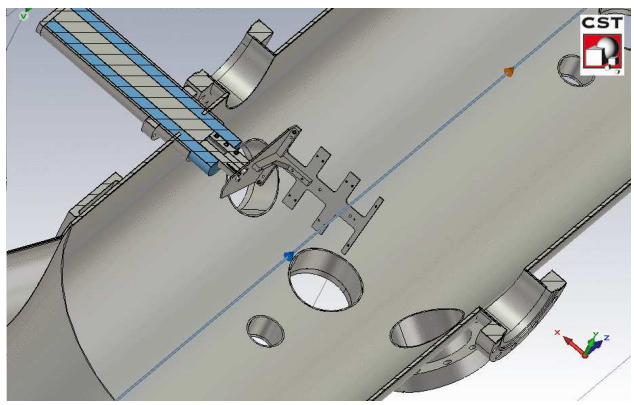


Figure 4: The detail of one horizontal target assembly. The vertical target assembly(the smaller hole at the bottom) was not included in the simulation.

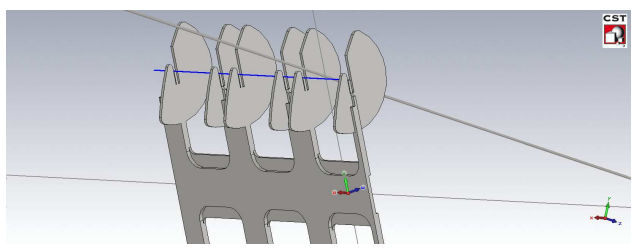


Figure 5: The details of the target frame fins. The shape is designed to have smooth curvature and enough clearance in the chamber. The half elliptical shape allows it to be mounted on every target, but a full elliptical shape should reduce the electric fields further.

Copyright © 2014 CC-BY-3.0 and by the respective authors

ISBN 978-3-95450-141-0

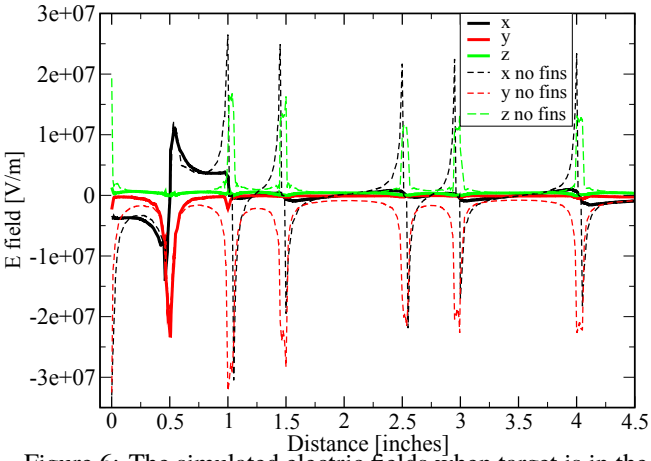


Figure 6: The simulated electric fields when target is in the center of beam (at 0.5 in location). Here z is along beam moving direction, y is the vertical direction and x is radial out direction. The solid lines are for the case with fins and the dashed lines are for the case without fins.

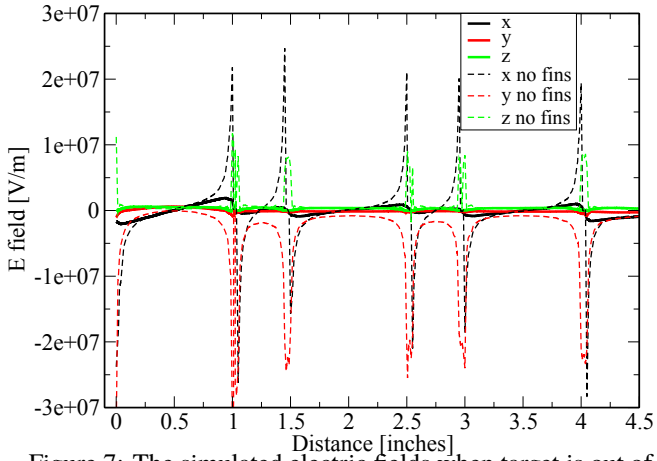


Figure 7: The simulated electric fields when target is out of beam. The coordinate system is the same as in Fig. 6.

In each case, the target with and without fins (as shown in Fig. 5) were simulated to see the effects. Note that the fins are in half elliptical shape and a slit in the middle allows it to be pushed into place. As Fig. 6 shows, the electric fields are very strong near the end of the target frames, even for the targets which are not in the beam. Further more, Fig. 7 shows that the electric fields are strong even when all targets are out of beam. These simulation results are consistent with the observation shown in Figs. 1-2, where the glowing light is visible for the target ends in the beam or out of beam. By comparing Figs. 6 and 7, it seems that the fields at all target ends are similar for both in and out of beam cases. The simulations suggest that the lifetime of targets not in use could be shortened. This was also consistent with the observation. As expected, the simulation results showed that the electric fields at the edge of target frames were greatly reduced for the case with fins. The reduction factor is about 10-20.

EXPERIMENTAL RESULTS

There was no polarized proton beam planned for 2014 and this also provided an opportunity to test the modification of target frame with other beams. Targets mounted on the frames with and without fins have been installed before the run started. To save time, a round shape aluminum fins were used (as shown in Fig. 8). It should have stronger effect than half elliptical one. Due to its shape, only four out of six target positions have the required clearance. A bunch of targets with and without fins were installed.

Both Au and He ion beams were used this year to compare the targets with and without fins. There is no chance for a carbon target to survive Au beam crossing. Instead, targets were put about 1.5 cm away from beam center at end of physics store. The glowing light is definitely stronger for

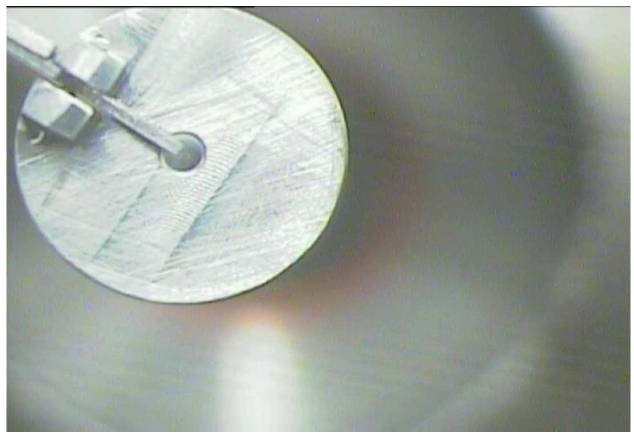


Figure 8: The fin used in the experiment test.

target frames without fins. Figs. 9 and 10 clearly showed the effect. When the targets were moved away from beam by more than 3 cm, the light disappeared for both type of targets. Unfortunately, due to the limiting space inside the polarimeter chamber, about half of the targets can not be parked that far from beam. Additional protections are needed for these targets.

Different Au beam peak current was used to compare the two type targets. The light is dimmer with smaller peak current. In all cases, the targets with fins have weaker glowing light. The voltage of 200 MHz RF cavity was also ramped down from 650 kV to 100 kV. The light disappeared for both targets with and without fins. This is expected, as the lower voltage corresponds to lower peak current. The induced electric fields are strongly peak current dependent.

For He beam, the charge is small enough, so that the carbon target can cross the beam and survive. The peak current for He beam is twice as high as Au beam. During the test, there was no glowing light from the ends of the targets with fins. Unfortunately, the targets without fins were broken during the target switching while all targets were outside beam. Two big light flashes were seen. It was

ISBN 978-3-95450-141-0

Copyright © 2014 CC-BY-3.0 and by the respective authors



Figure 9: The target with fins at position 1.5 cm away from beam.



Figure 10: The target without fins at position 1.5 cm away from beam.

confirmed that the two targets without fins were gone (no beam loss detected when the two targets crossed the beam), while the targets with fins survived. The target switch had been fine with gold beam, but gold beam has lower peak current. It could be that when the target frames moved to certain location, it generated a resonance condition. There is no simulation for this situation done yet. Nevertheless, it is encouraging that the targets with fins did get protection from this resonance condition. After this experiment, the target motion history in the past has been checked, since the peak current of proton beam is higher than He beam in general, and this could happen for proton beam, too. From the logged data in last run, we never switched targets at store between these two positions with beam at store.



Figure 11: A bright flash from the target without fins happened when switching targets. All targets were outside He beam during this operation.

SUMMARY

The pC CNI polarimeters in RHIC provide fast polarization (with polarization profile) measurements. The analyzing power of this polarimeter has been calibrated by the simultaneous polarization measurements in the absolute H-jet polarimeter at various energies. This polarimeter is ideal for high-energy proton polarimetry: fast measurement, low cost and compact size.

As intensity increases, the target lifetime becomes an important issue. Observed continuous glowing light from target ends outside beam implies that the temperature is high and this could damage target. The experimental results showed that the targets with fins do get weaker light, which in turn implies better lifetime. In addition, the target breakage of targets without fins gave another strong reason to install the fins as the fins can protect targets. The plan is to install the fins for all possible targets in the coming polarized proton operation.

REFERENCES

[1] I. Alekseev, *et al.*, NIM. **A499**, 291 (2003).

[2] J. Tojo, *et al.*, Phys. Rev. Lett. **89**, 052302 (2002).

[3] H. Okeda, *et al.*, Phys. Lett. **B638**, 450(2006).

[4] H. Huang and K. Kurita, AIP Proc. 868, 3(2006).

[5] W. Lozowski and J. Hudson, NIM. **A334** 173(1993).

[6] W. Lozowski, D. Steski, H. Huang, C. Naylor, NIM. **A590**, 157(2008).

[7] H. Wang, W. Guryn, H. Huang, D. Trbojevic, Proc. of PAC01, 1832(2001).

[8] https://www.cst.com/ .

Copyright © 2014 CC-BY-3.0 and by the respective authors

ISBN 978-3-95450-141-0

THE ELECTRON BACKSCATTERING DETECTOR (eBSD), A NEW TOOL FOR THE PRECISE MUTUAL ALIGNMENT OF THE ELECTRON AND ION BEAMS IN ELECTRON LENSES*

P. Thieberger#, F. Z. Altinbas, C. Carlson, C. Chasman, M. Costanzo, C. Degen, A. Drees, W. Fischer, D. Gassner, X. Gu, K. Hamdi, J. Hock, Y. Luo, A. Marusic, T. Miller, M. Minty, C. Montag, A. Pikin, S. White,
Collider Accelerator Department, Brookhaven National Laboratory, Upton, NY, U.S.A.

Abstract

The Relativistic Heavy Ion (RHIC) electron lenses being commissioned to attain higher polarized proton luminosities by partially compensating the beam-beam effect require good alignment of the electron and proton beams. These beams propagating in opposite directions in a 6 T solenoid have an rms width as small as 300 microns and need to overlap each other over an interaction length of about 2 m with relative deviations of less than ~50 microns. A new beam diagnostic tool to achieve and maintain this alignment is based on detecting electrons that are backscattered in close electron-proton encounters. Maximizing the production of these electrons ensures optimum beam overlap. The successful commissioning of these electron backscattering detectors (eBSDs) using 100 GeV/nucleon gold and ^{3}He beams is described. Future developments are discussed that could further improve the sensitivity to small angular deviations.

INTRODUCTION

The partial compensation of the beam-beam effect in RHIC is necessary for mitigating the limit imposed by this effect on the achievable proton-proton beam luminosities. Electron lenses (e-lenses) [1] consisting of low energy (in our case ~6 keV), high intensity (~1 A) magnetized electron beams, can in principle provide the precise non-linear focusing properties necessary to effect such compensations. After developments on a test bench [2], two such e-lenses have now been installed in the RHIC tunnel. In preparation for the 2015 RHIC polarized proton-proton run, commissioning of the RHIC e-lenses has been successfully accomplished [3] with the ion beams available during the 2014 run; namely 100 GeV/nucleon gold and 100 GeV/nucleon helium (^{3}He).

The precise alignment of the electron and ion beams is an important prerequisite for achieving maximum compensation. Over the 2 m interaction region in the ~6 T solenoid, the centers of these ~300 micron rms wide beams need to be separated by less than ~50 microns. The precision achievable with the installed beam position monitoring system [4] isn't quite sufficient for ensuring this result. As described before [5], electron beam electrons backscattered by the relativistic ions or protons (henceforth, ions) can provide the "luminosity" signal required for optimizing and maintaining this alignment.

After briefly reviewing the principle and design of the RHIC electron backscattering detectors (eBSDs), we show results from commissioning the eBSDs with relativistic gold (Au) and helium (^{3}He) beams. We present conclusions about their expected performance with proton beams.

* Work supported by Brookhaven Science Associates under Contract No. DE-AC02-98CH10886 with the U.S. Department of Energy
#pt@bnl.gov

PRINCIPLE OF THE METHOD

The lensing effect of an e-lens on the relativistic ions is due to the macroscopic electric and magnetic fields produced by the Gaussian-shaped electron beam. In other words, it is the collective long-range Coulomb interaction of the electrons with individual ions that affects the trajectory of these ions. The vast majority of the electron trajectories are only slightly affected since their trajectories are confined by a strong magnetic field. There is however a finite probability for ion-electron collisions with impact parameters that are so small as to produce a significant electron scattering angle imparting at the same time considerable momentum and energy to the scattered electrons. Large scattering angles, correlated with high energies, result in energetic electrons spiraling backwards (towards the electron gun) along the magnetic field lines. As described below, some of these backscattered electrons are intercepted and counted by a scintillation detector placed in air, behind a thin vacuum window.

To first order in the fine structure constant, the Coulomb scattering of relativistic electrons by nuclei is described by the Mott formula which in the rest frame of the nucleus is written as [6]:

$$\frac{d\sigma}{d\Omega} = \frac{Z^2}{4}\left(\frac{e^2}{E}\right)^2 \frac{1}{sin^4\left(\frac{\theta}{2}\right)} \times \left[1 - \left(\frac{pc}{E}\right)^2 sin^2\frac{\theta}{2}\right]$$

$$\times \left[1 + \frac{2E\, sin^2(\theta/2)}{M_A c^2}\right]^{-1} \times \left[1 - \frac{q^2 \tan^2(\theta/2)}{2M_A^2}\right]$$

where σ is the cross section, Z the atomic number , M_A the mass of the nucleus, e the elementary charge, E and p the energy and momentum of the electron in the frame of the nucleus, $\boldsymbol{\theta}$ the electron scattering angle in that frame and $\boldsymbol{q}$ the four momentum transfer coefficient. The first term is the classical Rutherford cross section and the last

ISBN 978-3-95450-141-0

Copyright © 2014 CC-BY-3.0 and by the respective authors

two of the three bracketed corrections (quantum, recoil and magnetic moment respectively) are negligible. Another correction that has been neglected is the one for Bremsstrahlung. A more complete theoretical treatment will probably be required to make good quantitative predictions, especially for even higher energy protons or ions.

Values of this cross section are computed at small angular intervals and then relativistic transformations to the laboratory frame of the cross sections, the angles and the energies lead to results such as plotted in Fig. 1. Such plots are useful for rough estimates of counting rates, but detailed comparisons are difficult due to the complicated nature of the spiraling electron trajectories.

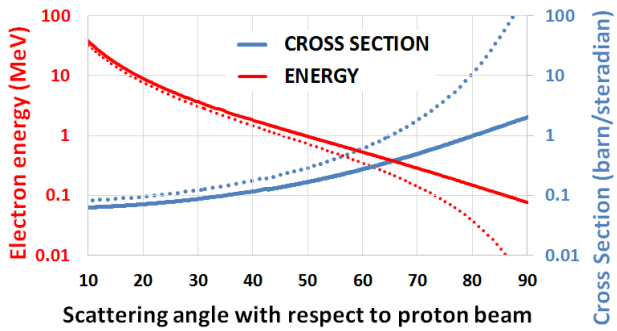


Figure 1: The solid lines show calculated energies and approximate scattering cross sections for 5 keV electrons backscattered by 250 GeV protons. The dotted lines correspond to the same quantities but for 10 eV electrons as a qualitative indication of energetic electrons generated by the interaction of the beam with the residual gas and/or with low energy electrons captured in the potential well of the beam. To obtain quantitative predictions of the effects of the residual gas, the correct treatment of the scattering and ionization of bound electrons will be required and has not yet been performed.

Figure 2 shows the simulated projected trajectories of two electrons backscattered by 250 GeV protons in a 5 T solenoid at angles of 50^0, one upwards and the other one downwards. As the electrons spiral towards the detector, the radii of their trajectories grow as they encounter lower fields. The upward drift of the trajectory envelopes is due to the horizontal bend in the magnetic field [7].

IMPLEMENTATION

Each e-lens was equipped with an eBSD consisting of a small plastic scintillator (7.4 × 7.9 × 20.6 mm^3) attached to a 1.2 m long light guide leading to a small magnetically shielded photomultiplier (PMT) tube (Hamamatsu R3998-02). The signals from this PMT reach the instrumentation rack through a ~90 m long 50 Ω coaxial cable and are amplified and connected to a fast discriminator, the output pulses of which are used to determine the counting rates. The light guide is necessary to keep the PMT far enough from the adjacent magnets so as to enable adequate shielding. This scintillation detector assembly is mounted in air in a vertical shaft at the bottom of which there is a 0.1 mm thick titanium alloy vacuum window facing the scintillator. The vertical position of the detector shaft can be selected so as to locate the bottom of the scintillator at any position from ~1 mm to ~26 mm from the edge of the primary electron beam. This position adjustment can be used as an intensity range selector. An insulated tungsten block (35 × 4.9 × 7.6 mm^3) with current detection provides some protection against electron beam heating should the position interlock and limit switch fail. Such a failure actually occurred during commissioning and a vacuum failure was avoided thanks to the tungsten block even though indirect heating was sufficient to melt the scintillator. Since the scintillation detector is in air it was easily replaced.

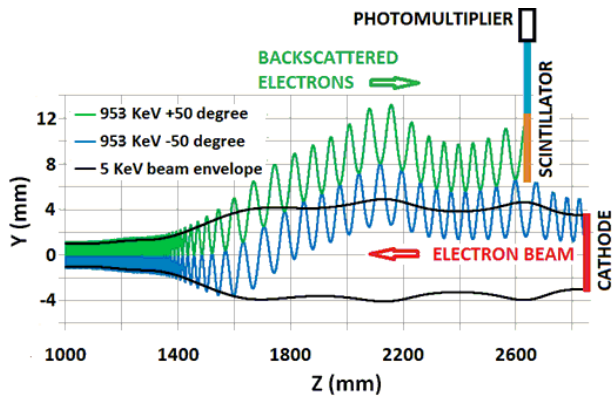


Figure 2: Example of computer simulated electron trajectories starting in a 5 T solenoid field to the left and propagating towards the cathode with some of the trajectories being intercepted by a scintillator (shown schematically). The upward drift of the trajectories is due to the horizontal bend of the magnetic field.

A cutaway drawing of the detector housing is shown in Fig. 3. The backscattered electrons traverse a thin insulated tungsten foil before penetrating the 0.1 mm thick titanium alloy vacuum window and depositing their energy in the plastic scintillator. Current measurement on the thin foil will be used to detect low energy electrons drifting back from the electron collector at the other side of the solenoid.

Copyright © 2014 CC-BY-3.0 and by the respective authors

ISBN 978-3-95450-141-0

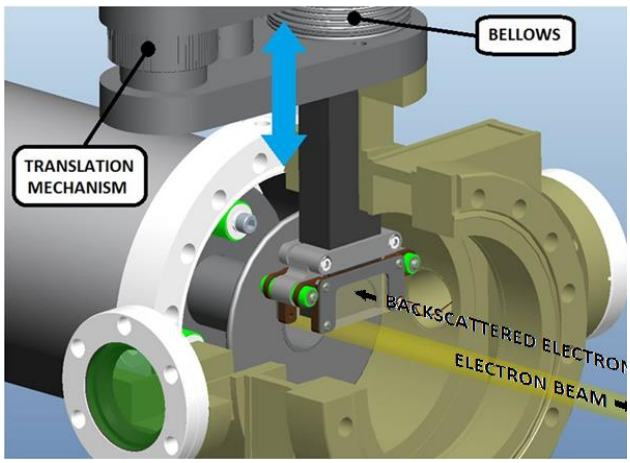


Figure 3: Cutaway drawing of the detector housing, the vertical translation mechanism and a thin tungsten foil located in front of the 0.1 mm thick titanium alloy vacuum window. The area of this window is 25.4 × 6.35 mm^2.

COMMISSIONING WITH GOLD AND He^3 BEAMS IN RHIC

The commissioning of the eBSDs was started during the 2014 100 GeV/nucleon gold-gold run. The first proof-of-principle horizontal and vertical beam separation scans are shown in Figs. 4 and 5. The measured widths are the sums in quadrature of the gold and electron beam widths.

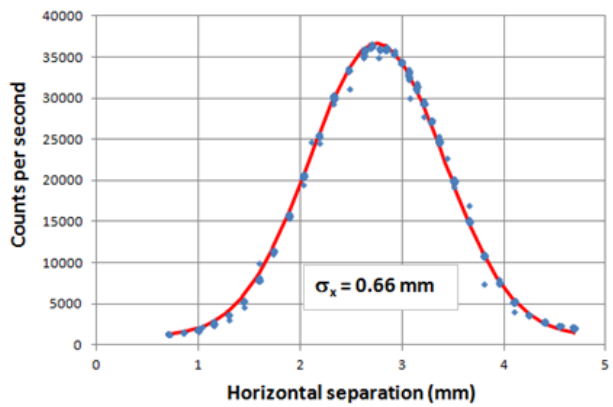


Figure 4: Horizontal beam separation scan obtained by steering the 5 keV electron beam with respect to the 100 GeV/nucleon gold beam.

Soon after obtaining these results, a beam alignment optimization system was implemented based on automatically maximizing both the horizontal and vertical eBSD counting rates. This system is based on a program (LISA) [8] that was developed and used for many years to maximize the luminosities for the RHIC experiments. At the colliding beam interaction points of the high energy physics program, coincidence rates from the zero degree calorimeters (ZDCs) [9] are maximized. Fig. 6 shows the counting rates observed during a manual LISA eBSD scan obtained by displacing the gold beam by means of a set of steering correctors forming a closed orbit bump.

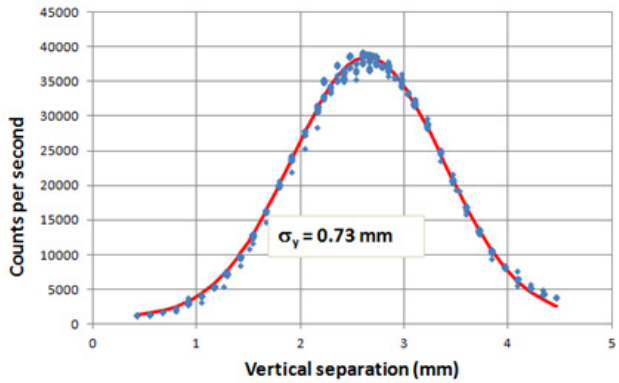


Figure 5: Vertical beam separation scan obtained by steering the 5 keV electron beam with respect to the 100 GeV/nucleon gold beam.

After the gold run was completed, there was a brief opportunity for commissioning the eBSD system with a ^{3}He beam. This was important since gold scattering cross sections are much larger than the cross sections for protons. The cross section for ^{3}He is only ~4 times larger, and this fact will be compensated by the higher proton beam intensities. In other words, the counting rates observed for ^{3}He should be similar to the ones expected for protons.

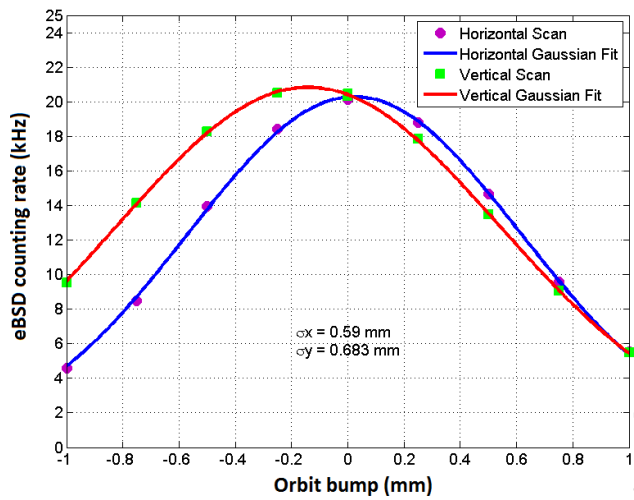


Figure 6: Manual beam separation scans obtained by steering the gold beam with the orbit bumps utilized for the automated alignment optimization system based on the LISA program [8]

During the He^3 run the vertical positioning mechanism was utilized for the first time since the counting rates with gold had always been so large that the fully retracted position had to be used. Figure 7 shows the counting rate as function of detector position for a 100GeV/nucleon ^{3}He beam consisting of 93 bunches with 4.7E10 ions per bunch and a 6 keV, 88 mA electron beam.

ISBN 978-3-95450-141-0

Copyright © 2014 CC-BY-3.0 and by the respective authors

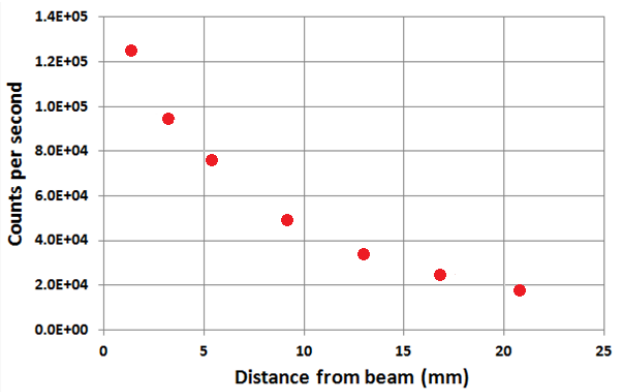


Figure 7: eBSD counting rates as function of detector position. These results were obtained with a 100 GeV/nucleon ^{3}He beam consisting of 93 bunches with 4.7E10 ions per bunch and a 6 keV, 88 mA electron beam.

In addition to obtaining total eBSD counting rates, one can also sort and store the counts as function of their time of arrival with respect to a bunch-synchronized clock or with respect to a revolution-synchronized clock. The first choice offers the possibility (at least in principle) of utilizing electron time of flight information to obtain longitudinally dependent luminosities which may be useful for detecting relative angular misalignments between the electron and ion beams. It remains to be seen if this is practical considering bunch lengths and time resolutions.

The second choice provides a very useful display of those bunches that are overlapped by a pulsed electron beam thus allowing convenient and accurate timing adjustments. It also provides display and measurements of back-ground counts due to the interaction of the ion beam with electrons of the residual gas.

During the 2014 run there were brief periods during which some of these ideas could be tested. A fast time digitizer [10] was utilized to obtain the results shown in Fig. 8. The background counts seen in the top plot are due to scattering of atomic electrons belonging to the residual gas. This counting rate is of course very sensitive to the quality of the vacuum. When a pulsed electron beam overlaps the last two bunches preceding the abort gap, the counting rates are ~20 times larger as seen at the bottom of Fig. 8. The small satellite peaks that appear to the left of the larger ones may be due to beam misalignment, but there was no time to investigate this issue further.

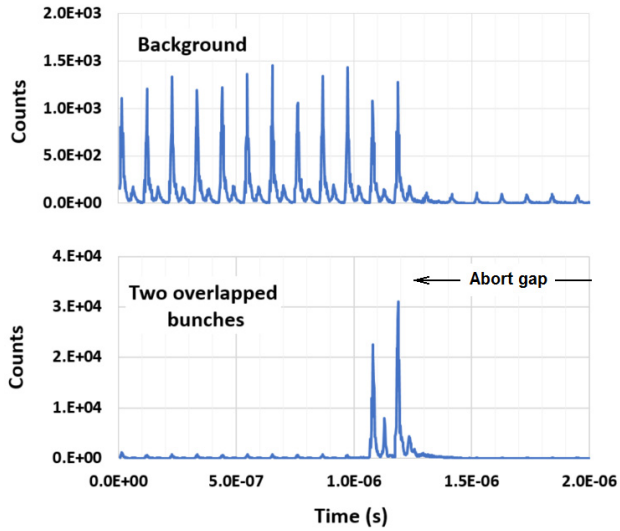


Figure 8: Time distributions with respect to a revolution synchronized clock of eBSD pulses accumulated without (top) and with (bottom) the presence of a 0.15 A pulsed electron beam overlapping the last two bunches. The background pulses are due to scattering of electrons of the residual gas. Note that the vertical scales differ by a factor ~20. The 100 GeV/nucleon gold beam intensity was 1.15 E9 per bunch. Data were accumulated for ~2 minutes for each of the distributions shown.

CONCLUSIONS

The successful commissioning of the eBSD detectors with gold and He^{3} beams indicates that it should be possible to achieve the stringent alignment required for the partial compensation of the proton beam-beam effect. Electron time-of-flight spectra similar to the ones shown in Fig. 8 but on a shorter time scale may aid in refining the angular alignment by providing some information regarding longitudinal position dependence of the luminosity contributions. More importantly, angular steering will be simplified in the future by rotating the beams around the centers of the e-lenses instead of a point between them.

The concept of using Coulomb scattered electrons as diagnostic probes for relativistic ion beams will probably find other applications. In particular, the hollow electron lenses suggested for beam halo control in the Large Hadron Collider [11] should be able to benefit from this technique. It could aid in centering the beams (minimizing the counting rate in that case) and in estimating and monitoring the intensity of the halo. Extremely good vacuum will be required to minimize the background counting rate generated by the interaction of the intense central part of the beam with the residual gas.

Copyright © 2014 CC-BY-3.0 and by the respective authors

ISBN 978-3-95450-141-0

REFERENCES

[1] W. Fischer, *et al.*, IPAC'10, p. 513, (2010), Kyoto, Japan, TUP065.

[2] X. Gu, *et al.*, "The electron lens test bench for the relativistic heavy ion collider at Brookhaven National Laboratory", Nucl. Instr. and Meth. in Phys. Res. A 743, pp. 56-67 (2013).

[3] W. Fischer, *et al.*, "First Experience with Electron Lenses for Beam-Beam Compensation in RHIC", IPAC2014, Dresden, Germany, to be published, and X. Gu *et. al.*, BNL-10090-2013-CP.

[4] D. M. Gassner, *et al.*, Proceedings of DIPAC2011, Hamburg, Germany, MOPD04, page 38.

[5] P. Thieberger, *et al.*, Proceedings of PAC'11, MOP209, p. 489.

[6] F. Halzen and A. Martin, *Quarks and Leptons*, John Wiley and Sons, (1984).

[7] Classical Electrodynamics, J. D. Jackson, John Wiley and Sons, 1962, page 417.

[8] A. Drees and T. D'Ottavio, Proceedings of EPAC 2004, Lucerne, Switzerland, page 911.

[9] C. Adler, *et al.*, "The RHIC Zero Degree Calorimeters", Nucl. Instr. and Meth. in Phys. Res. A 470, pp. 488-499 (2001).

[10] Agilent 53230A, Universal Frequency Counter/Timer, Agilent Technologies.

[11] G. Stancari *et al*., arXiv:1405.2033v3 [physics.acc-ph] and Fermilab Report TM-2572-APC (May 2014).

ISBN 978-3-95450-141-0

Copyright © 2014 CC-BY-3.0 and by the respective authors

PERFORMANCE AND UPGRADE OF THE FAST BEAM CONDITION MONITOR AT CMS

M. Hempel, DESY, Zeuthen, Germany*
B. Pollack, Northwestern University, Evanston, Illinois†
A. Bell, H. M. Henschel, O. Karacheban, W. Lange, W. Lohmann, J. L. Leonard,
M. Penno, S. Schuwalow, R. Walsh, DESY, Zeuthen, Germany
Dominik Przyborowski, University of Science and Technology, Cracow, Poland
David Peter Stickland, Princeton University, Princeton, New Jersey, USA
P. Bartowy, A. E. Dabrowski, R. Loos, V. Ryjov, A. A. Zagozdzinska, CERN, Geneva, Switzerland
K. Afanaciev, NC PHEP BSU, Minsk, Belarus
On behalf of CMS Collaboration

Abstract

The Fast Beam Condition Monitor (BCM1F) is a diamond based particle detector inside CMS. It consisted of 8 single-crystal chemical vapor deposition (sCVD) diamond sensors on both ends of the interaction point, and was used for beam background and luminosity measurements. The system has been operated with an integrated luminosity of 30 fb^{-1}, corresponding to a particle fluence of $8.78 \cdot 10^{-13}$ cm^{-2} (24 GeV proton equivalent). To maintain the performance at a bunch spacing of 25 ns and at the enhanced luminosity after the LHC Long Shutdown LS1, an upgrade to the BCM1F is necessary. The upgraded system features 24 sensors with a two pad metallization, a very fast front-end ASIC built with 130 nm CMOS technology, and new back-end electronics. A prototype of the upgraded BCM1F was studied in the 5GeV electron beam at DESY. Measurements were done on the signal shape as function of time, the charge collection efficiency as a function of voltage, and the amplitude as a function of the position of the impact point of the beam electron on the sensor surface. The preliminary results of this test-beam experiment and the status of the newly upgraded BCM1F will be presented.

BCM1F DURING OPERATION

BCM1F is a particle counter with nanosecond time resolution based on single-crystal chemical vapor deposition (sCVD) diamonds. Due to the linear dependence between detection probability and luminosity as shown in Figure 1, it is possible to use BCM1F as a luminosity monitor as well as a background monitor [1, 2].

During the first LHC running period from 2008-2012 BCM1F delivered online background and luminosity measurements as feedback for the CMS and LHC operation [3,4]. Since the data acquisition for BCM1F is decoupled from the main CMS DAQ, it could measure luminosity even before physics data was taken.

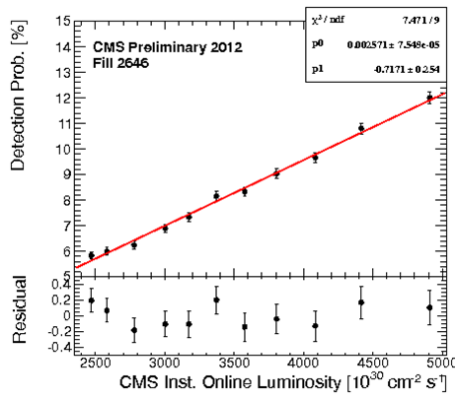


Figure 1: Particle detection probability as a function of luminosity.

MOTIVATION FOR THE BCM1F UPGRADE

The BCM1F modules are located around the beam pipe at a distance of 5 cm from the beam center. A particle fluence of $8.78 \cdot 10^{-13}$ cm^{-2} (24 GeV proton equivalent) at this position led to radiation damage of the laser diodes, which were used in the front-end electronics to convert the diamond sensor signal to an optical signal.

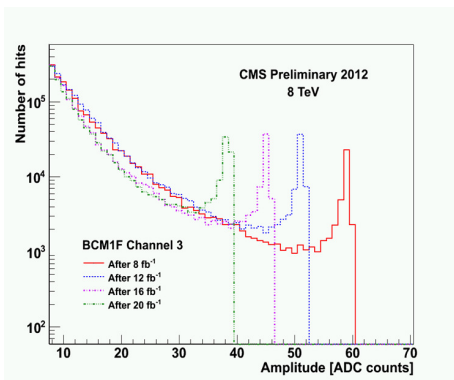


Figure 2: Decrease of the amplification measured by an ADC amplitude spectrum.

* maria.hempel@desy.de
† brian.lee.pollack@cern.ch

ISBN 978-3-95450-141-0

Copyright © 2014 CC-BY-3.0 and by the respective authors

The observation of the amplitude spectrum measured by an Analog-to-Digital converter (ADC) showed a decrease in the amplification as a function of integrated luminosity, as illustrated in Figure 2. This decrease in amplification lead to inefficiencies because smaller signals could not be detected. Additional inefficiencies occurred due to very large signals in the sensors, as shown in Figure 3.

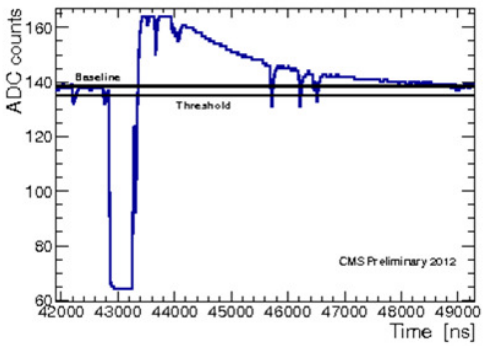


Figure 3: Amplitude as a function of time for large input signals.

These signals caused the front-end electronics to saturate for around 100 ns and signals could not be detected during this time. After the saturation, the amplitude shows an overshoot for a few μs. All signals that arrived during this time are detected with less efficiency.
Additionally, the proton bunch spacing for the future LHC run will be 25 ns, comparable to the peaking time of the amplifier. This potentially leads to pile-up of subsequent signals.

BCM1F FRONT-END UPGRADE

All BCM1F components are upgraded in order to match the demanding requirements corresponding to higher luminosity and smaller (25 ns) bunch spacing.

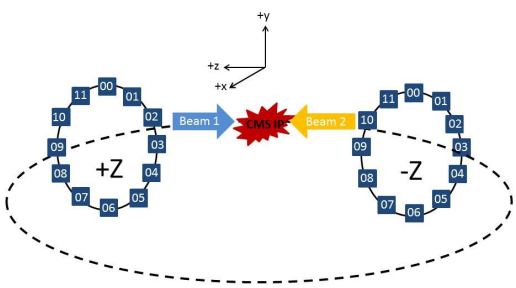


Figure 4: Upgraded BCM1F layout with 12, 2-pad sCVD sensors on each side of the CMS interaction point. Distance between the CMS interaction point and sensors is 1.8 m

Firstly, the number of sensors is increased from 8 to 24 sCVD in order to improve the acceptance of the background measurements. The new BCM1F layout is illustrated in Figure 4 and contains 12 sensors on each side of the interaction point. The distance between the sensors and interaction point will be the same as in the first running period at 1.8 m. Each sensor has a two pad metallization as shown in Figure 5 in order to decrease the count rate. The width of the gap between the two pads is between 5 and 25 μm.

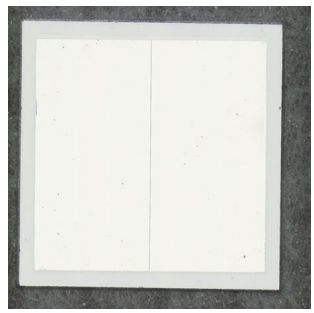


Figure 5: Two pad metallization of sCVD sensors.

A new dedicated front-end ASIC, developed at CERN in collaboration with the University of Science and Technology AGH Krakow, is based on 130 nm CMOS technology and includes a fast trans-impedance preamplifier with an active feedback, a shaper stage and a fully differential output buffer. A better charge-to-voltage conversion of 50 mV/fC is obtained (previously was 20 mV/fC). Measurements done in the laboratory show a FWHM of less than 10 ns as shown in Figure 6.

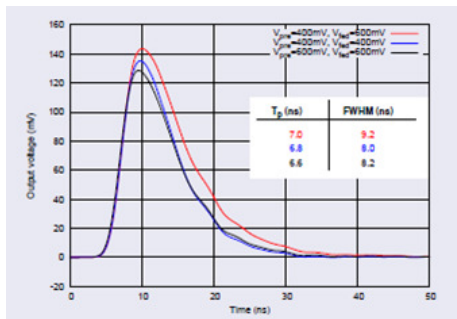


Figure 6: The ASIC output signal for various feedback and bias settings as a function of time for an injected test charge, which corresponds to one minimum ionizing particles.

In order to characterise the impact of overshoots, a very large signal was fed into the front-end ASIC and the response was measured. As can be seen in Figure 7, the amplitude shows fast baseline recovery after about 30 ns.

The upgraded carriage design, as shown in Figure 8, has two main parts: the C-shape, each of which holds 6 sensors and their corresponding front-end ASICs, and the flexible regions where the optical board will be placed. This design allows the placement of the analog opto-hybrid board (AOH) to be further away from the beam center (16 cm as opposed to 5 cm), which reduces the radiation load to the lasers.

A C-shape assembled with the electronic parts is shown in Figure 9. The six square gold pads will hold the sensors and supply the bias voltage.

ISBN 978-3-95450-141-0

Copyright © 2014 CC-BY-3.0 and by the respective authors

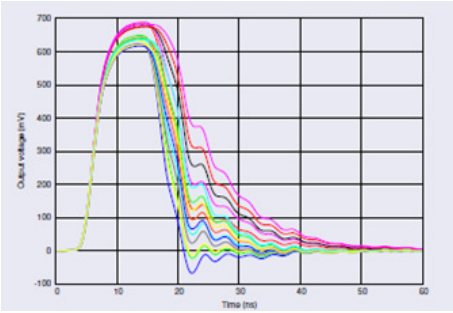


Figure 7: The ASIC output signal as a function of time for large (150 fC) injected input signals.

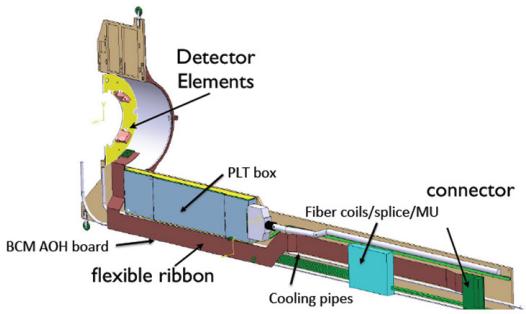


Figure 8: Upgraded carriage design with the C-shape and flexible parts that hold the sensors, front-end ASICs, and the optical board.

TESTS OF FRONT-END PARTS

Sensors and analog optical hybrid boards (AOHs) were characterised in the laboratory. The performance of a prototype detector, comprising of a sensor, front-end ASIC, AOH, and fast digitizer was measured in a test-beam.

Measurements in the Laboratory

The leakage currents were measured for the sensors as a function of bias voltage. A result is shown in Figure 10. The currents are in the pA range as expected, due to the very high band gap for diamonds 5.4 eV.

The charge collection efficiency (CCE), defined as the ratio between the measured charge and expected charge of the diamond at a given bias voltage, was measured. Figure 11 shows, as an example, the CCE as a function of bias voltage. A maximum CCE of around 95 % above 40 V was obtained.

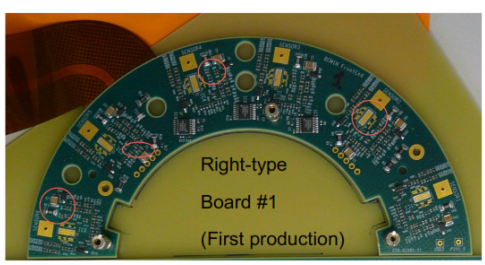


Figure 9: C-shape with mounted electronics.

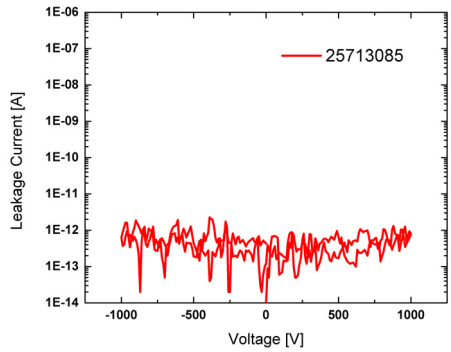


Figure 10: Measured leakage current as a function of bias voltage for an sCVD diamond sensor.

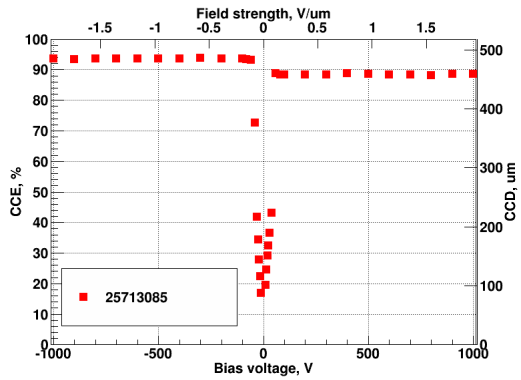


Figure 11: Measured CCE and charge collection distance (CCD) as a function of bias voltage for a sensor.

In order to determine the turn-on voltage and the linearity of the response of the laser, the output signal was measured as a function of the input voltage. The results are shown in Figure 12. Linearity up to 1.2 V input voltage is observed.

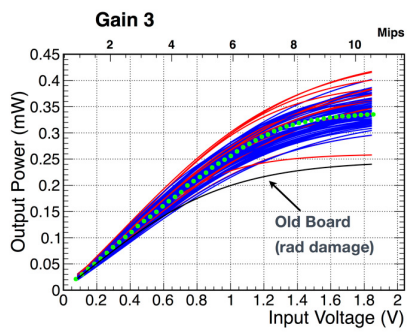


Figure 12: Response of the laser as a function of signal strength.

Test-Beam Results

The test-beam measurements were performed at DESY II using a 5 GeV electron beam at a rate of 100 Hz. The signals generated by the beam electrons were triggered by scintillators of 1 cm^2 effective area located before and after the

Copyright © 2014 CC-BY-3.0 and by the respective authors

ISBN 978-3-95450-141-0

test setup, and 6 Mimosa26 telescope planes were used to reconstruct the tracks of triggered electrons. The full readout chain, consisting of sensor, the front-end ASIC, and AOH was characterised.

A signal, measured by a sampling ADC, is shown in Figure 13. The amplitude of this signal corresponds to a minimum ionizing particle in a sensor with 80 %CCE. The FWHM of the signal is less than 10 ns, matching the design requirements.

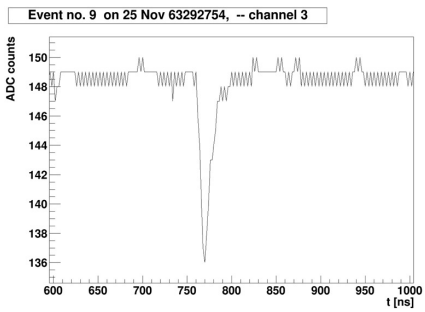


Figure 13: Signal from a triggered electron as a function of time.

A scan of the CCE as a function of the impact point of the electron beam was done to measure the uniformity of the response over the sensor surface. The result, shown in Figure 14, was a flat CCE of about 80 % over the metallised area. Charge sharing between the pads was observed in the region of the gap. However, the gap size was on the order of 5 μm, much less than the width of the charge sharing range.

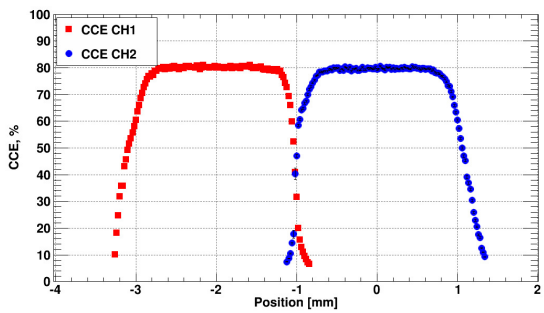


Figure 14: The CCE as a function of the position of the beam electron impact point.

An explanation of this observation is given by a simulation using the program called “Superfish” [5] that calculates the weighting potential of a sensor with two pads and a CCE of 80 %. The weighting potential, as discussed by Ramo [6] and H. Spieler [7], determines the coupling of a moving charge carrier at any position to an electrode.

The simulations were done setting the bottom pad of the sensor and the top right pad to 0 V, whereas the top left readout pad was set to 1 V, as illustrated in Figure 15. The uniform electrical field will force a free charge carrier to travel perpendicular to the read out pads.

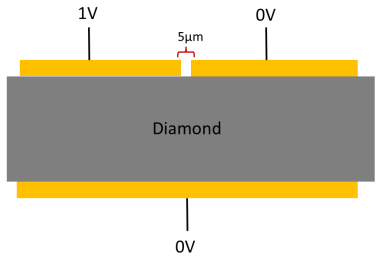


Figure 15: Sensor structure used in the Superfish simulations.

Figure 16 shows the comparison between the measurements of the left readout pad (red) and three different types of simulated weighting potentials. The green curve represents the prediction for a sensor that has a 20 % reduced CCE directly under the top pad. The magenta curve represents the prediction for a 20 % reduced CCE at the bottom pad, and the blue curve represents the due to a 10 % reduction at the top electrode and a 10 % reduction at the bottom electrode. The magenta curve does not agree with the measurements and thus that scenario can be excluded. The other two curves describe the test-beam results moderately well. It can be concluded that at least some of the inefficient sensor material is located close to the top readout pad.

SUMMARY

All components of the fast beam condition monitor, BCM1F, were upgraded, including the sensors, the front-end ASICs, and the mechanical structure. All front-end parts were tested in the laboratory and in a test-beam. The functionality of the full system was demonstrated and the relevant parameters match the requirements.

ISBN 978-3-95450-141-0

Copyright © 2014 CC-BY-3.0 and by the respective authors

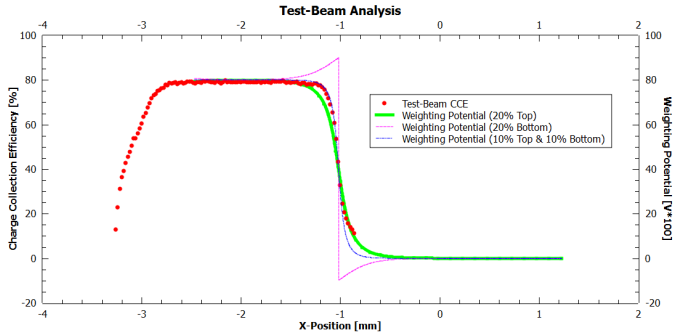


Figure 16: Comparison of the measurements and Superfish simulations of the charge sharing between the pads of a sensor with a charge collection efficiency of 80 %.

REFERENCES

[1] N. Odell, " Measurements of Luminosity and Normalised Beam-Induced Background Using the CMS Fast Beam Condition Monitor," Contribution to ICHEP2012, Melbourne, Australia, PoS(ICHEP2012)526

[2] A. Dabrowski, et al., " The Performance of the Beam Conditions and Radiation Monitoring System of CMS," Contribution to IEEE Nuclear Science Symposium and Medical Imaging Conference 2011, Valencia, Spain, CMS CR 2011/275

[3] A. J. Bell, " Fast Beam Conditions Monitor BCM1F for the CMS EXperiment," Nucl. Instrum. Methods Phys. Res., A 614 (2010) 433-438

[4] E. Castro, et al. " Application of Single Crystal Diamonds (scCVD) as Beam Coniditions Monitors at LHC," IBIC2012, Tsukuba, Japan, TUPA08

[5] R. F. Holsinger, et al. "SUPERFISH - A Computer Program for Evaluation of RF Cavities with Cylindrical Symmetry," Particle Accelerators 7 (1976) 213-222

[6] S. Ramo, "Currents Induced by Electron Motion," Proceedings of I.R.E. 27 (1939) 584-585
http://ieeexplore.ieee.org/stamp/stamp.jsp?tp=&arnumber=1686997

[7] H. Spieler, "Semiconductor Detector Physics," Oxford University Press 2005,
ISBN: 0-19-852784-5 978-0-19-852784-8

Copyright © 2014 CC-BY-3.0 and by the respective authors

ISBN 978-3-95450-141-0

SYNCHRONISATION OF THE LHC BETATRON COUPLING AND PHASE ADVANCE MEASUREMENT SYSTEM

J. Olexa, M. Gasior, CERN, Geneva, Switzerland

Abstract

The new LHC Diode ORbit and OScillation (DOROS) system will provide beam position readings with sub-micrometre resolution and at the same time will be able to perform measurements of local betatron coupling and beam phase advance with micrometre beam excitation. The oscillation sub-system employs gain-controlled RF amplifiers, shared with the orbit system, and followed by dedicated diode detectors to demodulate the beam oscillation signals into the kHz frequency range, subsequently digitized by multi-channel 24-bit ADCs. The digital signals are processed in each front-end with an FPGA and the results of reduced throughput are sent using an Ethernet protocol to a common concentrator, together with the orbit data. The phase advance calculation between multiple Beam Position Monitors (BPMs) requires that all DOROS front-ends have a common phase reference. This paper presents methods used to generate such a reference and to maintain a stable synchronous sampling on all system front-ends. The performance of the DOROS prototype synchronisation is presented based upon laboratory measurements.

INTRODUCTION

The DOROS system has been primarily designed and optimised for processing beam signals from the beam position monitors (BPMs) embedded into the jaws of the new LHC collimators [1]. The system will provide orbit readings used for the automatic positioning of the collimator jaws symmetrically around the beam, which will reduce the time needed to set-up the collimators and potentially improve the collimation efficiency. The Diode ORbit (DOR) system will be complemented by Diode OScillation (DOS) sub-system optimised for processing the beam oscillation signals. The DOS part will provide data that can be used for the measurement of local betatron coupling and the phase advance between the BPMs with micrometre beam excitation.

The simplicity of the DOROS system and its already proven sub-micrometre orbit resolution [2] made it a good candidate to complement the standard LHC BPM system. This system was designed for bunch-by-bunch trajectory measurements and is limited to an orbit resolution at the micrometre level. The DOROS system will therefore be installed on all BPMs close to the LHC interaction points, where a better orbit resolution will help in optimising the collision process. Electrode signals of these BPMs will be passively split and sent to both systems. This way the standard system will provide bunch-by-bunch beam trajectories while the DOROS will measure precisely beam orbits. In addition, the DOS part of the DOROS system will be capable of providing oscillation data with micrometre beam excitation for betatron coupling and phase advance measurements.

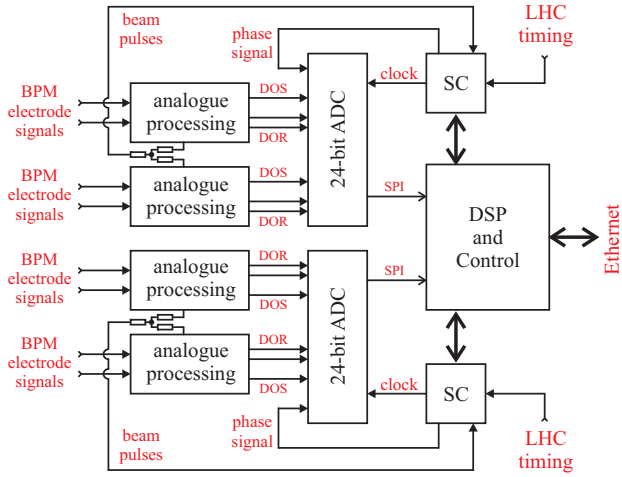


Figure 1: Block diagram of a DOROS front-end. Abbreviations: SC – synchronisation circuits, DOR – diode orbit, DOS – diode oscillation, SPI – serial peripheral interface link.

DOROS SYSTEM

The DOROS front-ends will be built as 1U 19" modules distributed around the LHC. Each front-end is foreseen to process signals from four BPM electrode pairs. Typically it will be up-stream and down-stream BPMs of two collimators or horizontal and vertical electrodes of two stripline BPMs [2]. The block diagram of one DOROS front-end is depicted in in Fig. 1.

The analogue processing channels of each electrode pair provide two low frequency orbit signals (DOR) proportional to the BPM electrode voltages, which are produced by compensated diode detectors [2], and one oscillation signal (DOS), resulting from the difference of the beam oscillation signals demodulated by diode peak detectors. All three signals are low-pass filtered and are digitized by a 24-bit ADC at the rate of the LHC revolution frequency (f_{rev}) of about 11.2 kHz. The subsequent digital signal processing (DSP) of the samples is implemented in an FPGA. The same FPGA provides the system control and timing as well as the Ethernet communication and data transmission to a common DOROS concentrator. The DOROS data transmission uses the same Ethernet protocol and the 25 Hz frame rate as the standard BPM system. The total DOROS data throughput is about 40 KB/s per front-end.

ISBN 978-3-95450-141-0

Copyright © 2014 CC-BY-3.0 and by the respective authors

In general, each LHC beam can have slightly different revolution frequency and therefore the LHC has two networks distributing the beam synchronous timing (BST). Since each DOROS front-end is foreseen to process simultaneously signals from both LHC beams, the digitalisation is done with two ADCs. As seen in Fig. 1, the ADCs are independently clocked with the signals obtained from dedicated synchronisation circuits (SC) blocks, each using an individual timing, which can come from either of the LHC timing networks.

The ADC selected for the DOROS system is of Σ/Δ architecture to obtain the 24-bit resolution and excellent linearity of the conversion. The ADC has been chosen for its very good performance for both DC and AC signals, required for the DOR and DOS systems, respectively. In addition each ADC accommodates 8 simultaneously sampled channels, fitting well to the DOROS architecture.

The DOS sub-system is based on synchronous demodulation of the beam oscillation signals [3] resulted from micrometre beam excitation at a constant frequency f_{exc}, typically chosen close to the betatron frequency f_β, which for the LHC is in the range 3.1 – 3.6 kHz for both horizontal and vertical planes. The oscillation phase advance is measured with respect to a local oscillator (LO) signal having exactly the same f_{exc} frequency as the beam excitation. This LO f_{exc} signal is generated with a direct digital synthesizer (DDS) [3] synchronised to a revolution frequency timing derived from the LHC BST and referred to as timing revolution frequency, f_{revT}. While the frequency of this signal is guaranteed to be the same in each DOROS front-end, it is not the case for its phase. The phase of f_{revT} in a particular DOROS front-end depends on its location around the LHC and the delay of the BST optical fibre link. Therefore, the f_{revT} signal phase must be aligned to the same beam bunch in each front-end, which will be done with a single bunch circulating in the machine. If the timing distribution does not change, in general this alignment needs to be performed once. This paper describes the circuitry and algorithms that will allow a reliable phase synchronisation of the timing f_{revT} derived from the LHC BST, with the focus on the synchronisation circuits accommodated in SC block in Fig. 1. The required accuracy of the phase advance measurements obtained from the DOS data is in the order of 0.1°, corresponding to some 80 ns at 3.6 kHz, the highest frequency at which the phase advance measurements will be typically done. The synchronisation between the DOROS front-ends should preferably be much better, in the order of 8 ns, equivalent to about 0.03° at f_{rev}. The described synchronisation was designed with the aim of achieving at least this accuracy.

SYNCHRONIZATION CIRCUITS

A diagram of the synchronisation circuits is shown Fig. 2. Its first block, a Beam Synchronous Timing receiver (BSTrx), decodes the LHC timing, distributed over fibre optics links from a single timing source. The block provides the bunch frequency f_{RF} (about 40.1 MHz)

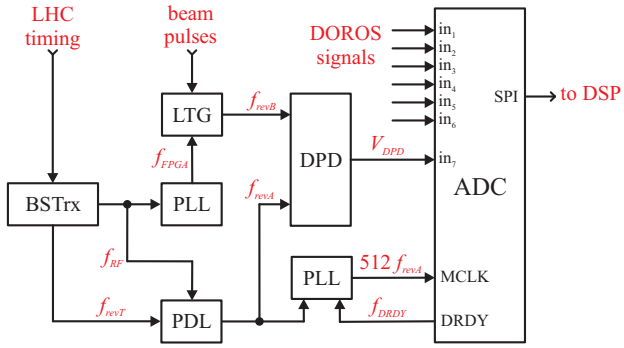


Figure 2: DOROS synchronisation circuits. BSTrx – beam synchronous timing receiver, LTG – local timing generator, PDL –programmable delay line, DPD – differential phase detector, MCLK – master clock, DRDY – data ready signal.

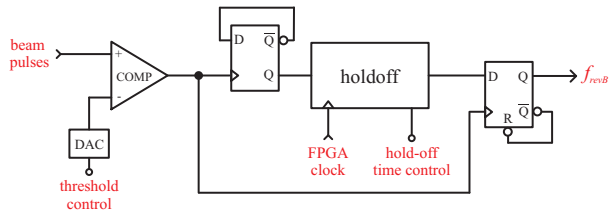


Figure 3: Block diagram of the Local Timing Generator (LTG).

which is multiplied by a factor of four in an FPGA PLL block to produce the FPGA global clock f_{FPGA} (about 160 MHz). The BSTrx block delivers also the earlier introduced timing revolution frequency signal f_{revT}, whose phase can be shifted by a Programmable Delay Line (PDL) to match the phase of the revolution frequency reference f_{revB}, which is derived from the beam pulses. The PDL provides the beam aligned revolution frequency reference f_{revA}, used as a phase reference for the PLL synchronising the ADC sampling signalled by the data-ready (DRDY) pulses. The PLL produce a low-jitter ADC master clock (MCLK), whose frequency is 512 times higher than f_{revA}, that is about 5.8 MHz. The PLL is optimised for low jitter and is based on a classical architecture with a charge-pump phase detector and a voltage controlled oscillator (VCO) built as an LC generator tuned with a varicap diode.

The beam reference f_{revB} is provided by a Local Timing Generator (LTG), synchronised by the beam pulses produced by a passive combination of the processed BPM electrode signals, as sketched in Fig. 1. The phase of the timing f_{revT} and beam f_{revB} signals is compared in a differential phase detector (DPD). This precise phase detector is designed in such a way that its output voltage read by one dedicated ADC channel has a maximum when the both input signals are phase-aligned. During the phase alignment procedure the delay of the PDL is adjusted to obtain a maximum voltage from the DPD.

Copyright © 2014 CC-BY-3.0 and by the respective authors

ISBN 978-3-95450-141-0

This way the phase-match condition does not depend on the input offset voltage of the ADC, which would otherwise cause an important error.

Local Timing Generator

The phase of the revolution frequency reference f_{revT} obtained from the LHC timing system in each DOROS front-end is foreseen to be synchronised with the beam with just one bunch circulating in the machine. However, the Local Timing Generator (LTG), schematically shown in Fig. 3, is designed to provide a beam revolution frequency reference f_{revB} synchronised to the same beam bunch regardless of the actual LHC bunch configuration. The LTG employs an asymmetry in the bunch train and locks to the first bunch following the largest gap in the bunch train. In the case of the physics beam the largest gap constitutes the so called abort gap, a 3 µs period with no bunches, corresponding to the risetime of the LHC dump kicker.

The operation of the LTG is based upon bunch pulses derived from the BPM electrode signals. The pulses are converted into short logic signals by a comparator and stretched in time by the following flip-flop. Once the LTG is already locked, the first bunch after the largest gap triggers the flip-flop generating a short pulse before being auto-reset. The same bunch starts the counter in the holdoff block, resetting also its output, which in turn disables the output flip-flop. The flip-flop gets enabled after the holdoff counter reaches the time falling already in the following bunch gap. The LTG locks to the first bunch after the largest gap when the holdoff time is set as

$$T_{holdoff} = T_{rev} - T_{largest\ gap} + \Delta T \qquad (1)$$

where $T_{rev} = f_{rev}^{-1}$ is the revolution period of about 88.9 µs, $T_{largest\ gap}$ is the time of the largest gap in the bunch train and ΔT is a small interval, typically a few ns.

The operation of the comparator can be optimised by changing its threshold voltage through a dedicated DAC.

Programmable Delay Line

The phase of the timing revolution frequency reference f_{revT} can be shifted with the resolution much better than one FPGA clock using the Programmable Delay Line (PDL), whose block diagram is shown in Fig. 4. The PDL is built from two parts: a raw delay, delaying the f_{revT} reference by a programmable number of f_{RF} clock cycles (25 ns) and a fine delay. The fine delay, which can be programmed in 100 ps steps, employs the feature of an FPGA PLL block, producing a delayed version of the f_{RF} timing, which clocks the raw delay block.

Differential Phase Detector

Since the phase measurement at the 0.01° level cannot be done with the FPGA logic, the measurement is performed with a specially designed Differential Phase Detector (DPD) built from discrete components and shown schematically in Fig. 5, together with simplified waveforms in the key nodes of the circuit. Such a phase detector delivers a DC voltage with the maximum value

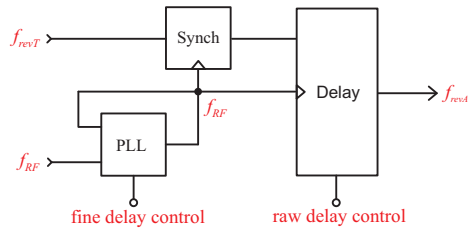


Figure 4: Programmable Delay Line (PDL). Abbreviations: Sync – synchronisation circuit.

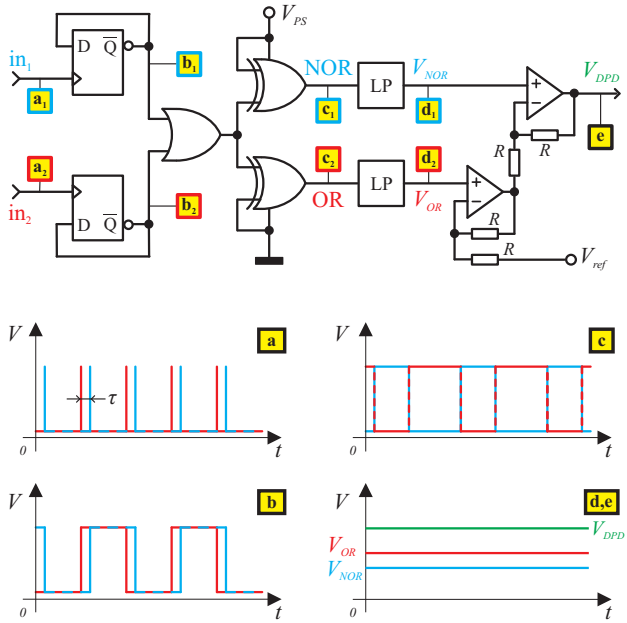


Figure 5: Block diagram of the Differential Phase Detector (DPD) and simplified waveforms in its key nodes. LP – low pass filter.

when the rising edges of the pulses at both DPD inputs coincide and the voltage is digitized by one channel of the DOROS ADC.

The pulses of both DPD inputs clock two flip-flops producing two signals with 50 % duty cycle, which conserve the delay τ between the two input signals. The flip-flops drive the inputs of an OR gate, followed by two XOR gates, working in a buffer and an inverter configuration, guarantying an equal delay for both, OR and NOR outputs. If both input signals have the same phase (i.e. $\tau = 0$), then the OR and NOR signals have equal 50 % duty cycles, which are converted by identical passive low pass (LP) filters into analogue voltages of exactly equal amplitude. The LP output signals are subtracted by a differential amplifier, whose output voltage, shifted by the ADC reference voltage (V_{ref}), is digitized by one channel of the ADC. The differential amplifier with the gain of two is built as a classical instrumentation amplifier with two op-amps.

ISBN 978-3-95450-141-0

Copyright © 2014 CC-BY-3.0 and by the respective authors

For $\tau \neq 0$ the OR duty cycle increases and NOR decreases, resulting in a decrease of the DPD output voltage. In general, the DPD output voltage V_{DPD} is

$$V_{DPD} = V_{ref} - V_{PS}\frac{|\tau|}{T_{rev}} \quad (2)$$

where $V_{PS} \cong 3.3$ V is the power supply of the CMOS XOR gates, defining the output high level. V_{PS} voltage influences the DPD gain but it is not the case for $\tau = 0$, where the DPD operation is the most important. In addition, V_{PS} can be measured by one ADC channel, which is switched by an analogue multiplexer between key nodes of the DOROS circuits.

Please note that according to (2) the phase difference of 0.01° changes the DPD output voltage only by some 90 µV. The DPD configuration is the only one found by the authors which was able to resolve such small phase changes.

LABORATORY MEASUREMENTS

The DOROS synchronisation was tested in a laboratory with locally generated signals and this paper presents some measurements of the most important blocks.

The functionality of the local timing generator was tested with beam pulses simulated with an arbitrary waveform generator in conditions representative of LHC beams. One such measurement is shown in Fig. 6, presenting the LTG holdoff output pulses (top trace in blue) triggered upon the first pulse after a larger gap in the pulse train (bottom trace in magenta). The LTG capability of locking to any asymmetry in the bunch train allows permanent monitoring of the synchronisation between the timing f_{revT} reference and the beam.

The performance of the differential phase detector is summarised on the plots in Fig. 7. In the first measurement the phase of the DPD input signals was changed in 200 ps steps. The steps, with the size selected for good plot readability, were produced using the programmable delay line, proving its good operation. The samples of the DPD output were averaged over 40 ms and 1 s intervals, corresponding to the standard processing applied to DOROS orbit samples. This way the DPD signal is processed and transmitted along with other DOROS samples.

In the second measurement the phase of the DPD input signals was kept constant for some 7 minutes. It can be seen that increasing the sample averaging by a factor of 25, from 40 ms to 1 s, only reduces the peak-peak noise by roughly a factor of 2. This indicates that the DPD output noise is dominated by low frequency content, which did not average out well over 1 s periods.

The peak-peak noise seen on the traces in Fig. 7 is of the order of the 200 ps steps, which corresponds to 0.0008° at f_{rev}. This resolution is by far sufficient for synchronising the DOROS units, with the goal of 0.01°. Please note that the phase noise of 200 ps_{pp} corresponds to some 7 μV_{pp} read by the ADC at the output of the DPD.

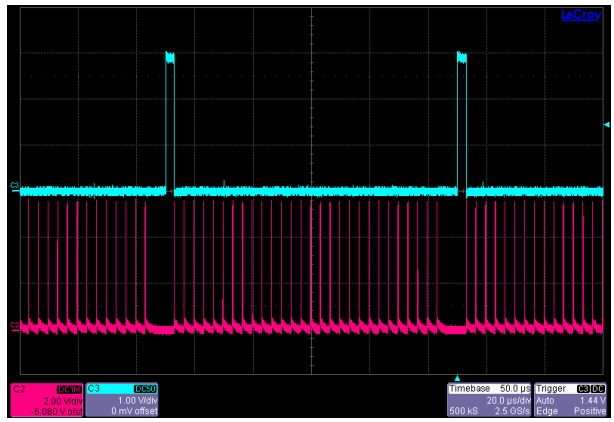


Figure 6: Laboratory testing of the local timing generator (LTG). Shown are the input and holdoff output waveforms in magenta and blue, respectively.

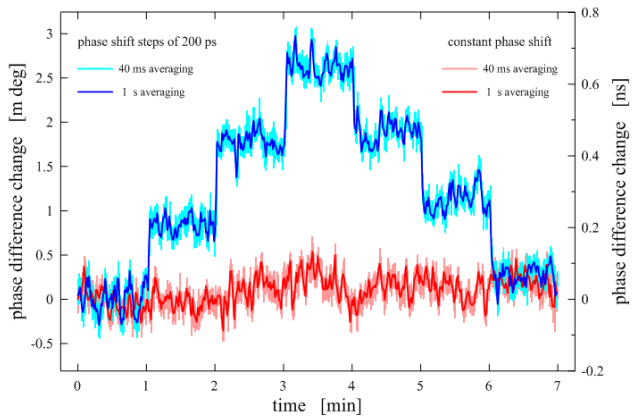


Figure 7: Response of the differential phase detector upon 200 ps delay steps (in cyan and blue) and the detector 7 minute stability (in red).

The jitter of the ADC master clock was measured to be about 5 ps_{RMS}. Its good quality resulted in the sampling jitter of about 30 ps_{RMS}, as measured on the data ready pulses.

CONCLUSIONS AND OUTLOOK

The timing and synchronization circuits are an important part of the DOROS system, particularly so for the phase advance measurement sub-system. For such measurements all DOROS front-ends need a common f_{revA} reference with the phase adjusted to the same bunch of the circulating beam. However, for the betatron coupling measurements the phase of the f_{revA} reference in each the system front-ends is not important and for the orbit measurements even its frequency does not matter.

For the phase advance measurements the revolution frequency reference f_{revT} derived from the LHC timing system needs to be aligned to the same beam bunch. As each LHC filling always starts from an injection of a low intensity pilot bunch, this bunch can be used for the

Copyright © 2014 CC-BY-3.0 and by the respective authors

ISBN 978-3-95450-141-0

timing alignment or its verification. In addition, the presented local timing generator is capable of deriving the revolution frequency reference from the LHC beam in practically all beam configurations. This reference can be used for a continuous monitoring of the phase of the adjusted timing reference f_{revA} by comparing the two signals using the differential phase detector, whose output is digitized in parallel to all other DOROS channels.

The presented differential phase detector allows measurements with a resolution in the order of 0.001º while the programmable delay line allows a fine adjustment of the timing f_{rev} reference in 100 ps steps. Both values are by far sufficient for achieving the synchronisation between the DOROS units at the 0.01º level.

After the LHC restart in 2015 the embedded BPMs of the 18 new collimators will operate with the DOROS system. In addition, DOROS front-ends will be installed on selected BPMs close to the LHC experiments, operating in parallel to the standard BPM electronics. This first DOROS operational installation, containing a few tens of front-ends, will allow its systematic testing and optimisation of its three measurement modes: orbit, local coupling and phase advance. The phase advance will be a real test bed for the performance of the presented DOROS synchronisation.

REFERENCES

[1] C. Boccard et al., "Embedded collimator beam position monitors", Proceedings of DIPAC 2011, Hamburg, Germany, CERN-BE-2011-023.

[2] M. Gasior et al., "BPM electronics based on compensated diode detectors – results from development systems", Proceedings of BIW 2012, Newport News, VA, USA, CERN-ATS-2012-247.

[3] J. Olexa et al., "Prototype system for phase advance measurements of LHC small beam oscillations", Proceedings of MAREW 2013, Pardubice, Czech Republic, CERN-ATS-2013-038.

Copyright © 2014 CC-BY-3.0 and by the respective authors

ISBN 978-3-95450-141-0

DUAL TRANSVERSE AND LONGITUDINAL STREAK CAMERA IMAGING AT ELSA*

M. Switka, F. Frommberger, P. Haenisch, M. Schedler and W. Hillert, ELSA, Bonn, Germany

Abstract

The electron pulse stretcher ring ELSA located at Bonn University provides 0.5–3.5 GeV polarized and non-polarized electron beams for external experimental stations. A streak camera system has been installed to capture time resolved images of beam dynamics ranging from nanoseconds to several milliseconds [1]. Particular attention was drawn to the capability of simultaneous imaging of both transverse beam dimensions, hence providing information of all spatial dimensions in one synchroscan or slow sweep measurement. Incoherent and coherent beam instabilities, especially at high stored beam currents, are subject of analysis due to the planned intensity upgrade towards 200 mA for standard operation. The current resolution performance of the imaging system and machine relevant measurements are presented.

INTRODUCTION

As streak cameras convert three dimensional light beam information into a two dimensional image with aspect on longitudinal resolution, the dimension of one transverse plane is always suppressed, either by the streak action or the narrow slit of the input optics. As for certain events interest arises for capturing dynamics in all three dimensions simultaneously, a method for dual transverse imaging at ELSA was introduced and demonstrated in [2]. In order to test the convenience of such a setup, a low-cost version was installed mostly utilizing equipment already available at the lab. Resolution limits were encountered primarily due to the limiting aperture of the optical system and for very short time windows due to limited light intensity. Furthermore, longitudinal instability behaviour was investigated through grow-damp measurements using the bunch-by-bunch feedback system (BBB). Attention was especially drawn to cavity temperature effects and decoherence observation.

BEAM MANIPULATION AND RECOUPLING

The primary lens of ELSA's *M7* optical synchrotron radiation diagnostic beamline focuses the visible synchrotron radiation onto the focal plane of the first lens of a relay line lens pair. The subsequent beam manipulation section in is illustrated in Fig. 1. The parallel light bundle is split by a 50 % beamsplitter, partially bypassing a Dove prism which rotates the beam transversally by 90°. Both light bundles, upright and flat, are recoupled onto the same light path with slight displacement and angular deviation. The second relay lens focuses the beam onto the streak camera's input slit (M_{tot} = 0.044). Hence the two perpendicular electron beam images are projected next to each other. In this setup, two main apertures restrict the resolution of transverse beam dynamics: The 0.15 × 4.41 mm^2 (v × h) large photo cathode limits the imaging of vertical light beam displacements. Secondly, the rectangular mirror downstream from the Dove prism imposes a horizontal aperture for the flat beam and a vertical aperture for the upright beam. Note that the original beam image orientation is upright.

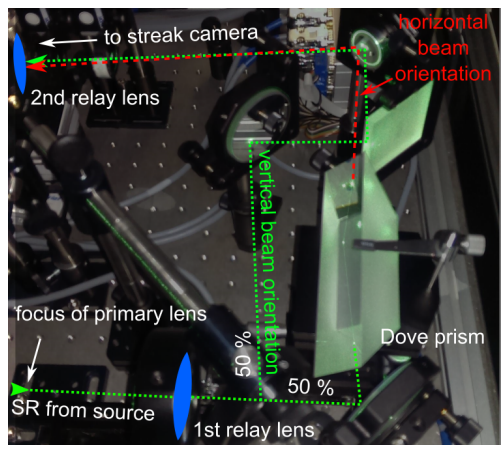


Figure 1: Optical setup for simultaneous imaging of both transverse beam dynamics. One part of the beam is rotated by 90° after exiting the Dove prism.

DUAL TRANSVERSE IMAGING

The streak camera used is the model C10910 by Hamamatsu [3]. Exemplary *slow sweep* measurements for the dual transverse imaging capability are shown in Fig. 2. Parts of

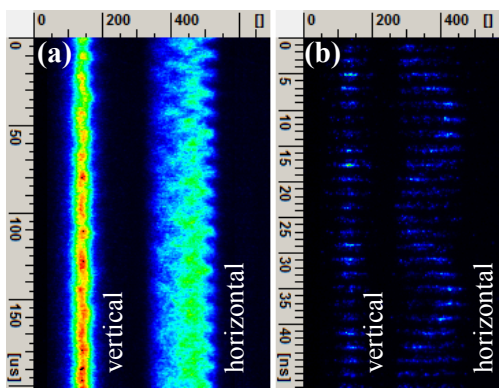


Figure 2: Dual transverse *slow sweep* images. Injection beam dynamics are captured at sufficient SNR (a) and single bunch resolution (b).

the injection process are captured where large horizontal

* Work supported by the DFG within SFB/TRR16.

Copyright © 2014 CC-BY-3.0 and by the respective authors

ISBN 978-3-95450-141-0

beam oscillations are expected. Image (a) shows vertical (left streak) and horizontal (right streak) beam dynamics during a time window of 200 µs where the signal-to noise ratio (SNR) is sufficient. Image (b) shows single bunches resolved during a time window of 50 ns. Due to the low irradiation time, the SNR is much lower, yet the horizontal betatron oscillations are observable including partial oscillation decoherence. Note that the intensity fluctuation of the vertical beam is due to the large horizontal oscillation amplitude, causing the signal to partially exceed the aperture perimeter. Further examples can be reviewed in [2].

LONGITUDINAL MEASUREMENTS

Grow-damp measurements were performed in dependency of different beam energies and cavity temperatures. The behaviour at coherent damping was imaged with single bunch resolution.

Obtaining Damping Rates

To utilize the streak camera as quantitative measurement device, data quality of grow-damp measurements was tested against the model for incoherent longitudinal damping:

$$\tau_s = \frac{2ET_{\mathrm{rev}}}{\Delta E_{\mathrm{SR}}\left(2+\frac{\alpha_c L}{2\pi R}\right)}, \qquad (1)$$

where E is beam energy, T_{rev} revolution period, $\Delta E_{\mathrm{SR}} \propto E^4/R$ energy loss per revolution, α_c momentum compaction, L the ring length and R the bending radius. For this purpose the beam was first stabilized with the BBB in storage mode. It was then excited longitudinally by switching off the BBB for a few milliseconds. The excitation process of the beam was synchronously monitored with the streak camera's *synchroscan* unit. Note that due to image symmetry in *synchroscan* mode only the upper half of the image is presented. Observation indicated that the duration of BBB down time had only negligible effect on the shape or amplitude of the excitation and the damping behaviour. The grow-damp measurements were performed between beam energies of 1 and 3 GeV. A typical measurement is illustrated in Fig. 3.

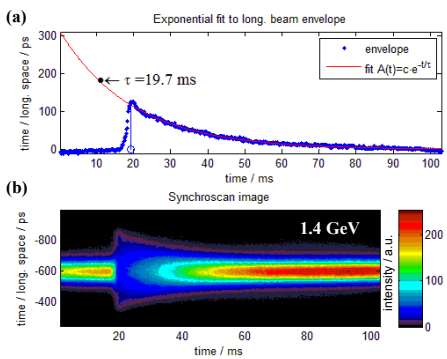


Figure 3: Exemplary grow-damp measurement at 1.4 GeV. An exponential decay function is fit to the upper envelope of the streak camera image.

In order to quantify the damping rate each column of the bitmap image was analyzed from top to bottom. The first value above noise threshold determines the longitudinal position of the beam envelope and links it to the underlying time grid. This assumes that only incoherent oscillations contribute to the amplitude which is only valid as an approximation due to the contribution of coherent oscillations seemingly enlarging the amplitude. However, analysis with the BBB's diagnostics showed a much faster decay of the coherent oscillation in comparison to the incoherent. In order to obtain the exponential fit the envelope of the initially damped beam marks the ground level. The data interval for the fit is set from maximum excitation to the end of the data set. The result is summarized in Fig. 4. The data shows

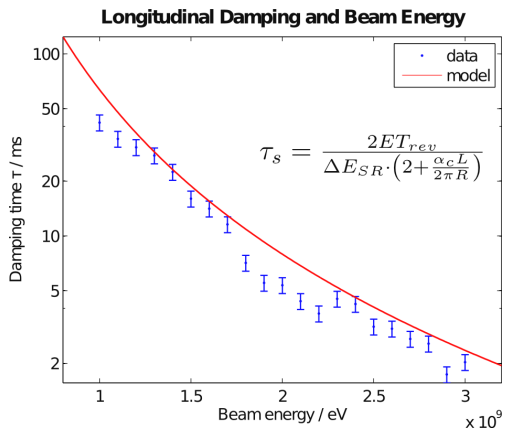


Figure 4: Damping rates at different beam energies.

sufficient agreement with the model. However, it appears that the measured damping time is systematically smaller than the expected value. Up to ten measurements were taken and averaged for one energy. A systematic error estimation of 10% is included, reflecting the effect of different threshold parameters on the damping time as well as the limited vertical pixel resolution.

Temperature Effects

At higher beam energies the shorter damping times prevent the built-up of large oscillation amplitudes which reduces the quality of the taken data. Furthermore, as heat load on the cavity body increases with beam energy, it was observed that the instability behaviour changed significantly with cavity temperature. An exemplary overview is given in Fig. 5, where the BBB down time was 10 ms and no down time repetition was manually set. The beam current was 80 mA.

The repetition rate of the instability occurrence increases to a maximum rate with rising temperature and decreases again as temperature rises further. The coherence duration, amplitude and rise time of the instability change significantly with temperature. At low temperatures a relatively slow collective rising behaviour is observable. At higher temperatures the instability is mostly visible due to instantly appearing incoherent oscillations with lower amplitude.

ISBN 978-3-95450-141-0

Copyright © 2014 CC-BY-3.0 and by the respective authors

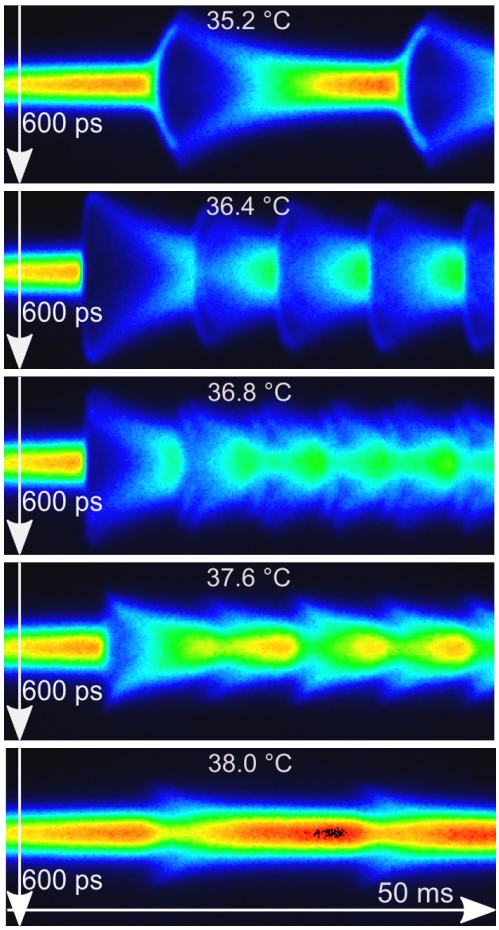


Figure 5: Damping and re-excitation behaviour for different cavity temperatures during grow-damp measurements in 1.9 GeV storage mode.

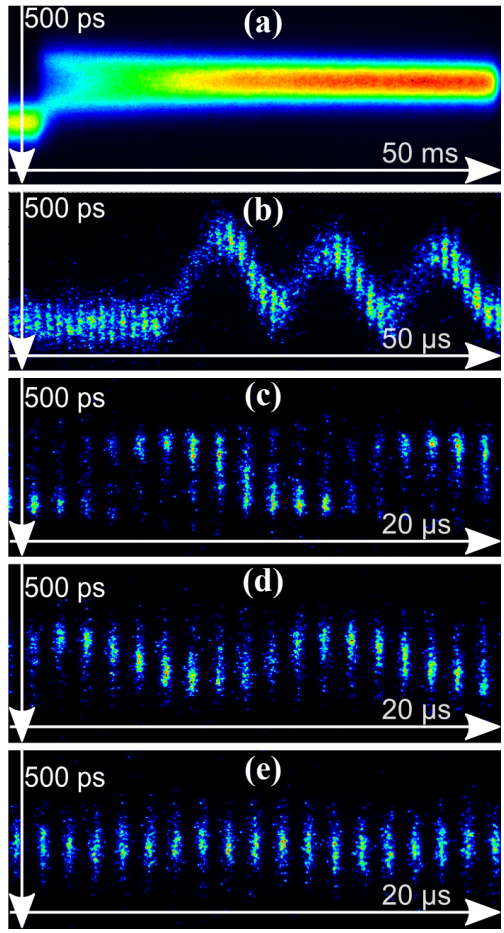


Figure 6: Single bunch oscillation behaviour after cavity phase jump.

Decoherence Observation

As individual bunch dynamics are not observable on millisecond time scales due to streak overlap, the BBB was used to remove all bunches but one. Aside, no instability growth was observed at BBB down time. Therefore the longitudinal oscillation was excited by an RF phase jump as visible in Fig. 6 (a). In (b) the instant of the phase jump is resolved with the maximum time window at which the bunch signals are yet distinguishable. The intensity fluctuation is likely caused by the limiting aperture. In order to gain maximum intensity the beam splitting section was removed and hence horizontal dispersive orbits were not resolved. Images (c) to (e) show the chronological evolution of the oscillation. In (c) the bunch distribution appears somewhat distorted which is likely an artifact due to aperture restriction. The broadening however is clearly visible as decoherence of the oscillation. The BBB is damping the coherent oscillation as visible in (d) and (e).

CONCLUSION

The intensity fluctuation due to the aperture limit has significant influence on the streak camera images. In order to clarify the appearance of artifacts observable as in Fig. 6 (c) both transverse planes need to be measured simultaneously. As beam intensity is not yet sufficient at the ELSA diagnostic beamline, dual transverse synchroscan measurements will be investigated after an aperture increase of the optical transfer line is completed.

REFERENCES

[1] M.T. Switka, et al., Streak Camera Imaging at ELSA, contribution IBIC 2013, Oxford

[2] M.T. Switka, et al., Synchrotron Radiation Diagnostics Performance at ELSA, contribution IPAC 2014, Dresden

[3] Hamamatsu Streak Camera C10910 data sheet: `http://www.hamamatsu.com/resources/pdf/sys/SHSS0016E07_C10910s.pdf`

Copyright © 2014 CC-BY-3.0 and by the respective authors

ISBN 978-3-95450-141-0

ELECTRON BEAM DIAGNOSTICS FOR SHORT PULSE FEL SCHEMES AT CLARA

S. Spampinati#, University of Liverpool and The Cockcroft Institute, Cheshire, U.K
D. Newton, University of Liverpool, Liverpool, U.K

Abstract

CLARA (Compact Linear Accelerator for Research and Applications) [1] is a proposed 250 MeV, 100-400 nm FEL test facility at Daresbury Laboratory. The purpose of CLARA is to test and validate new FEL schemes in areas such as ultra-short pulse generation, temporal coherence and pulse-tailoring. Some of the schemes that can be tested at CLARA depend on a manipulation of the electron beam properties with characteristic scales shorter than the electron beam and require a 30 - 50 µm modulation of the beam energy acquired via the interaction with an infrared laser beam in a short undulator. In this article we describe the electron beam diagnostics required to carry on these experiments.

INTRODUCTION

Some of the most advanced schemes proposed to improve FEL performance depend on a manipulation of the electron beam properties with characteristic scales of several coherence lengths and shorter than the electron beam [2, 3, 4]. We are interested to test, among other schemes, mode locking FEL and femto-slicing for the production of trains of short pulses [5, 6, and 7]. The implementation of these schemes at CLARA requires a 30 - 50 µm modulation of the beam energy acquired via the interaction with an infrared laser beam in a short undulator (modulator). The performance of these FEL schemes depend on this energy modulation. So monitoring the longitudinal phase space of the electron beam is important to perform and to realize these experiments. A deflecting cavity [8] installed in the last part of the FEL line will allow the longitudinal beam distribution to be observed on a screen placed after the dipole leading to the beam dump. Figure 1a shows the FEL line of CLARA, composed of a modulator, a dispersive section, seven radiators and an afterburner section. The afterburner is composed by a series of short undulators and delay chicanes. A possible layout of the diagnostic system placed at the end of the CLARA undulator from the afterburner is shown in Fig. 1b.

In this design, the electron beam is deflected vertically by the deflecting cavity. This deflection maps the electron beam longitudinal coordinate to the vertical coordinate on an intercepting screen after the spectrometer dipole magnet; the dipole converts the particle's energy to the screen horizontal coordinate. Consequently, the electron beam longitudinal phase space is imaged on the screen, and the energy modulation taking place in the modulator can be studied and optimized. Another interesting application of this diagnostic beam line could be the study of the FEL process taking place in the different operation modes of CLARA.

#simone.spampinati@cockcroft.ac.uk

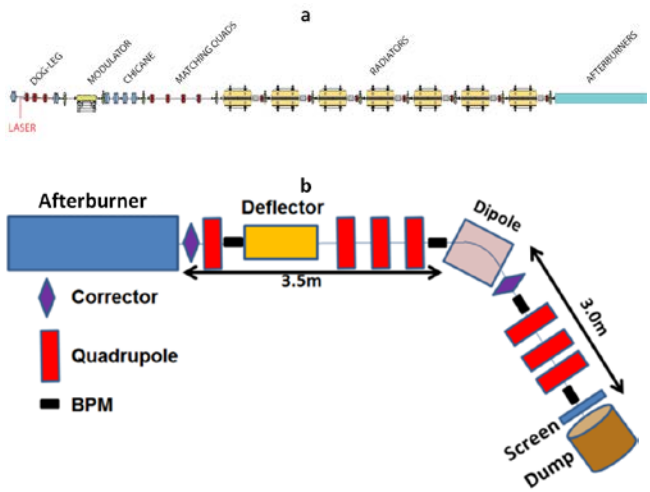


Figure 1: Top: FEl line of CLARA. Bottom: Layout of the phase space diagnostics composed by of a transverse deflector and an energy spectrometer.

OPTICS OPTIMIZATION AND RESOLUTIONS

The vertical beam size at the screen, after deflection, is [9]:

$$\sigma_y = \sqrt{\sigma_{y,0}^{\ 2} + (S\sigma_Z)^2} \qquad (1)$$

where $\sigma_{y,0}$ is the vertical beam size at the screen location without deflection, σ_z is the longitudinal beam size and S is the calibration factor representing the strength of the beam deflection [9]:

$$S = \frac{e_0 V k}{pc}\sqrt{\beta_{yS}\beta_{yD}}\left|\sin\Delta\Psi\right| \qquad (2)$$

here $k = \frac{2\pi}{\lambda}$ with λ = 10.01cm for an S-band cavity (frequency of 2.998 GHz). V_0 is the deflecting voltage, $\beta_{y,D}$ and $\beta_{y,S}$ are vertical betatron functions at the deflector and the screen, respectively. ΔΨ is the vertical

ISBN 978-3-95450-141-0

Copyright © 2014 CC-BY-3.0 and by the respective authors

betatron phase advance between the deflector and the screen. The size of the image of the beam detected on the screen will be increased by the system resolution (screen and CCD pixel size) and:

$$\sigma_y = \sqrt{\sigma_{y,0}{}^2 + \sigma_{screen}{}^2 + (S\sigma_Z)^2} \qquad (3)$$

where σ_{Screen} is the screen and CCD resolution.

The longitudinal resolution of the screen image, $\sigma_{L,r}$, can be defined as the ratio of the non-deflected beam size on the screen to the calibration factor S [10]:

$$\sigma_{L,r} = \frac{pc}{e_0 Vk|\sin\Delta\Psi|}\sqrt{\frac{\varepsilon_n}{\gamma\beta_{yD}} + \frac{(\sigma_{screen})^2}{\beta_{yS}\beta_{yD}}} \qquad (4)$$

The third term in equation 3 is equal to the quadratic sum of first two terms when $\sigma_z = \sigma_{L,r}$. The energy resolution of the spectrometer can be written as [10]:

$$\sigma_E = \sqrt{\frac{E^2}{\eta^2}\frac{\varepsilon_n\beta_x}{\gamma} + \frac{E^2}{\eta^2}(\sigma_{screen})^2 + (e_o Vk)^2\frac{\beta_y\varepsilon_n}{\gamma}} \qquad (5)$$

Here η is the horizontal dispersion at the screen. The first two terms represent the resolution of an energy spectrometer line, the third term is the energy spread induced by the deflector [11]. Equations 4 and 5 guide the optimization of the optics functions in the diagnostic beam line. The optimum phase advance between the deflector and the screen is $\Delta\psi = 90^\circ$. Large values of V and $\beta_{y,D}$ lead to a good longitudinal resolution but increase the energy resolution of the system via the induced energy spread. A large value of $\beta_{y,S}$ improves the total longitudinal resolution for a poor resolution screen but has to be narrowed to limit the total beam dimension on the screen given by equation 1. A small value of $\beta_{x,S}$ and a large value of η are required to have a good energy resolution.

STUDY OF BEAM ENERGY MODULATION

Figure 2 shows a possible optical solution, used to study the energy modulation (with a spatial period in the range 30-50 μm), from the entrance of the modulator to the screen. The radiators are at maximum gap and the intra-undulator quadrupoles are used along with the seven quadrupoles shown in Fig. 1 to give the required resolution. The optics shown are for beam energy of 150 MeV. The vertical betatron functions at the deflector and at the screen are 25 m and 0.95 m respectively. The calibration factor S, for a deflecting peak voltage of 5 MV and a RF frequency of 2.998 GHz, is ~10.2. The vertical rms beam size on the screen is 2.7 mm. The horizontal betatron function and dispersion at the screen are 1 m and 0.6 m. A longitudinal resolution of 4.7 μm and an energy resolution of 75 Kev are therefore achieved. A screen resolution of 20 μm is assumed.

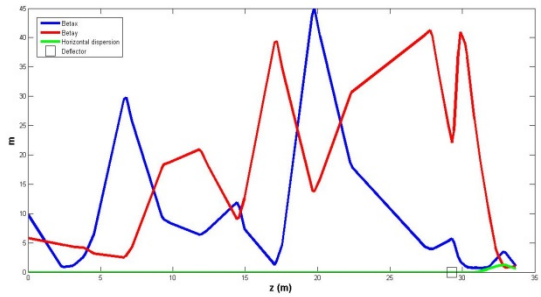


Figure 2: Possible optics from the exit of the modulator to the screen.

Similar optics and performances can be reached for beam energy of 250 MeV with a deflecting voltage of 7.5 MeV.

The reconstruction of the phase space requires short portions of the bunch to be resolved at the screen. An estimate of the length of these portions of the bunch, that can be resolved, can be obtained by using the following simple approach [1, 12]: A portion of the longitudinal density distribution is modelled by two identical Gaussians with different centres in the bunch at a distance Δz. The sigma of the two Gaussians is σ_{screen} /s. This longitudinal test density distribution is reproduced in Fig. 3a. At the screen the separation between the two Gaussians is S·Δz while the sigma is $\sqrt{(\sigma_{y,0})^2 + (\sigma_{screen})^2}$. The vertical profile of the image on the screen is reproduced in Fig. 3b.

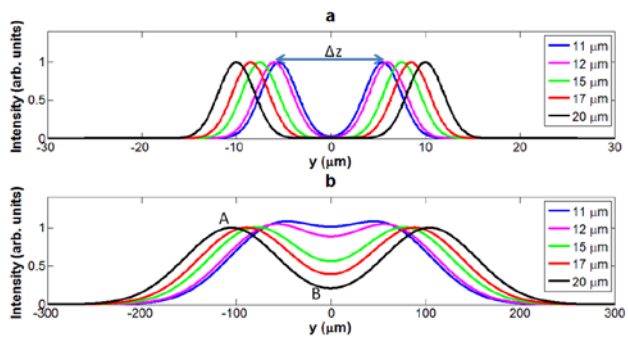


Figure 3: Top: Test longitudinal distributions represented by two Gaussians with a sigma of σ_{Screen} /S separated by a distance Δz. Bottom: Vertical profile on the screen for the distribution depicted above. A and B indicate respectively the values of the intensity of the peaks and of the central local minimum for any profile.

Copyright © 2014 CC-BY-3.0 and by the respective authors

ISBN 978-3-95450-141-0

Figure 4a shows the screen image obtained by simulation tracking the test distribution, it representing two Gaussians separated by 16 µm, from the deflector entrance to the screen. The vertical profile of the image on the screen is reproduced in Fig. 4b.

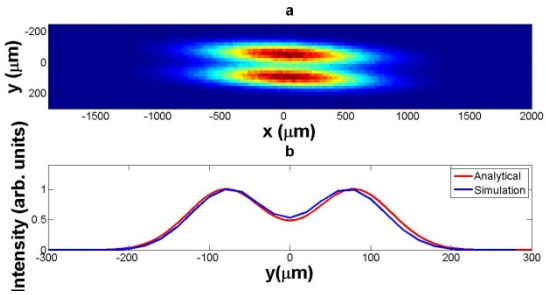


Figure 4: Top: screen image obtained by simulation tracking the test distribution, that it representing two Gaussians separated by 16 µm, from the deflector entrance. Bottom: Vertical profile on the screen.

We can define an intensity contrast IC as (A-B)/A (see Fig. 3b). This parameter quantify the visibility of the separation between the two Gaussians on the screen and for a given measurement system (optics, deflector, screen and CCD) it depends on the separation between the two Gaussians. IC equal to one means perfect visibility while IC equal to 0 means that the image of the two Gaussians are superimposed. The value of IC, for a given measurement system (optics, deflector, screen and CCD) depends on the separation between the two Gaussians. Thus a minimum distance between the two peaks is determined by fixing an intensity contrast. The intensity contrast as function of the distance between the two peaks is plotted in Fig. 5 for the system described above. A value of IC close to 0.5 is obtained when the two Gaussians in the beam distribution are at a distance of 15 µm. This is a first estimate of the minimum slice length detectable [1].

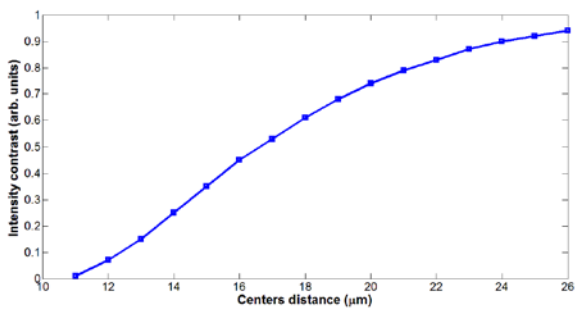


Figure 5: IC vs centers distance.

Simulations including the beam energy modulation in the modulator, the vertical deflection in the RF deflector and the beam transport up to the screen have been performed with the code ELEGANT [13] to test the performance of the diagnostic system introduced above. The parameters used in the simulations are listed in Table 1 and are taken from the CLARA CDR [1]. One-dimensional longitudinal space charge (LSC) and coherent synchrotron radiation (CSR) impedances are included in the simulations.

Table 1: Simulation Parameters

Parameter	Value	Unit
Macro-particles	$2 \cdot 10^6$	
Beam energy	150	MeV
Energy spread	50 (RMS)	Kev
Emittance	0.6 (RMS)	mm-mrad
Laser wavelength	40	µm
Laser pulse duration	500 (FWM)	fs
Laser pulse energy	10	µJ
Laser waist	2.5	mm
Deflecting frequency	2.998	GHz
Deflecting voltage	5	MV
Screen resolution	20 (RMS)	µm

Results of simulation are shown in Fig. 6. Fig. 6a shows the phase space after the interaction in the modulator (see Fig. 1) with the 40 µm laser. Fig. 6b shows the beam density distribution projected on the x-y plane at the end of the diagnostic beam line and it representing the screen image. The energy modulation is well evident as predicted above.

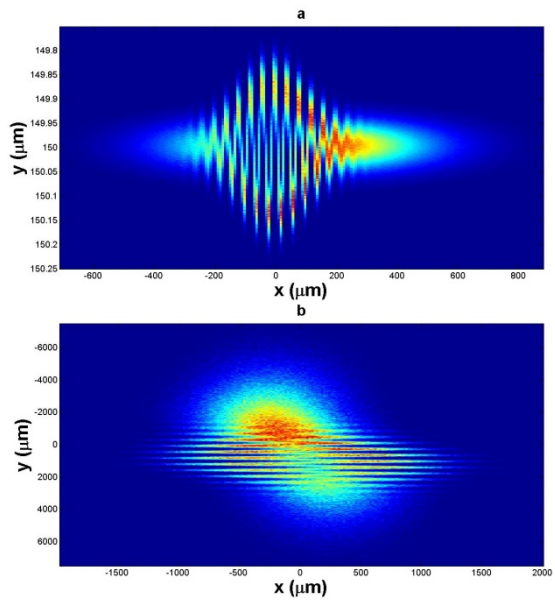


Figure 6: Top: Beam phase space after the interaction in the modulator (see Fig. 1) with the laser. Bottom: beam density distribution projected on the x-y plane at the end of the diagnostic beam line.

ISBN 978-3-95450-141-0

Copyright © 2014 CC-BY-3.0 and by the respective authors

We can now compere the beam energy modulation after the laser-electron interaction with the measurements on the screen. We can derive the beam energy modulation on the screen image by using the theoretical value of the calibration factor S (eq. 2) and of the horizontal dispersion at the screen location. Linear correlated energy spread induced by the deflector, LSC and CSR can be removed. The result is shown in Fig. 7 where the mean slice energy is plotted versus the slice longitudinal coordinate in the bunch. The red curve is the beam energy modulation derived by screen analysis (Fig. 6b) and the blue is the energy modulation present on the beam after the laser-electron interaction in the modulator (Fig. 6a). The agreement between the two curves is good.

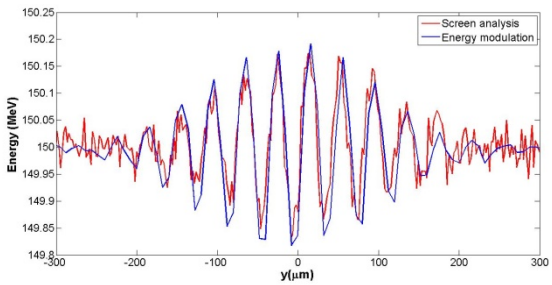


Figure 7: Beam energy modulation derived by the measurement analysis (red) compared with the one gained in the modulator (blue).

ENERGY MODULATION START UP

The interaction between the laser and the electron in the modulator requires a temporal and a spatial alignment of the two beams. The diagnostics so far described can be used to find the effects of the laser-electron interaction during these procedures.

A spatial pre-alignment can be done by aligning the long wavelength laser (30-50 μm) beam with the 800 nm laser that will be used in the seeding experiments [1] and aligning this laser beam with the electron beam on two OTR [14] or CROMOX (Al2O3:Cr) [15] screens placed at both ends of the modulator. Alternatively two OTR screens can be used to image directly the long wavelength laser beam and the electrons using a Pyro electric Array Camera instead of a CCD to look at the two screens. We have performed the same simulation of the energy modulation adding a transverse off-set and a tilt to the laser respect to electron beam trajectory in the modulator in order to estimate the required alignment tolerances. Figure 8 shows the phase space imaged on the screen when there are off-sets of 2 mm between the laser and the electron beam in both planes and the laser trajectory is tilted by 0.002 rad respect to the electron beam trajectory tilt. The laser modulation is still well evident. We can quantify these values of off-sets and tilt as the requirements for the initial alignment between the laser and the electron beam. This level of alignment can be reached rather easily with the pre-alignment. The alignment can be improved after having established the interaction using remote movable mirror to maximize the energy modulation on the screen.

In the same way a coarse overlapping (with an accuracy of 200-300 ps) in time between the two beam can be established recording on the same oscilloscope a signal for the electron beam coming from a BPM pickup and a signal for the laser from a photodiode placed on an optical table in the linac tunnel closer possible to the modulator and to each other. The temporal overlapping can be adjusted by scanning a delay line for the laser while observing the spectrometer screen.

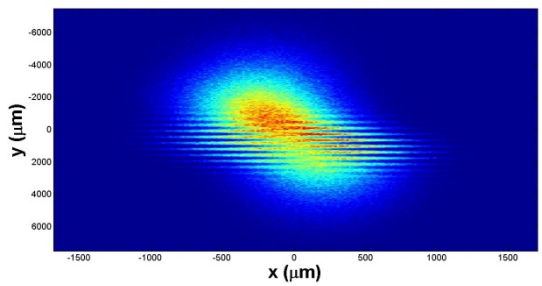


Figure 8: Beam imaged on the spectrometer screen as obtained by a simulation with the code Elegant for the parameter reported in Tb. 1 adding a relative laser-electron beam misalignment of 2 mm in both planes at the entrance of the undulator and a tilt of 2 mrad for the laser trajectory.

STUDY OF THE FEL INTERACTION

Recently a method to study FEL pulse length and fel intensity using a defector and an electron beam spectrometer has been proposed and applied to LCLS experiments [16, 17]. The beam phase space is measured with the FEL on and the FEL off. The application of the energy conservation principle permits to measure the temporal profile of the FEL pulse (E. vs t.) from the changes in the slice mean energy and energy spread induced by the lasing.

The diagnostics described above can be used to study the electron beam phase space with the FEL process on and off to apply this method. In this case the radiators are closed and the intra-radiator qudrupoles are set to ensure beta values required by FEL. We can use the quadrupoles placed after the last radiator to optimize the diagnostics resolutions according to eq. 4 and eq. 5. A quadrpupole in the middle of the afterburner has been considered in this case. A possible solution for the optics between the last radiator and the spectrometer screen is shown in Fig. 9. The vertical betatron functions at the deflector and at the screen are 60 m and 0.95 m respectively. The calibration factor S, for a defecting voltage of 5 MV and a RF frequency of 2.998 GHz, is ~16.2. The horizontal beta and dispersion at the screen are 1m and 0.6m.

Copyright © 2014 CC-BY-3.0 and by the respective authors

ISBN 978-3-95450-141-0

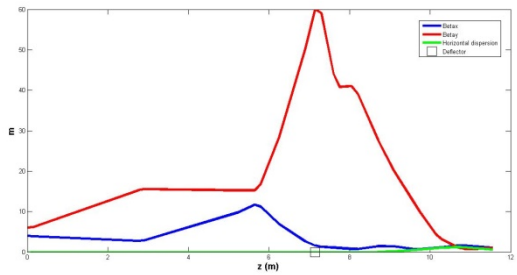


Figure 9: Possible optics from the exit of last radiator to the screen.

For this solution a longitudinal resolution of 3.3 μm and an energy resolution of 105 Kev are predicted by equations 4 and 5. A value of IC close to 0.5 is obtained for two features in the beam distribution separated by a distance of 10 μm as can be seen in Fig. 10.

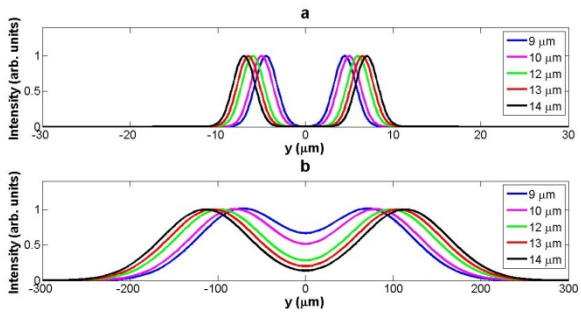


Figure 10: Top: longitudinal test distributions. Bottom: Vertical profiles at screen.

Simulations including the FEL process, using the codes GENESIS [18] and ELEGANT, will be performed.

CONCLUSIONS

We have presented results on the viability of post-FEL diagnostics on CLARA to study the phase space of the beam after the beam energy modulation required by mode locking and sliced FEL schemes. Their expected performance and simulations of their utilization have been presented.

ACKNOWLEDGEMENTS

This work is funded by STFC (Science and Technology Facilities Council, UK). We thank S. Di Mitri, P. Williams and N. Thompson for the careful reading and suggestions.

REFERENCES

[1] J. A. Clarke et al., JINST **9**, 05 (2014).
[2] A.A. Zholents, W.M. Fawley, Phys. Rev. Lett. **92**, 224801, (2004).
[3] E. Kur, D.J. Dunning, B.W.J. McNeil, J. Wurtele, A.A. Zholents, New J. Phys. **13**, 063012 (2011).
[4] D.J. Dunning, B.W.J. McNeil, N.R. Thompson, Phys. Rev. Lett. **110**, 104801 (2013).
[5] E.L. Saldin, E.A. Schneidmiller, M.V. Yurkov, Phys. Rev. ST Accel. Beams **9**, 050702 (2006).
[6] N. R. Thompson, B.W.J. McNeil, Phys. Rev. Lett. **100**, 203901 (2008).
[7] L. Giannessi et al., Phys. Rev. Lett. **106**, 144801 (2011).
[8] G. A. Loew, O.H. Altenmueller, SLAC, PUB-135, Aug. (1965).
[9] Y. Ding et al., "Ultra-short electron bunch and X-ray temporal diagnostics with an x-band transverse deflecting cavity", in Proc. 1st Int. Beam Instrumentation Conf., Tsukuba, Japan Accelerator (2012), TUPA41.
[10] Y. Ding et al., "Commissioning of the X-band Transverse Deflector for Femtosecond Electron / X-Ray Pulse Length Measurements at LCLS", in Proc. 4th Int. Particle Accelerator Conf., Shanghai, (2013), WEOBB201.
[11] M. Cornacchia, P. Emma, Phys. Rev. ST Accel. Beams **5**, 084001 (2002).
[12] P. Craievich et al., "A transverse RF deflecting cavity for FERMI@elettra project", in Proc. 8th European Workshop on Beam Diagnostics and Int. for Particle Accelerator Conf., Venice, (2007), TUPC10.
[13] M. Borland, ANL/APS Report No. LS-287 (2000).
[14] Z. Huang et al., Phys. Rev. ST Accel. Beams **13**, 020703 (2010).
[15] S. Spampinati et al., "Commissioning of the FERMI@ELETTRA Laser Heater", in Proc. 34th International Free-Electron Laser Conference, Nara, (2012), MOPD58.
[16] Y. Ding et al., Phys. Rev. ST Accel. Beams **14**, 120701 (2011).
[17] C. Behrens at al., Nature communications **5**, 3762 (2014).
[18] S. Reiche et al., Nucl. Instrum. Methods Phys. Res., Sect. A 429, 243 (1999).

Copyright © 2014 CC-BY-3.0 and by the respective authors

ISBN 978-3-95450-141-0

NEW MTCA.4-BASED HARDWARE DEVELOPMENTS FOR THE CONTROL OF THE OPTICAL SYNCHRONIZATION SYSTEMS AT DESY*

M. Felber#, M. K. Czwalinna, H. T. Duhme, M. Fenner, C. Gerth, M. Heuer, T. Lamb, U. Mavrič, J. Mueller, P. Peier, H. Schlarb, S. Schulz, B. Steffen, C. Sydlo, M. Titberidze, T. Walter, R. Wedel, F. Zummack, DESY, Hamburg, Germany
J. Szewinski, NCBJ, Świerk, Poland
T. Kozak, P. Prędki, K. Przygoda, TUL-DMCS, Łódź, Poland
E. Janas, ISE-WUT, Warsaw, Poland

Abstract

The optical synchronization group at DESY is operating and continuously enhancing their laser-based synchronization systems for various facilities which need femtosecond-stable timing. These include the free-electron lasers FLASH and the upcoming European XFEL as well as the electron diffraction machine REGAE (Relativistic Electron Gun for Atomic Exploration) and the future plasma acceleration test facilities (LAOLA and FLASHforward). One of the major upgrades under development is the migration of the entire electronic control hardware to the new MTCA.4 platform which was introduced as the new standard for accelerator control in many facilities worldwide. In this paper we present the applied modules and the topology of the new systems. Main advantages are a compact design with higher performance, redundancy, and remote management.

INTRODUCTION TO MTCA.4

MTCA is a novel electronic framework derived from the Advanced Telecommunication Computing Architecture (ATCA) [1]. MTCA.4 was released as an official standard by the PCI Industrial Manufacturers Group (PICMG [2]) in 2011 and is supported by the xTCA for physics group, a network of physics research institutes and electronics manufacturers. Its main improvements over the preceding standards are enhanced rear I/O connectivity and provisions for improved precision timing. MTCA.4 has inherited many of the advantages of ATCA including capabilities for remote monitoring, remote maintenance, hot-swap of components, and the option to duplicate critical components, making the standard highly modular and flexible. It also made the outstanding signal processing performance of ATCA systems more affordable and less demanding in terms of space requirements and energy consumption.

Major accelerator facilities worldwide currently evaluate the deployment of MTCA.4-based Low-Level Radio Frequency (LLRF) systems, either for extensions or upgrades of existing infrastructure or for the initial equipment of new facilities.

*This work has partly been funded by the Helmholtz Validation Fund Project MTCA.4 for Industry (HVF-0016)
#matthias.felber@desy.de

MTCA.4 System Architecture

A picture of an equipped MTCA.4 system is shown in Figure1. Fundamental components are the chassis which is available in different form factors and sizes, the power supply, a crate management controller (MCH), and CPU and hard drive.

For user applications specific analog and digital processing cards are used. From the front Advanced Mezzanine Cards (AMC) are inserted to the crate. There are various connections on the backplane which provide e.g. Gigabit Ethernet and PCI Express links between the slots and the MCH, dedicated clock and trigger distribution lines, and point to point links between the slots for fast real time communication between the cards. Additionally, there is the possibility to insert cards from the rear of the crate, so-called Rear Transition Modules (RTM) which connect to the according AMC board via the Zone 3 connector. This connection provides 60 differential pairs for analog or digital signals, which will be defined in the standard [3]. Often the cards have connectors for additional industrial standard piggy back boards like FPGA Mezzanine Cards (FMC) or IndustryPack (IP) modules.

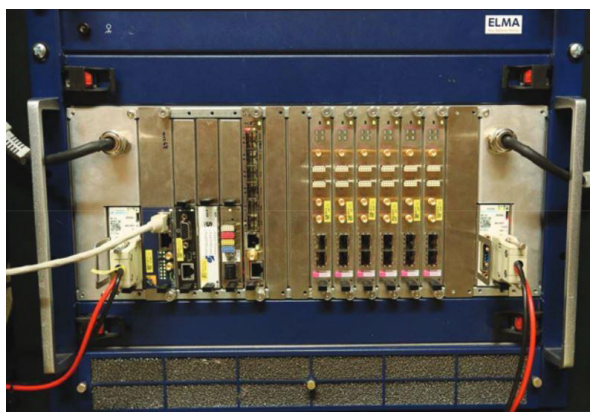


Figure 1: MTCA.4 crate equipped with AMC cards.

MTCA.4 AT DESY

In broad agreement between the involved groups, it was decided to use the MTCA.4 standard for the control electronics of the European XFEL. This involves the LLRF field control [4], timing system, diagnostics like beam position monitors [5] and camera readouts, and the optical synchronization system [6].

Copyright © 2014 CC-BY-3.0 and by the respective authors

ISBN 978-3-95450-141-0

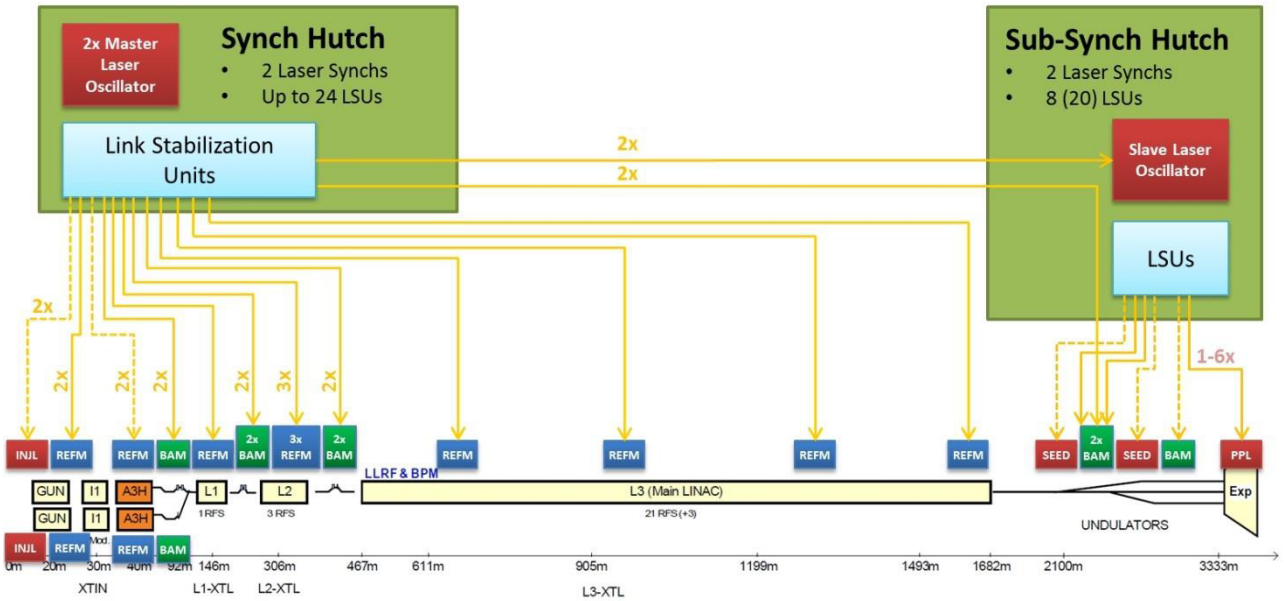


Figure 2: Schematic view on the optical synchronization system at the European XFEL.Up to 24 stabilized fiber links serve for laser synchronization, bunch arrival time monitor stations and RF reference generation modules. The sub-synch hutch located in the experimental hall serves further end stations.

In the course of the developments required for fulfilling the demanding tasks, the standard was further adapted and improved. Naturally also other facilities at DESY like for example the free-electron laser FLASH and the electron diffraction machine REGAE [7] migrate to MTCA.4.

In order to facilitate the development of new boards for extending the portfolio of applications and to ensure the availability of spare parts, DESY took the initiative for a better establishment of the MTCA.4 standard in industry. With substantial funding from the Helmholtz Association for a two-year validation project, DESY has developed novel, fully MTCA.4-compliant components to lower the barriers to adoption in a wide range of industrial and research use scenarios [8].

Most designs are licensed to industry partners who offer those components to their customers. This way it is easy for other institutes and companies to make use of the sophisticated designs (e.g. high speed digital or low noise analog cards) without the need for own developments or additional agreements.

THE OPTICAL SYNCHRONIZATION SYSTEMS AT DESY

FLASH was the first large scale accelerator facility worldwide using a laser-based synchronization system which was deployed in 2008/2009 [9, 10]. For the upcoming European XFEL a similar system is foreseen, scaled to the larger distances and incorporating major improvements. In both cases it provides a reference distribution on a femtosecond level in order to allow time resolution of pump-probe experiments with ultra-short FEL pulses [6].

The main applications of the optical synchronization system are precise bunch arrival time monitors (BAMs), synchronization of external lasers like the pump-probe laser or for FEL seeding, and provision of a precise reference for the LLRF system.

In smaller facilities like REGAE such a complex laser-based reference distribution is not applicable. Nevertheless they benefit from the developments e.g. for laser synchronization and especially the MTCA.4 hardware progress [7].

Synchronization System Architecture

A schematic representation of the synchronization system is shown in Figure 2. The master-oscillator (MO, not shown in the figure) distributes a stabilized 1.3 GHz reference to which the master laser oscillator (MLO), with a repetition rate of 216.7MHz (a sixth of the MO frequency), is locked. The MLO is a passively mode-locked erbium laser oscillator, emitting 200 fs long pulses at the telecom wavelength of 1.55 um. The stabilized pulse train from the MLO is split into multiple channels and guided to the individual link stabilization units (LSUs) through the free-space distribution (FSD). Each LSU actively stabilizes the effective length and therefore the transit time of its assigned optical link fiber, which can be conveniently guided through the entire FEL to stations obliged to femtosecond timing stability. Recently the stabilization of a 3.6 km long fiber link to 3.3 fs rms and 15 fs peak to peak (measured with an independent out-of-loop detector) was demonstrated over 25 hours. The link was operated under realistic conditions, laid out in an uncontrolled ambient environment [6].

ISBN 978-3-95450-141-0

Copyright © 2014 CC-BY-3.0 and by the respective authors

Bunch Arrival Time Monitor

The BAM uses a broadband pickup signal induced by the electron bunch which is sampled by the optical pulses of the synchronization system in an electro-optic modulator (EOM). Arrival time deviations modulate the amplitude of the optical pulse train. This amplitude modulation is converted to an electrical signal and read out with fast ADCs for further processing. This information can be used directly by the FEL experiments and it is used for a fast feedback to the LLRF system for correcting the amplitude of the accelerating modules with a low latency of only a few microseconds. The resolution of the BAM is charge dependent but typically in the order of a few femtoseconds even for bunch charges < 100 pC [11]. By this means the relative arrival time jitter of the FEL is reduced to 20 fs rms [12].

Laser Synchronization

The output of a stabilized fiber link serves as a reference for the synchronization of remote mode-locked laser oscillators. This happens usually in two steps: In the first step an RF signal is generated from each of both pulse trains of the reference and the oscillator. These are compared in an RF mixer (down converter) which provides an error signal proportional to the phase difference of the two inputs. A digital feedback controller stabilizes this phase difference by acting on the frequency/phase of the oscillator [13]. In a second step the two optical pulse trains are compared in a balanced optical cross correlator (OXC). This device combines the pulses in a non-linear crystal to generate second harmonic light whose amplitude is proportional to the timing difference. This information is then again used to stabilize the timing of the oscillator with respect to the reference. While the RF lock provides maximum flexibility and robustness it suffers from limited performance due to the noise and drift of components like the photo detector. The OXC provides maximum sensitivity and therefore the lowest achievable jitter but has the disadvantage of limited operating range and is therefore more sensitive to disturbances. Preliminary measurements show that sub-10 fs rms stability can be sustained over long time periods [10].

RF Reference

The beam-based longitudinal feedback for the stabilization of the bunch train with the help of the BAMs can provide only small corrections and therefore relies on an intrinsically stable LLRF control. For this reason the reference to which the LLRF system compares the field probe signals from the accelerating cavities must be as stable as possible. Coaxial RF distribution or a simple photo detector conversion from the optical reference is not sufficient in terms of noise and drift. Therefore a new approach was developed at DESY which resulted in the design of so-called REFM-OPT modules [14, 15]. In these modules the stabilized optical reference is compared with the local LLRF reference in an EOM. Phase deviations between the two are converted to an RF signal amplitude. This is further processed with analog electronics such that only a baseband signal is read out by the digital feedback controller. The feedback loop acts on a vector modulator or phase shifter to stabilize the RF reference with respect to the optical reference. The control takes place in the so-called TMCB board which is not a MTCA.4 module. The long-term stability is below 4 fs peak-to-peak [15].

Laser Synchronization at REGAE and LAOLA

As the REFM-OPT module incorporates a low jitter and low drift "Microwave vs. Optical PhasE Detector" (MOPED) between an optical and an RF signal the scheme can be as well used to stabilize a mode-locked laser oscillator with respect to an RF reference when an optical reference is not available and therefore the OXC is not applicable. Several challenges have to be overcome in the redesign of the setup to adapt it from the convenient telecommunication wavelength to the Titan:Sapphire laser wavelength of 800 nm [16].

INTRODUCTION OF USED MTCA.4 MODULES

The hardware modules required for the different tasks in the optical synchronization systems like signal detection, sampling, processing, and actuating are mostly generic and applicable in different setups and configurations. Only for a few very specific tasks individual boards were designed.

In this chapter most of the used modules are introduced with a short description.

SIS8300 Versatile FPGA (Virtex 5) AMC board with 10 channel 125 MSPS 16 bit ADCs and 2 fast DACs, developed in co-operation between DESY and the industry partner Struck GmbH [17].

FMC25 Versatile FPGA (Virtex 5) AMC board for data processing and FMC carrier with two high pin count FMC slots [18]. The board was developed at DESY and licensed to the company CAEN ELS d.o.o. [19].

FMC20 Low-cost FPGA (Spartan6) AMC board for interfacing with actuator modules and FMC carrier with two FMC slots. The board was developed at DESY and licensed to the company eicSys GmbH [20].

AD84 Generic analog IO RTM board with 8 channel 10 MSPS 16 bit ADCs and 4 channel DACs. The board was developed at DESY, not yet licensed to an industry partner [1].

DWC8300 10 channel low-noise down converter RTM board (0.7 GHz – 4 GHz). The board was developed at DESY and licensed to the company Struck GmbH [17].

PZT4 Generic 4 channel piezo driver and piezo sensor RTM board with switchable output range (up to ±80 V), internal DAC or external input, and internal or

Copyright © 2014 CC-BY-3.0 and by the respective authors

ISBN 978-3-95450-141-0

external power supply [21]. The board was developed at DESY and licensed to the company eicSys GmbH [20].

MD22 2 channel stepper motor driver FMC board with end-switch and encoder readout. The board is capable of driving up to 1.8 A coil current and supports 256 micro steps. It was developed at DESY and is licensed to the company eicSys GmbH [20].

AD16 Generic ADC FMC board with 16 channels up to 200 kSPS and 18 bits resolution. The board was developed at DESY and is not yet licensed to an industry partner [1].

LASIO Versatile, general purpose, low-cost IO FMC board with 39 IO pins. Each pin can be assigned to digital IO, gnd or alternate function like ADC, DAC, power supply, or UART (12 V) via Xilinx CPLD. The board was developed at DESY, not yet licensed to an industry partner [1].

DSBAM FMC board specially designed for the BAM readout. It incorporates 4 ADCs for two channel interleaved sampling at up to 250 MSPS with 16 bit resolution, and has photo diodes and clock generation on board [18].

SFP4 Generic 2-4 channel SFP+ GbE or fiber transmission FMC board. Board was developed at DESY, not yet licensed to an industry partner [1].

LASY RTM board under development at DESY specially for laser synchronization purposes. It is based on the down converter design but incorporates many laser specific inputs and features.

TOPOLOGY OF THE SYSTEMS

Laser Synchronization Electronics

The laser synchronization development is the most advanced and already used permanently at REGAE and at the third FLASH injector laser albeit with limited features compared to the anticipated final setup [7].

The RF signal generated from the laser pulse train is down-converted in the DWC8300 to an intermediate frequency which is sampled by the SIS8300. Additionally the baseband signal from an OXC or MOPED setup is fed to a second ADC. After phase detection and signal processing the feedback controller output is digitally transferred to the next slot in the crate where it is received by the FMC20. From here the PZT4 is addressed to drive the piezo in the laser cavity. If the required tuning exceeds the piezo range a coarse tuning step has to be performed. For the MLOs and the pump-probe lasers of the European XFEL (tuned by internal temperature change) this is done via the LASIO board, in all other cases the coarse tuning is done with a delay stage within the laser cavity driven by a stepper motor via the MD22.

Additional inputs of the down converter and later the LASY are used for bucket detection to set the correct absolute timing and for some other required monitoring and control signals.

For remote control the LASIO additionally provides all needed features for monitoring and driving the MLO's controller unit and for driving beam shutters.

As the PZT4 is capable of driving more than one piezo also laser oscillators with two piezos and/or two lasers oscillators can be synchronized with no additional hardware.

Fiber Link Stabilization Electronics

For serving the LSUs MTCA.4 offers a very compact and efficient solution because four links can be stabilized with only two slots in the crate. The heart of the LSU is an OXC whose signal is sampled by the AD84 (2 ADC channels per link). The processing is done with the FMC25 which computes the feedback controller output and, similar to the laser application, transmits the required actuator action to the FMC20. Again, this board addresses the piezo driver in the rear which drives a piezo-based fiber stretcher to compensate for the detected timing change in the link fiber by stretching a piece of it. Also here a delay stage is required for coarse tuning when the piezo stretcher reaches its limit. The delay stage is driven by the MD22. For a complete set of four LSUs all eight ADC inputs from the AD84, all four piezo driver outputs from the PZT4, and all four motor drivers on two MD22 FMCs mounted on the FMC20 are used.

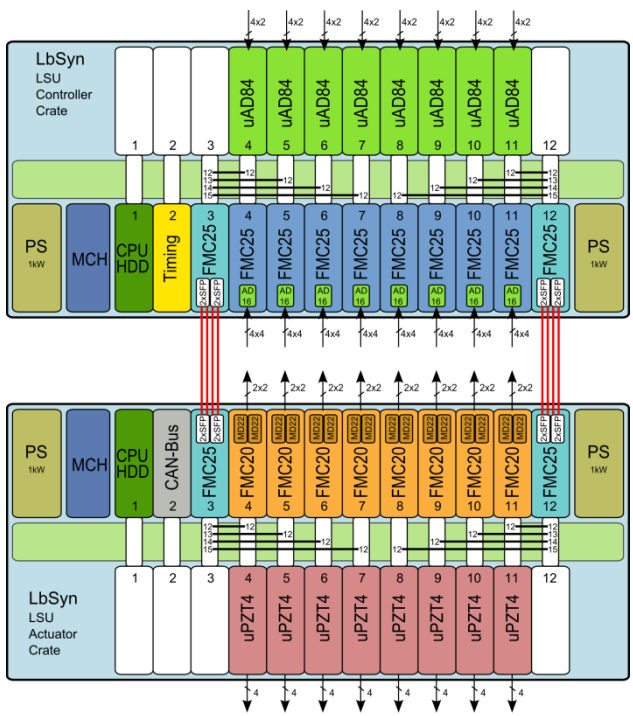


Figure 3: MTCA.4 setup for controlling up to 32 LSUs.

Additionally, the AD16 FMC mounted on the FMC25 carrier collects slow monitor signals like optical power levels and backup phase detector signals. Four slow ADC

ISBN 978-3-95450-141-0

Copyright © 2014 CC-BY-3.0 and by the respective authors

channels are available and used for one LSU, again fitting perfectly to the 16 channel ADC when controlling and monitoring four LSUs simultaneously.

In the baseline design of the European XFEL 23 LSUs are foreseen with the possibility for upgrades to more units. Despite the compact design this requires 12 crate slots which are not available as two slots are used by a timing module and the CPU. For this reason and to avoid distortions on the sensitive OXC detector signals by electromagnetic interference from the actuators (piezo = high voltage, stepper motor = sharp current spikes) the planned design foresees to physically separate the detector unit comprised of AD84 and FMC25+AD16 from the actuator unit comprised of FMC20+2xMD22 and PZT4. Figure 3 shows a schematic view of the complete setup ready for controlling max. 32 LSUs. The communication between the detector and the actuator crate is done via a FMC25 concentrator, collecting the signals from up to four FMC25 controller boards and sending them via a SFP4 module to the corresponding SFP4 on the FMC25 receiver board. From here the signals are distributed again to the FMC20 boards driving the actuators. To minimize the latency the complete communication happens via low latency point-to-point links on the crate backplane and direct fiber connections between the two SFP4s.

BAM Readout Electronics

The amplitude modulated laser pulses from the electro-optical BAM frontend setup are guided in fibers to the photo detectors placed on the DSBAM FMC module. Here, a sampling clock for the fast ADCs used for probing the pulse amplitudes is extracted. The FMC is placed on a FMC25 for processing the ADC data. Fast low-latency links are provided via SFP modules on the DSBAM to ship the arrival time information to the LLRF station for beam-based feedback correction.

Additionally, an FMC20 carrier with two MD22 motor driver cards is used to drive the delay stages in the BAM frontend.

CONCLUSION

The design topology of hardware modules required for signal detection, analog and digital processing and actuating in the optical synchronization systems was introduced. The systems are partly in the prototype state and partly already applied in the facilities. Further tests and the design and improvement of firmware and high level software i.e. control system servers is pursued in a couple of test setups. Within the next year the presented systems will be operational in FLASH, the European XFEL and other facilities.

REFERENCES

[1] MTCA website: http://mtca.desy.de
[2] PICMG website: http://www.picmg.org
[3] DESY, “Zone 3 Connector Pin Assignment Recommendation”; http://mtca.desy.de/recources/zone_3_recommendation/index_eng.html
[4] J. Branlard et al., “The European XFEL LLRF System”, IPAC 2012, MOOAC01
[5] F. Schmidt-Foehre et al., “First Tests with the Self-triggered Mode of the New MicroTCA-based Low-charge Electronics for Button and Stripline BPMs at FLASH”, IPAC 2014, THPME117
[6] C. Sydlo et al., “Femtosecond Timing Distribution for the European XFEL”, FEL 2014 THP090
[7] M. Felber et al., “Laser Synchronization at REGAE using Phase Detection at an Intermediate Frequency”, IPAC 2012, WEPPD048
[8] T. Walter et al., “Novel Crate Standard MTCA.4 for Industry and Research”, IPAC 2013, THPWA003
[9] F. Loehl et al., “Electron Bunch Timing with Femtosecond Precision in a Superconducting Free-Electron Laser”, Phys. Rev. Lett. 104, 144801 (2010)
[10] S. Schulz et al., “Past, Present and Future Aspects of Laser-Based Synchronization at FLASH”, IBIC 2013, WEPC32
[11] M. K. Czwalinna et al., “Performance Study of High Bandwidth Pickups Installed at FLASH and ELBE for Femtosecond-Precision Arrival Time Monitors”, FEL 2014, THP069
[12] C. Schmidt et al., “Feedback Strategies for Bunch Arrival Time Stabilization at FLASH Towards 10 fs”, FEL 2011, THPA26
[13] M. Felber et al., “Compact MTCA.4 Based Laser Synchronization”, IPAC 2014, TUPRI107
[14] E. Janas et al., “Design and Integration of the Optical Reference Module at 1.3 GHz for FLASH and the European XFEL”, IPAC 2014, WEPRI115
[15] T. Lamb, et al., “Femtosecond stable laser-to-RF phase detection for optical synchronization systems”, IBIC 2013, TUPC33
[16] M. Titberidze et al., “Novel Femtosecond Level Synchronization of Titanium Sapphire Laser and Relativistic Electron Beams”, IBIC 2014, MOPD12
[17] http://www.struck.de
[18] J. Szewinski et al., “MTCA Upgrade of the Readout Electronics for the Bunch Arrival Time Monitor at FLASH”, ICALEPCS 2013, THPPC140
[19] http://www.caenels.com
[20] http://eicSys.de
[21] K.P. Przygoda et al., “MTCA.4 Module for Cavity and Laser Piezo Operation”, IPAC 2014, THPRO105

Copyright © 2014 CC-BY-3.0 and by the respective authors

ISBN 978-3-95450-141-0

A DOUBLE-PRISM SPECTROMETER FOR THE LONGITUDINAL DIAGNOSIS OF FEMTOSECOND ELECTRON BUNCHES WITH MID-INFRARED TRANSITION RADIATION *

S. Wunderlich†, E. Hass, M. Yan and B. Schmidt, DESY, 22603 Hamburg, Germany

Abstract

Electron bunch lengths in the sub-10 fs regime and charges of a few tens of picocoulombs are parameters required for free-electron lasers [1] and are also a consequence from the intrinsic process in laser-driven plasma wake field acceleration [2]. Since the coherent spectrum of transition radiation of these bunches carries the information on the longitudinal bunch profile in the form factor, the spectroscopy of transition radiation is an attractive method to determine the electron bunch length. A double-prism spectrometer has been developed and demonstrated for the single-stage measurement of mid-infrared transition radiation between 2 µm and 18 µm. The spectrometer facilitates single-shot spectral measurements with high signal-to-noise ratio utilising a line array of mercury cadmium telluride detectors. In this contribution, we present the spectrometer and measurements of electron bunches at the Free-Electron Laser in Hamburg (FLASH) at DESY. The results are compared to established bunch length monitors which are a multi-stage grating spectrometer for transition radiation and a transverse deflecting structure accessing the longitudinal phase space of the electron bunches directly.

DIAGNOSIS OF ELECTRON BUNCHES WITH COHERENT RADIATION

The coherent spectrum of characteristic radiation from relativistic and charged particle bunches carries the information on the three-dimensional current profile encoded in the form factor. In other words, the complex form factor F yields the wavelength-dependent level of coherence in the emission of radiation, like coherent diffraction radiation (CDR), coherent synchrotron radiation (CSR) and coherent transition radiation (CTR). This project focuses on the latter, CTR.

Spectral Intensity of Coherent Radiation

The spectral intensity $U = U(\omega,\Omega)$ of transition radiation (TR) per solid angle Ω and wavelength ω can be described by

$$\frac{\mathrm{d}^2U}{\mathrm{d}\omega\,\mathrm{d}\Omega} \approx \frac{\mathrm{d}^2U_1}{\mathrm{d}\omega\,\mathrm{d}\Omega}\, N^2\, |F(\omega,\Omega)|^2 \qquad (1)$$

with, expressing the nature of coherent emission, the number of radiating particles squared, N^2, and the single-particle contribution U_1 [3]. The modulus of the complex form factor is denoted by $|F\,(\omega,\Omega)|$.

* The project has been supported by the BMBF under contract 05K10GU2 & FS FLASH 301.

† steffen.wunderlich@desy.de

Form Factor

The complex form factor

$$F = F\,(\omega,\Omega) = |F\,(\omega,\Omega)|\exp\,(i\Phi\,(\omega))$$

is the Fourier transform of the three-dimensional normalised charge density $\rho_{3\mathrm{D}}(\vec{r})$ in position space and can be expressed, at an observation distance much larger than the electron bunch extension, by

$$F(\omega,\Omega) = F(\vec{k}) = \int_{-\infty}^{\infty} \rho_{3\mathrm{D}}(\vec{r})\ \exp(-i\,\vec{k}\,\vec{r})\,\mathrm{d}\vec{r}.$$

A decomposition of $F(\omega,\Omega)$ into transverse and longitudinal components, F_t and F_l, is justified for a negligible coupling of the two planes [4].

The longitudinal form factor $F_l = F_l(\omega)$ now reflects a charge density in the direction of the movement of the high-relativistic particles

$$F_l = \int_{-\infty}^{\infty} \rho_l(t)\ \exp(-i\,\omega\,t)\,\mathrm{d}t \qquad (2)$$

Due to the high-relativistic motion of the particles, the influence of the transverse form factor is strongly suppressed. This allows to approximate $F(\omega,\Omega)$ by $F_l(\omega)$ in Equation (1) for sufficiently small transverse beam sizes [3].

Utilising F for Estimating the Bunch Length

Figure 1 shows examples of form factors on the beam axis of electron bunches with lengths (σ_l) in the femtosecond regime between 0.5 µm (≈ 1.5 fs) and 3 µm (≈ 10 fs). As depicted, the form factor shows a strong modulation with bunch length in the wavelength range between 2 µm and 20 µm. Hence, this range has been chosen for the region of interest of the prism spectrometer described in the following section.

According to Equation (2), the determination of the absolute value and the slope of the modulus of the form factor, $|F_l|$, allows the estimation of the bunch length and moreover, a time-domain current profile. However, the spectral phase $\Phi(\omega)$ of the complex form factor F cannot be acquired by intensity spectroscopy. Underlying several constraints, phase-retrieval processes [5–7] can access a possible temporal current profile and show an impressive accordance with direct time-domain diagnostics like a transverse deflecting structure (TDS) [4].

DOUBLE-PRISM SPECTROMETER

Compared to grating-based spectrometers, prism spectrometers yield bulk absorption in the prisms, but provide

ISBN 978-3-95450-141-0

Copyright © 2014 CC-BY-3.0 and by the respective authors

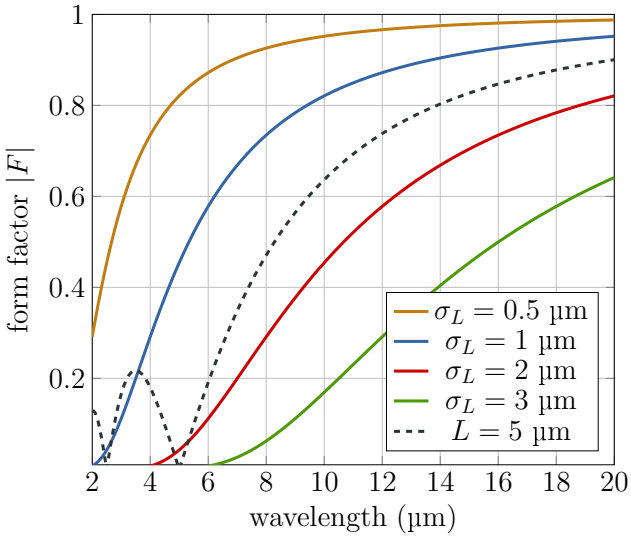


Figure 1: Examples of form factors on the beam axis resulting from a temporal Gaussian shape (*solid*) and rectangular shape (*dashed*) for widths σ_L and total length L, respectively, in the femtosecond regime.

a continuous dispersion without higher orders. For mid-infrared wavelengths, the polycrystalline compounds *KRS-5*, thallium bromo-iodide, and *zinc selenide* (ZnSe) offer a sufficient dispersion at a refractive index $n > 2.3$. In contrast to other prism spectrometer setups for beam diagnostics with coherent radiation [8,9], this particular spectrometer utilises an arrangement of two ZnSe prisms, as illustrated in Fig. 2, to achieve an integrated linear dispersion in the detector focal plane of approximately 32 mm for the wavelength range between 2 µm and 18 µm.

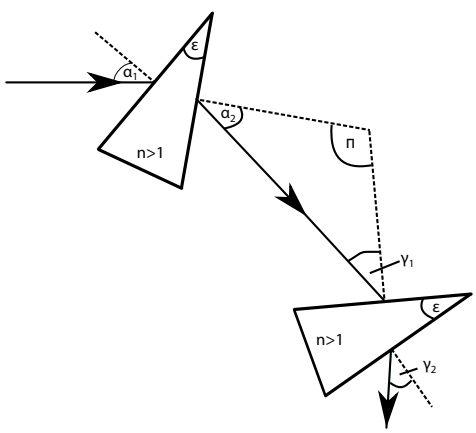


Figure 2: Schematic of the dispersive stage consisting of two consecutive ZnSe prisms.

The spectrometer is equipped with a 32 mm-wide line array of 128 mercury cadmium telluride (MCT) photoconductive detector elements [10], which is attached to a liquid nitrogen dewar to preserve a temperature of 77 K for low-noise operation. For mid-infrared wavelengths, MCT detectors yield a signal-to-noise ratio larger by a factor of 100 compared to pyro-electric radiation sensors utilised in similar spectrometers.

A chain of analogue and digital electronics, including a gated boxcar integrator and a built-in analogue-to-digital converter (ADC), allows a parallel and single-shot data acquisition up to a repetition rate of 50 kHz [11].

Response Function

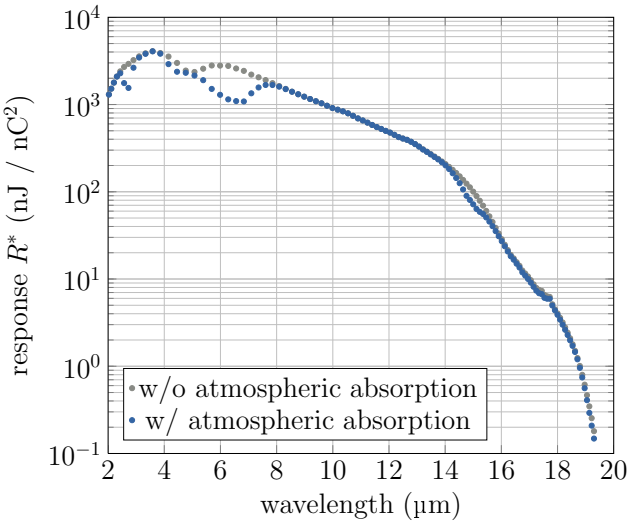


Figure 3: Spectrometer response function R^*.

The determination of the absolute form factor modulus imposes the knowledge of the so-called *response function*, $R = a \cdot R^*$, which expresses the connection of the detector signal, a digitised voltage amplitude, with the absolute TR intensity expected at the detector.

The function R^* covers the process of imaging of the source, driven by N particles with elementary charge e, onto the detector plane and the dispersive process due to the two prisms. In addition, transmissive and reflective losses of the bulk material and the ambient air have been considered. For the latter, data from the HITRAN database [12] have been used.

The response function is depicted in Figure 3, also showing the influence of 3.1 m of ambient air in the free-space beam transport onto the spectrum.

The second important constituent of R is the absolute intensity calibration a of the detector unit. The factor $a = G \cdot R_{\text{abs}}$ provides the conversion of the detector voltage signal S into an absolute irradiated intensity, R_{abs}, in units of Volts/Joules, times a *gain factor* G accounting for a variable electronic signal amplification.

$$|F| = \frac{1}{N\,e}\sqrt{\frac{S}{a \cdot R^*}} \tag{3}$$

Since the absolute detector calibration a is not yet available for mid-IR radiation pulses with pulse durations $\ll 1$ ns, a cross-calibration with a grating spectrometer with calibrated pyro-electric detectors will be performed. Details

Copyright © 2014 CC-BY-3.0 and by the respective authors

ISBN 978-3-95450-141-0

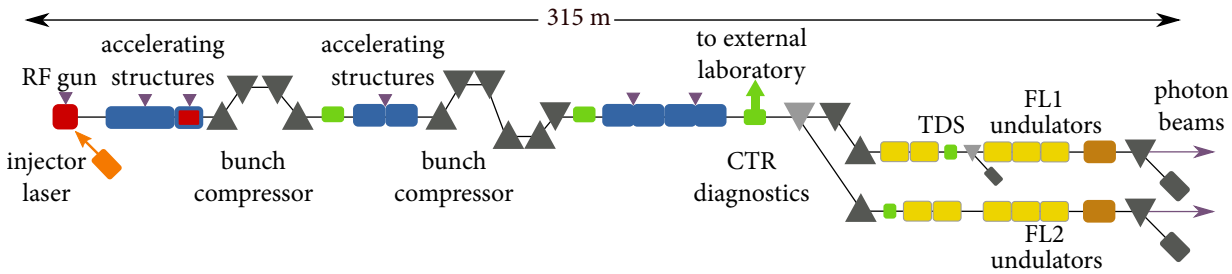


Figure 4: Overview of the FLASH FEL facility with the undulator beamlines FLASH1 (FL1) and FLASH2 (FL2). The locations of longitudinal diagnostics are indicated in *green*. Details can be found in [13].

will be presented later in this contribution. A calibration at an intensity and wavelength standard is in preparation.

EXPERIMENTAL SETUP

Measurements with the double-prism spectrometer have been taken at the free-electron laser (FEL) facility FLASH, at DESY in Hamburg, Germany [14]. The FLASH linear accelerator provides electron bunch trains with an energy up to 1.2 GeV, charges from a few tens of picocoulombs up to several nanocoulombs and electron bunch lengths down to < 50 fs at a repetition rate of 10 Hz. Due to the superconducting acceleration modules, the bunch trains can consist of a single bunch to 800 bunches at a spacing down to 1 µs.

The transition radiation source, consisting of a aluminium-coated silicon screen, is located at the end of the linac. The transverse beam size is approximately 200 µm (Gaussian, 1σ). The TR is guided into an external laboratory [15], where the double-prism spectrometer is accessible independently from the operation of the FEL. The beam transport line is kept in vacuum and sealed towards the spectrometer setup by a 3 mm thick zinc selenide window.

At the TR source, also a calibrated multi-stage grating spectrometer [3], CRISP4, is available. The dispersive section consists of two sets of four consecutive gratings spanning the wavelength range between (5 – 44) µm and (45 – 430) µm, respectively. The pyro-electric detectors utilised in the CRISP4 spectrometer are calibrated absolutely. As reported in [3] and [4], the measured form factors $|F|$ are in striking agreement with the transverse deflecting structure.

Referring to Figure 4, the transverse deflecting structure (TDS) at FLASH is located in front of the SASE undulators in the FLASH1 beamline, separated from the CTR source by electron beam transport and a dispersive section for energy collimation [16]. The TDS is a LOLA-type RF cavity [17] and offers a direct access to the time-domain current profile and the longitudinal phase space by streaking the bunch transversally, i.e. translating the longitudinal plane into a transverse plane, in combination with a dipole spectrometer.

MEASUREMENTS

The measurements presented in this section have been acquired in May 2014 complementary to studies of the CRISP4 spectrometer and the TDS.

Figures 5 and 6 depict the form factor modulus $|F|$ of measurements with the CRISP4 spectrometer and the double-prism spectrometer for two compression settings. The data of the latter diagnostic have been scaled according to Equation (3). The scaling factor a has been calculated for the two settings to $(5.47 \pm 0.68) \cdot 10^{-2}$ V/nJ and $(6.01 \pm 0.87) \cdot 10^{-2}$ V/nJ, respectively.

The form factors of the two spectrometers show a significant accordance in the range between 8.5 µm and 13.5 µm, which has been used to determine the scaling factor a. The striking similarity in the slope of $|F|$ and the values of a for the two settings within one standard deviation indicate an attractive performance of the prism spectrometer in comparison to the calibrated and established CRISP4. For these measurements, the peak signal-to-noise ratio in the double-prism spectrometer is approximately 200, while the pyro-electric sensors in CRISP4 are approaching their sensitivity limit, especially below approx. 10 µm.

At $\lambda = 8.77$ µm, a transition from the first to the second grating stage is visible in the CRISP4 signal [3]. The discontinuity in the CRISP4 trace can indicate an alignment issue. This is currently under investigation, as well as the discrepancy for wavelengths above 14 µm, where bulk absorption of zinc selenide has a significant contribution to the response function.

The bunch charges, measured with an integrated current transformer (ICT), are 232 pC (setting 1) and 146 pC (setting 2). The measurements have been taken at an electron beam energy of 970 MeV.

SUMMARY AND OUTLOOK

In this contribution, we present a double-prism spectrometer suitable for the longitudinal diagnosis of femtosecond electron bunches. The spectrometer is equipped with sensitive detectors extending a high signal-to-noise ratio to mid-infrared wavelengths. In combination with the double-prism design, the setup enables a single-stage measurement of coherent transition radiation in the wavelength range between 2 µm and 18 µm in a single shot.

The spectrometer has been set up and commissioned at the transition radiation source at FLASH at DESY. The results are in agreement with measurements of established diagnostics. A quantitative calibration in wavelength and intensity is currently in preparation.

ISBN 978-3-95450-141-0

Copyright © 2014 CC-BY-3.0 and by the respective authors

Thus, the spectrometer is qualified to face the challenges imposed by conventional and novel concepts of particle accelerators, both yielding bunch charges in the sub-10 pC regime and lengths below ten femtoseconds.

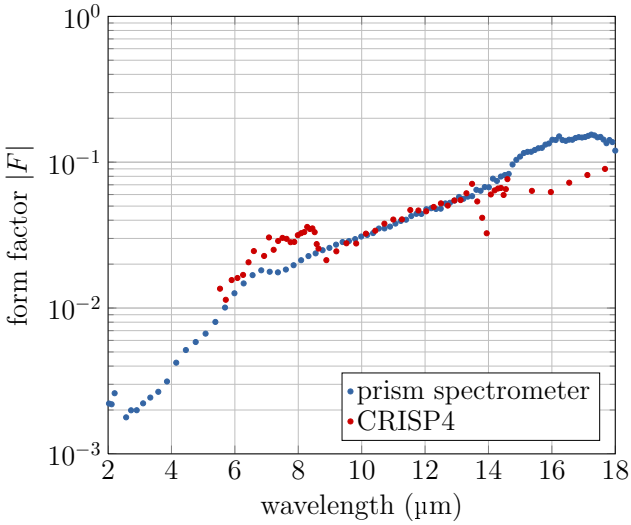


Figure 5: Comparison of the form factors at compression setting 1.

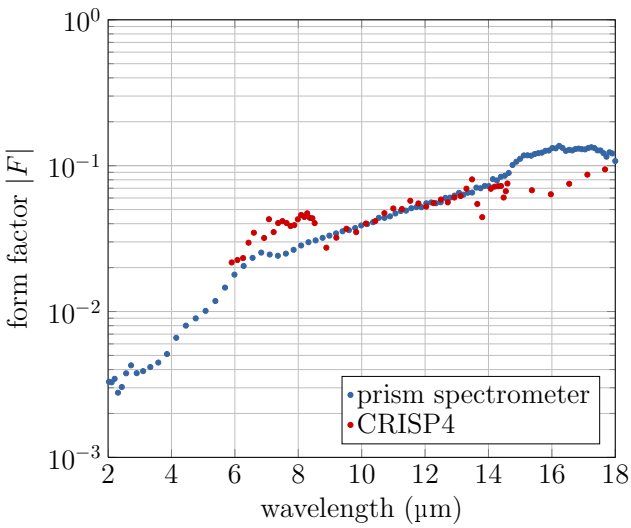


Figure 6: Comparison of the form factors at compression setting 2.

REFERENCES

[1] J. Rönsch-Schulenburg et al., Proceedings of FEL 2014, TUB04 (2014), to be published

[2] O. Lundh et al., Nature Physics 7, 219–222 (2011)

[3] S. Wesch et al., NIM A 665 (2011) 40–47

[4] E. Hass et al., Proceedings of IBIC 2013, MOPC37 (2013)

[5] R. Lai et al., NIM A, 397, 221-231 (1997)

[6] D. Pelliccia and T. Sen, "A two-step method for retrieving the longitudinal profile of an electron bunch from its coherent radiation", ArXiv preprint 1403.1233v1 (2014)

[7] S.I. Bajlekov, Phys. Rev. ST Accel. Beams 16, 040701 (2013)

[8] O. Zarini and A. Debus et al., DPG-Frühjahrstagung, Göttingen (Poster), T 129.17 (2013)

[9] T.J. Maxwell et al., Phys. Rev. Lett. 111, 184801 (2013)

[10] P. Norton, Opto-Electronics Review 10 (3), 159–174 (2002)

[11] InfraRed Associates, `http://www.irassociates.com/`

[12] L.S. Rothman et al., Journal of Quantitative Spectroscopy & Radiative Transfer 130 (2013) 4–50

[13] B. Schmidt, Proceedings of FEL 2006, THCAU01 (2006)

[14] J.R. Schneider, Journal of Physics B 43, 194001 (2010)

[15] S. Casalbuoni et al., Phys. Rev. ST Accel. Beams 12, 030705 (2009)

[16] V. Balandin et al., "Studies of the Collimator System for the TTF Phase 2", TESLA report 2013-17 (2013)

[17] C. Behrens and C. Gerth, Proceedings of FEL 2010, MOPC08 (2010)

Copyright © 2014 CC-BY-3.0 and by the respective authors

ISBN 978-3-95450-141-0

LONGITUDINAL PHASE SPACE TOMOGRAPHY USING A BOOSTER CAVITY AT THE PHOTO INJECTOR TEST FACILITY AT DESY, ZEUTHEN SITE (PITZ)

D. Malyutin*, M. Gross, I. Isaev, M. Khojoyan, G. Kourkafas, M. Krasilnikov, B. Marchetti, F. Stephan, G. Vashchenko, DESY, 15738 Zeuthen, Germany

Abstract

One of the ways to measure the longitudinal phase space of the electron bunch in a linear accelerator is a tomographic technique based on measurements of the bunch momentum spectra while varying the bunch energy chirp. The energy chirp at PITZ can be controlled by varying the RF phase of the CDS booster – the accelerating structure installed downstream the electron source (RF gun). The resulting momentum distribution can be measured with a dipole spectrometer downstream. As a result, the longitudinal phase space at the entrance of the CDS booster can be reconstructed.

In this paper the tomographic technique for longitudinal phase space measurements is described. Results of measurements at PITZ are presented and discussed.

INTRODUCTION

For successful operation of linac based Free Electron Lasers (FELs) there are quite stringent requirements on the electron beam quality: small transverse emittance, small energy spread and high beam peak current (high brightness) [1]. The measurements of the beam slice energy spread and current profile can be done using a transverse deflecting structure (TDS) [2] or using a tomographic technique [3, 4]. Both methods allow full longitudinal phase space characterization. With the current setup of the Photo Injector Test facility at DESY, Zeuthen site (PITZ), only the tomographic technique can be employed. A TDS, which is already installed in the beamline, is planned to be put into operation at the end of this year.

The PITZ facility was built as an electron source test stand [5] for FELs like FLASH and the European XFEL. The present PITZ beamline layout is shown in Fig. 1. The main components of the PITZ facility are a photocathode laser system, an RF photo-electron gun (first accelerating structure) surrounded by main and a bucking solenoids, a second accelerating structure – Cut Disk Structure (CDS) which is also called booster cavity; and three dipole spectrometers. One spectrometer is located in the low energy section downstream the gun (Low Energy Dispersive Arm – LEDA), a second one in the high energy section downstream the booster (the first High Energy Dispersive Arm – HEDA1), and the third one in the end of the PITZ beamline (the second High Energy Dispersive Arm – HEDA2). Additionally there are three Emittance Measurement Stations (EMSYs) and a transverse deflecting structure (TDS), Fig. 1.

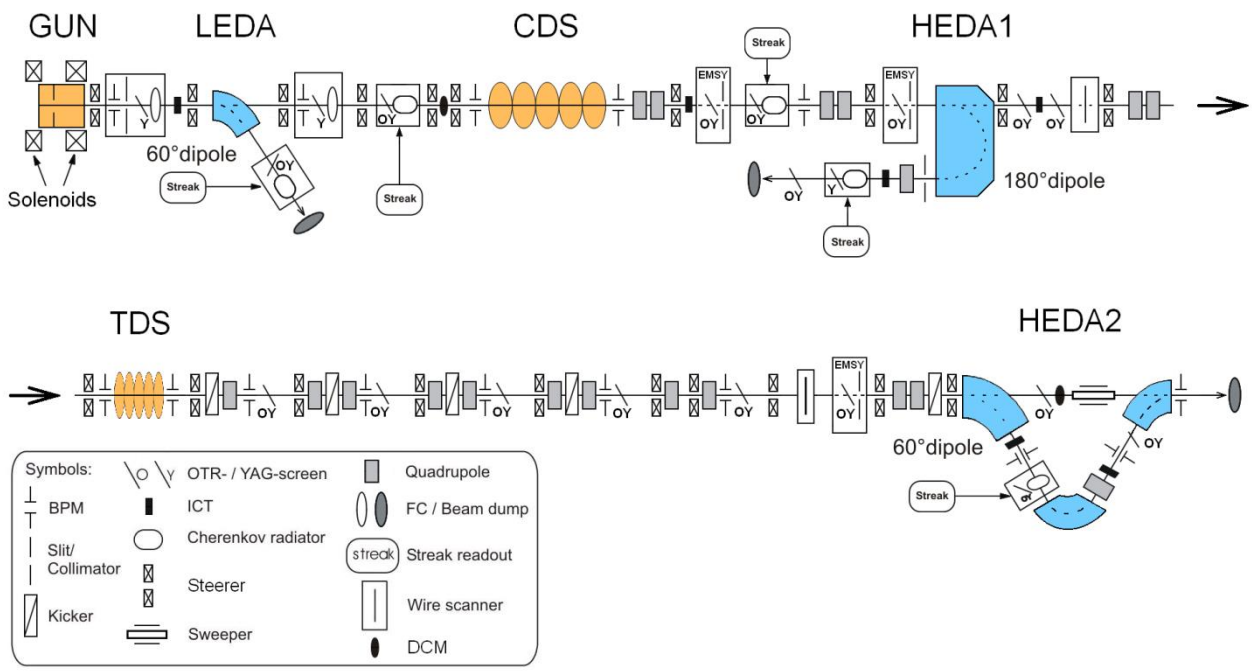


Figure 1: PITZ beamline layout. The beam propagates from left to right.

*dmitriy.malyutin@desy.de

ISBN 978-3-95450-141-0

Copyright © 2014 CC-BY-3.0 and by the respective authors

LONGITUDINAL PHASE SPACE TOMOGRAPHY

A tomographic technique can be used for measuring of the longitudinal phase space as the input projections for the reconstruction will correspond to momentum spectra where the bunch energy chirp has been varied [3]. The electron bunch current profile and slice energy spread can be extracted from the reconstructed longitudinal phase space and the longitudinal emittance can be calculated as well.

At PITZ, such measurements can be performed by varying the RF phase of the CDS booster. The momentum spectra measured downstream the booster at the HEDA1 or HEDA2 dispersive sections can be used to feed the tomographic reconstruction. Finally, the longitudinal phase space can be reconstructed using for example the Algebraic Reconstruction Technique (ART) [6].

Bunch Momentum Chirp

The acceleration of an ultra-relativistic electron bunch in an accelerating structure can be described as [7]:

$$p = p_0 + V \cdot \cos(\varphi), \quad (1)$$

where p_0 is the bunch initial momentum, V is the maximum momentum gain by the accelerating structure, φ is the RF phase of the structure relative to the maximum mean momentum gain (MMMG) phase and p is the bunch final momentum.

The bunch momentum chirp k induced by an accelerating structure can be calculated from Eq. (1) as a first time derivative with inverse sign:

$$k = -\frac{dp}{dt} = V\omega \cdot \sin(\varphi), \quad (2)$$

where $\omega = 2\pi f$ and f is the RF frequency in the structure.

Since the acceleration by the accelerating structure cannot cause full 90° rotation of the longitudinal phase space, the temporal resolution will be limited by the maximum momentum chirp applied to the bunch, the slice momentum spread in the bunch and the momentum resolution of the momentum distribution measurement system. The time resolution σ_t can be roughly estimated from the maximum momentum chirp $k_{\max}$ applied to the bunch:

$$\sigma_t = \frac{\sigma_\delta}{k_{\max}}, \quad (3)$$

where σ_δ is the electron bunch slice momentum spread. Here it is assumed that the resolution of the momentum measurement is much better (smaller) than the bunch slice momentum spread.

Bunch Length Estimation

The electron bunch length can quickly be estimated from the momentum phase scan without performing the time consuming tomographic reconstruction. But such estimation will be rough. For this one need to make maximum momentum spread of the bunch by going to the off-crest RF phase of the accelerating structure, which is still measurable by a dispersive section (spectrometer). Measuring this momentum spread the bunch length can be calculated by:

$$\delta_l = \frac{\delta_p}{k_0 + k_1} c, \quad (4)$$

where δ_l is the RMS bunch length, δ_p is the RMS momentum spread, k_0 is the initial momentum chirp (upstream the booster), k_1 is the momentum chirp induced by the booster cavity at the maximum measurable momentum spread and c is the speed of light. k_0 can be estimated using Eq. (2) with inverse sign at the phase with minimum momentum spread.

EXPERIMENTAL RESULTS

Experimental measurements of the longitudinal phase space were performed at PITZ for two laser temporal profiles Gaussian and flat-top. For each case the range of booster RF phases was chosen to have measurable bunch momentum distributions in the dispersive section (enough high intensity and bunch size within the observation screen) and usually it is chosen at about +/- 20 degrees around the MMMG phase.

For the first set of measurements a bunch charge of 20 pC was chosen and the photo cathode laser had a Gaussian temporal profile with FWHM length of 2.8 ps. Figure 2 shows the measured mean beam momentum and RMS momentum spread in the HEDA1 section as a function of the booster RF phase relative to the MMMG phase.

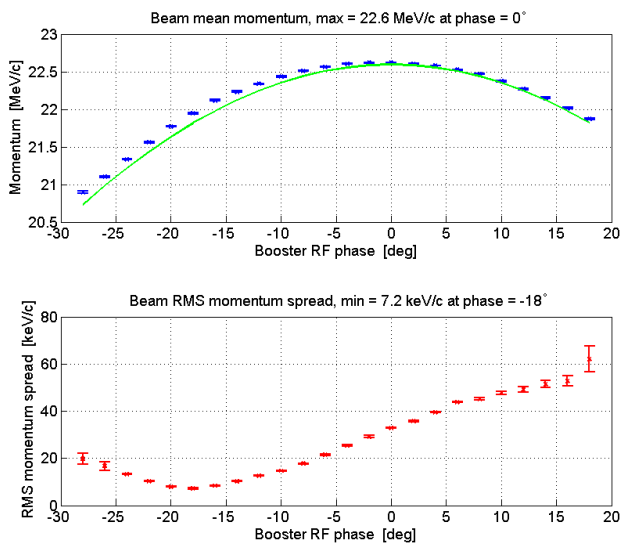


Figure 2: Top: the beam mean momentum as a function of the booster RF phase for 20 pC bunch charge and Gaussian laser temporal profile, blue dots with error bars show measurements; green curve shows acceleration model according Eq. (1). Bottom: RMS momentum spread shown as red dots with error bars, as a function of the booster RF phase.

The used booster RF phase range was from -28° to +18° with respect to the MMMG phase with a step width of 2 degrees. The maximum mean momentum gain from the

Copyright © 2014 CC-BY-3.0 and by the respective authors

ISBN 978-3-95450-141-0

booster cavity was V = (22.6 – 6.8) MeV/c = 15.8 MeV/c, where 22.6 MeV/c is the maximum mean momentum downstream the booster and 6.8 MeV/c is the maximum mean momentum downstream the gun. As a result, the maximum momentum chirp k_{max} at the RF phase of +18° calculated according to Eq. (2), is 40 keV/c/ps, for f = 1.3 GHz. The resulting temporal resolution σ_t of the reconstructed longitudinal phase space is about 0.25 ps or 75 μm for a slice momentum spread of the bunch σ_δ = 10 keV/c, Eq. (3). The result of the longitudinal phase space reconstruction using the ART algorithm is shown in Fig. 3.

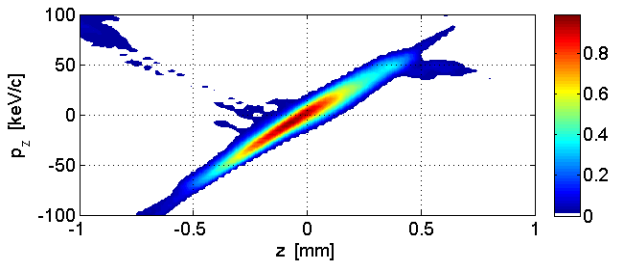


Figure 3: Reconstructed longitudinal phase space for a Gaussian temporal laser profile and 20 pC bunch charge.

Figure 4 shows the comparison of the bunch current profile, calculated from the reconstructed longitudinal phase space in Fig. 3, with the measured laser temporal profile. The current profile from Fig. 3 was calculated applying 15% charge cut to the reconstructed phase space in order to remove reconstruction artifacts.

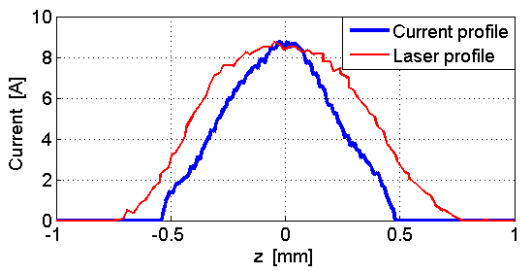


Figure 4: Current profile from Fig. 3, the blue curve, and the temporal laser profile, the red curve. The laser profile was scaled vertically to have the same amplitude as the current profile.

The calculated current profile is shorter than the laser profile (0.56 mm vs 0.86 mm at FWHM), due to three effects. Firstly, the charge cut applied to the phase space. Secondly, the weak tails of the distributions are not detected during the momentum measurements due to not perfect sensitivity of the measurement method. Thirdly, velocity bunching is taken place for low bunch charges at the initial acceleration in the gun when the electrons are started from the cathode surface. For the MMMG phase of the gun, the tail of the bunch sees a higher accelerating field than the head, resulting in bunch compression. For high charges the longitudinal space charge forces elongate the bunch.

The RMS bunch length calculated from the reconstruction is 0.22 mm. The rough estimation from the momentum phase scan (Fig. 2) using Eq. (4) for the bunch momentum spread at +18 degree of δ_p = 60 keV/c and for V = 15.8 MeV/c, k_0 = 40 keV/c/ps calculated at +18 degree and k_1 = 40 keV/c/ps calculated at -18 degree gives the estimated bunch length of 0.23 mm. This number is reasonably close to the obtained value from the reconstructed current profile.

A second set of measurements was done for a bunch charge of 20 pC and a flat-top laser temporal profile with a FWHM length of 17.4 ps. Figure 5 shows the measured beam mean momentum and RMS momentum spread in the HEDA1 section as a function of the booster RF phase, relative to the MMMG phase. The used booster RF phase range was from -23° to +22° with respect to the MMMG phase with a step width of 1 degree. The beam maximum mean momentum gain from the booster cavity was V = (22.3 – 6.8) MeV/c = 15.5 MeV/c.

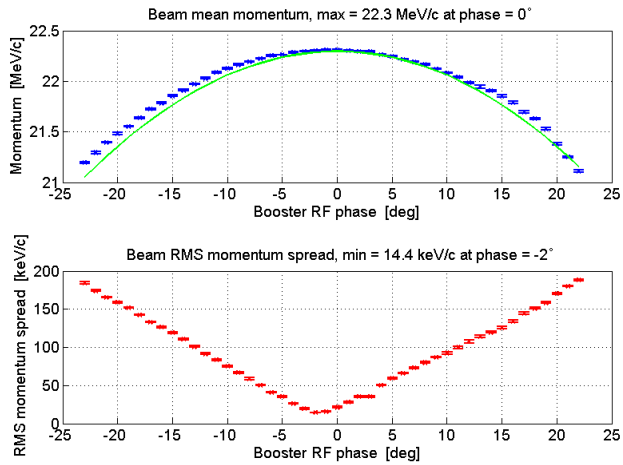


Figure 5: Top: the beam mean momentum as a function of the booster RF phase for 20 pC bunch charge and flat-top laser temporal profile, blue dots with error bars show measurements; green curve shows acceleration model according to Eq. (1). Bottom: RMS momentum spread shown as red dots with error bars, as a function of the booster RF phase.

The maximum momentum chirp applied to the bunch in this case is 47 keV/c/ps at the RF phase of +22 degree, yielding a temporal resolution of 0.21 ps or 63 μm. The reconstructed longitudinal phase space is shown in Fig. 6 and the comparison of the current profile with the laser profile is shown in Fig. 7.

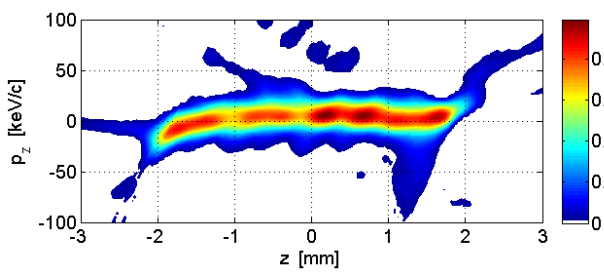


Figure 6: Reconstructed longitudinal phase space for flat-top temporal laser profile and 20 pC bunch charge.

Copyright © 2014 CC-BY-3.0 and by the respective authors

ISBN 978-3-95450-141-0

The laser profile in Fig. 7 was squeezed longitudinally to have the same length and scaled vertically to have the same amplitude as the current profile for better comparison (original laser profile is longer). The modulation structure of the laser profile is well reproduced in the current profile and in the reconstructed phase space.

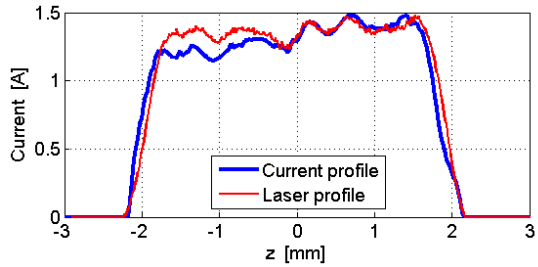


Figure 7: Current profile (the blue curve) and squeezed temporal laser profile (the red curve).

The RMS bunch length calculated from the reconstruction is 1.1 mm. The rough estimation from the momentum phase scan (Fig. 5) using Eq. (4) gives the same number.

CONCLUSION

The longitudinal phase space of the electron bunch can be measured using a tomographic technique by varying the RF phase of the acceleration structure. Such measurements were performed at the PITZ facility for two temporal laser profiles and 20 pC bunch charge. Reconstructed current profiles at low bunch charge are in good agreement with the measured temporal laser profiles, except that they are shorter due to velocity bunching. Temporal density modulations of the laser profile can be seen in the reconstructed longitudinal phase spaces. The bunch length can be quickly estimated from the momentum phase scan without performing the time consuming tomographic reconstruction.

REFERENCES

[1] P. Schmueser, M. Dohlus and J. Rossbach, *Ultraviolet and Soft X-Ray Free-Electron Lasers*. (Springer, 2008).

[2] P. Emma, *et al.*, A transverse RF Deflecting Structure for Bunch Length and Phase Space Diagnostics. LCLS-TN-00-12. 2000.

[3] H. Loos, *et al.*, "Longitudinal phase space tomography at the SLAC Gun Test Facility and the BNL DUV-FEL", Nucl. Instrum. Meth. A 528, (2004) 189.

[4] D. Malyutin, *et al.*, "First results of a longitudinal phase space tomography at PITZ", FEL2013, TUPSO47.

[5] F. Stephan, C. H. Boulware, M. Krasilnikov, J. Bähr, *et al.*, "Detailed characterization of electron sources yielding first demonstration of European X-ray Free-Electron Laser beam quality." Phys. Rev. ST Accel. Beams 13, 020704, (2010).

[6] A.C. Kak, M. Slaney, *Principles of Computerized Tomographic Imaging*, (IEEE Press, 1979).

[7] J. Le Duff, "*Dynamics and acceleration in linear structures*", CERN Accelerator School, Fifth General Accelerator Physics Course, Jyväskylä, Finland, 7–18 September 1992, CERN 94-01.

Copyright © 2014 CC-BY-3.0 and by the respective authors

ISBN 978-3-95450-141-0

NEW RESULTS OF FERMI FEL1 EOS DIAGNOSTICS WITH FULL OPTICAL SYNCHRONIZATION

M. Veronese*, E. Allaria, P. Cinquegrana, E. Ferrari, F. Rossi, P. Sigalotti, C.Spezzani,
Elettra-Sincrotrone Trieste, Trieste, Italy

Abstract

The electro optical sampling diagnostics (EOS) of the FERMI FEL has been recently upgraded with a full optical synchronization of its dedicated femtosecond fiber laser to the ultra-stable optical pulsed timing system of FERMI. For this purpose a dual synchronization electronics has been developed and installed. It exploits a mixed error signal derived from both optical to electrical conversion and from second harmonic generation based optical phase detection. For this second part a new optical setup including a cross correlator has been installed. The operation of the EOS has greatly benefited from the upgrade. The arrival time measurements have been compared with the ones from the bunch arrival monitor diagnostics (BAM) showing very good agreement. This new setup has also allowed to improve the bunch profile measurement. Some examples of measurement with ZnTe and GaP are presented. Finally, usability and operator friendliness of the new setup are also discussed.

INTRODUCTION

FERMI is a seeded free electron laser (FEL) operating in the spectral range from VUV to soft x-rays. It is based on a SLAC/BLN/UCLA type RF-gun, and a normal conducting LINAC, currently operated at 1.2 GeV (up to 1.5 GeV). Longitudinal compression is provided by two magnetic chicanes BC1 and BC2 (respectively at 300 MeV and 600 MeV). The FEL has two undulator chains, namely FEL1 [1] and FEL2 [2]. The first, FEL1, is a single cascade HGHG seeded free electron laser designed to provide ultrashort radiation pulses with energies up to hundreds of micro joules per pulse in the wavelength range from 100 nm to 20 nm. The second, FEL2, is a double cascade seeded system designed to reach 4 nm at the shortest wavelength, implementing the fresh bunch technique. Optimization of a seeded FEL is a multi-parameter optimization process. To reach an optimal FEL emission several conditions have to be met. All information pertaining the time of arrival and the temporal profile of the electron bunch are of crucial importance. For this reason an electro optical sampling (EOS) diagnostics station has been installed at the entrance of both the FEL undulators chains. This paper is focused on the FEL1 EOS (see Fig. 1). This device in based on a fiber laser oscillator installed in the tunnel and exploits the spatial encoding scheme. The FEL1 EOS initial operational experience has been described in [3]. We made a major upgrade to the locking of the laser with a full optical synchronization setup and electronics with the aim of improving the time jitter performances of the FEL1 EOS.

* marco.veronese@elettra.eu

EXPERIMENTAL LAYOUT

The layout of FEL1 chain, in the undulator hall, is depicted in Fig. 1. In the figure the electron beam travels from left to right and its trajectory is depicted in black. The seed laser is depicted as a red flash. The modulator undulator (MOD) is in light blue while the dispersive section is in green and radiator (RAD) undulators are in violet. After the last radiator the electron beam is bent towards the main beam dump while the FEL radiation travels towards the experimental hall. The EOS diagnostic station is installed just upstream the modulator and is depicted in yellow in Fig. 1.

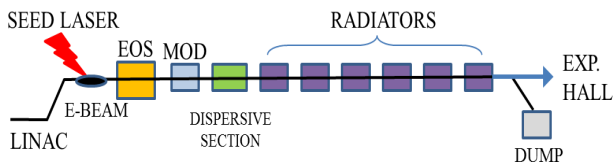


Figure 1: FERMI FEL1 layout.

The upgraded EOS optical layout is depicted in Fig. 2. The laser source is visible in the upper left part of the figure. It is a fiber laser (Menlosystems, TC780) delivering pulses at 780 nm wavelength with 110 fs duration, average power of 55 mW and repetition rate of 78.895 MHz. The pulses pass a delay line needed for fine time delay adjustments. Then the laser beam passes a Glan-Taylor polarizer (P) to improve polarization purity and a motorized zero order $\lambda/2$ waveplate for rotation of the polarization. The laser is focused on the electro optic (EO) crystals surface by a cylindrical lens (L2). The laser angle of incidence on the crystal is of 30 degrees with respect to the electron beam. This angle allows encoding temporal information in the spatial profile of the laser. After passing through the EO crystal the laser exits the vacuum chamber and passes through the polarization analysis optics. This is composed of two motorized waveplates ($\lambda/4$ and $\lambda/2$) and a Wollaston prism. They are adjusted to work in a cross polarizer configuration. The beam is then directed to the intensified charge-coupled device (ICCD) camera. Two lenses are set between the vacuum chamber and the ICCD camera to provide the necessary magnification. The vacuum 3-axis manipulator houses a ZnTe 1 mm thick crystal, a GaP 0.4 mm thick, a GaP 0.1 mm thick, an OTR screen and a YAG:Ce crystal. In the bottom part of Fig. 2 we show the coarse longitudinal alignment system. Coherent optical transition radiation (COTR) is used to set the correct ICCD gate delay. The extraction path for COTR radiation is depicted in violet.

ISBN 978-3-95450-141-0

Copyright © 2014 CC-BY-3.0 and by the respective authors

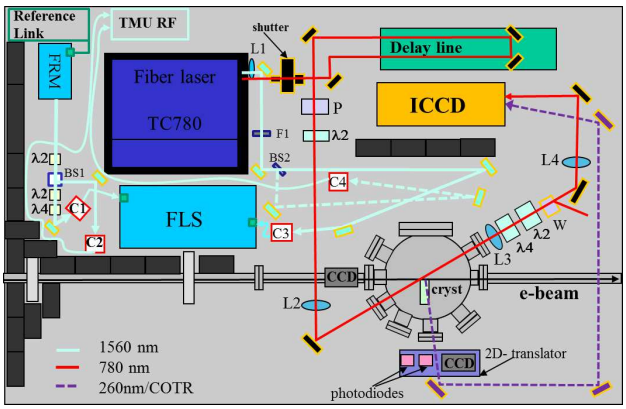


Figure 2: EOS optical table layout.

UPGRADES TO THE OPTICAL LAYOUT

To work as a time resolved diagnostics the EOS laser has to be phase locked to the pulsed optical timing system (OTS) of FERMI [4]. For this reason a dedicated phase reference fiber link for the EOS has been installed. The link delivers ultra stable pulses at 157.790 MHz with a wavelength of 1560 nm up to the end point of the link which is a Faraday rotator mirror unit (FRM). After the FRM the reference laser beam is in free space and it is split into and high power and a low power branches by a polarizing beam splitter (PBS). A $\lambda/2$ at the PBS entrance is used to control the power splitting ratio. The low power branch is fiber coupled by a collimator (C2) and used for RF locking. The high power branch is also fiber coupled via collimator (C1) and it is used for optical phase detection. The TC780 fiber laser is equipped with a secondary high power air output delivering 1560 nm pulses with a duration of about 350 fs. This beam is also split in two parts: one is used for optical phase detection (C3) while the other is sent via a fiber collimator (C4) to the locking electronics. The optical phase detection is performed via a Menlosystems fiber link stabilization (FLS) unit where the link and the reference pulses are cross correlated using a single crystal balanced detection scheme [5]. Both arms of the FLS have about 8 mW power on the second harmonic generation (SHG) crystal.

SYNCHRONIZATION ELECTRONICS

The optical equipment described above is used in a dual locking scheme where both RF locking and optical locking techniques are used at the same time. A layout of the synchronization electronics scheme is shown in Fig. 3. RF locking starts by converting laser and OTS link reference pulses to electrical signals extracting their common harmonics at 2.99801 GHz. Then the relative phase is detected by a heavily saturated RF mixer that produces a phase error signal which is used in the control loop. RF locking is very robust but does not give the needed performances in terms of time jitter and long term drifts. For this purpose optical locking in our case is added to RF locking. Both error signals from RF and optical phase detection are used for long term operation. The final proportional-integral (PI) controller is driven by weighting in the most efficient way RF and optical error signals. The control of the laser locking is achieved by two electronics units named TMU-RF and TMU-CU as described in [6]. This is the same electronics developed in-house for the synchronization of the FERMI photoinjector and seed femtosecond lasers. The TMU-RF

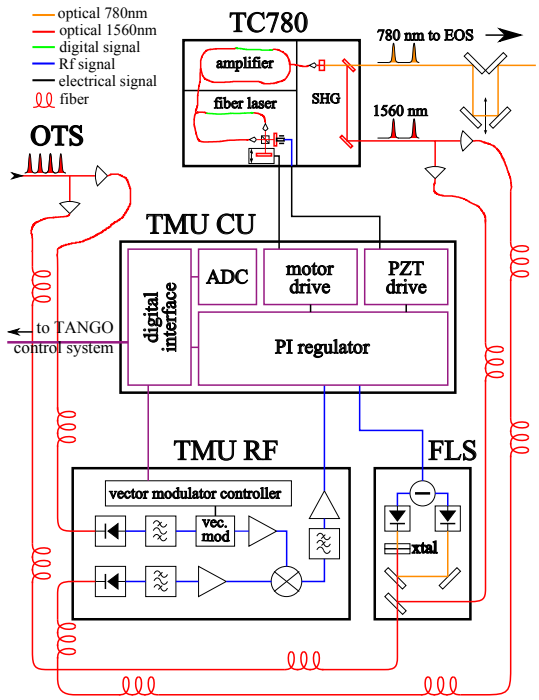


Figure 3: Synchronization scheme.

converts the optical signal from the fibers coming from either the link or the laser in RF signals. It performs a phase detection and generates an error signal which is fed to the TMU-CU. The TMU-CU controls the TC780 laser cavity stepper motor and piezo electric actuator to lock the phase of the laser to the reference link. Once this condition is reached the systems scans the time delay between laser and link to find the cross correlation position. This scan is done by deliberately changing the TC780 cavity frequency via a vector modulator acting on the RF converted signal from the laser while keeping it locked. The frequency difference causes a time slippage between the TC780 laser and the reference pulses. Once the cross correlation signal is found the delay is finely adjusted to reach the zero crossing. As a final step the PI loop controlling the locking is set to work at 80% based on the cross correlator signal reducing to 20% the weight of the RF error signal. The system is design to allow easy and remotely operated automatic synchronization of the laser. Moreover it provides all diagnostics information to the FERMI control system such as the optical power per each channel, the RF power per each channel, the error signal amplitudes, the 78.895 MHz and 2.99801 GHz phases as well as the frequency difference of the cavity, the cross correlator signal amplitude.

Copyright © 2014 CC-BY-3.0 and by the respective authors

ISBN 978-3-95450-141-0

LABORATORY TEST RESULTS

One of the goals of this upgrade was to improve the time jitter of laser and thus of the EOS arrival time measurement previously at the level of 80 fs rms, by exploiting the full optical synchronization. The new synchronization system was tested in the laboratory. The TC780 laser was locked to an external optical master oscillator (Menlosystems TC1550 fiber laser), to establish the new system performances. The

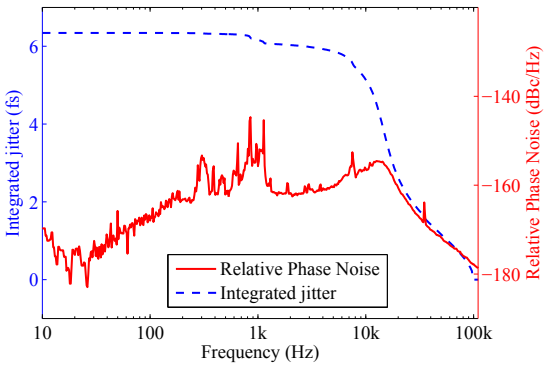


Figure 4: Phase noise data analysis of the TC780 laser locked to a TC1550 laser.

relative phase noise, measured in loop, is obtained from the output of cross- correlator, scaled by a conversion factor calculated from the cross- correlation signal slope. Data are acquired using a signal source analyzer (Agilent E5052B) used as a FFT analyzer. In Fig. 4 we show the measured phase noise curve in dBc/Hz (right axis and red solid curve) and the integrated jitter (left axis and blue dashed curve). The curve is then integrated up to 100 KHz which is the 3 dB cutoff limit of the bandwidth of the photodiode used in the cross-correlator. The total time jitter is of about 6 fs rms. After installation in the FERMI tunnel we performed again the phase noise measurement but this time with the laser locked to the stabilized pulsed fiber link. When locked to the reference fiber link the phase noise is the same within the error of the measurement which is about ±10%.

E-BEAM ARRIVAL TIME MEASUREMENTS

The performances of the EOS diagnostics after the described upgrade of the synchronization system have been tested on the electron beam of FERMI. We deliberately caused a change of arrival time of the electron bunch by modifying in a controlled way the electron trajectory in the first bunch compressor. During this operation we recorded shot by shot the bunch arrival time with the EOS and for comparison with the nearby bunch arrival monitor (BAM). An example of this kind of measurement is shown in Fig. 5. In this case we induced a modulation of the arrival time of about ± 400 fs and recorded the EOS and BAM measurements for the same FERMI electron bunch. In the upper plot, the horizontal axis of the figure is the FERMI bunch

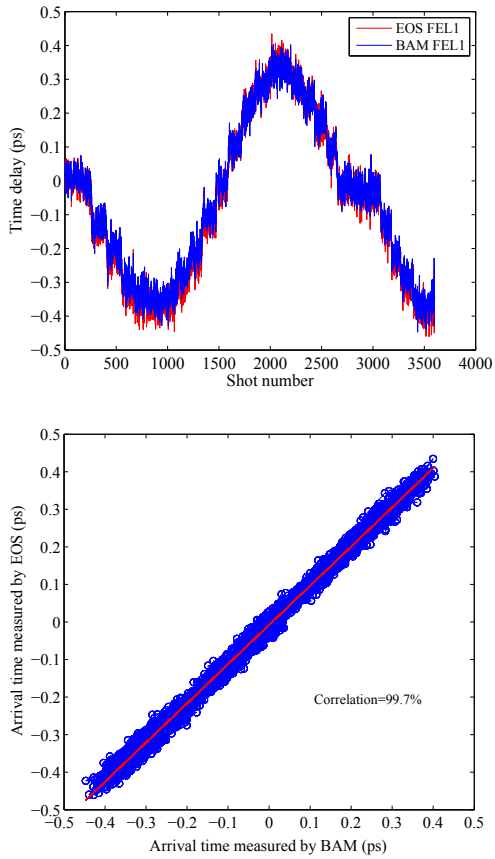


Figure 5: Upper plot EOS (red) and BAM (blue) arrival time vs bunch number. In the bottom plot we show EOS arrival time vs BAM arrival time.

number while on the vertical axis we have the time of arrival measurement performed with the BAM and the EOS. The data are plotted one versus the other in the lower plot an their correlation is of 99.7%.

PROFILE MEASUREMENTS

As described before, the EOS manipulator is equipped with three electro optic crystals: ZnTe 1mm thick, GaP 0.4mm thick and GaP 0.1mm thick. The ZnTe crystal is protected with a fused silica optical substrate coated with an high reflectivity coating to protect it from the seed laser in the event of a wrong steering. Since GaP has a higher damage threshold than ZnTe, no protection is installed. The ZnTe has a higher EO coefficients and thickness, thus single shot bunch profiles can easily be acquired. In Fig. 6 we present a typical sequence of profiles acquired at 10 Hz. In the figure the profiles are stacked adding an offset to improve image quality. The centroid position for each bunch is calculated and the rms deviation is the bunch arrival time jitter, typically of about 40 fs. The ZnTe offers the best signal to noise ratio but the temporal resolution is insufficient for accurate bunch profile measurements. For sub picosecond electron bunch profile measurements the best resolution in

ISBN 978-3-95450-141-0

Copyright © 2014 CC-BY-3.0 and by the respective authors

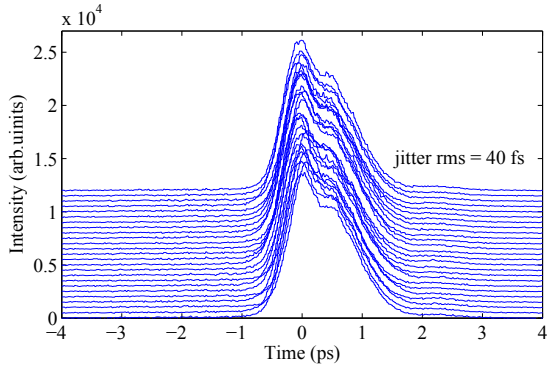


Figure 6: EO signal of 30 consecutive bunches (ZnTe).

FERMI EOS is obtained with the GaP 0.1 mm crystal because of its better frequency response and smaller thickness. The lower electro optic coefficient of GaP compared to ZnTe and the reduced thickness produce a lower rotation of the polarization. This means a lower EOS signal which of the same order of magnitude of the background and optimization of the waveplates is needed to maximize SNR. Also a subtraction of the background (unrotated polarization) is needed to obtain a bunch profile with no artifacts. As an example we show in Fig. 7 an EOS profile measurement with the GaP 0.1 mm thick, after background subtraction. In the figure we also show an asymmetric Gaussian fit of the profile. The FWHM of the profile is of about 1.15 ps but the profile sides have different slopes. The left side is much steeper and has a Gaussian sigma of 154 fs. All the

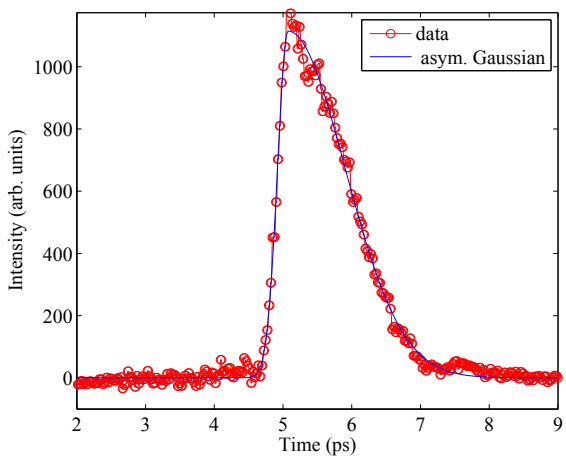


Figure 7: Bunch profile acquired with the GaP 0.1 mm crystal (in red) and asymmetric Gaussian fit (in blue).

information provided so far are based on a calibration of the temporal scale which converts ICCD pixels to picoseconds. The time calibration of the EOS for spatial encoding is usually performed comparing the transverse rms beam size of the laser on the crystal (σ_C) and the transverse rms beam size of the laser on the ICCD (σ_{ICCD}). For a given angle α between the electron beam and the laser propagation direction, the equivalent temporal sigma is defined as $\sigma_t = \sigma_C * \cos(\alpha)/c$ where c is the speed of light in the vacuum [7]. Knowing σ_t, the pixel to picosecond conversion is determined. The new ultra stable synchronization system has allowed us to devise another way to calibrate the EOS by scanning the position of the delay line while recording the beam profiles. Averaging over multiple shots we reduce the effect of the already small time jitter over the determination of the average e-beam temporal arrival time and in this way a direct time to pixel conversion can be performed. Both calibration methods have been tested. The first gives a calibration constant of 73 px/ps while the second 77 px/ps, in both cases an error from 5% to 10% is to be expected. In conclusion, we have installed a dual synchronization system that has greatly enhanced the usability and eased the operation of the EOS as well as allowed time of arrival jitter measurements with an accuracy level comparable to the one of the BAM. Also the profile measurements have benefited from the upgrade. We reported on the resolution of profile measurements, showing a value below 150 fs.

REFERENCES

[1] E. Allaria et al., "Highly coherent and stable pulses from the FERMI seeded free-electron laser in the extreme ultraviolet", Nature Photonics, 6, 699, (2012).

[2] E. Allaria et al., "Two-stage seeded soft-X-ray free-electron laser", Nature Photonics 7, 913, (2013)

[3] M.Veronese et al.,"First operation of the electro optical sampling diagnostics of the FERMI@Elettra FEL", Proc. IBIC2012, Tsukuba, Japan, pp. 449, (2012).

[4] M. Ferianis et al. "All-optical femtosecond timing system for the FERMI@Elettra FEL.", Proc. FEL2011, Shanghai, China, pp. 641, (2011).

[5] J. Kim et al., "Long-term femtosecond timing link stabilization using a single-crystal balanced cross correlator", Optics Letters 32, 1044 (2007).

[6] P. Sigalotti, et al., "Ultrafast laser synchronization at the FERMI@Elettra FEL", Proc. SPIE 8778, Advances in X-ray Free-Electron Lasers II: Instrumentation, 87780Q, (2013).

[7] A.L. Cavalieri, Ph.D. thesis, The University of Michigan, (2005).

Copyright © 2014 CC-BY-3.0 and by the respective authors

ISBN 978-3-95450-141-0

NEAR-SATURATION SINGLE-PHOTON AVALANCHE DIODE AFTERPULSE AND SENSITIVITY CORRECTION SCHEME FOR THE LHC LONGITUDINAL DENSITY MONITOR

M. Palm*, E. Bravin, S. Mazzoni, CERN, Geneva, Switzerland

Abstract

Single-Photon Avalanche Diodes (SPADs) monitor the longitudinal density of the LHC beams by measuring the temporal distribution of synchrotron radiation. The relative population of nominally empty RF-buckets (satellites or ghosts) with respect to filled bunches is a key figure for the luminosity calibration of the LHC experiments. Since afterpulsing from a main bunch avalanche can be as high as, or higher than, the signal from satellites or ghosts, an accurate correction algorithm is needed. Furthermore, to reduce the integration time, the amount of light sent to the SPAD is enough so that pile-up effects and afterpulsing cannot be neglected. The SPAD sensitivity has also been found to vary at the end of the active quenching phase. We present a method to characterize and correct for SPAD deadtime, afterpulsing and sensitivity variation near saturation, together with laboratory benchmarking.

INTRODUCTION

The LHC RF cavities operate at about 400 MHz (2.5 ns RF buckets), with a distance of at least 10 buckets between nominally filled buckets (main bunches). A fraction of the beam can be found in the nominally empty buckets, where they are called satellite or ghost bunches [1]. The number of particles in satellites and ghost bunches is typically less than four or five orders of magnitude lower than the main bunches. However, they can create background noise at the interaction points and, due to their large number, cause problems for luminosity calibration [1].

The purpose of the LDM is to measure the relative number of particles in the different buckets, via the synchrotron radiation emitted by the beam.

A schematic overview of the LHC LDM system (one per beam) that was installed during Run 1 is shown schematically in Fig. 1: an SPAD registers individual synchrotron radiation photons emitted from an undulator (below 2 TeV) or separation dipole (above 2 TeV). Their arrival times relative to the LHC turn clock are stored with 50 ps resolution, allowing a histogram over the longitudinal beam profile, with sufficient statistics, to be generated in a few minutes. The light intensity on the SPAD sensor can be adjusted by moving individual neutral density (ND) filters in or out of the light path. With little filtering, the average number of *photons* per ghosts is high, but the *counts* per ghost that are within one deadtime of a main bunch is reduced due to the deadtime of the detector. For heavy filtering, the availability of the detector is higher, but the number of photons per ghost

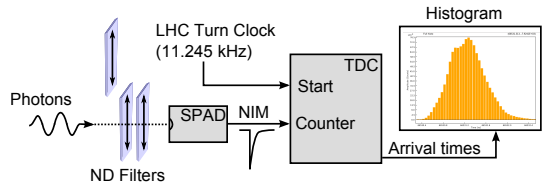


Figure 1: Schematic overview of the LDM system.

lower. The filtering strength should therefore be chosen to maximize the number of counts per ghost. A more detailed description of the system can be found in [1].

An example of part of the beam profile histogram measured by the LDM during Fill 3005 in 2012 is shown in Fig. 2 (integrating over 5 minutes, or 3.3 million turns). Two features must be taken into account when resolving the relative bunch population:

1. Reduced detector availability due to the detector deadtime.
2. Afterpulsing from main bunches, which is comparable to, or greater than, the signal from ghost and satellite bunches.

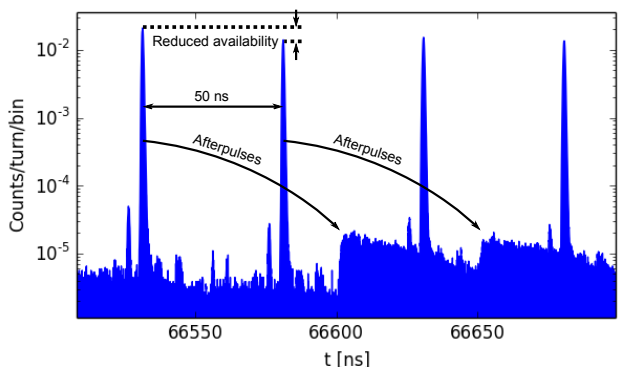


Figure 2: Part of the uncorrected profile histogram from fill 3005 (Beam 1). Main bunch separation is 50 ns. Satellites and ghosts are visible around the main bunches as smaller peaks.

The LDM sensors used in the LHC are of the PDM-series from Micro Photon Devices[1], with Peltier-cooling and integrated active quenching circuits. An identical spare detector was used for the characterization described in this paper, with the key figures summarized in Table 1.

* marcus.palm@cern.ch

[1] http://www.micro-photon-devices.com/

ISBN 978-3-95450-141-0

Copyright © 2014 CC-BY-3.0 and by the respective authors

Table 1: Characteristics of the Spare SPAD Used in Laboratory Tests (*= as measured in laboratory setup)

Photon detection efficiency	49% (550 nm)
Deadtime, τ	≈72 ns
Afterpulse probability	4%
Dark count rate	300 Hz*
Timing resolution (FWHM)	50 ps
Sensor diameter	50 µm

METHODS

Detector Characterization

The principle of active quenching is well described in e.g. [2]. After an avalanche occurs, the voltage over the SPAD is lowered below breakdown to quench the avalanche and allow most of the charge carriers that are trapped during the avalanche to be released. After about τ seconds, the deadtime, the voltage is restored.

Sensitivity It has been observed that as the voltage is restored after an avalanche, the relative probability for a photon or trapped charge carrier to trigger a new avalanche, $S[t]$, oscillates around its ideal, steady-state value of 1 during a few nanoseconds. To characterize this behavior, the SPAD was exposed to a laser pulse (<1 ns) and illuminated with a weak LED pulse (~100 ns) during the time where the voltage is restored. By comparing the response to the LED light with and without the initial laser pulse, $S[t]$ could be measured. The result is shown in Fig. 3. $T_{s,min}$ and $T_{s,max}$ indicate where $S[t]$ begins to increase from 0 and settles at 1. $S[t]$ is referred to as the sensitivity response profile.

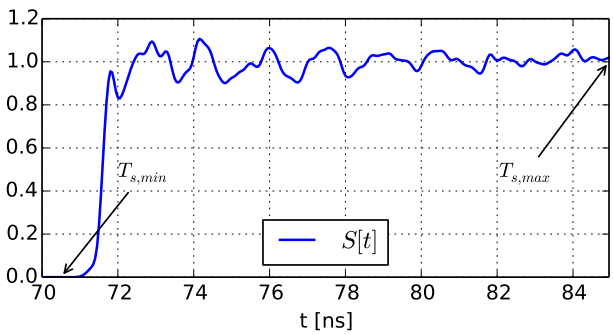


Figure 3: Sensitivity response profile after an avalanche at $t = 0$.

Afterpulsing We define $R[t]$ as the the probability that an avalanche at $t = 0$ will cause an afterpulse avalanche at time bin t, assuming there are no intermediate avalanches reducing the availability. To measure $R[t]$, the SPAD was exposed to a single laser pulse and the resulting afterpulse tail measured. When correcting the afterpulse tail for reduced availability and removing the constant background, the result is essentially an infinite series of convolutions between the initial laser profile $\delta[t]$ and progressively higher order afterpulses:

$$R_{tail}[t] = \delta[t] * (\underbrace{R[t]}_{\text{Primary}} + \underbrace{R[t] * R[t]}_{\text{Secondary}} + \ldots) \quad (1)$$

$R[t]$ is resolved by a deconvolution, and the result for the spare SPAD is shown in Fig. 4. Note that the fluctuations around t =72 ns corresponds to the same fluctuations seen in $S[t]$. The afterpulses were still measured several 100 µs after the initial laser pulse (inset, Fig. 4), albeit reduced by 4-5 orders of magnitude.

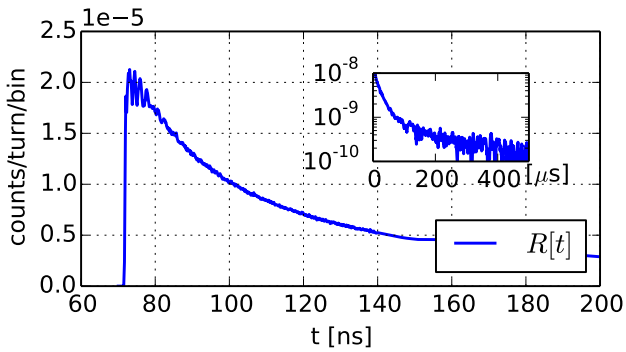


Figure 4: Single pulse afterpulse profile, $R[t]$.

Retrieving the Photon Rate

The goal of the correction algorithm is to retrieve the relative rate of photons striking the sensor. Avalanches registered in the histogram are assumed to have three causes: (1) Synchrotron radiation photons, $\gamma[t]$, (2) Afterpulses, $r[t]$, and (3) Background events (ambient photons, dark counts), $b[t] \ll 1$. Square brackets indicate an average number per time bin (50 ps) per turn. For a sufficiently long integration time, the measured histogram (divided by the number of turns), $a[t]$, contains the probability that an avalanche will be triggered in an individual time bin. The probability that no avalanche is measured (subscript m) in time bin t can then be written as:

$$1 - a[t] = P(\Gamma_m[t] + B_m[t] + R_m[t] = 0) \quad (2)$$

Here, $\Gamma_m[t]$, $R_m[t]$ and $B_m[t]$ are independent random variables from Poisson distributions with mean values $\gamma_m[t]$, $r_m[t]$ and $b_m[t]$. Note that these means are in general lower than $\gamma[t]$, $r[t]$ and $b[t]$, due to the detector deadtime. We introduce the *average sensitivity*, $h[t]$, as a scaling factor for the probability to measure an avalanche at t, as compared to an ideal detector that does not suffer from deadtime effects (similarly to what was done for deadtime correction in [1]). Setting $\Phi = \Gamma + B$, $h[t]$ relates Φ_m to Φ as (R_m is elaborated later):

$$P(\Phi_m > 0) = h[t]P(\Phi > 0) \quad (3)$$

For example if the first main bunch triggers an avalanche with 10% probability, $h[t]$ will be reduced to 0.9 immediately after the main bunch, reducing the number of avalanches from following ghosts and satellites by 10%. The probability that

Copyright © 2014 CC-BY-3.0 and by the respective authors

ISBN 978-3-95450-141-0

a Poisson-variable with mean λ is zero is $e^{-\lambda}$, from which Eq. 2 can be reshuffled (omitting the time-dependence of $b[t]$) to give:

$$\gamma[t] = -\ln\left[1 - \frac{1-(1-a[t])e^{r_m[t]}}{h[t]}\right] - b \qquad (4)$$

Average Sensitivity

In previous analyses of LDM data, the sensitivity response profile $S[t]$ has been modeled as a binary function switching from 0 to 1 after a constant number of time bins. With $S[t]$ in fact behaving as shown in Fig. 3, a more careful approach is needed. To estimate h in a particular time bin t_2, only avalanches in the interval $[t_2 - T_{s,max}, t_2 - 1]$ will have an impact ($S[t]$ is restored to 1 for earlier avalanches). This interval can be split into three regions as shown in Fig. 5. Since the minimum time between two avalanches is $T_{s,min}$, there are only five possible configurations, **a**-**e**, of preceding avalanches in the three regions, as summarized in Table 2. Their respective probabilities and resulting single-turn sensitivity at t_2 are denoted p_a-p_e and h_a-h_e. The average sensitivity $h[t_2]$ is the weighted sum $\sum p_i h_i$. Note that with an avalanche in I_2 or I_3, $h[t_2]$ is 0.

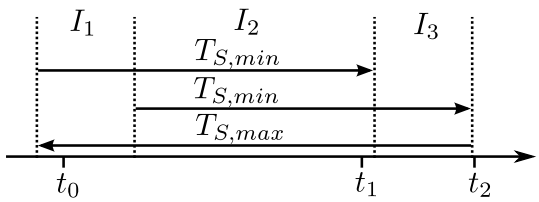


Figure 5: Regions considered to evaluate $h[t_2]$.

Table 2: Possible Avalanche Configurations in I_1-I_3 During a Single Turn (x=avalanche in region I_1, I_2 or I_3)

I_1	I_2	I_3	P	$h[t_2]$
-	x	-	p_a	$h_a[t_2] = 0$
x	-	-	p_b	$h_b[t_2] \neq 0$
x	-	x	p_c	$h_c[t_2] = 0$
-	-	x	p_d	$h_d[t_2] = 0$
-	-	-	p_e	$h_e[t_2] = 1$
			$\sum p_i = 1$	$h[t_2] = \sum p_i h_i[t_2]$

a: If there was an avalanche in I_2, there could not have been one in I_1 and there can be none in I_3. Since avalanches in the I_2-bins never occur in the same turn, the probability for this configuration, p_a, is given by a sum of $a[t]$ over I_2: $p_a = \sum_{t' \in I_2} a[t']$.

b: The probability of an avalanche at $t_0 \in I_1$ is $a[t_0]$. For this case to occur, there must be no subsequent avalanches up to $t_2 - 1$. Assuming that $h[t]$ is known for all $t < t_2$, we use the *corrected* avalanche rate, $a'[t]$:

$$a'[t] \equiv a[t]/h[t] \qquad (5)$$

to estimate p_b. Given an avalanche at t_0, the sensitivity at $t_1 > t_0$ is $S[t_1 - t_0]$ and subsequent avalanche probabilities are estimated as $S(t_1 - t_0)a'[t_1]$.

The probability of no avalanche in I_3, given an avalanche at t_0, is denoted $P(!I_3|t_0)$ and estimated to:

$$P(!I_3|t_0) = \prod_{t_1=t_0+T_{s,min}}^{t_2-1} (1 - S[t_1 - t_0]a'[t_1]) \qquad (6)$$

p_b is given by a sum over all $t_0 \in I_1$:

$$p_b = \sum_{t_0 \in I_1} a[t_0]P(!I_3|t_0) \qquad (7)$$

Finally, h_b is the weighted sum of $S[t_2 - t_0]$

$$h_b = \sum_{t_0 \in I_1} a[t_0]P(!I_3|t_0)S(t_2 - t_0)/p_b \qquad (8)$$

c: Given an avalanche in I_1, this is the complement of case **b**

$$p_c = \sum_{t_0 \in I_1} a[t_0]P(I_3|t_0) = \qquad (9)$$

$$= \sum_{t_0 \in I_1} a[t_0](1 - P(!I_3|t_0)) = \left(\sum_{t_0 \in I_1} a[t_0]\right) - p_b$$

d: The probability of an avalanche in I_3 is: $P(I_3) = \sum_{t_0 \in I_3} a[t_0] = p_c + p_d$. Therefore:

$$p_d = P(I_3) - p_c \qquad (10)$$

e: This is the last case, i.e:

$$p_e = 1 - (p_a + p_b + p_c + p_d) \qquad (11)$$

To evaluate $h[t_2]$ for all t_2 in the entire histogram, $h[t_2]$ must be evaluated iteratively since, since $h[t_2 - 1]$ and $a'[t_2 - 1]$ are used.

Afterpulse Rate

To estimate the rate of measured afterpulses, it is tempting to convolute $a[t]$ with $R[t]$ and then multiply with the average sensitivity $h[t]$. However, this would in general underestimate the afterpulsing rate where main bunches are closer than $T_{s,min}$ since two main bunches spaced by 25 or 50 ns will never cause an avalanche in the same turn. For example the rate of measured afterpulses from the first bunch in Fig. 2 is completely unaffected by the presence of the second main bunch, no matter how high its intensity. This single-turn correlation between a primary avalanche and its afterpulses therefore needs to be addressed. To evaluate how an avalanche at t_0 affects the measured rate of afterpulses at t_2, we therefore distinguish between *recent* afterpulses, $r_r[t]$, and *late* afterpulses, $r_l[t]$. The total afterpulse rate $r_m[t]$ is the sum $r_m[t] = r_r[t] + r_l[t]$.

ISBN 978-3-95450-141-0

Copyright © 2014 CC-BY-3.0 and by the respective authors

Recent afterpulses We define "recent" to mean $t_2 - t_0 \leq 2T_{s,min}$, i.e. about 140 ns in our case. Given an avalanche at $t_0 \in [t_2 - 2T_{s,min}, t_2 - T_{s,min}]$, an afterpulse at t_2 can occur only if there are no subsequent avalanches in the interval $[t_0 + 1, t_2 - 1]$. We estimate the probability for this to be:

$$P(![t_0 + 1, t_2 - 1]|t_0) = \prod_{t_1=t_0+1}^{t_2-1} 1 - S[t_1 - t_0]a'[t_1] \quad (12)$$

Here, the corrected avalanche rate $a'[t]$ is used. In the case of Fig. 2, the influence by the second main bunch on afterpulses from the first main bunch would be masked by the factor $S[t_1 - t_0]$.

Since no avalanches in $[t_2 - 2T_{s,min}, t_2 - T_{s,min}]$ can occur in the same turn, the total rate of recent afterpulses at t_2 is a straight sum over t_0:

$$r_r[t_2] = \sum_{t_0=t_2-2T_{s,min}}^{t_2-T_{s,min}} a[t_0]P(![t_0 + 1, t_2 - 1]|t_0)R[t_2 - t_0] \quad (13)$$

Late afterpulses For late afterpulses, the assumption is made that the gap between avalanche occurrence t_0 and afterpulse time t_2 is sufficiently large that the average sensitivity $h[t_2]$ can be used to estimate the afterpulse:

$$\begin{aligned} r_l[t_2] &= \textstyle\sum_{t_0<t_2-2T_{s,min}-1} a[t_0]R[t_2 - t_0]h[t_2] = \\ &= h[t_2] \times (a * \tilde{R})[t_2] \end{aligned} \quad (14)$$

where $*$ denotes discrete convolution and $\tilde{R}[t]$ is identical to $R[t]$, but with the contribution from recent afterpulses masked:

$$\tilde{R}[t] = \begin{cases} 0 & \text{if} \quad t \leq 2T_{s,min} \\ R[t] & \text{if} \quad t > 2T_{s,min} \end{cases} \quad (15)$$

RESULTS

Afterpulse Rate

In order verify the accuracy of the afterpulse rate, $r_m[t]$, the SPAD was illuminated with 300 laser pulses spaced at 25 ns with a repetition rate of 100 kHz to simulate the typical main bunch rate under operational conditions. The light was attenuated with neutral density (ND) filters of different strengths (0-2, corresponding to three orders of magnitude). Figure 6 shows the measured histogram, $a[t]$ (solid), and the predicted afterpulse rate, $r_m[t]$ (dashed), at the end of the pulse train. $r_m[t]$ and $a[t]$ are in excellent agreement up to ND1, where the number of counts per main bunch is about 0.13 (=0.2 at full availability). At this count rate (5.2×10^6/s), the availability in the pulse train is in general reduced by about 40%.

With ND0, the SPAD is close to saturation, but the counts per bunch are only marginally higher (0.15). The discrepancy between $a[t]$ and $r_m[t]$ can be explained by an SPAD feature unaccounted for in the current model. At the end of the deadtime, there is a time window of a few ns where the bias voltage is above breakdown, but the signal output is still inactive. Avalanches occurring in this window will be unaccounted for, causing an overestimation of $h[t]$. The quenching of these avalanches is also delayed, so that the longer lasting avalanche current will trap more charge carriers and increase the afterpulse rate.

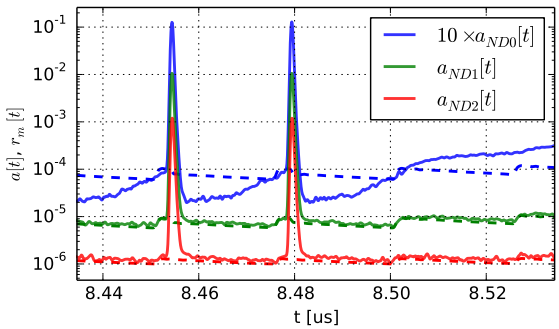


Figure 6: $a[t]$ (solid) and $r_m[t]$ (dashed) at the end of a 300 long 40 MHz pulse train. $a_{ND0}[t]$ is offset by a factor 10 for readability.

Photon Rate

In order to verify the correction algorithm, the SPAD was exposed to two pulsed lasers with different intensity, simulating operational conditions with 40 MHz high intensity "main bunches" with intermediate "ghosts" of about 2.4×10^{-5} times lower intensity. $a_{H+L}[t]$ in Fig. 7 shows the initial part of the pulse train. The afterpulsing between main bunches shows a larger variation than the amplitude of the "ghosts", with almost discontinuous jumps one τ after each main bunch. When removing the afterpulses to estimate $\gamma[t] + b$ (Eq. 4), the baseline between main bunches is flattened, which greatly facilitates estimation of ghost and satellite population. As there are inevitably some unregistered avalanches, the estimated baseline is slightly higher than the "true" background rate (as a reference, $a_L[t]$ shows the signal with only the low intensity laser on). The higher baseline, which is fairly stable, can be explained by late afterpulses accumulated from unregistered avalanches.

LHC LDM Data Correction

The correction algorithm has also been tested on some data sets from LHC Run 1. One example is shown in Fig. 8.

Uncorrected, the afterpulses alone produce a baseline variation between main bunches that is several times larger than the ghost and satellite signal. After correction, the baseline is flattened and the satellite and ghost bunch profiles are more apparent.

A gradual decrease of the corrected baseline between main bunches can be seen in the signal. This is an effect of the unregistered avalanches, which are more likely to happen where there are main bunches, and result in an overestimation of $h[t]$, with the effect that $r_m[t]$ is overestimated and $\gamma[t]+b$ consequently underestimated. The closer the window where avalanches can occur without being registered is to the main

Copyright © 2014 CC-BY-3.0 and by the respective authors

ISBN 978-3-95450-141-0

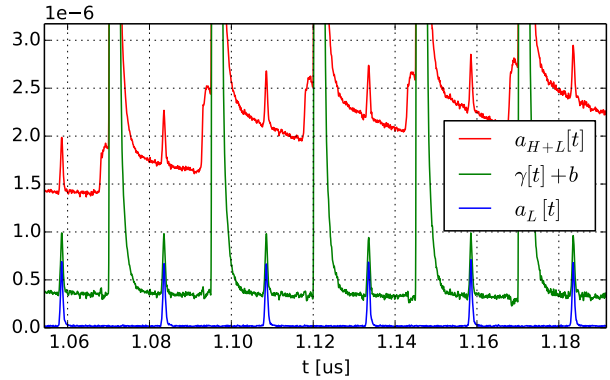


Figure 7: Initial part of LHC-like pulse train with intermediate ghosts (red: high+low intensity laser, blue: only low intensity laser, green: calculated $\gamma[t] + b$).

bunch separation (a multiple of 25 ns), the more enhanced this effect would be. It has been confirmed that the end of this window is very close to 75 ns. For Run 2, the deadtime of the SPADs has been adjusted to minimize this effect.

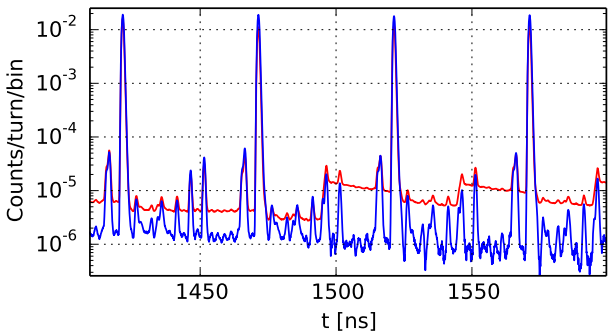


Figure 8: Raw (red) and corrected (blue) LDM data from fill 3005, Beam 2.

CONCLUSIONS

A model based characterizing the response of Single-Photon Avalanche Diodes has been developed to enable the removal of afterpulse signals to retrieve the underlying relative photon rate. Its accuracy and ability to distinguish between afterpulse and photon induced avalanches has been confirmed experimentally under LHC-like conditions at count rates over $5{\times}10^6$/s.

ACKNOWLEDGMENT

Many thanks to Georg Simmerle at MPD for his kind support and help in interpreting the data and behaviour of the SPADs, as well as for tuning the deadtime of the LDM detectors to our needs.

REFERENCES

[1] A. Jeff et al., "Longitudinal density monitor for the LHC", Phys. Rev. ST-AB, p. 032803 (2012) 15(3)

[2] F. Zappa et al., "Monolithic Active-Quenching and Active-Reset Circuit for Single-Photon Avalanche Detectors", IEEE Journal of solid-state circuits, p. 1298 (2003) 3(7)

Copyright © 2014 CC-BY-3.0 and by the respective authors

ISBN 978-3-95450-141-0

NOVEL FEMTOSECOND LEVEL SYNCHRONIZATION OF TITANIUM SAPPHIRE LASER AND RELATIVISTIC ELECTRON BEAMS

M. Titberidze*, F. Grüner, A.R. Maier, B. Zeitler, University of Hamburg, CFEL, Hamburg, Germany
M. Felber, K. Flöttmann, T. Lamb, H. Schlarb, C. Sydlo, DESY, Hamburg, Germany
E. Janas, Warsaw University of Technology, Warsaw, Poland

Abstract

Laser driven plasma accelerators are offering high gradient (~10-100 GV/m), high quality (low emittance, short bunch length) electron beams, which can be suitable for future compact, bright and tunable light sources. In the framework of the Laboratory for Laser-and beam-driven plasma Acceleration (LAOLA) collaboration at Deutsches Elektronen-Synchrotron (DESY) the external injection experiment for injecting electron bunches from a conventional RF accelerator into the linear plasma wave is in progress. External injection experiments at REGAE (Relativistic Electron gun for Atomic Exploration) require sub-20fs precision synchronization of laser and electron beams in order to perform a beam scan into the plasma wave by varying the delay between electron beam and laser pulses. In this paper we present a novel optical to microwave synchronization scheme, based on a balanced single output integrated Mach-Zehnder Modulator (MZM). The scheme offers a highly sensitive phase detector between a pulsed 800 nm Ti:Sa. laser and a 3 GHz microwave reference source. It is virtually independent of input laser power fluctuations and it offers femtosecond long-term precision. Together with the principal of operation of this setup, we will present promising preliminary experimental measurements of the new detector stability.

INTRODUCTION

Preparations for external injection experiments at REGAE facility for mapping the plasma wakefield are currently ongoing. At REGAE, electron bunches are generated by impinging commercial ultrafast (25 fs pulse duration) Ti:Sa. laser on a photo-cathode. Generated electrons are accelerated by S-band (resonance frequency f_{RF} = 2.9979 GHz) RF structure. Accelerated electrons reach maximum energy of ~ 5 MeV. Subsequently, electrons are longitudinally compressed down to 10 fs rms by S-band RF buncher using so called "ballistic bunching" technique, more details about REGAE can be found everywhere [1].

In order to deliver ultrashort electron bunches with femtosecond level accuracy for external injection purposes in a linear plasma wave, it is crucial to precisely synchronize photo-injector 83 MHz repetition rate 800 nm center wavelength Ti:Sa. laser oscillator to 2.9979 GHz RF source from Master Oscillator (MO).

Different approaches can be considered for synchronizing femtosecond laser pulses to RF reference signals: One could employ a so called direct conversion scheme which involves a fast photo-diode followed by an RF band-pass filter, used to extract a desired microwave signal from the laser pulse train. The phase difference between the RF reference and the microwave signal generated from the laser can be used to synchronize the latter. Currently, the direct conversion based down converter scheme is in daily operation at REGAE. General layout of the REGAE is shown in Fig. 1. It is clear form the block diagram that our reference source is RF Master Oscillator. Signals from MO are distributed to different sub-systems of the accelerator as well as to photo-injector laser for synchronization purposes.

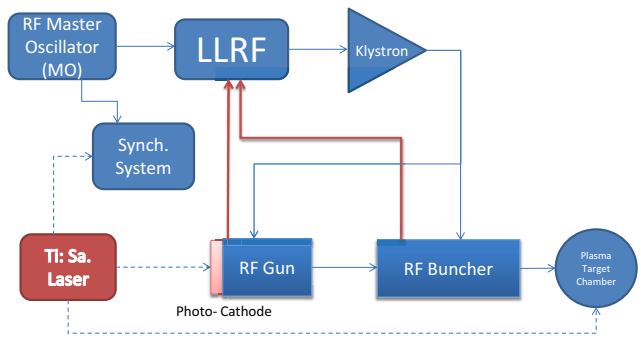


Figure 1: Layout of the RF and laser systems of REGAE.

In general, earlier mentioned direct conversion scheme suffers from AM/PM (amplitude modulation to phase modulation) effects in the photodiode, which can be as high as 1-3 ps/mW [2]. Another Laser to RF locking setup, which is highly accurate and very sensitive, uses an single output integrated electro-optical amplitude modulator (EOM, practically a Mach-Zehnder Intensity Modulator). The phase error between the laser pulse train and the RF reference causes an amplitude modulation of the laser pulse train, which can be detected with a photodiode much more accurately. The original idea of the new synchronization setup based on MZM was first published in 2011 [3] for RF stabilization purposes when the reference was laser itself. The scheme was realized for 1.3 GHz RF and 216 MHz repetition rate (FLASH and European XFEL frequencies) 1550 nm wavelength laser pulses and it showed very promising results ~ 15 fs peak-to-peak drift over 40 hours, the results were improved in 2013 where the experiment showed 3.6 fs peak-to-peak stability over 24 hours [4]. At REGAE, our reference is a 2.9979 GHz RF signal coming from RF Master Oscillator. Therefore, we

* mikheil.titberidze@desy.de

Copyright © 2014 CC-BY-3.0 and by the respective authors

ISBN 978-3-95450-141-0

want to precisely synchronize/lock the Ti:Sa. laser oscillator to our reference.

There is a conceptual difference between the setup what is presented in this paper and the one which was tested for FLASH and European XFEL [3, 4]. For FLASH and European XFEL setups, MZMs are available with dual outputs. The dual output configuration gives flexibility to overcome several significant challenges of the setup, such as splitting ratio mismatch between two pulse trains and DC bias drift of the MZM. Additionally, in dual output MZM one could quadruple the repetition rate of the pulse train by adding an extra delay to one of the outputs of the MZM which increases the sensitivity of the detector.

PRINCIPLE OF OPERATION

The idea is, to take the incoming laser pulse train and split it into two beams. After splitting, a time delay is introduced to one of the pulse trains. Both pulse trains (delayed and non-delay) are then recombined and guided into an integrated MZM. The time delay between laser pulses is chosen such that when 3 GHz reference is applied to the MZM, the pulses arrive on zero crossings with positive and negative slopes of the microwave reference signal. Ideally, when there is no timing jitter between two sources, laser pulses do not get any amplitude modulation. If there is a phase mismatch between the laser pulse train and the RF reference, the laser pulse arriving on the positive slope will see a positive voltage from the RF reference, while the laser pulse arriving on the negative slope will experience a negative voltage from the RF reference or vice versa, depending on the direction of the phase change. This will lead to an amplitude modulation of the optical pulse train. The modulated optical pulses can be represented as following:

$$P_{mod} = P_{in}\frac{\alpha}{2}\left(1+\cos\left(\frac{\pi(V_{in}-V_0)}{V_\pi}\right)\right) \qquad (1)$$

Where, P_{in} is an average power of input radiation to the MZM from the laser, V_0 and V_{in} are offset and input voltages respectively. V_π is a value of V_{in} needed to introduce a π phase shift, resulting full transmission to no transmission of the input optical power at the output of the MZM. α is an insertion loss of the MZM. Fig. 2 summarizes the idea of the new synchronization system.

In Fig. 2, upper sketch shows 3GHz RF signal from Master Oscillator (MO) is sampled by two pulse trains of 83 MHz repetition rate laser with a time delay T. The laser pulses are aligned with respect to RF signal such that they arrive on zero crossings as well as opposite slopes of the signal. Since, relative phase shift between two sources is zero, we do not observe any amplitude modulation.

On the other hand, lower sketch of Fig. 2 depicts the case when there is a timing jitter between microwave signal and a laser and it is converted into amplitude modulation of the laser pulses via MZM. Once the amplitude modulation is detected, it is possible to use this information to lock the laser to the 3 GHz RF reference.

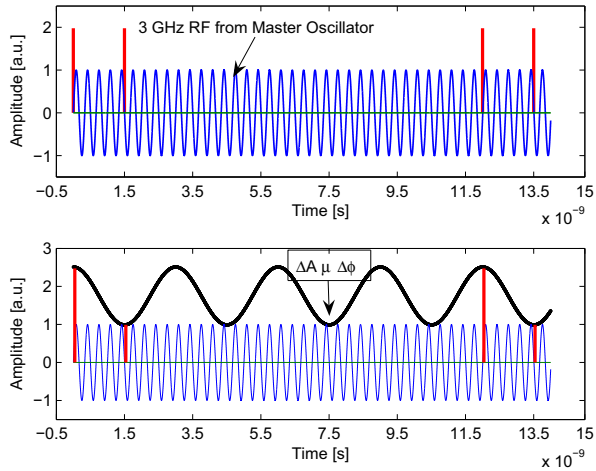


Figure 2: Conceptual representation of the modulated vs. non modulated laser pulses.

How to choose a Delay between Laser Pulse Trains and what is a Modulation Frequency?

It is crucial to define a correct time delay between two pulse trains of the Ti:Sa. after splitting. As we mentioned earlier there are several conditions which needs to be satisfied when choosing a time delay T. The separation of 83 MHz laser pulses cover 36 full periods of 3 GHz RF signal.

- Laser pulses should arrive opposite slopes of the RF.
- Product of harmonic of the laser N, and sub-harmonic of RF M should result 36.
- M has to be odd sub-harmonic of 3 GHz signal so laser pulses can experience opposite slopes of the RF.

For REGAE frequencies these conditions can be satisfied only by the following three combinations:

Table 1: Possible Combinations of Laser and RF Harmonics

Laser harmonic	RF sub-harmonic	Freq. f_{mod}
4	9	~ 333 MHz
12	3	~ 1000 MHz
36	1	~ 3000 MHz

From the table above, it is obvious that the best combination due to practical reasons is the first combination which results the modulation frequency of ~333 MHz. Since, $T = \frac{1}{2}T_{mod} = \frac{1}{2f_{mod}}$ the time delay between laser pulses should be ~ 1.5 ns.

REALIZATION OF THE EXPERIMENTAL SETUP

A new synchronization setup is based on free space optics as well as fiber optics since we use integrated MZM which has polarization maintaining fiber input and output. The detailed sketch of the setup is shown in Fig. 3.

ISBN 978-3-95450-141-0

Copyright © 2014 CC-BY-3.0 and by the respective authors

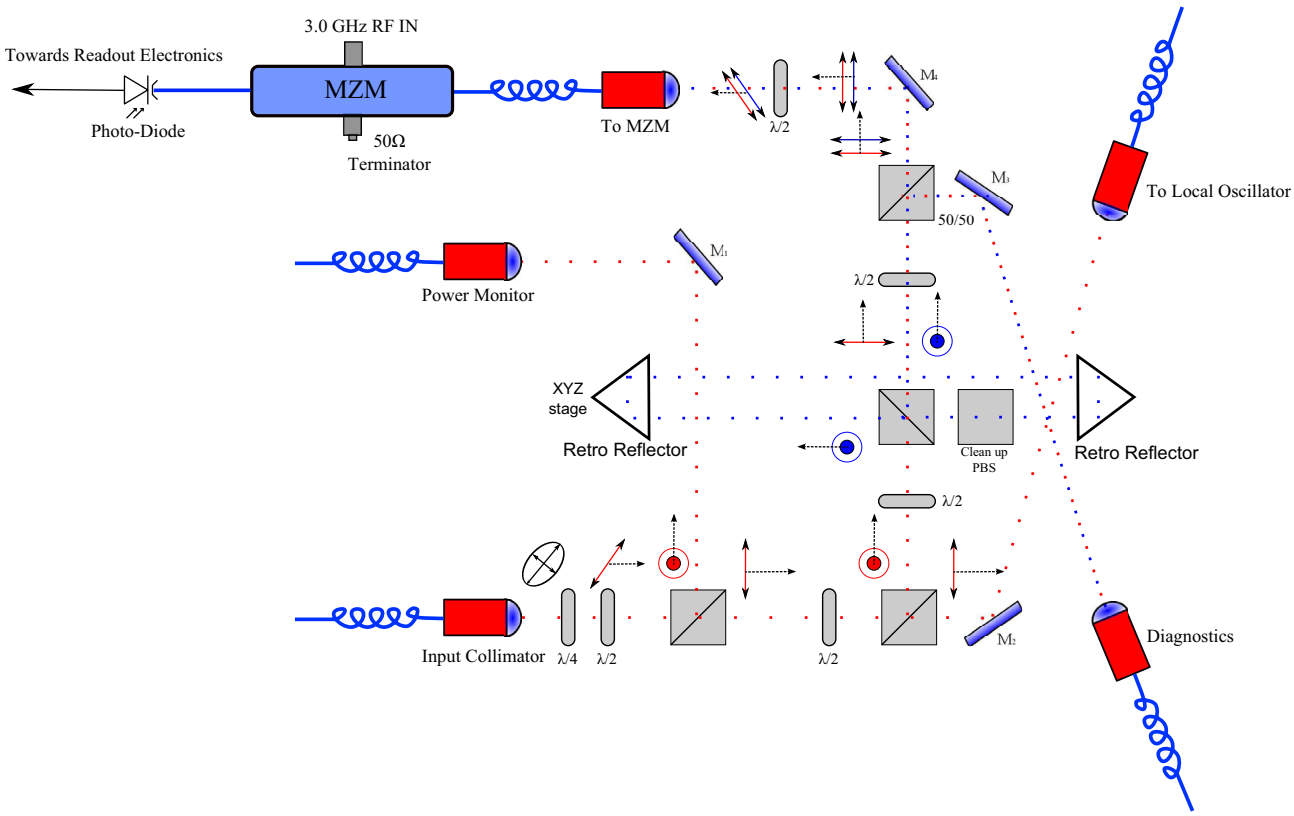


Figure 3: Optics part for novel laser to RF synchronization system.

The reader may observe that in Fig. 3 pigtailed fiber collimators are used throughout the setup. The major advantages of using them is that collimators output defined spot size of the laser beam, they are less sensitive to laser beam pointing and collimator to collimator incoupling efficiency can be more than 80% over distances up to 0.5 m. In Fig. 3, after the first collimator we have $\frac{\lambda}{4}$ waveplate to make sure that the input light after the collimator is linearly polarized. It is followed by two pairs of $\frac{\lambda}{2}$ waveplates and polarizing beam cubes (PBC) to tap off some light for diagnostics purposes. The third pair of wavepalate and PBC is the most important in this setup because it adjusts the splitting ratio of the delayed vs. non-delay pulse trains. The delayed pulse train passes through a pair of retro-reflectors and a PBC which is used for "clean up" purposes to remove the undesired polarization state which might be generated after the retro-reflectors. Afterwards both delayed and non-delayed pulse trains get combined using the same PBC which was used for splitting. After recombining the pulses the polarization states are orthogonal to each other and in order to make them collinear we need to rotate polarization states of both pulse trains by 45° using a $\frac{\lambda}{2}$ waveplate. This will result 50% optical power loss after the PBC. The pigtailed fiber collimator which is used for guiding both pulse trains into the MZM has a polarization maintaining fibre (PMF). MZM is build in a way that, it requires input light polarization state to be aligned to the slow axis of the PMF fibre. We do not know the orientation of the pigtailed fibre collimator in terms of its polarization axis (slow axis). Therefore, additional $\frac{\lambda}{2}$ waveplate is used to align the polarization state of the light to the slow axis of the PMF fibre. We can crosscheck it by measuring the maximum optical power at the output of the MZM. Both pulse trains passing the MZM undergo the insertion loss of the modulator which varies depending on the manufacturer of the modulator. In our case MZM was designed and manufactured by Jenoptik AG and the insertion loss of the modulator amounts to 6 dB of the input optical power. One can roughly estimate what fraction of the initial optical power do we obtain at the output of the MZM, taking into account all the losses we mention earlier in this discussion and it turns out to be ~ 10% of the total input power. The modulated pulses after the MZM are sent to fast photo-diode to convert the optical pulses into electric signals for further signal processing and ultimately detecting the amplitude modulation of it. Therefore, the desired input average optical power of the novel laser to RF synchronization setup should be around 10 mW. Fig. 4 below shows the commissioning process of the new synchronization setup.

In Fig. 4, red line shows the propagation of the optical pulse train from input collimator to output collimator including optical delay line made by a pair of retro-reflectors. An engineered baseplate [4, 5] is used for mounting the opto-mechanics. It is actively temperature stabilized using two Peltier elements connected to analog temperature controller from Team Wavelength. Additionally, special isolation is

Copyright © 2014 CC-BY-3.0 and by the respective authors

ISBN 978-3-95450-141-0

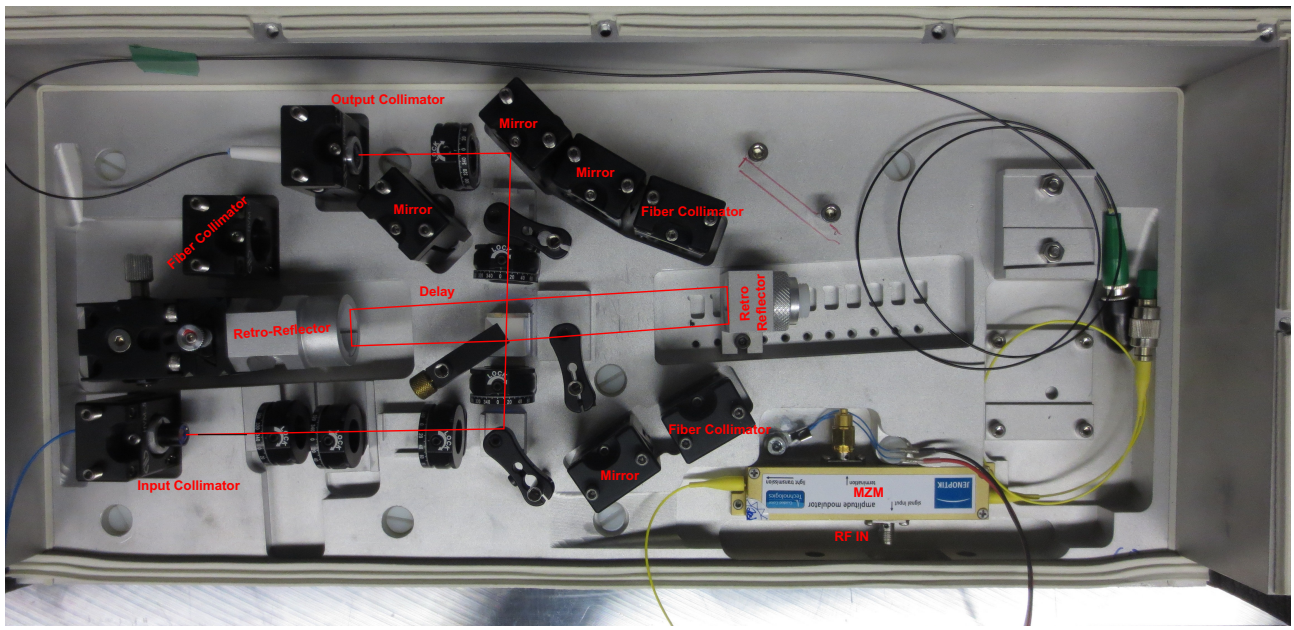


Figure 4: Commission process of the opto-mechanical setup for the novel synchronization system.

used to minimize the influence of the ambient temperature variations inside the box.

Fig. 5 shows the temperature stability of the two different positions of the baseplate measured over approximately 6 days. The measurement shows ambient temperature variation peak-to-peak more that 0.6 K, while the temperature changes near the MZM and across the baseplate are peak-to-peak 11 mK and 63 mK, resulting suppression factors of ~ 56 and ~ 10 respectively.

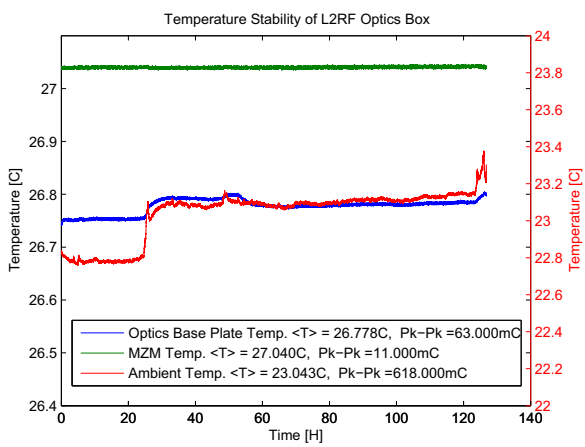


Figure 5: Temperature stability of the engineered baseplate.

ELECTRONICS SETUP FOR AMPLITUDE DETECTION

Once optical pulses are converted to electric signals via photo-diode, we need to filter out desired frequency line from the RF comb. As it was discussed earlier, the modulation frequency of the optical pulses is $\sim$ 333 MHz for REGAE frequencies. Therefore we employed 333 MHz RF bandpass filter and further amplified signal using low noise RF amplifiers. We decided to use an RF mixer for detecting the amplitude of the 333 MHz signal by mixing the signal to 333 MHz local oscillator (LO) which is also derived from the same laser oscillator pulse train. LO power should be high enough to saturate the mixer so small power fluctuations from the laser oscillator which will convert to amplitude variations of the LO signal can be neglected. Additionally, an electric phase shifter should be used to drive mixer as an amplitude detector. The schematics of the electronics setup for amplitude detection of 333 MHz signal is shown in Fig. 6. The diagram also shows how we plan to stabilize DC bias drift of the MZM and how to keep the working point of the modulator in a so called "quadrature bias point" or half transmission point.

Performance Measurements

The performance of the synchronization scheme will be limited by noise floor of the photo-diodes and read-out electronics. For that reason, we carried out baseband voltage noise measurements. For the measurement we used 1550 nm central wavelength Menlo Laser, InGaAs photodiodes and minicircuits RF components (Filters, Amplifiers). Optical power levels were set to $\sim$ 1 mW for both diodes. Agilent Signal Source Analyzer (SSA) was used to measure baseband voltage noise of the read-out electronics setup. Calibration constants K_φ were obtained by applying 1.3 GHz RF signal to the MZM. K_φ is used to convert integrated voltage noise to timing jitter (femtoseconds). Figure 7 shows the voltage noise and integrated timing jitter over the frequency range of 1 kHz to 10 MHz of the amplitude modulation read-out electronics for two different cases.

ISBN 978-3-95450-141-0

Copyright © 2014 CC-BY-3.0 and by the respective authors

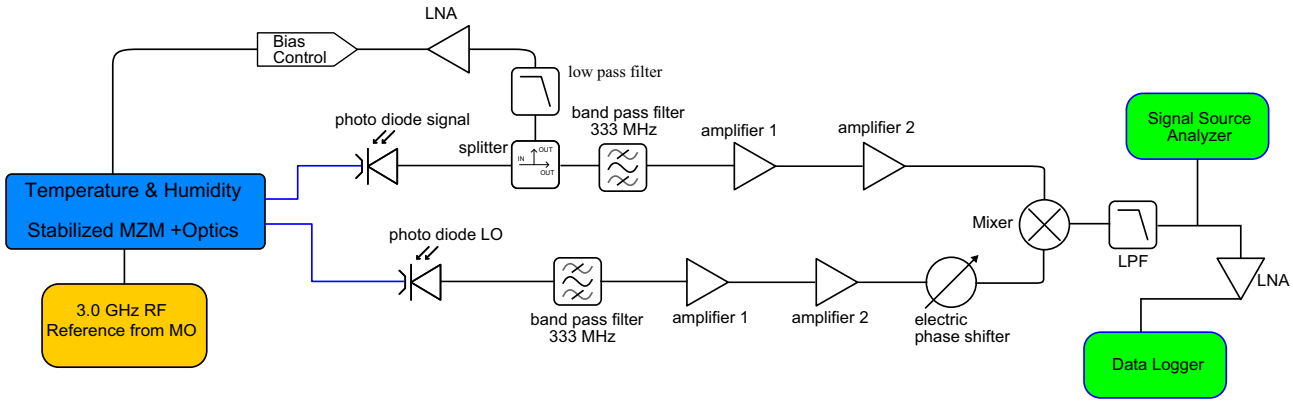


Figure 6: Schematics for amplitude modulation read-out electronics.

First we had two low noise RF amplifiers connected in series for signal amplification coming from the photo-diode which was getting signal from the MZM output. The calibration factor in this case was $K_\varphi = 0.3\frac{\mathrm{V}}{\mathrm{ps}}$, which results integrated timing jitter of $\Delta T_1 = 15.5$ fs. Adding one more low noise amplifier, definitely increases the noise floor of the signal, but on the other hand it also increases the calibration factor up to $K_\varphi = 6.2\frac{\mathrm{V}}{\mathrm{ps}}$ which compensates the higher noise floor and results almost factor of 2 smaller timing jitter $\Delta T_2 = 8.86$ fs.

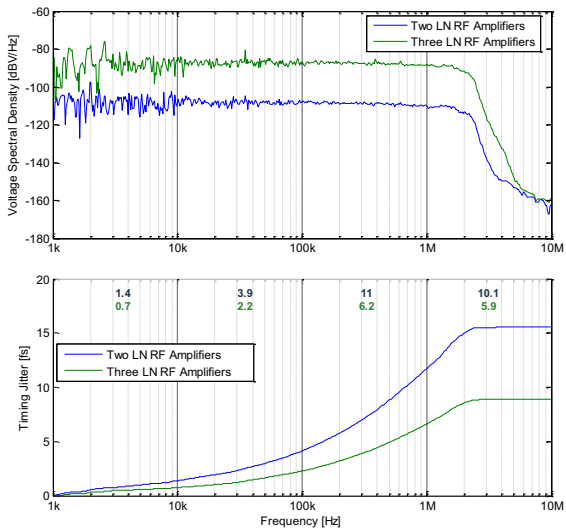


Figure 7: Baseband voltage noise (top) and Integrated timing jitter (bottom).

CONCLUSION AND FUTURE WORK

We presented novel synchronization system for locking Titanium Sapphire laser and 2.997 GHz RF reference with fs level of precision. The setup was discussed in great details and pointed out some of the technical challenges. Noise floor measurements of the read-out electronics show promising results. Next step is to test the single output MZM based setup in a real accelerator environment and lock the Ti:Sa. oscillator to the RF reference.

ACKNOWLEDGMENT

I would like to thank my supervisors Prof. F.Grüner and Dr. H.Schlarb, colleagues from DESY Lbsync group for their support. I also express my gratitude to REGAE external injection group as well as LUX team.

REFERENCES

[1] B. Zeitler et al., "Merging conventional and laser wakefield accelerators", Proc. SPIE 8779, doi: 10.1117/12.2019339 (2013).

[2] B. Lorbeer et al., "Noise and drift Characterization of Critical Components for the Laser Based Synchronization System at FLASH", Proc. DIPAC'07, Venice, Italy (2007).

[3] T. Lamb et al., "Femtosecond Stable Laser-to-RF Phase Detection using Optical Modulators", Proc. FEL'11, Shanghai, China (2011).

[4] T. Lamb et al., "Femtosecond Stable Laser-to-RF Phase Detection for Optical Synchronization Systems", Proc. IBIC'13, Oxford, UK (2013).

[5] E. Janas et al., "Design and Integration of the Optical Reference Module at 1.3 GHz for FLASH and the European XFEL", Proc. IPAC'14, Dresden, Germany (2014).

Copyright © 2014 CC-BY-3.0 and by the respective authors

ISBN 978-3-95450-141-0

CW BEAM STABILITY ANALYSIS IN TIME AND FREQUENCY DOMAIN

M. Kuntzsch#, HZDR, Dresden Germany, TU-Dresden, Dresden, Germany
U.Lehnert, R.Schurig, J. Teichert, M.Gensch, S. Kovalev, B. Green, P. Michel, HZDR, Dresden, Germany

Abstract

The continuous wave (CW) mode of operation enables a high bandwidth jitter analysis for different diagnostic devices. The measurement is only limited by the bunch repetition rate and the acquisition time, since the bunch train is not interrupted by a macro pulse. At ELBE various diagnostics capable for continuous data acquisition has been installed and used for an analysis of noise sources. This paper comprises measurements from a bunch arrival time monitor (BAM), results from a fast beam position monitor (BPM) installed in a dispersive section and the power spectra from a coherent transition radiation (CTR) source.

INTRODUCTION

General

The recent update of the ELBE accelerator included the installation of a new beamline section which will be used to compress the electron bunches to a duration of 100 fs at a charge of 1 nC. Two THz sources based on coherent transition or diffraction radiation und and an undulator source making use of the compressed bunches [1]. The bunch shaping is done in multiple stages by using two magnetic chicanes [2]. Along the new beamline path a couple of diagnostic stations have been set up to measure the beam properties. Figure 1 gives an overview on the ELBE accelerator and the recently installed femtosecond-beamline. The schematic shows the location of beam diagnostics used to generate the data presented in this letter.

Diagnostics

The bunch compression monitors (BCM) are measuring the power of diffraction radiation generated by the electron bunches travelling thru a hole in a silicon screen. The amplitude increases when the bunch length is reduced. Fast detectors are used to acquire qualitative bunch by bunch information [3][4].

Bunch arrival time monitors (BAM) are used to measure the timing jitter of the electron bunches with respect to an optical reference. The reference is provided by a low noise laser synchronization system. The laser pulse train is modulated by an electro-optical modulator driven by a high bandwidth beamline pickup. The arrival time information is coded into an amplitude modulation of the laser pulses and analyzed with single bunch resolution [5][6]. BAM and BCM are located between the broadband THz source and the undulator. In this section the bunch compression is optimized for the THz production and the diagnostics experiences the same jitter as the secondary sources.

In order to observe beam energy fluctuations a spectrum analyzer was used to measure the modulation of a fast analog BPM readout based on a logarithmic amplifier [7]. The BPM pickup was installed in the dispersive section right after the THz sources before entering the beam dump. Energy fluctuations are translated into position variations after the dipole magnet. By keeping the trajectory of the beam entering the dipole constant measurement artifacts caused by beam pointing could be minimized.

To measure the impact of beam instabilities on the secondary radiation, the power spectrum of the coherent diffraction radiation has been measured inside the THz laboratory. The measurement has been done with a high dynamic range spectrum analyzer connected to a fast pyro-electric detector radiated by the THz field.

All measurements are limited by the bunch repetition rate and the acquisition time. Noise components faster than half the bunch rate violate the Nyquist theorem and cause aliasing. Mirror frequencies have been identified by comparison to measurements at other repetition rates.

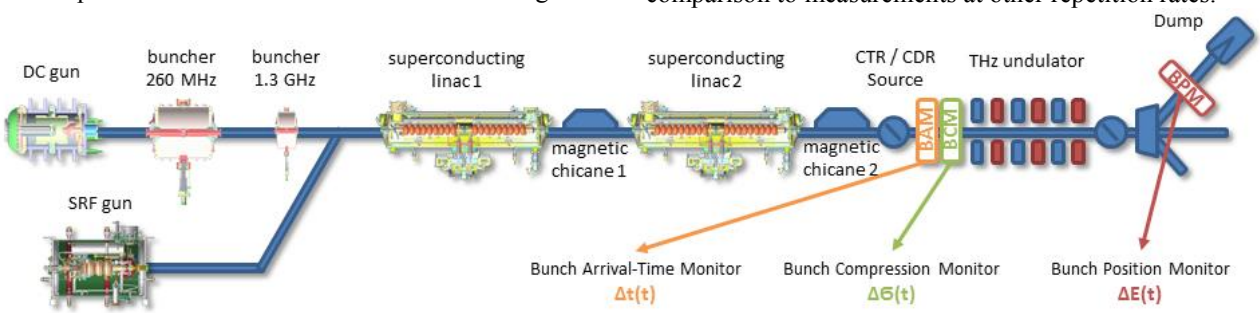


Figure 1: Schematic view on ELBE with two injectors, two superconducting accelerating cavies, magnetic chicanes for bunch compression and the THz sources. The diagnostics used to acquire the data for this contribution are highlighted, like bunch arrival time monitor, bunch compression monitor and energy dependent beam position monitor.

m.kuntzsch@hzdr.de

ISBN 978-3-95450-141-0

Copyright © 2014 CC-BY-3.0 and by the respective authors

NOISE ANALYSIS

BAM Results

The bunch arrival time monitor acquires the bunch information in time domain. By applying a Fourier transformation the information are transferred into frequency domain. Figure 2 shows the result for a 101 kHz beam at high compression in linear scale. Various fast spurs are visible above 15 kHz. The arrows mark frequency components which are also visible in the other measurements. The colors indicate spurs generated by the same noise components. For example 43 kHz as well as 17 kHz are introduced by an 84 kHz signal.

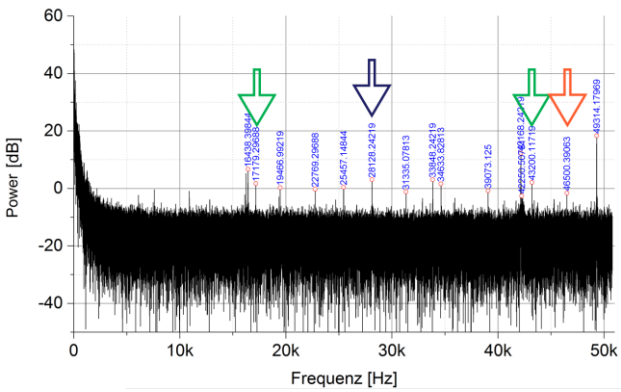


Figure 2: Bunch arrival time readout in frequency domain for a 101 kHz beam at 76 pC.

BPM Results

The energy dependent beam position measurement has been performed in parallel to the BAM measurements. Figure 3 shows the readout of the spectrum analyzer. 84 kHz and 28 kHz are mixed in the upper and the lower sideband of the 101 kHz carrier. The colors correspond to the same sources as in Fig. 2.

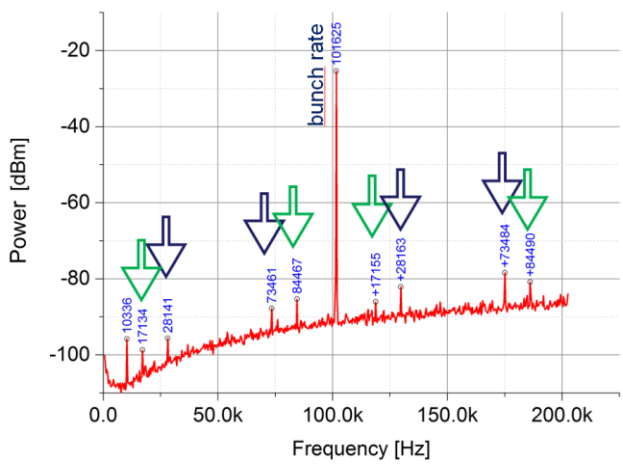


Figure 3: Power spectrum of the BPM readout. The 101 kHz carrier generated by the beam is modulated with repetitive spurs.

THz Power Spectrum

The THz power spectrum has been measured with a spectrum analyzer. The results shown in Fig. 4 indicate similar noise components as for the BPM and BAM measurements. In addition there is a major component visible at 56 kHz.

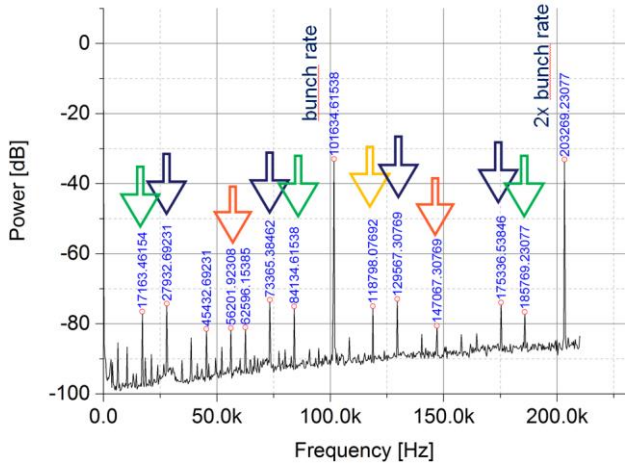


Figure 4: Power spectrum of the broadband THz source.

Summary of Analysis

The analysis of the three different beam diagnostic methods indicated similar noise components at 28 kHz, 56 kHz and 84 kHz which are all multiples of a common frequency. The equally spaced frequency components are most likely introduced by a single source. The amplitude of noise components varies from one method to other but they are always present. The frequency range of 28 kHz leads to the injector because fast fluctuation can barely be introduced by the superconducting cavities except for higher order modes.

IDENTIFICATION OF NOISE SOURCES

DC Gun and High Voltage Terminal

The DC gun at ELBE is using 235 kV to accelerate the electrons from the cathode. Figure 5 shows a schematic of the high voltage components. A resistor has been added to provide a measurement pickup to verify the voltage stability.

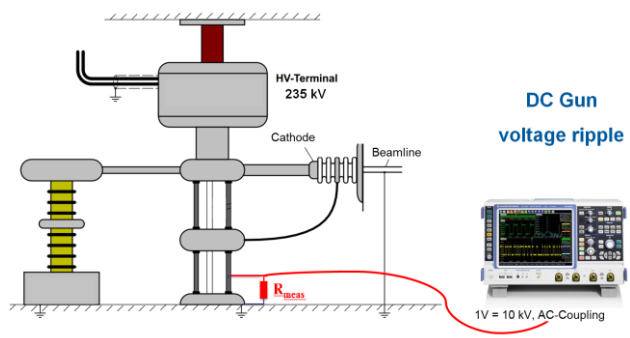


Figure 5: Schematic of the DC gun's high voltage terminal.

Copyright © 2014 CC-BY-3.0 and by the respective authors

ISBN 978-3-95450-141-0

Results

The measurement revealed instabilities of the high voltage terminal, which can be seen in Fig. 6 and Fig. 7. The ripple has a continuous sine component at 56 kHz and repetitive spurs at 28 kHz rate. The amplitude ripple of more than 2000 volt represents 0.85 percent of the static value.

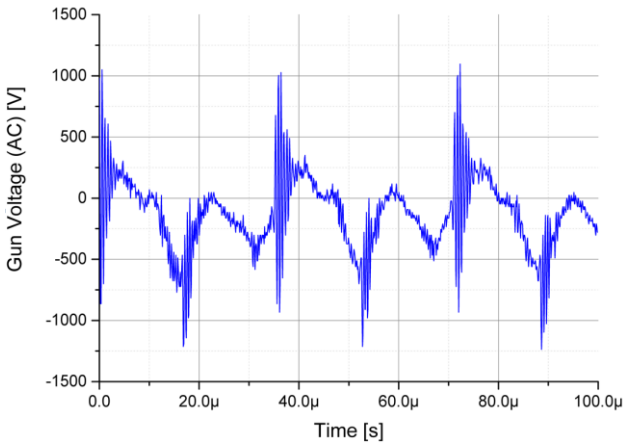


Figure 6: High voltage ripple in time domain with a 56 kHz sine component and bursts at 28 kHz rate.

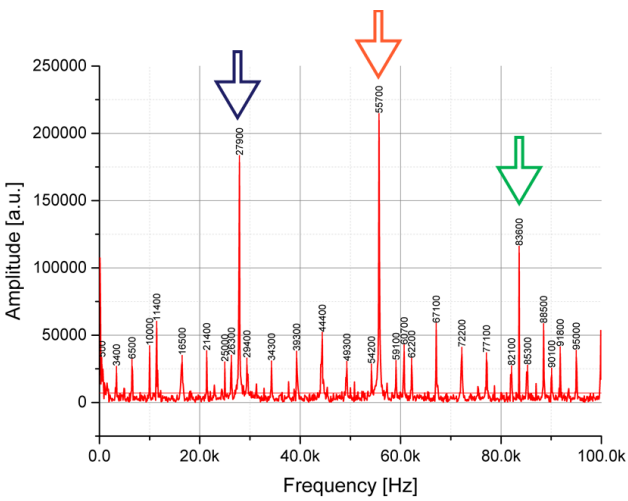


Figure 7: High voltage ripple in frequency domain. The measurement is dominated by 28 kHz and harmonic spurs

SUMMARY AND OUTLOOK

We demonstrated a combination of time and frequency domain measurements performed at ELBE. The high duty cycle enables a direct identification of noise sources indicated by their characteristic frequency. In particular the high voltage power supply for the ELBE DC gun has been revealed as one major contributor to the overall instabilities.

As a next step the high voltage power supply will be checked in order to identify the reason for the instabilities. The measured ripple which is outside of the device's specification might be due to damage caused by aging or radiation.

ACKNOWLEDGEMENT

S.K., B.G. and M.G. acknowledge support through the BMBF project INSEL (project number: 05K130DB).

REFERENCES

[1] M. Gensch et al. "THZ FACILITY AT ELBE: A VERSATILE TEST FACILITY FOR ELECTRON BUNCH DIAGNOSTICS ON QUASI-CW ELECTRON BEAMS", Proceedings of IPAC14, TUZA02

[2] U. Lehnert et al., "BUNCH COMPRESSION OF THE LOW-ENERGY ELBE ELECTRON BEAM FOR SUPER-RADIANT THz SOURCES", Proceedings of IPAC2014, Dresden, Germany, TUPRO044

[3] C. Behrens et al, "UPGRADE AND EVALUATION OF THE BUNCH COMPRESSION MONITOR AT THE FREE-ELECTRON LASER IN HAMBURG (FLASH), Proceedings od IPAC2010, Kyoto, Japan, MOPD090

[4] M. Kuntzsch et al. "ELECTRON BUNCH DIAGNOSTIC AT THE UPGRADED ELBE ACCELERATOR: STATUS AND CHALLENGES", Proceedings of IBIC2013, Oxford, United Kingdom, MOBL3

[5] F. Loehl et. al., "Electron Bunch Timing with Femtosecond Precision in a Superconducting Free-Electron Laser", Physical Review Letters PRL 104, 144801 (2010)

[6] M. Kuntzsch et. al., "Status of the femtosecond synchronization system at ELBE", BIW2012, Newport News, USA, MOBP03

[7] P. Evtushenko et al., "PERFORMANCE OF THE ELBE BPM ELECTRONICS" , Proceedings of DIPAC2003, Mainz, Germany, PT15

Copyright © 2014 CC-BY-3.0 and by the respective authors

ISBN 978-3-95450-141-0

SINGLE-SHOT ELECTRO-OPTICAL DIAGNOSTICS AT THE ANKA STORAGE RING*

N. Hiller, A. Borysenko, E. Hertle, V. Judin, B. Kehrer, A.-S. Müller, M.J. Nasse, P. Schönfeldt, M. Schuh, N.J. Smale, J.L. Steinmann, KIT, Karlsruhe, Germany
B. Steffen, P. Peier, DESY, Hamburg, Germany
V. Schlott, PSI, Villigen PSI, Switzerland

Abstract

ANKA is the first storage ring in the world with a near-field single-shot electro-optical (EO) bunch profile monitor. The method of electro-optical spectral decoding (EOSD) uses the Pockels effect to modulate the longitudinal electron bunch profile onto a long, chirped laser pulse passing through an EO crystal. The laser pulse is then analyzed with a single-shot spectrometer and from the spectral modulation, the temporal distribution can be extracted. The setup is tuned to a sub-ps resolution (granularity) and can measure down to bunch lengths of 1.5 ps RMS for bunch charges as low as 30 pC. With this setup it is possible to study longitudinal beam dynamics (e. g., microbunching) occurring during ANKA's low-α_c-operation, an operation mode with longitudinally compressed bunches to generate coherent synchrotron radiation in the THz range. In addition to measuring the longitudinal bunch profile, long-ranging wake-fields trailing the electron bunch can also be studied, hinting bunch-bunch interactions.

INTRODUCTION

During the low-α_c-operation of the ANKA storage ring at the Karlsruhe Institute of Technology, the momentum compaction factor α_c is reduced to compress the bunches longitudinally and thus generate coherent synchrotron radiation (CSR) in the THz range [1]. Previous streak camera measurements have shown a beam current dependent bunch lengthening and deformation effect at ANKA in this special operation mode [2, 3]. In addition, the emitted CSR exhibits a bursting behavior [4–6], which we believe to be caused by dynamic changes of the longitudinal bunch shape (e. g., microbunching). EOSD offers the possibility to measure the longitudinal bunch profile and its arrival time relative to the revolution clock (f_{rev} = 2.7 MHz at ANKA) with a sub-ps time resolution without averaging. First single-shot measurements with the setup have indicated the formation of substructures on the compressed bunches [7], and we have now performed systematic studies of this behavior for different accelerator conditions. Additionally, the EO near-field setup is sensitive to the vertically polarized component of the wake-fields generated by an electron bunch passing the setup. Studying the transverse wake-fields, which are coupled to the longitudinal ones, and comparing them to simulations, helps greatly to improve the simulation model for longitudinal wake-fields [8]. The observed wake-fields range further than our minimum bunch spacing of 2 ns and could influence a following bunch. An increase of CSR has previously been observed at ANKA when the ring impedance was changed by inserting a copper scraper in order to induce strong wake-fields [9].

METHOD

Electro-optical bunch length measurement techniques rely on the field-induced Pockels effect to modulate the longitudinal electron bunch profile onto a laser pulse passing through an EO crystal (further reference e. g., [10]). Figure 1 illustrates the working principle of EOSD.

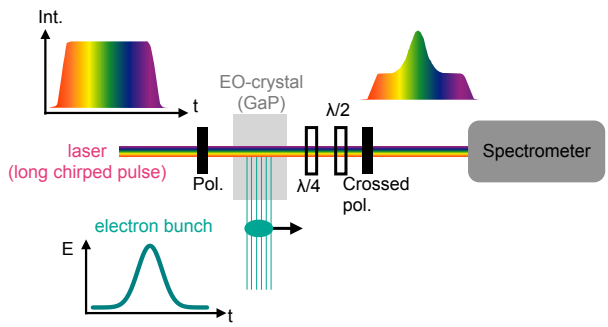


Figure 1: Schematic of EOSD (see text for details).

For the near-field measurements at ANKA, the EO crystal is brought close to the electron beam, so the direct Coulomb field of the bunch causes a modulation of polarization of the initially linearly polarized laser. This can be turned into an intensity modulation with the depicted optical components (quarter- and half-wave plates in combination with a crossed polarizer). Practically, the electric field of the bunch acts as a field-dependent phase retarder for the electric field of the laser pulse with the phase retardation being directly proportional to the field strength. For this to hold true, the crystal axis orientation, the direction of polarization of the Coulomb field and the laser need to be aligned in a specific way. Furthermore, the angles of the wave-plates need to be set in a way that the quarter-wave plate compensates the intrinsic birefringence of the the crystal and the half-wave plate regulates the transmission through the crossed polarizer (see e.g. [11] for a detailed description).
The laser system needs to be in sync with the bunch repetition rate and its delay with respect to the electron bunch

* This work is funded by the BMBF contract numbers: 05K10VKC, 05K13VKA.

Copyright © 2014 CC-BY-3.0 and by the respective authors

ISBN 978-3-95450-141-0

passing by needs to be adjustable to ensure temporal overlap between the laser pulse and the modulating electric field.

In order to demodulate the desired signal from the laser pulse, it is analyzed with a single-shot spectrometer and the temporal distribution of the electron bunch can be extracted from the spectral modulation by performing a time calibration measurement. For this time calibration measurement, we delay the laser pulse in well known steps - in our case electronically, with a programmable vector modulator - and measure the position of the centroid of the modulation within the spectrum as a function of the applied delay.

SETUP AT ANKA

The EOSD setup at ANKA consists of a laser system (EO-Laser), several single-mode and polarization maintaining fibers, the fiber-coupled EO-Monitor through which the laser beam is coupled into the UHV system of the storage ring, a set of detectors used to measure the modulated laser pulse, a beam position monitor (BPM) which we use as absolute timing reference, and a loss rate counter to ensure that the crystal is far enough from the electron beam to not cause any significant beam losses. Figure 2 illustrates the setup at ANKA and the individual components are described in more detail below.

We use an Yb-doped fiber laser system (RF synchronized oscillator, pulse picker and amplifier) developed at PSI [12] specifically for electro-optical bunch length measurements for SwissFEL and the European X-FEL. The laser oscillator is tuned to 62.5 MHz (23rd harmonic of f_{rev}) and the amplified laser pulses used for the experiment have a wavelength of around 1050 nm (60-80 nm FWHM) and a repetition rate tuned to 0.9 MHz ($f_{\mathrm{rev}}/3$).

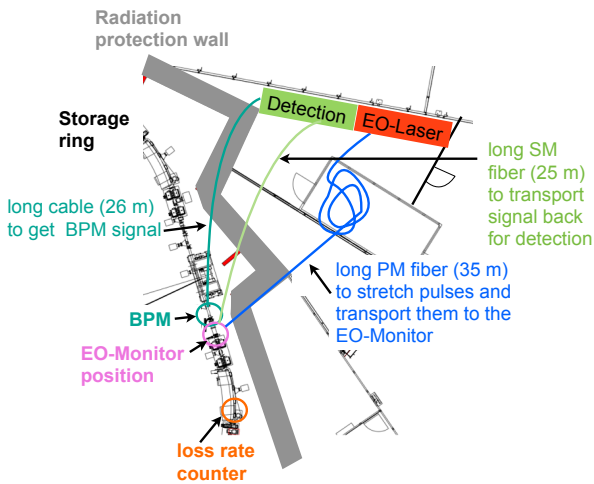


Figure 2: Near-field EOSD setup at ANKA.

The laser system is placed outside the radiation protection wall of the storage ring, the amplified laser pulses are then sent via a 35 m long polarization maintaining fiber to the EO-Monitor. The fiber-coupled EO-Monitor transports the laser beam into the UHV of the storage ring and back out to the laser hutch for analysis. It is based on a design from PSI [13, 14] which has been extended by a grating compressor to control the laser pulse length right before the pulses are sent to the EO crystal. Figure 3 depicts the in-vacuum components of the EO-Monitor. After the laser enters the UHV through a viewport, it is reflected by a silver coated prism used as a mirror and sent towards the 5 mm thick GaP crystal. The laser light enters the crystal through the front surface and is then reflected by its high-reflex coated back surface.

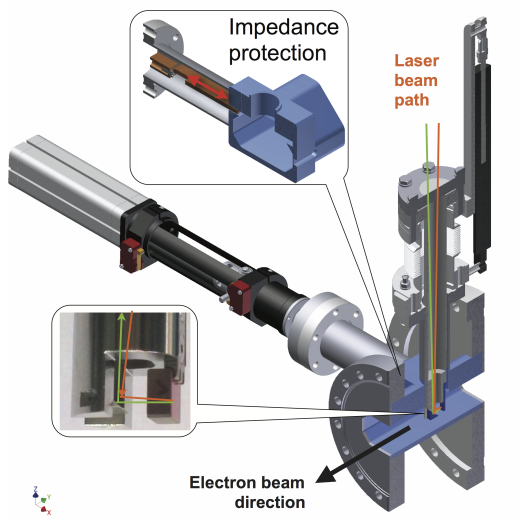


Figure 3: In-vacuum components of the EO-Monitor.

The modulation of the laser pulse by the electric field of the bypassing electron bunch happens when both the electron bunch and the laser pulse co-propagate in the crystal. The distance of the EO-crystal to the electron beam can be adjusted precisely via a linear motion feedthrough that moves not only the crystal, but also the whole EO-Monitor, this ensures that the optical delay remains unchanged when moving the crystal in. For operation at a storage ring, the EO-Monitor has been extended with a movable metallic shutter (impedance protection) that can fully cover the hole inside the UHV vacuum chamber to minimize impedance effects during normal user operation when the crystal is fully retracted from the beam pipe. With the current design, measurements are only possible during single- or dual-bunch operation because of thermal power generated by wake-fields (see [8]).

For the actual measurement, temporal overlap between the laser pulse and the electron bunch needs to be achieved inside the EO-crystal. To adjust the temporal overlap with an accuracy in the order of 1 ns, we use the direct signal of one of the four buttons of a nearby button BPM and compare its arrival time in relation to the signal of the laser pulses (measured with a fast photodiode) with an oscilloscope. The fine adjustment of the time delay (sub-ps accuracy) is then done with a step wise scan of the vector modulator that lets us delay the laser pulse very precisely while monitoring the amplitude of the modulated laser signal. Each time

ISBN 978-3-95450-141-0

Copyright © 2014 CC-BY-3.0 and by the respective authors

the synchronization between laser and RF is interrupted (e.g. when the laser is turned off), this procedure has to be repeated.

The detection of the modulated laser pulses in the laser hutch is done by either a fast InGaAs photodiode[1] in combination with an oscilloscope (for EOS, see below) or a grating spectrometer[2] (for EOSD). A more detailed description of the whole setup and measurement procedure can be found in [15]. The readout of the commercial line array inside of the spectrometer limits our acquisition rate of single-shot measurements to about 7 Hz.

Typical distances of the EO crystal from the electron beam are in the order of 5-6 mm (center of beam pipe to bottom tip of crystal) for which we detect no significant increase in the local beam loss rate with a very sensitive loss detector (lead glass scintillator coupled with a photomultiplier tube) that is placed in a dispersive section a few meters downstream of the EO-Monitor.

MEASUREMENT RESULTS

The results presented here are divided into single-shot bunch profile measurements obtained with EOSD and the study of long-ranging wake-fields measured with EOS.

Single-Shot Bunch Profile Measurements

Figure 4 shows longitudinal bunch profiles recorded for three different low-α_c-machine parameters. While plots b), c) and d) show single-shot profiles recorded with EOSD, plot a) shows bunch profiles recorded with our streak camera at approximately the same time as the profiles shown in b).

The error bands for the EOSD profiles in the plots give a measure of the one-σ-fluctuation retrieved from background measurements. They confirm that the bunch deformations and the substructures in the order of a few picoseconds are highly significant. While the data set in b) shows substructures on an otherwise rather smooth profile, the data set in d) for which the bunch charge was comparatively high shows rather triangular bunch shapes. For the data set in c), the bunch compression was not as high, and deformations and substructures do not seem to occur as strongly and frequently.

Figure 5 shows EOSD bunch profiles with the settings from a) and b) in Fig. 4, but for different bunch currents during the decay of a single bunch. While the substructures are clearly visible for the higher currents, they become less significant for lower currents. The average bunch length for the data set recorded at the lowest current (0.08 mA) was measured to be (3.31 ± 0.45 ± 0.24) ps (RMS) with the first uncertainty coming from the statistical fluctuations of fits to the 11 shots, and the second uncertainty coming from the fluctuation of the time calibration measurements for this fill.

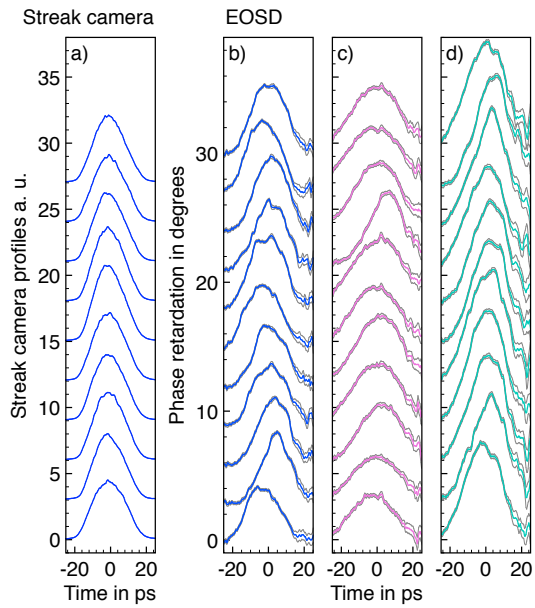


Figure 4: Bunch profiles for different machine settings. The curves have been displaced vertically for better visibility. a) Streak camera profiles for single images (averaged over 2700 bunch revolutions). b) Single-shot EOSD profiles recorded around the same time. Beam parameters for a) and b): Fully compressed beam (V_{rf} = 1.8 MV, f_s = 7.7 kHz) with 1.13 mA (418 pC) bunch current, average bunch length 8.79 ± 0.63 ps. c) Single-shot EOSD profiles for a slightly compressed beam (V_{rf} = 0.72 MV, f_s = 8.3 kHz) with 1.14 mA (422 pC) bunch current, average bunch length 13.56 ± 1.26 ps. d) Single-shot EOSD profiles for a heavily compressed beam (V_{rf} = 1.8 MV, f_s = 10.4 kHz) with a high beam current of 1.75 mA (648 pC), average bunch length 7.97 ± 0.81 ps.

Influence of Long-Ranging Wake-Fields on Following Bunches

The electro-optical setup is also sensitive to the vertically polarized component of the wake-fields trailing an electron bunch passing the setup. Typically, for this measurement we want to cover time periods in the order of a few nanoseconds, so single-shot measurements, which typically have a time window in the order of 50 ps, are not feasible, therefore only the peak amplitude of the whole laser pulse is measured while the delay between electron bunch and laser pulse is scanned step-wise. This averaging technique is referred to as electro-optical sampling (EOS). The top of Fig. 6 shows two such EOS measurements, one for a single-bunch in the accelerator and one for two consecutive bunches. For better comparison, the signals are normalized with the charges of the first bunches respectively. One can clearly see, that at the position of the second bunch (2000 ps), the wake-fields are still present. The plot on the bottom is a zoom into the time range around the first peak of the first bunches. Additionally, the signal from the second bunch (normalized

[1] EOT ET-3010
[2] Andor iDus A-DU490A-1.7

Copyright © 2014 CC-BY-3.0 and by the respective authors

ISBN 978-3-95450-141-0

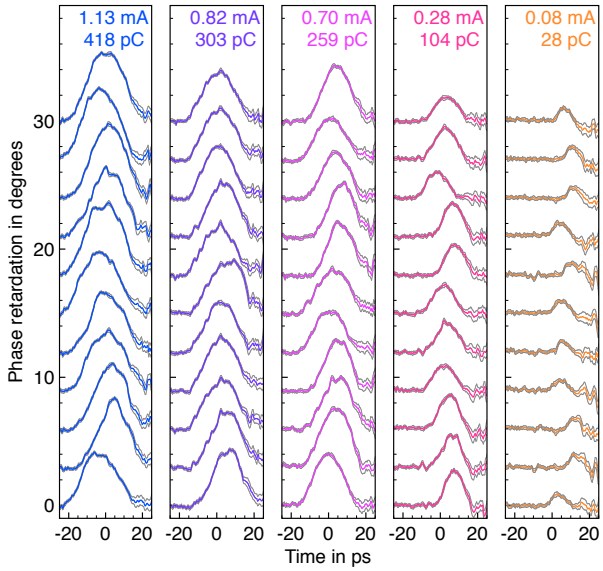


Figure 5: Single-Shot EOSD profiles for different beam currents during one fill (V_{rf} = 1.8 MV, f_s = 7.7 kHz).

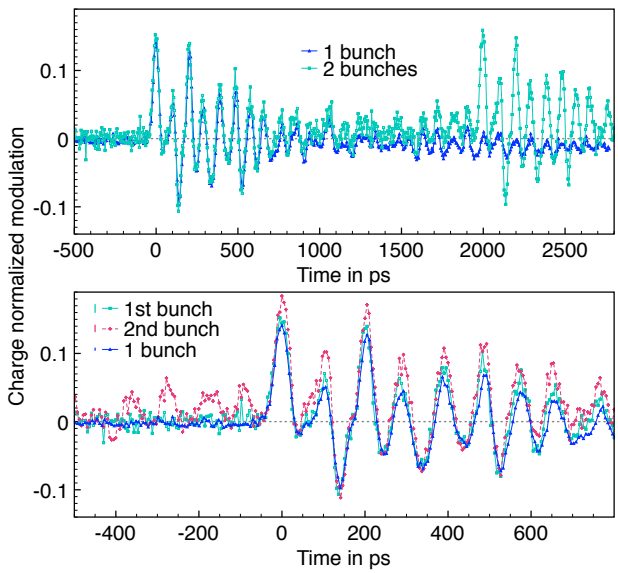


Figure 6: Top: Two EOS scans over a time range of 3 ns. One for a pure single bunch and one for a 2-bunch fill. The EOS-signal is normalized to the charge inside the first bunches. Bottom: Zoom into the region around the first peak for which in addition the signal of the second bunch has been displaced by -2 ns and has been normalized with the charge inside the second bunch.

with the bunch charge of the second bunch) is displaced by -2 ns, so all three signals can be compared easily. The second bunch shows a significantly higher signal than the first bunch and the corresponding measurement for just one bunch, which might be an indication of the influence of the wake-field of the 1st bunch on the 2nd bunch.

Clear indications of bunches influencing the bursting behavior of following bunches have previously been observed at ANKA [9] and this is believed to be caused by wake-fields. While the exact shape of the wake-fields we observe with EOS depends predominantly on the geometry of the in-vacuum setup holding the crystal [8], other structures in the storage ring (e. g., a scraper) could cause similar wake-fields, leading to bunch-bunch interactions.

CONCLUSION

We have successfully adapted the method of near-field EOSD measurements to work at a storage ring. Thus is ANKA the first storage ring in the world with a near-field single-shot EO bunch profile monitor allowing the acquisition of single-shot longitudinal bunch profiles with a sub-ps resolution (down to 330 fs granularity) down to bunch lengths of 1.5 ps RMS. The setup is sensitive enough to measure bunch charges as low as 30 pC. Measurements for different bunch compression settings have revealed the anticipated dynamic substructures on the bunch profiles and strong bunch deformations for high bunch charges. Furthermore, we have detected long-ranging wake-fields which could influence following bunches.

OUTLOOK

The acquisition rate of single-shot bunch profiles is currently limited by the readout rate of our commercial line detector inside the spectrometer. It is of great interest to compare the bunch substructures directly to the bursting behavior of the CSR; therefore we plan to increase the readout rate to at least 0.9 MHz, ideally even to the full 2.7 MHz repetition rate of ANKA. To achieve this, an ultra-fast readout system for an InGaAs-based line-array sensor is being developed in collaboration with the Institute for Data Processing and Electronics (IPE) at KIT [16].

ACKNOWLEDGMENTS

Many thanks to the entire technical staff both at PSI and ANKA who helped us to get the experimental setup running. Also many thanks to the beamline scientists of the IR, FLUO and SUL beamlines at ANKA who helped us with many little but important things.

REFERENCES

[1] A.-S. Müller *et al.*, "Far Infrared Coherent Synchrotron Edge Radiation at ANKA", RPAE038, Proc. PAC'05, Knoxville, TN, USA (2005).

[2] N. Hiller *et al.*, "Observation of Bunch Deformation at the ANKA Storage Ring", WEPEA020, Proc. IPAC'10, Kyoto, Japan (2010).

[3] N. Hiller *et al.*, "Status of Bunch Deformation and Lengthening Studies at the ANKA Storage Ring", THPC021, Proc. IPAC'11, San Sebastian, Spain (2011).

[4] V. Judin *et al.*, "Observation of Bursting Behavior Using Multiturn Measurements at ANKA", WEPEA021, Proc. IPAC10, Kyoto, Japan (2010).

ISBN 978-3-95450-141-0

Copyright © 2014 CC-BY-3.0 and by the respective authors

[5] M. Klein *et al.*, "Simulations of the Microbunching Instability at ANKA using a Vlasov-Fokker-Planck Solver", WEPC095, Proc. IPAC'11, San Sebastian, Spain (2011).

[6] V. Judin *et al.*, "Spectral and Temporal Observations of CSR at ANKA", TUPPP010, Proc. IPAC'12, New Orleans, LA, USA (2012).

[7] N. Hiller *et al.*, "Electro-Optical Bunch Length measurements at the ANKA Storage Ring", MOPME014, Proc. IPAC'13, Shanghai, China (2013).

[8] B. Kehrer *et al.*, "Numerical Wakefield Calculations for Electro-Optical Measurements", MOPME015, Proc. IPAC'13, Shanghai, China (2013).

[9] A.-S. Müller *et al.*, "Experimental Aspects of CSR in the ANKA Storage Ring", ICFA, Beam Dynamics Newsletter 57, p. 154-165 (2012).

[10] I. Wilke *et al.*, "Single-Shot Electron-Beam Bunch Length Measurements", Phys. Rev. Lett. Vol. 88, No. 12 (2002).

[11] B. Steffen, "Electro-Optic Methods for Longitudinal Bunch Diagnostics at FLASH", PhD thesis, University of Hamburg, Hamburg, Germany (2007).

[12] F. Müller *et al.*, "Ytterbium Fiber Laser for Electro-Optical Pulse Length Measurements at the SwissFEL", TUPD31, Proc. DIPAC'09, Basel, Switzerland (2009).

[13] B. Steffen *et al.*, "A Compact Single Shot Electro-Optical Bunch Length Monitor for the SwissFEL" TUPB42, Proc. DIPAC'09, Basel, Switzerland (2009).

[14] F. Müller *et al.*, "A Compact Electro Optical Bunch Length Monitoring System - First Results at PSI", WEPA09, Proc. FEL'10, Malmö, Sweden (2010).

[15] N. Hiller, "Electro-Optical Bunch Length Measurements at the ANKA Storage Ring", PhD thesis, Karlsruhe Institute of Technology (KIT), Karlsruhe, Germany (2013).

[16] L. Rota *et al.*, "An Ultrafast Linear Array Detector for Single-Shot Electro-Optical Bunch Profile Measurements", these proceedings, TUPD10, IBIC'14, Monterey, CA, USA (2014).

Copyright © 2014 CC-BY-3.0 and by the respective authors

ISBN 978-3-95450-141-0

ALS TIMING SYSTEM UPGRADE*

J. Weber#, C. Lionberger, E. Norum, G. Portmann, C. Serrano, E. Williams, Lawrence Berkeley National Laboratory, Berkeley, CA 94720, USA

Abstract

The Advanced Light Source (ALS) is in the process of upgrading its timing system as a part of the ALS Instrumentation and Controls Upgrade project. The timing system built upon construction of the machine at the beginning of the 1990s is still in operation today, and a replacement of the machine timing system is under way based on a commercially available solution, benefiting from 20 years of improvements in the fields of digital electronics and optical communications. An overview of the new timing system architecture based on a Micro-Research Finland (MRF) solution is given here.

INTRODUCTION

The primary function of the ALS timing system is to synchronize and sequence all systems required to deliver beam from the gun through the injection system to the storage ring. In addition, the timing system synchronizes diagnostics to the beam and provides controls for optimizing injection efficiency and selecting the operating mode.

The existing timing system has a centralized architecture that performs control and logic functions locally and distributes individual signals with coaxial or single-fiber optical cables. The hardware modules are primarily based on discrete ECL and TTL logic and reside in eurocard bins [1]. The remote control interface is provided by three embedded Intelligent Local Controllers (ILCs) [2] that communicate with the logic modules through the custom bin backplanes. The ILCs communicate with the rest of the control system through a multi-drop 2 Mb/s serial link connected to a Multibus I processor which now connects to the newer EPICS-based control system equipment.

The timing system upgrade is part of a larger Instrumentation and Controls Upgrade (ICU) project at the ALS to modernize controls, improve machine performance, and reduce vulnerability to single-point failures and aging equipment. Many of the ILCs have been replaced by a plug-compatible ILC Replacement Module (IRM) [3], but it was not feasible to use this solution for ILCs in systems such as the timing system where their usage is more specialized. The ICU project also includes new systems with timing requirements that could not be met by the existing system without significant changes to the infrastructure. Some of these systems, such as Beam Position Monitors (BPMs) based on the NSLS-II BPM architecture [4], rely on event-based timing, which the existing system does not support.

A survey of similar, more modern accelerator timing systems revealed that the most common commercial solution for event-based timing systems was based on Micro Research Finland (MRF) [5] hardware. In particular, NSLS-II had developed EPICS drivers for the MRF hardware in their timing system [6]. MRF hardware was chosen as the platform for the new ALS timing system to accelerate development by leveraging demonstrated commercial hardware with EPICS drivers.

Since the timing system has many existing clients that are not in the scope of the ICU project, interfaces to existing equipment had to be carefully considered to define the scope of the timing system upgrade. In general, timing logic and distribution infrastructure that could be slaved to a new trigger from the MRF system was retained. In particular, the existing sequencing and trigger generation system for the Linac, the trigger distribution infrastructure for Booster magnets, and the user timing and gating systems for beamlines will be slaved to the new MRF system.

The existing timing system relies on a measurement of the Booster dipole magnetic field to generate raw Booster injection and extraction field triggers, and then synchronizes them to the RF domain and the beam, as described here [7]. The new system uses time-based field triggers, so the field measurement was separated into a new diagnostic system. This system takes the field triggers as inputs and provides a "field" stamp of the measured field at the time of each field trigger, which is available for monitoring in the control system.

An additional challenge with this upgrade is commissioning a complex new system on a multi-user accelerator with minimal impact to experimenters. This constraint requires careful planning to minimize the risk of downtime during installation, testing, and commissioning of new system components. To accommodate this, where possible the project has been broken into several phases so new functions, features, and equipment can be tested in smaller groups. A bench test environment and a parallel machine test system have been set up so development can be demonstrated as fully as possible before migrating to production.

ARCHITECTURE

The ALS event system consists of a central Event Generator (EVG), event distribution using high speed serial transceivers, fiber optic cables, and electro-optical fanouts, and an array of Event Receivers (EVRs) placed as close to existing client signal inputs as feasible, or embedded in the system firmware of new clients. Each EVG and physical EVR resides in a VME crate with an IOC running EPICS connected to the ALS control system

*This work was supported in part by the U.S. Department of Energy under Contract Number DE-AC02-05CH11231.
#jmweber@lbl.gov

ISBN 978-3-95450-141-0

Copyright © 2014 CC-BY-3.0 and by the respective authors

via Ethernet. The physical EVRs generate analog triggers and clock signals for the various existing client systems. A block diagram of the timing system fiber optic network is shown in Figure 1.

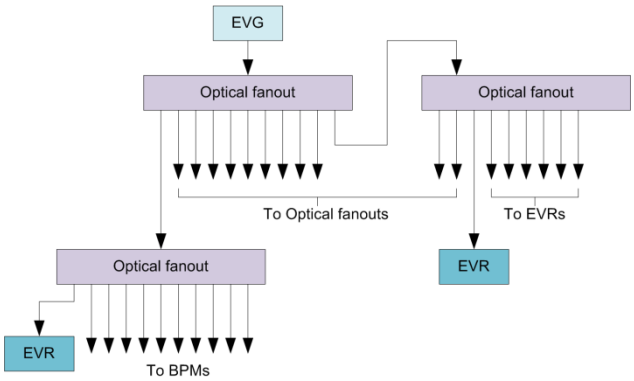


Figure 1: Timing System Event Link Block Diagram.

HARDWARE

A combination of commercial and custom hardware was used to construct this system. The commercial MRF components include the EVG (MRF VME-EVG-230), EVRs (VME-EVR-230RF), optical fanouts (VME-FOUT-12), as well as various MRF Universal I/O boards and carriers. MVME3100 CPU boards serve as IOCs. VME crates were built by Dawn (1U, 3U sizes) or Wiener (5U). All fiber optic trunk and patch cables are standard 50um OM3 multi-mode cables (typically aqua colored).

Two custom chassis were designed to provide signal and connector translations between the MRF outputs and existing client system inputs at several locations throughout the accelerator. The TTL Translation Rate Limit Chassis converts TTL signals on LEMO connectors to either differential TTL or differential NECL outputs on Twin BNC connectors. It also provides a hard-coded rate limit on all signals to protect clients against mis-setting the sequence rate in the EVG.

The CML Translation Chassis converts CML signals on a pair of LEMO connectors to TTL outputs on SMA connectors or differential NECL outputs on Twin BNC connectors. It also takes a raw 60Hz AC signal from the line cord and converts it to a TTL output on a LEMO connector, and a 500MHz sine wave on an SMA connector to a differential NECL output on a Twin BNC.

The Booster field diagnostic system consists of 2 IRMs with slightly modified firmware and some discrete TTL logic inside an ILC chassis.

Embedded Event Receiver

An MRF-compatible embedded event receiver was developed by NSLS-II and included in their accelerator instrumentation platform [8]. This platform serves as the Digital Front End (DFE) board in the NSLS-II BPM chassis, which was adopted for use in the new ALS BPMs.

The NSLS-II embedded EVR was modified so that the phase relationship between the EVG event clock and the EVR recovered clock is fixed, permitting synchronous RF-based clock recovery. In the ALS BPM, the recovered clock is used to regenerate the orbit clock that is the reference for the BPM ADC sampling clock.

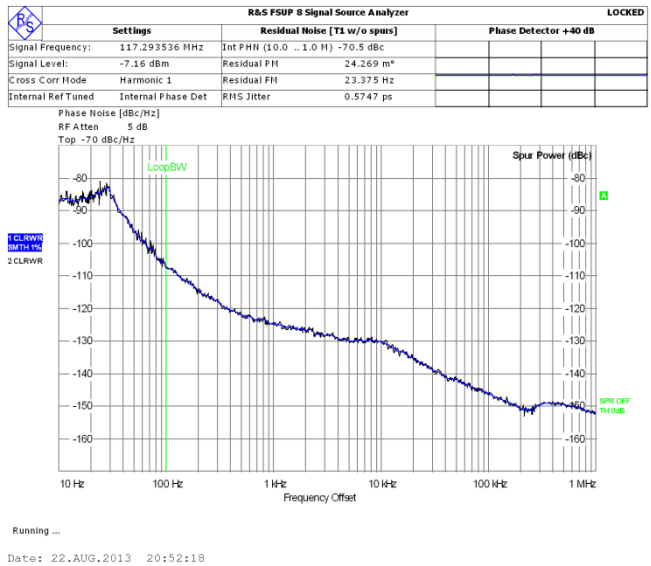


Figure 2: Embedded EVR Phase Noise.

A measurement of the ADC sampling clock phase noise using the embedded EVR as the PLL reference is shown in Figure 2, with a corresponding RMS jitter of less than 600ps. The SINAD of the BPM in this configuration was compared to the MRF EVR analog reference configuration. No degradation in performance was noted.

This modified embedded EVR has since been ported to the new ALS Bunch Current Monitor (BCM) system, where it is also used to derive an RF-synchronous reference for the sampling clock.

The embedded EVR was designed to use a Xilinx Virtex-6 series high speed transceiver [9]. However, it is possible to port the design to another Xilinx device family or different FPGA vendor by replacing only the hardware-specific portion of the EVR code. This EVR only requires an FPGA with a high speed serial transceiver supporting transfer rates of 20x the event clock rate (2.5Gb/s for ALS) connected to an SFP port and a local reference clock close enough in frequency to the event clock rate that it can be used as a reference for the transceiver clock recovery PLL.

SOFTWARE

The ALS Timing System IOCs run the MRFIOC2 EPICS device and driver support developed for the MRF hardware in the NSLS-II Timing System. NSLS-II also provided EDM engineering screens that control the MRF hardware at a low level. The IOC will provide support for the ALS event sequence control, as well as EPICS databases with ALS system-specific records. The high level interface will support EDM, Matlab, and other standalone applications to provide the array of functions and operational modes of the accelerator.

Copyright © 2014 CC-BY-3.0 and by the respective authors

ISBN 978-3-95450-141-0

Timestamping

The event system achieves accurate and precise timestamps by combining the accuracy of a GPS NTP server with the precision of the event link, as shown in Figure 3. The timing IOCs get GPS time from the NTP server via Ethernet at boot time. The server also sends a GPS-locked Pulse Per Second (PPS) trigger to the EVG. The EVG sends this trigger out on the event link to the EVRs, which resets the event clock tick counters and generates an interrupt to increment the seconds counter in the IOC. The IOC combines the NTP time at boot, the IOC seconds counter, and the EVR event clock tick counter to form a timestamp.

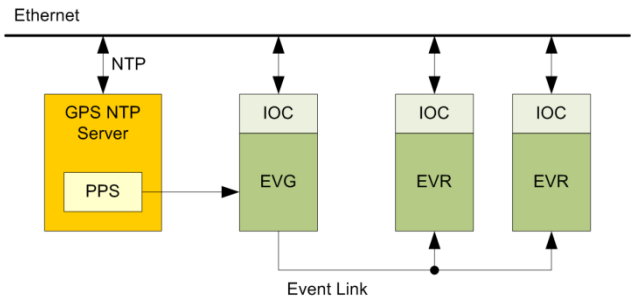


Figure 3: Event System Timestamping Block Diagram.

EVENT SEQUENCE

The Booster event sequence consists of a minimum of 7 event epochs, as shown in Figure 4. Before the Booster is ramped, some setup is required. Just over 200 ms before the start of the next sequence, the EVG sends the Setup Interrupt Event (event 62), which interrupts the master IOC (in the same crate). The interrupt triggers the IOC to read local EPICS records containing parameters defining the next sequence, reset the mode to default (no beam), and increment the sequence number.

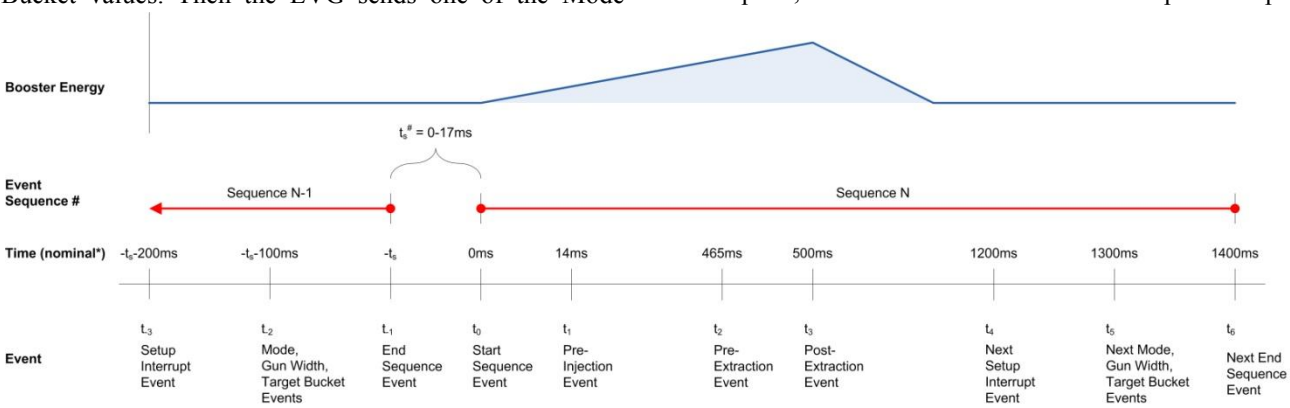
About 100 ms after the Setup Interrupt Event, the EVG sends 12 events (event 60 for binary 0, 61 for binary 1) that encode the Gun Width and Storage Ring Target Bucket values. Then the EVG sends one of the Mode Events (50-59). The modes cover the various anticipated operating modes of the accelerator, as defined in Table 1. EVRs that use these parameters load the values into their interrupt FIFOs. When the EVR IOCs receive these interrupts, they shift the values into their local parameters, and then use this information to set up trigger enables and delays for the next sequence.

Table 1: Mode Event Definitions

Event #	Definition
50	Enable Booster ramp triggers only (no beam)
51	Linac tuning
52	Booster tuning
53	BTS tuning
54	Enable all triggers
55	Custom (enable/disable triggers based on local PVs)
56-58	Reserved for future expansion
59	Disable all triggers

About 100 ms after the Mode Event is sent, the EVG sends the End Sequence Event (127). The EVG then waits for the next rising edge of the 60Hz line, followed by the rising edge of Coincidence Clock (COIC), which is generated by a free-running counter in the EVG. Once the EVG is synchronized to these signals, the next sequence can begin.

At the start of the sequence, the EVG sends out the Start Sequence Event 10 and enables the event sequence counter. Pre-Injection, Pre-Extraction, and Post-Extraction events are then sent according to the timestamps in the sequence table. After the Booster ramp is complete, the EVG sends the next Setup Interrupt



*Time values are approximate since events occur in multiples of 4/f_{RF} (~8ns).
#t_s= the variable time to synchronize to the AC Line (16.666ms) and then Coincidence Clock (~82us).

Figure 4: ALS Event Sequence Diagram. The event sequence number and event epochs are shown with respect to relative time and the Booster energy ramp.

ISBN 978-3-95450-141-0

Copyright © 2014 CC-BY-3.0 and by the respective authors

Event, and the cycle repeats. ALS Booster operation and timing constraints are described in more detail here [7].

CONCLUSION

The ALS timing system upgrade combines mature and widely used commercial hardware with custom hardware for ALS-specific functions and interfaces. This allowed a reduction in the scope of the project while providing a flexible, expandable and event-based timing master. Leveraging the NSLS-II embedded EVR firmware and MRFIOC2 EPICS support greatly accelerated development.

Building the RF-clock recovery into the embedded EVR reduced the number of MRF EVRs and physical connections needed, significantly reducing equipment installation, cost, and maintenance in the long-term. The embedded EVR can be included in any new instrumentation firmware requiring machine timing.

A flexible and configurable event sequence scheme provides support for existing and future modes of ALS operation. Timestamps are accurate and precisely synchronized across all timing system clients, providing a level of multi-system diagnostic data correlation previously unachievable at ALS.

Project Status

ALS timing system development is well underway. The majority of production hardware has been installed, but not yet commissioned. Currently, the MRF EVG feeds field triggers to the existing timing system and the field diagnostic system, and has been providing time-based field triggers during accelerator operations for nearly a year. The first production client to make use of the embedded receiver was the BCM system, commissioned earlier this year. The first set of new production BPMs were commissioned in the Storage Ring this summer, and the new timing system provides all BPM timing via embedded receivers. The majority of the remaining work involves implementing the event sequence scheme in the IOCs, developing ALS-specific databases, and implementing the high level control interface.

ACKNOWLEDGMENTS

The authors would like to thank Michael Davidsaver, Joe DeLong, and Joe Mead of Brookhaven National Lab for support of NSLS-II components, including the MRFIOC2 support package, the embedded timing receiver, and its usage in the NSLS-II BPM DFE firmware. The authors are also grateful to John Dusatko and Patrick Krejcik at SLAC for sharing advice and experience regarding the LCLS timing system. Finally, the authors acknowledge Mike Chin at LBL for providing guidance and measurement support during development of the embedded receiver and the timing interface to the ALS BPM, and Helen Chen, Rick Lellinger, and the rest of the technical support staff at ALS for their care and attention to detail in coordinating and installing all the new equipment and infrastructure required for this project.

REFERENCES

[1] M. Fahmie, “Design of the Advanced Light Source Timing System”, PAC’93, Washington, D.C.
[2] S. Magyary, et al., “Advanced Light Source Control System”, PAC’89, Chicago, IL.
[3] W. E. Norum, et al., “Advanced Light Source Control System Upgrade - Intelligent Local Controller Replacement”, ICALEPCS’13, San Francisco, CA.
[4] K. Vetter et al., “NSLS-II RF Beam Position Monitors”, PAC’11, New York, NY, 2011.
[5] Micro Research Finland, www.mrf.fi
[6] P. Cheblakov, et al., “NSLS-II Booster Timing System”, ICALEPCS’11, Grenoble, France.
[7] C. Serrano, J. Weber, “Timing of the ALS Booster Injection and Extraction”, ICALEPCS’13, San Francisco, CA.
[8] J. DeLong, “A Modular Architecture for Accelerator Instrumentation”, PAC’11, New York, NY.
[9] Xilinx, “Virtex-6 FPGA GTX Transceivers User Guide” (v2.6), July 27, 2011.

Copyright © 2014 CC-BY-3.0 and by the respective authors

ISBN 978-3-95450-141-0

BUNCH ARRIVAL TIME MONITOR FOR PAL-XFEL

J. Hong*, C. Kim, J.-H. Han, H.-R Yang, H.-S Kang, PAL, Pohang, Korea

Abstract

The X-ray Free Electron Laser project in Pohang Accelerator Laboratory (PAL-XFEL) requires high stability of bunch arrival time, and measurement resolution better than a few femtoseconds. The pickups of the electron Bunch Arrival time Monitor (BAM) for PAL-XFEL have been developed and simulated. The BAM pickups are based on an S-band monopole cavity with two coupling loops. The prototype BAM has been fabricated and installed downstream of the accelerating column at the Injector Test Facility (ITF) for PAL-XFEL. In this paper we will present the recent measurement results on the beam test of the BAM as well as a proposed strategy for developing the BAM for PAL-XFEL.

INTRODUCTION

PAL-XFEL requires high stability of bunch arrival time, and measurement resolution of bunch arrival time less than a few femtoseconds. The cavity type (monopole mode) BAM pickup is applied, which allows the detection of the bunch arrival time with a few femtoseconds. The BAM pickups are based on an S-band monopole cavity (LCLS type) with two coupling loop antennas. Figure 1 shows the geometry of the prototype BAM for PAL-XFEL. The prototype BAM

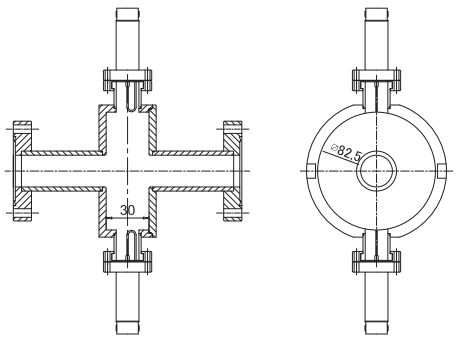


Figure 1: Prototype BAM geometry for PAL-XFEL.

pickup has been developed and installed downstream of the accelerating column at ITF [1] for PAL-XFEL. Figure 2 shows the photograph of the prototype BAM. The prototype BAM was tested for S-parameters and the results were compared to simulations. CST Microwave Studio is used to compute. Table 1 shows the resonance frequencies and their obtained quality factors. For the signal processing, the LLRF system is employed. Because the LLRF PAD is similar to electronics of the BAM. In the LLRF system, the RF signal is downconverted to the Intermediate Frequency (IF) signal while keeping the information of the preserved signal. The IF signal is sampled using by 16 bit Analog to Digital Converter (ADC) at a constant sampling rate of 238 MHz.

* npwinner@postech.ac.kr

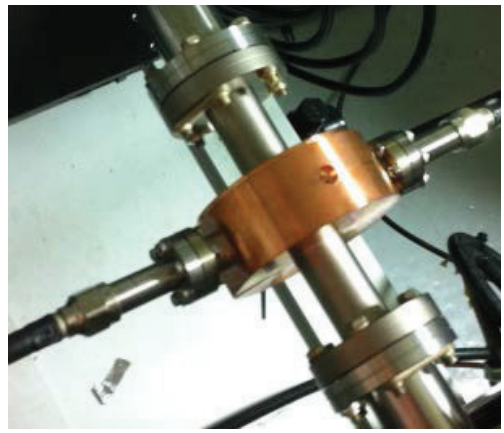


Figure 2: Photograph of the prototype BAM.

Table 1: BAM Pickup Parameters

Parameter	Value	Unit
Operating Frequency	2,823	MHz
Coupling Coefficient	0.1	
Quality Factor	10,000	

More detail on the LLRF system will be found in Ref. [2]. For the RF system, the RF frequency is 2,856 MHz, the LO frequency is 2,826.25 MHz, and then the IF frequency is 29.75 MHz. There frequencies are not well matched to the prototype BAM pickup.

SIGNAL PROCESSING

The schematic diagram of the signal processing is shown in Fig. 3. RF signal is firstly converted to IF signal and then directly digitized. If reference signal, $y_{\mathrm{Ref}}(t)$ and raw BAM signal, $y_{\mathrm{BAM}}(t)$ are:

$$\begin{aligned} y_{\mathrm{Ref}}(t) &= A_{\mathrm{Ref}}(t)\sin(\omega_{\mathrm{Ref}}(t)-\phi_{0,\mathrm{Ref}}), \\ y_{\mathrm{BAM}}(t) &= A_{\mathrm{BAM}}(t)\cos(\omega_{\mathrm{BAM}}(t)-\phi_{0,\mathrm{BAM}}), \end{aligned}$$

then IF signal, $y_{\mathrm{IF}}(t)$ can be written as:

$$y_{\mathrm{IF}}(t) = A_{\mathrm{IF}}(t)\cos(\omega_{\mathrm{IF}}(t)-\phi_{0,\mathrm{IF}}).$$

By using digital modulation the in-phase component, $I_{\mathrm{IF}}(t)$ and the quadrature-phase component, $Q_{\mathrm{IF}}(t)$ of the IF signal can be written as:

$$I_{\mathrm{IF}}(t) = \frac{A_{\mathrm{IF}}(t)}{2}\cos(\phi_{0,\mathrm{IF}}),\ Q_{\mathrm{IF}}(t) = \frac{A_{\mathrm{IF}}(t)}{2}\sin(\phi_{0,\mathrm{IF}}). \quad (1)$$

From Eq. 1, the amplitude, A_{IF} and the phase, $\phi_{0,\mathrm{IF}}$ can be calculated as:

$$A_{\mathrm{IF}}(t) = 2\sqrt{I_{\mathrm{IF}}^2+Q_{\mathrm{IF}}^2},\ \phi_{0,\mathrm{IF}} = \tan^{-1}\frac{Q_{\mathrm{IF}}}{I_{\mathrm{IF}}}.$$

ISBN 978-3-95450-141-0

Copyright © 2014 CC-BY-3.0 and by the respective authors

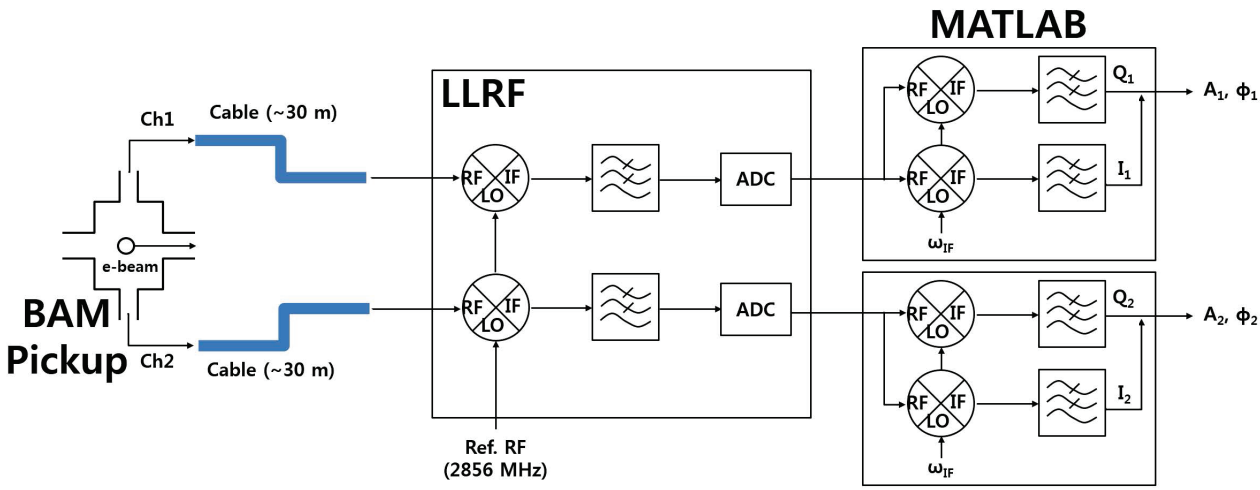


Figure 3: Schematic diagram for signal processing.

For down conversion and digital sampling, we used the LLRF system. MATLAB is used for digital signal processing. Figure 4 shows BAM signal processing data for 200 pC bunch charge. A 16 bit ADC can represent 65,536 (2^{16}) discrete voltage levels. Figure 4 a) shows the amplitude for one of the two pickup electrodes. In this figure the maximum voltage is about 4,096 (2^{12}) peak to peak. This value is so small because input voltage of ADC of the LLRF system is not matched to the voltage due to the prototype BAM pickup.

Using MATLAB simulation we have calculated BAM resolution as a function of signal error as shown in Fig. 5. In this figure, we can find that the resolution is proportional to BAM signal voltage.

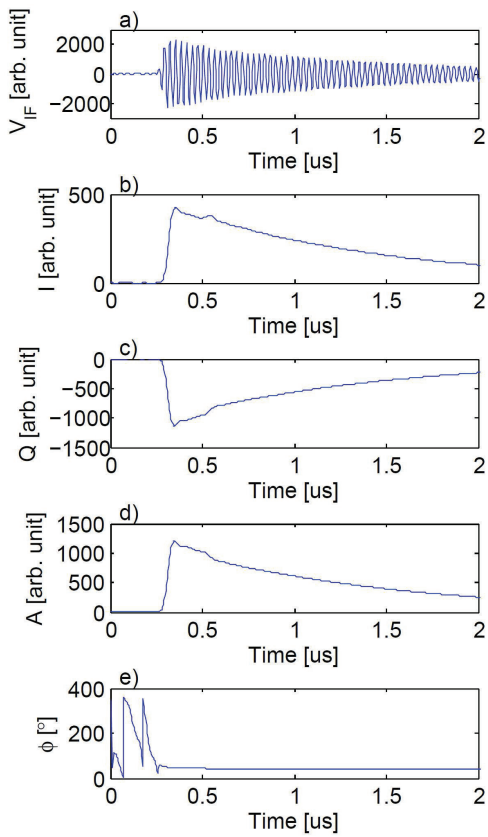


Figure 4: BAM signal processing data for 200 pC bunch charge; a) IF raw data, c) I data, d) Q data, e) amplitude data, and f) phase data.

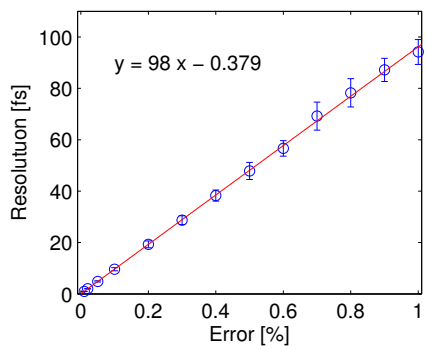


Figure 5: BAM resolution as a function of the signal error. The solid line represents a linear fit.

MEASUREMENT

The prototype BAM was installed at ITF and then tested with an electron beam. An RF signal is generated when an electron beam passes through the BAM cavity. The RF signal is collected with two pickups at the cavity cylindrical wall. The signals are processed using two channels of the LLRF system installed at the first RF station.

Charge dependence of BAM resolution is measured. By measuring the arrival-times with both pickup electrodes, the BAM resolution can be determined. The dependence of BAM resolution on bunch charge is shown in Fig. 6. Between 300 and 100 pC BAM resolution becomes worse slowly from 14.8 fs to 40.8 fs. Below 100 pC degradation is faster and at 20 pC it reaches 247 fs. The BAM resolution with bunch

Copyright © 2014 CC-BY-3.0 and by the respective authors

ISBN 978-3-95450-141-0

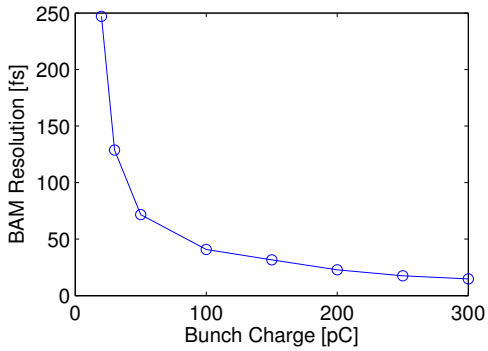


Figure 6: BAM resolution dependence on the charge.

charge of 200 pC is 22.8 fs. In this figure, BAM resolution is inversely proportional to bunch charge.

Using both timing systems (RF timing system and Optical timing system), long term stability test is performed. A long term bunch arrival time measurement with RF timing system is shown in Fig. 7. In this measurement the bunch charge is 200 pC, beam energy is 70 MeV. Figure 7 a) represents the beam arrival time variations measured by BAM. Figure 7 b) shows the bunch arrival time jitter calculated as deviation of instantaneous arrival time from a smoothed average. The rms jitter is 115 fs and the peak is 158 fs. This jitter accumulates in the gun-laser amplifier and in the transfer line sections following the stabilized laser oscillator. Figure 7 c) represents the resolution of the BAM. The average value of this signal is 24.2 fs. To minimize bunch arrival time jitter, an optical timing system is developed. A long term bunch arrival time measurement with the optical timing system is shown in Fig. 8. In this measurement the bunch charge is

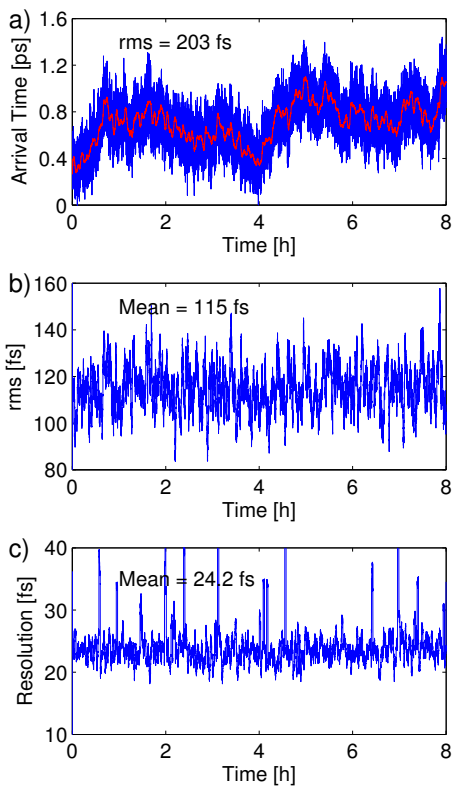


Figure 7: Stability measurement at the bunch charge of 200 pC with RF timing system; a) bunch arrival time, b) bunch arrival time jitter over 100 shots, and c) BAM resolution over 100 shots.

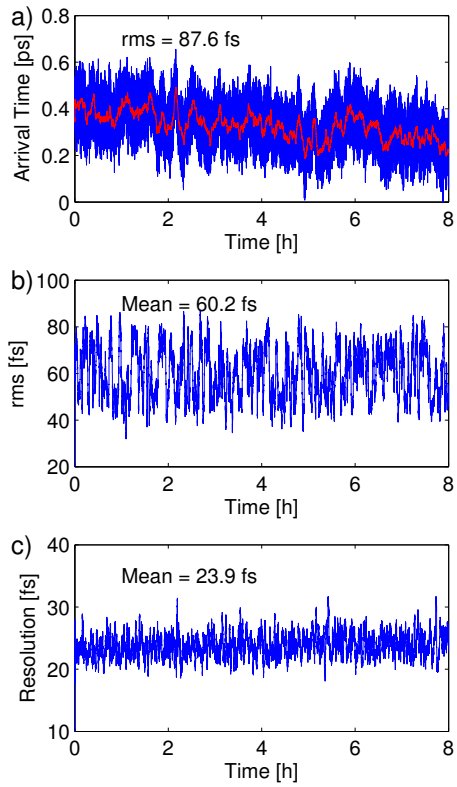


Figure 8: Stability measurement at the bunch charge of 200 pC with optical timing system; a) bunch arrival time, b) bunch arrival time jitter over 100 shots, and c) BAM resolution over 100 shots.

200 pC, beam energy is 70 MeV. Figure 8 a) presents beam arrival time variations measured by BAM. The rms jitter is 60.2 fs and the peak is 85.1 fs. The average value of BAM resolution is 23.9 fs. Initial measurements on long-term stability could be carried out yielding a BAM resolution of around 24 fs over a duration of 8 hours. Comparing the results in Fig. 7 and Fig. 8 the optical timing system is better than the RF timing system.

SUMMARY

In the first BAM measurements the bunch arrival time jitter was 115 fs with the RF timing system and 60.2 fs with

ISBN 978-3-95450-141-0

Copyright © 2014 CC-BY-3.0 and by the respective authors

the optical timing system over a duration of 8 hours without beam feedback. The calculation of BAM resolution was done by using the prototype BAM. In both timing systems the resolution of the BAM is 24 fs. This is larger than the desired value of a few femtoseconds. Probably the main limitation on the BAM resolution with the present setup are the BAM electronics (LLRF system). Studies on the BAM electronics are ongoing. Matching of the input voltage of the ADC will be processed, so that its full 16 bit range can be used independently on the bunch charge. A 16 bit ADC is in progress to improve the resolution and reduce the noise effect at low charge. Also, there are several ideas for improvement of the electronics, which could be implemented as patches. We hope that all these will provide for the required resolution of PAL-XFEL.

REFERENCES

[1] J.-H. Han et al., "Operation of PAL-XFEL Injector Test Facility", FEL'14, Basel, Switzerland, August 2014, WEB02 (2014), http://www.JACoW.org

[2] J. Hu et al., "Experimental Test of the Prototype LLRF Systems for PAL-XFEL", IPAC'14, Dresden, Germany, June 2014, WEPME078 (2014), http://www.JACoW.org

[3] K. Jung et al., "Femtosecond-stability Delivery of Synchronized RF-signals to the Klystron Gallery Over 1-km Optical Fibers", FEL'14, Basel, Switzerland, August 2014, THB03 (2014), http://www.JACoW.org

Copyright © 2014 CC-BY-3.0 and by the respective authors

ISBN 978-3-95450-141-0

BUNCH PATTERN MEASUREMENT VIA SINGLE PHOTON COUNTING AT SPEAR3*

Jeff Corbett†, Perry Leong and Linnea Zavala
SLAC National Accelerator Laboratory, Menlo Park, CA, 94025, USA

Abstract

SPEAR3 is a 3GeV storage ring light source with 500mA circulating beam current and a 5 minute top-up cycle. The bunch pattern contains 4 bunch 'trains' and a single timing pulse isolated by ±60ns dark space for laser pump/x-ray probe applications. In order to quantify the bunch pattern and charge purity of the probe pulse, a time-correlated single-photon counting system has been installed (TCSPC). In this paper we report on preliminary results using a photomultiplier tube with a commercial PicoHarp300 TCSPC device to identify bunch charge purity, afterpulse effects and top-up performance.

INTRODUCTION

SPEAR3 is an 18-cell, 234m circumference storage ring light source servicing 16 photon beam lines with up to 30 experimental endstations. The 476MHz RF system produces 372 RF buckets of which typically 280 contain charge bunches distributed in 4 bunch 'trains' separated by 30ns to minimize ion accumulation [1]. A single isolated timing pulse separated by ±60ns is available for time resolved pump/probe experiments using fast-gated detectors [2].

Charge injection into the 500mA electron beam takes place on a fixed 5 minute time interval. During each injection period the 10Hz booster synchrotron injects single-bunch pulses into consecutive SPEAR3 buckets until full current is restored. Each circulating bunch contains 1.4nC, or about 30 injection pulses (3% per shot). With a 9 hour electron beam lifetime, the periodic 1% beam loss is replenished by ~50 charge pulses containing 50pC each. Of significance, the arrival time of injected charge must be sufficiently accurate to avoid charge spill into adjacent buckets. The time separation between buckets is 2.1ns and the beam revolution time is 781ns (1.28MHz).

Historically a control room oscilloscope connected to a dedicated BPM was used to monitor the bunch pattern. More recently a PicoScope [3] was installed to enable remote viewing site wide. Although the 'scope solutions provide rough monitoring of the charge pattern, a more precise system is needed to measure bunch purity of the timing pulse and to study injector performance on a more quantitative basis. Furthermore, to remove unwanted charge, plans are underway to install x-y kicker magnets driven by the bunch-by-bunch feedback system [4].

In this paper we report on preliminary bunch pattern measurements using a Hamamatsu photomultiplier tube in conjunction with the PicoHarp300 TCSPC module [5].

*Work sponsored by US Department of Energy Contract DE-AC03-76SF00515 and Office of Basic Energy Sciences.
†corbett@slac.stanford.edu

The work follows directly from previous authors [6,7,8]. In short, for TCSPC, the PicoHarp300 records the time difference between the 1.28MHz storage ring orbit clock synchronization pulse (SROC) and single photon detection events. Upon integration, the resulting histogram displays the electron bunch pattern with potentially high resolution.

TCSPC DETECTOR CONFIGURATION

The PicoHarp300 was installed in the visible beam diagnostic laboratory at SPEAR3 [9]. At 500mA, the visible beam power is 0.5mW or about 10^{15} photons/sec. In order to reduce the count rate to ~1 count every 10 turns (7.8μs) the beam power incident on the PMT must be attenuated by 10 orders of magnitude. Most of the reduction was achieved by placing a small translatable pick-off mirror in the far beam halo. This arrangement also permits operation of other beam diagnostics in parallel. As shown in Fig. 1, redirected photons then pass through an ND filter and a 10nm bandpass filter inside a double-walled optical isolation box. A series of mirrors and irises serve to reduce background photon counts from ambient room light.

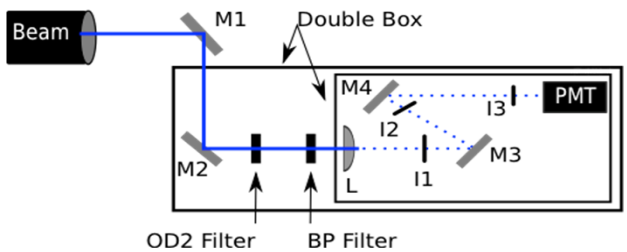


Figure 1: Schematic optical input system. The PMT has a dark count rate of 15 cps.

The PicoHarp300 was selected because it has two independent channels which can read up to 10^6 counts per second with 4ps time resolution [10]. Each channel requires a negative-going input pulse between 0V and -1V, and has a high resolution constant-fraction discriminator followed by time-to-digital conversion electronics (TDC) [10]. The 1.28MHz SROC is connected to Channel 1 as a timing reference (Sync port) after conversion from TTL to NIM in a commercial CAEN module.

Single photon detection was carried out using a Hamamatsu H7360-01 photon counting head [11]. The H7360-01 was selected based on experience with laser/SR cross-correlation bunch length measurements previously made in the diagnostics laboratory [12].

For each detected photon event, the H7360-01 outputs a single TTL pulse which is again converted to NIM and subsequently connected to PicoHarp300 Channel 2 (Signal port). Figure 2 shows the circuit schematic.

ISBN 978-3-95450-141-0

Copyright © 2014 CC-BY-3.0 and by the respective authors

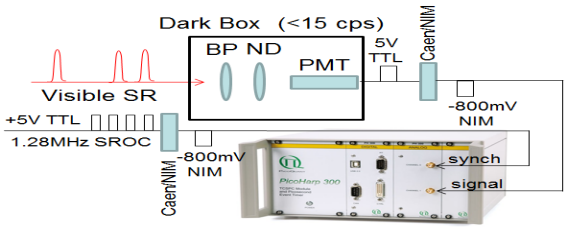


Figure 2: SROC and PMT input to PicoHarp300.

Operationally, the bin width of the PicoHarp300 histogram time axis can be set to multiples of 2ps across the 2^{16} wide horizontal time axis. For the 781ns one-turn time interval in SPEAR3, 16ps is the smallest bin size possible to record the entire beam profile in a single histogram.

Ideally, each pulse seen on the PicoHarp300 would be an exact, narrow spike localized in time; however, the counts actually 'land' in time distributed across a range of digitized bins. In order to maximize the number of counts in each bin while maintaining accuracy, a bin width of 32ps was typically used [13]. The maximum number of counts per bin is 2^{16} yielding in principle $1.5\text{x}10^{-5}$ contrast resolution. Operating with 3.3×10^{5} cps and 32ps bin width, the peak number of counts/bin was about 9,000 for 120s acquisition with the current detector configuration.

As an initial test of the TCSPC system, a single bunch was injected into SPEAR3. Figure 3 shows the resulting histograms for beam current values of 2, 4 and 6 mA. The narrow spike seen in the center was obtained by splitting the SROC signal, routing each copy through independent TTL-to-NIM conversion channels and detecting SROC 'counts' without the uncertainty of the PMT. This measurement indicates an overall 'impulse response' of approximately 32ps FWHM including timing jitter in the TTL-to-NIM conversion modules.

The actual bunch profile measurements exhibit a much wider profile of 800ps FWHM, and surprisingly a broad tail prior to the anticipated photon arrival time (Fig. 3). After conducting a series of tests it was determined the pulse broadening is due either to pulse conversion to TTL within the H7360-01 PMT electronics, or timing jitter on the SROC. When beam returns to the experimental station the source of pulse broadening will be further investigated and a higher time resolution detector acquired as needed.

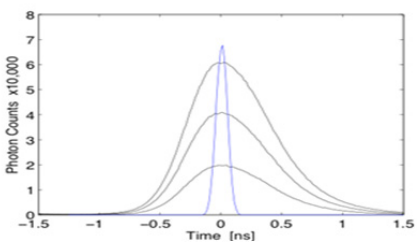


Figure 3: Histo gram for impulse response (32ps FWHM and single bunch measurement (800ps).

NOMINAL SPEAR3 BUNCH PATTERN

A typical measurement of the nominal 500ma bunch pattern is shown in Fig. 4 in both linear and logarithmic scale. As seen in Fig. 5, an 'afterpulse' is present 10ns following each electron bunch. The afterpulse is an electronic artifact located at a non-integer multiple of the 2.1ns bucket separation time and has 4ns duration. As a test, bunch patterns were generated by filling pairs of buckets at varying 2.1ns bucket intervals. By numerically identifying the afterpulse signature the artifact can be removed from the raw histogram data in software.

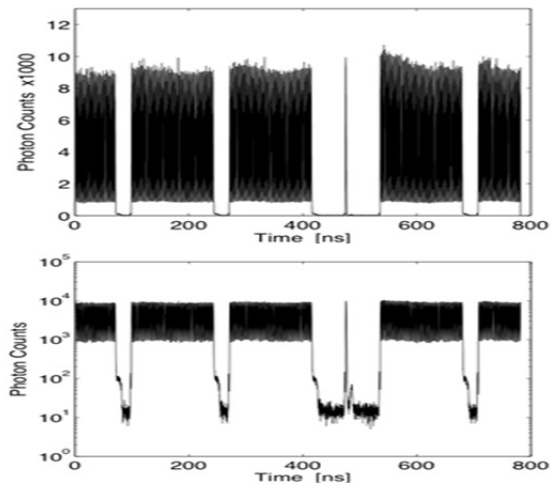


Figure 4: Nominal bunch pattern with four bunch trains and timing pulse. Linear scale (top) and log scale (bottom).

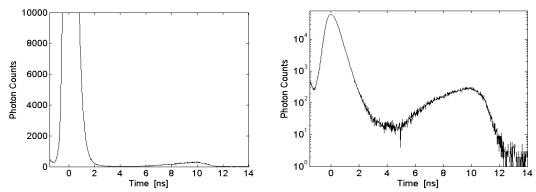


Figure 5: Afterpulse in linear and log scale.

DOUBLE-BUCKET INJECTION

Further examination of the timing bunch also reveals a second, upstream pulse with almost 1% amplitude relative to the timing bunch. Figure 6 shows the 'pre-pulse' in closer detail. In this case the pre-pulse is located exactly 2.1ns prior to the timing bunch and easily identified as charge spill during the injection process. To further study the source of the pre-pulse, the relative RF phase between SPEAR3 and the injector was varied.

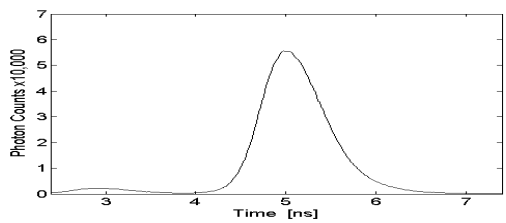


Figure 6: Injection charge spill into upstream bucket.

At first it was hypothesized the 'correct' phase setting would line up the injected charge exactly with the target SPEAR3 bucket and the pre-bunch would disappear. To the contrary, as the injection timing changed the spilled

Copyright © 2014 CC-BY-3.0 and by the respective authors

ISBN 978-3-95450-141-0

charge remained on one side or both sides of the target bunch depending on the injection time (Fig. 7).

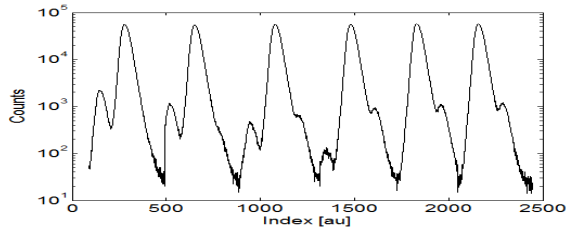


Figure 7: Evolution of double-bucket injection with varible timing between the injector and SPEAR3.

Archived oscilloscope images of the bunch fill pattern revealed the 'double bucket' was not present only days prior to the first PicoHarp300 measurements. Possible sources for the double bucket are outlined in Fig. 8. Likely candidates include jitter in the SPEAR3-to- injector timing system or multiple injector buckets. A less likely possibility the injector output pulse length may be longer than design causing charge injection into adjacent SPEAR3 buckets. Due to the observed systematic response to changes in injection timing it is unlikely the double buckets are due to steady-state diffusion between potential wells in longitudinal phase space. Longitudinal beam dynamics at injection is known to be complex [14] so the charge transfer could take place during the initial 5ms inject/damp cycle. Further tests will be made to correct the charge spill when beam operations resume.

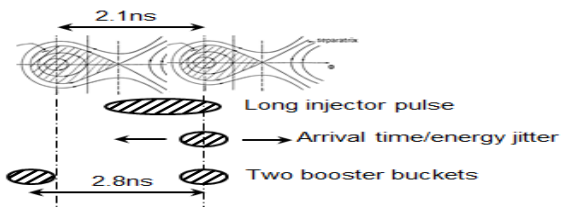


Figure 8: Potential double-bucket injection scenarios.

TOP-UP INJECTION

Injector performance across top-up cycles can be difficult to diagnose due to low bunch charge differential at each fill cycle. With present operating conditions, during each 5 min 'coasting beam' interval about 1% of the stored current is lost. Distributed across 280 buckets, each bunch loses 14pC or about 1/3 of the charge contained in a single injection pulse. Furthermore, with single-photon counting, the data integration time is of order 120 seconds or almost half the time interval between consecutive injection cycles.

In order to optimize the measurement, we positioned the TCSPC integration time to occur prior to each top-up cycle. In this way all 280 bunches decay for a full 5 minutes or more while the fresh 'top-up' charge decays at most 3-5 min. A schematic of the data acquisition timing is shown in Fig. 9.

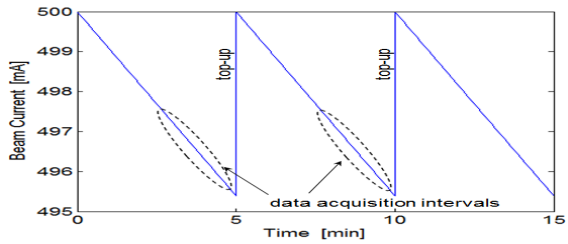


Figure 9: Timing diagram for top-up data acquisition.

A typical top-up data set is plotted in Fig. 10. The histogram in blue was acquired just before a top-up cycle while the red portion indicates target buckets after injection. By summing histogram bin counts across each 2.1ns bucket interval, a measure of differential bunch charge loss/gain can be found before and after top-up. The resulting change in integrated bin counts is plotted to the right in Fig. 10. Here the blue data indicates charge loss over a 5 minute time interval (bunches with no charge injection). The red data reflects top-up into ~50 target bunches followed by several minutes decay. The data are clearly quantitatively correct and will be further evaluated taking into account beam loss throughout the data acquisition time and enhanced intra-beam scattering in the top-up buckets which contain additional current.

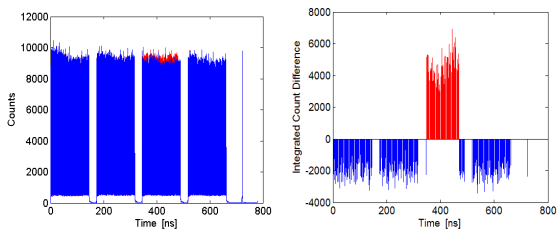


Figure 10: Bunch charge histogram before (blue) and afte topoff (red). Differential change in histogram count shown to right.

GUI DEVELOPMENT

The PicoHarp300 comes with both a graphical user interface and programming library compatible with a variety of languages. In order to provide additional interface functionality for operations staff, a complementary interface was developed in Matlab [15]. The gui mimics (see Fig. 11) the 'PlotFamily' interface used in conjuction with the Matlab Middlelayer for high level machine control [16]. Features of the interface include:

- Machine independence
- PicoHarp300 control
- data smoothing
- afterpulse deconvolution
- histogram difference capability
- display of desired bucket pattern
- intra-bucket histogram integration
- before/after top-up measurements
- measured bucket pattern report to EPICS
- pause/continue and additional data for histogram
- software timing shift to line up measurements with buckets as defined by main control system

ISBN 978-3-95450-141-0

Copyright © 2014 CC-BY-3.0 and by the respective authors

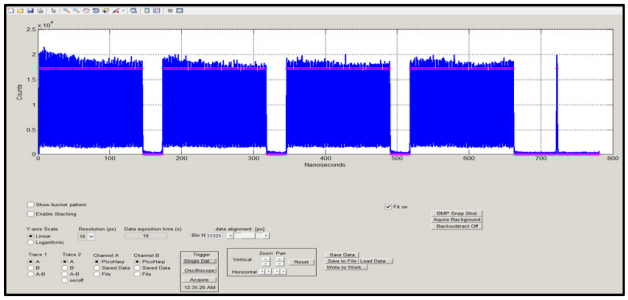


Figure 11: Matlab interface to PicoHarp300 for storage ring bunch pattern analysis.

SUMMARY

The PicoHarp300 accumulating real-time processor has been installed at SPEAR3 in conjunction with a Hamamatsu H7360-01 single photon counting PMT to measure the stored bunch pattern. Overall system performance is excellent. Histogram accumulation durations of 120sec with 32ps bin size were chosen make use of the PicoHarp300 dynamic range while maintaining good timing resolution and reasonable data acquisition times. Initial results produced a 800ps FWHM single-bucket histogram with the present PMT and timing system configuration. In the future this number must be decreased by at least a factor of 2 to better resolve individual buckets.

Preliminary measurements also revealed and error in the timing system leading to injected charge spill into adjacent buckets. By adjusting the relative RF phase between the injector and SPEAR3, the charge spill was observed to move from early- to late buckets. This problem will be corrected when beam operations resume.

Top-up measurements show that the TCSPC system can resolve both charge loss in coasting beam buckets over a single top-up cycle and single-pulse injection into target top-up buckets. Development of a machine-independent Matlab gui allows control of the PicoHarp300 with added functionality for storage ring operations. Individual bunch charge data can be posted to EPICS for history buffers, top-up control, single-bunch cleanout and monitoring of the probe pulse amplitude for pump/probe research.

ACKNOWLEDGEMENTS

This work was supported by Department of Energy contract DE-AC02-76SF00515. The authors gratefully acknowledge technical assistance from A.S. Fisher, D. Martin, W. Mok, S. Park, K. Tian and the SPEAR3 Operations staff.

REFERENCES

[1] L.Wang et al., 'Beam ion instability: measurement, analysis, and simulation', PRSTAB 16, 104402 (2013)

[2] J. Wittenberg et al., 'Bunch length measurements at SPEAR3 with time-resolved pump/probe experiments', IPAC11, San Sebastien, (2013).

[3] http://www.picotech.com/oscilloscope.html

[4] http://dimtel.com

[5] http://www.picoquant.com/

[6] T. Obina et al., 'Measurement of the longitudinal bunch structure in the PF positron storage ring with photon counting', NIMA 354, 204-214 (1995).

[7] C.A. Thomas et al., 'Bunch purity measurement for Diamond', Nucl. Instr. Meth. A 566 (2), 762 (2006).

[8] H. Wang, 'Bunch pattern measurements via single photon counting at SPEAR3', SULI Report (2011).

[9] J. Corbett et al., 'Visible light diagnostics for SPEAR3', SRI2009, Melbourne, (2009).

[10] PicoHarp 300 User's Manual and Technical Data, PicoQuant, Software version 2.2.

[11] T.A. Miller et al., 'Bunch length measurements with laser/SR cross-correlation', IPAC2010, Kyoto (2010).

[12] Hamamatsu Model H7360-01 Integrated photon counting head User Manual.

[13] L. Zavala, 'Time-correlated single photon counting for analysis of the electron bunch profile at SPEAR3', SULI Report (2014).

[14] J. Corbett et al., 'Injection beam dynamics in SPEAR3', BIW2010, Santa Fe, (2010).

[15] P. Leong, 'Electron cluster analysis using time-correlated photon counting', SULI Report (2014).

[16] G. Portmann et al., 'An accelerator control Middle layer', PAC2005, Knoxville, Tennessee (2005).

Copyright © 2014 CC-BY-3.0 and by the respective authors

ISBN 978-3-95450-141-0

DEVELOPMENT STATUS OF SINAP TIMING SYSTEM

M. Liu*, K. C. Chu, C. X. Yin, L. Y. Zhao, SINAP, Shanghai, China

Abstract

After successful implementation of SINAP timing solution at Pohang Light Source in 2011, we started to upgrade SINAP timing system to version 2. The hardware of SINAP v2 timing system is based on Virtex-6 FPGA chip, and bidirectional event frame transfer is realized in a 2.5Gbps fiber-optic network. In event frame, data transfer functionality substitutes for distributed bus. The structure of timing system is also modified, where a new versatile EVO could be configured as EVG, FANOUT or EVR with optical outputs. Besides standard VME modules, we designed PLC-EVR as well, which is compatible with Yokogawa F3RP61 series. Based on brand new hardware architecture, the jitter performance of SINAP v2 timing system is improved remarkably.

INTRODUCTION

Timing information with high precision is required to synchronize distributed devices and equipments in large accelerator facilities. Based on event timing mechanism, SINAP timing solution provides trigger pulses with programmable polarity, width and delay. Edge aligned clocks with variable fractional factors are integrated in output function as well. [1]

We started to develop SINAP timing system since 2007. The prototype of SINAP timing system was completed and tested at LINAC of SSRF in January 2010. Pohang Light Source adopts the system in its upgrade project, and first beam accumulation was realized in August 2011. [2] [3] Subsequently, we modified system design and improved performance in SINAP v2 timing system. The hardware development is completed so far. And we will implement the system for different project this year.

SYSTEM DESIGN

Thanks to rapid development of high-speed serial communication and FPGA technology, event timing system became the sophisticated solution for timing system in the large-scale accelerator facilities, especially for the 3rd generation light source. The main advantage of event timing system is that the required triggers and clocks could be transmitted in the uniform fiber-optic network. This means wherever the timing system fiber-optic network reaches, triggers and clocks could be provided. [4]

SINAP v1 Timing System

SINAP v1 timing system adopts classic star broadcast topology based on fiber-optic link of 2.5Gbps. Single event clock from 120MHz to 135MHz is supported. All of EVG (event generator), EVR (event receiver) and FANOUT are standard 6U VME modules. All output triggers delay could be adjusted with coarse resolution of event clock period. Optical triggers from front panel of EVR could be additionally adjusted with fine delay resolution of 1/20 event clock period and 5ps. Interrupt function is integrated in EVG and EVR. The event logic and VME local bus is realized in Virtex-4 FPGA chip and CPLD respectively. [5] The system structure is illustrated in Fig. 1.

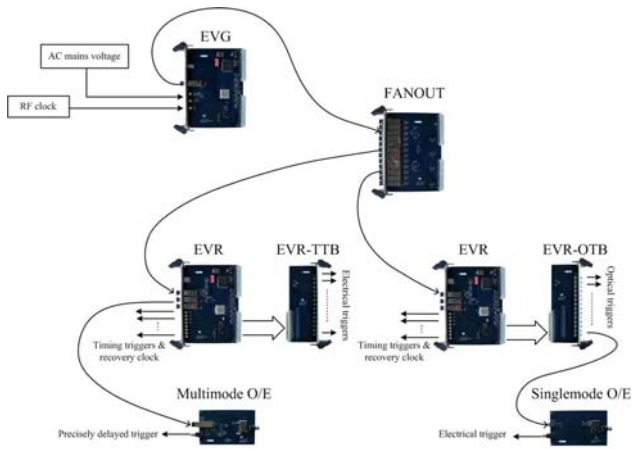


Figure 1: Structure of SINAP v1 timing system.

Software of the system is based on EPICS base 3.14.8.2 and vxWorks 5.5.1. During injection, the positions of all injection event codes stored in Sequence RAM of EVG are changed, but delay values of EVR output keep fixed. When transmission of all event codes is completed, an interrupt is generated in EVG, which makes a new list of event codes added to Sequence RAM. The whole mechanism is easy and efficiency. [6]

SINAP v2 Timing System

SINAP v2 timing system adopts similar topology based on fiber-optic network as well, but communication mode upgrades from simplex to duplex, which means that we could conduct deterministic data transfer and event distribution at the same time.

The frame format in the new version is illustrated in Fig. 2. One byte is for event code and the other byte is for data frame. Conventional distributed bus is abandoned, and all clocks are generated in EVR. Event clock from 60MHz to 135MHz is supported. EVG cascading function is supported. Two or more RF clocks are allowed to exist and synchronize output triggers in one single system consequently. Besides, all output triggers, no matter

*liuming@sinap.ac.cn

ISBN 978-3-95450-141-0

Copyright © 2014 CC-BY-3.0 and by the respective authors

electrical or optical, could be delayed with multiple resolution, including event clock, 1/20 event clock and 5ps.

1 byte	1 byte
trigger	data frame
K28.5	data frame
K28.5	data frame
K28.5	data frame
trigger	data frame
K28.5	data frame
⋮	⋮

Figure2: Frame format in SINAP v2 timing system.

The system structure is illustrated in Fig. 3. Types of hardware modules are simplified. Only two types of core modules, VME-EVO (event optical board) and VME-EVE (event electrical board), could form one complete system. They are standard 6U VME boards, and both of event logic and VME local bus are realized in one Virtex-6 FPGA chip. VME-EVO board could be flexibly configured as EVG, FANOUT or EVR with optical outputs by software. VME-EVE could only be used as EVR with electrical outputs. Both of VME-EVO (configured as EVR) and VME-EVE support feature of multi-channel backplane transition board.

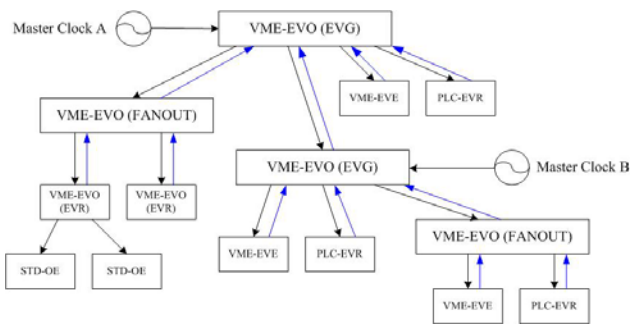


Figure 3: Structure of SINAP v2 timing system.

Additionally, the former one-channel Multimode Fiber OE module upgrades to four-channel STD-OE (stand-alone optical-to-electrical convertor), so as to achieve electrical isolation for critical equipments of high power. The module converts modulated optical triggers from VME-EVO (configured as EVR) to electrical triggers.

A new PLC-EVR was designed, which is compatible with Yokogawa F3RP61 series and suitable for low-cost applications. The module is one-slot width, and requires external 5V/3A DC power supply. Heat dissipation was specially considered to maintain the performance for long-term operation. We use an E^2PROM chip to restore essential information for configuration before normal operation. I/O register addressing mode is utilized in PLC software. Interrupt function is supported.

The four modules mentioned above are illustrated in Fig. 4.



Figure 4: Modules of SINAP v2 timing system.

Software in SINAP v2 timing system is similar to v1. Graphic interface is provided for basic operation and debugging with EDM.

TEST RESULTS

We made use of Tektronix TDS8000B oscilloscope and 80E03 Sampling Module to measure the short-term jitter between output trigger from EVR and RF reference clock. As shown in Fig. 5, the RMS jitter is about 10.1ps. By the way, the background short-term RMS jitter of the oscilloscope and sampling module is about 1.5ps.

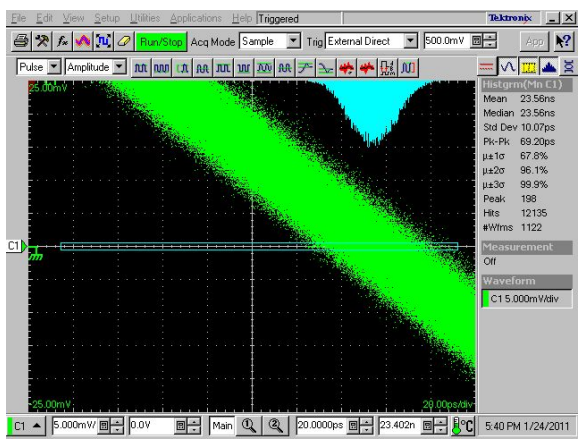


Figure 5: Jitter of SINAP v1 timing system.

For SINAP v2 timing system, we made use of the same test bench to measure the short-term jitter of output trigger from VME-EVE and RF reference clock. As

Copyright © 2014 CC-BY-3.0 and by the respective authors

ISBN 978-3-95450-141-0

shown in Fig. 6, the RMS jitter is about 6.3ps. The jitter performance of PLC-EVR is similar to VME-EVE. We measured the long-term jitter for 20 hours as well, which is about 8.3ps and illustrated in Fig. 7.

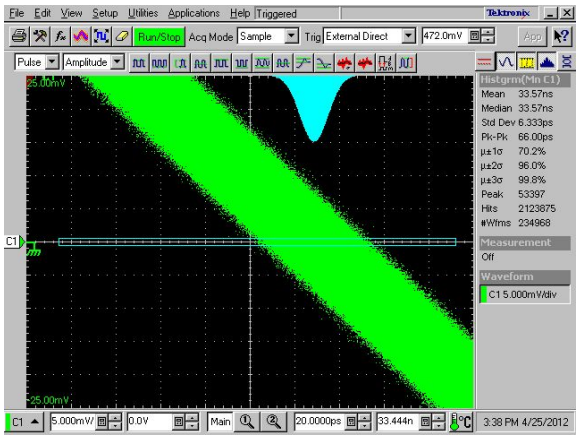


Figure 6: Jitter of SINAP v2 timing system.

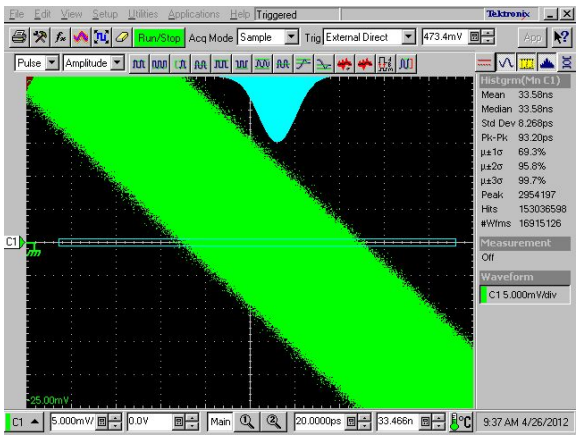


Figure 7: Jitter of SINAP v2 timing system with long-term drift.

CONCLUSION

As shown above, performance of SINAP v2 timing system is improved remarkably compared with v1 system. We designed a brand new firmware with Virtex-6 FPGA chip in the development of SINAP v2 timing system. Moreover, a lot of effort was done in dealing with ground bounce, which is often caused by high throughput of data in reading and writing VME bus.

After successful implementation at Pohang Light Source, SINAP timing system attracts the attention of many projects under construction or newly approved. SuperKEKB from Japan, ADS (Accelerator-Driven System) from China and CSNS (China Spallation Neutron Source) adopt the system as their timing solution. Shanghai Advanced Proton Therapy Project also considers the system as a competitive option.

With experience in research and design of SINAP timing system, we realized that it is barely possible to reach beyond magnitude of picoseconds for jitter performance in an electronics timing system. Therefore, we will focus on fiber-optic laser system to achieve lower jitter for accelerator facilities with higher requirement.

ACKNOWLEDGMENT

The authors would like to thank Cosylab d. d., Control System Laboratory from Slovenia for a complete professional test and a well-prepared user guide of SINAP timing system.

REFERENCES

[1] M. Liu, “Research of a New Timing System”, Doctoral Dissertation, 2010.
[2] S. J. Park, S. S. Park, W. H. Hwang et al., Proc. of LINAC’10 (2010) 698-702.
[3] S. Shin, S. Kwon, D-T. Kim et al., Proc. of IPAC’12 (2012) 1089-1091.
[4] Electronics Group, SINAP, “SINAP Timing System User Guide, Version 2”, 2012.
[5] M. Liu, C. X. Yin, L. Y. Zhao et al., Proc. of IPAC’10 (2010) 1396-1398.
[6] L. Y. Zhao, “The Status of SINAP Timing System”, EPICS Collaboration Meeting Fall 2012 (2012).

Copyright © 2014 CC-BY-3.0 and by the respective authors

ISBN 978-3-95450-141-0

DIAGNOSTICS OF AND WITH LASER-INDUCED ENERGY MODULATION AT THE DELTA STORAGE RING*

S. Khan†, S. Hilbrich, M. Höner, H. Huck, M. Huck,
C. Mai, A. Meyer auf der Heide, R. Molo, H. Rast, P. Ungelenk,
Center for Synchrotron Radiation (DELTA), TU Dortmund University, 44227 Dortmund, Germany

Abstract

DELTA is a 1.5-GeV synchrotron light source operated by the Center for Synchrotron Radiation at the TU Dortmund University. An interaction between electron bunches and femtosecond laser pulses is routinely used to generate ultrashort pulses of coherent synchrotron radiation at harmonics of the laser wavelength (coherent harmonic generation, CHG) as well as short and coherent pulses in the THz regime. The paper describes diagnostics methods to optimize the laser-electron overlap and to characterize the generated VUV and THz pulses. Furthermore, the laser-electron interaction can be employed as a beam diagnostics tool, e.g. to study the longitudinal steady-state bunch profile as well as dynamic properties during RF-phase modulation, which is applied to improve the beam lifetime.

INTRODUCTION

Synchrotron radiation (SR) sources based on electron storage rings [1] are complementary to high-gain free-electron lasers (FELs) [2] in various ways. The extreme peak brilliance of FELs has opened up new scientific opportunities, while the brilliance of SR sources, having increased by several orders of magnitude per decade, is still sufficient for many applications. Since high-gain FELs are based on linear accelerators, they serve only one experiment at a time with a relatively low pulse repetition rate, while SR sources are multi-user facilities producing very stable beams with a pulse rate of up to 500 MHz. The pulse duration of FELs is in the femtosecond regime allowing to study dynamic processes such as chemical reactions, structural and electronic changes in molecules or crystals, or fast magnetic phenomena, while the pulses from SR sources with a duration of 30 to 100 ps (FWHM) are inadequate for this purpose. Presently, four high-gain FELs are in user operation while about 50 SR sources exist worldwide. Reducing the pulse duration of SR sources by about three orders of magnitude would, therefore, increase the research opportunities for a very large user community.

While the electron bunches can be shortened to a few picoseconds by reducing the momentum compaction factor [3, 4], sub-picosecond SR pulses are obtained by extracting radiation from a small longitudinal fraction (a "slice") of long electron bunches [5]. To this end, the electron energy is modulated by the electric field of a femtosecond laser pulse co-propagating with the bunch in an undulator. The modulation has the periodicity of the laser wavelength, an envelope similar to the laser pulse shape, and an amplitude proportional to the square root of the laser pulse energy. Typically, Ti:sapphire laser systems are employed with a wavelength of 800 nm, a pulse energy of a few mJ and a repetition rate in the kHz range, leading to a modulation amplitude of 5-10 times the rms energy spread within a slice of 1/1000 of the bunch length. An undulator used for this purpose is called "modulator". The laser-induced energy modulation may be employed in several ways (Fig. 1):

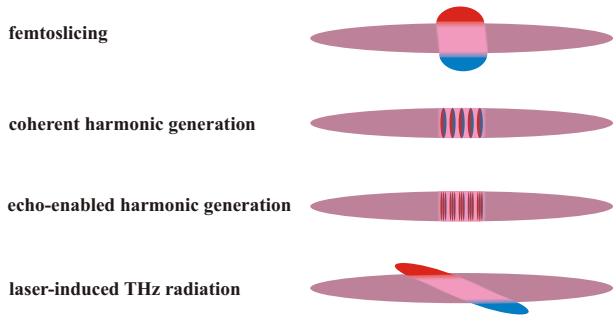


Figure 1: Laser-based methods to generate ultrashort SR pulses (see text). Note that the central "slice" of energy-modulated electrons (red and blue) is typically 1000 times shorter than the whole bunch.

- Off-energy electrons are transversely displaced in magnets such that their short SR pulse from a second undulator (the "radiator") can be separated spatially from the long pulse produced by the other electrons. In this "femtoslicing" scheme [6], the radiator wavelength can be tuned to any value. Even though incoherent SR from a small fraction of the bunch is rather weak and the laser pulse rate is 10^{-5} of the bunch rate, this scheme produces significant scientific results at the ALS in Berkeley/USA [7, 8], BESSY in Berlin/Germany [9, 10], and the SLS in Villigen/Switzerland [11, 12]. Another femtoslicing source is currently under commissioning at SOLEIL in Saint-Aubin/France [13].

- Using a dispersive chicane, the energy modulation may be translated into a periodic density modulation giving rise to coherent radiation at harmonics of the laser wavelength. Since the coherent SR intensity scales with the number of energy-modulated electrons squared [14], it is higher than the incoherent SR intensity from the rest of the bunch, and no spatial separation is required. This scheme, called CHG (coherent harmonic generation) [15], is restricted to harmonics $h < 10$ since

* Work supported by BMBF (05K13PEC), DFG (INST212/236-1), and by the state NRW.
† shaukat.khan@tu-dortmund.de

Copyright © 2014 CC-BY-3.0 and by the respective authors

ISBN 978-3-95450-141-0

Table 1: Parameters of the DELTA Short-Pulse Facility

beam energy	1.5 GeV
circumference (revol. frequency)	115.2 m (2.6 MHz)
multibunch / single-bunch current	130 / 20 mA
horizontal emittance	15 nm rad
relative energy spread	0.0008
rms bunch length (duration)	13 mm (43 ps)
laser wavelength	800 nm
pulse energy at 800 / 400 / 267 nm	8.0 / 2.7 / 1.0 mJ
laser repetition rate	1 kHz
laser pulse duration	45 fs
undulator period length	250 mm
modulator / radiator periods	7 / 7
maximum undulator parameter K	12
maximum chicane strength R_{56}	130 μm

the coherent SR intensity decreases exponentially with increasing harmonic number. The CHG principle was demonstrated in the 1980s [16], and recent implementations were accomplished at Elettra near Trieste/Italy [17], UVSOR in Okazaki/Japan [18], and DELTA in Dortmund/Germany [19].

- A density modulation following a twofold laser-electron interaction has been proposed as an FEL seeding scheme but may as well be used to generate ultrashort pulses in storage rings. Known as EEHG (echo-enabled harmonic generation) [20], the advantage over CHG is that the coherent SR intensity follows $I_{\mathrm{coh}} \sim h^{-2/3}$ and higher harmonics can be reached. EEHG has been demonstrated at two linac-based experiments at SLAC in Menlo Park/USA [21] and SINAP in Shanghai/China [22], and has been proposed for the storage rings SOLEIL [23] and DELTA [24].

- Due to the energy-dependent path lengths along the storage-ring lattice, the energy-modulated electrons leave a short dip in the longitudinal charge density giving rise to coherent radiation pulses in the terahertz (THz) regime over several turns, see e.g. [25]. These short and intense pules are used at several facilities (ALS, BESSY, SLS, UVSOR, DELTA) as energy-modulation diagnostics, but can also be employed for time-resolved far-infrared spectroscopy.

In the following, techniques used at the CHG facility at DELTA to diagnose and optimize the laser-electron interaction are described. Most of these methods are relevant to other short-pulse sources (CHG, EEHG, or femtoslicing) and to seeded FELs. In addition, laser-induced energy modulation can be used as a beam diagnostics tool, e.g. to sample the longitudinal charge distribution. Interacting only with 1/1000 of the electrons, the effect on the bunch is small but not always negligible. The energy modulation can, for example, trigger an instability leading to coherent THz bursts [26].

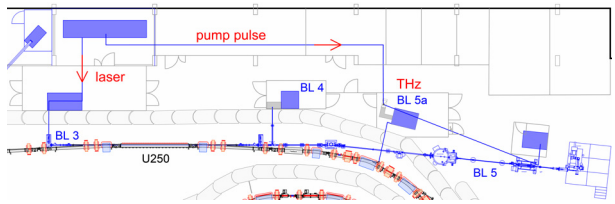


Figure 2: Short-pulse facility at DELTA comprising a laser system, the beamline BL 3 sending seed pulses to the undulator U250, the diagnostics beamline BL 4, the VUV beamline BL 5 and the THz beamline BL 5a.

THE SHORT-PULSE FACILITY AT DELTA

DELTA is a 1.5-GeV synchrotron light source operated by the Center for Synchrotron Radiation at the TU Dortmund University. A facility to generate ultrashort and coherent SR pulses in the VUV and THz regime was constructed in 2011 [19, 24]. Its footprint is shown in Fig. 2, relevant parameters are given in Tab. 1. Pulses from a femtosecond Ti:sapphire laser system or a harmonic thereof modulate the electron energy in the first 7 periods of the electromagnetic undulator U250 tuned to the seed wavelength, while 3 further periods are powered to form a dispersive chicane. The last 7 periods are tuned to a harmonic of the seed wavelength and act as radiator sending coherent pulses either via beamline BL 4 to a diagnostics hutch or to the experiment at BL 5. This beamline, operated by the Forschungszentrum Jülich, comprises a plane-grating monochromator and a photoelectron spectrometer with a 2-dimensional detector for spectral and angular sensitivity. In addition, a dedicated THz beamline (BL 5a) was constructed, which is equipped with an InSb bolometer, a fast $YBa_2CU_3O_{7-x}$ (YBCO) detector, and an FT-IR spectrometer using a Si bolometer as detector. An evacuated beam pipe allows to send laser pulses directly to BL 5 and BL 5a for pump-probe applications.

In the past, the undulator U250 was operated as a storage-ring FEL in optical-klystron configuration, lasing in the visible regime at reduced beam energies around 0.5 GeV [27]. New power supplies allow to tune the modulator to a seed wavelength of 800 nm at the nominal beam energy of 1.5 GeV, making CHG during user operation possible. Accelerator physics studies can be performed during 10 weeks/year and, in addition, in a shift following the Mo-Fr user operation at 20 weeks/year. During machine studies, CHG is predominantly performed in single-bunch mode with a current of up to 20 mA and a seed wavelength of 800 or 400 nm. In user operation, CHG was demonstrated using a hybrid fill pattern (120 mA multibunch plus a 10-mA single bunch). The final goal is seeding with 267 nm and generating ultrashort pulses at 53 nm for pump-probe experiments. As an upgrade, the 6 m long straight section of the U250 will be extended to 20 m by rearranging the dipole magnets in order to accommodate two new electromagnetic modulators (7 periods, period length 200 mm, to be delivered by the end of 2014) and the U250 as radiator for EEHG [28].

ISBN 978-3-95450-141-0

Copyright © 2014 CC-BY-3.0 and by the respective authors

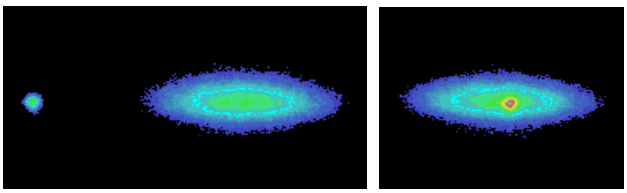


Figure 3: Streak camera images of a femtosecond laser pulse preceding the undulator radiation by 200 ps (left) and of overlapping pulses (right). The apparent laser pulse duration is given by the camera resolution.

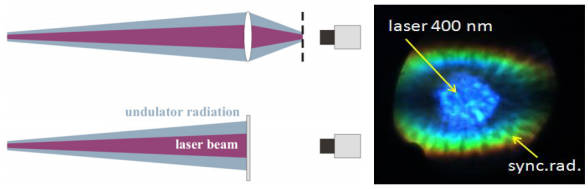


Figure 5: Two methods to image undulator and laser light with (top) or without (bottom) focusing. A typical screen image without focusing (right) shows the frequency-doubled laser as a blue spot surrounded by undulator radiation.

THE LASER-ELECTRON OVERLAP

For optimum energy modulation, a number of conditions must be met:

- The undulator spectrum must overlap with the laser spectrum, which is not critical due to the large undulator bandwidth. The electric field vector of the laser must be parallel to the electron motion in the planar undulator.

- The laser arrival time should be that of the bunch center. To this end, the laser oscillator is synchronized to the radio frequency (RF) of the storage ring by piezo-tuning the laser cavity, and the 1-kHz laser amplifier timing is set for the desired RF bucket by a revolution trigger which is vetoed for 1 ms. The laser timing was initially fine-tuned by delaying the RF signal using a mechanical phase shifter ("trombone"), but now a vector modulator is employed. The arrival time of SR from the modulator and the (strongly attenuated) laser pulse is measured using a fast photodiode and a streak camera (Fig. 3).

- The energy modulation depends critically on the spatial overlap of laser and electron bunch at the center of the modulator, but is less sensitive to angular errors. In the evacuated seed beamline BL 3, good control over position and angle is achieved by two mirrors with reproducible and backlash-free angular tunability (M1 and M2 in Fig. 4). Since the beam cannot be intercepted by screens in a storage ring, the transverse overlap is not easy to judge. Laser light and SR from the modulator is viewed on a screen without focusing (obtaining the overlap at the screen position) or, alternatively, using cameras equipped with lenses (obtaining the overlap at the focal point), see Fig. 5. Splitting the beam and using two screens at different positions or two different focal points, respectively, allows to obtain spatial and angular information (screen 1 and 2 in Fig. 4). In either case, the optical quality suffers from aperture limitations and from deformations or radiation damage of the light-extracting mirror.

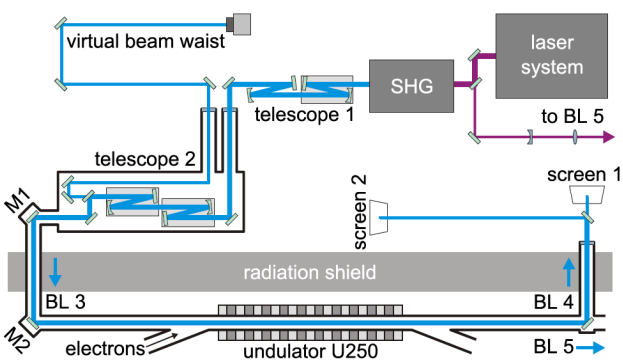


Figure 4: Laser beam path at DELTA with two mirror telescopes (currently under construction). Telescope 1 (in air) enlarges the laser beam, telescope 2 (in vacuum) provides the final focusing.

- The optimum laser waist position is usually at the modulator center. For an on-axis electron, the maximum energy change is obtained if the Rayleigh length is about 1/4 of the modulator length [29]. The finite electron beam size and a laser quality factor $M^2 > 1$, however, requires to increase the Rayleigh length $z_R = \pi w_0^2/\lambda$ and thus the $1/e^2$ laser waist radius w_0 in order to obtain a sufficient modulation averaged over all electrons. The waist size and position is controlled by changing the positions of focusing lenses or mirrors, usually associated with transverse "steering" of the laser beam. After focusing, leakage through a dielectric mirror is picked off and sent to a point at an equal distance as the modulator. This "virtual laser waist" is inspected by a CCD camera movable on a rail (Fig. 4).

- The laser pulse quality at the modulator is critical. It suffers from spherical aberrations and astigmatism from mirrors and lenses. The transition through lenses, vacuum windows, and even air causes focusing due to the intensity-dependent index of refraction ("B integral"), chirp due to group-delay dispersion, and chromatic aberrations. The wavefronts may be distorted by air turbulence and thermal effects in glass. In the configuration shown in Fig. 5, the first telescope in air enlarges the laser beam to reduce the power density on the vacuum window, while the second telescope in vacuum provides the final focusing.

The occurrence of coherent THz radiation detected by the InSb bolometer at beamline BL 5a is a very sensitive indicator of successful energy modulation [25], another one is the CHG signal.

Copyright © 2014 CC-BY-3.0 and by the respective authors

ISBN 978-3-95450-141-0

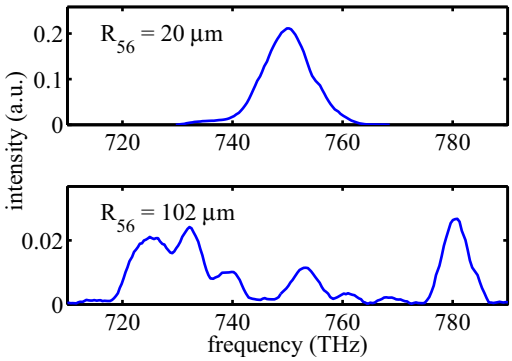


Figure 6: CHG spectra at 400 nm (frequency 750 THz) with the chicane set for optimum density modulation (top) and with a larger R_{56} value (bottom).

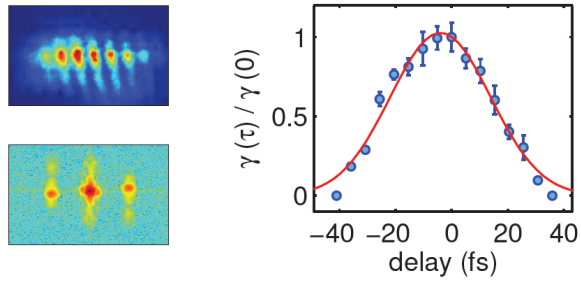


Figure 7: Double-slit pattern of 200-nm CHG radiation in real (left, top) and spatial frequency space (left, bottom), and dependence of the fringe visibility on the delay τ between light from the two slits. Here, $\gamma(\tau)$ is the ratio of the integrated intensities of a sideband and the central peak in frequency space.

The energy-modulation amplitude $\Delta E_{\max}$ can be measured by observing the beam lifetime while reducing the energy acceptance of the storage ring. This can be done using a scraper in combination with dispersion [9] or by reducing the RF voltage. In the case of CHG, optimum bunching is obtained at a constant value of $R_{56} \cdot \Delta E_{\max}/\sigma_E$, from which the modulation amplitude can be deduced. Here, σ_E is the energy spread and the chicane strength R_{56}, if uncertain, can be obtained from the fringe pattern of an optical-klystron spectrum, see e.g. [30].

CHARACTERIZATION OF RADIATION

A general issue when detecting CHG radiation is how to reject the strong co-propagating seed pulses. When seeding at a wavelength of 800 nm, CHG radiation at 400 nm passes a dielectric mirror coated for the seed wavelength. To study CHG pulses at shorter wavelengths, which would not pass a mirror substrate, several dielectric mirrors deflecting CHG radiation while transmitting the seed pulses are used in combination with bandpass filters.

The spectrum of spontaneously emitted (SE) undulator radiation and CHG pulses is measured using a Czerny-Turner-type monochromator followed by an avalanche photodiode (APD). For a selected wavelength, a digital oscilloscope records the CHG+SE intensity as well as the SE intensity at the following revolution without laser-electron interaction, observing a CHG-to-SE ratio of up to 10^3. The spectra obtained this way match those obtained by scanning the plane-grating monochromator in beamline BL 5 while recording the photoelectron yield or by using a CCD-line spectrometer [24]. In the latter case, the CCD records the whole spectrum at once but integrates over 2600 SE pulses for each CHG pulse. For the case of low harmonics, however, the strong CHG component is nevertheless visible. The SE spectrum has a width of $\Delta\nu/\nu \approx 1/N$ (FWMH), where $N = 7$ is the number of radiator periods, and shows fringes from the interference between the radiator and the corresponding harmonic of the modulator [30]. The CHG spectrum is narrower with a time-bandwidth product close to the Fourier limit, provided that the R_{56} transfer matrix element of the chicane is tuned for optimum density modulation (Fig. 6, top). As an example, a width of 2.6 nm (FWHM) was measured at BL 5 for 200-nm CHG radiation. Increasing the chicane strength leads to a broader CHG spectrum with interference fringes (Fig. 6, bottom), which can be explained by a more complex density modulation. The energy modulation follows the Gaussian shape of the laser pulse, and its maximum is overbunched, i.e. the optimum value of $R_{56} \cdot \Delta E_{\max}/\sigma_E$ is exceeded, if R_{56} is too large (see [32]).

The CHG pulse energy can be estimated from the observed CHG-to-SE ratio and the SE intensity measured with a powermeter. As an example, a pulse energy of 0.2 nJ was obtained at 200 nm (the 4th harmonic of 800 nm), corresponding to $2 \cdot 10^8$ photons per pulse [31]. The angular distribution of CHG and SE at a selected wavelength is obtained by scanning the radiation over the spectrometer entrance slit. In accordance with the respective spectral widths, the angular distribution of CHG is narrower than that of SE.

For radiation emitted by micro-bunched electrons, which is the case for FEL as well as CHG radiation, the coherence properties are of particular interest. In all coherence measurements, a fast-gated intensified CCD camera is essential in order to obtain sufficient single-shot intensity from a single turn without adding SE pulses [33]. The transverse coherence is studied using a classical double-slit setup followed by the camera after 1.3 m [32]. The visibility of interference fringes reduces with increasing slit separation, and the separation with 50% reduction defines the transverse coherence length. Here, the visibility $V = (I_{\max} - I_{\min})/(I_{\max} + I_{\min})$ can either be obtained by directly observing the maximum and minimum intensity in forward direction or by performing a 2-dimensional Fourier transform (Fig. 7, left). In spatial frequency space, the fringes appear as sidebands adjacent to a central peak, and their integral intensity is proportional to V [34]. A typical transverse coherence length of 1 mm is obtained at a distance of 10 m from the radiator.

The longitudinal coherence can be estimated from the off-axis fringe visibility in the double-slit pattern, but more accurate results are obtained from dedicated experiments.

ISBN 978-3-95450-141-0

Copyright © 2014 CC-BY-3.0 and by the respective authors

In one measurement, the length of one arm of a Michelson interferometer was varied while recording the interference pattern. Another experiment employed the double-slit setup with movable glass wedges to delay the light from one slit with respect to the other (Fig. 7, right). In either case, the longitudinal coherence length is derived from the dependence of the fringe visibility on the delay. In reasonable accordance with the measured spectral widths, a coherence length of 34 fs was obtained with both methods for CHG and 10 fs for SE [31, 32], where the SE spectrum was narrowed by a bandpass filter. Yet another approach to study the coherence is to record speckle patterns [35] of CHG pulses passing through a diffuse organic film. After successful application at FELs, e.g. [36], speckle measurements were performed at DELTA and are currently under analysis [37].

LONGITUDINAL BEAM DIAGNOSTICS

The longitudinal electron density distribution $\rho(t - t_0)$ can be sampled by moving the laser arrival time t relative to that of the bunch center (t_0) and recording either the CHG or coherent THz signal, both being proportional to ρ^2. The bunch length obtained this way is $\approx$ 100 ps (FWHM), in accordance with streak camera measurements [38]. The longitudinal fine structure imprinted on the bunch, i.e. the aforementioned "dip" which gives rise to coherent THz radiation, can be studied in the frequency domain by measuring the THz spectrum, and the results obtained at DELTA agree well with a model calculation [39]. Direct measurements in the time domain were not yet performed but can be done with sub-ps resolution by electro-optical sampling either in the far field [40] or in the near field [41].

The laser-induced energy modulation was also used to study dynamic changes of the bunch shape. A periodic modulation of the RF phase by twice the synchrotron frequency is routinely applied at DELTA to suppress longitudinal instabilities and to improve the beam lifetime [42]. Depending on the modulation amplitude, the bunch length changes periodically or the electrons populate two or even three "islands" rotating about each other in longitudinal phase space [43,44]. Two methods were applied to perform CHG while the RF-phase modulation was in operation [45]:

(a) The modulation frequency f_m was tuned close to an integer multiple (e.g. $n = 32$) of the laser repetition rate f_l such that the laser-electron interaction takes place at a slowly changing phase of the RF modulation. The CHG and THz signal oscillate on a typical time scale of a minute (Fig. 8), depending on the frequency difference $f_m - n \cdot f_l$.

(b) The modulation frequency was synchronized to the laser pulses by using a trigger at a rate of f_l to start a train of modulation cycles, and at the end of an integer number of cycles, the trigger starts the next train. In this case, a delay applied to the trigger selects a constant modulation phase at which the laser-electron interaction takes place.

Depending on f_m and the modulation amplitude, the beating behavior of the CHG and THz signal in method (a) can be in phase or 180° out of phase, as shown in Fig. 8. If the

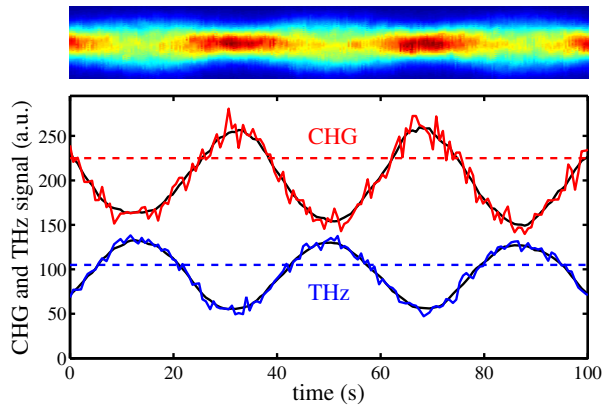


Figure 8: Streak camera image (top) and CHG/THz signal intensities versus time (bottom) in the presence of an RF-phase modulation (see text for details). The dashed lines indicate the respective steady-state values without modulation.

modulation is weak, the bunch length and energy spread oscillate in a countercyclical way. The CHG signal follows the electron density at the bunch center while the THz signal measured by the InSb bolometer decreases strongly with increasing energy spread. This assumption is confirmed when the laser arrival time is tuned away from the bunch center at which the electron density is larger when the bunch is shorter. If the laser pulse is delayed as to intercept the bunch tail, the interacting electron density is larger when the bunch is longer, and the CHG and THz signals are in phase.

While method (a) is convenient to study the full period of the RF phase modulation, method (b) is the one to be employed for CHG in user operation. In both cases, a CHG signal up to 30% larger than without modulation was observed suggesting that the bunch is temporarily shorter than its equilibrium length.

OUTLOOK

With several femtoslicing and CHG facilities in operation and the advent of seeded high-gain FELs [46], the laser-based manipulation and diagnostics of relativistic electron beams [47] has become a standard method, although achieving and maintaining an optimum laser-electron overlap is still a laborious task. Newly emerging schemes like EEHG [20] and other recently proposed ideas, e.g. phase merging [48], suggest that there is still room for improvement. Once this technology has matured, it may be possible to explicitly design a storage ring as a "pump-probe factory" with multiple laser-based short-pulse beamlines dedicated to ultrafast science.

ACKNOWLEDGEMENTS

It is a pleasure to thank our colleagues at DELTA and other institutes, particularly FZJ in Jülich, HZB in Berlin, DESY in Hamburg and KIT in Karlsruhe, for their continuous support and advice.

Copyright © 2014 CC-BY-3.0 and by the respective authors

ISBN 978-3-95450-141-0

REFERENCES

[1] Z.T. Zhao, "Storage Ring Light Sources", in *Reviews of Accelerator Science and Technology*, Vol. 3, edited by A. W. Chao and W. Chou, ISBN: 978-981-434038-0, World Scientific (2010), p. 57.

[2] P. Schmüser, M. Dohlus, J. Rossbach, S. Behrens, *Ultraviolet and Soft X-Ray Free-Electron Lasers*, ISBN: 978-3-31904080-6, Springer (2014).

[3] M. Abo-Bakr et al., "Brilliant, Coherent Far-Infrared (THz) Synchrotron Radiation", Phys. Rev. Lett. 90, 094801 (2003).

[4] A.-S. Müller et al., "Far-Infrared Coherent Synchrotron Edge Radiation at ANKA", Sync. Rad. News 19(3), 18 (2006).

[5] A. Zholents, "Electron-Beam-Based Sources of Ultrashort X-ray Pulses", in *Reviews of Accelerator Science and Technology*, Vol. 3, edited by A. W. Chao and W. Chou, ISBN: 978-981-434038-0, World Scientific (2010), p. 237.

[6] A. A. Zholents, M. S. Zolotorev, "Femtosecond X-Ray Pulses of Synchrotron Radiation", Phys. Rev. Lett. 76, 912 (1996).

[7] R.W. Schoenlein et al., "Generation of Femtosecond Pulses of Synchrotron Radiation", Science 287, 2237 (2000).

[8] A. Cavalleri et al., "Band-Selective Measurements of Electron Dynamics in VO_2 Using Femtosecond Near-Edge X-Ray Absorption", Phys. Rev. Lett. 95, 067405 (2005).

[9] S. Khan et al., "Femtosecond Undulator Radiation from Sliced Electron Bunches" Phys. Rev. Lett. 97, 074801 (2006).

[10] I Radu et al., "Transient Ferromagnetic-like State Mediating Ultrafast Reversal of Antiferromagnetically Coupled Spins", Nature 472, 205 (2011).

[11] P. Beaud et al., "Spatiotemporal Stability of a Femtosecond Hard–X-Ray Undulator Source Studied by Control of Coherent Optical Phonons", Phys. Rev. Lett. 99, 174801 (2007).

[12] S.L. Johnson et al., "Direct Observation of Non-fully-symmetric Coherent Optical Phonons by Femtosecond X-ray Diffraction", Phys. Rev. B 87, 054301 (2013).

[13] P. Prigent et al., "Progress on the Femto-Slicing Project at the Synchrotron SOLEIL", J. Phys.: Conf. Series 425, 072022 (2013).

[14] H. Wiedemann, "Particle Accelerator Physics", ISBN: 978-3-54049043-2, Springer (2007).

[15] R. Coisson, F.D. Martini, "Free-Electron Relativistic Scatterer for UV-Generation", in *Physics of Quantum Electronics: Free-Electron Generators of Coherent Radiation*, Vol. 9, edited by S. F. Jacobs et al., ISBN: 978-0-20105689-1, Addison-Wesley (1982), p. 939.

[16] B. Girard et al., "Optical Frequency Multiplication by an Optical Klystron", Phys. Rev. Lett. 53, 2405 (1984).

[17] E. Allaria et al., "Experimental Characterization of Nonlinear Harmonic Generation in Planar and Helical Undulators", Phys. Rev. Lett. 100, 174801 (2008).

[18] M. Labat et al., "Optimization of a Seeded Free-Electron Laser with Helical Undulators", Phys. Rev. Lett. 101, 164803 (2008).

[19] S. Khan et al., "Coherent Harmonic Generation at DELTA: A New Facility for Ultrashort Pulses in the VUV and THz Regime" Sync. Rad. News 24(5), 18 (2011).

[20] G. Stupakov, "Using the Beam-Echo Effect for Generation of Short-Wavelength Radiation", Phys. Rev. Lett. 102, 074801 (2009).

[21] D. Xiang et al., "Demonstration of the Echo-Enabled Harmonic Generation Technique for Short-Wavelength Seeded Free Electron Lasers", Phys. Rev. Lett. 105, 114801 (2010).

[22] Z.T. Zhao et al., "First Lasing of an Echo-Enabled Harmonic Generation Free-Electron Laser", Nature Photonics 6, 360 (2012).

[23] C. Evain et al., "Soft X-ray Femtosecond Coherent Undulator Radiation in a Storage Ring", New. J. of Phys. 14, 023003 (2012).

[24] S. Khan et al., "Generation of Ultrashort and Coherent Synchrotron Radiation Pulses at DELTA" Sync. Rad. News 26(3), 25 (2013).

[25] K. Holldack et al., "Femtosecond Terahertz Radiation from Femtoslicing at BESSY", Phys. Rev. Lett. 96, 054801 (2006).

[26] J.M. Byrd et al., "Laser Seeding of the Storage-Ring Microbunching Instability for High-Power Coherent Terahertz Radiation", Phys. Rev. Lett. 97, 074802 (2006).

[27] D. Nölle et al. "First lasing of the FELICITA I FEL at DELTA", Nucl. Inst. Methods A 445, 128 (2000).

[28] S. Hilbrich et al., "Upgrade Plans for the Short-pulse Facility at DELTA", Proc. of the Free Electron Laser Conference 2014, Basel, Switzerland, MPO087, http://jacow.org/.

[29] A.A. Amir, Y. Greenzweig, "Three-dimensional Theory of the Free-Electron Laser", Phys. Rev. A 34, 4809 (1986).

[30] D.A.G. Deacon et al., "Optical Klystron Experiments for the ACO Storage Ring Free Electron Laser", App. Phys. B 34, 207 (1984).

[31] M. Huck, dissertation, TU Dortmund University (in preparation).

[32] M. Huck et al., "Ultrashort and Coherent Radiation for Pump-probe Experiments at the DELTA Storage Ring", Proc. of the International Particle Accelerator Conference 2014, Dresden, Germany, 1848.

[33] A fast-gated iCCD camera was generously provided by B. Schmidt and S. Wunderlich (DESY Hamburg).

[34] A. Singer et al., "Spatial and Temporal Coherence Properties of Single Free-Electron Laser pulses", Opt. Express 20, 17480 (2012).

[35] J.W. Goodman, *Speckle Phenomena in Optics* ISBN: 978-1-93622114-1, Roberts & Company (2010).

[36] S. Lee et al., "Single-shot Speckle and Coherence Analysis of the Hard X-ray Free Electron Laser LCLS", Opt. Express 21, 24647 (2013).

[37] C. Gutt et al., "Femtosecond Speckle and Coherence Experiments ta the CHG Short-Pulse Facility DELTA", International Workshop on Phase Retrieval and Coherent Scattering, Evanston, USA (2014), P8.

[38] P. Ungelenk et al., "Recent Developments at the DELTA THz Beamline", Proc. of the International Particle Accelerator Conference 2012, New Orleans, USA, 768.

[39] P. Ungelenk et al., "Temporal and Spectral Observation of Laser-induced THz Radiation at DELTA", Proc. of the International Particle Accelerator Conference 2013, Shanghai, China, 94.

ISBN 978-3-95450-141-0

Copyright © 2014 CC-BY-3.0 and by the respective authors

[40] F. Müller et al., "Electro-optical measurement of sub-ps structures in low-charge electron bunches", Phys. Rev. ST - Accel. Beams 15, 070701 (2012).

[41] N. Hiller et al., "Status of Single-shot EOSD Measurement at ANKA", Proc. of the International Particle Accelerator Conference 2014, Dresden, Germany, 1909.

[42] S. Khan, J. Fürsch, P. Hartmann, T. Weis, "Studies and Control of Coupled-bunch Instabilities at DELTA", Proc. of the International Particle Accelerator Conference 2010, Kyoto, Japan, 2755.

[43] H. Huang et al., "Experimental Determination of the Hamiltonian for Synchrotron Motion with RF Phase Modulation", Phys. Rev. E 48, 4678 (1993).

[44] J. Byrd, W.-H. Chen, F. Zimmermann, "Nonlinear Effects of Phase Modulation in an Electron Storage Ring", Phys. Rev. E 57, 4706 (1998).

[45] A. Meyer auf der Heide et al., "Coherent Harmonic Generation at the DELTA Storage Ring: Towards User Operation", Proc. of the Free Electron Laser Conference 2014, Basel, Switzerland, TUP082.

[46] E. Allaria et al., "Highly coherent and stable pulses from the FERMI seeded free-electron laser in the extreme ultraviolet", Nature Photonics 6, 669 (2012).

[47] E. Hemsing, G. Stupakov, D. Xiang, A. Zholents "Beam by Design: Laser Manipulation of Electrons in Modern Accelerators", Rev. Mod. Phys. 86, 897 (2014).

[48] H. Deng, C. Feng, "Using Off-Resonance Laser Modulation for Beam-Energy-Spread Cooling in Generation of Short-Wavelength Radiation", Phys. Rev. Lett. 111, 084801 (2013).

Copyright © 2014 CC-BY-3.0 and by the respective authors

ISBN 978-3-95450-141-0

TIME DOMAIN PICKUP SIGNAL CHARACTERISATION FOR LOW CHARGE ARRIVAL-TIME MEASUREMENTS AT FLASH*

A. Angelovski†, A. Penirschke, R. Jakoby, Institut für Mikrowellentechnik und Photonik, TU Darmstadt, Germany
M.K. Czwalina, C. Sydlo, H. Schlarb, DESY, Hamburg, Germany
T. Weiland, Institut für Theorie Elektromagnetischer Felder, TU Darmstadt, Germany

Abstract

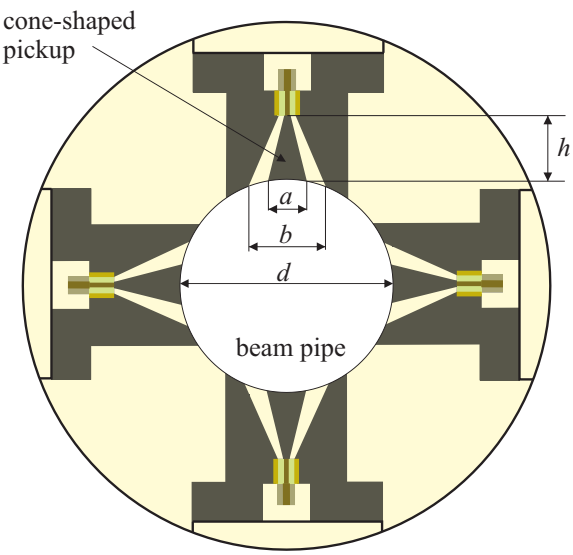
For the low charge operation mode at the European XFEL, high bandwidth cone-shaped pickups were developed as a part of the Bunch Arrival-time Monitors (BAMs). The simulation showed that the signal parameters of interest, the signal slope and bandwidth are improved by more than a factor of six compared to the state of the art pickups. The pickups are installed at FLASH for verification. In this paper, time domain measurements of the cone-shaped pickups at FLASH are presented. The pickup signal is recorded with a high bandwidth sampling oscilloscope. Two channel measurements are conducted with a single and a combined pickup signal in order to analyse the orbit and charge dependence. The measured time domain pickup signal wave form is compared with the full wave CST PARTICLE STUDIO as well as with the Agilent Advanced Design System (ADS) simulation.

INTRODUCTION

In order to measure the arrival-time of the electron bunches at FLASH, Bunch Arrival-time Monitors (BAMs) are installed as an integral part of the laser-based synchronisation (LbSyn) system [1,2]. A BAM comprises RF pickups, electro-optical and RF front-end and read-out electronics. The beam induced pickup signal modulates the amplitude an external laser pulse train in the Mach-Zender type electro-optical modulator (EOM). The reference timing is determined by the laser pulse sampling the pickup signal at the zero-crossing resulting with a zero amplitude modulation at the output of the EOM. An arrival-time jitter of the electron bunch and thus of the transient signal translates into a laser amplitude modulation. The arrival-time is deduced by comparing the amplitude of the modulated laser pulse to the adjacent ones. The sensitivity of the BAMs depends on the pickup signal slope steepness. This detection scheme provides for a time resolution of the arrival-time measurements of less then 10 fs for bunch charges above 500 pC. For the new European - XFEL a low charge operation mode is planed with bunch charges of 20 pC. As the bunch charge reduces below 200 pC, the time resolution of the BAMs decreases significantly [3]. For improving the time resolution for low charges the bandwidth of the BAMs is increased from the current 10 GHz to 40 GHz. The high bandwidth system provides for a beam induced signal with steeper slope compared to the low bandwidth one.

Cone-shaped Pickups

The cone-shaped pickups were developed in [4] as a part of the 40 GHz BAMs for low bunch charge operation of the European-XFEL. Figure 1 shows the cross-section of the pickups with dimensions.



a = 2.42 mm	h = 6 mm
b = 5.60 mm	d = 40.50 mm

Figure 1: Cross section of the cone-shaped pickup with dimensions [4].

The simulated slope steepens at the zero-crossing is 417 mV/ps and it is by a factor of six higher compared to signal slope of the current 10 GHz pickups [4]. The pickups are installed in FLASH for testing and evaluation as part of the BAMs for low charges.

In this paper we present the time domain measurements of the cone-shaped pickups at FLASH. A comparison between the measured wave forms and simulations is performed for validation of the results. The signal slope is evaluated for different bunch charges and orbit displacements.

* Work supported by the German Federal Ministry of Education and Research (BMBF) within Joint Project - FSP 302.
† angelovski@imp.tu-darmstadt.de

ISBN 978-3-95450-141-0

Copyright © 2014 CC-BY-3.0 and by the respective authors

TIME DOMAIN MEASUREMENTS OF THE CONE-SHAPED PICKUP SIGNAL

The measurements of the pickup signal are performed directly in the accelerator tunnel with a high bandwidth (50 GHz) sampling oscilloscope Tektronix DSA8300 with a 80E10 electrical sampling module. In order to avoid damages to the equipment due to radiation, the oscilloscope was enclosed in a lead box.

Measurement Setup

The beam induced pickup signal is recorded at the output of the RF signal path which includes RF coaxial cables, combiner and two attenuators. Figure 2 shows the measurement setup. In order to reduce the signal degradation due to the

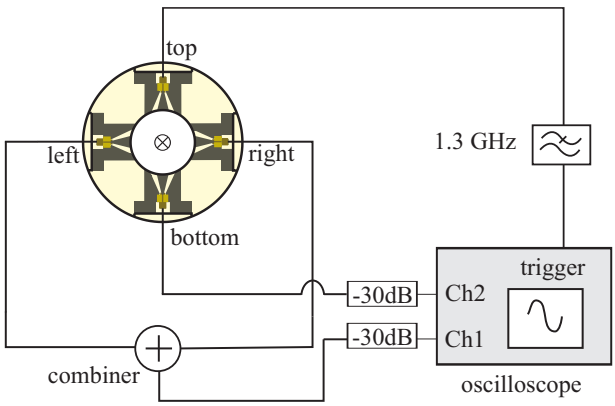


Figure 2: Measurement setup for the time domain measurements of the beam induced pickup signal.

cable length, the oscilloscope is mounted inside the beam tunnel. The left and right pickups (horizontal branch) are fed into a power combiner and the output is connected to the oscilloscope via 40 GHz phase stable RF cables (Phasemaster 160, Teledyne-Storm Microwave) through 30 dB attenuator for an over voltage protection. The bottom pickup (vertical branch) signal is recorded as a single while the top signal is connected to the trigger input via 1.3 GHz bandpass filter. The result from the measurements are given in the next subsections.

Comparison between Measurements and Simulation

In order to validate the measurement results a comparison between them and the outputs of two different simulation packages is performed. A full wave simulation with CST PARTICLE STUDIO delivers the beam induced signal at the output of the pickup while an Advanced Design System (ADS) simulation shows the signal at the end of the RF path. The pickup signal from the CST PARTICLE STUDIO is used as an input parameter for the ADS simulation and the measured S-parameters of the cables and the combiner are embedded into the building blocks. Figure 3 shows the schematics of the RF path for the ADS simulation. A

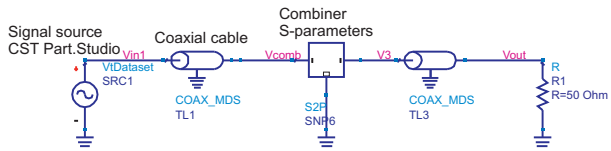


Figure 3: ADS schematics for the RF path simulation. The excitation signal is obtained with a CST PARTICLE STUDIO simulation.

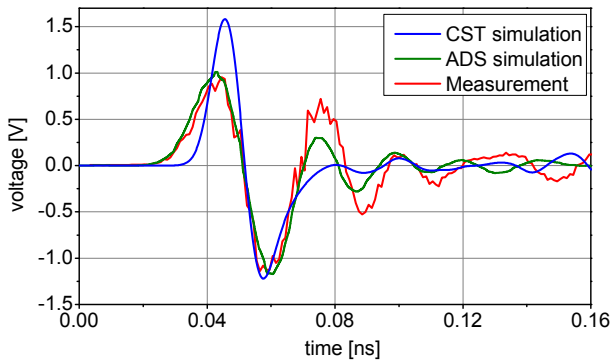


Figure 4: Simulation measurements.

comparison between the measured pickup signal for a bunch charge of 20 pC and two simulation outputs is shown in Fig. 4. It can be seen that the measured curve and the ADS simulation are in a good agreement with decreased slope and peak voltage compared to the CST PARTICLE STUDIO simulation. The second zero crossing signal visible in the ADS simulation and in the measurement as well as the slope reduction are as a result of the signal degradation in the RF path. The extracted parameters from the wave forms are given in Table 1.

Table 1: Comparison of the Pickup Signal Parameters for Measurement and Simulations

signal source	slope [mV/ps]	V_{pp} [V]
CST PARTICLE STUDIO	417	2.7
ADS	372	2.1
measurement	370	2.15

Bunch Charge and Orbit Sweep

The beam induced pickup signal is recorded for different bunch charges and orbit positions. Two channels of the oscilloscope simultaneously recorded the signals from the single pickup and the combined pickups. Figure 5 shows the pickup signal for a bunch charge sweep from 25 pC up to 215 pC. It can be seen that the peak voltage has a linear dependance from the bunch charge, i.e. 1.1 V for a bunch charge of 25 pC and 12.2 V for a bunch charge of 215 pC at both single and combined signal. The peak amplitude is the same for the single and the combined signal due to the

Copyright © 2014 CC-BY-3.0 and by the respective authors

ISBN 978-3-95450-141-0

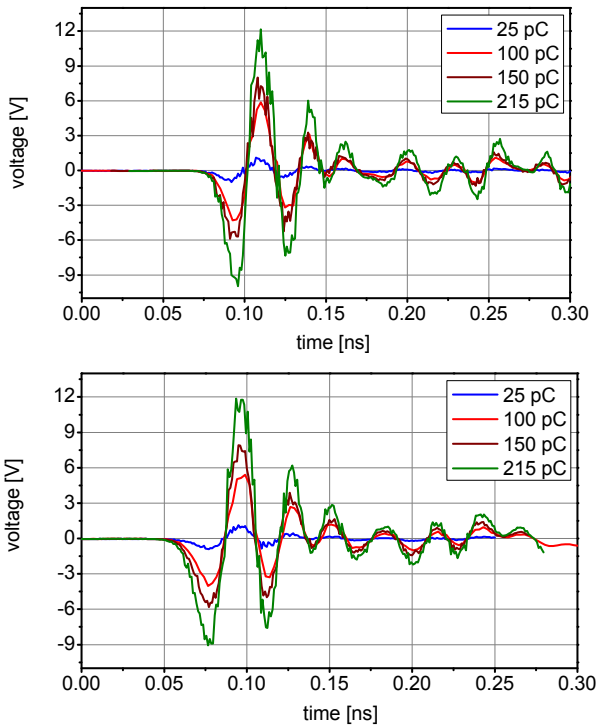


Figure 5: Measured beam pickup signal for bunch charge sweep from 25 pC to 215 pC. Top: Single pickup signal, bottom: combined pickup signal.

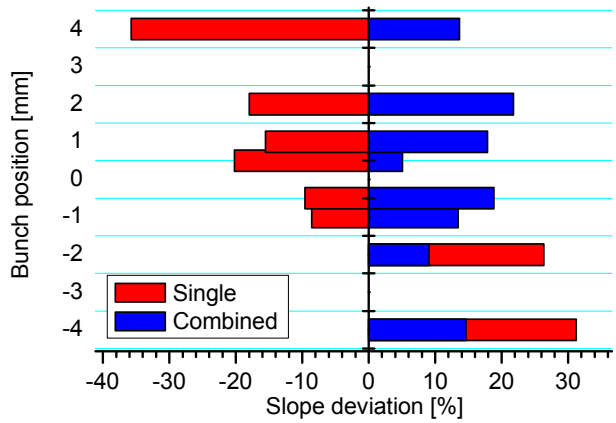


Figure 6: Simulation measurements.

losses of the power combiner at high frequencies (7 dB at 40 GHz).

Figure 6 shows the dependance of the signal slope from the bunch position. The pickup signal obtained from the single and the combined branch is recorded for a vertical orbit displacement measured with a BPM mounted behind the BAM pickups. As the electron bunch moves closer of further away to the pickups the induced voltage increases or decreases respectively as well as the signal slope. In case of a single signal the slope deviation is around 65 % in the full scan range compared to a centralised beam. The slope deviation decreases down to 20 % for the combined pickup signal. The voltage difference between the opposite pickups caused by the beam position change is compensated in the combiner resulting in a reduced slope dependance. This will decrease the uncertainty in the arrival-time detection of the BAMs.

CONCLUSION

The cone-shaped pickups for the high bandwidth low charge BAMs are installed at FLASH. The pickup signal is measured with an oscilloscope and the measurement data is compared to the simulations showing a good agreement between the wave forms. With a combination of the opposite pickups the slope dependance of the bunch position is significantly reduced which will lead to a decreased uncertainty of the bunch arrival-time measurements.

ACKNOWLEDGMENT

The authors would like to thank the company CST for providing the CST STUDIO SUITE software package.

REFERENCES

[1] F. Löhl *et al*. Phys. Rev. Lett. **104**, 144801 (2010).

[2] M. K. Bock, Ph.D. thesis,Universität Hamburg, (2012).

[3] M. K. Bock et al., "Benchmarking the Performance of the Present Bunch Arrival Time Monitors at FLASH," DIPAC 2011, Hamburg, May 2011, TUPD28, p. 365. (2011).

[4] A. Angelovski et al., Phys. Rev. ST Accel. Beams **15**, 112803 (2012).

Copyright © 2014 CC-BY-3.0 and by the respective authors

ISBN 978-3-95450-141-0

A BUNCH EXTENSION MONITOR FOR THE SPIRAL2 LINAC

J.L. Vignet, R. Revenko, GANIL, Caen, France

Abstract

Measurements of the bunch longitudinal shape of beam particles are crucial for optimization and control of LINAC beam parameters and maximization of its integrated luminosity. The non-interceptive bunch extension monitor for the LINAC of SPIRAL2 facility is being developed at GANIL. Five bunch extension monitors will be installed at the beginning of the LINAC between superconducting cavities. The principle of operation is based on the registration of x-rays induced by ions of accelerator beam interacting with a thin tungsten wire positioned on the beam path. The monitor consists of two parts: a system for wire insertion and positioning, and an x-ray detector based on microchannel plates (MCP). A detector prototype has been developed for three years and was tested using protons and heavy ions beams. The influence of the cryomodule operation on the diagnostic measurement was also studied.

INTRODUCTION

The SPIRAL2 project [1] is based on a multi-beam LINAC driver in order to allow both ISOL and low-energy in-flight techniques to produce RIB. A superconducting light/heavy-ion LINAC capable of accelerating 5 mA deuterons up to 40 MeV and 1 mA heavy ions up to 14.5 MeV/u is used to bombard both thick and thin targets. These beams could be used for the production of intense RIB by several reaction mechanisms (fusion, fission, transfer, etc.) and technical methods (ISOL, IGISOL, recoil spectrometers, etc.). The production of high intensity RIB of neutron-rich nuclei will be based on fission of uranium target induced by neutrons, obtained from a deuteron beam impinging on a graphite converter (up to 10^{14} fissions/s) or by a direct irradiation with a deuteron, ^{3}He or ^{4}He beam.

The accelerating RF of the LINAC [2] is 88.0525 MHz. It means that time distance between two bunches is 11.26 ns. The extension of the phase for bunch (±2σ) is 60˚ or ~1,6ns for bunch length. The LINAC can operate at continuous or pulsed mode with period of macropulse between 100 µs and 1s.

Correct adjustment of the LINAC is necessary for obtaining maximal intensity and luminosity on the target. Adjusting includes synchronization of phase for each acceleration section. For this reason, information about bunch length distribution is needed and will be obtained using a Bunch Extension Monitor (BEM). These diagnostic detectors will be placed inside the warm sections between superconducting acceleration cavities. Each warm section consists of two quadrupoles and diagnostic box placed in between. Five BEM will be mounted into the first five diagnostic boxes at the LINAC entrance where deuteron beam energy will be between 1.46 and 2.29 MeV.

BEM DESCRIPTION

Bunch extension monitor is a non-destructive beam diagnostic detector for estimation of the length of LINAC bunches. The principle of BEM measurement is based on registration of x-rays emitted from a thin tungsten wire due to the interaction with ions beam. All components of BEM should meet UHV requirements since the LINAC will be operated at 10^{-8} mbar. Moreover, all BEM materials must satisfy required purity conditions for preventing cavity pollution.

BEM Working Principle

The photons emitted from the tungsten wire will be produced due to ionization of atoms hit by beam ions. The ions can knock-out electrons from inner shells and produce electron vacancy. Electrons from outer shells fill this vacancy and emit the difference of energy of bound states as characteristic x-ray photons. The energies of emitted characteristic photon are unique for each element and in case of tungsten they are 60 keV and 11 keV for K- and L-shell ionization respectively. A two stage microchannel plates is used to produce photoelectrons and multiplied them. Output signal is transmitted through coaxial cable to the input of a constant fraction discriminator CFD 7174. Signal of accelerator RF comes to another channel of CFD. The two logical signals from CFD output are sent to a time-to-amplitude converter Ortec 566 as “start” and “stop” signals. The output signal from TAC (whose amplitude is proportional to the time difference) is digitized by multichannel analyzer CANBERRA Multiport II. The Schema of BEM electronics operation is presented in Fig. 1.

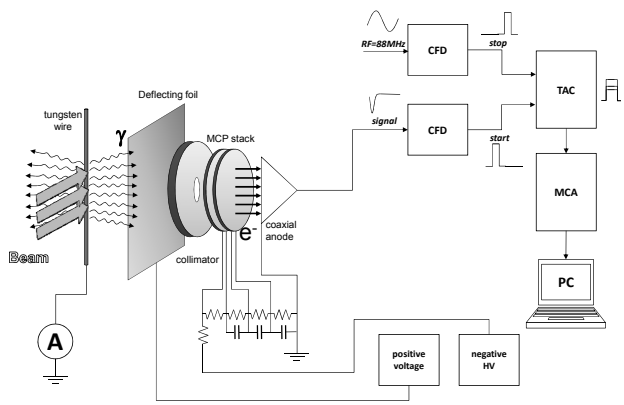


Figure 1: Principal schema of operation of BEM electronics.

X-rays of ^{55}Fe was used to measure the electronic temporal resolution. Output signal from detector prototype was transmitted through a long coaxial cable of 70 meters length and split in two signals. Both signals

Copyright © 2014 CC-BY-3.0 and by the respective authors

ISBN 978-3-95450-141-0

were going to CFD inputs with one of them delayed by 10 ns. Measured time resolution for electronics was 12 ps (FWHM) for MCP high voltage of 1.85 kV.

BEM Design

The BEM consists of two parts which are installed inside the diagnostic box that can be seen on Fig. 2.

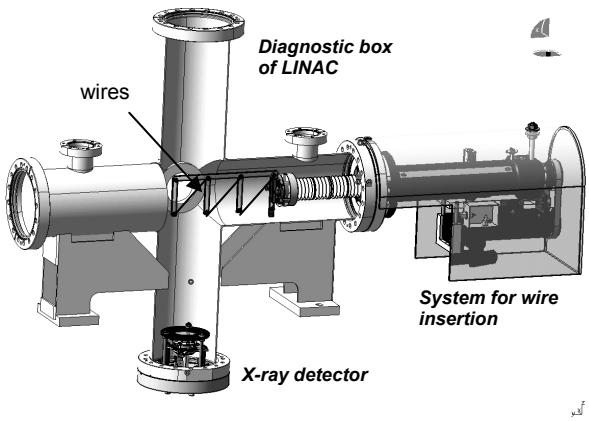


Figure 2: General view of BEM installed at diagnostic box of LINAC.

The first part of this detector is the system for wire insertion which allows inserting the wire into the beam with precision better than 100 µm. Three different tungsten wires of 150 microns diameter are fixed on a stainless steel frame. Each holder has dimensions 50mm × 50mm where tungsten wire is fixed along the diagonal. Wires of the next BEM are fixed at a perpendicular direction compared to the previous BEM wires to minimize beam distortion. Three wires are installed to have some spare in case of wire damaging without dismounting. The rod is moved by a brushless motor through a system of screw-nut mounted on air side of flange CF100.

The system for wire insertion allows also to perform measurements of current on the wire. Frame with tungsten wires is isolated and electrically connected through vacuum feedthrough on the flange. Current from the wire is measured by a card developed at GANIL and also used for measurements of current from Faraday Cups and slits.

The second part of BEM is the x-ray detector used for registration of photons emitted from wire. Two MCPs Hamamatsu F1551 (∅ 18mm) are used assembled in chevron configuration and provide gain up to 10^7 at applied voltage -2kV. For obtaining short signal front, the output electrons are collected by a fast readout coaxial anode of 50 Ohms impedance connected on the CF100 flange with N-type connector. Entrance of first MCP is covered by an 8 mm thick copper plate with a 4 mm hole. This collimator permits to select x-rays coming from the center of the wire.

To avoid background signals from ions coming from residual gas ionization, a deflecting grid polarized at +30V is positioned on the top of the collimator.

TEST OF PROTOTYPE

Test at GANIL on IRRsud Ligne

A test was performed at GANIL with a beam of $^{36}Ar^{+10}$ ions of 0,98MeV/n energy. A 60s acquisition time with 2.4 µA intensity has given the spectra shown Fig. 3 with a good signal over noise ratio.

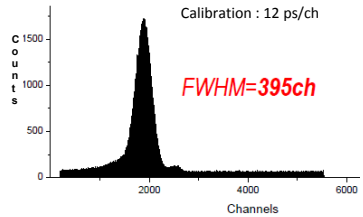


Figure 3: Measured bunch profile of $^{36}Ar^{+18}$ with 2.4 µA beam intensity (Value of MCP applied voltage of 1.95kV and time acquisition =60 s).

Bunch length measurements were done at various intensity up to 2.5 µA using a continuous wave beam with adapted voltage on MCP (see Fig 4). FWHM values are stable and the difference of the three curves is due to a different background subtraction for the FWHM calculation.

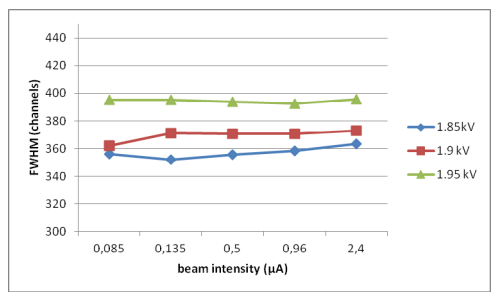


Figure 4: Measured FWHM bunch of $^{36}Ar^{+18}$ versus beam intensity.

Comparison with Theoretical Estimation

Results of the beam test were compared with analytical calculation of x-ray production from the wire (see Fig 5). To perform these calculations the cross section of tungsten wire was divided into small elemental cells. For each cell the value of ionization cross section was calculated. The cross-section can be implemented as a function of scaled velocity of projectile ion to velocity of electron on the shell V_{proj}/V_{elect} and can be represented through Gryzinsky function (see Eq.1) [3].

$$\sigma_{ionis}(E) = \frac{N \cdot Z^2 \cdot \sigma_0}{U^2} \cdot G(V) \qquad (1).$$

Where N is a number of electrons on the shell (K-shell=2, L-shell=8), Z is charge of projectile ion, U is binding energy of electrons at the given shell, $G(V)$ is a function of the scaled velocity $V=V_{proj}/V_{elect}$ and $\sigma_0 = \pi \cdot e_0 = 6.56 \times 10^{-14} cm^2 eV^2$

ISBN 978-3-95450-141-0

Copyright © 2014 CC-BY-3.0 and by the respective authors

To estimate the scaled velocity the value of beam energy loss is calculated in each cell. The attenuation of x-rays in the wire is also taken into account.

The total value of emitted photon from the wire can be obtained by summing the x-ray production in each cell [4]. The final expression for total number of photons emitted in solid angle ratio $\Omega/4\pi$ and registered by MCP can be written as:

$$Q = \frac{\Omega}{4\pi} \cdot \varepsilon \cdot N_{atoms} \cdot \omega_{k,l} \cdot \sum_{ij} I_{ij} \cdot \sigma_{ionis}\left(E(x_i)\right) \cdot e^{-\mu \cdot L_{ij}} \quad (2).$$

where $\Omega/4\pi$ is a solid angle ratio of detector, ε is the photon registration efficiency by MCP, N_{atoms} is the concentration of target atoms per cm^2, $\omega_{k,l}$ are fluorescence yields of photons for K-, L-shell ionizations, I_{ij} is number of incident ions of the beam at ij-cell per second, σ_{ionis} is ionization cross-section for K-,L-shells as function of incident ion energy, $exp(-\mu \cdot L_{ij})$ is x-ray attenuation.

The calculations (see Eq. 2) were done for both cases of ionization for K- and L- shell. The relative yield of photons due to ionization of L-shell is almost 10^5 times higher than for K-shell. For this reason, only the L shell calculation is shown in comparison with experimental results (see Fig. 5).

An experimental count rate comparison to the theoretical calculation has been made for different beam intensities and MCP applied voltage (see Fig. 5). Variation of the experimental count rate measurement is similar to the calculation curve but values are lower of these due to different parameters not take in count in the calculation like MCP opacity and gain.

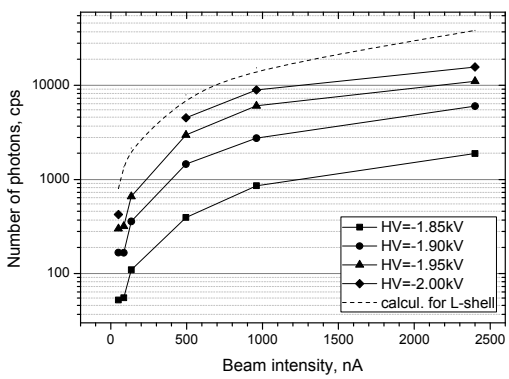


Figure 5: Comparison of count rates for different values intensities and applied voltage. Theoretical estimation of count rate due L-shell ionisation is presented.

Test of BEM Close to Cryomodule

To verify if x-rays emitted from the cavity could disturbed the BEM acquisition, a BEM has been mounted in a LINAC diagnostic box and connected to a SPIRAL2 cryomodule type B (with two superconducting cavities) (see Fig. 6). This test was performed at ORSAY IPN. The principle of operation for bunch extension monitor (BEM) is based on the registration of x-ray emitted from thin tungsten wire.. A superconducting cavity inside of cryomodule can produced x-rays due to electrons bremsstrahlung inside the cavity at high applied accelerating field. The emitted x-rays from cavity can be directly registered by BEM or can create x-rays on the wire and produce unwanted background in both cases.

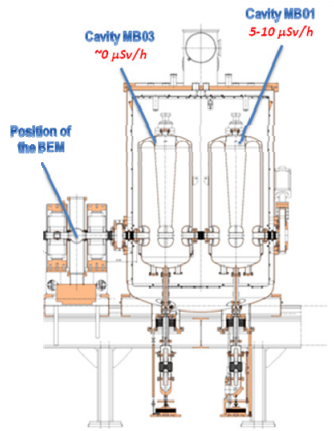


Figure 6: Installation of BEM set close to cryomodule B.

Two series of measurements for each cavity were carried out and average count rates were measured. Each series of measurements contains several points at different values of electric field gradient starting from zero and exceeding of nominal value (operating acceleration field value is 6.5 MV/m).

Also for each value of electric field gradient two measurements were done with inserted wire and without. The average count rate measured without insertion of the wire permits to estimate global x-ray background generated by cavity. The ratio of count rates obtained with inserted wire and without gives the number x-rays number emitted from the wire due to x-ray fluorescence.

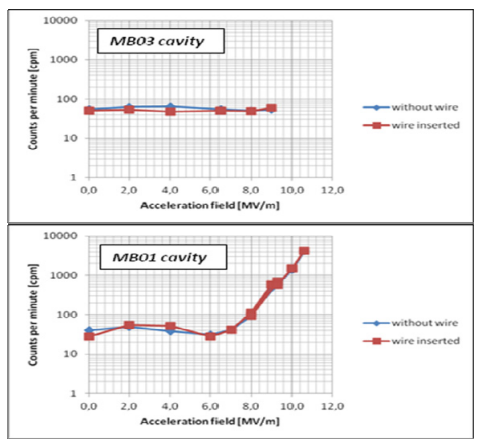


Figure 7: value of count rate emitted from cryomodule and detected by BEM.

At the maximum value of 10.6 MV/m, the count rate was about 50 Hz on the worst cavity (Fig. 7). This value

Copyright © 2014 CC-BY-3.0 and by the respective authors

ISBN 978-3-95450-141-0

is lower by about two to three orders of magnitude compared to normal conditions in beam.

SUMMARY

A prototype of non-interceptive beam diagnostic detector for bunch length measurements was developed. Test with proton and ions beams were performed in various conditions. The time resolution for detector and electronics is approximately 10 ps using analogical electronics. The results of test were compared with theoretical estimation of x-ray production. The test of BEM installed close to the cryomodule has shown that BEM measurements will not be perturbated by it during beam acceleration. A test with high intensity proton beam at SARAF facility is scheduled in October 2014 to estimate the maximum count rate possible with this detector. The set of the five BEM will be installed on the LINAC at the beginning of 2015.

ACKNOWLEDGMENT

This work is funded in frame of CRISP WP3T1 project.

REFERENCES

[1] http://www.ganil-spiral2.eu/
[2] D. Uriot et al., “Configuration de base du LINAC supraconducteur de SPIRAL2 V2.0”, Référence Spiral 2 I-013103/1 (2008).
[3] Michal Gryzinski, "Classical Theory of Atomic Collisions. Theory of Inelastic Collisions", Phys. Rev. V.138, 2A (1965) p.336.
[4] I. Orlic et al., "TTPIXAN - A Package of computer programs for quantitative thick target PIXE analysis", NIM B49 (1990) p166.

Copyright © 2014 CC-BY-3.0 and by the respective authors

ISBN 978-3-95450-141-0

THE BEAM INSTRUMENTATION AND DIAGNOSTIC CHALLENGES FOR LHC OPERATION AT HIGH ENERGY

O. R. Jones, CERN, Geneva, Switzerland

Abstract

This contribution will present the role of beam diagnostics in facing the challenges posed by running the LHC close to its design energy of 7TeV. Machine protection will be ever more critical, with the quench level of the magnets significantly reduced, so relying heavily on the beam loss system, abort gap monitor, interlocks on the beam position and fast beam current change system. Non-invasive profile monitoring also becomes more of a challenge, with standard synchrotron light imaging limited by diffraction and rest gas ionisation monitoring dominated by space charge effects. There is also a requirement to better understand beam instabilities, of which several were observed during Run I, leading to the need for synchronised bunch-by-bunch, turn-by-turn information from many distributed instrumentation systems. All of these challenges will be discussed along with the strategies adopted to overcome them.

INTRODUCTION

The first beam was injected into the LHC during tests in August 2008, with circulating beams established on the 10th September 2008. Nine days later disaster struck as a fault in one of the superconducting circuits led to the release of 600MJ of stored energy during a test of high current powering. It took over a year to recover from the damage caused by this event, with over 30 magnets needing to be repaired or replaced. After intensive investigations the source of this accident was concluded to be due to a faulty splice between the superconducting cables of neighbouring magnets. In addition it was found that for many magnets there was poor electrical and thermal conductivity between the superconducting cable and the copper stabiliser surrounding these joints. In the event of a magnet quench, when the superconductor becomes normal conducting due to overheating, these copper stabilisers take the full current until it can be safely extracted, a process which takes several minutes. Under such circumstances any poor contacts can lead to a thermal runaway, resulting in a similar accident to the one experienced in 2008. Due to these issues it was decided to initially run the LHC at half its design energy of 7TeV. This represents some 6kA in the main circuits, a current which was considered could be safely extracted even with such poor contacts still present in the machine.

The beam was back in the machine for commissioning on the 29th November 2009, with first physics collisions at 3.5TeV per beam occurring on 30th March 2010. This was the start of 3 years of nearly continuous LHC operation, culminating in the discovery of the Higgs boson on the 4th July 2012. During this time the stored beam intensity was gradually increased, with the energy also increased to 4TeV per beam in 2012. A total integrated luminosity of nearly 30fb^{-1} was accumulated over this period (Fig. 1), with the LHC ending the 2012 run reaching peak luminosities of 8×10^{34} cm^{-2}s^{-1}, close to its design value of 10^{34}.

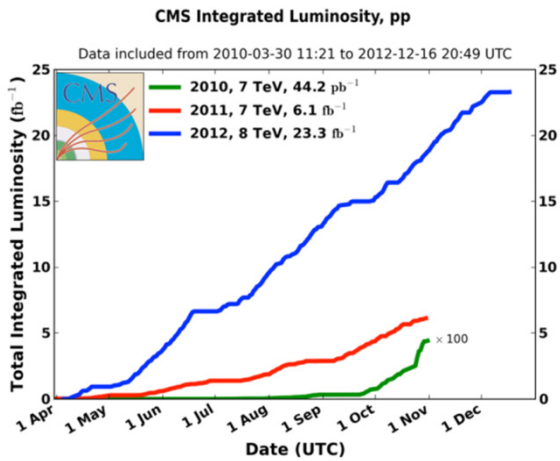


Figure 1: LHC performance during Run I.

In order for the LHC to work at, or close to, its nominal energy of 7TeV, major consolidation of all the superconducting circuits was necessary. Long Shutdown 1 (LS1) started on the 14th February 2013 with the aim of consolidating over 10,000 superconducting splices, reducing the effects of radiation to electronics and carrying out full maintenance on all equipment, including the majority of beam instrumentation systems.

At the time of writing, this consolidation work is complete and the LHC is in the process of being cooled to 1.9K before the start of hardware commissioning. The beam is currently expected back in March 2015, with the LHC foreseen to run at 6.5TeV for the remainder of that year.

The beam instrumentation and diagnostic systems of the LHC [1] worked remarkably well throughout Run I, and played an important part in the rapid commissioning and reliable operation of the machine. However many lessons have been learned and shortcomings identified, the majority of which have been addressed during the long shutdown. Run II of the LHC, at an energy close the design energy of 7TeV, will in addition bring its own challenges, and it is these that will be addressed in this contribution.

Copyright © 2014 CC-BY-3.0 and by the respective authors

ISBN 978-3-95450-141-0

THE CHALLENGES FOR RUN II OF THE LHC

The three main challenges for Run II of the LHC are:

- ***Operating at higher energy.*** It is currently foreseen that the LHC will start running in 2015 at a top energy of 6.5TeV, with the possibility to increase in later years towards 7TeV depending on the quench behaviour at high field of the main dipole magnets. At this energy the quench thresholds will be significantly reduced compared to Run I, meaning that the machine will tolerate much less beam loss. As can be seen from Fig. 2, a single pilot bunch of 5×10^9 protons is close to the material damage threshold at 7TeV while a quench can be incurred if less than one millionth of a nominal beam is lost over a 10ms period.

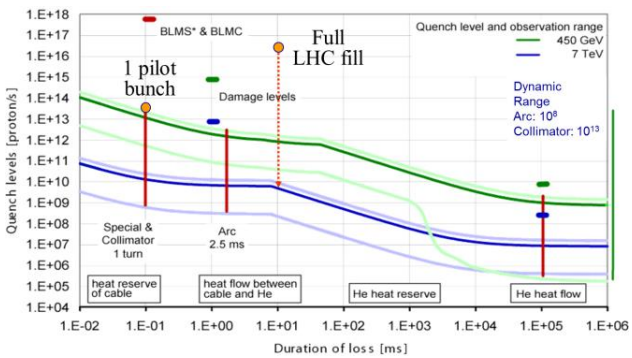


Figure 2: Estimated quench levels for the LHC at injection and top energy.

- ***Running with 25ns bunch spacing.*** During Run I the LHC was operating with a nominal bunch spacing of 50ns. Such a beam could be produced by the LHC injector chain with high brightness, and could be injected, accelerated and collided with little loss in the LHC. However, such a high intensity per bunch coupled with a low emittance, meant that the LHC experiments had to disentangle on average over 30 events per bunch crossing. In going to high energy and tighter focussing, this "pile-up" would become unacceptably large and hence operation at 25ns spacing is foreseen. This brings with it the problems related to enhanced electron cloud formation and beam induced RF heating due to the increase in total beam current.
- ***Coping with high brightness beams.*** While going to 25 bunch spacing is likely to reduce the brightness of the LHC bunches at injection (lower intensity and slightly larger emittance), the fact that they are accelerated to higher energy and hence reduced in size, will mean that at flat-top they will be significantly smaller than any beams produced during Run I. This will pose severe issues for the measurement of their emittances, required for the understanding and optimisation of the machine.

Each of these challenges will now be looked at in detail, with the role played by beam instrumentation and diagnostics in addressing them highlighted.

OPERATING AT HIGHER ENERGY

As stated previously, the main challenge of operating the LHC at higher energy is dealing with the reduced quench thresholds of the main dipole and quadrupole magnets. This poses two questions: how to deal with unidentified falling objects and how to ensure efficient collimation?

Dealing with Unidentified Falling Objects

Run I of the LHC was plagued by Unidentified Falling Objects (UFOs) creating beam losses that were large enough to trigger a beam abort by the BLM system[2]. In 2012, 20 beam dumps were identified to be associated with UFOs, with 14 of these occurring at 4TeV. In addition, some 17,000 candidate events were attributed to UFOs below the BLM threshold. The origin of these events is unclear, but as they appear at nearly all locations around the LHC they are believed to be the result of dust particles dropping into the vacuum chamber. The reduction of quench thresholds with energy will mean that at 6.5 – 7 TeV many more beam aborts can be expected. To buy some additional margin a relocation of the ionisation chambers of the beam loss monitoring system has been carried out during LS1 (Fig. 3).

Designed to protect the superconducting magnets from beam losses at maximum-beta locations, the original system had 3 ionisation chambers per beam and per quadrupole [3]. However, as UFOs can occur at any location, an event in one of the dipoles between two quadrupoles will result in a relatively small signal by the time the secondary shower reaches the beam loss monitor (BLM) sitting on the quadrupole. In order to avoid the dipole quenching, the BLM thresholds therefore have to be increased substantially, well above what is required to avoid quenches due to standard beam loss at the quadrupoles. After significant simulation work it was decided to move one of the BLMs per beam from the quadrupoles to the dipoles. This was found to leave sufficient redundancy to avoid quenches due to losses at the quadrupoles while gaining a factor 30 in sensitivity to UFO events occurring in the dipoles.

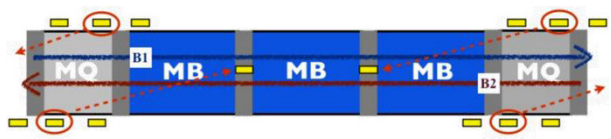


Figure 3: Relocation of beam loss system ionisation chambers (yellow) to optimise protection against UFOs. MQ - main quadrupole: MB - main bend (dipole).

While the beams will still be aborted should a large enough UFO even occur at 6.5-7TeV, the relocation of these BLMs will at least enable the thresholds to be set

ISBN 978-3-95450-141-0

Copyright © 2014 CC-BY-3.0 and by the respective authors

closer to what is required to avoid quenching in all magnets with losses generated by either a UFO event or via a standard loss scenario.

Ensuring Efficient Collimation

The cleaning efficiency necessary to ensure that any beam loss in the cold arc is maintained well below the quench threshold is ensured by a comprehensive collimation system (Fig. 4) [3]. A series of primary, carbon-jawed collimators scatter the transverse and longitudinal beam halo, which is then absorbed by secondary carbon collimators with slightly larger opening. Tungsten-jawed tertiary collimators near the experiments and various protection devices complete the collimator hierarchy, cleaning-up the remainder of the secondary halo and protecting against equipment failure, such as the misfire of the dump kickers. During Run I the gap in the 1.2m long jaws of the primary collimators was only 2.2mm.

Ensuring the correct set-up of these ~100 moveable devices and ensuring that the beam remains centred during long periods of operation is the job of the beam loss and beam position system respectively.

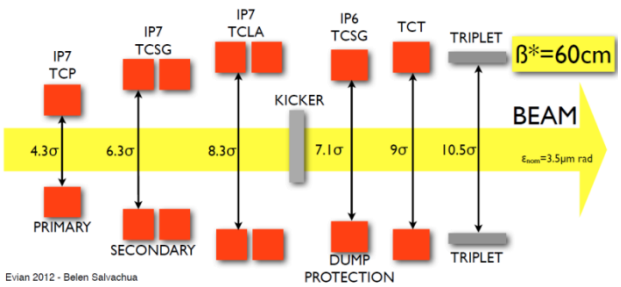


Figure 4: Collimation hierarchy in the LHC. Retraction in beam sigma for possible for operation at high energy.

Defining the Right Collimator Positions

Once a stable orbit has been defined, the setting up of the collimators is carried out using the LHC beam loss system [4], consisting of over 3000 ionisation chambers. With very low intensity beam in the machine, each collimator jaw is individually moved in until it touches the beam halo, inducing a loss spike which is detected in a neighbouring BLM. Initially this procedure took over a day to be performed for all collimators, but has since been reduced to less than one hour, thanks to the parallelisation of the task and an improved BLM data stream. Beam loss measurements are now published to the collimator control system at 12.5Hz, allowing the maximum 8Hz movement of the jaws.

Once centred, the collimation hierarchy is validated by so-called loss maps. This involves creating an artificial loss and monitoring the leakage of lost particles into the cold magnets using the complete BLM system. An example of such a loss map is shown in Fig. 5. It can be seen that the losses are all localised in the betatron and momentum cleaning collimation regions. The maximum leakage of lost particles into a cold magnet is less than 0.02%, within the design specifications.

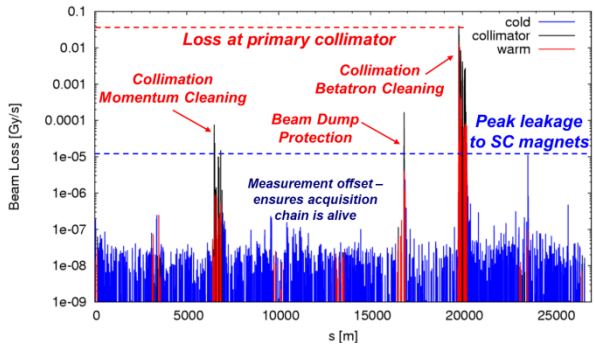


Figure 5: Example of an LHC loss map showing the measurements from all beam loss monitors around the LHC.

During LS1, all 16 tertiary collimators have been replaced by a design which includes embedded beam position monitors (Fig. 6) [5]. The settings of these collimators are linked to the amount of focussing possible in the experimental insertions. A better knowledge of the beam position at their location would enable safety margins to be reduced to allow tighter focussing, and hence higher luminosity.

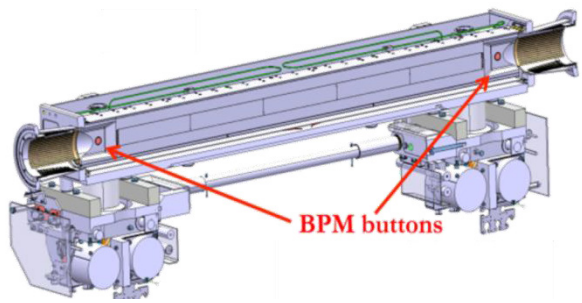


Figure 6: Design of the new LHC tertiary collimator with beam position monitors embedded within the jaw.

A prototype of such a collimator with embedded BPMs has been successfully tested in the CERN-SPS and showed that the time required to set-up the collimator to be centred within 10μm around the beam can be reduced to a mere 20 seconds [6]. The system uses two pairs of button pick-ups, one at the upstream and one at the downstream end of the collimator, slightly retracted from the face of the jaw. The signals are processed using compensated diode peak detector electronics, specially designed to give excellent resolution, < 100nm, for centred beams [7]. This electronics for accurate, high resolution orbit measurements has been so successful that it will now also be extended to work in parallel to the existing bunch-by-bunch orbit and trajectory system in critical locations.

Maintaining the Right Collimator Positions

Once the right collimator positions have been defined, the role of maintaining the beam in their centres is the job

Copyright © 2014 CC-BY-3.0 and by the respective authors

ISBN 978-3-95450-141-0

of the LHC beam position system [8]. This is comprised of 1054 beam position monitors, the majority of which (912) are 24mm button electrode BPMs located in all arc quadrupole cryostats. The remaining BPMs are enlarged (34mm or 40mm) button electrode BPMs mainly for the stand alone quadrupoles, or stripline electrode BPMs used either for their directivity in the common beam pipe regions or for their higher signal level in the large diameter vacuum chambers around the dump lines.

The beam position acquisition electronics is split into two parts, an auto-triggered, analogue, position to time normaliser which sits in the tunnel and an integrator/digitiser/processor VME module located on the surface. Each BPM measures in both horizontal and vertical planes, making a total of 2156 channels.

The data from all these channels is fed at 25Hz to a central orbit feedback system which, using a regularised SVD approach and a closed loop bandwidth of 0.1Hz, can maintain orbit stabilities of typically better than 70µm globally and 20µm in the arcs. The measured fill-to-fill reproducibility when going into collision at the ATLAS interaction point throughout 2012 is shown in Fig. 7. Whilst a slow drift of 80µm is seen to build-up over the year, the reproducibility from one fill to the next is excellent with the difference only 7µm rms.

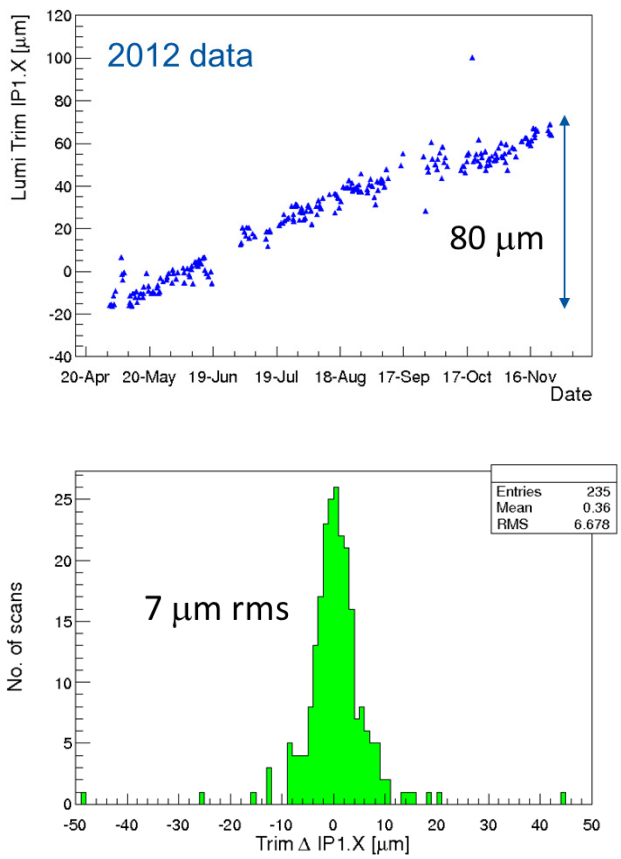


Figure 7: Orbit reproducibility going into collision at the ATLAS experiment as measured in 2012.

The main performance limitation of the orbit feedback is linked to an observed systematic position dependence on temperature that initially caused errors of greater than 300µm on the orbit measurements. This was reduced to the order of 100µm during Run I by regular calibration and applying temperature corrections to the data. To eliminate this problem for Run II, temperature controlled racks have been added to house the BPM surface electronics. These maintain a stable temperature to within ±0.2°C which should keep any orbit drifts below 10µm.

RUNNING WITH 25NS BUNCH SPACING

The main challenge of running with 25ns spaced bunches in the LHC will be dealing with the electron cloud that this generates [9]. This cloud of electrons is created due to secondary emission from the beam pipe wall, initially via ion bombardment or synchrotron radiation. As these electrons drift into the chamber they are accelerated by a passing bunch, hitting the opposite wall and creating more secondary electrons. This process is repeated with the following bunches, creating and avalanche of electrons, which eventually forms an electron cloud. Apart from creating a dynamic pressure rise and an additional heat-load for the cryogenic circuits, it also has an impact on beam quality, with the induced instabilities leading to particle loss and emittance growth.

For a given bunch spacing, the threshold at which this cloud can develop is given by the secondary electron yield of the wall material. This can be lowered by scrubbing the surface with a dense electron cloud, which is why many machines introduce scrubbing runs with high intensity beams at low energy. Moving from 50ns spacing to 25ns spacing significantly lowers the secondary electron yield threshold at which a significant electron cloud forms. It can therefore be expected that during Run II it will be even more important to be capable of observe instabilities, measure beam loss and monitor emittance growth.

Bunch by Bunch Diagnostics

Understanding the effects of the electron cloud and other instabilities can only be effectively done using bunch-by-bunch measurements. In the LHC nearly all instrumentation systems have therefore been designed to deliver such data, with many improvements carried out during LS1.

Two new types of fast beam current transformer have been installed to improve the bunch by bunch resolution of the existing system and remove the dependency on beam position and bunch length observed during Run 1 [10]: an integrating current transformer developed in collaboration with Bergoz Instrumentation [11] and a wall current monitor developed at CERN. Both are aimed at providing a bandwidth of up to ~100MHz, less than 0.1%/mm position dependence and 0.1% bunch length dependence.

The synchrotron light monitor is also capable of providing bunch by bunch diagnostics and has already been used extensively to study the effect of electron cloud on emittance blow-up. In this mode a Proxitronic Nanocam, HF4 S 25N NIR intensified via a multichannel

ISBN 978-3-95450-141-0

Copyright © 2014 CC-BY-3.0 and by the respective authors

plate between the photocathode and the camera sensor, is used in gated mode to scan through the individual bunches. The present acquisition chain (analogue camera ⇒ frame grabber ⇒ software) is limited to about 16 frames/s, which implies that it takes some 3 minutes to scan though all bunches. A plan to upgrade this to the maximum camera rate of 50 frames/s is foreseen in the near future.

Fig. 8 shows an example of bunch by bunch emittance measurements during the scrubbing run used to condition the machine against electron cloud effects at the start of 2011. Instabilities leading to increased emittance are clearly visible on one beam towards the end of the injected batches. These measurements were invaluable in quantifying the improvements made during the course of this conditioning. It has also been used to detect non-uniformity in the emittance of the beam coming from the LHC injectors, leading to an optimisation campaign which resulted in much better emittance uniformity.

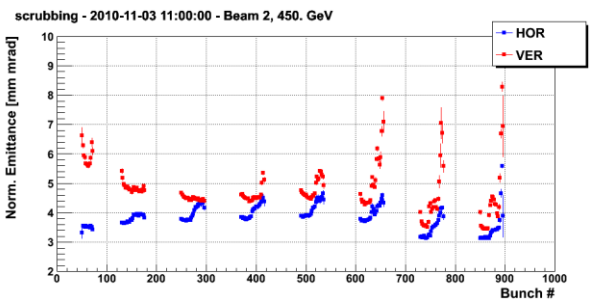


Figure 8: Bunch by bunch emittance showing the blow-up of some bunches due to electron cloud instabilities.

Intra-Bunch Diagnostics

Another important diagnostic to understand the origin of instabilities is intra-bunch measurement. During Run I various instabilities, leading to beam loss and emittance growth, were observed during the beta squeeze (while focussing the beam in the experiments) and whilst going into collision. Disentangling the many possible causes of these instabilities requires a detailed knowledge of their effect on the beam. Although general oscillation data showing that an instability had occurred was available during Run I, it was not possible to distinguish between coupled bunch and intra-bunch motion. The reason for this was twofold. Firstly there was no reliable trigger to freeze the acquisition buffers of the systems that were measuring bunch-by-bunch when the instability occurred. Secondly, the resolution of these systems was often insufficient to observe the instability before the beams were aborted.

To address these two points a new Multiband Instability Monitor (MIM) is being developed [12]. This system exploits the fact that the frequency spectrum of an unstable bunch will be modified depending on how it is oscillating. By measuring this frequency spectrum the modes of the oscillation can therefore be inferred.

The MIM under construction will measure the amplitude of the intra-bunch motion in 16 different frequency bands separated by 400MHz, from 0.4-6GHz. A stripline pick-up is used to provide the input signals, which then transit a 16 channel filter bank, before being converted to baseband by 16 parallel direct diode detection channels. This should give the system sufficient sensitivity to detect sub-micron oscillations, allowing it to both trigger other systems and give valuable information on the type of instability being observed.

COPING WITH HIGH BRIGHTNESS BEAMS

Beam Induced RF Heating

During Run I beam induced RF heating was observed on many pieces of equipment [13]. This effect comes about due to the intense LHC beams generating RF wakes in these structures, which are then amplified by the following bunches. If the cooling is insufficient, or the RF power absorbed too great this can have serious consequences. It has led to the failure of RF fingers, damage to the injection protection system and the overheating of injection kickers and forward physics experiments. In addition is resulted in the failure of the extraction mirror support for the synchrotron light monitor and a blistering of the mirror coating.

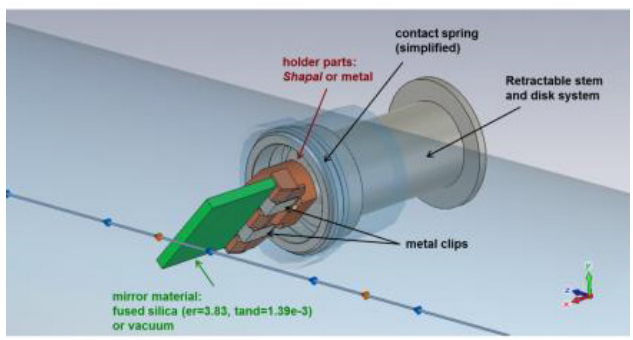


Figure 9: Original synchrotron light extraction mirror support. The metal holder, which was surrounded by ferrites, acted as an antenna, absorbing RF power from the beam and heating the complete structure.

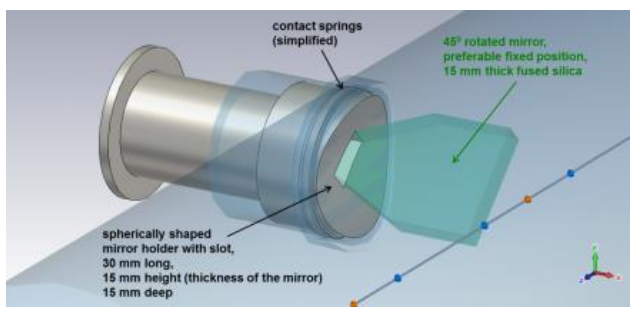


Figure 10: New synchrotron light extraction mirror support. A long mirror is held in place by a spherically shaped holder which maintains the continuity of the beam pipe.

Copyright © 2014 CC-BY-3.0 and by the respective authors

ISBN 978-3-95450-141-0

An intensive electromagnetic simulation campaign [14] showed that with the existing design (Fig. 9) the ferrites used to detune the cavity and absorb the RF power could be heated well above their Curie temperature. The assumption is that this then led to an overheating of the mirror and support. The best alternative found is shown in Fig.10. This still allows the mirror to be placed a few centimetres from the beam and uses the same extraction tank. The design significantly reduces the RF coupling to the beam, and should allow the structure to dissipate any heat generated via conduction and radiation. Such holders have now been produced (Fig. 11) and installed on both beam lines.

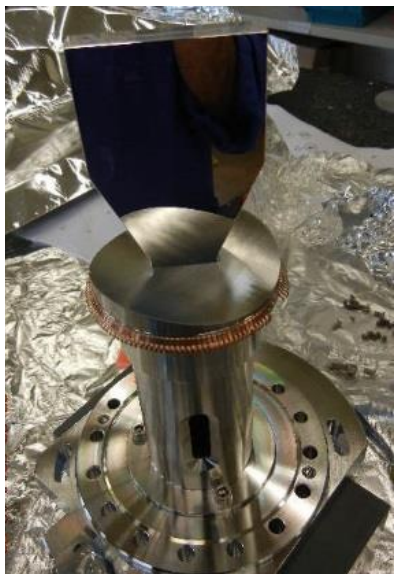


Figure 11: New synchrotron light extraction mirror and support.

Measuring Small Beam Sizes

During Run I, the LHC was equipped with 4 beam size measurement devices: optical transition radiation screens for the setting-up of injection and extraction; wire-scanners for absolute measurement and the calibration of the other devices; synchrotron light monitors; rest gas ionisation monitors. Each of the three devices used with circulating beam presented limitations, and will be further pushed to measure the even smaller beam sizes expected at 6.5-7TeV.

Wire-Scanners

The operation limits for the LHC wire-scanners during Run II are defined by the process of wire sublimation (Fig. 12) [15]. At the injection energy of 450GeV the limit sits at a total intensity of around 2.7×10^{13} protons. This was sufficient during Run I to measure the first full injected SPS batch of 144 bunches with 50ns spacing. However, it will not be sufficient to measure a full injected SPS batch of 288 bunches with 25ns spacing. In addition the limit at 6.5TeV has been calculated to be at 2.7×10^{12} protons, which is a mere 20 bunches. Dedicated runs will therefore be required to use the wire-scanners to cross calibrate the other devices.

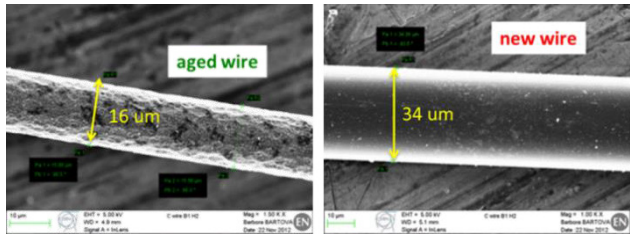


Figure 12: The effect of sublimation on the carbon wire of the LHC wire-scanners.

Synchrotron Light Monitor

With a new extraction mirror in place it is hoped that the imaging accuracy of the synchrotron light monitor will be much improved for Run II. In addition, wave-front distortion measurements using the Shack-Hartman mask method will be used to measure and correct for any remaining distortions. However, at 6.5-7 TeV the imaging will be dominated by diffraction. The optical system has therefore been redesigned to use ultra-violet (UV) compatible optics and a CCD camera with a UV sensitive photocathode, rather than the visible optics and camera used in Run I. Even so, when imaging in a narrow band at 250nm, the contribution from diffraction is estimated to be ~250μm compared to a beam size of only 180μm. A good understanding of the diffraction effects and all other distortions will therefore be necessary to extract an accurate absolute beam size from these images.

Due to the extent to which imaging is expected to be dominated by diffraction at 6.5-7TeV a new optical line has been added to perform interferometry, though a collaboration with KEK (Japan), SLAC (US) and CELLS-ALBA (Spain) [16]. This non-diffraction limited technique is widely used in electron machines with very small beam sizes and relies on the fact that the visibility of the interference pattern is dependent on the beam size. The results of simulations showing the expected interference patterns in the LHC at injection and top energy are shown in Fig. 13, with the dependence of the visibility on beam size presented in Fig. 14.

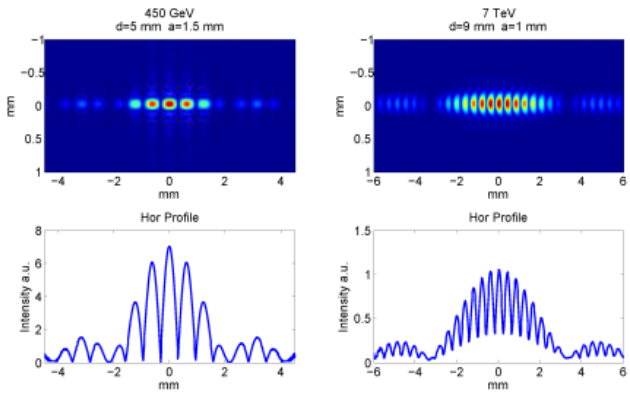


Figure 13: Simulation results showing the expected interference patterns from synchrotron radiation at injection and top energy.

Copyright © 2014 CC-BY-3.0 and by the respective authors

ISBN 978-3-95450-141-0

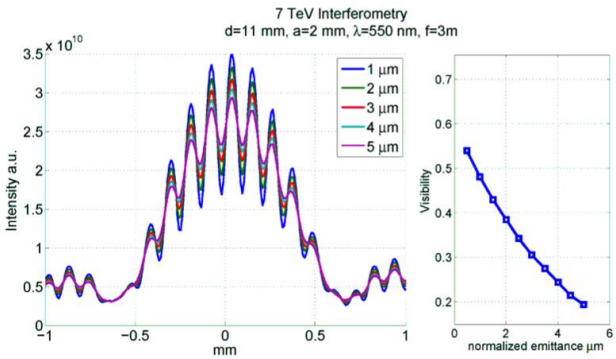


Figure 14: Simulation results showing the expected variation of visibility with beam size.

It is hoped that with the modifications to the extraction mirror and the standard imaging system, plus the addition of interferometry, the synchrotron light monitor will continue to give accurate beam size measurements during Run II.

Ionisation Profile Monitor

The LHC ionisation profile monitor (IPM) is based on electron collection using a 0.2 T guide magnet, a multi-channel plate for amplification and an optical readout from a phosphor screen with a radiation-hard camera [17]. While this monitor has worked well with Pb^{54+} ion beams, it was seen to suffer from severe image distortion during the proton energy ramp. This was suspected to be due to space-charge effects from the high brightness proton beams, something that was confirmed by simulations using the PyECLOUD code [18]. The distorted profile (Fig. 15) cannot currently be deconvoluted to extract the original profile, and the only real solution to this problem seems to be to increase the magnetic guide field to around 1T. This is not currently foreseen, and thus the IPM will only be used to measure Pb^{54+} ion beams during Run II. This was in any case its primary purpose as Pb^{54+} ion beams emit very little synchrotron light at the LHC injection energy of 450GeV.

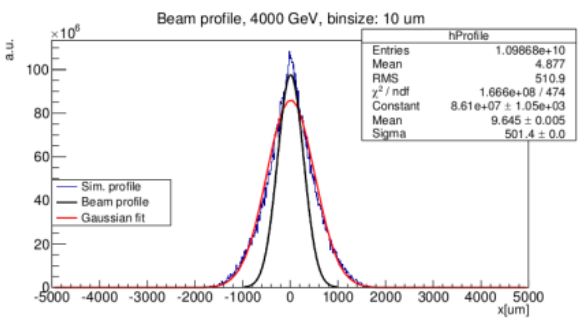


Figure 15: Profile as measured by the IPM at 4TeV showing the large distortion due to space charge.

Beam Gas Vertex Detector

The beam gas vertex (BGV) detector [19] is a new instrument being prototyped on one of the LHC beams after LS1, under the auspices of the High Luminosity LHC upgrade project. A collaboration between CERN, EPFL Lausanne (Switzerland), and RWTH Aachen (Germany) has been formed to design, develop, install and commission a demonstrator BGV system for the LHC by the end of 2015. This non-invasive beam gas interaction detector is based on developments for the LHCb experiment [20], where the vertex detector was successfully used with gas injection during Run I to measure 3D beam profiles during collisions for absolute luminosity determination [21].

Unlike for LHCb, where the detector is placed very close to the beam and can therefore only be used during stable beams in collision, the aim with the BGV detector was to design a robust instrument that could be used for beam size measurements for machine operation at all times in the LHC cycle. Its final specifications are to provide a relative bunch width measurement with 5% accuracy within 1 minute and an absolute average beam width measurement to an accuracy of 2% within the same time. For the demonstrator it was considered essential to maintain the functionality of real-time bunch-by-bunch profile measurements with a resolution of about 5 %, but within an increased 5 minute measurement interval, while the absolute accuracy requirement was relaxed to 10 %.

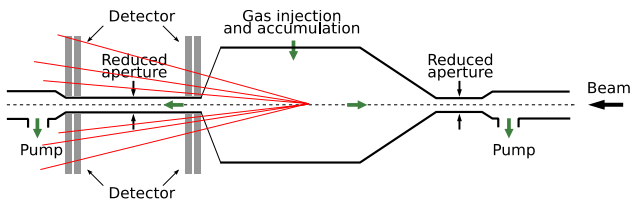


Figure 16: Principle of the beam gas vertex detector for transverse beam profile measurement.

The principle of the device is shown in Fig. 16. The LHC proton beam interacts with an injected gas volume to produce secondary particles. These are peaked in the forward direction and are tracked using a set of tracking detectors. By tracing back from the detected tracks the original vertex can be located, provided that the quantity of intervening matter is small enough to limit the amount of multiple-scattering.

The main subsystems are: a neon gas target at a pressure of 6×10^{-8} mbar, a thin aluminium exit window, tracking detector based on scintillating fibre modules read out by silicon photomultipliers, hardware and software triggers, and a readout and data acquisition system based on that used for LHCb. As the tracking detector is external to the vacuum chamber, no movable parts are needed. The final design is shown in Fig. 17.

Copyright © 2014 CC-BY-3.0 and by the respective authors

ISBN 978-3-95450-141-0

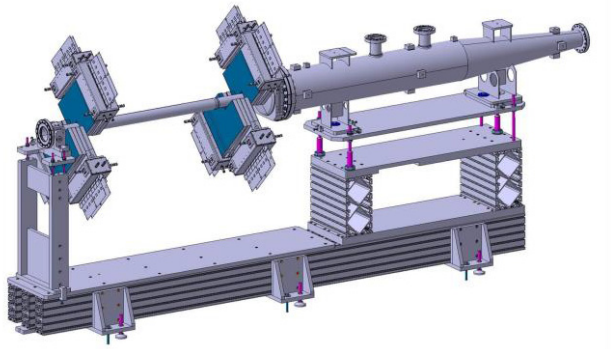


Figure 17: The demonstrator Beam Gas Vertex detector installed in the LHC during LS1.

SUMMARY

During the first long LHC shutdown nearly all beam instrumentation devices have been consolidated or upgraded with a few new additions installed, to cope with the challenges of the next 3 years of running at close to top energy.

After being dismounted for the repair work on the superconducting magnets, the BLMs have been re-installed in a configuration that should help cope with the threat of quenches due to unidentified falling objects. All the quench thresholds have also been updated with simulations and results and from tests performed at the end of the last run.

The BPM system sees the addition of temperature controlled racks for added measurement stability, embedded BPMs in collimators and the test of a new, high resolution diode orbit system for improved resolution at critical locations.

The synchrotron light monitor has a new extraction mirror that will hopefully eliminate the effects of beam induced RF heating suffered during Run I. It also sees the addition of a new interferometry line and the use of UV optics.

Instability monitoring will be provided by the new multi-band detector, while a new technique for non-invasive beam profile measurements will be tested with the beam gas vertex detector.

Other improvements include: a revamped schottky system for on-line chromaticity and bunch-by-bunch tune measurements, new fast beam current transformers for better bunch-by-bunch performance, and improved correction algorithms for the single photon counting longitudinal density monitor.

With the original LHC beam instrumentation already having shown its worth during Run I it is hoped that these upgrades and new additions will help meet the challenges of Run II.

REFERENCES

[1] R. Jones, “LHC Beam Instrumentation - Status and Challenges”, BIW06 (2006).

[2] T. Baer et al.,“UFOs in the LHC”, Proceedings of IPAC, San Sebastian, September 2011, TUPC137, p.1347-1350

[3] D. Wollmann et al., “First Cleaning With LHC Collimators”, TUOAMH01, IPAC10, Kyoto, Japan (2010).

[4] B. Dehning et al., “The LHC Beam Loss Measurement System”, PAC07 (2007).

[5] C. Boccard et al., “Embedded Collimator Beam Position Monitors”, MOPD18, DIPAC11, Hamburg, Germany (2011).

[6] G. Valentino et al., “Development and Beam Tests of an Automatic Algorithm for Alignment of LHC Collimators with Embedded BPMs”, THPFI063, IPAC2013, Shanghai, China (2013).

[7] M. Gasior et al., “BPM electronics based on compensated diode detectors - results from development systems”, BIW12, Newport News, USA (2012).

[8] E. Calvo et al., “The LHC Beam Position System”, DIPAC11, (2011)

[9] G. Iadarola and G. Rumolo, “Electron cloud in the CERN accelerators (PS, SPS, LHC)”, arXiv:1309.6795

[10] J-J. Gras et al., “Optimization of the LHC Beam Current Transformers for Accurate Luminosity Determination”, IPAC11, San Sebastian, Spain, (2011).

[11] D. Belohrad et al., “A New Integrating Current Transformer for the LHC”, IBIC14, Monterey, USA (2014 - these proceedings).

[12] R. Steinhagen, A Multiband-Instability-Monitor for High-Frequency Intra-Bunch Beam Diagnostics”, IBIC13, Oxford, UK, (2013).

[13] B. Salvant et al., “Update on Beam Induced RF Heating in the LHC”, TUPME032, IPAC13, Shanghai, China (2013).

[14] F. Roncarolo et al., “Electromagnetic coupling between high intensity LHC beams and the synchrotron radiation monitor light extraction system”, IPAC13, Shanghai, China (2013).

[15] M. Sapinski et al., “Carbon Fiber Damage in Particle Beam”, HB2010, Morschach, Switzerland, (2010).

[16] G. Trad, “A Novel Approach to Synchrotron Radiation Simulation”, IPAC14, Dresden, Germany, (2014).

[17] M. Sapinski et al., “The first experience with the Beam Gas Ionization Monitor”, IBIC 2012, Tsukuba, Japan, (2012).

[18] M. Patecki et al., “Electron Tracking Simulations in the Presence of the Beam and External Fields”, MOPWA034, IPAC13, Shanghai, China (2013).

[19] P. Hochev et al., “A Beam Gas Vertex detector for beam size measurement in the LHC”, IPAC14, Dresden, Germany (2014).

[20] M. Ferro-Luzzi, Nucl. Instrum. Methods Phys. Res., Sect. A 553, 388 (2005).

[21] LHCb Collaboration, J. Instrum. 7 P01010 (2012).

ISBN 978-3-95450-141-0

Copyright © 2014 CC-BY-3.0 and by the respective authors

MANAGING ELECTROMAGNETIC INTERFERENCE IN LARGE INSTRUMENTATION SYSTEMS*

M. Gruchalla, EG&G Division of URS, Albuquerque, NM 87110, USA
M. Thuot, Los Alamos National Laboratory (Retired), NM 87545, USA

Abstract

Implementing high-quality measurement systems in large test environments presents a number of unique challenges. And, these challenges are made even more interesting where new instrumentation systems are being implemented in existing legacy environments where there is little opportunity to modify the infrastructure. Often, Electromagnetic Interference (EMI) is encountered. This interference may be simply an annoyance when sufficiently low that data integrity is not severely compromised, but in many cases, perhaps most, EMI is so severe as to totally obscure the signals of interest. Various sources of EMI and common points of entry of are reviewed. Means of mitigation of EMI in the design and implementation of instrumentation systems in legacy environments are presented. Common sources of EMI potentially introduced by the instrumentation systems themselves are examined, and means of design to mitigate such self-induced interference are examined. Real-life examples are provided to demonstrate the EMI issues, and the effect of mitigation. It's all about the current – pretty much!

EMC vs EMI

Virtually everyone involved in instrumentation systems has encountered electronic noise that corrupts data acquisition. Two terms used in instrumentation venues in discussion of electromagnetic effects are Electromagnetic Compatibility ("EMC") and Electromagnetic Interference ("EMI"). Often it is found that these two terms are used somewhat interchangeably. This however is incorrect interpretation of the terms.

EMC is a goal to be achieved. EMI is a corrupting signal compromising competent collection of data signals. Very simply, the goal of EMC is to minimize EMI.

Specifically, the goal of EMC is to "minimize" EMI, but not to totally eliminate the EMI signals. Interfering signals need only be reduced to the level that allows competent collection of the signals of interest. Although it may be feasible to further reduce EMI, there is little to be gained in terms of the data acquisition, and there may be significant increases in cost and time.

EMC is most effectively managed in the initial design of a facility. At this point, such critical elements as grounding structures, placement of high-energy sources, instrumentation placement, high-energy cable parameters, high-energy cable routing, signal-cable parameters, signal-cable routing, conduit systems for carrying high-energy and signal cables, and virtually all other characteristics of the facility may be addressed to attempt to assure that interference is minimized.

However, typically the facility infrastructure is designed to support the mission, and the instrumentation systems simply must live in this environment. And in many cases, perhaps most, instrumentation systems must be implemented in facilities and systems that have been in place for a very long time, e.g., legacy systems.

STANDARDS AND REFERENCES

There are numerous EMC standards. A number of IEEE publications address the EMC topic, and one of the more common references is MIL-STD-461 [1]. In general, two specific types of emissions are considered: Radiated Emissions ("RE") and Conducted Emissions ("CE"). Similarly, two specific types of susceptibility are considered: Radiated Susceptibility ("RS") and Conducted Susceptibility ("CS").

Although standards are necessary and valuable, these simply define emissions allowable from a source, and the required tolerance to emissions of systems exposed to the allowed emissions. Standards tell you what you must do, but do not give you any guidance as to how to do it.

There are also numerous "How To" references providing insight into both control of emissions and minimizing EMI. One of the industry standards is *Noise Reduction Techniques in Electronic Systems* by Ott [2]. However, in many cases, these references are highly theoretical and very general, and it is often found that it is quite difficult to apply the guidance in "your" systems. And, often the guidance provided is more easily implemented in new designs, and more difficult in legacy systems. For example, just how does one implement a "single-point ground" and avoid "ground loops" in a new cable plant installation in a facility where cable plants are as much as a hundred meters long, and perhaps even much longer, and where all the high-energy cables and other potential noise sources are permanently in place?

CLASSIC EMC DESIGN PROCESS

There is no standardized process in applying EMC principles to minimize EMI. Every situation is unique, and must be examined independently based on the specific system elements and the operational requirements. However, the general design approach to assure EMC reviewed in many references is typically the control of the emissions at the source.

* This material is based upon work supported by the U.S. Department of Energy, Office of Science, Los Alamos National Laboratory under Contract No. DE-AC52-06NA25396.

Copyright © 2014 CC-BY-3.0 and by the respective authors

ISBN 978-3-95450-141-0

Several classic EMI mitigation approaches that are commonly suggested are listed in Table 1.

Table 1: Classic EMI Migration Approaches

At the Source	At the Receiver
Shielding	Shielding
Grounding	Grounding
Shielded Source Cables	Shielded Signal Cables
Shielded Signal Cables	Shielded Source Cables
Balanced Source Signals	Balanced Data Signals
Filtering	Filtering
	Separate Equipment Ground
	Cable Routing
	"Single-Point Ground"
	"Eliminate Ground Loops"
	Etc.

In general, all of these approaches listed in Table 1 are simply common sense. However, two of the items are particularly interesting: "Single Point Ground" and "Eliminate Ground Loops." Here again it is simple to direct that one should utilize a single-point ground, and should assure that all ground loops are eliminated, but actually following this advice is typically difficult if not impossible.

For example, how does one effect a single-point ground in a facility that is a kilometer or more in extent, and where the majority of the grounding in the facility is predetermined? And, just what is a ground loop? Why is it a problem? And even if a ground loop is discovered, can it be even be effectively broken, and if so, can it be broken without compromise of facility operations, or more specifically, broken without compromise of safety? So again, the advice may be sound, but not particularly useful since it may be impossible to implement.

UNDERSTANDING EMI

The very first task in EMC design and EMI mitigation is the understanding of EMI. What must be recognized is that one person's signal is another person's EMI.

For example, the signal of a nearby high-power radio transmitter may interfere with your television reception or the operation of other wireless devices. The high-power RF is of course the intended signal of the transmitter, but its effect on your systems is EMI. In this example, one would have no control whatsoever at the source.

Similarly, in big-physics systems, such as accelerator facilities, the overall design of the facility is primarily to support the physics. For example, the high-current, high-energy signals applied to bending magnets and kickers are signals necessary to competently operate the system. Any related signals that adversely affect data acquisition in the instrumentation are EMI. And here too, it may not be feasible to change the facility infrastructure at the source to reduce EMI at the instrumentation since that is determined by the needs of the physics.

In this paper, the author presents a somewhat non-traditional definition of EMI. In general, EMI is most often defined as something that is done to your system from various external sources. However, in many cases of EMI contamination of signals, the actual root cause of the EMI is internal to the instrumentation system itself. And, very often these are obscure, easily overlooked, and if not recognized, can be very difficult to control.

The author's definition of EMI in an instrumentation environment is simply:

EMI is *any* electrical signal adversely affecting data quality whether from external or internal sources

This statement may seem obvious and innocent enough, but as reviewed in the real-life examples below, some of what is identified as EMI in this paper is not all that obvious. And some may argue that such electrical effects are not actually EMI, even though the measurements are compromised by these unwanted electrical signals. However, based on this definition, any interfering electrical signal regardless of its source, or its nature, is defined by the author as EMI.

The most important aspect of control of EMI is developing a very accurate understanding of why EMI occurs. If the actual root cause of an EMI contamination is due to sources internal to the actual instrumentation system, but this is unrecognized, and one proceeds to try to locate and mitigate the EMI by examining and modifying external elements, the task will be exceedingly laborious, and very likely much less than successful.

There are no cookbook methods to EMI mitigation, and there is no one-size-fits-all configuration to assure adequate EMC in a complex system environment. Accordingly, all upfront EMC considerations in new facilities, and all EMI mitigation needed in legacy facilities, must be engineered for each specific case.

JUST WHAT IS EMI

To this point, the term "EMI" has been repeatedly referenced, but no actual sources have been identified. In general, EMI is a broad catchall term used whenever some electrical noise is encountered. So, just what are some the common sources of EMI?

One very common source of EMI is the result of noise on the AC power MAINS coupling into the instrumentation systems. Often this noise is from indeterminate sources. It is just there!

Other common sources of EMI are various infrastructure equipment within the facility. Some examples of such sources are high-energy power supplies, variable-speed motor drives, contactors, high-intensity discharge lighting, solid-state ballasts, other MAINS

ISBN 978-3-95450-141-0

Copyright © 2014 CC-BY-3.0 and by the respective authors

devices, and countless other equipment common in almost every facility.

But not all sources of EMI are external. Some EMI we do to ourselves internal to our instrumentation systems. Some typical examples of internal EMI sources are switch-mode power supplies, motor-drive systems driving various motive sensors such as wire scanners, and even digital electronics such as high-speed microcontrollers.

Almost any internal element can be a source of EMI, even very low-frequency sources, even DC sources, and even the signals themselves. Often these internal EMI sources are the most elusive to isolate, but can be straightforward to mitigate since one typically has reasonable control of the actual instrumentation system.

There are of course environmental sources of EMI. A typical example is lightning. Although this is a low duty-cycle transient, it is still quite significant since the instrumentation must at least survive even nearby strikes. And often this EMI occurs at the most inopportune time causing loss of data.

Also, less obvious environmental sources of EMI are earth currents, although technically not all are truly environmental. These can be due to true geological effects such as geopotentials between physical positions, such as between one point in a facility and another point in the facility far removed from the first. But more often these are related to such things as currents due to AC MAINS power distribution, currents induced in the ground structure of RF sources such as radio and television transmitters, as well as other wireless devices.

These are loosely termed environment since they live in the earth itself. And, due to the extremely low impedance typical of these sources, it is virtually impossible to eliminate, or even reduce, these EMI sources by shunting around the source, for example by installing massive ground buses and grounding straps. Further, the installation of such grounding features can actually inadvertently create ground loops. So, in some cases, the more one does to solve an EMI problem, the worse it gets.

Finally, one absolute boundary condition of EMI is first-principle noise, specifically thermal noise and shot noise. These noise sources are not typically viewed as EMI sources, but these fit very accurately in the EMI definition above. And, this EMI cannot be eliminated! However, these noise sources are a function of measurement bandwidth, and therefore only the bandwidth necessary to competently capture the data of interest should be utilized in order to minimize this EMI. And such bandwidth limiting is always a good practice in all instrumentation applications.

THE INSTRUMENTATION ENVIRONMENT

The actual instrumentation environment in which one is constrained to work directly affects the application EMC and EMI-mitigating principles.

As noted above, EMC is most effectively managed in new, purpose-built systems being designed and built from the ground up. Here the instrumentation team has some opportunity to affect the facility design to try to assure some acceptable degree of EMC. However, in many facilities, if not most, the actual purpose of the facility drives the infrastructure design. For example, in big-physics systems such as accelerators, the physics almost exclusively drives the design of the structures.

Legacy systems present a much greater challenge since virtually all EMI issues must be solved without any substantial changes to the infrastructure.

GROUNDING

Grounding is often a critical parameter in instrumentation systems, and is almost always the most controversial. What to ground, how, and where, is typically the source of lively debate.

Facility Grounding

However, typically very much of the grounding structure in a facility is predetermined and may not be altered. Safety grounding of all MAINS operated equipment may never be removed. Metal cable trays, metal conduits, counterpoise, and even the system being instrumented, such as an accelerator, are all grounded. Typically this facility grounding may not be altered in any substantial manner.

Sensor Grounding

Very many of the sensors utilized also are grounded. Specifically, the sensor output signal is presented single ended with respect to the conductive body. Two typical such sensors are shown in Fig. 1.



Figure 1: Typical Grounded Sensors.

The first sensor in Fig. 1 is a Bergoz Beam Current Monitor [3], and second is a T&M Research Products Current-Viewing Resistor (“CVR”) [4]. Both of these sensors are configured with a single-ended output connector tied to the conductive body, and the conductive body is also part of the sensor active element. Therefore, the grounding at the point of measurement is very often predetermined with sensors such as these.

Instrumentation Grounding

Grounding is also typically predetermined at the instrumentation. All MAINS-operated equipment is grounded to assure electrical safety. Although it is feasible to utilize fiber optics, high-isolation power supplies, and other means to provide isolation, these are

Copyright © 2014 CC-BY-3.0 and by the respective authors

ISBN 978-3-95450-141-0

often costly, complex, and can introduce reliability concerns, e.g., battery-operated equipment.

Instrumentation-Cable Grounding

It may seem that the instrumentation engineer has total discretion in grounding of instrumentation cabling. The basic question that then arises is just how to ground cabling, and to what?

Also, the instrumentation cabling is typically routed through metal conduits, along metallic cable trays, and even along walls and flooring that have embedded metallic structural members that are grounded. The cable routing itself results in capacitive coupling from the cable to ground. This effectively creates the dreaded ground loop inviting EMI coupling at higher frequencies.

SIMPLE EMI REAL-LIFE EXAMPLES

It is most useful to actually demonstrate several examples of EMI and to show specifically how this EMI finds its way into data systems. However, the next EMI examples may not seem appropriate for a tutorial on EMI, but hopefully after reviewing the cases, the reader will be convinced that these are indeed examples of EMI. It's all about the current – pretty much.

The author likes to use the CVR in real-life examples demonstrating often-unrecognized effects of EMI. The CVR is perhaps the simplest of sensors – it is simply a resistor, nothing more. And it has been suggested that "the CVR is so simple that one simply cannot do it wrong!"

Consider that measurement of the RF currents from 1 kHz to several megahertz is to be made on a magnet power supply using preinstalled 1 mOhm CVR devices as in Fig. 1. It is therefore important to know the frequency response of the sensor. This may be easily collected using a network analyzer. Figure 2 is a typical frequency-response measurement configuration.[1]

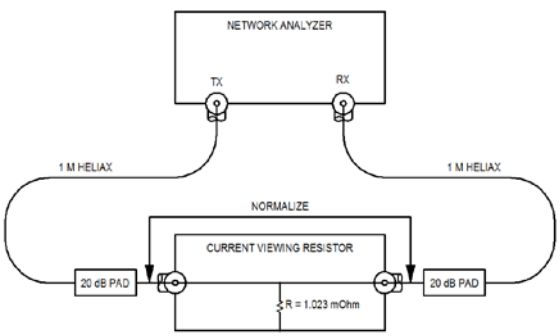


Figure 2: CVR Frequency Response Measurement.

One would expect the response of the CVR to be flat from DC to some break frequency, and then drop into the network analyzer noise floor. However, this is not the case. Figure 3 is the response actually observed.

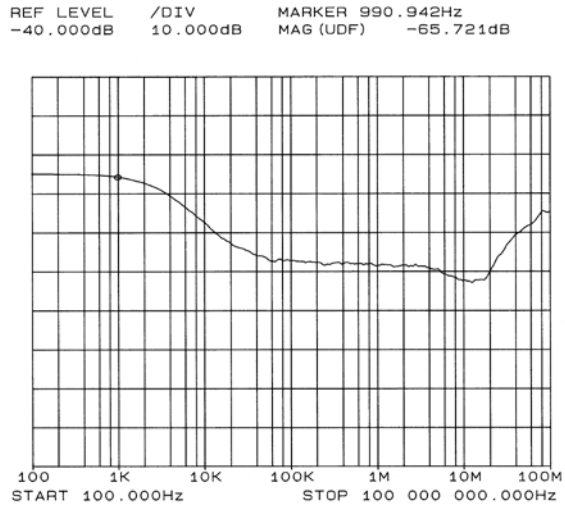


Figure 3: Apparent 1 mΩ CVR Frequency Response.

The response of Fig. 3 shows a quite serious anomalous response below nominally 100 kHz, and this extends to true DC. The DC resistance of this CVR is 1.023 mOhms. At 1 kHz and below, the apparent CVR impedance is 12.9 mOhms. Therefore, there is a 22 dB measurement error at 1 kHz, and all the way down to DC.

One might conclude from this response that the CVR is in some way defective, or perhaps even that the network analyzer is defective. However, this anomalous response is due to EMI, and EMI introduced by the measurement itself. But this EMI is not what is typically recognized as EMI, and therefore this EMI effect is easily overlooked.

If this CVR were used to record the frequency characteristics of the current of the magnet power supply, and this EMI contribution were not known, and the response of Fig. 3 were used as the "calibrated" response characteristic of the sensor, the results would be seriously in error at 1 kHz, specifically 22 dB in error, and this error would extend to DC. And since the CVR is so simple that one simply cannot use it wrong, it would prove very difficult to determine why the magnet power supply "appears" to be behaving in a strange manner.

This anomalous response is due to shield currents in the signal cables. To demonstrate this, again with a real-life example, the author removed the center pin and insulator from an SMA barrel connector, soldered an RF block into the connector to provide RF isolation between the two ports, and connected this in the test configuration of Fig. 2 as the test article in place of the CVR. This is shown in Fig. 4.

This test article now allows the signal-cable shields to be connected at the point of measurement, but with the center conductors open, and shielded from each other.

In this measurement, one expects the response to simply be the network analyzer noise floor since the center conductors of both the source and receiver cables are open and well shielded from each other at the point of

1. The 20 dB pads are utilized to assure that all signal cables are properly terminated since the test article presents a severe mismatch. With these pads included, the impedance seen by the signal cables is effectively the proper terminating impedance regardless of the characteristics of the test article.

ISBN 978-3-95450-141-0

Copyright © 2014 CC-BY-3.0 and by the respective authors

measurement. Figure 5 shows the actual response collected.

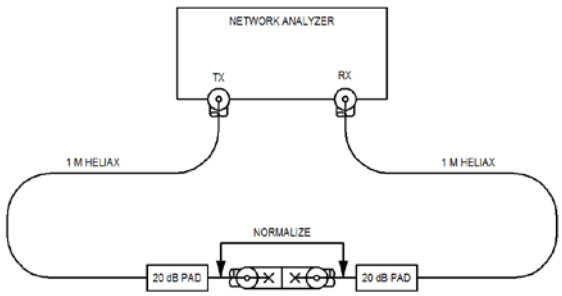


Figure 4: Cable-Current Artifact Measurement.

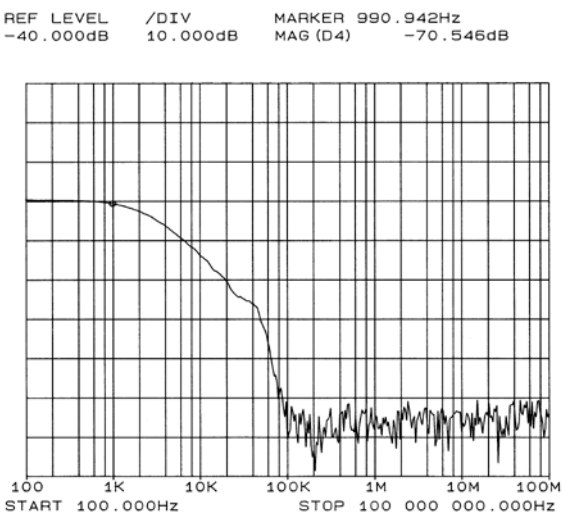


Figure 5: EMI Measurement Artifact.

The response of Fig. 5 looks suspiciously similar to that of the CVR in Fig. 3. And indeed this is an EMI signal. And this is the root cause of the anomalous response seen in Fig. 3.

This response is caused by shield currents. Current flows from the source, to the test article, through the terminating pad, and then returns on the shields of both the source and receiver cables. At low frequencies, the transfer impedance of the cable approaches simply the cable resistance. Therefore, a potential is developed on the "outside" of the receiver cable, and this potential is communicated to the center conductor through the terminating pad. The result is a potential, i.e., EMI, introduced into the receiver as witnessed by Fig. 5.

Oddly, the root cause of this form of EMI is the signal itself. This is not typically what is envisioned when the term EMI is used. But, based on the definition above, it is a corrupting electrical signal, and is therefore EMI by that definition. And, if one is not familiar with this type of EMI, measurement results as shown in Fig. 3 are very difficult to reconcile, and the EMI even more difficult to mitigate since the root cause is illusive.

Since the network analyzer connector grounds are electrically connected at the network analyzer, and the feed-line shields are also connected together at the test article, a "ground loop" is created. However, in this example, there is no external magnetic field penetrating the loop, so one would expect no worrisome shield currents. So, the shield currents would go undetected. And, even if one recognized this ground loop, it cannot be easily broken since the RF integrity of the measurement must be maintained. Also, if this ground loop were discovered, and the loop area were reduced by keeping the signal cables very near the network analyzer, there would be no change in the anomalous response, and it would be concluded that this ground loop is not the source of the EMI. And again the shield currents would go undetected.

If the shield currents can be reduced, the quality of the measurement may be improved very substantially. The frequency-response measurement of Fig. 3 was repeated, but with the addition of a simple common-mode isolator in the receiver signal line (the common-mode isolator is reviewed in detail below). The resulting response is shown in Fig. 6.

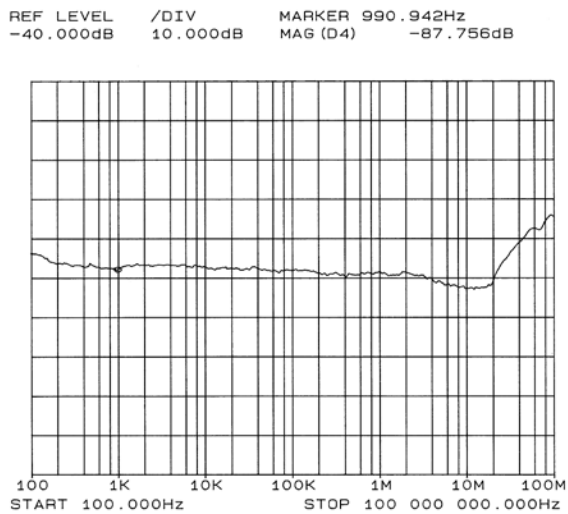


Figure 6: Improved 1 mΩ CVR Frequency Response.

At 1 kHz, the CVR impedance is now seen to be 1.024 mOhms, which agrees very well with the DC resistance measurement. The specific common-mode isolator utilized in the measurement of Fig. 6 was designed specifically for this example to provide just sufficient reduction of the EMI to allow accurate measurements down to just below the specified 1 kHz measurement specification. A small residual artifact of the EMI can still be seen at 100 Hz. This is an example of supressing EMI "just enough" to allow accurate capture of the data of interest. The EMI could be supressed farther, e.g., to allow measurements to lower frequencies, but the mitigation means would be more complex and more costly. The lower measurement goal of this example was specified as 1 kHz, and the response of Fig. 6 easily meets this requirement.

Copyright © 2014 CC-BY-3.0 and by the respective authors

ISBN 978-3-95450-141-0

To demonstrate that this EMI management is not dependent on the actual test article, the response of a nominal 250 µOhm CVR shown in Fig. 1 was recorded, and is shown in Fig. 7.

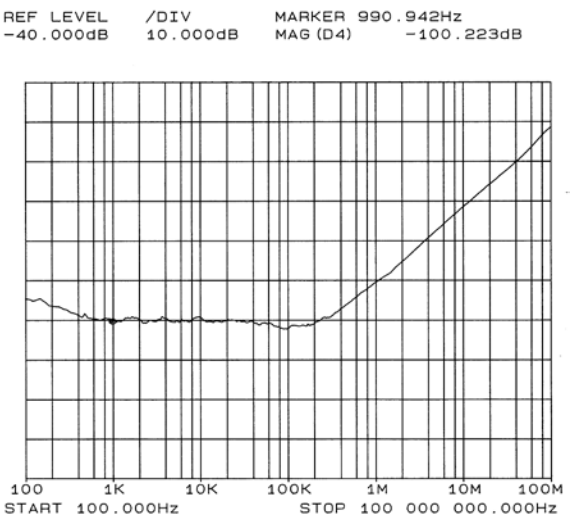


Figure 7: 243.3 µOhm CVR Response.

The DC resistance of this test article is 243.3 µOhms. At 1 kHz the impedance is 243.7 µOhms showing good agreement with the DC value.[2] Again in Fig. 7 the residual EMI artifact is seen at 100 Hz.

This specific CVR was selected for this example due to the network zero in the frequency response at nominally 200 kHz. This response characteristic is due to the equivalent series inductance of this CVR. This is an inherent characteristic of the sensor, and is not due to poor shielding effectiveness or EMI influencing the measurement. Below this zero frequency, this sensor is linear responding with a nominal 243.7 µOhm transimpedance, and above the zero frequency it responds as a derivative sensor.

For pulsed signals, this sensor will provide true representation of the pulse edges for transition times longer than nominally 1 µs. And for faster pulses the derivative response will differentiate the edges resulting in overshoot. This sensor and its response will be used again below in an actual measurement example.

Another real-life EMI example is a case where the author was asked to investigate why a high-power CVR was providing exceptionally-low readings of current in a simple MAINS current measurement. The simplified installation configuration is shown in Fig. 8.

The system configuration comprises a single-phase MAINS source supplying a load with the load return communicated through a CVR and returning to the source. Resistor R1 is the resistance of the MAINS bus work from the CVR to the source, R2 is the resistance of the oscilloscope power-cable safety ground from the oscilloscope to the source return and service bond, and Rsh is the resistance of the data-cable shield (~100 m RG58). And, the CVR device was found to actually be installed as shown in Fig. 8.

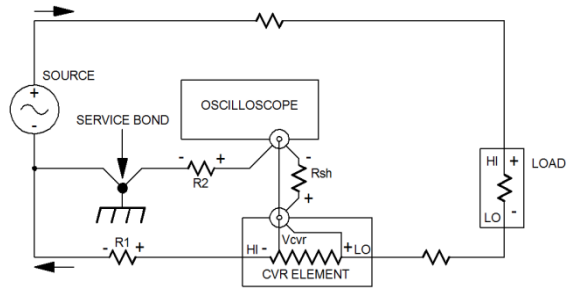


Figure 8: Actual Real-Life CVR Installation.

When the author examined the test data, not only was the CVR indicating a low current, but the sign of the current was inverted from that expected implying that current was actually flowing in reverse through the load, which could not occur in this test. And, since the CVR is such a simple sensor that one simply cannot use wrong, this was remarkable. But this was an obvious clue to the author as to the root cause of this errant reading. The root cause was simple EMI, but again not quite what one would typically recognize as EMI. The equivalent circuit of the measurement configuration of Fig. 8 is shown in Fig. 9.

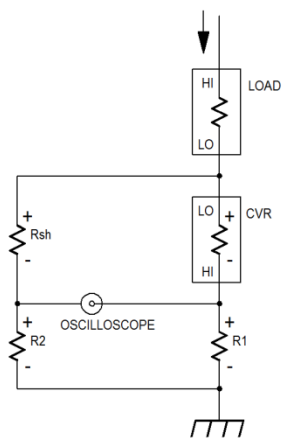


Figure 9: Measurement Equivalent Circuit.

Examining Fig. 9, it is seen that the resistors Rsh, R2, the CVR and R1 form a simple bridge configuration. Therefore, if the ratio of the data-cable shield resistance Rsh to the oscilloscope safety-ground resistance R2 were made exactly equal to the ratio of the CVR resistance to the bus-work resistance R1, not only would the indicated current be low, it would be exactly zero for any load current. This would not be a very good measurement of the load current!

And, since this is a simple bridge configuration, the sign of the indicted current at the oscilloscope can be

2. A network analyzer is not typically considered a high-accuracy instrument, perhaps ~0.1 dB, or on the order of 1 percent. The very close agreement of this measurement with the high-accuracy DC resistance measurement is coincidental.

ISBN 978-3-95450-141-0

Copyright © 2014 CC-BY-3.0 and by the respective authors

either true or inverted based on the relative values of the four resistances. It was this parasitic bridge configuration that resulted in the indicated current in the actual test being both low and inverted. It was simply a coincidence that the reversed installation of the CVR and the resistance ratios combined to indicate reverse current flow.

So, what does this example have to do with EMI? There is no EMI here! Or is there? First, it is noticed that there is the much-feared ground loop. Specifically the path from the service bond, through the bus-work resistance R1, through the CVR element, through the data cable shield resistance Rsh to the oscilloscope, and through the oscilloscope safety ground R2 returning to the service bond is a loop, a ground loop. However, since there are no external fields penetrating this loop, there is no problem since no loop currents can be induced.

The error results from a parasitic current, or in other words, EMI. This current is the current that flows in the data-cable shield resistance. The potential developed across the combined resistance of R1 and the CVR resistance drives current into the series combination of Rsh and R2. This results in shield current in the data-cable shield. This in turn results in a voltage drop across the data-cable shield. However, there is no corresponding voltage drop on the center conductor of the data cable. Therefore, the oscilloscope displayed data is in error by an amount equal to the voltage developed on the data-cable shield due to the shield current.

It may be argued that this is not really an example of EMI, but rather simply an example of poor instrumentation configuration. But, is not any case of EMI contamination a result of poor instrumentation configuration? Consider that instead of the source current causing the error in this example, a magnetic field linking the ground loop resulted in the same shield-current signal. There would be little argument that this would be a case of EMI contamination. Since the error is the same in both cases, both cases represent EMI contamination, and both fit the author's definition above.

This type of EMI can prove to be rather difficult to mitigate if not well understood. For example, consider that the ground loop is recognized, and it is simply *assumed* that the error is due external magnetic-field coupling to this loop, and accordingly various types of shielding are implemented. In fact, no amount of shielding will mitigate this EMI since it is not the result of a radiated emission, but rather is the result of a conducted emission. And, the conducted emission is due to the measurement configuration itself, and not from some external source.

This EMI could be mitigated simply by removing R2 opening the ground-return path from the oscilloscope to the facility ground, i.e., breaking the ground loop. This would very effectively eliminate the corrupting current in the data-cable shield, at least at low frequencies. However, R2 is the oscilloscope electrical safety ground, and which may not be broken under any circumstances.

It may be argued that this EMI problem may be mitigated by simply adding an isolation transformer to power the oscilloscope. However, electrical codes require all equipment grounds to be bonded together, so a bond is required across the isolation transformer, again completing the ground loop.

An obvious solution is a battery-operated oscilloscope totally floating with respect to the facility ground. This *may* work. But consider that this is a digital oscilloscope (as was the case in this real-life example), and that it has a digital output signal cable communicating the digital data to a host computer, and that this cable is a typical shielded digital data cable (which was also the case in this example). This digital data cable now again completes the ground loop, but here, in a large facility, the loop is likely very much larger than the original loop resulting in not only higher risk due to the conducted emission, but now has the increased risk of radiated emission is added.

Now, as the reader has likely concluded, the *obvious* root cause of the error in the CVR data is simply that the CVR is improperly connected in Fig. 8, indeed simply connected in reverse, and that the error is not truly due to EMI, but rather due simply to an incorrect implementation of the CVR. So, the CVR is so simple that one *almost* cannot use it wrong.

Figure 10 shows the CVR connected "correctly," specifically with its low terminal returning to the source. So, now life is good, and now confident that the CVR measurements are accurate, operations are resumed.

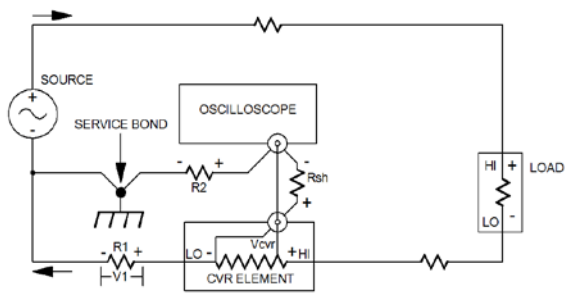


Figure 10: Another Real-Life CVR Installation.

To demonstrate that this configuration in Fig. 10 is now correct, and that the error introduced due to the improper installation of the CVR in Fig. 8 is now fully resolved, the instrumentation engineer performs a very simple qualification test with the following parameters:

Qualification-Test Parameters:

CVR = 100 μΩ,

R1 = ~65 μΩ, R2 = ~100 mΩ, Rsh = ~1 Ω,

Test Current = 1000 A P-P

The 1000 A P-P test current is applied, and the oscilloscope signal observed. The signal expected with the 1000 A P-P test current and the 100 μOhm CVR is 100 mV P-P. However, the oscilloscope display is found to be 159 mV P-P erroneously indicating that the current

Copyright © 2014 CC-BY-3.0 and by the respective authors

ISBN 978-3-95450-141-0

is 1590 A P-P. Again, the error is due to the current flowing in the data-cable shield. Installing the CVR "correctly" has not eliminated this EMI contamination.

If instead of actually preforming this qualification test, it was *assumed* that the issue had been resolved, and if an experiment specified a 1000 A load current, for example the current in a bending magnet in an accelerator, with 1000 A indicated at the instrumentation, the actual current would be 629 A. This could prove rather embarrassing if the beam happily escaped through the wall of the beam pipe due to an improper steering current.

So, the CVR is actually a very simple sensor where it is very easy to use it wrong, due to EMI.

These examples using a very simple sensor very clearly demonstrate the EMI issues caused by shield currents. And, these EMI issues extend from true DC to RF. In trying to eliminate the EMI corruption as seen in Fig. 3, if one is not aware of these currents, it would be very difficult to eliminate the EMI effects. So in cases of EMI in cables, ***it's all about the current – pretty much!***

SHIELDED-CABLE PROPERTIES

Two common terms used to specify cable-shielding properties are "shielding effectiveness" and "transfer impedance." Shielding effectiveness is typically defined in terms of fields, and therefore is often difficult to apply in real applications. However, transfer impedance is defined simply as the ratio of the potential developed on the signal conductors with respect to the shield, due to a current flowing on the shield, to the shield current. Both of these parameters may be directly measured.

Figure 11 shows the basic models for transfer impedance and shielding effectiveness. Note that no grounds are shown. Simply, there is a shield current, and a potential across the length of the shield. It is of no consequence how this current and potential are introduced, or whether the current is due to the potential, or the potential is due to the current. It is only of interest that these shield signals are present.

The transfer impedance is typically specified in units of Ohms per unit length. Shielding effectiveness is typically specified in terms of the ratio of fields, and specified in dB. The models for measuring both transfer impedance and shielding effectiveness, and the relationship between these two parameters, are also shown in Fig. 11.

Another useful cable-shield parameter is the Shield Reduction Factor K_r [5,6] defined simply as the ratio of the complex signal-conductor voltage induced by a voltage across the shield, to that complex shield voltage.

$$K_r \equiv {}^{V_d}/_{V_{sh}} = \frac{Z_t \cdot I_{sh} \cdot l}{Z_{sh} \cdot I_{sh} \cdot l} = \frac{(R_t + j\omega L_t) \cdot I_{sh} \cdot l}{(R_{sh} + j\omega L_{sh}) \cdot I_{sh} \cdot l}$$

But at DC, Z_t reduces to R_{sh}, so: $Z_t = (R_{sh} + j\omega L_t) \cdot l$

$$K_r = \frac{(R_{sh} + j\omega L_t)}{(R_{sh} + j\omega L_{sh})}$$

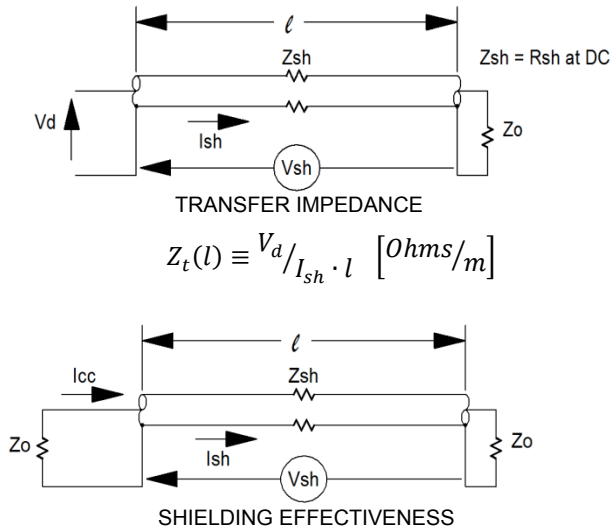


Figure 11: Cable Shielding Definitions [7]

At DC, K_r is unity, and there is no reduction provided by the shield. With frequency, the response characteristic will depend on the placement of the poles and zeros in the K_r expression. The simulated response of a nominal 2 m length of RG400 is shown in Fig. 12 expressed in terms of transfer impedance as a function of frequency.

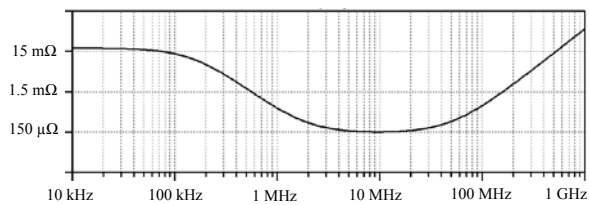


Figure 12: Simulated Z_t of 2 m RG400.

In Fig. 12 it is seen that Z_t is simply the shield resistance from DC to nominally 100 kHz, and therefor K_r is unity. With increased frequency, the Z_t first drops in magnitude, flattens, and then increases with a first-order response. This complex response is typical of all shielded cables, although the location of the poles and zeros will vary as a function of the shield construction.

A second network zero seen in Fig. 12 at nominally 30 MHz. This is due to leakage through the less than perfect shielding properties of the braided shield.

Terms like transfer impedance and shielding effectiveness are useful parameters to compare different materials, but just how does EMI outside a shielded cable actually couple to the signal conductors? It is not as mysterious as it is often portrayed. Figure 13 shows two models for two general sensor configurations.

The upper model of Fig. 13 is that of a low-resistance sensor, such as a magnetic-loop (B-Dot) beam position monitor. The lower model is that of a high-impedance sensor, such as a wire-scanner sense wire.

ISBN 978-3-95450-141-0

Copyright © 2014 CC-BY-3.0 and by the respective authors

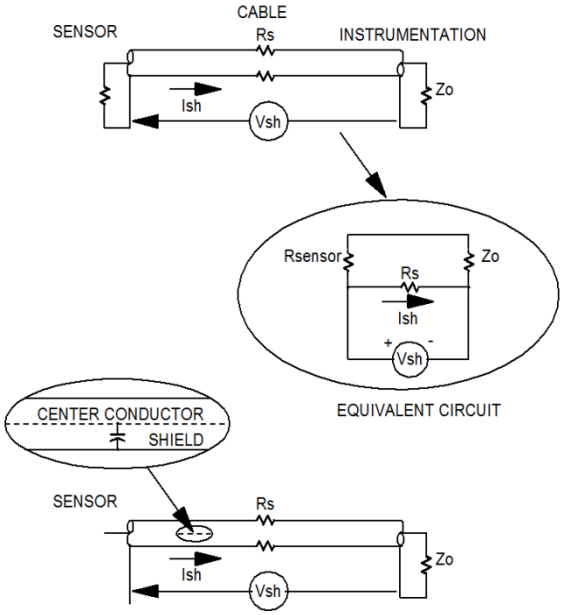


Figure 13: EMI Coupling into Shielded Cable.

The equivalent circuit of the upper model clearly shows that the source impedance and the load impedance (signal-conductor resistance is not shown) form a simple voltage divider driven by the shield voltage. This communicates shield voltage to the load.

It may seem that the lower model is immune to the effects of the shield voltage due to the open-circuit sensor. However, the capacitive coupling from the shield to the signal conductor form a reactive voltage divider comprising the cable capacitance and the load resistance again driven by the shield voltage that results in coupling of shield voltages to the signal conductor.

Figure 13 therefore demonstrates that the coupling of the EMI signal on the shield of a cable is very simply communicated to the signal conductor by simple voltage divider action.

EMI MITIGATION APPROACHES

As noted above, all EMI management is unique to each specific task. However, there are some general approaches that are useful to review.

Filtering

Filtering can be a very effective means of mitigating EMI, particularly were the EMI frequency signature is significantly out-of-band from the actual signals of interest, or presents as a very narrow spectral impulse, such as a radio station. As noted above, one should only utilize the bandwidth necessary to competently pass the signals of interest.

The means of applying a filter function must be carefully considered. For example, the actual instrumentation electronics itself is typically designed to band-limit signals to control noise by including a filter. Typically such a filter is placed at or near the analog output of the signal-processing path to effectively band limit all noise contributions, both that in the actual signal, e.g., EMI, as well as that inherent in the signal-processing path, e.g., thermal and shot noise.

For analog signal capture with such as an oscilloscope utilized to capture the analog data, in an attempt to minimize EMI, it is a common practice to add a "noise filter" immediately at the input to the oscilloscope. In cases of digital signal processing within the data channel itself, which is becoming quite common, it is a common practice to digitally filter the digital representation of the signal to provide band limiting. These are examples of types of post filtering.

Such post filtering does indeed band limit all noise at the output of the instrumentation signal-processing path. However this is not typically a very effective means of managing EMI, and can result in very puzzling data corruption. Although the noise is band limited at the output, there is no control of the signals input to the instrumentation. Where the EMI signals are out-of band with respect to the signals of interest, they are not observed. And where these signals are extremely high compared to the sensitivity of the data channel, the input circuitry can be easily driven out of both its normal-mode range and its common-mode range by the EMI signal. When this occurs, it may not be detectible in the instrumentation output signals since the actual EMI content at the output of the signal-processing path is removed by the post filter. However, the input circuitry is directly exposed to both the magnitude and spectral content of the EMI signal totally unfiltered.

This overdrive of the input circuitry of the instrumentation channel will result in non-linear response to the data signals. For less severe overdrive, one effect is that the channel gain appears mysteriously low. But in severe cases of overdrive, the data signals may be totally obscured as the input circuitry is driven hard into saturation at the frequencies of the EMI signal. Since the post filter removes all witness of the EMI signal, there is no evidence of an EMI contamination.

A real-life example is a typical field-mapping process where a very wide-bandwidth electric-field sensor was being used to observe signals over comparatively narrow frequency range using a network analyzer. The specific network analyzer being used had a frequency range of 9 kHz to 8.5 GHz. The frequency range of interest in the field-mapping task was 100 kHz to 100 MHz. The network analyzer frequency range is quite sufficient to capture the spectrum of interest. A comparatively low-level mapping signal was used, nominally 1 V/m, to prevent interference with nearby receivers as the network analyzer signal was swept over the test frequency range. To minimize noise to allow effective capture of the low-level mapping signal, the resolution bandwidth of the network analyzer was set to 1 Hz.

However, when the field mapping was complete, the results deviated very substantially from that expected. What was unknown about this environment was that there are a number of high-level RF sources, i.e., RF

Copyright © 2014 CC-BY-3.0 and by the respective authors

ISBN 978-3-95450-141-0

transmitters, operating nominally above 1 GHz in the vicinity, but that are not part of the actual facility being mapped, so these sources were unknown to the test personnel.

The signals from these sources are very effectively captured by the sensor, and since the frequency range of the network analyzer extends to 8.5 GHz, these signals pass directly into the network analyzer input into the first mixer. The network analyzer input circuitry is driven deep into limiting by these unknown signals.[3] The response to the in-band signals becomes extremely nonlinear resulting in inexplicable data records.

The foreign signals are true EMI. Although these signals are out-of-band with respect to the signals of interest, they still represent very serious EMI contamination since they unknowingly pass directly into the input of the instrumentation. The 1 Hz resolution bandwidth utilized is totally ineffective in controlling this EMI since this filter is a post-filter process, and typically is even applied after several heterodyne conversions within the network analyzer, or simply applied digitally in contemporary instruments. And, since the EMI is far out-of-band with respect to the spectrum of interest, it cannot be seen in the data records.

Based on experience, the author suspected out-of-band EMI. To do a "quick" diagnosis of the root cause of the unusual data records, the author utilized the network analyzer input attenuators. These attenuators are immediately at the input of the network analyzer and specifically before the first mixer or any active circuitry, and therefore attenuate all input-signal frequency components equally before the signal is presented to the input circuitry.

As the attenuators were engaged, it was observed that the output signal level did not follow the attenuation. For example, when a 10 dB attenuator was engaged, the signal level only dropped ~3 dB. This is due to the fact that even with the 10 dB attenuator, the input to the network analyzer was still being driven into limiting by the EMI signal, but simply somewhat less so.

One could of course add enough attenuation to reduce the EMI sufficiently low that the network analyzer input is no longer driven into nonlinear operation, but the actual signal then could not be observed.

In this case of out-of-band EMI contamination, once diagnosed, there was clearly no means to mitigate the EMI at the actual source, e.g., the offending RF transmitters. Therefore, the mitigation was necessary in the data acquisition. This issue was resolved by adding a sharp-cutoff low-pass filter with a corner frequency above 100 MHz, but below 1 GHz, at the input to the network analyzer thereby sufficiently reducing the EMI signals at the network analyzer input to prevent driving the network analyzer into nonlinear operation.

This specific real-life example of EMI contamination may seem a rather isolated example, and not really applicable in "typical" systems. However, the author has encountered this very EMI contamination in numerous cases. And, this type of EMI corruption is very insidious since it is for all practical purposes totally invisible. If one is not familiar with this type of EMI contamination, solving this type of EMI issue can prove very difficult.

The only reason that any problem was suspected at all in the field-mapping task of this example was that the nature of the facility had been very accurately modeled, and the field map had been very accurately computed analytically. The specific purpose of the physical mapping was to confirm the analytical predictions. When the test results did not match that expected from the analytical predictions, only then was some corrupting influence suspected. If this had been simply a task to map the field with no guidance as to what to expect, the errant data would have been accepted as accurate.

Capacitive Coupling

An approach that is occasionally used is full capacitive coupling of all of the data-cable conductors, including the shield. For example, at the point of measurement with a shielded cable, all the signal conductors and the shield would be capacitively coupled to the sensor. This of course will block any DC EMI, and it may be effective in blocking the MAINS first harmonic, but generally this approach is totally ineffective in eliminating higher frequency EMI components since these are simply passed through the capacitance with little of no attenuation.

Transformer Coupling

Total isolation seems the most logical approach to provide electrical isolation to reduce EMI. Transformer coupling provides near total isolation. However, inter-winding capacitive coupling allows high-frequency EMI to couple through the transformer. Also, the DC and low-frequency signal components are lost.

For wide-bandwidth applications, the coupling transformer must be carefully designed to competently pass the RF signals of interest while providing an adequate lower -3 dB frequency, and provide electric-field shielding between the primary and secondary, and magnetic shielding as well. These are often conflicting requirements in the design of the transformer. In general, suitable transformers may not be available as commercial parts, and therefore must be designed for the specific task. Transformer design, and specifically wide bandwidth RF transformer design, is in general a rather specialized art.

Fiber-Optic Signaling

Fiber-optic isolation also seems an attractive mitigation approach. And this can be quite effective in applications where EMI is extremely high, such as in electromagnetic-pulse environments.

However, fiber-optic systems tend to be costly and somewhat complex, and typically do not provide response to DC. Additionally, typically the optical transmitter at the point of measurement must be powered, which requires some type of power source having very high

3. These out-of-band signals can easily be of sufficient magnitude to damage the sensitive input circuitry of instruments such as network analyzers and spectrum analyzers.

ISBN 978-3-95450-141-0

Copyright © 2014 CC-BY-3.0 and by the respective authors

isolation, not only with respect to the instrumented system, but also with respect to the AC MAINS. Also, where a large number of channels are needed, fiber-optics can be a very costly approach.

Balanced Signalling and Twisted Pairs

A very useful approach to management of EMI is the use of balanced signals, e.g., as utilized in digital networks using standard unshielded, twisted pair ("UTP"). However, although the signal is accurately presented as the differential signal between the two conductors of the pair, EMI may, and often does, introduce such high common-mode signals that the receiver is driven far out of its useful common-mode range.

Since a UTP cable has no shield, the question of how to ground a cable shield is not an issue. But since UTP has no shield, the opportunities for mitigating EMI are severely reduced.

EMI mitigation in many applications, such as typical office environments, is provided by the use of coupling transformers in the communication equipment. However, since any DC signal component is lost with transformer coupling, a specific digital signal encoding that has a zero DC component, such as 8b10b, must be utilized.

This is not necessarily a difficult constraint to meet, but if a coupling transformer is arbitrarily introduced in an attempt to solve some EMI issue in a digital signal path, and the digital signaling does not have a zero DC component, very odd results can occur, such as random corruption of the received data with certain symbol sequences where the DC error results in the inability of the receiver to competently decode the digital signal.

And again the root cause of this data corruption is essentially invisible, and therefore extremely difficult to diagnose if one is not aware of this possible root cause.

In cases such as this, one could spend an inordinate amount of time trying to solve the data-corruption issue by further reducing EMI, but unsuccessfully. The actual original EMI corruption may have been very effectively eliminated by the introduction of the transformer isolation, but due to the nature of the signaling protocol, a totally different problem was introduced unrelated to EMI. Accordingly, further EMI reduction will have no effect in solving the data-corruption issue, and may even worsen the data corruption. This can be a very frustrating exercise.

Shielded Cabling

Shielded cable is perhaps the most common mitigation means utilized to control EMI. Shields *can be* effective for both multi-conductor cables as well as basic coaxial cables. And, for RF signals above even a few kilohertz, coaxial cabling is typically required to preserve signal integrity.

However, as reviewed above, any current that flows on the shield due to EMI excitation will to some extent couple EMI into the signal path. Cables with high shielding effectiveness are typically specified, but often the shielding effectiveness is never high enough. Also, cables having the lowest possible transfer impedance, such as with solid shields, may be utilized, but here too often the transfer impedance is never low enough. Even where the shield is solid, and even if many skin depths thick, EMI current on the shield can couple into the signal path. So, just having a "very good" cable will not assure elimination of EMI coupling.

Triaxial Cabling

Triaxial cables can be very effective in controlling EMI. The two shields of the triaxial configuration are electrically independent, as opposed to double-shield configurations. There are often lively discussions concerning how to "ground" the shield of even simple shielded coaxial cables. And the discussions become even more interesting when the second independent shield of the traixial configuration is introduced. It is not unusual to see both shields of a triaxial cable simply tied together and "grounded" in some manner thought to be optimal. This configuration effectively converts the triaxial configuration to a double-shield configuration, as provided in such as RG400, RG223, and numerous others including the class of cabling utilizing a combination of a wrapped foil shields and a braided shields.

If implemented effectively, the outer shield of a traixial cable carries virtually all the EMI current that would normally present on the shield of the actual signal path, eliminating, or at least greatly reducing, corrupting shield current on the signal-path shield. However, in many applications the legacy environment may not provide a useful means to use triaxial cabling effectively.

Steel Conduit

An excellent means of EMI mitigation is the use of steel conduits to carry both source and signal cabling, but in separated conduits. Such a conduit provides both another independent layer of shielding many skin depths thick, and also acts as a choke tending to reduce common-mode currents on its internal conductors at low frequencies.

The question still arises as to grounding of the conduit. In some cases, such as conduits carrying MAINS conductors, grounding is specified by safety codes. In legacy facilities the actual grounding configuration of conduits may be unknown. For example, where conduits pass through walls and floors, are the conduits bonded to the structural steel of the facility?

Also, it is often suggested that the low impedance of the conduct will eliminate "ground potentials" between the ends of the conduit. However, this is not typically the case. The impedance of the conduit is not really all that low, and particularly at higher frequencies. Also, the conduit effectively forms a ground loop with nearby grounds, such as facility structural steel, ground mats, counterpoise, etc., and this ground loop is formed even if the conduit is not "grounded" at all due to capacitive coupling to grounded structures.

Copyright © 2014 CC-BY-3.0 and by the respective authors

ISBN 978-3-95450-141-0

Common-Mode Isolator

As stated previously, "it's all about the current – pretty much." Currents that flow on the outside of a shielded cable will couple to the signal conductors as demonstrated in the real-life examples above. In general the end-point potentials between the ends of a shielded cable are more of less fixed and cannot be effectively reduced. This is true for both electric-field coupling, i.e., antenna-type coupling, and magnetic-field coupling, i.e., ground loops. And this is also true of virtually all conducted emissions as well.

In the examples above reviewing transfer impedance and shielding effectiveness, no actual grounding of the cable shields is shown. All the analyses are based simply on the fact that shield currents and potentials are present on the cable shield. How the currents and potentials are introduced on the shield is of no consequence. It is only of concern that such signals are present.

To reduce the EMI coupled to the signal conductors, the shield currents must be reduced. This may be accomplished in some cases by selective grounding of the cable shield, but in a large extended facility, it must be expected that the ground structure is not equipotential. Also, even if there are no intentional grounds, capacitive coupling will still introduce ground coupling. And, in the case of unshielded cabling, such as UTP, there are no cable shields.

One means to reduce shield currents is to increase the shield impedance. This actually seems counterintuitive based on the earlier review of transfer impedance where it is implied that the shield impedance should be made as low as possible. However, that reduction of shield impedance was based simply on some current flowing in the shield. Reducing the shield impedance tends to reduce the potential developed on the shield, and in turn reduces the potential coupled to the signal conductors.

Alternately, if the shield current can be reduced, the coupling is also reduced. An example of this approach is grounding of a signal-cable shield only at one end. The shield impedance is effectively made infinite, but only for low frequencies. Such single-ended grounding eliminates direct conducted susceptibility, but higher frequencies still couple through capacitive coupling and electric-field coupling. Also, this is ineffective if there is direct coupling of the signal conductors to grounded structures, such as grounded sensors and grounded instrumentation. And again, in the case of such as UTP, there is no shield to be utilized in any manner.

One approach that can prove very effective in the management of EMI for both shielded and unshielded cabling is the use of the common-mode isolator ("CMI"). The CMI is perhaps the least complex, least costly, and least difficult to implement of all EMI suppression approaches. Because of these properties, it is a very useful device to implement in the initial efforts to control EMI where EMI issues are encountered in legacy environments, and also a useful device to consider in new facility designs as well as simply an inexpensive EMI-management measure.

The CMI is nothing more than a very simple 1:1 turns-ratio transformer. There are many different CMI configurations, but perhaps the simplest is shown in Fig. 14.

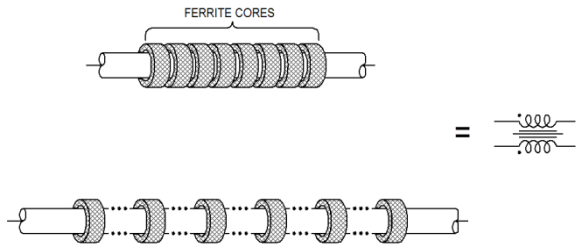


Figure 14: Examples of Common-Mode Isolators.

The CMI configuration of Fig. 14 comprises a number of high-permeability ferrite cores threaded onto the signal cable to be protected. The cores may be placed in close proximity as in the upper model, or placed periodically along the cable as in the lower model. The author uses both of these configurations in virtually all instrumentation in electromagnetic-pulse ("EMP") tests where the pulsed fields are extremely high, even approaching the breakdown of air, and with very fast transition times on the order of several nanoseconds.

The CMI actually provides two services. As noted, it increases the shield impedance which tends to reduce shield currents. But also, the CMI forces the voltage along the shield and signal conductors to be equal by adding mutual inductance. As a result, any AC potential above the lower cut-off frequency of the CMI that is introduced into the measurement due to shield voltage is also introduced in series with the signal conductors effectively subtracting the shield potential from the measured signal. This can be seen in the models of Fig. 11. In both models, if there is a shield voltage, all of part of this voltage will appear on the signal conductor. However, if a voltage source exactly equal to the shield voltage is placed in series with the signal path, the effect of the shield voltage is eliminated.

To objectively demonstrate the value of the CMI in a real-life example, the measurement of Fig. 5 was repeated both without and with a CMI. These measurements are shown in Fig. 15.

The upper trace in Fig. 15 is the same as that of Fig. 5. Any signal spectral content below nominally 100 kHz will be seriously compromised by the EMI introduced due to the shield currents in the signal cables.

A simple CMI similar to that of the upper model in Fig. 14 was placed in the source signal cable.[4] The lower trace in Fig. 15 is the resulting response with the CMI in place.

4. This CMI comprises a nominal 10 cm length to 0.250 semi-rigid 50-Ohm cable, terminated in female Type-N connectors, and with ten high-permeability cores placed on the cable.

ISBN 978-3-95450-141-0

Copyright © 2014 CC-BY-3.0 and by the respective authors

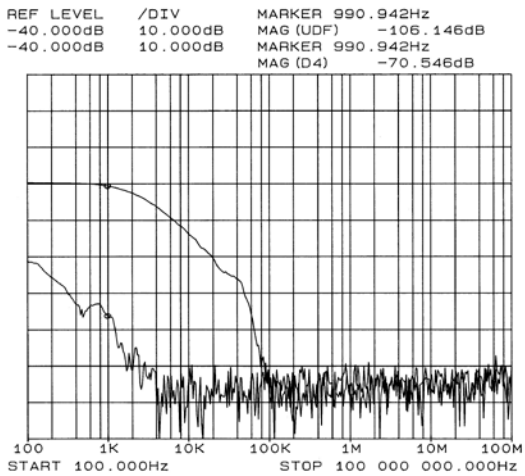


Figure 15: Performance of Common-Mode Isolator.

The CMI has very significantly reduced the EMI well below that without the CMI. At nominally 2 kHz, the EMI artifact has been reduced by almost 50 dB. And, at the 1 kHz lower measurement specification from the example above, the EMI is reduced by more than 36 dB.

As another real-life example, specifically in a time-domain measurement, the author constructed a simple pulse generator capable of delivering a nominally square current pulse having a rise time on the order of 500 ηs, a pulse width of ~50 μs, and a peak current of ~1600 A into a short circuit. The leading edge of the pulse exhibits a good first-order response with no overshoot, and the pulse exhibits a nominal ~10-percent droop over the pulse width.

This pulse generator was battery operated to assure a fully isolated source, and configured to drive the 250 μOhm CVR characterized in Fig. 7 above. The CVR was "correctly" installed such that the common terminal of the CVR and that of the pulser were common.[5] The CVR output was connected to one input of an oscilloscope with a nominal 1 m length of RG400, and terminated in 50 Ohms at the oscilloscope. A standard oscilloscope probe was connected to a second channel, the probe ground lead was tied directly to the common of the CVR output connector, and the probe was place "near" the pulse generator output switch to capacitively couple a sample of the switch transition voltage simply to provide a trigger and a time reference. The common node at the pulser and CVR was not tied to anything other than the signal cables. Finally, a 1 Ohm wide-bandwidth current transformer was placed on the signal cable from the CVR to the oscilloscope, and connected to a third channel of the oscilloscope to witness any common-mode current flowing on the CVR cable.

5. At these high currents, the current-carrying structures are quite large. In this simple experiment, the ground structure is a brass plate 12 mm thick and ~150 mm, wide and nominally ~300 mm total length. Also, the entire experimental structure is configured as a parallel-plate transmission line with ~0.2 mm dielectric spacing to minimize the parasitic inductance of the system.

From the frequency response of the CVR shown in Fig. 7, the high-frequency response exhibits a response zero at nominally 200 kHz. Therefore, the response expected of the CVR to the pulsed current signal is a slight overshoot at the leading edge of the response due to the CVR response zero, and then a reasonably smooth response with a nominal ten-percent droop due to the pulse-generator characteristic. The response of the CVR in this configuration is shown in the first image in Fig. 16.

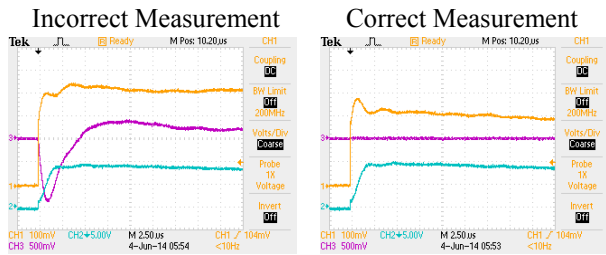


Figure 16: Example of Common-Mode Isolation.

The upper trace (400 A/Div) in the images of Fig. 16 is the CVR output, the lower trace is the timing reference, and the center trace (500 mA/Div) is the current-transformer output.

The response shown in the first image is not at all that expected. The peak current is nominally 1600 A as expected based on the known pulse-generator characteristics and the known CVR low-frequency characteristics. However, there is no overshoot at the leading edge, and indeed there is a noticeable dribble-up. This is not an acceptable response. Also, the late-time response shows virtually no droop in the signal. This too is an unacceptable response since it is known that the input pulse exhibits droop, and that the CVR response is well behaved below its response zero at 200 kHz.

The current transformer shows a nominal 1.3 A common-mode current flowing on the CVR signal cable. It is this current, a true EMI signal, that is corrupting the measurement.

The CMI used for the measurement in Fig. 15 has a nominal 250 μH inductance, and was installed in the CVR signal line and same signals captured. These signals with the CMI are shown in the second image of Fig. 16. In this image the peak current is ~1400A with overshoot seen on the leading edge of the CVR response witnessing the CVR zero, as expected. Also, there is a nominal ten-percent droop witnessing the droop in the pulse-generator response, also as expected. And, the current on the CVR signal cable is virtually zero.[6]

Therefore, the first image in Fig. 16 is seriously in error. But the only reason that the author is aware that this is an erroneous measurement is that the characteristics of the CVR, specifically the frequency response, and that of the pulse shape of the pulse

6. The actual current was observed as <5 mA, but for ease of visual comparison of the two images, the same scales are used for both.

Copyright © 2014 CC-BY-3.0 and by the respective authors

ISBN 978-3-95450-141-0

generator, specifically the transition time and pulse droop, are known. The author designed this experiment specifically to demonstrate how EMI can unknowingly corrupt a very simple measurement, even in a well-controlled bench environment.

If one were unaware of these CVR and pulse-generator parameters, and for example were tasked to capture the response of the pulse generator using this CVR, and no CMI were utilized, the very poor result would be obtained suggesting that the pulse generator exhibits a small degree of dribble-up on the leading edge, but provides a reasonably flat late-time characteristic, both incorrect. Similarly, if the task were instead to capture the CVR response using the pulse generator, the erroneous result would totally conceal the CVR zero, also a serious error.

The logical question to ask is: How is this EMI error introduced in such a simple and apparently well-controlled experiment? It's the current, not "pretty much," but absolutely. Clearly as shown in the first image of Fig. 16, a substantial common-mode current flows on the shield of the CVR signal cable. And this current induces a corresponding potential into the measurement as reviewed above.

But, how is this current introduced on the signal cable in this "well-controlled" experiment? The answer is obvious, well almost. It is due to a ground loop. The loop path is from the oscilloscope ground at the connection of the CVR signal cable, to the CVR output connector common, to the oscilloscope probe ground lead, and back to the oscilloscope ground through the probe-cable shield.

But how is this ground loop excited? This is a case of radiated susceptibility. The magnetic field due to the pulser current links to this ground loop. This results in a current in the loop, and therefore a common-mode current in the CVR signal cable. If there were no second ground connection, i.e., no probe ground, there would be no path to create a common-mode current, and virtually all shield common-mode current would be eliminated. With the second ground connected, a loop is created resulting in current flow from the CVR output common to the oscilloscope. This current is a common-mode current, and in both the CVR signal cable as well the oscilloscope-probe cable.

This then raises the question of "to ground or not to ground?" For example, if the probe ground were disconnected, the ground-loop problem would be eliminated, and a true response would be observed for the CVR signal. However, if the probe ground lead were disconnected, the voltage measurement of the probe would be severely compromised. So, for competent measurement of both the current and voltage signals, both the signal-line ground path and the probe ground path must be fully intact. In other words, one must live with this ground loop. Also note that in this example, the safety ground of the oscilloscope is of no consequence.

Therefore, rather than attempting to eliminate the ground loop with heroic measures, such as perhaps a fiber-optic data system, the CMI was utilized to highly attenuate the common-mode current around the loop, and to force any shield voltage artifact across the signal-line shield to be introduced in series with the signal on the signal conductor.

This very basic experiment demonstrates both how easily an apparently simple measurement using a very simple sensor can be quite seriously compromised by EMI, even in an apparently well-controlled experimental environment, and how effective the simple CMI is in eliminating the EMI influence.

The basic concept of the CMI is not that unusual. Figure 17 is a photograph of an actual CMI installed in an operational system.

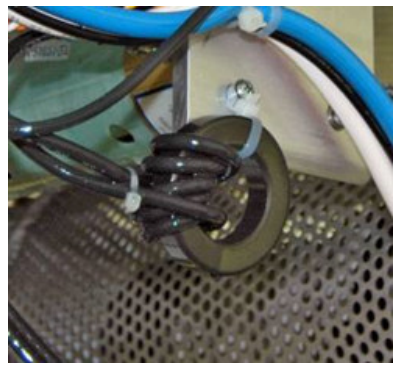


Figure 17: Multi-Turn Common-Mode Isolator.

This CMI utilizes six turns on a large high-permeability ferrite core. The advantage of this multi-turn configuration is that the inductance, and in turn the impedance, increases as turns squared. Therefore, at first examination, to achieve the same result as this CMI but using the configurations of Fig. 14, it would seem that 36 cores would be required. However, the much smaller cores of Fig. 14 will typically exhibit an inductance factor greater than that of the larger core of Fig. 17. In practice, the same inductance may be achieved with perhaps ten to fifteen of the smaller cores.

However, there is a critical deficiency in the CMI of Figure 17. The cable from the two isolated sides of the CMI are tightly tied together. This results in high capacitive coupling shunting around the CMI, and at higher frequencies, the effect of the CMI is diminished, or even totally frustrated. In the configurations of Fig. 14, the two CMI ports remain very well isolated.

Also, another subtle issue with the CMI in Fig. 17 is the resistivity of the ferrite core. Typically a Manganese-Zinc ("MnZn") material, or even a high-permeability metallic material in a tape-wound core, would be utilized to provide the highest-possible inductance. The MnZn materials, and more so metallic core materials, exhibit a very low resistivity. Therefore, the core itself provides a capacitive coupling path among all the turns. This too can seriously compromise the performance of this CMI at higher frequencies. A Nickel-Zinc ("NiZn") material, that typically exhibits a much higher resistivity, could be utilized, but the inductance factor of the NiZn materials is very much lower than that of the MnZn materials

ISBN 978-3-95450-141-0

Copyright © 2014 CC-BY-3.0 and by the respective authors

resulting in a much lower inductance reducing the effectiveness of the CMI at lower frequencies.

The low resistivity of the MnZn core material is of little consequence in the CMI configurations of Fig. 14.

The common-mode isolator is equally as simple as the current-viewing resistor, but as with the current-viewing resistor, it can be implemented incorrectly regardless of its simplicity.

A FINAL OBSERVATION

Where did all this 180 Hz (or 150 Hz) come from?

The author has been asked on numerous occasions to help resolve a puzzling EMI issue were the signals are contaminated with a predominately 180 Hz artifact. And, the author is assured that: "We have nothing operating at 180 Hz!"

This artifact is due to summing of the third-harmonic currents of the 3φ AC Power MAINS. This is easily seen with a bit of trigonometry.

Sum of Fundamental Phase Current I^1 :

$$I^1{}_{SUM} \equiv I^1{}_A + I^1{}_B + I^1{}_C$$
$$|I^1{}_A| = |I^1{}_B| = |I^1{}_C| \equiv |I^1{}_0|$$
$$I^1{}_A = |I^1{}_0| \angle 0$$
$$I^1{}_B = |I^1{}_0| \angle 120$$
$$I^1{}_C = |I^1{}_0| \angle 240$$
$$I^1{}_{SUM} = 0$$

Sum of Third-Harmonic Phase Current I^3 :

$$I^3{}_{SUM} \equiv I^3{}_A + I^3{}_B + I^3{}_C$$
$$|I^3{}_A| = |I^3{}_B| = |I^3{}_C| \equiv |I^3{}_0|$$
$$I^3{}_A = |I^3{}_0| \angle 0$$
$$I^3{}_B = |I^3{}_0| \angle 360 = |I^3{}_B| \angle 0$$
$$I^3{}_C = |I^3{}_0| \angle 720 = |I^3{}_C| \angle 0$$

$$I^3{}_{SUM} = 3 \cdot |I^3{}_0| \angle 0$$

These simple computations show that even if all phase currents of all harmonics are perfectly balanced, which is rarely the case, the vector sum of the harmonic phase currents do not all sum to zero. Specifically, in this example, it is seen that the magnitudes of the three third-harmonic currents all add directly resulting in a third-harmonic current the sum of which is a factor of three greater than that of each phase. This is also true of the various higher-order harmonics.

This third-harmonic current flows in the neutral of the 3φ MAINS distribution, and since the MAINS neutral is connected to ground at some point, this current can, and commonly does, escape into the ground system. Also, the higher frequencies of these harmonic currents result in a higher degree of coupling into surrounding structures, such as building structures and instrumentation cabling.

A very quick and simple assessment to determine if some EMI signal is MAINS related is by using an oscilloscope. While observing the EMI signal, simply switch the oscilloscope trigger to "LINE TRIGGER." Anything that "stands still" is related to the MAINS distribution, either directly or indirectly.

CONCLUSIONS

Electromagnetic Interference, EMI, is eventually encountered by anyone working with data acquisition systems, data communication systems, and virtually any other system requiring high-quality communication of information. There is no cookbook solution, and no one-size-fits-all approach to mitigating EMI. Every EMI issue is unique, and all EMI mitigation must be engineered for each specific application. The goal of EMI mitigation is to reduce the effects sufficiently to reduce interference to acceptable levels. It is not typically economical, or even feasible, to totally eliminate EMI.

EMI is commonly due to coupling from external sources, such as MAINS equipment, RF sources such as radio transmitters, and many other sources, often which cannot be identified. But often the interference is due to internal coupling from such as switch-mode power supplies, or even high-speed digital electronics. And, EMI may be introduced by the measurement-system itself. The root cause of EMI is often unrecognized, and the source misdiagnosed leading to substantial difficulty in achieving adequate mitigation. The nature and root cause of interference signals must be very well understood before any attempt at mitigation is begun. And this is why virtually all EMI solutions must be engineered to each specific case. And: *It's all about the current – pretty much!*

REFERENCES

[1] US Department of Defense, *Requirements for the Control of Electromagnetic Interference Characteristics of Subsystems and Equipment*, MIL-STD-461F, December 10, 2007.

[2] H.W. Ott, *Noise Reduction Techniques in Electronic Systems 2nd Edition*, (New York: Wiley, 1988).

[3] Bergoz Instrumentation, website: http://www.bergoz.com/index.php?option=com_content&view=article&id=23&Itemid=469

[4] T&M Research Products, website: http://www.tandmresearch.com

[5] M. Mardiguian, "Simple Method for Predicting a Cable Shielding Factor, Based on Transfer Impedance," (Plymouth Meeting: ITEM Media, 2012), EMC Directory and Design Guide.

[6] M. Mardiguian, *EMI Trouble Shooting Techniques*, (Boston: McGraw Hill, 2000).

[7] E.F. Vance, *Coupling to Shielded Cables*, (New York: Wiley, 1978).

Copyright © 2014 CC-BY-3.0 and by the respective authors

ISBN 978-3-95450-141-0

DIAGNOSTICS FOR HIGH POWER ACCELERATOR MACHINE PROTECTION SYSTEMS*

S. Lidia#, Facility for Rare Isotope Beams, Michigan State University, East Lansing, MI, USA

Abstract

Modern hadron accelerators create and transport beams that carry MW-scale power or store GJ-scale energy. The Machine Protection Systems (MPS) that guard against both catastrophic failures and long-term performance degradation must mitigate errant beam events on time scales as short as several microseconds. Measurement systems must also cope with detection over many orders of magnitude in beam intensity to adequately measure and respond beam halo loss. Other issues, such as radiated signal cross-talk, also confound and complicate delicate measurements. These requirements place enormous demands on the MPS beam diagnostics and beam loss monitors. We will review the current state of MPS diagnostic systems for this class of accelerator, including SNS, ESS, FRIB, LHC, J-PARC, and SPIRAL-II. Specific designs and key performance results will be presented and discussed.

INTRODUCTION

Trends in modern accelerators push at the boundaries of beam energy (LHC, ILC), beam power (Fig. 1) and brightness [1][2]. Accelerator based neutron-generating facilities (SNS, JPARC, PSI, LANSCE) have pushed the frontier of proton beam power to 1 MW, with 5 MW beams in development [ESS]. For heavy ion beams, the frontier will be advanced by more than two orders of magnitude to 400 kW at FRIB [FRIB]. High energy hadron colliders have pushed the frontier of stored proton beam energy from 1-3 MJ (SPS, RHIC, HERA, TEVATRON) to 140 MJ (LHC, design goal 360 MJ).

Key technology development has powered the push at high intensity frontier [1]. Continuing improvements in SRF accelerator and large-scale cryogenics enable efficient, high gradient acceleration and robust operation. Ion source, RFQ, and low energy beam transport produce intense, high charge state, high brightness, CW beams. High power charge strippers and beam collimators accept many kWs of beam power. Rapid-cycling booster synchrotrons accept and accumulate high intensity beams and then accelerate with minimal losses. High power beam targets and radiation resistant magnets operate are necessary to handle the intense thermal and radiation fields generated. Finally, loss detection and machine protection techniques are crucial to prevent damage from prompt, fast events and to monitor and control chronic losses from small ($<10^{-4}$-10^{-6}) fractions of the beam power.

*This material is based upon work supported by the U.S. Department of Energy Office of Science under Cooperative Agreement DE-SC0000661, the State of Michigan and Michigan State University.
#lidia@frib.msu.edu

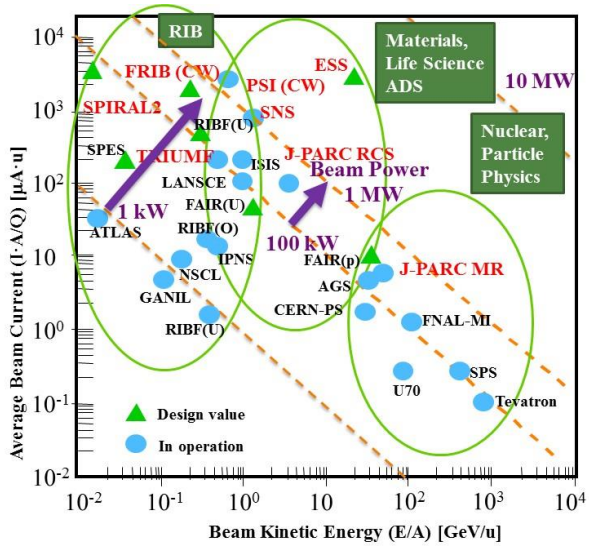


Figure 1: Development of high power hadron accelerators. [1].

MACHINE PROTECTION SYSTEM BASICS

Machine protection systems exist to avoid prompt and long-term damage to the accelerator and experimental instrumentation, to minimize the number of false trips that limit production, and to provide evidence of failures or fault events when interlock systems stop beam operation [3][4].

Machine failures can derive from several sources. Hardware failures can include power supply trips, magnet or cavity quench, RF trips and low-level control loss, loss of vacuum, etc. Control system failures include incorrect calibrations and settings updates, trigger mistiming and timing distribution errors, feedback malfunctions. Operational sources include tuning and steering errors, and administrative controls on beam mode and machine state. Beam instabilities at high current or high brightness can develop quickly and damage components.

The time response for MPS interdiction ranges over many orders of magnitude. Fast protection systems (FPS) serve to protect against prompt damage from beam impacts. Typical FPS response times can vary from several to some hundreds of microseconds, and reflect thermodynamic changes of accelerator materials caused by errant beams. Run permit systems (RPS) operate on a slower time scale, from milliseconds to many seconds, typically, and are used to verify machine state and identify conditions that may lead to unintended damage or long term irradiation effects that limit personnel access. As accelerator facilities may function

ISBN 978-3-95450-141-0

Copyright © 2014 CC-BY-3.0 and by the respective authors

in many different operating modes with varying thresholds for beam induced damage, the complete machine protection system must be flexible and configurable.

Accelerator Prompt Damage Capacities

Hadron beam loss effects in materials depend strongly on species, energy, and intercepting materials. High energy hadrons (greater than some 100's GeV/u) can generate cascades of secondary particles that lead to deep (several m) penetration and energy deposition. Material damage as well as quenching of cryogenic components can occur.

Lower energy hadron beams (10's to 100's MeV/u) deposit their energy primarily on the surface of components, which can lead to local temperature increase. Plastic deformation and rapid melting can occur when the energy deposition exceeds 10 kJ. Penetration range of low and medium energy hadrons is shown in Fig. 2 below.

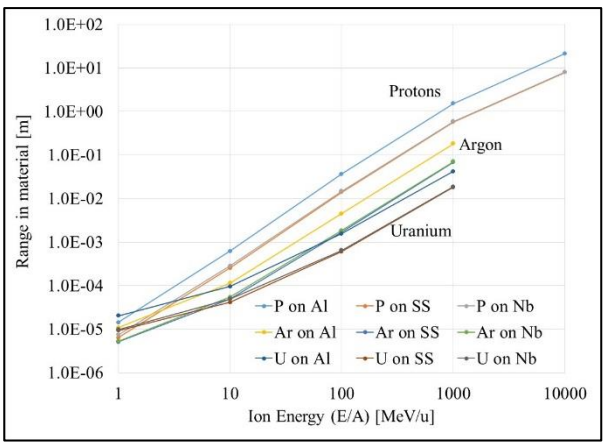


Figure 2: Penetration range for H, Ar, and U ions onto Al, stainless steel, and Nb from SRIM [5].

The time to failure for beamline components is necessary to understand in order to define the MPS fast response requirements. Figure 3 shows the time to failure of Nb and stainless components in the FRIB complex [6][7] when U ions are accelerated. ANSYS [8] calculations of energy deposition, thermal transport, and material stress.

In SRF cryomodules, power losses can generate additional heat load and induced quenches. Particle losses on or near SRF cavity surfaces can degrade the surface resistance, introduce defects and field emission sites, and affect the local gas distribution. These latter effects can degrade the operational gradient of the cavity by lowering the cavity Q-factor, and interfere with the low-level operation of the cavity rf controls.

MPS Fast Detection Times

The required detection time scales for errant beam detection in existing and proposed high power facilities are shown in Table 1. Current development of machine protection systems require 'not OK' signals to be generated within 1-10 μs.

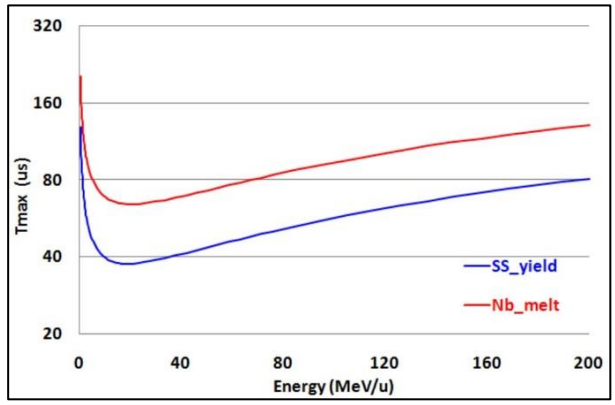


Figure 3: Time to failure for Nb and stainless steel components driven by 2mm, 8.4 pμA U beam. [6]

Table 1: Errant Beam Detection Time Scale Limits

	Ion	Energy [MeV/u]	Beam Power [MW]	Detection time limit [μs]
PSI	H^+	590	1.3	few 100
SNS	H^-/H^+	1000	1-2	5-10
ESS	H^-/H^+	2000	5	1-2
SPIRAL-2	D/HI	20	0.2	10
FRIB	HI	200	0.4	10
JPARC-MR	H+	$3\ 10^4$	0.75	10
LHC	H^+	$7\ 10^6$	$4\ 10^6$	80

Slow Loss Generation and Detection

Slow beam losses can be generated when the tails of the beam distribution are intercepted at the vacuum chamber walls, when primary beam particles scatter from residual gases, and other causes. These chronic, low-level losses lead to activation of components and limit access to the beam line.

Previous experience at high power facilities [9] [10] have indicated that a loss of 1 W/m corresponds to activation levels about 100 mR/hr. More recent measurements at SNS [11] (Fig. 4) have demonstrated activation rates of 30-40 mR/hr corresponding to beam power ~1 MW. This can be compared to the LANSCE experience of 100 mR/hr with 780 kW beam power.

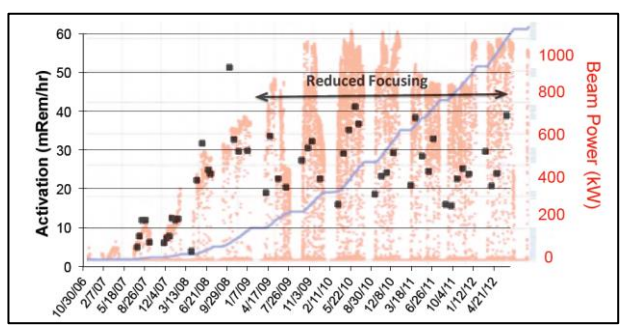


Figure 4: Residual activation in the SNS SCL [11].

Copyright © 2014 CC-BY-3.0 and by the respective authors

ISBN 978-3-95450-141-0

At most facilities, the baseline detection and background requirements are set in the range 0.5-1 W/m. Improvements in beam orbit and halo control, and improved detection thresholds are sought to decrease the slow loss rates to 0.1 W/m or lower.

Challenges and Opportunities

There are significant issues and multiple areas for diagnostic development in support of machine protection systems at contemporary high intensity hadron machines: development of systems with high dynamic range sensitivity that must contend with high radiation fields and EMI environments; development of fast and robust reporting and control networks, with low false-trip rates; simulations and modelling of radiation fields from slow and prompt beam losses, and the distribution of loss patterns from specific fault events.

QUANTITIES MEASURED WITH DIAGNOSTIC INSTRUMENTATION

Various quantities are utilized as inputs to the machine protection system. These parameters measure and gauge the behaviour of the beam and the performance of accelerator components, and compare against known or anticipated thresholds.

Beam loss monitors are employed to directly monitor the prompt radiation fields produced by the accelerator components (eg. rf cavities, distribution lines and sources) as well as the secondary particle fields generated by primary beam impact onto the vacuum chamber walls. Gamma and neutron detectors are common in medium to high energy facilities. Techniques to detect hadronic showers can also be useful in that they may indicate threshold energy levels in primary beams, and may be more advantageously staged further from the vacuum chamber.

Direct beam measurements will indicate normal or errant behavior that may require interdiction of the beam, by dumping the stored beam and preventing the source chain from injecting or producing new beam, until the problem is resolved. Specific beam measurements include average and peak current (intensity), beam orbit, beam halo, micro pulse duration, and spot size.

Vacuum monitoring is critical to preserve the operational lifetime of superconducting rf (SRF) cavities. Vacuum gauges are employed for leak detection as well as for any slow changes in the background gas pressure due to beam (and secondary) particle impacts on the vacuum chamber walls.

Cryogenic system monitors are used to detect changes in the overall thermal loading budget, indicating changes in source terms. Heat load source changes can result from changes in forward or reflected rf power (and the formation of standing waves in distribution lines), increased radiative heat loads in cryogenic devices due to changes in rf beam loading, and from beam particle interception on limiting apertures. Quench detection circuits monitor for changes in the superconducting state of magnet windings, or the Q-factor of SRF cavities. Low-level rf (LLRF) digital monitors are employed to detect fast (~μs) changes in SRF cavity field amplitudes, forward/reflected power, and phase.

Normal conducting magnet power supplies are typically monitored with DC current transformers (DCCTs) that detect changes in supplied current to magnet coils, which may result in changes to the beam orbit or focusing. Changes to DCCT readings may interlock the beam.

PROMPT RADIATION GENERATION ALONG ACCELERATOR CHAIN

Radiation production along the accelerator chain exhibits derives from several sources.

Background sources of gamma radiation are produced by high field rf cavities, couplers, transmission lines and rf sources. These photons interact with detectors, vacuum chamber walls and other components to generate electrons and increase overall background noise levels. Measured background levels can be in excess of 1 Rem/hr [12][13].

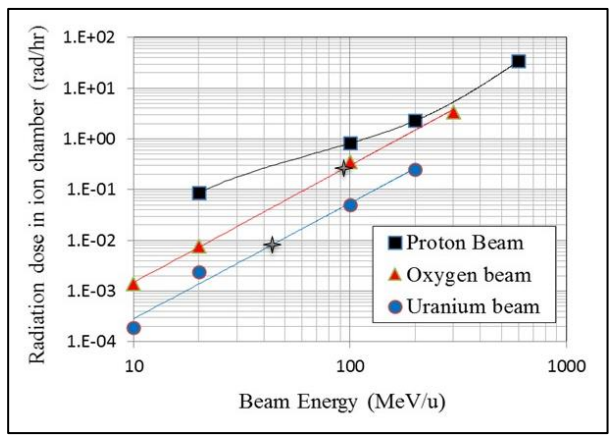


Figure 5: Gamma ray dose at 30cm from cryomodule. Power loss is normalized to 1 W/m. Pencil beam with 3mrad angle was uniformly distributed along 150m long linac segment.[12]

Beam induced radiation fields include gamma, neutron, and hadronic cascades. The fields are produced when a primary beam particle collides with the vacuum chamber, insertable diagnostics, or background gas molecules. The production rates are strongly dependent on primary beam energy.

Gamma ray doses generated with several hadron beams in the FRIB accelerator, modelled by GEANT4 [14], are shown in Fig. 5. The beam losses are assumed to be 1 W/m distributed uniformly along a 150-m linac section. For heavy ion beams, the prompt gamma radiation dose can easily be masked by background gamma sources at beam energies below a few 100s MeV/u.

ISBN 978-3-95450-141-0

Copyright © 2014 CC-BY-3.0 and by the respective authors

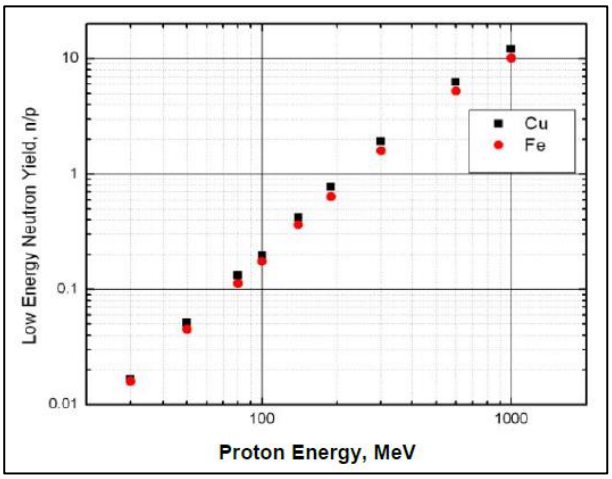


Figure 6: Evaporation neutron yield from a copper target as a function of incident proton energy. [15]

The collision of high energy hadron beams with beamline components and background gases precipitates various nuclear interactions. Neutron evaporation [16] is the main source of neutrons in hadron machines. Low energy neutron transport processes [17] describe the propagation and thermalization of neutrons in materials and detectors. Neutron production rates from evaporation processes of protons onto copper and iron are shown in Fig. 6. Neutron fluxes from heavy ion beam losses (uniform 1W/m) also exhibit energy and species dependence (Fig. 7).

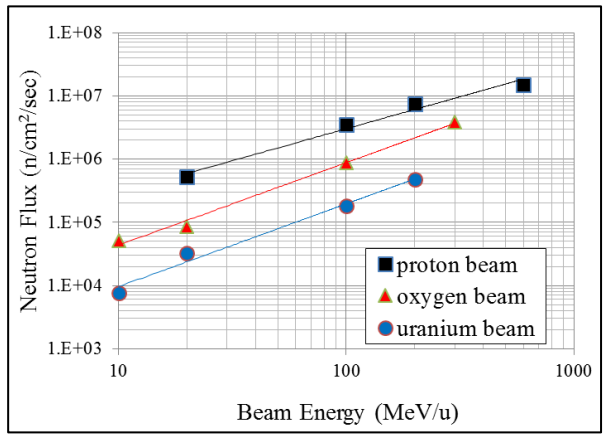


Figure 7: Neutron flux normalized to 1W/m loss. [12].

Hadronic cascades or showers generate a mixed radiation field of gammas, lepton, and hadrons. These showers can, in principle, be modeled with Monte Carlo codes [14][18][19][20][21]. A recent benchmark study [22] was performed at the CERN-EU High Energy Reference Field Facility (CERF) to calibrate LHC beam loss monitors. FLUKA generated spectra were presented in [23], Fig. 8 below.

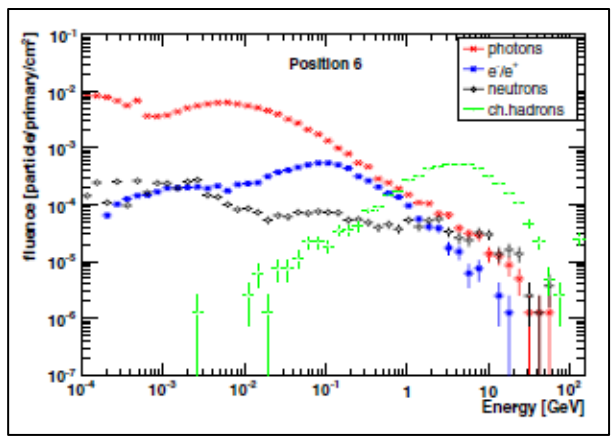


Figure 8: FLUKA hadron spectra from high energy proton beam bombardment [23].

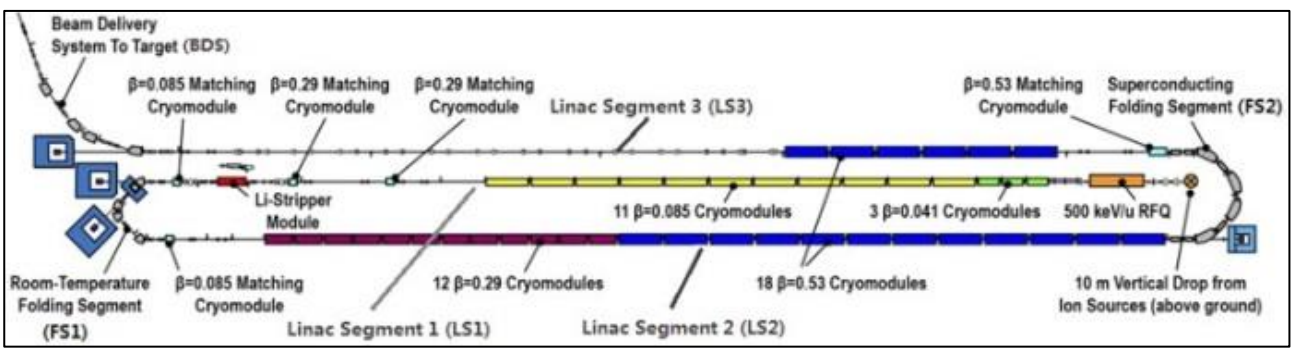


Figure 9: FRIB drive accelerator layout, showing the folded, 'paperclip' geometry.

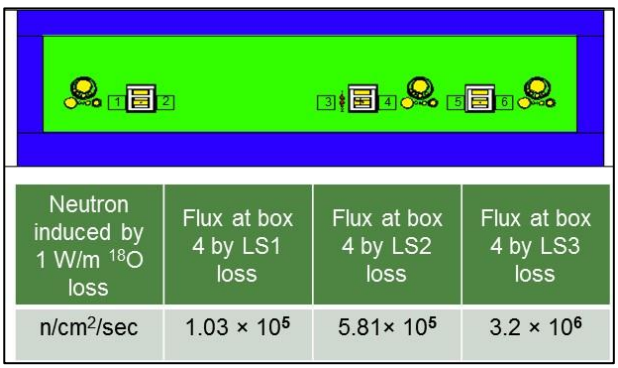
Copyright © 2014 CC-BY-3.0 and by the respective authors

ISBN 978-3-95450-141-0

Crosstalk Effects

Compact, low energy, high intensity hadron accelerators, especially those attached to existing campuses or facilities, can encounter crosstalk issues when the higher energy portions of the beamline are brought into close proximity with the lower energy portions. A current example is the 'paperclip' design of the FRIB drive linac, Fig. 9.

In the FRIB case, the drive linac is separated into 3 segments, with the lowest energy segment (LS1) placed between the two higher energy ones (LS2, LS3). Uniform beam losses of 1 W/m have been simulated with GEANT [14] and PHITS [19]. Figure 5 shows the gamma radiation dose rate at 30 cm from the cryomodule. The crosses indicate the strength of the radiation field at LS1 due to losses occurring in LS3. At these beam loss rates, ionization chambers along LS1 would be overwhelmed by signal from LS3. A similar situation exists for the neutron field, where the LS3 signal detected at LS1 exceeds the LS1 signal by ~30 times (Fig. 10).



Neutron induced by 1 W/m ^{18}O loss	Flux at box 4 by LS1 loss	Flux at box 4 by LS2 loss	Flux at box 4 by LS3 loss
n/cm^2/sec	1.03 × 10^5	5.81× 10^5	3.2 × 10^6

Figure 10: Neutron crosstalk effects in FRIB linac, modeled with PHITS [12]. The top figure shows a cross section of the beamline.

SIMULATIONS AND MODELING

The design, development, and implementation of diagnostic systems for machine protection require extensive evaluation of fault modes, risk analyses, and beam loss events and spill patterns.

Predicted radiation power levels from low level beam spill processes can be modelled with radiation transport codes [14][18[19][20][21] (Fig. 11) to estimate dose rates at various sections of the machine.

To assess risk from infrequent, prompt fault events due to component failure or mistuning, beam spill patterns need to be generated and analyzed [25][26][27]. Spill pattern maps (Fig. 12) can aid in the placement of in-vacuum diagnostics and passive protection devices to limit damage to sensitive components.

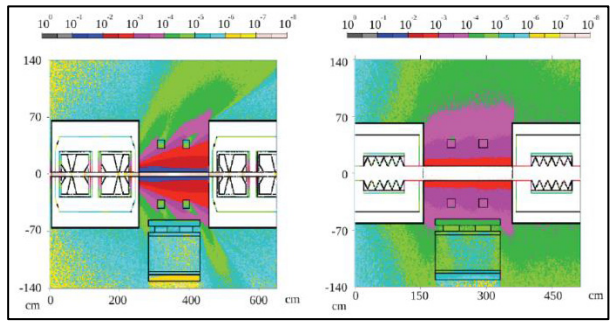


Figure 11: Radiation field power density (Gy/sec) in the ESS linac from uniform 1 W/m losses at 200 MeV (left) and 2 GeV (right) [24].

Once constructed, a comprehensive atlas of spill pattern maps can be incorporated into a machine learning framework [25][28] to optimize the placement of beam loss monitors and their networking, and in the post-mortem analysis of fault events.

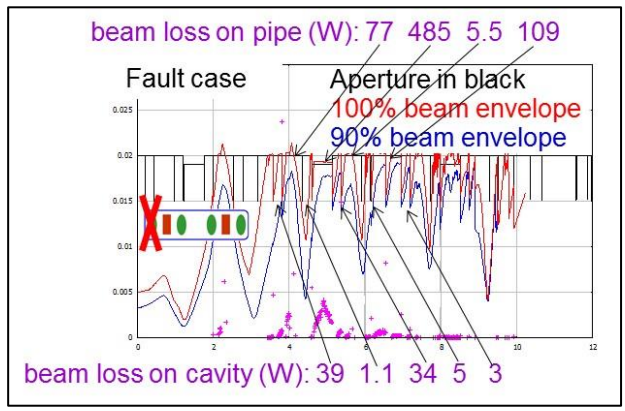


Figure 12: Beam loss map in the FRIB linac due to single cavity failure. [26].

BEAM LOSS MONITORS

We describe various beam loss monitor instrumentation techniques currently employed at high power facilities. This follows the excellent tutorial by Zhukov [15].

Ionization Chambers

Ion chambers are the main type of loss monitors used in hadron machines. These are gas-filled chambers containing an electrode pair with applied high voltage. Multiple ion chambers are typically strung together on a common high voltage supply. When operated in the ionization mode, the chamber sensitivity is largely insensitive to HV fluctuations.

Small ion chambers (Fig. 13) have been designed and optimized for various machines. The SNS ionization chamber [29] has a volume of 133 cm^3 of argon gas. At a HV bias of -2 kV the chamber sensitivity is 70 nC/rad. The response time for charge collection can be ~1-2 μs.

Copyright © 2014 CC-BY-3.0 and by the respective authors

ISBN 978-3-95450-141-0



Figure 13: SNS type ionization chamber. [29]

A larger chamber developed for LHC [30] is shown in Fig. 14. The LHC chamber was developed in collaboration with the Institute for High Energy Physics (Protvino, Russia). The detector is filled with N_2 at 100 mbar overpressure. The 50-cm-long, 9-cm-diameter chamber is constructed with parallel aluminium plates, separated by 0.5 cm. The 1.5 L volume provides a sensitivity of ~54 μC/Gy at 1500 V bias. The response time is approximately 300 ns for electrons and 80 μs for ions. The electron mode is compatible with fast detection requirements for high intensity hadron machines.

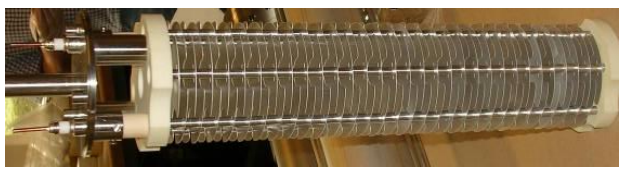


Figure 14: The LHC ionization chamber. [30]

Secondary Emission Monitors

At locations with very high loss rates, the high sensitivity of the ion chambers can lead to saturation and charge pile-up. Secondary emission monitors (Fig. 15) exhibit lower sensitivity, thus extending the detection dynamic range when used to complement ionization chambers. The center electrode of the 3-electrode is titanium rather than aluminium to take advantage of the greater stability of the secondary emission coefficient with integrated radiation dose [31].

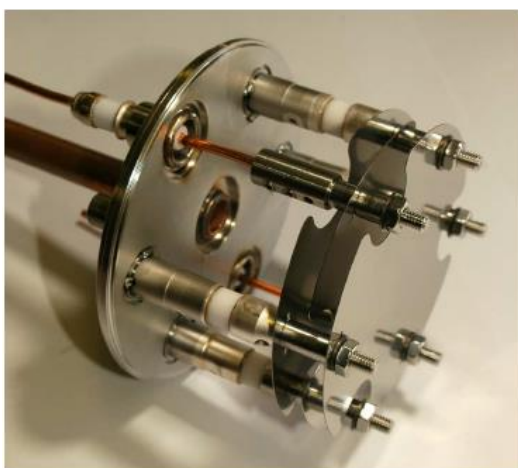


Figure 15: Secondary emission chamber developed for LHC magnet quench protection.[32].

Scintillation-Based Detectors

Scintillation based schemes typically employ photomultiplier tubes that increase gain by 10^5-10^8 with applied HV. The wide variety of scintillation materials available allow for optimization to detect specific types of radiation. Many crystalline and powder scintillating materials [33] have excellent efficiencies at gamma detection, with decay time constants mostly in the 10s-100s ns. Pulse shape discrimination of the waveform is used to separate gamma and neutron signals. Plastic based scintillator materials containing ^{6}Li or ^{10}B are widely used to detect fast and thermal neutrons. These latter types are useful for discriminating neutron-producing beam losses from background gamma sources. Moderated detectors are relatively slow, but are sensitive to neutron fluxes over a wide range, 10^4-10^8 n/cm^2/s for the SBLM [34], suitable for monitoring slow beam losses.

Background Subtraction

Overall sensitivity to beam losses can be improved with background subtraction techniques. These can be implemented in hardware, software, or firmware. Dual beam loss monitors [34] are utilized that provide differential sensitivity to background gammas and beam-induced neutron signals. Beam loss monitor signals can also be acquired at rates that permit the discrimination between 'beam on' and 'beam off' events. Robust background subtraction can then be performed in software (see Fig. 16), which limits the time response to seconds. Firmware implementation can reduce the comparison time against a stored background waveform and recover μs-scale responsivity.

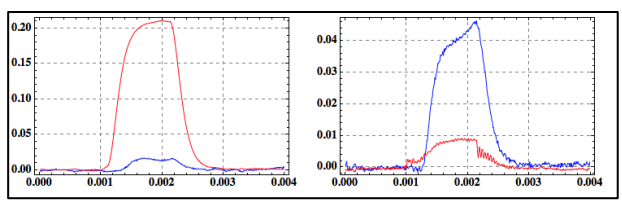


Figure 16: Background subtraction of SNS BLM waveforms, performed in software. Red traces are RF only waveforms, blue traces are beam loss only (ie. subtracted). [34]

Novel Schemes for In-Situ Cryogenic Detection

Detection of beam losses inside of cryomodules is critical to minimize damage to sensitive cavity surfaces, and to prevent quenching of magnets with large stored energy.

Recent work at LHC [35][46] have studied the feasibility of using silicon (300 μm) and CVD diamond (500 μm) in the cold mass at 1.9K to measure slow losses with sensitivities 0.1-10 mGy/s and response times <1 ms. Measured response times to Minimum Ionizing Particles (MIPS) were 2.5 ns and 3.6 ns for silicon and diamond, respectively, at liquid helium

Copyright © 2014 CC-BY-3.0 and by the respective authors

ISBN 978-3-95450-141-0

temperatures, allowing bunch by bunch resolution. Signal reduction factors were measured and calibrated to the expected LHC 20 year integrated dose (2 MGy). The expected degradation factor is 25 for silicon and 14 for diamond.

A system based on collection of charge carriers in liquid helium itself was also considered, as the material is self-healing and does not exhibit degradation from integrated dose. With an applied electric field of 200 V/mm, sensitivity of ~0.1 fC/cm/MIP was measured. Slow charge collection limits the time response to events longer than ~200 μs. A similar system has been developed and employed at Fermilab [37] (Fig.17).

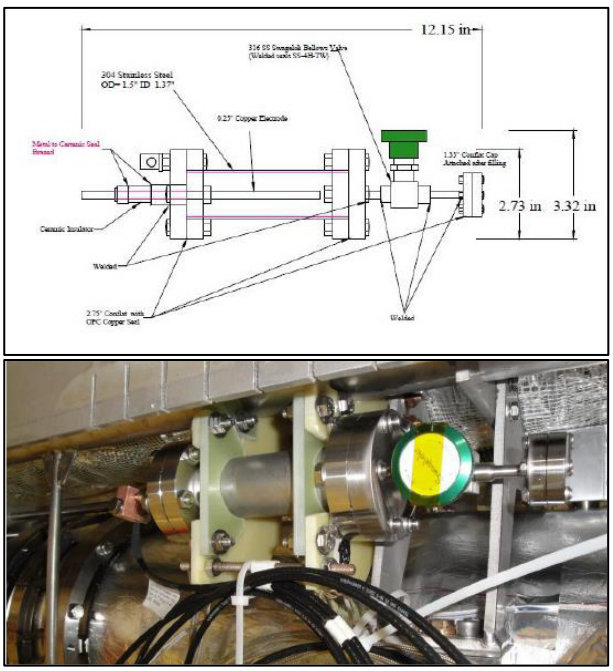


Figure 17: Cryogenic ionization chamber at ASTA [37].

Systems employing fast thermometry or calorimetry have been developed to monitor the temperature of cryogenic components and beamlines [38][39]. Resistance temperature detectors (Cernox RTDs) are employed to monitor the surface temperature of components.

Fast thermometry techniques are currently being explored to detect low level, slow beam losses at limiting apertures in cryomodules. ANSYS models can be used to predict the change in component temperature and time rate under beam thermal loading conditions (Table 2).

Table 2: Cryogenic Beam Loading Response

Rising time for 0.1K temperature difference from beam loss		
Beam loss in cryomodule	0.1 W/m	1 W/m
0.1K rising time	1 min	7 sec
Maximum temperature rising	1.83 K	8.9 K
Total rising time	30 min	20 min

Initial measurements of thermal loading and RTD pickups were conducted at FRIB [40]. Initial sensor response is encouraging for detection of several mK temperature rise with a time response of 10's seconds. Improvements to the sensitivity and time response are expected with higher sampling and averaging rates (1-10kHz).

DIRECT BEAM DIAGNOSTICS FOR FAST TIME SCALES

The measurement of beam properties themselves, on a suitably fast basis, can directly inform the machine protection system to cease beam production and to dump stored beam. Robust monitoring of beam current at the 1-10% level of the normal current on a fast time scale (several μs) is generally required to detect changes in the beam intensity that may require MPS interdiction. Beam position monitors, capacitive pickups, and current sensing interceptive devices near the limiting beam aperture can also provide reliable detection sensitivity. Modern FPGA electronics systems are gaining wide acceptance for fast and flexible beam loss detection and interface to MPS decision and control systems.

Beam Current Monitors (BCM)

Most current sensing of intense beams is conducted with AC or DC current transformers (ACCT, DCCT) with appropriate analog front end, analog-to-digital conversion, and digital signal processing (Fig. 18).

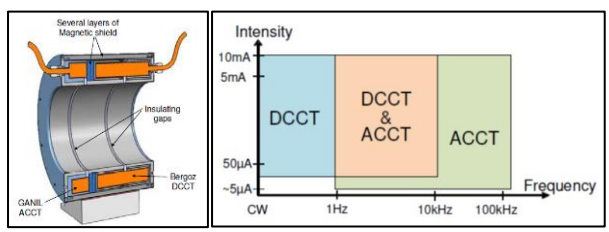


Figure 18: Hybrid ACCT/DCCT developed for SPIRAL-2 (left) and frequency response for DCCT and ACCT systems (right).[41].

The differences between ACCTs and DCCTs have important implications to their optimal use for tuning and MPS. DCCTs require offset correction and are limited in their high frequency response to slower current evolution (100s μs). However, they can more easily the presence and absence of beam. ACCTs have higher frequency response, and so can detect relatively fast changes in beam current (<10 μs), but they have no DC response and so must be periodically re-baselined to define the 'no current' condition. Additional signal conditioning is required to compensate for current 'droop' in the time response. [42]

Differential Beam Current Monitoring (DBCM)

The fast response of ACCTs has led to a demonstration of a fast MPS network to detect errant

ISBN 978-3-95450-141-0

Copyright © 2014 CC-BY-3.0 and by the respective authors

beams on the SNS linac [43], based on differential beam current monitoring (DBCM) between two spatially separated locations (Fig. 19).

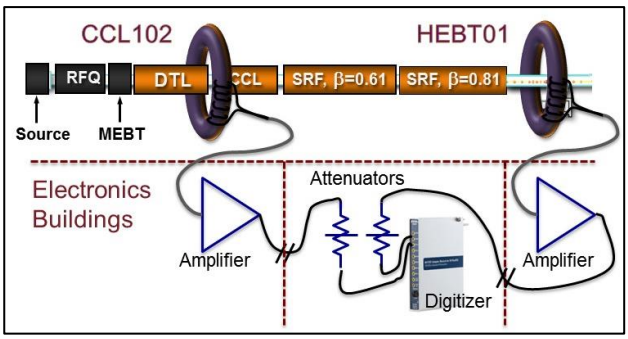


Figure 19: SNS differential beam current monitor.[43].

The SNS configuration consists of two wideband (1 GHz, 1 ms droop time constant) current transformers, and relatively long cable lengths (500-1200ft). The electronic platform consists of PXIe real-time controller with FlexRIO FPGA and 14-bit, 2-channel, 100MS/s digitizer. The FPGA processing performs the time-of-flight accounting for the beam and cable lengths, applies calibrations and corrects for drifts and droop in the transformer. The block diagram of the digital processing and interface with the MPS control is shown in Fig. 20.

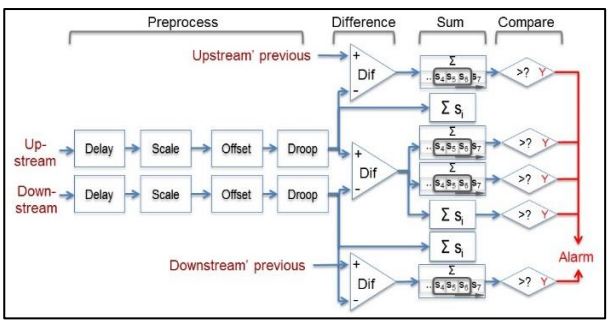


Figure 20: Digital processing of SNS DBCM. [43].

Similar systems are proposed for ESS, SPIRAL-2, and FRIB. In the SPIRAL-2 implementation the MPS control is based on a preset beam charge loss threshold rather than a beam intensity threshold [44]. The distribution of DBCM monitors for SPIRAL-2 is shown in Fig. 21, and the proposed distribution for FRIB in Fig. 22. The ESS implementation has been bench tested with a measured response time of 770 ns. Including additional delays from the analog electronics, digital filters and rear transition module to the μTCA chassis, the expected response time still meets the required 1-2 μs [45].

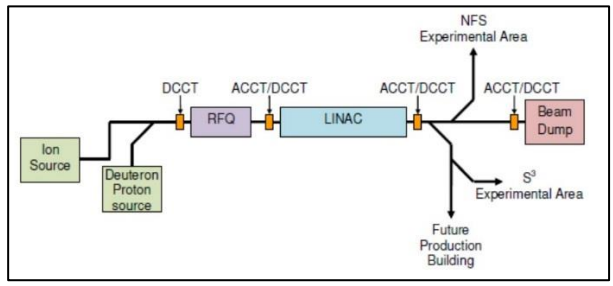


Figure 21: Distribution of beam current monitors in SPIRAL-2. [41].

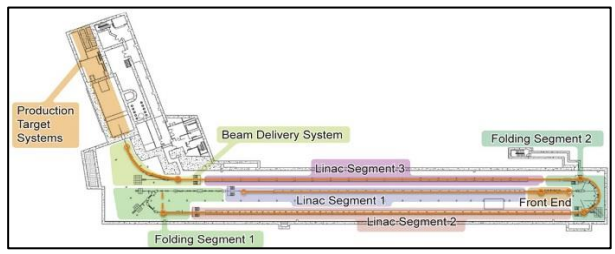


Figure 22: Distribution of beam current (open circles) in FRIB. [46].

Beam Position Monitors (BPM)

Beam position monitors are currently being developed and implemented in MPS applications. Besides fast orbit monitoring and deviation detection, recent studies at SNS have indicated how to include BPMs as part of a differential intensity monitoring system [47].

The SNS BPM current measurement scheme utilizes the digital sum signal from the four BPM capacitive sensors. The signal is processed within the FPGA to reconstruct the signal amplitude from the logarithmic amplifier. A final calibration is applied based on an existing BCM reference. The BPM and BCM signals are shown in Fig. 23.

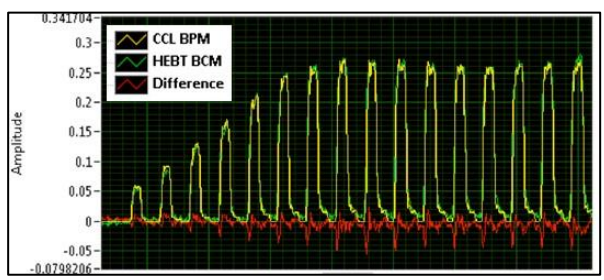


Figure 23: Cross-calibration of BPM and ACCT for differential intensity monitoring. [47].

Utilizing BPMs as intensity monitoring devices, and incorporating them into differential intensity monitoring schemes significantly increases the density of the monitoring network. However, limited linear apertures in the BPMs as well as low-beta effects [48] can increase the complexity of the required signal analysis, making the practical implementation of BPMs as intensity monitors problematic. Recent work has addressed possible schemes for implementing low-beta corrections [49].

Copyright © 2014 CC-BY-3.0 and by the respective authors

ISBN 978-3-95450-141-0

Halo or Loss Monitor Rings

Beam loss monitors based on radiation detection have limited sensitivity for low energy hadron beams (< 20 MeV/u). The FRIB design increases the problems for low energy beam loss detection by placing the lowest energy linac in close proximity to the highest energy linac. In this case, both ionization chamber and neutron detector instruments at the low energy side are swamped with signal from slow losses from the high energy linac.

The halo, or loss, monitor ring was designed as a minimally interceptive device [13], with high sensitivity (~0.1 nA) to small losses and fast response (<15 μs) for large losses. The device is designed to be mounted within a diagnostic box between two cryomodules, with inner aperture that approximately matches the limiting beam aperture in the cryomodule. Tests of the loss ring sensitivity were performed at the National Superconducting Cyclotron Laboratory. The FRIB loss ring design and measured sensitivity are shown in Fig. 24.

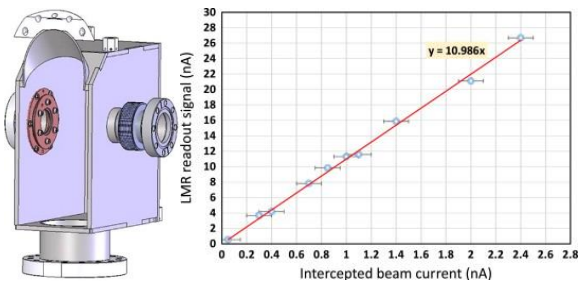


Figure 24: Installation and measured sensitivity of loss monitor ring. [13].

A comparison (Table 3) of the detected signal between the loss ring and the SNS ion chamber was made, in the case of uniform 1 W/m loss of uranium ions in the FRIB linac.

Table 3: Performance Comparison between Loss Monitor Ring and Ion Chamber. [13]

Loss Mode	Loss Source Location	^{238}U Energy / Charge [(MeV/u) / Q]	Loss Level [W/m]	Ion Chamber Signal [pA]	HMR Intercepted Beam [nA]
Slow loss	LS1	10 / 33+	1	0.003 *	72 **
	LS2	60 / 78+	1	0.3 *	29 **
	LS3	200 / 78+	1	4.2 ***	9 **
Fast loss	3rd ↕=0.29 cavity	20 / 78+	~1300 (in ~15m)	~7.0	29×10^3

* Assume the transfer function of ion chamber is 16.9 pA/R/hr (SNS).
** Assume HMR intercepts 1 W/m × 5 m beam power.
*** LS3 signal is calculated from loss in a superconducting structure.

A similar halo ring is currently employed at the PSI Ultra-Cold Neutron source beamline [50]. This implementation is segmented into 4 quadrants, with individual readouts. The signals are read and compared to a nearby current monitor. With proper tuning and collimation, the halo monitor should indicate 5% beam current interception.

An obvious criticism of employing intercepting devices near SRF cryomodules is the risk of material sputtering, beam scattering, and gas production due to primary beam ion collisions. Calculation of the time required to sputter Nb ring atoms onto the surface of a Nb cavity to the London penetration depth is in excess of 10^5 years. Recent studies of tungsten, niobium, and carbon wire sublimation close to superconducting cavities at SPIRAL-2 [51] have shown encouraging results for tungsten and niobium bursts, while burst of carbon led to clear quenches.

LAYERED DESIGN ASPECTS

Machine protection system diagnostics exhibit various sensitivities and time response to beam losses incurred along an accelerator chain. To mitigate risk and increase the probability of a robust detection scheme, a network of sensors is established. As previously discussed, existing machines utilize complementary beam loss monitors to improve dynamic range in high loss regions, and incorporate beam intensity difference measurements alongside traditional radiation loss detectors. Responsiveness to losses occurring over multiple time scales permits optimization of specific device or technique sensitivity to losses on particular time scales. Specific scales are chosen to overlap with physical or administrative time scales of greatest concern.

The loss monitor network scheme for FRIB is shown in Table 4. Fast and slow losses, in each segment of the accelerator chain, are separated, and the primary as well as backup detection schemes are indicated. At low energy, the primary fast detection schemes are based on direct beam monitoring, with secondary radiation monitoring appearing only as the primary beam energy increases to a suitable production threshold. The slow loss schemes are based on time averaged loss ring monitoring as well as thermal drift monitoring in cryomodules.

Table 4: FRIB Beam Loss Detection Layers

		LS1	FS1	LS2 low energy	LS2 high energy	FS2	LS3	BDS
Fast Loss	Primary	DBCM	DBCM	DBCM	DBCM	DBCM	DBCM	DBCM
< 35 μs	Secondary	HMR	HMR	HMR	BLM	BLM	BLM	BLM
	Tertiary				HMR	HMR	HMR	
Slow loss	Primary	HMR/Temp	HMR	HMR/Temp	BLM	BLM	BLM	BLM
> 100 ms	Secondary	HMR/Temp		HMR/Temp	HMR/Temp	HMR	HMR/Temp	
	Tertiary	Cryo		Cryo	HMR/Temp		HMR/Temp	
					Cryo		Cryo	

The LHC beam loss monitoring system is captured in the digital processing with 12 separate time scales extending from ½ turn (39 μs) to 84 s.

The layering of machine protection diagnostics and time scales with decision and control processes for SPIRAL-2 is shown in Fig. 25.

Copyright © 2014 CC-BY-3.0 and by the respective authors

ISBN 978-3-95450-141-0

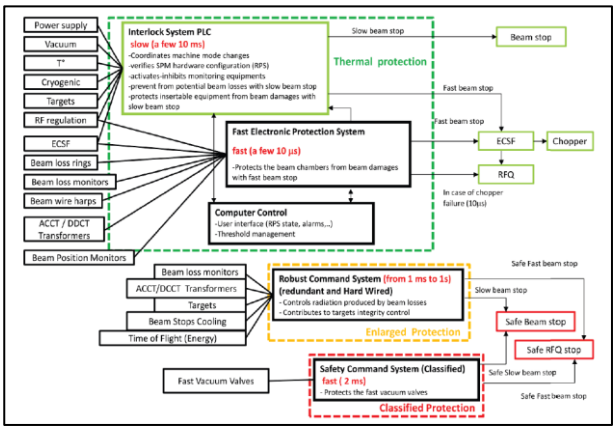


Figure 25: Components and layering of SPIRAL-2 machine protection system.[44].

SUMMARY

Elements of modern machine protection systems for high intensity hadron accelerators have been presented, emphasizing the types of diagnostic systems used and measurements that are required for a robust system.

ACKNOWLEDGMENT

The author would like to thank the participants of the 2014 Machine Protection Workshop for the discussion and presentations. Materials and discussions with additional individuals is gratefully acknowledged: Alexander Zhukov, Wim Blokland, Rudolf Doelling, Christophe Jamet, Marc Ross, Bernd Dehning, Doug McCormick, Zhengzheng Liu, Yan Zhang, Qiang Zhao, and Andreas Jansson.

REFERENCES

[1] J. Wei, "The very high intensity future," Proceedings of IPAC2014, MOYBA01, http://www.JACoW.org
[2] J. Wenninger, "State-of-the-art and future challenges for machine protection systems," Proceedings of IPAC2014, FRXCA01, http://www.JACoW.org
[3] J. Wenninger, Special CERN CAS, Feb. 2009.
[4] R. Schmidt, CAS, October 2011.
[5] http://www.srim.org/
[6] Y. Zhang, *et al.*, "Analysis of beam damage to FRIB driver linac," Proceedings of SRF2011, MOPO058, http://www.JACoW.org
[7] H. Takei and H. Kobayashi, J. Nucl. Sci. Tech. 42, (2005), p. 1032.
[8] www.ansys.com
[9] D. Gassner, *et al.*, "Spallation Neutron Source Beam Loss Monitor System," Proceedings of the 2003 Particle Accelerator Conference, p. 2447, http://www.JACoW.org
[10] R.A. Hardekopf, "Beam loss and activation at LANSCE and SNS," LA-UR-99-6825, Los Alamos National Laboratory, Los Alamos, NM, Sept. 1999.
[11] J. Galambos, *et al.*, "Increased understanding of beam losses from the SNS linac proton experiment," Proceedings of LINAC2012. MO2A02; http://www.JACoW.org
[12] Z. Liu, *et al.*, "Beam loss monitor system for the low-energy heavy-ion FRIB accelerator," Proceedings of IBIC2013, MOPC46; http://www.JACoW.org
[13] Z. Liu, *et al.*, "A new beam loss monitor for low-energy protons and heavy-ion accelerators," Nucl. Instrum. Methods Phys. A, *in press* (2014).
[14] Geant4 collaboration, "Geant4 Simulation Toolkit," http://geant4.web.cern.ch/geant4
[15] A. Zhukov, "Beam loss monitors (BLMs): Physics, simulations, and applications in accelerators," Proceedings of BIW10, THTNB01 (2010).
[16] V.E. Weisskopf and D.H. Ewing, Phys. Rev. 57, 472 (1942).
[17] ENDF/B-VI Summary Document, Report BNL-NCS-17541 (ENDF-201) (1991), P.F. Rose ed., National Nuclear Data Center, Brookhaven National Laboratory, Upton, NY, USA.
[18] A. Fasso, A. Ferrari, J. Ranft, *et al.*, "FLUKA: a Multi-Particle Transport Code," CERN-2005-10 (2005), INFN/TC_05/11, SLAC-R-773.
[19] Koji Niita, Tatsuhiko Sato, Hiroshi Iwase, *et al.*, "PHITS - a Particle and Heavy Ion Transport Code System," Radiation Measurements 41 (2006) 1080.
[20] N.V. Mokhov, "The Mars Code System User's Guide", Fermilab-FN-628 (1995).
[21] http://mcnp.lanl.gov
[22] M. Stockner, "Beam Loss Calibration Studies for High Energy Proton Accelerators," CERN-THESIS-2008-009, (2008).
[23] M.Stockner, *et al.*, 2006 IEEE Nuclear Science Symposium, N30-274, 1342-1345, (2006).
[24] L. Tchelidze, "Beam loss monitoring at the European Spallation Source," Proceedings of IBIC 2013, WEPC45; http://www.JACoW.org
[25] M. Jarosz, "Studies into beam loss patterns at European Spallation Source," Proceedings of IPAC2014, THPME165; http://www.JACoW.org;
[26] Q. Zhao, *et al.*, "FRIB accelerator beam dynamics design and challenges," Proceedings of HB2012, WEO3B01 (2012).
[27] R. Bruce, *et al.*, "Simulations and measurement of beam loss patterns at the CERN Large Hadron Collider," PR-STAB 17, 081004, (2014).
[28] A. Hofler, *et al.*, "Innovative applications of genetic algorithms to problems in accelerator physics," PR-STAB 16, 010101, (2013).
[29] R.L. Witkover and D. Gassner, "Design of an improved ion chamber for SNS," BIW2002, AIP Conf. Proc. 648, (2002), p. 337.
[30] E.B. Holzer, *et al.*, "Beam loss monitoring system for the LHC," IEEE-MIC '05, Puerto Rico, CERN-AB-2006-009 BI, (2005).

Copyright © 2014 CC-BY-3.0 and by the respective authors

ISBN 978-3-95450-141-0

[31] D. Kramer, "Design and implementation of a detector for high flux mixed radiation fields", CERN-THESIS-2008-090, (2008).
[32] D. Kramer, *et al.*, "Secondary electron emission beam loss monitor for LHC", Proceedings of DIPAC 2007, WEPC03; http://www.JACoW.org
[33] M. Nikl, "Scintillation detectors for x-rays", Meas. Sci. Technol. **17** (2006) R37-R54.
[34] A. Zhukov, private communication.
[35] C. Kurfuerst, *et al*., "Investigation of the use of silicon, diamond, and liquid helium detectors for beam loss measurements at 2 Kelvin," Proceedings of IPAC2012, TUOAB02; http://www.JACoW.org
[36] C. Kurfuerst, *Cryogenic Beam Loss Monitoring for the LHC*, CERN-THSIS-2013-232, (2013).
[37] A. Warner, private communication.
[38] D. Orris, *et al.*, "Fast thermometry for superconducting rf cavity testing," Proceedings of PAC07, WEPMN105; http://www.JACoW.org
[39] J. Knobloch, *et al.*, Rev. Sci. Instrum. 65, 3521 (1994).
[40] J. Ozelis, private communication.
[41] S. Leloir, *et al*., "Measurement and control of the beam intensity for the SPIRAL-2 accelerator," Proceedings of IBIC2013, WEPF33; http://www.JACoW.org
[42] R.C. Webber, "Charged particle beam current monitoring tutorial," AIP Conf. Proc. 333, (1995), p. 3-23.
[43] W. Blokland, C. Peters, "A new differential and errant beam current monitor for the SNS accelerator," Proceedings of IBIC13, THAL2; http://www.JACoW.org
[44] M-H. Moscatello, *et al.*, "Machine protection system for the SPIRAL2 facility," Proceedings of IPAC2012, WEPPD044; http://www.JACoW.org
[45] H. Hassanzadegan, "Design, implementation and preliminary test results of the ESS beam current monitor system," Proceedings of IPAC2014, THPME160; http://www.JACoW.org
[46] S. Lidia, private communication.
[47] W. Blokland, private communication.
[48] R.E. Shafer, "Beam position monitor sensitivity for low-β beams," AIP Conf. Proc. 319, (1994), 303-308.
[49] O. Yair, *et al.*, "FRIB beam position monitor pickup design," Proceedings of IBIC2014, TUPF16 (2014).
[50] B. Blarer, *et al.*, "The beam safety system of the PSI UCN source," Proceedings of DIPAC2011, MOPD03; http://www.JACoW.org
[51] R.Ferdinand, *et al*., "Tests of wire sublimations very close to SPIRAL 2 superconducting cavity," Proceedings of LINAC08, THP005; http://www.JACoW.org

ISBN 978-3-95450-141-0

Copyright © 2014 CC-BY-3.0 and by the respective authors

STUDY OF SCINTILLATION STABILITY IN KBR, YAG:CE, CaF_2:EU AND CSI:TL IRRADIATED BY VARIOUS-ENERGY PROTONS *

L. Y. Lin#, D. Leitner, C. Benatti, S. W. Krause, R. Rencsok, S. Nash, W. Wittmer,
NSCL, East Lansing, MI 48824, USA
G. Perdikakis, Central Michigan University, Mt. Pleasant, MI 48859, USA

Abstract

The luminescence of KBr, YAG:Ce, CaF_2:Eu and CsI:Tl scintillators induced with H_2^+ ion beams in the energy range of 600-2150 keV/u has been systematically measured as a function of irradiation time. The measurements showed that the luminescence of CsI:Tl and YAG:Ce remained constant within the 1-hour continuous irradiation. An initial fast drop of the luminescence on CaF_2:Eu was observed but the light output eventually approached a stable state under constant ion bombardment. We also observed that the light output of KBr initially increased and then degraded gradually with further irradiation. The CsI:Tl screen produced the highest scintillation yield and KBr the lowest.

INTRODUCTION

The wide use of scintillator screens in beam profile measurements and pepper-pot emittance systems has motivated a number of studies [1-4] on the scintillation stability under ion irradiation. The scintillation degradation caused by radiation damages can deteriorate the accuracy of beam width and emittance measurements. The degradation of luminescence can be attributed to many factors, some of which are related to the nature of the scintillator materials, the accumulated fluence, and the energy of bombarding particles. In a previous work [5], we have reported that the scintillation yield of single crystal YAG: Ce was significantly degraded under low-energy (28-58 keV) He^+ irradiation. By using the Birks model, we explained that the decrease of the observed light yield in YAG:Ce is the result of a competition between the creation of luminescence photons and displacement damage defects. The model allows to quantitatively explain how the degradation time depends on the bombarding energy in the low radiation energy range. The degradation of scintillation yield is reduced as the beam energy increases under low-energy bombardments.

In this report, our measurements were focused on investigating the scintillation stability of KBr, YAG:Ce, CaF_2:Eu and CsI:Tl single crystals under H_2^+ irradiation at the energies of 600-2150 keV/u. The scintillation materials and their optical properties [6] are listed in Table 1 together with their manufacturers and dimensional sizes. The choice of these materials was based on their availability and common use as diagnostics in low energy accelerators delivering low intensity beams.

Table 1: The Scintillator Materials under Study

Material	CsI:Tl	CaF_2: Eu	YAG: Ce	KBr
Density (g/cm^3)	4.51	3.18	4.55	2.74
Light yield photons/MeV	55,000	24,000	16,700	----
Thickness (mm)	1	1	1	2
Diameter (mm)	19	19	18	19
Manufacturer	SGC	SGC	MII	ICL

SGC: Saint-Gobain Crystals [7]
MII: Marketech International Inc. [8]
ICL: International Crystal Laboratory [9]

EXPERIMENTAL SETUP

The irradiation experiments were performed at the rare isotope ReAccelerator (ReA) facility of the National Superconducting Cyclotron Laboratory (NSCL) in Michigan State University (MSU). A H_2^+ beam from a stable ion beam injector was accelerated by a room temperature RFQ and the SRF linac, and then delivered to the scintillator target chamber installed in the ReA experimental hall, as shown in Fig. 1. The four different scintillator materials were held on a rotating target wheel inside the chamber under vacuum. A CCD camera (PCO

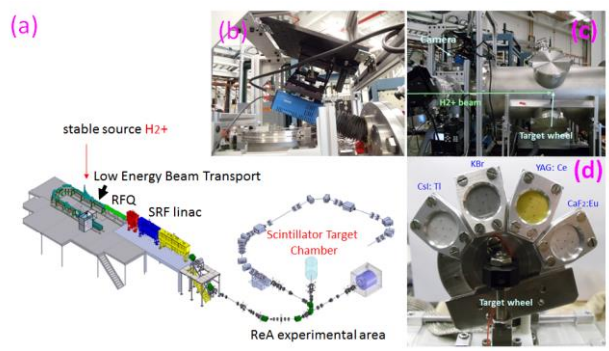


Figure 1: (a) Layout of the beam delivery to the scintillator target chamber in the ReA facility of NSCL. The experimental setup consists of (b) a CCD camera, (c) a target chamber and (d) a target wheel with four different scintillator screens.

*Supported by Michigan State University.
Lingy@frib.msu.edu

Copyright © 2014 CC-BY-3.0 and by the respective authors

ISBN 978-3-95450-141-0

1600) [10] mounted outside of the target chamber was used to record the light emitted from the scintillator screens in time increments of 4 seconds during ion irradiation. The width of the beam spots was about 5 mm and the beam current was not higher than 400 pA in order to prevent sample heating. The light yield for each measurement presented in this report was obtained by integrating the light output in a region of interest which was chosen to be the central brightest region of the irradiated beam spot. To allow the comparison of scintillation yield under varying scintillator materials and beam energies, the light yield was normalized by the beam current and camera exposure time.

RESULTS AND DISCUSSION

The initial beam spot observed from KBr, YAG:Ce, CaF_2:Eu and CsI:Tl under the same irradiation energy is compared in Fig. 2. Among the investigated materials, CsI:Tl produced the highest light yield and KBr produced the lowest. Due to the different light sensitivity for the materials under ion bombardment, the beam current was adjusted for each scintillator material to avoid blurring of the beam spot images due to photon scattering inside the crystal.

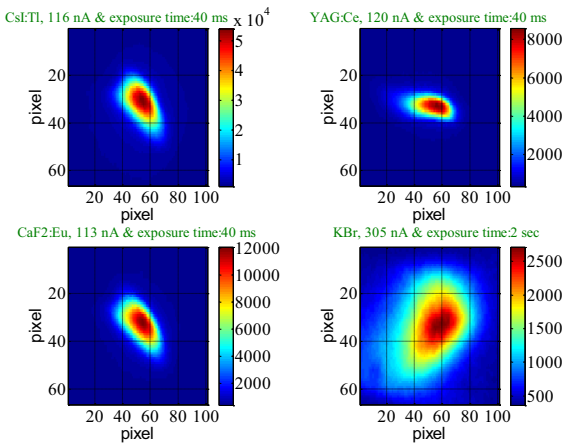


Figure 2: The initial beam spot image on CsI:Tl, CaF_2:Eu, YAG:Ce and KBr under H_2^+ irradiation at the beam energy of 2150 keV/u.

In Fig. 3, the scintillation response for CsI:Tl and YAG:Ce materials is shown as a function of irradiation time. In the investigated beam energy range of 600-2150 keV/u with less than 400 pA of beam current, a constant light output is observed from these two screens during 1-hour irradiation. The stable light yield suggests that the transparency loss of the scintillation photons inside the irradiated scintillators is negligible in the energy range and low radiation fluence of this study.

On the other hand, M. García-Muñoz et al. [11] have reported scintillation degradation of YAG:Ce during the irradiation of the deuterium ions and α-particles with the energies of 0.47-3MeV and the beam current of 30-60 nA. In addition, our previous study [5] showed that the YAG:Ce scintillator will rapidly degrade under He^+ irradiation at the beam energies of 28-58 keV and beam current of 100-500 pA. Thus it is important to note that the scintillation deterioration caused by radiation damages can be significant under low-energy or high-fluence irradiation.

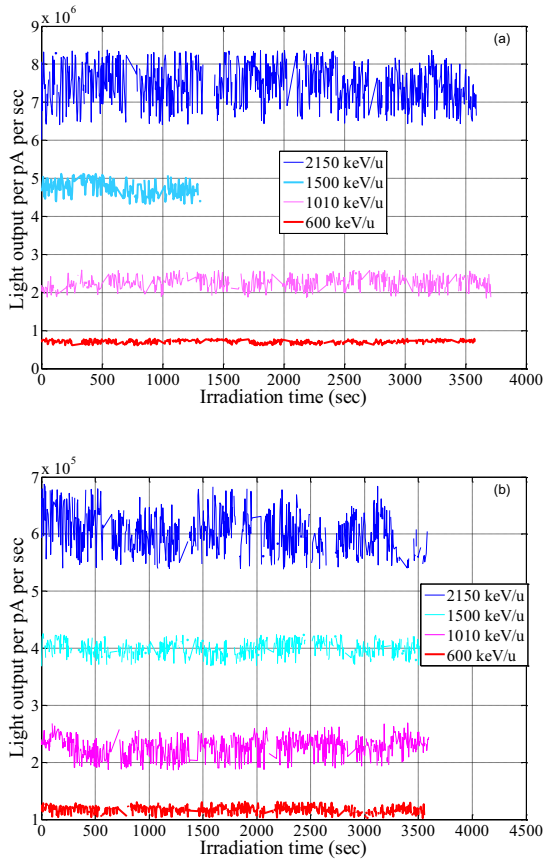


Figure 3: Light yield of (a) CsI:Tl and (b) YAG:Ce as a function of irradiation time at H_2^+ beam energies of 600-2150 keV/u.

Figure 4 shows the luminescence intensity of CaF_2:Eu as a function of irradiation time at the H_2^+ beam energies of 600-2150 keV/u. The light yield of CaF_2:Eu significantly drops in the beginning of irradiation and then approaches constant luminescence as irradiation continues. Figure 4 also shows that the initial degradation of CaF_2:Eu luminescence caused by irradiation cannot be recovered through a 10-minute radiation break. One of the suspected causes for a rapid initial decay in CaF_2:Eu luminescence may be due to a change of the charge state of the luminescence centers by energy transfer in CaF_2:Eu [12].

Copyright © 2014 CC-BY-3.0 and by the respective authors

ISBN 978-3-95450-141-0

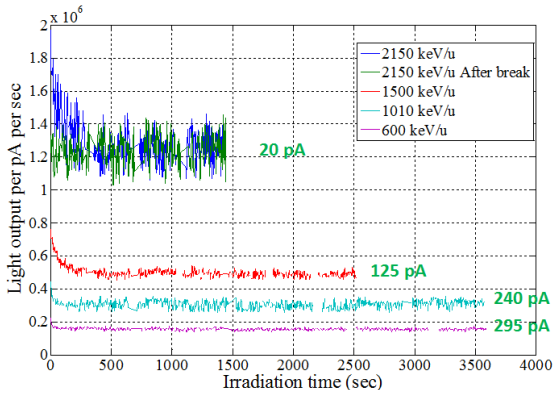


Figure 4: Light yield of CaF_2:Eu as a function of irradiation time at H_2^+ beam energies of 600-2150 keV/u. For 2150 keV/u, after 24-min irradiation (blue curve), a 10-min break was applied and followed by 24 minutes of the second-time irradiation (green curve).

The scintillation yield of KBr irradiated with H_2^+ ions at the beam energies of 600-2150 keV/u is plotted as a function of irradiation in Fig. 5. Among the investigated scintillators, the KBr is the only scintillator material that shows a relatively fast increase in the light yield in the beginning of H_2^+ irradiation, followed by a gradually decay. Since there is a region where luminescence intensity of KBr increases as a function of irradiation time, it indicates that the centers responsible for KBr luminescence are created by ion bombardment. Indeed, when the KBr sample was examined after irradiation, it was found that the irradiated areas on the KBr sample turned blue, as shown in Fig. 6, which adds evidence that color centers were created in the crystal during irradiation. It is known that F-centers in KBr can produce a band of optical absorption around 600 nm [13]; thus the blue color appeared on the irradiated spots demonstrates the F-center formation. The combination of F-centers with V-centers would be responsible for KBr luminescence [14].

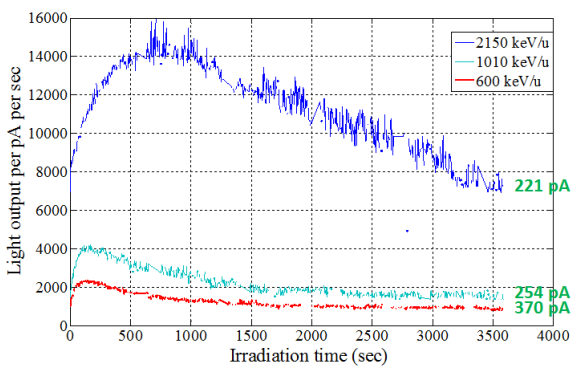


Figure 5: Light yield of KBr as a function of irradiation time at H_2^+ beam energies of 600-2150 keV/u.

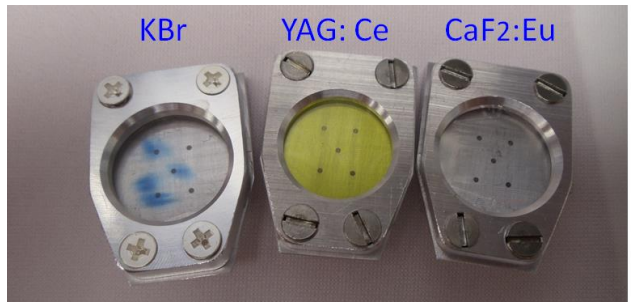


Figure 6: The KBr, YAG:Ce and CaF_2:Eu samples after ion irradiation. The KBr crystal shows damaged spots in blue colour.

CONCLUSION

KBr, YAG:Ce, CaF_2:Eu and CsI:Tl scintillator materials were investigated under H_2^+ irradiation for the beam energies from 600 to 2150 keV/u. CsI:Tl is the most sensitive material among all the investigated scintillators. The luminescence of YAG:Ce and CsI:Tl exhibits a stable behaviour under the beam energy and total particle fluence used for this measurements. For CaF_2:Eu scintillator, scintillation degradation at the beginning of irradiation was observed but then a constant luminescence during consequent irradiation was measured. Due to the radiation with bombarding ions, the KBr material shows noticeably radiation damages on the sample and an unstable behaviour in the light yield. The results of this study are essential for choosing a suitable scintillator screen to achieve precise beam width and emittance measurements at the rare isotope ReAccelerator facility. Further analysis and discussion will be presented in a future publication.

REFERENCES

[1] M. Ripert et al., "A low energy ion beam pepper pot emittance device", Proceedings of BIW10, Jefferson Lab, Santa Fe, USA, (2010).

[2] B. Walasek-Höhne et al., "Scintillating screen applications in beam diagnostics", WEOB01, Proceedings of DIPAC2011, Hamburg, Germany, (2011).

[3] E. Gütlich et al., "Scintillation screen investigations for high-current ion beams", IEEE Trans. Nucl. Sci. 57 (2010) 3.

[4] M. Strohmeier et al., "Development of a pepper-pot device to determine the emittance of an ion beam generated by electron cyclotron resonance ion sources", Rev. Sci. Instrum. 81, 02B710 (2010).

[5] L. Y. Lin et al., "Scintillation degradation of YAG: Ce under low-energy ion bombardment", JINST 6 P07010 (2013).

Copyright © 2014 CC-BY-3.0 and by the respective authors

ISBN 978-3-95450-141-0

[6] http://scintillator.lbl.gov/
[7] http://www.crystals.saint-gobain.com/
[8] http://mkt-intl.com/
[9] http://www.internationalcrystal.net/0002.htm
[10] http://www.pco.de/fileadmin/user_upload/db/products/datasheet/pco1600_20080805.pdf
[11] M. García-Muñoz et al., "Characterization of scintillator screens for suprathermal ion detection in fusion devices", JINST 6 P04002 (2011).
[12] S. J. Dhoble et al., "Effect of Bi ion on $Eu^{2+} \leftrightarrow Eu^{3+}$ conversion in CaF_2:Eu phosphors for RPL dosimetry", J. Mater. Sci. 46 (2011)7253.
[13] Y. Mitsushima et al., "Determination of the V4-center structure in KBr crystal by means of double alignment", Journal de Physique Colloques 37 (1976)C7.
[14] A. I. Bazhin et al., "Luminescence induced by ion impact on alkali-halide crystals at high temperatures (-160 to 200¤C)", Phys. Rev. B 14 (1976) 6.

Copyright © 2014 CC-BY-3.0 and by the respective authors

ISBN 978-3-95450-141-0

PULSED GREEN LASER WIRE SYSTEM FOR EFFECTIVE INVERSE COMPTON SCATTERING*

Arpit Rawankar#, School of High Energy Accelerator Science, Graduate University for Advanced Studies, Shonan International Village, Hayama, Miura, Kanagawa 240-0193, Japan
Tomoya Akagi, Alexander Aryshev, Yosuke Honda, Nobuhiro Terunuma, Junji Urakawa, High Energy Accelerator Research Organization [KEK], 1-1 Oho, Tsukuba, Ibaraki 305-0801, Japan
Didier Jehanno, Laboratoire de l'Accélérateur Linéaire [LAL], Orsay, France
Kazuyuki Sakaue ,Waseda University, 3-4-1 Okubo, Shinjuku, Tokyo, 169-8555, Japan

Abstract

Laser-Compton scattering has become an important technique for beam diagnostics of the latest accelerators. In order to develop technologies for low emittance beam, an Accelerator Test facility (ATF) was built at KEK. It consists of an electron linac, a damping ring in which beam emittance is reduced and an extraction line. For emittance measurement we developed a new type of beam profile monitor which works on the principle of Compton scattering between electron and laser light. In order to achieve effective collision of photon and electron, very thin size laser is required. Laser wire is one of such a technique to measure a small beam size. With green laser which is converted to second harmonics from IR pulsed laser, minimum beam waist is half of beam waist obtained using IR laser oscillator. Therefore, it is possible to obtain beam waist less than 5 μm (σ value) using green laser pulse, which is required for effective photon-electron collision. First pulsed IR seed laser is amplified with 1.5 meter long PCF based amplifier system. This high power pulsed IR laser is converted to second harmonics with a non-linear crystal. Pulsed green laser is injected inside four mirror resonator to obtain very small beam waist at IP (Interaction Point). Using a pulsed compact laser wire, we can measure 5 μm electron beam in vertical direction. From observed Compton signal profile, bunch length of electron beam is measured as 23.3$\pm$0.7 ps. Electron beam size in vertical plane is measured as 12.6$\pm$1.8 μm and vertical emittance is measured as 24.1 $\pm$ 6.8 pm-rad. Longitudinal bunch length and vertical beam size of electron beam was measured with pulsed laser wire system. We report the development of high power pulsed green generation and compact four mirror resonator parameters for effective Inverse-Compton scattering in this paper.

KEK-ATF DAMPING RING

Figure 1 shows the ATF-DR layout. The electron source is an RF gun with CsTe cathode driven by a mode-locked UV laser. The electron beam is accelerated to 1.28 GeV.

by the linear accelerator with RF cavity of 2856 MHz. After accelerated to 1.28 GeV, the electron beam is injected to the Damping Ring (DR). RF frequency of the DR is 714 MHz and the revolution frequency is 2.16 MHz.

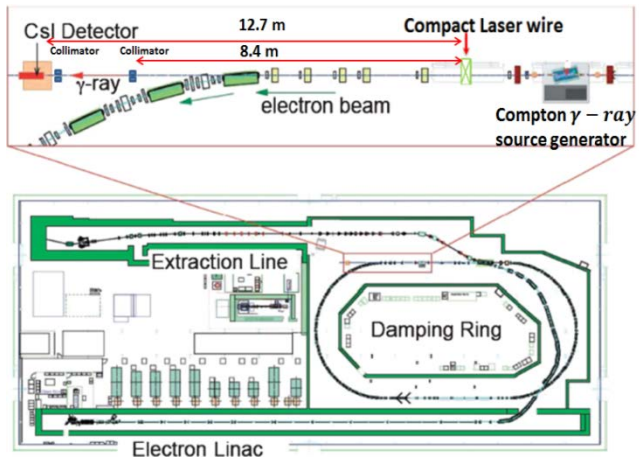


Figure 1: ATF DR layout.

COMPACT FOUR MIRROR CAVITY

The optical cavity assembly consists of four mirrors, mirror holder system and cyilindrical spacers which define length of cavity. In order to have precision control over cavity length, both plane mirror holders were supported by a piezo actuator through a disk type plate spring. Hollow piezo actuators are used for laser beam to pass through them. Four mirror optical cavity is designed for 532 nm wavelength. Distance between concave-concave mirror is kept at 102.8 mm and distance between plane-plane mirror is kept at 103.2 mm. A complex mirror alignment scheme as shown in fig. 2 and fig. 3 is used to keep side by side distance between plane and concave mirror to 29.2 mm [1]. All mirrors are fixed with angle tilt of 8°. The cavity angle of system which indicates laser pulse crossing angle is 16°. All mirrors used in cavity design are of 1 inch diameter. The radius of curvature for two concave mirror is 101.81 mm.

*Work supported by Quantum beam technology project of Japanese Ministry of Education, Culture, Sports, Science and Technology (MEXT)

arpit@post.kek.jp

ISBN 978-3-95450-141-0

Copyright © 2014 CC-BY-3.0 and by the respective authors

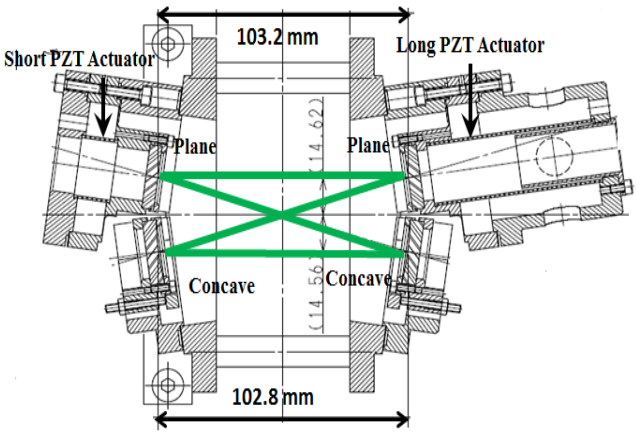


Figure 2: Cavity assemply and its mounting.

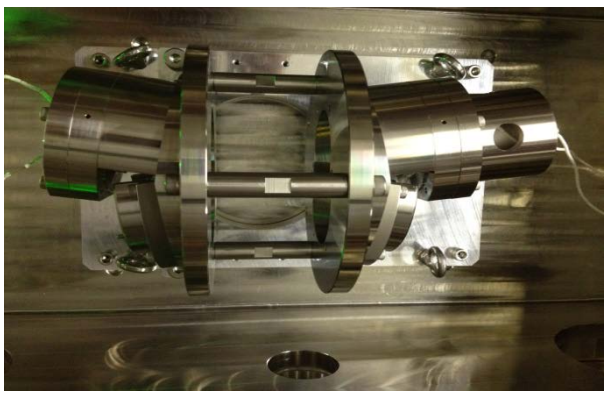


Figure 3: Four mirror cavity.

PCF BASED AMPLIFIER SYSTEM

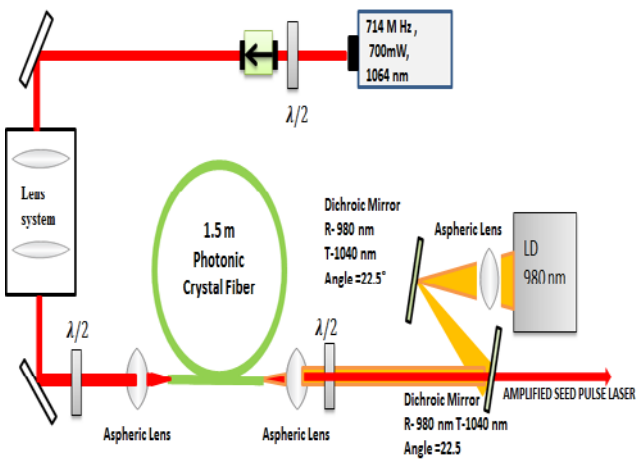


Figure 4: PCF Amplifier system setup.

For construction of system, we utilize 714 MHz mode locked laser as seed laser. The beam is focused to one end of PCF with the help of aspheric lens. At another end of PCF, pump light from laser diode is injected. Laser diode emits beam with wavelength 976 nm and has maximum power of 40 W. Special type of dichroic mirrors are used in this setup which have high reflectivity for 976 nm wavelength and high transmittance for 1064 nm beam [2]. The amplified seed laser and pump light are separated at dichroic mirror as shown in fig. 4. We used 1.5 meter long PCF for this experiment. Seed laser of 450 mW is amplified to 7 W in this setup. Thus total gain factor of 15.5 is achieved in this experiment. Figure 5 shows the amplification of seed laser with pump excitation power inside PCF.

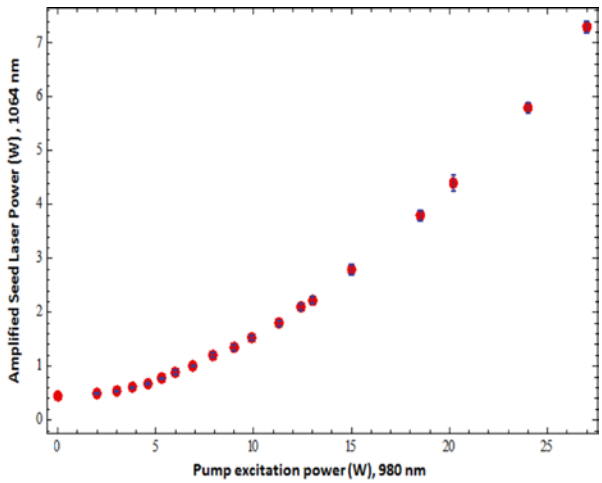


Figure 5: Amplification inside PCF.

PULSE GREEN GENERATION BY SHG

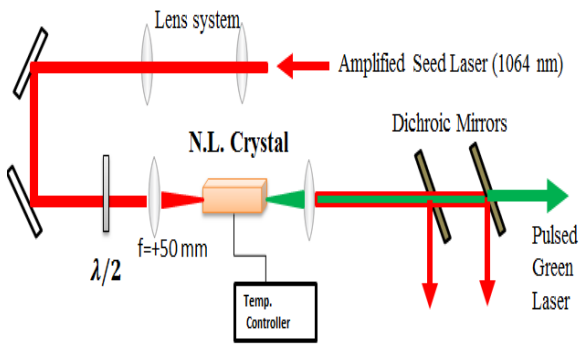


Figure 6: System setup for SHG.

High power pulsed IR laser is converted to second harmonics by 2nd order non-linear crystal. Figure 6 describes the system setup for second harmonics generation (SHG). Amplified seed laser obtained from PCF amplifier system has wavelength of 1064 nm. The first requirement for laser wire project was to obtain high power pulse green laser. Pulsed green laser was needed to achieve very small beam size and fast scanning of electron beam profile. The amplified beam from PCF pass through a half wave polarization plate to control the polarization direction required for SHG. The non-linear crystal has very small thickness so injection beam is sharply focused by using strong focusing lens. Crystal's

ISBN 978-3-95450-141-0

Copyright © 2014 CC-BY-3.0 and by the respective authors

temperature is set by a temperature controller which is connected with peltier device. It is very important to separate first harmonics from second harmonics of converted beam. The second harmonics generation setup is shown in fig. 6. Second harmonics generation efficiency depends on polarization control and operating temperature of crystal. 5 W of amplified seed laser is converted to 1.6 W of pulsed green laser as shown in fig. 7. Thus conversion efficiency of more than 32 % was obtained with non-linear crystal.

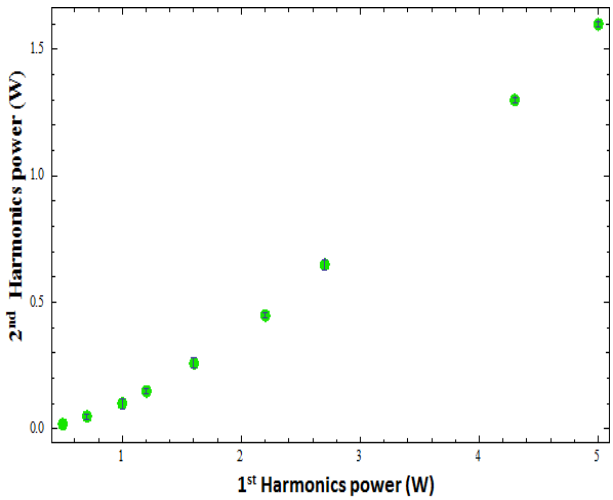


Figure 7: Second harmonics generation.

Generated pulsed green laser is input laser to compact four mirror cavity. Cavity length is scanned by piezo actuator and the resonance of optical cavity is obtained inside four mirror cavity.

POUND-DREVER-HALL FEEDBACK SCHEME

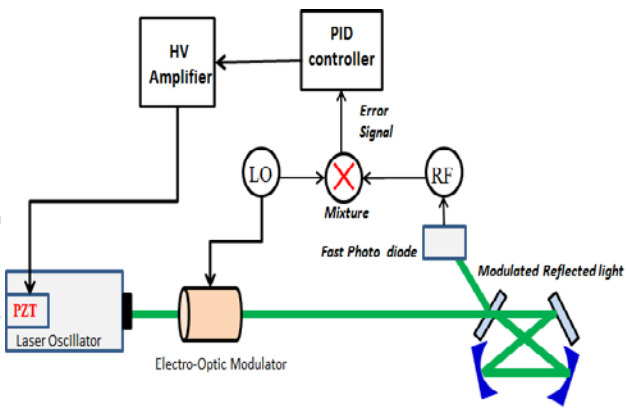


Figure 8: PDH feedback scheme.

Pound–Drever–Hall (PDH) laser frequency stabilization is a powerful technique for improving an existing laser's frequency stability [3, 46]. This arrangement is for locking a cavity to a laser. A phase modulated beam is sent to the cavity and fast photo diode detects the reflected light signal. This output after processing is applied to piezo actuator that controls the length of laser oscillator. The mixer compares the modulation signal of 15 MHz with the output of the fast photodiode, extracting the part that is at the same frequency as the modulation signal. This feedback signal is called error signal. Sending this error signal to the piezo actuator completes the feedback loop and locks the system on resonance as shown in fig. 8. Figure 9 shows error signal generated inside four mirror cavity. Error signal is given to PID controller. Proportional and integral gain of PID controller was tuned so that holding of resonance can be confirmed. PID controller output is given to Notch filter for removing electrical noise by rejecting higher bands of frequencies.

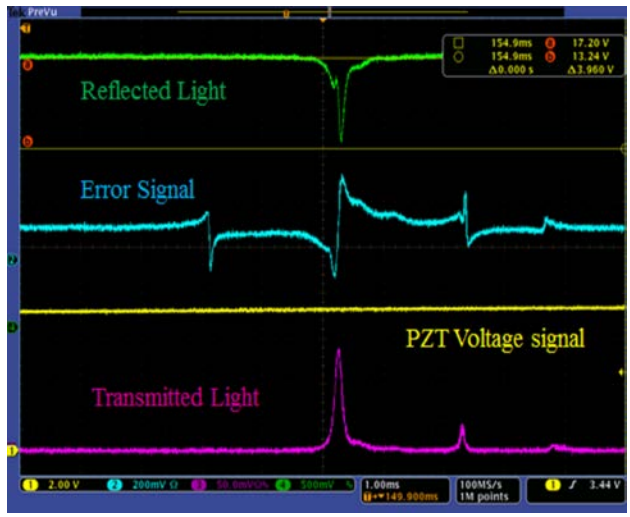


Figure 9: Error signal generation.

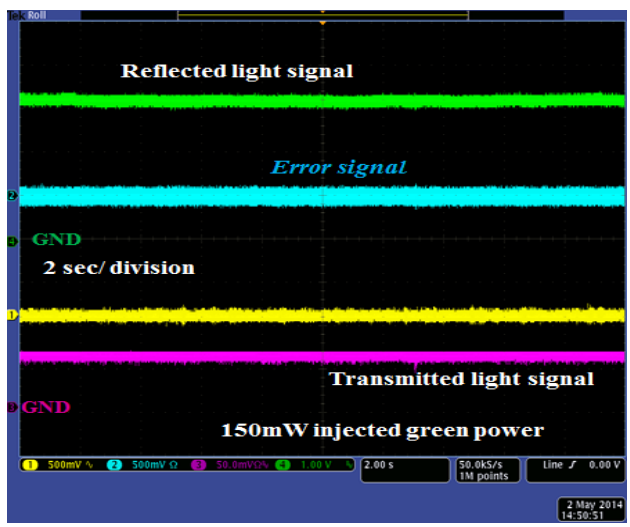


Figure 10: Holding of resonance inside four mirror cavity.

This output is amplified with high voltage amplifier and given to 714 MHz oscillator PZT. Transmitted light

Copyright © 2014 CC-BY-3.0 and by the respective authors

ISBN 978-3-95450-141-0

from four mirror cavity becomes stable and reflected light intensity reduces when cavity is locked. Figure 10 shows holding of resonance inside four mirror cavity with pulsed green laser. Stability of this system was confirmed for more than one hour during electron beam operation. The experiment with electron bunch is performed with 140 mW pulsed green power to the optical cavity.

The following table 1 shows measured values of four mirror optical resonator. The reflectivity of coupling plane mirror is 99.9 %, while the reflectivity of other plane mirror and two concave mirrors are 99.99%. The beam waist at IP is measured with transverse mode difference method [4]. The enhancement factor of 960 is measured at interaction point. The pulsed green power has large fluctuation at higher laser diode current. For stability of feedback, experiment with electron bunch is performed at low pulsed green power.

Table 1: Parameters of Four Mirror Optical Cavity

Parameter	Measured Value
Finesse	2315 ± 220
Min. beam waist (σ_s, σ_t)	$7\pm2\ \mu m,\ 13.4\pm3\ \mu m$
Enhancement factor	960
Storage power	17.5 W

ELECTRON BEAM SIZE & VERTICAL EMITTANCE ANALYSIS

The PDH feedback system was turned on to detect Compton signal. The ATF clock of 357 MHz was used during this experiment. Therefore, laser frequency signal of 714 MHz is converted to 357 MHz frequency signal with frequency divider and fed to phase detector. Because of this frequency division, two peaks are observed according to two cycles of laser pulse. Figure 11 show observed counting rate in the detector while changing the relative phase between electron beam and laser pulse with laser turned on. The enhancement of the counting rate was clearly measured at a particular phase which indicated photons from laser-Compton scattering [5]. The maximum Compton signal was observed at horizontal position of -0.0350 mm and vertical position of -1.164 mm. The vertical axis of 2-D scattered plot shows deposition of energy at detector which is read by ADC in terms of counts. The counts read by ADC is converted into energy deposited in MeV at detector. The horizontal axis shows phase in radians between electron bunch and laser pulse during collision experiment. We first obtain histogram plots of all verical scan position.

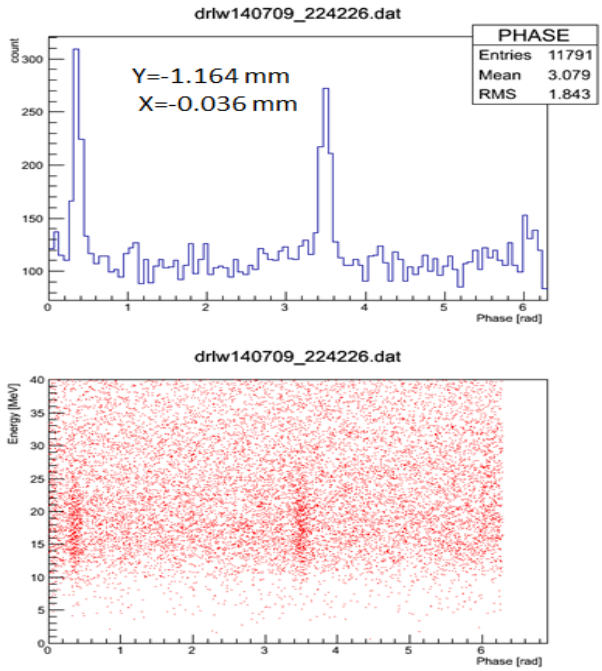


Figure 11: Compton signal observation.

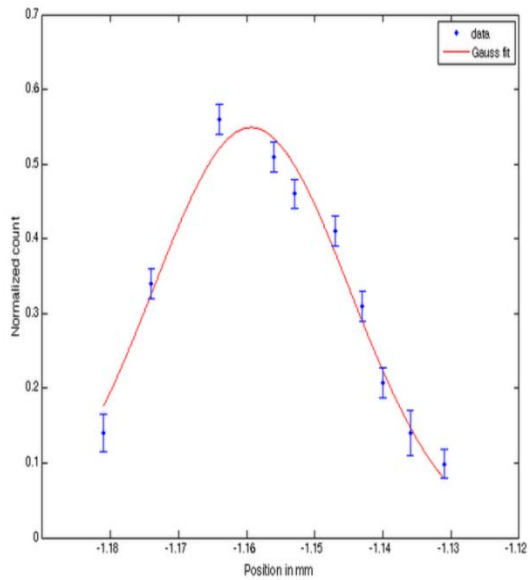


Figure 12: Normalized count with vertical scam position.

We calculate normalized count for all scan position as ratio of average peak count to average background level. The maximum S/N ratio is observed at -1.164 mm vertical scan position which is 0.56 ± 0.02. Similarly, we can calculate normalized count of other vertical scan positions with small error Figure 12 shows vertical scan result. All data of scan results are fitted to Gaussian function. The sigma value of observed Gaussian function is calculated as $14.4\pm1.3\ \mu m$, which is convolution of laser beam size and electron beam size. In particular, if

Copyright © 2014 CC-BY-3.0 and by the respective authors

ISBN 978-3-95450-141-0

both electron and laser beam are assumed to have Gaussian profiles with width σ_e and σ_{lw}, the observed profile is also Gaussian with width σ_{obs} expressed by

$$\sigma_{\mathrm{obs}}^2 = \sigma_{\mathrm{lw}}^2 + \sigma_{\mathrm{e}}^2 \qquad (1)$$

The laser wire beam waist is measured as $7\pm2\ \mu m$ using transverse mode difference method. The electron beam size can be determined as

$$\sigma_e = 12.6\pm 1.8\ \mu m.$$

We can estimate vertical emittance of beam with collected data. The beam size is basically given by equation

$$\sigma_y = \sqrt{\beta_y \epsilon_y} \qquad (2)$$

, where β_y is vertical β function at interaction point. Vertical β function at interaction point is 6.58 m. The vertical emittance value is calculated as 24.1 $\pm$6.8 pm-rad.

BUNCH LENGTH MEASUREMENT

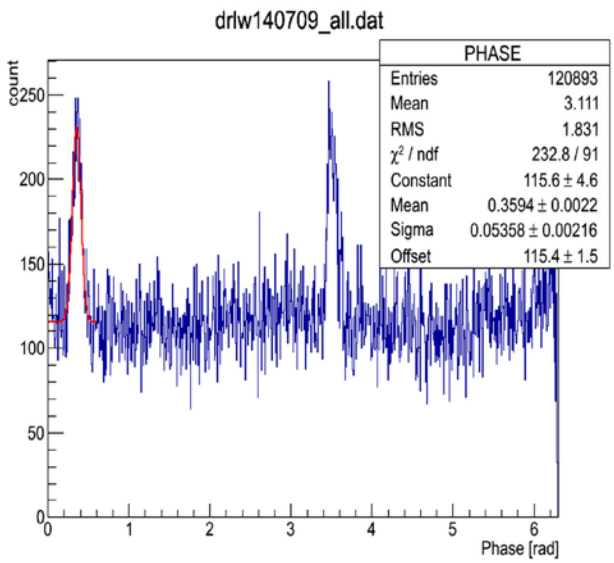


Figure 13: Gaussian fit on sum of all histogram data.

In order to measure bunch length of electron beam, we consider sum of all histogram data which are corresponding to particular vertical scan positions. The purpose is to estimate accuracy of phase measurement during our experiment. We can evaluate width of distribution for two peaks by Gaussian fitting as shown in fig. 13. We can calculate bunch length of electron beam by relative phase difference information. The laser pulse timing corresponds to mean value of the Gaussian distribution to the time of the maximum counting rate. Average value of bunch length was the convolution of the longitudinal length of the laser pulse ($\sigma = 3\ ps$) and electron bunch. Therefore, bunch length of electron beam can be calculated as

$$\sigma_z\ (ps) = \sqrt{23.5^2 - 3^2} = 23.3\ \pm 0.7\ \mathrm{ps}.$$

CONCLUSION

The longitudinal bunch length and vertical size of electron beam can be measured with relative phase difference measurement between electron bunch and laser pulse without frequency locking of laser pulse and electron RF frequency. This compact laser wire system can be used to store pulsed green power with small waist size.

REFERENCES

[1] A. Rawankar et al. “Design studies on compact four mirror laser resonator with mode-locked pulsed laser for 5 mm laser wire”, NIM -A, 2013, 700: 145-152.
[2] Y. Honda, PCF Amplifier, KEK internal report 2011/08/30.
[3] E. D. Black. An introduction to Pound-Drever-Hall laser frequency stabilization, Am. J. Phys, 1001, 69,79.
[4] Y. You, J. Urakawa, A. Rawankar, et al. “Measurement of beam waist for an optical cavity based on Guoy phase, NIM- A, 2012, 694: 6-10.”
[5] T. Okugi et al. “Evaluation of extremely small horizontal emittance”; Phys. Rev. Special Topics-Accelerator and Beams 2, 022801 (1999).

Copyright © 2014 CC-BY-3.0 and by the respective authors

ISBN 978-3-95450-141-0

TRANSVERSE PROFILE MONITORS FOR SwissFEL

Rasmus Ischebeck, Eduard Prat, Volker Schlott, Vincent Thominet, PSI, Villigen, Switzerland
Minjie Yan, DESY, Hamburg, Germany
Patrick Krejcik, Henrik Loos, SLAC, Menlo Park, CA, USA

Abstract

We have developed a beam profile monitor that allows us to measure two-dimensional electron beam profiles for highly compressed electron bunches. Such bunches have plagued profile measurements in optical transition radiation monitors in the past, because coherent radiation entering the optical system has invalidated the images and even destroyed cameras. The present design makes use of a scintillating crystal, and directs coherent transition radiation away from the optical axis by careful choice of the angle. When observing Snell's law of refraction as well as the Scheimpflug imaging condition, a resolution better than the thickness of the scintillator can be achieved. We will present here measurements performed at the SwissFEL Injector Test Facility and at the Linac Coherent Light Source. The high resolution and excellent sensitivity of this monitor make it ideal for installation in SwissFEL.

REQUIREMENTS ON TRANSVERSE PROFILE MONITORS FOR FREE ELECTRON LASERS

The slice emittance of the electron beam is among the most important parameters when designing a free electron laser, because it has a direct influence on the gain length. Second-generation X-ray FELs such as SACLA [1] or SwissFEL [2] achieve a much more compact footprint by basing their design on a lower energy than what has been implemented in first-generation FELs. This scheme requires a shorter undulator period, possible with in-vacuum undulators, as well as a smaller normalized emittance. The generation of these beams, as well as the diagnostics for the emittance are thus of primary interest. Slice emittance measurements are based on a transverse deflecting radiofrequency cavity, a quadrupole magnet lattice to control the phase advance, and a two-dimensional transverse profile monitor. Measurements of projected emittance can be performed without the deflector, and using a one-dimensional profile measurement, but sources of projected emittance growth may not need to affect the slice emittance, which is central to the FEL process in the undulators.

Developments in photocathode as well as thermionic electron guns have resulted in the generation of smaller and smaller emittances, which result in progressively smaller beam sizes, putting ever tighter requirements on the transverse profile monitors. In addition to increased requirements on resolution, an effect has occurred in recent years, which has hampered transverse profile measurements using optical transition radiation: highly compressed electron bunches have a pronounced longitudinal structure at sub-micrometer length scales, resulting in the coherent emission of optical transition radiation [3–7]. This coherent OTR (COTR) is several orders of magnitude brighter than the incoherent light that is proportional to the particle density.

SwissFEL will use wire scanners [8], as well as two-dimensional profile monitors that image scintillators inserted into the beam. Profile measurements with wire scanners are not affected by coherent emission effects, because the scattering process is based on individual collisions of the electrons with particles in the wire. Similarly, the scintillation process in materials such as cesium doped yttrium aluminum garnet (Ce:YAG) originates from individual excitations of the scintillator by the primary electrons. One has to be careful, however, as coherent transition radiation generated on the scintillator surface, or in-vacuum mirrors, might affect the measurement. This can happen in one of two ways: either it enters the imaging system directly, or it generates radiation with a sufficient photon energy to excite the scintillator.

The first effect can be avoided by delaying the acquisition in the detector until the prompt transition radiation has disappeared. This requires an effective shutter that opens on a nanosecond scale to catch the tail of the scintillation light. Such shutters are implemented by using microchannel plates, a method that increases the complexity of the camera significantly, leads to more frequent service intervals, and most importantly, leads to a loss in image quality through smearing of the image, as well as a non-uniform response. Another method consists of choosing the observation geometry such that the COTR is directed away from the camera. Care has to be taken in this case to not artificially degrade the resolution by imaging radiation from a scintillator with finite thickness. Another issue to take into account is a possible saturation of the scintillator for high-density beams.

RESOLUTION OF PROFILE MEASUREMENTS

The SwissFEL design aims for a normalized slice emittance of 180 to 430 nm. This results in beam sizes down to about 30 µm FWHM at the location of the profile monitors. The resolution of the imaging system was verified according to the ISO 12233 standard. The limiting resolution was found to be better than 8 µm (Figure 1).

The resolution of the optical system is however not the only factor determining the resolution for beam profile measurements. One has to take into account also the broadening inside the scintillator [9], as well as the imaging of a scintillating crystal of finite thickness [10]. The SwissFEL profile monitor takes into account the Snell-Descartes law of refraction [11], as illustrated in Figure 2. The observation angle

ISBN 978-3-95450-141-0

Copyright © 2014 CC-BY-3.0 and by the respective authors

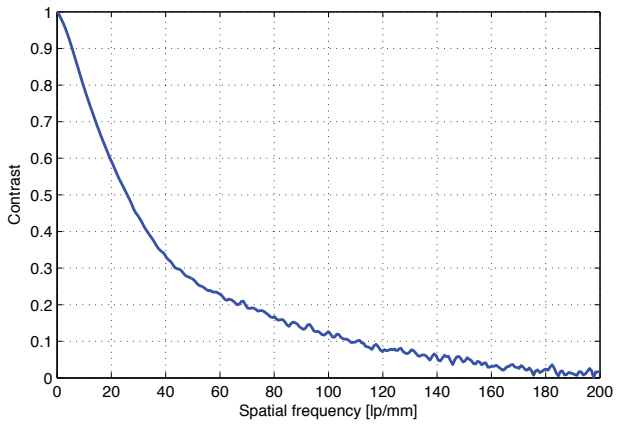


Figure 1: Measurement of the resolution of the imaging system used in the SwissFEL profile monitors.

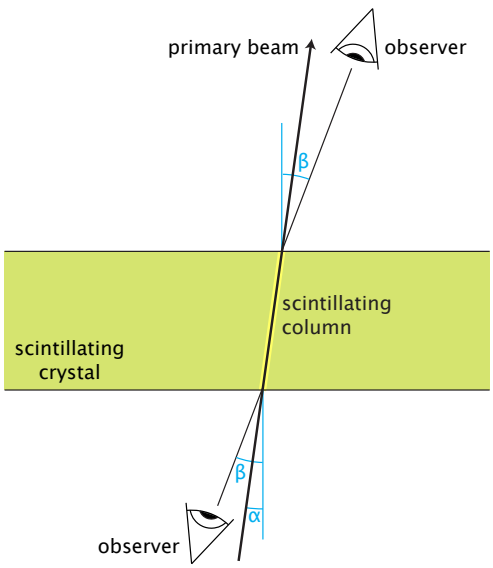


Figure 2: Imaging of the light-emitting column inside the scintillating crystal.

β is chosen such as:

$$\beta = -\arcsin(n \sin \alpha)$$

This minimizes the effect of the scintillator thickness on the image resolution.

By tilting the lens and/or the image detector (Figure 3), observing the Scheimpflug criterion [12], the entire scintillator can be imaged simultaneously. Considerations of lens aberrations and detector efficiency favor a small observation angle. The observation axis, on the same side to the normal of the crystal as the primary beam, is then relatively close to the beam, which may be difficult to set up if the primary beam is in vacuum and the detector in air. This difficulty has been overcome by using a flat in-vacuum mirror, shown in Figure 3 b.

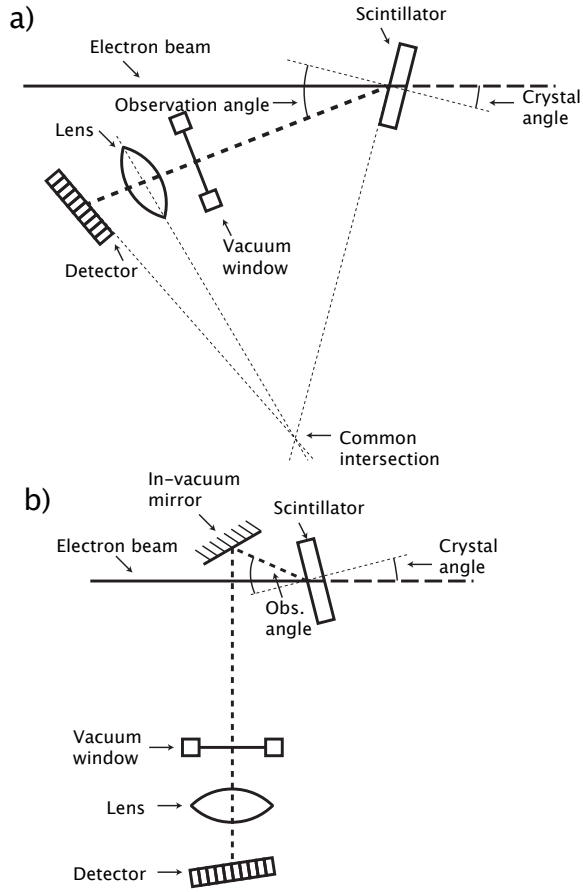


Figure 3: Imaging of scintillation radiation, observing the Snell-Descartes law of refraction as well as the Scheimpflug imaging condition.

DESIGN OF TRANSVERSE PROFILE MONITORS FOR SWISSFEL

We have completed the design of transverse profile monitors for SwissFEL. These monitors use a cerium doped yttrium aluminum garnet (Ce:YAG) scintillator, which is polishedon both sides. To avoid charge-up, the YAG is coated with indium tin oxide (ITO). The scintillator has a diameter of 20 mm, and two different observation geometries are implemented, to balance resolution with field-of-view.

For those monitors requiring high resolution, the scintillating crystal is positioned at an angle of 8.1° to the primary beam, and the in-vacuum mirror is placed such that the normal of the crystal has an angle of 15° to the optical axis of the camera. The screens are imaged by an $f = 200$ mm macro lens[1] to a CCD[2] or CMOS detector[3]. The magnification of the imaging system is 1 : 1.22, resulting in an effective pixel size on the scintillator of 7.9 µm. To fulfill the Scheimpflug imaging condition, the normal of the CMOS

[1] Nikon, Tokyo, Japan
[2] Basler AG, Ahrensburg, Germany
[3] PCO AG, Kelheim, Germany

Copyright © 2014 CC-BY-3.0 and by the respective authors

ISBN 978-3-95450-141-0

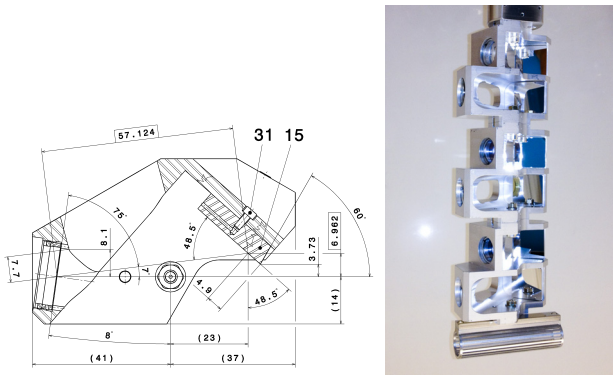


Figure 4: Screen holder for scintillating crystals. Left: technical drawing, including the scintillator to the left and the in-vacuum mirror to the top right. Right: photograph of the in-vacuum assembly of the first prototype, including two scintillators, two OTR screens and two alignment and calibration targets. At the bottom, an RF shield continues the beam pipe when the screen is not in use.

detector is tilted by 14° to the optical axis. At this angle, the microlens array on the chip can be used with only minor loss in efficiency. The field of view is horizontally constrained by the in-vacuum mirror[4] to ±3 mm.

A larger field of view is implemented by choosing an angle between the beam axis and the normal of the scintillator of 14.6°, and a corresponding observation angle of 30°. In this geometry, the in-vacuum mirror can be mounted at a distance of 8 mm to the beam axis, allowing to cover a field of view of 16 mm diameter.

The two monitors differ only in the screen holder, and in the placement of the lens and camera. A third model has been designed for use in the laser heater of SwissFEL, where light of a wavelength of 1040 nm is imaged with a hyperspectral lens[5] onto an IR-optimized CMOS detector[6].

The screens are mounted to an aluminum holder, shown in Figure 4. They can be positioned into the beam by means of a UHV translation stage. For the first prototype, installed in the SwissFEL Injector Test Facility, different scintillators (Ce:YAG[7], boron doped diamond[8], CRY019[9], and Cromox[10]) were compared to optical transition radiation generated on a 5 µm thick silicon wafer[11]. Out of these scintillators, the best resolution was achieved with Ce:YAG. The measured beam sizes were found to be comparable to the OTR measurements.

Two prototype monitors were built. One was installed in the SwissFEL Injector Test Facility, and one in the LCLS linac-to-undulator line [13]. Tests of the resolution were performed in the SwissFEL Injector Test Facility [14], and saturation of the scintillators as well as the effectiveness of COTR suppression was studied at the Linac Coherent Light Source (LCLS).

[4] LT Ultra, Herdwangen-Schönach, Germany
[5] Jenoptik Optical Systems, LLC, Jupiter, FL, USA
[6] Basler AG, Ahrensburg, Germany
[7] Crytur Ltd., Turnov, Czech Republic
[8] Diamond Materials GmbH, Freiburg, Germany
[9] Crytur Ltd., Turnov, Czech Republic
[10] BCE Special Ceramics, Mannheim, Germany
[11] University Wafers, South Boston, MA, USA

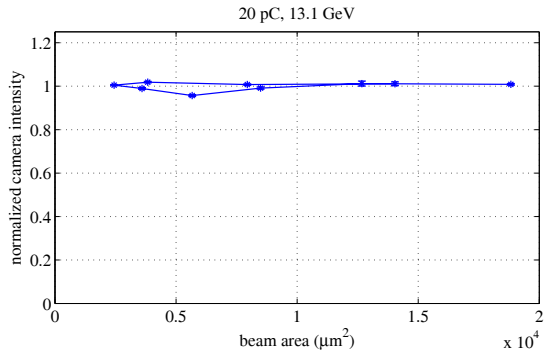


Figure 5: Total light emitted as a function of beam size.

SATURATION STUDIES

A possible disadvantage of scintillators as compared to optical transition radiation monitors is the saturation of the scintillator at high beam energies and densities. A measurement was performed by varying the transverse size of the electron beam while keeping the bunch charge constant. The measurement was performed with settings used for emittance measurements by a quadrupole scan. Scintillation light was collected by a camera, and integrated over a field of view large enough to cover the beam spot. The beam energy was 13.1 GeV, and a charge of 20 pC was used Saturation would show as a decrease of the total emitted light. As shown in Figure 5, the variation is less than 10% for the studied beam densities.

SUPPRESSION OF COHERENT OTR

The LCLS linac-to-undulator line is known for intense coherent OTR. Light intensities four orders of magnitude larger than the incoherently emitted light have been observed at this location, and focusing this light onto a CCD has resulted in a damaged sensor.

Since the scintillator is oriented at an angle of 8.1°, transition radiation from the front surface is emitted in a cone around an angle of 16.2°. The scintillation light is observed via the in-vacuum mirror, which is located on the other side of this emission cone.

The geometric suppression of coherent OTR has been tested by measuring the total emitted light as a function of compression. The charge for the present measurement was 20 pC, the beam energy 13.1 GeV. The compression was varied by changing the chirp of the acceleration, while keeping the beam energy constant. The resulting curve (blue line in Figure 6) shows no significant variation during this measurement.

The situation was somewhat different when the laser heater was switched off (red line in Figure 6). Here, an increase of 20% of the total emitted light was observed. It should be noted that this is not relevant to the nominal oper-

Copyright © 2014 CC-BY-3.0 and by the respective authors

ISBN 978-3-95450-141-0

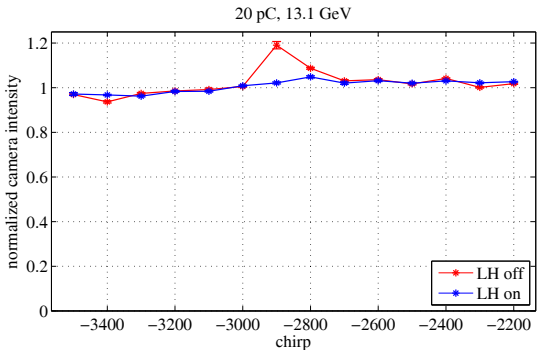


Figure 6: Total light emitted as a function of compression. Blue curve: nominal operation (laser heater on), red curve: laser heater off.

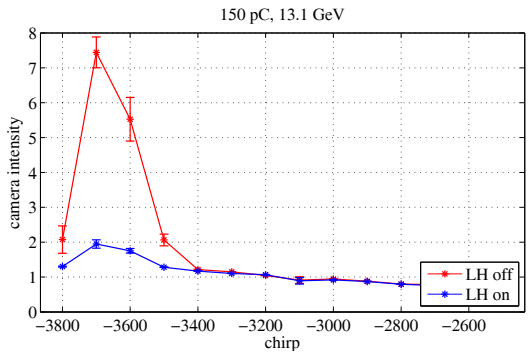


Figure 7: Total light emitted as a function of compression. Blue curve: nominal operation (laser heater on), red curve: laser heater off.

ation mode of LCLS, but it will be interesting nevertheless to explore what causes this increase. One theory is the emission of coherent radiation in the ultraviolet, which would cause the crystal to fluoresce. A comparison of different scintillating materials would allow further insight into this question.

For a bunch charge of 150 pC, the increase in light yield for full compression is more significant. Figure 7 shows a measurement with laser heater on (blue curve) and laser heater off (red curve). The light yield increases by almost an order of magnitude in the latter case.

CONCLUSION AND OUTLOOK

We have designed a transverse profile monitor for SwissFEL, which images light from a fluorescent crystal onto a CCD / CMOS detector. The resolution, saturation and COTR suppression of this monitor have been tested at the SwissFEL Injector Test Facility and at the LCLS linac-to-undulator line. Based on the results, we are confident that we can use this monitor to measure slice emittance at SwissFEL. Nonetheless, we will install wire scanners along the SwissFEL linac, as additional monitors to measure the projected emittance.

REFERENCES

[1] T Ishikawa, M Yabashi et al. A compact X-ray free-electron laser emitting in the sub-ångström region. *Nature Photonics*, 6(8):540–544, June 2012.

[2] SwissFELConceptual Design Report. Technical report, Paul Scherrer Institut, April 2012.

[3] R Akre et al. Commissioning the Linac Coherent Light Source injector. *Phys. Rev. ST Accel. Beams*, 11(030703), 2008.

[4] H Loos et al. Observation of Coherent Optical Transition Radiation in the LCLS Linac. *Proceedings of FEL08*, 13395, 2008.

[5] A H Lumpkin et al. Evidence for transverse dependencies in COTR and microbunching in a SASE FEL. *Nuclear Instruments and Methods in Physics Research Section A: Accelerators, Spectrometers, Detectors and Associated Equipment*, 507(1-2):200–204, July 2003.

[6] A Lumpkin, N Sereno, W J Berg, M Borland, Y Li, and S Pasky. Characterization and mitigation of coherent-optical-transition-radiation signals from a compressed electron beam. *Phys. Rev. ST Accel. Beams*, 12(8):080702, August 2009.

[7] D Ratner, Z Huang, and G Stupakov. Analysis of shot noise suppression for electron beams. *Phys. Rev. ST Accel. Beams*, 14(6):060710, June 2011.

[8] GL Orlandi et al. Design and Test of Wire-Scanners for SwissFEL. In *Proceedings of FEL2014, Basel, Switzerland*, 2014.

[9] G Kube et al. Inorganic Scintillators for Particle Beam Profile Diagnostics of Highly Brilliant and Highly Energetic Electron Beams. In *Proceedings of IPAC2012, New Orleans, Lousiana, USA*, 2012.

[10] R Ischebeck and V Thominet. Transverse Profile Imager for Ionizing Radiation. EP 2 700 979 A1, February 2014.

[11] Ibn Sahl. *On Burning Mirros and Lenses*. Unnamed publisher, 984.

[12] T Scheimpflug. Improved Method and Apparatus for the Systematic Alteration or Distortion of Plane Pictures and Images by Means of Lenses and Mirrors for Photography and for other purposes. *GB Pat. 1196*, 1904.

[13] P Emma et al. First lasing and operation of an ångstrom-wavelength free-electron laser. *Nature Photonics*, 4(9):641–647, 2010.

[14] R Ischebeck and E Prat. Transverse Profile Imager for Ionizing Radiation. Submitted for publication. 2014

Copyright © 2014 CC-BY-3.0 and by the respective authors

ISBN 978-3-95450-141-0

RADIATION SOURCES AND THEIR APPLICATION FOR BEAM PROFILE DIAGNOSTICS

G. Kube
DESY, Hamburg, Germany

Abstract

Radiation generated by high-energy particle beams is widely used for beam diagnostic purposes. Depending on the mechanism of radiation generation, the emitted wavelength range extends from the THz up to the X-ray region, thus allowing to measure beam profiles in the longitudinal and the transverse plane over a wide range. In this talk, basic considerations for radiation based profile measurements will be discussed with special emphasis on the mechanism of radiation generation and the impact on beam diagnostic measurements.

INTRODUCTION

Beam monitors probing the particle electromagnetic field are widely used in accelerator physics. The majority of them is sensitive to the particle near field, i.e. the field which is directly bound to the charged particle, and a usable signal is derived from the interaction of this field with the environment. Examples of this kind of monitors are beam position and beam current monitors. In an other type of monitors, information about the beam properties is generated from the fields which are separated from the charged particle itself. These freely propagating fields can be measured at large distances from the particle as radiation in a wide spectral range, even outside of the accelerator tunnel. Depending on the separation mechanism of the electromagnetic field, the process of radiation generation is named in a different way. Examples considered in the following are synchrotron radiation, transition radiation, diffraction radiation, parametric X–ray radiation, and Smith–Purcell radiation. A comprehensive overview of the radiation generation by ultra–relativistic particles can be found for example in the textbooks [1]– [4], actual topics in radiation physics are discussed at the RREPS conference series [5] or at the conference series *Charged and Neutral Particles Channeling Phenomena*.

All radiation mechanisms mentioned before are either widely applied or investigated in view of an applicability in the field of particle beam diagnostics in different ways. A vast number of information can be extracted from the radiation field, as for example beam energy, energy width and beam divergence, but in the following only beam profile measurements will be considered. In this context, the transverse beam profile diagnostics based on imaging with visible radiation is widespread, the focus will be on their description and the applied concepts (see also Ref. [6]). Besides beam imaging techniques, a measurement of the angular distribution can also be gathered to gain information about the transverse beam profile. Finally, coherent radiation diagnostics is a technique to determine both shape and length of a charged particle bunch by spectral investigation of the coherently emitted radiation.

Starting from imaging with classical light and a discussion about resolution, the radiation generation from ultra–relativistic particles is described in terms of the separation of the pseudo- or virtual photon field associated with the charged particle (Weizsäcker–Williams approximation [7,8]). In this picture, the various radiation processes appear as different ways to separate the virtual photons from the particle, and the formalism of classical imaging can simply be applied to the separated field. Examples are given for particle beam imaging, and the concept of beam size determination from the angular distribution is presented for different radiation sources. Finally, bunch length diagnostics based on coherent Smith–Purcell radiation is presented as an example.

IMAGE FORMATION AND RESOLUTION

In the case of particle diagnostics, the object from which the size has to be determined, i.e. the particle bunch, is not directly accessible because it is moving in a vacuum beam pipe in the accelerator tunnel. In this situation, radiation based diagnostics in general and imaging in particular helps to generate a replica of the object in a more comfortable environment, and the replica size (image) is adjusted to size of measuring device (CCD) with the help of an optical system (lenses). In the subsequent discussion about imaging, only aberration–free optical systems will be considered. Nevertheless, from classical optics it is known that even for imaging with a perfect lens, the image of a point source will never result in a point image because the uncertainty relation imposes a fundamental limit $\Delta x = \lambda/(2\sin\theta)$ with Δx the uncertainty in the location of the emission point, λ the wavelength of observation, and $\sin\theta$ the acceptance angle (numerical aperture) of the imaging lens. To be more precise, the point source image is the result of plane wave diffraction at a circular aperture (lens), and the intensity distribution in the image plane is described by the well known Airy disk (see eg. [9] or textbooks about classical optics). The resolution is usually expressed as the first minimum of the Airy disk

$$\Delta x = 0.61\frac{M\lambda}{\sin\theta} \qquad (1)$$

with the magnification factor M of the optical setup.

A deeper discussion of the resolution requires some basic knowledge of the image formation process. For this purpose a simple optical setup is considered as shown in Fig. 1. The common procedure is to calculate the intensity distribution of a point source in the image plane which is proportional to

ISBN 978-3-95450-141-0

Copyright © 2014 CC-BY-3.0 and by the respective authors

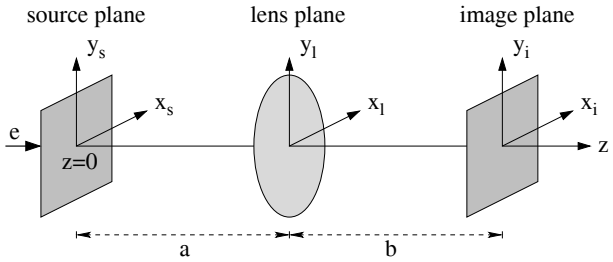


Figure 1: Scheme of the optical setup. Source and image planes are located at distances a, b from the perfect lens, the magnification of the system is $M = b/a$.

the absolute square of the electric fields in this plane. This point source image is referred to as Point Spread Function (PSF), and the PSF is characterizing the optical system properties. In analogy to the PSF definition in classical optics, the image generated in a radiation process from a single particle will be called PSF throughout the rest of this paper, being aware that in this case the PSF is not only determined by the optical system properties, but also by the particle properties (beam energy) which influence the radiation characteristics, e.g. the opening angle. The image of an extended object is obtained by a two–dimensional convolution of the source distribution with the PSF, and the resolution is the difference between source and image distribution for a magnification of $M = 1$.

In order to calculate the PSF, the electric field from the source plane has to be propagated through the optical system to the image plane, taking into account the interaction of each optical element. In the simple setup shown in Fig. 1, the source field distribution has to be propagated from the source plane to the lens entrance plane, from there to the lens exit plane, and then to the image plane. The propagation is performed in frame of scalar diffraction theory in Fresnel approximation, i.e. up to the quadratic phase term. With the target located at $z = 0$ the propagation from the source plane S_{src} to the lens input in a distance a is described by

$$E^{l_i}_{x_l,y_l}(\vec{r_l},\omega) = -i\,\frac{e^{ika}}{\lambda a}\, e^{i\frac{k}{2a}(x_l^2+y_l^2)} \ldots \quad (2)$$
$$\times \int_{S_{src}} \mathrm{d}^2 S_{src}\; E^{s}_{x_s,y_s}(\vec{r_s},\omega)\; e^{i\frac{k}{2a}(x_s^2+y_s^2)}\; e^{-ik\frac{x_s x_l + y_s y_l}{a}}$$

see for example Ref. [10]. The integration has to be carried out over the source plane Σ_s, and special care has to be taken to the integration limits. They may either be defined by the target dimensions or by the radiation field and will be annotated later in more detail. In the far field or Fraunhofer approximation $\frac{k}{2}(x_s^2 + y_s^2)_{max} \ll a$, the corresponding exponential in the integration can be omitted, and in this limit the field in the lens plane is proportional to the two–dimensional Fourier transformation of the source field distribution, c.f. Eq. (2). In the next step the resulting field Eq. (2) is propagated through the lens. In thin lens approximation the effect of the lens is described by introducing an additional quadratic phase shift [10], and the fields at the lens output are given by

$$E^{l_o}_{x_l,y_l}(\vec{r_l},\omega) = E^{l_i}_{x_l,y_l}(\vec{r_l},\omega)\; e^{-i\frac{k}{2f}(x_l^2+y_l^2)} \quad (3)$$

with f the focal length of the lens and $\frac{1}{f} = \frac{1}{a} + \frac{1}{b}$ the condition for imaging. In the next step, the field has to be propagated from the lens output to the image plane similar to Eq. (2), and finally the intensity distribution in the image plane

$$\frac{\mathrm{d}^2 W}{\mathrm{d}\omega \mathrm{d}\Omega} = \frac{c}{4\pi^2}\,(|E^i_{x_i}|^2 + |E^i_{y_i}|^2)\,. \quad (4)$$

has to be calculated. If the source field distribution is from a point source or from radiation of a single charged particle, this intensity distribution is representing the PSF.

Based on the concept of Fourier optics and the image generation

$$\text{Image} = \text{PSF} \otimes \text{Object} + \text{Noise}\,, \quad (5)$$

the process of imaging can be described in the frame of system theory, see also Fig. 2. In standard system theory the signals are one–dimensional, treated in the time/frequency domain, and system analysis is performed with a delta pulse. In the case of imaging one is dealing with two–dimensional signals (space coordinates), treated in the space/spatial frequency domain (line pairs per mm), and system analysis is performed with a point source.

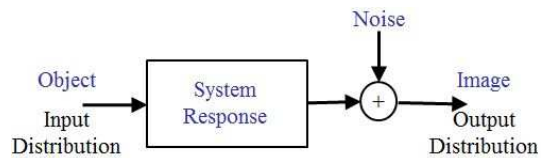


Figure 2: System approach to imaging. The system response is described by the PSF which acts on the input distribution to produce the output.

RADIATION GENERATION

To apply standard optical imaging techniques, the information about the particle beam charge distribution has to be converted in an optical intensity distribution which can be recorded by camera. In the selection of this conversion process, care has to be taken that (i) any resolution broadening introduced by the basic underlying physical process has to be small (i.e. the PSF of the physical process corresponding to the single particle resolution function should not dominate the total spatial resolution), and that (ii) the conversion process should be linear to avoid any deformation of the intensity distribution. There exist two principle possibilities for this conversion process, either to exploit the interaction of the beam particles with matter (used e.g. for scintillation screens or residual gas luminescent monitors), or the particle electromagnetic field has to be separated from the beam to be detected in the far field as radiation.

Copyright © 2014 CC-BY-3.0 and by the respective authors

ISBN 978-3-95450-141-0

While scintillators are widely used in particle beam diagnostics at hadron and electron accelerators [11], in the following only radiation based beam profile monitors will be considered. Therefore the process of radiation generation is shortly explained in this section in the frame of virtual photons: Considering an ultra–relativistic particle with an electric field which is relativistic contracted (i.e. mainly transversal), the degree of contraction is described by the field opening angle $1/\gamma$ with $\gamma = E/m_0c^2$ the Lorentz factor. Hadrons have a comparatively large rest mass and γ is much smaller than the one for electrons. Therefore radiation based monitors are the exception rather than the rule at hadron accelerators, and in the following only ultra–relativistic electron or positron beams are considered.

In the limiting case $\gamma \to \infty$ the field would be completely transversal and correspond to a plane wave (classical description of a photon). This situation occurs either by considering a particle with zero rest mass (i.e. a photon), or in the limiting case if the beam energy is increased into the ultra–relativistic regime. Due to the similarity between a real photon and the field of an ultra–relativistic particle, the action of this particle is described by so called virtual or pseudo photons. However, to measure radiation in the far field the virtual photon field bound to the beam particle has to be separated from the particle. In case of a circular accelerator this is achieved by a force acting on the charged particle which is caused by the magnetic field of accelerator (bending) magnets, and the resulting radiation is called *synchrotron radiation*. In case of a linear accelerator there is (per definition) no particle bending, but the separation can be achieved by acting on the virtual photons itself via structures that diffract the particle electromagnetic field away from the particle. The analogy between real and virtual photons can be exploited for better understanding: Real photons can be refracted resp. reflected at a surface, and the same holds for virtual photons. In this case the radiation is named *Forward/Backward Transition Radiation*. In classical optics the effect of edge diffraction is known, in the case of virtual photons the radiation effect is called *Diffraction Radiation*. Real photons can be diffracted at a grating, the same hold for virtual photons and the effect is called *Smith–Purcell Radiation*. Finally, high–energetic real photons (X–rays) are diffracted at a 3D structure of a crystal, and if a charged particle beam traverses such crystal *Parametric–X Radiation* is emitted.

SYNCHROTRON RADIATION

Synchrotron radiation (SR) is a versatile tool for beam profile measurements due to its non–destructive nature. While in principle SR from insertion devices or bending magnets can be utilized, in reality most accelerators use bending magnet radiation based profile monitoring because of space limitations. Due to the relativistic energy of the particles, the generated light has superior properties [12]: The process of radiation generation is non–invasive and the radiation spectrum is continuous from infrared up to X-rays. As consequence the photon energy can be freely chosen according to the monitoring problem. Typically the spectrum is characterized by the critical energy $\hbar\omega_c = \frac{3}{2}\hbar c\frac{\gamma^3}{\rho}$ with γ the Lorentz factor and ρ the dipole bending radius. The natural divergence of the radiation which depends on the polarization state is very small with a vertical opening angle of about $1/\gamma$ in case of horizontal ($\sigma-$) polarization.

In order to apply the formalism of image formation to the case of SR based diagnostics, the source field has to be determined. According to the geometry depicted in Fig. 3, the field of a moving charge is described by the Liénard–Wiechert potentials. The common way found in most textbooks about electrodynamics is to deduce the fields in the time domain

$$\vec{E}(t) = -e\left(\frac{(1-\beta^2)(\hat{n}-\vec{\beta})}{R^2(1-\hat{n}\cdot\vec{\beta})^3} + \frac{\hat{n}\times[(\hat{n}-\vec{\beta})\times\dot{\vec{\beta}}]}{cR(1-\hat{n}\cdot\vec{\beta})^3}\right)_\tau$$
$$\vec{H}(t) = (\vec{n}\times\vec{E})_\tau \ . \qquad (6)$$

which have to be evaluated at the retarded time $\tau = t - R(\tau)/c$. In the far field approximation, the first term in the sum which does not depend on the acceleration (the so called velocity term) is usually omitted because it scales quadratically with the distance to the observer. To get rid of the retarded time, the fields are transformed in the Fourier domain, and if the special case of a particle motion on a circular orbit is considered, the standard formulas for the SR fields are derived [12]. SR imaging investigations based on this field description are presented in Ref. [13].

However, the radiation fields derived in this way are only approximative because of the far field approximation. Furthermore, in this approach the emission is considered to originate from a single point, additional resolution broadening effects as depth–of–field and orbit curvature have to be introduced additionally [14, 15].

In the approach of Ref. [16] these contributions are included from the beginning. Starting point are again the Liénard–Wiechert potentials, but this time the potentials are Fourier transformed and the fields are derived in the

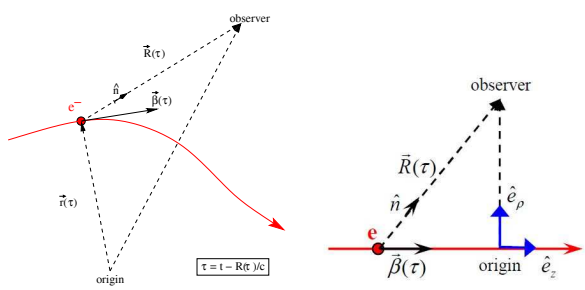


Figure 3: Geometry for the description of the Liénard–Wiechert fields for a particle in arbitrary (left) and linear (right) motion.

ISBN 978-3-95450-141-0

Copyright © 2014 CC-BY-3.0 and by the respective authors

frequency domain, resulting in an integral equation

$$\vec{E}(\omega) = -\frac{i\omega e}{c}\int_{-\infty}^{+\infty} \mathrm{d}\tau \left[\frac{\vec{\beta}-\hat{n}}{R(\tau)} - \frac{ic}{\omega}\frac{\hat{n}}{R^2(\tau)}\right] e^{i\omega(\tau+\frac{R(\tau)}{c})} . \tag{7}$$

The integration can be performed numerically with high accuracy using e.g. numerical near field calculations [16] in order to study resolution broadening effects. Codes like SRW [17] or SPECTRA [18] are freely available allowing computations preserving all phase terms that are necessary for further propagation of the radiation through optical components. In SRW, even propagation is implemented in the frame of scalar diffraction theory applying the methods of Fourier optics. Besides the numerical near field calculation, there exist also analytical approaches in which the disturbed wave front is characterized by an additional phase factor such that orbit curvature and depth–of–field influence can directly be included in the radiation field description [19–21].

A review of SR based diagnostics for transverse profile measurements is given in Ref. [22], therefore only some basic considerations for modern 3^{rd} generation light sources are discussed in the following. For these machines with natural emittances in the order of 1 - 5 nm.rad and an emittance coupling of 1 %, the task is to resolve few micrometer beam sizes. For PETRA-III at DESY (Hamburg, Germany) for example, the beam sizes which have to be measured amount $\sigma_x = 40\,\mu\mathrm{m}$ and $\sigma_y = 20\,\mu\mathrm{m}$. Recalling that the fundamental resolution limit depends on the acceptance angle ϑ, and that the limit in the acceptance is not dictated by the lens diameter but by the extremely small SR emission angle in vertical direction (with $\vartheta_{acc} = 1.7$ mrad for PETRA-III), observation in the visible spectral region ($\lambda = 500$ nm) would result in a vertical resolution of about 145 µm according to the uncertainty principle which is much larger than the beam size which has to be measured. Beam profile measurements based on visible SR are therefore fully diffraction limited at modern light sources.

The most straightforward way to overcome this limitation is imaging at smaller wavelength in the VUV, soft or even hard X–ray region. In this case the discussion about a monitor concept is reduced to the question about the appropriate imaging optics. In the case of imaging with focusing optics either reflective (Kirkpatrick–Baez mirror), diffractive (Fresnel zone plates) or refractive (compound refractive lens) optics can be used, and all these concepts are applied at different accelerator laboratories, see Ref. [22]. In the case of a non–focusing optics, the most prevalent device is the X–ray pinhole camera (see e.g. Ref. [23]). Besides the imaging schemes, other techniques are applied as the SR interferometer exploiting the spatial coherence of the radiation [24], the π–polarization imaging as a special case of PSF dominated imaging [25], and the coded aperture technique [26].

CONSTANT LINEAR MOTION

For the discussion about radiation based imaging techniques in linear accelerators, the electromagnetic field of a point particle in constant linear motion is considered as it is the case for an electron in a drift space. Again the particle field is given by the Liénard–Wiechert field in Eq. (6), however in this situation it is the second term in the sum (acceleration term) which vanishes because there is no acceleration per definition. Because of the rotational symmetry it is convenient to describe the geometry in the cylindrical coordinate system as shown in Fig. 3, right. In this system, the electric field can be expressed as [1]

$$\vec{E}(\rho,z,\omega) = \frac{e\alpha}{\pi v}\, e^{i\frac{\omega}{v}z}\left(\mathrm{K}_1(\alpha\rho)\,\hat{e}_\rho - \frac{i}{\gamma}\,\mathrm{K}_0(\alpha\rho)\,\hat{e}_z\right) \quad \text{with} \quad \alpha = \frac{2\pi}{\lambda\beta\gamma} \tag{8}$$

and K_0, K_1 the modified Bessel functions. While K_0 is already smaller than K_1, according to Eq. (8) in the ultra–relativistic limit $\gamma \to \infty$ the contribution from the longitudinal component can be completely neglected and the particle field exhibits the typical pancake structure. It is this field which is associated with the pseudo photons in order to describe the different radiation generation mechanisms.

With increasing distance ρ from the beam orbit, the field shrinks following the K_1 dependency. It is convenient to assign a value to the radial field extension ρ_{ext} by setting the argument of the Bessel function equal one, i.e.

$$\rho_{ext} = \frac{\lambda\beta\gamma}{2\pi} \approx \gamma\lambda . \tag{9}$$

In a descriptive way the virtual photon field is interpreted as a radial field disc with the radius ρ_{ext}. The angular distribution of the virtual photon field is given by

$$\frac{\mathrm{d}^2W}{\mathrm{d}\omega\mathrm{d}\Omega} = \frac{e^2}{\pi^2 c}\frac{\theta^2}{(\gamma^{-2}+\theta^2)^2} . \tag{10}$$

These photons associated to the charged particle beam possess therefore a characteristic double lobe structure with a central minimum, and it is this structure which is imprinted to the real photons (radiation) when the field is separated from the beam.

The pseudo photon approach presented here in a descriptive way implies a simplification in the sense that only the transverse field components are considered. In Refs. [27,28] the contribution of the longitudinal component was taken additionally into account, allowing an extension of the theory to low particle beam energies and arbitrary inclination angles. This was done either by developing a vector electromagnetic theory for transition and diffraction radiation, or by applying Kirchhoff's method to a flat target. As it was shown, significant differences are to expect if the beam energy is low and/or the target inclination angle is large (i.e. in the case of near grazing incidence). However, these are not the cases under investigation here, and therefore the application

Copyright © 2014 CC-BY-3.0 and by the respective authors

ISBN 978-3-95450-141-0

of the simplified pseudo photon method is justified for the subsequent discussion.

In the following sections, different methods to separate the field Eq. (8) from the particle in the ultra–relativistic limit are introduced, and the application of these radiation sources is discussed in view of beam diagnostics.

OPTICAL TRANSITION RADIATION

If a charged particle passes the boundary between two media with different dielectric constants, a broad band electromagnetic radiation is produced which is named transition radiation. For beam diagnostic purposes the visible part of the radiation (Optical Transition Radiation, OTR) is used and an observation geometry in backward direction is mainly chosen such that the screen has an inclination angle of 45° with respect to the beam axis, and observation is performed under 90°. In a typical monitor setup the beam is imaged via OTR using standard lens optics, and the recorded intensity profile is a measure of the particle beam spot. OTR has the advantage that it allows a fast single shot beam profile measurements, and the radiation output scales linearly with the bunch intensity (neglecting coherent effects).

In the case of OTR, the separation mechanism corresponds to the direct reflection of pseudo photons at the screen surface which acts as a mirror and which is assumed to be a perfect conductor for simplicity (otherwise the Fresnel coefficients have to be taken into account). In this reflection process, the virtual photons absorb momentum from the screen and are released from the charged particle, transformed into real photons (radiation) which can be measured at large distances as OTR. The reflection does not modify the field properties, therefore the incoming virtual and outgoing real photons are described by Eq. (8) and consequently have the same angular distribution Eq. (10).

An interesting point which goes beyond the scope of this paper is that the surrounding field of the stripped electron, moving with constant velocity inside the screen material, will be reconstructed. This reconstruction does not happen immediately and results in interesting effects, affecting e.g. the ionization loss as discussed in Ref. [29]

For a discussion about OTR based beam imaging in view of the PSF calculation, the formalism derived in the section about image formation has to be applied to the OTR field Eq. (8) in the ultra–relativistic limit, i.e neglecting the longitudinal component. Before doing so, two aspects have to be considered: (i) In the propagation integral Eq. (2), the integration has to be performed over the source plane. Particular care has to be payed concerning the integration limits, the geometrical screen dimensions and the radial field extension according to Eq. (9) have to be balanced between each other. This is especially important for high beam energies and wavelengths in the THz region where the radiation properties may be dominated by the screen boundaries. (ii) Assuming that the field contributing to the imaging process is originating from an area in the source plane which is given by the finite extension of the pseudo photon disc. With this area, an upper limit for the contribution of the quadratic phase factor in Eq. (2) can be given, i.e. for which cases this factor has to be taken into account or not. For this purpose, the spatial coordinates in that phase term which indicates the near field (Fresnel) diffraction are replaced by the source extension from Eq. (9), i.e.the phase is rewritten in the form

$$\exp\left(i\frac{k}{2a}[x_s^2+y_s^2]\right)=\exp\left(i\frac{k}{2a}\rho_{ext}^2\right)=\exp\left(i\pi\frac{\gamma^2\lambda}{a}\right)\ .$$

The quadratic phase term has to be taken into account if $a \leq \gamma^2\lambda$, which is nothing else than the range estimation for the pre–wave zone [30]. On the other hand the contribution can be omitted in the case $a \gg \gamma^2\lambda$, resulting in the wave zone condition. Therefore special care has to be taken at ultra–relativistic beam energies.

The OTR PSF is calculated based on the propagation of the pseudo photon field through the optical system Fig. 1. Details about this calculation can be found in Refs. [31]– [35] for different cases and examples. For observation in the wave zone and with the assumption for the angular acceptance of the optical system $\theta_m \gg \gamma^{-1}$, the PSF can be written as

$$\begin{aligned} I_{PSF} &\sim \zeta^{-2}\left[\zeta/\gamma\,\mathrm{K}_1(\zeta/\gamma)-\mathrm{J}_0(\zeta\theta_m)\right]^2 \\ &\sim \zeta^{-2}\left[1-\mathrm{J}_0(\zeta\theta_m)\right]^2 \end{aligned} \qquad (11)$$

with $\zeta = 2\pi R_i/(M\lambda)$, R_i being the space coordinate in the image plane, λ the wavelength of observation and M the magnification of the optical system. The second equations holds in the ultra–relativistic limit, and it is interesting to note that the OTR imaging properties are independent of the beam energy in this limit.

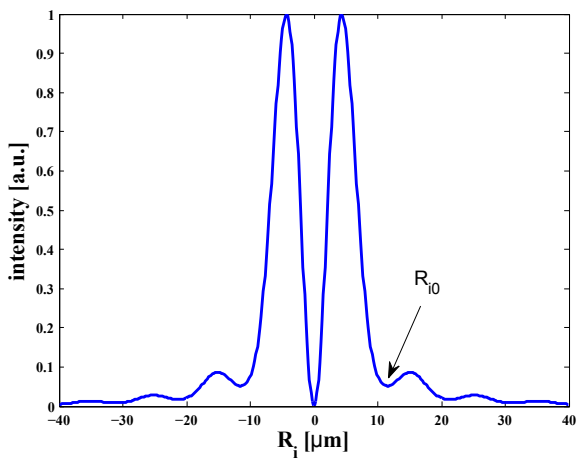


Figure 4: Calculated OTR PSF for a 855 MeV electron beam and observation with a 2" lens diameter at λ = 500 nm, assuming 1:1 imaging.

Figure 4 shows a calculated PSF according to Eq. (11). As can be seen, the PSF exhibits an interference structure similar to the Airy disc with a central minimum, indicating the origin from a pseudo photon field. Similar to the classical resolution definition for the Airy disc, it is possible to express

ISBN 978-3-95450-141-0

Copyright © 2014 CC-BY-3.0 and by the respective authors

the OTR resolution R_{i0} as the first non–central minimum of the PSF as shown in Fig. 4, resulting in

$$R_{i0} = 1.12\frac{M\lambda}{\theta_m} \ . \qquad (12)$$

In comparison to SR where the resolution in vertical direction is limited by the angular distribution, in the case of OTR the angle θ_m is defined by the optical system because the OTR angular distribution contains sufficient intensity at larger angles. It is interesting to compare the OTR resolution with the one of a classical point source from Eq. (1). As can be seen, the latter is about a factor of two better than the one of OTR. Therefore care has to be taken while speaking about the resolution of an OTR monitor, it is not only the optical system resolution.

Transverse beam profile imaging in electron linacs is widely based on OTR as standard technique [36]. While this type of monitor prevails in electron machines covering an energy range from 10 keV [37] up to 30 GeV [38], it was also applied in proton accelerators [39, 40] and for heavy ion beam diagnostics [41]. Recent advances in OTR based beam diagnostics are summarized in Ref. [42].

Unfortunately there are physical limitations that make the method ineffective for reliable diagnostics in modern accelerators. Microbunching instabilities in high–brightness electron beams of modern linac–driven free–electron lasers (FELs) can lead to coherence effects in the emission of OTR, thus rendering it impossible to obtain a direct image of the particle beam and compromising the use of OTR monitors as reliable diagnostics for transverse beam profiles. The observation of coherent OTR (COTR) has been reported in the meantime by several facilities [43, 44]. While the use of inorganic scintillators is an alternative scheme to overcome this limitation [45], beam profile imaging with transition radiation in the EUV region is an interesting concept because it results additionally in a better resolution due to the smaller wavelength. A first proof–of–principle experiment measuring at a wavelength of $\lambda = 19.6$ nm was reported in Ref. [46].

An interesting option to measure sub–micron beam sizes with OTR is the application of PSF dominated imaging.

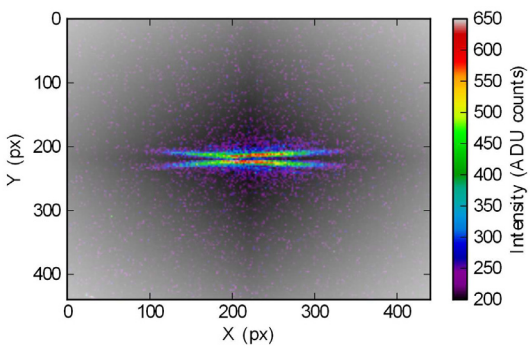


Figure 5: PSF dominated OTR beam image taken with a linear polarizer and a (550±20) nm optical filter. Image courtesy P. Karataev (RHUL), see also Ref. [47]

While in standard imaging one strives to minimize the PSF contribution such that the image is a true replica of the object, in PSF dominated imaging the object size is much smaller that the PSF, and the image is dominated by the PSF properties. In the case of OTR, a non–zero beam size results in a smearing out of the central PSF minimum, and the beam size is determined from the image contrast. The first proof–of–principle experiment was reported in Ref. [48], in the meantime the authors succeeded in measuring a minimum beam size of (0.754 ± 0.034) µm with this method [47], see also Fig. 5.

OPTICAL DIFFRACTION RADIATION

OTR beam size diagnostics has the disadvantage that it requires the interaction of the beam with the screen. However, due to the high power density of modern high brightness beams, the energy deposition in the screen may lead to a damage of the device. Therefore the development of non–intercepting methods is essential. In this context Optical Diffraction Radiation (ODR) is an interesting candidate. This kind of radiation is generated if a charged particle beam passes close to a diffracting structure like an edge or a slit, and the physics of DR is well known in the literature, see e.g. Refs. [1, 49] and the references therein. In the subsequent discussion and similar to OTR, only backward emitted ODR will be considered because it is more convenient for beam diagnostic applications.

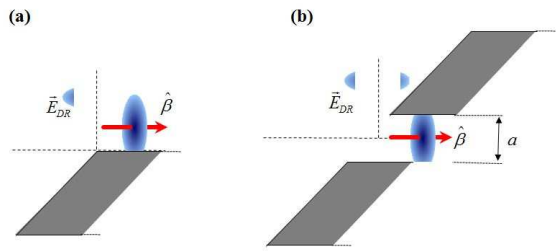


Figure 6: An ultra–relativistic electron with typical pancake field distribution passes close to (a) a metallic edge or (b) a slit in a metallic screen. Parts of the field are diffracted away and can be measured as radiation.

The mechanism of radiation generation is similar to the one of OTR and sketched in Fig. 6. But in the case of ODR it is not the complete pseudo photon field which is diffracted away, only a part of it is released from the electron. Therefore the ODR intensity will be lower than the one of OTR. Keeping in mind the radial field extension Eq. (9), it is obvious that the distance from the electron to the edge resp. the slit size a in Fig. 6 should be within the range of ρ_{ext} in order to efficiently generate ODR. Furthermore, in the limit $a \ll \rho_{ext}$ there is no difference between ODR and OTR.

In principle ODR can be generated at any kind of aperture. However, the use of rectangular slit shapes is advantageous because the mathematical description is simplified due to the translational invariance with respect to one coordinate, and the slit size itself can be considered as infinitely long

Copyright © 2014 CC-BY-3.0 and by the respective authors

ISBN 978-3-95450-141-0

with respect to ρ_{ext}. As consequence, the beam size in only one dimension can be deduced from an ODR measurement.

For the PSF calculation of ODR based imaging, the formalism introduced before and described in the case of OTR has to be applied, taking into account the finite integration limits imposed by the slit dimensions in the source plane. Theoretical investigations about ODR imaging from a slit and a single edge are described in Refs. [32, 50]. It is intuitively clear that if only a part of the pseudo photon field is released, as it is the case in ODR, it is not the full beam image which is generated because the PSF contains information only in the region where the screen acts as a mirror, cf. the discussion in Ref. [50]. Nevertheless it is possible to deduce information about the beam size in the direction parallel to the slit edge (in the following the horizontal or x direction) under the assumption that the beam has a Gaussian shape and that the distance between edge and beam axis is known. In Refs. [51, 52] relative horizontal beam sizes were measured by cross–calibrating the projected ODR image intensities with previously measured OTR ones.

In order to deduce beam size information, instead of using the ODR image the angular distribution from a slit can also be exploited. In this case, the coordinate corresponding to the direction of the displacement of the beam from the slit edge is of relevance (in the following the vertical or y coordinate). Information about the beam size can be extracted from a measurement of the visibility, i.e. the ratio between the maximum intensity and the intensity in the central minimum which is smeared out due to the non–zero beam size σ_y. However, the ODR angular distribution is not only influenced by the beam size, but also by the beam offset from the slit center and by the beam divergence. While the beam offset can be controlled by a complementary diagnostic device as for example a BPM, the divergence has to be determined independently. Different schemes are proposed as discussed e.g. in Refs. [53, 54]. In order to overcome this ambiguity, in the pioneering experiment [55] a beam with very low divergence was used such that only the additional position dependence had to be taken into account which could be controlled by independent beam position measurements. With this method the authors measured beam sizes down to about 10 µm [56].

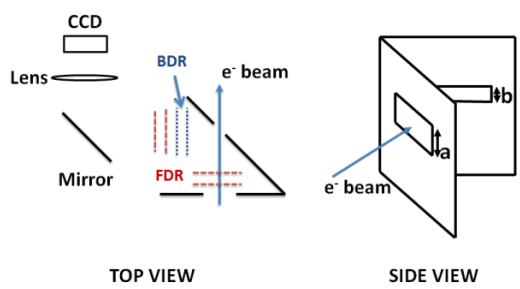


Figure 7: Setup of the ODRI experiment, explanation see text. Image courtesy A. Cianchi (INFN and Univ. Rome), see also Ref. [60].

Interferometric measurements are suitable methods to study beam divergences. ODR as well as ODTR interferometers are proposed and already in use, c.f. Refs. [57, 58]. However, this report is restricted to the application of beam profile measurements, but there is one interferometric technique to measure also beam sizes σ_y. In the Optical Diffraction Radiation Interference (ODRI) setup [59] a system of two slits with different widths is used, c.f. Fig. 7. The Forward Diffraction Radiation (FDR) from the first slit which acts additionally as a shielding mask against SR background interferes with the Backward Diffraction Radiation (BDR) from the second slit. The choice of the different slit widths allows to place the second slit within the formation length of the first one without nearly complete cancellation of the interference, thus resulting in a very compact target setup. Furthermore, the slit centers are slightly off–centered, introducing a small asymmetry in the interference pattern which helps to resolve the ambiguities. Using a complex fit routine, the contributions from beam size, beam divergence and offset can be disentangled. Figure 8 shows an example of an ODRI angular distribution measurement together with the fit to the data, demonstrating the high quality of the method. In a recent publication [60], vertical beam sizes measured with the ODRI method and with conventional OTR imaging were compared from a quadrupole scan, resulting in a very good agreement in both beam sizes and deduced vertical emittance.

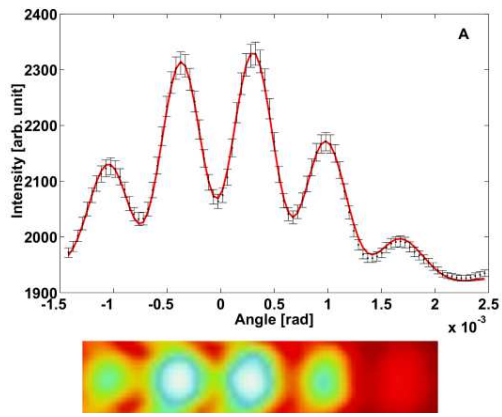


Figure 8: Top: Angular distribution of ODRI radiation with superimposed fit. Bottom: 2D angular distribution raw data. Image courtesy A. Cianchi (INFN and Univ. Rome), see also Ref. [60].

PARAMETRIC X–RAY RADIATION

Parametric X–Ray Radiation (PXR) is emitted when a relativistic charged particle beam crosses a crystal, and the radiation process can be understood as diffraction of the virtual photon field associated with the particles at the crystallographic planes. As result, radiation is emitted in the vicinity of directions satisfying the Bragg condition. Because of the discrete momentum transfer from the crystal planes which is characterized by the reciprocal lattice vector

ISBN 978-3-95450-141-0

Copyright © 2014 CC-BY-3.0 and by the respective authors

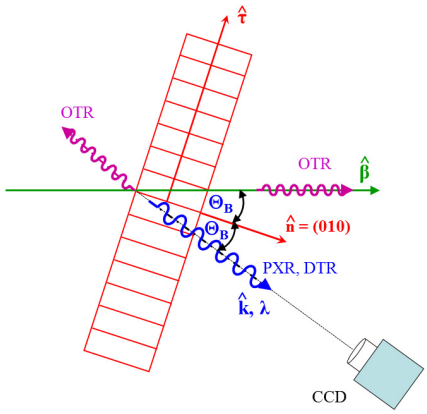


Figure 9: Sketch of the PXR geometry.

$\vec{\tau}_{hkl}$, PXR exhibits a line spectrum. The energy of the PXR lines is determined by the momentum conservation

$$\vec{p}_i = \vec{p}_f + \hbar\vec{\tau}_{hkl} + \hbar\vec{k} \tag{13}$$

with $\vec{p}_{i,f}$ the electron momentum in the initial and final state and $\hbar\vec{k}$ the associated photon momentum. Keeping in mind that the electron energy loss is given by the momentum difference projection onto the electron velocity $\delta E = (\vec{p}_i - \vec{p}_f) \cdot \vec{v}$, and that the energy loss is transferred to the emitted photons, i.e. $\delta E = \hbar\omega_{hkl}$, the energy of the PXR lines is derived as

$$\hbar\omega_{hkl} = \hbar c \frac{|\vec{\beta} \cdot \vec{\tau}_{hkl}|}{1 - \sqrt{\varepsilon}\,\vec{\beta} \cdot \hat{k}} \tag{14}$$

with $\vec{\beta} = \vec{v}/c$ the vector of the reduced electron velocity and ε the crystal dielectric constant which is in the order of 1 for X–rays, see also Fig. 9. PXR is originating from a Bragg diffraction of pseudo photons, therefore their angular distribution exhibits properties of these virtual photons, i.e. it has a double–lobe structure with a characteristic opening angle of

$$\Delta\theta = \sqrt{\left(\frac{1}{\gamma}\right)^2 + \left(\frac{\hbar\omega_p}{\hbar\omega}\right)^2} \tag{15}$$

together with the characteristic central minimum. The width of this structure is larger because the radiation is generated inside the crystal, therefore material properties influence the characteristics which is indicated by the plasma frequency ω_p.

PXR for beam diagnostics was independently proposed in Refs. [61, 62]. Besides the smaller radiation wavelength and the better resolution, the usage of PXR is advantageous because it is emitted from crystallographic planes inside the radiator which usually have a certain inclination angle with respect to the crystal surface, thus allowing a spatial separation from a possible COTR background which is directly generated at the surface. Disadvantage is the PXR radiation yield which is typically 1 – 2 orders of magnitude smaller than the one from transition radiation. Different schemes were proposed by the different authors: (i) imaging with an appropriate X–ray optics, (ii) bringing either the detector itself close to the target, or a scintillator converting X-rays into visible light which can be read out by a conventional CCD, and (iii) exploiting the properties of the angular distribution.

In Ref. [63] the successful imaging with an X–ray pinhole camera was reported. However, the exposure time of the detector (image plate) was 3.5 hours corresponding to an integration of 12600 beam shots. The previously reported measurement [62] to bring the image plate close to the emission point suffered from the large background contributions. In the experiment reported in [64] a scintillator was placed close to the target, but even no beam image could be observed because of the low intensity. In the same experiment the angular PXR distribution was investigated in view of sensitivity on the beam size. The measured angular distributions showed a dependency on the electron beam size, thus in principle allowing to extract information about the transverse beam profile. A preliminary analysis of these distributions indicated that not only PXR was emitted from the crystal, but in addition radiation components with narrower opening angles significantly contributed to the measured intensities. These additional radiation contributions can be interpreted as higher–order diffracted PXR, Diffracted Bremsstrahlung, or Diffracted Transition Radiation originating from the crystal entrance surface and also Bragg reflected by the crystallographic planes. As consequence additional studies are required to investigate the applicability of PXR for beam profile diagnostics.

SMITH-PURCELL RADIATION

Smith–Purcell radiation (SPR) is emitted when an electron beam passes a diffraction grating at a fixed distance close to its surface, and the radiation mechanism can be understood as diffraction of the incoming pseudo photon field at the grating structure. The grating with spacing D represents a one–dimensional Bravais structure, thus offering a discrete momentum $\hbar n\frac{D}{2\pi}$. Similar to PXR, the momentum conservation can be exploited leading to the SRP dispersion relation

$$n\lambda = D(\beta^{-1} - \cos\theta) \tag{16}$$

with n the diffraction order and θ the observation angle as measured between grating surface and outgoing photon, c.f. Fig. 10.

This dispersion relation is a necessary condition for SPR identification, but it is not sufficient because it describes

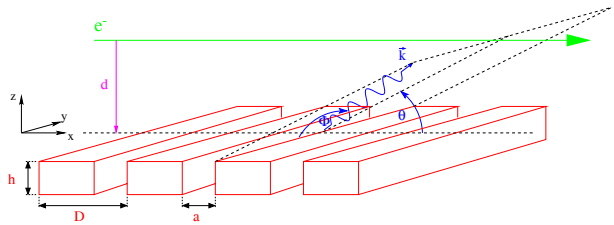


Figure 10: Sketch of the SPR geometry.

Copyright © 2014 CC-BY-3.0 and by the respective authors

ISBN 978-3-95450-141-0

only the relative phase difference between an electron and an emitted photon. Keeping in mind that the beam passes the grating at a certain distance d, it is the pseudo photon field extension which uniquely determines this radiation source. While the fields scale by Eq. (9), the intensity scales with the square of the fields resulting in a characteristic decay constant $h_{int} = \frac{\lambda\beta\gamma}{4\pi}$. In Ref. [65] it is demonstrated how these SPR characteristics can be used to discriminate against background radiation.

A general overview about SPR in view of particle beam diagnostics is given in [66]. An SPR based transverse beam profile measurement is described in this reference, but as a one–dimensional scanning method it was never intended and designed to be used for this purpose, therefore it may never compete with other radiation based profile measurements described before. Furthermore, in Ref. [67] the use of SPR as a high–resolution position sensor for ultra relativistic electron beams was proposed, but the most promising application seems to be for longitudinal profile diagnostics as described in the next section.

COHERENT RADIATION DIAGNOSTICS

A method widely applied for bunch length diagnostics is Coherent Radiation Diagnostics (CRD) [68]. Radiation is emitted coherently if the wavelength is in the order of the bunch length, i.e. information about bunch length and shape is encoded in the emission spectrum which is exploited in CRD. In case of coherent emission, the spectral intensity is strongly amplified which can be expressed in the following form:

$$\frac{\mathrm{d}U}{\mathrm{d}\lambda} = \left(\frac{\mathrm{d}U}{\mathrm{d}\lambda}\right)_1 \left(N + N(N-1)|F(\lambda)|^2\right) \qquad (17)$$

$$\text{with } F(\lambda) = \int_{-\infty}^{\infty} \mathrm{d}z\, S(z)\, e^{-2\pi i z/\lambda}.$$

Here $(\mathrm{d}U/\mathrm{d}\lambda)_1$ is the single particle emission spectrum, N the number of particles in the bunch, and $F(\lambda)$ the bunch form factor which is related to the normalized bunch profile $S(z)$ via a Fourier transform. According to Eq. (17), from a measurement of the spectral intensity and with knowledge of the single electron spectrum together with the bunch charge, the form factor can be determined. Inverting the Fourier transform results in the reconstructed bunch profile $S(z)$. The situation is more complex because it is the magnitude $|F(\lambda)|$ of the form factor which is determined rather than the complex form factor itself. Reconstruction is possible only if both amplitude and phase are available. Although a strict solution of this phase–reconstruction problem is not possible, a so–called minimal phase can be constructed with the Kramers–Kronig relation which gives a handle to solve this problem satisfactory. A detailed treatment of this problem can be found e.g. in Ref. [69].

In principle any kind of coherent radiation can be used as a radiation source. Measurements were performed with coherent synchrotron radiation, transition radiation, and diffraction radiation. The resolution of CRD is limited to about 100 fs, mainly caused because of uncertainties in the spectral reconstruction. Drawback of CRD is that the radiation sources are polychromatic, i.e. a spectrometer is required for the spectral decomposition which is usually a scanning device and does not allow single–shot measurements. In this context the development of multi–stage spectrometers (see e.g. Ref. [70]) is a very interesting alternative.

SPR is an other promising alternative because the radiation source is dispersive by itself. The idea to use this kind of radiation for CRD was discussed several years ago [71, 72]. In the last years, a series of experiments was published performed by a group of authors at different accelerators in an energy range from 1.8 MeV up to 28.5 GeV [73]– [76]. These experiments demonstrate the potential to use SPR in view of CRD with the possibility to perform even single shot diagnostics.

However, there is one critical point in connection with SPR based CRD which is related to the knowledge of the exact theory describing the single particle emission spectrum in Eq. (17). In Ref. [77] a comparison of the various theories is given, demonstrating that there are discrepancies of orders of magnitude in the prediction especially at higher beam energies.

SUMMARY

In this report, some basic applications of radiation phenomena and their physical background in view of particle beam diagnostics are presented. While some of these radiation mechanisms like SR and OTR became already a standard method for beam profile monitors, ODR for transverse and SPR for longitudinal measurements are already applied but not yet established. The application of PXR is rather new in this field, but nevertheless a stimulating phase of experiments is expected during the next years.

ACKNOWLEDGMENT

The author acknowledges stimulating discussions and help in the preparation of this report to A.P. Potylitsyn (TPU), A. Cianchi (INFN and Univ. Rome), P. Karataev (RHUL), D. Nölle, N.A. Potylitsina–Kube and K. Wittenburg (DESY).

REFERENCES

[1] M.L. Ter–Mikaelian, *High–Energy Electromagnetic Processes in Condensed Media*, Wiley–Interrscience, New York (1972).

[2] A. I. Akhiezer and N.F. Shul'ga, *High–Energy Electrodynamics in Matter*, Gordon and Breach Publishers, Amsterdam (1996).

[3] P. Rullhusen, X. Artru, P. Dhez, *Novel Radiation Sources using relativistic Electrons*, World Scientific, Singapore (1998).

[4] A.P. Potylitsyn, *Electromagnetic Radiation of Electrons in Periodic Structures*, Springer Tracts in Modern Physics 243, Berlin Heidelberg (2011).

[5] Radiation from Relativistic Electrons in Periodic Structures, `http://rreps.tpu.ru/`

ISBN 978-3-95450-141-0

Copyright © 2014 CC-BY-3.0 and by the respective authors

[6] A.H. Lumpkin, Proc. BIW'12, Newport News, April 2012, TUBP02 (2012).

[7] C.F. von Weizsäcker, Z. Phys. 88 (1934) 612.

[8] E. J. Williams, Phys. Rev. 45 (1934) 729.

[9] E. Hecht, *Optics*, 2nd ed., Addison–Wesley, Reading, Massachusetts (1990).

[10] J.W. Goodman, *Introduction to Fourier Optics*, 3rd ed., Roberts & Company Publishers, Colorado (2004).

[11] B. Walasek–Höhne and G. Kube, Proc. DIPAC'11, Hamburg, May 2011, WEOB01 (2011).

[12] A. Hofmann, *The Physics of Synchrotron Radiation*, Cambridge University Press, Cambridge 2004.

[13] A. Hofmann and F. Méot, Nucl. Instr. and Meth. 203 (1982) 483.

[14] Å. Andersson and J. Tagger, Nucl. Instr. and Meth. A 364 (1995) 4.

[15] G. Kube *et al.*, Proc. BIW'04, Knoxville, May 2004, AIP Conf. Proc. 732 (2004) p.350.

[16] O. Chubar, Rev. Sci. Instrum. 66 (1995) 1872.

[17] O. Chubar and P. Elleaume, Proceedings of the EPAC'98, Stockholm, June 1998, (1998) p.1177.

[18] T. Tanaka and H. Kitamura, J. Synchrotron Rad. 8 (2001) 1221.

[19] R.A. Bosch, Nucl. Instr. and Meth. A 431 (1999) 320.

[20] O. Chubar *et al.*, Nucl. Instr. and Meth. A 435 (1999) 495.

[21] G. Geloni *et al.*, *Paraxial Green's functions in Synchrotron Radiation theory*, DESY 05-032, ISSN 0418-9833 (2005).

[22] G. Kube, Proc. DIPAC'07, Venice, May 2007, MOO1A03 (2007).

[23] C. Thomas *et al.*, Phys. Rev. ST Accel. Beams 13 (2010) 022805.

[24] T. Mitsuhashi, Proc. of BIW'04, Knoxville, May 2004, AIP Conf. Proc. 732 (2004) p.3.

[25] V. Schlott *et al.*, Proc. IBIC'13, Oxford, September 2013, TUPF09 (2013).

[26] J.W. Flanagan *et al.*, Proc. DIPAC'11, Hamburg, May 2011, WEOB03 (2011).

[27] A.G. Shkvarunets and R.B. Fiorito, Phys. Rev. ST Accel. Beams 11 (2008) 012801.

[28] D.V. Karlovets and A.P. Potylitsyn, Nucl. Instr. and Meth. B 266 (2008) 3738.

[29] N.F. Shul'ga and S.V. Trofymenko, Phys. Lett. A 376 (2012) 3572.

[30] V.A. Verzilov, Phys. Lett. A 273 (2000) 135.

[31] M. Castellano and V.A. Verzilov, Phys. Rev. ST Accel. Beams 1 (1998) 062801.

[32] A.P. Potylitsyn, Proc. NATO Workshop *Advanced Radiation Sources and Applications*, Nor-Hamberd, Springer, New York (2006), p.149.

[33] D. Xiang and W.-H. Huang, Nucl. Instr. and Meth. A 570 (2007) 357.

[34] G. Kube, *Imaging with Optical Transition Radiation, Transverse Beam Diagnostics for the XFEL*, TESLA-FEL Report 2008-01 (2008).

[35] G. Stupakov, *Image Formation by Incoherent and Coherent Transition Radiation from Flat and Rough Surfaces*, SLAC-PUB-14758 (2011).

[36] R.B. Fiorito and D.W. Rule, Proc. BIW'93, Sante Fe, October 1993, AIP Conf. Proc. 319 (1994) p.21.

[37] R.B. Fiorito *et al.*, Proc. PAC'07, Albuquerque, June 2007, FRPMS033 (2007).

[38] P. Catravas *et al.*, Proc. PAC'99, New York, March/April 1999, (1999) p.2111.

[39] O.V. Afanasyev *et al.*, Proc. BIW'06, Batavia, May 2006, AIP Conf. Proc. 868 (2006) p.534.

[40] V.E. Scarpine *et al.*, Proc. BIW'06, Batavia, May 2006, AIP Conf. Proc. 868 (2006) p.473.

[41] B. Walasek-Höhne *et al.*, Proc. HB 2012, Beijing, China, September 2012, THO3C01 (2012).

[42] R.B. Fiorito, Proc. PAC'09, Vancouver (BC), May 2009, TU3GRI02 (2009).

[43] H. Loos *et al.*, Proc. FEL'08, Gyeongju, August 2008, THBAU01 (2008).

[44] S. Wesch and B. Schmidt, Proc. DIPAC'11, Hamburg, May 2011, WEOA01 (2011).

[45] G. Kube *et al.*, Proc. IPAC'12, New Orleans, May 2012, WEOAA02 (2012).

[46] L.G. Sukhikh *et al.*, Proc. IPAC'12, New Orleans, May 2012, MOPPR019 (2012) and submitted to Phys. Rev. ST Accel. Beams.

[47] K. Kruchinin *et al.*, J. Phys.: Conf. Series 517 (2014) 012011 and Proc. IBIC'13, Oxford, September 2013, WEAL2 (2013).

[48] P. Karataev *et al.*, Phys. Rev. Lett. 107 (2011) 174801.

[49] A.P. Potylitsyn, M.I. Ryazanov, M.N. Strikhanov, A.A. Tishchenko, *Diffraction Radiation from Relativistic Particles*, Springer Tracts in Modern Physics 239, Berlin Heidelberg (2010).

[50] D. Xiang *et al.*, Phys. Rev. ST Accel. Beams 10 (2007) 062801.

[51] A.H. Lumpkin *et al.*, Phys. Rev. ST Accel. Beams 10 (2007) 022802.

[52] P. Evtushenko, *et al.*, Proc. BIW'08, Tahoe City, May 2008, WECOTC01 (2008).

[53] R.B. Fiorito and D.W. Rule, Nucl. Instr. and Meth. B 173 (2001) 67.

[54] N.A. Potylitsina–Kube and X. Artru, Nucl. Instr. and Meth. B 201 (2003) 172.

[55] P. Karataev *et al.*, Phys. Rev. Lett. 93 (2004) 244802.

[56] P. Karataev *et al.*, Nucl. Instr. and Meth. B 227 (2005) 158.

[57] R.B. Fiorito *et al.*, Phys. Rev. ST Accel. Beams 9 (2006) 052802.

[58] M.A. Holloway *et al.*, Phys. Rev. ST Accel. Beams 11 (2008) 082801.

[59] A. Cianchi *et al.*, Phys. Rev. ST Accel. Beams 14 (2011) 102803.

Copyright © 2014 CC-BY-3.0 and by the respective authors

ISBN 978-3-95450-141-0

[60] A. Cianchi *et al.*, accepted for publication in New Journal of Physics (2014).

[61] A. Gogolev, A. Potylitsyn, G. Kube, J. Phys. Conference Series 357 (2012) 012018.

[62] Y. Takabayashi, Phys. Lett. A 376 (2012) 2408.

[63] Y. Takabayashi and K. Sumitani, Phys. Lett. A 377 (2013) 2577.

[64] G. Kube *et al.*, Proc. IPAC'13, Shanghai, May 2013, MOPME011 (2013).

[65] G. Kube *et al.*, Phys. Rev. E 65 (2002) 056501.

[66] G. Kube, Proc. DIPAC'03, Mainz, May 2003, IT09 (2003).

[67] G. Doucas *et al.*, Nucl. Instr. and Meth. A 474 (2001) 10.

[68] O. Grimm, Proc. PAC'07, Albuquerque, June 2007, THYC02 (2007).

[69] O. Grimm and P. Schmüser, TESLA-FEL Report 2006-03 (2006).

[70] S. Wesch *et al.*, Nucl. Instr. and Meth. A 665 (2011) 40.

[71] M.C. Lampel, Nucl. Instr. and Meth. A 385 (1997) 19.

[72] D. Nguyen, Nucl. Instr. and Meth. A 393 (1997) 514.

[73] G. Doucas *et al.*, Phys. Rev. ST Accel. Beams 5 (2001) 072802.

[74] G. Doucas *et al.*, Phys. Rev. ST Accel. Beams 9 (2006) 092801.

[75] V. Blackmore *et al.*, Phys. Rev. ST Accel. Beams 12 (2009) 032803.

[76] H.L. Andrews *et al.*, Phys. Rev. ST Accel. Beams 17 (2014) 052802.

[77] D.V. Karlovets and A.P. Potylitsyn, Phys. Rev. ST Accel. Beams 9 (2006) 080701.

Copyright © 2014 CC-BY-3.0 and by the respective authors

ISBN 978-3-95450-141-0

NOVEL EMITTANCE DIAGNOSTICS FOR DIFFRACTION LIMITED LIGHT SOURCES BASED ON X-RAY FRESNEL DIFFRACTOMETRY

M. Masaki#, Y. Shimosaki, S. Takano, M. Takao
Japan Synchrotron Radiation Research Institute (JASRI/SPring-8), Hyogo, Japan

Abstract

A novel emittance diagnostics technique with high sensitivity using X-ray Fresnel diffraction by a single slit has been developed to measure micron-order electron beam sizes at insertion devices (IDs) of photon beamlines. The X-ray Fresnel diffractometry (XFD) is promising for diagnostics especially of a so-called diffraction limited storage ring with ultra-low emittance. The XFD observes a double-lobed diffraction pattern that emerges by optimizing the single slit width. The principle is based on a correlation between the depth of a median dip in the double-lobed pattern and the light source size at the ID. The validity of the new technique was theoretically and experimentally studied. The achievable resolution of the XFD will be also discussed.

INTRODUCTION

In recent years, a diffraction limited storage ring (DLSR) [1] as ring-based future light sources has been extensively and intensively discussed, aiming to drastically boost the average brilliance and the transverse coherence by orders of magnitude compared with existing storage rings. In the DLSR, due to inevitable field errors of strong quadrupole and sextupole magnets, unwanted distortion of lattice functions and local betatron coupling may result in a different light source size at each X-ray photon beamline. One of the most important things for synchrotron light sources is to maximize the light performance at photon beamlines for user experiments. Therefore, measurements of electron beam sizes at the ID source points will be more crucial for securing the absence of degradation of brilliance and transverse coherence of radiation at the beamlines. So far, various techniques have been developed to measure the micron-order vertical beam sizes, for examples, π-polarization imaging method [2], method using a vertical undulator spectra [3], widely used X-ray pinhole cameras (XPCs) e.g. [4], an X-ray imaging method using Fresnel zone plates [5][6] and interferometric techniques [7][8]. However, these methods are not necessarily as readily applicable as they are to emittance diagnostics of all the ID sources of the beamlines. Therefore, development of a new emittance diagnostics technique universally applicable to all the ID beamlines is necessary. We have developed a novel emittance diagnostic method, X-ray Fresnel diffractometry (XFD) [9]. It is capable of resolving a micron-order beam size at the ID source point with high sensitivity and available at typical photon beamlines equipped with a 4-jaw slit and a monochromator.

masaki@spring8.or.jp

PRINCIPLE OF XFD

The XFD observes a double-lobed diffraction pattern that emerges by optimizing a single slit width A under given conditions of distance L from a source point to the slit, distance R from the slit to an observation point, and the observing wavelength λ (Fig. 1). The principle of XFD is based on the correlation between the depth of the median dip in the double-lobed pattern and the light source size; i.e., the dip becomes shallow with growth in the source size. The only requirement for light sources is that the radiation should be a spherical wave with a flux distribution wider than the slit width. Therefore, the XFD is applicable to both most types of ID sources and bending magnet sources.

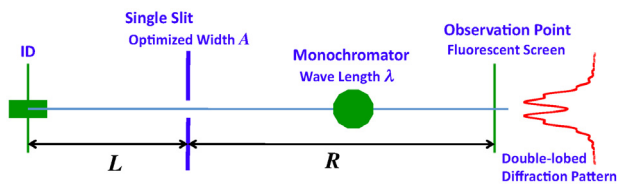


Figure 1: Layout of ID source size measurement using the XFD.

In a one-dimensional case for simplification, a point spread function (PSF) at the observation point is expressed by the following Fresnel integral,

$$I(y,y_e) \propto \left| \int_{-A/2}^{A/2} \sqrt{I_s(y_s - y_e)} \exp\left[i \frac{\pi}{\lambda} \left\{ \frac{1}{L} + \frac{1}{R} \right\} \left\{ (y_s - y_e) - \frac{L(y - y_e)}{L+R} \right\}^2 \right] dy_s \right|^2 \quad (1)$$

where the function $I_s(y_s\text{-}y_e)$ is the radiation flux distribution at the slit, y_e, y_s and y are an electron position at source point, coordinates on the slit and the screen, respectively. An optimized slit width to obtain the double-lobed diffraction pattern is given by a following formula derived from a destructive interference condition of the light at the center (y=0),

$$A \approx \sqrt{7\lambda \frac{LR}{L+R}}. \quad (2)$$

The distance between two lobe peaks, i.e., the pitch P, is expressed as follows from a constructive interference condition of the light,

Copyright © 2014 CC-BY-3.0 and by the respective authors

ISBN 978-3-95450-141-0

$$P = 2\lambda\frac{R}{A} = 2\sqrt{\frac{\lambda}{7}\frac{R(L+R)}{L}}. \quad (3)$$

The PSF of Eq. (1) is shifted by $-(R/L)y_e$ depending on the electron position y_e at the source point. This shift creates sensitivity to changes in the electron beam size. While, the small electron orbit angle y'_e at the source point has little effect on the PSF, because a spherical phase distribution of the radiation on the slit is independent of the orbit angle. Therefore, an electron beam angular divergence, if it is smaller than 10 μrad (r.m.s.), has little influence on the observed diffraction patterns.

The XFD scheme needs the monochromatic X-ray. According to a numerical analysis, the peak-to-peak photon bandwidth narrower than $\Delta\lambda/\lambda \sim 2\%$ is necessary to be negligible distortion of the PSF with the finite bandwidth. A widely-used silicon (111) as a monochromator crystal generates an X-ray beam with the photon bandwidth of 10^{-4} sufficiently narrower than 2%.

The undulator and wiggler radiations have light properties required by XFD. The wavefront is well-approximated by a spherical wave with a parabolic phase distribution around a longitudinal light axis. Furthermore, the flux of the on-axis resonant wavelength has an intensity distribution with a flat top wider than the slit width of several tens of microns [10].

SIMULATION FOR SOURCE SIZE MEASUREMENT AT DLSR

The source size measurement using the XFD at a DLSR photon beamline has been simulated. We assumed a distance of L = 25 m from source to slit, R = 25 m from slit to observation screen, and an X-ray energy of 40 keV. The double-lobed diffraction pattern with the deepest dip is formed when the slit width is 52 μm from Eq. (2). Figure 2 shows the calculated PSF assuming a constant $I_s(y_s\text{-}y_e)$ and its convolution with Gaussian-distributed sources. The peak-to-valley intensity ratio I_v/I_p of the median dip has a high sensitivity to micron-order changes in the root mean square (r.m.s.) source size of less than 10 μm, corresponding to vertical electron beam sizes at the ID source points, where a vertical emittance from 10 to 20 pm.rad and a vertical betatron function of several meters are assumed. In Fig. 3, the peak-to-valley ratios I_v/I_p as a function of the source size are shown as sensitivity curves for three different X-ray energies of 40, 16, and 7.2 keV, where the slit width is optimized for each X-ray energy. The observing X-ray energy can be tuned by a beamline monochromator depending on the range of measuring source sizes. The XFD using photon energy of 7.2 keV is also applicable to the measurement of horizontal source sizes of about 20 μm corresponding to an ultra-low horizontal emittance of about 100 pm.rad of DLSR.

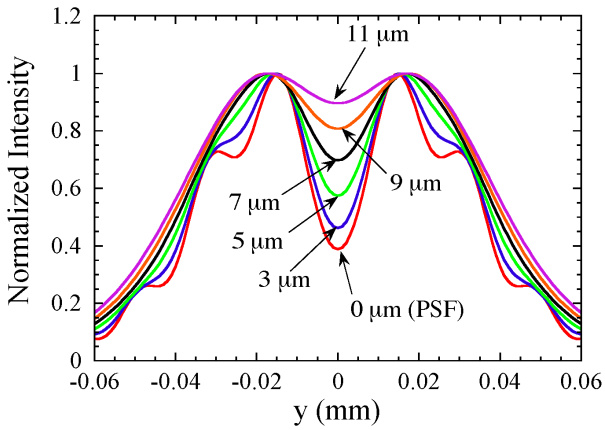


Figure 2: The calculated PSF and its convolution with Gaussian-distributed sources having sizes from 3 to 11 μm (r.m.s.), assuming X-ray energy of 40 keV, distances of 25 m from source to slit and slit to observation screen.

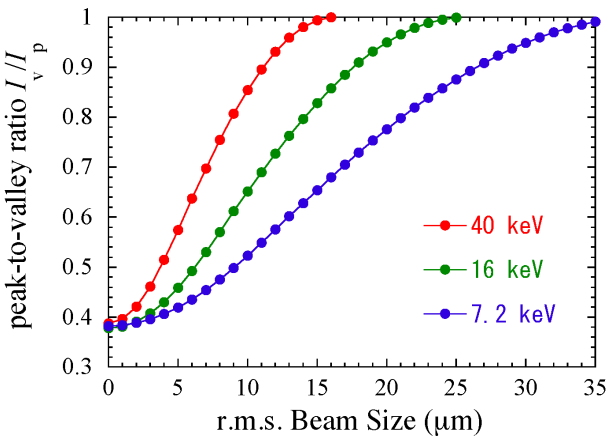


Figure 3: Calculated sensitivity curves at some X-ray energies. Red, green and blue dots show the curves at 40, 16 and 7.2 keV, respectively.

EXPERIMENTAL STUDY AT SPRING-8

We have confirmed XFD's sensitivity to changes in the source sizes experimentally by observing the double-lobed Fresnel diffraction patterns for some different vertical beam emittances at an ID source point. The measurements were performed at the SPring-8 diagnostics beamline (BL05SS) [10] with a planar undulator (ID05) [11]. The beamline front-end slit is located at a distance of 26.8 m from the source point, and 65.4 m from the slit to the observation position. The double-lobed patterns were observed by a high-resolution X-ray imaging system (HAMAMATSU), which consists of a P43 fluorescent screen, an imaging optics with lenses, and a CCD camera. The resolution of the imaging system was calibrated by sharpness of observed edge a stainless steel wire of 0.5 mm diameter placed in front of the system. The result was 6.8 μm (r.m.s.) in scale at the

Copyright © 2014 CC-BY-3.0 and by the respective authors

ISBN 978-3-95450-141-0

ID05 source point. The measuring integration time was set at a minimum of 1 ms to reduce the influence of the vibration of the cryogenically cooled monochromator crystals. An X-ray energy of 7.2 keV for the fundamental harmonic radiation with a deflection parameter K = 0.46 was selected by the monochromator. The X-ray energy was fine-tuned to 7.167 keV in the range of the spectrum band of the harmonic radiation to maximize the vertical flat top width of an observed flux distribution with the fully opened front-end slit. From Eq. (2), the optimized vertical slit width is 150 μm, which was consistent with the experimentally adjusted width to provide the deepest median dip in the observed double-lobed pattern. A narrow horizontal slit of 200 μm was also empirically adjusted to provide the deepest dip as well as the vertical slit. Figure 4 shows four examples of Fresnel diffraction images observed at different operation points of the storage ring by moving horizontal betatron tunes, both with and without the skew quadrupole magnetic fields for XY betatron coupling correction. The double-lobed structures are clearly observed in the vertical direction; however, in the horizontal direction, the diffraction patterns are smeared out due to the large horizontal emittance. The vertical line-projected profiles of the four 2D images are shown in Fig. 5.

To evaluate the vertical beam sizes at ID05 from the observed double-lobed patterns, the PSF of this experimental setup is needed. In a strict calculation of the PSF, the vertical flux distribution $I_s(y_s\text{-}y_e)$ given in Eq. (1) needs to include contributions of off-axis and off-resonant radiations coming from the horizontal emittance and the energy spread of electron beam, respectively. The flux distribution calculated at 7.167 keV assuming a single electron of zero horizontal emittance and zero energy spread does not include those contributions. However, since a rigorous treatment of the effects of the horizontal emittance and the energy spread requires very elaborate computation, we assumed the measured flux distribution at 7.167 keV with a fully opened vertical slit as $I_s(y_s\text{-}y_e)$. The experimental flux distribution effectively includes the contributions of the off-axis and off-resonant radiations. Using the PSF based on the measured flux distribution, the vertical beam sizes were evaluated by fitting Gaussian source convolved with the PSF to the experimental line-projected profiles. The fitted function $f(y)$ is expressed as,

$$f(y) = C\int_{-\infty}^{\infty} I(y,y_e)\exp\left[-\frac{(y_e - y_0)^2}{2(\sigma_{y,e}^2 + \sigma_{res}^2)}\right]dy_e, \quad (4)$$

where the fitting free parameters are a normalization factor C, a center position y_0, a vertical electron beam size $\sigma_{y,e}$ at a source point. The parameter σ_{res} is the imaging system resolution of 6.8 μm (r.m.s.) mentioned above. The smallest in the evaluated beam sizes is 8.1 μm (r.m.s.) for the red profile with the deepest dip in Fig. 5. To analyze the red data, a comparison between the experimental profile and calculated profiles for some beam sizes deviating from the best-fitted size of 8.1 μm is shown in Fig. 6. The function, Eq. (4) with beam size deviations of 0.5 μm step is calculated. The deviation of at least 0.5 μm looks distinguishable from the best-fitted curve. We conclude that light source size smaller than 10 μm (r.m.s.) was successfully resolved, and the resolution was in the order of sub-micron (~0.5 μm).

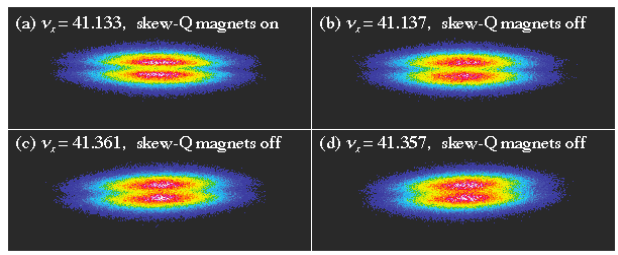


Figure 4: Double-lobed diffraction images observed at four different vertical emittances, changing operation points with different horizontal betatron tunes ν_x, turning skew quadrupole magnets on and off.

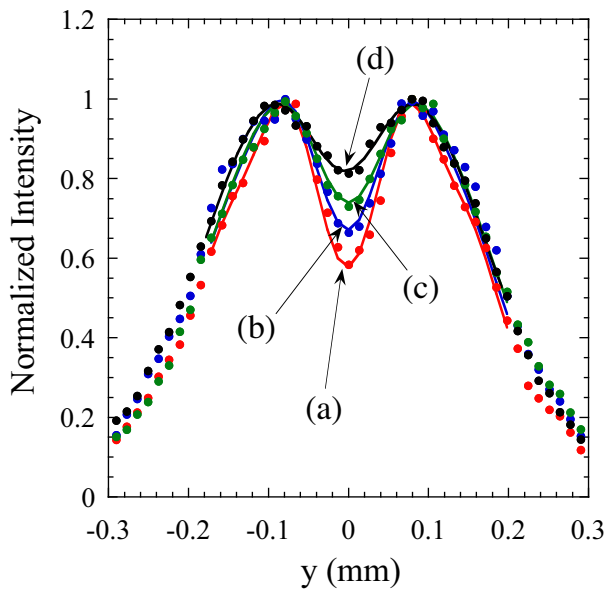


Figure 5: Normalized vertical line-projected profiles (dots) of the four 2D images, their fitted curves (solid lines) by Gaussian source distributions convolved with the PSF. Red, blue, green, and black correspond to (a), (b), (c) and (d) in Fig. 4, respectively.

We also simultaneously measured vertical beam sizes at two separate bending magnet sources using the X-ray beam imager (XBI) [6] by a Fresnel zone plate and the 2D-interferometer [8] by a diffraction mask with four circular apertures instead of a double slit. Figure 7 shows the comparison between three measurements using XFD, XBI and 2D-interferometer, where the beam sizes are

Copyright © 2014 CC-BY-3.0 and by the respective authors

ISBN 978-3-95450-141-0

normalized by the square root of the vertical betatron functions at each source point. The black solid line in Fig. 7 shows the case where the global betatron coupling model is a good approximation, viz. the XY emittance coupling ratio is independent of the position along the storage ring. The correlation between three measurements has a trend along the black linear line. However the scatters of data around the black line are larger than the error bars. We deduce the scatters to be an influence of the local betatron coupling resulting in position-dependent XY emittance coupling ratio along the ring.

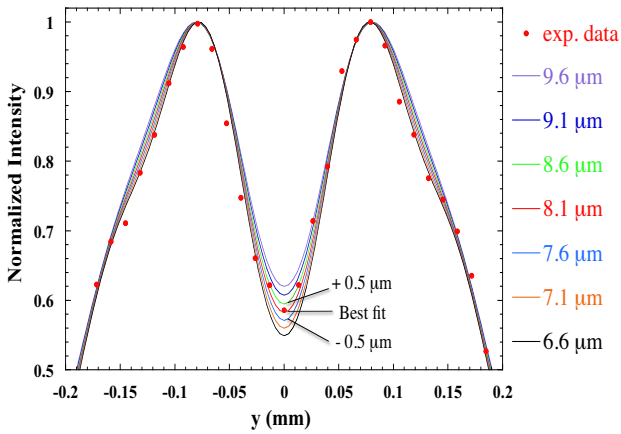


Figure 6: Comparison between the experimental data with the deepest dip and calculations for beam sizes deviating from the best-fitted size of 8.1 μm. The deviations are 0.5 μm step.

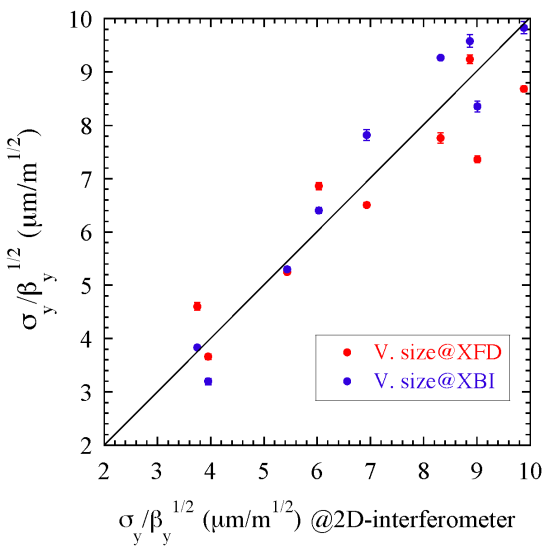


Figure 7: Comparison between results of the simultaneous measurements by XFD at the ID05 source, X-ray beam imager (XBI) and 2D-interferometer at two separate bending magnet sources. The X-axis is the result of 2D-interferometer. On the Y-axis, Red and blue dots indicate the results by XFD and XBI, respectively. The black line shows a correlation on the global betatron coupling model.

TWO-DIMENSIONAL MEASUREMENT FOR FUTURE LIGHT SOURCES

The XFD technique, obviously, can be expanded to two-dimensional measurement. We simulated a two-dimensional scheme with the capability of simultaneous measurement of the horizontal and vertical beam sizes. Assuming a 150 μm square slit, distances 26.8 m from source to slit, 65.4 m from slit to observation screen and X-ray energy of 7.2 keV, a calculated 2D point spread function is shown in Fig. 8. As an example for finite source size, Figure 9 shows a diffraction pattern convoluted by the 2D Gaussian source with the horizontal and vertical sizes of 20 μm (r.m.s.) and 10 μm (r.m.s.), respectively. From cross sections of this 2D pattern, we can obtain the double-lobed profiles in the horizontal and vertical directions, independently. Especially for future light sources such as diffraction limited light sources with ultra-low emittance, the horizontal emittance is expected to be small, comparable to the vertical emittance. For such a case, this two-dimensional scheme will be effective.

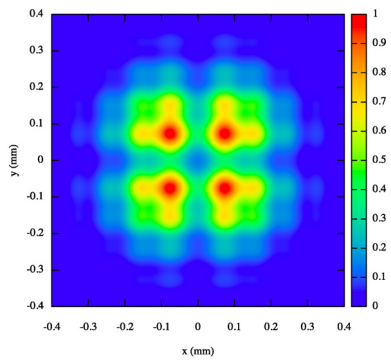


Figure 8: 2D point spread function by assuming a 150 μm square slit, X-ray energy of 7.2 keV and the distances 26.8 m from source to slit, 65.4 m from slit to observation point.

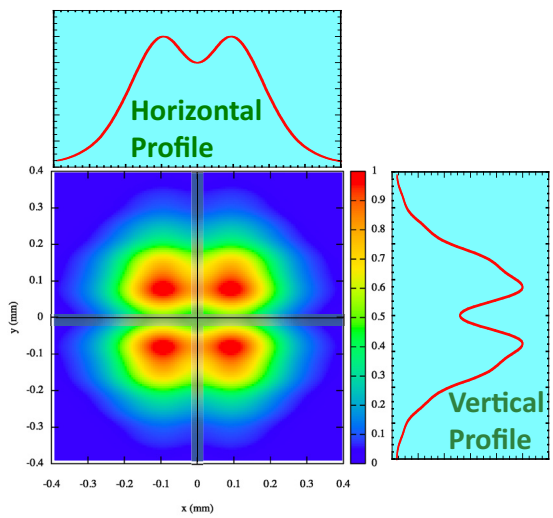


Figure 9: A 2D pattern convoluted by Gaussian source distribution with the horizontal and vertical sizes of 20 μm (r.m.s.) and 10 μm (r.m.s.), respectively.

ISBN 978-3-95450-141-0

Copyright © 2014 CC-BY-3.0 and by the respective authors

ACHEIVABLE RESOLUTION OF XFD

We discuss the achievable resolution of XFD, and compare it with a widely-used and conventional X-ray pinhole camera (XPC). For both cases, a straightforward way to improve the resolution is to place the slit or pinhole close to the source point. For example, we assume that the slit (pinhole) can be placed at a distance of 3 m for both cases, and the observation point is to be 9m from the slit (pinhole), and X-ray energy is 40 keV. In both cases, the PSFs and their convolutions with Gaussian-distributed sources are calculated for the optimized slit width of 22 μm for XFD and pinhole sizes of 13 μm for XPC. As shown in Fig. 10, when the source size is 1 μm (r.m.s.), in the XFD, the bottom intensity of the dip rises by 26 % compared to the PSF. On the other hand, in the XPC case, the FWHM width of the convoluted pattern broadens by 8 % compared to the PSF. The rise of the bottom intensity in the XFD with increasing source size is obviously more sensitive than the broadening of the FWHM width in the XPC. Therefore, we can see that XFD has a higher sensitivity to changes in micron-order source sizes than the XPC, and the example of Fig. 10 (a) indicates that XFD can resolve even sub-micron source sizes.

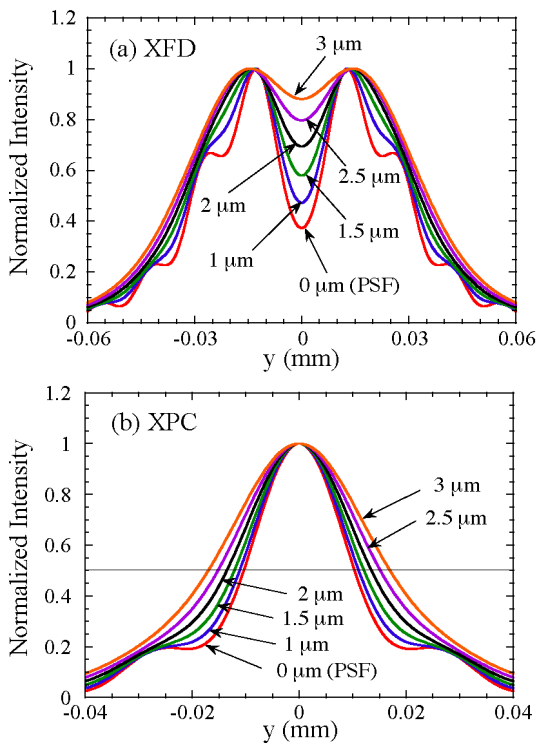


Figure 10: The diffraction patterns for the Gaussian source sizes from zero to 3 μm (r.m.s.). (a) XFD case with a slit width of 22 μm and (b) XPC case with a pinhole size of 13 μm are shown.

CONCLUSION

We have developed a new emittance diagnostics technique, X-ray Fresnel Diffractometry (XFD) to measure micron-order beam size at ID source point. Experimental Study at SPring-8 have shown that XFD is sensitive to micron–order change in the beam size at the ID source point and the light source size smaller than 10 μm (r.m.s.) was successfully resolved with sub-micron resolution. The XFD with an optimized setting has potential to resolve sub-micron beam sizes. This new method is a promising emittance diagnostic technique to maximize the performance of ring-based next-generation light sources.

ACKNOWLEDGMENTS

We would like to thank Dr. T. Watanabe for fruitful discussions and his useful comments, and Nano-forensic Science Group of SPring-8 for their kindness in allowing us to use a high-resolution X-ray imaging system for this experiment.

REFERENCES

[1] R. Hettel and M. Borland, Proceedings of NA-PAC2013, Pasadena, CA, USA, p. 19, (2013).
[2] A. Andersson, *et al.*, Nucl. Instrum. Methods Phys. Res. A, 591, p. 437, (2008).
[3] K.P. Wootton, *et al.*, Phys. Rev. Lett. 109, 194801 (2012).
[4] C. Thomas, *et al.*, Phys. Rev. ST-AB, 13, 022805 (2010).
[5] H. Sakai, *et al.*, Phys. Rev. ST-AB, 10, 042801 (2007).
[6] S. Takano, *et al.*, Nucl. Instrum. Methods Phys. Res. A, 556, p. 357, (2006).
[7] T. Mitsuhashi, *et al.*, Proceedings of DIPAC 2001, Grenoble, France, p. 26 , (2001).
[8] M. Masaki and S. Takano, J. Synchrotron. Rad., 10, p. 295, (2003).
[9] M. Masaki, *et al.*, submitted to Phys. Rev. ST-AB.
[10] S. Takano, *et al.*, Proceedings of IBIC 2012, Tsukuba, Japan, p. 186, (2012).
[11] M. Masaki, *et al.*, Proceedings of SRI 2009, Melbourne, Australia, in AIP Conf. Proc.,Vol.1234, p. 560, (2010).

Copyright © 2014 CC-BY-3.0 and by the respective authors

ISBN 978-3-95450-141-0

MEASUREMENTS OF SMALL VERTICAL BEAMSIZE USING A CODED APERTURE AT DIAMOND LIGHT SOURCE

C. Bloomer, G. Rehm, Diamond Light Source, Oxfordshire, UK
J.W. Flanagan, KEK, Tsukuba, Ibaraki, Japan

Abstract

Diamond Light Source produces a low emittance 3 GeV electron beam which is now regularly operated at 8 pm rad vertical emittance. This corresponds to a vertical beamsize of just 13 µm in the dipole, which is at a high vertical beta location and routinely used for observing the synchrotron radiation using a pinhole camera. Deconvolution of the images from the pinhole camera to maximise resolution is limited by uncertainty regarding the precise shape of the pinhole, resulting in uncertainty on its computed point spread function. Recently a coded aperture has been installed which offers the potential to improve upon the traditional pinhole measurement by offering both higher resolution and increased flux seen through a larger total aperture, however, at the cost of significantly more complex analysis of the recorded images. A comparison of results obtained using the coded aperture and those achieved using the conventional pinhole is presented.

INTRODUCTION

Diamond Light Source (DLS) is a third generation light source, nominally operating with a vertical beam size of 13 µm (0.3 % coupling) through the dipole arcs. Measurements of the transverse beam size are typically made by imaging the synchrotron radiation source point using a pinhole camera. A 25 µm x 25 µm square pinhole, located in air, is used to image the source for storage ring currents from below 1 to 300 mA. X-rays are passed from the vacuum chamber to air through a 1.0 mm aluminium window. They pass through the pinhole located at 3.8 m from the source, to a 200 µm thick LuAG:Ce screen located at 9.1 m from the pinhole. The total path length through air is 9.2 m. The spectrum of the synchrotron radiation is filtered by both the aluminium window and the 9.2 m of air, leading to a peak energy seen at the LuAG:Ce screen of 26 keV. Vertical electron beam size resolutions of better than 1 µm for 1 ms exposure time are achievable [1] [2].

To obtain a beam size measurement with this resolution the pinhole image must be deconvolved with the point spread function (PSF) of the system. At this bandwidth the resolution of the measurement is limited by uncertainty in the PSF, obtained analytically from the pinhole dimensions and scintillator screen properties [1]. Photon flux is sufficiently high that the statistical noise seen on the pinhole camera image for 300 mA stored beam is negligible compared to the errors in the calculated PSF. However, a 1 ms exposure time integrates several electron beam orbits of the DLS storage ring (circulation frequency = 534 kHz). Beam size measurements at turn-by-turn, or even bunch-by-bunch bandwidths require much shorter exposure times, reducing the observed photon flux. For short enough exposure times the statistical counting noise from the small number of photons passing through the pinhole would dominate the measurement errors.

To open up the potential to make beam size measurements of individual bunches with sufficient resolution (better than 1 µm for 13 µm vertical beam size), various alternative 'large aperture' approaches have been proposed. These aim to overcome the limitations in flux seen through the small aperture of a traditional pinhole camera [3].

CODED APERTURE

One such proposal is an adaptation of the coded aperture. This was first introduced as a tool for X-ray astronomy, originally using a collection of randomly distributed pinholes to produce an image that is made up of many overlapping images, unrecognisable as the original object. Figure 1 shows how the coded aperture operates. With knowledge of the location of each of the pinholes it is possible for the complex overlapping pinhole images to be unscrambled (originally described as 'rectification' in early papers, more commonly referred to as 'deconvolution' or 'decoding' in the modern era). This can be carried out either using optical techniques, or digitally using Fourier transforms [4] [5].

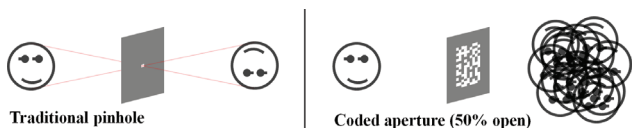


Figure 1: Left: The operation of a traditional pinhole camera. Right: A coded aperture with randomly distributed pinholes, and the resultant overlapping images.

Later, pseudo-random pinhole arrays ('uniformly redundant arrays') were introduced, with pinhole locations chosen such that they exhibit favorable properties for deconvolution [6]. The open aperture of these arrays can be up to 50 % of the total aperture size, giving them the ability to image very low intensity sources, or to image high intensity sources at very high bandwidths.

A vertical beam size monitor using a coded aperture has been proposed and developed for bunch-by-bunch measurements at SuperKEKB and CESR-TA [7] [8]. A 59 element 1-dimensional array produced for use at SuperKEKB has been installed for tests at DLS, intercepting the synchrotron radiation fan at the location of an existing X-ray pinhole (in air). In order to verify the performance of the analysis techniques that have been developed at KEK,

ISBN 978-3-95450-141-0

Copyright © 2014 CC-BY-3.0 and by the respective authors

images of the synchrotron radiation have been observed through the coded aperture using a CCD camera for a variety of beam sizes at 1 ms exposure times.

The coded aperture installed at DLS is a uniformly redundant array featuring an 18.2 µm thick gold mask on a 625 µm thick silicon substrate, with a 10 µm 'pixel pitch' (the smallest array element). It is important that the exact dimensions of the mask itself are known so that the point response function can be accurately calculated. Thus, the dimensions and the quality of the mask edges are measured by the manufacturer after production, and verified using a scanning electron microscope (SEM). Figure 2 shows the coded aperture, it's dimensions, and an example of one such SEM image.

For simplicity of manufacturing and analysis, 1-dimensional coded apertures have been produced for beam size measurements, capable of imaging the beam in one dimension. Since the vertical beam size is more challenging to measure than the horizontal (due to its smaller extent), and can be controlled via an adjustment of the emittance coupling ratio, the coded aperture has been oriented to measure this dimension (although it should be noted that it would, in principal, be possible to utilize a full 2-dimensional coded aperture in order to measure both the vertical and horizontal beam size).

A schematic of the coded aperture beamline layout is shown in Fig 3.

EXTRACTING ELECTRON BEAM PARAMETERS FROM THE CODED APERTURE IMAGES

Decoding of Coded Aperture Images

True deconvolution of coded aperture images in order to restore the original image is computationally expensive, and dependant on very precise knowledge of the aperture dimensions and PSF. Typically, if there are N elements in the coded aperture pattern, and M pixels on the detector used, then the deconvolution requires $N^2 \cdot M^2$ operations (multiplications) [9]. At DLS the X-ray images from the coded aperture are intercepted by a LuAG:Ce screen, and the fluorescence from this screen is recorded using a standard IEEE1394 (firewire) CCD camera with 1024x768 pixels. Assuming that the vertical X-ray beam image can be represented by single column of pixels from the camera, this results in some $59^2 \cdot 768^2 \approx 2e^9$ operations to decode the 1-dimensional beam profile. Binning can be used to reduce computation time at the expense of input resolution. Clearly the decoding of even 1-dimensional coded aperture images represents a computational challenge, but this is not insurmountable.

A greater problem is that coded aperture imaging and deconvolution as used in X-ray astronomy generally operates far from the diffraction region, and with uniform mask illumination. In the case of decoding images from synchrotron radiation sources diffraction and inhomogeneous

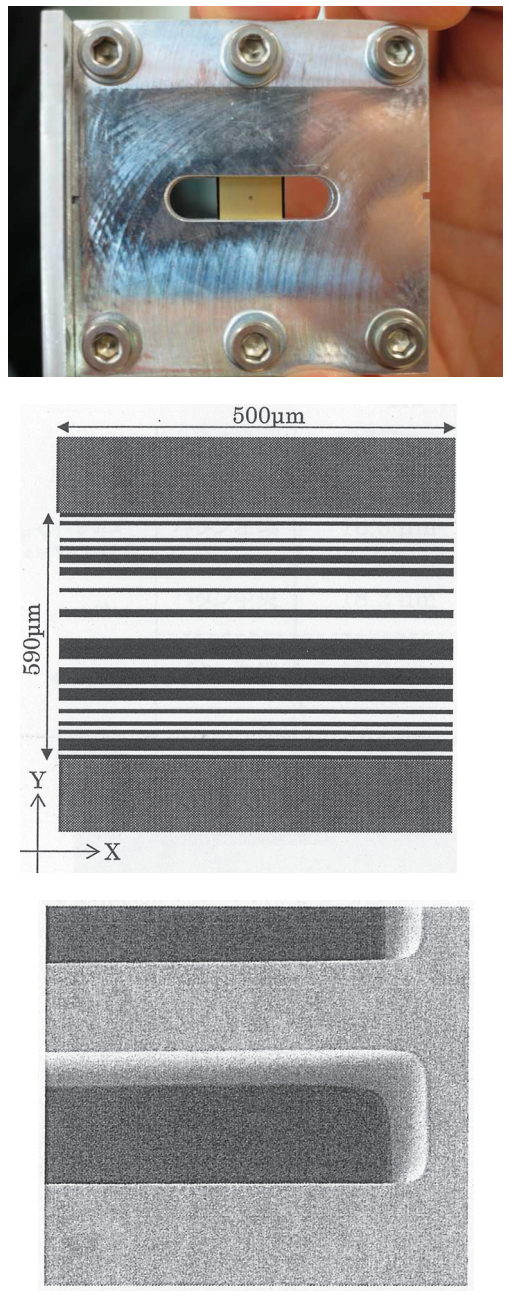


Figure 2: Top: The coded aperture mounted in an aluminium holder. The square gold mask is visible in the centre of the holder. Middle: The mask design. Bottom: An SEM image of the coded aperture at 5000x magnification.

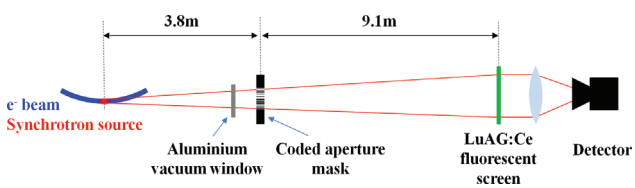


Figure 3: Basic schematic layout of the coded aperture beamline.

Copyright © 2014 CC-BY-3.0 and by the respective authors

ISBN 978-3-95450-141-0

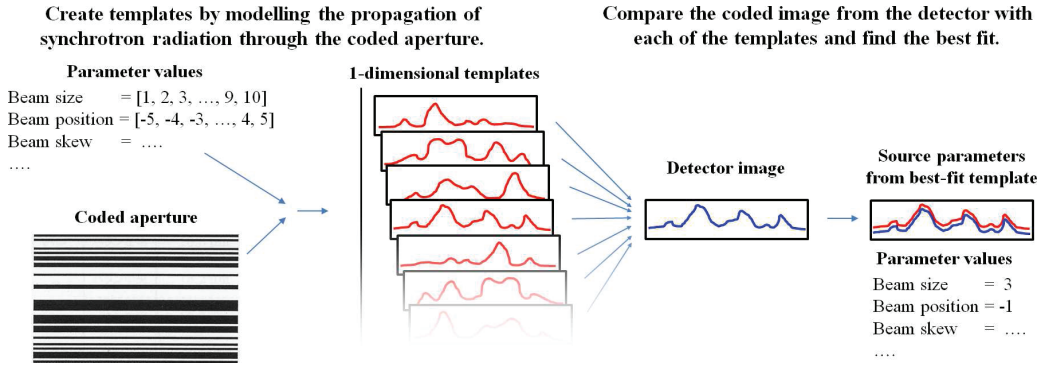


Figure 4: The process used to find the source parameters from the detected image.

illumination of the aperture (as well as X-ray scattering and noise) can prevent the recovery of the image [11] [3].

Fitting Coded Images to Pre-calculated Templates

As a perfect deconvolution of the 'coded image' to restore the original image is difficult or impossible, an alternative method of analysing the coded image is used in order to extract the electron beam parameters. Models of the expected flux seen through the coded aperture are produced for several initial electron beam parameters. The measured X-ray flux at the detector is then compared to these models.

The distribution of synchrotron radiation is well understood [10], and thus it is possible to model the projection of the synchrotron radiation wavefront through the coded aperture and simulate the flux seen at each pixel on the detector. One must take into account the spectra of the radiation, and the resulting attenuation and phase shifts due to the materials and path lengths along the beamline.

The simulation accounts for energy filtering from the aluminium vacuum window, from the 9.2 m of air along the beam path, as well as that from the silicon substrate of the coded aperture. The gold mask blocks the majority of the X-ray photons striking it, but what does pass through the mask is responsible for the observed scattering. This technique is discussed in detail in [8] (*Methods and tools*), and [11] (*Simulation Method*). At DLS we are employing the method described by Flanagan *et al* in [11].

A large number of 1-dimensional templates corresponding to different values of the initial source parameters are pre-calculated, and the measured coded image is compared to each of the templates, searching for a 'best-fit' using a least-squares method. The variable parameters for the pre-calculated templates include vertical position offsets between the source and the coded aperture, as well as vertical offsets between the coded aperture and the detector. Also included as variables are the size, the skewness, and the kurtosis of the source. A range of differing values for detector 'pedestal' (baseline offset) are also used. Assuming that pre-calculated templates are created with ~10 different values for each of these variables, the resulting number of 1-dimensional 768 pixel fits to perform will be ~$1e^6$. This is certainly a non-trivial number, yet it is still offers an improvement over attempting a direct decoding of the coded image.

The electron beam parameters are recovered from the coded image by identifying the template with the best-fit to the detected beam profile, as shown in Fig. 4. As the precision of the results is dictated by the size of the intervals between those values used to generate the templates, improved accuracy can be obtained by specifying a range of parameter values with smaller increments, re-generating a new set of templates, and running the fit again.

Figure 5 shows examples of the coded images captured by the camera for 1 ms exposure time for two different vertical beam sizes at DLS. Figure 6 shows the detected flux for a single column from such an image for nominal beam conditions, along with the simulated flux seen at each pixel of our detector for a range of simulated vertical beam sizes.

Each column of the camera image may be fit individually to the generated templates, and the beam size obtained from each column can be averaged to give a more precise measurement. The template generation and fitting is performed on a 16-core computer, with 64GB of available memory. Typically, some 100,000 templates have been utilised for fitting images obtained at DLS, taking a few

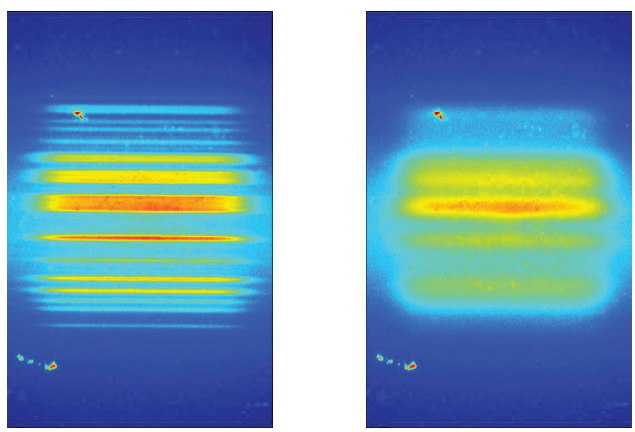


Figure 5: Images of the synchrotron radiation, as viewed through the coded aperture, acquired by the camera. Left: 6.1 µm vertical e^- beam size, σ_y (0.1 % coupling, κ). Right: 25.6 µm vertical e^- beam size, σ_y (1.1 % coupling, κ).

ISBN 978-3-95450-141-0

Copyright © 2014 CC-BY-3.0 and by the respective authors

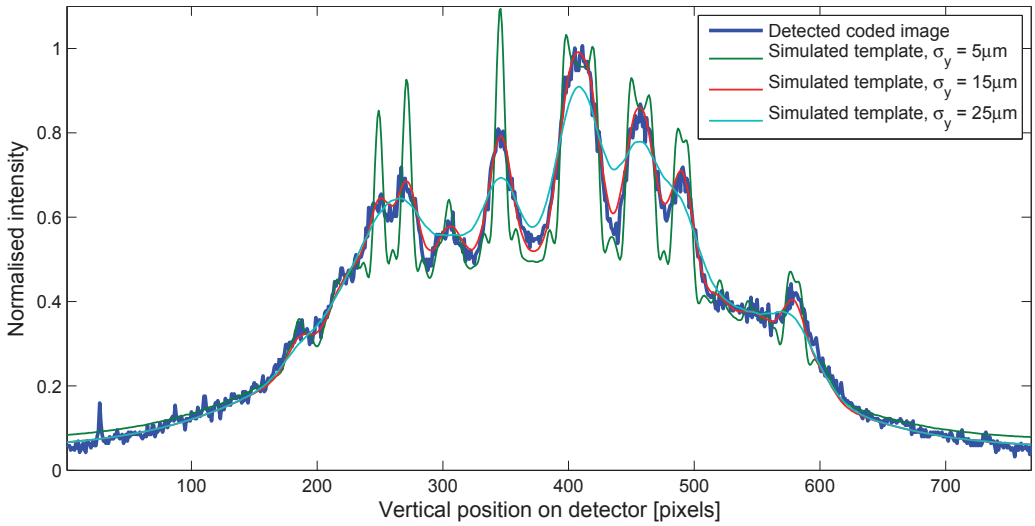


Figure 6: The detected flux for nominal beam conditions (~0.3 % coupling, κ) as seen by a single column of pixels from the camera, plotted along with the generated templates for flux seen at each detector pixel for three different vertical source sizes, σ_y.

10s of seconds to generate. The fitting itself is faster, taking <10 s to fit a few hundred columns from a coded image image with 100,000 templates. If faster fitting is required, processing times could be reduced by shrinking the range of values used to generate the templates. (In the case at DLS where fitting time is essentially unconstrained, memory becomes the limiting factor. This limits the number of templates that can be generated).

COMPARISONS OF CODED APERTURE AND PINHOLE MEASUREMENTS

Pinhole cameras are currently relied upon to give an accurate electron beam size measurement at DLS [1]. The vertical beam size can be changed by altering the currents through the skew quadrupoles, and thus the results of the coded aperture measurements and fitting routine can be compared with those obtained from existing pinhole measurements for a range of beam sizes. The very fine control of the electron beam size available at DLS also allows for smaller beam sizes than were available during the earlier CESR-TA tests, down to ~7 µm.

The measurement was carried out using a 'slow', 1 ms exposure time camera system, differing from that carried out at CESR-TA, and from that planned for SuperKEKB, where a 'fast' 1-dimensional diode array, capable of MHz, bunch-by-bunch, bandwidth is used. This 'slow' camera system has the disadvantage that bunch-by-bunch or turn-by-turn measurements are impossible as the 1 ms exposure time integrates some ~500 turns, but the advantage of an excellent signal-to-noise ratio at high spatial resolution. Thus, a detailed comparison of the actual beam distribution with the modelled templates can be made.

Figure 7 shows the electron beam size measurements from the coded aperture fit plotted against beam size measurements from a pinholes camera measuring synchrotron

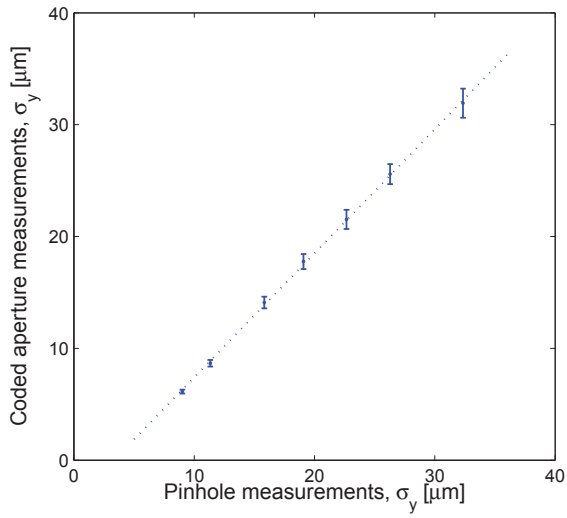


Figure 7: A plot comparing the vertical electron beam size measurements calculated from pinhole images, and calculated from from coded aperture images. A best fit line is shown.

light from the same dipole. It is interesting to note that while the results generally correlate, the coded aperture measurements give a consistently smaller beam size than the pinhole camera. The reasons for this are not clear. At 7 µm beam size the error bars on the coded aperture measurement (the standard deviation measured from fitting each column from the coded aperture image) are ~0.3 µm.

CONCLUSIONS

The coded aperture measurements of vertical electron beam size correlate well with those measured by the existing pinhole cameras at DLS, although unexplained differences in the measured beam size are observed. The coded aperture

Copyright © 2014 CC-BY-3.0 and by the respective authors

ISBN 978-3-95450-141-0

measurements consistently give a smaller beam size than that found using the pinhole camera. Resolution of the coded aperture system is found to be on par with that obtained with the pinhole cameras, although the clear discrepancies between the measurements of the two systems require further investigation.

Analysis of the coded aperture images by fitting the detector output to pre-calculated templates is preferable to attempting to fully decoding the images. It is possible to produce simulated flux distributions closely matching that seen at each pixel on the detector, even at high spatial resolution. This gives confidence that the technique works correctly.

With the use of a higher bandwidth detector the measurement should be feasible at turn-by-turn bandwidths with acceptable resolution. 1-dimensional diode arrays offer the required bandwidths and noise properties to realise this measurement, though developing such an array capable of imaging X-rays at >20 keV still represents a challenge. The potential to observe vertical beam size instabilities at turn-by-turn rates has the potential to open up new accelerator physics experiments at DLS, and it is hoped that such a system can be realised in the coming years.

REFERENCES

[1] C. Thomas et al., "X-ray pinhole camera resolution and emittance measurement", Physical Review ST Accelerators and Beams, Vol. 13, 022805, 2010.

[2] C. Thomas et al., "An X-ray pinhole camera with a range of defined apertures", Proceedings of BIW, 2012.

[3] C. Thomas et al., "Large aperture X-ray monitors for beam profile diagnostics", Proceedings of IBIC, 2013.

[4] R.H. Dicke, "Scatter-hole cameras for X-rays and gamma rays", The Astrophysical Journal, Vol. 153, 1968.

[5] J.G. Ables, "Fourier transform photography: a new method for X-ray astronomy", Proceedings of the Astronomical Society of Australia, 1968.

[6] E.E Fenimore et al., "Coded aperture imaging with uniformly redundant arrays", Applied Optics, "Vol. 17, 1978.

[7] J.W. Flanagan et al., "Single-shot resolution of X-ray monitor using coded aperture imaging", Proceedings of DIPAC, 2011.

[8] J.P. Alexander et al., "Vertical beam size measurement in the CESR-TA e^+ e^- storage ring using X-rays from synchrotron radiation", Nuclear Instruments and Methods in Physics Research A, Vol. 748, 2014.

[9] K. Byard., "Fast decoding algorithms for coded aperture systems", Nuclear Instruments and Methods in Physics Research A, Vol. 754, 2014.

[10] K.J. Kim, "Characteristics of synchrotron radiation", AIP Conference Proceedings, Vol. 1, 1989

[11] J.W. Flanagan et al., "Performance of coded aperture X-ray optics with low emittance beam at CESRTA", Proceedings of PAC, 2009.

Copyright © 2014 CC-BY-3.0 and by the respective authors

ISBN 978-3-95450-141-0

A QUANTUM GAS JET FOR NON-INVASIVE BEAM PROFILE MEASUREMENT

A. Jeff, CERN, Geneva, Switzerland & University of Liverpool, U.K.
E.B. Holzer, T. Lefèvre, CERN, Geneva, Switzerland.
V. Tzoganis, C. Welsch, H. Zhang, Cockcroft Institute, Daresbury & University of Liverpool, U.K.

Abstract

A novel instrument for accelerator beam diagnostics is being developed by using De Broglie-wave focusing to create an ultra-thin neutral gas jet. Scanning the gas jet across a particle beam while measuring the interaction products, the beam profile can be measured. Such a jet scanner will provide an invaluable diagnostic tool in beams which are too intense for the use of wire scanners, such as the proposed CLIC Drive Beam.

In order to create a sufficiently thin jet, a focusing element working on the de Broglie wavelength of the Helium atom has been designed. Following the principles of the Photon Sieve, we have constructed an Atomic Sieve consisting of 5230 nano-holes etched into a thin film of silicon nitride. When a quasi-monochromatic Helium jet is incident on the sieve, an interference pattern with a single central maximum is created. The stream of Helium atoms passing through this central maximum is much narrower than a conventional gas jet. The first experiences with this device are presented here, along with plans for further tests.

INTRODUCTION

The Compact Linear Collider (CLIC) will use a novel two-beam acceleration scheme to collide electrons and positrons at up to 3TeV [1]. Energy is extracted from a very intense, lower energy Drive Beam (DB) using specially designed RF structures, and transferred to the less intense, high energy colliding beams.

Table 1: Relevant Parameters for the CLIC Drive Beam

Beam Energy	to 2.4 GeV
Beam Current	4.2 A
Pulse Length	140 μs
Bunch Length	13 ps
Bunch Separation	2 ns
Repetition Frequency	50 Hz
Normalised Emittance	150 mm mrad

High intensity beams pose a challenge for beam diagnostics, since all instruments must be non-interceptive. In addition, the short bunch length and separation envisaged for the CLIC DB will generate substantial high-frequency wake fields which can interfere with beam measurements. A number of solutions are being explored, including synchrotron radiation for the high-energy part of the DB. The gas jet monitor described here is a promising option for the lower energy section of the DB accelerator, as well as for other planned high-intensity accelerators.

BEAM GAS IONISATION

Residual gas ionisation is used as a diagnostic tool in many accelerators [2][3]. A charged particle beam ionises a fraction of the residual gas present in the beam pipe. If an electric field is applied across the beam pipe, the ions and the liberated electrons are accelerated away from the beam in opposite directions. A position sensitive detector is used to image either the ions or the electrons, and thus measure the beam profile. Throughout the discussion below we refer for clarity to ion collection; however the conclusions remain valid if the electrons are collected instead.

In order for this technique to be accurate, the position at which the ions are generated must be mapped onto the detector, that is, the ions should fly in a straight line. In reality, however, this is not quite true. Firstly, the ions are created with a certain initial momentum. Secondly, the electromagnetic field of the beam will influence their trajectory. Thus, the profile of ions arriving at the detector will not exactly match the beam profile.

In order to reduce this effect, a magnetic field may be added parallel to the electric field. In this case, the ions follow a helical path which, if the gyroradius is sufficiently small, may be taken to approximate a straight line. In the case of a very intense beam, however, the space charge field may be so strong that a small gyroradius cannot be guaranteed. Numerical methods can be used to correct for this effect [4] but the resolution of the profile is in consequence reduced.

GAS JET MONITOR

Gas jet monitors have been developed at NIRS and J-Parc [5] in order to decrease the measurement time and allow 2-d profile measurements at a single point. A planar gas jet or ‘gas curtain’ crosses the beam pipe. The curtain is tilted at 45° and acts like a screen when combined with an electric field for ion extraction. The pressure of the gas jet is locally much higher than the residual gas pressure, so that sufficient ions for beam profile measurement with a given accuracy are collected in a shorter time. The jet passes through the beam pipe into a collection chamber, so that the beam vacuum is not substantially affected.

Copyright © 2014 CC-BY-3.0 and by the respective authors

ISBN 978-3-95450-141-0

The gas jet is generated by allowing high-pressure gas to expand through a small-aperture nozzle and then pass through a series of skimmers. The small skimmers separate the jet generator into a number of chambers, and each chamber is separately pumped so that the pressure drops by several orders of magnitude in each successive chamber. After the second skimmer, the jet operates in the molecular regime, where the mean free path of the gas molecules is much longer than the chamber dimensions. In this regime, each gas molecule can be regarded as a projectile, which flies in a straight line until it hits the chamber surface. A final shaped aperture is used to make the planar jet.

A further development from the same group is the focusing of the neutral gas jet using a non-linear magnetic field [6]. Oxygen is used due to the larger magnetic moment of the O_2 molecule. A highly non-linear field is applied using short-period multi-pole magnets. This magnetic focusing allowed an increase, by a factor of 2, of the gas density in the plane of the curtain, and a small reduction in the gas jet thickness. However, such non-linear effects are inherently small, and an extremely large magnetic field gradient would be necessary to achieve stronger focusing.

COCKCROFT INSTITUTE TEST STAND

A gas jet test stand has been set up at the Cockcroft Institute, U.K., in order to demonstrate and optimise the gas jet generation [7]. The gas jet is generated using the nozzle and skimmer method described above, and the nozzle is moveable, so that the effect of changing the nozzle-skimmer distance can be investigated. The test stand was designed as a demonstration monitor for an Ultra-low energy Storage Ring [8], where a non-interceptive monitor is required and must operate in extremely high vacuum in order to preserve the beam lifetime.

The gas jet is generated by a circular orifice of 30 µm diameter, and two conical skimmers with open diameters of 180 µm and 400 µm. The orifice can be supplied with either Nitrogen or Helium at a variable pressure up to 12 bar. Finally a rectangular skimmer is used to shape the curtain jet before it enters the interaction chamber. The interaction chamber (located where the beam pipe would be if the jet monitor were installed at an accelerator) contains a series of circular electrodes which are used to generate a homogeneous vertical electric field. An electron gun with an energy of up to 5 keV is used to ionise the gas. Ions are then extracted by the electric field onto two Multi-Channel Plate photomultipliers (MCPs), arranged in chevron configuration to provide a gain of up to 10^6. The electrons released by the MCPs are then accelerated onto a phosphor screen, which is imaged using a CCD camera. The whole setup is illustrated in Fig. 1.

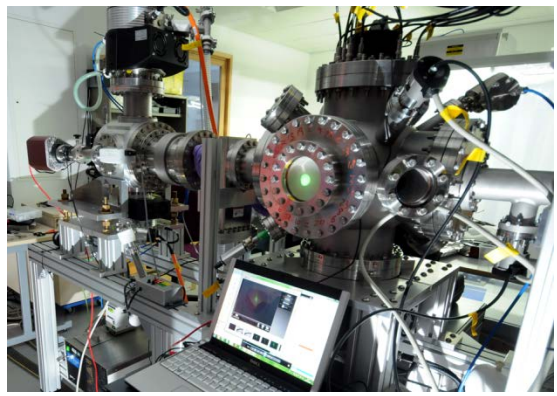


Figure 1: The gas jet test stand at the Cockcroft Institute. The jet generator is on the left, the interaction chamber on the right. The electron beam is seen on the side phosphor screen, while the MCP / Phosphor assembly for imaging of the extracted ions is at the top.

The differential pumping scheme of the gas jet is shown in Fig. 2 and is described in greater detail in [9]. It can be seen that a reduction in pressure by 12 orders of magnitude is achieved between the gas inlet and the interaction chamber.

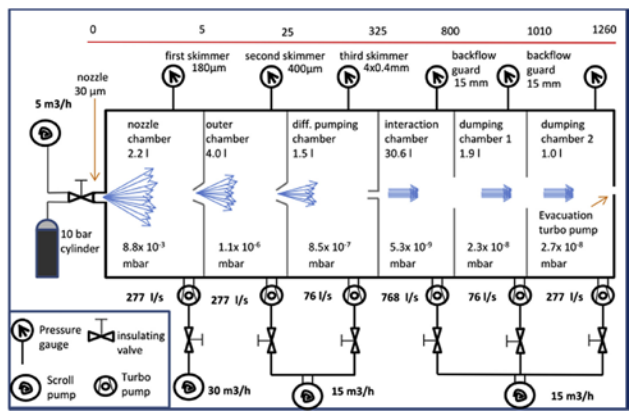


Figure 2: Differential pumping scheme and chamber pressures in the gas jet test stand.

Generation of the gas jet was recently demonstrated [10]. A typical image of the MCP / phosphor screen is shown in Fig. 3. Two separate lines are clearly visible. The line on the left is due to ionisation of the residual gas. As the electron beam passes through the chamber, residual gas ions are generated and then move vertically due to the extraction field. There is some spreading due to the initial thermal motion of the gas, so the line is broader than the true width of the electron beam. The line on the right is due to ionisation of the gas jet. The gas jet is traveling with a speed of around 500 ms^{-1} for Nitrogen or 1000 ms^{-1} for Helium. This horizontal motion continues as the ion is accelerated vertically, resulting in a parabolic path, and a separation of the two lines. The gas jet line is considerably brighter, due to the higher density of the gas jet, and thinner due to the relatively small velocity spread in the gas jet.

ISBN 978-3-95450-141-0

Copyright © 2014 CC-BY-3.0 and by the respective authors

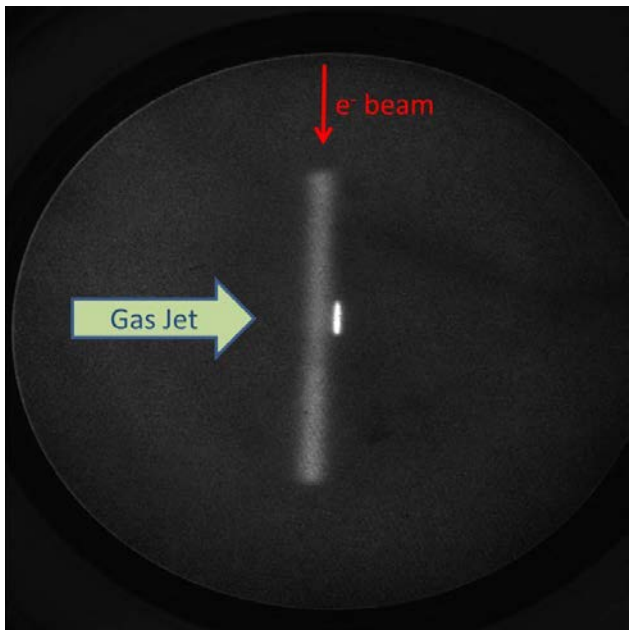


Figure 3: Typical image on the phosphor screen. The longer, fainter line is ions from the residual gas in the chamber; the shorter, brighter line is ions from the gas jet.

The jet acts like a 'thick' screen, since ionisation can occur anywhere in the intersection volume of the beam and jet. This affects the resolution of the monitor. Specifically, for a jet of thickness t, the point spread function (PSF) is stretched by a factor $\sqrt{2}t$ along the axis perpendicular to both the beam and the jet; the resolution along the axis parallel to the jet is not affected. The gas jet appears as a streak instead of a circular profile because the gas jet thickness is larger than the beam size.

By scanning the electron beam vertically through the gas jet, a rough cross-section of the gas jet density can be reconstructed, and the average thickness of the jet is estimated to be 2 mm. A more accurate method for measuring the jet density profile is currently being commissioned. This consists of an ionisation vacuum gauge which is inserted into the gas jet on a 3-axis translation stage. The gauge is covered on the side facing the gas jet by an aluminium shield with a thin slit through which the gas jet can pass. By scanning the slit through the gas jet we will be able to measure the density profile.

Each of the chambers is equipped with a vacuum gauge, and the effect of the gas jet on the pressure in each chamber can be examined. As expected, the pressure in the nozzle chamber and the outer jet chamber (i.e. between the nozzle and 1st skimmer, and between the two skimmers) increases linearly with the gas inlet pressure. Thanks to the differential pumping scheme and the efficient collection of the gas jet in the dumping section, however, the pressure in the interaction chamber increases only slightly, as shown in Fig. 4.

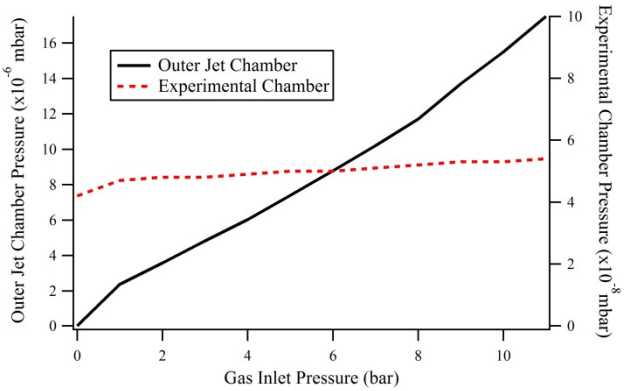


Figure 4: Dependence of the chamber pressure on the gas inlet pressure. Solid black line, left axis: pressure in the outer jet chamber. Dashed red line, right axis: pressure in the experimental chamber.

In order to reduce even further the load on the beam vacuum system, the jet can be operated in pulsed mode. A fast solenoid valve is attached to the gas inlet line. If the gas inlet is simply closed, the gas jet continues operating for some time, as the gas pipe slowly empties through the orifice. Instead, a two-way valve is used. When the valve is in the 'off' position, the orifice is connected to a vacuum pump, quickly emptying the high-pressure gas. The valve has a switching time of approximately 20 ms and can be operated at up to 20 Hz. As an example, Fig. 5 shows the operation of the gas jet at 1 Hz with a 50% duty cycle. The brightness of the gas jet line on the phosphor screen closely follows the operation of the valve. The gas jet rise time could not be precisely measured since the CCD camera was only capable of 10 fps. The pressure in the differential pumping chamber and the dump chamber are also shown. It can be seen that the pressure rises asymptotically over a few hundred μs, and then falls just as quickly to its original value.

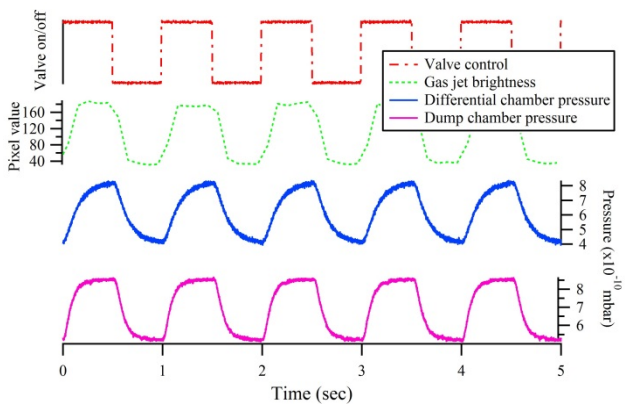


Figure 5: Operation of the jet in pulsed mode. Traces from top to bottom: Valve control, average pixel brightness of the gas jet line, pressure in the differential pumping chamber, pressure in the jet dumping chamber.

QUANTUM GAS JET

Due to the thickness of the gas jet as well as the space charge effects from an intense beam, it is unlikely that a

Copyright © 2014 CC-BY-3.0 and by the respective authors

ISBN 978-3-95450-141-0

monitor based on the curtain gas jet will achieve a sufficiently small resolution to measure sub-mm beams such as the CLIC DB. Instead, we propose to develop a gas jet scanner. A thin pencil beam must be generated and is then moved through the beam to measure the profile. The device would be analogous to a wire scanner, but since it is minimally interceptive it can be scanned much more slowly.

The beam intensity at each position could be derived by extracting and counting ions, as with the current setup. However the trajectory of the ions would not be important, since the position information is provided by the gas jet position, so the profile measurement would not be affected by space charge. Alternatively, reliance on charged particles could be eliminated altogether by recording the beam losses during the gas jet scan or by detecting bremsstrahlung photons.

In order to achieve a thin gas jet with a diameter below 100 μm, a novel focusing method is being developed for the generation of the gas jet. The quantum wavefunction of the neutral gas atoms is used to generate an interference pattern with a single maximum, which acts as an ultra-thin gas jet. A similar technique has been used successfully to create a neutral-Helium matter-wave microscope [11]. A Fresnel Zone Plate (FZP) was used to create a focal spot of 2 μm FWHM.

A Fresnel Zone Plate consists of a series of alternating open (transmitting) and closed (blocking) concentric rings. The width of the rings is chosen such that the path difference of a wave/particle passing through adjacent open rings to reach the focal point is equal to one wavelength. This is achieved if the open rings are centered at radii

$$r_n = \sqrt{nf\lambda}$$

where f is the focal length of the FZP and λ is the wavelength to be focused. Since only the relative path length is important, n may begin at any number, so long as it is incremented by 2 for each successive open ring.

The rings become narrower the further from the center they are, such that the area of each ring is the same. In addition, the resolution of the FZP is approximately equal to the width of the smallest (outermost) zone. Thus, it is desirable to have as many zones as possible, in order to maximize the transmitted power and produce a tight focus. However, for a small wavelength the zones must be extremely small in order to produce an acceptable focal length, so that manufacturing constraints limit the number of zones which can be produced.

The focal length for a given FZP is inversely proportional to the wavelength. Thus, FZPs suffer from large chromatic aberration if the wave to be focused is not monochromatic.

In order to use this particle-wave focusing, a conventional Helium jet will be generated using the current setup. However, the final skimmer will be replaced with the diffractive focusing plate. During the expansion of the jet from the orifice, the gas is adiabatically cooled. Almost all the thermal motion of the gas atoms is converted into forward motion of the gas jet, leaving a very small velocity spread. Thus, the jet can be considered to be almost monochromatic. The average thermal momentum of a gas atom is derived from the Maxwell-Boltzmann distribution:

$$\bar{p} = \sqrt{\frac{8kTm}{\pi}}$$

where k is Boltzmann's constant, T is the gas temperature and m is the molecular mass. The de Broglie wavelength of a particle depends on its momentum,

$$\lambda = {}^{h}/_{p} = \sqrt{\frac{h^2\pi}{8kTm}}$$

where h is Planck's constant. It can be seen that in order to make the wavelength as large as possible, a light gas species should be chosen. For Helium at 300K, λ=0.08 nm.

FZPs are used at similar wavelengths for x-ray focusing. However, x-ray FZPs are usually constructed from metal rings attached to an x-ray transparent substrate. In the case of the gas-focusing FZP, the open zones must allow gas atoms to pass, so no substrate can be used. For the matter-wave microscope, the plates were etched from a thin film of silicon nitride, and struts were added in order to support the inner zones [12].

We propose to simplify the production process by using a different focusing plate based on the photon sieve [13]. In the photon sieve, the concentric rings of the FZP are replaced with a series of small circular holes. Each hole is centered at the radius of an open zone in the equivalent FZP. The two plates are compared in Fig. 6. It can be seen that since there are no completely cut rings in the photon sieve, struts are not necessary.

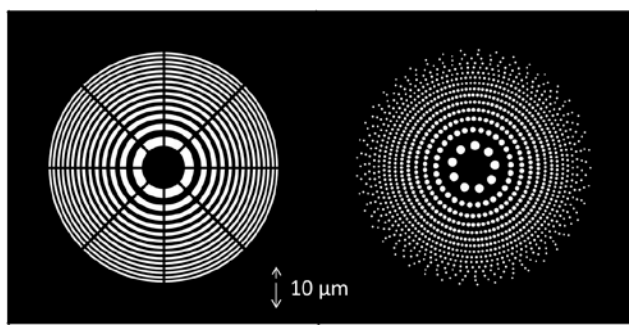


Figure 6: Comparison of an FZP and a photon sieve, both giving a focal length of 0.5m for λ=0.08nm.

It has been shown that a photon sieve with the same number of zones can create a sharper focus than the equivalent FZP. In addition, the sharp cut-off at the edge of the FZP causes higher-order diffraction which leads to side-lobes close to the focal spot. In a photon sieve, the intensity of side-lobes can be reduced if the fraction of each ring that is filled with holes is gradually reduced. The sieve is then said to be apodised [14].

Taking the above considerations into account, an 'atomic sieve' has been designed, applying the principle of the photon sieve to quantum matter-wave focusing.

ISBN 978-3-95450-141-0

Copyright © 2014 CC-BY-3.0 and by the respective authors

The atomic sieve consists of 5230 holes, the smallest having a diameter of 80 nm and the largest 1.5 µm. The holes are etched into a 2 µm membrane of silicon nitride. The plates are currently under production, a Focused Ion Beam image of one of the test plates is shown in Fig. 7.

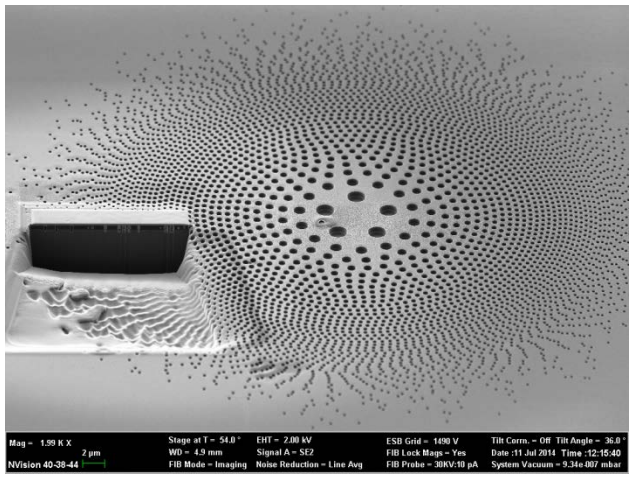


Figure 7: Focused Ion Beam image of the atomic sieve in production. The large hole on the left of the image has been cut into this test plate in order to check that the holes completely penetrate the silicon nitride film.

CONCLUSION

The test setup at the Cockcroft Institute has demonstrated reliable gas jet operation, and can be used for profile measurement in both continuous and pulsed mode. Thanks to efficient dumping of the jet and differential pumping in the jet generator, the effect on the beam vacuum system is small. However, due to the thickness of the jet it is not suitable for measuring beams of less than a millimetre.

For measurement of smaller beams with intense space charge, a new gas jet scanner is proposed. A focusing method based on the de Broglie wavelength of the neutral gas atoms will be used to produce a thin pencil jet. A focusing plate based on an apodised photon sieve has been designed. This 'atomic sieve' is under production and will be tested later this year.

REFERENCES

[1] M. Aicheler, P. Burrows, M. Draper, T. Garvey, P. Lebrun, K. Peach, et al., "A Multi-TeV linear collider based on CLIC technology: CLIC Conceptual Design Report", CERN, Geneva (2012).

[2] W. DeLuca, "Beam detection using residual gas ionization", IEEE Trans. Nucl. Sci. NS-16 (1969) p813.

[3] M. Sapinski, W. Andreazza, B. Dehning, A. Guerrero, M. Patecki, R. Versteegen, "The first experience with LHC beam gas ionization monitor", Proc. IBIC, Tsukuba (2012).

[4] J. Egberts, P. Abbon, H. Deschamps, F. Jeanneau, J. Marroncle, J. Mols, et al., "Development of the LIPAc ionization profile monitor", Proc. DITANET, Seville (2011).

[5] Y. Hashimoto, Y. Fujita, T. Morimoto, S. Muto, T. Fujisawa, T. Honma, et al., "Development of a non-destructive beam profile monitor using a gas sheet", Proc. PAC, Chicago (2001) p. 1631–1633.

[6] T. Fujisawa, Y. Hashimoto, T. Morimoto, Y. Fujita, "Multi-pole magnets to focus an O2 sheet beam for a non-destructive beam-profile monitor", Nucl. Instrum. Meth. A **506** (2003).

[7] M. Putignano, C.P. Welsch, K. Kuehnel, "Design of a nozzle-skimmer system for a low perturbation ionization beam profile monitor", Proc. DIPAC, Basel (2009).

[8] M. Putignano, D. Borrows, C.P. Welsch, "Experimental characterization of a flexible ionization monitor for transverse profile measurement in the USR", Proc. BIW, Newport News (2012).

[9] V. Tzoganis, A. Jeff, C.P. Welsch, "Gas dynamics considerations in a non-invasive profile monitor for charged particle beams", Vacuum **109** (2014) p417–424.

[10] V. Tzoganis, C.P. Welsch, "A non-invasive beam profile monitor for charged particle beams", Appl. Phys. Lett. **104** (2014).

[11] M. Koch, S. Rehbein, G. Schmahl, T. Reisinger, G. Bracco, W.E. Ernst, et al., "Imaging with neutral atoms: a new matter-wave microscope", J. Microsc. **229** (2008).

[12] T. Reisinger, S. Eder, M.M. Greve, H.I. Smith, B. Holst, "Free-standing silicon-nitride zoneplates for neutral-helium microscopy", Microelectron. Eng. **87** (2010) p1011–1014.

[13] L. Kipp, M. Skibowski, R. Johnson, R. Berndt, "Sharper images by focusing soft X-rays with photon sieves", Nature **414** (2001).

[14] A. Sabatyan, P. Roshaninejad, "Super-resolving random-Gaussian apodized photon sieve", Appl. Opt. **51** (2012) p6315–6318.

Copyright © 2014 CC-BY-3.0 and by the respective authors

ISBN 978-3-95450-141-0

NSLS-II RF BEAM POSITION MONITOR-SYSTEM TEST AND INTEGRATION

Danny Padrazo, Anthony Caracappa , Weixing Cheng , Christopher Danneil, Al Dellapenna , Kiman Ha, Marshall Maggipinto, Joseph Mead, Om Singh, Kurt Vetter
Brookhaven National Laboratory, Upton, NY 11973, USA

Abstract

The NSLS-II Synchrotron Light Source is a state of the art 3GeV electron storage ring currently in the process of commissioning at Brookhaven National Laboratory. The RF Beam Position Monitors (RF BPM) are one of the key diagnostics systems required for a successful and efficient commissioning. There are more than 250 RF BPM installed in the injector and storage ring. Each RF BPM was fully tested, first under laboratory environment, and then after installation utilizing a built in pilot tone signal source. These successful tests provided a solid base for the integrity of the RF BPM system, prior to the start of beam commissioning. This paper will describe tests performed and results of system integration.

INTRODUCTION

Beam stability is a key factor in meeting the specifications for intensity and brightness designed to be delivered by NSLS-II. The multi-bunch stored beam condition for vertical and horizontal resolution, as well as long term stability must be less than 200nm. The NSLS-II BPMs are installed in thermally stabilized racks which are regulated to +/- 0.1 degree C of operating rack temperature, which is essential to meet the stability requirement [1,2]. This paper will detail the implementation of various test procedures designed and performed on each BPM receiver (Fig. 1) pre and post installation.

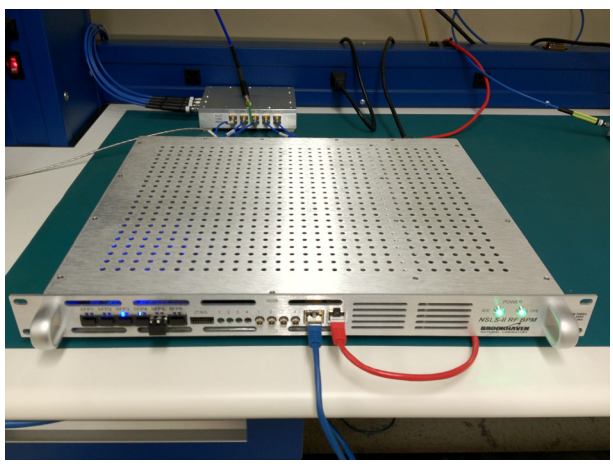


Figure 1: NSLS-II RF BPM production unit.

PILOT TONE COMBINER

An integral part of testing depends on implementation of the on board Pilot Tone Synthesizer, which generates a CW signal that is phase locked to the machine clock and is connected to the Pilot Tone Combiner module (PTCM) – shown in Fig. 2. This module is a custom design consisting of a passive RF board mounted in an aluminum enclosure and resides in the tunnel, near the BPM PUE and is connected via custom SIO2 Semi-Rigid Cables. The PTCM is characterized by comprehensive S-Parameter measurements, where S21 channel to channel variations are removed via automatic calibration routine, which maps the pilot tone to the received beam signal via measured S21[1,2].

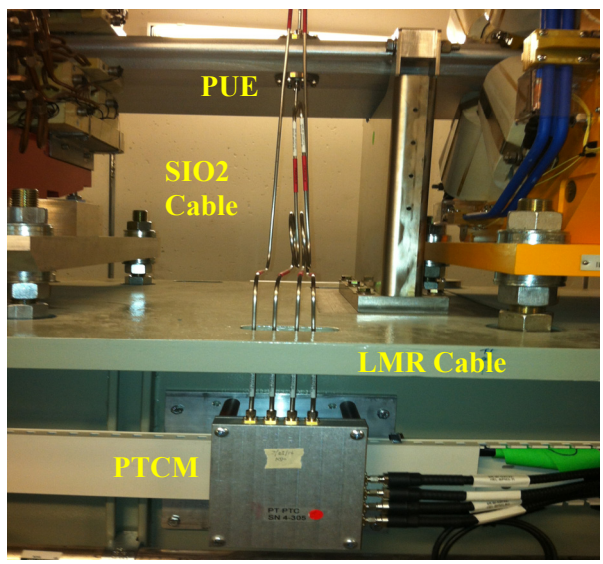


Figure 2: Pilot Tone Combiner Module (PTCM).

PRE/POST-INSTALLATION TESTING

Testing is conducted in a controlled laboratory environment using a custom test setup including VME based event/timing system, data acquisition, and post processing. MATLAB and Python based scripts have been developed to execute routines to test key functions and features of the BPM receiver. Performance tests procedures are first completed on each Analog Front End Board (AFE) using a dedicated receiver chassis populated with a Digital Front End Board (DFE). System testing is accomplished using custom routines developed to capture data for all three

Copyright © 2014 CC-BY-3.0 and by the respective authors

ISBN 978-3-95450-141-0

phases of functional tests, and utilizes the on board Pilot Tone Synthesizer as a CW source. The data is then organized, plotted and archived on per unit bases. Test results are stored in PDF, HTML, or screen shot images using MATLAB publishing feature. System integration tests are performed when BPM receivers are installed, and are run using EPICS to test network communications as well as IOC functionality and is presented using Control System Studio (CSS) as the user interface. High level applications are developed to run via Control System Studio (CSS) via a dedicated BPM IOC Server, with the added benefit of remote access to all of the BPM receivers installed in the accelerator [3]. These tools are used pre and post installation for lab based tests as well as integration tests and commissioning. Engineering panels for CSS have been developed to easily control parameters of each BPM in real-time. Figure 3 shows one of the CSS Engineering panel.

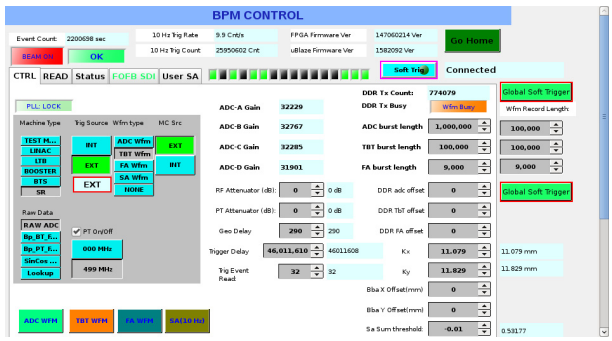


Figure 3: CSS Engineering panel for BPM control.

There are 3 phases of testing performed on each BPM receiver prior to installation. Each phase tests have several scripts performing various tests, as shown in Table 1.

PHASE 1 TEST

Communication interface and Firmware verification - This test is Python based and reports the IP address, MOXA port assignment, Mode, Firmware version, and PLL status – as shown in Fig. 4. Each RF BPM is parametrically configured for Single-Pass, Booster, and Storage Ring application. They are assigned a unique IP address and is mapped to a geographical location at NSLS-II. Upon power up, the BPM is examined to determine proper configuration mode. The ip address and MOXA port are manually configured. The firmware version , PLL status, ip, and port assignment is obtained by executing Phase 1 test script. Each BPM is automatically configured to one of three operational modes, as all three operational modes are derived from the storage ring revolution frequency.

Table 1: Stages of Testing and Routines

Description	Script	Output
Phase 1 Test	PYTHON	
Serial Communication	bpm_status.py	MOXA ip/port #
Network Communication	bpm_status.py	BPM Receiver ip
Firmware Version	bpm_status.py	FPGA/ublazer ver #
PLL/Machine Clk Present(378KHz)	bpm_status.py	PLL status T/F
Phase 2 Test	MATLAB	
117MHz Phase Noise(Jitter)	R&S FSUP	VCXO/PLL output
ADC Raw Data(117MHz Sample Rate)	test2.m	A-D, Sum Plot
Frequency Domain	test2.m	dbFs vs. Freq plot
Time Domain	test2.m	Samples vs. Counts plot
TBT Data(378KHz(SR), 1.89MHz(BR)	test2.m	A-D,X,Y Plot
FA Data (10KHz)	test2.m	A-D,X,Y Plot
SA Data (10Hz)	CSS	A-D,X,Y Plot
Phase 3 Test	MATLAB	
Cable Orientation Verification	test2.m	A-D FFT Plot
Static Gain Calibration	Static_gain_cal.m	
Intensity Dependence	Intensity_sweep_test.m	



Figure 4: Phase 1 test data (Communication/Firmware Verification).

Copyright © 2014 CC-BY-3.0 and by the respective authors

PHASE 2 TEST

ADC_Raw Histogram Data, ADC_Raw Data in Time & Frequency Domain, TBT_Position, FA Position, and 117MHzPhase Noise (Jitter) plot – These tests are MATLAB based and are performed on each receiver both as a lab test, as well as a site test after installation, and compiles raw data to plot Time and frequency domain response of each ADC channel output, as well as 10KHz FA position data, and TBT position data. The test setup is fairly elaborate (shown in Fig. 5) and essentially a representation of operations configuration. The site test is performed when all BPMs are installed in the rack and cabled with production hardware.

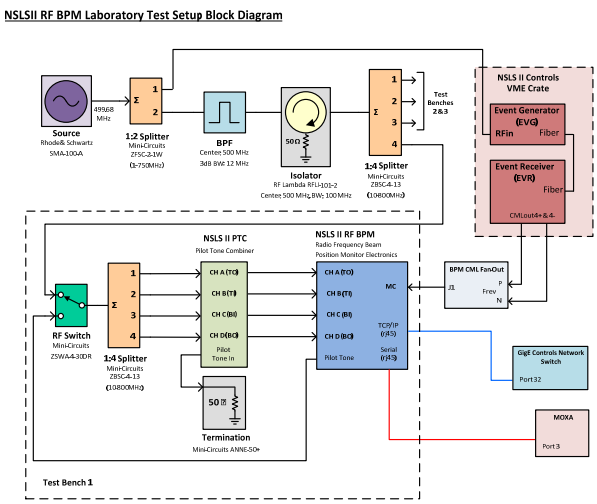


Figure 5: Phase 2 Test set up.

All test scripts are run local to racks via portable laptop computer. EPICS based applications via CSS engineering panels can also be used as a cross check during this phase of site testing, and is part of the integration testing requirement. A Noise jitter plot for the VCXO/PLL output is also produced using a Rhode & Schwarz FSUP Signal Source Analyzer. Figures 6-10 show the plots of data for phase 2 test.

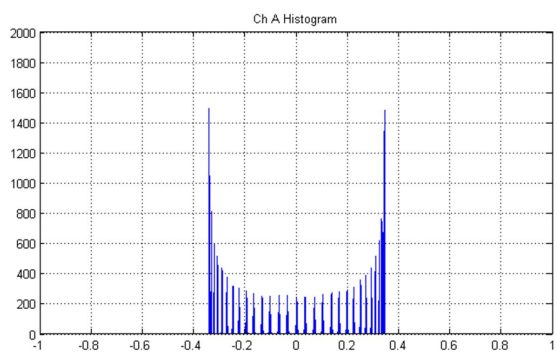


Figure 6: Phase2 data - channel A ADC raw histogram.

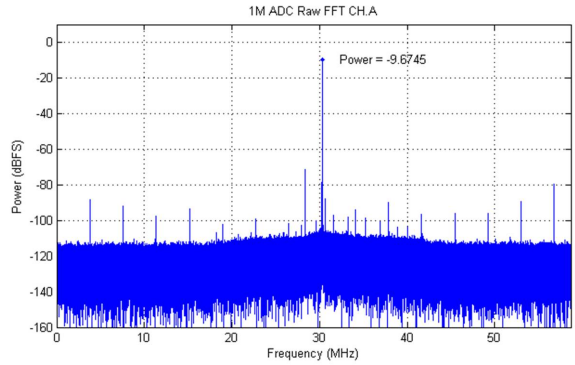


Figure 7: Phase data - channel A- ADC raw.

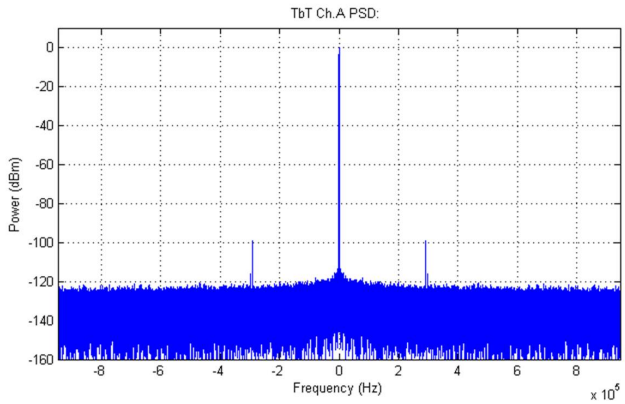


Figure 8: Phase 2 data - channel A - TBT Pwr dBm.

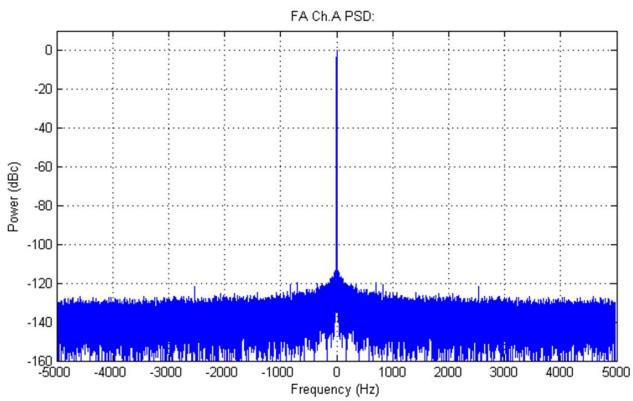


Figure 9: Phase 2 data - channel A FA Pwr.

Copyright © 2014 CC-BY-3.0 and by the respective authors

ISBN 978-3-95450-141-0

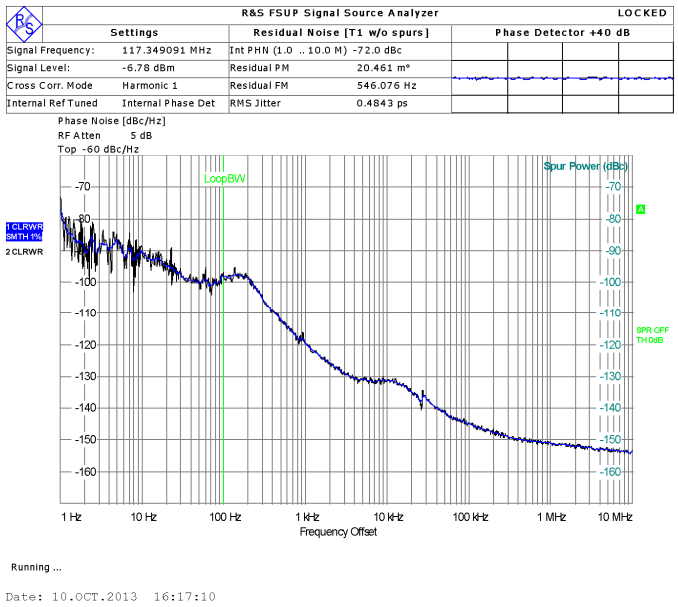


Figure 10: Phase 2 data -117MHz phase noise.

PHASE 3 TEST

Cable Orientation Verification (COV), Static Gain Calibration (SGC), and Intensity Dependence Test (IDT) - There are 3 separate MATLAB routines developed to perform these tests, and is part of site wide system integration. In addition the on-board Digital Step Attenuators are used for the SGC and IDT test respectively. The COV test is performed to certify all cable connections between the PUE and receiver, and is pilot tone based. The SGC test is performed to calculate the offsets due to channel-channel AFE amplifier gain differences. The IDT routine quantifies the performance of each channel as a function of position vs. signal power over the range of the Digital Step Attenuator in the Pilot Tone Synthesizer (0-31db), in 1db increments, and uses the PT as CW source. The hardware setup is identical for both SGC and IDT; and is shown in Fig. 11.

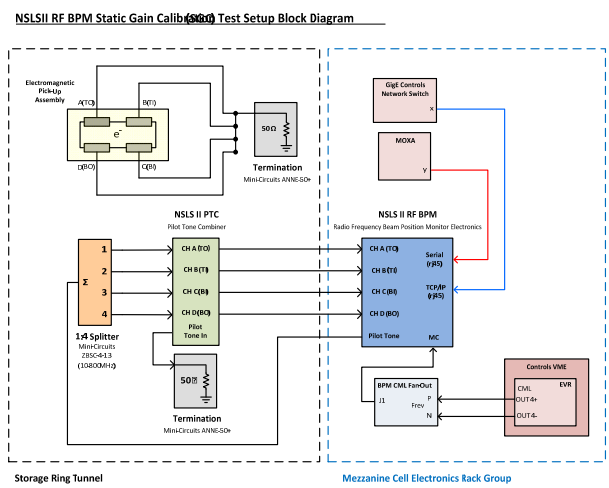


Figure 11: Phase 3 SGC/IDT test setup.

Cable Orientation Verification (COV)- A Process was implemented to address cable orientation verification. This helps insure that cables were connected correctly between PUE and receiver inputs. The NSLS-II BPM system consists of three distinct transmission line sets including phase matched, low loss SIO2 and LMR Coaxial cable, as well as phased matched custom patch cables in the rack. In addition, various adaptors are incorporated in these connections, and comprise over 6 thousand connections system wide. An elegant simple solution was developed using either an external CW source or the on board Pilot Tone Synthesizer and external attenuators installed as follows; Channel A(TO) = 0db, Channel B(TI) = -10db, C(BI) = -20db, D(BO) = -30db. The power level plots in Fig. 12, provided by MATLAB script illustrates 1:1 mapping of all channels in Frequency domain.

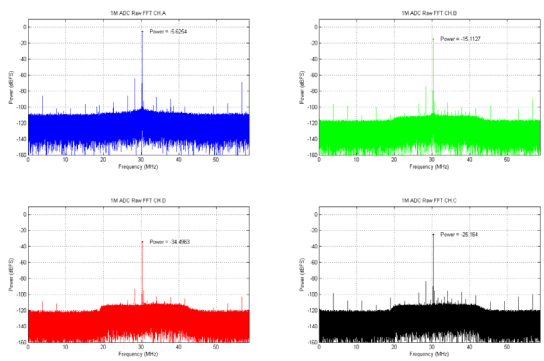


Figure 12: Phase 3 data - Pwr dBFs vs. freq.

Static Gain Calibration (SGC)- To address differences in the channel-channel AFE amplifier gain, which could result in significant offsets to the calculated position values, a MATLAB based test and calibration process was developed. The pilot tone drive through a calibrated 1:4 splitter is supplied at the tunnel PTC. The power is then measured at the receiver. The MATLAB routine selects one of the four channels as

Copyright © 2014 CC-BY-3.0 and by the respective authors

unity. The difference between the remaining three and unity channel is calculated. This process is repeated in 1dB increments from 0db to 20dB using the available digitally controlled attenuators. A 21:5 element matrix is generated with weighting coefficients for each channel, across the gain set range and shown in Table 2 below.

Table 2: Static Gain Coefficient Matrix

	A	B	C	D
0	32597	31789	**32767**	31993
1	32553	31772	**32767**	31972
2	32569	31807	**32767**	31992
3	32531	31794	**32767**	31971
4	32551	31786	**32767**	31979
.				
.				
15	32304	31552	**32767**	31722
16	32117	31366	**32767**	31624
17	32094	31352	**32767**	31597
18	32120	31395	**32767**	31598
19	32097	31382	**32767**	31598
20	32124	31379	**32767**	31605

Figure 13 shows that position variation has been reduced to less than 1 micron after applying the SGC.

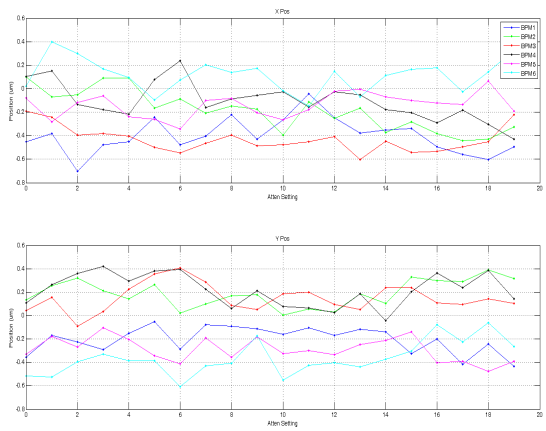


Figure 13: Position Vs attenu ator after applying static gain calibration.

Intensity Dependence Test (IDT)- Intensity dependence test is pilot tone based and is performed on each BPM site wide as a measure to test performance specification of 200 um stability in its linear range. It is the same hardware setup as the SGC test, and implements a custom MATLAB script. The on board Pilot Tone Synthesizer is used as a CW source and the Digital Step Attenuator is varied from (0-31db), in 1db increments. Figure 14 shows a typical intensity dependence and rms noise with power range of 40 dB.

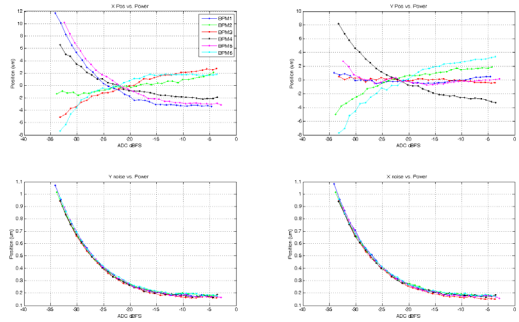


Figure 14: Phase 3 Intensity Dependence Data.

SUMMARY

Beam position Monitor system test and integration procedures including custom software routines and data capture, contributed to a methodology that provided effective and successful diagnostics for system level testing both pre and post installation in preparation for Storage ring commissioning. This streamlined efforts to meet system requirements as well as schedule for operations readiness. An exhaustive set of test procedures proved to produce a very high yield of working production units, as well as insuring system integrity site wide. This also provided a means to characterize and catalog performance of each BPM unit prior to installation. This data was also depended on as baseline measure for integration testing, as to ensure that design specifications were met.

REFERENCES

[1] Kurt Vetter, "NSLS-II RF Beam Position Monitor", PAC11, New York, USA, (2011).
[2] Kurt Vetter, "NSLS-II RF Beam Position Monitor Update", BIW12, Newport News, VA, USA, (2012).
[3] Kiman Ha, "NSLS-II Beam Position Monitor Embedded Processor and Control System," ICALEPCS11, Grenoble, France, (2011).

Copyright © 2014 CC-BY-3.0 and by the respective authors

ISBN 978-3-95450-141-0

PROPOSED PULSE STRETCHING OF BPM SIGNALS FOR THE POSITION DETERMINATION OF VERY SHORT AND CLOSELY SPACED BUNCHES*

P. Thieberger#, S. Brooks, C. Hamdi, R. Hulsart, G. Mahler, M. Minty, R. Michnoff and D. Trbojevic
Collider Accelerator Department, Brookhaven National Laboratory, Upton, New York, U.S A.

Abstract

A proposal for a future ultra-relativistic polarized electron-proton collider (eRHIC) is based in part on the transport of multiple electron beams of different energies through two FFAG beam transports around the 3834 m long RHIC tunnel circumference in order to recirculate them through an Energy Recovery Linac (ERL) for their stepwise acceleration and deceleration. For each of these transports, the beams will travel in a common vacuum chamber horizontally separated from each other by a few mm. Determining the position of the individual bunches is challenging due to their very short length (~12 ps rms) and their temporal proximity (less than 4 ns in some cases). Providing pulses adequate for accurate sampling is further complicated by the less-than-ideal response of long coaxial cables. Here we propose two approaches to produce enhanced, i.e. stretched, pulse shapes of limited duration; one based on specially shaped BPM electrodes and the other one on analog integration of more conventional stripline BPM signals. In both cases, signals can be generated which contain relatively flat portions which should be easier to sample with good precision without requiring picoseconds timing accuracy.

INTRODUCTION

A plan is being developed for replacing the Relativistic Heavy Ion Collider (RHIC) by a high energy electron proton collider (eRHIC) [1]. The proton beam would be accelerated and stored in one of the existing RHIC rings while the 16 GeV or 21 GeV electrons would be accelerated and decelerated in multiple passes through an Energy Recovery Linac (ERL) [1, 2]. The present design calls for two electron beam transport arcs, located in the RHIC tunnel, both based on a Fixed-Field Alternating Gradient (FFAG) lattice design [1]. There would thus be several electron trajectories within each of these two FFAG arcs, slightly displaced horizontally and nominally at the same vertical height. Figure 1 shows an example of a short portion of such trajectories through a set of three FAG magnets in the "high energy" FFAG beam transport.

Accurately monitoring the positions of these beams at multiple locations around the arcs is a major challenge because some of these very short bunches (~12 ps rms) are separated in time by less than 4 ns, and because no beam position monitor (BPM) pick up electrodes (PUEs) may overlap the orbit plane due to the intense synchrotron radiation. Various alternative options are being considered to mitigate these difficulties, such as providing so called pilot bunches, well separated in time from the regular bunch sequence and also the possible use of synchrotron radiation generated in or near the visual range to measure orbit positions with optical systems.

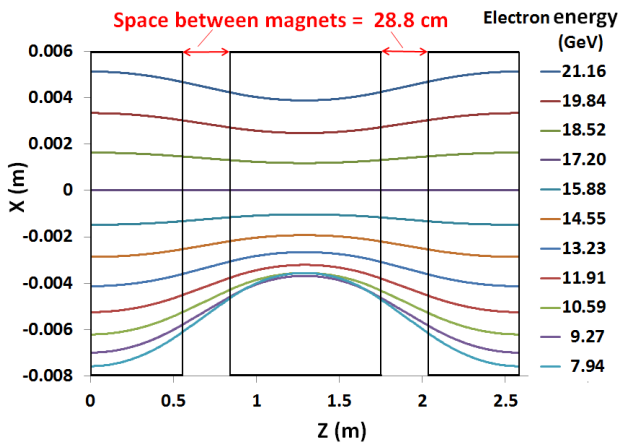


Figure 1: Electron trajectories in one cell of the high energy FFAG beam transport [1].

Here we have started to address these issues by performing Particle Studio [3] simulations for two preliminary designs of possible BPM configurations, one based on a set of conventional "button" pickup electrodes (PUEs) and the other one on a new design of tapered stripline PUEs designed in an attempt to mitigate an additional challenge, namely the result of sample timing errors. This last problem is particularly severe when closely-spaced bunches make it impossible to use conventional filters [4] with long enough time constants so as to provide pulse maxima that are flat enough to be accurately sampled and digitized.

DESCRIPTION OF THE MODELS

The two models used for the Particle Studio simulations are shown in Figs. 2 and 4. In both cases, the left and right tubular parts of the vacuum chamber cross sections will have cooled walls to absorb the power generated by the intense synchrotron radiation.

The tapered striplines shown in Fig. 4 are designed to receive a linearly increasing and decreasing induced charge as the "pancaked shaped" (Lorentz-contracted)

* This material is based upon work supported by the U.S. Department of Energy, Office of Science, Brookhaven National Laboratory under Contract No. DE-AC02-98CH10886.
# PT@BNL.GOV

Copyright © 2014 CC-BY-3.0 and by the respective authors

electromagnetic field traverses over them. The output current from one of these pick-up electrodes, which is proportional to the derivative of these induced charges, will therefore show relatively flat portions amenable to accurate digitization without the use of additional filters. To what extent this can be achieved will be indicated by the simulation results shown in the next section.

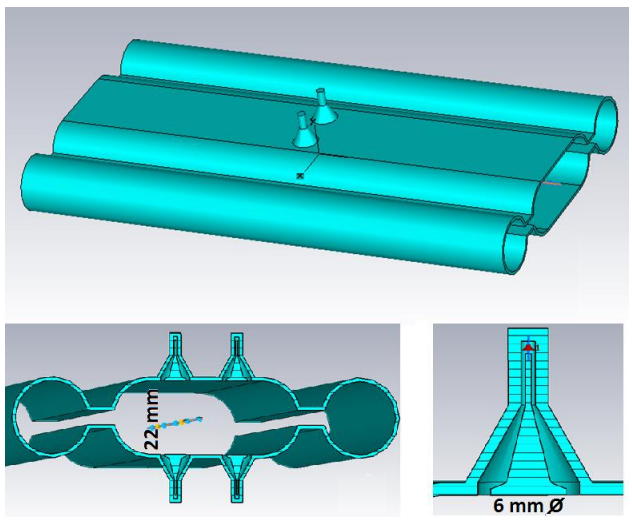


Figure 2: Model used for the Particle Studio simulations of a BPM consisting of four 6 mm diameter button-type PUEs. The unusual positions are chosen so as to allow synchrotron radiation to escape and also to accommodate the ± ~5 mm horizontal orbit locations.

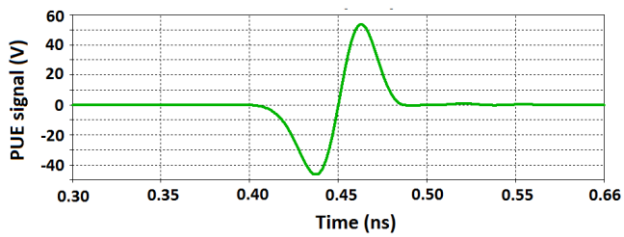


Figure 3: Particle Studio simulated button type PUE signal generated on a 50 Ω load for a centered, 4 mm rms long fully relativistic (v=c) bunch containing 3.1E10 electrons (~ 5 nC).

As mentioned above, the conventional configuration of two horizontal and two vertical PUEs cannot be implemented for this application. What is also unusual is that the design orbits are not horizontally centered. The two quantities that will be computed in this case to measure the horizontal and vertical positions will each necessarily contain all four voltage values obtained from the PUEs. Naming these values UL, UR, DL and DR, where U stands for up, D for down, L for left and R for right we will calculate the ratios Qx and Qy as most indicative of the horizontal and vertical position respectively:

$$Q_x = \frac{(UL+DL)-(UR+DR)}{UL+UR+DL+DR} \quad \text{and} \quad Q_y = \frac{(UL+UR)-(DL+DR)}{UL+UR+DL+DR}$$

The sum of the four signal amplitudes in the denominators provide the required intensity normalization. How these quantities correlate with the actual positions will be determined below from the simulations. Experimental calibrations would be performed for an actual system to allow the determination of real positions.

The simulated signal amplitude response for the button BPM is shown in Fig. 3 assuming bunch parameters of the FFAG-based eRHIC design. For detection of the pilot bunches the signals the PUE signals will be filtered and sampled using conventional electronics as described for example in Reference [4].

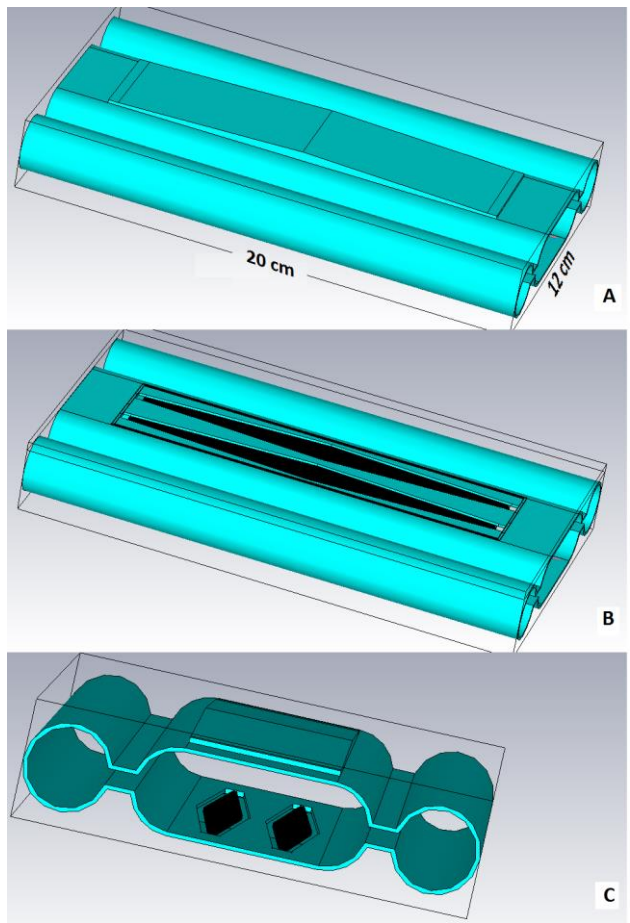


Figure 4: Model used for the Particle Studio simulations of a BPM consisting of four tapered striplines. A) External view. At the top, one sees the inclined ground plane used to maintain the stripline's 50 Ω impedance in spite of its varying width. B) The top ground plane has been removed and one sees the two top tapered striplines (black). C) End view showing the two bottom striplines.

SIMULATED RESPONSES OF THE TAPERED PUEs

The Particle Studio simulations were performed with the model shown in Fig. 4 using a 12 ps rms bunch containing 3.1E10 electrons which corresponds to a

Copyright © 2014 CC-BY-3.0 and by the respective authors

ISBN 978-3-95450-141-0

charge of ~5 nC. The trajectory positions were varied in 1 mm steps from -6 to 6 mm horizontally (x direction) and from 0 to 3 mm vertically (y direction). The signals from one of the PUEs as functions of x are shown in Fig. 5 for y=0. The short positive and negative peaks seen in the signals (see Fig. 5) are due to the fact that the PUEs cannot end in sharp points. In fact these 150 mm long PUEs are 10 mm wide in the center and 1mm wide at their ends.

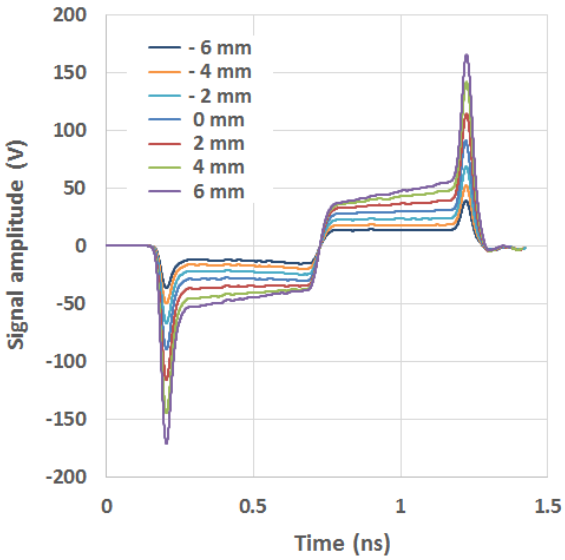


Figure 5: Simulated signals generated on a 50 Ω load connected to one end of one of the PUEs shown in Fig. 4 for vertically centered bunches containing 3.1E10 electrons (~5 nC). The horizontal orbit positions are varied from -6 mm to +6 mm in 1 mm steps.

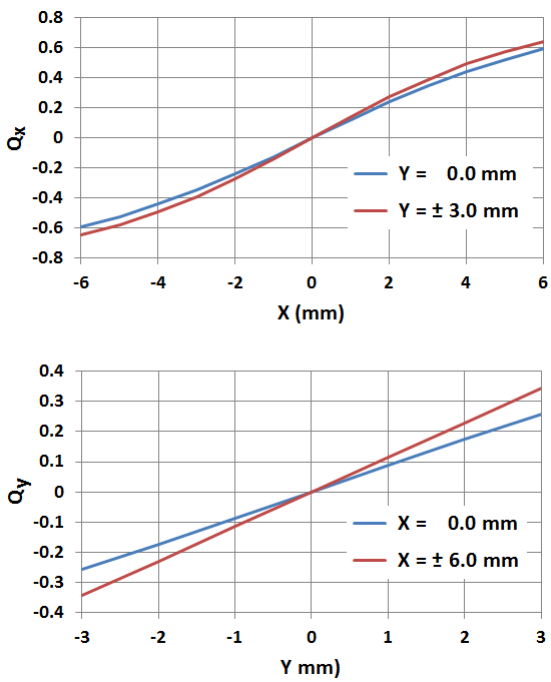


Figure 6: Horizontal (top) and vertical (bottom) calibration curves obtained from the simulations when the orbit was either centered or at its extreme position in the other plane.

Figure 6 shows calibration curves obtained by using the quantities *Qx* and *Qy* defined above, calculated by using the pulse amplitudes at the centers of the relatively flat negative portions of the signals (see Fig. 5). For each of these cases we show two calibration curves; one with the trajectory centered in the other plane and the second one with the trajectory at its extreme position in the other plane

We see from Fig. 6 that the ***x***-calibration depends on the value of ***y*** and vice versa. This can be seen in a more comprehensive way in Fig. 7 which shows the mapping of the ***Qx*** and ***Qy*** values onto the corresponding ***x*** and ***y*** coordinates

The mapping "pincushion" distortion shown in Fig. 7 is also present for other types of BPMs. In the present case it is particularly important to take into account two-dimensional mapping since some of the nominal orbits are horizontally displaced by as much as ± ~5 mm.

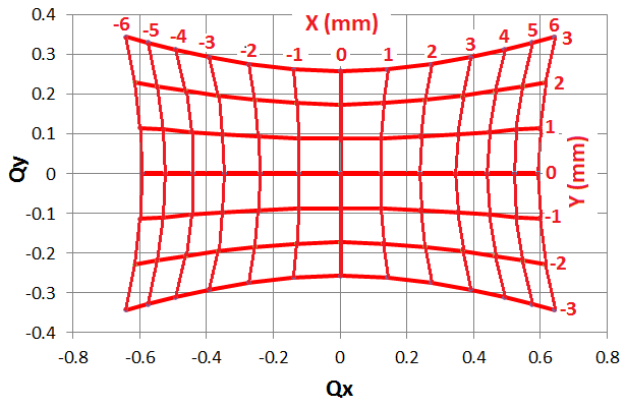


Figure 7: Mapping of the ***Qx*** and ***Qy*** ratios calculated from the tapered stripline PUE signal amplitudes (see text) onto the corresponding ***x*** and ***y*** beam position coordinates.

POSITION MEASUREMENT SENSITIVITY TO TIMING ERRORS

The slopes of the signals shown in Fig. 5 increase gradually as the horizontal distance from the center increases. These slopes will result in measurement errors if there are sampling-time fluctuations. The sensitivities to sampling-time errors are shown in Figs. 8 and 9. Figure 8 shows this sensitivity as function of horizontal position obtained using the simulated data of Fig. 5 by sampling values of the negative part of the pulses (blue points) and of the positive part (red points). The slope of the signals are of opposite sign and therefore the errors at each value of x are opposite too. These calculations were performed assuming a sampling time length of 100 ps and thus averaging the values between 0.4 and 0.5 ns for the negative part and between 0.9 and 1.0 ns for the positive one. Then both of these intervals were shifted by 10 ps to establish the timing sensitivity.

Copyright © 2014 CC-BY-3.0 and by the respective authors

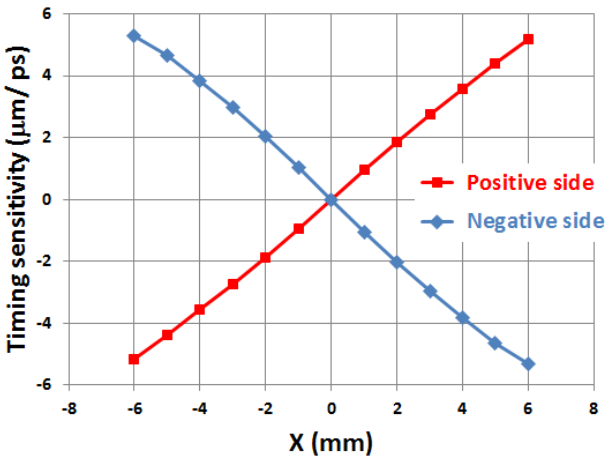


Figure 8: Sensitivity of simulated horizontal position measurements to sampling-time fluctuations. These relatively small time dependences are due to the slope of the positive and negative portions of the pulses seen in Fig. 5.

The worst cases (for large x values) of ~5 µm per ps are similar to values observed with regular BPMs and much longer bunches. Averaging these two position results at each value of x largely eliminates the sampling time sensitivity providing the sampling time errors are common to both measurements. The residual sensitivities of these average positions are shown in Fig. 9.

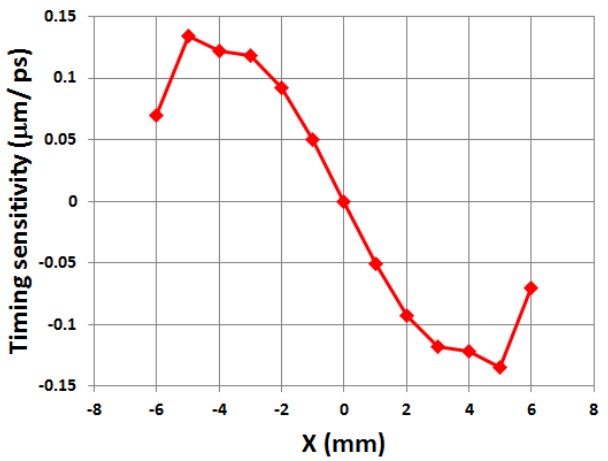


Figure 9: Residual timing sensitivity of positions obtained by averaging values obtained by sampling negative and positive parts of the signals shown in Fig. 5 (see text).

CONCLUSIONS

The multiple eRHIC electron orbits in the proposed lattice of the Non-Scaling FFAG spread out horizontally over ± 5 mm, and the presence of intense synchrotron radiation requires a somewhat unusual BPM PUE configuration. We have shown how positions can be obtained for such configurations and we have analyzed in detail the type of two-dimensional measurement distortions that will need to be corrected in software.

For the extremely short eRHIC electron bunches, the tapered stripline BPM could, at least in principle, generate signals amenable to accurate sampling and digitization without the use of conventional filters. This may allow accurate position measurements of bunches separated by as little as 2 ns for the present design. The major issue that hasn't been addressed here is how the performance will be affected by the coaxial cable response if the digitizer can't be located very close to the BPM.

A possible alternative to the tapered stripline BPM that has not been investigated in detail is a BPM based on straight (not tapered) striplines used in conjunction with signal integrators. Yet another possible modification of both of these designs would consist in replacing the "floating" PUEs considered here with ones half as long and grounded at one end. The calibration issues for all of these alternative designs would be the same as studied here. Experiments as well as further simulations will be required to make progress towards a final design.

REFERENCES

[1] E. C. Aschenauer, et.al. , eRHIC Design Study: An Electron-Ion Collider at BNL. arXiv:1409.1633 [physics.acc-ph].

[2] D. Kayran et. Al. Proceedings of PAC11, New York, NY (2011) THP006.

[3] Particle Studio by CST – Computer Simulation Technology: https://www.cst.com/products/cstps

[4] S. R. Smith, "Beam Position Monitor Engineering", Proc. 7th Beam Instrumentation Workshop (BIW 96) : http://slac.stanford.edu/cgi-wrap/getdoc/slac-pub-7244.pdf

Copyright © 2014 CC-BY-3.0 and by the respective authors

ISBN 978-3-95450-141-0

OVERVIEW OF THE GEOMETRICAL NON-LINEAR EFFECTS OF BUTTON BPMS AND METHODOLOGY FOR THEIR EFFICIENT SUPPRESSION

A. A. Nosych, U. Iriso, A. Olmos, ALBA CELLS, Barcelona, Spain
M. Wendt, CERN, Geneva, Switzerland

Abstract

This paper describes an overview of the geometric non-linear effects common to beam position monitors (BPMs) installed in the accelerators and a methodology to correct for these effects. A typical characteristic curve of a pick-up is linear within a limited range from the BPM origin. At larger offsets the non-linearity of the curve is more pronounced and gets worse if the button diameter is small with respect to the beam pipe diameter. The general real-time linearization methods usually utilize linear correction combined with a simplistic polynomial, which may lead to inaccuracies in their limited application. We have developed a more rigorous methodology to suppress the non-linear effects of the BPMs through electromagnetic (EM) simulations and 2D fitting approximations. The focus is mainly on standard button pick-ups for the electron (ALBA) and proton machines (LHC).

INTRODUCTION

BPMs are among the most important and numerous parts of a diagnostics system of any particle accelerator. Accelerators require constant beam orbit monitoring in order to control the quality of passing beams and allow various feedback systems to improve it. Usually beams travel close to geometrical centers of BPMs on their way, following the optimal "golden" orbit. However, beams are sometimes intentionally steered away from the optimal orbit, whether it is to increase the crossing angle in order to improve luminosity of a collider (LHC), or to study the non-linear magnetic field components of a storage ring (ALBA).

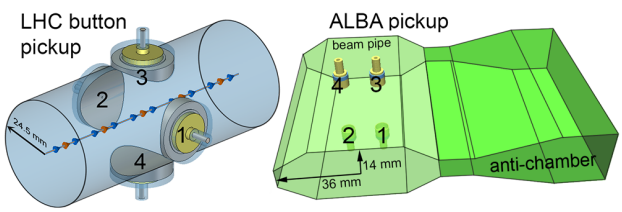


Figure 1: 3D models of a typical LHC curved-button pickup and a standard pickup of ALBA.

Every beam position reading of a BPM is subject to non-linear errors. The non-linear behavior of a BPM pickup is caused by its geometrical design and the resulting errors are more pronounced at larger beam offsets from the BPM origin. In this paper we will describe two standard BPM geometries, one belonging to LHC: a proton collider, and another to ALBA: a synchrotron light source (both geometries are shown in Fig. 1). After discussing the modeling and simulation process we will summarize non-linear effects of the BPMs' characteristic response for different signal treatments, and address results of an efficient non-linearity correction using high-order surface (2D) polynomials.

MODELLING AND MAPPING A BPM

Left in Fig. 1 is a common 4-button (arranged 90^o apart) pickup mounted on a beam pipe of circular cross-section (radius $R_{\mathrm{lhc}} = 24.5$ mm) belonging to the LHC. Right in Fig. 1 is a flat-button BPM used in ALBA, a 3 GeV synchrotron light source, with 2 pairs of buttons located above and below the beam, which travels in a hexagonal beam pipe of 72×28 mm transversely ($R_{\mathrm{alba}} = 36$ mm).

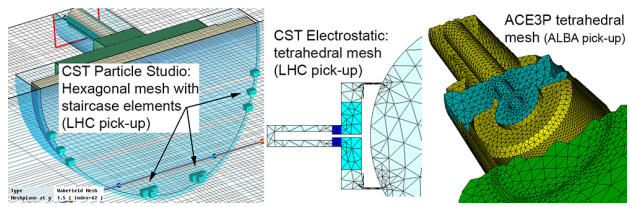


Figure 2: Meshing BPM buttons with hexahedral mesh of CST Particle Studio and tetrahedral meshes of CST Electrostatic and ACE3P.

As usual in light sources, parts of ALBA vacuum chamber include the anti-chamber used for photons. Depending on location in the storage ring, the anti-chamber has different dimensions; one of them is shown in Fig. 1 right. Here the beam pipe loses its symmetry in Y plane; however, we have studied 2 types of anti-chambers attached to the same BPM module, and have not observed any noticeable effect on BPM sensitivity. Hence, in our studies we consider all types of ALBA beam pipes symmetric, omitting the anti-chamber.

To simulate BPM response of the LHC button in time-domain we have initially used CST Particle Studio [1]. We have found that for 3D geometry with small curved elements (e.g. a curved button and a curved vacuum gap around it, Fig. 2 left) the hexahedral mesh of CST PS is not very efficient: in pursuit to approximate curves by orthogonal edges, the mesh cells greatly multiply in numbers (at least 6M mesh cells for this BPM), leading to lengthy simulations: it took 25 minutes on a desktop PC with 2x3.5 GHz CPU and 8 Gb RAM to simulate a single beam transit.

To avoid this time waste we have switched to the Electrostatic solver of CST in "semi-2D" mode [2], using the tetrahedral mesh with more accurate approximation of curved elements. The solver itself does not allow a true 2D input, so we introduce a 1 mm thick "slice" of the BPM with magnetic

Copyright © 2014 CC-BY-3.0 and by the respective authors

ISBN 978-3-95450-141-0

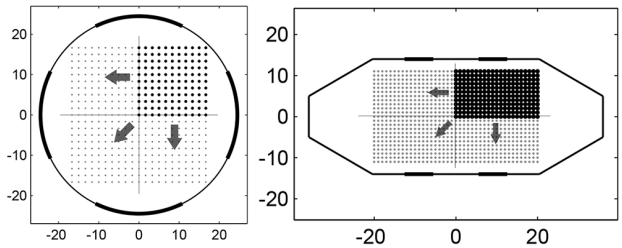


Figure 3: Mapping layout of LHC (left) and ALBA (right) BPMs with equidistant grid covering the first quadrant of the coordinate system.

boundaries at the z-planes (Fig. 2 middle). The electrostatic potentials are then evaluated for one BPM electrode and, due to symmetries, restored for others by mirroring/rotation. The obtained potentials are then combined for the normalized horizontal/vertical potential, which is equivalent to the normalized line charge (the beam) position. A single simulation maps the entire BPM in seconds.

To simulate the ALBA pick-up we have used the 3D time-domain solver (T3P) of ACE3P [3], which also offers tetrahedral meshing (Fig. 2 right) and quick (within minutes) simulations on parallel CPU clusters. The BPM was excited with a single relativistic bunch excitation (Q=3.4E-10 C, σ_τ=5 mm). To simulate the BPM response as a function of beam position, a beam displacement parameter sweep within a quadrant in the transverse plane (as shown in Fig. 3) was executed in T3P using the transverse beam coordinates (x, y) as iteration parameters with constant step size. At each beam position the peak voltage $V_{i=1,2,3,4}$ of every BPM port was logged. Due to 4-fold symmetry of the ALBA BPM, the mapped quarter-grid is then mirrored (taking into account appropriate sign swaps) to reproduce a full map, thus describing behavior of the entire BPM. We have stayed with a 41×23 grid ($\pm 20 \times \pm 11$ mm) for the ALBA BPM, and a 21×21 grid ($\pm 17 \times \pm 17$ mm) for the LHC pickup. The initial choice of grid size, step size and number of grid points is open; however, it has an impact on the quality of beam position linearization and area of efficient correction.

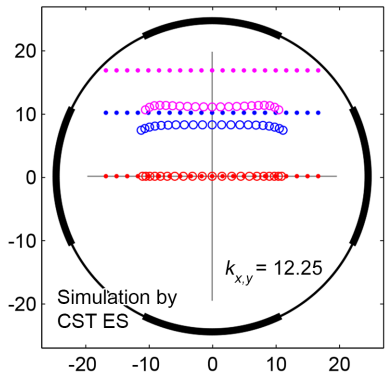
We consider the 3D approach as the default technique, as it accurately takes all beam-induced effects (e.g. resonances, non-TEM effects, etc.) into account. Analysis of the mentioned tools for BPM modelling was previously discussed in [2] in more detail.

NON-LINEARITY TREATMENT

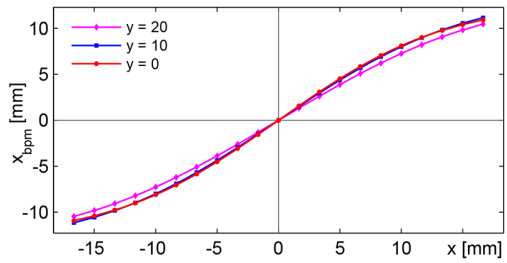
By comparing the signals of opposite sets of electrodes, a beam intensity independent, normalized beam position signal can be deduced. There are several ways to restore the beam position from 4-button BPM signals due to distinct button arrangements in considered geometries. We will show three examples of common linear signal treatments.

Difference over Sum

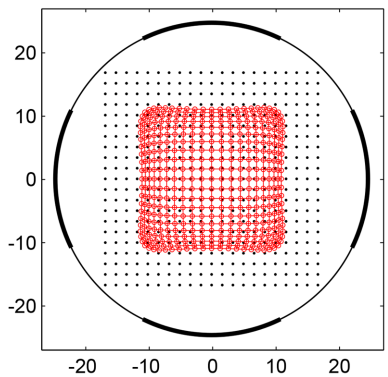
In a simplistic symmetric BPM button arrangement around a circular vacuum chamber (LHC case), the pickup response can be approximated by a wall-current model, where the normalized position characteristic in the XY plane is described in general by



(a) Horizontal beam sweeps for 3 vertical displacements.



(b) Characteristic curves of the beam sweeps above.



(c) Mapped grid of $(x^{lhc}_{dos}, y^{lhc}_{dos})$.

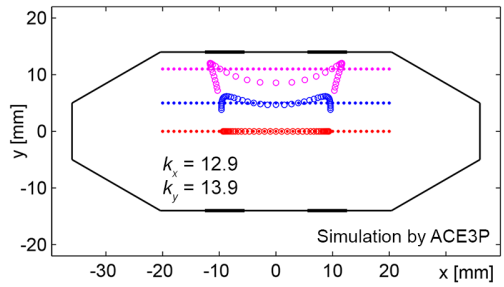
Figure 4: Results of DOS application to LHC BPM map.

$$x^{lhc}_{dos} = k_x \times \frac{V_1 - V_2}{V_1 + V_2}\,, \quad y^{lhc}_{dos} = k_y \times \frac{V_3 - V_4}{V_3 + V_4} \qquad (1)$$

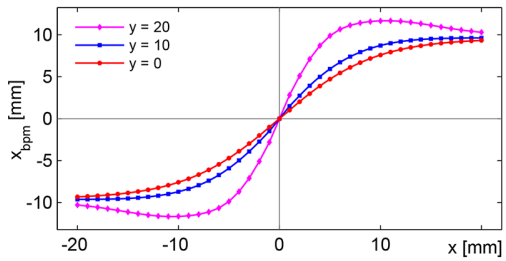
Here k_x, k_y are the linear calibration constants to mm, and in fact, for circular beam pipes they are approximated by $k_{x,y} = R/2$ [2]. Equation 1 represents a classic linear approach, usually referenced as the Difference Over Sum (DOS), its application is plotted in Fig. 4 for horizontal sweeps at fixed vertical offsets and for a full mapped grid of the LHC BPM. Here the linear region of $k_{x,y}$ is within $x, y = \pm 7$ mm.

Copyright © 2014 CC-BY-3.0 and by the respective authors

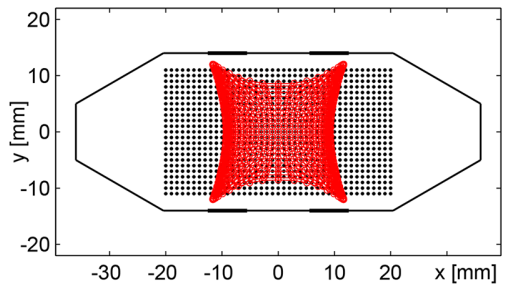
ISBN 978-3-95450-141-0



(a) Horizontal beam sweeps for 3 vertical displacements.

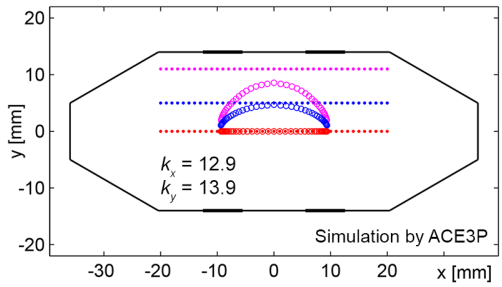


(b) Characteristic curves of the beam sweeps above.

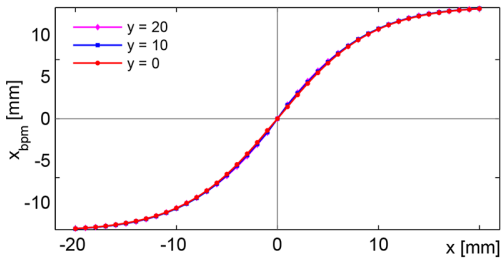


(c) Mapped grid of $(x^{\text{alba}}_{\text{dos}}, y^{\text{alba}}_{\text{dos}})$.

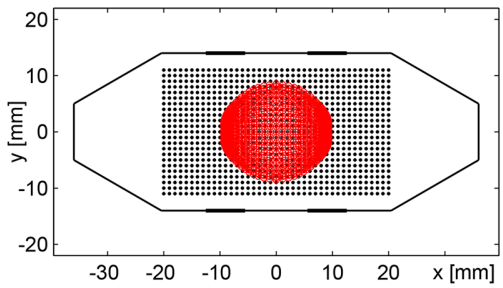
Figure 5: Results of DOS application to ALBA BPM map. Anti-chamber is not shown.



(a) Horizontal beam sweeps for 3 vertical displacements.



(b) Characteristic curves of the beam sweeps above.



(c) Mapped grid of $(x^{\text{alba}}_{\text{diag}}, y^{\text{alba}}_{\text{diag}})$.

Figure 6: Diagonal treatment of ALBA BPM map.

Due to button placement in the ALBA BPM, a modification of DOS is used to normalize the electrode signals [4]:

$$x^{\text{alba}}_{\text{dos}} = k_x \times \frac{V_3 + V_1 - V_4 - V_2}{V_1 + V_2 + V_3 + V_4} \tag{2}$$

$$y^{\text{alba}}_{\text{dos}} = k_y \times \frac{V_3 + V_4 - V_2 - V_1}{V_1 + V_2 + V_3 + V_4} \tag{3}$$

Here $k_{x,y}$ can be approximated by the slope of the characteristic curve (linear part of it) for each axis separately, e.g. the red curve ($y = 0$) for $|x| \leq 5$ mm in Fig. 5(b) can provide a corresponding constant k_x. However, this approach has limited application due to strong cross-coupling between X and Y offsets and non-linear behavior of k_x and k_y already for arbitrary beam offsets.

Diagonal Treatment

By using a so-called "diagonal" treatment [5, 6] of the ALBA BPM signals

$$x^{\text{alba}}_{\text{diag}} = \frac{k_x}{2} \times \left[\frac{V_3 - V_2}{V_3 + V_2} - \frac{V_4 - V_1}{V_4 + V_1}\right] \tag{4}$$

$$y^{\text{alba}}_{\text{diag}} = \frac{k_y}{2} \times \left[\frac{V_3 - V_2}{V_3 + V_2} + \frac{V_4 - V_1}{V_4 + V_1}\right] \tag{5}$$

a much smaller coupling within the central part of the BPM is obtained. A pair of constant calibration factors $k_{x,y}$ can provide linearization for an arbitrary beam offset within $x, y = \pm 5$ mm, as can be observed in Fig. 6(b): for three different beam sweeps the characteristic curves are almost identical. Compared to previous DOS treatment, the diagonal approach is favorable for BPMs where the buttons are not located along the transverse axis, and beams stay within the close vicinity of beam pipe center.

POLYNOMIAL CORRECTION

Linear analysis demonstrates that no electrode configuration of a button BPM can supply a perfect linear beam position response. Their position sensitivity is not only non-linear, particular for large beam displacements, but the maps

Copyright © 2014 CC-BY-3.0 and by the respective authors

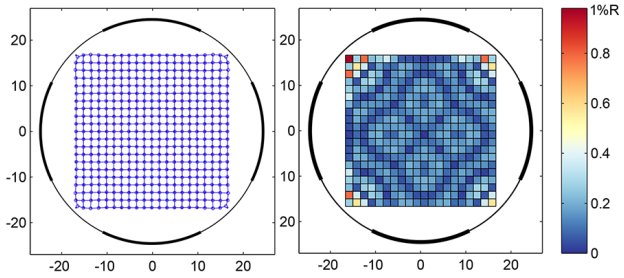


Figure 7: 9th-order polynomial correction of LHC BPM grid $(x^{\mathrm{lhc}}_{\mathrm{dos}}, y^{\mathrm{lhc}}_{\mathrm{dos}})$ (right), and its error map (left).

in Figs. 4(c)-6(c) also show a "pin-cushion" effect, indicating cross-coupling between XY planes. In a general case of an arbitrary BPM cross-section, the position characteristic of the pickup cannot be approximated by a closed analytical form, and therefore must be evaluated in a different way.

Based on the studies done in [2,7] for LHC stripline BPMs, we have applied the polynomial fitting technique to both considered pickups. Applying a mapping scheme, a pair of polynomial functions (one per each plane) of the following form allows to adequately compensate non-linearity of the BPM response within the considered mapped grid, taking into account the cross-coupling:

$$F^{\mathrm{x,y}}_{pq}(x_{bpm}, y_{bpm}) = \sum_{i,j=0}^{p,q} C^{\mathrm{x,y}}_{ij} x^i_{bpm} y^j_{bpm} \qquad (6)$$

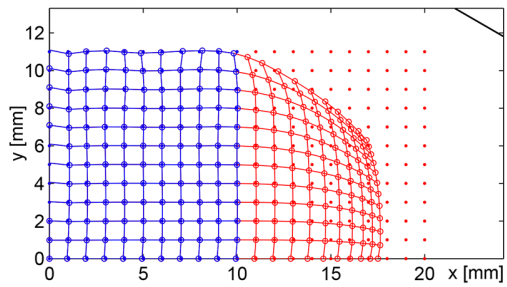
Here $C^{\mathrm{x,y}}_{ij}$ is a set of calculated coefficients per each corresponding plane X and Y, p and q are maximum powers of each variable, and (x_{bpm}, y_{bpm}) are the uncorrected sets of beam position values, i.e. $(x^{\mathrm{lhc}}_{\mathrm{dos}}, y^{\mathrm{lhc}}_{\mathrm{dos}})$, $(x^{\mathrm{alba}}_{\mathrm{dos}}, y^{\mathrm{alba}}_{\mathrm{dos}})$ or $(x^{\mathrm{alba}}_{\mathrm{diag}}, y^{\mathrm{alba}}_{\mathrm{diag}})$. We have determined that already low-power polynomials provide sufficient quality of correction. For brevity, here we will focus only on the 9th-order polynomials.

An absolute error map is defined as distances (in mm) between initial beam positions and corrected positions by the polynomial. For convenience, it is displayed as color-coded map with error values normalized to the aperture R, such that all error values above 1% of R are colored in red.

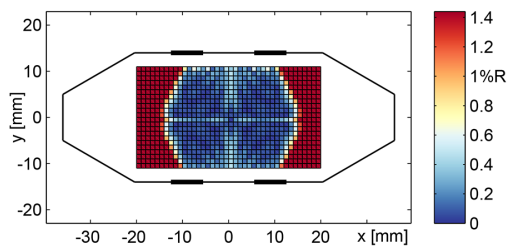
Figure 7 shows application of the calculated polynomial to the LHC BPM grid: the corrected map and its 2D error. Here, an overall quality of correction is well below 75 μm (0.3% of R_{lhc}) except the grid corners, where the beam is unlikely to drift.

Partial Correction

In any accelerator the beam is typically allowed to circulate within limited offsets from the beam pipe center. Larger drift will be detected by interlock BPMs and the beam will be automatically dumped. For the first study on ALBA BPM, consider the "beam allowed" limit as 21×23 points ($\pm 10 \times \pm 11$ mm) - a subset of previously defined grid. By including the limited grids of both DOS (Eq. 2) and diagonal (Eq. 4) normalization types in the polynomial routine, we calculate 9th-order polynomials which are efficient only in the "allowed" area. Figures 8(a,b) and Figures 9(a,b) show a zoom into the corrected maps and errors after applying these polynomials corresponding to DOS or diagonal-type grids. Here blue points belong to the "beam allowed" area, included in the polynomial fits, while red ones were ini-

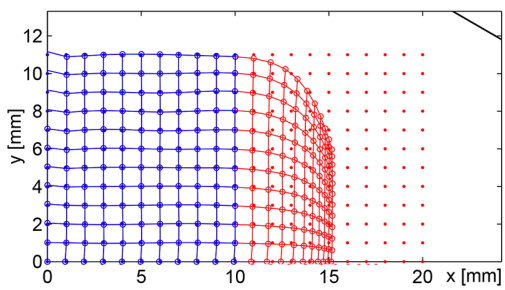


(a) Corrected grid of $(x^{\mathrm{alba}}_{\mathrm{dos}}, y^{\mathrm{alba}}_{\mathrm{dos}})$ (zoom),

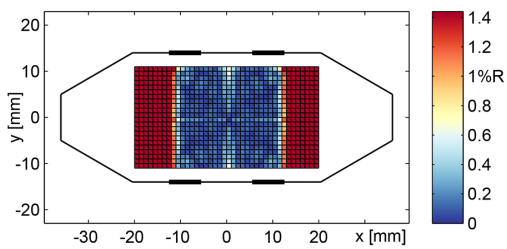


(b) and its error map.

Figure 8: 9th-order polynomial correction of partial ALBA BPM grid after DOS signal treatment.



(a) Corrected grid of $(x^{\mathrm{alba}}_{\mathrm{diag}}, y^{\mathrm{alba}}_{\mathrm{diag}})$ (zoom),

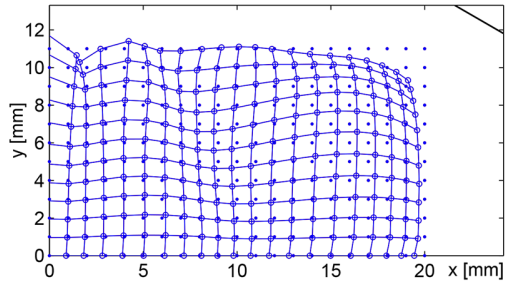


(b) and its error map.

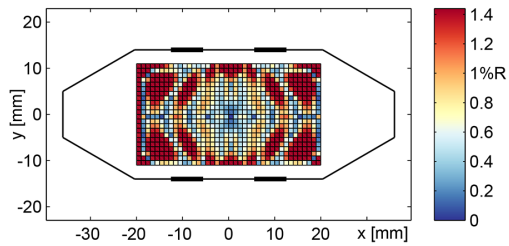
Figure 9: 9th-order polynomial correction of partial ALBA BPM grid after diagonal signal treatment.

Copyright © 2014 CC-BY-3.0 and by the respective authors

ISBN 978-3-95450-141-0

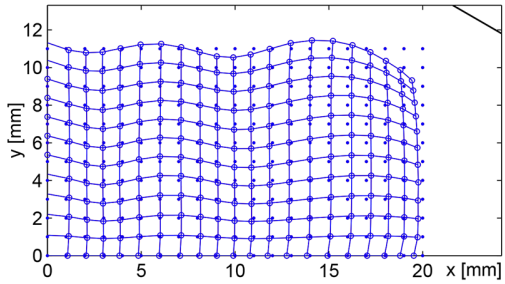


(a) Corrected grid of $(x^{\text{alba}}_{\text{dos}}, y^{\text{alba}}_{\text{dos}})$ (zoom),

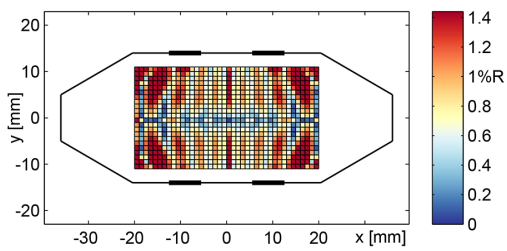


(b) and its error map.

Figure 10: 9th-order polynomial correction of a full ALBA BPM grid after DOS normalization.



(a) Corrected grid of $(x^{\text{alba}}_{\text{diag}}, y^{\text{alba}}_{\text{diag}})$ (zoom),



(b) and its error map.

Figure 11: 9th-order polynomial correction of a full ALBA BPM grid after diagonal normalization.

tially excluded. The overall correction efficiency for both normalization types is under 200 μm (0.6 % of R_{alba}).

Complete Correction

Limiting the BPM map can be useful to gain linearization accuracy in the central area of a BPM, when the correction beyond is not important. Larger-scale correction can be done by deriving a polynomial based on the maximal mapped grid of points. Results of such approach (also for 9th-order polys) are shown in Figs. 10 and 11 for both normalization types of ALBA BPM.

There is a clear reduction of accuracy seen in both error maps, especially along the axes in Figs. 10(b) and 11(b). To avoid this one could increase the polynomial powers, possibly, at the cost of some processing speed on the fly. We consider testing it in the future.

CONCLUSIONS AND OUTLOOK

In this work we analyzed several types of geometrical non-linear effects which deteriorate the BPM response of two standard BPM pickups. We demonstrated the results of efficient suppression of these effects by surface polynomials, calculated by combining EM simulations with 2D fitting. This methodology has great potential to be applied for any BPM of a modern accelerator.

However, testing these polynomials with actual real-time beam orbit monitoring is a challenge because it is difficult to produce large amplitude orbits. For historical (and simplicity) reasons the calibration of 1100 LHC BPMs before 2013 was limited to a 5th-order 1D polynomial, which was sufficient for most operational situations, except for several critical BPMs near the collision points. The correction of all LHC BPM families will be replaced by proper 2D polynomials after 2015. At the moment all 120 BPMs of ALBA are using linear BPM calibration with constant calibration factors. For studies of non-linear correction, the data will be analyzed off-line during upcoming machine studies.

REFERENCES

[1] CST Studio: http://www.cst.com

[2] A. A. Nosych and M. Wendt, "Analysis of Geometric Non-Linearities of LHC BPMs by 2D and 3D Electromagnetic Simulations", PRST-AB (to be published).

[3] ACE3P Suite: www-group.slac.stanford.edu/acd/

[4] R. W Helms. and G. H. Hoffstaetter, "Orbit and optics improvement by evaluating the nonlinear beam position monitor response in the Cornell Electron Storage Ring", Phys. Rev. ST Accel. Beams, vol. 8, issue 6, 2005.

[5] A. Olmos et al., "Matlab code for BPM button geometry computation", Proc. DIPAC 2007, pp. 186-188, 2007.

[6] A. Stella, "Analysis of DAΦNE BPM with a boundary element method", DAΦNE Technical Note, INFN, 1997.

[7] A. A. Nosych, "Geometrical non-linearity correction procedure of LHC beam position monitors", EDMS doc. no. 1342295, CERN, 2014.

Copyright © 2014 CC-BY-3.0 and by the respective authors

NUMERICAL CALCULATIONS FOR THE FAIR PROTON LINAC BPMS

C. Simon#, V. Bellego CEA-Saclay/DSM/Irfu, Gif sur Yvette, France,
M. Almalki, P. Forck, W. Kaufmann and T. Sieber, GSI, Darmstadt, Germany

Abstract

Fourteen Beam Position Monitors (BPMs) will be installed along the FAIR Proton Linac. These monitors will be used to determine the beam position, the relative beam current and the mean beam energy by time of flight (TOF). A capacitive button type pickup was chosen for its easy mechanical realization and for the short insertion length which is important for the four BPMs locations of the inter-tank sections between the CH-cavities. Depending on the location, the BPM design has to be optimized, taking into account an energy range from 3 MeV to 70 MeV, limited space for installation and a 30 mm or 50 mm beam pipe aperture. This paper reports wake field numerical simulations performed by the code CST PARTICLE STUDIO to design and characterize the BPMs. Response time of monitors are presented and results of calculations for various pickup-geometries are discussed taking into account different beam velocities.

INTRODUCTION

The FAIR Project [1] (Facility for Antiprotons and Ions Research), built at GSI Darmstadt, requires a Proton Linac [2] which has to provide the primary proton beam for the production of antiprotons. This Linac will operate at a frequency of 325 MHz. It will deliver a 70 MeV beam at a current limit of 70 mA with a repetition rate of 4 Hz for injection into the SIS 18. The main beam parameters are listed in Tab. 1.

Table 1: FAIR Proton Linac Parameters

Parameter	Value
Final energy	70 MeV
Pulse current	70 mA
Protons per pulse	7.10^{12}
Macro pulse length	30 to 100 µs
Repetition rate	4 Hz
Trans. beam emittance	4.2 µm (tot. norm.)
RF-frequency	325.224 MHz

The fourteen Beam Position Monitors (BPMs) will be installed along the Linac as shown Fig. 1.

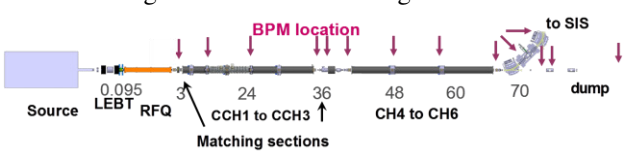


Figure 1: Distribution of Beam Position Monitors along the Linac.

#claire.simon@cea.fr

At nine locations the vacuum chamber aperture is 30 mm. Due to the different requirements, monitors installed in the transfer section, the dump and between the two dipoles will have a vacuum chamber aperture of 50 mm.

The same type of button electrode is foreseen along the Linac with an energy varying from 3 MeV to 70 MeV and a change of vacuum chamber geometry.

The main measurement is to determine the beam displacement, with a spatial resolution of 0.1 mm averaged on a macro pulse of 36 µs duration, by calculating the ratio of the difference over sum voltage between two opposite buttons. The sum signal from a BPM can be also used as a relative measurement for the beam current. An important application at a proton Linac comprising of novel CH-cavities is the determination of the beam energy after each DTL tank which can be calculated via the time of flight determination of a bunch between two BPMs. For this time measurement, an accuracy of 8.5 ps has to be achieved corresponding to a phase resolution of 1°.

The main parameters are summarized in Tab 2.

Table 2: FAIR Proton Linac BPM Parameters

Parameter	Value
Beam pipe diameter	30 mm intertank section, 50 mm transfer lines
Length	50 mm
Beam energy	From 3 MeV to 70 MeV
Bunch frequency	325.225 MHz
Beam pulse length	36 µs nominal
Bunch length	150 ps typical
Average current	35 mA nominal, max 70 mA
Position resolution (RMS)	100 µm averaged on a macro pulse of 36 µs
Operation range	± 5 mm
Phase resolution	1° averaged on a macro pulse of 36 µs

LAYOUT

Beam dynamics requirements and compactness of the beamline require that some BPMs (at four locations) will be an integral part of the inter-tank section between the CH cavities [2]. In this context and after having performed some preliminary simulations [3], a capacitive button type BPM with buttons of 14 mm diameter was chosen for its easy mechanical realization and short

Copyright © 2014 CC-BY-3.0 and by the respective authors

ISBN 978-3-95450-141-0

insertion length to fit into the inter-tank sections of the CH-cavities.

This device is composed of 4 electrodes called "buttons" mounted by welding on the vacuum pipe. Those feedthroughs consist of a central conductor with a button electrode and a SMA-type connector with a characteristic impedance of 50 Ω. The field on the inner wall of a beam pipe induces a surface wall current which will generate a voltage on the pickup electrodes.

A first prototype and mechanical design, inserted in the inter-tank section, shown in Fig. 2 is in fabrication state [4]. The housing will be in stainless steel 316LN to avoid magnetic problems. Commercial 14 mm pickups, fabricated by Kyocera, were chosen (Fig. 3).

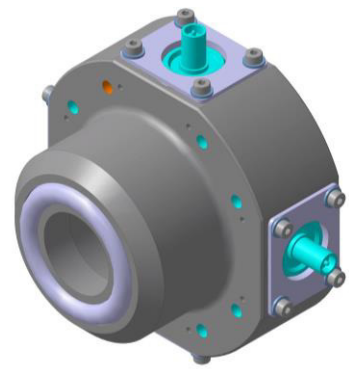


Figure 2: Design of the button BPM installed in the CH-inter-tank section.



Figure 3: Kyocera button – diameter 14 mm.

ELECTROMAGNETIC SIMULATIONS

To improve and extend calculations of the signal response of the monitors, new numerical simulations were performed using a geometrically simplification of the 14 mm Kyocera buttons and different beam properties. The code CST PARTICLE STUDIO with the wake-field solver [5] on a hexahedral mesh is used where the excitation source is defined by a Gaussian-shaped longitudinal charge distribution.

To use the same type of electrode on all BPMs along the linac, BPMs simulations with two beam pipes are shown Fig. 4. The amplitude on a button for a BPM with an aperture of 50 mm will be half of a BPM with an aperture of 30 mm. In the pre-amplifier design, those results will be taken into account.

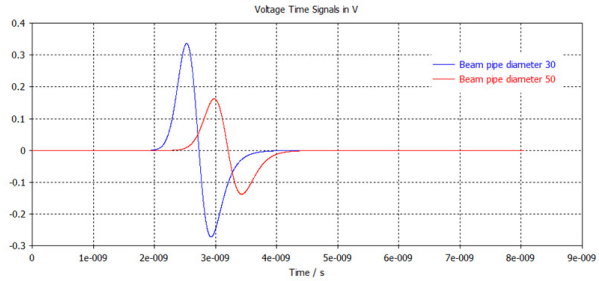


Figure 4: BPM output voltage for two different apertures used on the linac (bunch length 150 ps, β=0.37, 35 mA).

The time and frequency responses of the pick-up were obtained at different beam velocities, namely 0.08, 0.27 and 0.37, while the longitudinal RMS bunch size varies within 60-650 ps range. The results show that the signal amplitude reduces with the length of bunch as shown in Fig. 5. There is a factor 10 between 60 ps and 650 ps. The case, with a long bunch length at $\beta = 0.37$ will give the lowest signal amplitude. Those simulations show that for the electronics, a large dynamic range will be necessary.

At low energy with $\beta = 0.08$, for bunches shorter than 100 ps, the solution becomes instable. Higher order modes have to be considered which requires denser mesh and, therefore, a longer simulation time.

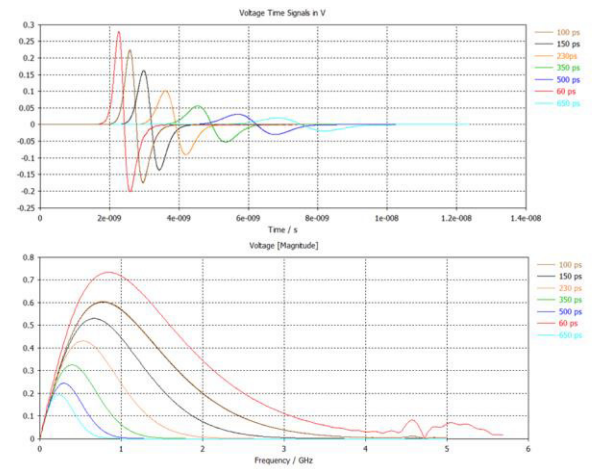


Figure 5: BPM output voltage for different bunch lengths beam pipe = 50 mm, β=0.37, 35 mA.

Sensitivity and non-linearity response analysis are important parts for a button BPM design. Sensitivity depends on the button diameter, the horizontal and the vertical separations of the buttons, and the distance to the beam.

For the investigation of the position sensitivity and the pickup non-linearity response versus the beam position, the position of the simulated beam (excitation) is moved horizontally and vertically in 1 or 2 mm steps in a range of ± 8 mm. The positions in each directions are calculated from amplitudes of the signals induced in the opposite BPM electrodes using the 'delta-over-sum' method. As depicted in Fig. 6, the operation frequency has more influence at low beta on the sensitivity and linearity.

Copyright © 2014 CC-BY-3.0 and by the respective authors

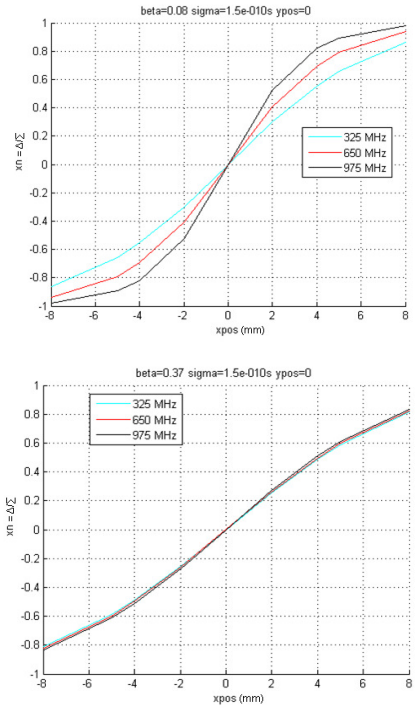


Figure 6: Horizontal beam position calculated using 'delta-over-sum' method at different frequencies with $\beta = 0.08$ and $\beta = 0.37$ for a bunch length = 150 ps. Vacuum aperture: 30 mm, button diameter: 14 mm.

To crosscheck the results of the CST simulations, a comparison with a theoretical estimation of the sensitivity [6] for a low-beta button-type BPM and 2-dimentional approximation is presented in Table 3. The agreement between the simulated and analytical results is reasonable.

Table 3: Comparison of Simulated and Analytical Sensitivities in Units of dB/mm

		Simulation	Theoretical Estimation
E=3 MeV (β=0,08)	325 MHz	2,69	2,67
	650 MHz	3,74	3,71
	975 MHz	5,00	5,05
E=35 MeV (β=0,27)	325 MHz	2,29	2,28
	650 MHz	2,41	2,39
	975 MHz	2,59	2,56
E=70 MeV (β=0,37)	325 MHz	2,27	2,26
	650 MHz	2,33	2,31
	975 MHz	2,42	2,40

To estimate linearity and sensibility, simulations are done with different bunch lengths. For the same pick-up design and the same beta value, the linearity and sensibility are identical compared to the bunch length. These numerical results coincide, as expected, to the results for the analytical investigations in [6] for each individual Fourier component.

To improve the performances of this button BPM, different pickup geometries are simulated.

Figure 7 compare signals with a button height varying from 1 mm to 4 mm and show that signal read by one button decreases with the thickness of the pickup. Button thickness (height) increases the button capacitance in respect to the shield. A modification of the thickness changes also the capacitance and therefore the cut-off frequency. This capacitance is critical and can cause mismatch through the structure.

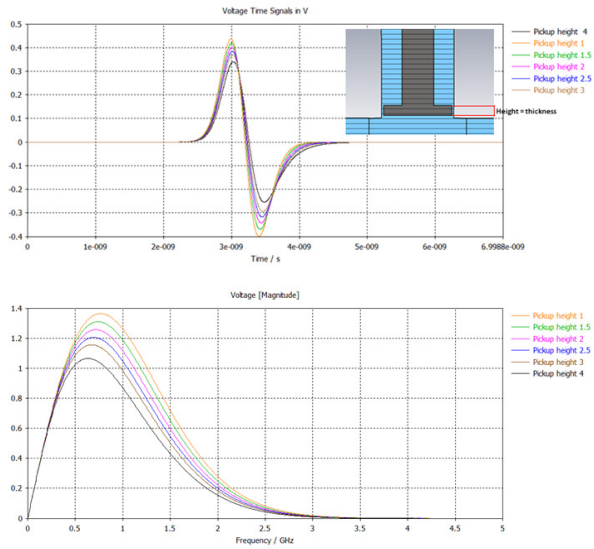


Figure 7: BPM output signals for different height of button given in units of mm. Beam pipe = 30 mm, button diameter: 14 mm β=0.27 for a bunch length = 150 ps, 35 mA.

In the BPM design, gap between the button and inner wall of the BPM housing represents a transmission line. Some resonant modes can be generated, trapped and can deposit power in the button [7]. In general, this power could lead to heating and damages the button and the ceramic insulator or the resonator mode can disturb the beam original beam signal. To minimize the trapped mode impedance; i.e. the transmission line, a thick button (see detail in Fig. 7) and a small gap to the outer housing are preferred with the disadvantage of increasing capacitance and, consequently, lower signal strength.

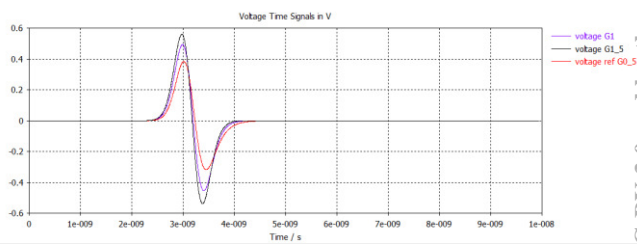


Figure 8: BPM output signals read by one electrode with the gap varying from 0.5 to 1.5 mm. Beam pipe = 30 mm, button diameter: 14 mm, β=0.27 for a bunch length = 150 ps, 35 mA.

Copyright © 2014 CC-BY-3.0 and by the respective authors

ISBN 978-3-95450-141-0

Simulations presented Fig. 8 show the influence of the gap between the button and the inner wall of beam pipe on the signal amplitude read by one electrode. The Kyocera button has a 0.5 mm gap.

The thickness and the gap of button influence the capacitance value. Figure 9 presents some capacitance values calculated for different button geometries.

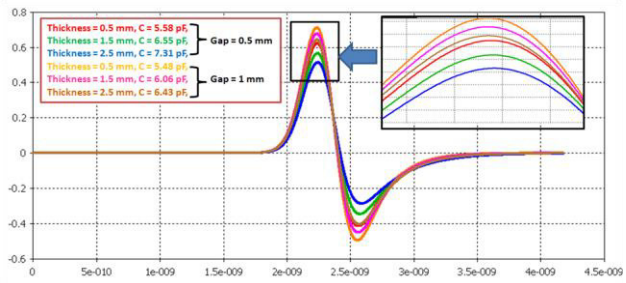


Figure 9: BPM output signals read by one electrode with different button geometries. Beam pipe = 30 mm, button diameter = 14 mm, β=0.37 for a bunch length = 100 ps, 35 mA.

CONCLUSION

Beam Position Monitors are essential devices for the beam-based alignment and diagnostic of the FAIR Proton Linac accelerator.

The BPM electrical performance was numerically simulated with CST Particle Studio. Although the low-energy affects the quality of the measurement, button BPM sensitivity on the beam energy and the frequency results demonstrated good agreement with the theoretical estimation.

A prototype of the BPM with 30 mm aperture is produced at CEA and will be characterized on a test bench with a coaxial wire to verify the results obtained with the simulations.

ACKNOWLEDGMENTS

We thank our colleagues from GSI for their support and the fruitful discussions on the integration of the BPMs. We, also, wish to acknowledge our colleagues from CEA Saclay for their advices and their help on this project and in particular persons who participated to the mechanical design of the next prototype.

REFERENCES

[1] ”FAIR Baseline Technical Report”, GSI Darmstadt, Germany, 2006

[2] L. Groening et al., “FAIR Technical Design Report for proton Linac”, March 2009, https://edms.cern.ch/document/994418/1.

[3] C. Simon et al., “Design status of Beam position monitors for the fair proton Linac” DIPAC11, Hamburg, Germany.

[4] M. Almalki et al., “The mechanical design of the BPM inter-tank for p-Linac at FAIR “, IPAC14, Dresden,Germany

[5] www.cst.com

[6] R. E. Shafer, “Sensitivity of PUs for low beta beams,” BIW93, Santa Fe, USA

[7] P.Cameron et al., “BPM Button Optimization to Minimize Distortion Due to Trapped Mode Heating”, PAC09, Vancouver, Canada

Copyright © 2014 CC-BY-3.0 and by the respective authors

PRODUCTION PROCESS FOR THE EUROPEAN XFEL RE-ENTRANT CAVITY BPM

C. Simon#, C. Boulch, P. Carbonnier, P. Contrepois, P. Daniel-Thomas, F. Eozenou, Y. Gasser, F. Gouit, O. Napoly, J. Novo, C. Servouin CEA-Saclay/DSM/Irfu, Gif sur Yvette, France
J. Kruse, D. Noelle, M. Schalwat, S. Vilcins- Czvitkovits, DESY, Hamburg, Germany
N. Rouvière, J.-P. Prestel, CNRS, IN2P3, Orsay, France

Abstract

As In-Kind contributor to the E-XFEL project, CEA is committed to the procurement of around one third (31) cold beam position monitors (BPM) of the re-entrant RF cavities type and to the assembly on the Saclay site of the 101 cryomodules of the superconducting linac. Each cryomodule is equipped with a beam position monitor connected to a quadrupole at the high-energy end of the cavity string. The industrial process of those BPMs, used in an ultra-clean environment at cryogenic temperature, includes several steps and involves a quality control in collaboration with industrial partners. This paper describes the different steps of the re-entrant cavity BPM fabrication process: machining, copper coating, thermal treatment, EB welding, cleaning and mounting in clean room on the quadrupole. Problems encountered and the lessons learnt will be also reported.

INTRODUCTION

The European XFEL [1] is an X-ray free electron laser user facility currently under construction in Hamburg, Germany. This accelerator has a superconducting 17.5 GeV main linac based on the TTF technology and is composed of 101 cryomodules including the injector module. Each module includes a string of eight 1.3 GHz RF cavities, followed by a BPM connected to a superconducting quadrupole. As In-Kind contributor to the E-XFEL project, CEA is committed to the integration on the Saclay site of the 101 cryomodules [2] as well as to the procurement of the magnetic shielding, superinsulation blankets and 31 cold re-entrant cavities beam position monitors (BPM). The others cold BPMs will be button BPMs and are not discussed here [3].

These re-entrant BPMs cavities have been studied and prototyped at CEA [4]. They are composed of two parts of stainless steel welded together to form a resonator. The production of the re-entrant cavities has been transmitted to a company named Gavard & Cie which is in charge of mechanical fabrication. Pickups and RF re-entrant BPM cavities are provided by the CEA/Saclay and sent to DESY to be mounted on the quadrupole inside an ISO4 cleanroom.

In this paper, the industrial process is reported with a description of different steps. In addition, difficulties met during production are discussed. Design and architecture of the re-entrant BPM electronics, developed by a collaboration of CEA/Saclay/Irfu, DESY and PSI, are not discussed here [5].

#claire.simon@cea.fr

GENERAL DESCRIPTION

In the XFEL accelerator modules, 31 cold re-entrant cavity BPMs will be installed. Independent of the type, all cold BPMs will have a common mechanical interface and the same specifications presented in Table 1.

Table 1: Cold BPM Parameters

Parameter	Value
Beam pipe diameter	78 mm
Length	170 mm
Single bunch resolution (RMS)	50 µm
Operation range for maximum resolution	± 3 mm
Transverse Alignment Tolerance (RMS)	300 µm

The re-entrant BPM will be connected to a cold quadrupole at the high-energy end of the cavity string as illustrated Fig. 1.

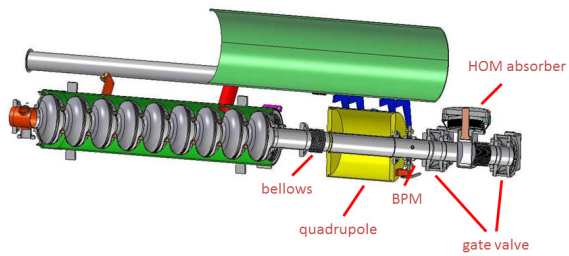


Figure 1: Layout of the XFEL cryomodule downstream end.

The length of this BPM is 170 mm to respect constraints imposed by the cryomodule and its aperture is 78 mm (see Fig. 2). It is composed of two parts, in stainless steel, welded together by electron beam welding (EB). Flanges are machined out of the same blocks to get the alignment tolerances. The alignment is done by dowel pins with respect to the cold magnet.

Each antenna, which is a combination of stainless steel, molybdenum and alumina Al2O3 ceramic brazed, is mounted on the cavity via a CF16 flange. They have to pass cryogenic shocks and to fulfil the conditions of Ultra High Vacuum (UHV). They have been manufactured by SCT (Société des Céramiques Techniques) [6]. Four copper-beryllium radio-frequency contacts are also welded in the inner cylinder of the cavity to ensure the electrical conduction between the feedthrough inner conductors and the cavity.

Copyright © 2014 CC-BY-3.0 and by the respective authors

ISBN 978-3-95450-141-0

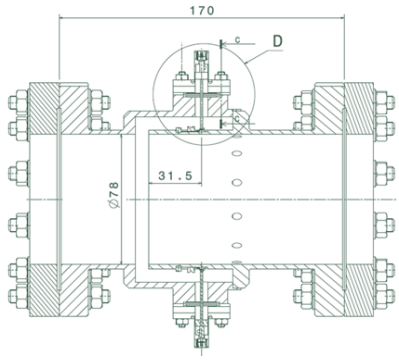


Figure 2: Drawing of the re-entrant cavity BPM.

FABRICATION PROCESS

Two prototypes have been produced by different companies and a pre-series of one + six units has been ordered to validate the process. The 30 BPMs have been machining together but EB welding is done in series of 6.

Gavard & Cie is in charge of machining and the whole of market of re-entrant BPM under the supervision of the CEA. Major aspects of going to industrial production of re-entrant BPM are summarized in Table 2.

Table 2: Fabrication Process of Re-entrant Cavity BPM

Process	Carried out by
Firing 950° for 2 h	Industry
Machining of feedthroughs	Industry- Specialist of brazing
Machining of two parts composing the RF cavity	Industry
Cu plating	Industry
Vacuum firing	Industry
US bath	Industry
RF contacts welding	Industry
EB welding	Industry
Final machining	Industry
Cleaning + RGA + leak test	CEA
N2 shocks on feedthroughs + leak test	Industry + CEA
RF measurements	CEA
Packing to transport to DESY	CEA
Final cleaning + RGA	DESY
Mounting	DESY

Stainless steel material has been ordered according the DESY specifications. In order to avoid hydrogen out-gassing, a heat treatment at 950 °C for 2 hours according the UHV specifications is applied to the two already machined parts, composing the BPM cavity. Since it is connected to a cold magnet, the BPM will be at a temperature close to the 4 K level and will be mounted in a clean room. For an effective cleaning, twelve holes of 5 mm diameter are drilled at the end of the re-entrant part.

To check the machining, Three-Dimensions (3-D) and roughness (Ra) measurements are carried out at the manufacturer.

Copper Coating

To reduce the cryo-losses, a 12 µm thick copper coating is deposited on the inner beam pipe. A thickness of 1 µm of Nickel is used to do the adhesion with the stainless steel. This copper coating is carried out by electro deposition in an acid bath by Protec [7]. Before to validate this process, several tests have been done:

- adhesion test by thermal shock
- desorption measurement
- electrical resistivity measurements and RRR calculation

Special tools (Fig. 3) have been manufactured to protect the parts no copper plating and to avoid the using of resin mask which is prohibited in a clean environment.



Figure 3: Copper coating BPM tools.

After the copper coating process, thickness measurement is done on each piece.

To check the copper surface and test the contact of copper and steel, pieces are put in an Ultra-Sonic (US) bath with ultrapure water and a vacuum firing at 300 °C for one hour is carried out. The acceptance is done by visual check inspection.

Weldings

Aspit [8] is in charge of weldings. Four RF contacts in CuBe are welded on the re-entrant part.

The two parts composing the BPM are mounted together with a special tool (Fig. 4) using some cupped washers to keep, during the Electron Beam (EB) welding, a coaxiliaty around 50 µm between the two blocks. During the welding, measurement with an electronic comparator is done.

Copyright © 2014 CC-BY-3.0 and by the respective authors



Figure 4: BPM mounted with its equipment used during EB welding.

Checking and Acceptance Tests

The industry is responsible up to the delivery of BPMs to Saclay. There, some acceptance tests are performed:

- Visual Inspection
- Leak test
- Residual Gaz Analysis (RGA). Acceptance criteria are given by the Ultrahigh-vacuum conditions [9]
- RF measurements as shown Fig. 5

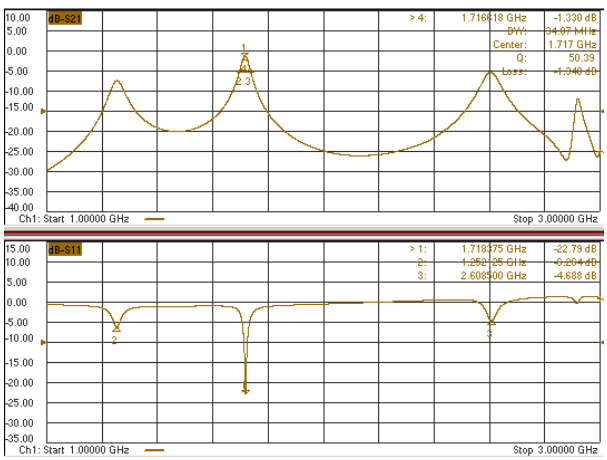


Figure 5: RF characteristics.

The RF measurements are done in laboratory and are presented in Table 3.

Table 3: BPM RF Characteristics

	Frequency (MHz)	**Q_{ext}**
	Measured in lab.	Measured in lab.
Monopole mode	1253	23.5
Dipole mode	1720	50.5

Frequencies of monopole and dipole modes of twelve first BPMs have a difference around 2 MHz maximum and the variation of the quality factor is well in specification.

Once the acceptance tests validated, the re-entrant BPM is sent to DESY to be assembled with the quadrupole.

Preparation and Mounting

At DESY, BPMs are cleaned in an ultra-sonic bath, rinsed by ultra-pure water and controlled by vacuum leak check and RGA by DESY MDI group. Cleaning and assembly of components requires cleanliness of UHV conditions as well as condition of particle free surfaces.

They are pre-assembled and mounted, by MKS group, with the quadrupole unit in an ISO4 cleanroom. HPR (High Pressure Rinsing) and RGA are carried out on the unit. Then, feedthroughs are mounted on the BPM and a test, to check the contact between the CuBe spring and the antennae pin is done with an ohmmeter.

After assembling, the BPM Quadrupole Unit (BQU) is put in a special box made for a transport under ISO4 conditions and for being able to absorb shocks during the transport to CEA Saclay where it will be mounted on the string cavity [10].

INDUSTRIAL FABRICATION

During the industrial process, several difficulties occurred:

On the prototypes, the coaxiality was around 70 µm while a coaxiality around 50 µm was asked. A special tool was made to equip the BPM during the EB welding and to guarantee a coaxiliaty in the specification.

Concerning the copper coating some problems appeared:

- On the first prototype, varnish was used to protect parts no copper coating. Even with a good cleaning, some black particles stayed. That's why a special tool was made to avoid the use of resin.
- On the second prototype: a problem is occurred during the HPR. After the HPR, drying is done "naturally" (no drying with compressed air is used). Due to the oxidation, some black marks have been seen on the copper coating. Copper coating was damaged. Some added tests have been carried on others BPMs to check the copper coating but no problem occurred. We didn't understand what happened.

On the prototypes, some problems are appeared during the mounting of antennae. If there isn't touch between the antennae and the RF contact, RF characteristics can be modified. This contact need to be checked with an ohmmeter.

Around 10 % of the feedthroughs production has a black area on the flange where a graphite frame was used during the brazing. Hypothesis is that some of them underwent cementation (carburation). The analysis of those pickups confirmed that carbon elements were more abundant in the "black" part. After, the cleaning of those feedtroughs with a detergent ElmaClean 115C, black traces are appeared on the flange where the graphite frame was mounted. A machining and etching were done to remove black parts then by a cleaning in an US bath with ethanol.

On the first prototype, frequencies shifted by around 10 MHz in comparison with the simulation results and the

Copyright © 2014 CC-BY-3.0 and by the respective authors

ISBN 978-3-95450-141-0

measurements done on the re-entrant BPM installed on the FLASH linac [5]. This difference could be due to the cavity geometry. That's why on the next ones, tolerances were tightened and RF measurements are used in the quality control process of the series.

FABRICATION

Several prototypes have been manufactured by different companies to qualify them. To avoid different problems, a strict control is carried out for the different steps during the fabrication process.

In 2009, one first prototype has been installed in a prototype cryomodule.

Since the first prototype, CEA Saclay received thirteen BPMs, seven BPMs are already mounted on quadrupole and are in a BQU. Four BPMs are already mounted in a cryomodule. Figure 6 shows a re-entrant BPM mounted on the cavity string.



Figure 6: Re-entrant BPM mounted in an XFEL cryomodule.

CONCLUSION

Strict quality control has to be carried out for the different steps to receive BPMs within the performances. The mostly of problem are now solved and the mounted in the BQU can continue. Several BPMs are already mounted in some BQU and on cryomodules. Production of re-entrant BPM will be finished at the end of September.

ACKNOWLEDGMENT

We thank our colleagues of MDI and MKS groups from DESY for their support and their fruitful discussions. We would like to thank the different companies with which we worked on this project and find new solutions to improve the fabrication process. We, also, wish to acknowledge our colleagues from CEA Saclay for their advices and their help on this project.

REFERENCES

[1] E. Vogel et al., "Integration of the European XFEL accelerating modules", SRF 2013, Paris France 2013.

[2] C. Madec et al., "The Challenge to Assemble 100 Cryomodules for the European XFEL", SRF 2013, Paris, France 2013.

[3] D. Lipka et al., "Button BPM Development for the European XFEL", DIPAC'11, Hamburg, Germany, 2011.

[4] C. Simon, et al., "Performance of a reentrant cavity beam position monitor", Physical review special topics – accelerators and beams 11, 082802 (2008).

[5] C. Simon et al., "Status for the re-entrant cavity Beam Position Monitor for the XFEL project", BIW10, Santa Fe, United States.

[6] Société des Céramiques Techniques, http://www.sct-ceramics.com/

[7] Protec, http://www.protec-groupe.com/

[8] Aspit, http://www.aspit.fr/

[9] U.Hahn, K. Zapfe, General DESY UHV Guidelines for Vacuum components, DESY Report, Vacuum 005/2008.

[10] M. Schalwat et al., "Set up of production line for XFEL beam position monitor and quadrupol units for cavity string assembly at CEA", SRF13, Paris.

Copyright © 2014 CC-BY-3.0 and by the respective authors

COMMISSIONING OF THE ELECTRONICS FOR HOM-BASED BEAM DIAGNOSTICS AT THE 3.9 GHz ACCELERATING MODULE AT FLASH*

N. Baboi#, O. Hensler, T. Wamsat, DESY, Hamburg, Germany
L. Shi, University of Manchester, Manchester, UK and DESY, Hamburg, Germany
N. Eddy, B. Fellenz, FNAL, Batavia, IL, USA
P. Zhang, CERN, Geneva, Switzerland

Abstract

Transverse Higher Order Modes (HOM) excited by electron beams in the 3.9 GHz accelerating cavities at FLASH may damage the beam quality. They can be reduced by extracting their energy through special couplers and by aligning the beam in the cavity. Electronics has been designed at FNAL for monitoring some of the potentially most damaging HOMs. This may be used for beam centering and therefore reducing the HOM effects. Moreover, the signals can be potentially calibrated into beam offset, so that they could be used as beam position monitors (HOM-BPM). The specifications of the monitors have been defined during an extensive study on the 4-cavity accelerating module installed at FLASH. Signals around 5.46 GHz have been chosen for higher precision measurements. However these signals propagate into the entire 1.2 m long module. Therefore in addition modes at about 9.06 GHz were selected for localized measurements in each cavity. The electronics has been recently installed at FLASH. The initial experience with this electronics is presented in this paper. The signals can already be used for centering. Some instability in the signals has been observed and the cause has to be further investigated.

INTRODUCTION

Higher Order Modes (HOM) excited by electron beams when traversing accelerating cavities can be used for beam alignment [1]. This is beneficial to the beam quality since in this way the transverse HOMs are reduced and therefore also their potentially damaging effect on the beam. HOMs can also be used as beam position monitors (BPM), similar to cavity BPMs. In particular dipole modes are very suitable due to the linear dependence of their strength on the beam offset.

The principle has been demonstrated in the past at the FLASH linac at DESY, Hamburg [1,2], using special HOM-BPM electronics built at SLAC and installed at forty 1.3 GHz cavities. One issue remains, namely that the calibration is instable [3]. However this affects only the functioning as a BPM, the raw HOM signals are used to align the beam.

Recently, electronics has been built at FNAL for the four 3.9 GHz cavities at FLASH. This paper presents the first beam experience with this electronics at FLASH. The challenges in comparison to the one for the 1.3 GHz cavities will be underlined.

*The work is part of EuCARD-2, partly funded by the European Commission, GA 312453.
#nicoleta.baboi@desy.de

The FLASH Injector

Figure 1 shows schematically the injector of the FLASH linac [2]. The electron bunches produced by the photo-gun pass the first accelerating module (ACC1), containing eight 1.3 GHz cavities, and then the third harmonic module (ACC39), containing four 3.9 GHz cavities, before going through the first bunch compressor. The 3.9 GHz cavities are used to linearize the energy spread along the bunch needed in the compression process. Magnets and beam monitors, such as charge, position and phase monitors are not shown.

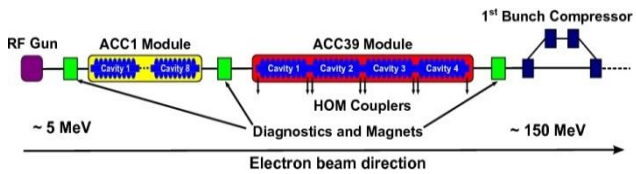


Figure 1: Layout of the FLASH injector. (The accelerating cavities are not to scale: the 3.9 GHz cavities are about 3 times smaller than the 1.3 GHz ones.)

The Third Harmonic Module

The arrangement of the 3.9 GHz cavities in ACC39 is shown in Figure 2. Each cavity has a power coupler and two couplers for HOM-damping. Two of the cavities, C1 and C3, are oriented with the power coupler downstream, the others have it upstream. The HOM-couplers are named with the cavity (C) and coupler (H) number, with H1 being on the power coupler side.

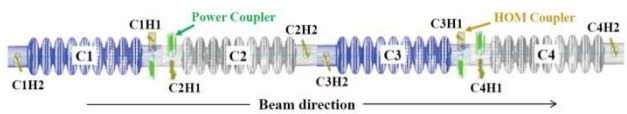


Figure 2: The arrangement of the 3.9 GHz cavities in the ACC39 cryo-module.

The HOMs in the 3.9 GHz cavities are much stronger than in the 1.3 GHz cavities due to the smaller aperture. This makes the need to align the beam in the cavities, and therefore avoid exciting transverse modes, more important. This is also the main reason why the beam pipes are larger than 1/3 of the beam pipes for 1.3 GHz cavities. This allows most modes to propagate along the entire module, and be damped by all couplers. On the

Copyright © 2014 CC-BY-3.0 and by the respective authors

ISBN 978-3-95450-141-0

other hand, this makes the spectrum much more crowded so that basically no isolated HOM can be filtered out. Also, with propagating modes one cannot measure the beam locally in each cavity, as it is done for the 1.3 GHz cavities. However modes in a narrow frequency range around 9.06 GHz, in the 5th dipole band, are trapped in the cavity, as a previous study with test electronics has found [4,5]. These modes can be used for alignment of the beam and position measurements in each cavity, at the expense of a lower resolution. For a measurement with a higher precision, the most suitable proved to be propagating modes around 5.5 GHz, in the 2nd dipole band.

HOM-BPM DOWNMIX ELECTRONICS

Downmix electronics shown in Figure 3 have been built to study modes of interest in 2nd and 5th dipole bands. The electronics consist of one 5 GHz PLL and one 9 GHz PLL each of which are locked to a FLASH low level RF 81MHz reference and programmable in 9 MHz steps over a 100 MHz range in each pass band. There are three 5 GHz and seven 9 GHz downmix. 1 of each is connected to a phase monitor pickup to allow an independent beam measurement of the system phase. The system can be configured remotely via a CAN Bus serial interface.



Figure 3: Front of the HOM-BPM electronics.

The block diagram for a downmix channel is shown in Figure 4. Each channel has a 100 MHz BW input filter centered on the band of interest. As the characteristics for each HOM coupler vary, there are programmable attenuators before the mixer to optimize the signal levels into the mixer. The mixer is a single sideband mixer with an IF of 30 MHz with 20 MHz bandwidth. For the beam commissioning, the LO frequencies are set to 9.027 GHz and 5.434 GHz to select HOMs around 9.058 GHz, and respectively 5.465 GHz.

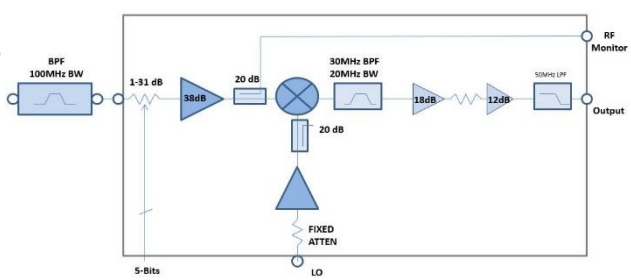


Figure 4: Block diagram of a downmix channel.

BEAM MEASUREMENTS

The HOM-BPM electronics has recently been installed at FLASH. The downmixed signals are send to a SIS8300 digitizer card via a SIS8900 card [6] placed in a MTCA crate [7]. A so-called scope server was installed to transfer the digitized signals from the SIS8300 card to the control system [8]. The sampling rate of the digitizer is 108 MHz. After adjusting the LO and the attenuation level for each channel, signals could be readily observed. Examples of 5 and 9 GHz signals are shown in Figure 5. Such signals can be already be used for beam alignment.

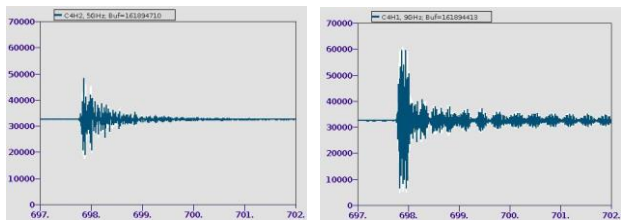


Figure 5: Raw signals from C1H2 (5 GHz channel) and C1H1 (9 GHz) from the control system.

During a dedicated beam time, the behavior of the signals with the transverse beam position has been studied. Two BPMs, one upstream and one downstream ACC39 have been used for beam position reference. The RF in the module has been switched off, while the quadrupoles have been cycled to zero field. In this way a drift space was created between the BPMs.

While placing the beam at various transverse positions in a somewhat equidistant grid, the signals from all channels of the HOM electronics have been recorded synchronously to the beam charge, position and phase readings. 5 pulses have been read for each position. One scan with 25 beam positions has been made first and the data was used for signal calibration. A second scan, with 16 positions within a smaller range is used for characterization of the system (validation data).

Figure 6 shows the beam position interpolated at the module center. A range of roughly 0.25 mm in the x plane and ±3.5 mm in y was covered. The strong difference is that with the used steerer magnets a divergent trajectory in y was obtained, while in x the beam was crossing the axis in ACC39. The x range was larger at the outmost cavities.

Figure 7 shows the waveforms obtained for all 25 beam position in the calibration scan from both 5 GHz channels (a), and the corresponding spectra obtained by Fourier transforms (b). One notices the variation in amplitude of the various modes with the beam position.

Copyright © 2014 CC-BY-3.0 and by the respective authors

ISBN 978-3-95450-141-0

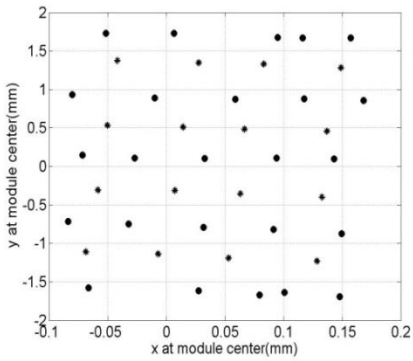


Figure 6: The beam positions as calculated at the module center from the two BPMs. One (larger) scan has been made for calibration data (dots), and another for validation data (stars).

The most relevant information from the HOM data has been extracted with a SVD-based technique [1,4]. By linear correlation against the beam position a matrix has been obtained for calibration of the HOM signals into beam position.

The RMS error obtained by applying this calibration matrix to the data used for obtaining it is a first indicator on how good the data is, and if the electronics behaves as expected. Another RMS error is obtained when applying this matrix to the validation data. Note that this RMS error is not the resolution of the HOM electronics, since it is obtained for a large beam position range.

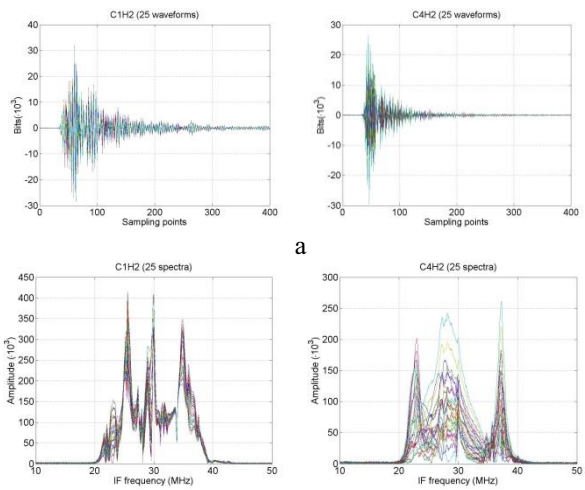


Figure 7: Waveforms (a) measured from the 5 GHz channels (C1H2 and C42H2) and the corresponding HOM spectra (b) obtained by Fourier transform.

Similarly, Figure 8 shows the waveforms from three of the 9 GHz channels (a) and their corresponding spectra (b). Note that the waveforms and spectra vary dramatically from coupler to coupler, due to the fabrication differences and different couplers.

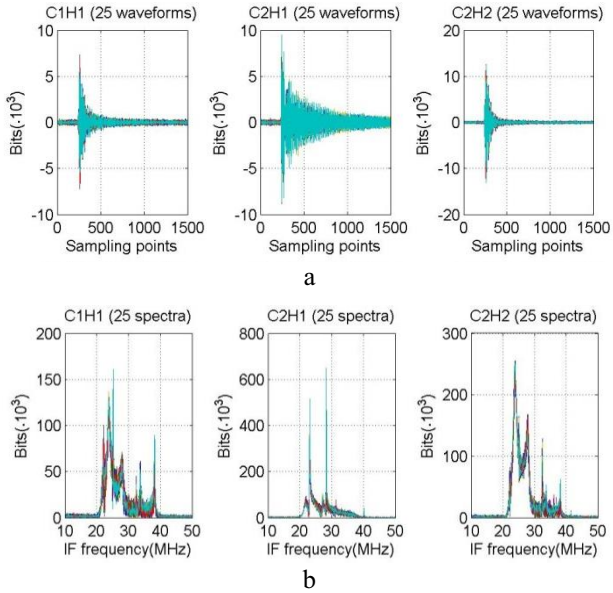


Figure 8: Waveforms (a) measured from three 9 GHz channels (C1H1, C2H1 and C2H2) and the corresponding HOM spectra (b) obtained by Fourier transform.

Figure 9 shows the beam position in the middle of the module as calculated from the BPM readings (blue) and as obtained from the calibration of the HOM signals (red). The two waveforms from the 5 GHz channels (see Figure 7) have been concatenated. The dots for each beam pulse are connected with each other. The RMS error obtained for the calibration data is 12 μm for x and 41 μm for y. Similar values are obtained for the validation data. The results are in agreement to the expected values (below 50 μm) from previous studies [4,5]. The y values are larger due to the large scan range. Similar values are obtained when using the signals from each coupler individually.

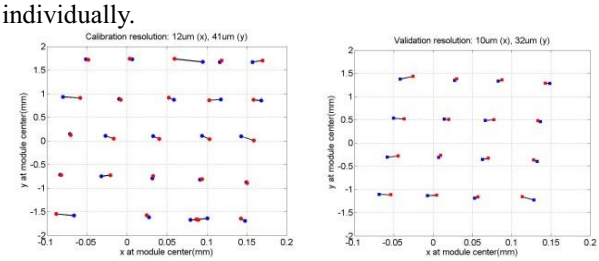


Figure 9: RMS errors obtained from calibration (left) and validation (right) data for the concatenated 5 GHz channels. Each beam position as interpolated from the BPMs (blue) is connected to the resulting position from the HOM signals (red).

Values below 100 μm are expected for each 9 GHz channel. However we obtain values between 20 and hundreds of μm rms. Table 1 summarizes the results for the 9 GHz channels. For cavities 2 and 3 also the results with concatenated waveforms are shown.

Copyright © 2014 CC-BY-3.0 and by the respective authors

ISBN 978-3-95450-141-0

Table 1 RMS Error Obtained for the 9 GHz Channels

	Calibration Data		Validation Data	
Channel	**x [µm]**	**y [µm]**	**x [µm]**	**y [µm]**
C1H1	21	104	23	124
C2H1	31	649	27	435
C2H2	22	103	17	98
C2	*10*	*59*	*12*	*89*
C3H2	35	196	55	123
C3H1	16	164	35	79
C3	*13*	*260*	*25*	*118*
C4H1	46	131	46	116

The RMS errors obtained for the x plane are all very good, below 50 µm, but mostly above 100 µm for y. This cannot be all explained by the larger scan range, since such scans have been used before with good results [4]. Some instability of the signal has been observed sometimes in some of the channels, and this may be the reason for the bad results. In different beam scans even higher values also for the x plane were obtained. Further investigations are necessary before continuing with the work.

CONCLUSIONS AND OUTLOOK

Downmix electronics has been designed and installed at all four 3.9 GHz cavities at FLASH. Dipole modes at 9058±10 MHz are used for beam alignment and position measurement in each cavity, while modes at 5465±10 MHz are used for more precise measurements. The best RMS error obtained so far by moving the beam in a relatively wide range is of the order of 12 and 40 µm (x and y planes) for 5 GHz modes. For the 9 GHz channels the error is below 50 µm for the x plane and above 100 µm in the y plane. It is not yet clear why we cannot reproduce the results with the test electronics, particularly for the 9 GHz channels. Investigations on the stability of the signals in the HOM-BPMs electronics are planned. However the raw signals can already be used for beam alignment.

This electronics serve also as a prototype for the electronics developed for the 3.9 GHz cavities at the European XFEL [9].

ACKNOWLEDGMENT

We are grateful to the operators and coordinators of FLASH for making these measurements possible.

REFERENCES

[1] S. Molloy et al., Phys. Rev. ST-AB 9, 112802 (2006).
[2] K. Honkavaara et al., “FLASH: First Soft X-ray FEL Operating Two Undulator Beamlines Simultaneously”, WEB05, FEL2014, Basel, 2014.
[3] L. Shi et al., “Stability Study of the Higher Order Mode Beam Position Monitors at the Accelerating Cavities at FLASH”, TUPF10, IBIC 2014, Monterey, CA, USA, 2014.
[4] P. Zhang, “Beam Diagnostics in Superconducting Accelerating Cavities: The Extraction of Transverse Beam Position from Beam-Excited Higher Order Modes”, Springer Thesis, 2013.
[5] N. Baboi et al., “HOM Choice Study with Test Electronics for use as Beam Position Diagnostics in 3.9 GHz Accelerating Cavities in FLASH”, Proc. IBIC2012, Tsukuba, p. 364, 2012.
[6] http://www.struck.de/sis8300.html; http://www.struck.de/sis8900.html
[7] http://www.picmg.com; http://mtca.desy.de/
[8] http://tesla.desy.de/doocs/doocs.html
[9] T. Wamsat et al., “First Tests of a uTCA-Based Downconverter Electronic for 5GHz Higher Order Modes in Third Harmonic Accelerating Cavities at XFEL”, TUPF12, IBIC 2014, Monterey, CA, USA, 2014.

Copyright © 2014 CC-BY-3.0 and by the respective authors

FLASH UNDULATOR BPM COMMISSIONING AND BEAM CHARACTERIZATION RESULTS

D. Lipka*, N. Baboi, D. Noelle, G. Petrosyan, S. Vilcins, DESY, Hamburg, Germany
R. Baldinger, R. Ditter, B. Keil, W. Koprek, R. Kramert, G. Marinkovic, M. Roggli, M. Stadler,
PSI, Villigen, Switzerland†

Abstract

Recently, the commissioning of FLASH2 has started, a new soft X-ray FEL undulator line at the DESY FLASH facility. In the FLASH2 undulator intersections, the beam positions are measured by 17 cavity beam position monitor (CBPM) pick-ups and electronics [1] developed for the European XFEL (E-XFEL). In addition four CBPMs are available at FLASH1 for test and development. The new CBPM system enables an unprecedented position and charge resolution at FLASH, thus allowing further analysis and optimization of the FLASH beam quality and overall accelerator performance. Results of first beam measurements as well as correlations with other FLASH diagnostics systems are reported.

INTRODUCTION

Beam position monitors (BPM) are an essential tool for the operation of a Free-electron laser (FEL). In the European X-FEL, cavity BPMs with sub-micron noise and drift are used for the alignment of the electron beam with the photon beam in the undulator area [2]; for a detailed description of a cavity BPM see [3, 4].

In addition to the undulator CBPMs with 10 mm aperture and 100 mm length, a second CBPM type with 40.5 mm aperture and 255 mm length will be installed in some locations in the warm beam transfer lines where the resolution of the standard button BPMs is not sufficient. A test area for the verification of the performance of both CBPM types has been installed at FLASH1 after the last undulator, see Fig. 1. The CBPM electronics, including its embedded FPGA firmware and software, is provided in an In-kind contribution from PSI, see Fig. 2. Both CBPM types have the same electronics because the BPM pickups have the same frequency of 3.3 GHz and similar loaded Q for their position and reference resonator.

In addition to FLASH1, a second undulator beamline FLASH2 [5] has been built to extend the capability of the FLASH soft X-ray FEL facility [6]. For the FLASH2 CBPMs, a pre-series for E-XFEL are used, with the BPM pickups provided by DESY and the electronics from PSI. In this report the results of CBPM measurements at FLASH1 and FLASH2 are reported, including comparisons with other monitors.



Figure 1: CBPM test-stand at FLASH1 with three undulator CBPMs (right) and one 40.5 mm beam pipe diameter CBPM (left). The beam passes the pickups from right to left. Each CBPM can be moved in both transverse directions with remote movers.

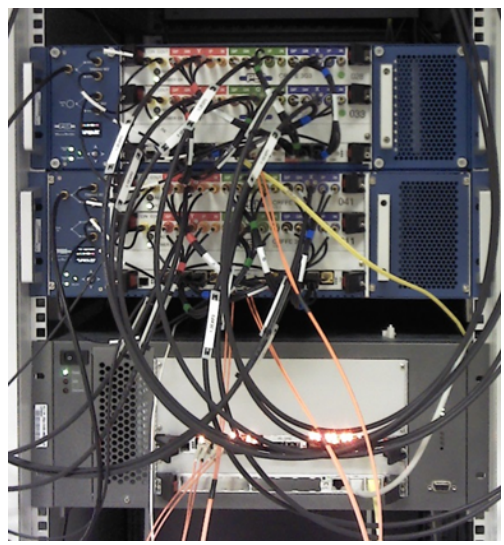


Figure 2: CBPM electronics provided by PSI for FLASH1 and FLASH2. For testing and verification purposes, the system was connected in parallel to the DOOCS based control system of FLASH, and also to EPICS based control system hardware provided by PSI for the commissioning of the systems.

CBPM AT FLASH1

The resulting position and charge values provided by the PSI electronics are transferred to the FLASH control system via an additional communication server. A rough calibra-

* dirk.lipka@desy.de
† This work was partially funded by the Swiss State Secretariat for Education, Research and Innovation SERI

Copyright © 2014 CC-BY-3.0 and by the respective authors

ISBN 978-3-95450-141-0

tion was done for the charge and position readings using a nearby Toroid and remotely controlled transverse movers for each CBPM, see Fig. 1. To calibrate the position readings more exactly a beam jitter independent method from [3] is extended to the four CBPMs in the test area described in the following. Assume z_i are the installed positions of each CBPM i next to each other with only drift space in between where each CBPM can move by m_i, see Fig. 3. Each CBPM

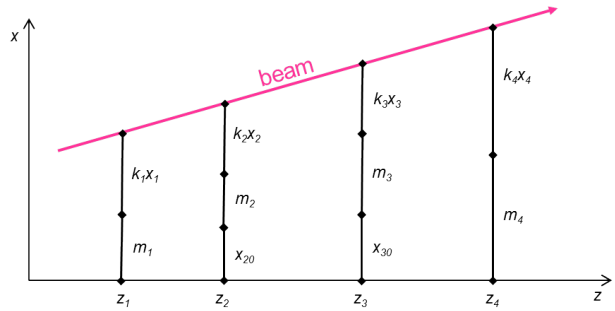


Figure 3: Sketch for the calculation of the calibration.

delivers a position x_i which has to be corrected by a constant k_i (the method is explained for horizontal plane but is used for the vertical plane y too). Both middle CBPMs are allowed to have a relative offset x_{20} and x_{30} with respect to a line between all four BPMs. This results in a condition to be fulfilled:

$$\frac{(k_2x_2 + m_2 + x_{20}) - (k_1 + m_1)}{z_2 - z_1 = z_{12}} = \frac{(k_4x_4 + m_4) - (k_3x_3 + m_3 + x_{30})}{z_4 - z_3 = z_{34}}.$$

Reordering the equation to

$$\frac{m_2 - m_1}{z_{12}} + \frac{m_3 - m_4}{z_{34}} = \frac{k_1x_1 - k_2x_2 - x_{20}}{z_{12}} + \frac{k_4x_4 - k_3x_3 - x_{30}}{z_{34}}$$

such that the right side can be written in vectors

$$= \begin{pmatrix} \frac{x_1}{z_{12}} & -\frac{x_2}{z_{12}} & -\frac{x_3}{z_{34}} & \frac{x_4}{z_{34}} & -\frac{1}{z_{12}} & -\frac{1}{z_{34}} \end{pmatrix} \begin{pmatrix} k_1 \\ k_2 \\ k_3 \\ k_4 \\ x_{20} \\ x_{30} \end{pmatrix}.$$

For several measurements the first vector becomes a matrix P and the vector with the mover positions a vector $\vec{M}$ such that the equation is rewritten to $\vec{M} = P\vec{k}$, where $\vec{k}$ contains the unknown calibration values. The solution is $\vec{k} = P^{-1}\vec{M}$. To solve the equation system at least 6 measurements at different mover positions m_i have to be performed.

This method was applied to the four CBPMs at the FLASH1 test area. Each CBPM was moved separately with about 200 μm step size, see Fig. 4. For each CBPM, 5 steps

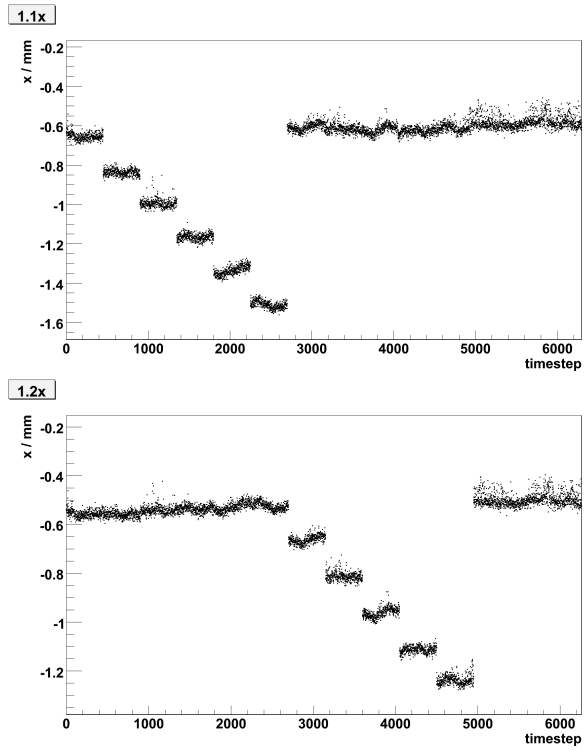


Figure 4: Position readings for different mover positions in x for first (1.1x) and second (1.2x) CBPM.

were used, with 450 position and charge measurements for each step. The histogram in Fig. 5 shows an example from the resulting calibration table that we obtained from the measurement. In this example, the approximate calibration

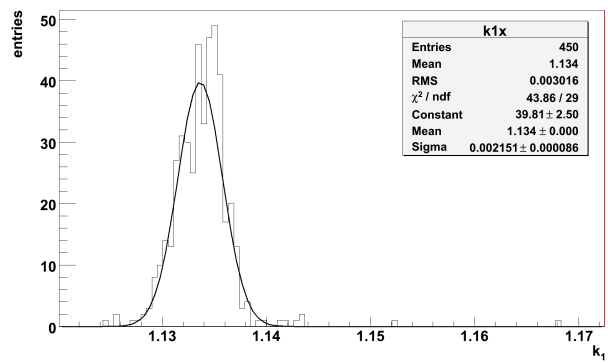


Figure 5: Histogram for different calculated correction values of first CBPM in horizontal direction with Gaussian fit.

obtained from the pre-beam measurements differs by ~13% from the more accurate beam-based calibration.

With the calibrated CBPM of the test-stand one can measure the beam positions and compare them with each other. The 3 BPM method is applied which is described in detail in [3]. Here two BPMs are used to predict the position at the third BPM. The difference from measured and predicted value results in a residual; one example of a residual

Copyright © 2014 CC-BY-3.0 and by the respective authors

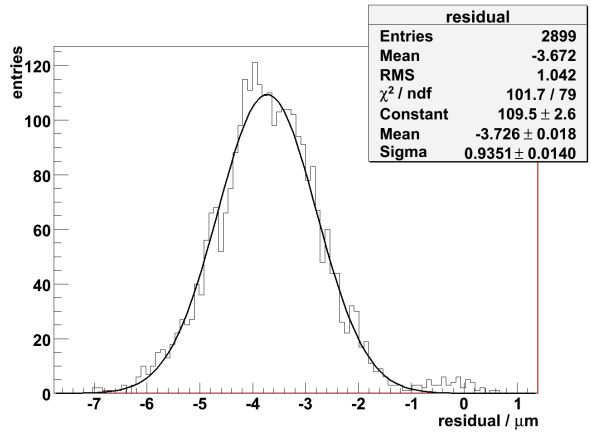


Figure 6: Residuals at a mean beam offset of 0.46 mm and charge 240 pC with Gaussian fit.

histogram is shown in Fig. 6. The Gaussian fit delivers a standard deviation which is used with a geometric factor (see [3]) to calculate the CBPM noise. The noise for both transverse planes are shown in Fig. 7 for different beam offsets at a charge of about 240 pC. The noise is increasing with the

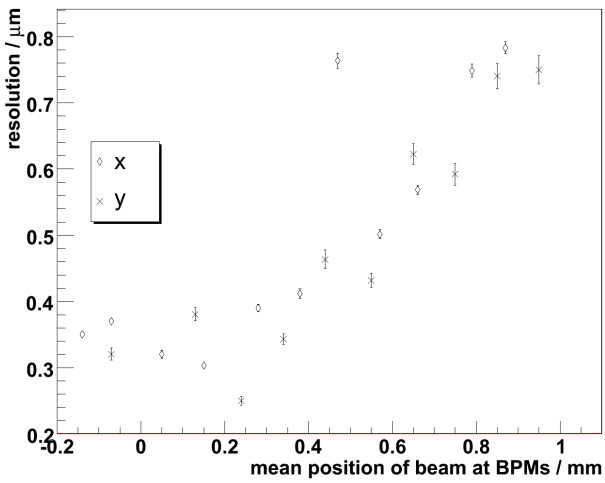


Figure 7: Resolutions of the undulator CBPMs at FLASH1 for different mean beam offsets in x and y for a charge of about 240 pC.

beam offset as expected, since the normalization of the position cavity to the reference cavity signal causes noise of the position that increases with larger beam offsets. For E-XFEL, the required single-bunch position noise for a stable beam with constant charge is below 1 μm for ±0.5 mm measurement range and 0.1 - 1 nC bunch charge. This requirement is already fulfilled by the E-XFEL pre-series electronics used in FLASH1 and FLASH2, where further improvements for the final system are expected by improved calibration and signal processing techniques. In addition one can compare the measured charge values of each CBPM and correlate them to calculate the charge resolution; for 240 pC charge, a resolution of 0.13 pC was obtained.

CBPM AT FLASH2

In FLASH2 17 CBPMs of an E-XFEL pre-series are installed between the undulators, see Fig. 8. In addition to

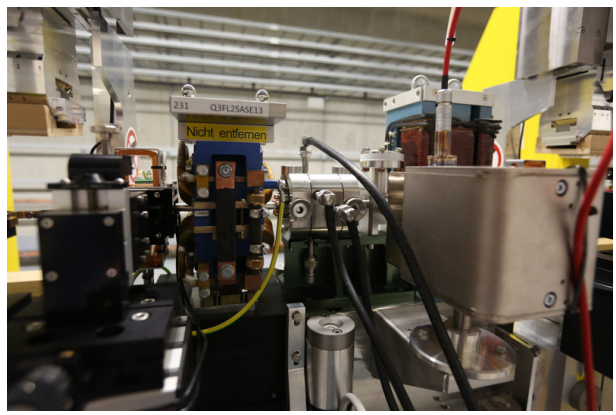


Figure 8: Undulator CBPM in an intersection of FLASH2.

supporting FLASH2 user operation, this gives the opportunity to get experience with the operation and beam-based calibration of a CBPM system in a working accelerator before E-XFEL is commissioned. The electronics for 4 CBPMs (provided by PSI) is shown in Fig. 9. Before first beam, the CBPMs have already been pre-calibrated, using e.g. measured RF properties of the pickups and cables, and signal generators for the electronics. Therefore, to get first beam position and charge readings, only the suitable trigger delay needed to be adjusted. The electronics also has a self-triggered mode using the reference cavity signal, but since the signal threshold may not always be reached during first commissioning (e.g. when the beam is lost somewhere), the external trigger was used.

Since the CBPMs are already integrated into the DOOCS control system (with a parallel EPICS system from PSI for test and verification), CBPM measurements could be compared with other FLASH diagnostics and subsystems.

For the absolute calibration of the CBPM charge measurement, the standard FLASH Toroid charge monitor was used. Thanks to a good pre-calibration, only a correction of 2.9% was necessary (except one CBPM with a correction of 21%, where maybe a measurement of the cable attenuation failed); this indicates that maybe the position calibration may have similar small corrections between pre- and beam calibration.

To get a first impression of the BPM system at FLASH2 the charge reading values are compared with Toroids. A mean charge value for each bunch is calculated such that the deviation due to a single monitor noise is negligible, except one monitor under test. This results in a difference between expected and measured charge for the monitor under test, see an example in Fig. 10. The standard deviation from the Gaussian fit shows the sum from systematical and statistical measurement errors, defined here as *sum error*. For all

Copyright © 2014 CC-BY-3.0 and by the respective authors

ISBN 978-3-95450-141-0

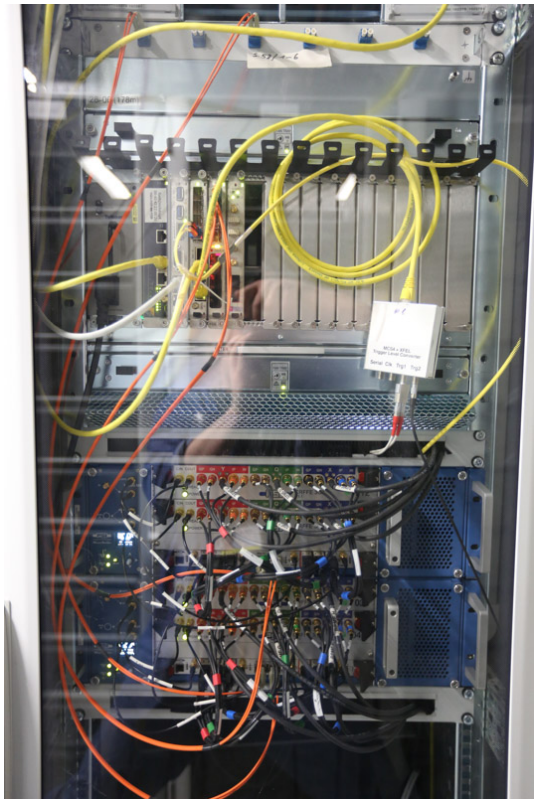


Figure 9: Undulator electronics for FLASH2 provided by PSI at the bottom part with 4 front-ends. Above is a μTCA crate with an FPGA/SFP board for the communication between PSI electronics and FLASH control system via fiber optic multi-gigabit links.

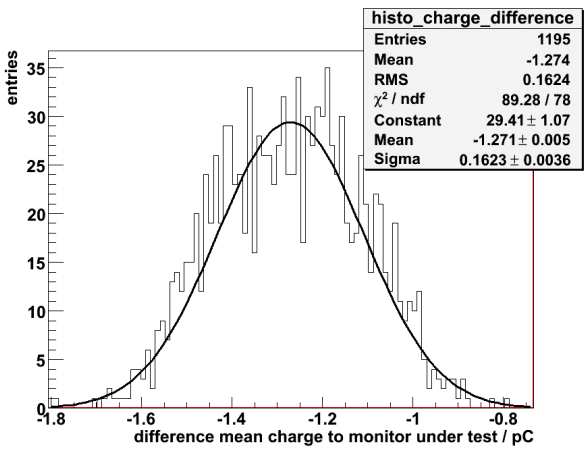


Figure 10: Difference between mean charge value to the monitor under test: here CBPM with the monitor number 19 with Gaussian fit at a charge of about 100 pC.

charge monitors these are shown in Fig. 11. All values above 0.6 pC are delivered by Toroids; therefore the CBPMs deliver better sum errors than standard charge monitors and are between 0.1 and 0.17 pC for a charge of 100 pC.

To obtain the position sum error (including statistical and systematical errors) two button BPMs after the accelera-

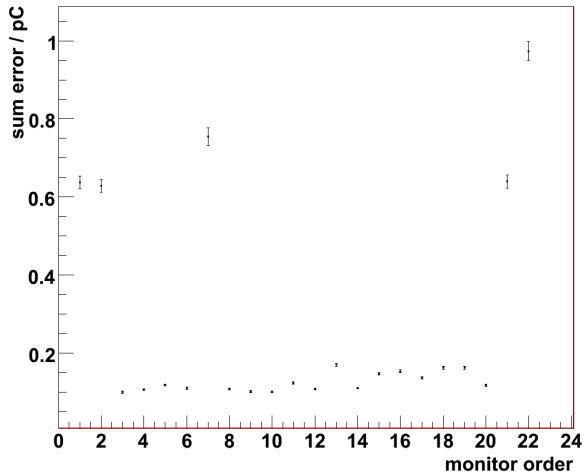


Figure 11: Sum of statistical and systematic errors of charge monitor correlation at FLASH2 at a charge of about 100 pC, with active automatic gain control of the CBPMs, ordered according beam direction. Values above 0.6 pC are from Toroids, values below from CBPMs.

tion modules and all CBPMs at FLASH2 are used. Here a correlation is calculated between each BPM and the BPM under test; the difference between expected and measured position value is obtained, for a reference of this method see [7]. An example of a difference histogram of one CBPM is shown in Fig. 12. All position sum errors of the BPMs

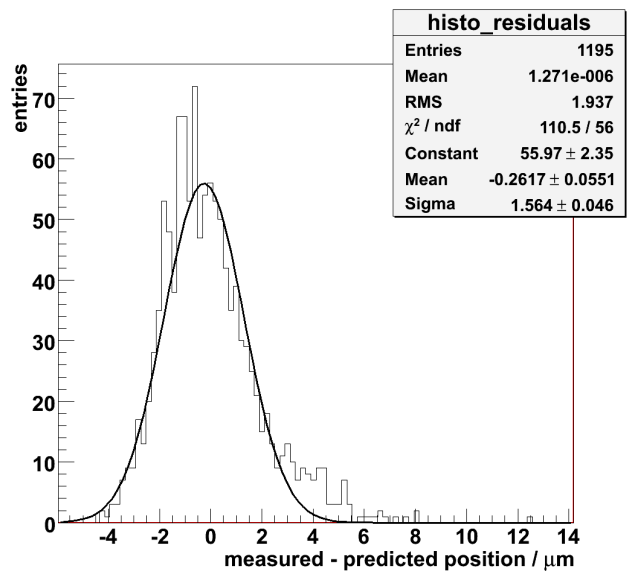


Figure 12: Difference between expected and measured position with Gaussian fit of a CBPM with monitor number 4 for position error calculation at the horizontal plane.

are shown in Fig. 13. Due to different beam positions, e.g. vertical sum error vs. mean beam position (see Fig. 14), the sum error is different at each CBPM, similar to the results shown in Fig. 7. As expected the sum error of the

Copyright © 2014 CC-BY-3.0 and by the respective authors

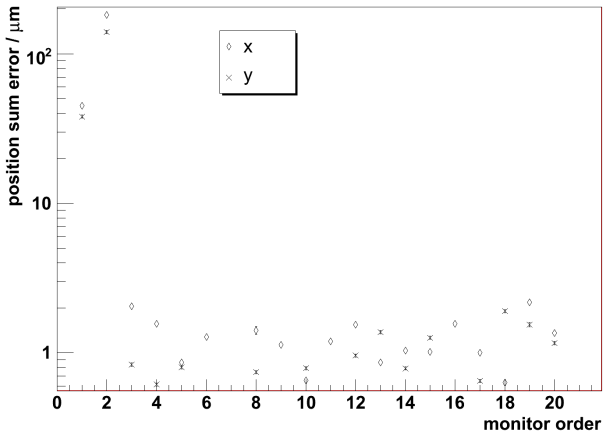


Figure 13: Sum error of BPM correlation at FLASH2 in both transverse planes for a charge of about 100 pC. The first two monitors are button BPMs, otherwise the order of CBPMs is similar to Fig. 11.

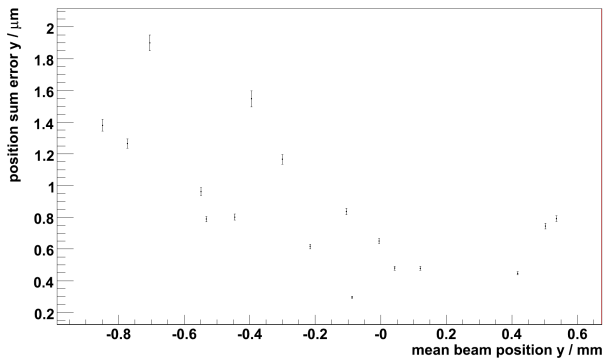


Figure 14: Sum error of CBPM correlation measurement at FLASH2 at the vertical plane with a charge of about 100 pC as a function of mean beam position.

correlation is much better for the CBPMs compared to the button BPMs. The sum error obtained for the CBPMs has several contributions. While the CBPM measurement in FLASH1 was done with constant attenuator settings (like later for the E-XFEL undulators), the CBPMs in FLASH2 were operated in a preliminary commissioning mode where a feedback loop permanently adapted the attenuators of the RFFE channels to the strongly varying charge and beam positions that may occur during first beam commissioning of an accelerator. Since the attenuators of the CBPMs were so far only approximately calibrated, the frequent changes of the attenuators caused systematic measurement errors of position and charge that usually dominate the sum error. In case of large beam position changes, the ADCs of the BPMs may saturate, which is indicated by the BPMs via a valid flag but not yet recorded by the control system, which also contributes to the measurement error. Finally, mechanical vibrations of the CBPM pickups or systematic errors of the measurement method itself (e.g. due to dispersive effects or X/Y rotation of pickups that has so far not been accounted for) can contribute to the overall error. A more detailed analysis of the individual contributions is in progress, where the goal is to minimize systematic contributions to the BPM measurement error via improved lab-based and beam-based calibration methods [8], leaving thermal RFFE noise and ADC resolution as dominating factors.

SUMMARY

The development of the CBPM system for the European XFEL is in an advanced state. An E-XFEL pre-series version of the CBPM pickups and electronics has been installed and tested in FLASH1 and FLASH2, and already fulfills the requirements for E-XFEL. Future activities will focus on improvement of lab and beam-based calibration techniques, as well as on improved automated range control and digital signal processing to further improve the CBPM system performance.

REFERENCES

[1] M. Stadler et al., "Low-Q Cavity BPM Electronics for E-XFEL, FLASH 2 and SwissFEL", *these Proceedings*, IBIC14, Monterey, US (2014).

[2] B. Keil et al., "The European XFEL beam position monitor system", IPAC, Kyoto, Japan, (2010). `http://cern.ch/AccelConf/IPAC10/papers/mope064.pdf`

[3] S. Walston et al., "Performance of a high resolution cavity beam position monitor system", NIM A 578, 1-22 (2007). `https://www.bnl.gov/edm/review/files/references/SWalston.NIMA578.2007.1.pdf`

[4] D. Lipka. "Cavity BPM Designs, Related Electronics and Measured Performances", DIPAC09, Basel, Switzerland (2009). `http://accelconf.web.cern.ch/AccelConf/d09/papers/tuoc02.pdf`

[5] N. Baboi, D. Noelle, "Commissioning of the FLASH2 Electron Beam Diagnostics in Respect to its use at the Europoean XFEL", *these Proceedings*, IBIC14, Monterey, US (2014).

[6] K. Honkavaara et al., "FLASH: First Soft X-Ray FEL Operating two Undulator Beamlines Simultaneously", WEB05, FEL, Basel, Switzerland (2014).

[7] N. Baboi et al., "Resolution studies at beam position monitors at the FLASH facility at DESY", BIW06, Fermilab, US (2006).

[8] B. Keil et al., "Beam-Based Calibration and Performance Optimization of Cavity BPMs for SwissFEL, E-XFEL and FLASH-II", *these proceedings*, IBIC14, Monterey, US (2014).

Copyright © 2014 CC-BY-3.0 and by the respective authors

ISBN 978-3-95450-141-0

DESIGN, DEVELOPMENT AND COMMISSIONING OF A MTCA-BASED BUTTON AND STRIP-LINE BPM SYSTEM FOR FLASH2

Bastian Lorbeer*, Frank Schmidt-Föhre, Nicoleta Baboi, Ludwig Petrosyan
DESY, Hamburg, Germany

Abstract

The FLASH (Free Electron Laser in Hamburg) facility at DESY (Deutsches Elektronen-Synchrotron) in Germany has been extended by a new undulator beam line called FLASH2 to provide twice as many experimental stations in the future [1]. After the acceleration of the electron bunch train up to 1.2 GeV, a part can be kicked into FLASH2, while the other is going to the old undulator beam line. In order to tune the wavelength of the SASE (Self Amplified Spontaneous Emission), the new line is equipped with variable gap undulators. The commissioning phase of FLASH2 started in early 2014 and continues mostly parasitically during user operation in FLASH1. One key point during first beam commissioning is the availability of standard diagnostic devices such as BPM (Beam Position Monitor) [2]. In this paper we present the design and first operational experience of a new BPM system for button and strip-line monitors based on MTCA.4 [3]. This is referred to as LCBPM (low charge BPM) in contrast to the old systems at FLASH initially designed for bunch charges of 1 nC and higher. We summarize the recent analog and digital hardware development progress [4, 5] and first commissioning experience of this new BPM system at FLASH2 and present a first estimation of its resolution in a large charge range from 1 nC down to 100pC and smaller.

INTRODUCTION

The demand for beam time at the user facility FLASH increased substantially in the past. In order to fulfill this need the FLASH facility has been extended by a new undulator beam line for SASE generation called FLASH2. The charge delivered to FLASH2 can be adjusted independently from the old FLASH facility with an independent laser. FLASH2 has been ready for electron beam commissioning in March 2014, has seen the first beam on 4th March and was able to deliver SASE for the first time on 20 August 2014 [6, 7]. This was done simultaneously during SASE delivery in the FLASH1 undulator beam line. The electron beam delivered to FLASH2 is accelerated within the same RF (Radio Frequency) pulse in the FLASH facility up to 1.2 GeV after approximately 150 m and is then kicked into the FLASH2 tunnel. One part of the diagnostics in FLASH2 are button and strip-line monitors at 16 locations in the machine utilizing new MTCA.4 electronics designed by us [4, 5]. Challenges in the development of this system are the resolution requirement of 50 µm, operation at charges well below 100 pC and a high bunch repetition rate of up to 4.5 MHz. This is compatible with the requirements for the European XFEL [8]. The hardware development status and operation experience with these new systems are summarized in this paper.

* bastian.lorbeer@desy.de

OVERVIEW

The new FLASH2 undulator beam line runs in parallel to the old FLASH1 undulator beam line which can be seen in Figure 1. It is divided into several sections namely EXTRACTION, SEED, SASE, BURN, and DUMP section with button and strip-line monitors in different locations. Most

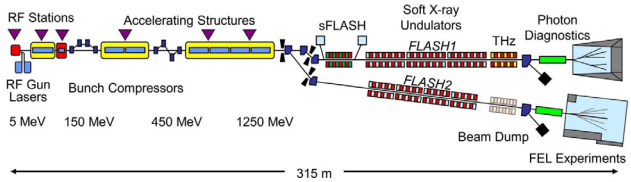


Figure 1: Section overview FLASH.

of the LCBPMs are distributed along the EXTRACTION section at the beginning of FLASH2 with nine BPMs and the rest of 4 BPMs are in the BURN/DUMP section. Due to space limitations in the SASE section three button BPMs have been installed here as well instead of using the more preferable cavity BPMs which offer the required resolution for orbit tuning in the SASE section [9, 10]. A variety of different beam pipe diameters for the button BPMs and a few refurbished strip-line BPMs with different RF cable lengths ranging from 35 to 58m installed in the machine required the development of a very robust but also flexible BPM electronics. The button type design is the same as for the European-XFEL that has been reported in [11]. Table 1 summarizes all types of BPMs for which the electronics are currently in operation. Electromagnetic field simulations [12] delivered the monitor constants. An overview of

Table 1: Types of Beam Position Monitors Installed in FLASH2 and Corresponding Monitor Constants

Type	amount	Diameter	Monitor constant
button	2	40 mm	10.6 mm
button	4	34 mm	9.06 mm
button	3	100 mm	23.84 mm
strip-line	4	44 mm	8.678 mm
in-air	1	100 mm	31.25 mm
button	3	10 mm	2.55 mm

the connections between the BPMs and readout electronics can be seen in Figure 2.

Copyright © 2014 CC-BY-3.0 and by the respective authors

ISBN 978-3-95450-141-0

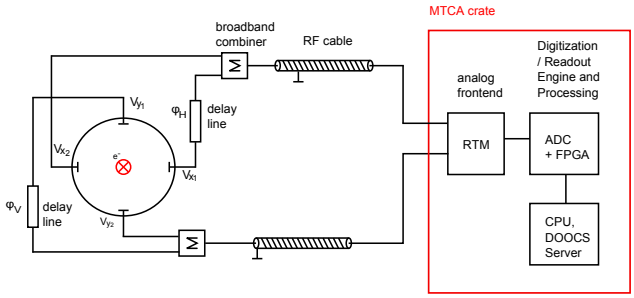


Figure 2: Overview Beam Position Monitor System.



Figure 3: Rear Transition Module RF front-end.

The beam excited RF signals in the horizontal and vertical plane are combined after a delay of 100 ns to suppress interference with the next bunch in the train. This so-called Delay Multiplex Single Path Technology (DMSPT) [13, 14] method has been successfully in operation for many years in HERA[1] at DESY. It successfully proved to suppress the common mode EMI disturbances on the RF cable from the tunnel to the electronic racks. It also reduces the number of necessary ADC (Analog Digital Converter) channels for each BPM. The electronics for signal conditioning and processing are separated into an analog and digital card. The two cards are housed in a MTCA.4 crate. The position calculation takes place in the Firmware on the digital card and is given by the normalized difference of the signal on opposite electrodes [15]. This position information can then be read from a device server which can display the position in a panel.

ELECTRONICS

Analog Electronics

The BPM signals delivered to the electronics rack have a rise-time, fall-time, and duration in the order of a few 100 ps. Since it is very difficult to sample such a signal even at a high sample rate, these signals are pre-conditioned for digitization and processing on a custom made RF module. This makes it also easier to sample the signal and achieve the necessary resolution of the entire BPM system. Such a RF module has been designed and developed following the specifications of the MTCA.4 standard for RTM (Rear Transition Module). Each RTM has two RF channels that can measure beam position from one BPM using the delay-line multiplex method. A picture of the analog RF front-end is shown in Figure 3.

The filtering and amplification in the RF receiver signal path has been designed in a way to guarantee a dispersion free signal transport. This has been done to avoid interference between the two signals of each plane and to increase the integrity of the original signals along the signal path. The signal paths consists of a cascade of amplifiers and step attenuators and a peak-hold detector circuitry with a discharge switch. The peak amplitude from the amplified RF signal is detected with a Schottky diode and its value is tracked by a capacitor. The discharging of the hold capacitor takes place after a time of approximately 40 ns and is adjusted by the timing settings in the custom made firmware. A picture of a single RF channel is shown in Figure 4.

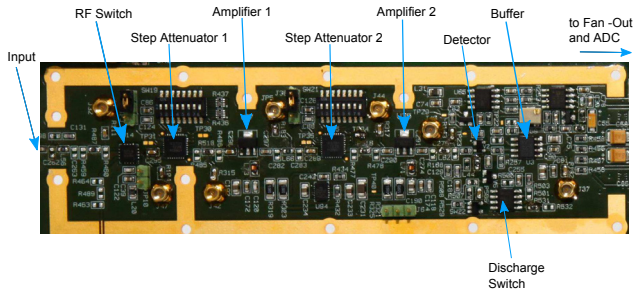


Figure 4: Single channel RF front-end.

The functionality of the electronics at low charge requires high gain in the receiver channel. The maximum gain of a single RF channel is on the order of 38 dB with a 3 dB bandwidth of approximately 600 MHz. Primarily the two step attenuators are used to adjust the signal strength for different charges with a dynamic range higher than 60 dB, while the step attenuator 2 can also be used to optimize the position measurement resolution for large beam offsets. Currently the information for signal level attenuation is loaded manually into the step attenuators. Before the analog signal is digitized it is distributed in a fanout stage for sampling by four ADCs in parallel for optional averaging. The analog bandwidth at the output of the fanout stages is approximately 230 MHz.

Digital Electronics

The digitization and signal processing takes place on a digitizer board containing ten ADC channels and a FPGA (Field Programmable Gate Array) [16]. The analog RF front-end and the digitizer board are connected to each other via a high speed connector keeping the signal integrity with the required analog bandwidth up to the ADCs. The pre-conditioned analog signals are buffered and filtered in front of the ADC channels and are then digitized by 16Bit at a rate of 125MSPS. The custom made firmware (FW) on the FPGA is operating in real time and delivers bunch by bunch information at its output registers. The FW contains registers to adjust the step attenuators on the analog RF

[1] Hadron Elektron Ring Anlage

ISBN 978-3-95450-141-0

Copyright © 2014 CC-BY-3.0 and by the respective authors

front-end and a state machine to control the discharge of the hold capacitors on the analog board. The FW can operate in four different modes of which two are capable to work independently from the timing system as described in [5]. The timing coupled FW operating mode uses the bunch train trigger, ADC clock, and charge information as delivered by the timing system. This mode is the most stable from all modes. An AGC (Automatic gain control) based on the charge information will adjust the step attenuators on the RF front-end for optimized position reading resolution. This mode is currently under development and intended to be the most stable mode. The mode currently in operation at FLASH2 is the so called quasi-autarcic mode. In this mode the FW receives an external pre-trigger from the timing system. All other bunch related timings such as the hold capacitor discharging signal on the RTM, and the calculation of the bunch position are derived from this initial trigger inside the FW. The ADC clock is also generated locally independent of the FLASH2 timing system.

SYSTEM INTEGRATION

Crate System and Timing

The analog and digital cards for all 16 BPMs have been installed in 19" MTCA.4 crates with twelve AMC slots on the front and ten RTM slots on the back side. A maximum of five BPMs are installed in each crate to minimize interference between the neighbouring cards. Two of the crates in operation carry five, one carries three, and one carries four BPM electronics. The power module, the MCH (management carrier hub), the CPU and timing system receiver board and the digitizers are installed on the front side of the crate. The trigger from the timing system to the digitizer is delivered on a dedicated line on the backplane. The crates are located in a technical site next to the FLASH2 tunnel in climatized racks. An example installation for five BPMs from the EXTRACTION section in FLASH2 is shown in Figures 5 and 6.

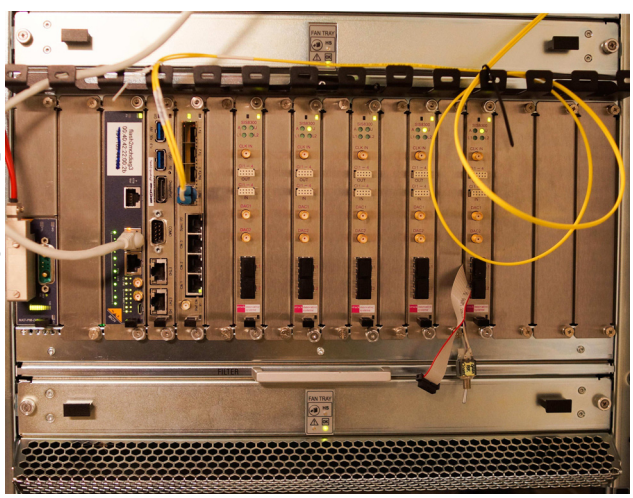


Figure 5: Front View of a MTCA crate carrying five LCBPMs at FLASH2.

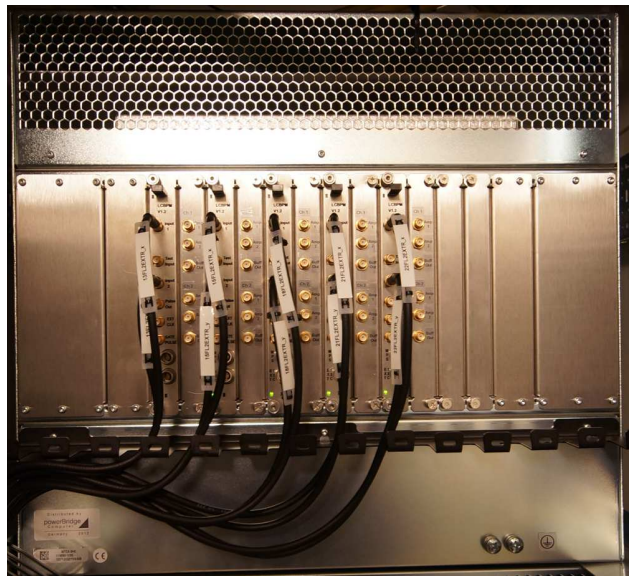


Figure 6: Rear View of a MTCA crate carrying five LCBPMs at FLASH2.

Driver and Software

The position information calculated in the Firmware is read out by a customized driver from a PCIe bus system to which all modules are connected in the crate. The links on this PCIe bus can be configured in the MCH. A device server application running on the system CPU is polling FW registers on the digitizers, which are connected via the PCIe bus. This server can be accessed remotely over ethernet and its content can be visualized by use of control system panels.

MEASUREMENTS

A typical distribution of position readings over 200 pulses from a strip-line BPM is shown in Figure 7 and 8. This measurement has been taken at a charge of 36 pC measured at a beam charge monitor located closest to the BPM. Similar results have been taken at higher charges up to 300pC which indicates that the electronics is not at its resolution limit. It is possible to steer the beam through an aperture of $+/-10$ mm for most BPMs without the need to adjust the second step attenuator. For both planes a standard deviation around 20 µm has been obtained.

The standard deviation for all BPMs in the extraction section is below 50 µm at charges lower than 50 pC for a centered beam but increases in the dump section to values in the order of 100 µms. In the current setup the three BPMs in the SASE section do not deliver sufficient signal amplitude for measurements. This will be overcome with additional pre-amplification of the BPM signal in the future. The fulfillment of the specifications for 50 µm position resolution at charges well below 100 pC has been shown for single-bunch operation at bunch repetition rates up to 1 MHz in the current state of commissioning. Increased BPM performance can be expected from bunch synchronous measurements from all FLASH2 BPMs in order to remove the correlated electron beam jitter from the position readings.

Copyright © 2014 CC-BY-3.0 and by the respective authors

ISBN 978-3-95450-141-0

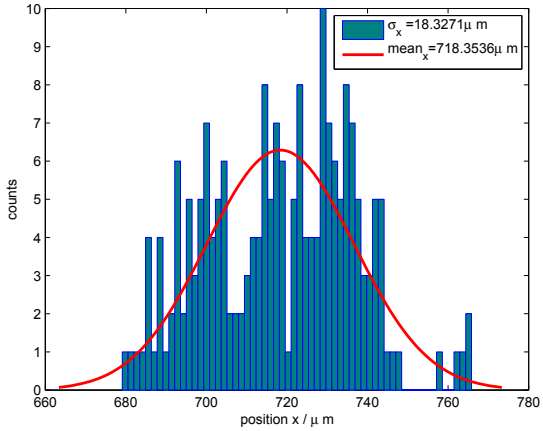


Figure 7: Position fluctuations in x direction for a strip-line BPM located in the FLASH2 EXTRACTION section.

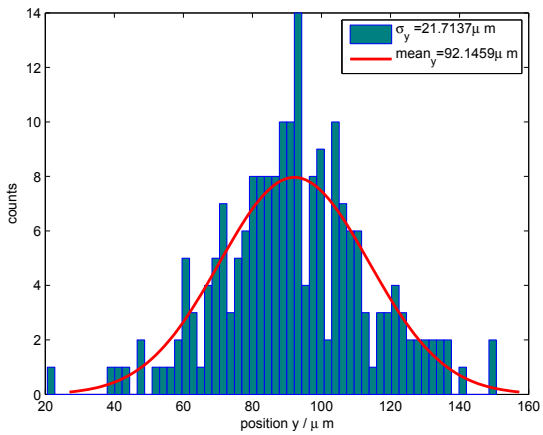


Figure 8: Position fluctuations in y direction for a strip-line BPM located in the FLASH2 EXTRACTION section.

SUMMARY

A new type of MTCA.4 based Beam Position Monitor System for button and strip-line monitors has been designed, developed and successfully installed in FLASH2. The system has been a useful tool during first commissioning and SASE production of the machine [17] and ongoing machine commissioning [18]. It operates at charges down to 35 pC and lower and has a large headroom for operation at higher charges due to the high dynamic range given by the two step attenuators.

OUTLOOK

The LCBPM system will be developed further to become more operator friendly for standard machine operation. This includes additional Firmware, device server and middle layer server upgrades. The performance will be analyzed as soon as data can be taken synchronously from all BPMs. In the future the system will replace the existing BPM system for the rest of FLASH which has been designed for a charge of 1 nC. Further increased BPM performance is expected by the implementation of the fully timing coupled mode. Additional pre-amplifiers will also enable LCBPM measurements in button BPM systems in the SASE section of FLASH2.

ACKNOWLEDGMENT

We acknowledge the support from our MDI colleagues Rudolf Neumann, Jörg Neugebauer, Jorgen Lund-Nielsen, Dirk Lipka for hints, discussions, installation, and simulations. We also acknowledge the support for system integration from Christoph Stechmann, Olaf Hensler and Kay Rehlich from MCS group.

REFERENCES

[1] http://flash2.desy.de

[2] N.Baboi et al., THIXB1, "Commissioning of the FLASH2 Electron Beam Diagnostics in Respect to its use at the European XFEL", *these Proceedings*, IBIC14, Monterey, US (2014).

[3] PICMG MTCA.4 Revision 1.0, "MicroTCA Enhancements for Rear I/O and Precision Timing", August 22, 2011 http://www.picmg.com

[4] B. Lorbeer et al., TUPA19, IBIC2012, Tsukuba, Japan.

[5] F. Schmidt-Föhre et al., THPME117, IPAC2014, Dresden, Germany.

[6] S. Schreiber, B. Faatz, "First Lasing at FLASH2", presented at 36th Int. Free-Electron Laser Conf., Basel, 2014.

[7] K. Honkavaara et al., "FLASH: First Soft X-ray FEL Operating Two Undulator Beamlines Simultaneously", in Proc. 36th Int. Free-Electron Laser Conf., Basel, 2014, WEB05.

[8] D. Nölle, "The European XFEL Beam Position Monitor System", Conceptual Design Report, Rev.1.00, June 15 2010

[9] M. Stadler et al., "Low-Q Cavity BPM Electronics for E-XFEL, FLASH 2 and SwissFEL", *these Proceedings*, IBIC14, Monterey, US (2014).

[10] D. Lipka et al., "FLASH Undulator BPM Commissioning and Beam Characterization Results", *these Proceedings*, IBIC14, Monterey, US (2014).

[11] D. Lipka et al., "Button BPM Development for the European XFEL", MOPD19, Proceedings of DIPAC2011, Hamburg, Germany.

[12] Dirk Lipka, private communication.

[13] Rudolph Neumann, private communication.

[14] F. Schmidt-Föhre et al., "BPM system upgrades in the Petra 3 Pre-accelerator chain during the 2008 shutdown", MOPD20, Proceedings of DIPAC09, Basel, Switzerland.

[15] G. Vismara et al., "From Narrow to Wide Band Normalization for Orbit and Trajectory Measurements", Presented at BIW-98, 8th Beam Instrumentation Workshop, SLAC, USA, 4-7 May 1998.

[16] SIS8300, "MTCA for Physics digitizer", August 2011, http://www.struck.de

[17] M. Scholz et al., "Optics Measurements At FLASH2", FEL2014, BASEL, Switzerland.

[18] Bart Faatz, private communication.

Copyright © 2014 CC-BY-3.0 and by the respective authors

ISBN 978-3-95450-141-0

CALIBRATION OF OLYMPUS/DORIS BEAM POSITION MONITORS

U. Schneekloth, N. Görrissen, G. Kube, J. Neugebauer, R. Neumann, F. Schmidt-Föhre
DESY, Hamburg, Germany

Abstract

The goal of the OLYMPUS experiment is a precise measurement of the ratio of the positron-proton and electron-proton elastic scattering cross sections in order to quantify the effect of two-photon exchange. The experiment was performed using intense beams of electrons and positrons stored in the DORIS ring at Deutsches Elektronen Synchrotron in Hamburg, impinging on an un-polarized, internal, hydrogen gas target. An essential ingredient of the experiment is a precise determination of the luminosity, which requires a precise knowledge of the beam position of both beam species. During DORIS operation cylindrical button beam position monitors, read out by two independent electronics systems, were mounted up- and downstream of the target chamber. After the end of operation, the readout systems were cross-calibrated. The BPMs were then calibrated using a test-stand, consisting of a wire scanner assembly. The beam was simulated by applying an RF signal to the wire. This paper describes the calibration principles and test setup, together with the results compared to the expected BPM response.

INTRODUCTION

The OLYMPUS experiment at DESY [1] aims to determine this two-photon contribution by measuring the ratio of the positron-proton to electron-proton cross sections. The experiment was performed at the DORIS storage ring, with 2 GeV electron and positron beams impinging on an un-polarized, internal, hydrogen gas target. For the aimed-for precision of the experiment, the beam position was required to be known on the 0.1 mm level, since it directly affects the acceptance of the detector systems.

During DORIS operation the beam position at the OLYMPUS target chamber was measured by two beam position monitors (BPMs), mounted up- and downstream of the target chamber. The BPMs consisted of four cylindrical pickup buttons of 10.8 mm diameter in a cylindrical 60.3 mm diameter beam pipe. The BPMs were readout by two independent electronics: the standard DORIS electronics (so-called Neumann electronics) [2] and the commercially available Libera Brilliance+ readout system [3]. Both readout systems use the same measurement principle: the beam position is calculated as $X = k_x((V_a + V_d) - (V_b + V_c))/\Sigma - X_{offset}$ and similarly for Y, where V_i is the voltage at pickup electrode i, k_x a calibration constant and Σ the sum of the four voltages. However, the signal processing is quite different. The Neumann electronics does serial signal processing (Delay-line Multiplex Single Pass Technology). The four analog signals are passed through a delay line and are then sent to the same ADC. A gain/attenuation correction in done is steps of 1 dB. In constrast, the Libera electronics uses parallel signal processing, including RF channel switching, amplitude compensation, phase equalization and automatic gain control. Calibration constants k_x and k_y for the standard DORIS vacuum chamber profile were determined by measurements many years ago. For the present cylindrical BPMs the constants were calculated using a boundary element method as described in [4].

Data from both readout systems were stored in the DORIS accelerator archive. All of the Neumann data were stored in the OLYMPUS slow control data base, whereas the Libera data were only available for the last part of the data taking period.

The goal of the present studies was: calibrate the up- and downstream BPMs, i.e. determine the zero-positions and the response to the wire position, check whether there was a dependence on the beam current (wire input signal) and beam species (pulse polarity), and to transform the beam position (wire position) into the OLYMPUS coordinate system. In addition, the two different readout electronics were cross-calibrated, in order to get consistent beam position information for the complete running period.

SETUP OF BPM TEST STAND

The calibration of the OLYMPUS/DORIS BPMs was done on a vertical BPM test-stand, based on an original design by Paul-Scherrer-Institute (PSI), Villigen, Switzerland. The original test stand construction was comprised of a vertically oriented segment of the beam tube containing a single button-type BPM chamber, fixed by a flange on a holder-table at the lower end of the setup. A thin wire-antenna, stretched by an oil-damped steel-weight at its lower end, is fixed in a N-type RF-connector, that is placed at the outer end of a horizontal wire-holder plate attached to a x/y- micrometer-portal-guide (mover) on top of the C-shaped steel holder-frame of the test-stand. The wire-antenna is driven by an appropriate pulsed or cw RF-generator-signal via the N-connector. A solid RF-ground connection between the RF-connector and the fixed beam-tube enables an optimum conduction of the RF-signal, avoiding an instable transition of the characteristic impedance between signal source cable and antenna. The present setup incorporated a second button BPM chamber, located below the first one on the upper end of the structure. During the pre-tests, the signal originally driving the antenna by a tuned, typically 2 ns long button-type pulse-signal of 40 V, turned out to be too low for the Libera electronics. After changing the source generator setup to a sinusoidal 500 MHz-cw-signal and optimization

Copyright © 2014 CC-BY-3.0 and by the respective authors

ISBN 978-3-95450-141-0

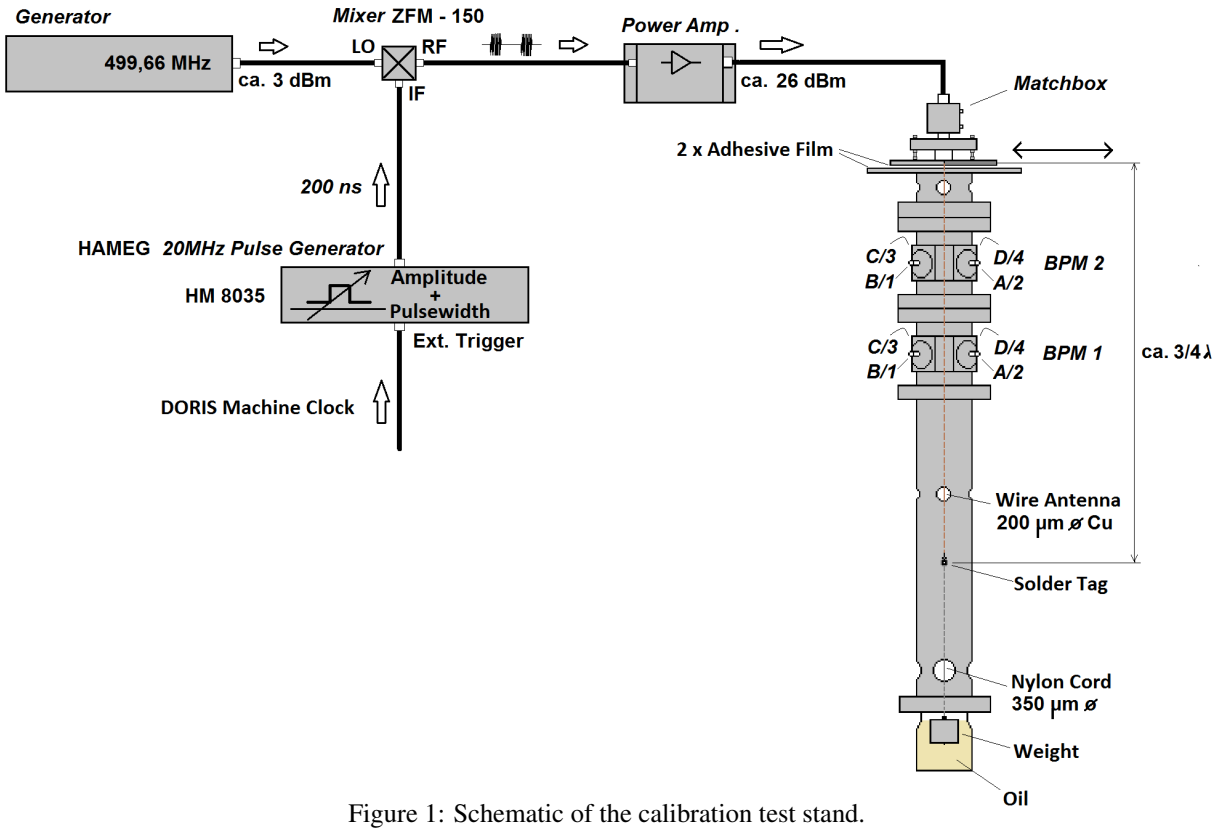


Figure 1: Schematic of the calibration test stand.

of the incoupling signal- and ground-conduction, sufficient RF-signal-level was coupled from the wire-antenna to the BPM-electrodes to drive the electronics.

CALIBRATION MEASUREMENTS

Several calibration measurements were performed, where the wire was usually kept in the center of the BPMs in one coordinate and scanned in steps of 1 mm up to ± 10 mm in the other coordinate. The maximum deviation of the BPM readings w.r.t the wire positions were ±0.9 mm at the extreme wire positions of ±10 mm, where the maximum deviation from a straight line fit was ±0.4 mm. Individual positions were reproducible to about 3 μm. Note, that geometry and alignment corrections were not applied to the BPM readings.

Scans in x for y positions of +2, 0 and -2 mm were done and compared to the calculations using a boundary element method [4]. The shape of the deviation of measured BPM readout positions from the true positions as a function of the true values are very well described by the calculations, as shown in Fig. 2. A small rotation of 20 mrad was applied to the data. At 1 mm the measurements and calculations agree within 5μm. The largest disagreement, at 5 mm, is about 0.1 mm. This could be due to a misalignment of the BPMs w.r.t. the test stand, fabrication tolerances or due to asymmetries in the cabling or readout electronics.

In order to check a possible dependence on the beam current, the level of the input pulse was varied over a factor of 6. No systematic dependence on the signal level was observed. The readout positions were stable with a standard deviation of 1.3 μm. The dependence on the input signal polarity was checked by injecting a bipolar pulse into the BPM cables with and without an inverting transformer. The measured BPM readings were equal within about 5 μm, which is well below the requirements of the OLYMPUS experiment. This was an important check, since the experiment relies on a precise measurement of the luminosity ratio for positron and electron beams.

In addition, several scans in steps of 0.2 mm over a range of 1 mm were performed for various x and y values, which corresponded to the beam positions during DORIS operation. The deviations w.r.t. to the wire positions were within a few μm.

CROSS-CALIBRATION OF ELECTRONICS

During beam operation, the BPMs in the interaction region were read out by two independent readout systems, providing significantly different beam position, as shown in Fig. 3. This was caused by the very different treatment of the BPM signals in the readout systems. In particular, the standard DORIS readout (Neumann) used the first negative part of the pulse, which is obviously different for electron beam and the inverted positron beam signals. Whereas the Libera electronics performed a narrow bandwidth analysis of the RF pulse, which is by design independent of the pulse polarity. This was confirmed by the measurements

Copyright © 2014 CC-BY-3.0 and by the respective authors

ISBN 978-3-95450-141-0

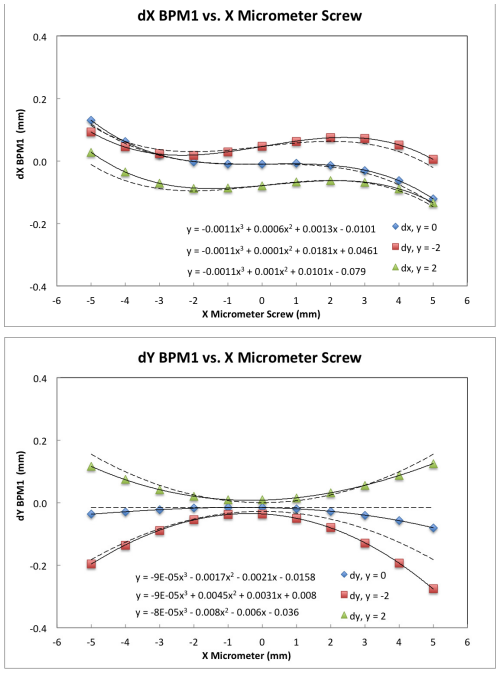


Figure 2: Deviation of the measured (calculated) BPM readout from the true position as a function of the wire position. Top figure: deviation in x for x movements for three y values. Bottom figure: deviations in y. Also shown is a 3rd order polynomial fit to the data.

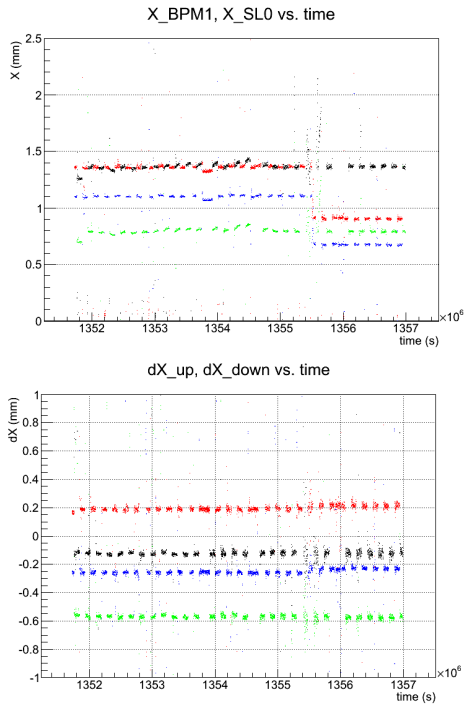


Figure 3: Top: Upstream horizontal Libera and Neumann BPM positions as function of time for e^+ and e^- beams (fall running period Oct. 2012 to Jan. 2013.) Bottom: Difference of Neumann and Libera horizontal positions vs. time. Data are from the DORIS accelerator archive.

as described above. The Neumann values were available in the OLYMPUS slow control system for the full running period, but unfortunately, the Libera values were only stored for part of the fall run. Corrections were therefore determined for the Neumann readout.

The difference of Neumann and Libera positions as a function of time was quite stable, as plotted in Fig. 3. Other effects like the beam current dependence were relatively small. Steps of 30 μm in the Libera positions were observed for beam current drops of 4 - 5 mA, i.e. 5% of the beam current, when the beam position was fixed by the feed back system using the Neumann BPM information. During stable fills, the position was stable within 15 μm. The Neumann Libera differences were quite substantial, from 0.1 to 1.4 mm depending on the BPM channel, and were simply added as offsets to the Neumann values. These offsets were stable within 15 μm over the full running period, except for one BPM channel which showed a somewhat larger deviation during the initial run.

CONCLUSIONS

BPM position deviations from the true position are quite substantial at large positions, 0.9 mm at 10 mm wire positions. They are very small for small position, a few μm for 0.5 mm offsets. The BPM response is in very good agreement with the calculations. No significant dependence on the input signal level and the signal polarity was observed. The readout systems were cross-calibrated, resulting in offsets for the Neumann electronics.

The survey of the wire, BPMs and target chamber locations [5] was used to transform the BPMs positions into the OLYMPUS coordinate system [6]. The uncertainties of the calibrated BPM data are within the requirements of the OLYMPUS experiment.

ACKNOWLEDGEMENTS

We gratefully acknowledge the contributions of R. Bacher, J. Bernauer, U. Laustroer, M. Noak, J. Wilgen and K. Wittenburg to this work.

REFERENCES

[1] R. Milner et al., "The OLYMPUS Experiment", NIM **A741**, 1 (2014).

[2] R. Neumann, private communication; F. Schmidt-Föhre et al., "BPM System Upgrades in the PETRA III Pre-Accelerator Chain during the 2008 Shutdown", DIPAC09, Basel, Switzerland.

[3] Libera+ Brilliance Electron beam position processor, Instrumentation Technologies,d.d., Solkan, Slovenia.

[4] G. Kube, "Sensitivity Estimation for the PETRA-III Beam Position Monitors based on a Boundary Element Method", DESY Technical Note 07-01 (2007); G. Kube, M. Werner "Signal Level Calculation for the PETRA III Beam Position Monitor System", DIPAC 2007, Venice, Italy

[5] M. Noak et al., private communication.

[6] J.C. Bernauer, private communication.

Copyright © 2014 CC-BY-3.0 and by the respective authors

STABILITY STUDY OF THE HIGHER ORDER MODE BEAM POSITION MONITORS AT THE ACCELERATING CAVITIES AT FLASH*

L. Shi [a,b,#], N. Baboi [a], R.M.Jones [b]
[a] DESY, Hamburg, Germany, [b] The University of Manchester, UK

Abstract

When electron beams traverse an accelerating structure, higher order modes (HOMs) are excited. They can be used for beam diagnostic purposes. Both 1.3 GHz and 3.9 GHz superconducting accelerating cavities at FLASH linac, DESY, are equipped with electronics for beam position monitoring, which are based on HOM signals from special couplers. These monitors provide the beam position without additional vacuum components and at low cost. Moreover, they can be used to align the beam in the cavities to reduce the HOM effects on the beam. However, the HOMBPM (Higher Order Mode based Beam Position Monitor) shows an instability problem over time. In this paper, we will present the status of studies on this issue. Several methods are utilized to calibrate the HOMBPMs. These methods include DLR (Direct Linear Regression), and SVD (Singular Value Decomposition). We found that SVD generally is more suitable for HOMBPM calibration. We focus on the HOMBPMs at 1.3 GHz cavities. Techniques developed here are applicable to 3.9 GHz modules. The work will pave the way for HOMBPMs of the E-XFEL (European X-ray Free Electron Laser).

INTRODUCTION

FLASH (Free-electron-LASer in Hamburg) [1] is a FEL (Free Electron Laser) facility to generate XUV (Extreme Ultraviolet radiation) and soft X-ray by the so-called SASE (Self Amplified Spontaneous Emission) process from energetic electron beam bunches. The beam is accelerated by seven 1.3 GHz modules that each of them has eight TESLA cavities working at 1.3 GHz and one 3.9 GHz module with four 3.9 GHz cavities. Each cavity has two HOM (Higher Order Mode) couplers to minimise the effects from the beam excited HOMs. The HOMs are brought out of the module to room temperature via cables.

There are in total 78 channels of HOM signal. All channels are equipped with independent down converter electronics. For the 1.3 GHz modules, electronics are designed by SLAC. The electronics designed by Fermilab for the 3.9 GHz module are being commissioned.

HOMBPMs have been demonstrated good performance [2, 5]. They have a great potential to reduce the number of conventional BPMs which are relative expensive along the linac. This is especially desirable for facilities which have long linac such as ILC [3] etc.

*The work is part of EuCARD[2], partly funded by the European Commission, GA 312453
liangliang.shi@desy.de

However, we found in the past that the HOMBPM systems at FLASH are not stable. They perform good after immediate calibration but the results become inconsistent after some time, from several hours to days.

In this paper, we first briefly present the basic principle of a HOMBPM and procedures for its calibration. Then we move to the methods we used to calibrate them. The results are shown in the last section. Future work and final remarks conclude the paper.

PRINCIPLE OF HOMBPM

When an electron beam traverses a cavity, HOMs are excited. We can classify them by the azimuthal dependence into 'Monopole', 'Dipole' etc. [4].

Among these modes, dipole modes have linear dependence on the beam offset relative to the electrical centre of the cavity [5].

A dipole mode at around 1.7 GHz has been selected for such purpose in the TESLA cavity since it has strong coupling to the beam. Thus it provides high sensitivity to the beam position offset [5].

Figure 1 shows a block diagram of a HOMBPM system.

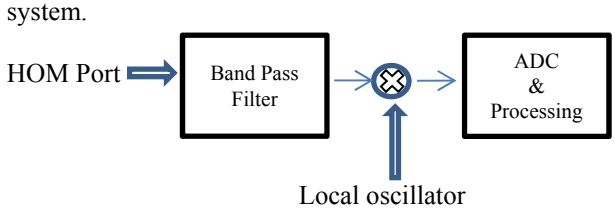


Figure 1: Block diagram of HOMBPM system.

The HOM signal is band filtered at around 1.7 GHz and down mixed with a signal from local oscillator. The signal is sampled and further transmitted to DOOCS (Distributed Object Oriented Control System) [6]. A user defined program was developed to perform data acquisition and post processing.

DATA DESCRIPTION AND MODEL OVERVIEW

Based on the HOMBPM system described above, the HOM data were gathered over half a year and are still under monitoring. The data was taken normally when FLASH operated in single bunch mode. The bunch repetition rate is 10 Hz. Most datasets were taken parasitically and we have four datasets that we moved the beam in a wide range. The data includes bunch charge from toroid readouts, the beam position from two cavity BPMs located upstream and downstream of the accelerating module and HOM signals from both HOM

Copyright © 2014 CC-BY-3.0 and by the respective authors

ISBN 978-3-95450-141-0

couplers. This paper is based on data from accelerating module 5.

The main reason for the resolution drift of a HOMBPM is that it needs to 'remember' the complete information of past beam positions in order to interpret a new beam position inside a cavity.

HOMBPM needs to be calibrated in order to make it be able to predict the beam position inside the cavity. When directly using the amplitudes of a dipole signal, one loses the phase information. Therefore, the whole waveform is used. Due to the linear dependence between the dipole signal and the beam offset, linear regression was performed to correlate the measured dipole waveform and the beam position from BPMs used for calibration.

The data is arranged in a matrix form as shown in equation 1.

$$\begin{bmatrix} d_{11} & \cdots & d_{1n} \\ \vdots & \ddots & \vdots \\ d_{m1} & \cdots & d_{mn} \end{bmatrix} \begin{bmatrix} C_{11} & C_{12} \\ \vdots & \vdots \\ C_{n1} & C_{n2} \end{bmatrix} = \begin{bmatrix} X_{11} & Y_{11} \\ \vdots & \vdots \\ X_{m1} & Y_{m1} \end{bmatrix} \quad (1)$$

Each row in the data matrix (d_{ij}) corresponds to one dipole waveform and the number of rows is the number of measurements available in a dataset. An additional column was placed in the data matrix to capture the intercept in the linear regression model.

The position matrix (X Y) was obtained by interpolating the beam position inside the cavity from the two BPMs. The calibration matrix C_{ij} obtained by linear regression is the knowledge of beam positions that calibration process can build into the HOMBPM.

Based on what it will actually be put in the data matrix, the model can be classified into DLR and SVD.

Each dataset is partitioned into two parts: one for calibration of the HOMBPM; the other independent part is used for validating its performance.

In this paper, the process of obtaining the calibration matrix is called training since we repeated the process several times from data mining point of view. The application of the calibration matrix to the validation dataset is called validation.

CALIBRATION PROCEDURE AND METHODS

An example of dipole signal from HOM coupler 2 of cavity 1 module 5 is shown in Fig. 2.

The signals from HOM ports are mixed with a so-called calibration signal from electronics which has nothing to do with the beam position [5].

Due to the trigger delay, there is a certain part (around 1 μs) of signal at the beginning of a measured dipole waveform dominated by the calibration signal from the electronics.

The calibration signal was removed from the dipole signal by fitting the sinusoid waveform. The filtered dipole signal was further pre-processed to remove the transient part and a time window of fixed width was applied to the waveform to select the part of dipole for regression. The motivation is mainly to avoid over training.

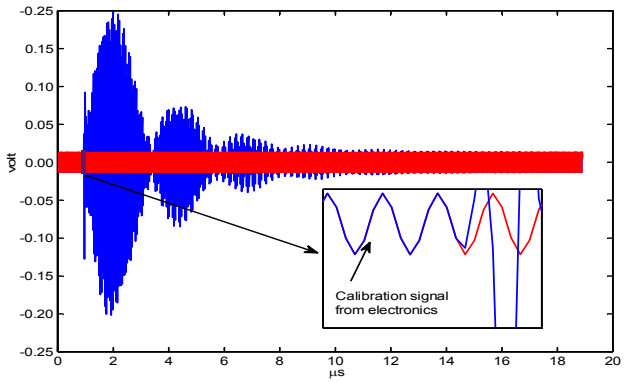


Figure 2: Dipole signal from HOM coupler 2 of 1st cavity at module 5. The calibration signal is highlighted with red colour and has a pure sinusoidal waveform.

In the DLR method, the pre-processed dipole signals are directly put in the data matrix. We can also transform the dipole signals and put them in the data matrix. In this paper, the transformed dipole mainly refers to the representation of a dipole signal by eigenmodes. The eigenmodes can be obtained via SVD (Singular Value Decomposition).

DLR

In the DLR method, we put the pre-processed dipole signal in the rows of a data matrix as shown in equation 2.

$$\begin{bmatrix} Dipole_{11} & 1 \\ \vdots & \vdots \\ Dipole_{m1} & 1 \end{bmatrix} \begin{bmatrix} C_{11} & C_{12} \\ \vdots & \vdots \\ C_{n1} & C_{n2} \end{bmatrix} = \begin{bmatrix} X_{11} & Y_{12} \\ \vdots & \vdots \\ X_{m1} & Y_{m2} \end{bmatrix} \quad (2)$$

In our analysis, the number of columns is fixed to 301 and the number of measurements (rows) varies from a few hundred to a few thousand, depending on the datasets.

The data was partitioned into training and validation parts based on ten folds cross validation. 90% of the data is used for training purpose and the other 10% of the data was used for validation. We repeated the training process 10 times to potentially use all the datasets for validation so that the model obtained is unbiased.

The resolution of HOMBPM for one dataset is defined as the RMS (Root Mean Square) of the difference between the position predicted from the model and the position interpolated from two BPMs.

Because we partitioned the dataset ten times, the average of the ten RMS values was treated as the resolution we can obtain for the HOMBPM from the dataset. The standard deviation of these ten RMS values was regarded as the model fluctuation. In Fig. 3 and Fig. 4, we show the obtained results for the training and validation datasets respectively. The result is based on the signals from HOM coupler 2 of the 1st cavity in module 5.

Copyright © 2014 CC-BY-3.0 and by the respective authors

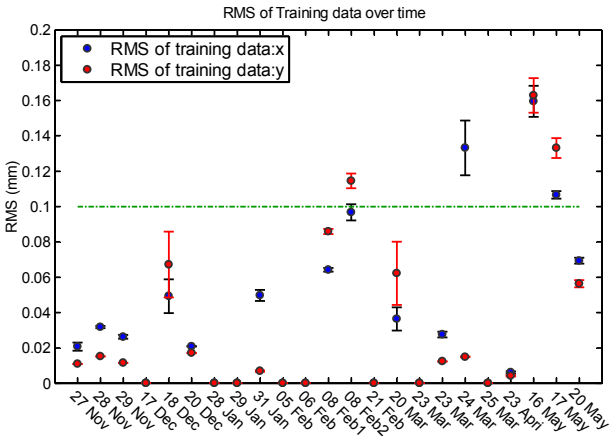


Figure 3: Resolution distributions of training datasets.

We can observe that several datasets were over trained (eg.17 Dec, 28 Jan, and 29 Jan) because the number of measurements available is less than number of regressors in the DLR model. In such case, the model generally also loses the power of prediction which can be observed in the wide fluctuation of the resolution for the validation datasets in Fig. 4.

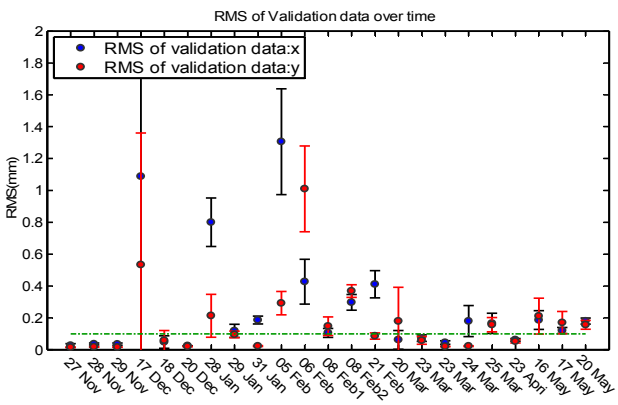


Figure 4: Resolution distributions of validation datasets.

Based on the Fig. 3 and Fig. 4, we can observe that some datasets can be better described by the DLR model (better resolution), but others show relatively worse resolution even if we exclude the results due to over training. The resolution of the HOMBPM spreads over hundreds of μm. We put a 100 μm green line in both plots. This is our first target to achieve. Even better resolution (~10 μm) has been demonstrated in the past [2]. Due to the instability problem, the resolution can easily drift to hundreds of μm.

The model is simple to implement, but the drawback is that it needs more measurements to avoid over training. Due to the parasitic nature of the study, this is sometimes not possible. To better exploit the datasets obtained, the technique of multivariate data reduction was used. We tried several data mining techniques, but found that SVD method is more suitable for the task due to the intrinsic relation to the physical modes as we will discuss below.

SVD

SVD (Singular Value Decomposition) or principal component analysis are widely used for MIA (Model Independent Analysis) in computer science and physics. They are closely connected and mathematically equivalent.

From physics point of view, each dipole signal has two polarizations with the same resonant frequency if the cavity is cylindrically symmetric. In reality, these two polarizations are degenerated due to the broken symmetry by the couplers (power and HOM) and imperfections of the cavity.

In Fig. 5, we show the spectrum of a typical dipole signal based on 2048 points FFT (Fast Fourier Transform).

The frequency was reconstructed based on the sampling frequency of 108.3 MHz. We can observe the frequency gap between the two polarizations.

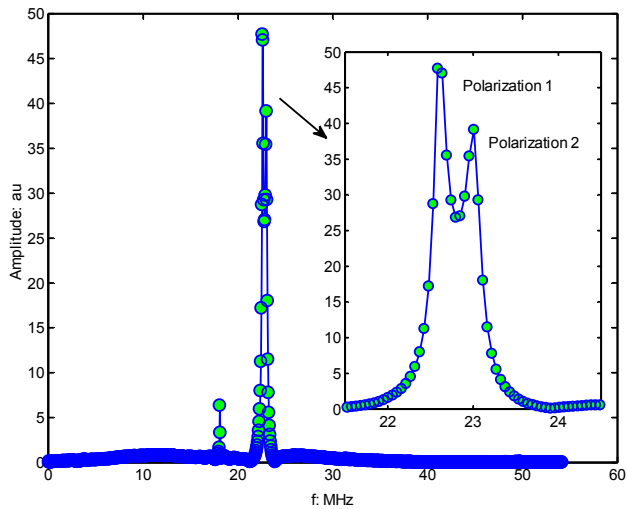


Figure 5: FFT of dipole waveform from Fig. 2. The sampling frequency is 108.3 MHz.

These two polarizations have linear dependence on the beam offset. One example is shown in Fig. 6.

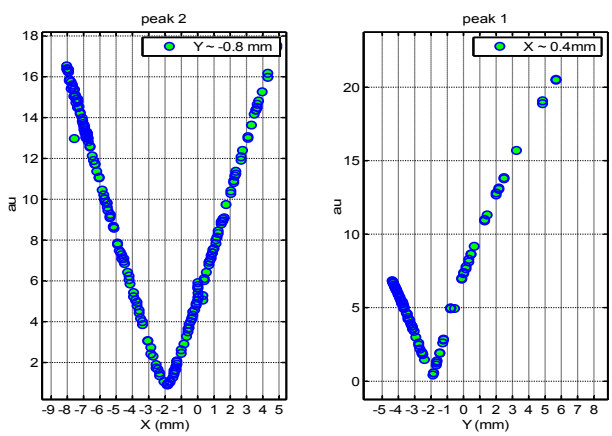


Figure 6: Position dependence of two polarizations (1) Y is about -0.8 mm; (2) X is about 0.4 mm.

Copyright © 2014 CC-BY-3.0 and by the respective authors

ISBN 978-3-95450-141-0

Details of SVD discussion for HOMBPM calibration can be found in [5]. Normally the modes discovered by SVD or MIA are modes in the vector space. There is a great difficulty to correlate these modes in vector space with the HOMs that have physical meaning. However, there is a correspondence between the two polarizations (when they are excited) and the first two modes discovered by SVD method. These modes are referred as Eigen-dipoles in this paper. Eigen-dipole is a general term to describe the modes discovered by SVD method used in our calibration. Fig. 7 shows that the physical dipole spectrum and the first two modes discovered by SVD method. The spectrum was obtained by 2048 points FFT of a dipole waveform.

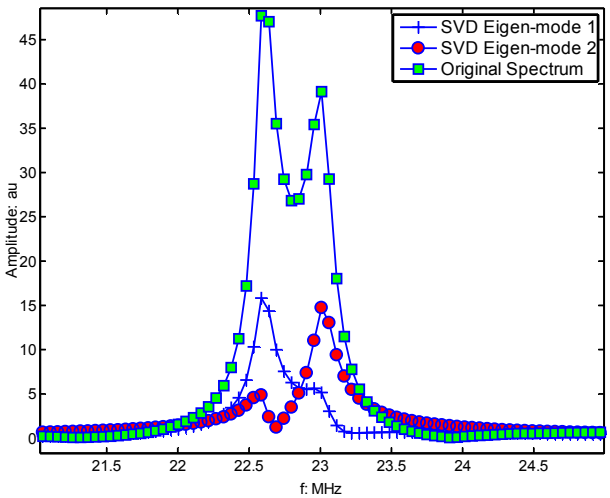


Figure 7: The identification of SVD modes and two polarizations of a dipole signal.

Amplitudes of these dipoles can be calculated via projecting the dipole waveforms onto Eigen-dipoles [2]. The amplitudes were arranged in the data matrix.

$$\begin{bmatrix} Amplitudes_{11} & 1 \\ \vdots & \vdots \\ Amplitudes_{m1} & 1 \end{bmatrix} \begin{bmatrix} C_{11} & C_{12} \\ \vdots & \vdots \\ C_{n1} & C_{n2} \end{bmatrix} = \begin{bmatrix} X_{11} & Y_{12} \\ \vdots & \vdots \\ X_{m1} & Y_{m2} \end{bmatrix} \quad (2)$$

Amplitudes in equation 2 refer to the amplitudes obtained in the space spanned by these Eigen-dipoles. The number of columns depends on the number of Eigen-dipoles used for the calibration. In our case, the number is fixed at 10 because we found 10 Eigen-dipoles are enough for calibration. So the number of columns in the data matrix is 11 in equation 2.

The results based on SVD method are displayed in Fig. 8 and Fig. 9 respectively.

Based on the SVD method, basically we removed the issue of over training. When the X position cannot be trained well (larger resolution than Y position), it also cannot predict well in X position (validation), and vice versa.

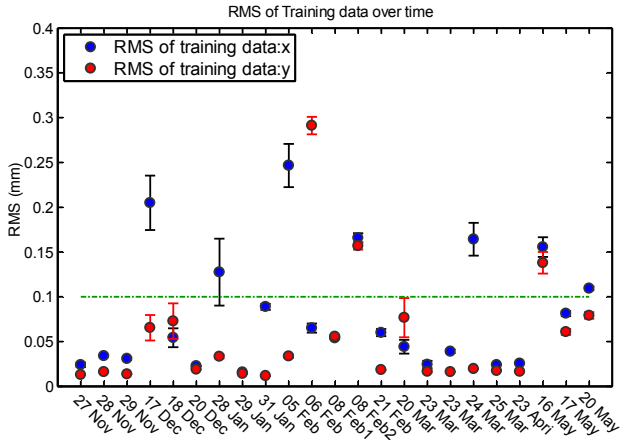


Figure 8: RMS distributions of training datasets over time based on SVD method. Top 10 Eigen-dipoles were used.

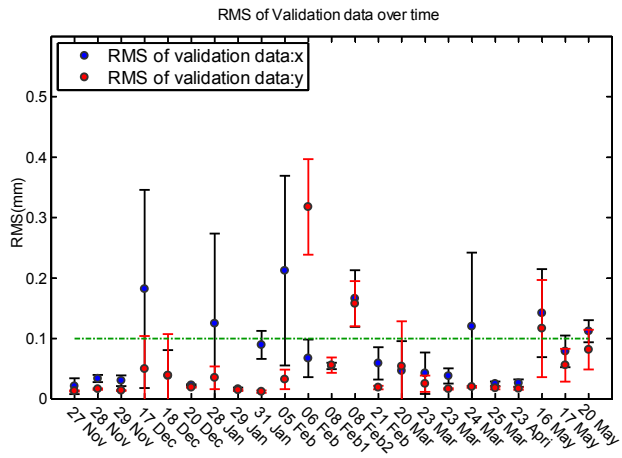


Figure 9: RMS distributions of validation datasets based on SVD method. Top 10 Eigen-dipoles were used.

From the error bar we observe that some datasets are sensitive (larger error bar) to the data partition, while others are not that sensitive.

We also can observe that the resolution varies hundreds of μm as we found with DLR method.

RESULTS SUMMARY OF DLR, SVD

The HOMBPM based on either DLR or SVD methods shows a spread of resolution over time. A summary of the calibration results based on DLR and SVD for is shown in Fig. 10.

After excluding the over trained results, both methods show resolution below 200 μm for most datasets. The resolution for calibration datasets varies a few hundred micro meters in both methods. For some datasets, we get hundreds of μm resolution in training datasets. Thus the resolutions obtained for the validation datasets are low or fluctuate widely.

Copyright © 2014 CC-BY-3.0 and by the respective authors

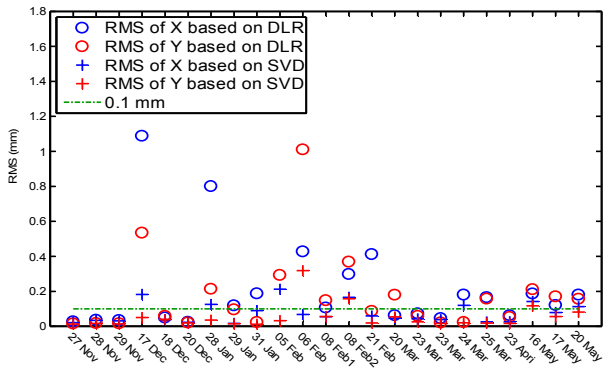


Figure 10: DLR and SVD summary. Only the mean values are displayed. The over trained results are also displayed in the plot.

In general, the SVD method performs better. When the resolution of the HOMBPM in X is worse than in Y in one method, it is also true in other method. That means both methods captured the essential information from the HOM data. However, there are two datasets (16 May, 17 May) showing inconsistency with this. We have not found out the reason yet.

Since the beam position is a strong factor in the formation of dipole signals, we plot the interpolated beam position over dates in Fig. 11.

The resolution of the HOMBPM varies a lot on some datasets. These datasets correspond to the case when the beam moves in a wider range and the beam position patterns show large gaps. One explanation would be that in such cases the HOMBPM cannot interpolate or extrapolate the position over the gap well.

One obvious drawback of such calibration scheme is that the HOMBPM is sensitive to the cavity BPMs used and their technical problems.

CONCLUSION AND OUTLOOK

We observed that the resolution changes (hundreds of μm) over time based on the same methods. We also saw a discrepancy between the two methods used, DLR and SVD, on the same datasets. Generally SVD performs better than DLR due to its intimate relationship to physical HOMs. We plan to use the SVD method to pre-select dipole waveforms before they can be used for calibration. We need to minimise the influence from the cavity BPMs.

Some unusual results are not completely understood yet.

Future work will focus on the stability of the dipole spectrum study. Data acquisition and analysis will continue for the 1.3 GHz modules. Recently we are commissioning the electronics of HOMBPM for 3.9 GHz module [7].

ACKNOWLEDGMENT

We thank FLASH team for the great supports for the work.

REFERENCES

[1] http://flash.desy.de/
[2] S.Molloy, "High precision superconducting cavity diagnostics with higher order mode measurements" PRST-AB 9, 112802 (2006).
[3] https://www.linearcollider.org/
[4] R.Wanzenberg, TESLA 2001-33, 2001.
[5] J.Frisch, "Electronics and algorithms for HOM based beam diagnostics",AIP Conf.Proc, 868 (2006) 313-324.
[6] http://tesla.desy.de/doocs/doocs.html
[7] N.Baboi et al., "Commissioning of the Electronics for HOM-based Beam Diagnostics at the 3.9 GHz Accelerating Module at FLASH", IBIC2014, Monterey, TUPF10 (2014).

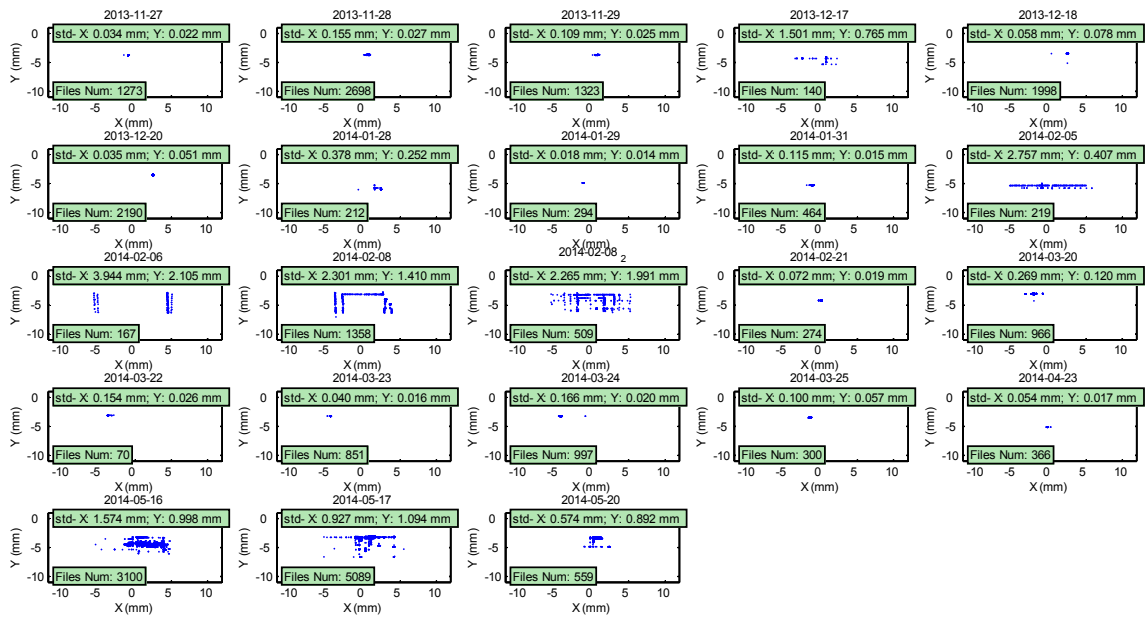


Figure 11: Interpolated beam position pattern over dates.

ISBN 978-3-95450-141-0

Copyright © 2014 CC-BY-3.0 and by the respective authors

MECHANICAL DESIGN OF CRYOGENIC VACUUM FEEDTHROUGHS FOR XFEL BUTTON BPMS

S. Vilcins, D. Lipka, DESY, Hamburg, Germany

Abstract

The European XFEL is a 4th generation synchrotron radiation source, currently under construction in Hamburg. Based on different Free-Electron Laser and spontaneous sources and driven by a superconducting accelerator, it will be able to provide several user stations with photons simultaneously.

Due to the superconducting technology in the accelerators modules many components have to operate at liquid helium temperature.

This poster will concentrate on high frequency ultra-high vacuum feedthroughs used for the beam position monitors of the cryogenic accelerator modules. Main emphasis will be put on the design of these feedthroughs, their material composition and the production process. The capability to be used under these very special conditions was investigated with FEM simulations, as well as with a test procedure. The results of these simulations will be presented; the tests and their results will be explained in detail.

INTRODUCTION

In particle accelerators like European XFEL (E-XFEL) many feedthroughs are used to monitor the electromagnetic field to determine and verify the actual beam position. At the European XFEL the Beam Position Monitors (BPM's) operate under two different ambient conditions, one under normal room temperature and the other one in a cryogenic environment, at ~4K. The cold button BPMs are installed close to the superconducting accelerator structures. Therefore they have to fulfil strict ultra-high vacuum and particle cleanliness requirements.

Many companies offer vacuum feedthroughs. Here the focus is on feedthroughs suitable for RF applications.

Such feedthroughs are coaxial structures, on one side with a pin, open conductor or button; on the other side a connector. In between there is a coaxial vacuum barrier, composed of inner and out conductor with dielectric material in between, providing the required leak tightness. Properties and geometry of the system has to be chosen such that they match to the required impedance of the coaxial system. The choice of isolation material is open to a wide field of materials. The usual technical ceramic materials are classified in three big groups, the oxide-ceramic (ZnO, LiO, SiO, Al_2O_3,), silicate ceramics (Stealit or porcelain) and non-oxide ceramics (Si_3N_4, BN or SiC).

The goal is to develop custom designed feedthroughs with well defined RF properties for accelerator applications at low temperatures and minimum particle emission. Therefore it is essential to understand the design principles and the mechanical characteristics of feedthroughs and BPM systems. Feedthrough prototypes installed on a test BPM at PSI, Fig. 1. The design of custom made feedthroughs requires, besides deep understanding of the RF requirements, other skills like knowledge in mechanical design and fabrication as well as some material science. Nowadays the extensive use of simulation tools help to speed up the design for the mechanical layout of a complete BPM [1], [2].

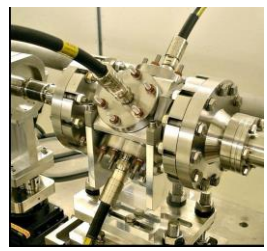


Figure 1: Cold button BPM mounted at SwissFEL test injector*.

R&D DESIGN PROPERTIES

The European XFEL is a 17.5 GeV superconducting linear accelerator with 71 button BPM's installed in superconducting cryostats next to the cold quadruple at temperatures about 4K. The beam pipe apertures of these BPMs is 78 mm, the length is 170 mm.

The BPM bodies, feedthroughs, cables have to deposit only negligible heat load into the cryogenic environment. High losses will increase the cryogenic cooling power and will raise the operation costs [3]. BPM body and button have to have high surface conductivity in order to minimize ohmic losses of high frequency HOM fields in the superconducting cavities. Therefore, all parts are copper plated or made from copper.

The nominal bunch charges of E-XFEL are between 0.1 and 1 nC. The BPMs must be able to measure position of single bunches with 220 ns spacing, in trains of up to 2700 bunches, and a repetition rate of 10 Hz. Train-by-train rms position resolution averaged over the bunch train was specified to be better than 10 µm, single bunch resolution should be better than 50 µm [4].

Mechanical robustness was the leading criterion. Vacuum tightness at 330 K and liquid helium temperature, as well as during cool down and warming up cycles and thermal-shock resistance are main design issues. Further requirements were implied due to the particle cleanliness requirements and the conformity to assembly procedures in the clean rooms. Therefore, the flange was designed for the so called diamond shaped aluminium gaskets, used for E-XFEL cavity string assembly. Due to the vicinity of the superconducting quadruple of the model as well as the cavities strict requirements on nonmagnetic materials had

*This photography is provided by Daniel Treyer, PSI, Swiss.

Copyright © 2014 CC-BY-3.0 and by the respective authors

ISBN 978-3-95450-141-0

to be fulfilled. As required nonmagnetic material, thermal-shock resistance, robust design and full metal sealing were following by the cleanroom requirements of cleaning and assembling.

According to the vacuum and particle cleanliness requirements for the E-XFEL cryogenic environment the "diamond shaped" aluminium gasket also were required for the module string assembly for flanges.

A market analysis has shown no suitable commercial feedthroughs, therefore new development was started. First steps were simulations using CST [5].

Step by step approach:

1. Simulate loss factor
2. Simulate temperature gradients with different materials to decide for the best material combination. This is an iterative process, due to temperature dependency of the thermal conductivity of the materials. (here some steps have to be done because thermal conductivity is a function of temperature and CST provides only one conductivity per material)
3. Tolerance studies of feedthrough in order to meet the requirement: S11< -10dB up to 2.5 GHz also with fabrication tolerances
4. Simulate BPM property: determine the monitor constant
5. Tolerance studies: change position of button and monitor the button signal and data processing to obtain offset. The deepness of the buttons tolerance can be directly converted into a position offset which affects the BPM accuracy: requirement 0.1 mm
6. Based on the design from different companies the design is reviewed with the simulation (frequency domain solver for reflection including mechanical tolerance influence on reflection, thermal simulation for temperature)

The RF simulation results were used as the input for mechanical design and the material composition for prototyping feedthroughs.

PROTOTYPING

The prototyping phase covered the main project management work. In this phase the scope properties have to be distinguished and completed for procurement process to start a call for tender.

The RF designer has to work close with the mechanical design engineer and the material experts, to choose suitable materials, proper matching glass/ceramics to metal, appropriate fabrication processes with feasible mechanical tolerances. In this phase the RF simulation work grows up to an extensive calculation volume.

After the prototype design was finished all relevant mechanical properties have been defined, the design was finally evaluated by an FEM simulation, to check the mechanical conditions for the combination of feedthrough flanged to the BPM body in the relevant temperature range, especially at cryogenic conditions. The cryogenic requirements were checked by FEM simulations done by the company Novicos [6], Hamburg, Germany. Figure 2 shows simulations of thermo cycles between 330 k and 4 K. One critical aspect is to select the proper coefficients of thermal expansion (CTE) for the material composition; which combination of titanium, copper, stainless steel to oxide ceramic or non-oxide ceramic has the best reliability under the specified conditions?

The relative big difference of the CTE for stainless steel and aluminium-oxide-ceramic of about a factor of two was the issue to have this FEM simulation for stainless steel and Al_2O_3. The CTE of titanium is just in the range of aluminium-oxide ceramic. For the FEM analysis it was a critical point to use the correct CTE for the cryogenic temperature**. Due to high costs the FEM analysis was done for stainless steel, only.

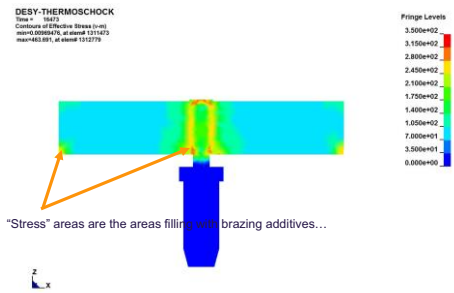


Figure 2: Thermo shock-analysis during cold/warm phases, stress of pin/ceramic/shell material (Novicos, Hamburg).

Based on the experience with cryogenic feedthroughs in the HERA proton ring brazing technology was chosen for the production process in order to have a "soft" buffer material to compensate the different CTE during cool down or warm up phases of XFEL modules. The allowed materials for the fabrication have been titanium or high quality stainless steel (316L/LN) for outer shell and flange. Titanium was preferred, because its CTE is closer to aluminium oxide ceramics.

For hermetic sealed ultra-high vacuum applications using brazing technology aluminium-oxide ceramic (Al_2O_3) was chosen to be the dielectric or isolation material. It allows brazing to copper, stainless steel and also titanium can braze too.

Finally molybdenum was defined to be the material of the inner pin. The material for the button, on the vacuum-side, was not defined at the time of the prototypes, due to unfinished wake loss simulations. A threaded end was a good compromise to test suitable materials.

The design of the feedthrough has to be robust with respect of all following handling steps like cleaning, drying, leak check, assembling and connection to cables.

**Properties of material at low temperature (Phase I), Victor J. Johnson.

Copyright © 2014 CC-BY-3.0 and by the respective authors

ISBN 978-3-95450-141-0

Therefore an N-connector for the cryogenic connecting cabling was selected.

Thermal-shock resistance and permittivity of the isolation barrier were the two important issues.

From those the resistance to thermal shock for operation under cryogenic conditions is the main topic. Therefore a cryogenic test process was defined. A controlled shock test in liquid nitrogen was required for quality check process before delivery to DESY.

The open call for tender resulted in a few quotations. Two companies fulfilled the required parameters. One company quoted a design in high alloy stainless steel and the other in titanium. An amount of 20 pre-series feedthroughs was ordered from both suppliers. The detailed test procedure will be described in the following.

TEST PROCEDURES

This passage describes all test procedures done for the prototypes and the series productions. Visual check of pin and connector centre alignment, purity of the feedthroughs and functionality of the gasket surface were the first steps. The alignment of button, pin and air-side connector were checked and the flatness and roughness of the sealing area. The packaging and UHV cleanliness were inspected followed by first leak checks. To ensure traceability, every feedthrough was individually labelled with part number, production date and company label. The critical mechanical tolerances were inspected by means of 3D measurements of random chosen parts.

For the cryogenic test the prototype items were assembled to a test vacuum vessel, inserted into a cryostat to be flooded with liquid helium. The mechanical test adapter is shown in Fig. 3. Ten cryogenic cycles were driven from 330 K up to 4 K in 20-30 min per cycle. Approximately 30 min at low temperature followed by a quick warm up in few minutes. The vacuum inside the test adapter was monitored during the tests, in order to detect temporary leakage at certain temperatures.

For the series production the test procedure was simplified. The feedthroughs were placed on horizontal multilevel table, shown in Fig. 4. The cryostat was flooded with liquid helium and the setup stayed under liquid helium for more than two hours, sometimes overnight.



Figure 3: Vacuum test adapter for cryogenic tests under vacuum with continuous leak check in a vertical cryostat.

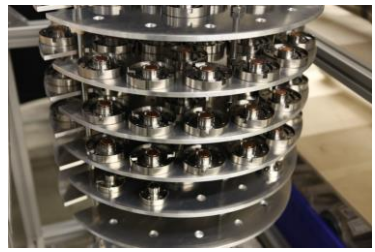


Figure 4: Multilayer table to “cryogenic-check” the serial production of feedthroughs.

The cryogenic tests ended with an individual leak check of each feedthrough. The next step was the check of RF properties. The reflection and transmission coefficients at the desired frequency were measured in a special mechanical setup with an automated procedure using a network analyzer. After this procedure the feedthroughs with similar transmission within the working frequency range of 0.3 to 2.5 GHz were paired.

The final step is the cleaning in a cleanroom, according to the particle cleanliness requirements for the E-XFEL cavity environment. The items are cleaned, starting with ultra-sonic bath cleaning with Tickopur R33, rinsing with clean alcohol and purging in ultra-pure water, until the resistance of the bath exceeds 12 MΩ. The parts are dried under pure air in a full metal oven up to 100 °C for several hours. The final step is particle counting and documentation of the results. Then the parts are packed in pairs and ready for assembly to the BPM bodies in a cleanroom class 4. Documentation of each BPM is available in the E-XFEL documentation using EDMS [7].

The electrical center of BPM depends on the position of the two pairs of feedthroughs with respect to the beam axis. The relevant mechanical tolerances were calculated during the design process. A FEM simulation and practical test were done with the prototype parts to optimize the assembly. The feedthrough flange has to be precisely mounted to fulfill the required tolerances.



Figure 5: Assembling of feedthroughs with torque wrench in classroom class 4.

Copyright © 2014 CC-BY-3.0 and by the respective authors

ISBN 978-3-95450-141-0

A further aspect for the assembly is to guaranty the leak tightness under cryogenic conditions for a long time. Based on FEM analysis results from Paolo Michelato [8], the aluminum gaskets have by squeezed approximately 0.3 mm to ensure safe tightening.

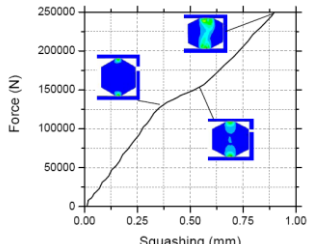


Figure 6: The deformation of the gasket cross section is shown. First step is the elastic to plastic zone. The distribution of equivalent plastic strains is shown at three different levels for alloy Al 5754.

SERIAL PRODUCTION

This passage describes the process steps of the series production. After all parts of pre-production were tested from both vendors, some changes and revaluations have been made.

The material of the button was defined to be copper and to be welded to the inner pin. The number of screws of the flange connection was increased from six to eight. Some changes for vacuum aspects were made and some tolerance changes were corrected due to the results of RF measurements.

The visual inspection in the last step before delivery was defined more precisely and the packaging was changed asking more robust boxes. After all drawings and specifications were updated, a restricted call for tender for the series production of 320 parts was send to both suppliers of the pre-production. The serial production was placed at the company providing the feedthrough shell in titanium, decided on the price. At beginning of the production a start-up meeting was held at the company, to fix all the production processes, quality assurance measurements and the delivery schedule. A jour-fix was agreed for monthly communication. The first lot arrived at DESY after 4 months. After 14 month the series production was complete.

PROJECT MANAGEMENT EFFORTS AND COMPETENCES

This task covered the complete project work for a R&D project including the fabrication a large scale of costumer designed feedthroughs in industry.

The phase plan with milestones has to elaborate and a work breakdown structure (PSP) has to be developed. Furthermore the evaluation of total cost and resources has to be done. The PSP integrates all working steps with a detailed description, effort and process activities. After them a net plan is derived of the PSP. These process steps will become time units of each work packet. The net plan showed the critical path of the project. The first version of the plan showed that the delivery will be months later than the requested milestone of pre-installation. Therefore other options had to be investigated. The leading documents are very often the technical documents and specifications, but they are not sufficient for project success. Important is a total quality management, a complete documentation, claim and change management.

RESULTS

The results are divided in technical and organizational aspects. After four months ramp-up time of the serial production, the production went very equally.

The RF simulation results defined all mechanical tolerances and in several iteration steps all critical aspects were fixed in the drawings and technical specifications. The wake losses simulations showed that copper is the proper material for the button of serial productions. The results of the RF measurements and simulation for the feedthroughs agree well. The mechanical changes were very small.

The FEM simulation of the cryogenic conditions and the excellent results of the cryogenic tests for the prototype items of both suppliers prove that the design is sufficiently robust. All forty prototypes feedthroughs passed the tests. The FEM simulation showed also a button position movement due to thermo cycles below 0.05 mm. Furthermore the deformation of the aluminum gaskets are in the correct tolerance range for a vacuum connection and don´t exceed the yield strength limit. The sealing area of the feedthrough flange was well defined and very painstakingly and carefully inspected.

The feedthrough assembly under cleanroom conditions had a good correlation to the mechanical FEM calculation. This tightening torques guaranty also the squeezing of the gasket within 0.3 mm. Due to these tests a special titanium stud-bolt was designed and ordered to reduce the friction during assembly under particle clean conditions, implying very clean surfaces with minimum abrasion. General frictional forces are not included in the values to be found in publications or specification for bolts, nuts and screwed connections. Therefore the practical test in cleanroom environment with different material compositions gave a very good matching between stainless steel BPM body and high-tensile titanium stud-bolts of Ti6 Al 4V. The grade 5 titanium with more than 1200 N/mm^2 tensile strength is excellent for applications in a cleanroom because of the minimum abrasion. This material is made for aerospace applications and can be hardening and has a very adherent oxide layer. The second important result was to increase the amount of bolts in the feedthrough flange from six to eight, to guaranty the accuracy of 0.1 mm feedthrough assembling.

The brazing technology of titanium or high-alloy stainless steel to metallized aluminum-oxide-ceramic provided sufficient stability for the cryogenic application. The ten successfully cycles for the pre-series items promise robustness for the long reliable operation of the cold linac modules. The feedthroughs of the series delivery were only cycled three times to avoid aging.

Copyright © 2014 CC-BY-3.0 and by the respective authors

ISBN 978-3-95450-141-0

The design of the feedthrough is robust with respect of all following handling steps like cleaning, drying, leak check, assembling and connection to cables. Therefore an N-connector for the cryogenic connecting cabling was selected. A part of project success was due to practiced project management competences. Due to the item identification numbers the traceability for each part is given, and used in the E-XFEL documentation processes.

Only few parts had not the necessary cleanness. Some leavings of glass blasting process were inspected or the brazing process. Furthermore few parts had a misaligned copper button or damaged outer connector. The covering boxes from one vendor of prototypes were not sufficient for this product.

CONCLUSIONS

Make in house or buy from industry is very often a serious question. Though it seems to be easy to buy good feedthroughs commercially in the market, lot colleagues think about this question. It is true that many vendors or suppliers can produce feedthroughs and you have only to answer which provider is the best for you.

The R&D of a costumer designed feedthrough can extend to a very complex project taking more time and efforts you will expect. If no real experts on RF simulations, matching feedthrough and front end electronics and mechanical skills in feedthrough and vacuum design, fabrication and project management are available, it will be smarter to buy and not to make in – house developments. Only with a good idea, a team of post docs or temporary staff will run in trouble.

It took 4 years to develop the cryogenic Feedthroughs for E-XFEL from the idea to the last shipment, and the final quality checks. Special attention has to be given to the feedthroughs which need to be produced with high precision and high quality in parallel or even before the mechanical design and electronic readout concept. A detailed specification with all requirements including beam parameters, environmental performance is fundamental.

The leading technology for this project was brazing of metallized ceramic to titanium. The colleagues from CERN used the same technology for the cold feedthroughs of LHC [9].

Under implementation of project management competences the project targets like budget, specifications, time schedule, procurement processes, change management and quality management are better controlled and get more reliable.

Based on the pre-production experience the series production went unobstructed. Therefore, pre-production for a R&D project like this is essential.

OUTLOOK

Based on the experience with the feedthrough for the cryogenic environment, a second project was started to develop and produce also a custom made feedthrough, especially suited to the requirements of linac driven facilities like E-XFEL. The design takes advantage of the relaxed restrictions from low average current machines and low synchrotron radiation or wake field power impacts. This allowed for a design with much better signal properties.

Although the cold feedthroughs were based on brazing technology the decision of fabrication of the warm feedthroughs went to glass to metal sealing technology in microprocessor-controlled furnaces. With this technology non oxide-ceramic-compositions with metals like high-alloy stainless steel or titanium can melt together. These glasses can have very low porosity, low or negative thermal expansion coefficients, low dielectric loss, a better permittivity than oxide-ceramics, high mechanical strength, very high thermal-shock resistance and high abrasion resistance to chemical substrates.

The diameter and the thickness which have big effects to the RF performance could be designed smaller. The normal voltage standing-wave ration losses are typical in the range from 1.1 to 1.3 for higher frequency for commercially feedthroughs. Furthermore this field of non-oxide ceramic is much larger as expected.

Meanwhile, also this project was finished successfully and 1400 feedthroughs of this type have been produced in collaboration with company VACOM in Jena, Germany.

ACKNOWLEGEMENT

The author would like to thank all the colleagues, especially from the groups MKS and MVS, suppliers and vendors for their support, motivation, help, constructive and interesting discussion. And also a special thanks to Dirk Nölle for his assistance to this paper.

REFERENCES

[1] D.Lipka et al, Button BPM Development for the European XFEL, proceedings, DIPAC2011, Hamburg, Germany.
[2] M.Tobiyama, BPM Electrode and high power feedthrough-special topics in wideband feedthrough, proceedings, IBIC 2012, Tsukuba, Japan.
[3] D.Lipka and S.Vilcins, BPM's from design to real measurements, proceedings, IPAC 2014, Dresden, Germany.
[4] D.M. Treyer et al, Design and beam test results of button BPM's for the European XFEL, proceedings, IBIC 2013, Oxford, UK.
[5] Computer Simulation Technoloty (CST), http://www.cst.com
[6] Novicos (Noise and vibration concepts), Hamburg, Germany. http://novicos.de/
[7] EDMS, Engineering Data Management Service used at DESY, Hamburg, Germany.
[8] Paolo Michelato, Improved Standard Cavity. Fabrication, SRF Meeting, LNL, Oct. 19 – 21, 2005
[9] Christian Boccard, Design Choices for the cold LHC-BPMs, CARE Meeting, Lüneburg, Germany, November 30- December 1 2006.

Copyright © 2014 CC-BY-3.0 and by the respective authors

FIRST TESTS OF A MICRO-TCA-BASED DOWNCONVERTER ELECTRONIC FOR 5GHz HIGHER ORDER MODES IN THIRD HARMONIC ACCELERATING CAVITIES AT THE XFEL†

T. Wamsat*, N. Baboi, Deutsches Elektronen-Synchrotron DESY, Hamburg, Germany

Abstract

Beam excited higher order modes (HOM) in 3.9GHz accelerating cavities at the European XFEL are planned to be used for beam position monitoring. The specifications of the monitors have been defined during an extensive study on the 3.9GHz module at FLASH. Selected HOMs for precision measurement are located around 5440MHz and 9040MHz. An electronics developed by FNAL has been recently installed at FLASH and provides a basis for the XFEL electronics.

The paper will present the design and first test of the hardware for the MicroTCA standard used for the XFEL. The hardware consists of three different Rear Transition Modules (RTM), two four channel downconverter RTMs (5GHz and 9GHz) and a third RTM with two phase locked loop synthesizers on board for LO generation. Presently the 5GHz and the PLL RTMs are under construction. The first measurements with these cards will be presented.

INTRODUCTION

The European X-ray Free Electron Laser 3.9GHz accelerating cavities are located right after the 1.3GHz injector module before the first bunch compressor, as shown in Fig. 2 [1]. The module is similar to the ACC39 module built by FNAL for the Free Electron Laser Hamburg (FLASH) [2], containing four third harmonic cavities.

The XFEL 3.9GHz module consists of eight cavities each with two HOM couplers respectively as shown in Fig. 3. We want to equip four couplers, the respective outer two, with electronics for modes around 5440MHz and fourteen for modes at 9060MHz suitable for beam monitoring as obtained in tests at FLASH ACC39 [3].

System Overview

At the XFEL the MicroTCA.4 [4] standard will be used. Figure 1 shows the planned fully equipped MicroTCA crate, consisting of five four channel downconverter RTMs with its particular SIS8300 AMC card [5]at the other side (not visible), one for the 5.44GHz modes and four 9.06GHz boards. We also see the HOM-PLL (Higher Order Mode Phase Locked Loop) RTM with a DAMC2 [6] card on the other side (not visible) to generate the LO-frequency and the uLOG for LO amplification and distribution over the MicroTCA backplane. [7]

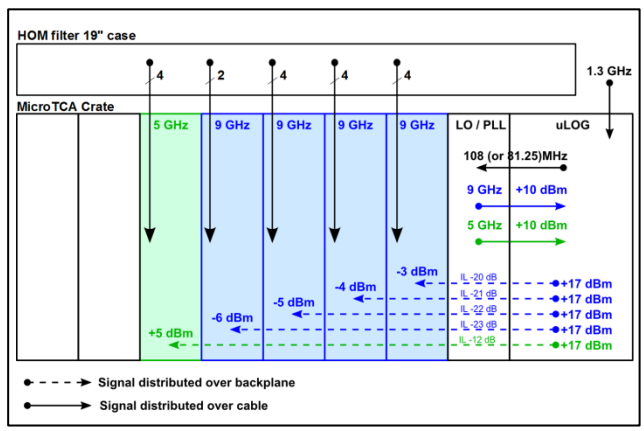


Figure 1: Overview over the complete system installation.

Above the crate there is a case which contains the HOM selecting bandpass filters for each channel. The outputs of the HOM coupler will be connected to the HOM filters.

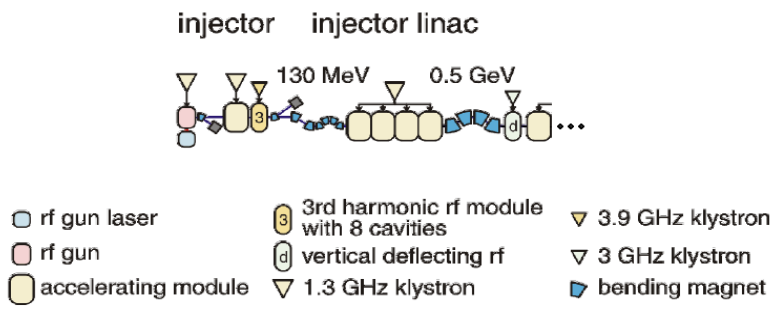


Figure 2: Schematic layout of the European XFEL injector [1].

†The work is part of EuCARD-2, partly funded by the European Commission, GA 312453

*thomas.wamsat@desy.de

Copyright © 2014 CC-BY-3.0 and by the respective authors

ISBN 978-3-95450-141-0

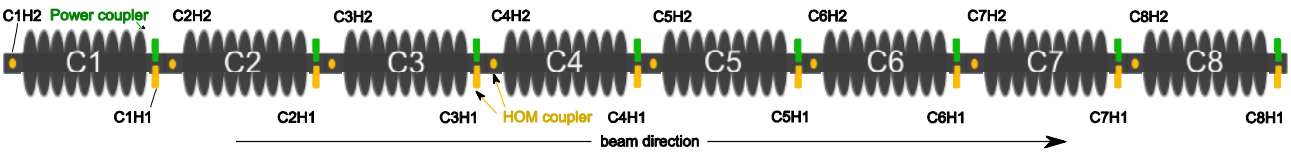


Figure 3: Cavity arrangement inside the module.

HOM FILTER CASE

The HOM bandpass filters are too big (compare Fig. 5) to include them on the RTM board, so we had to put them in an extra case. The benefit is that we could use the downconverter cards for other frequencies, if there is any application for it in the future.

A sketch of the HOM filter box is shown in Fig. 4. Since the modes around 5.44GHz propagate in whole of the module, only two cavities, the outmost ones, are planned to be connected to the 5GHz RTM. For monitoring the beam position in each single cavity we use the 9.06GHz modes, since these are trapped in each cavity. According to former studies, the respective outer couplers are not suitable, so that we need only 14 channels instead of all 16. Two signals from the outmost cavities (C1H1 and C8H2) will be split for monitoring both 5 and 9GHz modes, so that we have 18 output signals in total.

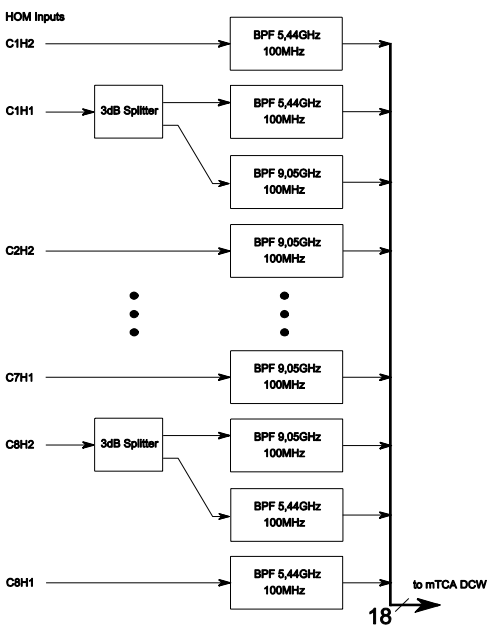


Figure 4: HOM filter case overview.

The already completed HOM filter case is shown in Fig. 5.



Figure 5: HOM filter case.

PLL SYNTHESIZER

The designed HOM-PLL (Higher Order Mode Phase Locked Loop) RTM includes two PLL synthesizers generating 5GHz and 9GHz accordingly. Figure 6 shows its block diagram.

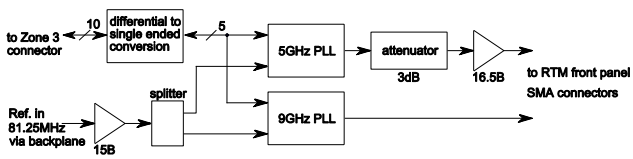


Figure 6: HOM PLL block diagram.

The Zone3 connector on the MicroTCA middle plane passes the signals from the DAMC2 AMC to the HOM-PLL RTM. The DAMC2 card includes a FPGA which manages the PLLs and provides the link to our control system.

The chosen VCO (Voltage Controlled Oscillator) for the 5GHz PLL has an operating range from 5 to 5.5GHz and the 9GHz VCO from 8.6 to 10.2GHz. In operation we set the PLLs to fixed frequencies needed to downconvert the particular HOMs but we are able to change them easily. To reach the needed input power for the uLOG (compare Fig. 1) power, we have to amplify the 5GHz LO signal. The output power of the 9GHz part is high enough and does not need additional amplification.

As reference frequency we use 81.25MHz. The PLL needs at least -6dBm at its input, so we put an amplifier and attenuator in front of the PLL input to adjust the power (the attenuators in front of the reference input are not shown in Fig. 6)

Copyright © 2014 CC-BY-3.0 and by the respective authors

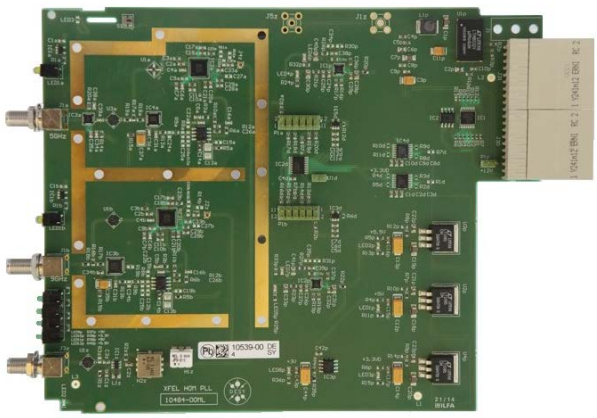


Figure 7: HOM-PLL RTM.

In Fig. 7 we see the finished HOM-PLL RTM. The uncoated lines delimit the PLL and VCO (Voltage Controlled Oscillator), on top of these lines a metallic case will be placed to protect the electronic from external effects. Only the top side of the RTM is assembled with components.

HOM PLL Test

The setup for the HOM-PLL test is shown in Fig. 8. A signal generator provides the reference frequency of 81.25MHz for the PLL. A PC is used to tune the settings of the PLL, a spectrum analyser shows the output signal.

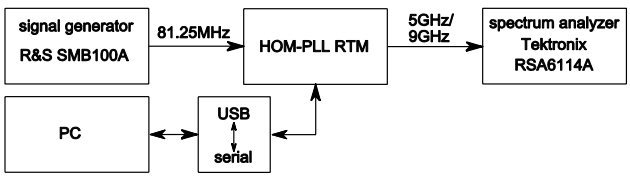


Figure 8: HOM-PLL RTM test setting.

Figure 9 shows the 5GHz output. The output power is less than expected at ca. 5dBm. We also see sidebands but they are almost 60dB below the carrier signal and should have no negative effects.

.

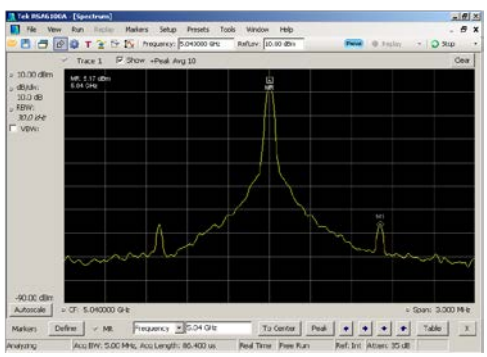


Figure 9: HOM-PLL 5GHz output.

Figure 10 shows the 9GHz output. The output power is very small at -3.7dBm. We have to find out if the signal is possibly too noisy but it is 30 dB below the carrier.

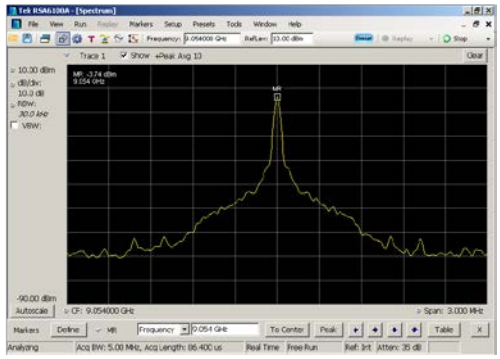


Figure 10: HOM-PLL 9GHz output.

To reach the needed output power of +10dBm we will place external amplifiers at the output and if needed attenuators for adjustment. A power connection for them is already provided on the synthesizer card.

DOWNCONVERTER CARD

Altogether we have 18 channels we want to use: four channels at 5.44GHz and 14 channels at 9.06GHz. We put four channels onto one RTM so we need only one card for the 5GHz and four cards for the 9GHz signals (compare to Fig. 1).

Figure 11 shows the general arrangement of a downconverter card. The LO frequency from the PLL-RTM will be applied over the RF backplane connector. For tests in the laboratory it is possible to connect the LO also via an SMA connector at the front panel. The signal from the HOM filters will be connected via SMA cables (circled with dotted line).

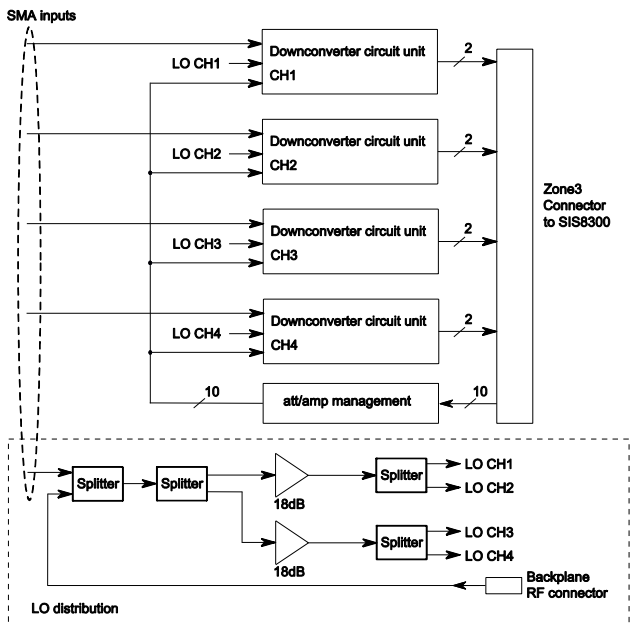


Figure 11: Block diagram of a downconverter card.

The 5GHz Downconverter Circuit

The 5GHz downconverter is arranged as shown schematically in Fig. 12. There is a step attenuator

Copyright © 2014 CC-BY-3.0 and by the respective authors

ISBN 978-3-95450-141-0

settable from 0.5-31.5dB in 0.5db steps at the beginning of the chain. The following 15dB amplifier can be switched off in case of high input amplitude. This chain has a tuneable input range of 46dB to ensure the required input level for the mixer to reach the optimum power level for the ADC at the end.

The bandpass filter (BPF) behind the mixer determines the intermediate frequency (IF) of 30MHz with a bandwith of 20MHz. According to the LO frequency, different areas of the spectrum within the 100MHz bandwith of the input filter can be downconverted.

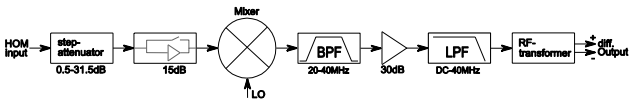


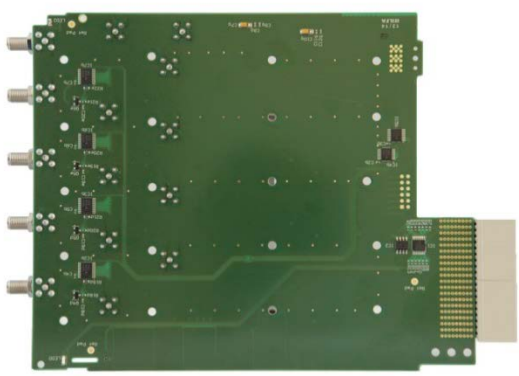
Figure 12: Block diagram of 5GHz downconverter channel.

The IF amplifier increases the IF power to reach the required input level for the ADC. The low pass filter (LPF) decreases the noise at the end. The RF-transformer changes the single ended signal to a differential signal needed by the ADC.

The design of the 5GHz RTM has been finished and a manufactured card can be seen in Fig. 13. One can easily notice the 4 channels. The uncoated lines on the top create space to place a metallic case on top of the RF electronic.



(a)



(b)

Figure 13: HOM downconverter: bottom side (a) and top side (b).

The 9GHz Downconverter Circuit

The 9GHz downconverter has almost the same arrangement as the 5GHz one. They only differ at the beginning of the chain as it can be seen in Fig. 14.

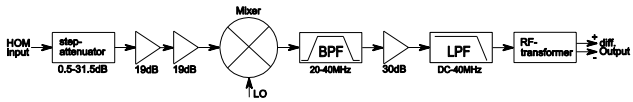


Figure 14: Block diagram of 9GHz downconverter channel.

Due to the higher amplification needed for the lower power signals of the 9GHz modes as against to the 5GHz modes, the 9GHz circuit will have an input range of 70.5dB.

The electronic of the 9GHz card is very similar to the 5GHz RTM. It will be manufactured after finishing tests with the 5GHz card.

Downconverter Tests

The 5GHz downconverter card was recently manufactured. A soldering issue with the footprint of the mixer component was found and it seems that it will have to be remade.

The test setting looks like mapped in Fig. 15.

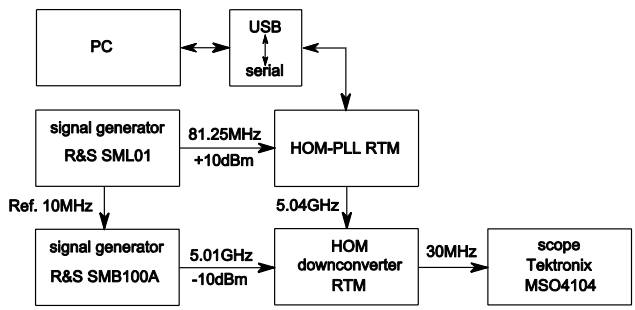


Figure 15: HOM downconverter test setup.

Even if we cannot measure anything at the scope, because the mixer does not work, we checked the input signals of the mixer. The LO frequency at the mixer input (compare Figs. 12 and 14) with +10dBm input power to the card is -6dBm (see Fig. 16). The mixer should work with this amount of power.

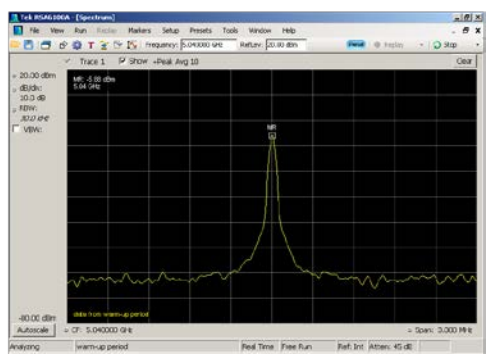


Figure 16: Measured power at mixer input.

Copyright © 2014 CC-BY-3.0 and by the respective authors

We also checked the efficiency of the step attenuator and amplifier. With maximum amplification (without attenuation) with an input power of -10dBm we reach -15dBm at the mixer input (see Fig. 17).

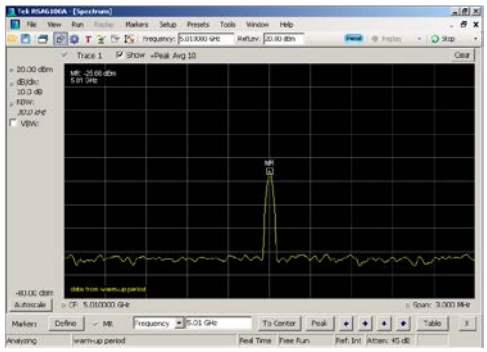


Figure 17: Signal input power at mixer (proportion 1/10).

We must add 10dBm to the measured signal as the point of measurement is connected via an 1 to 10 divider, whereas Fig. 16 shows the correct power because of using a connector cutting the following structure and connecting it directly to the spectrum analyser.

CONCLUSION

The PLL card is working well and is ready to use. Unfortunately the 5GHz downconverter card does not work yet and needs to be remade. After the successful testing of the new 5GHz card, the 9GHz card will be designed. The difference between both cards is very small so the design of the 9GHz one will be very fast.

OUTLOOK

The following step will be to test the whole system under real conditions with beam at FLASH and compare to the electronic from Fermilab.

It is planned to eventually implement the beam position calculation, now being made with a MATLAB code, in the FPGA on the Struck SIS8300 digitizer card, and thus speed up to information transferred to the control system.

REFERENCES

[1] K. Floettmann, et al., in Proc. SRF2005, FRA06 (2005).
[2] http://flash.desy.de
[3] P. Zhang, “Beam Position Diagnostics with Higher Order Modes in Third Harmonic Superconducting Accelerating Cavities”, (2013), ISBN 978-83-7814-070-2.
[4] MicroTCA® is a trademark of PICMG, MTCA.4 specifications: http://www.picmg.org
[5] “SIS8300 MTCA for Physics Digitizer User Manual Rev. 1.05”, October 17, 2011, http://www.struck.de.
[6] For a description of the DAMC2 card: http://fe.desy.de/fea/projects/tca_developments/damc2/
[7] U. Mavric, et al., IPAC2014, WEPME069, (2014).

ISBN 978-3-95450-141-0

Copyright © 2014 CC-BY-3.0 and by the respective authors

DIAMOND-BASED PHOTON BPMS FOR FAST ELECTRON-BEAM DIAGNOSTICS IN SYNCHROTRON RADIATION SOURCES

M. Antonelli, G. Cautero, D. Giuressi, S. Lizzit, R. H. Menk,
Elettra – Sincrotrone Trieste S.C.p.A., Trieste, Italy
A. De Sio, E. Pace, Università degli Studi di Firenze, Firenze, Italy
M. Di Fraia, Università degli Studi di Trieste, Trieste, Italy

Abstract

Electron-beam stability is amongst the primary concerns in current Synchrotron Radiation (SR) sources; in particular, in third-generation SR facilities high-brightness beamlines using undulator radiation are extremely sensitive to electron-beam oscillations. Orbit stabilization has been intensively addressed in the past years and many SR machines have been equipped with a Fast Orbit Feedback (FOFB) based on electron Beam-Position Monitors (eBPMs).

On the other hand, photon Beam-Position Monitors (pBPMs), besides providing beamline users with crucial calibration data, are also a useful tool for keeping the electron beam under control, by monitoring position and intensity of the delivered radiation. The machine control system can take advantage of this information in order to improve the stability of the electron-beam.

A diagnostic beamline, utilizing a couple of fast pBPMs based on single-crystal CVD diamond detectors, has been built and inserted into the central dead-end outlet of one of Elettra's bending-magnets. Tests have been carried out both during normal machine operations and by deliberately moving the orbit during dedicated shifts. Owing to the outstanding properties of diamond in terms of speed and radiation hardness, the results show how the aforementioned system allows the beam position to be monitored with sub-micrometric precision at the demanding readout rates required by the FOFB. The radiation hardness of the sensors allows the operation over extended periods of time without special maintenance.

Therefore, this system is particularly suited for storage-ring sections lacking in electron-beam monitoring and the tested diagnostic line represents a demonstrator for future implementation of pBPMs at several bending-magnet front ends of Elettra.

INTRODUCTION

In modern SR facilities electron-beam monitoring and stabilization are amongst the primary concerns. In particular, the high-brightness beamlines using undulator radiation are the most sensitive to electron-beam oscillations occurring in 3rd-generation light sources [1]. Therefore, such machines are equipped with specific control systems, like the FOFB, based on the measurements of the eBPMs implemented along their storage rings [2].

Despite such stabilization measures and owing to a number of instability sources, the resulting photon beam can exhibit residual fluctuations in terms of both position and intensity. These phenomena can be detected by utilizing pBPMs, which are capable of simultaneously estimating the intensity and the position of the emitted beam passing through. Fast pBPMs inserted in beamlines are well-suited for either *a posteriori* data calibration or real-time adjustment in beamline experiments [3]. Nevertheless, the information provided by such detectors is useful for the electron-beam diagnostics and it can be integrated into the FOFB [4]. In particular, if pBPMs are installed upstream from the beamline optics, their measurements are directly related to the status of the electron beam as they are not affected by any instability imputable to optical elements (such as mirrors, monochromators, etc.).

Amongst the available technologies for the production of fast and semitransparent *in situ* pBPMs, diamond grown by Chemical Vapour Deposition (CVD) is one of the most suitable materials owing to its outstanding physical properties. Because of its high bond energy it can withstand the high dose rates occurring in 3rd- and 4th-generation SR sources and its low atomic number renders it semitransparent to X-rays. Besides, due to its high energy gap, intrinsic diamond is an insulator with low thermal noise at room temperature, while its high electron and hole mobility allows charge to be collected faster than in many other active materials [5, 6].

With the aim to provide Elettra's future FOFB with additional information stemming from state-of-the-art diamond pBPMs, a diagnostic beamline has been built at the central outlet of one of Elettra's bending magnets. The present document reports on the main features of the implemented line, its monitoring performances and its long-term reliability.

DIAGNOSTIC BEAMLINE

At Elettra, each bending magnet was originally designed with a three-way radiation pipe. The lateral outlets became then the anchoring points for the implemented user beamlines, while the central ones remained unused. The presented diagnostic line has been built at one of those central dead-end outlets in order to continuously monitor the photon beam without interfering with normal beamline operations. This prototype has been completely accommodated inside the shielding wall of the storage ring, between the pipes of the 10.1L and 10.1R beamlines, as shown in Fig. 1. This solution has imposed stringent space constraints, which have been met due to the compact size of the diamond pBPMs.

Copyright © 2014 CC-BY-3.0 and by the respective authors

ISBN 978-3-95450-141-0

This diagnostic line features an overall length of about 5 m and it is hooked up to the main shutter of front end 10.1, through a 2-mm-thick water-cooled aluminium window located approximately 4 m downstream from the source point. Due to its geometry, the window accepts (horizontally) about 1 mrad of the beam cone. Moreover, it separates the UHV of the storage ring from the vacuum of this demonstrator line and it serves as X-ray filter to reduce the heat load on the CVD detectors.

Half meter downstream from the Al window, a remotely controlled beam shutter is situated in order to block the beam whenever it is required. Other 80 cm further downstream, the line incorporates a motorized slit system, which allows the beam to be shaped and cleaned in horizontal and vertical direction, respectively. The upstream pBPM (D1) is placed 1.3 m upstream from the slits (i.e. 6.6 m from the source), followed by the downstream pBPM, which is 2.4 m apart from it (i.e. 9 m from the source).

In particular, with such arrangement the system can work in a *camera obscura* geometry, which has been adopted, in order to circumvent the complications caused by the wide horizontal emission angle of the bending magnet. During normal operations, both apertures are narrowed; thus, the slit system acts as a pinhole and D1 is not strictly necessary for the position monitoring. However, the vertical slits can be opened completely, allowing the beam through for its entire vertical size. In such case, the position information of D1 is required in combination with that of D2 to estimate the vertical position of the source.

Outside the shielding wall, a PC-based control system (DAQ) allows acquiring and processing of pBPM data for testing and beam monitoring through a convenient graphical user interface. Furthermore, the DAQ controls motors and biasing modules, allowing for both detector realignment and beam shaping.

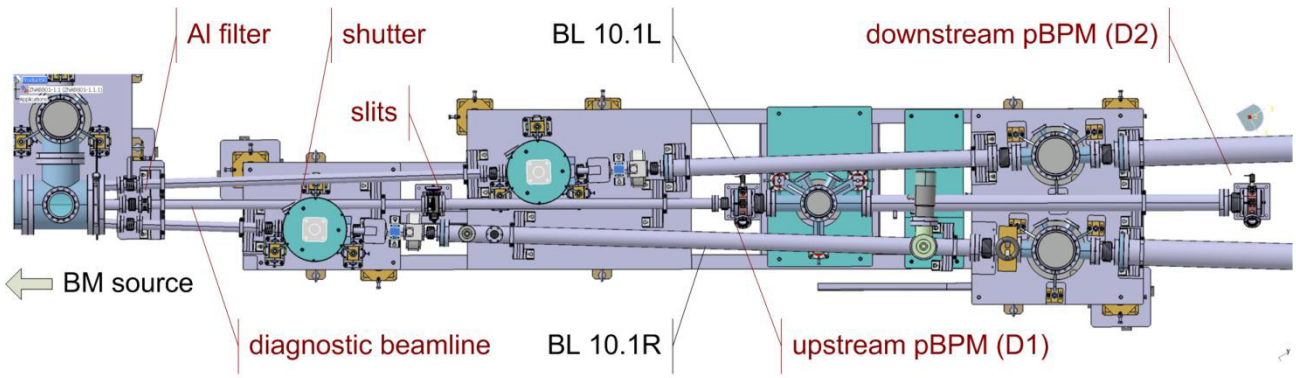


Figure 1: Top view of bending-magnet front end 10.1 at Elettra. The diagnostic beamline is represented by the central pipe between beamlines 10.1L and 10.1R. The main components are labelled in red (upstream to downstream, i.e. left to right): Al filter, beam shutter, motorized slits, upstream pBPM (D1), downstream pBPM (D2).

DIAMOND-BASED PHOTON BPMS

The upstream detector D1 is based on a 50-µm-thick, freestanding, single-crystal CVD diamond. This sensor is a 4.7×4.7 mm^2 die, mechanically grinded and lapped from a 500-µm-thick base material. Front and back surfaces have been coated with 100-nm-thick Al electrodes on top of 100-nm-thick diamond-like-carbon layers. A four-quadrants (*quad*) structure has been created by segmenting the front electrode through a lithographic process, leaving a 100-µm-wide gap between quadrants.

The sensor of the downstream pBPM differs from D1 in terms of thickness and electrode material. It consists of a standard, 500-µm-thick, single-crystal CVD diamond coated with Cr-Au electrodes. It features the same area and *quad* geometry as D1. The lower thickness of D1 reduces its absorption, allowing most of the photons to be transmitted towards D2.

Each of these devices is glued and wire-bonded onto a printed-circuit carrier board and mounted on an X-Y movable stage, which is, in turn, accommodated into a CF-63-flanged, UHV-compatible detector chamber. These carrier boards are electrically connected via BNC and SMA feedthroughs for biasing and readout, respectively. In order to acquire the photo-generated currents, these readouts are then fed into AH501B picoammeters[1]. While these instruments allow the signals to be sampled at a maximum rate of 6.5 kHz, the diamond pBPMs described above can detect incoming photons with much higher time resolutions; they are capable of monitoring SR beams on a bunch-by-bunch basis, even at a 500-MHz repetition rate [7].

PERFORMANCES

In order to evaluate the position-encoding capabilities of the system, some preliminary characterizations have been carried out. The slit aperture has been fixed to 300×300 $µm^2$; as mentioned, with such setup the system works in a *camera obscura* configuration both horizontally and vertically. Mesh and linear scans of the detectors have been performed during normal machine

1http://iloweb.elettra.eu/index.php?page=_layout_prodotto&id=141&lang=en

Copyright © 2014 CC-BY-3.0 and by the respective authors

ISBN 978-3-95450-141-0

operations.

D2 has been moved with respect to the stationary photon beam by utilizing the stepper motors coming with the detector chamber. At a sampling rate of 10 Hz the pBPM has estimated the relative beam displacement (with *difference-over-sum* method) with a precision of 124 nm. As shown in Fig. 2, the linear range extends for approximately 400 µm.

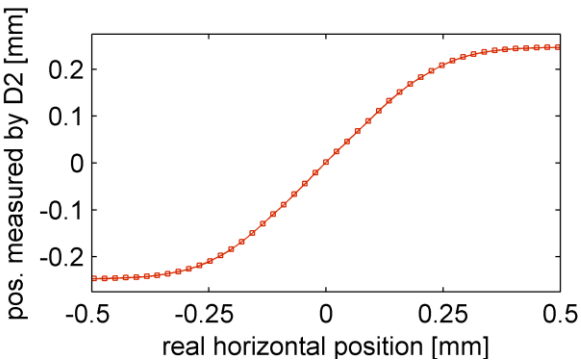


Figure 2: Horizontal position estimated by D2 during a horizontal translation of its movable stage.

In this case, to a first approximation, the 10-kHz precision can be estimated in 3.9 µm. As a matter of comparison, with a 10-Hz acquisition rate, a precision of 72 nm is theoretically expected in such flux conditions. However, it must be pointed out that the acquired data are dominated by systematic errors such as stepping precision, slow beam movements, etc.

Analogous linear scans have been performed during dedicated shifts by deliberately moving the electron beam while keeping the detectors in position (horizontal case shown in Fig. 3). In this case, the position estimated by D2 has shown a similar trend, except for a quasi-periodic deviation from the linear interpolation. When applying an unsharp filter in the linear part of the curve confined by the red vertical lines, an undulation with a period of about 260 µm and an amplitude of about 15 µm becomes prominent. In principle the unsharp filter (measured values minus the line-fit values) reveals the deviation of the electron beam position from the photon beam position. Interestingly, this deviation follows in sufficient approximation a Sinc function which is the Fourier transform of a box function of width B, with a zero crossing at about $2B$ = 60 µm. Eventually this is not surprising since the beam position was sampled through the pinhole with a step width B of exactly 30 µm. In this configuration, according to the Nyquist sampling theorem, the maximum resolvable spatial frequency is 60 µm. Since in such bending-magnet section the electron-beam position is not directly measurable with the eBPMs, it is estimated through a non-linear fit on the simulated optics. Therefore, this result justifies the hypothesis that the interpolation algorithm of the eBPMs introduces such undulation.

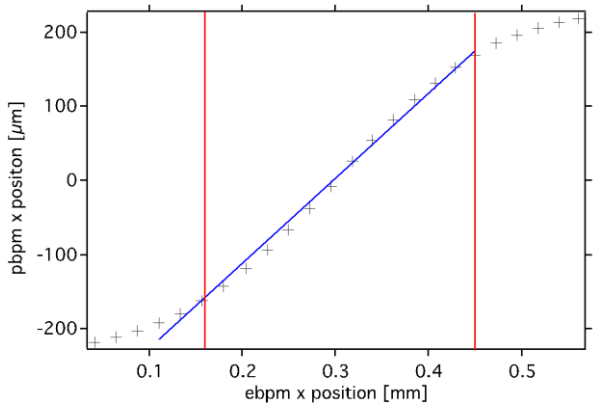


Figure 3: Horizontal position estimated by D2 versus eBPM estimation during deliberate motion of the electron beam. The crosses represent the measured data, the blue line is a linear fit within the linear range (delimited by by red lines).

It is worth mentioning that, due to the small vertical emission angle (about 100 µrad at 2 GeV), the slit aperture cuts specific portions out of the Gaussian vertical beam profile. This turns into a significant flux decrease for wide vertical beam movements and, as a consequence, a reduction in precision. In future, the vertical aperture is likely to be increased in order to avoid these effects; as explained above, in such case the vertical position has to be estimated by the combined readings of D1 and D2.

Test at a 6.5-kHz sampling rate have also been carried out during normal machine operations (2 GeV, 300 mA). A typical trace of the vertical position estimated by D2 is reported in Fig. 4 and its Fast Fourier Transform (FFT) is shown in Fig 5.

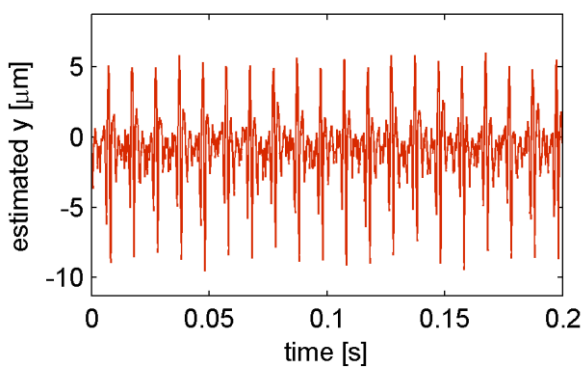


Figure 4: Vertical position estimated by D2 at a sampling rate of 6.5 kHz.

A periodic pattern with a σ_{RMS} of about 2 µm is prominent and superimposed with a stochastic uncertainty of about 500 nm, which can be considered as the resolution limit for the system at the aforementioned acquisition rate and photon flux. The FFT reveals a number of systematic components contributing to such fluctuations. In particular, significant contributions at 17 Hz and 23.5 Hz (imputable to water cooling) are visible;

Copyright © 2014 CC-BY-3.0 and by the respective authors

besides this, 100-Hz fluctuations and harmonics are prominent (noise from correctors).

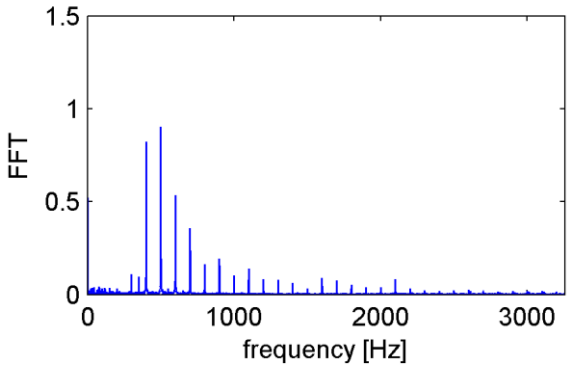


Figure 5: FFT magnitude of vertical position estimated by D2 at a sampling rate of 6.5 kHz.

For what concerns intensity monitoring, the photon flux can be directly estimated through the sum of the acquired photo-currents. With a machine current of 300 mA this gives 20 nA and 0.19 µA for D1 and D2, respectively, with a precision better than 1%. Since only sparse data on radiation damage of this kind of CVDs caused by long-term exposure with x-rays is available in literature, the demonstrator was operated continuously over a period of 9 months. The total current remained reasonably constant over the span of time with respect to a given machine energy (Fig. 6); this is an important point with a view to future applications of CVDs in FOFB systems.

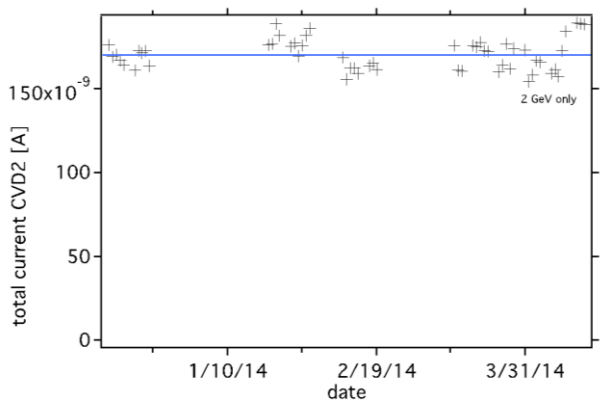


Figure 6: Long-term stability of the intensity monitoring of D2 for normal machine operations at 2 GeV (measured data reported as crosses).

CONCLUSIONS

In its first 9 months of operation the diagnostic-line demonstrator has turned out to be a reliable instrument, allowing for surveillance of bending-magnet radiation with high relative intensity resolution (better 1%) and high position resolution (better than 1 µm) at a maximum frame rate of 6.5 kHz. In order to include these diamond-based pBPMs in a FOFB system, the maximum frame rate should be increased to 10 kHz; this requires some refinements on the readout electronics, which can be implemented without major problems.

REFERENCES

[1] A. Galimberti et al., Nuclear Instruments and Methods A 477, 317 (2002).
[2] M. Lonza et al., Proceedings of the 10th ICALEPCS, Geneva, Switzerland, PO2.011-2, 2005.
[3] T. Scarvie et al., Infrared Physics & Technology 45, 403 (2004).
[4] T. Schilcher et al., Proceedings of DIPAC'05, Lyon, France, POW015, 2005.
[5] J. Morse et al., Journal Synchrotron Radiation 17, 456 (2010).
[6] M. Antonelli et al., Proceedings of SPIE 8504, San Diego, USA, 85040D, 2012.
[7] M. Antonelli et al., Nuclear Instruments and Methods A 730, 164 (2013).

Copyright © 2014 CC-BY-3.0 and by the respective authors

ISBN 978-3-95450-141-0

NEWLY DEVELOPED 6mm BUTTONS FOR THE BPMS IN THE ESRF LOW-EMITTANCE-RING

B.K. Scheidt, ESRF, Grenoble, France

Abstract

For the small beam pipe of the BPMs in the LE-ring a development of 6mm button-UHV-feedthroughs was launched and has resulted in the delivery of a total of 27 prototypes from both the Kyocera and the PMB-ALCEN companies. These buttons are flat, without skirt, with a central pin of Molybdenum ending in a male SMA connector. Among these prototype units are versions with Copper, Steel and Molybdenum material for the button itself, with the aim of assessing possible different heat-load issues. All design considerations, that are compatible with a further button reduction to 4mm, will be presented next to issues of costs, mechanical tolerances and feasibility.

DESIGN ASPECTS OF THE SMALL BPM BUTTONS-FEEDTHROUGHS

The European Synchrotron Radiation Facility has decided to replace its existing double-bend-achromat lattice for 7-bend-achromat lattice that aims to reduce the horizontal emittance from 4 to below 0.15nm·rad. [1]

In this new Ring a total of 288 BPM stations (9 in each of the 32 cells) are foreseen with beam-pipe diameters much reduced with respect to the dimensions in the present Ring. The Fig.1 shows the cross-section of two examples of the preliminary design.

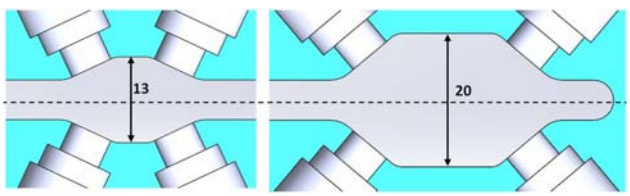


Figure 1: Cross sections of two different future BPMs.

In the existing Ring at total of nearly a thousand of buttons of 10mm diameter (but in BPM cross-sections of 70x34mm) have been successfully used for over 22 years for BPM purposes in a reliable way, i.e. without failures on the UHV aspects, or on the RF-signal pick-up aspects. This reliability issue was important to inspire the design of the new buttons.

For the new BPMs a diameter of 6mm for the button was decided and the study and the realisation of such button were pursued with two independent companies : Kyocera (Japan) and PMB-ALCEN (France). [2, 3]

The pictures in Figs.2 and 3 show the design of the entire button and feedthrough. The main characteristics can be resumed as follows :

- The button, the UHV feedthrough and the (male) SMA connector are all self-contained in one housing that can be (circularly) welded to its lodging hole of the BPM block. This design has successfully served the ESRF for its present ring and also avoids fully the use of vacuum flanges.
- The button (6mm diameter, 4mm height) is without skirt. It is brazed to the central pin and has a support ring (3mm) to the ceramic (but not brazed).
- The central conductor is of Molybdenum and forms the central pin of a standard SMA connector.
- The ceramic disk is of Alumina (Al2O3) and of 9mm diameter and 2.5mm height.
- The housing (13mm outer diameter) is of Stainless Steel.
- The concentricity specifications are at 50um between the button and the outside of the housing.

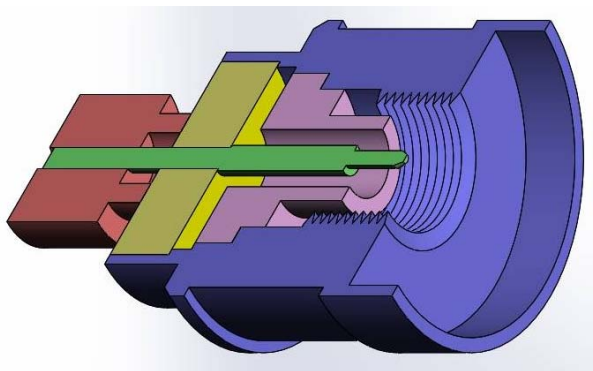


Figure 2: illustration of the button, central-pin-conductor, ceramic isolation, (male) SMA connector and housing.

All parts are prepared, assembled and then brazed according to the specific methods and technology of each of the two companies. The mechanical tolerances, and notably the concentricity, are accepted by each company as part of the final specifications at delivery.

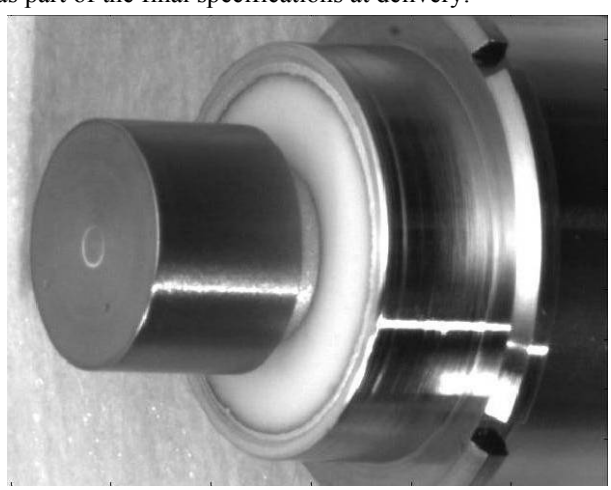


Figure 3: Photograph showing one unit with the 6x4mm button, its central pin welding and its support to the ceramic, and the UHV side of the housing.

Copyright © 2014 CC-BY-3.0 and by the respective authors

The design of the outer body features two cylindrical rings at 9.5mm distance that should facilitate and ease these final delicate operations of correctly inserting it into its lodging hole and then properly welding it. These final operations (done by non-specialists) thereby avoid both the use of special tools or jigs and the risks of mal-positioning by twists or movements at the time of the welding.

The lower ring contains 4 small grooves to facilitate vacuum pumping.

The absence of the skirt (as present with today's buttons at the ESRF) was motivated by the possibility to maintain tight mechanical tolerances on both the buttons' concentricity and that of its lodging hole in the BPM block. The lodging hole, at the section of the button has a diameter of 6.5mm so the nominal gap around the 6mm button is 250um. With the (non-)concentricity specification at 50um we believe that this will not lead to any significant variations of the RF pick-up characteristics, or the heat-load issues.

The absence of the skirt also totally avoids any RF wake-field losses arising from the annular slot around the skirt. [4]

The values of any (non-)concentricity were easily measured, one by one, using a simple optical set-up after inserting the unit under test into a standard reception (or "dummy") hole. Out of a total of 27 delivered units we found the worst case at slightly above 60um, with a resolution/precision of the measurement set-up of about 10um. The Fig.4 shows two examples of images taken of 2 different buttons in that dummy lodging hole.

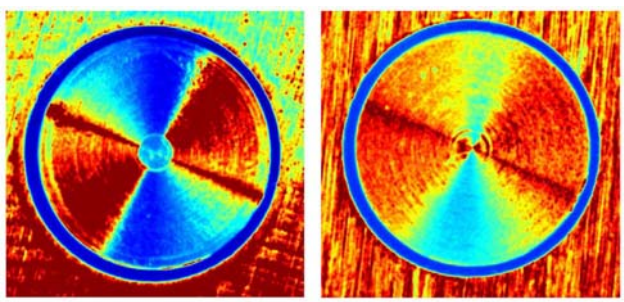


Figure 4: high-contrast images showing the 6mm button and the 250um gap around it, for a non-perfect (left) and close-to-perfect (right) concentricity.

Buttons of Steel, Molybdenum and Copper

The choice of material suitable for the button, but also for the central conductor pin, is mainly influenced by considerations of how much power the button could possibly absorb due to effects of RF fields trapped under different electron beam conditions (i.e. charge and bunch-length), and of the heat conductivity aspects that determine how any button heat-load will evacuate to the outside (i.e. BPM block).

The precise calculation of power absorption due to any RF trapping is far from straight-forward.

However, since the present Ring will still be operating for about 4 more years, and with beam conditions (total current, current per bunch, bunch length) quasi identical to that for the new Ring, we are going to use that opportunity by implementing a Test-BPM-Chamber in one of the straight sections. Not only does this make it possible to assess the button and BPM characteristics with beam now (as reported below) but also to follow-up carefully its behaviour over a time-scale of months and years.

This chamber holds three identical BPMs, adjacent at 60mm longitudinal distance, and each with 4 identical buttons. The only difference between the 3 BPMs is the material of the button. In agreement with the manufacturers we opted for buttons of Stainless Steel, Molybdenum and Copper.

RESULTS OBTAINED WITH 3 ADJACENT TEST BPMS IN TODAYS RING

The ID25 straight section offered sufficient space for the insertion of a Test-BPM-Chamber that itself holds three identical BPMs in the centre and tapered sections on both sides as shown in Fig.5. Not shown are a set of 4 bellows (2 on either side) and a motorized translation table that allows displacing the whole chamber +/-3mm in both planes from its central position.

Note that this translation system is presently not precisely calibrated and was therefore not (yet) used for K-factor and coupling measurements as described further below. However independent and precise position transducers will be installed later and shall then allow such measurements.

The cross-section of that BPM (conceived autumn 2013) is shown in Fig.6 and is different from that of today's foreseen geometries of real future BPM blocks (and shown in Fig.1) simply because of the past year's evolution of the possible vacuum chamber designs. Nevertheless, that Test-BPM cross-section is a good compromise between the two different BPMs, and it will be adequate to fully assess the behaviour and characteristics of these new 6mm buttons.

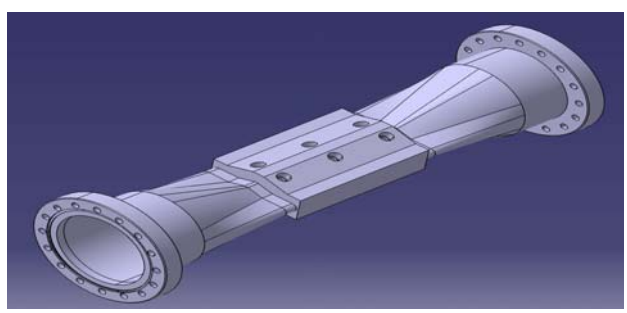


Figure 5: The Test-BPM-Chamber installed in the ID25 straight section of our Ring with 3 adjacent BPMs.

Copyright © 2014 CC-BY-3.0 and by the respective authors

ISBN 978-3-95450-141-0

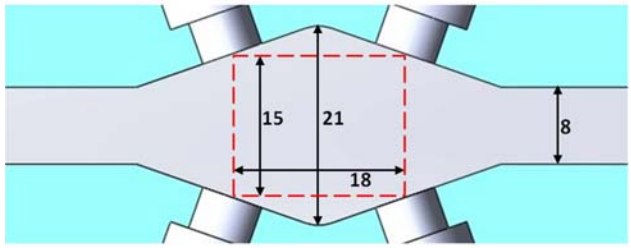


Figure 6: the BPM cross-section in the Test-Chamber.

No Heat-load Issues Measurable on any Button

During 1 week after the installation, all the 12 buttons have been equipped with a small sleeve that slides onto the central male-SMA pin. This sleeve has a small thermocouple integrated and the electric signal from that (via 2 thin wires) is acquired to measure the temperature on this point. This simple temperature measurement system is devised so to keep thermal inertia to a minimum and to obtain a temperature indication of this central pin-conductor with an absolute precision of about 1C and resolution of a fraction of that.

Such similar temperature measurement system had already been installed on the 4 buttons of a different BPM block in our Ring. This former Feedback-BPM block (adjacent to the ID straight section chambers) has a button size of 9.5mm, with a skirt (so also an annular slot around this skirt) and the internal vertical height of the chamber is only 10 mm. Horizontally and longitudinally the 4 buttons are arranged such that the distance between the beam and the centre of the button is only 9.4mm. This geometry is believed to provide rather favourable conditions of heating induced by beam and RF fields. The temperature readings obtained indeed confirm that heating occurs on these buttons since the differential temperature (with respect to the body of the BPM block) of these central conductor pins was evaluated at about 38C for a beam current of 200mA.

Today, doing exactly the same measurements on the 12 pins of the buttons of our Test-BPM-Chamber, we found no measurable temperature effect. The body of the chamber (measured by independent thermocouples) itself heats up from 23C (no beam) to about 35C (200mA) but the 12 measurements on the button-pins show no differential temperature rises. By consequence no difference between the 3 different button materials is measurable.

This method is not perfect since it measures on the pin and not on the button itself. From the design in Fig.2 it can be easily deduced that a considerable amount of (hypothetical) heat deposited in the button would be evacuated by the ceramic disk and then the housing etc. So any temperature rise on the pin only reveals a fraction of that on the button itself. Nevertheless, temperature rises on the pins of these former F-BPM buttons are clearly measureable while measurements with the same method on the new 6mm buttons show no effect at all. We therefore believe that there is no risk of heating issues with these buttons in our foreseen BPM blocks.

First Results from the RF Signals and the Beam Position Measurements Characteristics

The 12 button signals of these 3 BPMs have been connected to a set of 3 Libera-Brilliance units in an electronic cabinet via RF cables (RG-223) of about 25m length. The RF input of the Liberas is preceded by a 3dB attenuator and a 40MHz bandpass filter as is the case for all the other 224 units of our BPM system for beam position measurement and slow & fast orbit control.

The first measurements with beam allowed us to compare the strength of the RF signal (352.2MHz) generated by the 6mm buttons to that of the standard (10mm) buttons in our BPMs. This RF signal is about a factor 0.7 compared to that of the standard BPMs.

The coherency (also often expressed as the Q value of the BPM) of the 4 signals also looks satisfactory on each of the 3 BPMs.

The conversion of the relative strength of the RF signals measured on each of the 4 buttons into the position of the electron beam is usually done by the simple delta / sum formula. For e.g. the vertical plane this z coordinate equals : $Kz * (A+B-C-D) / (A+B+C=D)$.

At the time of starting the acquiring the RF signals from these Test-BPMs with real beam we had not yet made any calculation or approximation of these Kx and Kz factors. However, it was relatively straight forward to obtain these values by measuring the responses from the 3 test BPMs while making a set of precise beam displacement bumps in that ID25 section.

The ID25 straight section has two standard BPMs on its extreme ends : BPM C24/7 up-stream and BPM C25/1 down-stream. The distance between these 2 standard BPMs is 6015mm and the (1rst or up-stream) BPM in the Test-BPM-Chamber is at 1026mm distance from the C24/7 BPM. There is no magnetic element between these 2 standard BPMs. Moreover their K-factors are precisely known (error <2%) from independent measurements in the past [5].

By applying a pre-qualified local bump, using three adjacent steerers in that region, the beam's transverse displacement AND the beam's angular path can be determined by readings of these C24/7 and C25/1 BPMs. The so caused beam displacement in the 3 Test-BPMs is then simply calculated from the known geometrical distances. In the horizontal plane this was done for 21 different values : from -1mm to +1mm in 0.1mm steps. For the vertical plane we limited this range to 11 steps from -0.5 to +0.5mm.

This real beam displacement is then compared to the value yielded by the Test-BPMs in which a preliminary K-factor had been applied. After this the correct K-factor can be established which turned out to be 6.43mm for Kx and 12.44 for Kz.

Copyright © 2014 CC-BY-3.0 and by the respective authors

These values have later been confirmed (within 1% error margin) by initial theoretical calculations of the electromagnetic field distributions in our BPM design using the CST Studio Suite software. [6]

But the scope and interest of this measurement go beyond finding these K-factors only for the centre of the BPM block : The linearity of these same factors can be assessed precisely when the beam is no longer close to the BPM centre. Having done the horizontal beam displacements over a +/-1mm range from the centre allows to see how the Kx factor varies over this range.

In each of the following figures the results of the 3 BPMs are shown by the 3 different colours (black, blue and red) of the curves.

The results shown in Fig.7 are for a beam displacement around the BPM centre : the Kx value varies only slightly (1.5%) from typically 6.43 to 6.53 for a 1mm displacement from centre.

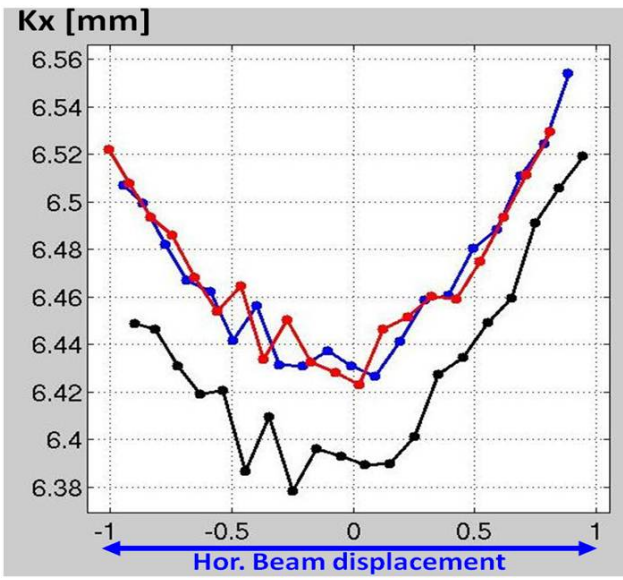


Figure 7: the variation of the Kx factors as function of the horizontal offset between the beam and the BPM centre.

The Fig.8 now shows the resulting value of Kx when the beam is about 2mm (both horizontally and vertically) away from the BPM centre. The K-factor now varies by about 18% (from 6.4 to 7.5).

In other words, the simple delta / sum formula is no longer adequate to convert the 4 button signals into beam position coordinates of reasonably good precision.

The 2nd effect of the too simplistic formula for the geometry of the BPM and its buttons is that it produces coupling between the 2 orthogonal planes. For instance the coupling from a (pure) horizontal beam displacement to a (fake) vertical beam motion is shown in Fig.9.

The green curve shows the vertical tilt of the beam displacement itself, i.e. a horizontal beam bump also produces some vertical bump but it can be measured independently by these 2 standard BPMs of C24/7 and C25/1. Please note that the 3 curves of BPM coupling have not been corrected for this.

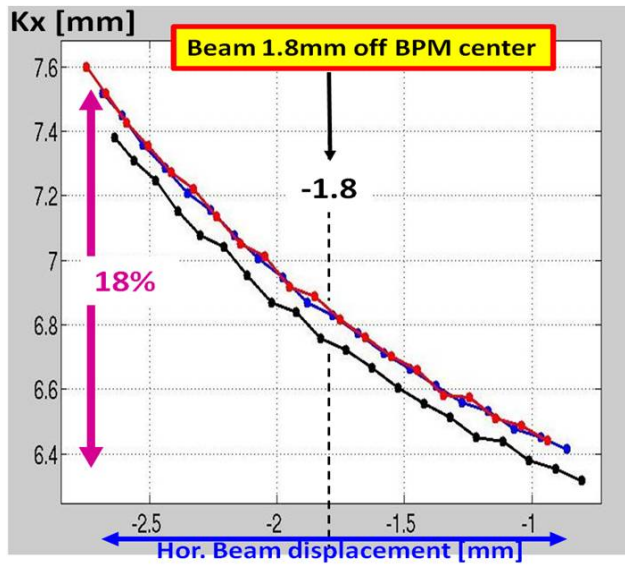


Figure 8: the Kx factor variation as in Fig.7 but now for a 2mm (both planes) offset between beam and BPM centre.

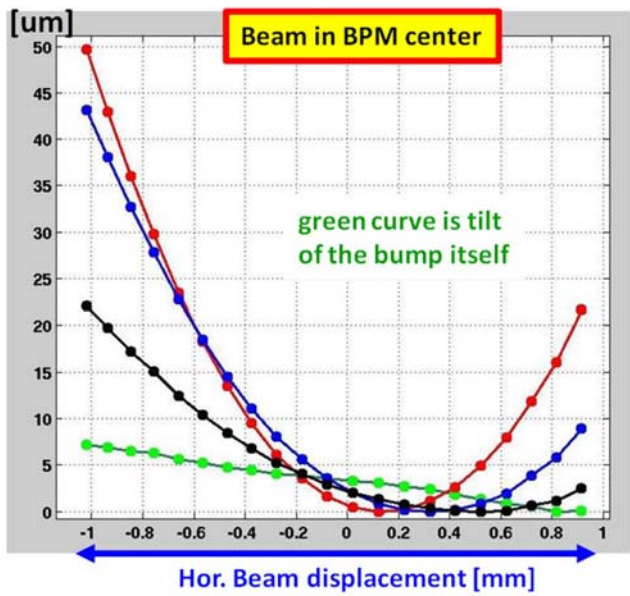


Figure 9: the coupling of the hor. beam displacement into (fake) vertical motion, for a centred beam.

The same coupling (hor. to vert.) was also measured with an offset (roughly 1.8mm for both planes) between the beam and the BPM centre. The results of that are shown in Fig.10 : The coupling now reaches strong values up to 300um but quite different for the three BPMs. This can be (partly) explained by the fact that the vertical offset of the three BPMs was quite different : i.e. +0.4, 0 and -0.6mm for respectively the up-stream, middle and down-stream BPMs. This could be explained by a vertical tilt of the BPM-Test-Chamber but this is not yet verified.

Copyright © 2014 CC-BY-3.0 and by the respective authors

ISBN 978-3-95450-141-0

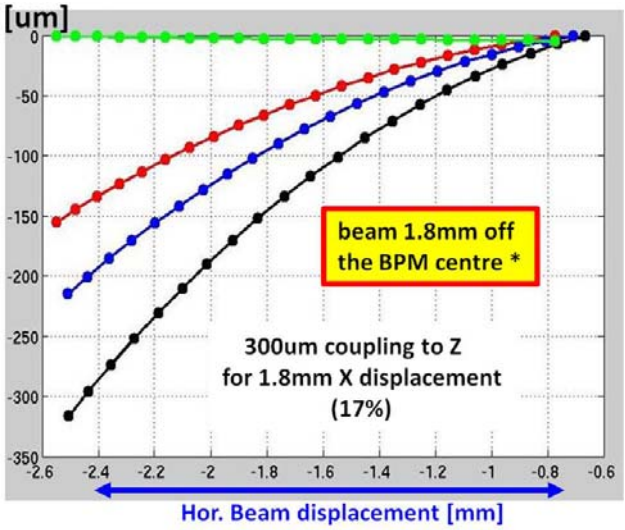


Figure 10: the coupling of the hor. beam displacement into (fake) vertical motion, for an 1.8mm off-centred beam.

Measurements of the (dis-)linearity of the Kz factor and of the coupling from vertical-to-horizontal plane have also been performed, as a function of offset between the beam and the BPM-centre. These are not reported here but lead essentially to the same observation of the restrictions of that simple delta / sum formula for beam coordinate calculation from the 4 buttons signals.

PRELIMINARY CONCLUSIONS AND FUTURE DEVELOPMENTS

The prototypes of new 6mm BPM buttons have been realised by two independent companies and have meet their specifications.

Subsequently integrated into a BPM chamber they have shown satisfactory characteristics and behaviour in tests of (only) 2 weeks since the installation in the Ring in August 2014. Both their RF characteristics for the use as a BPM system, and their apparent immunity to significant heat-load problems have been assessed.

Further measurements on the beam to characterise the BPM geometry will soon be possible in a straight forward manner and compatible with normal conditions under User operation. This is needed to obtain a precise "mapping" of that BPM geometry and for which a precisely calibrated motorized translation system will be used instead of the above beam bump methods.

In parallel, the simulations and calculations with the CST tools will be pursued for also different beam offsets from the BPM centre. This will be used to compare and validate a simulation model and then to apply it also the BPM geometries of the two real BPMs.

The simplistic delta / sum formula shows significant limitations and restrictions in terms of linearity and coupling, even for moderate offsets between the beam and the BPM centre.

The 6mm diameter button seems a good compromise so far but if simulations would show that a smaller diameter (down to 5 or even 4mm) would yield a more acceptable dislinearity & coupling when using simple delta / sum formulas (which have their own advantages) then technically both companies have confirmed that they can reduce the button diameter without any major change to the rest of the feedthrough itself.

ACKNOWLEDGMENT

The author expresses thanks to N.Benoist and B.Ogier for their precious help on the design and the mechanics of the test BPM chamber, and to G.Rehm, L.Goirand and E.Plouviez, for useful discussions and assessment of the design concepts of the button feed-through, and to the latter for the recent simulations of the K-factors of the Test-BPMs and the future BPM geometries.

Thanks are also extended to the ESRF vacuum group for the preparation and installation of the test BPM chamber in the Storage Ring, and to B.Joly, F.Taoutaou and F.Epaud for installing the BPM cables & Libera electronics and the systems for temperature measurement.

REFERENCES

[1] J-L.Revol et al., "ESRF Upgrade Phase 2 Status", IPAC'14, Dresden, May 2014. http://accelconf.web.cern.ch/AccelConf/IPAC2014/papers/mopro055.pdf

[2] Kyocera, Fine Ceramics, Beam-Position-Monitors http://global.kyocera.com/prdct/fc/product/category/metalize/metalize004.html

[3] PMB-ALCEN, 13790 Peynier - France http://www.pmb-alcen.com/en/ceramic-metal#traversees

[4] A.Morgan and G.Rehm, "Quantifying dissipated power from wake-field losses in diagnostic structures", MOPF23, IBIC'13, Oxford, September 2013.

[5] private communication, L.Farvacque, beam dynamics group, ESRF

[6] Computer Simulation Technology, Darmstadt-Germany https://www.cst.com/Applications/MWandRF

Copyright © 2014 CC-BY-3.0 and by the respective authors

FIRST RESULTS WITH THE PROTOTYPES OF NEW BPM ELECTRONICS FOR THE BOOSTER OF THE ESRF

B.K. Scheidt, ESRF, Grenoble, France

Abstract

The 25 year old BPM electronics of the ESRF's Booster (200MeV to 6GeV, 300m, 75 BPM stations) are in process of replacement with new modern acquisition electronics. The design and development of this acquisition system was done in collaboration with the Instrumentation Technologies company and has resulted in a commercial product under the name Libera-Spark. It contains RF filtering & amplification electronics in front of 14 bit & 125MHz ADCs for 4 channels, followed by a (Xilinx ZYNQ) System_on_Chip for all processing, that also includes the possibility of single bunch filtering directly on the ADC data. It is housed in a compact and robust module that is fully powered over the Ethernet connection and which facilitates its installation close to the BPM stations thereby avoiding long RF cabling. For simplicity and cost economic reasons this Spark is without PLL and adjustable RF attenuators since not needed for Booster BPM applications, but possible in elaborated versions for other applications. Two prototypes were fully tested with beam and the results in terms of resolution & stability were assessed since delivery in January.

THE ESRF BOOSTER RING AND MOTIVATION FOR NEW BPM SYSTEM

The European Synchrotron Radiation Facility operates a 200 MeV linear Pre-Injector and a full energy fast cycling Booster synchrotron that accelerates the electron beam to the 6GeV energy in an acceleration period of 50millisec before extraction to the 2nd transferline and subsequent injection into the Storage Ring. This Booster presently still uses the original power supplies for the magnets that function with a resonant "white-circuit" at 10Hz cycling frequency, producing biased sine wave currents in these magnets. That magnet's power supply system will be replaced in 2015 by ramping power converters, with a minimum cycling rate of 250ms (150ms ramping up and 100ms ramping down), followed by a partial re-commissioning of the Booster.

The Booster has a circumference of 300m and contains 75 BPM blocks with each 4 buttons of 10mm diameter in a circular chamber of 60mm internal diameter. The 4 buttons are angularly distributed with 4 equal 90deg angle shifts between them, but with a 45deg angle offset with respect to horizontal and vertical planes. The so-called K factor for this BPM geometry is 21.5mm when using the simple delta/sum algorithm for calculating the beam position from the 4 RF signal strengths measured at the buttons.

The RF signal amplitude, at the sma connector of the button feedthrough, is about 300uV rms for 1mA of Booster current. The RF frequency is 352.2MHz and the maximum nominal current 5mA in so-called long-pulse (from Linac) which produces a bunch-train of 352 bunches. However, the Booster also operates routinely in multi-single bunch configurations with only 1 to 5 bunches and typical currents between 0.1 and 0.5mA.

Motivation for the New BPM Electronics with Improved Functionality and Performance

The old electronics and acquisition system had no functionality for Turn-by-Turn measurements and could only perform 6 punctual measurements in the 50millisec acceleration cycle. These old electronics have an RF multiplexer in close vicinity to the BPM block (hence inside the Booster Tunnel) and the rest of the electronics in permanently accessible cabinets, but at RF cable lengths varying between 20 and 60meters. [1]

A few years ago 2 Libera-Brilliance units were installed to perform the signal acquisition of the RF signals from 2 BPM blocks and had been helpful to demonstrate the benefits of more performing BPM measurements, notably serving as a new Booster tune measurement system. However, the Libera system is specifically designed for Storage Ring BPM requirements with incorporated functionalities that have strictly no application in a Booster BPM system with only a beam duration of a fraction of a second.

The search for an alternative, but also more cost-effective, system for the acquisition of the 4 weak RF signals aimed at simplifying the concept to a strict minimum but yet achieving Turn-by-Turn measurement functionality even for (low current) single bunch fillings. A completely new hardware design that needs no maintenance (passive cooling, no disc, power over ethernet) was elaborated by the Instrumentation Technologies company and resulted in a new and now commercial, product, named as Libera Spark [2, 3].

FUNCTIONAL DESCRIPTION OF SPARK

The main features of the Spark device can be resumed as follows :

- 4 channels digitizer for weak RF signals.
- Adequate signal processing for the calculation of the 4 signal strengths, comprising I , Q and Sum values, the beam-position values, and this all for data-rates reduced to Turn-by-Turn rate and lower, and this also optimized for specific (single-bunch) filling patterns
- Efficient and straight-forward interface (SCPI commands) for the control & read-out via Ethernet.
- Suitable and compact chassis & housing, with Power-over-Ethernet (IEEE802.3af standard).

Copyright © 2014 CC-BY-3.0 and by the respective authors

ISBN 978-3-95450-141-0

The Fig.1 shows a block diagram with, on the analogue (left-) side, the four inputs (sma-connectors) followed by RF bandpass filters and RF amplifiers. The total RF gain is such that the subsequent 14bit ADCs reach their full scale (+/-8192 counts) for an RF input level at -40dBm (2.2mV rms). There is no variable RF gain (or attenuation) implemented since for even the highest beam currents in the Booster the ADCs will be below this full range, and this even if the RF cable length between the BPM block and the Spark is only a few meters long (i.e. installation of the Spark inside the Booster tunnel).

The ADCs are running at about 108MHz and so the BPM's RF signal (352.2MHz) is frequency under-sampled inside the 7th Nyquist zone. The exact ADC sample rate should be 108 times per Booster orbit revolution (is 1.000574MHz) but it should be noted that this frequency is determined by a programmable crystal oscillator (XO) which is not locked to any of the real frequencies (RF or Orbit) of the Booster itself. It is therefore up to the user to set (at reboot of the device) the XO such that indeed 108 samples per turn are obtained and further delivered to the Digital Down-Convertor that is realised in the FPGA section and that converts to Turn-by-Turn data rate.

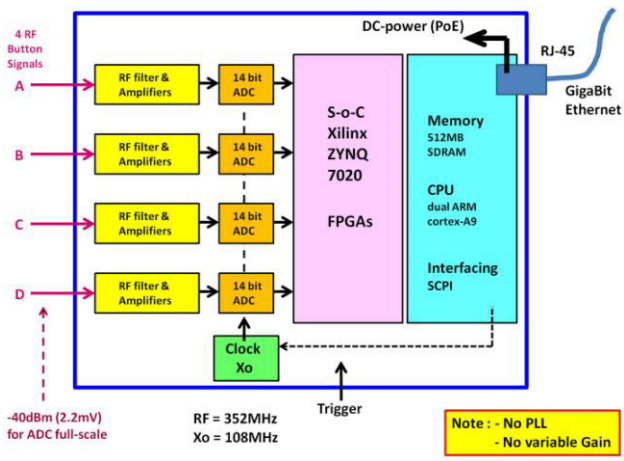


Figure 1: Block diagram of the Spark [um].

The omission of a PLL mechanism (needing itself additional externally provided timing signals) was motivated for both simplification and cost-reduction reasons, and it can be shown (see subsection on synchronisation) that for the short duration of the beam in the Booster (50millisec) such PLL is not needed.

The device can boot via network (using TFTP protocol) or alternatively from a micro-SD memory card (not shown in the above diagram).

SIGNAL PROCESSING THAT COVERS VARIABLE NEEDS AND APPLICATIONS

The Fig.2 shows the scheme of signal processing with the Digital Down Convertor (DDC) that provides a quadrature demodulation on each of the 4 channels, at the XO frequency, producing the I and Q signals at Turn-by-Turn (TBT) rate. This TBT buffer is used to further calculate the absolute signal strengths of the 4 channels and the X and Z position values (using the simple delta/sum formula), taking into account the K factor and possible offsets. A similar, but slower rate buffer is also available at TBT divided by 64.

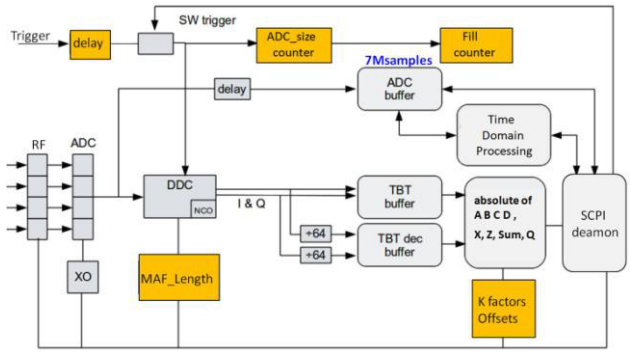


Figure 2: Signal Processing Scheme, the orange blocks indicate input parameters.

The DDC allows applying a pre-filtering on the ADC samples to be used in the subsequent TBT generation of data flow. A parameter called MAF_Length can be set to an integer value below the (ADC_to_TBT) decimation rate of 108. This makes it possible to only select those ADC samples that contain a real RF beam signal as is the case in single-bunch filling patterns. This example is further illustrated in Fig.3 where 432 ADC samples that represent 4 Turns are depicted (in black) together with a possible configuration of that MAF filter in blue. Per orbit turn only the 35 samples defined by the MAF are used in further processing while the other (73) are discarded. It is noted that the ADC buffers (upto 7Msamples each, i.e. representing 65millisec) themselves are available.

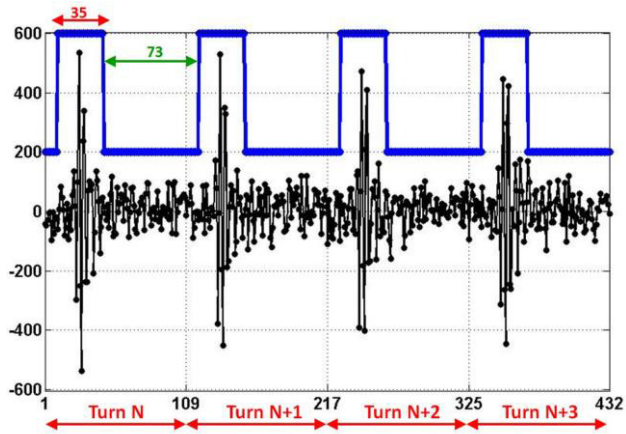


Figure 3: MAF filtering on the digitized RF signal with partial beam fill patterns (in this case single bunch).

Trigger and Synchronisation Issues

The trigger signal plays an important role in the precise timing of T-b-T data, also in the absence of a PLL on the ADC clock. This trigger (after a settable trigger delay) defines the start of the first Turn and also the start of the

Copyright © 2014 CC-BY-3.0 and by the respective authors

MAF filter (if used). It can be shown that if the crystal oscillator is not exactly at 108 times the RF frequency then the MAF window will drift away from its position with respect to the RF beam signal. E.g. at each new trigger the MAF will initially (meaning for the first number of turns) be correctly positioned (as shown in Fig.3), but no longer at much later turn numbers. One should keep in mind here that in a system with 75 BPMs, and each with an individual and free-running crystal oscillator, that such non-rigorous synchronisation between T-b-T data of all stations could limit the usefulness or lead to misinterpretations.

However, the exact frequency values of each Xo in a system with 75 BPMs can be simply determined by an FFT on the retrieved ADC data buffers (of any of the 4 channels) when taken with a circulating beam in the Booster. Any differences of the real Xo frequency with respect to the set-value can then be corrected individually and a next acquisition should confirm then that all Xos are now sufficiently close in real values, and that consequently the T-b-T data of all stations is in phase, even 50millisec after the Trigger.

The stability of the Xo frequencies over a longer span of time (days, weeks) has been assessed satisfactorily with the 2 available prototypes and it is therefore expected that such adjustment work on the Xos is not needed regularly. For a rapid estimation of this effect please note that a differential of 1E-5 between two Xos results in a 0.5us offset after 50millisec (i.e. half a Booster orbit turn after the full acceleration cycle).

It is further noted that the Booster RF frequency is completely identical to that of the Storage Ring, and the latter has daily fluctuations of about 20Hz (i.e. 6E-8) due to (12hrs) tidal effects, and long-term variations of about 200Hz (6E-7).

RESOLUTION, REPRODUCIBILITY AND SIGNAL LEVEL DEPENDANCY

The 2 prototypes have first been measured in the laboratory with a CW RF signal source on their performance of resolution, reproducibility and long-term stability, and their dependence of the beam position values on the RF signal strength at the 4 inputs.

For this the input signal level was programmed with steps of 5dB from -70dB to -40dBm (every 100sec), and a record of 1600 values (0.1sec) of the X and Z buffers (64-decimated-TbT, i.e. 16KHz rate) was taken every 2sec. The average and rms values were calculated on each buffer (with K-factor at 10mm), and this yields 50 values at each distinct level. The whole measurement sequence was repeated for >20hours so to also assess any slow drifts of these position readings. The Fig.4 illustrates only one such sequence covering a period of 700*2=1400sec (23min). The top plot shows the sum signal recorded while the two middle plots the X and Z values (for each prototype), and the bottom plot the 4 rms noise values (X & Z, both units).

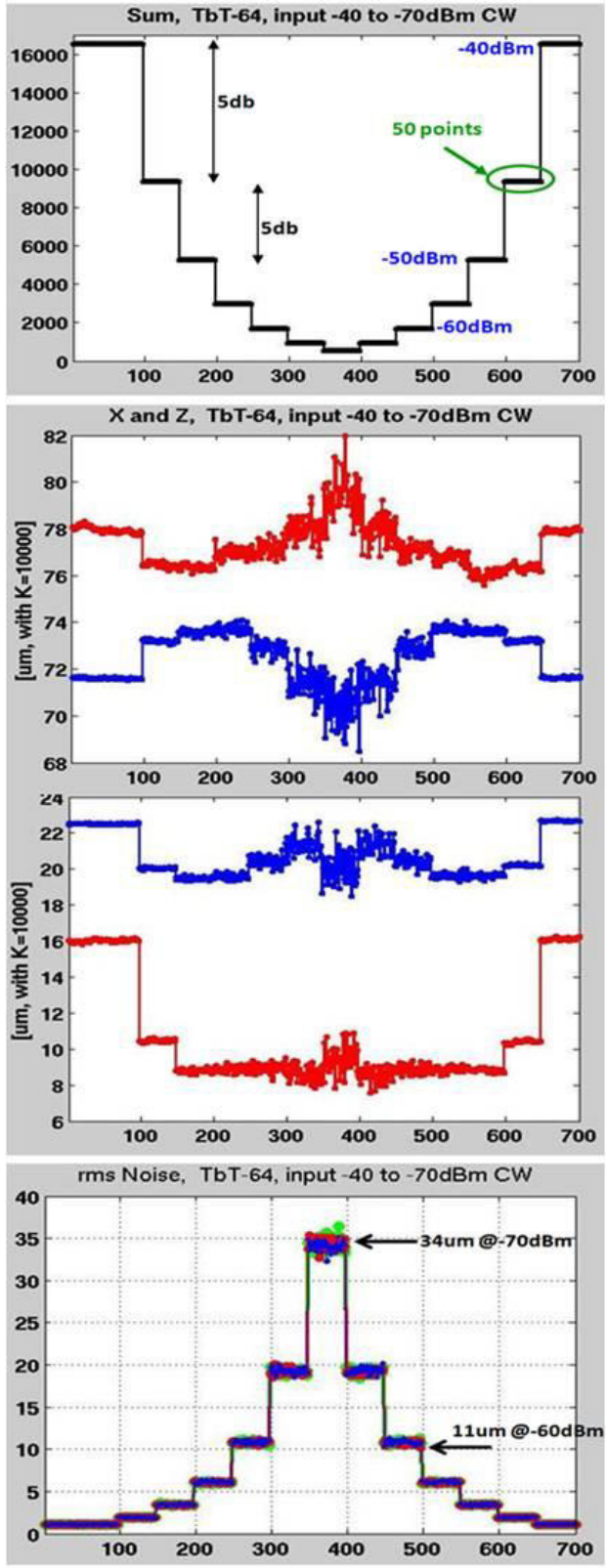


Figure 4: recordings over 23min showing from top to bottom values of Sum (i.e. Signal Level), X (blue) and Z (red) of both units, and rms noise. All data taken from the 16KHz rate buffers and with CW RF power at inputs, and with K-factor at 10mm.

Copyright © 2014 CC-BY-3.0 and by the respective authors

ISBN 978-3-95450-141-0

The results can be resumed by the following figures : The shift of beam position value due to a different level of RF input signal (also called Beam-Current-Dependence) is 3, 3, 3, 8um (x1, x2, z1, z2) for -40 to -70dBm.

The noise (for 16KHz rate output) is 1.1, 3.4, 11 and 34 um rms (average of X & Z) for input levels of respectively -70, -60, -50, -40dBm.

As stated above, the measurement sequence was continued for more than 20hours to also assess any drifts over such a time-span. Such drifts were in the order of 1um (rms) on both units, for both planes.

TURN-BY-TURN MEASUREMENTS IN EARLY CYCLE OF THE BOOSTER

The 2 units have been connected to two Booster BPM blocks using RF cable lengths of about 20m. This allowed verifying the signal levels and some general performance aspects. This also made it possible to measure the beam position directly after the injection of a single bunch (0.1mA current) into the Booster, and on the 1MHz Turn-by-Turn rate and also using the MAF filtering as described above. The latter assures the acquisition of true (i.e.no-smearing between turns) T-b-T position data with the best noise performance.

The betatron tune values of the beam oscillations can be calculated by a simple FFT on that T-b-T data. It was done in slices of 1000 Turns (i.e. 1millisec), and over the first 8millisec after injection. In Fig.5 an image of such tune data (from 1 BPM) shows of a single injection the excursions of both tunes visible over this 8ms period.

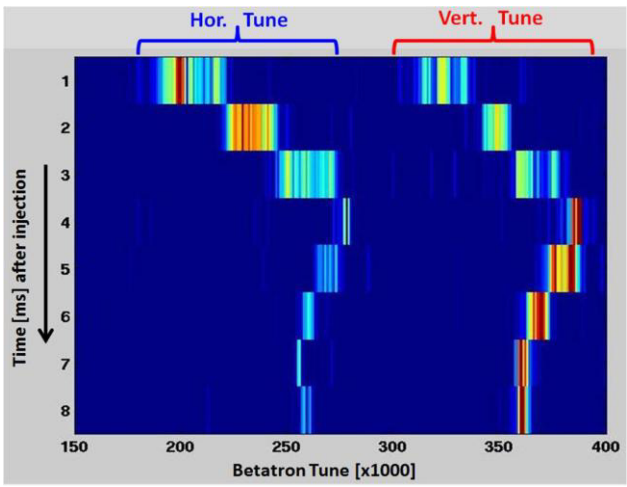


Figure 5: The tune behaviour in both planes of the injected beam during the first 8ms, in 8 slices of 1ms.

When repeating such tune measurements at successive injections the shot-to-shot stability of the Booster's magnet currents can be assessed. Obtained results are shown in Fig.6 over 40 shots with 2 independent BPMs (and Sparks) measuring the horizontal tune at 4ms after injection, in a window of 1ms. The result difference between the two systems is typically below 5E-4 (on a tune of ~0.27).

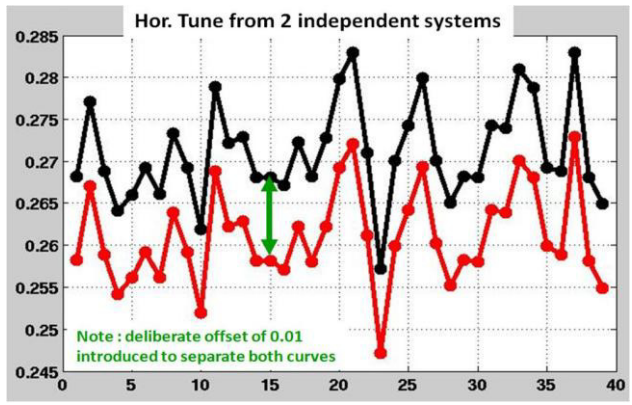


Figure 6: The horizontal tune stability, measured by 2 independent BPMs, over 40 shots at 4ms after injection.

INSTALLATION OF A FULL SYSTEM AND FURTHER DEVELOPMENTS

End of this year 75 units will be installed progressively. Their installation inside the Booster tunnel with short (2m) RF cables from their BPMs is considered but not yet decided. Radiation dosimetry measurements are performed since a few months at specific points to help such decision, while also similar electronics have been exposed since months and are being monitored for any malfunctioning caused by received dose. If the risk of radiation damage is judged too high then installation outside the tunnel is possible but at the expense of lower sensitivity and higher noise levels.

The satisfaction with these prototypes has stimulated the conception of a more complete device that includes a PLL, variable RF attenuators and a 40Hz data-stream output (not depending on triggering). The realisation is presently undertaken and will be available in early 2015.

ACKNOWLEDGMENT

The author wishes to thank the company for making the development of this versatile instrument possible, and their staff for understanding our specific BPM needs and their ability to satisfy these requirements in a short development time with the realisation of a modern, versatile and powerful device. Thanks are also expressed to F.Epaud for taking full care of the Tango device-server and the computer control aspects.

REFERENCES

[1] B.K.Scheidt and F.Loyer, "ESRF Synchrotron Injector BPM System", EPAC'92, Berlin, March 1992. http://accelconf.web.cern.ch/AccelConf/e92/PDF/EPAC1992_1121.PDF

[2] G.Jug et al., "Development of Compact Electronics dedicated to BPM System in Injectors and Boosters", IBIC'13, Oxford, September 2013. http://accelconf.web.cern.ch/AccelConf/IBIC2013/papers/wepc18.pdf

[3] Instrumentation Technologies, http://www.i-tech.si/

Copyright © 2014 CC-BY-3.0 and by the respective authors

FRIB BEAM POSITION MONITOR PICK-UP DESIGN*

Oren Yair#, Jenna Crisp, Gerlind Kiupel, Steven Michael Lidia, Robert C. Webber, Facility for Rare Isotope Beams (FRIB), Michigan State University, East Lansing, MI 48824 USA

Abstract

The heavy ion linac under construction at Michigan State University as part of the Facility for Rare Isotope Beams requires a Beam Position Monitoring System with dual-plane pick-ups at 147 locations. Four different pick-up designs will be used with apertures of 40, 50, 100, and 150 mm. The 40 mm BPMs are designed to operate at cryogenic temperatures, as 39 are bolted to superconducting RF cavities and reside in the insulating vacuum of the cryomodule. The other designs serve only room temperature locations. Requirements, designs, analyses, tests, and status is reported

INTRODUCTION

The Facility for Rare Isotope Beams (FRIB) will be a new national user facility for nuclear science, funded by the Department of Energy Office of Science (DOE-SC), Michigan State University (MSU), and the State of Michigan. Under construction on campus and operated by MSU, FRIB will provide intense beams of heavy ions to produce rare isotopes. A heavy ion superconducting linac capable of accelerating ions up to Uranium with energies higher than 200 MeV/u and beam power up to 400 kilowatts will be used. The primary time structure for beam ranges from 50 μs pulses at 1 Hz to nearly CW beam with 100Hz 50 μs notches. The bunch rate will be 20.125, 40.25, or 80.5 MHz and the velocity will range from 3.3 to 50% the speed of light.

With 100 μA beam current, the required BPM system accuracy is ±0.4 mm and resolution is 0.1 mm. Accuracy includes survey errors with respect to the designed beam orbit, linearity and electrical center in the BPM, cable mismatch, amplifier impedance and gain, and receiver errors. Accuracy addresses the ability to thread the beam safely through the linac while preserving aperture. BPM stability reduces the frequency of beam based alignment and aperture scans used to identify and maintain optimum beam orbit.

Resolution is focused on the ability to measure changes while tuning. This allows measurement of the machine lattice and helps identify irregularities or failures in other accelerator components. The relevant time period for resolution is a day.

The BPM system will also be used to identify optimum accelerating cavity phase by measuring beam time of flight.[1] With 100 μA beam current, the required phase accuracy is ±2 degrees at 80.5MHz with 0.5 degree resolution.

Beam intensity will be measured with the BPM system as well. Sensitivity to position and bunch length is problematic. Accuracy of a few percent should be possible for reasonable beam conditions.[2][3]

BPM PICK-UP RESOLUTION

Split plate style BPMs are inherently more linear [4] than button or stripline BPMs. However, split plate and stripline designs require additional complexities to hold the electrodes in position. The single support point characteristic of button BPMs alleviates problems with differential expansion at cryogenic temperatures.

Button BPMs are both non-linear and dependent on the position in the orthogonal plane. A general rule of thumb is that the button width should be about 60° wide leaving a 30° gap between buttons. Buttons with a flat face rather than one that aligns with the inside surface of the BPM aperture are simpler and less expensive to make, yet, provide good response.

Position and resolution near the center of a button bpm of diameter D is estimated below. The D/π scale factor is only an approximation but is reasonably accurate over 1/3rd of the aperture.

$$Pos \approx \frac{D}{\pi}\frac{A-B}{A+B} \quad mm \qquad Pos_N \approx \frac{D}{\pi\sqrt{2}}\frac{V_N}{V_{button}} \quad mm$$

The voltage induced on a BPM electrode can be estimated from its geometry, beam current, and button impedance.[5] The image current has equal but opposite charge on the inside of the beam pipe and follows the beam. The image current flowing onto the button as the beam enters the BPM must come off of the button as the beam exits. The time difference is the combination of the beam flight time and the signal delay time across the button. The fraction of image current intercepted by a button is d/4D. The BPM output is nearly an ideal current source as the voltage induced on the button is not sufficient to change the beam current. For bunches reasonably short compared to the period of the frequency being measured, $I(\omega) \approx 2I_{avg.}$

*This material is based upon work supported by the U.S. Department of Energy Office of Science under Cooperative Agreement DE-SC0000661, the State of Michigan and Michigan State University. Michigan State University designs and establishes FRIB as a DOE Office of Science National User Facility in support of the mission of the Office of Nuclear Physics.

#yair@frib.msu.edu

Copyright © 2014 CC-BY-3.0 and by the respective authors

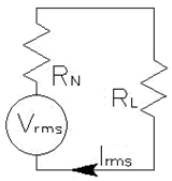
ISBN 978-3-95450-141-0

$$I_{button}(t) \approx \frac{d}{4D}\left\{I_{beam}\left(t+\frac{\Delta t}{2}\right)-I_{beam}\left(t-\frac{\Delta t}{2}\right)\right\} \qquad \Delta t = \frac{d}{c}\left(1+\frac{1}{\beta}\right)$$

$$I_{beam}(t) = 2I_{avg}\sin\omega t \qquad \sin(\alpha+\beta)-\sin(\alpha-\beta) = 2\cos\alpha\sin\beta$$

$$V_{button}(t) = Z_{button}\frac{d}{4D}2I_{avg}2\sin\frac{\omega d}{2c}\left(1+\frac{1}{\beta}\right)\cos\omega t$$

An optimum digital receiver would have sufficient gain so that the error associated with the least significant bit projected to the BPM output is less than that contributed by thermal noise. The total thermal noise power spectral density is provided below. Total noise rather than available noise is appropriate as the BPM equivalent voltage source impedance is small.



$$k = 1.3806488\times10^{-23}\frac{joule}{molecule-K}$$

$$for\ T = 290°K \qquad (0°C = 273.16°K)$$

$$for\ R_N = R_L \quad P_{N\,available} = kT = -174.0\frac{dbm}{Hz}$$

$$for\ R_N << R_L \quad P_{N\,total} = 4kT = -168.0\frac{dbm}{Hz}$$

The effective number of bits (ENOB) for an analog to digital converter (ADC) provides a good estimate for the equivalent noise level at the input. ENOB is the number of bits required for an ideal ADC to provide the measured signal to noise ratio (SNR) of the part.

$$V_N\,rms = \frac{ENOB}{2}\sqrt{\frac{1}{T}\int_0^T\left(t\frac{2}{T}-1\right)^2 dt} = \frac{ENOB}{2\sqrt{3}}$$

Total noise includes the amplifier noise figure, cable loss, ADC error, and thermal noise. The phase and beam current noise levels can be found from the estimated position noise.

$$Pos \approx \frac{D}{\pi}\frac{A-B}{A+B}\ \ mm \qquad Pos_N \approx \frac{D}{\pi\sqrt{2}}\frac{V_N}{V_{button}}\ \ mm$$

$$for\ V_{button} = Q + jI \qquad Q >> I \quad Q_N << Q \quad I_N >> I$$

$$\varphi_N = atan\frac{I+I_N}{Q+Q_N} \approx \frac{I_N}{Q} = \frac{\sqrt{4}V_N}{4V_{button}} = \frac{V_N}{2V_{button}}\ \ rad$$

$$\frac{180}{\sqrt{2}D}Pos_N \ \ \text{deg}$$

$$\frac{Int_N}{Int_{avg}} = \frac{\sqrt{4}V_N}{4V_{button}} = \frac{\pi}{\sqrt{2}D}Pos_N$$

Fermilab digital receiver	
14	bit ADS6445
12.12	ENOB
-71.2	dbfs SINAD
78.06061	MHz
2	Vpp at input
182	fSec max clock jitter

1.4	db cable loss (125ft LDF1-50)
6	db noise fig
40	db gain at end of cable
37000	Hz BW 4.3 uSec tc
856	samples per measurement
52.14	nVrms ADC equiv error at bpm
403.5	nVrms 4kT equiv noise at bpm
406.9	nVrms total equiv noise at bpm

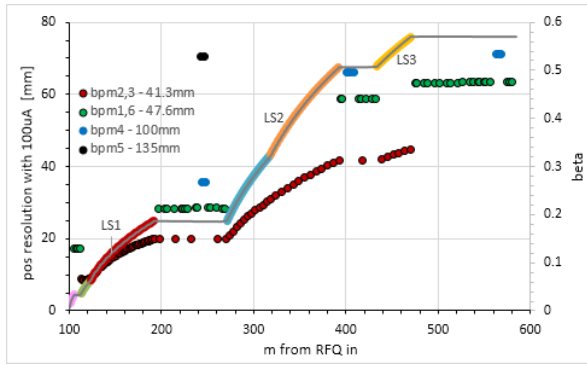


Figure 1: Calculated position resolution for all FRIB BPMs taking into account bandwidth, amplifier gain and noise figure, cable loss, thermal noise, and ADC error.

Figure 1 includes the effect of beam velocity or β in the estimate of image current. For non-relativistic beams, the electric field has an opening angle of about 1/γ. A CST studio model was used to determine the image current for a point charge in a round pipe for various beam velocities, $\sigma_t \approx 0.563D/2\gamma$ as shown in Figs. 2 & 3. [6] For FRIB, the actual bunch length is nearly insignificant for estimating the image current length. The amplitude of the first two rf harmonics, 80.5 and 161MHz are only affected by β in the first 10m of the linac.

A digital receiver with 41.3mm ID BPMs is sufficient to provide the required accuracy and resolution. If necessary, resolution could be improved by limiting the bandwidth at the expense of response time.

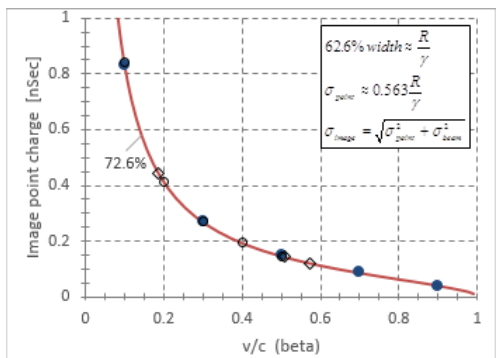


Figure 2: Length of the image current induced by a point charge. CST studio model.

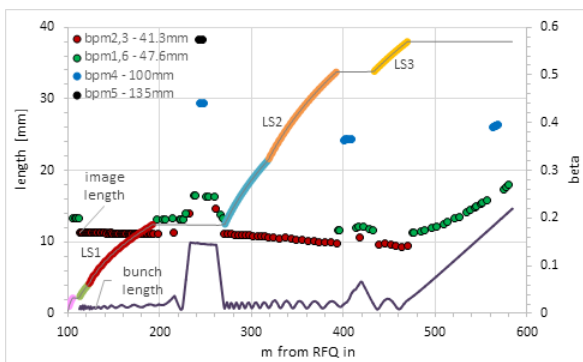


Figure 3: Image current length at all of the FRIB BPMs.

Copyright © 2014 CC-BY-3.0 and by the respective authors

To verify calculation, two prototype BPMs with 35mm aperture and 20mm buttons where installed in ReA3.[7] Fermilab provided digital BPM receivers and interfaced the VME crate running VXWorks to the EPICS control system. Figure 4 shows for each trigger, an array of 2048 measurements each with 37 kHz bandwidth was recorded while beam intensity was scanned from 0.08 µA to 9.6 µA. The standard deviation compares well with the estimate below.

Fermilab digital receiver	1.3 db cable loss (125ft LDF1-50)
14 bit ADS6445	1 db noise fig
12.12 ENOB	81 db gain at end of cable
-71.2 dbfs SINAD	37000 Hz BW 4.3 uSec tc
78.06061 MHz	856 samples per measurement
2 Vpp at input	0.46 nVrms ADC equiv error at bpm
182 fSec max clock jitter	224.3 nVrms 4kT equiv noise at bpm
	224.3 nVrms total equiv noise at bpm

1 uCoul/sec avg Ibeam

161MHz component, error includes cable, amp, thermal & adc noise

	rms bunch lgth				34.9		20 mm dia
beta	MeV/u	rms deg	image mm	uVrms-bpm	um-rms	deg-rms	uA-rms
0.04630	1	7.5	10.5	5.2	336.6	1.23	0.086
0.08006	3	7.5	11.6	4.0	445.9	1.63	0.114

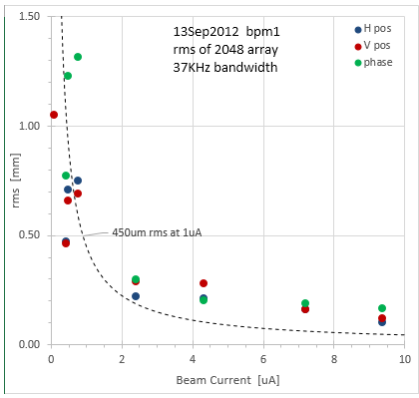


Figure 4: Rms variation in measured beam position in ReA3 for various beam currents. The actual beam measurement matches the estimated value, 450 µm at 1µA.

RESULTS

CST studio was used to evaluate methods to correct linearity as shown in Fig. 5. The polynomial has only odd terms for in axis correction (anti-symmetric) and even terms for the orthogonal axis (symmetric). With polynomial correction the error over 2/3rds of the aperture is 50 µm rms.

$$polynomial \qquad D_{bpm} = 41.3mm \qquad d_{but} = 20mm$$

$$R = \frac{D_{bpm}}{\pi}\frac{a-c}{a+c}$$

$$H_{pos} = p_0 + p_1 R_H + p_3 R_H^3 + p_5 R_H^5 + p_{12} R_H R_V^2 + p_{32} R_H^3 R_V^2$$

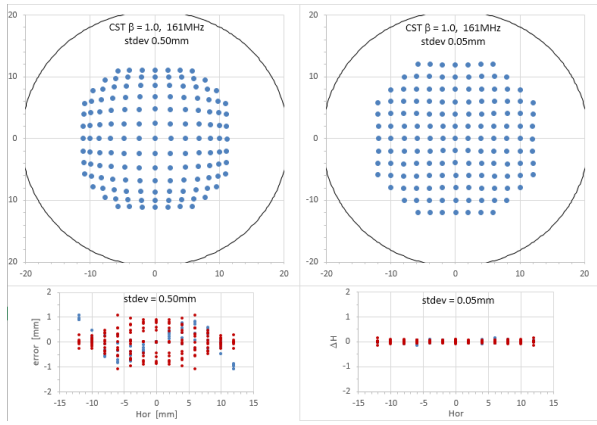


Figure 5: CST studio results with β = 1.0. Linear scaling on left (D/π) and polynomial scaling on the right. The error is shown in the lower plots.

To validate the CST model 3 of the 4 prototype BPMs were scanned with a wire at Fermilab.[8] Using the same polynomial coefficients the error over 2/3rds the aperture was 80 µm rms for all 3 BPMs at both 80.5 and 161MHz. However, the wire measurement sensitivity was 1.8% higher than our CST model. We compared the CST model with β = 1 to the same model but excited with a 1mm wire terminated in 230Ω rather than a particle beam. The model using the wire was 1% higher than with a particle beam as shown in Fig. 6. We believe the 1.8% difference is caused by capacitive coupling to the wire.

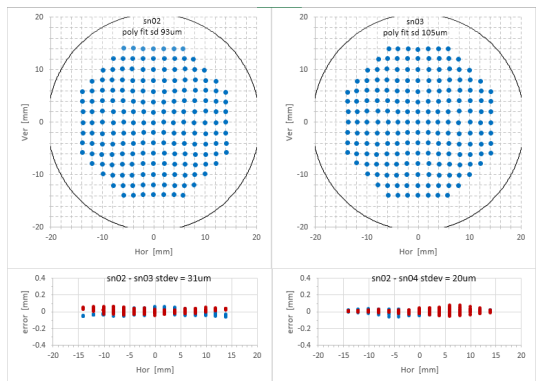


Figure 6: Wire map of sn02 and sn03 BPMs. The rms difference between measured and programmed wire positions is 100 µm. The rms difference between any two wire measurements is less than 50 µm, lower plots.

S One of the acceptance criteria involves measurement of $_{21}$ between all four buttons. The measurement can be compared to a simple electrical model to reveal the coupling capacitance between buttons and the capacitance to ground as shown in Fig. 7. The 3.3 pF to ground and 50Ω load have a corner frequency of 1GHz, well above the 161MHz component used to measure position. The results are kept in the traveler so that the BPM can be evaluated at a later time. We anticipate checking all cold BPMs before sealing the cryomodule.

Copyright © 2014 CC-BY-3.0 and by the respective authors

ISBN 978-3-95450-141-0

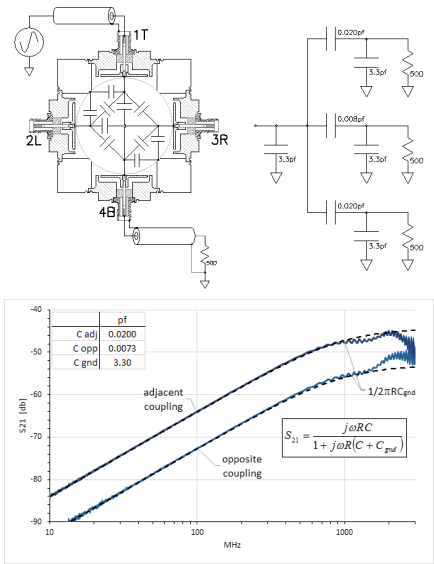


Figure 7: S_{21} measured between buttons to verify capacitance.

EFFECT OF β

With low β, the electric field lines spread out resulting in longer, slower image current, and reduced high frequency content. This effect depends on the proximity to the button and produces a position dependent frequency response. This effect can only be measured with beam or using an electromagnetic field model as β ≈ 1.0 for a signal traveling along a wire. [9]

As shown in Fig. 8 at injection into the FRIB linac, β equals 0.03275 and the measured position would be 50% too large without correction for β shown in Fig. 9 & 10. By the end of the first linac segment, β equals 0.18647 and the effect is only 2%. The effect is linear near the center of the BPM, as shown in Fig. 11 [6][10].

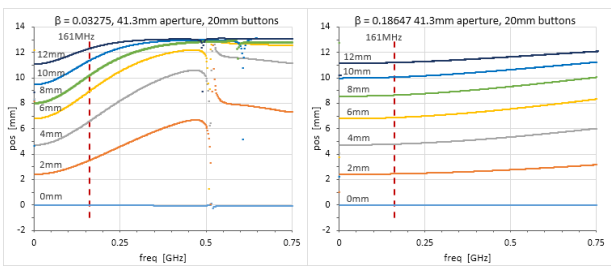


Figure 8: CST calculated position (D/pi)(A-B)/(A+B) versus frequency for β = 0.03275 and 0.18647. At 0.5 GHz the beam flight time and button diameter are ½ period.

$$pos \approx \left(\frac{1}{1+G}\right)\frac{D}{\pi}\frac{A-B}{A+B}$$

$$G = 0.0347\left(\frac{\omega}{\beta c}\frac{D}{\gamma}\right)^2 - 0.00181\left(\frac{\omega}{\beta c}\frac{D}{\gamma}\right)^3$$

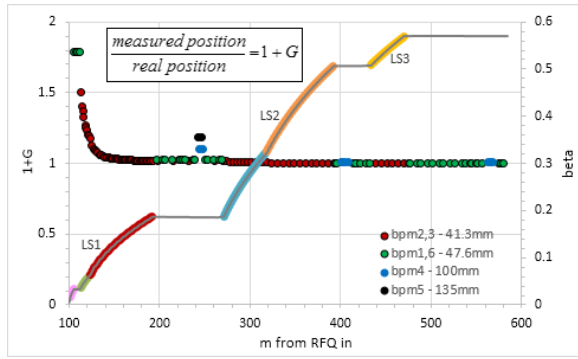


Figure 9: Linear β correction factor for all BPMs in FRIB.

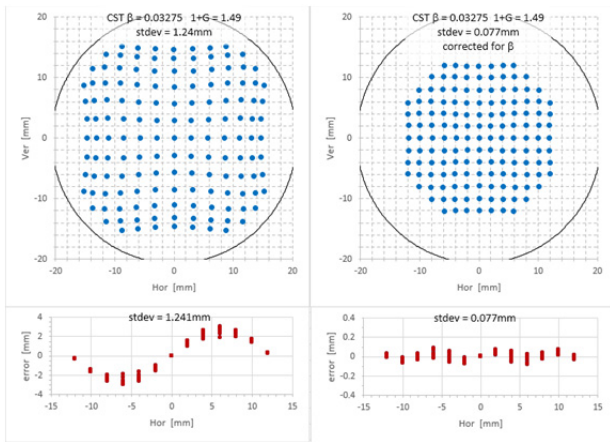


Figure 10: CST model with β = 0.03275. The β = 1 polynomial is used to correct linearity. Plot on right uses a polynomial to correct for β before correcting linearity.

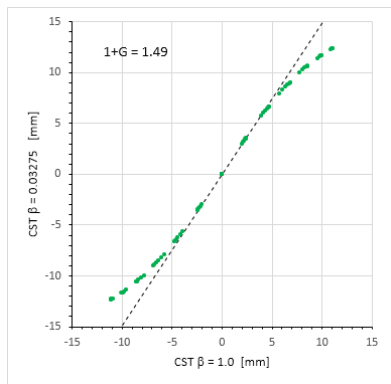


Figure 11: CST model comparing β = 0.03275 and β = 1.

DESIGN DESCRIPTION AND STATUS

The four different BPM designs required for FRIB have nominal apertures of 40, 50, 100, and 150 mm.

40 mm Aperture Design

We moved forward early with the cold 40 mm pick-up design to be prepared to support the cryomodule schedule. The 40 mm aperture BPMs as shown in Fig. 12 include those that will operate at cryogenic temperatures. This design is based on strict cryogenic requirements and interfaces of the device. All stainless steel material will be 316L. The residual magnetic field must be less than 50

Copyright © 2014 CC-BY-3.0 and by the respective authors

mG near the superconducting rf cavities. Four 20 mm SMA buttons are used, one on each face.



Figure 12: 41.3mm ID 20mm diameter button BPM manufactured to FRIB specifications by Solid Sealing Technology.

The axial length is set based on the location of the superconducting cavity and solenoid. Due to a tight clearance between the cavity and solenoid flanges, the BPM needs a bellows to compress roughly .5" for installation. The housing includes a machined flange to avoid extra welds that will throw off the BPM alignment. It will also include through clearance holes that allow for easy installation and cleaning. We will use steel-jacketed SiO_2 cables to connect the BPM to a four-port flange in the vacuum vessel with 50 Ohm feedthroughs with SMA connectors on the vacuum side and N-type connectors airside.

50 mm Aperture Design

The 50 mm design will have a similar housing design to the 40 mm design and the same 20 mm buttons. The only difference will be that the housing grows due to the increase in aperture. Two versions will be installed depending on the mechanical interface to the adjacent beam pipe component, so either a beam pipe or a bellows will be welded to the BPM housing.

100 mm and 150 mm Aperture Design

The 100 mm aperture BPMs are still in the preliminary stages as shown above in Fig. 13 with two different design variations. One possibility is a housing similar to the 40 and 50 mm apertures using 20 mm buttons. These will include a bellows welded to the housing.

The second design variation has an elliptical aperture to match the beam pipe in two locations of the linac with four split plates with two feedthroughs on top and bottom. [4] The two 150 mm BPMs will likely use this design which may be scaled down for the ten 100 mm BPMs.

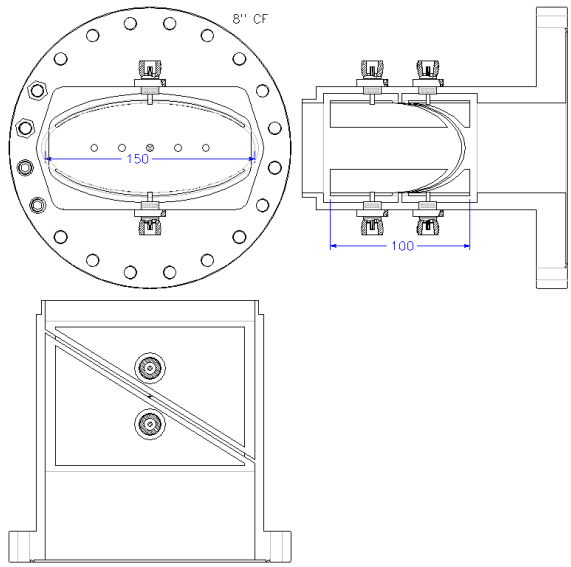


Figure 13: Conceptual design of the 150 mm split plate BPM. Only two are required for FRIB.

NEXT STEPS

Conceptual designs of the 100 and 150 mm BPMs are complete. Discussion with vendors is required to verify practical realization.

SUMMARY

Solid Sealing Technologies (SST) helped design, tolerance, and manufacture BPMs using buttons welded to the BPM body that are clean room compatible with superconducting rf cavities and have less than 50 mG residual magnetic field. First articles received are of excellent quality and consistency.

A consistent 1.8% gain error was measured by comparing BPM wire mapping to CST studio model using a particle beam. The difference was partially understood with a 0.8% difference between CST models with a wire and with a particle beam.

The BPM pick-up design meets the physics and mechanical requirements of FRIB and is well understood. The 20 mm button will be used in 135 of the 147 BPMs required. The models and wire measurements demonstrate that polynomials for correction of geometry and low β provide high accuracy and resolution for position, phase, and beam intensity.

ACKNOWLEDGMENT

We would like to thank Jim Fitzgerald at Fermilab for mapping the BPMs with a wire.

Copyright © 2014 CC-BY-3.0 and by the respective authors

ISBN 978-3-95450-141-0

REFERENCES

[1] B. Durickovic, D. Constan-Wahl, J. Crisp, G. Kiupel, S. Krause, D. Leitner, S. Nash, R. Rencsok, J. Rodriguez, R. Webber, W. Wittmer, "RF Cavity Phase Calibration Using Electromagnetic Pickups", NA-PAC2013 Proc., Pasadena, USA, 1334, (2013).

[2] M. Wendt, "Overview of Recent Trends and Developments for BPM Systems", DIPAC2011 Proc., Hamburg, Germany, 18-22, (2011).

[3] R.E. Shafer, "Beam Position Monitoring", AIP Conf. Proc. 212, 26-58 (1990).

[4] P. Kowina et al.,"Optimisation of 'Shoe-Box Type' Beam Position Monitors Using the Finite Element Methods", DIPAC2005 Proc., Lyon, France, 114-6, (2005).

[5] C. J. Bouwkamp and N. G. De Bruijn, "The Electrostatic Field of a Point Charge Inside a Cylinder, in Connection with Wave Guide Theory", J. Appl. Phys. 18, 562 (1947).

[6] A. Lunin , N. Eddy, T. Khabiboulline, V. Lebedev, V. Yakovlev, "Development of a Low-Beta Button BPM for PXIE Project", IBIC2013 Proc., Oxford, UK, 392-5,(2013).

[7] J. Crisp, D. Constan-Wahl, B. Durickovic, G. Kiupel, S. Krause, D. Leitner, S. Nash, J. A. Rodriguez, T. Russo, R. Webber, W. Wittmer, N. Eddy, C. Briegel, B. Fellenz, D. Slimmer, M. Wendt, "Beam Position and Phase Measurements of Microampere Beams at the Michigan State University ReA3 Facility", NA-PAC2013 Proc., Pasadena, USA, 1187, (2013).

[8] J. Fitzgerald, J. Crisp, E. McCrory; G. Vogel, "BPM testing, analysis, and correction", AIP Conf. Proc. 451(1), 370-7 (1998).

[9] P. Kowina, P. Forck, W. Kaufmann, P. Moritz, F. Wolfheimer, T. Weiland, "FEM Simulations – A Powerful Tool for BPM Design", DIPAC2009 Proc., Basel, Switzerland, 35-7, (2009).

[10] R.E. Shafer, "Beam Position Monitor Sensitivity for Low-β Beams", AIP Conf. Proc. 319, 303-8, (1994);

Copyright © 2014 CC-BY-3.0 and by the respective authors

DEVELOPMENT OF A BUTTON BPM FOR THE LCLS-II PROJECT*

A. Lunin#, T. Khabiboulline, N. Solyak, V. Yakovlev
FNAL, Batavia, IL 60510, USA

Abstract

A high sensitivity button BPM is under development for a linac section of the LCLS-II project. Since the LCLS-II linac will operate with bunch charge as low as 10 pC, we analyse various options for pickup button and feedthrough in order to maximize the BPM output signal at low charge regime. As a result the conceptual BPM design is proposed including an analytical estimation of the BPM performance as well as numerical simulation with CST Particle Studio and ANSYS HFSS. Both numerical methods show a good agreement of BPM output signals for various design parameters. Finally we describe the signal processing scheme and the electronics we are going to use.

INTRODUCTION

Achieving a low beam emittance is one of key factors for reliable operation of the LCLS-II project [1]. In order to preserve a low emittance during beam transportation through the superconducting linac, Beam Position Monitors (BPM) will be installed in every cryomodule with a quadrupole. These BPMs will be used to monitor the beam orbit and provide transverse beam position data for beam steering. Since the "cold" BPMs are the only beam instruments inside the cryogenic sections of the linac, therefore a high reliability of the BPM systems is essential. Some of the specific requirements of the cold BPMs are listed below:

• The space inside the cryomodule for installation is limited to ~180 mm length and ~200 mm transverse size (with feedthrough). The beam pipe aperture is circular, having 78 mm diameter.

• The BPM has to operate under ultra-high vacuum (UHV) conditions, and in a cryogenic environment at a temperature of ~2. 10 K.

• A cleanroom class 100 certification is required to prevent pollution of the nearby SC cavities.

The LCLS-II linac can operate in a variety of regimes with parameters of electron beam shown in Table 1. A single bunch (bunch-by-bunch) resolution of < 100 μm at 10 pC is required to preserve the low emittance by applying dispersion-free orbit correction methods during single short operation. The BPM ability to perform at low charge regimes also allows for troubleshooting and diagnostics during the linac commissioning procedure, but can be guaranteed only nearby (± 1...2 mm) the electrical center of the BPM pickup.

Based on the above requirements the choice of BPM is limited mostly to beam orbit monitoring with button BPM pickups due to its compactness, simple mechanical design and reliability. The large button cold BPM from the European XFEL is an existence proof of a design that has been successfully integrated into a cryomodule [2], which should be able to meet the resolution requirements here, but this has not been demonstrated at the low bunch charge expected and puts much more strenuous requirements on electronics processing scheme.

Table 1: Electron Beam Parameters of the LCLS-II Linac

Operation Mode	CW
Beam Energy	4 GeV
Bunch charge	10 ÷ 300 pC
Bunch length, rms	0.6 ÷ 53 μm
Emittance (at 100 pC, normalized)	~ 0.3 μm
Bunch rate	< 0.93 MHz

Thus, the design of the cold XFEL BPM with large 20 mm diameter buttons was chosen as a prototype pickup for beam diagnostic in the LCLS-II cryomodule [3]. According to the baseline scheme of a signal processing the frontend electronic will downmix the button signal in the pass band around 1 GHz comparing to 1.5 GHz ÷ 2.3 GHz frequency band used for the XFEL cold BPM [4]. Despite the simplicity of a processing scheme at low frequencies there are pro and contra arguments of working around 1 GHz instead of 2 GHz: a) the pickup will produce fewer signals, b) the RF bandpass filters and pickup cables will have smaller losses, c) signal of L-band linac may leak into the BPM [5]. While items a) and b) may compensate each other depending on the actual pickup cable parameters, prevention of effect c) requires that the upper bandwidth should be reduced significantly below 1.3 GHz. This might directly compromise usable signal level and, thus, the position noise. Because the exact relation of position noise versus bandwidth remains to be determined we don't limit ourselves with a design of low frequency button pickup only and propose the optimal geometry of a button and feedthrough assembly for 2 GHz also as a backup option.

GENERAL ASPECTS OF THE BUTTON TYPE PICKUP EM DESIGN

Relativistic charged particles moving inside a hollow metal beam pipe is followed by a pancake like electromagnetic field with longitudinal extension of the bunch size itself. The field on the inner wall of a beam pipe is diffracted on the button gap and induces wakefield travelling in the beam pipe and rf signal radiating through

* Operated by Fermi Research Alliance, LLC under Contract No. De-AC02-07CH11359 with the United States Department of Energy.
#lunin@fnal.gov

Copyright © 2014 CC-BY-3.0 and by the respective authors

ISBN 978-3-95450-141-0

pickup ports. For long or low beta bunches with limited frequency spectrum a simplistic analytical model [6] can be used, while short relativistic require numerical simulations in order to obtain accurate BPM response at frequencies above 1 GHz.

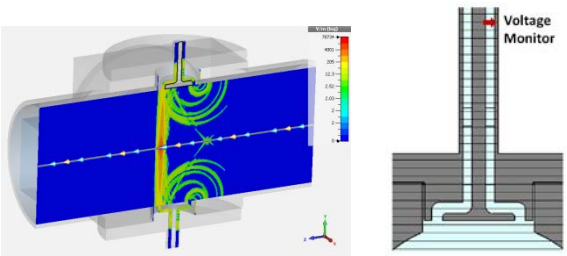


Figure 1: CST model of the button pickup (right) and a snapshot of the instant electric field induced by 1 mm bunch.

We chose the button size of 20 mm diameter with 3 mm gap similar to the cold XFEL BPM design. For numerical simulations we use the time domain CST wakefield solver [7]. The CST 3D model is illustrated in Figure 1 with a snapshot of the instant electric field induced by an interaction of the 1 mm bunch with a button pickup. In order to prevent signal reflections the model has multimode port boundary conditions at the ends of the beam pipe and coaxial lines. The BPM output signal is recorded with voltage monitor defined at the end of coaxial line.

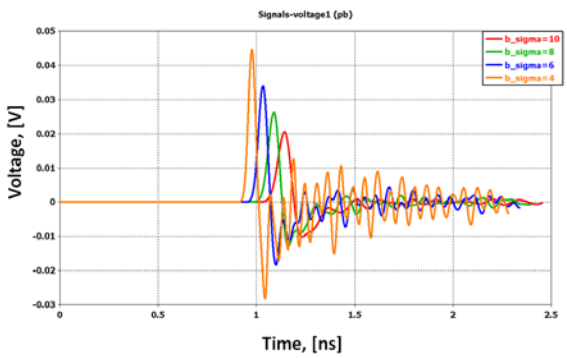


Figure 2: Time domain BPM output signals produced by 1pC bunch with different lengths.

Simulation a response of a short sub-millimeter bunches in time domain requires very dense mesh (> 100M cells) and, thus, results in a long calculation time. Therefore we started with simulation of the BPM response depending on the bunch length for the simple case where the button is loaded to the ideal 50 Ω coaxial line. The result is shown in Figure 2 as BPM output signal versus time. Since the diameter of the output coaxial is small (~ 7÷8 mm), the cutoff frequency of the second propagating mode in the coaxial is above 20 GHz which is higher than simulated bunch bandwidths. Hence, most of the power is radiated through coaxial line as the lowest TEM mode. Therefore one can define the instant power in coaxial as $P_{inst} = U^2/R$, where U is an instant voltage and R is the impedance of coaxial line. Integrating the instant power over the time we obtain the total energy radiated through the pickup port:

$$E_{port} = \int_0^{t_{end}} P_{inst}(t)dt \qquad (1)$$

Based on Eq. 1 we calculated the amount of rf power radiated to all four coaxial port of the pickup depending on a bunch length and compared this value with the total power loss found by the wake loss factor simulation. The result for the maximum bunch charge of 300 pC and 1MHz repetition rate of the LCLS-II linac is illustrated in Figure 3. The dotted blue line corresponds to analytical approximation of the loss factor based on diffraction theory [8]. Only fraction of the total power lost by bunch is radiated to pickup ports. One can extrapolate that this fraction would be below 20÷25 % for the bunch size of tens microns.

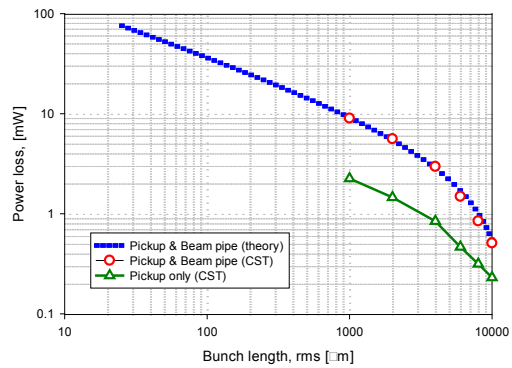


Figure 3: Full (blue and red) and relative (green) power losses generated by the 300 pC and 1MHz pps electron beam passing through the Ø20 mm button BPM.

The FFT transform of a time domain voltage signal *u(t)* preserver the Parsevals identity with omega:

$$\int_{-\infty}^{\infty} |u(t)|^2 dt = \int_{-\infty}^{\infty} |U(\omega)|^2 d\omega \qquad (2)$$

Therefore applying the FFT transformation we can plot the signal energy spectrum density normalized to the total amount of energy radiated through the pickup port (see Figure 4).

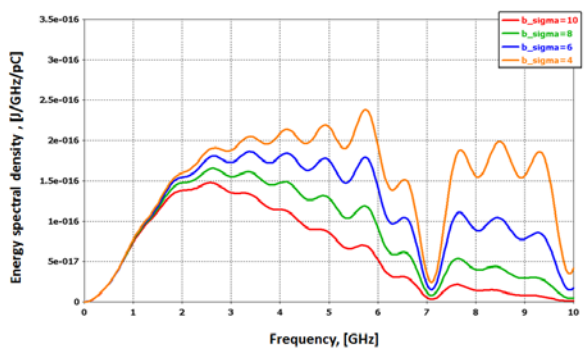


Figure 4: BPM output signals spectral density for various bunch lengths.

Copyright © 2014 CC-BY-3.0 and by the respective authors

One can see that the energy spectral density at low frequencies (< 2 GHz) is weakly dependent on the bunch length. Therefore, we chose the bunch of 4 mm rms size for further analysis as a good compromise between accuracy and a simulation time.

PICKUP RF FEEDTHROUGH OPTIMIZATION

New version of the C100 feedthrough for the 1.3 GHz cavity HOM coupler has been recently redesigned by JLAB in order to meet to the LCLS-II parameters [9]. The feedthrough assembly is shown in Figure 5. This feedthrough meets all UHV and cryogenic requirements and can be easily adapted to the cold button BPM design. Thus, we took it as a prototype for our simulations.

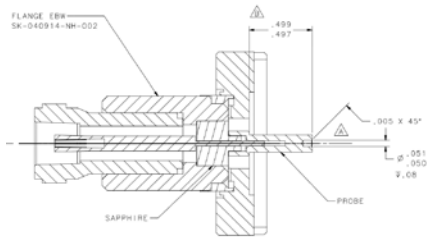


Figure 5: C100 feedthrough for the HOM coupler developed by JLAB.

At first, we analysed the matching of the original JLAB feedthrough. Calculated reflection coefficient is shown in Figure 6 as a red S_{11} curve. The feedthrough demonstrates broadband matching up to about 4 GHz which satisfies the HOM damping goal. Next we modified the original feedthrough for better matching around the 1.1 GHz central frequency in order to improve the BPM performance when a low frequency (~ 1 GHz) signal processing scheme is applied. Blue curve in Figure 6 shows a reflection from the modified feedthrough #1.

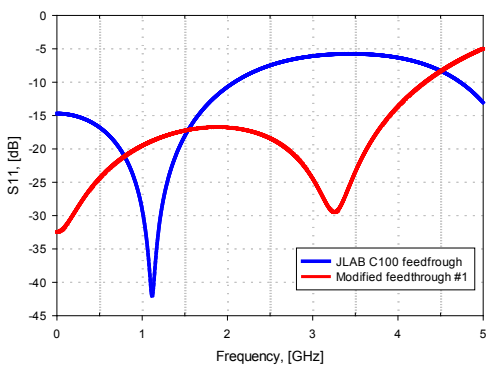


Figure 6: Reflection coefficients of original (red) and modified (blue) JLAB feedthrough.

We used then both variants, original and modified #1, of vacuum rf feedthroughs for ultimate CST time domain simulation of BPM output signals. The simulation results are presented in Figure 7 in forms of signal spectral densities. The spectral density of the BPM signal produced by button loaded to the ideal 50 Ω coaxial line is shown as green curve for the comparison. One can see that the spectral density is almost flat for this case while signals passed through feedthroughs with ceramic window contain quite broadband and low-Q resonances resulting local gain of the spectral density. This effect can be explained by the signal reflections introduced by the ceramic window, which travel back and forth between window and button and, hence, creating a local standing wave. While it difficult to form such a resonance at low frequencies around 1 GHz, it looks feasible to do it at frequency of 2 GHz. For verification we modified the C100 feedthrough again and used ANSYS HFSS eigenmode solver for finding optimal feedthrough geometry [10]. Figure 8 illustrates the final result of optimization, a low-Q resonance at 2 GHz frequency.

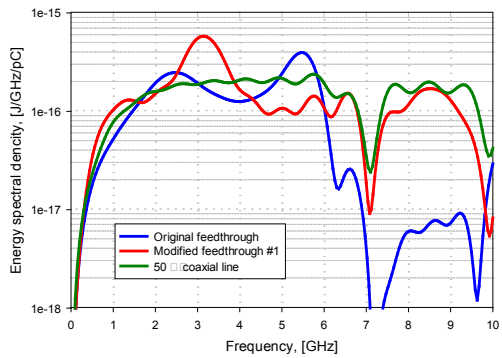


Figure 7: BPM signal spectral density for original (blue) and modified (red) ceramic feedthrough and for the ideal 50 Ω line (green).

Graphic visualisations of proposed feedthrough modifications #1 and #2 are presented in Figure 9. Finally we performed the BPM simulation with the feedthrough #2 attached and compared results obtained for the feedthrough #1. The time domain signals and their spectral densities are shown in Figure 10 and 11 respectively.

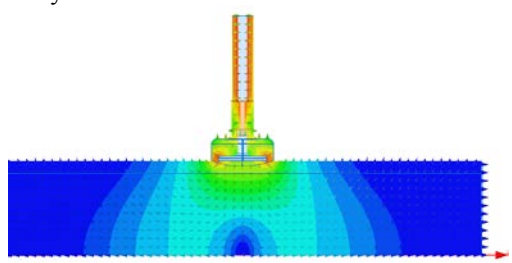


Figure 8: Low-Q resonance of button and modified feedthrough #2 at frequency of 2 GHz.

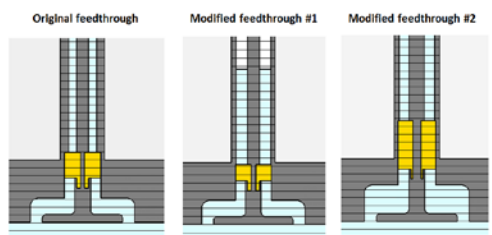


Figure 9: CST models of various ceramic feedthroughs with attached Ø20 mm button used for BPM simulations.

Copyright © 2014 CC-BY-3.0 and by the respective authors

ISBN 978-3-95450-141-0

Based on results of BPM signal spectral densities simulation it is possible to estimate particular amounts of energy captured by the readout electronics in given frequency bandwidth. Integrated pulse energies at the pickup coaxial output are summarized in the Table 2 for 10 pC bunch charge.

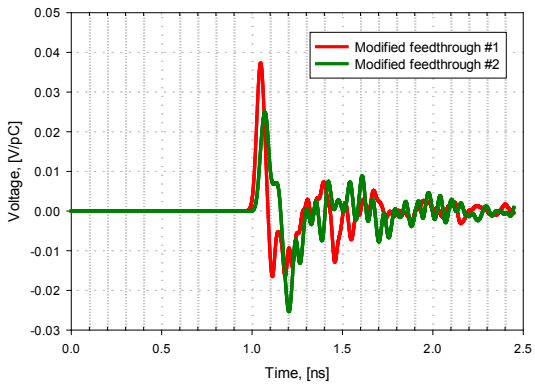


Figure 10: Time domain signals of the button BPM with modified feedthrough #1 and #2.

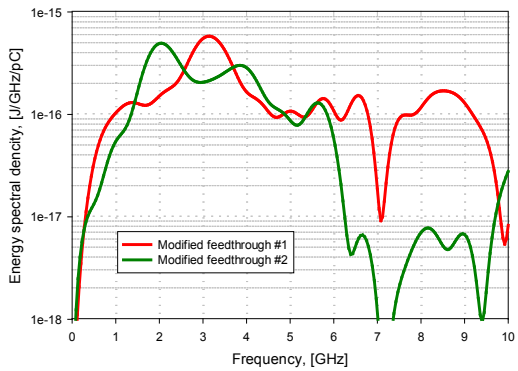


Figure 11: Signal spectral densities of the button BPM with modified feedthrough #1 and #2.

Table 2 Pulse Energy for 10 pC Bunch at Pickup Output

Feedthrough Type	Captured pulse energy, [fJ]	
	Frequency range 0÷1.3 GHz	Frequency range 1.5÷2.3 GHz
Original C100	4	13
Modified #1	8	12
Modified #2	4	35

Further detailed study of BPM signal transmission and processing, including losses in rf cables and readout electronics performance, is needed in order to estimate the feasibility to have the BPM signal noise below the LCLS-II requirements for low charge single bunch resolution.

READOUT ELECTRONICS

The standard BPM readout electronics for LCLS II will measure position, intensity, and phase using direct digital down-conversion scheme at ~ 1 GHz button signal. A simplified block diagram is shown in Figure 12. A 2D polynomial fit to the difference over sum in each plane will be used to correct position and intensity for nonlinearities in the button pickup shown here.

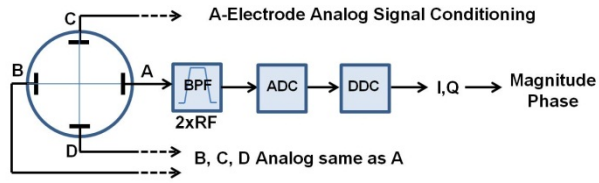


Figure 12: Block diagram for BPM electronics.

The high performance signal processing scheme used by XFEL is a backup option depending on actual configuration of connecting cables and operating of electronics frontend.

SUMMARY

A button-type BPM will be used in the LCLS II cryomodule. We presented two possible conceptual BPM designs based on the C100 HOM feedthrough developed at JLAB and optimized for signal processing at 1 GHz and 2 GHz passbands respectively. Further evaluation of BPM signal transmission and readout electronics performance is needed in order to make a final decision and meet the LCLS-II requirements for low charge single bunch position resolution.

ACKNOWLEDGEMENT

The author would like to thank Daniel Treyer (PSI) and Dirk Lipka (DESY) for useful discussion and comments.

REFERENCES

[1] LCLS-II Conceptual Design Report, SLAC Report, LCLSII-1.1-DR-0001-R0, 2014.
[2] D. Lipka et al., "Button BPM Development for the European XFEL", MOPD19, DIPAC2011, Hamburg, Germany, 2011.
[3] J. Frisch et al., "Electron Beam Diagnostics and Feedback for the LCLS-II", THB04, Proceedings of FEL2014, Basel, Switzerland, 2014.
[4] D.M. Treyer et al., "Design and Beam Test Results of Button BPMs for the European XFEL" DESY Report DESY-2041-01447, 2013.
[5] D.M. Treyer, PSI, private communications.
[6] A. Lunin et al., "Development of a Low-Beta Button BPM for PXIE Project", TUPC14, IBIC2013, Oxford, UK, 2013.
[7] www.cst.com
[8] K. Bane, "Wakefields of Very Short Bunches in an Accelerating Cavity", SLAC-PUB-4441, 1987.
[9] N. Huque and E. Daly, "C100 HOM Feedthru Modification for LCLS-II", JLAB Internal Report, 2014.
[10] www.ansys.com

Copyright © 2014 CC-BY-3.0 and by the respective authors

BEAM POSITION MONITOR ELECTRONICS UPGRADE FOR FERMILAB SWITCHYARD*

P.Stabile#, J. S. Diamond, J.A. Fitzgerald, N. Liu, D. K. Morris, P. S. Prieto, J. P. Seraphin
FERMILAB, Batavia, IL, 60510, USA

Abstract

The beam position monitor (BPM) system for Fermilab Switchyard (SY) provides the position, intensity and integrated intensity of the 53.10348MHz RF bunched resonant extracted beam from the Main Injector over 4 seconds of spill. The total beam intensity varies from $1x10^{11}$ to $1x10^{13}$ protons.

The spill is measured by stripline beam postion monitors and resonant circuit. The BPMs have an external resonant circuit tuned to 53.10348MHz.

The corresponding voltage signal out of the BPM has been estimated to be between -110dBm and -80dBm.

INTRODUCTION

During current operation the Main Injector accelerates beam to 120Gev and extracted to the Switchyard (SY). Beam is extracted at the MI52 area, transported through P1, P2 and P3 beam lines, and then steered to the original Switchyard beam line where it traverses Enclosures B, C and the F-manholes, finally arriving to the Target [1].

Extraction is implemented by the half-resonant integer mode and is regulated by a quadrupole circuit (QXR) to resonantly extract beam over 4 seconds.

The typical spill intensities vary from $1x10^{11}$ protons to $1x10^{13}$ protons per machine cycle with the protons distributed into 486 of the 588 53.10348MHz RF buckets that make up the machine's circumference. Extracting $1x10^{13}$ protons over 4 sec accounts for $2.5x10^{12}$ protons per second (pps). With a revolution frequency of the machine equal to 90.312KHz (53.10348MHz/588), a total of $27.68x10^{6}$ protons are extracted per turn ($2.5x10^{12}$pps/90.312KHz). Dividing the number of protons per turn by the number of buckets a total of $56.95x10^{3}$ protons per bunch can be estimated. Extracting $1x10^{12}$, using the same calculations, accounts for $5.695x10^{3}$ protons per bunch

SYSTEM DESCRIPTION

The stripline BPMs have a pair of detector plates, facing each other inside the beam pipe.

The plate capacitances are equal to 65pF and the plate-to-plate capacitance is 8pF.

In order to resonate at the desired extraction frequency three inductors were added to the circuit (Figure 1) [2].

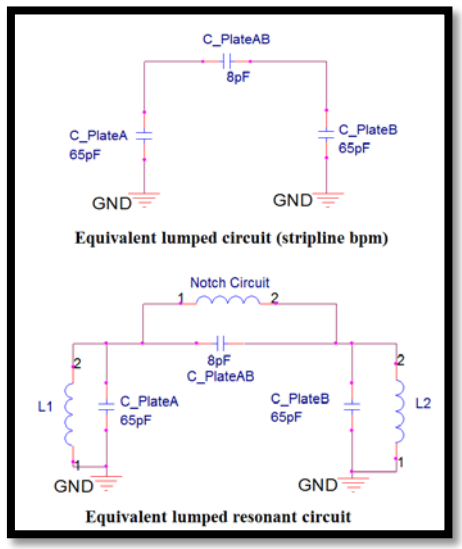


Figure 1: Equivalent circuit for resonant BPM.

During extraction the particle beam can be considered as a current generator at 53.10348MHz (flat top extraction frequency). The signal power detected by the position detector can therefore be increased by raising the detector shunt impedance for the Fourier components of beam current that are chosen (for simplicity the detector is tuned for the n=1 Fourier component).

The detectors are tuned to resonate at the RF frequency of 53.10348 MHz, with a resulting increase of detector shunt impedance from 50Ω to 9.5 KΩ and a Q of around 190.

The original beam position monitor system for the SY was first designed in 1985 [3] and then installed in 1986.

The new designed electronic system consists of:

1. Detectors (Resonant BPMs).
2. RF Transition Board (Analog Front-End).
3. Digitizer (Digital Acquisition and Processing).
4. MVME 5500 Single Board Computer (Software interface).

Figure 2 shows a block diagram of the SY electronic system.

* This work was supported by the U.S. Department of Energy under contract No. DE-AC02-07CH11359.

stabile@fnal.gov

Copyright © 2014 CC-BY-3.0 and by the respective authors

ISBN 978-3-95450-141-0

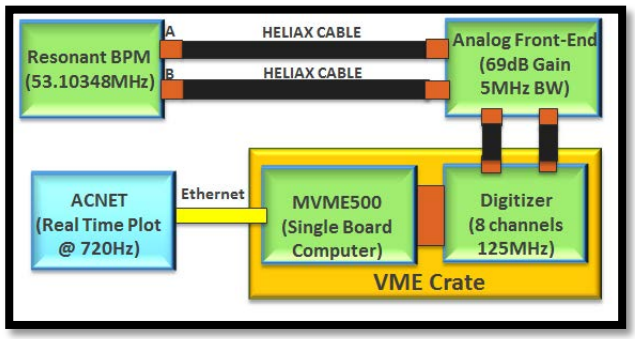


Figure 2: SY electronics schematic block.

Resonant BPMs

Two different types of resonant BPMs [4] are installed in the beam line:

- A short beam detector (7" plate length, $< \lambda/4$).
- A long detector (1 meter plate length, $\lambda/4$).

Figure 3 and Figure 4 show a view of the short type.

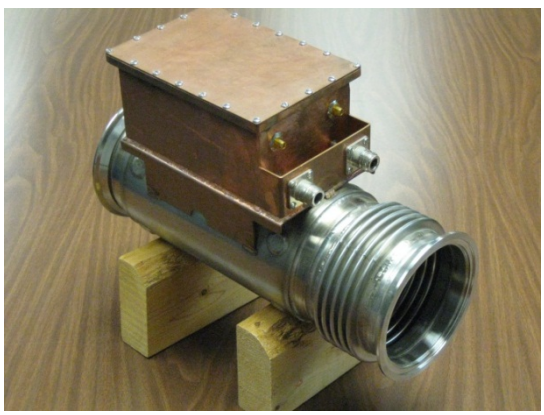


Figure 3: Short BPM detector (1).



Figure 4: Short BPM detector (2).

The detector body, or beam pipe, is schedule 40 304 stainless pipe of 4.056" I.D. The curved detector plates are copper, supported off the pipe bore by G-10 spacers.

A shorted coax hardline $< \lambda/4$ long is used in the 1 meter detector. In the short detectors, where much more inductance is needed in a limited space, the inductor has been built using a supported copper single-layer solenoid.

Referring to BPM design notes [5] and considering the cylindrical geometry of the detectors, the first harmonic of the output voltage, per electrode, for a centred beam is given by:

$$V_1 = 2.41\times10^{-10} N_p vrms \quad (1)$$

N_p is the number of protons per bunch. The sensitivity of the BPMs is calculated to be:

$$\left(\frac{V_a}{V_b}\right)_{dB} = 0.67x \quad (2)$$

Where x is the distance the beam is displaced from the detector canter. Actual wire measurements show the sensitivity to be between 0.57dB/mm and 0.63dB/mm.

Analog Front-End

The analog front-end is composed by a RF analog board using a cascade of three RF low noise amplifier (total gain of 69dB). Due to the low signal to noise ratio (SNR~12dB) the noise figure of the amplifiers is a key parameter in the design. The amplifier chosen for this application reports by datasheet a noise figure of 0.7dB. A 53.10348MHz band pass filter with a 5MHz bandwidth has been added to the signal path to improve the SNR.

Since the bunch charge range is between $56.95\text{x}10^3$ and $5.59\text{x}10^3$ protons, the voltage range at the analog front-end input can be estimated to be between $13.72\mu V_{rms}$ (-84dBm) and $1.38\mu V_{rms}$ (-106dBm) per plate per bunch. To connect the BPM plates to the analog front-end ½' heliax cables are used.

A prototype of the analog board amplifying the resonant BPM signal is currently being used to measure the intensity and the position of the beam extracted from the Main Injector.

A new transition board is being layed-out. While the current board reads only one BPM, the new one will be able read the signal from 4 BPMs at the same time (8 analog channels). A 6-bit digital attenuator is added to the signal path to compensate differences between channels

The new design will also include a communication interface between the analog board and the crate controller processor using a CAN bus interface.

Digital Acquisition and Processing

A digitizer (8 channel, 125MHz, designed at Fermilab) acquires the output signal of the analog front-end.

The signal is first sampled at 122.162935MHz (~2.3 times the fundamental frequency of the beam signal) through a 14 bit ADC and then scaled to 16 bits. The

Copyright © 2014 CC-BY-3.0 and by the respective authors

data is then down converted to base band and digitally filtered obtaining the in phase (I) and in quadrature (Q) components (Figure 5). The total pass/stop band of the filter has been designed to be 2KHz/5KHz.

The digital processing architecture is composed by:

- NCO: 32bits, center frequency 53.10348MHz
- Scale Register on 8 bit
- CIC: Decimation by 2048;
- CFIR: 24 Taps, Decimation by 2, Pass band 4KHz, Stop Band 10KHz;
- PFIR: 32 Taps, Decimation by 2, Pass band 2KHz, Stop Band 5KHz;
- 3 Gain blocks;

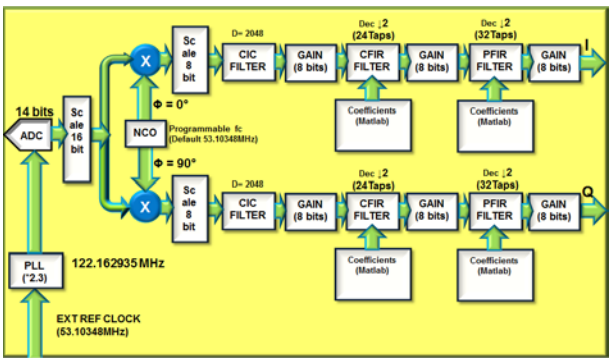


Figure 5: Digital Signal Processing Block diagram 1.

Figure 6 shows a block diagram of the data processing following the signal processing.

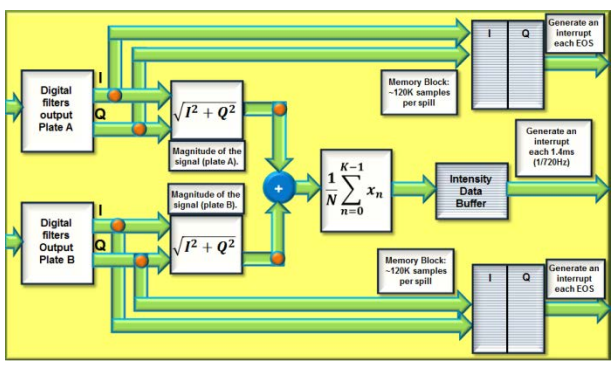


Figure 6: Digital Signal Processing Block diagram 2.

The throughput of the I and Q generated for each of the two plates of the BPM is 14912K samp/sec. The digitizer board saves I and Q data in a memory buffer and makes them available to be copied and stored in a database by the firmware. The data is automatically overwritten at the next extraction cycle. The calculated square root of sum of squares of I and Q data for each BPM is averaged (N=18) and then saved in a buffer accessible by the main processor. The final update rate to plot is in real time with intensity and position data fixed to 720Hz.

The digital filtering and signal processing is the biggest improvement of the new system over the the old one. A desired signal bandwidth can be re-programmed and modified simply re-loading the FPGA firmware and the intensity and position can be plotted in “real time” during the extraction.

Software Interface

One or more digitizers exist in a VME crate with an MVME 5500 Single Board Computer (SBC) running custom software and a Fermilab built clock decoder. To the Fermilab accelerator controls system (ACNET) this collection of hardware and software is known as a "front-end". Several front-ends are required to accommodate a large number of BPMs dispersed over the SY beam line. The front-end computer runs the VxWorks real-time operating system, which is common practice for data acquisition applications at Fermilab. An effort is underway to port the front-end software to Linux.

The primary responsibility of the front-end software is to arm the digitizers before the slow spill begins then read down-converted samples from the digitizers, calculate positions and present them to the control system. Several graphical applications already exist that the user can utilize to display, log and analyze data once it is has been captured by the front-end. Real-time plotting of position and intensity is provided by averaging every 18 down converted samples to match the capability of the control system (720Hz). The full 4 seconds of down converted samples are collected in the digitizer's memory during the slow spill. After the end-of-beam event all of the samples collected from the digitizers in the front end are transferred to the computer's memory and can then be saved to a file or downloaded via the control system for analysis.

RESULTS

Figure 7 shows the measured beam being extracted (I:702RI) by one the 4 BPMs installed in the P1 line compared to the amount of beam extracted (I:BEAM).

A total efficiency of 93%, I:702EFF (I:702RI/I:BEAM21) for the Main Injector extraction has been measured during spill.

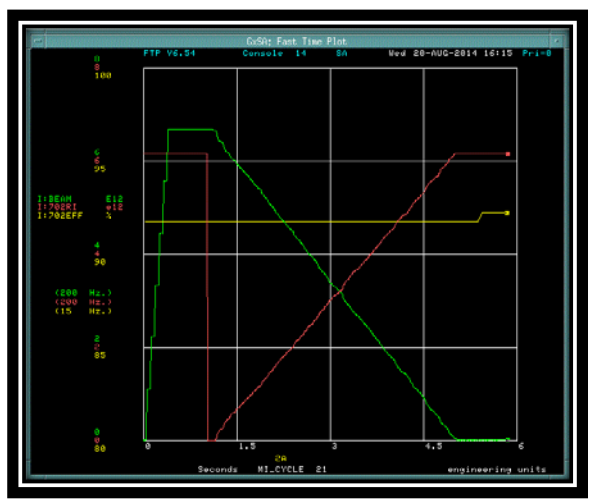


Figure 7: Beam extraction intensity measurement.

Copyright © 2014 CC-BY-3.0 and by the respective authors

ISBN 978-3-95450-141-0

More tests were run to characterize the resolution of the BPMs. In Figure 8 one of these tests is shown. The total beam intensity in the machine was equal to 5.48e12 and, at the end of the spill, 1.31e11 protons (2.4% of the total beam) were sent to the abort line. A drop of 2% in efficiency was recorded by the intensity monitor.

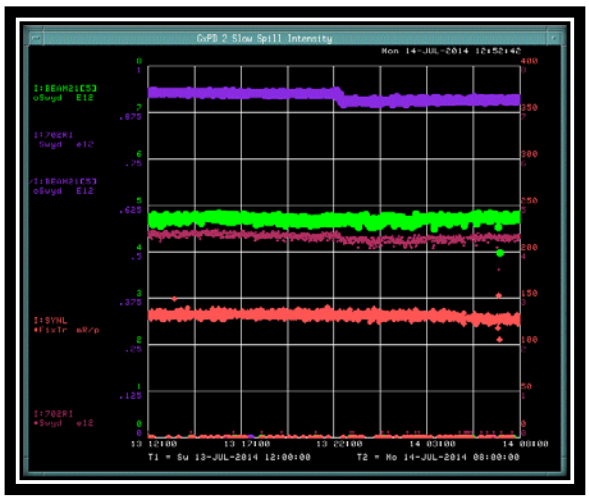


Figure 8: Spill efficiency drop of 2%.

The error in resolution is around 0.4 to 0.5% for the intensity measurements.

Figure 9 shows a sweep in the percentage of beam extracted. I:TORO03 is the amount of the beam going to the abort line and I:702RI is the intensity measured.

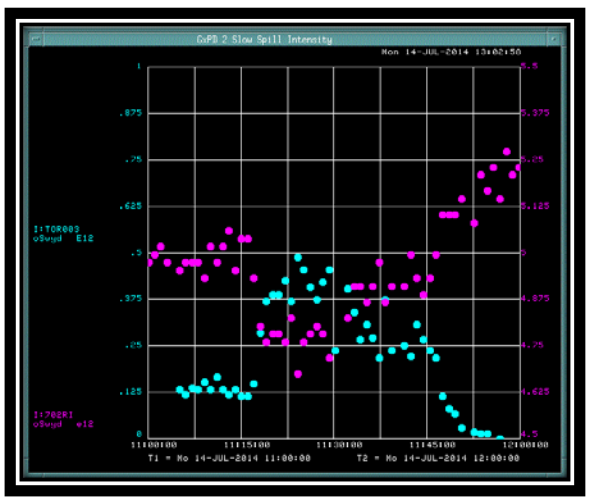


Figure 9: Beam extracted vs Beam going to the abort line.

To verify the validity of the position recorded by the BPM, a multiwire has been placed in the beam line to compare the results. In Figure 10 the comparison between two vertical BPMs (702 and 714) and the multiwire is shown.

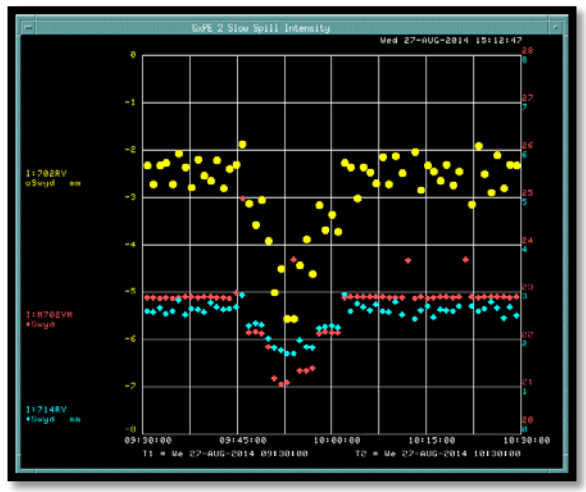


Figure 10: Multiwire vs BPMs vertical position comparison.

During these measurements the vertical beam position was deflected. The results show how both vertical BPMs follow the variation in position of the beam and how these results match with the results from the multiwire.

CONCLUSION

An upgrade of the old SY electronics system has been prototyped and tested. Results show a resolution for the intensity measurement around 0.4/0.5%. The resonant BPM have been proven also good results in position measurement. A new prototype to improve the performances of the system is currently at the layout stage and is expected to be ready for the coming fall.

ACKNOWLEDGMENT

The authors would like to acknowledge all of the Instrumentation and Main Injector group for their support with this work.

REFERENCES

[1] Switchyard Rookie Book “Fermilab Doc BD version 3.3”.

[2] Q, Kerns et.al., Tuned Beam Position Detectors 1987 Particle Accelerator Conference Session T47, and for his hours on RF theory and techniques.

[3] R. Fuja et. al., Electronics Design for the Fermilab Switchyard beam Position Monitor System Session T21

[4] R. Shafer et. al., Fermilab Energy Doubler Beam Position Detector, IEEE Transactions on Nuclear Science, Vo. NS-28, No. 3, June 1981, pp. 2290-2292.

[5] R. Shafer “BPM Notes” and discussion, guidance and patience.

Copyright © 2014 CC-BY-3.0 and by the respective authors

NSLS2 VISIBLE SYNCHROTRON LIGHT MONITOR DIAGNOSTIC BEAMLINE COMMISSIONING*

W. Cheng#, B. Bacha, H. Xu, Y. Hu, O. Singh
NSLS-II, Brookhaven National Laboratory, Upton, NY 11973

Abstract

Visible Synchrotron Light Monitor (SLM) beamline has been designed and constructed at NSLS2 storage ring, to characterize the electron beam profile at various machine conditions. Due to careful alignment, SLM beamline was able to see the first light even before beam circulating the ring. Besides a normal CCD camera to monitor the beam profile, streak camera and gated camera are used to measure the longitudinal and transverse profile to understand the beam dynamics. Measurement results from these cameras will be present in this paper.

INTRODUCTION

NSLS2 is a third generation light source at Brookhaven National Laboratory. The 3GeV low emittance storage ring has been commissioned with beam recently. Average current of 50mA beam was able to be stored in the ring with superconducting RF cavity [1]. While electrons pass through the bending magnet, broadband synchrotron radiation will be generated. This can be used to measure the transverse and longitudinal profile.

Visible synchrotron light monitor (SLM) diagnostic beamline utilizes the radiation from C30 BM-B, which is the second dipole after injection straight. Nominal source point is ~2.75mrad into the dipole. The beamline has acceptance of +/-1.5mrad horizontal and +/-3.5mrad vertical. Visible light from the dipole synchrotron radiation will be reflected by in-vacuum mirror. The visible light is guided into SLM hutch located on the C30 experimental floor. There are various optics setups on the 4'x10' optical table, currently there are three branches setups: CCD camera branch; fast gated camera branch and streak camera branch. Visible light can be guided to different cameras. More information on the diagnostic beamline design can be found at [2].

Figure 1 shows the installed beamline and optical table setups. Radiations from the dipole pass through the fixed aperture, which defines the source point and horizontal/vertical apertures. Upstream of the fixed mask are vacuum gate valve (GV) and bending magnet photon shutter (BMPS). These two components are standard for NSLS2 beamlines which can be used to shut down the photon whenever needed. Most high energy photons are blocked by the thin absorber called "cold finger". The cold finger has vertical aperture of +/-0.5 mrad. Most of the power will be blocked by the cold finger so that downstream first mirror sees less than 1W of power at 500mA. The cold finger is controlled through a linear motor and stage. It can be fully retracted or tracking the electron beam position with 10um resolution. In vacuum first mirror reflect the visible (and near infrared) light 90 degree out of the vacuum window. The mirror was made from Glidcop with Aluminum coating. Both first mirror and vacuum window have flatness better than 50nm, which is about 1/10 of interesting wavelength. Visible light is then reflected by three 6'' diameter in air mirrors on to the experiment floor, where a dark room and 4'x10' optical table are located. Synchrotron light first gets focused on the optical table with 6'' achromatic lens. Focal length of the lens is 2.25 m. Light is then guided to different cameras using beam splitter and reflection mirrors.

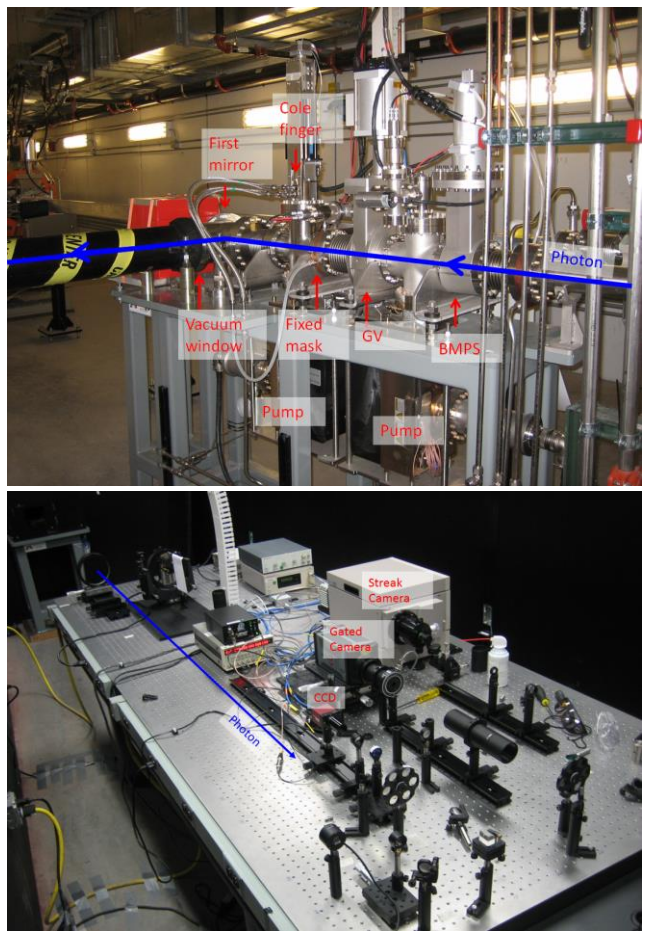


Figure 1: (top) Installed visible synchrotron light monitor (SLM) beamline components inside the NSLS2 storage ring tunnel; (bottom) Optical table setup in the SLM hutch.

* This material is based upon work supported by the U.S. Department of Energy, Office of Science, Brookhaven National Laboratory under Contract No. DE-AC02-98CH10886.
#chengwx@bnl.gov

Copyright © 2014 CC-BY-3.0 and by the respective authors

ISBN 978-3-95450-141-0

FIRST LIGHT

During installation of the visible SLM beamline, precise laser alignment was carried out to align the mirror. The laser was shot backward from the optical table to align the light to source point. First light was observed in the SLM hutch at the very early stage of storage ring commissioning. Figure 2 shows the first synchrotron light on NSLS2 experimental floor captured on Apr-02. Electron beam was going around the ring for about 1 turn. The CCD the camera was able to see synchrotron light radiated from the first turn. The camera trigger was synchronized triggered with injection kickers trigger. 4x4 binning helped to improve signal noise ratio. Injection charge reading was about 1nC at BtS ICT2, right before the storage ring injection straight. The image was not focused. That's why two bright spots appears on the image, dark band in the middle is the cold finger shadow. Fine optics adjustment was carried out once the hutch was granted safe to access.

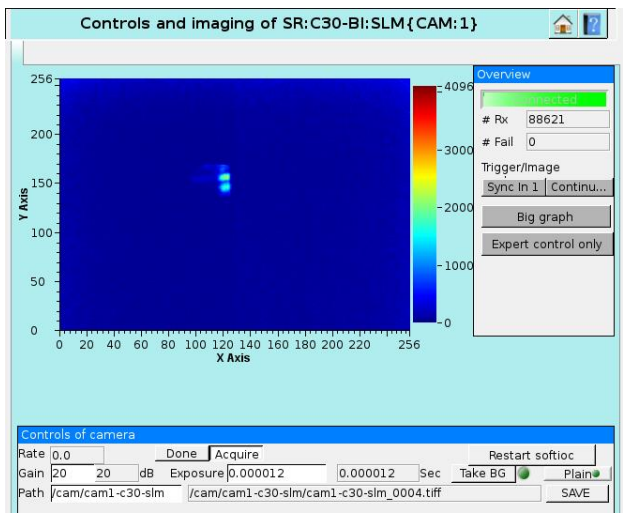


Figure 2: First light observed in the SLM hutch, Apr-02-2014. Beam was circulating the ring 1-2 turns.

TRANSVERSE PROFILE

Once beam was stored in the ring and fault studies showed no radiation hazard in the SLM hutch, fine optics adjustment was able to be carried out. Figure 3 shows a CCD image screenshot at 1.5mA stored beam.

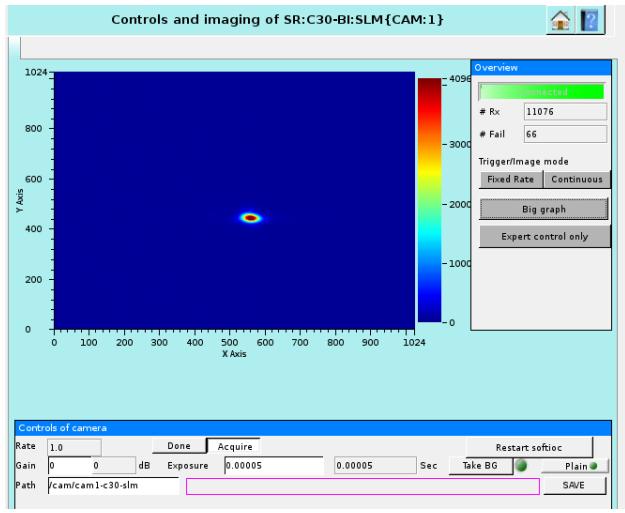


Figure 3: CCD camera image with 1.5mA stored beam.

Optics (de)magnification factor was calibrated by creating a parallel local bump near the SLM source point, while detecting how many pixels moved on the CCD image centroid. Local bump height were recorded from nearby BPMs and calculated based on distance of BPMs to source point. Horizontal local bump calibration results are shown in Fig. 4. Fitting the slope, one gets ~8 um/pixel which means 1 pixel on the CCD is corresponding to 8um at the source point. Vertical local bump calibration gave the same slope.

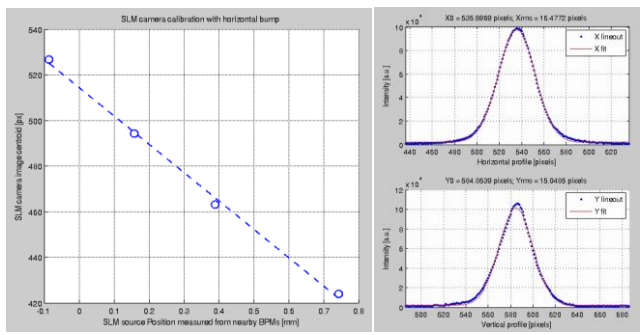


Figure 4: (Left) Visible SLM CCD camera calibration using local bump near the source point. (Right) Gaussian fitting of CCD measured profile.

CCD measured profile can be fitted to Gaussian distribution. Based on the above calibration, beam sizes at the source point can be measured. Right plot in the figure gives an example of Gaussian fitting. Horizontal beam size was fitted to be ~ 15.5 pixels, which was corresponding to 124 um at the SLM source point. Vertical beam size was not able to be measured using visible light due to diffraction limit. It can be measured with x-ray diagnostic beamline which will be commissioned shortly.

Copyright © 2014 CC-BY-3.0 and by the respective authors

ISBN 978-3-95450-141-0

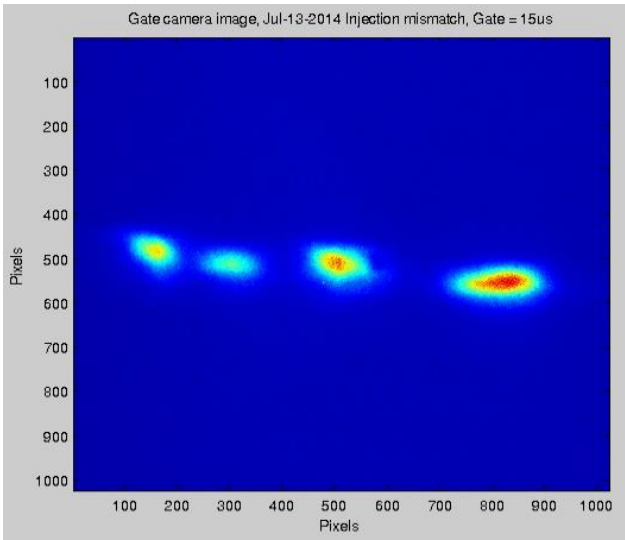


Figure 5: First several turns profile captured using gated camera after injection kicker.

Gated camera has been preliminary tested. The camera has minimum gate width of 3ns and repetition rate up to 1MHz. It's possible to capture NSLS2 storage ring single bunch profile in consecutive turns. Figure 5 shows first 4-5 turns profile captured using gated camera. Beam was kicked with mis-matched injection kickers. Camera was trigger synchronized with injection kickers and the gate width was set to 15us.

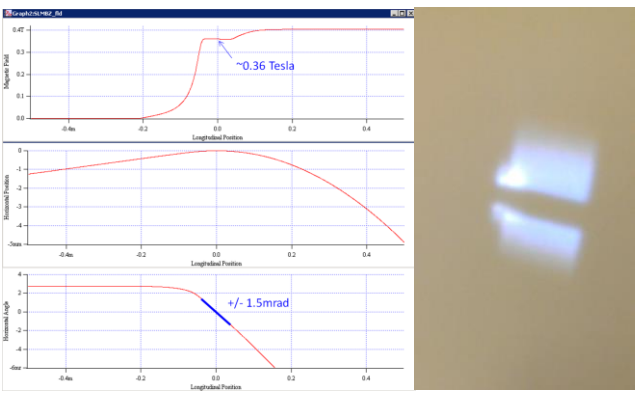


Figure 6: (Left) Magnetic field and beam trajectory near the SLM source point. (Right) Unfocused beam light image.

SLM beamline source point is in the dipole edge field. It was a concern of seeing edge radiation. SRW tracking was carried out during design stage and it was confirmed that the beamline will accept edge radiation in the visible light range. Shown in Fig 6 are the dipole field and beam trajectory near the SLM source point. Nominal SLM source point of 2.75mrad into the dipole will see magnetic field of 0.36 Tesla. Horizontal opening of +/-1.5mrad of the beamline will accept light mostly from the plateau. For the NSLS-II storage ring bending magnet radius R = 25m; detecting wavelength λ = 500nm; synchrotron radiation natural open angle $\theta_{SR} \sim 0.45(\lambda/R)^{1/3}$ = 1.2 mrad. It's no surprise that edge radiations from this dipole and the upstream dipole will be seen. With stored beam we have noticed bright spots on the unfocused profile. Figure 6 right side image shows the unfocused light in the SLM hutch. Left side bright images are likely coming from the dipole edge field radiation.

LONGITUDINAL PROFILE

Streak camera has been used for longitudinal profile measurements. The camera is Hamamatsu C5680 with 2ps resolution, it includes synchroscan and dual sweep modules. Synchroscan frequency is at 125MHz, which is 1/4 of NSLS2 storage ring RF frequency. The sweeping clock signal is getting from master oscillator through long Heliax cables. Phase jitter of the clock signal was measured to be less than 1ps.

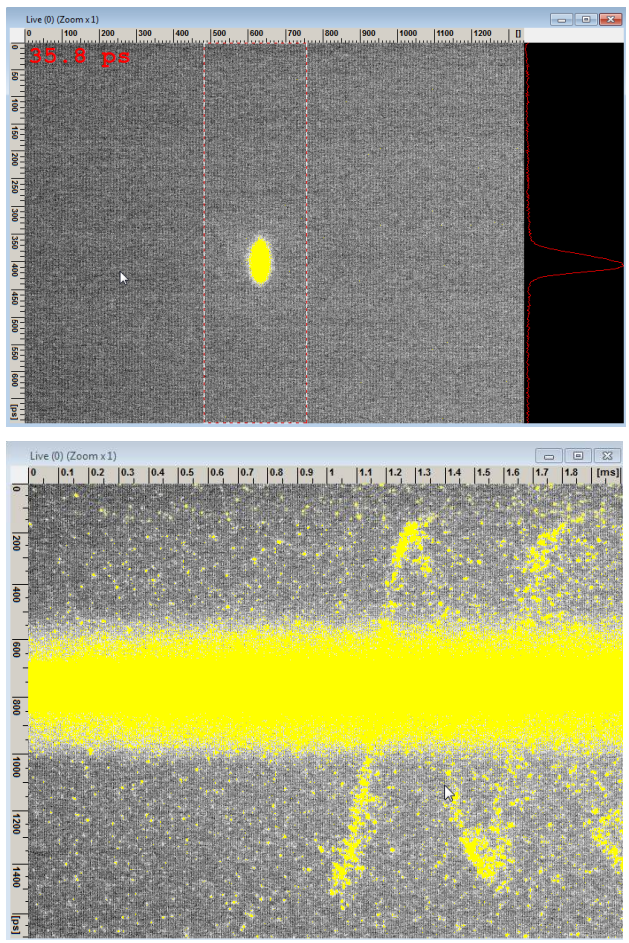


Figure 7: (Top) Streak camera image in synchroscan mode, 0.22mA single bunch was stored in the ring. (Bottom) Streak camera image in dual sweep mode, one can see injection beam came with phase mis-match.

Figure 7 images were two typical streak camera snapshots. The top one was in synchroscan mode. Beam was stored at ~0.22mA in single bunch. In dual sweep mode, as seen in the bottom snapshot, the camera was external triggered with injection signal. There were stored beam and injecting beam came in with phase mis-match. Injected beam was doing synchrotron oscillation around

ISBN 978-3-95450-141-0

Copyright © 2014 CC-BY-3.0 and by the respective authors

synchronous phase. This can be used as direct observation of injection beam phase or energy mis-match.

Longitudinal bunch distribution was measured at different single bunch current and RF gap voltage. Figure 8 top plots the streak camera measured profiles at Vrf = 1200kV. Single bunch was stored at 0.1mA steps up to threshold current ~ 1.1mA. Profile peak height was scaled to bunch current. Vertical instability was observed at ~ 0.6mA [1,3]. As the single bunch current increasing, due to broadband impedance (short range wakefield), bunch length increasing due to reactive impedance. Meanwhile resistive impedance in the ring makes the bunch lean towards bunch head at higher current. Skewed Gaussian distribution function was used to fit the measured profile [5,6], as shown in Eq. (1).

$$I(t) = I_0 + I_1 \exp\left\{-\frac{1}{2}\left(\frac{(t-t_0)}{[1+\mathrm{sgn}(t-t_0)A]\sigma}\right)^2\right\} \quad (1)$$

Where I_0 and I_1 are offset and amplitude respectively, A is asymmetric factor, t_0 is peak location and σ is bunch length related parameter. At low bunch currents where there is little skew of the profile, we can set A = 0 to reduce numerical noise. It's a standard normal distribution in this case. Fitted results are plotted as solid lines.

RMS bunch length can be calculated from:

$$\sigma_t = \left\langle (t-\langle t\rangle)^2 \right\rangle^{1/2} = \left[1+\left(3-\frac{8}{\pi}\right)A^2\right]^{1/2}\sigma \quad (2)$$

In which <t> is the bunch center of mass

$$\langle t\rangle = \mathrm{mean} = t_0 + 2\sqrt{\frac{2}{\pi}}A\sigma \quad (3)$$

Curves in Fig. 8 middle plot are fitted bunch length from the above equations, at five different RF gap voltages. The highest RF voltage was limited at 1200kV using superconducting cavity. Bottom plot in the figure gives the bunch centroid (synchronous phase) drifts towards the head, at Vrf = 1200kV. Fit the data points up to 0.6mA gave 12.3 ps/mA slope, from which the loss factor was calculated to be ~ 17 V/pC. Further measurement and analysis are needed to characterize the longitudinal broadband impedance of the ring.

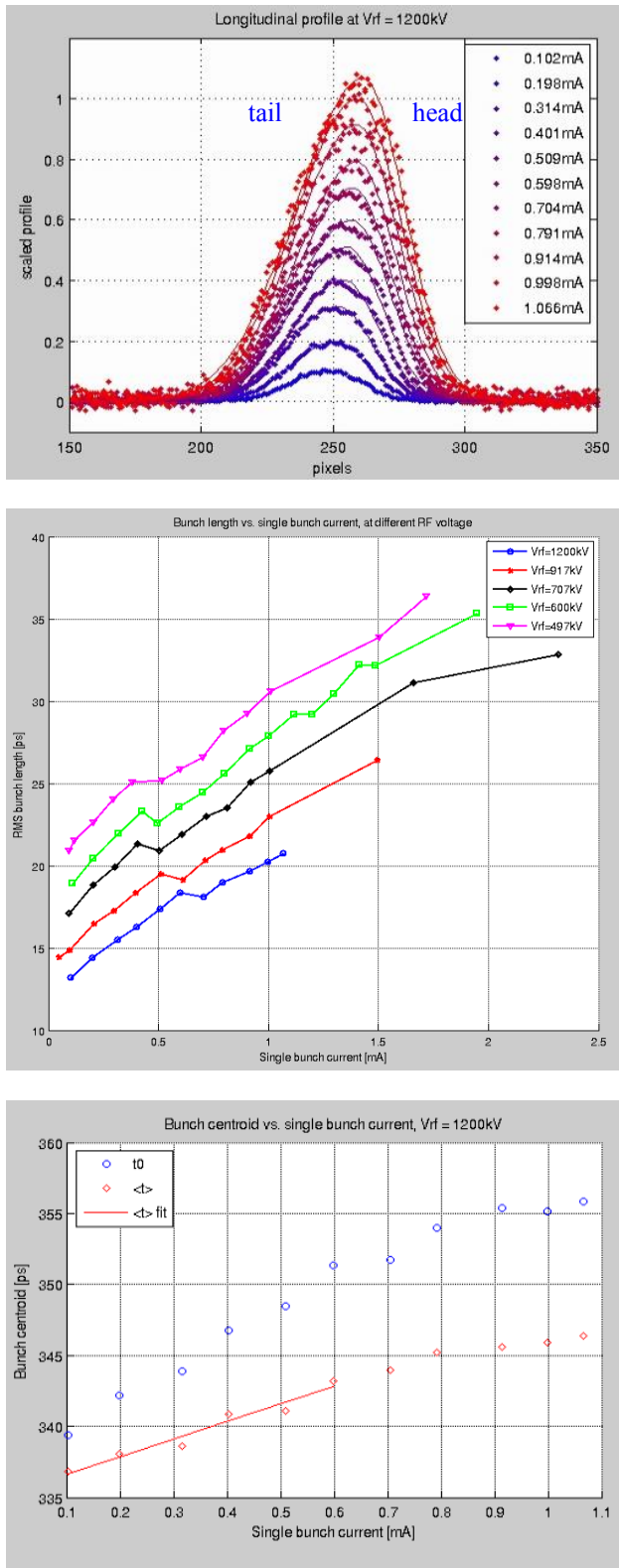


Figure 8: (top) single bunch profile measured at different single bunch current, Vrf = 1200kV. (middle) RMS bunch length vs. current results measured at five different RF voltages. (bottom) Synchronous phase drift as bunch current increasing at Vrf = 1200kV.

Copyright © 2014 CC-BY-3.0 and by the respective authors

ISBN 978-3-95450-141-0

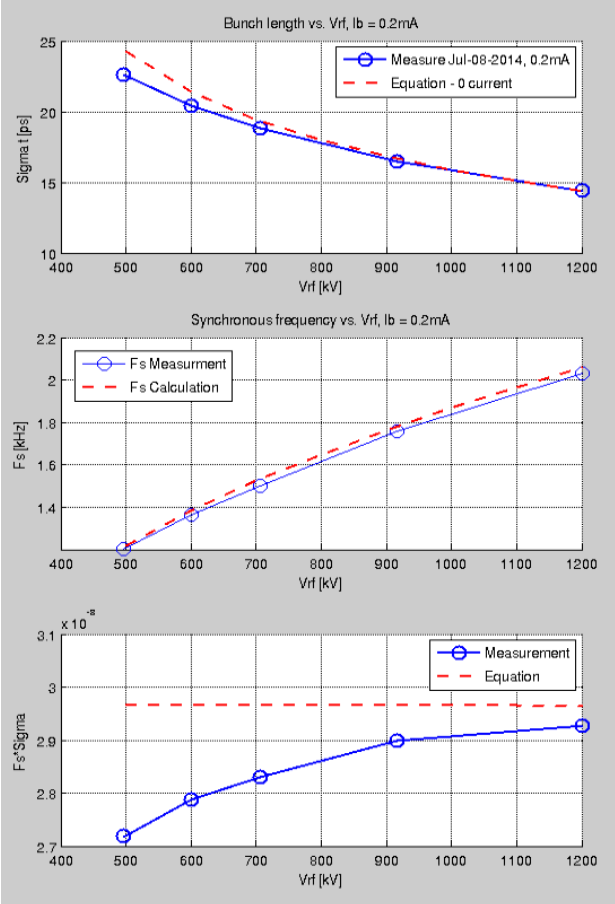


Figure 9: Measured bunch length, synchronous frequency at different RF voltages, bunch current was fixed at ~0.2mA.

Bunch length and synchronous frequency has the relations as shown:

$$\sigma_t = \frac{\alpha}{2\pi f_s}\left(\frac{\sigma_E}{E}\right) \quad (4)$$

Where momentum compaction factor α = 3.627e-4, relative energy spread σ_E/E is ~ 0.0514% for NSLS2 lattice (no damping wigglers). If the RF voltage varied at a fixed single bunch current, measured synchronous frequency and bunch length should follow the Eq. (4). This can be used to measure the energy spread, assume momentum compaction factor is known.

Synchronous frequency can be measured from BPM turn by turn data spectrum at dispersion locations. Figure 9 shows the bunch length and synchronous frequency at different RF voltages. Product of bunch length and synchronous frequency varied by less than 10%, result in good agreement to Eq. (4).

SUMMARY

Visible SLM diagnostic beamline has been designed, constructed and commissioned at NSLS2 storage ring. Camera setups have been used frequently to monitor the transverse and longitudinal profile. Streak camera bunch length measurements were able to be carried out during single bunch shifts. These measurements are essential to characterize and optimize the NSLS2 storage ring. Future developments using the visible light are underway for more advanced diagnostics.

The author thanks the NSLS2 diagnostics group and commissioning team members.

REFERENCES

[1] W. Cheng, et al., "NSLS2 Diagnostic Systems Commissioning and Measurements", this conference
[2] W. Cheng, "Synchrotron Light Monitor System for NSLS-II", BIW'2010.
[3] W. Cheng, et al., "Commissioning of Bunch-by-bunch Feedback System for NSLS2 Storage Ring", this conference, IBIC'2014, Monterey CA, USA
[4] O. Chubar, P. Elleaume "Accurate and Efficient Computation of Synchrotron Radiation in the Near Field Region", SLM beamline SRW tracking carried out with help from Dr. Oleg Chubar.
[5] W. Cheng, et al., "Streak Camera Measurements with High Current in PEP-II and Variable Optics in SPEAR3", BIW'2008.
[6] R. Holtzapple, et al., "Single Bunch Longitudinal Measurements at the Cornell Electron-Positron Storage Ring", PRST-AB, Vol.3, 034401 (2000).

Copyright © 2014 CC-BY-3.0 and by the respective authors

ISBN 978-3-95450-141-0

BEAM SIZE MEASUREMENTS USING SYNCHROTRON RADIATION INTERFEROMETRY AT ALBA

L. Torino, U. Iriso, ALBA-CELLS, Cerdanyola, Spain
T. Mitsuhashi, KEK, Tsukuba, Japan

Abstract

First tests to measure the transverse beam size using interferometry at ALBA showed that the measurement reliability was limited by the inhomogeneous light wavefront arriving at the double slit system. For this reason, the optical components guiding the synchrotron radiation have been exchanged, and detailed quality checks have been carried out using techniques like the Fizeau interferometry or Hartmann mask tests. We report the results of the analysis of the optical elements installed in the beamline, and the beam size measurements performed using double slit interferometry in both horizontal and vertical planes.

INTRODUCTION

ALBA is a 3 GeV third generation synchrotron light source operative for users since 2012 [1].

Due to the machine small emittance it is not possible to measure the beam size by using a simple imaging system because of the diffraction limit. Measurements of the beam size are nowadays routinely performed using a x-ray pinhole camera [2]. In order to have a second reliable measurement of this parameter the double slit synchrotron radiation interferometry technique (SR interferometer) [3] has been proposed and is still under development. Preliminary tests were performed at the diagnostic beamline Xanadu using the already existing optical components which quality was not good enough to provide the best results [4].

In this report we describe the improvement of the beamline optical components and the tests performed to ensure their quality. We also report some results of the interferometry measurements.

THE SR INTERFEROMETER

The main parameters of the ALBA lattice that determine the transverse beam size at the source point are listed in Table 1.

Table 1: ALBA Lattice Parameters

	x	y
β	0.299 m	25.08 m
Dispersion	0.04 m	0 m
Energy spread	0.001 01	—
Emittance	4.6 nm	0.023 nm
Beam size	53.6 µm	23.9 µm

One of the most common techniques to measure beam sizes in this range is the SR interferometer. Using a double slit interferometer the degree of spatial coherence of the synchrotron radiation produced by the beam is measured, from where the beam size can be inferred. A sketch is presented in Fig. 1.

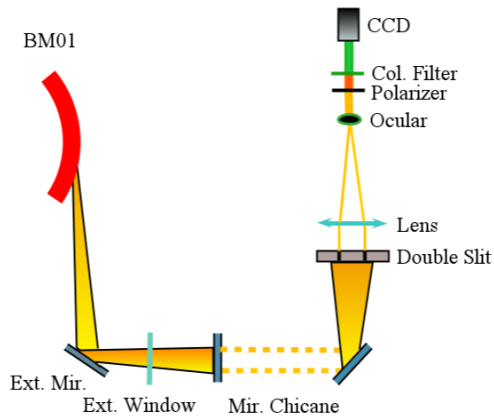


Figure 1: Sketch of the SR interferometer setup at ALBA. The optical path is composed by 6 mirrors in atmospheric pressure. The extraction mirror is set in the vacuum.

The visible part of the radiation produced by the electron beam passing through a bending magnet (BM01) is extracted by an in-vacuum mirror located at 8.635 m from the source and at $\simeq$ 6 mm from the beam orbit plane. In this way the extraction mirror is not in contact with hard x-rays that may compromise its characteristics. Only the radiation produced with a positive angle with respect to the beam orbit plane is collected, for this reason the mirror is said to be an "half-mirror". The light is extracted through a window and guided out from the tunnel up to the optical table in the beamline by 6 mirrors. The interferometer system is composed by a double slit aperture that produces the interferogram. The width of the slits is 1 mm and the height is chosen depending on the quantity of light needed. The separation between the two slits is variable from 8 mm to 22 mm. Immediately after the double slit an apochromat (BORG ED500) lens with focal length of 500 mm and flatness $\frac{\lambda}{10}$ is located. After the focal point an ocular (Takahashi MC LE 18 mm) is introduced to magnify the image. A polarizer and a 540 nm narrow bandpass color filter (width 10 nm) both from Thorlabs are used to select the σ radiation polarization and energy. Finally the interferogram is captured by a CCD camera whose pixel size is 3.75 µm × 3.75 µm.

WAVEFRONT ERROR

In order to obtain good measurements the wavefront error due to the quality of the optical components has to be

Copyright © 2014 CC-BY-3.0 and by the respective authors

ISBN 978-3-95450-141-0

minimized. Previous measurements showed that optical components of Xanadu were not suitable to obtain good measurements [4]. For this reason the extraction mirror, the extraction window and all the mirrors of the optical path were changed. The quality of each component was tested before the installation.

In particular the most critical component of the diagnostic beamline is the extraction mirror. This mirror is located in-vacuum and is designed for ultra-high vacuum and high temperature (bake-outing at 80 °C). To prevent the deformation due to over heating the mirror is provided with thermocouples that measure directly the temperature at its bottom. A motorized system allows to move the mirror vertically in and out from the radiation fan, down to 5 mm from the orbit plane. The routine position is set to 6 mm.

Old Xanadu Beamline

Xanadu beamline was not meant to perform precise optical measurements such as interferometry. The mirrors used before the beamline upgrade to bring the light to the optical table were aluminum with 2" diameter from Thorlabs. They were small with respect to the radiation fan and cut the radiation at the border.

The extraction mirror was made of copper and with a designed flatness of $\frac{\lambda}{2}$. The mirror had not been measured before the use, but it was clear that the wavefront reaching the beamline was strongly deformed. To measure the wavefront deformation caused by all the transport line a Hartmann mask was used.

The Hartmann mask is a thin plate over which little holes are present (Fig. 2). In particular the one used for this measurements has a matrix of (10×10) holes of 1 mm diameter spaced by 5 mm directly irradiated by synchrotron radiation. Generally the mask is used to find the focal position of optical system (specially in astronomy) but can also be used to reconstruct a wavefront after the propagation through the optical components of the transport line by converting the complex wavefront in light rays . The wavefront error is obtained by averaging the difference between the positions of the centroid of the rays after the propagation, and the position obtained considering only the wavefront (without optical components). Details on the calculations ant the theory can be found in [5]. The result for the wavefront reconstruction when using the old Xanadu mirror is shown in the first picture of Fig. 3 and the result of the calculation provides a wavefront error of $\frac{\lambda}{3}$.

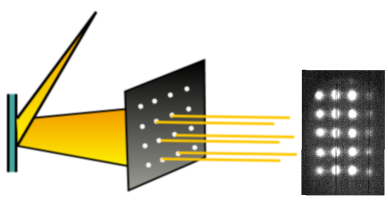


Figure 2: Sketch of the Hartmann mask working principle and a real data acquisition.

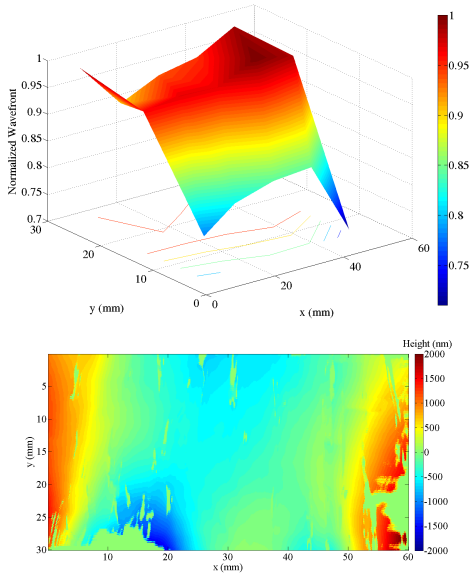


Figure 3: Wavefront reconstruction and Fizeau analysis for the old Xanadu extraction mirror.

Direct measurements of the extraction mirror flatness were performed in the ALBA optical laboratory using a Fizeau interferometer (second picture in Fig. 3). The flatness over all the mirror is around λ. Note that the flatness of the whole mirror may introduce a wavefront error worst with respect the one measured with the Hartmann mask. This is because the second measure is an approximation, and also because in this case a smaller region of the mirror is considered: the one intercepted by visible light.

It is worth mentioning that after the extraction of the old mirror the presence of some scratches compatible with a crystalline growth were evident. Moreover clear structures were visible at bare eye in the vertical direction. Further analysis shows actually that the growth is compatible with nano-crystalline diamond (see **APPENDIX**).

New Xanadu Beamline

First, all the transport mirrors were substituted by 4" mirrors always by Thorlabs with a designed flatness of $\frac{\lambda}{10}$. Also the extraction window was manufactured specially for ALBA by Torr Scientific and its flatness measured with the Fizeau interferometer was found to be $\frac{\lambda}{20}$ in the region of interest. Due care was taken to obtain a parallelism better than 5 arcsec (< 3 arcsec measured).

The new extraction mirror was produced by Thales-SESO: it is again made out of copper with a nickel coating called "kanigen" aided to protect the Cu from oxidation. The requested flatness was $\frac{\lambda}{10}$ and the 3 thermocouples feedback system to prevent overheating is also present. After the mounting on the actual mechanical support, the mirror was measured with the Fizeau interferometer and the obtained flatness is $\frac{\lambda}{7}$. Results are presented in the first picture of Fig. 4.

ISBN 978-3-95450-141-0

Copyright © 2014 CC-BY-3.0 and by the respective authors

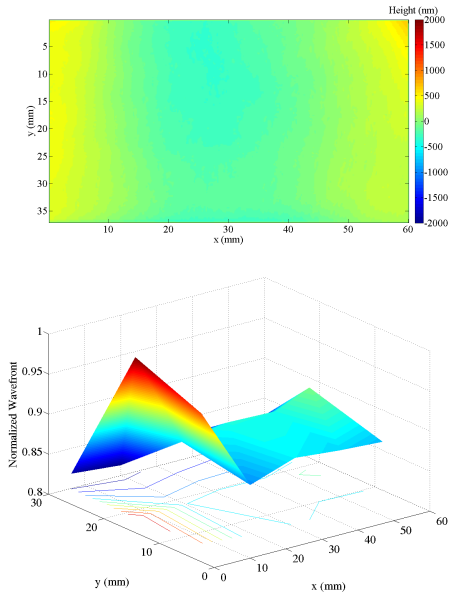


Figure 4: Fizeau analysis and wavefront reconstruction of the new extraction mirror. The color scale is the same as in Fig. 3.

The mirror appears a bit deformed on the sides because of the design of the mechanical holder, for this reason it is important to point out that the measurement were performed with the mirror mounted, in this way it is possible to directly compare the Fizeau results with the one obtained from the Hartmann mask. The wavefront deformation caused by the whole transport line, measured with the Hartmann mask is presented in the second picture of Fig. 4. The wavefront is much flatter than the one from the old mirror presented in Fig. 3 and provides an approximate wavefront error of $\frac{\lambda}{8}$.

A simple test of the good quality of the transport line can be performed using the synchrotron radiation and a three holes mask to check whether, using a focusing lens, the three rays collapse in a single spot at the focal position. The progression to find the lens focal point is shown in Fig. 5 and shows a very good quality for the transport line.

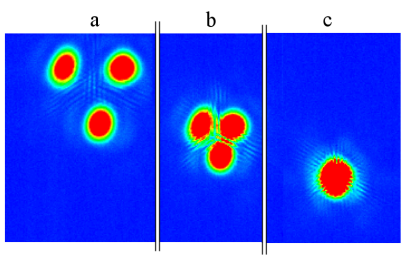


Figure 5: Test performed with a three holes mask to check the quality of the transport line. The rays produced collapse in a single spot at the focal point showing a good quality of the optical components.

In summary, the analysis of the optical components shows that the flatness of the whole mirror, measured with the Fizeau interferometer, is improved from $\frac{\lambda}{1}$ to $\frac{\lambda}{7}$ and that the total wavefront error, measured with the Hartmann mask, from $\frac{\lambda}{3}$ to $\frac{\lambda}{8}$.

BEAM SIZE MEASUREMENTS

After the upgrade of the Xanadu beamline beam size measurements were performed. The apparatus was already described in the previous sections, a typical interferogram with a slit separation of 16 mm is presented in Fig. 6.

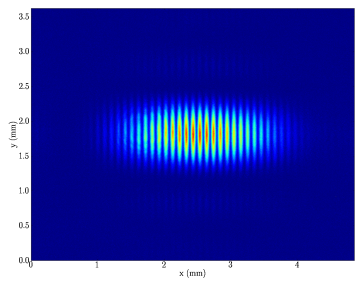


Figure 6: Typical interferogram obtained using the setup described in the first section.

The cross section of the interferogram is described theoretically by:

$$I = I_0 \left\{ \mathrm{sinc}\left(\frac{2\pi a x}{\lambda f}\right)\right\}^2 \times \left\{1 + V\cos\left(\frac{2\pi D x}{\lambda f}\right)\right\} \quad (1)$$

where I_0 is the sum of the intensity of the radiation coming from the two slits, a is the half width of the slit aperture, f is the distance between the double slits and the interference plane, D is the slit separation and V is the absolute value of the complex degree of spatial coherence (visibility). Equation 1 is used to fit the cross section of the interferogram. The theoretical equation dos not foresee the use of the ocular, for this reason the parameter related with the image magnification, f, is let as a free parameter in the fit. The same happens with I_0 since it is not possible obtain the value in advance. The other free parameter is the visibility V and extracting it from the fit it is possible to compute the beam size:

$$\sigma = \frac{\lambda L}{\pi D}\sqrt{\frac{1}{2}\ln\frac{1}{V}} \quad (2)$$

where L is the distance between the source and the double slits. Figure 7 shows an example of the fit result.

Horizontal Beam Size

Several data were taken with different slits separations. For each slit separation D several data acquisitions were taken to study the fluctuation of the result. First results showed that the measurement was not stable. Beam size result for different slit separation D are the green dots in Fig. 8, the value on the plot was calculated averaging over several

Copyright © 2014 CC-BY-3.0 and by the respective authors

ISBN 978-3-95450-141-0

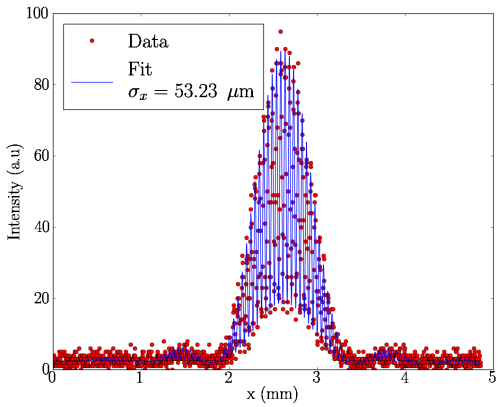


Figure 7: Fit of the cross section of the interferogram showed in Fig. 6. The expected result for the horizontal beam size is 53.6 µm as reported in Tab. 1

acquisitions and the error bar considering the standard deviation from the average. The cause of this error in the beam

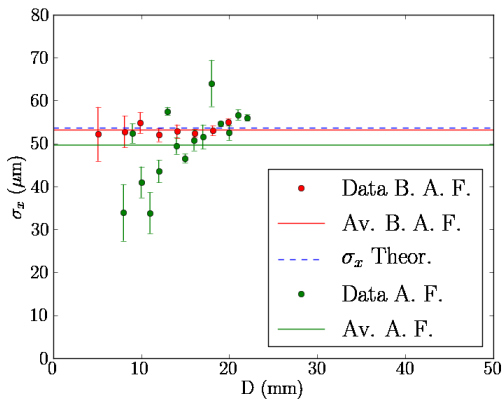


Figure 8: Horizontal beam size as a function of the slit separation blocking the air flux (red dots, average beam size 53.1 µm) and without (green dots, average 49.6 µm).

size was mainly caused by the vibration in the optical path. In particular these vibrations may be caused by air flowing between the tunnel and the Xanadu beamline through the hole driven in the shielding wall, probably due to a pressure gradient. Two neutral density filters were used to block the air flux between the tunnel and the beamline. Using this setup, measurements are more stable.

An example of the 100 data acquisitions for the horizontal beam size measurement with $D = 16$ mm is shown in Fig. 9. The final beam size average on a value that is very close to the expected one. Again the measurement was repeated for different slit separations. The results are presented in red dots in Fig. 8. for all the D the beam size result is compatible with the expected one, which indicates a Gaussian beam profile.

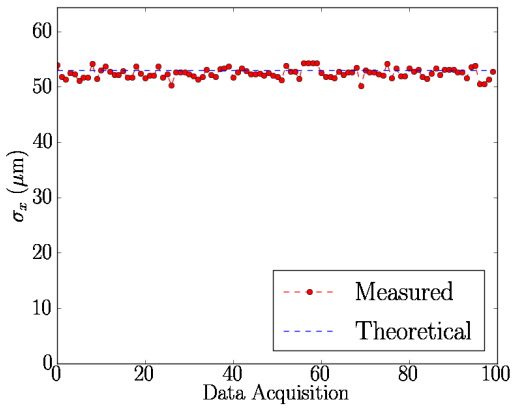


Figure 9: Trend of the fitted horizontal beam size for 100 acquisitions.

Vertical Beam Size

Synchrotron radiation is not homogeneous vertically and moreover, since the radiation is cut from the extraction half-mirror, the footprint reaching the beamline is affected from Fresnel diffraction and presents some darker zone. For these reasons the intensity of the radiation at the double slit position is not the equal in the two slits and the imbalance of the intensities must be taken into account [6]. Including this imbalance effect, the visibility is given by in Eq. 2 the simple visibility V has to be substituted by:

$$\gamma = \frac{I_1 + I_2}{2\sqrt{I_1 I_2}} \times V \tag{3}$$

where I_1 and I_2 are the intensities at each single slit of the double slit.

Several measurements were taken for different slits separations but unfortunately, for timing reasons, it was not possible to reproduce tests blocking the air flux as in the horizontal plane. For this reason for each set of measurement, only the minimum of the resulting beam sizes is considered in Fig. 10. Results still have to be improved by stabilizing the air flux.

On the other hand simulations show that the use of not monochromatic radiation strongly affect the interferogram shape for small beam sizes, for this reason the fitting algorithm has to be improved [7].

Vibration in the Optical Path

Small displacement in the mirror, or air turbulence along the optical path may change wavefront direction, which in turn produce deformation in the interferograms.

We estimate these effects by studying the displacement of the interferogram centroid during consecutive data acquisitions. The CCD exposure time is fixed to 15 ms. If the light wavefront is moving during the exposure time, several interferograms are superimposed and may cause the increasing of the visibility. Comparing standard deviation of the average position of the centroid with respect to the oscillation period

ISBN 978-3-95450-141-0

Copyright © 2014 CC-BY-3.0 and by the respective authors

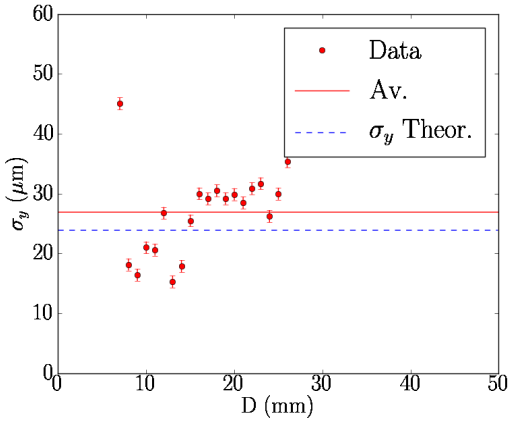


Figure 10: Vertical beam size as a function of the slit separation. The average beam size measurement is 26.9 µm, 15% larger with respect to the expected one.

of the interferogram ($\frac{2\pi D}{\lambda f}$, from Eq. 1), it was possible to have an idea of how influent was the effect which should wash out the interferogram in both horizontal and vertical direction. Figure 11 shows the ratio between the two values at different slits separations: the centroid vibration varies between 10% and 70% of the oscillation period. In both cases the displacement is large and may cause the instability of the results observed previously.

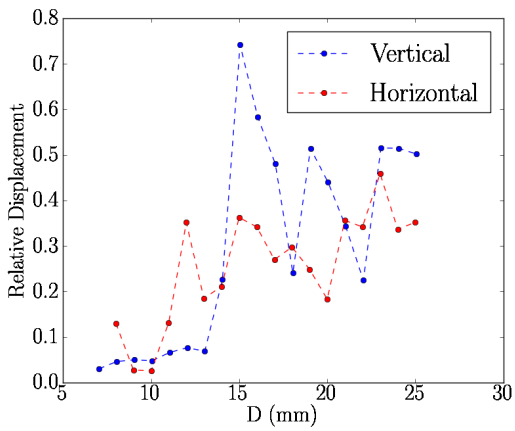


Figure 11: Ratio between the displacement in 15 ms and the period of the interferogram at different slit separation.

A further upgrade of the Xanadu beamline is taking place to prevent these effects. On top of it, we plan to use a fast CCD camera to obtain the spectrum of the interferogram vibrations to better understand their origin.

CONCLUSION

In order to obtain reliable beam size measurements using the SR interferometer, Xanadu beamline underwent to several upgrades. A better in-vacuum mirror and larger mirrors for the transport light were installed. The quality of the wavefront reaching the beamline had been carefully analyzed and strongly improved. Moreover blocking the air flux from the tunnel to the beamline allowed to obtain good and stable results for the horizontal beam size. Unfortunately this test could not be performed for the vertical beam size measurements.

In case of small beam sizes, as the one corresponding to the vertical plane, the fitting algorithm is not yet fully developed to deal with the effect of non monochromatic light. Further theoretical and practical studies will be performed in the near future.

ACKNOWLEDGMENT

We wants to thanks J. Nicolas, M. Llonch J. Ladrera, E. Pellegrin, M. Gonzalez (ALBA-CELLS), J. Pasquaud (ESRF) and all the technical staff of ALBA for their valuable help. This project is funded by the European Union within the oPAC network under contract PITN-GA-2011-289485.

APPENDIX

When the Xanadu beamline was upgraded the old in-vacuum mirror was extracted and a crystalline growth was observed on the surface. Experiments were performed together with the ALBA Experiments group to understand the nature of the growth. Results from a Raman scattering experiment shows that the growth is compatible with a nano-crystalline carbon-like-diamond structure. The results are show in Fig. 12 together with results published in literature. The peak at 1332 cm^{-1} is typical of the diamond and the one present at 1550 cm^{-1} is typical of carbon. The total structure is comparable with the footprint of nano-crystalline carbon-like-diamond. Further studies will be performed to understand the nature of the growth and prevent it if possible.

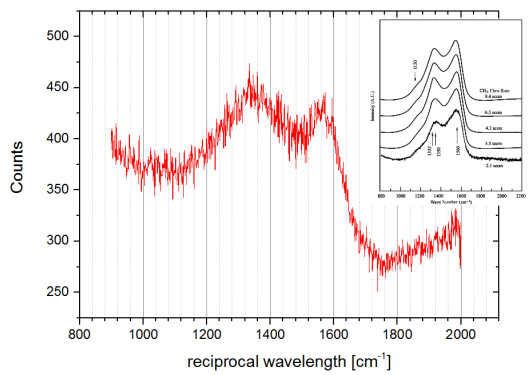


Figure 12: Raman spectrum of the old Xanadu mirror (in red) and spectra taken from the literature (inserted) [8].

REFERENCES

[1] F. Perez, "First Year Operation of the ALBA Synchrotron Light Source", IPAC2013, Shanghai, June 2013, MOPEA055 (2013)

[2] U. Iriso, "Beam size and emittance measurements using the ALBA Pinhole", AAD-SR-DI-PINH-01.

Copyright © 2014 CC-BY-3.0 and by the respective authors

ISBN 978-3-95450-141-0

[3] T. Mitsuhashi, "Measurement of small transverse beam size using interferometry", DIPAC'2001, Grenoble, May 2001, IT06 (2001)

[4] U. Iriso, L. Torino and T. Mitsuhashi, "First Transverse Beam Size Measurements Using the Interferometry at ALBA", IBIC2013, Oxford, September 2013, MOPF01 (2013)

[5] T. Mitsuhashi. "SR Monitor – Special topics", BIW2012, Newport News, April 2012, TUAP02 (2012)

[6] M.J. Boland, T. Mitsuhashi. and K.P. Wootton "intensity imbalance optical interferometer beam size monitor", IBIC2012, Tsukuba, September 2012, WECC03 (2012)

[7] A. Arinaga et al. "KEKB beam instrumentation systems", Nuclear Instruments and Methods in Physics Research A 499 (2003) 100–137

[8] Z.L. Wang, Y. Liu and Z. Zhang "Handbook of Nanophase and Nanostructured Materials", (Kluwer Academic PublishersPlenum Publishers, 2003)

Copyright © 2014 CC-BY-3.0 and by the respective authors

ISBN 978-3-95450-141-0

CHARACTERIZATION OF THE LASER BEAM FOR HHG SEEDING

S. Ackermann*, B. Faatz, DESY, Hamburg, Germany
V. Miltchev, University of Hamburg, Hamburg, Germany

Abstract

Recently free-electron laser (FEL) facilities around the world have shown that the direct seeding approach can enhance the spectral, temporal and coherence properties of the emitted radiation as well as reducing the fluctuations in arrival time and output energy. To achieve this, a photon pulse of the desired wavelength ("seed") is overlapped transversely and temporally with the electrons in the undulator to start up the FEL process from a defined radiation pulse rather than from noise. To benefit from the advantages of this technique, the energy of the seed has to exceed the energy of the spontaneous emission. The ratio between these two energies is strongly influenced by the seed beam properties. In this contribution, we will present simulations on the achieveable power contrast in dependence on the beam quality of the seed, and compare the results to the experimental data of the seeded FEL experiment ("sFLASH") at DESY, Hamburg. Additionally we show a way of creating FEL seed pulses for simulation purposes from Hermite-Gaussian generating functions.

INTRODUCTION

In order to benefit from the advantages of the high-harmonic generation ('HHG') direct seeding approach one has to ensure good quality of the external photon pulse ('Seed') as the energy transfer between the electrons and the electromagnetic field is strongly depending on the photon pulse wave front properties [7], which is in principle accessible through measurement, for example using a Shack-Hartmann wavefront sensor [9]. In an FEL the direct measurement of the wavefront distortions in the vicinity of the undulator is challenging due to limited space, or even excluded, e.g. if the beam pipe is small [2]. The M^2 -value [1] can be easily measured by focus scan technique [11] in the laser lab. In this contribution, we present simulations showing the importance of the M^2 -value onto the FEL output power as well as a method for the estimation of the M^2 -value using modal decomposition of single transverse intensity profiles similar to [5]

NUMERICAL SIMULATION SETUP

These studies have been carried out using the time-dependent 3D FEL code "GENESIS 1.3, v2" [14]. The electron beam line considered in the simulations is similar to the FLASH2 beam line of the FEL facility FLASH at DESY, Hamburg, Germany [6], [8]. Table 1 contains all important simulation parameters.

Table 1: Simulation Parameters and Ranges used in the Numerical Simulation

Electron beam		
Peak current	I_{max}	2.5 kA
Beam size	σ_{x}	100 μm
	σ_{y}	49 μm
Bunch Length (rms)	σ_{z}	30 μm
Energy	E	700 MeV
Energy spread	σ_{E}	500 keV
Normalized emittance	$\epsilon_{\mathrm{x,n}}$	1.4 mm · mrad
	$\epsilon_{\mathrm{y,n}}$	1.4 mm · mrad
HHG pulse		
Temporal shape		Gaussian
Wavelength	λ_{HHG}	37.6 nm
Pulse energy	E_{HHG}	70 pJ
Peak power	$P_{\mathrm{max,HHG}}$	2.5 kW
Duration (rms)	τ_{HHG}	12 fs
Undulators		
Lattice		FODO
Number of undulators		3
Undulator period	λ_{u}	31.4 mm
Periods per undulator	$_{\mathrm{periods}}$	76
Undulator intersection	L_{drift}	91.36 cm
Max. K parameter (rms)	K_{rms}	2.0

The goal of these simulations is to show the FEL output power at the end of the beam line as a function of the seed laser pulse quality in terms of M^2 . It has been assumed that the waist of the incoming seed pulse is located at the entrance of the first undulator module. For all simulations the waist size has been set to the value yielding the maximum FEL output power with an M^2 =1, namely 55 μm. Field distribution files containing seeds with different M^2 -values have been generated by superposition of different Hermite-Gaussian modes. The direct-search numerical algorithm [13] has been used to find amplitude and phase of the contributing modes to fullfill the following boundary conditions:

- The waist size has to be 55 μm.
- The total seed power equals 2.5 kW, see Table 1.
- M^2 is equal to the desired M^2 -value for **both** planes.
- In order to keep the axial symmetry of the multimode seed field, only TEM$_{mn}$ modes with even *n,m* are considered.

A large number of sets of Hermite-Gaussian modes exist fulfilling the aforementioned boundary conditions - we

* sven.ackermann@desy.de

Copyright © 2014 CC-BY-3.0 and by the respective authors

ISBN 978-3-95450-141-0

pick the one consisting of the smallest possible number of higher order modes. This is implemented in the numerical algorithm, which starts with the fundamental mode and higher order modes are being added in steps of one to the field only if a solution with the desired M^2 could not be found.

FEL OUTPUT POWER VS. SEED PULSE M^2 -VALUE

The simulation results have been summarized in Figure 1 with the power contrast $\frac{P_{pk}-\langle P_{SASE}\rangle}{\langle P_{SASE}\rangle}$ as the figure of merit. P_{pk} stands for the peak output power for the seeded FEL, $\langle P_{SASE}\rangle$ for the SASE power time averaged over the FEL photon pulse. As expected, the contrast has a maximum

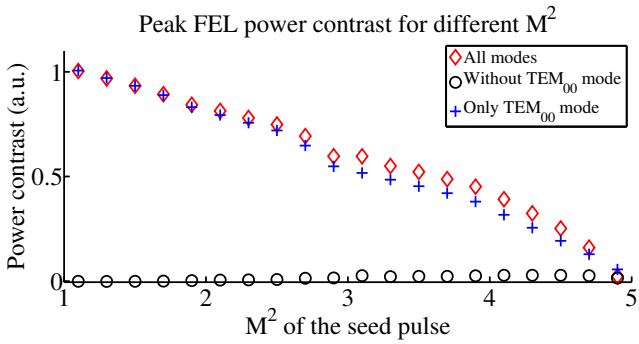


Figure 1: Seeded FEL power contrast vs. M^2 of the seed pulse.

at M^2 =1 with a maximum contrast of about 20 and drops rapidly to 0 at an M^2 of about 5. In order to give a proper interpretation of these results, all the higher order modes in the seed field distributions have been taken out except the fundamental. The simulations have been repeated and the results are plotted in Figure 1. The comparison between the seeding with the full modal content and the TEM_{00} only shows that mainly the fundamental mode contributes to the seeded FEL output power. One can say that the fundamental mode almost exclusively defines the reachable power contrast, while higher order modes do not seem to contribute anyhow. In order to support this conclusion, a simulation has been done using only the higher order modes. The results, also shown in Figure 1 show that FEL seeded with such fields have almost zero output contrast compared to SASE, meaning SASE is still the dominating radiation process. The drop in the FEL power contrast can be understood if one sees that the TEM_{00} mode size is reduced when the waist size is kept constant while higher order modes are added, leading to inefficient coupling between electron and the seed pulse. Additionally, since higher order modes require to carry some energy, less energy is avaible for the fundamental mode, decreasing the power contrast further. In the exponential growth regime, the FEL works as a linear amplifier, so that the characteristics of the plot should be independentfrom the longitudinal position inside the undulator as long as one stays in this mode. One has to not that in the simulation power contrast is the figure of interest, while for the photon users usually the energy contrast counts. The energy contrast can be estimated by scaling the power contrast ratio between SASE photonp pule length. In addition, this simulation allows to see the influence of the M^2 of the seed on the M^2 of the FEL. Out simulation gives an M^2 at the end of the FEL of 1.38 and independent from the initial M^2 . This means that the FEL does not benefit from seeding in terms of transverse photon beam quality.

MODAL RECONSTRUCTION OF INTENSITY PROFILES

Due to space restrictions in the vincinity of the undulator it is very challenging to measure the M^2 at the undulator, and therefore rarely done. M^2 is usually measured using the focus scan technique [11]. In [10] a different method is suggested to obtain M^2 -values from single transverse intensity profiles using decomposition into certain sets of modes. Provided that an observation screen is at the waist of the seed beam, this method can offer an estimate of the M^2 of the seed pulse and only requires little space. The field amplitudsme can be considered as superposition of Hermite-Gaussian functions [10], which in the one-dimensional case is:

$$G_n(x) = \left(\frac{2}{\pi}\right)^{\frac{1}{4}} \frac{1}{\sqrt{2^n n! w(z)}} H_n\left(\frac{\sqrt{2}x}{w(z)}\right) \exp\left(-\frac{x^2}{w^2(z)}\right) \tag{1}$$

The two dimensional approach has been derived in [15] where the two-dimensional intensity distribution in the waist is given by

$$I(x,y) = \sum_{n,n',m,m'=0}^{\infty} [A_{nm} G_n(x) G_m(y) \times A^*_{n'm'} G_{n'}(x) G_{m'}(y)] \tag{2}$$

Here one exploits the fact that the generalized Guoy phase (Eq. (5c) in [15]): is zero at the waist. Assuming that all modes are independent from each other, the time-averaged intensities can be added which means that the elements $A_{nm}A_{n'm'} = c_{nm}\delta_{nn'}\delta_{mm'}$ where δ_{mn} is the Kronecker symbol. The time-averaged intensity Eq. (2) can then be written as

$$\bar{I}(x,y) = \sum_{n,m=0}^{\infty} \left(c_{nm} G_n^2(x) G_m^2(y)\right) \tag{3}$$

where c_{nm} are the weights representing the intensity content of the individual modes. These coefficients can be calculated as shown in [10] using the Fourier transform $\tilde{I}(p_x, p_y)$ of the intensity distribution where p_x, p_y are the space-frequency variables.

$$c_{nm} = C_0 \int_0^{\infty}\int_0^{\infty} \left[\tilde{I}(p_x,p_y)\Psi_m\left(\pi^2 w_0^2 p_x^2\right) \times \Psi_n\left(\pi^2 w_0^2 p_y^2\right) p_x p_y \mathrm{d}p_x \mathrm{d}p_y\right] \tag{4}$$

ISBN 978-3-95450-141-0

Copyright © 2014 CC-BY-3.0 and by the respective authors

where $\Psi_n(t) = L_n(t)\exp\left(-\frac{t}{2}\right)$ with L_n the n-th order Laguerre polynomial. The constant C_0 is a normalization factor which is used to adjust the total power of the reconstructed field to the measured one. Although the method provides unique solutions for the power content coefficients, in practice one has to set an upper limit for the expected highest mode number. This means that the summation in Eq. (3) does not go to infinity but is limited to upper summation bounds $n_{\max}, m_{\max}$. In the following analysis of experimental data, we set a threshold where the reconstructed intensity profile yields more than 95% of the original intensity which was the case for $n_{\max} = 8$. The upper bounds depend on the considered profile and has to be adjusted for each particular case. It is worth noting that the precise calculation of M^2 requires high number of modes as noted in [15]. However, the higher order modes tend to have very small intensities, close to the noise level of the detector, and therefore it is difficult to obtain a precise estimate for their power intensity coefficients from experimental data. From this point of view the choice of n_{max}, m_{max} is a compromise between the need to correctly measure M^2 and the desire to keep the measurement error small. These issues have been covered in the discussion on the measurement errors in the section below. In our analysis the waist size w_0 of the fundamental mode is a free parameter which can be fitted using maximum likelihood approach using the following numerical algorithm: One starts with some initial guess for w_0 and one computes the mode content coefficients c_{nm} where $n, m = 0...n_{\max}$. Based on these coefficients, one calculates the intensity distribution $\hat{I}$ using Eq. (3). Further the algorithm adjusts w_0 until the difference $\left(\bar{I} - \hat{I}\right)^2$ reaches a minimum.

COMPARISON TO EXPERIMENTAL RESULTS

We have used this method to analyze the 38 nm HHG seed pulse at the sFLASH direct seeding experiment [12, 4]. The transverse intensity profile at the waist shown in Figure 2. As one can easily see, the intensity distribution is tilted and asymmetric. There are three possible sources for this [3].

- The first is the injection beam line which transports the seed pulse from the harmonics source to the undulators, which rotates the beam by about 11°, thus introducing coupling between x and y.
- Astigmatism out of the source, as experimentally studied in [12], is the second one.
- Third, the NIR laser beam used for the production of the harmonics is also already astigmatic, imprinting this property to the produced seed pulse.

All of these lead to odd modes contributing to the intensity distribution. Since in our analysis two-dimensional Fourier transform of the intensity distribution has been done, the decomposition algorithm is not restricted to even modes and can also be used to determine the modal content of arbitrary intensity profiles.

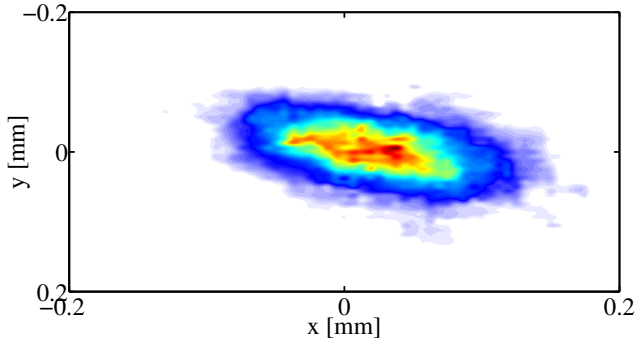


Figure 2: Transverse intensity distribution of the 38 nm HHG seed beam used at the direct seeding experiment sFLASH.

The power content coefficients which are the result of the modal decomposition, are shown in Figure 3. With this power coefficients one can calculate M^2 of the field. The first option is to use the formula derived in [15] which directly relates the beam quality factor to the power content coefficients:

$$M^2 = \frac{\sum_{n,m=0}^{\infty}((2m+1)c_{nm})}{\sum_{n,m=0}^{\infty} c_{nm}} \quad (5)$$

Applying Eq. (5) yields $M_x^2 = 2.45$ and $M_y^2 = 2.39$. This result is in a very good agreement with the result obtained with the second possible option which is to numerically propagate the field over a certain distance and thus obtain the dependence of the beam size versus longitudinal position $w(z)$ and then analyze this date in the same way as a focus scan technique by exploiting the formula $M^2 = \frac{\pi w_0}{\lambda z}\sqrt{w^2(z) - w_0^2}$. One can estimate the M^2 of the HHG seed beam to be $M_x^2 = 2.2 \pm 0.6$ and $M_y^2 = 2.0 \pm 0.6$. The error of 28% consists of two contributions: Uncertainties in the determination of the wavelength and beam size due to finite camera pixel size where studied in Monte Carlo simulation yielding an error of about 20%. This Monte Carlo simulation works as follows: A random set of modes is generated and the corresponding intensity profile calculated, which is then transformed to a discrete distribution on a grid with the size of the camera pixels and a intensity resolution corresponding to the bit-depth of the camera. Noise is added afterwards. Then, the modal decomposition is applied. An uncertainty of 10% in the wavelength has been assumed, which is similiar for all pixels. This procedure has been repeated 10^5 times and the resulting values are plotted in Fig. 4. Another error to the measurement is introduced if the measurement has not been done directly at the waist position. This error source has been also studied by scanning the z-position. Within one Rayleigh length this leads to an error of 20% or less.

Copyright © 2014 CC-BY-3.0 and by the respective authors

ISBN 978-3-95450-141-0

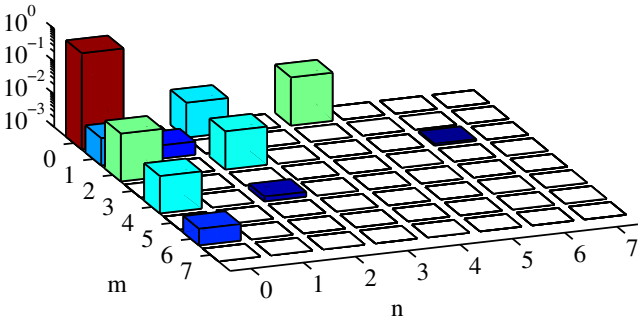


Figure 3: Power content coefficients c_{nm} of the harmonics beam shown in Fig. 2. The TEM_{00} mode is with around 90% of the overall intensity the strongest mode. Power content coefficients smaller than 10^{-3} are colored white.

Both errors may be summed up quadratically as they are independent of each other, leading to a error of about 28%. However, since the real waist size of the fundamental is unknown and one is not necessarily dealing with partially coherent beams, the calculated M^2 -value can only be a qualitative estimate although values calculated with this method are comparable to each other and within errorbars in good agreement with focus scan technique values.

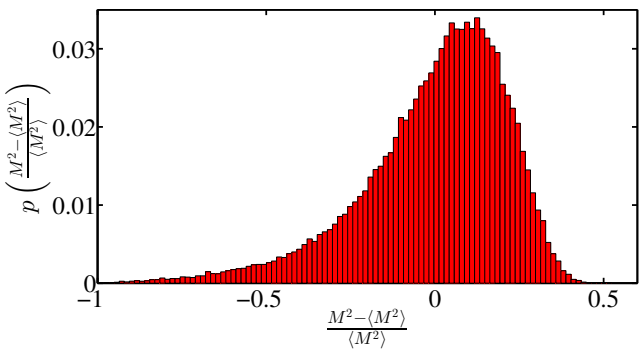


Figure 4: Probability distribution of the M^2 values determined using Monte Carlo simulation.

An input field distribution for GENESIS has been prepared using the measured profile shown in Figure 2 and the FEL performance has been calculated for the parameters listed in Table 1. Figure 5 shows the power contrast after the fourth undulator along the bunch. The simulated contrast is in a good agreement with the expected value for an M^2 of 2.2 in Figure 1 and also agrees with the experimentally measured energy contrast reported in [4]. In order to compare the results one has to stress that the ratio between the SASE photon pulse length and the seed pulse length is about 4. FEL pulse energy was $(1.3 \pm 0.5)\,\mu$J while the unseeded SASE pulse had an energy of about 300 nJ. The duration of the seeded FEL pulse is determined by the duration of the seed pulse of approx. 15 fs while the duration of the region in the bunch suited for SASE was 60 fs, measured using a transverse deflecting cavity. Shot-to-shot fluctuations have been averaged out.

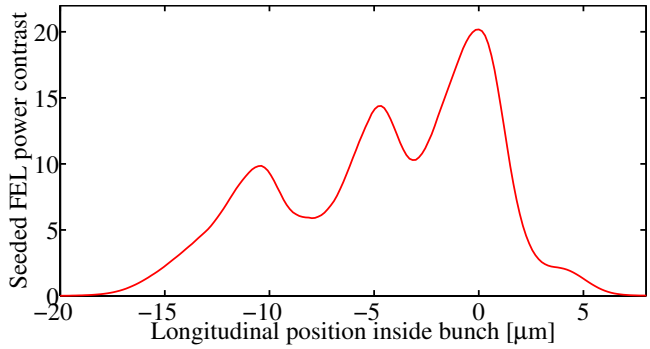


Figure 5: Power contrast along the internal bunch coordinate s.

CONCLUSION

It has been shown that the influence of the M^2 onto the power contrast is of high importance for the performance of a seeded FEL facility. The power contrast decreases strongly with M^2 , reaching 0 at an M^2 of about 5. Results of the studies of this dependence are in good agreement with the experimental data from "sFLASH", the HHG direct seeding experiment at FLASH. A method to obtain M^2 value has been discussed and used to evaluate properties of the HHG seed beam at FLASH. Seed pulse field distribution files have been generated. Therefore the modal content that has been reconstructed from intensity profiles. Those profiles were taken during the successful seeding. Simulation using these field distributions deliver results which are in good agreement with measured data.

REFERENCES

[1] *How to (Maybe) Measure Laser Beam Quality*, volume 17 of *OSA Trends in Optics and Photonics*. Optical Society of America, 1998.

[2] *Undulator system for a seeded FEL experiment at FLASH (WE5RFP070)*, Proceedings of the Particle Accelerator Conference 2009, 2009.

[3] *Commissioning results of the photon-electron diagnostics unit at aFLASH (MOPD54)*, Proceedings of the DIPAC2011, 2011.

[4] S. Ackermann et al. Generation of coherent 19 nm and 38 nm radiation at a free-electron laser directly seeded at 38 nm. *Physical Review Letters*, 111(11):114801, 2013.

[5] Sven Ackermann, Bart Faatz, and Velizar Miltchev. Modal analysis of a seeded free-electron laser. *Phys. Rev. ST Accel. Beams*, 16:100702, Oct 2013.

[6] W. Ackermann et al. Operation of a free-electron laser from the extreme ultraviolet to the water window. *Nat Photon*, 1(6):336–342, June 2007.

[7] R. Bachelard et al. Wavefront analysis of nonlinear self-amplified spontaneous-emission free-electron laser harmonics in the single-shot regime. *Physical Review Letters*, 106(23):234801, 2011.

ISBN 978-3-95450-141-0

Copyright © 2014 CC-BY-3.0 and by the respective authors

[8] B. Faatz et al. Flash ii: Perspectives and challenges. *Nuclear Instruments and Methods in Physics Research Section A: Accelerators, Spectrometers, Detectors and Associated Equipment*, 635(1, Supplement):S2 – S5, 2011.

[9] J. Gautier et al. Optimization of the wave front of high order harmonics. *The European Physical Journal D*, 48(3):459–463, 2008.

[10] F. Gori et al. Intensity-based modal analysis of partially coherent beams with hermite—gaussian modes. *Opt. Lett.*, 23(13):989–991, Jul 1998.

[11] Thomas F. Johnston. Beam Propagation (M2) Measurement Made as Easy as It Gets: The Four-Cuts Method. *Appl. Opt.*, 37(21):4840–4850, 1998.

[12] Th. Maltezopoulos et al. A high-harmonic generation source for seeding a free-electron laser at 38 nm. *Applied Physics B*, pages 1–10, 2013.

[13] J. A. Nelder and R. Mead. A simplex method for function minimization. *The Computer Journal*, 7(4):308–313, 1965.

[14] S. Reiche. GENESIS 1.3: a fully 3D time-dependent FEL simulation code. *Nuclear Instruments and Methods in Physics Research, Section A: Accelerators, Spectrometers, Detectors and Associated Equipment*, 429:243–248, 1999.

[15] P. Sprangle, H.P. Freund, B. Hafizi, and J.R. Penano. Optical Beam Quality in Free-Electron Lasers. *IEEE Journal of Quantum Electronics*, 45:218–222, 2009.

Copyright © 2014 CC-BY-3.0 and by the respective authors

ISBN 978-3-95450-141-0

LINEAR FOCAL CHERENKOV-RING CAMERA FOR SINGLE SHOT OBSERVATION OF LONGITUDINAL PHASE SPACE DISTRIBUTION FOR NON-RELATIVISTIC ELECTRON BEAM *

K. Nanbu#, K. Kashiwagi, H. Hinode, Y. Shibasaki, T. Muto, I. Nagasawa, S. Nagasawa,
K. Takahashi, C. Tokoku, A. Lueangaramwong, H. Hama,
Electron Light Science Centre, Tohoku University, Sendai, Japan

Abstract

Test accelerator as a coherent Terahertz (THz) source (t-ACTS) has been constructed at Tohoku University, in which generation of intense coherent THz radiation from sub-picosecond electron bunches will be demonstrated. Since final electron bunch length of accelerated beam is mostly dictated by the longitudinal phase space distribution at the exit of electron-gun, Measurement of initial electron distribution in the longitudinal phase space is indispensable for stable production of very short electron bunches. A novel method for measurement of electron kinetic energy applying a velocity dependence of the opening angle of Cherenkov light from a radiator medium has been proposed for relatively lower energy electrons. Combined use of a streak camera and a "turtle-back" mirror designed specifically that confines the Cherenkov light onto a linear focal line may allow us to observe the longitudinal phase space distribution directly. In this report, we describe the concept and designing of the linear focal Cherenkov-ring (LFC) camera system, as well as the current status of the system development.

t-ACTS PROJECT

In the t-ACTS project, the intense coherent THz radiation will be generated from an undulator and an isochronous accumulator ring via producing sub-picosecond bunches [1, 2, 3]. The t-ACTS consists of a thermionic cathode rf gun, an alpha magnet and a 3-meter-long accelerating structure, and velocity bunching scheme in the accelerating structure is being used for generate the sub-picosecond electron bunches. The thermionic rf gun composed of two independent cavities is capable of manipulating the beam longitudinal phase space, named an Independently-Tunable Cells (ITC) RF gun [4]. Employing a scheme of velocity bunching in the travelling-wave accelerating structure, the bunch compression will be performed [5]. The longitudinal phase space distribution at the exit of the rf-gun governs the final bunch length of electron beam after the bunch compression process, so that production of proper initial electron distribution in the longitudinal phase space is crucial to achieve very short electron bunch length of hundreds femtosecond.

*Work supported by JSPS KAKENHI Grant Numbers 24651096, 25790078.
#nanbu@lns.tohoku.ac.jp

LINEAR FOCAL CHERENKOV-RING CAMERA

Concept and Principle

In order to confirm directly whether the proper longitudinal phase space of the beam created by the ITC-RF gun for bunch compression, the LFC camera has been developed [6, 7].

The Cherenkov light is widely used for beam diagnostics and particle counters in high energy physics experiments. It is well known that the Cherenkov angle θ_c is inversely proportional to the particle velocity β (= v/c) as

$$\cos\theta_c = \frac{1}{n(\omega)\beta}, \qquad (1)$$

where n(ω) is the refractive index of the Cherenkov radiator medium at a radiation frequency. Since the Cherenkov angle contains information of the charged particle velocity, the photons having the same Cherenkov angle has to be focused onto an identical focal position of a detector in order to identify the particle momentum. If the focal points of different Cherenkov angles can be placed on a straight line, the momentum distribution of the beam will be observed at once. Furthermore, if information on relative arrival times onto the Cherenkov

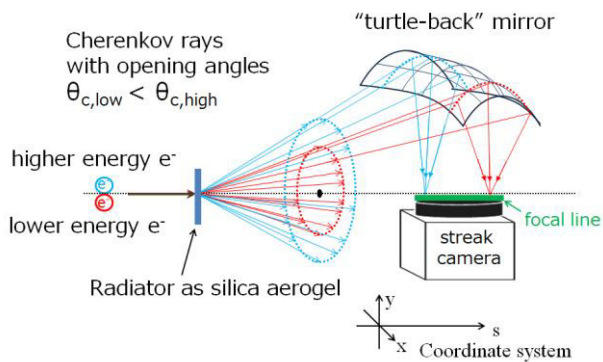


Figure 1: Conceptual drawing of the LFC camera. Electron emits the Cherenkov light when through the radiator made by silica aerogel. The turtle-back mirror is used to resolve the Cherenkov rays with the different opening angles with specific focal positions along a focal line. The streak camera can detect the relative arrival time of the rays with sub-picosecond time resolution.

ISBN 978-3-95450-141-0

Copyright © 2014 CC-BY-3.0 and by the respective authors

radiator for each particle is preserved, we are able to perform direct observation of the longitudinal phase space distribution by using a high-resolution streak camera.

Figure 1 shows schematic principle of the LFC-camera. The LFC- camera is composed of a Cherenkov radiator, turtle-back mirror, and optical devices such as a streak camera. The turtle-back mirror gathers photons emitted some part of azimuthal angle in the Cherenkov ring and confines onto the longitudinal axis. Surface of the turtle-back mirror is parabolic in the s-axis and spherical in the x-axis (shape of mirror looks like a turtle's carapace, so named the turtle-back mirror).

Design and Manufacturing the Turtle-back Mirror

The reflecting surface of the turtle-back mirror is expressed by a following formula

$$x^2 + y^2 - \left(-\frac{1}{2A} s^2 + \frac{A}{2} \right)^2 = 0 \quad \left(A \equiv \sqrt{y_0^2 + s_0^2} + y_0 \right). \quad (2)$$

The origin of the coordinate is the center of the radiator medium. The parabolic curve can resolve Cherenkov ray with the different Cherenkov angles. Role of the spherical curve is to confine the Cherenkov light on the s-axis, in other words focus it in the x-direction. The parameter A of the turtle-back mirror is crucially important for the energy resolution at the LFC camera [8], meanwhile the parameter A makes little impact on the time resolution. The parameter A is a magnification factor of the energy resolution, nothing but that the energy resolution can be optimized when optimum and larger A is selected. On the other hand, the small A leads an advantage in fabrication, Physical size of the turtle-back mirror limits the tolerance of machining error.

Momentum and time resolutions of the LFC camera for measuring longitudinal phase space at the exit of the rf-gun are required to be less than 1 keV/c and 1 ps, respectively. As a result, the parameter A of 350 mm was chosen, in which the momentum in a range from 2.294 to 2.412 MeV/c can be observed with sufficient resolution by the streak camera having a photon entrance slit of 3 mm width.

A prototype turtle-back mirror was fabricated for proof-of principle experiment. Since distortion caused during machining on the fabricated mirror surface may critically affect the resolution, an aluminium block cut to the eight pieces and assembled together with a special jig was lathed along its central axes to shape the parabolic curve. The mirror surface was polished and coated by vacuum aluminium evaporation

Performance Test of the Turtle-back Mirror

To evaluate the momentum and time resolutions caused by the surface roughness of the turtle-back mirror, roughness parameters such as the amplitude of the roughness and the correlation length are required. We measured the surface profile of the turtle-back mirror using a contact type surface profilometer (Talysurf PGI 1250A).

The surface of a high quality commercial plain mirror was also measured to compare with the turtle-back mirror. Figure 2 shows measurement results of surface profilometer. The roughness of the turtle-back mirror was deduced by Fourier transform. Roughness analysis result indicates a root-mean-square amplitude of the roughness per correlation length is 0.00032. Using a ray trace calculation it was found out that the momentum resolution is degraded from 1.05 keV/c to 7 keV/c. On the other hand, the commercial plane mirror roughness was measured to be as low as 0.000016. Consequently, it is concluded the surface of the turtle-back mirror is not well manufactured and must be improved for sufficient momentum and time resolution.

In order to confirm the parameter A of the turtle-back mirror, we have measured the parameter A as follows.

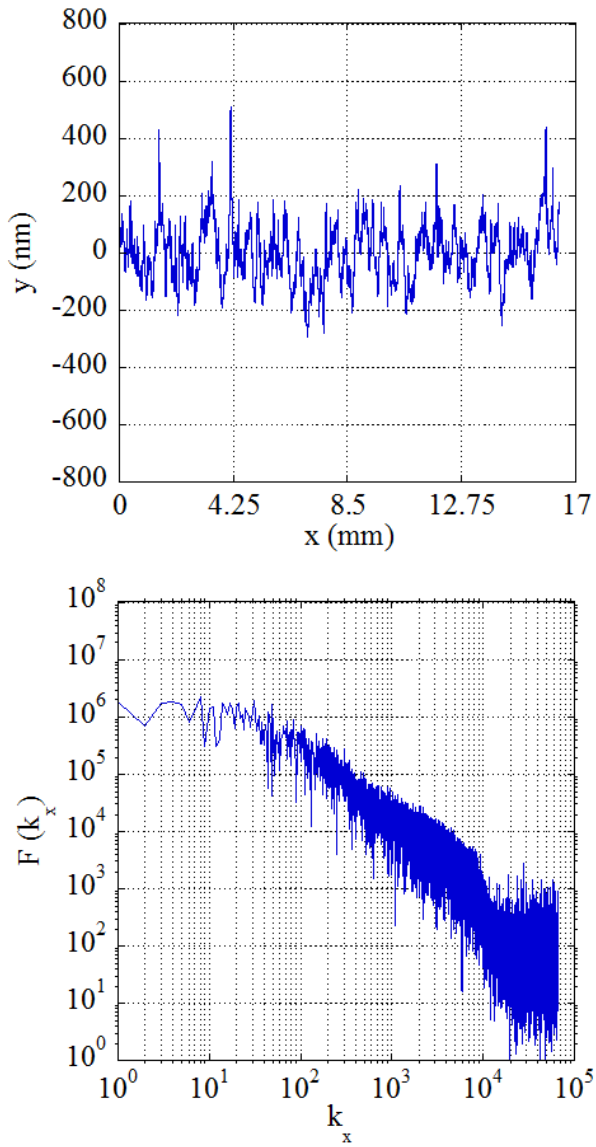


Figure 2: (upper) one-dimensional surface profile of the turtle-back mirror along the x-direction (lower) Fourier spectrum of the surface profile.

Copyright © 2014 CC-BY-3.0 and by the respective authors

ISBN 978-3-95450-141-0

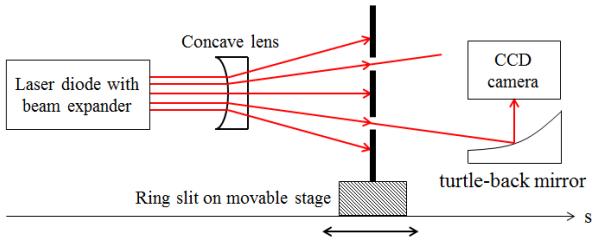


Figure 3: Schematic view of the parameter A measurement. The opening angle of laser is varied by moving the ring slit position along the s-axis.

We have used a ring-like diverging laser light instead of the Cherenkov light as shown in Fig. 3. It makes possible to generate the particular opening angle (represented by the Cherenkov angle θ_c) by changing the position of the ring slit on the translation stage. The CCD camera is placed on the focal line above the turtle-back mirror to acquire the focal position and the focal profile for respective opening angles. Measurement were performed for a wide range of the opening angle, and the derived parameter A was 349.50±0.13 mm, while target value is 350 mm. Although the roughness of the prototype mirror surface is quite insufficient, overall shape of the mirror is well manufactured. Surface polishing by a precision machinery technique will be performed.

CHERENKOV RADIATOR

Silica Aerogel

The LFC-camera employs the Cherenkov radiator placed in vacuum to avoid the electron scattering in vacuum windows. The radiator medium is required to have high transparency as well as low refractive index around 1.05, so that we have chosen the hydrophobic silica aerogel with extremely low density [10].

Accuracy of Electron Momentum

Since the LFC camera employs the silica aerogel in vacuum as Cherenkov radiator, if the refractive index of silica aerogel in vacuum is different from an atmospheric one, there should be some ambiguity in measured electron momentum. It was reported that refractive index of aerogel in vacuum is changed by approximately 2% compared with atmospheric one [9].

The focal position of the turtle-back mirror is expressed as

$$s_f(\beta) = A \cdot n \cdot \beta \left[1 - \sqrt{1 - \left(\frac{1}{n \cdot \beta} \right)} \right], \qquad (3)$$

where $s_f(\beta)$ is the position of the focal line along the s-axis for the Cherenkov photon emitted from the electron with a velocity β and n is the refractive index of the Cherenkov radiator. The turtle-back mirror converts the Cherenkov angle to the focal position of the focal line. Figure 4 shows a plot of $s_f(\beta)$ and its derivative as a function of the electron momentum p. If refractive index

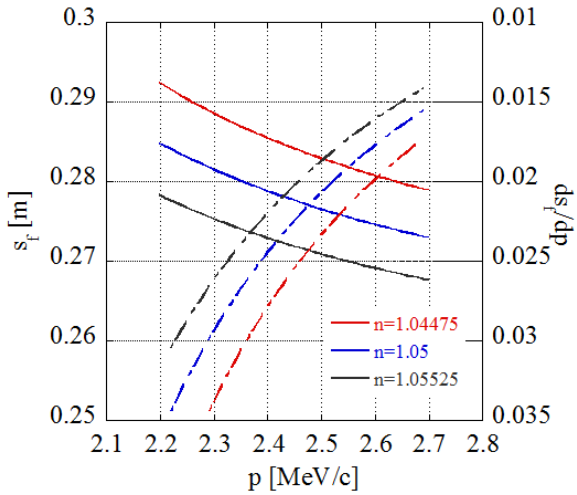


Figure 4: Solid lines denote the variation of focal positions for different refractive indices of the radiator medium calculated using Eq. (3). Dotted lines indicate those derivatives of the focal position with respect to the momentum p.

of the radiator in vacuum differs by as low as 0.5% compared with the one at atmospheric pressure, the position on the focal line is shifted about 10 mm, which is equivalent to a change of the momentum of 250 keV/c. Absolute value of the in-vacuum refractive index of silica aerogel is crucial to calibrate the electron momentum observed by the LFC-camera.

Refractive Index Measurement

Number of method for measurement of the refractive index, such as a minimum deviation angle method, a critical angle method and a v-block method, have been developed for many years. However, these methods are not much suitable for measurement of the thin silica aerogel. Therefore, we performed measurement of the thin silica aerogel refractive index by detecting an optical path difference using a Mach-Zehnder interferometer [11]. The optical path difference Δd at the rotation angle θ is expressed as

$$\Delta d = t\left(n\cos\theta_r - \theta_i\right) - t \cdot \left(n - 1\right), \qquad (4)$$

where θ_i is an incident angle, θ_r is a reflecting angle. The refractive index n at the optical path difference Δd can be derived as

$$n = -\frac{(m\lambda)^2 + 2t(m\lambda - t)(\cos\theta_i - 1)}{2t\left\{t(\cos\theta_i - 1) + m\lambda\right\}}, \qquad (5)$$

where λ is a wavelength of laser, m is an order of interference. Figure 5 shows the schematic of interferometer for refractive index measurement. Rotating angle of the silica aerogel is being controlled by a stepper motor (1 step = 0.001125deg). The silica aerogel is installed on the rotary manipulator via a special holder in the vacuum chamber.

ISBN 978-3-95450-141-0

Copyright © 2014 CC-BY-3.0 and by the respective authors

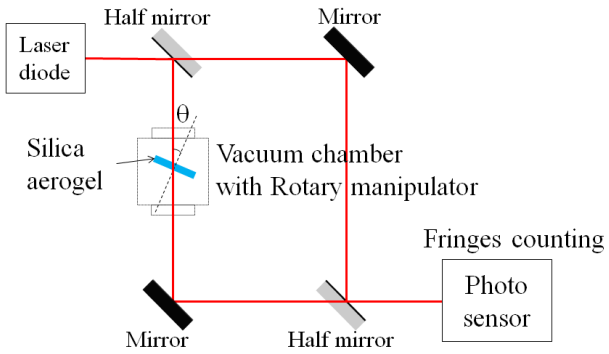


Figure 5: The interferometer for refractive index measurement. A silica aerogel is placed in the vacuum chamber with a rotary manipulator. It is possible to rotate in vacuum. A light source for interferometer is a diode laser with a laser beam expander and a photodiode with an amplifier is used to detect the laser light interference.

Two silica aerogels, referred in the following as the Sample 1 and Sample 2 one, have been measured. The rotation angle was varied between -45° to +45° in steps of 0.01125°. Measured interfered spectrum was analysed by second-order polynomial curve fitting, and then the optical path difference was derived. The refractive index of samples was calculated using Eq. (5) applied for a 10^{th} order interfered spectrum. The average value of refractive index deduced from 6 times measurements carried out for each sample was listed in Table 1.

Table 1: Measurement Result

	Atmospheric pressure	**Vacuum (3×10^{-5}Pa)**	**Difference value**
Sample 1	1.0448(13)	1.0440(20)	0.0008(23)
Sample 2	1.0488(6)	1.0450(6)	0.0038(8)

It was found out the measured value for the sample 2 at the atmospheric pressure is in good agreement with a refractive index of 1.049 that was already derived using a mass density. This suggests the measurement system has sufficient performance for lower refractive index case such as n ~ 1.05.

We have not observed significant difference for the refractive index in vacuum from one at the atmospheric pressure for the sample 1. Though the refractive index in vacuum of the sample 2 obviously diminished from the one at the atmospheric pressure, the difference of 0.4 % is pretty small. This experimental result indicates a structural change of the silica aerogel due to the vacuum pressure is unlikely because the aerogel was manufactured by a water-free hydrophobic treatment [12].

CONCLUSION

A novel beam diagnostic system for direct measurement of longitudinal phase space distribution (the LFC-camera) has been studied and developed. Characteristics of the prototype turtle-back mirror was investigated. The large surface roughness of the turtle-back mirror degrades the momentum resolution to up to 7 keV, while the predicted it is 1 keV resulted from perfect system condition. The measured parameter A was indicated 349.50±0.13 mm, which is in good agreement with a designed value of 350 mm. According to the measurement with Mach-Zehnder interferometer, the refractive index of aerogel in vacuum diminishes by 0.36% from one in the atmospheric pressure, which may shift the absolute momentum by 200 keV/c. However, we have confirmed the refractive index of the silica aerogel can be known beforehand, so that calibration of the electron momentum observed by LFC-camera is possible with sufficient accuracy.

ACKNOWLEDGEMENT

The authors thank the Industrial Technology Institute of Miyagi Prefectural Government for the mirror surface measurement. We appreciate Dr. M. Tabata of Chiba University for providing the silica aerogel samples.

REFERENCES

[1] H. Hama et al., N. J. of Phys. 8 (2006), 292.
[2] H. Hama and M. Yasuda, Proc. of FEL2009, (2009), 394.
[3] F. Hinode et al., Nucl Instr. and Meth., A 637 (2011), S72.
[4] T. Tanaka et al., Proc. 27th Int. FEL Conf., Stanford (2005), 371.
[5] F. Miyahara et al., Proc. of IPAC'10, (2010), 4509.
[6] H. Hama et al, Proc of BIW10, (2010), TUCNB03.
[7] K. Nanbu et al., Proc. of FEL2011, (2011), 576.
[8] A. Lueangaramwong, "Development of Linear Focal Cherenkov-ring Camera for Direct Observation of Longitudinal Phase Space of Non-relativistic Electron Beam", Master's thesis, Tohoku University, 2014.
[9] D. Richter et al., Nucl Instr. and Meth., A 513 (2003), 635.
[10] A. Lueangaramwong, et al., Proc, of PASJ10, (2013), 194.
[11] Laser Handbook second edition, The Laser Society of Japan, (2005), 72.
[12] M. Tabata, et al. Nucl Instr. and Meth., A 623 (2010), 339.

Copyright © 2014 CC-BY-3.0 and by the respective authors

ISBN 978-3-95450-141-0

OPTICAL SYSTEM FOR ESS TARGET PROTECTION

M. Donna, T. Grandsaert, M. Göhran, R. Linander,
Thomas Shea, Cyrille Thomas*, ESS, Lund, Sweden

Abstract

One specificity of the ESS accelerator and target is that a high power and ultra low emittance proton beam is sent straight onto a Tungsten target. The high power density proton beam from the ESS linac will damage any material it meets. Thus a strategy to protect the target and the target area has to be deployed: the proton beam on target will be defocused and swept, distributing homogeneously the power density on an area 10^4 times larger than its non defocused area. On its way towards the target, the beam goes through two windows: the proton beam window (PBW) separating the high vacuum of the accelerator to the 1-bar He filled area of the target monolith; and the target window (TW) marking the entrance area of the target wheel. In this paper, we present the PBW imaging system, one of the proton beam diagnostics to be developed for imaging the proton beam current density deposited in the PBW. We will describe the expected performance of the imaging system in order to satisfy the PBW protection requirement. We will also describe the radiative processes which could be used as the source of the imaging system. Finally, we will describe the necessary condition and hardware for the implementation of a protection system for both the PBW and TW.

INTRODUCTION

The ESS Linac is designed to deliver a proton beam on a tungsten target for the production of neutrons. The emittance of the beam is 0.7 mm.mrad and its average power is 5 MW [1]. As a result, the natural beam size at the end of the linac, thus on target, is expected to be 2-3 mm, and would damage the target instantaneously. The strategy chosen to prevent this is twofold: the beam is defocused and swept linearly across a large area on the target [2]. The results is a dilution of the proton current density on the PBW and target by a factor 10^4, bringing the density bellow the damaging threshold (0.110 mA/cm^2 on PBW). However, each proton beam macro-pulse, a train of one million proton bunches, 2.86 ms long with more than 10^{15} protons in total, can potentially damage the PBW and TW if the defocusing and rastering condition are not fulfilled. In order to monitor the proton beam current density distribution of each macro-pulse, we will implement redundant diagnostics [2]. One of these will be to perform an image of the beam passing through the PBW. Each image will show the current density distribution which can be recorded, analysed in such a way that not only the degradation state of the PBW can be monitored and anticipated, but also any fault of the rastering system can be detected and beam abort before the next macro-pulse. In the following, we will present the imaging system performance required for PBW protection, together with the constraints from the high radiation environment of the target. We will also mention the possible sources to be used, emerging from the interaction of the protons with the surface of the PBW. Finally, we will draw the necessary condition for the PBW protection to occur, and present the possible hardware and software to implement such a protection system.

* cyrille.thomas@esss.se

IMAGING SYSTEM EXPECTED PERFORMANCE

The imaging system for the PBW has to meet performance for protection of the PBW, but also, to overcome the constraints due to the hard radiation environment. The PBW is large, with $250 \times 110\,\mathrm{mm}^2$. The first optical element of the imaging system can be placed at 2.65 m from the PBW, 65 mm above or bellow the proton beam axis. The optical system has to go through a 4 m high plug, the Proton Beam Instrumentation Plug (PBIP), in order to exit the high radiation area of the target; then the optical path has to run another 7 m toward a radiation safe environment for camera and people. In total the distance from the PBW to the image sensor is close to 15 m. The size of the sensor imposes magnification less than $m = 0.2$. The resolution is specified to be of the order of 1 mm or less. The transmission must be optimised not only to permit single shot macro-pulse imaging, but also reliable analysis on the images. The distortion of the image must also be minimised to render image fidelity and avoid additional image processing prior analysis of the current density distribution. Finally, because the first optical elements are in radiation environment, the optical path goes through the radiation shield and thus its integrity must remain. In addition, the first optical elements must be remote handled during installation and removal after been degraded by long exposure to the hadronic shower. The expected performances described above translate into optical characteristics, which in turn, can be summarised with a reduced number of these characteristics. The position of the PBIB and the necessary small aperture to maintain the shield integrity define the maximum numerical aperture (NA) of the optical system. The first mirror aperture can be of the order of 100 mm, which define NA ≈ 0.19. The optimum resolution (R), without aberration of the optical system, is also determined by NA, by means of the well-known formula: $R = \frac{\lambda}{2NA}$, with λ the wavelength at which the object is imaged. So taking into account the requirements of 1 mm resolution or less, at $\lambda = 550\,\mathrm{nm}$, NA $> 3 \cdot 10^{-4}$. For the power transmission (T), NA also plays a role. In our case, the first mirror of the system is the defining aperture, so the best expected power transmission, without accounting for the reflectance of the mirrors, is simply given by the solid angle under which the first mirror sees the object. For a cir-

ISBN 978-3-95450-141-0

Copyright © 2014 CC-BY-3.0 and by the respective authors

cular aperture, T = 1 − cos(arcsin(NA)). So the larger NA, the larger the transmission. With NA ≈ 0.19, T ≈ $1.6 \cdot 10^{-4}$. Finally, one must account for the Depth of Field (DoF), due to the source plane non orthogonal to the main optical axis. Similar to the R, DoF is associated to NA: DoF = λ/NA^2. As is well-known, a larger DoF imposes a lesser resolution (i.e. a larger R). Optical system performance for the imaging system are summarised in Table 1.

Table 1: Summary of the Optical System Properties as Given by the ZEMAX Primary Design and Compared to the Expected Conceptual Approach

	Expected Values		ZEMAX Design
Mag.	0.05 - 0.2		0.085
NA_{eff}	R < 1 mm DoF > 1 mm T > 0.01	> 0.0003 < 0.022 > 0.14	0.01
DoF (mm)	> 4		5
R (μm)	< 1000		30
Δ_{PSF} (mm)	< 1		2-4
Geo. T			$5 \cdot 10^{-5}$

ZEMAX Design

The design of the optical system is mainly done using ZEMAX [3]. The system is divided in three parts, a primary imaging system, which constitute a 3-mirror system block. Their function is to make a first intermediate image of the PBW. Then a series of also 3-mirror block relay imaging systems, to carry the image to the radiation safe area. The last system block performs the image on the camera. This way, by splitting the system in small blocks, we may control aberration and field distortion. With the three mirrors assembly, we should be able to satisfy Petzval condition for each block assembly, and eventually for the whole system assembly. However, in our preliminary design, shown in Fig. 1, we have introduced afocal system block assembly to save distance and keep a small number of mirrors. By doing this, we also introduced coma aberration, and field distortion, which reflects in the Δ_{PSF} value shown in the Table 1. This will have to be corrected in the next design iteration.

Proton Current Density Source

There are several sources to take into account for the imaging of the proton current density distribution: the Optical Transition Radiation (OTR) occurring at the interface between the PBW and the He-filled atmosphere of the Target monolith; the luminescence from specific coating of the PBW; the proton induced fluorescence from the He gas. The OTR is likely to be excluded: the OTR yield from Al to air per 2 GeV proton per unit steradian over the whole visible range is of the order of 10^{-7}. A macro-pulse would generate ≈ 10^8 photons over 2 π steradian. The transmission of the optical system associated with NA, Table 1, excludes the possibility to get any sensible information by means of OTR. The yield from luminescence is much brighter than OTR; there are several possible coating to be used. For example, the typical yield for a Cr:Al2O3 coating is of the order of 10^2 photons per steradian [4]. It is thus expected to get 10^{11} photons per macro-pulse on the sensor. With this level of photon intensity a large signal to noise ratio is expected with the possibility to not only perform single shot image of the macro-pulse, but also it may permits faster acquisition at 10^4 images per second. Finally, the proton induced fluorescence of He-gas may lead to similar photon yield. However, this source is longitudinally extended and provides an additional challenge to the imaging system, which would have either to have infinite depth of field or be telecentric. Both would impose a rather small NA, perhaps incompatible with the resolution requirements.

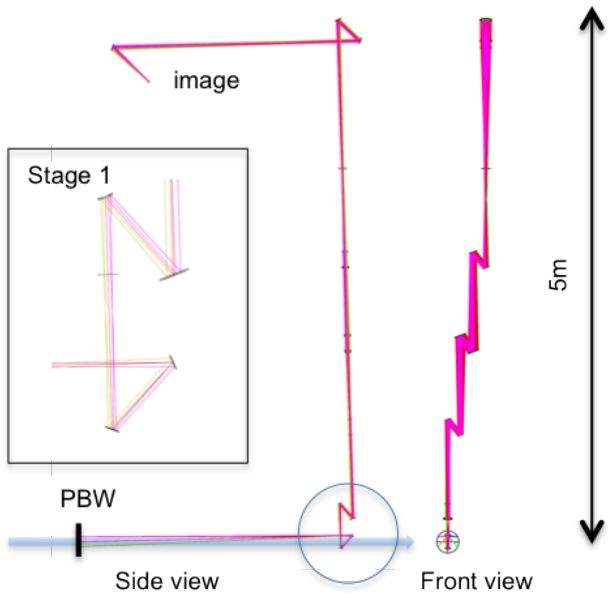


Figure 1: Optical imaging system preliminary design. The proton beam is shown by the semi-transparent arrow; the primary imaging assembly in the inset. The distance between PBW and first mirror is 2.65 m. On the top, the visible beam exits the monolith through a viewport (not shown) and then is finally focused on the image sensor.

IMAGE FAILURE MODE DETECTION

The typical image to be seen from one macro-pulse been swept in horizontal and vertical axes, with a saw-tooth signal of frequency 40 and 29 kHz in Hor. and Vert. respectively, is shown in Figure 2. To generate this image we build a model of the rastering beamlet throught the window. The 4 raster magnets induce a sawtooth motion on both horizontal and vertical axes of the center of mass of the beamlet. With no rastering, the r.m.s beam size is expected to be 12 × 4 mm. So we can generate the image of the current density by summing 2D-Gaussian distributions with their centre of mass

Copyright © 2014 CC-BY-3.0 and by the respective authors

ISBN 978-3-95450-141-0

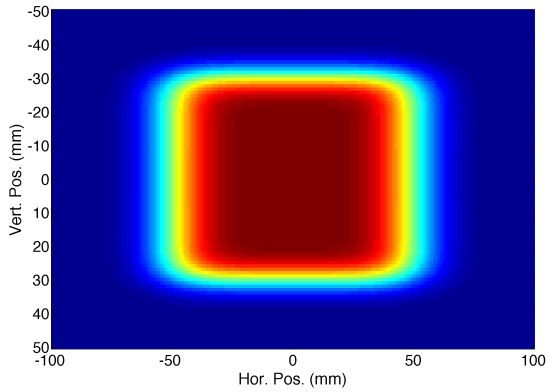


Figure 2: Image of the current density under normal operation.

moved using the parametric equations generated by the raster motion:

$$C_i = B_{0,i} + 2\frac{B_i}{\pi}\arcsin\left(\sin\left(2\frac{\pi}{p_i}t\right)\right) \quad (1)$$

with C_i the centre of mass in the plane i (Hor. or Vert.), $B_{0,i}$ the initial offset of the beam at the time $t = 0$, B_i the amplitude of the motion given by the strength of the magnets, p_i the period of the motion in the plane i, and t the time during which the motion occurs.

In addition, the intensity of the beamlet Gaussian distribution is also time dependent.

This model allows to investigate almost all possible failing modes. For instance, off-centered beam in one or both axis, deflection amplitude not matching the required one, in one or both axis; sweeping may stop at any time through the motion, etc.

In order to be able to detect any of the possible faults, we build the following detection model: the image of the beam with the required condition is generated, and can be compared with the running condition, e.g. beamlet size, beam motion amplitude. Then during commissioning and operation, this generated reference image may be used and compared with each and every image of the macro-pulses. The comparison to be made is given by:

$$r = \sqrt{\sum_{i,j}\frac{\left(\frac{A_{ij}^{PBW}}{A_{ij}^{ref}} - 1\right)^2}{n_x n_y}} \quad (2)$$

with A_{ij}^{PBW}, A_{ij}^{ref} the matrix elements of the real macro-pulse image and the reference image respectively; $n_{x,y}$ the number of lines and columns of the images. r is then a number between 0 and 1.

Some of the possible failure mode are illustrated in Fig. 3. We have assumed a mismatch of the amplitude of the centroid motion induced by the 4 raster magnets. The curves represent the cases in which the horizontal, the vertical, and then both axis amplitudes are smaller than the set values. The

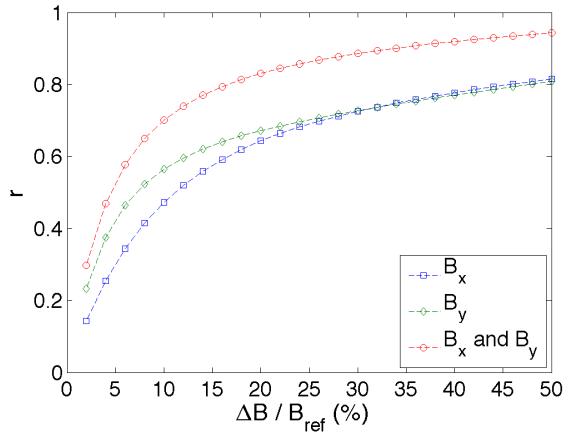


Figure 3: Image residual as given by Eq. 2 for several test failures involving magnet power supply been smaller than the targeted values. The horizontal axis shows the relative difference of the motion amplitude to the nominal one.

calculation of r from Eq. 2 shows for all considered cases, deviation of 5% of the amplitudes of the raster magnets intensities leads to a residual larger than $r \geq 0.2$. Obviously, further investigation of the model is required. We show here that wrong motion amplitude can be detected. However, robustness of the model needs to be demonstrated. In such a case, we will conclude the model and the test to be applicable for the protection of the PBW and the target.

HARDWARE AND FPGA FOR MPS

As discussed above, images of the proton beam current density distribution must be acquired and processed within a single shot period to permit the protection of the PBW. For that, the real-time response of the data acquisition board must be evaluated. In this section, we discuss how the image data is taken to the FPGA digitizer board in the µTCA.4 crate, that equip a Xilinx component, and then elaborated in order to have a response fast enough to satisfy the Machine Protection System (MPS) requirements.

Firstly, the camera interface protocol needs to be selected within existing standardization committees and standards, e.g. Camera Link and Camera Link HS, GigE Vision, USB3 Vision, EMVA 1288, Fire Wire, CoaXPress, and others; at this point in time, the choice of the protocol yet has to be done. It depends strongly on the sensor/camera choice. Intimate to this choice is the selection of a specific board: it can be either FPGA Mezzanine Card (FMC), or Rear Transition Modules (RTM), depending on the selected platform. In addition, once the board is chosen, the connection technology is defined. For instance, the relative decoding/encoding intellectual property is designed to extract the image data from the protocol frame, and to interface the controls for the specific camera. Further integration has to take into account the image data format delivered by a specific camera (RGB24/32, IUV, etc..) and pixel order. This operation of conversion and pixel re-ordering can also be implemented in the FPGA

ISBN 978-3-95450-141-0

Copyright © 2014 CC-BY-3.0 and by the respective authors

processing board, before making any further elaboration. At this point the raw image data, after this pre-elaboration, is stored in memory and can be collected from EPICS for archiving purpose. The next FPGA board operation is frame processing. Two possible scenario are anticipated. The first one is to acquire a single shot image during the passage of a single macro-pulse. This corresponds to the acquisition and processing of the images discussed in the previous section. The second one, is to acquire a series of images shot during the passage of a macro-pulse. This can be done with a fast camera that can be triggered and operated in burst mode. The typical camera speed in view for this acquisition mode is of the order of $20 \cdot 10^3$ frames per second. In this mode, the processing of the images will give information on the beamlet within a macropulse. This is not discussed here. In both acquisition modes, the FPGA board has to be triggered and synchronised with the ESS timing system (essentially a Timing Receiver board). It is required for the FPGA board to control the camera, and to select the images to be acquired and processed.

The image processing to be implemented into the FPGA board will be the following: firstly, the images acquire will have to be normalised to the maximum image intensity. Then the image will be compared to the generated reference image in order to produce the test scalar r (Eq. 2). Finally r will be compared to a threshold producing a boolean value for the MPS trigger.

Normalisation of the acquired images can be implemented following several possible sequences of operation: one of these is to find the largest pixel intensity, then scale the reference image, prior to the division and subtraction operations. However, the exact final sequence of operations will be defined by the time cost of the total operation to produce r. For example, to perform the division it is possible to use the LogiCORE IP Divider Generator, in High Radix implementations that uses the XtreamDSP slices; using the dual-port block RAM, it is possible to write the data in the memory, coming from the pre-elaboration, at the protocol rate, while it is possible to read out, to perform the residual calculation, at an higher rate to reduce the latency of the algorithm. The division in Eq. 2 could be done again using the LogiCORE IP Divider Generator, but could be also a simple factor 2 scaling, in case that the window dimension ($n_x n_y$) is a power of 2. The accumulation is performed using a XtreamDSP slices, and the calculation of the square root is performed using the Xilinx LogiCORE IP CORDIC. A schematic of the FPGA architecture is shown in Fig. 4. It illustrates the essential functionality to be provided by the FPGA board. It includes the acquisition operation of the images, and their processing to extract the boolean value for the MPS trigger. The processing of the fast acquisition frames during one macro-pulse is not treated here. however, the FPGA architecture would be essentially the same, to permit MPS trigger within one macro-pulse.

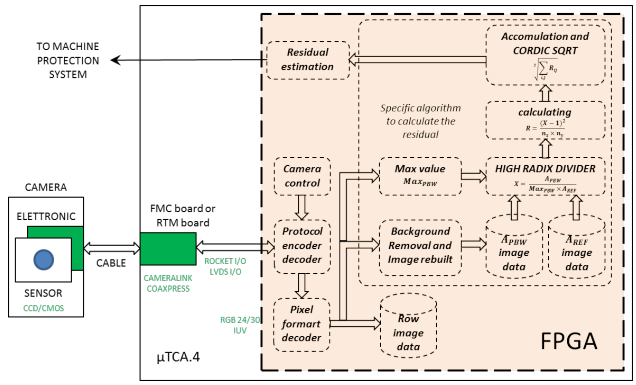


Figure 4: FPGA Architecture.

CONCLUDING REMARKS

For the monitoring and protection of the PBW and TW, we are designing a complex optical system which satisfies image performance together with Target shield requirements. As in any optical system, NA drives the imaging performance. With the requirements drawn, we expect NA ≈ 0.01 to satisfy DoF and resolution requirements. However, This is done to the detriment of the geometrical transmission, and thus imposes a high source radiation yield. This might be satisfied by specific luminescent coating. For instance, Cr:Al2O3 coating may generate enough photons for imaging, but it has a decay time comparable to the macro-pulse duration. This might be an issue and it needs to be addressed. We have developed a model of the expected proton beam density distribution during the rastering operation. This model can be used to investigate all possible failure modes. The model, once validated will be implemented in the FPGA for the image processing and for MPS trigger. Finally, we designed the core architecture for the camera control and FPGA code to be developed, identifying all elements and functionality required for PBW and TW window monitoring and protection.

REFERENCES

[1] M. Eshraqi, H. Danared, D. McGinnis, "Design Options of the ESS LINAC", Proceedings of IPAC2013, THPWO072, pages 3921–3923, Shangai, 2013.

[2] T.J. Shea, C. Bohme, B. Cheymol, S. Gallimore, H. Hassanzadegan, E.J. Pitcher, H. Thomsen, "Proton Beam Measurement Strategy for the 5 MW European Spallation Source Target", Proceedings of IBIC2013, TUPC02, pages 349–352, 2013.

[3] www.zemax.com

[4] T.J. Shea, C. Maxey, T.J. Mcmanamy, D. Feldman, R. Fiorito, A. Shkvarunets, "Status of Beam Imaging Developments for the SNS Target", Proceedings of DIPAC2009, MOOC04, pages 38–40, 2009.

Copyright © 2014 CC-BY-3.0 and by the respective authors

ISBN 978-3-95450-141-0

DISTINCT TRANSVERSE EMITTANCE MEASUREMENTS OF THE PXIE LEBT*

R. D'Arcy†, B. Hanna, L. Prost, V. Scarpine, A. Shemyakin, J. Steimel
Fermilab, Batavia, IL 60510, USA

Abstract

PXIE is the front-end test stand of the proposed PIP-II initiative i.e. the first step towards a CW-compatible, pulsed H- superconducting RF linac upgrade to Fermilab's injection complex. The test stand for this machine will be built step-wise; the Ion Source and Low-Energy Beam Transport (LEBT) are currently in place, with the RFQ and MEBT due for installation 2015.

The initial LEBT configuration under investigation in this paper is comprised of a D-Pace Filament-driven H- source and a single downstream solenoid, accompanied by a number of beam-diagnostic tools. The emittance studies expounded are performed via two methods: a position-angle phase-space sweep using an Allison-type emittance scanner; a solenoid corrector-induced transverse beam shift, impinging the bunch on an isolated, biased diaphragm. A detailed comparison of the two results is outlined.

INTRODUCTION

The proposed plan to upgrade Fermilab's injection complex consists of designing and building a CW SRF H- Linac. At its initial stage this is known as the Proton Improvement Plan II (PIP-II), to be used in pulsed mode. Front end components crucial for CW operation will be tested at an accelerator called, for historical reasons, PXIE [1], composed of a D-Pace [2] filament-driven H- ion source; a Low Energy Beam Transport (LEBT) section; a CW 2.1 MeV RFQ; a Medium Energy Beam Transport (MEBT) section; two SRF cryomodules (HWR and a SSR1); a High Energy Beam Transport (HEBT); and a beam dump. Figure 1 shows a schematic of the proposed beamline. The content of this paper will concern itself with the initial beam diagnostic results of the LEBT, namely the emittance measurements with two methods: Allison scanner and solenoid scans at the same beam conditions of, in part, a current of 2 mA. For a more detailed outline of the experiment, and its current status, please refer to [3].

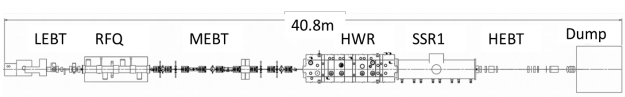


Figure 1: The proposed PXIE beamline.

LOW ENERGY BEAM TRANSPORT

The LEBT section of PXIE began with installation of the 30 keV H- ion source, producing beam in either pulsed (0.001 − 16 ms at 10 Hz) or CW mode with a beam current of 0.1 − 10 mA. Since then the beamline has been installed incrementally with the addition of a first solenoid, along with beam diagnostic tools, at the start of 2014. Once this initial layout was commissioned, the addition of two further downstream solenoids was completed in mid-2014. The data taking and results included in this paper are for the initial one-solenoid layout previously described, displayed in more detail in Fig. 2.

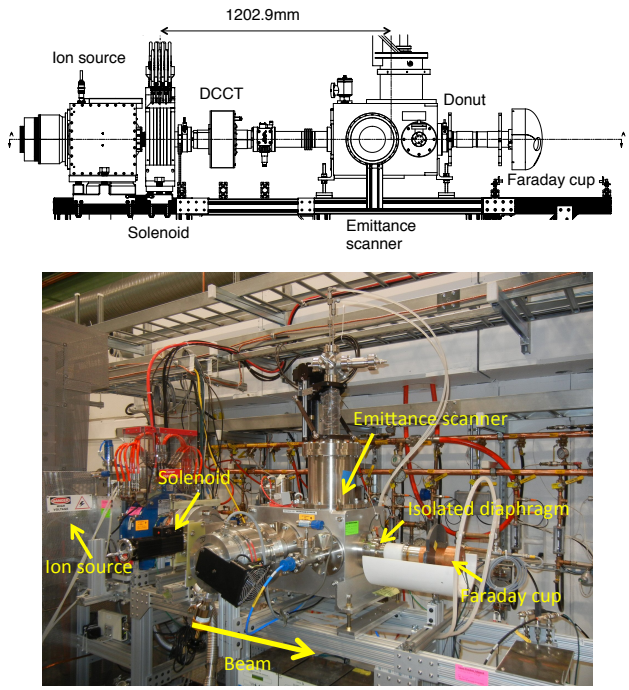


Figure 2: A schematic and photograph of the LEBT section constructed at the time of data taking for this paper.

ALLISON EMITTANCE SCANNER

The main tool to measure the beam emittance in the layout shown in Fig. 2 is the Allison Emittance Scanner. The Allison scanner was designed and built in collaboration with SNS and is based upon the original proposal in 1983 by P. Allison et al. [4]. The pictorial representation of the scanner, copied from [5], is shown in Fig. 3. The scanner measures the phase portrait of the beam in one dimension (vertical in the reported case). The scanner assembly consists of two slits, a Faraday cup with a suppressor electrode, and two de-

* Operated by Fermi Research Alliance, LLC, under Contract DE-AC02-07CH11359 with the U.S. DOE.
† rtpdarcy@fnal.gov

Copyright © 2014 CC-BY-3.0 and by the respective authors

ISBN 978-3-95450-141-0

flection plates placed symmetrically with respect to the slits. The spatial coordinate of a phase slice is determined by the position of the entrance slit and is adjusted by a step motor moving the entire assembly. The slice angle is determined by the voltage V applied between plates. In approximation of a negligible slit size, particles can pass through both slits only when their initial angle x' with respect to the scanner axis is

$$x' = \frac{VL}{4g_e U} \quad , \tag{1}$$

where L is the effective length of the plates, g_e is the effective gap between the plates, and qU the energy of the ion. For the PXIE LEBT Emittance Scanner (with voltage applied symmetrically to each plate $V/2$ = 1000 V, L = 96 mm, g_e = 8.9 mm, and U = 30 kV) the scanner can operate over an angular range of ±180 mrad and a spatial range of ±30 mm.

The scanner's Faraday cup signal goes to a 16-bit, ±10 V ADC, which for the primarily unipolar signal has a dynamic range of 3×10^4. The secondary electrons from the Faraday cup are suppressed by the field of the suppressor electrode, typically biased at -100 V. The voltage of the deflecting plates is swiped at 10 Hz.

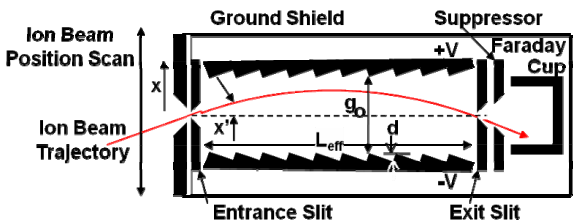


Figure 3: Pictorial representation of the Allison scanner, with a demonstration of the bending properties of the electric plates [5]. The deflecting plates are stair-cased with a depth d to prevent impacting particles from being scattered into the back slit.

Ultimate spatial resolution can be determined by the step size of the motor drive (0.01 mm) or by the entrance slit size (0.2 mm). The angular resolution is dictated by the slit size. As a measure of the angular resolution one can consider the RMS size of a distribution that would be measured with these slits for a beam slice with zero angular scatter. For the size of the second slit of 0.5 mm, such estimation gives 1.5 mrad. In practice, however, the granularity of the measured phase portraits was determined by the need for a reasonably low measuring time (approx. 3 mins) for a typical scan with 31 points over a 30 mm shift by 61 points over a 60 mrad angle sweep.

Note that the main modification of the PXIE emittance scanner with the previous SNS design [5] is an added capability of operating in DC mode. For that, the entrance slits are made of the Molybdenum alloy TZM and bolted to the water-cooled stainless steel body with a Carbon foil in between. Simulations[1] predict a safe operation with a DC 10 mA (300 W) beam focused to a spot with RMS size as low as 3 mm. So far, the minimum size in measurements of 10 mA beam was 3 mm RMS without any indications of performance deterioration.

Calibration

The spatial calibration for the emittance scanner was performed using a spring gauge, with a resolution of 10 µm, placed at the top of the shaft. This measured the movement of the scanner box as related to the number of steps made by the motor. The conversion of motor steps to distance travelled was found to be accurate and reproducible to less than a percent.

Uncertainty in the angular calibration is related to the values in Eq. 1. This model includes the calibration of the plate voltage and ion energy as well as the relationship between the voltage and the electric field integral along the ion trajectory (the ratio of L/g_e). However, we found a way of a direct calibration, which uses the dipole correctors built into each solenoid for shifting the beam in two orthogonal directions. The fields of the correctors have been measured, and their deflecting properties were independently verified using beam shifting with respect to the donut (see the next section) and using the bottom part of the emittance scanner as a scraper. It allowed finding combinations of the currents in two correctors (at a given solenoid current) that would kick the beam either horizontally or vertically by a known amount (within 1%). A vertical kick results in both a shift Δx of the beam centroid at the location of the emittance scanner slit and a change of the angle centroid by

$$\Delta x' = \frac{\Delta x}{L_{\mathrm{sol->es}}} \quad , \tag{2}$$

where $L_{\mathrm{sol->es}}$ is the distance between the centre of the correctors and the entrance slit.

Substituting initially the effective values of the gap and length in Eq. 1 by their geometrical values, and assuming that the ion energy and the plate voltage follow exactly to settings, one can record the spatial and angular positions of the beam centroid as measured by the emittance scanner at various vertical kicks. Comparing the slope of the measured line $\Delta x' = f(\Delta x)$ with the known value of $L_{\mathrm{sol->es}}$ = 1.203 m, one can correct the coefficient used by the program to make them agree (Fig. 4). The uncertainty of angle calibration with this procedure is determined primarily by the scatter of data in Fig. 4 and is approx. 2%.

Pulse Analysis

The PXIE Ion Source is CW but, due to the introduction of a modulator at the extraction electrode, the beam may be pulsed with duration of 0.001-16 ms and frequency up to 60 Hz. The pulse mode is preferable at the commissioning stage to decrease the chances of damage to the machine.

[1] The scanner design and simulations were made by M. Alvarez and J. Gaynier.

Copyright © 2014 CC-BY-3.0 and by the respective authors

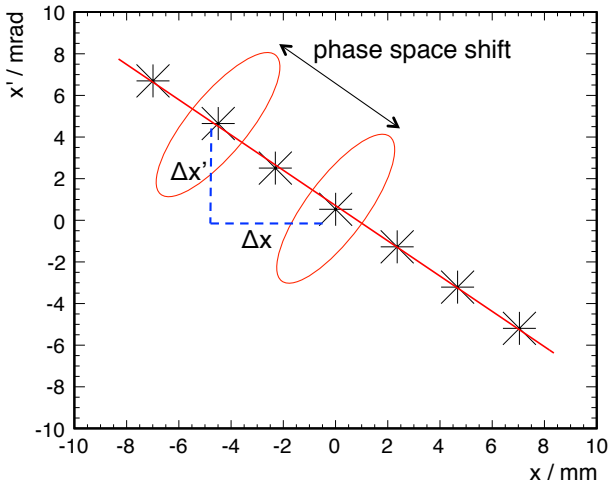


Figure 4: Phase space shifts of the centroids caused by the vertical kicks by the solenoid dipole correctors.

The emittance scanner analysis package can analyse both DC and pulsed beams, breaking down the structure of each timing window into individual time slices. Each pulse is sampled at a rate of 1 MHz so, for example, a slice size of 10 µs would produce an array of data averaged across 10 measurements, thus reducing the statistical noise between pulses. The plot in Fig. 5 demonstrates the evolution of both the RMS beam size and normalised emittance across a 400 µs pulse with 25 µs slices. In this figure both parameters plateau at approximately 300 µs suggesting a neutralisation time slightly shorter than this. All data reported further were taken at the back end of the 400 µs pulse.

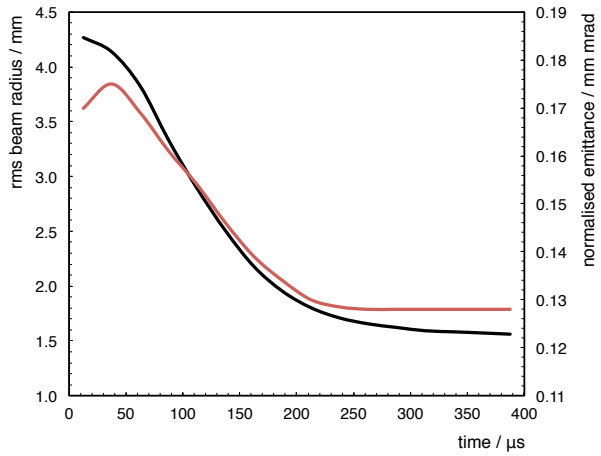


Figure 5: A graphical representation of the evolution of the RMS beam size (black) and normalised emittance (red) along a 400 µs, 5 mA H- pulse.

Initial Results

The emittance scanner is controlled by a Labview [6] package which operates the HV supplies and stepper driver and reads the thermocouples, Faraday cup, etc. After calibration of the emittance scanner, data were parsed into bespoke analysis software. In the pulsed mode, the instrumental background is subtracted using the data recorded before the pulse triggers - the default time window being 100 µs. In addition, a user-specified cut (in percents of the maximum signal) is applied to remove from the signal a beam-related background that might not come directly from the primary ions. After this threshold cut a centering routine was utilised. Figure 6 gives an example of a 2 mA beam phase portrait after applying such a procedure, as well as the collapsed profile plots for both the spatial and angular axes. The normalised RMS emittance value (with a 1% threshold cut) for this distribution is $\epsilon_{\mathrm{RMS}} = 0.074 \pm 0.002$ mm.mrad. For a perfectly double-Gaussian beam the RMS and the 39% emittance are equal. The 39% emittance for this distribution is $\epsilon_{39\%} = 0.053 \pm 0.002$ mm.mrad. The enlarged RMS emittance is due to the S-shaped phase space structure, with tails pulled off from the core. Such S-shaped emittances are normal for low-energy ion beams, where aberrations in the extraction system and lenses cause the outer part of the beam to over focus [7].

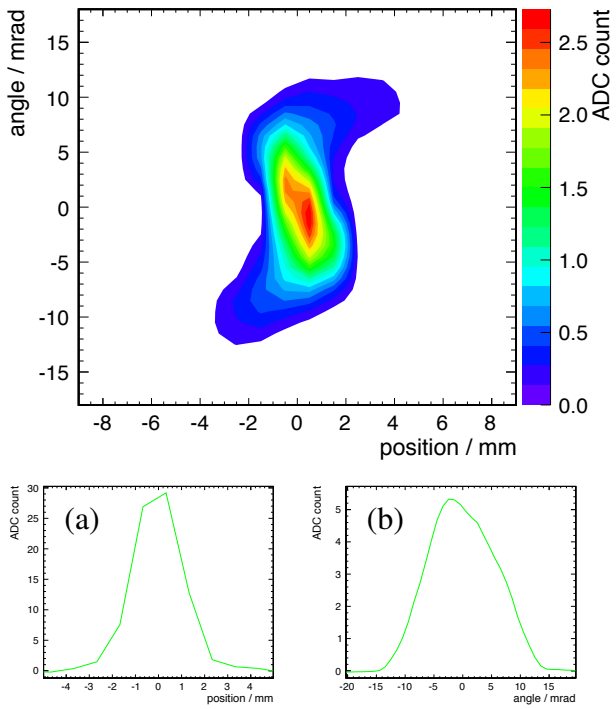


Figure 6: The phase space, as recorded by the Allison scanner, for a 2mA H- beam. Also shown are the collapsed profiles of the a) x-, and b) x'-axes. The background cut is 1%.

Core Emittance Calculation

A widely used procedure to characterise the beam core e.g. in 1D spatial distribution, is to fit its central part to a Gaussian curve. The analog of such procedure for a phase portrait is to fit its central area with a function that is Gaus-

Copyright © 2014 CC-BY-3.0 and by the respective authors

ISBN 978-3-95450-141-0

sian in both angular and spatial dimensions. The procedure was implemented as follows:

- Twiss parameters α, β, and γ are calculated from the recorded phase space data using 0% cut,
- Action [8] is calculated for each (x, x') data point as

$$J = \frac{1}{2}(\gamma x^2 + \alpha x x' + \beta x'^2) \quad , \tag{3}$$

- The data points are ordered according to their action. The percentage of beam outside of a given action is calculated as a function of action,
- The portion of the function corresponding to low action is fitted to

$$N(J) = e^{\frac{-J}{\epsilon_{\text{core}}}} \quad , \tag{4}$$

with ϵ_{core} as the only free parameter, which we will refer to as the core emittance.

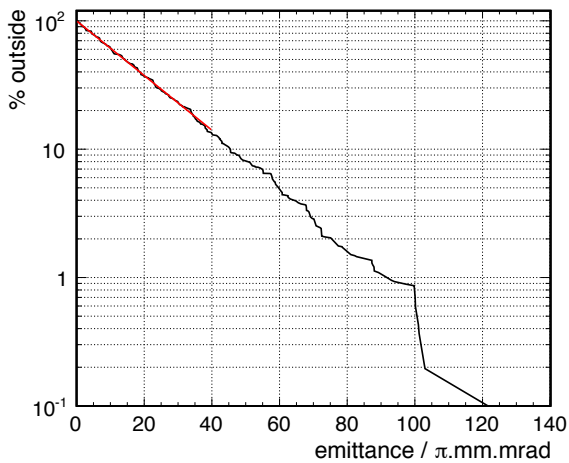


Figure 7: The percentage of beam outside a given emittance value for the phase space distribution of Fig. 6. An exponential fit to the initial straight section yields a value for the core emittance.

An example of such a plot and fit can be seen in Fig. 7. The value of the fitted core emittance $\epsilon_{\text{core}} = 0.082 \pm 0.003$ mm.mrad is 10% larger than the RMS emittance calculated in the previous section. This is due to the beam phase tails falling faster than assumed by the double-Gaussian distribution and is related to a non-Gaussian spatial profile at the ion source. We find the notion of a core emittance useful to describe the brightness of the beam core because it is significantly more rigorously defined and depends less on the choice of the threshold cut than the RMS emittance, as illustrated by Fig. 8.

SOLENOID SCAN METHOD

An alternative way to measure the beam emittance is to measure the beam size at various solenoid currents and compare these data with a propagation model. In the setup of Fig. 2, the beam size measurement can be performed

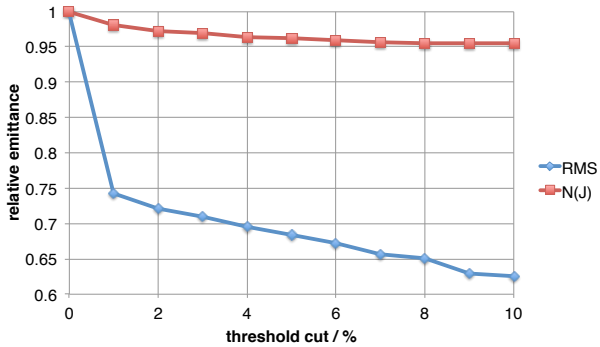


Figure 8: A graphical comparison of the evolution of both the RMS and core emittance across a range of threshold cuts, each normalised by their respective maximum value.

using the dipole correctors incorporated into the solenoid design and an electrically isolated, 18 mm ID diaphragm (also known as the 'donut') in front of a Faraday cup. When the beam is moved by the dipole correctors across the donut, it successively impinges one side of the donut, passes into the Faraday cup, and comes to the opposite side of the donut (Fig. 9). If the scan trajectory passes the donut centre, fitting of it simultaneously gives the information about calibration of the corrector strength (shift per Ampere), position of the centre in the direction of the scan, and the beam size. Strictly speaking, fitting requires solving an integral equation to reconstruct the beam density distribution. To simplify the procedure, fitting was done assuming either constant density or Gaussian distribution. The difference in the RMS beam size reconstructed with these two fits did not exceed 20%. For the Gaussian case, the portion of the beam current that passes to the Faraday cup $I(x, R, \sigma)$ is fitted as follows:

$$I(x,R,\sigma) = \frac{1}{\pi}\int_{\frac{-R-x}{\sqrt{2}\sigma}}^{\frac{R-x}{\sqrt{2}\sigma}} e^{-u^2}\left[\sqrt{\frac{R^2}{2\sigma^2} - \left(u + \frac{x}{\sqrt{2}\sigma}\right)}\right] \mathrm{d}u \, , \tag{5}$$

where R is the donut radius, x the centre position of the beam relative to the centre of the donut, and σ the RMS beam size. By centering the beam by hand before making a corrector scan the only free parameter from the fit is the RMS beam size.

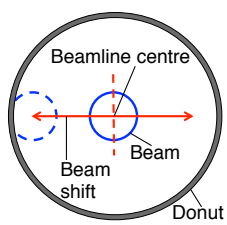


Figure 9: Illustration of the beam motion across the donut.

An example of a corrector scan can be seen in Fig. 10, with the fit denoted by the red curve. The beam size resulting from the fit is $\sigma = 1.35$ mm. This process may then be repeated for a series of solenoid currents creating a relation

Copyright © 2014 CC-BY-3.0 and by the respective authors

between the solenoid current and the RMS beam size. An example of this relation can be seen in Fig. 11.

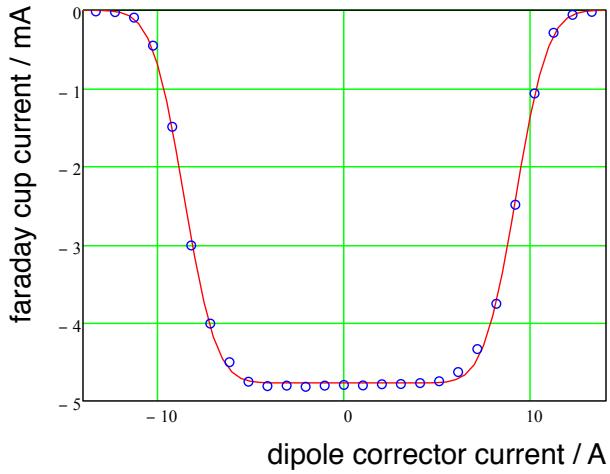


Figure 10: Beam current reaching the Faraday cup versus the dipole corrector current. Blue circles are measurements, and the solid red curve is the fit. Beam current is 2 mA. The beam is preliminarily centered in the opposite direction. The data were recorded at the end of 0.4 ms pulse.

For extracting the emittance we used the simplest propagation model that includes only a solenoid, approximated by a thin lens with the equivalent dependence of the focusing strength on the solenoid current $f(I_{\mathrm{sol}}) = \frac{k}{I_{\mathrm{sol}^2}}$, and a drift space with no space charge

$$\sigma^2 = \sigma_0^2 + 2\sigma_0\sigma_0' L + \left(\frac{\epsilon^2}{\sigma_0^2} + \sigma_0'^2\right)L^2 \quad , \qquad (6)$$

where L is the distance between the lens and the centre of the donut, and $\sigma_0' = \frac{\sigma_0}{f(I)} - \sigma'$. The free parameters of this fit are therefore σ_0, σ', and ϵ. The emittance obtained from such a fit to data in Fig 11 is $\epsilon = 0.084$ mm.mrad. The propagated statistical error is several percent, but the uncertainty related to the model itself is significantly larger, probably ~10 %. The emittance value agrees with that derived for a 2 mA beam using the emittance scanner.

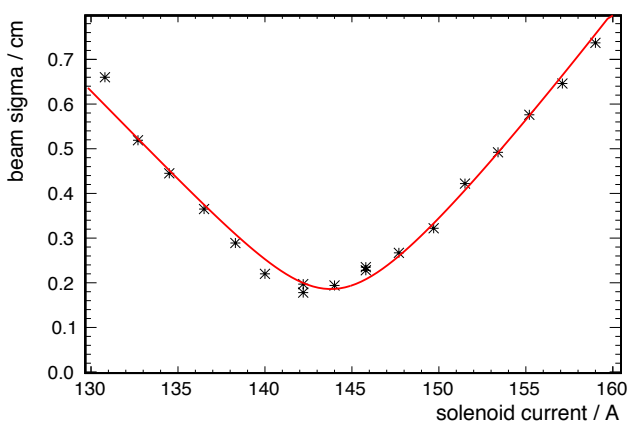


Figure 11: Beam size as a function of solenoid current with a fit used to derive the emittance of the beam.

CONCLUSIONS AND PLANS

1. Two methods of measuring the beam emittance have been successfully commissioned and used at the PXIE LEBT one-solenoid assembly in a long-pulse mode, with an Allison-type emittance scanner and the solenoid scan, which we consider being complimentary. The solenoid scan method doesn't require sophisticated equipment and the emittance value can be measured for any direction. On the other hand, the emittance scanner provides a detailed phase portrait, and its emittance figure doesn't depend on the prechosen distribution model. The results obtained with these two methods agree within the error margin.

2. The angle measurement of the emittance scanner was calibrated to 2% accuracy.

3. The introduced notion of the core emittance allows estimating the brightness of the beam core in a manner weakly affected by the choice of the threshold cut.

The commissioned diagnostic tools are now used in the three-solenoid beamline both in pulse- and DC-modes to optimise the beam for future injection into the RFQ in 2015.

ACKNOWLEDGEMENTS

Thanks go to Martin Stockli, Willem Blokland, et al. from SNS at ORNL who designed the original Allison scanner, wrote the Labview code to operate the machine, and provided technical knowledge during all phases of commissioning. Thanks also go to Matt Alvarez, Sali Sylejmani, and Jared Gaynier for building and installing the machine, simulating beam-induced thermal effects, and constantly providing expert mechanical support. Finally the authors of the paper would like to thank Dave Slimmer for his work with updating the Labview code.

REFERENCES

[1] V. Lebedev *et al.*, *An 800 MeV Superconducting Linac to Support Megawatt Proton Operations at Fermilab*, Proc. of LINAC14, Geneva, Switzerland (2014), THIOA05.

[2] D-Pace, Inc. `http://www.d-pace.com`.

[3] A. Shemyakin *et al.*, *Status of the Warm Front End of PXIE*, Proc. of LINAC14, Geneva, Switzerland (2014), THPP056.

[4] P. Allison, J. Sherman, D. Holtkamp, *An emittance scanner for intense low-energy ion beams*, IEEE Trans. Nucl. Sci. NS-30 (1983).

[5] M. Stockli *et al.*, *Low Energy Emittance Studies with the new Allison Emittance Scanner*, Proc. of PAC09, Vancouver, Canada (2009), TH6REP012.

[6] National Instruments, Inc. `http://www.ni.com/labview/`

[7] M. Stockli, *Measuring and Analyzing the Transverse Emittance of Charged Particle Beams*, Proc. of BIW06, Fermilab, Batavia, USA (2006), CP868.

[8] S.Y. Lee, *Accelerator Physics*, World Scientific, Singapore (1999), p.51.

Copyright © 2014 CC-BY-3.0 and by the respective authors

ISBN 978-3-95450-141-0

ELECTRON BEAM PROFILER FOR THE FERMILAB MAIN INJECTOR*

R. Thurman-Keup#, M. Alvarez, J. Fitzgerald, C. Lundberg, P. Prieto,
FNAL, Batavia, IL 60510, USA
W. Blokland, ORNL, Oak Ridge, TN 37831, USA

Abstract

The long range plan for Fermilab calls for large proton beam intensities in excess of 2 MW for use in the neutrino program. Measuring the transverse profiles of these high intensity beams is challenging and generally relies on non-invasive techniques. One such technique involves measuring the deflection of a beam of electrons with a trajectory perpendicular to the proton beam. A device such as this is already in use at the Spallation Neutron Source at ORNL and a similar device will be installed shortly in the Fermilab Main Injector. The Main Injector device is discussed in detail and some test results and simulations are shown.

INTRODUCTION

Traditional techniques for measuring the transverse profile of proton beams typically involve the insertion of a physical object into the path of the proton beam. Flying wires for instance in the case of circulating beams, or secondary emission devices for single pass beamlines. With increasing intensities, these techniques become difficult, if not impossible. A number of alternatives exist including ionization profile monitors, gas fluorescence monitors, and the subject of this paper, electron beam profile monitors.

The use of a probe beam of charged particles to determine a charge distribution has been around since at least the early 1970's [1-3]. In those examples, the charge distribution was a plasma, and the probe beam was electrons. Later, the concept was applied to ion beams at a number of facilities [4-6]. At CERN a version using a probe beam of ions was used to average over the bunch structure of the proton beam in the SPS [7]. A variation on the technique was the use of an electron probe beam to measure the longitudinal charge distribution in an electron injector at BINP [8]. The most recent incarnation of this technique is a profile monitor in the accumulator ring at SNS [9,10].

An Electron Beam Profiler (EBP) has been constructed at Fermilab and will be installed shortly in the Main Injector. The Main Injector is a proton synchrotron that can accelerate protons from 8 GeV to 120 GeV for use by a number of neutrino experiments, and eventually several muon-based experiments. The protons are bunched at 53 MHz for a typical rms bunch length of 1-2 ns. In this paper we discuss the design of the EBP and present some studies of the electron beam.

THEORY

The principle behind the EBP is just electromagnetic deflection of the probe beam by the target beam under study (Fig. 1).

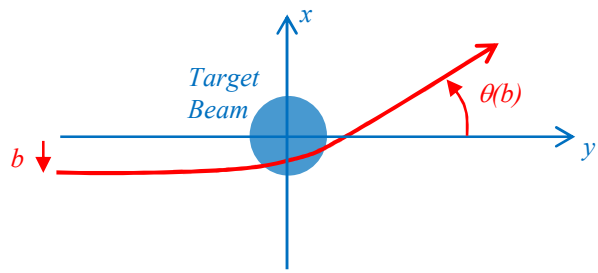


Figure 1: Probe beam deflection (red) for some impact parameter b.

If one assumes a target beam with $\gamma \gg 1$, no magnetic field, and $\rho \neq f(z)$, then the force on a probe particle is

$$\vec{F}(\vec{r}) \propto \int d^2\vec{r}'\rho(\vec{r}')\frac{(\vec{r}-\vec{r}')}{|\vec{r}-\vec{r}'|^2}$$

and the change in momentum is

$$\Delta\vec{p} = \int_{-\infty}^{\infty} dt\ \vec{F}\big(\vec{r}(t)\big)$$

For small deflections, $\vec{r} \approx \{b, vt\}$, and the change in momentum is

$$\Delta\vec{p} \propto \int_{-\infty}^{\infty} dx' \int_{-\infty}^{\infty} dy'\ \rho(x',y') \cdot \int_{-\infty}^{\infty} dt\ \frac{\{b-x', vt-y'\}}{(b-x')^2+(vt-y')^2}$$

where {} indicates a vector. For small deflections, $\vec{p} \approx \{0, p\}$ and $\theta \approx \frac{|\Delta\vec{p}|}{|\vec{p}|}$. The integral over time can be written as $\mathrm{sgn}(b - x')$ leading to an equation for the deflection

$$\theta(b) \propto \int_{-\infty}^{\infty} dx' \int_{-\infty}^{\infty} dy'\,\rho(x',y')\,\mathrm{sgn}(b-x')$$

If one takes the derivative of $\theta(b)$ with respect to b, the sgn function becomes $\delta(b - x')$ leading to

$$\frac{d\theta(b)}{db} \propto \int_{-\infty}^{\infty} dy'\,\rho(b,y')$$

which is the profile of the charge distribution of the beam. Thus for a Gaussian beam, this would be a Gaussian distribution and the original deflection angle would be the error function, $\mathrm{erf}(b)$. This of course is true only to the extent that the above assumptions are valid.

*Operated by Fermi Research Alliance, LLC under Contract No. De-AC02-07CH11359 with the United States Department of Energy.
#keup@fnal.gov

Copyright © 2014 CC-BY-3.0 and by the respective authors

EXPERIMENTAL PROCEDURE

There are a number of techniques for obtaining $\theta(b)$. A fast scan of the electron beam diagonally through the proton bunch (Fig. 2) can in principle achieve a measurement in one pass of the bunch. This requires a deflection of the electron beam in a period that is much shorter than the proton bunch. For the Main Injector, this would be sub-nanosecond and may be difficult to achieve.

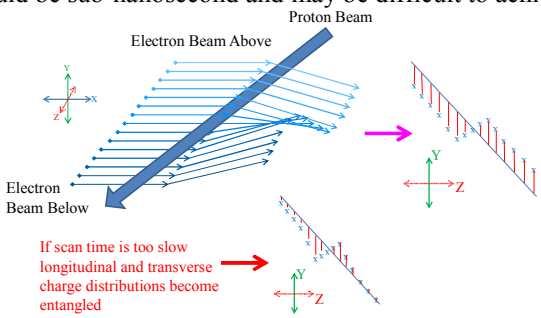


Figure 2: Fast scan of the electron beam though the proton beam. One can see the erf-like deflection from the baseline.

A second method involves slowly stepping the electron beam through the proton beam and recording a deflection value on each turn of the proton bunch (Fig. 3). In this method the electron beam is stationary each time the proton bunch passes, and then is moved to the next impact parameter.

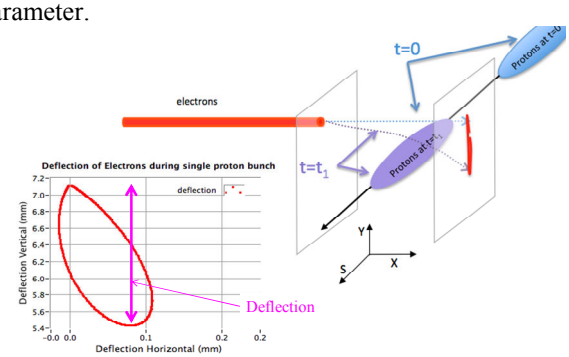


Figure 3: Trajectory followed by a stationary electron beam as the proton bunch passes by. There is some deflection along the proton beam direction due to the magnetic field of the proton beam, but it is much smaller than the deflection transverse to the proton beam.

A variation on the slow scan is to scan quickly along the proton beam direction and slowly transverse to the beam (Fig. 4). This provides a measurement of the longitudinal profile at each step as well as the transverse profile.

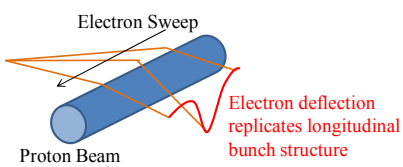


Figure 4: Deflection when the electron beam is scanned along the direction of the proton bunch with a duration equalling the bunch structure.

APPARATUS

The device (Fig. 5 and Fig. 6) that was constructed for the Main Injector consists of the EGH-6210 electron gun from Kimball Physics, followed by a cylindrical, parallel-plate electrostatic deflector, and terminating in a phosphor screen.

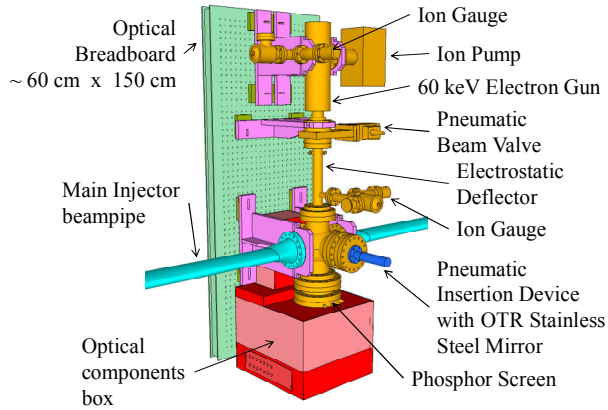


Figure 5: Model of the EBP showing the main components.

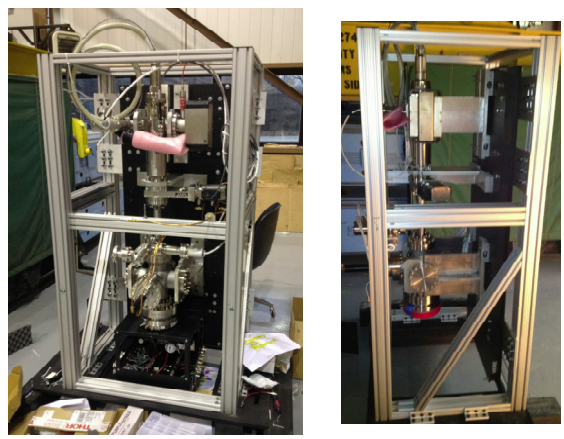


Figure 6: Assembled device front and side views.

The gun (Fig. 7) is a 60 keV, 6 mA, thermionic gun with a LaB_6 cathode, that can be gated from 2 μs to DC at a 1 kHz rate. The gun contains a focusing solenoid and four independent magnet poles for steering/focusing. The minimum working spot size is <100 μm. The electrostatic deflector (Fig. 7) contains 4 cylindrical plates that are 15 cm long and separated by ~2.5 cm.Following the electrostatic deflector is the intersection with the proton beamline. There is a pneumatic actuator at this point with a stainless steel mirror for generating optical transition radiation (OTR) to be used in calibrating the electron beam. After the proton beam intersection there is a phosphor screen from Beam Imaging Systems (Fig. 7). It is composed of P47 (Y_2SiO_5:Ce3+) with an emission wavelength of 400 nm, a decay time of ~60 ns and a quantum yield of 0.055 photons/eV/electron. The phosphor screen has a thin conductive coating with a drain wire attached.

Copyright © 2014 CC-BY-3.0 and by the respective authors

ISBN 978-3-95450-141-0

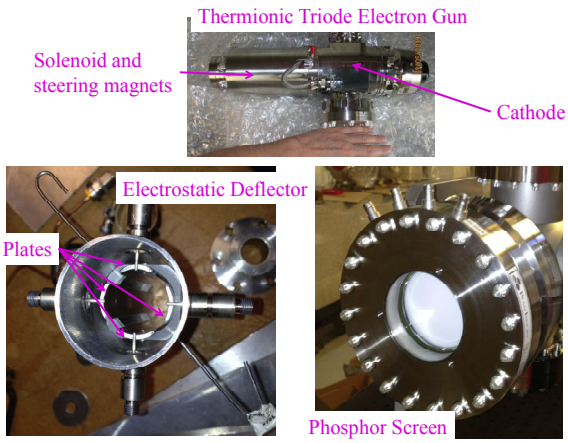


Figure 7: Left) Inside view of the electrostatic deflector showing the cylindrical parallel plates. Right) Phosphor screen mounted in an 8 in Conflat flange. A drain wire is attached between the screen and one of the SHV connectors.

Both the OTR and the phosphor screen are imaged by a single intensified camera system (Figs. 8 and 9). The source is chosen by a mirror on a moving stage. Each source traverses a two-lens system plus optional neutral density filters or polarizers before entering the image intensifier (Hamamatsu V6887U-02). The output of the intensifier is imaged by a Megarad CID camera from Thermo-electron with a C-mount lens.

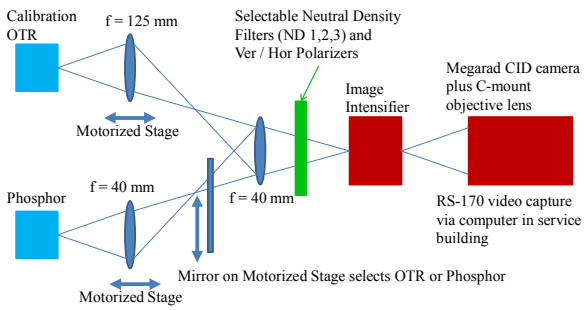


Figure 8: Optical paths followed by the OTR light and the phosphor screen light. Of the two lenses in each path, one is shared.

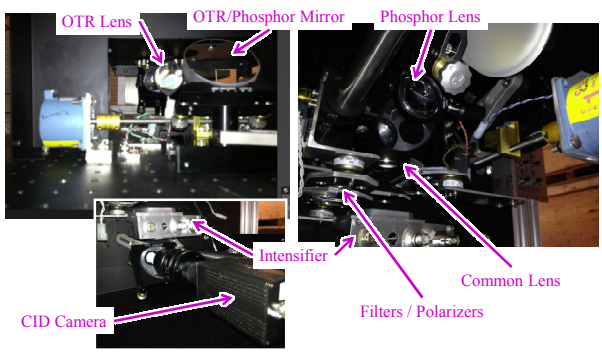


Figure 9: Optical components mounted inside box. The top left picture is looking vertically along the OTR line. The top right picture shows the phosphor path.

TEST STAND RESULTS

Electron Gun

The initial test stand was setup to test characteristics of the electron gun. It consisted of a pair of YAG:Ce screens used to measure the spot size and divergence to verify the manufacturer's specifications and for use in the simulation (Fig. 10).

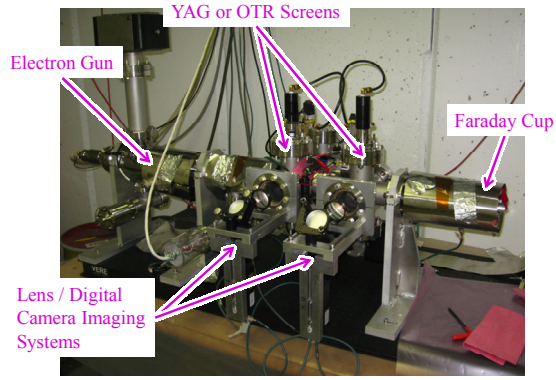


Figure 10: Initial test stand for measuring beam parameters.

The beam measurements were carried out using the solenoidal magnet in the gun to focus the beam at the first screen (Fig. 11), allowing a measurement of the emittance of the electron beam.

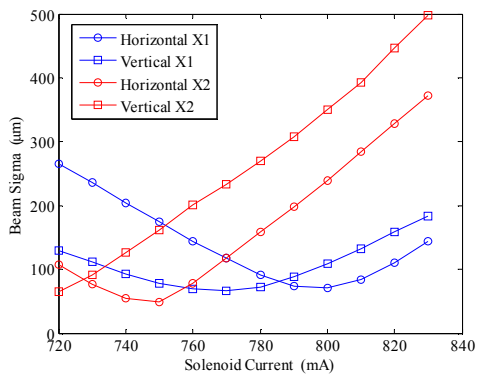


Figure 11: Horizontal and vertical rms beam sizes at the first (blue) and second (red) crosses in the test stand. The electron beam was ~50 keV and 1 μA onto YAG:Ce screens.

Following the intial measurements, the YAG:Ce screens were replaced with stainless steel mirrors to enable running at 1 mA beam currents. Measurements from these currents are shown in (Fig. 12) and are larger as might be expected.

Electrostatic Deflector

The electrostatic deflector was designed to deflect the electron beam from one side of the phosphor screen to the other. One would like to minimize the voltage required for the deflector while also minimizing the length of the deflector. Unfortunately, physics doesn't work that way. A reasonable compromise is the 15 cm-long plates, for

Copyright © 2014 CC-BY-3.0 and by the respective authors

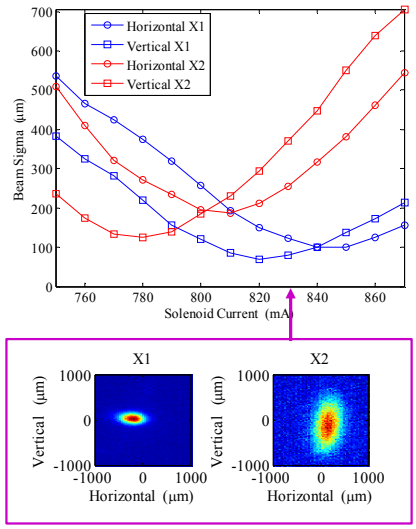


Figure 12: Horizontal and vertical rms beam sizes at the first (blue) and second (red) crosses in the test stand. The measurements are from OTR taken at ~50 keV and 1 mA beam current onto the stainless steel mirrors.

which ±400 V on each plate is more than sufficient to deflect a 15 keV beam. The deflector was tested with ~150 V with a sweep time of 80 ns. The result on the phosphor screen is shown in (Fig. 13). There appear to be focusing effects during the sweep, but the magnitude of the sweep is roughly correct.

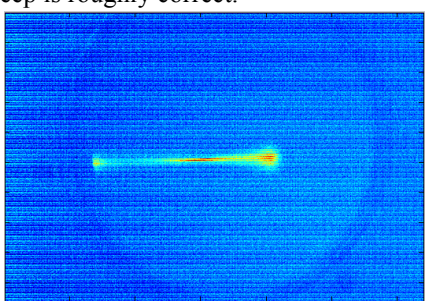


Figure 13: Trace of the electron beam on the phosphor screen for a deflecting voltage of ~150 V. This image was not taken with the design optics. It was taken with just a camera and objective lens. The beam started off the screen on the left side and was then swept to the right.

SIMULATIONS

Electron Beam

Simulations of the electron beam were developed both at SNS and Fermilab. The SNS calculations (as seen in Fig. 3 and Fig. 14) showed that the measured profile was within 2% of the actual profile. This simulation was based on the slow stepping method.

At Fermilab, an electron beam simulation was developed in MATLAB to track electrons through the deflector and proton beam to the phosphor screen. The simulation starts with the measured emittance of the electron gun and propagates the beam through the deflector electric field, calculated via POISSON, and

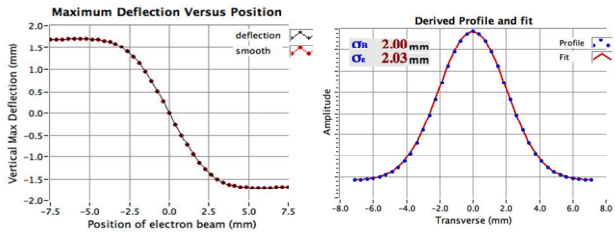


Figure 14: Deflection plot of electron beam, and the derivative of it, showing agreement to better than 2%.

through the electric and magnetic fields of a proton bunch. Presently, the electric fields of the deflector have no edge effects since POISSON is a 2-D calculation. The time dependence of the deflector field is handled by a linear scaling of the POISSON fields. The time dependence of the proton bunch position however, is fully accounted for in evaluating the fields at a given point in time. This simulation was focused on the third method, using fast sweeps along the proton direction while slowly stepping through the proton beam. Some results of this simulation are shown in (Fig. 15).

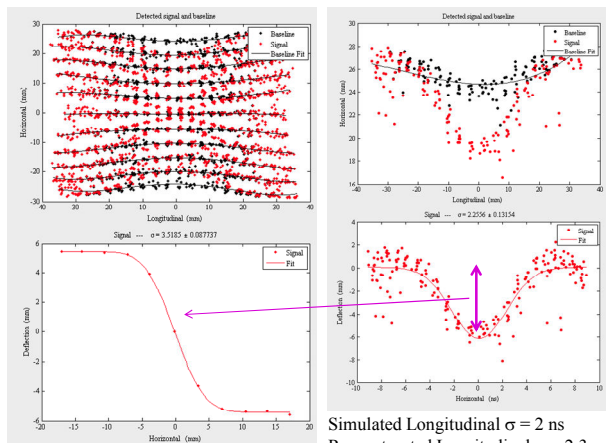


Figure 15: Simulated deflection data for varying impact parameters. The black points are baseline deflections with no beam. They result from the non-uniform deflector field. Each point represents a single electron with the random spread given by the measured emittance.

Optics

Since the imaging optics contain relatively fast lenses, and the source size is large, ray tracing was used to determine the optical acceptance of the phosphor screen at the input to the image intensifier. The face of the phosphor screen was randomly populated with light rays heading in random directions. These rays were traced through the optics to the image intensifier to produce an acceptance map. One can see from (Fig. 16) that the acceptance is quite uniform over most of the phosphor screen.

Copyright © 2014 CC-BY-3.0 and by the respective authors

ISBN 978-3-95450-141-0

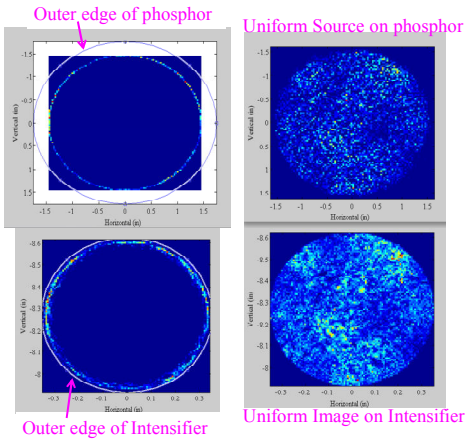


Figure 16: Ray tracing from source (top) to image planes (bottom) to determine aperture (left) and uniformity (right).

External Magnetic Fields

External magnetic fields are a serious problem for low energy electron beams. From calculations, a 2 G transverse field will deflect the 15 keV electron beam by 100 mm from gun to phosphor screen. This makes the device inoperable. Figure 17 shows the magnetic fields from the Main Injector magnet busses which are located ~50 cm from the electron beam. The busses run in pairs to mostly cancel the magnetic fields, but there are still low levels remaining.

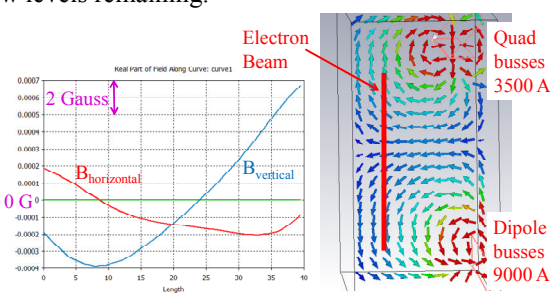


Figure 17: CST simulation of magnetic field from magnet busses along the line of the electron beam. The horizontal component is most important as the electron beam is vertical. The maximum horizontal field is 2 G.

ACKNOWLEDGMENT

The authors would like to acknowledge the help of the Main Injector, Mechanical Support, and Instrumentation departments for all their assistance in readying this device.

REFERENCES

[1] P.D. Goldan, Phys. Fluids 13 (1970) 1055
[2] C.H. Stallings, J. Appl. Phys. 42 (1971) 2831.
[3] C.W. Mendel Jr., Rev. Sci. Instrum. 46 (1975) 847.
[4] J. Shiloh et al., Rev. Sci. Instrum. 54 (1983) 46.
[5] V. Shestak et al., TRIUMF Design Note, TRI-DN-87-36 (1987).

One solution that will be tried is to surround the electron beam with mumetal shielding. Bench tests seem to indicate that 3 layers of mumetal should be sufficient to eliminate problems from the magnetic field. In addition, calculations with CST (Fig. 18) show the mumetal as being effective. However, a previous attempt to shield an electron cloud measurement from the same bus fields was not very successful. If the mumetal does not work, further shielding of the busses may be required. The device at SNS has a low-μ shield as well as a high-μ shield.

SUMMARY

An electron beam profiler has been built for the Main Injector at Fermilab and will be installed during the current multi-week shutdown. It will measure the horizontal profile of the Main Injector proton beam during normal operations and provide a secondary profile measurement to the Ionization Profile Monitor.

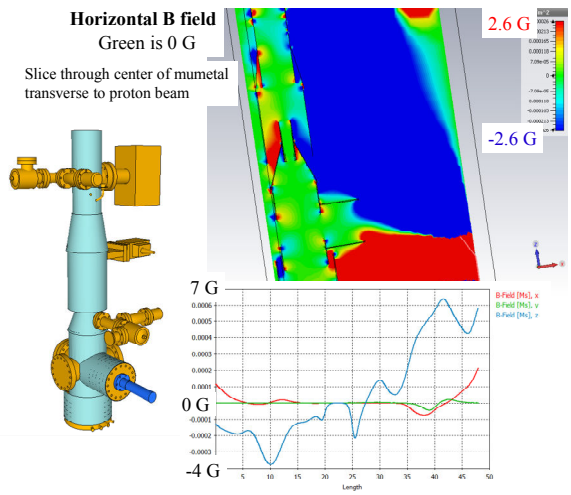


Figure 18: Model of mumetal wrap. The intensity plot is a CST simulation of the magnetic field inside the mumetal shield. The residual horizontal fields (red and green in the lower plot) are significantly less than 1 G with the exception of the ends.

[6] P. Gross et al., "An Electron Beam Probe for Ion Beam Diagnosis", EPAC'90, Nice, June 1990, p. 806.
[7] J. Bosser et al., Nucl. Instrum. Methods Phys. Res. A 484 (2002) 1.
[8] A.A. Starostenko et al., "Non-Destructive Singlepass Bunch Length Monitor: Experiments at VEPP-5 Preinjector Electron Linac", 18th ICHEP, Tsukuba, March 2001.
[9] A. Aleksandrov et al., "Feasibility Study of Using an Electron Beam for Profile Measurements in the SNS Accumulator Ring", PAC05, Knoxville, May 2005, p. 2586.
[10] W. Blokland and S. Cousineau, "A Non-Destructive Profile Monitor for High Intensity Beams", PAC'11, New York, March 2011.

Copyright © 2014 CC-BY-3.0 and by the respective authors

TERAHERTZ AND OPTICAL MEASUREMENT APPARATUS FOR THE FERMILAB ASTA INJECTOR*

R. Thurman-Keup#, A.H. Lumpkin, J. Thangaraj, FNAL, Batavia, IL 60510, USA

Abstract

ASTA is a facility at Fermilab that, once completed, will consist of a photoinjector with two superconducting capture cavities, at least one superconducting ILC-style cryomodule, and a small ring for studying non-linear, integrable beam optics. This paper discusses the layout for the optical transport system that will provide THz radiation to a Martin-Puplett interferometer for bunch length measurements as well as optical radiation to an externally located streak camera, also for bunch length measurements. It will be able to accept radiation from two synchrotron radiation ports in the bunch compressor, a diffraction/transition radiation screen downstream of the compressor, and a transition radiation screen after the spectrometer magnet for measurements of energy-time correlations.

INTRODUCTION

The Advanced Superconducting Test Accelerator (ASTA) is a facility that has been constructed at Fermilab for advanced accelerator research [1-3]. It consists of a photoinjector followed by an ILC-type cryomodule and a small ring called IOTA (Integrable Optics Test Accelerator) for studying non-linear optics. Recently, the initial photoinjector beamline was completed and rf tests of the cryomodule reached the ILC design goal in 7 of the 8 cavities, with one cavity just short of it. The plan for the photoinjector is to run it at 20-25 MeV while the beamline from the cryomodule to IOTA, and the corresponding accelerator enclosure are completed. At some point in time, the photoinjector will receive a second capture cavity (currently being repaired) which will increase the energy to around 50 MeV The photoinjector will support a number of small user experiments, some of which are already planned. When the full beamline to IOTA has been completed, the photoinjector will provide beam to IOTA to map out the optics of the ring. In support of photoinjector operations and experiments, there will be an optical / THz transport system with a number of instruments including a Martin-Puplett interferometer, and a Hamamatsu streak camera. This paper will describe the plan for this system.

ASTA

The ASTA injector (Fig. 1) starts with a 1.3 GHz normal-conducting rf photocathode gun with a Cs_2Te coated cathode. The photoelectrons are generated by a YLF laser at 263 nm that can provide several μJ per pulse [4]. Following the gun are two superconducting 1.3 GHz capture cavities that accelerate the beam to its design energy of around 50 MeV. Initially only the second capture cavity will be in place giving an energy of 20-25 MeV. After acceleration there is a section for doing round to flat beam transforms, followed by a magnetic

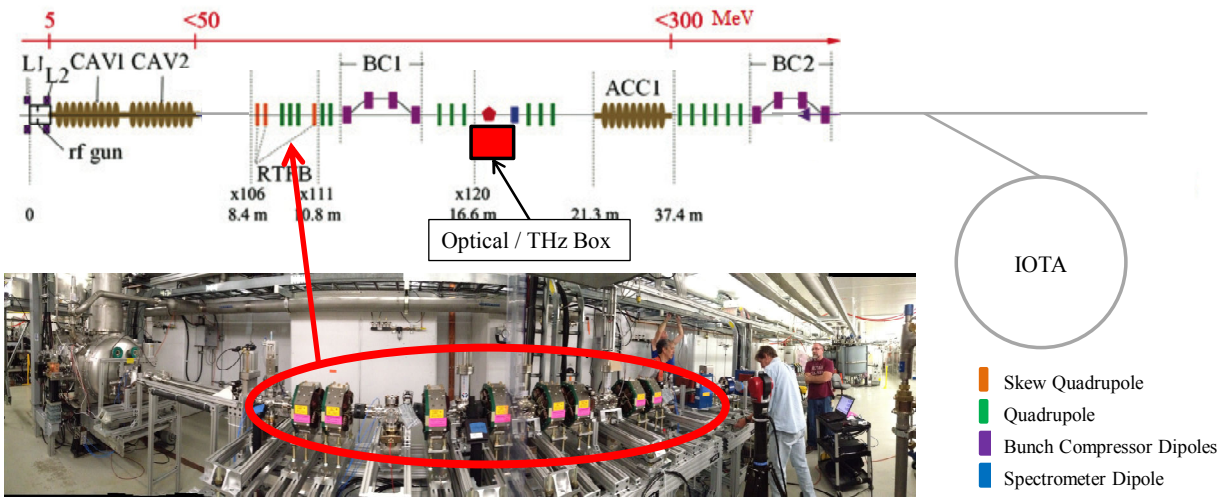


Figure 1: ASTA beamline layout. L1 and L2 are the gun solenoids. CAV1 and CAV2 are the capture cavities. Presently only CAV2 is installed. The section titled RTFB is the round-to-flat beam transform section which is followed by the magnetic bunch compressor BC1. The next section contains space for user experiments and is the location of the optical / THz system. ACC1 is the ILC-type cryomodule.

*Operated by Fermi Research Alliance, LLC under Contract No. De-AC02-07CH11359 with the United States Department of Energy.
#keup@fnal.gov

ISBN 978-3-95450-141-0

Copyright © 2014 CC-BY-3.0 and by the respective authors

bunch compressor and a short section that can accommodate small beam experiments. At the end of the experimental section is a spectrometer dipole which can direct the beam to the low energy dump. If the beam is not sent to the dump, it enters the ILC-type cryomodule where it gets up to 250 MeV of additional energy. It can then be sent to a high energy dump, or to the IOTA ring. Table 1 lists the typical expected beam parameters for ASTA.

Table 1: Expected Beam Parameters for ASTA

Parameter	Value
Energy	50 – 300 MeV
Bunch Charge	0.02 – 5 nC
Bunch Frequency	3 MHz
Macropulse Duration	≤ 1 ms
Macropulse Frequency	0.5, 1, 5 Hz
Transverse Emittance	0.1 – 100 μm
Longitudinal Emittance	5 – 500 μm
Peak Current	3 – 10 kA

OPTICAL AND TERAHERTZ INSTRUMENTATION SYSTEM

The optical / THz instrumentation system (OTIS) is located near the low energy dump. The transport system is constructed of stainless steel pipes and flanges purchased from GVC.net and normally used in the food industries (breweries, dairy, etc…). Figure 2 shows a 3-D model of the layout. There will be four source points for the radiation. One each from dipoles 3 and 4 in the bunch compressor, one from a cross (X121) in the user experiment section, and one from the cross (X124) in the low energy dump beamline that normally measures the energy spread.

The source points in the bunch compressor will provide coherent synchrotron edge radiation (CER) from the entrance of the corresponding dipole magnets (Fig. 3). The CER is generally in the high GHz / low THz region [6]. For 50 MeV beam it will also be possible to observe optical synchrotron radiation (OSR) from these points with an intensified or cooled camera. At 20 MeV the optical intensity is too low to observe.

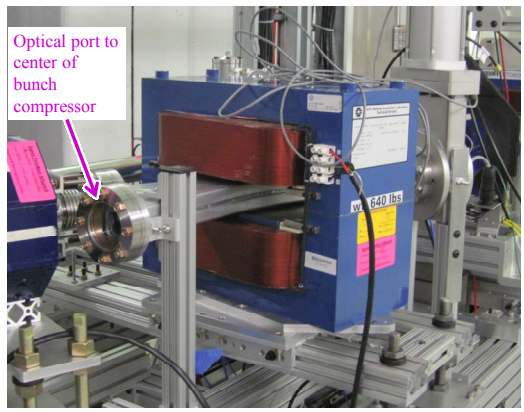


Figure 3: Second dipole in bunch compressor showing the optical entrance port to the center leg of the chicane. The beamline through the dipole is X shaped.

The source point at X121 consists of an aluminized, silicon wafer on a rotatable and translatable actuator (Fig. 4). The wafer can be inserted all the way into the beam to generate both coherent transition radiation (CTR) and optical transition radiation (OTR). The screen can also be extracted partly, with its edge a few mm above the beam, to generate coherent diffraction radiation (CDR).

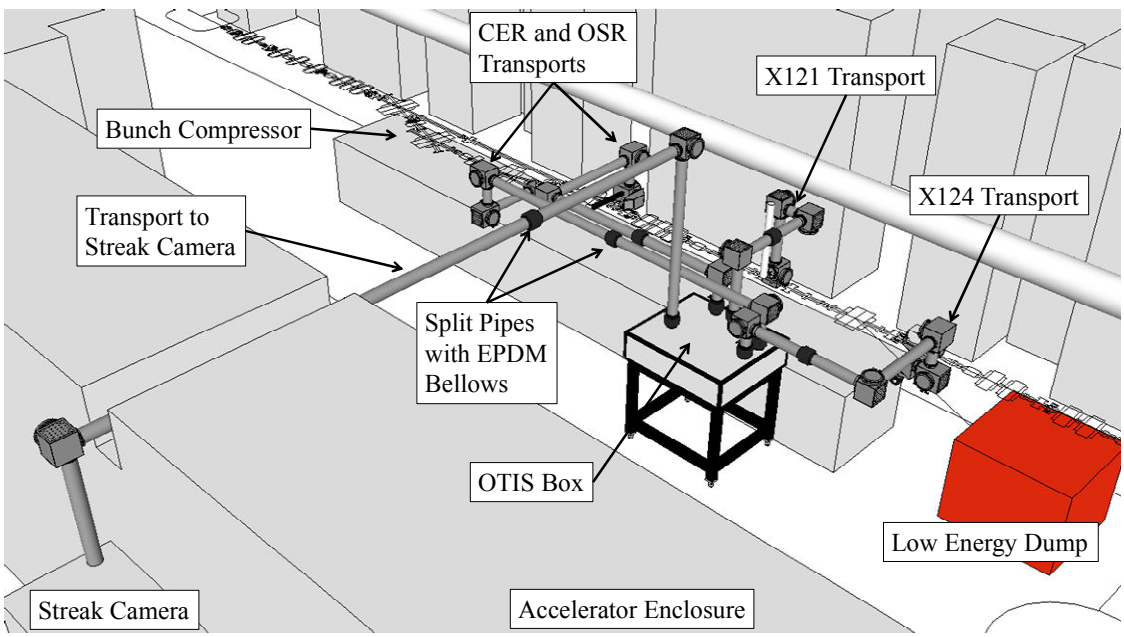


Figure 2: OTIS transport pipes just after the bunch compressor.

Copyright © 2014 CC-BY-3.0 and by the respective authors

ISBN 978-3-95450-141-0

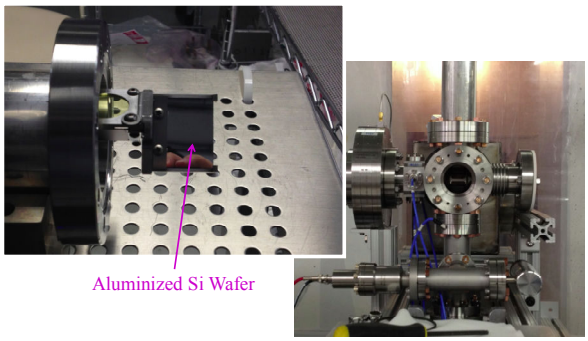


Figure 4: Left) X121 actuator retracted; OTR wafer is visible. Right) X121 cross with actuator installed.

The source point at X124 is also an aluminized, silicon wafer that will provide OTR (Fig. 5). This location is normally used to obtain the energy spread since it lies after the spectrometer dipole.

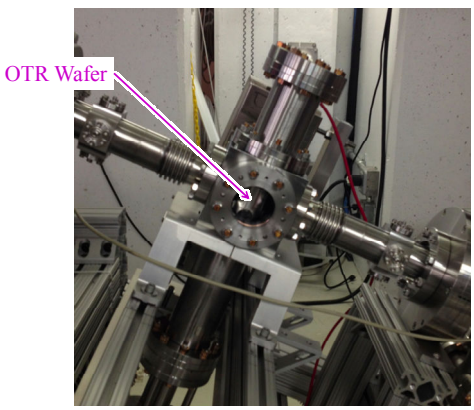


Figure 5: X124 cross in downward beamline to dump. There will be an optics system attached to this side of the cross.

All the sources converge to the OTIS box containing translatable mirrors to switch between the various inputs (Fig. 6). There are effectively three outputs from the box: Hamamatsu streak camera, Martin-Puplett interferometer (Fig. 6) which is housed inside the OTIS box, and a user experiment location which is also inside the box. All four inputs (plus one spare) are able to be switched to any of the outputs. Additionally, radiation sent to the interferometer or streak camera is split via a dielectric mirror such that the optical light is sent to the streak camera while the THz radiation continues to the interferometer.

The transport lines will consist of stainless steel, 4" diameter pipes with quick disconnect flanges (Tri-clamp). In the bunch compressor, light is extracted through a single crystal quartz viewport. Since space is limited at these ports, a small box with one or two flat mirrors is attached to the port to redirect the radiation to a more readily accessible location (Fig. 7). The radiation is then collimated by a pair of 3" diameter, 90° off-axis, parabolic, aluminium coated, UV-enhanced mirrors located in stainless steel boxes (Fig. 8). A pair is needed

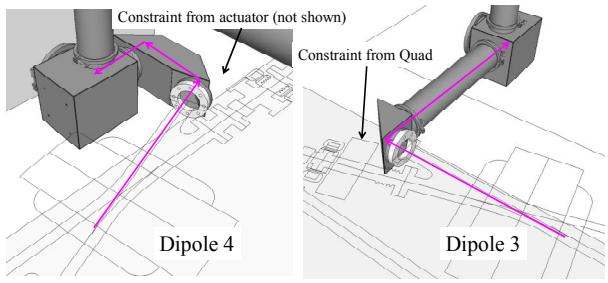


Figure 7: The two compressor source port boxes.

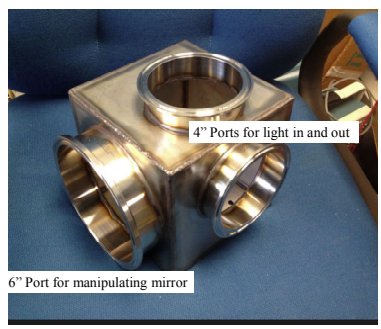


Figure 8: Stainless steel mirror box.

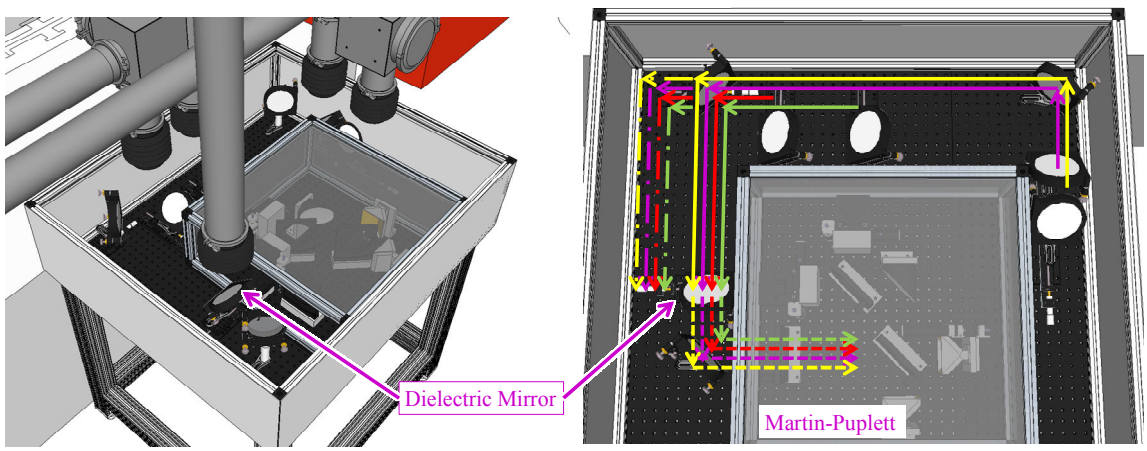


Figure 6: Left) 3-D model of OTIS box. Right) The colors indicate source, Yellow – X124, Purple and Red – Compressor, Green – X121. Solid lines go to the streak camera. Dashed lines go to the interferometer, Dot-Dash lines go to the user area in the box.

ISBN 978-3-95450-141-0

Copyright © 2014 CC-BY-3.0 and by the respective authors

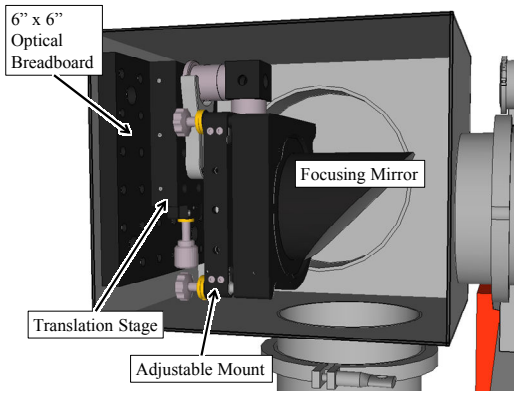


Figure 9: Off-axis parabolic optics in stainless steel box.

since the focal length of the mirrors is much smaller than the closest distance to the dipole source point. The mirrors are mounted in an adjustable mirror mount which sits on a translatable stage to enable both direction and focusing adjustments (Fig. 9).For X121, the light is also extracted through a single-crystal-quartz viewport (Fig. 10). Here it is not necessary to have two focusing mirrors, since the mirror can be positioned at its focal point.

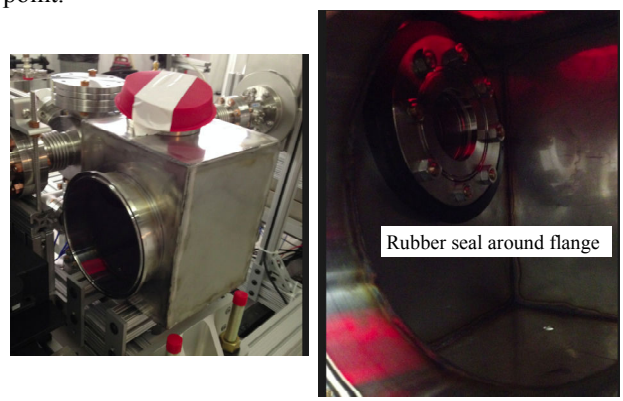


Figure 10: Stainless steel box mounted over flange on X121. Box is sealed around flange with a Uniseal gasket.

At X124, the only accessible extraction point is through the optics arm for the normal camera imaging system (Fig. 11). A beam-splitting pellicle will split the OTR light between the normal camera and OTIS.

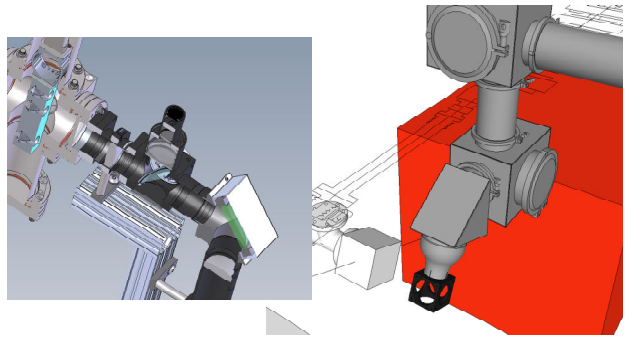


Figure 11: OTIS extraction from X124. Left) Normal camera optics cross section. Right) Attachment point of OTIS transport line.

Ninety degree bends in the transport are handled by 4"-diameter, flat, aluminium-coated, UV-enhanced mirrors mounted in an adjustable mount. To enable the system to be disassembled when access to the beamline is needed, the longer pipes are cut in two and have an EPDM bellows between them.

The streak camera will be located outside the accelerator enclosure. The pipe running to the streak camera goes through one of the penetrations to the outside where the streak camera is housed in a small enclosure (Fig. 12).

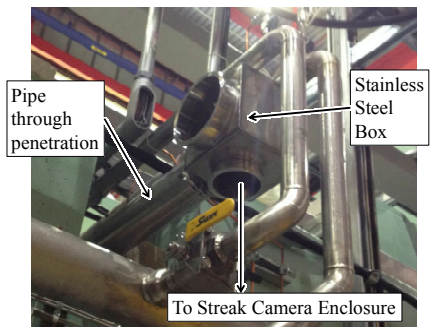


Figure 12: Penetration pipe and mirror box before the streak camera.

ALIGNMENT

The OTIS setup has many mirrors which forces one to consider how to align everything such that light gets from one end to the other (Fig. 13). For the bunch compressor

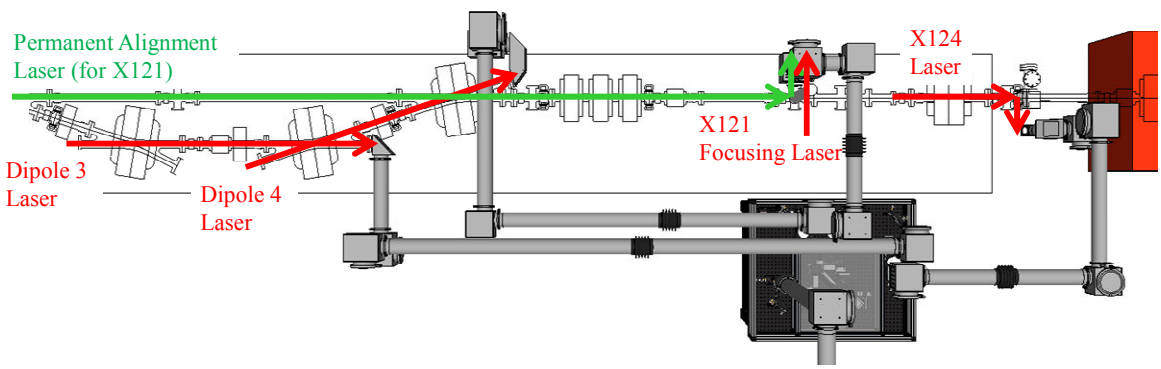


Figure 13: Laser paths for alignment purposes. Dipole 3 and 4 and X124 lasers will do both focusing and alignment.

Copyright © 2014 CC-BY-3.0 and by the respective authors

ISBN 978-3-95450-141-0

and X124 ports, a laser will be directed down the beamline with its waist at the location of the radiation source point. The mirrors will then be adjusted first for directionality and then for focus with the process iterated as necessary. At X121, a permanent alignment laser upstream will be used to set the directionality, while a local laser will be used to adjust the focusing.

INSTRUMENTATION

There are several end points of the optical and THz radiation including a Hamamatsu streak camera and a Martin-Puplett interferometer, both of which are used for bunch length measurements. In addition there is a space for a user instrument which initially will be used for testing a THz spectrometer based on a CsI crystal.

Streak Camera

The streak camera [5] is a Hamamatsu C5680 mainframe with S20 PC streak tube that can accommodate a vertical sweep plugin unit and a horizontal sweep unit or blanking unit. The device is fitted with all-mirror input optics enabling the assessment of the UV OTR component as well as the visible light OTR. The mirror optics also mitigate the streak image blurring due to the inherent chromatic temporal dispersive effects of the lens-based input optics for broadband sources such as OTR. The unit is also equipped with the M5675 synchroscan unit with its resonant circuit tuned at 81.25 MHz so the streak image would have jitter of less than 1 ps from the system itself.

Interferometer

The Martin-Puplett interferometer is a polarizing-type interferometer with wire grids as the polarizer and beam splitters (Fig. 14). The wire grids are 10 μm diameter Tungsten wires with a 45-μm wire spacing. The device uses THz frequencies to determine the bunch length. The relative capabilities of the streak camera and interferometer are listed in Table 2.

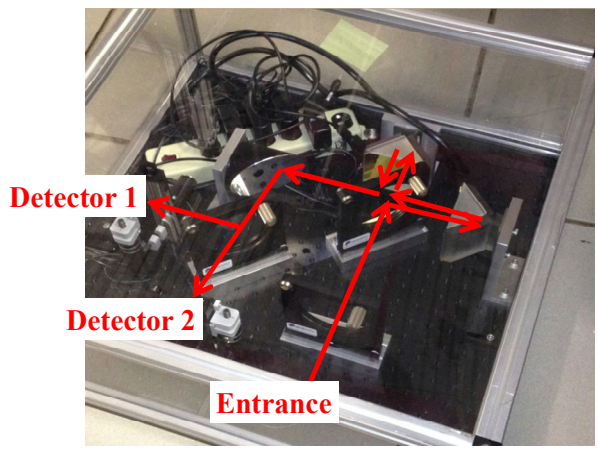


Figure 14: Interferometer light path. The THz is split and recombined from different path lengths. The interference determines the frequency content which in turn determines the bunch length.

Table 2: Bunch Length Capabilites

Device	Range (σ)	Charge Needed
Streak Camera	≥ 0.5 ps	8-10 nC
Martin-Puplett	0.1 – 1 ps	10 – 50 nC

SUMMARY

A system for distributing THz and optical light from four separate source points to three measurement points has been designed and is in the process of being constructed at Fermilab's ASTA facility. This system will enable both bunch length measurements for operational purposes and a variety of other experiments relating to both THz and optical radiation.

ACKNOWLEDGMENT

The authors would like to thank both the Accelerator and Technical divisions for their efforts in constructing and installing this system.

REFERENCES

[1] P. Garbincius et al., "Proposal for an accelerator R&D user facility at Fermilab's Advanced Superconducting Test Accelerator (ASTA)", Fermilab-TM-2568, October 2013.
[2] J. Ruan et al., "Commissioning Status of the Advanced Superconducting Accelerator at Fermilab", IPAC14, Dresden, June 2014, WEPRI058.
[3] A.H. Lumpkin et al., "Commissioning status of the ASTA facility at Fermilab", FEL14, Basel, August 2014, TUP075.
[4] J. Ruan et al., "Commission of the Drive Laser System for Advanced Superconducting Test Accelerator", IPAC13, Shanghai, 2013, WEPME057.
[5] A.H. Lumpkin et al., "Commissioning of a Dual-sweep Streak Camera with Applications to the ASTA Photoinjector Drive Laser", FEL14, Basel, August 2014, MOP021.
[6] J.C.T.Thangaraj et al., Phys. Rev. ST Accel. Beams 15 (2012) 110702.

Copyright © 2014 CC-BY-3.0 and by the respective authors

ISBN 978-3-95450-141-0

THIRD GENERATION RESIDUAL GAS IONIZATION PROFILE MONITORS AT FERMILAB*

J.R. Zagel#, M. Alvarez, B. Fellenz, C. Jensen, C. Lundberg, E. McCrory, D. Slimmer, R. Thurman-Keup, D. Tinsley, FNAL, Batavia, IL 60510, USA

Abstract

The latest generation of IPM's installed in the Fermilab Main Injector and Recycler incorporate a 1 kG permanent magnet, a newly designed high-gain, rad-tolerant preamp, and a control grid to moderate the charge that is allowed to arrive on the anode pick-up strips. The control grid is intended to select a single Booster batch measurement per turn. Initially it is being used to allow for a faster turn-on of a single, high-intensity cycle in either machine. The expectation is that this will extend the Micro Channel Plate lifetime, which is the high-cost consumable in the measurement system. We discuss the new design and data acquired with this system.

INTRODUCTION

Previous generations of residual gas ionization profile monitor's (IPM's) have been in operation, both at Fermilab and other laboratories, for many years [1-3]. The second-generation system applied a fixed permanent magnetic field, and polarity change to collect electrons to reduce space charge effects in the measurement [4]. Its field quality, while sufficient to improve the measurements, was not quite 1 kG, and required 4 feet of beam line to accommodate the magnetic unit. Two primary issues that arise have been the Micro Channel Plate (MCP) lifetime, and saturation effects of too much charge required from them. The third generation is designed to improve on these deficiencies, Fig. 1.

MEASUREMENT TIMING

The new system uses a timing module that combines the function of our Universal Clock Decoder (UCD), and the VME RF Timing module (VRFT). This module decodes the lab-wide timing 10 MHz clock (TCLK), the machine specific, beam synchronous clock (BSYNC), and a Machine Data (MDAT) Reference System, and outputs a clock trigger. Utilizing this board, we can generate a trigger on a specific machine state, and a particular machine clock cycle that then enables the beam synchronous clock pulses to gate our ADC's. The resolution of this trigger is one 53 MHz bunch. One sample per turn is generally acquired for a range of turns specified in the measurement specification. Multiple samples per turn is also a supported mode of operation.

* Operated by Fermi Research Alliance, LLC under Contract No. De-AC02-07CH11359 with the United States Department of Energy.
# zagel@fnal.gov

WHAT'S NEW

The new system incorporates the improvements added to the Fermilab Tevatron IPM [5] along with a few new features. Three new installations have been accomplished

New Magnet Design

The new magnet is designed using $SmCo_5$ permanent magnets. This material was chosen to give the highest residual magnetic field (Br) with the lowest variation in temperature dependence, at a reasonable cost and availability. A standard brick is 1" by 2" by 1/2". The magnet was intended to provide 1 kG in the detector area, with the return flux half upstream and half downstream, and shimmed, such that the beam sees a total integrated field of zero. The magnet is 31.5"L x 14"D with a minimum aperture of 4.25" to allow for a 4" diameter beam pipe suitable to both horizontal and vertical planes in the Main Injector and Recycler. Magnet design, modeling, and measurement details have been presented in [6].

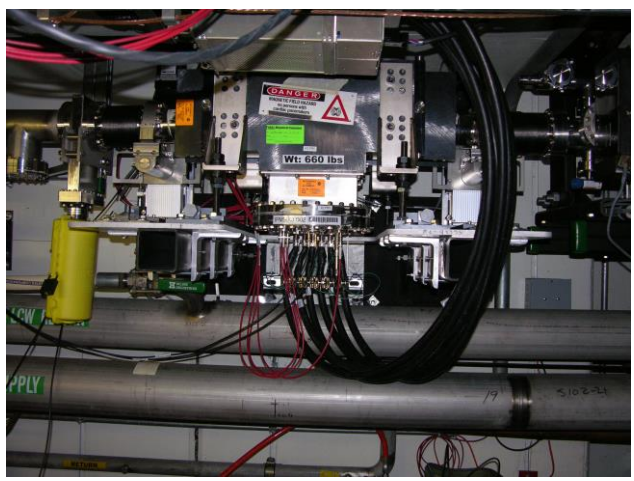


Figure 1: Recycler Vertical Installation.

Anode Strip Board

The anode strip pick-up board for both Main Injector and Recycler is a ceramic circuit board with 120 copper strips spaced at 0.5mm. The copper occupies 80% of that pitch with 20% space between strips. All signals are connected via 20 pin, ceramic mounted, quick release connectors. A multilayer flexible circuit delivers these signals to 6 front flange feed through connectors. A "Flash Test" strip has been added to the bottom of the

Copyright © 2014 CC-BY-3.0 and by the respective authors

board to facilitate testing of the full analog signal path integrity. This strip is designed to be a 50Ω strip line that can be pulsed from outside of the tunnel.

Control Grid

The third major improvement is the addition of a "Control Grid" that is placed on the beam side of the MCP's. The function of this control grid is to trap electrons and force them either upstream or downstream, outside of the detector area.

The grid material is electroformed nickel, 20 lines per inch with 0.00363" diameter wire, and open area of 86% . It is supported in a 316L stainless steel frame to cover the MCP aperture.

The control grid is kept at the full clearing field voltage until the batch of interest is passing through the detector. It is then pulsed to ground to allow the electrons to pass, un-deflected, on to the MCP. With the capacitance of this grid and a 600 Ohm source impedance, the rise time is 100 nsec. The external cable adds approximately 100 pF per meter.

Our batch structure is a string of 84 bunches, which represents a single full Booster turn. Up to 6 full Booster batches can be populated in Main Injector, leaving one equivalent 84 bunch length gap, for extraction kicker rise time. These 84 bunches constitute a 1.6 µsec batch. Ideally we plan to enable the grid slightly before the first bunch in the batch of interest arrives and shut it down after the last bunch passes.

Pre-Amplifier

The fourth major improvement is a redesigned preamplifier that lives within 2 meters of the detector. The preamp input will see all of the charge induced onto the anode strips and amplifies it to a reasonable voltage for transmission outside the tunnel. It has radiation tolerant parts, and is mounted away from the plane of the beam to further reduce particle bombardment, Fig. 2.

The amplifier was designed with a 100 Ohm input impedance, and a bandwidth of 1.2MHz providing sufficient rise time for the 1.6 µsec batch length, but also a high frequency signal rejection at 53 MHz. An OPA846 was chosen for the two stages for its low input voltage noise, high bandwidth, dc accuracy and output drive.

The amplifiers have an overall voltage gain of 5000 into 50 Ohms and an input impedance of 100 Ohms that together form a trans-impedance of 500 kOhm. The analog front end is set to +/- 1.5 Volts full scale. At the input of the amplifier is a 1.2 MHz low pass filter to reduce the beam's 53 MHz RF signal that couples onto the strips, this was measured to be less than -80dB. The low bandwidth of the amplifier in effect integrates the charge of each batch (up to 84 populated bunches).

Twenty channels are placed on a single board, in a single wide NIM module with six of these modules in a NIM crate to make a total of 120 channels per IPM system. Coupling between channels has been measured to be less than -56dB. The crate was placed in the tunnel close to the IPM detector to reduce noise on the signals.

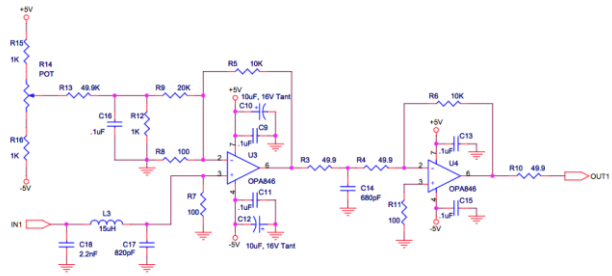


Figure 2: IPM Pre-Amplifier 2014 design.

Analog to Digital Converter

A new series of VME Analog to Digital Converter's (ADC) has been designed by the Fermilab Accelerator Instrumentation Department. The boards produced for the IPM system are populated with 16 channels of 14 bit 80 MHz parts. Also on board is a Field Programmable Gate Array (FPGA) that allows us great flexibility in our data acquisition. We sample multiple times during a gate that is centered on the batch of interest, and then average those samples to obtain a single recorded value for that batch for that particular turn. The sample depth is limited only by the amount of memory installed on the board, and the processing time desired for a result.

In addition, the FPGA also has an MDAT frame decoder that supplies our system with the intensity of the beam in the machine and the energy of the machine at the time that the analog data is sampled. A total of 96 Channels are digitized to create the beam profiles.

LabVIEW™ Front End Software Enhancements

We have added new features to the third generation IPM program to enhance utility and usability, Fig. 3.

The 2D display now has XY cursors enabled. When the Y cursor is moved, the new sample number is captured and used to initiate a single turn analysis. The X cursor destination (channel) is displayed below the X axis scale as an aid for identifying individual channels of interest.

There is now a running total stored and displayed that represents the amount of time high voltage has been applied to the micro channel plate. This number, in conjunction with the S/N (dB) is provided to help analyze micro channel plate lifetime.

A MCP accumulated plate charge correction button is available for the 2D display. This correction assumes there is no significant change in amplitude, sigma, or position from the reference sample (default sample 500). The correction is for visualization purposes only and is not used in the single or multi-sample analysis.

Channel data values above or below predetermined limits are now automatically eliminated from display in the Single Turn analysis plot. Limits are established using the specifications of the ADC and the expected normal data range. Channels outside this range are still represented in the 2D raw data display.

Position and sigma FFT data is now reported to ACNET devices in addition to the front panel display.

Copyright © 2014 CC-BY-3.0 and by the respective authors

ISBN 978-3-95450-141-0

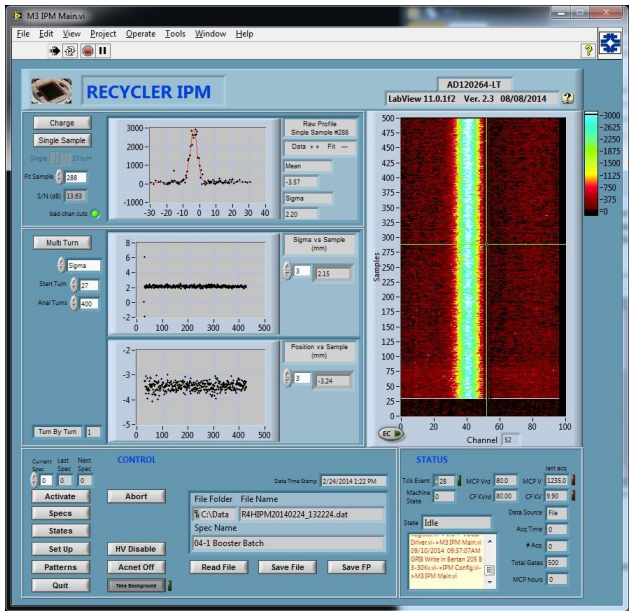


Figure 3: LabView™ User interface.

Movable Detector

The detector vacuum vessel is mounted on a pair of linear slides at each end that allow us to change the area of the MCP that is exposed to beam. Initially we can change the alignment of the detector to the beam by skewing the unit a few degrees from end to end. We take data to verify the alignment that yields the minimum sigma measured during stable beam conditions. This also facilitates moving the unit to a different spot on the MCP after every few weeks of operations.

There is a total travel of 3.8 cm centered on the proton beam. However, we can position the vacuum vessel much farther into the magnet to provide extra clearance when we need to remove the detector for maintenance.

Moving the vacuum vessel without changing the position of the magnet means that the beam is exposed to the same magnetic field.

Maintenance Enhancement

A major step forward is the addition of isolation valves immediately adjacent to the instrument both upstream and downstream. The detector can be isolated from the rest of the beam pipe for removal and replacement of the MCP. This minimizes the time for vacuum recovery after maintenance. A cross with a pump out port and an ion pump is installed inside the isolation valves. To vent the instrument, we let it up to dry nitrogen before opening it to atmosphere.

MEASUREMENT CAPABILITY

A total of 96 Channels are digitized to create the beam profiles. Depending on the number of cables coming up from the tunnel, some anode strips are skipped at the tails to provide for a good fit.

These instruments are generally used for injection matching. A detailed analysis is performed on the first 500 turns after injection to look for either sigma oscillations, indicating a betatron oscillation, or position oscillations, indicating beam was injected off orbit.

OBSERVED PERFORMANCE

The control grid, at full clearing field voltage, is effective at diverting over 90% of the electrons formed by ionization from bunches other than the desired measurement. We currently have the ability to switch the control grid from our service buildings, allowing us to start a measurement soon after decoding the appropriate clock events. Turn on time is about 7.25 µsec. Revolution time in both Main Injector and Recycler is on the order of 11.1 µsec.

High voltage switches are available in the commercial market that will provide fast rise times at 10 kV for the low capacitance load of this grid. The peak current is limited to 12 Amps by a series resistance. These switches are built using MosFET technology, but are not radiation tolerant. Switching the control grid for the batch measurement is not yet possible as switching time is dominated by the capacitance of the 100-150 foot cables from service building to tunnel. We are looking for a place in an alcove where we could potentially build a somewhat shielded enclosure to house the switches.

CONTROL GRID SIMULATION

The IPM simulation is a MATLAB program that tracks the ionization particles from their point of production to some arbitrary stopping point. It utilizes the time-dependent electric and magnetic fields of the proton bunches as they pass through the IPM region. It also includes the calculated magnetic field of the IPM magnet from OPERA, and the 2-D electric field of the IPM as calculated via POISSON. Ionization particles with energy E are generated from a $1/E^2$ distribution. Fig. 4 shows the drift of the ionization electrons when the IPM is gated on. This is the normal behaviour.

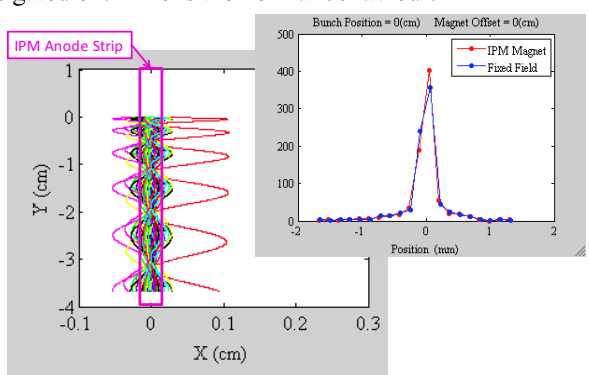


Figure 4: Plot of electron drift lines. All electrons start from the same point and take about 1.7 ns to drift to the bottom. The inset plot shows the distribution of particle positions at the bottom. Most of them are contained within a single anode strip.

When the grid is gated off, the field lines are as shown in Fig. 5.

Copyright © 2014 CC-BY-3.0 and by the respective authors

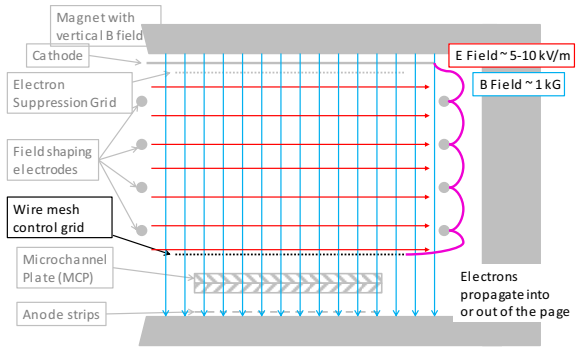


Figure 5: Field lines when the control grid is gated off. The crossed electric and magnetic fields produces motion in the perpendicular direction. In this case that is along the proton beam line.

The simulation results of the drift lines for the gated-off case are shown in Fig. 6. The electron drift velocity along the proton beam line in the simulation is ~8 cm/μs compared to ~10 cm/μs estimated analytically assuming a uniform electric and magnetic field and no protons. This velocity implies that the ionized electrons will drift out of the region of the MCP in ~1 μs.

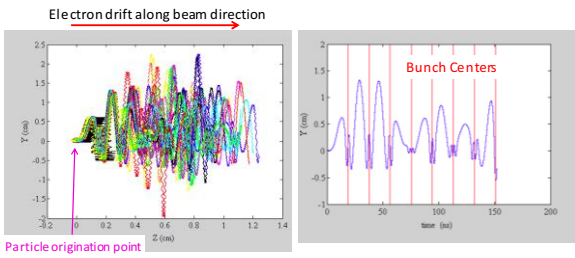


Figure 6: Drift trajectories of electrons with the control grid gated off. The plot on the right shows the trajectory of a single electron where one can see the constraining of the trajectory that occurs when a proton bunch passes by.

The drift trajectories of the ions are shown in Fig. 7. Ions that encounter the grid are not directly a problem, however if they generate secondary electrons on the far side of the control grid, those would then accelerate toward the MCP and could partially negate the benefits.

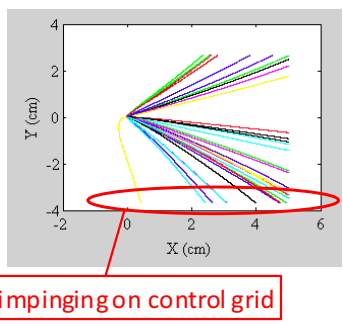


Figure 7: Ion trajectories with control grid gated off. Since they are heavy, they are relatively uninfluenced by the electric and magnetic fields. The elapsed time to reach the control grid was ~1.5 μs.

CONCLUSION

The improvements detailed all contribute to the goal of making a better measurement while at the same time extending micro channel plate lifetime. We still have work to do to design a cost effective way of switching high voltages, at 100 kHz, in the Fermilab tunnels. This work continues.

ACKNOWLEDGMENT

The authors would like to acknowledge all the work of the Fermilab Technical Division for their efforts in designing, building, and testing our new magnet for this project. In addition, we could not have gotten this far without the collaborations with other individuals at various laboratories as cited in the reference section below. Lastly, we acknowledge the efforts of many technicians who spent many hours in the assembly, testing, vacuum certification, and installation of the instruments.

REFERENCES

[1] J. R. Zagel, *et al.*, "Operational Use of IPM's at Fermilab", BIW 2010, Santa Fe, NM, USA.

[2] R. Connolly, *et al.*, "Residual-Gas-Ionization Beam Profile Monitors In RHIC," PAC 2005, C05-05-16.1, p230, Knoxville, KY, USA.

[3] K. Wittenburg, "Experience with the Residual Gas Ionization Beam Profile Monitors at the DESY Proton Accelerators", Proc. 1992 EP AC., 24.3.-28.3, Berlin, Germany and DESY HERA 92-12

[4] J. R. Zagel, *et al.*, "Permanent Magnet Ion Profile Monitor at the Fermilab Main Injector", PAC 2001, pp1303-1305, Chicago, IL, USA, June 2001.

[5] A. Jansson, *et al.*, "The Tevatron Ionization Profile Monitors", 12th Beam Instrumentation Workshop, Fermilab, Batavia, IL, USA, 2006.

[6] V. Kashikhin, *et al.*, "Permanent Magnet for a Beam Profile Monitor", 23rd International Conference on Magnet Technology (MT-23), Boston, MA ,USA, July 2013, IEEE Trans. Appl. Supercond. 24 (2014) 501004.

Copyright © 2014 CC-BY-3.0 and by the respective authors

ISBN 978-3-95450-141-0

OPTIMIZATION OF BEAM INDUCED FLUORESCENCE MONITORS FOR PROFILE MEASUREMENTS OF HIGH CURRENT HEAVY ION BEAMS AT GSI

C. Andre, P. Forck, R. Haseitl, A. Reiter, R. Singh, B. Walasek-Hoehne,
GSI Helmholtzzentrum für Schwerionenforschung GmbH, Germany

Abstract

To cope with the demands of the Facility for Antiproton and Ion Research (FAIR) for high current operation at the GSI Heavy Ion Linear Accelerator UNILAC non intercepting methods for transverse beam profile measurement are required. In addition to intercepting diagnostics like Secondary Electron Emission Grid (SEM-Grid) or scintillating screens, the Beam Induced Fluorescence (BIF) Monitor, an optical measurement device based on the observation of fluorescent light emitted by excited nitrogen molecules, was brought to routine operation. Starting with the first installations in 2008 and consequent improvements, successively six monitors were set up in the UNILAC and in the transfer line (TK) towards the synchrotron SIS18. BIF is used as a standard diagnostic tool to observe the ion beam at kinetic energies between 1.4 and 11.4 MeV/u. Beside the standard operation mode where the gas pressure is varied, further detailed investigations were conducted. The BIF setups were tested with various beam parameters. Different settings of camera, optics and image intensification were applied to improve the image quality for data analysis. In parallel, the light yield from different setups was compared for various ions, charge states, beam energies and particle numbers.

INSTALLATIONS

Along GSI linear accelerator UNILAC and transfer line, six BIF monitors are installed. Each monitor consists of two perpendicularly mounted image intensified camera systems to measure transversal beam profiles in horizontal and vertical plane simultaneously (see Figure 1 and Table 1). The monitors are placed to observe changes of the beam due to stripping or acceleration. Profiles and positions of a single linac pulse can be observed at all positions without beam distortions.

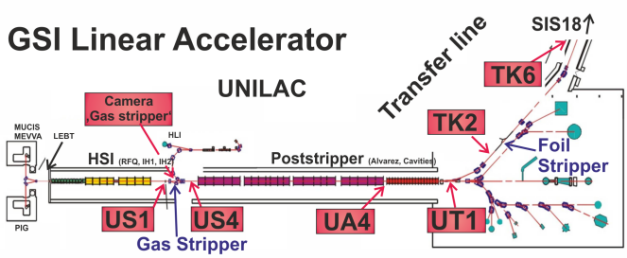


Figure 1: Locations of BIF monitors along GSI Linear Accelerator.

In addition, a regular CCD camera observes beam induced fluorescence at the gas stripper to control the gas flux. Here, different charge states of the same beam can be observed within one image.

Table 1: BIF Installations and Typical Beam Parameters

BIF		US1	US4	UA4	UT1	TK2	TK6
CCD coupling	H	T	R	T	R	T	T
	V	T	R	T	R	T	R
Energy [MeV/u]		1.4	1.4	11.4	11.4	11.4	11.4
Typical charge states :							
Argon		1+	11+	11+	11+	11+	18+
Nickel		2+	14+	14+	14+	14+	26+
Tantalum		4+	24+	24+	24+	24+	62+
Uranium		4+	28+	28+	28+	28+	73+

DETECTOR SETUP

The BIF principle and the detailed setup (hardware, optics, readout and control) of the system is described in [1]. To observe the fluorescence of the ion beam interaction with the nitrogen gas molecules at lowest gas pressures, image intensified camera systems (ICCD) are required, preferably with a 2-stage multichannel plate (MCP) to enable single photon counting. ProxiVision® developed two custom designed camera types; a fiber-taper coupled CCD (T) where the CCD chip is glued to the taper and a relay-lens coupled CCD (R) with c-mount standard (Figure 2, Table 1).

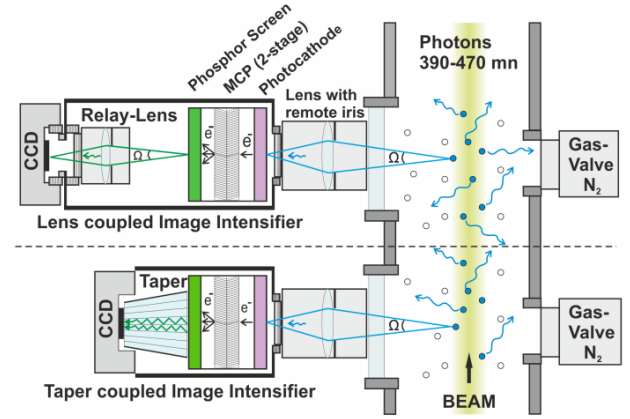


Figure 2: Types of Image Intensified Camera Systems.

Copyright © 2014 CC-BY-3.0 and by the respective authors

Fiber-tapered cameras intrinsically offer a higher light yield due to the higher coupling efficiency between phosphor and CCD chip, whereas relay-lens coupled systems are easier for maintenance e.g. malfunctioning CCD cameras screwed on the c-mount can easily be replaced without removing the image intensifier from the beam line installation. Thus, the relay-lens coupled camera systems are preferred for permanent installations in the future. Currently, both types of image intensifier systems are set up in the UNILAC (see Table 1).

Prior to installation, each camera lens was separately calibrated and the light transmission can be chosen relative to the fully opened iris (100 %, f-stop 1.4).

All images of the CCD cameras are recorded in 8 bit.

SIGNAL EVALUATION

Operational parameters for BIF to gain signal strength and quality are the N_2 gas pressure, the iris opening and the MCP high voltage. By setting MCP and iris in a proper way, both systems can be used for profile measurements in

- Event counting (EC) mode
  Requires a high intensifier gain for efficient single photon detection and relies on bright, well separated event signatures.
  The captured image, after defining a threshold, is converted to a binary image and checked for connected components of minimum 2 neighbouring pixels, so called events. Each event has vertex (x/y), where profiles are projections of the vertices in the vertical plane. The total light yield is the number of counted events N_{EC} in the image.
- Charge collection (CC) mode
  The intensifier gain is adjusted to avoid camera saturation at the expense of some detection efficiency. Here, the overlap of detected events is not a problem as long as no saturation occurs.
  A background is calculated by the outer region of the image and subtracted from each pixel. The total light yield N_{CC} is obtained by integration over the CCD matrix after background subtraction. Profiles are projections of the matrix in the vertical plane.

The two different modes ideally demand for specific settings of the complete camera system. Figure 3 shows typical images for both analysis modes.

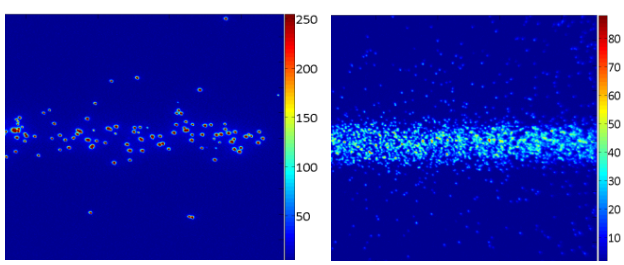


Figure 3: Typical images for counting mode (left) and for charge collection (right).

For a comparison in Figure 4, both ways of data analysis were performed for images with different iris settings under constant beam conditions and camera settings. For the CC mode, the maximum grayvalues were ~120, thus saturation of pixels was excluded. For the EC mode, the events were clearly separated for counting for an almost closed iris and the threshold was manually adjusted for each measurement. The resulting curves normalise to the lowest iris setting of the event counts.

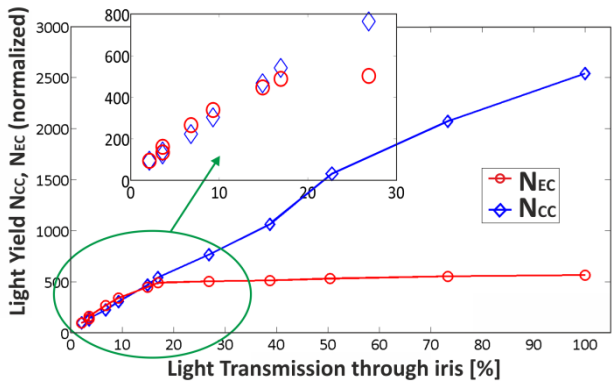


Figure 4: Comparison of event counting mode and charge collection mode for varied iris opening. Beam parameters: US4, N^{4+} beam, 1.4 MeV/u, $8.4 \cdot 10^{11}$ ppp, $5 \cdot 10^{-6}$ mbar N_2 pressure.

The obtained results (Figure 4) clearly show that the dynamic range of the N_{CC} mode is a factor of 5 larger than the N_{EC} mode. For these images and beam settings, the events start to overlap at ~200 events in an image.

Figure 5 shows an image with defined ROI, where consistent projections in both modes were obtained. For the charge collection mode, a background was subtracted and no pixels were saturated. Within the ROI, the N_{EC} was ~130.

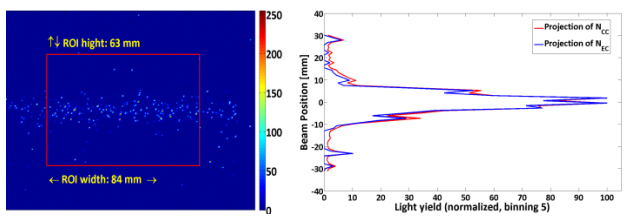


Figure 5: Raw image and projections in the CC and EC-mode, both binned by a factor of 5. Beam parameters: TK6, Ta^{24+} beam, 11.4 MeV/u, $3.8 \cdot 10^{10}$ ppp, $5 \cdot 10^{-6}$ mbar N_2 pressure.

For images with fewer events, integration over several pulses is possible to obtain a reasonable profile. Especially to depict the beam position of a single linac pulse from images with low signal, the charge collection mode is more sensitive. Figure 6 shows a projection of few, slight grey events in the CC mode (pixel value on events ~50, subtracted background and binned by a factor of 5) and the corresponding profile of a SEM-Grid. Both systems are in good agreement.

Copyright © 2014 CC-BY-3.0 and by the respective authors

ISBN 978-3-95450-141-0

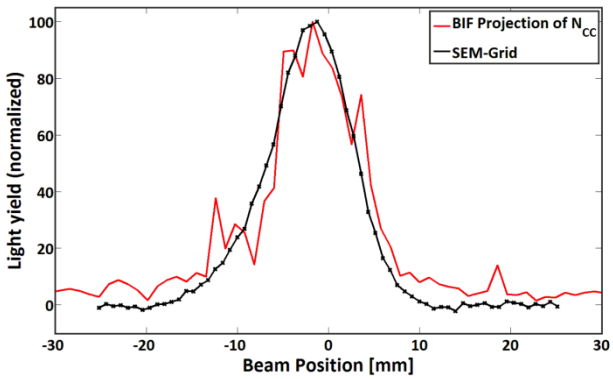


Figure 6: Comparison of the beam position at TK2, measured by BIF and a SEM-Grid. Beam parameters: U^{39+} beam, 11.4 MeV/u, $3 \cdot 10^{10}$ ppp, $5 \cdot 10^{-6}$ mbar N_2 pressure.

BIF IN OPERATION

For the usage of BIF as a beam diagnostic monitor, a wide range of ions, particle numbers and charge states as well as different beam positions have to be covered. This demands for a high dynamic of the detector and robust and reliable analysis of the image data. Where the event counting mode strongly depends on user defined parameters, e.g. the threshold has to be set case by case, the charge collection mode uses fixed settings for all parameters of the CCD and image intensifier. For each individual detector, appropriate settings of MCP high voltage, iris opening and CCD gain were determined by tests to achieve small events with grayvalues around 100 and saved in an initialization file. Hence, the charge collecting mode is more suitable and preferred for standard operation (see Figure 4).

The software 'Profile View' [2] that is used by the operating crew for beam position and profile measurements offers a 'User Mode', where the N_2 gas pressure as the operational parameter can be varied stepwise up to a maximum of $5 \cdot 10^{-6}$ mbar. For the user mode, all other settings are loaded from the initialization file. The Profile View GUI (Figure 7) shows the horizontal and vertical beam positions for three BIF detectors simultaneously. To determine the beam position and profile width, a projection of the raw image data in the CC-mode without background subtraction is sufficient. For a better profile appearance, an additional smoothing is provided. During beam alignment with BIF, ongoing experiments can continue without any disturbance.

An additional 'Expert Mode' enables to view and save the raw images. Here, further settings for gas pressure, MCP high voltage and the iris opening can be applied. Beside this, the expert has remote access to all parameters of the CCD (gain, integration time …) and the timing of all the devices. The 'Expert Mode' is mainly used for experiments, system calibration and diagnostic inspection, if unexpected signals occur and a 2-dimensional view of the beam trajectory is necessary.

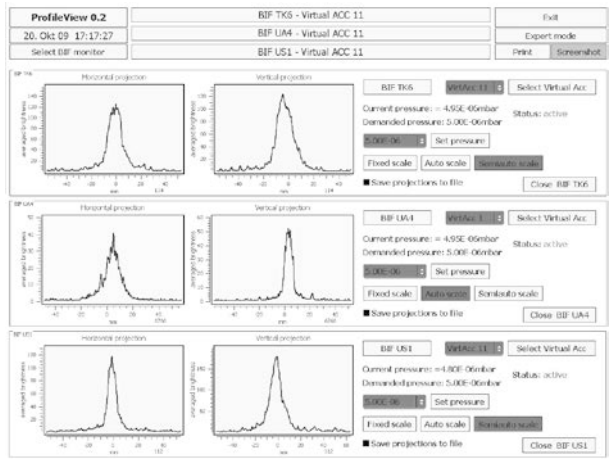


Figure 7: GUI of Profile View for operating.

COMPARISON OF NORMALIZED SIGNALS

BIF data was recorded over years during routine operation, by using the given beam parameters and settings. Unfortunately, dedicated UNILAC beam times for BIF with specified beam conditions are quiet rare. During most data acquisitions, only the settings of the detector itself could be varied for different studies, e.g. the behaviour of the gas pressure, of the iris opening or the MCP high voltage. These experiments and results can be found in [3], [4].

Here, the recorded data of multiple beam times at all BIF installations positions (see Table 1) with varying camera settings, N_2 pressure settings and beam parameters (ions, charge states, current) were compared, after normalization based on the Bethe-Bloch scaling [5]. Though optics, mechanics and hardware of all setups was kept identical, the characteristics of the Image Intensified Camera Systems varies according to the type of photocathode, their quantum efficiency, the overall gain of the MCPs and the type of coupling (see Figure 2). Thus, the event signature of all camera systems slightly deviates. Hence, for this comparison, preferably images with clearly separated events were chosen to be analysed in the EC-mode. Counting here is an advantage, because if the MCP high voltage was set to a reasonable value and the events appear clearly and separated on the CCD chip, one can assume an efficiency of ~1 for each electron reaching the the MCP and triggers an avalange, independently of the exact MCP voltage, the CCD gain and the type of coupling. For a relative comparison of the different measurements, the counted events N_{EC} of each image have to be normalized as follows.

The number of expected events N_{EC}, as described in [5-7] is defined as

$$N_{EC} = N_{Ions} \cdot \rho \cdot x \cdot \frac{N_A}{A} \cdot \sigma \cdot \varepsilon_{Iris} \cdot \varepsilon_{Detector} \quad (1)$$

$$\sigma(E) \propto {}^{dE_P}/_{dx}(E) \cdot q^2 \quad (2)$$

Copyright © 2014 CC-BY-3.0 and by the respective authors

Where

N_{Ions}	number of incident beam ions (ppp)
ρ	mass density of the target
x	observation length in beam direction; here fixed by a constant image ROI
N_A	Avogadro number
A	mass number of the target
σ	cross section
ε_{Iris}	iris opening (resp. light transmission)
$\varepsilon_{Detector}$	a global constant for each detector, including the solid angle for an open iris, the efficiencies of the flange, the iris, the photocathode and the penetration into the multichannel plate
E_P	kinetic proton energy
$^{dE_P}/_{dx}(E)$	differential proton energy loss for energy E
q	charge state of the ion

For a relative comparison of the measurements, constant values of Equation (1) for x, N_A/A and $\varepsilon_{Detector}$ can be neglected.

$$N_{EC} \propto N_{Ions} \cdot \rho \cdot {}^{dE_P}/_{dx}(E) \cdot q^2 \cdot \varepsilon_{Iris} \quad (3)$$

The following parameters are given for each measurement and taken into account for normalization:

N_{Ions}	known for the beam pulse
ρ	calculated from the nitrogen gas pressure
ε_{Iris}	iris opening of the calibrated lens

For the UNILAC energy of 11.4 MeV/u with a constant $^{dE_P}/_{dx}$ [8], the number of events is proportional to the q^2.

$$N_{EC} \propto q^2 \quad (4)$$

Figure 8 shows the normalized number of events N_{EC} for different detectors and ions. Each data point is the average number of counted events over 100-150 images with corresponding standard deviation, where each set of images was checked for consistency by testing different threshold settings. The data was normalized in respect to the gas pressure, the iris opening, the particle number, the differential energy loss and to the square of the ion charge state.

After normalization, N_{EC} data scatter within a factor of three between the measurements of Ar^{10+} to Ta^{62+} (Figure 8). Since the q^2 ratio between these charges would be a factor of ~40, a factor of three here seems reasonable. The data were taken on different detectors in parallel to standard operation and the detector settings were not optimized for EC mode. Beside this, the pulse-to-pulse beam current was not recorded in parallel, so an average value for each series of images was taken for the normalization. Also the true gas pressure at different locations can vary, depending on the installation in the chamber. The results presented in Figure 8 acceptably support the q^2 dependency for various ions at the energy of 11.4 MeV/u and show a consistency of the individual detector settings.

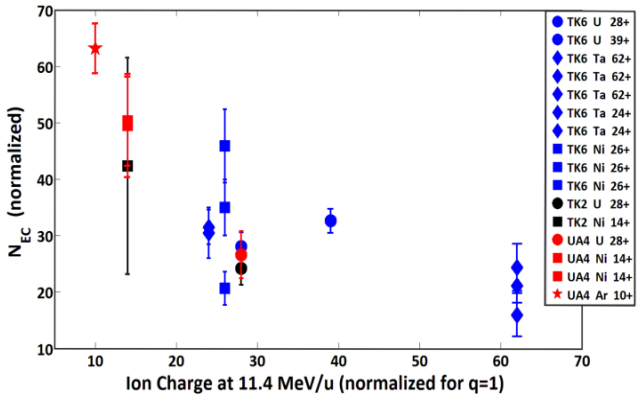


Figure 8: Counted events (data normalized on q=1 and on the particular measurement settings) for various measurements on different BIF installations.

During one dedicated experiment, a direct comparable measurement could be performed with a tantalum beam, once stripped at the stripper foil to Ta^{62+} and unstripped with Ta^{24+}. At the BIF installation TK6 horizontal and vertical images could be taken of both charge states without any changes of the detector settings, gas pressure and so on. All detector characteristics, defined by $\varepsilon_{Detector}$ can be neglected, e.g. the fact, that the horizontal camera system is a fiber-tapered one, whereas the vertical camera system is relay-coupled. To use the same images for both modes of data analysis, the camera parameters were chosen carefully to have maximum 100 events and grayvalues < 150 in an image. By this, beside the event counting mode, also the total light yield in the charge collecting mode could be compared for both tantalum charge states (see Figure 9).

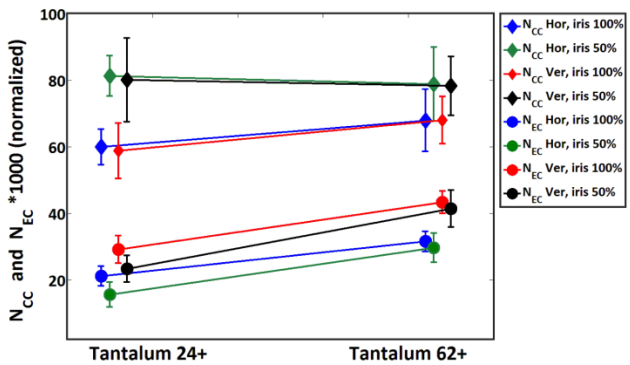


Figure 9: Number of collected charges and counted events (normalized on q=1 and on the particular measurement settings) for Ta^{24+} and Ta^{62+} beam in TK6. The lines present corresponding data sets.

Figure 9 strongly supports the q^2 dependency for the CC and EC mode. The deviation of a few percent is acceptable and could derive from the iris calibration that also shows a hysteresis curve or be due to the usage of an average current value for one data set.

Copyright © 2014 CC-BY-3.0 and by the respective authors

ISBN 978-3-95450-141-0

CONCLUSION

BIF detectors are non-invasive and able to measure the beam position and achieve transversal beam profiles at 6 dedicated positions in the UNILAC within one beam pulse. A systematic check of the alignment over the whole linac and transfer line can be done with the BIF monitors.

The installed BIF detectors offer a reliable and robust measurement of beam position and transversal profiles for high current beams. For operation, the data analysis is done in the charge collecting mode as a projection of the raw image, which offers a high dynamic and sufficient accuracy, even without background subtraction. Hence, the event counting mode seems less practical and more complex for daily operation, because the quality of the counting strongly depends on the settings of the threshold and on overlapping events.

For a relative comparison between different BIF systems with deviating characteristics of the image intensified camera systems, the event counting mode turned out to be more appropriate. Settings of MCP voltage or camera gain can be neglected if clear bright events on the CCD are achieved. At the UNILAC energy of 11.4 MeV/u, the q^2 dependency of normalized N_{EC} signals of multiple different measurements and detectors could be shown.

A further dedicated experiment at 11.4 MeV/u of a tantalum beam at two different charge states strongly supports the q^2 dependency on the basis of the applied normalization. Similar results that also support the q^2 dependency were published by T. Tsang [7] for relativistic ions of different charge states.

OUTLOOK

For future installations at GSI linear accelerators and in the High Energy Beam Transport (HEBT) lines of FAIR, numerous non intercepting profile measurements, e.g. BIF are demanded. For permanent installations, the relay-coupled image intensified cameras are preferred, due to the better maintenance. Beside the lower overall intensity on the CCD chip which can be compensated by higher MCP voltages, the appearance of the events is smaller with a better distribution.

The normalization is a first step for automized detector setting generation for multiple beam production with shot-by-shot changes of ion species. This will get more important for future installations in linear accelerators and the HEBT of FAIR.

ACKNOWLEDGMENT

Thanks to all my colleagues at GSI for help with the BIF setups, data acquisition and analysis.

REFERENCES

[1] C. Andre et al., “Beam induced Fluorescence (BIF) Monitors as a Standard Operating Tool”, DIPAC 2011, Hamburg, Germany, p. 185

[2] R. Haseitl et al., “ProfileView – A Data Acquisition System for Beam Induced Fluorescence Monitors”, DIPAC 2009, Basel, May 2009, p. 134

[3] F. Becker et al., "Beam Induced Fluorescence (BIF) Monitor for Transverse Profile Determination of 5 to 750 MeV/u Heavy Ion Beams ", DIPAC 2007, Venice, May 2007, p. 33

[4] F. Becker, “Non-destructive Profile Measurement of intense Ion Beams”, PhD-thesis, Darmstadt, 2009

[5] A. Variola et al., “Characterization of a Non-destructive Beam Profile Monitor using Luminescent Emission”, Physical Review Special Topics - Accelerators and Beams 10 (2007), August, Nr. 122801, S. 1–14

[6] D. Sober et al., “An Introduction to Cross Section”, Physics 537/635, January 2005 (rev. 2007)

[7] T. Tsang et al., “Residual Gas Fluorescence Monitor for Relativistic Heavy Ions at RHIC”, Physical Review Special Topics - Accelerators and Beams 16 (2013), Nr. 102802, S. 1-7

[8] http://www.srim.org

Copyright © 2014 CC-BY-3.0 and by the respective authors

CUPID: NEW SYSTEM FOR SCINTILLATING SCREEN BASED DIAGNOSTICS

B. Walasek-Höhne, C. Andre, H. Bräuning, A. Bräuning-Demian, R. Haseitl,
T. Hoffmann, R. Lonsing, A. Reiter, C. Schmidt, M. Schwickert
GSI Helmholtzzentrum für Schwerionenforschung GmbH, Darmstadt, Germany

Abstract

The Facility for Antiproton and Ion Research (FAIR) with its wide range of beam parameters poses new challenges for standard beam instrumentation like precise beam imaging. To cover the various foreseen applications for standard scintillating screen based diagnostics, a new technical solution was required.

CUPID (Control Unit for Profile and Image Data) is a new system for scintillating screen imaging, which is based on the data acquisition framework for FAIR. It includes digital image acquisition, remote control of the optical system (focus and iris; camera setup and power) and a graphical user interface (GUI). CUPID is also designed to work with different imaging devices like GigE cameras or video cameras using frame grabber cards. In this paper we report on the first results with this novel system during routine beam operation.

For imaging applications in the high radiation environment of the heavy ion synchrotrons radiation-hard cameras are required. One possible candidate for such cameras at FAIR is the CCIR MegaRAD3 from Thermo Fischer Scientific. We describe here our first results with this camera, which has been installed at the SIS18 extraction point, where a high radiation level is present.

CUPID SYSTEM

CUPID is a new, fully FAIR-conformal system for standard scintillating screen based beam diagnostics including pneumatic drive, data acquisition, slow control of parameters like focus and iris and graphical user interface. The new system, installed and commissioned at several GSI High Energy Beam Transport Lines (see Figure 1) in the beginning of this year, is now used in standard accelerator operation.

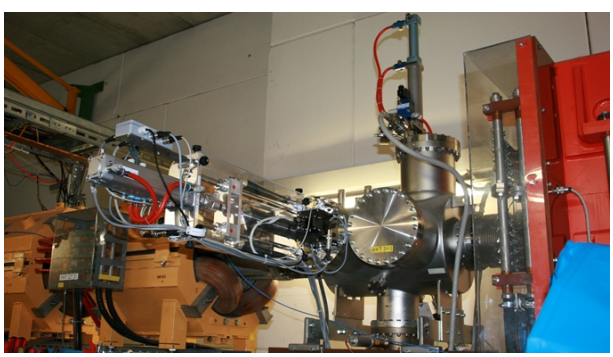


Figure 1: Scintillating Screen installation at High Energy Beam Transport Lines.

The scintillating screens with typically 120 mm diameter, made of Chromox or phosphor P43, are mounted on a pneumatic drive in vacuum. Special markers on the screen holder are used to calibrate the image and convert pixels into beam position and size in millimeters. The scintillating screens are typically (but not exclusively) mounted under 45° with respect to the beam axis and the optical axis of the camera. The camera is operated outside the vacuum chamber and views the screen through a UV-glass flange.

A LED can illuminate the scintillating screen for diagnostic purposes or recalibration of the optical system.

With the exception of the pneumatic drives, the direct hardware access (camera readout, lens control etc.) is based on FESA, the CERN Front-End Software Architecture [1]. Image acquisition, lens control and camera power are implemented as different FESA classes. Because CUPID is designed to work with different imaging hardware, a dedicated image acquisition FESA class is written for each imaging system supported. Using the inheritance mechanism in FESA a new imaging device can be easily incorporated in the system. The imaging base class contains all common code, like image manipulation (rotation, mirroring) and computations (profiles, intensity histogram, moments of the intensity distribution). It also provides the code to save raw images to disk (local or via network) as standard bitmap files. In addition, it enforces the common interface between the imaging FESA class and the CUPID GUI. The derived FESA class for the specific imaging device only implements the specific code to set up the device and acquire the images.

The decision to implement image acquisition, lens control and camera power as separate FESA classes (and thus devices) has the advantage, that single components can easily be exchanged or even removed. It is currently the responsibility of the GUI, to connect to the different FESA classes and hide this diversity from the operator. In the future FAIR control system, the paradigm proposed by the accelerator control system department is to treat all components as a single device and access it via a single FESA class. This is not contradictory to the approach used currently in the CUPID system. Using the 'association' feature of FESA, the single device paradigm can be implemented by creating a simple wrapper FESA class acting as a middle tier between the separate FESA classes now in use and the future control system.

The standard camera installed is the IDS uEye UI-5240SE-M [2], which is a digital GigE camera equipped with the radiation tested e2v CMOS sensor [3] with 1280 by 1024 pixel. A camera internal area-of-interest limits the image to

Copyright © 2014 CC-BY-3.0 and by the respective authors

ISBN 978-3-95450-141-0

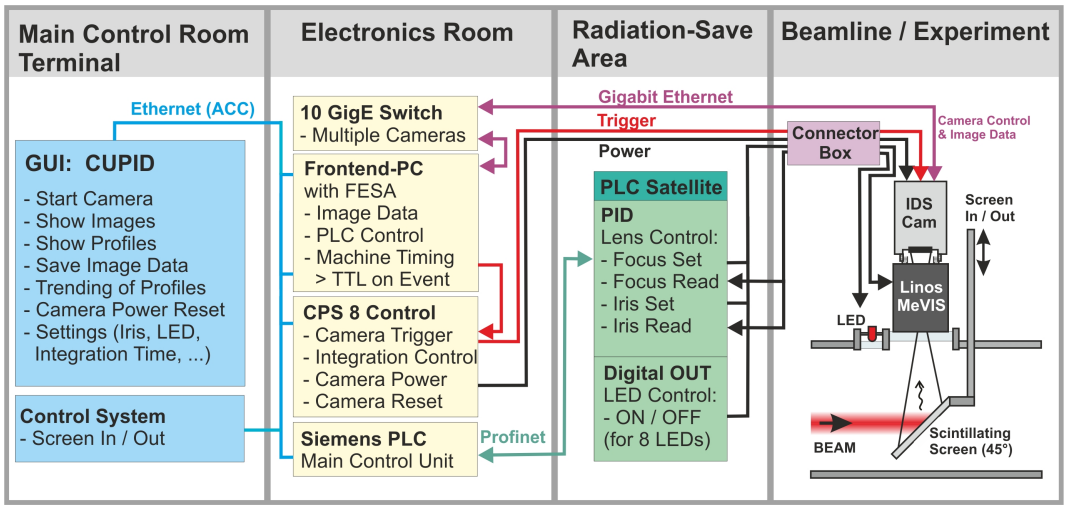


Figure 2: CUPID: overview of electronic devices and communication scheme.

the size of the scintillating screen and reduces the amount of data transferred already in the camera. Grouped according to their location,the cameras are connected via a HP Procurve 10 Gigabit Ethernet switch to a Kontron PCI 761 Industrial PC. The PC is equipped with an additional 10 Gigabit network adapter to provide a private network for the camera readout. The PC also runs the FESA classes and provides the link via the accelerator network to the GUI. The performance of the system reached more than 15 frames per second at full resolution with one active camera and a single connected client. Besides the IDS uEye camera, the Allied Vision Technology GC650 GigE camera has also been integrated in the CUPID system. It has been used in machine experiments with an image intensifier. Currently, a FESA class is under development to acquire images from an IDS FALCONquattro frame grabber card to be used with a radiation hardened camera from Thermo Fischer Scientific (see next section).

Power supply and remote reset for up to eight digital cameras are realized by the in-house developed Camera Power Supply controller CPS8. The CPS8 is based on an Arduino single-board microcontroller [4] and controlled via Ethernet. By sending simple ASCII commands the controlling FESA class sets the power of any attached camera. It can also obtain the power status of each connected camera. In addition, the CPS8 distributes hardware triggers to the cameras either from an external input or self-generated.

The standard installation for CUPID uses a Linos MeVis-Cm lens with 16 mm focal length, motorized iris and lens control with potentiometers to read back actual positions [5]. A Siemens PLC (main unit and satellites) handles control of focus and iris motors, read and set by a PID controller (FM355C). In addition, digital outputs (SM322) of the PLC control the LED to illuminate the phosphor P43 target (Prox-iVision) respectively Chromox (BCE Ceramics) for calibration issues. A dedicated FESA class using the CERN IEPLC [6] library provides access to the PLC from the CUPID GUI.

Conforming to FAIR requirements, the GUI (see Figure 3) is written in Java. It displays the acquired image (corrected for camera orientation), the profiles, the intensity histogram as well as integral data like total brightness, centre of intensity in the reference coordinate system and full-width-half-maximum of the profiles. The GUI is also responsible for the conversion of pixels into millimetres. The corresponding conversion factors are stored with the FESA class and sent to the GUI with each profile or image. Because the scintillating screen is tilted 45° with respect to the camera's optical axis, the image suffers from perspective distortion. This means that the x and y positions in mm are a function of both, x_p and y_p the pixels positions. Because profiles are obtained by integrating the image pixels along the y (or x) axis, for the profile display the position in mm (x and y respectively) are assumed to be dependent only on the corresponding pixel coordinate (x_p and y_p):

$$\begin{aligned} x &= m_x(x_p - x_0) \\ y &= m_y(y_p - y_0) \end{aligned}$$

Here m_x and m_y are the average scaling factors in mm per pixel in x and y. The error due to perspective distortion is less than 5 mm at the edges of the scintillating screen with 120 mm diameter.

The GUI provides the possibility to overlay a grid with 5 mm line spacing over the image. In addition, the coordinates of any pixel under the mouse cursor are displayed not only in pixels but also in mm. For the grid and the cursor display, the conversion is calculated according to (for the x-axis):

$$\begin{aligned} x'_p &= x_p - x_0 \\ y'_p &= y_p - y_0 \\ m &= m_x + m_{xx}x'_p + m_{xy}y'_p \\ x &= mx'_p \end{aligned}$$

Thus for each pixel coordinate a scaling factor m in x is calculated, which depends on the pixels x and y coordinate.

Copyright © 2014 CC-BY-3.0 and by the respective authors

m_{xx} is the change of the scaling factor in x with the pixel's x coordinate x_p (i.e. $\Delta m_x/\Delta x_p$) and m_{xy} is the change with y_p (i.e. $\Delta m_x/\Delta y_p$). Depending on the orientation of the scintillating screen, in general either m_{xx} or m_{xy} is zero. The conversion for the y axis is performed accordingly. However, it should be noted, that this more elaborate calibration noticeably improves the accuracy of the beam position only at the outer regions of the scintillating screen.

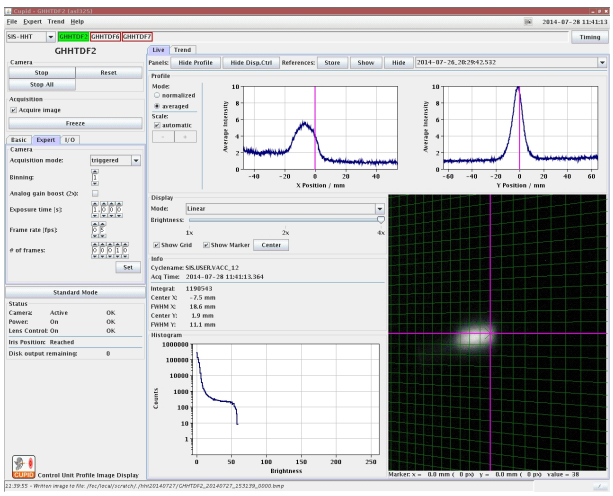


Figure 3: CUPID GUI with an image of 7×10^9 protons at 4 GeV on Chromox screen.

For basic operation the camera controls are reduced to changing the opening of the iris and switching on or off the illuminating LED. An expert mode provides more detailed control like changing the exposure time, the binning of the image or requesting the raw images to be automatically saved to disk by the FESA class. It also allows to change the acquisition mode. The CUPID system provides three acquisition modes, which may either be realised in hardware or in software by the FESA class. The two most important ones are 'free run' and 'triggered'. In 'free run' the camera continuously acquires images with the specified exposure time and frame rate. The acquired images are displayed in the GUI as they arrive in real time. In the 'triggered' mode, the image acquisition is triggered by a machine event of the accelerator (for example at beam extraction). At the time of the trigger, a single image is acquired by the FESA class and displayed by the GUI. An extension of the 'triggered' mode is the 'sequence' mode, which acquires a predefined number of images with the specified frame rate after a trigger is received.

The CUPID system is currently running successfully at 16 different points in the GSI high energy beam transport lines. In daily operation it was used to image several beams from protons up to uranium with various beam energies and intensities. The generally positive feedback by the operating team highlights the simple usage of the GUI and the advanced features of the new system. The work experience gathered so far confirms CUPID as the standard for scintillating screen based beam instrumentation at GSI and FAIR.

RAD-HARDENED CAMERA TESTS

Technological advances in solid state camera design provide a wider choice of equipment for beam instrumentation. However, our previous experience with CCD based cameras has shown that their performance degrades during operation due to the background radiation (γ, neutrons, etc.) produced by the heavy ion beam (see Figure 4). Any semiconductor device operating in a radiation field can undergo degradation due to radiation damage effects. Energetic particles incident on the semiconductor bulk lose their energy to ionising and non-ionising processes as they travel through a given material. The ionising processes involve electron-hole pair production and subsequent energy deposition (dose) effects. The non-ionizing processes result mainly in displacement damage effects, i.e. displaced atoms in the detector bulk and hence defects in the semiconductor lattice like vacancies and interstitials. More details can be found in [7].

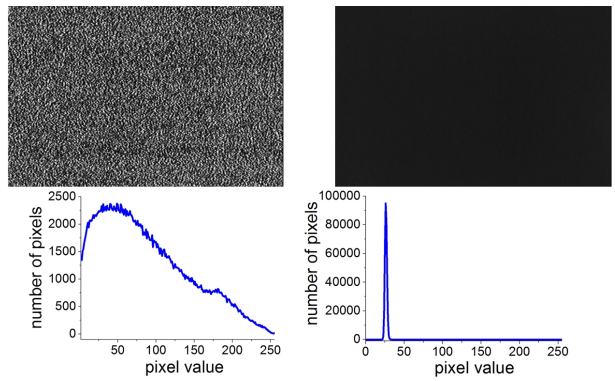


Figure 4: Dark image of the standard CCD camera Sony XC-ES30 (upper left) and new radiation-hardened solid-state CID camera MegaRad3 (upper right) after few weeks of irradiation with its corresponding histograms of pixel brightness below (bottom right, bottom left, respectively).

In the GSI SIS18 extraction point a great variety of particles with energy of up to few GeV/u is present. At this location, where a high radiation level is observed, the CCIR MegaRad3 (8726DX7) radiation-hardened solid-state CID (Charge Injection Device)-based camera [8] was installed in 2013. According to the manufacturer [9] this device is tolerant to gammas, neutrons, high energy electrons and proton radiation to at least 3 MRad. Only in tests up to 14 MRad a noticeable degradation in the image quality has been reported by the manufacturer.

In our tests, the camera has been placed near the SIS18 extraction. The camera is continuously running since November 2013. The accumulated dose impinging on the camera has been monitored by thermoluminescent dosimeters placed next to the camera. During this test, we found the image quality to be nearly the same after eight months of exposure to neutrons (accumulated dose: 55 Sv) and γ (accumulated dose: 33 Sv) radiation. As shown in Figure 4 and Figure 5, no significant change in camera performance like loss of contrast and resolution was observed. A standard

Copyright © 2014 CC-BY-3.0 and by the respective authors

ISBN 978-3-95450-141-0

CCD camera at the same position was out of order due to irradiation within two weeks of operation. The dark image of a standard CCD camera at a position with lower radiation level is shown in Figure 4.

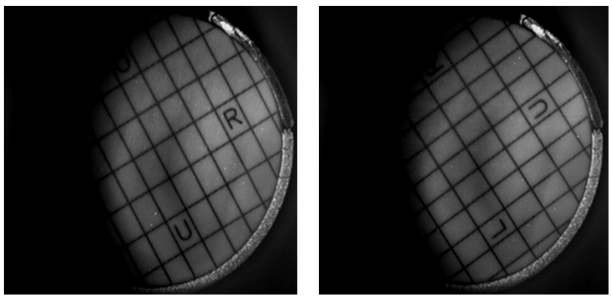


Figure 5: Original pictures of scintillating screen target with progressive level of accumulated dose. No loss of contrast was observed. Left: before test, right: after 8 months beam operation at SIS18.

Our first test with this radiation-hardened solid-state CID-based camera is very promising. This device exhibits a significant improvement for operation in a radiation rich environment as compared to the CCD and CMOS-based cameras. The performed tests show that the camera is not sensitive to radiation damage on the level observed at GSI. This makes this camera suitable for use in precise and reliable profile monitors of high energy heavy ion beams in the vicinity of beam extraction points, targets or beam dumps as well as other higher radiation environments expected at FAIR.

SUMMARY

The Facility for Antiproton and Ion Research (FAIR) poses new challenges for standard beam instrumentation like precise beam imaging over a wide range of beam parameters, radiation hardness, etc. CUPID, a new, fully FAIR-conformal system for standard scintillating screen based diagnostics was developed, commissioned and employed in routine beam operation at GSI. CUPID includes digital imaging, a remote controllable optical system, mechanical drive and easy to use GUI. Based on FESA it is expected to seamlessly integrate into the future control system of FAIR.

In addition, we reported on our first experiences with a radiation hardened CID-based camera. The camera is working in the SIS18 extraction point at a high radiation level. After 10 months of operation no deterioration or loss in the camera features were observed. This device exhibits a significant improvement for operation in radiation rich environments as compared to standard CCD-based cameras.

CUPID and the radiation hardened camera are the first beam instrumentation devices for FAIR used in routine operation with beams from proton to uranium. Results and feedback from the operating team promises a successful operation at FAIR.

ACKNOWLEDGEMENT

It is a pleasure to acknowledge cooperation of the GSI operating team, beam instrumentation and radiation protection departments.

REFERENCES

[1] R. Haseitl et al., "Development of FESA-based Data Acquisition and Control for FAIR", DIPAC 2010, http://www.JACoW.org/

[2] IDS Imaging Development Systems GmbH, http://en.ids-imaging.com/

[3] B. Dryer et al., "Gamma radiation damage study of 0.18 μm process CMOS sensors", http://core.kmi.open.ac.uk/download/pdf/16915

[4] Arduino, http://www.arduino.cc

[5] Linos MeVis-Cm lens, http://www.qioptiq-shop.com/Praezisionsoptik/Machine-Vision-Solutions/LINOS-Machine-Vision-Objektive/MeVis-Cm-motorisiert.html

[6] F. Locci et al., "IEPLC framework, automated communication in a heterogeneous control system environment", ICALEPCS 2013, http://www.JACoW.org/

[7] S. Hutchins et al., "Radiation tests on solid state cameras for instrumentation", DIPAC 2005, http://www.JACoW.org/

[8] Thermo Fisher Scientific, Inc., http://www.thermoscientific.com/content/tfs/en/products/charge-injection-device-cid-cameras.html

[9] S. Bhaskaran, "Research and development efforts at CIDTEC cameras and imagers", 3rd DITANET School 2011, http://indico.cern.ch/event/112220/contributions/

Copyright © 2014 CC-BY-3.0 and by the respective authors

PERFORMANCE DEMONSTRATION OF THE NON-INVASIVE BUNCH SHAPE MONITOR AT GSI HIGH CURRENT LINAC*

B. Zwicker, C. Dorn, P. Forck, O. Kester, P. Kowina, T. Sieber, GSI, Darmstadt, Germany

Abstract

At the heavy ion LINAC at GSI, a novel scheme of a non-invasive Bunch Shape Monitor has been tested with several different ion beams at 11.4 MeV/u and beam currents in the range from 80 to 1000 µA. Caused by the beam impact on the residual gas, secondary electrons are liberated. These electrons are accelerated by an electrostatic field, transported via a sophisticated electrostatic energy analyzer and an rf-deflector, acting as a time-to-space converter. Finally a MCP amplifies the electrons and the electron distribution is detected by a CCD camera. For the applied beam settings this Bunch Shape Monitor is able to obtain longitudinal profiles down to 250 ps RMS width with a resolution of 34 ps, corresponding to 0.5° of the 36 MHz accelerating frequency. Systematic parameter studies for the device were performed to demonstrate the applicability and to determine the achievable resolution. The background contributions, as originated by x-rays, are investigated.

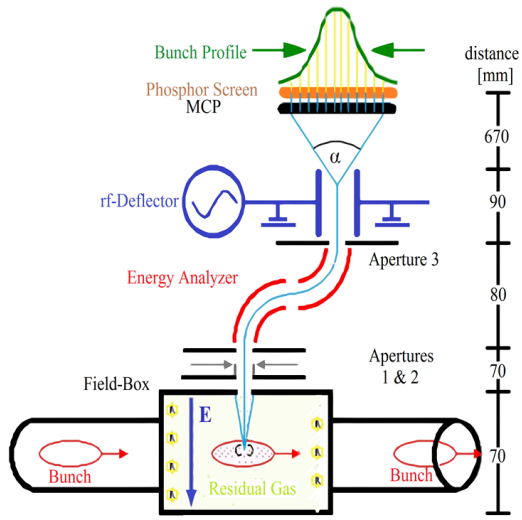


Figure 1: Schematic illustration of the non-invasive BSM

MOTIVATION

Within the FAIR-Project [1] a proton LINAC [2] is scheduled as a new injector for the SIS18 synchrotron at GSI. The p-LINAC will provide 70 MeV and 70 mA current in addition to a compact construction. Due to the high energy deposition for conventional intersecting Bunch Shape Monitors [3, 4] a novel design is foreseen. The new detector for the longitudinal bunch structure with a phase resolution of 1°, with respect to the 325 MHz acceleration frequency, is intended to ensure proper longitudinal matching of the accelerating structures. The presented device is a recommissioning of the non-intercepting Bunch Shape Monitor presented in [5].

WORKING PRINCIPLE

The non-invasive Bunch Shape Monitor (BSM) prototype is based on secondary electrons, which are freed by the interaction of beam ions and the residual gas. Figure 1 provides a schematic illustration. These electrons are accelerated towards an aperture by an external homogeneous electrostatic field of 4.2 kV/mm. Using side strips parallel to the electrodes the electric field is leveled. To further reduce the divergence of the secondary electrons (SEs) two apertures with a distance of 70 mm are used. The aperture width can be remotely adjusted between 0.1 mm and 2 mm. After passing these apertures the electrons are filtered by two 90° cylindrical electrostatic energy analyzers with a bending radius of 30 mm. Two similar analyzers are used to bend the SE beam back in original direction for mechanical reasons. The applied voltages are ±5.5 kV for the opposite cylinder segments. A third aperture is placed 10 mm away from the edge of the second analyzer to enable a point-to-point focusing from the entrance to the exit slit. After a drift of 90 mm the SEs reach a radio frequency (rf) driven deflector coupled to the accelerating frequency. The rf-deflector works as a time-to-spatial converter. Each electron is deflected in dependence to its time of arrival. Two deflectors with different resonance frequencies are available. One is operating at a frequency of 36 MHz for long bunches and the other one for short bunches at the third harmonic at 108 MHz. Both deflectors are 800 mm long parallel wires corresponding to $\lambda/4$ for high field strength. The maximum power applicable is 100 W at 36 MHz and 50 W at 108 MHz in pulses of 6 ms duration. The deflected SEs, after a 670 mm flight, are spatially detected by a Chevron MCP (Hamamatsu F2226-24P) with an effective diameter of 77 mm and finally monitored by a P20 phosphor screen. The illuminated spots on the phosphor screen are observed by a CCD camera (PCO 12 Bit SensiCam, CCD chip of 640×480 pixel). In addition, the deflector has a second function as a focusing electrostatic einzel-lens by a common DC-voltage of maximal 6000 V on the deflector's plates. Between the rf-deflector and the MCP a 1 cm thick stainless steel plate is inserted as a x-ray shield for the MCP detector.

COMPENSATION OF THE BEAM DEFLECTION

While operating the BSM the applied E-Field affects the ion beam. For an 11.4 MeV U^{28+} beam with an applied voltage of -31 kV (resulting in a field strength of 420 V/mm) the

* Supported by EU-Project CRISP, WP3 T1 Non-intercepting bunch shape monitors

Copyright © 2014 CC-BY-3.0 and by the respective authors

ISBN 978-3-95450-141-0

beam deflection is about 140 µrad according to CST based calculations, for a proton beam it is higher with 400 µrad. The present monitor location at UNILAC leads to a typical 50 % beam loss at the entrance of SIS18 at GSI facility, due to over stressing the synchrotron's acceptance. For a foreseen operation within a LINAC the beam deflection must be minimized. Compensation electrodes have been built and designed. It was mandatory to upgrade the device without changing the existing vacuum chamber. The design of appropriate compensation requires a field simulation by CST finite elements code shown in Fig. 2.

Due to the lack of available insertion space (two thirds occupied by the Field-Box), the optimal design for complete compensation is not an option. Best suited is an identical Field-Box with opposite polarity, split it into equal halves and put in front and behind of the original Field-Box. This approach requires not available space, but with the help of a CST based simulation a more sophisticated design was chosen, which stays as close as possible with this solution and achieves sufficient compensation. Finally the selected design is a product of contrary objectives, achieving sufficient homogeneous high field strength with a fixed voltage of -31 kV and avoiding any material in a symmetry axis coaxial to the beam axis, at least 55 mm in diameter (iris size in front of the BSM). Capacitor plates with fixed distance are here inapplicable. In order to achieve a necessary field strength of 620 V/mm in comparison to 420 V/mm of the Field-Box a distance of maximum 50 mm is needed. To avoid material within the 55 mm safety buffer zone the capacitor plates are bent in the middle with a 60 mm diameter (see Fig. 2). Also for E-field leveling purposes electrode lamellas are attached at the fringes of the capacitor. The compensation f of the

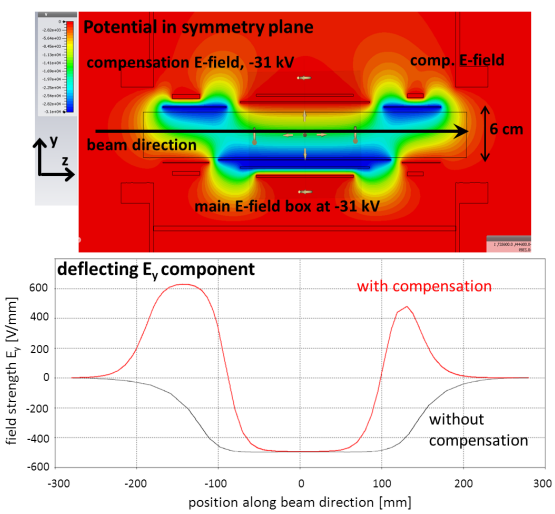


Figure 2: The upper image shows a CST finite element code based calculation of the potential distribution of the Field-Box inside the symmetry plane along the beam axis. The lower image shows the un-compensated and compensated E_y-field component along the beam axis.

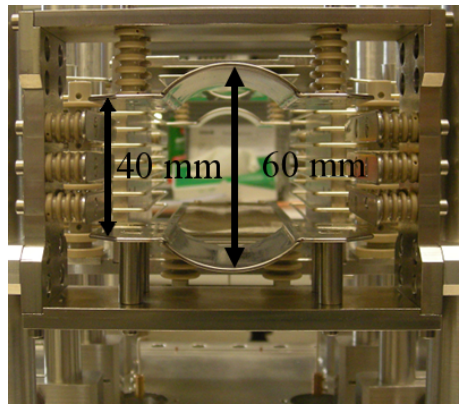


Figure 3: One of two compensation capacitors with its bended 60 mm opening. The polarity is swapped by applying the voltage to the upper plate instead of the lower one like the Field-Box does.

beam deflection is calculated with Equation (1).

$$f = \frac{\int E_y \text{ (compensated)} \cdot dz}{\int E_y \text{ (un-compensated)} \cdot dz} \quad (1)$$

Along a beam path the field components for the compensated and non-compensated case are integrated, then the quotient f of both integrals is formed. The results for different beam paths are represented in Fig. 4 as a contour plot. According to the results a deflection of 48 µrad within a 50 mm diameter is still present for a 11.4 MeV proton beam and 17 µrad for a U^{28+} beam at the same energy per nucleon. The majority of the ion beam trajectories are sufficiently compensated. Beam based tests showed no detectable deflection or beam loss at the GSI synchrotron by using Beam Position Monitors.

EXAMPLE OF BUNCH SHAPE MEASUREMENTS

Using the BSM different bunch shapes were determined ranging from 1531 ps RMS down to 240 ps RMS. An example for the image of the MCP detector is depicted in Fig. 5.

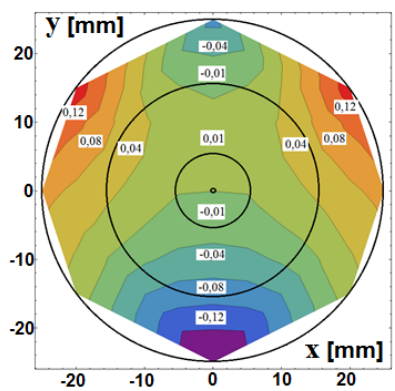


Figure 4: Contour plot of deflection in ion beam direction after compensation. Positive values indicate over compensation in relation to original value and direction.

Copyright © 2014 CC-BY-3.0 and by the respective authors

The image is represented in pseudo colors to enhance contrast, while operating and adjusting the device. By projecting the spatial distribution over the axis of deflection the bunch shape including background is obtained. A second measurement is taken with identical setup besides the absence of the bunch signal by blocking the SEs with totally closed apertures. After equalizing the background level on both MCP images by averaging and comparing them at the fringe areas, where no bunch signal is expected, the background image can be subtracted from the other. The result of this procedure is also shown in Fig. 5.

To further proof the BSMs capabilities a measurement with different bunch shapes has been setup. By using a single gap resonator, mounted 60 m upstream of the monitor location, as a re-buncher for the beam with the right phase and sufficient strong amplitude, the bunch shape can be stretched or compressed. By systematical manipulation of the rf-amplitude inside the single gap resonator the longitudinal focal length can be varied and the bunch shape is modified. See Fig. 6 for the results of the measurement.

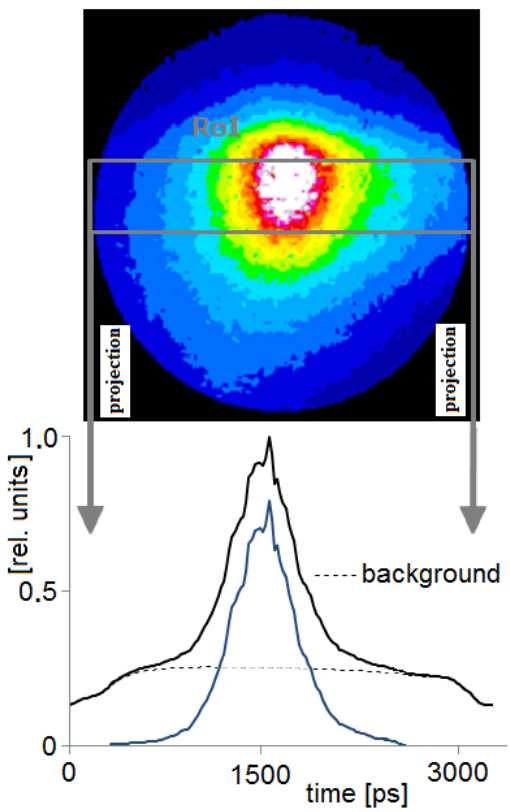


Figure 5: The MCP detector is shown in pseudo colors. By performing a projetion over the axis of deflection, a bunch structure, including background, is obtained. Furthermore, a background only measurement allows the substraction of the background. Parameters: RMS of 290 ps, Ni^{28+}, I = 900 µA, t_{pulse} = 180 µs, P = $5{\cdot}10^{-6}$ mbar, 32 averages, phase calibration: 21 ps/pixel.

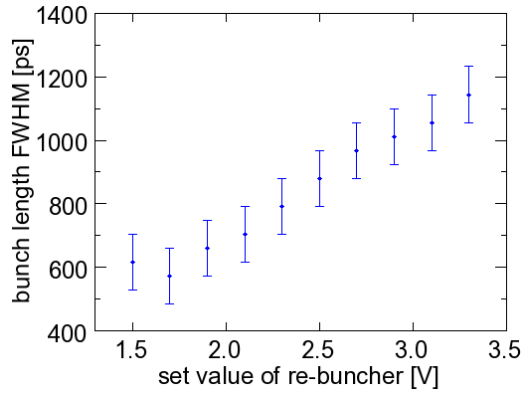


Figure 6: Bunch shape variation by the action of a re-buncher 60 m upstream of the BSM location. By varying the rf-amplitude of the re-buncher different bunch shapes from 570 ps FWHM to 1150 ps FWHM have been detected.

CALIBRATION PROCEDURE

In order to determine the longitudinal time structure of a bunch, a calibration has to be done and the resolution has to be determined [6]. The deflection angle and therefore the position of a detected electron depends on the amplitude and phase of the driving frequency of the rf-deflector. For a given amplitude the rf-phase is shifted by a preset degree corresponding to a certain time delay and regarding the displacement of the distribution, the phase calibration is done. In Fig. 7 the phase calibration is shown with a maximum of 100 W applied rf-power and the 36 MHz resonator. The high rf-power means broader spatial distributions and therefore allows to investigate more details with the same resolution. Depending on the bunch length, which might vary for different beam parameter settings, the rf-power can be varied

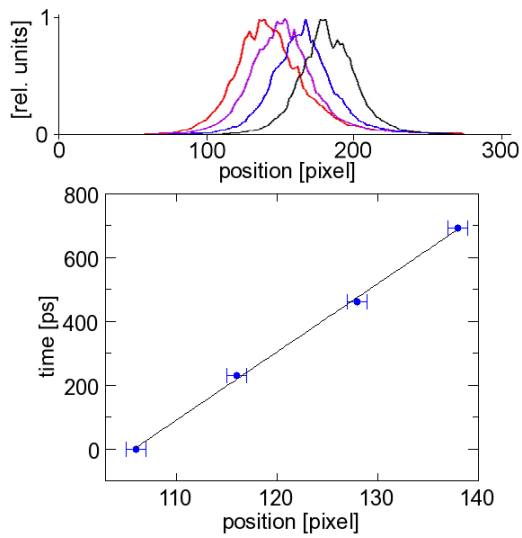


Figure 7: The upper image shows different measurements with 3° @ 36 MHz phase shift. The lower image shows the center of distribution plotted over their position lead to a calibration of (21.3 ± 0.5) ps/pixel.

ISBN 978-3-95450-141-0

Copyright © 2014 CC-BY-3.0 and by the respective authors

to match the image of the bunch to the MCP size, leading to an optimal resolution. For each rf-power setting a new calibration must be performed.

DETERMINATION OF RESOLUTION

With only DC voltage applied to the rf-deflector, working as an electrostatic einzel-lens, the image properties can be investigated. Figure 8 shows a determination of the focus width and the corresponding voltage. With an aperture setup of 0.5 mm, 1 mm respectively, a minimum RMS of 0.6 mm was achieved. With a pixel width of 0.45 mm the total resolution is about 25 ps RMS for the rf-power as used for Fig. 7.

BACKGROUND INVESTIGATION

For further improvements of the BSM the source of the background was investigated. Here we refer to a background, which is statistically distributed over the entire MCP area and can therefore not be caused directly by the SE from the interaction of the beam and the residual gas. As a first step the residual gas pressure is varied from $5 \cdot 10^{-8}$ to $5 \cdot 10^{-6}$ mbar and determine the signal level for the entire area of the MCP. The apertures are closed to exclude SE contribution. Figure 9 shows a linear correlation between the pressure and the average background level for the attainable pressure range of $p \geq 5 \cdot 10^{-8}$ mbar. From this we can conclude that the background is generated locally within less than ±1 m around the BSM where the gas pressure is increased. It is not originated by beam losses in this area which would be independent of the gas pressure. The intensity within the bunch image is averaged and shown in terms of signal-to-noise ratio in Fig. 9. Even though the pressure is varied over about two orders of magnitude, the signal-to-background ratio varies only within a factor of 2. From a second measurement, described in the next paragraph, we assign the main source of background to x-rays generated in the E-field.

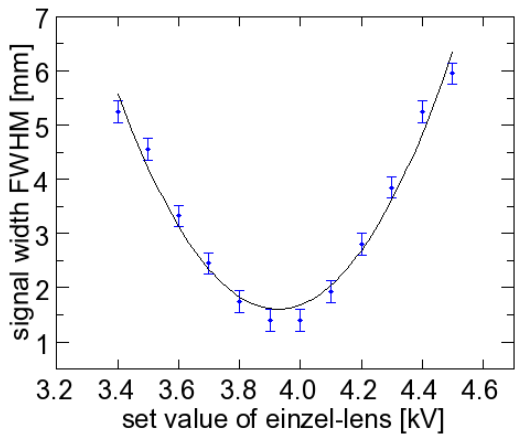


Figure 8: Focus width depending on the applied voltage on the einzel-lens, the solid line is a parabola fit. Parameters: Apertures 0.5 mm, 0.5 mm and 1 mm opened, 11.5 kV driving potential, 16 averages, $5 \cdot 10^{-6}$ mbar. The Field-Box bottom plate is used as SE source for higher intensity purposes.

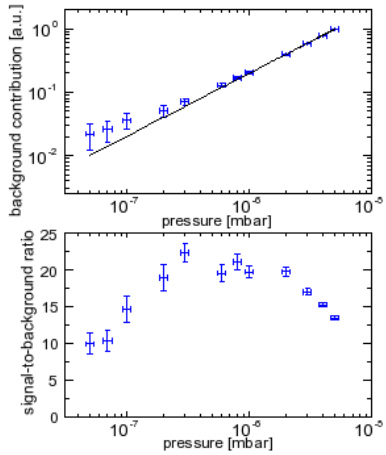


Figure 9: Upper image: First measurement of the pressure contribution to the background. Over two magnitudes the distribution is in good agreement with a linear fit. Lower image: Signal-to-background ratio with open apertures showing a variation of only a factor of two over full range. Parameters: N^{7+}, I = 900 µA, t_{pulse} = 180 µs, 20.5 kV driving potential, MCP = 1600 V, 16 averages, apertures closed for upper image.

To confirm the presence of x-rays, the applied voltage to the E-field box was varied from 2 kV to 30 kV. The background, distributed statistically on the entire MCP area, grows for increasing voltages as shown in Fig. 10. This is interpreted in terms of x-rays for the following reason: The interaction of the beam and the residual gas leads to electrons, which are accelerated towards a slit and energy analyzer by the applied field (top side in Fig. 1). But only a very small fraction is transmitted through the slits, with

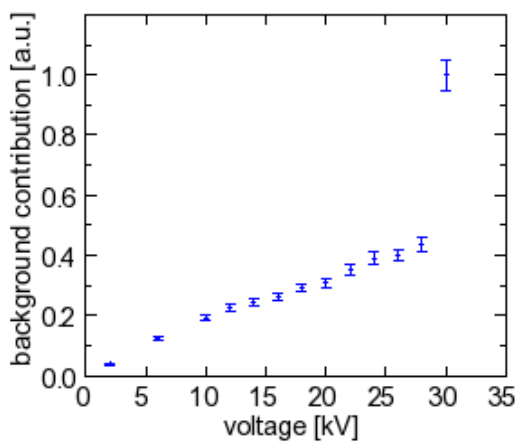


Figure 10: Background (no SE contribution) increases with the applied voltage. Parameters: N^{7+}, I = 900 µA, t_{pulse} = 180 µs, $1 \cdot 10^{-6}$ mbar, MCP = 1600 V, 8 averages, apertures closed.

Copyright © 2014 CC-BY-3.0 and by the respective authors

the majority of electrons hits the metal plate of the box and potentially creates x-rays. Moreover, the residual gas ions are accelerated towards the negative biased plate (bottom plate in Fig. 1) and by hitting the bottom plate secondary electrons are emitted for the surface, which are then accelerated toward the top plate of the E-field box. These electrons are accelerated by the full potential and finally they create additional x-rays when hitting the top plate. X-rays created by this effect seem to be the dominate source for the background, because the creation probability and the x-ray energy depends on the electron's kinetic energy, which is given by the applied voltage. This conclusion is supported by the fact that the signal-to-background ratio is basically independent from vacuum pressure, see Fig. 9. To suppress a large part of the electrons liberated by the residual gas ions, a grid is mounted close to the bottom electrode with a transmission of 90 % and biased to a proper potential of 3.44 kV between the grid and the ground plate. Further investigations have been performed and the analysis of the recorded data is ongoing.

SUMMERY AND OUTLOOK

A novel device for bunch shape measurement was tested in detail concerning its application at the high current ion LINAC and can be used with some modification at the FAIR proton LINAC:

- The non-invasive BSM has performed high quality measurements for the longitudinal bunch profile from 1200 ps RMS down to 240 ps RMS.
- Shorter bunches can potentially be resolved because the resolution for high rf-power can be chosen to be about 25 ps corresponding to 0.5° of the 36 MHz acceleration frequency. It is an advantage of the used technology that the resolution can be chosen with the help of the rf-power and the aperture settings.
- The background was investigated; it is caused by x-rays created by the secondary electrons or further electrons caused by the residual gas ion impact on the HV bottom plate. For a bunch length determination with sufficient averages, this over the entire MCP-detector statistically distributed background can reliably be subtracted. However a better shielding of the MCP-detector has to be installed.
- The related signal-to-background ratio is more than sufficient for a reliable bunch length determination with an adequate resolution and enables good statistics with only 16 averages per profile measurement. Therefore the acquisition time decreases below one minute.
- For the FAIR proton LINAC a higher deflection frequency of 325 MHz will be used. The achieved phase resolution of 0.5° will be preserved i.e. a required time resolution of 10 ps or less.

ACKNOWLEDGMENT

We would like to thank several colleagues of the LOBI department at GSI. First we appreciate the help of H. Graf from the mechanical workshop. We also like to thank A. Reiter for his guidance and support, T. Giacomini for his expended advices and T. Milosic for discussion and assistance.

REFERENCES

[1] O. Kester, "Status of the FAIR Facility," IPAC'13, Shanghai, May 2013, TUXB101, p. 1085, http://www.JACoW.org

[2] L. Groening et al., "Status of the FAIR 70 MeV Proton Linac," LINAC'12, Tel-Aviv, September 2013, THPB034, p. 927, http://www.JACoW.org

[3] A. Feschenko, "Technique and Instrumentation For Bunch Shape Measurements", RuPAC'12, Saint-Petersburg, September 2012, FRXOR01, p. 181, http://www.JACoW.org

[4] A. Feschenko et al., "Bunch Shape Monitors With RF Scanning of Low Energy Secondary Electrons," Workshop on Bunch Shape Measurment, Lund, February 2013. https://indico.esss.lu.se/indico/contributionDisplay.py?contribId=1&confId=44

[5] P. Forck et al., "Measurements with a Novel Non-intercepting Bunch Shape Monitor at the High Current GSI-LINAC," DIPAC'05, Lyon, June 2005, POM010, p. 48, http://www.JACoW.org

[6] B. Zwicker et al., "Test of a Non-Invasive Bunch Shape Monitor at GSI High Current LINAC," IBIC'13, Oxford, September 2013, MOPC36, http://www.JACoW.org

Copyright © 2014 CC-BY-3.0 and by the respective authors

ISBN 978-3-95450-141-0

YAG:Ce SCREEN MONITOR USING A GATED CCD CAMERA

Takashi Naito#, Toshiyuki Mitsuhashi
KEK, 1-1 Oho, Tsukuba, Ibaraki 305-0801, Japan

Abstract

Due to its good spatial resolution, the YAG:Ce screen monitor is often used for small beam profile measurement in the Linac and beam transport line. We constructed a high-resolution YAG:Ce screen monitor at KEK-ATF2 for the observation of small size beam. We tested two types of screen, one is ceramic (sintered alumina powder) YAG:Ce and the other is single crystal YAG:Ce. Both screens have 50μm thickness. To escape from the Synchrotron radiation(SR) from the upstream and the Coherent Optical radiation(COTR), we applied delayed timing of the gate for the CCD camera. A microscope having a spatial resolution of 4.3μm is set outside of vacuum chamber to observe the scintillation light from the YAG:Ce screen. The results of the difference between the two screens, the camera performance with delayed gate and the optical performance of microscope will be presented in this paper.

INTRODUCTION

The low emittance beams using the state-of-the-art technology are generated and accelerated in recent electron accelerators for the FELs and the collider machines. The beam monitors are required to have a high resolution to measure the small beam size. Screen monitor is often used to measure the transvers profile at the linac and the beam transport. Usually, a chromium doped Alumina (AF995R, Desmaruquest Co.) fluorescent plate is used for the screen material. Recently, the other materials are tested and used to improve the resolution. We developed a high resolution screen monitor using YAG:Ce for the momentum spread measurement at KEK-ATF2 beam line.

ATF2 is a test beam line to develop the final focus system for the International Linear Collider. The beam test is carried out to realize 37nm of the vertical beam size [1]. The ultra-low emittance beam is supplied from the damping ring(DR). The energy is 1.3GeV and the design emittances for horizontal and vertical are 1.3nm and 10pm, respectively. The momentum spread is one of the key parameters of the beam. In the DR, the intra-scattering effect increases the momentum spread, which is a function of the beam emittance and the bunch charge. The momentum spread is calculated from the horizontal beam size at the large dispersion location,

$$X = \sqrt{\left(\sqrt{\varepsilon_x \bullet \beta}\right)^2 + \left(\eta \frac{\Delta p}{p}\right)^2} \ .$$

where, X is the horizontal beam size, ε_x is the horizontal emittance, β is the beta function, η is the dispersion function and Δp/p is the momentum spread. The first parentheses can be ignored in the case of the large dispersion. The dispersion function can be measured by the horizontal beam position change when the RF is changed. At the ATF2, the dispersion function at the screen monitor location is about 0.5m. When the momentum spread is assumed at 6 x 10^{-4}, the horizontal beam size is estimated to be 300μm. However, the fluorescent screen does not have enough resolution to measure the beam size. OTR monitors are used at the downstream of the ATF2, however, OTR does not have enough light yield at the low bunch charge. We decided to employee YAG:Ce screen. YAG:Ce has a good scintillation property at 550nm wavelength. We tested two types of screen, one is ceramic (sintered alumina powder) YAG:Ce [2] and the other is single crystal YAG:Ce [3]. Both screens have 50μm thickness.

The hardware design and the beam test results are described in the following sections.

HARDWARE

Fig. 1 shows the schematic layout of the YAG:Ce screen monitor(YSC). The screen is inserted into the beam orbit at a 45-degree horizontal direction by the air actuator. The CCD observes the scintillation light of the screen from a perpendicular direction. The screen has an oblique angle (45 degrees) for the beam and the horizontal beam image is magnified by $\sqrt{2}$. The benefit of using the oblique angle is that, 1) the optical system can fully focus on the screen when the beam position moved, 2) the reflection of the synchrotron radiation (SR) and coherent optical radiation (COTR) can mostly be avoided, which are reflected to a 90-degree direction. Avoiding the COTR is a significant problem for the FEL application [4]. In the case of the ATF2, the CTOR is negligible small.

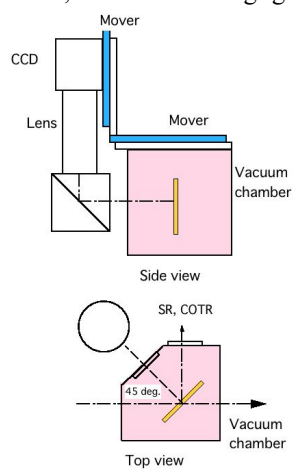


Figure 1: Schematic layout of YSM.

takashi.naito@kek.jp

Copyright © 2014 CC-BY-3.0 and by the respective authors

There is a limitation for the minimum observable image size in the horizontal direction. The beam comes across the screen at the oblique angle of 45 degrees. The CCD observes the scintillation light from the surface to the deep side, because YAG:Ce is almost transparent. Even if the beam has zero-μm in horizontal, the observed image size is limited to the screen thickness. Consequently, the observed image size becomes a convolution of the thickness of the screen and the incident beam size. Fig.2 shows the calculation of the incident beam size and the observed image size in the case of 50μm thickness screen. The beam size is limited to 50μm.

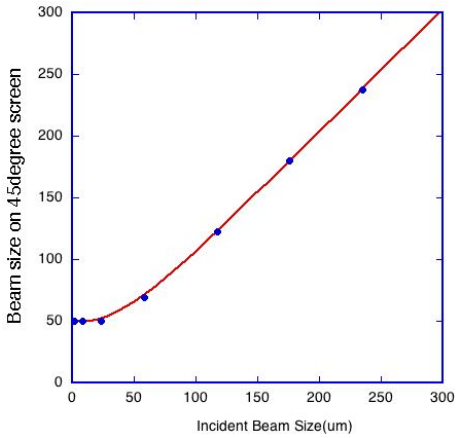


Figure 2: Calculation of the horizontal beam size at oblique angle of 45 degrees screen in the case of 50μm thickness.

Lens System

The scintillation light is delivered to the CCD using a 90-degree reflective mirror and a zoom lens. The reflective mirror is used for changing the optical axis and avoiding the X-ray on the CCD. A zoom lens (TS-93022: Sugito Co.) is used for the lens. The parameter of the lens is summarized in Table 1.

Table 1: Parameters of the *Lens(SUGITOH TS-93022)*

Magnification ratio	0.38~3
Diameter of lens	38mm
Focus length	165 mm
Focal depth	0.3mm
Resolution	4.3μm

The CCD sits on three directional movers to adjust the horizontal/vertical positions, and the focus. The observation area is 1.6mm x 1.2mm at the maximum magnification ratio. The focal depth of the lens is longer than the thickness of the screen. The lens can focus from the surface to the deepest area of the screen. The resolution is estimated from the Fourier transform of the modulation transfer function of the lens. The distribution of the point spread function (PSF) differs a little bit from the Gaussian distribution. The Gaussian fit of the PSF peak area is defined to the resolution.

Characteristics of the Gated CCD Camera

The SR and the COTR exist only during the duration of the bunch length. The YAG:Ce has 100ns of the scintillation time [5][6]. To distinguish the SR, COTR and the scintillation light, a gate function of the image intensifier was used [4]. Image intensifier is an expensive device, so we tried to use the commercially available CCD with an electric shutter. To check the gate function of the electric shutter, we measured the very short laser light by scanning the gate timing.

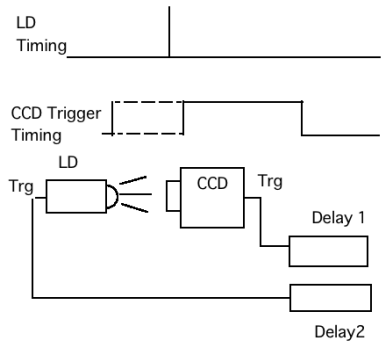


Figure 3: Measurement setup of the gate characteristics of the CCD.

Figure 3 shows the setup of the measurement. The light of the laser diode (Hamamatsu C4725, the duration of the pulse light: 30ps) was observed with the CCD in the electric shutter mode. The light intensity of the image was plotted when the trigger timing was scanned. CCD IGV-B0610M(IMPREX Co.) is used for the test. The exposure time in this measurement was 2μs. The measurement result is shown in Fig.4.

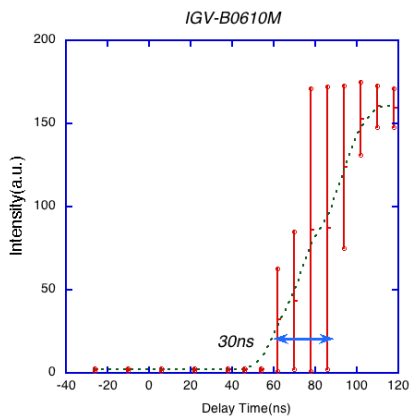


Figure 4: Gate characteristics of IGV-B0610M.

The exposure timing of the CCD has an asynchronous jitter for the external trigger. The start timing of the exposure is synchronized with the internal clock. The external trigger is not synchronized with the internal clock. The width of the jitter corresponds to a period of the internal clock. IGV-B0610M uses a 40MHz clock. The jitter exists at least 25ns. The measurement result shows that: 1) the exposure timing starts with a 50ns delay from the trigger, 2) the exposure includes about 30ns of jitter and 3) the rise time of the exposure is at

Copyright © 2014 CC-BY-3.0 and by the respective authors

ISBN 978-3-95450-141-0

60ns. If the beam timing is set to just before the exposure, the SR and the COTR can be avoided and the scintillation light of YAG:Ce can be measured using this CCD.

BEAM MEASUREMENT

Horizontal Beam Size Measurement

The example of the measured beam profile is shown in Fig. 5 and the current dependence of the horizontal beam size is shown in Fig. 6.

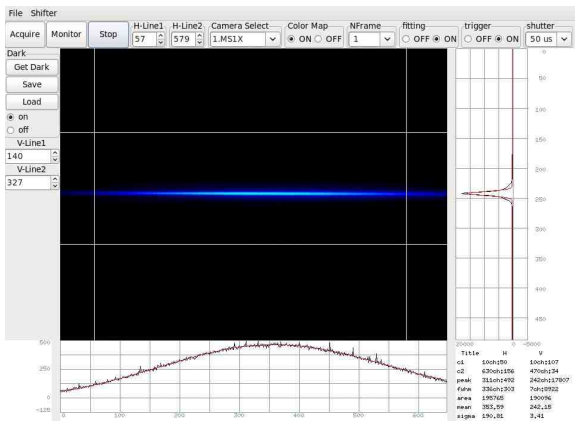


Figure 5: Example of the measured profile with the YSM.

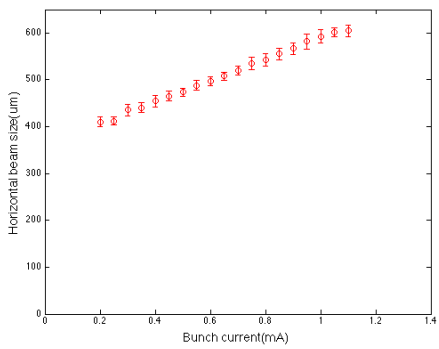


Figure 6: Current dependence of the horizontal beam size.

The horizontal beam size was changed from 600 to 400μm when the current changed from 1.2 to 0.2mA. The measurement error did not increase even at low current, which means the measurement kept a good signal-to-noise ratio.

Vertical Beam Size Measurement

To confirm the resolution of the YSM, the vertical beam size was measured when the focus strength of the upstream quadruple magnet was changed. The estimated vertical beam size at this measurement is several-μm.

We tested three of the YAG:Ce screens, 1) ceramic YAG:Ce with a 100μm thickness, 2) ceramic YAG:Ce with a 50μm thickness, 3) crystal YAG:Ce with a 50μm thickness [3][4]. The projections of the vertical profile at the minimum beam size condition are shown in Fig. 7. The measured beam sizes were 1) 13.9μm, 2) 8.6μm, 3) 7.0μm, respectively. There are some enlargement effects,

a) Blurring effect of the screen
b) Resolution of the lens c)
Saturation effect of the screen

There was a clear difference between 1) and 2) beam sizes. The difference of the thickness contributes to the blurring effect. The scintillation light emits in all directions. The scintillation light from the deep side of the screen spreads to the transverse direction. The effect is stronger than in a thick screen. Especially, the profile of 1) has a larger tail.

There was not a clear difference between 2) and 3) beam sizes. Lumpkin et. al. reported that crystal has better resolution than ceramic [7]. We used a small grain size ceramic, 2μm [3]. It is assumed that the scattered reflection inside of the screen is small in our case.

In the case of 3), the measured beam size was affected by the resolution of the lens. The beam size takes into account the resolution of the lens that was estimated at 5.5μm, which almost agreed with the estimation.

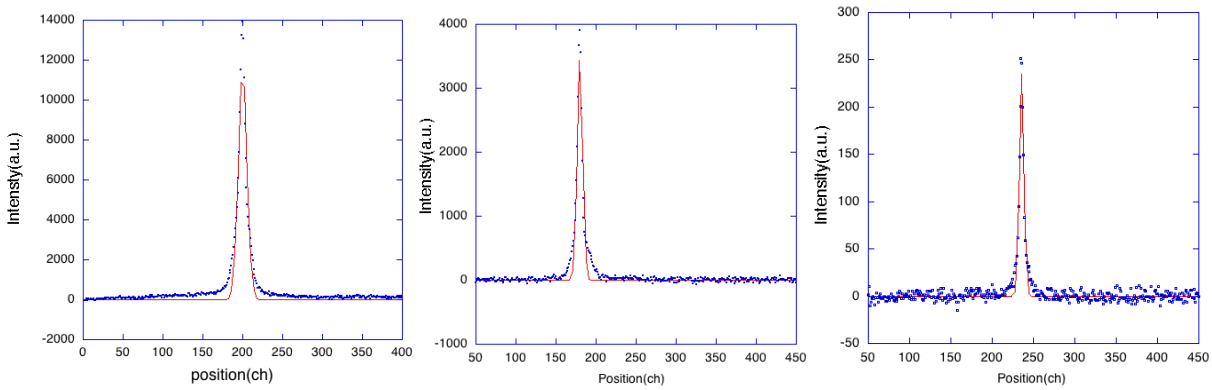


Figure 7: 1) Ceramic YAG:Ce 100μm thickness(left) σ_y=13.9μm, 2) Ceramic YAG:Ce 50μm thickness(center) σ_y=8.6μm, 3) Crystal YAG:Ce 50μm thickness(right) σ_y =7.0μm(right).

Copyright © 2014 CC-BY-3.0 and by the respective authors

It is difficult to check the saturation effect by this measurement. As described in the previous section, this location has a large dispersion function. The beam size is very large for the horizontal direction. The density of the beam is not so high compared to the other location. We moved the YSM to a no-dispersion location and measured the profile. Fig. 8 shows the example of the image. The horizontal profile of the center is clearly saturated. The saturation of the beam density was estimated at 0.25pC/μm^2.

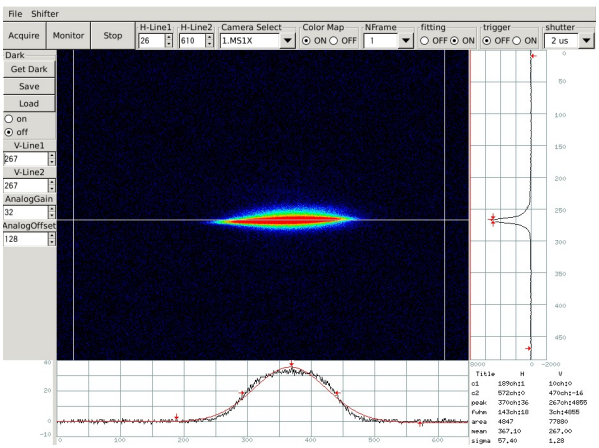


Figure 8: Example of the saturated beam profile.

Gate Timing of the CCD

The beam profile was measured as a function of the gate timing. Fig 9 shows the scintillation light intensity and the vertical beam size as a function of the gate timing. The gate timing of the electric shutter opened at 0μs and the gate width of the electric shutter was at 2μs. The timing scan corresponds to observe the tail part of the scintillation with a 2μs window. The scintillation light intensity almost agreed with YAG:Ce scintillation characteristics. The measured vertical beam size was not dependent on the gate timing, which means that the tail of the scintillation light has the same information of the beam profile except for the light intensity. The beam size could be measured over 500ns after the beam timing. The light intensity of the CCD can be controlled adjusting the gate timing.

SUMMARY

We developed a screen monitor using YAG:Ce screen(YSM) for the momentum spread measurement of the KEK-ATF2 beam line. The YSM could measure the horizontal beam size with a good signal-to-noise ratio, which means the YSM has enough performance for the momentum spread measurement. The minimum beam sizes for the vertical direction were: 1) ceramic YAG:Ce 100μm thickness: σ_y=13.9μm, 2) ceramic YAG:Ce 50μm thickness: σ_y=8.6μm, 3) crystal YAG:Ce 50μm thickness: σ_y=7.0μm, respectively. The saturation of the YSM was 0.25pC/μm^2.

The gate function of the CCD was tested with the test bench and the beam test. The gate function can be applicable for avoiding the SR and COTR.

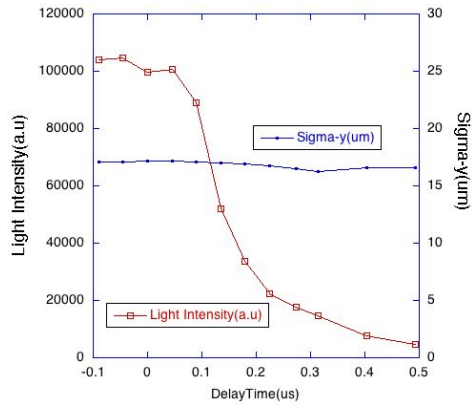


Figure 9: The scintillation light intensity and the measured vertical beam size as a function of the gate timing of the CCD.

ACKNOWLEDGMENT

We acknowledge to Professors S.Yamaguchi, A.Yamamoto and K. Oide for their encouragement. We also thank to the members of the ATF group for giving machine time for testing of the monitor.

REFERENCES

[1] ATF collaboration, “ATF2 Proposal”, KEK Repoert 2005-2, August 2005.
[2] http://www.konoshima.co.jp
[3] http://www.crytur.cz
[4] C. Behrens, et al., “ Electron beam profile imaging in the presence of coherent optical radiation effects”, PRST-AB 15, 062801, 2012.
[5] W. Chewpraditkul, et al., IEEE Transactions on Nuclear Science, Vol. 56, No. 6, Dec 2009, pp3800-3805.
[6] T. Yanagida, et al., IEEE Transactons on Nuclear Science, Vol. 52, No. 5, October 2009, pp1836-1841.
[7] A. H. Lumpkin, et al., “Upgrades of beam diagnostics with application to emittance to mittance-exchange experiments” PRST-AB 14, 060704, 2011.

Copyright © 2014 CC-BY-3.0 and by the respective authors

ISBN 978-3-95450-141-0

VACUUM IMPROVEMENT OF BUNCH SHAPE MONITOR FOR J-PARC LINAC*

A. Miura#, Y. Kawane, N. Ouchi,
J-PARC Center, Japan Atomic Energy Agency, Tokai, Ibaraki, 319-1195, JAPAN
T. Miyao, J-PARC Center, High Energy Accelerator Research Organization, KEK, Tsukuba, Ibaraki, 305-0801, JAPAN

Abstract

Bunch shape monitors (BSMs) have been developed and installed in the summer of 2012 at the upstream part of new Annular-ring Coupled Structure Linac (ACS) section. Because a problem of the vacuum degradation was found during the BSM operations, BSMs were once dismounted from the beam line and the off-line baking operations with outgas analysis had been performed to reduce the vacuum pressure of BSM surrounding. The impacts of the bias voltage to the target wire and static lens, and the RF power to the deflector were examined in the vacuum test. Finally, we propose the additional vacuum system arrangement for the installation of BSM to the beam line. This paper describes the vacuum test results of BSMs and the additional vacuum system arrangement for the BSM installation.

INTRODUCTION

In the upgrade project in J-PARC to establish the 1 MW at the experimental laboratories connected to the upstream Linac and Rapid Cycling Synchrotron, we have two big projects as the energy upgrade from 181-MeV Linac to 400-MeV Linac and the front end improvement using new RF ion source and replacing of the upgraded Radio Frequency Quadrupole Linac (RFQ) cavity. To meet with the 400 MeV, 21 ACS cavities have been developed and installed in the beam line, and to meet with this installation, we have developed the beam monitors for the ACS cavity tuning. Because the acceleration frequency of ACS cavities is 972 MHz which is three-fold higher than that of upstream RF cavities, we need to take longitudinal matching at the upstream part of new ACS beam line.

We started the development of BSM for the J-PARC Linac in corroboration with the Institute of Nuclear Research, Russian Academy of Science (INR, RAS). After three years since the project started, three BSMs were completed to be fabricated. In the summer of 2012, prior to the installation of ACS cavities, we installed all three BSMs at the upstream of the new ACS section in order to conduct some test measurement using 181-MeV beams. During the BSM measurements, a problem of the degradation in vacuum conditions was found. One reason for this problem is the dark current resulting in desorption of absorbed gas molecules. And another reason is outgas released from materials when the high voltage and RF power were supplied for the electro-static lens and RF deflector, respectively. In order to evaluate and mitigate this problem, BSMs were once dismounted from the beam line and the off-line baking operations with outgas analysis had been performed to avoid the degradation of the vacuum in the summer of 2013. The impacts of the bias voltage to the target wire and static lens, and the RF power to the deflector were examined in the vacuum test.

Finally the improved arrangement of the vacuum system to install the BSM is also proposed. We will install a BSM in at the upstream of the ACS again in the summer of 2014 with additional vacuum arrangement. This paper describes the vacuum degradation of the BSMs, results of the vacuum test, and the proposed arrangement of vacuum system.

VACUUM DEGRADATION AT BEAM LINE

Longitudinal pulse width measurements were done with the beam energy of 181 MeV, the beam pulse current of 15 mA, the pulse duration of 100 μs, and the pulse repetition rate of 1 Hz [1]. During the measurement, several problems connected with the influence on the vacuum have been found. Before the BSM installation, vacuum pressure at the upstream part of ACS section is around 1.0e-6 Pa.

The first one was connected with too big excitation power of BSM power amplifier. It was observed that the vacuum degraded over 1.0e-4 Pa which is the machine protection level in J-PARC Linac immediately after supplying RF power to the deflector. Decreasing of the magnitude of the input RF signal immediately removed the influence on the vacuum.

The second problem was a vacuum degradation in the case of multipactoring in the RF deflector at the operating mode. This discharge occurred when the high voltage potential was not supplied to the deflector electrodes. The software had been modified to suppress this degradation. RF is switched on only during the measurements.

The third effect is an influence of a dark electron current from the target. The electrons are accelerated and bombard the surfaces resulting in desorption of the absorbed gas molecules. The effect was observed immediately after supplying high voltage potential. After conditioning for several days the effect almost decreased and it became possible to make measurement with the potential of -10 kV. After installation and beam line tuning, beam line pressure didn't recover the previous level because of the malfunction of the closest ion pump.

Above influences had been met at the beam line. We have examined the vacuum test for BSMs with additional pumps.

#akihiko.miura@j-parc.jp

Copyright © 2014 CC-BY-3.0 and by the respective authors

ISBN 978-3-95450-141-0

STRUCTURE OF BSM

BSM consists of the body, RF deflector, steering magnet, actuator and electron detector in Fig. 1. An RF deflector and an actuator which holds a target wire are vertically installed against the beam axis on the body. Secondary electron past through the doubly installed collimators on the RF deflector travels to the pipe connected to the electron detector [2].

We supply the constant high voltage to focus the secondary electron trajectories from the feed-through set. There are ceramic spacers to support the electrodes

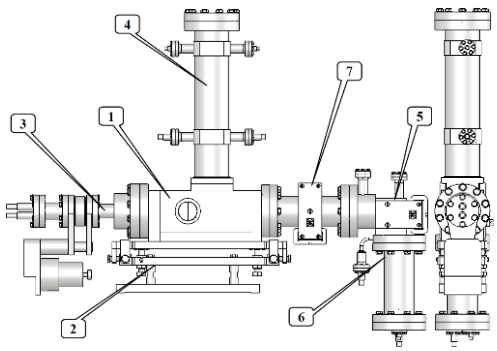


Figure 1: Over View of BSM (1- body, 2- support, 3- target actuator, 4- RF deflector, 5- bending magnet, 6- electron detector, 7- steering magnet).

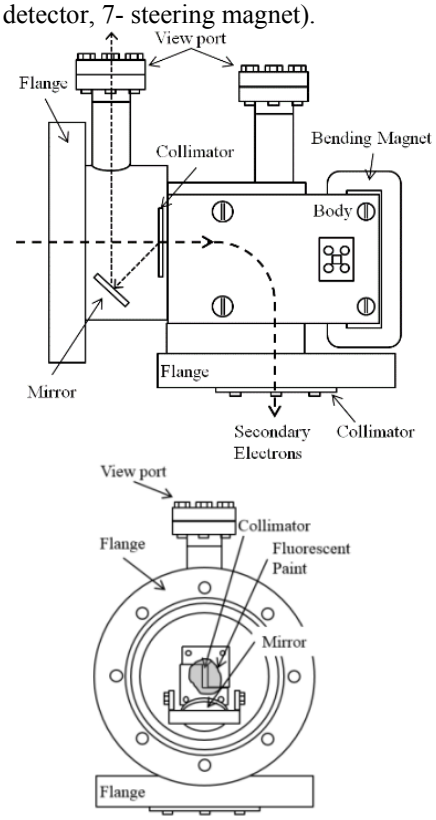


Figure 2: Schematic View of Bending Magnet. Dashed line in the side view shows the secondary electron trajectory.

spacing in the deflector pipe. These structural characteristics depend on the low conductance of pumping rate. For the coarse tuning of secondary electron trajectories, we can directory observe the electron trajectory from the two view port located at the bending magnet part in Fig. 2. We use the thermal electrons emitted from the target wire by supplying the electrical current. When the electron trajectory is out of double collimators, electrons hit the fluorescent paint to release the light of fluorescence. The path width inside the bending magnet is almost 10 mm with the collimators at the both sides. Finally, secondary electrons past through some collimators and bending magnet reach the electron multiplier.

As shown in Fig. 1 and 2, there are some collimators and structural parts which prevent from the gas flow. This is thought to cause a low pumping rate. The bias high voltage to the static lens and target wire, and RF power input are the main parameters of the BSM measurement, they are also key parameters for the vacuum degradation.

VACUUM TEST

Target Vacuum Pressure

Vacuum pressure around BSM should be around or under the pressure of the ACS cavities, because the vacuum degradation is a potential hazard of the cavity condition. Assuming the vacuum accident, pumping time to reach the normal vacuum pressure should be consistent to that of the cavities. We decided the target vacuum pressure under 5.0e-7 Pa and the pumping time to reach under 1.0e-6 Pa is faster than a week by referring the cavity records [3].

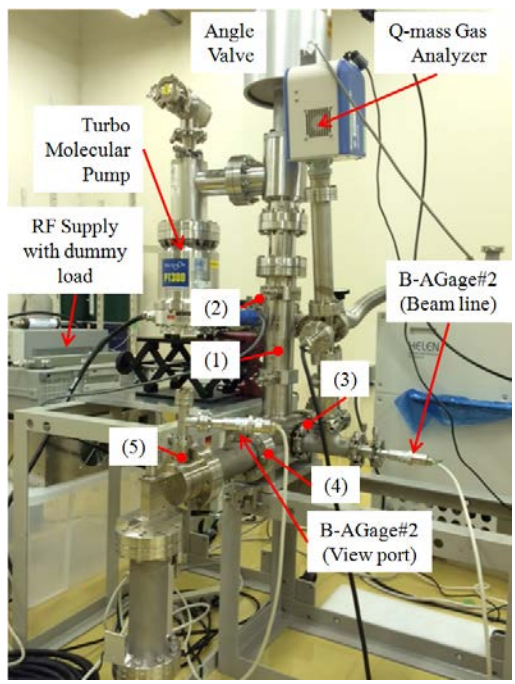


Figure 3: Set-up of vacuum test using BSM#1 in Test bench.

Copyright © 2014 CC-BY-3.0 and by the respective authors

ISBN 978-3-95450-141-0

Set-up of the Vacuum Test

We use an additional turbo molecular pump (TMP) for a BSM vacuum test. We assume the realistic beam line layout of the pump arrangement, the TMP is located above the quadrupole magnets. The vacuum test set-up consists of a turbo molecular pump (TMP), the heating devices, a Q-mass analyzer, two vacuum gage (B-A gage) which are set at the end of beam line and the view port, a high voltage supplier and an RF power supply with a dummy load. High voltage supplier can put a DC voltage and pulsed RF power can input the RF deflector. Numbers in brackets are the points for temperature measurement (Fig. 3).

Baking of BSM

Tape-shaped heaters are put on the surface of the RF deflector, nipples, pipe between the body and bending magnet, pipe of actuator, pipe of electron detector and around an angle valve. Baking temperature is carefully decided. Metallic and ceramic parts can be sustained up to 200 deg. C, but vacuum seal and cramps should be under 100 deg. C. Maximum baking temperature at six points are below. These numbers are corresponding in the numbers in Fig. 3.

(1) Surface of RF deflector: 175 ^{0}C
(2) SHV connector on RF deflector: 60 ^{0}C
(3) KF40 Flange (Beam line): 70 ^{0}C
(4) ICF114 Flange between body and pipe: 180 ^{0}C
(5) Surface of first view point: 150 ^{0}C

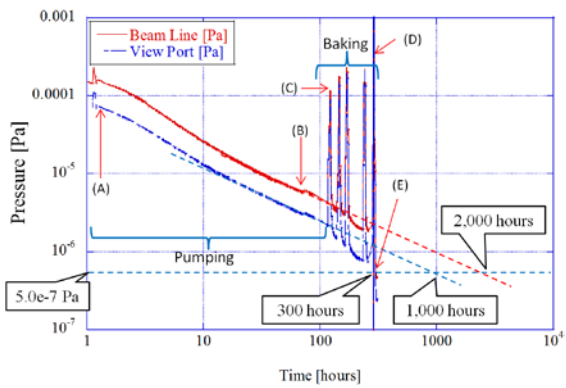


Figure 4: Initial pumping speed of BSM and acceleration of time for the target vacuum level.

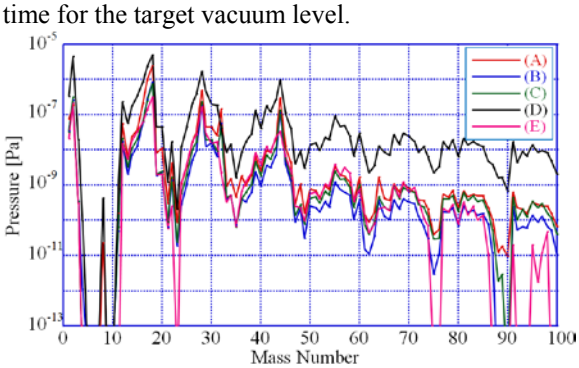


Figure 5: Gas components of at pumping and baking time. Heavier hydro carbons can be removed by baking. Symbols (A) to (E) are the timings of gas analysis, which are shown in Fig. 4.

Initial Pumping Rate and Baking Effect

Trend on the pumping speed of a BSM using a TMP is shown in Fig. 4. Estimated time to the target vacuum pressure is over 1,000 hours. The time can be accelerated to about 300 hours by baking five times. As the mass peak of the outgas components seen in Fig. 5, before the baking, the gas mainly consisted of the air components. During the high temperature, heavy hydrocarbons are removed. After baking, mass number 2, 18, 28, 32 and 44 are the conspicuously reduced.

Effect by Static Lens

After pumping, a lens high voltage was scanned from 0 to -10 kV. Usual setting value is -8.3 kV. Although the scan range covers with the higher voltage, no effect with the high voltage was found in Fig. 6. In the beam line measurement, no big pressure increase was found by supplying the lens high voltage. This result agreed with the experience at beam line.

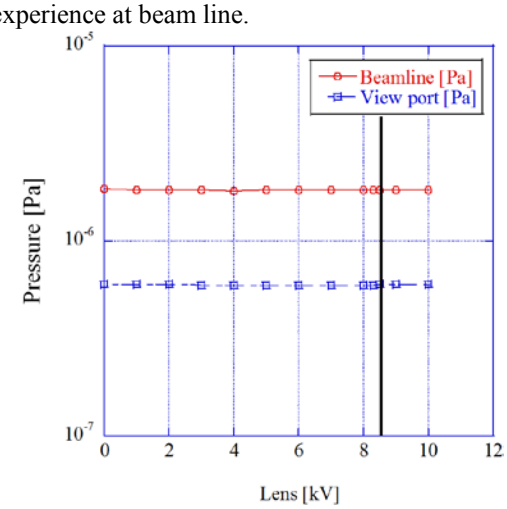


Figure 6: Lens HV Dependence on Gas Pressure. There is no dependence on the lens HV (DC). This lens DC is the negative potential.

Effect by RF Power for Deflector

Pulsed (100 μs) RF power was supplied from 0 to 13 W. Usual setting value is 10 W for BSM, but estimated input power is attenuated in the long transport cable to 6 - 7 W. The vacuum pressure increase was slightly observed from 2 W, but the dependence of the RF Power is not strongly connected on the vacuum pressure (Fig. 7). At the beam line test, we input too much power to the RF deflector and the vacuum degraded immediately. The RF amplitude was tuned to the half, we observed the immediate reduction of the vacuum pressure. This results didn't show a strong dependence, but we have already improved to suppress this degradation by the software modification. The software controls the RF input only during the measurements.

Effect by Target HV

The target high voltage was scanned from 0 to -13 kV. Usual setting value is -10.0 kV. The very big out gassing was observed from -7.0 kV (in Fig. 8). At the beam line

Copyright © 2014 CC-BY-3.0 and by the respective authors

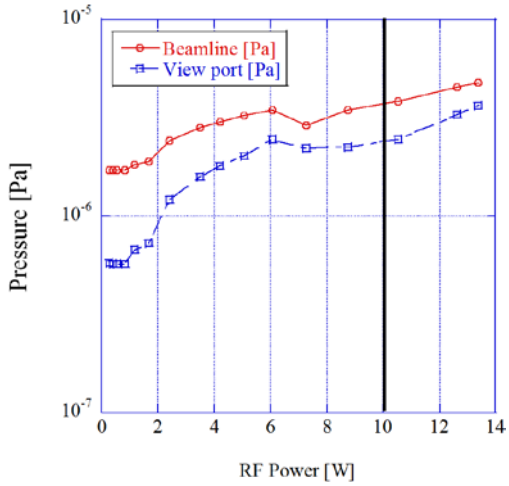


Figure 7: RF power dependence on gas pressure. There is small dependence on the RF power.

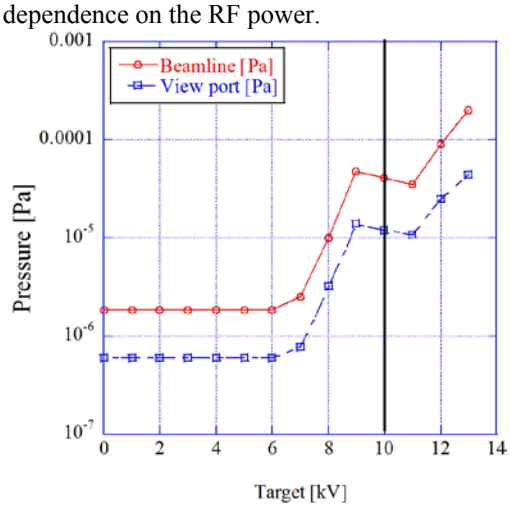


Figure 8: Target HV dependence on gas pressure. The effect strongly starts from -7 kV. This bias voltage is negative.

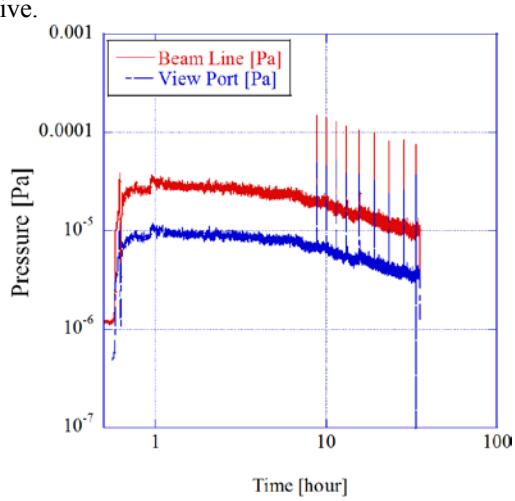


Figure 9: Target wire conditioning with HV supply. Pressure depends on the conditioning.

measurement, the intensity of the effect also depended on the value of the target potential and normally started at around -7 kV. This result is agreed with this result.

High voltage was supplied from 0 to -13 kV and the voltage was kept at -10 kV for over 35 hours for the wire conditioning. Vacuum pressure was decreased gradually with time (Fig. 9). About 10 hours has passed, electrical discharge is seen. After conditioning of the target wire, the dependence of high voltage supply to the target wire is improved to about one order in Fig. 10.

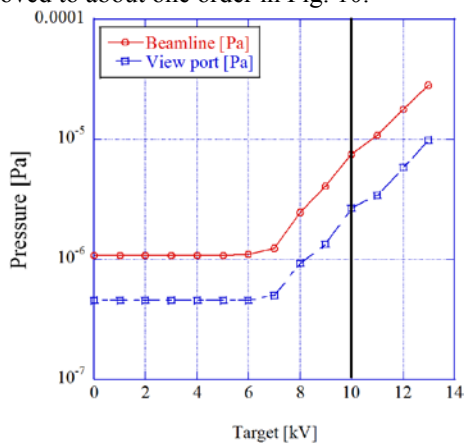


Figure 10: After conditioning of target wire. The effect is drastically improved. These data were taken with Q-mass analysis. Pressure with Q-mass analysis is usually higher than that without Q-mass analysis.

Improved Vacuum Pressure in the Test

After cooled from the finishing the baking and the target wire conditioning, we turned off the target HV and Q-mass analyzer to check the achieved pressure level. As the results, vacuum pressure reached 5.99e-7 at beam line and 3.08e-7 Pa at view port. High voltage to the target wire was supplied again from the lowest pressure, the pressure was recovered from the original level. Because the recovered pressure level after conditioning was already improved, impact of the pressure increasing is not so seriously high. After purging with dry nitrogen gas to confirm the pumping rate again (Fig. 11), the estimated time to 5.0e-7 Pa is almost half as initial condition in Fig. 4. After baking once, and turned off the target HV and Q-

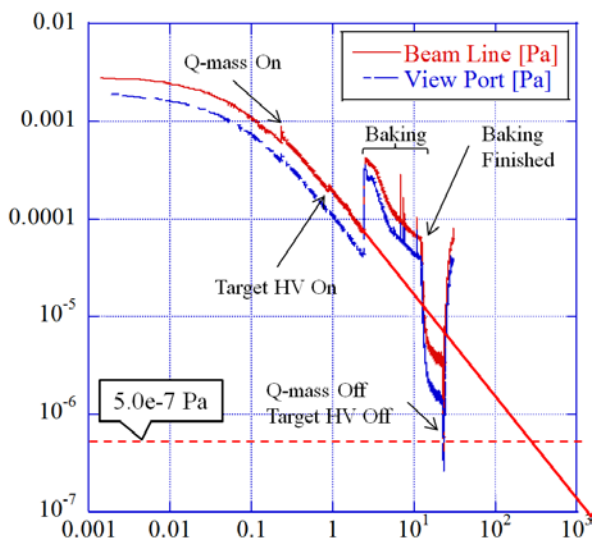


Figure 11: Pumping Speed after Baking. Once dry nitrogen gas was purged inside the BSM, pumping stated again.

Copyright © 2014 CC-BY-3.0 and by the respective authors

ISBN 978-3-95450-141-0

mass analysis, time to achieve 5.0e-7 Pa is about 30 hours. Actually the vacuum pressure reached 4.05e-7 at beam line and 2.74e-7 Pa at view port. This result is enough for the target level. But the target HV turned on again, the pressure level was recovered to the original level to the 3.50e-6 at beam line and 9.38e-7 Pa at view port. Because the HV impact still remained, further conditioning were required.

VACUUM SYSTEM IMPROVEMENT

Original BSM has no vacuum equipment, but the installation of BSM caused some vacuum degradation. We have examined the vacuum test with the high voltage supply and RF power input using additional vacuum pump. When the high voltage supply and RF power are off, the target vacuum level was almost achieved. But the vacuum level with high voltage was recovered to another pumps will be installed closer to the beam line to remove the impact of the high voltage supply.

CONCLUSION

Because there are some narrow slits inside the BSM, vacuum conductance is suppressed. Low conductance will require a quite long time to reach the operational vacuum condition. An additional pump and baking can accelerate the pumping speed. HV supply and RF supply have the impact of vacuum increasing. Baking with the target conditioning (supplying HV) is effective for the vacuum improvement. Further improvement will bring the better condition. Supplying period of RF power is limited only for the measurement by software improvement. Limitation of HV supplying is only for the pulse duration (supplying term is set for slightly longer than the macro pulse). Using the shorter pulse duration for the measurement.

We can successfully take various vacuum data for installation of BSM. But this is not enough for all three BSMs. We will continue to improve the vacuum system of BSM.

ACKNOWLEDGMENT

The authors would like to acknowledge the specialists to perform and support the vacuum test and new vacuum system arrangement. We would like to give special thanks to Drs. A. V. Feschenko and A. N. Mirzojan of INR, Russia for the fruitful advice and discussions. Drs. K. Hasegawa, Y. Hori, M. Kinsho, N. Hayashi, H. Ao, J. Tamura and J. Kamiya of J-PARC for useful discussions and helps. Also, we would like to give special thanks to the engineers M. Yoshikawa, M. Mayama (Mitsubishi Electric System & Service Co. Ltd.) and Y. Nemoto (Nihon Advanced Technology Co. Ltd.).

REFERENCES

[1] A. Miura, et. al., “Bunch Shape Measurement of 181 MeV Beam in J-PARC Linac", Special Volume of Proceedings of J-PARC Symposium, Journal of the Physical Society of Japan (JPSJ), to be published in April, 2015,

[2] A. V. Feschenko, "Methods and Instrumentation for Bunch Shape Measurements", Proc. Part. Acc. Conf. PAC 2001, Chicago, p. 517 (2001).

[3] H. Ao, et. al., “Annular-ring Coupled Structure Linac for the J-PARC Linac Energy Upgrade”, Proceedings of IPAC13, THPWO036, Shanghai, China, 2013.

Copyright © 2014 CC-BY-3.0 and by the respective authors

AN ULTRAFAST LINEAR ARRAY DETECTOR FOR SINGLE-SHOT ELECTRO-OPTICAL BUNCH PROFILE MEASUREMENTS

L. Rota, M. Caselle, N. Hiller, A.-S. Müller, M. Weber,
Karlsruhe Institute of Technology (KIT), Karlsruhe, Germany

Abstract

A new spectrometer system has been developed at ANKA for near-field single-shot Electro-Optical (EO) bunch profile measurements with a frame rate of 5 Mfps. The frame rate of commercial line detectors is limited to several tens of kHz, unsuitable for measuring fast dynamic changes of the bunch conditions. The new system aims to realize continuous data acquisition and over long observation periods without dead time. InGaAs or Si linear array pixel sensors are used to detect the near IR and visible spectrum radiation. The detector signals are fed via wire-bonding connections to the GOTTHARD ASIC, a charge-sensitive amplifier with analog outputs. The front-end board is also equipped with an array of fast ADCs. The digital samples are then acquired by an FPGA-based readout card and transmitted to an external DAQ system via a high-speed PCI-Express data link. The DAQ system uses high-end Graphics Processors Units (GPUs) to perform a real-time analysis of the beam conditions. In this paper we present the concept, the first prototype and the low-noise layout techniques used for fast linear detectors.

INTRODUCTION

During the low-α_c-operation at the ANKA storage ring at the Karlsruhe Institute of Technology, the momentum compaction factor α_c is reduced to compress the bunches longitudinally and thus generate Coherent Synchrotron Radiation (CSR) in the THz range [1]. The emitted CSR exhibits a bursting behavior [2–4], which is caused by dynamic changes of the longitudinal bunch shape (e. g., microbunching). To study these dynamic changes, single-shot measurements with a sub-ps resolution are required.

The method of Electro-Optical Spectral Decoding (EOSD) offers the possibility to measure the longitudinal bunch profile and its arrival time relative to the revolution clock with a sub-ps time resolution without averaging. For EOSD, the field induced Pockels effect inside an electro-optical crystal is used to modulate the temporal profile of the electron bunch onto a laser pulse. Subsequently this laser pulse is detected with a commercial InGaAs line array inside an optical spectrometer and from the spectral modulation the bunch profile can be extracted.

First single-shot measurements with the EOSD setup at ANKA have indicated the formation of substructures on the compressed bunches [5, 6]. In principle, EOSD, offers the possibility to measure the longitudinal bunch profile on a turn-by-turn basis (f_{rev} = 2.7 MHz at ANKA) because the laser can easily be adjusted to the ANKA revolution frequency. The laser system at ANKA operates at 1050 nm, so an InGaAs based line array is required. The acquisition rate of the commercial InGaAs line arrays, however, is limited to the low kHz range [7] thus it is not possible to monitor fast dynamic changes of the longitudinal bunch profile. For this reason a fast spectrometer is being developed at KIT and the target frame rate has been set to 5×10^6 frames per second (Mfps) to make it also applicable to other facilities such as XFEL and ELBE for which the repetition rates are higher. The final system must also be able to perform some on-line analysis of the bunch conditions in order to be used as a real-time and non-destructive diagnostic tool.

DESIGN CONCEPT

The architecture of the new spectrometer system is shown in Fig.1. The system consists of a mezzanine card where the detector (a), the front-end electronics (b) and the ADCs (c) are mounted, an FPGA-based high-throughput readout board (d) and an external DAQ system (e).

Two different detectors technologies can be used to detect the modulated spectral response over different frequency ranges: an InGaAs linear array for the near IR and an uncoated Si linear array for visible light. The final version of the system will be based on a 1D detector with 512 pixels and a pitch of 50 μm.

The detector's output signals are fed via high density fine-pitch wire-bonding connections to the front-end electronics. A low temperature fine pitch wire-bonding technology is required. Therefore, an ultrasonic wedge-to-wedge alluminium wire with a diameter of 25 μm has been choosen.

Eight GOTTHARD ASICs [8] developed by PSI are used as charge-sensitive pre-amplifiers. Although the GOTTHARD has been developed for a Si microstrip detector, it can also be used with different detectors thanks to its automatic and adaptive gain selection stage. The current version of the GOTTHARD (v1.4) has 128 inputs and 4 outputs. A group of 32 inputs is connected to one output through a distributed multiplexer, clocked at 32 MHz. Therefore, a maximum frame rate of 1 Mfps can be achieved. A new GOTTHARD version (v1.6) with 8 analog outputs and an operating maximum frequency of 50 MHz is currently being submitted to the foundry. The new version allows to achieve a maximum frame rate of 3.1 Mfps. In order to meet the requirement of 5 Mfps with a linear array of 512 pixels, a special routing is required: each GOTTHARD chip will be connected to the detector in interleaving mode, and only 64 inputs of each chip will be used. In this way each output serves 8 pixels. With a reset after 8 clock cycles, a frame rate of up to 6.25 Mfps can be realized.

Copyright © 2014 CC-BY-3.0 and by the respective authors

ISBN 978-3-95450-141-0

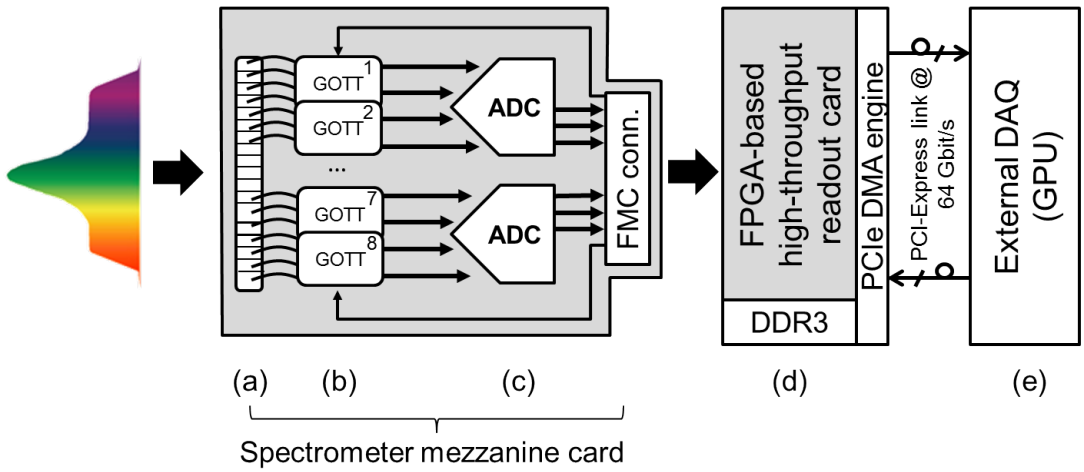


Figure 1: Architecture of the novel spectrometer.

The front-end card is completed by an array of fast ADCs and an high-density Samtec FMC connector.

The FPGA-based back-end card acquires the digital samples from the mezzanine card and performs a preliminary data analysis. A dedicated input stage is used to control and synchronize the GOTTHARD chips and the ADCs. The FPGA firmware includes several IP cores developed at KIT which are already employed in different experimental setups [9] and [10]. In particular, the system will use a DDR3 memory interface for temporary data storage and a PCI-Express Direct Memory Access (DMA) architecture [11] to transfer data to an external DAQ system with a throughput of up to 64 Gbit/s.

The setup is completed by a real-time data processing stage based on high-end Graphics Processors Units (GPUs) for an on-line monitoring of the beam conditions. The final system aims to realize continuous data acquisition without any dead time and will be controlled by a dedicated software.

FIRST PROTOTYPE OF THE SPECTROMETER MEZZANINE CARD

A first prototype of the spectrometer mezzanine card with a target frame rate of 1 Mfps is being developed to study the most critical aspects of the system.

The bias voltage of the detector can be supplied by an external source. In this way the voltage can be carefully adjusted to achieve the best performance in both the detector and the GOTTHARD input stage. Also, the electrical properties the wire-bonding connection between each pixel and the analog front-end must be carefully characterized and optimized with a dedicated layout. The working parameters of the GOTTHARD must then be calibrated to minimize the Equivalent Noise Charge (ENC) of the system.

The first prototype will also be used to further develop the FPGA firmware, the GOTTHARD's control logic, the algorithms for the on-line data analysis and the software interface.

The mezzanine card mounts a single InGaAs linear array detector provided by Xenics, with 256 pixels and 50 μm pitch. The detector has been according to the operational wavelength of the laser that is used in the experimental setup for EO bunch profile measurements at ANKA. The detector's bias voltage can be supplied from an accurate external source through an SMA connector mounted on the board.

Two GOTTARD v1.4 chips are connected to the InGaAs detector. The analog samples are digitized by an AD9252 ADC with 8 channels and a 14-bit resolution, operating at 32 MS/s. A FMC connector is used to connect this card with the readout board.

The back-end board mounts a Xilinx Virtex6 device. The FPGA firmware architecture consists of a DDR3 memory interface for temporary data storage, an on-line data analysis stage and a PCI-Express DMA engine, capable of sustaining

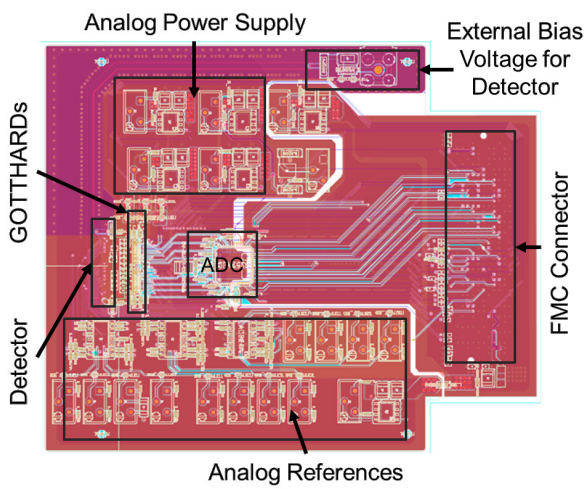


Figure 2: Layout of the spectrometer mezzanine card.

Copyright © 2014 CC-BY-3.0 and by the respective authors

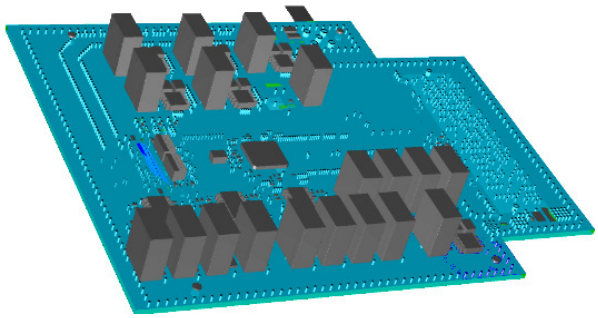


Figure 3: Rendering of the spectrometer mezzanine card.

the required throughput of 3.6 Gbit/s (14 bits × 8 channels @ 32 MS/s).

Low-noise Layout Techniques

Several low-noise layout design practices have been employed in order to achieve the best noise performance and reduce electromagnetic interference (EMI). To isolate the digital circuitry from the analog part, two separate grounds are used (as can be seen in Fig. 2). An inductor located below the ADC connects the two grounds and provides the required common voltage reference. Multiple ground planes are used, and signal pairs are router near their respective planes in order to reduce the signal's return current path. All the power planes and the critical traces (including the external detector bias voltage) have been filtered, routed between the corresponding ground planes and shielded with via guard fences (Fig. 3). Decoupling capacitors are placed near the components to filter the power supply and the analog references. These capacitors also act as a low-impedance source for dynamic currents, thus minimizing the switching noise.

The high-speed digital signals (maximum clock frequency = 330 MHz) have been routed using differential coplanar waveguide transmission lines with controlled impedance. To avoid signal reflections on these traces, series termination resistors have been placed near the outputs pins.

CONCLUSIONS AND FUTURE WORK

In this paper we have described the design concepts of a novel spectrometer based on an InGaAs detector and operating with a frame rate of up to 5 Mfps. A first prototype of the front-end board is currently being developed in order to study the critical parts of the front-end board. The system will be tested at the ANKA synchrotron light source to characterize the InGaAs linear array detector and its compatibility with the GOTTHARD chip. The board will then be integrated in the novel EO setup currently under development at ANKA.

ACKNOWLEDGMENTS

The authors would like to thank Aldo Mozzanica, Bernd Schmitt and Christian Ruder from the Paul Scherrer Institute (PSI).

REFERENCES

[1] A.-S. Müller *et al.*, "Far Infrared Coherent Synchrotron Edge Radiation at ANKA", RPAE038, Proc. PAC'05, Knoxville, TN, USA (2005).

[2] V. Judin *et al.*, "Observation of Bursting Behavior Using Multiturn Measurements at ANKA", WEPEA021, Proc. IPAC10, Kyoto, Japan (2010).

[3] M. Klein *et al.*, "Simulations of the Microbunching Instability at ANKA using a Vlasov-Fokker-Planck Solver", WEPC095, Proc. IPAC'11, San Sebastian, Spain (2011).

[4] V. Judin *et al.*, "Spectral and Temporal Observations of CSR at ANKA", TUPPP010, Proc. IPAC'12, New Orleans, LA, USA (2012).

[5] N. Hiller *et al.*, "Single-Shot Electro-Optical Diagnostics at the ANKA Storage Ring", these proceedings, MOPD17, IBIC'14, Monterey, CA, USA (2014).

[6] N. Hiller *et al.*, "Electro-Optical Bunch Length measurements at the ANKA Storage Ring", MOPME014, Proc. IPAC'13, Shanghai, China (2013).

[7] Sensors Unlimited, "2048R InGaAs Linescan Camera", http://www.sensorsinc.com/products/detail/gl2048-r-ingaas-linescan-camera, 2014

[8] A. Mozzanica *et al.*, "The GOTTHARD charge integrating readout detector: design and characterization", C01019, JINST, 7, 2012.

[9] M. Caselle *et al.*, "A Picosecond Sampling Electronics "KAPTURE" for Terahertz Synchrotron Radiation", these proceedings, MOCZB1, IBIC'14, Monterey, CA, USA (2014).

[10] U. Stevanovic *et al.*, "Control System and Smart Camera with Image Based Trigger for Fast Synchrotron Applications", Proc. RT2014, Osaka, JAP (2014).

[11] L. Rota *et al.*, "A New DMA PCIe Architecture for Gigabyte Data Transmission", Proc. RT2014, Osaka, JAP (2014).

Copyright © 2014 CC-BY-3.0 and by the respective authors

ISBN 978-3-95450-141-0

LANSCE 1L HARP DATA ACQUISITION SYSTEM UPGRADE*

J. Sedillo, J. Nguyen, J.D. Gilpatrick, M. Gruchalla, LANL, Los Alamos, NM 87545, USA

Abstract

The 1L Harp is the last beam diagnostic preceding LANSCE's 1L Target, the neutron source of LANSCE's Lujan Center, and consists of two orthogonal planes of stationary sense wires for monitoring the beam distribution prior to its arrival at the target. A new data acquisition system has been developed for the 1L Harp that features a National Instruments compactRIO contained within a BiRIO chassis hosting electronic circuits for signal conditioning and a new feature for sense wire integrity monitoring. Hardware design, software architecture, and preliminary data acquisition results will be described.

INTRODUCTION

The 1L harp is a fixed-position, beam diagnostic sensor for measurement of the beam's transverse profiles immediately prior to impingement on the 1L target. The sensor is composed of three planes of silicon-carbide (SiC) fibers; two sense planes for measuring horizontal and vertical beam profiles, and a bias plane for attraction of secondary electrons. Each sense plane is composed of seventeen, 0.079-mm diameter sense fibers spaced at 6-mm intervals. All fibers connect to individual 10 pF capacitors at one end and a cable plant at the other end for signal transmission to the data acquisition system [1] as shown in Fig. 1.

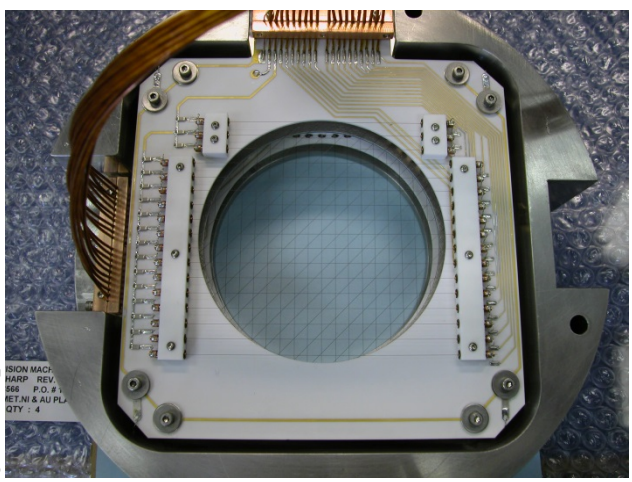


Figure 1: 1L Harp Sensor [1].

PRINCIPLE OF OPERATION

The 1L harp operates on the principle of secondary electron emission resulting from the interaction of the particle beam with the harp's sense wires. As the high-energy (800 MeV) H+ particle beam passes through the fiber's SiC material, electrons are forcefully removed from the fiber's surface into free space, leaving a positive charge gain within the fiber. The positive voltage resulting from the fiber's loss of electrons attracts a flow of electron current from the signal conditioning circuit to the sense wire, neutralizing the charge difference. This current and its associated net charge are transformed by the signal conditioning circuitry into a voltage signal proportionally related to the charge. Since the particle beam's transverse particle density is generally Gaussian, each fiber in the plane receives a different concentration of beam flux. This beam flux translates into secondary electron emission differences resulting in charge differences at the signal conditioning circuitry and finally a voltage difference at the ADC dedicated to each sense wire. Plotting the resulting voltages as a function of the fiber's relative position creates a Gaussian profile corresponding to the beam's transverse particle density.

Beam parameters at the 1L Harp are listed in Table 1. From the properties of the beam and the SiC fiber; application of the Bethe-Bloch formula described by Loveland in [2], with a ionization potential of 180 eV for SiC [3], and applying the Sternglass theory across the surface of a SiC fiber at beam center yields an expected negative charge loss of 484 picocoulombs.

Table 1: 1L Harp Beam Properties

Beam Property	Value
Beam species	H+
Beam energy	800 MeV
Longitudinal current profile	Triangular
Pulse duration	300 ns
Peak current	33.3 A
Transverse RMS	12.5 mm
Bunch charge	5 μCoulombs

SYSTEM HARDWARE

Data Acquisition System/ EPICS IOC

The data acquisition hardware consists of a National Instruments compactRIO with interfaces to three AFE (Analog Front End) boards and one integrity board housed within a BiRIO chassis as shown in Fig. 2. Logic signals for beam synchronization and AFE control connect to the compactRIO through a single NI-9401

*Work supported by the U.S. Department of Energy under contract DE-AC52-06NA25396.

Copyright © 2014 CC-BY-3.0 and by the respective authors

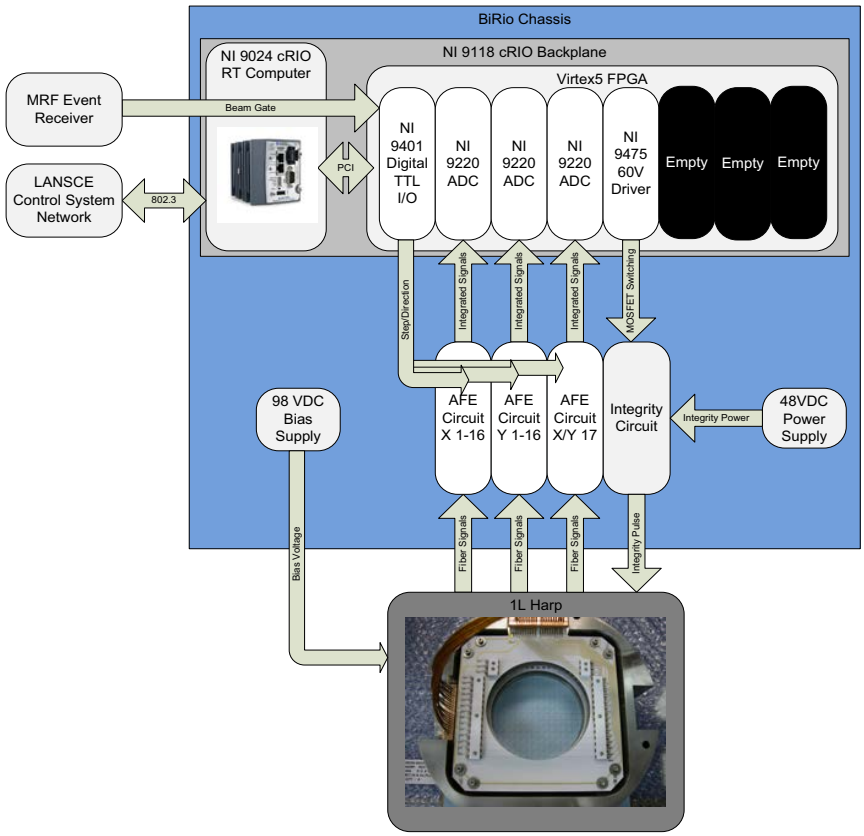


Figure 2: 1L Harp Data Acquisition System Hardware Diagram.

TTL logic module. Signals generated by the AFEs are digitized by three NI-9220 analog-to-digital conversion (ADC) modules. Finally, one NI-9475, 60V-source module is incorporated for integrity pulse generation. Additional circuitry includes a 98-volt power supply for the harp bias plane.

Beam Signal Conditioning Subsystem/Analog Front End (AFE)

1L Harp signals are integrated by AFE circuits depicted in Fig. 3. At the core of each circuit is a subcircuit of a Texas Instruments, ACF2101 dual switched integrator [4]. The ACF2101 provides on-die capacitors and multiplexing circuitry for integration, select, reset, and hold operations. Set at 100pF, the on-die capacitor is capable of measuring up to 1 nanocoulomb of positive charge before the integrator saturates. Low-pass filters with 40-kHz corners are applied before the ACF2101's as an anti-aliasing precaution. For this application, a beam pulse measured on the center fiber is expected to result in a negative 4.84-volt signal output from the integrator. Beam integration time is variable and can be set by the control logic signals applied to the ACF2101s. Additionally, the state of integration is reset after the measurement has been made to prevent interference to subsequent pulse measurements. The final value of each signal's integration is applied to the beam profile for observation. Figure 4 shows one of the system's three AFE circuits. This board contains eight ACF2101 integrators for processing sixteen, 1L Harp channels. Connections to the AFE board include the Harp sensor interface shown on the left of the board, a power connector shown on the top-center, a control connection to the right of the power connector, and the output connector to the ADC on the right.

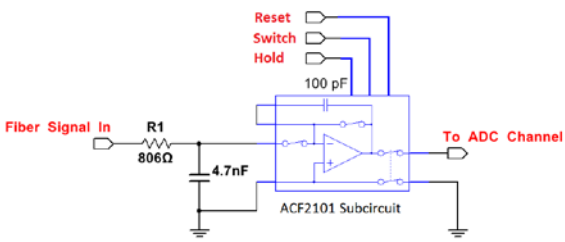


Figure 3: Circuit for one AFE channel.

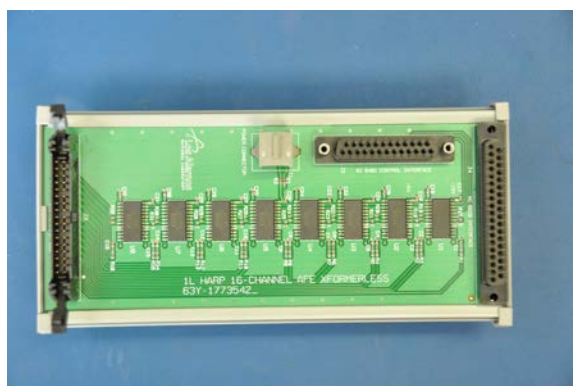


Figure 4: 16-Channel AFE.

Copyright © 2014 CC-BY-3.0 and by the respective authors

ISBN 978-3-95450-141-0

Integrity Subsystem

As beam-induced sense wire damage is a prevalent problem with harp diagnostics, a wire integrity subsystem has been incorporated for monitoring the continuity of the sense wires. The 1L Harp hardware accomplishes this by generating a 48-volt, square pulse to the 10 pF capacitor-end of the fibers. The 10 pF capacitors are applied in series to each wire at the harp and function to AC-couple the 48 volt pulse to the fiber. As the pulse translates through the capacitor-fiber circuit, it is attenuated to a signal on the order of 20 mV with an expected charge displacement of 480 picocoulombs. Measurement of this signal occurs in the same manner as the beam signal; via charge integration by the AFEs. Through this method, an acceptable integrity signal can be read as -4.8 volts by the ADCs. Adjusting the integrity pulse width and ACF2101 integration time allows for adjustment of the integrity signal received.

SYSTEM SOFTWARE

FPGA Software Architecture

1L Harp sense wire data acquisition starts with the compactRIO's FPGA and its associated I/O modules. The FPGA program consists of two parallel operations shown in Fig. 5. Process 1 simultaneously monitors the beam

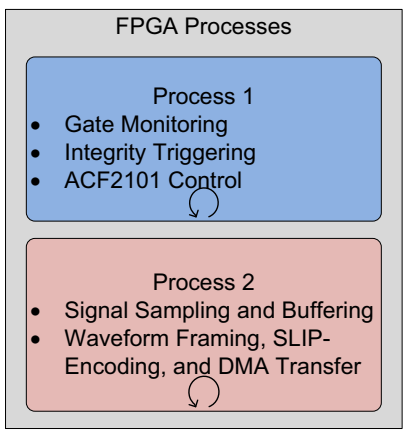


Figure 5: The compactRIO FPGA program architecture.

synchronization signal and applies the drive signals for all ACF2101 integrators via the NI-9401 module. Since the beam gate has a narrow, 300ns pulse width, the NI-9401 must sample at its fastest operating rate of 10 MHz to achieve 2-3 samples per pulse. When the gate has been detected by this process, a flag is set, notifying process 2. The primary purpose of the process 2 is to continuously sample the wire signals at the maximum ADC sampling rate of the NI 9220 modules. Once notified of a gate, this process will save the set number (typically 2) of pre-gate-edge samples and acquire a set amount (typically 8) of post-gate-edge samples across all 34 channels. Each set of samples spanning all 34 channels is framed, SLIP-encoded [5], and streamed over the DMA channel to the compactRIO RT computer. Once all prescribed samples have been streamed; a final, SLIP-encoded trailer frame is transferred over the DMA buffer. In addition to demarcating the end of a waveform set, the trailer frame distinguishes whether the data is a set of beam waveforms or a set of integrity waveforms.

Waveforms obtained by the compactRIO RT system generally have a monotonically-decreasing nature resulting from the charge integration process of the ACF2101. As a result of this, the final value of each integrated waveform represents the total accumulated charge for that channel and provides the best relative comparison between channels since the output signal-to-noise ratio improves with the time over which the integration occurs. It is for this reason that the final value of each channel's integrated waveform is represented in the transverse profile.

Integrity Process

The integrity process operates in a similar manner as that of the beam data acquisition process. Subtle differences include the manner in which the integrity process is triggered and how the integrity data is differentiated from beam data as it is transferred through the DMA channel. Since beam signals are characterized by a 20Hz pulse rate with 150 µs-long width, an opportunity for triggering an integrity acquisition presents itself within the remaining 49 ms of dead signal time. FPGA process 1 derives a virtual gate signal for process 2 by calculating the period of the last beam gate cycle and then adding half of that period to the time the next beam gate is expected to occur. This permits the integrity process to non-invasively interleave the integrity process between beam cycles.

RT Software Architecture

The software developed for the compactRIO's RT system consists of the two threads depicted in Fig. 6. The compactRIO RT computer utilizes a real-time (RT) process for deterministically extracting AFE/ADC

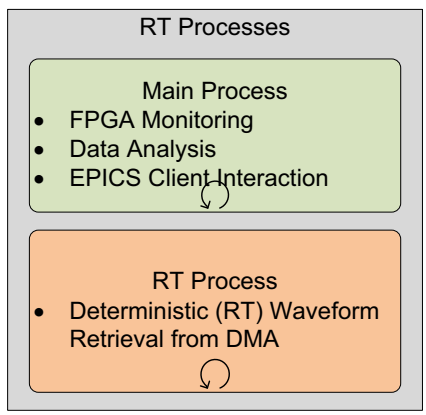


Figure 6: The compactRIO RT program architecture.

Copyright © 2014 CC-BY-3.0 and by the respective authors

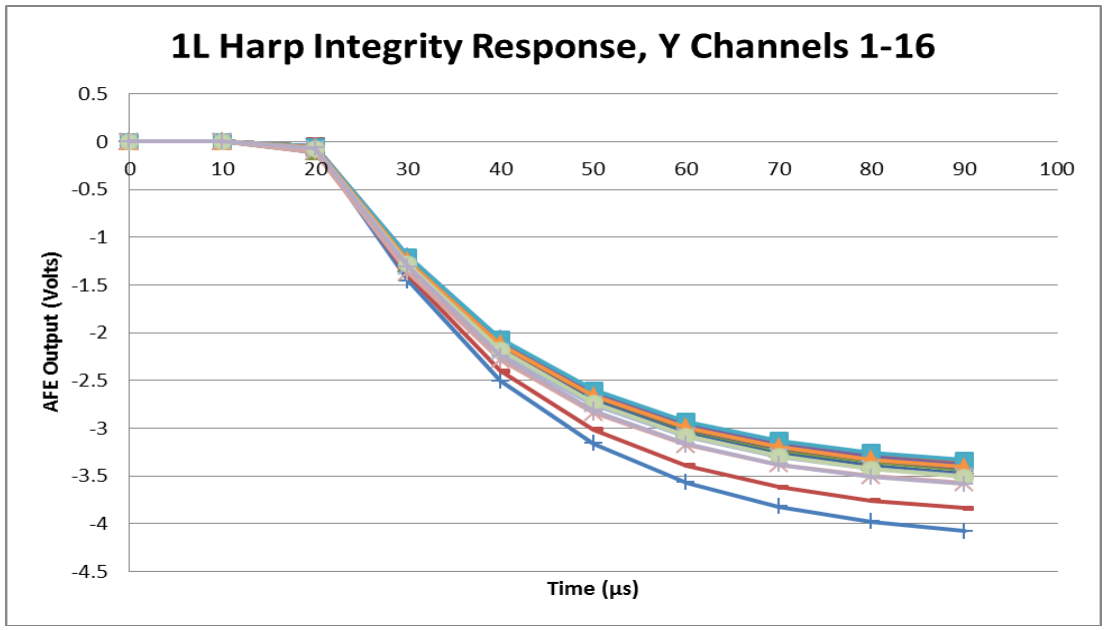


Figure 7: System Integrity Response.

waveforms from the DMA (Direct Memory Access) channel to ensure the DMA channel does not overflow. The data stream extracted from the DMA channel is reframed, SLIP-decoded, and transferred to an appropriate analysis routine within the "Main Process." The main process loads the analyzed data (transverse profiles for beam data and pass/fail results for integrity data) into EPICS process variables for observation by LANSCE operations staff.

PERFORMANCE

Initial testing of this system has yielded the data presented in Fig. 7. This data was captured by the system's compactRIO and represents sixteen channels of one AFE's response to an integrity pulse through the 1L Harp sensor. The results follow the expected negative integration pattern approaching -4.8 volts. In the final analysis, this data will be translated from volts to coulombs through the ACF2101's 100-pF integrating capacitance relationship.

Beam data has not yet been obtained since the LANSCE accelerator has been offline during the development of this system. However, beam data is expected to follow the similar response shape as the integrity signal with the final amplitude approaching -4.8 volts at the beam's transverse peak. When compared to the maximum measureable limit of -10-volts/1000-picocoulombs, the nearly -5 volts of peak expected output provides this system with a favorable 5-volt/500-picocoulomb operating margin.

REFERENCES

[1] J.D. Gilpatrick et al.,"LANSCE Harp Upgrade: Analysis, Design, Fabrication, and Installation," TUPSM014, BIW'10, Santa Fe, May 2010: http://www.JACoW.org.

[2] W.D. Loveland et al. *Modern Nuclear Chemistry*, (Hoboken: John Wiley & Sons, 2006), 502.

[3] Y. Zhang et al., "Electronic Stopping Powers in Silicon Carbide," Physical Review B 69, 205201 (2004).

[4] ACF2101 Data Sheet. www.ti.com/product/acf2101

[5] J. Romkey, "A Nonstandard For Transmission of IP Datagrams Over Serial Lines: SLIP," IETF RFC1055, http://tools.ietf.org/html/rfc1055.

Copyright © 2014 CC-BY-3.0 and by the respective authors

ISBN 978-3-95450-141-0

DEVELOPMENT OF NON-INVASIVE ELECTRON BEAM POSITION MONITOR BASED ON COHERENT DIFFRACTION RADIATION FROM A SLIT*

Y. Taira#, R. Kuroda, M. Tanaka, H. Toyokawa, AIST, Tsukuba, Japan
K. Sakaue, Waseda Univ., Tokyo, Japan
H. Tomizawa, RIKEN Harima Institute, Japan

Abstract

Diffraction radiation is emitted when a charged particle passes through in the vicinity of a boundary between two media with different dielectric constants. An aperture, a slit, and an edge are used for diffraction radiation target. It is theoretically suggested that an asymmetry of a spatial distribution of diffraction radiation appears by changing the beam trajectory with respect to the center of a rectangular slit. We have developed the beam position monitor using the coherent diffraction radiation generated when a sub-picosecond electron beam passes through the rectangular slit. A theoretical background of the diffraction radiation emitted from the slit and experimental results will be reported.

INTRODUCTION

Generation of an ultra-short pulsed electron beam with a bunch length of few hundreds of femtoseconds and below 100 fs is key technique of accelerator science; that are generation of intense terahertz radiation [1] and x-ray free electron lasers (X-ray FEL) [2]. Many techniques for beam diagnostic have been developed so far.

Diffraction radiation (DR) is used as a non-invasive beam diagnostic and can be used to measure beam energy, transverse size, divergence, and position [3]. DR is generated when a charged particle moves in the vicinity of a boundary between two media with different dielectric constants with a condition of $d < \gamma\lambda/2\pi$, where d is the distance between the edge of the medium and the electron, γ is the Lorentz factor of the electron beam, and λ is the observed wavelength of DR [4]. An aperture, a slit, and an edge can be used as DR devices.

Recently, three-dimensional electron bunch charge distribution (3D-BCD) monitor has been proposed for the X-ray FEL by H. Tomizawa [5-6]. It is based on Electro-Optical (EO) multiple sampling (multiplexing) with a manner of spectral decoding. Here, three hollow EO detectors surround the electron beam axis azimuthally and are installed at three detection points on the beam axis. To simplify the monitor system of the 3D-BCD, the basic concept of the DR beam position monitor was proposed [5]. The electron bunch's center of mass and incident angle at the central EO detector of 3D-BCD is defined by the EO detectors of both ends. We investigated the feasibility of the concept of this novel monitor.

Our facility, S-band compact electron linac at the National Institute of Advanced Industrial Science and Technology (AIST) [7] is the beam energy of 40 MeV. If we observe an optical diffraction radiation with the wavelength of 500 nm, the distance d must be smaller than 6 μm. This value will be much smaller than the beam size. Therefore it is necessary to observe the longer wavelength of DR for realistic measurements.

Coherent radiation emits when the wavelength of the radiation is comparable to or longer than the electron bunch length. The frequency spectrum of coherent radiation is mainly depended on a bunch form factor described as

$$f(\omega) = \left| \int_{-\infty}^{\infty} \rho(t) \exp(i\omega t) \mathrm{d}t \right|^2, \quad (1)$$

where ω is the angular frequency of coherent radiation, $\rho(t)$ is the particle distribution, and t is time. If $\rho(t)$ is assumed to a Gaussian particle distribution of bunch length σ (rms), the form factor is expressed as

$$f(\omega) = \exp\left(-\sigma^2\omega^2\right). \quad (2)$$

Consequently, the frequency spectrum of coherent radiation is strongly depended on the bunch length σ. For example, if the bunch length is 200 fs, coherent radiation up to the frequency of 2 THz (wavelength of 150 μm) is coherently enhanced. If we observe the wavelength of 150 μm of the CDR, the distance d must be less than 2 mm. This condition is useful for the CDR measurement. Therefore, CDR can be used to measure electron bunch length, energy, transverse size, divergence, and position.

In this paper, we focus on the measurement of the beam position using the CDR emitted from a rectangular slit. A theoretical background and experimental results will be reported. We have successfully detected the beam position by measuring the asymmetry of the spatial distribution of CDR.

DIFFRACTION RADIATION GENERATED FROM A RECTANGULAR SLIT

Theoretical equations concerning with the DR emitted from the rectangular slit are described in Ref. [4]. The DR field generated by a charged particle passing through a rectangular slit opening in a rectangular screen can be described as

$$E_{x,y}^{DR}(a_{out}, b_{out}) = E_{x,y}^{TR}(a_{out}, b_{out}) - E_{x,y}^{TR}(a_{in}, b_{in}). \quad (3)$$

where the indices x and y are the horizontal and vertical polarization components at the detector coordinates, a_{out}

*Work supported by JSPS KAKENHI Grant Number 26246046.
#yoshtiaka-taira@aist.go.jp

Copyright © 2014 CC-BY-3.0 and by the respective authors

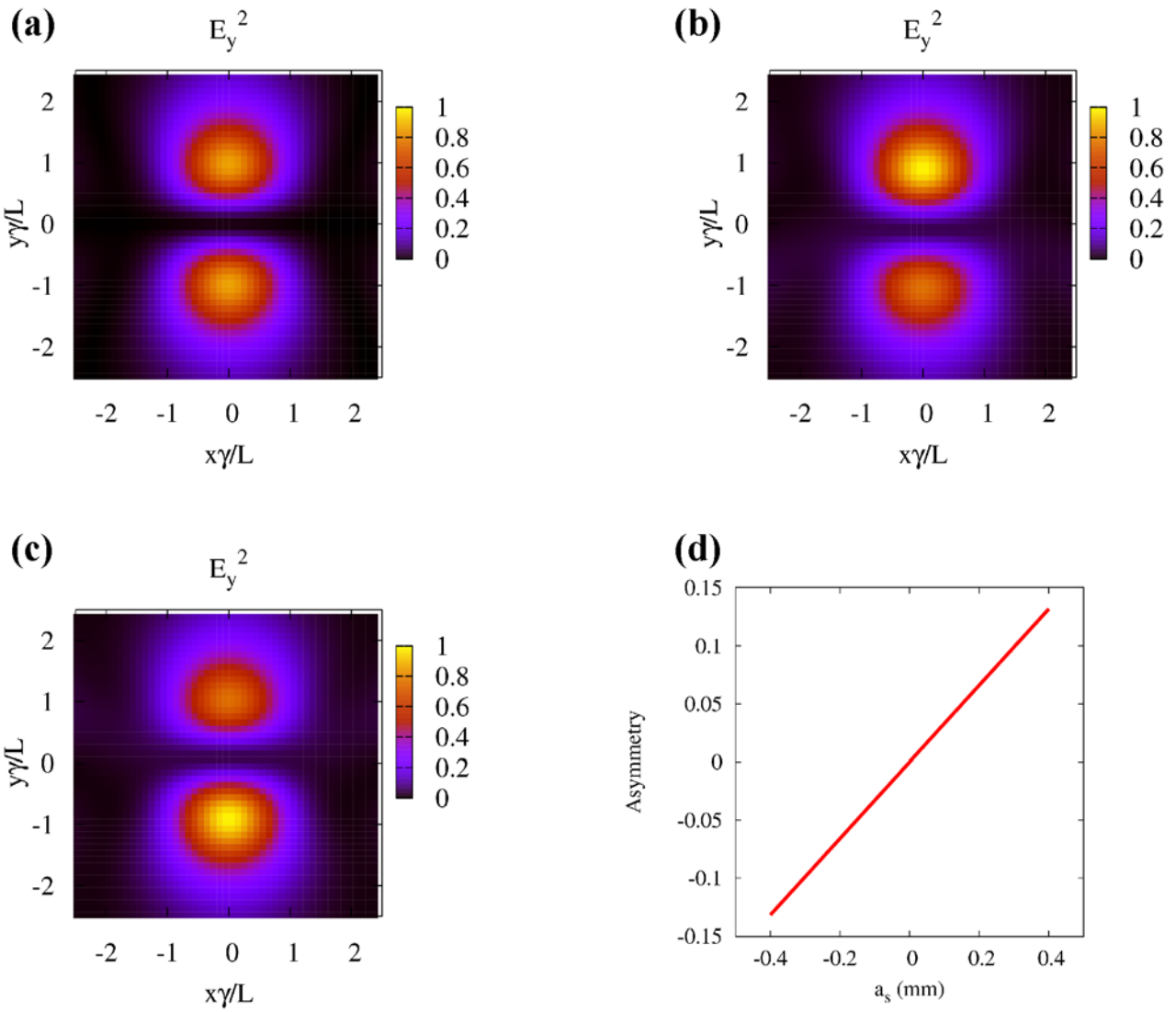


Figure 1: Normalized spatial distribution of vertically polarized DR calculated for different offsets of the electron beam trajectory with respect to the slit center derived from Eqs. (3) – (5). (a) a_s = 0.0 mm, (b) a_s = -0.4 mm, and (c) a_s = 0.4 mm. (d) Asymmetry in the plane x = 0.

and b_{out} are the screen dimensions along the y-axis and x-axis, respectively, a_{in} and b_{in} are the slit dimensions along the y-axis and x-axis, respectively. E^{TR} is the transition radiation (TR) field including pre-wave zone effect generated by a rectangular screen and is described as

$$E_{x,y}^{TR}(a_{out}, b_{out}) = -\frac{R_{x,y}}{4\pi^3}\frac{ek^2}{\gamma L}\int_{-a_{out}/2+a_s}^{a_{out}/2+a_s} dy_s \int_{-b_{out}/2+b_s}^{b_{out}/2+b_s} dx_s \times \frac{x_s, y_s}{\sqrt{x_s^2+y_s^2}} K_1\left(\frac{k}{\gamma}\sqrt{x_s^2+y_s^2}\right) \times \exp\left\{\frac{ik}{2L}(x_s^2+y_s^2) - \frac{ik}{L}(x_s x + y_s y)\right\} \quad (4)$$

Here R_x and R_y are the Fresnel reflection coefficients, e is the elementary charge, k is the wave number, L is the distance from the slit to the detector plane, a_s and b_s are the offsets of the electron trajectory with respect to the slit center along the y-axis and the x-axis, respectively, x_s and y_s are the coordinates of the target surface, and K_1 is the modified Bessel function of the second kind, respectively.

The spectral angular distribution of the DR energy is calculated to be

$$\frac{d^2W^{DR}}{d\omega d\Omega} = 4\pi^2 L^2\left(\left|E_x^{DR}\right|^2 + \left|E_y^{DR}\right|^2\right). \quad (5)$$

Here, $d\Omega = dxdy/L^2$. We can calculate the spatial distribution of DR emitted from the slit by using Eqs. (3) - (5).

Figure 1 show the normalized spatial distribution of vertically polarized DR calculated for different offsets of the electron beam trajectory with respect to the slit center derived from Eqs. (3) - (5) and spatial distribution asymmetry as a function of the offsets. The asymmetry of

Copyright © 2014 CC-BY-3.0 and by the respective authors

ISBN 978-3-95450-141-0

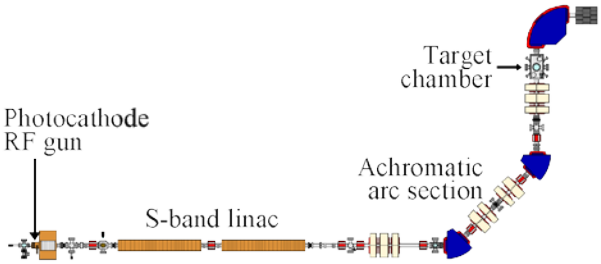


Figure 2: Schematic illustration of the S-band compact electron linac at AIST.

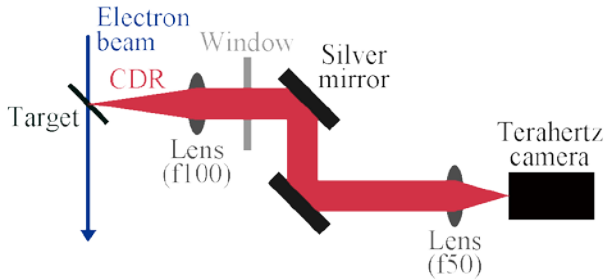


Figure 3: Schematic illustration of the spatial distribution measurement of CDR generated from the rectangular slit using the terahertz camera.

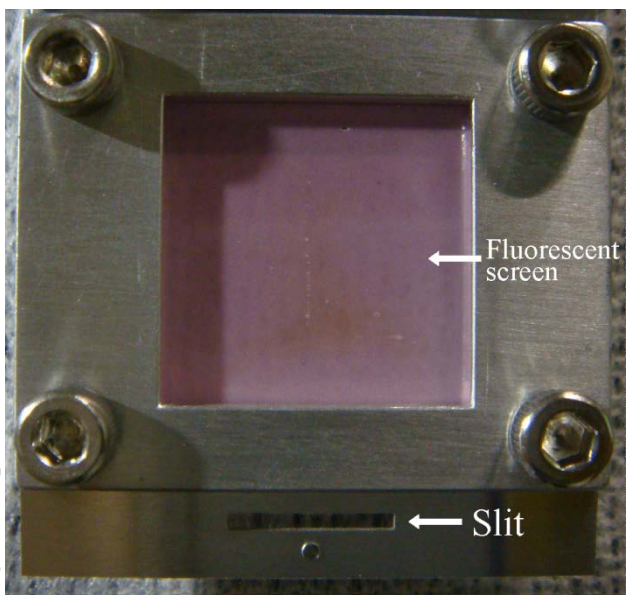


Figure 4: Slit target for CDR.

the spatial distribution was calculated by the following equation:

$$A = \frac{I_{\max}^{y<0} - I_{\max}^{y>0}}{I_{\max}^{y<0} + I_{\max}^{y>0}}. \quad (6)$$

Here $I^{y<0}_{\max}$ and $I^{y>0}_{\max}$ are the maximum intensity in the range of $y < 0$ and $y > 0$ in the plane $x = 0$. The calculation parameters are as follows: $\gamma = 80$; $\lambda = 150$ μm; $L = 790$ mm; $a_{out} = b_{out} = 20$ mm; $a_{in} = 1$ mm; $b_{in} = 10$ mm; $b_s = 0$ mm; and $R_x = R_y = 1.0$. One can see that the asymmetry appears by changing the offsets and reaches 0.13 at the offsets of ± 0.4 mm.

EXPERIMENTAL SETUP

We have developed a non-invasive beam position monitor using a rectangular slit at an S-band compact electron linac (Fig. 2) at AIST. The S-band compact electron linac consists of a Cs_2Te laser photocathode RF gun, a linear accelerator, and an achromatic arc section. Electron beam of 20 micro-bunches separated by 10.5 ns was generated in the RF gun. The bunch charge is 0.6 nC/bunch. Then the electron beam was accelerated up to 40 MeV at two accelerating tubes and passed through the achromatic arc section for bunch compression. The achromatic arc section consists of two 45-degree bending magnets and four quadrupole magnets. The electron beam was compressed to less than 300 fs at the achromatic arc section and then passed through the slit target inside a target chamber shown in Fig. 2.

We measured the spatial distribution of CDR using a terahertz camera (NEC, IRV-T0831) as shown in Fig. 3. The target mounted on a linear manipulator was inclined 45-degree to the electron-beam axis. Backward CDR was emitted perpendicularly to the electron beam axis and extracted into the atmosphere from the vacuum through a z-cut quartz window.

The terahertz camera contains an uncooled micro-bolometer focal plane array (FPA). The structure of focal plane array and the absorption mechanism of the terahertz radiation are explained in detail in Ref. [8]. Specifications of the terahertz camera are as follows [9]: pixel format, 320 x 240; pixel pitch, 23.5 μm; frequency range, 1 - 7 THz; frame rate, 30 Hz; and Noise equivalent power (NEP), <100 pW.

Figure 4 shows a rectangular slit target. A target was made the hole of 10 mm x 1 mm in a 0.5 mm thick aluminium plate. Horizontal size of the hole is much larger than the vertical size. In order to observe the CDR with the terahertz camera, the beam trajectory and the beam size of the electron beam have to be adjusted. First, we checked the spatial distribution of coherent transition radiation (CTR) emitted from the fluorescent screen and metal screen. The beam parameters were adjusted to obtain the ring profile of CTR [10]. Then, we measured the spatial distribution of CDR using the slit. The slit position was moved at 100 μm step in the vertical direction in the range of ± 400 μm from the slit center.

RESULT AND DISSCUSSION

Figure 5 shows the spatial distribution of CDR measured with the terahertz camera for two electron beam trajectory offsets with respect to the slit center and the line intensity distribution. The spatial distribution was clearly changed by changing the electron beam trajectory with respect to the slit center. A total count of a

Copyright © 2014 CC-BY-3.0 and by the respective authors

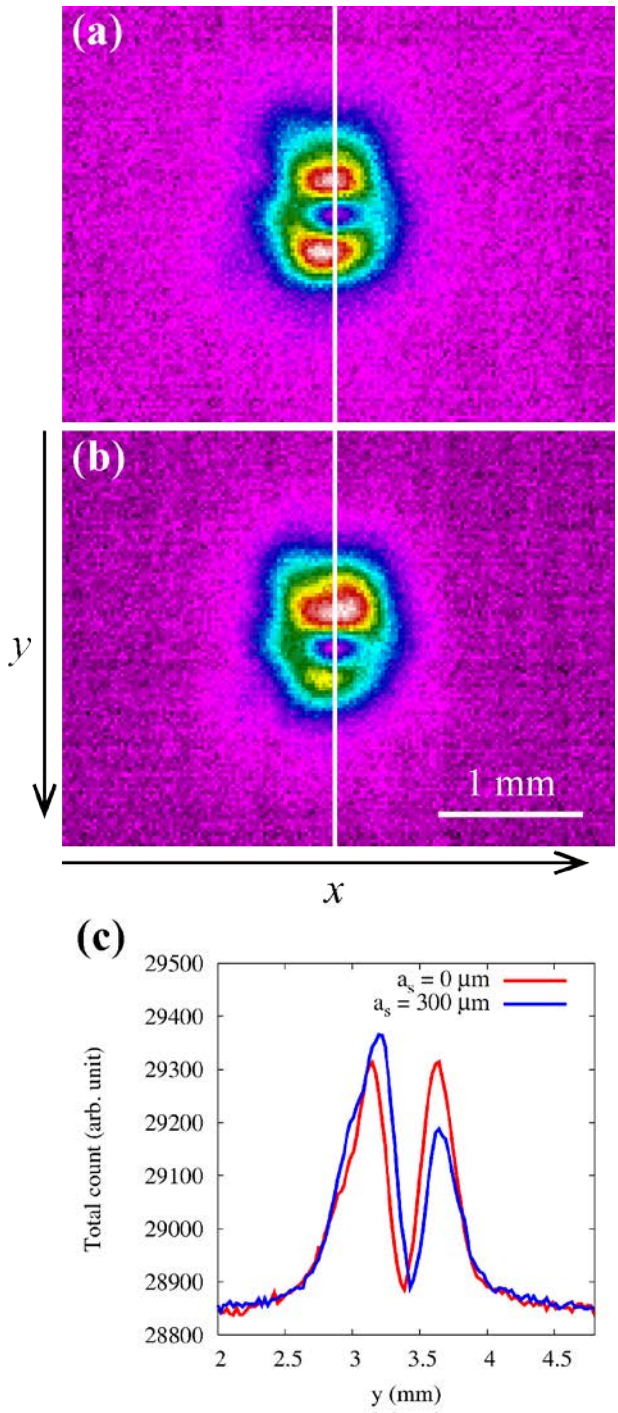


Figure 5: Spatial distribution of CDR measured with the terahertz camera. The electron beam trajectory offsets with respect to the slit center as (a) 0 μm and (b) 300 μm, respectively. (c) The line intensity distribution given in (a) and (b), respectively.

background, where y < 2.5 mm and 4.5 mm < y, is not reduced to zero as shown in Fig. 5 (c). This is due to the NEP of the FPA.

Figure 6 shows the asymmetry of the spatial distribution of CDR in the vertical direction as a function of electron beam offsets with respect to the slit center. It

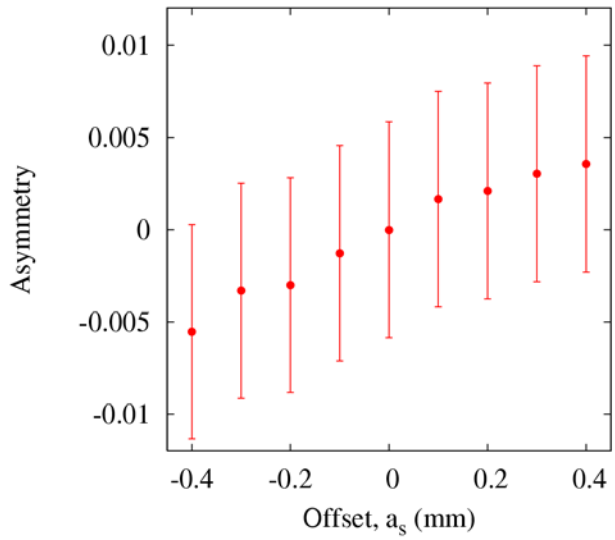


Figure 6: Asymmetry of the spatial distribution of CDR in the vertical direction as a function of electron beam offsets with respect to the slit center.

was clearly observed that the asymmetry depends on the electron beam offsets. Nevertheless, a discrepancy of the asymmetry between the measurement data and the calculated value shown in Fig. 1 (d) was observed. This discrepancy is because of the NEP. If the asymmetry is calculated by considering that the base line of Fig. 5 (c) is zero (the origin), the asymmetry is increased to 0.2 at the offset of 300 μm. This value is twice as much as the calculated value as shown in Fig. 1 (d). However, detailed data analysis has to be performed for a precise comparison.

CONCLUSION

We have developed the non-invasive beam position monitor by observing the asymmetry of the spatial distribution of CDR emitted from the rectangular slit. The spatial distribution was measured with the terahertz camera by changing the slit position with respect to the electron beam trajectory. The asymmetry as a function of electron beam offset with respect to the slit center was clearly observed. This technique can measure the absolute position of an electron beam and can be widely used as a beam position monitor even in high energy electron beam with the energy up to 1 GeV. We will develop the bunch length and beam size measurement technique using the CDR. To improve the contrast of spatial radiation profiles measured with the terahertz camera, we are planning to use a gating THz camera with low NEP for the next step.

REFERENCES

[1] G. L. Carr et al., Nature 420 (2002) 153.
[2] Y. Inubushi et al., Phys. Rev. Lett. 109 (2012) 144801.
[3] R. B. Fiorito et al., Nucl. Instr. Meth. B, 173 (2001) 67.
[4] P. Karataev et al., Phys. Rev. ST- AB, 11 (2008) 032804.
[5] H. Tomizawa et al., Proc. FEL2010 (2010) 445.
[6] H. Tomizawa et al., Proc. IBIC2013 (2013) 1.

Copyright © 2014 CC-BY-3.0 and by the respective authors

ISBN 978-3-95450-141-0

[7] R. Kuroda et al., Nucl. Instr. and Meth. A 637 (2011) S30.
[8] N. Oda, Comp. Rend. Phys. 11 (2010) 496.
[9] N. Oda et al., Proc. of SPIE 8363 (2012) 83630A.
[10] Y. Taira et al., Vib. Spec. in press 2014.

Copyright © 2014 CC-BY-3.0 and by the respective authors

ISBN 978-3-95450-141-0

EXPERIENCE WITH AND STUDIES OF THE SNS* TARGET IMAGING SYSTEM

W. Blokland, ORNL, Oak Ridge, TN 37831, USA

Abstract

The Target Imaging System (TIS) shows the size and position of the proton beam by using a luminescent Cr:Al2O3 coating on the SNS target. The proton beam hitting the coating creates light, which is transferred through mirrors and optical fibers to a digital camera outside the high radiation area. The TIS is used during operations to verify that the beam is in the right location and does not exceed the maximum proton beam peak density. This paper describes our operational experience with the TIS and the results of studies on the linearity, uniformity, and luminescence decay of the coating. In the future, tubes with material samples might be placed in front of the target for irradiation studies. The simulations of placing tubes in the front of target coating and the effect on the beam width and position measurements are also discussed.

INTRODUCTION

Spallation Neutron Source

The Spallation Neutron Source (SNS) uses short and intense pulses of neutrons for materials research. These neutron pulses are created through a spallation process by hitting the mercury filled target with 1 GeV protons pulses. The SNS accelerator creates these proton pulses and must steer them to the target within ±4 mm vertically and ±6 mm horizontally of the target center and with a maximum size and peak density to prevent a premature end of life of the target.

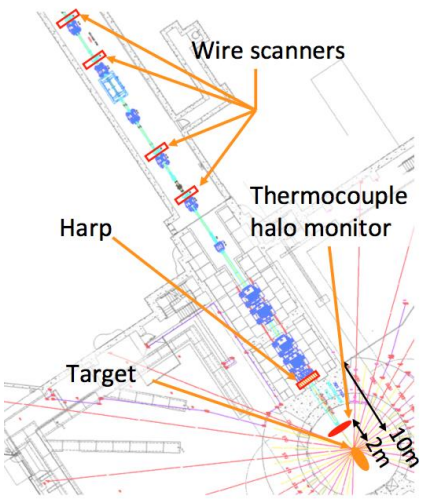


Figure 1: The locations of RTBT instrumentation.

*ORNL/SNS is managed by UT-Battelle, LLC, for the U.S. Department of Energy under contract DE-AC05-00OR22725

The Ring to Target Beam Transfer line (RTBT) Wizard program uses wire scanners and harp profiles to calculate the beam size and steering for the initial setup using low power beam. During neutron production with full beam power, the harp still provides profile data to verify the beam profiles but it is approximately 10 meters away and cannot, on its own, fully determine the location of the beam on the target. Thermocouples located at the Proton Beam Window (PBW), are only two meters away from the target, indicate only the halo of the beam. The beam halo is not necessarily symmetric and thus not a good measurement of the profile size or center position of the beam. Figure 1 shows the locations of the instrumentation. The Target Imaging System has been created to deal with these limitations.

Target Imaging System

The TIS measures the position and profile of the beam right on the target nose cone using a luminescent coating. The light produced by the protons hitting the coating is guided using mirrors, lenses, and a rad-hard fiber bundle to a camera outside of the high radiation area [1-5]. Figure 2 shows an example of the acquired image. The coating has fiducial markers that are measured before installation of the target and then used to calibrate the image obtained by the camera. Once calibrated, the TIS can determine the widths, peak density, and center of the beam on the target.

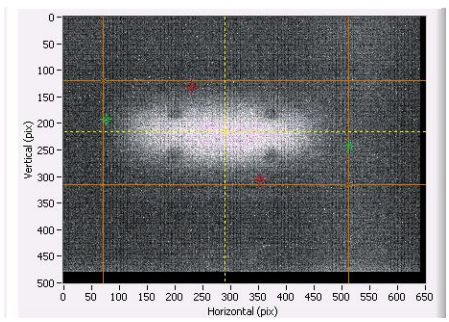


Figure 2: Image of beam on target.

OPERATION

Operators track the results of the TIS during the neutron production runs and adjust the beam trajectory if needed. Figure 3 shows the Target Errant Beam Control screen tracking the center of the beam on the target. The red circles are the individual measurements while the blue circles are the average positions. This shows a peak-to-peak noise of about 1 mm. The bottom part of the figure shows the magnets that can be adjusted to steer the beam if needed. This screen, created by the operators, is always visible in the control room and, in addition to being watched by the operators, also monitored by errant beam

Copyright © 2014 CC-BY-3.0 and by the respective authors

ISBN 978-3-95450-141-0

alarm software. While the TIS is not required for beam operations, it is still treated as a critical system that can only be tolerated to be offline for short time periods of time. During such time the Harp and thermocouple measurements are used to confirm that the beam has not undergone major changes. No beam downtime has been assigned to the TIS, but it has required a restart of the analysis or a reboot of the camera, a few times a year. The system runs mostly without interaction, however the camera's exposure and gain, as well as the analysis fit parameters have to be adjusted during the luminescence decay. The camera has to be replaced about once a year, as it does suffer minor radiation damage since it is located in a (low) radiation area.

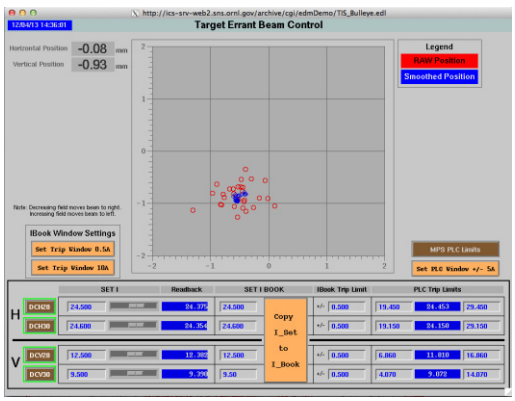


Figure 3: Errant Beam Control Screen.

STUDIES

Position Dependency on Power

Operators noted that during beam power ramping, the TIS reported positions consistently changed by about 1-2 mm in both planes but that the harp reported positions did not change. This points to a problem with the TIS, specifically to a movement of the first mirror pointing at the target. This first mirror is attached to the PBW and the PBW varies in temperature with the beam power. Different calibrations were done at low and high power, confirming that the image alignment does change. This calibration requires human interaction and takes at least 10 minutes each or even days, if we want to analyze thousands of pictures to study trends. New code was written to automatically find the fiducial markers in the images.

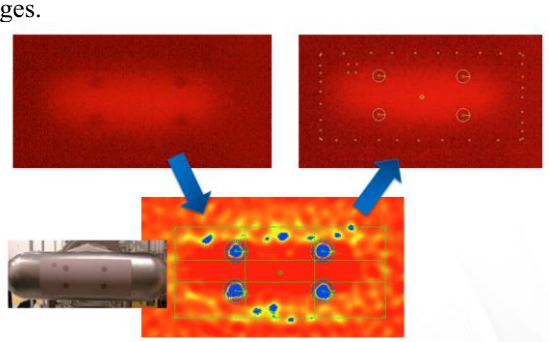


Figure 4: Automatic finding of fiducials.

This process is shown in Figure 4. Algorithms from the LabVIEW Vision toolkit first smooth and enhance the contrast of the original image (top left image) to show the markers more clearly (bottom image) followed by a circular edge finder to determine the center of each fiducial (bottom image). The locations of the fiducials and outlines are then drawn onto the origin image (right top image) and saved to a file. The software can analyze a thousand images within minutes.

To study the dependency of the TIS beam position on beam power, the TIS was set to save an image every second right after a beam outage while the beam power value, the harp and TIS reported positions, and the PBW cooling water temperatures were logged by the SNS Archiver. The data is plotted in Figure 5.

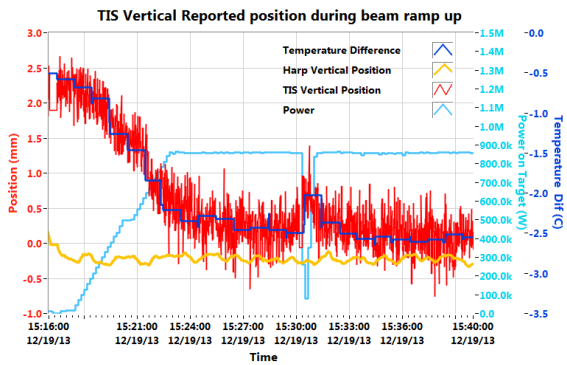


Figure 5: TIS vertical beam position (red).

The TIS reported vertical position trace (red) shows the change in reported position as the beam is turned on and ramped up in power. The beam power trace (light blue) shows the ramping up of the beam power. Initially, even though the beam pulse has the full charge, the power is very low as there is only one beam pulse per second. The harp reported vertical position (yellow) does not change while the beam is ramping up in power. The difference in temperature of the PBW cooling (dark blue) correlates well with the TIS reported position and shows that the increasing beam power heats the PBW.

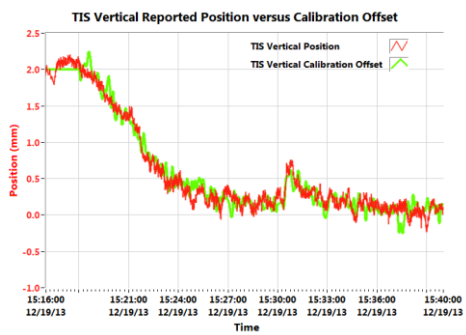


Figure 6: TIS vertical beam position (red) versus the calibration offset (green).

About 1800 images were analyzed to determine the calibration during the beam ramp up. Figure 6 shows the results for the vertical calibration offset. Both the reported

Copyright © 2014 CC-BY-3.0 and by the respective authors

vertical beam position and vertical calibration offset are low-pass filtered to show the trends. The curves closely follow each other, including the peak at 15:31, at which time the beam was temporarily interrupted.

These results lead us to conclude that the TIS position variation is due to the mirror moving and given the correlation with the temperature difference curve, that this is most likely due to heat stress.

Luminescence Decay

The selection of the luminescent coating material was based on early studies [2,4] and the brightest material was picked. However, the brightness was found to decay rapidly at production intensities. An initial study in [2,4] roughly shows the decay in luminescence. To further study the decay, and also while preparing to study new coatings, software was created to automatically correct the measured intensity based on camera exposure time, beam intensity, and image background level. The results are plotted in Figure 7 with data from 15 to 27, October 2013. This shows that the luminescence decays very quickly. The decay of the coating is mostly likely due to F-center formation, which saturates within 100-200 MWhrs. Because most of the damage (displacements per atom: dpa) is due to the more uniform backscattered neutrons, up to 85%, the coating decay is also more uniform and within a factor of two edge to center [4].

We plan to use this software tool to determine the different decay behaviors once we have different coating materials on the same target. The coating will be evaluated not only for its luminescence and decay rate, but also for how equally it decays, edge to middle, and when the decay curve flattens in order to end up with a uniform luminescence.

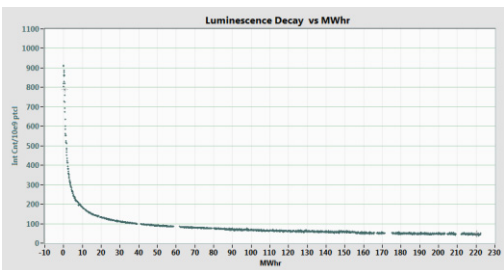


Figure 7: Luminescence decay.

Uniformity Scanning

The accuracy of the TIS estimates of beam position and size also depends on the uniformity of the luminescence across the coating. To study the uniformity, we scan a small pencil beam across the coating and measure the light response. This study has been done before but it has now been automated to speed up the process. A script steers the beam, using up to 10 magnets, while the TIS acquires and saves the images. Because the pencil beam is mostly off-center, it can only be up to approximately 1/300 of the full production beam. This gives very low intensity light that is barely visible by the camera and is affected by noise and light leakage and can only be done with a fresh coating early in the decay curve. The new analysis program first finds the approximate center location of the pencil beam and then positions the projections area around the center. The profiles are calculated by summing the image pixels both vertically and horizontally within the projection areas, as shown in Figure 8, indicated by the light blue boxes. The resulting profiles are shown on the right of the figure. The red traces represent the fits to the large area while the blue traces represent the fits to the narrow boxes and result in a more accurate location and peak intensity estimate.

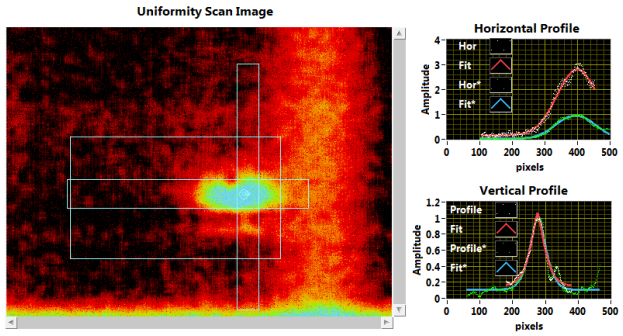


Figure 8: Estimating the pencil beam intensity and position.

The result, intensity versus position (pixel), is shown in the top of Figure 9. There are about 1.8 pixels per mm. The red curve shows that the vertical position is only changing by a few pixels as intended for the horizontal scan. The total variation in intensity is about ±12.5%. However, the noise in the measurement is significant, and, given the low intensities of the light emitted, estimated to contribute about half of that variation. We hope to perform more accurate studies in the future. The bottom half of the figure shows a 3D plot of the scans with the axes representing pixels. The fiducial markers are visible in the plot.

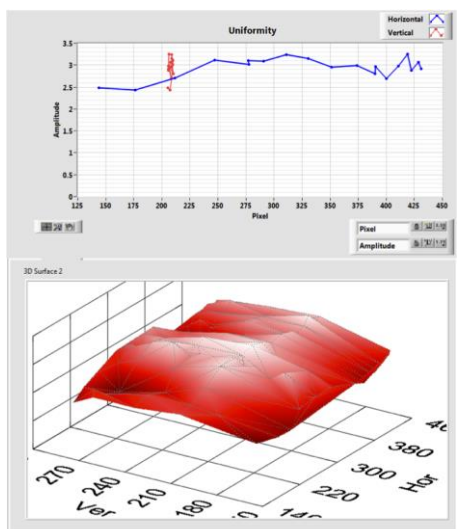


Figure 9: Results of a horizontal scan on top and the overall results on the bottom.

Copyright © 2014 CC-BY-3.0 and by the respective authors

ISBN 978-3-95450-141-0

FMITS Effect on TIS Estimates

A feasibility study is ongoing to build an irradiation facility for fusion materials called the Fusion Material Irradiation Test Facility (FMITS) at SNS [6]. The goal is to study material damage from neutrons such as the impact of He and H transmutation products. The materials to study would be placed inside tubes in front of the target partially blocking the view of the target Imaging System, shown in Figure 10.

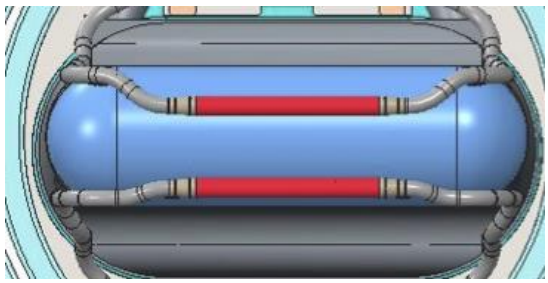


Figure 10: Drawing of the FMITS tubes (red) in front of the target nose cone.

As part of this feasibility study, the effect of the tubes on the TIS is being studied using simulations. To simulate the tubes blocking the light from the coating, the normal TIS program was modified to insert horizontal blackout regions across the image. The tubes can be simulated to be completely black or have partial light to simulate that the tubes have a luminescent coating.

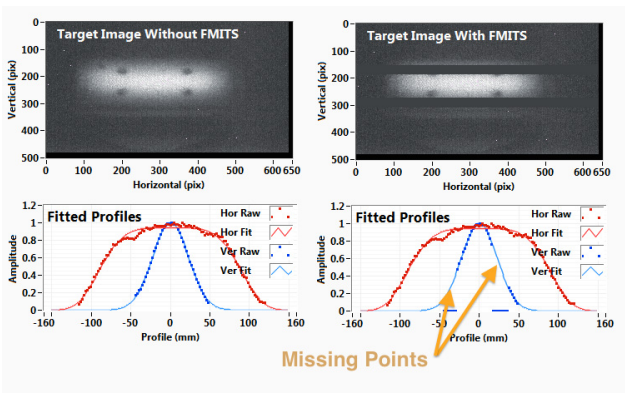


Figure 11: On the left top the typical TIS image and on the right the simulated image with FMITS tubes in front, the bottom shows the resulting profiles.

Figure 11 shows, on the right, such a simulation with the tubes completely black. The tubes are horizontal and don't affect the horizontal profile because that profile is calculated from an area in between the tubes. The vertical profile is affected as the tubes cross through its profile area. A good estimate can still be made of the profile by excluding the points affected and this is shown in the figure's profile plots. The location of the tubes can change depending on the requested exposure ratios to protons and neutrons. The most likely positions have the tubes asymmetrically positioned, as shown in the figure. Because of the asymmetry, the vertical profile still has points on one of the tails, which helps with the accuracy of the estimates.

The results of analyzing many images are shown in Figure 12. Two simulations are done. The first simulation, shown in the top half of the figure, has the tubes in their standard asymmetric locations, where one tube blocks the tail and one tube blocks part of the right side, but not the tail, of the profile. In the second simulation, shown in the bottom half of the figure, the tubes block both tails. The results show that if only one tail is blocked, the estimates in the vertical profile widths differ by about 2-3%, while the noise in the jitter remains about the same. When both tails are blocked, the estimates in the width are still off by about 2-3%, but now the variation in the estimates has doubled. Position variations were found to be less than 0.5 mm, slightly less than the TIS reported position noise. In either case, it shows that the FMITS won't incapacitate the TIS but does degrade the performance by a few percent, though the accuracy remains acceptable.

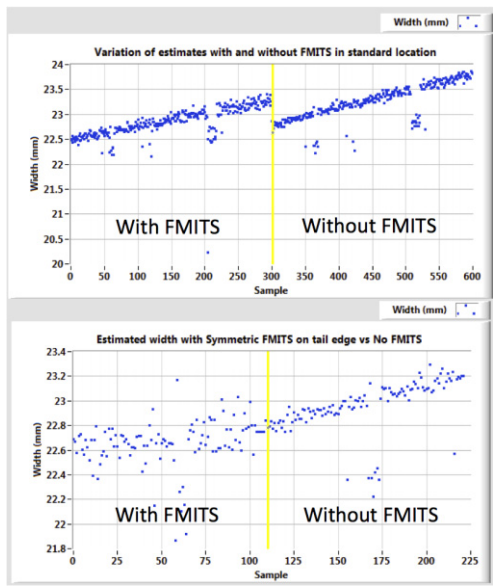


Figure 12: The results of analyzing images with or without the FMITS in different locations.

Simulations in which the FMITS tubes have some coating on the tubes were performed but none of the results of incorporating this light led to acceptable results at this point. Further simulations are planned. An additional problem with using light from the FMITS tubes is that the replacement of the FMITS tubes and target will be done at different times, thus getting coatings at different parts of their luminescence decay curves. We still are considering putting a coating on the FMITS tubes, as a sudden decrease in light can indicate overheating of the tubes. Another issue to resolve is that the tubes can block the fiducial markers. The target coating might have to be designed with additional markers so that a calibration can always be performed.

Copyright © 2014 CC-BY-3.0 and by the respective authors

ISBN 978-3-95450-141-0

CONCLUSION

The TIS is an essential tool for day-to-day operations and initial setup of the accelerator. A newly created analysis tool automatically determines the calibration and can potentially be used to automatically correct the mirror movement. The uniformity scan has been automated and sped up by using a script to steer the beam and an analysis program to study the uniformity of the coating. A request for higher power off-centered beam pulses has been approved and we hope to do better scans in the future, although these scans can still only be done early in the decay curve.

The tool to plot the decay curve versus MWhrs on target will help to study future coating materials. The goal is to find a material that has high luminescence throughout its exposure but also changes equally edge to center. Thus an quick saturation in the decay curve could be better than a slow one if that means that the whole of the coating reaches a decayed but uniform response quickly.

Initial studies with the FMITS tubes in front the target nose cone show that the TIS can still function despite the blocked light. Future simulation studies and a mockup of a target nose cone with tubes in front of it with a complete optical path are planned.

ACKNOWLEDGMENT

The author likes to acknowledge the work by Andrei Shishlo for creating the script, Charles Peters for assisting with the uniformity scans, and V. Graves for the FMITS drawing. Many other people have been involved with designing and building the Target Imaging System.

REFERENCES

[1] T. Shea, *et al.*, "Status of Beam Imaging Developments for the SNS Target", DIPAC 2009. Basel, Switzerland, May 25-27, (2009).

[2] T. Shea, *et al.*, "Installation and Initial Operation of an On-Line Target Imaging System for SNS", ICANS 2010.

[3] W. Blokland, *et al.*, "SNS Target Imaging System Software and Analysis", Proceedings of BIW10, Santa Fe, New Mexico, US, May 2-6, (2010).

[4] T.J. McManamy, *et al.*, "Spallation Neutron Source Target Imaging System Operation", Proc. AccApp '11, Knoxville, April 3-7, (2011).

[5] L. C. Maxey, *et al.*, "A hybrid reflective/refractive/ diffractive achromatic fiber-coupled radiation resistant imaging system for use in the Spallation Neutron Source (SNS)", Proc. SPIE 8142, Hard X-Ray, Gamma-Ray, and Neutron Detector Physics XIII, September 27, 2011, doi: 10.1117/ 12.894125.

[6] R. Battle, *et al.*, SNS Fusion Materials Irradiation Test Station (FMITS) Feasibility study, SNS-ISDD-NSD-TD-0001/R00, July 1, (2014).

Copyright © 2014 CC-BY-3.0 and by the respective authors

ISBN 978-3-95450-141-0

DEVELOPMENT OF THE TRANSVERSE BEAM PROFILE MONITORS FOR THE PAL-XFEL*

I. Y. Kim†, J. Choi, H. Heo, C. Kim, G. Mun, B. Oh, S. Park, H. S. Kang,
Pohang Accelerator Laboratory (PAL), Pohang, 790-834, Republic of Korea

Abstract

The PAL-XFEL is an X-ray free electron laser under construction at the Pohang Accelerator Laboratory (PAL), Korea. In the PAL-XFEL, the electron beam can make coherent optical transition radiation (COTR) due to the microbunching instability in the compressed electron beam. In order to obtain transverse beam profiles without the COTR problem, we are developing scintillating screen monitors (with the geometric suppress method) and wire scanners. In this paper, we report test results at the test facility and progress in the development of the screen monitor and the wire scanner for the PAL-XFEL.

INTRODUCTION

Transverse beam profile diagnostics in electron linacs is widely based on optical transition radiation (OTR) as standard technique which is observed in backward direction when a charged particle cross the boundary between two media with different electrical properties. Unfortunately, microbunching instablities in high-brightness electron beam of modern linac-driven free-electron lasers (FELs) can lead to coherent effects in the emission of OTR. Because of this reason it is not possible to obtain a direct image of the particle beam. In order to allow the beam profile measurements in the presence of microbunching instabilites, there are solutions has been studied. First is to use scintillation screens instead of transition radiation and another is wire scanner [1, 2].

To successful commissioning, the transverse beam profile monitors which is not affected by COTR effect are necessary. In this reason we are studying scintillating beam profile monitors and wire scanners.

In this article, we report test results with transverse profile monitor installed at the injection test facility (ITF) and the new profile monitors design for PAL-XFEL.

MEASUREMENTS

The screen monitors and wire scanner which is used to acquire beam profie installed at the ITF. The screen monitor is operating for beam diagnostics. The Fig. 1 shows screen montor and wire scanner installed at the end of beamline.

ITF Screen Monitor

The RadiaBeam Technologies's Integrated Beam Imaging System II (IBIS-II) was installed at the ITF. This screen target is 100 μm thick YAG:Ce scintillator which is installed normal to the beam direction and 200 nm aluminized silicon wafer for mirror was installed 45 deg with respect to the beam axis. The BAUMER GigE cameras with 5M pixels and a 2/3 inch CCD sensor are used to obtain electron beam image. The electron beam image with this screen is shown in Fig. 2. The beam size was obtained with σ_x = 0.57 ± 0.03 mm and σ_y = 1.00 ± 0.05 mm.

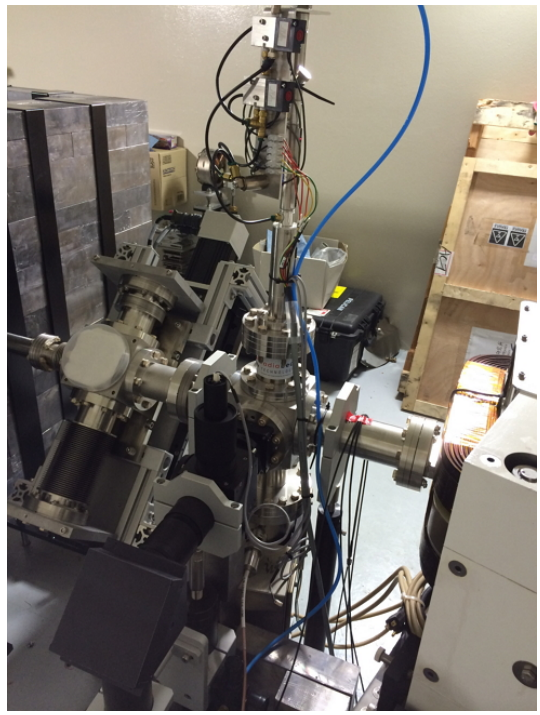


Figure 1: The wire scanner (Left) and screen monitor (Right) station.

ITF Wire Scanner

A wire scanner measures the average, projected beam profile in one plane over several successive beam pulses. The wire scanner was installed at the diagnostic section which was manufactured by RadiaBeam Technologies. This is consist of a wire card with three 25 μm thick tungsten wires and a ball-screw linear stage [3]. And the radiation intensity of the beam at a wire position determined by silica optical fiber with Photomultiplier (PMT). The schematic layout of measurement system are shown in Fig 3. The electron beam loss signal (shown Fig. 4) is pulse width is about 5 μsec.

Beam profile measurement and analysis were performed. Because of the motor controller is not yet integrated with timing system, it takes a few minutes to get a set of beam profile. The electron beam operation condition which is

* Work supported by MSIP, Korea
† ilyoukim@postech.ac.kr

Copyright © 2014 CC-BY-3.0 and by the respective authors

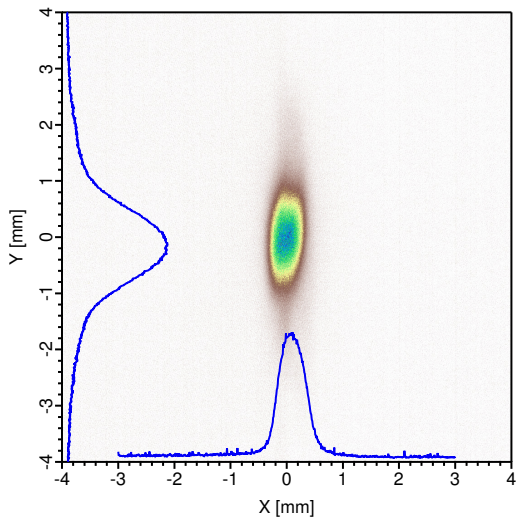


Figure 2: The Beam image with YAG:Ce scintillator and projected profile.

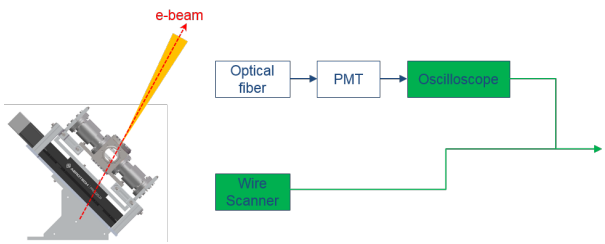


Figure 3: The wire scanner measurements diagram.

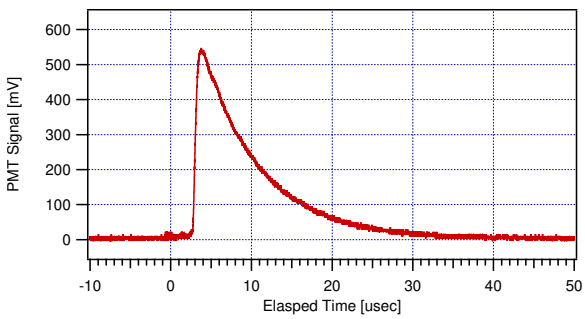


Figure 4: The beam loss signal.

obtained beam profile with wire scanner (shows in Fig. 5) is the same with beam image of Fig. 2. The beam size was obtained with σ_x = 0.63 ± 0.09 mm and σ_y = 0.92 ± 0.02 mm with wire scanner. The measurement value with wire scanner was good agreemen with the value of beam image.

XFEL SCREEN MONITOR

The Screen monitor for PAL-XFEL will be consisted of scintillator target and vacuum mirror for imaging without COTR effect. The YAG:Ce scintillator has been used to electron beam imaging which is will be saturated for high energy and high flux beam current [4]. And the LYSO:Ce was not saturated and very good linearity depend on beam

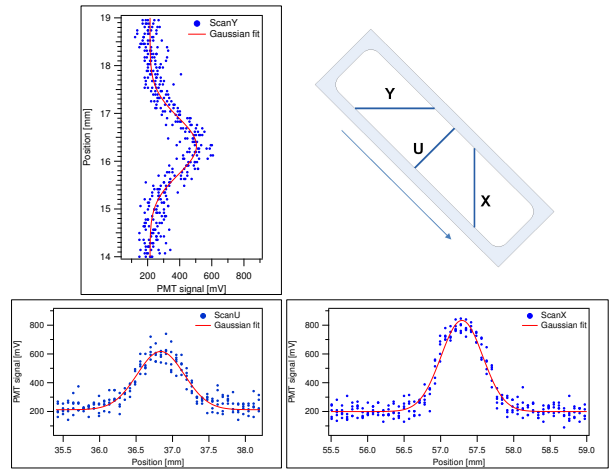


Figure 5: The wire scanner measurements.

charge [5]. Because of this reason we choose LYSO:Ce for scintillator and also will be adapted the RF shield to minimize the wake field due to the structure of chamber. And we have limited space for installation because of this reason we apply mirror in vacuum for guide the scintillation light to CCD camera. In order to minimize depth-of-focus effects, we will apply the Scheimpflug principle. Fig. 6 shows the geometric scheme for screen monitor between ITF screen and XFEL screen.

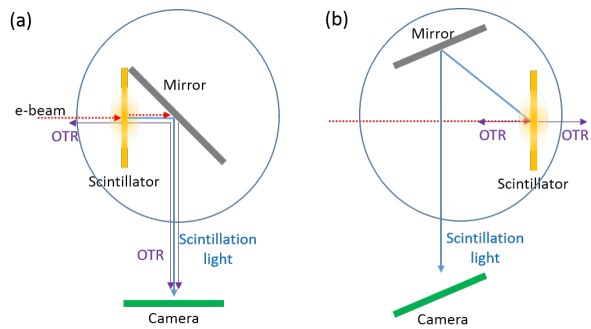


Figure 6: The geometric scheme for screen monitor. (a) ITF Screen Monitor and (b) XFEL Screen Monitor.

XFEL WIRE SCANNER

The wire scanner for XFEL is on going design with Linear servo motor to minimize the vibration from the step motor stage [2].

SUMMARY

The screen monitor and wire scanner will be updated for PAL-XFEL facility.

REFERENCES

[1] G. Kube et al., "Inorganic Scintillators for Particle Beam Profile Diagnostics of Highly Brilliant and Highly Energetic Electron Beams", WEOAA02, IPAC'12, New Orleans, USA (2012).

Copyright © 2014 CC-BY-3.0 and by the respective authors

ISBN 978-3-95450-141-0

[2] P. Krejcik et al., "Evaluation of New, Fast Wire Scanner Designs for the LCLS", TUPG035, BIW'12, Virginia, USA (2012).

[3] M. Harrison et al., "Design of a Fast, XFEL-quality Wire Scanner", MOPWA080, IPAC'13, Shanghai, China (2013).

[4] A. Murokh et al., "Limitations on Measuring a Transverse Profile of Ultradense Electron Beams with Scintillators", p1333, PAC'01, Chicago, USA (2001).

[5] C. Wiebers et al., "Scintillating Screen Monitors for Transverse Electron Beam Profile Diagnostics at the European XFEL", WEPF03, IBIC'13, Oxford, UK (2013).

Copyright © 2014 CC-BY-3.0 and by the respective authors

ISBN 978-3-95450-141-0

AC COUPLING STUDIES AND CIRCUIT MODEL FOR LOSS MONITOR RING*

Zhengzheng Liu#, Jenna Crisp, Steven Lidia, Facility for Rare Isotope Beams (FRIB),
Michigan State University, East Lansing, MI 48824, USA

Abstract

As a follow-up study to the initial design of FRIB Loss Monitor Ring (previously named Halo Monitor Ring [1]), we present recent results of coupling studies between the FRIB CW beam and the Loss Monitor Ring (LMR). While a ~33 kHz low-pass filter was proposed to attenuate high-frequency AC-coupled signals [1,2], the LMR current signal may still contain low frequency signals induced by the un-intercepted beam, for example, by the 50μs beam notch that repeats every 10ms. We use CST Microwave Studio to simulate the AC response of a Gaussian source signal and benchmarked it to analytical model. A circuit model for beam-notch-induced AC signal is deduced and should put a ~33pA (peak) bipolar pulse on the LMR at 100Hz repetition rate. Although its amplitude falls into our tolerable region, we could consider an extended background integration to eliminate this effect.

INTRODUCTION

Loss Monitor Ring (LMR), or previously called Halo Monitor Ring, is described in Ref [1, 2] as a metal ring with carefully specified aperture designed to intercept ions that are likely to be lost further downstream. While the to-be-lost particles hit and stop in the ring, most of the beam passes through it. Therefore three dominating signals are generated: primary current by the impacting ions, secondary emission current by the escaped electrons, and AC-coupled current induced by the beam. The former two signals are low frequency signals, which we want to measure as beam losses [2]. Therefore we need to eliminate the AC-coupled signal and ensure it is insignificant in our data acquision.

Considering FRIB CW beam structure, it can be generally layered as mini pulses and macro bunches: The mini pulses have a 100 Hz repetition rate and 50μs pulse spacing, which is required by the AC beam current monitor; the macro bunches, inside the mini pulse, have a repetition rate of 80.5 MHz with variable pulse spacing. To attenuate the macro-bunch induced signal that is in MHz range, we can use a ~33 kHz low pass filter to attenuate it [2]. However, the 50μs notch of mini pulse could induce some fake data in low frequency range that we want to estimate and find solutions.

Since the CST computation of μsec excitation is extreme long, we first simulated a nano-seconds Gaussian pulse in CST Microwave Studio and benchmarked the result with our analytical models. The validated model will then be applied to calculate the 50μs notch induced signal. According to the estimation, the induced signal is not critical but could put some fake background samples. Integration for an extended time period might help and we are investigating other schemes to release the concern.

* This material is based upon work supported by the U.S. Department of Energy, Office of Science, Facility for Rare Isotope Beams under Cooperative Agreement No. DE-SC0000661

liuz@frib.msu.edu

EM SIMULATION FOR AC-COUPLING

There are generally two ways to simulate the AC-coupled signal: CST Microwave analysis that simulates an excitation signal through the capacitive pick-up; or Particle Studio that simulates a Gaussian bunch through the ring. Since we are interested in low frequency response rather than MHz range, nonrelativistic bunch is not our concern. Therefore we use CST Microwave Studio to help build the circuit model for LMR.

Geometry Modelling of LMR

Figure 1 shows an example of the basic LMR design [2]. The niobium ring, which intercepts lost particles, is sandwiched by two copper plates, one for electric field shielding and the other one attached on the wall to remove heat. The mounting and shielding rings are electrically connected to the chamber. Ceramic or sapphire washes are used to electrically isolate the Niobium ring while thermally connecting it to the chamber through the mounting ring.

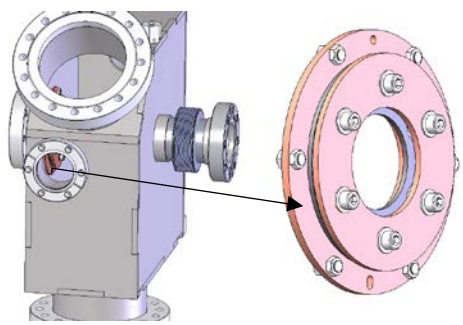


Figure 1: Basic mechanical design of LMR.

We modeled the basic LMR geometry in CST, as shown in Figure 2. The diagnostics box was simplified to a rectangular box and the bolts were smaller than the holes on niobium ring for electric isolation. Ceramic washers were attached on both sides of the niobium ring, as good dielectric material with reasonable thermal conductivity. A wire was set across the box with 220Ω approximate characteristic impedances at both ends.

EM Simulation

To measure the induced AC signal, we located a discrete ports (50Ω) from niobium intercept to grounded

ISBN 978-3-95450-141-0

Copyright © 2014 CC-BY-3.0 and by the respective authors

plate, as shown in Figure 2. The source signal is the default Gaussian excitation in Microwave Studio, specified for frequency range 1.5 GHz. And we assume all the washers to be 96% Alumina (ceramic) with ε_r=9.4.

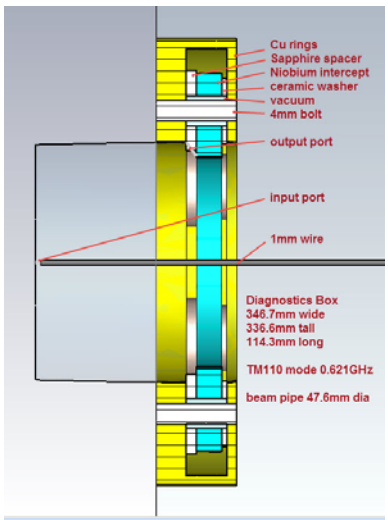


Figure 2: Cross-section view of LMR model in CST.

For convenience in labelling, we named the source port that drives source signal to be port 1, and the output port that connects Niobium ring to ground to be port 2. Figure 3 shows the voltage simulated at port 2, in logarithmic unit.

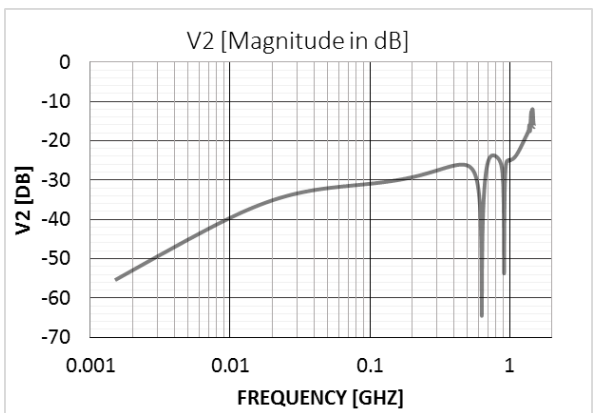


Figure 3: Simulated output voltage V_2 in the frequency domain, full bandwidth. The result is normalized to the source signal.

According to the diagnostics box dimension in Figure 2, the first fundamental mode of the box is TM110 with cut-off frequency 0.621 GHz, while the corner frequency for 50Ω 150pf RC circuit is only 0.021 GHz. Therefore the oscillations close to 1GHz should be caused by the box. At the same time, attachment of LMR perturbs the fundamental mode and brings in a little frequency shift, as shown in Figure 4.

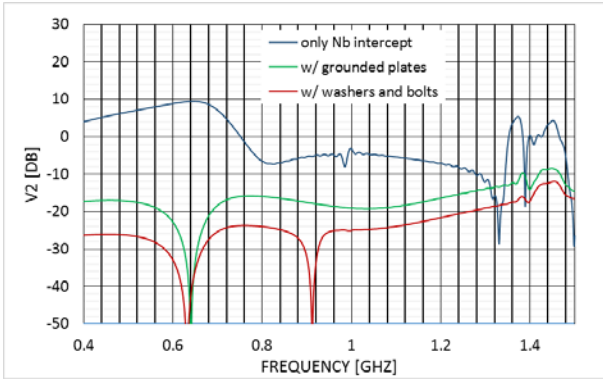


Figure 4: Comparison of output voltages with different structures of LMR. Different colours correspond to a) only niobium intercept, b) adding grounded copper plates, c) adding washers and bolts.

Analytical Model Benchmarking

As implied in Figure 3, in lower frequencies, the LMR could be taken as linear electrical network system, or simply a capacitive pick up ring, which could be described as Figure 5.

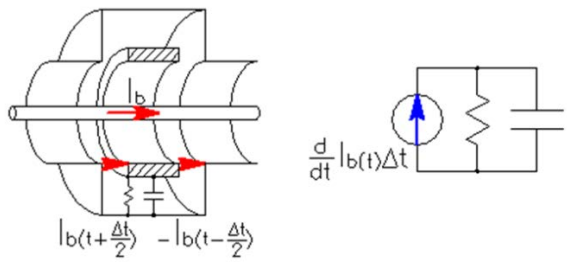


Figure 5: Model for capacitive pick-up.

Therefore the calculation of output voltage V_{ring} in the model becomes straight-forward:

$$V_{ring} = 2R_{ring} I_{wire} \sin\frac{\omega l_{eff}}{2c}\left(1+\frac{1}{\beta}\right) \quad (1)$$

where

$$R_{ring} = \frac{R}{1+j\omega RC}. \quad (2)$$

For the simulated LMR structure, R is set to be 50Ω, C is estimated to be ~150 pf and β=1. The actual length of the niobium ring is 5mm, but the effective length is longer. We adjust the effective length l_{eff} in the expression of V_{ring} to match the simulation in low frequencies. Figure 6 shows a perfect match between the calculated V_{ring} (dash line) and simulated V_2 (solid trace), where we assumed the effective ring length is 8.5mm.

Copyright © 2014 CC-BY-3.0 and by the respective authors

ISBN 978-3-95450-141-0

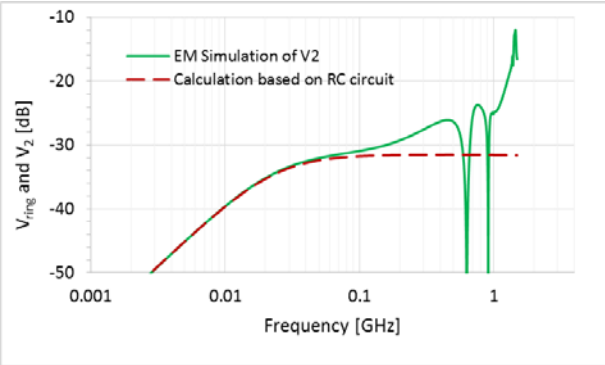


Figure 6: Calculated V_{ring} (dash line) matches simulated V_2 (solid line), by assuming the effective length l=8.5mm in the analytical model. Complete LMR structure is presented.

We did the same calculation & matching for the cases in Figure 4: niobium ring only and with copper plates. The estimated capacitances are 3 pf and 40 pf respectively. Figure 7 and 8 shows the matching result with effective length l=21mm and 8.5mm respectively. Also implied from Figure 6 to Figure 8, we could observe the necessity of a good shielding for LMR, which greatly reduces the effective LMR length by confining the field locally.

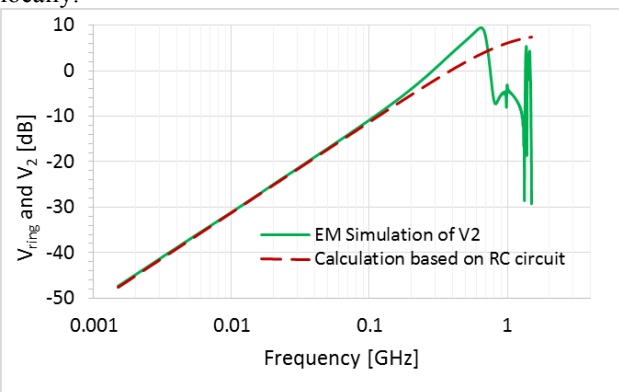


Figure 7: Calculated V_{ring} (dash line) matches simulated V_2 (solid line), by assuming the effective length l=21mm in the analytical model. Only Niobium ring is presented.

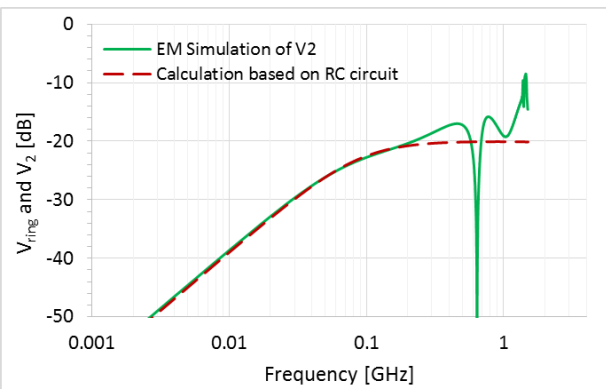


Figure 8: Calculated V_{ring} (dash line) matches simulated V_2 (solid line), by assuming the effective length l=8.5mm in the analytical model. Partial LMR structure (without washers and bolts) is presented.

LMR AC Signal Estimation

As we benchmarked the analytical model, we can use Equation 3 to estimate the induced current for the 50μs notch.

$$I_{notch}(\omega) = 2I_{avg}\frac{\Delta t_{Notch}}{T}\frac{\sin\left(\frac{\omega\Delta t_{Notch}}{2}\right)}{\frac{\omega\Delta t_{Notch}}{2}}$$

$$\frac{I_{ring}}{I_{beam}} = 2\sin\frac{\omega l}{2c}\left(1+\frac{1}{\beta}\right) \approx \frac{\omega l}{c}\left(1+\frac{1}{\beta}\right) \qquad (3)$$

$$I_{ring} = \frac{1}{2}\frac{I_{ring}}{I_{beam}}I_{notch}$$

We plug in parameters β=0.033 and l=8.5mm into Equations (3). The average current at LS1 is 0.35mA. The Iring/Inotch could be think as a high pass filter, which has a bandwidth of 6.4 kHz. Combined with the 33 kHz loss pass filter that we plan to use, the final induced current will be ~33pA, as shown in Figure 9.

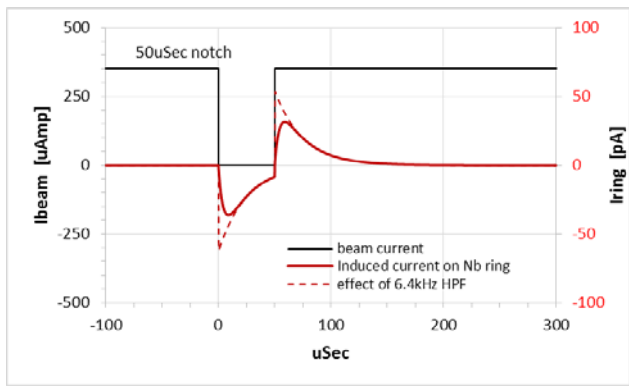


Figure 9: Induced beam current in time domain (red trace), as the effect of a 6.4 kHz high pass filter and 33 kHz loss pass filter.

CONCLUSION

As a follow-up study of LMR, we considered the effect of AC-coupling by FRIB mini pulse structure, which has a 50μs notch at 100Hz. Since it is too time-consuming to directly simulate the AC response for μs pulse in CST, we instead simulated a nano-second Gaussian excitation signal. Analytical model was benchmarked with the Gaussian excitation and effective ring length is obtained for different LMR structures. With the validated analytical model, we calculated the induced current for a 50μs rectangular pulse and it gives ~33pA induced current for 0.35mA average beam current at LS1. Compared with LMR desired detection limit 100pA ± 50pA, it is still tolerable. It, however, brings some fake background when we take the samples in the notch for background subtraction. Integration in an extended time could help.

Copyright © 2014 CC-BY-3.0 and by the respective authors

ISBN 978-3-95450-141-0

ACKNOWLEDGMENT

This material is based upon work supported by the U.S. Department of Energy Office of Science under Cooperative Agreement DE-SC0000661, the State of Michigan and Michigan State University. The authors want to thank Zhihong Zheng for the help on CST modelling. The authors would also like to thank Dylan Constan and Bob Webber for the fruitful discussions.

REFERENCES

[1] Z. Liu et al., "Ion Chambers and Halo Rings for Loss Detection at FRIB", Proc. of IPAC2012, p. 969-971 (2012)

[2] Z. Liu et al., "A New Beam Loss Detector for Low-Energy Proton and Heavy-Ion Accelerators", NIM-A, to be published. (2014)

Copyright © 2014 CC-BY-3.0 and by the respective authors

ISBN 978-3-95450-141-0

BEAM LOSS MONITOR AT SUPERKEKB

Hitomi Ikeda*, Mitsuhiro Arinaga, John Walter Flanagan, Hitoshi Fukuma and Makoto Tobiyama,
KEK, High Energy Accelerator Research Organization, Ibaraki 305-0801, Japan

Abstract

We will use beam loss monitors for protection of the hardware of SuperKEKB against unexpected sudden beam losses. The sensors are ion chambers and PIN photo-diodes. The loss monitor system provides an important trigger to the beam abort system. We can optimize the threshold of the abort trigger by checking the beam information at each abort event. This paper explains the overall system of the SuperKEKB beam loss monitors including the damping ring (DR).

INTRODUCTION

The KEKB collider is being upgraded to SuperKEKB in order to get higher luminosity. The beam energy of the Low Energy Ring (LER) is 4 GeV for positrons, and that of the High Energy Ring is 7 GeV for electrons. The beam currents are 2.6 A in HER and 3.6A in LER. LER injection system includes a 1.1 GeV DR [1, 2]. The machine parameters of SuperKEKB are shown in Table 1. In order to get 40 times higher luminosity than that of KEKB, the beam currents will be increased 2 times higher than at KEKB and the beam size at the interaction point will be further squeezed with a large crossing angle. The first beam is expected in FY 2015.

Table 1: Machine Parameters of SuperKEKB

Parameter	LER	HER	DR	unit
Energy	4.0	7.0	1.1	GeV
Max. bunch charge	14.4	10.4	8	nC
No. of bunches	2500		4	
Circumference	3016		135.5	m
Max. stored current	3.6	2.6	0.07	A
Horizontal damping time	58	29	10.9	ms
x-y coupling	0.27	0.28	5	%
Emittance (h)	3.2	4.6	42.5	nm
Emittance (v)	8.64	12.9	3150	pm
Bunch length	6.0	5.0	6.53	mm
βx*/βy*	32/0.27	25/0.30		mm
Crossing angle	83			mrad
Luminosity	$8x10^{35}$			$cm^{-2}s^{-1}$
RF frequency	509			MHz

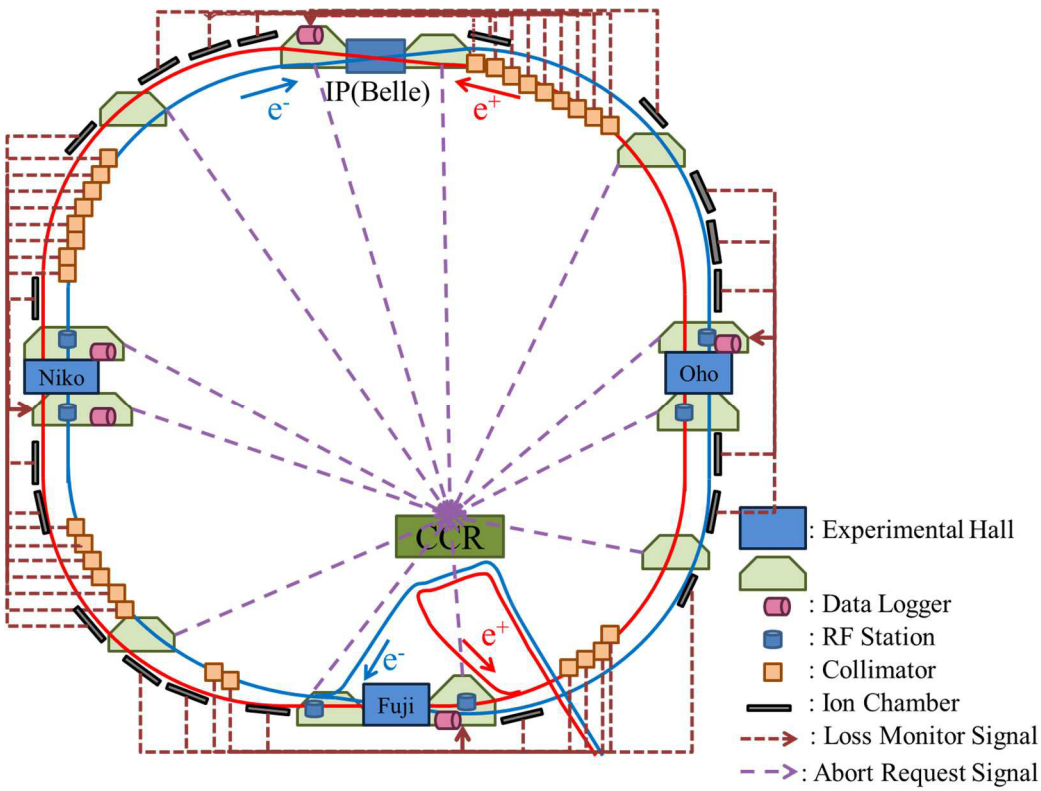


Figure 1: The overall system of the SuperKEKB beam loss monitor.

*hitomi.ikeda@kek.jp

ISBN 978-3-95450-141-0

Copyright © 2014 CC-BY-3.0 and by the respective authors

The beam loss rates at SuperKEKB were simulated and predicted to be 10mA/s and 7.2mA/s at the LER and the HER, respectively [3]. They are 50 times higher than that of KEKB. The beam will be lost at the interaction region and collimators mainly. Beam loss monitors (BLMs) must protect the Belle II detector and the accelerator hardware components against unanticipated beam loss caused by beam instabilities. Typical beam loss rates at KEKB were 10 mA/ms and 10mA/μs in the case of BLM aborts caused by ion chambers and PIN photo-diode sensors, respectively. An example of a beam loss abort is shown in Fig.2. Since the dangerous beam loss rate which triggers the beam abort and could cause the hardware damages will be much larger than the expected beam loss rate at SuperKEKB, the abort system at KEKB will work at SuperKEKB even in large background due to the beam loss by adjusting a threshold level of the abort trigger. We decided to use the same beam loss monitor system as the KEKB system [4], which consists of ion chambers and PIN photo-diodes. The overall system of the BLM is shown in Fig. 1. BLM signals from the whole rings are collected at four local control rooms (LCRs). An interlock signal from each BLM generates a beam abort. The number of channels is approximately 200 in the tunnel. Table 2 shows the number of BLM in the main ring (MR) and DR. We use the data loggers which are installed at 5 LCRs in order to diagnose whether the abort is correctly requested by BLM and other sensors or not [5].

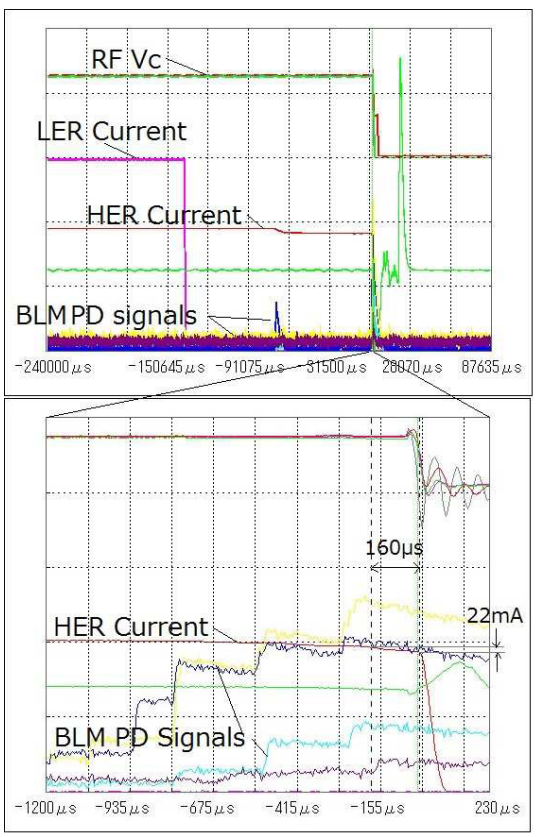


Figure 2: An example of a beam loss monitor abort at KEKB. HER beam loss was 22mA within 160μs. PIN photo-diodes generated an abort signal.

Table 2: Number of Beam Loss Monitors at SuperKEKB

Sensor	MR	DR
IC	105	40
PD	101	-
Optical fiber	-	optional

ION CHAMBER

The ion chambers (ICs) are reused sensors that were used for KEKB. The 5-m long chambers are mounted in cable racks on the outer wall along the tunnel. The IC is a Fujikura FC-20D co-axial cable. The inner and outer conductors are separated by an air gap. The high voltage at the outer conductor is 200V. The typical drift time over which a positive ion is collected at the inner conductor is 1 ms. The resulting current is sent to a readout electronics which include an integrator and an amplifier as shown in Fig. 3. Each module handles eight channels. The amplifier gain can be selected to be 1, 10 or 100. The RC time constant also can be selected to be 10, 100, 300 or 1000 ms. The IC is sensitive down to a loss of around 0.1mA/s. An interlock signal is generated and a beam abort is requested when the beam loss level exceeds a threshold that is set for each channel. The loss signal is buffered and sent to a 16-bit 64 channel ADC (DGX 18K14B) and logged at 1 Hz. The same signal is sent to a data logger with a higher sampling-rate just after any beam abort.

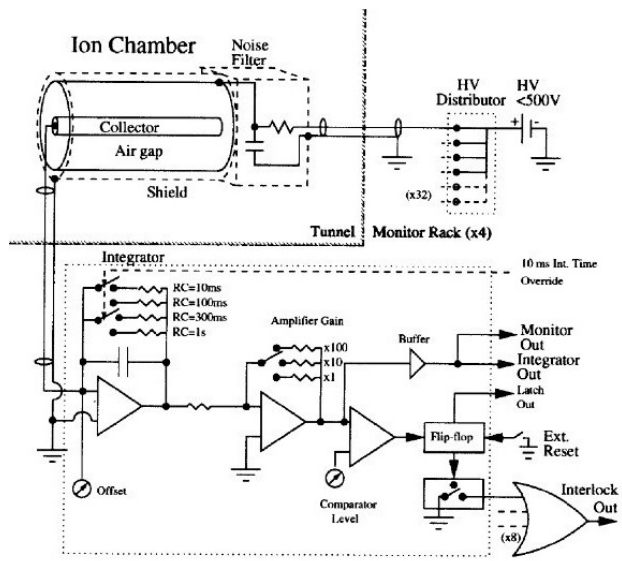


Figure 3: Block diagram of the readout electronics for the ion chambers [4].

Copyright © 2014 CC-BY-3.0 and by the respective authors

ISBN 978-3-95450-141-0

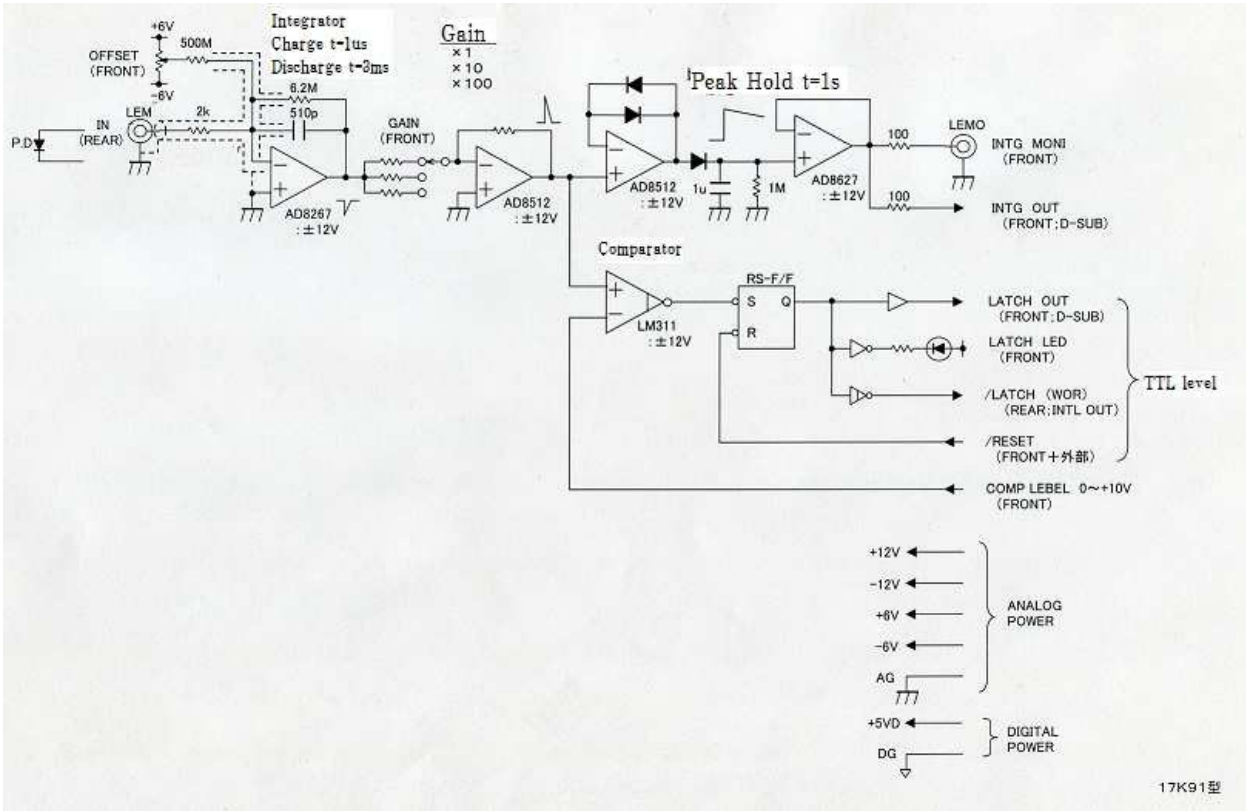


Figure 4: Block diagram of the readout electronics for the PIN photo-diodes.

PIN PHOTO-DIODE

Collimators are installed in the beam line in order to protect the BelleII detector from lost particles. The number of collimators is 13 and 16 for the LER and the HER, respectively. High current beam can damage the collimator itself when the beam orbit changes rapidly. PIN photo-diodes (PDs) with high speed and high radiant sensitivity (BPW34) are used as sensors for the BLM since the interlock signal from an IC is not fast enough to protect the collimator. The cross section of the PD is 2.65mm× 2.65mm. Two PDs are put in an aluminium box and insulated by Kapton tape. We put 4 boxes around a collimator to detect beam loss in all directions. The rise time of the PD is 60 μs, which is determined by the capacitance of the signal cable (30 nF for a 400 m cable) and an input resistor of 2 kΩ. The readout electronics are shown in Fig. 4. The peak hold circuit is for logging the signal by ADC and the comparator is for the interlock signal. The interlock signal is generated within a few turns after beam loss happened. The PD signal can protect the hardware from a localized rapid beam loss, and it is possible to distinguish in which ring the beam loss happened. We will install PDs in several locations where we expect localized beam loss, including collimator sections as shown in Fig. 5. The signal flow after the readout module is the same as for the IC signal.



Figure 5: Examples of PIN photo-diodes which are put (a) on the collimator and (b) near bellows at KEKB.

ISBN 978-3-95450-141-0

Copyright © 2014 CC-BY-3.0 and by the respective authors

LOGGER SYSTEM

The abort diagnostic system is based on a high-sampling-rate data logger that records BLM and other signals at the moment of beam abort [5]. Data loggers are located in five LCRs where BLM signals and RF cavity signals are collected. The logged time period is 600 ms and 300 ms. The sampling intervals are 5 μs and 1μs for the two logging times, respectively. Beam intensity, signals from the RF cavities, beam phase showing deviation of synchronous phase, and injection trigger timing signals are logged along with BLM signals. These fast signals are useful to diagnose the cause of the beam abort. The recorded data are sent to the central control room (CCR) via the KEK internal network. The information is ready for inspection within a few minutes after the abort. By analysing the data, the reason for beam loss and the beam abort are identified.

DAMPING RING

The DR LM is not used for an interlock signal giving a beam abort. It is used for commissioning, injection tuning and monitoring in routine operation. Regarding the injection efficiency of the DR, the normal beam loss is estimated to be 2.5% near the injection point and 2.7% in all other arc sections. Alternatively, around 20% of loss is expected in a collimator. It is necessary to have enough sensitivity when greater than the expected loss occurs.

ICs are reused sensors that were used at the KEKB linac. They are 9 m long FC-20D co-axial cables. The cross section of the DR IC is shown in Fig. 6. This is similar to the MR IC. The IC will be mounted on the cable rack or the magnet. A readout electronics consists of an integrator and an amplifier, same as for the MR IC. The amplifier gain can be selected to be 1, 10,100 or 1000. The signal caused by beam loss at DR is expected to be smaller than that of the MR, since the DR beam current and beam energy are smaller.

Signal level of the IC was simulated by the electromagnetic shower code EGS5 [6]. In the simulation a beam chamber was assumed to be a rectangle with aluminium walls of 6 mm thick. Two iron blocks with 5 cm thick separated by 30 cm along the beam axis were placed around the chamber to simulate magnets. The IC with an aluminium conductor of 1.8 mm thick, 5 m long and with a shape of a square of 22.5 mm on a side was placed 1 m apart from the beam axis horizontally and vertically. Positrons of 1.1 GeV horizontally hit a side of the chamber wall. The code counted the number of electrons, positrons and photons that entered the IC. The number of the ions created in the IC was calculated from the stopping power and the mass attenuation coefficient in the air. The ionization constant for the air was assumed to be 34 eV. The result shows that 2.7×10^5 ions are created for 1×10^5 incident electrons. This means 1.1×10^8 lost positrons, that is 0.2 % of the maximum bunch population, gives output voltage of the ion chamber of 0.1 V assuming that the gain of 100 and the capacitance of the integrator of 47 nF.

The planned setup has enough sensitivity. The signal is sent to ADC which is the same as that used for the MR LM, and logged by the SuperKEKB logging system. PIN photo-diodes and optical fibers also will be installed to check the beam loss situation in detail as backups.

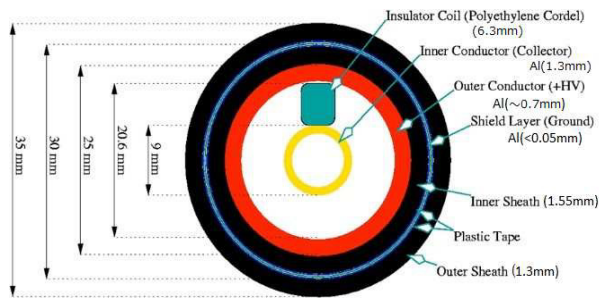


Figure 6: Cross section of the Ion Chamber.

CONCLUSION

Preparation of the BLM of the SuperKEKB is in progress for a start-up in FY 2015. The BLM system is based on the KEKB BLM system. Most of the sensors and the readout electronics are re-use from KEKB. The number of MR channels is increased, and electronics are partially modified for the DR.

REFERENCES

[1] M. Kikuchi et al., Proceedings of IPAC'10, Kyoto, Japan, TUPEB054 (2010).
[2] N. Iida et al., Proceedings of IPAC'11, San Sebastian, Spain, THYA01 (2011).
[3] Y. Funakoshi, talk given at the KEKB review committee (2013).
[4] M. Arinaga et al., KEKB Accelerator Papers, NIM. A499 (2003).
[5] M. Arinaga et al., Prog. Theor. Exp. Phys. 03A007(2013).
[6] H. Hirayama et al., "The EGS5 Code System", SLAC-R-730 and KEK Report 2005-8 (2005).

Copyright © 2014 CC-BY-3.0 and by the respective authors

ISBN 978-3-95450-141-0

REAL-TIME DISPLAY SYSTEM FOR THE OPTICAL FIBER BEAM LOSS MONITOR FOR THE PHIL AND THOMX FACILITIES

I. Chaikovska*, N. Delerue, A. Variola,
Laboratoire de l'Accélérateur Linéaire, CNRS-IN2P3, Université Paris-Sud XI, Orsay, France

Abstract

Fiber monitors are an attractive beam loss diagnostics tool. They are based on the detection of the electromagnetic shower produced by the beam losses. Cherenkov radiation is produced by the electromagnetic shower charged particles within the multimode fibers attached to the vacuum chamber. This radiation is consequently converted to an electrical signal containing the information about the position and intensity of the beam losses. Therefore, a system based on fibers installed alongside the whole accelerator together with a signal detection system forms a continuous, real-time Fiber Beam Loss Monitor (FBLM). In this context, the FBLM is a very useful tool for the commissioning and beam alignment. In this article we report on the development of the real-time display system for the FBLM at PHIL (PHotoInjector at LAL, Orsay, France) as a prototype of the beam loss monitor for the ThomX project, the compact Compton based X-ray source under construction in Orsay

INTRODUCTION

ThomX is a project proposed by a colaboration of French institutions and one company to build an accelerator based compact X-ray source in Orsay (France) [1]. The main goal of the project is to deliver a stable and a high energy X-ray beam (up to 90 keV) with a flux of the orders of 10^{11} – 10^{13} photons per second generated by the Compton backscattering process. At present, the ThomX machine is under construction.

The ThomX accelerator facility is composed by the linac driven by 2998 MHz RF gun, a transfer line and a compact storage ring where the collisions between laser pulses and relativistic electron bunches result in the production of the X-rays. Low energy, compactness and lack of the operation experience make such type of the machine very difficult to operate and, especially, to commission. In this context, a reliable beam loss monitor able to locate the losses will be indispensable for the commissioning (tuning of the linac and the transfer line to optimize the injection, setting-up of the ring working point) and further operation of the machine.

Nowadays, the beam loss monitor technology based on the optical fibers is established. Hereafter, we will describe the FBLM installed at PHIL facility as a prototype for the ThomX machine. PHIL is a photoinjector driven by the 2998 MHz RF gun [2]. The beam line consists of the three solenoids, a pair of steerers and a dipole (see Figure 1). Among the diagnostics tools are the ICTs, YAG screens, Cherenkov radiation monitor and a Faraday cup. Some of the ThomX and PHIL machine parameters are listed in Table 1.

A real-time display system for the FBLM is being developed for the future commissioning and operation of the PHIL and ThomX machine. It presents an application having the convenient GUI to control the FBLM equipment and helping easily locate beam losses along the accelerator.

Table 1: PHIL and ThomX Electron Beam and Machine Parameters

Description	PHIL	ThomX	Units
Beam energy	5	50 – 70	MeV
Bunch charge	< 1.5	1	nC
Bunch length (rms)	> 3.5	3.7 (injector) 30 (ring)	ps ps
Beam energy spread (rms)	< 2 – 3	< 1	%
Repetition frequency	5	50	Hz
Machine length	~ 5	~ 5 (injector) ~ 13 (transfer line) ~ 18 (ring)	m m m

PRINCIPLE OF THE BEAM LOSS DETECTION

The detection principle of the beam losses is based on the production of Cherenkov radiation in the optical fiber attached to the vacuum chamber by the electromagnetic shower generated when the main beam hits the vacuum chamber or any obstacle. The secondary charged particles produce Cherenkov radiation provided that the velocity of that particles are greater than the phase velocity of light in the fiber core material. Consequently, the Cherenkov light is converted to an electrical signal containing the information about the position and intensity of the beam losses.

The Cherenkov light is emitted along a cone with an opening angle defined by the velocity of the particle and the refractive index of the fiber core. Light yield is proportional to $1/\lambda^2$, where λ is a wavelength of the Cherenkov radiation and depends on the direction at which the particle crosses the fiber. A detailed description of the Cherenkov radiation process including production, photon yield, probability for the photon to be captured and guided by the fiber, photon detection, etc. has been extensively worked out in the framework of the Cherenkov fiber calorimetry [3].

* chaikovs@lal.in2p3.fr

ISBN 978-3-95450-141-0

Copyright © 2014 CC-BY-3.0 and by the respective authors

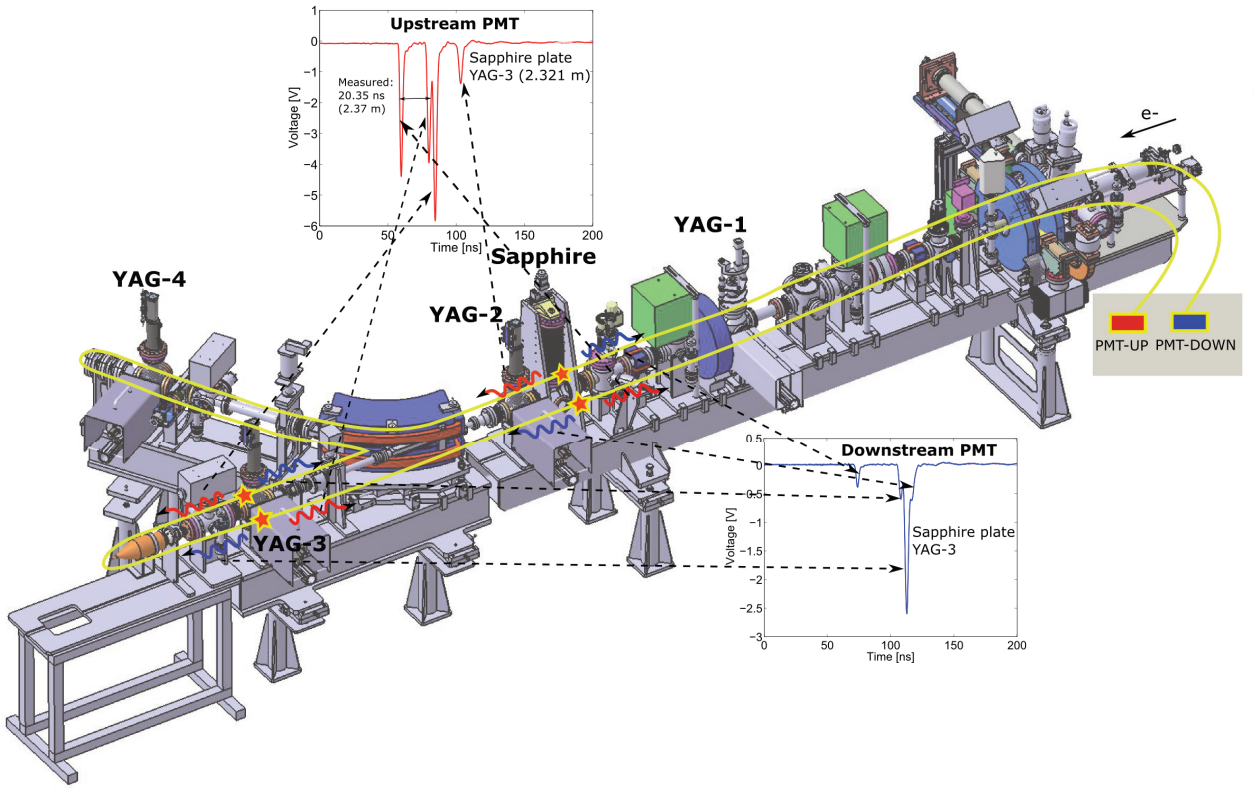


Figure 1: Scheme of the FBLM installed at PHIL. The red stars indicate the positions of the loss points at Sapphire plate and YAG-3 locations. In this case, two plots illustrate the typical beam losses measured by the upstream and downstream PMTs.

Although the strength of the signal detected is proportional to the beam loss intensity, it is also dependent on the type and mass of the material within which the electromagnetic shower is developed. Various beam line elements and hardware will cause the signal variations since the fiber has to be pulled around such components. This, together with the absorption of the signal by the fiber as it transmits to the detector makes difficult to extract the exact amount of the beam loss and use the FBLM to measure the absolute intensity of the losses.

The time calibration of the FBLM can be accomplished by several techniques [4]. The one, adopted by our scheme uses the beam loss signal produced by inserting a known device such as the vacuum valve, collimator, screen, etc. as the reference. Knowing the speed of light in the fiber, one can calibrate the oscilloscope display (time between the beam losses measured in seconds) to real distance along the accelerator (distance between the beam losses measured in meters). In our case, the speed of light in the fiber was measured to be 0.63 c (0.19 m/ns), where c is a speed of light in vacuum. This calibration gives that every meter along the accelerator is 8.6 ns on the oscilloscope. Therefore, by measuring the time between the reference and the unknown beam loss signal and dividing it by 8.6 ns/m one can determine the location in meters from the reference to the unknown beam loss point.

As mentioned before, in some locations due to the beam line elements the fiber covers a slightly longer path than the beam line. The further measurements are done from the reference, the greater chance for the error to penetrate into the measurements. This results in the deterioration of the FBLM accuracy. Therefore, to reduce the errors in the absolute loss position measurements, it is required to have as many references as possible. Moreover, the fiber should be placed as close to the beam pipe as allowed by the geometry of the beam line components.

FBLM INSTALLATION

Fibers for the FBLM

The fiber installed at PHIL facility is made by the LEONI Fiber Optics GmbH. It belongs to the Hard Plastic Clad Silica (HPCS) fibers which combines fused silica glass core and polymer cladding consisting of a fluorinated acrylate. Numerical aperture of the HPCS fibers can go up to 0.49. This kind of the fibers are positioned as a cost-effective alternative to the silica/silica glass fibers. As far as radiation hardness is concerned, the fibers with plastic core/cladding suffer from radiation damages. Radiation damage of the optical fibers can be an issue because it will degrade the light propagation. Therefore, depending on the expected radiation level the fibers having silica glass core and cladding are preferable (e.g. AS600/660UVST, LEONI Fiber Optics) [5].

The fibers used at PHIL have a 600 μm fused silica glass core, 630 μm of optical cladding made from polymer and 950 μm Tefzel® jacket. Since the jacket surrounding the

Copyright © 2014 CC-BY-3.0 and by the respective authors

ISBN 978-3-95450-141-0

fiber is transparent, the fibers have been covered with heat shrinking tube. Attenuation of the fibers has been estimated to be several tenths of dB/meter at 405 nm. The cost of the HPCS fiber is about 4 euros per meter.

Detection and Data Acquisition Systems

In order to detect the Cherenkov light, the fiber has to be coupled with a photon detector. For this, two ends of the fiber have been connecterized by using the FC type connectors. The photon detectors employed are the photosensor modules H10721-01 manufactured by Hamamatsu Photonics containing the PMT and a built-in high-voltage power supply circuit. The sensitivity in the wide range 230-870 nm and a short rise time of about 0.6 ns result in a very fast loss signal allowing us to resolve the location of beam losses that are very close together (~7 cm).

The PMTs can be used to read out the signal from both fiber terminations. However, the better time resolution is obtained by using the signal from the PMT placed at the upstream end of the fiber. In this case, the Cherenkov light produced moves opposite to the beam direction and provides better information about the position of the beam losses since the peaks corresponding to the multiple loss point are more distant apart compared to the ones read out by the downstream PMT (see Figure 1).

At PHIL, two PMTs are currently used to crosscheck the FBLM system and initially, to calibrate the speed of light in the fiber. In future, the downstream PMT could be replaced either by the reflector providing additional information to determine the exact location of the beam losses or by the LED to monitor from time to time the fiber efficiency.

The FBLM signal is displayed and recorded by using a LeCroy WavePro 740Zi 40 Gs/s oscilloscope with 4 GHz bandwidth located near the detection system behind the PHIL. The acquisition is driven by the external trigger being the 5 Hz laser light signal measured by the photodiode. Remote control of the oscilloscope is used to adjust the display parameters at different beam loss regimes.

MEASUREMENTS AT THE PHIL FACILITY

The fiber with a length of 25 meters was installed alongside the vacuum chamber to cover continuously the total length of the photoinjector from both sides (see Figure 1). The fiber ends are coupled to the PMTs mounted on the board and shielded by lead and black screens against the parasitic signals.

Four YAG screens and Sapphire plate have been used to calibrate and generate the beam losses at PHIL. Figure 2 illustrates the beam loss profile from two successive beam loss points at the Sapphire plate and YAG-2 screen locations. Two peaks spaced by ~3 ns defines time resolution of the FBLM. However, more advanced approach can be taken to disentangle the pile-up and improve the FBLM resolution.

Moreover, during the operation, it turned out that the FBLM can be served as a tool to characterise the dark current.

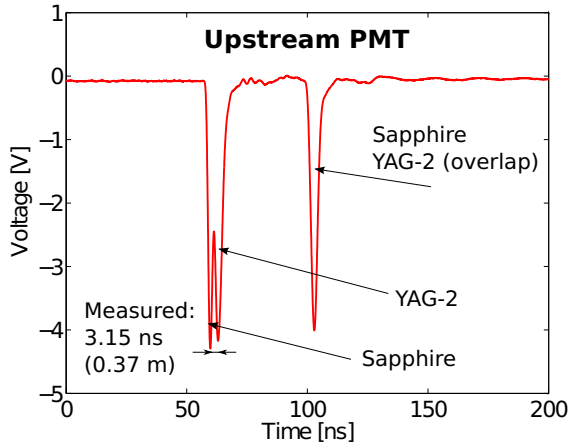


Figure 2: Beam loss signal (averaged) generated by the Sapphire plate and the YAG-2 screen spaced by 0.282 m.

Figure 3 shows the signal acquired during the dark current studies (RF photogun laser is OFF).

One can notice the whole RF pulse reconstructed by the beam loss signal. The detection limit of the system has been observed to be well below 1 pC that has been also confirmed by measuring the FBLM sensitivity hitting directly the fiber with the electron beam.

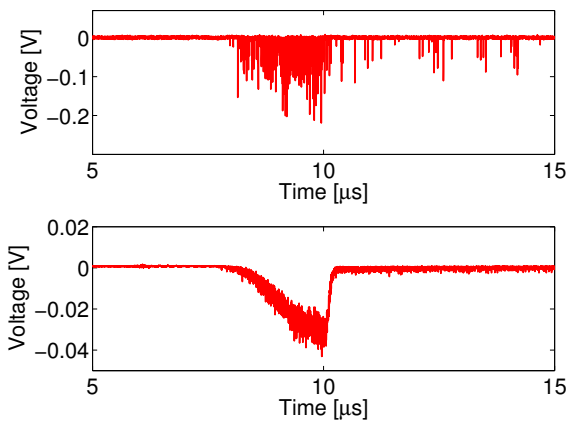


Figure 3: Beam loss signal generated by the dark current (60 MV/m). The RF pulse duration is 3 μs which is clearly visible on the waveform. Top: one acquired waveform. Bottom: averaging over several waveforms.

REAL-TIME DISPLAY SYSTEM FOR THE FBLM

Real-time display system for the FBLM is now under development. It is designed to provide a practical and simple interface to analyse the acquired waveforms and give the estimated location of the beam loss.

The FBLM application will mainly be served as an auxiliary tool during the machine commissioning, tuning and operations. The preliminary version of the FBLM real-time display system to be tested at PHIL is shown on Figure 4. It will offer the following possibilities for the user:

ISBN 978-3-95450-141-0

Copyright © 2014 CC-BY-3.0 and by the respective authors

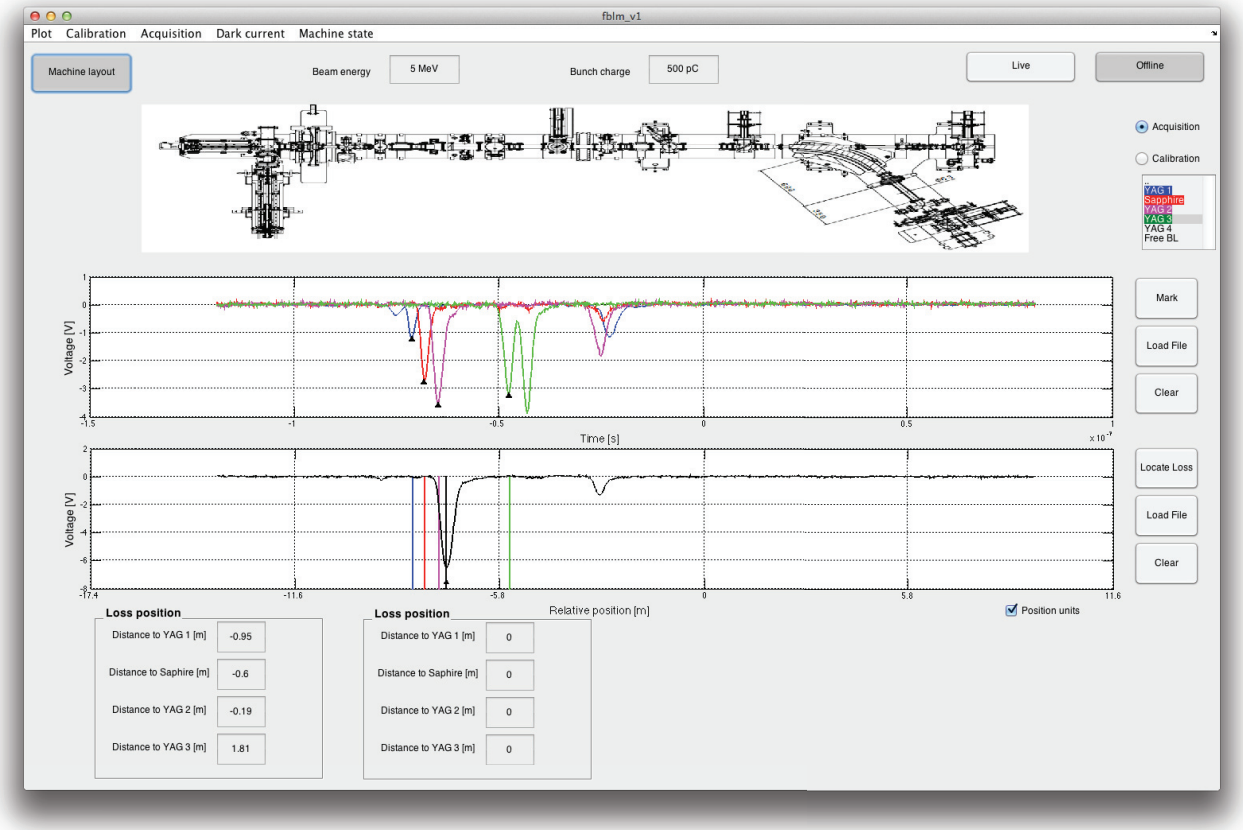


Figure 4: Preliminary view of the real-time display system GUI to be used at PHIL facility.

- acquisition and display of the raw waveforms together with the main machine parameters
- performing the FBLM calibration procedure using the available devices (e. g. YAG screens, sapphire plate, etc.)
- using the calibration, locating the beam losses and search for their relative position along the accelerator
- saving the data and calibration, loading that ones from the previous runs which allows to compare the machine states from run to run
- live acquisition as well as the possibility to conduct offline analysis if needed
- performing the dark current studies.

To be consistent with the ThomX machine control system which will use Matlab Middle Layer [6] to connect the low level control system to the high level applications written mainly in Matlab, the GUI of the FBLM real-time display system is developed on the Matlab platform.

SUMMARY AND FUTURE PLANS

FBLM is a powerful tool in locating the beam losses with a good enough accuracy and evaluating changes in the beam operation along whole accelerator. The measured position accuracy allows resolving the beam losses occurring as close as 30 – 40 cm with the 25 m fiber along the vacuum chamber. Geometry of the fiber installation gives partial information about the loss spatial distribution.

As the next step, we would like to test another type of the fiber (AS600/660UVST, LEONI Fiber Optics). Although this kind of the fibers has smaller numerical aperture, they are less sensitive to radiation and have the better transmission characteristics. The final choice of the fiber used for the ThomX machine will be made based on the results obtained.

To benefit fully from the FBLM operation, the real-time display system is being developed. Soon, this application will be tested at PHIL. This will require to establish the connection with PHIL control system in order to access the machine parameters. Possibility to test and operate the FBLM at the PHIL facility will allow optimising the content and GUI of the FBLM real-time display system. Eventually, operation of the FBLM application allows substituting an appropriate data acquisition system for the oscilloscope which will facilitate its integration into the machine control system.

In the framework of the ThomX project, the optical fiber will be installed to monitor the losses along the linac, the transfer line and the ring. Auxiliary calibration procedure will be envisaged for the commissioning phase. The current

Copyright © 2014 CC-BY-3.0 and by the respective authors

ISBN 978-3-95450-141-0

FBLM real-time display system will be modified to meet all the requirements and features of the ThomX machine.

ACKNOWLEDGMENT

The authors would like to thank the PHIL group for help and possibility to perform the presented studies, Leonid Burmistrov and Doug McCormick for useful discussions. In particular, we acknowledge the operator team for their help during the FBLM test at the PHIL facility.

REFERENCES

[1] A. Variola, A. Loulergue, F. Zomer, *"ThomX Conceptual Design Report"*, LAL RT 9, 28 (2010).

[2] M. Alves, C. Arnault, D. Auguste, J.-L. Babigeon et al. *"PHIL photoinjector test line"*, Journal of Instrumentation 8 (01), T01001 (2013).

[3] P. Gorodetzky, D. Lazic, G. Anzivino et al, *"Quartz fiber calorimetry"*, Nuclear Instruments and Methods in Physics Research Section A, 361 (1), 161-179 (1995).

[4] T. Obina, Y. Yano, *"Optical-fiber beam loss monitor for the KEK photon factory"*, Proceedings of IBIC12, Tsukuba, Japan (2012).

[5] D. Sporea, A. Sporea, S. O'Keeffe, D. McCarthy, E. Lewis, *"Optical fibers and optical fiber sensors used in radiation monitoring"*, Selected Topics on Optical Fiber Technology, 978-953 (2012).

[6] J. Corbett, G. Portmann, and A. Terebilo, *"Accelerator control middle layer"*, Particle Accelerator Conference, 2003. PAC 2003. Proceedings of the. Vol. 4. IEEE, 2003.

Copyright © 2014 CC-BY-3.0 and by the respective authors

ISBN 978-3-95450-141-0

INSTALLATION OF A BEAM LOSS MONITORING SYSTEM AT THE S-DALINAC*

L. Jürgensen#, U. Bonnes, C. Burandt, M. Fischer, F. Hug, T. Kürzeder, N. Pietralla, R. Stegmann, M. Steinhorst, Technische Universität Darmstadt, Germany

Abstract

The S-DALINAC is the superconducting linear accelerator of the Institut für Kernphysik at Technische Universität Darmstadt (Germany). In order to get a short-time response about occurring beam losses and their locations a new system based on PIN-diodes was installed. The readout of the commercially available beam loss monitors is done via an in-house developed system compatible to our EPICS-based control system. The system and the results of the commissioning will be presented in this paper.

INTRODUCTION

Since 1987 the S-DALINAC serves nuclear- and astrophysical experiments at TU Darmstadt [1]. It is fed by either a thermionic gun or a photoemission gun which delivers a spin-polarized electron beam [2]. After pre-acceleration up to an energy of 10 MeV by the injector module the electron beam can either be used for experiments at the Darmstadt High Intensity Photon Setup (DHIPS) [3] or it is guided through a 180°-arc to enter the main linac. By passing the linac up to three times the maximum energy of about 130 MeV can be reached. The beam current can be adjusted from several pA up to 60 µA.

In order to improve the accelerator's performance and also to decrease the contamination of the surrounding by undetected beam losses, a beam loss monitoring system has been set up. Comparable machines are using several different monitors based on e.g. ionizing chambers, scintillators, glass fiber or semiconductor detectors. The requirements for an operation at the S-DALINAC are sensitiveness for (secondary) electrons, easy mounting and space-saving dimensions. In addition the detectors should provide a short-time readout in order to provide the operator with direct feedback for an improved beam tuning.

Beam Losses at the S-DALINAC

At the S-DALINAC beam losses typically occur because of small misalignments in the beam line or deviations in the magnetic fields. Therefore part of the beam is lost in the walls of the vacuum chamber. Depending on the electron's initial energy the produced secondary radiation can penetrate and activate the beam tube and surrounding equipment.

BEAM LOSS MONITORING SYSTEM

Originally designed and implemented at HERA [4] the chosen Beam Loss Monitor (BLM) is currently manufactured and distributed by Bergoz Instrumentation [5]. The beam loss detection is based on a coincidence setup of two PIN-photodiodes interacting with ionizing radiation. The coincidence reduces the zero counting rate caused by the dark currents of the photodiodes. The operating principle is shown in Fig. 1.

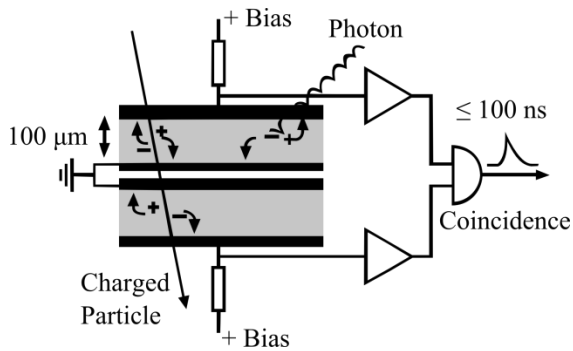


Figure 1: Operating principle of the Beam Loss Monitor [5].

Figure 2 shows the BLM circuit board with highlighted PIN-diodes of the BPW34 type. During operation the upper half is shielded from light and electromagnetic noise by a metal enclosure. The overall size is 69 x 34 x 18 mm³. To increase sensitivity, the original type of PIN-diodes can be exchanged by larger diodes.

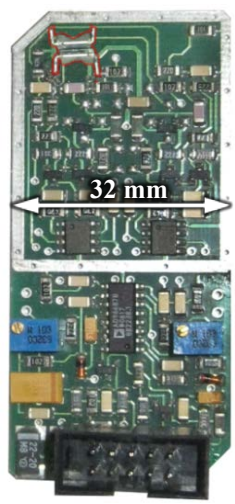


Figure 2: BLM circuit board with PIN-diodes at the upper left part.

*Work supported by BMBF through under contract No. 05K13RDA.
#ljuergensen@ikp.tu-darmstadt.de

Copyright © 2014 CC-BY-3.0 and by the respective authors

ISBN 978-3-95450-141-0

To adjust the level of amplification for each diode separately, two potentiometers (in blue) are included. The BLM is supplied via the 10-pin connector with ± 5 V and + 24 V. Positive TTL pulses with rates up to 10 MHz are driven towards the used counter. Its radiation hardness has been tested for up to 10^8 Rad [5].

In-house Developed Readout Electronics and Supply Unit

For easier integration into the existing, EPICS-based [6], accelerator control system at the S-DALINAC [7], readout electronics and voltage supply unit has been developed in-house. The supply, which is also including differential line-drivers, can be seen in Fig. 3. Each BLM needs its own supply unit within a maximum distance of 5 m. The conditioned pulses are sent to the counting cards located outside the accelerator hall. The maximum driving rate is 20 MHz while the BLM itself is limited to 10 MHz. The signal transport is done via standard Cat5 twisted-pair cable.

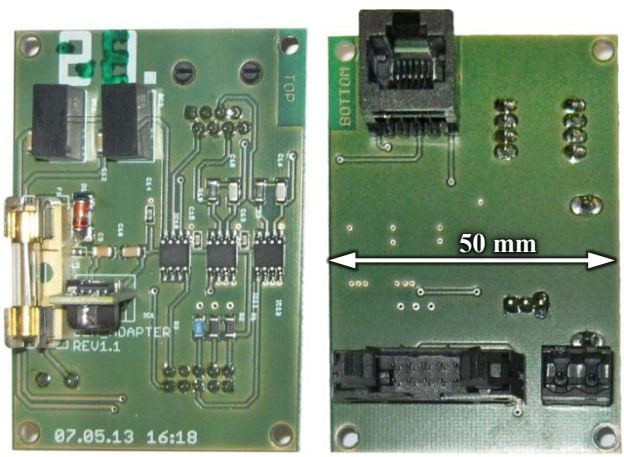


Figure 3: Back and front of BLM supply unit including the differential line-drivers.

Each counting card provides two input channels. The front panel indicates the actual counting rates by flashing LEDs. The longest readout interval of this device is $^1/_7$ s.

Integration into the EPICS-based Accelerator Control System

For easy integration into the existing, EPICS-based control system, the fast counting cards are designed to be compatible to the existing in-house developed QM07 multipurpose-measurement system. Hence the occurring count rates can be transferred to the control room via the already existing EPICS IOC. Control System Studio (CSS) [8] is used to allow the operator to access most of the data. For practical use an overview of the floor plan was combined with small displays showing the actual measured beam loss rate at each monitored position. CSS also offers to make customized changes if necessary with very small effort. So it is common to draw a special user interface, only including the BLMs which are important for this special operating mode. One example for the DHIPS mode of our accelerator control system is given in Fig. 4.

The window contains the beam current at the radiation production targets in the upper half. The current is measured by two separate plates. By recording the ratio of both, deviations of the beam energy can be indicated. The chart in the middle shows the beam current over the last 30 minutes. The two fields below display the concurrent beam loss rate behind the injector module. The recorded beam loss rate is drawn in the small charts below and can be archived optionally.

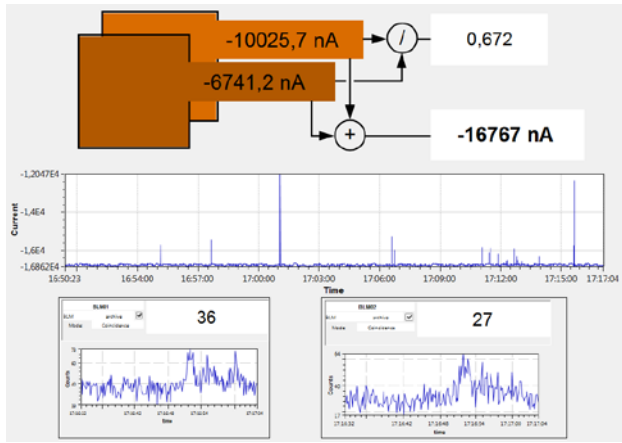


Figure 4: Customized CSS window for DHIPS experiments showing the beam current at the radiation production targets in the upper half and the beam loss rate behind the injector cryostat below. Slow changes over time are indicated by the two charts.

Calibration

For the purpose of adjusting the levels of amplification for each diode separately, the counting card supports disabling one channel of the coincidence set-up to measure the other's zero counting-rate. After adjusting the amplification levels, the 20 BLMs for the S-DALINAC were calibrated with a radioactive source (^{60}Co, 60 MBq) normalizing the BLM count rates [9]. Factors between 0.5 and 2 were tolerated; otherwise the amplifier gains were changed again. Using this normalization, it is possible to mount several BLMs at the same position around the beam tube to gain information about the direction of deviation of the beam from the ideal orbit.

BLM set up and first Commissioning

The threshold for particle detection is around 1 MeV [10]. This prohibits measuring beam loss before acceleration above this threshold. Hence at the S-DALINAC these BLMs are sensitive from the first superconducting acceleration stage on. The space-saving BLM can be mounted easily, e.g. by a cable tie to the beam tube. For this reason changing the monitored positions is possible on short notice. An overview plan of the currently monitored positions is given in Fig. 5.

ISBN 978-3-95450-141-0

Copyright © 2014 CC-BY-3.0 and by the respective authors

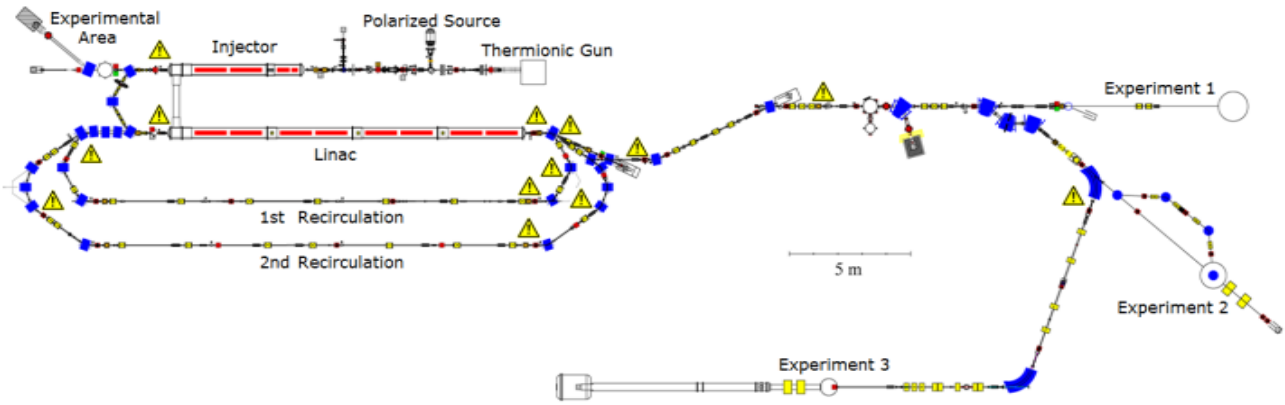


Figure 5: Floor plan of the S-DALINAC, including the experimental area. Positions of BLMs are indicated using exclamation marks (⚠).

The 10 MeV injector module's exit is prepared with two BLMs, one on the right side, the other one on the top. Also the 40 MeV Linac module is monitored with several BLMs. At the entrance, three BLMs are mounted, while four are mounted right behind its exit. By the use of more than one BLM at a single position, more information can be gained, e.g. about the direction the beam deviates from its ideal orbit. The BLMs turned out to be a very helpful feature, not only for safety reasons during the operation, but also while optimization of the tuning parameters, the beam loss rates give information about the right settings.

By recording the rates for extended periods, drifts and charging effects have been monitored which have not been noticed before and were corrected later on. As an example an image of a short-period charging effect can be seen in the screenshot in Fig. 6.

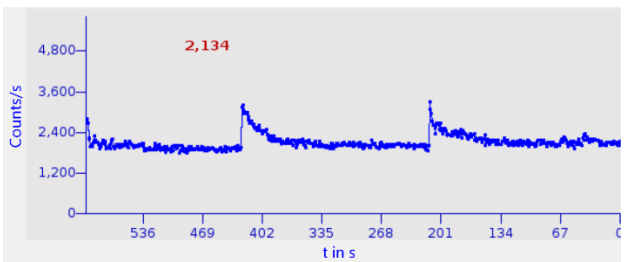


Figure 6: CSS window showing BLM rates over 10 min. An unnoticed charging effect could be discovered.

FUTURE PLANS

The S-DALINAC is a superconducting, recirculating electron linac and is showing transverse beam break up. This occurs already at low threshold currents of some µA. Several methods to counteract the beam break up are to be experimentally investigated [11] in future in order to gain information for future high current Energy Recovering Linacs (ERLs). For these measurements the beam loss monitoring system shall be spread around the accelerator to indicate the effect of each setting to the beam break up limit.

CONCLUSION

The new beam loss monitoring system of the S-DALINAC provides on-line beam loss rates which can be visualized and archived in several ways, using EPICS and CSS. The flexibility gives the option to change the monitored positions within a few minutes. Not only for operation safety, but also for efficient and fast beam tuning, the installed system is a useful, non-destructive tool.

ACKNOWLEDGEMENTS

We thank our electronic workshop, essentially Dipl.-Ing. Uwe Bonnes for the design of our electronics and the BMBF under contract No. 05K13RDA for financial support.

REFERENCES

[1] A. Richter, EPAC '96, Sitges (1996) 110.
[2] Y. Poltoratska *et al.*, J. Phys.: Conf. Ser. 298 (2011) 012002.
[3] K. Sonnabend *et al.*, Nucl. Instr. & Meth. A 640, (2011) 6.
[4] K. Wittenburg, EPAC'90, Nice, 90-11 (1990).
[5] Beam Loss Monitor User's Manual, Bergoz Instrumentation, 2001.
[6] Experimental Physics and Industrial Control System, http://www.aps.anl.gov/epics/.
[7] C. Burandt, *et al.*, Proceedings of ICALEPCS '13, (2013) 332.
[8] Control System Studio, http://cs-studio.sourceforge.net/.
[9] R. Stegmann *et al.*, Proceedings of IPAC '12. (2012) 804.
[10] K. Wittenburg, CERN Accelerator School, 2007.
[11] F. Hug, *et al.,* Proceedings of ERL '13. (2013) 97.

Copyright © 2014 CC-BY-3.0 and by the respective authors

ISBN 978-3-95450-141-0

CRYOGENIC BEAM LOSS MONITORS FOR THE SUPERCONDUCTING MAGNETS OF THE LHC*

M. R. Bartosik†, B. Dehning, M. Sapinski, CERN, Geneva, Switzerland
C. Kurfuerst, Technische Universität, Vienna, Austria
E. Griesmayer, CIVIDEC, Vienna, Austria
V. Eremin, E. Verbitskaya, IOFFE, St. Petersburg, Russian Federation

Abstract

The Beam Loss Monitor detectors close to the interaction points of the Large Hadron Collider are currently located outside the cryostat, far from the superconducting coils of the magnets. In addition to their sensitivity to lost beam particles, they also detect particles coming from the experimental collisions, which do not contribute significantly to the heat deposition in the superconducting coils. In the future, with beams of higher energy and brightness resulting in higher luminosity, distinguishing between these interaction products and dangerous quench-provoking beam losses from the primary proton beams will be challenging. The system can be optimised by locating beam loss monitors as close as possible to the superconducting coils, inside the cold mass in a superfluid helium environment, at 1.9 K. The dose then measured by such Cryogenic Beam Loss Monitors would more precisely correspond to the real dose deposited in the coil. The candidates under investigation for such detectors are based on p^+–n–n^+ silicon and single crystal Chemical Vapour Deposition diamond, of which several have now been mounted on the outside of cold mass of the superconducting coil in the cryostat of the Large Hadron Collider magnets. This contribution will present the mechanical and electrical designs of these systems, as well as the results of their qualification testing including results of a cryogenic irradiation test.

INTRODUCTION

Motivation

The magnets close to the LHC interaction points (IPs) are exposed to high irradiation from the collision debris. It has been shown in Fluka simulation [1] that with the present configuration of the installed Beam Loss Monitoring (BLM) in this region, the ability to measure the energy deposition in the coil is limited because of this debris, masking the real beam loss signal (see fig. 1).

The particle showers from beam loss measured by the present BLM configuration are partly shielded by the cryostat and the iron yoke of the magnets. The system can hence be optimised by locating beam loss monitors as close as possible to the elements that need protecting. This is what is foreseen for the High Luminosity LHC (HL-LHC) upgrade,

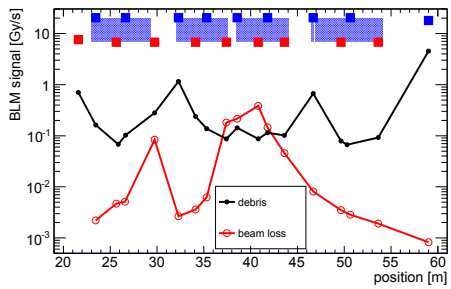


Figure 1: Doses in the coil and signal in the existing BLMs; black: BLM signal from collision debris (one point for each BLM); red: BLM signal from quench-provoking losses inside second central superconducting quadrupole magnet in the focusing triplet (Q2B).

where the BLM will be located near the superconducting coils inside the cold mass of the magnets in superfluid helium at a temperature of 1.9 K [2] (see fig. 2, courtesy of P. Ferracin)).

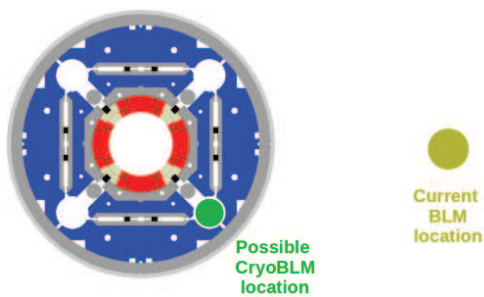


Figure 2: Cross section of a large aperture superconducting insertion magnet (MQXF) foreseen for HL-LHC with the current BLM placement and the future possible Cryogenic BLM location shown.

The advantage being that the dose measured by the Cryogenic BLM would more precisely correspond to the dose deposited in the superconducting coil [3].

Cryogenic BLM Requirements

From the mechanical point of view the main challenges of the Cryogenic BLM system is the low temperature of 1.9 K and 20 years, maintenance free operation [3]. Furthermore the Cryogenic BLM needs to work in a magnetic field of 2 T and at a pressure of 1.1 bar, and capable of withstanding a fast pressure rise up to 20 bar in case of a magnet quench.

* This research project has been supported by a Marie Curie Early Initial Training Network Fellowship of the European Community's Seventh Framework Programme under contract number (PITN-GA-2011-289485-OPAC).

† marcin.bartosik@cern.ch

ISBN 978-3-95450-141-0

Copyright © 2014 CC-BY-3.0 and by the respective authors

The electronic requirements, for a detector, are that is linear between 0.1 and 10 mGy/s and has a response time faster than 1 ms. Simulations of detector response were performed to estimate the allowable distance between the detector and amplifier and the best associated resistor and capacitor parameters. All the selected detector technologies are based on ionisation with subsequent charge carrier transport within the detector bulk material. The candidates under investigation are p^+-n-n^+ silicon [4] and single crystal Chemical Vapour Deposition (scCVD) diamond [5] detectors.

CRYOGENIC RADIATION TEST

The Cryogenic BLM specifications represents a completely new and demanding set of criteria that has never been investigated in such a form before. A certain knowledge about radiation hardness of particle detector is available for the temperature of outer space (2.7 K), from the requirements of space based experiments, but little is known for detectors below this temperature. The main unknown is the combination of the cold environment with a total ionizing radiation dose of 2 MGy. This is why the first radiation-hardness test of the diamond and the silicon detectors in liquid helium environment were recently performed at CERN [6].

Setup

The main aim of the cryogenic irradiation test was to investigate the radiation hardness of ionizing radiation detectors in liquid helium at 1.9 K. After careful preparations, the irradiation experiment was performed in the Proton synchrotron (PS) IRRAD beam line T7 in the East Experimental Area at CERN. This beam line is frequently used for sample irradiation and detector performance tests [7].

The detectors under investigation were:

- Single crystal CVD diamond with a thickness of 500 μm, an active area of 22 mm^2 and gold as metallisation material.
- p^+-n-n^+ silicon wafers with a thickness of 300 μm, an active area of 23 mm^2 and aluminium as metallisation material.

The T7 beam line provides protons with a particle momentum of 24 GeV/c. The beam intensity is 1.3 10^{11}protons/cm^2 per spill with an rms beam size at the samples location of about 1 cm^2. The spill duration is between 400 ms and 450 ms.

For the final implementation in the LHC, direct current (DC) measurements are required. It was therefore decided to characterise radiation hardness of the detectors by looking at DC measurements. These measurements were performed using a Keithley 6517, which enabled a high voltage bias to be applied while measuring the current at the same time. A LabVieW was written for data acquisition.

Results

At the end of the irradiation a total integrated fluence of 1.22 10^{16} protons/cm^2 was reached, corresponding to an integrated dose of about 3.26 MGy for the silicon and 3.42 MGy for the diamond detectors. The bias voltage could be switched from -400 V to +400 V for all detectors.

The silicon has a larger signal than the diamond at the beginning of irradiation, but the situation changes rapidly (see fig. 3). The reduction in signal corresponding to 20 years of LHC operation (2 MGy) is of a factor of 52 ±11 for the silicon device at 300 V and of a factor of 14 ±3 for the diamond detector at 400 V.

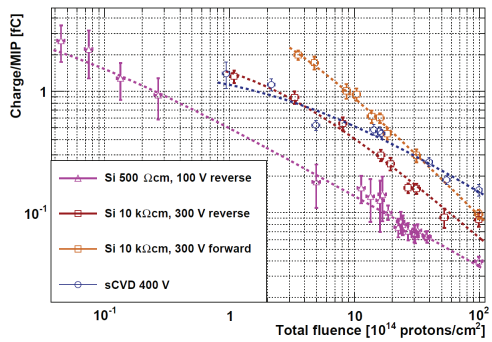


Figure 3: Degradation curves of scCVD diamond detector at 400 V compared with 10 kΩcm silicon detector at 300 V and 500 Ωcm silicon at 100 V reverse as reference curve [3].

In liquid helium, the major downside of silicon detectors compared to diamond, its high leakage current, disappears. The leakage current for the silicon remains below 100 pA at 400 V, even under forward bias for an irradiated diode. However, the diamond is seen to perform better for very high fluence and suffers less variation in its output.

INSTALLATION OF CRYOGENIC BLMS ON THE OUTSIDE OF THE COLD MASS OF THE LHC MAGNETS

As a safety critical system, the long term stability of the BLM detectors is a high priority criterion. It has therefore been decided to install several Cryogenic BLMs on the outside of cold mass of existing LHC magnets.

During Long Shut-down 1 (LS1) four cryogenic radiation detectors were mounted on the outside of the cold mass containing the superconducting coils in the cryostat of two LHC dipole magnets. These four detectors consisted of one 500 μm scCVD diamond detector (see fig. 4, place nr 1), one 100 μm silicon detector (see fig. 4, place nr 2) and two 300 μm silicon detectors (see fig. 4, places nr 3 and 4).

Two types of detector holders were also used, one Al_2O_3 based ceramic holder for one of the scCVD diamond detectors (see fig. 5) and seven FR-4 glass-reinforced epoxy laminate based holders for the other locations (see fig. 6). Taking into consideration that the final Cryogenic BLMs have to be available, reliable and operate for 20 years radiation hard connectors, feedthroughs and semi-rigid coaxial cables were used.

Copyright © 2014 CC-BY-3.0 and by the respective authors

ISBN 978-3-95450-141-0

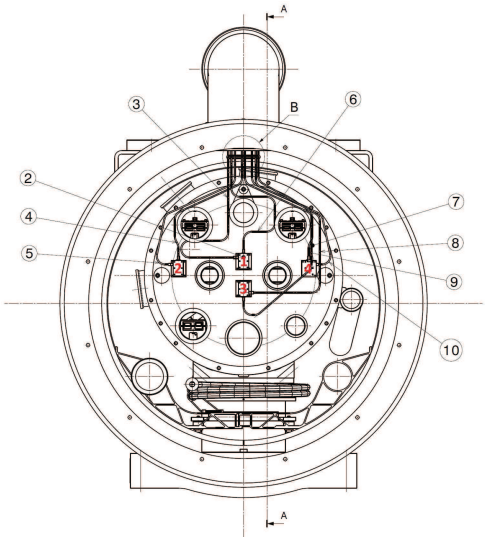


Figure 4: Cross section of an LHC dipole magnet showing the outer cryostat, the inner cold mass housing the superconducting coils and the position of cryogenic radiation detectors on the end of the cold mass.

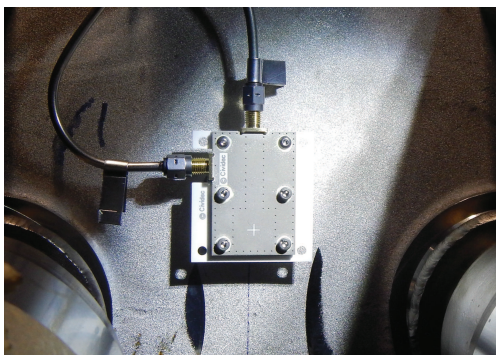


Figure 5: scCVD diamond detector mounted using a ceramic based holder.

Tests

A multistep testing procedure was performed on all detectors. Before installation the detector holders were immersed into liquid helium to test their low temperature resistance. During the installation the detectors were checked using ionizing radiation (see fig. 7), and, for the silicon detectors, using visible light.

After the interconnection between the two magnets where the detectors were located was closed and the cryostat were under vacuum a Current-Voltage (IV) curve measurement of the detectors was performed. The results (see fig. 8 and 9) show that the leakage current is at a reasonably low level, which should allow the measurement of beam losses with a high signal to noise ratio.

These first cryogenic radiation detectors installed in operational, superconducting LHC magnets will not only allow the behaviour of the detectors to be tested in realistic conditions, but also determine the validity of the integration in a setup at 1.9 K, in a magnetic field and under vacuum.

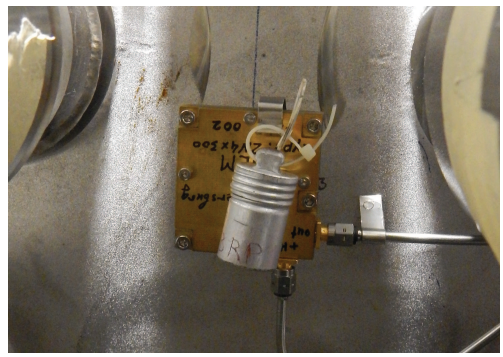


Figure 6: p^+-n-n^+ silicon detector mounted using an FR-4 glass-reinforced epoxy laminate based holder during testing with a gamma-radiation source (capsule).

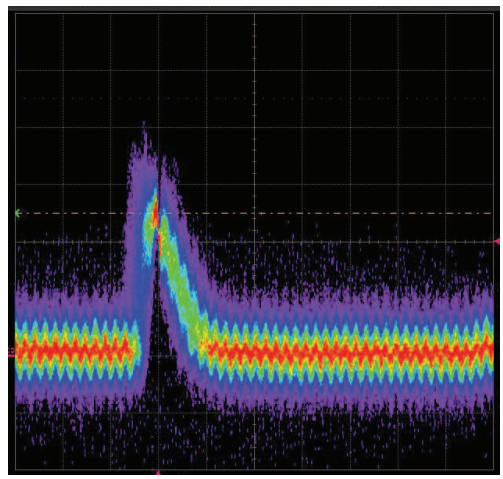


Figure 7: Beta-radiation induced signal from a scCVD diamond cryogenic radiation detector in the LHC magnet (80 mV on vertical and 40 ns on horizontal scale).

First results with beam are expected in early 2015, when the LHC starts its second operational run.

ACKNOWLEDGMENT

The project efforts have been supported by: Cryogenic Laboratory team at CERN (especially: J. Bremer, T. Eisel

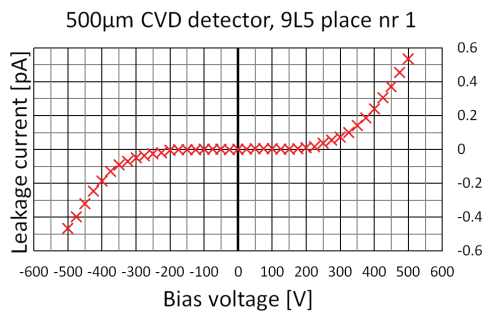


Figure 8: Leakage current of scCVD radiation detector as measured in a LHC superconducting dipole magnet at a temperature of 295 K.

ISBN 978-3-95450-141-0

Copyright © 2014 CC-BY-3.0 and by the respective authors

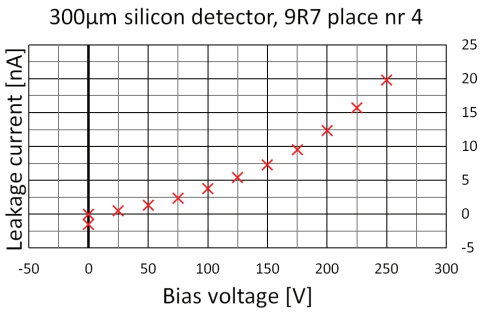


Figure 9: Leakage current of p^+-n-n^+ silicon radiation detector as measured in an LHC dipole magnet at a temperature of 295 K.

and, T. Koettig), C. Arregui Rementeria, A. Mereghetti, E. Griesmayer (CIVIDEC Instrumentation GmbH), C. Weiss, L. Gatignon, M. Glaser, F. Ravotti, RD39 collaboration (especially: J. Haerkoenen, E. Verbitskaya and P. Luukka), E. Guillermain, H. Pernegger, H. Jansen, V. Parma, T. Renaglia and a number of Beam Instrumentation group members at CERN.

REFERENCES

[1] A. Mereghetti, M. Sapinski et al., Estimation of thresholds for the signals of the BLMs around the LHC final focusing triplet magnets, Proceedings of IPAC 2012, CERN-ATS-2012-093.

[2] C. Kurfuerst et al., Investigation of the use of Silicon, Diamond and liquid Helium detectors for Beam Loss Measurements at 2K, Proceedings of IPAC 2012, p. 1080, ISBN 978-3-95450-115-1, New Orleans, USA, May, 2012.

[3] C. Kurfuerst, Cryogenic Beam Loss Monitoring for the LHC, PhD thesis.

[4] M. R. Bartosik, et al., Characterisation of SI detectors for the use at 2K, Proceedings of IPAC 2013, Shanghai, China.

[5] C. Kurfuerst, et al., Radiation tolerance of cryogenic beam loss monitor detectors, Proceedings of IPAC 2013, Shanghai, China.

[6] C. Kurfuerst, et al., Operation of Silicon, Diamond and Liquid Helium Detectors in the Range of Room Temperature to 1.9 Kelvin and After an Irradiation Dose of Several Mega Gray, Proceedings of IBIC 2013, Oxford, UK.

[7] M. Glaser, L. Durieu, C. Leroy, M. Tavlet, P. Roy and F. Lemeilleur, New irradiation zones at the CERN-PS, Nucl. Instr. and Methods, vol. A 426, pp. 72-77, 1999.

Copyright © 2014 CC-BY-3.0 and by the respective authors

ISBN 978-3-95450-141-0

LCLS BEAM DIAGNOSTICS*

H. Loos†, SLAC, Menlo Park, CA 94025, USA

Abstract

An extensive set of beam diagnostics has been one of the factors in the successful commissioning and operation of the Linac Coherent Light Source (LCLS) x-ray FEL over the last seven years. The originally developed and installed diagnostics were geared towards measuring the electron beam parameters of the LCLS design specifications. Since then, a number of improved and new diagnostics has been implemented to accommodate a much wider range of beam parameters and to overcome the challenges of diagnostics for a high brightness electron beam. Plans for the diagnostics of the high repetition rate LCLS-II project and ongoing developments will also be discussed.

INTRODUCTION

The Linac Coherent Light Source (LCLS) free electron laser facility is based on the last km of the existing SLAC linear accelerator using normal conducting copper accelerating structures providing a multi-GeV electron beam at a rate of up to 120 Hz feeding a 100 m long undulator system to generate soft and hard x-rays [1]. The facility has been operating since 2009 delivering up to about 5 mJ photon pulse energy to users during 9 user runs. A comparison of the LCLS baseline performance goals and the presently achieved operational parameters can be found in Table 1.

Over the past years the range of the available electron beam parameters has been significantly widened and new capabilities have been added to the FEL which poses enhanced demands on the existing diagnostics or made the development of new diagnostics necessary. As the baseline LCLS diagnostics has been extensively described in [2, 3], this paper will focus on recent developments. Among them, upgrades to BPM signal processing hardware and RF cavity BPM tests, improvements to the charge measurements, a new wire scanner design to significantly reduce emittance measurement durations and beam tuning time, a beam profile screen less susceptible to coherent radiation effects, and instrumentation to measure the shortest bunches single-shot using coherent radiation detection as well as an X-band deflecting cavity will be presented.

Recently, a new facility, LCLS-II [4], is being planned to enhance the existing LCLS capabilities by providing a MHz rate electron beam from a superconducting accelerator operating at 1.3 GHz feeding two undulator systems to simultaneously generate soft and hard x-ray beams and to generate shorter photon wavelengths using the existing LCLS-I linac, superseding the former LCLS-II project based on using an existing fraction of the normal-conducting (NC) SLAC 2-mile copper linac. The planned performance parameters can also be found in Table 1 where values in parentheses refer to the Cu-linac.

While the LCLS-II project design benefits from diagnostics improvements already underway, several key parameters of LCLS-II present new challenges to beam diagnostics [5]. The MW beam power greatly limits the use of intercepting diagnostics such as screens and wires which makes it necessary to incorporate low rate diagnostics beam lines into the machine design. Furthermore, the MHz beam rate requires very fast acquisition hardware and software to provide real-time beam pulse synchronized data for machine tuning and fast beam-based feedback systems. Diagnostics developments as they pertain to LCLS-II will be addressed throughout the paper.

BEAM CHARGE MEASUREMENT

The absolute charge measurement at LCLS is designed to be done with a number of toroids distributed at various locations from the injector through the undulator area which then serve as cross-calibration for all the BPM charge measurements. During the initial LCLS commissioning the readings were questionable and an existing toroid still installed from the SLC was used to provide the

Table 1: LCLS and LCLS-II Parameters

	LCLS		LCLS-II
	Baseline	**Operation**	**(Cu)**
RF frequency (GHz)	2.856		1.3
Repetition rate (Hz)	120	$1-120$	10^6
Beam energy (GeV)	$4.3-13.6$	$2.4-15.4$	4
Bunch charge (nC)	0.200 & 1	$0.02-0.25$	0.1
Bunch length rms (μm)	20	$<2-50$	8
Emittance norm. (μm)	1.2	$0.13-0.5$	0.4
X-ray energy (keV)	$0.83-8.3$	$0.25-10.5$	$0.2-5$ $(1-25)$
X-ray pulse energy (mJ)	<2	<4.7	<2.2
X-ray pulse length (fs)	230	$<5-500$	60

* Work supported by DOE contract DE-AC02-76SF00515
† loos@slac.stanford.edu

ISBN 978-3-95450-141-0

Copyright © 2014 CC-BY-3.0 and by the respective authors

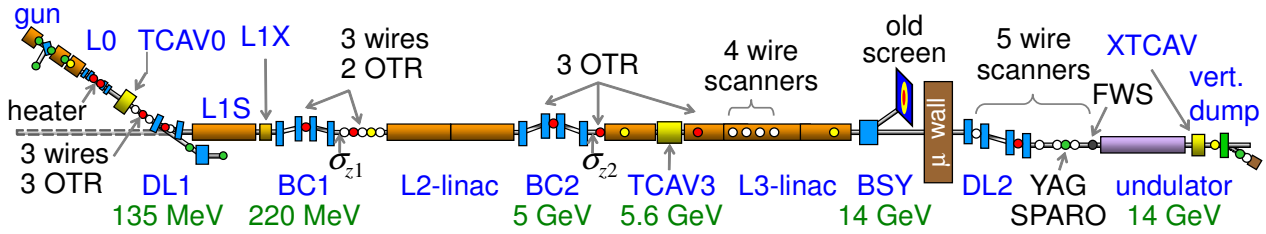


Figure 1: LCLS diagnostics layout. FWS (fast wire scanner), YAG (SwissFEL profile monitor), SPARO (Single-shot bunch length monitor), and XTCAV (X-band transverse deflector) indicate locations of diagnostics discussed in the text.

absolute LCLS bunch charge measurement. Although the toroids had been calibrated using a known test charge, the charge measurements since have shown systematic variations of up to 15% between toroids at the same bunch charge level, and pulse to pulse noise levels of up to 4%, whereas the strip line BPM charge measurement shows typically 0.05% noise at 150 pC. An upgrade project was launched, originally for the normal conduction LCLS-II project, to reach 1% absolute charge accuracy and better than 1% noise to be tested with two toroids in the beam transport line to the undulators. The improved electronics include a 10X amplifier with integrated remote calibrator located in the tunnel at the toroid, differential cables for the up to 500 ft cable run to the service building housing the controls racks, and instead of the previously used Acromag IP330 ADC now a charge ADC, the Caen QDC965A VME module, which is already used for data acquisition of beam loss monitor PMT signals, and which has a 12 bit digitizer with a high and a low signal automatic range selection.

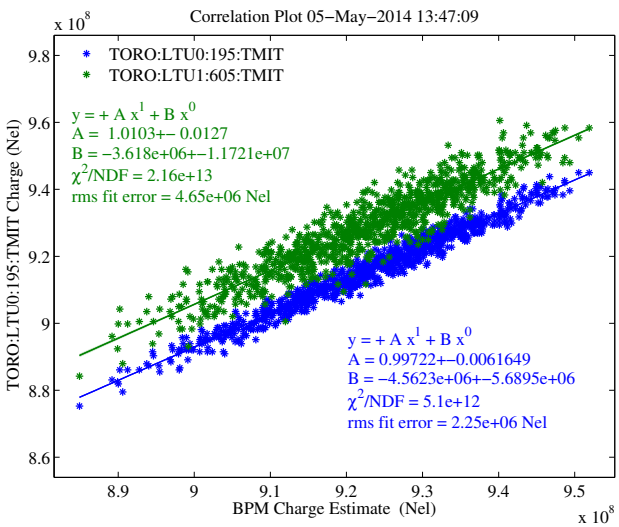


Figure 2: Charge measurement comparison with new toroid electronics and data acquisition. The toroid charge at the two locations is compared to the mean charge measured with two nearby BPMs during an 8 s long duration.

The new system shows the desired performance as can be seen in Fig. 2. The two independently calibrated toroids agree to about 1% with each other on the absolute charge and agree to better than 1% to the mean charge reported by the two nearby BPMs. The noise is significantly reduced by about a factor 10 to 0.2–0.5%.

For the LCLS-II charge measurement, one important parameter is the average machine current which will be measured with integrated current transformers like the Bergoz Turbo-ICT, and which will be located in the injector and bunch compressor areas and in each of the beam lines downstream of a beam spreader distributing the beam to the different undulators. A sensitivity down to 1 μA is required for low charge operation. An independent charge measurement will be provided by a Faraday cup at the end of the low rate diagnostic line in the LCLS-II injector.

BEAM POSITION MEASUREMENT

Several development projects for potential upgrades of the LCLS beam position monitor hardware and analog and digital processing electronics using the μTCA architecture have been undertaken over the past several years, which were also driven by diagnostics requirements for the former Cu-linac based LCLS-II project.

Stripline Beam Position Monitors

The existing LCLS strip-line BPM receiver electronics [6] was designed to process signals from a single BPM in one crate containing an analog front end (AFE) operating at 140 or 200 MHz with a 7 MHz bandpass filter and 16 bit digitizers. A new BPM receiver and digitizer electronics for strip-line BPMs have been developed in the past years and a test crate has been installed and is operating with first 3 [7] and now 4 BPMs in the L3 linac [8]. The new SLAC built AFE operates at 300 MHz where the strip-line response is higher and has 15 MHz bandwidth. Similar to the previous system, amplifiers and two variable attenuators provide the necessary dynamic range for operation at different bunch charges and a calibration pulse is feed into the stip-lines for self-calibration between beam pulses. A Struck SIS8300 16 bit ADC clocked at 109 MHz is used to sample the signal waveforms. A total of 8 BPMs can be processed in a single 12 slot crate.

The performance of the new system of 3 BPMs is shown in Fig. 3 for a range of 12–350 pC bunch charge. Compared

Copyright © 2014 CC-BY-3.0 and by the respective authors

ISBN 978-3-95450-141-0

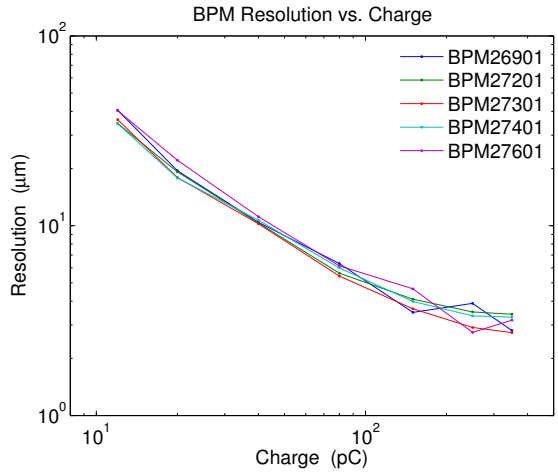


Figure 3: Stripline BPM resolution with new compact μTCA receiver for bunch charges from 12–350 pC. The first and last BPM 26901 and 27601 equipped with standard LCLS BPM electronics show similar performance.

to neighboring BPMs with a standard receiver the BPMs processed with the new system show almost identical resolution and have been reliably operating for almost 2 years. It remains an open issue that the measured resolution is the same although the processing frequency is better suited to the strip-line length and the bandwidth has been doubled.

Cavity BPMs

In collaboration with Pohang Accelerator Laboratory a new X-band cavity BPM and receiver electronics is being tested in the LCLS undulator beam line adjacent to one of the existing ANL built X-band RF BPMs [9]. The new BPM has been designed and built by PAL [10] and is designed to use 4th harmonic of accelerator frequency at 11.424 GHz compared to standard LCLS undulator cavity BPMs operating at 11.384 GHz to enable arbitrary S-band bucket fill pattern for potential LCLS-I multi-bunch operation. Figure 4 shows the PAL cavity BPM which has the usual monopole reference and dipole cavity but uses coaxial feed-through instead of an RF window and waveguide as implemented for the ANL BPMs.

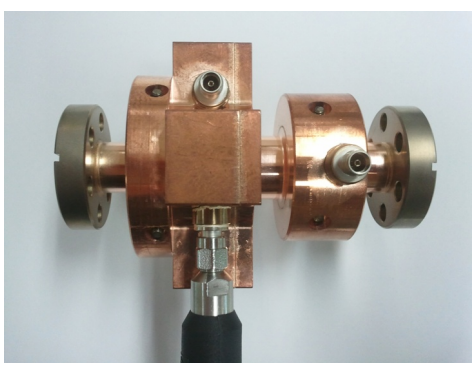


Figure 4: PAL XFEL RF X-band cavity BPM.

The new down-mix receiver [11] avoids the hydrogen poisoning occuring with the existing RF-BPM receivers which leads to gain deterioration and is designed for low cost using COTS circuits and a wide frequency range 11–13 GHz with only the input filters limiting the bandwidth to 200 MHz. The receiver chassis is located in close proximity to the BPM, and the down-mixed signals are then digitized upstairs of the undulator hall with a μTCA system similar to the strip-line BPMs using a 4 channel SIS digitizer at 119 MHz. The system schematic is shown in Fig. 5.

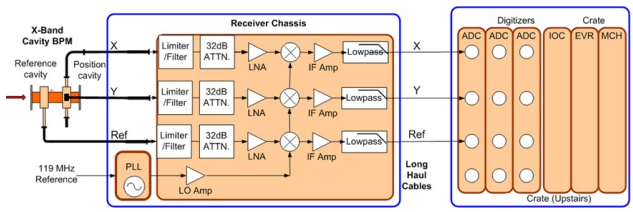


Figure 5: X-band cavity BPM receiver schematic. The μTCA crate is located outside the undulator hall whereas the receiver chassis is close to the BPM.

Two different cavities installed about 20 cm downstream of the last undulator RF-BPM and supported by the same girder have been tested with beam so far over the last year. The best resolution data achieved is shown in Fig. 6 for the horizontal plane of the first PAL RF-BPM installed with a resolution slightly below 400 nm at 150 pC bunch charge, which is well below the original design goal of 1 μm for LCLS-II, but is not as good as the resolution of most of the installed ANL RF-BPMs. The elevated noise presently limiting the resolution has since been traced to a bad power supply in the receiver chassis which has been upgraded and beam tests will take place late September at the start of the next LCLS run.

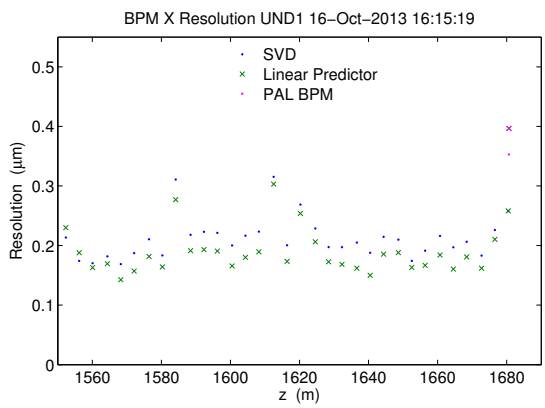


Figure 6: PAL XFEL cavity BPM resolution compared to 33 undulator cavity BPMs measured at 13.4 GeV and 150 pC. The PAL BPM is located at 1680 m and indicated in magenta.

Tests are also underway to use the new receiver with the ANL built BPMs for performance comparison which re-

ISBN 978-3-95450-141-0

Copyright © 2014 CC-BY-3.0 and by the respective authors

quires little modification of the receiver to accommodate the different cavity frequency and the waveguide input.

LCLS-II BPMs

The MHz beam rate and the 10 pC low end of the planned charge range pose the main design issues for the LCLS-II accelerator. Strip-line BPMs with about 30 μm resolution at the low charge suffice for most of the normal conducting part of the beam transport. In critical locations where much better resolution is necessary as for energy measurement, fast transverse feedback, beam jitter correction at wire scanners, and undulators, RF cavity BPMs will be installed with X, S, or L-band frequency depending on the measurement function and required beam pipe aperture. Cold button BPMs can be used inside the cryo-modules as a 100 μm resolution is sufficient due to the large aperture of the modules. The high beam rate requires fast processing for several diagnostics and controls elements which will be addressed with the development of a common processing platform [5] including device specific analog front end, fast digitizer, and FPGA data processing, which is then connected to fast timing, machine protection, and fast feedback networks.

BEAM PROFILE MEASUREMENT

Measurements of the transverse size and profile of the electron beam are routinely performed to yield information about the beam's transverse or—via bend magnets and deflecting cavities—longitudinal phase space distribution needed to tune the machine settings to match the design phase space or to optimize beam parameters throughout the accelerator. During the initial LCLS commissioning strong visible coherent effects (COTR) due to the high brightness of the beam were observed on the optical transition radiation (OTR) screens [12] which rendered them insufficient for beam profile measurements at most locations of the accelerator. Several methods of mitigating the COTR effect as well as using and upgrading wire scanners have been explored.

Fast Wire Scanner

As wire scanners are now the predominant transverse profile measurements at LCLS, the originally installed SLC-style scanners suffer from several shortcomings which are being addressed with a new design, based on a linear motor [13]. The SLC-style scanners have a wire card mounted to a shaft which is supported on one end and are driven by a stepper motor. The shaft moves at a 45° angle to the horizontal and has wires oriented horizontally and vertically to sample the respective planes, and a wire at 45° perpendicularly to the scan motion to measure x-y coupling. This setup leads to transverse oscillations of the wire positions up to 10s of μm which could be greatly reduced by implementing either gear reducers or micro-stepping. The achievable speed of less than 1 mm/s means however that a scan of both transverse profiles at a single wire takes more than a minute and a full emittance measurement requiring scans at four wire locations in the beam line takes several minutes.

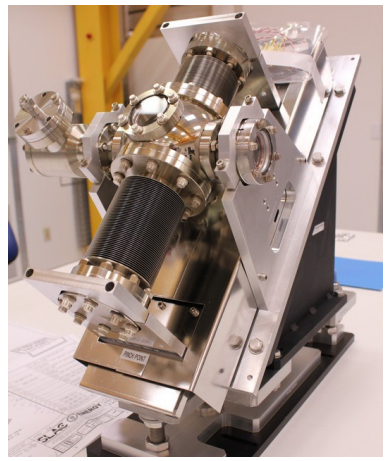


Figure 7: Fast Wire scanner prototype. The beam enters through the right port. Visible are the 45° support stand, the μ-metal shield covering the linear motor, and the two bellows and 6-way cross housing the wire card.

The new fast wire scanner (FWS) design shows in Fig. 7 is normally operated at a maximum speed of 100 mm/s with speeds of 400 mm/s or more being possible by use of a linear motor. It employs a dual bellow design to equalize vacuum forces and to provide a rigid support of the wire card equipped with 3 wires similar to the SLC design. An absolute encoder gives beam synchronous pulse-to pulse wire position data with sub-μm resolution over the 50 mm actuator stroke. First tests of a FWS installed upstream of the LCLS undulators back-to-back to an existing SLC-style wire scanner show identical beam size measurements, but the scan of both planes takes only a few seconds (see Fig. 8).

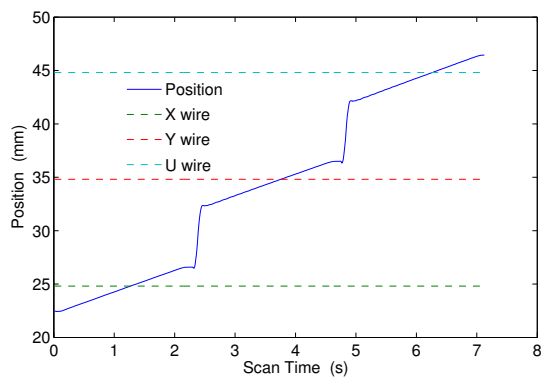


Figure 8: Fast wire scanner motion profile. The solid line shows the encoder read back of the card position, whereas the dashed lines indicate the electron beam intercept position of the respective wire on the card.

Copyright © 2014 CC-BY-3.0 and by the respective authors

ISBN 978-3-95450-141-0

At the initial tests of the first fast wire scanner prototype with the electron beam being set up to generate x-rays in the undulators, a drop in the FEL pulse energy was observed, as can be seen in Fig. 9. The drop did not only happen at the point where the carbon wire intercepts the electron beam, but during the entire time when the motor position was away from the initial position. The drop was correlated to orbit oscillations in the undulators of up to 25 μm, which is equivalent to the rms electron beam size in the undulators. The orbit kick was originating from the fast wire scanner with magnetic field integral changes of about 20 μTm depending on the position of the linear motor.

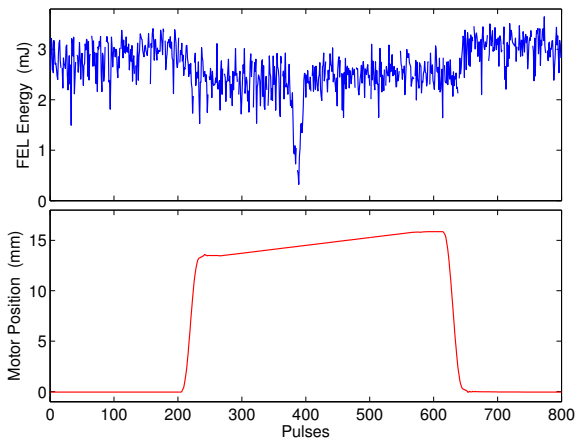


Figure 9: Drop in FEL pulse energy during fast wire scanner prototype scan at 12.4 GeV beam energy. The main dip around pulse number 390 occurs when the electron beam intercepts the carbon wire.

Subsequently, a μ-metal shield was retrofitted to cover the linear motor and the improved version shows field integral changes over most of the scan range below 1 μTm, which is sufficient to guarantee beam steering of less than 10% of the rms beam size at all LCLS wire scanner locations. Plans to replace most of the existing LCLS wire scanners are underway.

A similar design is planned to be used for LCLS-II to enable beam size measurements in the main beam line where the beam repetition rate of up to 1 MHz necessitates much higher scan speeds as the SLC-style scanner provides. A main concern is damage to the wires from the MW beam power. Initial studies of the heat deposition and transport in the wire are based on damage studies of carbon wires in the SLC wire scanners [14]. Figure 10 shows simulations of the relative temperature increase in a 34 μm thick carbon wire during a scan at 240 mm/s wire speed and 40 μm beam size at 0.6 MHz beam repetition rate for various values of thermal diffusivity found in the literature for carbon wires. The final temperature increase in the case of no cooling is due to the heat deposited from the integrated charge density impinging on the wire during the scan, which was chosen to be equivalent to the charge density where no damage occured according to [14]. Due to the 45° geometry the actual motor speed needs to be larger than 340 mm/s which has been demonstrated with the present FWS design.

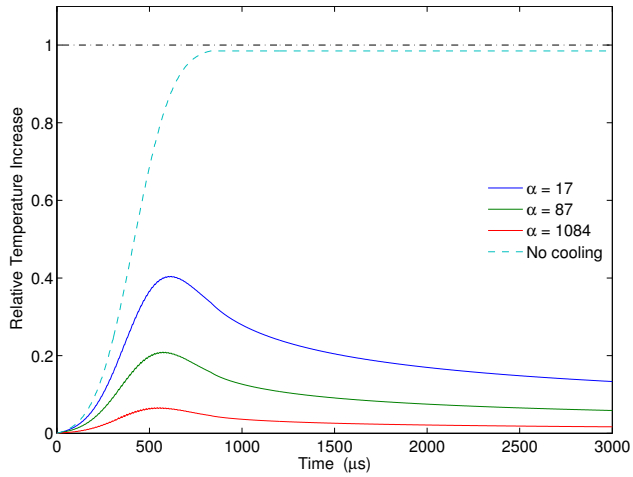


Figure 10: Simulation of carbon wire temperature increase during wire scan. The increase is normalized to the final temperature at the end of the scan assuming no cooling. The thermal diffusivity α is given in mm^2/s.

OTR and YAG Screens

During the initial LCLS commissioning, the OTR screens downstream of the bunch compressors were deemed unusable due to the observed COTR effect [12], but the screens in the injector prior to any bend magnets remained useful as the OTR intensity response was linear with charge. After the installation of the laser heater and its chicane magnets [15] the COTR effect was considered tolerable due to the small R_{56} of 8 mm of the chicane. Recent investigations [16] comparing wire scanner and OTR screen measurement show that the emittance measured with the injector OTR screen agrees well with the wire scanner measurement if the chicane is off. If it is turned on with the heater laser still blocked the emittance is however underestimated by 30%.

Figure 11 shows typical OTR spectra at 135 MeV and 150 pC taken with a transmissive grating placed in front of the lens of the OTR CCD camera. It shows a smooth incoherent OTR spectrum with the chicane off, and a factor 2 higher light intensity with the chicane on, but the heater laser blocked. The COTR effect is much reduced when the heater laser is enabled by adding uncorrelated energy spread to the beam and reducing the micro-bunching instability. The temporal modulation of the electron beam at 766 nm in the laser heater undulator by the laser also causes a modulation at the second harmonic at 383 nm which can be seen in the figure. In both cases when the chicane on on the additional light is emitted preferably in the core of the beam, hence underestimating the true beam size. Emittance measurements for normal beam tuning which requires the laser heater chicane to be on have been regularly done with

ISBN 978-3-95450-141-0

Copyright © 2014 CC-BY-3.0 and by the respective authors

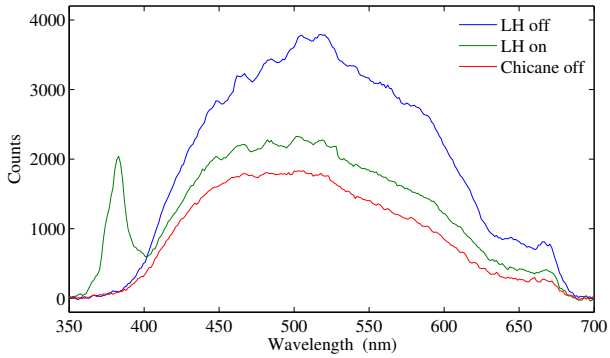


Figure 11: Injector OTR light spectrum for different laser heater (LH) configurations at 150 pC charge. LH on is the normal LCLS operating mode, LH off has the laser beam of the heater blocked, and chicane off also has the chicane bend magnets turned off.

the heater laser blocked as the additional light at the second harmonic was affecting the beam size measurements. Although a suitable optical filter could narrow the spectrum collected by the camera to the central part where the intensity with the laser heater on is only enhanced by about 25%, such a measurement resulted in the beam emittance still underestimated by 30%. The standard injector emittance measurement has now been done for the last year with the adjacent wire scanner. A proper 2-D single shot screen setup needed for reliable time resolved emittance measurements in the LCLS injector remains an open issue as YAG:Ce scintillators saturate at the small beam sizes there [2], but crystals with lower scintillation yield might offer a possible solution.

One method to avoid coherent visible radiation to affect beam profile measurements is to use a screen of a fluorescent crystal rather than an OTR screen, and to have a non-specular viewing geometry so that transition radiation emerging from the crystal surface at a specular reflection angle with respect to the electron beam axis does not enter the camera. Such a screen with various upgrades has been installed for several years in the LCLS main dump line replacing an OTR screen where the YAG crystal is tilted by 7° to the electron beam axis, thus effectively reflecting upstream coherent light away from the camera.

A beam profile monitor with a new fluorescent screen observation geometry developed at the Paul Scherrer Institut (PSI) is now being tested at LCLS [17] at GeV beam energies in a location upstream of the undulators (see Fig. 1). This location was chosen because an OTR screen at approximately the same location had shown in the past the strongest COTR effect with up to 5 orders of magnitude enhancement due to strong bunching at visible wavelengths from the micro-bunching instability. Furthermore, the location enables to measure final slice emittance and bunch length just before the beam enters the undulators by using the deflecting cavity in the main linac.

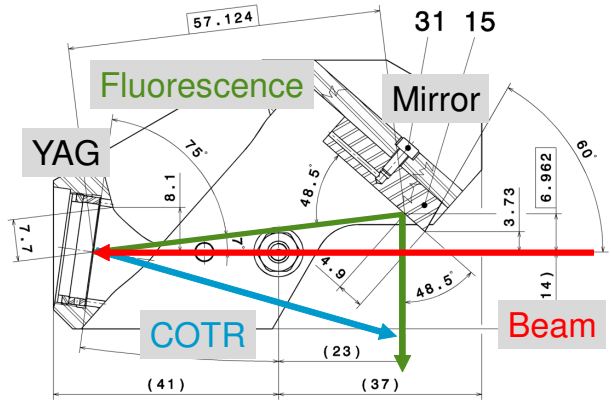


Figure 12: Schematic of the SwissFEL YAG screen.

In the new design shown in Fig. 12, the YAG crystal normal is tilted by 8° to the electron beam axis and the viewing angle of 7° is chosen for optimal resolution so that the line of sight from the camera is in line with the line of fluorescence emitted where the electron beam passes through the crystal, taking refraction at the crystal surface into account. The tilted object geometry is accounted for by tilting the CCD with respect to the lens according to the Scheimpflug principle so that the entire crystal plane can be in focus.

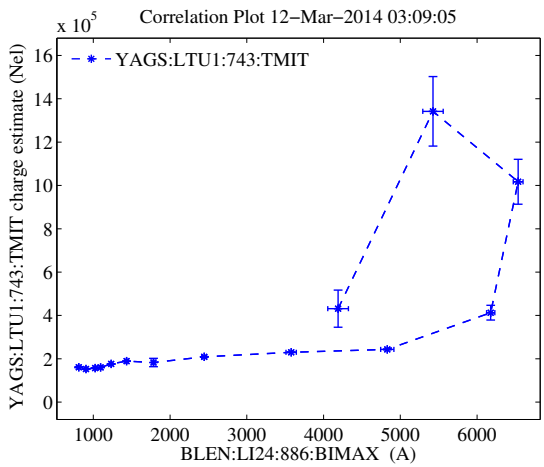


Figure 13: Total CCD counts from SwissFEL YAG screen for different bunch compressions at 160 pC.

The YAG crystal thickness plays a crucial factor in the operation of the profile monitor as the crystal initially installed was 100 µm thick and due to the resulting beam loss the machine protection system only allowed 0.5 Hz operation. The presently installed 30 µm thick crystal now enables 10 Hz beam rate with the beam parked on the tune-up dump before the undulators. Beam sizes as small as 45 µm could be observed to date. Studies of the COTR effect have been made by observing the beam spot brightness while varying the bunch compression (see Fig. 13) which show at full compression a small coherent enhancement of 10–15% for a 20 pC bunch charge at both 4 and 13 GeV.

Copyright © 2014 CC-BY-3.0 and by the respective authors

ISBN 978-3-95450-141-0

This is reduced to 5% with the laser heater on. Furthermore, at this low charge no fluorescence saturation effect is observable. At 160 pC coherent effects are more pronounced; with the laser heater off a 10 times enhancement is observed which reduces to factor 2.5 with the laser heater enabled. A slight saturation of the fluorescence at 180 pC could be inferred from a 10% drop in light emission during a scan of an upstream quadrupole. Recently, a yellow filter was installed to narrow the observed spectral range to the green YAG fluorescence to block potential coherent radiation at longer visible wavelengths and first tests indicate considerably less coherent enhancement. Further details of the studies done so far of the profile monitor can be found in [17].

As this design has proven to reduce the COTR effect from many orders of magnitude to a percent effect, it is now being considered for the LCLS-II diagnostics as beam profile monitors in the low energy diagnostics line and for use at low beam rate in the main accelerator beam line and the transport lines to the two undulators.

Overlap Diagnostics

A combination device of a wire scanner and a fluorescent YAG screen is being used for the soft x-ray self-seeding experiment (SXRSS) [18] where after 8 undulators a four dipole chicane separates the electron beam from the x-ray beam, and a setup of a grating and three mirrors acts as a monochromator for the x-rays. A special diagnostics was needed which simultaneously can measure the transverse position of both the electron beam and the x-ray beam at two different locations downstream of the chicane/monochromator setup, so that both beams which are diverted from their straight trajectories can be steered back onto the same axis to enable further FEL amplification in the downstream undulators. As only a YAG screen can sufficiently measure the position of the x-rays of at this point only a few nJ pulse energy, but radiation protection for the undulators prohibits the use of such a crystal for electron beam diagnostics, the beam overlap diagnostic (BOD) device shown in Fig. 14 has been developed which combines a 20 µm thick 10 mm square YAG crystal and two crossed 40 µm thick carbon wires. With an electron beam size of 30 µm rms in the undulators and an x-ray spot size as small as 30 µm an overlap precision of the same value is needed.

In normal beam operation the device is retracted and both beams pass through the cut-out in the left part. A stepper motor with sub-µm encoder resolution and 1 µm position repeatability provides horizontal motion and when inserted, the nominal electron beam axis is indicated by the cross-hair between the vertical wire and the YAG crystal to the right, leaving 1.5 mm clearance of the electron beam to the crystal. The whole card assembly can be viewed with a CCD camera having about 10 µm pixel resolution via a fixed 45° annular mirror in front of the card with a 9 mm hole to provide sufficient stay clear. Two such diagnostics are installed in the inter-spaces upstream of undulators 10

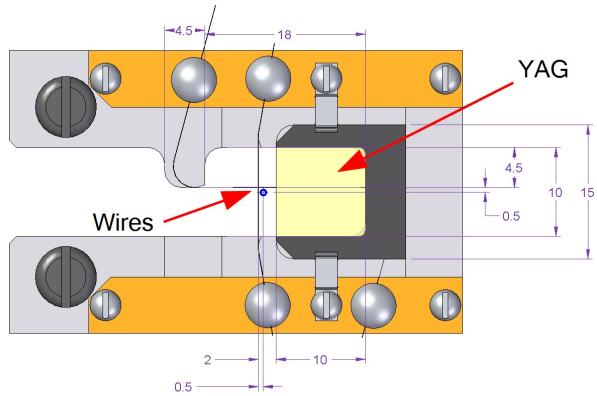


Figure 14: Soft x-ray self-seeding beam overlap diagnostic card. Nominal beam position is at the cross-hair in the center, electron beam position is measured with the adjacent horizontal and vertical wires, and x-ray position with the YAG crystal to the right.

(BOD10) and 13 (BOD13) and supported by the respective girders while the SXRSS setup replaced the undulator located on girder 9.

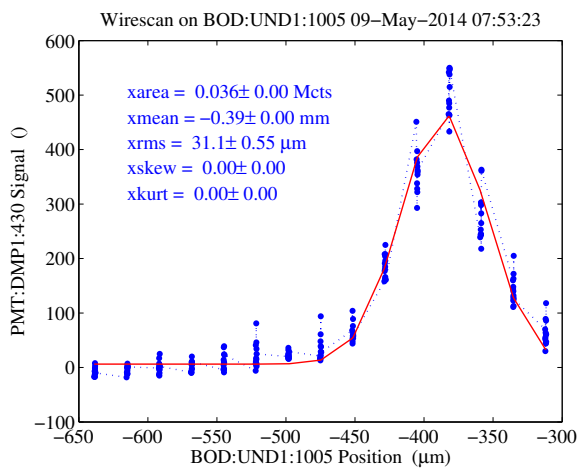


Figure 15: Electron beam position measurement with the BOD.

The electron beam position relative to the wires can be obtained by moving the position of the supporting girder horizontally or vertically, and by recording the electron beam loss signal when the wire is hit, which is shown in Fig. 15. The such established distance between the wires and the electron beam can then be used to determine the pixel coordinates in the camera image of both wires and YAG crystal, and finally to determine the separation between the electron and x-ray beams. The x-ray beam has to be steered away from its nominal position via one of the monochromator mirrors to be visible on the YAG crystal. Once the separation is measured on both screens, the x-ray beam is steered onto the electron beam position using the measured response function of the x-ray mirrors.

Figure 16 shows the camera image of the first overlap

ISBN 978-3-95450-141-0

Copyright © 2014 CC-BY-3.0 and by the respective authors

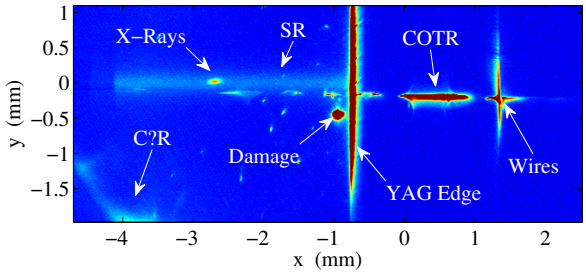


Figure 16: Typical image of the girder 10 BOD diagnostics with the YAG crystal occupying the left and the wires the right part. The annotations indicate the various features visible in the image (see text).

diagnostics. Besides the x-ray spot a number of undesired features are visible which are generated solely by the electron beam. While the synchrotron radiation stripe (SR) is generated from the last bend in the upstream SXRSS chicane and shows steady intensity, the remaining features fluctuate significantly in intensity from shot to shot with up to 100 times the x-ray intensity. The wires can be seen as COTR or coherent optical diffraction radiation (CODR) is generated at the carbon surface where the electron beam is near the wire. The edge of the YAG crystal and a damaged spot are visible by the same mechanism. The radiation labeled "C?R" is however not fully understood. Highly coherent diffraction radiation reflected of the smooth YAG surface would be emitted under small angles to the electron beam and pass through the upstream annular mirror and not be seen by the CCD; however, coherent UV components of this radiation might stimulate fluorescence in the crystal which would be emitted at all angles.

The fluctuating nature of most of the undesired radiation, which is even more pronounced at the second diagnostics, makes it necessary to subtract a background averaged over dozens of images with the x-ray beam blocked. The resulting x-ray to electron beam separation could thus be measured with the required precision to achieve self-seeding [19].

BUNCH LENGTH MEASUREMENT

The generation of shorter and shorter bunches of the high brightness LCLS accelerator in low charge mode to durations of a few fs makes the development of adequate diagnostics necessary as the one originally installed for LCLS was intended for a nominal bunch length not shorter than 20 fs rms. Two such systems have been commissioned during the past year, a single-shot spectrometer (SPARO) and an X-band deflecting cavity, to measure the temporal bunch properties close to the undulators.

Coherent Radiation Monitor

As coherent radiation spectra based electron bunch length measurements were originally applied to 100s of femtosecond or ps long bunches requiring far-infrared techniques, the few μm rms and shorter bunches at LCLS generate coherent radiation in the near infrared to mid-infrared or even visible spectrum. A single-shot bunch length monitor has been developed at LCLS as a prism spectrometer for the 1–40 μm wavelength range using a KRS-5 prism [20]. As shown in Fig. 17, OTR light from a 1 μm thick Al foil at a location upstream of the undulators is imaged onto a pyroelectric line sensor with 128 elements. The present setup is disruptive to normal beam operation, but could be relocated to non-invasively detect coherent edge or synchrotron radiation from a bend magnet in the upstream beam transport line.

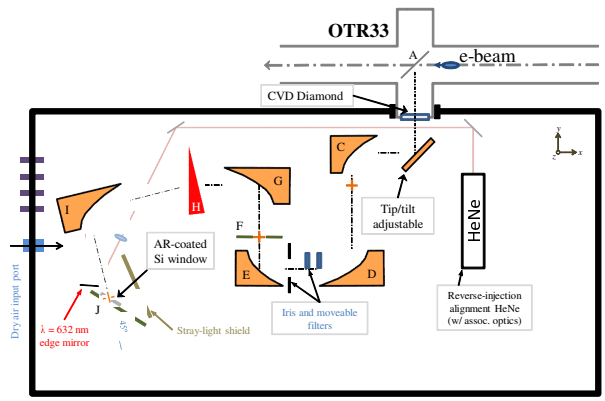


Figure 17: Single-shot mid-IR prism spectrometer.

The use of a prism enables a straightforward coverage of the necessary more than one order of magnitude wavelength range needed for bunch shape reconstruction using a Kramers-Kronig phase retrieval algorithm, however, the resolution is lower than with a grating, and due to the wavelength dependent material dispersion, the resolution and efficiency is also non-uniform and varies considerably over the wavelength range. As the measured spectrum is the product of the bunch form factor of interest with the optical system transmission and spectrometer efficiency, this unknown transfer function needs to be known in order to determine the bunch form factor and eventually the bunch length and temporal distribution. Suitable broadband and calibrated sources are not available to determine the transfer function, so it was found by setting the accelerator to a range of bunch lengths and fitting the measured spectra to a single unknown transfer function and simulated bunch form factors matching the different accelerator settings [20] giving a useful result for wavelengths between 1–20 μm.

Figure 18 shows for four different accelerator bunch compression settings the spectra corrected by the transfer function with extrapolations between 500 cm^{-1} and zero wavenumber where the spectrometer response is too weak, and also the reconstructed bunch profiles at 150 pC and

Copyright © 2014 CC-BY-3.0 and by the respective authors

ISBN 978-3-95450-141-0

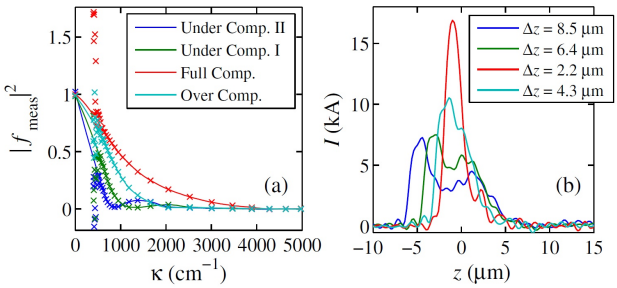


Figure 18: Bunch form factors (a) measured with single-shot prism spectrometer and temporal shape reconstructions (b), adapted from [20].

13.4 GeV. The shortest bunch length is 2.2 μm FWHM, but at a low charge of 10 pC bunch lengths below 2.2 μm FWHM could be observed. The 150 pC result is consistent with a 1 μm rms bunch length measured with the XTCAV (see below) under similar beam conditions. On the long bunch side, lengths of up to 18 μm FWHM could also be observed.

For LCLS-II the non-interceptive bunch length monitors will also be essential for the fast longitudinal feedback. The average THz radiation power becomes 1000 times higher with otherwise similar beam properties as for the LCLS-I monitors. The single shot bunch length detection necessary at MHz rate becomes a dynamic range issue as attenuating the average power could lower the pulse energy below the noise level. Possible cooling schemes and pyroelectric detector damage thresholds are presently being explored.

Deflecting Cavity

In order to improve the time resolution of the existing S-band deflecting cavity in the L3 linac of about 5 μm to be able to measure much shorter bunch lengths and resolve finer features in the bunch shape an X-band deflecting cavity was proposed a few years back which would provide a factor 10 or better resolution from the 4 times higher RF frequency and the much higher field gradient possible. Such a cavity was build, installed and finally in 2013 commissioned, and is located downstream of the undulators in the beam line leading to the main beam dump [21]. At this location the diagnostics is non-interferring with FEL user operation as only the spend beam after lasing is affected; it also provides longitudinal phase space information through the dispersion of the bend magnet by viewing the beam downstream of the magnet via a YAG screen as shown in Fig. 19.

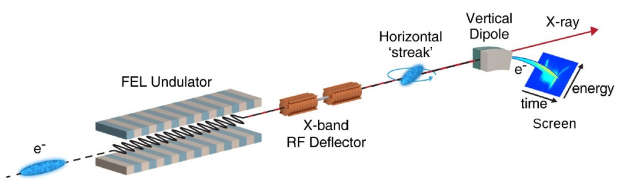


Figure 19: Diagram of the XTCAV diagnostic layout in the undulator dump line, adapted from [21].

The streaking capacity can be seen in Fig. 20 showing beam sizes at the ±90° and XTCAV off setting at 4.2 GeV beam energy and the 20 pC low charge configuration at about half the maximum RF field, where the unstreaked intrinsic beam size corresponds to 1 μm resolution via the streak or calibration factor of 55 and a bunch length of 1.41 μm can be obtained. The highest resolution of 1 fs at full RF power has been achieved at soft x-ray beam energies, whereas the resolution at hard x-ray energies is 4 fs.

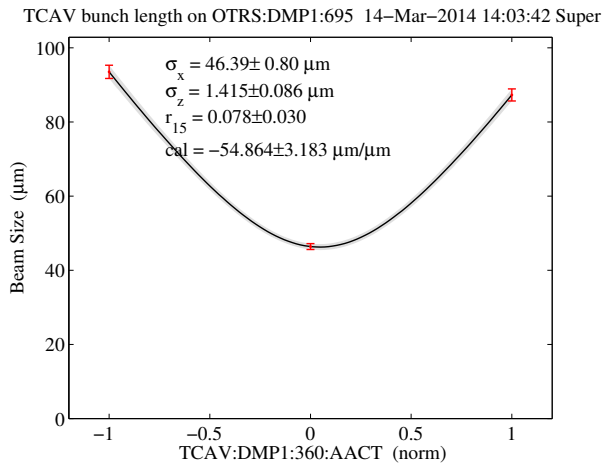


Figure 20: XTCAV bunch length measurement at 4.2 GeV and 20 pC. The three data points for the bunch length fit correspond to settings of −90°, off, and +90°.

The main purpose for this development was however the possibility to observe the dynamics of the longitudinal phase space evolution of the electron beam during the lasing process in the undulators as the electrons lose energy due to the interaction with the growing x-rays pulse. The time resolved loss in beam energy is directly proportional to the x-ray power distribution, and the increase in slice energy spread is also related to the x-ray temporal pulse shape. Figure 21 shows a phase space snapshot during soft x-ray beam operation at 4.5 GeV. Details of the x-ray pulse analysis can be found in [21]. These beam images can now be streamed to the x-ray experimental DAQ system to provide offline pulse to pulse x-ray pulse length information. Work is in progress to perform the image analysis in real-time to make this information available at 120 Hz rate [22].

An improved calibration based on absolute measurements with the deflecting cavity in the L3 linac for the relative bunch length monitor after the second bunch compressor [3] which is used in the 120 Hz longitudinal beam based feedback was implemented in Sep. 2013 and could now be cross-checked with the absolute bunch length measurement using the higher resolution XTCAV. The relative error shown in Fig. 22 is only 5% on average over 1 decade of bunch length.

ISBN 978-3-95450-141-0

Copyright © 2014 CC-BY-3.0 and by the respective authors

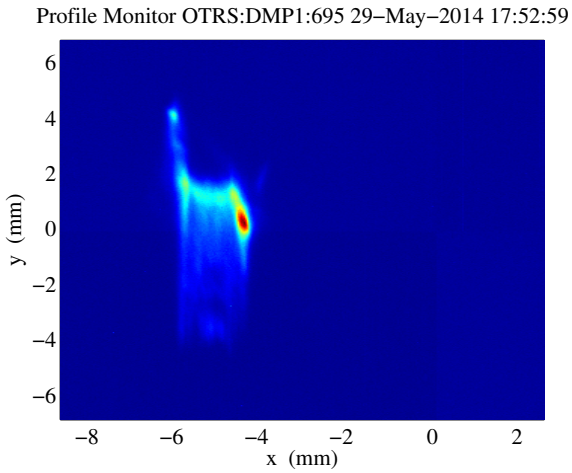


Figure 21: XTCAV measurement of electron beam phase space during soft x-ray self seeding operation. The time is horizontal and the energy vertical. The beam occupying the area below the main brighter part of the beam represents electrons participating in the lasing process.

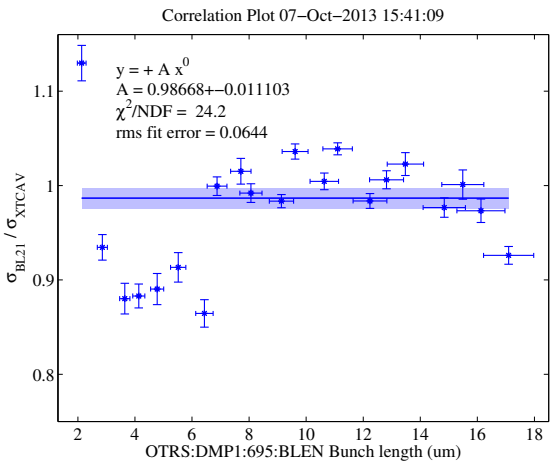


Figure 22: Comparison of post BC2 relative bunch length monitor calibration with XTCAV absolute measurements for 150 pC. The beam energy at the XTCAV was 10.4 GeV.

Besides the x-ray pulse shape determination, the XTCAV has since proven to be an invaluable tool for machine tuning and for many beam physics studies, as the suppression of micro-bunching by the laser heater, or the emittance spoiling of temporal parts of the beam with a slotted foil, or the dynamics of two-bunchlet beam operation can be observed. To further reduce the time resolution, an X-band SLED system as RF pulse compressor is under development, which will double the RF field in the XTCAV and enable 2 fs resolution at hard x-ray beam energies.

ACKNOWLEDGMENT

I wish to acknowledge the many contributions from colleagues at SLAC and collaborators elsewhere to the developments and results presented here first. For the toroid development I thank Dave Brown, Shantha Condamoor, and Ray Larsen, for the PAL RF BPM collaboration Sandeep Babel, Changbum Kim, Patrick Krejcik, Sonya Hoobler, Andrew Young, and Charlie Xu, and for the fast wire scanner project Scott Anderson, Marc Campell, Antonio Cedillos, Mitch D'Ewart, Patrick Krejcik, Rick Iverson, and Ziga Oven.

REFERENCES

[1] P. Emma *et al.*, Nature Photonics 4 (2010) 641.

[2] H. Loos *et al.*, "Operational performance of LCLS beam instrumentation," Proceedings of BIW 2010, Santa Fe, NM, May 2010, p. MOIANB01 (2010).

[3] H. Loos, "LCLS accelerator operation and measurement of electron beam parameters relevant for the x-ray beam," Proceedings of SPIE, 8778, p. 87780J (2013).

[4] P. Emma *et al.*, "The linear accelerator design for the LCLS-II FEL facility," Proceedings of FEL 2014, Basel, Switzerland, Aug. 2014, p. THP025 (2014).

[5] J. Frisch *et al.*, "Electron beam diagnostics and feedback for the LCLS-II," Proceedings of FEL 2014, Basel, Switzerland, Aug. 2014, p. THB04 (2014).

[6] E. Medvedko *et al.*, "Stripline beam position monitors for LCLS, BIW08, Tahoe City, CA, USA, May 2008, TUPTPF037, p. 285 (2008).

[7] C. Xu *et al.*, "Design of an ultra-compact stripline BPM receiver using microTCA for LCLS-II at SLAC,"' Proceedings of IBIC2013, Oxford, UK, WEPC23, p. 731 (2013).

[8] C. Xu *et al.*, "Commissioning results of MicroTCA.4 stripline BPM system," WEPD17, Proc. IBIC 2014, (2014)

[9] S. Smith *et al.*, "Commissioning and performance of LCLS cavity BPMs," Proceedings of PAC 2009, Vancouver, BC, May 2009, p. TU3GRC05 (2009).

[10] H. Choi *et al.*,"About BPMs to be used for PAL-XFEL," Proceedings of IBIC2013, Oxford, UK, MOPC25, p. 112 (2013).

[11] A. Young, J. Dusatko, S. Hoobler, J. Olsen, T. Straumann, C. Kim, "Performance measurements of the new X-band cavity BPM receiver," Proceedings of IBIC2013, Oxford, UK, WEPC24, p. 735 (2013).

[12] H. Loos *et al.*, "Observation of coherent optical transition radiation in the LCLS linac," Proceedings of FEL 2008, Gyeongju, Korea, Aug. 2008, p. THBAU01 (2008).

[13] P. Krejcik, M. Campell, N. Fong, J. Frisch, H. Loos, "Evaluation of new, fast wire scanner designs for the LCLS," BIW 2012, Newport News, VA, April 2012, TUPG035, pp. 210-212 (2012).

[14] C. Field, D. McCormick, P. Raimondi, M. Ross, "Wire Breakage in SLC Wire Profile Monitors," Proceedings of BIW 1998, Stanford, CA, May 1998, AIP Conf. Proc. 451, pp. 440-445 (1998).

[15] Z. Huang *et al.*, Phys. Rev. ST Accel. Beams 13 (2010) 020703.

Copyright © 2014 CC-BY-3.0 and by the respective authors

ISBN 978-3-95450-141-0

[16] F. Zhou, K. Bane, Y. Ding, Z. Huang, H. Loos, "Further Understanding of the Linac Coherent Light Source Injector Emittance," Proceedings of FEL 2014, Basel, Switzerland, Aug. 2014, p. THP031 (2014).

[17] R. Ischebeck, E. Prat, V. Schlott, V. G. Thominet, P. Krejcik, H. Loos, M. Yan, "SwissFEL beam profile monitor," TUCYB3, Proceedings of IBIC 2014, (2014)

[18] Y. Feng *et al.*, "System design for Self-Seeding the LCLS at Soft X-Ray Energies," Proceedings of FEL 2012, Nara, Japan, Aug. 2012, p. (2012)

[19] J. Amann *et al.*, "Soft X-ray Self Seeding at the Linac Coherent Light Source," manuscript in preparation.

[20] T. J. Maxwell, C. Behrens, Y. Ding, A. S. Fisher, J. Frisch, Z. Huang, H. Loos, Phys. Rev. Lett. 111 (2013) 184801.

[21] C. Behrens *et al.*, Nature Commun. 5 (2014) 3762.

[22] L. Piccoli, Y. Ding, P. Krejcik, T. J. Maxwell, "Real Time Image Processing for Bunch Length Reconstruction with the XTCAV at the LCLS," MOPD22, Proceedings of IBIC 2014, (2014)

Copyright © 2014 CC-BY-3.0 and by the respective authors

ISBN 978-3-95450-141-0

DIRECT (UNDER) SAMPLING VS. ANALOG DOWNCONVERSION FOR BPM ELECTRONCS*

M. Wendt#, CERN, Geneva, Switzerland

Abstract

Digital signal processing by means of undersampling the analog signal has become a popular method for acquiring beam position monitor signals. This presentation discusses the technique and its principle limitations, presents today's technical limits (e.g. in terms of performance of available ADCs), and provides an outlook for the future. It will also try to compare the technique with more tradition analog downmixing and signal processing methods

INTRODUCTION

Beam position monitors (BPM) are the workhorse of the beam diagnostics for every particle accelerator, linear, circular or transport lines, operating with leptons, hadrons or ions. A system of many, synchronized BPMs, distributed along the accelerator's beam-line allows the observation of the beam orbit, and, using well adapted read-out electronics, enables the extraction of a manifold of relevant information of the performance of the accelerator and it's beam quality. It is the optimization of BPM pickup, read-out electronics and data acquisition system, matched to the properties of accelerator and beam, which defines performance, quality and reproducibility of this important beam instrumentation system.

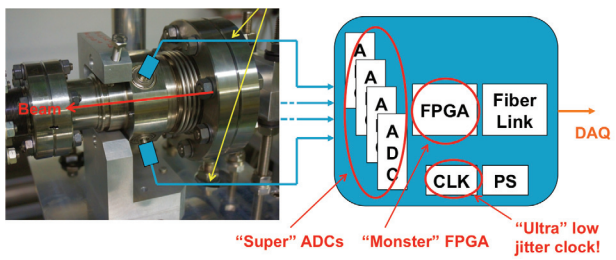


Figure 1: The ultimate digital BPM read-out electronics?

While the combination of both, the BPM pickup and the read-out electronics defines the ultimate performance in terms of resolution and long-term stability, most of the progress on these parameters have been made in recent years due to improvements in the read-out electronics, namely by adapting digital technologies, with profits taken from the commercial and military chip developments. Fig. 1 illustrates a provocative, "all digital" BPM electronics, using "super" ADCs and other equivalent components, hooked directly to the pickup electrodes.

Even with todays most advanced semiconductors, this idea is not feasible. Analog and RF components are still required in the signal path to guarantee the expected BPM performance, and to keep the costs reasonable, as the accelerator has to be equipped with many, sometimes more than 1000 beam position monitors, e.g. the LHC [1].

This work focuses on aspects of present technologies for BPM read-out electronics, trying to evaluate how much analog RF electronics is still necessary, and what can and should be accomplished digitally. A more general summary on trends and developments for BPM systems has been published some years ago [2].

BEAM SIGNALS

Understanding the beam properties, and the signals and characteristics of the BPM pickup is mandatory to specify and develop the optimal, best-suited read-out electronics.

Broadband BPM Pickups

A typical broadband BPM pickup consists out of symmetrically arranged RF antennas, typically "button" or stripline-like electrodes, which interact to the electromagnetic field of the passing beam.

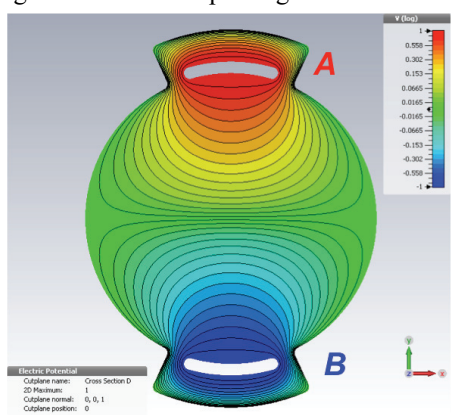


Figure 2: Equipotentials of a stripline BPM.

Figure 2 shows the cross-section of a stripline BPM with symmetrically arranged electrodes, for simplicity only the vertical ones. Plotted are the equipotentials for a potential difference between the electrodes, which indicate contour lines of beam positions giving constant signal amplitudes A and B. The beam displacement, or beam position is measured by detecting the asymmetry of these amplitudes, and normalizing them such that the beam position measurement is independent from the absolute signal level, as this varies with the beam intensity:

$$\text{norm. beam position} \propto \frac{A-B}{A+B}. \qquad (1)$$

The output signal of a BPM electrode or pickup is given by

#manfred.wendt@cern.ch

Copyright © 2014 CC-BY-3.0 and by the respective authors

ISBN 978-3-95450-141-0

$$V_{elec}(x,y,\omega) = s(x,y)Z(\omega)I_{beam}(\omega) \quad (2)$$

where $Z(\omega)$ is the frequency dependent transfer impedance of the BPM electrode, and $s(x,y)$ is a sensitivity function which reflects the geometry of the beam pickup, thus the position characteristic. For broadband BPM pickups $s(x,y)$ is frequency independent, but nor for resonant BPMs.

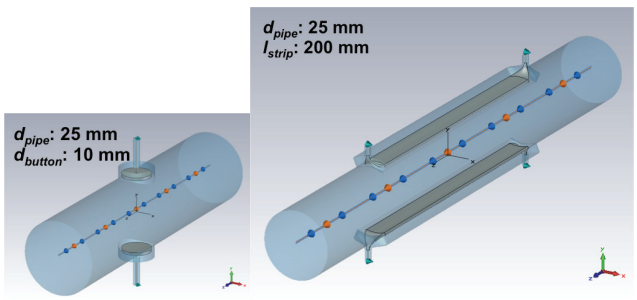


Figure 3: "Button" (left) and stripline (right) BPM pickups.

The transfer impedance $Z(\omega)$ of a BPM electrode can be estimated analytically, e.g. for a "button" electrode:

$$Z_{button}(\omega) = \phi R_{load}\left(\frac{\omega_1}{\omega_2}\right)\frac{(\omega_1/\omega_2)}{1+(\omega_1/\omega_2)^2} \quad (2)$$

$$\text{with: } \omega_1 = \frac{1}{R_{load}C_{button}}, \quad \omega_2 = \frac{c_0}{2r_{button}}, \quad \phi = \frac{r_{button}}{4r_{pipe}}$$

and for a stripline electrode:

$$Z_{strip}(\omega) = i\phi Z_0 e^{-i\frac{\omega l_{strip}}{c_0}}\sin\left(\frac{\omega l_{strip}}{c_0}\right) \quad (2)$$

However, a quick numerical analysis, e.g. here accomplished by using the *CST Studio Suite* wakefield solver, will give directly output signal of the BPM electrode for a specific beam condition. Figure 3 shows the geometries of the analysed button and stripline BPMs. The simulated beam bunch was *Gaussian*, with n=10^{10} electrons, σ=25 mm, travelling at v=c_0 on an orbit with a vertical offset (x=0, y=+1 mm).

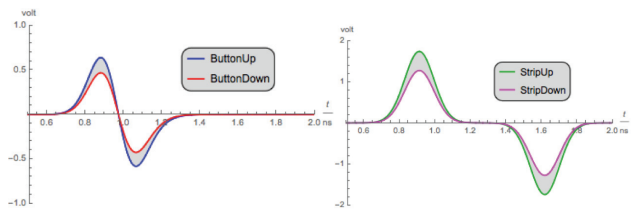


Figure 4: Time domain output signals of the button (left) and stripline (right) BPM electrodes for a single bunch passing with a +1mm vertical beam offset.

Figure 4 shows the time domain output signals from both, button and stripline electrodes. As of the vertical beam offset, the signal amplitude of the upper electrode is larger for both pickup styles. However, the shape of the signal waveform is different, also the amplitudes of the stripline BPM electrodes are higher. In both cases, the single bunch response is a short, differentiated pulse waveform in the nano-second regime, i.e. for most of the time there is no signal ("0" volt) if bunches are spaced far.

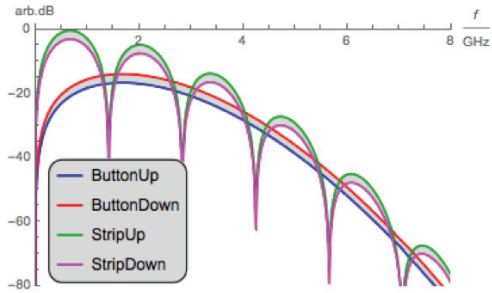


Figure 5: Frequency domain representation of the signals of Fig. 4, scaled to arbitrary dB.

Figure 5 shows the frequency domain representation of the signals of Fig. 4, scaled to dB. Noticeable, for both BPM styles the amplitude difference between the output signals of the electrodes is ~2.7 dB, and is constant over the entire output frequency spectrum. The stripline BPM outputs higher signal levels, particular at lower frequencies, e.g. at 500 MHz the stripline signal level is ~20 dB higher compared to the button electrode.

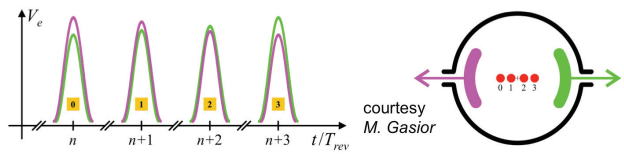


Figure 6: Turn-by-turn beam oscillations at the BPM.

Figure 6 illustrates the amplitude modulation of the BPM electrode signals due to the transverse bunched beam oscillations on a turn-by-turn basis. Both BPM electrodes deliver a high, common-mode signal, defined by the beam intensity, amplitude modulated by a small beam displacement signal, defined by the amplitude of the position modulation. A simple case of the dipole moment spectrum of a single bunch in a ring accelerator, observed by a BPM can be estimated to [3]:

$$Z(\omega)I_{beam}(\omega) = D(\omega) =$$

$$= \omega_{rev}A_0\sum_{n=-\infty}^{+\infty}\delta\left[\omega-\left(n\omega_{rev}+\omega_\beta\right)\right]e^{-\frac{(\omega-\omega_\beta-\omega_\xi)^2\sigma_\tau^2}{2}} \quad (3)$$

and provides much more relevant information of accelerator and beam quality than just the static orbit.

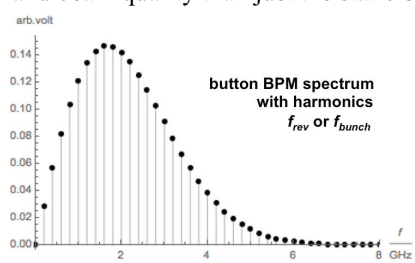


Figure 7: Button electrode spectrum for periodic bunches.

Figure 7 shows the same button electrode signal spectrum, now in linear scaling of the magnitude, and

ISBN 978-3-95450-141-0

Copyright © 2014 CC-BY-3.0 and by the respective authors

sampled with f_{rev} or f_{bunch}, as of the periodic repetition of the bunched beam. In practice the signal spectrum may be more complex. The beam formatting often produces batches of bunches with gaps, bunches of different intensities, etc. The accelerator has non-linearities that lead to coupled oscillations, and the oscillation amplitude of each particle in a bunch, as wells as of each bunch may be different.

Resonant BPM Pickups

A cylindrical resonator of radius R and length l has eigenmodes at frequencies:

$$f_{mnp} = \frac{1}{2\pi\sqrt{\mu_0\varepsilon_0}}\sqrt{\left(\frac{j_{mn}}{R}\right)^2 + \left(\frac{p\pi}{l}\right)^2} \qquad (4)$$

and with added beam pipe ports, can be operated as beam excited, passive cavity BPM. The beam couples to the longitudinal components of the E-field of the eigenmodes, for dimensions $l<2R$ the TM_{010} is the fundamental monopole mode, sensitive to the beam intensity, while the TM_{110} lowest dipole mode is proportional to beam displacement and intensity.

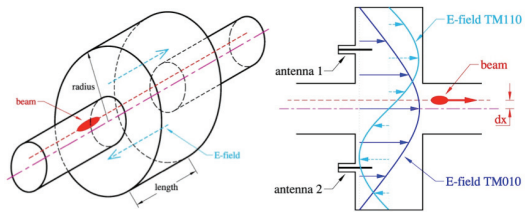


Figure 8: Beam excited, passive cylindrical resonator operating as cavity BPM.

Figure 8 illustrates the principle of operation. A simple pin antenna is used to detect the signal, however, to benefit from the high resolution potential of this BPM type a more sophisticated signal coupling schema needs to be implemented.

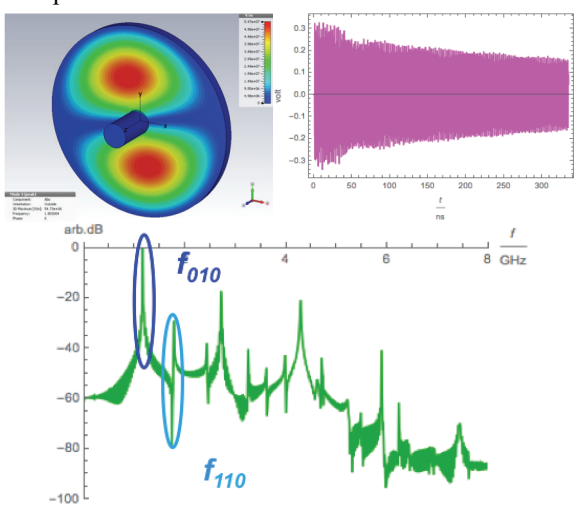


Figure 9: Cavity BPM signals.

Using the same bunch properties as for the broadband BPM examples, Fig. 9 shows the dipole mode of a simplistic cavity BPM resonator of dimensions R = 100 mm, l = 10 mm, and the resulting time domain output signal for the y = +1 mm displaced beam (upper trace). For computation time reasons, the simulation was truncated at 350 nsec, therefore the corresponding frequency spectrum (lower plot) shows some artefacts. However, the important modes at $f_{010} \approx 1.15$ GHz and $f_{110} \approx 1.8$ GHz can be clearly identified.

As of the presence of many unwanted modal components in the output signal, the processing of the cavity BPM signals has substantially different objectives, compared to those of the broadband BPMs. For the cavity BPMs, analog RF and microwave electronics are necessary, the backend and DAQ technologies may nevertheless be quite similar to that of a button or stripline BPM, and based on digital signal processing.

Signal Processing Objectives

The processing of the BPM pickup signals has two main objectives

- ***Normalization*** Extract beam intensity independent displacement information, e.g. by relating difference and sum signal information from the BPM electrode pair. This can be accomplished by using analog RF techniques, e.g. Δ-Σ (180^0) or 90^0-hybrids, logarithmic amplifiers, etc. or by mathematical manipulation of the digitized signals of the individual electrodes.
- ***Processing of broadband signals, decimation*** The BPM pickup signals need to be conditioned for digitalization, which includes filters, gain stages and switchable attenuators, as well as analog down-conversion. In the digital domain the data needs to be further demodulated, decimated and filtered to the appropriate level, e.g. synchronized turn-by-turn position data, high resolution narrowband beam orbit data, etc.

To ensure stable BPM operation, the BPM electronics may include calibration or test signals, or switching elements to compensate drift effects of individual channels that otherwise would result in "electronic offsets". The signal processing may also provide valuable beam intensity and/or beam phase (timing) information at each BPM station. Location and other design aspects of the BPM read-out electronics should minimize the cable length (expenses) between BPM pickup and electronics, which also will improve the performance.

BPM SIGNAL PROCESSING

Figure 10 shows the main building blocks of a typical BPM station. An analog signal conditioning section is required to adapt the signals for quantization at the ADC. Today, most of the BPM signal processing objectives can be accomplished in the digital domain (digital signal processing and data acquisition blocks). The question to answer is, how much analog technology is still required for the signal conditioning. The BPM block schematics

Copyright © 2014 CC-BY-3.0 and by the respective authors

ISBN 978-3-95450-141-0

also indicate some of the necessary auxiliary elements, e.g. calibration section, clock-, timing-, and trigger signals, power supplies, etc.

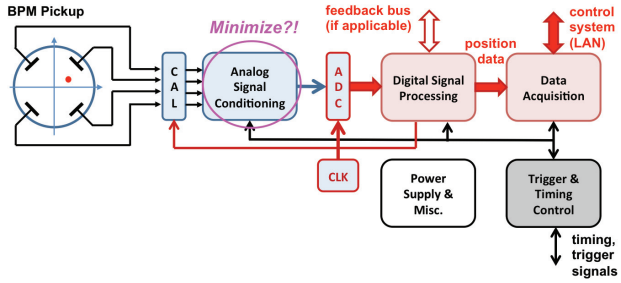


Figure 10: BPM building blocks.

Analog BPM Example: The Multiplexed Heterodyne Receiver

Let us define a BPM read-out system based on analog signal processing as electronics system, which utilizes all the normalization, demodulation, filtering and other signal gymnastics of the pickup signals before the digitalization. Now the requirements for the ADC, in terms of sampling rate, analog bandwidth and dynamic range are substantially reduced, on the costs of more complex analog and RF electronics. An overview of the various analog signal-processing schemas is given in [4].

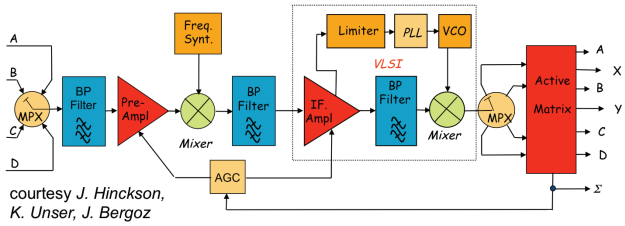


Figure 11: Analog heterodyne receiver based BPM electronics.

MPX Heterodyne Receiver A prominent example of BPM signal processing based on analog and RF electronics uses the heterodyne receiver concept, see Figure 11 [5]. It basically follows the classical radio receiver schema, the input signal is band-pass filtered, amplified and down-converted to an intermediate frequency (IF). The IF signal is further filtered, amplified, and finally detected by a synchronous demodulator. To scope with drift effects of analog components, the four BPM electrode signals are time multiplexed on a single receiver. An active matrix temporary stores the information and executes the normalization using operational amplifiers. The system operates with a narrow bandwidth and provides a high resolution (~1 μm) beam orbit measurement, however, no turn-by-turn beam positions.

RF Mixer The analog RF mixer is a key element for downconversion and demodulation of RF signals. The ideal mixer multiplies the RF input signal

$$y_{RF}(t) = A_{RF}\sin(\omega_{RF}t + \varphi_{RF})$$

with the LO signal from a local oscillator

$$y_{LO}(t) = A_{LO}\sin(\omega_{LO}t + \varphi_{LO})$$

which results in upper and lower sideband signals at $f_{IF}=f_{RF}\pm f_{LO}$:

$$y_{IF}(t) = \frac{1}{2}A_{LO}A_{RF}\left\{\sin\left[(\omega_{RF}-\omega_{LO})t+(\varphi_{RF}-\phi_{LO})\right] + \sin\left[(\omega_{RF}-\omega_{LO})t+(\varphi_{RF}-\phi_{LO})\right]\right\}$$

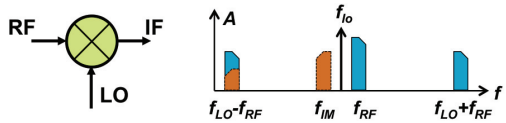


Figure 12: Analog RF mixer as downconverter.

For frequency conversion applications the mixer can be used as down-converter in a heterodyne receiver, typically $f_{RF}>f_{LO}$, or as demodulator or phase detector in homodyne operation with $f_{RF}=f_{LO}$. If no special care is taken, e.g. image rejection, the mixer will also down-convert the band at the image frequency, $f_{IM}=f_{LO}-f_{RF}$, which would be converted as indistinguishable alias to f_{IF} (see Figure 12). The "real" mixer is based on the non-linear characteristics of the *Schottky* diode,

$$I = I_0\left(e^{V/V_T}-1\right)$$

which results in additional mixing frequencies, giving $f_{IF}=mf_{RF}\pm nf_{LO}$. Particular care has to be taken to avoid unwanted mixing products appearing in the IF-band, e.g. filters, image rejection (SSB) mixing, etc.

BPMs Read-out Electronics Based on Analog and Digital Signal Processing Elements

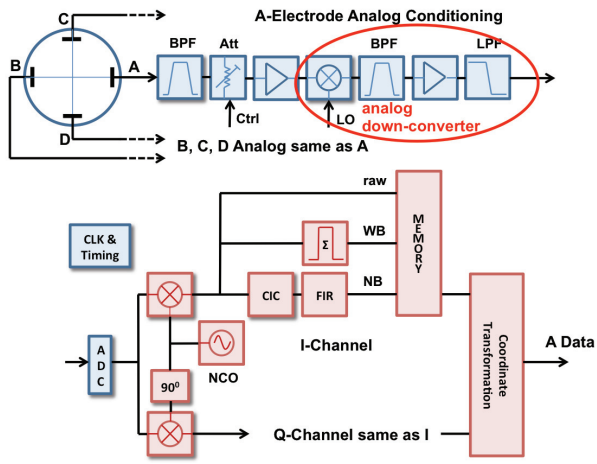


Figure 13: Schema of BPM read-out electronics, 1-out-of-4 channels shown.

Figure 13 shows the block diagram of a typical BPM read-out electronics for broadband BPM pickups, i.e. button or stripline monitors, heavily based on digital signal processing elements (only 1-out-of-4 channels is depicted). Often, the analog downconverter, highlighted in the analog signal conditioning section, is not required,

ISBN 978-3-95450-141-0

Copyright © 2014 CC-BY-3.0 and by the respective authors

and a direct under-sampling to based-band demodulation is preferred.

The processing of the BPM signals in digital domain provides several advantages compared to analog schemes:

- Better reproducibility and stability of the beam position measurement, i.e. robust to environmental conditions (temperature, humidity, etc., however, not necessarily to radiation), no aging or drift effects, deterministic (no noise or statistical effects on the position information).
- Flexibility, i.e. modification of FPGA firmware, control registers or DAQ software allows to adapt the measurement to different beam conditions or operational requirements.
- Often the digital signals processing gives a better performance to the position measurement, e.g. higher resolution and stability, also because there is no analog equivalent to digital filters and data processing elements.

However, digital signal processing is not always better. The latency of the pipeline ADCs, quantization and clock jitter effects, as well as dynamic range and bandwidth limitations can degrade the performance substantially, or may limit the application. Also, to fully benefit from the digital technologies, the implementation often tends to be more complex than analog signal processing techniques, and require more manpower, costs and development time.

"Ringing" Bandpass Filter Even with state-of-the-art ADCs the time compressed BPM signals (Fig. 4) cannot be directly quantized with a sufficient dynamic range.

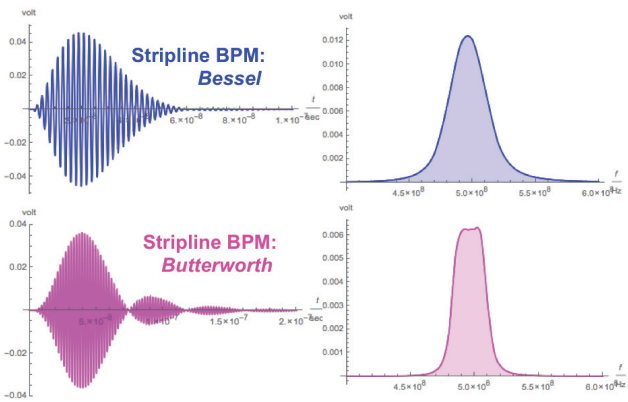


Figure 14: "Ringing" bandpass filter.

As Figure 13 indicates, a bandpass filter located in front of the ADC si used to " stretch" the BPM signal to a "ringing" sinusoidal waveform. Figure 14 shows two different types of filters, Bessel and Butterworth, both excited by the single bunch response of the stripline BPM. Both filters operate at f_{center} = 500 MHz (bandwidth f_{3dB} = 25 MHz), the Butterworth filter shows a steeper response in the frequency domain, but as seen, gives additional ringing of the envelope in the time domain, that is why usually a design with linear group delay (*Bessel*, *Gaussian*, time domain designs) is preferred.

As the signal level reduces substantially because most energy of the input signal is rejected, a gain stage is switched into the signal path (Fig. 13), often in combination with a switchable RF attenuator to provide operational flexibility in terms of beam intensity range.

In case of multibunch operation, with a bunch spacing $t_{bunch}<t_{rise}$ of the filter rise time, a constructive signal pile-up effect has to be taken into account. Figure 15 shows the resulting signals for different bunch spacing's for our stripline BPM / *Bessel* filter example.

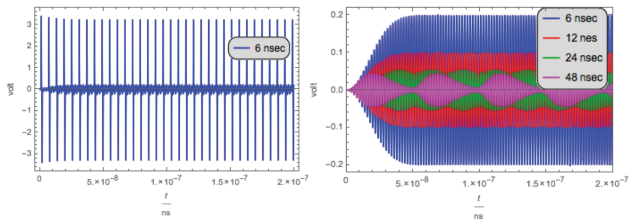


Figure 15: Multibunch signal pile-up effect, left: input signal (t_{bunch}=6ns), right: output signal for different bunch spacing's

Analog-Digital Converter (ADC) The ADC is the central element of the BPM signal processing, and has a major impact on the concept and overall performance of the BPM read-out system.

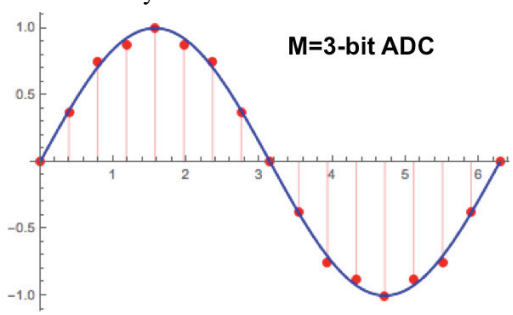


Figure 16: Quantization of a sinusoidal signal with a 3-bit ADC.

The ADC quantizes the continuous input signal waveform at equidistant spaced time samples. The digital output data is discrete in amplitude and time. The LSB voltage (resolution), $Q=V_{FSR}/2^M$ is given by the number of bits M and the full-scale range voltage V_{FSR}. Figure 16 shows the quantization effect for a 3-bit ADC on a sinusoidal signal. For M=14 or 16-bit, and V_{FSR} = 1 volt the LSB voltage is Q = 61 µV (14-bit) or 15 µV (16-bit), demanding stable reference and supply voltages.

The maximum achievable dynamic range due to the quantization error is than given by

$$SQNR = 20\log_{10}\left(2^M\right) \quad (5)$$

which is 84 dB for 14-bit, and 96 dB for 16-bit ADCs.

However, in practice the dynamic range is limited due to the aperture jitter t_a of the clock signal, and degrades with higher frequency f of the input signal (see Fig. 17):

$$SNR = -20\log_{10}\left(2\pi f t_a\right) \quad (6)$$

Copyright © 2014 CC-BY-3.0 and by the respective authors

ISBN 978-3-95450-141-0

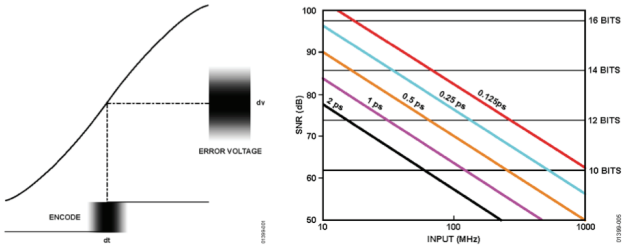


Figure 17: ADC SNR limit due to aperture (clock) jitter.

Following our example with a frequency $f \approx 500$ MHz of the input signal, and assuming an excellent low clock signal jitter of $t_a = 0.25$ ps, the dynamic range would be limited to $SNR = 62$ dB, equivalent to EOB = 10.3 (effective number of bits).

On the positive side, the BPM signal processing correlates the samples of 2 or 4 ADCs for the position data, by clocking them with the same signal. This correlates the aperture jitter, thus ensures reasonable small errors on the position measurement, even in presence of a rather large jitter of the clock signal.

Table 1: Performance of ADCs

Type	Res. bit	f_s MSPS	BW MHz	$SNR@f_{in}$ dB@MHz
AD9652	16	310	485	72@170
AD9680	14	1000	2000	67@170
LTM9013*	14	310	300*	62@150
ADC16DX..	16	370	800	69@150
ADS5474	14	400	1280	70@230

* has an analog I-Q mixer integrated, $0.7 < f_{in} < 4$ GHz

As of the time of writing (September 2014), there is a large variety of fast sampling ADC chips available. Table 1 summarizes a few examples of 14 and 16-bit ADCs, comparing a few performance parameters. All these ADCs follow the so-called "pipeline" architecture, a chain of T&Hs, ADCs and DACs converting the signal in a pipeline manner until the desired quantization resolution is reached. The pipeline ADC requires a constant clock frequency, and typically has a rather long latency until the digitized data reaches the output register. Often these ADCs have two or more channels on a single chip with very little cross talk, e.g. for direct I-Q sampling. Some chips include analog components, e.g. analog mixers, gain stages, filters, etc.

Sampling Theory A band-limited signal $x(t)$, $B=f_{max}$, can be fully reconstructed from the sampled amplitude values, if the sampling frequency $fs \geq 2f_{max}$ (Nyquist-Shannon theorem, [6]). The reconstruction of $x(t)$ by $x_n=x(nT)$ is based on the sinc-function (with $T=1/f_s$):

$$x(t) = \sum_{n=-\infty}^{+\infty} x_n \frac{\sin \pi(2 f_{\max} t - n)}{\pi(2 f_{\max} t - n)} = \sum_{n=-\infty}^{+\infty} x_n \operatorname{sinc} \frac{t - nT}{T} \quad (7)$$

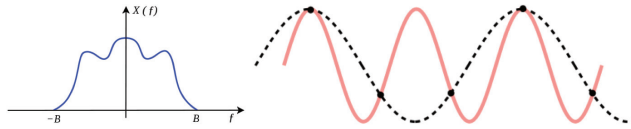


Figure 18: Band-limited signal (left), and sampling of a sinusoidal signal (right).

As Fig. 18 (left) shows, f_{max} of the band-limited signal is the frequency, where the signal level practically reaches zero, it is not the frequency defined by the 3 dB bandwidth!

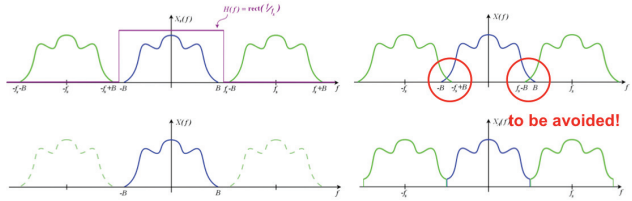


Figure 19: Aliasing effects.

The samples, e.g. of a sinusoidal signal of frequency f cannot be distinguished from an alias signal of same waveform, amplitude and phase, but twice the frequency, $2f$ (Fig. 18, right), in general: $f_{alias}(N)=|f-Nf_s|$. In the frequency domain this effect shows up as an image band (see Fig. 19, left). For the signal recovery based on eq. (7) a rectangular lowpass filter can be used to eliminate the unwanted image bands, however, if $fs<2f_{max}$ the bands overlap, and the reconstruction will fail (Fig. 19, right).

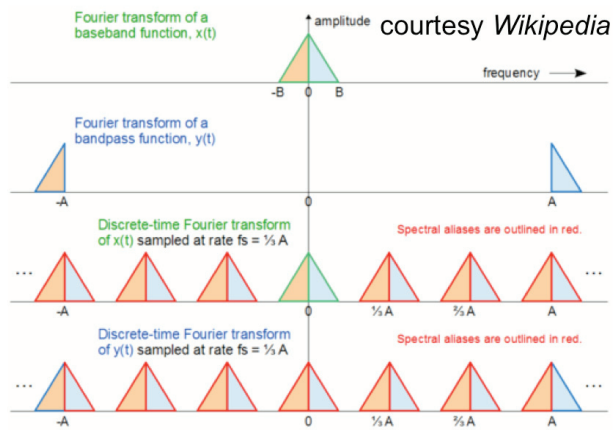


Figure 20: Bandpass or under-sampling.

A bandpass signal of $f_{hi}=A$ and $f_{lo}=A+B$ (see Fig. 20) can be down-converted to base-band (demodulated) if:

$$\frac{2 f_{hi}}{n} \leq f_s \leq \frac{2 f_{lo}}{n-1} \text{ with: } 1 \leq n \leq \left| \frac{f_{hi}}{f_{hi} - f_{lo}} \right| \quad (8)$$

Figure 20 illustrated the bandpass sampling for $f_s=f_{hi}/3$, showing the aliasing bands due to the undersampling. Figure 21 (left) demonstrates the undersampling concept on the single bunch Bessel filter response, with $T = 4$ ns, $f_s = 200$ MHz, $f_{hi}/f_{lo} = 550/450$ MHz, $n = 5.5$.

ISBN 978-3-95450-141-0

Copyright © 2014 CC-BY-3.0 and by the respective authors

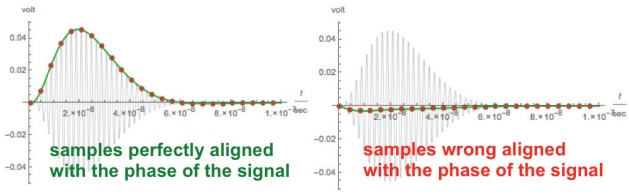


Figure 21: Undersampling of the 500 MHz Bessel filter single bunch response.

I-Q Sampling Figure 21 also demonstrates, the reconstruction requires the samples well aligned to the waveform, i.e. the phase between f_s and f_{in}. Applying the concept of I-Q sampling (see Fig. 22) on a sinusoidal waveform will avoid that problem [7]:

$$y(t) = A\sin(\omega t + \varphi_0)$$
$$y(t) = \underbrace{A\cos\varphi_0}_{\equiv I}\sin\omega t + \underbrace{A\sin\varphi_0}_{\equiv Q}\cos\omega t \qquad (9)$$

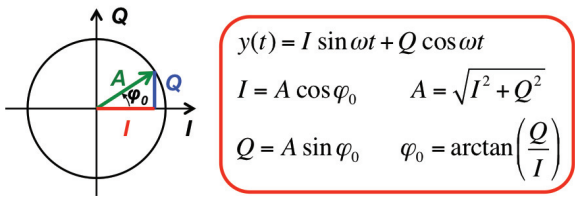


Figure 22: Concept of I-Q sampling.

The in-phase (I) and quadrature-phase (Q) components of the counter-clockwise rotating phasor of a sinusoidal frequency f are sampled with $f_s = 4f$. The signal amplitude A, as well as the phase φ_0 can be deduced independent of the relative phase (timing) between f_s and f. Figure 23 shows the principle (left), and the example on our 500 MHz Bessel filter response (right).

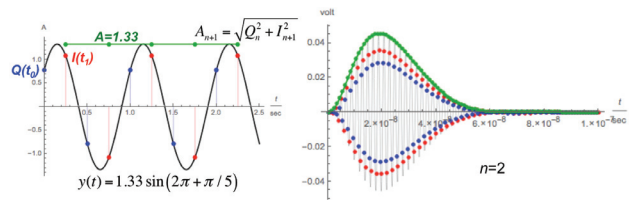


Figure 23: I-Q sampling of a sinusoidal signal (left), and of a 500 MHz Bessel filter response signal (right).

Direct Down-Converter (DDC) The I-Q sampling is applied in the digital down-converter (DDC), which converts the band-limited RF or IF signal to baseband (quadrature demodulation) and also serves for data reduction (filtering and decimation). Figure 24 shows the building blocks of a DDC [7]:

- A fast oversampling ADC
- A numerically controlled oscillator (NCO), based on a direct digital frequency synthesizer (DDS)
- Digital mixers ("ideal" multipliers)
- Decimation lowpass filters for anti-aliasing and data reduction, e.g. based on CIC and/or FIR filters.

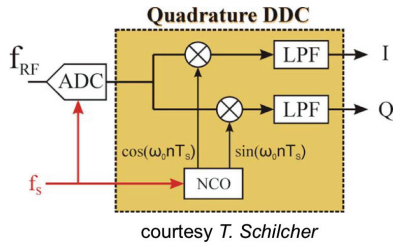


Figure 24: Building blocks of a digital down-converter.

Cascaded Integrator Com (CIC) Filter Because of the economical implementation, a decimating cascaded integrator comb filter (CIC) is often the preferred lowpass filter in the DDC impementation. It consists out of N integrators, a decimator R, and N comb filters (Fig. 25), forming a stable FIR filter with a sinc-function like transfer response [8]:

$$H(f) = \left(\frac{\sin \pi M \dfrac{f}{f_{out}}}{\sin \dfrac{\pi}{R}\dfrac{f}{f_{out}}} \right)^N \qquad (10)$$

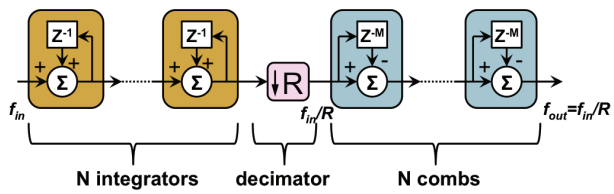


Figure 25: Cascaded integrator comb filter (CIC).

Figure 25 shows the architecture of the CIC filter. The output data rate (frequency) is decimated by $f_{out} = f_{in}/R$. Figure 26 (left) plots the frequency response of eq. (10). The differential delay M of the comb sections defines the location of the zeros, $f_0 = k\, f_{out}/M$. Care has to be taken on the aliasing / image bands of the CIC filter around: $(i\text{-}f_c) \le f \le (i\text{+}f_c)$, see Fig. 26 (right). Typically one or more FIR filters follow the CIC filter, one optimized to compensate the CIC passband drop.

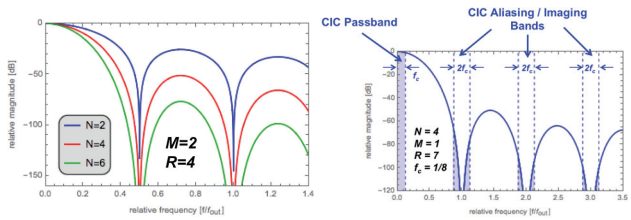


Figure 26: Cascaded integrator comb filter (CIC).

Signal/Noise (*S/N*) and BPM Resolution At the first gain stage (amplifier) of the analog signal conditioning (Fig. 13), the minimum noise voltage is expected to be:

$$v_{noise} = \sqrt{4k_B T R \Delta f} \qquad (11)$$

Copyright © 2014 CC-BY-3.0 and by the respective authors

ISBN 978-3-95450-141-0

For the single bunch example of the stripline BPM / *Bessel* bandpass, with $R = 50\ \Omega$, $\Delta f = 25$ MHz, $T = 300$ K the theoretical noise voltage computes $v_{noise} = 4.55\ \mu V$ (-93.83 dBm). The signal-to-noise ratio is $S/N = \Delta v/v_{noise}$, with Δv being the BPM voltage signal at the amplifier input, reflecting a signal change due to the change of the beam position (Δx, Δy). At $f = 500$ MHz, the signal level for our example is $v \approx 22.3$ mV (-20 dBm). This results in a $S/N \approx 4900$ (73.8 dB), which would be the required dynamic range to resolve the theoretical resolution limit of the BPM. Using the sensitivity of ~2.7mm/dB of the stripline BPM, this corresponds to $\Delta x = \Delta y \approx 0.66\ \mu m$.

In practice there are several factors that will reduce this theoretical *S/N* limit, e.g. insertion losses between BPM pickup and amplifier (cables, connectors, bandpass filter, couplers, etc.) and the noise figure of the 1st amplifier. Also, a useable *S/N* needs to be >0 dB. As a result the practically achievable *S/N* for this signal bunch signal is ~10 dB lower, and the corresponding resolution will be in the 2…3 µm regime.

Several factors can still improve the BPM resolution:

- Increase the signal level, e.g. by modifications of the pickup (larger electrodes, smaller beam pipe aperture), higher beam intensity.
- Increase the measurement (integration) time, and/or apply statistics on periodic signals or data, e.g. reduce the filter bandwidth in analog and/or digital sections ($S/N \sim 1/\sqrt{BW}$), apply data filtering by averaging ($S/N \sim \sqrt{n}$).

ANALOG VS. DIGITAL DOWN-CONVERSION

Processing the BPM electrode signals individually requires a large dynamic range. Linearity is the most important system aspect. Present ADC technologies are limited to ~70 dB of linear dynamic range, this is not sufficient for most BPM applications. At minimum, a set of gain stages and switchable attenuators has to be foreseen to extend to the necessary dynamic range, also a slow automatic gain control (AGC) feedback is an option.

An analog heterodyne down-converter for each channel, in front of the ADC (Fig. 13), will complicate the RF signal engineering, but offers also some advantages, e.g. allows the sampling in the 1st Nyquist passband (no undersampling), relaxes RF input filter requirements, relaxes ADC and clock signal requirements, and may even relax some cables requirements in case the analog RF hardware can be installed near the beam pickups (transfer the IF signals via long cables). Beside additional analog and RF hardware, we also may suffer from additional aliasing effects due to the frequency mixing, which count against this solution.

What is better? To some extend it is a matter of taste and engineering preference, but sure requires a very detailed analysis for the specific case to answer this question. For beam pickups operating at microwave frequencies, e.g. cavity BPM, a RF heterodyne receiver stage in front of the digital electronics certainly is still necessary.

BPM PERFORMANCE

Applying and optimizing the discussed BPM signal-processing principles may lead to excellent performance of BPM systems. Depending of the specific case and the BPM requirements, better-tailored and advanced techniques should be followed, particular in the digital sections.

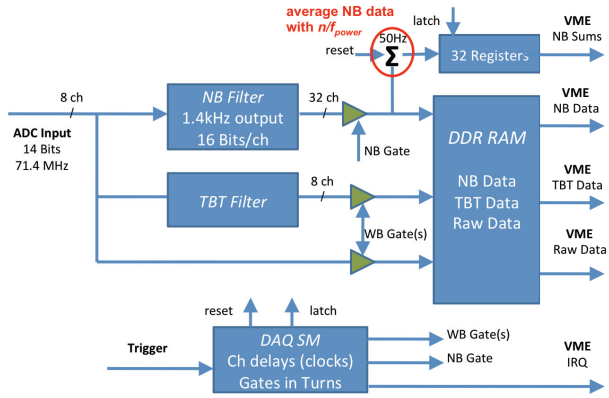


Figure 27: Digital signal processing for the ATF BPMs.

Figure 27 highlights the averaging feature of narrowband position data in multiples of the power-grid frequency, implemented at the digital signal processing for the ATF damping ring BPMs. This ensures clean, high-resolution beam position measurements, independent from the integration timing to the power grid frequency. Turn-by-turn and narrowband beam studies verified the ATF BPM performance, validating the measured optics functions (β-function, beating and phase advance) with the accelerator optics models [9].

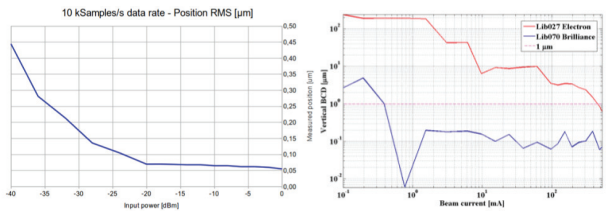


Figure 28: BPM performance *Libera Brilliance +*.

Figure 28 shows the performance of the *Libera Brilliance +* (*Instrumentation Technologies*) BPM system, at higher input signal levels the position resolution in narrowband (0.01…1 kHz) mode is <50 nm (left), and the measured beam position is independent over a three decades of beam intensity (right). Applying a crossbar switch technique to eliminate drift and aging effects in the analog sections of the Libera BPM electronics, a <100 nm stability over 14 hours could be demonstrated [10].

ISBN 978-3-95450-141-0

Copyright © 2014 CC-BY-3.0 and by the respective authors

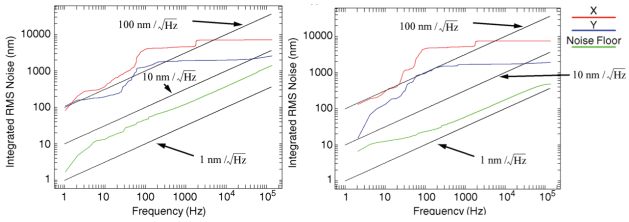


Figure 29: S/N performance of "home-brew" vs. commercial digital BPM electronics.

Figure 29 compares the performance of "home-brew" digital BPM read-out electronics to an earlier version of the commercial Libera system, noise floor and resolution performance show quite similar behaviour [11].

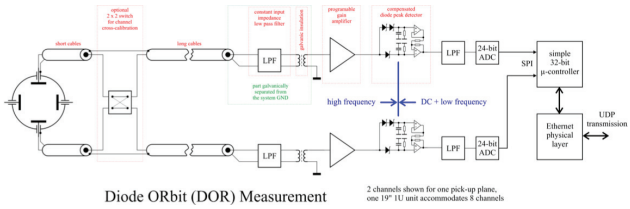


Figure 30: Beam orbit measurement based on diode detectors.

Advanced, and to some extend complex digital signal processing techniques demonstrated very high resolution and stability, however, pure analog BPM signal processing with minimalistic circuits can achieve similar results [12]. Figure 30 shows the schematics of beam orbit electronics based on a compensated diode detector, which demonstrated a resolution of <20

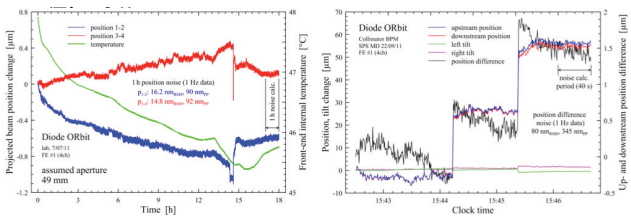


Figure 31: Performance of analog beam orbit read-out electronics based on compensated diode detectors.

REFERENCES

[1] E. Calvo Giraldo, et al., "The LHC Beam Position System: Performance during 2010 and Outlook for 2011", Proc. of DIPAC 2011, Hamburg, Germany, 2011, pp.323-325; http://www.JACoW.org

[2] M. Wendt, "Overview of Recent Trends and Developments for BPM Systems", Proc. of DIPAC 2011, Hamburg, Germany, 2011, pp.18-22; http://www.JACoW.org

[3] R. H. Siemann, "Spectral Analysis of Relativistic Bunched Beams", Proc. of BIW 1996, Argonne, IL, U.S.A., 1996, pp.3-22

[4] G. Vismara, "Signal Processing for Beam Position Monitors", Proc. of BIW 2000, Cambridge, MA, U.S.A., 2000, pp.36-60

[5] J. A. Hinkson, K. H. Unser "Precision Analog Signal Processor for Beam Position Measurements in Electron Storage Rings", Proc. of DIPAC 1995, Travemünde, Germany, 1995

[6] Wikipedia, "Nyquist-Shannon Sampling Theorem", http://en.wikipedia.org/wiki/Nyquist-Shannon_sampling_theorem

[7] T. Schilcher, "Digital Signal Processing for RF Applications", Digital Signal Processing CAS 2007, Sigtuna, Sweden, 2007, pp.249-283

[8] E. B. Hogenauer, "An Economical Class of Digital Filters for Decimation and Interpolation", IEEE Trans. on Acoustics, Speech and Signal Processing, vol. ASSP-29, No. 2, April 1981, pp.155-162

[9] Y. Renier, et al., "Turn-by-Turn BPM Data Analysis from the ATF Damping Ring", CLIC Workshop 2013, Geneva, Switzerland, 2013

[10] P. Leban, *Instrumentation Technologies*, private communications

[11] G. Decker, "Beam Position Monitors: How to Meet the Specifications of the Most Recent Accelerators", Proc. of IBIC 2013, Oxford, UK, 2013, pp.623-629; http://www.JACoW.org

[12] M. Gasior, et al.,"BPM Electronics based on Compensated Diode Detectors – Results from Recent Development Systems", Proc. of BIW 2012, Newport News, VA, U.S.A., 2012, pp.44-46; http://www.JACoW.org

Copyright © 2014 CC-BY-3.0 and by the respective authors

ISBN 978-3-95450-141-0

DEVELOPMENT OF A MODIFIED SIX-PORT DISCRIMINATOR FOR PRECISE BEAM POSITION MEASUREMENTS*

A. Penirschke†, T. Mahn, A. Angelovski, M. Hansli, R. Jakoby TU Darmstadt, Darmstadt, Germany

Abstract

For the European XFEL, new energy beam position monitors (EBPM) based on planar transmission lines where designed for energy measurements in the dispersive section of bunch compressor chicanes. The EBPM consists of transversely mounted stripline pickups in a rectangular beam pipe section and a signal detection scheme which measures the phases of the pulses at the ends of the pickup [1]. It allows simultaneous measurements of the beam energy and arrival-time. The EBPM needs a high dynamic range over the sensor length of 183 mm and high resolution of less than 20μm. Both, the dynamic range and the resolution depend on the operation frequency. Due to phase ambiguity, a low frequency is required for the high dynamic range whereas a high frequency is needed for the high resolution.

This paper presents the development of a RF readout electronic based on a modified six-port discriminator as a low-cost alternative to the readout electronics based on the MTCA.4 platform for the EBPM [2]. Based on the six-port, the beam position can be determined by means of the phase difference between the received signals from both ends of the transmission line pickup.

The six-port discriminator is a linear passive component, first developed in the 70's for accurate measurements of complex reflection coefficients in microwave network analysis [3]. It typically consists of two hybrid couplers and two power dividers or one Wilkinson power divider and three -3dB hybrid couplers. For the measurement of the difference of two signals excited from a single source one of the hybrid coupler can be omitted. The advantage of the six port is the fact that accurate phase measurements can be performed at microwave and millimeter wave frequencies only by amplitude measurements. This paper shows the principle of operation, developed prototype, and first test results.

INTRODUCTION

The rapid increase of computational power in the last decades made various possibilities of digital measurements available. As a result of this development well developed analog measurement techniques are only of minor importance today. For some applications, there is a more simple solution in the analog domain that is worth to be considered. This paper evaluates whether phase difference measurements are realizable using a analog six-port reflectometer circuit and determines the achievable phase resolution.

The six-port reflectometer, first mentioned in publications in the 1970's by Engen [3], never became commonly spread although many possible application fields exist. Application fields are amongst others measurement devices , communication receivers or sensors in automotive radar systems. This diversity comes from the relatively simple circuit design and the ability to scale the six-port circuit to almost any frequency [4]. The name already implies that the device has six connections whereof two are input ports and four are output ports. The superposition of the two input signals is internally phase shifted in the reflectometer. As a result four different powers at the outputs can be measured and further processed. Phase shifts can be realized by different types of couplers which makes the six-port reflectometer a relatively large but completely passive circuit structure.

One advantage of the six-port reflectometer is the direct application in the RF frequency range. Many applications like the MTCA.4 platform use signals in the RF range and down-convert them to an intermediate frequency for processing purposes [2]. In contrast the six-port reflectometer only needs one ADC for every output which is twice as many as a common receiver structure with I/Q-circuit has. A drawback using a reflectometer is the necessity of narrow bandpass filters for the RF signals, that can be easier realized at intermediate frequencies.

COPLANAR WAVEGUIDE ENERGY BEAM POSITION MONITOR

The operation of the European XFEL will require multiple special diagnostic tools to study the properties of the electron bunch. For the longitudinal properties Energy Beam Position Monitors (EBPMs) are utilized at three different locations along the European XFEL LINAC. Here the EBPM consists of two transversely mounted striplines and signal detection system, which measures the phases of the pulses emerging from both ends of the pickup in the dispersive section of a bunch compressor chicane [5]. The bunch energy can be determined from the phase differences that are directly proportional to the beam position by the formalism of the bunch compressor [6]. The principle of operation is visualized in Fig. 1 that shows a realized EBPM utilized with transversely mounted open coaxial lines in FLASH. The phase difference between the measured phases on the left and right side is direct proportional to the bunch position. The measurement resolution is defined by the minimum detectable phase-difference between both pulses. The phase of the pulse is defined by the phase constant of the transmission line. Without any distortions on the transmission line the phase constant is directly proportional to the fre-

* The authors would like to thank the CST AG for providing the CST Software Package.

† penirschke@imp.tu-darmstadt.de

ISBN 978-3-95450-141-0

Copyright © 2014 CC-BY-3.0 and by the respective authors

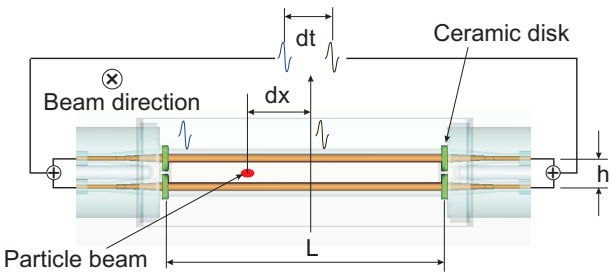


Figure 1: CAD model of the EBPM installed in the second bunch compressor at FLASH.

quency of operation and thus the phase-difference between both ends of the line. The measurement resolution is limited by the maximum operation frequency of the pickup, the limitations of the detection electronics and the length of the active sensor region which imposes the wavelength, below which the phase detection will be no longer unique [2]. The mechanical and electrical requirements for future EBPMs at the European XFEL differs significantly from the ones at FLASH. The opening of the rectangular beamline section is increased from $L = 183$ mm, $H = 8$ mm for FLASH to $L = 400$ mm, $H = 40.5$ mm for XFEL and at the same time the minimum detectable bunch charge is reduced from 1 nC for FLASH to 20 pC for XFEL. First results of planar transmission line pickups as a baseline for the XFEL EBPM monitor were presented in [7]. A possible upgrade of the EBPM by a quasi-grounded coplanar waveguide that combines the advantages of microstrip transmission lines and coplanar waveguide structures is shown in [1]. Compared to the microstrip design the grounded CPW line is the more complex design and even more difficult to mount within a vacuum environment. To make the CPW approach applicable for usage in accelerators, the CPW structure needs to be adapted to fulfill the vacuum requirements. In the proposed structure, the vias are exchanged by two metallic walls. Furthermore the metallic walls are shifted to the edge of the ground strips on the top layer as shown in Fig. 2. For

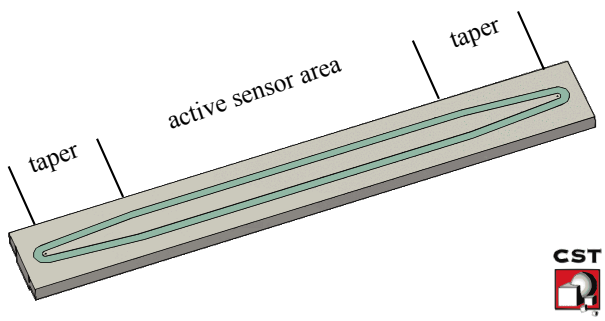


Figure 2: Simulation model of the quasi-grounded CPW structure.

maintaining the 50 Ω geometry, the gap between the line and the ground layer was increased slightly compared to a standard grounded CPW line. To match the wave impedance for the smaller line width, either the gap needs to be reduced for a constant substrate thickness or the thickness needs to be reduced for a constant gap. The matching to the transition is performed by a tapered reduction of the substrate thickness due to the parasitic effects in the transition section.

SIX-PORT REFLECTOMETER DESIGN

There are different possible implementations of a six-port reflectometer. The selected design is based on the measurement configuration from Engen [8], depicted in Fig. 3 in black and Grey color. It consists of a directional coupler, a rat-race coupler and three branch line couplers. For the

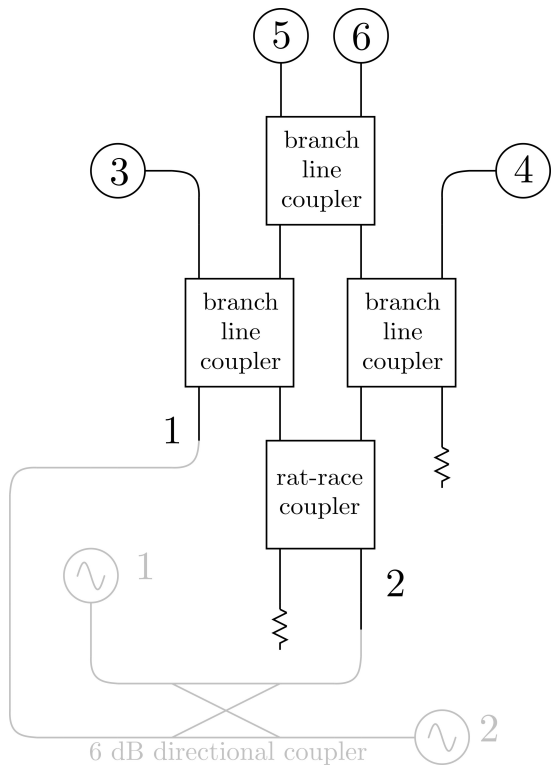


Figure 3: General circuit design for measurement purposes (Grey), and modified circuit design (black).

direct measurement of the signal difference of two signals, the structure can be simplified. The directional coupler at the input (grey color) can be omitted. The output values can be calculated from the input signals. The parameter a describes the amplitude of the incoming wave from port 1,

Copyright © 2014 CC-BY-3.0 and by the respective authors

ISBN 978-3-95450-141-0

while b is the amplitude for the wave from port 2.

$$\text{Port 1} : 2a \tag{1}$$

$$\text{Port 2} : 2b \tag{2}$$

$$\text{Port 3} : \frac{\sqrt{3}}{2}a - \frac{\sqrt{3}}{\sqrt{2}}b \tag{3}$$

$$\text{Port 4} : \frac{\sqrt{3}}{2}a \tag{4}$$

$$\text{Port 5} : \frac{\sqrt{3}}{2\sqrt{2}}a + \frac{\sqrt{3}}{2}b - j\frac{\sqrt{3}}{2\sqrt{2}}a \tag{5}$$

$$\text{Port 6} : \frac{\sqrt{3}}{2\sqrt{2}}a - j\frac{\sqrt{3}}{2\sqrt{2}}a - j\frac{\sqrt{3}}{2}b \tag{6}$$

It is visible that every output port has a different phase, which is a necessary criterion for the function of the six-port reflectometer. It can be seen that port 4 is only dependent on the incoming wave a, so that it can be used as a reference port.
The simulation of the circuit models were done with *Agilent Advanced Design System*, afterwards the ADS layouts were used to build 3D models in *CST Microwave studio*. The model is depicted in Fig. 4

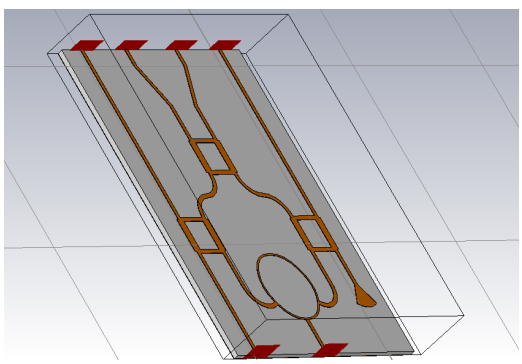


Figure 4: 3D model of the Six port reflectometer.

In order to proof the functionality, a phase shifter was added to input port 2 to obtain a phase sweep from 0° to 360° in 5° steps. The goal was to find a range were the detected power is as high as possible and second the power should vary as much as possible, to enable a more precise measurements. A suitable solution is the range of about 50° to 80°, as shown in Fig. 5.

As a substrate, *Rogers RT/duroid 6010* with a relative permittivity $\epsilon_r = 10.8$ and a thickness of 1.28 mm was chosen. A high relative permittivity is necessary to keep the dimensions of the circuit small. The connection to the circuit is done using SMA connectors with a flat and short pin that has a width that matches the line width of the six-port. For a stable connection a metal frame was build and the circuit board has been soldered onto it. Figure 6 shows a photo of the finished six-port reflectometer.

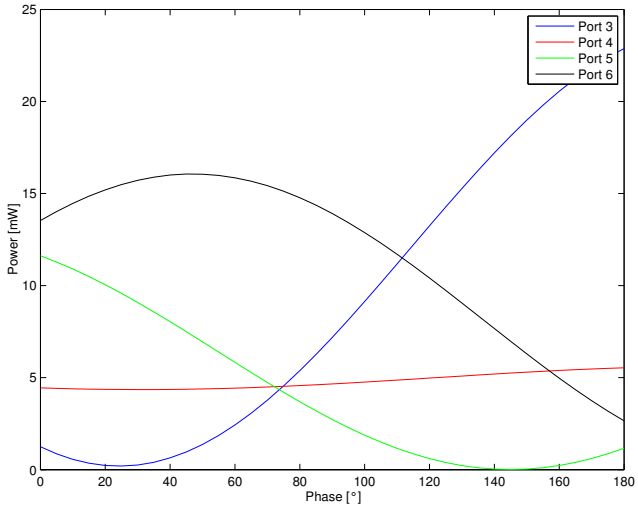


Figure 5: Output power versus phase difference of the six-port reflectometer.

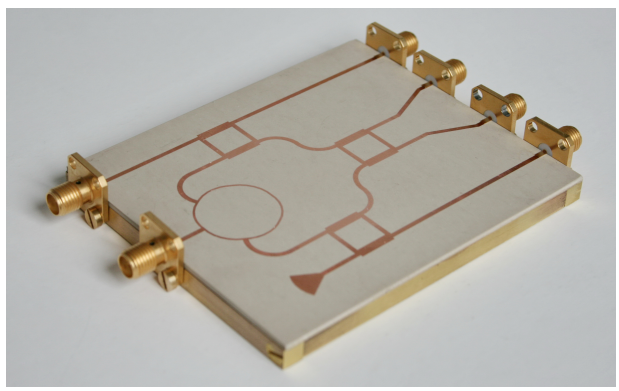


Figure 6: Photo of the six-port reflectometer design.

IMPLEMENTATION

In the application, the six port has to deal with pulses rather than single frequencies. This can be achieved applying band pass filters for the desired frequency range to its inputs which will make the superposed signals in the reflectometer less distorted. A direct processing in the RF domain

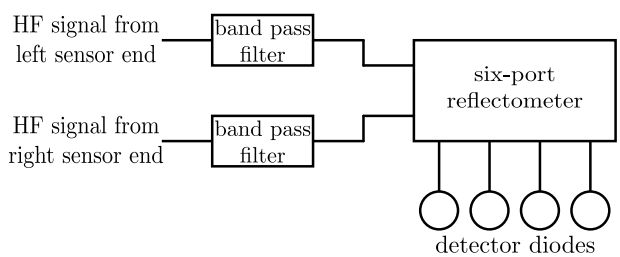


Figure 7: block diagram of the approach.

makes downconversion to an intermediate frequency range redundant and the signal can be directly led into the input ports of the six-port circuit. At every output a detector diode or a comparable circuit is installed to read the power level. This approach is depicted as a block diagram in Fig.7. For

ISBN 978-3-95450-141-0

Copyright © 2014 CC-BY-3.0 and by the respective authors

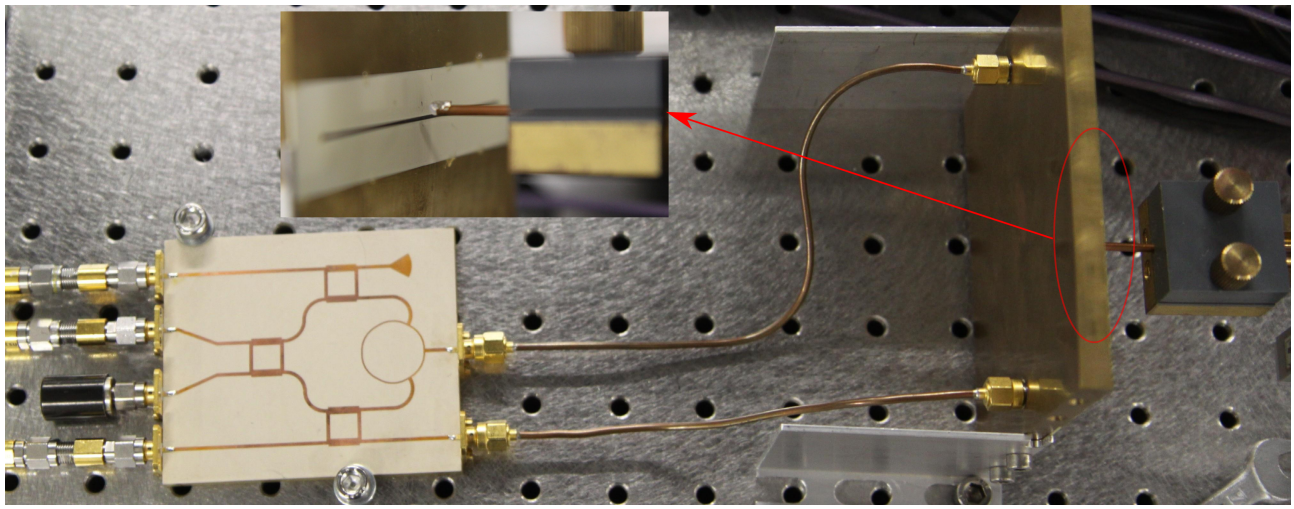


Figure 8: Measurement setup.

single-bunch measurements in multibunch operation mode, which will be the standard operation mode of the XFEL, the beam induced sensor signal shaped is a derivation of Gaussian bunches. This makes a instantaneous measurement necessary. A six-port reflectometer has the ability to detect these pulses, if the time resolution of the overall system is small enough [9]. Especially the detector circuit and plays an important role here.

PHASE DIFFERENCE MEASUREMENTS

The phase difference at both output ports of the sensor originates from the beam induced signal at the transmission line sensors. Since the particle beam only covers a small part of the sensor's width the induced signal is primary induced at a single point along the transmission line. As a result, electromagnetic waves propagate to both ends of the sensor where K-connectors are positioned. If the particle beam is not centered, the propagation time to the ends will differ, which leads to a phase mismatch, that can be detected with the six-port reflectometer.

An important information is the maximal phase difference that is achieved when the particle beam is near one of the sensor's terminations. The total length to both connections is about 183 mm. The propagation speed of the wave in the transmission-line substrate c depends on its electromagnetic properties of the used Rogers RO3010 substrate. It has a relative permittivity $\epsilon_r = 10.2$.

$$c = \frac{c_o}{\sqrt{\epsilon_r \mu_r}} = \frac{2.998 \cdot 10^8 \mathrm{m\,s^{-1}}}{\sqrt{10.2 \cdot 1}} \approx 93.87 \cdot 10^6 \mathrm{m\,s^{-1}} \quad (7)$$

Using the equations

$$\Delta t = \frac{\Delta l}{c} \quad (8)$$

and

$$\Delta t = \frac{\Delta \phi}{\omega} = \frac{\Delta \phi}{2\pi f} \quad (9)$$

the phase difference for a non-centered particle beam can be calculated.

The measurement setup to test the six-port reflectometer is shown in Fig. 8.

The beam induced excitation is modeled with a small coupling loop in the vicinity of the transmission line. The coupling loop is mounted A 3D Micropositioner to adjust the induced signal with μm precision. Due to the limited adjustable range, less than a quarter of the sensor length could be measured. The obtained results are shown in Fig. 8 Evaluating port 4, it can be clearly seen that the transmission line sensor is not fully matched to the six-port reflectometer. The reflections cause a power variation of more than 3dBm. Nevertheless a change in detected power of more than 15dBm for port 3 and 35dBm for port 5 could be observed.

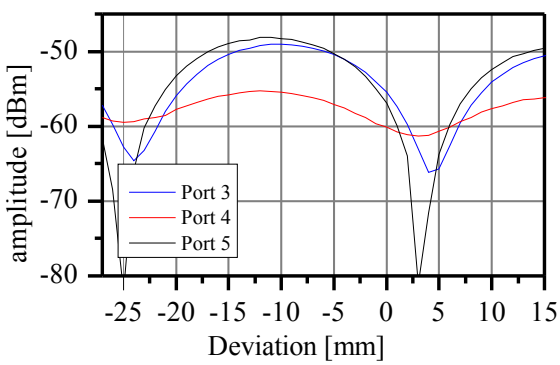


Figure 9: Detected power versus beam offset for ports 3,4 and 5 at a 3GHz.

The investigation of the minimum detectable phase shift and thus beam position requires a much lower step size in lateral direction. Figure 10 shows the measurement results obtained with a step size of 100μm. The amplitude variation for port 4 is less than 1dBm, for port 3 8dBm and port 5

Copyright © 2014 CC-BY-3.0 and by the respective authors

ISBN 978-3-95450-141-0

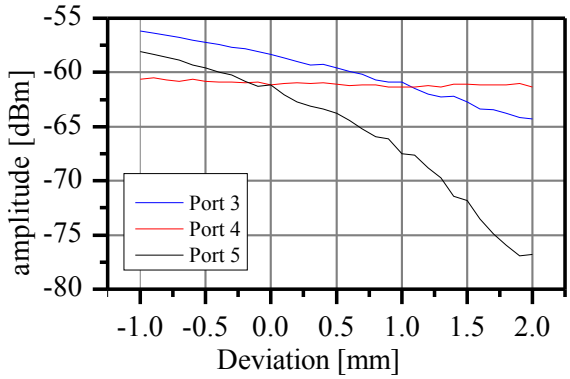


Figure 10: Detected power versus narrow beam offset for ports 3,4 and 5 at a 3GHz.

more than 20dBm for a beam offset of 3mm. This results in a sensitivity of more than 5dBm/mm taking into account a quadratic behavior.

CONCLUSION

A simple and passive read out scheme the EBPM Pickup structures for energy measurements of free-electron lasers such as FLASH or XFEL was introduced. The EBPM needs a high dynamic range over the sensor length of 183 mm and high resolution of less than 20μm. Both, the dynamic range and the resolution depend on the operation frequency. Due to phase ambiguity, only the readout scheme for high resolution was simulated using Agilent ADS as well as CST Microwave studio. For validating the obtained simulation results a prototype was build and a series of measurements were conducted with a non-hermetic prototype of a EBPM Pickup structure.

The proposed design provides a sensitivity of more than 5dBm/mm beam offset for a mean value of -60dBm for the non hermetic test setup. For the high resolution of less than 20μm a sensitivity of 0.1dB at the given power level is sufficient. A standard power meter fulfills this requirements typically down to -70dBm.

Although a measurement of all four output ports was not possible at the same time, it could be confirmed, that the six-port reflectometer enables precise measurements of phase and amplitude differences.

REFERENCES

[1] A. Penirschke, A. Angelovski, R. Jakoby, “Grounded Coplanar Waveguide Transmission Lines As Pickups For Beam Position Monitoring In Particle Accelerators”, TUPC29, IBIC 2013, Oxford, UK, 2013.

[2] U. Mavric, M. Felber, Ch. Gerth, W. Jalmuzna, A. Piotrowski, H. Schlaarb, “Preliminary measurement results of the upgraded Energy BPM at FLASH”, Moppr017, IPAC2012, May 2012, New Orleans, Louisiana, USA, p.813-815.

[3] G.F. Engen, C.A. Hoer, “Application of an arbitrary 6-port junction to power-measurement problems”, IEEE Transactions on Instrumentation and Measurement, 1972, vol.21, no.4, pp 470–474.

[4] A. Koelpin, G. Vinci, B. Laemmle, D. Kissinger, R. Weigel, “The six-port in modern society”, Microwave Magazine, IEEE, 2010, vol.11, no.7, pp 35-47.

[5] K. Hacker, “Measuring the Electron Beam Energy in a Magnetic Bunch Compressor”, PhD Thesis, Hamburg, 2012.

[6] P. Castro, “Beam trajectory calculations in bunch compressors of TTF2”, DESY Technical Note 03-01, April 2003.

[7] A. Angelovski, A. Penirschke, R. Jakoby, “Planar Transmission Lines BPM for horizontal Aperture Chicane for XFEL”, MOPA47, IBIC 2012, Tsukuba, Japan, 2012.

[8] G.F. Engen, “An improved circuit for implementing the six-port technique of microwave measurements”, Microwave Theory and Techniques, IEEE Transactions on, IEEE, 1977, vol. 25, pp .1080-1083.

[9] Y. Demers, R.G. Bosisio, F.M. Ghannouchi, “Repetitive and single shot pulse microwave six-port reflectometer”, IEEE Transactions on Instrumentation and Measurement, 1990, vol. 39, no. 1, pp. 195–200.

Copyright © 2014 CC-BY-3.0 and by the respective authors

ISBN 978-3-95450-141-0

NSLS-II RF BEAM POSITION MONITOR COMMISSIONING UPDATE

Joseph Mead#, Anthony Caracappa, Weixing Cheng, Christopher Danneil, Joseph DeLong, Al DellaPenna, Kiman Ha, Bernard Kosciuk, Marshall Maggipinto, Danny Padrazo, Boris Podobedov, Om Singh, Yuke Tian, Kurt Vetter
NSLS-II, Brookhaven National Laboratory, Upton, NY 11973, USA

Abstract

The National Synchrotron Light Source II (NSLS-II) is a third generation light source currently in the commissioning stage at Brookhaven National Laboratory. The project includes a highly optimized, ultra-low emittance, 3GeV electron storage ring, linac pre-injector and full energy booster synchrotron. Successful commissioning of the booster began in November 2012, followed by the ongoing commissioning of the NSLS-II 3GeV electron storage ring which began in March 2014. With those particles first injected came a value realization of the in-house developed RF Beam Position Monitor (RF BPM). The RF BPM system was envisioned and undertaken to meet or exceed the demanding applications of a third generation light source. This internal R&D project has since matured to become a fully realized diagnostic system with over 250 modules currently operational. Initial BPM performance and applications will be discussed.

INTRODUCTION

NSLS-II, a 3 GeV ultra-low emittance third generation light source, currently in the commissioning stage of construction at Brookhaven National Laboratory [1,2]. It includes a 200MeV LINAC, LINAC to Booster (LtB) transfer line, 200MeV to 3GeV Booster, Booster to storage ring (BtS) transfer line and 3GeV storage ring [3,4]. Injector commissioning was conducted from Nov 2013 to Feb 2014 and 3GeV ramped beam was established in the booster at the end of 2013. Storage ring commissioning began in March 2014 and 25mA of stored beam was achieved by May 2014. After a 2 month shutdown to install the super-conducting RF cavity, commissioning resumed at the end of Jun 2014 for a few weeks and the goal of 50mA of stored beam was achieved by mid July 2014. Commissioning is expected to resume in October of 2014. The NSLS-II storage ring is equipped with 180 RF BPMs (2 per each multipole girder, 3 multipole girders per ring cell) plus a number of "specialized" BPMs, 4 in injection straight, and (eventually) two or more per every ID straight.

BPM ELECTRONICS OVERVIEW

The NSLS-II RF BPMs incorporate the latest technology available in the RF, Digital, and Software domains. A single design has been achieved that strives to meet all NSLS-II operational requirements for all the injection components as well as the storage ring. During the linac and then booster commissioning BPMs performed very well, easily meeting the corresponding specifications. However, it is the storage ring performance specs, especially the resolution and long term drift that impose the strictest requirements [5]. The architecture of the rf bpm electronics has been carefully conceived to provide robust design with substantial flexibility to serve as a platform for other systems.

The rf bpm electronics system consist of 1) a chassis, housing an analog front-end (AFE), digital front-end (DFE) & power supply (PS) modules, shown in Fig. 1; and 2) a pilot tone combiner (PTC) module mounted in the tunnel near rf buttons, shown in Fig. 2.



Figure 1: NSLS-II RF bpm electronics chassis.

The AFE topology is based on band-pass sampling architecture which subsamples the 500MHz impulse response of the SAW band-pass filter at ~117MHz. The response of the filter produced for a single bunch results in an impulse of approximately 30 samples or ~300ns in length. Coherent timing is derived from an external 378 KHz revolution clock via differential CML. An analog phase-locked loop is used to synchronize VCXO ADC clock synthesizer [7,8]. The received revolution clock is transmitted to the DFE to serve as a time reference for the DSP engine.

The DFE is responsible for all DSP of the button signals and communication of the results with the control system. The DFE is based on a Xilinx Virtex-6 Field Programmable Gate Array (FPGA). The fixed-point DSP engine calculates TbT position based on a single-bin DFT algorithm. The FOFB 10KHz data and 10Hz slow acquisition data are derived directly from the TbT calculation.

The bpm system is parametrically configured for single-pass, booster or storage ring. The digital signal processing (DSP) architecture is also generic; all three operational modes use the same firmware.

*Work supported by DOE contract No: DE-AC02-98CH10886.
#mead@bnl.gov

Copyright © 2014 CC-BY-3.0 and by the respective authors

ISBN 978-3-95450-141-0

The bpm's in a cell communicate with an industrial PC running an EPICS IOC via TCP/IP [6]. The communication protocol supports waveform monitoring for ADC raw data waveform (117 MHz), single pass, turn by turn waveform (TbT, 378 kHz), fast waveform (FA, 10 kHz) and slow data (SA, 10 Hz). The ADC raw, TbT and FA data is triggered on demand and supports a large 1 million sample history buffer (~32 Mbytes). Table 1 provides a summary for all data transfer capabilities.

Table 1: RF Bpm Data Transfer Capabilities

Data Type	Mode	Max Length
ADC Data	On-demand	256Mbytes or 32M samples per channel simultaneously
Single-Pass	Streaming	800hr circular buffer (1Hz Injection)
TbT	On-demand	256Mbytes or 5 M samples Va,Vb,Vc,Vd, X,Y,SUM, Q, pt_va,pt_vb,pt_vc,pt_vd
FOFB 10KHz	Streaming via SDI Link & on demand	Streaming - X,Y,SUM; For on demand: 256 Mbytes or 5 Msamples. Va,Vb,Vc,Vd, X,Y, SUM, Q, pt_va,pt_vb,pt_vc,pt_vd
Slow Acquisition 10Hz	Streaming and On-demand	80hr circular buffer Va,Vb,Vc,Vd, X,Y,SUM, Q, pt_va,pt_vb,pt_vc,pt_vd
System Health	Streaming & on-demand	80hr circular buffer AFE temp, DFE temp, FPGA Die temp, PLL lock status, SDI Link status

The PTC, shown in Fig. 2, is a passive module located on the girder below the rf button. A 1 m SiO2 cable connects the rf button to the PTC module. A pilot tone generated on the AFE is carried out to the PTC module via a 5th cable, which is coupled into each of four forward beam signal channels. The pilot tone was to be used to provide dynamic calibration to mitigate long term drift. However, test has shown that the bpm long-term stability (< 200 nm) has been achieved by the use of highly stable ±0.1 °C thermally regulated racks. The pilot tone now is only used for system diagnostics and integration without beam [9].

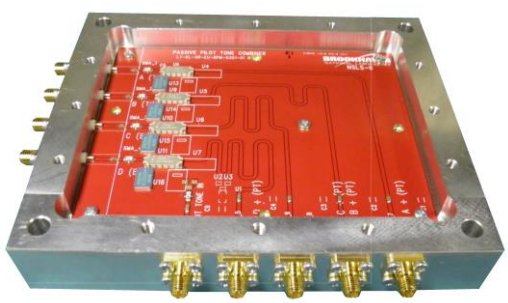


Figure 2: Pilot Tone Combiner (PTC).

BPM COMMISSIONING RESULTS

Initial tests were conducted to measure the performance of the bpm's, but due to limited time and administrative limits (25 mA total beam current towards the end of this commissioning period) the specs could not be fully tested. However, significant progress in verifying the resolution performance of BPMs was achieved at lower currents. Extrapolating these results to higher beam currents we should easily meet the resolution specifications. Separately, due to lack of time, no long term drift studies have been performed and these will be scheduled later.

Resolution Measurements

BPM resolution measurements were performed using a dedicated BPM button assembly located on girder 2 in cell 28. This assembly is not used in normal operations but was rather instrumented with an electronics module specifically for this test. The module was connected to the 4 bpm buttons using a combiner/splitter assembly to make the measurements independent of transverse beam motion. The connection scheme sums the 4 button signals with a 4:1 combiner and then splits the summed signal using a 1:4 splitter, which are then connected to the 4 input channels of the electronics. With this connection scheme each of the 4 channels of the electronics will see the same signal and electronics performance can be measured independent of beam motion.

The resolution measurements were performed using three different fill patterns; single bunch, 50 bunches, and approximately a 60% fill (~800 bunches). For each of these fill patterns beam was injected into the storage ring and then allowed to naturally decay. To help speed up the decay process, scrapers were inserted to a position which limited the beam life-time to approximately 15-30 minutes. Data was then collected from the BPM approximately every 5 seconds along with the beam current from the DCCT. The data collected from the BPM was; raw ADC data (1Mpts), TbT data (10Kpts), and FA data (18Kpts). Over 100 data files were collected for each fill pattern as the beam decayed. Figure 3 shows the resulting ADC data for each of the fill patterns.

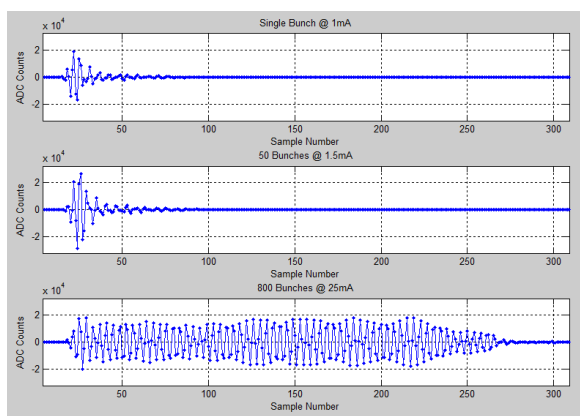


Figure 3: Raw ADC data for different fill patterns.

ISBN 978-3-95450-141-0

Copyright © 2014 CC-BY-3.0 and by the respective authors

The single bunch resolution performance of the electronics is shown in Figure 4 for TbT data and in Figure 5 for FA data. The digitizer on the BPM has 16 bits of resolution so the maximum value is 3.2767 x 10^4. The maximum ADC value of each of the four channels was found and the mean value of these maximums is plotted on the ordinate of the resolution plots. At the time of these tests the maximum single bunch beam current that could be stored in the ring was about 1mA, which was not enough to bring the ADC's of the electronics to full scale, so the full scale resolution could not be measured. At around ½ full scale the resolution is about 12um for TbT data and 2um for FA data. A resolution gain of a factor of six is expected from TbT positions to FA positions, since the bandwidth reduction is a factor of 38.

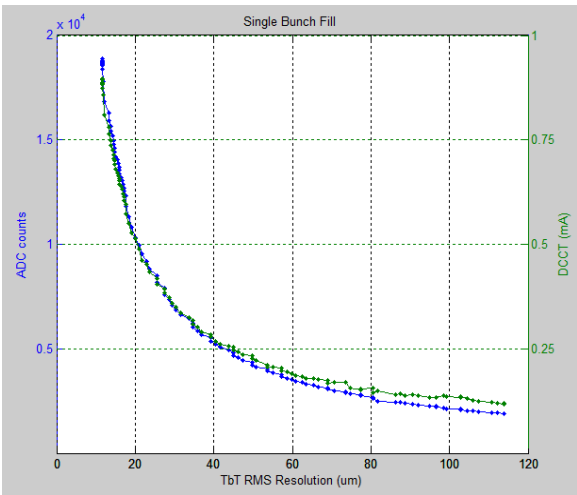


Figure 4: TbT data resolution with single bunch.

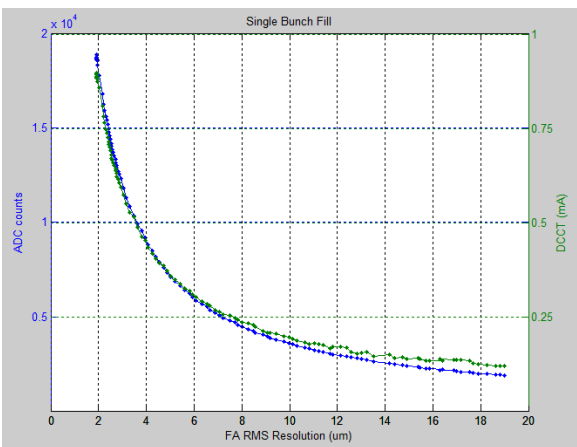


Figure 5: FA data resolution with single bunch.

For a 50 bunch fill pattern the results are shown in Figure 6 for TbT data and in Figure 7 for FA data. With this fill pattern the BPM's reached saturation at about 1.6mA of beam current. At full scale the resolution was measured at 7um for TbT data and just over 1um for FA data.

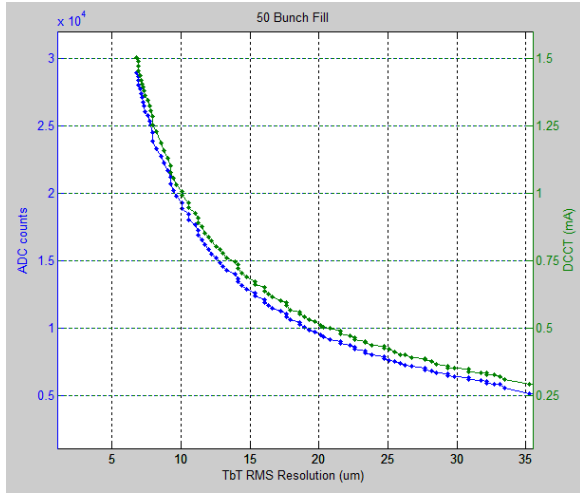


Figure 6: TbT data resolution with 50 bunches.

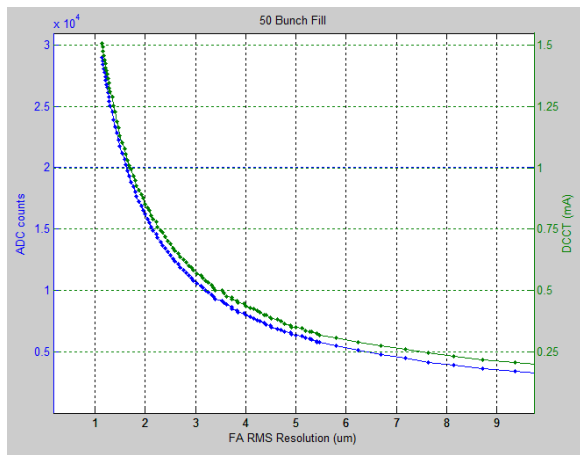


Figure 7: FA data resolution with 50 bunches.

The final measurement was done with a fill pattern of about 800 bunches, or 60% fill. The limiting factor for this test was the administrative limit of 25mA maximum beam current, so the BPM's didn't quite reach their full scale range. At beam currents above 15mA the results became irregular as the maximum ADC count values began to fluctuate greatly between data sets and stopped monotonically increasing as beam current continued to increase. This can be seen in Figures 8 and 9. Above 15mA of beam current the maximum ADC values smear out, which could be an indication of longitudinal instabilities at these higher beam currents. Even with these issues the TbT resolution easily meets the specification of < 3um rms with an 80% fill.

Copyright © 2014 CC-BY-3.0 and by the respective authors

ISBN 978-3-95450-141-0

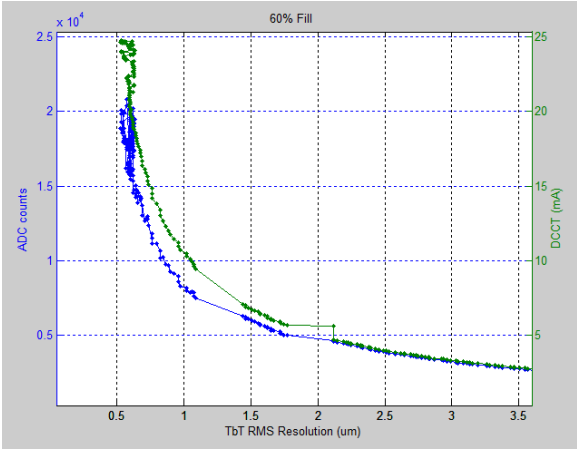


Figure 8: TbT data resolution with 60% fill pattern.

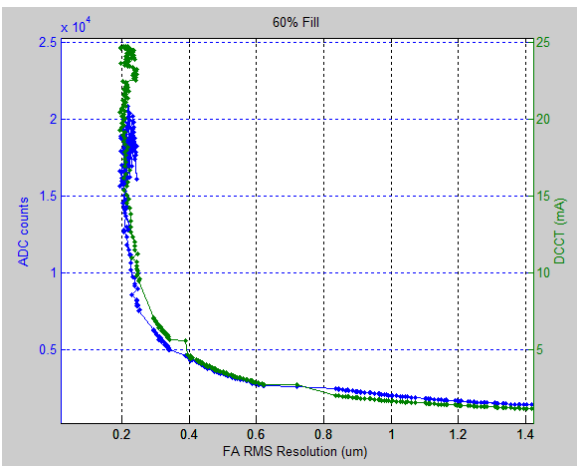


Figure 9: FA data resolution with 60% fill pattern

Timing Adjustment

The Beam Position Monitor Electronics calculates a single horizontal and vertical position for every revolution. To function correctly the electronics needs to have its timing signals properly adjusted. This involves the adjustment of two different delay values, one being a fine adjustment and one a coarse adjustment. The fine adjustment, called the geographic delay, provides a delay of the machine clock (Frev) signal which is received from the timing system. The delay resolution is approximately 8.5ns, which is the ADC sampling clock period, and the range of the delay is a single revolution, which is 2.6us. The machine clock signal provides the critical signal to instruct the DSP engine to begin a new position calculation. For every machine clock signal received a new position calculation is performed. The function of this delay is to provide a knob to the user to permit compensation for various cabling delays and beam transit delays between BPM's, thus allowing all BPM's in the ring to perform their position calculation on the same bunches. The BPM calculates a new position for every revolution, but unless a trigger signal is received via the timing system, the results are not saved to memory. This is where the coarse adjustment, called the trigger delay, comes into play. This value delays the trigger signal so that the desired revolutions of the beam are saved to memory. Once a trigger is received the next N ADC samples and position calculations are saved to memory. For the storage ring BPM's this value was found to be a value of 10,795,750 which corresponds to an actual delay of about 92ms to properly align to the first injected revolution. The timing was done experimentally, one BPM at a time, using the CSS panel shown below in figure 10. This CSS panel helped streamline the operation by allowing changes and showing the results for an entire cell. In theory, all trigger delays should be equal, and only the geographic delays should change as a function of its location in the ring. For most cases this was found to be true, but some anomalies were discovered. The reason we believe is from timing cables with inverted polarity, plus perhaps cell to cell timing discrepancies. We are currently investigating these issues. Regardless, the flexibility of the BPM timing architecture permitted us to overcome these issues and still properly align the timing. All 180 storage ring BPM's were successfully timed in and operational in under 2 hours.

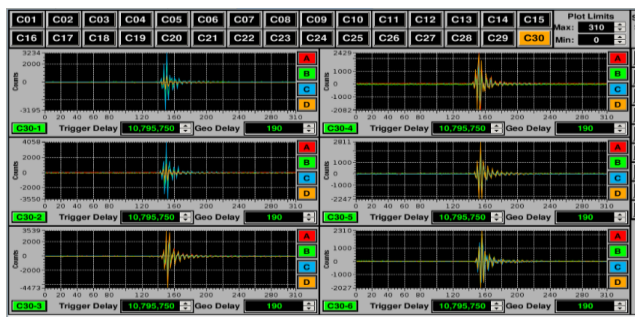


Figure 10: BPM Timing CSS Panel.

Triggering Modes

The flexibility of the BPM architecture permits it to be triggered in various modes and configurations. The raw ADC data, turn-by-turn (TbT) data, and Fast Acquisition (FA) data are all on-demand data streams and are only available to the user if a trigger signal is received by the BPM. After the trigger signal is received, up to millions of data points from each data stream are stored to the large DDR memory on the BPM. Depending on beam conditions, the trigger scenarios may vary. During the initial operation when first turn was being attempted, the BPM's were set to trigger on the booster extraction event (Event 66). In that scenario, the BPM's could capture the data for the first few million turns after injection. After stored beam was achieved the BPM's were set to trigger on the 1 Hz event (Event 32), so that BPM data would be constantly refreshed to users. In this mode limited record lengths are available do to the communication of long waveforms through the control system. If a user wanted to capture a single shot, long data record, the BPM's can be placed into internal trigger mode and then issued a global single shot event. In this mode the BPM's will trigger only once, to allow time for large records to be

ISBN 978-3-95450-141-0

Copyright © 2014 CC-BY-3.0 and by the respective authors

offloaded from the local DDR memory through the control system and to the high level applications. These were the main triggering modes of operation used during commissioning. About halfway through commissioning it was observed that if the targeted injection bucket was greater than 200, the BPM's would start reporting positions on incorrect turns. After discussions with the timing system experts, it was learned that the timing of this event (66) was relative to targeted bucket and therefore moved with respect to the machine clock. Since different BPM's need different geographic delays, this timing shift could cause inconsistent results between BPM's. The problem was solved by adding another event (47) to the timing system which always has a fixed timing relationship to the machine clock.

SUMMARY

BPMs were by far the most heavily used diagnostics during the commissioning. A great number of high level applications make use of BPM data. These include, to name just a few, stored beam orbit measurement, correction, and (slow) feedback (typically using SA data); various linear lattice diagnostics tools (LOCO from SA, tune measurement from TbT, etc.); dynamic aperture and other non-linear lattice diagnostics tools relying on kicked TbT beam response and many others.

It is also worth emphasizing, that even without running any sophisticated tools, the ability to quickly check BPM ADC signals at any ring location or glance through minimally processed TbT data around the ring was absolutely crucial for the ring commissioning. For instance, the very first turn around the ring was closed and confirmed simply by looking at ADC-sum BPM signals all around the ring. Similarly, an aperture in cell 10 (which later turned out to be a hanging RF seal) was first suspected from the fractional drops of kicked beam TbT BPM sum signal which persistently showed up on BPMs at that particular location [10].

So far the overall experience with BPMs was very positive, especially after additional triggering modes were added. Of course, as is typical for any commissioning, we did encounter and fixed some of the newly discovered issues with the BPM system. During the SR commissioning proper, the hardware issues with BPMs turned out pretty minimal, i.e. two units (out of 236) had to be replaced because of a failed PLL module. Rather, the majority of the issues were related to the communication between the BPMs to the IOCs as well as from the IOCs to the rest of the control system. Most of these issues were not anticipated prior to the commissioning but rather resulted from the evolution of the requirements from the BPM users, which naturally evolved during the commissioning.

Additional BPM system commissioning studies must be performed in the future. Even though the initial BPM resolution measurement results are very encouraging, to fully verify the compliance with the specs, similar measurements should be repeated at higher currents, as well as with long bunch trains (when stable). When larger amounts of dedicated beam time are provided, long term drift studies should also be performed. In addition, studies to characterize orbit sensitivity to the fill pattern changes and as well as to the changes of BPM attenuation should be performed (the latter have only been done with the pilot tone, not real beam). These will allow us to decide whether automated adjustments of BPM attenuation should be implemented in the control system, and if so, how. Another important issue for physics applications is the correction of the non-linearity at large transverse beam displacements (this is unrelated to the BPM electronics). So far the linearity is corrected using the coefficients obtained from BPM button geometry (essentially solving the Laplace equation). Experimental verification of these would be extremely beneficial, and it could be accomplished, for instance, by comparing the BPM readout with large transverse beam offset vs. the positions on the nearby flag.

REFERENCES

[1] NSLS-II preliminary design report", http://www.bnl.gov/nsls2/project/PDR
[2] F. J. Willeke, "Status of NSLS-II project", PAC11, New York, USA, (2011).
[3] T. Shaftan, "Status of NSLS-II Injector", IPAC13, Shanghai, China, (2013).
[4] R. Fliller, "Results of NSLS-II Linac Commissioning", IPAC13, Shanghai, China, (2013).
[5] S. Krinsky, "Accelerator physics challenges for the NSLS-II Project", PAC09, Vancouver, Canada, (2009).
[6] Kiman Ha, "NSLS2 beam position monitor embedded processor and control system", ICALEPCS11.
[7] K. Vetter, "NSLS-II RF beam position monitor", PAC11, New York, USA, (2011).
[8] K. Vetter, "NSLS-II RF beam position monitor update", BIW12, Newport News, Virginia, USA, (2012).
[9] O. Singh, "NSLS-II BPM and fast orbit feedback system", IBIC13, Oxford, UK, (2013).
[10] W. Cheng, "NSLS2 Diagnostic Systems Commissioning and Measurements", IBIC2014, Monterey, CA, USA, (2014).

Copyright © 2014 CC-BY-3.0 and by the respective authors

ISBN 978-3-95450-141-0

STATUS OF THE SIRIUS RF BPM ELECTRONICS

S. R. Marques#, R. A. Baron, G. B. M. Bruno, F. H. Cardoso, L. A. Martins, J. L. Brito Neto, L. M. Russo, D. O. Tavares, LNLS, Campinas, SP, Brazil

Abstract

A modular and open-source RF BPM electronics based on the PICMG® MicroTCA.4 and ANSI/VITA 57.1 FMC standards is being developed to be used at Sirius, a 3 GeV low emittance synchrotron light source under construction in Brazil. This paper reports on the latest development advances focusing on bench tests of the second version of the RF front-end and evaluation of the electronics with beam at SPEAR3 (SSRL/SLAC). The interface of the BPM electronics with the orbit feedback system is also discussed.

INTRODUCTION

Sirius is a new 3 GeV synchrotron light source under construction in Brazil [1], targeting a 0.28 nm.rad natural emittance. Storage ring commissioning has been rescheduled and should occur in the 1st semester of 2018.

The Sirius RF BPM electronics is composed of a low noise RF front-end (RFFE) which process the signals coming from RF BPM pick-ups and a typical FPGA-based digital receiver employing direct RF sampling technique and further difference-over-sum algorithm to extract beam position information. The RFFE uses the "switching electrode" principle [2] to compensate for low frequency drifts originated in the RF chains. Instead of multiplexing the four BPM signals into one single RF chain or using a full four-by-four crossbar switching scheme [3], only diagonal BPM antenna signals are switched, as seen in [4].

The system is modular, based on proven industrial standards and is being developed as an open source project. Information on technical choices and hardware and software structures were detailed in the past [5, 6, 7].

During the last year, effort to consolidate the hardware has been done by the development team. Open questions about performance limitations were solved and a new spin of the RFFE and ADC boards was concluded.

Bench tests revealed the current BPM electronics performance status. In addition, beam tests performed at SPEAR3 (SSRL/SLAC) showed the operation of the electronics with realistic broadband BPM signals.

The MicroTCA.4-based digital platform, composed of CPU and FPGA boards for readouts and fast orbit feedback (FOFB) implementation, is currently being integrated and will be detailed in future work.

SYSTEM REQUIREMENTS

BPM electronics specification is mainly driven by beam orbit stability requirements. At Sirius, the most stringent electron beam stability requirement is given by the vertical beam size at the center of the longer straight sections, namely 1.94 µm. In order to achieve position stability better than 5% of this beam size within a 0.1 Hz to 1 kHz bandwidth, the corresponding vertical plane RMS orbit disturbance shall be lesser than 97 nm. By allocating half of this budget to orbit distortions exclusively caused by electronic and mechanical BPM noise, which is transferred to the beam through the fast orbit feedback loop, a 69 nm RMS orbit disturbance specification was derived for BPMs.

Simulations with the Sirius storage ring show that a factor of 0.72 translates uncorrelated RMS noise in all storage ring BPMs to an RMS orbit disturbance at each of the long straight sections. Hence the 69 nm orbit distortion specification derived above can be relaxed to 95 nm when translated to noise on the BPMs. From this resulting number, a 50 nm upper bound RMS BPM noise is reserved for mechanical vibration on the BPM stands, thus leaving 80 nm RMS noise (or resolution) budget for the BPM electronics itself.

Table 1 summarizes BPM electronics resolution specification alongside more general requirements for the Sirius's BPM system. The numbers have been reviewed since last publications [6].

Table 1: Requirements of Sirius RF BPM Electronics

Parameter	Value
Resolution (RMS) @ 0.1 Hz to 1 kHz	< 80 nm
Resolution (RMS) @ turn-by-turn full bandwidth	< 3 µm
1 hour position stability (RMS)	< 0.14 µm
1 week stability (RMS)	< 5 µm
Beam current dependence (decay mode)	< 1 µm
Beam current dependence (top-up mode)	< 0.14 µm
Filling pattern dependence	< 5 µm
First-turn resolution (RMS)	< 0.5 mm
Horizontal/Vertical plane coupling	< 1%

HARDWARE IMPROVEMENTS

The tests carried out in 2013 [6] were performed with the first versions of the RFFE and ADC boards, which has partially fulfilled specifications. The following sections describe the modifications made since then.

RF Front-End Board

The RFFE v1 board concept consisted of an analog front-end in which several calibration and compensation schemes (channels switching, pilot tone and temperature control) were available for comparative tests [8]. The RFFE v2 was designed as a cost-optimized board in

#sergio@lnls.br

ISBN 978-3-95450-141-0

Copyright © 2014 CC-BY-3.0 and by the respective authors

which only the most effective calibration schemes were present. The major changes on RFFE v2 are listed below:

- Improvement of noise figure by reducing 6 dB on insertion loss before the first amplifying stage.
- A low pass filter has been added before the diagonal switching circuit in order to avoid high peak voltages on the RF switches.
- Reduction in the number of RF amplifiers per channel, from 3 to 2, and in the number of RF programmable attenuators per channel, from 2 to 1.
- Reduction in the number of temperature control elements in each RF diagonal channel. Only one temperature controller per diagonal pair of channels has been placed close to the devices upstream of the RF diagonal switching scheme. Temperature control has proved necessary only for those elements upstream of the RF switches, such as low pass filters and matching network.
- Redesign of the diagonal switching scheme using DPDT RF switches. The switching response time was decreased by a factor of 100, from 2 µs to 20 ns (90% stabilization time).

Figure 1 shows the RFFE v2 prototype emphasizing one of the RF channel pairs.

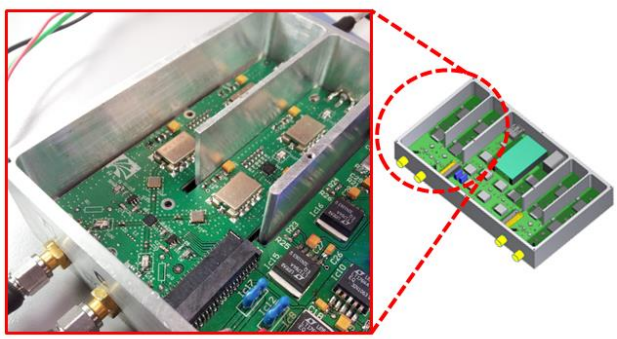


Figure 1: RFFE v2 prototype board. The dimensions of the prototype aluminum box are 20 cm x 11.5 cm.

An important shortcoming of the RFFE v2 was the reduction in dynamic range due to the removal of an amplification stage of the RF chain. An additional amplification stage will integrate the final version of the RFFE, currently under development.

FMC ADC Board

Two variants of FMC (FPGA Mezzanine Card) four-channel fast ADC boards were designed and produced since the very early stages of the project, differing by the data converters in use: LTC2208 (130 MS/s ADC) or ISLA216P25 (250 MS/s). Efforts have been concentrated on the former board, on which a few hardware modifications have been implemented:

- RF traces at signal inputs were carefully symmetrized.
- The ADC LTC2208 matching network was improved resulting in 2.5 dB reduction in insertion loss at 500 MHz, keeping the S_{11} parameter lower than -20 dB.
- Lower additive phase noise RF switch has been used as reference clock selector.
- Standard ADC digital LVPECL clock terminations were adopted, slightly improving SFDR performance by ~2 dB.

EXPERIMENTAL SETUP

Figure 2 shows the setup used in all tests herein described. This test platform does not rely on the MicroTCA digital hardware platform which has been developed for the final BPM system [7], although FPGA digital signal processing firmware and control software are kept essentially the same. The described setup is based on a FPGA development kit and a small form factor mini-ITX PC board with PCI Express connectivity, to allow easy transportation of the system for different environments. Several RF signal and external clock sources were used across the tests.

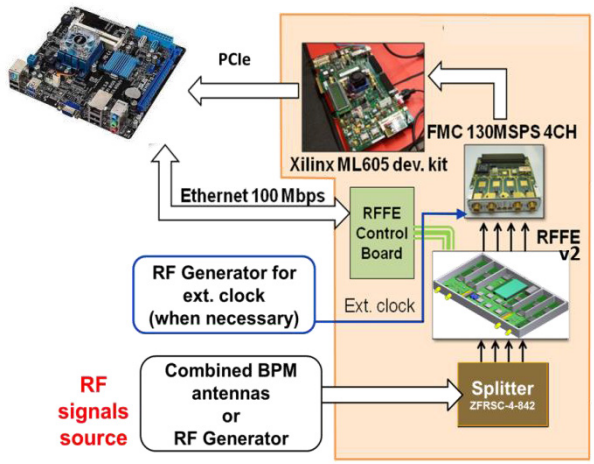


Figure 2: Block diagram of the setup used for the BPM electronics test.

PERFORMANCE IMPROVEMENTS

Previous tests with the Sirius BPM electronics have already met filling pattern dependence and temperature dependence specifications. On the other hand, resolution and beam current dependence (BCD) performance figures were only partially within specifications [6]. In 2014 several laboratory tests were carried out in order to understand the referred limitations and find solutions for improvements. The following sections show the results of such effort.

Unless otherwise noted, all bench tests herein presented have been performed using two locked R&S SMA100A RF signal generators for both clock and signal inputs. Centered beam was simulated by splitting by four the generated signal. The switching frequency was made identical to the FOFB data rate frequency (~110 kHz).

Resolution

From RFFE v1 to v2, the following facts have led to improvements on resolution performance:

Copyright © 2014 CC-BY-3.0 and by the respective authors

ISBN 978-3-95450-141-0

- Due to wrong FPGA calibration of delays between ADC clock and data paths, one of the four channels had one clock cycle delay relative to the others, resulting in a loss of correlation between diagonal channels and hence reducing the diagonal switching effectiveness. The correction of this issue has improved resolution performance.
- Faster RF switches allowed swapping the RFFE channels at higher rates thus reducing the loss of signal power and guaranteeing smooth transition of signal phase when transitioning switches' states.
- Noise figure has improved due to RFFE circuit redesign.

Figure 3 shows the resolution in function of input power obtained after the improvements. An integration bandwidth of 2 kHz and a BPM geometric factor of $k = 10$ mm have been used to allow comparison with previous results. It has been measured for centered beam with optimized RFFE attenuator values. The 80 nm resolution specification could be reached for input power levels higher than -25 dBm, corresponding to a beam current above 200 mA at Sirius.

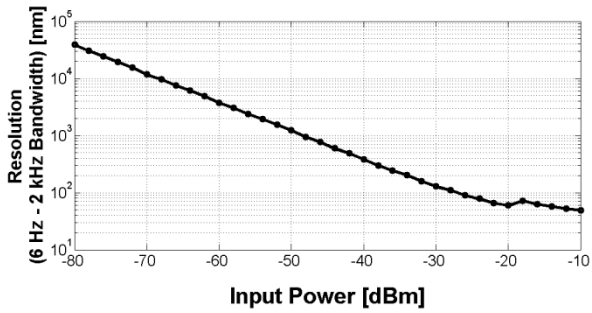


Figure 3: Resolution in function of input power.

The integrated RMS noise for two input power levels, -10 dBm and -20 dBm, with diagonal switching on and off, is showed in Fig. 4. The noise suppression effect of the switching is more evident at lower frequencies.

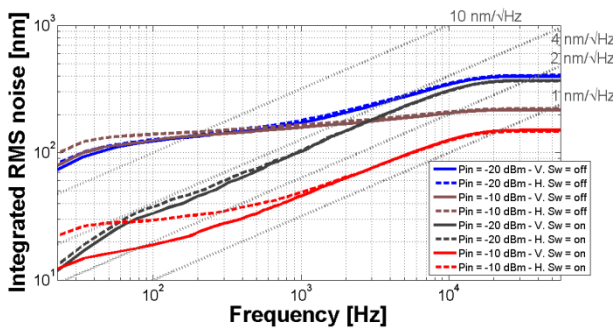


Figure 4: Integrated RMS noise for different input power and diagonal switching scenarios.

Beam Current Dependence

BCD tests were recently performed using new data acquisition software, with longer buffers and automated acquisition, which has made it possible to evaluate beam position average value with less uncertainty at lower input power conditions.

The long range BCD simulating a beam decay mode operation is depicted in Fig. 5. It shows that the ±1 µm requirement is satisfied for input power levels above -45 dBm, corresponding to a beam current of approximately 20 mA at Sirius. Nonlinear behavior of the RF chains, in the order of ~0.001 dB, is responsible for these observed BCD characteristics.

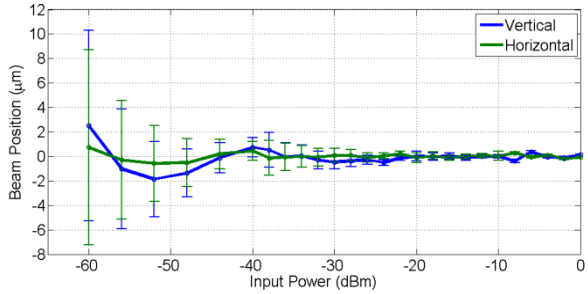


Figure 5: Long range BCD for centered beam.

The short range BCD for five different input power levels, from -40 dBm to -10 dBm, was also verified and met the ±0.14 µm top-up operation requirement with considerable margin, as can be seen in Fig. 6.

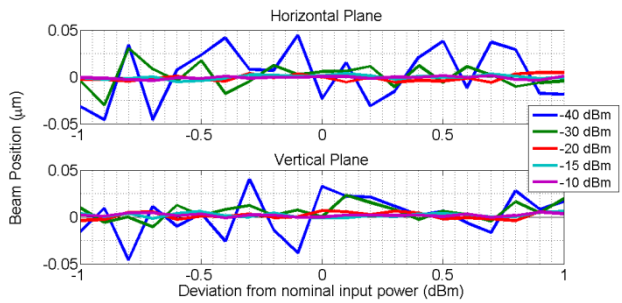


Figure 6: Short range BCD for centered beam.

TESTS WITH BEAM

In March 2014, tests with beam were performed at SPEAR3 storage ring in order to verify system performance under realistic conditions. Figure 7 shows the test setup used for the tests, essentially the same as depicted in Fig. 2.

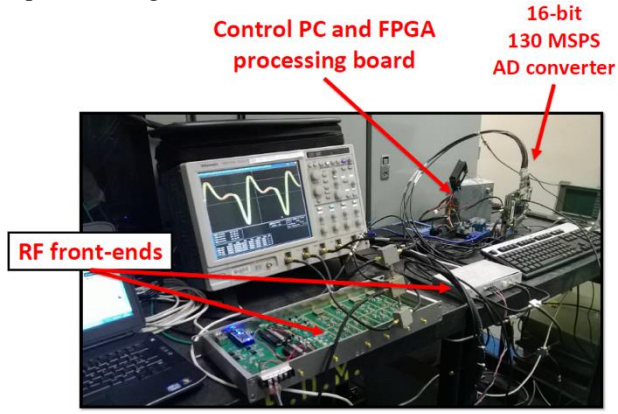


Figure 7: Setup used for the tests with beam at SPEAR3.

Four beam signals coming from a spare button BPM were combined and then split by four with a broadband

ISBN 978-3-95450-141-0

Copyright © 2014 CC-BY-3.0 and by the respective authors

splitter in order to emulate a perfectly stable beam. The ADCs external clock input was sourced by a 64.02 MHz sine wave clock locked to the beam frequency coming from SPEAR3's timing system. This clock frequency was chosen by convenience since it was readily available. The tests were performed under the following beam conditions:

- Parasitically to user beam: a 500 mA stored beam current relying on top-up refills every 5 minutes with standard filling pattern. The beam's first RF harmonic at 476 MHz provided -13 dBm power at the BPM electronics inputs. Different sets of external attenuators were used to emulate different beam currents.
- Accelerator physics shift: a 200 mA stored beam, low alpha mode with 4.5 ps RMS bunch lengths with a variety of filling patterns. No external attenuator was used.

Figure 8 shows the integrated RMS noise values for four situations where the input power was kept nearly the same in order to keep the same RFFE attenuators configuration (except for a 0 dBm generator experiment also showed for reference).

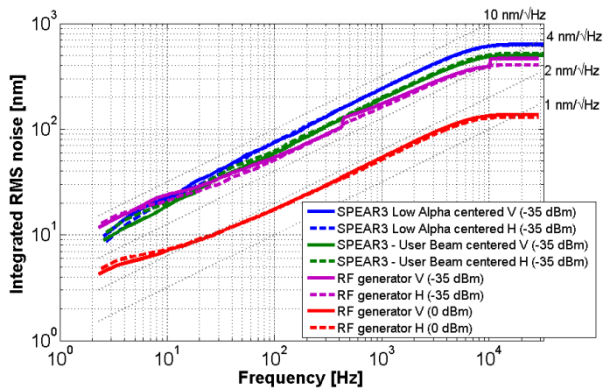


Figure 8: Integrated RMS position noise for four different conditions: (i) SPEAR3 beam in low alpha mode (200 mA), (ii) SPEAR3 beam during user shift (500 mA), (iii) RF generator R&S SMB100A at -35 dBm, and (iv) RF generator R&S SMB100A at 0 dBm.

Integrated RMS beam position noise for SPEAR3 low alpha beam shows that even for bunch lengths as short as 4.5 ps there is no relevant intermodulation products in the spectrum which could affect the beam position measurement at the FOFB data rate. Since the natural bunch length of Sirius is expected to be roughly 9 ps, this can be considered as a worst case scenario with considerable margin. Moreover, coaxial BPM signal cables at Sirius (LMR195) are expected to have higher dispersion than those used at SPEAR3 (LMR240), thus providing additional filtering of beam's RF harmonics.

EXTENDED DISCUSSION

RF Channels Switching Mechanism

As it will be shown in this section, the usage of the diagonal switching scheme virtually eliminates electronic noise originated from the RF chain downstream of the switches. Long term and flicker noise drifts on RF channels' gain are almost completely compensated and hence puts the ultimate beam position resolution limitation on the ADC clock source's phase noise and on long term drifts of all elements upstream of the RFFE diagonal switching.

A practical criterion to distinguish the high, medium and low frequency ranges is described below and is based on the coherence function of channels' noise when the diagonal switching mechanism is active.

The coherence function of two signals, x and y, is defined as $C_{xy}(f) = \frac{|P_{xy}(f)|^2}{P_{xx}(f)P_{yy}(f)}$, where $P_{xx}(f)$ and $P_{yy}(f)$ are the Power Spectral Density (PSD) of signals x and y, respectively, and $P_{xy}(f)$ is the Cross Power Spectral Density (CPSD) of both signals. The coherence function measures how well frequency components of the two signals are correlated with each other.

Figure 9 shows the coherence for all combinations of channels when the diagonal switching scheme is turned on or off. The test has been performed with 0 dBm input power and considered a typical configuration of RFFE attenuators, satisfying both resolution and BCD requirements.

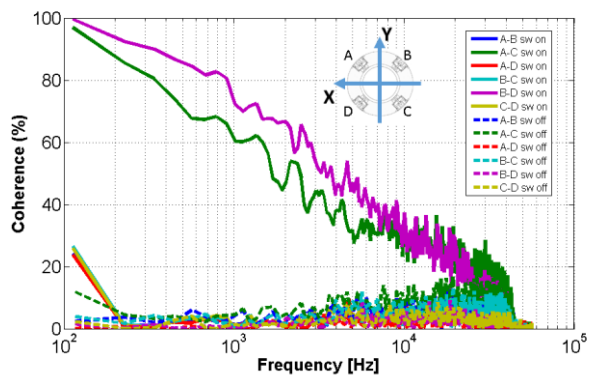


Figure 9: Coherence function between pairs of antenna baseband signal additive noise at FOFB data rate (~110 kHz). BPM signals naming convention is indicated.

It can be noted that the switching scheme is responsible for introducing coherence between the diagonal channel pairs (A-C and B-D) from DC to approximately 40 kHz. For frequencies below 100 Hz, coherence is better than 95%. A rough classification can be thus proposed:

- Low frequency range (from DC to ~100 Hz): noise is dominated by long term drifts and flicker noise of elements downstream of the switches; all drifts on RF channels are considered to be vanished due to common mode noise rejection in difference-over-sum position calculation algorithm.
- Medium frequency range (from ~100 Hz to 40 kHz): the higher the frequency the higher is the noise contribution of uncorrelated RF channel gain and ADC clock phase noise.
- High frequency range (from ~40 kHz to a few GHz): noise is dominated by clock jitter integrated over the

Copyright © 2014 CC-BY-3.0 and by the respective authors

ISBN 978-3-95450-141-0

~40 kHz to the ADC clock input bandwidth (typically a few GHz).

This result shows that the switching scheme could be used to compensate for noise from very low frequency up to roughly half of the switching frequency, including clock phase noise and long term gain drifts originated in the RFFE chains, such as RF amplifiers' flicker noise.

Reference Clock

Although the bench tests herein presented have been performed with ADC clocks directly sourced by RF signal generators, preliminary results showed that position measurement resolution is not significantly degraded when the PLL-based clock synthesizer available on the FMC ADC boards is used. This result was already expected, since the switching mechanism introduces high coherence below the chosen PLL bandwidth, 300 Hz. On the other hand, white noise introduced by Si571 VCXO and clock distribution broadband jitter (from 30 kHz to 3 GHz) is not significant (< 250 fs) and is responsible for a resolution performance degradation of less than 10 nm.

Orbit Feedback and BPM Delay

The BPM system was conceived with a strong focus on its integration with the FOFB system. A 1 kHz cross-over frequency performance goal for closed-loop orbit feedback was established in order to allow disturbance attenuation greater than 20 dB for frequencies below approximately 100 Hz. Combined fast steering magnets, power supplies and vacuum chamber response was optimized for a -3 dB bandwidth above 10 kHz for kick amplitudes below 25 µrad, making closed-loop latency the most critical parameter for performance optimization.

The fundamental limiting factor in terms of FOFB latency was found to be the accelerator-wide sensors and actuators data distribution. Detailed calculations showed that the usage of multigigabit digital communication through FPGAs and efficient network topology would allow a theoretical minimum latency of ~5.3 µs for Sirius, out of which ~2.5 µs would come from light propagation through several optical fibers along half storage ring circumference (250 m). The calculations considered frame headers, checksums and FPGA logic overheads, as well as a factor of 2 fiber length safety margin. Considering additional margin in the latency budget, a goal of 10 µs latency for a complete data distribution cycle was determined.

Given that scenario, BPM delay, typically dominated by decimation filters group delay, should be ideally made comparable to (or lesser than) the data distribution latency. A preliminary performance goal of 10 µs BPM group delay was thus established. In order to reach this number, the FOFB update rate was set to 115 kHz (turn-by-turn rate divided by 5), which allows reaching 8.64 µs of BPM group delay with a simple Cascaded Integrator-Comb (CIC) decimation filter with two sections and one differential delay. Refinements to help lower the BPM delay, either by improving the decimation filter response or increasing the FOFB update rate, are under study.

CONCLUDING REMARKS

Several refinements on the Sirius RF BPM electronics, mainly on the analog part of the design, led to significant performance improvements. Critical specifications are now met with exceeding performance. The electronics has undergone tests with short length beam at SPEAR3 and proved to keep its performance figures with broadband BPM signals.

The third spin of the RFFE board has been launched to provide higher input power dynamic range and final enclosure form factor based on industrial standards. LTC2208-based FMC ADC board is in advanced development stage and should not require new hardware modifications. After the conclusion of this new R&D cycle, scheduled to be concluded by the end of the 2nd semester of 2014, the RFFE and ADC hardware efforts will be redirected for pre-series production of a complete Sirius's storage ring superperiod BPM system (12 BPMs) and long term reliability tests with beam at LNLS UVX storage ring.

Substantial integration work on the digital back-end will take place in the 2nd semester of 2014 and throughout 2015.

ACKNOWLEDGMENTS

The authors would like to thank Jean-Claude Denard, Boris Keil, Andrej Košiček, Jim Sebek and Grzegorz Kasprowicz for the always insightful discussions about BPM systems, and Donald J. Martin, Jim Sebek, Fernando da Silva Rafael and Antonio Carlos de Lira for their support during the technical visit to SLAC.

REFERENCES

[1] L. Liu et al., "Update on Sirius, the new Brazilian light source", IPAC'14, Dresden, June 2014, p. 191 (2014).

[2] R. Biscardi, J. W. Bittner, "Switched Detector for Beam Position Monitor", PAC'1989, Chicago, March 1989, p. 1516 (1989).

[3] U. Mavrič, "Innovative RF Design Unites Benefits of Multiplexed and Multi-channel System", BIW'2004, Knoxville, May 2004, p. 373 (2004).

[4] B. Keil et al., "Development of New BPM Electronics for the Swiss Light Source", Tsukuba, October 2012, p. 399 (2012).

[5] Sirius BPM project at the Open Hardware Repository: http://www.ohwr.org/projects/bpm/wiki

[6] D. O. Tavares et al., "Development of the Sirius RF BPM Electronics", IBIC'2013, Oxford, September 2013, p. 63 (2013).

[7] D. O. Tavares et al., "Development of an Open-Source Hardware Platform for Sirius BPM and Orbit Feedback", ICALEPCS'13, San Francisco, October 2013, p. 1039 (2013).

[8] R. A. Baron et al., "Development of the RF Front-End Electronics for the Sirius BPM System", IBIC'2013, Oxford, September 2013, p. 673 (2013).

Copyright © 2014 CC-BY-3.0 and by the respective authors

ISBN 978-3-95450-141-0

A SQUID-BASED BEAM CURRENT MONITOR FOR FAIR / CRYRING*

R. Geithner #, Helmholtz-Institut Jena, Germany & Friedrich-Schiller-Universität Jena, Germany
T. Stöhlker, Helmholtz-Institut Jena, Germany & Friedrich-Schiller-Universität Jena, Germany &
Helmholtzzentrum für Schwerionenforschung, Darmstadt, Germany
R. Neubert, P. Seidel, Friedrich-Schiller-Universität Jena, Germany
F. Kurian, H. Reeg, M. Schwickert,
GSI Helmholtzzentrum für Schwerionenforschung, Darmstadt, Germany

Abstract

A SQUID-based beam current monitor was developed for the upcoming FAIR-Project, providing a non-destructive online monitoring of the beam currents in the nA-range. The Cryogenic Current Comparator (CCC) was optimized for lowest possible noise-limited current resolution together with a high system bandwidth. This CCC should be installed in the CRYRING facility, working as a test bench for FAIR. In this contribution we present results of the completed CCC for FAIR/CRYRING and also arrangements that have been done for the installation of the CCC at CRYRING, regarding the cryostat design.

INTRODUCTION

The high energy beam transport lines (HEBT) at FAIR require a non-intercepting, absolute and precise detection of high brightness, high intensity primary ion beams as well as low intensities of rare isotope beams. The expected beam currents in these beam lines are in the range of few nA up to several µA for continuous as well as bunched beams [1]. This requires a detector with a low detection threshold, a high resolution, and as well as high bandwidth from DC to several kHz.

A superconducting pick-up coil and SQUID system are the main components of a Cryogenic Current Comparator. Superconducting pick-up coils allow the detection of DC magnetic fields created by continuous beams without applying modulation techniques. A SQUID acting as current sensor for the pick-up coil enables the detection of lowest currents. Therewith the CCC optimally fulfils the requirements for the FAIR beam parameters.

DESIGN AND WORKING PRINCIPLE

The CCC [2, 3, 4] consists of a meander-shaped niobium shielding, a toroidal niobium pick-up coil with a ferromagnetic core, a toroidal matching transformer also including a ferromagnetic core and an LTS SQUID with the appropriate SQUID-electronics (see Fig. 1).

* Work supported by GSI Helmholtzzentrum für Schwerionenforschung, Darmstadt, Germany and Helmholtz-Institut Jena, Germany

rene.geithner@uni-jena.de

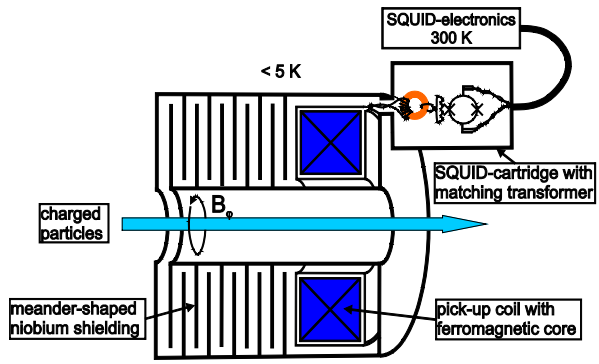


Figure 1: Circuit diagram of the CCC.

The azimuthal magnetic field of the particle beam passes the ceramic gap in the beam line and is guided to the pick-up coil by the meander-shaped shielding whereby all other external magnetic field components are strongly attenuated [3, 5].

Sensitivity Optimization

The total intrinsic noise of the entire CCC is composed by the intrinsic noise of the SQUID itself and its electronics, as well as the magnetization noise of the embedded coils. The spectral current density $\langle I^2 \rangle$ of a coil coupled to the input coil L_I of a SQUID at a temperature T can be calculated with the Fluctuation-Dissipation-Theorem (FDT) and the measured frequency-dependent serial inductance $L_S(\nu)$, respectively. With the serial resistance $R_S(\nu)$ in the equivalent circuit diagram of a real coil, $R_S(\nu)$ represents the total losses [6, 7]:

$$\langle I^2 \rangle = 4k_B T \int \frac{R_S(\nu)}{\left(2\pi\nu\left(L_I + L_S(\nu)\right)\right)^2 + \left(R_S(\nu)\right)^2} \qquad (1)$$

As one can see in Equation (1) the current noise decreases if $L_S(\nu)$ is as high as possible and, secondly, $R_S(\nu)$ remains low over the whole frequency range.

From preliminary investigations [5, 7] we found that the nanocrystalline ferromagnetic material Nanoperm [8] shows very satisfying results matching our requirements. A single-turn Niobium toroidal pick-up coil was electron-beam welded around a Nanoperm M764 core. This pick-up coil has an outer diameter 260 mm, an inner diameter of 205 mm and a width of 97 mm.

A possibility for optimization of the overall current sensitivity of the SQUID detector is the use of a matching transformer with optimized winding ratio and core material.

Copyright © 2014 CC-BY-3.0 and by the respective authors

ISBN 978-3-95450-141-0

For a transformer the current gain in the short-circuit case only depends on the winding ratio, $I_2/I_1 = n_1/n_2$.

However, the CCC with a matching transformer can be described as a series connection of two burdened transformers (see Fig. 2) [4].

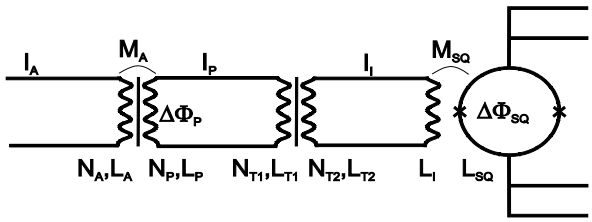


Figure 2: Schematic circuit diagram of the CCC with pick-up coil L_P, matching transformer L_{T1}, L_{T2}, SQUID input coil L_I and SQUID L_{SQ}.

The ratio of the screening currents, I_A, seen by the pick-up coil L_P, and the current through the input coil of the SQUID, I_I, depends on the winding ratio N_{T1}/N_{T2} of the matching transformer, on the inductances L_P of the primary pick-up coil and L_{T1} respectively L_{T2} of the matching transformer, and the input coil of the SQUID, L_I.

$$\frac{I_I}{I_A} = \frac{N_{T1}}{N_{T2}} \cdot \frac{1}{1+\frac{L_I}{L_{T2}}} \cdot \frac{N_A}{N_P} \cdot \frac{1}{1+\frac{L_{T1}L_I}{(L_{T2}+L_I)L_P}} \qquad (2)$$

Setting $N_A = N_P = N_{T2} = 1$, $L_{T1} = N_{T1}^2 \times L_{T2}$, $L_I = 0.46$ µH and $L_P = 103$ µH, I_I/I_A can be plotted as a function of L_{T2} and N_{T1}. There is an optimal number of windings, $N_{T1,\,opt} = 15$, for $L_{T2} = 0.46$ µH where the current gain factor has a maximum of $I_I/I_A = 5.0$. The differences with an unburdened transformer can be seen at this point where the current gain N_{T1}/N_{T2} (= 15/1) should be 15.

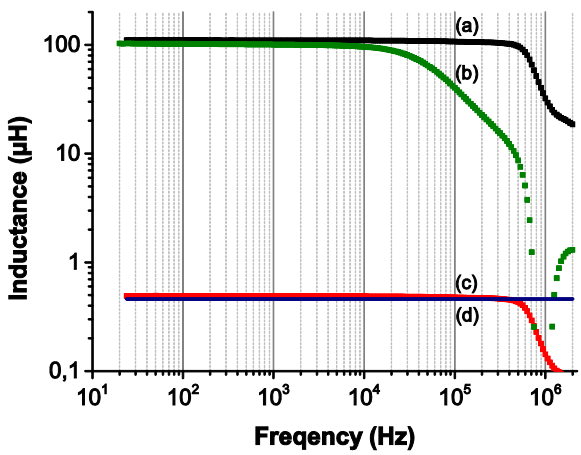


Figure 3: L_S (ν) at 4.2 K for the welded toroidal pick-up coil with Nanoperm M764 core (a), and the primary (b) respectively secondary (c) coil of the matching transformer with Vitrovac 6030 core as well as the SQUID input coil inductance (d).

The dependence on the inductance of the secondary coil of the matching transformer saturates for L_{T2} higher than 0.46 µH which is the inductance of the input coil of the SQUID. Regarding these results the matching transformer was customized by applying 15 turns respectively 1 turn of niobium wire to a selected Vitrovac 6030 [4, 9] core.

Figure 3 shows the frequency dependence L_P (ν) at 4.2 K of the FAIR-CCC's single-turn toroidal pick-up coil with Nanoperm M764 core and the primary L_{T1} (ν) with $N_{T1} = 15$ respective secondary coil L_{T2} (ν) with $N_{T2} = 1$ of the matching transformer with Vitrovac 6030 core. The frequency characteristics of serial inductance L_S (ν) and the serial resistance R_S (ν) of the coils were measured with a commercial Agilent E4980A LCR-Meter [8].

The inductance of the pick-up coil of $L_P = 103$ µH matches quite well to the inductance of the matching transformer's primary coil $L_{T1} = 110$ µH as well as the inductance of the matching transformer's secondary coil $L_{T2} = 0.49$ µH to the inductance of the SQUID input coil of $L_I = 0.46$ µH. Inserting these measured values in Eq. (2) yields an overall current gain factor of 5.1. It could be shown that the inductance of the welded coil with the Nanoperm M764 core is almost constant for frequencies below 10 kHz (see (b) in Fig. 3). L_{T1} respectively L_{T2} (see (b), (c) in Fig. 3) are even constant up to 400 kHz which promises high system bandwidths.

EXPERIMENTAL RESULTS

For the presented results of the completed FAIR-CCC including its matching transformer, a SQUID sensor 'CP2 blue' from the manufacturer Supracon [10] in combination with a 'XFF-1' readout electronics from the manufacturer Magnicon [11] were used.

Step Function Response

Figure 4 shows the response of the completed FAIR-CCC with matching transformer to a rectangular current signal of 2 µA (a), 1 µA (b), 200 nA (c), 100 nA (d), 20 nA (e), and 10 nA (f) applied to a beam simulating wire along the beam axis with the help of a battery powered current source. The response is plotted as the magnetic flux seen by the SQUID in units of the magnetic flux quantum Φ_0 as calculated from the output voltage and the flux sensitivity of the SQUID system. The flux sensitivity was adjusted to 0.103 V/Φ_0 and the bandwidth of the SQUID system to 217 kHz. There is no low pass filter or time averaging used in the output circuit of the CCC. From this curves it is also visible that there is close to zero drift in the CCC signal during a time span of at least 5 s. The smoothing at the rising edge of the signal at higher currents (curve (a)) appears due to the use of a 10 Hz low-pass filter in the input to prevent RF-interferences and is not a characteristic of the CCC.

Copyright © 2014 CC-BY-3.0 and by the respective authors

ISBN 978-3-95450-141-0

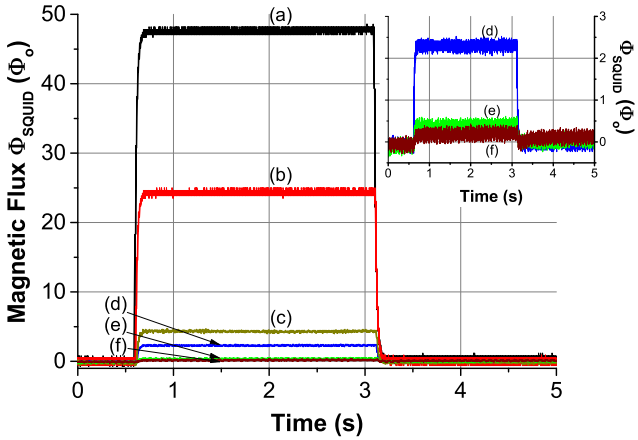


Figure 4: Response of the completed FAIR-CCC with matching transformer to a rectangular current pulse of 2 µA (a), 1 µA (b), 200 nA (c), 100 nA (d), 20 nA (e), and 10 nA (f) applied to a beam simulating wire along the beam axis (insert with magnified scale).

Figure 5 depicts the peak-to-peak value of the step function response in units of the magnetic flux quantum versus the applied calibration current between 10 and 2000 nA, which is linear over the plotted range. This graph displays another advantage of the CCC. Using a simple wire along the beam axis or an additional wire coil around the pick-up coil enables an easy calibration with a linear response. From the responses to the different current pulses an overall current sensitivity of 42 nA/Φ_0 could be calculated. In the case of the direct coupled pick-up coil the current sensitivity was 190 nA/Φ_0. The overall current sensitivity therefore was enhanced by a factor of 4.5 using the matching transformer compared to the direct coupled pick-up coil.

Figure 6 shows the step function response of the CCC to a calibration current of 14 nA with a low slew rate of the applied signal.

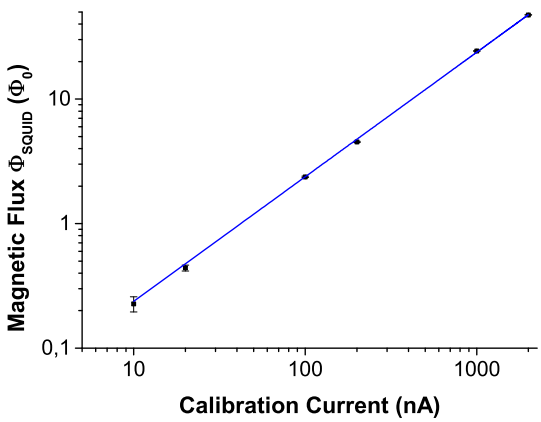


Figure 5: The plot of the peak-to-peak value of the step function response of the completed FAIR-CCC vs. calibration current shows a linear transfer function.

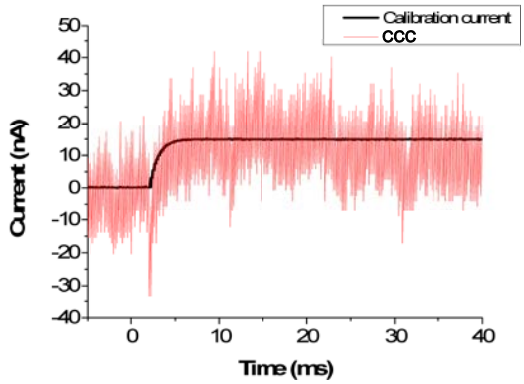


Figure 6: Response of the completed FAIR-CCC with matching transformer (red curve) to a current pulse of 14 nA applied to a beam simulating wire along the beam axis (black curve).

It is shown that the CCC signal follows the calibration current instantaneous and delivers the same amplitude with the calculated overall current sensitivity from Fig. 5. The smoothing at the rising edge of the calibration current is caused by the limited bandwidth of the battery powered current source. When test signals with higher slew rates from a battery powered current source with a higher bandwidth are applied, the slew rate of the signal exceeds the maximum slew rate of the CCC and an overshooting appears (see Fig. 7). For the signals shown in Fig. 7 the SQUID electronics in the FLL-mode is able to stabilize the working point and the peak-to-peak values of the measured CCC signals correspond to the measured current values from the battery powered current source. For signals with higher slew rates it might happen, that the SQUID electronics in the FLL-mode adjusts to another working point and flux jumps in the CCC signal may appear.

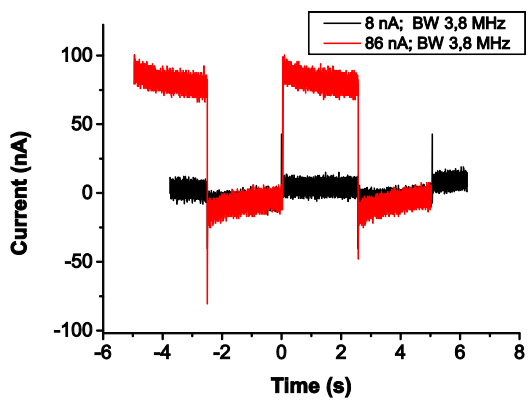


Figure 7: Response of the completed FAIR-CCC with matching transformer to a current pulse of 8 nA (black curve) and 86 nA (red curve) applied to a beam simulating wire along the beam with higher slew rates.

Copyright © 2014 CC-BY-3.0 and by the respective authors

ISBN 978-3-95450-141-0

Noise Measurements

The output voltage noise density of the SQUID electronics was measured by an HP 89410A vector signal analyzer. The current noise density was calculated using the flux and current sensitivity of the setup.

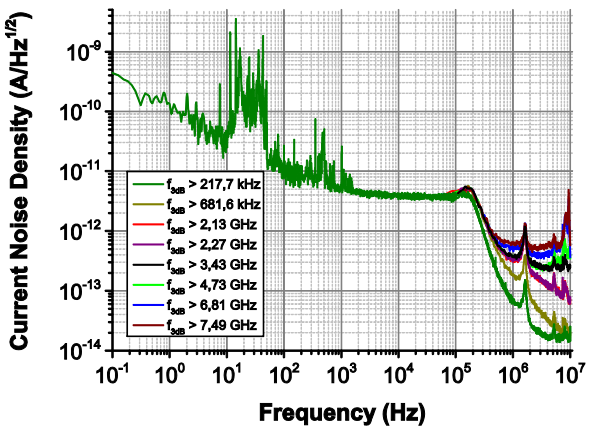


Figure 8: Current noise density of the FAIR-CCC with matching transformer for several SQUID system bandwidths.

Figure 8 shows the measured current noise density of the FAIR-CCC with matching transformer using the Supracon's SQUID sensor CP2 blue and Magnicon's XFF-1 SQUID electronics. The current noise density was measured to be 35 pA/Hz$^{1/2}$ at 7 Hz and to 3,5 pA/Hz$^{1/2}$ at 10 kHz, cf. Fig. 8. The total noise of the completed FAIR-CCC is calculated to be 3 nA in the frequency range from 0.2 Hz to 10 MHz.

Due to the limited bandwidth of the battery powered current source it was not feasible to measure the bandwidth of the CCC directly. Regarding the frequency dependent inductances of the coils in Fig. 3, it turns out that the bandwidth of the CCC will be limited by this behaviour. To estimate the bandwidth, noise measurements with several Gain-Bandwidth-Product settings at the SQUID electronics were performed. The 3dB-bandwidth of the SQUID system varies from 217 kHz to 7.49 GHz. All noise figures have a decrease at 200 kHz in common, thus a CCC bandwidth of 200 kHz is estimated. But this needs to be proved by direct measurements.

There appears an additional noise contribution in the frequency spectrum current from 10 Hz to 1 kHz. These so called microphonic effects are caused by the coupling of mechanical vibration of the underground as well as pressure and temperature variations of the helium bath into the CCC. These interactions are not clarified yet and need further investigations.

The results will be directly implemented into the development of a cryostat with local liquid helium supply in order to reduce microphonic effects by damping of mechanical vibrations and, additionally, a pressure and temperature stabilization.

CONCLUSION AND OUTLOOK

The Cryogenic Current Comparator has shown its capability as a beam intensity monitor for ions as well as electrons [12, 13]. It is shown that the transfer function is linear over a wide measurement range. Using an additional wire along the beam axis or around the pick-up coil, that enables an easy and absolute calibration method. Using Nanoperm M764 material, the current noise density of the pick-up coil was reduced by a factor of 2 to 5 compared to previous installations. Including the matching transformer enhances the overall current sensitivity by a factor of 4.5 without increasing the current noise density. The total current noise in the frequency range from 0.2 Hz to 10 MHz calculated to be 3 nA. Minimizing the additional noise due to the microphonic effects should reduce the total noise further more.

This enables the detection of beam currents below 1 nA with the help of filter techniques which means approximately 10^9 ions/spill of $^{238}U^{28+}$ respectively 28×10^9 protons/ spill for slow extraction with t_{spill} = 5 s. Using fast SQUID systems as well as broadband core materials enables time resolved measurements to explore the spill structure of the beam. The estimated CCC bandwidth is 200 kHz still needs to be verified by direct measurements. Together with the improved resolution the sensitivity to coasting beams qualifies the CCC as a well suited instrument for beam diagnostics at FAIR.

The next steps will be the estimation of the CCC slew-rate to qualify the CCC for beam diagnostics of bunched beams with high slew rates. This CCC prototype should be implemented in the CRYRING as test bench for FAIR. Therefore, a cryostat will be designed and fabricated with special focus on damping of mechanical vibrations and a pressure and temperature stabilization, as well as a local helium supply.

REFERENCES

[1] Conceptual Design Report, Darmstadt, 2000, http://www.gsi.de/GSI-Future/cdr/
[2] I. K. Harvey, Rev. Sci. Instrum. 43 (1972) 11, p 1626.
[3] K. Grohmann, H. D. Hahlbohm, D. Hechtfischer, and H. Lübbig, Cryogenics 16 (1976) 10, pp. 601.
[4] R. Geithner, R. Neubert, W. Vodel, M. Schwickert, H. Reeg, R. von Hahn, and P. Seidel, IEEE Trans. Appl. Supercond. 21 (2011) 3, pp. 444-447.
[5] R. Geithner, W. Vodel, R. Neubert, P. Seidel, F. Kurian, H. Reeg, M. Schwickert, Proc. of IBIC 2013, Oxford, UK, TUPF32, 545, 2013.
[6] H. P. Quach, T. C. P. Chui, Cryogenics 44 (2004) 6, pp. 445.
[7] R. Geithner, D. Heinert, R. Neubert, W. Vodel, P. Seidel, Cryogenics 54 (2013), pp. 16-19.
[8] MAGNETEC GmbH, Industriestrasse 7, D-63505 Langenselbold, Germany.
[9] VACUUMSCHMELZEGmbH & Co. KG, GruenerWeg 37, D-63450 Hanau, Germany.

ISBN 978-3-95450-141-0

Copyright © 2014 CC-BY-3.0 and by the respective authors

[10] Supracon AG, An der Lehmgrube 11, 07751 Jena, Germany.
[11] Magnicon GmbH, Barkhausenweg 11, 22339 Hamburg, Germany.
[12] A. Peters, W. Vodel, H. Koch, R. Neubert, H. Reeg, C. H. Schroeder, AIP Conf. Proc. 451 (1998), pp. 163-180.
[13] R. Geithner, R. Neubert, W. Vodel, P. Seidel, K. Knaack, S. Vilcins, K. Wittenburg, O. Kugeler, and J. Knobloch, Rev. Sci. Instrum. 82 (2011), 013302.

Copyright © 2014 CC-BY-3.0 and by the respective authors

ISBN 978-3-95450-141-0

MEASUREMENT OF BEAM LOSSES AT THE AUSTRALIAN SYNCHROTRON

E. Nebot del Busto, M. Kastriotou, CERN, Geneva, Switzerland; University of Liverpool, Liverpool, UK,
M. J. Boland, ASCo, Clayton; The University of Melbourne,
P. D. Jackson, University of Adelaide, Adelaide,
R. P. Rasool, The University of Melbourne, Australia
E. B. Holzer. CERN, Geneva, Switzerland,
J. Schmidt, Albert-Ludwig Universitaet Freiburg, Freiburg, Germany
C. P. Welsch Cockcroft Institute, Warrington, Cheshire; University of Liverpool, Liverpool, UK

Abstract

The unprecedented requirements that new machines are setting on their diagnostic systems is leading to the development of new generation of devices with large dynamic range, sensitivity and time resolution. Beam loss detection is particularly challenging due to the large extension of new facilities that need to be covered with localized detector. Candidates to mitigate this problem consist of systems in which the sensitive part of the radiation detectors can be extended over long distance of beam lines. In this document we study the feasibility of a BLM system based on optical fber as an active detector for an electron storage ring. The Australian Synchrotron (AS) comprises a 216 m ring that stores electrons up to 3 GeV. The Accelerator has recently claimed the world record ultra low transverse emittance (below pm rad) and its surroundings are rich in synchrotron radiation. Therefore, the AS provides beam conditions very similar to those expected in the CLIC/ILC damping rings. A qualitative benchmark of beam losses in a damping ring-like environment is presented here. A wide range of beam loss rates can be achieved by modifying three beam parameters strongly correlated to the beam lifetime: bunch charge (with a variation range between 1 uA and 10 mA), horizontal/vertical coupling and of dynamic aperture. The controlled beam losses are observed by means of the Cherenkov light produced in a 365 $\mu\ m$ core Silica fber. The output light is coupled to different type of photo sensors namely: Metal Semiconductor Metal (MSM), Multi Pixel Photon Counters (MPPCs), standard PhotoMulTiplier (PMT) tubes, Avalanche PhotoDiodes (APD) and PIN diodes. A detailed comparison of the sensitivities and time resolution obtained with the different read-outs are discussed in this contribution.

THE AUSTRALIAN SYNCHROTRON AS A DAMPING RING TEST FACILITY

The compact linear collider CLIC [1] foresees two 20 km main linacs accelerating electrons and positrons up to 3 TeV. In order to provide an instantaneous luminosity on the order of $5 \cdot 10^{+34}\ cm^{-2}\ s^{-1}$, the beam spot at the interaction point shall reach unprecedentedly low nanometer sizes. This is only achievable with ultra low emittance beams at the entrance of the linac that account for the large contribution coming from the particle sources, particularly the positron source, and the emittance growth budget up to the interaction point. The Damping Rings (DR) designed to cool down the CLIC beams [2] comprise a 412 m ring built of FODO cells in the long straight section and Theoretical Minimum Emittance (TME) in the arcs with the use of two half cells for dispersion suppression. Superconducting wigglers aim to decrease the damping times to the 2 ms level, values well below the 20 ms imposed by the 50 Hz CLIC repetition rate. This constrains the requirements on time response of beam instrumentation. Moreover, the low foreseen longitudinal emittances triggers a set of single bunch collective effects typically not observable in electron machines. Hence, the measurement of beam parameters on a bunch by bunch basis imposes a tighter requirement on the time resolution of the instrumentation systems.

The Australian Synchrotron (AS) [3] is a third generation light source consisting of a 100 MeV linac, a 100 MeV to 3 GeV Booster and a 3 GeV Storage Ring (SR). The SR comprises 14 Double Bend Achromat (DBA) cells where a 200 mA beam is circulated in pulses of approximately 600 ns when flling 300 out of the 360 buckets. As it is shown in table 1, there are many similarities between the parameters of the AS and the CLIC damping rings. In particular, the AS has recently measured vertical normalized emittances comparable to those expected in CLIC. Moreover, the synchrotron provides good fexibility to modify some of its nominal parameters to approach those of the DR. For instance it is feasible to reduce the pulse length to CLIC like values by keeping nominal beam charge. Hence, this facility provides a great opportunity to test and develop instrumentation targeting requirements for the DR of the future collider.

OPTICAL FIBER BEAM LOSS MONITORS: THE EXPERIMENTAL SETUP

The use of optical fbers, once restricted to waveguides for the transport of information, is increasingly being adopted in the beam instrumentation feld. The light generated inside an optical fber due to the crossing of ionizing radiation may be used as a tool for Beam Loss Monitoring

ISBN 978-3-95450-141-0

Copyright © 2014 CC-BY-3.0 and by the respective authors



(a) Storage Ring scrapers (far left), Beam Loss Monitors behind dipole (far right).



(b) Optical f ber installed in the outer side of the bending magnet, beam from left to right (top view).

Figure 1: Beam loss monitor set-up in the AS.

Table 1: Comparison Between Some of the Parameters of the AS and CLIC DR.

Parameter	AS	CLIC DR
Energy (GeV)	3.0	2.86
Intensity (elec)	$9.0 \cdot 10^{+11}$	$1.28 \cdot 10^{+12}$
Number of bunches	300	312
Pulse length (ns)	600	156
Circ. length (m)	216	427.5
f_{rev} (MHz)	1.38	0.73
Bunch spacing (ns)	2	0.5
$\gamma\epsilon_x$ (nm rad)	58708	472
$\gamma\epsilon_y$ (nm rad)	< 5	4.8

(BLM) [4, 5]. Two main advantages raise from the use of Optical f ber based BLM (OBLM) systems:

- The active ionizing radiation detector can be distributed over large sections of beam lines. This prevents missing the observation of beam losses at otherwise uncovered locations and it minimizes the number of required sensors (and hence acquisition systems) and therefore the cost of the system.

- OBLM systems can provide position reconstruction of the original location of the beam loss with resolutions down to a few tens of centimeters [6].

The light generation mechanism inside the optical f ber can be of various origins, namely: scintillation, f uorescence, thermoluminescence, radioluminescence, etc. In this contribution, we concentrate on Cherenkov light generated when charged particles cross the f ber with speed higher than the phase velocity of light in the core medium. As a reference number, the Cherenkov light generating energy thresholds for electrons and positrons (which account for the largest fraction of the charge component of the showers) crossing a quartz f ber is 186 keV [7].

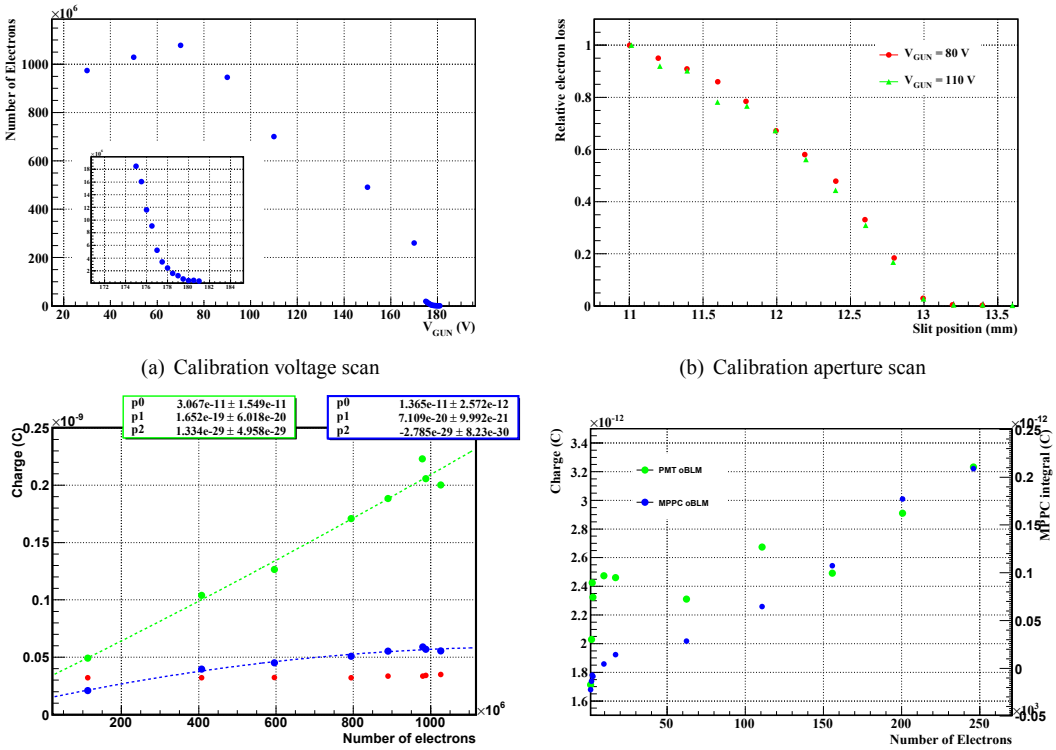
Two 7 m long optical f bers with 365 μm diameter SiO_2 core were located on the horizontal plane of the outer side of the beam. A third f ber with reduced diameter core (200 μm) was also available and provided the possibility to test three photo sensor within the same experiment. All three f bers were enclosed into a tube to shield from ambient light and were situated near the f rst bending magnet in sector 11. This location was selected as the easiest position to produced controlled beam losses since the beam scrapers are situated approximately 1.5 m upstream of the front face of this bending magnet, as shown in f gure 1(a). The f ber enclosing plastic tube run parallel for the length of the magnet, as seen in Figure 1(b) and it immediately deviated upwards from the horizontal plane toward the roof of the accelerator tunnel where it was extracted to the upper level. A 14400 pixels 3x3 mm^2 active area Multi Pixel Photon Counter (MPPC) and a Photo Multiplier Tube (PMT) were coupled to the end of the two 365 μm f bers. The light output of the third 200 μm f ber was directed via focusing lens to the 25 μm active area of an Avalanche Photo Diode (APD). The readout signals were observed via a 10 bit Analog to Digital Converter (ADC) or via fan in/fan out pulse discriminator and scaler as pulse counting mode electronics.

SINGLE SHOT BLM CALIBRATION

The prototype OBLM system was calibrated by directing a single bunch beam onto a fully closed scraper in the SR. The f rst challenge to overcome was the determination of the number of charges hitting the intercepting device. The measurements of the DC current transformer were not available as the beam did not even complete a single turn from the injection point. Intensity measurements from the Booster ring and transfer lines did not provide enough accuracy due to the diff culty of a precise determination of the injection eff ciencies. Moreover, the lower current beams injected into the machine reached values either near or signif cantly below the noise level of the current measuring in-

Copyright © 2014 CC-BY-3.0 and by the respective authors

ISBN 978-3-95450-141-0



(a) Calibration voltage scan

(b) Calibration aperture scan

(c) Voltage scan. APD (red), PMT (green), MPPC (blue).

(d) Aperture scan

Figure 2: Beam intensity and integrated signals observed during voltage and aperture scans.

struments. Therefore, a calibration exercise was performed to determine the number of particles that could be injected in the SR in a single shot. Two parameters were modified to achieve the largest possible range, namely: the voltage of the grid in the electron gun and the position of the energy selection slits in the Booster To SR (BTS) transfer lines. For a given set of parameters, a certain number of single injections were accumulated in the SR where the intensity was measured with the DC current transformer. Thereafter, the beam was scraped out of the ring and the measurement for the subsequent set of parameters was conducted.

Figure 2(a) summarizes the results achieved during the voltage gun calibration. Note that the number of accumulated shots needed to be increased from 10 to 40 when the gun voltage was above 170 V and up to 100 above 175 V due to the non linear relation between the voltage and the number of charges. The larger number of charges corresponds to the low voltage range with a maximum at 80 V of $1.1 \cdot 10^{+9}$ electrons. From this point the tendency is an approximately linear decrease up to voltages of 170 V. After this value a somewhat exponential decrease is observed and a minimum of $6 \cdot 10^{+5}$ electrons is measured for $V_{gun} = 182V$. Similarly, Figure 2(b) presents the results of the slit grid scan. In this case the measurement was conducted for two independent gun voltages, 80 V and 110 V, to verify the reproducibility of the result. The graphic shows the charge loss relative to the upper and lower BTS slits in their nominal position, i.e. 11.0 mm.

Subsequently, a similar scan was executed with both the horizontal and vertical scrapers in the SR fully closed. Figure 3 shows the evolution of the signals over time for the three OBLMs for a gun voltage of 150 V. A single peak appears in all cases, which indicates that the position of the scrappers ensured that all the charges were fully stopped within the first turn. A clear distortion is observed on the APD signal, which was expected to provide a TTL output. This is attributed to the frequency cutoff introduced by the nearly 90 m of coaxial cables bringing the signals from the photo sensors to the ADC. The effect is also observable on the tail end of the MPPC and PMT signals, as they extent over several hundreds of nanoseconds. The performance in terms of time response of the MPPC and PMT detectors with respect to each other is inferred from the raise time of the pulse, which stands at 10 and 15 nanoseconds respectively.

In order to compare the sensitivity of the three detectors, a numerical integration of the signals acquired with the ADC was computed. Figure 2(c) presents the results obtained during the voltage scan, i.e, for injected charges ranging from 100 million to 1 billion electrons. The APD shows a flat response with beam charge. This is expected since the output of the system is a (binary) TTL signal. The tendencies of the PMT and MPPC integrals are slightly different. Even though in both cases there is an increasing behaviour, the PMT shows a more linear evolution. In both cases, a second degree polynomial was fit to the data.

ISBN 978-3-95450-141-0

Copyright © 2014 CC-BY-3.0 and by the respective authors

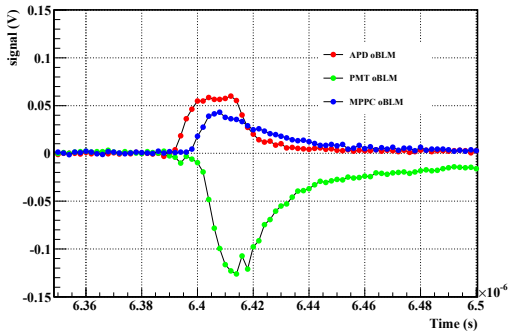


Figure 3: Signals observed in the three OBLMs during an injection of 500k electrons

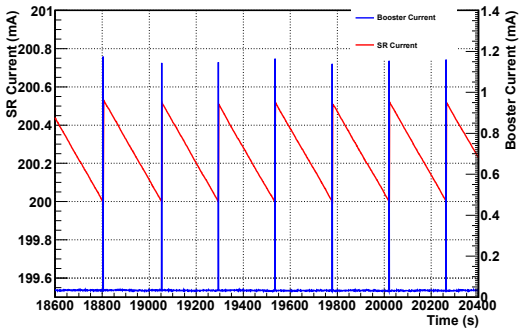


Figure 4: Booster and SR current measurement during topup injections

While the second order coeff cient for the PMT is compatible with zero, the MPPC gets a clearly negative value. This is compatible with expected saturation effects when the number of incident photons exceeds the number of available pixels within the illuminated area. The summary of the results obtained for the low charge range are shown in Figure 2(d). Only the MPPC and PMT signals are shown as the APD OBLM did not observe any pulses during irradiation. This is attributed to the lower diameter core of the optical f ber for this particular OBLM [1] as well as to potential ineff ciencies on the light coupling from the f ber to the small active active area of the APD. The PMT OBLM seem to show a good linearity down to 150k electrons. This is established as the sensitivity limit with the rest of the values attributed to the dark count of the system. The MPPC signals seem to be sensitive to much lower beam charges, down to 10k electrons, despite similar expected gain. This is understood as the MPPC readout was equipped with a 30 dB amplif er in the low charge BTS scan. Moreover, this is in agreement with the more suited single photon counting capabilities of the MPPC.

TOPUP INJECTION LOSSES

The AS works on topup mode to keep a constant nominal current of 200 mA circulating in the SR ring and continuously provide synchrotron light to the different beam lines. Figure 4 compares the intensity measurement in the SR with the fast intensity measurement performed in the Booster for 7 consecutive injections. While the SR intensities indicate an increase of 0.5 mA immediately after injection, the booster measurement provides 1.1 mA, which accounting for the Booster (SR) 216 (360) harmonic number it should provide 0.66 mA in the SR. This indicates, assuming typical injection eff ciencies of 80 %, that around 0.028 mA ($1.25 \cdot 10^{+9}$ electrons) are lost around the ring within the f rst several turns. The sensitivity of the OBLM system to injection losses was tested during operation of the facility by triggering on the electron gun. For this measurement, the 365 μm f ber coupled to the PMT and MPPC detectors were compared to the signals observed by a slow NaI scintillator and a $NE102$ plastic scintillators both coupled to PMTs and located 2 m downstream of the optical f ber.

A very good shot to shot reproducibility of the signals was observed. As an example, one of the triggers is presented in Figure 5(a), where the full time range of 2 ms corresponds to 2777 turns. In all four detectors there is a clear modulation effect where the maximum of the signals peaked around every 100 μs. This becomes more evident when performing a frequency analysis. In the power spectrum the modulation effect is clear with a 11 kHz frequency line followed by the higher order harmonics at shown in Figure 5(b). This was attributed to the synchrotron tune of the machine. Figure 5(c) presents the power spectrum in a wider range (up to 2 MHz) where some other substructure can be observed. The second most clear line that appears corresponds to 1.388 MHz which is the revolution frequency of the SR. The two side bands around f_{rev} are located at a $\Delta f = 400$ kHz. This can be attributed to the horizontal tune of the machine. The two peaks observed around 200 kHz and 400 kHz may be also related to the horizontal and vertical tune.

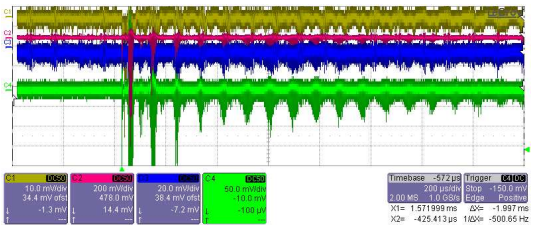
DYNAMIC APERTURE AND BETATRON COUPLING INDUCED LOSSES

Two types of controlled losses were generated over a user-like f ll, i.e. 200 mA f lled within 300 RF buckets. The dynamic aperture was squeezed by changing the sextupole currents. The lifetime variation changed from 1 hour to over sixty. Despite the observation of some activity in the BLMs, no conclusion could be drawn due to the fact that the collected signals were dominated by high frequency noise picked up in the coaxial cables going from the detectors to the ADC. The skew quadrupoles settings were also modif ed to increase the vertical emittance from 1 pm

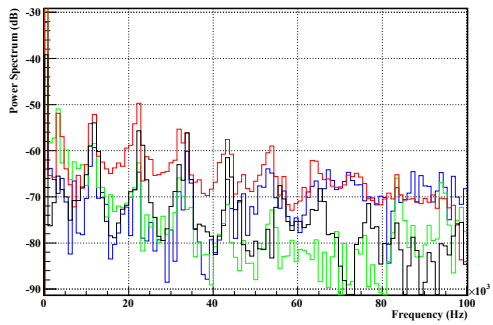
[1] In [7] it is demonstrated that the Cherenkov photon yield produced in an optical f ber is proportional to the square of the core diameter

Copyright © 2014 CC-BY-3.0 and by the respective authors

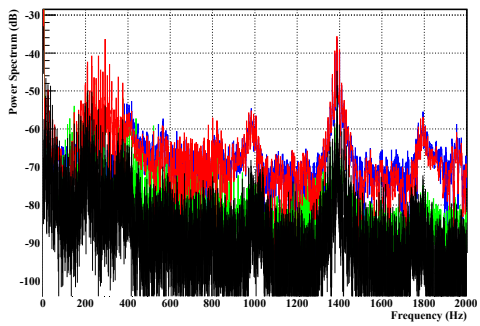
ISBN 978-3-95450-141-0



(a) Signals for the 4 detectors



(b) Power spectrum for the 4 detectors (0, 100kHz)



(c) Power spectrum for the 4 detector (0,2MHz)

Figure 5: Beam losses and derived power spectrum for NaI (black), NE102 (red), PMT (green) and MPPC (blue).

to 2 nm. Again, the noise dominated and no conclusions could be extracted from this test.

For the very last exercise, the ADC acquisition system was brought within a meter of the detectors to avoid the collection of noise though the cable length. Moreover, the SR was filled with a CLIC like beam. The 200 mA were injected in dedicated RF buckets so the length of the whole pulse did not exceed 150 ns. Figure 6 shows a measurement of the Fill pattern during the experiment. With this conditions of intensity and pulse length the, settings of the skew quadrupoles were modified in order to change the betatron coupling. Eleven different skew quad settings were tried to achieve vertical emittances of 1 pm, 2 pm, 5 pm 10 pm, 20 pm, 50 pm 100 pm, 200 pm 500 pm, 1 nm and 2 nm. For every setting the signals in the BLMs were acquired via ADC over a period of 2 μs. A MPPC and a PMT were checked as potential OBLM systems and a NaI scintillator was used as benchmarking detector. For each skew quad

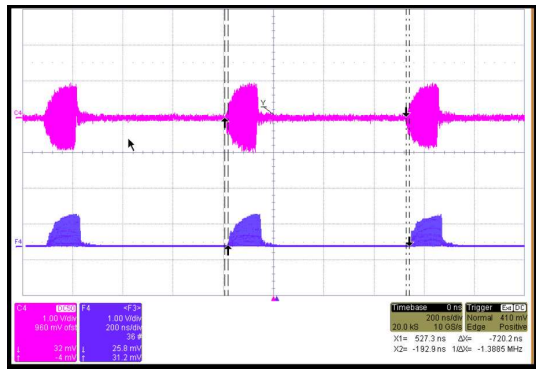


Figure 6: CLIC like pulse measured with the Fill pattern monitor

settings 8 acquisitions were taken. Figure 7 shows the numerical integration for all channels as a number of recorded pulse. The three plots correspond to the identical skew setting scans but with position of the upper and lower blade of the vertical scrapper at 13 mm, 14 mm and 15 mm respectively. The amount of losses seem to increase steadily with the emittance. Moreover, the tendency is clearer for the 15 mm case as the the scraper is located closer to the beam.

SUMMARY AND CONCLUSIONS

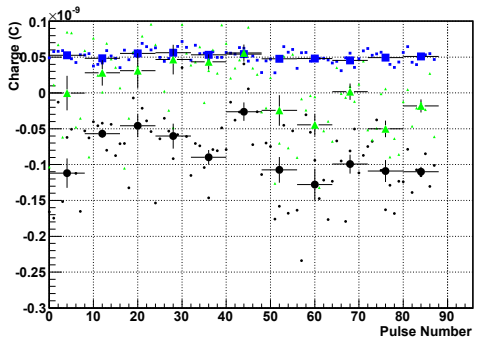
The AS has demonstrated to be an ideal facility to perform research and development for beam instrumentation for the DR of future linear colliders. Some of its main parameters are very similar to those of the CLIC DR and it provides flexibility so other parameters can approach CLIC DR conditions. An OBLM system has been calibrated under single shot conditions and it has demonstrated to be sensitive to beam losses down to a few ten thousand electrons. Moreover, the system was able to clearly determine beam losses generated during the topup process as well as to measure the synchrotron tune and provide indications of the feasibility to measure vertical and horizontal betatron tunes. The system was able to measure beam losses generated by modifying the betatron coupling in a CLIC-like fill and there were no indication of observation of synchrotron radiation despite that fact that the optical fiber was installed in the outer side of a bending magnet.

ACKNOWLEDGMENTS

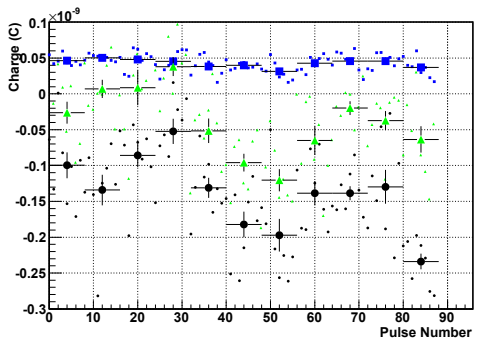
This work was supported by the Royal Society via the International Exchanges Scheme. We would like to express our thanks to CERN and ASLS for providing the equipment and dedicated beam time necessary for achieving the results presented here.

Copyright © 2014 CC-BY-3.0 and by the respective authors

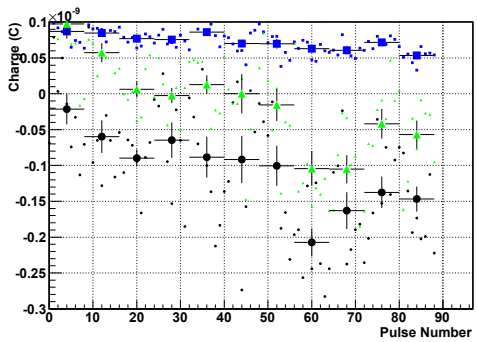
ISBN 978-3-95450-141-0



(a) Scrapper at 13mm



(b) Scrapper at 14mm



(c) Scrapper at 15mm

Figure 7: NaI (black), PMT-OBLM (green) and MPPC- OBLM (blue) BLM signals observed during the coupling scan. The solid points represent an average over all mea- surements for a given coupling. The small dotsshowindi-vidualmeasurements.

REFERENCES

[1] CLIC Collaboration, "A multi-TeV linear collider based on CLIC technology", CLIC Conceptual Design Report. Volume 1 Technical Report. CERN, Geneva 2012.

[2] "Conceptual design of the CLIC damping Rings", Y. Papaphilippou et. al. New Orleans 2012. IPAC12.

[3] J. Boldeman, D. Einfeld, Nucl. Instr. and Meth., A 521, 2004, p. 306-317.

[4] "Optical Fiber Based Beam Loss Monitor for Electron Storage Rings", T. Obina. September 2013, Oxford, IBIC13.

[5] "Fiber Optic sensors at accelerators: Considerations and Pitfalls", J. Kuhnhenn, May 2013. Vienna. 3rd OPAC topical Workshop on Beam Diagnostics.

[6] "Instrumentation for machine protection at femi@elettra", L. Froehlich et. al. Hamburg. DIPAC11.

[7] "Cherenkov Fibers for Beam Loss Monitoring at the CLIC Two Beam Module", J. Van Hoorne, June 2012. CERN-THESIS-2012-112.

Copyright © 2014 CC-BY-3.0 and by the respective authors

ISBN 978-3-95450-141-0

A TOROID BASED BUNCH CHARGE MONITOR SYSTEM WITH MACHINE PROTECTION FEATURES FOR FLASH AND XFEL

M. Werner*, T. Lensch, J. Lund-Nielsen, R. Neumann, D. Noelle, N. Wentowski,
DESY, Hamburg, Germany

Abstract

For the superconducting linear accelerators FLASH and XFEL, a new toroid based charge measurement system has been designed as a standard diagnostic tool. It is also a sensor for the bunch charge stabilization feedback and for machine protection. The system is based on MTCA.4 technology and will offer a high dynamic range and high sensitivity. The machine protection features will cover recognition of poor transmission between adjacent toroid sensors, bunch pattern consistency checks, and protection of the beam dumps. The concept, an overview of the algorithms, and the implementation will be described. A summary of first operation experience at FLASH will be presented.

INTRODUCTION

In the FLASH accelerator, toroid based Beam Current Monitor (BCM) systems have been used from the beginning.

Other requirements came up when the beam current increased due to the increasing number of bunches per RF pulse and a redundancy for the beam loss monitors (BLMs) became mandatory. Namely, pairs of beam current signals had to be applied for transmission interlocks. At this time, a "Toroid Protection System" (TPS) was developed [1] to detect beam losses by analysing the amplitude differences within toroid pairs. The TPS used the existing analogue toroid signals as inputs, and in addition to the control system digitizers, separate ADC and FPGA based data processing chains were implemented in a dedicated box. Connections to the Control System were avoided so as to insure maximum safety against unintended changes.

When beam current stability became an issue, a beam current feedback system was developed [2], again with the analogue toroid signals as inputs. It was realized by still another FPGA based system, providing a fast digital fibre connection to the injector.

Another application of the toroid signals was the beam loading compensation for the cavities realized by the LLRF group [3].

For the new European XFEL [4], it was desired to implement all this functionality into a single system, creating even more requirements.

For the x-ray cameras in the experiments, a "veto" signal is required to disable data acquisition for improper bunches.

For the protection of sensitive components, it is necessary to check that the integrated bunch charge is below a certain limit and that the bunches are directed to the correct branches of the beamline.

Since the exchange of a damaged beam dump is a major issue, dedicated protection algorithms were desired for the different kinds of dumps (three main beam dumps and two diagnostic dumps at the XFEL).

Another important topic is the ability of the system to work (with some restrictions) if the control signals from the machine timing system (clock, trigger) are not available or corrupted. In this case, the system should still measure the bunch charge (with relaxed precision) and the safety must be maintained.

*Matthias.Werner@desy.de

HARDWARE SETUP

The hardware consists of the toroid device, the front-end device (signal combiner, filter, amplifier) and the MTCA backend (see Fig. 1). The front-end device will be contained in a box together with a test pulse generator close to the toroid, the backend will be composed of a dedicated Rear Transition Module (RTM) in combination with a commercial 10 channel 125 MSPS digitizer board (Struck SIS8300-L2), housed in an MTCA.4 crate. The digitizer board will communicate over the MTCA backplane with the CPU in the crate, and the CPU will be part of the control system within an Ethernet network. The digitizer modules offer an FPGA for fast data processing and direct communication over Gigabit links with a speed of up to 6.25 Gb/s with other modules.

High Dynamic Range Feature

For the possibility of extending the dynamic range to a value above the dynamic range of the ADC, a two-channel arrangement will be implemented with two amplifiers of different gains, see Fig. 1. The high gain amplifier will provide improved SNR for low signals [5]; the low gain amplifier is still in the linear range for high amplitudes.

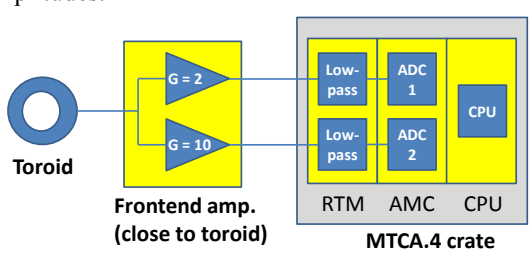


Figure 1: Hardware setup with high dynamic range feature (simplified).

OPERATION MODES

The system offers two basic operation modes: a self-triggered mode and a timing-triggered mode.

ISBN 978-3-95450-141-0

Copyright © 2014 CC-BY-3.0 and by the respective authors

Self-triggered Mode

This mode has to be used if correct clock and trigger signals from the timing system are not yet available in the commissioning phase and as a fallback in case of a timing system failure. In this mode bunches are detected by a threshold comparison of the digitized and pre-processed signal. This requires a bunch amplitude above a certain limit for reliable detection, and the precision is reduced because of the missing synchronization between bunch arrival times and ADC sampling.

In addition a technical alarm is issued to the MPS system to stop the (multi-bunch) machine operation.

Timing-triggered Mode

The timing-triggered mode can be used if the timing information (clock, trigger and bunch pattern) is available. This mode offers the full performance and is mandatory for multi-bunch operation with activated MPS.

MACHINE PROTECTION FEATURES

The BCM system is an important alarm supplier to the Machine Protection System (MPS) [6] and will offer the following features:

Differential Interlock

The main system to protect the XFEL and FLASH accelerator against extended beam losses will be the Beam Loss Monitor (BLM) system, based on scintillator panels connected to photomultipliers. While BLMs are very sensitive, they are localized – so losses at hidden locations can be invisible to BLMs. A BCM based transmission interlock can overcome this constraint, and it can also provide redundancy to the BLM system - therefore it was decided to implement this functionality. The principle is illustrated in Fig. 2. If a beam loss happens in a section between two BCM devices, the downstream BCM will show less charge than the upstream BCM (disregarding secondary emission inside the beam pipe). The amplitudes will be transmitted digitally via optical fibre links between the BCM devices. If the difference (calculated in the upstream BCM) is too big, an alarm will be generated with latency below 1µs to stop the beam via the MPS system.

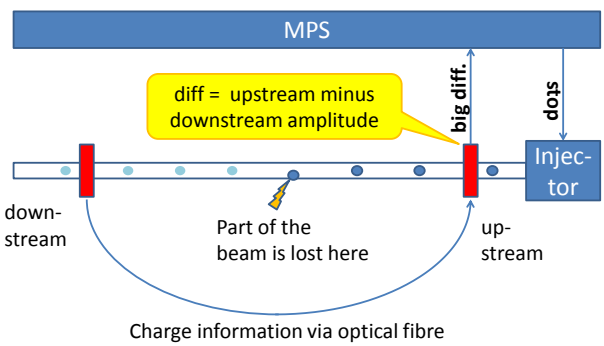


Figure 2: Principle of the differential interlock: a beam loss between two BCMs leads to reduced amplitude at the downstream BCM.

To monitor the whole accelerator, a chain of differential interlocks can be installed, see Fig. 3.

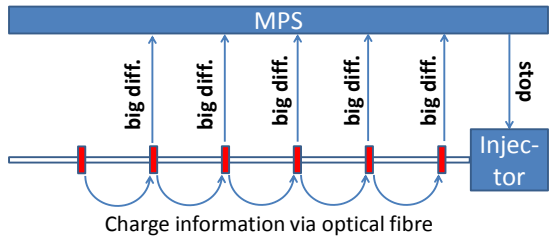


Figure 3: Non-interlaced differential interlock chain.

If a single BCM in this arrangement fails, it cannot any more receive and transmit the bunch charge information, so two sections between BCMs are "invisible". To avoid this risk, a redundant arrangement will be used in XFEL and FLASH with two interlaced optical fibre chains, see Fig. 4. A single failure of any BCM except the leftmost and the rightmost device will not affect the safety of the whole system.

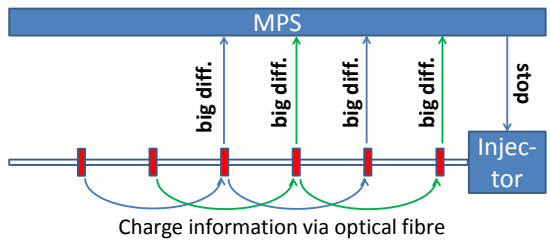


Figure 4: Interlaced differential interlock chain.

The differential interlock can also be applied to branches of the beam pipe. In this case the receiving BCM has to provide two fibre link inputs – one for either branch. A simple method to check for beam losses would be to add the signals from the two branches arithmetically and compare with the common signal before the branch. However, at XFEL and FLASH the direction of each bunch is known in advance from the bunch pattern (see next chapter) – this information can be used to decrease the noise. The principle is shown in Fig. 5 for the non-interlaced case and in Fig. 6 for the interlaced case.

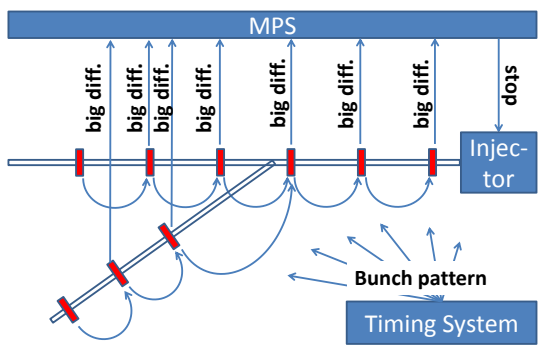


Figure 5: Differential interlock for a branch.

Copyright © 2014 CC-BY-3.0 and by the respective authors

ISBN 978-3-95450-141-0

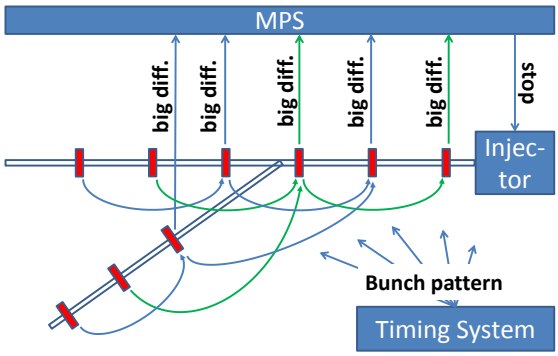


Figure 6: Interlaced differential interlock for a branch.

Bunch Pattern Consistency Check

The Timing System transmits information ("bunch pattern") about the destination of each bunch to all BCMs and other diagnostic devices ahead of each macropulse. For safe operation of the accelerator, the bunch pattern announced by the Timing System has to be consistent with the real bunch pattern.

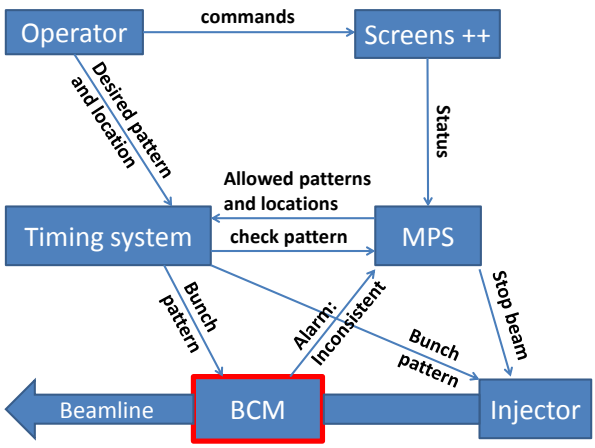


Figure 7: Bunch pattern consistency check.

The bunch pattern will be derived from the operation requirements, combined with the restrictions from the MPS, and then transmitted to all devices (see Fig. 7). So the injector generates bunches according to the bunch pattern. Every BCM can check if the announced bunch pattern is consistent with the pattern in the corresponding accelerator section. If bunches appear in wrong accelerator sections or time slots, the MPS will stop the injector.

Direct Protection of XFEL Dumps

Three main dumps and two diagnostic dumps will be installed in the XFEL accelerator. While any of the main dumps can absorb about 50% of the design beam power, the diagnostic dumps are very limited in beam power and current [7]. For every dump a dedicated BCM exists which monitors only the beam going to this dump. If the limit is exceeded, the beam will be stopped.

Indirect Protection of XFEL Diagnostic Dumps

One of the two diagnostic dumps in the XFEL is very delicate – only a given integrated charge (corresponding to only a few bunches) is allowed per macropulse in order to stay below the damage level. For the direct protection discussed above, the beam stop latency would be too large due to the given distance between BCM and injector, see chapter "Reaction times" in [6].

To overcome this problem, the indirect protection can be applied, using a BCM directly behind the injector. The bunch pattern informs the system which bunches are designated for the delicate dump. Only these bunches are used for the protection algorithm. Then the latency is very short because of the small distance between BCM and injector.

For first operation, a slow bending magnet will be used to steer the beam into the diagnostic dump or not. So the status of this magnet will be communicated via the MPS to the Timing System where the bunch pattern information will be composed, see Fig. 8.

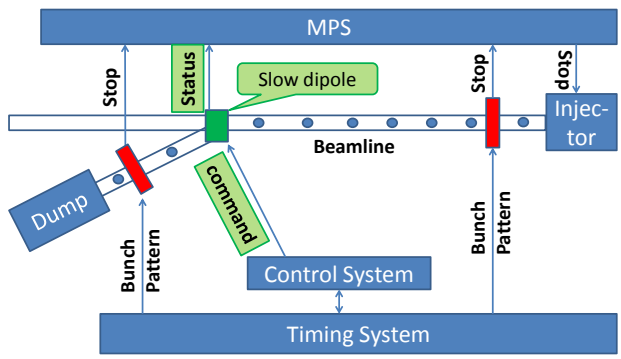


Figure 8: indirect protection of XFEL diagnostic dumps with beam steering by a slow dipole.

For later operation, it is desired to pick out bunches for the diagnostic dump by a fast kicker. This needs another protection scheme: The command to kick a bunch will be communicated by the bunch pattern from the Timing System to the kicker. The bunch pattern will also inform the BCM that this bunch will be steered to the diagnostic dump, see Fig. 9.

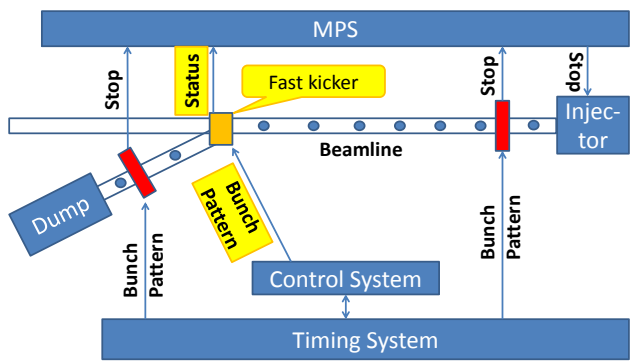


Figure 9: indirect protection of XFEL diagnostic dumps with beam steering by a fast kicker.

Copyright © 2014 CC-BY-3.0 and by the respective authors

ISBN 978-3-95450-141-0

Detection of too High Charge

If the charge exceeds a limit given by the bunch pattern telegram from the timing system, an alarm is triggered.

CHARGE CALCULATION ALGORITHMS

Basic Charge Calculation

For the current standard BCM implementation in FLASH, raw ADC samples (sampling frequency 108.333 MHz, bunch synchronous) are transmitted to a CPU where the bunch amplitudes are calculated in software. The algorithm [8] is shown in Fig. 10: At first, 4 samples are averaged to get the baseline value. Then 2 (optional 3) samples are ignored. The following 3 (optional 4) samples are averaged, and from this average the baseline value is subtracted to get the bunch charge.

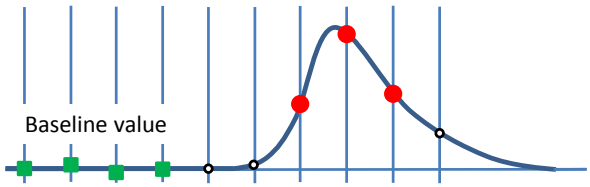


Figure 10: Basic charge calculation algorithm as currently implemented in software at the FLASH accelerator.

Improved Amplitude Calculation

The result of the basic charge calculation depends to some degree on sampling timing, especially on the time difference between the top of the curve and the center sampling point. To mitigate this dependence, a second order parabola fit algorithm can be used [9], [10]. More algorithms are currently under consideration.

Automatic Sampling Point Correction

In addition to a more precise integral of the signal, the parabola fit algorithm also generates an estimate for the time difference between the top of the curve and the center sampling point. For the new XFEL BCM system, it is foreseen to use this value to fine tune the ADC sampling phase, as also implemented in [9], [10]. This time tracking algorithm can be combined with the basic or improved amplitude calculation.

FIRST OPERATION AT FLASH

First data acquisitions have been demonstrated in the FLASH accelerator with a commercial RTM (Struck SIS8900), connected to a SIS8300 digitizer board, using the self-triggered mode. The basic charge calculation algorithm (see above) was implemented in FPGA firmware together with a maximum search algorithm and a threshold comparator. A bunch is detected if a given trigger threshold is exceeded and a local maximum is found. The algorithm waits for the first bunch of each macropulse and then outputs values at a rate of 9 MHz – this is the granularity in which bunches can occur. If no bunch is detected, the algorithm outputs a zero value. During the test, the bunch repetition rate in FLASH was 1 MHz and Fig. 11 shows that the algorithm correctly shows this rate: bunches were detected at index 0, 10, 19, 28, 37 … which corresponds to the 1 MHz bunch spacing in 111 ns (1 / 9 MHz) units. The displayed variations of the amplitude (order of ± 4%) are caused by two effects: fluctuations of the beam charge and imperfectness of the basic charge calculation algorithm in connection with the self-triggered mode.

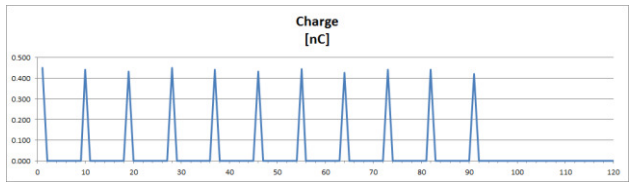


Figure 11: FPGA processed data from FLASH operation with 11 bunches at 1 MHz. Unit of X-axis: 111 ns buckets.

OUTLOOK

The development of a new RTM for the BCM system is under way and the features described above will be implemented in firmware as needed by the upcoming XFEL commissioning and operation. After successful commissioning in the lab, the XFEL Injector and the FLASH facility can be used for further functional verification, and finally the system is foreseen to be the standard BCM solution for XFEL and FLASH.

ACKNOWLEDGMENT

The authors wish to thank their colleagues Zlatan Pisarov, Klaus Knaack and Bastian Lorbeer for fruitful discussions and support in the project.

REFERENCES

[1] A. Hamdi et al., “Toroid Protection System for FLASH”, WEPC19, Proc. DIPAC2007, http://jacow.org/.
[2] Private communication with Christian Schmidt, Lukasz Butkowski and Martin Killenberg, group MSK, DESY.
[3] Beam loading compensation realized by group MSK, DESY.
[4] “The European X-Ray Free-Electron Laser”, Technical design report, July 2007, DESY 2006-097.
[5] M. Werner et al., “Sensitivity optimization of the standard beam current monitors for XFEL and FLASH II”, MOPD65, Proc. DIPAC2011, http://jacow.org/.
[6] S. Karstensen et al., “XFEL Machine Protection System (MPS) based on uTCA”, TUCOCA01, Proc. ICALEPCS 2013, http://jacow.org/.
[7] Private communication with Michael Schmitz and Norbert Tesch, DESY.
[8] Private communication with Kay Rehlich and Olaf Hensler, group MCS, DESY.
[9] M. Stadler et al., “Beam test results of undulator cavity BPM electronics for the European XFEL,” TUPA27, Proc. IBIC 2012, p. 406, http://jacow.org/.
[10] Private communication with Goran Marinkovic and Markus Stadler, PSI.

Copyright © 2014 CC-BY-3.0 and by the respective authors

ISBN 978-3-95450-141-0

UPGRADE OF THE FAST BEAM INTENSITY MEASUREMENT SYSTEM FOR THE CERN PS COMPLEX

D. Belohrad*, J.C. Allica, M. Andersen, W. Andreazza, G. Favre,
N. Favre, L. Jensen, F. Lenardon, W. Vollenberg, CERN, Geneva, Switzerland

Abstract

The CERN Proton Synchrotron complex (CPS) has been operational for over 50 years. During this time the Fast Beam Current Transformers (FBCTs) have only been repaired when they ceased to function, or individually modified to cope with new requests. This strategy resulted in a large variation of designs, making their maintenance difficult and limiting the precision with which comparisons could be made between transformers for the measurement of beam intensity transmission. During the first long shutdown of the CERN LHC and its injectors (LS1) these systems have undergone a major consolidation, with detectors and acquisition electronics upgraded to provide a uniform measurement system throughout the PS complex. This paper discusses the solutions used and analyses the first beam measurement results.

INTRODUCTION

The CERN PS complex is a chain of accelerators producing accelerated beams for the Super Proton Synchrotron (SPS), and subsequently for the Large Hadron Collider (LHC). In addition it delivers a wide range of particle beams to the secondary experimental areas.

The complex (Fig. 2) is comprised of the proton and the heavy ion linear accelerators ($LINAC_{II}$, $LINAC_{III}$), the Proton Synchrotron Booster (PSB) and the Proton Synchrotron (PS). Transfer lines transport the beams from the CPS accelerators to the appropriate targets (e.g. the On-Line Isotope Mass Separator ISOLDE), to the experimental areas (e.g. the Antiproton Decelerator AD), and for further acceleration to the SPS.

The transfer of particle beams nearly always involves some beam loss which has to be minimised. The beam transfer efficiency is calculated from the measured beam intensities at various locations in the accelerator complex. The beam intensity measurement in the CPS transfer lines is provided by the FBCTs, as shown in Fig. 2.

The FBCTs were installed during the construction of the accelerator chain and they were only repaired or modified when they ceased to function, or to cope with new requests. This resulted in a large variety of FBCTs designs, acquisition techniques and calibration methods. This state of affairs limited the accuracy of the transfer efficiency estimate to no better than 5%.

In 2010 the CPS FBCTs were equipped with new acquisition systems. The originally used analogue integrators were replaced by digital signal processing [1]. This improved the calculation accuracy of the transfer efficiency to ≈ 2%. A further improvement could be only achieved by upgrading the FBCTs and their calibration methods.

During LS1, a major upgrade of the FBCTs for the PS complex was therefore performed. Twelve out of 21 old FBCTs measuring the bunched beams at the PSB extraction were replaced (the red boxes in Fig 2), with the remaining FBCTs foreseen to be upgraded during LS2 in 2018.

MECHANICAL CONSTRUCTION

The FBCT Toroid

The major issue associated with the design of the new FBCT for the PS complex was the choice of the measurement toroid. From past experience, it was known that the currently used toroids provided a beam position dependent signal which adversely affected the absolute accuracy of the intensity measurement. A collaboration was set up with Bergoz Instrumentation to design a toroid mitigating this problem. An iterative design process resulted in the fabrication of a new type of large-aperture toroid (210 mm) having an imperceptible beam position dependence. To achieve this the toroid's measurement bandwidth had to be lowered from the usual GHz range to 120 MHz. This 120 MHz bandwidth is sufficient to provide the bunch to bunch transfer line beam intensity measurements (droop ≈0.25%/μs) for the beams with bunch spacing greater than 100 ns. Using this toroid to measure the beams with bunch spacing of 25 ns (the LHC beams) requires further signal treatment

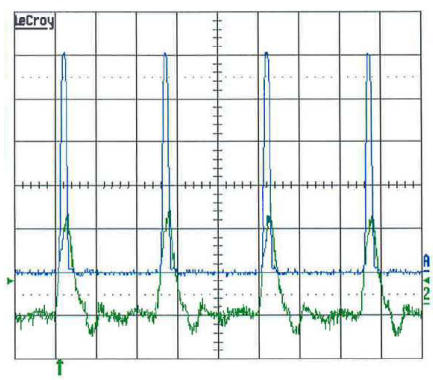


Figure 1: The impulse response of the 1:40 FBCT toroid. The blue trace shows the input signal fed through an antenna. The green trace shows the toroid output signal. The time scale is 10 ns/div.

* david.belohrad@cern.ch

ISBN 978-3-95450-141-0

Copyright © 2014 CC-BY-3.0 and by the respective authors

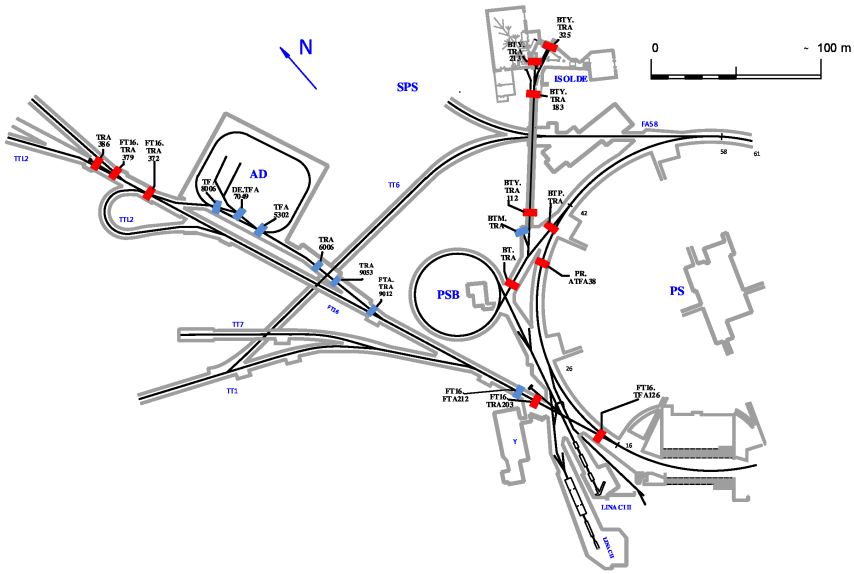


Figure 2: The FBCTs in the CERN PS complex. Twelve FBCTs have been upgraded during the LS1 (shown as the red boxes), the remaining FBCTs will be upgraded during the LS2 (shown as the blue boxes).

in the digital domain as the toroid's output signal transient extends beyond 25 ns (Fig. 1).

The FBCT Housing

The complete FBCT assembly is shown in Fig. 3. The toroid (orange) and the calibration turn (dark blue) are housed in two magnetic shieldings. Each shielding is made of two 1 mm thick μMetal sheets rolled and forged to form a shell. To restore the shielding efficiency, the μMetal was thermally treated for 1 hour at 1080 °C and naturally cooled. Both shieldings are separated by fibre glass spacers (green) to maintain their respective positions. The spacers also improve the mechanical stability of the assembly.

The shielding and the toroid assembly are inserted into the outer shell (brown) which serves as a mechanical housing. The shell is fabricated from the pure iron, commercially known as Armco. The shell provides a well-defined, low-impedance path for the beam induced wall image current. An excellent electrical contact between the body parts and the vacuum chamber is achieved by plating the Armco with a 25 μm layer of silver. The Armco's high magnetic saturation (2.15 T) and permeability (μ_r = 300-500) provide an additional layer of magnetic protection. The initial permeability can be further increased by thermal treatment (μ_r = 3500 - 6000). Hence the FBCT housing was thermally treated for 1 hour at 870 °C and cooled down in a furnace at 100°C per hour.

The Vacuum Chamber

The FBCT body is installed over the vacuum chamber. The design of the vacuum chamber differs for the various installation locations, but the ceramics-bellow assembly inside the cavity of the FBCT is always present (Fig 3). This

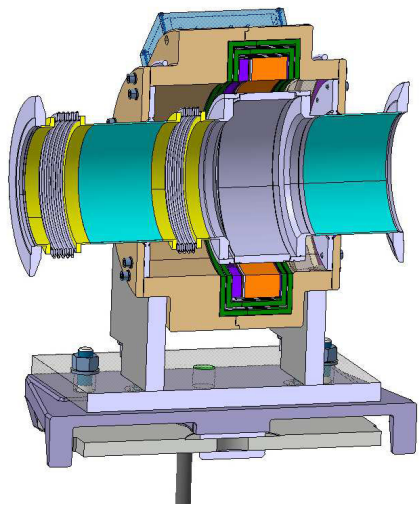


Figure 3: The CATIA model of the FBCT. The toroid is shown in the orange colour.

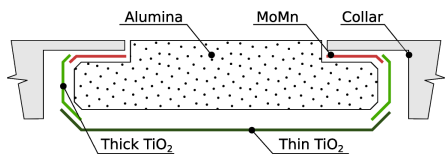


Figure 4: The cross-section of the ceramics showing the deposited layers.

ceramic insert forces the wall image current to flow through the Armco body making the magnetic field of the particle beam to be visible to the toroid. The bellow internal to the housing relaxes the transversal forces applied to the ceramic,

Copyright © 2014 CC-BY-3.0 and by the respective authors

ISBN 978-3-95450-141-0

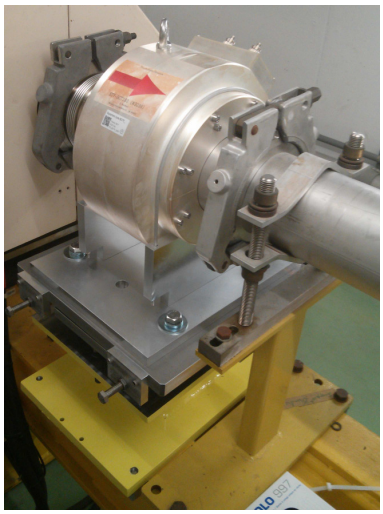


Figure 5: The upgraded FBCT BTY.TRA183.

while the presence of the bellow outside the FBCT cavity depends of the surrounding equipment in the PS complex.

The ceramic insert is composed of two copper collars and a 98% pure alumina ring (Al_2O_3, Fig. 4). The ceramic's extremities were factory covered by a Molybdenum-Manganese coating, which was sintered onto the Alumina surface. This provided a metal contact layer for the brazing of the collars, which were fabricated from OFE copper. Kovar could not be used, as simulations performed using the Maxwell code showed that the magnetic properties of Kovar could induce a significant magnetic coupling with magnetic fields external to the toroid.

To ensure that there was no electrostatic charge build-up on the ceramics, a titanium (Ti) coating with a resistance of 20-25 Ω end-to-end was deposited on the inside surface. The resistance value chosen was a compromise between reducing the ringing of the FBCT signal and not causing too much attenuation.

Due to technological limitations the assembly had to be constructed in three steps. First a thick Ti layer was deposited on the sides of the ceramic (resistivity of ≈2 Ω). The collars were then brazed in a second step, and the final resistivity was achieved by depositing a thin Ti layer of ≈20 Ω. Further oxidation of the deposited layer in air then causes an increase of the total stable layer resistance to the final 20-25 Ω.

One of the FBCTs, assembled and installed in the CPS, is shown in Fig. 5 (corresponding to BTY.TRA183 shown in Fig. 2).

ANALOGUE-FRONT END AND ACQUISITION SYSTEM

To maximise the signal to noise ratio (SNR) of the FBCT signal, there is an analogue front-end installed in the vicinity of each FBCT[1]. This consists of a 6 dB resistive splitter and an amplifier. One of the splitter outputs is fed directly into the acquisition system and provides a low-gain measurement. The other is amplified (G = 30 dB) to provide high-gain measurements. The bandwidth of this channel is limited to 18 MHz due to the operational amplifiers used. The amplifier and the splitter are implemented on a single PCB using commercially available components with current feedback amplifiers (THS3001) used to achieve the required amplification.

The analogue signals are transported to the acquisition systems outside the accelerator tunnels, using 7/8" foam-filled non-corrugated coaxial cables The cable type chosen ensures a minimum signal loss over the cable length, which for some FBCTs exceeds 400 m.

The FBCT acquisition system uses the 6U VME form-factor Transformer Integrator Card (TRIC) [1] to sample the analogue signals, compare them to the calibration signals, and compute the total beam charge. The TRIC is equipped with two 100 MSPS ADCs providing two independent acquisition channels. These are connected to the high and low gain signals coming from the front-end electronics through additional 3 MHz low-pass filters. The filters extend the width of the raw signals (σ = 1 - 5 ns) so they can be sampled using a 100 MHz sampling system, and still allow bunch to bunch measurements for the beams spaced by 100 ns or more.

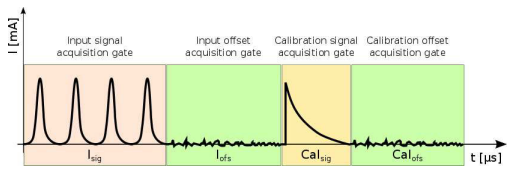


Figure 6: The TRIC sampling windows.

The total beam charge is calculated in the TRIC using measurements from four independent acquisition windows as shown in Fig. 6. The simple sum of all the samples within each window is used to estimate the integral in the measured intervals. The four intervals correspond to the beam signal, its offset without beam, the calibration signal and its associated offset. The measured offsets are subtracted from the measured beam and calibration signals to improve the immunity from low-frequency signal fluctuations and FBCT droop. The total measured charge is calculated using following equation:

$$N_q = \frac{I_{sig} - I_{ofs}}{Cal_{sig} - Cal_{ofs}} \cdot Cal_q, \quad (1)$$

where the $I_{[sig,ofs]}$ and the $Cal_{[sig,ofs]}$ are the integrals of the respective intervals shown in Fig. 6, and Cal_q corresponds to the charge generated by a calibrator.

As the PS complex provides beams differing in number of bunches, amplitudes and intensities, all the TRIC window gates have to be set-up separately for each beam.

[1] Except for the ISOLDE FBCTs due to too high ambient radiation damaging the electronics.

ISBN 978-3-95450-141-0

Copyright © 2014 CC-BY-3.0 and by the respective authors

CALIBRATION

The absolute accuracy of the measurement is primarily determined by the absolute accuracy of the calibrator and the coupling of the FBCT calibration turn to the FBCT measurement winding.

The FBCT calibrator forms an integral part of the TRIC. To calibrate the FBCTs, the TRIC charges a capacitor to a known voltage and then discharges it into the FBCT calibration winding to provide a reference calibration signal Cal_{sig}.

This calibration method was preferred over a pulsed current source generator due to its simplicity. The absolute accuracy of the calibrator is mainly determined by the quality of the capacitor used and the precise knowledge of its capacitance and the applied voltage.

The FBCT calibration turn is formed using 8 parallel single-turn windings distributed equidistantly over the toroid circumference. The windings are connected together using a set of resistors so that the entire structure looks like a single 50 Ω terminated calibration turn when measured at the SMA connector. The structure is manufactured on a single PCB and is installed on the side of the toroid (Fig. 7) to minimise the mechanical forces applied to the resistors.



Figure 7: The installed calibration winding.

In order to further improve the accuracy of the transfer efficiency measurements, the TRICs in the PS complex were cross-calibrated. This was done in the laboratory during the reception testing of the TRICs. One master TRIC was used to generate a calibration signal, which was consecutively injected into all the tested TRICs as a measured signal. The tested TRICs used their on-board calibrators to estimate the injected calibration signal intensity as if it was the beam signal. If the calibrators of all the TRICs were the same, there would be no difference seen in the calculated intensities. However, due to the accuracy of the calibrators, the measurement results differ. Sixteen fabricated TRICs showed a difference ranging from -3.07% to 1.2% (σ=1.14%) with respect to the mean value calculated over the entire batch.

The calculated differences were used to correct the calibration factors by multiplying Cal_q in Eq. (1) by a correction factor, so that the measurements of the injected calibration signals for all TRICs were equal.

The authors acknowledge that the presented cross-calibration method requires improvements, since it requires the testing of all cards at once. This is difficult when the TRICs are already installed in the CPS. A study is currently ongoing to see how a DC current source could be used to independently cross-calibrate the TRICs.

SOFTWARE DESIGN

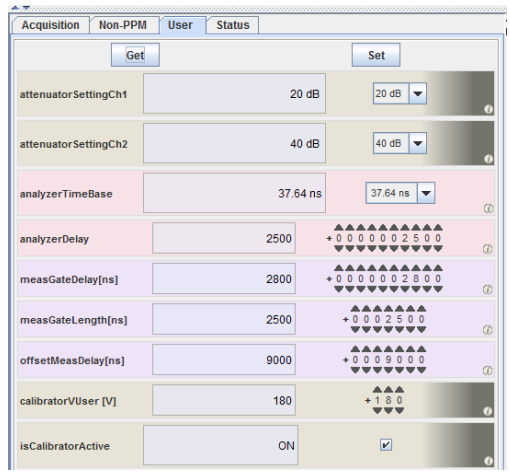


Figure 8: Screen-shot from expert application provided to control settings specific to one selected cycle.

The control system at CERN uses the concept of "devices" whereby the name of any given BCT device is derived from the specific beam-line, its type and position. As an example of this convention BTY.BCT183 measures the total intensity in number of charges in the BTY transfer-line from the PSB to ISOLDE (Fig. 2). The real-time software maps a physical BCT detector to one controls device through one TRIC module. This simplifies the integration in the control system. Two real-time (RT) actions are used for the acquisition:

1. "Prepare" which sets up the TRIC modules with the next acquisition and calibration parameters. The timing event is chosen such that the execution of the RT action finishes safely before the external fast trigger to launch the acquisition arrives. Typical execution times per controls device is of the order of a 1 ms. The operational settings are split into two categories:

   (a) Cycle specific settings, examples of which can be seen in Fig. 8, and typically involve the attenuation for each of the two channels and the measurement gate delay and duration.

   (b) Cycle independent settings, such as those for the calibrator.

2. "Acquire" which checks that the acquisition has completed and then reads the values from the different acquisition modes. The data is normalised using the acquired offset and gain values. The internal analyser

Copyright © 2014 CC-BY-3.0 and by the respective authors

ISBN 978-3-95450-141-0

(Fig. 10) is used for verifying that the settings are correct, i.e. that the gates are correctly set-up with respect to the beam and that the ADC is not saturated.

FIRST MEASUREMENT RESULTS

The upgrade of the CPS FBCTs started in August 2013 with the last FBCT installed in April 2014. They were then tested without beam using measurements of noise in the machine. This permitted the complete acquisition chain to be verified, as the input signal, including the calibration pulse, could be displayed. Such a measurement for the low-gain signal inputs is shown in Fig. 9. The histogram depicts the data published to the CERN control system and to the logging databases.

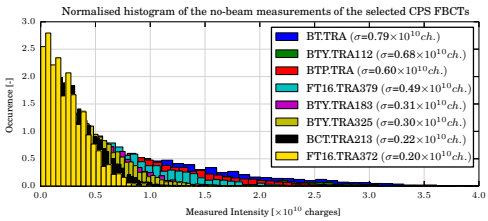


Figure 9: The normalised histogram of the low-gain channel noise measurements of the selected FBCTs installed in the PS complex.

The first beam measurements were taken in mid-2014, when the PSB re-started. The integrating gates had to be correctly set up for all the FBCTs and all different beam types, as shown e.g. in Fig. 10 for the BTY.TRA325. The picture shows a beam well fitted into the signal measurement gate, followed by the signal offset measurement gate, the calibration pulse gate and the corresponding calibration offset gate.

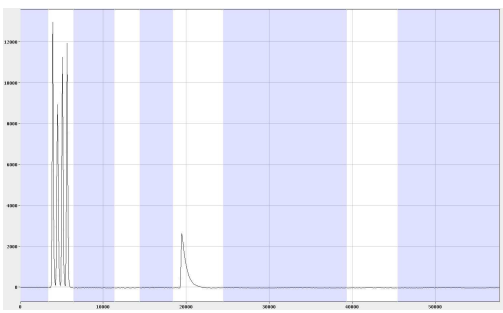


Figure 10: The correctly set up FBCT measurement for the ISOLDE BTY.TRA325. The four measurement gates (white background) identify the regions where the beam signal, its offset, calibration signal and the calibration offset are measured. The picture shows the measurement of the 4 bunches extracted from the PSB to the ISOLDE (Fig. 2). Even when using 3 MHz low-pass filter the four individual bunches can be clearly identified.

During the commissioning, it was found that some of the FBCTs diverge from the optimal behaviour shown in Fig. 10. Such an example, the measurement of BTY.TRA213, is depicted in Fig. 11. The figure shows a low-frequency fluctuation of the baseline, resulting in a deterioration of the absolute accuracy. This issue is currently being investigated, but is believed to originate from an electro-magnetic coupling of the FBCT to the dipole magnet installed nearby (< 20cm).

The long-term drift shown in Fig. 11 cannot be suppressed using the offset subtraction due to the ratio of the drift period and the measurement gate lengths. However, as this is a systematic effect, it can be suppressed using additional signal treatment in the digital domain. An algorithm subtracting the low-frequency baseline drifts is currently being tested in the CERN LINAC$_4$ and if it works, it will added to the PS complex intensity measurements.



Figure 11: A low-frequency fluctuation of the base line in the BTY.TRA213.

SUMMARY

As the CERN injector complex re-starts after the long shutdown, the newly installed fast beam current transformers are currently being set-up for the different types of accelerated beams. First measurements indicate that the systems are fully functional, but additional tuning will, however, be required to achieve optimal measurement accuracy. This mainly concerns the FBCTs installed in the vicinity of magnets, as these magnets induce low-frequency baseline drifts that are not effectively suppressed by the currently used base-line restoration algorithm. The method for cross-calibration of the individual TRIC acquisition boards, to maintain a relative accuracy between transformers at the 1also has to be improved. Following the success of this consolidation, the remaining transformers are now foreseen to be upgraded during Long Shutdown 2 in 2018, which will result in a standardised installation of FBCTs throughout the injector complex.

REFERENCES

[1] A. Monera et al., “Upgrade of the CERN PSB/CPS Fast Intensity Measurements”, DIPAC 2011, Hamburg, Germany

ISBN 978-3-95450-141-0

Copyright © 2014 CC-BY-3.0 and by the respective authors

A CRYOGENIC CURRENT COMPARATOR FOR THE LOW ENERGY ANTIPROTON FACILITIES AT CERN

M. Fernandes*, The University of Liverpool, U.K. & CERN, Geneva, Switzerland
J. Tan, CERN, Geneva, Switzerland,
C.P. Welsch, Cockcroft Institute & The University of Liverpool, Liverpool, U.K.

Abstract

Several laboratories have shown the potential of using Superconducting QUantum Interference Device (SQUID) magnetometers together with superconductor magnetic shields to measure beam current intensities in the sub-micro-Ampere regime. CERN, in collaboration with GSI, Jena university and Helmholtz Institute Jena, is currently working on developing an improved version of such a current monitor for the Antiproton Decelerator (AD) and Extra Low ENergy Antiproton (ELENA) rings at CERN, aiming for better current resolution and overall system availability. This contribution will present the current design, including theoretical estimation of the current resolution; stability limits of SQUID systems and adaptation of the coupling circuit to the AD beam parameters; the analysis of thermal and mechanical cryostat modes.

LOW-INTENSITY BEAMS CURRENT MEASUREMENT

Low-intensity charged particle beams present a considerable challenge for existing beam current diagnostics [1], this is particularly significant for coasting beams with average current below 1 μA which is the minimum resolution of DC Current Transformers. Other monitors, such as AC Current Transformers or Schottky monitors are able to measure low-intensity beam currents, but neither can simultaneously provide an absolute measurement, with a high current and time resolution, which is at the same time independent of the beam profile, trajectory and energy.

At CERN's low-energy antiproton decelerators, the AD and the ELENA (currently under construction) rings, circulate both bunched and coasting beams of antiprotons with average currents ranging from 300 nA to 12 μA [2]. Having a current measurement with the above mentioned characteristics would benefit the machine operation and optimization.

To meet these requirements, a low-temperature SQUID-based Cryogenic Current Comparator (CCC) is currently under development. Similar devices have already been developed for electrical metrology [3], and later for beam current measurements in particle accelerator [4]. The current, a collaboration between CERN, GSI, Jena University and Helmholtz Institute Jena aims to make this a fully operational device, with a prototype foreseen to be tested in the AD machine at CERN in 2015.

*Funded by the European Unions Seventh Framework Programme for research, technological development and demonstration under grant agreement no 289485.

The main design specifications for the monitor are: beam current resolution < 10 nA; and measurement bandwidth > 1 kHz.

Overview of the Functioning Principle of the CCC

The CCC (see Fig. 1) works by measuring the magnetic field induced by the particle beam current. This field is concentrated in a high-permeability ferromagnetic pickup core, from which it is coupled into a Superconducting QUantum Interference Device (SQUID). These are highly sensitive magnetic flux sensors that permit sensing the weak fields created by the beam. A superconducting magnetic shield structure around the pickup-core, as described in [4, 5], renders the coupled magnetic field nearly independent of the beam position and makes the system practically immune to external magnetic field perturbations.

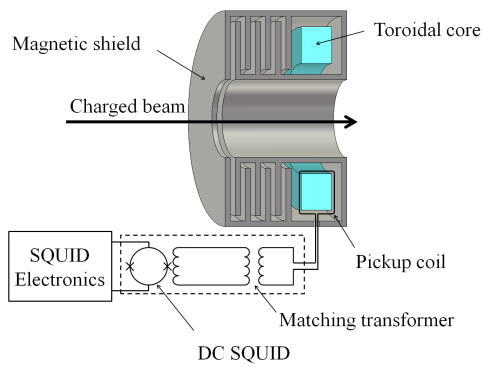


Figure 1: Schematic of the CCC.

CCC MONITOR DIMENSIONING

The AD CCC will in a first phase use a superconducting shield and pickup core developed by Jena University and Helmholtz Institute Jena. This core has a single turn inductance $L_P = 104\,\mu$H, while the SQUID device [1] has the following parameters, input coil self-inductance $L_i = 1\,\mu$H and mutual inductance $M_i = 3.3\,\phi_0/\mu$A [2].

Coupling Circuit and Resolution

The circuit such as the one depicted in Fig. 2 will be used to couple the beam current signal into the SQUID. The transfer function of this circuit, defined as the change

[1] Manufactured by Magnicon GmbH.

[2] $\phi_0 = 2.0678 \times 10^{-15}$ Wb is the magnetic flux quantum which is the unit commonly used for magnetic flux when dealing with SQUID systems.

Copyright © 2014 CC-BY-3.0 and by the respective authors

ISBN 978-3-95450-141-0

in the flux coupled to the SQUID per unit change in beam current $S_{I_B} = \Phi_S(t)/I_B(t)$, excluding the RC-shunt, is given by:

$$S_{I_B} = \left[\frac{M_i M_P M_f}{(L_P + L_1)(L_2 + L_i) - M_f^2} \right], \qquad (1)$$

where M_P is the mutual inductance between the beam current and the pickup core coil self-inductance L_P, M_f is the mutual inductance of the matching transformer and $L_{1,2}$ are the respective primary and secondary self-inductances (see Fig. 2).

Since the pickup core is made of a high-permeability material one can assume that $M_P \approx L_P$, provided that L_P is a single-turn coil. To optimally couple the signal to the SQUID, a matching transformer is used to adapt the high inductance of the pickup core with the much smaller inductance at the SQUID input. Optimizing S_{I_B} for the known values of L_P and L_i, and assuming a coupling factor of $k = 0.9$ one obtains:

- $L_1 = 239\,\mu\text{H}$
- $L_2 = 2.29\,\mu\text{H}$
- $S_{I_B} = 10.5\,\phi_0/\mu\text{A}$

Using a high inductance pickup core is desirable since it maximizes the signal coupling, but not if this increase in the inductance is obtained by increasing the number of turns in the secondary coil of the pickup-core, since then this would be acting as a current transformer with current transformation ratio $1/N_P$. The only options left are to increase the size of the core or the magnetic permeability of the ferromagnetic material.

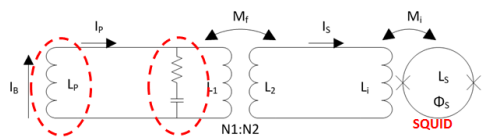


Figure 2: Circuit coupling beam current into SQUID magnetic flux density. In red are the elements with a low-pass effect.

Nanocrystaline soft magnetic materials are good candidates since these have very high real permeability and exhibit low losses particularly at low-frequencies. Additionally, different studies [6] have shown that these materials keep most of their magnetic properties when cooled down to 4.2 K. The material of the pickup core to be used in the first phase AD installation is Nanoperm [3]. Fig. 3 shows the complex permeability measurements performed by [7].

The permeability curves can be fitted to good agreement, with a first-order relaxation Debye model, provided that a

[3] Produced by Magnetec GmbH.

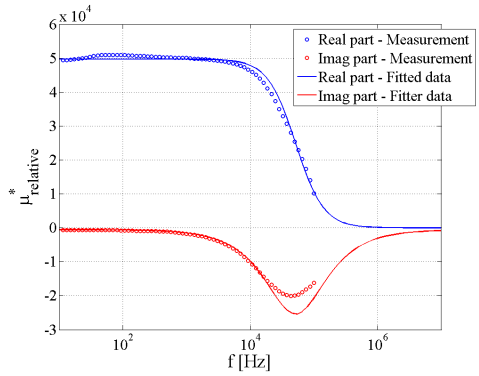


Figure 3: Complex relative permeability of Nanoperm ferromagnetic cores. Measurements [7] and curve fitting.

constant imaginary term is added in order to account for the $1/f$ spectral noise behaviour at low frequencies [8].

$$\mu_r^*(f) = 1 + \frac{K_{spin}}{1 + i\frac{f}{f_{spin}^{res}}} - iK_{1/f} \qquad (2)$$

The obtained values for this model parameters are $K_{spin} = 49700$ for the DC magnetic susceptability, $K_{1/f} = 556$ for the DC imaginary magnetic permeability, and $f_{spin}^{res} = 51.5\,\text{kHz}$ for the resonant frquency of the spin magnetic moment.

The current resolution of the monitor will be fundamentally limited by the different noise contributions. The intrinsic noise level of the SQUID plus its read-out electronics for modern low-noise devices is of the order of $1.2\,\Phi_0/\sqrt{\text{Hz}}$, with corner frequency at $\leq 1\,\text{Hz}$. Using the fitted complex permeability functions, shown in Fig. 3, it is possible to calculate the induced noise from the ferromagnetic material via the fluctuation-dissipation theorem [9, 10]. This results in Eq. 3, where L_0 is the value of an equivalent air-inductor, L_i is the load inductance connected to the ferromagnetic core coil, T is the temperature and k_B is the Boltzman constant.

$$< I_C^2 >_{PSD} = \frac{4k_B T}{\omega L_0} \left(\frac{\mu''(\omega)}{[L_i/L_0 + \mu'(\omega)]^2 + \mu''(\omega)^2} \right) \qquad (3)$$

The calculated noise spectral density from the pickup core, as well as the SQUID and read-out electronics is shown in Fig. 4. These are calculated as flux coupled to the SQUID.

External noise sources may also adversely impact the measurement resolution. Particularly in an accelerator environment, where many possible sources of mechanical vibrations, stray magnetic fields, and RF interference are present. The magnitude of these noise components can only be accurately known from measurements at the installation location. Nevertheless one can estimate the impact on the current resolution by assuming different values for an additional constant spectral noise component that accounts for all the external perturbations.

Combining the different noise components and parameterising the environmental noise contribution, the achiev-

ISBN 978-3-95450-141-0

Copyright © 2014 CC-BY-3.0 and by the respective authors

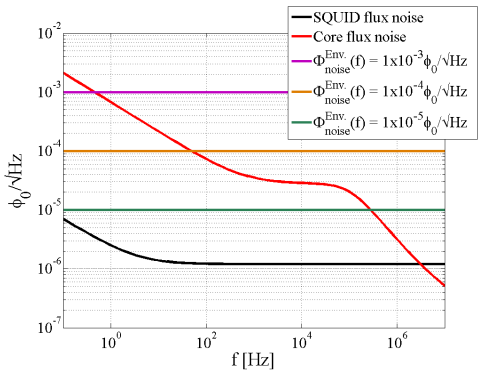


Figure 4: Spectral density of the expected magnetic flux noise coupled to the SQUID.

able beam current resolution (considering a bandwidth of 1 kHz) can be estimated. The results are shown in Fig. 5. Assuming that $\Phi^{env.}_{noise} = 1 \times 0^{-3}\phi$ (purple curve) the ex-

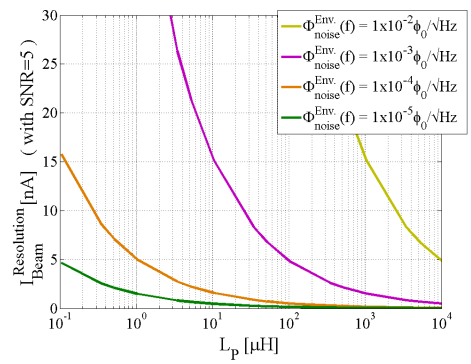


Figure 5: Expected noise-limited beam current resolution as a function of the pickup inductance, taking into account the known SQUID and core components, and assuming different values for the combined unknown average environmental sources.

pected current resolution for $L_P = 100\,\mu$H, with $SNR = 5$, is 5 nA, which complies with the specification.

Values for the first CCC monitor installation at GSI, reported in [4], using an older SQUID technology, and with a less performant magnetic core and shield, indicate noise density values of $2 \ldots 23 \times 10^{-4}\,\phi_0/\sqrt{\text{Hz}}$. Recent measurements, performed at GSI with a CCC installed in a beam line, and equipped with a modern SQUID system, indicate much smaller noise figures, with perturbation peaks of the order of $10^{-5}\,\phi_0/\sqrt{\text{Hz}}$ and noise floor $10^{-6} \ldots 10^{-5}\,\phi_0/\sqrt{\text{Hz}}$, over a frequency range from 10 Hz to 10 kHz. This indicates that considering an average environment noise of $\Phi^{env.}_{noise} = 10^{-4}\,\phi_0/\sqrt{\text{Hz}}$ (orange curve in the plots) is a good conservative estimation.

Flux-Locked-Loop (FLL) and Slew-rate Limitations

SQUID devices are unparalleled in the sensitivity they exhibit to magnetic flux variations. The model chosen for the AD monitor has a maximum value of $2579\,\mu\text{V}/\phi_0$. However, this only holds in small regions of the periodic $V(\Phi)$ transfer function. To linearise this response and increase its dynamic range most common readout schemes implement a flux feedback loop - a so called Flux-Locked Mode (FLL) - as shown in Fig. 6. This keeps the SQUID

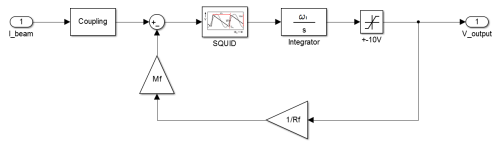


Figure 6: SQUID readout Flux-Locked Mode.

operating at a constant working point ($\Phi_{\text{SQUID}} = \text{constant}$), while the measurement output is given by the output voltage of the integrator. The bandwidth of the system in FLL readout mode is given by

$$f_{BW} = \frac{V_\Phi M_f}{R_f} f_I, \tag{4}$$

where, M_f is the mutual inductance of the SQUID feedback coil, R_f is the feedback resistance converting output voltage into feedback current, and f_I is the gain of the preamplifier and integrator.

In order for the SQUID to be able to track input signals with a high slew-rate, while keeping a constant working point and avoiding the occurrence of flux jumps, the closed loop bandwidth (given by Eq. 4 and typically limited to a few MHz) needs to be high enough for the feedback loop to react in a short time, driving the error signal ($\Phi_e = \Phi_{signal} - \Phi_{feedback}$) close to 0. However, if the bandwidth is too high, this will increase the amplitude of the amplified noise that is fed-back into the SQUID, increasing the probability of fast changing flux signals that cannot be compensated by the feedback loop, thus imposing a limit on the maximum bandwidth that can be set for the FLL loop. The condition for stable operation can be conservatively defined to be

$$|\delta\Phi_e| < \phi_0/2. \tag{5}$$

Assuming a Gaussian distribution for the total noise, it is possible to calculate the maximum allowed slew rate as a function of the FLL bandwidth [11]. This is shown for different average spectral noise density values in Fig. 7. In this calculation the maximum allowed flux-jump rate was assumed to be 1 per hour. This is considered reasonable as a calibration of the CCC can be performed before the start of each AD cycle, which has the duration of 85 s.

If one considers an average $\Phi_{noise} = 10^{-5}\,\phi_0/\sqrt{\text{Hz}}$, the stability region for the system will be roughly bounded by:

Copyright © 2014 CC-BY-3.0 and by the respective authors

ISBN 978-3-95450-141-0

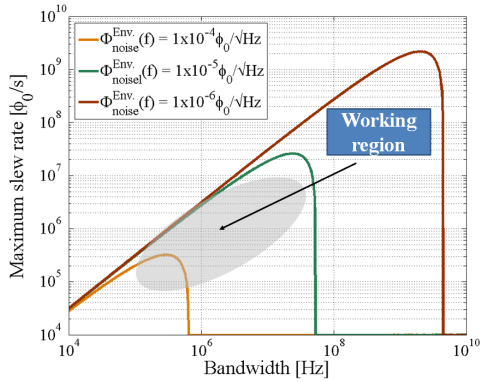


Figure 7: Maximum slew-rate for different RMS SQUID flux noise levels as a function of the FLL loop bandwidth, for a flux jump rate < 1/hour.

- Slew rate limit for input signal: $d\phi/dt < 5\,\mathrm{M}\phi_0/\mathrm{s}$
- FLL loop bandwidth limit: $f_{3dB} < 20\,\mathrm{MHz}$

During AD beam injection, when the average current jumps from 0 to 12 μA, the slew-rate is $400\,\mathrm{M}\phi_0/\mathrm{s}$. This can be reduced by decreasing the flux coupling or by low-pass filtering before the SQUID input. The latter is preferable since it does not entail a loss of current resolution. Given this, the design includes an RC-shunt in the coupling circuit, with [4] $R = 1\,\Omega$ and $C = 10\,\mu$F, which has the effect of attenuating the input with a second-order filter as shown in Fig. 8.

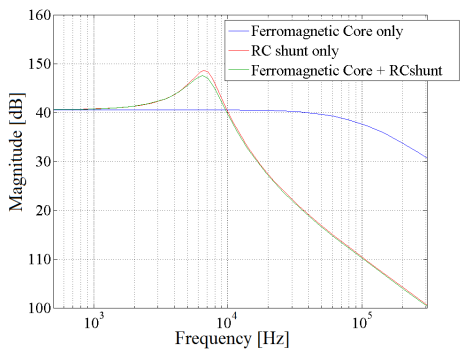


Figure 8: Coupling circuit transfer function with low-pass filtering effect from frequency dependent permeability, RC-shunt, and both combined.

When the injected AD beam couples to the SQUID through this coupling circuit, the maximum slew-rate is reduced to $3\,\mathrm{M}\phi_0/\mathrm{s}$. The resonant peak will cause an overshoot on the signal to be measured but the settling time (to within 1%) is calculated to be 0.45 ms, considered acceptable compared to the overall measurement bandwidth requested for the monitor.

[4]The largest capacitance available for small-sized capacitors at cryogenic temperatures is $\leq 1\,\mu$F.

It should also be mentioned that the delays t_d introduced by the different components in the FLL loop, which are normally dominated by the cables connecting the SQUID device to the room-temperature electronics, may be another source of instability depending on the cable length. Keeping $f_I t_d < 0.08$, as explained in [12], results in the maximal flat frequency response and guarantees that the phase margin at the cut-off frequency does not come close to possibly unstable values. For a 1 m cable the typical delay is of the order of ~ 10 ns resulting in a maximum achievable value of $f_I = 20\,\mathrm{MHz}$ [5] for systems with electronics at room-temperature.

CRYOSTAT DESIGN

A new cryostat is being developed at CERN to house the CCC monitor and allow for its integration in the AD-ring. The main requirements for this cryostat are:

- Long term operation at 4.2 K
- Annular cryostat with the inner wall of the vacuum vessel acting as the beam pipe
- Ceramic insulating rings to break the beam image current and allow magnetic coupling to the outside
- A supporting structure optimised for stiffness and mechanical resonances to minimise perturbation of the CCC
- Accessibility of the CCC without the need to break the beam vacuum

The CCC will be cooled by a liquid Helium (LHe) bath supplied by an external re-condensation unit based on a pulse tube cryocooler. The evaporated He will be circulated through the radiation shield to cool it down to an intermediate temperature of $50 - 70$ K, after which it will return into the re-condensation unit for liquefaction. This will enable stand-alone operation, with no need for periodic refills with LHe. Modern, commercially available, pulse tube cryocoolers can provide up to 1 W of cooling power at 4.2 K. Integrated re-condensing units, are slightly less efficient, providing cooling powers ranging from > 0.3 W to > 0.8 W [6]. Fig. 9 shows a longitudinal cut through the different vessels of the cryostat. The two most challenging aspects of the design are:

- The proximity of components between the CCC (ID 185 mm) and the beam pipe (OD 103 mm), where, two sets of ceramic isolator rings and associated bellows are required to prevent the flow of beam image currents.
- The design of the LHe vessel support structure which should be both stiff and have low thermal conductivity.

[5]With increased t_d the FLL bandwidth is in fact slightly increased with $f_{3dB} = 2.25 f_{I,\mathrm{max}}$ [12].

[6]Example of single cryocooler units developed by Cryomech.

ISBN 978-3-95450-141-0

Copyright © 2014 CC-BY-3.0 and by the respective authors

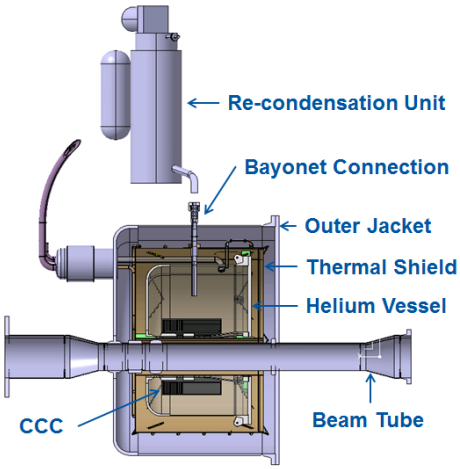


Figure 9: Cryostat longitudinal view

It has been decided to use Kevlar 49 cables rather stainless steel bars to support to LHe vessel due to Kevlar's superior heat conductivity to stiffness relationship. The known sources of mechanical perturbations originate in the cryocooler ($f < 2$ Hz) and the He compressor connected to the re-condensation unit ($f = 50$ Hz). The design of the support structure therefore tries to increase its first resonant frequency above the 50 Hz. This can be achieved by increasing the number of support cables and their diameter. However this will also increase the heat in-leak. In order to optimize the support structure, an analysis combining the structural mode frequencies and the heat load was performed as a function of the number supporting Kevlar cords and their diameter. The results are shown in Fig. 10. A

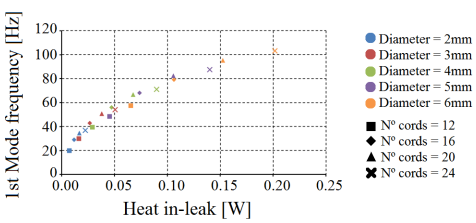


Figure 10: Frequency of the first mechanical mode versus the heat load into the 4.2 K vessel for different number of Kevlar support cables and cable diameter.

support structure with a total of 16 support cables, of 4 mm diameter was found to be a good compromise, resulting in a first mode frequency close to 60 Hz while maintaining a small heat load.

The total estimated heat load, shown in table 1, in the 4.2 K surface equals 0.422 W, corresponging to an Helium evaporation rate of 14 l/day. Modern recondensing units with a single pulse tube cryocooler can generate from > 10 l/day to > 27 l/day, depending on model and working conditions.

Table 1: Estimated Heat Load for Radiation Shield Surface (at 50 K) and LHe Vessel Surface (at 4.22 K).

	50 K [W]	**4.2 K [W]**
Kevlar supports (16×)	0.5864	0.0473
Bayonet + Safety Valve	3.6065	0.1832
Cryostat instrumentation	0.8185	0.0527
Heater wires	0.0195	0.0004
SQUID cabling	0.0162	0.1798
Total	**5.0471**	**0.4219**

CONCLUSIONS

The design and dimensioning of the main parts of a prototype CCC monitor for the AD machine at CERN has been presented. The expected performance based on theoretical analysis, as well as analysis of stability conditions required for its reliable operation, were evaluated. The conclusion is that considering all the particularities of this monitor it should be possible to construct a system for the AD-ring that meets the requirements. In addition a stand-alone cryogenic system has been designed that should allow maintenance free-operation during AD running.

This theoretical analysis of the CCC performance will provide a good basis for the benchmarking of this monitor once it is installed for beam tests in 2015.

ACKNOWLEDGMENT

The authors would like to acknowledge the work and support of Andrew Lees, Torsten Koettig and Conor Sheehan from CERN's TE-CRG group, who are providing the cryogenic system design, including the cryostat mechanical design. I would also thank Febin Kurian from GSI, Ren Geithner from Helmholtz Institute Jena and Ralf Neubert from Jena University for the fruitful discussions. Finally I acknowledge the oPAC network support which has made this work possible.

REFERENCES

[1] D. Belohrad, "Beam Charge Measurements," WEOC01, DIPAC2011 proceedings.

[2] M.F. Fernandes, "Cryogenic Current Comparator as Low Intensity Beam Current Monitor in the CERN Antiproton Decelerators," MOPF25, IBIC2013 proceedings.

[3] I.K. Harvey, Rev. Sci. Instrum. 43 (1972) 1626.

[4] A. Peters et al., "A cryogenic current comparator for the absolute measurement of nA beams," BIW98, Standford, May 1998, (p. 163), AIP conference proceedings.

[5] K. Grohmann et al., Cryogenics 16(10) (1976) 601.

[6] A. Steppke et al., "Application of LTS-SQUIDs in Nuclear Measurement Techniques," IEEE Transactions on Applied Superconductivity 19(3), p. 768 (2009).

[7] R. Geithner et al., Cryogenics 54 (2013) 16.

Copyright © 2014 CC-BY-3.0 and by the respective authors

ISBN 978-3-95450-141-0

[8] G. Durin et al., "Low temperature properties of soft magnetic materials: Magnetic viscosity and 1/f thermal noise," Journal of Applied Physics 73(10), p. 5363 (1993).

[9] S. Vitale et al., "Thermal magnetic noise in rf SQUIDS coupled to ferromagnetic cores,". Journal of Applied Physic 65(5), p. 2130 (1989).

[10] N. R. Hutzler et al., "Low temperature, high frequency permeability of Metglas 2714A and its potential for use as a core material for EMI filters," Cryogenics 47(5-6), p. 279 (2007).

[11] R. H. Koch, "Maximum theoretical bandwidth and slewrate of a dc SQUID feedback system," IEEE Transactions on Appiled Superconductivity 7(2), p. 3259 (1997).

[12] D. Drung and M. Muck, "Chapeter 4: SQUID Electronics", In: J. Clarke and A. Braginski, *The SQUID Handbook. Vol. I: Fundamentals and Technology of SQUIDS and SQUID Systems. Materials and Manufacturing Processes, (Weinheim: Wiley-VCH, 2005).*

Copyright © 2014 CC-BY-3.0 and by the respective authors

ISBN 978-3-95450-141-0

SIMULATION OF THE BEAM DUMP FOR A HIGH INTENSITY ELECTRON GUN

A. Jeff , CERN, Geneva, Switzerland & University of Liverpool, U.K.
S. Doebert, T. Lefèvre, CERN, Geneva, Switzerland
K. Pepitone, CEA, Le Barp, France

Abstract

The CLIC Drive Beam is a high-intensity pulsed electron beam. A test facility for the Drive Beam electron gun will soon be commissioned at CERN. In this contribution we outline the design of a beam dump / Faraday cup capable of resisting the beam's thermal load.

The test facility will operate initially up to 140 keV. At such low energies, the electrons are absorbed very close to the surface of the dump, leading to a large energy deposition density in this thin layer. In order not to damage the dump, the beam must be spread over a large surface. For this reason, a small-angled cone has been chosen. Simulations using geant4 have been performed to estimate the distribution of energy deposition in the dump. The heat transport both within the electron pulse and between pulses has been modelled using finite element methods to check the resistance of the dump at high repetition rates. In addition, the possibility of using a moveable dump to measure the beam profile and emittance is discussed.

INTRODUCTION

The Compact Linear Collider (CLIC) will use a novel two-beam acceleration scheme to collide electrons and positrons at up to 3TeV [1]. Energy is extracted from a very intense, lower energy Drive Beam (DB) using specially designed RF structures, and transferred to the less intense, high energy colliding beams.

In order to prove the feasibility of generating such an intense electron beam, a new test stand will be installed at CERN during 2015. Only the electron gun is to be tested, so the beam will remain unbunched and at low energy. Some relevant parameters are shown in table 1.

Table 1: Relevant Parameters for the CLIC Drive Beam Test Stand

Beam Energy	100 – 140 keV
Beam Current	4.2 A
Pulse Length	150 μs
Pulse Population	4 x 10^{15} e^-
Pulse Energy	88 J
Repetition Frequency	1 - 50 Hz
Beam Emittance	12 mm mrad
Beam size at dump	σ=2.5mm

The high beam current means that stopping the beam is not trivial. Low energy electron beams are stopped very quickly in almost all materials, so the density of energy deposition close to the surface is extremely high. Thus, a beam dump must be designed to safely absorb the beam by distributing the heat load over as large a surface as possible.

In addition, the test stand aims to demonstrate the stability of the electron gun. Both the current flatness during a pulse and the charge variation between pulses should be below 0.1%. Thus, the beam current must be measured with a resolution at least at this level.

BEAM DUMP DESIGN

The depth profiles for energy deposition by the electron gun beam in various materials are shown in figure 1, assuming that the beam is incident normal to the surface. Since the energy is deposited in a very thin layer, the energy deposition density, and therefore the temperature rise, will be very large. The integrated peak energy deposition during the pulse is shown in figure 2 for the most promising materials. It can be seen that for the nominal current, no material can survive the full pulse. Thus, the beam must be incident at a shallow angle in order to dilute the beam.

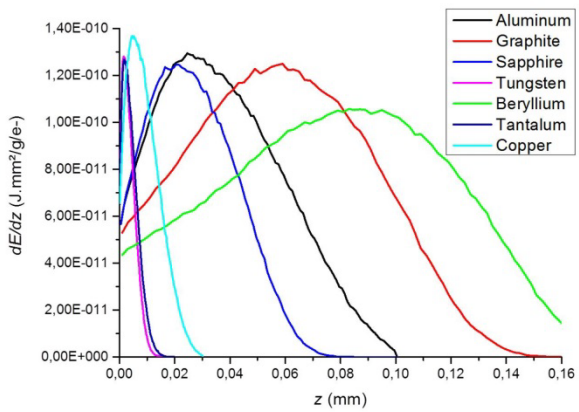


Figure 1: Energy deposition profiles for a 140 keV electron beam incident normal to the surface, for various materials, normalised to the material density.

Copyright © 2014 CC-BY-3.0 and by the respective authors

ISBN 978-3-95450-141-0

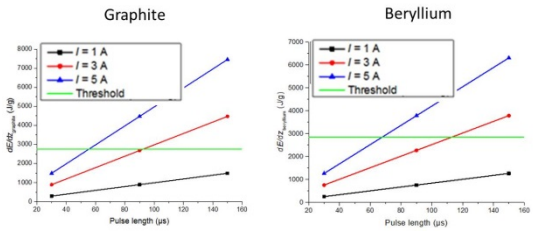


Figure 2: Integrated energy deposition during the pulse.

It can be seen that Beryllium had the best performance. However, its toxicity considerably increases the difficulty and cost of manufacture. Graphite performs almost as well and has a considerable advantage in terms of safety. Graphite is therefore retained as the material for the beam dump. The physical properties of amorphous graphite are shown in table 2.

Table 2: Physical Properties of Amorphous Graphite (at 300K where applicable) [2]

Density	1.8 g / cm^3
Specific Heat Capacity	0.76 J / g K
Thermal Conductivity	100 W / m K
Thermal Expansion Coefficient	4.0 x10^{-6} / K
Sublimation Temperature	3900 K

The high specific heat capacity, which also rises with temperature, means that graphite can accept 7.9 kJ / g before reaching its sublimation point. In reality, however, the stress caused by the sudden thermal expansion would destroy the graphite at a much lower temperature. Thermo-mechanical stress due to sudden heating ΔT is given by

$$Stress = E\ \alpha\ \Delta T\ f(\nu)$$

where E is the Young's modulus, α the coefficient of thermal expansion, and ν Poisson's ratio. The nature of $f(\nu)$ depends on whether the problem is considered in 1, 2 or 3 dimensions.

During heating some parts of the graphite feel compressive stress and other regions feel tensile stress. The graphite to be used in the dump construction has a strength of 120 MPa (compressive) and 40 MPa (tensile). However it is estimated that the repeated stress cycles will reduce the dump lifetime if the maximum stress exceeds 32 MPa [3]. This equates to a maximum single-shot temperature rise of $\Delta T \approx 1100$ K.

Despite the favourable properties shown above, the intensity of the beam is sufficiently high to destroy the graphite if it hits the surface at right angles. If the beam is incident at an angle θ to the surface, the area over which the beam is spread is increased by a factor of $1/\sin\theta$. In order to maximise this area, a small-angled cone has been chosen for the beam dump. The baseline design is shown in figure 3. A graphite cone of 12 mm thickness is mounted in a copper block. The copper is provided with water cooling in order to take away the excess heat. The cone has an open diameter of 50 mm and a length of 500mm, giving a half-angle of 2.86°.

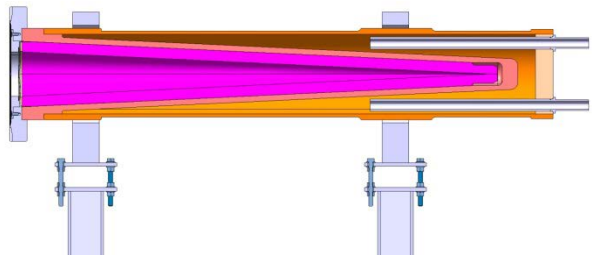


Figure 3: Design of the proposed beam dump. The inner cone is graphite, while the outer block is made of copper.

ENERGY DEPOSITION SIMULATIONS

The range of 140 keV electrons in graphite is given by the ESTAR database as 180 μm [4], calculated according to the Continuous Slowing Down Approximation (CSDA). However, this range is measured along the trajectory of the electron. Since the electron transport in this regime is dominated by multiple scattering, the penetration depth is in fact considerably smaller than the CSDA range.

Furthermore, if the electron hits the surface with a small angle, it has a large probability of being scattered out of the material as shown in figure 4. In the case of a conical dump, this does not mean that it escapes the dump but that it is re-incident in another location. The mean penetration depth is decreased, since the electron has a lower energy on its second hit. Since electrons are only being 'swapped' between different locations inside the cone, there is no spreading out effect due to backscattering, unless the beam is incident off-axis.

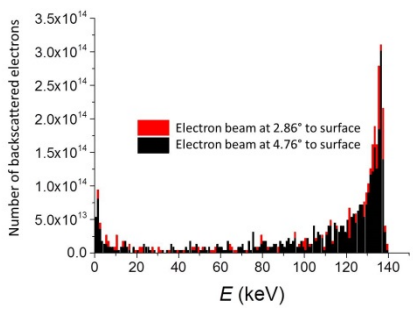


Figure 4: Energy spectrum of electrons exiting the graphite after scattering. A pulse of 4x10^{15} electrons incident at a small angle on a graphite surface was simulated.

In order to calculate the energy deposition profile, simulations have been carried out using the Geant4 code [5]. The simulations were carried out using either a gaussian or uniform circular beam, incident on-axis to a graphite cone of variable opening angle. The backscattered electrons are also tracked, so that the derived energy deposition profile includes the effect of re-incident electrons. For each event, the energy deposition is scored, its distance from the surface of the cone is calculated, and it is added to a histogram. The Geant4 step length is limited to a maximum of 1 μm in order to

ISBN 978-3-95450-141-0

Copyright © 2014 CC-BY-3.0 and by the respective authors

increase the accuracy of the profile. It can be seen from figure 5 that the effective range of the electrons strongly reduces at small angles. This is mostly due to the effect of backscattered electrons.

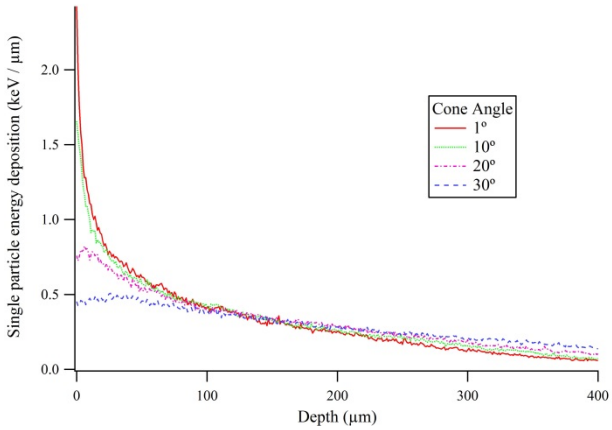


Figure 5: Energy deposition profiles for a beam of 140 keV electrons hitting a graphite cone of various angles.

The energy deposition profile is then normalised to the expected beam flux. The beam at the dump is expected to be Gaussian with a diameter (±2σ) of 10 mm. This equates to a charge density in the center of the beam of 1.5 mC / cm^2, integrating over one pulse. However, the conical surface dilutes the charge density by a factor of $1/\sin\theta$. In the baseline dump design the cone half-angle of 2.86° gives an effective charge density of 75 µC / cm^2. The dependence of the effective range on the cone angle acts in opposition to the dilution effect, giving an unexpected relationship for the peak energy deposition, as shown in figure 6. It can be seen that the worst case is for a cone of 10-20°.

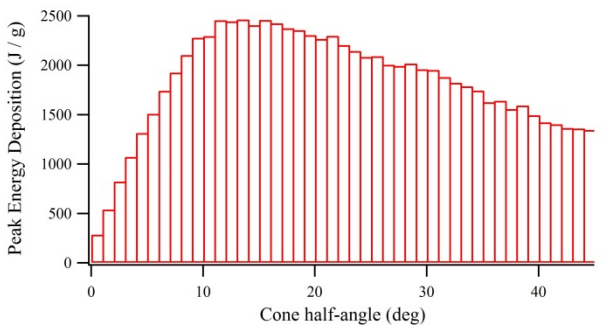


Figure 6: Peak energy deposition versus cone angle, taking account the beam parameters and the dilution effect of the angled surface.

THERMAL SIMULATIONS

The diameter of the beam is much larger than the depth over which the energy is deposited. Thus, it is possible to treat the heat transport problem as 1-dimensional, under the conservative assumption that the diffusion of heat parallel to the surface is negligible compared to that normal to the surface.

We used a simple finite element method to estimate the temperature profile of the graphite. In each time step,

1) If the beam is on, heat is deposited according to the profile computed above using geant4.

2) Heat is radiated from the first (surface) bin.

3) Heat is transported from each bin to its two neighbours according to the temperature difference between them.

The size of the bins and the timestep were chosen to be sufficiently small that the results are independent of small changes in these values. The specific heat capacity of graphite is strongly dependent on temperature (figure 7), and the temperature calculation must take this into account.

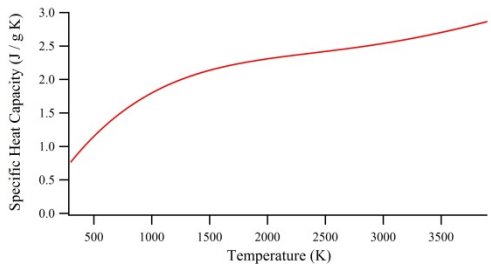


Figure 7: Specific heat capacity of graphite.

First, we look at the heat transport within the 150 µs of the beam pulse. The thermal diffusion length μ of a material is given by

$$\mu(t) = 2\sqrt{kt/C\rho} \approx 200\mu m$$

where k is the thermal conductivity, C the specific heat capacity and ρ the density [6]. Since the beam energy is deposited in a layer comparable in thickness to the diffusion length, we can predict that the heat transport will be significant even in this short time period, and will reduce the peak temperature reached. This is confirmed by the simulation as shown in figure 8.

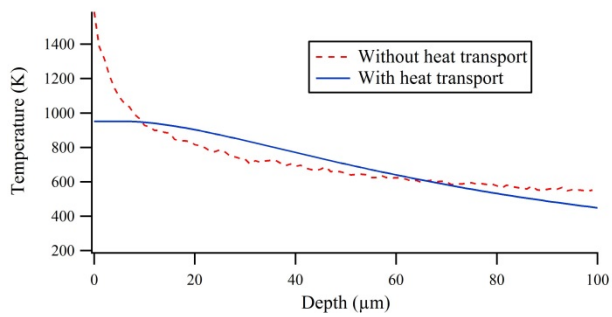


Figure 8: Temperature profile of the graphite at the end of a single beam pulse, with and without simulation of the heat transport.

Secondly, we look at the temperature evolution over several pulses. We simulate the most demanding case of operation at 50 Hz. It is necessary to make several assumptions about the transfer of heat from the graphite into the copper block. We assume that the water cooling system will be able to maintain the temperature rise in the copper block to a maximum of 50 K. At 50Hz the average power deposited by the beam is over 5 kW, so the design

Copyright © 2014 CC-BY-3.0 and by the respective authors

ISBN 978-3-95450-141-0

of the cooling system is not trivial, but it will not be discussed in this paper. With this condition, and taking a conservative value for the thermal conductivity across the graphite/copper boundary, we can see from figure 9 that the maximum temperature stabilises after a few shots.

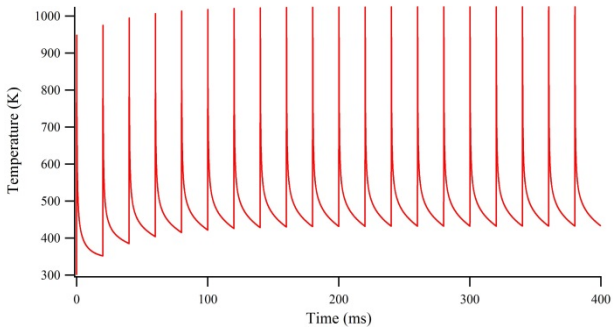


Figure 9: Peak temperature in the beam dump when exposed to the electron beam at 50Hz.

CURRENT MEASUREMENT

In order to measure the beam current, three options have been considered, and a final decision is yet to be reached.

1. Isolate the Whole Dump

In order to use the beam dump as a Faraday Cup, it must be electrically isolated. The three main points of contact are the beam pipe, the mechanical supports, and the cooling water circuit. The latter in particular is difficult from an engineering point of view. In addition, due to the considerable size of the dump, care must be taken to extract the current in such a way as to preserve the signal integrity.

2. Isolate the Graphite Plates Only

An alternative solution is to electrically isolate the graphite plates from the copper cooling block. Naturally, a good thermal contact is still required, so the insulating material must have a high thermal conductivity as well as a large electrical resistance. Shapal [7] fulfils these requirements as well as being relatively easy to machine. Its thermal properties being similar to those of graphite (see table 3) it should be possible replace the 12mm thick graphite cone with two 6mm thick nesting cones, the first of graphite and the second of Shapal, without affecting the thermal performance of the dump.

Table 3: Thermal Properties of Shapal [7]

Thermal Conductivity	90 W / m K
Thermal Expansion Coefficient	5.1 x10^{-6} / K
Maximum Temperature	2200 K

However, it is difficult to assure a good thermal contact between two large surfaces in vacuum. A large pressure must be exerted in order to maximise the thermal conduction between the two materials. By adding a layer of Shapal, we create two interfaces, graphite-Shapal and Shapal-copper, thus increasing the risk of a poor thermal contact.

3. Beam Current Transformer

Given the technical difficulties of isolating the dump, it may be more practical to separate the functions of beam dump and current measurement. In this case the dump would be preceded by a beam current transformer which would measure the current entering the dump, and the dump itself would not have to be electrically isolated.

CONCLUSION

A test stand for the electron gun of the CLIC Drive Beam will be installed at CERN. This paper presents the design of the beam dump for this high-intensity beam. No material can withstand the beam at normal incidence. Instead, a conical dump is proposed. We have shown that the dump can withstand the beam energy deposition even at the highest repetition rate of 50Hz.

ACKNOWLEDGEMENTS

Thanks to Jean-Marc Scigliuto of the CERN design office for the technical drawing of the dump.

REFERENCES

[1] M. Aicheler et al., “A Multi-TeV linear collider based on CLIC technology: CLIC Conceptual Design Report”, Geneva, 2012.
[2] Data Sheet, Ringsdorff Specialty Graphite, www.sglgroup.com (Accessed 26/08/2014).
[3] F. Carra, A. Dallocchio, “LINAC4 3MeV Test Stand : Thermo-Mechanical Fatigue Analysis of the SLIT”, Geneva, 2010.
[4] ESTAR database, NIST, physics.nist.gov/PhysRefData/Star/Text/ESTAR.html (Accessed 25/08/2014).
[5] S. Agostinelli et al., “Geant4 - a simulation toolkit”, Nucl. Instrum. Meth. A 506 (2003) 250–303.
[6] E. Marín, “Characteristic dimensions for heat transfer”, Lat. Am. J. Phys. Educ. 4 (2010).
[7] http://www.shapal.info/physicalproperties/, (Accessed 26/08/2014).

Copyright © 2014 CC-BY-3.0 and by the respective authors

ISBN 978-3-95450-141-0

A NEW INTEGRATING CURRENT TRANSFORMER FOR THE LHC

D. Belohrad, M. Krupa, P. Odier, L. Søby, CERN, Geneva, Switzerland
J. Bergoz, F. Stulle, Bergoz Instrumentation, Saint-Genis-Pouilly, France

Abstract

The existing Fast Beam Current Transformers of the LHC have been shown to exhibit both bunch length and bunch position dependency. A new Integrating Current Transformers (ICT) has therefore been developed in collaboration with Bergoz Instrumentation to address these issues. As goals a 0.1%/mm beam position dependency and 0.1% bunch length dependency were specified, along with a bandwidth of 100 MHz. This paper describes the principles of ICT operation and presents the laboratory measurement results obtained with the first prototypes at CERN.

INTRODUCTION

The present fast beam intensity measurements for the LHC rings are provided by four Fast Beam Current Transformers (FBCT), two per ring. They measure both bunch-by-bunch and total turn-by-turn beam intensities. The LHC proton bunch intensity varies from 5e9 to 1.3e11 charges with nominal bunch spacing of 25ns and up to 2808 bunches. While operational needs are covered by the present performance of the LHC FBCTs, the needs of the LHC experiments in terms of knowledge of the absolute bunch to bunch population during luminosity calibration puts more stringent demands on the intensity measurements accuracy. In addition to providing bunch by bunch intensity information, the FBCTs also send signals to the Machine Protection System (MPS), via the LHC Fast Beam Current Change Monitor (FBCCM). The FBCCM [1] calculates the magnitude of the beam intensity signal provided by the FBCT, looks for a change over specific time intervals, and triggers a beam dump interlock if losses exceed an energy-dependent threshold. The present FBCTs exhibit bunch-length and beam-position dependencies (Figure 1), which exceed the requirements for luminosity calibration and the LHC MPS. It was therefore decided to develop new intensity monitors with minimized bunch-length and beam-position dependency.

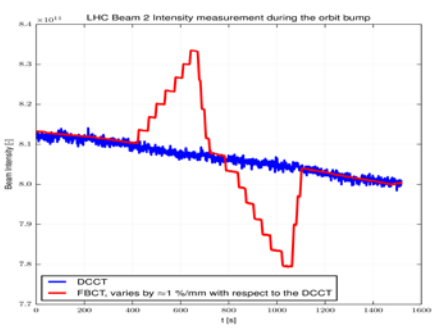


Figure 1: Beam position dependency in present LHC FBCTs with an orbit bump of ± 4mm.

PRINCIPLE OF OPERATION

The Integrating Current Transformer (ICT) and its respective read-out electronics are designed for accurate measurement of the bunch charge. To accomplish this, almost all information about the longitudinal bunch shape is sacrificed. Its working principle is based on the fact that the value of a pulse's time integral is contained in the lower end of its frequency spectrum. A precise bunch charge monitor may disregard information about the longitudinal bunch shape, which is contained in the high frequency part of the spectrum. That means, its bandwidth can be a lot narrower than the pulse spectrum.

This fundamental principle can be understood from the Fourier transform of a current pulse i(t), e.g. a particle bunch:

$$I(f) = \int_{-\infty}^{+\infty} i(t)\, e^{-i\,2\pi\, f\, t}\, dt \qquad (1)$$

For f = 0 we obtain:

$$I(0) = \int_{-\infty}^{+\infty} i(t)\, dt = q \qquad (2)$$

Eq. 2 proves that the value of the time integral of a current pulse i(t), i.e. its charge q, is carried by the DC component of the pulse spectrum. The ICT exploits exactly this principle, though reality is more complicated than this idealistic description.

A passive current transformer, including the ICT, can never transmit the DC component of the spectrum. In fact, any spectral content below the lower cut-off frequency is lost. The effect in time-domain is a droop, i.e. the signal amplitude drops with a certain time constant. To obtain a proper charge value, the integration time must be shorter than this time constant. Of course this implies that the output pulse length must be shorter than the time constant; speaking in frequency-domain terms the upper cut-off frequency must be sufficiently high.

A practical limit of the low frequency cut-off for the ICT has been chosen to be 500 Hz, which at LHC is sufficiently low for the Base Line Restitution (BLR) circuit to work correctly during batch injections of up to 288 bunches spaced by 25ns. The BLR corrects for any base line drifts before bunch integration.

Even though the information about the bunch charge is contained in the very low frequency components, the bandwidth of the ICT has to be wide enough to perform bunch-by-bunch measurements. In order to fulfil this requirement the ICT output pulse must settle at a steady baseline before the monitor is excited by the next bunch. The nominal bunch spacing in the LHC is 25 ns and a safe higher cut-off frequency of a bunch charge monitor was estimated to be in the order of 100 MHz.

Copyright © 2014 CC-BY-3.0 and by the respective authors

ISBN 978-3-95450-141-0

Limiting the upper cut-off frequency and thus neglecting higher frequency components in the beam spectrum is beneficial as the beam-position and bunch-length dependent components are mainly present in that region. Moreover, as the signal frequency increases, core permeability and magnetic coupling diminish and core losses get stronger. Spurious resonances also become more likely.

Disregarding the high frequency effects mentioned above, the ICT can be described as an ideal transformer with three windings: the beam is the primary winding, the box with the integrating capacitors is the secondary winding and the wire wound on the core is the tertiary winding, see Figure 2. The two magnetic cores of the ICT, of which only one is wound, are enclosed in a box with gap that is closed by capacitors C_2. The read-out winding is terminated by a resistor R_3.

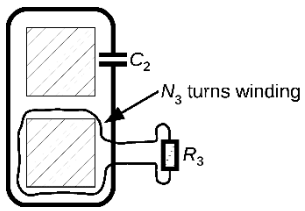


Figure 2: Cut through an ICT with an unwound core (top) and a read-out core with the read-out winding (bottom). The beam passes outside the box which encloses the cores.

Assuming that all the components of the ICT sketched in Fig. 1 are perfect and disregarding the unwound core, the voltage over the load resistor can be calculated by applying standard transformer equations:

$$U_{R3}(\omega) = -\frac{1}{N_3} I_1 \left(\frac{1}{i\,\omega\,L_3} + \frac{1}{R_3} + \frac{i\,\omega\,C_2}{N_3^2} \right)^{-1} \qquad (3)$$

where I_1 is the amplitude of an incoming harmonic current, ω is the signal angular frequency and L_3 is the inductance of the read-out winding. Eq. 3 is in fact the response of a damped parallel resonant circuit.

While this equation properly describes the basic ICT functioning, it is insufficient to describe the output waveform as seen in Figure 3. At the very least the imperfect magnetic coupling of the windings should be taken into account. This can be described by inductances in series with the windings. Although their values will be very small, they do have an important influence on the output waveform, especially on resonances.

One would arrive at the same result by adding parallel capacitors to a standard transformer output. But such a design is prone to spurious resonances and position dependence. Unwound cores and capacitors over the box gap are therefore included as they modify signal propagation from the beam to the read-out winding. They help to ameliorate imperfections.

LABORATORY MEASUREMENTS

Bergoz Instrumentation delivered two ICTs to CERN in 2013, which were then thoroughly tested prior to their installation on the LHC. They are now pending beam measurements in early 2015.

Measurement Setup

The test bench used for all measurements performed by CERN, with the exception of beam position dependency measurements, was based on a 50 Ω transmission line consisting of the LHC beam pipe with a ceramic insert, an inner conductor and conical transitions maintaining the line impedance on each end of the beam pipe. The distinct difference to the actual LHC beam pipe is the lack of a thin metallisation layer on the ceramic insert in the laboratory test bench which serves as a bypass for the high-frequency end of the beam spectrum.

The ICT was excited by bunch-like pulses from custom made avalanche generators [2]. The equivalent bunch intensity delivered was in the order of a few 1e9 protons per pulse similar to an LHC pilot bunch. Although these pulses were not Gaussian and were followed by some fast decaying reflections they were believed to be a good approximation of an LHC bunch.

For each measurement, 100 ns of the test bench input and output signals as well as the ICT output response were recorded with a 12-bit, 1 GHz analogue bandwidth oscilloscope running in the Random Interleaved Sampling (RIS) mode with an equivalent sampling rate of 125 GS/s. The pulse integration, where necessary, was performed offline [3]. A satisfying signal to noise ratio was achieved by averaging, resulting in an integration precision of the order of 0.1%.

Pulse Response and Sensitivity

The pulse response of the ICT is shown in Figure 3 for a 250 mA peak current pulse of about 500 ps (one sigma length) injected into the test bench. This corresponds to a bunch consisting of approximately 2e9 protons i.e. 320 pC of electric charge. The ICT output pulse amplitude reached 220 mV yielding an ICT sensitivity of approximately 0.7 V_{peak}/nC. For the ultimate LHC bunch of 3e11 protons the ICT is therefore expected to output pulses with amplitudes exceeding 30 V.

The main output pulse is 7 ns long and followed by damped oscillations lasting some 25 ns. It was attempted to reduce the oscillations by applying different reflective and absorptive filters but no better results could be achieved.

The ICT was designed to perform precise bunch by bunch intensity measurements in the LHC where the nominal bunch spacing is 25 ns. Therefore the amount of charge leaking into the next bunch slot had to be measured and is shown in Figure 4. These integrals were obtained from the data seen in Figure 3.

Copyright © 2014 CC-BY-3.0 and by the respective authors

ISBN 978-3-95450-141-0

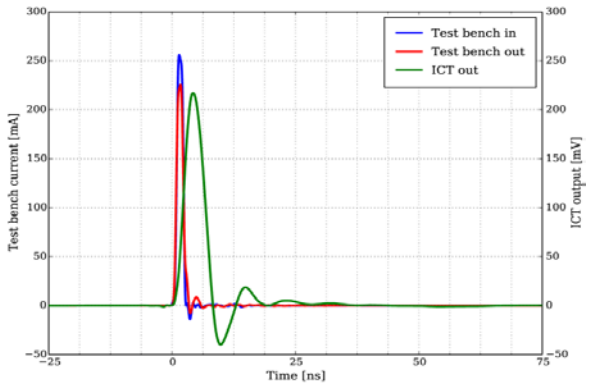


Figure 3: Time response of the ICT to an LHC bunch-like pulse.

The numbers on the top of each graph show how much of the total charge has been accumulated when looking at the first three 25 ns bunch slots. During laboratory evaluation the ICT was demonstrated to confine 98.6% of the total pulse integral within the first 25 ns slot, with the output pulse integral at 100% after 60 ns. This means that there is an influence on the two bunch slots following the main bunch slot. Nevertheless, it must be noted that the charge leakage is deterministic and can be accounted for in signal the processing.

The bandwidth of the ICT was measured to span over five decades up to 100 MHz. The lower cut-off frequency is at around 550 Hz, which translates into a droop of 0.35%/µs.

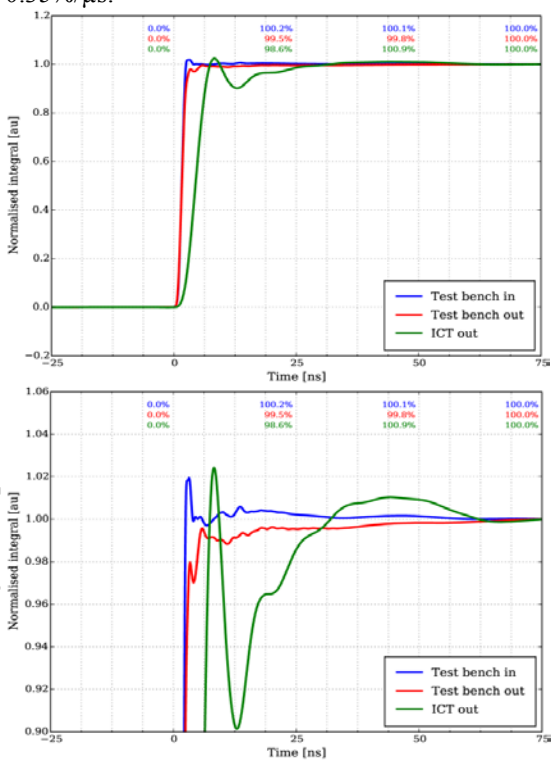


Figure 4: Normalised time integral of the ICT output pulse, with a zoom in to the region of interest in the lower plot.

Beam Position Dependency

In order to study the beam position dependency of the ICT a non-coaxial test bench of similar dimensions as the LHC beam pipe was designed and assembled at CERN. The inner conductor of the 300 Ω transmission line was off-centred by 7 mm which translated to about 20% of the beam pipe radius. The line was matched to 50 Ω on either end to minimise possible reflections. The test bench was evaluated to provide viable results up to a few 100 MHz.

To simplify the measurements the ICT orientation was fixed. The beam position dependency of the monitor was measured by radially displacing the inner conductor with respect to the monitor. This was done by rotating the antenna azimuthally in steps of 30 degrees. The signals of interest were integrated over 100 ns to account for any possible charge leakage into the following bunch slots.

The results seen in Figure 5, shows that the ICT exhibits no quantifiable beam position dependency down to the 0.1% level, the limit given by the measurement set-up, for radial displacements of up to 7mm. From Figure 5, it can also be seen that when rotating the antenna the transmission in the antenna changes, due to imperfect impedance matching.

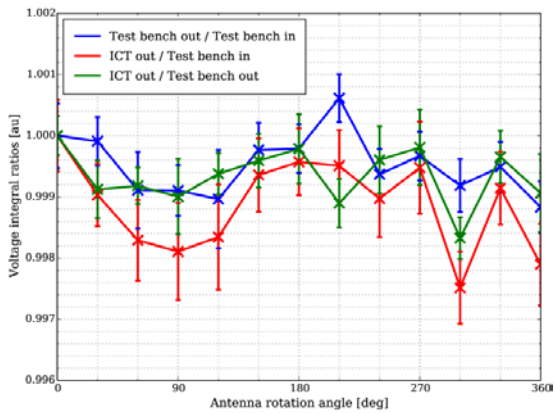


Figure 5: Measured beam position dependency.

Bunch Length Dependency

The avalanche generators used to test the system allowed the standard deviation of the pulse to be controlled with a resolution of about 50 ps. However, since they maintained their amplitude, the total pulse charge was different for each measured bunch length. Hence, in order to estimate the ICT bunch length dependency, the ratio of the ICT output integral to the transmission line output integral was computed for each tested bunch length. Similarly to the beam position dependency measurements, both integrals were obtained over 100 ns.

Pulses with standard deviations of approximately 250, 300, 350 and 500 ps were generated as input to the coaxial setup. These values were chosen to simulate the typical range of LHC bunch lengths, which during normal operation have an RMS bunch length in the order 300 ps.

The ratio of the integrals remained constant over this entire range down to the 0.1% accuracy given by the test

Copyright © 2014 CC-BY-3.0 and by the respective authors

ISBN 978-3-95450-141-0

set-up. In addition, the percentage of electric charge contained within the first 25 ns of the ICT output pulse was not observed to be influenced by the pulse length. The charge leakage into the following bunch slots is therefore believed to be independent of the bunch length.

CONCLUSIONS AND OUTLOOK

Two ICTs manufactured by Bergoz Instrumentation were installed in the LHC in June 2014, and are pending measurements with beam by beginning of 2015. The new design, which has been optimized to reduce beam position and bunch length dependency on the measured intensities, is based on filtering frequencies above 100 MHz before the signal reaches the magnetic readout toroid. Laboratory tests have shown very promising results, with less than 0.1%/mm beam position dependency, and 0.1% bunch length dependency. The charge leakage from one bunch slot to the next is slightly higher than desired and will need to be corrected for.

ACKNOWLEDGMENT

The authors would like to thank M. Gasior for his input to the discussions and his invaluable help in the design of the test circuit.

REFERENCES

[1] J. Belleman, D. Belohrad, L. Jensen, M. Krupa, A. Topaloudis, “The LHC Fast Beam Current Change Monitor”, WEPF29, IBIC 2013, Oxford, UK, Sept 2013.
[2] M. Krupa and M. Gasior “Application of Avalanche Generators in Laboratory Measurements”, MIXDES 2014, Lublin, Poland, June 2014, http://www.mixdes.org
[3] M. Krupa and M. Gasior “Precise Digital Integration of Fast Analogue Signals Using a 12-bit Oscilloscope”, IBIC 2014, these proceedings.

Copyright © 2014 CC-BY-3.0 and by the respective authors

ISBN 978-3-95450-141-0

OPTIMIZATION OF A SHORT FARADAY CUP FOR LOW-ENERGY IONS USING NUMERICAL SIMULATIONS*

A. Sosa†, E. Bravin, E. D. Cantero, CERN, Geneva, Switzerland
C. P. Welsch, Cockcroft Institute, Warrington, Cheshire,
The University of Liverpool, Liverpool, United Kingdom

Abstract

ISOLDE, the heavy-ion facility at CERN is undergoing a major upgrade with the installation of a superconducting LINAC that will allow post-acceleration of ion beams up to 10 MeV/u. In this framework, customized beam diagnostics are being developed in order to fulfil the design requirements as well as to fit in the compact diagnostic boxes foreseen. The main detector of this system is a compact Faraday cup that will measure beam intensities in the range of 1 pA to 1 nA. In this contribution, simulation results of electrostatic fields and particle tracking are detailed for different Faraday cup prototypes taking into account the energy spectrum and angle of emission of the ion-induced secondary electrons.

INTRODUCTION

The High Intensity and Energy (HIE) upgrade of the Isotope On-Line DEvice (ISOLDE) facility at CERN aims to increase the energy and intensity of the radioactive ion beams currently available on site. From the beam energy standpoint, an increase from the present 3 MeV/u to 10 MeV/u is foreseen for ions with a mass-to-charge ratio of A/Q≤4.5. The present room-temperature LINAC (known as REX) will be replaced with a superconducting LINAC with up to six cryomodules containing a total of 32 Nb-sputtered quarter-wave resonators [1]. All beam diagnostic devices will be installed in purpose-built diagnostic boxes, located in every inter-cryomodule region and along designated points in the High Energy Beam Transfer lines (HEBTs). A total of 15 diagnostic boxes (seven in the LINAC and eight in the HEBT) are required for the complete upgrade. The number and type of diagnostic devices in each box is different depending on the location in the accelerator. Beam intensity, transverse beam profile and beam position can be measured at each diagnostic box location. Other devices available in some boxes include a silicon detector, sets of collimators, beam attenuators and stripping foils.

COMPACT FARADAY CUP

Faraday cups are well known devices with a simple and reliable technique for measuring absolute beam intensities, but optimizing a Faraday cup for a specific set of beam parameters, especially with low-intensity ion beams remains challenging [2]. The Faraday cup used in the current REX-ISOLDE LINAC has been redesigned into a much shorter version in order to fit in the short (58 mm long) diagnostic boxes of HIE-ISOLDE. The Faraday cup to be used in HIE-ISOLDE should be 30 mm in diameter to cover the full beam aperture (max. beam sizes in HIE-ISOLDE are 1σ=5 mm). The initial prototype (Prototype 1), shown in Fig. 1(a), is just a rescale of the original design and has a repeller ring and ground ring measuring 1.5 mm in length, and a 2.5 mm thick collector electrode, the whole enclosed in a metallic housing. The collector electrode and repeller ring of the first prototype are made of stainless steel (AISI 316L [3]), the body is made of aluminium (6082) and the insulators are made of VESPEL© SP-1 [4].

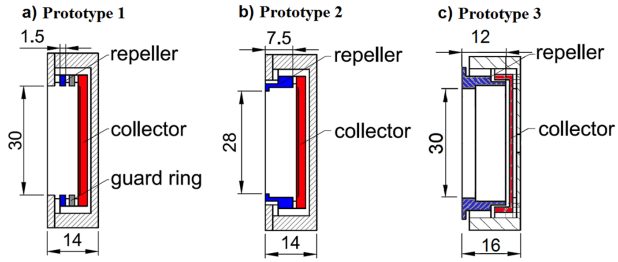


Figure 1: Schematic of the different Faraday cup prototypes developed for HIE-ISOLDE.

ELECTROSTATIC SIMULATIONS

Numerical simulations have been done in order to assess the design of the cups, analysing the electrostatic potential distribution and the secondary electron emission. CST Particle Studio [5] was used to study the electrostatic fields and track secondary electrons in these cups. When the repeller ring is biased at a given voltage, the electrostatic potential in the central axis of the Faraday cup varies according to the length and inner diameter of the repeller ring. The electrostatic potential is a maximum on the surface of the repeller ring and has a minimum value in the centre of the cup, corresponding to the beam axis.

In Fig. 2 the potential distribution for the initial HIE-ISOLDE Faraday cup prototype biased at -60 V is shown. The compact geometry of the FC results in only -5 V in the centre when the repeller ring is biased to a voltage of -60 V. As this repeller voltage is insufficient to contain

*This project has received funding from the European Union's Seventh Framework Programme for research, technological development and demonstration under grant agreement no 264330.

† alejandro.garcia.sosa@cern.ch

Copyright © 2014 CC-BY-3.0 and by the respective authors

ISBN 978-3-95450-141-0

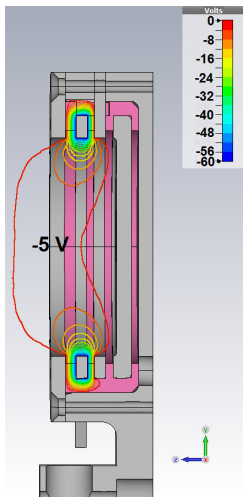


Figure 2: Electrostatic potential distribution for the Prototype 1 Faraday cup biased at -60 V.

secondary electron emission, a modification of the existing Faraday cup was done to test the effect of a longer repeller ring, resulting in Prototype 2.

Prototype 2 is composed of a 7.5 mm repeller ring, with the aim of increasing the potential in the centre of the cup, and a reduced aperture of 28 mm at the cost of measuring a smaller maximum beam size. Its potential distribution biased at -60 V (Fig. 3) shows an increased potential in the cup's centre of -22 V. In this cup the guard ring was removed because of the limited space available.

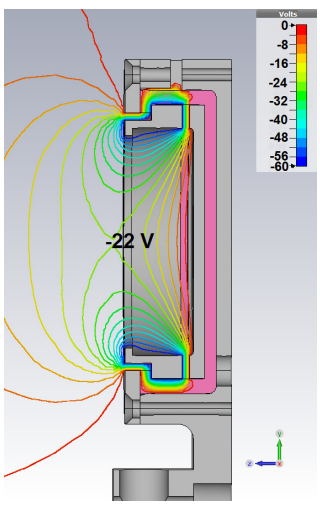


Figure 3: Electrostatic potential distribution for the Prototype 2 Faraday cup biased at -60V.

Taking advantage of the maximum length available for the Faraday cup inside the diagnostics box (16 mm) and going in the same direction of increasing the length of the repeller ring, as well as redesigning and optimizing all other parts, Prototype 3 was built.

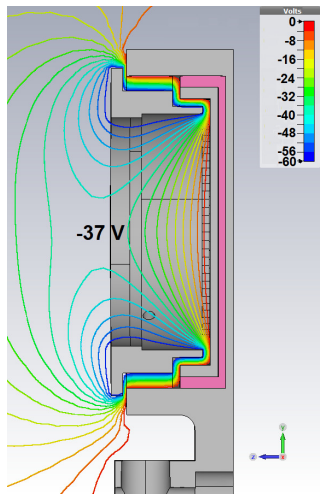


Figure 4: Electrostatic potential distribution for the Prototype 3 Faraday cup biased at -60 V.

Prototype 3 has a 12 mm repeller ring and covers the full 30 mm beam aperture. The thickness of the collector electrode, insulator and back of the FC body is 1 mm. As shown in Fig. 4, biasing the repeller ring at -60 V the potential barrier in this design is -37 V, well beyond the typical energy peak of secondary electron emission (<20 eV) [6].

PARTICLE TRACKING & LOSS PROBABILITY

Particle tracking simulations using CST were run to study the charge loss probability of the different Faraday cup prototypes when emitting electrons at different emission energies and angles from a beam-sized surface centred on the collector electrode. Loss probability was defined as the percentage of secondary electrons escaping the collector electrode over the total amount of secondary electrons emitted from the collector surface. In all simulations, 10^4 electrons were emitted simultaneously from a circular surface source of 3 mm in diameter facing the aperture of the Faraday cup, as the critical area for the escape of electrons is precisely the centre of the cup. It is not possible to simulate ion-induced electron emission, hence the use of the electron source in the cup.

The loss probability values for each Faraday cup prototype were obtained by counting the number of electrons that do not return to the collector electrode and dividing this by the total number of electrons emitted. This was performed for many different configurations, sweeping the electron emission energy (0 to 500 eV) and the repeller ring voltage (0 to -500 V) for several electron emission angle cones (0°, 45° and 90°) relative to the beam axis. Electrons are emitted in random angles within that cone, but not necessarily isotropically. Very few previous studies exist about ion-induced electron emission for this particular projectile-target combination and energy range. However,

Copyright © 2014 CC-BY-3.0 and by the respective authors

ISBN 978-3-95450-141-0

similar studies suggest that the angular distribution of the emitted electrons follows a cosine law [7].

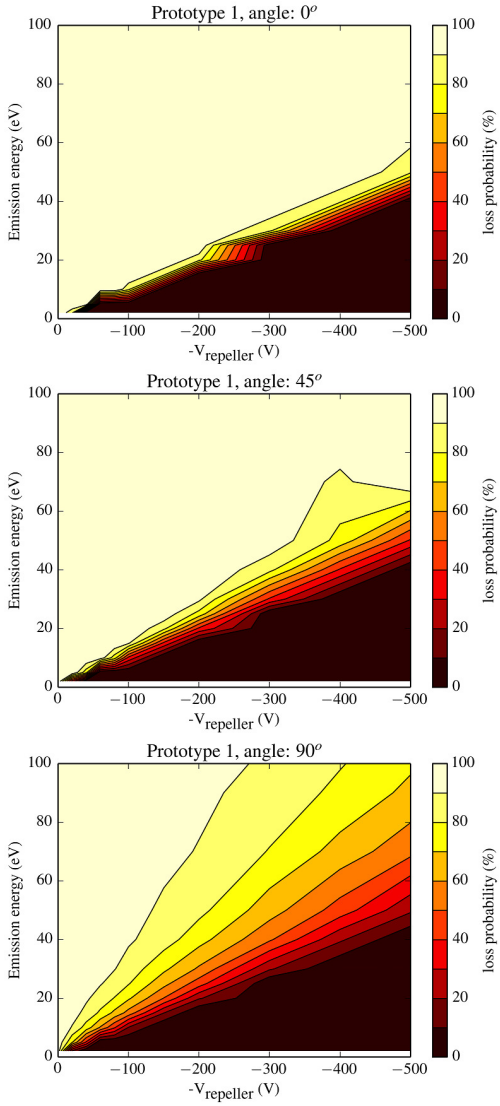


Figure 5: Loss probability of Prototype 1 at different emission energies, repeller ring voltages and maximum emission angle cones of 0°, 45° and 90°.

SIMULATION RESULTS

Prototype 1

In the case of Prototype 1 (see Fig. 5), the loss probability is 100% at an emission energy of 20 eV and 0° emission angle. Even biasing the repeller ring at voltages up to -100 V the loss probability only decreases to about 80% in the case of an emission angle cone of 90°. This would lead to false beam intensity measurements in the FC, making the device inaccurate.

Prototype 2

The design of Prototype 2 greatly improves the retention of electrons in the collector. As shown in Fig. 6, all electrons emitted at 20 eV would be retained by the cup at voltages beyond -100 V for all emission angles. In the case of a 90° emission angle, distortions in the general behaviour may be due to secondary electron emission in other metal parts of the FC such as the repeller ring.

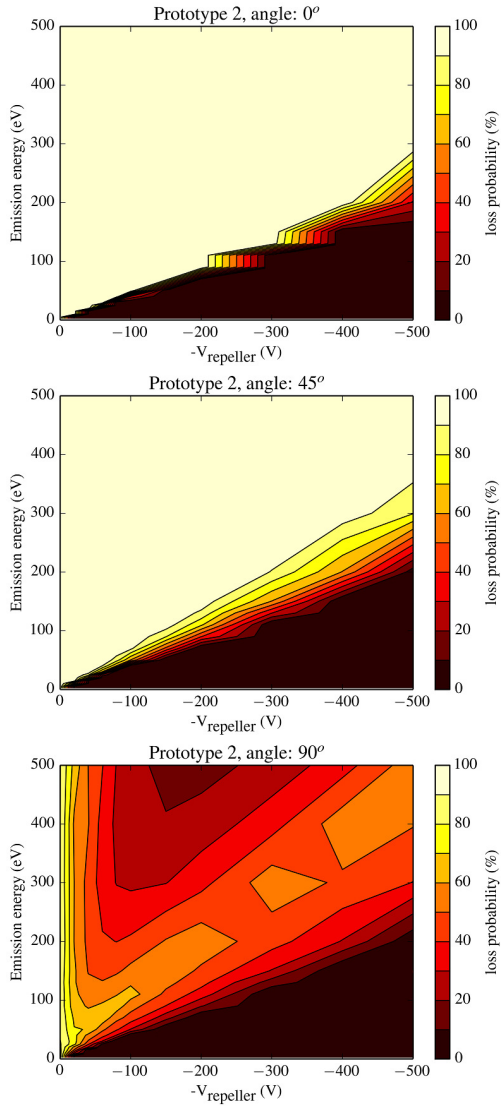


Figure 6: Loss probability of Prototype 2 at different emission energies, repeller ring voltages and maximum emission angles of 0°, 45° and 90°.

Prototype 3

The simulation results for Prototype 3, shown in Fig. 7, indicate a 0% loss probability at lower voltages compared to Prototype 2. The geometry of Prototype 3 also shows 0% loss probability at -500 V in the case of electrons with an emission energy up to 300 eV.

CONCLUSIONS & OUTLOOK

A short Faraday cup has been developed at CERN to measure low-energy ion beam intensities and, when used

Copyright © 2014 CC-BY-3.0 and by the respective authors

ISBN 978-3-95450-141-0

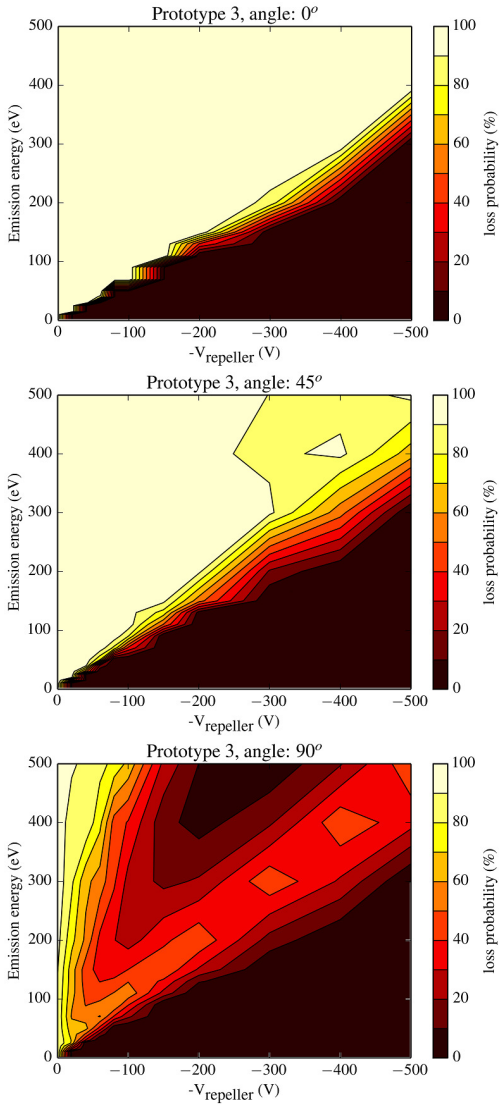


Figure 7: Loss probability of Prototype 3 at different emission energies, repeller ring voltages and maximum emission angles of 0°, 45° and 90°.

together with the slit scanner, the transverse beam profile and position. This is the main beam instrumentation system for the HIE-ISOLDE project. An extension of the repeller ring in the longitudinal direction has been shown to eliminate the loss of secondary electrons from the Faraday cup even for relatively low bias voltages. All prototypes discussed in this contribution have been built and tested using ion beams with a mass-to-charge ratio A/q≤4.5. Further work on estimating the electron yield and their energy spectrum for this particular target-projectile combination is in progress.

ACKNOWLEDGEMENTS

The authors would like to thank the technical staff from the beam instrumentation group at CERN for their support and help throughout this development project.

REFERENCES

[1] Sosa, A., Fraser, M. A., Kadi, Y., Welsch, C. P., Galipienzo, J., Bravin, E., ... & Larman, A. (2012, May). Beam instrumentation for the HIE Isolde linac at CERN. In Conf. Proc. (Vol. 1205201, No. CERN-ATS-2012-091, p. MOPPR048).

[2] Harasimowicz, J., Welsch, C. P., Cosentino, L., Pappalardo, A., & Finocchiaro, P. (2012). Beam diagnostics for low energy beams. Physical Review Special Topics-Accelerators and Beams, 15(12), 122801.

[3] American Iron and Steel Institute: http://www.steel.org/

[4] Vespel parts and shapes, DUPONT: http://www.dupont.com/products-and-services/plastics-polymers-resins/parts-shapes/brands/vespel-polyimide.html

[5] CST Particle Studio, http://www.cst.com/Content/Products/PS/Overview.aspx

[6] Hasselkamp, D., Hippler, S., & Scharmann, A. (1986). Ion-induced secondary electron spectra from clean metal surfaces. Nuclear Instruments and Methods in Physics Research Section B: Beam Interactions with Materials and Atoms, 18(1), 561-565.

[7] Hasselkamp, D. (1992). Kinetic electron emission from solid surfaces under ion bombardment. In Particle Induced Electron Emission II (pp. 1-95). Springer Berlin Heidelberg.

Copyright © 2014 CC-BY-3.0 and by the respective authors

ISBN 978-3-95450-141-0

DOSIMETRY OF PULSED BEAMS IN PROTON THERAPY

J. Van de Walle, Y. Claereboudt, G. Krier, D. Prieels, IBA, Louvain-la-Neuve, Belgium
G. Boissonnat, J. Colin, J.-M. Fontbonne, LPC, Caen, France

Abstract

In the proton therapy system ProteusONE™ by Ion Beam Applications, the superconducting synchro-cyclotron provides intense proton pulses of 230 MeV in 10μs and with a repetition rate of 1 kHz. In these conditions, the large gap (few mm's) air-filled ionization chambers at the exit of the proton gantry suffer from recombination losses. Since these ionization chambers are crucial to control the dose delivered to the patient, these recombination losses have to quantified pulse-by-pulse. The concept of an "asymmetrical ionization chamber" has been introduced at the exit of the gantry to be able to do this.

INTRODUCTION

In order to reduce the cost of proton therapy systems, Ion Beam Applications has developed in recent years the ProteusONE™ system, which consists of a compact superconducting synchro-cyclotron (S2C2) [1] and a compact, iso-centric rotating gantry [2], which rotates 220 degrees around the patient. A layout of this gantry is shown in Figure 1. The S2C2 delivers a pulsed proton beam at 230 MeV with a repetition rate of 1kHz and a pulse duration of 10 μs. The concept of pulsed beam is ideally suited for Pencil Beam Scanning (PBS), a technique by which the tumor volume is scanned with a fixed size (typically 3 mm) proton beam with varying energy and intensity per irradiated voxel. The proton charge in each pulse in PBS treatments has to be measured with high precision.

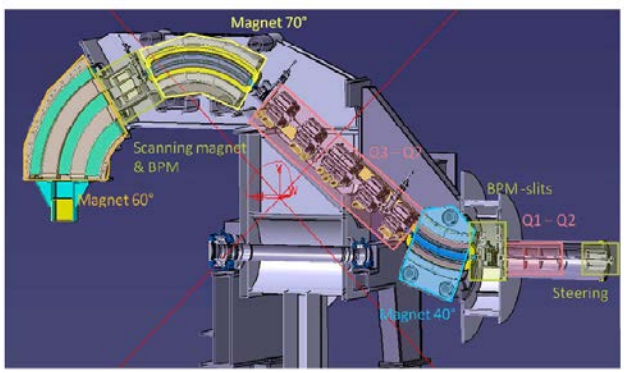


Figure 1 : Layout of the ProteusONE™ compact gantry. The ionization chambers are located at the exit of gantry, after the 60° magnet.

Air-filled ionization chambers (IC's) are used at the exit of the rotating gantry, with a typical surface area of 200x300 mm^2 and gap sizes of a few mm. This large surface area is needed to cover the full irradiation area. The charge collection times in these IC's is typically a few hundred μs, much more than the proton pulse of 10 μs. Recombination losses of the created electron-ion pairs in the air-filled IC's cannot be avoided with the pulse intensities needed to irradiate a tumor volume, which can go as high as 10 pC/pulse. To ensure an accurate measurement of the pulse intensity in PBS, these recombination losses have to be quantified on a pulse-by-pulse base. The concept of an "asymmetric ionization chamber" (AIC) has been introduced at the gantry exit to enable this.

THE ASYMMETRIC IONIZATION CHAMBER (AIC)

A schematic layout of the asymmetric ionization chamber (AIC) is shown in Figure 2. It consists of two ionization chambers with different gap sizes, d_1 and d_2. One such ionization chamber is in itself divided in two parts : the grounding foil is placed in between two high voltage foils and the detector signal is read from this grounding foil. For recombination calculations, only a distance d_1 has to be considered, the gain of ICi (i=1,2) in Figure 2 is given by :

$$G_i = \frac{2 d_i S \rho}{W}$$

where S is the stopping power of protons for a given energy, ρ is the density of air in the IC and W is the ionization potential of air. The measured charge in ICi ($Q_{det,i}$) is given by :

$$Q_{det,i} = G_i Q_{IN} \varepsilon_i$$

where Q_{IN} is the incident proton charge, which is the quantity of interest and ε_i is the efficiency of ICi, which is determined by recombination losses in the air-filled IC. The ratio of the two measured charges ($Q_{det,}$) is given by

$$R = \frac{Q_{det,1}}{Q_{det,2}} = \frac{d_1}{d_2}\frac{\varepsilon_1}{\varepsilon_2} = R_0 \frac{\varepsilon_1}{\varepsilon_2} \quad (1)$$

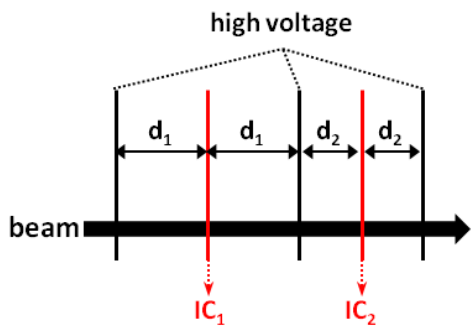


Figure 2 : Schematic layout of the asymmetric ionization chamber. It consists of two ionization chambers with different gap sizes (d1 and d2).

Copyright © 2014 CC-BY-3.0 and by the respective authors

ISBN 978-3-95450-141-0

where R_0 is the ratio of the gap sizes. From Eq. (1) it is clear that the ratio of detected charges equals the ratio of the gap sizes of the two IC's, in case recombination losses are negligible. If recombination losses are non-negligible, this ratio will be lower ($R<R_0$). A theoretical description of recombination losses for pulsed radiation in air filled ionization chambers can be found in [3]. Here, the expression for the theoretical efficiency of an IC will be given as :

$$\varepsilon_i = p_i + \frac{1}{u_i}\ln[1 + (1 - p_i)u_i] \quad (2)$$

where p_i is the free electron fraction in ICi and depends on the applied high voltage and the gap size. More details and a parameterization of this free electron fraction can be found in [4]. The parameter u_i is given by :

$$u_i = \frac{\mu d_i^2 r}{V} \quad (3)$$

where V is the applied voltage, μ is a constant (see [3] for details) and r is the charge density of positive ions liberated per radiation pulse. The relation between the parameters u_1 and u_2 for one radiation pulse is just simply

$$u_1 = u_2\, d_1^2/d_2^2 \quad (4)$$

The principle point of the AIC is that the measured ratio of charges (R in Eq. (1)) has a direct link to the parameter u_i which appears in Eq. (2). The exact knowledge of the quantities μ and r in Eq. (3) is thus not needed. This is very important, since the charge density r depends strongly on the details of the beam spot size and intensity, which varies during proton beam treatments. The relation between the ratio of detected charges R, the parameter u_i for one specific IC (in this case u_1) and the efficiency of this IC is illustrated in Figure 3 for the case of an AIC with d_1=4.97 mm and d_2=2.92 mm.

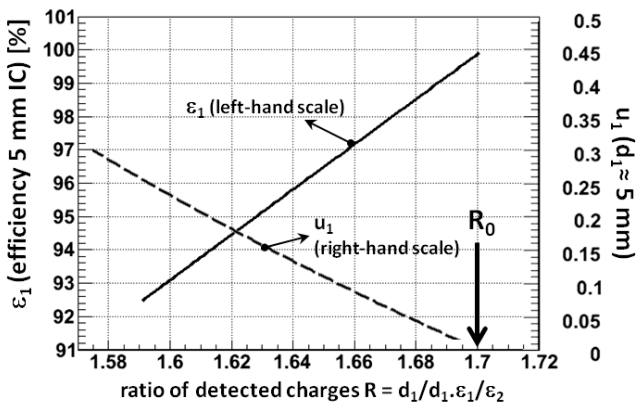


Figure 3 : relation between the ratio of detected charges in an AIC, the efficiency of a specific IC and the parameter "u" for this IC. In this case the (measured) gap sizes for the AIC are : d_1=4.97 mm and d_2=2.92 mm.

From Figure 3 it can be seen that a linear relation exists between the efficiency of the IC's and the ratio of detected charges. An approximate expression of the efficiency can thus be written as :

$$\varepsilon_i' = 1 - CF_i\left[1 - \frac{R}{R_0}\right] \quad (5)$$

where the constant CF_i is given by :

$$CF_i = \left\langle \frac{(1-\varepsilon_i)}{1-\frac{\varepsilon_1}{\varepsilon_2}} \right\rangle \quad (6)$$

The brackets indicate that the average is taken over the relevant measurement range for the AIC. This range is given by the minimum ratio which is expected for a typical treatment sequence (varying pulse intensities and energies). For example, if one considers the AIC from Figure 3 and the minimum measured ratio would be 1.6, the corresponding range of u_1-values will be 0 to 0.23. The efficiencies appearing in Eq. (6) are calculated with Eq. (2) using u-values in the range specified above. Eq. (3) provides the possibility to deduce the efficiency of the IC's from the ratio of measured charges in both IC's, comprising the AIC.

EXPERIMENTS AND RESULTS

A series of experiments was performed to check the validity of the approximate expression for the efficiencies of the IC's (Eq. (5)).

Three experiments are described below. The first two experiments were conducted with a 228 MeV proton beam from the Cyclone™ 230. In order to obtain a pulsed proton beam with a pulse duration much lower than the collection time of ions in the few mm IC's (typically few

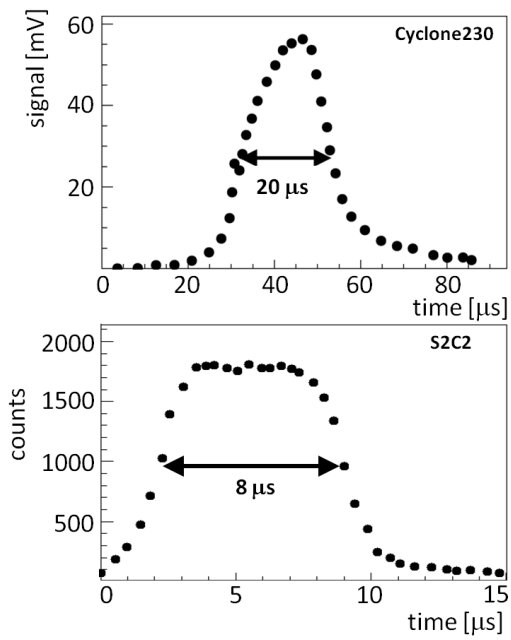


Figure 4 : measured time profile of the proton beam pulse from the Cyclone™ 230 with pulsed RF.

ISBN 978-3-95450-141-0

Copyright © 2014 CC-BY-3.0 and by the respective authors

100 μs), the RF of the cyclotron was pulsed and a beam pulse of about 20 μs was obtained. The last experiment was conducted with the prototype S2C2, which provides intrinsically a pulsed beam at 1 kHz and with a beam pulse duration of around 10 μs. Pulse time profiles obtained with both accelerators are shown in Figure 4.

Nitrogen Filled AIC

In the first experiment, the AIC was flushed with nitrogen (N_2) gas. Since N_2 is a non-electronegative gas, the electrons liberated during the ionization process do not get attached to ions during their drift towards the electrode (the free electron fraction in Eq. (2) is 1) and the efficiency is expected to be 100%. This hypothesis was tested as a function of applied high voltage, beam intensity and beam spot size. The gap sizes of the N_2 filled AIC were 4.98 mm and 4.05 mm. In case both IC's are 100% efficient, the ratio of detected charges should be 1.23. The results are shown in Figure 5.

Only for a 2 mm (1-σ Gaussian) beam spot and low high voltages the efficiency of N_2 filled IC's drops below 100%. Ongoing studies confirm this observation from first principles and this drop in collection efficiency is attributed to space charge effects.

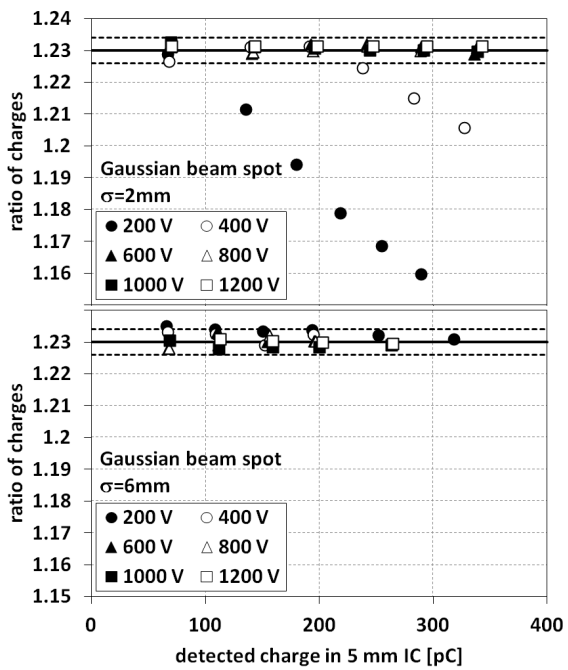


Figure 5 : the ratio of detected charges in the nitrogen filled AIC (d_1=4.98 mm, d_2=4.05 mm) as a function of increasing pulse intensity and for different voltages for a Gaussian beam spot with 1-sigma size of 2 mm (top) and 6 mm (bottom).

Air Filled AIC

In a second experiment, the efficiency of an air-filled AIC was measured as function of the incident proton bunch intensity. This was done by a stack of 2 AIC's, where the first AIC was filled with air and the second AIC was flushed with N_2. A sketch of the setup is shown in the top part of Figure 6. On both AIC's a high voltage of 1.2 kV was applied and the beam spot size was 2 mm. The N_2 filled AIC was used to determine the incoming proton pulse intensity, since this AIC is 100% efficient. The exact gap sizes of the N_2 filled AIC were d_1=4.93 mm and d_2=2.96 mm (providing a ratio R_0 of 1.67) and for the air filled AIC d_1=5.07 mm and d_2=2.96 mm (providing a ratio R_0 of 1.71). The ratio of detected charges in both the air- and N_2-filled AIC's is shown with the open symbols in the top part of Figure 6. In the N_2-filled AIC, the ratio is constant and equal to R_0, as expected from a 100% efficient IC, whereas the ratio drops in the air filled AIC with increasing pulse intensity.

The efficiency of the 3 mm and 5 mm IC in the air-filled AIC was obtained by dividing the measured charges in both IC's by their gain and by the incoming charges as detected by the N_2-filled AIC. These efficiencies are shown in the middle part of Figure 6 as a function of incident proton charge per pulse. The full lines represent

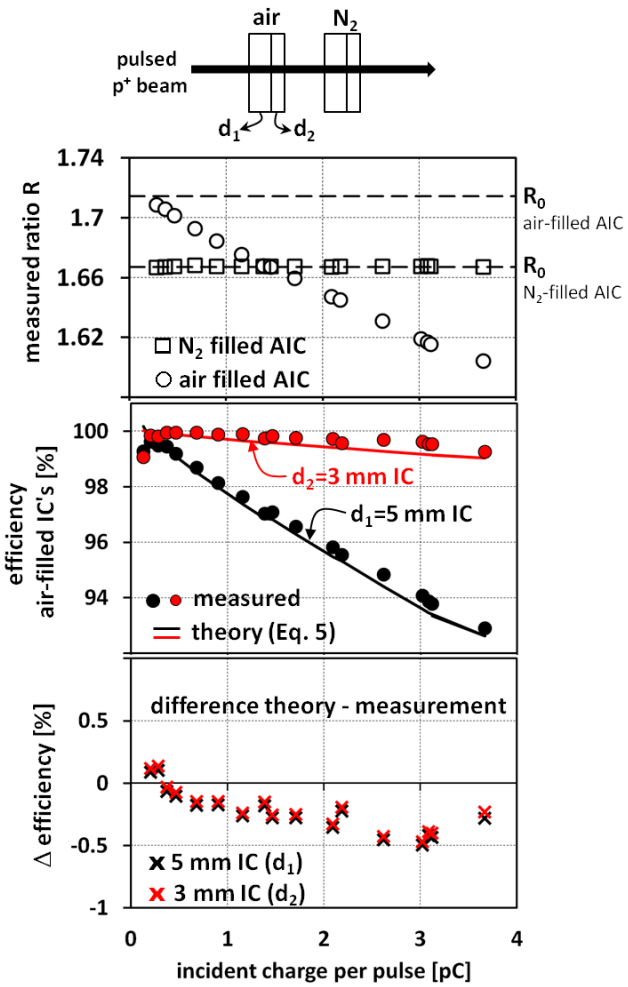


Figure 6 : (top) measured charge ratios in the air- and N_2 filled AIC. (middle) experimental efficiencies (dots) for both IC's (3 mm and 5 mm) in the air-filled AIC. The approximate efficiencies from Eq. (5) are shown with the full lines. (bottom) the difference between measured and approximated efficiencies from Eq. (5).

Copyright © 2014 CC-BY-3.0 and by the respective authors

ISBN 978-3-95450-141-0

the approximate efficiencies obtained from Eq. (5), only utilizing the detected ratio and the constant factors CF_1=1.14 and CF_2=0.15, which were calculated with Eq. (6). The averaging in Eq. (6) was done over the range where the ratio given by Eq. (1) remains above the experimentally observed minimum ratio (R = 1.6, see top part of Figure 6).

The crosses in the bottom part of Figure 6 indicate the differences between the measured efficiencies and the approximate efficiencies of the 3 and 5 mm IC's comprising the air-filled AIC. An accuracy better than 0.5% is obtained.

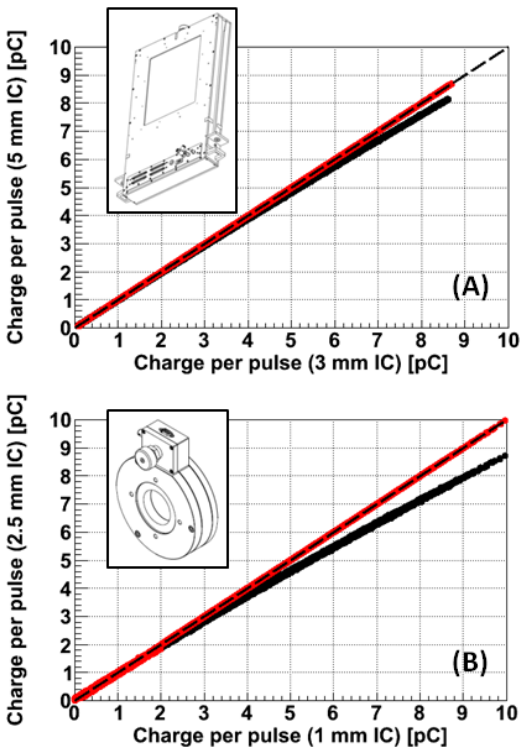


Figure 7 : Measured charge per pulse in the largest gap IC versus the measured charge per pulse in the smallest gap IC before (black) and after (red) a correction was applied for the approximate efficiency (Eq. 3).

In a last experiment, a large area (600 cm^2) air-filled AIC with gap sizes of d_1=5.07 mm and d_2=2.96 mm was tested in pulsed beam from the prototype S2C2. At the same time, a small area (60 cm^2) AIC with gap sizes d_1=2.48 mm and d_2=0.86 mm was tested. Both AIC's are shown in the insets in Figure 7. The latter AIC will be used at the exit of the S2C2 to measure the exit pulse charge from the accelerator prior to injection to the gantry. The high voltage on this AIC is 400 V. This lower voltage will lower drastically the efficiency of the largest gap IC and this AIC is thus a good candidate to test the validity of the Eq. (5).

Figure 7 shows the measured charge per pulse (measured charge divided by the gain of the IC) of the largest gap IC versus the smallest gap IC for both AIC's. The top figure shows this for the 5 mm IC versus the 3 mm IC and the bottom figure for the 2.5 and 1 mm IC. It is clear that for increasing pulse intensity, recombination losses start to become more pronounced for the largest gap sizes. When the measured charge per pulse is corrected for the efficiency of the IC by using Eq. (5), the red line is obtained and it is clear that both IC's measure the same amount of incident proton charge, illustrating the accurate estimation of the efficiency.

The top part of Figure 8 shows in detail the measured ratio of charges in the large area AIC and is illustrative of the expected performance of this AIC in the gantry. The red line in this figure was obtained from the recombination theory (Eq. (2)), where the parameter u (u_1 and u_2) was calculated for both IC's. In this case, only the beam spot size (and thus the positive ion density in the IC) was a fitting parameter. The theory reproduces nicely the ratio over the full range of pulse intensities. The fitted spot size is a factor 2.5 larger than the actual spot size. The exact reason for this is still under investigation.

The bottom part of Figure 8 shows the efficiencies of both IC's in the large area AIC. The lower black symbols are the efficiencies of the large gap IC and the red symbols are the efficiencies of the smallest gap IC. The dashed blue curves are the theoretical efficiencies calculated with Eq. 2, from which the red curve in the top figure results. Important to note is that the smallest gap IC (3 mm) provides efficiencies of >99% over the full range.

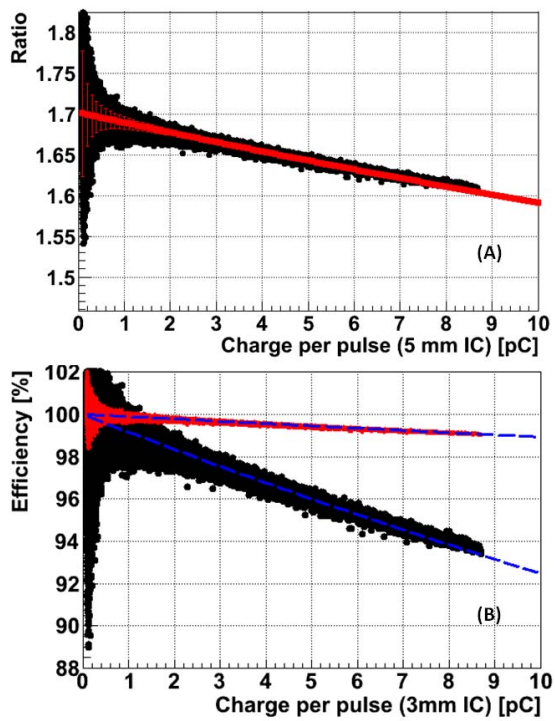


Figure 8 : (A) measured ratio in the air-filled large area AIC with S2C2 pulsed beam. The red line is the calculated ratio using the efficiencies from Eq. 2 where the beam spot size was the only fitted parameter. (B) The efficiencies (Eq. 5) from the observed ratio for both 3 mm and 5 mm IC's and the theoretical efficiencies calculated with Eq. 2 (blue dashed lines).

ISBN 978-3-95450-141-0

Copyright © 2014 CC-BY-3.0 and by the respective authors

CONCLUSION

Recombination losses in the large gap and large surface air-filled ionization chambers (IC's) at the exit of the gantry have to be quantified on a pulse-by-pulse base. Experiments have provided the absolute efficiencies of the air-filled IC's and these have been compared to approximated efficiencies, where only the measured ratio of charges is used as input. The experiments are well reproduced by these efficiencies and recombination losses can be corrected for up to 10 pC/pulse, the typical clinical range with the ProteusONE^{TM} system.

REFERENCES

[1] W. Kleeven *et al.*, Proceedings of the 20th International Conference on Cyclotrons and their Applications, MO4PB02, (2013)
[2] E. Pearson *et al.*, IEEE Transactions on Applied Superconductivity, Vol. 24, Issue 3 (2013)
[3] J.W. Boag *et al.*, Phys. Med. Biol. **41**, 885-897 (1996)
[4] R.F. Laitano *et al.*, Phys. Med. Biol. **51**, 6419-6436 (2006)

Copyright © 2014 CC-BY-3.0 and by the respective authors

ISBN 978-3-95450-141-0

INTRODUCTION TO THE TEST RESULT OF TURBO-ICT IN PAL-ITF*

H. Choi†, M.S. Chae, S.-J. Park, H.-S. Kang
Department of Accelerator, PAL-XFEL, Pohang, Korea

Abstract

Pohang Accelerator Laboratory (PAL) built a PAL-ITF (Injector Test Facility) at the end of 2012 to successfully complete PAL-XFEL (X-ray Free Electron Laser) in 2015. The PAL-ITF is equipped with various kinds of diagnostic equipment to produce high-quality electron bunches. The three main parameters that an injection testing facility should measure are charge, energy and emittance. Although integrated current transformer (ICT) and Faraday Cup were installed to measure beam charge, the noise generated in a klystron modulator not only interrupted accurate measurement but prevented low charges under tens of pC from being measured. Due to the changes in the overall voltage level of ITF, integration of ICT measured value failed to maintain perfect accuracy in terms of methodology (measured value continuously changed by +/- 5pC). Accordingly, to solve the noise problems and accurately measure the quantity of electron beam charge, Turbo-ICT was installed. [1] This paper focuses on the processes and test result of electric bunch charge quantity measurements using Turbo-ICT.

PURPOSE OF BCM INSTALLATION

As shown in Figure 1, A charge generator or a device which accelerates or uses charge has its absolute amount of charge. In other words, knowing the amount of charge which a charge generator produces and a charge accelerator or a charge-based device uses would allow users to check where charge loss occurs and to decide the final amount of charge they will be supplied with. The coulomb (C) is a unit of electrical charge and is also the derived unit of International System (Système International d'unités, SI) of Unit. A bunch charge monitor (BCM) shall be installed after it is calibrated to measure the absolute amount of charge.

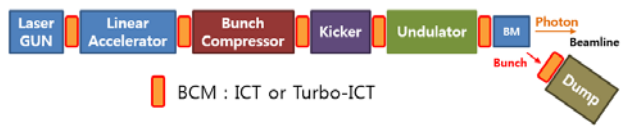


Figure 1: Locations where BCM installation is required.

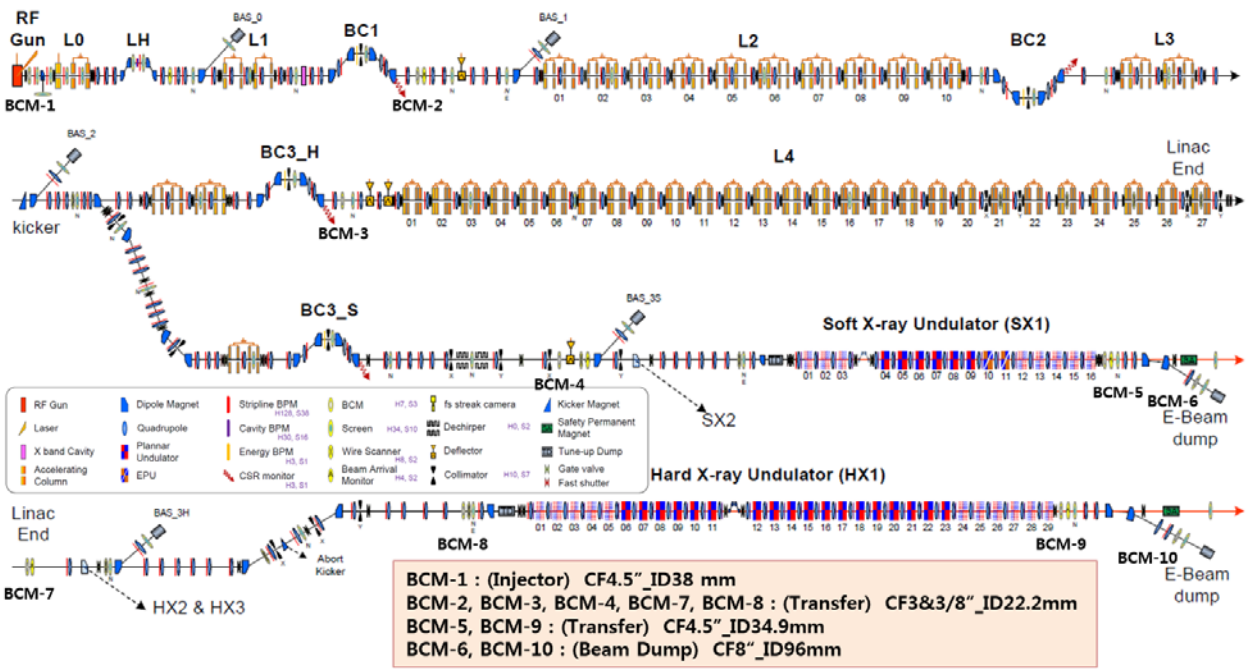


Figure 2: Locations of BCM installed on PAL-XFEL.

As shown in Figure 2, Ten BCMs are installed on PAL-XFEL: Laser gun generator, the rear part of a bunch compressor with the possibility of charge loss, Kicker-based bunch branch part, the end of a linear accelerator (Starting point of an undulator), the end of an undulator, and beam dump part. A BCM is a calibrated device for measuring the absolute amount of charge. Sometimes Stripline-BPM Sum Value and Cavity-BPM Reference Value are complementarily used to measure the amount

* Work supported by the Ministry of Science, ICT and Future Planning (MSIP) in Korea.
† choihyo@postech.ac.kr

ISBN 978-3-95450-141-0

Copyright © 2014 CC-BY-3.0 and by the respective authors

of charge. Monitoring the fluctuation in the amount of charge using BCM and BPM can systematically record and control the locations of charge loss on XFEL and contribute to improving XFEL performance. To minimize the fluctuation in the amount of charge and ensure steady and stable supply of charge, BCM readings are transmitted to a laser system through Fast Feed-forward Network.

The Figure 3 is an important parameter required by the beamline experiments. The flux related to charge.

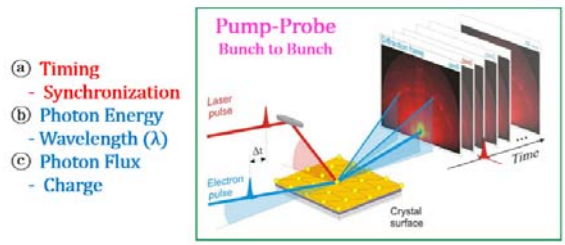


Figure 3: Important parameter on the Pump-Probe.

When installing a BCM on an accelerator (20mm in internal diameter), ICT-CF3"3/8-22.2-40-UHV-Turbo1-316LN-H with 22.2mm in internal diameter will be used to minimize the influence of Wakefield by spatial change. The layout of ICT-CF3"3/8 shown in Figure 4.

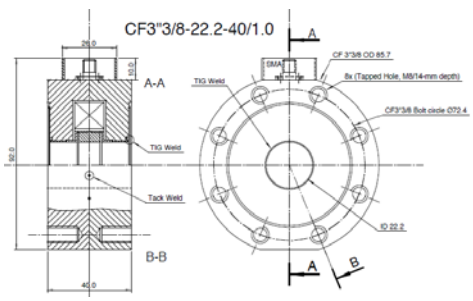


Figure 4: Bergoz's ICT-CF3"3/8 Drawing.

ICT ORGANIZATION AND PRINCIPLE OF PHYSICAL MEASUREMENT

As show in Figure 5, BCM system consists of (1) integrating current transformer (ICT), (2) cables, (3) electronic integrators, and (4) interface electronics to the control system. [2]

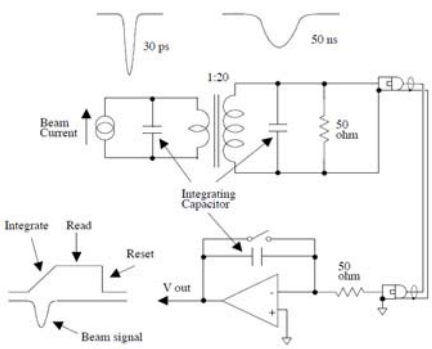


Figure 5: Simplified diagram of a BCM.

As the physical concept of pickup is important to all the beam diagnostic systems, understanding the physical concepts of a BCM is important to designing and operating suitable electronics. [3] As show in Figure 6, A toroidal core is a piece of magnetic material (Amorphous cobalt alloy cores) and plays the same role as a magnet when the magnetic field, which is generated when the beam bunch passes, induces magnetic flux momentarily. Then the magnetic flux flowing in the toroidal core is proportional to the amount of charge in the beam bunch. [4][5][6]

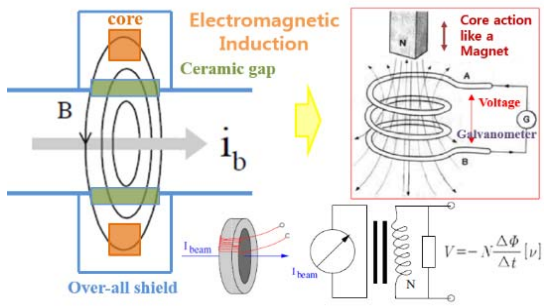


Figure 6: Concept of core induction in the magnetic field generated in an electron beam.

As show in Figure 7, if magnetic flux flows around toroidal cores, varying magnetic fields cause electromagnetic induction. The induced electromotive force is subject to Michael Faraday's Law: The induced electromotive force in any closed circuit is equal to the time rate of change of the magnetic flux through the coils and the number of turns of coil. The electrical properties of ICT which measures the charge amount of beam bunch depends on core properties and turns ratio. Based upon the facts, pickup's equivalent circuit is made and an electrical circuit diagram for ICT measurement is designed. [7][8]

Copyright © 2014 CC-BY-3.0 and by the respective authors

ISBN 978-3-95450-141-0

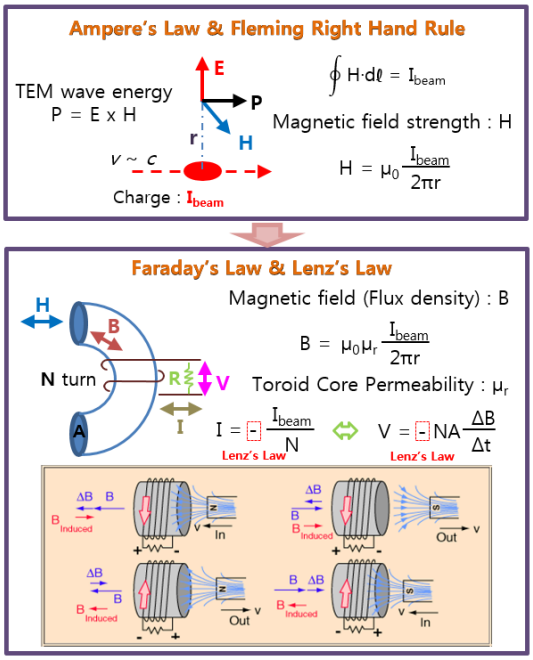


Figure 7: Physical principle of ICT.

As show in Figure 8, the area of pulse generated by beam bunch is equal to the charge amount. If the amount of charge increases, the induced current may have rise and droop time owing to the physical properties of pickup. As shown in the below figure, the readings of ICT output voltage reveals that ICT output pulse extends more widely towards time axis than beam pulse. To get the precise value of charge amount in ICT, integrate ICT output pulse area in DAQ.

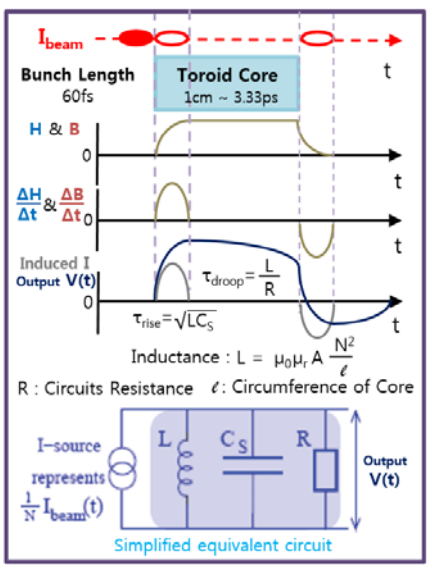


Figure 8: Output voltage of ICT

TURBO-ICT ORGANIZATION AND PRINCIPLE OF OPERATION

As show in Figure 9, Turbo-ICT system consists of (1) In-flange Integrating Current Transformer, (2) BCM SMA-SMA radox cable, and (3) BCM-RF-E & RF-Shielded powered chassis.

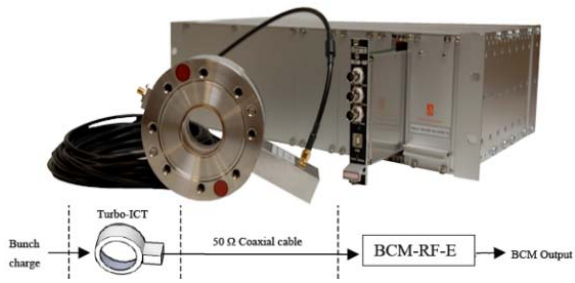


Figure 9: Simplified diagram of a Turbo-ICT.

The charge amount of PAL-XFEL ranges between 1~200pC (Max. 300pC). An improved system like Turbo-ICT is required to measure the small amount of charge in XFEL. First of all, ICT induces a small amount of charge and the output pulse is relatively low. As the amount of charge fluctuates greatly owing to modulator noise, it is difficult to measure its amount precisely by transmitting a low voltage of current in ICT through cables. To solve this problem, the Turbo-ICT use a bandpass filter to limit the output bandwidth to small band 180MHz. The result is a short resonance at 180MHz that is amplified in a low noise amplifier before transmission. It show on Figure 10. [9]

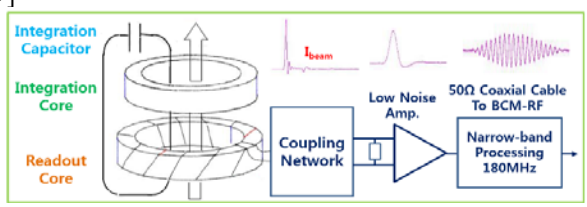


Figure 10: Turbo-ICT Pickup.

As show in Figure 11, Inside BCM-RF-E are a filter which removes noise infiltrating ICT signals and Log. Envelope detector for logarithmic signal. Log scale increase the detector dynamic range of input signal. The PIC integrated on BCM-RF for digital output on USB port. The micro-calibration of related electronic circuits is done by Bergoz's precision electric charge measuring system. [10]

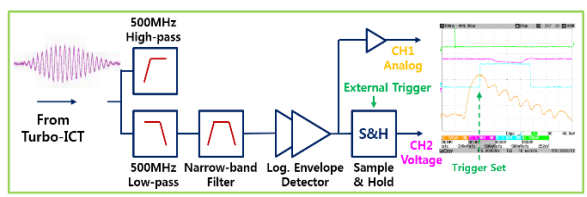


Figure 11: BCM-RF-E.

Timing synchronization is required to measure the charge amount of beam bunch in BCM-RF-E. For this purpose, event trigger signals are authorized in BCM-RF-E. There are three ways of reading charge amount in BCM-RF-E: (1) Read output waveform in CH1 or (2) calculate it according to a given equation after reading

ISBN 978-3-95450-141-0

Copyright © 2014 CC-BY-3.0 and by the respective authors

DC value in CH2, and (3) LabVIEW GUI program on USB cable.

As show in Figure 12, Bergoz's support the useable LabVIEW GUI (graphical user interface) program for configuration setting and beam charge monitoring of Turbo-ICT.

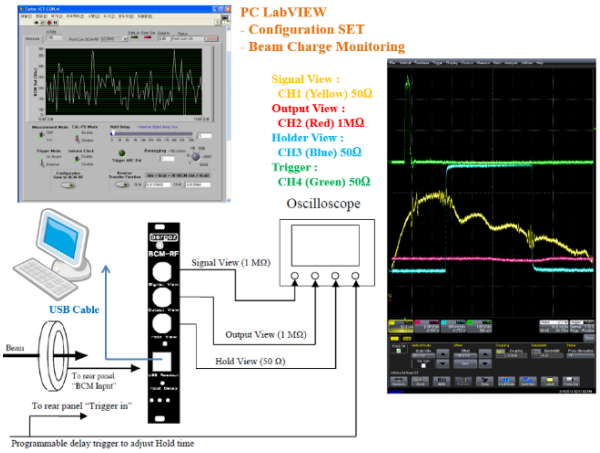
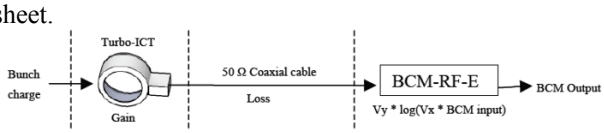


Figure 12: Configuration set and charge monitoring.

Turbo-ICT is manufactured by the purchaser production (custom make) method. All components of Turbo-ICT including cables should be carefully managed as a concept of set. The calculation formula of Turbo-ICT charge amount is shown in Figure 13. Parameters for calculation are included in suppliers' calibration data sheet.



Direct transfer function:

BCM Output = Vy * log((Bunch charge * Gain charge * Loss) / Vx)

Calibration Factor for the PAL-ITF Turbo-ICT

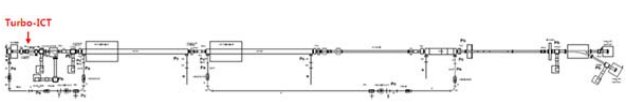
```
Sample and Hold mode :
Turbo-ICT input charge(pC) = Qcal*10^(BCM Out(V)/Ucal)
Qcal = 0,015766
Ucal = 0,817896
```

Input charge (pC) = 0.015766 X 10^(BCM Out (V) / 0.817896

Figure 13: Calculation formula of Turbo-ICT charge amount.

PAL-ITF INSTALLATION & TEST RESULTS

The requirements of PAL-XFEL is: (1) 300pC (the minimum charge amount for measurement is uncertain owing to noise in a modulator), (2) Bunch repetition rate 60Hz, and (3) bunch length 60fs. This time not ordered the two-bunch mode.



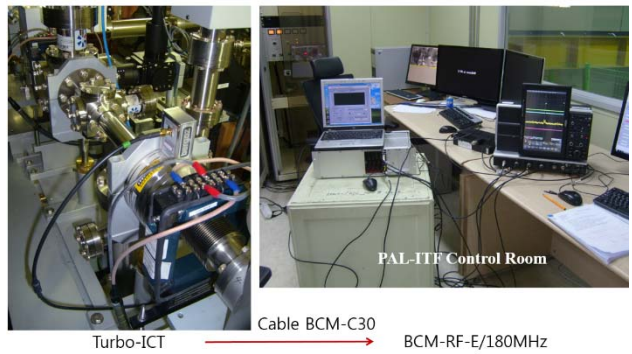


Figure 14: Turbo-ICT installed on PAL-ITF.

As shown in Figure 14, a Turbo-ICT was installed on PAL-ITF and Gun's output charge amount was measured together with Stripline-BPM while changing the Half-wave plate angle of the laser system. It shown on Figure 15.

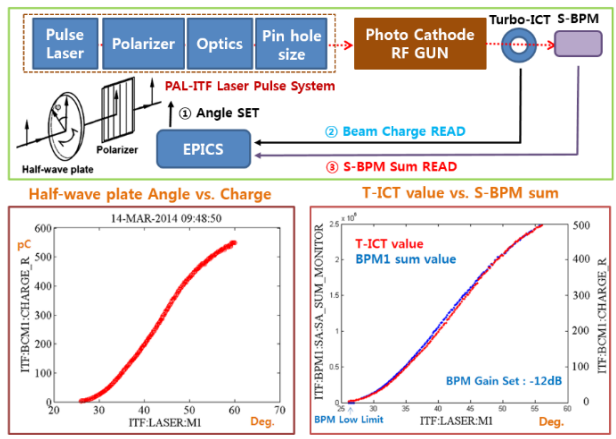


Figure 15: Turbo-ICT following charge control by laser system and BPM Sum value measurement results.

Figure 16 show the modulator noise problem. Turbo-ICT's minimal range of measurement for charge amount is limited by the noises of peripherals including Klystron Modulator. The results of tests on PAL-ITF have shown that in spite of modulator noise's influence it met the requirements of PAL-XFEL, or 1~200pC (Max. 300pC). The test result shown on Figure 17.

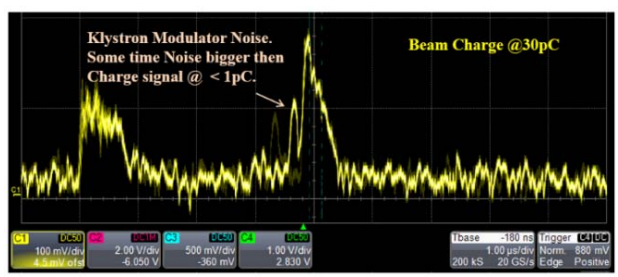


Figure 16: Influence of Klystron modulator Noise.

Copyright © 2014 CC-BY-3.0 and by the respective authors

ISBN 978-3-95450-141-0

Turbo-ICT input charge (pC)	BCM Out (V)
426,5501	3,640
307,9428	3,516
220,0240	3,384
152,2194	3,254
108,7602	3,140
78,3376	3,021
55,0136	2,886
39,3070	2,766
27,2251	2,645
19,6097	2,536
14,0110	2,414
9,6265	2,275
6,8781	2,161
4,9542	2,055
3,4274	1,930
2,4489	1,810
1,7178	1,685
1,2387	1,579
0,8851	1,477
0,6123	1,363
0,4375	1,260
0,3155	1,157
0,2198	1,064

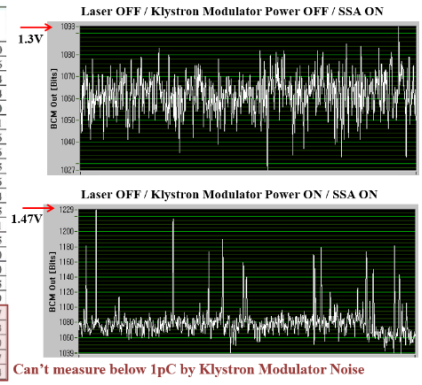


Figure 17: Problems of Klystron modulator noise and measured value of Turbo-ICT on PAL-ITF.

ACKNOWLEDGMENT

Thanks to Mr. Julien Bergoz, Mr. Sébastien Artinian, Mr. Frank Stulle and all the colleagues of the Bergoz Instrumentation. They are support many things for implementation Turbo-ICT on PAL-ITF.

REFERENCES

[1] H. Choi, et al., "Presentation about Results Produced After Measuring PAL-ITF Beam Diagnostic Instruments", IPAC 2014, THPRO021
[2] Jim Hinkson, "ALS Beam Instrumentation – Beam Charge Monitoring", July 1998
[3] Alex Chao, et al., "Handbook of Accelerator Physics and Engineering", 2nd Edition, World Scientific Pub Co Inc.
[4] J.-C. Denard, "Beam Current Monitor", CERN-2009-005
[5] W.Blokland, "Beam Current Monitors", USPAS 2009
[6] R.C. Webber, "Tutorial on Beam Current Monitoring", BIW 2000
[7] P. Forck, "Beam Instrumentation and Diagnostics", JUAS 2012
[8] Hyper Physics, http://hyperphysics.phy-astr.gsu.edu/
[9] S. Artinian, et al., "Development and First Tests of a High Sensitivity Charge Monitor for SwissFEL", IBIC 2013, MOPB87
[10] S. Artinian, et al., "Goubau Line and Beam Characterization of Turbo-ICT for SwissFEL", IPAC 2013, MOPME005

Copyright © 2014 CC-BY-3.0 and by the respective authors

ISBN 978-3-95450-141-0

RANGE VERIFICATION SYSTEM USING SCINTILLATOR AND CCD CAMERA SYSTEM

N. Saotome#, Y. Hara, K. Mizushima, R. Tansho, Y. Saraya, T. Furukawa, T. Shirai, and K. Noda,
National Institute of Radiological Sciences, Chiba, Japan

Abstract

For the daily QA of the energy scanning delivery, quick and easy range verification system is required. In this work, we have developed range verification system using scintillator and CCD (charge-coupled device) camera. From the comparison of the several methods, edge detection method is best for range detection. Accuracy of range detection for the system is within the 0.2 mm. Reproducibility of the range is within 0.1 mm. Our range check system has shown to be capable of quick and easy range verification with sufficient accuracy.

INTRODUCTION

At NIRS, three-dimensional irradiation with carbon-ion pencil-beam scanning has been performed from 2011 [1]. We have been commissioning the irradiation method that employs more than 200 multiple beam energies supplied by synchrotron instead of the energy degraders [2]. Since carbon ion deposits most of their energy in the last final millimeters of their trajectory, the accuracy of the beam energy/range is required for carbon ion treatment especially for using scanning method. ICRU78 recommend checking the range constancy for daily QA. Recommended relative accuracy of range measurements is less than 0.5 mm [3].

In the current daily QA at NIRS, Few-points depth dose measurement using ionization chamber is employed for range verification. It takes about 1 minute for a measurement of one energy beam. In order to apply the range check for multiple energy beams, quick and easy range verification system is required. The purpose of this work is to develop range verification system using scintillator and CCD camera and to estimate the accuracy of the range verification using the system.

MATERIALS AND METHODS

Experimental Setup

The scintillator and CCD system is shown in Fig. 1. The system is consisted of a scintillator block, CCD camera, and opaque (black) box. Light distribution is detected by CCD camera through a mirror. The optical path length between the scintillator and lens is 400 mm. The system was placed on the treatment couch. The center of the scintillator was placed at isocenter.

A EJ-200 plastic scintillator block was selected for pure tranceparent block, similar density with human body, and matching wavelength of maximum emission for CCD camera. The size of cylindrical scintillator block was 200 mm diameter ×100 mm thickness. For shading the light from the treatment room, the scintillator was wrapped by light blocking sheet. The CCD camera (Type BU-41L, 1360x1024 pixels, Bitran Corp., Japan) was installed on the light-shielding house. The spatial-resolution of the system is 0.2 mm/pixels.

#naosao@nirs.go.jp

Image Acquisition

All measurement was performed at fixed vertical beam line. Total 131 energy carbon beams with mini ridge filter that were in the range from 56 to 332 MeV/n were measured sequentially. The data acquisition of the CCD camera was synchronized with irradiation. We measured pencil-beam having intensities between 8×10^7 and 1.6×10^8 particles per second. Measurement time is 0.1 sec for all energy.

Image Processing

Measured two-dimensional images were processed by in-house program developed by c++. The workflow of image processing is shown in Fig. 2. After the background correction and median filter, projection on one-dimensional axis is performed.

Range Scaling Factor

The common reference point of range is distal 80% of the dose distribution. However the system measures the range not with the dose distribution but with the light distribution. Archambault *et al*. concluded that the distal 80% minimized discrepancies between expected and measured ranges for proton beam [4]. Fukushima *et al*. also use 80% and obtained great result [5]. To our knowledge, there is no published report of clinical carbon range measurement with scintillator. In order to select the best reference point on a light distribution, the authors compared two range detection methods using several parameters.

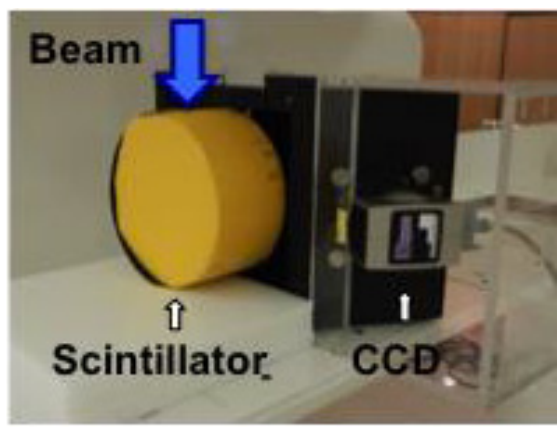


Figure 1: Layout of the scintillator and CCD system.

Copyright © 2014 CC-BY-3.0 and by the respective authors

ISBN 978-3-95450-141-0

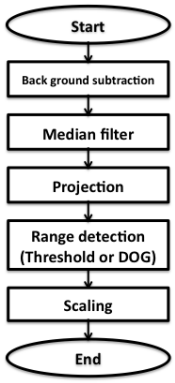


Figure 2: Workflow of the image processing.

One is threshold method (TH); the threshold positions set by 30, 50, 60, 70, 80, and 90% of maximum value on the projected line are identified. The other is difference of Gaussian (DOG) method; DOG method is widely used in edge detection field instead of Laplacian filter [6]. Using DOG method, range position is determined by zero-crossing position in the difference between small-Gaussian smoothed image and large-Gaussian smoothed images. Sigmas for small and large Gaussian are 1 and 1.5 pixels respectively. As shown in Fig. 3, only the high-frequency edge position is enhanced when relative small sigma is used. In this work, range-scaling factor is applied. The Range Shifter (RSF) that gave us the least deviation from the expected relative range for all RSF thickness is then used for all range measurements.

RESULT

Depth Brightness Distribution

Fig. 4 shows the example of the depth brightness distribution acquired with the system. Measurement time was about 5 seconds for one energy beam. Peak-plateau ratio was small due to quenching effect and absorption of the light within the scintillator block.

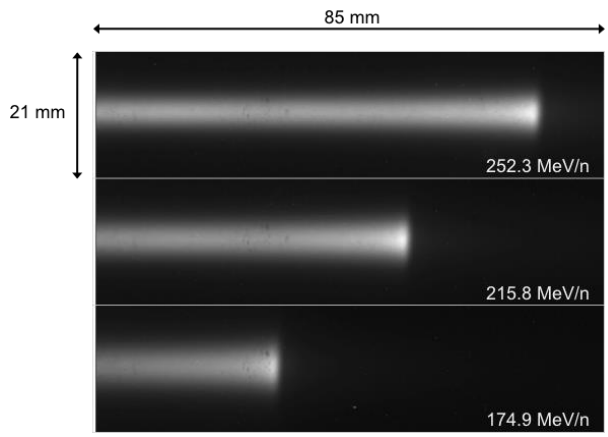


Figure 4: Example of the depth brightness distribution acquired with CCD camera.

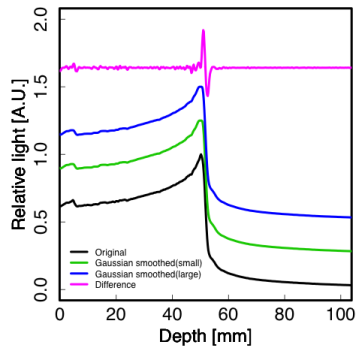


Figure 3: Instruction of the DOG method.

Range Scaling Factor Using Range Shifter

The RSF plates with thickness from 0.5 to 4 mm was inserted upstream of the system. Reference depth dose distribution measured by ion chamber and depth brightness distribution with/without RSF measured by the system were shown in Fig. 5. All curves were normalized at highest point. As it can be seen, the brightness distribution was clearly separated by the RSF thickness. The relative range was determined by range between the without RSF and with RSF. Comparison of the relative range between RSF thickness and relative range determined by DOG method was shown in Fig. 6. Relative range differences from the expected range were very small. Standard deviation was less than 0.05 mm for all measurements. Summary of mean difference and standard deviation for all range detection methods were listed in Table 1. It was found that differences of relative range are very small with many method but using DOG method minimized differences between expected and measured ranges.

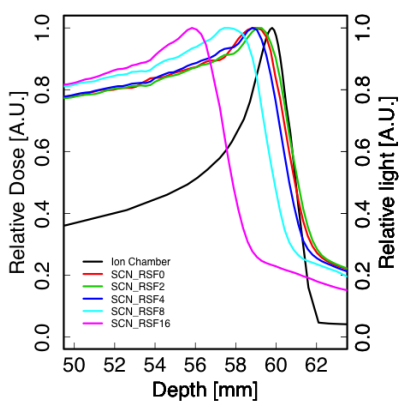


Figure 5: Comparison between the reference depth dose measured by ionization chamber and relative light output shifted by RSF.

Copyright © 2014 CC-BY-3.0 and by the respective authors

ISBN 978-3-95450-141-0

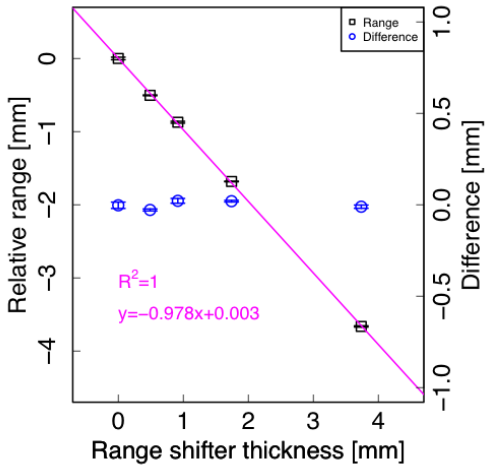


Figure 6: Comparison of the relative range with range shifter thickness.

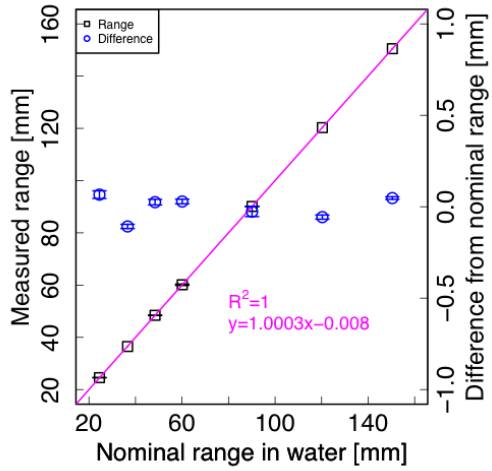


Figure 7: Measured range using DOG method and difference from nominal range.

Table 1: Comparison of the Difference Between RSF Thickness and Measured Relative Range Using Threshold and DOG Method.

Method	Mean Difference [mm]	Standard deviation [mm]
TH_30%	0.003	0.033
TH_50%	0.002	0.030
TH_60%	0.002	0.029
TH_70%	0.001	0.028
TH_80%	-0.001	0.037
TH_90%	0.000	0.043
DOG	0.000	0.022

Table 2: Comparison of the Difference from Nominal Range Changing Using Threshold and DOG Method.

Method	Mean Difference [mm]	Standard deviation [mm]
TH_30%	0.015	0.296
TH_50%	-0.011	0.078
TH_60%	-0.011	0.071
TH_70%	-0.011	0.068
TH_80%	-0.014	0.072
TH_90%	-0.018	0.078
DOG	-0.003	0.055

Depth Measurement

Comparison of the nominal carbon range in water and the range measured in the scintillator system with DOG method is shown in Fig.7. The pencil beam with range in water between 24 mm and 150 mm were employed. Summary of mean difference and standard deviation for all range detection methods were listed in Table 2. The measured range is closed to the nominal range in water for all energies. It was found that differences of range were very small with many method but using DOG method minimized differences between expected and measured ranges. The mean difference between the nominal and the measured with DOG method range -0.003±0.055 mm (1 SD). The maximum discrepancy was 0.108 mm.

CONCLUSION

In this work, range verification system using scintillator and CCD camera has been developed. We have shown that the range of carbon pencil beam can be determined with subminiature accuracy with some image processing. We have found that Edge detection method (DOG) is minimized discrepancies between expected and measured ranges for carbon beam.

It was supposed to be a result of the change of shape due to quenching effect. Since the system determine the range with short time and sufficient accuracy, it seems be that the system has potential to play the daily range check system.

REFERENCES

[1] T. Furukawa, *et al.*, “Performance of the NIRS fast scanning system for heavy-ion radiotherapy”, Med. Phys., 37 (11), 5672-5682, (2010).
[2] Y. Iwata, *et al.*, “Multiple-energy operation with extended flattops at HIMAC”, NIM. A, 624, 33-38, (2010).
[3] ICRU Report 78, Journal of the ICRU, Vol 7, No 2.
[4] L. Archambault, *et al.*, “Verification of proton range, position, and intensity in IMPT with a 3D liquid scintillator detector system”, Med. Phys. 39 (3), 1239-1246, (2012).
[5] Y.Fukushima, *et al.*, “Development of an easy-to-handle range measurement tool using a plastic scintillator for proton beam therapy”, Phys. Med. Biol., 51, 5927–5936, (2006).
[6] D. Mark, *et al.*, “Theory of edge detection”, Proc. R. Soc. Lond. B, 207, 187-217, (1980)

Copyright © 2014 CC-BY-3.0 and by the respective authors

ISBN 978-3-95450-141-0

A DIAGNOSTICS OF ION BEAM FROM 28GHz ELECTRON CYCLOTRON RESONANCE ION SOURCE

Jung-Woo Ok# ,Byoung Seob Lee ,Seyong Choi ,JungBae Bahng, Jin Yong Park, Seong Jun Kim, Jonggi Hong, Chang Seouk Shin, Jang-Hee Yoon, Mi-Sook Won,
Korea Basic Science Institute(KBSI), Busan, Korea

Abstract

A neutron radiography facility utilizing a 28 GHz superconducting electron cyclotron resonance (ECR) ion source and a heavy ion accelerator is now under construction at Korea Basic Science Institute (KSBI). In order to generate a proper energy distribution of neutron, a lithium ion beam is considered. It will be accelerated up to the energy of 2.7 MeV/u by using a radio frequency quadrupole (RFQ) and drift tube linear (DTL) accelerator. The 28 GHz superconducting ECR ion source, which is the state of the art of an ion beam injector, has been built to produce the lithium ion beam. The ion beam of 12 keV/u would be extracted to low energy beam transport (LEBT) system, which is comprised of several types of electromagnets to focus and deliver the beam, effectively. After transporting an ion beam through LEBT, RFQ once accelerates the ion beam from 12 to 500 keV/u. Finally, we can achieve the final beam energy after accelerating at the DTL. Before the ion beam is delivered to accelerator, the requirements should be satisfied to confirm the status of beam. For this, we developed the instruments in the diagnostic chamber in the middle of LEBT system to observe the beam dynamics. An analyzing electromagnet, slits, wire scanners and faraday cup will be used to perform a diagnosis of ion beam characteristics. We will present and discuss the experimental results of ion beam profile and the current after selecting are required charge state.

INTRODUCTION

For the research facility based on accelerator technology at KBSI, a 28 GHz superconducting ECR ion source, a LEBT system, and linear accelerators are under development [1]. Recently, ECR plasma ignition was successfully implemented using 28 GHz superconducting ECR ion source [2]. Since then, a ion beam extraction from ECR ion source is scheduled to experiment. In the ion beam extraction test, the beam properties will be measured using various diagnostic technique. Figure 1 shows the layout of the KBSI Accelerator research facility. The first application to the KBSI accelerator research facility is neutron radiography. For the generation of neutron, the inverse kinematics technique is considered. In this method, a lithium beam accelerated up to 2.7 MeV/u will impact the hydrogen gas target, then the neutron will be generated. In order to accelerate lithium beam, radiofrequency quadrupole and drift tube linear accelerator will be used.

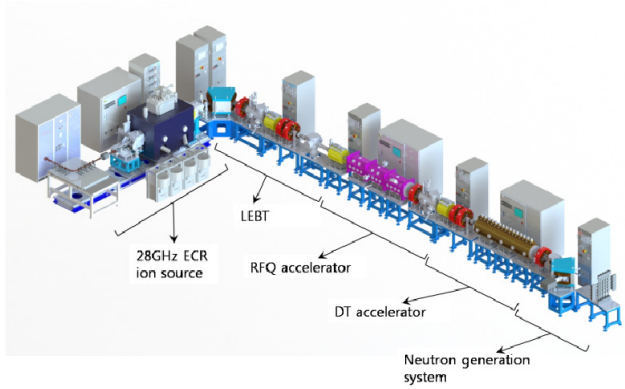


Figure 1: The layout of the KBSI accelerator research facility.

Also, for the beam transmission from ECR ion source to RFQ a LEBT system is designed. The schematic of LEBT system is showed in Figure 2.

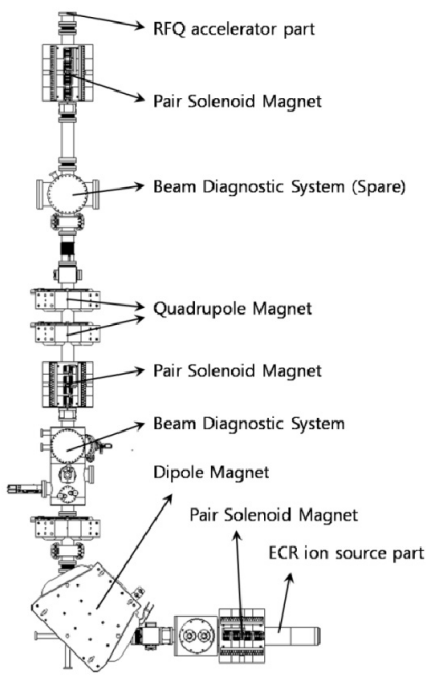


Figure 2: The schematic of LEBT system.

#jwo @kbsi.re.kr

ISBN 978-3-95450-141-0

Copyright © 2014 CC-BY-3.0 and by the respective authors

The details of the LEBT system are presented next section.

LOW ENERGY BEAM TRANSMISSION SYSTEM

In order to satisfy the requirement for the input beam of RFQ, the LEBT system is designed. The whole LEBT system consists of a dipole magnet, three pair solenoids, three quadrupole magnets, four steering magnets, and two diagnostic chamber (1 spare). For the LEBT design, the TRANSPORT code is used[3]. The initial beam parameters are shown in table 1.The results of beam transport simulation are shown in the Figure 3. The abbreviation of Sol, D, BM, DG, QM is pair solenoid, drift tube, dipole magnet, diagnostic chamber, and quadrupole magnet, respectively. In Figure 3, the total length of the LEBT is 7 m and the calculated maximum beam size is around 4 cm. The elements of the LEBT are fabricated based on the results.

Table 1: The Initial Beam Parameters

Particle	Lithium
Mass	7
Charge	3
Energy	12 keV/u
Emittance	0.2 π mm mrad
Current	1.0 mA

The beam is extracted from 28 GHz superconducting ECR ion source, ate that time unwanted charge states particles and ions are included. A dipole magnet is used to separate these undesirable particles. After dipole magnet, beam devices in diagnostic system measure the beam profile, emittance and current. The description of the diagnostic system will be discussed in the next section.

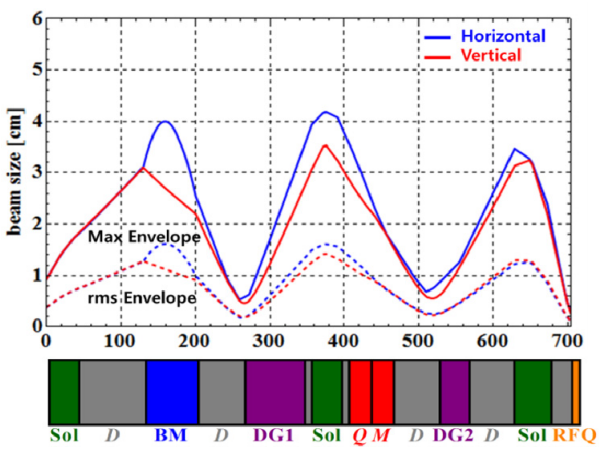


Figure 3: The beam optics simulation results using TRANSPORT code.

DIAGNOSTICS SYSTEMS

A various diagnostic devices are prepared in LEBT system. The whole name, the purpose of use and the number of devices are listed in table 2. The number of slit is two due to the horizontal and vertical position.

Table 2: List of Beam Diagnostic Equipments

Device		#
Slit	Beam separation	2
Screen	position and size	1
Wire scanner	Transverse emittance	1
Faraday cup	Current	1

The photo of equipments inserted into diagnostic chamber is shown in the Figure 4.

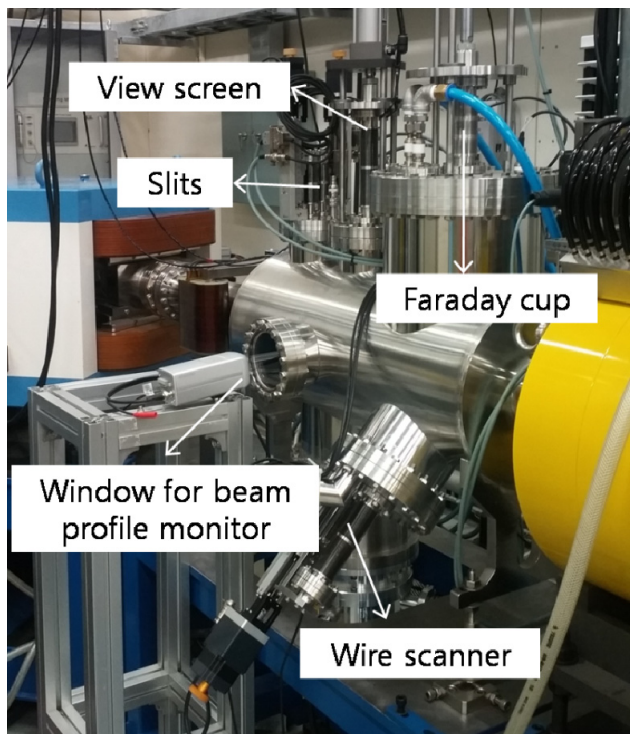


Figure 4: The photo of diagnostic chamber with measuring devices.

View Screen

In order to monitor the beam profile we have decided to use a view screen in the diagnostic chamber. The use of view screen is easy and simple method. The screen is comprised of stainless steel plate which tilts to 45° as compared with beam axis for beam profile observation. The stainless steel screen is designed with pin holes for calibration of beam position. The fabricated screen is shown in the Figure 5. Also, CCD camera for beam profile monitoring and a movable stage is installed as a part of view screen in the Figure 4.The Y_2O_2S is selected

Copyright © 2014 CC-BY-3.0 and by the respective authors

ISBN 978-3-95450-141-0

as a doping material, which has a high brightness in low beam energy regime and a short decay time.

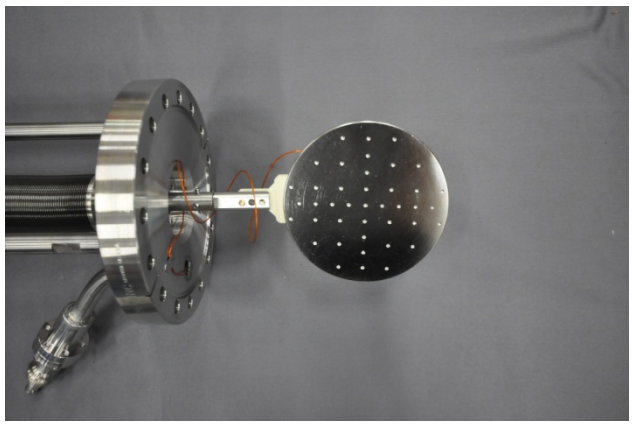


Figure 5: The photo of view screen with pin holes.

Faraday Cup

For the beam current monitoring, a faraday cup is designed. Faraday cup is inherently a destructive device and it measures beam intensity with collection of charge. Therefore, faraday cup has to absorb a full beam power and it can be used for beam dump. We multi-functionally choose both charge collection and beam dump in faraday cup design. The diameter of cup is also decided considering a beam size from LEBT simulation. In order to measure precisely beam intensity, a suppress electrode with voltage from -100 V to -500 V and a confinement of secondary electron emission from the inside of the cup is considered. A water cooling channel also is inserted in the body of faraday cup to take away a heat caused by an interaction between beam and cup. Figure 6 shows the results of faraday cup simulation.

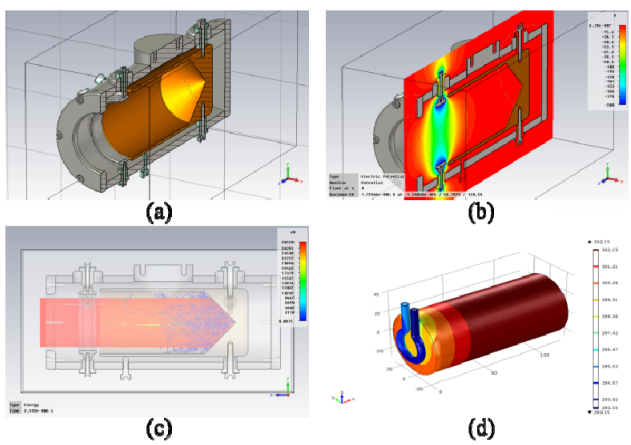


Figure 6: The simulation results of Faraday cup 3D model (a), potential distribution (b), secondary electron tracking (c), temperature distribution with cooling channel (d).

Based on the simulation results, the faraday cup is fabricated and it is shown in the Figure 7. In order to reduce a noise, de-ionised water is flowed for cooling and a electrically isolated ground is adopted. For a movement in the diagnostic chamber, movable stage also is inserted.

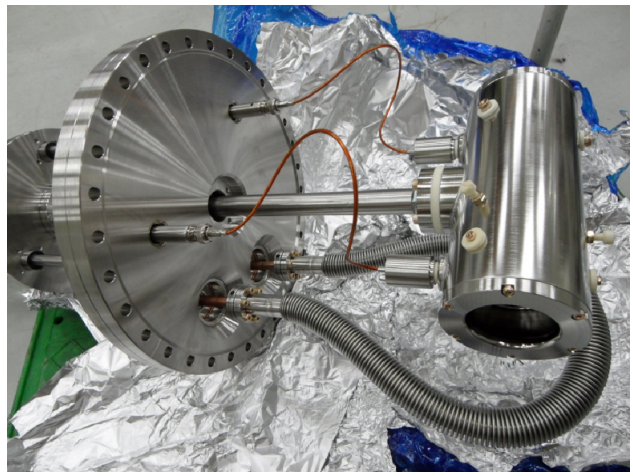


Figure 7: The photo of the fabricated faraday cup.

Wire Scanner

A wire scanner is used to measure a beam profile due to the it's silmple structure and high resolution. In order to measure beam profile, wire scanner sweaps a beam using a thin tungstenwire. A step moter and bellows are adopted for a wire movement of up and down. The wire has thickness of 0.1 and the minimum step of the step motor is 0.1 mm. These thin wire and small step garantee a high resolution when beam profile is measured. We use three wires for wire scanner. The three wires measurement provides projection signal as well as correlation, and twiss alpha information from a single measurement. The manufactured wire scanner with three wire is shown in th Figure 8.

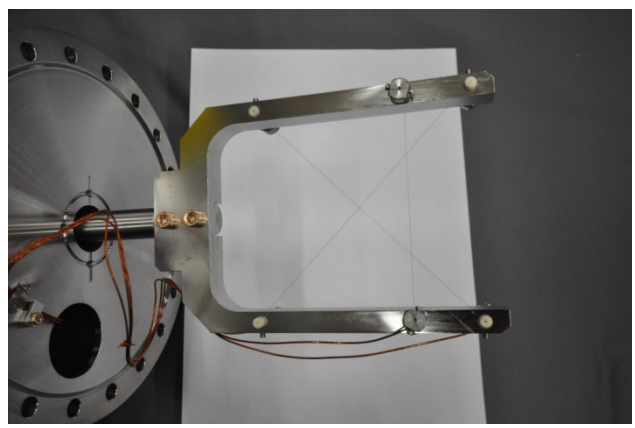


Figure 8: The photo of wire scanner with three wire.

For a verification of performance of the fabricated wire scanner and the measurement program, a pilot test is carried out at Research Center for Nuclear Physics (RCNP) in Japan [4] before operating our 28 GHz superconducting ECR ion source and LEBT system. The measured beam particle is $O^{7+}$with 30 eμA. The measured vertical and horizontal emittance using the fabricated slits and wire scanner is 137.1and 185.8 π mm mrad and previous emittance using RCNP's measurement system is 152.2 and 208.5 π mm mrad, respectively. The gap

ISBN 978-3-95450-141-0

Copyright © 2014 CC-BY-3.0 and by the respective authors

between the measured emittance values is come from the different data calibration method and the different measuring position between devices. However, the effect of the both factors on the results is small. Therefore, the measured emittance data from fabricated wire scanner is well matched up with a RCNP beam emittance data from existing measurement device in RCNP.

CONCLUSION

A 28 GHz ECR plasma is generated at KBSI and ion beam will be extracted soon. In order to measure ion beam properties extracted from 28 GHz superconducting ECR ion source, a beam diagnostic systemis prepared. Diagnostic devices consist of view screen, slits, faraday cup, and wire scanner. Each device is fabricated and installed in diagnostic chamber in LEBT. A pilot test of wire scanner is carried out at RCNP in Japan and the results are well matched with RCNP's emittance measurement data. After beam extraction from KBSI 28 GHz ECR ion source, the diagnostic system will be applied to analyse the ion beams.

ACKNOWLEDGMENT

This work was supported by Korea Basic Science Institute (KBSI) grant (D34300).

Thanks to Prof. Kichiji Hatanaka in Osaka university for help and advice for beam emittance measurement at RCNP.

REFERENCES

[1] J.-H. Yoon et al., “Development of compact linear accelerator in KBSI”, Rev. Sci. Instrum., 83, 02A315 (2012).

[2] M.-S. Won et al., “The First Plasma Ignition of 28 GHz Superconducting ECR Ion Source At KBSI” ECRIS2014, Nizhny Novgorod (Russia), August (2014).

[3] K.L. Brown et al., "TRANSPORT: A computer program for designing charged particle beam transport systems", SLAC-91 (1983).

[4] https://www.rcnp.osaka-u.ac.jp/

Copyright © 2014 CC-BY-3.0 and by the respective authors

ISBN 978-3-95450-141-0

THE STATUS OF BEAM DIAGNOSTICS FOR THE HIE-ISOLDE LINAC AT CERN*

E. D. Cantero†, W. Andreazza, E. Bravin, A. Sosa
CERN, Geneva, Switzerland

Abstract

The HIE-ISOLDE project aims at upgrading the CERN ISOLDE radioactive ion beam facility for higher beam intensities and higher beam energies. New beam diagnostic devices have to be developed as part of this upgrade, in particular for the measurement of intensity, energy, transverse and longitudinal profiles, and transverse emittance. The beam energy ranges from 300 keV/u to 10 MeV/u and beam intensities are between 1 pA and 1 nA. Faraday cups will be used for the measurement of the beam intensity while silicon detectors will be used for the energy and longitudinal profile measurements. The transverse profiles will be measured by moving a V-shaped slit in front of a Faraday cup and the beam position will be calculated from the profiles. The transverse emittance can be measured using the existing REX-ISOLDE slit and grid system, or by the combined use of two scanning slits and a Faraday cup. The final design of the mentioned devices will be presented in this contribution, including the results of the experimental validation tests performed on prototypes during the last two years.

INTRODUCTION

A major upgrade of the on-line isotope mass separator facility ISOLDE at CERN is taking place since 2010 under the HIE-ISOLDE project [1]. The technical challenges for beam diagnostics include the development of new instruments for low-intensity ion beams with energies up to 10 MeV/u. Moreover, in the inter-cryomodules regions of the superconducting LINAC, the longitudinal space available for beam instrumentation is very limited (58 mm) due to restrictions coming from the beam optics design. As a consequence all the devices need to be designed with a very compact geometry.

The diagnostic requirements of HIE-ISOLDE beams are [2]:

- Beam intensity measurements: an absolute accuracy of 1 %, for pilot beams of stable ions such as oxygen and neon, with intensities in the range of 10 pA to 1 nA.
- Transverse profile and position measurements: an accuracy of 10 % in the beam size measurement and of $\pm$ 0.1 mm in the beam position determination. Beam sizes are in the range of 1 to 5 mm (1 σ_{rms}).
- Longitudinal profile measurements: the energy spread and bunch length should be measured with resolutions of $<$1 % (2σ) and $<$100 ps respectively.
- Transverse emittance meter: a target accuracy of $\pm$ 20 % is expected, for beam currents up to 1 nA.

DIAGNOSTIC BOXES

The installation of stage 1 for the HIE-ISOLDE LINAC includes two cryomodules with five cavities each. It is scheduled to deliver the first beams for physics in October 2015. More cryomodules will be added at a later stage, increasing the beam quality and final energy per nucleon.

A total of five short Diagnostic Boxes (DBs) and eight long DBs will be required for the accelerator and its two transfer lines to the experiments. Their location is schematically presented in Fig. 1. The short DBs are located between the cryomodules and have a very compact design in the longitudinal direction compared to the long DBs. All DBs include a Faraday Cup (FC) and a scanning slit that will be used for the beam intensity and transverse profile measurements. All DBs are also equipped with circular and/or vertical collimators for beam cleaning purposes, with four DBs including carbon stripping foils to allow modification of the beam charge state. Two DBs will contain silicon (Si) detectors for longitudinal beam profile measurements.

In Fig. 2 a cutaway drawing of a short DB is presented. The modular, six port design of the box allows up to five instruments or devices to be attached, with one port reserved for the vacuum system. A FC, scanning slit and collimator blade with four circular collimators are shown, with the remaining extra ports available for the installation of a Si detector and a blade with stripping foils. The main tank is an octagonal-shaped box machined from a single block of 316L stainless steel, with a beam pipe aperture of 40 mm. Top and bottom faces are integrated with alignment and support devices respectively.

The position of the various devices is controlled by means of linear actuators driven by stepper motors. As the precision on the positioning of the scanning slit is critical for the accuracy of the transverse beam profiles measurements, a special mechanism was designed for that movement, which includes a robust guiding system with two rods. The plane of movement of the scanning slit, collimators and stripping foils is located slightly upstream of the plane of movement of the FC and the Si detector, al-

*The research leading to these results has received funding from the European Commission under the FP7-PEOPLE-2010-ITN project CATHI (Marie Curie Actions - ITN). Grant agreement No. PITN-GA-2010-264330.
† esteban.cantero@cern.ch

ISBN 978-3-95450-141-0

Copyright © 2014 CC-BY-3.0 and by the respective authors

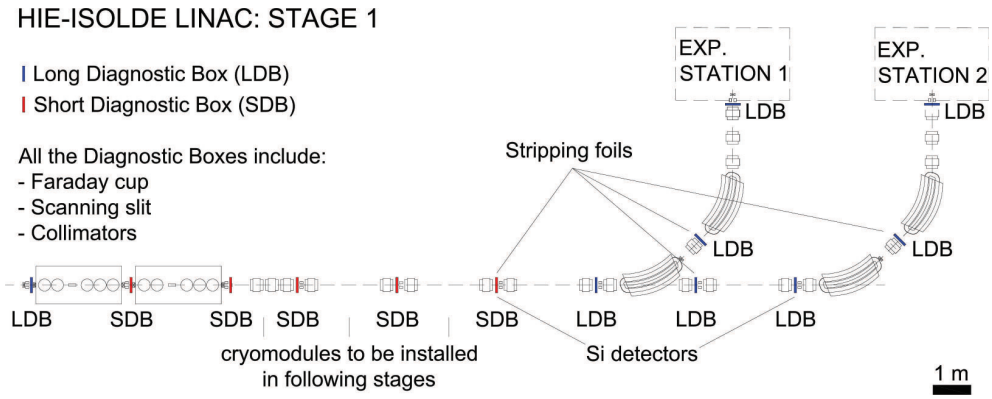


Figure 1: Location of the diagnostic boxes in the HIE-ISOLDE LINAC and High Energy Beam Transfer lines.

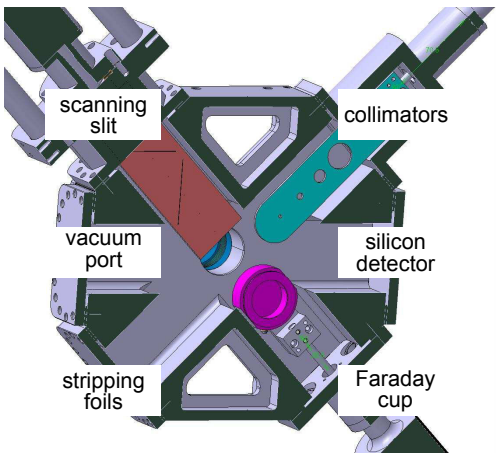


Figure 2: Cutaway drawing of the short diagnostic box with instruments inside.

lowing the insertion of one collimating or stripping device in front of a detector in the same box.

BEAM INTENSITY

The beam intensities will be measured with Faraday cups, of which the final designs are presented in Fig. 3. The diameter of the cup aperture is 30 mm. The collector plate will be connected to a current-sensitive preamplifier and the repeller cylinder will be biased to -100 V in order to suppress the loss of low-energy secondary electrons. The material chosen for the metallic parts is aluminium, while the insulators will be Vespel® (polyimide). The design of the short FC (which will be used in the short DBs) included an extensive research and development campaign as its geometry does not respect the usual aspect ratio of FCs (with a longitudinal length of the collector similar to the FC aperture diameter for increasing the geometrical capture of the secondary charges). Both cups have been tested with beams of energies and composition similar to the ones that will be used on HIE-ISOLDE, using the REX-ISOLDE [3] accelerator at CERN and the ISAC-II accelerator at TRIUMF [4]. The results obtained (Figs. 4 and 5) satisfy the requirements in terms of beam intensity measurements accuracy.

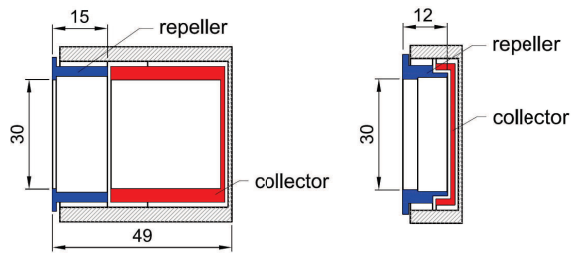


Figure 3: Final design of the HIE-ISOLDE Faraday cups (distances in mm). Left: long FC. Right: short FC.

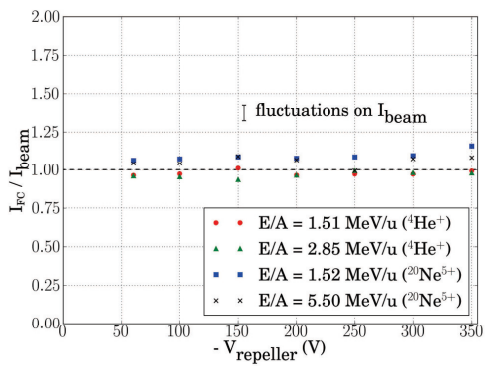


Figure 4: Beam current measurements with the HIE-ISOLDE long Faraday cup.

TRANSVERSE PROFILE AND POSITION

The transverse beam profiles will be determined by moving vertical and horizontal collimators in front of a FC detector. The so-called scanning slit is comprised of an aluminium blade (3 mm thick) that is inserted at 45° of the vertical with a V-shaped slit drilled onto it. A picture of a prototype blade, which will be inserted in one of the diagonal ports of the diagnostic box, is shown in Fig. 6.

The moving blade acts as a scanning collimator that stops any particle that does not have the currently selected

Copyright © 2014 CC-BY-3.0 and by the respective authors

ISBN 978-3-95450-141-0

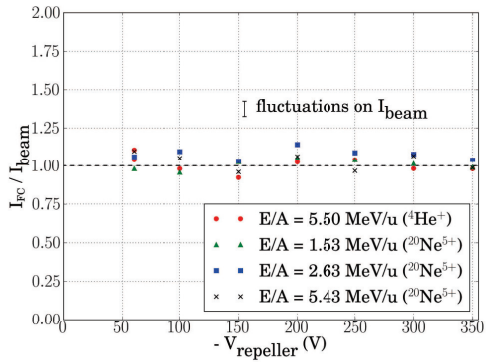


Figure 5: Beam current measurements with the HIE-ISOLDE short Faraday cup.

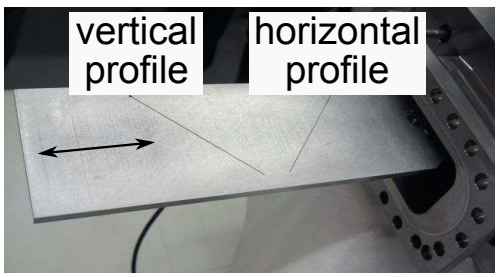


Figure 6: Scanning slit for HIE-ISOLDE. An aluminium blade with a V-shaped slit is moved at 45° of the vertical to collimate the beam, in order to obtain the transverse beam profiles by measuring the transmitted beamlet intensity as a function of the blade position.

horizontal (or vertical) position. By registering the FC signal for different slit positions a direct measurement of the transverse beam profile is obtained. Fig. 7 shows a vertical beam profile obtained with a REX-ISOLDE beam (E/A = 2.85 MeV/u and A/q = 4, mostly $^{20}Ne^{5+}$) with a total beam current I_{beam} = 18 pA. The presented beam profile was acquired with a prototype scanning slit which had an slit width of 0.2 mm. Montecarlo simulations of beam profile measurements were performed with a selection of simulated HIE-ISOLDE beams, determining an optimal slit width of 1 mm for the final design. The larger slit width as compared to the one used in the prototype tests will increase the amplitude of the acquired signal without introducing major distortions in the beam profile and size determination. The transverse position of the beam is calculated directly from the measured profiles.

LONGITUDINAL PROFILE

The longitudinal beam profiles, i.e. the energy spread and bunch length, will be measured using two silicon detectors from CANBERRA (model PIPS TMPD50-16-300RM). Details about experimental tests of those detectors, including energy and timing spectrometry and their application to the cavity phase tuning, can be found in [5]. By acquiring the time of arrival of the particles at two different locations of the beam transfer line, absolute time of flight measurements are obtained and can be used for calibrating the energy per nucleon of the beam. With the present solution using Si detectors, timing measurements with both detectors cannot be done at the same time. An alternative solution using annular Si detectors is under analysis.

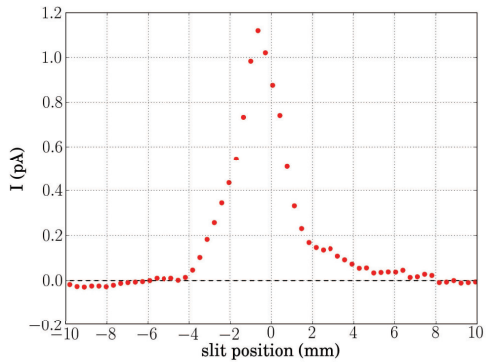


Figure 7: Vertical profile of a REX-ISOLDE low intensity beam, obtained with a prototype scanning slit of 0.2 mm width.

TRANSVERSE EMITTANCE

The transverse emittance measurements will be done using the existing REX-ISOLDE emittance meter based on the slit and grid method [6]. As a complementary solution, a two-slit scan technique can be implemented using two diagnostic boxes. The achievable resolution for the emittance measurements using the two slits was studied by means of Montecarlo simulations. A diagram representing the main simulation parameters is presented in Fig. 8. The initial beam current is I_{beam}. The slit positions (horizontal or vertical) are x_1 and x_2, the width of the slit is w and the distance between the slits is d. A Faraday cup placed downstream of the second slit detects the transmitted particles. By scanning the slits in turn and recording the transmitted intensity the profile of each beamlet can be reconstructed, from which the emittance can then be calculated. Noise contribution is simulated with the addition of a current I_{noise} to the collected intensity I_{FC}.

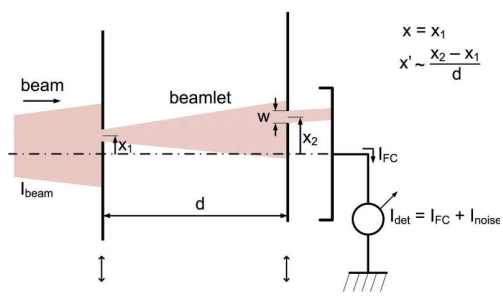


Figure 8: Schematic representation of the two slits-emittance measurement.

ISBN 978-3-95450-141-0

Copyright © 2014 CC-BY-3.0 and by the respective authors

The simulations performed included scans of the two slits in both horizontal and vertical directions. Typical HIE-ISOLDE beams measurements were studied, with I_{beam} in the range 100 to 1000 pA and an added noise contribution I_{noise} with standard deviation 0.1 pA, for three different slit widths (w = 0.2, 0.5 or 1 mm). The separation between the slits was d = 2.6 m, which is the distance between consecutive DBs in the HEBT lines. For the data analysis, an algorithm including a threshold was applied to reduce the influence of noise in the final evaluation of the emittance. In all the studied cases a slit width of 1 mm was found to be optimal. With such a slit width value, the transverse emittance was simulated to be measurable within the requirements for beams with intensities $I_{beam} \geq 400$ pA.

ACTUATORS TEST

The position accuracy of the linear actuator for the movement of the scanning slit of the HIE-ISOLDE DBs was characterised using a prototype short DB designed and built by the company AVS [7]. The mechanism includes two guiding rods and a lead screw, with a full stroke of 135 mm. To test the system a specially designed blade was mounted on the actuator and the transverse position monitored with a camera-based optical system while moving the actuator. The blade had two slits of 0.2 mm width at 45° from the axis of movement and six holes of 0.1 mm diameter drilled in the axis that were used for monitoring the transverse position of the blade. Two optical viewports were mounted on the beam pipe flanges of the DB vacuum tank to allow the installation of a light source and a CCD camera on either sides of the tank. Their supports were independent and mechanically detached from the DB support to avoid coupling any vibration generated by the actuator movement to the optical devices. The position of the slit was controlled by means of a stepper motor. The system also included limit switches and a temperature monitor connected to the external casing of the stepper motor.

The test procedure consisted of tracking the position of the drilled holes for different blade positions while it was moved at speeds of up to 10 mm/s. When the scanning blade crossed the beam aperture, the light passing through the drilled holes (or the slits) was detected by the camera. By analysing the size and position of the light spots frame by frame, the displacements of the blade due to mechanical vibrations were determined. To better reproduce operating conditions these tests were carried out under high vacuum conditions ($P \sim 2 \cdot 10^{-6}$ mbar). After several measurements at different blade speeds, it was concluded that the reproducibility in the positioning of the blade is better than 20 μm. This value allows the determination of transverse beam profile and position within the requirements of the functional specification [2].

ELECTRONICS AND CONTROLS

A new VME board has been designed, built and tested to control the devices on each diagnostic box. It has the capability of controlling up to eight stepper motors, as well as the complete acquisition chain of a FC (DAC/ADC, gains, integration time selection, external trigger, and a programmable high voltage power supply). A new front-end preamplifier has also been produced for the measurement of beam intensity with the FC. In addition, two main Front End Software Architecture (FESA) [8] servers have been developed specifically for HIE-ISOLDE to handle the beam intensity acquisition, the collimator movement, and the energy and time spectra obtained with the Si detectors.

ACTUAL STATUS AND FUTURE WORK

The design of the instruments for the HIE-ISOLDE project has been finalised. Tests with prototypes have been performed with all the devices, showing that they fulfill all the functional specifications. The production of the fully assembled diagnostic boxes (six short and nine long) is currently in its final stages, with contracts signed with external companies. The series production of the electronic cards and preamplifiers will be delivered in October 2014. Installation of the equipment in the HIE-ISOLDE hall is forseen to start at the beginning of 2015, with commissioning with beam scheduled to start in July 2015.

ACKNOWLEDGEMENT

We would like to thank R. E. Laxdal and M. Marchetto from TRIUMF for their collaboration during the FC tests in August-September 2013, and the support of J. M. Carmona, J. Galipienzo and J. Reyes from AVS [7] during the scanning slit actuator test in February 2014. Support by our colleagues S. Bart Pedersen, S. Burger, D. Lanaia and D. Voulot from CERN is also gratefully acknowledged.

REFERENCES

[1] The HIE-ISOLDE Project at CERN, https://hie-isolde.web.cern.ch

[2] M. Fraser et al., "Functional specification of the beam diagnostic boxes for HIE-ISOLDE", CERN EDMS Id: 1213401.

[3] The REX-ISOLDE post-accelerator, http://isolde.web.cern.ch/rex-isolde

[4] TRIUMF, Canada's national laboratory for particle and nuclear physics. The TRIUMF Isotope Separator and Accelerator (ISAC) facility, http://www.triumf.ca/

[5] F. Zocca et al., Nucl. Instrum Meth. in Phys. Res. A **672**, 21 (2012).

[6] J. Dietrich et al., "High sensitive beam emittance analyzer," EPAC'02, Paris, June 2002, THPRI115, p. 1864.

[7] Added Value Solutions. Pol. Ind. Sigma Xixilion, Kalea 2, Bajo Pabellon 10. 20870 Elgoibar, Gipuzkoa. Spain. http://www.a-v-s.es/

[8] M. Arruat et al., "CERN Front-End Software Architecture for Accelerator Controls", ICALEPCS2003, Gyeongju, Korea, October 2003, WE612, p. 342.

Copyright © 2014 CC-BY-3.0 and by the respective authors

ISBN 978-3-95450-141-0

STATUS OF THE STANDARD DIAGNOSTIC SYSTEMS OF THE EUROPEAN XFEL

D. Nölle for the E-XFEL Diagnostic Team, DESY, Hamburg, Germany

Abstract

The European XFEL, an X-ray free-electron-laser user facility based on a 17.5 GeV superconducting linac, is currently under construction close to the DESY site at Hamburg. DESY is in charge of the construction of the accelerator. This contribution will report the status of the standard diagnostic systems of this facility. The design phase has finished for all main systems; most of the components are in production or are already produced. This paper will show details of the main systems, their installation issues and will report on the further time schedule. Furthermore, the preparation of the commissioning of the RF gun with beam will be presented.

INTRODUCTION

The European XFEL facility (E-XFEL) is currently under construction in Hamburg [1]. The facility is organized and will be operated as an international company with shares hold by the countries participating in the construction, either with cash or in-kind contributions. DESY acting for the German Ministry of Science and Education is the biggest shareholder of this company, and is taking the leadership of the Accelerator Construction Consortium, that is in charge to build and operate the accelerator.

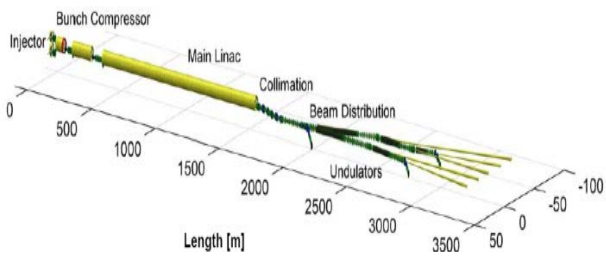


Figure 1: Layout of E-XFEL.

The core of the facility is the 17.5 GeV superconducting accelerator, able to supply up to 5 undulator systems with electrons simultaneously. The corresponding 5 photon beamlines transport the radiation into an experimental hall, with a distance of about 3.3 km to the gun (Fig.1). The overall facility will be installed in a tunnel system at an underground level between 28 and 7 m. Due to superconducting RF the machine is able to run long RF pulses at a repetition rate of 10 Hz each containing up to 2700 bunches. The beam distribution within the bunch train is enabled by a fast kicker septum system, capable to split the long bunch train into two sub-trains. Arbitrary bunch patterns out of this sub-trains are possible using a beam dump kicker to kick out bunches not requested by the users. This scheme was very recently successfully demonstrated at the FLASH facility with the first lasing of the FLASH2 beamline, simultaneously while FLASH was continuing to provide long bunch SASE delivery for users [2]. The electron beams are then send to X-ray SASE Undulator systems of up to 200 m length to produce intense photon pulses down to 0.5 Å at mJ level. One of the two main beamlines provides 2 SASE undulators for hard and soft X-ray production in a sequence, the other starts with only a hard X-ray system and has the option to be upgraded either with spontaneous radiation sources for hard X-rays or with soft X-ray laser sources. Due to the installation in a tunnel, all the electronics has to be installed close to the machine. Racks shielded by about 20 cm of heavy concrete will be used.

The project is now entering the installation phase [3]. All underground buildings are completed and the technical infrastructure is almost finished. The first of the 101 accelerator modules is installed in the tunnel. About 10 more are currently under test at the Accelerator Module Test Facility (AMTF) at DESY. Newly assembled modules are coming almost every week from the assembly facility at CEA, Saclay. Concerning the installation of the warm beamline, the assembly of the girder systems for the injector and bunch compressor sections has started.

The project time schedule foresees, to continue commissioning of the RF gun system this fall, to complete the injector and start commissioning in late spring 2015, the main accelerator should be completed about 1 year later, so that commissioning can start in summer 2016. The goal to get first photons is set to the end of 2016 and first lasing to spring 2017. First user operation with some relaxed operation parameters should be possible about 1 year after the start of the commissioning.

The work package of standard diagnostics is taking care of all systems needed as standard tools in bigger quantities, as described in Table 1. More special monitors, usually for longitudinal diagnostics are within the scope of the special diagnostics work package. In the standard diagnostics work package, the systems are either provided by DESY as the main contributor or as projects with in-kind contributions from PSI, CEA or IHEP Protvino. PSI, CEA and DESY are providing the BPM system as a collaborative effort [4], and IHEP has delivered the mechanical components of the BLM system [5]. In general the status of the different systems is advanced and within the current global time schedule. Therefore, also the diagnostics have entered the installation phase, details

Copyright © 2014 CC-BY-3.0 and by the respective authors

ISBN 978-3-95450-141-0

on each system and on the different machine sections will be given in the following chapters.

DIAGNOSTIC SUB-SYSTEMS

Since the E-XFEL is based on a superconducting linac, all vacuum systems close to the cavities have to fulfil Class 100 or ISO 5 cleanliness requirements. Therefore, cleaning and assembly of all parts in general takes place in clean rooms. Components used inside the cryo-modules have even to be cleaned to Class 10 or ISO 4 specifications (Fig.2).



Figure 2: Assembly of button BPMs in cleanroom environment.

The control system standard of E-XFEL is µTCA.4. Therefore, most of the electronic developments are based on MTCA.4[6].

Table 1: Overview on Diagnostic Devices

Device	Injector	Main Linac	SASE Lines
Cold BPMs*	2	100	
Button BPMs	11	104	111
Cavity BPMs 10 mm			103
Cavity BPMs 40.5 mm	3	18	5
Toroids	4	17	15
Dark Current Monitors	2	7	
Faraday Cups	3		
Simple Screens (45°)	6	4	4
Screens	1	26	16
Off Axis Screens	4	8	
Wire Scanners		3	9
Beam Loss Monitors	8	92	250
Dosimetry Sensors	10	200	500

* 31 Reentrant Cavity BPMs, 71 Cold Button BPMs

BPM System

The BPM system for E-XFEL is an in-kind contribution of the BPM collaboration by PSI, CEA and DESY. DESY is in charge of the BPM RF-pickups, except the re-entrant cavity BPM. CEA provides the re-entrant cavity BPMs together with the corresponding RF front end electronics[7]. PSI takes care of the entire electronics - RF front ends and digital back ends - except the re-entrant cavity BPMs [4].

The button BPM is the working horse of the E-XFEL. Two different types of buttons are used. One with a button diameter of 20 mm has a very robust design and was designed for applications in the cryogenic environment [8]. Extensive tests at liquid helium temperature have proven the robustness of this feedthrough design. Flat flanges for diamond edge aluminium gaskets are used to be compatible with the flange system of the E-XFEL cryo-modules. The BPM body with 78 mm diameter and 170 mm length (Fig.3) has the same external interfaces to the module as the re-entrant cavity BPM, so that both fit to the module design. Alignment of the cold BPMs to the vessel of the module´s superconducting quadrupole is done by means of dowel pins. BPMs of both types are routinely assembled to “BPM quadrupole units” About 20 of them are already delivered to CEA for module production.

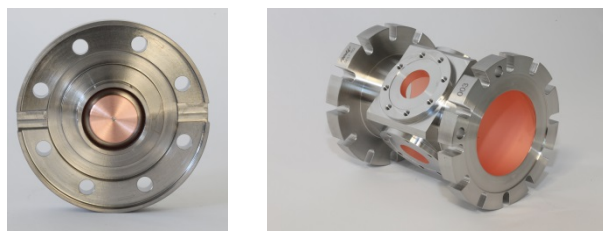


Figure 3: Cold button BPM: Feedthrough and body.

The second feedthrough type with 16 mm buttons was optimized to provide high signal levels, in order to face the challenge of low charge operation [9]. It is used in all warm button BPMs with different beam pipe diameters from the standard 40.5 mm beam pipe to the dump lines with a diameter of 200 mm (Fig. 4). The BPMs are rotated by 45° around the beam axis, so that no synchrotron radiation should hit the buttons. All feedthroughs are delivered. The production of the bodies of all warm button BPMs was done in-house. Cleaning, assembly and final vacuum checks are done on demand. Several BPMs are already installed in the tunnel.



Figure 4: “Warm” button BPM components.

Beam tests at FLASH and the PSI test accelerator using the BPM electronics from PSI have demonstrated a

Copyright © 2014 CC-BY-3.0 and by the respective authors

ISBN 978-3-95450-141-0

resolution of 30 µm for the cold button and 11 µm for the standard 40.5 mm BPM at 20 pC. Within the nominal charge range of E-XFEL (0.1-1 nC) the resolution is 5 µm (cold) and 3 µm for the warm button BPMs [10].

For the warm beamlines also 2 types of cavity BPMs have been designed and built [11]. Both types work at a frequency of 3.3 GHz. The material is stainless steel resulting in a rather low Q of about 70. This design was chosen to be able to cleanly separate the signals at bunch repetition frequencies up to 4.5 MHz. Both types will use the same electronics provided by PSI. The 40.5 mm cavity BPMs type shown on a injector girder in Fig. 5, will also be part of the fast transverse intra bunchtrain feedback of the E-XFEL, which will be provided by PSI as an in-kind contribution [12].

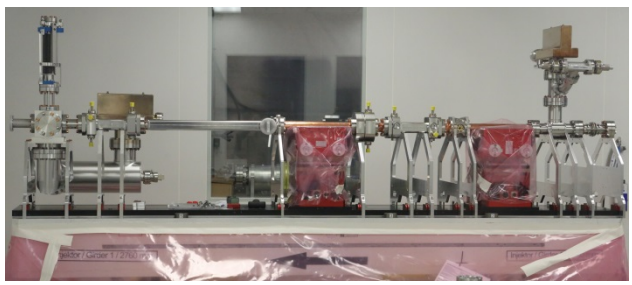


Figure 5: XFEL girder with two 40.5 mm cavity BPMs during assembly in the clean room.

The BPM for the 10 mm beam pipe, designed for the Undulator sections, is much more compact, since crosstalk between reference and dipole cavity is much smaller. A part of the production of the 140 BPMs is installed in the FLASH2 beamline (Fig.6), and has already been commissioned there [13, 14].

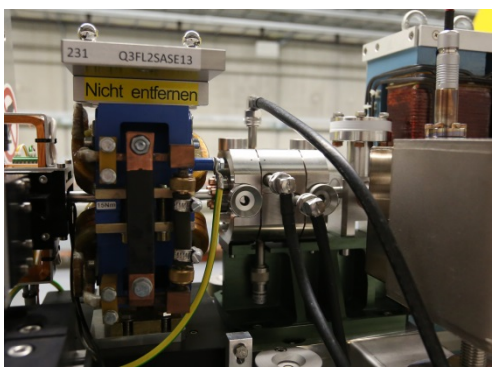


Figure 6: XFEL cavity BPM of the Undulator type installed in an Undulator intersection of the FLASH2 beamline.

Close collaboration with industry and QA actions including RF measurements at the manufacturers´ site resulted in a series production of 140 BPMs of the 10 mm type and 30 BPMs with a beam pipe diameter of 40.5 mm, all within the specification [11].

Measurements at FLASH, FLASH2 and the PSI test injector showed that the resolution of the 10 mm type is about 0.5 µm and for the 40.5 mm type about 1 µm in the standard operational range of 0.1 to 1nC of the E-XFEL. Even at a charge as low as 2 pC a resolution of 11 µm was measured for the undulator type BPM [15].

Charge Measurements

Apart from of faraday cups in gun region, the E-XFEL will use standard DESY toroids and dark current monitors [16] for charge measurements.

The main charge monitor system of E-XFEL is based on the so called toroids, DESY´s standard AC current transformers used in all transfer lines and also at the FLASH facility. Beside the refinement of the front-end electronics like development of a new amplifier and adding a test pulse generator, the main development step was to go to µTCA. The design includes online bunch by bunch data processing in an FPGA and fast digital data links. The fast communication links allow to use two toroid stations for low latency transmission validation, and can also be used for communication to other customers like laser controls or low level RF system. Furthermore bunch pattern validation and detection of too high charge is provided by bunch by bunch FPGA processing. Interlocks detected by the toroids are reported by a special low latency interface to the machine protection system [17].

X-FEL uses 36 of these devices, always located at the beginning and end of a logical section of the machine and at all the branches. The vacuum hardware ready for installation, the front-end is being built while the back-end is in the final development phase.

The dark current monitors are based on 1.3 GHz stainless steel cavities. They use the pile up resulting from summing up the signals coming from the low charged dark current buckets coming in phase at the RF repetition rate of 1.3 GHz. This scheme allows the detection of dark currents in the nA range. In addition, also the signal of the regular bunches can be seen, so that charge measurements with some fC resolution are possible. 9 of these monitors will be installed, the resonators are available; the series production of the electronics will finish in fall this year.

Beam Size Measurements

Due to the compressed bunches X-ray FELs very easily run into the problem of coherent radiation emission from screens, the so called COTR. Furthermore, the E-XFEL will use long bunch trains with up to 2700 bunches per train. These two requirements together with the need of 10 µm resolution for the screens was the driver for the beam size measurement system, using scintillating screens and (fast) wire scanners.

The high resolution screens have the LYSO:Ce target oriented perpendicular to the beam axis, so that COTR will be reflected back into the beam pipe [18]. The camera is looking to the scintillating light from the screen under an angle of 45°. Using the Scheimpflug principle the field of depth is extended almost over the entire screen. 1:1 magnification together with a large chip CCD camera gives a field of view of 12.9 mm x 9.6 mm. The

ISBN 978-3-95450-141-0

Copyright © 2014 CC-BY-3.0 and by the respective authors

screen holder allows to place up to 2 targets and a calibration screen, one of the screens can be an off axis screen, allowing to kick single bunches out of the long train to this target. The system was successfully tested at FLASH, and is now also in use at the FLASH2 beamline (Fig.7).

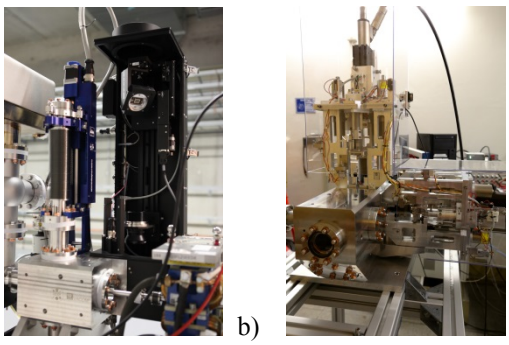


Figure 7: E-XFEL screen station and wire scanner.

a) Screen station installed in FLASH2 with the optics box opened. One can see the lens and the camera in Scheimpflug configuration.
b) Wire scanner with horizontal and vertical scanner in the vacuum chamber. The ports in front of the scanner are used to install a screen system like the one shown in part a) of the figure

In addition E-XFEL will have 4 wire-scanner systems, each consisting of 3 stations, so that emittance and twiss parameters can be measured without touching the magnets. Each station consists of one fast scanner for the horizontal and one for the vertical plane. The scanners are driven by linear motors and move on trigger within 800 µs and 1 m/s speed through the beam (slow scans are also possible). The wire should withstand 100 bunches at 1 nC, so that fast scans are always possible The mechanics of the scanners is in production, and the µTCA based electronics is in the final development phase [19].



Figure 8: Pair of type X-FEL type BLMs installed in the FLASH2 beamline.

Beam Loss Monitoring and Dosimetry

With an average beam power of up to 600 kW CW, E-XFEL has to have an effective protection against beam loss, in order to avoid damage and to keep activation to reasonable low limits. Therefore about 350 beam loss monitors [5] and a network of about 700 dosimetry sensors will be installed [20].

The BLM system is based on the classical scheme using scintillators read out by PMTs (Fig.8). Two types, plastic scintillators and quartz rods, detecting Cherenkov light are used. The signals from 8 BLMs are digitized on a µTCA rear transition module and are then processed in a FPGA on the AMC backend on a bunch by bunch time scale. If different interlock conditions are violated, a signal is issued to the machine protection system. Beside of the single bunch, few bunch and integral loss alarms processed in the FPGA, a fast single bunch alarm based on an analogue comparator is also included. The latency of the BLMs is few ns for the analogue channels and some 100 ns for the alarms processed in the FPGA.

The dosimetry system [20] will be based on RadFet sensors. It consists of internal sensors, positioned on a special FMC carrier board on other electronics, like the µTCA AMC boards of the machine protection system or in the BPM crates of EXFEL. These sensors will be at the same position like “other” electronics, and therefore will deliver a dose map of the electronic racks. The FMC carrier has a field bus interface to the outside. It allows to connect outside sensors via the so called “Dosibox”. Several of these boxes can be connected to a bus line, each connecting to up to 4 sensors. Cable lengths up to 20 m are possible. These external sensors will be place at critical devices like the undulators. From the point of sensitivity two ranges will be covered, for low dose regions inside the shielding of the electronic racks the sensitivity will be in the mGy range, while the external sensors will work with some Gy resolution. For a future upgrade, the possibility to include neutron sensors is foreseen in the design.

ACCELERATOR INSTALLATION

Currently the installation of the technical infrastructure is almost finished, but the injector and the main accelerator tunnel are ready for the installation of accelerator components. Fig. 9 shows the first accelerator module, which was recently installed in the tunnel.



Figure 9: First E-XFEL accelerator module installed in the tunnel.

Copyright © 2014 CC-BY-3.0 and by the respective authors

ISBN 978-3-95450-141-0

In the injector building, the RF gun with the warm beamline between the gun and the first module is installed and the commissioning has started in September 2014. This first about 1.5 m long beamline, shown in Fig. 10, contains BPMs, screens, charge and dark current monitors.

The remaining warm beamline in the injector is currently being installed. The next step will be the assembly of the girder system for the bunch compressors.

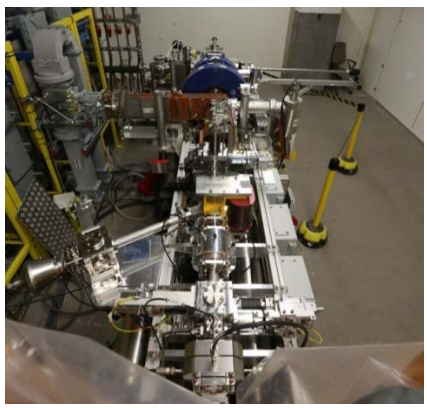


Figure 10: RF gun with first about 1.5 m long beamline installed in the injector building.

TIME SCHEDULE

After completion of the cryogenic infrastructure of the injector and the availability of the 3.9 GHz third harmonic structure the injector will start operation in late spring 2015. There will be about one year time for intensive commissioning of the injector. The goal is, to have the full range of operation parameters from the injector available after this time. Since almost all devices are used in the injector this intense commissioning process covers also most of the diagnostics. In mid-2016 the installation of the entire facility will be finished, and cool down of the linac will start. First photons should be possible by the end of 2016, and lasing in the X-ray regime is scheduled for spring 2016.

CONCLUSION

The diagnostic system for E-XFEL is well on track. The vacuum hardware is produced and ready for installation. The electronics systems are close to production. Even if the start-up of the complete facility is still two years ahead the commissioning work already has started, since cavity BPMs, screens, BLMs and toroids of the E-XFEL type are part of the FLASH2 beamline and have been commissioned there [13,14]. Furthermore, the E-XFEL injector has started the operation of the RF gun. After studies with RF only, production of photoelectrons will follow within the next weeks.

ACKNOWLEDGMENT

This paper gives an overview over the work done within the standard diagnostic work package. Therefore it represents the contributions of many people of the project team. The author would like to thank all contributors to this work package as well as all people in the E-XFEL project helping to get the entire machine ready for installation and commissioning.

REFERENCES

[1] The European XFEL, Technical Design Report, http://www.xfel.eu/documents/technical_documents
[2] S. Schreiber et al., “First Lasing at FLASH2”, FEL 2014, Basel.
[3] M. Hüning, “Status of the European XFEL”, IPAC 2013, Shanghai.
[4] B. Keil et al., “The European XFEL beam position monitor system”, IPAC 2010, Kyoto.
[5] A. Kaukher et al., “XFEL Beam Loss Monitor System”, IBIC 2012, Newport News
[6] MTCA.4, www.picmg.org, 2014.
[7] C. Simon et al., “Production Process for the XFEL Re-Entrant Cavity BPM”, IBIC 2014, Monterey.
[8] S. Vilcins et al., “Mechanical Design of Cryogenic Vacuum Feedthroughs for X-FEL Button BPM’s” , IBIC 2014, Monterey.
[9] D. Lipka et al., “Button BPM Development for the European XFEL”, DIPAC 2011, Hamburg.
[10] D. Treyer et al., “Design and Beam Test Results of Button BPMs for the European XFEL BPM Electronics”, IBIC 2013, Oxford
[11] D. Lipka et al., “BPMs from Design to real Measurement”, IPAC 2014, Dresden.
[12] B. Keil et al., “Design Status of the European X-FEL Transverse Intra Bunch Train Feedback”, IBIC 2012, Tsukuba.
[13] N. Baboi et al., “Commissioning of the FLASH2 Electron Beam Diagnostics in Respect to its use at the European XFEL”, IBIC 2014, Monterey.
[14] D. Lipka, “FLASH Undulator BPM Commissioning and Beam Characterization Results”, IBIC 2014, Monterey.
[15] M. Stadler et al., “Low-Q Cavity BPM Electronics for E-XFEL, FLASH-II and SwissFEL”, IBIC 2014, Monterey.
[16] D. Lipka et al., “Dark Current Monitor for the European XFEL”, DIPAC 2011, Hamburg.
[17] M. Werner et al., “A Toroid Based Bunch Charge Monitor System with Machine Protection Features for FLASH and XFEL”, IBIC 2014, Monterey.
[18] C. Wiebers et al., “Scintillating Screen Monitors for Transverse Electron Beam Profile Diagnostics at the European XFEL”, IBIC 2013, Oxford.
[19] T. Lensch, “Wire Scanner Installation into the MicroTCA Environment for the European XFEL”, IBIC 2014, Monterey.
[20] D. Nölle et al., “Test and Measurements with the Embedded Radiation-Monitor-System Prototype for Dosimetry at the European XFEL”, IPAC 2012, New Orleans.

Copyright © 2014 CC-BY-3.0 and by the respective authors

ISBN 978-3-95450-141-0

ALGORITHM TO IMPROVE THE BETA-FUNCTION MEASUREMENT AND ITS EVALUATION IN STORAGE RINGS LATTICES

A.C. García B.*, Universidad Nacional de Colombia, Bogotá, Colombia

Abstract

In any beam-line, one of the basic measurements in the beam-diagnostics is the measurement of the Beta-Function. This can be achieved, in Storage Rings, by taking the tune change obtained when varying the intensity of quadrupoles, or by using the matrix response to fit the corresponding parameters, or by shaking the beam to obtain a betatron motion. In accelerators like the LHC, the Beta-Function measurement is done from the Phase Advance Measurement using the Transfer Matrix. In this paper, a study of a new algorithm or numerically approximation for this measurement is presented, as well as the results of simulations on LHC and CLIC lattices. The deduced and implemented algorithm takes into account a fraction of the both transverse planes measurements. A random (uniform) deviation of the MAD-X phase values is taken to obtain the measured values and then used to study the Beta Function measurement for a different amount of orbits. There are observed cases where the improvement is close to 30% and 50% compare to a traditional method.

INTRODUCTION

The measurement of the Beta Function in accelerators is an important task during the commissioning, because all the properties of the focusing structure are described and calculated using the Twiss functions or Courant-Snyder parameters. For any beam-line, in colliders and transport lines of high energy particles, the horizontal and vertical Beta functions determine the transverse beam sizes that change around the storage ring. During the beam-diagnostics, to know the twiss parameters implies, in general, to be able to determine all the dynamic beam parameters. [1],[2],[3].

One of the techniques used to measure the beta-function in colliders or storage rings, is by using the tune shift induced by quadrupole excitation, this consists in *to detect the shift in the betatron tune as the strength of an individual quadrupole magnet is varied*, pag. 17 on [4]. The theoretical expression is obtained from the trace of the corresponding transport matrix for the entire ring multiplied by the perturbation matrix, which represents the effect of the gradient change. In the simplified final expression, each transverse beta function depends on the tune change in the corresponding plane, the gradient change, and constants. A specific variation of this method, using two symmetric placed quadrupoles, allows measuring the beta-function at the interaction point in colliders [5].

* acgarciab@unal.edu.co,ac.garcia412@uniandes.edu.co

A second method is given by shaking the beam to obtain a betatron motion. The betatron oscillations are measured with multi-turn beam position monitors (BPMs) and *the beta function is calculated from the betatron phase advance between three adjacent BPMs*, pag. 21 on [4]. Theoretically, from the Transfer Matrix on element to element, one can obtain a set of two independent equations with the information of three BPMs. The final expression involves the matrix elements depending of the designed optics and the $\tan$ value of the measured phase advances. The α measure can also be obtained with this procedure.

Additionally, having a betatron motion in the beam-line allows measuring the Beta Function using an interpolation of the twiss functions between the BPMs. In this way, the matrix response is used to fit the corresponding parameters assuming that the magnetic gradients in the transfer line model between the monitors 1 and 3 are perfect. The theoretical expressions are similar of what was discussed for the previous method. Computers are used to calculate the fit, where the measured variables are normalized to create a symmetric covariance matrix to be solved by least squares. The final expression depends on the measured phase advances and Beta Function in the BPMs. [1], [5].

Another simple method is to measure the orbit change when a steering corrector magnet is excited at different values. This method use a BPM nearby the corrector, and it is where the beta function value is obtained. The theory involves the expression of the closed-orbit distortion in the presence of a single dipole kick. The final beta function measurement if obtained from the $\tan$ value of the tune, the closed-orbit distortion, the steering error value and constants. [4], [2].

For instance, in the LHC the measurement of the Beta Function for the relativistic beams is performed by using the second method described above, eq. (1) in [6].

THEORY

During the measurement of any optical quantity in an accelerator, it is expected to have a correspondence between the model scenario and what is measured at the machine. Using the transfer matrix for the beta function measurement, it is found that the following should be fullfilment

$$\cot \Delta\Phi_{1,2}^{ide} - \cot \Delta\Phi_{1,3}^{ide} = \cot \Delta\Phi_{1,2}^{meas} - \cot \Delta\Phi_{1,3}^{meas} \quad (1)$$

where, Φ are the phase advance in the transverse plane, at the three different longitudinal positions 1, 2 and 3; the labels *ide* and *meas* stand for the 'ideal' and 'measured' scenarios, respectively. The discrepancies among the model phase advances, or 'ideal' values, and the ob-

Copyright © 2014 CC-BY-3.0 and by the respective authors

ISBN 978-3-95450-141-0

served or 'measured' values, are then propagated to the beta function measurement.

The proposed new algorithm is to correlate both planes to a common factor, which as before it is expected to be true. It implies the following:

$$\frac{\cot\Delta\Phi^{x,ide}_{1,2}-\cot\Delta\Phi^{x,ide}_{1,3}}{\cot\Delta\Phi^{y,ide}_{1,2}-\cot\Delta\Phi^{y,ide}_{1,3}}=\frac{\cot\Delta\Phi^{x,mea}_{1,2}-\cot\Delta\Phi^{x,mea}_{1,3}}{\cot\Delta\Phi^{y,mea}_{1,2}-\cot\Delta\Phi^{y,mea}_{1,3}} \quad (2)$$

This allows counting on the coupling that could interfered in the Beta Function measurement. In this way, the improvement algorithm consist of take into account the information of both planes. Therefore, there exists an optical function that would be called ρ from where the β function can be measured.

$$\beta^{x,measure} = \rho_z[\cot\Delta\Phi^{y,ide}_{1,2}-\cot\Delta\Phi^{y,ide}_{1,3}] \quad (3)$$

$$\beta^{y,measure} = \rho_z[\cot\Delta\Phi^{x,ide}_{1,2}-\cot\Delta\Phi^{x,ide}_{1,3}] \quad (4)$$

Additionally an optimization based on the possibility of small deviations of the expected values, turns into a problem of mathematical geometry which I solved to be

$$\rho_z=\begin{cases}\beta^{z,ide}\frac{\tau(x,2)\pm\cot\Delta\Phi^{x,mea}_{1,2}}{\tau(y,2)\pm\cot\Delta\Phi^{y,mea}_{1,2}} & \text{or}\\ \beta^{z,ide}\frac{\tau(x,2)\pm\cot\Delta\Phi^{x,mea}_{1,3}}{\tau(y,2)\pm\cot\Delta\Phi^{y,mea}_{1,3}}\end{cases} \quad (5)$$

where $\tau(z,m)=\cot\Delta\Phi^{z,mea}_{m-1,m}-\cot\Delta\Phi^{z,mea}_{m-1,m+1}$ and its depends on how close the measure fraction is close to the ideal fraction. These differences, although small quantities, are also what may improve the measurement when high noise (meaning a high deviation of the phase advanced) is presented.

The approach described in eq.(5) is not obtained from a statistical quantity, or based in them, as most of the traditional methods does. Although, the combinations of the above equations imply that the fitting is done to obtained the number 1.

TRANSFER MATRIX REMARK

The Transfer Matrix that allows measuring the Beta-Function in a collider, is given by:

$$\begin{pmatrix}\sqrt{\frac{\beta_f}{\beta_i}}(\cos\phi_{fi}+\alpha_i\sin\phi_{fi}) & \sqrt{\beta_f\beta_i}\sin\phi_{fi}\\ -\frac{1+\alpha_i\alpha_f}{\sqrt{\beta_f\beta_i}}\sin\phi_{fi}+\frac{\alpha_i-\alpha_f}{\sqrt{\beta_f\beta_i}}\cos\phi_{fi} & \sqrt{\frac{\beta_f}{\beta_f}}(\cos\phi_{fi}-\alpha_f\sin\phi_{fi})\end{pmatrix} \quad (6)$$

When applying to three adjacent BPMs, the value of the beta function at the first lattice element can be obtained as a function of the matrix elements, on the first row of the matrices that transfer from the element 1 to 2, and from 1 to 3, usually called m_{11}, m_{12} ,n_{11}, and n_{12}, respectively, [7]. See the details of the theory development for LEP [1] and the application at LHC in [6].

RESULTS ON LATTICES

The proposed new algorimth is tested on the lattices examples for two storage rings, using the standard software MAD-X [8] by a comparison with the traditional way to obtain the beta function measurement. The lattice source code is obtained from the MAD-X examples at [9].

The storage rings optics choose for this paper are the LHC and CLIC. In the optics corresponding to the CLIC lattice, a ring of 357.46 m of length is simulated, to a tune correspondence of 72.69 2π rad in the horizontal plane and 35.42 2π rad in the vertical plane. The maximum beta function at those planes are 30.00 m and 9.21 m, respectively. The beam consists of 3.1×10^9 positrons. For the LHC case, the simulated sequence is the Beam1, which is composed by 1.15×10^{11} protons in a ring of 26658.88 m length. The protons have an energy of 450 GeV, reaching a horizontal tune of 64.28 2π rad with a maximum beta function of 592.8 m, and a vertical tune of 59.31 2π rad with a maximum beta function of 611.97 m.

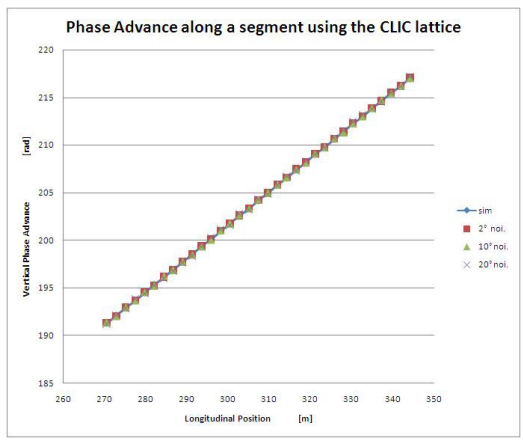


Figure 1: Phase Advances for a sector of the CLIC lattice, without and with noise for 2, 10 and 20 degrees of deviation, for the Y plane.

To obtain the measurement for the comparison, just a sector of each ring is used. In the cases for the CLIC lattice, 35 BPMS are taken into account, while for the LHC, 39 BPMs located at the arcs 4 and 5 are used. This is to have a difference in the phase advance in between the adjacent BPMs, and therefore having a better analysis on the Beta Function measurement.

The 'ideal' values during this test corresponds to the quantities obtained using the *twiss* function of MAD-X. These values are obtained for the phase advances and the Beta Fuction in both transverse planes.

The 'measured' values are interpreted as the total value of each 'ideal' phase advance plus or less a deviation according with a random uniform distribution. Three maximum deviations are studied, those values are 2.0, 10.0 and 20.0 degrees. The deviation value is half equally distributed around the 'ideal' values, to give as positive as negative deviations. These values are obtained using the

ISBN 978-3-95450-141-0

Copyright © 2014 CC-BY-3.0 and by the respective authors

random library of PYTHON [10].

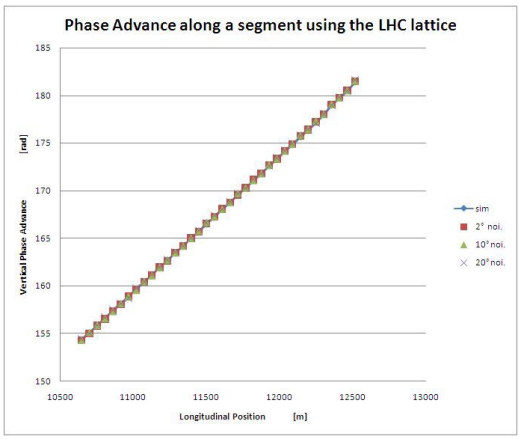


Figure 2: Phase Advances for a sector of LHC lattice , without noise and with noise of 2, 10 and 20 degrees.

Figures 1 and 2 shows the corresponding 'ideal' and 'measured' phases advances, for the studied cases in the plane Y using the CLIC and LHC optics, respectively. The *ide* values are denoted by the label "sim" and linked with a line. The *meas* values are presented using points of different colors for the studied deviations and denoted by adding the label "noi".

The plots for the two storage rings lattices are straight lines with a positive slope as expected. Similar plots were obtained in the horizontal plane, for both lattices. Evenmore the noise is almost not perceptive to the eye.

Using the noised phase advance values at three adjacent locations the equations (3) and (4) are applied to the corresponding transverse plane to obtain the Beta Function, as well as the traditional equations given by eq.(6) to obtain the same quantity, along the segment of the ring.

The measured value of the beta function is affected by the noised phase advances as presented in figures 3 and 4, for the different lattices. In the plots the noise is now perceptible. The notation used is the label "sim" for the ideal beta, label "t" for the traditional β- measurement, label "a" for the new algorithm, and together with the numbers 2, 10 and 20 according with the distribution used for the noise.

For each beta measurement a relative error to the ideal beta is obtained. And for the entire segment a global relative error, denoted by $Err.$, is asociated to be the average of the errors at the different locations. Each particular noised segment is going to be called an orbit, and with different random numbers used each time, different noised segments are obtained.

Taking different orbits Tables 1 and 2 are constructed, for each lattice independently. The first columnn is the studied case label, it corresponds with the amount of simulated noise and the type of theory used for the β measurement; the notation is the same as explained for Figures 3 and 4. The second and third column are the average of the global error, in each transverse plane with its corresponding uncertainty. The forth a final column contains the number of orbits used to obtained the average of the global error.

For the 2 degrees cases the new algorithm has a small increment of the global error % compare to the traditional way, in both cases the LHC and CLIC, this could be explain by the fact than a very small amount of noise presented does not favors the use of the both noise planes to do the Beta measurement. Specifically for the LHC cases, the results show that both -t and -a approaches are on the same order to make the measurement.

Table 1: Beta Fuction Err. Using CLIC Lattice

Case.	$Err. < \beta_x >$ [%]	$Err. < \beta_y >$ [%]	Num. Orb.
20-t	14.0064 ± 0.47	21.5973 ± 1.1	10
20-a	11.1688 ± 0.46	11.3702 ± 0.54	10
20-t	14.0898 ± 0.20	21.0753 ± 0.37	100
20-a	10.4034 ± 0.14	10.4941 ± 0.14	100
20-t	14.4705 ± 0.063	20.8487 ± 0.11	1000
20-a	10.5313 ± 0.046	10.6460 ± 0.046	1000
10-t	6.6708 ± 0.2369	10.1476 ± 0.35	10
10-a	8.6858 ± 0.34	8.9647 ± 0.35	10
10-t	6.9188 ± 0.093	9.9884 ± 0.14	100
10-a	8.8234 ± 0.10	8.9866 ± 0.10	100
10-t	6.8664 ± 0.029	10.0190 ± 0.050	1000
10-a	8.7920 ± 0.031	8.9517 ± 0.031	1000
2-t	1.4010 ± 0.062	1.9980 ± 0.11	10
2-a	2.4296 ± 0.097	2.4272 ± 0.098	10
2-t	1.3594 ± 0.018	2.0168 ± 0.031	100
2-a	2.4009 ± 0.040	2.4002 ± 0.040	100
2-t	1.3584 ± 0.0056	1.9917 ± 0.010	1000
2-a	2.3827 ± 0.012	2.3823 ± 0.012	1000

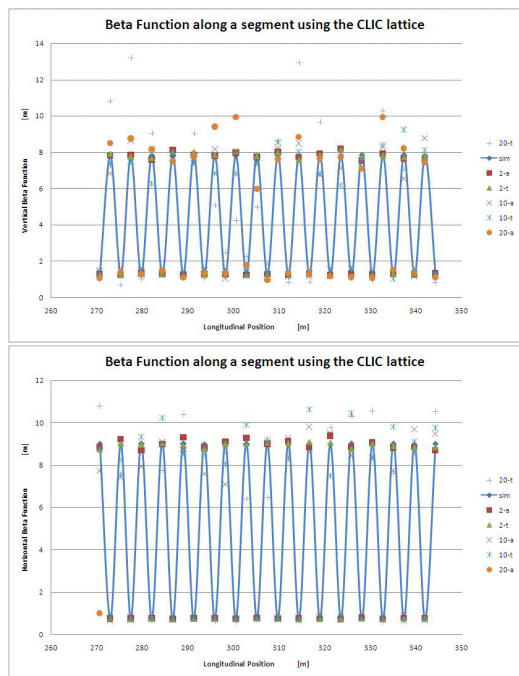


Figure 3: Beta Functions for a sector of the CLIC lattice, without and with noise for 2, 10 and 20 degrees of deviation.

With 10 degrees of noise, for the CLIC lattice the behaivor of the global error for the vertical plane is oppossed

Copyright © 2014 CC-BY-3.0 and by the respective authors

ISBN 978-3-95450-141-0

with respect to the horizontal plane. Err always increases by an amount of 20% of the traditional method by using the new algorithm for the horizontal plane, but it always decreases for the vertical plane by an amount of 10% of the traditional one.

Using the LHC lattice, for all the cases with 10 degrees noise, the new algorithm (-a) decreases the global error Err, to value close to 30% each time, compare with the traditional way to do the measurement for both planes.

With a noise of 20 degrees, for both lattices, it is found that the average of the global error is decreasing when using the new algorithm compare to the traditional one. This is expected, if the new algorithm is over stabilized values for the fraction of noise, and without favored to a particular plane. The reported values imply that percents of 26 and 49 for the horizontal and vertical planes for CLIC, and 29 to 27 for the horizontal and vertical planes for LHC, are reduced in the global error, when the new algorithm is applied compare with the traditional one.

Taking the average of the β function at each location before taking the global error, it is not studied in here to have the completed effect of the noise. Taking that average will reduced the noise in advance.

Table 2: Beta Fuction Err. Using LHC Lattice

Case.	$< Err.\beta_x >$ [%]	$Err.\beta_y >$ [%]	Num. Orb.
20-t	23.9845 ± 1.6	21.0685± 0.53	10
20-a	16.0208 ± 0.94	15.6167± 0.70	10
20-t	22.8245± 0.53	22.7674 ±0.37	100
20-a	16.7904± 0.45	16.3095± 0.37	100
20-t	22.3585± 0.16	22.7038± 0.12	1000
20-a	16.9809± 0.15	16.5626± 0.11	1000
10-t	10.4422± 0.43	11.2105± 0.65	10
10-a	7.1806± 0.54	7.1872± 0.57	10
10-t	10.3884± 0.16	11.0943± 0.17	100
10-a	7.2590± 0.15	7.2989± 0.15	100
10-t	10.4041± 0.055	10.9358± 0.054	1000
10-a	7.5054± 0.053	7.4269± 0.051	1000
2-t	1.9998± 0.075	2.1757± 0.12	10
2-a	2.2319± 0.051	2.2607± 0.058	10
2-t	2.0484± 0.033	2.1714± 0.033	100
2-a	2.2017± 0.027	2.2133± 0.027	100
2-t	2.0329± 0.010	2.1555± 0.010	1000
2-a	2.2014± 0.0092	2.2127± 0.0090	1000

In general, in all cases, the observed uncertainty of the global error is reduced or keeping in the same level as using the traditional way to do the measurements.

Nevertheless it is possible to run the new algorithm to calculate the beta function for the entire ring. The observed advantage is that there are few times when the measurements can be done with the new algorithm, in comparison with the old case. This could means that the difference in the phase advance is less restricted in new algorithm case.

Further studies could determine at which conditions the new algorithm favors, and to stablished the differences when using the traditional fitting processes, and or the fact that both plane measurements are involved. This would depend in the tunes of the accelerator used and the distance between the elements from whre the measurement is done.

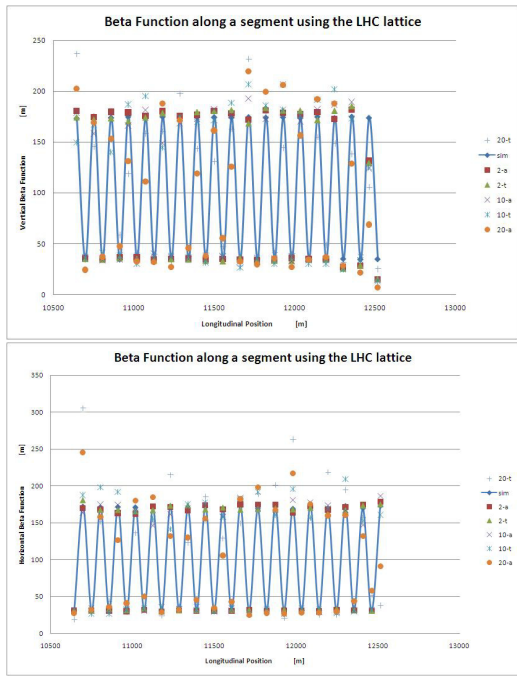


Figure 4: Beta Functions for a sector of the LHC lattice , without and with noise for 2, 10 and 20 degrees of deviation.

CONCLUSION

The algorithm introduced in this paper allows reducing the noise presented when performing the Beta Function measurement. In applications to the LHC Mad-X lattice, it is found cases where the improvement is close to 30% compare to the traditional one, when the noise is 10^o or 20^o; using the CLIC Mad-X lattice a reduction close to 25% and 50% are observed with a noise of 20^o . Althought further studies are needed to establish the ideal conditions for its application in real machines, this new algorithm could serve as a complement and/or improvement to the traditional technique.

ACKNOWLEDGMENT

I would like to thank B. Podobedov (at BNL), for his comments and criticisms to this manuscript. Also, to all my instructors and professors at the U.S. Particle Accelerator School and to the directors of my theses at the different institutions, thanks for the source of inspiration.

REFERENCES

[1] P. Castro, Luminosity and beta function measurement at the electron-positron collider ring LEP. Doctoral Thesis, CERN SL/96-70(BI) 1996.

[2] Helmut Wiedemann. Particle Accelerator Physics, Third Edition. Springer, 2007, USA. (Pag 159).

ISBN 978-3-95450-141-0

Copyright © 2014 CC-BY-3.0 and by the respective authors

[3] S.Y. Lee. Accelerator Physics, Third Edition. 2012. World Scientific, Singapore. (Pag47).

[4] F. Zimmermann. Measurement and Correction of Accelerator Optics. Beam Techniques, Beam Control and Manipulation., SLAC-PUB-7844, June 1998. (Pag 22, Pag. 418-422).

[5] Michiko G. Minty and Frank Zimmermann. Beam Techniques, Beam Control and Manipulation. Lectures given at the US Particle Accelerator School, June 14-25, 1999. (Pag 18).

[6] M. Aiba, R. Calaga, A. Morita, R. Tomas and G. Vanbavinckhove. Optics Correction in the LHC. Proceedings of EPAC08, Genoa, Italy. WEPP025.

[7] Notes and slides from the US Particle Accelerator School, course Beam-Based Diagnostics. June 2012.

[8] CERN-BE/ABP Accelerator Beam Physisc Group. MAD - Methodical Accelerator Design, MAD-X is the successor of MAD-8 and was first released in June 2002, http://mad.web.cern.ch/mad/ , CERN.

[9] Frank Schmidt. CERN-BE/ABP Accelerator Beam Physisc Group. MAD-X example for the Touschek Effect. 2008. http://frs.home.cern.ch/frs/mad-X_examples/touschek/

[10] The Python Software Foundation, 9.6. random — Generate pseudorandom numbers. www.python.org and https://docs.python.org/2/library/random.html

Copyright © 2014 CC-BY-3.0 and by the respective authors

ISBN 978-3-95450-141-0

ERROR ANALYSIS FOR PEPPERPOT EMITTANCE MEASUREMENTS REDUX: CORRELATED PHASE SPACES*

S. Lidia[#†], K. Murphy[‡], Lawrence Berkeley National Laboratory, Berkeley, CA, USA

Abstract

Recently, Jolly *et al.* presented an analysis of the rms emittance measurement errors from a first principles approach [1]. Their approach demonstrated the propagation of errors in the single-plane rms emittance determination from several instrument and beam related sources. We have extended the analysis of error propagation and estimation to the fully correlated 4-D phase space emittances obtained from pepperpot measurements. We present the calculation of the variances using a Cholesky decomposition approach. Pepperpot data from recent experiments on the NDCX-II beamline are described, and estimates of the emittances and measurement errors for the 4-D as well as the projected rms emittances in this coupled system are presented.

INTRODUCTION

Jolly, *et al.* [1] recently published an analysis of the data acquisition and uncertainty estimation of beam emittances derived from pepperpot measurements. There, they presented a first principles methodology for propagating measurement errors into the nonlinear functions of position, angle and beamlet intensity that are typically used to calculate the horizontal or vertical root-mean-squared (rms) emittances. Estimates of measurement errors were discussed that stemmed from the practical implementation of the pepperpot measurement system. The dominant sources of measurement error were the spacing of holes in the pepperpot mask; the camera resolution and drift distance between mask and scintillation screen; and beam intensity variation and background intensity noise levels. Additional errors in the measurement system were not included, so that the estimates of uncertainty represent lower limits on the total error.

A pepperpot image and its correlations to the background mask can be utilized to estimate the complete 4-D phase space emittance by analyzing all 10 independent correlation terms in the 4-D beam matrix. In this paper we extend Jolly, *et al.*'s formalism to estimate the uncertainty of the 4-D emittance and related quantities that include the correlations between the horizontal and vertical phase spaces. The results of this analysis can be applied to coupled systems found in solenoidal or skew quadrupole transport lattices, and beams that carry significant canonical angular momentum.

*This work was supported by the Director, Office of Science, Office of Fusion Energy Sciences, of the U.S. Department of Energy under Contract No. DE-AC02-05CH11231.

#lidia@frib.msu.edu
†Presently at Facility for Rare Isotope Beams, Michigan State University.
‡Presently at Department of Physics, University of Chicago.

CORRELATED PHASE SPACES

The 4-D beam covariance matrix is constructed from the density-weighted, rms product averages of the beam distribution,

$$\Sigma_4 = \begin{pmatrix} \langle xx \rangle & \langle xx' \rangle & \langle xy \rangle & \langle xy' \rangle \\ \langle xx' \rangle & \langle x'x' \rangle & \langle x'y \rangle & \langle x'y' \rangle \\ \langle xy \rangle & \langle x'y \rangle & \langle yy \rangle & \langle yy' \rangle \\ \langle xy' \rangle & \langle x'y' \rangle & \langle yy' \rangle & \langle y'y' \rangle \end{pmatrix} \quad (1)$$

Here, the individual product terms are defined by

$$\langle fg \rangle = \frac{\sum_i \rho_i f_i g_i}{\sum_i \rho_i}, \quad (2)$$

where the index i labels the coordinates in the 4-D space of {x, x', y, y'} and ρ is the local beam density in that space. We assume that the 10 unique terms are linearly-independent of each other.

The 4-D beam matrix can be expressed in the symmetric, block form that reveals the separate, Cartesian sub-spaces as well as the correlation between them,

$$\Sigma_4 = \begin{pmatrix} \Sigma_x & C \\ C^T & \Sigma_y \end{pmatrix}. \quad (3)$$

We note that other representations [2,3] are also used.

The definitions of rms emittances follow from the determinants of the beam matrix. The determinant and emittance of the 2-D Cartesian (sub-)phase space has the well known definition:

$$\det \Sigma_x = |\Sigma_x| = \langle xx \rangle \langle x'x' \rangle - \langle xx' \rangle^2 = \tilde{\varepsilon}_x^2 . \quad (4)$$

We carry the definition to the 4-D space and 4-D emittance:

$$\tilde{\varepsilon}_4^2 = |\Sigma_4|. \quad (5)$$

To compare the equivalent beam quality defined by the 4-D emittance measure, we define an equivalent 2-D emittance

$$\tilde{\varepsilon}_2^2 = |\Sigma_2| = |\Sigma_4|^{1/2}. \quad (6)$$

For transversely uncoupled phase spaces, $\Sigma_4 = \begin{pmatrix} \Sigma_x & 0 \\ 0 & \Sigma_y \end{pmatrix}$, and $|\Sigma_2| = |\Sigma_x||\Sigma_y|$ so that $\tilde{\varepsilon}_2^2 = \tilde{\varepsilon}_x \tilde{\varepsilon}_y$.

We utilize the equivalent 2-D rms emittance measure, $\tilde{\varepsilon}_2$, as a basis of comparison with the single-plane rms

ISBN 978-3-95450-141-0

Copyright © 2014 CC-BY-3.0 and by the respective authors

emittances, $\tilde{\varepsilon}_x$ and $\tilde{\varepsilon}_y$. We will also make use of the following definition of normalized, edge emittances, $\varepsilon_a = 4\gamma\beta\tilde{\varepsilon}_a$, where $\tilde{\varepsilon}_a$ is any of the above mentioned 2-D or single plane rms emittances.

CHOLESKY DECOMPOSITION OF BEAM COVARIANCE MATRIX

The analysis of error propagation from known measurement uncertainties into the 4-D or equivalent 2-D emittance measures can be made more computationally tractable if a matrix factorization is utilized. The Cholesky decomposition [4] is unique for positive-definite, symmetric, square matrices. This factorization produces a product of a lower-diagonal matrix (L) with its transpose, an upper diagonal matrix (L^T). Here, we opt to use a variant of the Cholesky decomposition, $A = LDL^T$, where A is the original matrix, and D is a block diagonal form.

The decomposition of the 4D beam covariance matrix

$$\Sigma_4 = \begin{pmatrix} \Sigma_x & C \\ C^T & \Sigma_y \end{pmatrix} = LDL^T = \begin{pmatrix} \mathrm{I} & 0 \\ S & \mathrm{I} \end{pmatrix} \begin{pmatrix} D_1 & 0 \\ 0 & D_2 \end{pmatrix} \begin{pmatrix} \mathrm{I} & S^T \\ 0 & \mathrm{I} \end{pmatrix} \tag{7}$$

With this decomposition, $|\Sigma_4| = |D_1||D_2|$. In terms of the Cartesian sub-spaces and correlation matrix C,

$$D_1 = \Sigma_x\,, \tag{8}$$

$$D_2 = \Sigma_y - C^T\left(\Sigma_x{}^{-1}\right)^T C. \tag{9}$$

This last form has its determinant expressed in terms of the elementary products as

$$|D_2| = \left(\langle yy\rangle - \frac{\nu_1}{|\Sigma_x|}\right)\left(\langle y'y'\rangle - \frac{\nu_4}{|\Sigma_x|}\right) - \left(\langle yy'\rangle - \frac{\nu_2}{|\Sigma_x|}\right)^2, \tag{10}$$

where

$$\nu_1 = \langle xy\rangle^2\langle x'x'\rangle - 2\langle xy\rangle\langle xx'\rangle\langle x'y\rangle + \langle xx\rangle\langle x'y\rangle^2,$$

$$\nu_2 = \langle xy\rangle\langle x'x'\rangle\langle xy'\rangle - \langle xy\rangle\langle xx'\rangle\langle x'y'\rangle + \langle x'y\rangle\langle xx\rangle\langle x'y'\rangle - \langle x'y\rangle\langle xx'\rangle\langle x'y'\rangle,$$

$$\nu_4 = \langle xy'\rangle^2\langle x'x'\rangle - 2\langle xy'\rangle\langle xx'\rangle\langle x'y'\rangle + \langle xx\rangle\langle x'y'\rangle^2. \tag{11}$$

ANALYSIS OF VARIANCE

The calculation of the combined variance proceeds typically [5]. A function, f, with independent variables (x, y, z, . . .), has a variance, σ_f^2, defined by $\sigma_f^2 = \left(\frac{\partial f}{\partial x}\right)^2\sigma_x^2 + \left(\frac{\partial f}{\partial y}\right)^2\sigma_y^2 + \left(\frac{\partial f}{\partial z}\right)^2\sigma_z^2 + . . .$, where the variance in the measurement of the independent variables is given by σ_x^2, σ_y^2, etc.

We calculate the variance of the 4-D beam matrix determinant, against the set of independent variables: $\langle xx\rangle$, $\langle x'x\rangle$, $\langle x'x'\rangle$, $\langle xy\rangle$, $\langle xy'\rangle$, $\langle x'y\rangle$, $\langle x'y'\rangle$, $\langle yy\rangle$, $\langle yy'\rangle$, and $\langle y'y'\rangle$.

$$\sigma_{|\Sigma_4|}^2 = \sum_{\langle ab\rangle}\left(\frac{\partial|\Sigma_4|}{\partial\langle ab\rangle}\right)^2\sigma_{\langle ab\rangle}^2, \tag{12}$$

where $\langle ab\rangle$ is a member of the set of 10 linearly-independent products.

The variance of the equivalent 2-D emittance is determined by applying the linear uncertainty estimation to (6)

$$\sigma_{\tilde{\varepsilon}_2}^2 = \sum_{\langle ab\rangle}\left(\frac{\partial\tilde{\varepsilon}_2}{\partial\langle ab\rangle}\right)^2\sigma_{\langle ab\rangle}^2 = \sum_{\langle ab\rangle}\left(\left[\frac{d\tilde{\varepsilon}_2}{d|\Sigma_4|}\right]\left[\frac{\partial|\Sigma_4|}{\partial\langle ab\rangle}\right]\right)^2\sigma_{\langle ab\rangle}^2 = \sum_{\langle ab\rangle}\left[\frac{1}{4|\Sigma_4|^{\frac{3}{4}}}\right]^2\left(\left[\frac{\partial|\Sigma_4|}{\partial\langle ab\rangle}\right]\right)^2\sigma_{\langle ab\rangle}^2 \tag{13}$$

$$\sigma_{\tilde{\varepsilon}_2}^2 = \frac{\sigma_{|\Sigma_4|}^2}{16|\Sigma_4|^{\frac{3}{2}}} \tag{14}$$

NDCX-II PEPPERPOT DESIGN AND MEASUREMENTS

The NDCX-II facility permits user experiments in the warm, dense matter regime, where matter is isochorically heated near solid density to temperatures in the eV range. Ion beams compressed to ns-scale pulse duration and focused with mm-scale spots onto micron-scale thickness targets can accomplish this task of target heating within the characteristic time of hydrodynamic expansion of the target material. The detailed physics design [6] and engineering [7] of the NDCX-II accelerator facility have been previously described. The first stage of beamline commissioning demonstrated the successful tuning of the beam transport lattice and the accelerating waveforms to deliver 30-50 nC, with normalized edge emittance of 1-2 π-mm-mrad, and to compress the pulse duration from ~600 ns at injection to <50 ns (FWHM) at the target plane [8].

The diagnostic end station houses the main complement of intercepting beam diagnostics, depicted in Fig. 1. The full instrumentation package includes a deep Faraday cup (14.2 cm long by 12 cm wide with a 10 cm entrance aperture), a horizontal slit and slit-cup analyzer, a vertical slit and slit-cup analyzer, a pepperpot mask and a 10.16-cm (4-inch) square optical scintillator (100 μm thick Al_20_3). A fast gated (~30 ns minimum), image intensified (ICCD) camera (Princeton Instruments PI-MAX II, 16-bit, 512x512 CCD array) is rear-mounted to collect the

Copyright © 2014 CC-BY-3.0 and by the respective authors

ISBN 978-3-95450-141-0

fluorescence signal from the scintillator plate. The deep Faraday cup is differentially biased to reject incoming electrons entrained with the ion beam, as well as to collect secondary electrons emitted during the ion current collection. The collector plane of the deep Faraday cup and the front surface of the scintillator coincide with the experimental target plane. Various planar targets may be mounted at the end of the scintillator/Faraday cup paddle. High voltage SHV feedthroughs allow bias potentials to be applied to the Faraday cup and slit cup suppressor and collector electrodes, and to the bias mesh on the upstream face of the optical scintillator. Capacitive dividers allow low amplitude beam-induced signals to be acquired from the high voltage biased electrodes.

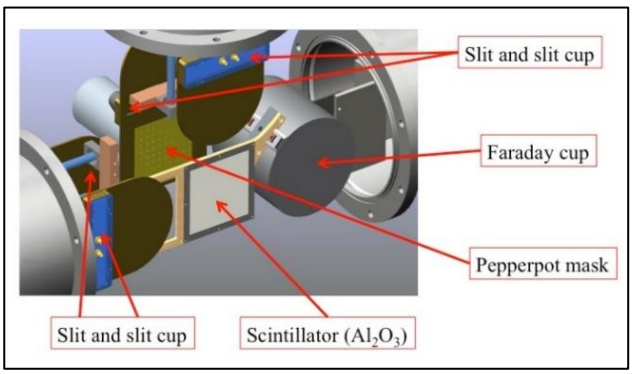


Figure 1: NDCX-II diagnostic end station.

The pepperpot mask (Fig. 2) and associated scintillator diagnostic has been designed and initially optimized to function with the high perveance, ~50-350 keV lithium ions. The mask is fabricated from 12.7 μm 304 stainless steel, and holds a rectangular pattern of 0.254 mm (0.010-inch) diameter holes spaced 3.81 mm (0.150-inch) apart (center-to-center). A scintillator screen is rigidly attached to the pepperpot mask holder, and spaced 17.5 mm downstream from the mask.

Analysis of the pepperpot images is accomplished utilizing a custom Python analysis routine: (i) beam-derived images and background images (resolution 4.7 pixels/mm) are obtained with defined gate windows around the beam current peak; (ii) background images are subtracted from beam-generated images; (iii) a Sobel filter [9] is applied to further assist in discriminating peaks from background; (iv) the images peaks are mapped to the known grid pattern to generate spatially correlated offsets and construct the 4-D transverse phase space; (v) background level cuts are applied based on calculating the Courant-Snyder invariant for each peak (equivalent to an L_{2} metric in phase space) and rejecting outlying, 'unphysical' peaks [10]; and (vi) the final values for the emittances and their uncertainties are calculated.

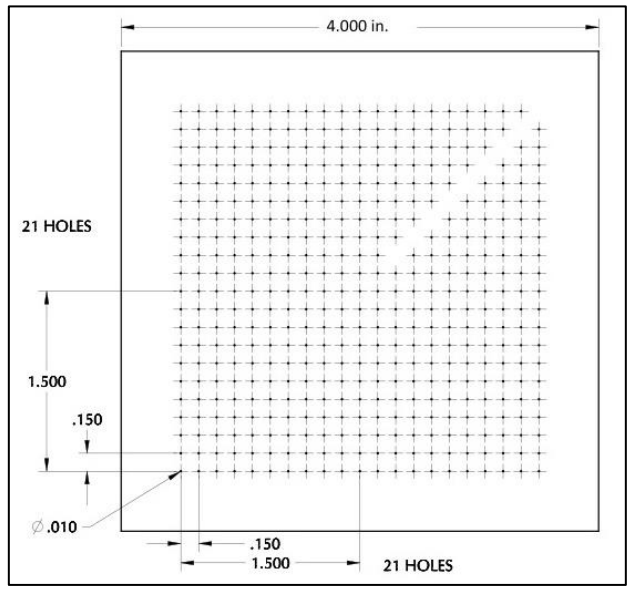


Figure 2: Pattern for the NDCX-II pepperpot mask.

The systematic measurement uncertainties, $\sigma_x^2, \sigma_{x\prime}^2, \sigma_y^2, \sigma_{y\prime}^2$, are determined from the geometry of the pepperpot mask, camera resolution, and scintillator standoff distance.

$$\sigma_x^2 = \sigma_y^2 = \frac{(hole\ spacing)^2}{12} + \frac{(resolution)^2}{12} \quad (15)$$

$$\sigma_{x\prime}^2 = \sigma_{y\prime}^2 = \frac{\left(\tan^{-1}\left[\frac{1}{resolution * standoff}\right]\right)^2}{12} \quad (16)$$

In the NDCX-II pepperpot, the systematic errors are 1.1 mm (σ_x, σ_y) and 3.5 mrad ($\sigma_{x\prime}, \sigma_{y\prime}$).

The variation in intensity is calculated for each pixel in the image region of interest (ROI). Equal numbers of images are acquired with the beam present as are background images without beam. Average values and their variances are calculated on a pixel-by-pixel basis for both the beam image and the background sets. The variance in intensity at each pixel is then determined by $\sigma_{\rho_i}^2 = \sigma_{image_i}^2 + \sigma_{background_i}^2$, where the index i labels each individual pixel. The calculation of the variances of the product terms, eqn. (2), is given in the Appendix.

Pepperpot Image Analysis

Results of the pepperpot analysis are shown in Figs. 3, 4, 5 below. The background subtracted image is shown in Fig. 3 alongside the mapping of the pixel intensity onto the transverse coordinate space (x-y). The horizontal $(x - x')$ and vertical $(y - y')$ phase spaces are shown in Fig. 4. Finally, the velocity-space distributions are shown in Fig. 5. Here the angular momentum is defined as $j_i = x_i y'_i - x'_i y_i$, where the index i labels individual beamlets in the pepperpot image.

Copyright © 2014 CC-BY-3.0 and by the respective authors

ISBN 978-3-95450-141-0

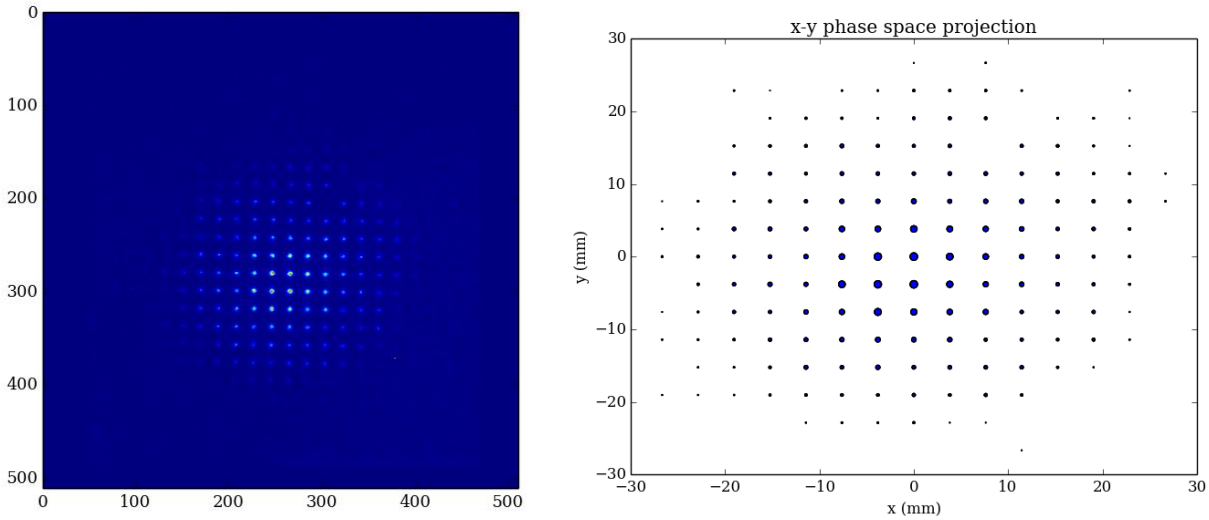


Figure 3: Pepperpot false color intensity image (left) and mapping (right).

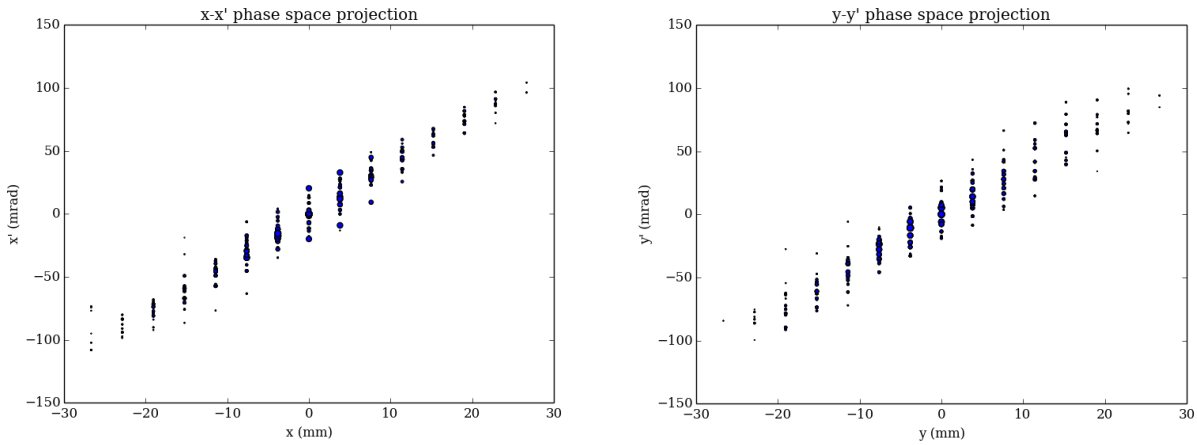


Figure 4: Cartesian phase space projections in the horizontal (left) and vertical (right) planes.

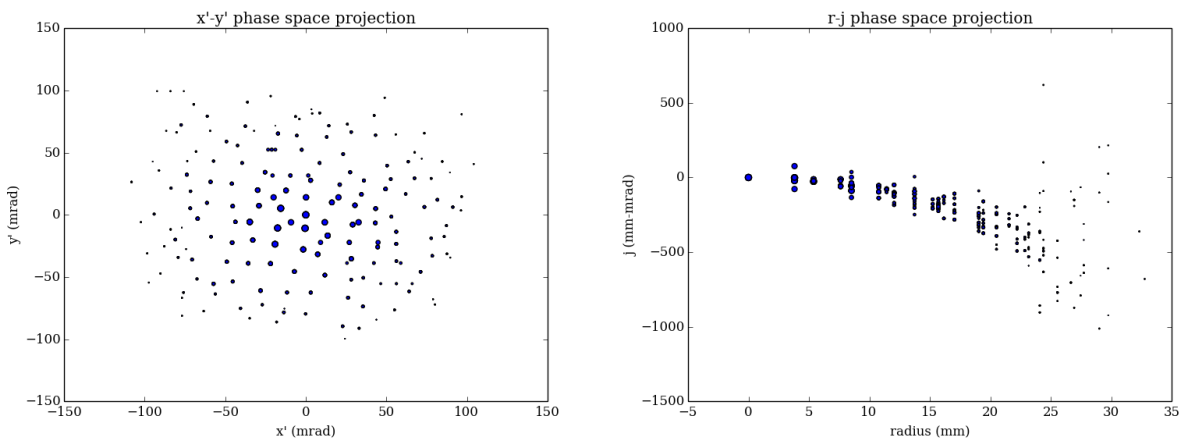


Figure 5: Velocity space (left) and angular momentum correlation (right).

Copyright © 2014 CC-BY-3.0 and by the respective authors

ISBN 978-3-95450-141-0

Emittance Measurements

We apply the variance analysis to determine the uncertainties present in the emittance measurements as the beam focus is changed by varying the strength of the final focus magnet. The results of the scan are shown in Fig. 6. We can see that the uncertainties in the emittance measurement vary as the beam is focused - the uncertainties increase significantly as the waist moves from downstream of the pepperpot mask to upstream of the mask.

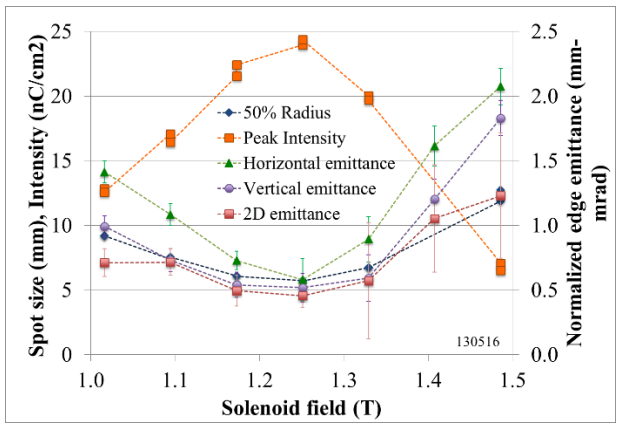


Figure 6: Variation of beam intensity, spot size, and emittances at the target plane with change in the final focus solenoid peak field.

We seek to understand the contributions of the individual measurement errors to the overall measurement uncertainty. To do so we recalculate the total uncertainties while sequentially equating all but one of the errors to zero. The results are shown in Fig. 7. We see that the relative influence of the position error increases, and that of the angle error decreases, as the beam is brought to a waist at the mask location. The opposite trend is observed as the waist moves upstream. The relative influence of the intensity error remains essentially constant for a converging beam, but increases as the waist moves farther upstream.

SUMMARY

We have performed the construction of the uncertainty in the fully correlated 4-D emittances from errors inherent in pepperpot measurements. We have demonstrated the effect of individual errors on measurements of correlated beams.

ACKNOWLEDGMENT

We would like to acknowledge the assistance of William Ghiorso in designing and fabricating the pepperpot mask used in the emittance measurements, and Wayne Greenway and Tak Katayanagi for fabricating and modifying the NDCX-II target diagnostics.

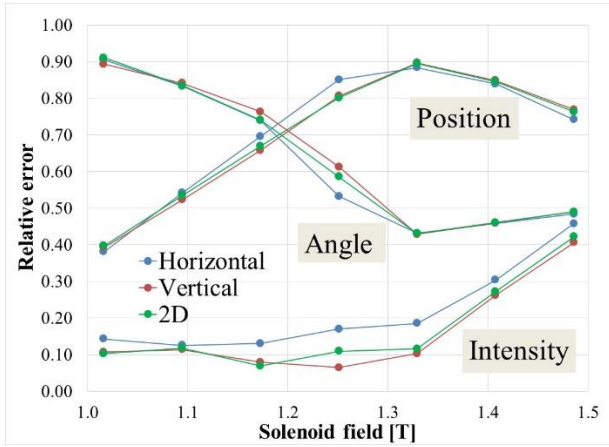


Figure 7: Contribution of the individual measurement errors to the emittance uncertainties. The total uncertainty is the quadrature sum of components.

APPENDIX: PRODUCT UNCERTAINTY

The net uncertainty in the product terms are derived.

$$\langle fg \rangle = \frac{\sum_i \rho_i f_i g_i}{\sum_i \rho_i} \tag{A1}$$

$$\sigma^2_{\langle fg \rangle} = \sum_i \left\{ \left(\frac{\partial \langle fg \rangle}{\partial \rho_i} \right)^2 \sigma^2_{\rho_i} + \left(\frac{\partial \langle fg \rangle}{\partial f_i} \right)^2 \sigma^2_{f_i} + \left(\frac{\partial \langle fg \rangle}{\partial g_i} \right)^2 \sigma^2_{g_i} \right\} \tag{A2}$$

$$\sigma^2_{\langle fg \rangle} = \sum_i \left\{ \sigma^2_{\rho_i} \left[\frac{f_i g_i}{\sum_k \rho_k} - \frac{\langle fg \rangle}{(\sum_k \rho_k)^2} \right]^2 + \sigma^2_{f_i} \left[\frac{\rho_i g_i}{\sum_k \rho_k} \right]^2 + \sigma^2_{g_i} \left[\frac{\rho_i f_i}{\sum_k \rho_k} \right]^2 \right\} \tag{A3}$$

REFERENCES

[1] S. Jolly, *et al.*, Proceedings of DIPAC'09, WEOA03, Basel, Switzerland, (2009); http://www.JACoW.org
[2] A. Burov, S. Nagaitsev, and Ya. Derbenev, Phys. Rev. E 66, 016503, (2002).
[3] D.A. Edwards and L.C. Teng, IEEE Trans. Nucl. Sci. 20, 885, (1973).
[4] Press, W. H.; Flannery, B. P.; Teukolsky, S. A.; and Vetterling, W. T., *Numerical Recipes in FORTRAN: The Art of Scientific Computing, 2nd ed*. Cambridge University Press, pp. 89-91, (1992).
[5] John R. Taylor, *An Introduction to Error Analysis*, *2nd ed.,* University Science Books, (1997).
[6] A. Friedman, *et al.*, Phys. Plasmas 17, 056704, (2010).
[7] W. Waldron, *et al.*, Nucl. Instrum. Methods Phys. Res. A733, pp. 226-232, (2014).
[8] S. Lidia, submitted to PRSTAB, (2014).
[9] John C. Russ, *The Image Processing Handbook, 4th ed.*, CRC Press, (2002).
[10] M. Stockli, R.F. Welton, R. Keller, Rev. Sci. Instrum. 75, 1646, (2004).

Copyright © 2014 CC-BY-3.0 and by the respective authors

ISBN 978-3-95450-141-0

PRECISE DIGITAL INTEGRATION OF FAST ANALOGUE SIGNALS USING A 12-BIT OSCILLOSCOPE

M. Krupa*, M. Gasior, CERN, Geneva, Switzerland

Abstract

An accurate laboratory characterization of beam intensity monitors requires a reliable integration of analogue signals simulating beam pulses. This poses particular difficulties when a high integration resolution is necessary for short pulses. However, the recent availability of fast 12-bit oscilloscopes now makes it possible to perform precise digital integration of nanosecond pulses using such instruments. This paper describes the methods and results of laboratory charge measurements performed at CERN using a 12-bit oscilloscope with 1 GHz analogue bandwidth and 2.5 GS/s sampling.

INTRODUCTION

The study of using 12-bit oscilloscopes as a high resolution digitiser has been considered for a laboratory characterisation of new intensity monitors currently being developed for the LHC restart in 2015 [1]. These monitors, operating according to the current transformer principle, provide signals proportional to the beam current, which are then integrated to measure the charge of each bunch of the circulating beam. Precise laboratory characterisation of such monitors requires time domain integration of nanosecond pulses with a relative accuracy better than 1 %. This value is considered as the accuracy limit of the analogue integrators used operationally at the LHC. The analogue integrators will be soon replaced by a digital system being developed, however, which was not yet available for the laboratory measurements of the new intensity monitors.

The study and results presented in this paper are based on oscilloscope measurements of nanosecond pulses from a fast pulse generator. Therefore, they are believed to be applicable also in domains outside the beam intensity instrumentation, where measurements of precise integrals of short pulses are necessary.

SET-UP AND OSCILOSCOPE

The pulses simulating beam bunches in the measurements discussed in this paper were generated by a custom-made avalanche generator delivering pulses with the amplitude of about 25 V and 0.5 ns full-width-at-half-maximum (FWHM) [2]. The pulse rise and fall times are about 0.3 ns, resulting in the frequency spectrum with the high cut-off around 1 GHz. Longer pulses required in the measurements were obtained by stretching the 0.5 ns pulses using a few commercial low pass filters. This way the total integral of the pulses, simulating the charge of a circulating bunch, was kept constant while the shapes of the pulses varied significantly.

* michal.krupa@cern.ch

All data studied in this paper were acquired using a 12-bit oscilloscope with 1 GHz analogue bandwidth and running in the Random Interleaved Sampling (RIS) mode with the maximal equivalent sampling rate of 125 GS/s. In this mode, the final waveform is a result of many acquisitions performed with the sampling clock having a random phase with respect to a common stable trigger. The phase of the sampling clock is measured with respect to the trigger for each acquisition by a precise time-to-digital converter (TDC), with the time resolution defining the RIS equivalent sampling rate. Then all RIS records are aligned according to the precise sampling phase measurement obtained from the TDC. The RIS scheme requires that the sampled signal is repetitive and the trigger event is identical for every acquisition, both of which conditions were satisfied in the discussed measurements. The RIS mode allowed increasing the oscilloscope native time resolution of 400 ps by a factor of 50, which was very important for the presented studies.

Before using the oscilloscope for signal integration, the instrument itself was characterised. In order to check the oscilloscope channel symmetry, the same signal from the avalanche generator was successively injected into each of the four inputs and sampled in the same manner. The absence of RF signal splitters in the measurement setup removed sources of systematic errors introduced by the inevitable asymmetry of the splitters themselves, which is at the percent level even for precise devices.

Results of the symmetry measurement are shown in Fig. 1. The measurements were performed consecutively assuring stable measurement conditions. The acquired samples were manually aligned on the time axis to

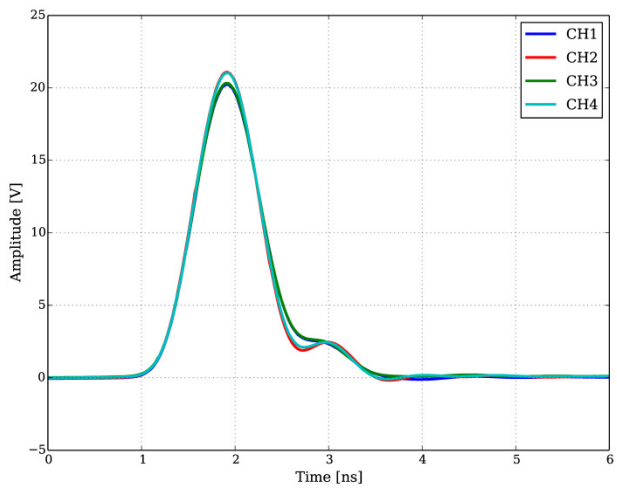


Figure 1: Measurement of the oscilloscope channel symmetry. Same input signal was acquired with consecutive channels.

Copyright © 2014 CC-BY-3.0 and by the respective authors

ISBN 978-3-95450-141-0

achieve the best signal overlapping. Nevertheless, significant discrepancies between the oscilloscope channels can be observed. In particular, channels are more symmetric in pairs 1 and 3 as well as 2 and 4, than in other combinations. The differences between the channels are shown in Fig. 2. The vertical axis denotes the relative difference between the channels scaled to the pulse amplitude. Both offset and gain asymmetry of the channels are visible. While the offset error (below 0.5% of the full scale, FS) can be easily corrected by measuring its value with no input signal, the only way to correct the gain error (up to 5% FS for the "more asymmetric channels") is to use a calibration reference with a well-known and stable amplitude.

The difference between the high-resolution 12-bit instrument used for the measurements described in this paper and an "ordinary" 8-bit oscilloscope is illustrated in Fig. 3. The 8-bit samples are simulated by taking the original 12-bit samples and clearing their 4 least significant bits. The resolution improvement offered by the 12-bit oscilloscope is very significant and probably opens a new era in laboratory oscilloscope measurements.

Please note that the 1 GHz bandwidth of the used oscilloscope results in its rise time of about 0.3 ns, the same as the rise time of the fastest pulses used in the discussed measurements. This modifies the shapes of the recorded pulses but does not influence the drawn conclusions based always on relative measurements.

INTEGRATION

The different pulses used to study the digital integration are shown in Fig. 4. Due to its large amplitude, the generator output signal was attenuated by 43 dB with 18 GHz attenuators, lowering it to the level representative for intensity monitor characterisation. Whenever applicable, the presented plots are corrected to take into account this attenuation, like in Fig. 4. The 0.8 ns pulse is the direct pulse from the avalanche generator while the remaining 5 pulses were obtained by low-pass filtering of the 0.8 ns pulse.

In order to improve the quality of the integrated signals, the generator pulses were averaged 400 times using the oscilloscope internal averaging prior to undergo digital integration. After some attempts of using the oscilloscope built-in option of calculating signal integrals, this idea was abandoned due to its limited accuracy, most likely due to the lack of a proper offset suppression. All presented integration was performed as a post-processing of the acquired signal records, with particular attention on the accurate correction of the oscilloscope offset errors.

In order to optimally use the oscilloscope ADC, the vertical sensitivity of the instrument was set to utilise at least 50 % of the available dynamic range in all the following integral measurements. This is why the 0.8, 1.2 and 1.5 ns pulses were measured with the scope gain set to 160 mV full scale, while the remaining 2.1, 2.5 and 3.4 ns pulses with the full scale of 80 mV.

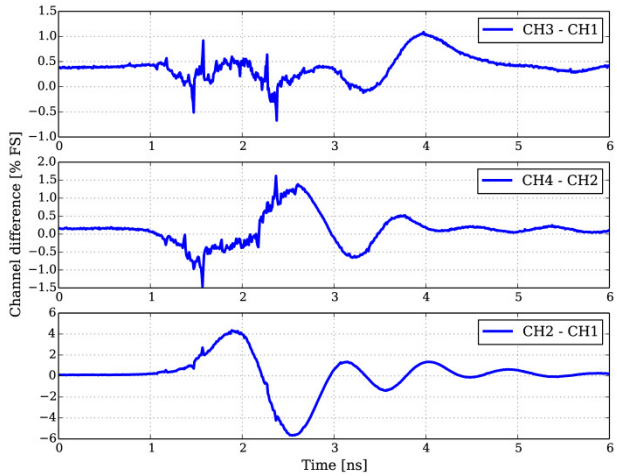


Figure 2: Measurement of oscilloscope channel symmetry. Shown are relative differences of the waveforms of Fig. 1.

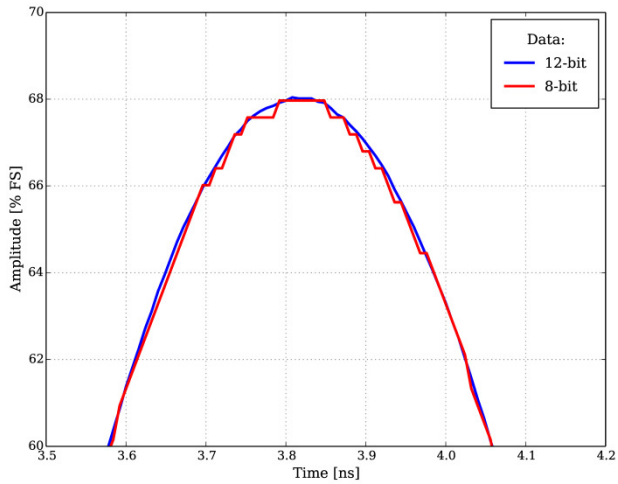


Figure 3: Comparison of the same signal with 12-bit and 8-bit resolution, zoom on the top of the pulse.

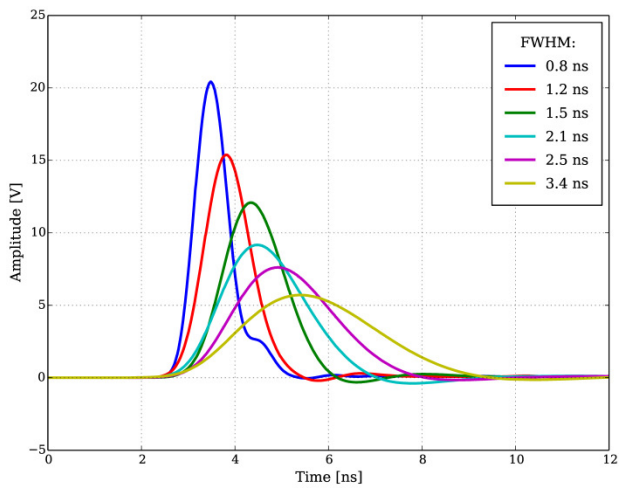


Figure 4: Pulses undergoing digital integration. The 0.8 ns pulse comes directly from the avalanche generator and the other pulses were produced using low-pass filters.

Copyright © 2014 CC-BY-3.0 and by the respective authors

ISBN 978-3-95450-141-0

Table 1: Relative Difference Between the Integrals of the Native 12-bit Records and their 8-bit Equivalents

Pulse FWHM [ns]	Used filter [MHz]	ADC usage [% FS]	Integral difference [%]
0.8	**none**	90.8	2.9
1.2	470	68.8	3.6
1.5	300	54.7	3.9
2.1	200	84.7	3.1
2.5	155	68.8	3.0
3.4	120	51.8	2.7

Table 2: Effect of the Sampling Rate and the Integration Method for the 3.4 ns Pulse

Sampling rate [GS/s]	12-bit integration error [%]		8-bit integration error [%]	
	trapez	rectangle	trapez	rectangle
125	**reference**	0.00	2.7	2.7
64	0.01	0.01	2.7	2.7
16	0.07	0.07	2.7	2.7
4	0.08	0.09	2.7	2.7
1	0.14	0.17	2.6	2.6
0.5	0.87	0.71	2.8	2.8

For each measurement 12500 samples were recorded over a time window of 100 ns with the resolution of 8 ps. The samples of the first 10 ns preceding the actual pulse were used in the post-processing as a reference for offset suppression. All the integral measurements were performed with the same oscilloscope channel.

Three main contributors to the accuracy of a digital integral were studied, with the results described in this chapter, namely the ADC resolution, the sampling rate and the used integration algorithm.

To study the effect of the ADC resolution each signal was acquired and integrated using the trapezoidal method. Then from these records acquired with the native 12-bit resolution their 8-bit equivalents were produced, by clearing the 4 least significant bits, and such 8-bit records were also integrated. Table 1 summarises the obtained integral relative differences. The table also lists the cut-off frequency of the low-pass filter used to stretch the integrated pulse and the usage of the ADC dynamic range. The ADC usage was calculated as the ratio of the peak-to-peak signal amplitude to the full scale of the oscilloscope for the vertical gain used in the measurement.

The difference between the 12-bit and 8-bit integrals varies between 2.7 and 3.9 %. For the three shorter pulses the decreasing usage of the ADC seems to be the source

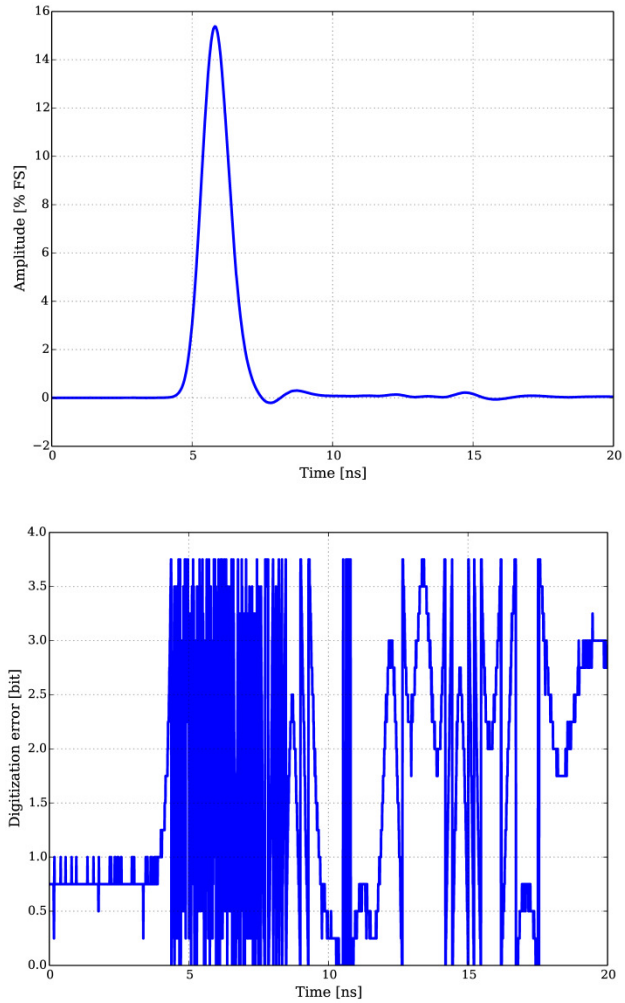


Figure 5: 8-bit dataset computed from the 12-bit dataset for the 1.2 ns pulse (top). Bits of error per sample of the 8-bit dataset obtained by comparing it to the 12-bit data (bottom).

of the increasing difference. However, for the remaining wider pulses this is no longer the case and the difference becomes smaller as the pulse stretches. The measurements show that the 8-bit resolution of the integrated signals causes an error in the order of 4 % and this is the quantified advantage of the 12-bit oscilloscope.

The source of such a large difference between the 12-bit and 8-bit integrals is demonstrated in Fig. 5 on the example of the 1.2 ns pulse, shown in the top plot for the time range taken for the integral calculation. The bottom plot shows the difference between the original 12-bit and its 8-bit version. The largest difference is close to 4-bits and its changes are related to the rate of change of the analysed pulse. The difference is the smallest during the time before the pulse for which the channel error was supressed. It is not the case for the time after the pulse, where a large difference can be seen, just changing slower than for the pulse. Therefore, the difference of the 12-bit and 8-bit integrals depends on the choice of the

Copyright © 2014 CC-BY-3.0 and by the respective authors

ISBN 978-3-95450-141-0

integration interval. The used 20 ns integration window was chosen as the value close to the one used by the analogue integrators of the LHC intensity monitors as well as their digital successors under development.

Table 2 summarises the results concerning the influence of the sampling rate and the integration method. All the integrals were calculated upon the longest 3.4 ns pulse with the rectangle and trapezoidal methods and, as in the previous measurements, on both the original 12-bit and the "artificial" 8-bit records acquired with six different sampling rates. All lower sampling rates were produced by decimating the only "truly measured" 125 GS/s record. The 12-bit trapezoidal integral of this original record was taken as the reference for all error computations.

As seen in the table, there is no significant difference between the trapezoidal and rectangle integrals for neither the 12-bit nor the 8-bit data for all the studied sampling rates. The sampling rate can be reduced by some two orders of magnitude before the integration error exceeds 0.1 %. This leads to the conclusion that once the sampling rate is sufficient for a given signal length, further increasing the sampling rate does not improve significantly the integrals. On the other hand, the additional four bits of vertical resolution improved the accuracy of the integrals for each sampling rate by more than 2.5 %.

CONCLUSIONS

The recent availability of fast 12-bit oscilloscopes opens a new era in laboratory measurements, for which the higher signal resolution plays an important role. It was certainly the case for the laboratory evaluation of the LHC intensity monitors, whose output signals have to be integrated with high resolution to quantify their performance [1].

As presented in the paper, the 12-bit oscilloscopes offer a much better accuracy of charge measurement than the standard 8-bit instruments, limited to a few percent for the cases studied in the paper. It was found that the post-processing integration of 12-bit signal records can be by far more accurate than the results obtained with the oscilloscope built-in integration functions, which suffer from the influence of the offset error. As demonstrated, this error can be efficiently suppressed in an adequate post-processing.

The very interesting Random Interleaved Sampling (RIS) acquisition mode, allowing achieving a very fast equivalent sampling rates, was used to study the influence of the sampling rate on the accuracy of the signal integrals. It was found that the rectangle and trapezoidal integration methods give very similar results.

All the presented integral measurements were relative and performed with the same oscilloscope channel. This way the results and the conclusions were independent of the oscilloscope gain. If absolute charge measurements are required, then the oscilloscope gain must be calibrated with a precise reference.

REFERENCES

[1] D. Belohrad, J. Bergoz, M. Krupa, L. Soby, F. Stulle, "A New Integrating Current Transformer for the LHC", in proceedings IBIC 2014, WEPF06, (2014)

[2] M. Krupa, M. Gasior, "Application of Avalanche Generators in Laboratory Measurements", MIXDES 2014, Lublin, Poland, June 2014, http://www.mixdes.org

ISBN 978-3-95450-141-0

Copyright © 2014 CC-BY-3.0 and by the respective authors

FAST TRANSVERSE PHASE SPACE MEASUREMENT SYSTEM FOR GUNLAB – A COMPACT TEST FACILITY FOR SRF PHOTOINJECTORS

J. Völker*, T. Kamps, HZB, Berlin, Germany

Abstract

Superconducting radiofrequency photo electron injectors (SRF guns) are promising electron sources for the next generation of electron linear accelerators. The energy recovery linac (ERL) bERLinPro will employ a 1.5 cell 1.3 GHz SRF gun cavity with normal conducting high quantum efficiency photocathode to produce a 100mA CW electron beam with high brightness. We are currently working on a compact test beamline (GunLab) to investigate the phase space of the extracted electron beam and to optimize the drive laser as well RF parameters. The motivation for GunLab is to decouple the SRF gun development from the ERL development. The goal is to measure not only the complete 6 dimensional phase space of the extracted and accelerated bunches but also to investigate dark current and beam halo. In this paper we will discuss unique features of GunLab for the phase space measurements.

MOTIVATION

GunLab is an independent and optimized beamline to characterize electron guns and to investigate different phase space measurement systems for space charge dominated electron bunches at low energies up to 3.5 MeV. A schematic overview is shown in Fig. 1.

A pulsed drive laser extracts electron bunches from a normal conducting photocathode inside a superconducting RF cavity (SRF gun) which accelerates them up to 3.5MeV. A superconducting solenoid will be used to focus the divergent beam and for emittance compensation at a reference point. To investigate the phase space of the bunches as a function of SRF gun and drive laser settings and solenoid focusing strength we want to use a fast phase space measurement system. The longitudinal phase space will be measured by a combination of transverse deflecting cavity (TCAV) [1] and spectrometer dipole [2]. For measurements of the transverse phase space we want to use a combination of two opposite directed steerer magnets (the scanner magnet) and a slit mask. The scanner magnet moves the beam parallel to the beam axis over the slit.

In this paper specification and realization of the scanner system is discussed.

Parameters of GunLab

The expected beam parameters are determined by the injector setup.

A detailed report about the estimated beam parameter as a function of the injector parameters you can find here [3]. Table1 shows the range of the estimated beam parameter.

Table 1: SRF Gun Setup and Expected Beam Parameters

Parameter	Value
Drive laser pulse length	3. . .16 ps (FWHM)
Transversal laser shape	FlatTop
Drive laser repetition rate	1.3 GHz
Macro pulse repetition rate	10 Hz
SRF gun frequency	1.3 GHz
Electric peak field	30 MV/m
Bunch exit energy	1 . . . 3 MeV
Rel. energy spread	0.2%. . . 5%
Bunch charge	0 . . . 100 pC
Bunch length	2. . .10 ps (rms)
Max. Average current	4 μA
Normalized emittance	0.4. . . 10 mm mrad

TRANSVERSE PHASE SPACE MEASUREMENT

We want to observe the projected and the sliced transverse phase space of the electron bunches with dedicated techniques.

Projected Transverse Phase Space

A direct method to investigate the projected transverse phase space is a pepperpot or a slit mask. The slit samples narrow emittance dominated beamlets out of a space charge dominated beam. For a slit scan the scanner-magnet deflects the beam parallel to the beam axis and through a slit which has a stable position in the middle of the beam tube. The achievable frequency of such a measurement is limited by the power supply[1] for the magnets and the measurement system downstream, which can be a second slit-scanner with a Faraday-Cup (electronic measurement) or for small beam currents a view screen (optical measurement). For the optical measurement the CCD is the limiting factor for the measurement frequency.

Sliced Transverse Phase Space

As another technique to reconstruct the transverse phase space we will perform a slice emittance measurement. Therefore a TCAV together with two quadrupole magnets are installed in GunLab. The developed TCAV is an one cell cavity which can deflect the beam in two directions. For the slice emittance measurement the quadrupoles minimize the beam dimension in one direction on a screen downstream the TCAV. In a second step the TCAV streaks

* jens.voelker@helmholtz-berlin.de

[1] For magnets with low inductivities DC power supplies can achieve a frequency up to 1 kHz.

Copyright © 2014 CC-BY-3.0 and by the respective authors

ISBN 978-3-95450-141-0

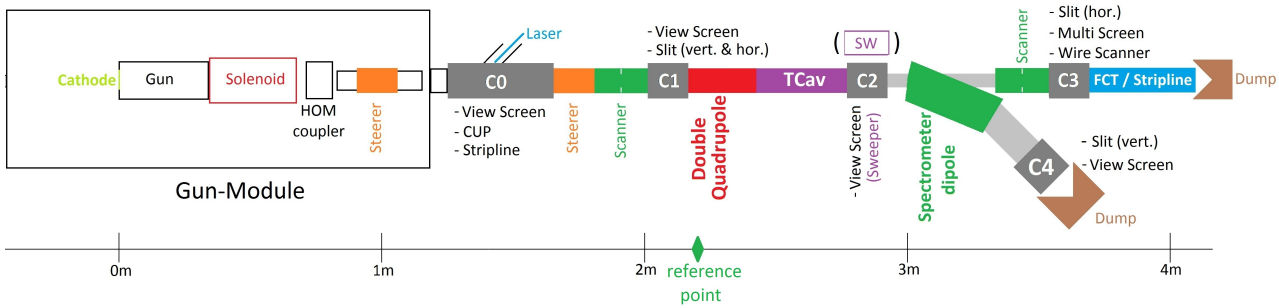


Figure 1: Schematic view of GunLab.

the electron bunch. The resulting image on the screen consist of the temporal distribution in streaked direction and one transverse distribution in the perpendicular direction. The temporal resolution of the slices is a convolution of the beam width in streak direction and the longitudinal profile. The resolution has to be constant for the complete double quadrupole scan. For such a scan the setting of both quadrupole strengths pass a definite function which produce a constant focal length in the streaked direction. Only the beam width in the perpendicular direction changes which will be used to reconstruct the phase space of each slice.

A problem for both methods could be that the used dipole and quadrupole magnets can have a significant impact on the linearity of phase space by non-perfect magnetic fields. The remanent magnetic field is an additionally problem in case of magnets with a yoke. These fields can kick and distort the beam also when the magnet is switched off. A solution are coil dominated magnets for example cos(nθ)-coils. They work without yoke and can produce magnetic fields with suppressed higher magnetic field orders (Sextupole, Dekapole, etc). Therefore cos(θ)-coils as scanner magnets and cos(2θ)-coils as quadrupole magnets are the most promising method for fast projected and sliced emittance measurements without negative influence of the electron phase space.

SHORT COIL DOMINATED MAGNETS

Coil dominated magnets consist of non magnetic materials, hence only the current distribution defines the magnetic field, which can be described as a sum of magnetic multipoles. One example for a coil dominated magnets are the so called cos($n\theta$)-magnets. In theory they produce perfect magnetic n-poles by an azimuthal current distribution around an infinity long round tube which follows a cos(nθ)-function. All but the amplitude of the n-th multi-pole are suppressed. For designing a real magnet one is limited by the dimensions of the cables and it is only possible to approximate these functions. Thereby the resulting magnetic field is not this perfect n-multi-pole any more. Furthermore the used cables need a connection to each other (end caps). The shape of these end caps and the azimuthal distribution of the cables have to be optimized to get a coil designs which produce dipole or quadrupole fields and suppress other multi-poles.This is only possible with the direct calculation of the three dimensional field of the complete magnet.

Field Calculation

The three dimensional magnet field of a coil was calculated by the Biot-Savart law. Therefore the coil was divided into N wires with m_i elements. These elements are straight short line segments with a current I which produce a magnetic field at the position $\vec{P}$. If we neglect material effects the magnetic field could be calculate by [4]:

$$\vec{B}(\vec{P}) = \frac{\mu_0 I}{4\pi} \frac{|\vec{r}_1| + |\vec{r}_2|}{|\vec{r}_1||\vec{r}_2| + \vec{r}_1\vec{r}_2} \frac{\vec{r}_1 \times \vec{r}_1}{|\vec{r}_1||\vec{r}_2|}$$

with $\vec{r}_1$ and $\vec{r}_2$ as the start and end points of the line segment relative to the point $\vec{P}$. These formula can be easily implemented and parallelized in a numerical program like MATLAB.[2]

Geometry of the Line Segments

The next step is the calculation of the positions of each wire of the coil especially for the coil end cap. The main elements of the coil are the wires along the beam pipe which are positioned on a cylinder with the radius R_0 at angle positions θ. For the calculation of the coil end caps we can imagine, that the wires are positioned on the two dimensional surface of the beam pipe. There the wire should follow an elliptical shape with a and b as the principal axes:

$$\begin{aligned} \vec{R}_{2d} &= (a\cos(\phi)\ ,\ b\sin(\phi)) \\ \Rightarrow \vec{R}_{3d} &= \left(R_0 \cos(\frac{R^{(1)}_{2d}}{R_0})\ ,\ R_0 \sin(\frac{R^{(1)}_{2d}}{R_0})\ ,\ R^{(2)}_{2d} \right) \end{aligned}$$

The parameter a can be substituted with the azimuth angle times the beam pipe radius $a = R_0\alpha = R_0(\frac{\pi}{2} - \theta)$.

The next step of the coil design is the transformation of this 2d geometry on the surface of the beam pipe to a real thick magnet coil.

Realization with Copper Foils

The construction should consist of copper foils instead of thick wires. Because with this foils we need only a small

[2] The final code was tested with models which can be calculated analytically.

ISBN 978-3-95450-141-0

Copyright © 2014 CC-BY-3.0 and by the respective authors

number of windings and we achieve a more compact wire package as with round wires. The foil will be spooled on an aluminum yoke with the negative contour of the innner coil part. The spin-off of foils is the more complex design of the end caps. Each wire has to be skewed to follow the defined path on the beam tupe. You can see an example of this effect in Fig. 2. It shows the position and rotation of one thin copper foil on the tube. This rotation angle β on top of the tube is given by the binormal unit vector of the function $\vec{R}_{3d}$ and can be calculated in our case to

$$\tan(\beta) = \frac{b}{R_0 \alpha^2}$$

This angle and his dependency of the parameter α and b which differ for each foil winding in one coil has to consider for the numerical design. For a more detailed overview about the geometry of the end caps see [4].

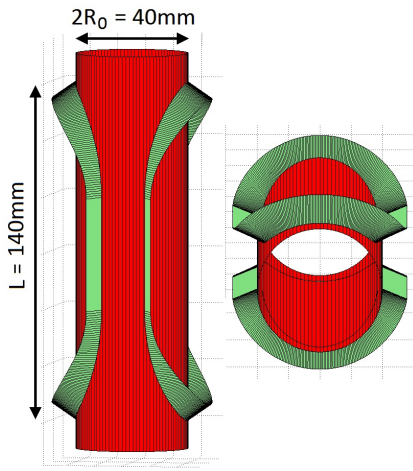


Figure 2: Example for the winding of one wire for Scanner coil (green) on the beam pipe (red).

DESIGN OF THE COSθ-COILS

We apply a numerical minimization of the unwanted beam effects to find the best parameter values for the distribution angle θ, the end cap radius b and the coil thickness d.[3] It is not possible to observe the effects of the magnets by a longitudinal integration of the resulting fields. Therefore the calculated 3d field of the scanner coils or the quadrupoles was implemented as 3d-fields in the tracking code ASTRA [5]. These method shows the real impact on the phase space of the electrons by the magnetic fields. The calculated dipole fields were implemented as a complete Scanner magnet which consist of two dipole coils with the same distance as in the beamline at GunLab (150 mm). For each magnet we observed the average error of the phase space for a given initial electron distribution, which is a zero-emittance, zero-space-charge electron distribution with a rectangle shape in the transverse plane. The average error is than the normalized χ^2-value which is defined as $\chi^2 = \Sigma_i^N (x_i^{(f)} - x_i^{(i)})^2/N$ with the particle number N and the initial $x_i^{(i)}$ and final $x_i^{(f)}$ positions in the phase space. Fig. 3 show χ^2 as a function of d, b and θ_0 for a steerer magnet with a length of 140 mm. Table 2 show the parameter of the dipole and quadrupole magnets which have the minimal effects on the beam.

[3] In normal cases L could be also an independent parameter for the optimization, but for GunLab the overall Length for the magnets is limited which means that L depends on the other 3 parameters.

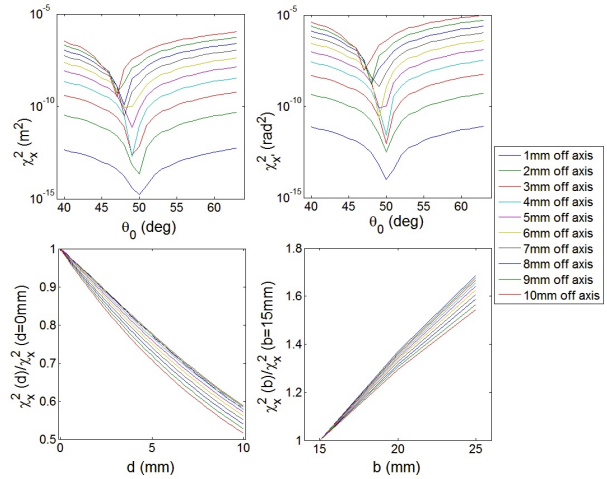


Figure 3: χ^2-values vs Parameter of the Scanner coil.

Table 2: Parameter for the Optimal Coil Dominated Magnets for GunLab

Parameter	**cosθ**	**cos2θ**
θ_{int}	96°	74°
R_0	15 mm	10 mm
d	> 8 mm	> 20 mm
L_{coil}	140 mm	80 mm

EMITTANCE MEASUREMENT WITH THE SLIT-SCANNER

The final scanner coils will be placed in GunLab in front of the slit. Both coils are separated longitudinal with 150 mm (peak to peak) and serially connected (identical absolute magnetic fields but with negative sign). The electron beam enters the first scanner coil centered to the beam pipe and will be deflected by a small angle and re-deflected by the the second scanner so that the beam exits the scanner parallel to the beam pipe axis but off-axis. For a better resolution of the divergence measurement the slit width should be as small as possible, but did not block to much signal. As a good solution it is planed to take a slit width of 100μm. The first tests at GunLab will be done with small average beam currents so that the width of the beamlets has to observed with the optical method. This can be done with luminescent screens in a distance of 700 mm or 1600 mm downstream the slit position. The transverse emittance follows from

Copyright © 2014 CC-BY-3.0 and by the respective authors

ISBN 978-3-95450-141-0

the method of second moments with the measured position, beam width and intensity values of the different beamlets.

Transverse Emittance - Method of the Second Moments

The transverse emittance of the electron beam is defined as

$$\varepsilon = \sqrt{< x^2 >< x'^2 > - < xx' >^2}$$

The second moments of the beam ($< x^2 >$,$< x'^2 >$,$< xx' >$) can be calculated by the position ζ_n and the width σ_n of the n-th beamlet on the screen at the distance L behind the slit:

$$\begin{aligned} < x^2 > &= \Sigma_n A_n (x_n - < x >)^2 \\ < x'^2 > &= \Sigma_n A_n (\delta_n^2 + (x'_n - < x' >)^2) \\ < xx' > &= \Sigma_n A_n (x_n x'_n - < x >< x' >) \end{aligned}$$

with the normalization factor A_n, the beam offset x_n at the slit, the divergence $\delta_n = \sigma_n / L$ and the correlated divergence of the beamlet $x'_n = (\zeta_n - x_n)/L$. $< x >= \Sigma_n A_n x_n$ and $< x' >= \Sigma_n A_n x'_n$ are the average values of x_n and x'_n. In case of an optical measurement with a luminescent screen the normalization factor is the ratio of the intensity of the single image to the sum of all images. This method together with the final scanner design was tested by simulations to estimate the uncertainty for the real measurements

Numerical Test of the Emittance Measurement

These simulations consist of tracking electron bunches with 10^5 particles with different transverse emittance and without space charge effects. This simulations was also done with ASTRA. Therefore we define 25 different amplitudes of the magnetic fields in the Scanner coils which deflects horizontally the beam between ≈ -6 and $\approx +6$ mm offset (≈ 0.5 mm step size). At the position of the slit only particle was taken into account which passes the range of the slit width ($\pm 50 \mu$m relative to axis). These particles were tracked a second time through a drift space to the position of the screen. The average position, width and the intensity (number of particles) of the beamlets were used to reconstruct the horizontal emittance of the original bunch. Fig. 4 shows the relative variations of the calculated transverse emittances to theme of the original bunch in front of the slit. The error bars in red and black and the blue line are the numerical and systematic uncertainties of this simulations and the slit scan method with a 100μm slit width. This illustrate that the influence of the magnets to the emittance measurement is not significant to numerical uncertainties, which are less then 1%. More expensive simulations to reduce the numerical error are work in progress.

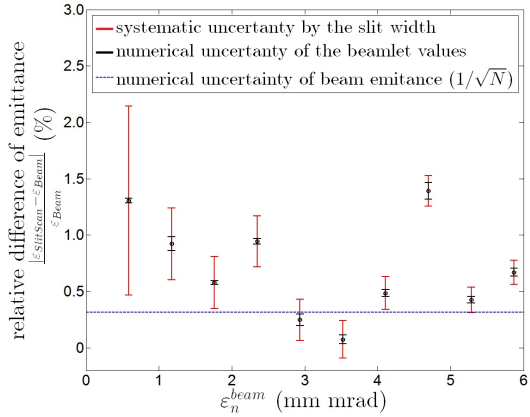


Figure 4: Relative differences between beam emittances and measured emittances by slit scanner.

SUMMARY AND OUTLOOK

A fast transverse phase space measurement system was developed for the new SRF gun test facility at HZB - GunLab. This slit-scanner consist of two cosθ coil magnets which moves the beam parallel to the beam axis over a slit. We presented the calculation and optimization procedure for the magnets and the influences to the measurements. Furthermore we sketch out that also quadrupole magnets based on the cos(nθ)-coils works and will be used for slice emittance measurements at GunLab. The next steps are the construction, field measurements and tests with beam. This should be done in the next half year so that we can start with beam measurement at GunLab in summer 2015.

REFERENCES

[1] A. Ferrarotto et al.,IPAC'14, June 2014, THPME105.

[2] I.Y.Vladimirov et al., IPAC'14, June 2014, THPME150.

[3] J. Völker et al., IPAC'14, June 2012, MOPRI020.

[4] S. Russenschuck, "Field Computation for Accelerator Magnets", (Weinheim, WILEY-VCH Verlag GmbH & Co., 2010), *ISBN: 978-3-527-40769-9*

[5] K. Floettmann et al., http://www.desy.de/mpyflo/

Copyright © 2014 CC-BY-3.0 and by the respective authors

ISBN 978-3-95450-141-0

ELECTRON CLOUD DENSITY MEASUREMENTS USING RESONANT MICROWAVES AT CESRTA*

J.P. Sikora†, CLASSE, Ithaca, New York 14853 USA
S. De Santis, LBNL, Berkeley, California 94720 USA

Abstract

Hardware has recently been installed in the Cornell Electron Storage Ring (CESR) to extend the capability of resonant microwave measurement of electron cloud density. Two new detector locations include aluminum beam-pipe in a dipole magnet and copper beam-pipe in a field free region. Measurements with both positron and electron beams are presented with both beams showing saturation of the electron cloud density in the aluminum chamber. These measurements were made at CESR which has been reconfigured as a test accelerator (CESRTA) with positron or electron beam energies ranging from 2 GeV to 5 GeV.

INTRODUCTION

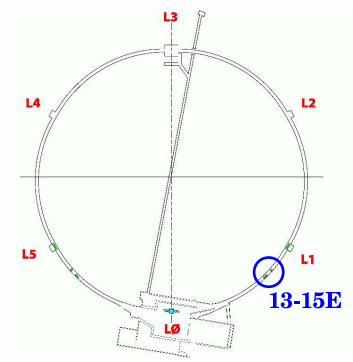


Figure 1: This sketch of the CESR storage ring shows the location of the 13-15E region where the the new measurement hardware is installed.

The Cornell Electron Storage Ring (CESR) has a circumference of 768 m and supports positron or electron beams with bunch populations of up to 1.6×10^{11} particles/bunch (10 mA/bunch) with total beam populations of 3.8×10^{12} particles/beam. Beam energies range from roughly 2 GeV to 5 GeV. The CESR test accelerator program (CESRTA) includes the study of the build-up and decay of electron cloud (EC) density [1], which in this storage ring is dominated by the photo-electrons that are produced by synchrotron radiation. A number of techniques have been used to measure EC density at different locations in CESR [2], including microwave measurements.

To use microwaves for EC density measurements, the microwaves are coupled into and out of the beam-pipe as described in Ref. [3] and shown in Fig. 2, typically using electrodes designed for the beam position monitor (BPM) system. If the response of the beam-pipe is resonant, the presence of the electron cloud will shift the resonant frequency slightly as given in Eq. 1 where n_e is the local EC density and E the local electric field of the microwaves, ϵ_0 is the vacuum permittivity, e is the charge and m_e the mass of an electron. The integral is taken over the resonant volume V of the section of beam-pipe. If the beam-pipe is excited at a fixed frequency near resonance and the electron cloud is periodic, as with a train of bunches in a storage ring, the result is modulation sidebands above and below the excitation frequency. The EC density can be calculated from the amplitude of the sidebands as described in Ref. [3]. This technique is also referred to as the resonant TE wave method [4, 5, 6].

$$\frac{\Delta\omega}{\omega_0} \approx \frac{e^2}{2\varepsilon_0 m_e \omega_0^2} \frac{\int_V n_e E_0^2 dV}{\int_V E_0^2 dV} \quad (1)$$

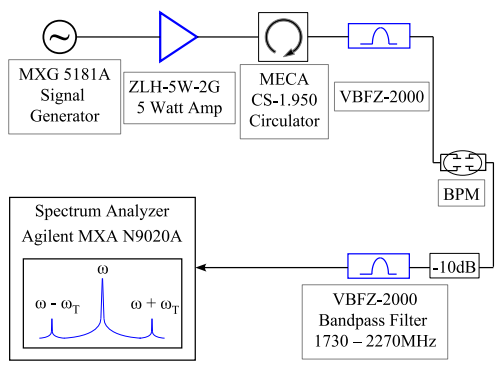


Figure 2: The hardware provides a drive signal to excite the beam-pipe at near a resonant frequency. The response will be phase modulated by the periodic EC density.

HARDWARE

The instrumentation needed to make the measurement is a signal generator and a 5 W amplifier to provide the drive and a spectrum analyzer to measure the sideband amplitudes. Filters and a circulator are also used to protect the instruments from the signal produced by the beam. We have recently added a set of high bandwidth relays that will allow the remote selection of three locations for connection to the drive and receive instruments during accelerator operation. Similar connections have already been made in other parts of the storage ring [7].

* This work is supported by the US National Science Foundation PHY-0734867, PHY-1002467 and the US Department of Energy DE-FC02-08ER41538, DE-SC0006505.

† jps13@cornell.edu

Copyright © 2014 CC-BY-3.0 and by the respective authors

ISBN 978-3-95450-141-0

Microwaves are routed to and from the BPM electrodes at the three locations using low loss Andrew LDF4-50A coaxial cable and coaxial relays as shown in Fig. 3. The relays are Dynatek model 06-133k10 coaxial switches that were part of the original beam position monitor system in CESR.

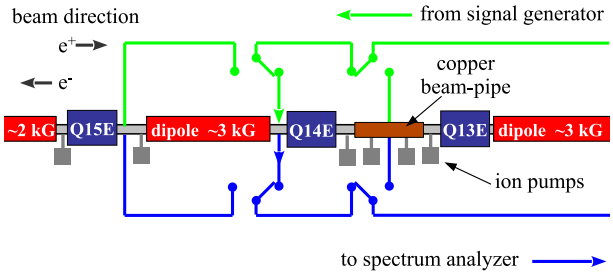


Figure 3: Microwaves are routed to and from three detectors in the storage ring using low-loss cable and rf relays.

Standing Wave Patterns

Microwave resonances are generated by changes in the beam-pipe geometry that produce reflections of the microwaves, especially near the cutoff frequency of the beam-pipe. Known reflectors of microwaves are the longitudinal slots that connect ion pumps to the beam vacuum space in the aluminum chamber of the CESR ring. Figure 4 shows some of the relevant dimensions of the 13-15E section of beam-pipe, including the locations of the ion pumps. Also shown is a copper test chamber in the straight section between Q13E and Q14E.

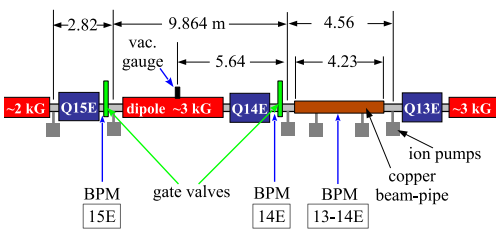


Figure 4: Sketch of the 13-15E section of beam-pipe with some dimensions. The BPMs used to couple microwaves in/out of the beam-pipe are labelled.

Figure 5 shows the response at the section between 13-14E. In this case, the resonances follow the expected $f^2 = f_c^2 + (nc/2L)^2$ pattern of a waveguide with its ends shorted having a cutoff frequency f_c and a length L with n the number of half wavelengths in the standing wave. Matching the measured response to the expected response gives a cutoff frequency f_c of 1.756 GHz for the copper beam-pipe with a length L of 4.23 m. This length is very close to the measured distance between transitions in the beam-pipe from the copper to the aluminum chamber. The aluminum beam-pipe in CESR is made from an extrusion whose cutoff frequency has been determined to be 1.896 GHz by similar measurements made in another part of the storage ring.

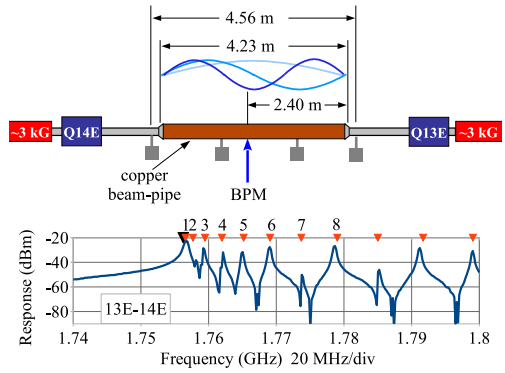


Figure 5: The response of the 13-14E section of beam-pipe has a series of resonances that are consistent with a shorted waveguide having a cutoff frequency of 1.756 GHz and a length of 4.23 m, matching the dimensions of the copper chamber. The calculated frequencies are shown as triangles with the larger dark triangle the cutoff frequency f_c.

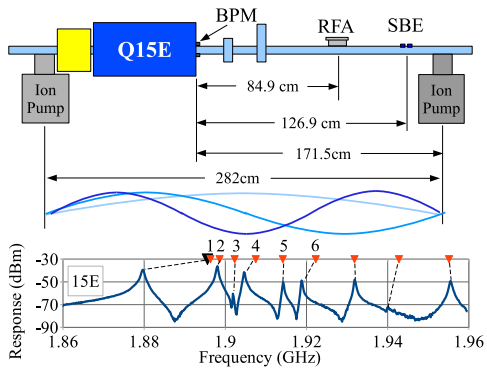


Figure 6: The response of the 15E section of beam-pipe shows frequencies similar to that of a shorted waveguide. The expected values are shown as triangles with dotted lines connecting them to possible corresponding peaks.The dark triangle is the cutoff frequency.

Figure 6 shows the response at the section that includes 15E. In this case the response is similar to the response expected from a shorted section of waveguide, but there are some notable differences. Since this section is constructed with a standard CESR aluminum extrusion, the cutoff frequency is taken to be 1.896 GHz. Using the 2.82 m distance between the ion pumps as the length of the resonant section, the expected resonant frequencies are plotted as triangles in Fig. 6. The lowest resonance is well below the cutoff frequency and several of the resonances are below the predicted values. A conjecture is that the gate valve near the middle of this section of beam-pipe and close to the drive point has a strong influence on the resonant series. The inner dimensions of the valve are somewhat wider than the beam-pipe to prevent synchrotron radiation from striking the valve body directly. This wider dimension lowers the cutoff frequency within the valve and can result in a resonance below the cutoff frequency of the surrounding beam-

ISBN 978-3-95450-141-0

Copyright © 2014 CC-BY-3.0 and by the respective authors

pipe. For frequencies above cutoff, this larger volume at the gate valve will lower the frequency of any resonance that has significant field at that longitudinal position.

Figure 7 shows the response when driving the BPM at 14E. Using the known cutoff frequency of the aluminum extrusion, the plot also shows the expected resonances using two different lengths: 9.86 m is the distance between the nearest ion pumps and 5.64 m is the distance from the ion pump nearest to the drive point to a vacuum gauge port in the middle of the dipole. Neither of these lengths gives a reasonable match to the measured response. As in the case of 15E, the lowest resonance is below the cutoff frequency, probably due to the influence of the nearby gate valve. Further modeling, or special measurements will be needed in order to understand the nature of the standing waves in this section.

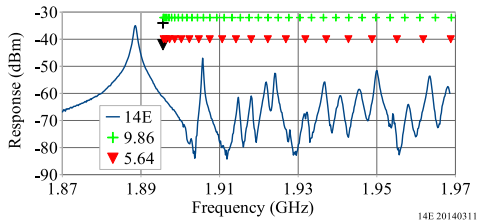


Figure 7: The response of the 14E section of beam-pipe does not match well the model of a shorted section of waveguide. Triangles show the location of resonances that might be expected with the given beam-pipe geometry.

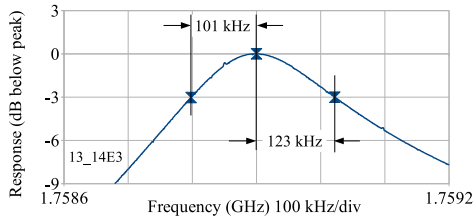


Figure 8: This detail of the response of the 13E-14E section of beam-pipe shows the asymmetry of the second resonance.

Table 1: Q Values for Beam-pipe Resonances

Resonance	f_0 (GHz)	$\pm\Delta f$ (kHz)	Q
13-14E1	1.7563150	-285/250	3277
13-14E2	1.7588850	-101/123	7852
13-14E3	1.7617530	-83/95	9897
13-14E4	1.7646210	-95/105	8824
13-14E5	1.7686440	-118/129	7132
13-14E6	1.7782610	-148/144	6089
14E1	1.88822	-438/440	2146
14E2	1.90535	-144/147	6571
15E1	1.879351	-358/342	2686
15E2	1.897685	-215/200	4584
15E3	1.90430	-176/187	5261
15E4	1.91390	-153/164	6057
15E5	1.91847	-133/171	6312

Calibration

Several auxiliary measurements are needed in order to obtain a calibration of the EC density for a given sideband amplitude: the Q of the resonances, an estimate of the time development of the periodic EC density as well as estimates of the uniformity of the EC density over the resonant volume. For a given maximum EC density, the sideband amplitudes will be determined by the envelope of the changing EC density vs. time and the Q of each resonance. Also, since the microwave resonance extends over some length of beam-pipe and the EC density can change over that length, it is important to understand the effect that this change in density has on the measurement.

The Q of a resonance can be obtained by measuring the frequency difference Δf between the resonance peak f_0 and where the response is lower by 3 dB. Then $Q = f_0/(2\Delta f)$. Figure 8 shows the response of a particular resonance where the value of Δf is not the same above and below the resonant frequency. This is presumably due to the presence of nearby resonances that make the response asymmetric. Our present analysis does not take this into account; the average of the upper and lower values of Δf is used. Table 1 shows the measured -3 dB points and the corresponding Qs for the different resonances.

With a fixed drive frequency near resonance, the periodic EC density will produce phase modulation sidebands whose amplitudes are given by the EC density's time structure. The periodic EC density versus time is convolved with the response time of the resonance ($\tau = 2Q/\omega_0$), when calculating the periodic phase. The simplest approximation is to begin with a rectangular EC density, which has a fixed value for the duration of the bunch train and is zero otherwise. This approximation has given normalized sideband amplitudes that are about 10% higher when compared with the shape given by ECLOUD simulations [8]. For the measurements discussed in this paper, only the first sidebands of each resonance will be used, assuming the rectangular approximation in the calculation of the EC density.

Equation 1 shows that if the EC density n_e is uniform over the resonant volume, the shift in frequency $\Delta\omega/\omega$ will be proportional to that uniform density. If the EC density varies over the volume, the meaning of the calculated value will need some interpretation. Figure 9 shows the effect that an EC density $n_e(s)$ that changes with the position s has on the quantity $n_e(s)E_0^2(s)$. In this case, we set $E_0(s)$ to be a half sine wave over the resonant length L. The frequency shift $\Delta\omega$ will be proportional to the integral of the resulting curve.

It can be shown that a linear change in EC density from one end of the resonant section to the other gives the following result: the magnitude of the frequency shift $\Delta\omega$ will correspond to the EC density at the midpoint of the

Copyright © 2014 CC-BY-3.0 and by the respective authors

ISBN 978-3-95450-141-0

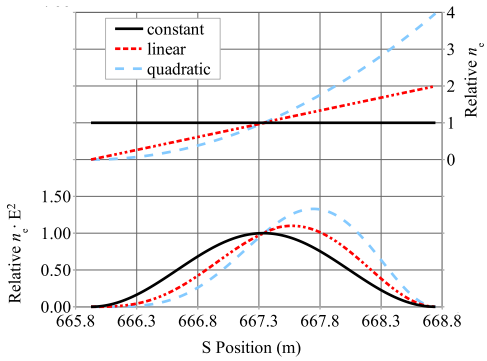


Figure 9: An EC density that changes over the length of the resonant section will change the local value of $n_e(s)E_0^2(s)$.

resonance length, as if that density were uniform over the volume. If the change in EC density is non-linear over the resonance length, the corresponding frequency shift would have to be calculated by integrating Eq. 1. This effect is shown in Fig. 9.

In the CESR storage ring, the source of cloud electrons is almost exclusively from photo-electrons. So we make the approximation that the EC density is proportional to the photon rate at each location along the resonant length. This ignores, for example, the effect that magnetic fields will have on EC density. Figure 10 shows the relative photon rates at 13-14E for both positrons and electrons along with the span of the resonant section and its center.

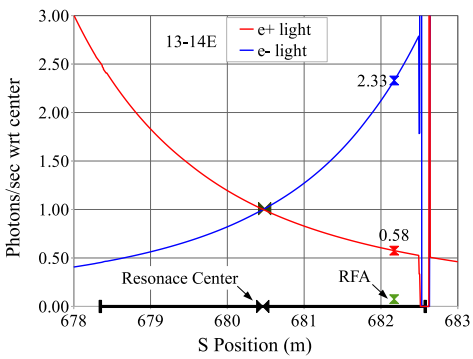


Figure 10: Estimates of the relative photon rates from positrons and electrons are show versus position in the section from 13-14E, normalized to the rate at the resonance center. Also shown is the location and rates at a retarding field analyzer (RFA) in the same section of beam-pipe.

DATA

Data was taken with 5.3 GeV beams of 20 bunches spaced by 14 ns for both positrons and electrons. The analysis of the data uses the rectangular approximation for the EC density, having a length of 266 ns with a revolution period of 2562 ns. The Q values are taken from Table 1. The EC density is taken to be proportional to the local photon rate and the normalized integral – using the relative photon rates as in Fig. 10 – is used to calculate a correction to the EC density and obtain the value at the center of the resonant length. This correction is made for each resonance and is different for positrons and electrons since the synchrotron light distribution is different. For the 15E data, the corrections are between 3% and 10%; for the 13-14E data, the corrections vary from 6% to 18% due to the higher non-linearity of the EC density. For 14E, since the standing wave pattern is not understood, a correction for a varying EC density was not made.

Data from the 13E-14E Section

Data from the 13-14E section with a positron beam is shown in Fig.11 for six resonances in the copper chamber. There is a roughly 30% range of values for EC density, depending on the resonance used. If $E_0^2(s)$ of the resonance is symmetric, the measurements at each resonance should give the same result provided that the change in EC density along the length of the resonance has been compensated correctly.

The result with an electron beam is shown in Fig.12, where the EC density is generally lower than for positrons. For both positrons and electrons, the EC density increases roughly linearly with beam current.

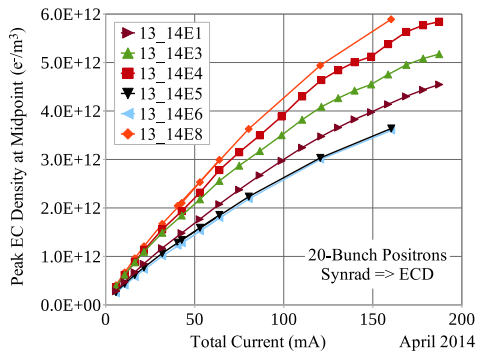


Figure 11: Data taken at 13-14E with a positron beam using six different resonances.

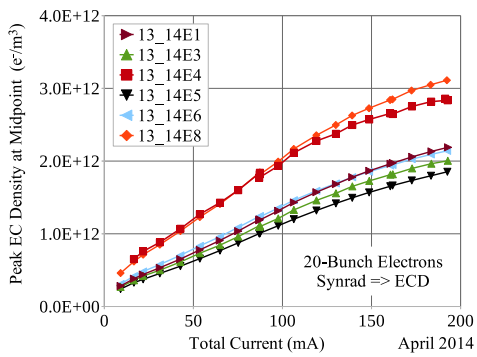


Figure 12: Data taken at 13-14E with an electron beam using six different resonances.

ISBN 978-3-95450-141-0

Copyright © 2014 CC-BY-3.0 and by the respective authors

Data from the 14E Section

At 14E, data was taken using only the two lowest resonances, with both positron and electron data appearing in Fig.13. The electron data shows an interesting curvature at the lowest currents and all of the data appears to saturate with higher currents. In this case, the EC density obtained from the two resonances is different by a factor of two for both the positron and electron beams. This data has not been corrected for a varying EC density over its resonant length, since the resonant length is not known. Further work is required to understand data from this section.

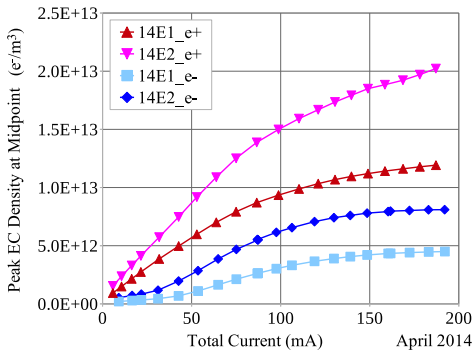


Figure 13: Data take at 14E with both positrons and electrons using the two lowest peaks of Fig.7.

Data from the 15E Section

At 15E, data was taken using five resonances of Fig. 6. The positron data in Fig.14 shows saturation at higher beam currents and a variation of about 25% between values of EC density obtained by the different resonances. The electron data of Fig.15 shows varying degrees of saturation.

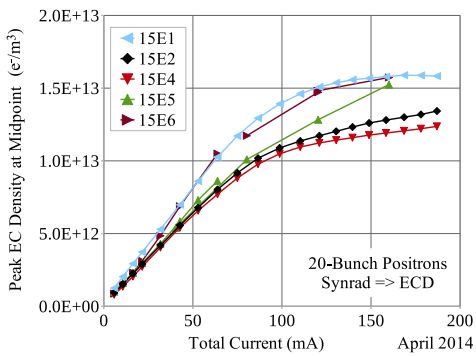


Figure 14: Positron data taken at 15E using five resonances.

CONCLUSIONS

A new section of the CESR ring has been instrumented so that EC density data can be taken at three different drive/receive points using the resonant microwave method.

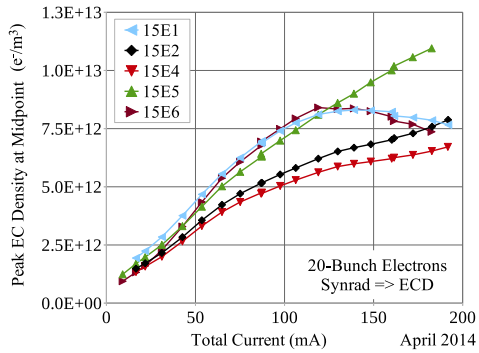


Figure 15: Electron data taken at 15E using five resonances.

Corrections have been made in the calibration through approximate Q measurements and an estimate of the variation in the EC density along the resonant length. A better understanding of the standing wave patterns is needed, especially at 14E. The data obtained also have a number of features that need further explanation, including variations in the measured density with different resonances in the same chamber.

REFERENCES

[1] G.F. Dugan, *et al.*, ICFA Beam Dynamics Newsletter No. 50, J. Urakawa and W. Chou, Eds. (2009).

[2] "The CESRTA: Phase I Report," Tech. Rep. CLNS-12-2084, LEPP, Cornell University, Ithaca, NY (Jan. 2013). http://www.lns.cornell.edu/public/CLNS/2012/

[3] J.P. Sikora, *et al.*, Nucl. Instrum. Methods Phys. Res., Sect. A **754**, pp. 28-35 (2014), http://dx.doi.org/10.1016/j.nima.2014.03.063, Preprint, arXiv:1311.5633 [physics.acc-ph].

[4] J. P. Sikora, *et al.*, "Resonant TE Wave Measurements of Electron Cloud Densities at CESRTA," in Proc. of IPAC'11, San Sebastián, Spain, August 2011, TUPC170, p.1434, (2011).

[5] J. P. Sikora, *et al.*, "TE Wave Measurement and Modeling," in *Proceedings of ECLOUD 2012, La Biodola, Elba, Italy*, edited by R. Cimino, G. Rumolo, F. Zimmermann, CERN-2013-002, CERN, Geneva, Switzerland, 2013, p. 193-200, arXiv:1307.4315 [physics.acc-ph].

[6] J.P. Sikora, *et al.*, "Resonant TE Wave Measurement of Electron Cloud Density Using Multiple Sidebands", in Proc. of IBIC'13, Oxford, United Kingdom, September 2013, TUPF34, (2013).

[7] J. P. Sikora, S. De Santis, K. Hammond, "TE Wave measurements at CESRTA," in *Proceedings of ECLOUD 2010, Ithaca, NY*, edited by Karl Smolenski, Cornell University, Ithaca, NY, 2013, p. 95-99.

[8] J.P. Sikora, *et al.*, "Cross-calibration of Three Electron Cloud Density Detectors at CESRTA," *these proceedings*, THCXB1, IBIC'14, Monetrey, CA, USA, (2014).

Copyright © 2014 CC-BY-3.0 and by the respective authors

ISBN 978-3-95450-141-0

DOSIMETRIC VERIFICATION OF LATERAL PROFILE WITH A UNIQUE IONIZATION CHAMBER IN THERAPEUTIC ION BEAMS

Y. Hara#, T. Furukawa, K. Mizushima, R. Tansho, N. Saotome, Y. Saraya, T. Shirai and K. Noda,
National Institute of Radiological Sciences, Chiba, JAPAN

Abstract

It is essential to consider large-angle scattered particles in dose calculation models for therapeutic ion beams. However, it is difficult to measure the small dose contribution from large-angle scattered particles. Therefore, we developed a parallel-plate ionization chamber consisting of concentric electrodes (ICCE) to efficiently and easily detect small contributions. The ICCE consists of two successive ICs with a common HV plate. The former is a large plane-parallel IC to measure dose distribution integrated over the whole plane, the latter is a 24-channel parallel-plate IC with concentric electrodes to derive the characteristic parameters describing the lateral beam spread. The aim of this study is to evaluate the performance of the ICCE. By taking advantage of the characteristic of ICCE, we studied the recombination associated with lateral beam profile. Also, we measured a carbon pencil beam in several different media by using ICCE. As a result, we confirmed the ICCE could be used as a useful tool to determine the characterization of the therapeutic ion beams.

INTRODUCTION

The application of charged particles such as proton and carbon-ion beams for radiotherapy has been increased interest around the world. One solution to make optimal use of therapeutic ion beams and to provide flexible dose delivery is three-dimensional (3D) pencil-beam scanning technique [1-3]. It has been utilized since 2011 at the Heavy Ion Medical Accelerator in Chiba (HIMAC), operated by the National Institute of Radiological Sciences (NIRS) [4]. In the scanning irradiation method, since the 3D dose distribution is achieved by superimposing doses of individually weighted pencil beams determined in the treatment planning, the dose calculation must be more accurate.

In dose calculation, the lateral beam spread due to multiple scattering that elemental pencil beams undergo in matter is generally assumed by a single-Gaussian model. However, the dose contributions from large-angle scattered (LAS) particles are not properly modeled in the single Gaussian. When the field size is too small for scattered particle equilibrium, it has been reported that the single-Gaussian model cannot express the reduction of the doses at the center of the field [5-7]. Therefore, several studies have proposed the expression for pencil beams of the sum of two or three Gaussians [8-11]. The parameterization of LAS particles by the multi-Gaussian model works very well. Generally, it is necessary to measure the small dose contributions from the LAS particles to derive the parameters. To efficiently and easily measure the small dose contributions, we developed a unique parallel-plate ionization chamber with concentric electrodes (ICCE) [12]. Since the sensitive volume of each channel is increased linearly with radial distance, it is possible to efficiently and easily detect small contributions from the LAS particles.

In this paper, both the measurement using the ICCE and the validity of simplified parameterization of LAS particles are described.

#y-hara@nirs.go.jp

MATERIALS AND METHODS

Specification of the ionization chamber with the concentric electrodes

The detailed design of the ICCE was reported previously [12]. Only a simplified explanation is given here. The ICCE consists of two successive ICs with a common HV plate: a large plane-parallel IC to measure dose distribution integrated over the whole plane and a 24-channel parallel-plate IC with concentric electrodes to derive the characteristic parameters describing the lateral beam spread. Figure 1 shows a schematic of measurement system with concentric electrodes. The design of the concentric electrodes is based on the Rayleigh distribution transformed by the bivariate circular Gaussian distribution into polar coordinates. To increase the output at the large off-axis position, we increased the width of the electrode from 0.2 mm to 5.3 mm as a function of radius.

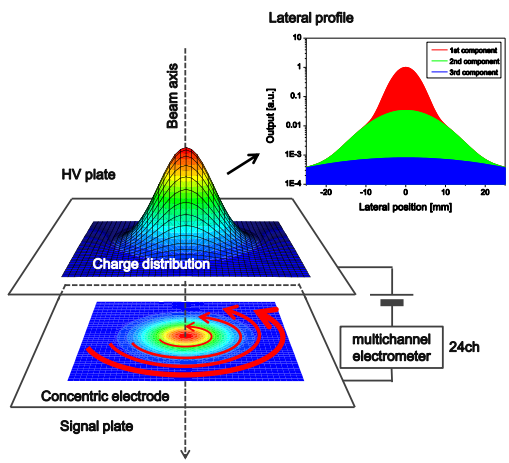


Figure 1: Schematic of the ICCE and lateral profile of carbon-ion expressed by the three-Gaussian model.

The large plane IC should have enough effective area to intercept all particles scattered. The diameter of the chamber is 150 mm. The gap between the HV plate and

ISBN 978-3-95450-141-0

Copyright © 2014 CC-BY-3.0 and by the respective authors

each signal plate is 2 mm. This chamber is freely open to the atmosphere, where the fill gas is ambient air. Since stray leakage current must be kept to a minimum to preserve accuracy, the signal electrodes were surrounded by annular guard rings.

Simplified parameterization of LAS particle

The characteristic parameters describing the lateral spreads can be derived from the outputs measured by the ICCE. The measured results can be fitted using three-Rayleigh function that transformed three-Gaussian model into polar coordinates as follows:

$$R(r;\sigma) = \int_{-\pi}^{\pi} \frac{r}{2\pi\sigma^2} \exp\left(-\frac{r^2}{2\sigma^2}\right) \mathrm{d}\theta = \frac{r}{\sigma^2} \exp\left(-\frac{r^2}{2\sigma^2}\right),$$

$$F(z,r;t) = \left(1 - \sum_{i=2}^{3} f_i\,(z;t)\right) R_1\left(r;\sigma_1(z;t)\right) + \sum_{i=2}^{3}\left(f_i(z;t) R_i(r;\sigma_i)\right),$$

where r is the distance from the central point. $f_i(z;t)$ is the fraction of the integrated dose assigned to the i-th Rayleigh distribution at a given depth z, for the range shifter plate of thickness t. R_i is the Rayleigh distribution equal to describing the lateral beam spread of the i-th component with the standard deviation σ_i. Here, we assumed the first component describing three-Rayleigh was dominated by the primary ions. Therefore, lateral beam spread and the fraction of primary ions in the regions beyond the maximum range are set to zero. On the other hand, in the regions beyond the maximum range of primary ions, i.e. in the tail regions, the dose distribution is dominated by dose contribution due to the second and third components. Additionally, the lateral spreads of the second and third components were approximated as invariant with respect to the depth.

Experimental set up

All experiments were performed with a ^{12}C pencil beam in the new treatment facility at NIRS-HIMAC, equipped with all the instruments indispensable for 3D scanning irradiation, including a scanning magnet, range shifter, ridge filter and beam monitors [3]. For depth scanning, the hybrid depth scanning method [13] was employed, in which 11 beam energies ranging from 140 MeV/u to 430 MeV/u were used in conjunction with the range shifter.

Measurement with the ICCE

The ICCE was enclosed in a polymethylmetacrylate (PMMA) waterproof shell so that it could be inserted into the water phantom. The large plane-parallel IC and 24-channel IC were each connected to a Unidos universal dosimeter and two Multidos multichannel dosimeters (both, PTW Freiburg, Germany). The typical high-voltage working value is +1 kV. The ICCE was immersed into a water phantom and scanned in the beam direction by a motor drive. Both the Rayleigh-like dose distribution of the carbon pencil beam and the integrated dose could be simultaneously measured. Additionally, to verify the reduction of the collected ions due to the general ion recombination, we measured the saturation curves for various applied voltage ranging from +50 V to +1 kV.

Measurement for the target volume

To prove that three-Gaussian model with the parameters by simplified parameterization adequately describes reality, we measured the lateral dose distributions for the target volume of 60 × 60 × 80 mm^3. The lateral dose distribution was measured with a pinpoint ionization chamber (PTW31015) which has a sensitive volume of 0.03 cm^3 connected to a Unidos at the center of a spread-out Bragg peak (SOBP) in water in the horizontal direction from 0 to 100 mm.

Measurement for different media

To investigate the influence of nuclear reaction caused by ^{12}C passing through different media, we measured the depth dose distributions and the lateral dose distributions for non-water materials. Non-water materials (water, 40% K_2HPO_4, lard, milk) put into container with thickness of 150 mm is set in front of a water phantom. The ICCE was immersed into a water phantom behind the non-water material. These measurements were repeated at various depths.

RESULTS AND DISCCUSION

Saturation curves of ICCE for different electrodes

In Fig. 2, the measured saturation curves are compared with the saturation curves calculated by a calculation model [14] based on the Boag theory [15] for different lateral positions. All calculations could reasonably reproduce the measured distribution. We confirmed the differences of the ion collection efficiency at different lateral positions. This result was attributed to the difference of ionization density dependent on lateral position.

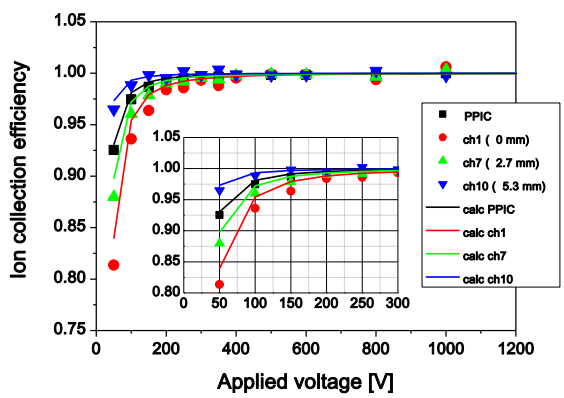


Figure 2: The measured saturation curves (symbols) are compared with the calculated ones (solid lines). PPIC indicates a large plane-parallel IC.

Copyright © 2014 CC-BY-3.0 and by the respective authors

ISBN 978-3-95450-141-0

Verification of parameters describing the LAS particles

Figure 3 shows the lateral dose distribution measured by the ICCE at the Bragg peak. The open squares show the fit of the measured results to three-Rayleigh function using the derived parameters of the lateral beam spreads and the fraction factors. The other symbols represent the first, second and third components of the lateral dose distribution fitted by three-Rayleigh function, respectively. In Fig. 4, the depth dose distribution and parameters describing the LAS particles at various depths are shown. As shown in Fig. 4 (b) and (c), while the lateral beam spreads of the second and third components were approximated as invariant with respect to the depth, the fraction factors of the second and third components change steeply from the distal-falloff region to the tail region. Since the fraction of the third component increases as a function of depth, it seems that the third component represents the lighter fragments from a qualitative viewpoint.

To verify the precision of the derived parameters, we calculated the correction factor for the field-size dependence of the doses, "predicted-dose scaling factor" (PDSF) [5, 6]. The PDSF was derived as a ratio of the averaged dose within the target volume optimized with the single-Gaussian form of the pencil beam model to one recalculated with the three-Gaussian model. The dose distribution of 1 Gy was optimized for three target volumes. Figure 5 shows the PDSF for three field sizes. The difference between the PDSF calculated with σ_2 and σ_3 changed as a function of depth and the one calculated with σ_2 and σ_3 by approximated as invariant with respect to the depth was 0.1%. As shown in Fig. 6, the calculation using the three-Gaussian model was in good agreement with the measured results. These results show that the simplified parameterization of LAS particles adequately describes the correction for the field-size dependence of the doses.

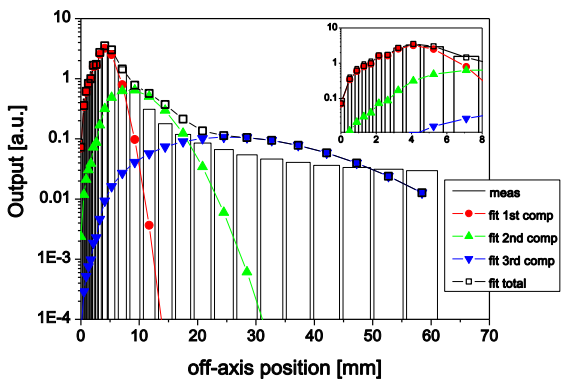


Figure 3: The lateral dose distributions of a 430 MeV/u carbon-ion beam measured at the Bragg peak are shown with the solid line. Each width of the bar charts formed by the solid line represents the widths of the electrodes. Each symbol represents each component of the lateral dose distribution fitted by three-Rayleigh function.

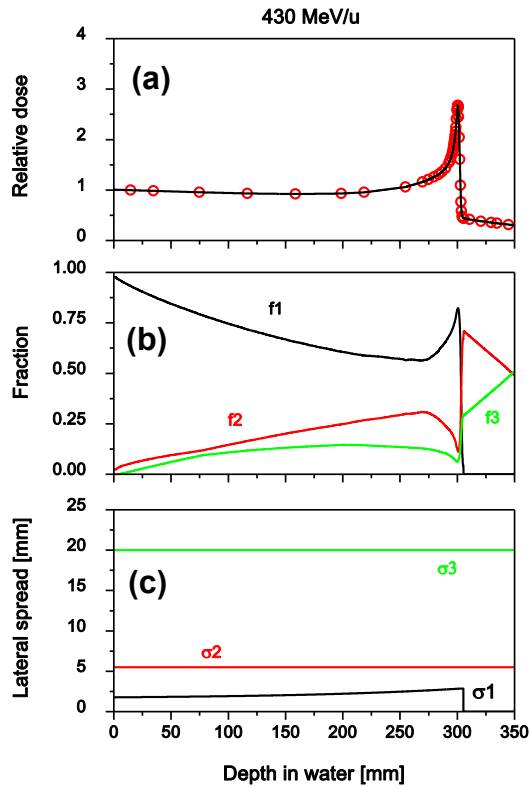


Figure 4: (a) Depth dose distributions measured (open circles) and calculated (solid line). (b) The fraction factors of the first, second and third components fitted by three-Rayleigh function. (c) The lateral beam spreads of the first, second and third components fitted by three-Rayleigh function.

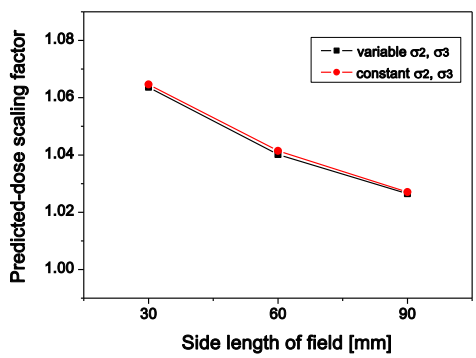


Figure 5: The PDSF for the target volumes of 30 × 30 × 80, 60 × 60 × 80, 90 × 90 × 80 mm^3. The closed squares represent the values calculated with σ_2 and σ_3 changed as a function of depth. The closed circles represent the values calculated with σ_2 and σ_3 by approximated as invariant with respect to the depth.

ISBN 978-3-95450-141-0

Copyright © 2014 CC-BY-3.0 and by the respective authors

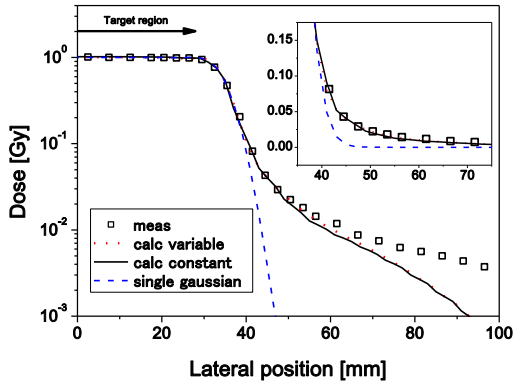


Figure 6: The measured lateral dose distributions (open squares) are compared with those calculated using the three-Gaussian model (solid line) with σ_2 and σ_3 by approximated as invariant with respect to the depth. For comparison, the calculations using the three-Gaussian model with σ_2 and σ_3 changed as a function of depth (dotted line) and the calculations using the single-Gaussian model with the PDSF (dashed line) are plotted. The target volume was 60 × 60 × 80 mm^3.

Nuclear reaction caused by ^{12}C passing through different media

Figure 7 shows the depth dose distributions for a 400 MeV/u carbon-ion beam measured in water behind non-water material. For milk, the depth dose distribution was almost identical as the one for water. For lard, the Bragg-peak height was 4.5% lower than that for water. This observation suggests that the loss of primary carbon ions in the lard due to nuclear reactions is less than that in water. We also observed a 7.0% increase of the Bragg-peak height for 40% K_2HPO_4 compared with that for water. The correction method of the depth dose distribution to account for the dosimetric errors in patient-dose calculations has been reported by Inaniwa et al [16] in detail. As shown in Fig. 8, there is a slight difference between the lateral dose distribution measured in water and those in non-water material. However, these differences are of no clinical significance.

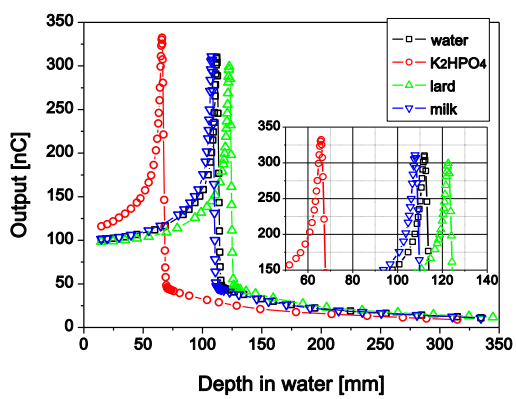


Figure 7: The depth dose distributions measured in water behind non-water material.

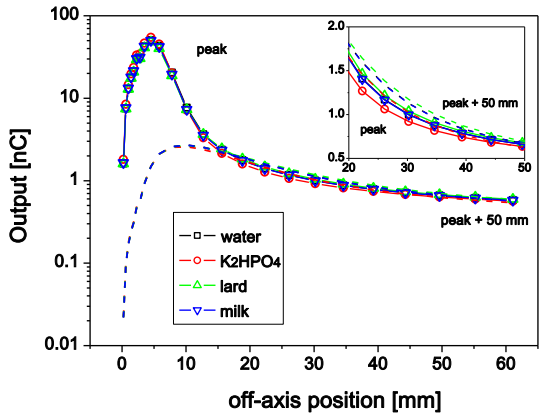


Figure 8: The lateral dose distributions measured in water behind non-water material at Bragg peak (symbols) and peak + 50 mm (dashed lines).

CONCLUSIONS

We evaluated a unique ionization chamber with concentric electrodes as a useful tool to determine the characterization of the therapeutic ion beams. Simplified parameterization with ICCE makes it possible to easily obtain the parameters describing LAS particles, while maintaining the dose calculation accuracy. Therefore, it will lead to shortened measurements for pencil beam datasets in the commissioning stage. Additionally, it can be easily applied to proton pencil beams. Since it is not necessary to scan the pencil beams, it may also be used for broad-beam delivery systems.

REFERENCES

[1] E. Pedroni et al., Med. Phys. 22 (1995) 37.
[2] Th. Haberer et al., Nucl. Instrum. Methods Phys. Res. A 330 (1993) 296.
[3] T. Furukawa et al., Med. Phys. 37 (2010) 5672.
[4] Y. Hirao et al., Nucl. Phys. A 538 (1992) 541.
[5] E. Pedroni et al., Phys. Med. Biol. 50 (2005) 541.
[6] T. Inaniwa et al., Med. Phys. 36 (2009) 2889.
[7] Y. Kusano et al., Med. Phys. 34 (2007) 4016.
[8] Y. Li et al., Med. Phys. 57 (2012) 983.
[9] J. Schwaab et al., Phys. Med. Biol. 56 (2011) 7813.
[10] O. Sawakuchi et al., Phys. Med. Biol. 55 (2010) 3467.
[11] Y. Kusano et al., Med. Phys. 34 (2007) 193.
[12] Y. Hara et al., Med. Phys. 41 (2014) 021706.
[13] T. Inaniwa et al., Med. Phys. 39 (2012) 2820.
[14] R. Tansho et al., in these proceedings
[15] J. W. Boag et al., Br. J. Radiol. 23 (1950) 601.
[16] T. Inaniwa et al., accepted to Phys. Med. Biol.

Copyright © 2014 CC-BY-3.0 and by the respective authors

ISBN 978-3-95450-141-0

DEVELOPMENT OF THREE-DIMENSIONAL DOSE VERIFICATION SYSTEM USING A FLUORSCENT SCREEN IN ION BEAM THERAPY

Y. Hara#, T. Furukawa, K. Mizushima, N. Saotome, Y. Saraya, R. Tansho, T. Shirai, K. Noda,
National Institute of Radiological Sciences, Chiba, JAPAN
E. Takeshita, Kanagawa Cancer Center, Kanagawa, JAPAN

Abstract

For quality assurance (QA) of therapeutic ion beams, QA tool having high spatial resolution and quick verification is required. The imaging system with a fluorescent screen is suitable for QA procedure. We developed a quick verification system (NQA-SCN) using a fluorescent screen with a charge-coupled device (CCD) camera for the sake of two dimensional dosimetry. The NQA-SCN is compact size to attach to irradiation port and water column. Several types of corrections were applied to the raw image obtained by the NQA-SCN. Our goal is to use the NQA-SCN for three-dimensional dose verification. In carbon-ion therapy, the fluorescent light is decreased by suffering from quenching effect due to the increased linear energy transfer (LET) in the Bragg peak. For the use of three-dimensional dose verification, as a first approach, we investigated the quenching effect of carbon-ion beam in water. Also, to evaluate the performance of NQA-SCN, we carried out experiments concerning QA procedures.

INTRODUCTION

Recently, to make the best use of physical and biological characteristics of therapeutic ion beam, three-dimensional (3D) pencil-beam scanning technique [1-3] has been implemented at some facilities. It has been utilized since 2011 at the Heavy Ion Medical Accelerator in Chiba (HIMAC), in the National Institute of Radiological Sciences (NIRS) [4]. In the scanning irradiation method, since the 3D dose distribution is achieved by superimposing doses of individually weighted pencil beams, any change in the scanned beams will cause a significant impact on the irradiation dose. Therefore, quality assurance (QA) procedures and tools for making refined measurements to verify the characteristics of the pencil beams (e.g. size and position) must be developed. For this purpose, we developed a verification system using a fluorescent screen with a charge-coupled device (CCD) camera, which we called the QA-SCN [5, 6], originally proposed by Boon et al [7, 8]. The QA-SCN is a very useful tool for QA of scanned ion beam because of a high spatial resolution and a quick verification at many points in the irradiation field.

On the other hands, in NIRS, the rotating gantry has developed to improve the dose conformity and less sensitivity to range uncertainties [9]. While the rotating gantry can be rotated 360 degrees, there are small errors due to gantry angle dependence of beam. Thus, a verification system which can be attached on the gantry nozzle is necessary for the commissioning of the rotating gantry and its QA. However, the QA-SCN is large to cover wide viewing field and heavy to maintain rigid. Additionally, the fluorescent light is decreased by suffering from quenching effect due to the increased linear energy transfer (LET) in the Bragg peak. It is difficult to use the QA-SCN for verification of 3D dose distribution in water. To overcome these problems, we developed the NQA-SCN. The NQA-SCN is very compact size. As a first approach, we investigated the response of the NQA-SCN to carbon-ion for various doses, dose rate and different linear energy transfer (LET) values. In this paper, the results of the QA measurements obtained by using the NQA-SCN are described.

#y-hara@nirs.go.jp

MATERIALS AND METHODS

Design of NQA-SCN

A schematic of NQA-SCN system was shown in Fig. 1. The NQA-SCN consists of a fluorescent intensifying screen, a CCD camera, a mirror, camera controllers and a dark box to protect against surrounding light. The mirror is located at 60 degrees relative to the beam axis. The distribution of fluorescent light is reflected by a mirror and is observed by a CCD camera, which is installed at -60 degrees relative to the beam axis. The path length to the CCD camera from the fluorescent screen is about 400 mm. The CCD camera installed in the NQA-SCN is the type BU-41L (Bitran Corp., Japan). The CCD resolution is 1360 × 1024 pixels and the pixel size of the CCD is 6.45 μm × 6.45 μm. The CCD camera allows for the measurements of a 2D light output with a large dynamic range by digitizing optical signals at 14 bits. To decrease thermal noise, the CCD chip is cooled to -1°C by the Peltier cooling unit. A focal length of a lens (V. S. Technology Corp., Japan) is 12 mm. To block direct fluorescent light from the screen, the light shield is placed near the lens. The viewing field and the aperture of the dark box cover an irradiation field of 220 × 220 mm^2. A fluorescent intensify screen, which the phosphor (ZnS: (Ag, Al)) with thickness of about 40 μm is coated on FR-4 board with thickness of 500 μm, is mounted at the entrance face. To verify a light yield difference for different screen positions depending on the coating thickness, we also used the two different types of screen for the flat field correction described later.

Copyright © 2014 CC-BY-3.0 and by the respective authors

ISBN 978-3-95450-141-0

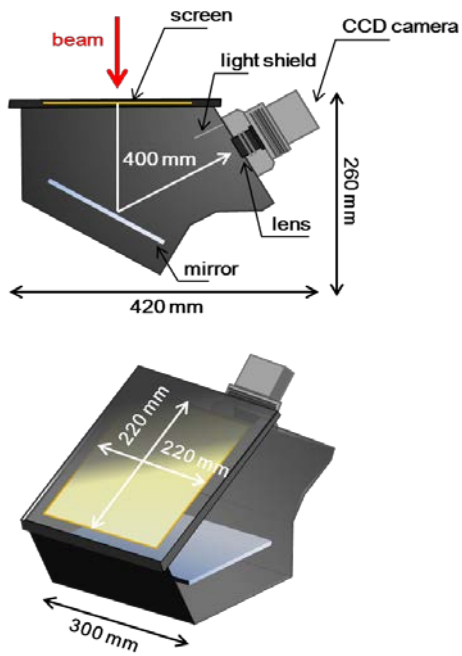


Figure 1: Schematic of the NQA-SCN system.

Image Correction Process

Figure 2 shows the flow chart of the image correction process. After the irradiation, all of the detected images are transferred to a data server at once, and the image processing is started. First, the background data are subtracted from the original image. The background noise level and its time dependence were measured. The background noise level was an almost constant without dependent on measured time. To suppress any spike noises, we apply a median filter in a 3 × 3 window to the image after subtraction. For both rotation correction and distortion correction, a simple correction formula correlated with lateral positions, x and y was applied [6]. To derive the parameters for this formula, we used the calibration board made of aluminum. The calibration board has multiple small holes (121 holes), which are located every 20 mm on the plane. The size of a hole is φ0.2 mm. Figure 3 shows layout of rotation and distortion correction with the calibration board. As shown in Fig. 4, the distortion caused by the lens was derived from the difference between geometric positions of holes and the center of gravity obtained by natural light passed through multiple holes. Simultaneously, the pixel spacing is converted to the actual spacing in millimeters. To convert the pixel spacing of the images into an actual size, the values are fitted to above formula as lateral positions, x and y. To reduce the variations of the output caused by lens vignetting and the difference in the thickness of the screen, we apply the flat field correction by using the radiochromic film Gafchromic EBT2 film as a reference. Figure 5 shows profiles of a uniform irradiation field without the flat field correction. To check the variations of the output due to positions, we compared the result measured by ZnS: (Ag, Al) with that obtained with the other fluorescent screen (Type HG-M2, Gd2O2S: Tb, Fujifilm Corp., Japan) in this figure. The result measured by ZnS: (Ag, Al) fluctuate due to a weak fluorescent light. However, this fluctuation is tolerable for verification of the uniformity. Although the result measured by Gd2O2S: Tb was affected by the difference in the thickness of the screen, the difference between the result by ZnS: (Ag, Al) and that by EBT2 was within 3% at 1-sigma. Therefore, in this study, the flat field correction was not used.

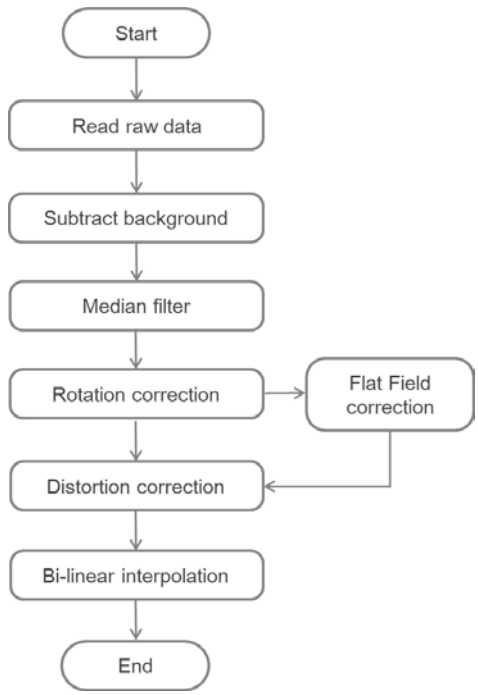


Figure 2: Flow chart of image correction process.

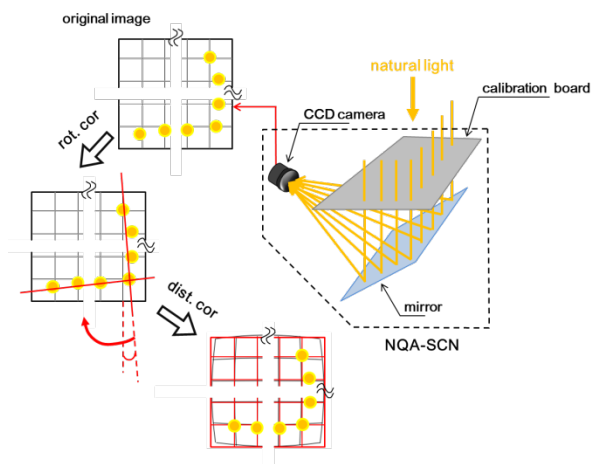


Figure 3: Schematic of the rotation correction and the distortion correction. Parameters for both corrections are derived from the image obtained with the calibration board.

Copyright © 2014 CC-BY-3.0 and by the respective authors

ISBN 978-3-95450-141-0

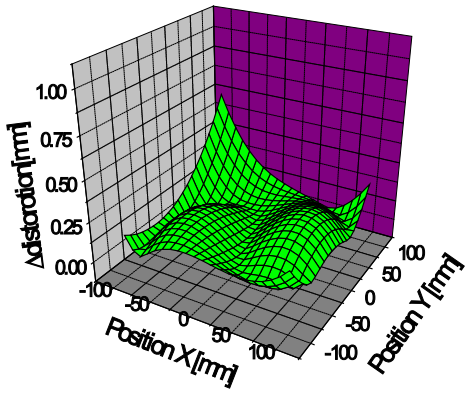


Figure 4: Difference between the center of gravity measured with the calibration board and the prescribed lateral positions.

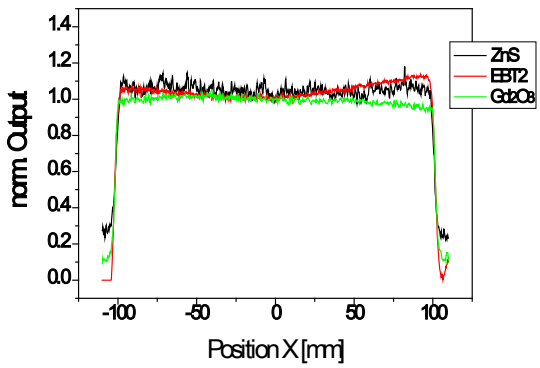


Figure 5: The profiles of a uniform field measured by the two different fluorescent screens and EBT2.

Experimental Setup

All experiments were performed in the new treatment facility at NIRS-HIMAC, equipped with all the instruments indispensable for 3D scanning irradiation, including a scanning magnet, range shifter, ridge filter and beam monitors [3]. For depth scanning, the hybrid depth scanning method [10] was employed, in which 11 beam energies were used in conjunction with the range shifter.

For measurement in water, as shown in Fig. 6, the NQA-SCN was attached to an accordion-type water phantom. The accordion-type water phantom was reported previously [11]. Only a simplified explanation is given here. Measurement depth for the accordion-type water phantom can be changed from 30 mm to 300 mm by remote control.

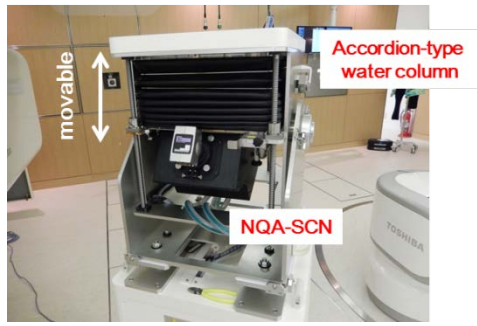


Figure 6: Photograph of experimental setup for the depth dose distribution in water.

RESULTS AND DISCUSSION

The first step was to check the linearity of dose, dose rate and LET in relation to light output. We measured the fluence with the NQA-SCN positioned on the isocenter without any water phantom. Figure 7 shows the linearity of applied dose and light output for single spot irradiation with three different incident energies. Even in small count region, the relation between dose and light output for three different energies is linear. Linearity for different dose rate is shown in Fig. 8. We confirmed that the relation for different dose rate turned out to be linear.

Several types of QA measurements must be performed to check the beam position, 2D intensity modulation and the effect of hysteresis for therapeutic scanned ion beams. The scanned beam position is directly affects the delivered dose distribution. Thus, we confirmed the accuracy of the position for scanned beam by using the NQA-SCN. Figure 9 shows differences between the measured and prescribed positions for irradiation fields, ±80 mm. The results show the accuracy of ±0.2 mm at 1-sigma. To verify the dose dependence of the beam size, we derived the size from the measured results of the spot irradiation. The variation of the beam size was less than 0.06 mm at 1-sigma.

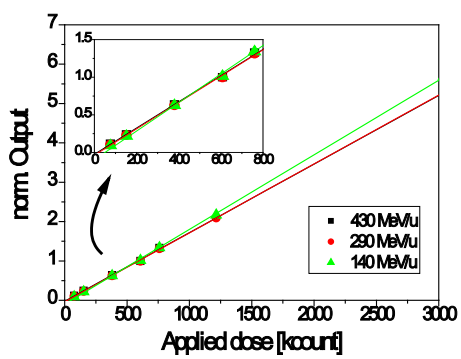


Figure 7: Linearity of applied dose and light output for single spot irradiation with different incident energy: 430, 290, 140 MeV/u.

ISBN 978-3-95450-141-0

Copyright © 2014 CC-BY-3.0 and by the respective authors

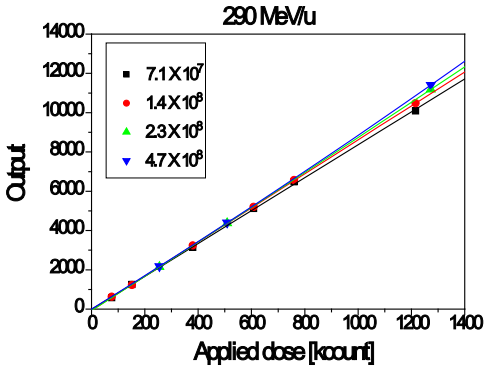


Figure 8: Linearity of applied dose and light output for single spot irradiation with different dose rate.

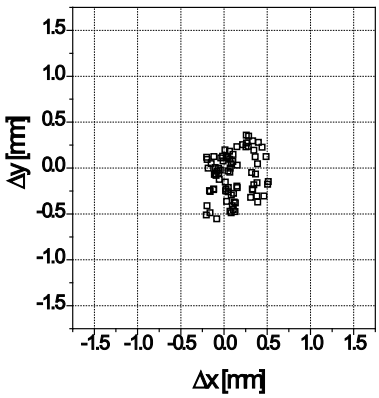


Figure 9: Differences between the measured and prescribed position obtained by using a large spot irradiation field, ±80 mm.

To measure the depth brightness distribution in water, the NQA-SCN was attached to an accordion-type water phantom in Fig. 6. Even for water phantom attached the NQA-SCN, the speed of a change in depth keeps 5 mm/s. Figure 10 shows the depth brightness distribution measured by the NQA-SCN. In same figure, the measured brightness distribution is compared to depth dose distribution measured by the large-plane ionization chamber (IC) [12]. NQA-SCN data was normalized to match the IC data at a depth of 30 mm. Compared to the result measured by the IC, the increase of quenching effect was significant for the LET dependence of the light output toward the Bragg peak region. For correct of quenching effect [13], we derived a ratio the result measured by NQA-SCN to that measured by the IC. The ratio increased steeply from the distal-falloff region to the tail region. It seems that dose contribution in the tail region is dominated by the lighter fragments with low LET from a qualitative viewpoint. While the depth brightness distribution was normalized to 1 at the entrance region, LET dependence of light output at the entrance region is small, as shown in Fig. 7. Effective area of the NQA-SCN is larger that of IC, background noise of the NQA-SCN at entrance may be overestimated.

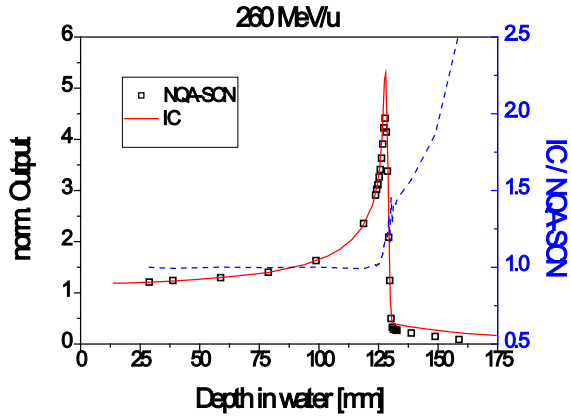


Figure 10: The depth brightness distribution in water (open square) and the depth dose distribution measured by the ionization chamber (solid line). Both distributions normalized at a depth of 30 mm. The dashed line shows a ratio the result measured by NQA-SCN to that measured by the ionization chamber.

CONCLUSIONS

We developed the compact dose verification system with a fluorescent screen and a CCD camera, so-called the NQA-SCN. We confirmed that the NQA-SCN could be used as a useful tool for QA procedures of therapeutic scanned ion beam. Additionally, we investigate the response of the NQA-SCN to carbon-ion for doses, dose rate and LET. In further research, we will assess the performance of the NQA-SCN for 3D dose verification.

REFERENCES

[1] E. Pedroni et al., Med. Phys. 22 (1995) 37.
[2] Th. Haberer et al., Nucl. Instrum. Methods Phys. Res. A 330 (1993) 296.
[3] T. Furukawa et al., Med. Phys. 37 (2010) 5672.
[4] Y. Hirao et al., Nucl. Phys. A 538 (1992) 541.
[5] E. Takeshita et al., Nucl. Instrum. Methods Phys. Res. B 269 (2011) 2936.
[6] Y. Hara et al., J. Kor. Phys. Soc., 63 (2013) 1446.
[7] S. N. Boon et al., Med. Phys. 24 (1998) 464.
[8] S. N. Boon et al., Med. Phys. 27 (2000) 2198.
[9] Y. Iwata et al., Nucl. Instrum. Methods Phys. Res. B 317 (2013) 793.
[10] T. Inaniwa et al., Med. Phys. 39 (2012) 2820.
[11] T. Furukawa et al., Med. Phys. 40 (2013) 121707.
[12] Y. Hara et al., Med. Phys., 41 (2014) 021706.
[13] N. Saotome et al., "Development of 3D dose verification system for scanned ion beam at HIMAC," EPAC 2008, Genoa, Italy, 1830.

Copyright © 2014 CC-BY-3.0 and by the respective authors

ISBN 978-3-95450-141-0

A FAST QUADRUPOLE MAGNET FOR MACHINE STUDIES AT DIAMOND

A. F. D. Morgan, G. Rehm, Diamond Light Source, Oxfordshire, UK

INTRODUCTION

Fast quadrupolar magnets (FQM) have been demonstrated in various schemes for increasing the coupled bunch instability thresholds [1] [3] [8], and for measuring the tune shift of transverse quadrupolar oscillation [5] [6], thus probing the transverse quadrupolar impedance [7]. Operationally they have been used to suppress quadrupole mode instabilities on injection at several machines [2] [4].

Due to machine upgrades, a ceramic vessel installed in the Diamond storage ring has become temporarily available for use. We decided to take advantage of this situation by designing and installing a simple air core quadrupole magnet which can operate at the fundamental quadrupolar frequencies for the horizontal (217kHz) and for the vertical plane (384kHz), as well as at the revolution frequency of the machine (533kHz).

Using this magnet we hope to be able to probe hitherto unexplored behaviours of the Diamond machine with the aim of improving our understanding of non centre of mass motions of the beam.

DESIGN AND REALISATION

After assessing several different coil geometries in a 2D EM simulation program a simple solution of two flat coils, on the top and on the bottom of the ceramic vessel was chosen. By driving the current in opposite directions in the two coils a quadrupolar field can be generated. Figure 1 shows the expected field distribution.

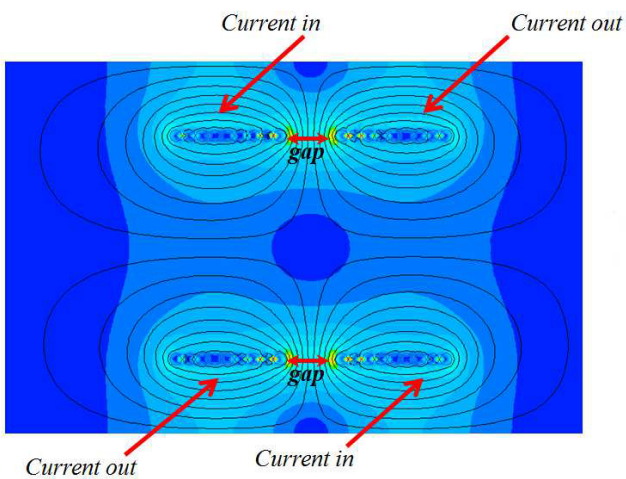


Figure 1: Simulated geometry of the magnet showing the expected quadrupolar field distribution.

The simulations showed that there should be as may turns as possible in order to increase the magnetic field, and also there should be as small a gap along the centre as possible in order to have a high field gradient. The number of turns on each coil was limited by the available space, and the wire radius set practical limits on the centre gap. The final magnet ended up being a pair of 14 turn coils with an 8mm centre gap, made of 2mm diameter enamelled copper wire.

Using these parameters to inform the model we calculated the horizontal and vertical field gradients as being 61mT/m and 64mT/m respectively (Fig.2). These field gradients are sufficient to drive growth and overcome radiation damping.

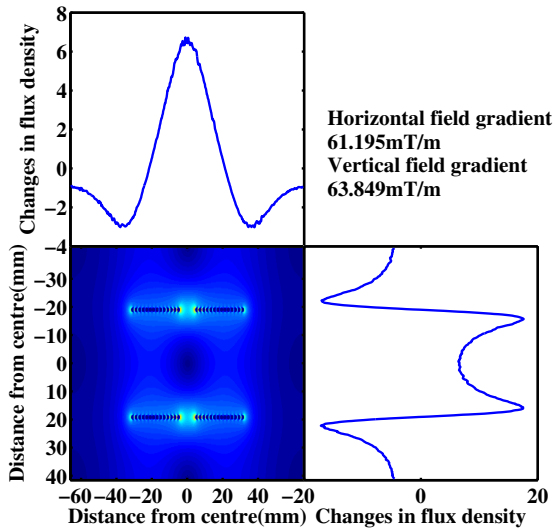


Figure 2: Simulated field gradients of the final magnet.

The coils were bonded in place on non-conductive boards. Using a simple frame, the boards were mounted around the ceramic vessel, as shown in Fig.3.

We planned to use an RF 50Ω amplifier as the power source. In order to match it well to the coils and so maximise the current flowing we decided to drive the coils as part of a resonator circuit. However this also has the effect that the system becomes narrow band and needs to be tuned to a frequency of interest. There are currently 3 operating modes, being tuned to either the vertical or horizontal quadrupole resonance frequencies to enable studies of tune shifts, or tuned to the revolution frequency in order to investigate transverse multibunch instability thresholds. In order to switch modes we change resonant circuits.

ISBN 978-3-95450-141-0

Copyright © 2014 CC-BY-3.0 and by the respective authors

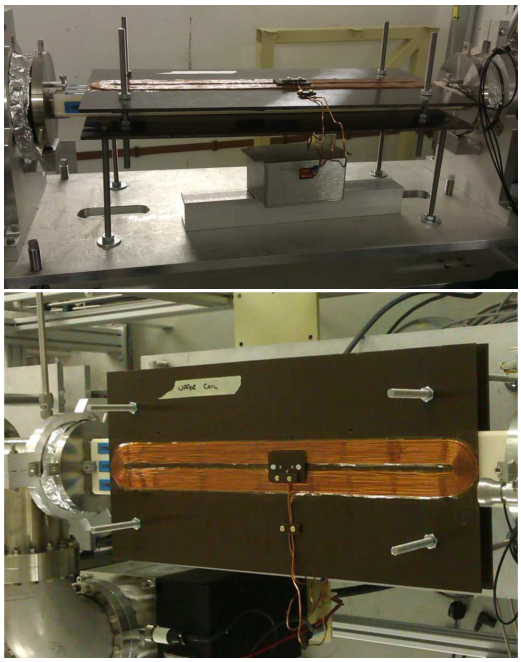


Figure 3: The fast quadrupole magnet in situ.

In order to go from simulation to a practical, tuned magnet, we followed the following procedure. First we simulated and build a test resonant circuit. The EM simulation gave an estimate of the resistance and inductance of the coils but did not include any effect from the ceramic vessel and the associated metallic coating. The circuit was assembled in situ around the ceramic vessel and the resonant frequency was measured. The circuit simulation was then adjusted to bring its predictions in line with the measured data. This allowed us to characterise the coil/ceramic subsystem as a set of resistance and inductance values.

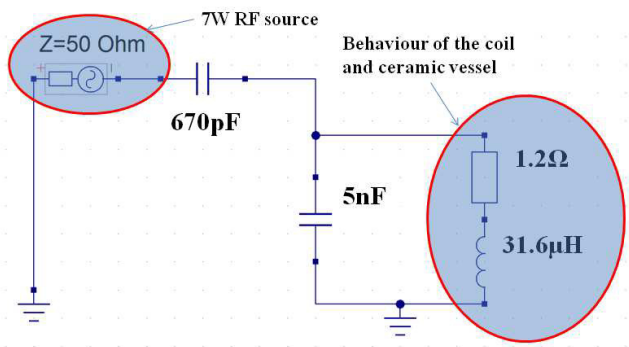


Figure 4: Circuit tuned for the vertical quadrupolar resonance.

Once the system had been characterised, the three desired resonant circuits were designed such that the system would resonate at the desired frequency in situ. An example circuit is shown in Fig.4, and a comparison of simulation and measurement is shown in Fig.5.

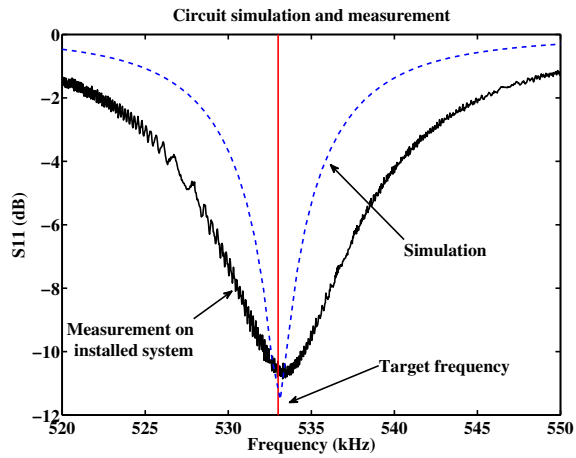


Figure 5: Simulation and measurement for the 533kHz resonator circuit.

INITIAL RESULTS

In order to test the system we tuned it to the vertical quadrupole resonance. The machine was set up with low current to reduce any detuning effects. The coupling was also lowered in order to achieve a reduced vertical beam size, which would make us more sensitive to any changes in beam size.

We measured the effect of the new magnet by recording the vertical beam size as reported by our two pinhole cameras and the results are shown in Fig.6.

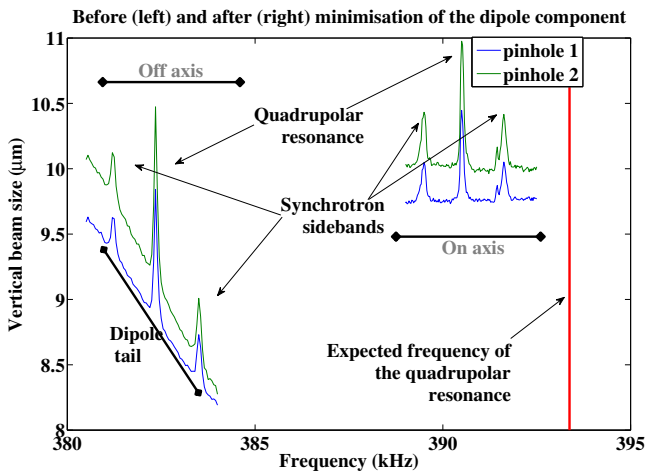


Figure 6: Initial results showing clear quadrupole resonances with associated synchrotron sidebands and how they relate to the expected quadrupolar resonance frequency.

We scanned the excitation frequency of the fast quadrupole magnet around twice the betatron frequency, which is the expected frequency for the quadrupole resonance. Initially we saw a quadrupolar resonance along with associated synchrotron sidebands superimposed on the tail of the dipole resonance.

Copyright © 2014 CC-BY-3.0 and by the respective authors

ISBN 978-3-95450-141-0

In order to reduce the dipolar component we changed the orbit through the fast quadrupole magnet to make the beam pass through its centre. This caused a tune shift which we corrected using our standard procedures. After this the quadrupole resonance was still at a different frequency. It did however show that the dipole component had been removed. The baseline beam size is higher probably due to slightly higher coupling which resulted from the orbit changes.

FUTURE PLANS

The quadrupolar tune shift with orbit change indicates that there is more to be understood. In the coming months, our planned investigations broadly fall into two categories. Firstly, determining how the quadrupolar tunes react to changes in various machine parameters, notably current, and also how this behaviour differs from the dipolar tune behaviour. Secondly, by using the system to apply a chirp to the beam so that each bunch has a slightly different resonant frequency to its neighbour, we hope to reduce the effect of coupled bunch instabilities and increase the instability thresholds.

More generally, work is needed to speed up the measurement such that the proposed parameter scans are practicable. By increasing the camera acquisition rate and more fully automating the measurement we expect to have a much more responsive measurement system, thus making our planned experiments more tractable.

REFERENCES

[1] R. D. Kohaupt, “Single beam instabilities in DORIS”, PAC1975.

[2] V. Chohan et. al. “Measurement of coherent quadrupole oscillations at injection into the antiproton accumulator”, EPAC1990.

[3] S. Sakanaka and T. Mitsuhashi, “Construction of an RF Quadrupole magnet for suppressing transverse coupled-bunch instabilities”, PAC1991.

[4] F. M. Bieniosek and K. Fullett, “Measurement and reduction of quadrupole injection oscillations in the Fermilab antiproton accumu- lator”, PAC1995.

[5] S. Sakanaka et. al. “Measurement of the transverse quadrupole-mode frequencies of an electron bunch in the KEK photon factory”, PAC2003.

[6] S. Sakanaka et. al. “Measurement of the vertical quadrupolar tune shift in the photon factory storage ring”, EPAC2004.

[7] S. Sakanaka et. al. “Measurement of quadrupolar tune shifts after the reconstruction of the photon factory storage ring”, PAC2007.

[8] S. Sakanaka et. al. “Measurement of quadrupolar tune shifts under multibunch operations of the photon factory storage ring”, EPAC2008.

Copyright © 2014 CC-BY-3.0 and by the respective authors

ISBN 978-3-95450-141-0

THE BROOKHAVEN LINAC ISOTOPE PRODUCTION FACILITY (BLIP) RASTER SCANNING UPGRADE*

R. Michnoff#, Z. Altinbas, P. Cerniglia, R. Connolly, C. Cullen, C. Degen, D. Gassner, R. Hulsart, R. Lambiase, L. Mausner, D. Raparia, P. Thieberger, M. Wilinski,
Brookhaven National Laboratory, Upton, NY, USA

Abstract

Brookhaven National Laboratory's BLIP facility produces radioisotopes for the nuclear medicine community and industry, and performs research to develop new radioisotopes desired by nuclear medicine investigators. A raster scanning system is being installed to provide a better distribution of the H^- beam on the targets, allow higher beam intensities to be used, and ultimately increase production yield of the isotopes. The upgrade consists of horizontal and vertical dipole magnets sinusoidally driven at 5 kHz with 90 deg phase separation to produce a circular raster pattern, and a suite of new instrumentation devices to measure beam characteristics and allow adequate machine protection. The instrumentation systems include multi-wire profile monitors, a laser profile monitor, beam current transformers, and a beam position monitor. An overview of the upgrade and project status will be presented.

INTRODUCTION

The purpose of the raster system currently under development at BNL's BLIP facility is to "paint" the H^- beam on the target in a circular pattern in order to provide a more even distribution of beam on the target material. At present, with a Gaussian beam profile, targets such as RbCl melt only in the region of highest beam intensity. This causes a large local density reduction leading to reduced and erratic production yield. The improved rastered beam distribution is expected to result in higher yield of the produced isotopes, especially the critical isotope Sr-82.

The BLIP H^- beam parameters are shown in table 1.

Table 1: BNL LINAC H^- Beam Parameters at BLIP

Energy options:	66, 116, 139, 181, 200 MeV
Repetition rate:	6.67 Hz
Pulse width:	450 microseconds
Peak beam current:	50 milliAmps
Max integrated current:	135 microAmps

The plan is to raster the beam in a circular pattern on the target at 5 kHz, which corresponds to 2.25 revolutions per 450 microsecond beam pulse. A repeating pattern as follows will be generated: 3 consecutive beam pulses at a radius of 19.5 mm, then 1 pulse at a 6.5 mm radius (ref. Fig. 1). Flexibility will be provided to vary the radius value and the number of beam pulses for each radius. In this manner near uniform deposition on the target can be achieved.

The concept of the BLIP raster system is based on the system that has been in operation at the Los Alamos National Laboratory Isotope Production Facility (IPF) [1]. However, several differences exist between the facilities, including increased magnet power requirements at BLIP due to a larger kick angle (3.3 milliRadians for BLIP, 1.5 milliRadians for IPF), and rastering with 2 different radii at BLIP for improved beam distribution.

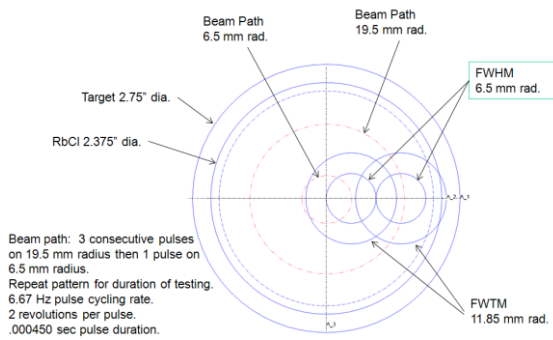


Figure 1: Diagram of circular raster pattern on target.

VACUUM COMPONENTS

The layout of the new BLIP beamline section is shown in Fig. 2. To the extent possible, aluminum components are used instead of stainless steel because aluminum has a shorter half-life and will present fewer activation issues in this high radiation area. The high radiation is primarily caused by back-scattering off the beryllium window that is used to isolate the upstream higher vacuum section from the downstream lower vacuum section.

Most the beam-line pipe is 8" OD. A 6.5" ID graphite collimator will be installed just upstream of the raster magnet to protect the magnet from being damaged by mis-steered particles, and a 4.5" ID graphite collimator just upstream of the multi-wire/LPM crosspiece to protect the beam current transformers. The BPM pipe is 8" OD with 4.5" ID pickups. Graphite is installed between the BPM pickups and the inner pipe wall to help shield the beam current transformers from backscattered particles from the beryllium window. Three aluminium bellows will be installed to facilitate assembly and alignment. A viewport section is in place for thermal imaging of the beryllium window in the future. Included in the viewport section is an electron suppressor ring that will prevent backscattered electrons from interfering with the BPM and current transformer measurements.

* Work supported by Brookhaven Science Associates, LLC under Contract No. DE-AC02-98CH10886 with the U.S. Dept. of Energy
#michnoff@bnl.gov

Copyright © 2014 CC-BY-3.0 and by the respective authors

ISBN 978-3-95450-141-0

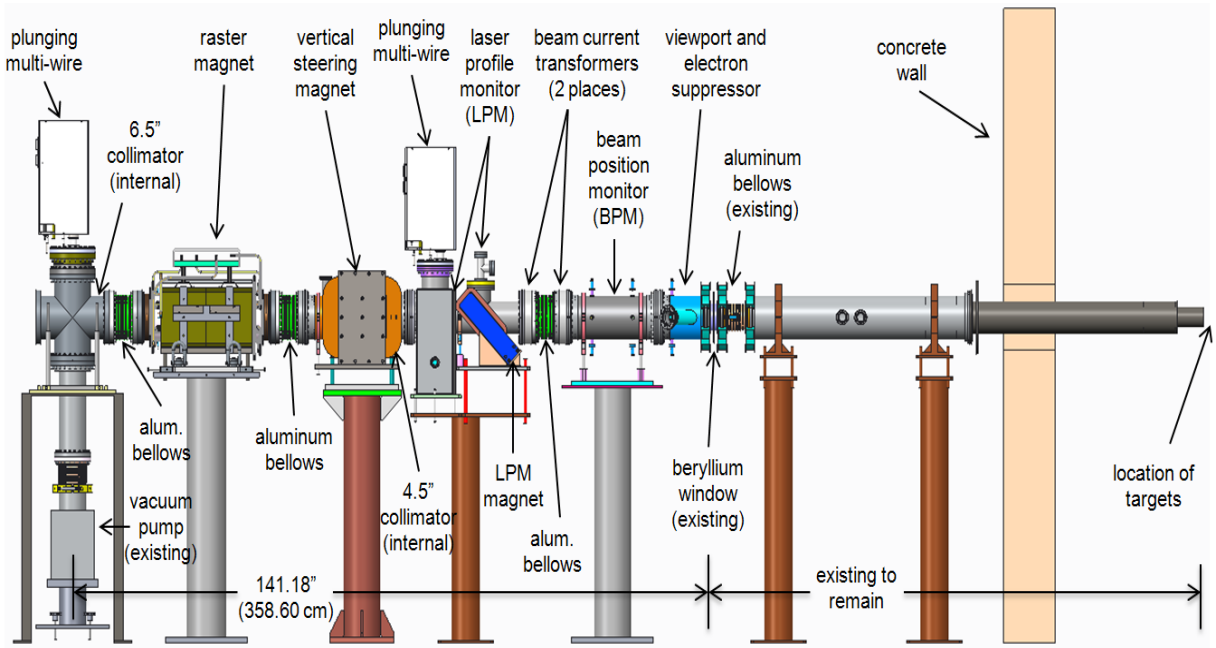


Figure 2: New BLIP beam-line layout.

RASTER MAGNET

The raster magnet consists of one horizontal pair and one vertical pair of water-cooled coils wound on an 8" OD ceramic beam tube with transitions to stainless steel flanges at each end. The coil/tube assembly is housed in ferrite (Fig. 3). A ceramic beam-tube was selected to limit eddy currents produced by the 5 kHz sinusoidal oscillations of each magnet coil. The interior of the ceramic beam tube has a thin conductive coating to dissipate static charge. Four small coils will be installed in the magnet to monitor the induced magnetic field.

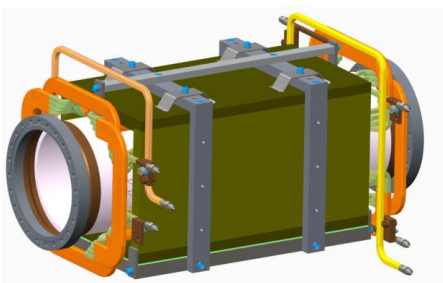


Figure 3: Image of BLIP raster magnet assembly.

RASTER MAGNET POWER SUPPLIES

The horizontal and vertical raster magnets will be driven continuously with a sine wave at 5 kHz and 90 deg. phase separation to provide the circular beam pattern. The amplitude of the signal will control the radius of the beam motion.

Pacific Power Source model 160AMX-UPC12 6 KVA power amplifiers will be used in combination with a custom-designed resonant circuit to deliver 225 A RMS (318 A peak), 470 V RMS (664 V peak), 105 KVA apparent power to the magnet [2]. 4/0 gauge Litz wire with polyimide insulation for radiation resistance will be used. Litz wire was selected because it has much lower resistance than standard wire at our 5 kHz operating frequency.

The power supply controls will be based on National Instrument's PXIe system and Labview. With a Q of about 50, slight frequency shifts off resonance will result in significant amplitude decrease. Therefore, frequency feedback loops will be implemented to keep the frequency on resonance. Software feedback loops will also be used for amplitude control. Other functions of the controls include maintaining 90 deg. phase separation between the horizontal and vertical signals, and interlock safeties for magnet over-temperature, low cooling water flow, etc.

MULTI-WIRE PROFILE MONITORS

Two plunging multi-wire devices manufactured by Princeton Scientific will be installed at the locations shown in Fig. 2. One is upstream of the raster magnet to provide profiles of the non-rastered beam, and the other is downstream of the raster magnet to provide profiles of the rastered beam. The combination of these two devices can also be used to provide a measurement of the beam trajectory angle through the beam-line.

The upstream device is mounted on a 10" OD flange with 7.74" ID pipe and has a stroke of 200 mm, with 300 mm distance from the beam axis to the mounting flange. The downstream device is mounted on an 8" OD flange with 5.75" ID pipe and has a stroke of 150 mm, with 240 mm distance from the beam axis to the mounting flange.

Each multi-wire unit consists of 32 horizontal and 32 vertical tungsten wires, with diameter 0.1 mm and spacing of 3.175 mm. Kapton-coated copper wiring will

ISBN 978-3-95450-141-0

Copyright © 2014 CC-BY-3.0 and by the respective authors

be used internal to the device and brought to 50-pin D-sub connectors with PEEK insulator.

The devices will be pneumatically controlled to plunge into the beam path for a limited time period while the profile measurement is taken. This will extend the longevity of the wires by preventing extended exposure to the beam. The existing BLIP multi-wire device has been problematic because it is stationary in the beam path and must be replaced approximately every two years due to broken wires from continuous beam exposure.

BNL Collider-Accelerator department standard 8-channel integrator modules will be used to process the signals (Advanced Technology Laboratories, Inc part number 22490001). One channel will be connected to each wire, for a total of 128 integrator channels (32 wires per plane, 2 planes per device, 2 devices).

LASER PROFILE MONITOR (LPM)

One laser profile monitor will be installed at the location shown in Fig. 2. This device is very similar to the LPM that is currently installed at the BNL LINAC upstream of the BLIP beam-line [3]. Valuable operational experience was gained with the existing LINAC LPM during the FY2014 beam run.

The purpose of the LPM is to produce profiles of the rastered beam. While this is similar in function to the multi-wire units, the LPM does not have components in the beam path that can be damaged by the beam. The expectation is that the LPM will produce profile measurements approximately several times an hour.

The LPM uses the Quantel Ultra 50 Q-switched Nd:YAG 100 mJ/pulse laser, with 10 ns pulse width. The laser is triggered once per 450 microsecond beam pulse, and will be stepped horizontally and vertically across the beam to provide average profiles for each plane. An average of many beam pulses will be taken at each laser position. Three Arun Microelectronics Ltd. LTVL100-UHV radiation hardened translation stages will be used - one to sweep the horizontal mirror, one to sweep the vertical mirror and one to insert/retract the mirror that directs the laser to each plane. The LPM chamber and optics/motor assembly is shown in Fig. 4.

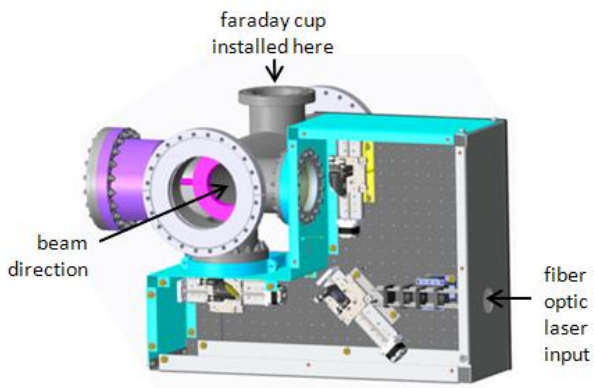


Figure 4: BLIP LPM chamber and optics/motor assembly.

A detector magnet powered by a Sorenson DCS-20-60, 0-20V, 0-60A power supply directs electrons released by the laser to a faraday cup that uses a Stanford Research SR-570 current preamplifier and Tektronix MDO3034 oscilloscope for measurement. Standard VME controls hardware will be used for motor control, triggering, and digital and analog I/O; and Labview will be used for sequencing the profile scans. A Modicon momentum PLC will be used for the Sorenson power supply control.

BEAM CURRENT TRANSFORMERS

Two Bergoz model ACCT-CF10"-147.6-40-UHV-CAW1-H beam current transformers will be installed. These devices are flange mounted with 10" OD and 5.75" ID. The Bergoz ACCT-E-RM-100mA-WB electronics module will be used to convert the current transformer signal to an analog voltage, where +/-5V output corresponds to +/-100mA beam current. Radiation hardened 20 meter cable was purchased from Bergoz for the connection from the current transformer in the beam tunnel to the electronics module in the control room.

BEAM POSITION MONITOR (BPM)

A split cylinder, electrostatic-type capacitive pickup BPM has been custom-designed for the BLIP beam-line and modelled after the BNL AGS Booster BPM [4]. An image of the internals of the device is shown in Fig. 5. A calibration ring is provided for each plane to allow a simulated signal to be induced on the pickups for testing and calibration of the electronics. The 4.5" ID end pieces will help maintain straight field lines at the end of the pickups before the transition to the 8" OD pipe.

BPM measurements will be challenging because for the lower energy operation the 200 MHz RF beam structure is not expected to be present since significant debunching occurs when the beam travels the long distance between the last driving RF tank and the BPM.

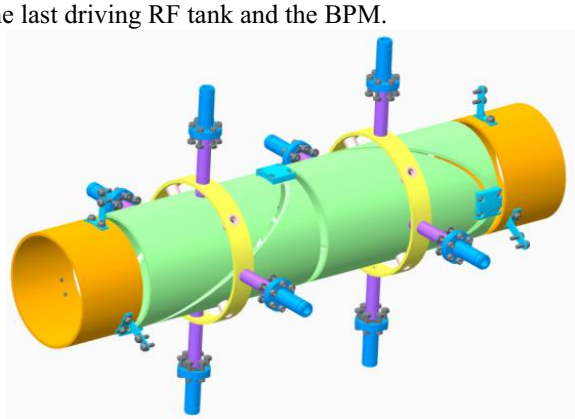


Figure 5: Image of BLIP BPM internal components.

A high input resistance, high gain electrometer-type analog circuit has been designed to measure the low energy debunched beam. An independent circuit will be used to measure the higher energy beam when the 200 MHz RF structure is present. Custom electronic hardware will be designed to process the BPM measurements and may be used to provide an interlock output signal to the beam inhibit system when the beam position is not rastering as expected.

Copyright © 2014 CC-BY-3.0 and by the respective authors

ISBN 978-3-95450-141-0

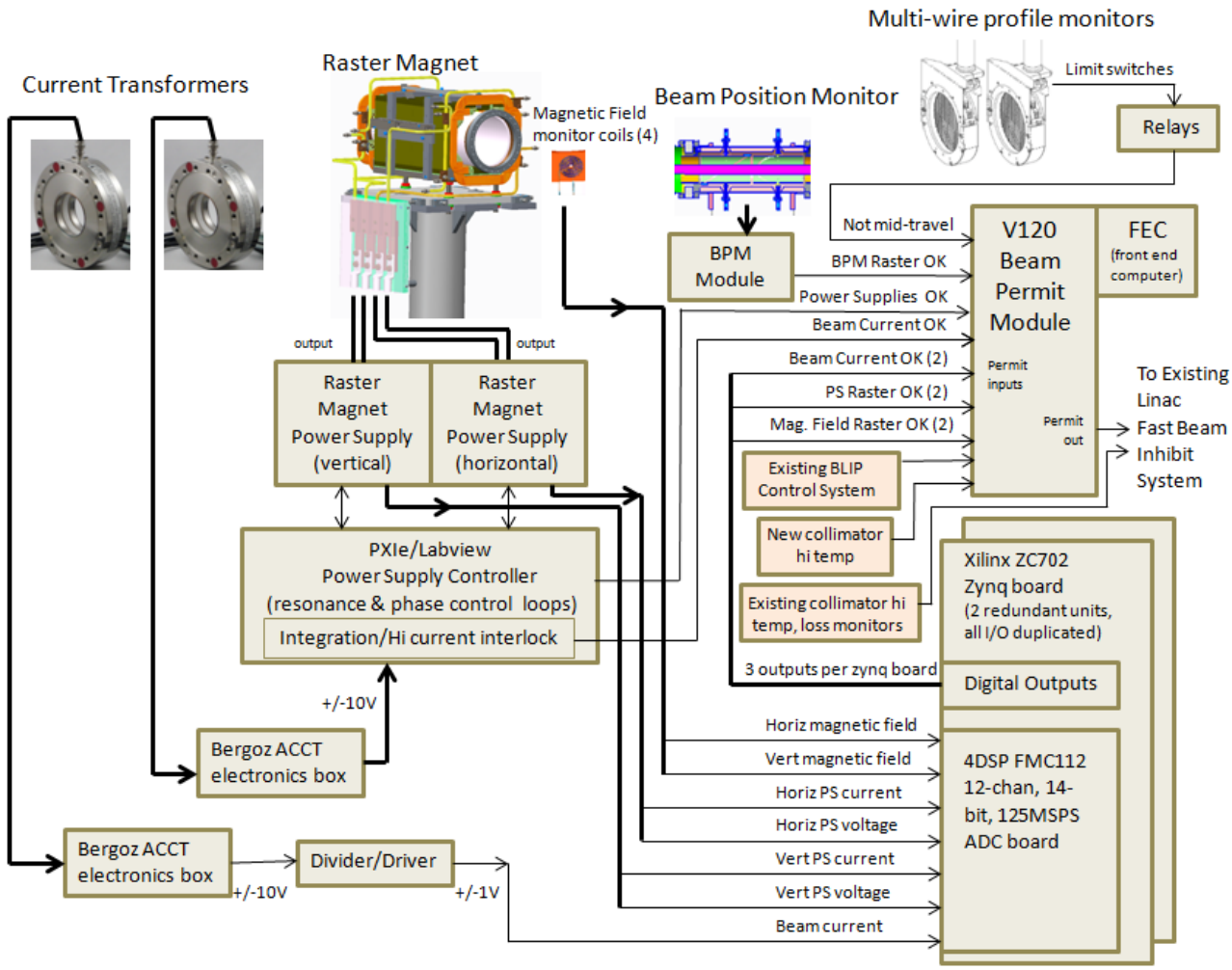


Figure 6: BLIP beam interlock system block diagram.

BEAM INTERLOCK SYSTEM

The purpose of the beam interlock system is a combination of machine protection and target failure prevention (Fig. 6). The present system uses a signal from the existing BLIP control system to inhibit the beam when alarm conditions occur. This signal is also used as a beam ready signal to allow beam to the BLIP targets, and is connected via a hard-wire cable to the LINAC fast beam interrupt (FBI) system.

Other direct signals to the existing LINAC FBI system include loss monitors and high temperature limits from thermocouples on the beam pipe where collimators are installed. These thermocouples are used as an indication that the beam is far off-center.

The signal from the existing BLIP control system will be rerouted into a standard BNL-designed VME-based V120 beam permit module [5]. This module will also be used to accommodate additional new signals as shown in the block diagram (Fig. 6).

Two redundant Xilinx ZC702 modules, each with a 12-channel, 125MSPS analog input module (4DSP FMC112) and 5 channel digital output module (FMC-DIO), running linux and custom gate array code will provide real-time processing of power supply, magnetic field and beam current signals to interlock the beam if any of the following conditions are not satisfied.

- Rastering is enabled and the horizontal and vertical raster magnet magnetic fields have the expected amplitude, 5 kHz sine wave, and 90 deg. phase separation.
- Rastering is enabled and the horizontal and vertical power supply currents have the expected amplitude, 5 kHz sine wave, and 90 deg. phase separation.
- Rastering is disabled and the beam current is below the programmed threshold.

The last condition is required for operating modes where beam rastering is not desired. In this case, the beam current is monitored and will cause the beam to be inhibited if the current exceeds a programmed threshold level in order to prevent target failure with high current beam.

Copyright © 2014 CC-BY-3.0 and by the respective authors

ISBN 978-3-95450-141-0

The FMC112 analog signals will also be capable of being displayed and logged via standard facility control system software tools.

The power supply control system and the BPM electronics module will also be capable of interlocking the beam. For redundancy, processing for one of the two beam current transformers will take place in the Labview PXIe system and can also inhibit the beam.

In addition, thermocouples will be installed on each quadrant of the 2 new collimator sections and will be capable of inhibiting the beam if any collimator temperature exceeds a programmed threshold, indicating that beam is far off-center.

Another signal will be provided to inhibit the beam if either multi-wire device is in the mid-travel position. This will guarantee that the frame of the multi-wire is not in the beam path when beam is present.

INSTALLATION PLAN

With the exception of the raster magnet and the associated power supplies, the entire new beam-line will be installed during the fall of 2014. A dummy spool piece will be installed in place of the raster magnet. The raster magnet and associated power supply will be installed one year later during the fall of 2015. This early installation of the beam-line and instrumentation will allow a full operational year to commission the instrumentation systems prior to beam rastering. The full system implementation is expected to be operational during early 2016.

STATUS

As of September 2014, nearly all of the required beam components have been received and are being mocked-up in the lab prior to installation in the tunnel (Fig. 7). The goal of the mock-up is to find and correct issues that arise prior to installation in the high radiation tunnel, thus limiting worker exposure during the tunnel installation.

The electronic equipment for the upgrade including the raster magnet power supplies, and instrumentation and control hardware will be installed in the BLIP control room, which is located above the end of the beam-line. Facilities work is in progress as shown in Fig 8.

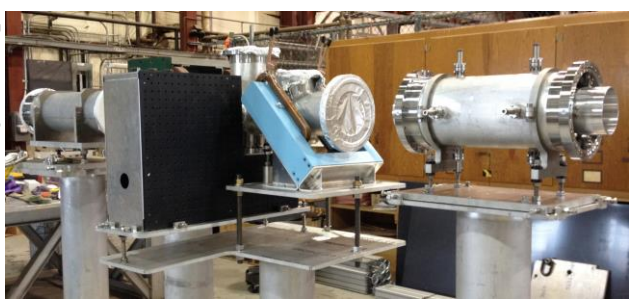


Figure 7: Beginning of mock-up of new BLIP beamline section including from left to right, the dummy raster magnet spool piece, the LPM with optics box (black side) and detector magnet (blue), and the BPM. Beam direction is left to right.

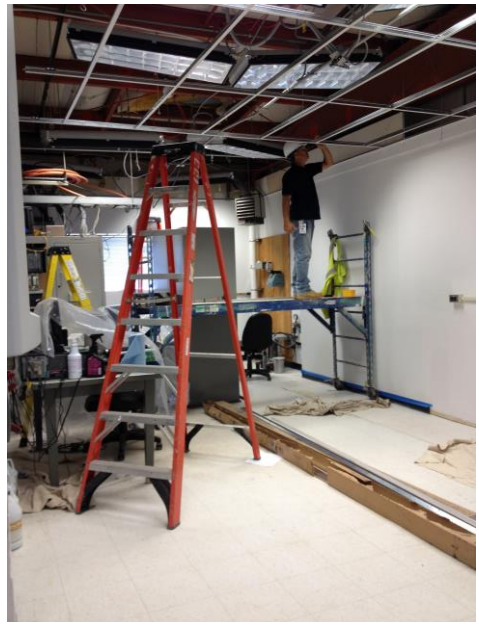


Figure 8: Photo of work in progress in the BLIP control room on September 8, 2014 where 7 new equipment racks will be installed to house the new electronics. Facilities work includes upgraded power, new ceiling and lighting, new air conditioning system, and cable trays.

ACKNOWLEDGEMENTS

The authors would like to thank H. Ashby, N. Baer, C. Biscardi, B. Briscoe, L. Carboni, A. Curcio, C. Dawson, L. DeSanto, L. Evers, C. Ho, R.D. Lehn, V. LoDestro, J. Nalepa, H. Palacios, W. Pekrul, S. Pontieri, R. Schoenfeld, J. Saetta, L. Taddonio, C. Trabocchi, and A. Weston for their engineering and technical support, and K. Mirabella and R. VanWormer for their project controls support. We would also like to thank Marc Garland and Michelle Shinn from the DOE for their overall guidance and project support.

REFERENCES

[1] K.F. Johnson, *et al.*, "Commissioning and Initial Operation of the Isotope Production Facility at the Los Alamos Nuetron Science Center (LANSCE)," EPAC 2004, Lucerne, Switzerland, (2004).

[2] R. Lambiase, Z. Altinbas, "Circular Beam Scanning Power System for Isotope Production Upgrade," IECON 2014, Dallas, Texas, USA, (2014).

[3] R. Connolly, *et al.*, "A Detector to Measure Transverse Profiles and Energy of an H^- Beam Using Gas Stripping and Laser Photo Neutralization," 2012 *JINST* 7 P02001.

[4] D. J. Ciardullo, *et al.*, "The AGS Booster Beam Position Monitor System," PAC 1991, San Francisco, CA, USA, (1991).

[5] C. R. Conkling, Jr., "RHIC Beam Permit and Quench Detection Communication System," PAC 1997, Vancouver, BC, Canada, (1997).

Copyright © 2014 CC-BY-3.0 and by the respective authors

ISBN 978-3-95450-141-0

FAILURE MODE AND EFFECTS ANALYSIS OF THE BEAM INTENSITY CONTROL FOR THE SPIRAL2 ACCELERATOR

C. Jamet #, S. Leloir, T. André, B. Ducoudret, G. Ledu, S. Loret, C. Potier de Courcy,
GANIL, Caen, France

Abstract

The first phase of the SPIRAL2 project includes a driver and its associated new experimental areas (S3 and NFS caves). The accelerator, located in Caen (France), is based on a linear solution composed of a normal conducting RFQ and a superconducting linac. Intense primary stable beams (deuterons, protons, light and heavy ions) will be accelerated at various energies for nuclear physics.

The beam intensity monitoring is a part of the control of the operating range. A high level of requirements is imposed on the intensity control system. In 2013, a Failure Mode and Effects Analysis (FMEA) was performed by a specialized company helped by the GANIL's Electronic Group. This paper presents the analysis and evolutions of the electronic chain of measurement and control.

INTRODUCTION

In the first phase, the SPIRAL2 driver will be able to accelerate and deliver beams of protons, deuterons and ions with q/A=1/3 to NFS (Neutron for Science) and S3 (Super Separator Spectrometer) experimental rooms. Table 1 shows the main beam characteristics.

Table 1: Beam Specifications

Beam	P	D+	Ions (1/3)
Max. Intensity	5 mA	5mA	1 mA
Max. Energy	33 MeV	20 MeV/A	14.5 MeV/A
Max. Power	165 kW	200 kW	43.5 kW

Beam diagnostics are installed along the accelerator in order to measure and control continuously beam parameters and transmission losses [1],[3]. Beam intensity and transmission levels are measured by non-interceptive transformers ACCT and DCCT.

To obtain the commissioning authorization, the SPIRAL 2 project has to demonstrate and prove to the French Safety Authority that these devices which monitor the operating range of the facility are built in respect of the quality assurance rules.

To respond to this request, a FMEA (Failure Mode and Effects Analysis) of the intensity and transmission monitors was performed in 2013 by a French company, Ligeron®, specialized in the safety system developments.

Results, conclusions of this FMEA and the uncertainties of the measurement chains are presented in this paper.

REQUIREMENTS

Global Functions

The functions of the non-interceptive intensity measurements are:

- ✓ Tune the beam,
- ✓ Control and monitor the beam intensity at the LINAC exit,
- ✓ Control and monitor the intensity between several points of the accelerator (transmissions),
- ✓ Control the intensity quantity sent to the Beam Dump Linac over 24 hours.

Tuning Requirements

The initial operating ranges for beam intensity were:

- ✓ for proton and neutron beams: from 0,15 to 5 mA
- ✓ for heavy ions (Q/A=1/3) : from 0,15 to 1 mA

"Voltmeter" function: Measure the beam intensity average
"Oscilloscope" function: Visualize the beam intensity in time. Time resolution: few µs

MPS Requirements

The SPIRAL2 Machine Protection System is based on three technical subsystems [2], [4]:

- ✓ One dedicated to thermal protection (TPS), which requires a fast electronic protection system,
- ✓ One dedicated to enlarged protection (EPS), based on robust technologies consisting of a PLC associated with a redundant hard-wired system. It controls the operation domain of the facility from the safety point of view (beam intensities and energies)
- ✓ One dedicated to classified protection (CPS), which protects the vacuum safety valves of the facility.

Enlarged Protection System Requirements

Beam intensity control at the linac output:

- ✓ Intensity levels: 5 mA on the Linac Beam Dump, 1 mA in the S3 experimental room, 50 µA in the NFS experimental room
- ✓ Response time: 1 s

Beam intensity transmission:

- ✓ Level: 250 µA (maximum losses to limit the radiologic level outside the accelerator area)
- ✓ Response time: 1 s

Intensity at the linac output for the activation control of the Linac Beam Dump:

- ✓ Intensity levels: from 11 µA to 5 mA
- ✓ Response time: 10 s

ISBN 978-3-95450-141-0

Copyright © 2014 CC-BY-3.0 and by the respective authors

Thermal Protection System Requirements

Beam intensity control:

- ✓ Intensity levels: 10 µA to 5 mA
- ✓ Response time: 10 ms

Beam intensity transmission:

- ✓ Levels: less 1 µA to 5 mA
- ✓ Response time: from 35 µs (5 mA)

BEAM INTENSITY AND TRANSMISSION CONTROLS

A DCCT and three ACCT-DCCT blocs will be installed along the accelerator. These diagnostics measure the intensity in the LEBT, MEBT, and in the HEBT at the linac exit and at the entrance of the Beam Dump.
The transmissions of the MEBT, Linac and Linac added to HEBT will be also monitored.

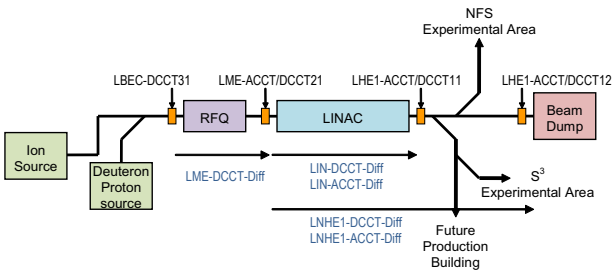


Figure 1: Beam Intensities and transmissions.

ACCT and DCCT diagnostics are complementary. The DCCT, a commercial device, measures the intensity of continuous and chopped beams (response time around 50 µs for a bandwidth of 10 kHz). The minimum intensity measured is around a few dozens of µA without offset compensation.

The ACCT chain is faster with a response time inferior to 1 µs (bandwidth superior to 300 kHz). Its intensity accuracy is better than 10 µA. However, against these benefits must be weighed a disadvantage, a chopped beam is necessary.

MEASURING CHAIN DESCRIPTION

ACCT-DCCT bloc

Two kinds of transformers are used to measure the beam intensity by a non-interceptive method, DCCT (NPCT) and ACCT. A Bergoz NPCT and a homemade ACCT, inside a magnetic shield, compose an ACCT-DCCT bloc.

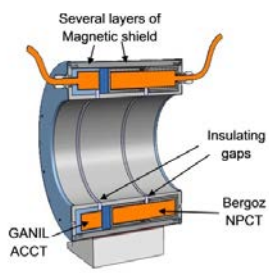


Figure 2: ACCT-DCCT bloc section.

Transformer descriptions:
DCCT: NPCT-175-C030-HR
ACCT: Torus: Nanocristaline, Turn ratio: 300:1
Internal diameter: 184 mm, External diameter: 220 mm

Three shielding layers (Armco, Mu-metal and copper) protect the sensors from external electromagnetic fields.
A vertical shield plate between AC and DC sensors is installed to minimize the disturbance produced by the DCCT magnetic modulator on the ACCT.

ACCT Measuring Chain

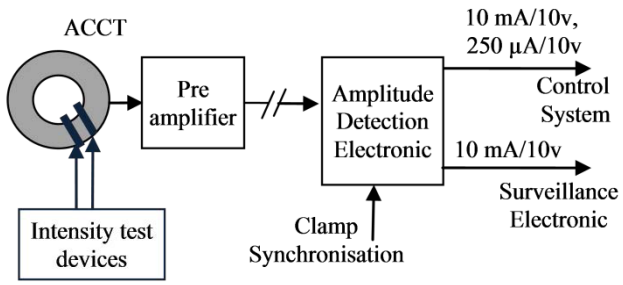


Figure 3: ACCT chain.

The preamplifier was developed to reduce the ACCT low frequency cut-off up to few 10 mHz and decrease the low drop.
The low drop is the gradual fall of the ACCT signal during a constant pulse beam. The low drop uncertainty is proportional to the pulse duration.

The amplitude detection electronic is synchronized to a signal "Clamp synchronization" which memorizes the voltage level when the beam is not present and subtracting the memorized value.
The board has different outputs with two gains 1 and 40 and two bandwidths: 0,5 Hz (low frequency) and 250 kHz (high frequency).

DCCT Measuring Chain

A thermal regulation maintains the temperature at 40 °C ±1°C in order to decrease the effect of the temperature variation on the offset value.

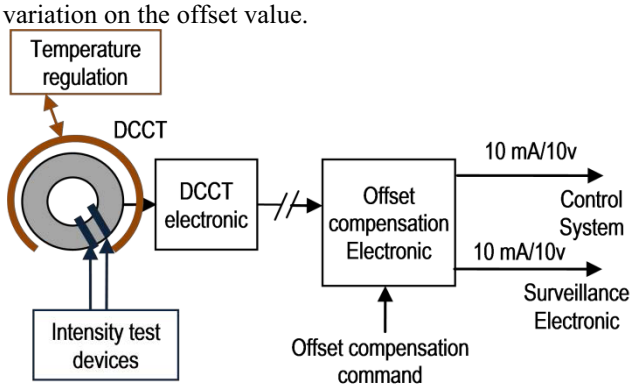


Figure 4: DCCT chain.

Copyright © 2014 CC-BY-3.0 and by the respective authors

ISBN 978-3-95450-141-0

An electronic offset compensation is planned to reset the offset at each start of a new beam tuning. The command is done manually.

INTENSITY SURVEILLANCE BOARD

Requirements

The main board requirements are the following:

- ✓ The surveillance of the average current independently of the duty cycle of the beam chopper (duty cycle period of 200 ms or 1s)
- ✓ a response time of 35 µs with an input level of 5mA

To respond to these 2 requirements, the chosen solution was to build an electronic which integrates the current over a duty cycle period.

Operating Principle

The electronic board realizes a moving integration by using a VFC, a delay of 200 ms or 1 s and a pulse down/up counter [5].

The ACCT or DCCT signal is converted into a pulse frequency. Continually, a counter adds up the pulses and removes the delayed pulses (Figure 5). The delay corresponds to the time interval of integration. This time is equal to a multiple of the chopper period. The counter value is then representative of the input average signal.

A microcontroller is used to perform the counting function and monitor the other thresholds with less reliability but more flexibility. The microcontroller manages the other functions like the communication between the electronics and the control system.

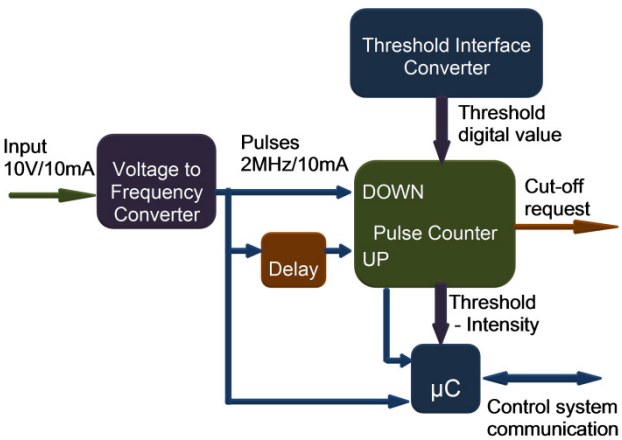


Figure 5: Integrator synoptic.

To generate the alarm signal, the counter starts at the threshold value and its inputs are inverted (count down the pulses and count up the delayed pulses). Therefore, the counter value is equal to the threshold value minus the integrator value.

A negative value of counter is equivalent to the threshold exceeded. In that case, the cut-off request is the sign bit of the counter.

MEASUREMENT RESULTS

Measurement Uncertainty

The MPS controls require knowing the absolute value of the beam intensities. The threshold values must take into account the measurement uncertainty.

The influence quantities in the total uncertainty are:

- ✓ Offset
- ✓ Noise
- ✓ External Electromagnetic field
- ✓ Linearity and accuracy of the gain
- ✓ Temperature drifts (only DCCT)
- ✓ Low drop (only ACCT)
- ✓ Slew rate
- ✓ Time lag between two chains (for transmission measurements)

The measured uncertainties for ACCT and DCCT are presented in the Table 2.

Table 2: Uncertainties

Sources of uncertainty	ACCT	DCCT
Linearity*	0.1%	0.6%
Offset vs. Temperature* ΔT = 1°C	-	10 µA
Integrator Offset	0.5 µA	0.5 µA
External magnetic field max. **	1,5 µA	-
Noise	3nA/√Hz	200nA/√Hz
Low drop ***	-	-
Slew rate	5µs	50µs

* measured by the GANIL test bench
** Measured with the I surveillance board
*** Low drop effect removed by an optimised sample & hold

Noise and fluctuations

For the beam tuning, the ACCT devices will be used to measure the low beam intensity. The main characteristic concerns the resolution the fineness of measurements limited by the noise.

The global chain with the detection board and the "I surveillance" board gives these first results.

The ACCT range of fluctuation is ±1,5 µA with a scale of ±10 mA. These fluctuations are due mainly to the 50 Hz perturbation (in laboratory).

The DCCT fluctuation value is ± 1,5 µA in a short time (few minutes). The offset changes slowly in function of the temperature. The offset variation is measured at ±10 µA for a regulated temperature of ±1°C.

Copyright © 2014 CC-BY-3.0 and by the respective authors

ISBN 978-3-95450-141-0

With a scale of ±250 µA and a 50 Hz reduction, the first ACCT measurements give a resolution better than ±0,5 µA.

The gain dispersion between the different chains limits the transmission accuracy. Tests are underway to adjust the gains in order to obtain the smallest gain difference.

FAILURE MODE AND EFFECTS ANALYSIS RESULTS

The Aim of the FMEA consists to verify that the intensity and transmission control respond to the requirements of the EPS. The risks are to underestimate the beam intensities and transmissions.

The determinist analysis consisted to study the effects of failure modes on the safety functions. The failure mode identification was realized from functional and physical descriptions of the control chains.

The FMEA results show dangerous failures and give three categories of recommendations:

- ✓ Technical recommendations
- ✓ Recommendations to establish periodical controls
- ✓ Recommendations to establish operating procedures

Technical Recommendations

The main technical recommendations are to add surveillances of the hardware functions (saturation detections, timing controls, power supply controls, and temperature regulation control) and add verifications by the microcontroller of the correct writing of the thresholds in the surveillance boards. All these surveillances are added and set off the cut-off request in case of activation. All these recommendations were taking account in the new design of the electronic devices.

An authorisation is now necessary to send a test, to enter a threshold and to deduct the DCCT offset. This authorisation is given when the beam is stopped in the LEBT.

Periodical Controls

These controls are the following:

The control of the measurement chain consists in injecting test currents in the test coil. The measured values and the threshold overrun have to be controlled.

Each hardware control has to be tested. In the new electronic design of the surveillance boards, a connection between each board and a test box is planned.

A control of the thermal regulation is also asked.

Operating Procedures

After each intervention on the beam pipe near ACCT-DCCT blocs, a verification of the beam intensity measurement is intended with the beam presence.

After each threshold modification, a remote verification of the threshold value is done by an operator.

CONCLUSION

The FMEA performed in 2013 and the conception review organised in the beginning of 2014 validated the final design of the intensity and transmission controls. The last prototypes are currently under test. The definitive manufacturing of the overall chain is planned for the end of this year.

The experience of FMEA is quite positive. The analysis has helped to define precisely the requirements, to develop an electronic more robust and to adapt this design to the recommended controls.

REFERENCES

[1] C. Jamet *et al*., “Injector Diagnostics Overview of SPIRAL2 Accelerator”, DIPAC2007, Venice, Italy.

[2] M-H. Moscatello *et al*., “Machine Protection System for the SPIRAL2 Facility”, IPAC2012, New Orleans, Louisiana, USA.

[3] C. Jamet *et al*., “Beam Intensity and Energy Control for the SPIRAL2 Facility”, LINAC2012, Tel-Aviv, Israel.

[4] C. Berthe *et al.*, Machine Protection System for the SPIRAL2 Facility, ICALEPS2013, San Francisco, CA, USA.

[5] S. Leloir *et al.*, Measurement and control of the beam intensity for the SPIRAL2 Accelerator, IBIC 2013, Oxford, England.

Copyright © 2014 CC-BY-3.0 and by the respective authors

ISBN 978-3-95450-141-0

PROGRESS ON THE BEAM ENERGY MONITOR FOR THE SPIRAL2 ACCELERATOR

W. Le Coz#, C. Jamet, G. Ledu, S. Loret, C. Potier de Courcy, D. Touchard, GANIL, Caen, France
Y. Lussignol, IRFU, Saclay, France

Abstract

The first part of the SPIRAL2 project entered last year in the end of the construction phase at GANIL in France. The facility will be composed of an ion source, a deuteron/proton source, a RFQ and a superconducting linear accelerator. The driver is planned to accelerate high intensities, 40 MeV deuterons up to 5 mA and heavy ions up to 1 mA.

A monitoring system was built to measure the beam energy on the BTI line (Bench of Intermediate Test) at the exit of the RFQ. As part of the MEBT commissioning, the beam energy will be measured on the BTI with an Epics monitoring application.

At the exit of the LINAC in the HEBT, another system should measure and control the beam energy. The control consists in ensuring that the beam energy stays under a limit by taking account of the measurement uncertainty. The energy is measured by a method of time of flight; the signal is captured by non-intercepting capacitive pick-ups.

This paper describes the BTI monitor interface and presents the system evolution following the design review of the HEBT monitor.

INTRODUCTION

The beam energy will be measured on BTI which is directly placed at the RFQ exit to qualify the beam properties in front of the LINAC. The beam energy at the LINAC exit in the HEBT will be also measured for the beam tuning and the energy control. The energy is monitored in order to ensure the respect of the accelerator operating range and the thermal protection of the machine. The energy is measured by a method of time of flight (TOF) [1].

Beam time structure may vary by using a slow chopper or a single bunch selector. The duty cycle of the slow chopper is included between 1/10000 and 1/1 with a frequency of 1 Hz and 5 Hz. The intensity beam will range from a few 10 µA to 5 mA.

As the energy control is part of the safety functions, Failure Modes and Effects Analysis (FMEA) and the measurement uncertainty are required on this control device.

BEAM ENERGY MEASUREMENTS

The energy monitor is composed by three electrodes installed along the beam line, the energy is calculated by a time of flight method (TOF).

In 2014, before the final installation, the BTI was assembled at the IPHC laboratory (Fig. 1) for mechanical verifications.

#lecoz@ganil.fr

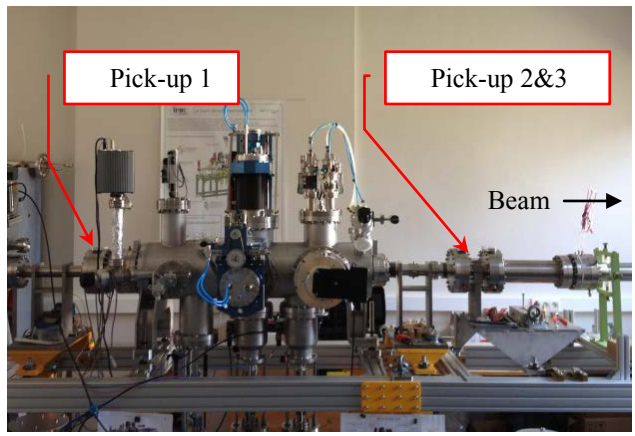


Figure 1: Electrodes along the BTI.

The first unit includes the Pick-up1 and the second unit is composed by the Pick-up2 and 3 (Fig. 2). The pick-up3 is designed to determine the number of bunches between the two first pick-ups. The length between the second and the third pick-up is calculated to be smaller than the distance between two bunches.

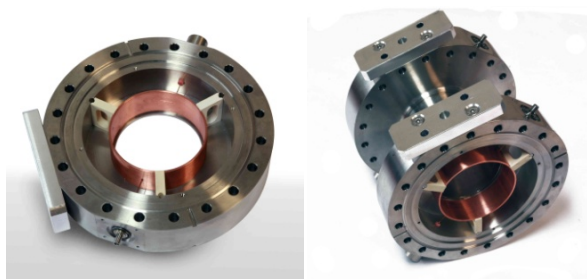


Figure 2: Pick-up1, Pick-up2&3.

The HEBT required performances are the following:
- Intensity range: from 10 µA to 5 mA
- Energy range: from 2 MeV/A to 33 MeV/A
- Response time: 1 s
- Required accuracy:
  +/-1 per mille for the beam tuning
  +/-1 per cent for the beam control

ELECTRONIC DESCRIPTION

The phase measurement of the TOF is based on an electronic system which realizes the lock-in amplifier function [2]. The signals come from three pick-up electrodes. The phase of the first harmonic is measured by the TOF device.

Copyright © 2014 CC-BY-3.0 and by the respective authors

ISBN 978-3-95450-141-0

The TOF electronic system (Fig. 3) is composed by :

- ADCs card with a clock part
- FPGA board
- Microcontroller board
- High Frequency Amplifier
- Alarm board

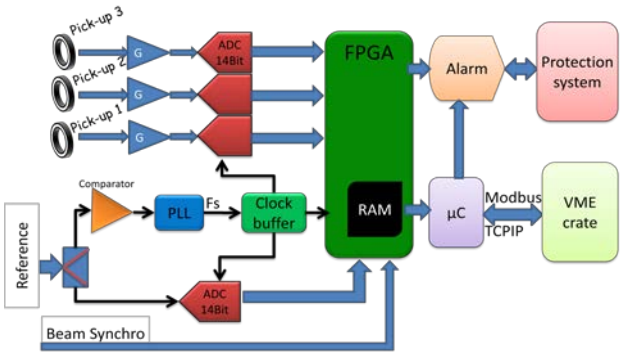


Figure 3: Electronic synoptic.

BTI MONITOR INTERFACE

The graphical interface of the BTI device is composed of a dedicated CSS/BOY project associated to EPICS TOFApp module and iocTOF IOCs.

The module application contains the EPICS interface with the measurement system of the energy by time of flight. This module is created on the SPIRAL2 EPICS skeleton. The module can run with the systems VxWorks and Linux IOCs. Concerning the final control system for the SPIRAL2 facility, the application is accommodated on an IOC VME VxWorks. For tests in laboratory, the application is running under IOC Linux.

The Modbus-TCP protocol is used for the communication between the EPICS IOC and the TOF measurement system connected together via Ethernet. The Modbus operations of reading and writing are done with EPICS Modbus driver developed by the University of Chicago [3].

An electronic test device allows injecting a test signal directly on each probe. The test commands are sent and read by a VME ADAS ICV196 board.

This GUI (Fig. 4) allows us to adjust the sample size in the average calculations. From the x and y coordinates of the measured vector, the phase and the amplitude of the signal on each probe are deduced. The application gives two information which allow us to calculate the ion velocity: the phase and the number of bunches between probes 1 and 2. Then knowing the mass of the accelerated ion, the beam energy and its standard deviation can be calculated.

The delay compensation between the three chains is done by injecting this test signal. The interface is used for calibration operation like offset deduction.

The graphical interface is composed of few tabs. A histogram tab allows seeing the dispersion and the distribution (Fig. 5) of measurements, and its evolutions.

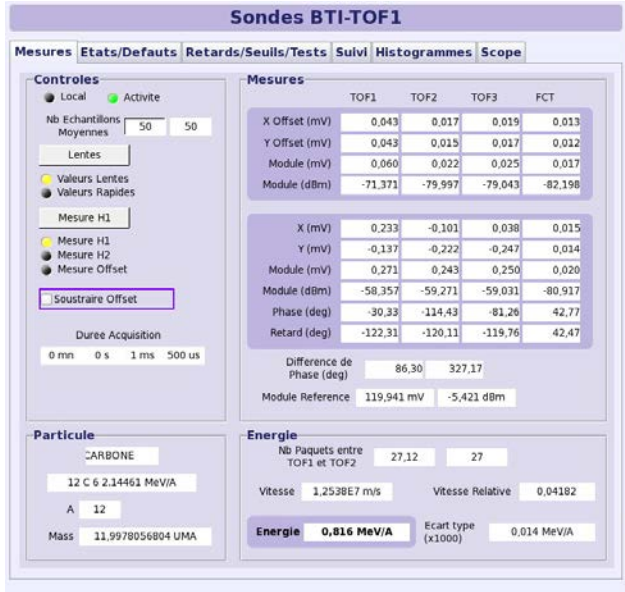


Figure 4: Energy measurement.

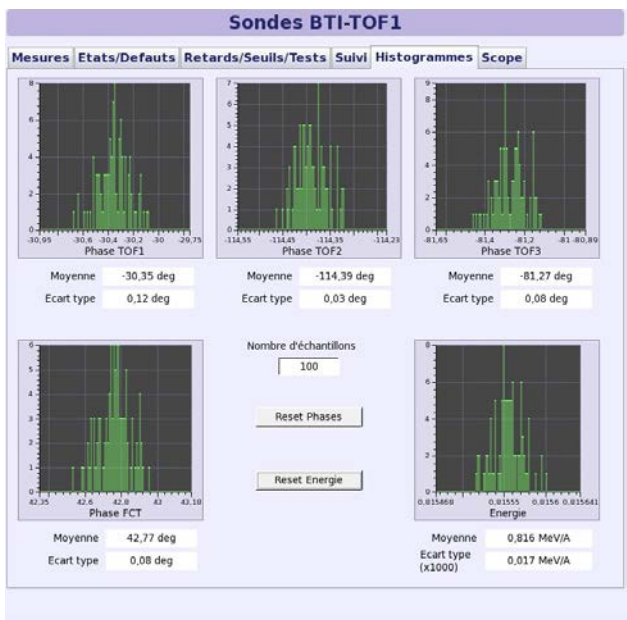


Figure 5: Statistic measurements.

SINGLE PULSE TEST BENCH

A single bunch selector, installed in the MEBT, will reduce the bunch repetition rates by a factor of 100 to 10000 [4]. This working mode was tested in laboratory.

The beam is simulated by injecting a signal in a coaxial line at 88 MHz (Fig. 6).

The three signals which come from the probes are measured by the TOF device.

The energy measurements are realized after the offset and delay compensation.

Copyright © 2014 CC-BY-3.0 and by the respective authors

ISBN 978-3-95450-141-0

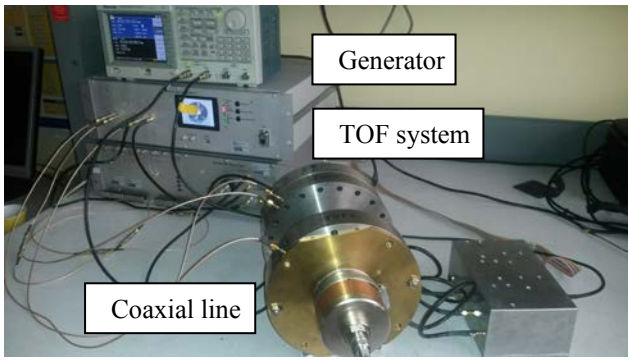


Figure 6: Single pulse test bench.

To simulate the single bunch selector, a generator with two outputs at the same frequency is used. The first output corresponds to the RF frequency (Fig. 7: green curve) and the second (Fig. 7: yellow curve) to the pulse. The generator allows us to select a single bunch mode.

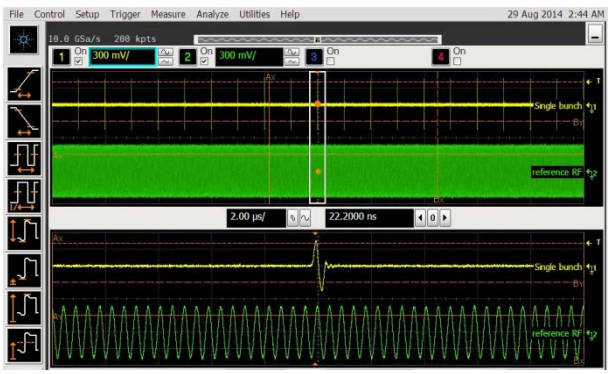


Figure 7: Single bunch mode.

The TOF device measures the energy of the high intensity beam.

As the energy is calculated from the average values of the signal phases, the repetition rates decrease the average module and increase the phase uncertainty.

The beam intensity average has to be higher than 10 µA that means an intensity peak higher than 1 mA for a bunch repetition rate of 100.

ALARM CONTROL SYSTEM

The energy measurement is non interceptive, in order to control continuously beam parameters and beam losses.

Alarm System

The TOF alarm management system is based on a microcontroller, which calculates the beam velocity. This velocity is compared to a threshold of the Enlarged Protection System (EPS) and to thresholds of the Thermal Protection System (TPS) [5].

The EPS threshold is defined following the operation schedule. An alarm is sent by the TOF device to the EPS when the velocity exceeds this threshold.

TPS thresholds are calculated from the beam velocity measured and memorized during the beam tuning at the LINAC exit. A fork of few percents in plus and in minus gives a maximum and minimum thresholds. When the velocity exceeds the maximum threshold or is less than the minimum, a cut-off request is sent to the TPS.

Threshold Guarantee

For each new beam, the thresholds have to be sent to the HEBT TOF device. Following the FMEA [6], a robust transfer protocol was developed to guarantee that the threshold values used by the energy control device are correct.

The thresholds for beam loss detection have to be recalculated for each beam, due to the specificity of SPIRAL2, which accelerates a large range of beams, with various intensities and energies. The general control system calculates these thresholds.

CONCLUSIONS

Currently, two TOF systems are realized to be used during the MEBT commissioning in the BTI (Bench of Intermediate Test). The monitor interface is operational and will allow us to qualify the beam at the RFQ exit.

The TOF electronic digitalization, which works with under sampling, can measure beam phases in the single bunch mode.

Following the FMEA and the design review in 2014, the HEBT electronic device is under development. The new design is an upgrade of the BTI device.

REFERENCES

[1] C. Jamet *et al.*, "Phase and amplitude measurement for the SPIRAL2 Accelerator", DIPAC09, Basel, Switzerland.

[2] W. Le Coz *et al.*, "SPIRAL2 Beam energy measurement", DIPAC11, Hamburg, Germany.

[3] CARS EPICS IOC Software, Mark Rivers, University of Chicago http://cars9.uchicago.edu/software/epics/

[4] Di Giacomo et al., "Measurements of the first rf prototype of the spiral2 single bunch selector", IPAC12, New Orleans, USA.

[5] C. Berthe *et al.*, "Machine Protection System for the SPIRAL2 Facility", ICALEPS2013, San Francisco, CA, USA.

[6] W. Le Coz et al., "Measurement and Control of THE Beam Energy for the SPIRAL2 Accelerator", IBIC13, Oxford, England.

Copyright © 2014 CC-BY-3.0 and by the respective authors

ISBN 978-3-95450-141-0

STUDY OF GENERAL ION RECOMBINATION FOR BEAM MONITOR USED IN PARTICLE RADIOTHERAPY

R. Tansho#, T. Furukawa, Y. Hara, K. Mizushima, N. Saotome, Y. Saraya, T. Shirai and K. Noda
National Institute of Radiological Sciences, Chiba, Japan

Abstract

For particle radiotherapy, accurate dose measurement using a beam monitor of an ionization chamber (IC) is essential to control prescribed dose to a tumor. General ion recombination is one of the most impact factors on the accurate dose measurement. The Boag theory predicts the general ion recombination effect on ionization current under the condition that ions are uniformly generated throughout the gas volume. For the particle radiotherapy using a pencil beam scanning system, however, the ions generated by the pencil beam is not uniform. We have developed a calculation code for accurate prediction of the general ion recombination effect for the pencil beam scanning system. The calculation code is called as division calculation method. The division calculation method takes into account the different ionized charge density in the beam irradiation area by dividing the ionization distribution into many sub-elements. The general ion recombination effect in each sub-element is calculated by the Boag theory. The calculation accuracy was verified by comparison of the saturation curve, which is the curve of applied voltage versus measured current, between measurements and calculation results. We measured the saturation curves by using a parallel plate IC and a cylindrical IC. We confirmed that the calculated saturation curves were good agreement with the measured curves. The division calculation method is effective tool to accurately predict the saturation curve for the pencil beam scanning system.

INTRODUCTION

Carbon ion radiotherapy has been attracted for a cancer treatment due to the characteristic depth-dose distribution with Bragg peak. Dose localization at the Bragg peak is utilized for concentrated irradiation to a tumor. To optimize dose distribution in the tumor, a 3D pencil beam scanning system [1, 2] has been developed at the new treatment research facility in National Institute of Radiological Sciences (NIRS) [3]. The pencil beam scanning system scans the pencil beam laterally by two scanning magnets and longitudinally by variable energy changes and using range shifters. Main and sub flux monitors of an ionization chamber (IC) are also used to control prescribed dose to the tumor. Since the discrepancy between the prescribed dose and the irradiated dose leads to the worse treatment results, accurate dose measurement in the flux monitors is essential.

General ion recombination is one of the most impact factors on the accurate dose measurement. The saturation curve, which is the curve of applied voltage versus measured current, represents the reduction rate of the collected ions with reducing the applied voltage due to the general ion recombination. Accurate prediction of the saturation curve is important to design the proper specifications of the IC such as applied voltage, gap length and kind of gas to obtain the saturation current.

We can predict the saturation curve by Boag theory [4-6]. The Boag theory assumed that ions are uniformly generated throughout the gas volume in the IC. However, the ionized charge distribution generated by the pencil beam is not uniform and the distribution is modeled by the 2-dimensional Gaussian form.

In this paper, we present a calculation method giving the accurate saturation curve for ions generated by the pencil beam.

MATERIALS AND METHODS

Calculation Methods

For a parallel plate IC, the Boag theory gives an ion collection efficiency f at an applied voltage V [V] by following formulae:

$$f = \frac{1}{1+\frac{\xi^2}{6}} \tag{1}$$

$$\xi = 2.01 \times 10^7 \left(\frac{d^2 \sqrt{q}}{V} \right) \tag{2}$$

where d [m] is the gap length between the electrodes of the IC and q [C m^{-3} s^{-1}] is ionized charge density per a unit of time. Since the ion collection efficiency f depends on the ionized charge density q, accurate estimation of the

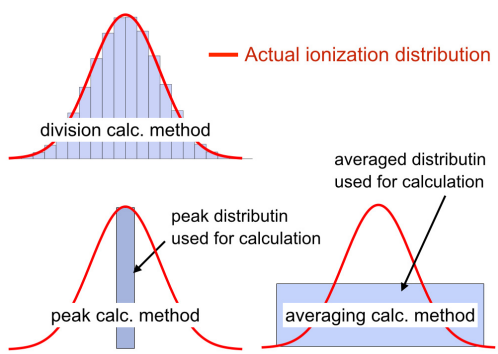


Figure 1: The different calculation methods to estimate the ionized charge distribution generated by the pencil beam irradiation.

Copyright © 2014 CC-BY-3.0 and by the respective authors

ISBN 978-3-95450-141-0

q is important. According to the Boag theory, the ionized charge density of the 2-dimensional Gaussian form is averaged in the range of the beam irradiation area. We call this calculation method "averaging calculation method". However, the averaging method does not take into account the different charge density within the beam irradiation area. Thus it is expected that the averaging method underestimates the applied voltage required to obtain the saturation current. It is undesirable because the IC designed by using the averaging method does not obtain the saturation current due to the insufficient applied voltage.

Taking the highest charge density around the beam center is the most safety method to determine the applied voltage for obtaining the saturation current. We call this calculation method "peak calculation method". However the peak method overestimates the applied voltage required to obtain the saturation current. It complicates the design of the IC due to the unnecessary high-applied voltage.

To calculate the saturation curve for the actual ionized charge density, we divided the ionization distribution of the 2-dimensional Gaussian into many sub-elements and assumed that the charge density in the each sub-element is uniform. We calculated the saturation curve for ions in the each sub-element by using the Boag theory. Then the saturation curve of the ions in the whole irradiation area was obtained by weighted average of the saturation curves in the each sub-element. We call this calculation method "division calculation method". The conceptual schemes of the three calculation methods are represented in Figure 1.

In the averaging calculation method, we defined the beam irradiation area as a circle with the radius of 3 σ of the pencil beam. In the division calculation method, we divided the beam irradiation area of the circle into sub-element with area of 0.1 × 0.1 mm^2. The peak calculation method used the ionized charge density in the sub-element at the beam center for the calculation.

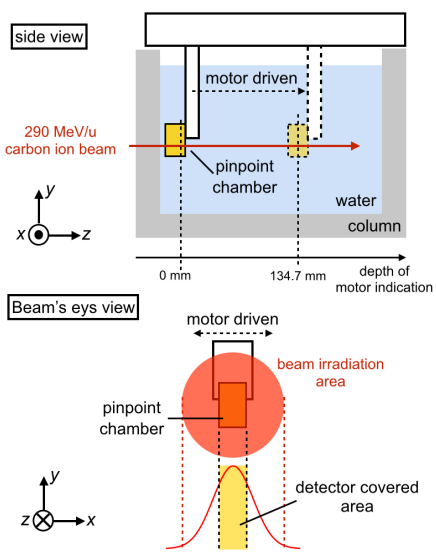


Figure 2: Experimental arrangement using a cylindrical pinpoint ionization chamber.

Experimental Arrangement

The saturation curves calculated by the three different calculation methods were compered with those measured by using two types of IC: a parallel plate IC and a cylindrical IC. The measurements were repeated three times in a single condition and compared the average value with the calculation results.

Parallel Plate Ionization Chamber (PPIC), the purpose of this experiment was verification of the calculation accuracy of the division calculation method by comparison of the saturation curve obtained by the measurement and by other the two calculation methods. We used a parallel plane ionization chamber (PPIC). The PPIC design was the same of the existing flux monitors [3]. The PPIC consisted of an anode of signal foil and two cathodes of wire mesh. The gap between the anode and each cathode was 5 mm. The PPIC was operated in air at atmospheric pressure. We used carbon ion beam with 430 MeV/u extracted from Heavy Ion Medical Accelerator in Chiba (HIMAC) and irradiated the pencil beam to the PPIC. We measured the saturation curves with the different beam intensities in the range of applied voltage from -100 V to -2,800 V. The beam intensities of 4.6×10^7, 2.8×10^8, 4.1×10^8 and 8.3×10^8 particles per second (pps) were used. The pencil beam was modeled to the Gaussian with 2 mm rms for the calculations.

Cylindrical Pinpoint Ionization Chamber (CPIC), the calculation accuracy of the division method was verified more in detail. We measured a part of the ionized charge in the irradiation area of the pencil beam by using a cylindrical pinpoint IC (CPIC) developed by PTW Freiburg GmbH (PTW 31015). The experimental arrangement using the CPIC is shown in Figure 2. We defined that the beam direction is z-direction and the x-y plane is the perpendicular plane to the z-direction. The lateral size of the CPIC was smaller than the lateral beam spread of the pencil beam. The center position of the CPIC was arranged at $(x, y) = (0, 0)$ mm corresponding to the beam center in water. We moved the chamber location in the z-direction by using a motor drive unit and the saturation curves were measured at the motor indicated depth of 0 and 134.7 mm. The depth of 134.7 mm was estimated at the depth corresponding to the depth of the Bragg peak. Then we also drove the chamber location in x-direction from 0 to 10 mm at the each depth and measured the saturation curve at each lateral position. We used the pencil beam of carbon ion with 290 MeV/u and measured the saturation curve in the range of applied voltage from 40 to 400 V.

We calculated the ion collection efficiency in the CPIC by using equation (1) and (2). For a cylindrical chamber, d in the equation (2) is obtained by following formulae:

ISBN 978-3-95450-141-0

Copyright © 2014 CC-BY-3.0 and by the respective authors

$$d = (a-b)K_{cyl} \quad (3)$$

$$K_{cyl} = \sqrt{\frac{(a/b+1)}{a/b-1}\frac{\ln(a/b)}{2}} \quad (4)$$

where a is the radius of the outer electrode and b is the radius of the central electrode. For the CPIC we used, a and b were assigned with 0.15 mm and 1.45 mm, respectively. The size of the lateral beam spread was 2.2 mm rms at the depth of 0 mm and 2.6 mm rms at the depth of 134.7 mm.

RESULTS AND DISCUSSIONS

Parallel Plate Ionization Chamber

The Figure 3 (a) and (b) are the comparisons of the measured saturation curves with the curves calculated by the three calculation methods. The Figure 3 (a) is the comparisons for the beam intensity of 2.8×10^8 pps, and Figure 3 (b) is the comparisons for the beam intensity of 8.3×10^8 pps. The small lower right graphs in the both Figures 3 (a) and (b) are close-ups in the curve rising region. The saturation curves are normalized by the value at the applied voltage of 2500 V. Since uncertainty of the measurements is estimated to be within 0.1% rms and the error bar is smaller than the maker size, the error bars are not displayed in the Figure 3.

We confirmed that the saturation curves calculated by the division method are the best agreement with the measured curves in the all calculated saturation curves. We also found that the applied voltage reaching to the saturation level is different depended on the calculation methods. The difference of the applied voltage was attributed to the different ionized charge density used by each calculation method. Then the difference observed for high intensity beam irradiation was larger than that observed for low intensity beam irradiation. It indicates that the division method is more effective when the beam intensity is higher.

Cylindrical Pinpoint Ionization Chamber

Figure 4 is the comparison of the saturation curves between measurements and calculation results of the division method at different depths in water. The Figure 4 (a) and (b) are the comparisons of the saturation curves when the lateral center position of the CPIC is $(x, y) = (0, 0)$ mm and (5, 0) mm, respectively. The error bar of measurements corresponds to the 2 times the rms error. The saturation curves are normalized by the averaged value between the applied voltage of 250 V and 400 V.

When the CPIC was located at the beam center, the saturation curves calculated by the division method were good agreement with measured curves (Figure 4 (a)). In contrast, when the CPIC was located at off beam axis, some discrepancies were observed even in the saturation region (Figure 4 (b)). In addition, the Figure 4 (b) indicated that the ion collection efficiencies measured at depth of 0 mm around the low applied voltages region are higher than the efficiencies in the saturation region.

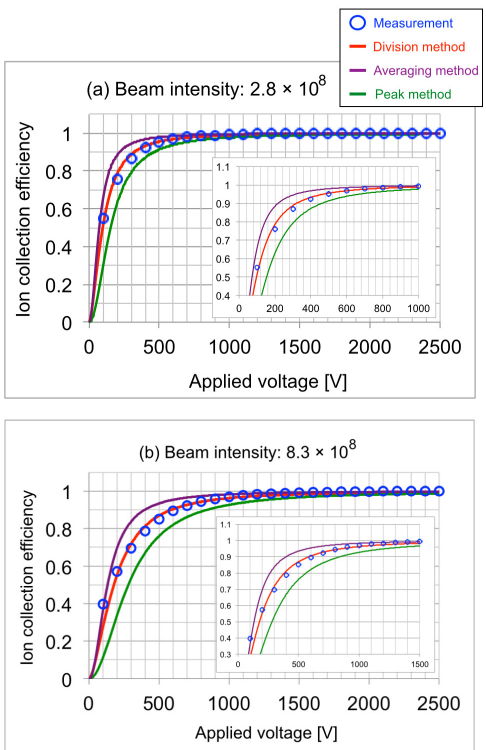


Figure 3: Comparisons of the saturation curves between measurements and calculation results obtained by using different calculation methods for the parallel plate ionization chamber.

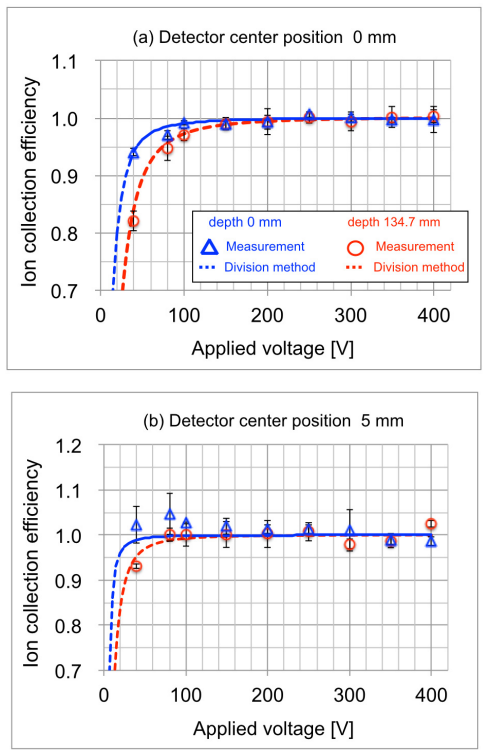


Figure 4: Comparisons of the saturation curves between measurements and calculation results obtained by using the division method for the cylindrical pinpoint ionization chamber.

Copyright © 2014 CC-BY-3.0 and by the respective authors

ISBN 978-3-95450-141-0

It is possible that the misalignment of the detector center position caused the inexplicable measured saturation curve. When the detector was located at x = 5 mm, the detector covered a part of penumbra region of the Gaussian and the ion collection efficiency can sensitively varied with the slight variation of the detector center position. Then we estimated the influence of the variation of the detector center position on the saturation curve. In the division calculation method, we shifted the detector center position between (x, y)=($\pm$0.3, 0) mm with a sampling pith of 0.1 mm and calculated the saturation curve at each lateral position. Figure 5 is the same comparison of the saturation curve represented by the Figure 4 (b). The comparisons at z = 0 mm and 134.7 mm in the Figure 4 (b) are separated to the Figure 5 (a) and (b), respectively. The error bar indicates the variation range of the measured value with variation of x =$\pm$0.1 mm of the detector center position. With the variation of the detector center position between x = 0.1 mm and -0.1 mm, the measurement results varied about $\pm$6〜9%. The calculated saturation curves were consistent with the measured curves including the misalignment of the detector center position with x = $\pm$0.1.

CONCLUSIONS

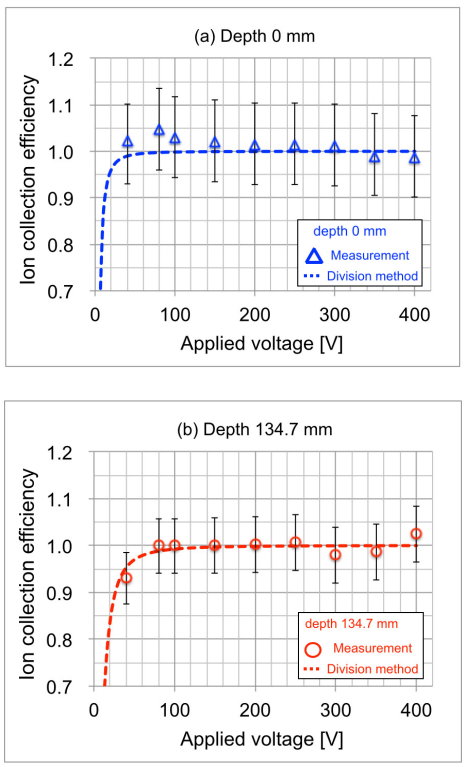


Figure 5: Comparisons of the saturation curves between measurements with the position error and calculation results obtained by using the division method. This is the same comparison represented by the Figure 4 (b). The error bar indicates the variation rage with variation of the detector center position with (x, y) = ($\pm$0.1, 0.0) mm.

We have developed the division calculation method to accurately calculate the saturation curve for a pencil beam scanning system. We confirmed that the saturation curves calculated by the division method are good agreement with those measured by the PPIC. We also verified in detail the calculation accuracy of the division method by comparing with the saturation curves measured by the CPIC. We found that the calculated saturation curves are consistent with measured curves including the misalignment of the detector center position. The division method is effective tool to calculate the general ion recombination effect on the measured current for the pencil beam scanning system.

REFERENCES

[1] Th. Haberer, *et al.*, Nucl. Instrum. Methods. A 330 (1993), 296.
[2] E. Pedroni, *et al.*, Med. Phys. 22 (1995) 37.
[3] T. Furukawa, *et al.*, Med. Phys. 37 (2010) 5672.
[4] J. W. Boag et al, Br. J. Radiol. 23 (1950) 601.
[5] J. W. Boag et al, Br. J. Radiol. 25 (1952) 649.
[6] J. W. Boag, *Dosimetry of ionizing radiation*, (New York: Academic Press, 1897), 169.

ISBN 978-3-95450-141-0

Copyright © 2014 CC-BY-3.0 and by the respective authors

SENSOR STUDIES FOR DC CURRENT TRANSFORMER APPLICATION

E. Soliman, K. Hofmann, Technische Universität Darmstadt, Darmstadt, Germany
H. Reeg, M. Schwickert, GSI Helmholtzzentrum für Schwerionenforschung GmbH, Darmstadt, Germany

Abstract

DC Current Transformers (DCCTs) are known since decades as non-intercepting standard tools for online beam current measurement in synchrotrons and storage rings. In general, the measurement principle of commonly used DCCTs is to introduce a modulating AC signal for a pair of ferromagnetic toroid. A passing DC ion beam leads to an asymmetric shift of the hysteresis curves of the toroid pair. However, a drawback for this measurement principle is found at certain revolution frequencies in ring accelerators, when interference caused by the modulating frequency and its harmonics leads to inaccurate readings by the DCCT. Recent developments of magnetic field sensors allow for new approaches towards a DCCT design without using the modulation principle. This paper shows a review of different kinds of usable magnetic sensors, their characteristics and how they could be used in novel DCCT instruments.

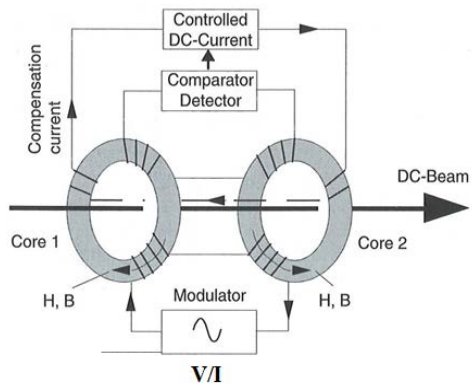


Figure 1: Conventional DCCT Block diagram [2].

INTRODUCTION

Commonly, DCCTs are the main tool in synchrotrons and storage rings for online monitoring of DC beam currents. The SIS100 heavy ion synchrotron will be the central machine of the FAIR (Facility for Antiproton and Ion Research) accelerator complex currently under construction at GSI. Beam operation at SIS100 requires a novel DCCT device with large dynamic range and high accuracy [1]. Currently a Novel DCCT (NDCCT) based on modern magnetic field sensors is under development at GSI. Main motivation for this research project is to investigate different commercially available magnetic field sensors with regard to their applicability for reliable beam current measurements with the goal to simplify the device as compared to the conventional DCCT setup.

Figure 1 presents the schematic of a conventional DCCT sensor, consisting of two symmetrical toroid and modulator/demodulator circuit. In this setup the modulator circuit drives the two cores to magnetic saturation with a 180º phase shift. In case a DC current passes through the two cores the magnetic flux density generated in the cores is shifted asymmetrically. The sum of the total magnetic flux of the two cores is proportional to the DC current amplitude. A feedback circuit is used to compensate the change in the magnetic flux inside the cores to reach zero flux. The output current signal of the feedback circuit is a direct measure for the DC current passing the DCCT [3].

Besides many quality characteristics, a major disadvantage of this design is the fact that for precise beam current measurements the magnetic properties of the two ring cores must be perfectly matched, which requires an intricate manufacturing process. A second drawback of this setup, especially for the usage at SIS100, is the fact that the modulation frequency is 20 kHz; when the beam's basic revolution frequency or harmonics are the same as the even harmonics of the modulating frequency interference occurs. Therefore, the current measurement of a conventional DCCT becomes erroneous without notification to the user.

Thus, the requirement for a simpler DCCT assembly with a single core and without using the modulation technique came up. The principle for current sensing in the NDCCT is using commercially available integrated circuit magnetic field sensors. The sensitivity of modern sensors is sufficient to directly measure the magnetic field as generated by the DC ion beam current, without the need of using the modulation technique.

In Fig.2 a schematic view of an open loop NDCCT is depicted. The NDCCT consists of a high permeability slotted flux concentrator which allows for easy installation of the setup around the ceramic gap without breaking the vacuum. The magnetic sensor is placed inside the air gap of the flux concentrator.

*Work supported by BMBF; Project. No.: 05P12RDRBG between GSI and TU Darmstadt

Copyright © 2014 CC-BY-3.0 and by the respective authors

ISBN 978-3-95450-141-0

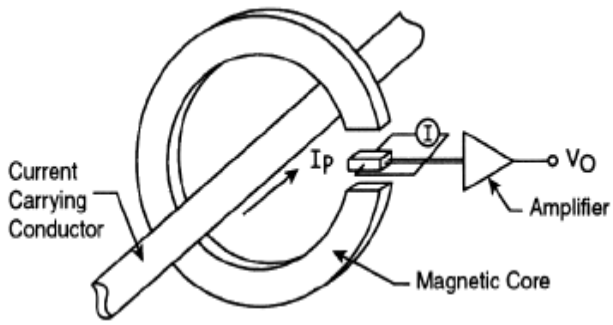


Figure 2: Schematic of NDCCT [4].

The magnetic sensor output voltage is proportional to the magnetic field inside the air gap. Additionally, an amplifier is implemented on the sensor PCB to amplify the output signal to increase sensitivity. Different types of commercially available magnetic sensors ICs were tested for magnetic field detection.

A conventional Hall sensor does not meet the NDCCT requirements due to a relatively low sensitivity and high power consumption. Today, different types of magneto-resistance (MR) sensors are commercially available. They have higher sensitivity and consume lower power than Hall sensors. In addition they are available in different IC packages like SOP8 and DFN8 ones, even as bondable dies. In the following we present an overview of MR sensor types and discuss their applicability for the NDCCT design.

MAGNETORESISTANCE SENSORS

MR sensors are based on a quantum mechanical magnetoresistance effect. The MR effect refers to the change of the material's electrical resistivity in response to a change of an external magnetic field. This change in the material's resistivity was found to be about 5% percent maximum in ferromagnetic materials, but could be enhanced significantly in thin film multilayer structures of alternating ferromagnetic/non-magnetic materials.

There are three main types of MR sensors:

- Anisotropic Magneto-Resistance (AMR),
- Giant Magneto-Resistance (GMR)
- Tunnelling Magneto-Resistance (TMR).

The three sensor types vary in their multilayer structure. The functional structure is identical for all MR sensors. Four thin film resistors form a Wheatstone bridge. If an external magnetic field is applied the resistor's value changes and consequently the output voltage of the bridge changes as well.

In Fig.3 and Fig.4 the physical and functional structures of GMR and TMR sensors are given. The difference between GMR and TMR is that the GMR has two shielded resistors in the bridge and this causes unipolar output voltage in contrast to the bipolar output voltage of the TMR.

The MR sensors are available from different companies. AMR IC sensors are produced by Honeywell Company [7], GMR by NVE Company [5] and TMR by Dowaytech Company [6]. All sensors are available in SOP8 packages, except for TMR which is also available in DFN8 package.

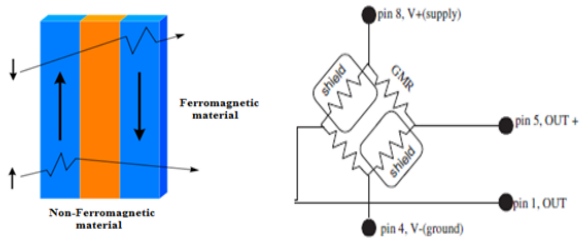


Figure 3: GMR Physical and Functional Structures [5].

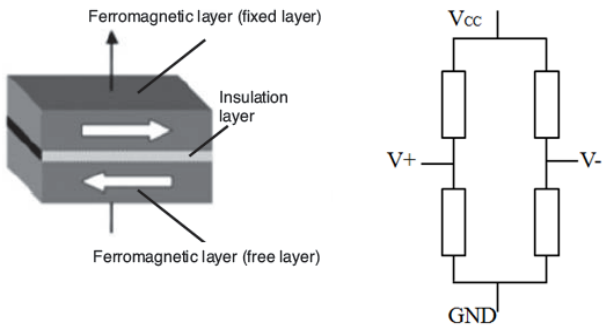


Figure 4: TMR Physical and Functional Structures [6].

MR SENSORS STUDY FOR NDCCT

In an earlier research project at GSI on the NDCCT a comparison between different commercial types of AMR and GMR sensors had been performed [8]. The result was that the GMR sensor from NVE Company [5] has a higher sensitivity to the magnetic field inside the air gap as compared to AMR. In addition, different types of GMR sensors from NVE were investigated and the best performance was reported for the AA002 type [8]. At the time of the study the TMR sensors were not yet available so the study didn't include them

To continue investigating the MR sensors two PCBs were fabricated to compare the performance of GMR and TMR sensors. Fig.5 and Fig.6 show the PCBs for GMR and TMR, respectively. The PCB contains a MR sensor and an instrumentation amplifier to amplify the output signal of the voltage bridge generated by the sensor. The amplifier gain was set to 10.

The GMR sensor is from NVE (type AA002), and the TMR sensors are available in two types, MMLH45F and MMLP57F, each with a different sensitivity. As stated in the TMR datasheets; the sensitivity of MMLH45F and MMLP57F is 12mV/V/Oe and 4.9mV/V/Oe. As for the GMR, the AA002 sensitivity is 3mV/V/Oe. To calculate the magnetic flux density inside the air gap of the flux

ISBN 978-3-95450-141-0

Copyright © 2014 CC-BY-3.0 and by the respective authors

concentrator the following formula was derived:

$$B_{gap} \approx \mu_o \frac{I}{d}. \quad (1)$$

Where B_{gap} is the magnetic field inside the air gap in Tesla, μ_o is the vacuum permeability in T.m/A, I is the beam current and d is the air gap width in m, ($\mu_r >> 1$).

As a first step towards characterising the PCBs of GMR and TMR sensors, a test of the sensors functionality using a permanent magnet was done. The value of the magnetic field at the sensor was measured using a Hall probe (Steingröver FH48). The DC output voltage of the PCB is measured versus the magnetic field by varying the distance between the permanent magnet and the magnetic sensor PCB. The results for the GMR and TMR sensors types are shown in Fig.7, 8 and 9, respectively. The measurement results are fitted linearly for positive and negative values separately. The standard error between the measurement points and the fitted curve is given as bar data points with scale on the right Y-axis of the graph.

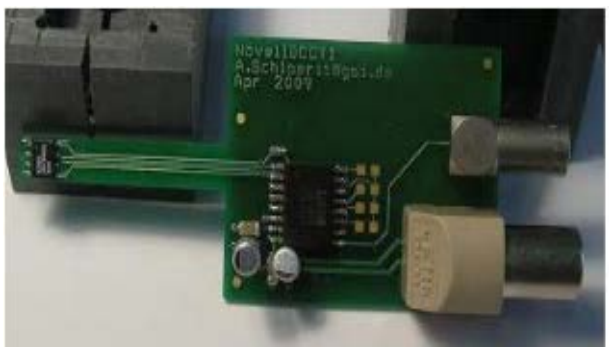


Figure 5: GMR Test PCB.

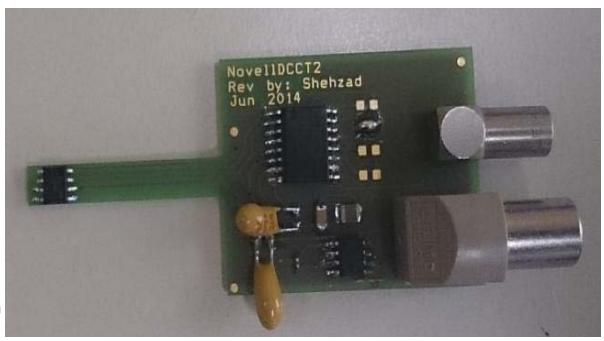


Figure 6: TMR Test PCB.

The results showed that both TMR sensors have bipolar transfer characteristics as expected, in contrast to the GMR sensor. TMR sensors have higher sensitivity compared to the GMR. Also with the use of the op-amp both types of TMR sensors display a comparable sensitivity.

If equation (1) were used to calculate the DC current needed to have a magnetic field value of ±1.25mT in a 10mm air gap width, then the current value will be ±10A.

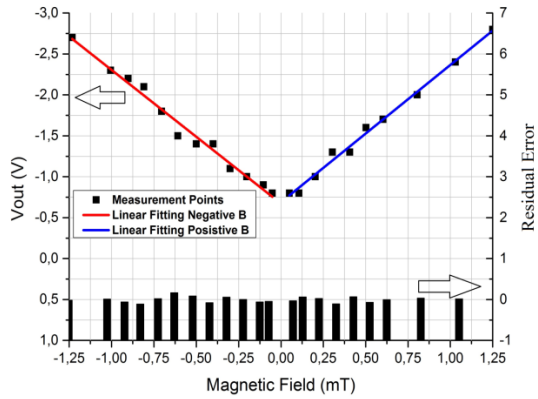


Figure 7: GMR PCB Output Voltage.

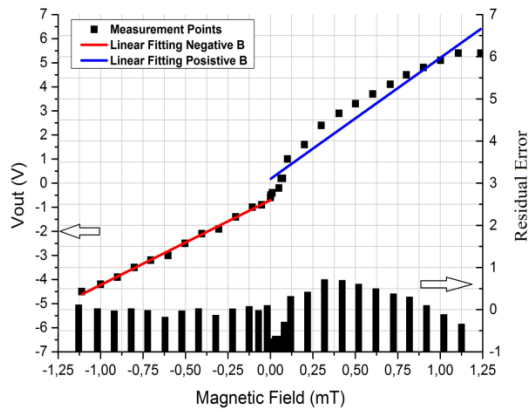


Figure 8: TMR MMLP57FP PCB Output Voltage.

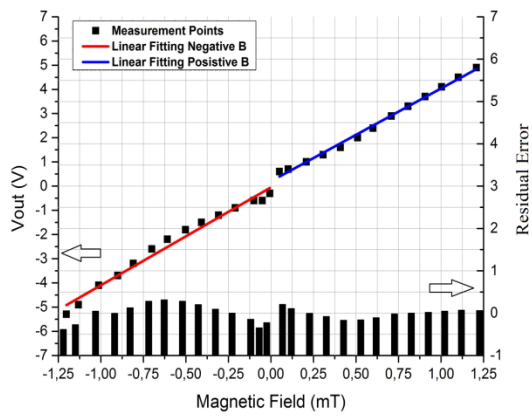


Figure 9: TMR MMLH45F PCB output Voltage.

Table 1 contains the slope of the measurement fitting curves and standard error present in Figs. 7, 8 and 9. It shows the sensitivity of the PCB's output voltage toward the magnetic field variation.

Copyright © 2014 CC-BY-3.0 and by the respective authors

ISBN 978-3-95450-141-0

Table 1: Sensitivity of PCB Output Voltage to Magnetic Field

Sensor	Negative B		Positive B	
	Slope (V/mT)	Error	Slope (V/mT)	Error
GMR AA002	1.671	0.0492	-1.633	0.0652
TMR MMLP57F	3.522	0.0661	5.025	0.3359
TMR MMLH45F	4.047	0.1697	3.837	0.0842

NDCCT DC WIRE TEST

A test setup has been prepared for the NDCCT. As shown in Fig.10 it consists of a ring core flux concentrator from VAC Company (Vitrovac '6025F'). The flux concentrator permeability is very high (above 100000) and the width of the air gap is 10 mm, the inner and outer diameter is 200 mm and 250 mm, respectively. A mechanical support was produced to hold the flux concentrator. In addition a soft iron box in Fig. 10 for shielding covers the whole NDCCT test setup. A DC current was generated in a conducting wire at the centre of the core. The wire was terminated with a 50Ω load. The purpose of the test was to measure the resolution of the NDCCT. An Agilent signal generator was used to generate the DC current. The values of the generated current are ±50mA and this will produce a magnetic field of ±0.0625mT inside a 10 mm air gap width.

The experimental result for the test setup using the two types of the TMR PCB is shown in Fig. 11 and 12 for the SOP8 MMLH45F and MMLP57F, respectively. The results shown in Fig. 11 and 12 are the output voltage of the PCB used to test the TMR sensors versus the input DC current generated in the wire at the centre of the flux concentrator. The corresponding magnetic flux density's value in the ring core air gap is shown on the upper X-axis of the figure. The sensitivity of the NDCCT is given by the slope of the curves shown in Fig. 11 and 12. The sensitivity of the TMR MMLH45F and MMLP57F sensors PCB are 0.382 V/A and 0.189 V/A respectively.

As stated in this paper's introduction, the TMR fabricating Company additionally offers another package than the regular SOP8 (MMLP57FP), that is to say the MMLP57F sensor in a DFN8 package (MMLP57FD). This new package has a width of only 3 mm, hence halving the air gap's width to 5 mm. In Fig. 13 the two packages of the TMR sensor are shown (6 mm x 3 mm x 1.5 mm and 3 mm x 3 mm x 0.75 mm). A special PCB for the DFN8 package was fabricated at GSI to test the sensor response against DC input current variation. This PCB is shown in Fig. 14.



Figure 10: NDCCT Test Setup.

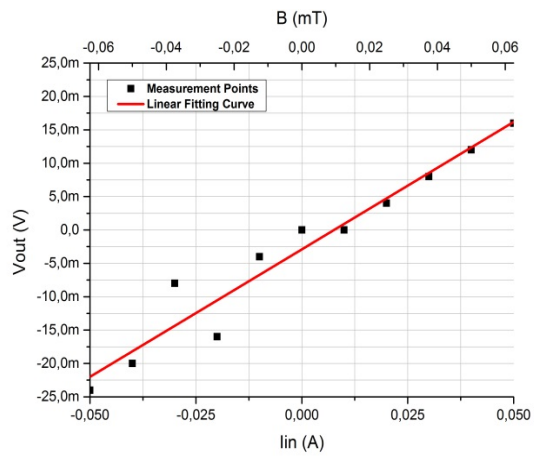


Figure 11: Output voltage of the DC wire test for TMR MMLH45F (Standard Error: 0.03102).

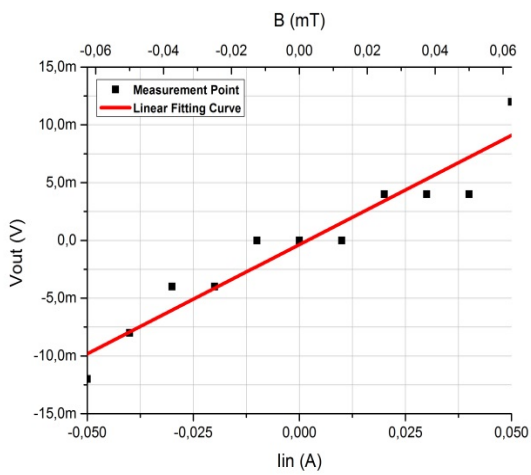


Figure 12: Output voltage of the DC wire test for TMR MMLP57FP (Standard Error: 0.01939).

ISBN 978-3-95450-141-0

Copyright © 2014 CC-BY-3.0 and by the respective authors

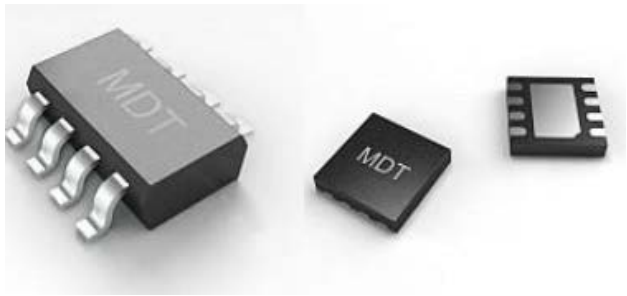


Figure 13: TMR MMLP57F packages [6].

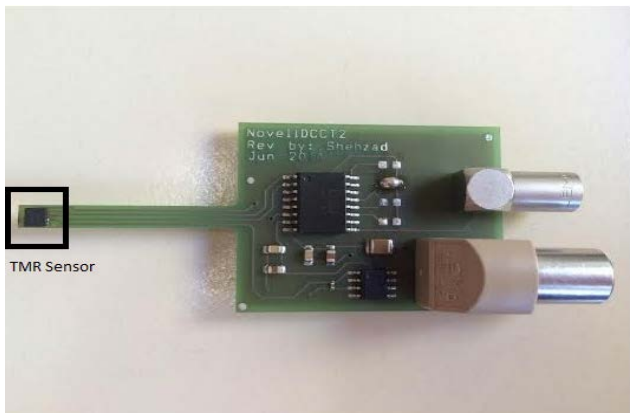


Figure 14: MMLP57FD customized PCB.

The DC wire test was done using the DFN8 package. The PCB width used for this sensor is reduced from 10mm to 5mm and thus the air gap size is halved. For example, ±50mA DC current will generate ±0.125mT in a 5 mm air gap width. The experimental result of the MMLP57FD TMR sensor is shown in Fig.15. The output voltage of the PCB is plotted versus the input current and the magnetic field generated in the air gap on the lower and upper X-axis, respectively. The sensitivity of the NDCCT setup is given by the slope of the curve, i.e. 0.416 V/A. The MMLP57FD sensor shows twice the sensitivity compared to the MMLP57FP sensor.

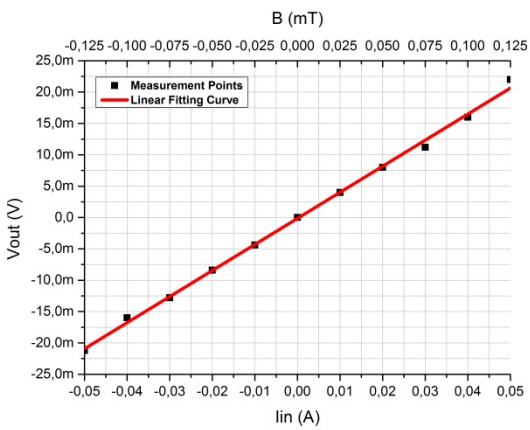


Figure 15: Output voltage of the DC wire test for MMLP57FD (Standard error: 0.00645).

CONCLUSION

A NDCCT based on the use of MR sensors is currently under development at GSI for the FAIR project. The NDCCT measures the DC current stored in the synchrotrons and storage rings by sensing the magnetic field generated by the ion beam current using MR sensors.

A comparative study of TMR and GMR sensors was performed to evaluate the advantages and disadvantages for the NDCCT design. As expected the TMR showed a bipolar transfer characteristics and higher sensitivity than the GMR sensor. Also different types of TMR sensors were examined to find the most sensitive type. The MMLH45F TMR sensor from Dowaytech Company is the most sensitive one according to the datasheets and the experimental results. A test setup for the NDCCT was built at GSI. The magnetic field generated by a DC current was measured using different TMR sensor types.

OUTLOOK

Future work for the NDCCT is to study the design for higher DC beam current values by using a power amplifier in the setup. The second step will be to add extra circuitry to measure the AC component of the NDCCT. A feedback system is foreseen to improve the device linearity and frequency response. Noise analysis and measurement is currently under investigation.

ACKNOWLEDGMENT

I would like to thank all my colleagues at GSI beam instrumentation department and at TU Darmstadt for their support during the test setup.

REFERENCES

[1] M. Schwickert et al., “Beam Diagnostic for SIS100 at FAIR”, DIPAC’11, May 2011, p. 41 (2011); http://www.JACoW.org
[2] S. Zorzetti, “Digital Signal Processing and Generation for a DC Current Transformer for Particle Accelerators”, BE/BI CERN.
[3] P. Forck, “Lecture Notes on Beam Instrumentation and Diagnostics”, Joint University Accelerator School, January – March 2013.
[4] Bob Mammano, “Current Sensing Solutions for Power Supply Designers”, Texas Instruments.
[5] http://www.nve.com/index.php
[6] http://www.dowaytech.com/en/
[7] http://sensing.honeywell.com/
[8] M. Häpe et al., “High Dynamic Magnetic Beam Current Measurements by Means of Optimised Magneto-resistance Sensor Engineering”, DIPAC’05, May 2005, p. 102 (2005); http://www.JACoW.org

Copyright © 2014 CC-BY-3.0 and by the respective authors

ISBN 978-3-95450-141-0

OBSERVATIONS OF THE QUADRUPOLAR OSCILLATIONS AT GSI SIS-18

R. Singh, P. Forck, P. Kowina, GSI, Darmstadt, Germany
W.F.O. Müller, J.A. Tsemo Kamga, T. Weiland, TEMF, Technische Universität Darmstadt, Germany
M. Gasior, CERN, Geneva, Switzerland

Abstract

Quadrupolar or beam envelope oscillations give valuable information about the injection matching and the incoherent space charge tune shift. An asymmetric capacitive pick-up was installed at GSI SIS-18 to measure these oscillations. In this contribution, we present the simulations performed to estimate the sensitivity of the quadrupolar pick-up to the beam quadrupolar moment and compare it with respect to other pick-up types installed at SIS-18. Further, dedicated beam measurements are performed to interpret the quadrupolar signal under high intensity conditions.

INTRODUCTION

A symmetric pick-up is shown in Fig. 1 along with a Gaussian beam with centroid at $\bar{x}$, $\bar{y}$ and rms dimensions $\bar{\sigma}_x$, $\bar{\sigma}_y$. The image current induced by the beam at the pick-up (PU) electrodes is derived in [1] and reproduced here,

$$J_{\text{image}}(a,\theta) = \frac{I_{beam}}{2\pi a}\left\{1 + 2\left[\frac{\bar{x}}{a}\cos\theta + \frac{\bar{y}}{a}\sin\theta\right] + 2\left[\left(\frac{\bar{\sigma}_x^2 - \bar{\sigma}_y^2}{a^2} + \frac{\bar{x}^2 - \bar{y}^2}{a^2}\right)\cos 2\theta + 2\frac{\bar{x}\bar{y}}{a^2}\sin 2\theta\right] + \text{higher order terms}\right\} \quad (1)$$

On a symmetric pick-up, the four plate signals are obtained for $\theta = 0$, $\pi/2$, π and $3\pi/2$ radians. The second order component that contains beam width information is referred to as the "quadrupole moment" and is given by,

$$\kappa = \bar{\sigma}_x^2 - \bar{\sigma}_y^2 + \bar{x}^2 - \bar{y}^2 \quad (2)$$

To extract the quadrupole moment from the pick-up electrode signals (denoted by U referring to the voltages induced), the electrodes are connected in the following "quadrupolar" configuration,

$$\Xi_q = (U_r + U_l) - (U_t + U_b) \quad (3)$$
$$= Z \cdot I_{beam}\left(\frac{\bar{\sigma}_x^2 - \bar{\sigma}_y^2 + \bar{x}^2 - \bar{y}^2}{a^2} + \text{higher order terms}\right)$$
$$\Xi_s = (U_r + U_l + U_t + U_b) \quad (4)$$
$$= Z \cdot I_{beam}$$

where Z is the transfer impedance of the pick-up and Ξ_q is the quadrupolar signal and when Ξ_q is normalized to the sum signal of all electrodes Ξ_s, it is referred to as the normalized quadrupolar signal.

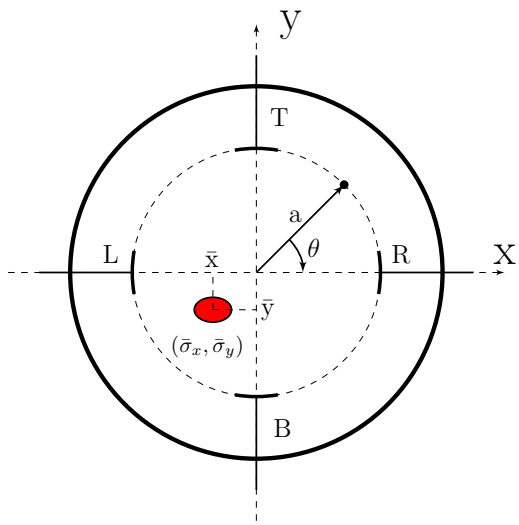


Figure 1: Symmetric pick-up for the analytical calculations.

Quadrupole signal monitors were first suggested as non-invasive emittance monitors at SLAC [1]. In synchrotrons, the quadrupole monitors were initially used to detect the injection mismatch causing envelope oscillations. It was also used to estimate the space charge dependent detuning [2] based on theoretical and numerical works [3,4]. Special pick-up designs and signal processing schemes were developed at CERN-PS to use quadrupolar pick-ups as regular emittance monitors [5].

At GSI SIS-18, quadrupolar beam transfer function (BTF) measurements were performed to get a direct measure of incoherent tune shift [6]. Due to unavailability of appropriate non-linear pick-ups int those studies, a new asymmetric pick-up was developed for SIS-18 [7]. There were recent studies which focussed on the signal processing methods to suppress the dipole contributions in the quadrupolar signal [8].

The first section of this paper summarizes the simulations performed to compare the sensitivities of various pick-up types installed at SIS-18 to the quadrupolar moment. The second section details the present installation of the quadrupolar pick-up, its data acquisition and the signal processing. The final section presents the beam experiments and results.

Copyright © 2014 CC-BY-3.0 and by the respective authors

ISBN 978-3-95450-141-0

PICK-UP GEOMETRY AND SIMULATIONS

For the typical SIS-18 operation, the longitudinal extent of beam is much larger in comparison to the pick-up electrode length, therefore it can be well approximated by the pick-up 2D geometry and its properties can be determined electrostatically. The pick-up was simulated using the electrostatics solver in the simulation software CST EM Studio. The pick-up design used for the simulation is depicted below in Fig. 2.

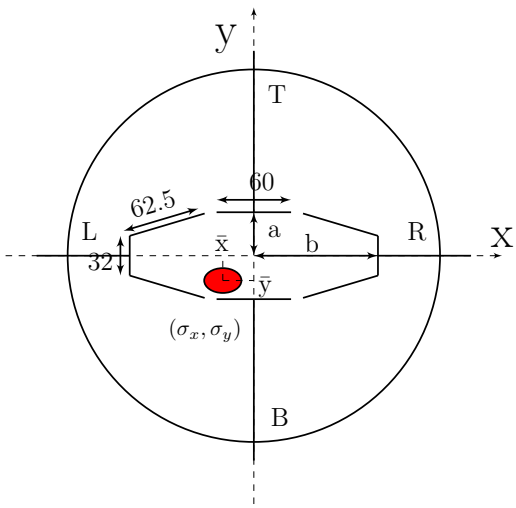


Figure 2: Front view of the pick-up design; a = 35.3 mm, b = 100.3 mm, length of the electrodes in longitudinal plane L = 216 mm [9]. All the lengths are in mm units.

In the simulation, the quadrupolar signal is obtained for each transverse horizontal beam size σ_x varying from 7.5 mm to 25 mm, while the transverse vertical beam size σ_y is kept constant at 7.5 mm. The initial values of simulated range are typical for the SIS-18 injection. The normalized quadrupolar signal Ξ calculated with CST EM Studio is shown in Fig. 3(a). It is obtained by using the difference over sum method (using Eq. 3),

$$\Xi = \frac{\Xi_q}{\Xi_s} = \frac{U_R + U_L - U_T - U_B}{U_R + U_L + U_T + U_B}$$

where U_R, U_L, U_T and U_B are defined as in the previous section.

It can be expressed as $\Xi = m_q\ (\sigma_x^2 - \sigma_y^2) + \Xi_0$, where m_q denotes the pick-up quadrupolar sensitivity and Ξ_0 is the value of the quadrupolar signal for a round and centered beam. Ξ_0 is a pick-up geometry dependent constant. $m_{q,asym} = 6.6 * 10^{-5}$ /mm^2 is determined using the linear regression method with the coefficient of determination $R^2 = 0.997$. The dipolar sensitivities for this pick-up were calculated in [9].

Comparison with Other Pick-ups

Another symmetrical pick-up is under operation in SIS-18 which is similar to the depiction in Fig. 1 with a =100 mm.

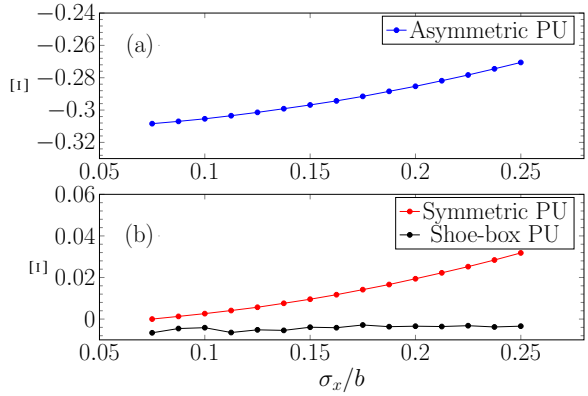


Figure 3: Quadrupole signal from the pick-ups as a function of σ_x/b; $\sigma_y/b = 0.075$, b = 100 mm.

However, it has rectangular plates with dimensions of 60 × 110 mm^2 opposed to the smaller cylindrical plates shown in Fig. 1. The sensitivity of the pick-up is calculated by the same method as for asymmetric pick-up. Figure 3(b) shows the normalized quadrupolar signal with respect to the beam dimension in the horizontal plane. The sensitivity calculated from the graph is $m_{q,sym} = 5.55 * 10^{-5}$/mm^2 with a coefficient of determination R^2 of 0.998. Similarly the sensitivity of the typical SIS-18 BPMs i.e. shoe-box pick-ups [10] is also calculated as $m_{q,sb} \approx 0$ from the graph shown in Fig. 3(b). The shoe-box pick-ups are optimized for linear response to change in the beam position, thus all the higher order components including the quadrupolar terms are strongly suppressed. The transfer impedance (Z) of the mentioned pick-ups roughly scale with their lengths and are calculated for a relativistic beam i.e. $\beta \approx 1$ as $Z_{asym} \approx 19\,\Omega$, $Z_{sym} \approx 13\ \Omega$ and $Z_{sb} \approx 7\ \Omega$.

The asymmetric pick-up (shown in Fig. 2) proves to be a good option to be used a quadrupolar pick-up due to 20% higher sensitivity compared to symmetric pick-up as well as high transfer impedance. The shoe-box BPMs which are used as beam position monitors (BPM) at SIS-18 are not sensitive to the quadrupolar moment at all.

DATA ACQUISITION AND SIGNAL PROCESSING

The signals from the asymmetric pick-up (shown in Fig. 2) are individually connected to diode based peak detectors [11]. The peak detectors strongly suppress the common mode due to the monopolar component of the beam signal. The time constant of the peak detector plays an important role in the common mode suppression. The outputs of the peak detectors from the opposite plates are added using passive power combiner. The output of each of these combiners are connected to a differential amplifier, such that "quadrupole configuration" Eq. 3 is obtained. This ensures effective suppression of the dipolar signal. The resulting signal is amplified by 45 dB and low pass filtered with a 3 dB cut-off of ≈ 1 MHz.

Copyright © 2014 CC-BY-3.0 and by the respective authors

ISBN 978-3-95450-141-0

The minimum detectable quadrupole moment oscillations of the beam can be estimated by the noise model of the peak detectors and the amplifiers. A full derivation of a comparable system can be found in [11]. The measured output noise from the amplifiers after the default gain of 45 dB is 0.6 mV rms. The quadrupolar sensitivity of the asymmetric pick-up was calculated as $m_{q,asym} = 6.6 * 10^{-5}$ /mm^2 and transfer impedance $Z_{asym} = 19\ \Omega$ in the previous section. For a beam current of $I_{beam} = 1$ mA and a quadrupolar moment κ oscillation of amplitude 0.01 mm^2 p-p, the quadrupole signal amplitude after 45 dB amplification is,

$$\Xi_q = Z_{asym} * I_{beam} * m_{asym} * \kappa * 180 = 40\ \mu\text{V p-p} \quad (5)$$

Thus, the quadrupolar moment oscillation of amplitude 0.1 mm^2 p-p for a 1 mA beam current can be detected from the power spectral density of 512 turn-by-turn quadrupolar signal with a signal to noise ratio of 6 dB. One should note that the quadrupolar signal is not normalized to the beam intensity.

INTERPRETATION OF THE QUADRUPOLAR PICK-UP SIGNAL

The quadrupolar signal was measured for various beam intensity levels. Due to unavailability of a suitable quadrupolar exciter during these measurements, we utilized the injection mismatch to "excite" the beam size oscillations.

Injection Mismatch and Beam Oscillations

Injection mismatch is undesired in general since it leads to beam emittance dilution [12]. There are various sources of beam mismatch during injection.

1. If the beam phase space has a different orientation with respect to synchrotron twiss parameters at its injection point, the beam is said to have a "beta" mismatch. The beta mismatch leads to coherent envelope oscillations in the plane of mismatch at approximately twice the tune frequency (explained later in this section) [3, 4].

2. If the beam is not injected on the closed orbit, there is a position mismatch leading to oscillations at the betatron tune frequency (Q_x, Q_y).

3. Another source of mismatch is the dispersion at the point of injection, leading to beam size oscillations at the tune frequency [13].

The multi-turn injection in the horizontal plane at GSI SIS-18 leads to an inherently mismatched beam in the horizontal plane leading to a combination of various mismatches and all of them contribute to the quadrupolar moment of the beam. The resulting coherent oscillations are usually "Landau" damped due to frequency spread in a few hundred turns.

If the beam position and envelope is oscillating due to the injection mismatch, the quadrupolar moment in Eq. 2 obtains a time dependence,

$$\kappa(t) = {\sigma_x}^2(t) - \sigma_y^2(t) + x^2(t) - y^2(t) \quad (6)$$

While expanding Eq. 6, we perform the following simplifications,

- We consider only the even modes for an anisotropic beam [4] since the sensitivity of the quadrupolar pick-up oriented with the beam pipe is very reduced for the odd (or coupled) modes.
- The contribution caused by dispersion to the beam size is negligible compared to that of beam emittance, therefore we ignore the dispersion mismatch component.
- The frequency spread in the beam which leads to decoherence of beam oscillations is also ignored.

Figure 4 shows the beam position and beam envelope variation for a KV beam at two time instants.

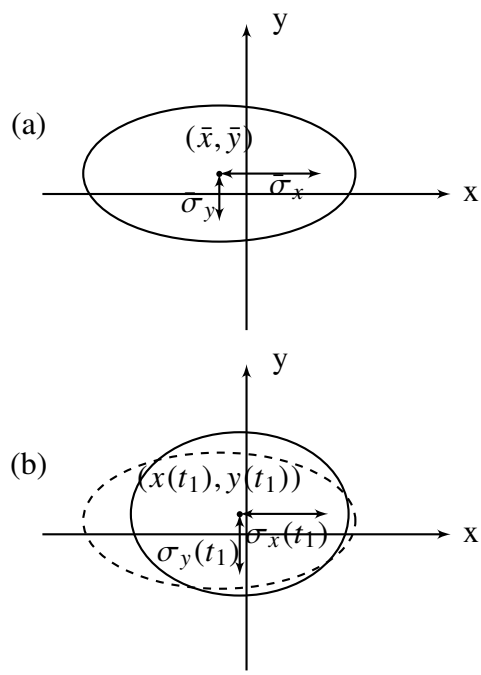


Figure 4: (a) Schematic showing the transverse profile of a stationary KV beam. (b) Schematic showing the excited beam at an arbitrary time t_1 performing beam position and envelope oscillations in both planes in comparison with the initial state (dashed).

If the initial beam position oscillation amplitudes are given by a_x and a_y, and beam envelope oscillation amplitudes are given by a_{xx} and a_{yy}, the time dependence of beam position and beam size can be written as,

$$\begin{aligned} \sigma_x(t) &= \bar{\sigma}_x + a_{xx}\cos(2\pi Q_{coh,1}t) \\ \sigma_y(t) &= \bar{\sigma}_y + a_{yy}\cos(2\pi Q_{coh,2}t) \\ x(t) &= \bar{x} + a_x\cos(2\pi Q_x t) \\ y(t) &= \bar{y} + a_y\cos(2\pi Q_y t) \end{aligned} \quad (7)$$

Copyright © 2014 CC-BY-3.0 and by the respective authors

ISBN 978-3-95450-141-0

Substituting Eqs. 7 into Eq. 6 and ignoring second order terms of beam envelope oscillations, we obtain,

$$\kappa(t) = \bar{\sigma}_x^2 + 2\bar{\sigma}_x a_{xx}\cos(2\pi Q_{coh,1}t) - \bar{\sigma}_y^2 - 2\bar{\sigma}_y a_{yy}\cos(2\pi Q_{coh,2}t) + \bar{x}^2 + 2\bar{x}a_x\cos(2\pi Q_x t) + \frac{{a_x}^2}{2}(1+\cos(2\pi 2Q_x t)) - \bar{y}^2 - 2\bar{y}a_y\cos(2\pi Q_y t) - \frac{{a_y}^2}{2}(1+\cos(2\pi 2Q_y t)) \quad (8)$$

The frequency of the even coherent quadrupolar modes $(Q_{coh,1}, Q_{coh,2})$ for a KV beam is given by [6],

$$Q_{coh,1} = 2Q_{x0} - (1.5 - 0.5\frac{\sigma_x}{\sigma_x+\sigma_y})\Delta Q_{sc,x}$$
$$Q_{coh,2} = 2Q_{y0} - (1.5 - 0.5\frac{\sigma_y}{\sigma_x+\sigma_y})\Delta Q_{sc,y} \quad (9)$$

Under no space charge conditions, $Q_{coh,1} = 2Q_{x0}$ and $Q_{coh,2} = 2Q_{y0}$ where Q_{x0}, Q_{y0} are the low intensity tunes or the "bare" tunes of the synchrotron. The coherent betatron tune Q_x, Q_y of a coasting beam are shifted due to dipolar wall impedances given by $\Delta Q_{coh(x,y)}$. The coherent tune is not directly affected by space charge. The coherent tune shifts ΔQ_{coh} for a coasting beam at injection in SIS-18 are negligible compared to incoherent tune shifts ΔQ_{sc} [14], therefore we assume $Q_x \approx Q_{x0}$ and $Q_y \approx Q_{y0}$.

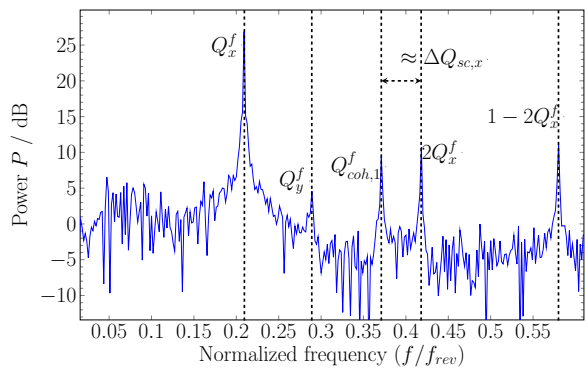


Figure 5: Typical spectrum of the quadrupolar signal for a high intensity beam immediately after injection with $I_{beam} \approx 6$ mA and other parameters given in Table 1.

Figure 5 shows an example of the baseband spectra of the quadrupolar signal for $I_{beam} \approx 6$ mA and other parameters given in Table 1. The horizontal axis shows the measured frequencies normalized to revolution frequency f_{rev}. The superscript in Q_x^f denotes fractional part of horizontal tune. In the spectra, frequency peaks expected from Eq. 8 are clearly seen. The presence of horizontal and vertical tunes suggest position mismatch in both planes. A peak at twice the horizontal tune is also clearly seen. Only one of the coherent envelope oscillation modes ($Q_{coh,1}$) is visible suggesting that the beam was well "beta" matched in the vertical plane. The spacing between $Q_{coh,1}$ and $2Q_x^f$ peaks is approximately the incoherent tune shift in horizontal plane ($\Delta Q_{sc,x}$) as expected by Eq. 9.

Experiments

Careful measurements were performed to see a systematic effect of beam intensity on the quadrupolar signal spectrum. The current was increased in steps from the UNILAC without affecting the parameters of SIS-18 multi-turn injection, and the frequency spectrum of the quadrupolar signals were recorded at several intensities. Table 1 shows the important beam parameters.

Table 1: Measured Parameters for N^{7+} Beam Experiment

Parameters	Value
W_{kin} (MeV/u)	11.45
I_{beam} (mA)	$\approx 0.6 - 6$
$\varepsilon_x, \varepsilon_y$ (2σ) (mm-mrad)	32,51
Q_{x0}, Q_{y0}	4.21,3.3

The beam profile measurements were performed in parallel using the Ionization profile monitor (IPM). The measured beam profiles were found to be independent of the current level. The incoherent space charge tune shift can be estimated using the beam parameters,

$$\Delta Q_{sc} = \frac{qI_{beam}R}{2\pi\epsilon_0 c W_0 \gamma_0^2 \beta_0^3 (\varepsilon_x + \sqrt{\varepsilon_x \varepsilon_y}\frac{Q_{x0}}{Q_{y0}})} \quad (10)$$

with $\varepsilon_x, \varepsilon_y$ as the rms emittance of the equivalent K-V distribution, q the particle charge and $W_0 = \gamma_0 m_0 c^2$ the rest energy, γ_0 and β_0 are the relativistic parameters and R is the synchrotron radius.

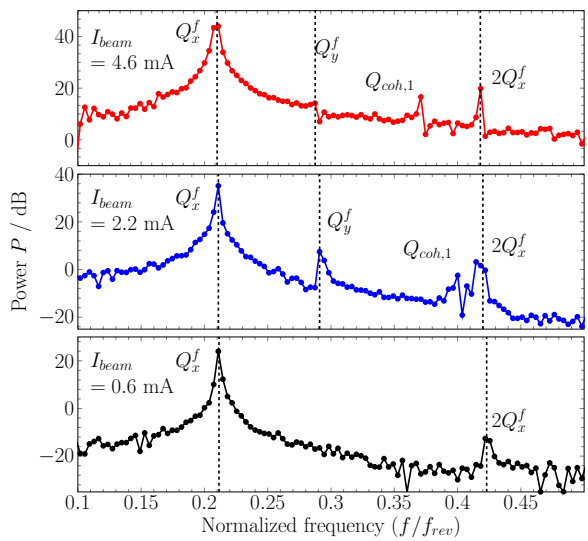


Figure 6: Shift of coherent quadrupole mode $Q_{coh,1}$ with beam current.

Figure 6 shows the spectrum at three intensities. For lowest intensity (Fig. 6 bottom), the calculated $\Delta Q_{sc,x}$ using Eq. 10 is ≈ 0.004, and the $Q_{coh,1}$ is difficult to distinguish from the $2Q_x^f$ line. Thus, we are unable to resolve the beam position and beam envelope oscillations. As the current is

Copyright © 2014 CC-BY-3.0 and by the respective authors

increased to 2.2 mA (Fig. 6 middle), the component resulting from beam size oscillations i.e $Q_{coh,1}$ separates from the $2Q_x^f$ peak and moves toward lower frequency as predicted by Eq. 9.The $\Delta Q_{sc,x}$ calculated is 0.017 in this case and roughly corresponds to the frequency shift. On further increase of beam current i.e. I_{beam} = 4.6 mA (Fig. 6 top), the $Q_{coh,1}$ peak moves further as a function of $\Delta Q_{sc,x}$ which is calculated to be 0.037. This procedure can be used as a direct method to measure ΔQ_{sc}.

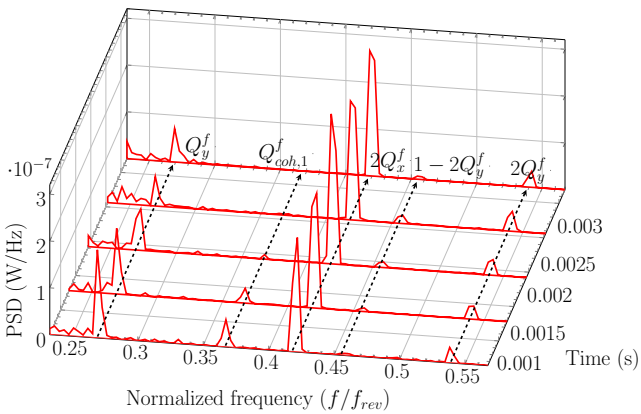


Figure 7: Quadrupolar signal spectra from Fig. 6 (top) over time. The quadrupolar mode $Q_{coh,1}$ damps much faster than the corresponding dipolar mode $2Q_x^f$.

The waterfall plot in Fig. 7 shows the evolution of frequency spectra over time immediately after injection. The first spectra is the same as the spectra in Fig. 6 for I_{beam} = 4.6 mA. The quadrupolar mode damps in $\approx$ 1 ms which corresponds to $\approx$ 200 turns at injection. One can note that the position related oscillations resulting in peaks at Q_y^f, $2Q_y^f$ and $2Q_x^f$ sustain for at least until 1000 turns, which hint towards a weaker damping mechanism against these oscillations.

SUMMARY AND OUTLOOK

The asymmetric pick-up installed at SIS-18 was simulated and compared with other installed pick-ups in terms of the quadrupolar sensitivity. Peak detectors were used to suppress the common mode signal, and pick-up electrode signals were connected in quadrupolar configuration to suppress the dipolar signal. This followed by low noise amplifier made our measurements very sensitive to coherent quadrupolar moment oscillations. Coherent quadrupolar oscillations were excited due to injection mismatch, and a clear correlation of the quadrupolar mode frequency shifts with the space charge tune shift was observed. Direct measurement of space charge tune shift by this method will be used to optimize the machine working point such that coherent dipole or quadrupole modes do not encounter any strong machine resonances. It can also be used as a diagnostic for efficient injection matching. Further work concerning installation of a quadrupolar exciter at SIS-18 is foreseen.

ACKNOWLEDGEMENT

We would like to emphasize the contribution of P. Moritz, who passed away on September 19th, 2014. The asymmetric pick-up used in this contribution is just one among his numerous scientific and technical developments, which are being continuously and successfully used at GSI.

REFERENCES

[1] R. Miller et al., "Non invasive emittance monitor", PAC'83, Washington, 1983.

[2] M. Chanel et al., "Study of beam envelope oscillations by measuring the beam transfer function with quadrupolar pick-up and kicker", EPAC'96, Sitges, 1996.

[3] W. Hardt, "On the incoherent space charge limit for elliptic beams", CERN/ISR/Int. 300 GS/66.2.

[4] I. Hofmann, "Stability of anisotropic beams with space charge", Physical Review E 57 (4), 4713.

[5] A. Jansson et al., "Noninvasive single-bunch matching and emittance monitor", Phys. Rev. ST Accel. Beams 5, 072803.

[6] R. Baer et al., "Measurement of space-charge-induced frequency shifts of quadrupolar beam oscillations in the SIS", NIM-A 415 460—463, 1998.

[7] Private communication with P. Moritz, GSI.

[8] J.A.Tsemo Kamga et al., "New method for reducing the contribution of the beam position in the quadrupolar signal", GSI Scientific report 2012.

[9] J. Latzko et al., "Simulations of the position sensitivity for SIS18 capacitive BPM with non-standard geometry", GSI scientific report 2013.

[10] P. Kowina et al., "Optimization of "Shoe-box type" beam position monitors using the finite element methods", DIPAC 2005, Lyon, France.

[11] M. Gasior et al., "The principle and first results of betatron tune measurement by direct diode detection", LHC-Project-Report-853 ; CERN-LHC-Project-Report-853, 2005.

[12] M.J Syphers et al., "Injection mismatch and phase space dilution", FNAl report, FN-458, 1987.

[13] M. Minty et al., "Injection envelope matching in storage rings", Proc. 1995 Part. Acc. Conf. and Intl. Conf. on High Energy Accel (Dallas, TX, 1995) 536.

[14] R. Singh et al., "Interpretation of transverse tune spectra in a heavy-ion synchrotron at high intensities", Phys. Rev. ST Accel. Beams 16, 034201, 2013.

Copyright © 2014 CC-BY-3.0 and by the respective authors

ISBN 978-3-95450-141-0

CONCEPTUAL DESIGN OF ELLIPTICAL CAVITY BEAM POSITION MONITORS FOR HEAVY ION STORAGE RINGS

M. S. Sanjari*, X. Chen, P. Hülsmann, Yu. A. Litvinov, F. Nolden, J. Piotrowski, M. Steck, Th. Stöhlker, GSI Darmstadt, 64291, Darmstadt, Germany

Abstract

Over 50 years in the history of accelerator physics, RF cavities have been used as beam position and intensity monitors. Their structure has been extensively discussed across numerous papers reporting their successful operation (a review can be found in [1]).

The application of RF cavities as pickups has recently been extended to include radioactive ion beam (RIB) facilities and heavy ion storage rings. These pickups allow very sensitive, accurate, and quick characterisation of ion beams and turn out to be indispensable tools in nuclear as well as atomic physics experiments. A notable example is the resonant pickup in the ESR at GSI Darmstadt [2] where single ion detection was achieved for lifetime measurements of radioactive nuclides [3]. A similar cavity pickup was installed in CSRe in IMP Lanzhou [4].

Usually, cavity pick-ups in dipole mode are used to accomplish position sensitive measurements. These achieve high sensitivities for small aperture machines (see e.g. [5] and [6]). In this work, we describe a novel conceptual approach that utilizes RF cavities with an elliptical geometry. While allowing a high precision determination of the position and intensity of particle beams, it has to cope with design restriction at heavy-ion storage rings such as large beam pipe apertures. The latter becomes inevitable at facilities aiming at storing large-emittance beams as e.g. planned in the future Collector Ring (CR) of the FAIR project at GSI Darmstadt.

THEORY OF OPERATION

Schottky Noise Analysis

Schottky noise analysis is meanwhile a well established method in beam diagnostics in storage rings, providing valuable information on beam characteristics. While transversal Schottky noise signals contain information on tune and chromaticity, longitudinal signals can be used for the determination of the revolution frequency and momentum spread of the beam. In an in-ring experimental scenario, longitudinal Schottky signals can be used to identify different nuclear species circulating in the storage ring. Using the fundamental relation of mass to charge ratio and the frequency resolution in storage rings [7], one can measure different nuclear masses by comparing the frequency difference with known reference nuclides. Using time resolved Fourier analysis, it is possible to monitor an unstable isotope in order to determine its lifetime. A more detailed account on mass and lifetime measurement in storage rings using the Schottky signal analysis can be found in [7].

Schottky noise signals are random processes. The power spectral densities show frequency bands around multiples of the beam revolution frequency [8]. These bands contain the same amount of power, and although increasing frequency affects their width and height, they essentially carry the same information about the beam. So provided that the recorded Schottky signal is mixed down into base band, an experimental event which causes a frequency change Δf (a decay event, isomeric states, determination of mass, beam cooling, jitter, etc.) is better resolved at higher harmonics for a given recording time Δt. In other words, for a required frequency resolving power, one needs a shorter recording time.

RF Cavities as Schottky Pick-Ups

Microwave cavities possess a set of eigenmodes, each oscillating at their corresponding eigenfrequency. Each of these modes ν can be thought of as an electrical resonator containing an ideal RLC element [9], each of which can be described by its frequency f_ν, Q value Q_ν and shunt impedance $R_{sh,\nu}$:

$$P_{diss,\nu} = \frac{U_\nu^2}{R_{sh,\nu}} = \frac{1}{2}\frac{U_\nu^2}{R_\nu} \tag{1}$$

where U_ν is the induced voltage after the passage of the particle, and $P_{diss,\nu}$ is the dissipated power to that mode and R_ν is the resistor in the equivalent RLC circuit. For the Q value we have

$$Q_\nu = \frac{\omega_{0\nu} W_\nu}{P_{diss,\nu}} \tag{2}$$

where $\omega_{0,\nu}$ is the angular eigenfrequency and W_ν is the energy stored in the mode. Instead of the shunt impedance, it is often useful to use a material independent version of it which is normalized to the Q value. It is often called *R/Q*, the *characteristic impedance* or *geometric factor* in units of ohms

$$\left(\frac{R_{sh}}{Q}\right)_\nu = \left(\frac{\widehat{R_{sh}}}{Q}\right)_\nu \Lambda_\nu(\beta)^2 \tag{3}$$

where $\Lambda_\nu(\beta)$ is the so called *transit time factor* as a function of the relativistic β of the beam. The hat shows the ideal characteristic impedance for a cavity with zero length and a beam travelling with the speed of light.

The signals from a beam of particles can be used to excite a microwave cavity . The resulting standing waves can

* s.sanjari@gsi.de

Copyright © 2014 CC-BY-3.0 and by the respective authors

be coupled out of the cavity by using a loop antenna. At critical coupling the output power of a single particle at the harmonic m is [9]

$$\langle P_{out}\rangle|_{mf_r} = \langle P_{diss}\rangle|_{mf_r} = (Ze)^2 f_r^2 \widehat{R_{sh,\nu}} \Lambda(\beta)^2 \quad (4)$$

Use of RF cavities as pick-ups allows for sensitive detection of particles whenever one of the resonant frequencies of the cavity matches with a harmonic of the beam. For intensity measurements a longitudinally sensitive detector can be designed using a circularly cylindrical shallow pillbox, with connected beam pipes, which oscillates at its fundamental oscillating mode TM010 (see e.g. [2]). By properly choosing the dimensions, and allowing for mechanical detuning of the cavity, the above requirements for sensitive particle detection can easily be met.

TRANSVERSAL SENSITIVITY

The R/Q Map

The characteristic impedance R/Q is an integrated quantity along the axis of the resonator (z axis). Nevertheless, its value depends not only on the transit time factor as seen in equation (3), but also on the transversal position of the beam [10]. The latter is due to the distribution (pattern) of the z component of the electric field in the specified mode. One can plot the R/Q values versus the transversal position in 3D which results in an *R/Q map* clearly showing the sensitivity of the mode for different transversal offsets.

Generalization to Elliptical Cross Section

The shallow circularly cylindrical cavity has, as expected, a nearly flat R/Q map around the beam pipe center. This makes it suitable for intensity measurements. For position sensitive detection, the desired R/Q map should show no variation on one axis, whereas a linear dependency on the perpendicular axis is needed. This would resemble a tilted plane. Two consecutive detectors would be able to cover the transversal plane, if they are placed orthogonally with respect to each other.

One of the best candidates that can show this kind of R/Q map is the TM010 mode of a pillbox cavity with an *elliptical* cross section. The equations governing the elliptical cavities do not depend on the standard Bessel functions any more, but need to be generalized. A detailed account can be found in [11].

Simulations show that the TM010 mode pattern of the electric field shows the same falloff as the circular TM010 mode as the radial distance increases in the direction of circumference. By contrast to the circular case, since the boundaries along the major elliptical axis are further away, a less steep variation is visible in this direction, whereas the electric field approaches zero much faster in the direction of the minor axis.

By putting the beam pipe off center along the direction of the minor axis (see Figure 1), one can make use of the steep *one sided* falloff of the fields while benefiting from the two sided slow variation in the direction of major axis.

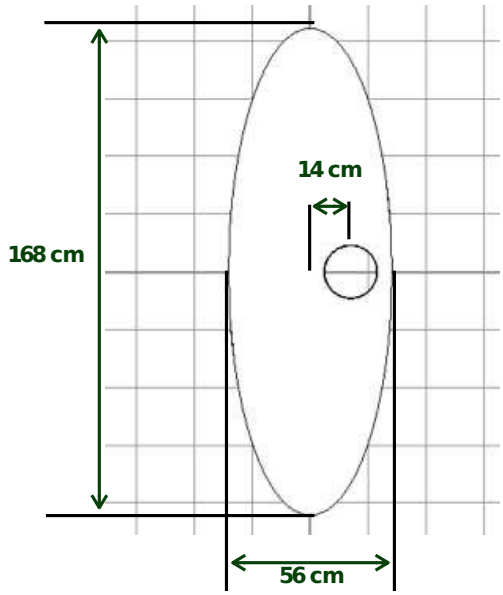
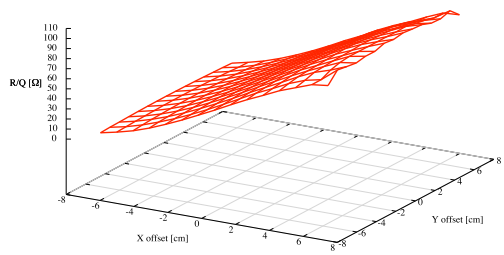
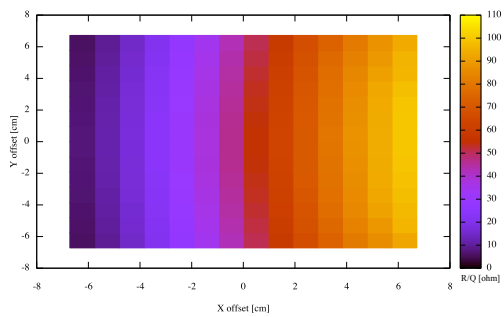


Figure 1: The simulated elliptical cavity.

Simulations using Microwave Studio® show that due to the large aperture, the beam pipe itself has a flattening effect, so that the net effect is a an almost constant field amplitude along the major axis.



(a) First



(b) Second

Figure 2: 3D and top view of the R/Q map of the simulated elliptical cavity in the region around the center of the beam pipe.

The resulting R/Q map of such a cavity is nearly a tilted flat plane (see Figure 2) as was required for transversal detection in the previous section. This approach has many advantages. The fundamental monopole mode is dominant and can be excited easily. While a strong monopole mode

Copyright © 2014 CC-BY-3.0 and by the respective authors

ISBN 978-3-95450-141-0

poses difficulties for designs that utilize dipole mode geometries and needs to be dealt with, in the present design it becomes an advantage. Dealing with higher order modes (HOM) is easier than suppressing the fundamental mode.

Single Particle Position Detection

The elliptical cavity described in this work is by nature a monopole mode cavity since it is operating in its fundamental TM010 mode. The information on the position of the particles is hidden in the amplitude of the coupled signal. For single particle position detection, it is necessary to make a level detection on the mixed down signal from the cavity. This information can be plotted versus time, with the same granularity as the usual time resolved Fourier analysis of the recorded signal. The resulting multi-diagram will show all three values (frequency, x position and y position) versus time.

CONCLUSION AND OUTLOOK

In this work we describe a novel method for position sensitive particle detection of coasting beams in heavy ion storage rings, using a hollow microwave cavity with an elliptical cross section. Simulations show the desired trend in the characteristic impedance. Two such detectors can cover the two dimensional XY plane. The design specifically allows large beam pipe apertures like those found in GSI's ESR and FAIR's future storage rings such as CR.

This is a work in progress, so many optimizations are still needed especially with regard to specific design parameters limited by the target storage ring in order to achieve the flattest possible R/Q map at the location of installation. This in turn should be the place with the highest dispersion. The detection method needs to be optimized to include multi-particle detection.

ACKNOWLEDGMENT

M.S.S. acknowledges partial support by the Alliance Program of the Helmholtz Association (HA216/EMMI). X.C. acknowledges support of the European Union under contract number PITN-GA-2011-289485. The authors thank I. Schurig, F. Caspers, P. Kowina, S. A. Litvinov and A. Mostacci for fruitful discussions.

REFERENCES

[1] X. Chen, GSI-Report-2014-3 (2104).

[2] F. Nolden et. al., Nucl. Inst. Meth. A, 659 (2011) 1 p. 69.

[3] P. Kienle, F. Bosch et. al., Phys. Lett. B 726 (2013) 45, p. 638.

[4] J. X. Wu et. al., Nucl. Inst. Meth. B 317 (2013) p. 623.

[5] J. Inoue et. al., Phys. Rev. ST 11 (2008) 062801.

[6] J-H. Su et. al., Chin. Phys. C 37 (2013) 1 p. 017002.

[7] F. Bosch and Yu. A. Litvinov, Int. J. Mass. Spec. 349-250 (2013) p. 151.

[8] S. Chattopadhyay, CERN84-11, CERN (1984).

[9] M. S. Sanjari, PhD, Thesis Goethe University Frankfurt (2013).

[10] D. Whittum and Yu. Kolomensky, Rev. Sci. Inst. 70 (1999) 5 p. 2300.

[11] C. W. H. Yeh, PhD, Thesis California Institute of Technology (1962).

Copyright © 2014 CC-BY-3.0 and by the respective authors

HIGH POSITION RESOLUTION AND HIGH DYNAMIC RANGE STRIPLINE BEAM POSITION MONITOR (BPM) READOUT SYSTEM FOR THE KEKB INJECTOR LINAC TOWARDS THE SuperKEKB

R. Ichimiya#, T. Suwada, M. Satoh, F. Miyahara, K. Furukawa, KEK, Tsukuba, Japan

Abstract

The SuperKEKB accelerator is now being upgraded to bring the world highest luminosity ($L=8x10^{35}/cm^2/s$). Hence, the KEKB injector linac has to produce low emittance and high charge electron (20 mm mrad, 7 GeV/c^2, 5 nC) and positron (20 mm mrad, 4 GeV/c^2, 4 nC) beam, respectively. In order to achieve these criteria, the accelerator structure has to be aligned within 0.1 mm position error. Since BPMs are essential instruments for beam based alignment (BBA), it is required to have one magnitude better position resolution to get enough alignment results. We have begun to develop high position resolution BPM readout system with narrow bandpass filters (fc = 180 MHz) and 250 MSa/s 16-bit ADCs. It handles two bunches with 96 ns interval separately and has a dynamic range from 0.1 nC to 10 nC. To compensate circuit drift, two calibration (x-direction and y-direction) pulses are output to the BPM electrodes between beam cycles (20 ms). Since it needs to achieve not only high position resolution but also good position accuracy, overall nonlinearity within ±0.02 dB is required and the system has to have more than ±5 mm accurate position range. We confirmed the system performance with a 3-BPM resolution tests at KEK Injector Linac and it turned out that the system has 3 μm position resolution. We plan to install this system during 2015 summer shutdown.

INTRODUCTION

KEK Injector Linac is now being upgraded as a part of SuperKEKB accelerator complex [1] to achieve $L = 8x10^{35}$ /cm^2/s luminosity, both electron and positron beam emittance have to be 20 mm mrad. To perform the BBA stably, BPMs are required to have one magnitude better position resolution than the required alignment accuracy. To accomplish <10 μm position resolution, we have designed dedicated narrow bandpass filter (BPF) type readout circuitry with 250 MSa/s 16 bit pipeline ADC (AD9467-250 [2]). As the SuperKEKB injector injects electron / positron beams into four different energy rings (SuperKEKB HER/LER, PF and PF-AR) simultaneously, we employed electrical attenuators to keep enough dynamic range.*

BPM readout system has to have not only high position resolution (σ < 10 μm) but also good position accuracy. There are many sources of position error, especially input channel gain drift from each BPM electrode is one of dominant sources. To compensate this, calibration pulse generator [3] is implemented. A calibration pulse from one electrode is equally divided into adjacent electrodes with coupling capacitance (see Fig. 1). By calculating both channel output power, channel gain ratio can be monitored and compensated.

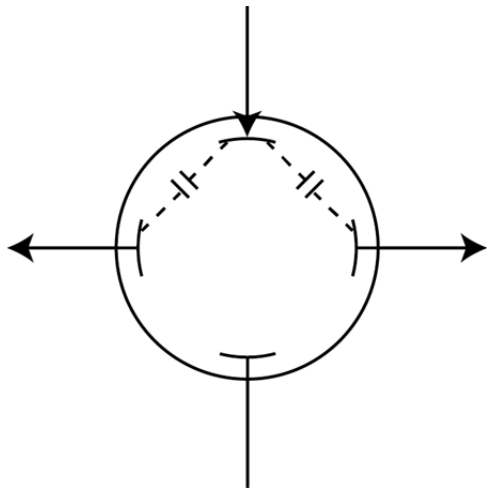


Figure 1: BPM calibration scheme is illustrated. Calibration tone is provided to the top electrode and induced pulses are generated on both adjacent electrodes with coupling capacitance.

HARDWARE IMPLEMENTATION

Baseline design of this BPM readout system has been reported at previous IBIC2013 conference [4]. Hence, we report updates from the last design here.

As discussed in previous section, we need to handle the signal with high linearity to achieve target position resolution (σ < 10 μm). It turned out that first prototype has following rooms to be improved:

At first, helical coils are needed to precise tuning, so it is not suitable for high linearity application. Therefore, we changed BPF centre frequency to 180 MHz so that we can use normal LC filters. Figure 2 shows the photograph of the prototype of the BPM readout board, Figure 3 shows block diagram of 2nd prototype BPF board. The latter BPF performs waveform shaping (burst length = 60 ns) and limits the bandwidth (22 MHz). The former BPF (BW=60 MHz) is for anti-aliasing at the ADC.

In addition, the latter amplifier is the critical device that limits the overall linearity. Therefore, we tested three RF amplifiers shown in Table 2. As shown in Fig. 4 an ADL5536 (Analog Devices (AD)), which have the highest output third-order intercept point (OIP3), has optimal (flat) linearity.

Figure 5 shows the BPF output waveform and ADC sampled data points. Waveform is stretched to about

* ryo@post.kek.jp

Copyright © 2014 CC-BY-3.0 and by the respective authors

ISBN 978-3-95450-141-0

60 ns length (<96 ns) so that enough data points can be sampled. 180 MHz as BPF center frequency locates at 250 MHz ADC[2]'s 2nd Nyquist zone (Under sampling condition).

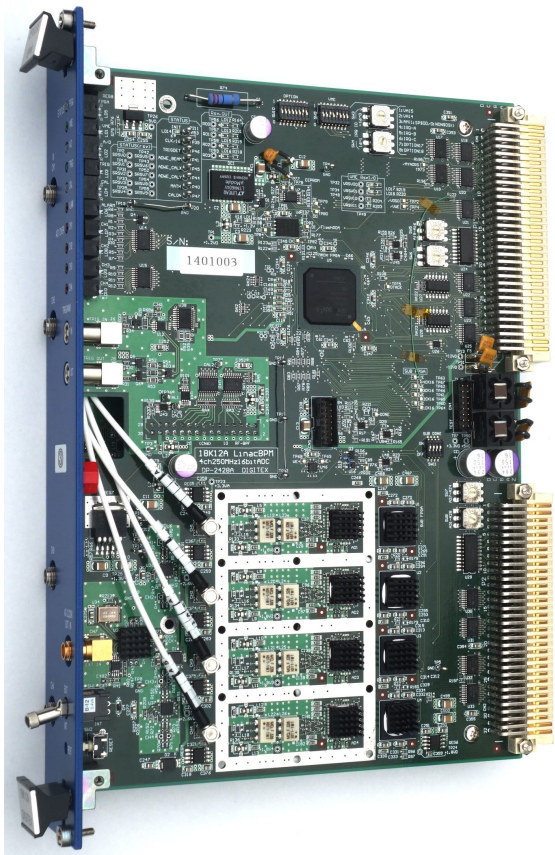


Figure 2: An photograph of prototype of BPM readout board (called 18K12A) is shown. This is a double width module. A BPF board is attached on bottom of a main (ADC) board. The output from BPF board is fed to the main board via four coaxial cables.

Then, we changed ADC input circuit from active circuit (with a RF amplifier) to passive circuit (with transformers) not to limit the linearity.

In addition, we took following improving steps to increase effective number of bits (ENOBs) of the ADC, which relates to the position resolution:

1. It is known that smaller ADC clock jitter contributes higher ENOBs. Hence, we changed standard AT cut crystal oscillator to SAW oscillator (known as low jitter output).
2. Eliminates ADC Clock delay chip (EP195) that gives additional clock jitter.

Finally, we increased calibration pulse generator output power to more than 40 dBm so that we can get enough S/N with the large inner diameter BPM for positron (ϕ = 63 mm, normal BPM has ϕ = 27 mm).

Table 1: Design Differences

Prototype	1st (18K12)	2nd (18K12A)
BPF Frequency	300 MHz	180 MHz
BPF structure	Bessel Filter with helical coils + anti-aliasing filter	Bessel filter with LC + Butterworth filter for anti-aliasing
Cal. power	> 36 dBm	> 40 dBm
ADC Clock	AT cut	SAW (low jitter)
Clock delay	Yes	No
ADC Input	Active circuit	Passive circuit

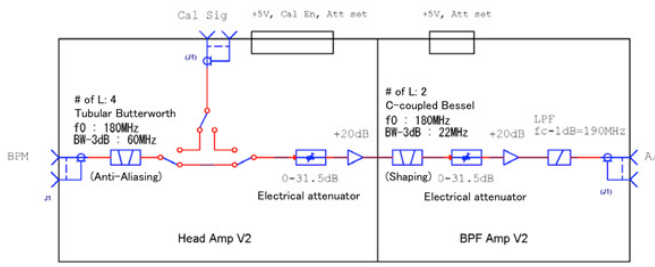


Figure 3: Block diagram of Band Pass Filter board (one channel is shown). It equips calibration pulse input selector. First Butterworth filter (60 MHz) cut tails that exceed ADC's Nyquist window (125 MHz – 250 MHz) and second Bessel filter (22 MHz) forms total bandwidth and burst length (60 ns). Each stage has an electrical attenuator and an amplifier to set an adequate level.

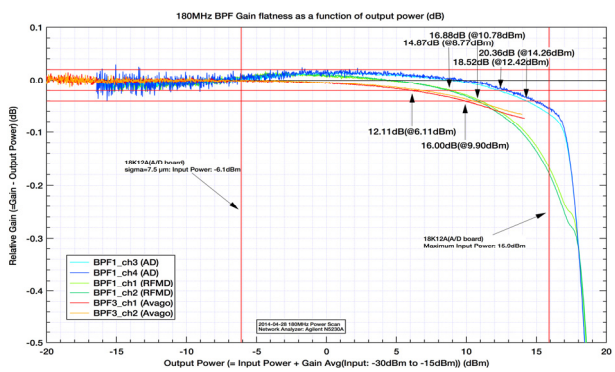


Figure 4: Amplifier linearity curve in the BPF circuitry is shown. AD (Blue) shows wide linearity, Avago (Red) shows moderate characteristics and RFMD (Yellow) shows narrow linearity.

Copyright © 2014 CC-BY-3.0 and by the respective authors

Table 2: Amplifier Comparison

Device	P1dB	Gain	OIP3	NF	Technology
SBB5089Z (RFMD) [5]	20 dB	20.8 dB	37.5 dB	4.3 dB	InGaP HBT.
ADL5536 (AD) [6]	19.6 dB	19.8 dB	45.0 dB	2.6 dB	GaAs HBT.
MGA-30689 (Avago) [7]	22.4 dB	14.3 dB	43.0 dB	3.0 dB	GaAs pHEMT.

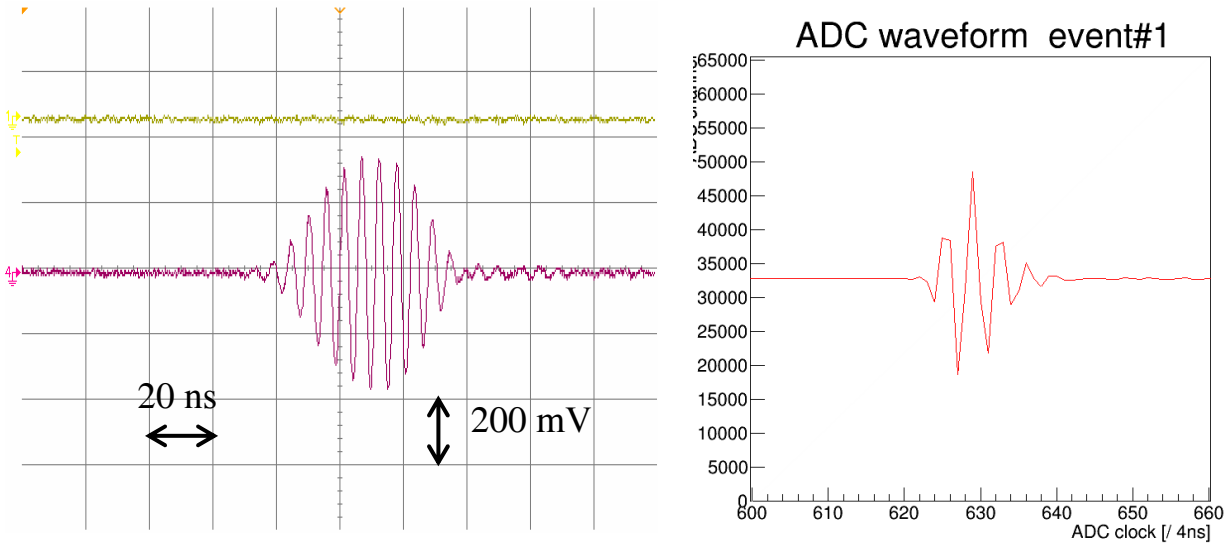


Figure 5: (a) BPF output waveform and (b) ADC sampled data points (2nd Nyquist zone under sampling).

PERFORMANCE TEST

Linearity / Resolution Check

In order to estimate linearity and position resolution of the BPM readout system, we performed linearity and resolution test. Instead of beam emulated impulse generator signal, 180 MHz CW is used. Because we'd like to keep the signal level stable as much as possible. Since accurate signal level is the key of these test, we used an Agilent J7211B Step attenuator, which has 0.03 dB repeatability. We calibrated it with a network analyzer. To provide beam equivalent ADC sampled data points, we used 96 ns Hanning window, which gives similar waveform with Fig. 5 (b).

Figure 6 shows test results with this setup: position resolution (upper plot) and channel power linearity (lower plot). At best condition, we can get about 1 μm position resolution. However, actual beam passes through at offset position from the BPM center, which gives unequal channel power between opposite channels. Therefore, we have to set an appropriate operation point, which allows ±5 mm position range (14 dB range is required).

Our requirement conditions for this system are:

1. Position resolution is less than 10 μm,
2. Linearity is within ±0.02 dB.

We find 24 dB ranges is agreed to these condition in the Fig. 6, so we can set an appropriate operation point that allows ±5 mm position range.

Amplifier Gain Time Drift

For the BPF output amplifier candidates, we also measured amplifier gain time drift in a thermostatic chamber (25±0.1°C) for 286 hours (11.9 days).

Measurement results are shown in Fig. 7. Although each channel power time drift ratio is up to 1.6% order, this is very curious phenomenon that these amplifiers have long time range gain drift even they are stored in a thermostatic chamber.

MGA-30689 (Avago) shows largest gain drift (1.6% (0.14 dB) / 11.9 days). On the other hand, ADL5536 (Analog Devices) shows smallest gain drift (0.6% (0.05 dB) / 11.9 days). Only MGA-30689 has pHEMT (FFT structure) and ADL5536 and SBB5089 have HBT (Bipolar structure). The difference of the amplifier structure may contribute these gain drift differences.

With this result and linearity measurements discussed in the previous section, we have decided to employ the ADL5536 for the BPF amplifier.

Copyright © 2014 CC-BY-3.0 and by the respective authors

ISBN 978-3-95450-141-0

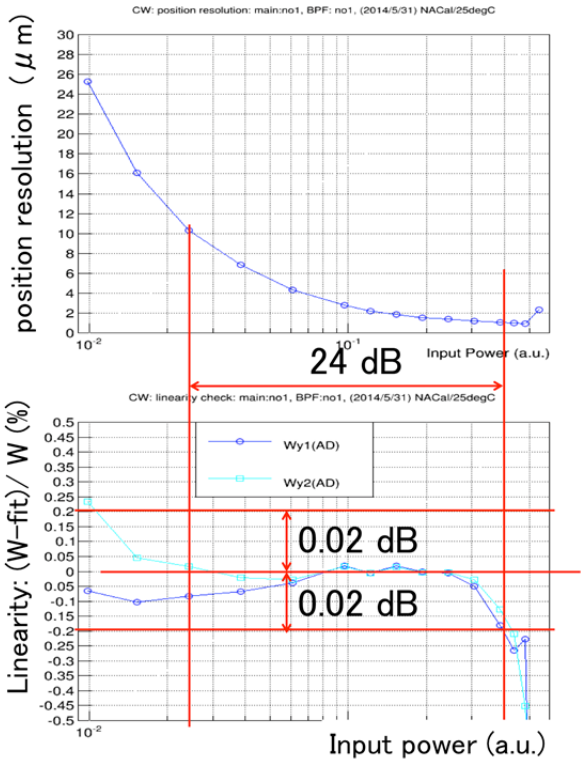


Figure 6: Upper plot shows BPM readout system resolution at ideal condition. Lower plot shows system linearity: we have 24 dB with ±0.02 dB linearity range.

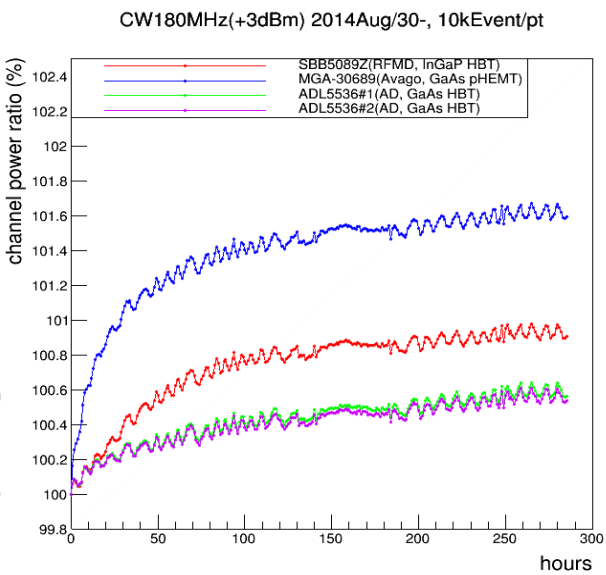


Figure 7: Amplifier gain drift is shown. Vertical axis is normalized channel power and horizontal axis is elapsed time. DUTs were tested in a thermostatic chamber.

3-BPM Resolution Tests

In order to make a decision to fabricate this readout system, we performed a 3-BPM resolution tests at KEK Linac. We used adjacent three BPMs (SP52-4, SP54-4 and SP56-4).

When we assume linear lattice, arbitrary three BPM positions x_1, x_2 and x_3 are given as:

$$x_3 = Ax_1 + Bx_2 + C.$$

Here, we can get (A, B, C) with a multiple regression analysis from N set of (x_{1n}, x_{2n}, x_{3n}) with N-times trials. Therefore residual can be given (corresponds to Fig. 8 right) :

$$\sigma^2 = \frac{1}{N}\sum_{n=1}^{N}\{x_{3n} - (Ax_{1n} + Bx_{2n})\}^2.$$

Assuming three BPM's position resolutions are same, the position resolution is given:

$$\sigma_x = \sqrt{\frac{\sigma^2}{1 + A^2 + B^2}}.$$

We took 3500 events data at 12.5 Hz, with changing Y steering magnet current in each 500 events. Figure 8 shows (left) reconstructed position to measured position, (right) residual distribution.

From the last formula and data, we got 3 μm position resolution.

SUMMARY AND FUTURE PLAN

We have developed a BPM readout system with high position resolution (σ < 10 μm) and high accuracy with a gain calibration system. In order to achieve these criteria, high linearity (±0.02 dB linearity) and large dynamic range (>14 dB) is required.

We performed 3-BPM resolution tests to demonstrate the readout system can be used at real environment and we got 3 □m position resolution.

We plan to fabricate total 100 units within this fiscal year (till March 2015) and install at 2015 summer shutdown.

ACKNOWLEDGMENT

Through this BPM readout system development, we thank Dr. Steve Smith, Dr. Andrew Young at SLAC and Dr. Makoto Tobiyama at KEK for their kind suggestions and advice in design and development. We also thank Mr. Kyosuke Yamada of Digitex Lab. Co. Ltd. (PCB), Mr. Morishige Aoyama of Sanko-sha Inc. (RF) and Mr. Takehito Koui of Skywave Co. Ltd. (FPGA) for developing this readout system with us.

Copyright © 2014 CC-BY-3.0 and by the respective authors

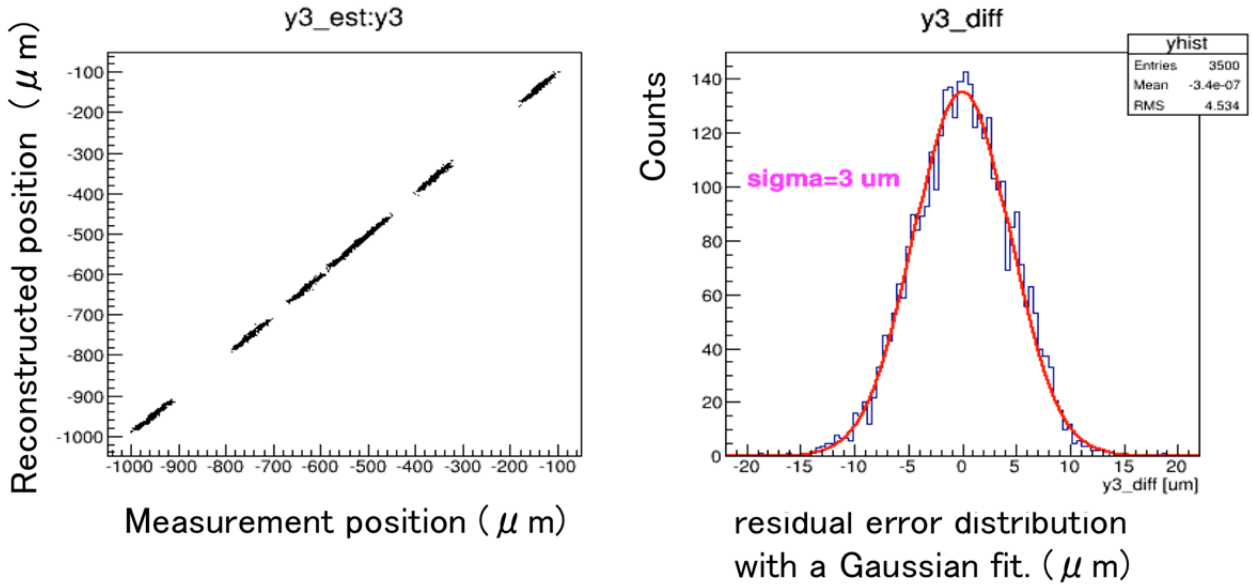


Figure 8: Left plot shows reconstructed position vs. measured position. Right plot shows residual error distribution histogram.

REFERENCES

[1] M. Masuzawa, in Proceedings of the First International Particle Accelerator Conference (IPAC'10), Kyoto, 2010, pp. 4764–4768.

[2] Analog Devices, 16-bit, 200 MSPS/250 MSPS Analog-to-Digital Converter AD9467 Data Sheet: http://www.analog.com/static/imported-files/data_sheets/AD9467.pdf

[3] S. R. Smith et al., "LCLS Stripline BPM System Commissioning", in Proceedings of the 23rd Particle Accelerator Conference (PAC'09), Vancouver, Canada, 2009, pp4027-4029.

[4] R. Ichimiya et al., "Development of High Precision Beam Position Monitor Readout System with Narrow Bandpass Filter for the KEKB Linac towards the SuperKEKB", Proceedings of the IBIC2013, pp.698-701.

[5] RFMD, 50 MHz to 6000 MHz, Cascadable Active Bias InGaP HBT MMIC Amplifier SBB5089Z Data Sheet: http://www.rfmd.com/CS/Documents/SBB5089ZDS.pdf

[6] Analog Devices, 20 MHz to 1.0 GHz, IF Gain Block ADL5536 Data Sheet: http://www.analog.com/static/imported-files/data_sheets/ ADL5536.pdf

[7] Avago Technologies, 40 MHz to 3000 MHz, Flat Gain High Linearity Gain Block MGA-30689 Data Sheet: http://www.avagotech.co.jp/docs/AV02-1876EN

Copyright © 2014 CC-BY-3.0 and by the respective authors

ISBN 978-3-95450-141-0

IMPROVEMENT OF DATA TRANSFER SPEED OF LARGE MEMORY MONITORS

M. Tobiyama*, KEK Accelerator Laboratory, 1-1 Oho, Tsukuba 305-0801, Japan, and
Graduate University for Advanced Studies (SOKENDAI), 1-1 Oho, Tsukuba 305-0801, Japan

Abstract

Beam monitors with long memories will be widely used in SuperKEKB accelerators. Since the slow data transfer time of such devices usually limits the operational performance, improvement of the transfer rate is required. Two kind of devices, VME-based modules and Ethernet-based modules have been developed. On the VME-based devices such as turn-by-turn position monitors for damping ring or long bunch oscillation monitors, MBLT and BLT transfer method have been implemented. For the Ethernet based system, such as the gated turn-by-turn monitors (TbT), SiTCP has been implemented on the FPGA and the EPICS device support for SiTCP has been developed. The improvement of the data transfer speed with the long-term reliability will be presented.

INTRODUCTION

With the rapid development of digital technology, it is much easier to implement large memory in the beam monitor system since late 1990's where we had designed the beam monitor devices for KEKB accelerators. As new accelerators with strongly improved performance such as SuperKEKB need much detailed information of the beam to achieve the design characteristics, the number and scale of the beam monitors with long memory becomes much larger than that of KEKB accelerators.

On the other hand, the environment of the beam instrumentation such as the selection of the field bus tends to be fairly conservative mainly due to saving of the design and construction efforts and costs. For example, in SuperKEKB beam instrumentations, though we newly introduce MTCAs and modules with direct Ethernet connection in some limited sections, we will still use the legacy bus such as VMEbus, VXIbus and GP-IB.

In the operational view, it is needless to emphasize the importance of the fast data acquisition and the fast data processing to minimize loss time of the operation. For example, during the operation of the KEKB collider, we have used the VMEbus based bunch oscillation recorders (BOR) with total 20 MB of memory which enables us to record the 4k turns of bunch oscillations for all the buckets in the ring [1]. We have also used the same recorders with limited address space of 5120 bytes for the bunch current monitors (BCMs). The BORs have been used for the post-mortem analysis of the beam abort and the machine developments such as the detailed analysis of the beam oscillation coming from intra-bunch oscillation due to electron cloud instabilities [2]. BCMs have been used to support the injection bucket selection systems to realize the equally filled bunch filling. As the EPICS system we had mainly used during the KEKB operation (R313) did not support larger array than 4k bytes, we needed to store the data to the remote disk directly from the IOC through the fairly slow Ethernet line (10base connection). Typical data transfer time from the BOR to the disk was 5 min to 10 min depending on the network traffic and the CPU usage of the host workstation with the remote disks. Of course that kind of waiting time was painful for all of us and had spoiled the efficiency of the machine operation.

For the SuperKEKB accelerators, we have developed the beam instruments with improved data transfer speed. Two kind of devices, the VMEbus based modules and direct Ethernet connection modules will be shown here. Table 1 shows the main parameters of SuperKEKB accelerators, main rings (LER and HER) and the positron damping ring (DR).

Table 1: Main Parameters of SuperKEKB Rings

	HER/LER	DR
Energy (GeV)	7/4	1.1
Circumference(m)	3016	135.5
Beam current (A)	2.6/3.6	0.07
Number of bunches	2500	4
Single bunch current (mA)	1.04/1.44	18
Bunch separation (ns)	4	>98
Bunch length (mm)	5/6	6
RF frequency (MHz)	508.887	
Harmonic number (h)	5120	230
T. rad. damping time (ms)	58/43	11
L. rad. damping time (ms)	29/22	5.4
Number of BPMs	466/444	83
Number of TbT monitors	135/135	83

VMEBUS BASED SYSTEM

Though the specifications and the expected performance of the VMEbus system might not be so modern [3], still the system have many strong points as:

- Board size fits most of our purpose as the beam instrumentation devices.

*makoto.tobiyama@kek.jp

Copyright © 2014 CC-BY-3.0 and by the respective authors

- Fairly simple bus interface and bus protocol. Bus interface could be realized with a simple CPLD-based logic ICs.
- There exist enough accumulation of usable resources such as already developed boards and operational experiences. It is still possible to obtain commercial boards with reasonable price.

In SuperKEKB, though the CPU (IOC) will be replaced from old PPC6750 to MVME5500, the VMEbus systems will still be used as the main field bus. The EPICS system will also be upgraded from R313 to R314 with VxWorks 6.8.2 which intrinsically supports large waveforms more than 20 MB. Therefore, it is a big concern about the total data transfer rate and the rate-limiting part in the data acquisition system.

Beam Position Detector for Damping Ring

In the normal operation mode of the DR, we inject one or two positron bunches of 1.1 GeV from the linac, damp the emittance during at least 40 ms of revolution, then eject them to the latter half of the linac to accelerate the beam up to 4 GeV. As the maximum repetition rate of the positron injection to the LER will be 50 Hz, 2nd set of positron bunches (single or two) will be injected 20 ms after the previous injection. It is therefore not suitable to use a narrowband position detector which needs longer accumulation time. We have developed the turn-by-turn beam position detector based on log-ratio method on the single VMEbus board (18K11) with the memory size of 32k to 256k words per channel which corresponds the recording time of 14.5 ms to 118 ms [4]. As there will be four BPM handling stations in the ring, one station needs to handle 20 to 22 BPMs. We will prepare two VME64x (without P0 connector) subracks for each station: one VME subrack contains 10 to 11 18K11s. Figure 1 shows the 18K11s in a VME64x subrack with a MVME5500 CPU as an IOC.

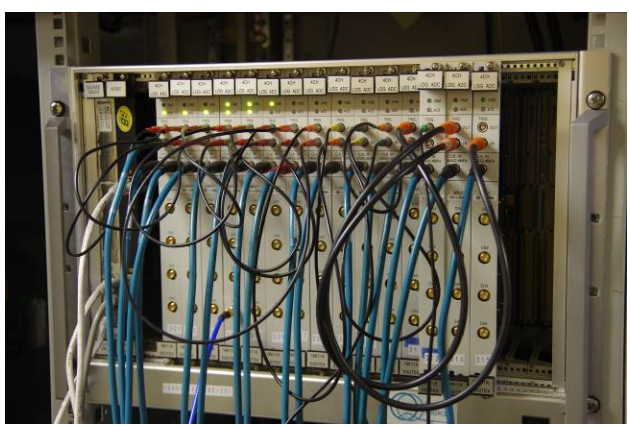


Figure 1: Log-ratio beam position monitor system (18K11) at the calibration station.

The data transfer speed of MVME5500 CPU with simple I/O mode (AM=0x0d) has been measured using a VME bus analyzer (HP 16500C or Agilent 16803A + FuturePlus FS3100) as shown in Fig. 2. The normal data accessing cycle is around 2 μs, that means it needs more than 0.15 s to transfer 4ch of 32k turns of data to the IOC. If we install 10 of 18K11s in one VME subrack, maximum repetition rate of the measurement will be smaller than 0.5 Hz.

To speed up the data transfer from 18K11 to the VME IOC, we have implemented A32 supervisory 64-bit block transfer (MBLT, AM=0x0C) defined by VME64 specification to 18K11 and developed the control code for UNIVERSEII PCI to a VME bridge chip on MVME5500 CPU. In the code, we at first transfer the specified memory block of the VMEbus module to the SDRAM of the CPU local memory using MBLT(VME) and DMA(CPU), then transfer them to EPICS waveform data.

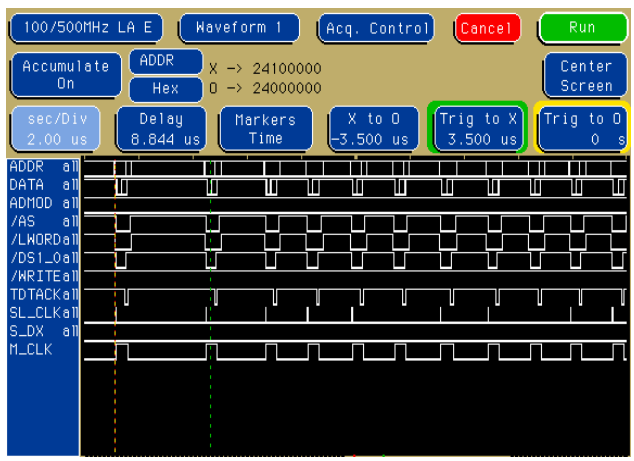


Figure 2: A32 supervisory data access using MVME5500. Typical bus access interval was around 2 μs.

By using the MLBT access, the bus access interval has shrunk down to 500 ns as shown in Fig. 3. During the MBLT cycle, CPU at first places the start address and the AM code of 0x0C (A32 MBLT) on the bus. After the return of DTACK signal of the slave board (18K11), MBLT cycle starts by handshake using DS0/1 and DTACK, and will continue up to the specified number of cycles (up to 256 cycles in one time).

In the real operation, 18K11 starts the data acquisition with the external hardware trigger signal, then initiates the VMEbus interrupt (IRQ) after filling the specified memory length to require data transfer to the IOC. Typical response time of IRQ to the start of the data transfer was about 24 μs. Data transfer of 32k turns of 4-ch data from 18K11 to the IOC took about 17 ms. After the raw data transfer, it converts the raw channel-mixed data array to EPICS waveform with the form of X, Y positions which needs about 7 μs. In case of 12-boards for one VME subrack, it needs roughly 0.3 s to transfer all 32k data. We will have enough margin for the 1 Hz system cycle even in the case of 64k turns (= 29 ms of beam position) of data acquisition.

Copyright © 2014 CC-BY-3.0 and by the respective authors

ISBN 978-3-95450-141-0

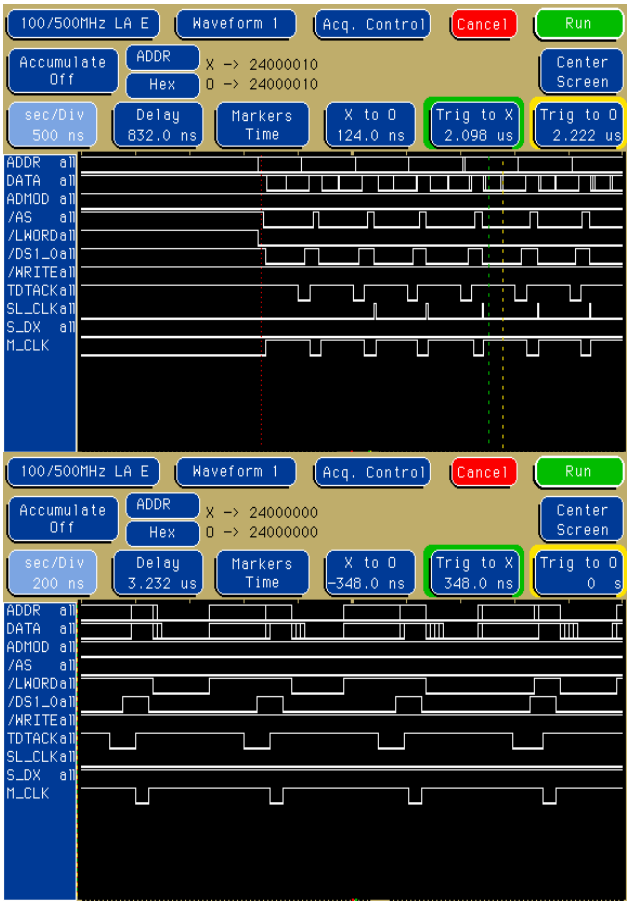


Figure 3: A32 MBLT access. Typical data bus access interval has shrunk to 500 ns (upper). The bus control has been controlled by the DTACK and DS0/1 during the MBLT cycle.

Bunch Current Monitor and Bunch Oscillation Recorder

In colliders such as SuperKEKB, the equalization of the bunch current is very important not only to suppress the instabilities, but also to maintain high luminosity with acceptable beam lifetimes. To control the bunch current during the injection process, it is necessary to measure the bunch currents and decide which bucket should be injected by the next pulse within the injection period, which is 20 ms at the maximum injection rate [5].

The transient behaviour of the beam just after closing or opening of the bunch feedback loop reveals many important characteristics of the coupled-bunch motions as well as the performance of the feedback systems (transient-domain analysis of the instability) [6]. Also the bunch motions just before the beam abort shows the cause of beam abort such as the growth of the instability or sudden beam kick by the miss-fire of the pulsed magnets (post-mortem analysis of the beam abort).

In KEKB, we have prepared 8-bit large scale memory boards with the memory size of 20 MB (the bunch oscillation recorder: BOR) for each planes (X, Y, and longitudinal) and the bunch current monitor board (BCM) that have same hardware structure as BOR but limited memory address space down to 5120 bytes.

In case of BCM of KEKB, the data transfer speed of 5120 bunches to IOC and reflective memory was about 1.4 ms under PPC6750 IOC with EPICS R313. As the minimum injection interval was 20 ms, there existed enough time to process the bucket selection before the next injection.

On the other hand, the data transfer of 20 MB of data from BOR to IOC took about 16 s with D16 data transfer mode. Because of fairly slow network (10base) coming from PPC6750, the data transfer from IOC to the remote disk (tftp protocol) on the host CPU took about 5 to 10 min depending on the total traffic on the network. As we normally took X and Y positions after the beam abort, it needed at least 10 min before the restart of the BOR systems. The situation became much worse when we took many BOR data in a short period such as machine study of electron cloud [2]; it needed huge time to store the data due to terribly increased network traffic between the IOC and the host CPUs.

We have developed new BCM/BOR system (18K10) based on fast FPGA technology [7]. It mainly consists of a fast 8-bit ADC (MAX108), a Spartan6 (XC6SLX45) daughter card with the form of a SO-DIMM card (Mars MX1), and VME-IF CPLDs and ICs. They are mounted on a double width, 6U VME card. For the BCM mode, as it is not needed to have large memory space, we have implemented the FPGA code to use only the block memory on the Spartan6 FPGA. For the BOR mode, as the MX1 board has 128MB of a DDR2 SDRAM, we have implemented the FGPA code to use the external DDR2 memory. The memory size for SuperKEKB mode (h=5120) could be 4k turns (20 MB) to 16k turns (80 MB) with the current configuration. Figure 4 shows the photo of the 18K10 BCM/BOR. As we designed 18K10 as the simple VME module which completely separates the address lines and data lines, it was difficult to implement MBLT on the board. We therefore implemented only simple A32 block transfer mode (AM=0x0f). The IRQ mean response time was 8.9 μs and the data transfer started after 36.5 μs of the IRQ. In the BCM mode, transferring 5120 bytes to IOC took only 1.1 ms.

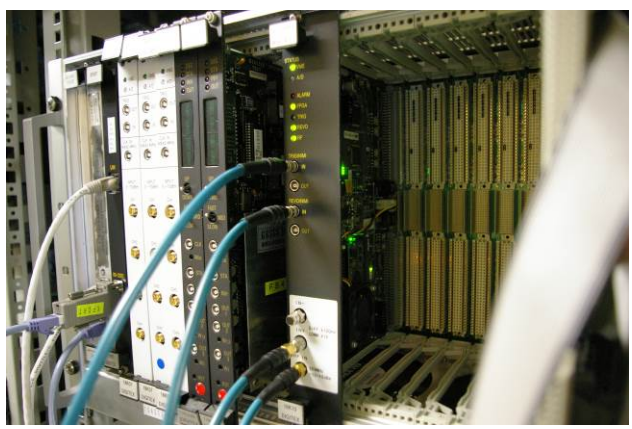


Figure 4: 18K10 bunch current /bunch oscillation monitor.

Copyright © 2014 CC-BY-3.0 and by the respective authors

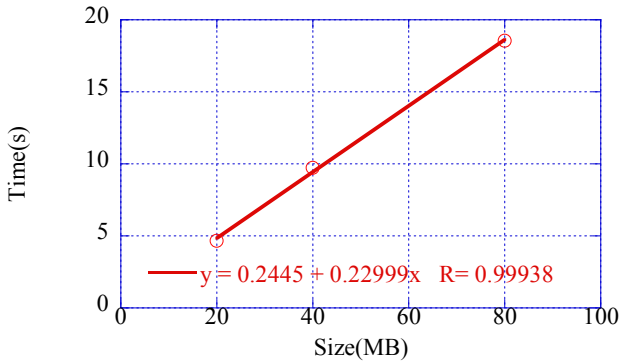


Figure 5: Measured data transfer time from 18K10 to IOC.

For the large data transfer on BOR mode, we have measured the transfer time of 20, 40, 80 MB of data using the VMEbus analyzer as shown in Fig. 5. It roughly shows 4 Mbytes/s data transfer rate.

We have also measured the data transfer speed from the IOC to the remote network disk (NAS, Thecas N8900 with 10GbE IF) mounted using NFS. Though the network speed from MVME5500 IOC to the local edge switch was limited by GbE, the other part, from the edge switch to the NAS, was connected with 10GbE so that we have expected full GbE speed. Figure 6 shows the measured data transferring time measured by the VME bus analyzer.

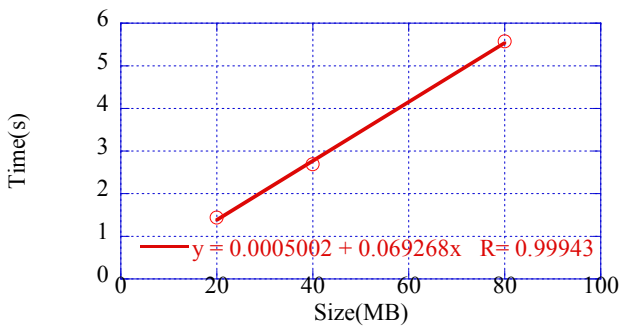


Figure 6: Measured data transfer time from 18K10 to NAS.

It needed less than 6 sec even in the case of 80 MB of data transfer. Though the total time needed to store the large 18K10s data is much shorter than that of old BOR and, waiting time, say 7 sec per one plane (20 MB) might be acceptable, it is obvious that data transfer in the VME system is the strong limiting factor of the total data transfer.

ETHERNET BASED SYSTEM

We have developed the gated turn-by-turn monitor (1421B) mainly to measure the beam optics (phase advance between the BPMs) during the collision using non-colliding bunch without feedback, and to measure the injection beam orbit [8]. It has four independent channels, each of them consists of a fast RF switch, a log-ratio beam signal detector, and a 14-bit ADC. Timing generation, data acquisition and data transfer is controlled by a Spartan6 FPGA (XC6SLX100T). Raw and calculated position data up to 1M turns per channel is stored in the DDR3 SDRAM. The block diagram and the photo of 1421B are shown in Fig. 7 and 8. We plan to install 12 to 15 1421Bs in one local control room under one server controlled by EPICS (R314.12.3) on CentOS 6.5-64bit system.

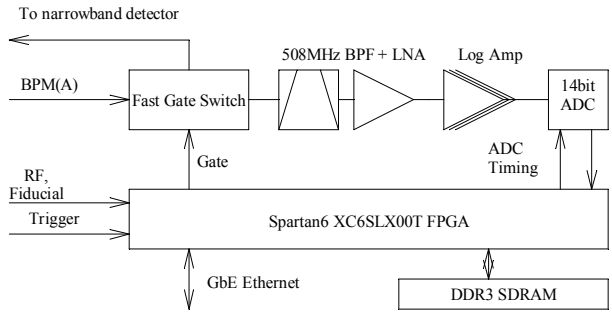


Figure 7: Block diagram of the gated turn-by-turn detector (1421B).

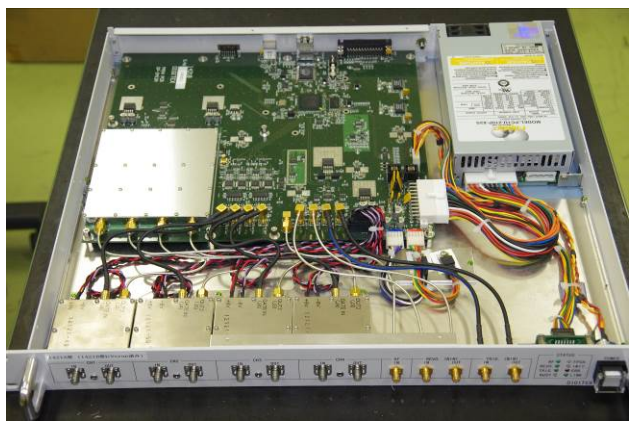


Figure 8: Photo of the 1421B gated turn-by-turn monitor.

Giga-bit Ethernet connection is used to control the system. We at first implemented a MicroBlaze soft processor on the Spartan6 FPGA to handle the commands from the server, and to transfer the data to the server through Ethernet. The measured data transfer rate has been found unexpectedly slow on the prototype system even in the case of 1:1 direct connection through a GbE non-intelligent SW-hub. To transfer 0.5 M turns of data of 4-channels which corresponds 5 sec of turn-by-turn data, it took about 44 s. Even by taking into account the data structure, the data transfer rate was only 2Mbit/s. For injection tuning, typically less than 32 turns of data transfer, or short data around 4k, that slow transfer might be acceptable. Nevertheless it is surely unacceptable to wait longer transfer time during operation. As it is suspected that the MicroBlaze is the main time-limiting principal, we have decided to implement SiTCP [9].

SiTCP supports hardware TCP/IP Ethernet communication from 10Mbps to 1Gpbs Ethernet with features:

- High speed communication stable at the upper limit of TCP.

Copyright © 2014 CC-BY-3.0 and by the respective authors

ISBN 978-3-95450-141-0

- Slow control function using UDP.
- Small circuit scale.
- Provided as FPGA library (Xilinx only: no source code available).

The SiTCP was originally developed in KEK and has been technology-transferred to Bee Beans Technology Co. Ltd. (BBT) [10]. The cost per module (mostly registration fee for MAC address) is not expensive. We have also implemented the firmware uploading function through Ethernet which enables us much faster rewriting of a SPI-flash than using JTAG connection. We have kept MicroBlaze to handle or monitor slow data handling in the FPGA, which is not controlling Ethernet communication, such as UART communication, which helps to set the IP address at the very beginning of the operation or after miss-setting the IP address. The booting time of the 1421B is less than 2 s, fairly fast enough. The communication and automatic negotiation with 1000baase and 100base has been confirmed to be OK.

On SiTCP, it is needed to use UDP as the slow control, such as setting some parameters or reading simple parameters, and TCP for larger data transfer. As existing framework provided by EPICS, such as ASYN, does not fit for the device support of SiTCP device, we have developed a mixed socket communication code as the EPICS device support to communicate with 1421B.

During the initialization of the device support, it generates communication threads (t1421ComXX) with the same number of 1421B to connect. In the normal command such as writing or reading short data, the record support at first posts the communication request to the t1421ComXX thread. The communication thread sends command to 1421B through UDP and receives the response also through UDP. It sends the response data to the record support through a callback thread.

In the case of large data transfer, the waveform record support also at first posts the communication request to the t1421CommXX thread. This time the thread tries to open the TCP socket and checks the DMA ready status of 1421B (if failed, it closes the socket and tries again), sends the DMA request through UDP, and receives the data through TCP. After receiving all the data, it closes the TCP socket and sends the data to the record support through a callback thread.

The data transfer rate has been measured using a software timer on the host PC. It was about 400MBPS from 1421B to the host, and about 280MBPS from the host to 1421B under GbE connection. As this asymmetry comes from the intrinsic structure of SiTCP, enough data transfer rate has been realized.

We have also examined long-term, fairly higher load (frequent large data transfer) test on 1421B and the server. During the test, we have encountered several unexpected communication errors and hung-ups of 1421B mainly during the TCP data transfer. As SiTCP is black box for us, we have implemented error handling and recovery functions in the communication thread. Though the error rate has been greatly reduced after this, it still remains communication hung-ups with very rare rate, say, once a week. We are discussing with BBT and also planning to implement a remote reboot function on the 1421B firmware.

SUMMARY

We have examined the fast data transfer on VMEbus and direct Ethernet devices. For the VMEbus devices, the 18K11 log-ratio beam position detector for DR and the 18K10 bunch current and bunch oscillation recorder, MBLT and BLT defined VME64 has been applied and more than 8 times of faster data transfer on MBLT case has been shown. Also the data transfer from IOC to the remote disk has been improved by the faster network (10GbE) and fast NAS and has shown about 300 times faster rate than that of KEKB.

For the direct Ethernet connection devices (1421B gated turn-by-turn monitor), we have implemented SiTCP to remove huge overheads in the FPGA code. The data transfer speed has been increased about 100 times than before. Also the EPICS device support routine to handle mixed UDP and TCP communication on SiTCP has been developed and has shown excellent performance.

The DMA data transfer code on MVME5500 has been developed by Mr. T. Okazaki of East Japan Institute of Technology Co., Ltd. (e-JAPAN IT Co., Ltd.). The EPICS device support for SiTCP has been written by Mr. Y. Iituka of e-JAPAN IT Co., Ltd. Implementation of SiTCP on the 1421B FPGA has been done by Skywave Co. Ltd. The author would like to thank Dr. T. Obina and Dr. H .Uchida for the discussion of SiTCP implementation. The author thanks colleagues of the SuperKEKB beam instrumentation group for numerous supports on the development.

REFERENCES

[1] M. Tobiyama, E. Kikutani, Phys. Rev. ST Accl. Beams 3, 012801 (2000).
[2] J. W. Flanagan, et. al., Phys. Rev. Lett. 94, 054801 (2005).
[3] W. D. Peterson, “The VMEbus Handbook”, ISBN 1-885731-08-6.
[4] H. Ikeda, et. al., in proceedings of IBIC2013, Oxford, UK. p.53 (2013).
[5] E. Kikutani, et. al., in proceedings of ICALEPS99, Trieste, Italy (1999).
[6] M. Tobiyama, et. al., Phys. Rev. ST Accl. Beams 9, 012801 (2006).
[7] M. Tobiyama and J. W. Flanagan, in proceedings of IBIC2012, Tsukuba. (2012)
[8] M. Tobiyama, et. al., in proceedings of IBIC2013, Oxford, UK. p295 (2013).
[9] Tomohisa Uchida, IEEE Trans. Nucl. Sci. Vol 55, No.3, p.1631, (2008).
[10] http://www.bbtech.co.jp/

Copyright © 2014 CC-BY-3.0 and by the respective authors

EVALUATION OF LIBERA SINGLE PASS H FOR ESS LINAC*

M. Cargnelutti, M. Žnidarčič, Instrumentation Technologies, Solkan, Slovenia
H. Hassanzadegan, ESS AB, Lund, Sweden

Abstract

The Beam Position Monitor system of the ESS linac will include in total more than 140 BPM detectors of different sizes and types. The resolution and accuracy of the position measurement with the nominal 62.5 mA beam current and 2.86 ms pulse width need to be 20 μm and 100 μm respectively, and those of the phase measurement are 0.2 deg and 1 deg respectively. The BPM system also needs to work successfully under off-optimal conditions, ex. with a de-bunched beam, or with the current and pulse width being as low as 6 mA and 10 μs respectively. Options for the implementation of the ESS BPM electronics include: 1) a custom or commercial front-end card combined with a commercial digitizer with in-house developed firmware and 2) a fully commercial off the shelf system.

Libera Single Pass H is an instrument intended for phase, position and charge monitoring in hadron and heavy ion LINACs. The instrument was tested at the ESS laboratory, to prove the feasibility of operation with ESS beam conditions. To give a realistic picture of the device performance, different testing setups were evaluated, including all the signal and environment conditions foreseen for the final ESS linac operation. The results present resolution, precision and accuracy evaluations, as well as stressful long-term and stability tests. This paper presents the achieved results of the Libera Single Pass H for the ESS beam parameters.

INTRODUCTION

During the evaluation of Libera Single Pass H, every parameter that was supposed to influence the instrument performance was treated as a degree of freedom. The measurements were carried out at the ESS laboratories within a 6 weeks time-frame, and the complete report on which this article is based, can be found in [1].

To determine the operating conditions in which the instrument is required to work (input signal levels and dynamic range, temperature variations), the analysis of the ESS beam and BPM characteristics was particularly useful, and it is presented in the next section. The third session explains how parameters like *resolution*, *precision*, *accuracy* are calculated, and for each one a definition is provided. Later on, a basic test setup for the measurements is presented, introducing the role of the most significant components.

Finally the phase and position measurements results are discussed and compared with the ESS requirements.

*This project has received funding from the European Union's Seventh Framework Programme for research, technological development and demonstration under grant agreement no 289485

ESS BUTTON BPMS

The ESS linac will include BPM detectors of different sizes and types, and a detailed overview is given in [2]. However, most of the detectors will be of electrostatic button type and according with the beam pipe size they will be of two different diameters: 60 and 100 mm. Table 1 introduces some ESS significant parameters which are useful to understand the signal characteristics.

Table 1: ESS Beam and BPM Parameters

Parameter	Value	Unit
RF frequency	352.21 and 704.42	MHz
Bunch repetition rate	352.21	MHz
Pulse repetition rate	14	Hz
Pulse duration	0.01 - 2.86	ms
Pulse current	6.25 – 62.5	mA
BPM diameter	60 and 100	mm
Button diameter	24 and 40	mm
Button capacitance	5.2	pF
Beam max displacement (with ref. to beam pipe)	50	%

It is possible to notice that even if the RF frequency changes from 352.21 to 704.42 MHz passing from the spokes section to the super-conductive linac, the bunch repetition rate remains the same. In terms of the BPM signals, this means that the fundamental harmonic is always at 352.21 MHz, and the other components are multiples of it.

Considering the Libera SPH capabilities, the instrument processes the first and the second harmonic, providing phase and position measurements for both of them.

BPMs Signal Levels

To estimate the signal levels coming from the BPMs, an analytical model of the beam and detectors is used. The expected signal levels for both harmonics are calculated according with the value of the influential parameters. Most are listed in Table 1: geometrical properties, beam current and b-factor all influence the amplitude of the BPM outputs. Considering the extreme cases, with a beam in the centre of the pipe:

- First harmonic ranges from -3.55 to -27.98 dBm
- Second harmonic ranges from -1.13 to -25.56 dBm

On the base of the same model, if the beam is 50% off-centred the signal coming from the closest button gains 8.72 dB while the opposite one loses 8.72 dB.

Copyright © 2014 CC-BY-3.0 and by the respective authors

ISBN 978-3-95450-141-0

Environment Conditions

The instrument analog part (filters, amplifiers, ADCs) is particularly sensitive to the environment conditions changes, especially temperature and humidity. The maximum drift in temperature foreseen at ESS for the instrumentation is 5 degrees. The same temperature variation was reproduced during the long-term measurements.

MEASUREMENT DEFINITIONS

This chapter introduces some parameters which are important to benchmark a measurement device. Examples are *resolution*, *precision* and *accuracy*. These concepts are widely used in this article, and for clarity reasons they are presented below, according with ISO Guide 99 [3].

Libera Single Pass H is intended for phase, position and charge measurements [4]. Starting from the four BPM signals, position is calculated using *delta-over-sum* formulas. The phase is measured against a fifth input, a pure sine tone used as a reference. The four phases measured using each input are then averaged. Charge measurements are not considered in this scope.

In its normal working conditions, Libera SPH samples the input signals at 125 MHz, with 16 bit ADCs. After the raw ADC data is processed by the *digital-down-conversion* (DDC) algorithm, phase and position samples are provided with 1 MHz rate. This means that at each trigger, for a 2.86 ms macropulse it is possible to acquire up to 2860 phase and position samples from the buffer. If not differently specified, all the presented results are based on the analysis of 2000 samples per trigger.

Resolution

It's defined as the "*Smallest change in a quantity being measured that causes a perceptible change in the corresponding indication*". For a digital instrument, resolution can be limited either by the digitization process (e.g. number of ADC bits) or the signal noise. With 16 bit ADCs, noise can be considered as the limiting factor.

Position and phase resolution is evaluated with the standard deviation, calculated from the samples acquired within a single trigger acquisition.

Precision

It's defined as "*Closeness of agreement between indications or measured quantity values obtained by replicate measurements on the same or similar objects under specified condition*". Each trigger acquisition can be seen as an independent measurement under similar conditions. From each acquisition, the mean value is calculated from 2000 acquired samples. The precision is evaluated as the standard deviation of the mean values obtained from 100 independent measurements.

Accuracy

It's defined as "*Closeness of agreement between a measured quantity value and a true quantity value of a measurand* ". Assuming the real value of the measurand is known, the accuracy is evaluated as the difference between the mean value of an acquisition and the real value.

Stability

The idea behind stability measurements is to evaluate how a given measured quantity is influenced by other factors which can be the phase, position, input signal level, temperature, etc... When the instrument stability is evaluated over time, then the term "*long-term stability*" is used. In all cases, stability is quantified considering the maximum peak-to-peak variation of the measurement.

SETUP WITH 4-WAY SPLITTER

In order to evaluate the performance of an instrument that elaborates the signals coming from the accelerator BPMs, such signal conditions need to be simulated. One possibility is to start from a suitable RF source and split the signal with a 4-way splitter. By controlling the properties of the inputs and outputs (e.g. harmonic components, power levels, etc...) it is possible to simulate several situations which are foreseen in the accelerator according with beam current, position displacement and so on. The only drawback in this configuration is the fact that it is not possible to evaluate the position accuracy.

Figure 1 introduces the setup described above, used for measurements in centred beam conditions (all the four inputs have roughly the same amplitude). Apart from the trigger signal, all the Libera inputs are obtained from the same RF source, a sine tone at 352.21 MHz. On the reference signal path, the analog phase shifter is used to control the phase difference between inputs and reference. On the BPM signal path, the pulse-generating diode provides a signal which contains also the second harmonic, a good approximation of the BPM signals. Attenuators are used both to control the signal level and

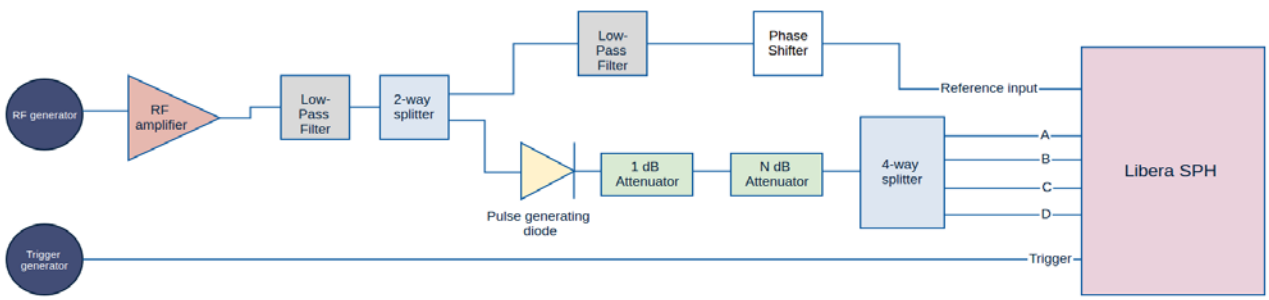


Figure 1: Block diagram of the measurement setup used for measurements with centred beam conditions.

Copyright © 2014 CC-BY-3.0 and by the respective authors

to reduce the signal reflections caused by the diode, since its impedance is not perfectly matched to 50 Ohm. Low-pass filters are used to clean out the unwanted harmonic components from the reference input signal.

MEASUREMENT RESULTS

This section presents part of the results achieved with the setup described above: for the whole set of measurements refer to [1]. Figure 2 shows the resolution of phase and position measurements as the four Libera inputs are lowered, starting from the reference level – 0 dB on the X axis. Both the first harmonic component (left) and the second (right) are considered.

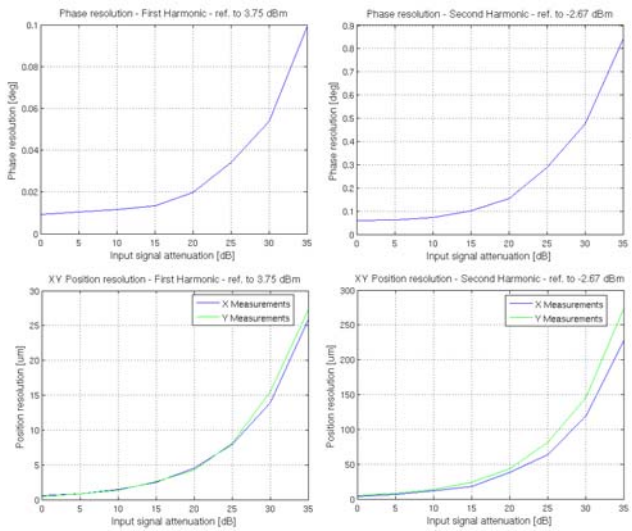


Figure 2: Phase and position resolution measurements.

Considering the measurement results, it is important to keep in mind that the phase shift measured at the second harmonic is two times the shift which affects the first harmonic. Consequently all the results should be divided by a factor of two.

Furthermore, the unit which was used for the measurements has a standard RF front-end with a bandwidth limited by the analog filters to 575 MHz. This attenuates the level of the input signal at the second harmonic. Substantial improvements are expected using an RF front-end tailored on the signal frequencies foreseen at ESS.

Another interesting measurement with this setup is the phase accuracy. Using the line stretcher in the reference signal path, it is possible to shift the phase up to 56.85 deg for the first harmonic, and up to 113.43 deg for the second. This range is divided in 17 equal steps and measurements are performed for each step. In order to evaluate the accuracy of the instrument, the phase shifter was first characterized with a Vector Network Analyser having an accuracy of 0.2 deg in these signal conditions.

Figure 3 presents the results for both harmonics: plots on the left show the total phase shift, while those on the right present the shift introduced by each shifter step. Again, the 2nd harmonic measures should be divided by 2. Single step plots show a non-linearity of the shifter, having the same profile for both VNA and Libera SPH.

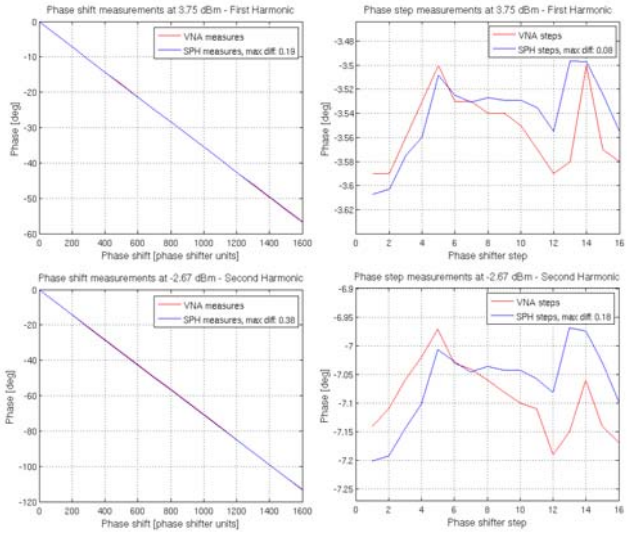


Figure 3: Phase accuracy measurements.

The measurements are then repeated lowering the input signal level and the results proved to be within the requirements in all the BPM expected signal range.

Another important evaluation is the long-term temperature stability. In order to evaluate it, the instrument was left running with the same input signal conditions for 24h.

A room temperature variation of 6-7 ºC was induced by leaving the window open. Figure 4 presents the temperature profile measured with the sensors located in the RF front-end. The acquired phase and position signals show a similar profile, with peak-to-peak variations reported in Table 2.

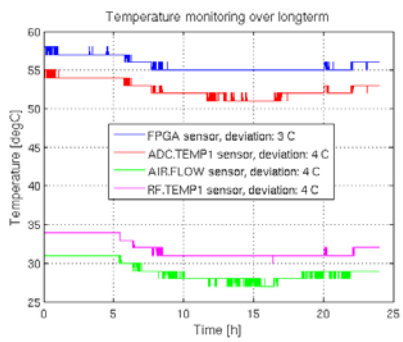


Figure 4: Long-term measurement temperature profiles.

Copyright © 2014 CC-BY-3.0 and by the respective authors

ISBN 978-3-95450-141-0

Table 2: Long-term Phase and Position Variations

Parameter	Peak-to-peak	Unit
Phase - 1st harmonic	0.13	deg
Phase - 2nd harmonic	0.42	deg
X pos. - 1st harmonic	1.52	mm
X pos. - 2nd harmonic	18.49	mm
Y pos. - 1st harmonic	0.83	mm
Y pos. - 2nd harmonic	12.75	mm

SETUP WITH BPM TEST-BENCH

In order to evaluate the position measurement accuracy, a possibility is to use a BPM test-bench: a device which consists of a section of the beam pipe with a BPM in the middle of it. Inside of the pipe, the beam is simulated with current impulses which pass through a wire, exciting electromagnetic signals which are captured by the BPM pickups. Mechanical slides can be used to control the wire position, offering the possibility to calibrate the instruments and perform the position measurements. Figure 5 shows the BPM test-bench designed and assembled at ESS.

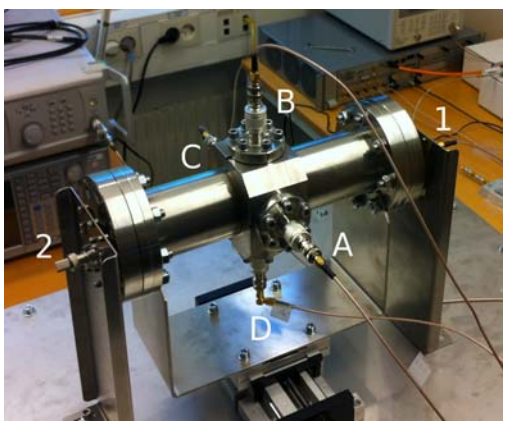


Figure 5: BPM test-bench used at ESS.

Ports 1 and 2 are the wire connectors, while ports A,B,C and D are the BPM outputs which are connected to the instrument. The pipe and BPM diameters are 60 mm and the slide enables to move the wire only in the horizontal plane, with a range of [-15 mm, +15mm] with reference to the centre, and 50 mm resolution.

The system was first characterized with the VNA, which measured an insertion loss (i.e. modules of S_{A1} and S_{C1}) around 48 dB, mainly due to the impedance mismatch between the wire input and the pipe. Because of this limitation, only the first harmonic was usable for the measurements, with a maximum level of -26 dBm (with the wire in the centre of the pipe). The Libera SPH calibration consisted in two steps:

- Using the slide, the wire was centred in the pipe, according with the instrument readout from the ADCs.
- The sensitivity parameter (K_X) was set in order to have a linear region between -5 and +5 mm.

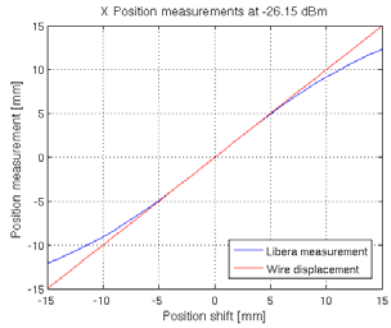


Figure 6: Position measurements with BPM test-bench.

Finally, the whole range between -15 and +15 mm was divided in 1 mm steps where to perform the measurement. Figure 6 presents the X position acquired in the whole horizontal range, while Figure 7 presents the accuracy in the linear region, estimated considering the slide position as the real value. These measurements have shown that the accuracy will be better than 100 mm in the linear region and beyond that, it will degrade due to the BPM non-linearities.

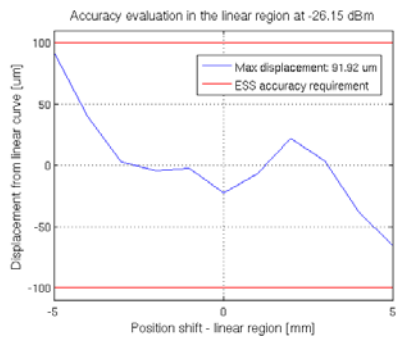


Figure 7: Position accuracy within the BPM linear region.

CONCLUSIONS

This article presents the measurements performed at the European Spallation Source with the Libera Single Pass H instrument. The purpose of the tests was to prove the feasibility of operation according with the ESS beam conditions.

The BPMs analytical models and the foreseen accelerator beam parameters provided enough information to identify the characteristics of the BPM signals which are expected at the instrument input. In order to evaluate the instrument performance, these signal conditions were reproduced in the ESS lab by using different tools and test-setups.

Resolution, precision, accuracy and stability of phase and position measurements were first defined and then evaluated in different conditions, playing with all the influential parameters in a multidimensional field.

The achieved results show that Libera SPH with a standard RF front-end meets the ESS requirements in almost all the conditions, providing accurate results with a good temperature stability. Even better performance is

Copyright © 2014 CC-BY-3.0 and by the respective authors

expected with an RF front-end tailored to the ESS machine parameters.

REFERENCES

[1] M. Cargnelutti, "Libera Single Pass H – Evaluation Measurements at ESS" - http://www.i-tech.si/file/download/355_d510aadf9bf0/stat

[2] H.Hassanzadegan, A. Jansson, A.J. Johnasson, R. Zeng, K. Strnisa, A.Young, "System Overview and Design Considerations of the BPM System of the ESS Linac", Proceedings of IBIC 2013, Oxford, UK.

[3] Philip Stein, "All you ever wanted to know about resolution – How to calculate measurement resolution's contribution to an uncertainly budget", Quality Progress, July 2011.

[4] Libera SPH page - http://www.i-tech.si/accelerators-instrumentation/libera-single-pass-h/benefits_3

Copyright © 2014 CC-BY-3.0 and by the respective authors

ISBN 978-3-95450-141-0

BEAM JITTER SPECTRA MEASUREMENTS OF THE APEX PHOTOINJECTOR*

H. Qian#, J. Byrd, L. Doolittle, Q. Du, D. Filippetto, G. Huang, F. Sannibale, R. Wells, J. Yang,
LBNL, Berkeley, CA 94720, USA

Abstract

High repetition rate photoinjectors, such as APEX at LBNL, are one of the enabling technologies for the next generation MHz class XFELs. Due to the higher repetition rate, a wider bandwidth is available for feedback systems to achieve ultra-stable machine and beam performance. In a first step to improve APEX beam stability, the noise spectra of the APEX laser beam and electron beam are characterized in terms of amplitude and timing. Related feedback systems are also discussed.

INTRODUCTION

The Advanced Photo-injector Experiment (APEX) is for demonstration of MHz repetition rate high brightness electron beam injection for the next generation high repetition rate free electron lasers [1]. APEX is staged in 3 phases. In phase 0, the 186 MHz normal conducting (NC) RF gun was successfully conditioned to achieve CW operation at nominal beam energy (750 keV) with low vacuum pressure performance (10^{-11} – 10^{-9} Torr). In phase I, several high QE photocathodes are being tested to demonstrate 0.3 mA beam current, and 6D beam phase space will be characterized at gun energy. In phase II, beam brightness will be more reliably demonstrated after being compressed by a buncher and accelerated by a 30 MeV NC pulsed linac.

Due to CW RF operation and MHz beam rep. rate, a wider bandwidth (BW) is available for feedback system, so ultrastable operation of the next generation FELs is being pursued [2]. Since photoinjector is one of the main noise sources, a tighter stability requirement has been put on photoinjectors like APEX, as shown in Table 1. With Phase I installed and in operation, efforts to characterize and improve APEX RF, laser and electron beam stability have been initiated.

Table 1: LCLS-II Injector Stability Requirements [3]

Injector Stability Parameters	RMS Tolerance
Bunch charge	1%
Timing jitter at injector exit	25 *f*s
Electron beam energy	0.01%
$\Delta x/\sigma_x$ and $\Delta y/\sigma_y$	1%

GUN RF STABILITY

Compared with the high frequency NC RF guns, APEX gun is special in terms of RF dependence of electron beam stability. Due to a low resonant frequency of 186 MHz, 1 degree of RF phase corresponds to 15 ps, which makes the electron beam energy much less sensitive to laser-RF timing jitter. Due to relatively low energy of 750 keV and inverse square dependence of drift space R_{56} on beam energy, beam arrival jitter before the linac booster becomes much more sensitive to RF amplitude jitter. In this sense, APEX gun behaves more like a DC gun.

In order to achieve the 25 *f*s arrival jitter at injector exit, the gun RF amplitude jitter is at least 7×10^{-5} rms without considering other jitter sources. Two feedbacks are implemented on the APEX gun RF, one is a slow feedback based on the cavity frequency tuner to keep the gun frequency on tune, and the other is a fast feedback based on the low level RF (LLRF) drive to keep the gun RF amplitude and phase stable [4]. A close-loop measurement shows gun RF amplitude and phase jitters are reduced to 2×10^{-4} and 0.01 degree respectively, as shown in Fig. 1, and gun dark current energy jitter measurement shows consistent result. The closed-loop amplitude stability of 2×10^{-4} includes strong components from a few lines at 6667 Hz, 6690 Hz, and 9672 Hz, which are out of the feedback BW. These lines show up in forward power and cavity pickup measurements, open and closed loop. Work is ongoing to identify and then eliminate the source of these lines in order to get below 10^{-4} RF amplitude stability.

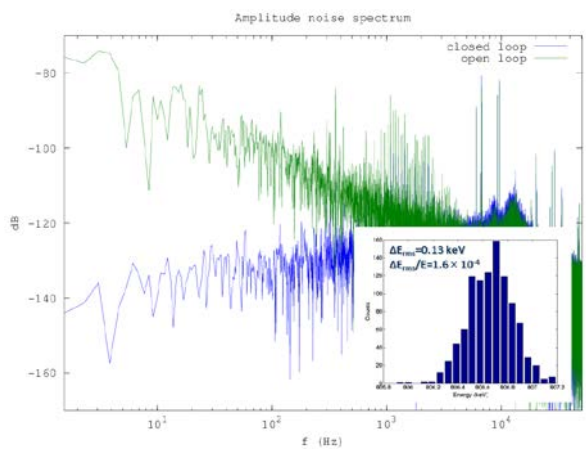


Figure 1: Gun RF amplitude jitter open and close loop (2×10^{-4}), insert shows consistent dark current energy jitter.

*This work was supported by the Director of the Office of Science of the US Department of Energy under Contract no. DEAC02-05CH11231
#hqian@lbl.gov

Copyright © 2014 CC-BY-3.0 and by the respective authors

LASER STABILITY

APEX phase I started with a homemade ~1 W 1MHz Yb doped fiber laser sitting in air without environment regulations [5]. In order to improve the laser stability, a laser enclosure with AC control was built and in operation recently. Besides, a commercial ~1.7 W 1 MHz fiber laser from CALMAR is under commissioning to replace the homemade fiber laser. In the following, both the old and new fiber laser stability will be presented.

Laser Energy Jitter

The long term stability of the old homemade laser has shown 100% fluctuation between day and night due to peak to peak (p-p) temperature fluctuations of ~4 degree C [6]. After installation of the AC enclosure, the p-p temperature fluctuation has dropped to ~1 degree C. A slow feedback based on a motorized continuous neutral density filter to stabilize either laser energy (laser power meter) or beam current (ICT) was also implemented, and close-loop long term stability has shown significant improvement from both the laser and beam performance (~2%) [7, 8]. The long term stability of the commercial laser is expected to be better.

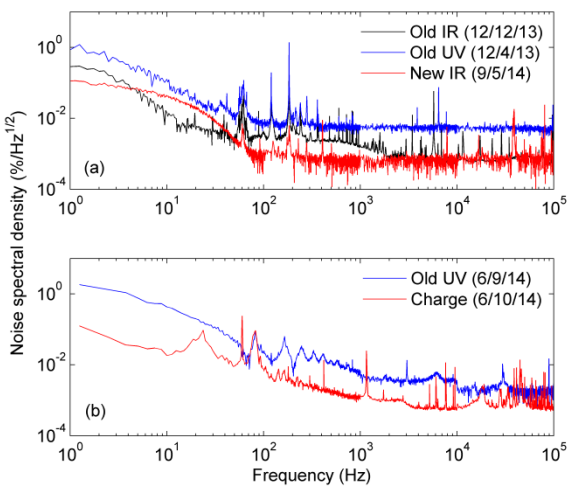


Figure 2: Noise spectral density of (a) APEX laser energy and (b) beam charge at 0.3 mA operation.

Fast feedback based on Pockels cell to reduce fast laser energy jitter was also developed elsewhere, which is effective but sacrifice half the IR energy and downstream harmonic generation efficiencies [9]. To decide whether such a fast feedback is necessary for APEX, the fast noise spectra of the laser energy are measured at DC band of the photodiode signal by a 100 kHz FFT analyser. The DC value of the photodiode signal is ~3 mV, and two photodiode signals of the same laser are used to do cross correlation in order to remove part of the noise induced by photodiode or FFT analyzer. Our measurements show, cross correlations reduce the measured noise below ~100 Hz by ~ 30% compared with no cross correlation.

Energy jitter of both the old laser and new laser are measured as shown in Fig. 2 (a), and integrated noise of old IR, old UV and new IR between 1 Hz and 100 kHz are shown in Table 2. The noise spectra of the three lasers share some common features, such as high noise below 100 Hz, 60 Hz and its harmonic peaks, and high noise above 10 kHz, probably due to pump laser noise. Compared with the homemade laser, the commercial laser is much cleaner below 10 kHz, and integrated noise is reduced by ~60%; the new laser is a bit noisier between 10 kHz and 100 kHz, and two dominating peaks at 38.9 kHz and 80.6 kHz contribute 0.54%, which are out of the BW of even a fast feedback [9]. Understanding and then eliminating the two peaks are very important to further reduce the fast noise of the new laser.

Table 2: UV Energy and Charge Jitter

Frequency (Hz)	Old IR (12/12/13)	New IR (9/5/14)	Old UV (6/9/14)	Charge (6/10/14)
$10^5 \sim 10^4$	0.41%	0.61%	0.68%	0.45%
$10^4 \sim 10^3$	0.26%	0.07%	0.39%	0.13%
$10^3 \sim 10^2$	0.35%	0.03%	0.43%	0.07%
$10^2 \sim 10^1$	0.08%	0.11%	1.2%	0.42%
$10^1 \sim 10^0$	0.36%	0.21%	3.1%	0.17%
$10^5 \sim 10^0$	0.70%	0.66%	3.4%	0.66%

Laser Timing Jitter

Even with a perfect gun and linac RF, the APEX laser timing jitter has to be below 100 *f*s in order to beat the 25 *f*s arrival jitter spec at injector exit. The APEX laser oscillator repetition rate (37.14 MHz) corresponds to the 5th subharmonic of the gun RF frequency, so 5th harmonic of the laser oscillator signal detected by photodiode is locked to the LLRF reference. Two phase lock loops have been implemented, one is a slow piezo actuator, and the other is a fast piezo actuator, both controlling the same end mirror of the laser cavity. Taking the gun RF phase feedback as an example, even with a good feedback, laser phase noise is expected to be limited by ~0.01 degree at 186 MHz, which corresponds to ~150 *f*s and cannot meet the 100 *f*s spec. When the 1.3 GHz LLRF board is built for the downstream linac, the 35th harmonic of the oscillator signal can be used to solve the problem.

In reality, the phase noise of the APEX laser oscillator is much worse than the gun RF phase noise. Before the AC installation, an in-loop timing jitter of ~3 ps has been measured for the homemade laser with the FPGA based LLRF board, and the big timing jitter was attributed to a bad design of the oscillator piezo mount stage. Its transfer function was measured with a piezo actuator step excitation, as shown in Fig. 3, which reveals a lot of dominating mechanical resonance peaks in the mounting stage. To avoid feedback instabilities, the feedback gain coefficients have to be kept low which limit the feedback effectiveness.

Copyright © 2014 CC-BY-3.0 and by the respective authors

ISBN 978-3-95450-141-0

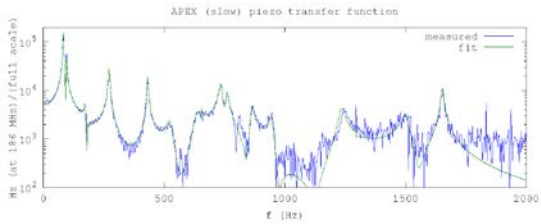


Figure 3: Transfer function of APEX old laser oscillator slow piezo.

After the AC enclosure was installed, the old laser oscillator was relocated and showed much worse phase noise. Signal Source Analyzer is used to measure the absolute phase noise, and a homemade mixer based analog phase detector combined with the FFT analyzer is used to measure relative phase noise between the 5th harmonic of laser signal and LLRF ~186 MHz drive signal. Both SSA and phase detector show a laser timing jitter of ~60 ps from 10 Hz to 100 kHz, and ~6 ps from 1 kHz to 100 kHz, see Fig.4 (a). Similar peaks show up in the laser phase noise spectra as in the laser slow piezo transfer function, such as 82.5 Hz, 92.5 Hz, 420 Hz and so on. The reason why the old laser phase noise is getting much worse after relocation both at the low frequency end and high frequency end is still not well understood.

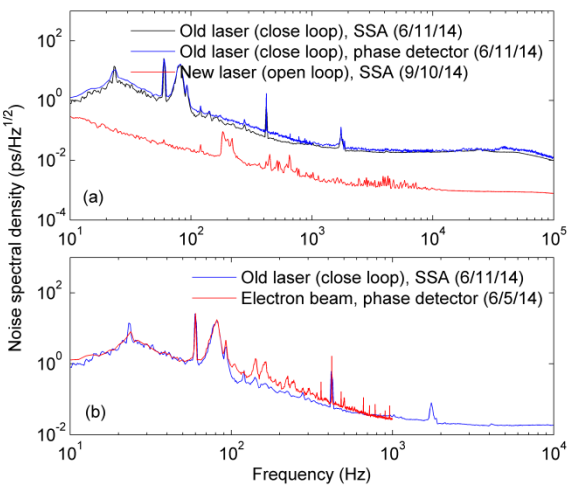


Figure 4: Noise spectral density of (a) APEX laser timing and (b) electron bunch arrival timing.

The new CALMAR fiber laser was installed and is now under test. A new piezo voltage amplifier is being purchased in order to measure its transfer function and lock the new laser to the LLRF reference. The absolute phase noise of the new laser in open loop is measured by SSA, and is already much better than the old laser, as shown in Fig. 4 (a). Integrated timing jitter between 10 Hz and 1 kHz is 0.9 ps, which is expected to be taken care of after phase locking, and timing jitter between 1 kHz and 1 MHz is ~0.44 ps, which is distributed, and becomes the limitation to achieve the 25 *f*s jitter at APEX injector exit. Work is still ongoing to understand this high frequency noise.

ELECTRON BEAM STABILITY

With the homemade phase detector, the 190th harmonic of the APEX BPM (at gun exit) sum signal mixed with the ~186 MHz LLRF drive is used to measure the bunch charge jitter when two signals are in phase, and arrival timing jitter when in quadrature. The main issue with the measurement is that the band-passed BPM signal is relatively low even with the 0.3 mA average beam current, and its signal to noise ratio (SNR) is ~60 dB when considering only thermal noise in the 100 kHz BW, which limits amplitude and timing jitter resolution to be ~0.1% and ~0.9 ps. This resolution is enough to characterize the current electron beam jitter, but becomes difficult for beam arrival jitter when new laser is used.

Fig. 2 (b) and Fig. 4 (b) show preliminary electron beam jitter when running with the old laser system. The beam arrival jitter at the BPM location is ~55 ps between 10 Hz and 1 kHz, whose noise spectra follow exactly the laser phase noise. With the new laser on line, the beam arrival jitter is expected to reduce below ps at gun exit.

The beam charge jitter is surprisingly smaller than the UV energy jitter (Fig. 2 (b)), and their noise spectrum shapes look very different. The charge noise spectrum shows a pronounced peak at 24 Hz which is not seen in the laser energy curve, but a feature of the beam arrival jitter and laser timing jitter curve (see Fig. 4). Based on that peak, it's evaluated that the BPM signal and the LO signal at the mixer are not exactly in phase when measuring charge jitter, but are ~4 degrees off, so part of the phase noise is coupled into the charge jitter curve, which means the real charge jitter could be even smaller than 0.66% between 1 Hz and 100 kHz. One possibility is that 300 pC photoemission is already at the space charge saturation region with current laser beam size, so that charge jitter is not sensitive to laser energy jitter, which is to be tested by measuring the QE curve near 300 pC.

CONCLUSION

Various feedbacks and tools have been developed to measure and improve APEX photoinjector stability. Preliminary efforts on gun RF stability have shown one order of magnitude improvement, and new commercial laser and related feedbacks are under commissioning to further reduce the electron beam jitter.

REFERENCES

[1] F. Sannibale et al., Phys. Rev. ST Accel. Beams 15 (2012) 103501.
[2] J. Byrd, TUOANO01, FEL'13.
[3] T. Raubenheimer, "LCLS-II SCRF Injector System Physics Requirement Document" (2014).
[4] G. Huang et al., Proceedings of IPAC'12, page 3488.
[5] J. Feng et al., Proceedings of IPAC'12, page 2537.
[6] F. Sannibale et al., Proceedings of NAPAC'13, page 709.
[7] D. Filippetto et al., Proceedings of FEL'13, page 255.
[8] F. Sannibale et al., Proceedings of IPAC'14, page 727.
[9] F. Loehl et al., Proceedings of IPAC'11, page 523.

Copyright © 2014 CC-BY-3.0 and by the respective authors

DEVELOPMENT OF A HIGH SPEED BEAM POSITION AND PHASE MONITORING SYSTEM FOR THE LANSCE LINAC*

H. Watkins#, J.D. Gilpatrick, R. McCrady, LANL, Los Alamos, NM 87544, USA

Abstract

The Los Alamos Neutron Science Center (LANSCE) is currently developing beam position and phase measurements (BPPMs) as part of the LANSCE risk mitigation project. BPPM sensors have been installed in the 805-MHz linac and development of the monitoring electronics is near completion. The system utilizes a high speed digitizer coupled with a field programmable gate array (FPGA) mounted in a VPX chassis to measure position, phase and bunched-beam current of a variety of beam structures. These systems will be deployed throughout the LANSCE facility. Details of the hardware selection and performance of the system for different timing structures are presented.

INTRODUCTION

Development efforts at LANSCE over the last year have been focused on creating a new electronics system to measure the beam position, bunched-beam current and phase of particles for the variety of time structures and species accelerated in the LANSCE 805-MHz side coupled linac. This system will replace the legacy ΔT system used during accelerator tune-up and also provide valuable transverse beam information during beam production which is not currently monitored.

ARCHITECTURE

The design of the system requires capturing signals from 4-electrodes of a beam position and phase monitor (BPPM) along with the accelerator reference signal. The signals are then conditioned to 201.25MHz RF waves. The five signals are then digitized and analyzed by a digital signal processor (DSP) to convert waveforms to position, phase and bunched-beam current. Processed data is provided to the end user through channel access managed by EPICS. [1] The system architecture is shown in Figure 1.

A high speed digitizer was selected to capture data at a 4-nanosecond time increments in order analyze beam position and phase variations that occur throughout the 1 millisecond pulse cycle. A field programmable gate array (FPGA) is being used for the DSP to analyze these signals in different timing modes such as long pulse (50 µsec), short pulse (150 nsec), and single shot (1 nsec).

A soft core processor, which resides in FPGA fabric, is used to store the results to the EPICS database for use by beam operators and other users.

Timing for synchronous measurements between BPPMs and beam specific information is provided by an event receiver connected to the master timer via optical links. The BPPM results are then stamped with the timing and beam species information prior to submission to the EPICS database. A real time operating system is used to collect data and match it with the correct timing information for each cycle of the beam.

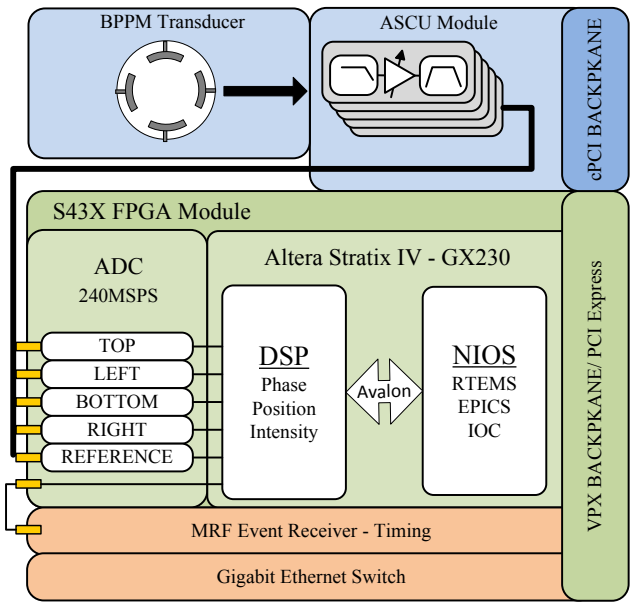


Figure 1: BPPM architecture.

REQUIREMENTS

The requirements for the BPPM system were broken up into two main regimes. The first regime is phase requirements that translate to time of flight (ToF) and energy measurements. These measurements are used to determine the phase set points for the acceleration modules. The second regime is position measurements that determine the transverse location of the beam centroid [2, 3].

*Work supported by the U.S. Department of Energy, Contract No. DE-AC52 06NA25396

hwatkins@lanl.gov

Copyright © 2014 CC-BY-3.0 and by the respective authors

ISBN 978-3-95450-141-0

Phase Requirements

Phase requirements were driven by the existing system which provides good measurements but many of its components have reached end of life. The original specification for this system required a ToF accuracy of 13.8psec which is approximately 1 degree at 200-MHz [3].

In addition the system must be capable of taking simultaneous measurements between two sensors to support tuning and provide results at 120-Hz operation.

Position Requirements

Position requirements did not have a legacy specification but were driven by experience with other BPM's at LANSCE such as the proton storage ring. Requirements were set based on what would be useful to users tracking problems with other systems, beam optimization and analyzing variation in positions over small time increments. Table 1 below details the requirements for signal levels, precision, accuracy, averaging and range.

Table 1: BPPM Requirements [4]

	Long Pulse	Short Pulse	Single Pulse
Minimum Charge	5 pC (1 mA peak)	5 pC	30 pC
Maximum Charge	100 pC (20 mA peak)	100 pC	150 pC
Phase Precision	0.25 deg	1.0 deg	n/a
Phase Accuracy	1.0 deg	2.0 deg	n/a
Averaging Window	50 us	150 ns @ 2.8 MHz	n/a
De-bunch Range	18 dB	n/a	n/a
Position Precision	0.1 mm	0.1 mm	
Position Accuracy	1.0 mm	1.0 mm	2.0 mm
Transducer Radius	50% (13 mm)	50%	
Phase Resolution	1 µdeg	1 µdeg	n/a
Position Resolution	1 µm	1 µm	1 µm

These requirements set the overall dynamic range listed in Table 2.

Table 2: Dynamic Range Budget

Charge range	26 dB
De-bunch range	18 dB
Max Current, position range	4 dB
Noise Floor Margin	10 dB
Total Dynamic Range	**58 dB**

In addition to these requirements some additional features were requested and will be supported by the new system.

- In-situ calibration of path losses
- Single pulse measurement capability
- EPICS timed and flavoured data
- Provide data to multiple clients

DEVELOPMENT

Analog-to-Digital Converter

The dynamic range requirement set the ADC performance specification for a minimum effective number of bits (ENOB) at 10-bits. This led to the choice of using the TI ADS62P49 analog-to-digital converter since it met both the ENOB requirements and the high speed sampling requirement. This 8-channel digitizer was available as an off the shelf part from 4DSP in a FPGA mezzanine carrier (FMC) form factor [5], allowing it to be interfaced to an Altera Stratix IV FPGA carrier [6].

Figure 2 shows how these two boards become a single module that is placed in a VPX chassis. This module is the main payload card for the design. It does all the digitizing, DSP analysis, system configuration, software execution and EPICS control.

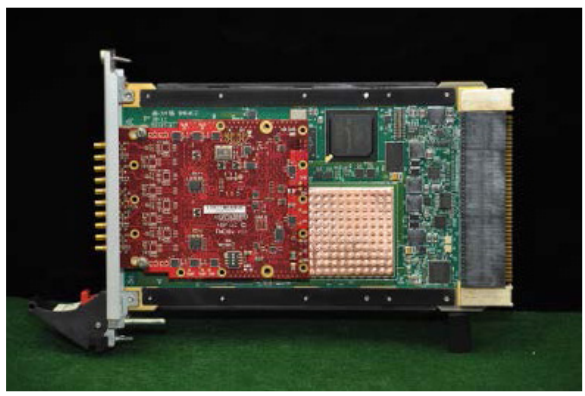


Figure 2: FPGA carrier with ADC mezzanine card.

Analog Conditioning

An analog-signal conditioning unit (ASCU) was developed in house to condition the BPPM's beam doublet signals to fall within the amplitude and frequency range of the ADC inputs. The ADC's full scale range is 2 Vp-p or +10 dBm. Typical BPPM signals for 1mA peak beam are -40 dBm with maximum signal at 20mA peak reaching -10 dBm. To optimize the headroom of the ADC the ASCU not only filters the beam doublets to pass 201.25-MHz but increases gain by 20-dB to take full advantage of the ADC's range.

Digital Signal Processing

The main effort has been in developing and testing the DSP algorithm. This is an under-sampling architecture where the sampling bandwidth is high enough to show

Copyright © 2014 CC-BY-3.0 and by the respective authors

modulation effects of the 201.25-MHz signals but analysis is performed in the FPGA on the aliased signal at 38.75-MHz. The reference signal is sampled and then split into its in-phase and quadrature-phase (IQ) components. This is then used to convert the electrode signals to separate IQ signals. These IQ components can then be used to calculate phase and amplitude for each electrode. Phases are then averaged for all four electrodes and amplitudes are used in a look up table that interpolates the position based on amplitude maps of the sensor.

Timing

The timing network triggers synchronous measurements of BPPM systems. Distributing this timing to all BPPM's allows for a single beam pulse to be measured as its travels down the linac. These timing cards are manufactured by Micro-Research Finland. This system is able to pass triggering information every 10 nanoseconds and provide timestamp and beam species information over the optical link.

Network

The network link is passed from the network switch in the chassis over PCI express to the other payload slots in the VPX chassis. This allows an EPICS IOC running on the FPGA's soft-core processor to communicate over the LANSCE network.

Figure 3 shows the four cards that make up the full system architecture.



Figure 3: ASCU, FPGA, timing and network cards.

TESTING

Testing was done to measure both the position and phase performance of the system. Phase performance testing used a 5-channel phase locked synthesizer to provide simulated beam signals from each electrode and a reference signal. All five channels were phase aligned and calibrated prior to testing.

Position was measured on a wire map system, used previously to characterize BPPM probes. This wire map system has laser micrometers for alignment and the positional error is less than 5 microns. This system simulates beam by exciting a wire with RF energy at 201.25-MHz. A 3-axis table then moves the wire through a mapped sequence inside the clear aperture of the probe.

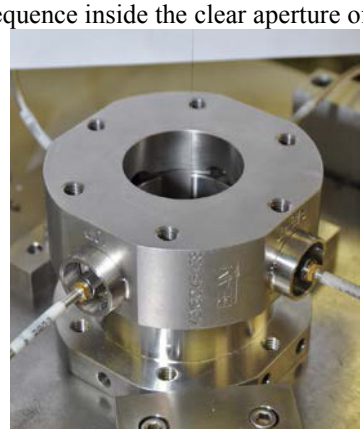


Figure 4: BPPM mounted to wire map table.

Initial testing of the DSP algorithm showed an oscillation in position and phase accuracy across a 360 degree phase sweep. Two problems were causing this oscillation. It was shown in Matlab simulations that an oscillation of the position could occur given a DC offset on the reference signal [7]. This first problem was fixed by turning on the DC cancellation mode of the ADC and using an extra sample in the quadrature calculation.

The second problem found was isolation in the ADC card between channels. The reference signal comes in at a high level and the ADC channels adjacent to the reference were picking up interference. The reference signal was moved to a separate ADC chip with a spare channel spaced in between. This solution provided enough isolation to remove any oscillations in position and phase.

PERFORMANCE

Phase

Results of accuracy, precision and linearity are given below for a 50-dB signal level sweep in power and 360-degree phase sweep.

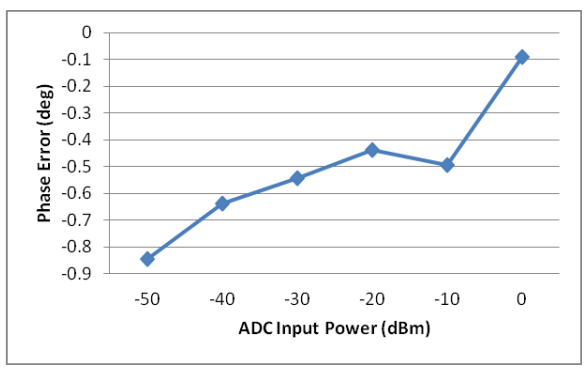


Figure 5: Phase accuracy (< 1.0 deg).

Copyright © 2014 CC-BY-3.0 and by the respective authors

ISBN 978-3-95450-141-0

Results in Figure 5 show the phase accuracy requirement of 1 degree is able to be met down to -50 dBm referenced to the ADC input for long pulse mode.

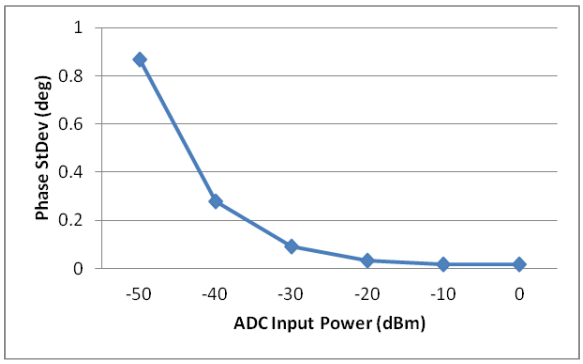


Figure 6: Phase precision (< 0.25 deg).

Phase precision graph in Figure 6 shows that the requirement of 0.25 degrees can be met down to -40 dBm. Typical electrode power for tuning is -35 dBm at the input of the ASCU. If the ASCU is set to 15dB of gain the system can meet the precision specification.

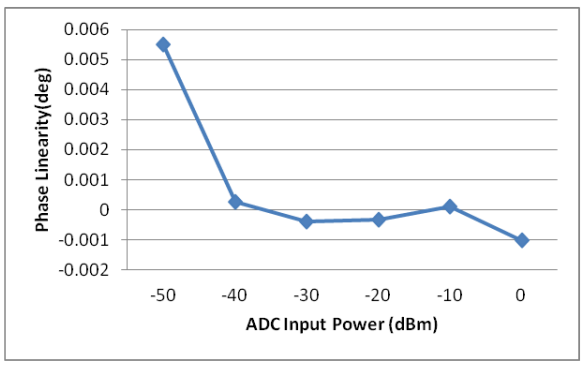


Figure 7: Phase linearity vs ADC input power.

Phase linearity did not have a specific requirement but is shown in Figure 7 to demonstrate how well the algorithm responds to increments in phase. The delta T procedure ultimately uses the relative difference in phase when the tank acceleration is on and off to determine the correct phase set point.

Position

Results for position accuracy and precision are displayed below. Position results were taken in a 13mm radius map in 1mm steps. Power levels for this test were taken at -25 dBm at probe center from each electrode. This level is about 10-dB lower than what would be expected for long pulse tuning beam in the accelerator.

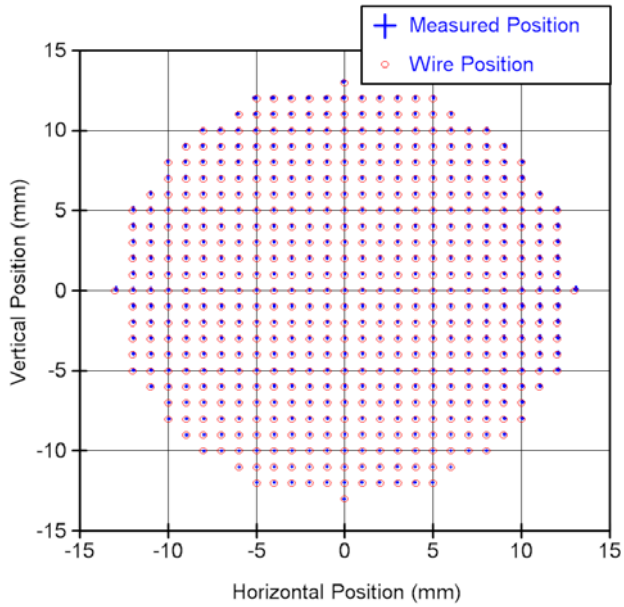


Figure 8: Wire position vs. measured position.

Figure 8 shows measurements on an actual BPPM sensor where the red circles are the commanded position of a thin tungsten wire. The blue + sign's center is the measured position by the BPPM electronics, with error bars showing the standard deviation. The precision is difficult to recognize in the plot since it is so small in comparison to the incremental step of 1-mm. Results are well within specifications for up to a 50% radius of the BPPM.

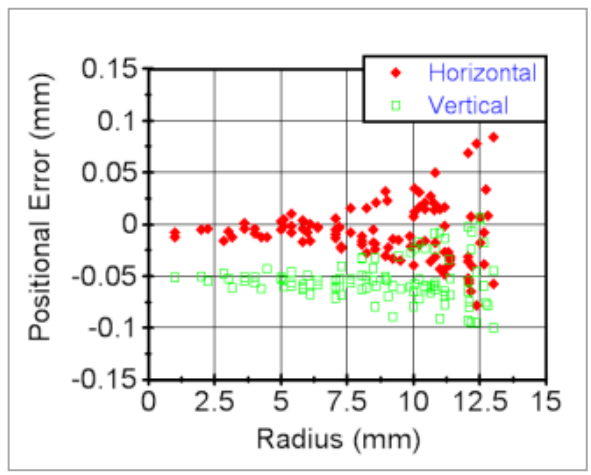


Figure 9: Position accuracy (< 1mm).

The positional error graph in Figure 9 shows that accuracy and precision of the system degrades as beam centroid approaches the outer radius of the aperture. This is expected given that the electrode power opposite the position change is being reduced in power level and is more susceptible to noise.

Copyright © 2014 CC-BY-3.0 and by the respective authors

ISBN 978-3-95450-141-0

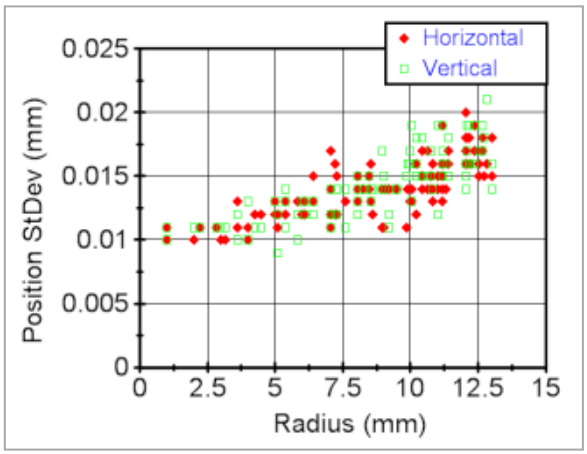


Figure 10: Position precision (< 0.1mm).

The position precision graph in Figure 10 shows that 0.1-mm of precision is achievable. Precision decreases slightly as beam approaches the outer limit of the aperture. Precision also degrades as the input level to the ADC is reduced. Figure 11 shows that the 0.1-mm precision requirement can be met as long as signal levels stay above -40 dBm. To achieve lower levels of sensitivity the gain of the ASCU will be increased.

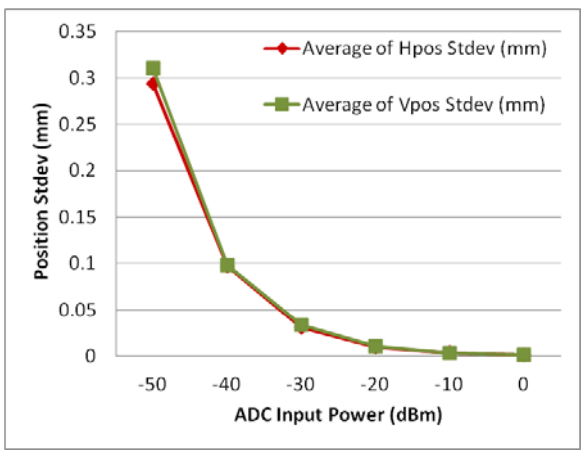


Figure 11: Position precision vs. ADC input.

These results were all taken with 30-µsecond averaging where the DSP is analyzing results every 1 µs. Accuracy and precision may show a slight improvement once the averaging is increased to 50 µs and the ASCU unit is placed in front of the ADC. These results are based on the long pulse mode of the DSP. The short pulse and single pulse modes need to be fully characterized along with actual beam measurements.

SOFTWARE INTEGRATION

The remaining steps to get this system deployed and data provided to the accelerator operators is the software components. There are two main areas that need to be integrated. The NIOS II soft-core processor must be instantiated in the FPGA design with the DSP code. Once the NIOS is able to collect data from the DSP and stamp it with timing information it is ready for upload to the EPICS database. This will allow multiple clients to subscribe to BPPM data for the variety of beam species and timing flavours that exist at LANSCE.

CONCLUSION

A high-speed beam position and phase monitoring system has been developed at LANSCE that meets all the intended requirements. There is still some work left to complete final deployment to the beam line that should be completed in early FY15. In all, approximately 40 systems will be deployed along the LANSCE SCL with proposals of extending this system to LANSCE's isotope production facility and proton storage ring.

REFERENCES

[1] R. McCrady, H. Watkins. "BPPM Design Review" Presentation, September 2013.
[2] J.D. Gilpatrick "Proposed beam position and phase measurements for the LANSCE LINAC" DIPAC, Venice, 2007, TUPB10, p. 78 (2004).
[3] I. H. Campbell, "LAMPF DELTA-T Hardware Review".
[4] R. McCrady. "Requirements for measurements of beam position and phase in the LANSCE risk mitigation project" Personal Email, September 2013.
[5] 4DSP, "FMC108 high pin count FMC ADC, 8-channel 14-bit ADC – 250MSPS" FMC108 datasheet, www.4dsp.com.
[6] Bittware, "S4-3U-VPX Commercial & Rugged Altera Stratix IV GX 3U VPX Board with Optional VITA 57 FMC for I/O" S43X datasheet, May 2014.
[7] Matlab R2012b. Mathworks Inc, Massachusetts, USA, 2012.

Copyright © 2014 CC-BY-3.0 and by the respective authors

ISBN 978-3-95450-141-0

FRONT END CONCEPT FOR A WAKE FIELD MONITOR

M. Dehler, M. Leich, S. Hunziker, PSI, Villigen PSI, Switzerland

Abstract

Wake field monitors (WFMs) are used to directly measure the alignment between beam and RF accelerating structure via the transverse higher mode spectrum. As a sub task of the EuCARD^2 project, we are developing a front end for the monitors of the multipurpose X band structure installed at the SwissFEL Injector Test facility (SITF) at PSI. We plan to use electro optical technology offering strong advantages in the robustness to interference and radiation, and in the ease of signal transport. We present the concept of the device, discuss the theoretical performance in terms of noise. For a proof of principle, we built a basic system, which we tested together with the existing monitors with beam at SITF.

INTRODUCTION

Inside RF accelerating structures, the level of transverse wake fields responsible for emittance dilution is determined by the alignment between structure and beam. Wake field monitors (WFMs) are devices for the direct measurement of this effect by coupling to the transverse higher order modes (HOM) excited by the offset beam. This is specially of interest for X band structures used in low to medium energy accelerators like free electron lasers, where the beam degradation due to transverse single bunch wake fields is a much bigger concern.

For structure with HOM damping like those developed for the CLIC project, suitable signals can be extracted from the HOM couplers. More classical structures, like the multipurpose X band structures [1,2] developed in a collaboration between PSI, CERN and Sincrotrone Trieste, use special pickup geometries to couple to the internal wake fields inside the structure.

As part of the EuCARD^2 project [3]), we are in the process of developing front ends for these class of devices, to be used for the existing wake field monitors installed in SITF at PSI [4] and FERMI at Sincrotrone Trieste. Given the relatively high frequency and large bandwidth and the need to operate the front end in a radiation environment, we decided not to use a classical RF front end, but to use an electro-optical approach, which promises the following advantages:

- Technology already used in space communications, so there is considerable experience concerning the radiation hardness of the device.
- Use of optical fibers vs. hollow wave guides in classical RF, which are cheaper, more flexible to put, have much larger bandwidths, are ideal to carry signal over long distances and have virtually no problem with electromagnetic interference.
- Only minor amount of hardware exposed to the radiation in the tunnel, essentially only an optical modulator and a microwave limiter near the structure.
- Off the shelf components available for bandwidths up to 40 GHz (practically tested even up to 1.5 THz)
- Possible secondary applications for break down monitors, wide band wall current pickups etc.

Measurement Principle

Wake field monitors are not isolated devices, but integrated parts of RF acceleration structures, whose transverse wake fields they are measuring. Fig. 1 shows the inner volume of such a structure, which we are using as a signal source for the front end.

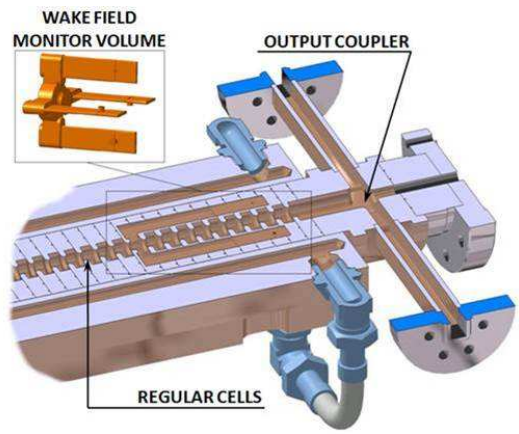


Figure 1: Wake field monitor inside a cutoff accelerating structure.

It is a 72 cell traveling wave structure working at the European X Band frequency of 11.9985 GHz. Its design employs a large iris, $5\pi/6$ phase advance geometry, which minimizes transverse wake field effects while still retaining a good efficiency. Its function in the FEL projects at PSI and Sincrotrone Trieste is actually not to accelerate the beam, but to compensate nonlinearities in the longitudinal phase space of the beam caused by prior acceleration stages [5].

One of the characteristics of its constant gradient structure design is the smooth variation of the cell dimensions along the structure, which compensates for internal losses and keeps the gradient of the fundamental mode constant. This leads to a spread of the synchronous frequency of the position dependent dipole modes over the 15-16 GHz region. Upstream, an offset beam will excite lower dipole mode frequencies than downstream. Also, the modes will not extend throughout the structure, but will be confined. To capture as much information as possible, two sets of monitors are used, one in the middle coupling to dipole modes in the upstream

Copyright © 2014 CC-BY-3.0 and by the respective authors

ISBN 978-3-95450-141-0

half of the structure and a second towards the downstream end for the other part. The fundamental limit for the monitor resolution is given by the precision of the internal alignment between individual cells [1]. We expect values below 10 μm.

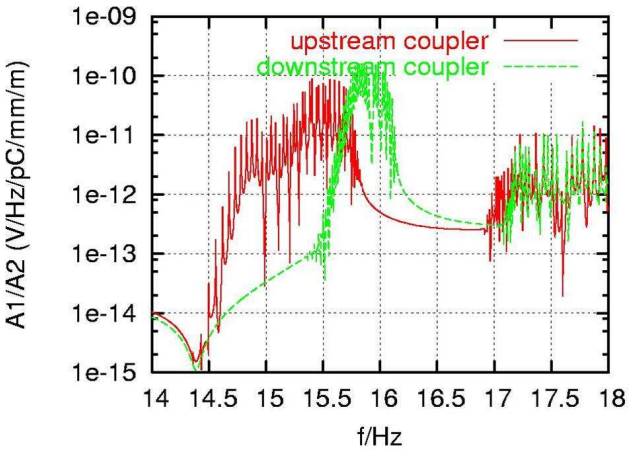


Figure 2: Theoretical WFM signal spectrum.

As the signals of interests are in the sub-milliwatt range, while the fundamental mode is powered with tens of megawatts, an important criterion in the design of the WFM is to eliminate any coupling of the fundamental mode into the monitor output. Furthermore we would like to see a purely position dependent signal, meaning that there should be no trace of higher order longitudinal modes. This was achieved by the coupling geometry shown in Fig. 1. A hollow waveguide is coupled to the coupling cavity so, that it rejects any longitudinal modes by symmetry. The chosen cutoff frequency further attenuates any trace of the fundamental 12 GHz before transitioning into a coaxial feed-through. The calculated spectra of the upstream and downstream WFMs are shown in Fig. 2.

For the signal levels, we measured peak amplitudes of 10 V/nC/mm [6], which, taking into account signal distortions and reflection in the measurement setup, correspond relatively well with the value of 6 V/nC/mm of the equivalent circuit model (which omits high order dipole bands) and 4 V/nC/mm obtained with a full model calculation using CST Microwave Studio [7].

A WFM is comparable to a classical cavity BPM in that respect, that we have position dependent signals, but there is an important difference. The WFM signal is directly proportional to the wakes and so to the degradation of the beam. The golden orbit with respect to the structure is given by minimizing the WFM readings, whereas a BPM needs a secondary procedure like e.g. beam based alignment to get a reference position. The WFM acts also as a self diagnostic tool for the accelerating structure: if amplitudes stay elevated at the minimum, problems with the internal alignment (bends, kinks and randomly displaced resonators) are probably the reason.

FRONT END CONCEPT

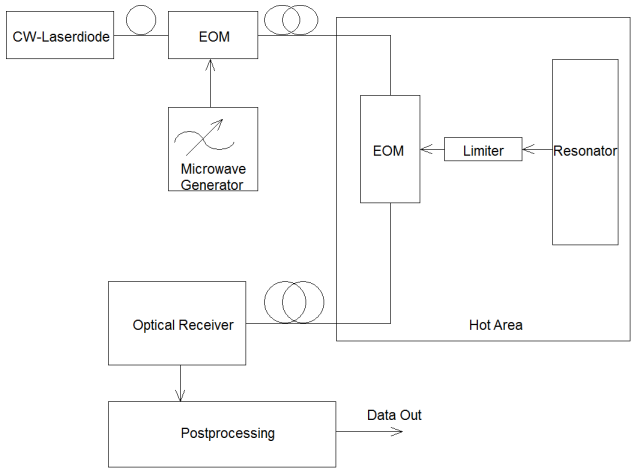


Figure 3: Layout of electro optical front end.

Basically, the front end is a down converter based on optical components as shown in Fig. 3. We have an optical source consisting of a very low noise laser diode, whose output is intensity modulated with a CW local oscillator signal of 12-15 GHz using a first electro-optical modulator (EOM). This is followed by a second modulator fed with the WFM signal. The resultant optical signal is converted back to an electronic output by a photo diode, where only the down converted part of the spectrum is used for further post processing.

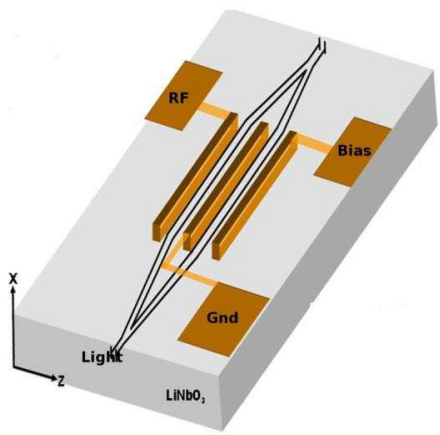


Figure 4: Electro optical modulator.

Fig. 4 shows the schematic layout of such an EOM. Essentially, it is a Mach Zehnder Interferometer: The incoming polarized light is split in two paths going through a Lithium Niobate crystal. Applied electrical fields change the phase delay of the light going through the signal, one path is modulated by the signal, the other by a DC bias and the recombination of both paths at the end of the modulator result in a phase to amplitude conversion of the signal. By a suitable choice of the DC bias, we can change the characteristics of the EOM from classical amplitude modulation to quadrature type [8].

Copyright © 2014 CC-BY-3.0 and by the respective authors

ISBN 978-3-95450-141-0

In practice, only the second modulator needs to be in the tunnel and be exposed to radiation. The supporting circuitry consists of an input filter, eliminating unwanted spectral information and a microwave limiter to protect the modulator from overload. The bias is supplied externally via a heavily shielded cable. All the other parts, laser diode, LO, photo diode and post processing electronics can be placed suitably outside the tunnel. The signal attenuation in an optical fiber is very small, so distances of several hundred meters pose no problem.

System Considerations

Comparing the efficiency of analog fiber optical transmission systems with the direct transmission of Rf via TEM-lines or waveguides, the noise behavior of optical transmission systems is one of the main distinctive features.

Main contributors to the overall noise in a optical system are the shot noise due to the detectable quantum nature of light and the relative intensity noise (RIN) of the laser source commonly used in these systems. Additionally, thermal noise has to be added like in direct transmission systems.

The effect of thermal noise, relatively minor here and not shown, usually is much stronger in RF based systems, since the transmission losses are very high also over comparably short distances affecting the signal to noise ratio (SNR).

A noise calculation for an analog optical transmission system with amplitude modulation including the effects of all the kinds of noise described above can be performed using [9–11], resulting in a SNR mainly depending on the optical power level.

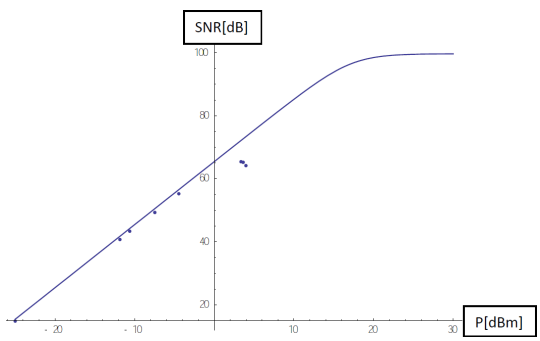


Figure 5: SNR versus optical drive power (modulation index 9.63%, bandwidth 20 kHz).

Calculated and measured SNR are shown in relation to the optical power level in the photo diode in Fig. 5. The measurements have been performed with a single modulator, the modulation index has been controlled by a measurement with an optical spectrum analyzer (m=0.0963). It was done using a R&S FSEK30 spectrum analyzer at a resolution bandwidth of 20kHz and a single mode fiber pigtailed photo diode. For a double modulation, as used in the front end, the effective modulation index, which is the product of the pre-modulation factor (with the LO) and the signal modulation, needs to be used.

For the photo diode used, saturation starts to degrade the SNR optical power levels in excess of 3 dBm. With the components presently in use, there is no sense in boosting the optical power at the diode to level higher than around -5dBm. Fig. 6 shows the relation between SNR and bandwidth.

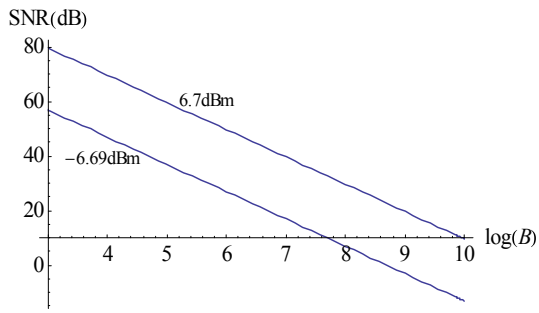


Figure 6: Theoretical S/N ratio versus bandwidth for two different optical drive powers.

Components

An important feature of the proposed front end architecture is the robustness to radiation damage, which means essentially the robustness of the electro optical modulator to this effect.

In standard semiconductors, the main effect consists in a slow destruction of the PN junction in the doped semiconductor by the radiation leading to an ever larger leakage current crossing the barrier. In an electro optical modulator, we donâĂŹt have any transition of this type. Exposing the Lithium Niobate in the EOM to radiation will lead to an ever larger number of defects in the crystal structure of the material. The optical beam carrying the signal will get scattered at these defects and become attenuated. The modulator gets blind and its optical return loss worsens.

For our system, we chose the Photline modulator type MX-LN-2, which, in order to validate its suitability for space application, was tested by the manufacturer among other things for its radiation hardness [12]. The modulators were exposed to 60 MeV protons with a dose density of $10^{11} p/cm^{\hat{A}}$š and γ rays from Co^{60} source with a dose rate of 36 rad/h, the total integrated dose was 10 krad. The samples were successfully tested at various temperatures with respect to their optical return loss, which was supposed to stay above 38 dB.

For the CW laser source, we use the 1772 high power laser diode provided by Emcore. Its special feature is a very low relative intensity noise (RIN) of -163dB/Hz at a output power level of 17dBm.

As a photo receiver a photo diode from Albis Optoelectronics of the type PQW18A with a responsitivity of 0.87A/W was used. It is pigtailed with a single mode optical fiber. We used a version, where the RF signal output is shunted with 50 Ohms. The bias is supplied via a RC-low pass circuit.

Copyright © 2014 CC-BY-3.0 and by the respective authors

Electronic Post-processing

At the output of the photo diode, we plan to have three different signals paths to allow specialized measurements:

As an operator signal, we need to measure the power of the complete signal. Required is a high sensitivity for low signal levels giving a high precision for the structure alignment in combination with a large dynamic range. A logarithmic detector offers the right approach to this problem. To that end, we are currently evaluating the type HMC602LP from Hittite, which seems to be a suitable choice with a bandwidth of 8 GHz, a RF threshold level (detection limit) of -65 dBm and a dynamic range of 72 dB. One of the beam tests shown later was performed using this device.

The measurement of internal misalignments of the structure needs a detector with a high sensitivity, while not requiring such a high dynamic range, since the structure itself should be well aligned for this type of measurement. We plan to look at scan the spectrum (corresponding to the scan for local offsets inside the structure), by having a varying LO frequency in combination with a fixed band pass filter after the photo diode. Their level and envelope will be measured by tunnel diode detectors. We are planning to use a component with built-in low noise preamplifier from Herotek (DTA1-1880A), which offers a detection threshold of -80 dBm with a high sensitivity of 1V/μW. Devices for test and evaluation are now in house and under evaluation.

At last, there is still need for an expert type signal, basically the raw output signal of the photo diode with some minimum filtering and amplification.

BEAM TESTS

A validation of the raw WFM signals was already done and is described in [6]. We built a proof of principle system containing the electro-optical system as shown in Fig. 3, which allows to measure one WFM channel. After testing it in the lab with sinusoidal signals, we connected it to the WFM pickup of the X band structure installed in SITF. The LO frequency used was 15 GHz. The accelerating structure containing the wake field monitors sits on movers, which allow to shift and tilt the structure with respect to the beam. All measurements were done with a LeCroy SDA816zi digital scope, featuring 18 GHz bandwidth and 40 GS/s sample rate, which allowed also to record the raw signals from the structure.

Fig. 7 compares the output of the raw RF signals from the WFM with the signal of the electro-optical front end, where the signals were scaled to the same sensitivity. Both measurements are strongly dominated by the digitization noise of the scope. Nonetheless the EOM signal (out of the photo diode) shows a more pronounced minimum, corresponding to a resolution of 20 μm at the measured bunch charge of 140 pC to be compared to a value of 37 μm for the raw signal.

Using the logarithmic detectors described above improves the situation still more, since we do a detection of the signal envelope giving an output signal with a strongly reduced

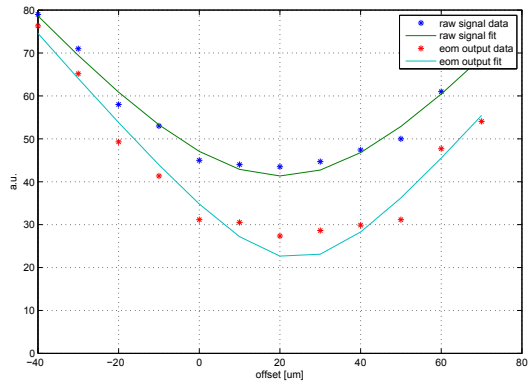


Figure 7: Comparison of raw signal output versus photo diode signal as a function of beam offset inside structure.

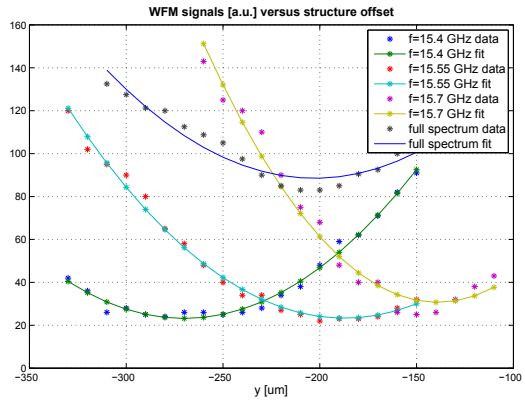


Figure 8: Spectral scan showing structure tilt, the curve with the full spectrum gives the average offset, while the filtered data shows the offset of different segment (15.4 GHz upstream end, 15.55 GHz near cell 18, 15.7 GHz in the middle of the structure.

bandwidth of 10 MHz. These were used for a rather interesting experiment, whose results are shown in Fig. 8. Here the structure was tilted with respect to the beam. For the upstream monitor, which receives wake field signals from the first half of the structure, it means, that regardless of the offset, while the structure may be centered e.g. in the middle, there are always parts of the structure at an offset generating wake field signals. This means for the full signal, that we see a relatively flat minimum as we move the beam versus the structure.

But now, the frequencies of the excited spectrum are correlated with the position along the structure (described in more detail e.g. in [1]. If we filter out parts of the spectrum, we should be able to see the offsets of individual segments inside the structure. This was done here, a band pass with 100 MHz bandwidth was inserted between photo diode and logarithmic detector. We measured at three frequencies, 15.4 GHz (corresponding to the upstream end), 15.55 GHz (moving in by a quarter) and 15.7 GHz (roughly in the middle of the structure). The corresponding curves show minima

Copyright © 2014 CC-BY-3.0 and by the respective authors

ISBN 978-3-95450-141-0

at offsets of -270, -190 and -140 μm, which is a perfect illustration of this effect.

The filter bandwidth used here is still relatively wide. We are in the process of ordering narrow band filters with a bandwidth of 10 MHz (corresponding to the bandwidth excited by an individual resonator inside the structure). In combination with the high sensitivity tunnel diode detectors described above, we hope to obtain a far better resolution of this type of measurement, possibly enabling us to see the internal cell to cell alignment of the accelerating structure.

SUMMARY AND OUTLOOK

Wake field monitors couple directly to the transverse wake field inside RF accelerating structures and are excellent device to measure structure alignment to the beam. We describe a concept for the front end for their wide bandwidth signals in the 15 GHz range.

For the architecture, we follow an electro-optical approach, where signal down conversion and transport is done in the optical domain. This offers significant advantages in terms of radiation hardness of the required components. Also, the signal transport happens over relatively cheap optical fibers with minimum attenuation and signal distortion even over longer distances. When looking at the signal to noise behavior, the most important criterion is to have a sufficient optical drive power to stay out of the region, where photon shot noise becomes visible.

For a proof of principle, we built a simplified system for one signal channel, which was subsequently tested with beam. Using just the internal scope functionality, we obtained already a resolution of 20μm at a bunch charge of 140pC. Scaling this to the nominal SwissFEL bunch charge of 200 pC, this gives us already 14 μm. We did also first tests using a wide band logarithmic detector to post process the electronic output from the photo diode. With this setup, we were able to do first tests of advanced measurement options – we were able to clearly distinguish offsets of individual segments inside the accelerating structure.

Next steps are the evaluation of high sensitivity tunnel diode detectors, which we plan to use to measure internal structure misalignment. Also, we have equipment on order for the digital control and readout, which we need to make the scans for frequencies and offset really functional.

ACKNOWLEDGMENTS

The research leading to these results has received funding from the European Commission under the FP7 Research Infrastructures project EuCARD^2, grant agreement no.312453.

The authors would like to thank Masamitsu Aiba, Thomas Schietinger and Simona Bettoni for their support with the beam measurements, whose results were shown here.

REFERENCES

[1] M. Dehler et al., "*X*-Band RF Structure with Integrated Alignment Monitors", Phys. Rev. ST Accel. Beams 12, 062001 (2009)

[2] M. Dehler et al., "A Multi Purpose X Band accelerating structure", IPAC 2012, New Orleans, USA, MOOBC003 p. 70 (2012)

[3] http://eucard2.web.cern.ch/

[4] M. Pedrozzi (ed.), "250 MeV Injector Conceptual Design Report", PSI Report 10-05 (2010)

[5] G. D'Auria et al., "RF Activation and Preliminary Beam Tests of the X-Band Linearizer at the FERMI@ELETTRA FEL Project", IPAC 2012, New Orleans, USA, TUPPP054 p. 1721 (2012)

[6] M. Dehler et al., "Wakefield Monitors in a Multi Purpose X Band accelerating structure", IBIC 2013, Oxford, UK, WEBL3, p. 3771 (2014)

[7] http://www.cst.de/

[8] J.M. Senior, "Optical Fiber Communication Systems, Principles and Practice", Prentice Hall Int. (UK) Ltd, 3 ed., 2009.

[9] H. Al-Raweshidi and S. Komaki (eds.), "Radio over fiber technologies for mobile communications networks", Artech House, Boston/London, 2002.

[10] C.H. Cox, "Analog optical links: theory and practice", Cambridge Univ. Press, Cambridge, 2004.

[11] Gao, Yu, "Nichtlineare Verzerrungen und Rauschstörungen in faseroptischen Uebertragungssystemen mit Subträgermultiplexierung", Diss. ETH Nr. 10814, Zürich, 1994.

[12] http://www.photline.com/product/view/37/

Copyright © 2014 CC-BY-3.0 and by the respective authors

BEAM-BASED CALIBRATION AND PERFORMANCE OPTIMIZATION OF CAVITY BPMS FOR SwissFEL, E-XFEL AND FLASH2*

B. Keil, G. Marinkovic, M. Stadler, Paul Scherrer Institute, Villigen, Switzerland
D. Lipka, DESY, Hamburg, Germany

Abstract

SwissFEL, the European XFEL (E-XFEL) and FLASH2 all use dual-resonator cavity beam position monitors (CBPMs) [1,2,3]. The CBPM electronics that is built by PSI has a larger number of calibration parameters that need to be determined in order to maximize the CBPM system performance. Beam measurements with the BPM electronics have been made in BPM test areas at the SwissFEL test injector and FLASH, as well as at FLASH2 where 17 E-XFEL type CBPMs have recently been installed in the undulator intersections. The CBPMs are pre-calibrated in the lab using an automated test and calibration system [4], and then the final calibration is done with beam. This report discusses beam-based methods to optimize the system performance by improving the pre-beam system calibration as well as the mechanical alignment of the BPM pickup position and angle.

PICKUPS

CBPM pickups with two resonators are the standard choice for measuring and stabilizing the beam orbit with highest resolution and lowest drift in the undulators of free electron lasers (FELs). The reference resonator measures the bunch charge, while the position resonator provides the product of bunch position and charge. The bunch position is thus obtained by normalizing position to reference resonator amplitude for the relevant monopole (reference) and dipole (position) modes, with a scaling factor that depends on the usually variable attenuation of the RF front-end (RFFE) input channels. All of the above mentioned FELs have CBPMs with cylindrical resonators and mode-selective couplers in the position resonator, where the frequencies of position and reference cavity modes are identical, thus minimizing the impact of frequency-dependent gain drift on the position readings.

Since the above mentioned FELs can also have several bunches with rather short bunch spacing (222ns for E-XFEL and FLASH, 28ns for SwissFEL), comparatively low loaded quality factors Q_L were chosen (see Table 1). This minimizes bunch-to-bunch crosstalk and keeps the effort and latency of the digital signal processing low, as required for the E-XFEL Intra Bunch Train Feedback (IBFB) [5]. Only in the SwissFEL undulators that have single bunches with 100Hz repetition rate, the CBPM pickups have a higher Q of ~1000 [6]. All E-XFEL CBPMs and the SwissFEL injector and linac CBPMs have stainless steel pickups with ~3.3GHz nominal frequency, which is safely below the cut-off frequency of the different beam pipe diameters. This allows using the same low-Q CBPM electronics for all machines [4,7]. In the following, the pickups will be named according to their beam pipe aperture, where e.g. CBPM16 is the 16mm aperture pickup of the SwissFEL linac.

Table 1: Overview of CBPM Pickups

	F [GHz]	Q_L	Aper-ture [mm]	Length [mm]
E-XFEL Transfer	3.300	70	40.5	255
E-XFEL/FLASH2 Undulators	3.300	70	10	100
SwissFEL Linac and Injector	3.284	40	38	255
	3.284	40	16	100
SwissFEL Undul.	4.855	1000	8	100

The E-XFEL CBPM10 and CBPM40 pickups developed by DESY have already been produced. First beam in the E-XFEL injector is expected spring 2015, first beam in the main linac end 2016. For the SwissFEL BPM pickups designed by PSI, the CBPM38 production is finished, while the CBPM16 pickups are ready for series production that will start shortly. Prototypes of the BPM8 pickup have recently been tested successfully with beam [6], where we have made a 3.3GHz stainless steel version with Q_L~200 and a 4.8GHz copper-steel hybrid version with Q_L~1000. Until recently the steel version had been the baseline since it is simpler and could have been operated with the standard 3.3GHz electronics with minor changes. However, after successful fabrication and test of the 4.8GHz pickup we made it the baseline version due to its higher expected resolution both at high charge (due to higher Q) and very low charge (due to higher sensitivity that improves with higher frequency). First beam in the SwissFEL injector is scheduled for end 2015, first main linac beam for end 2016.

Presently, three E-XFEL CBPM10 and three CBPM40 pickups are installed at the SwissFEL Injector Test Facility SITF at PSI, one more CBPM40 and three CBPM10 at FLASH1. At SITF, also one SwissFEL CBPM38, one CBPM16 and two CBPM8 (steel and copper version) are installed, see Figure 1. While these pickups are only intended for testing (with stripline and button BPMs used as "working horses" for normal machine operation), the recently installed 17 CBPM10 systems in the FLASH2 undulator intersections are needed for machine operation, but are also still part time

* This work has partially been funded by the Swiss State Secretariat for Education, Research and Innovation SERI.

Copyright © 2014 CC-BY-3.0 and by the respective authors

ISBN 978-3-95450-141-0

available for tests since FLASH2 is still in the commissioning phase and does not yet have users.

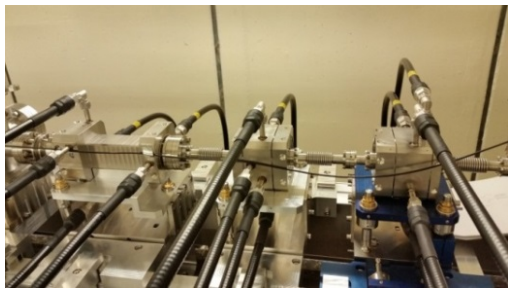


Figure 1: SwissFEL CBPM38 (left), CBPM8 with Q_L=1000 (middle) and CBPM8 with Q_L=200 (right).

The horizontal (X) and vertical (Y) position of two CBPM10 at SITF and all four CBPMs at FLASH1 can be adjusted within a range of > ±1mm via motorized 2D mover stages with sub-micron resolution encoders, while all other CBPM pickups at SITF and FLASH1 require manual X and Y position measurement and adjustment.

The pickup angles dX/dS, dY/dS and dY/dX (where S is the longitudinal coordinate) are also measured and adjusted manually for all pickups.

ELECTRONICS

The CBPM electronics for the E-XFEL, FLASH2 and SwissFEL low-Q pickups has an RFFE (see Figure 2) that mixes the 3.3GHz ringing signals of the pickup down to baseband. The bandpass and variable gain input stage of the RFFE reference and position input channels (that have a symmetric design) is followed by an IQ mixer and a lowpass/bandpass stage. The on-board local oscillator (LO) for the I/Q mixer is normally synchronized to an external bunch-synchronous reference clock, with an internal backup oscillator that automatically takes over when the external clock fails. The I and Q output signal pulses of the RFFE have some 10ns length and are sampled by high-speed 16-bit ADCs with differential inputs. The bunch-synchronous ADC clock is also generated by the RFFE. The ADC output signals are processed by an FPGA board that provides interfaces to control, timing, feedback and machine protection systems.

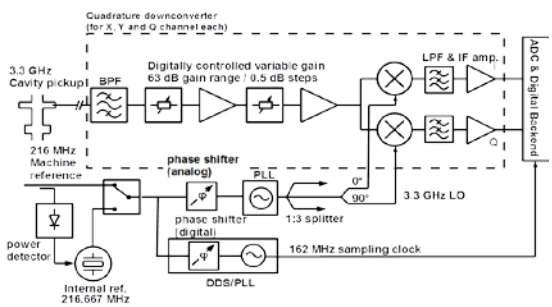


Figure 2: Simplified schematics of low-Q CBPM RFFE electronics, showing only one of its three input channels.

The FPGA board also controls various ADC and RFFE parameters (LO and ADC clock frequency and phase, temperature stabilization set points, ...) and stabilizes the IQ signal phases (via LO phase shifter) and ADC clock phase (via DDS-phase shifter) by FPGA-based digital feedback loops. An optional automatic range control (ARC) adapts the attenuators of the RFFE to varying input signal levels, thus minimizing ADC-related position and charge noise.

Recently, electronics for 17 CBPMs have been installed at FLASH2, a new soft X-ray undulator line at the DESY FLASH FEL facility. In addition, also the four FLASH1 CBPMs and all 3.3GHz CBPMs at SITF are equipped with the same electronics, except for the SwissFEL low-Q RFFEs at SITF where the output (IF) stage has been slightly modified (by soldering different filter components) in order to reduce the bunch-to-bunch crosstalk for the very short bunch spacing of 28ns.



Figure 3: Cavity BPM electronics for two BPMs. Two RFFEs (top) and the FPGA carrier board with ADC mezzanines (bottom) are inserted into a customized crate from the front side. Power supply module and boards with SFP+ transceivers etc. are plugged in from the rear side.

BEAM BASED CALIBRATION AND DIGITAL SIGNAL PROCESSING

The CBPM system has a number of parameters that need to be calibrated in order to obtain accurate data in physical units for beam position and charge. Our general strategy is to determine these parameters first with lab equipment as good as possible with reasonable effort, and then to make a more accurate beam-based calibration where needed. For the beam-based calibration, one can compare the BPM readings either with other monitors or encoders of motorized BPM pickup movers, or with other BPMs, utilizing the fact that the information provided by the BPM system is usually redundant, where the position and charge at the location of one BPM (or the derivative or other functions of these quantities) can be predicted using the other BPMs or monitors. This allows determining calibration parameters by tuning them such that the difference between prediction and measurement is minimized.

Absolute Position Calibration

In contrast to button or stripline BPMs, CBPMs have a larger uncertainty of the absolute scaling factors that convert signal amplitudes to millimeters. While the scaling factor for button and stripline BPMs can usually be determined entirely from the pickup geometry, the

Copyright © 2014 CC-BY-3.0 and by the respective authors

factor for the CBPM position depends on the overall gain and attenuation of the whole signal path, from pickup resonator via RF feedthrough and cables to RFFE and ADC. Any unknown loss on this path changes the scaling factor, thus it can usually just be pre-determined by lab measurement of BPM components with a limited accuracy in the order of typically ~10%, depending on system design, measurement tools and methods.

For the SwissFEL undulator CBPMs, the position scaling factors can be determined beam-based via motorized BPM pickup movers and encoders for all CBPMs. In the SwissFEL injector, linac and transfer lines, as well as in the whole E-XFEL, the CBPMs do not have motorized movers for cost reasons (except one CBPM10 in E-XFEL). The scaling factors for these BPMs will be determined using beam optics models and cross-comparisons with screens, wire scanner monitors, or other BPMs with motorized movers.

Absolute Charge Calibration

Both in E-XFEL and SwissFEL, the CBPMs will also be used as charge monitors, since they can measure relative charge variations with high resolution of typically 0.05% at higher bunch charges. The absolute calibration of the BPM charge scaling factor will be done by comparing the BPM readings with dedicated charge monitors that have a more accurate absolute calibration, e.g. toroids, where care must be taken that the beam loss between BPM and toroid during calibration is negligible.

Digital Signal Processing

Figure 4 shows show the algorithm that calculates beam position (X and Y) and charge (Q) from the ADC raw values. In order to achieve a desired overall IBFB feedback loop latency of ~1µs or less, the algorithm was implemented in VHDL on the BPM FPGA board. An FPGA-based feedback automatically tunes the ADC clock phase such that the RFFE output pulses always have one sample exactly at their top. This sample is then used to calculate the beam position and charge, using some samples before the pulse to perform baseline subtraction and thus eliminate any low-frequent noise. An optimal algorithm that uses all samples would only improve the noise by ~30% and was thus not (yet) implemented. The ADC phase feedback shifts the clock phases of reference and position signals together using a DDS clock generator on the RFFE, e.g. for compensation of beam arrival time or machine reference clock drifts. The alignment of the ADC sampling phases relative to each other is only done once, using programmable delay shifters on the ADC board. After determining the signal amplitudes of the I and Q channels, Cartesian-to-polar conversion is performed. The resulting amplitude and phase (A,φ) for position and reference channel have systematic "IQ imbalance" errors, since the gains of I and Q channel are not exactly identical and since their phase difference is not exactly 90°. This IQ amplitude and phase imbalance is corrected digitally by the FPGA, using a lookup table obtained from an automated lab calibration system [4] which also determines the attenuation of the variable attenuators in the RFFE. Over their 63dB range they can be changed in steps of 0.5dB, where small deviations of nominal and real attenuation cause small systematic measurement errors (i.e. steps) of X, Y and Q readings when the attenuators are changed (see below).

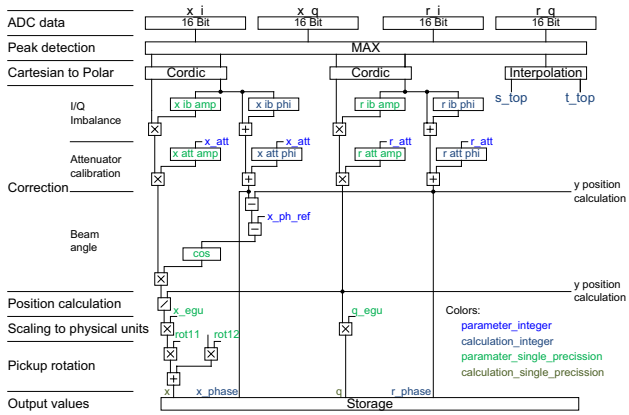


Figure 4: Simplified data flow of the CBPM signal processing algorithm.

Varying the attenuation also causes a shift of the phase delay between RFFE input and output. This is also calibrated in the lab and corrected by the FPGA firmware. The resulting IQ angle is thus attenuation-independent and can be used for the so-called beam angle correction. This correction digitally suppresses a systematic measurement error of the beam position, caused by the undesired beam angle signal, which is a position cavity signal component caused by a relative angle dX/dS or dY/dS between beam and longitudinal pickup axis. The dominant cause of this angle signal is the mechanical misalignment of the pickup.

Without digital angle signal correction, the 2-dimensional amplitude vectors (I_x,Q_x) and (I_y,Q_y) are the sum of a vector proportional to the product of beam position and charge, and of an orthogonal vector proportional to the product of beam angle and charge, e.g. for the X plane $(I_x,Q_x) = (I_{x_pos},Q_{x_pos}) + (I_{x_ang},Q_{x_ang})$. The angle signal sensitivities for the different pickups are shown Table 2, where the unit µm/mrad means that a pickup angle misalignment of 1mrad results in a beam angle signal as large as the (orthogonal) beam offset signal would be for 1 µm.

For large beam offsets, the beam angle signal usually causes a negligible error of the beam position. However, when moving the beam position from larger positive values through zero, without beam angle correction the calculated beam position would not reach zero, but converge from larger values to e.g. +16µm for an 1mrad misalignment of CBPM40, and then jump to -16µm when the beam crosses the pickup axis. In order to avoid this, the FPGA algorithm e.g. for X projects (I_x,Q_x) to a unit vector that is orthogonal to the beam angle signal (and parallel to the beam position signal) before performing the Cartesian-to-polar conversion (see Figure 4). This unit

Copyright © 2014 CC-BY-3.0 and by the respective authors

ISBN 978-3-95450-141-0

vector is obtained by rotating the IQ vector for the reference channel by a fixed angle. This angle is determined with beam, using the fact that the unit vector and (I_x,Q_x) are (nearly) parallel for large beam offsets. Thanks to the above mentioned correction of the attenuation-dependent IQ phase, the unit vector stays orthogonal to the beam angle signal for any attenuation.

Table 2: CBPM pickup angle sensitivities, expected alignment errors after beam-based mechanical realignment (SwissFEL: For shimming-based / screw-based adjustment), and resulting beam angle signal.

	Angle Sensi-tivity [µm/ mrad]	Angle Alignment Error [mrad]	Angle Signal [µm]
E-XFEL CBPM10	1.0	<0.2	0.2
E-XFEL CBPM40	16	<0.2	3.2
SwissFEL CBPM8	5.2	0.1 / 0.02	0.5 / 0.1
SwissFEL CBPM16	4.3	0.1 / 0.02	0.4 / 0.1
SwissFEL CBPM38	15.5	0.04 / 0.01	0.6 / 0.16

Beam Based Pickup Angle and Offset Calibration

The X and Y offset of the CBPM pickups will be calibrated beam-based using well-established beam based techniques like dispersion free steering or ballistic methods, where only measurements of relative beam movements are required to determine the offset of the CBPM. For the mechanical offset of the pickup, laser-tracker based alignment allows reaching offsets well below 100µm with respect to the nominal beam trajectory, where the beam-based alignment then allows to verify the initial alignment and correct it where needed.

However, despite digital beam angle error correction we intend to perform beam-based correction of the pickup angle misalignment in order to improve the initial laser-tracker based alignment, aiming to reduce the beam angle signal to an equivalent <1µm beam offset (see Table 2). This makes sure that, even without perfect calibration e.g. of the attenuation-dependent IQ phase shifts, the remaining angle-induced beam position error is negligible compared to the sub-micron BPM position noise and drift requirements for FEL undulators and IBFB CBPMs [1,2].

When the X beam position moves from large positive values through zero and then to large negative values, φ_x changes by 180°. Figure 5 shows a plot of φ_x vs. X, measured with beam for three CBPM10 installed at SITF, where φ_x was normalized to 0° at X=0mm. At φ_x=±45°, the two orthogonal vectors (I_{x_pos},Q_{x_pos}) and (I_{x_ang},Q_{x_ang}) have the same length, thus the beam angle is simply the beam position (calculated with active angle correction) where $\varphi_{x=}$=45°, divided by the beam angle sensitivity. While the first and third pickup have mechanical misalignments of about 2mrad and 3mrad, the second BPM10 pickup has a much larger value of about 22mrad. For SwissFEL and E-XFEL, the angles of the CBPM pickups will be measured with beam, and then corrected manually. For SwissFEL, most BPMs have fixed supports where pickup angle and positions are adjusted via shimming plates. Some SwissFEL BPMs are equipped with a support where angle and offset can be adjusted via differential screws (see Figure 1). Table 2 shows the expected angle alignment errors and resulting angle signal amplitudes after beam-based calibration and realignment.

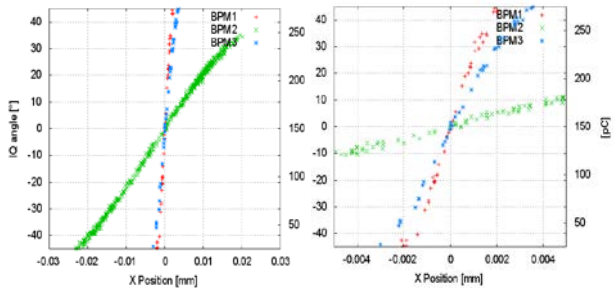


Figure 5: Measurement of IQ vector phase vs. beam position (same data with different X scales).

Beam Based Attenuator Calibration

In our baseline concept, we plan to operate E-XFEL and SwissFEL CBPMs with fixed attenuator settings for each accelerator operation mode, e.g. 10pC short bunch and 200pC standard SwissFEL operation mode. A coarse lab-based calibration of IQ imbalance and attenuators for each operation mode would already be sufficient, since the beam arrival time jitter is extremely low, and the IQ signal phase is nearly constant due to the LO phase feedback. Therefore, the beam-based calibration is only needed to determine and correct the absolute scaling factors for charge and position (for each operation mode), the pickup offsets and angles, as well as the angle between reference and position IQ vector as required for the above mentioned angle signal suppression (and to determine the sign of the beam position).

However, for 1st beam commissioning or accelerator test shifts where large beam position and charge variations may occur, it would be useful to use many or all of the 125 attenuator settings of each RFFE channel, with an automated range control (ARC) that adjusts the attenuators automatically such that the ADC signal levels are reasonably high but still do not saturate, thus minimizing ADC-related position and charge noise automatically for any beam position and charge. After implementing a first very simple version of such an ARC on the FPGA board, we have made a coarse calibration of the attenuators in the lab with a pulsed signal generator, using the signal generator set value for calibration. Then we improved the lab-based calibration with beam, using a least-square fit of the attenuator correction factors for the different attenuator settings, such that the errors (steps) caused by attenuator changes are minimized. At first, tests at FLASH with nearly constant bunch charge were performed. During the measurement, the ARC changed the position channel attenuators many times due to larger beam movements, e.g. for Y between 7 and 14dB. The reference channel attenuators were not changed due to the

Copyright © 2014 CC-BY-3.0 and by the respective authors

nearly constant charge. With the coarse lab-based calibration, the Y position RMS error (calculated by correlating three CBPMs) was about 650nm RMS, which is about 3 times larger than without ARC. After beam-based calibration, the noise with and without active ARC was nearly identical and about 220nm RMS.

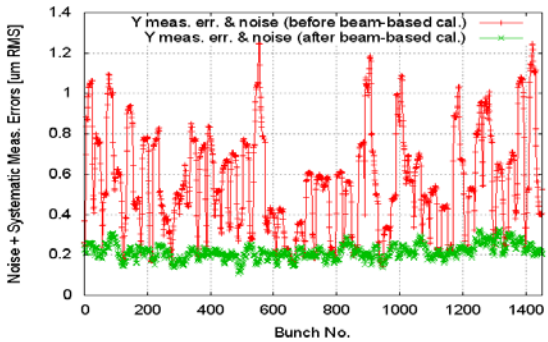


Figure 6: Floating average of the Y RMS measurement error (noise plus systematic errors due to switching attenuators etc). of FLASH CBPMs vs. bunch number before and after beam-based calibration of attenuators, calculated by correlating the readings of three CBPM10.

As mentioned above, the phase delay of the attenuators and thus the angle of the (I,Q) vector of the RFFE output signals depends on their attenuation. This also causes systematic attenuation-dependent errors when the IQ imbalance is not perfectly calibrated. Beam tests have shown that with our present lab-based calibration, we still have ~1% IQ imbalance [4]. It should however be noted that the beam-based calibration of the scaling factors we did for each attenuator setting does not only correct the attenuation, but also any remaining IQ imbalance at the same time.

The left plot in Figure 7 shows the charge ratio of two adjacent CBPM10 before (red) and after beam-based calibration, measured at SITF while the bunch charge was ramped down from 180pC to 75pC. After beam-based calibration, the previous errors of >1% were reduced to a relative charge noise of ~0.05%, that we also measure at constant charge and fixed attenuators. The right plot in Figure 7 shows the reduction of the position measurement error due to the beam-based calibration. In contrast to the measurement above at FLASH, the beam position at SITF was affected not only by the changing attenuators in the position channels of the RFFE, but also by the changing reference channel attenuators. However, also here the beam-based attenuator calibration resulted in a strong reduction of attenuator-dependent systematic errors from more than 2000nm RMS to 670nm RMS, using a measurement range of about ±400µm.

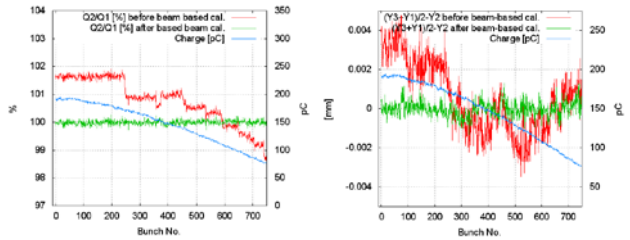


Figure 7: Left: Charge ratio of adjacent CBPM10 before and after beam-based calibration. Right: Difference between predicted and measured position at a CBPM10 at SITF, using adjacent CBPM10 for the prediction, before (red) and after (green) beam-based calibration.

SUMMARY AND OUTLOOK

The status, calibration and signal processing concept, and first beam-based calibration results for the low-Q CBPM systems for E-XFEL, FLASH2 and SwissFEL were presented. First beam tests have shown that our lab-based calibration of the CBPM electronics can be significantly improved with beam, making the switching of the RFFE attenuators basically invisible. Although this is not necessary for the baseline FEL operation modes where the attenuators will normally have fixed values, the improved calibration enhances the system performance for non-standard modes e.g. during 1st beam commissioning or accelerator test shifts.

We now plan to improve our present coarse lab-based calibration, e.g. by splitting the RF generator signals to several CBPM electronics, and then calibrating the RFFE attenuation and IQ imbalance by correlating readings of several CBPM electronics like we did for the beam-based calibration. Combined with an optimization of the pulse shape and spectrum of our lab signal pulse generator, we are aiming to further minimize the difference between lab- and beam-based calibration results.

REFERENCES

[1] B. Keil et al., *"The European XFEL Beam Position Monitor System"*, Proc. IPAC'10, Kyoto, Japan, 2010.

[2] B. Keil et al., *"Design of the SwissFEL BPM System"*, Proc. IBIC'13, Oxford, UK, 2013.

[3] D. Lipka et al., *"Flash Undulator BPM Commissioning and Beam Characterization Results"*, Proc. IBIC 2014, Monterey, CA, USA, 2014.

[4] M. Stadler et al., *"Low-Q Cavity BPM Electronics for E-XFEL, FLASH-II and SwissFEL"*, Proc. IBIC 2014, Monterey, CA, USA, 2014.

[5] B. Keil, *"Design Status of the European X-FEL Intra Bunch Train Feedback"*, Proc. IBIC'12, Tsukuba, Japan. 2012.

[6] M. Stadler et al., *"Development of the SwissFEL Undulator BPM System"*, WEPD13, IBIC'2014, Monterey, CA, USA, 2014.

[7] M. Stadler et al., *"Beam Test Results of Undulator Cavity BPM Electronics for the European XFEL"*, Proc. IBIC'12, Tsukuba, Japan, 2012.

Copyright © 2014 CC-BY-3.0 and by the respective authors

ISBN 978-3-95450-141-0

LOW-Q CAVITY BPM ELECTRONICS FOR E-XFEL, FLASH-II AND SwissFEL*

M. Stadler#, R. Baldinger, R. Ditter, B. Keil, F. Marcellini, G. Marinkovic, M. Roggli, M. Rohrer
PSI, Villigen, Switzerland
D. Lipka, D. Nölle, S. Vilcins, DESY, Hamburg, Germany

Abstract

PSI has developed BPM electronics for low-Q cavity BPMs that will be used in the E-XFEL and FLASH2 undulators, as well as in SwissFEL injector, linac and transfer lines. After beam tests at the SwissFEL test injector (SFIT) and FLASH1, a pre-series of the electronics has been produced, tested and commissioned at FLASH2 [1]. The design, system features, signal processing techniques, lab-based test and calibration system as well as latest measurement results are reported.

INTRODUCTION

The European XFEL (E-XFEL) has a superconducting 17.5GeV main linac that will provide trains of up to 2700 bunches, with 0.1-1nC bunch charge range, 600µs train length, ≥222ns bunch spacing, and 10Hz train repetition rate. A kicker/septum scheme can distribute fractions of the bunch train to two main SASE undulator lines followed by "secondary undulators" for spontaneous or FEL radiation. The E-XFEL will provide SASE radiation down to below 0.1nm wavelength and supports arbitrary bunch patterns within a bunch train, with bunch spacing of n*111ns, where n is an integer >1.

The cavity BPM electronic system is being developed at PSI [2, 3, 4]. For detailed performance measurements of the E-XFEL undulator BPM system an array of 3 pickups have been installed both at the SwissFEL injector test facility [3] and FLASH1 [1]. 22 E-XFEL undulator BPM systems have recently been installed at the FLASH2 section [1].

CAVITY PICKUP

The 3.3 GHz cavity pickups used for FLASH2 and EXFEL undulator and transfer line sections were designed at DESY [5]. Sensitivity parameters are given in Table 1.

Table 1: EXFEL Cavity BPM Pickup Parameters (10mm Beam Pipe Aperture)

	position cavity (TM110 mode)	reference cavity (TM010 mode)
Resonant frequency	3300 MHz	3300 MHz
Sensitivity	2.8 mV/nC/µm	42 V/nC
Cavity loaded-Q	70	70
Aperture	10mm (undulator) and 40.5mm (transfer line)	

markus.stadler@psi.ch

* This work was partially funded by the Swiss State Secretariat for Education, Research and Innovation SERI

Due to the low bunch rate of only 28ns (double-bunch operation) the cavity pickup used in the SwissFEL linac and transfer line sections have a loaded-Q (Q_L) factor of 40. SwissFEL undulator BPMs use high-Q cavities with a Q_L of ~1000 and a frequency of 4.8 GHz.

Table 2: SwissFEL low-Q cavity pickup data

	BPM38	BPM16
Frequency (GHz)	3.284 GHz	3.284 GHz
Min. bunch separation (ns)	28 ns	28 ns
loaded-Q	40	40
aperture	38 mm	16 mm
Sensitivity (reference resonator in mV/nC/µm)	5.7	7
Sensitivity (position resonators in V/nC)	66	135

BPM ELECTRONICS

The present BPM electronics prototype consists of:

- The RF front-end electronics (RFFE): One I/Q downconverter for reference, x- and y-position signal channel, using a common LO synthesizer, and an ADC sampling clock synthesizer. Active local temperature stabilizer circuits are employed on the RFFE PCBs for drift reduction.
- 6-channel, 16-bit 160MS/s analog-to-digital converters for all RFFE I and Q baseband differential output signals.
- Digital signal processing hardware ("GPAC" board) for signal processing and interfacing to control, feedback, timing and machine protection systems.

Detailed description of the overall electronics is given in [2, 3, 5].

RF Frontend (RFFE)

The simplified block diagram of the RFFE electronics used is shown in Figure 1. The basic principle of the BPM electronics and cavity design is based on [3].

Copyright © 2014 CC-BY-3.0 and by the respective authors

ISBN 978-3-95450-141-0

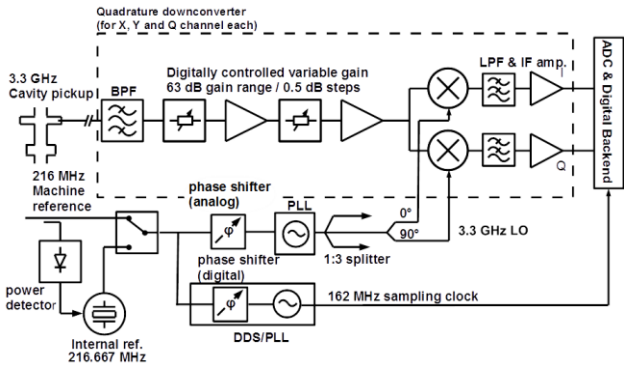


Figure 1: Simplified downconverter block diagram (one channel).

An input band pass filter selects the cavity signal components around 3.3GHz. The filter is followed by a programmable gain section.

The quadrature downconverter operates with a programmable LO frequency of ~3.3GHz. The LO is locked to a machine reference signal that has a stable phase relative to the electron bunch. This signal is 216.666 MHz at EXFEL and 142.8 MHz for SwissFEL.

In order to provide a bunch-synchronous sampling a second PLL is synthesizing the ADC clock signal of ~160 MHz from the machine reference signal.

This reference signal may be replaced by that of an internal crystal oscillator running at the same nominal frequency. This internal oscillator is automatically switched on in case the external clock fails, detected by measuring the *reference* signal power, or it can be switched on manually.

When the local reference crystal oscillator is activated the BPM system is not synchronized to the beam arrival any more. This "emergency" mode was implemented in order to still be able to get approximate beam position readings (with less accuracy compared to the nominal mode) when the reference clock distribution in the accelerator fails.

A programmable phase shifter for the LO is used to keep the reference cavity signal constant at 45 degrees by a feedback algorithm implemented on an FPGA on the GPAC. The phase shifter can also be set manually, which is used to measure and calibrate the I/Q imbalances of the downconverter.

The BPM electronics automatically adjusts the ADC sampling phase so that one sample is always at the top of the RFFE output pulse [3]. An FPGA on the GPAC board controls a direct digital synthesizer (DDS) on the RFFE that performs both phase shifting and frequency division prior to the final multiplication up to the sampling frequency.

SwissFEL and EXFEL RFFEs

SwissFEL linac and transfer line BPM systems use essentially the same RFFE boards. The SwissFEL prototype systems presently under test at the SwissFEL Test Injector Facility (SITF) only differ from the E-XFEL RFFE in the choice of filter parameters in the baseband section in order to accommodate for the lower loaded-Q.

The SwissFEL undulator BPM systems is planned to use dual-resonator high-Q cavities (Q_L~1000) with ~ 4.8 GHz operating frequency. High-Q cavities are appropriate here because the undulator section operates in single bunch mode only.

GAIN AND I/Q IMBALANCE CALIBRATION

As in every analog system the RFFE electronics shows systematic imperfections in both the downconverter section (I/Q imbalance) and the variable attenuator (DSA) section (attenuator setting inaccuracies). Both imperfections are suppressed by applying correction look-up tables before the sampled data is entering the position and charge calculation algorithms on the GPAC FPGAs.

The look-up tables are generated by a laboratory set-up in the first place. Because of differences between a real machine environment and the laboratory set-up a beam-based post calibration is planned [6].

Pre-calibration is performed for the following parameters:

- The I/Q gain and phase imbalance of the analog downconverter
- The gain setting of the digital step attenuators
- The overall gain factors relating vector magnitudes (in digits) to position (in mm) and charge (in pC)

In the following, we will describe a preliminary pre-calibration procedure that we so far have used for the E-XFEL pre-series electronics installed at FLASH1/2 and PSI, as well as possible improvements for the final calibration scheme to be used for the E-XFEL series version of the CBPM system.

Calibration Set-Up

The basics of the set-up used for the RFFE pre-calibration in the laboratory can be seen in Figure 2.

The synthetic pickup RF pulses are generated by an RF signal generator with wideband modulation capabilities. It is modulated by a baseband pulse resembling an exponential decay with a decay time constant of 7ns. This simulates a cavity loaded quality factor (loaded-Q) of 70.

The RF signal is then split equally into 3 parts and (after isolation) connected to the RFFE RF inputs.

A measurement Windows PC controls the MBU crate via LAN and the signal generator via GPIB.

The calibration procedure is implemented into MATLAB software. The control of RFFE and MBU functionality is provided by EPICS.

After pre-calibration all calibration data are stored into an EEPROM located on the RFFE board.

Copyright © 2014 CC-BY-3.0 and by the respective authors

ISBN 978-3-95450-141-0

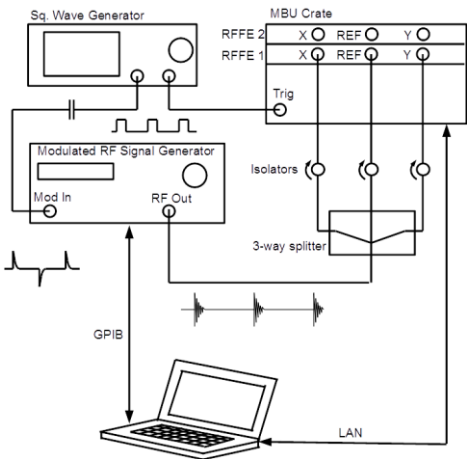


Figure 2: Principle of Laboratory Calibration Set-Up.

Downconverter Imbalance Calibration

The laboratory pre-calibration starts with measuring and the I/Q imbalance of the downconverter. During this step the signal phase is swept by stepping the internal phase shifter over a range >360 degrees in steps of ~10 degrees. The phase angles and the magnitudes of the resulting baseband signals are recorded. Finally a look-up table (1 degree steps) is generated that corrects for the imbalance. Angle values in between the steps are linearly interpolated.

Attenuator Calibration

After the I/Q imbalance has been corrected the digital step attenuators (DSA) that are determine the overall gain of the RFFE input channels are calibrated. The goal is to precisely know the actual gain setting of the RFFE channels. Ideally no change in charge or position reading should be seen after the RFFE gain has been changed.

During attenuator calibration the previously determined I/Q-imbalance correction is turned on. The DSA is swept from 0dB to 50dB in 1dB steps. At each step the magnitude of the IF vector is recorded. By comparing the measured attenuation to the nominal attenuator setting a correction (calibration) table is generated.

The signal phase change at each attenuator step is also measured and recorded and stored in a calibration table, which is important for the so-called beam angle correction explained below.

Overall Scale Factor Calibration

The final calibration step is to determine additional three numbers that relate the vector signal amplitudes (in digits) to position (in mm) and charge (in pC).

This step uses a signal generator setting of known RF pulse amplitude at the RFFE inputs. This amplitude has previously been determined using a fast oscilloscope. The scale factors are determined to show a charge and position that would result from a nominal cavity pickup with nominal sensitivities for reference and position channels with the same RF output signal amplitude as the synthetic pulse.

Beam Based Calibration

Beam tests at FLASH2 have shown that absolute position and charge readings are typically within a few percent of their true values. Beam based calibration methods may be used to increase absolute precision [6].

SIGNAL PROCESSING

Presently, the position calculation algorithm only uses a single sample at the top of the RFFE output signal pulse, as well as some samples of the baseline before the pulse to suppress common mode variations of the signal baseline. RF and sampling phase are stabilized using algorithms briefly described in [3]. Phase and amplitude drifts of the reference signal or the beam arrival time are compensated automatically via digital feedbacks of the GPAC.

From the raw ADC data the vector magnitudes and vector phases are calculated. The vector magnitudes are then multiplied each by a value stored in the I/Q calibration table. Finally, the resulting vector magnitude information is used to calculate the beam charge and the beam positions in x and y direction.

BEAM TEST RESULTS

I/Q Imbalance Calibration

Under nominal operation the BPM is synchronized to the beam arrival. The relative vector angle between reference and position channel is constant. However, before commissioning this relative angle is not known due to differences in pickup cable length, which cannot practically be avoided. Furthermore, the digitally programmable attenuators used on the RFFE have a phase delay that depends upon the programmed attenuation value. Therefore, the relative phase angles between the RFFE channels may change after a different charge or position range has been selected by reprogramming the attenuators. Relative phase shifts result in amplitude errors due to phase and amplitude imbalance occurring in the analog downconverter. In order to minimize this effect the imbalance (I/Q imbalance) is compensated using a look-up table. This table is initially generated by pre-calibration. The final calibration, if required, is done beam-based.

The pre-calibration using the laboratory calibration set-up is tested with beam by turning the LO phase feedback loop off and sweeping the LO phase of the downconverters over 360° using the internal LO phase shifter. Relating the charge reading to a second charge reading from a second BPM the deviation can be evaluated. Figure 3 shows an example of a beam measurement where the charge of one BPM is seen to depend upon the actual LO phase angle.

Copyright © 2014 CC-BY-3.0 and by the respective authors

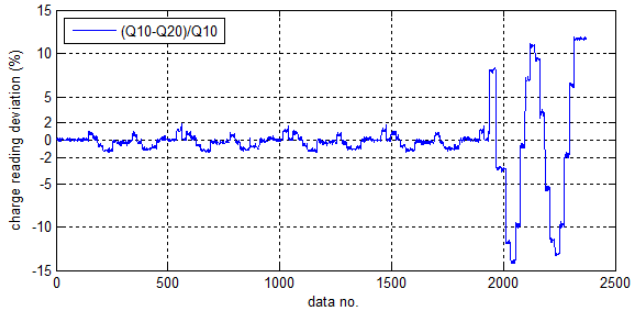


Figure 3: Pre-Calibration imbalance correction (calibration turned off for data points 1900 and higher).

As can be seen the pre-calibration is good to roughly ±1%. The final accuracy can be reached after application of beam based calibration procedures [6].

Attenuator Pre-Calibration

If the charge readings of several BPMs are compared while the gain of one BPM is stepped one ideally sees no steps in the charge readings.

After pre-calibration there is still a charge reading depending on the gain setting (Figure 4). This remaining difference may be reduced further beam-based.

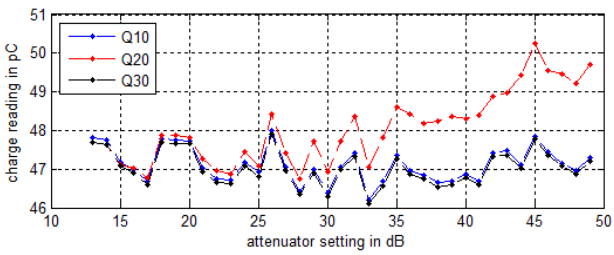


Figure 4: Charge Reading versus attenuator setting. The attenuator of BPM20 (red lines) was stepped.

Electronics Linearity

Since position and reference channel are identical (except an extra attenuator at the input of the reference channel), charge measurements were used to assess the nonlinearity of the RFFE input channels.

The reference channel linearity is measured in the following way: At a given beam charge the reference attenuator of the BPM under test (TBPM) is set such that its reference channel nearly saturates. A second BPM, the reference BPM (RBPM) has its reference attenuator set to a value about 20dB higher than that of the TBPM. It is assumed that the RBPM with its low amplitude does operate within its linear range, since nonlinear deviations are typically expected to occur at high signal amplitudes. Figure 5 shows beam measurements using 4 BPMs at SITF. BPM 40 (green curve in Figure 5 is the reference BPM).

Plotting the charge reading of the test BPM against the reading of the reference BPM now shows any nonlinear behaviour. However, Figure 6 suggests a good linearity over the full signal range with deviations from the linear fit being smaller than ±1%.

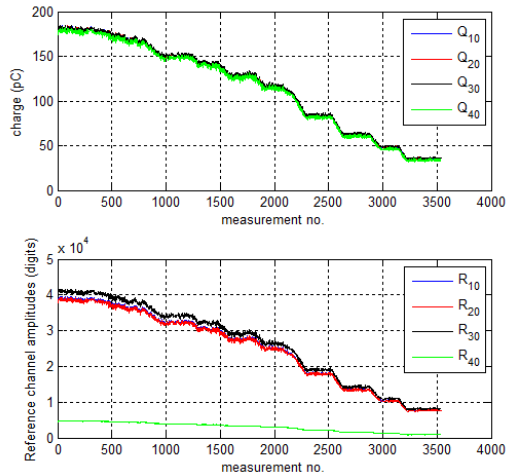


Figure 5: Linearity Measurement (charge readings and IF output amplitudes).

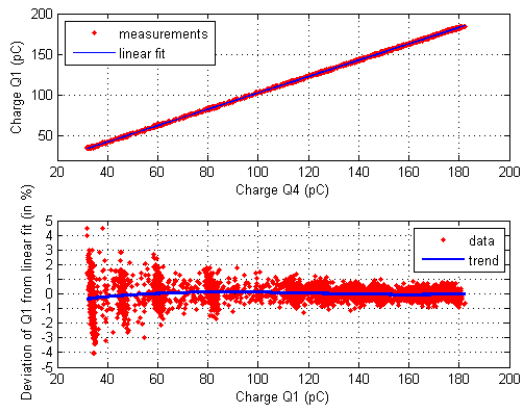


Figure 6: Deviation of the charge reading from linear fit.

Position Resolution

Position resolution is measured using the method described in [3].

The single bunch position resolution requirement for EXFEL undulator BPM systems is 1µm rms within a measurement range of ±500µm and within the charge range 100pC to 1nC.

Figure 7 shows the results of resolution measurements taken at SITF and at three different beam charges: 30pC, 100pC and 200pC. Higher charges were not available. All measurements used a full-scale position range of ±600µm. Position resolution is better than 1µm rms for all charges above 30pC and at all beam offset positions within this measurement range.

Similar measurements using EXFEL undulator BPMs at higher beam charges have been undertaken at FLASH1 (DESY, Hamburg) and are reported in [1].

Copyright © 2014 CC-BY-3.0 and by the respective authors

ISBN 978-3-95450-141-0

Results generally agree in the fact that resolution requirements of EXFEL and FLASH2 BPM electronics are met or exceeded by the present PSI cavity BPM system.

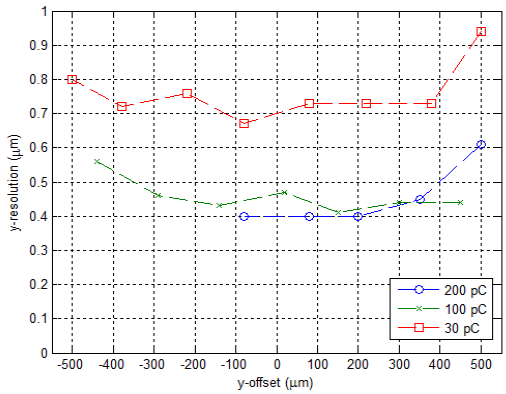


Figure 7: Measured position resolution for a ±600µm measurement range at different beam charges (EXFEL undulator BPMs).

It is worth noting that the position resolution is predictable by theory quite precisely. In contrast to this almost all other important BPM parameters, as for example temperature drift, linearity, or final accuracy, are far less predictable. An isolated view on the BPM resolution alone is therefore not considered adequate to characterize the performance of a BPM system.

Positon Temperature Drift (Lab Measurement)

The temperature drift of the ratio of position to reference channel amplitude (=position drift) has been measured under controlled laboratory environment using a similar set-up as seen in Figure 2. The room temperature was raised slowly over several degrees. The position reading and temperature of a nearby and not actively stabilized RFFE were logged and plotted against each other.

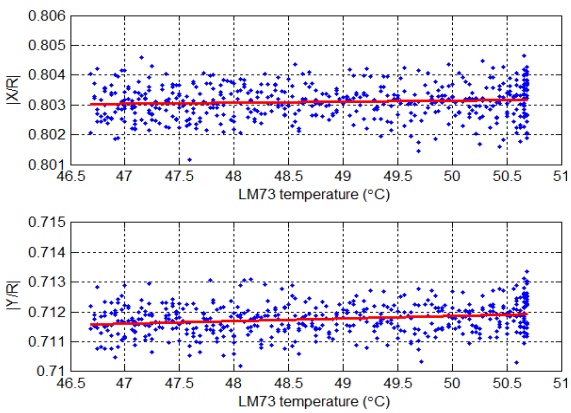


Figure 8: Position Reading (internal units) vs. Temperature.

It is found that the position reading drifted less than 0.01% per degree of ambient temperature change. At the upper precision range demanded by EXFEL this would result in a position drift of 50nm per °C. Further drift tests are pending.

CONCLUSION

We described the new cavity BPM electronics that is presently installed at FLASH2, which is a pre-series of the E-XFEL version. A set-up used to pre-calibrate the BPM electronics in the laboratory has been described. Finally some beam measurement results taken at the SwissFEL Injector test facility were presented. The results indicate adequate position resolution, in agreement with earlier measurements, good electronics linearity and temperature stability.

The laboratory pre-calibration method presently in use is able to bring the absolute accuracy to within a few percent. Possible improvements of pre-calibration results are discussed in [6].

In order to improve the calibration beyond what is already reached by laboratory based pre-calibration it is suggested to use beam-based procedures at commissioning of the BPM system.

REFERENCES

[1] D. Lipka et al: "*Flash Undulator BPM Commissioning and Beam Characterization Results*", these proceedings, TUPF07, IBIC 2014, Monterey, California, USA, 2014.

[2] B. Keil, et al.: "*The European XFEL Beam Position Monitor System*", Proc. IPAC, Kyoto, Japan, 2010.

[3] M. Stadler et al.: "*Beam Test Results of Undulator Cavity BPM Electronics for the European XFEL*", Proc. IBIC12, Tsukuba, Japan, 2012.

[4] B. Keil et al., *"A Generic BPM Electronics Platform for European XFEL, SwissFEL and SLS"*, Proc. IBIC12, Tsukuba, Japan, 2012

[5] D. Lipka, et al.: "*Cavity BPM Designs, related Electronics and Measured Performances*", Proc. DIPAC'09, Basel, Switzerland, 2009.

[6] B. Keil, et al.: *"Beam-Based Calibration and Performance Optimization of Cavity BPMs for SwissFEL, E-XFEL and FLASH-II"*, these proceedings, WEPD11, IBIC 2014, Monterey, California, USA, 2014.

Copyright © 2014 CC-BY-3.0 and by the respective authors

DEVELOPMENT OF THE SWISSFEL UNDULATOR BPM SYSTEM

M. Stadler#, R. Baldinger, R. Ditter, B. Keil, F. Marcellini, G. Marinkovic, M. Roggli, M. Rohrer
PSI, Villigen, Switzerland

Abstract

For SwissFEL, two types of cavity BPMs are used. In the linac, injector and transfer lines, low-Q dual-resonator cavity BPMs with a loaded-Q factors (Q_L) of ~40 and 3.3GHz mode frequency allow easy separation of the two adjacent bunches with 28ns bunch spacing. For the undulators that receive only single bunches from a beam distribution kicker with 100Hz repetition rate, dual-resonator BPM pickups with higher Q_L are used. The baseline version for the undulator BPMs is a stainless steel pickup with Q_L=200 and 3.3GHz frequency. In addition, an alternative version with copper resonators, Q_L=1000 and 4.8GHz frequency has been investigated. For all pickups, prototypes were built and tested. The status of pickup and electronics development as well as the latest prototype test results are reported.

INTRODUCTION

Due to different apertures in different parts of SwissFEL, three different BPM pickups are needed. While the injector and linac have BPM pickup apertures of 38mm ("BPM38") and 16mm ("BPM16), the undulator BPMs have 8mm ("BPM8").

Injector and Linac BPMs

The planned cavity BPM system for injector and linac is similar in architecture to that already developed by for E-XFEL and FLASH2 [1,2,3,4]. In order to independently measure position and charge of the two bunches with 28ns spacing (compared to 222ns for E-XFEL), the SwissFEL BPM38 and BPM16 pickups have a lower Q_L of ~40, compared to Q_L=70 for E-XFEL. The signal frequency is f_o=3.284 GHz for BPM38 and BPM16, which is still safely below the cut-off frequency of the larger (38mm aperture) beam pipe. Moreover, this frequency is an integer multiple of the machine reference clock frequency (142.8MHz), where the bunch spacing is four reference clock periods. As a result, both bunches have (nearly) the same IQ phase, which simplifies the algorithms for BPM signal processing and local oscillator phase feedback (see ref [3]). Finally, the choice of this frequency also allows direct reuse of large parts of the E-XFEL cavity BPM electronic system that also work at 3.3GHz (with a similar aperture of 40.5mm for the warm E-XFEL beam transfer lines), thus minimizing the development effort.

For Q_L=40 and f_o=3.284 GHz the resulting decay time $\tau=Q_L/(\pi \cdot f_o)$ of the BPM38 and BPM16 pickup signals is 3.9 ns. After 28ns, the cavity signal is decayed to <0.1% of the initial amplitude before the second bunch arrives, thus causing only negligible RF crosstalk between bunches. In order to be able to use the same 160MSPS ADCs like for E-XFEL, the RFFE shapes the output pulses for the two bunches such that enough samples for a sufficiently accurate computation of the beam position are available, using a simple algorithm in the BPM electronics FPGAs to eliminate any bunch-to-bunch crosstalk caused by the pulse shaper. Compared to pickups with high Q where overlapping pickup signals can have constructive or destructive interference, the low-Q RFFE output pulse shaper only causes small overlap of baseband amplitude signals, where a simple (scalar) subtraction of the overlapping signal pulses is sufficient to supress bunch-to-bunch crosstalk, without the necessity to use phase information.

The RMS noise requirements of the SwissFEL linac BPMs is <5µm for the 16mm aperture cavity and <10µm for the 38mm cavity (see Table 1) at 10-200pC bunch charge. Tests with a slightly modified E-XFEL BPM electronics have already demonstated sub-micron resolution for a BPM16 prototype pickup installed at the SwissFEL Injector Test Facility SITF [1].

Undulator BPMs

The BPMs in the SwissFEL undulator intersections have higher resolution and precision requirement than the linac and injector sections (see Table 1). From the experience gained with the E-XFEL and FLASH2 cavity BPM system we decided to use BPM pickups of the same basic structure, but with higher Q_L. The main reasons for this decision are:

1. In contrast to EXFEL, the SwissFEL undulators are operated in single bunch mode with 100Hz repetition rate, therefore we do not need a low Q_L to avoid bunch-to-bunch crosstalk of pickup output signals.
2. With higher Q_L, more data samples are available per bunch when using a similar ADC sampling rate. This reduces the impact of ADC noise on the BPM position noise and thus increases the ratio of measurement range to noise (for higher bunch charges), which is typically ~1000 for Q_L~40-70.
3. Direct digital quadrature downconversion from a finite IF frequency is able to eliminate systematic measurement errors due to phase and amplitude imbalance. Position and charge readings are thus less sensitive to sampling phase or bunch arrival fluctuations, increasing robustness and overall accuracy.

markus.stadler@psi.ch

Copyright © 2014 CC-BY-3.0 and by the respective authors

ISBN 978-3-95450-141-0

Table 1: SwissFEL BPM Pickup Specifications (EXFEL undulator pickup shown for comparison only)

Type	Aperture (mm)	Q_L	Freq. (GHz)	Bunch spacing	Resonator Sensitivity		RMS Position Noise (µm)	Location
					Reference (V/nC)	Position (mV/nC/µm)		
BPM8	8	200	3.284	1 bunch 100Hz	47.5	5.2	<1	Undulators
BPM8	8	1000	4.855	1 bunch 100Hz	58	4.3	<1	Undulators
BPM16	16	40	3.284	28ns (2 bunch mode)	135	7.1	<5	Injector/Linac
BPM38	38	40	3.284	28ns (2 bunch mode)	66	5.7	<10	Injector/Linac
EXFEL	10	70	3.3	222ns	45	2.8	<1	Undulators

It should be noted that choosing a higher Q_L (for a given pickup geometry, by having weaker coupling) does not affect the BPM position noise at very low bunch charges, or at higher bunch charges and small measurement ranges where RFFE noise dominates over ADC noise.

UNDULATOR PICK-UP DESIGN AN STATUS

Recently we have successfully tested two BPM8 undulator pickup prototypes at the SwissFEL Injector Test Facility (SITF) with beam: One made from stainless steel, with Q_L~200 and f=3.284GHz, and one with copper resonators and an outer stainless steel hull with Q_L~1000 and f=4.855GHz (see Figure 1).After getting experience with the production and confirming that the copper version can be produced on time and on budget, we decided to use it in the SwissFEL undulators since it allows to reach better resolution than the 3.3GHz steel version both at high charge (due to the higher Q_L) and at low charge (due to the higher frequency that improves sensitivity for a given decay time). A detailed discussion of further design considerations may be found in [1].

The design of the SwissFEL cavity pickup was based on the experience gained during the E-XFEL cavity BPM project over the last few years - as is true for the entire PSI SwissFEL BPM activities. The pickup bodies for BPM38, BPM16 and the BPM8 version with Q_L=200 are all made from stainless steel (316LN). Details of the design are given in [1,5,6,7]. Q_L=200 is a compromise between the goals of having a high Q_L and keeping the resistive losses reasonably low. In order to reach a much higher Q_L of ~1000, we designed a BPM8 pickup with copper resonators.

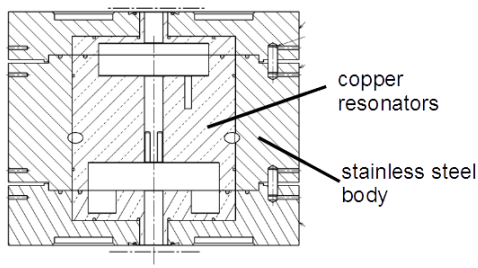


Figure 1: Cross-section of BPM8 Q_L=1000 pickup.

As shown in Figure 1 the pickup has an outer hull and vacuum flanges made from stainless steel, while the inner part with the resonators is made from copper. This combines the advantages of copper resonators – easy machining and low losses – with the advantages of stainless steel for the outer part of the pickup – easy welding of the RF feedthroughs, and solid vacuum flanges.

Table 2: Status of SwissFEL cavity BPM pickups

Cavity	Quantity for at SwissFEL	Status
BPM16	111	Prototype installed at SwissFEL Test Injector Facility (SITF). Test OK, series production started
BPM38	6	Prototype installed at SITF. Test OK. Production started
BPM8 (Q_L=200) or BPM8 (Q_L=1000)	27	Prototype installed at SITF. Preliminary Test OK Prototype installed at SITF. Preliminary test OK.

Copyright © 2014 CC-BY-3.0 and by the respective authors

During production, the copper block is first brazed into the steel hull. After machining the three body parts, they are brazed together. Then the glass ceramic RF feedthroughs are welded to the body, followed by a final vacuum test. The current status of the SwissFEL cavity pickups is summarized in Table 2.

All SwissFEL undulator BPM8 pickups will be horizontally and vertically adjustable using high-precision motorized movers. This allows absolute calibration of the undulator BPM position during operation. The BPM16 and BPM38 pickups will have supports that can only be adjusted manually for cost reasons.

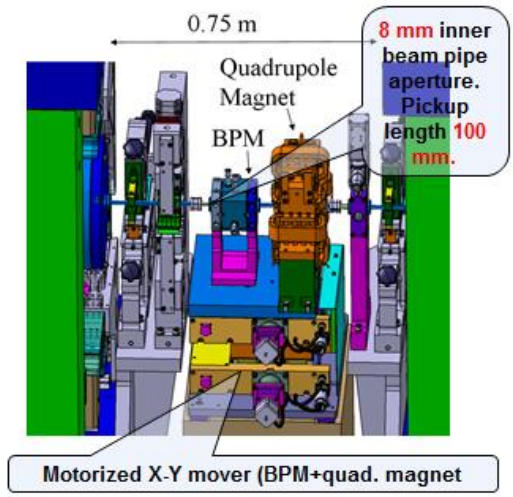


Figure 2: SwissFEL undulator BPM8 pickup in an undulator intersection, mounted together with a quadrupole magnet on a motorized 2D mover stage.

LOW-Q & HIGH-Q RF FRONT-END ELECTRONICS

To process the BPM38 and BPM16 pickups signals, a slightly modified version of the already existing E-XFEL cavity BPM RF electronics will be used [3,4]. A block diagram of this electronics is shown in Figure 3.

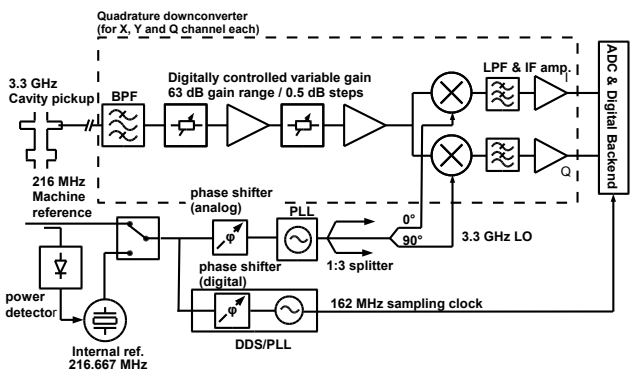


Figure 3: RFFE electronics use for low-Q BPM.

The short RF pulse signal (compared to the ADC sampling interval) produced by a low-Q pickup makes it adequate to use analog I/Q downconversion. If high-Q cavities are used it becomes however more attractive to do the downconversion in the digital domain. A block schematics of the BPM8 electronics (with 3.3GHz and Q_L=200 or 4.8GHz and Q_L=1000) is shown in Figure 4.

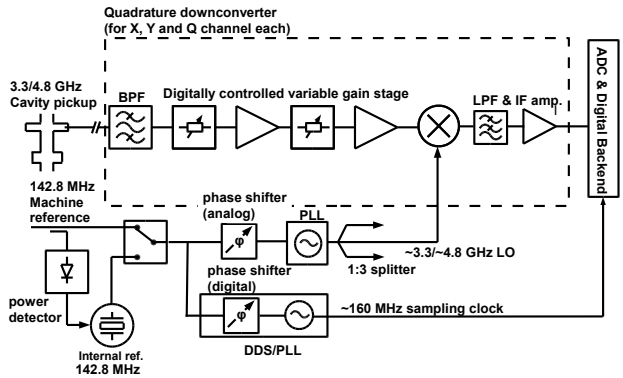


Figure 4: High-Q RFFE electronics.

Instead of using an I/Q downconverter, a single mixer is sufficient to convert the pickup signals to an IF frequency of ~40MHz. The IF portion (downstream of the mixers) uses different filter characteristics, which represents only a slight change in circuit design compared to the low-Q RFFEs.

For the 3.3GHz BPM8 pickup, large parts of the E-XFEL / FLASH2 CBPM electronics could have been reused due to the same signal frequency. For the 4.8GHz version that is now the baseline for SwissFEL, parts in the RFFE input stage (filters, amplifiers, mixers) need to be adapted or exchanged in order to support the higher frequency. The development of the 4.8GHz RFFE is in progress. Presently we are using synthetic high-Q cavity signals from a signal generator at 3.3 GHz together with the present 3.3GHz EXFEL cavity BPM RFFE electronics which can thus generate the same output signals like the future 4.8GHz version. This allows tests of the high-Q firmware and digital signal processing in parallel to the development of a new 4.8GHz RFFE.

LOW-Q BPM SIGNAL PROCESSING

The low-Q BPM systems need to process data under multi-bunch operation. In case of the EXFEL BPM systems there is a need to process the data with minimal processing latency. Presently, only one ADC sample at the very top of the RFFE output signal is used for calculation of vector magnitude and vector angle [3, 4].

However, while this approach provides minimal latency for the E-XFEL intra-bunch train feedback, it is also "wasting" the information contained in other sampling points of nonzero magnitude. Collecting the information of all sampling points by applying matched filter technique can reduce the position noise of the BPMs by approximately 30%. Since the present system performance already meets the E-XFEL requirements, the implementation of such a filter – that will cause a

Copyright © 2014 CC-BY-3.0 and by the respective authors

ISBN 978-3-95450-141-0

moderate increase of the system latency - is planned for a future firmware version.

The signals from SwissFEL BPM16 and BPM38 (both having a loaded-Q factor of ~40) are captured using the same approach and, in large parts, identical hard- and firmware as is used in the EXFEL/FLASH2 cavity BPM systems. Figure 6 shows double bunch signal from BPM16 under real beam conditions at SITF.

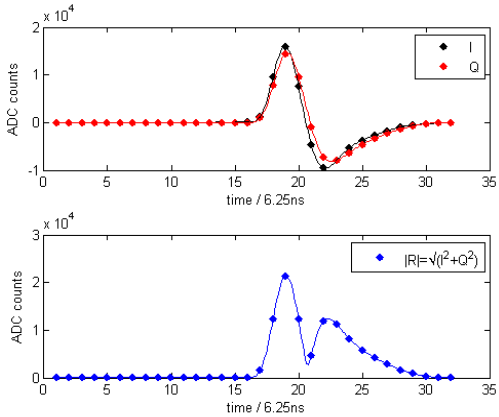


Figure 5: Low-Q signals and sample values (EXFEL electronics [4]).

As can be seen only the sampling points at the top have optimal signal-to-noise ratio. Therefore, a matched filter processing would increase resolution only by about 30%. The process of RF phase and sampling phase alignment (described in [3]) for SwissFEL BPM38 and BPM16 are identical to the EXFEL cavity BPM system.

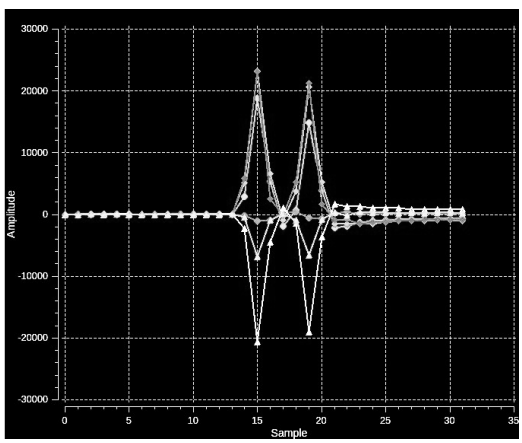


Figure 6: Screen showing the ADC samples of BPM16 (Q_L=40) at SITF in two-bunch mode (28ns bunch spacing).

HIGH-Q BPM DATA PROCESSING

For the planned SwissFEL high-Q undulator cavity BPM system it is intended to apply digital quadrature downconversion from a cavity signal that has previously been mixed by the RFFE to an IF frequency of ~40MHz. Figure 7 shows a principle diagram of the data processing chain. The ADC samples of the IF pulse waveform are stored in an array. The stored values are then parallel multiplied by an array of data containing a sine or cosine waveform, thus representing a numerical controlled oscillator. Afterwards the resulting values are processed by a FIR low-pass filter in order to remove the sum frequency content. This FIR filter may also implement a matched filter at the same time. The filter output is then fed to the interpolation and peak-detection algorithm from where vector magnitude and phase is extracted. The firmware following this stage is intended to be similar in large parts to the already existing implementation of the EXFEL/FLASH2 cavity BPM system. A first version of the high-Q BPM signal processing algorithm has been implemented in software on the generic E-XFEL BPM FPGA board that is also suitable for SwissFEL [1,3]. Laboratory and beam tests at PSI are ongoing.

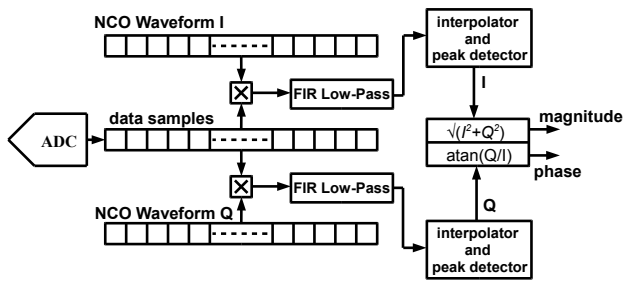


Figure 7: High-Q signal processing scheme.

PICKUP BEAM TESTS

Waveform and signal frequency spectra for SwissFEL and E-XFEL BPM pickups have been measured under real beam conditions at SITF. Figure 8 through Figure 11 shows the signal of the reference and position cavity for the two prototypes of the SwissFEL undulator BPM pickups.

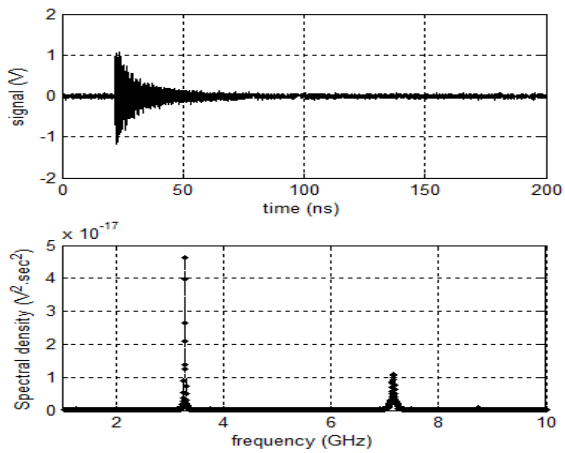


Figure 8: BPM8 (Q_L=200, 3.284GHz) Reference Signal waveform and spectrum (8 GHz oscilloscope).

Figure 12 shows the results from the preliminary implementation of the intended high-Q BPM signal processing (Figure 7) using the EXFEL RF electronics of Figure 3. The top screen contains the raw signal samples from I- and Q output at an intermediate IF frequency of

Copyright © 2014 CC-BY-3.0 and by the respective authors

~40MHz. Only the I-waveform is used for further processing. The NCO waveforms are seen in the screen below. The bottom screen shows the output of the FIR filter stages, representing the in phase and quadrature component from which vector magnitude and vector angle are calculated. The FIR filter in this example has been chosen to implement a low-pass section followed by a matched filter.

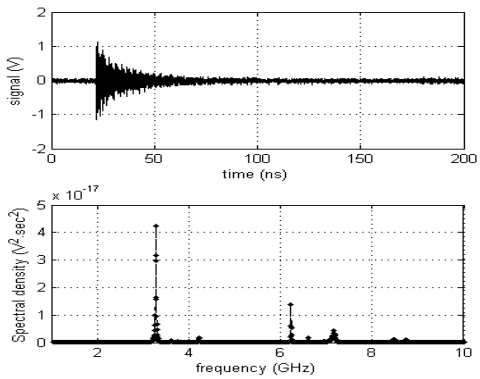


Figure 9: BPM8 (Q_L=200, 3.284GHz) Position Cavity Signal Waveform and Spectrum (8 GHz oscilloscope).

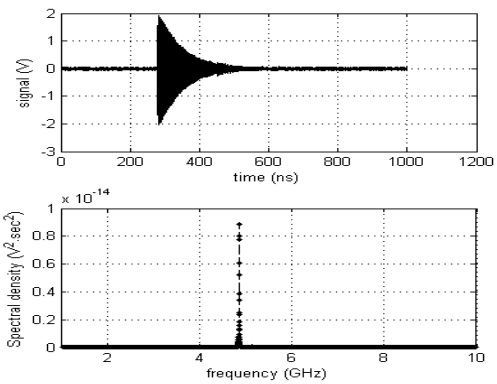


Figure 10: BPM8 (Q_L=1000, 4.855GHz) Position Cavity Signal Waveform and Spectrum (6 GHz oscilloscope).

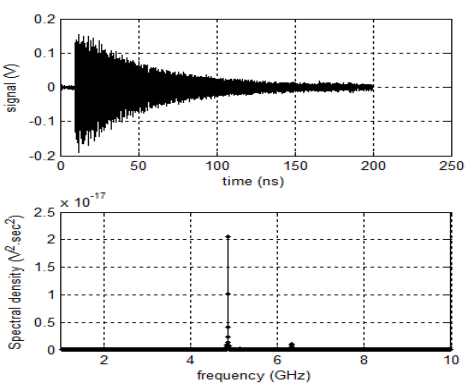


Figure 11: BPM8 (Q_L=1000, 4.855GHz) Position Cavity Signal Waveform and Spectrum (6GHz oscilloscope).

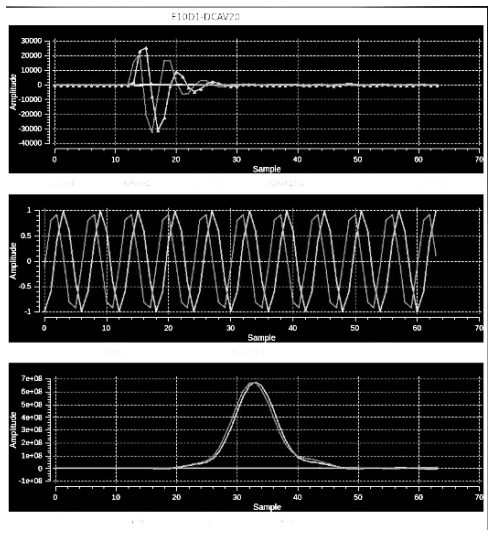


Figure 12: BPM8 (Q_L=200) Test System Waveform Window.

SUMMARY

An overview or the planned SwissFEL undulator BPM system has been given. A comparison to the existing EXFEL/FLASH2 BPM system has been made. The intended high-Q signal processing scheme has been described. Finally beam measurements of two SwissFEL undulator BPM pickup prototypes with Q_L values of 200 and 1000 have been presented.

Test and development activities on this high-Q BPM system are ongoing at PSI using EXFEL cavity BPM electronics and a preliminary signal processing implementation on a E-XFEL BPM FPGA board.

REFERENCES

[1] B. Keil, et al.: *"Design of the SwissFEL BPM System"*, proc. IBIC13, Oxford, UK, 2013.

[2] B. Keil, et al.: "*The European XFEL Beam Position Monitor System*", proc. IPAC, Kyoto, Japan, 2010.

[3] M. Stadler, et al.: *"Low-Q Cavity BPM Electronics for E-XFEL, FLASH-II and Swiss-FEL"*, these proceedings.

[4] M. Stadler, et al.: *"Beam Test Results of Undulator Cavity BPM Electronics for the European XFEL"*, proc. IBIC12, Tsukuba, Japan, 2012.

[5] F. Marcellini, et al.: *"Design of Cavity BPM Pickups for SwissFEL"*, proc. IBIC12, Tsukuba, Japan, 2012.

[6] D. Lipka, et al.: *"Cavity BPM Designs, Related Electronics and Measured Performance"*, proc. DIPAC09, Basel, Switzerland, 2009.

[7] H. Maesaka, et al.: *"Development of the RF Cavity BPM of XFEL/SPRING-8"*, proc. DIPAC09, Basel, Switzerland, 2009.

Copyright © 2014 CC-BY-3.0 and by the respective authors

ISBN 978-3-95450-141-0

COMMISSIONING RESULTS OF MICROTCA.4 STRIPLINE BPM SYSTEM*

C. Xu#, S. Allison, S. Hoobler, D. J. Martin, J. Olsen, T. Straumann, A. Young,
SLAC National Accelerator Laboratory, Menlo Park, CA 94025, USA
H. Kang, C. Kim, S. Lee, G. Mun
Pohang Accelerator Laboratory, Pohang, Kyungbuk, Korea

Abstract

SLAC National Accelerator Laboratory is a premier photon science laboratory. SLAC has a Free Electron Laser (FEL) facility that will produce 0.5 to 77 Angstroms X-rays and a synchrotron light source facility. In order to achieve this high level of performance, the beam position measurement system needs to be accurate so the electron beam bunch can be stable. We have designed a general-purpose stripline Beam Position Monitor (BPM) system that has a dynamic range of 10pC to 1nC bunch charge. The BPM system uses the MicroTCA (Micro Telecommunication Computing Architecture) for physics platform that consists of a 14bit 250MSPS ADC module (SIS8300 from Struck) that uses the Zone 3 A1.0 classification for the Rear Transition Module (RTM). This paper will discuss the commissioning result at SLAC LINAC Coherent Light Source (LCLS), SLAC Sanford Synchrotron Radiation Lightsource (SSRL), and Pohang Accelerator Laboratory (PAL) Injector Test Facility (IFT). The RTM architecture includes a band-pass filter at 300MHz with 30 MHz bandwidth, and an automated BPM calibration process. The RTM communicates with the AMC FPGA using a QSPI interface over the zone 3 connection.

NEW ELECTRONICS AND TEST SUITE

The test result presented at IBIC 2013 was conducted using a 16bit 125MSPS SIS8300 ADC module. After the conference, more tests were done using the 14bit 250MSPS ADC module on LCLS-I. In addition, more tests were moved to automate testing to decrease testing time and increase accuracy by eliminating operator error.

250MSPS ADC Module

With a 250MSPS ADC, the BPM electronic was able to capture two times the waveform data. With the faster ADC, a 30MHZ band-pass filter replaced the 15MHz band-pass filter used for the original electronic.

A narrower band-pass filter will produce a ringing signal with less amplitude comparing to a wider band-pass filter. By using a wider band-pass filter, it will increase the dynamic range of the BPM electronics by the square-root of the bandwidth factor (i.e., in our case $\sqrt{2}$). Figure 1 shows the comparison between 125MSPS system and 250MSPS resolution difference.

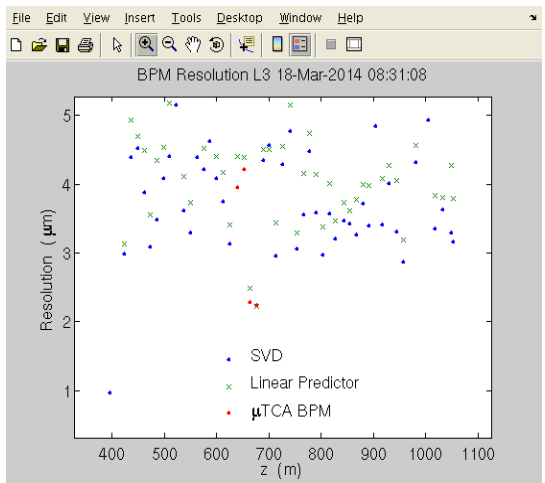


Figure 1: Resolution measurement with both 125Msa/s and 250Msa/s ADCs shown in red.

Automated Test Suite

To decrease the testing time for the eight BPM systems, an automated test suite was created using MATLAB and Python script. Each module was tested for signal to noise ratio (SNR), effective number of bits (ENOB), linearity test (IP3), attenuator linearity test, and simulated beam resolution. Two Agilent vector generators were controlled via SLAC intranet. The operator has the ability to choose between the full test and individual tests. Each test records the board serial number of the date the test is performed. Comparing to the original test duration, the test suite reduced the testing time by 75%. In addition, test results can be accessed later if needed.

POHANG ACCELERATOR LABORATORY – INJECTOR TEST FACILITY

In preparation for the new PAL FEL, PAL has constructed an injector test facility (ITF) to test instruments like TCAVs, modulators, BPMs, and other accelerator components. PAL asked SLAC to build seven BPM systems for the PAL ITF. The ITF is composed of two Kystrons and one TCAV for beam

*This work supported by the U.S. Department of Energy, Office of Science, SLAC National Accelerator Laboratory under Contract No. DE-AC02-76SF00515 and WFOA13-197.

#charliex@slac.stanford.edu

Copyright © 2014 CC-BY-3.0 and by the respective authors

profile monitoring. The operating conditions were the Klystrons voltages set between 35kV to 40kV with L0a set to 116 degrees and L0b set to 90 degrees. The beam energy was between 45MeV to 70Mev. [2] Figure 2 shows the Klystron layout of the ITF.



Figure 2: PAL ITF gallery layout.

Deployment

The work for the PAL BPM system was developed under a Work For Others (WFO) agreement [1]. SLAC was responsible for developing the BPM electronics for PAL. PAL was responsible for developing the stripline BPMs and providing a test facility to measure the performance. There are seven BPM instruments in the entire ITF. Figure 4 illustrates the first four BPMs are mounted rotated 45 degree, the last four BPMs are non-rotated and each BPM is mounted on a motor mover system. Three member of SLAC's BPM team traveled to PAL in June and deployed seven BPM systems. Figure 3 illustrates the mTCA BPM electronics and the BPMs at the end of the ITF.



Figure 3: microTCA BPM system installed at PAL ITF.

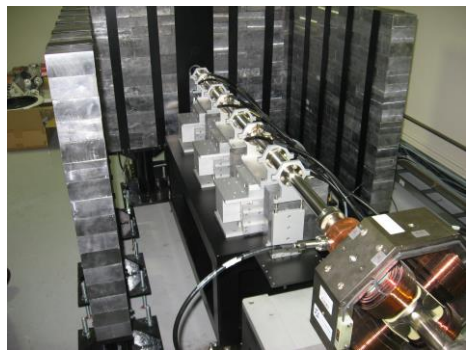


Figure 4: Stripline BPMs inside PAL ITF.

Verification

Both SLAC's BPM and PAL's ITF team verified the performance of the SLAC BPM electronic. Several tests were performed at PAL's ITF. Each board's resolution was tested using a single BPM. Figure 5 shows at 200pC beam energy, the BPM electronic produced approximately 1.7micron resolution.

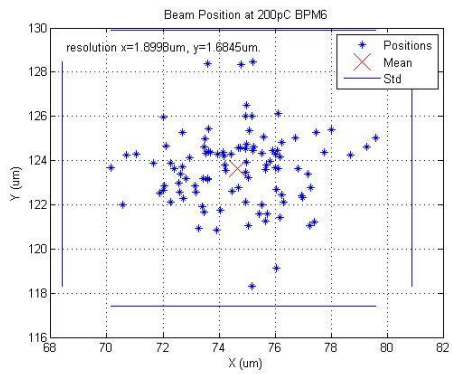


Figure 5: Example of single board resolution.

Beside the single board resolution, resolution was also tested using all seven BPMs. By using the data from all the BPMs, the beam position jitter could be removed by using both the linear predictor method and single value decomposition method. Figure 6 illustrates at 10pC beam energy the BPM electronic yielded 10micron resolution. Figure 7 shows at 200pC, the BPM electronic yielded ~3micron resolution.

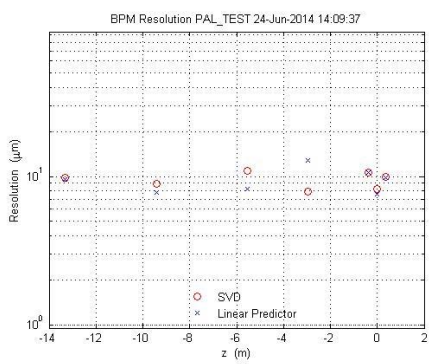


Figure 6: Multi-BPM resolution test at 10pC.

Copyright © 2014 CC-BY-3.0 and by the respective authors

ISBN 978-3-95450-141-0

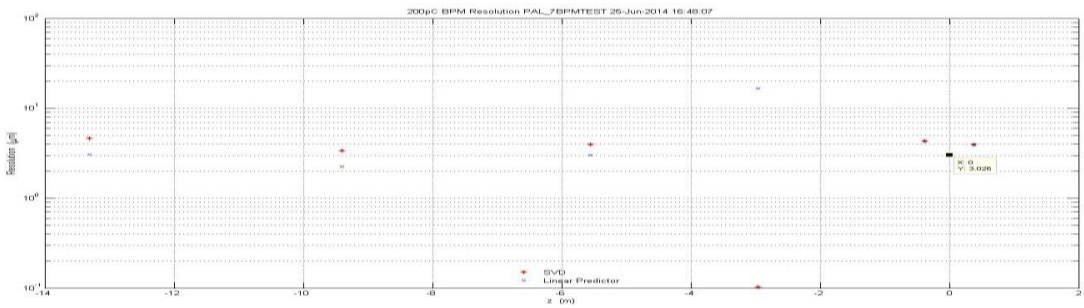


Figure 7: Multi-BPM resolution test at 200pC.

In addition to resolution tests, a series of linearity tests were performed. The BPMs that were mounted on movers have both X-axis and Y-axis mover. To verify the linearity of the electronic, the beam position was recorded while the mover swept both X-axis and Y-axis in 5mm steps. (See Figure 8 & 9) The data shows good linearity correlation over +/-1mm range.

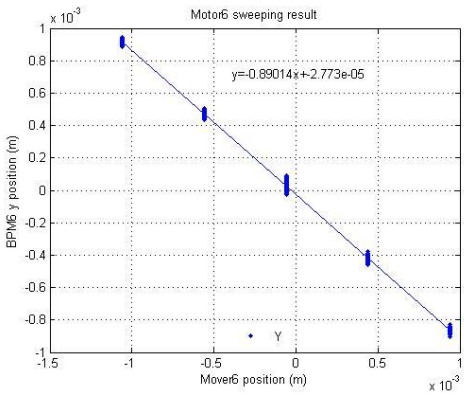


Figure 8: Y-axis BPM sweep.

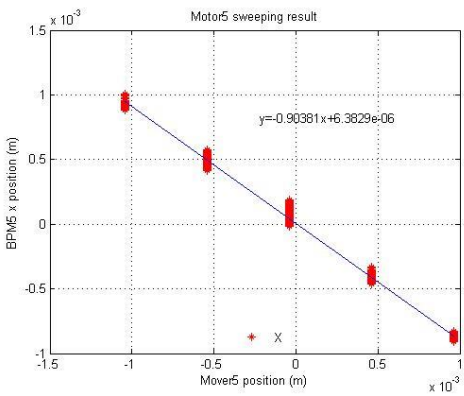


Figure 9: X-axis BPM sweep.

Summary of Test Results

Ordinarily, the BPM system is used to qualify the beam quality. When the BPM system needs to be qualified, the beam needs to be stable and predictable. After several days of testing, data shown the ITF beam has a large beam jitter due to low beam energy and the beam had a significant energy spread. The figure 10 illustrates this condition.

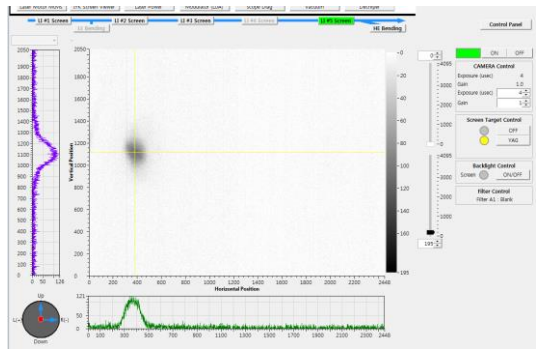


Figure 10: PAL ITF 200pC beam profile [1].

This made the resolution test difficult. Despite having difficulty qualifying the beam resolution, both PAL and SLAC's team were satisfied with the results of 10um at 10pC and between 3 and 5um resolution at 200pC.

STANFORD SYNCHROTRON RADIATION LIGHTSOURCE

After reviewing the initial test result of the 125MSPS BPM electronic, SSRL decided to upgrade two of the BPMs. The two mTCA BPMs are in the BTS (booster-to-SPEAR) transport line that is part of the injector. BTS is between the booster ring that boosts the energy of the beam from the LINAC to 3GeV and the SPEAR ring. Specifically, the BPMs are at the end of BTS where it is critical to know the exact location of the beam in order to have the best injection into SPEAR. The system has been deployed at SSRL during the summer downtime. It is now waiting for beam testing when the facility restarts during October 2014, (See Figure 11).

Copyright © 2014 CC-BY-3.0 and by the respective authors

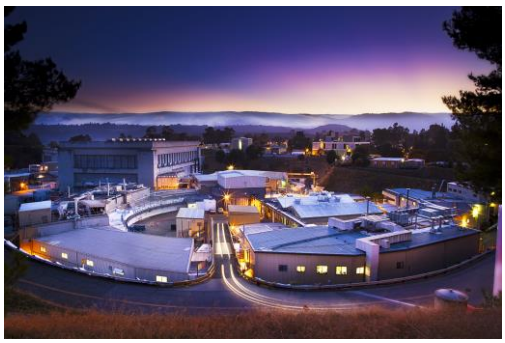


Figure 11: SSRL SPEAR.

CONCLUSION

SLAC's MicroTCA.4 based BPM system has been deployed at SLAC's LCLS, SSRL facility and PAL's ITF during 2014. Test results show the system is robust and meets the performance requirement of various facilities. To improve the analysis of the BPM resolution the code needs the linear predictor MATLAB subroutine to include or exclude the complex values. SLAC and PAL will collaborate in building 144 more stripline BPM electronics for their LINAC for their XFEL. We anticipate the system will be deployed in March of 2015.

ACKNOWLEDGEMENTS

The author would like to acknowledge the contribution of PAL's ITF team for their continuous effort in providing us with four days of beam time for the SLAC's BPM and Controls team to make the deployments successful. In addition, the continuous technical support from Wiener, NAT, and Struck Innovative System has allowed us to quickly troubleshoot infrastructure issue. This is greatly appreciated by SLAC's BPM team.

REFERENCES

[1] DOE/ SLAC WFO 13-197.a2 agreement.
[2] Private communication with So-Jeung Lee.

Copyright © 2014 CC-BY-3.0 and by the respective authors

ISBN 978-3-95450-141-0

BPM DATA CORRECTION AT SOLEIL

N. Hubert, B. Béranger, L. S. Nadolski, Synchrotron SOLEIL, Gif-sur-Yvette, France

Abstract

In a synchrotron light source like SOLEIL, Beam Position Monitors (BPM) are optimized to have the highest sensitivity for an electron beam passing nearby their mechanical center. Nevertheless, this optimization is done to the detriment of the response linearity when the beam is off-centered for dedicated machine physic studies. To correct for the geometric non-linearity of the BPM, we have applied an algorithm using boundary element method. Moreover the BPM electronics is able to provide position data at a turn-by-turn rate. Unfortunately the filtering process in this electronics mixes the information from one turn to the neighboring turns. An additional demixing algorithm has been set-up to correct for this artefact. The paper reports on performance and limitations of those two algorithms that are used at SOLEIL to correct the BPM data.

INTRODUCTION

BPM Block Description

SOLEIL BPM blocks have been designed to optimize the position measurement resolution for a centred beam. Its geometry is the same as the one that is generally used in the other parts of the machine (all arcs) for impedance reasons. Aperture is 84 mm in horizontal and 25 mm in vertical. Electrodes are circular buttons of 10 mm diameter spaced by 16 mm in horizontal and 25 mm in vertical (Fig. 1).

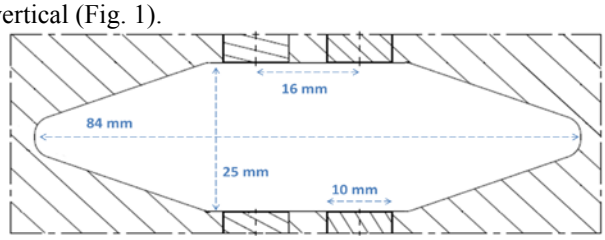


Figure 1: Cross section of a BPM. Design optimizes the resolution in the centre of the chamber.

Non Linear BPM Response

The beam position measurement is given by the usual "difference over sum" method:

$$X_{POS} = K_X \times \frac{(\Phi_A + \Phi_D) - (\Phi_B + \Phi_C)}{\Phi_A + \Phi_B + \Phi_C + \Phi_D} \quad (1)$$

$$Z_{POS} = K_Z \times \frac{(\Phi_A + \Phi_B) - (\Phi_C + \Phi_D)}{\Phi_A + \Phi_B + \Phi_C + \Phi_D} \quad (2)$$

With Φ_i the potential read on electrode (A, B, C and D), and K_X, K_Z the geometric factor for each transverse plane.

This commonly used formula is linear for a centred beam but becomes strongly nonlinear in the horizontal plane when the beam goes to large amplitudes, typically above ±2 mm (Fig. 2).

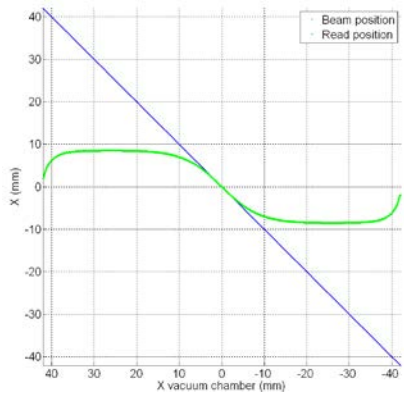


Figure 2: Read beam position (green) with respect to the real beam position (blue) in the horizontal plane for a centred beam in vertical plane. Linear region is limited to ± 2mm around the BPM centre.

CORRECTION OF THE NON LINEAR BPM RESPONSE

Theoretical Reconstruction

Beam position can also be reconstructed from the potential read on the four electrodes. The method used is based on a preliminary theoretical calculation of the BPM response [1, 2, 3]: knowing the theoretical beam position, potential on the four electrodes is calculated using the Poisson equation and the boundary element method. This step requires the definition of a mesh to slice the vacuum chamber wall into elementary parts. Then, in a second step the theoretical BPM response is inverted using the standard Newton method. This method gives a very good beam position reconstruction (Fig. 3) for a large area (~± 15 mm in H, ~±8 mm in V around the BPM centre), compared to the difference over sum method.

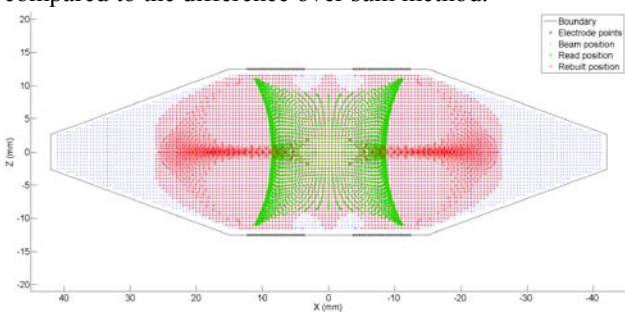


Figure 3: Reconstruction of the position of the beam (blue points) using the difference over sum method (green points) and the Newton inversion (red points).

Copyright © 2014 CC-BY-3.0 and by the respective authors

ISBN 978-3-95450-141-0

In small areas (lob shapes) close to the buttons, the convergence does not work. It is because one of the points in the iterative process goes outside the vacuum chamber and in this case, convergence is lost. An additional checking has been implemented in the algorithm to retrieve any iterative point from the outside to the internal side of the vacuum chamber. With this correction, reconstruction in all the centre area of the BPM is almost perfect with an error close to the numerical resolution (Fig. 4).

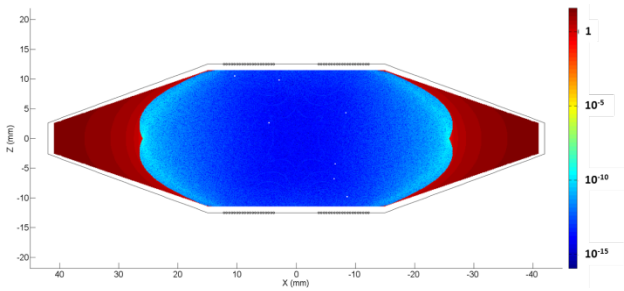


Figure 4: Error between the theoretical beam position and the rebuild position using boundary element and Newton inversion method with the additional lob correction. In the area of interest (±15mm in H, ± 10 mm in V around the BPM centre), the error is below 10^{-10} mm

At large horizontal amplitudes the iterative process for Newton method cannot converge as it has to cross an area (crescent-like shape on left and right sides on Fig. 4) where the Jacobian cancels out in the mathematical resolution: because of this singularity no mathematical solution is founded. Nevertheless by choosing a starting point (for the iterations) on the good side of the crescent, the reconstruction works fine. The number of iterations to reconstruct with an error below 10^{-6} is less than ~15 for any point in the vacuum chamber except on this crescent (Fig. 5). Overall this method is much faster than directly solving the Poisson equation using a mesh code for static electromagnetic problem.

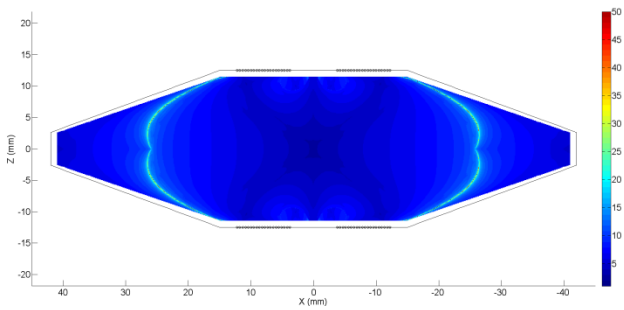


Figure 5: Number of iterations required to reach a reconstruction with an error below 10^{-6}. The convergence cannot be reached for the points located on areas with a crescent shape.

Experimental Reconstruction

Reconstruction of theoretical data is done using the same mesh as the one used to calculate the BPM response. In this case, whatever the mesh granularity, the reconstruction error is always very good. Nevertheless, in the case of experimental data, the mesh granularity that is chosen impacts the results of the reconstruction because of self-consistency between the simulation and the reconstruction model. The area where the reconstruction is the most sensitive to the mesh definition is on the horizontal wall (few % errors), then on the oblique wall (~ % errors), and has finally little influence far from the BPM centre on the vertical wall. The reconstruction dependence to the mesh definition shows an asymptotic value when the mesh becomes infinitely thin (Fig. 6).

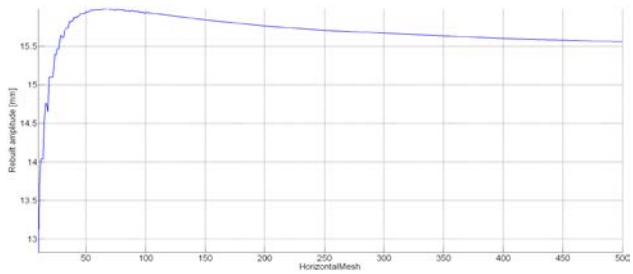


Figure 6: Dependence of the reconstruction to the mesh definition. Case of the horizontal plane reconstruction for a mesh between 10 and 500 points on the horizontal wall. Reconstruction reaches an asymptotic value for an infinitely small mesh granularity.

Intuitively, the most accurate reconstruction is done for an infinitely thin mesh. But the computation time needed to reconstruct with a large number of points (>200) to define the mesh increase drastically. Nevertheless, this dependence can easily be fitted by equation (3):

$$f(x) = C_1 + \frac{C_2}{x + C_3} \qquad (3)$$

where x is the number of points in the mesh. Actually, the reconstruction can be done with a reasonable (~100) number of points in the mesh and then post-corrected.

A dedicated experiment on the machine has been carried on to verify the efficiency of the reconstruction: horizontal beam position has been scanned from 0 to 15 mm with static bumps (limited to 15 mm by the horizontal physical acceptance), and reconstructed position has been compared to how much the scraper has to be moved to maintain a lifetime (on purpose) reduced to 1 hour (case 1) or 2 hours (case 2) (Fig. 7).

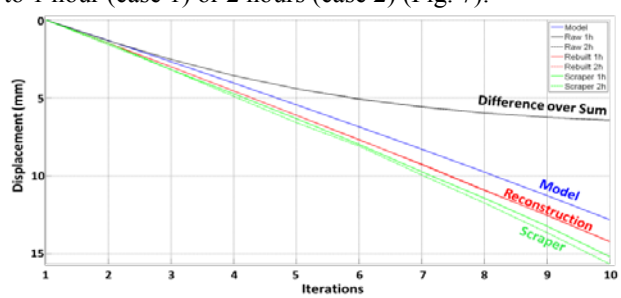


Figure 7: Good agreement between the position reconstruction (red) and an experimental check using the

Copyright © 2014 CC-BY-3.0 and by the respective authors

ISBN 978-3-95450-141-0

scraper (green) or the model (blue), compared to the usual difference over sum method results (black).

DEMIXING OF THE TURN-BY-TURN BPM ELECTRONICS DATA

SOLEIL BPM Electronics is able to provide position data at the revolution frequency sampling rate. Nevertheless, due to internal filtering when decimating ADC samples (at 109 MHz) down to turn-by-turn data (at 846 kHz), those samples are not independent and contain information from more than one turn. This phenomenon can be seen looking at the impulse response of the BPM electronics. This has been registered on the sum signal of the BPMs when the beam is doing only one turn in the storage ring, and killed at the end of the turn (Fig. 8).

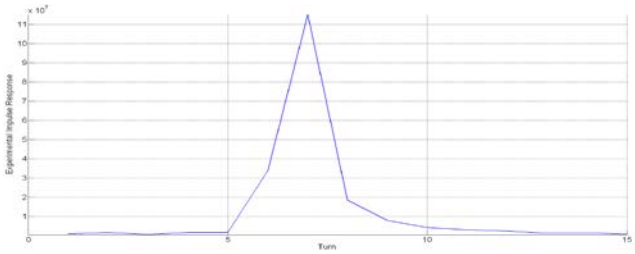


Figure 8: Impulse response of the BPMs measured when the beam is doing only one turn in the storage ring. Electronics filters over ~6 turns to produce turn-by-turn samples.

A correction algorithm has been developed in order to correct for that "mixing", based on the method described in [4]: as each turn-by-turn sample is a linear combination of ADC samples, a correction filter can be built from the impulse response. This is done in the frequency domain by inverting the Fourier transform of the impulse response. Then, going back to the time domain the resulting filter can be convoluted with the position data to make the turns independent (Fig. 9).

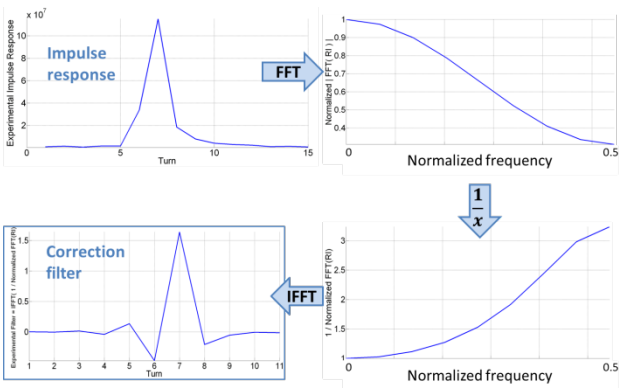


Figure 9: Construction of the correction filter. The fast Fourier transform of the impulse response is inverted and then brought back to the time domain to obtain the correction filter to be convoluted with the turn-by-turn data.

This demixing correction can be combined with the correction of the nonlinear BPM response in the case the turn-by-turn data are used to measure the beam position at large amplitudes (Fig. 10).

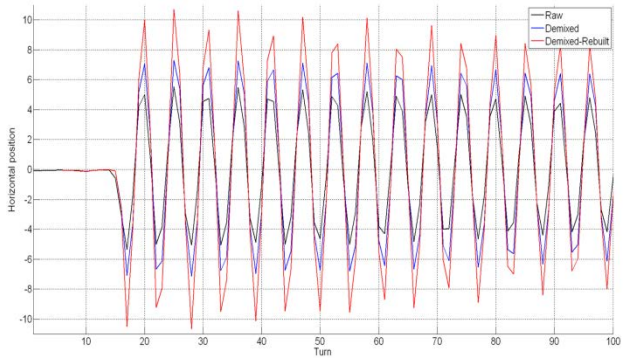


Figure 10: Turn-by-turn BPM corrections in the case of a response to a pinger magnet in the horizontal plane. Raw data (black curve) are first demixed (blue curve) and then corrected for the non-linearities (red curve).

CONCLUSION

Dedicated algorithm have been developed to correct for: the non-linearities induced by the BPM block geometry when the beam is at large amplitude, and for the mixing of the information between neighbouring turns for turn-by-turn data that are computed by the electronics. Both corrections give satisfactory results and are used for the machine physics studies.

ACKNOWLEDGMENT

This paper reports the result of the work performed by Benoît Beranger during its Master-internship at SOLEIL. The authors would also like to thank Guenther Rehm for the helpful discussions about demixing principle and trainee Foued Talbi for his initial work on the BPM response based on boundary condition method.

REFERENCES

[1] T. SHINTAKE et al., «Sensitivity calculation of beam position monitors using boundary element method,» *Nuclear Instruments and Methods in Physics Research,* pp. 146-150, 1987.

[2] A. Stella, «Analysis of the Dafne beam position monitor with a boundary element method,» *Dafne Technical Note CD-10, December 19th,* 1997

[3] R. W. Helms et al, Phys. Rev. ST Accel. Beams 8, 062802 (2005).

[4] R. Bartolini et al., "Calibration of the nonlinear ring model at the Diamond Light Source", Phys. Rev. ST Accel. Beams 14, 054003 (2011).

Copyright © 2014 CC-BY-3.0 and by the respective authors

DESIGN OF A NEW BLADE TYPE X-BPM

N. Hubert, N. Béchu, J. Dasilvacastro, L. Cassinari, J-C. Denard, M. Labat, J-L. Marlats, A. Mary,
Synchrotron SOLEIL, Gif-sur-Yvette, France
S. Marques, R. Neuenschwander, LNLS, Campinas, Brazil

Abstract

A new photon Beam Position Monitor (X-BPM) design has been developed in collaboration between the Brazilian Synchrotron Light Laboratory (LNLS) and SOLEIL Synchrotron [1]. This blade-type X-BPM has been carefully studied in order to minimize beam current dependence and temperature dependence. The main advantage of the design is a better stability compared to the standard X-BPMs initially installed at SOLEIL. This new design is used for the new X-BPMs installed at SOLEIL and is being considered for the bending magnet front-ends of the future SIRIUS [2] light source. A first "double" unit has been constructed by LNLS for the two canted Anatomix and Nanoscopium SOLEIL beamlines, and has been installed at SOLEIL in May 2014. Design and first results are presented.

INTRODUCTION

X-BPMs are used in synchrotron machines to monitor the photon beam position in the beamline frontend. They are composed of a stand and a head that supports four blades placed in the photon beam halo (Fig. 1).

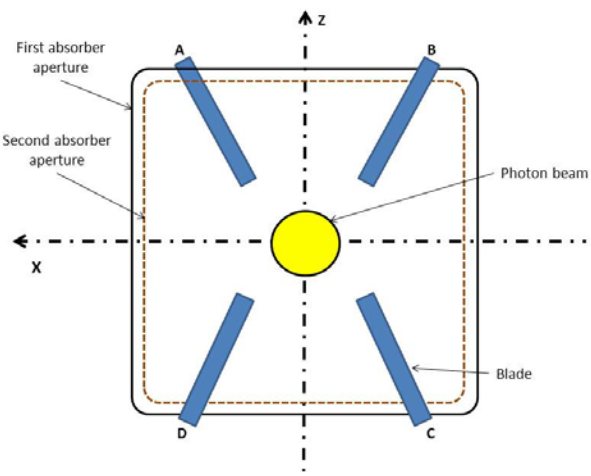


Figure 1: Layout of an X-BPM using blade signals for position measurements of a photon beam produced by an insertion device.

Taking benefit of the photoemission principle, the photon beam will create on each blade a current that vary with the distance between the beam and the blade. The centre of mass of the photon beam is then deduced using the classical difference over sum equation:

$$X_{POS} = K_X \times \frac{(I_A + I_D) - (I_B + I_C)}{I_A + I_B + I_C + I_D} \quad (1)$$

$$Z_{POS} = K_Z \times \frac{(I_A + I_B) - (I_C + I_D)}{I_A + I_B + I_C + I_D} \quad (2)$$

With I_i the current read on blade (A, B, C and D), and K_X, K_Z the horizontal and vertical geometric factors, for photon beams produced by an undulator. In the case of bending magnet or wiggler photon beams, only the vertical position is measured by two pairs of blades.

At SOLEIL, 21 X-BPMs are already installed on undulator beamline frontends, whereas 11 are installed on bending magnets/wiggler beamline frontends.

At LNLS, in total, four X-BPMs are installed, two X-BPMs in the U11 undulator front-end and other two in the bending magnet X-Ray diagnostics beamline.

STABILITY REQUIREMENTS

In its original design, the X-BPM was made of a head supported by a stand, both made of stainless steel (Fig. 2). This design was subject to mechanical deformation in case of temperature variations like tunnel air temperature drifts or changes in the heat load deposited on the X-BPM by the beam. As a consequence, photon beam position reading could be impacted by a few µm, in particular during the few tens of minutes following a reinjection (in case of beam loss).

For beamlines requiring a high stability, the stand has been made of INVAR to reduce its vertical expansion. This expansion was consequently reduced from 3 µm (stainless steel) to 0.3 µm (invar) for a 0.2 °C temperature variation.

Then it has also been decided to study a new X-BPM head to minimize the position dependence to the heat load variations. This work has been done in collaboration between SOLEIL and LNLS.

Since a 3rd generation light source is currently under construction at LNLS, the new concept of XBPM has been considered as candidate solution for all bending magnet beamline front-ends and possibly for some undulator beamlines.

MECHANICAL DESIGN

When designing the new X-BPM head, efforts have been focussed on an optimized power dissipation to minimize the effect on the position measurement.

Symmetrical Thermal Expansion

In its new design, the X-BPM head presents a (beam) axial symmetry, and is fixed to the stand by a cradle in the beam plane. The heat load deposited by the beam is supposed to be homogeneous around its axis which is true

Copyright © 2014 CC-BY-3.0 and by the respective authors

ISBN 978-3-95450-141-0

at least for a centred beam. The resulting thermal expansion of the head material will also be symmetric to the beam axis and cancelled when calculating the beam position using formulae (1) and (2).

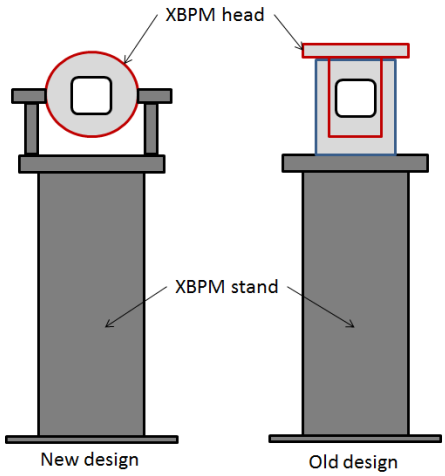


Figure 2: X-BPM head (in red) and stand in old and new designs. Whereas the old X-BPM head was plunging into the vacuum chamber, the new one is supported by a cradle and presents an axial symmetry to cancel the thermal expansion effect in the position calculation.

Heat Load

The heat load deposited by the beam is absorbed by a mask integrated in the X-BPM head. This 30 mm long mask is made of copper and water cooled. The blade support, also made of copper (32 mm), is isolated from the mask and water cooled also. Temperature sensors equip the two copper pieces that are brazed on stainless steel parts, forming the X-BPM head (Fig. 3).

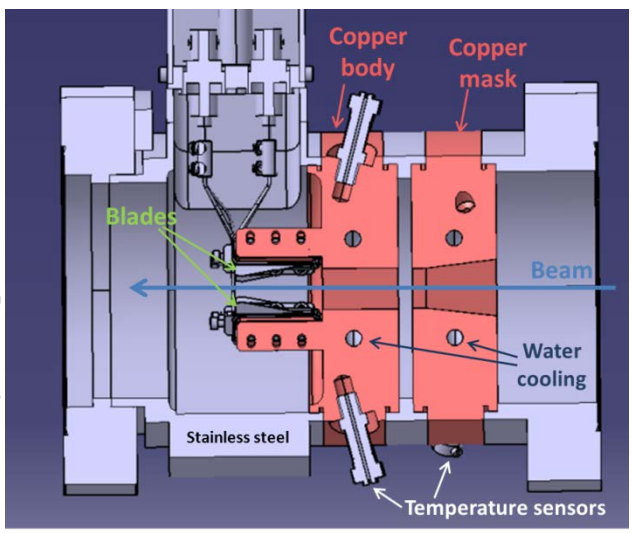


Figure 3: Different pieces of the X-BPM head: mask and body are both made of copper but separated to avoid thermal exchanges. A water cooling circuit is used to extract heat load.

Blades are electrically isolated from the copper body on which they are fixed. Insulator used is Aluminium Nitride ceramics that have a good thermal conductivity to extract

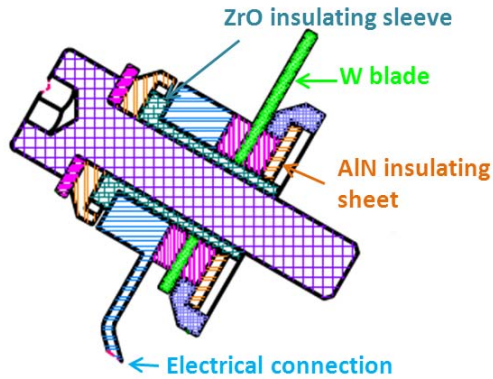


Figure 4: The stack made for blade insulation preserves a good thermal conductivity to extract the heat load deposited by the beam on the blade.

Compacity

With the old XBPM design, an additional absorber (with its associated pumping port) had to be installed upstream in order to protect the XBPM head from unwanted missteered beam. This new design integrates the absorber (mask), saving an additional pumping port and pump, and is only 191 mm long.

MANUFACTURING

It has been decided to manufacture a double unit head to take benefit of the already existing X-BPM INVAR stand installed on the double canted SOLEIL beamlines Nanoscopium and Anatomix (Fig. 5).

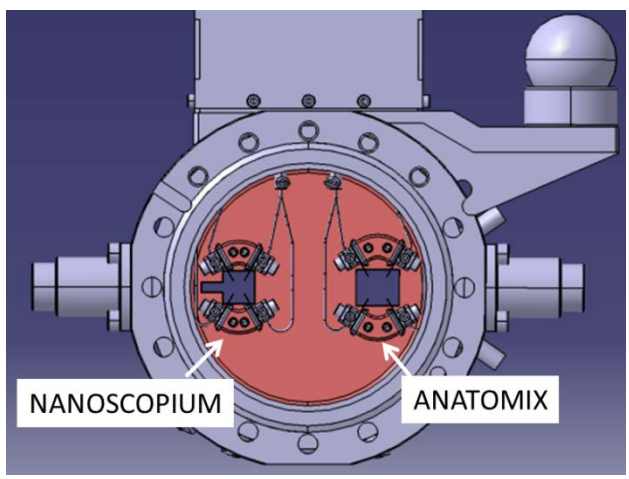


Figure 5: Double unit X-BPM head that has been manufactured for testing on the canted Anatomix and Nanoscopium SOLEIL beamlines.

The manufacturing has been done at LNLS workshop, including brazing and electrical discharge machining (EDM) operations.

Copyright © 2014 CC-BY-3.0 and by the respective authors

PERFORMANCES

The new double unit X-BPM was installed in May and commissioned in July 2014. We first calibrated the XBPM response and then analysed its performances in terms of stability.

The calibration consists in the experimental measurement of the geometric factors K_X and K_Z for each X-BPM unit, which finally enables to get an absolute measurement of the photon beam centroid position. The simplest method consists in displacing the X-BPM unit around the photon beam, but this new X-BPM is not mounted on translation stages as previous SOLEIL's X-BPMs. We displace instead the electron beam on parallel orbits. The displacement amplitude is about +/- 0.25 mm in both planes by steps of 0.05 mm. For the Anatomix X-BPM we found a coefficient of K_X =5.1 in the horizontal and K_Z =2.9 in the vertical plane. For the Nanoscopium X-BPM, we found a coefficient of K_X =2.64 in the horizontal and K_Z =1.68 in the vertical plane. The Nanoscopium coefficients are slightly lower than those of Anatomix because the Anatomix undulator is closer to the X-BPM, allowing higher intensity on the blades and therefore higher sensibility.

The X-BPM stability performances were evaluated using the following procedure:

- The X-BPM is initially "stable": i.e. operated in nominal conditions (at constant current in the synchrotron and constant incident photon flux from the insertion device) for several hours. In these conditions, we can assume that all X-BPM components are thermalized.
- Cooling: The insertion device gap is opened to cool down the X-BPM unit. Every ten minutes the gap is closed for a couple of seconds in order to probe its response during this process.
- Heating (1): Once cooled, the insertion device gap is closed again to observe the heating of the X-BPM by the photon beam.
- Heating (2): The electron beam is finally killed for more than 30 minutes in order to cool both the X-BPM and the whole synchrotron. And after re-injection and closure of the insertion gap, we observe the X-BPM together with the machine stabilization.

In order to ease the stability analysis of the X-BPM unit itself, we compare the X-BPM position measurement to the position predicted by the BPMs measurement using a projection in the X-BPM plane. We compared those measurements to those performed on the previous X-BPM, which was also double unit though only equipped with blades on the Nanoscopium unit. A trend of the experimental session for the characterization of the Nanoscopium unit is presented in Figure 6. The results are summarized in Table 1.

Table 1: Performances in terms of stabilization of the Nanoscopium X-BPM. Difference between position measured by the XBPM and the projection of the eBPM at the XBPM location is evaluated and time needed to stabilize.

		H	V
Nanoscopium			
Old Design	XBPM – eBPM projected	**12 µm** stabilized in **20 min**	**27 µm** stabilized in **30 min**
New Design	XBPM – eBPM projected	**26 µm** stabilized in **5 min**	**24 µm** stabilized in **15 min**

Thanks to the new X-BPM design, the time required by the X-BPM measurement to stabilize after machine injection and/or insertion device gap closing has been reduced and is found below 15 minutes i.e. two to four times shorter than with the old design. The time to stabilize the machine itself after injection is now the limiting factor in terms of stability.

COSTS ANALYSIS

The first X-BPM heads of SOLEIL were designed and manufactured by the FMB company (Germany) [3]. The stands were designed by SOLEIL and manufactured in France. The use of INVAR instead of steel or 316L to improve the thermal stability of the X-BPM also caused a huge increase of the material cost. A stand in INVAR is 3 times more expensive than a stand in stainless steel. Because of the lower quantity of INVAR, the price difference of an X-BPM head in INVAR instead of 316L is negligible. But the manufacturing of the head in INVAR caused other issues. All SOLEIL front-end vacuum chambers are 316L and baked up to 250°C. Using a copper ring to link a 316L with an INVAR flange, with respectively $12*10^{-6}$ K^{-1} and $1.2*10^{-6}$ K^{-1} thermal expansion coefficients, causes systematic leakages at the junction after baking. To prevent such situation, baking is locally reduced at 150°C but was still considered inconvenient by the vacuum group. The manufacturing in 316L according to the new design therefore also presented advantages in terms of operation at SOLEIL. The first XBPM head unit based on the new design has been manufactured at LNLS. Since then, SOLEIL ordered two additional "single unit" XBPM to private companies, we could compare the price of an old and new design head in 316L. The difference is negligible. But we do no longer need to install an absorber before the XBPM since it is included in the new head design, which corresponds to a money save of approximately 10.000 €.

Copyright © 2014 CC-BY-3.0 and by the respective authors

ISBN 978-3-95450-141-0

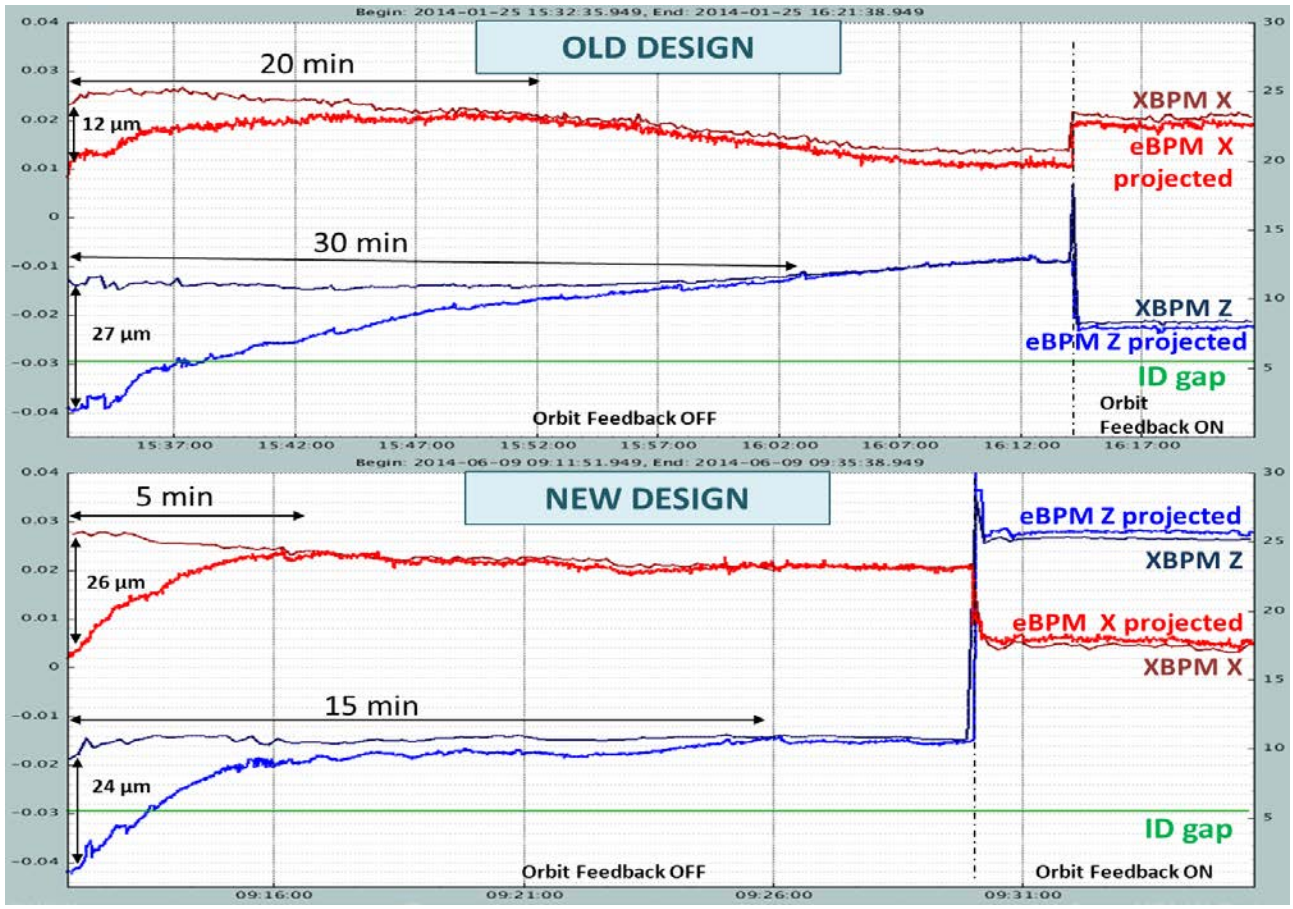


Figure 6: Stability comparison of the Nanoscopium X-BPM: (Up) for the old design and (bottom) for the new design in both horizontal and vertical plane. Stabilization time of the measurement after an injection from 0 to 430 mA has been reduced in both planes with the new design.

CONCLUSION

A fruitful collaboration between LNLS and SOLEIL has been set up to design a new blade type X-BPM head. The main goal which was an improvement of the thermal stability compared to already existing designs, preserving the manufacturing budget, has been achieved. This new design is now used for the new X-BPM to be installed at SOLEIL (already two more units have been manufactured) and is supposed to be used for the bending magnet X-BPM of the future SIRIUS light source.

ACKNOWLEDGMENT

Authors would like to thank SOLEIL and LNLS legal and purchase department for their work establishing the Memorandum of Understanding between our two institutes. We also would like to express our gratitude to the LNLS technical and engineering groups, especially to our colleagues from mechanical designs, materials engineering and mechanical workshop groups.

REFERENCES

[1] L. Nadolski, et al., “SOLEIL Operation and On-going Projects”, MOPRO051, IPAC’14, Dresden, Germany. (2014).

[2] L. Liu et al., “Update on Sirius, the New Brazilian Light Source”, MOPRO048, IPAC’14, Dresden, Germany, (2014).

[3] FMB Berlin XBPM design: http://www.fmb-berlin.de/attachments/article/117/BPM_for_ID_Radiation.pdf

Copyright © 2014 CC-BY-3.0 and by the respective authors

COMMISSIONING OF THE ALBA FAST ORBIT FEEDBACK SYSTEM

A. Olmos, J. Moldes, R. Petrocelli, Z. Martí, D. Yepez, S. Blanch, X. Serra, G. Cuni, S. Rubio,
ALBA-CELLS, Barcelona, Spain

Abstract

The ALBA Fast Orbit FeedBack system (FOFB) started its commissioning phase in September 2013, when all the required hardware was installed and the development of different controls for the feedback started. This report shows our experience tuning the different parameters to setup the system, together with vibration and beam noise measurements at different conditions. Finally, the present results and future steps for this system are described.

FOFB DESCRIPTION

ALBA Synchrotron machine is an already running facility providing beam for users in decay mode (2 injections per day). Even though ALBA has been demonstrated to be a low noise machine, the near use of a Top-up injection mode [1] will demand a better and faster feedback than the current Slow Orbit FeedBack (SOFB). Description of the FOFB layout and the different devices of the system has been already presented on IBIC13 [2]. A description of what have been done during the commissioning and the bottlenecks we have found is reported here.

Correction Calculation and GUI

Most of the effort and time during the last year has been dedicated to the development of the correction code and all required controls associated infrastructure. Correction algorithm runs on the 16 distributed CPUs where the Beam Position Monitors (BPMs) data is transferred to and the new setpoints for the correctors power supplies are computed. Testing of different CPUs has been performed in order to find the ideal hardware to match the FOFB requirements. Performance of one and two cores CPUs has been demonstrated to be not sufficient, since some of the 100 us loops of the FOFB are lost when using these CPUs [3]. Final solution using 4 cores CPUs matches the requirements, especially after the distribution of the different processes to the different cores: one core to do BPMs position data reading, another to perform correction calculation and power supplies interfacing and the other cores to take care of interruptions, handling of operating system, …

Each CPU runs a C correction code that retrieves the position data from the PMC FPGA Board [2]. Correction computation is based on broadly used SVD algorithm and a PI loop controller. 16 TANGO device servers are running on the 16 cPCI crates hosting the CPUs, while a high level device server controls the whole system. A preliminary Graphical User Interface (GUI) has been developed for the commissioning phase of the FOFB, from where we can start/stop the feedback system and set the PI and RF frequency loops parameters (Fig. 1).

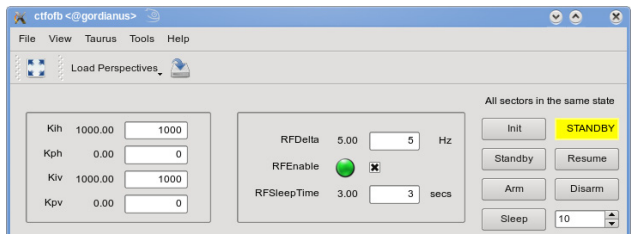
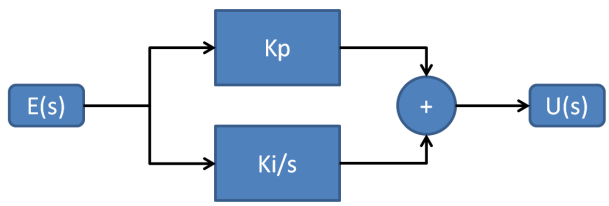


Figure 1: Commissioning FOFB GUI.

PI Controller

Different implementations of the PI loop after the SVD calculation have been tested, being the one showed on Fig. 2 the implementation that gave best results.



$$U(n) = U(n-1) + A0 * E(n) + A1 * E(n-1)$$

$$A0 = (Ki * Ts / 2) + Kp$$

$$A1 = (Ki * Ts / 2) - Kp$$

Figure 2: PI loop implementation.

Last version of the correction code has separated PI loops for horizontal and vertical plane, since the feedback requirements and beam noise are different depending on the plane.

RF Frequency Control

Our intention is to run just the FOFB during operation, without SOFB. That means that the control of the RF frequency has to be moved from the SOFB, running nowadays as a Matlab MiddleLayer routine, to the FOFB system. Decision has been taken to implement a routine on the high level FOFB device server that monitors the dispersive pattern on the correctors and changes RF frequency in case it is needed. Minimum frequency step and the correction periodicity will be modified from the main FOFB GUI.

System Limitations

Related with the RF frequency control, one of ALBA limitations is that we don't have fast and slow correctors, so the RF frequency cannot be handled in separate power supplies from the FOFB correction.

Copyright © 2014 CC-BY-3.0 and by the respective authors

ISBN 978-3-95450-141-0

Another limitation is that we cannot have a readback of the current from the correctors power supplies, since the time needed to handle the PCI interruptions and acknowledgments occupies too much of the PCI bus time and spoils the performance of the correction loop. The FOFB system is based on the assumption that the correction setpoint sent to the power supply is properly applied.

The electronics layout in the cPCI crate forces the transfer of position data from the PMC FPGA Board to the CPU to go through two PCI bridges. The use of Burst mode data transfer should allow this communication to be done in about 20 us, but that's not the case. For whatever reason not yet understood, burst mode stops after 2 transfer cycles and starts again. Not being capable to use the Burst mode, ALBA FOFB system can only warranty that half of the BPMs data cycles are processed, reducing the handling of position data from 10 kHz to 5 kHz rate.

CORRECTION RESULTS

Two different setups have been used for the time being to analyze the performance of the FOFB system: using a trim coil power supply as a beam perturbation source and closing an Insertion Device.

Trim Coil Excitation

A programmed waveform on a horizontal trim coil power supply has been used as beam excitation. The waveform is built as a combination of sinewaves at frequencies 1.2, 3.6, 12, 36 and 120 Hz. That setup was widely used on the days when we were finding the proper tuning of the PI loop parameters (Kp and Ki).

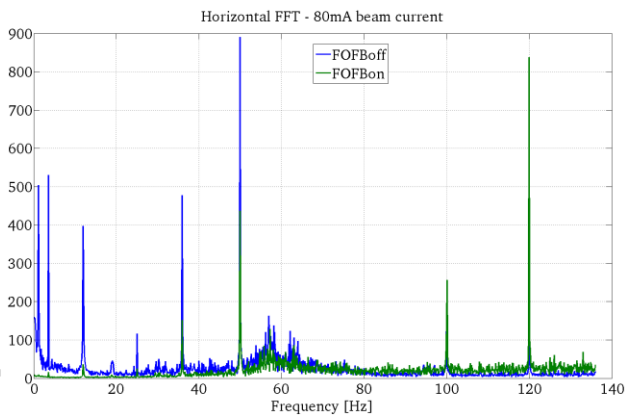


Figure 3: Horizontal FFT of beam position when FOFB was ON and OFF. Trim coil components are identified at 1.2, 3.6, 12, 36 and 120 Hz.

Figures 3 and 4 show the correction capabilities of the FOFB system on an 80 mA beam when using PI loop gains of Kp=0 and Ki=1000. In the FFT spectrum one can identify the components create by the trim coil. The other perturbations at 19 and 25 Hz are from the beam and their sources have not been yet found.

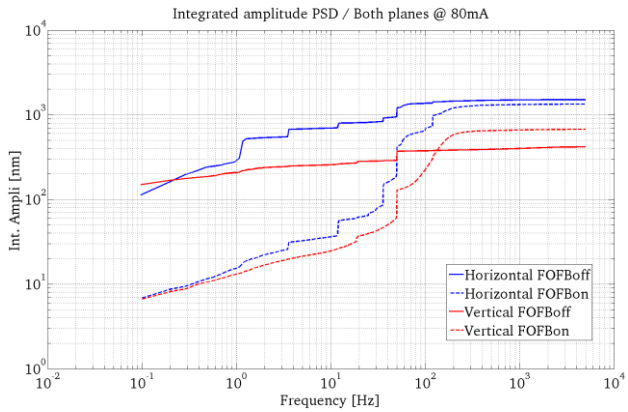


Figure 4: Integrated spectrum of both planes, with FOFB running or not. Beam is excited at different frequencies using a trim coil power supply.

The system properly reduces the contribution of the low frequency components and starts to increase their amplitude for frequencies above ~100 Hz.

Correction of ID Perturbation

ALBA has one super-conducting wiggler, one multipole wiggler, two in-vacuum undulators and two apple-type undulators. For the time being, only the effect of the in-vacuum undulator of XALOC beamline has been analyzed. Figure 5 shows the horizontal and vertical position of the 88 BPMs under different FOFB and ID movement combinations.

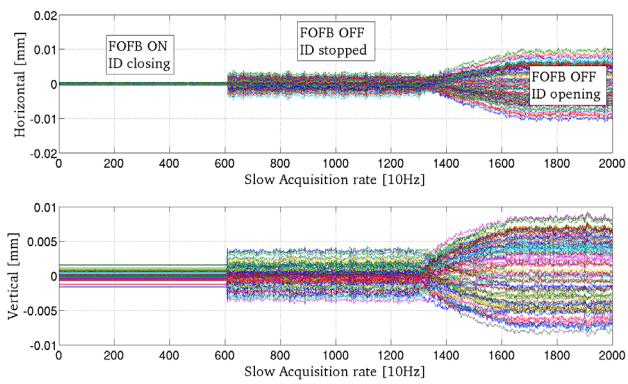


Figure 5: BPMs position when closing/opening the ID.

One can see the overall position correction to the centre of the BPM and also the noise reduction well below the micrometre level, but on a slow rate time scale (10 Hz).

FOFB performance at higher frequencies under same scenario can be seen on Fig. 6 and 7. Integrated noise over the frequency is showed for the BPMs close by the ID and at the source point, typically better since it's usually at the centre of the straight section hosting the ID. FOFB specifications commonly refer to beam stability below 10% of the beam size and beam angle below 10% of beam divergence at the source point. For the particular case of XALOC beamline, the 10% specification refers to position stability below 13.73 um/0.65 um and angle stability below 5.14 urad/0.53 urad for horizontal and vertical planes respectively. Both position and angle

Copyright © 2014 CC-BY-3.0 and by the respective authors

ISBN 978-3-95450-141-0

stability specs at the source point are accomplished at any given frequency when using ALBA FOFB.

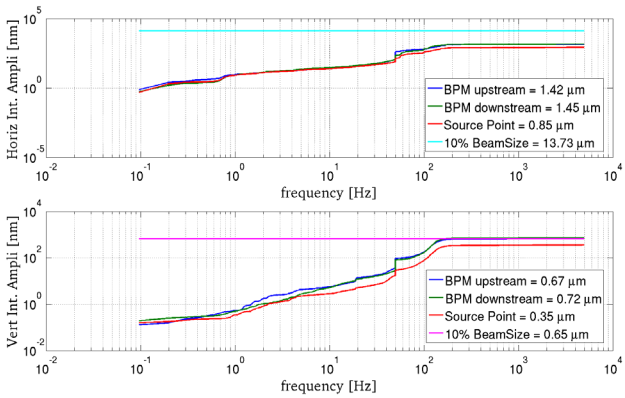


Figure 6: Beam position stability at source point wrt specification of 10% of beam size.

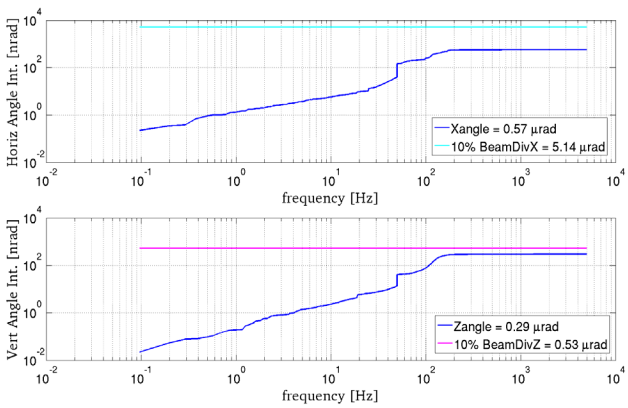


Figure 7: Beam angle stability at source point wrt specification of 10% of beam divergence.

PROBLEMS AND IMPROVEMENTS

Commissioning phase of any system is the time to face problems and to try different solutions and improvements. Here we report about some of them.

Wrong Corrector Setting

After a long shutdown period in April'14, the FOFB behavior was completely spoiled for unknown reasons. Figures 8 and 9 show a performance comparison before and after the shutdown when running the FOFB on a 15 mA beam. No problem was seen when FOFB was OFF. After discussion with Diamond colleagues, they suggested to do a tracking of all the correctors setpoints calculated by the FOFB. That needed some extra programming to be able to store 10 seconds of data on all 176 correctors at a 5 kHz rate and post-process it. The analysis of the data showed that one particular vertical corrector was introducing the perturbation to the beam on the region around 30 Hz (Fig. 10). Deeper investigation on that corrector power supply confirmed that its internal PI regulator was not properly configured.

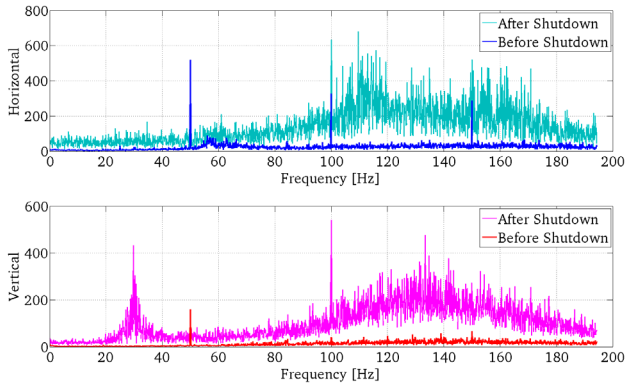


Figure 8: FFT spectrum comparison before and after the shutdown when running the FOFB @ 15 mA beam.

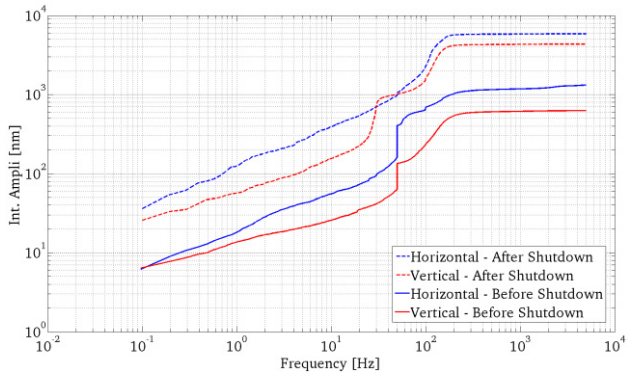


Figure 9: Integrated spectrum comparison before and after the shutdown when running the FOFB @ 15 mA beam.

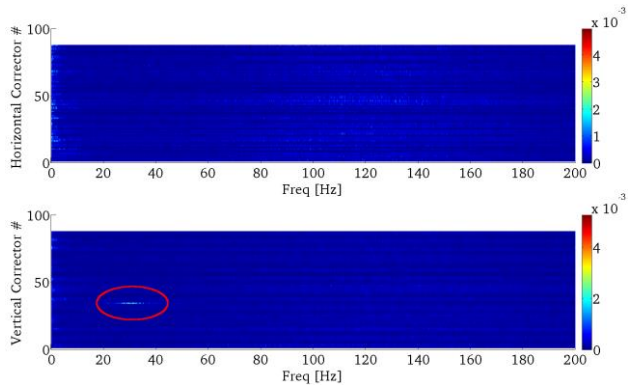


Figure 10: Frequency map of the 88H and 88V correctors setpoints calculated by the FOFB.

Kickers Pulse Suppression

ALBA aims to run in Top-Up mode by the end of 2014, with periodic injections every 10 minutes at a 3 Hz rate. Until now, while running in decay mode, the effect of the injector on the beam orbit has not been an issue since shutters were closed and beamlines not operating during the injection. The study of the effect of the injection kicker magnets on the orbit has revealed a horizontal perturbation near the mm at some BPMs, especially if the injection bump is not properly closed. First tests of Top-up injection together with FOFB showed an orbit

ISBN 978-3-95450-141-0

Copyright © 2014 CC-BY-3.0 and by the respective authors

distortion after the kicker pulse due to the FOFB system, which tries to correct the high frequency kicker pulse perturbation (and obviously it cannot).

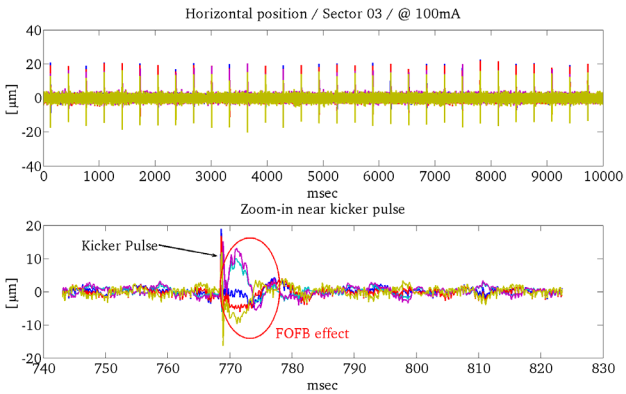


Figure 11: Kicker pulse position distortion and FOFB effect seen on 5 BPMs.

Figure 11 shows the position distortion due to the 3 Hz kicker pulses during a 10 seconds injection. Plot at the bottom is a zoom-in version near one of the kicker pulses. It can be seen both the kicker pulse position perturbation and the effect of the FOFB system trying to correct that perturbation. Figures 12 and 13 show how the noise reduction changes when FOFB and injector are running or not.

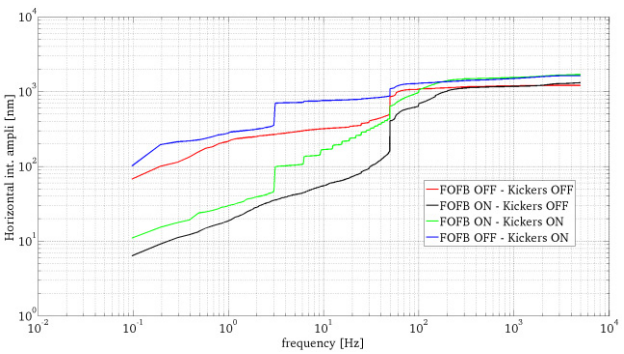


Figure 12: Horizontal comparison for different FOFB and injector status.

The 3 Hz and its harmonics can be clearly seen on the spectrum and are not properly corrected by the FOFB. Even under these conditions, the FOFB is capable to correct the perturbations inside specs up to 200 Hz (10% Vertical Beam size is 0.65 um).

We tried the system to ignore the kicker pulse by defining position limits beyond which the FOFB should not correct, but first attempts ran without success and just degraded the FOFB performance.

Correctors Bandwidth

One of the last improvements we have tried is the modification of the correctors power supplies bandwidth. Intention is to push a bit forward the correction capabilities of the FOFB loop, aiming to have a better high frequency correction.

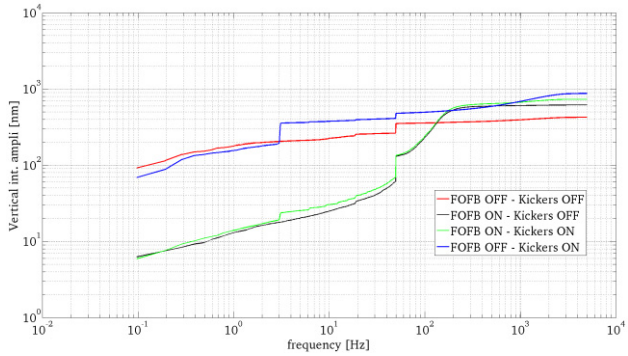


Figure 13: Vertical comparison for different FOFB and injector status.

Figure 14 shows the preliminary results we obtained just before summer shutdown. Improvement is little but confirms that we are on the good way. Note that test has been done on a 15 mA beam, so results will be better (lower noise) on a standard 100-150 mA beam.

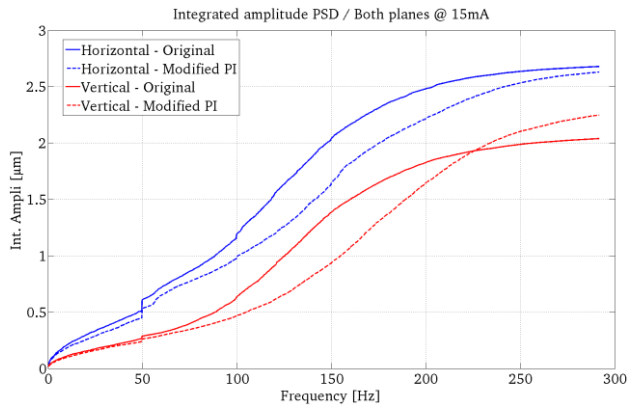


Figure 14: Integrated spectrum improvement when using the modified PI regulator for the correctors power supplies on a 15 mA beam.

NEXT STEPS AND FUTURE PLANS

Filtering of 50 Hz Component

The 50 Hz perturbation is the main contributor to the noise spectrum in our storage ring and its reduction will improve the FOFB overall performance. Even though the system already meets the ALBA FOFB specifications, intention is to implement a Notch-type filter on the computation CPU to go further. The way to do it is nowadays under discussion.

Interlocking of the FOFB

The main pending task regarding the commissioning of the FOFB is to ensure the loop reliability. On such a fast system, the failing of a BPM or a corrector power supply leads to an immediate beam loss due to wrong beam steering. Checks and limitations on position values and correctors setpoints have to be implemented at a 5k Hz rate in order to interlock the FOFB system in a controlled

Copyright © 2014 CC-BY-3.0 and by the respective authors

ISBN 978-3-95450-141-0

way and do not kill the beam. Recovery of FOFB operation after such an interlock is also to be defined.

Upgrade of the FOFB System

The use of already obsolete electronics and the system limitations we found since day one pushed us to think on a future system upgrade. Main purpose of the upgrade is the replacement of the PMC-FPGA board, hosting the BPMs position reading, and the replacement of the CPU, in charge of the correction calculation.

The upgrade will be done in two phases. First phase will change the current Micro-Research EVR-230 FPGA boards [2] by AFC2310-A0 electronics from IOxOS [4]. This first phase upgrade will bring following improvements:

- Better FOFB redundancy and reliability since new electronics have 2 SFP ports to be used as optical links for BPMs position data transfer (current electronics do only have one SFP port).
- More powerful and longer lifetime Xilinx Virtex-6T FPGA (current Virtex-II FPGA is obsolete)
- Increase of position transfer speed to 10 kHz to have a higher FOFB bandwidth (now we run at 5 kHz).
- Two input ports could be used to synchronize the FOFB in all sectors and to disable the correction during the duration of the injection kicker pulses.

The main tasks that have to be done on phase I are the integration of the Diamond Communication Controller [5] on the new boards and the migration of the correction computation from the CPU to the FPGA.

Upgrade phase II is based on the modification of the correctors power supplies interfacing. Intention is to migrate the controllers of the correctors that are embedded on the IP modules to the new FPGA. To accomplish that, a modification on the cPCI crates has been done to use the backplane I/O connector to drive the correctors power supplies. An intermediate board will be needed to change signals from electrical to optical.

Pictures of the IOxOS boards are showed on Fig. 15. A total of 20 boards have been already received (16 needed + 4 spares), together with the SFP-optical transceivers.



Figure 15: New PMC-FPGA board from IOxOS (side and front views).

SUMMARY

The ALBA FOFB has showed its correction capabilities and has demonstrated that matches its specifications. Different problems have been faced during the commissioning phase and some improvements have been already implemented. Deeper testing of the system and programming developments are still to be done, especially on all referring to reliability and time to recover after a failure. The plan for the future upgrade is on the way and main devices for that are already on the site.

ACKNOWLEDGMENT

We would like to thank the organizers and attendants of the first DEELS workshop at ESRF [6] for the fruitful discussions we have with them before, after and during the workshop.

REFERENCES

[1] M. Pont, *et al.*, “Top-Up Operation at ALBA Synchrotron Light Source”, IPAC14, Dresden, Germany, (2014).
[2] A. Olmos, *et al.*, “First Steps Towards a Fast Orbit Feedback at ALBA”, IBIC13, Oxford, UK, (2013).
[3] X. Serra, *et al.*, “Fast Orbit Feedback Implementation At ALBA Synchrotron”, ICALEPCS 2013, San Francisco, CA, USA, (2013).
[4] www.ioxos.ch
[5] I.S. Uzun, *et al.*, “Initial Design of the Fast Orbit Feedback System for Diamond Light Source”, ICALEPCS 2005, Geneva, Switzerland, (2005).
[6] http://www.esrf.eu/home/events/conferences/deels-2014-workshop.html

Copyright © 2014 CC-BY-3.0 and by the respective authors

ISBN 978-3-95450-141-0

NEW FEATURES AND MEASUREMENTS USING THE UPGRADED TRANSVERSE MULTIBUNCH FEEDBACK AT DIAMOND

G. Rehm, M.G. Abbott, A.F.D. Morgan, Diamond Light Source, Oxfordshire, UK

Abstract

A Transverse Multi-Bunch Feedback has been used in the Diamond Storage Ring for the stabilization of instabilities since 2007. Following a recent upgrade of the FPGA code and EPICS layer, a set of new features is now available to support operation and machine development: Firstly, a bunch by bunch choice of feedback filter allows for better stabilization of a single high charge bunch in a hybrid fill pattern. Secondly, complex grow-damp experiments are now possible using a sequencer of internal states allowing precise measurements of the damping rates on a mode by mode basis. Thirdly, a phase locked loop excitation and detection has been implemented to allow both extremely fast (kHz update rates) and extremely precise tracking of the betatron tune frequencies. Finally, short FIR filters on the ADC input and DAC output enable a fine tuning of the impulse response to provide maximum bunch to bunch isolation, as for instance required for efficient bunch cleaning.

INTRODUCTION

At Diamond we stabilise transverse oscillations of the bunches with two FPGA based Transverse Multi-Bunch Feedback (TMBF) processors, one operating horizontally, one vertically. Each processor is a Libera Bunch-by-Bunch from Instrumentation Technologies [1], packaged as a 1U unit containing 4 14-bit ADCs running at 125 MHz, a Virtex-II Pro FPGA clocked at 125 MHz, a 14-bit DAC running at 500 MHz, and an embedded Single Board Computer (SBC) ARM microprocessor running Linux to provide the control system.

The system was delivered as a basic development platform with interfacing software on the Linux board and a layer of FPGA code for interfacing to the external signals and the processor board. The initial implementation of the Transverse Multi-Bunch Feedback (TMBF) processor was done at Diamond [2] based on work at the ESRF [3]. The Diamond implementation consists of FPGA code together with an EPICS driver running on the embedded processor board.

Diamond has been using transverse multibunch feedback since 2007 [4]. The firmware and software have continued to develop and include functionality beyond the pure feedback action required for suppression of multibunch instabilities, most importantly a numerically controlled oscillator (NCO), which can be used to excite bunches and detect their oscillation in phase with the excitation.

The developments described in this paper provide support for more detailed measurements, finer control, and more complex experiments. In particular, the following major functionality has been added in a recent upgrade of FPGA and EPICS firmware:

- Input (ADC) and Output (DAC) gain pre-emphasis using a 3 point FIR to compensate the frequency response of various system components.
- Program sequencing, allowing a sequence of different control parameters to be applied to the beam at the same time as data capture.
- Tune detection and fast following via a phase locked loop (PLL) excitation of either one or many bunches.
- Concurrent swept tune measurements on up to four individual bunches.
- Separate feedback parameters for individual bunches. For example, we can now use one feedback filter for the hybrid bunch and a different filter for the rest of the fill.

Details of the implementation have been previously published [5, 6]. This paper will present results from some of the new types of measurements and operational modes that are enabled by the new features of the TMBF.

FREQUENCY RESPONSE CORRECTION

If a TMBF is employed purely for stabilisation using a turn-by-turn FIR filter applied to each bunch individually, this may be understood as a time invariant linear response system (within the linearity limits of the hardware). As such, the only effect of the broadband frequency response from DC to half sampling frequency will be a variation of damping efficiency as a function of frequency or mode number.

However, once different filters or even excitations are applied to individual bunches, the system is no longer time invariant. In that case, it becomes important to ensure the frequency response is as flat as possible (impulse response as sharp as possible). It is also not sufficient to apply a round trip frequency response correction just in one place (for instance before the DAC), as this would compensate for all errors (also from the ADC) by applying a corrected impulse response to the bunches. Instead, there need to be separate corrections before the DAC (to compensate for the effects of the DAC, power amplifier and strip lines), and after the ADC (to compensate for the effects of the hybrids, low level RF and ADC). In this way maximum isolation between bunches both in acting on them and in reading back their position can be achieved.

We have shown previously how we optimised the impulse response (equivalent to optimising the frequency response)

Copyright © 2014 CC-BY-3.0 and by the respective authors

ISBN 978-3-95450-141-0

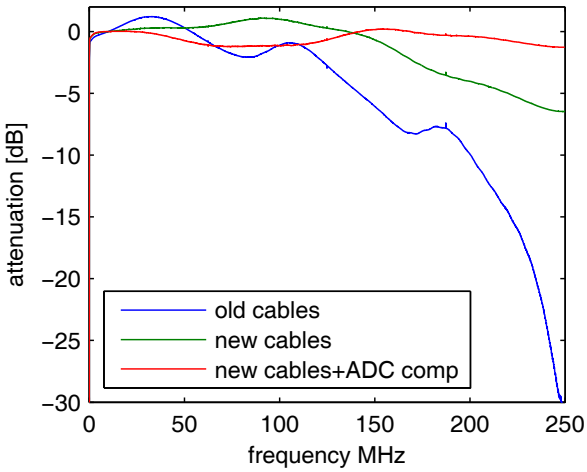


Figure 1: Round trip attenuation of TMBF electronics (DAC connected to ADC) for different cables and ADC compensation filter.

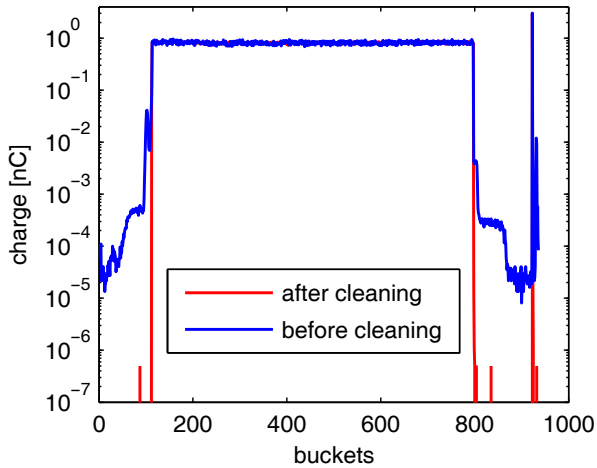


Figure 2: Fill pattern before and after bunch cleaning.

using a 3-point FIR in front of the DAC [5]. With this optimisation in place, we then looped back the DAC output into the input of the TMBF electronics. As the Libera TMBF is based on 4 separate 125MS/s ADCs, the signal has to go through a resistive splitter (to be broadband down to DC) and 4 short cables. When we measured the round trip frequency response using the swept excitation and I/Q detector (essentially a digitally controlled vector network analyser), we found unexpected structure (bumps in the frequency response at 30, 110, 190 MHz) and a sharp drop off at the highest frequencies (see Figure 1). It turned out the resistive splitter and following cables were not matched well enough, and the overall length was not optimised. With new cables, splitters, and the correct length, the frequency response improved significantly, and in line with what can be expected as roll-off from the ADC sampling window. The 3-point FIR after the ADC was then used to flatten the response further, the final result is flat within -1.2/+.2 dB.

COMBINED TUNE MEASUREMENT AND BUNCH CLEANING

In operation we use a Numerically Controlled Oscillator (NCO) with a programmable sweep function together with a numerical I/Q mixer and accumulator for continuous measurement of the betatron tune oscillation frequency [7,8] with minimal disturbance to the beam by exciting only one bunch.

A new feature now allows to extend this beyond a simple sweep into a sequence of up to 7 'states', each of which can be a swept or fixed frequency (or no) excitation, and have the output of the I/Q mixers recorded or discarded. In practice this has been used for 'permanent bunch cleaning' of the fill pattern: Dark current from the LINAC gets accelerated through the booster and causes a low background of charge injected into a train of bunches before and after the actual 'single bunch' that is used for filling and top-up injection. However, for some time resolved beamline experiments it is essential to keep a single bunch (in a hybrid or camshaft fill pattern) as clean as possible. To this end, we have implemented the following sequence of states:

1. Excite all 'unwanted' bunches with full amplitude on the vertical plane while sweeping **backwards** over the betatron resonance frequency. Stabilise all other bunches using feedback. Discard I/Q data.

2. Excite one 'designated' bunch with small amplitude to measure betatron tune frequency by recording I/Q data and finding peak. Stabilise all other bunches using feedback.

3. Stabilise all bunches using feedback until next sequence run is triggered.

It should be emphasised that this process can take place permanently during user operation without any noticeable disturbance of the beam. To this end, it is important that DAC pre-emphasis is used and the gain is switched from +1 to -1 before and after the single bunch so not to excite it [5]. In this way, even the regular injections into unwanted buckets during top-up operation can be cleaned away immediately (Figure 2).

FAST SCANNING OF TRANSVERSE MODE DAMPING

In order to assess the damping (or growth) rates of individual transverse multi-bunch modes there are in principle two methods commonly referred to [9, 10]:

- The feedback is switched off for a short period (or even inverted to drive all modes), then the feedback is turned back on. Bunch-by-bunch data is recorded from the point of switching off the feedback to some point after switching it back on to observe both growth

ISBN 978-3-95450-141-0

Copyright © 2014 CC-BY-3.0 and by the respective authors

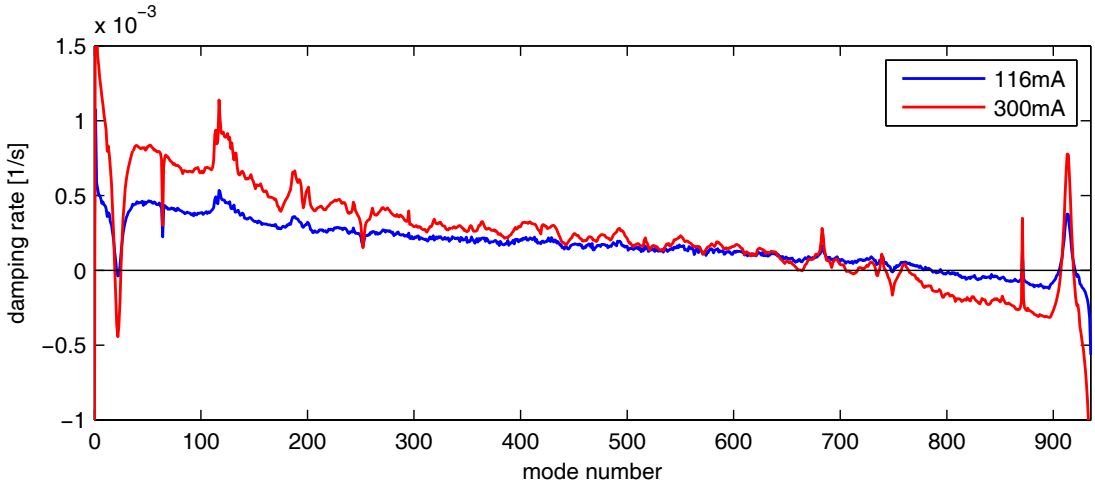


Figure 3: Natural damping rates of all vertical modes as a function of beam current in a uniform fill pattern, with chromaticity set to 0.

and damping. This data is then transferred to an off-line analysis, which disseminates it mode by mode and analyses the individual growth rates. The limitation of this approach is that it will only show those modes which are unstable without active damping (or a few more if gain inversion is used). However, it is a very fast experiment which will require only a disturbance lasting typically a few ms.

- An individual mode is excited using the NCO, this is followed by a period of a bunch-by-bunch recording during which after some delay the feedback is switched on again. Both the natural damping (or growth) and the active damping are recorded, however, only for one specific mode. This experiment then needs repeating for each mode. If bunch-by-bunch data is recorded the volumes of data created by the whole process can be quite large.

The second method has the ability to probe the damping times of each individual mode, no matter how close to instability it is. In the past, it would however been typically prohibitively slow to run through the repeated process of exciting, recording and data transferring for the typically high number of modes (there are 936 modes at DLS). We have significantly sped up this process (which is, at least with our current hardware, dominated by data transfer times) by two means:

- Instead of recording bunch-by-bunch data, we use the I/Q detector to determine the complex amplitude of the probed mode on a turn by turn basis. In our case, this reduces the amount of data to be stored and transferred for a typical scan of 936 modes of 750 turn grow-damp experiment from 1.3 GB to 5.6 MB.

- Rather than performing one grow-damp experiment each and then transferring the data, we store all the I/Q data in the on board memory, and only read out once all modes have been scanned. The multi state sequencer has been extended to repeat with a programmable list of offset frequencies to this end. Thus a full scan of all 936 modes can be performed within 1.3s, plus a further 2s for data transfer and analysis.

The collected data is then analysed by assuming an exponential decay of the mode amplitude (that is the magnitude of the turn-by-turn I/Q data). A straight line fit to the logarithm of the magnitude is used to calculated the damping or growth rate, which is then plotted per mode. As these experiments can be repeated rapidly, it is now possible to scan parameters (like beam current, fill pattern, chromaticity) and see the effect on the damping rates in near real time.

Figure 3 shows an example of the vertical damping rates as a function of beam current. It is clearly visible that more modes become unstable and the growth rates of the unstable modes (with negative damping rate) become larger (more negative). The overall slope across modes and the two distinct features at mode numbers 23 and 913 are understood from beam dynamics as a result of the resistive wall wake field. On the other hand, narrow features like at mode number 64 require further investigation, even if not currently leading to an instability, as these indicate narrow band resonators for instance as a result of long range wake fields.

FAST TUNE FOLLOWING USING PLL

Our normally used method of swept excitation and detection to determine the betatron tune frequency [7] will typically measure the tune once per second. However, we have noticed that the betatron tunes exhibit continuous and fast small movements with a standard deviation of $\approx 10^{-4}$ fractional tune units. These can be investigated in more detail using a tune following mechanism employing a PLL.

In this method, we continue to excite one or many bunches using the NCO, but rather than sweeping the NCO frequency, we detect the phase of the oscillating

Copyright © 2014 CC-BY-3.0 and by the respective authors

ISBN 978-3-95450-141-0

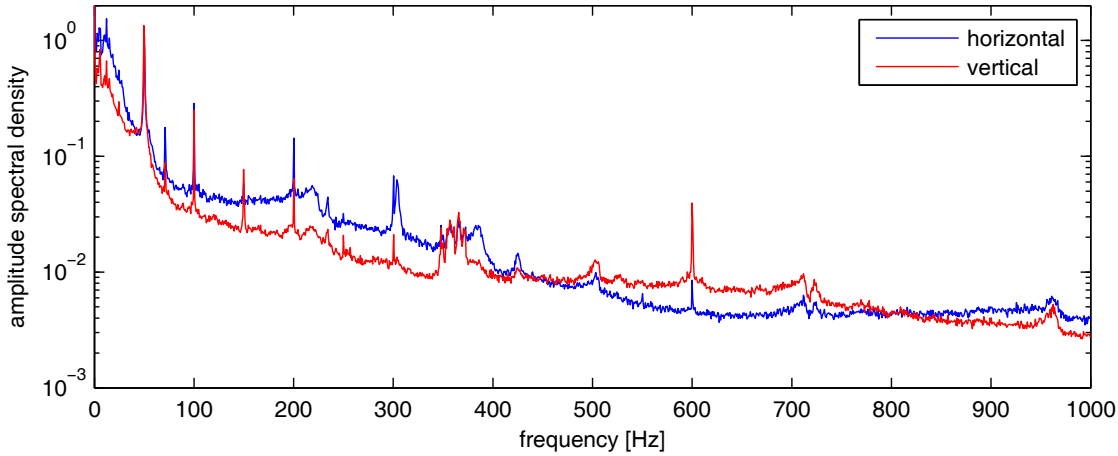


Figure 4: Spectra computed from betatron tune frequency data recorded using the PLL.

bunches relative to the excitation, low pass filter and feed it back through a proportional-integral controller to the NCO frequency. The number of turns observed to detect the phase is configurable, but in a typical setup we measure for 100 turns thus giving us a tune frequency reading every 187 μs. The tune frequency readings are stored in a 4096 point buffer which can then be conveniently read out every time it updates to collect a long term record of tune stability at high update rate.

Figure 4 shows the amplitude spectral density calculated from a 1 million point long record covering a total duration of 3 minutes. For this particular graph, the large number of points was split into 128 blocks which have been fourier transformed individually and then power averaged to produce spectra with precise amplitude densities rather than ultra fine frequency resolution. The spectra show that most of the movement of the betatron tunes is at low frequencies of a few 10 Hz, similar to orbit motion. There are also distinct lines at mains frequency and its harmonics.

The PLL tune measurement can also be used to measure the tune with higher precision by low pass filtering the stream of measurements, thus tracking the average tune value. This improves the uncertainty of tune measurements from 10^{-4} as achieved using the swept excitation (limited by tune motion during the sweep) to better than 10^{-5} at an update rate of once per second.

CONCLUSIONS

We presented some examples of the new types of measurements that have been enabled by a firmware development and upgrade of our existing TMBF system. The fundamental concept of the excitation using NCO and I/Q detection of bunch oscillations has been made more flexible by implementing complex sequences of excitations and PLL controlled tracking of the excitation. In particular, we expect the method of fast scanning of transverse mode damping times to be extensively used in probing transverse impedance of the storage ring and gathering a better understanding of the driving terms of instabilities.

REFERENCES

[1] Instrumentation Technologies, *Libera Bunch-by-Bunch*, `http://www.i-tech.si`.

[2] A.F.D. Morgan, G. Rehm, I. Uzun, *First Tests of the Transverse Multibunch Feedback at Diamond*, DIPAC 2007

[3] E. Plouviez, P. Arnoux, F. Epaud, J. Jacob, J.M. Koch, N. Michel, G.A. Naylor, J.-L. Revol, V. Serriere, D. Vial, *Broadband Bunch by Bunch Feedback for the ESRF using a Single High Resolution and Fast Sampling FPGA DSP*, EPAC 2006.

[4] A.F.D. Morgan, G. Rehm, I. Uzun, *Performance and Features of the Diamond TMBF System*, EPAC 2008.

[5] M.G. Abbott, G. Rehm, I. Uzun, *Capability Upgrade of the Diamond Transverse Multibunch Feedback*, IBIC 2013.

[6] M.G. Abbott, *Extending the Capabilities of the Transverse Multibunch Feedback Processor at Diamond*, Libera Workshop 2014, `http://www.i-tech.si/file/download/333_a8fc22df128d`

[7] I. Uzun, M.G. Abbott, M.T. Heron, A.F.D. Morgan, G. Rehm, *Operational Status of the Transverse Multibunch Feedback System at Diamond*, ICALEPCS 2011.

[8] G. Rehm, M.G. Abbott, A.F.D. Morgan, J. Rowland, I. Uzun, *Measurement of Lattice Parameters Without Visible Disturbance to User Beam at Diamond Light Source*, BIW 2010.

[9] D. Teytelman, *Architectures and Algorithms for Control and Diagnostics of Coupled-Bunch Instabilities in Circular Accelerators*, PhD thesis, SLAC report 633.

[10] S. Prabhakar, *New Diagnostics and Cures for Coupled-Bunch Instabilities*, Phd thesis, SLAC report 554.

Copyright © 2014 CC-BY-3.0 and by the respective authors

ISBN 978-3-95450-141-0

UPGRADE DEVELOPMENT PROGRESS FOR THE CERN SPS HIGH BANDWIDTH TRANSVERSE FEEDBACK DEMONSTRATION PROCESSOR*

J. E. Dusatko, J. M. Cesaratto, J.D. Fox, C.H. Rivetta
SLAC National Accelerator Laboratory, Menlo Park, CA, USA
W. Hofle, CERN, Geneva, Switzerland
S. De Santis, LBL, Berkeley, CA, USA

Abstract

A high bandwidth feedback demonstrator system has been developed for proof of concept transverse intra-bunch closed loop feedback studies at the CERN SPS. The system contains a beam pickup, analog front end receiver, signal processor, back end driver, power amplifiers and kicker structure. The main signal processing function is performed digitally, using very fast (4 GS/s) data converters to bring the system signals into and out of the digital domain. The digital signal processing is itself implemented in an FPGA allowing for maximum speed and flexibility. The signal processor is a modular design consisting of commercial and custom components. This approach allowed for a rapidly-developed prototype to be delivered in a short time with limited resources. Initial beam studies at the SPS using the system prior to the CERN long shutdown one (LS1) have been very encouraging. Building on this success, we are planning several key upgrades to the system, including the signal processor. This paper describes these key upgrades and reports on their progress.

OVERVIEW AND UPGRADES TO THE DEMONSTRATION SYSTEM

The high-current operation of the SPS for HL-LHC injection will require mitigation of possible Ecloud and TMCI driven intability effects [1]. A single-bunch wideband digital feedback system (Fig. 1) was initially commissioned in November 2012 and used through the February 2013 SPS LS1 shutdown. During the CERN LS1 interval we are upgrading the Demonstration system to add functions necessary to validate a full-featured control system.

PHASE I UPGRADES

The Demo system [3] was rapidly developed in 2012 and the first operational version included a snapshot mode that captures 32000 turns of digitized bunch motion. This data can be processed offline to study beam motion in the frequency domain and see changes in the beam motion as the feedback parameters are varied. The original studies contained some hard to understand narrowband spectral features that were not from the beam, but instead from interactions with the SPS RF and timing systems, as well as some internal digital clocks which were visible roughly 8 - 10 dB above the digitizer noise floor. As part of the upgrade, the A/D boards were relocated within the system chassis, grounded to a common copper plate and the narrowband interferring signals are now neglible. Additional studies and development of the RF and sampling clock signals have also been completed and we anticipate the next round of measurements to be free of the spurious interferring signals.

The beam dynamics measurements use an excitation/response formalism with chirps applied to the beam while the response is recorded. In these first measurements the existing 4 GS/s excitation system [2] was used to excite the beam with an analog summation of the feedback signal into the power amplifier input. These measurements required careful synchronization and alignment of the excitation system, feedback system and beam signals. As an upgrade, we have integrated the excitation system function within the demo system, so that the same system clocks drive the excitation sequence and the DSP aquistion and filter functions, so the summation of the excitation signal and filter output is now a digital addition with controlled saturation and gain.

The second major improvement is a phase-locked loop for system clocks. The DAC device (Maxim Semi MAX19693) does not have a mechanism to resynchronze its 4:1 input data mux, for many frequency domain applicationsthis is not a concern. This arbitrary synchronization meant that the excitation sytem and DSP processing had to be manually timed for each set of measurements, or after any interruption of the system power or clocks. The upgraded system uses a phase lock technique to adjust the phase of the input clocks to the D/A so that the divided parallel data clock is always consistently syncronized to the beam. This important upgrade makes the system timing repeatable and consistent from measurement to measurement. It also provides a path for a future upgrade allowing energy ramping and compensation for vaiations in synchronous phase and system timing with acceleration. In conjunction with the new operating modes, the system operator's interface has been simplified and expanded.

WIDEBAND KICKER STRUCTURES AND POWER AMPLIFIERS

A kicker structure to apply correction fields to the beam is a critical system function. A July 2013 design report

* Work supported by the U.S. Department of Energy under contract # DE-AC02-76SF00515 and the US LHC Accelerator Research Program (LARP).

Copyright © 2014 CC-BY-3.0 and by the respective authors

ISBN 978-3-95450-141-0

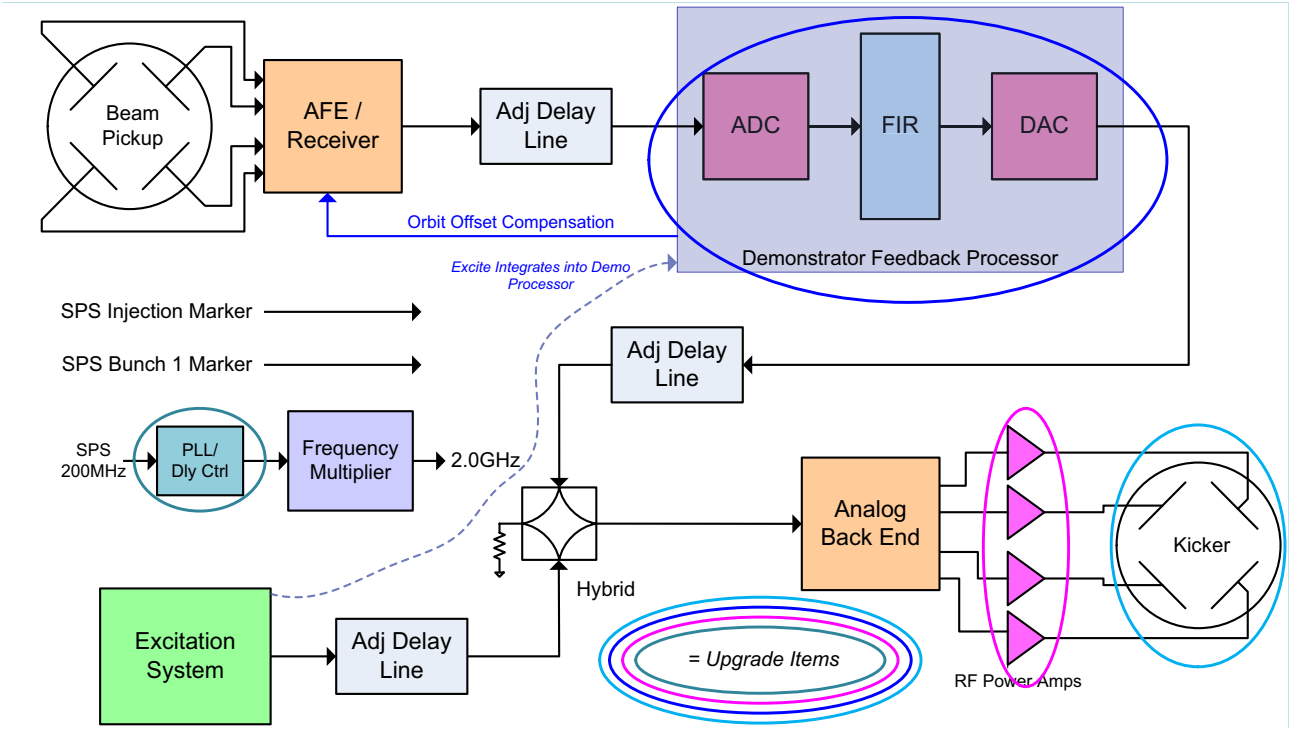


Figure 1: System block diagram highlighting the expansion in progress to the Demonstration system. The first expansions include combining the excitation and feedback functions within the DSP processing, the new wideband kicker structures and amplifiers, and the improvements to the high speed timing and synchronization to the SPS RF. The second phase of expansions will add control for a short 16 bunch train, and allow control of a special adjecent bucket scrubbing fill. Subequent efforts will increase the dynamic range of the input A/D functions through improved orbit offset rejection techniques, and implement synchronization of the beam/kicker signals throughout an energy ramp cycle.

summarized requirements and three possible technical implementations [4]. The stripline design is more mature, and three stripine kicker prototypes have been fabricated by CERN with the first kicker installed in August 2014. Figure 3 shows the first stripline kicker just before final assembly and installation. The slotline design is in the optimization phase, but should be fabricated starting winter 2015.

Either wideband kicker design requires suitable RF amplifiers to drive them. We have studied commercial RF amplifiers for possible use, with criteria of linear phase response and clean time response. After evaluating 8 possible amplifers, we have selected a 5 - 1000 MHz 250 Watt RF amplifier for the first tests with the new stripline kickers. Procurement is underway to have a pair available for beam tests in early 2015.

SECOND PHASE UPGRADES

A second upgrade is planned for integration at CERN starting January 2015. In this phased upgrade we will expand the system beyond the single bunch control capability to allow control of 16 bunches at the 25 ns separation. A related upgrade will implement control of two consecutive buckets (5 ns separation) used in special scrubbing fill.

The receiver $\Delta\Sigma$ processing generates individual bunch slice error signals, but orbit offset still appears and must be budgeted in the input dynamic range (the offsets are removed by the filter processing and do not appear at the output). We are exploring two co-methods to increase the input dynamic range through orbit offset rejection.

TECHNOLOGY IMPLEMENTATION ROADMAP

The goal of developing a full-function instability control system for the SPS is envisaged to span two generations of prototype hardware. Fig.2 shows a multi-year program to expand the Demonstration system, validate the kicker and control technologies, and learn from the SPS MD experiments. We plan future reconfiguration of the Demonstration system to allow studies of both IIR and FIR filter approaches. Additionally the dual ADC structure of the system can be split to allow two independent pickups, with each running at a reduced 2 GS/sec. rate. This path would allow measurements and system tests of the two pickup method if the simulations suggest the control is more robust at the higher effective sampling rates from two pickups.

In parallel, we want to explore a second hardware platform, based on a higher sampling rate A/D and D/A processing system, with associated higher-capacity FPGA processing functions. This increased processing capacity may be needed to support architectures with multiple pickups, or possible two-channel processing streams which use both the Δ signal (beam motion) and the Σ signal (bunch

ISBN 978-3-95450-141-0

Copyright © 2014 CC-BY-3.0 and by the respective authors

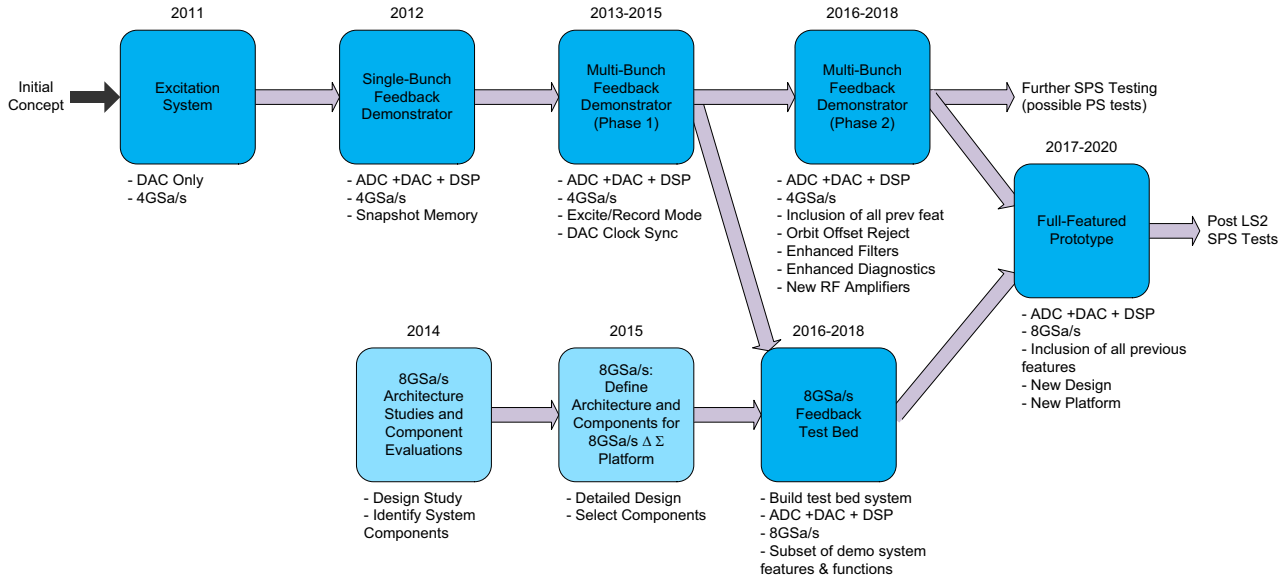


Figure 2: The technology development plan for the LARP Wideband Feedback effort, showing the path of expansion of the Demonstration system, and a parallel technology path with a higher sampling rate. We anticipate that the operational experience from the demonstrator system will guide the features to be implemented in the full-featured prototype in 2017.

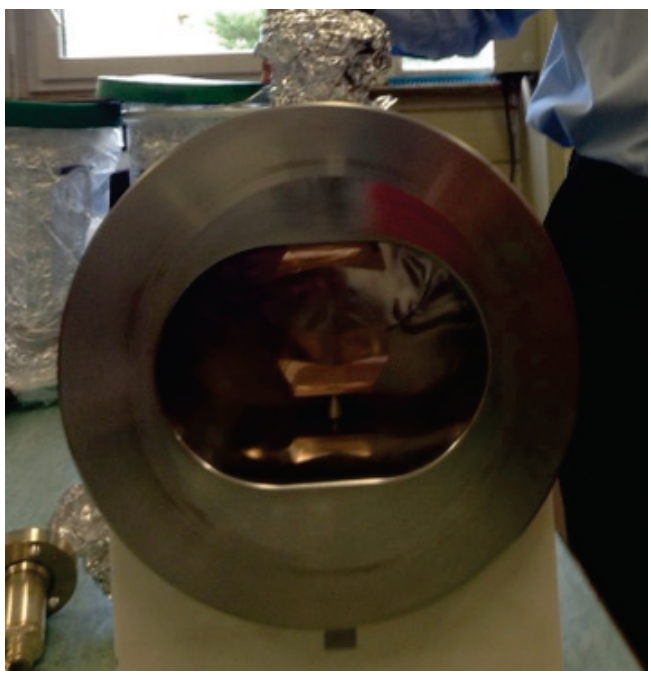


Figure 3: The first completed stripline kicker module for installation in SPS. The beam line vacuum system has been developed to allow 3 stripline kickers, as well as two slotline kickers, for beam testing. Dummy vacuum sections are in place to allow rapid and efficient installations of the third stripline kicker and a future slotline kickers.

charge) as part of the computation of a correction signal.

SUMMARY AND PLANS FOR NEXT MD STUDIES

The upgraded demonstration system will be recommissioned at the SPS in Fall 2014, with the new wideband kickers starting in 2015. We should be able to demonstrate control of 16 bunch trains and study the necessary bandwdiths for the pickup and kicker functions. Studies, and comparisons with beam instability simulations, are vital to predict the operation and margins of this beam feedback at the anticipated HL intensities and filling patterns. We plan on continuing to add features to the demonstration prototype while in parallel developing the platform for the full-featured prototype system to be commissioned after the LS2 shutdown.

ACKNOWLEDGEMENTS

We thank A. Bullitt ,J. Goldfield, S. Uemura,E. Montesinos, and SLAC Controls I&C-EE and ARD, CERN ABP group, the US LHC Accelerator Research Program and the US-Japan Cooperative Program in High Energy Physics for support.

REFERENCES

[1] E. Shaposhnikova, "Intensity Upgrade Plans for CERN-LHC Injectors", 42nd ICFA Advanced Beam Dynamics Workshop Nashville, Tenn., USA, 2008, CERN-AB-2008-065.

[2] J. D. Fox, *et al.*, "A 4.2GS/sec. Synchronized Vertical Excitation System for SPS Studies - Steps Toward Wideband Feedback", IPAC 2012.

[3] J. E. Dusatko, *et al.*, "The Hardware Implementation of the CERN SPS Ultrafast Feedback Processor Demonstrator", MOPC28, IBIC 2013.

[4] J. M. Cesaratto, *et al.*, "SPS Wideband Transverse Feedback Kicker: Design Report," SLAC-R-1037.

Copyright © 2014 CC-BY-3.0 and by the respective authors

ISBN 978-3-95450-141-0

BUNCH-BY-BUNCH FEEDBACK SYSTEMS AT THE DELTA STORAGE RING USED FOR BEAM DIAGNOSTICS*

M. Höner†, S. Khan, M. Sommer
Center for Synchrotron Radiation (DELTA), TU Dortmund University, Dortmund, Germany

Abstract

At the 1.5-GeV electron storage ring DELTA operated by the TU Dortmund University, a bunch-by-bunch feedback system was installed in 2011. Since then, it is in operation for different beam diagnostic purposes. A fast analysis of bunch-position data allows a real-time multibunch mode analysis during machine operation. In addition, the data analysis can be triggered by external events, e.g. beam losses or the injection process. In this paper, a feedback-based method to measure the damping times of multi-bunch modes is presented. Furthermore, a chromaticity-dependent single-bunch instability is analyzed. Finally, the use of the feedback system in the presence of an RF-phase modulation is presented.

INTRODUCTION

In 2011, a digital bunch-by-bunch feedback system [1] was installed at the 1.5-GeV electron storage ring DELTA (Fig. 1, Table 1) for beam diagnostics purposes [2, 3] and to suppress longitudinal and transverse coupled-bunch instabilities. The system comprises processing units for the longitudinal, horizontal and vertical plane as well as a common frontend and backend. In user operation, ~144 out of 192 buckets are filled with a beam current up to 130 mA (3/4 filling pattern). Longitudinal coupled-bunch modes show up above a current threshold of ~75 mA, while transverse instabilities are rarely observed. A modulation of the RF phase is routinely applied [4, 5] to suppress longitudinal instabilities and to improve the beam lifetime by reducing the mean electron density and thus the rate of Touschek scattering.

Ultrashort radiation pulses in the VUV and THz regime are generated since 2011 by an interaction of femtosecond laser pulses with an electron bunch of enhanced current [6]. For this purpose, the storage ring is either filled with a single bunch during dedicated machine shifts or with a hybrid filling pattern (an additional bunch in the gap of the 3/4 filling pattern). One purpose of the longitudinal feedback system is to suppress longitudinal oscillations of the bunch interacting with the laser pulses.

In addition, the feedback system is used to provide post-mortem data on the bunch motion preceding beam losses [3] and to study the beam dynamics under various circumstances. One example is to record the bunch motion during the injection process [2, 3], other more recent examples are descibed below.

* Work supported by the BMBF (05K13PEC).
† markus.hoener@tu-dortmund.de

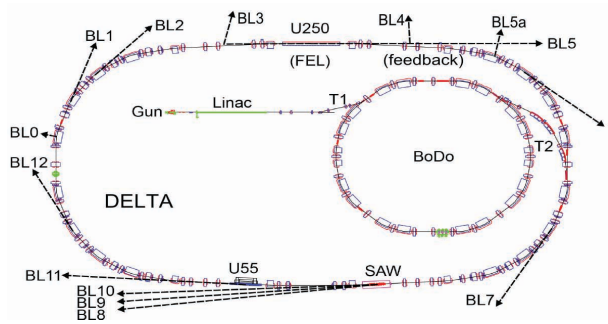


Figure 1: Overview of the DELTA facility including the storage ring and its booster synchrotron (BoDo).

Feedback Setup

To extract the horizontal, vertical and longitudinal position of every single bunch, the signals from a beam position monitor with four symmetrically arranged buttons are combined in a hybrid network to extract the horizontal and vertical differential signal as well as the sum signal. The three resulting signals are stretched using a two-cycle comb-filter in the feedback frontend and are mixed with a 1.5-GHz reference signal. The resulting signals are filtered by a low-pass filter. Using phase shifters and attenuators, the mixed signals can be adjusted to be either phase sensitive (longitudinal position) or amplitude sensitive (transverse position). Finally, the signals are digitized by 12-bit ADCs in the feedback processing units. By applying a 24-tap FIR filter on consecutive input data, the output signals are created, which are converted to analog signals driving the power amplifiers and the corresponding kicker structures [7]. In the longitudinal plane, the output signal is mixed up to 1.5 GHz in the feedback backend before being sent to the amplifier. In addition to an FIR-filter, the processing units include a frequency generator, which allows to send a dedicated RF signal to the beam, e.g. to excite specific multibunch modes, as shown in the next section.

Table 1: Storage Ring Parameters

parameter	value
revolution frequency	2.6 MHz
RF frequency	500 MHz
nominal RF power	25 kW
maximum beam current (multibunch)	130 mA
maximum beam current (single bunch)	20 mA
synchrotron frequency	15.7 kHz
fractional horizontal tune	0.10
fractional vertical tune	0.28

ISBN 978-3-95450-141-0

Copyright © 2014 CC-BY-3.0 and by the respective authors

DAMPING TIMES OF COUPLED-BUNCH MODES

To determine the damping rates of all $h = 192$ multibunch modes at DELTA, the following measurement scheme was applied [8]. Below the instability threshold, i.e. well below 75 mA, all bunches are excited by the feedback drive signal corresponding to a dedicated multibunch mode. Then the excitation is switched off for a few milliseconds and the oscillation is damped. The measurement was repeated for all multibunch modes. From an exponential fit to the damping time of each multibunch mode, its respective damping rate can be obtained. Figure 2 shows one example measurement for mode no. 20 in time domain (a), in frequency domain (b) and the resulting damping rates of all 192 modes (c). As expected from analytical calculations, the pairs of modes μ and $h \quad \mu$ show an anti-correlated behaviour. While one mode is damping slower, the other is damping faster than the zero-current value. This can be understood by calculating the multibunch growth rate for two example modes following the analytical expression given by [9]

$$\frac{1}{\tau_\mu} = \frac{hNe^2\eta}{2\omega_s ET_0^2} \sum_{p=\ \infty}^{\infty} \omega(p)\mathrm{Re}Z_\parallel \quad \omega(\mathrm{p})) \qquad (1)$$

with $\omega(p) = ph\omega_0 + \mu\omega_0 + \omega_s$, the revolution frequency ω_0, the synchrotron frequency ω_s, the number of electrons in each bunch N, the electron charge e, the slippage factor η, the beam energy E and the revolution time T_0. For a narrowband impedance $Z_\parallel$ with center frequency $\mu\omega_0$, as an example, the growth rate for multibunch mode μ is positve, while the growth rate of mode $h \quad \mu$ is negative, while all other multibunch modes are not effected by the impedance. Since several narrowband impedances, e.g. higher-order modes of the accelerating cavity, interact with the beam, many of the multibunch modes are affected and are damping faster or slower than the zero-current value.

Beam Current Dependence

To study the current dependence of the damping rates, the measurements shown above were repeated for different beam currents below the instability threshold. The damping rates of several modes with high or low damping rates are plotted as a function of the beam current in Fig. 3. Linear fits for each mode allow to extrapolate to the zero-current damping rate, which should be identical for all multibunch modes. The resulting zero-current damping rate of about $1/\tau = 0.4/\mathrm{ms}$ differs from the synchrotron radiation damping rate of $1/\tau = 0.23/\mathrm{ms}$. This might be explained by the fact that the feedback system is only capable to detect the center-of-mass motion, which damps faster than the incoherent motion. This effect can also be seen by comparing the feedback data with data from a streak camera, which is discussed in the next section.

Comparison With Streak Camera Data

In addition to studying the bunch dynamics with the feedback system, the longitudinal bunch oscillation can be observed with a streak camera. In this measurement, the beam is stabilized by negative feedback and only excited by positive feedback for a time interval of 8 ms. The resulting oscillation is observed with the streak camera and the feedback system simultaneously, both being are triggered by a common clock signal. In Fig. 4a, the streak camera image is shown where the abscissa extends over several ms, while the ordinate shows the bunch length on a scale of several 100 ps. When the positive feedback is enabled, the bunches start to oscillate longitudinally. The actual oscillation of the bunches is not resolved on the given timescale, but results in a broadening of the apparent bunch length. In Fig. 4b, the rms value of a Gaussian fit to the bunch profile is plotted on the same time scale together with the amplitude of longitudinal bunch oscillations observed by the feedback system. There is a good general agreement between the position data

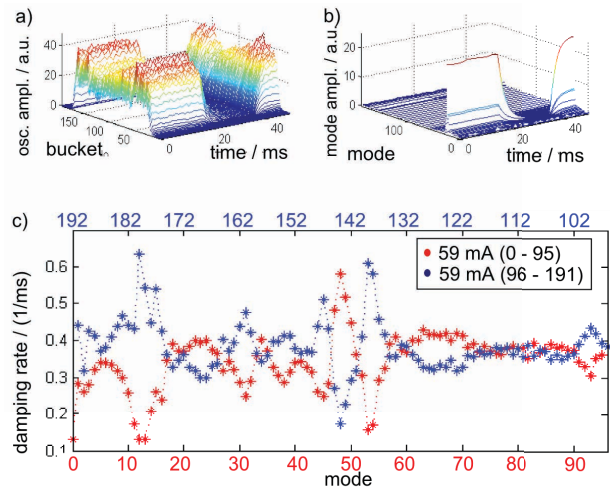


Figure 2: Bunch oscillation amplitudes for one example mode in time domain (a) and frequency domain (b). The excitation is switched off for several ms. The observed damping rates (c) of all longitudinal coupled-bunch modes are plotted in red (modes 0-95) and blue (modes 96-191).

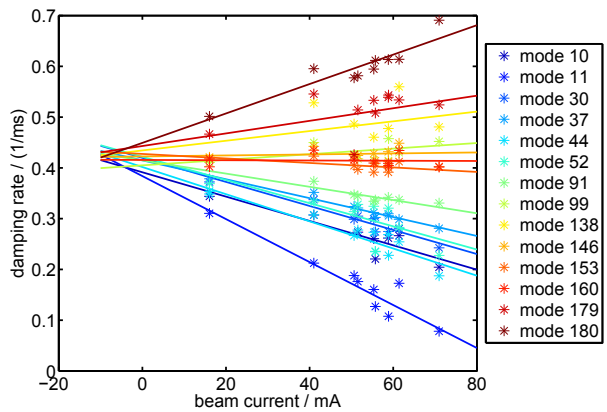


Figure 3: Damping rates of selected coupled-bunch modes as function of the beam current. Linear fits to the data points of each mode allow an extrapolation to the zero-current damping rate.

Copyright © 2014 CC-BY-3.0 and by the respective authors

ISBN 978-3-95450-141-0

taken with these two different tools except for the difference in the rising and falling slope of the signals which can be explained by the fact that the feedback system detects only the bunch centroid, while the streak camera images the whole charge distribution (e.g. [10]). Since the bunch centroid is damped faster, the slopes are steeper in the feedback data than in the streak camera curve.

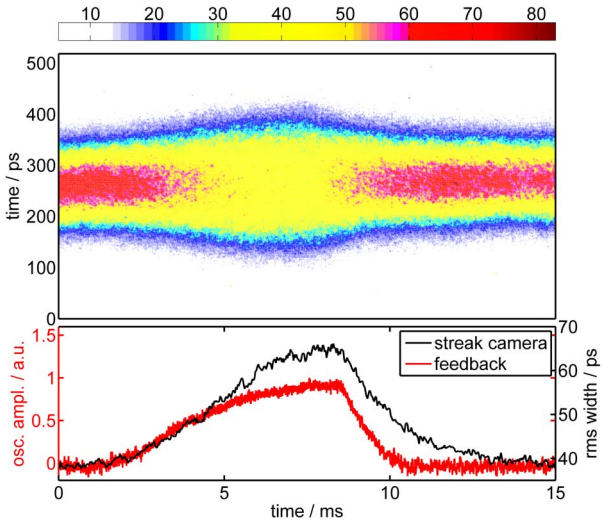


Figure 4: Streak camera image of a temporarily excited beam (top) with color-coded light intensity. The width of the apparent bunch length from the streak camera image and the oscillation amplitudes obtained by the feedback system are plotted on a common scale (bottom, see text for details).

SINGLE-BUNCH INSTABILITY

Besides using the bunch-by-bunch feedback system to study multibunch effects, it was used to observe the bunch oscillation during single-bunch operation. In this example, the chromaticity of the DELTA storage ring was varied by reducing the strength of sextupol magnets to excite single-bunch instabilities. The chromaticity was measured by changing the RF frequency by several kHz and detecting the change of the betatron tune $Q_{x,y}$. From a linear fit to the extracted data, the chromaticity can be determined according to

$$\xi_{x,y} = -\alpha \cdot f_{RF} \cdot \frac{dQ_{x,y}}{df_{RF}} \qquad (2)$$

with the momentum-compaction factor α and the RF frequency f_{RF}. While the chromaticities at DELTA are typically slightly positive $\xi_y \sim 2$ and $\xi_x \sim 3$, with reduced sextupoles they are reduced and the vertical chromaticity becomes negative, which gives rise of an oscillation of the single bunch. By reducing the sextupole strength further, the negative vertical chromaticity is increased, which leads to an increase of the the growth rate of the single-bunch oscillation. In Fig. 5a-d, two example measurements for different chromaticities and the corresponding exponential fits are plotted. Figure 5e shows the linear dependence of the growth rate on the chromaticity $\frac{1}{\tau} \sim -\xi$.

The growth of the oscillation saturates at a certain level due to the dependence of the betatron frequency on the oscillation amplitude, which leads to a collapse of the oscillation. As the growth rate increases, the periodicity of the single bunch oscillations becomes shorter because the saturation level is reached earlier. The linear dependence of the observed single-bunch growth rate on the chromaticity, can be interpreted as head-tail instability. For a negative chromaticity, the head-tail mode zero which can be detected by a centroid motion of the bunch has a positive growth rate (e.g. [9]).

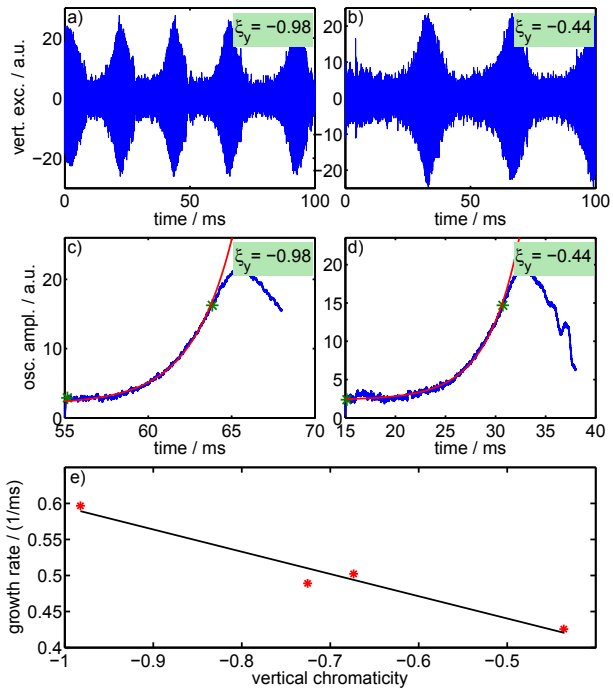


Figure 5: Vertical oscillation of a single bunch plotted in time domain for two different vertical chromaticities (a/b). The signal was high-pass filtered to suppress slow orbit fluctuations and the DC offset. An exponential fit to the envelope of the oscillation within the green marks yields the growth rate (c/d). The growth rate shows a linear dependence on the chromaticity (e).

FEEDBACK DURING RF-PHASE MODULATION

The DELTA short-pulse facility, based on the Coherent Harmonic Generation principle (CHG) [6] was constructed in 2011. Here, femtosecond laser pulses interact with a short slice within an electron bunch to create ultrashort, coherent VUV radiation pulses. In addition, coherent THz radiation is created [11]. During machine studies, ultrashort pulses are generated in single-bunch mode. In order to operate the short-pulse facility during multibunch user mode, a hybrid fill pattern was tested, injecting a high-current single bunch into the gap of the multibunch fill. Furthermore, an RF-phase modulation is routinely employed in user operation to

ISBN 978-3-95450-141-0

Copyright © 2014 CC-BY-3.0 and by the respective authors

increase the beam lifetime. The high-current single bunch is not only disturbed by this modulation but also performs center-of-mass oscillations due to coupled-bunch instabilities. Therefore, the longitudinal bunch-by-bunch feedback was used to stabilize the single bunch without acting on the other bunches. To study the influence of the RF-phase modulation and the bunch-by-bunch feedback on the beam lifetime and the laser-induced THz and CHG signal, these parameters were observed over several minutes for different configurations. If the RF phase is not modulated and the feedback system is switched off, the laser-induced signals are relatively high, while the beam lifetime is about 11 hours (see Fig. 6). If the RF-phase modulation is switched on, the beam lifetime is improved but the laser-induced signals are reduced by up to 30%. Finally, stabilizing the high-current single bunch using the longitudinal bunch-by-bunch feedback unit, does not affect the beam lifetime, but brings the laser-induced signals to their optimum level. Even though the signal fluctuations are slightly increased, the feedback system allows to generate ultrashort pulses during user operation without compromising the beam lifetime. As shown in Ref. [12], a synchronization of the laser to the RF-phase modulation can even increase the laser-induced signal.

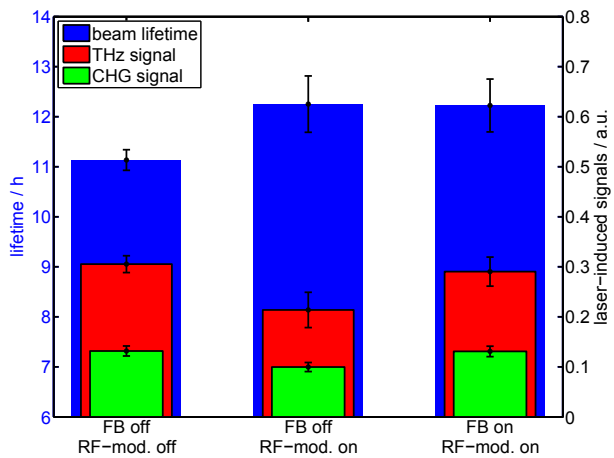


Figure 6: Laser-induced THz radiation (green), laser-induced CHG radiation in the VUV regime (red) and beam lifetime (blue) for different feedback and RF-phase modulation configurations: without feedback and RF-phase modulation (left), with phase modulation (center) and with both, feedback and phase modulation (right). The error bars indicate the fluctuation of the respective value during a time interval of several minutes.

SUMMARY AND OUTLOOK

The bunch-by-bunch feedback system is a powerful tool to study coupled-bunch and single-bunch instabilities. A beam-current-dependent measurement of the damping time of all coupled-bunch modes was performed and shows a linear dependence on the beam current. The measured damping rates indicate the relative strength and frequency of longitudinal impedance contributions folded into the baseband of the RF-frequency. The use of the longitudinal bunch-by-bunch feedback system in hybrid filling mode yields promising results to achieve a mode of operation, with a high beam lifetime while generating laser-induced VUV and THz radiation with optimum intensity.

ACKNOWLEDGMENT

It is a pleasure to thank our colleagues at DELTA as well as ANKA, BESSY and ELSA for their continuous support. The project has profited strongly from the expertise of D. Teytelman (Dimtel Inc.).

REFERENCES

[1] Dimtel Inc., http://www.dimtel.com.

[2] M. Höner et al., "Bunch-by-Bunch Feedback sytems at the DELTA Storage Ring", in Proc. 3rd Int. Particle Accelerator Conf. 2012, New Orleans, USA, 807.

[3] M. Höner et al., "Beam Diagnostics by using Bunch-by-Bunch Feedback sytems at the DELTA Storage Ring", in Proc. 4th Int. Particle Accelerator Conf. 2013, Shanghai, China, 485.

[4] S. Khan et al., "Studies and Control of Coupled-Bunch Instabilities at DELTA", in Proc. 1st Int. Particle Accelerator Conf. 2010, Kyoto, Japan, 2755.

[5] N.P. Abreu et al., "Longitudinal Dynamics with RF Phase Modulation in the Brazilian Electron Storage Ring", Phys. Rev. ST Accel. Beams 9,124401 (2006).

[6] S. Khan et al., "Generation of Ultrashort and Coherent Synchrotron Radiation Pulses at DELTA", Sync. Rad. News 26, issue 3, 25 (2013).

[7] S. Khan, T. Knuth, "Longitudinal and transverse Feedback Kickers for the BESSY II Storage Ring", in Proc. 18th Particle Accelerator Conf. 1999, New York, USA, 1147.

[8] M. Höner et al., "Investigation of Beam Instabilities at DELTA using Bunch-by-Bunch Feedback Systems", in Proc. 5th Int. Particle Accelerator Conf. 2014, Dresden, Germany, 3486.

[9] A. Chao, "Physics of Collective Beam Instabilities in High Energy Accelerators", New York, NY: Wiley & Sons (1993).

[10] M. Switka et al., "Synchrotron Radiation Diagnostics Performance at ELSA", in Proc. 5th Int. Particle Accelerator Conf. 2014, Dresden, Germany, 3471.

[11] P. Ungelenk et al., "Studies of Ultrashort THz Pulses at DELTA", in Proc. 5th Int. Particle Accelerator Conf. 2014, Dresden, 1936.

[12] A. Meyer auf der Heide et al., "Coherent Harmonic Generation at the DELTA Storage Ring: Towards User Operation", in Proc. 36th Int. Free-Electron Laser Conf. 2014, Basel, MOP087, http://jacow.org/.

Copyright © 2014 CC-BY-3.0 and by the respective authors

ISBN 978-3-95450-141-0

COMMISSIONING OF BUNCH-BY-BUNCH FEEDBACK SYSTEM FOR NSLS2 STORAGE RING*

W. Cheng#,1, B. Bacha[1], D. Teytelman[2], Y. Hu[1], H. Xu[1], O. Singh[1]
[1] NSLS-II, Brookhaven National Laboratory, Upton, NY 11973
[2] Dimtel Inc., San Jose, CA 95124

Abstract

Transverse bunch by bunch feedback system has been designed to cure the coupled bunch instabilities, caused by HOM, resistive wall or ions. The system has been constructed, tested and commissioned with beam. Preliminary studies show that the feedback system can suppress single bunch instability as well as coupled bunch instabilities. Mode analysis of the unstable coupled bunch motion reveals fast ion instability exist even at relative low current.

INTRODUCTION

As the newest third-generation light source, NSLS2 at Brookhaven National Laboratory has been constructed and commissioned recently. 50mA stored beam has been achieved without insertion devices [1]. Insertion devices commissioning and user operation will follow in the near future. NSLS2 storage ring will have < 1nm.rad horizontal emittance by using weak dipoles together with damping wigglers. For the storage ring of 792m circumference, geometric impedance, resistive wall impedance and ion effects are expected to be significant. A transverse bunch-by-bunch feedback system has been designed to suppress the coupled bunch instabilities. More information can be found in previous papers [2,3].

Pickup signals for transverse feedback system are coming from button BPMs. Broadband RF front end electronics detect the bunch to bunch positions separated by 2ns, which is then digitized and processed to get the correction signal. The correction signal can be precisely timed to act on the individual bunches come back in one turn. Dimtel's iGp12 digitizer [4] was selected for NSLS2 bunch by bunch feedback. It has EPICS driver and graphical operation panel integrated and other diagnostic features like bunch cleaning, transfer function measurement and others.

High power amplifiers from Amplifier Research are fully controlled through LAN/RS232 gateway remotely. Amplifier gain, forward power, reverse power and other status can be monitored/controlled from the CSS panel. There are temperature sensors installed on the stripline kicker feed-throughs and chambers. These RTD's temperature data will supply health information of the kicker, especially when the machine is running at high current.

*Work supported by DOE contract No: DE-AC02-98CH10886.
#chengwx@bnl.gov

KICKER PERFORMANCE

As the feedback actuator, stripline kicker was designed to have sufficient high shunt impedance and minimized beam impedance. The stripline kicker has two 30cm long plates housed in round chamber with inner radius ~ 39mm. The chamber inner surface and plates are copper coated. Each plate was fed by a 500W broadband amplifier though 1/2'' Heliax cables.

Figure 1 shows one assembled stripline kicker and its TDR measurement result. Between the cursors were the 30cm (1ns) plate. The plate was matched to 50 Ohm. The dip was coming from vacuum feedthrough ceramic seal.

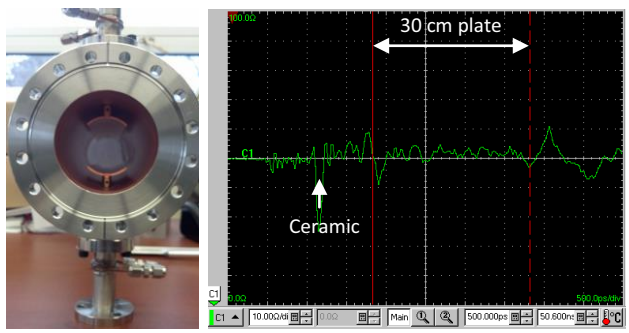


Figure 1: Assembled Stripline kicker (left) and TDR measurement response (right).

Installed stripline frequency response, together with high power amplifier, long Heliax cables and 500W attenuator, were measured using network analyzer, as shown in Fig. 2. In the working frequency range of 0-250 MHz, gain flatness is about 3dB. Phase response is less than 5 degrees difference in the range.

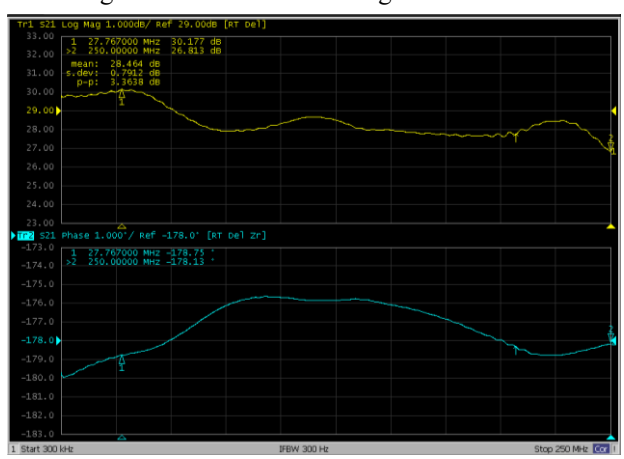


Figure 2: Network analyzer measured amplitude and phase response, including high power amplifier, stripline kicker, Heliax cables and attenuator.

Copyright © 2014 CC-BY-3.0 and by the respective authors

ISBN 978-3-95450-141-0

CURE BUNCH INSTABILITIES

Single bunch instability was observed at around 0.7mA. Vertically beam was getting unstable at higher single bunch current. About 1mA threshold current was measured for normal +2/+2 chromaticity. This instability was observed with normal conducting 7-cell PETRA-III cavity [5], as well as super conducting single cell cavity. Measuring the transfer function at different single bunch current reveals that vertical instability happened when the vertical betatron sideband met the low sideband (likely -fs sideband). Shown in Fig. 3, are the transfer function measurement results at various single bunch current. As the current increasing, horizontal betatron frequency didn't change much, while the vertical betatron peak moved towards lower frequency and eventually met the smaller peak at ~ 84.3 kHz.

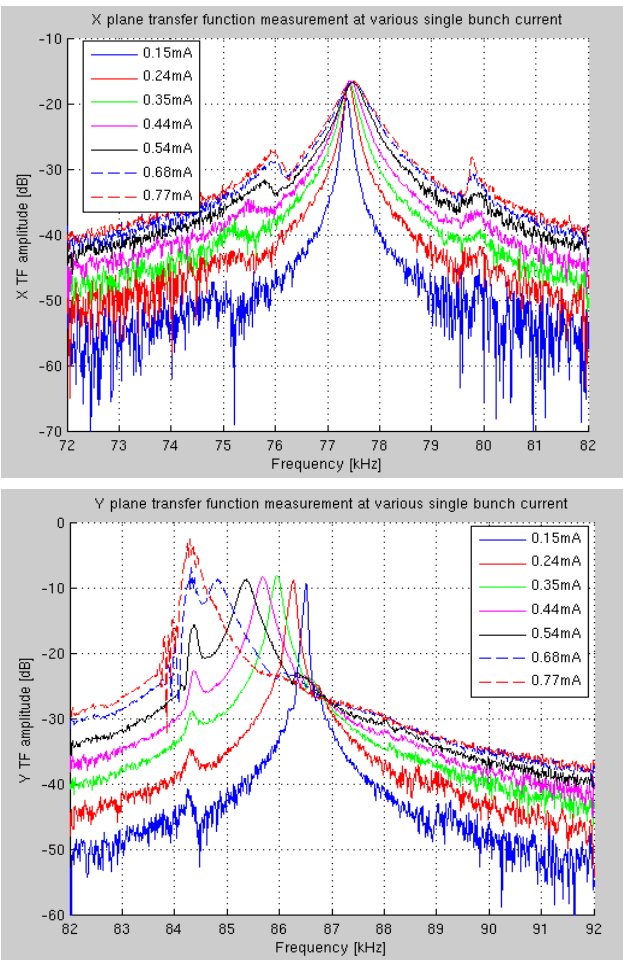


Figure 3: Single bunch transfer function measurement at various bunch current for horizontal (top) and vertical (bottom) plane.

It's an interesting observation that 3dB bandwidth of the transfer function was increasing as the single bunch current increased. Determined from the Fig. 3 spectrum, Fig. 4 plots the peak frequency and 3dB bandwidth change at different bunch current. Horizontally the tune peak didn't vary much with the current. Vertically tune decreased at higher single bunch current, the slope was fitted to be -2.92 kHz/mA (or fraction tune v_y slope of 0.0077/mA). This agrees with the results measured with other methods [1]. Besides the peak drift, from the transfer function measurement, one can see that 3dB bandwidth was increasing linearly with single bunch current. This indicates the incoherent tune spread in the bunch was increased at higher single bunch current.

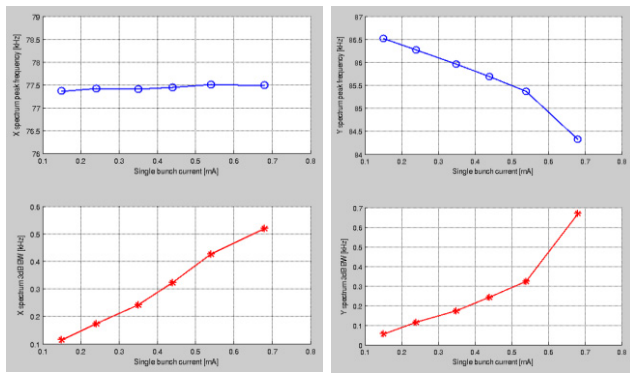


Figure 4: Transfer function spectrum peak frequency and 3dB bandwith change at different single bunch current.

After optimizing the transverse feedback loop parameters, the loop was first closed in single bunch mode. Vertical single bunch instability was suppressed and more than 6mA can be stored in one bunch, until the vacuum pressure elevated and sent out alarms.

In multi-bunch fill, when the stored beam was above 20mA, coupled bunch instabilities were observed. These instabilities are considered to be ion related. The feedback system was able to suppress them in both x/y planes. Figure. 5 shows the BPM turn by turn position and its spectrum with and without feedback. The data was recorded at 44mA stored in ~1040 buckets. Note that bunch to bunch current varies. Without transverse bunch by bunch feedback, beam centroid RMS motion was about 11 um for both planes. Turning on the feedback helped suppress the betatron oscillations. As can be seen on the power spectrum density plots, betatron sidebands were suppressed by more than 60 dB. Beam RMS motion was about 6.3um horizontally and 2.6um vertically. Horizontal motion was higher due to longitudinal energy jittering coupled through dispersion. The integrated lower frequency motions were 1.2/1.9 um RMS (<1 kHz).

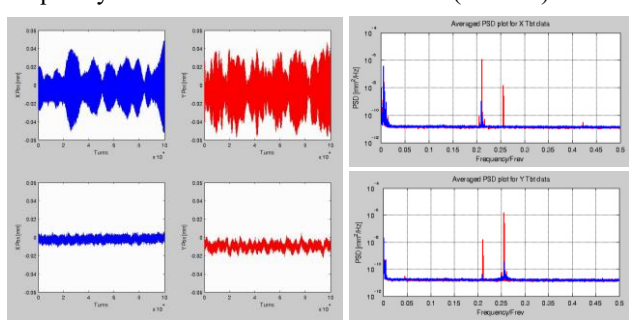


Figure 5: (left) BPM X/Y TbT data from one of the storage ring BPM C30BPM1; (right) BPM TbT data spectrum averaged from 180 BPMs, red traces were spectrum with bunch-by-bunch feedback OFF and blue trances with feedback ON.

Copyright © 2014 CC-BY-3.0 and by the respective authors

ISBN 978-3-95450-141-0

BUNCH CLEANING

Individual bunches can be knocked out using the integrated bunch driving functions. Highly purified single bunch will be one of the operational modes for timing related experiments. We tested the bunch cleaning using vertical bunch by bunch feedback as the vertical aperture is smaller in the ring. Due to tune dependency on bunch current and oscillation amplitude, bunch needs to be excited across the betatron tune, the sweeping range and sweeping speed was adjusted to knock out the bunch effectively. Fig. 6 shows the filling pattern after bunch cleaning. Initially there was 20 consecutive bunches filled in the ring, separate by 2ns RF period. One single bunch was able to be kicked out with little effect on nearby bunches. In the figure, the top snapshot shows bunch #9 was cleaned. Bunches were able to be knocked out in user defined patterns. For example the bottom snapshot in the figure shows bunches was kicked out every three buckets. Red arrows indicate where knocked out bunches were located.

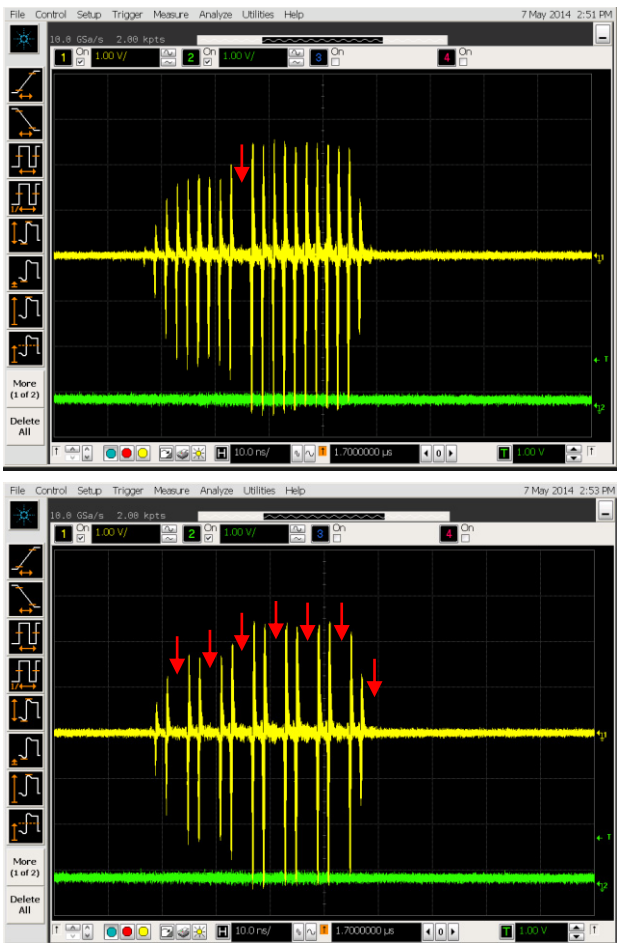


Figure 6: With an initial fill of 20 consecutive bunches, bunches at arrow locations were knocked out using vertical plane bunch excitation. (top) bunch #9 was kicked out; (bottom) bunches were kicked out every three buckets.

At this point, NSLS2 storage ring filling pattern is not well controlled. The filling pattern is mainly determined by the multi-bunch pattern from the injector. The non-uniform bunch train was placed into different RF buckets of the ring. To have an even filling pattern, overlap between injection shots may be a simply approach. Bunch cleaning function can be used to clean the unwanted bunches. Arbitrary filling pattern can be achieved by setting the proper bunch excitation mask.

Filling pattern shown in Fig 6 was using the pickup signals from button BPM. Two diagonal button signals were sent to a broadband hybrid, the SUM signal from the hybrid was feed to the 20GHz real time oscilloscope. Limited by electronics and digitizer, dynamics range of the filling pattern monitor system is typically around 10^-3. Touschek scattering in NSLS2 storage ring will be a dominant effect, the scattered electrons can be re-captured by nearby buckets. To check the bunch purity with higher dynamics ranges (six orders of magnitude or better), a new bunch purity measurement system based on single photon counting method is needed, see for example reference [6,7].

ION EFFECT

Mode analysis of acquired position data for all bunches reveals broadband beam unstable modes when the feedback was OFF. The graph in Fig. 7, compares the spectrum with and without bunch-by-bunch feedback. Beam was filled in 80% of 1320 buckets with total current of 49mA. 1024 turns' data of all 1320 buckets was used to get the spectrum. The plot shows vertical plane amplitude of the first 150 '+' or '-' unstable modes ($m \times Frev \pm f_{\beta y}$). When feedback was turned ON, most of the betatron sidebands were suppressed. With feedback OFF, several humps appeared on the broadband spectrum, which is typically ion-induced spectrum.

In multi-bunch fill, storage ring typical average vacuum pressure was around 1 nTorr. Residual gases are mainly composed of H2, CH4, CO and CO2. Fig. 8 shows a typical residual gas analyzer (RGA) measured results. There are 30 RGAs installed in the ring, one per cell. In the figure was the RGA result from Cell 15 with beam stored at 10mA.

Considering a condition similar to what's shown in Fig. 6, where 80% buckets were filled, assume a total current of 50mA evenly distributed in 1040 buckets, one can calculate the ion frequencies [2,8]. With this filling pattern, the ion critical mass (see Eq. 1) is quite low. All the ions can be trapped in the electron beam potential.

$$A_{crit} = \frac{N_b r_p c T_b}{2\sigma_{x,y}(\sigma_x + \sigma_y)} = \frac{N_b r_p L_{sep}}{2\sigma_{x,y}(\sigma_x + \sigma_y)} \quad (1)$$

Where N_b is number of particles per bunch; r_p is proton classical radius ~ 1.5×10^{-18} m; A is atomic mass of ion; T_b (or L_{sep}) is bunch separation and σ_x σ_y the RMS beam size.

ISBN 978-3-95450-141-0

Copyright © 2014 CC-BY-3.0 and by the respective authors

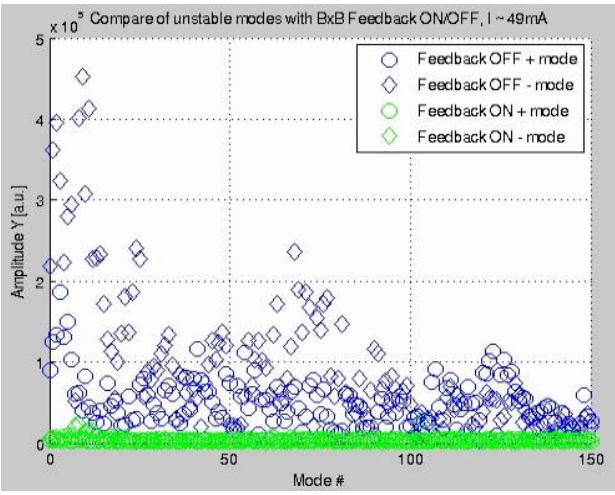


Figure 7: Comparison of vertical mode amplitude with and without bunch-by-bunch feedback.

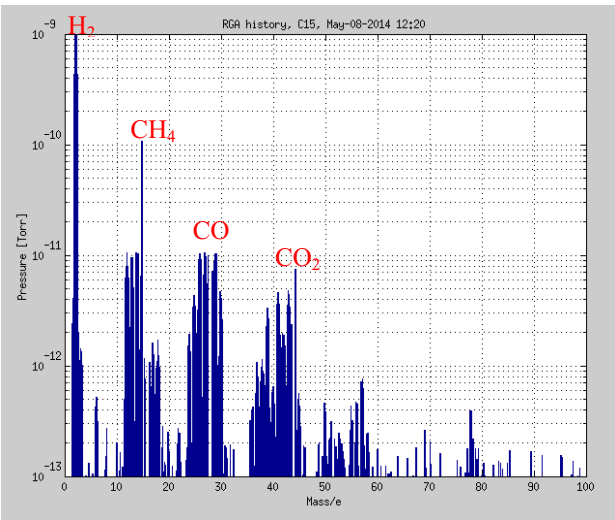


Figure 8: Typical residual gas analyzer (RGA) measured results with beam stored in the ring.

Table 1 lists the dominant ions and their oscillation frequency. Ion frequency depends on bunch current as well as beam sizes, hence it varies along the ring, as expressed in Eq. (2).

$$\omega_{ion} = 2\pi f_{ion} = \left[\frac{2N_b r_p c}{A\sigma_{x,y}(\sigma_x + \sigma_y)T_b} \right]^{1/2} \quad (2)$$

Table 1: NSLS2 Ions and their Effects

	H_2	CH_4	CO	CO_2
Atomic mass	2	16	28	44
Cross section [Mbarn]	0.35	2.1	2.0	2.92
Ion freq. Hor. [MHz]	13.6	4.8	3.6	2.9
Ion freq. Ver. [MHz]	47.3	16.7	12.6	10.0

What's shown in the table is averaged value in the super cell. Fig. 9 gives an example of CO+ ion frequencies in the super cell. Horizontal/vertical emittance of 2/0.01 nm.rad was used. Beam sizes were calculated from the baseline lattice without damping wigglers. From Eq. (2), ion frequency changes at different beam current. It has been observed that unstable hump moved to lower frequency when 20mA was stored in the same 80% fill pattern. Transient measurement indicated that the tail bunches in the long bunch train had larger oscillation amplitude. This is another indication of instability caused by ions.

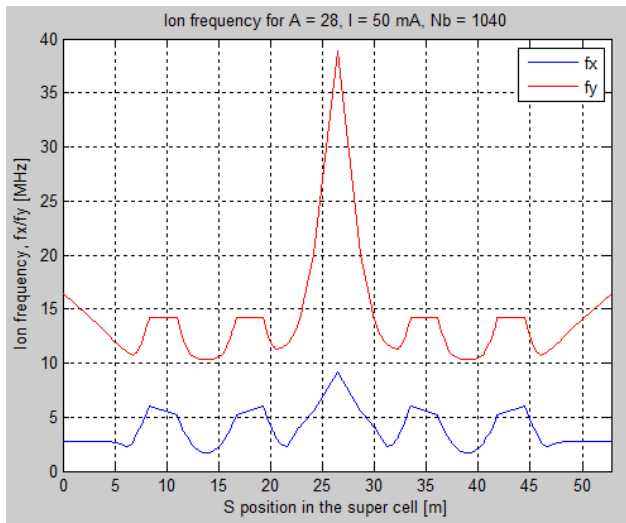


Figure 9: Ion frequency for CO^+ in one of NSLS2 storage ring super cell.

Compare the ion frequencies to the measured unstable mode in Fig. 7, it's likely that unstable modes around #125 was caused by trapped H_2 ions. Other unstable modes at lower frequency were possibly induced from heavier ions. It's worth to point out that ion frequencies calculated in Table 1 are valid for evenly distributed filling pattern, while the real machine filling pattern was not well controlled. Further studies with even filling pattern will be carried out to better understand the ion phenomena.

Besides the transverse mode analysis, with a third digitizer detecting the BPM Sum signal, one can study the longitudinal beam motion behavior. During the NSLS2 storage ring phase 1 commissioning, 7-Cell PETRA-III type normal conducting cavity was used. The cavity was full of HOMs. It was revealed from the bunch by bunch phase data that cavity HOM was making the beam unstable longitudinally. Varying the cavity temperature moved the HOM frequency.

Copyright © 2014 CC-BY-3.0 and by the respective authors

ISBN 978-3-95450-141-0

SUMMARY

Transverse bunch by bunch system has been designed, constructed and commissioned at NSLS2 storage ring. The system helped to suppress the coupled bunch instabilities as well as single bunch instability. Preliminary mode analysis indicate ion induced instability was observed even at 20mA stored beam (~0.02mA per bunch). Further systematic studies are necessary to better understand the ion instabilities. Besides its major role of curing instabilities, the feedback system supplies a wealth of data for diagnostics. The feedback system was tested to knock out un-wanted bunches so that arbitrary filling pattern or highly purified single bunch can be stored in the ring.

We thank the NSLS2 diagnostics group and commissioning team members for various help during installation, testing and commissioning the system.

REFERENCES

[1] W. Cheng, et al., "NSLS2 Diagnostic Systems Commissioning and Measurements", IBIC14
[2] W. Cheng, "NSLS2 Transverse Feedback System Design", BIW'2010.
[3] W. Cheng, et al., "Stripline Kicker Design for NSLS2 Storage Ring", PAC'11.
[4] http://www.dimtel.com/
[5] A. Blednykh, et al., "NSLS-II Commissioning with 500MHz 7-Cell PETRA-III Cavity", IPAC'2014
[6] T. Obina, et al., "Measurement of the Longitudinal Bunch Structure in the Photon Factroy Positron Storage Ring with a Photon Counting Method", Nucl. Instru. Methods A354 (1995).
[7] C. Thomas, et al., "Bunch Purity Measurement for Diamond", Nucl. Instr. Methods A566 (2006).
[8] T. Raubenheimer, F. Zimmermann, "Fast beam-ion instability, I. Linear Theory and Simulation", Phys. Rev. E52 (1995).

Copyright © 2014 CC-BY-3.0 and by the respective authors

ISBN 978-3-95450-141-0

COMMISSIONING OF THE FLASH2 ELECTRON BEAM DIAGNOSTICS IN RESPECT TO ITS USE AT THE EUROPEAN XFEL

N. Baboi# and D. Nölle, DESY, Hamburg, Germany,
for the electron beam diagnostics team

Abstract

This report presents the first operation experience of the electron beam diagnostics at FLASH2. FLASH2 is a new undulator line at the FLASH linac at DESY. Most electron beam diagnostics installed, like the beam loss monitors, cavity beam position monitors, toroids, beam halo monitors, have been designed for the European XFEL, and will provide operational experience beforehand. A few systems, as for example the button beam position monitors and the ionization chambers, have been developed for FLASH. The controls use the new MTCA.4 standard. Both linacs, FLASH and the European XFEL, require similar performance of the diagnostics systems. Many beam parameters are similar: bunch charge of 0.1 to 1 nC, pulse repetition frequency of 10 Hz, while others will be more critical at the XFEL than the ones currently used at FLASH, like the bunch frequency of up to 4.5 MHz. versus 1 MHz. The commissioning of FLASH2 and its diagnostics is ongoing. The beam monitors have accompanied the first beam through the linac, fine tuning for some systems is still to be done. The achieved performance will be presented in view of their use at the European XFEL.

INTRODUCTION

The FLASH linac at DESY, Hamburg has recently been upgraded with a second undulator beamline, FLASH2, in order to increase the number of user beamlines [1,2]. FLASH is a Free Electron Laser (FEL) based on Self Amplified Spontaneous Emission (SASE-FEL). It produces ultra-short, highly intense photon beams typically in the range from 45 down to 4.2 nm.

In order to make use of the synergies between the FLASH facility and the European X-ray Free Electron Laser (E-XFEL) [3], many of the diagnostics components installed in FLASH2 are the same or similar to the ones developed for the E-XFEL [4,5]. Some are similar to the old FLASH components, and others have been designed especially for FLASH2. This paper gives an overview of the diagnostics installed in FLASH2 and reports on the first operational experience.

Overview of the FLASH Linac

Figure 1 shows schematically the layout of FLASH. Two independent lasers are sent to the Cs_2Te cathode, placed on the back plane of the 1.5-cell RF-gun, to produce, within the same RF pulse, the beam for each of the two electron beamlines, FLASH1 and FLASH2. In the following FLASH will denote either the whole facility or the common, accelerating part.

The electron beam is accelerated to an energy of up to 1.25 GeV by 7 cryo-modules, each containing 8 TESLA cavities, operating at 1.3 GHz (in yellow in the figure). One third-harmonic cryo-module containing four 3.9 GHz cavities (in red), placed after the first 1.3 GHz module, is used to linearize the energy chirp. Two magnetic chicanes are used to compress the bunches, down to the order of 100 fs and below, in order to achieve the peak currents needed for the FEL process.

A kicker-septum system is used to extract part of the beam pulse into the FLASH2 line. The kicker rise time of ca. 30 µs determines the minimum gap between the beams for FLASH1 and FLASH2, which are within the same pulse. The electrons produce the FEL beam in FLASH1 within six 4.5 m long fixed-gap undulators. The photon wavelength is varied by changing the electron energy. A seeding experiment, sFLASH, is also placed in the FLASH1 beamline.

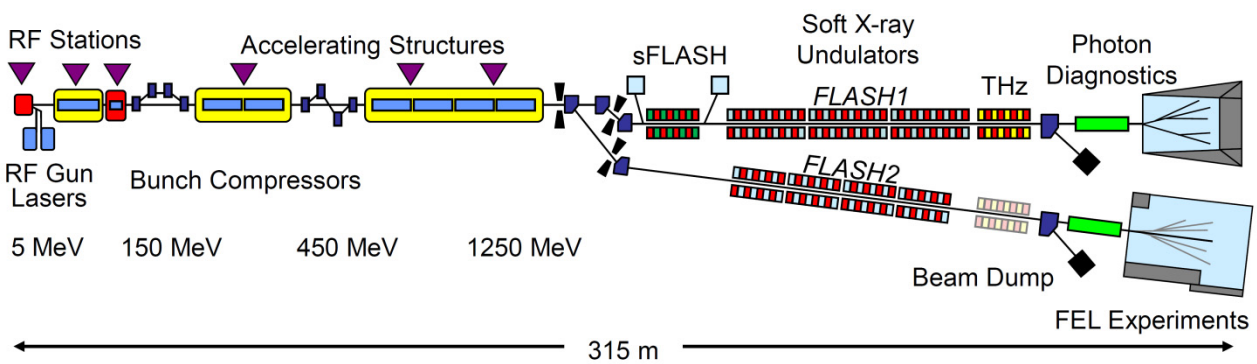


Figure 1: Schematic of the FLASH facility with the two undulator beamlines, FLASH1 and FLASH2 [1].

#nicoleta.baboi@desy.de

Copyright © 2014 CC-BY-3.0 and by the respective authors

ISBN 978-3-95450-141-0

Twelve 2.5 m long variable gap undulators are used to produce the FEL beam in FLASH2. In this way one can vary the wavelength of the photons produced independent of FLASH1. In addition also small differences of the acceleration gradient for pulses for the two beamlines can be provided if they are within the optics acceptance.

After each undulator beamline, the electrons are sent to a dump, while the photons pass a diagnostics section, followed by the user beamlines. On request THz radiation can be produced in a special undulator, placed after the SASE undulators in FLASH1. A similar undulator is planned to be installed in the FLASH2 beamline as well.

The construction of the new experimental hall has been finalized in spring 2014 and now the photon beamlines are under construction.

The European XFEL has similar requirements, using the same type of accelerating cavities, gun, pulse structure, controls etc. Table 1 lists some main design parameters for the E-XFEL and typical operational parameters for FLASH. Most E-XFEL components will have to deal with a bunch frequency of up to 4.5 MHz, as compared to currently a maximum value of 1 MHz at FLASH. While FLASH has been designed for bunch charges of 1 nC and higher, and runs usually with charges well above 100 pC, the XFEL operation is specified for 0.1 to 1 nC, but precautions have been taken, that the diagnostics is also capable to work at charges down to 20 pC.

Table 1: Typical Parameters of the E-XFEL and FLASH

Parameter	E-XFEL	FLASH
Max. energy [GeV]	17.5	1.25
Pulse repetition rate [Hz]	10 (25**)	10*
Max. bunch frequency [MHz]	4.5	1
Max. pulse duration [μm]	600	800
Bunch charge [nC]	0.1 - 1	0.1 - 1
Photon wavelength [nm]	0.05 – 6	4.2 - 45

* FLASH2 operates often at 1 Hz to reduce activation

** The RF should able to work at 25 Hz with reduced gradient

DIAGNOSTICS OVERVIEW

As mentioned before, many diagnostic systems installed in FLASH2 have been designed for the European E-XFEL, whose electron gun has recently started commissioning. Some components have been designed for FLASH2, but are based on similar concepts, e.g. same type of electronics crates and timing system. Therefore the experience gained by commissioning and operating these systems in FLASH will be a great benefit for the E-XFEL operation. It is expected to contribute to a faster commissioning of these components in the larger linac and may help for a better performance. The beam time for commissioning and machine studies at the E-XFEL will be limited, and some more restrictions on beam conditions apply. At FLASH these conditions are somewhat more relaxed.

Table 2 gives a brief overview of the diagnostics systems and numbers installed in FLASH2 in comparison to the number of (same or similar) components to be installed in the E-XFEL. There are toroids, used for measuring the charge, screen stations, beam position monitors (BPMs) of various types, beam loss monitors (BLMs), and beam halo monitors (BHMs). Other monitors present in both linacs belonging to the so-called special diagnostics, as for example the bunch compression monitors and the beam arrival time monitor, are not discussed in this paper. In addition to the diagnostic item used for both machines, additional types will be installed in the E-XFEL only, such as the wire scanners and dosimeters, and some diagnostics of the same type, but with different geometry and aperture, as for example cavity BPMs with 40.5 mm aperture. Other systems installed in FLASH2, like the ionization chambers in the dump area, the Cherenkov fibers along the undulator section, are not present in the E-XFEL and are not shown in the table either. The apertures given in the table are true for components which are identical or very similar in both linacs (vacuum part and electronics). More details on each type of component are given later in the paper.

Table 2: Number of Standard Diagnostics Components in the E-XFEL and FLASH2 (similar components installed in FLASH1 are also counted).

Monitor Type	Aperture [mm]	E-XFEL	FLASH2	FLASH1
Toroid	40.5, 44, 100	36	5	
Screen station	40.5, 100	64	7	
Screen on dump window		3	1	
Cavity BPM	10	101	17	3#
Button BPM*	10 - 100	>300	12	4
Stripline BPM*	34, 44	-	4	
BLM	-	>300	~56	
BHM	100	4	1	1

Cavity BPMs installed in FLASH1 for tests

* Different electronics, based on the same principle, in FLASH2 (designed at DESY) and the E-XFEL (design at PSI)

General Characteristics

We mention here a few common characteristics for most new diagnostic systems: They deliver bunch by bunch measurements and are designed for lower charge than the older FLASH components, well below 1 nC.

The two photo-injector lasers can deliver bunch trains with different bunch number, repetition frequency and bunch charge for the two beamlines within the same RF pulse. Figure 2 shows an example of a possible pulse

ISBN 978-3-95450-141-0

Copyright © 2014 CC-BY-3.0 and by the respective authors

structure. A gap between the two parts of the train of at least 30 µs is needed for the rise time of the kicker. While the diagnostics should deliver a measurement for both trains, they do not have to give optimal performance for both.

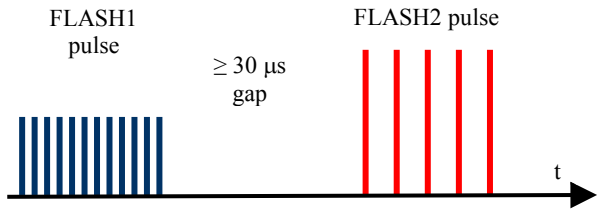


Figure 2: Example of different pulse structures and bunch charges within a FLASH bunch train for the FLASH1 and FLASH2 undulator beamlines.

A new timing system [6] and the E-XFEL type machine protection system [7] deliver the necessary flexibility for the operation of two beamlines.

The electronics is, in general, based on the MTCA.4 technology [8]. This has the advantage of having a modular architecture, redundant power, well defined management, high availability. On the other hand it's a rather new technology, this bringing some challenges with it: there is lack of experience and some components are still being optimized. Nine MTCA crates have been installed for diagnostics at FLASH2, and several others at FLASH and FLASH1.

All electronics in FLASH2 is installed in a technical corridor which is parallel to the accelerator tunnel. The situation will be different in the 2 km long E-XFEL tunnels, where the electronics has to be installed in racks inside the accelerator tunnel. This situation requires very reliable and remotely manageable systems, since maintenance is restricted to scheduled accesses or will cause downtime of the facility.

Diagnostics Commissioning

When talking about the commissioning of the components of an accelerator, one usually thinks of the last step: the commissioning with beam. However at least as important is the sometimes called "cold" commissioning, i.e. the work being made previously to the first beam through that component:

- Check the monitors (mostly the vacuum parts): visual and electrical check of components, short, symmetry etc.;
- Check cables: sometimes damage occurs after installation;
- Check and preliminary set up of electronics: check individual components (in many cases MTCA-components) and how they work together; check availability and quality of signals, like timing, IT; use test pulses;
- Test servers;
- Make sure operating panels are made and working;
- Pre-calibrate components with values from theory or laboratory measurements.

More than one time we discovered that one or more components were not available or accessible due to e.g. connection problems or server limitations. It is probably unavoidable that some problems occur, but through careful preparation one can reduce such cases.

The initial commissioning with beam is made in parallel with the commissioning of the accelerator. That is when the electronics settings and timing are roughly adjusted, in order to search for first beam signals. Later the fine adjustment is made, often during dedicated beam time.

First Beam in FLASH2

All main diagnostics components were available for the first beam attempt in FLASH2 on March 4. Even if not all were in the foreseen state yet, all were able to evaluate the beam charge, position, transverse profile and losses.

Figure 3 shows a photo of the first part of the FLASH2 extraction region. Part of the septum can be seen in the bottom of the picture. One notices the small separation of the two beamlines. About 4 m after the septum one can see the optics box of the first screen station in FLASH2. This is followed by a toroid, which is just in front of a sextupole (in yellow). In front of the screen there is a stripline BPM mounted in a quadrupole. BLMs are distributed along the beamline (cannot be seen in the figure). These are the diagnostics elements that played a major role during the first operation looking for beam.



Figure 3: First part of the FLASH2 extraction beamline (right) together with part of the FLASH1 beamline (left).

Copyright © 2014 CC-BY-3.0 and by the respective authors

ISBN 978-3-95450-141-0

The work started with carefully setting the linac parameters in order to have stable SASE radiation in FLASH1 from two bunches, each generated by one of the injector lasers. The beam energy was about 700 MeV. Then the kicker was switched on to separate the two bunches in front of the septum by about 20 mm (corresponding to a kick of 2.2 mrad), as theoretically required for injection into FLASH2. Figure 4 shows two bunches on the screen at the septum entrance. The central one is for FLASH1, and the upper one to be extracted into FLASH2.

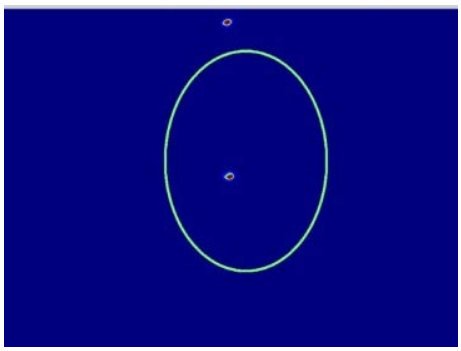


Figure 4: Two beam spots, for FLASH1 (center) and FLASH2 (up), separated by about 20 mm, are seen on the screen before the septum.

After the screen has been removed, and after some steering was applied, beam losses were seen by the first BLMs in FLASH2. Figure 5 shows the raw signal from a BLM about 6 m after the separation. The signal at 780 μs is caused by the FLASH2 bunch, the one at 700 μs are losses from the first bunch continuing its path in FLASH1 (seen here due to the small geometrical separation). One notices also a plateau in the losses, which is caused by the dark current kicked into the FLASH2 beamline.

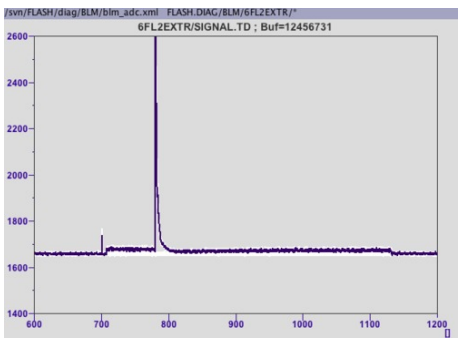
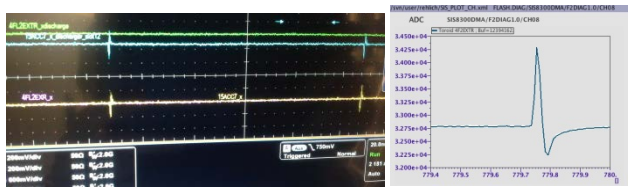


Figure 5: Raw BLM signal from a BLM at 6 m into the FLASH2 extraction. The horizontal axis is time in μs, the vertical one is in arbitrary units.

While BLM signals show that the beam is nearby, it's not clear if the beam was transported in the FLASH2 beamline, or just lost at the beginning. The first BPM (Figure 6a) and the first toroid (Figure 6b), at 4 m inside FLASH2, showed that indeed there was beam at this location. The raw BPM signals are measured by an oscilloscope. On each curve, the signals from two opposite pickups are displayed, one of them being delayed by an additional cable. The beam was roughly centered on the BPM.



a b

Figure 6: Signals from the first BPM (a) and toroid (b) in FLASH2. a: The yellow (lowest) and blue (middle) curves on the scope show each the two signals from two opposite pick-ups of the BPM at 4 m; b: Raw toroid signal from an ADC.

The screen nearby (see Figure 3) was inserted in the chamber and after some adjustments the image was visible on this screen (Figure 7).

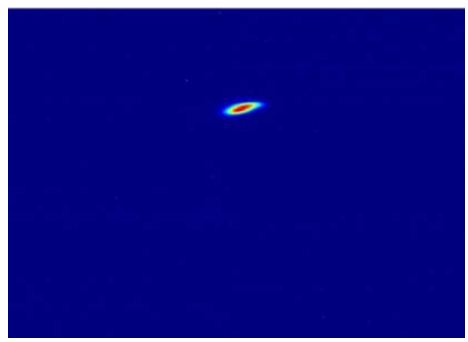


Figure 7: First beam seen on the first screen in the FLASH2 beamline.

While the first beam at the beginning of the FLASH2 beamline was obtained very quickly, it was impossible to get it much further downstream during this first beam time. Later it became clear that a collimator was blocking the beam path, due to some missing connection in the control system. During the following allocated beam times one was able to go further and further into the beamline, so that on May 23 the beam could be transported to the dump. Parallel operation of the two beamlines has meanwhile become routine.

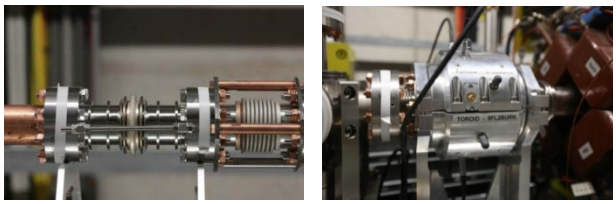
The following sections describe each diagnostic system.

CHARGE MONITORS

The charge monitoring is based on AC current transformers, called toroids, developed at DESY and used in all accelerators on site. In Figure 8 one can see a ceramic gap (a) in FLASH2, over which the transformer housing, or toroid body, is mounted (b). The body is made of two halves so that it can be installed without breaking the vacuum.

Copyright © 2014 CC-BY-3.0 and by the respective authors

ISBN 978-3-95450-141-0



a b

Figure 8: Toroid installed in FLASH2: ceramic gap (a) and toroid (b).

A MTCA-based readout system, containing front-end and back-end electronics, has been designed for the E-XFEL and FLASH and is now under test [9]. The front-end electronics contains a signal combiner, a filter and an amplifier and will be placed close to the toroid. The back-end electronics will be placed in the MTCA-crate and contains a rear transition module (RTM) in combination with a SIS8300 digitizer [10]. This system will offer a high dynamic range and high sensitivity, and includes a test pulse generator for remote testing of the entire signal chain.

Until the E-XFEL system is ready to be installed, an intermediate solution was adopted for all 5 toroids of FLASH2 (see Figure 9). The signals from the 4 toroid pickups are summed up. A preliminary version of the front-end electronics has been installed close to the pickups in the tunnel. CAT cables bring the differential signals to the MTCA crate.

So-called adapter RTMs convert the differential signal to a single ended signal, that is delivered to the ADC, which accepts amplitudes of ±1 V. From here, the signals go to the SIS8900 RTM, which passes the signal to a SIS8300 ADC card [10], in the same slot of the MTCA crate. The sampling rate is 108.3 MHz.

Two toroids in FLASH have also been equipped with the new electronics. With this system a resolution below 1 pC rms has been measured, while the FLASH systems have a resolution around 3 pC.

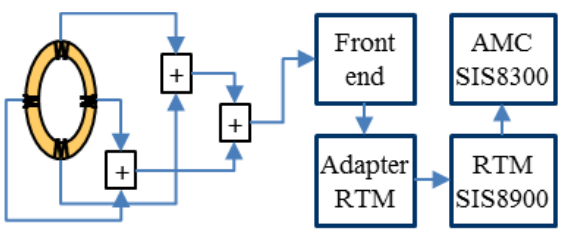


Figure 9: Schematics of the toroid system at FLASH2.

Figure 10 shows a typical raw signal from a toroid in FLASH2. For the moment the signal processing is made in the server. This integrates typically 4-5 points along the signal (between the red lines) and subtracts the base line (evaluated over 4-5 samples, between the yellow lines). Later the processing will be made in the FPGA.

The result of the integration procedure proved to be quite insensitive (to % level) to changes in the sampling point of the order a couple of ns [11]. However, in order to improve even further, it is intended to implement in the final system an automatic correction procedure to optimize the timing of ADC and signal [9].

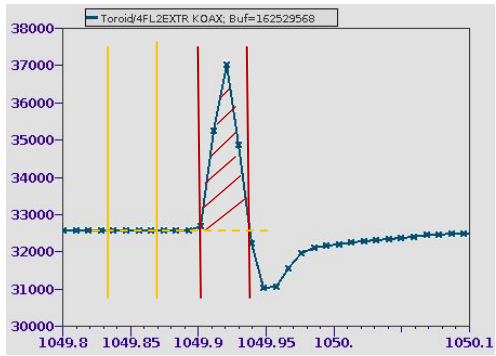


Figure 10: Example of raw toroid signal.

The charge readings are an important part of the machine protection system. A transmission interlock is planned as for the E-XFEL [9]. For the time being, as a temporary solution, the Toroid Protection System (TPS) system developed for FLASH is used [12]. Each of three modules compare the (analogue) signals from a pairs of toroids, one at the beginning and the other at the end of each linac section: FLASH (the common part), FLASH1, and FLASH2. Each TPS module generates an alarm when the difference of single bunch signals or the integrated charge loss is higher than a threshold value. Also a low charge alarm is send when a bunch is expected, but no charge, or too low charge is measured.

This system configuration however has a gap in the septum region, where the machine protection relies only on the beam loss monitors. This gap will be closed as soon as the E-XFEL system becomes available. This system will be able to deal with the distribution of beam into several branches.

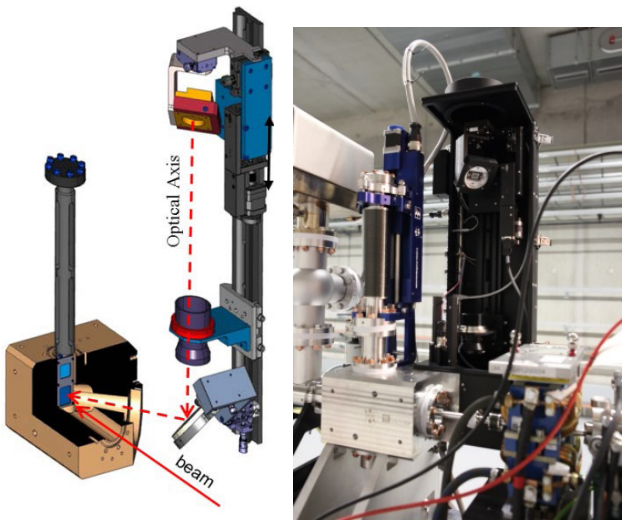
SCREENS

The screens are an essential component for the beam characterization and tuning. For the E-XFEL and FLASH a resolution of 10 μm over the entire field of view is required. One concern when designing the screens was avoiding coherent optical transition radiation (COTR) first observed with ultra-short bunches at LCLS [13]. Based on a series of tests with various scintillating materials, LYSO:Ce screens with a thickness of 200 μm were chosen [14].

Figure 11a shows the layout of the screen system, composed of vacuum chamber, mover and optic box. The beam image created by luminescence on the screen, which is mounted perpendicular to the beam axis, is observed under 45 deg. Potential COTR radiation is reflected back into the beam pipe and thus is geometrically suppressed. In addition to the scintillator, a calibration target is also installed in the system and can be moved into the field of view. A CCD camera is used for visualization. In order to extend the depth of field, the Scheimpflug principle is used. An installed station in FLASH2 is also shown in Figure 11b.

Copyright © 2014 CC-BY-3.0 and by the respective authors

ISBN 978-3-95450-141-0



a b

Figure 11: Layout of a screen system (a) and installed station (b) in FLASH2.

Laboratory tests gave a resolution of 5.4 μm, which is well within the requirement. Two versions are installed in FLASH: most of the stations have an optical magnification of 1:1 while the stations requiring a large field have a magnification of 1:2.

Figure 4 shows the two beams, in the center for FLASH1 and the upper one for FLASH2 on a screen with wide field of view, just before the septum. The separation between the two beams is about 2 cm. Another screen of the same type, with a beam chamber of 100 mm diameter has been installed in the dump line.

In Figure 7 one can see the beam observed for the first time on the first, standard screen in FLASH2, in the extraction region, with a magnification of 1:1.

A special luminescent screen, a Chromox ceramic with a thickness of 1 mm, is placed at the dump vacuum window [15]. An optical system looks at the screen through a special port placed upstream. After commissioning it is expected that this system delivers constantly an image of the beam at the dump.

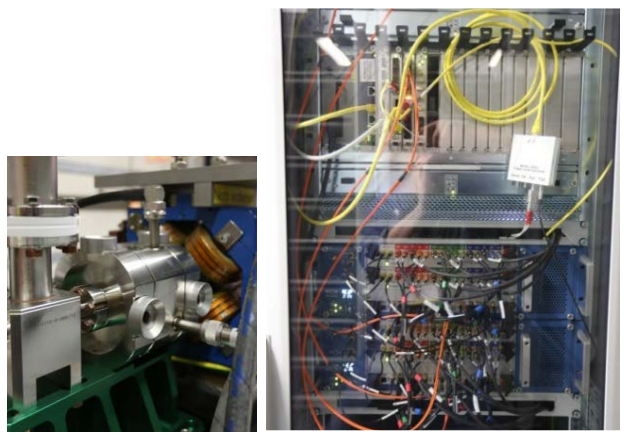
BUNCH POSITION MONITORS

Cavity BPMs (CBPM) have been installed in the undulator section. Button BPMs and several stripline BPMs have been installed in the remainder of the electron beamline.

Cavity BPMs

17 CBPMs, developed for the E-XFEL have been installed in the undulator section [16]. Figure 12a shows a CBPM installed in FLASH2. The monitors have a total length of 100 mm and an aperture of 10 mm. Each BPM has a dipole and a reference cavity, both with a resonant frequency of 3.3 GHz and a low quality factor of around 70. Due to the low Q it is possible to separate the signals of consecutive bunches, even at E-XFEL bunch repetition rates of 4.5 MHz. The monopole resonator is needed to normalize the charge, and to provide a phase reference to determine the beam offset sign. Two antennas are mounted for the horizontal signal and two for the vertical one in the dipole resonator, for symmetry reasons. Only one per plane is connected to a cable for readout, while the opposite pickup is terminated with a load. The reference cavity has one pickup for monitoring of the monopole signal.

The electronics has been built by PSI in a modular way [17,18]. Each Modular BPM Unit (MBU) contains up to 2 RF front ends (RFFE), each of these serving one cavity BPM (see Figure 12b). The RFFE mixes the 3.3 GHz signals from the pickups down to baseband. 16-bit 160 MS/s ADCs are used for the six I and Q signals. A digital signal processing board ("GPAC" board) is used for signal processing and interfacing with the control system. The interfacing to the DOOCS system is done using a FPGA-FPGA bridge between FPGAs located on the GPAC board and on a DAMC02 card [19] installed in a MTCA crate. Both crates are connected by optical fibers.



a b

Figure 12: CBPM installed in FLASH2 (a) and electronics rack (b) with 2 MBUs (lower crates) and a MTCA crate with DAMC02 card for the CBPMs.

Three further CBPMs of the E-XFEL prototype development have been installed in FLASH1 for tests. For a beam charge of 0.24 nC a resolution below 1 μm rms was measured even for a beam offset of 1 mm. This is well within the required resolution of 2 μm rms* for a beam offset between ±0.5 mm and charges above 0.1 nC, as specified for FLASH2.

The CBPMs deliver also a measurement of the bunch charge. The resolution measured at the FLASH1 CBPMs for a bunch charge of 0.24 nC is 0.13 pC.

Button and Stripline BPMs

Button BPMs with the E-XFEL aperture of 40.5 mm and with FLASH standard beam pipes of 34 mm, both with button feedthroughs of 16 mm diameter have also

* Note that the requirement at the XFEL is 1 μm rms, but was somewhat relaxed at FLASH since the cables are much longer, of maximum about 15 instead of 6 m, due to the placement of the electronics outside of the tunnel.

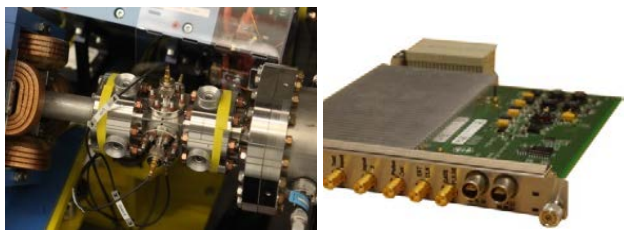
ISBN 978-3-95450-141-0

Copyright © 2014 CC-BY-3.0 and by the respective authors

been installed in FLASH2 (see Figure 13a). In addition at 3 locations in the undulator section, where space did not allow for installation of CBPMs, small, finger-like feedthroughs have been installed in the beam pipe, like the ones in the FLASH1 undulator section. Furthermore, 4 stripline BPMs installed inside quadrupoles yokes have been placed in FLASH2 [20].

A special electronics based on the MTCA standard has been designed for these both types of BPMs. This is called low charge BPM (LCBPM) electronics [21], in contrast to the old monitors in FLASH, designed for charges of 1 nC and higher.

The signals from two opposite BPM pickups are send through the same cable, one of them with a delay of 100 ns, to a RTM module (see Figure 13b). This pre-conditions the short signals, by filtering and using a peak detector, so that it is possible for an ADC to sample them. A cascade of amplifiers enables the fine tuning of the signal amplitude for best performance for each charge and beam offset range. The resulting signals are fanned out to 4 outputs for digitization.

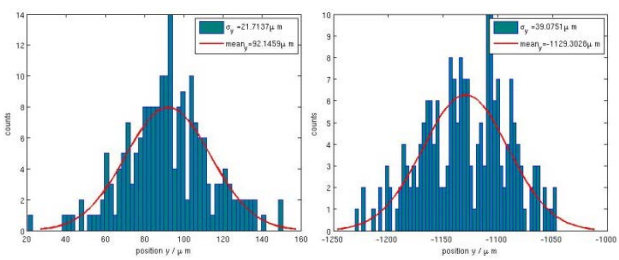


a b

Figure 13: Button BPM (a) and RTM card for button and stripline BPMs (b).

SIS8300 cards [10] are used for digitization and digital data processing. The electronics processes bunch by bunch data in an FPGA. Therefore it is suited to be used in low latency feedback and interlock systems.

Figure 14 shows the residuals measured for a stripline and a button BPM in FLASH2 for a bunch charge of 36 pC, measured over 200 pulses. A sigma of about 22 µm is obtained for the stripline, and about 40 µm for the button BPM is obtained.



a b

Figure 14: Residuals of the BPM display for a stripline (a) and a button (b) BPM in FLASH2.

Note that due to the measurement principle the beam jitter is included in this number. Even with beam jitter included the values already are close to the specifications. A resolution of 30 µm rms is generally required from the BPMs in FLASH, apart from the undulator sections, while at the E-XFEL the requirement is in general 50 µm rms.

BEAM LOSS MONITORS

The beam loss monitor (BLM) system developed for the E-XFEL [22] is also installed at FLASH2. Figure 15 shows schematically one BLM unit. The electrons hitting the beam pipe produce secondary radiation which then passes through a scintillator, placed in a cylinder protecting against surrounding light. The rod is opto-mechanically interfaced to a photomultiplier (PMT). The high voltage (HV) of the order of hundreds of volts, needed to power the PMT is produced by a circular printed circuit board placed at its base. This is made with Cockcroft-Walton multipliers powered by an oscillator. The signal from the PMT is send to the readout electronics (RTM), which stretches the pulse and controls the HV. The signal is then digitized and sent to a DAMC02 board, where low latency digital data processing is done [19]. Part of the analogue signal is sent to comparators, to provide single bunch alarms with lowest possible latency. The digital data processing in the FPGA of the DAMC02 can generate one of the following alarms: single bunch alarm, when the signals of individual bunches pass a threshold; multi bunch alarm, when a certain number of bunches pass a threshold; and integration alarm, when the integral of the BLM signal has reached a threshold. The settings of the fast comparator signal path are also controlled by the FPGA. If either an analog or a digital alarm is generated, this is sent to the machine protection system (MPS). The latency of the BLM electronics is on the order of 100 ns.

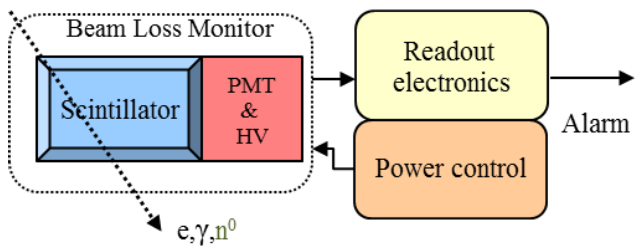


Figure 15: Schematic of a BLM unit.

Figure 16 shows a photo of a scintillating rod (a), of printed circuit boards (b) and of two BLMs mounted left and right of the beam pipe in the undulator section (c). A typical signal in the control system from a BLM is shown in Figure 5.

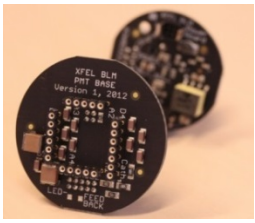
Note that in the septum area, both for FLASH1 and for FLASH2, the MPS relies only on the BLM system, therefore in this area particular care has to be taken.

Copyright © 2014 CC-BY-3.0 and by the respective authors

ISBN 978-3-95450-141-0



a



b



c

Figure 16: Scintillating rod of a BLM (a), printed circuit boards mounted in the PMT housing (b), and two BLMs mounted in FLASH2.

Cherenkov Monitors

The permanent magnets of the undulators are sensitive to radiation and therefore they have to be protected. Complementary to the BLMs installed between the undulators, optical fibers are to be installed inside the vacuum chambers of the undulators, right and left from it [23]. The radiation produced by electrons hitting the beam pipe produces Cherenkov light which is collected by PMTs mounted at the upstream end of the fibers. This system is similar to the one in FLASH1, but with newly designed electronics. The system has not yet been commissioned. At FLASH1 it has proven to be very helpful in setting up the machine and reducing the overall losses. At the E-XFEL a different system, based on dosimeters has been adopted instead [24].

BEAM DUMP INSTRUMENTATION

Several types of monitors ensure that the high power electron beam is safely dumped. The part installed inside or around the vacuum pipe is the same as in FLASH1, while the electronics have been redesigned using the MTCA standard and using synergies to the E-XFEL BLM development.

Figure 17 shows the dump vacuum chamber. The beam coming towards the dump passes along the last 2 m before the vacuum window among 4 ionization chambers placed symmetrically in tubes around the beam pipe (with red caps in the figure). 4 fused silica fibers are installed next to them, in the same pipes (not in the figure). After passing the vacuum window, of which a part can be seen as well, the beam generates signals in the loops of a magnetic BPM and the sensors (placed under protecting caps) of a beam halo monitor.

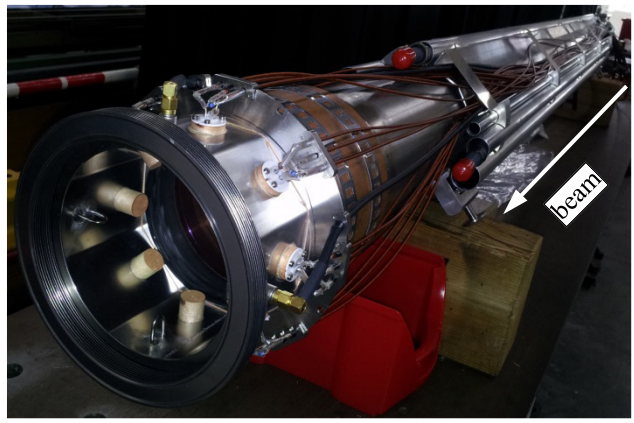


Figure 17: The dump vacuum chamber with pipes for BLM fibers and ionization chambers. At the closer end is the vacuum window. The caps of the beam halo sensors and the loops of the magnetic BPM placed after the vacuum window (in beam direction) can also be seen.

The individual systems are still under commissioning and are briefly described in the following.

Cherenkov BLMs

Four fused silica fibers are symmetrically installed along the last 2 m of the beamline [25]. These produce Cherenkov radiation, which is then coupled to PMTs and read out using the same electronics as for scintillator-based BLMs.

Ionization Chambers

Air filled Heliax cables are used as ionization chambers, like in FLASH1 [25]. They are installed next to the BLM fibers. Their downstream ends covered by red caps can be seen in Figure 17.

The electronics has a large dynamics range, from 10^{-4} to 10^{4} μA, like the one for FLASH1. The form factor has been adapted to MTCA standard, and the front end was placed on an RTM.

Such ionization chambers will not be used at the E-XFEL.

Beam Halo Monitor

Four pCVD diamond and four artificial monocrystalline sapphire sensors, placed inside protecting caps, constitute the beam halo monitor (BHM) [26] (see Figure 17 and Figure 18). It has the same design as the one in FLASH1. To avoid the risk of vacuum leaks due to additional feedthroughs in this difficult environment, it is placed after the vacuum window in a Nitrogen-flooded area. The sensors are operated as solid state ionization chambers and were proven in tests to be radiation hard.

The front-end signal shaping electronics is placed in the tunnel, close to the BHM. The signal is then bought to an RTM and DAMC02 card. The RTM and the firmware are quite similar to the ones for the BLMs.

ISBN 978-3-95450-141-0

Copyright © 2014 CC-BY-3.0 and by the respective authors

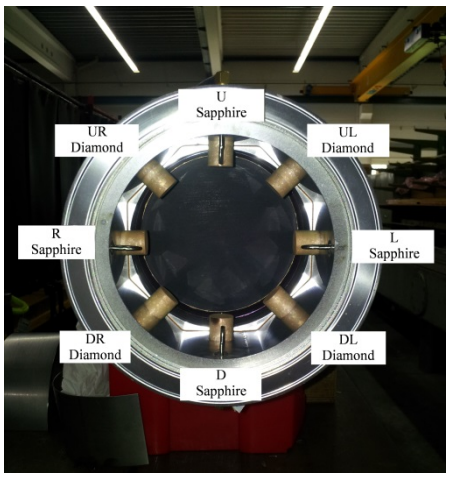


Figure 18: Diamond and sapphire sensors of the BHM placed in protecting caps.

Similar BHMs will be used also in the dumps of the E-XFEL, with the difference that the sensors will be placed outside of the beam pipe.

Magnetic BPM

Out of fear of vacuum leaks at the pickups, no BPM has been placed in the beam pipe closely before the dump window, but after it, next to the BHM sensors in an area is filled with dry Nitrogen [27]. In order to avoid signals from ions, it was decided to use the magnetic field of the bunches, sampled with wire loops for monitoring. The signals are read with the LCBPM electronics. Such a BPM will not be used in the E-XFEL.

OTHER DIAGNOSTICS

Monitors for longitudinal bunch diagnostics have also been built into the FLASH2 beamline and are here only listed: a beam arrival monitor [28], a bunch compression monitor [29], and a coherent transition radiation monitor [30]. These are yet to be commissioned. Similar monitors will be also built into the E-XFEL.

SUMMARY

Many beam monitors built in the new FLASH2 undulator beamline have been designed for the E-XFEL, some were specially designed for FLASH2 and some have been copied from similar older systems in FLASH. Some systems have been fully commissioned (like the screen stations), some are still under commissioning (like the BPMs) or have a temporary solution (toroid system).

In spite of lots of work remaining to be made, recently the first lasing was obtained in FLASH2 [1,31]. The electron beam energy was 680 MeV and the photon wavelength was 40 nm. FLASH1 was producing FEL radiation at the same time, with 250 bunches per pulse, at a wavelength of 13.5 nm.

Meanwhile routine operation of FLASH2 in parallel to FLASH1 has become routine [32]. The experience gained with E-XFEL systems at FLASH2 will surely contribute to a faster and easier commissioning of the European XFEL.

ACKNOWLEDGMENT

This paper is a brief summary of the work of many people from several institutes. We thank the many colleagues who gave input and made comments to this paper.

REFERENCES

[1] K. Honkavaara et al., “FLASH: First Soft X-ray FEL Operating Two Undulator Beamlines Simultaneously”, WEB05, FEL2014, Basel (2014).
[2] M. Vogt et al., “Status of the Free Electron Laser User Facility FLASH”, IPAC2014, Dresden, p. 938 (2014).
[3] M. Hüning, “Status of the European XFEL”, IPAC2013, Shanghai, p. 2058 (2013).
[4] D. Nölle, “Status of the Standard Diagnostic Systems of the European XFEL”, WEPF14, IBIC2014, Monterey (2014).
[5] N. Baboi et al., “Electron Beam Diagnostics for FLASH II”, DIPAC2011, Hamburg, p. 53 (2011).
[6] K. Rehlich, “Recent Hardware and Software Achievements for the European XFEL”, THCOBB02, ICALEPCS2013, San Francisco (2013).
[7] S. Karstensen et al., “XFEL Machine Protection System (MPS) Based on uTCA”, ICALEPCS2013, San Francisco, p. 906 (2013).
[8] H. Schlarb et al., “Novel Crate Standard MTCA.4 for Industry and Research”, IPAC2013, Shanghai, p. 3633 (2013); http://www.picmg.com; http://mtca.desy.de/
[9] M. Werner et al., “A Toroid Based Bunch Charge Monitor System with Machine Protection Features for FLASH and XFEL”, WEPF02, IBIC2014, Monterey (2014).
[10] http://www.struck.de/sis8300.html; http://www.struck.de/sis8900.html
[11] R. Neumann, Private communication.
[12] A. Hamdi et al., “Toroid Protection System for FLASH”, DIPAC 2007, Venice, p. 349 (2007).
[13] H. Loos et al., “Observation of Coherent Optical Transition Radiation in the LCLS Linac”, FEL08, Gyeongju, p. 485 (2008).
[14] C. Wiebers et al., “Scintillating Screen Monitors for Transverse Electron Beam Profile Diagnostics at the European XFEL”, IBIC2013, Oxford, p. 807 (2013).
[15] J. Good et al., “An Electron Beam Detector for the FLASH II Beam Dump”, IBIC2013, Oxford, p. 814 (2013).
[16] D. Lipka et al., “FLASH Undulator BPM Commissioning and Beam Characterization Results”, TUPF07, IBIC2014, Monterey (2014).
[17] M. Stadler et al., “Low-Q Cavity BPM Electronics for E-XFEL, FLASH-II and SwissFEL”, WEPD12, IBIC2014, Monterey (2014).

Copyright © 2014 CC-BY-3.0 and by the respective authors

ISBN 978-3-95450-141-0

[18] B. Keil et al., "Beam-Based Calibration and Performance Optimization of Cavity BPMs for SwissFEL, E-XFEL and FLASH2", WEPD11, IBIC2014, Monterey (2014).
[19] http://fe.desy.de/fea/projects/tca_developments/damc2
[20] D. Nölle et al., "TTF2 Beam Monitors, Bunch Charge and Phase Measurements", LINAC 2004, Lübeck, p. 435 (2004).
[21] B. Lorbeer et al., "Design, Development and Commissioning of a MTCA-Based Button and Strip-Line BPM System for FLASH2", TUPF08, IBIC2014, Monterey (2014).
[22] A. Kaukher et al., "XFEL Beam Loss Monitor System", BIW2012, Newport News, p. 35 (2012).
[23] W. Goettmann et al., "Beam Profile Measurement with Optical Fiber Sensors at FLASH", DIPAC 2007, Venice, p. 123 (2007).
[24] F. Schmidt-Föhre et al., "Tests and Measurements with the Embedded Radiation-monitor-system Prototype for Dosimetry at the European XFEL", IPAC 2012, New Orleans, p. 4041 (2012).
[25] N. Baboi et al., "New Electron Beam Diagnostics in the FLASH Dump Line", BIW10, Santa Fe, p. 420 (2010).
[26] A. Ignatenko et al., "Beam Halo Monitor for FLASH and the European XFEL", IPAC2012, New Orleans, p. 816 (2012)
[27] D. Lipka et al, "Magnetic Coupled Beam Position Monitor for the FLASH Dump Line", BIW10, Santa Fe, p. 214 (2010).
[28] A. Angelovski et al., "Time Domain Pickup Signal Characterisation for Low Charge Arrival-Time Measurements at FLASH", MOPD25, IBIC2014, Monterey (2014).
[29] C. Behrens et al., "Upgrade and Evaluation of the Bunch Compression Monitor at the Free-Electron Laser in Hamburg (FLASH)", IPAC'10, Kyoto, p. 912 (2010).
[30] S. Wesch et al., "Fast Bunch Profile Monitoring with THz Spectroscopy of Coherent Radiation at FLASH", BIW2012, Newport News, p. 256 (2012).
[31] S. Schreiber, B. Faatz, "First Lasing at FLASH2", FEL 2014, Basel, (2014).
[32] S. Ackermann et al., "Simultaneous Operation of Two FEL Undulator Beamlines at FLASH", MOPF22, IBIC2014, Monterey (2014).

Copyright © 2014 CC-BY-3.0 and by the respective authors

ISBN 978-3-95450-141-0

CROSS-CALIBRATION OF THREE ELECTRON CLOUD DENSITY DETECTORS AT CESRTA*

J.P. Sikora†, J.R. Calvey, J.A. Crittenden, CLASSE, Ithaca, New York, USA

Abstract

Measurements of electron cloud density using three detector types are compared under the same beam conditions at the same location in the Cornell Electron Storage Ring (CESR). Two of the detectors sample the flux of cloud electrons incident on the beam-pipe wall. The Retarding Field Analyzer (RFA) records the time-averaged charge flux and has a retarding grid that can be biased to select high energy electrons. The Shielded Button Electrode (SBE) samples the electron flux without a retarding grid, acquiring signals with sub-nanosecond resolution. The third detector uses resonant microwaves and measures the electron cloud density within the beam-pipe through the cloud-induced shift in resonant frequency. The analysis will include comparison of the output from POSINST and ECLOUD simulations of electron cloud buildup. These time-sliced particle-in-cell 2D modeling codes – simulating photoelectron production, secondary emission and cloud dynamics – have been expanded to include the electron acceptance of the RFA and SBE detectors in order to model the measured signals. The measurements were made at the CESR storage ring, which has been reconfigured as a test accelerator (CESRTA) providing electron or positron beams ranging in energy from 2 GeV to 5 GeV.

INTRODUCTION

The Cornell Electron Storage Ring (CESR) has a circumference of 768 m and supports positron or electron beams with energies from 2 GeV to 5 GeV. Bunch populations can be as high as 1.6×10^{11} particles/bunch (10 mA/bunch) with total beam populations of 3.8×10^{12} particles/beam.The storage ring has been used as part of a test accelerator program (CESRTA) that includes the measurement of electron cloud (EC) density and mitigation techniques. A number of devices have been installed for EC density measurements at the locations shown in Fig. 1.

The subject of this paper is a comparison of the measurements made with different devices at the same location. Section 15E, shown in Fig. 2, includes a retarding field analyzer (RFA), a shielded button electrode (SBE) and connections for resonant microwave measurements. The RFA and the SBE sample the flux of electrons onto the wall of the beam-pipe, while resonant microwaves are sensitive to the EC density within the beam-pipe volume.

* This work is supported by the US National Science Foundation PHY-0734867, PHY-1002467 and the US Department of Energy DE-FC02-08ER41538, DE-SC0006505.

† jps13@cornell.edu

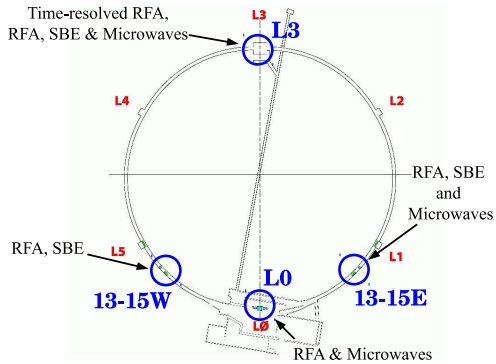


Figure 1: This sketch of the CESRTA storage ring shows the location of electron cloud detectors, including the group at 15E used in this study.

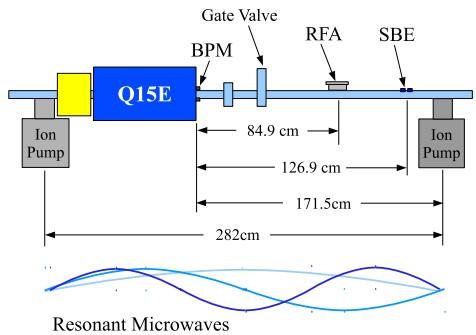


Figure 2: The 15E section of the CESR storage ring contains an SBE, an RFA and a resonant section of beam-pipe.

RETARDING FIELD ANALYZER

Figure 3 shows the conceptual layout of the RFA [1]. Cloud electrons can enter the detector through an array of small holes in the beam-pipe wall. Nine positively biased collectors are arranged horizontally. The current is time averaged to give a DC current measurement. There is a grid between the holes and the collectors which can be negatively biased to prevent lower energy electrons from impacting the collectors. In a typical measurement, the currents are measured as a function of the grid bias voltage in order to gain information about the energy distribution of the cloud electrons. A plot of such a measurement is given in Fig. 4 showing that most of the electrons are of relatively low energy, but there are some electrons at the central collectors with energies above 200 eV.

SHIELDED BUTTON ELECTRODE

The SBE also has a pattern of holes that allow electrons to enter the detector, shown in Fig. 5, but the collector provides

Copyright © 2014 CC-BY-3.0 and by the respective authors

ISBN 978-3-95450-141-0

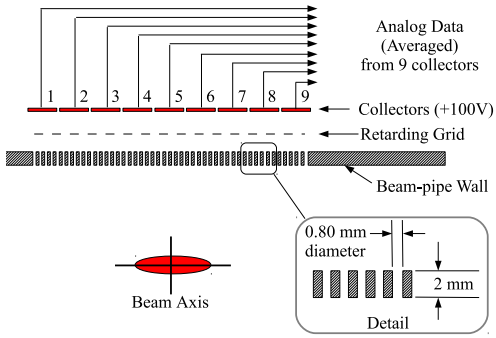


Figure 3: An array of holes in the beam-pipe wall allows cloud electrons to enter the detector. A retarding grid can be biased to suppress electrons with energies below the bias voltage. The array of collectors is arranged horizontally to record the transverse dependence of the current.

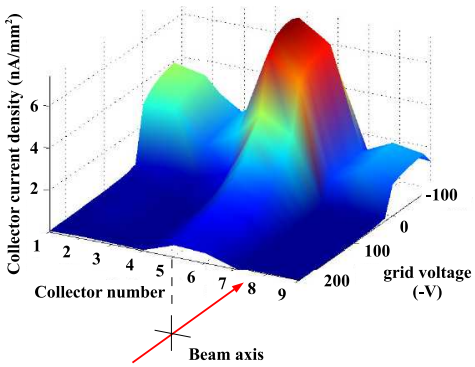


Figure 4: Data from the RFA shows the current versus transverse position for values of the retarding voltage from -100 to 200V. The beam is a 45-bunch train of 5.3 GeV positrons with 14 ns spacing at 1.25 mA/bunch. Collector 1 is toward the outside of the ring.

time-resolved measurements [2, 3]. The collector is of the same design as the buttons used in the beam position monitor (BPM) system, except that it is located behind the array of holes. The depth to diameter ratio of 3:1 (used for both the SBE and the RFA) is effective in suppressing the direct beam signal. The collector is biased at +50 V and the signal is capacitively coupled to +20 dB of amplification and a digital oscilloscope.

Figure 6 shows data from the SBE with two equally populated bunches of 5.3 GeV positrons spaced at 28 ns. The signal from the first bunch comes primarily from photo-electrons since the 2562 ns revolution time of the storage ring is long compared to the lifetime of the electron cloud. The arrival of the second bunch produces a signal from the photo-electrons, but also accelerates into the detector some of the electron cloud produced by the first bunch.

SIMULATION CODES

Two simulation codes are used in the analysis of data taken with these devices. Both are particle-in-cell time-sliced

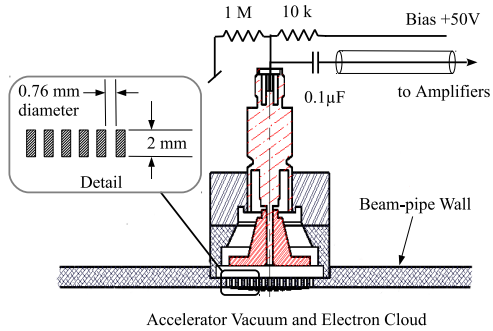


Figure 5: The SBE also has an array of holes that allow electrons to enter the detector. There is no retarding grid and the collector is biased at +50 V.

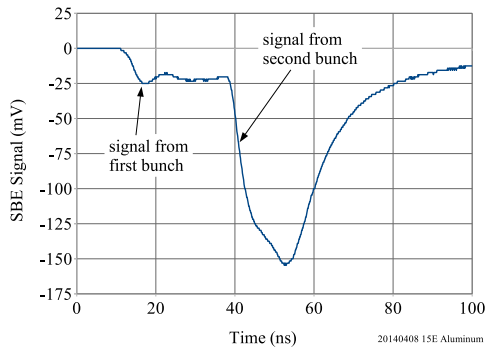


Figure 6: Data from the SBE with two bunches of 5.3 GeV positrons at 3 mA/bunch (4.8×10^{10} e^+/bunch) spaced by 28 ns.

codes that model the buildup of the electron cloud. The models include the simulation of photo-electron generation, the effect of electrostatic fields by the beam and the cloud, as well as detailed modeling of the interaction of the electrons with the vacuum surface.

The POSINST simulation code [4] was developed at Lawrence Berkeley National Laboratory (LBNL) and the Stanford Linear Accelerator (SLAC) beginning in the 1990s. It has been used in understanding EC effects in PEP-II at SLAC, the Large Hadron Collider (LHC) at CERN and the Advanced Photon Source at Argonne National Laboratory as well as in the design of the damping ring for the International Linear Collider (ILC) [5–7]. The parameters of POSINST are used in fitting the EC buildup model to the data measured with the RFA [8]. This requires that the detector response is included in the model.

The ECLOUD code [9] was developed at CERN in the 1990s for simulating EC buildup at the CERN LHC, SPS, and PS. It has also been used at CESRTA [3, 10] and in the design of the ILC damping ring [7]. The parameters of ECLOUD are used in fitting the EC buildup model to the data measured with the SBE. A model of the SBE detector response is included when matching the modeled signal to the data.

ISBN 978-3-95450-141-0

Copyright © 2014 CC-BY-3.0 and by the respective authors

Both simulation codes require as input the synchrotron radiation photon rate and absorption site distribution on the vacuum chamber wall. We have used the simulation code SYNRAD [11] to calculate photon rates based on the CESR lattice and ring geometry. In addition, we used the SYNRAD3D [12] code to obtain the photo-electron production site distribution, since it includes photon tracking, absorption, and scattering on the beam-pipe wall, both diffuse and specular, based on beam-pipe geometry and surface roughness parameters.

An important difference between the ECLOUD and POSINST codes is in the algorithm for generating secondary electrons. In ECLOUD, each macroparticle-wall collision produces a single secondary macroparticle, whose charge is scaled by the secondary yield. In POSINST, each collision can generate up to nine secondary macroparticles (depending on the secondary yield), each with its own energy and emission angle. Another difference between the codes is that ECLOUD provides for different quantum efficiency values for scattered and unscattered photons.

RESONANT MICROWAVES

An alternate technique for measuring EC density is the use of resonant microwaves [13–15]. When microwaves are coupled into the beam-pipe the response will often be resonant, especially near the cutoff frequency of the beam-pipe. At 15E, reflections produced by the longitudinal slots at two ion pumps generate standing waves between them. Microwaves are coupled into and out of the beam-pipe using the buttons of a BPM between these pumps. The resonant response is shown in Fig. 7. An EC density within the beam-pipe will shift the resonant frequencies slightly, as given by Eq. 1.

$$\frac{\Delta\omega}{\omega_0} \approx \frac{e^2}{2\varepsilon_0 m_e \omega_0^2} \frac{\int_V n_e E_0^2 dV}{\int_V E_0^2 dV} \qquad (1)$$

With a short train of bunches in the storage ring, this shift will be periodic. With a fixed drive frequency near resonance, the periodic shift in resonant frequency will produce phase modulation sidebands at the revolution frequency above and below the drive frequency. A sketch of the measurement setup is shown in Fig. 8. In the case of 15E, five of the numbered resonances of Fig. 7 are excited and the phase modulation sidebands are measured for each resonance.

MEASURING EC DENSITY

Each of these techniques has challenges in obtaining an absolute EC density from the measured data. The signals from the RFA and SBE do not have a simple relation to the EC density, so modeling is necessary to infer the density from the measurements.

There are many physical parameters in the ECLOUD and POSINST simulations that are used for the SBE and RFA respectively. These include the photon distribution, quantum efficiency, secondary yield as a function of energy, and the angular and energy distributions of the emitted electrons.

Changes in each parameter affect the simulated signal in ways that have considerable overlap, so that it can be difficult to optimize individual parameters. As shown in the Fig. 9 and Fig. 10, the optimized model provides an approximate agreement with the measurement. As a result, fitting the simulation parameters to the data is not straightforward.

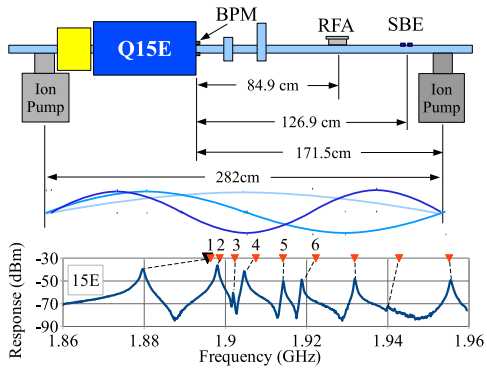


Figure 7: At 15E, reflections from the longitudinal slots at two ion pumps generate a resonant response when the beam-pipe is driven with microwaves at the BPM between them. The five labelled resonances are used in the measurement of EC density.

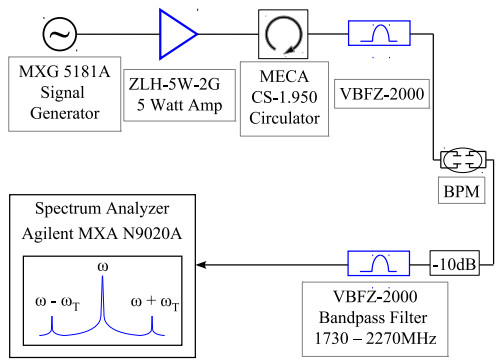


Figure 8: This sketch shows the configuration of instruments used in making resonant microwave measurements.

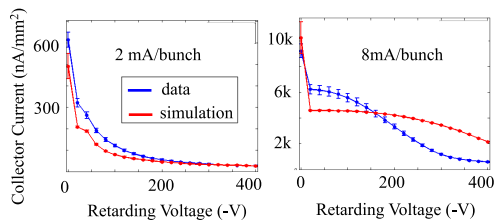


Figure 9: The POSINST simulation output is plotted along with the measured collector currents versus retarding voltage on the RFA. The 8 mA simulation matches the scale of the data, but not the energy distribution.

The microwave measurement of EC density has its own challenges. As described in Ref. [13], a number of steps are

Copyright © 2014 CC-BY-3.0 and by the respective authors

ISBN 978-3-95450-141-0

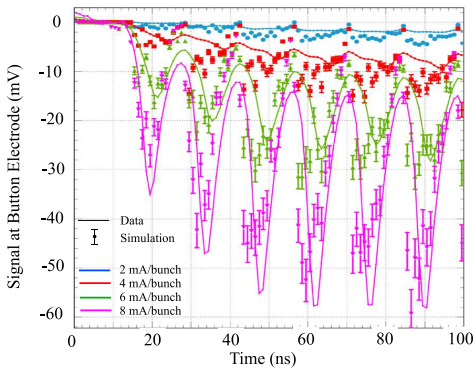


Figure 10: This detail of the ECLOUD simulation output is plotted along with the measured signal from the SBE. The fit to the measured data looks reasonable at 8 mA/bunch, but at lower bunch currents the simulated signal is larger than the data.

needed to relate an EC density to the measured sideband amplitudes: the EC induced frequency shift becomes a phase shift, but a convolution with the damping time of the resonance is needed; the Fourier components of the resulting phase modulation are calculated with their corresponding modulation sideband amplitudes. In addition to the measured sideband amplitudes, additional measurements or estimates need to be made in order to carry out the calculations: the Q of the resonances, the EC density versus time, and the EC density versus position within the resonant section of beam-pipe [16].

The EC density can vary considerably over the length of the resonant section. While the RFA and the SBE measurements are localized to within a few centimeters of those detectors, the microwave measurement is an average over its length, weighted by E^2. An estimate for the change in EC density versus position is needed to relate the measurements at the three detectors.

We use the approximation that the EC density will be proportional to the synchrotron radiation photon rate. This ignores the effects of magnetic fields and the possible saturation of the cloud at high photon rates. Figure 11 shows the relative photon rates predicted by SYNRAD for positrons and electrons. The photon rates are normalized to the rate at the longitudinal center of the resonance. Since the RFA and SBE are localized measurements, their values can be scaled by their relative photon rates for comparison. The microwave resonant region and its center are shown at the bottom of the plot, along with the positions of the RFA, SBE and the longitudinal center of the resonance.

This EC density approximation can be used to calculate a correction to the microwave measurements in order to obtain the EC density at the center of the resonant section. If the EC density is either constant or changing linearly along the resonant length, Eq. 1 is unchanged. If the change in EC density is not linear with longitudinal position, a correction is needed. For the 15E resonances, this correction is only a few percent. Once the value at the center of the resonance has been obtained, it can be scaled to find the EC density values at the RFA and SBE.

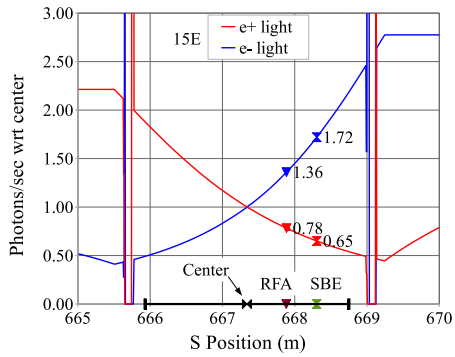


Figure 11: The relative photon rates from positron and electron beams are shown normalized to the rate at the center of the microwave resonance at 15E.

COMPARISON

For this comparison, data was taken in the 15E aluminum chamber with a 20-bunch train of positrons at 5.3 GeV having bunch currents of 2, 4, 6 and 8 mA (total currents from 40 to 160 mA). At each current step, data was taken with the three detectors.

Using the approximation that the EC density is proportional to the photon rate, the measurements are scaled to the position of the SBE. For the microwave measurements, the EC density versus time from the ECLOUD simulation is used to calculate the Fourier spectrum.

The EC density versus time for both simulations at 8 mA/bunch is shown in Fig. 12. The growth and decay rates are similar, although the peak EC density from ECLOUD is lower by about 40%. In Fig. 13 the peak EC densities at four currents are plotted for the simulations and for the microwave measurements. The density derived from the ECLOUD simulation is lower than the POSINST and microwave values by about 40% over this current range. The densities given by microwave measurements vary depending upon the resonance used over a range that is also about 40%.

FUTURE WORK

Verification of the models in both the POSINST and ECLOUD simulations should continue over a wide range of beam energies, bunch populations, magnetic fields and vacuum chamber surfaces. This will ensure that results are applicable to a variety of accelerators and provide robust predictions. Work on resonant microwaves should include improvements in the measurement of Q, the microwave E^2 electric field distribution and the compensation for changes in EC density with position.

REFERENCES

[1] J.R. Calvey *et al.*, Nucl. Instrum. Methods Phys. Res., Sect. A **760**, p. 86-97 (2014), `http://dx.doi.org/10.`

ISBN 978-3-95450-141-0

Copyright © 2014 CC-BY-3.0 and by the respective authors

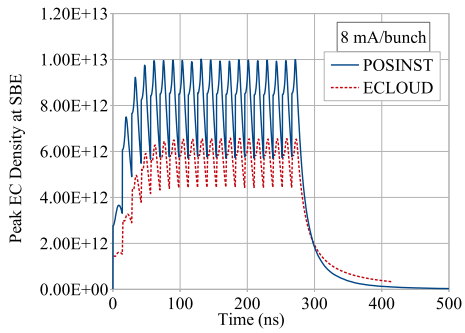


Figure 12: The EC density versus time from POSINST and ECLOUD at 8 mA/bunch are plotted with both scaled to the location of the SBE.

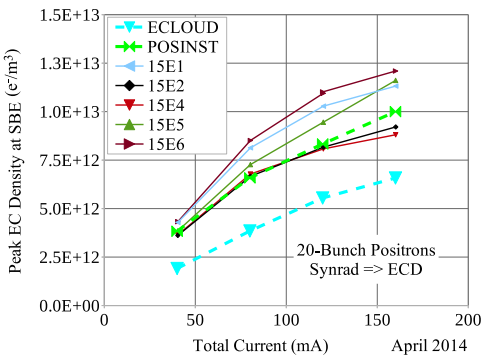


Figure 13: The EC density output from POSINST and ECLOUD are plotted with microwave measurements for five resonances shown in Fig. 7. All measurements are scaled to the location of the SBE as described in the text.

1016/j.nima.2014.05.051, Preprint, arXiv:1402.7110 [physics.acc-ph].

[2] J.A. Crittenden *et al.*, Nucl. Instrum. Methods Phys. Res., Sect. A **749**, p. 42-46 (2014), http://dx.doi.org/10.1016/j.nima.2014.02.047, Preprint, arXiv:1311.7103 [physics.acc-ph].

[3] J.A. Crittenden, J.P. Sikora, "Electron Cloud Buildup Characterization Using Shielded Pickup Measurements and Custom Modeling Code at CESRTA," in *Proceedings of ECLOUD 2012: Joint INFN-CERN-EuCARD-AccNet Workshop on Electron-Cloud Effects, La Biodola, Elba, Italy*, edited by R. Cimino, G. Rumolo, F. Zimmermann, CERN-2013-002, CERN, Geneva, Switzerland, 2013, p. 241-250, arXiv:1307.4013 [physics.acc-ph].

[4] M.A. Furman, M.T.F. Pivi, "Probabilistic Model for the Simulation of Secondary Electron Emission," Phys. Rev. ST Accel. Beams **5**, 124404 (Dec. 2002).

[5] M.A. Furman, G.R. Lambertson, "The Electron Cloud Instability in the Arcs of the PEP-II Positron Ring," in Proceedings of MBI97: International Workshop on Multibunch Instabilities in Future Electron and Positron Accelerators, Tsukuba, Japan, 1997, Y. H. Chin, Ed. (1997), KEK Proceedings 97-17, p. 170.

[6] M.A. Furman, "The Electron-Cloud Effect in the Arcs of the LHC," Tech. Rep. LHC Project Report 180/LBNL-41482/CBP Note 247, CERN, Geneva, Switzerland (May 1998).

[7] J.A. Crittenden *et al.*, "Investigation into Electron Cloud Effects in the International Linear Collider Positron Damping Ring," Phys. Rev. ST Accel. Beams *17*, March 2014, 031002.

[8] J.R. Calvey *et al.*, "Measurement and Modeling of Electron Cloud in a Field Free Environment Using Retarding Field Analyzers," Phys. Rev. ST Accel. Beams **17**, June 2014, 061001, arXiv:1402.7110.

[9] F. Zimmermann, G. Rumolo, K. Ohmi, "Electron Cloud Build Up in Machines with Short Bunches," ICFA Beam Dynamics Newsletter **Nr. 33**, eds. K. Ohmi & M. Furman (2004).

[10] J.A. Crittenden *et al.*, "Progress in Studies of Electron-Cloud-Induced Optics Distortions at CESRTA," in Proceedings of IPAC10, Kyoto, Japan (2010).

[11] D. Sagan, "Design and Applications of the Bmad Library for the Simulation of Particle Beams and X-rays," in *11th International Computational Accelerator Physics Conference, Rostock-Warnemünde, Germany* (2012).

[12] G.F. Dugan, D. Sagan, "SYNRAD3D Photon Propagation and Scattering Simulations," in *Proceedings of ECLOUD 2012: Joint INFN-CERN-EuCARD-AccNet Workshop on Electron-Cloud Effects, La Biodola, Elba, Italy*, edited by R. Cimino, G. Rumolo, F. Zimmermann, CERN-2013-002, CERN, Geneva, Switzerland, 2013, p. 117-129.

[13] J.P. Sikora *et al.*, Nucl. Instrum. Methods Phys. Res., Sect. A **754**, pp. 28-35 (2014), http://dx.doi.org/10.1016/j.nima.2014.03.063, Preprint, arXiv:1311.5633 [physics.acc-ph].

[14] J.P. Sikora *et al.*, "TE Wave Measurement and Modeling,"in *Proceedings of ECLOUD 2012: Joint INFN-CERN-EuCARD-AccNet Workshop on Electron-Cloud Effects, La Biodola, Elba, Italy*, edited by R. Cimino, G. Rumolo, F. Zimmermann, CERN-2013-002, CERN, Geneva, Switzerland, 2013, p. 193-200, arXiv:1307.4315 [physics.acc-ph].

[15] J.P. Sikora *et al.*, "Resonant TE Wave Measurement of Electron Cloud Density Using Multiple Sidebands," in Proceedings of IBIC'13, Oxford, United Kingdom, September 2013, TUPF34, (2013).

[16] J.P. Sikora *et al.*, "Electron Cloud Density Measurements Using Resonant Microwaves at CESRTA," *these proceedings*, WEPF21, IBIC'14, Monetrey, CA, USA (2014).

Copyright © 2014 CC-BY-3.0 and by the respective authors

ISBN 978-3-95450-141-0

PERFORMANCE EVALUATION OF THE INTRA-BUNCH FEEDBACK SYSTEM AT J-PARC MAIN RING

K. Nakamura, Kyoto University, Kyoto, Japan
M. Tobiyama, T. Toyama, M. Okada, Y.H. Chin, T. Obina, T. Koseki, H. Kuboki
KEK, Ibaraki, Japan
Y. Shobuda, JAEA, Ibaraki, Japan

Abstract

An intra-bunch feedback system has been developed at J-PARC (Japan Proton Accelerator Complex) Main Ring (MR) for suppression of head-tail motions and reduction of particle losses. This system consists mainly of a BPM, a signal processing circuit (iGp12), power amplifiers, and stripline kickers. These components were fabricated and installed to MR in April of 2014. This system successfully suppressed internal bunch motion caused by injection kicker errors in the 3GeV constant-energy operation, It also achieved a shorter damping time than that by the bunch-by-bunch feedback system, which is currently used in the routine operation. Comparisons with simulations confirm that internal motion is actually suppressed by intra-bunch feedback system.

INTRODUCTION

The J-PARC is composed of three proton accelerators: the 400MeV linear accelerator (LINAC), the 3 GeV Rapid Cycling Synchrotron (RCS), and the Main Ring (MR) Synchrotron. The main parameters are listed in Table 1. At the J-PARC MR, transverse instabilities have been observed at the injection and during the acceleration. The present narrowband bunch-by-bunch feedback system (BxB FB) is effectively suppressing these transverse dipole oscillations [1]. But the BxB feedback system can damp only the whole bunches, and internal bunch oscillations have been still observed, which is causing additional particle losses [2]. To suppress intra-bunch oscillations, a more wideband and advanced feedback system (named the intra-bunch feedback system) has been developed.

Table 1: Main Parameters of J-PARC Main Ring

Circumference	1568m
Injection Energy	3GeV
Extraction Energy	30GeV
Repetition Period	2.48s
RF Frequency	1.67-1.72 MHz
Number of Bunches	8
Synchrotron Tune	0.002-0.0001
Betatron Tune (Hor./Ver.)	22.41/20.75

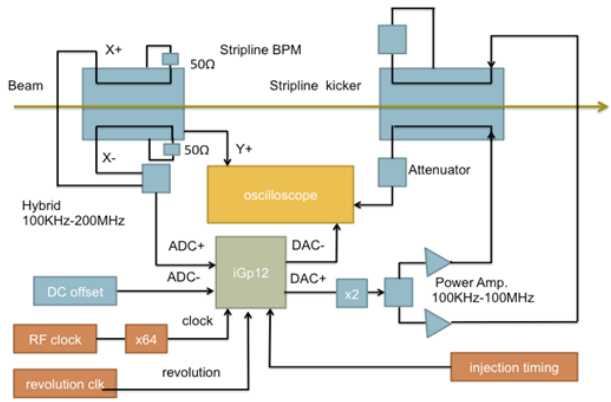


Figure 1: Schematic of the intra-bunch feedback system.

INTRA-BUNCH FEEDBACK SYSTEM

Figure 1 shows the schematic of the intra-bunch feedback system. It is composed mainly of three components: a BPM (Fig. 2), a signal processing circuit (iGp-12) and kickers (Fig. 3). The signal processing circuit detects betatron oscillation of bunches using signals from the BPM and calculates feedback signals. These feedback signals are sent to the kickers through the power amplifiers.

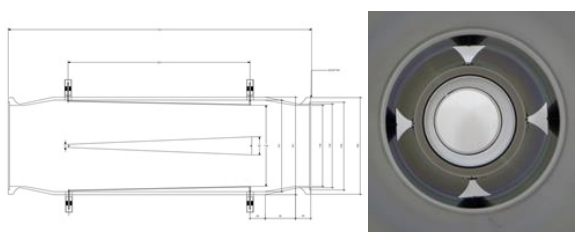


Figure 2: Side (left) and front (right) views of BPM.

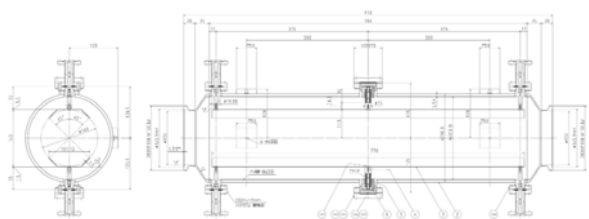


Figure 3: Kicker design.

Copyright © 2014 CC-BY-3.0 and by the respective authors

ISBN 978-3-95450-141-0

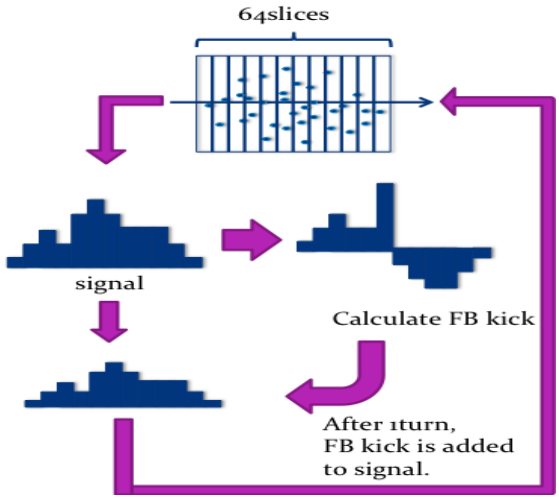


Figure 4: Schematic view of simulation.

PERFORMANCE TESTS WITH 3 GeV BEAM

We tested the performance of the new feedback system with 3GeV beams. The beam parameters are listed in Table. 2. The results are shown in Figs. 6, 7 and 8. We found that the intra-bunch feedback can damp betatron oscillations faster than the BxB FB system and is quite effective to suppress internal bunch motions [3]. To assess the performance of the feedback system further, we developed a macro particle simulation code and compare its results with measurements.

Table 2: Parameters at the Beam Test

Beam intensity(/pulse)	2.7×10^{13}
Number of bunches	1
Bunch width	150ns
chromaticity	+0.5
Twiss parameter : alpha	-0.45896
Twiss parameter : beta	15.5835
Horizontal offset x/x'	0.001/0.0
Initial longitudinal distribution tau/delta	Gaussian/Gaussian

SIMULATION METHOD

Macro particles of 6400 are used in this simulation. Each RF bucket is divided into 64 slices. Particle positions are calculated turn by turn and put into each slice to make a dipole current signal. From this signal, FB kicks are calculated through the n tap FIR filter (n=4 or 8), and after 1 turn, the kicks are added to the signal (Fig. 4). The equation of motion is given in Eq. (1) - (4). Wake fileds, space charge effects and nonlinear effects are not included. The filter coefficients are given in Eq. (5) and (6). In case of BxB FB system, only the peak of BPM signal is used. On the other hand, the intra-bunch FB filters each slice. Here we note that the BxB FB system uses BPM signal directly, and the peak of "differentiated" signal is used. But in the intra-bunch feedback system, the signal process module integrates the BPM signals before filtering. The same parameters are used as for the beam test.

$$\tau_{n+1} = \tau_n - \frac{\eta}{\beta c}\Delta s \delta_n \quad (1)$$

$$\delta_{n+1} = \delta_n + \frac{\beta c}{\eta}\left(\frac{\nu_{s0}}{R}\right)^2 \Delta s \tau_{n+1} \quad (2)$$

$$\begin{pmatrix} x_n \\ x'_n \end{pmatrix} = \begin{pmatrix} \cos\mu + \alpha\sin\mu & \beta\sin\mu \\ -\gamma\sin\mu & \cos\mu - \alpha\sin\mu \end{pmatrix} \begin{pmatrix} x_n \\ x'_n \end{pmatrix} \quad (3)$$

$$\mu = 2\pi(\nu_{\beta x} + \xi\delta_n) \quad (4)$$

$$b[n] = \sin((n\text{-}1)\omega T_s + \Delta\phi) - \Delta \quad (5)$$

$$\Delta = \frac{1}{N_{tap}}\sum_{n=0}^{N_{tap}-1} \sin(n\omega T_s + \Delta\phi) \quad (6)$$

THE CALACTERISTICS OF FEEDBACK SYTEMS

Figure 5 shows the signals and the mean positions of each slice. Signals are superimposed every turn from the 250th turn. In both the BxB FB and the intra-bunch FB systems, feedback signals are calculated from the dipole moment. Thus, the intra-bunch FB system cannot kick slices at the exterior of the bunch effectively, and as a result, the mean positions at the bunch exterior have larger amplitudes than those at the bunch center.

OSCILLATION AMPLITUDE

Figure 6 shows the time revolution of center slice of the bunch. The left figures are for experimental results and the right ones are for simulations. It can be clearly seen that the intra-bunch FB system damps oscillations faster than the BxB FB system. This tendency qualitatively agrees with the experiments. The damping time in the simulation is about 100 turns. This also agrees with the experiments. The experimental results when the feedback is off shows damping of signals, indicating the existence of additional damping mechanisms, such as non-linear effects or wake fields. More elaborate simulation models are needed for accurate evaluations. Figure 7 shows the spectrograms of the oscillation amplitudes. They also show good agreements with the experiments.

INTERNAL MOTIONS

In Fig. 8, the delta signal motions are plotted every 5 turns after the 200th turn from the perturbation kick. In simulations, an artificial offset is added to match with the experiment. Good agreements are seen between the simulations and the experiments. Figure 9 is the waterfall plot of this motion. The delta signals are FFTed for 200 turns and only the amplitudes of betatron frequency (~75kHz) are plotted here for each slice.

Copyright © 2014 CC-BY-3.0 and by the respective authors

ISBN 978-3-95450-141-0

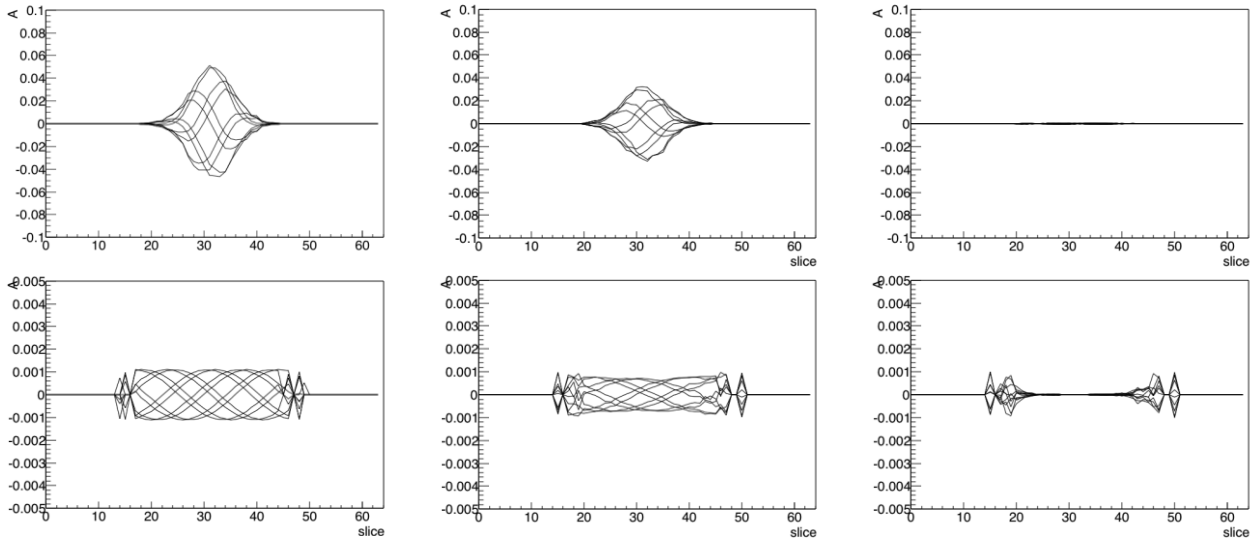


Figure 5: The delta signal motion and the mean position around at the 250th turn. The top figures are for the delta motion (Left: FBs off, Middle: BxB FB on, Right: intra-bunch FB on) and the bottom ones are for the mean positions (Left: FBs off, Middle: BxB FB on, Right: intra-bunch FB on).

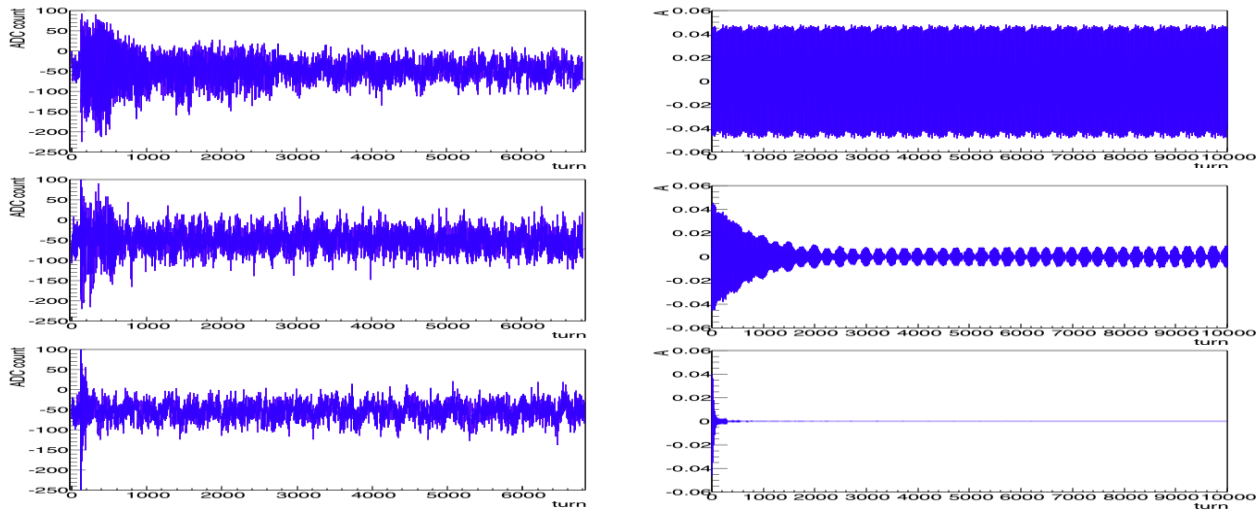


Figure 6: Time revolution of the center slice of the bunch (the 30th slice). The left figures are the experimental results (Top: FBs off, Middle: BxB FB on, Bottom: intra-bunch FB on) and the right ones are the simulations (Top: FBs off, Middle: BxB FB on, Bottom: intra-bunch FB on).

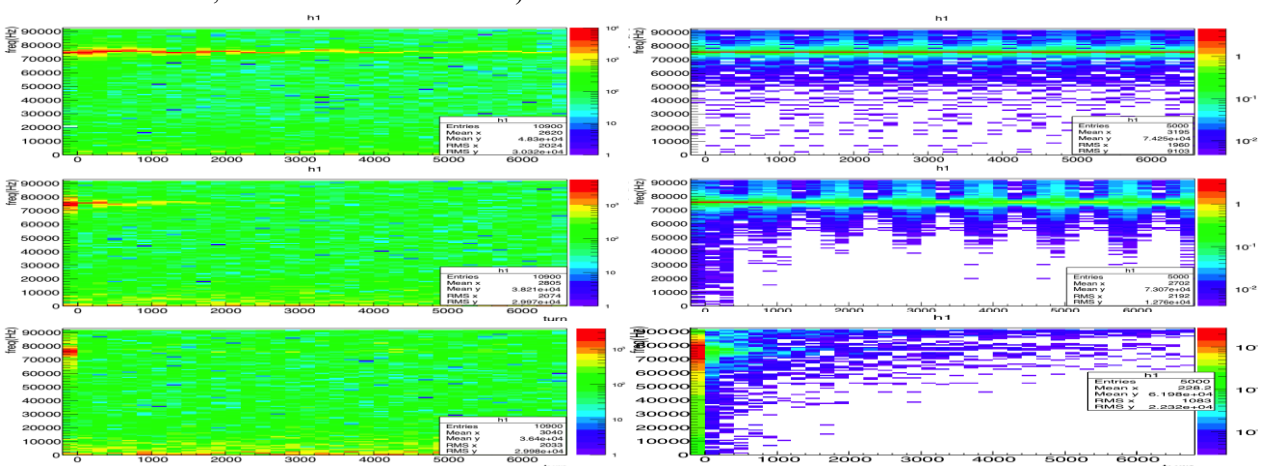


Figure 7 Spectrograms of the center slice of the bunch (the 30th slice). The left figures are the experimental results (Top: FBs off, Middle: BxB FB on, Bottom: intra-bunch FB on) and the right ones are the simulations (Top: FBs off, Middle: BxB FB on, Bottom: intra-bunch FB on).

ISBN 978-3-95450-141-0

Copyright © 2014 CC-BY-3.0 and by the respective authors

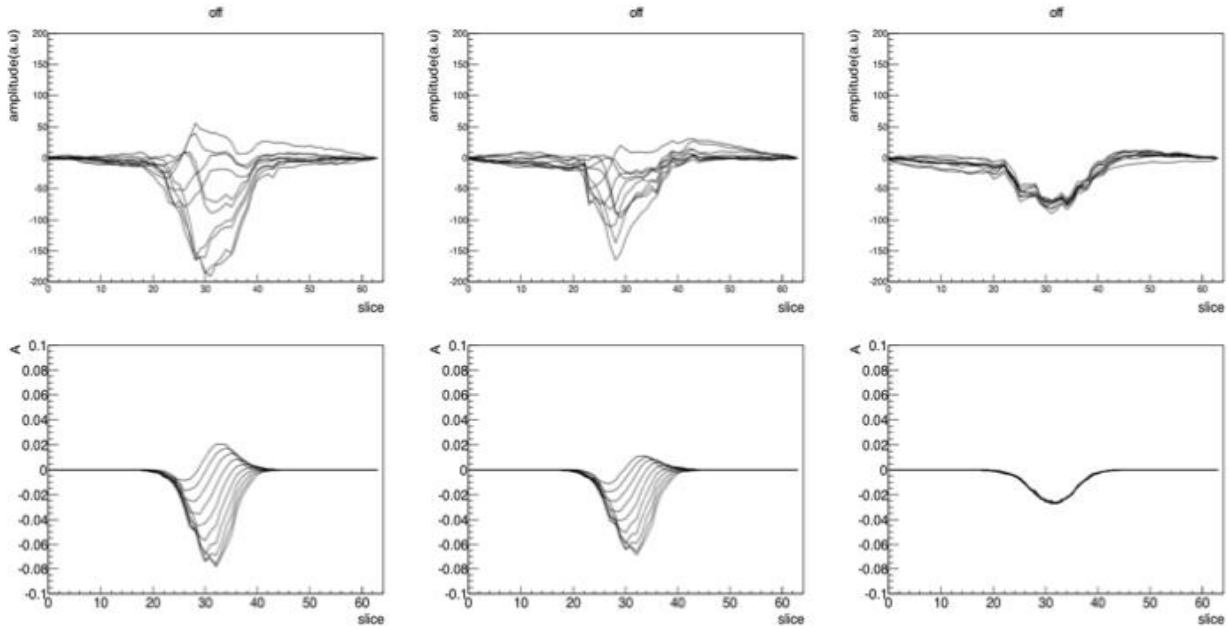


Figure 8: The delta signal motion around 250th turn after a perturbation kick. The top figures are for the experimental results (Left: FBs off, Middle: BxB FBon, Right: intra-bunch FB on) and the bottom ones are for the simulations (Left: FBs off, Middle: BxB FB on, Right: intra-bunch FB on).

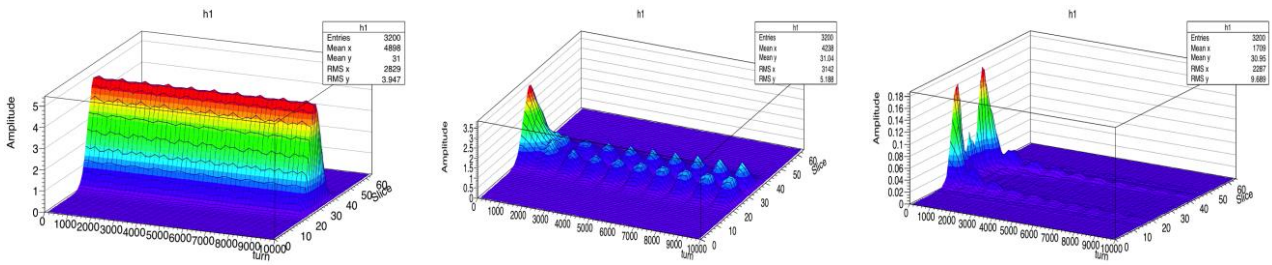


Figure 9: The waterfall plot of simulations (Left: FBs off, Middle: BxB FB on, Right: intra-bunch FB on).

GAIN AND DAMPING TIME

We tried to search for the maximal gain to damp betatron oscillations. The gain 2.0 x 10^{-4} is the maximum for the intra-bunch FB system and the gain 3.125 x 10^{-6} is for the BxB FB system. At those values, the damping time is about 40 turns and 2000 turns for these system respectively for them. Even a larger feedback gain might be available with the intra-bunch FB system.

SUMMARY

We made very simple simulations, and confirmed that they qualitatively reproduce the experimental results of the intra-bunch FB system. We plan to add more effects such as wake fields, the space charge and the multi-bunch effects for more accurate evaluations.

REFERENCES

[1] Y. Kurimoto, *et al.*, "Bunch by bunch feedback system in J-PARC MR", DIPAC2011, Hamburg, May 2011, p482, (2011).

[2] Y. H. Chin, *et al.* ,"Analysis of transverse instabilities observed at J-PARC MR and their suppression using feedback systems" NA-PAC2013, Pasadena, September-October 2013, p.27, (2013).

[3] K. Nakamura, *et al.* , "Intra-bunch feedback system in The J-PARC Main Ring", IPAC2014, Germany, June,(2014).

Copyright © 2014 CC-BY-3.0 and by the respective authors

ISBN 978-3-95450-141-0

List of Authors

Bold papercodes indicate primary authors

— A —

Abbott, M.G. WEPD24
Abela, R. MOPF31
Ackermann, S. **MOPF22**, **TUPF25**
Afanaciev, K. MOPD03
Akagi, T. TUCYB2
Aleksandrov, A.V. MOCYB3
Alekseev, I.G. MOPD01
Allaria, E. MOPD10
Allica, J.C.A. WEPF03
Allison, S. WEPD17
Almalki, M.H. TUPF04
Altinbas, Z. MOPD02, WEPF26
Alvarez, M.L. TUPD02, TUPD04
Andersen, M. WEPF03
Andre, C. **TUPD05**, TUPD06
Andre, T.A. WEPF28
Andreazza, W. WEPF03, WEPF13
Angelovski, A. **MOPD25**, WECYB1
Antonelli, M. **TUPF13**
Ardana-Lamas, F. MOPF31
Arinaga, A. TUPD22
Arnold, A. MOPF27
Arsov, V.R. MOCZB2, MOPF31
Aryshev, A.S. TUCYB2
Aschenauer, E.C. MOPD01
Atoian, G. MOPD01
Aumeyr, T. MOPF14
Ayvazyan, V. MOPF22

— B —

Baboi, N. **TUPF06**, TUPF07, TUPF08, TUPF10, TUPF12, **THIXB1**
Bacha, B. MOIZB1, TUPF21, WEPD27
Bahng, J. WEPF12
Baldinger, R. MOPF31, TUPF07, WEPD12, WEPD13
Baron, R.A. WECYB3
Bartosik, M.R. **TUPD25**
Bazilevsky, A. MOPD01
Béchu, N. WEPD22
Bell, A.I. MOPD03
Bellego, V. TUPF04
Belohrad, D. **WEPF03**, WEPF06
Béranger, B. WEPD21
Bergoz, J.F. WEPF06
Berrig, O.E. MOPF16
Billing, M.G. MOPF14
Blanch-Torné, S. WEPD23
Blednykh, A. MOPF07
Blokland, W. TUPD02, **TUPD13**
Bloomer, C. **TUCZB2**
Bobb, L.M. **MOPF14**
Boissonnat, G. WEPF08
Boland, M.J. WECZB3
Bonnes, U. TUPD24
Boorman, G.E. MOPF15
Borysenko, A. MOPD17
Bosco, A. MOPF15
Boulch, C. TUPF05
Bräuning, H. TUPD06
Bräuning-Demian, A. TUPD06
Braun, H.-H. MOPF31
Bravin, E. MOPF14, MOPF15, MOPD11, WEPF07, WEPF13
Brooks, S.J. TUPF02
Brosi, M. MOCZB1
Bruno, G.B.M. WECYB3
Buechi, F. MOCZB2
Burandt, C. TUPD24
Burtowy, P.R. MOPD03
Byrd, J.M. WEPD08

— C —

Calvey, J.R. THCXB1
Calvi, M. MOPF31
Cantero, E.D. WEPF07, **WEPF13**
Caracappa, A. TUPF01, WECYB2
Carbonnier, P. TUPF05
Cardoso, F.H. WECYB3
Cargnelutti, M. **WEPD07**
Carlson, C. MOPD02
Caselle, C.M. **MOCZB1**, TUPD10
Caspers, F. MOPF16
Cassinari, L. WEPD22
Cautero, G. TUPF13
Cerniglia, P. WEPF26
Cesaratto, J.M. WEPD25
Chae, M.S. WEPF09
Chaikovska, I. **TUPD23**
Chasman, C. MOPD02
Chen, J. MOPF30
Chen, X. WEPD03
Cheng, W.X. **MOIZB1**, TUPF01, **TUPF21**, WECYB2, **WEPD27**
Cheng, Y.-S. MOPF30
Chilingaryan, S.A. MOCZB1
Chin, Y.H. THCXB2
Chiu, P.C. MOPF30
Choi, H. J. **WEPF09**
Choi, J.Y. TUPD16
Choi, S. WEPF12
Chu, K.C. MOPD23
Cinquegrana, P. MOPD10

ISBN 978-3-95450-141-0

Copyright © 2014 CC-BY-3.0 and by the respective authors

Claereboudt, Y. WEPF08
Coffee, R.N. WEIZB1
Colin, J. WEPF08
Connolly, R. **MOPF02**, MOPF09, WEPF26
Contrepois, P. TUPF05
Conway, J.V. MOPF14
Corbett, W.J. **MOPD21**
Costanzo, M.R. MOPF08, MOPD02
Crisp, J.L. TUPF16, TUPD21
Crittenden, J.A. THCXB1
Cullen, C. WEPF26
Cuní, G. WEPD23
Czwalinna, M.K. MOPD07, MOPD25

— D —

D'Arcy, R.T.P. **TUPD01**
Da Silva Castro, J. WEPD22
Dabrowski, A.E. MOPD03
Dalesio, L.R. MOPF20
Daniel-Thomas, P. TUPF05
Danneil, C. TUPF01, WECYB2
Dawson, W.C. MOPF02
De Long, J.H. WECYB2
De Santis, S. WEPF21, WEPD25
De Sio, A. TUPF13
Degen, C. MOPD02, WEPF26
Dehler, M.M. **WEPD10**
Dehning, B. MOPF16, TUPD25
Delerue, N. TUPD23
Delfs, A. MOPF13
Della Penna, A.J. **MOPF03**, TUPF01, WECYB2
Denard, J.-C. WEPD22
Di Fraia, M. TUPF13
Diamond, J.S. TUPF19
Ditter, R. MOPF31, TUPF07, WEPD12, WEPD13
Döbert, S. WEPF05
Dolenc Kittelmann, I. MOPF17
Donna, M. TUPF27
Doolittle, L.R. WEPD08
Dorn, C. TUPD07
Drees, K.A. MOPD02
Dritschler, T. MOCZB1
Du, Q. WEPD08
Ducoudret, B. WEPF28
Duhme, H.T. MOPD07
Dusatko, J.E. **WEPD25**

— E —

Eddy, N. TUPF06
Emery, J. MOPF16
Éozénou, F. TUPF05
Eremin, V. TUPD25
Erny, C. MOPF31
Eyser, O. MOPD01

— F —

Faatz, B. MOPF22, TUPF25
Favre, G. WEPF03
Favre, N. WEPF03
Fedotov, A.V. MOPF05
Felber, M. **MOPD07**, MOPD12
Fellenz, B.J. TUPF06, TUPD04
Feng, Y. WEIZB1
Fenner, M. MOPD07
Fernandes, M.F. **WEPF04**
Fernando, A. MOPD01
Ferrari, E. MOPD10
Filippetto, D. WEPD08
Fischer, M. TUPD24
Fischer, W. MOPF08, MOPD02
Fite, J.M. MOPF02
Fitzgerald, J. TUPF19, TUPD02
Flanagan, J.W. TUCZB2, TUPD22
Flöttmann, K. MOPD12
Fontbonne, J.-M. WEPF08
Forck, P. TUPF04, TUPD05, TUPD07, WEPD01
Fox, J.D. WEPD25
Frak, B. MOPF08
Frei, F. MOPF31
Fritz, D.M. **WEIZB1**
Frommberger, F. MOPD05
Fukuma, H. TUPD22
Furukawa, K. MOPF28, WEPD04
Furukawa, T. WEPF10, WEPF23, WEPF24, WEPF30

— G —

Ganter, R. MOPF31
García-Bonilla, A.C. **WEPF16**
Gąsior, M. MOPD04, WEPF18, WEPD01
Gasser, Y. TUPF05
Gassner, D.M. MOPF04, **MOPF05**, MOPF08, MOPD01, MOPD02, WEPF26
Geithner, R. **WECZB1**
Gensch, M. MOPD15
Gerth, C. MOPD07
Gharibyan, V. MOPF13
Gibson, S.M. MOPF15
Gilpatrick, J.D. TUPD11, WEPD09
Giuressi, D. TUPF13
Göhran, M. TUPF27
Görrissen, N. TUPF09
Gorgisyan, I. MOPF31
Gouit, F. TUPF05
Grandsaert, T.J. TUPF27
Green, B.W. MOPD15
Griesmayer, E. MOPF15, TUPD25
Groß, M. MOPD09
Gruchalla, M.E. **TUTUB1**, TUPD11
Grüner, F.J. MOPD12
Gu, X. MOPF08, MOPD02

Copyright © 2014 CC-BY-3.0 and by the respective authors

ISBN 978-3-95450-141-0

— H —

Ha, K. MOIZB1, TUPF01, WECYB2
Hänisch, P. MOPD05
Hama, H. TUPF26
Hamani, M. MOPF16
Hamdi, K. MOPD02, TUPF02
Han, J.H. MOPD19
Hanna, B.M. TUPD01
Hansli, M. WECYB1
Hara, Y. WEPF10, **WEPF23**, **WEPF24**, WEPF30
Haseitl, R. TUPD05, TUPD06
Hass, E. MOPF22, MOPD08
Hassanzadegan, H. WEPD07
Hauri, C.P. MOPF31
Hempel, M. **MOPD03**
Henschel, H.M. MOPD03
Hensler, O. TUPF06
Heo, H. TUPD16
Hertle, E. MOPD17
Heuer, M. **MOCZB3**, MOPD07
Hilbrich, S. MOPD24
Hiller, N. MOCZB1, **MOPD17**, TUPD10
Hillert, W. MOPD05
Hinode, F. TUPF26
Hock, J. MOPD02
Höfle, W. WEPD25
Höner, M. MOPD24, **WEPD26**
Hoffmann, T. TUPD06
Hofmann, K. WEPF31
Hofmann, T. **MOPF15**
Holzer, E.B. TUCZB3, WECZB3
Honda, T. MOCYB2
Honda, Y. TUCYB2
Hong, J.G. WEPF12
Hong, J.H. **MOPD19**
Hoobler, S. L. WEPD17
Hsu, K.T. **MOPF30**
Hsu, S.Y. MOPF30
Hu, K.H. MOPF30
Hu, Y. MOIZB1, **MOPF20**, TUPF21, WEPD27
Huang, C.H. MOPF30
Huang, G. WEPD08
Huang, H. MOPF02, **MOPD01**
Huang, J.Y. **MOPF04**
Hubert, N. **WEPD21**, **WEPD22**
Huck, H. MOPD24
Huck, M. MOPD24
Hülsmann, P. WEPD03
Hug, F. TUPD24
Hulsart, R.L. MOPF05, TUPF02, WEPF26
Hunziker, S. **MOCZB2**, MOPF31, WEPD10

— I —

Ichimiya, R. MOPF28, **WEPD04**
Iida, N. MOPF28
Ikeda, H. **TUPD22**
Ikeno, M. MOPF28
Iriso, U. MOPF10, TUPF03, TUPF23
Irwin, K.D. **MOIXB3**
Isaev, I.I. MOPD09
Ischebeck, R. **MOPF31**, **TUCYB3**

— J —

Jackson, P.D. WECZB3
Jakoby, R. MOPD25, WECYB1
Jamet, C. **WEPF28**, WEPF29
Janas, E. MOPD07, MOPD12
Jansson, A. MOPF17
Jao, S.E. MOPF02
Jeff, A. **TUCZB3**, **WEPF05**
Jehanno, D. TUCYB2
Jensen, C.C. TUPD04
Jensen, L.K. WEPF03
Jones, O.R. **TUIXB1**
Jones, R.M. TUPF10
Judin, V. MOCZB1, MOPD17
Jürgensen, L.E. **TUPD24**
Juranic, P.N. MOPF31

— K —

Kaiser, M.G. MOCZB2
Kaji, H. MOPF28
Kalinkin, D. MOPD01
Kamps, T. WEPF19
Kang, H.-S. MOPD19, TUPD16, WEPF09, WEPD17
Karacheban, O. MOPD03
Karataev, P. MOPF14
Kashiwagi, S. TUPF26
Kastriotou, M. WECZB3
Kaufmann, W. TUPF04
Kawane, Y. TUPD09
Kayran, D. MOPF05
Kehrer, B. MOPD17
Keil, B. MOPF31, TUPF07, **WEPD11**, WEPD12, WEPD13
Kester, O.K. TUPD07
Kewisch, J. MOPD01
Khabiboulline, T.N. TUPF18
Khan, S. **MOPD24**, WEPD26
Khojoyan, M. MOPD09
Kim, C. MOPD19, TUPD16, WEPD17
Kim, I.Y. **TUPD16**
Kim, S.J. WEPF12
Kiupel, G. MOPF19, TUPF16
Klose, K. MOPF22
Kopmann, A. MOCZB1

ISBN 978-3-95450-141-0

Copyright © 2014 CC-BY-3.0 and by the respective authors

Koprek, W. MOPF31, TUPF07
Kosciuk, B.N. **MOPF07**, WECYB2
Koseki, T. THCXB2
Kourkafas, G. MOPD09
Kovalev, S. MOPD15
Kowina, P. TUPD07, WEPD01
Kozak, T. MOPD07
Kramert, R. MOPF31, TUPF07
Krasilnikov, M. MOPD09
Krejcik, P. TUCYB3
Krier, G. WEPF08
Krouptchenkov, I. MOPF13
Kruchinin, K.O. MOPF15
Krupa, M. WEPF06, **WEPF18**
Kruse, J. TUPF05
Kube, G. **TUIZB1**, TUPF09
Kuboki, H. THCXB2
Kuczerowski, J. MOPF16
Kürzeder, T. TUPD24
Kuntzsch, M. **MOPD15**
Kuo, C.H. MOPF30
Kurfuerst, C. TUPD25
Kurian, F. WECZB1
Kuroda, R. TUPD12

— L —

Labat, M. WEPD22
Lamb, T. MOPD07, MOPD12
Lambiase, R.F. WEPF26
Lange, W. MOPD03
Le Coz, W.LC. **WEPF29**
Ledu, G. WEPF28, WEPF29
Lee, B.S. WEPF12
Lee, D. MOPF30
Lee, S.J. WEPD17
Lee, T.H. **WETUB1**
Lefèvre, T. MOPF14, TUCZB3, WEPF05
Lehnert, U. MOPF27, MOPD15
Leich, M. WEPD10
Leloir, S.L. WEPF28
Lemke, H. WEIZB1
Lenardon, L. WEPF03
Lensch, T. **MOPF13**, WEPF02
Leonard, J.L. MOPD03
Liao, C.Y. MOPF30
Lichtenberg, G. MOCZB3
Lidia, S.M. **TUIYB1**, TUPF16, TUPD21, **WEPF17**
Lin, L.Y. **TUCYB1**
Linander, R. TUPF27
Lionberger, C.A. MOPD18
Lipka, D. **TUPF07**, TUPF11, WEPD11, WEPD12
Litvinenko, V. MOPF05
Litvinov, Yu.A. WEPD03
Liu, C. MOPF09
Liu, M. **MOPD23**
Liu, N. TUPF19
Liu, Y. MOCYB3
Liu, Z. **TUPD21**
Lizzit, S. TUPF13
Llorente Sancho, D. MOPF31
Löhl, F. MOPF31
Lohmann, W. MOPD03
Lonsing, R. TUPD06
Loos, H. TUCYB3, **WEIXB1**
Loos, R. MOPD03
Lorbeer, B. **TUPF08**
Loret, S. WEPF28, WEPF29
Lu, P.N. **MOPF27**
Lueangaramwong, A. TUPF26
Lumpkin, A.H. TUPD03
Lund-Nielsen, J. WEPF02
Lundberg, C.E. TUPD02, TUPD04
Lunin, A. **TUPF18**
Luo, Y. MOPD02
Lussignol, Y. WEPF29

— M —

Maggipinto, M.A. MOIZB1, MOPF03, TUPF01, WECYB2
Mahler, G.J. MOPD01, TUPF02
Mahn, T. WECYB1
Mai, C. MOPD24
Maier, A.R. MOPD12
Makdisi, Y. MOPD01
Malyutin, D. **MOPD09**
Marcellini, F. MOPF31, WEPD12, WEPD13
Marchetti, B. MOPD09
Marinkovic, G. MOPF31, TUPF07, WEPD11, WEPD12, WEPD13
Marlats, J.L. WEPD22
Marques, S.R. **WECYB3**, WEPD22
Martí, Z. WEPD23
Martin, D.J. WEPD17
Martins, L.A. WECYB3
Marusic, A. MOPD02
Mary, A. WEPD22
Masaki, M. **TUCZB1**
Mausner, L.F. WEPF26
Mavrič, U. MOPD07
Mazzoni, S. MOPF14, MOPD11
McCrady, R.C. WEPD09
McCrory, E.S.M. TUPD04
Mead, J. MOIZB1, MOPF03, TUPF01, **WECYB2**
Meng, W. MOPF02
Menk, R.H. TUPF13
Meyer auf der Heide, A. MOPD24
Michel, P. MOPD15
Michnoff, R.J. MOPF02, MOPF05, TUPF02, **WEPF26**

Copyright © 2014 CC-BY-3.0 and by the respective authors

ISBN 978-3-95450-141-0

Miller, T.A. MOPF05, **MOPF08**, MOPD02
Miltchev, V. TUPF25
Minty, M.G. MOPF04, MOPF05, **MOPF09**, MOPD02, TUPF02
Mitsuhashi, T.M. TUPF23, TUPD08
Miura, A. **TUPD09**
Miyahara, F. **MOPF28**, WEPD04
Miyao, T. TUPD09
Mizushima, K. WEPF10, WEPF23, WEPF24, WEPF30
Moeller, S.P. WEIZB1
Mok, W.Y. MOPD21
Moldes, J. WEPD23
Molo, R. MOPD24
Monoszlai, B. MOPF31
Montag, C. MOPD02
Morgan, A.F.D. **WEPF25**, WEPD24
Morris, D.K. TUPF19
Müller, A.-S. MOCZB1, MOPD17, TUPD10
Mueller, J.M. MOPD07
Müller, W.F.O. WEPD01
Mun, G. TUPD16, WEPD17
Murcek, P. MOPF27
Murphy, K. WEPF17
Muto, T. TUPF26

— N —

Nadolski, L.S. WEPD21
Nagasawa, I. TUPF26
Nagasawa, S. TUPF26
Naito, T. **TUPD08**
Nakamura, K.G. **THCXB2**
Nanbu, K. **TUPF26**
Napoly, O. TUPF05
Nasse, M.J. MOPD17
Nebot Del Busto, E. **WECZB3**
Nemesure, S. MOPD01
Nesterenko, I.N. MOPF19
Neto, J.L.B. WECYB3
Neubert, R. WECZB1
Neuenschwander, R.T. WEPD22
Neugebauer, J. TUPF09
Neumann, Re. WEPF02
Neumann, Ru. TUPF09
Newton, D. MOPD06
Nguyen, J.D. TUPD11
Noda, K. WEPF10, WEPF23, WEPF24, WEPF30
Nölle, D. MOPF13, TUPF05, TUPF07, WEPF02, **WEPF15**, WEPD12, THIXB1
Nogami, T. MOCYB2
Nolden, F. WEPD03
Norum, W.E. MOPD18
Nosych, A.A. **MOPF10**, **TUPF03**
Novo, J. TUPF05

— O —

Obina, T. MOCYB2
Odier, P. WEPF06
Oh, B.G. TUPD16
Ok, J.W. **WEPF12**
Okada, M. THCXB2
Okazaki, T. MOPF28
Olexa, J. **MOPD04**
Olmos, A. TUPF03, **WEPD23**
Olsen, J.J. WEPD17
Orel, P. MOCZB2
Orlandi, G.L. MOPF31
Ouchi, N. TUPD09
Ozkan, C. MOPF31

— P —

Pace, E. TUPF13
Padrazo, D. MOIZB1, **TUPF01**, WECYB2
Palm, M. **MOPD11**
Park, J.Y. WEPF12
Park, S.J. TUPD16, WEPF09
Patthey, L. MOPF31
Pedrozzi, M. MOPF31
Peier, P. MOPF31, MOPD07, MOPD17
Pelzer, M. MOPF13
Penirschke, A. MOPD25, **WECYB1**
Penno, M. MOPD03
Pepitone, K. WEPF05
Petrocelli, R. WEPD23
Petrosyan, G. TUPF07
Petrosyan, L.P. TUPF08
Petzold, L. MOCZB1
Pfeiffer, S. MOCZB3, MOPF22
Pietralla, N. TUPD24
Pikin, A.I. MOPF08, MOPD02
Pinayev, I. MOPF05
Piotrowski, J. WEPD03
Piselli, E. **MOPF16**
Poblaguev, A. MOPD01
Podobedov, B. WECYB2
Pollack, B.L. MOPD03
Pollet, P. MOPF31
Portmann, G.J. MOPD18
Potier de courcy, C. WEPF28, WEPF29
Prat, E. TUCYB3
Prędki, P. MOPD07
Prieels, D. WEPF08
Prieto, P.S. TUPF19, TUPD02
Prost, L.R. TUPD01
Przyborowski, D. MOPD03
Przygoda, K.P. MOPD07

— Q —

Qian, H.J. **WEPD08**

ISBN 978-3-95450-141-0

Copyright © 2014 CC-BY-3.0 and by the respective authors

— R —

Raasch, J. MOCZB1
Radovic, M. MOPF31
Raich, U. MOPF15
Raparia, D. WEPF26
Rassool, R.P. WECZB3
Rast, H. MOPD24
Rawankar, A.A. **TUCYB2**
Reeg, H. WECZB1, WEPF31
Rehm, G. **MOIYB1**, TUCZB2, WEPF25, **WEPD24**
Reiter, A. TUPD05, TUPD06
Revenko, R.V. MOPD26
Rivetta, C.H. WEPD25
Rivkin, L. MOPF31
Rodriguez Esparza, S. **MOPF19**
Roggli, M. MOPF31, TUPF07, WEPD12, WEPD13
Rohrer, M. MOPF31, WEPD12, WEPD13
Romann, A. MOCZB2
Roncarolo, F. MOPF15
Roose, C. **MOPF17**
Ross, M.C. **MOIXB2**
Rossi, F. MOPD10
Rota, L. MOCZB1, **TUPD10**
Rouvière, N. TUPF05
Rubio-Manrique, S. WEPD23
Russo, L.M. WECYB3
Ryjov, V. MOPD03

— S —

Sagehashi, H. MOCYB2
Sakaue, K. TUCYB2, TUPD12
Salvant, B. MOPF16
Sanjari, M.S. **WEPD03**
Sannibale, F. WEPD08
Saotome, N. S. **WEPF10**, WEPF23, WEPF24, WEPF30
Sapinski, M. TUPD25
Saraya, Y. WEPF10, WEPF23, WEPF24, WEPF30
Satoh, M. MOPF28, WEPD04
Sautier, R.S. MOPF16
Scarpine, V.E. TUPD01
Schalwat, M. TUPF05
Schedler, M. MOPD05
Scheidt, K.B. **MOCYB1**, **TUPF14**, **TUPF15**
Schlarb, H. MOCZB3, MOPD07, MOPD12, MOPD25
Schlott, V. MOCZB2, MOPF31, MOPD17, TUCYB3
Schmickler, H. MOPF14
Schmidke, W.B. MOPD01
Schmidt, B. MOPD08
Schmidt, C. TUPD06
Schmidt, J. WECZB3
Schmidt-Föhre, F. TUPF08, TUPF09
Schneekloth, U. **TUPF09**
Schönfeldt, P. MOPD17
Scholz, M. MOPF22
Schreiber, S. MOPF22
Schuh, M. MOPD17
Schulz, S. MOPD07
Schurig, R. MOPD15
Schuwalow, S. MOPD03
Schwickert, M. TUPD06, WECZB1, WEPF31
Sedillo, J.D. **TUPD11**
Seidel, P. WECZB1
Seletskiy, S. MOPF07
Seraphin, J.P. TUPF19
Serra-Gallifa, X. WEPD23
Serrano, C. MOPD18
Servouin, C. TUPF05
Shea, T.J. TUPF27
Shemyakin, A.V. TUPD01
Shi, L. TUPF06, **TUPF10**
Shibasaki, Y. TUPF26
Shimosaki, Y. TUCZB1
Shin, C.S. WEPF12
Shirai, T. WEPF10, WEPF23, WEPF24, WEPF30
Shobuda, Y. THCXB2
Shoji, M. MOPF28
Sieber, T. TUPF04
Siegel, M. MOCZB1
Sigalotti, P. MOPD10
Sikora, J.P. **WEPF21**, **THCXB1**
Simon, C.S. **TUPF04**, **TUPF05**
Singh, O. MOIZB1, MOPF03, MOPF20, TUPF01, TUPF21, WECYB2, WEPD27
Singh, R. TUPD05, **WEPD01**
Slimmer, D. TUPD04
Smale, N.J. MOCZB1, MOPD17
Smith, S.R. **MOIXB1**, **THIYB1**
Søby, L. **WEPF06**
Soliman, E. **WEPF31**
Solyak, N. TUPF18
Sommer, M. WEPD26
Sosa, A.G. **WEPF07**, WEPF13
Spampinati, S. **MOPD06**
Spezzani, C. MOPD10
Stabile, P. **TUPF19**
Stadler, M. TUPF07, WEPD11, **WEPD12**, **WEPD13**
Steck, M. WEPD03
Steffen, B. MOPD07, MOPD17
Stegmann, R. TUPD24
Steimel, J. TUPD01
Steinhorst, M. TUPD24
Steinmann, J.L. MOCZB1, MOPD17
Stepanov, A.G. MOPF31
Stephan, F. MOPD09

Copyright © 2014 CC-BY-3.0 and by the respective authors

ISBN 978-3-95450-141-0

Steski, D. MOPD01
Stettler, J. MOPF31
Stickland, D.P. MOPD03
Stöhlker, T. WECZB1, WEPD03
Straumann, T. WEPD17
Stulle, F. WEPF06
Summers, T. MOPF09
Suwada, T. MOPF28, WEPD04
Svirida, D. MOPD01
Switka, M.T. **MOPD05**
Sydlo, C. MOPD07, MOPD12, MOPD25
Szewiński, J. MOPD07

— T —

Taira, Y. **TUPD12**
Takahashi, K. TUPF26
Takai, R. **MOCYB2**
Takano, S. TUCZB1
Takao, M. TUCZB1
Takeshita, E. WEPF24
Tan, J. WEPF04
Tanaka, M. TUPD12
Tanaka, M. MOPF28
Tanimoto, Y. MOCYB2
Tansho, R. WEPF10, WEPF23, WEPF24, **WEPF30**
Tavares, D.O. WECYB3
Teichert, J. MOPF27, MOPD15
Tepikian, S. MOPF02, MOPF04, MOPF09
Terunuma, N. TUCYB2
Teytelman, D. WEPD27
Thangaraj, J.C.T. TUPD03
Thieberger, P. MOPF04, **MOPD02**, **TUPF02**, WEPF26
Thomas, C.A. **TUPF27**
Thominet, V.G. TUCYB3
Thuot, M. TUTUB1
Thurman-Keup, R.M. **TUPD02**, **TUPD03**, TUPD04
Tian, K. MOPD21
Tian, Y. WECYB2
Tiessen, H. MOPF13
Tinsley, D.G. TUPD04
Titberidze, M. MOPD07, **MOPD12**
Tobiyama, M. MOCYB2, TUPD22, **WEPD05**, THCXB2
Tokoku, C. TUPF26
Tomizawa, H. TUPD12
Torino, L. **TUPF23**
Touchard, D.T. WEPF29
Toyama, T. THCXB2
Toyokawa, H. TUPD12
Trbojevic, D. TUPF02
Tsang, T. MOPD01
Tsemo Kamga, J.A. WEPD01
Tsoupas, N. MOPF04
Tzoganis, V. TUCZB3

— U —

Ungelenk, P. MOPD24
Urakawa, J. TUCYB2

— V —

van de Walle, J. **WEPF08**
Variola, A. TUPD23
Vashchenko, G. MOPD09
Veness, R. MOPF16
Vennekate, H. MOPF27
Verbitskaya, E. TUPD25
Veronese, M. **MOPD10**
Vetter, K. MOPF03, TUPF01, WECYB2
Vignet, J.L. **MOPD26**
Vilcins, S. TUPF05, TUPF07, **TUPF11**, WEPD12
Völker, J. **WEPF19**
Vogelgesang, M. MOCZB1
Vollenberg, W. WEPF03
Vuitton, C. MOPF16

— W —

Walasek-Höhne, B. TUPD05, **TUPD06**
Walsh, R. MOPD03
Walter, T. MOPD07
Wamsat, T. TUPF06, **TUPF12**
Watkins, H.A. **WEPD09**
Webber, R.C. TUPF16
Weber, J.M. **MOPD18**
Weber, M. MOCZB1, TUPD10
Wedel, R. MOPD07
Weiland, T. MOPD25, WEPD01
Wells, R.P. WEPD08
Welsch, C.P. TUCZB3, WECZB3, WEPF04, WEPF07
Wendt, M. TUPF03, **WEIYB1**
Wentowski, N. WEPF02
Werner, M. MOPF13, **WEPF02**
White, S.M. MOPD02
Wilinski, M. MOPF05, WEPF26
Williams, E.C. MOPD18
Wittenburg, K. MOPF13
Won, M. WEPF12
Wu, C.Y. MOPF30
Wuensch, S. MOCZB1
Wunderlich, S. **MOPD08**

— X —

Xiang, R. MOPF27
Xu, C. **WEPD17**
Xu, H. MOIZB1, MOPF20, TUPF21, WEPD27

— Y —

Yair, O. **TUPF16**
Yakovlev, V.P. TUPF18
Yan, M. MOPD08, TUCYB3
Yang, H. MOPD19

ISBN 978-3-95450-141-0

Copyright © 2014 CC-BY-3.0 and by the respective authors

Yang, J. WEPD08
Yano, Y. MOPF28
Yépez, D. WEPD23
Yin, C.X. MOPD23
Yip, K. MOPD01
Yoon, J.H. WEPF12
Young, A. WEPD17

— Z —

Zagel, J.R. **MOCYB4**, **TUPD04**
Zagozdzinska, A.A. MOPD03
Zannini, C. MOPF16
Zeitler, B. MOPD12
Zelenski, A. MOPD01
Zhang, H.D. TUCZB3
Zhang, P. TUPF06
Zhao, L.Y. MOPD23
Zhu, D. WEIZB1
Zhukov, A.P. **MOCYB3**
Zimmer, C.M. MOPF04
Žnidarčič, M. WEPD07
Zocca, F. MOPF15
Zorzut, S. MOCZB2
Zummack, F. MOPD07
Zwicker, B. **TUPD07**

Copyright © 2014 CC-BY-3.0 and by the respective authors

ISBN 978-3-95450-141-0

Institutes List

AGH University of Science and Technology
Kraków, Poland
- Piotrowski, J.

AGH
Cracow, Poland
- Przyborowski, D.

AIST
Tsukuba, Ibaraki, Japan
- Kuroda, R.
- Taira, Y.
- Tanaka, M.
- Toyokawa, H.

Albert-Ludwig Universität Freiburg
Freiburg, Germany
- Schmidt, J.

ASCo
Clayton, Victoria, Australia
- Boland, M.J.

BERGOZ Instrumentation
Saint Genis Pouilly, France
- Bergoz, J.F.
- Stulle, F.

BNL
Upton, Long Island, New York, USA
- Altinbas, Z.
- Aschenauer, E.C.
- Atoian, G.
- Bacha, B.
- Bazilevsky, A.
- Blednykh, A.
- Brooks, S.J.
- Caracappa, A.
- Carlson, C.
- Cerniglia, P.
- Chasman, C.
- Cheng, W.X.
- Connolly, R.
- Costanzo, M.R.
- Cullen, C.
- Dalesio, L.R.
- Danneil, C.
- Dawson, W.C.
- De Long, J.H.
- Degen, C.
- Della Penna, A.J.
- Drees, K.A.
- Eyser, O.
- Fedotov, A.V.
- Fernando, A.
- Fischer, W.
- Fite, J.M.
- Frak, B.
- Gassner, D.M.
- Gu, X.
- Ha, K.
- Hamdi, K.
- Hock, J.
- Hu, Y.
- Huang, H.
- Hulsart, R.L.
- Jao, S.E.
- Kalinkin, D.
- Kayran, D.
- Kewisch, J.
- Kosciuk, B.N.
- Lambiase, R.F.
- Litvinenko, V.
- Liu, C.
- Luo, Y.
- Maggipinto, M.A.
- Mahler, G.J.
- Makdisi, Y.
- Marusic, A.
- Mausner, L.F.
- Mead, J.
- Meng, W.
- Michnoff, R.J.
- Miller, T.A.
- Minty, M.G.
- Montag, C.
- Nemesure, S.
- Padrazo, D.
- Pikin, A.I.
- Pinayev, I.
- Poblaguev, A.
- Podobedov, B.
- Raparia, D.
- Schmidke, W.B.
- Seletskiy, S.
- Singh, O.
- Steski, D.
- Summers, T.
- Tepikian, S.
- Thieberger, P.
- Tian, Y.
- Trbojevic, D.
- Tsang, T.
- Tsoupas, N.
- Vetter, K.
- White, S.M.
- Wilinski, M.
- Xu, H.
- Yip, K.
- Zelenski, A.
- Zimmer, C.M.

ISBN 978-3-95450-141-0

Copyright © 2014 CC-BY-3.0 and by the respective authors

BTU
Cottbus, Germany
- Lohmann, W.

CEA/DSM/IRFU
France
- Carbonnier, P.
- Contrepois, P.
- Éozénou, F.
- Gasser, Y.
- Lussignol, Y.
- Napoly, O.
- Novo, J.
- Servouin, C.
- Simon, C.S.

CEA/IRFU
Gif-sur-Yvette, France
- Bellego, V.
- Boulch, C.
- Gasser, Y.

CEA
Gif-sur-Yvette, France
- Daniel-Thomas, P.
- Gouit, F.
- Pepitone, K.

CELLS-ALBA Synchrotron
Cerdanyola del Vallès, Spain
- Blanch-Torné, S.
- Cuní, G.
- Iriso, U.
- Martí, Z.
- Moldes, J.
- Nosych, A.A.
- Olmos, A.
- Petrocelli, R.
- Rubio-Manrique, S.
- Serra-Gallifa, X.
- Torino, L.
- Yépez, D.

CERN
Geneva, Switzerland
- Allica, J.C.A.
- Andersen, M.
- Andreazza, W.
- Bartosik, M.R.
- Belohrad, D.
- Berrig, O.E.
- Bravin, E.
- Burtowy, P.R.
- Cantero, E.D.
- Caspers, F.
- Dabrowski, A.E.
- Dehning, B.
- Döbert, S.
- Emery, J.
- Favre, G.
- Favre, N.
- Fernandes, M.F.
- Gąsior, M.
- Hamani, M.
- Hofmann, T.
- Holzer, E.B.
- Höfle, W.
- Jeff, A.
- Jensen, L.K.
- Jones, O.R.
- Kastriotou, M.
- Krupa, M.
- Kuczerowski, J.
- Lefèvre, T.
- Lenardon, L.
- Loos, R.
- Mazzoni, S.
- Nebot Del Busto, E.
- Odier, P.
- Olexa, J.
- Palm, M.
- Piselli, E.
- Raich, U.
- Roncarolo, F.
- Ryjov, V.
- Salvant, B.
- Sapinski, M.
- Sautier, R.S.
- Schmickler, H.
- Søby, L.
- Sosa, A.G.
- Tan, J.
- Veness, R.
- Vollenberg, W.
- Vuitton, C.
- Wendt, M.
- Zagozdzinska, A.A.
- Zannini, C.
- Zhang, P.
- Zocca, F.

CFEL
Hamburg, Germany
- Grüner, F.J.
- Maier, A.R.
- Zeitler, B.

CIVIDEC Instrumentation
Wien, Austria
- Griesmayer, E.

Copyright © 2014 CC-BY-3.0 and by the respective authors

ISBN 978-3-95450-141-0

Cockcroft Institute
Warrington, Cheshire, United Kingdom
- Newton, D.
- Sosa, A.G.
- Spampinati, S.
- Tzoganis, V.
- Welsch, C.P.
- Zhang, H.D.

Cornell University (CLASSE), Cornell Laboratory for Accelerator-Based Sciences and Education
Ithaca, New York, USA
- Billing, M.G.
- Calvey, J.R.
- Conway, J.V.
- Crittenden, J.A.
- Sikora, J.P.

DELTA
Dortmund, Germany
- Hilbrich, S.
- Huck, H.
- Huck, M.
- Höner, M.
- Khan, S.
- Mai, C.
- Meyer auf der Heide, A.
- Molo, R.
- Rast, H.
- Sommer, M.
- Ungelenk, P.

DESY Zeuthen
Zeuthen, Germany
- Groß, M.
- Hempel, M.
- Henschel, H.M.
- Isaev, I.I.
- Karacheban, O.
- Khojoyan, M.
- Kourkafas, G.
- Krasilnikov, M.
- Lange, W.
- Leonard, J.L.
- Malyutin, D.
- Marchetti, B.
- Penno, M.
- Stephan, F.
- Vashchenko, G.

DESY
Hamburg, Germany
- Ackermann, S.
- Ayvazyan, V.
- Baboi, N.
- Czwalinna, M.K.
- Delfs, A.
- Duhme, H.T.
- Faatz, B.
- Felber, M.
- Fenner, M.
- Flöttmann, K.
- Gerth, C.
- Gharibyan, V.
- Görrissen, N.
- Hass, E.
- Hensler, O.
- Heuer, M.
- Klose, K.
- Krouptchenkov, I.
- Kruse, J.
- Kube, G.
- Lamb, T.
- Lensch, T.
- Lipka, D.
- Lohmann, W.
- Lorbeer, B.
- Lund-Nielsen, J.
- Mavrič, U.
- Mueller, J.M.
- Neugebauer, J.
- Neumann, Re.
- Neumann, Ru.
- Nölle, D.
- Peier, P.
- Pelzer, M.
- Petrosyan, G.
- Petrosyan, L.P.
- Pfeiffer, S.
- Schalwat, M.
- Schlarb, H.
- Schmidt, B.
- Schmidt-Föhre, F.
- Schneekloth, U.
- Scholz, M.
- Schreiber, S.
- Schulz, S.
- Shi, L.
- Steffen, B.
- Sydlo, C.
- Tiessen, H.
- Titberidze, M.
- Vilcins, S.
- Walsh, R.
- Walter, T.
- Wamsat, T.
- Wedel, R.
- Wentowski, N.
- Werner, M.
- Wittenburg, K.
- Wunderlich, S.
- Yan, M.
- Zummack, F.

Dimtel
San Jose, USA
- Teytelman, D.

ISBN 978-3-95450-141-0

Copyright © 2014 CC-BY-3.0 and by the respective authors

DLS
Oxfordshire, United Kingdom
- Abbott, M.G.
- Bell, A.I.
- Bloomer, C.
- Bobb, L.M.
- Morgan, A.F.D.
- Rehm, G.

Duke University
Durham, North Carolina, USA
- Huang, J.Y.

EBG MedAustron
Wr. Neustadt, Austria
- Kurfuerst, C.

EJIT
Hitachi, Ibaraki, Japan
- Okazaki, T.

Elettra-Sincrotrone Trieste S.C.p.A.
Basovizza, Italy
- Allaria, E.
- Antonelli, M.
- Cautero, G.
- Cinquegrana, P.
- Ferrari, E.
- Giuressi, D.
- Lizzit, S.
- Menk, R.H.
- Rossi, F.
- Sigalotti, P.
- Spezzani, C.
- Veronese, M.

ELSA
Bonn, Germany
- Frommberger, F.
- Hänisch, P.
- Hillert, W.
- Schedler, M.
- Switka, M.T.

EPFL
Lausanne, Switzerland
- Ardana-Lamas, F.
- Gorgisyan, I.
- Hauri, C.P.
- Rivkin, L.

ESRF
Grenoble, France
- Scheidt, K.B.

ESS
Lund, Sweden
- Dolenc Kittelmann, I.
- Donna, M.
- Grandsaert, T.J.
- Göhran, M.
- Hassanzadegan, H.
- Jansson, A.
- Linander, R.
- Roose, C.
- Shea, T.J.
- Thomas, C.A.

Fermilab
Batavia, Illinois, USA
- Alvarez, M.L.
- D'Arcy, R.T.P.
- Diamond, J.S.
- Eddy, N.
- Fellenz, B.J.
- Fitzgerald, J.
- Hanna, B.M.
- Jensen, C.C.
- Khabiboulline, T.N.
- Liu, N.
- Lumpkin, A.H.
- Lundberg, C.E.
- Lunin, A.
- McCrory, E.S.M.
- Morris, D.K.
- Prieto, P.S.
- Prost, L.R.
- Scarpine, V.E.
- Seraphin, J.P.
- Shemyakin, A.V.
- Slimmer, D.
- Solyak, N.
- Stabile, P.
- Steimel, J.
- Thangaraj, J.C.T.
- Thurman-Keup, R.M.
- Tinsley, D.G.
- Yakovlev, V.P.
- Zagel, J.R.

FRIB
East Lansing, Michigan, USA
- Crisp, J.L.
- Kiupel, G.
- Lidia, S.M.
- Lin, L.Y.
- Liu, Z.
- Nesterenko, I.N.
- Rodriguez Esparza, S.
- Webber, R.C.
- Yair, O.

Copyright © 2014 CC-BY-3.0 and by the respective authors

ISBN 978-3-95450-141-0

FSU Jena
Jena, Germany
- Neubert, R.
- Seidel, P.

GANIL
Caen, France
- Andre, T.A.
- Ducoudret, B.
- Jamet, C.
- Le Coz, W.LC.
- Ledu, G.
- Leloir, S.L.
- Loret, S.
- Potier de courcy, C.
- Revenko, R.V.
- Touchard, D.T.
- Vignet, J.L.

GSI
Darmstadt, Germany
- Almalki, M.H.
- Andre, C.
- Bräuning-Demian, A.
- Bräuning, H.
- Chen, X.
- Dorn, C.
- Forck, P.
- Haseitl, R.
- Hoffmann, T.
- Hülsmann, P.
- Kaufmann, W.
- Kester, O.K.
- Kowina, P.
- Kurian, F.
- Litvinov, Yu.A.
- Lonsing, R.
- Nolden, F.
- Reeg, H.
- Reiter, A.
- Sanjari, M.S.
- Schmidt, C.
- Schwickert, M.
- Sieber, T.
- Singh, R.
- Steck, M.
- Stöhlker, T.
- Walasek-Höhne, B.
- Zwicker, B.

HAW
Hamburg, Germany
- Lichtenberg, G.

HIJ
Jena, Germany
- Geithner, R.
- Stöhlker, T.

HZB
Berlin, Germany
- Kamps, T.
- Völker, J.

HZDR
Dresden, Germany
- Arnold, A.
- Gensch, M.
- Green, B.W.
- Kovalev, S.
- Kuntzsch, M.
- Lehnert, U.
- Lu, P.N.
- Michel, P.
- Murcek, P.
- Schurig, R.
- Teichert, J.
- Vennekate, H.
- Xiang, R.

I-Tech
Solkan, Slovenia
- Cargnelutti, M.
- Orel, P.
- Žnidarčič, M.
- Zorzut, S.

IAP
Frankfurt am Main, Germany
- Kester, O.K.
- Zwicker, B.

IBA
Louvain-la-Neuve, Belgium
- Claereboudt, Y.
- Krier, G.
- Prieels, D.
- van de Walle, J.

IOFFE
St. Petersburg, Russia
- Eremin, V.
- Verbitskaya, E.

IOQ
Jena, Germany
- Geithner, R.
- Stöhlker, T.

IPN
Orsay, France
- Rouvière, N.

Copyright © 2014 CC-BY-3.0 and by the respective authors

ISBN 978-3-95450-141-0

ITEP
Moscow, Russia
- Alekseev, I.G.
- Svirida, D.

J-PARC, KEK & JAEA
Ibaraki-ken, Japan
- Toyama, T.

JAEA/J-PARC
Tokai-mura, Japan
- Kawane, Y.
- Miura, A.
- Ouchi, N.
- Shobuda, Y.

JAI
Egham, Surrey, United Kingdom
- Aumeyr, T.
- Bobb, L.M.
- Karataev, P.

JASRI/SPring-8
Hyogo-ken, Japan
- Masaki, M.
- Shimosaki, Y.
- Takano, S.
- Takao, M.

KEK
Ibaraki, Japan
- Akagi, T.
- Arinaga, A.
- Aryshev, A.S.
- Chin, Y.H.
- Flanagan, J.W.
- Fukuma, H.
- Furukawa, K.
- Honda, T.
- Honda, Y.
- Ichimiya, R.
- Iida, N.
- Ikeda, H.
- Ikeno, M.
- Kaji, H.
- Koseki, T.
- Kuboki, H.
- Mitsuhashi, T.M.
- Miyahara, F.
- Miyao, T.
- Naito, T.
- Nogami, T.
- Obina, T.
- Okada, M.
- Sagehashi, H.
- Satoh, M.
- Shoji, M.
- Suwada, T.
- Takai, R.
- Tanaka, M.
- Tanimoto, Y.
- Terunuma, N.
- Tobiyama, M.
- Urakawa, J.
- Yano, Y.

KIT
Karlsruhe, Germany
- Borysenko, A.
- Brosi, M.
- Caselle, C.M.
- Chilingaryan, S.A.
- Dritschler, T.
- Hertle, E.
- Hiller, N.
- Judin, V.
- Kehrer, B.
- Kopmann, A.
- Müller, A.-S.
- Nasse, M.J.
- Petzold, L.
- Raasch, J.
- Rota, L.
- Schuh, M.
- Schönfeldt, P.
- Siegel, M.
- Smale, N.J.
- Steinmann, J.L.
- Vogelgesang, M.
- Weber, M.
- Wuensch, S.

Korea Basic Science Institute
Busan, Republic of Korea
- Choi, S.
- Hong, J.G.
- Kim, S.J.
- Lee, B.S.
- Ok, J.W.
- Park, J.Y.
- Shin, C.S.
- Won, M.
- Yoon, J.H.

Kyoto University
Kyoto, Japan
- Nakamura, K.G.

Kyungpook National University
Daegu, Republic of Korea
- Bahng, J.

Copyright © 2014 CC-BY-3.0 and by the respective authors

ISBN 978-3-95450-141-0

LAL
Orsay, France
- Chaikovska, I.
- Delerue, N.
- Jehanno, D.
- Variola, A.

LANL
Los Alamos, New Mexico, USA
- Gilpatrick, J.D.
- McCrady, R.C.
- Nguyen, J.D.
- Sedillo, J.D.
- Thuot, M.
- Watkins, H.A.

LBNL
Berkeley, California, USA
- Byrd, J.M.
- De Santis, S.
- Doolittle, L.R.
- Du, Q.
- Filippetto, D.
- Huang, G.
- Lionberger, C.A.
- Murphy, K.
- Norum, W.E.
- Portmann, G.J.
- Qian, H.J.
- Sannibale, F.
- Serrano, C.
- Weber, J.M.
- Wells, R.P.
- Williams, E.C.

LNLS
Campinas, Brazil
- Baron, R.A.
- Bruno, G.B.M.
- Cardoso, F.H.
- Marques, S.R.
- Martins, L.A.
- Neto, J.L.B.
- Neuenschwander, R.T.
- Russo, L.M.
- Tavares, D.O.

LPC
Caen, France
- Boissonnat, G.
- Colin, J.
- Fontbonne, J.-M.

National Institute of Radiological Sciences
Chiba, Japan
- Saraya, Y.

NC PHEP BSU
Minsk, Belarus
- Afanaciev, K.

NCBJ
Świerk/Otwock, Poland
- Szewiński, J.

NIRS
Chiba-shi, Japan
- Furukawa, T.
- Hara, Y.
- Mizushima, K.
- Noda, K.
- Saotome, N. S.
- Shirai, T.
- Takeshita, E.
- Tansho, R.

NSRRC
Hsinchu, Taiwan
- Chen, J.
- Cheng, Y.-S.
- Chiu, P.C.
- Hsu, K.T.
- Hsu, S.Y.
- Hu, K.H.
- Huang, C.H.
- Kuo, C.H.
- Lee, D.
- Liao, C.Y.
- Wu, C.Y.

NU
Evanston, Illinois, USA
- Pollack, B.L.

ORNL
Oak Ridge, Tennessee, USA
- Aleksandrov, A.V.
- Blokland, W.
- Liu, Y.
- Zhukov, A.P.

Copyright © 2014 CC-BY-3.0 and by the respective authors

ISBN 978-3-95450-141-0

PAL
Pohang, Kyungbuk, Republic of Korea
- Chae, M.S.
- Choi, H. J.
- Choi, J.Y.
- Han, J.H.
- Heo, H.
- Hong, J.H.
- Kang, H.-S.
- Kim, C.
- Kim, I.Y.
- Lee, S.J.
- Mun, G.
- Oh, B.G.
- Park, S.J.
- Yang, H.

PSI, Villigen
Villigen, Switzerland
- Leich, M.

PSI
Villigen PSI, Switzerland
- Abela, R.
- Ardana-Lamas, F.
- Arsov, V.R.
- Baldinger, R.
- Braun, H.-H.
- Buechi, F.
- Calvi, M.
- Dehler, M.M.
- Ditter, R.
- Erny, C.
- Frei, F.
- Ganter, R.
- Gorgisyan, I.
- Hauri, C.P.
- Hunziker, S.
- Ischebeck, R.
- Juranic, P.N.
- Kaiser, M.G.
- Keil, B.
- Koprek, W.
- Kramert, R.
- Llorente Sancho, D.
- Löhl, F.
- Marcellini, F.
- Marinkovic, G.
- Monoszlai, B.
- Orlandi, G.L.
- Ozkan, C.
- Patthey, L.
- Pedrozzi, M.
- Pollet, P.
- Prat, E.
- Radovic, M.
- Rivkin, L.
- Roggli, M.
- Rohrer, M.
- Romann, A.
- Schlott, V.
- Stadler, M.
- Stepanov, A.G.
- Stettler, J.
- Thominet, V.G.

PU
Princeton, New Jersey, USA
- Stickland, D.P.

RIKEN SPring-8 Center
Sayo-cho, Sayo-gun, Hyogo, Japan
- Tomizawa, H.

Royal Holloway, University of London
Surrey, United Kingdom
- Aumeyr, T.
- Boorman, G.E.
- Bosco, A.
- Gibson, S.M.
- Karataev, P.
- Kruchinin, K.O.

SINAP
Shanghai, People's Republic of China
- Chu, K.C.
- Liu, M.
- Yin, C.X.
- Zhao, L.Y.

SLAC
Menlo Park, California, USA
- Allison, S.
- Cesaratto, J.M.
- Coffee, R.N.
- Corbett, W.J.
- Dusatko, J.E.
- Feng, Y.
- Fox, J.D.
- Fritz, D.M.
- Hoobler, S. L.
- Irwin, K.D.
- Krejcik, P.
- Lemke, H.
- Loos, H.
- Martin, D.J.
- Moeller, S.P.
- Mok, W.Y.
- Olsen, J.J.
- Rivetta, C.H.
- Ross, M.C.
- Smith, S.R.
- Straumann, T.
- Tian, K.
- Xu, C.
- Young, A.
- Zhu, D.

Copyright © 2014 CC-BY-3.0 and by the respective authors

ISBN 978-3-95450-141-0

Sokendai
Ibaraki, Japan
- Rawankar, A.A.
- Terunuma, N.
- Urakawa, J.

SOLEIL
Gif-sur-Yvette, France
- Béchu, N.
- Béranger, B.
- Cassinari, L.
- Da Silva Castro, J.
- Denard, J.-C.
- Hubert, N.
- Labat, M.
- Marlats, J.L.
- Mary, A.
- Nadolski, L.S.

Stanford University
Stanford, California, USA
- Lee, T.H.

TEMF, TU Darmstadt
Darmstadt, Germany
- Müller, W.F.O.
- Tsemo Kamga, J.A.
- Weiland, T.

The University of Liverpool
Liverpool, United Kingdom
- Jeff, A.
- Nebot Del Busto, E.
- Newton, D.
- Sosa, A.G.
- Tzoganis, V.
- Welsch, C.P.
- Zhang, H.D.

The University of Melbourne
Melbourne, Victoria, Australia
- Boland, M.J.
- Rassool, R.P.

Tohoku University, Research Center for Electron Photon Science
Sendai, Japan
- Hama, H.
- Hinode, F.
- Kashiwagi, S.
- Lueangaramwong, A.
- Muto, T.
- Nagasawa, I.
- Nagasawa, S.
- Nanbu, K.
- Shibasaki, Y.
- Takahashi, K.
- Tokoku, C.

TU Darmstadt
Darmstadt, Germany
- Angelovski, A.
- Bonnes, U.
- Burandt, C.
- Fischer, M.
- Hansli, M.
- Hofmann, K.
- Hug, F.
- Jakoby, R.
- Jürgensen, L.E.
- Kürzeder, T.
- Mahn, T.
- Penirschke, A.
- Pietralla, N.
- Soliman, E.
- Stegmann, R.
- Steinhorst, M.

TUB
Beijing, People's Republic of China
- Yang, J.

TUL-DMCS
Łódź, Poland
- Kozak, T.
- Prędki, P.
- Przygoda, K.P.

UMAN
Manchester, United Kingdom
- Jones, R.M.

UNAL
Bogota D.C, Colombia
- García-Bonilla, A.C.

Uni HH
Hamburg, Germany
- Grüner, F.J.
- Maier, A.R.
- Miltchev, V.
- Schuwalow, S.
- Titberidze, M.

University of Adelaide
Adelaide, Australia
- Jackson, P.D.

Università degli Studi di Firenze
Firenze, Italy
- De Sio, A.
- Pace, E.

ISBN 978-3-95450-141-0

Copyright © 2014 CC-BY-3.0 and by the respective authors

Università degli Studi di Trieste
Trieste, Italy
- Di Fraia, M.
- Ferrari, E.

URS
Albuquerque, New Mexico, USA
- Gruchalla, M.E.

Warsaw University of Technology, Institute of Electronic Systems
Warsaw, Poland
- Janas, E.

Waseda University
Tokyo, Japan
- Sakaue, K.

Copyright © 2014 CC-BY-3.0 and by the respective authors

ISBN 978-3-95450-141-0